

# 中草藥研究中心

2019 年 9 月 1 日~2020 年 12 月 31 日

## (上)論文集



**CHANG GUNG UNIVERSITY OF SCIENCE AND TECHNOLOGY**

長庚科技大學  
中草藥研究中心  
2019年9月1日~2020年12月31日  
論文集  
目 錄

序號	期刊論文	學校主要 負責教師	頁碼
1.	Hsieh, H.-L., Tsai, M.-M. Tumor progression-dependent angiogenesis in gastric cancer and its potential application. World Journal of Gastrointestinal Oncology 11(9): 686-704; 2019.	蔡明明、 謝喜龍	1
2.	Liu, C.-H., Liu, Y.-X., Kumari, M., Wu, W.-C. Multivariate analysis of metabolic parameters and optimization of antibody production using high cell density hybridoma in hollow fiber bioreactors. Biotechnology Letters 41(8-9): 963-977; 2019.	劉繼賢	20
3.	Lee, C.-W., Chi, M.-C., Peng, K.-T., Chiang, Y.-C., Hsu, L.-F., Yan, Y.-L., Li, H.-Y., Chen, M.-C., Lee, I.-T., Lai, C.-H. Water-soluble fullereneol C60(OH)36 toward effective anti-air pollution induced by urban particulate matter in HaCaT cell. International Journal of Molecular Sciences 20(17): 259; 2019.	李江文	35
4.	Chang, Z.-Y., Chen, C.-C., Liu, H.-M., Yeh, Y.-C., Lin, T.-Y., Lee, T.-Y., Huang, T.-H. Positive effects of Ger-Gen-Chyn-Lian-Tang on cholestatic liver fibrosis in bile duct ligation-challenged mice. International Journal of Molecular Sciences 20(17): 4181; 2019.	黃澤宏	55
5.	Liu, F.-C., Yu, H.-P., Chen, P.-J., Yang, H.-W., Chang, S.-H., Tzeng, C.-C., Cheng, W.-J., Chen, Y.-R., Chen, Y.-L., Hwang, T.-L. A novel NOX2 inhibitor attenuates human neutrophil oxidative stress and ameliorates inflammatory arthritis in mice. Redox Biology 26: 101273; 2019.	黃聰龍	67
6.	Kao, H.-H., Kuo, C.-Y., Chen, K.-S., Chen, J.-P. Preparation of gelatin and gelatin/hyaluronic acid cryogel scaffolds for the 3D culture of mesothelial cells and mesothelium tissue regeneration. International Journal of Molecular Sciences 20(18): 4527; 2019.	陳志平	84
7.	Hsiao, C.-Y., Yang, S.-C., Alalaiwe, A., Fang, J.-Y. Laser ablation and topical drug delivery: a review of recent advances. Expert Opinion on Drug Delivery 16(9): 937-952; 2019.	蕭千祐、 方嘉佑	104
8.	Wang, P.-W., Lin, T.-Y., Hung, Y.-C., Chang, W.-N., Yang, P.-M., Chen, M.-H., Yeh, C.-T., Pan, T.-L. Characterization of fibrinogen as a key modulator in patients with wilson's diseases with functional proteomic tools. International Journal of Molecular Sciences 20(18): 4528; 2019.	潘台龍	120
9.	Lin, J.-Y., Kung, Y.-A., Shih, S.-R. Antivirals and vaccines for Enterovirus A71. Journal of Biomedical Science 26(1): 65; 2019.	施信如	137



10.	Huang, S.-Y., Huang, C.-H., Chen, C.-J., Chen, T.-W., Lin, C.-Y., Lin, Y.-T., Kuo, S.-M., Huang, C.-G., Lee, L.-A., Chen, Y.-H., Chen, M.-F., Kuo, R.-L., Shih, S.-R. Novel Role for miR-1290 in Host Species Specificity of Influenza A Virus. <i>Molecular Therapy - Nucleic Acids</i> 17: 10-23; 2019.	施信如	147
11.	Yang, H.-C., Wu, Y.-H., Yen, W.-C., Liu, H.-Y., Hwang, T.-L., Stern, A., Chiu, D.T.-Y. The Redox Role of G6PD in Cell Growth, Cell Death, and Cancer. <i>Cells</i> 8(9); 2019.	吳依璇、 黃聰龍、 趙崇義	161
12.	Chen, M.-H., Hsu, J.-W., Huang, K.-L., Su, T.-P., Li, C.-T.a,b, Lin, W.-C., Tsai, S.-J., Cheng, C.-M., Chang, W.-H., Pan, T.-L., Chen, T.-J., Bai, Y.-M. Risk and coaggregation of major psychiatric disorders among first-degree relatives of patients with bipolar disorder: a nationwide population-based study. <i>Psychological Medicine</i> 49(14): 2397-2404; 2019.	潘台龍	190
13.	Chen, Y.-F., Chen, W.-F., Wen, Z.-H., Hwang, T.-L., Zhang, Z.-J., Sung, P.-J. New bioactive $\Delta^{11}(17)$ -furanoeunicellins from an octocoral <i>Cladiella</i> sp. <i>Phytochemistry Letters</i> 33: 31-35, 2019.	黃聰龍	198
14.	Wang, P.-W., Wu, T.-H., Lin, T.-Y., Chen, M.-H., Yeh, C.-T., Pan, T.-L. Characterization of the Roles of Vimentin in Regulating the Proliferation and Migration of HSCs during Hepatic Fibrogenesis. <i>Cells</i> 8(10); 2019.	潘台龍	203
15.	Lu, Y.-J., Chuang, E.-Y., Cheng, Y.-H., Anilkumar, T.S., Chen, H.-A., Chen, J.-P. Thermosensitive magnetic liposomes for alternating magnetic field-inducible drug delivery in dual targeted brain tumor chemotherapy. <i>Chemical Engineering Journal</i> 373: 720-733; 2019.	陳志平	223
16.	Huang, P.-S., Wang, C.-S., Yeh, C.-T., Lin, K.-H. Roles of thyroid hormone-associated microRNAs affecting oxidative stress in human hepatocellular carcinoma. <i>International Journal of Molecular Sciences</i> 20(20): 5220; 2019.	林光輝	237
17.	Chen, C.-T., Chen, C.-H., Sheu, C., Chen, J.-P. Ibuprofen-loaded hyaluronic acid nanofibrous membranes for prevention of postoperative tendon adhesion through reduction of inflammation. <i>International Journal of Molecular Sciences</i> 20(20): 5038; 2019.	陳志平	261
18.	Liu, Y.-C., Yeh, C.-T., Lin, K.-H. Molecular functions of thyroid hormone signaling in regulation of cancer progression and anti-apoptosis. <i>International Journal of Molecular Sciences</i> 20(20): 4986; 2019.	林光輝	280
19.	Chiang, C.-C., Cheng, W.-J., Korinek, M., Lin, C.-Y., Hwang, T.-L. Neutrophils in Psoriasis. <i>Frontiers in Immunology</i> 10: 2376; 2019.	黃聰龍	307
20.	Chen, P.-Y., Wu, C.Y.-J., Fang, J.-H., Chen, H.-C., Feng, L.-Y., Huang, C.-Y., Wei, K.-C., Fang, J.-Y., Lin, C.-Y. Functional Change of Effector Tumor-Infiltrating CCR5+CD38+HLA-DR+CD8+ T Cells in Glioma Microenvironment. <i>Frontiers in Immunology</i> 10: 2395; 2019.	方嘉佑	319

21. Wang, T.-H., Chen, C.-C., Huang, K.-Y., Shih, Y.-M., Chen, C.-Y. High levels of EGFR prevent sulforaphane-induced reactive oxygen species-mediated apoptosis in non-small-cell lung cancer cells. *Phytomedicine* 64: 152926; 2019. 陳琦媛 333
22. Liou, C.-J., Dai, Y.-W., Wang, C.-L., Fang, L.-W., Huang, W.-C. Maslinic acid protects against obesity-induced nonalcoholic fatty liver disease in mice through regulation of the Sirt1/AMPK signaling pathway. *FASEB Journal* 33(11): 11791-11803; 2019. 劉倩君、黃文忠 340
23. Shalumon, K.T., Liao, H.-T., Kuo, C.-Y., Wong, C.-B., Li, C.-J., Mini, P.A., Chen, J.-P. Rational design of gelatin/nanohydroxyapatite cryogel scaffolds for bone regeneration by introducing chemical and physical cues to enhance osteogenesis of bone marrow mesenchymal stem cells. *Materials Science and Engineering C* 104: 109855; 2019. 陳志平 353
24. Weng, J.-R., Huang, T.-H., Lin, Z.-C., Alalaiwe, A., Fang, J.-Y. Cutaneous delivery of [1-(4-chloro-3-nitrobenzenesulfonyl)-1H-indol-3-yl]-methanol, an indole-3-carbinol derivative, mitigates psoriasiform lesion by blocking MAPK/NF- $\kappa$ B/AP-1 activation. *Biomedicine and Pharmacotherapy* 119: 109398; 2019. 方嘉佑 372
25. Lee, K.-F., Tsai, M.-M., Tsai, C.-Y., Huang, C.-G., Ou, Y.-H., Hsieh, C.-C., Hsieh, H.-L., Wang, C.-S., Lin, K.-H. DEK is a potential biomarker associated with malignant phenotype in gastric cancer tissues and plasma. *International Journal of Molecular Sciences* 20(22): 5689; 2019. 林光輝 384
26. Wang, T.-H., Leu, Y.-L., Chen, C.-C., Shieh, T.-M., Lian, J.-H., Chen, C.-Y. Psorachromene Suppresses Oral Squamous Cell Carcinoma Progression by Inhibiting Long Non-coding RNA GAS5 Mediated Epithelial-Mesenchymal Transition. *Frontiers in Oncology* 9: 1168; 2019. 陳琦媛 403
27. Tsai, Y.-F., Chen, C.-Y., Chang, W.-Y., Syu, Y.-T., Hwang, T.-L. Resveratrol suppresses neutrophil activation via inhibition of Src family kinases to attenuate lung injury. *Free Radical Biology and Medicine* 145: 67-77; 2019. 黃聰龍 415
28. Wu, M.-F., Shu, C.-C., Wang, J.-Y., Yan, B.-S., Lai, H.-C., Chiang, B.-L., Wu, L.S.-H., Yu, C.-J. NLRP3 inflammasome is attenuated in patients with Mycobacterium avium complex lung disease and correlated with decreased interleukin-1 $\beta$  response and host susceptibility. *Scientific Reports* 9(1): 12534; 2019. 賴信志 426
29. Huang, T.-H., Wu, A.T.H., Cheng, T.-S., Lin, K.-T., Lai, C.-J., Hsieh, H.-W., Chang, P.M.-H., Wu, C.-W., Huang, C.-Y.F., Chen, K.-Y. In silico identification of thiostrepton as an inhibitor of cancer stem cell growth and an enhancer for chemotherapy in non-small-cell lung cancer. *Journal of Cellular and Molecular Medicine* 23(12): 8184-8195; 2019. 黃澤宏 436
30. Wang, I.-L., Hsiao, C.-Y., Shen, J., Wang, Y., Huang, C.-C., Chen, Y.-M. The effects of Jilin sika Deer's (Cervus dybowski) tendon liquid supplementation on endurance drop jumps performance, biochemistry profile of free boxing players. *Journal*

of Ethnopharmacology 245: 112119; 2019.

31. Zhang, Z.-J., Wang, Y.-H., Chen, S.-R., Peng, B.-R., Yang, S.-N., Hu, C.-C., Fang, L.-S., Hwang, T.-L., Sung, P.-J. Novel secoeunicellins produced by an octocoral *Cladiella* sp. *Tetrahedron Letters* 60(49): 151300; 2019. 黃聰龍 458
32. Lu, C.W., Lin, T.Y., Wang, S.J., Huang, S.K. Asiatic acid, an active substance of *Centella asiatica*, presynaptically depresses glutamate release in the rat hippocampus. *European Journal of Pharmacology* 865:172781; 2019. 王素珍 462
33. Huang, W.-C., Ting, N.-C., Huang, Y.-L., Chen, L.-C., Lin, C.-F., Liou, C.-J. *Helminthostachys zeylanica* water extract ameliorates airway hyperresponsiveness and eosinophil infiltration by reducing oxidative stress and Th2 cytokine production in a mouse asthma model. *Mediators of Inflammation* 2020: 1702935; 2020. 黃文忠、林傳福、劉倩君 470
34. Wu, L.-C., Chen, C.-C., Lin, C.-H. Synthesis and thermal characteristic of liquid crystalline polyoxetane containing trans-stilbene side group. *Polymers* 12(1): 185; 2020. 林志鴻 485
35. Huang, W.-C., Liou, C.-J., Shen, S.-C., Hu, S., Hsiao, C.-Y., Wu, S.-J. Luteolin Attenuates IL-1  $\beta$ -Induced THP-1 Adhesion to ARPE-19 Cells via Suppression of NF- $\kappa$ B and MAPK Pathways. *Mediators of Inflammation* 2020: 9421340; 2020. 黃文忠、劉倩君、蕭千祐、吳淑如 496
36. Kumari, M., Liu, C.-H., Wu, W.-C. Oligochitosan modified albumin as plasmid DNA delivery vector: Endocytic trafficking, polyplex fate, in vivo compatibility. *International Journal of Biological Macromolecules* 142: 492-502; 2020. 劉繼賢 511
37. Yang, S.-C., Tsai, Y.-F., Pan, Y.-L., Hwang, T.-L. Understanding the role of neutrophils in acute respiratory distress syndrome. *Biomedical Journal*; 2020. in press 黃聰龍 522
38. Li, Y.-C., Tanapichatsakul, C., Pripdeevech, P., Hwang, T.L., Kuo, P.-C., Tzen, J.T.C. Characterisation of teaghrein-like principles from Assam tea cultivated in Thailand. *Natural Product Research*; 2020. in press 黃聰龍 530
39. Hsieh, H.-L., Liu, S.-H., Chen, Y.-L., Huang, C.-Y., Wu, S.-J. Astragaloside IV suppresses inflammatory response via suppression of NF- $\kappa$ B, and MAPK signalling in human bronchial epithelial cells. *Archives of Physiology and Biochemistry*; 2020. in press 謝喜龍、吳淑如 537
40. Jose, G., Shalumon, K.T., Chen, J.-P. Natural polymers based hydrogels for cell culture applications. *Current Medicinal Chemistry* 27(16): 2734-2776; 2020. 陳志平 547
41. Yang, H.-C., Stern, A., Chiu, D.T.-Y. G6PD: A hub for metabolic reprogramming and redox signaling in cancer. *Biomedical Journal*; 2020. in press 趙崇義 590
42. Liao, H.T., Lai, Y.-T., Kuo, C.-Y., Chen, J.-P. A bioactive multi-functional heparin-grafted aligned poly(lactide-co-



- glycolide)/curcumin nanofiber membrane to accelerate diabetic wound healing. *Materials Science and Engineering C*: 111689; 2020.
43. Hung, Y.-C., Wang, P.-W., Lin, T.-Y., Yang, P.-M., You, J.-S., Pan, T.-L. Functional Redox Proteomics Reveal That *Salvia miltiorrhiza* Aqueous Extract Alleviates Adriamycin-Induced Cardiomyopathy via Inhibiting ROS-Dependent Apoptosis. *Oxidative Medicine and Cellular Longevity* 2020: 5136934; 2020. 潘台龍 613
  44. Kuo, P.-C., Tai, S.-H., Hung, C.-C., Hwang, T.-L., Kuo, L.-M., Lam, S.H., Cheng, K.-C., Kuo, D.-H., Hung, H.-Y., Wu, T.-S. Antiinflammatory triterpenoids from the fruiting bodies of *Fomitopsis pinicola*. *Bioorganic Chemistry*: 104562; 2020. 黃聰龍 628
  45. Ma, J., Chan, C.-C., Huang, W.-C., Kuo, M.-L. Berberine inhibits pro-inflammatory cytokine-induced IL-6 and ccl11 production via modulation of stat6 pathway in human bronchial epithelial cells. *International Journal of Medical Sciences* 17(10): 1464-1473; 2020. 黃文忠、郭敏玲 639
  46. Chung, H.-M., Chang, Y.-M., Wang, W.-H., Chen, J.-J., Hwang, T.-L., Sung, P.-J. Rumphellolide K, a novel C-3/8 ether linkage caryophyllane from *rumphella antipathes*. *Heterocycles* 100(9); 2020. 黃聰龍 649
  47. Chan, C.-M., Hsiao, C.-Y., Li, H.-J., Fang, J.-Y., Chang, D.-C., Hung, C.-F. The inhibitory effects of gold nanoparticles on VEGF-A-induced cell migration in choroid-retina endothelial cells. *International Journal of Molecular Sciences* 21(1):109; 2020. 蕭千祐、方嘉佑 655
  48. Chen, Y.-H., Chin, H.-K., Peng, B.-R., Chen, Y.-Y., Hu, C.-C., Zheng, L.-G., Huynh, T.-H., Su, T.-P., Zhang, Y.-L., Wen, Z.-H., Hwang, T.-L., Wu, Y.-C., Sung, P.-J. Survey of briarane-type diterpenoids – Part VII. *Heterocycles* 100(6): 857-870; 2020. 黃聰龍 666
  49. Su, T.-P., Kuo, T.-J., Yang, S.-N., Lee, G.-H., Lee, Y.-T., Wang, Y.-C., Chen, J.-J., Wen, Z.-H., Hwang, T.-L., Sung, P.-J. 11 $\beta$ ,20 $\beta$ -Epoxybriaranes from the gorgonian coral *Junceella fragilis* (Ellisellidae). *Marine Drugs* 18(4): 18040183; 2020. 黃聰龍 678
  50. Lan, M.-Y., Hsu, Y.-B., Lan, M.-C., Chen, J.-P., Lu, Y.-J. Polyethylene Glycol-Coated Graphene Oxide Loaded with Erlotinib as an Effective Therapeutic Agent for Treating Nasopharyngeal Cancer Cells. *International journal of nanomedicine* 15: 7569-7582; 2020. 陳志平 688
  51. Khan, M., Huang, Y.-A., Kuo, C.-Y., Lin, T., Lu, C.-H., Chen, L.-C., Kuo, M.-L. Blocking pannexin1 reduces airway inflammation in a murine model of asthma. *American Journal of Translational Research* 12(7): 4074-4083; 2020. 郭敏玲 702
  52. Huang, P.-S., Chang, C.-C., Wang, C.-S., Lin, K.-H. Functional roles of non-coding RNAs regulated by thyroid hormones in liver cancer. *Biomedical Journal*; 2020. in press 林光輝 713

53. Wang, T.-H., Chen, C.-C., Leu, Y.-L., Lee, Y.-S., Lian, J.-H., Hsieh, H.-L., Chen, C.-Y. Palbociclib induces DNA damage and inhibits DNA repair to induce cellular senescence and apoptosis in oral squamous cell carcinoma. *Journal of the Formosan Medical Association*; 2020. in press 謝喜龍、陳琦媛 726
54. Vo, T.T.T., Lee, C.-W., Wu, C.-Z., Liu, J.-F., Lin, W.-N., Chen, Y.-L., Hsu, L.-F., Tsai, M.-H., Lee, I.T. Surfactin from *Bacillus subtilis* attenuates ambient air particulate matter-promoted human oral cancer cells metastatic potential. *Journal of Cancer* 11(20): 6038-6049; 2020. 李江文 737
55. Lin, T.-L., Lu, C.-C., Lai, W.-F., Wu, T.-S., Lu, J.-J., Chen, Y.-M., Tzeng, C.-M., Liu, H.-T., Wei, H., Lai, H.-C. Role of gut microbiota in identification of novel TCM-derived active metabolites. *Protein and Cell*; 2020. in press 賴信志 749
56. Gong, Y.-N., Tsao, K.-C., Hsiao, M.-J., Huang, C.-G., Huang, P.-N., Huang, P.-W., Lee, K.-M., Liu, Y.-C., Yang, S.-L., Kuo, R.-L., Chen, K.-F., Liu, Y.-C., Huang, S.-Y., Huang, H.-I., Liu, M.-T., Yang, J.-R., Chiu, C.-H., Yang, C.-T., Chen, G.-W., Shih, S.-R. SARS-CoV-2 genomic surveillance in Taiwan revealed novel ORF8-deletion mutant and clade possibly associated with infections in Middle East. *Emerging Microbes and Infections* 9(1): 1457-1466; 2020. 施信如 766
57. Yen, W.-C., Wu, Y.-H., Wu, C.-C., Lin, H.-R., Stern, A., Chen, S.-H., Shu, J.-C., Tsun-Yee Chiu, D. Impaired inflammasome activation and bacterial clearance in G6PD deficiency due to defective NOX/p38 MAPK/AP-1 redox signaling. *Redox Biology* 28: 101363; 2020. 吳依璇、趙崇義 776
58. Hsu, C.-C., Fu, T.-C., Huang, S.-C., Chen, C.P.-C., Wang, J.-S. Increased serum brain-derived neurotrophic factor with high-intensity interval training in stroke patients: A randomized controlled trial. *Annals of Physical and Rehabilitation Medicine*; 2020. in press 王素珍 787
59. Senghore, T., Wang, W.-C., Chien, H.-T., Chen, Y.-X., Young, C.-K., Huang, S.-F., Yeh, C.-C. Association of XRCC2 rs2040639 with the survival of patients with oral squamous cell carcinoma undergoing concurrent chemoradiotherapy. *Gene* 145283; 2020. 簡暉慈 795
60. Tseng, C.-P., Huang, Y.-L., Chang, Y.-W., Liao, H.-R., Chen, Y.-L., Hsieh, P.-W. Polysaccharide-containing fraction from *Artemisia argyi* inhibits tumor cell-induced platelet aggregation by blocking interaction of podoplanin with C-type lectin-like receptor 2. *Journal of Food and Drug Analysis* 28(1): 115-123; 2020. 謝佩文 802
61. Peng, B.-R., Lai, K.-H., Chang, Y.-C., Chen, Y.-Y., Su, J.-H., Huang, Y.M., Chen, P.-J., Yu, S.S.-F., Duh, C.-Y., Sung, P.-J. Sponge-Derived 24-Homoscleranes as Potent Anti-Inflammatory Agents. *Marine Drugs* 18(9): 434; 2020. 張祐嘉 811
62. Jose, G., Shalumon, K.T., Liao, H.-T., Kuo, C.-Y., Chen, J.-P. Preparation and characterization of surface heat sintered nanohydroxyapatite and nanowhitlockite embedded poly (Lactic-

co-glycolic acid) microsphere bone graft scaffolds: In vitro and in vivo studies. *International Journal of Molecular Sciences* 21(2): 528; 2020.

63. Chiang, C.-C., Cheng, W.-J., Lin, C.-Y., Lai, K.-H., Ju, S.-C., Lee, C., Yang, S.-H., Hwang, T.-L. Kan-Lu-Hsiao-Tu-Tan, a traditional Chinese medicine formula, inhibits human neutrophil activation and ameliorates imiquimod-induced psoriasis-like skin inflammation. *Journal of Ethnopharmacology* 246: 112246; 2020. 黃聰龍 843
64. Kamel, N.M., Helmy, M.W., Abdelfattah, E.-Z., Khattab, S.N., Ragab, D., Samaha, M.W., Fang, J.-Y., Elzoghby, A.O. Inhalable Dual-Targeted Hybrid Lipid Nanocore-Protein Shell Composites for Combined Delivery of Genistein and All-Trans Retinoic Acid to Lung Cancer Cells. *ACS Biomaterials Science and Engineering* 6(1): 71-87; 2020. 方嘉佑 857
65. Chi, L.-M., Hsiao, Y.-C., Chien, K.-Y., Chen, S.-F., Chuang, Y.-N., Lin, S.-Y., Wang, W.-S., Chang, I.Y.-F., Yang, C., Chu, L.J., Chiang, W.-F., Chien, C.-Y., Chang, Y.-S., Chang, K.-P., Yu, J.-S. Assessment of candidate biomarkers in paired saliva and plasma samples from oral cancer patients by targeted mass spectrometry. *Journal of Proteomics* 211: 103571; 2020. 余兆松 874
66. Peng, B.-R., Lai, K.-H., Chen, Y.-Y., Su, J.-H., Huang, Y.M., Chen, Y.-H., Lu, M.-C., Yu, S.S.-F., Duh, C.-Y., Sung, P.-J. Probing anti-proliferative 24-homoscalaranes from a sponge *Lendenfeldia* sp. *Marine Drugs* 18(2): 76; 2020. 賴奎宏 885
67. Yu, H.-P., F.-C.a,b, Umoro, A., Lin, Z.-C., Elzoghby, A.O., Hwang, T.-L., Fang, J.-Y. Oleic acid-based nanosystems for mitigating acute respiratory distress syndrome in mice through neutrophil suppression: How the particulate size affects therapeutic efficiency. *Journal of Nanobiotechnology* 18(1): 25; 2020. 黃聰龍、方嘉佑 895
68. Hu, C.-C., Lin, N.-C., Peng, B.-R., Chen, Y.-Y., Wen, Z.-H., Chang, Y.-C., Lee, G.-H., Wu, Y.-C., Sung, P.-J. New trihydroxybriarane diterpenoids from an octocoral *Briareum* sp. *Phytochemistry Letters* 35: 23-27; 2020. 張祐嘉 911
69. Liu, C.-H., Lee, G.-W., Wu, W.-C., Wang, C.-C. Encapsulating curcumin in ethylene diamine- $\beta$ -cyclodextrin nanoparticle improves topical cornea delivery. *Colloids and Surfaces B: Biointerfaces* 186: 110726; 2020. 劉繼賢 916
70. Chao, C.-C., Lee, C.-W., Chang, T.-M., Chen, P.-C., Liu, J.-F. CXCL1/CXCR2 paracrine axis contributes to lung metastasis in osteosarcoma. *Cancers* 12(2): 459; 2020. 李江文 925
71. Wang, C.C., Ho, Y.H., Hung, C.F., Kuo, J.R., Wang, S.J. Xanthohumol, an active constituent from hop, affords protection against kainic acid-induced excitotoxicity in rats. *Neurochemistry International* 133: 104629; 2020. 王素珍 941
72. Liu, C.-C., Chou, Y.-S., Chen, C.-Y., Liu, K.-L., Huang, G.-J., Yu, J.-S., Wu, C.-J., Liaw, G.-W., Hsieh, C.-H., Chen, C.-K. 余兆松 950



- Pathogenesis of local necrosis induced by *Naja atra* venom: Assessment of the neutralization ability of Taiwanese freeze-dried neurotoxic antivenom in animal models. *PLoS Neglected Tropical Diseases* 14(2): e0008054; 2020.
73. Abdelaziz, H.M., Elzoghby, A.O., Helmy, M.W., Abdelfattah, E.-Z.A., Fang, J.-Y., Samaha, M.W., Freag, M.S. Inhalable Lactoferrin/Chondroitin-Functionalized Monoolein Nanocomposites for Localized Lung Cancer Targeting. *ACS Biomaterials Science and Engineering* 6(2): 1030-1042; 2020. 方嘉佑 970
  74. Leu, Y.-L., Wang, T.-H., Wu, C.-C., Huang, K.-Y., Jiang, Y.-W., Hsu, Y.-C., Chen, C.-Y. Hydroxygenkwanin suppresses non-small cell lung cancer progression by enhancing EGFR degradation. *Molecules* 25(4): 941; 2020. 陳琦媛 983
  75. Chen, B.-S., Lee, H.-C., Lee, K.-M., Gong, Y.-N., Shih, S.-R. Enterovirus and Encephalitis. *Frontiers in Microbiology* 11: 261; 2020. 施信如 995
  76. Yu-Ju Wu, C., Chen, C.-H., Lin, C.-Y., Feng, L.-Y., Lin, Y.-C., Wei, K.-C., Huang, C.-Y., Fang, J.-Y., Chen, P.-Y. CCL5 of glioma-associated microglia/macrophages regulates glioma migration and invasion via calcium-dependent matrix metalloproteinase 2. *Neuro-Oncology* 22(2): 253-266; 2020. 方嘉佑 1010
  77. Chen, C.-Y., Chen, C.-C., Chuang, W.-Y., Leu, Y.-L., Ueng, S.-H., Hsueh, C., Yeh, C.-T., Wang, T.-H. Hydroxygenkwanin Inhibits Class I HDAC Expression and Synergistically Enhances the Antitumor Activity of Sorafenib in Liver Cancer Cells. *Frontiers in Oncology* 10: 216; 2020. 陳琦媛 1024
  78. Wu, C.-H., Chen, C.-Y., Yeh, C.-T., Lin, K.-H. Radiosensitization of hepatocellular carcinoma through targeting radio-associated microRNA. *International Journal of Molecular Sciences* 21(5): 1859; 2020. 林光輝 1037
  79. Hsu, C.-C., Fu, T.-C., Huang, S.-C., Wang, J.-S. High-intensity interval training recuperates capacity of endogenous thrombin generation in heart failure patients with reduced ejection fraction. *Thrombosis Research* 187: 159-165; 2020. 王鐘賢 1051
  80. Hsiao, Y.-C., Lin, S.-Y., Chien, K.-Y., Chen, S.-F., Wu, C.-C., Chang, Y.-T., Chi, L.-M., Chu, L.J., Chiang, W.-F., Chien, C.-Y., Chang, K.-P., Chang, Y.-S., Yu, J.-S. An immuno-MALDI mass spectrometry assay for the oral cancer biomarker, matrix metalloproteinase-1, in dried saliva spot samples. *Analytica Chimica Acta* 1100: 118-130; 2020. 余兆松 1058
  81. Lee, W.-R., Lin, Y.-K., Alalaiwe, A., Wang, P.-W., Liu, P.-Y., Fang, J.-Y. Fractional Laser-Mediated siRNA Delivery for Mitigating Psoriasis-like Lesions via IL-6 Silencing. *Molecular Therapy - Nucleic Acids* 19: 240-251; 2020. 方嘉佑 1071
  82. Yeh, J.-Y., Shyu, Y.-C., Lee, S.-Y., Yuan, S.-S., Yang, C.-J., Yang, K.-C., Lee, T.-L., Sun, C.-C., Wang, L.-J. Comorbidity of Narcolepsy and Psychotic Disorders: A Nationwide Population-Based Study in Taiwan. *Frontiers in Psychiatry* 11: 205; 2020. 徐于喬 1083

83. Liou, C.-J., Chen, Y.-L., Yu, M.-C., Yeh, K.-W., Shen, S.-C., Huang, W.-C. Sesamol alleviates airway hyperresponsiveness and oxidative stress in asthmatic mice. *Antioxidants* 9(4): 295; 2020. 劉倩君、黃文忠 1092
84. Chen, Y.-M., Chiu, W.-C., Chiu, Y.-S., Li, T., Sung, H.-C., Hsiao, C.-Y. Supplementation of nano-bubble curcumin extract improves gut microbiota composition and exercise performance in mice. *Food and Function* 11(4): 3574-3584; 2020. 蕭千祐 1109
85. Chang, C.-H., Ahmed, A.F., Yang, T.-S., Lin, Y.-C., Huang, C.-Y., Hwang, T.-L., Sheu, J.-H. Isolation of Lobane and Prenyleudesmane Diterpenoids from the Soft Coral *Lobophytum varium*. *Marine Drugs* 18(4): 223; 2020. 黃聰龍 1120
86. Ho, S.-Y., Chiu, C.-H., Huang, Y.-C., Chen, C.-J., Lien, R., Chu, S.-M., Huang, C.-G., Tsao, K.-C., Shih, S.-R., Hsu, J.-F. Investigation and successful control of an echovirus 11 outbreak in neonatal intensive care units. *Pediatrics and Neonatology* 61(2): 180-187; 2020. 施信如 1137
87. Lee, C.-W., Su, Y.-H., Chiang, Y.-C., Lee, I.-T., Li, S.-Y., Lee, H.-C., Hsu, L.-F., Yan, Y.-L., Li, H.-Y., Chen, M.-C., Peng, K.-T., Lai, C.-H. Glycofullerenes inhibit particulate matter induced inflammation and loss of barrier proteins in HaCaT human keratinocytes. *Biomolecules* 10(4): 514; 2020. 李江文 1145
88. Lu, C.W., Lin, T.Y., Wang, S.J. 11-Keto- $\beta$ -Boswellic Acid Attenuates Glutamate Release and Kainic Acid-Induced Excitotoxicity in the Rat Hippocampus. *Planta Medica* 86(6): 434-441; 2020. 王素珍 1168
89. Wang, T.-H., Wu, C.-C., Huang, K.-Y., Chuang, W.-Y., Hsueh, C., Li, H.-J., Chen, C.-Y. Profiling of subcellular EGFR interactome reveals hnRNP A3 modulates nuclear EGFR localization. *Oncogenesis* 9(4): 40; 2020. 陳琦媛 1176
90. Yu, H.-P., Liu, F.-C., Lin, C.-Y., Umoro, A., Trousil, J., Hwang, T.-L., Fang, J.-Y. Suppression of neutrophilic inflammation can be modulated by the droplet size of anti-inflammatory nanoemulsions. *Nanomedicine* 15(8): 773-791; 2020. 黃聰龍、方嘉佑 1190
91. Chen, H.-A., Ma, Y.-H., Hsu, T.-Y., Chen, J.-P. Preparation of peptide and recombinant tissue plasminogen activator conjugated poly(Lactic-co-glycolic acid) (PLGA) magnetic nanoparticles for dual targeted thrombolytic therapy. *International Journal of Molecular Sciences* 21(8): 2690; 2020. 陳志平 1209
92. Huang, P.-S., Lin, Y.-H., Chi, H.-C., Tseng, Y.-H., Chen, C.Y., Lin, T.-K., Yeh, C.-T., Lin, K.-H. Dysregulated FAM215A Stimulates LAMP2 Expression to Confer Drug-Resistant and Malignant in Human Liver Cancer. *Cells* 9(4); 2020. 林光輝 1232
93. Yeh, Y.-C., Huang, T.-H., Yang, S.-C., Chen, C.-C., Fang, J.-Y. Nano-Based Drug Delivery or Targeting to Eradicate Bacteria for Infection Mitigation: A Review of Recent Advances. *Frontiers in Chemistry* 8: 286; 2020. 方嘉佑 1252

94. Lin, T.-L., Shu, C.-C., Chen, Y.-M., Lu, J.-J., Wu, T.-S., Lai, W.-F., Tzeng, C.-M., Lai, H.-C., Lu, C.-C. Like Cures Like: Pharmacological Activity of Anti-Inflammatory Lipopolysaccharides From Gut Microbiome. *Frontiers in Pharmacology* 11: 554; 2020. 賴信志 1274
95. Yang, S.-C., Wang, Y.-H., Tsai, Y.-F., Chang, Y.-W., Wu, T.-S., Ho, C.-M., Hwang, T.-L. A synthesized heterocyclic chalcone inhibits neutrophilic inflammation through K<sup>+</sup>-dependent pH regulation. *FASEB Journal* 34(5): 7127-7143; 2020. 黃聰龍 1283
96. Lai, Y.-W., Wang, S.-W., Hu, Y.-Y., Hwang, T.-L., Cheng, M.-J., Chen, I.-S., Sung, P.-J., Chen, J.-J. Anti-inflammatory alkaloids from the root bark of *Hernandia nymphaeifolia*. *Phytochemistry* 173: 112326; 2020. 黃聰龍 1300
97. Chang, Y.-C., Lai, K.-H., Kumar, S., Chen, P.-J., Wu, Y.-H., Lai, C.-L., Hsieh, H.-L., Sung, P.-J., Hwang, T.-L. 1H NMR-based isolation of anti-inflammatory 9,11-secosteroids from the octocoral *sinularia leptoclados*. *Marine Drugs* 18(5): 271; 2020. 張祐嘉、  
吳依璇、  
謝喜龍、  
黃聰龍 1307
98. Lin, Y.-C., Lin, J.-J., Chen, S.-R., Hwang, T.-L., Fang, S.-Y., Korinek, M., Chen, C.-Y., Lin, Y.-S., Wu, T.-Y., Yen, M.-H., Wang, C.-H., Cheng, Y.-B. Clerodane diterpenoids from *callicarpa hypoleucophylla* and their anti-inflammatory activity. *Molecules* 25(10): 2288; 2020. 黃聰龍 1317
99. Alalaiwe, A., Lin, C.-F., Hsiao, C.-Y., Chen, E.-L., Lin, C.-Y., Lien, W.-C., Fang, J.-Y. Development of flavanone and its derivatives as topical agents against psoriasis: The prediction of therapeutic efficiency through skin permeation evaluation and cell-based assay. *International Journal of Pharmaceutics* 581: 119256; 2020. 蕭千祐、  
方嘉佑 1327
100. Al-Sayed, E., Ke, T.-Y., Hwang, T.-L., Chen, S.-R., Korinek, M., Chen, S.-L., Cheng, Y.-B. Cytotoxic and anti-inflammatory effects of lignans and diterpenes from *Cupressus macrocarpa*. *Bioorganic and Medicinal Chemistry Letters* 30(10): 127127; 2020. 黃聰龍 1339
101. Li, C.-Y., Chang, C.-C., Tsai, Y.-H., El-Shazly, M., Wu, C.-C., Wang, S.-W., Hwang, T.-L., Wei, C.-K., Hohmann, J., Yang, Z.-J., Cheng, Y.-B., Wu, Y.-C., Chang, F.-R. Anti-inflammatory, Antiplatelet Aggregation, and Antiangiogenesis Polyketides from *Epicoccum sorghinum*: Toward an Understating of Its Biological Activities and Potential Applications. *ACS Omega* 5(19): 11092-11099; 2020. 黃聰龍 1344
102. Liu, Y.-C., Yeh, C.-T., Lin, K.-H. Cancer Stem Cell Functions in Hepatocellular Carcinoma and Comprehensive Therapeutic Strategies. *Cells* 9(6); 2020. 林光輝 1352
103. Cheng, C.-Y., Haque, A., Hsieh, M.-F., Hassan, S.I., Faizi, M.S.H., Dege, N., Khan, M.S. 1,4-disubstituted 1h-1,2,3-triazoles for renal diseases: Studies of viability, anti-inflammatory, and antioxidant activities. *International Journal of*



104. Lee, T.-H., Chen, J.-L., Liu, P.-S., Tsai, M.-M., Wang, S.-J., Hsieh, H.-L. Rottlerin, a natural polyphenol compound, inhibits upregulation of matrix metalloproteinase-9 and brain astrocytic migration by reducing PKC- $\delta$ -dependent ROS signal. *Journal of Neuroinflammation* 17(1): 177; 2020. 蔡明明、王素珍、謝喜龍 1398
105. Lin, S.-L., Lin, Y.-H., Chi, H.-C., Lin, T.-K., Chen, W.-J., Yeh, C.-T., Lin, K.-H. A Novel Long Non-Coding RNA-01488 Suppressed Metastasis and Tumorigenesis by Inducing miRNAs That Reduce Vimentin Expression and Ubiquitination of Cyclin E. *Cells* 9(6); 2020. 林光輝 1411
106. Huang, S.-S., Chen, T.-Y., Deng, J.-S., Pao, L.-H., Cheng, Y.-C., Chao, J. An Ethnobotanical Study on Qīng-Cǎo-Chá Tea in Taiwan. *Frontiers in Pharmacology* 11: 931; 2020. 鮑力恆 1428
107. Kuo, P.-C., Wu, Y.-H., Hung, H.-Y., Lam, S.-H., Ma, G.-H., Kuo, L.-M., Hwang, T.-L., Kuo, D.-H., Wu, T.-S. Anti-inflammatory principles from *Lindera aggregata*. *Bioorganic and Medicinal Chemistry Letters* 30(13): 127224; 2020. 黃聰龍 1441
108. Huang, S.-L., Chang, T.-C., Chao, C.C.K., Sun, N.-K. Role of the TLR4-androgen receptor axis and genistein in taxol-resistant ovarian cancer cells. *Biochemical Pharmacology* 177: 113965; 2020. 孫念康 1445
109. Kuei Huang, S., Lin, T.-Y., Wang, S.-J. Tapentadol Suppresses Glutamatergic Transmission and Neuronal Firing in Rat Hippocampal CA3 Pyramidal Neurons. *Pharmacology* 105(7-8): 445-453; 2020. 王素珍 1457
110. Zhang, Y.-L., Chiang, C.-C., Lee, Y.-T., Wen, Z.-H., Wu, Y.-C., Wu, Y.-J., Hwang, T.-L., Wu, T.-Y., Chang, C.-Y., Sung, P.-J. Briarenols Q-T: Briaranes from a cultured octocoral *Briareum stechei* (Kükenthal, 1908). *Marine Drugs* 18(8): 383; 2020. 黃聰龍 1466
111. Lu, C.-H., Chen, C.-M., Ma, J., Wu, C.-J., Chen, L.-C., Kuo, M.-L. DNA methyltransferase inhibitor alleviates bleomycin-induced pulmonary inflammation. *International Immunopharmacology* 84: 106542; 2020. 郭敏玲 1476
112. Cheng, C.-Y., Lin, Y.-K., Yang, S.-C., Alalaiwe, A., Lin, C.-J., Fang, J.-Y., Lin, C.-F. Percutaneous absorption of resveratrol and its oligomers to relieve psoriasiform lesions: In silico, in vitro and in vivo evaluations. *International Journal of Pharmaceutics* 585: 119507; 2020. 鄭靜宜、方嘉佑、林傳福 1483
113. Yang, C.-L., Wu, H.-C., Hwang, T.-L., Lin, C.-H., Cheng, Y.-H., Wang, C.-C., Kan, H.-L., Kuo, Y.-H., Chen, I.-S., Chang, H.-S., Lin, Y.-C. Anti-inflammatory and antibacterial activity constituents from the stem of *Cinnamomum validinerve*. *Molecules* 25(15): 3382; 2020. 黃聰龍 1497
114. Chen, M.M., Chiu, C.-H., Yuan, C.-P., Liao, Y.-C., Guo, S.-E. Influence of environmental tobacco smoke and air pollution on fetal growth: A prospective study. *International Journal of*

115. Huang, C.-G., Lee, K.-M., Hsiao, M.-J., Yang, S.-L., Huang, P.-N., Gong, Y.-N., Hsieh, T.-H., Huang, P.-W., Lin, Y.-J., Liu, Y.-C., Tsao, K.-C., Shih, S.-R. Culture-based virus isolation to evaluate potential infectivity of clinical specimens tested for COVID-19. *Journal of Clinical Microbiology* 58(8): e01068-20; 2020. 施信如 1519
116. Liu, Y.-C., Kuo, R.-L., Shih, S.-R. COVID-19: The first documented coronavirus pandemic in history. *Biomedical Journal* 43(4): 328-333; 2020. 施信如 1527
117. Huang, H.-I., Lin, J.-Y., Chiang, H.-C., Huang, P.-N., Lin, Q.-D., Shih, S.-R. Exosomes facilitate transmission of enterovirus A71. *Journal of Infectious Diseases* 222(3): 456-469; 2020. 施信如 1533
118. Anilkumar, T.S., Lu, Y.-J., Chen, J.-P. Optimization of the preparation of magnetic liposomes for the combined use of magnetic hyperthermia and photothermia in dual magneto-photothermal cancer therapy. *International Journal of Molecular Sciences* 21(15): 5187; 2020. 陳志平 1547
119. Gaber, M., Elhasany, K.A., Sabra, S., Helmy, M.W., Fang, J.-Y., Khattab, S.N., Bekhit, A.A., Teleb, M., Elkodairy, K.A., Elzoghby, A.O. Co-Administration of Tretinoin Enhances the Anti-Cancer Efficacy of Etoposide via Tumor-Targeted Green Nano-Micelles. *Colloids and Surfaces B: Biointerfaces* 192: 110997; 2020. 方嘉佑 1570
120. Tang, K.-W., Lin, Z.-C., Wang, P.-W., Alalaiwe, A., Tseng, C.-H., Fang, J.-Y. Facile skin targeting of a thalidomide analog containing benzyl chloride moiety alleviates experimental psoriasis via the suppression of MAPK/NF- $\kappa$ B/AP-1 phosphorylation in keratinocytes. *Journal of Dermatological Science* 99(2): 90-99; 2020. 方嘉佑 1581
121. Chen, C.-Y., Fang, J.-Y., Chen, C.-C., Chuang, W.-Y., Leu, Y.-L., Ueng, S.-H., Wei, L.-S., Cheng, S.-F., Hsueh, C., Wang, T.-H. 2-O-Methylmagnolol, a Magnolol Derivative, Suppresses Hepatocellular Carcinoma Progression via Inhibiting Class I Histone Deacetylase Expression. *Frontiers in Oncology* 10: 1319; 2020. 方嘉佑 1591
122. Hu, H.-C., Li, C.-Y., Tsai, Y.-H., Yang, D.-Y., Wu, Y.-C., Hwang, T.-L., Chen, S.-L., Fülöp, F., Hunyadi, A., Yen, C.-H., Cheng, Y.-B., Chang, F.-R. Secondary metabolites and bioactivities of *aspergillus ochraceopetaliformis* isolated from *anthurium brownii*. *ACS Omega* 5(33): 20991-20999; 2020. 黃聰龍 1604
123. Fang, J.-Y., Tang, K.-W., Yang, S.-H., Alalaiwe, A., Yang, Y.-C., Tseng, C.-H., Yang, S.-C. Synthetic Naphthofuranquinone Derivatives Are Effective in Eliminating Drug-Resistant *Candida albicans* in Hyphal, Biofilm, and Intracellular Forms: An Application for Skin-Infection Treatment. *Frontiers in Microbiology* 11: 2053; 2020. 方嘉佑 1613

124. Chiang, M.-H., Liang, C.-J., Lin, L.-C., Yang, Y.-F., Huang, C.-C., Chen, Y.-H., Kao, H.-L., Chen, Y.-C., Ke, S.-R., Lee, C.-W., Lin, M.-S., Chen, Y.-L. miR-26a attenuates cardiac apoptosis and fibrosis by targeting ataxia–telangiectasia mutated in myocardial infarction. *Journal of Cellular Physiology* 235(9): 6085-6102; 2020. 李江文 1626
125. Li, S.-L., Wu, H.-C., Hwang, T.-L., Lin, C.-H., Yang, S.-S., Chang, H.-S. Phytochemical investigation and anti-inflammatory activity of the leaves of *Machilus japonica* var. *kusanoi*. *Molecules* 25(18): 4149; 2020. 黃聰龍 1644
126. Cheng, C.-Y., Vo, T.T.T., Lin, W.-N., Huang, H.-W., Chuang, C.-C., Chu, P.-M., Lee, I.-T. Nrf2/HO-1 partially regulates cytoprotective effects of carbon monoxide against urban particulate matter-induced inflammatory responses in oral keratinocytes. *Cytokine* 133: 155185; 2020. 鄭靜宜 1658
127. Lin, T.-Y., Wang, P.-W., Huang, C.-H., Yang, P.-M., Pan, T.-L. Characterizing the relapse potential in different luminal subtypes of breast cancers with functional proteomics. *International Journal of Molecular Sciences* 21(17): 6077; 2020. 潘台龍 1668
128. Chen, P., Kuo, L., Wu, Y., Chang, Y., Lai, K., Hwang, T. BAY 41-2272 attenuates CTGF expression via sGC/cGMP-independent pathway in TGFβ1-activated hepatic stellate cells. *Biomedicines* 8(9): 330; 2020. 張祐嘉、黃聰龍 1684
129. Alalaiwe, A., Lin, Y.-K., Lin, C.-H., Wang, P.-W., Lin, J.-Y., Fang, J.-Y. The absorption of polycyclic aromatic hydrocarbons into the skin to elicit cutaneous inflammation: The establishment of structure–permeation and in silico–in vitro–in vivo relationships. *Chemosphere* 255: 126955; 2020. 方嘉佑 1699
130. Al-Sayed, E., Korinek, M., Esmat, A., Chen, G.-Y., Cheng, Y.-B., Hsieh, P.-W., Chen, B.-H., Hwang, T.-L. Anti-inflammatory, hepatoprotective and antioxidant activity of ellagitannin isolated from *Melaleuca styphelioides*. *Phytochemistry* 177: 112429; 2020. 謝佩文、黃聰龍 1713
131. Liu, J.-F., Lee, C.-W., Lin, C.-Y., Chao, C.-C., Chang, T.-M., Han, C.-K., Huang, Y.-L., Fong, Y.-C., Tang, C.-H. CXCL13/CXCR5 interaction facilitates VCAM-1-dependent migration in human osteosarcoma. *International Journal of Molecular Sciences* 21(17): 6095; 2020. 李江文 1723
132. Lu, Y.-J., Wang, Y.-H., Sahu, R.S., Chen, J.-P., Dash, B.S., Chung, P.-J., Yang, H.-W., Chuang, E.-Y., Hwang, T.-L. Mechanism of nanoformulated graphene oxide-mediated human neutrophil activation. *ACS Applied Materials and Interfaces* 12(36): 40141-40152; 2020. 黃聰龍 1736
133. Chi, H.-C., Tsai, C.-Y., Wang, C.-S., Yang, H.-Y., Lo, C.-H., Wang, W.-J., Lee, K.-F., Lai, L.-Y., Hong, J.-H., Chang, Y.-F., Tsai, M.-M., Yeh, C.-T., Wu, C.H., Hsieh, C.-C., Wang, L.-H., Chen, W.-J., Lin, K.-H. DOCK6 promotes chemo- and radioresistance of gastric cancer by modulating WNT/β-catenin signaling and cancer stem cell traits. *Oncogene* 39(37): 5933- 蔡明明、林光輝 1748



5949; 2020.

- |      |   |                     |      |
|------|---|---------------------|------|
| 134. | Liou, C.-J., Wu, S.-J., Shen, S.-C., Chen, L.-C., Chen, Y.-L., Huang, W.-C. Phloretin ameliorates hepatic steatosis through regulation of lipogenesis and Sirt1/AMPK signaling in obese mice. <i>Cell and Bioscience</i> 10(1): 114; 2020.  | 劉倩君、<br>吳淑如、<br>黃文忠 | 1765 |
| 135. | Wu, C.-H., Yeh, C.-T., Lin, K.-H. Thyroid hormones suppress FOXM1 expression to reduce liver cancer progression. <i>Oncology Reports</i> 44(4): 1686-1698; 2020.  | 林光輝                 | 1779 |
| 136. | Lu, Y.-J., Lan, Y.-H., Chuang, C.-C., Lu, W.-T., Chan, L.-Y., Hsu, P.-W., Chen, J.-P. Injectable thermo-sensitive chitosan hydrogel containing CPT-11-loaded EGFR-targeted graphene oxide and SLP2 shRNA for localized drug/gene delivery in glioblastoma therapy. <i>International Journal of Molecular Sciences</i> 21(19): 7111; 2020.   | 陳志平                 | 1792 |
| 137. | Liu, Z.-H., Huang, Y.-C., Kuo, C.-Y., Kuo, C.-Y., Chin, C.-Y., Yip, P.K., Chen, J.-P. Docosahexaenoic acid-loaded polylactic acid core-shell nanofiber membranes for regenerative medicine after spinal cord injury: In vitro and in vivo study. <i>International Journal of Molecular Sciences</i> 21(19): 7031; 2020.   | 陳志平                 | 1820 |
| 138. | Mykhailenko, O., Korinek, M., Ivanauskas, L., Bezruk, I., Myhal, A., Petrikaite, V., El-Shazly, M., Lin, G.-H., Lin, C.-Y., Yen, C.-H., Chen, B.-H., Georgiyants, V., Hwang, T.-L. Qualitative and quantitative analysis of Ukrainian iris species: A fresh look on their antioxidant content and biological activities. <i>Molecules</i> 25(19): A4; 2020.   | 黃聰龍                 | 1839 |
| 139. | Chiang, C.-C., Korinek, M., Cheng, W.-J., Hwang, T.-L. Targeting Neutrophils to Treat Acute Respiratory Distress Syndrome in Coronavirus Disease. <i>Frontiers in Pharmacology</i> 11: 572009; 2020.  | 黃聰龍                 | 1863 |
| 140. | Ebada, S.S., Al-Jawabri, N.A., Youssef, F.S., El-Kashef, D.H., Knedel, T.-O., Albohy, A., Korinek, M., Hwang, T.-L., Chen, B.-H., Lin, G.-H., Lin, C.-Y., Aldalaie, S.M., Disi, A.M., Janiak, C., Proksch, P. Anti-inflammatory, antiallergic and COVID-19 protease inhibitory activities of phytochemicals from the Jordanian hawksbeard: Identification, structure-Activity relationships, molecular modeling and impact on its folk medicinal uses. <i>RSC Advances</i> 10(62): 38128-38141; 2020. | 黃聰龍                 | 1877 |
| 141. | Virly, Chiu, C.-H., Tsai, T.-Y., Yeh, Y.-C., Wang, R. Encapsulation of $\beta$ -Glucosidase within PVA Fibers by CCD-RSM-Guided Coelectrospinning: A Novel Approach for Specific Mogroside Sweetener Production. <i>Journal of Agricultural and Food Chemistry</i> 68(42): 11790-11801; 2020.   | 邱群惠                 | 1891 |
| 142. | Lee, K.-M., Gong, Y.-N., Shih, S.-R. Methods for detection and study of virus-derived small RNAs produced from the intramolecular base-pairing region of the picornavirus genome. <i>Methods</i> 183: 4-12; 2020.   | 施信如                 | 1903 |
| 143. | Jose, G., Lu, Y.-J., Hung, J.-T., Yu, A.L., Chen, J.-P. Co-delivery of cpt-11 and panobinostat with anti-gd2 antibody conjugated  | 陳志平                 | 1912 |

immunoliposomes for targeted combination chemotherapy. *Cancers* 12(11): 3211; 2020.

144. Hsu, S.K., Hung, C.F., Yang, H.C., Weng, J.R., Wang, S.J. TCD, a triterpenoid isolated from wild bitter gourd, reduces synaptosomal release of glutamate and protects against kainic acid-induced neuronal death. *Food and Function* 11(11): 9858-9867; 2020. 王素珍 1937
145. Lu, C.-W., Lin, T.-Y., Chiu, K.-M., Lee, M.-Y., Huang, J.-H., Wang, S.-J. Silymarin inhibits glutamate release and prevents against kainic acid-induced excitotoxic injury in rats. *Biomedicines* 8(11): 486; 2020. 王素珍 1947
146. Lu, C.W., Lin, T.-Y., Yang, H.C., Hung, C.F., Weng, J.R., Chang, D.C., Wang, S.J. [1-(4-chloro-3-nitrobenzenesulfonyl)-1H-indol-3-yl]-methanol, an indole-3-carbinol derivative, inhibits glutamate release in rat cerebrocortical nerve terminals by suppressing the P/Q-type  $\text{Ca}^{2+}$  channels and  $\text{Ca}^{2+}$ /calmodulin/protein kinase A pathway. *Neurochemistry International* 140: 104845; 2020. 王素珍 1969
147. Yang, H.-C., Yu, H., Ma, T.-H., Tjong, W.-Y., Stern, A., Chiu, D.T.-Y. Tert-butyl hydroperoxide (Tbhp)-induced lipid peroxidation and embryonic defects resemble glucose-6-phosphate dehydrogenase (g6pd) deficiency in *c. elegans*. *International Journal of Molecular Sciences* 21(22): 8688; 2020. 趙崇義 1977
148. Chang, Y.-C., Chiang, C.-C., Chang, Y.-S., Chen, J.-J., Wang, W.-H., Fang, L.-S., Chung, H.-M., Hwang, T.-L., Sung, P.-J. Novel Caryophyllane-Related Sesquiterpenoids with Anti-Inflammatory Activity from *Rumphella antipathes* (Linnaeus, 1758). *Marine drugs* 18(11); 2020. 張祐嘉、黃聰龍 1988
149. Li, M.-L., Chen, B.-S., Shih, S.-R. Editorial: Viral Encephalitis. *Frontiers in Microbiology* 11: 599257; 2020. 施信如 1998
150. Nguyen, D.D., Lai, J.-Y. Advancing the stimuli response of polymer-based drug delivery systems for ocular disease treatment. *Polymer Chemistry* 11(44): 6988-7008; 2020. 賴瑞陽 2000
151. Lee, T.-H., Liu, P.-S., Tsai, M.-M., Chen, J.-L., Wang, S.-J., Hsieh, H.-L. The COX-2-derived PGE2 autocrine contributes to bradykinin-induced matrix metalloproteinase-9 expression and astrocytic migration via STAT3 signaling. *Cell Communication and Signaling* 18(1): 185; 2020. 蔡明明、王素珍、謝喜龍 2021
152. Chiang, C.-C., Li, Y.-R., Lai, K.-H., Cheng, W.-J., Lin, S.-C., Wang, Y.-H., Chen, P.-J., Yang, S.-H., Lin, C.-C., Hwang, T.-L. Aqueous extract of kan-lu-hsiao-tu-tan ameliorates collagen-induced arthritis in mice by inhibiting oxidative stress and inflammatory responses. *Life* 10(12): 313; 2020. 黃聰龍 2034
153. Li, H.-J., Wu, N.-L., Pu, C.-M., Hsiao, C.-Y., Chang, D.-C., Hung, C.-F. Chrysin alleviates imiquimod-induced psoriasis-like skin inflammation and reduces the release of CCL20 and antimicrobial peptides. *Scientific Reports* 10(1): 2932; 2020. 蕭千祐 2051

154. Elzoghby, A.O., Abdelmoneem, M.A., Hassanin, I.A., Abd Elwakil, M.M., Elnaggar, M.A., Mokhtar, S., Fang, J.-Y., Elkhodairy, K.A. Lactoferrin, a multi-functional glycoprotein: Active therapeutic, drug nanocarrier & targeting ligand. *Biomaterials* 263: 120355; 2020. 方嘉佑 2064
155. Yang, S.-C., Hsu, C.-Y., Chou, W.-L., Fang, J.-Y., Chuang, S.-Y. Bioactive Agent Discovery from the Natural Compounds for the Treatment of Type 2 Diabetes Rat Model. *Molecules (Basel, Switzerland)* 25(23); 2020. 方嘉佑 2085
156. Lee, T.-L., Lee, M.-H., Chen, Y.-C., Lee, Y.-C., Lai, T.-C., Lin, H.Y.-H., Hsu, L.-F., Sung, H.-C., Lee, C.-W., Chen, Y.-L. Vitamin D Attenuates Ischemia/Reperfusion-Induced Cardiac Injury by Reducing Mitochondrial Fission and Mitophagy. *Frontiers in Pharmacology* 11: 604700; 2020. 李江文 2103
157. Yeh, K.C., Hung, C.F., Lin, Y.F., Chang, D.C., Pai, M.S., Wang, S.J. Neferine, a bisbenzylisoquinoline alkaloid of *Nelumbo nucifera*, inhibits glutamate release in rat cerebrocortical nerve terminals through 5-HT<sub>1A</sub> receptors. *European Journal of Pharmacology* 889: 173589; 2020. 王素珍 2120
158. Chen, Y.-H., Chang, Y.-C., Chen, Y.-H., Zheng, L.-G., Huang, P.-C., Huynh, T.-H., Peng, B.-R., Chen, Y.-Y., Wu, Y.-J., Fang, L.-S., Su, J.-H., Hsu, C.-M., Sung, P.-J. Natural Products from Octocorals of the Genus *Dendronephthya* (Family Nephtheidae). *Molecules (Basel, Switzerland)* 25(24); 2020. 張祐嘉 2130
159. 蔡書憲(Shu-Hsien Tsai)；鄭潔穎(Jie-Ying Zheng)；簡全基(Chuan-Chi Chien)；李士畦(Shih-Chi Lee)；鄭俊昇(Chun-Shen Cheng)；范植軒(Chin-Hsuan Fan)；李明怡(Ming-Yi Lee)。在農業循環經濟浪潮下柑橘類檸檬皮渣之再利用技術現況及展望(Current Status and Prospects on Reuse Technology of Citrus Limon Waste in The Agricultural Circular Economy)。長庚科技學刊 32 期: 125 - 137; 2020. 李明怡 2156



## Tumor progression-dependent angiogenesis in gastric cancer and its potential application

Hsi-Lung Hsieh, Ming-Ming Tsai

**ORCID number:** Ming-Ming Tsai (0000-0002-4495-6616); Hsi-Lung Hsieh (0000-0001-8302-2472).

**Author contributions:** The author contributed to this paper with conception and design of the study, literature review and analysis, drafting and critical revision and editing, and final approval of the final version.

**Supported by** the Ministry of Science and Technology, Taiwan, No. MOST 106-2320-B-255-005 and No. MOST 107-2320-B-255-003; Chang Gung Medical Research Foundation, Taoyuan, Taiwan, No. CMRPF1G0011, No. CMRPF1G0251, No. CMRPF1I0031, No. CMRPF1H0051, and No. CMRPF1I0041; and Chang Gung University of Science and Technology, Taoyuan, Taiwan, No. ZRRPF3H0131.

**Conflict-of-interest statement:** No potential conflicts of interest. No financial support.

**Open-Access:** This article is an open-access article which was selected by an in-house editor and fully peer-reviewed by external reviewers. It is distributed in accordance with the Creative Commons Attribution Non Commercial (CC BY-NC 4.0) license, which permits others to distribute, remix, adapt, build upon this work non-commercially, and license their derivative works on different terms, provided the original work is properly cited and the use is non-commercial. See: <http://creativecommons.org/licenses/by-nc/4.0/>

**Hsi-Lung Hsieh, Ming-Ming Tsai**, Research Center for Chinese Herbal Medicine, College of Human Ecology, Chang Gung University of Science and Technology, Taoyuan 333, Taiwan

**Hsi-Lung Hsieh, Ming-Ming Tsai**, Department of Nursing, Division of Basic Medical Sciences, Chang-Gung University of Science and Technology, Taoyuan 333, Taiwan

**Hsi-Lung Hsieh**, Department of Neurology, Chang Gung Memorial Hospital, Taoyuan 333, Taiwan

**Ming-Ming Tsai**, Department of General Surgery, Chang Gung Memorial Hospital, Chiayi 613, Taiwan

**Corresponding author:** Ming-Ming Tsai, PhD, Associate Professor, Department of Nursing, Division of Basic Medical Sciences, Chang-Gung University of Science and Technology, 261 Wen-hwa 1 Road, Taoyuan 333, Taiwan. [mmtsai@mail.cgu.edu.tw](mailto:mmtsai@mail.cgu.edu.tw)

**Telephone:** +886-3-2118999

**Fax:** +886-3-2118866

### Abstract

Despite improvements in the early diagnosis, prognosis and therapeutic strategies for gastric cancer (GC), human GC remains one of the most frequently diagnosed malignant tumors in the world, and the survival rate of GC patients remains very poor. Thus, a suitable therapeutic strategy for GC is important for prolonging survival. Both tumor cells themselves and the tumor microenvironment play an important role in tumorigenesis, including angiogenesis, inflammation, immunosuppression and metastasis. Importantly, these cells contribute to gastric carcinogenesis by altering the angiogenic phenotype switch. The development, relapse and spreading of tumors depend on new vessels that provide the nutrition, growth factors and oxygen required for continuous tumor growth. Therefore, a state of tumor dormancy could be induced by blocking tumor-associated angiogenesis. Recently, several antiangiogenic agents have been identified, and their potential for the clinical management of GC has been tested. Here, we provide an up-to-date summary of angiogenesis and the angiogenic factors associated with tumor progression in GC. We also review antiangiogenic agents with a focus on the anti-vascular endothelial growth factor receptor (VEGFR)-mediated pathway for endothelial cell growth and their angiogenesis ability in GC. However, most antiangiogenic agents have reported no benefit to overall survival (OS) compared to chemotherapy alone in local or advanced GC. In phase III clinical trials, only ramucirumab (anti-VEGFR blocker) and apatinib (VEGFR-TKI blocker) have

**Manuscript source:** Invited manuscript

**Received:** March 15, 2019

**Peer-review started:** March 18, 2019

**First decision:** June 5, 2019

**Revised:** July 5, 2019

**Accepted:** August 19, 2019

**Article in press:** August 19, 2019

**Published online:** September 15, 2019

**P-Reviewer:** Huang L, Tanabe S

**S-Editor:** Ma YJ

**L-Editor:** A

**E-Editor:** Qi LL



reported an improved median overall response rate and prolonged OS and progression-free survival outcomes as a 2nd-line agent combined with chemotherapy treatment in advanced GC. By providing insights into the molecular mechanisms of angiogenesis associated with tumor progression in GC, this review will hopefully aid the optimization of antiangiogenesis strategies for GC therapy in combination with chemotherapy and adjuvant treatment.

**Key words:** Gastric cancer; Angiogenesis; Vascular endothelial cell; Angiogenic phenotype switch; Anti-angiogenesis; Tumor dormancy

©The Author(s) 2019. Published by Baishideng Publishing Group Inc. All rights reserved.

**Core tip:** Tumor angiogenesis in gastric cancer (GC) and antiangiogenic therapies for GC, including information from their preclinical and/or application to clinical trials, are discussed. The antiangiogenic strategies for advanced GC include decreasing the expression of proangiogenic ligands and their receptors, increasing the level of angiogenic inhibitors, and directly targeting the inner walls of endothelial cells. Here, the antiangiogenic strategies mainly focus on decreasing the expression of vascular endothelial growth factor-mediated pathway constituents for advanced GC in phase III clinical trials. Thus, this review provides a brief description of various tumor angiogenic factors for the purposes of diagnosis, prognosis and therapeutics and describes the antiangiogenic agents that are currently being investigated in preclinical and phase III clinical trials. Hopefully, according to the molecular mechanism of tumor angiogenesis, we highlight the accuracy of the diagnosis and prognosis and the selection of the most appropriate therapy for GC patients.

**Citation:** Hsieh HL, Tsai MM. Tumor progression-dependent angiogenesis in gastric cancer and its potential application. *World J Gastrointest Oncol* 2019; 11(9): 686-704

**URL:** <https://www.wjgnet.com/1948-5204/full/v11/i9/686.htm>

**DOI:** <https://dx.doi.org/10.4251/wjgo.v11.i9.686>

## INTRODUCTION

Gastric cancer (GC) has a high incidence throughout the world and a high mortality rate associated with malignant tumors<sup>[1-3]</sup>. GC might not cause any clinical symptoms at the early stage, resulting in the fact that GC is rarely detected at the early stage<sup>[2,3]</sup>. However, the five-year survival outcome for late-stage GC patients is only approximately 20%-30% after initial diagnosis<sup>[4]</sup>, and gastrectomy is the major common treatment for GC. Thus, to improve the low survival outcome, it is necessary to develop novel therapeutic strategies for GC<sup>[5]</sup>.

In recent decades, studies on the molecular mechanism of tumor development have focused on the genetic or epigenetic changes in tumor cells, such as the emergence of cancer stem cells (CSCs), epithelial-mesenchymal transition (EMT) and the expression of microRNAs (miRNAs)<sup>[6]</sup>. However, several studies conducted in recent years found that the tumor microenvironment (TME) strongly influences tumor growth and progression and revealed that the tumor-host interactions determine tumor progression<sup>[7,8]</sup>. The TME contains extracellular matrix and stromal cells, including ECs, tumor-associated fibroblasts and tumor-associated immune/inflammatory cells, which can regulate tumor progression through autocrine/paracrine cytokines or factors. Furthermore, cancer cells can support the angiogenesis of ECs, and ECs can also help cancer cell proliferation by releasing growth factors. Tumor-associated immune/inflammatory cells can control cancer cell proliferation and metastasis under different conditions, and cancer cells might induce immune cell dysfunction as well as proinflammatory cytokine release. Exosomal miRNAs can alter normal fibroblasts into TAFs for tumor survival, and TAFs can promote tumor proliferation and metastasis. Thus, the TME is also involved in multiple processes, including tumor angiogenesis, inflammation, immunosuppression and metastasis, as shown in **Figure 1**<sup>[9,10]</sup>.

In 1971, Dr. Folkman and Klagsbrun<sup>[11]</sup> provided a novel theory stating that all phases of rapid tumor growth are dependent on tumor angiogenesis. At present, it is known that tumor angiogenesis plays a key role in tumor progression, and the

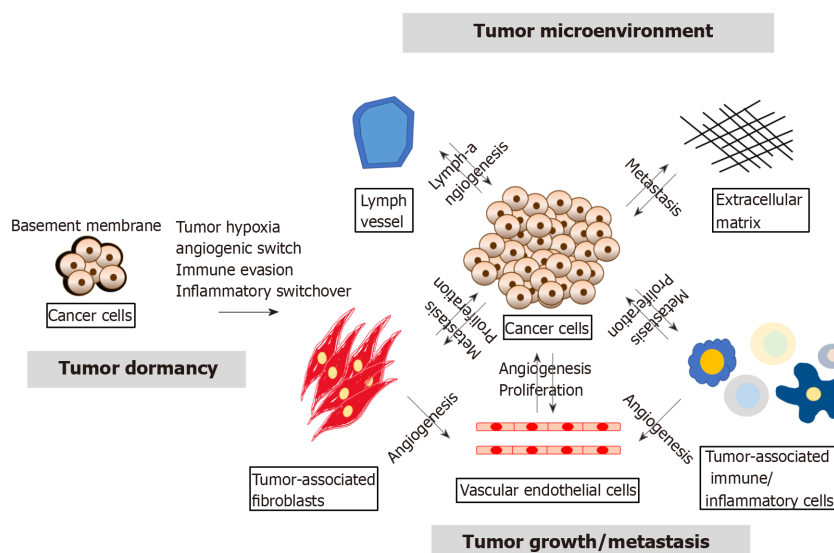


**Figure 1** The tumor microenvironment regulates tumor growth, relapse and metastasis. Tumor dormancy can be induced in malignant cancer through several mechanisms, such as epigenetic or genetic changes (cancer stem cells, epithelial-mesenchymal transition, and miRNAs) in the tumor, tumor hypoxia, the angiogenic switch, immune evasion and inflammatory switchover. A change in the tumor microenvironment can facilitate tumor growth/relapse/metastasis and thereby permit the tumor to exit from dormancy through interaction with endothelial cells, tumor-associated fibroblasts, tumor-associated immune/inflammatory cells and the extracellular matrix.

angiogenic switch is necessary for tumor growth, relapse and metastasis. Herein, we provide a review of tumor-associated angiogenesis, explore the molecular regulation of angiogenesis, and discuss various antiangiogenic drugs and their potential applications based on preclinical and phase III clinical trials for GC.

## MOLECULAR REGULATION OF TUMOR ANGIOGENESIS IN GC

An increasing number of studies has revealed that tumor growth is strongly associated with tumor angiogenesis<sup>[12]</sup>. Tumor growth, relapse and metastasis should turn on the “angiogenic switch” to induce tumor growth to a size greater than 1-2 mm. Numerous signals (*e.g.*, epigenetic changes, the TME, CSCs, EMT, and miRNAs) can disturb tumor dormancy, resulting in local tumor proliferation/recurrence or metastasis at a secondary site<sup>[13]</sup>. The “angiogenic switch” is regulated by angiogenic activators and inhibitors<sup>[14,15]</sup>, and the timing of the “angiogenic switch” can occur before, during or after tumor progression. As will be discussed in the following sections (Table 1), recent studies have shown that the available knowledge on the induction and molecular regulation of tumor angiogenesis has grown rapidly, and several growth factors, growth factor receptors, cytokines and signaling pathways have been identified in GC.

## TRANSCRIPTION FACTORS

### *Hypoxia and hypoxia-inducible factor*

**Preclinical trial:** First, the basement membrane in growing tumor cells is injured locally, and tumor cells immediately experience destruction and hypoxia. Tumor hypoxia is a major force that triggers tumor angiogenesis and activates the expression of hypoxia-inducible factor-1 (HIF-1), which then induces the expression of various proangiogenic factors, including vascular endothelial growth factor (VEGF) and vascular endothelial growth factor receptor (VEGFR), in cancer cells<sup>[16-19]</sup>. Moreover, HIF-2 isoforms have similar functions as HIF-1, but HIF-2 mainly activates the expression of erythropoietin (EPO) in kidney and liver cells<sup>[20]</sup>. Overall, HIF-1 is known as a potential target of anticancer therapy in many cancers<sup>[21]</sup>. In addition, treatment with HIF-1-specific inhibitors has been studied in animal models, and it has been shown that this treatment results in slowed growth of tumors, decreased

Table 1 Regulators of tumor angiogenesis in gastric cancer and their use in antiangiogenic therapy

Biological category	Gene name	Regulator of pro-/anti angiogenic types	Antiangiogenic drug	Drug direct target	Preclinical trials; cell line ( <i>in vitro</i> )/animal ( <i>in vivo</i> )	Clinical application	
						Expression levels in GC patients	Prognostic factors (proangiogenic biomarker)
Transcription factor	Hypoxia HIF <sup>[16-19,22-25]</sup>	Activator	NSAID <sup>[82]</sup>	COX-1, COX-2 inhibitor	•	ND	ND
Growth factor	VEGF family <sup>[26-38]</sup>	Activator	Aflibercept <sup>[22]</sup>	Anti-VEGF-A	•	VEGF-A, C	Lymph node metastasis (VEGF-A, C)
				Anti-PIGF		overexpression <sup>[21,41-47]</sup>	Distant metastasis (VEGF-A)
							Poor survival (VEGF-A)
	PIGF <sup>[29,30,35,48]</sup>	Activator	Bevacizumab <sup>[83-89]</sup>	Anti-VEGF-A	•	ND	ND
			IFN <sup>[90]</sup>	Anti-IFNR	•	ND	ND
			Rapamycin <sup>[91]</sup>	Anti-rapamycin kinase	•	ND	ND
			Neovastat <sup>[92]</sup>	Anti-VEGF	•	ND	ND
			Aflibercept <sup>[22]</sup>	Anti-VEGF-A	•	PIGF	ND
Growth factor receptor	FGF, EGF, HGF, IGF <sup>[31,52-55]</sup>	Activator	IFN <sup>[93]</sup>	Anti-IFNR	•	ND	ND
	PDGF <sup>[56,57]</sup>	Activator	SU6668	Multiple receptor	•	ND	ND
	VEGFR <sup>[32,33]</sup>	Activator	Orantinib <sup>[94]</sup>	TKI			
			Ramucirumab <sup>[95-97]</sup>	Anti-VEGFR2	•	ND	ND
			Regorafenib <sup>[98,99]</sup>	VEGFR TKI	•	ND	ND
			Apatinib <sup>[98,99]</sup>	VEGFR TKI	•	ND	ND
			Foretinib <sup>[98,99]</sup>	VEGFR TKI	•	ND	ND
			SU5416	Multiple receptor (KDR/FGFR/PD GFR)	•	ND	ND
			SU6668		•		
			Orantinib <sup>[94]</sup>		•		
			Pazopanib <sup>[100]</sup>	Multiple receptor TKI	•	ND	ND
			Sorafenib (Nexavar) <sup>[101,102]</sup>	Multikinase inhibitor (the serine/threonine kinase Raf and receptor tyrosine kinases)	•	ND	ND
			Sunitinib (Sutent) <sup>[103,104]</sup>	Multitargeting TKI	•	ND	ND
			Telatinib	Multitargeting TKI	•	ND	ND
			Erbitux (Cetuximab) <sup>[105]</sup>				
	GP130 IL-6R <sup>[58]</sup>	Activator	ND	ND	•	ND	ND
Cytokine	Her2/Neu <sup>[59-62]</sup>	Activator	Trastuzumab <sup>[59,62]</sup>	Anti-Her2/Neu	•	ND	ND
	Ang-1,3,4 <sup>[63,64,66-73]</sup>	Activator	ND	ND	•	Ang-1,2	Lymph node metastasis
	Ang-2 <sup>[65,66]</sup>	Activator				overexpression <sup>[74-77]</sup>	Liver metastasis
	IL-6 <sup>[58]</sup>	Inhibitor					Poor survival
	IL-6 <sup>[58]</sup>	Activator	ND	ND	•	ND	ND



	IL-8 <sup>[37,106]</sup>	Activator	ND	ND	•	ND	ND
	IL-17 <sup>[78]</sup>	Activator	ND	ND	•	ND	ND
	Tryptase <sup>[79,80]</sup>	Activator	ND	ND	•	Tryptase overexpression <sup>[81]</sup>	ND
ECM	MMP <sup>[92]</sup> , <sup>[107,108]</sup>	Activator	Marimastat <sup>[107,108]</sup> Bay 12-9566 AG3340 Neovastat <sup>[92]</sup>	MMP inhibitor	•	ND	ND

GC: Gastric cancer; ND: Not determined; •: Determined; VEGF: Vascular endothelial growth factor; VEGFR: Vascular endothelial growth factor receptor; TKI: Tyrosine kinase inhibitor.

angiogenesis and minor vessel maturation<sup>[22]</sup>. Stoeltzing *et al*<sup>[23]</sup> obtained similar results using the dominant negative form of HIF-1 in GC. Chronic infection with *Helicobacter pylori* induces DNA damage by generating reactive oxygen species (ROS) in GC cells<sup>[24]</sup>. Overaccumulation of ROS might stimulate HIF-1 accumulation and aid tumor angiogenesis in GC<sup>[25]</sup>.

## PROANGIOGENIC LIGANDS AND RECEPTORS

### VEGF family

**Preclinical trial:** Growing cancer cells encourage the growth of new blood vessels by secreting VEGF and VEGFR into the surrounding TME, and secreted VEGF binds to VEGFR on the outer surface of ECs. ECs are activated by the VEGF signaling pathway, and this activation induces the growth, survival, vascular permeability and migration of ECs to encourage tumor angiogenesis<sup>[26]</sup>. To date, various cytokines and a major proangiogenic factor of ECs have been found to be members of the VEGF-A family. The VEGF (homodimers) family of growth factors contains VEGF-A, B, C, D and E and placental growth factor (PIGF), and during angiogenesis<sup>[27,28]</sup>, these growth factors bind to and activate the tyrosine kinase receptors (TKRs) VEGFR-1, VEGFR-2, and VEGFR-3, which are specifically expressed on the surface of ECs and have different affinities for the ligands. Consequently, the downstream TKR signaling proteins activate proliferation-mediating signaling pathways, such as the phosphatidylinositol 3 kinase (PI3K)/AKT, protein kinase C (PKC), and mitogen-activated protein kinase (MAPK; p38 and p42/44) pathways<sup>[29-31]</sup>. In general, VEGF-A binds to VEGFR-1 and VEGFR-2, PIGF and VEGF-B bind to VEGFR-1, and VEGF-C and VEGF-D bind to VEGFR-2 and VEGFR-3<sup>[32-34]</sup>. Carmeliet *et al*<sup>[35]</sup> reported that among the VEGFs, the *vegfa* gene can lead to embryonic lethality due to serious vascular defects after the loss of only a single allele in mice<sup>[34-36]</sup>. An *in vitro* tube formation assay using GC cells cocultured with human umbilical vein endothelial cells (HUVECs) demonstrated proangiogenesis function due to the upregulation of VEGF in GC cells<sup>[37]</sup>. In a rat model, the blockage of VEGF by a specific siRNA led to reduced proliferation and cell cycle arrest<sup>[38]</sup>. Moreover, the coreceptor of neuropilins in signaling pathways is activated by other growth factors or VEGFs, and neuropilins bind several growth factors and enhance their function; however, the molecular mechanisms affected by neuropilins remain unclear<sup>[39,40]</sup>. The above data indicate that GC cells possess proangiogenic abilities by secreting angiogenic cytokines to both stimulate ECs and to support their own growth in an autocrine manner. Furthermore, the growth and invasion of GC cells are mainly controlled by the VEGF-mediated pathway.

**Clinical application:** These discoveries from *in vitro* and animal models were confirmed in GC patients, and their diagnostic or prognostic abilities were tested in GC patients. Through ELISA, significantly higher preoperative plasma or serum VEGF levels were detected in GC patients compared with healthy control subjects. Importantly, a clinicopathological analysis revealed that higher VEGF expression in the plasma or serum of GC patients was significantly associated with advanced stage, distant metastasis and worse survival outcomes<sup>[21,41-47]</sup>.

### PIGF

**Preclinical trial:** PIGF is another member of the VEGF family and plays a proangiogenic role in the progression of some tumors<sup>[29,30,35,48]</sup>. Akrami *et al*<sup>[49,50]</sup> reported that the knockdown of PIGF in AGS and MKN-45 cells inhibited the



proliferation, self-renewal capacity, MMP activity, transcription activity and migration of these cells.

**Clinical application:** Higher PIGF and VEGF levels were detected by ELISA in GC tissues compared with paired noncancerous mucosa tissues. A clinicopathological analysis showed that higher expression of only PIGF in GC patients was significantly associated with tumor stage, distant metastasis and worse survival outcomes [51].

### ***Fibroblast growth factors, epidermal growth factor, hepatocyte growth factor, and insulin-like growth factor***

**Preclinical trial:** The fibroblast growth factor (FGF) family is a large cytokine family, and some of these cytokines, *e.g.*, FGF-1/-2, bind to different fibroblast growth factor receptors, *e.g.*, FGFR 1-4, to activate the PI3K/AKT/mTOR (mammalian target of rapamycin) pathway. Furthermore, these cytokines can regulate tumor angiogenesis, proliferation, migration and antiapoptosis/survival activities both *in vitro* and *in vivo* [31,52-54]. epidermal growth factor (EGF), hepatocyte growth factor (HGF) and insulin-like growth factor (IGF) reportedly stimulate proangiogenic, proliferation and survival activities similarly to those induced by VEGF [55].

### ***Platelet-derived growth factor***

**Preclinical trial:** Pericytes and smooth muscle cells secrete platelet-derived growth factor (PDGF)-BB, which then binds to PDGFR- $\beta$  and thereby modulates tumor angiogenesis in ECs [56,57].

### ***GP130, interleukin-6, and interleukin-6R***

**Preclinical trial:** In a mouse model, the blockage of GP130 inhibits tumor development in the epithelium of the glandular stomach *via* the STAT 1/3-mediated angiogenesis pathway. These results suggest that the TME and cancer cells secrete interleukin-6 (IL-6) *via* autocrine or paracrine binding to GP130 or IL-6R [58].

### ***Human epidermal growth factor receptor 2/Neu (HER-2/neu) and EGFR***

**Preclinical trial:** In tumor cells, EGF binds to EGFR and HER-2/neu to activate the PI3K/AKT and RAS-MAPK-mediated pathways, which are involved in the overexpression of VEGF-A. The secretion of VEGF-A from cancer cells can be mediated through the activation of various signaling pathways. Furthermore, these factors act as central regulators of tumor growth and tumor angiogenesis in GC [59-62].

### ***Angiopoietin-1, 2, 3, and 4 (Ang-1, -2, -3, and -4)***

**Preclinical trial:** Ang-1, -2, -3, and -4 biologically serve as growth factors for ECs and can strongly regulate competitive interaction with TIE-2 (TKR), which is expressed on the surface of ECs [63,64]. The binding of Ang-1 to TIR-2 activates TIE-2 phosphorylation *via* the Ang-1/Tie2-cascade pathway and is involved in the proliferation, migration, inflammation and survival of ECs. Ang-2 is then released from activated ECs and serves as a significant antagonist [65,66]. Additionally, TIE-1 (an orphan receptor) can form a complex with TIE-2 to form heterodimers and compete with Ang-1/TIE-2 interactions and thereby promote inflammation in ECs [66-69]. Inhibition of Ang-1 or Ang-2 shows similar inhibition of cell proliferation in GC cell lines [70-73].

**Clinical application:** Blank *et al* [74] found that high expression levels of Ang in serum and tissue from GC patients are associated with poor survival. In addition, the Ang/VEGF ratio in GC and esophageal cancer patients serves as an independent proangiogenic biomarker for the clinical response to chemotherapy [75]. Another group of researchers found that Ang-2 can serve as an independent predictor of OS and liver metastasis in GC patients [76]. Moreover, Aktaş *et al* [77] found that VEGF, PIGF, and Ang-1 are strongly correlated with OS; thus, these angiogenesis prognostic indices (APIs) could predict survival outcomes in GC patients.

### ***IL-8***

**Preclinical trial:** Tumor-infiltrating macrophages secrete IL-8 and upregulate VEGF to activate EC angiogenesis in GC, as demonstrated in an *in vitro* assay [37].

### ***IL-17***

**Preclinical trial:** IL-17 stimulates the STAT3-mediated angiogenesis pathway to upregulate VEGF in GC [78].

### ***Tryptase***

**Preclinical trial:** Tumor-infiltrating mast cells (TIMs) secrete tryptase by binding to proteinase-activated receptor-2 (PAR-2) and then produce VEGF to stimulate tumor angiogenesis and EC proliferation, as demonstrated through *in vitro* and *in vivo*

assays<sup>[79,80]</sup>.

**Clinical application:** TIMs can release tryptase *via* PAR-2 activation and are involved in tumor angiogenesis. Ammendola *et al*<sup>[81]</sup> suggested that an increased mast cell density positive for tryptase (MCDPT) and a higher general vascularized area are related to poor survival outcome and can thus serve as potential targets in both primary tumor and lymph node metastases in GC patients.

## RESULTS FROM PRECLINICAL AND CLINICAL STUDIES OF ANTIANGIOGENIC THERAPIES FOR GC

According to the results of studies on the molecular mechanism of tumor angiogenesis, we can develop a novel antiangiogenic strategy that could reduce tumor angiogenesis and limit tumor growth instead of eradicate the tumors and thereby delay the progression of precancer/primary lesion to metastases/aggressive cancers. The purpose of antiangiogenesis therapy is not to directly target cytotoxic tumor cells but rather block the supply of oxygen, growth factors and nutrition from blood vessels<sup>[109]</sup>. Thus, this section will focus on several tumor angiogenic factors that could serve as potential targets for antiangiogenic drugs that are currently being investigated in preclinical (the section only highlights the most common antiangiogenic drugs; Table 1) and clinical studies on GC patients. Due to the metabolic changes and stemness of malignant cells lacking oxygen supply in various tumors, tumors appear to escape antiangiogenic therapy within a short time owing to the manipulation of alternative pathways<sup>[110]</sup>, vasculogenic imitation<sup>[111]</sup> and recruitment of bone marrow-derived cells<sup>[112,113]</sup>. Various clinical trials have not shown a statistically significant extension of survival outcomes. Thus, most of the antiangiogenesis strategy can be ineffective. In phase III clinical trials, only ramucirumab (anti-VEGFR) and apatinib (VEGFR-TKI) have reported to improve ORR and prolong OS and PFS outcomes when used as a 2nd-line regimen combined with chemotherapy treatment in advanced GC (Table 2).

## INHIBITORS OF PROANGIOGENIC LIGANDS AND RECEPTORS

### **Bevacizumab (avastin, genentech, rhumad)**

**Preclinical trial:** As demonstrated in a preclinical model, this drug, which is a recombinant monoclonal antibody against VEGF-A, serves as a powerful and effective antiangiogenesis agent in several cancers<sup>[83-85]</sup>. An *in vitro* study revealed that treatment with bevacizumab reduced cell growth and pro-apoptosis in GC cell lines<sup>[86]</sup>. Yamashita-Kashima *et al*<sup>[87]</sup> performed an *in vivo* study and found that bevacizumab could be effective against GC and select biomarkers in the MKN-45 human gastric xenograft model. A study with mouse models revealed that treatment with bevacizumab significantly reduced the tumor size<sup>[88,89]</sup>. In the future, we will explore the effects of the antibody-mediated blockage of VEGF-mediated tumor angiogenesis in GC to obtain a more in-depth understanding.

**Clinical trial:** Ohtsu *et al*<sup>[114]</sup> explored the effect of bevacizumab, which is a VEGF blocker. The AVAGAST clinical trial indicated that the 1st line treatment of advanced GC patients (multiethnic population) with bevacizumab in combination with chemotherapy (Cisplatin; Cis/Capecitabine; Cap) resulted in significantly improved ORR ( $P = 0.0315$ ) and extended PFS ( $P = 0.0037$ ) outcomes compared with those achieved with chemotherapy alone (Table 2). However, the AVATAR clinical trial showed that the 1st line treatment of advanced GC patients (China) with bevacizumab in combination with chemotherapy (Cis/Cap) did not significantly prolong the survival outcomes compared with those achieved with chemotherapy alone<sup>[115]</sup>. In contrast, Ma *et al*<sup>[116]</sup> assessed the effects of bevacizumab in combination with chemotherapy (Docetaxel; Doc/Oxaliplatin; Oxa/5-FU) compared with those of the 1st line treatment of chemotherapy alone in advanced GC patients (China) and observed significantly improved ORR ( $P = 0.0436$ ) and extended PFS ( $P = 0.013$ ) outcomes compared with those achieved with chemotherapy alone. The other group, the ST03 clinical trial, showed that the perioperative treatment of advanced GC patients (United Kingdom) with bevacizumab in combination with chemotherapy (Cis/Cap/Epirubicin; Epi) had no positive results compared with those achieved with chemotherapy alone<sup>[117]</sup>. However, the differences in the outcomes achieved after bevacizumab treatment among the different populations remain unknown.

**Table 2 Overview of phase-III clinical trials in gastric cancer including vascular endothelial growth factor, vascular endothelial growth factor receptor and vascular endothelial growth factor receptor tyrosine kinase inhibitor blockers**

Tar-get C Cate- gory	Blockers	Country	Cancer type	Setting	Treat- ment	N	ORR (%)	DCR (%)	PFS (mo)	OS (mo)	Top 5 adverse events	Ref.
							HR (95% CI) <i>P</i> value	<i>P</i> value	HR (95% CI) <i>P</i> value	HR (95% CI) <i>P</i> value		
Anti- VEGF	Bevacizumab (Monoclonal Ab)	Multiethnic Asia-Pacific  Europe  Pan-America	•Metastatic GC	1st-line	Bevacizumab	387	46%	76.90%	6.7	12.1	Neutropenia	AVA-GAST <sup>[114]</sup>
			Unresectable locally advanced GC		+Cis/Cap						Febrile neutropenia	
			Recurrent GC								Anemia	
		China	Gastro-esophageal junction GC		Placebo	387	37.40%	67.70%	5.3	10.1	Decreased appetite	AVA-TAR <sup>[115]</sup>
					+Cis/Cap		<i>P</i> = 0.0315	ND	<i>P</i> = 0.0037	<i>P</i> = 0.1002	Diarrhea	
			Metastatic GC	1st-line	Bevacizumab	100	40.70%	75.30%	6.3	10.5	Vomiting	
		China	Unresectable locally advanced GC		+Cis/Cap						Neutropenia	[116]
			Recurrent GC								Nausea	
			Gastro-esophageal junction GC		Placebo	102	33.70%	72.10%	6	11.4	Anemia	
					+Cis/Cap		<i>P</i> = 0.348	ND	<i>P</i> = 0.4709	<i>P</i> = 0.5567	Intestinal obstruction	
			Unresectable locally advanced GC	1st-line	Bevacizumab	40	65%	30%	15.2	17.6	Nausea	
					+Doc/Oxa/5-FU						Vomiting	
Anti- VEGFR	Ramucirumab (Monoclonal Ab)	United Kingdom			Placebo	40	42.50%	42.50%	12.3	16.4	Leukopenia	(United Kingdoms Medical Research Council ST03) <sup>[117]</sup>
					+Doc/Oxa/5-FU		<i>P</i> = 0.0436	ND	<i>P</i> = 0.013	<i>P</i> = 0.776	Decreased hemoglobin	
			Resectable GC	Peri-operative	Bevacizumab	530	ND	ND	ND	48.10%	Lethargy	
			Esophago gastric junction GC		+Cis/Cap/Epi						Nausea	
			Lower esophageal junction GC								Neutropenia	
											Diarrhea	
		Multiethnic North America, Europe, Australia, New Zealand, Asia	Advanced gastric GC	2nd-line	Ramucirumab	238	3%	49%	2.1	5.2	Fatigue	REG-ARD <sup>[118]</sup>
			Gastro-esophageal junction GC		+ Pla/5-Fu						Abdominal pain	
											Decreased appetite	
											Vomiting	

		South and Central America, India, South Africa, Middle East		Placebo	117	3%	23%	1.3	3.8	Constipation		
				+ Pla/5-Fu								
						ND	<i>P</i> = 0.76	<i>P</i> < 0.0001	<i>P</i> = 0.047			
		Multiethnic	Advanced gastric GC	2nd-line	Ramucirumab	330	28%	80%	4.4	9.63	Fatigue	RAIN-BOW <sup>[119]</sup>
		North and South America	Gastro-esophageal junction GC		+ Pac						Neuropathy	
		Europe									Decreased appetite	
		Australia,			Placebo	335	16%	64%	2.86	7.4	Abdominal pain	
		Asia			+ Pac						Nausea	
							<i>P</i> < 0.0001	<i>P</i> = 0.0001	<i>P</i> < 0.0001	<i>P</i> = 0.0169		
		Multiethnic	Metastatic GC	1st-line	Ramucirumab	326	41.10%	81.90%	10.2	11.2	Neutropenia	RAIN-FALL <sup>[120]</sup>
		North America	Gastro-esophageal junction GC		+ Cis/5-Fu						Anaemia	
		Europe									Hypertension	
		Japan			Placebo	319	36.40%	76.50%	9.2	10.7	Palmar-plantar erythrodysesthesia syndrome	
					+ Cis/5-Fu						Fatigue	
							<i>P</i> = 0.17	<i>P</i> = 0.095	<i>P</i> = 0.4	<i>P</i> = 0.68		
VEGF	apatinib	China	Metastatic GC	3rd-line	Apatinib	176	2.84	42.05	2.6	6.5	Hand-foot syndrome	<sup>[121]</sup>
TKI			Advanced GC								Proteinuria	
			Gastro-esophageal junction GC								Hypertension	
					Placebo	91	0	8.79	1.8	4.7	Myelosuppression	
							<i>P</i> < 0.001	<i>P</i> = 0.1695	<i>P</i> < 0.001	<i>P</i> = 0.0149	Nausea and vomiting	

A  $P$  value less than 0.05 indicates statistical significance according to the Mann-Whitney  $U$  test. VEGF: Vascular endothelial growth factor; VEGFR: Vascular endothelial growth factor receptor; TKI: Tyrosine kinase inhibitor; ORR: Median overall response rate; DCR: Median disease control rate; PFS: Median progression-free survival; OS: Median overall survival; Cis: Cisplatin; Cap: Capecitabine; Doc: Docetaxel; Oxa: Oxaliplatin; 5-FU: 5-Fluoropyrimidin; Epi: Epirubicine; Pla: Polylactic acid; Pac: Paclitaxel; HR: Hazard ratio; CI: Confidence interval.

### Interferon, rapamycin, and neovastat

**Preclinical trial:** The interferon family contains multifunctional cytokines that exhibit antiviral and antitumor properties, induce regulatory cell apoptosis and immune responses and inhibit proangiogenic factors. Abdel-Rahman *et al.*<sup>[90]</sup> evaluated bevacizumab in combination with other anticancer agents, such as mTOR inhibitors and interferon (IFN), as a more effective treatment for gastrointestinal tract and pancreatic tissues. Preclinical and clinical trials showed that other mTOR inhibitors, such as rapamycin, also display antiangiogenic activity in GC<sup>[91]</sup>. Moreover, Neovastat is a multifunctional drug that blocks VEGF, MMPs and proapoptotic activity in ECs. One MMP inhibitor (Marimastat) has been shown to induce positive outcomes in

phase III clinical trials with advanced GC patients. The other MMP inhibitors are continuing to be investigated in clinical trials<sup>[92]</sup>.

**Clinical trial:** A clinical phase II trial showed that the treatment of advanced GC patients with interferon-alpha 2B (IFN) and folinic acid (FA) in combination with 5-fluorouracil (5-FU) chemotherapy also resulted in significantly prolonged PFS outcomes compared with those achieved with chemotherapy alone<sup>[122]</sup>. Al-Batran *et al*<sup>[123]</sup> demonstrated that mTOR-mediated inhibitors (*e.g.*, rapamycin) blocked the growth of GC cells and delayed tumor progression in cell lines and mouse models. Additionally, the mTOR inhibitor rapamycin has also yielded better survival outcomes in phase I/II studies of metastatic GC patients than do treatment without rapamycin.

### **Ramucirumab**

**Preclinical trial:** Ramucirumab is a VEGFR-2-targeted monoclonal antibody that inhibit VEGFR-2 signaling. An *in vitro* study showed that treatment with ramucirumab also inhibited cell growth and promoted apoptosis in GC cell lines and animal models<sup>[95,96]</sup>. Thus, both bevacizumab and ramucirumab inhibit VEGF-mediated pathways in GC. Additionally, an *in vivo* study showed that the effects of combination therapy involving anti-VEGFR and anti-EGFR agents resulted in a significantly decreased tumor size in a GC mouse model<sup>[97]</sup>.

**Clinical trial:** Fuchs *et al*<sup>[118]</sup> attempted to explore the effect of ramucirumab, which blocks VEGFR signaling. The REGARD clinical trial indicated that the treatment of advanced GC patients (multiethnic) with ramucirumab in combination with chemotherapy (Plr/5-Fu) resulted in significantly extended PFS ( $P < 0.0001$ ) and OS ( $P = 0.047$ ) outcomes compared with those achieved with placebo. Moreover, the RAINBOW clinical trial showed that the treatment of advanced GC patients (multiethnic) with ramucirumab in combination with chemotherapy (Paclitaxel; Pac) also resulted in significantly improved ORR ( $P < 0.0001$ ) and DCR ( $P < 0.0001$ ), extended PFS ( $P < 0.0001$ ) and OS ( $P = 0.0169$ ) outcomes compared with those achieved with chemotherapy alone<sup>[119]</sup>. In contrast, the RAUNFALL clinical trial showed that the treatment of advanced GC patients (multiethnic) with bevacizumab in combination with chemotherapy (Cis/5-Fu) had no positive results compared with those achieved with chemotherapy alone<sup>[120]</sup>. Ramucirumab was approved by the United States Food and Drug Administration (FDA) in 2014 as a 2nd-line treatment of advanced GC due to the REGARD and RAINBOW clinical trials and has beneficial effects on PFS and OS for advanced GC.

## **DIRECT ACTION ON ECs**

### **Regorafenib, apatinib, and foretinib**

**Preclinical trial:** Regorafenib, apatinib and foretinib belong to the family of multitargeting TKIs. Blockage of the effects of VEGF by silencing RNA in GC cell lines led to reduced tumor volume after implantation of these GC cells into nude mice<sup>[98]</sup>. The same effect was observed in mice treated with apatinib after tumor grafting<sup>[99]</sup>.

**Clinical trial:** First, Li *et al*<sup>[121]</sup> explored the effect of apatinib, which VEGFR TKI blockade. A 116 clinical trial (3<sup>rd</sup> line) indicated that the treatment of advanced GC patients (China) with apatinib resulted in significantly improved ORR ( $P < 0.001$ ), extended PFS ( $P < 0.001$ ) and OS ( $P = 0.0149$ ) outcomes compared with those achieved with placebo. In a phase II study, the tumor-angiogenesis inhibitor regorafenib, which targets VEGFR, TIE and multiple kinases, was evaluated in advanced GC patients, and the results showed that treatment with this inhibitor resulted in significantly prolonged PFS outcomes compared with those achieved with placebo<sup>[124]</sup>. Thus, regorafenib will be investigated in a phase III study. However, another antiangiogenic drug, foretinib, which inhibits VEGFR2 and TIE-2, did not yield any benefits in the survival outcomes of GC patients<sup>[125]</sup>. In addition, Shan *et al*<sup>[126]</sup> reviewed information from clinical trials evaluating antiangiogenic agents (with a focus on multitargeting TKIs) in advanced GC and found that only apatinib yielded a positive effect on PFS.

### **Orantinib (SU5416, SU6668), Pazopanib, Sorafenib (Nexavar), Sunitinib (Sutent), Telatinib (Erbix, Cetuximab)**

**Preclinical trial:** Orantinib (SU5416 SU6668)<sup>[94]</sup>, pazopanib<sup>[100]</sup>, sorafenib (Nexavar)<sup>[101,102]</sup>, sunitinib (Sutent)<sup>[103,104]</sup> and telatinib (Erbix, Cetuximab)<sup>[105]</sup> block tyrosine kinases and belong to the family of multitargeting TKIs. Suppressing the effects of VEGF by silencing RNA in GC cell lines led to decreased tumor



angiogenesis and growth after these cells were implanted into nude mice.

**Clinical trial:** Chen *et al*<sup>[71]</sup> summarized the results from clinical trial phase II studies of antiangiogenic drugs, including VEGF ligands, VEGFRs and multitarget TKIs, in advanced GC. The treatment of advanced GC patients with orantinib<sup>[127]</sup>, pazopanib<sup>[128,129]</sup>, sorafenib<sup>[130-133]</sup>, sunitinib<sup>[134-136]</sup>, telatinib<sup>[137-141]</sup> and vandetanib resulted in significantly extended OS and PSF.

#### **Aflibercept**

**Preclinical trial:** Aflibercept traps VEGF and PlGF *in vivo* and is currently being investigated in a clinical trial (NCT01747551) as a supplement to standard chemotherapy for GC patients<sup>[22]</sup>. In addition to VEGF-specific inhibition, the effect of HIF-1 blockage has been investigated in animal models in several studies. The treatment of subcutaneous xenografts with an inhibitory HIF-1 compound results in smaller and less vascularized tumors after implantation into nude mice.

#### **Trastuzumab**

Seidman *et al*<sup>[62]</sup> reported that the antibody trastuzumab blocks the Her2/neu receptor through the RAS-MAPK proliferation signaling pathway. A log-rank test showed improved survival outcomes in breast cancer patients. The comparison of two different Her2 and VEGF inhibitors revealed that the effect of tumor growth inhibition on Her2-overexpressing GC xenografts through the combination of Her2 and VEGF inhibitors was better than that achieved with either inhibitor alone<sup>[59]</sup>.

#### **Nonsteroid anti-inflammatory drugs**

In an animal model, nonsteroid anti-inflammatory drug (NSAID)-mediated cyclooxygenase (COX) inhibition resulted in reduced tumor angiogenesis, and decreased HIF-1 expression was detected in GC cells after treatment with NSAIDs<sup>[25]</sup>.

## **OTHER ASSOCIATED CHEMOTHERAPIES**

In clinical phase trials, cancer patients are typically administered combination therapy consisting of antiangiogenic agents with chemotherapeutic agents. However, antiangiogenic therapy sometimes elicits several adverse effects, such as hypertension<sup>[142,143]</sup> or proteinuria<sup>[144]</sup>, but the factors responsible for these adverse effects remain unknown. In general, the results from several studies on some antiangiogenic therapies, such as the inhibition of VEGF, Ang-1 and PlGF, indicate that antiangiogenic therapy not only inhibits EC migration and proliferation but also enhances chemotherapy ability. Hwang *et al*<sup>[145]</sup> indicated that the inhibition of VEGFR enhances paclitaxel sensitivity in GC cells. Another group of researchers showed that the upregulation of HIF-1 promotes chemotherapy and the antiapoptosis ability in GC cells by inducing miR-27a- or p53- and NF-κB-mediated pathways<sup>[146-148]</sup>. Additionally, compared with normal blood vessels, tumor vessels exhibit heterogeneity, versatility, high permeability and vascular properties that benefit chemotherapy<sup>[149]</sup>. Thus, antiangiogenic therapy could exert an adjuvant effect in chemotherapy.

## **CONCLUSION**

Tumor angiogenesis involves a complex multistep process. In general, the available knowledge indicates that proangiogenic and pro-oncogenic (such as proliferation, anti-apoptosis, migration and invasion) pathways are linked to each other. Thus, tumor angiogenesis occurs at different stages of tumor progression, including tumor growth, metastasis and recurrence. This connection can be clearly observed by the administration of combination therapy against angiogenic and proliferative pathways, such as the VEGF-, EGFR- and STAT3-mediated pathways<sup>[16-19,31,52-54,58]</sup>. These transcription factors regulate cell growth, migration and angiogenesis in multiple ways.

First, we investigated the expression of angiogenic factors in GC through preclinical trials [cell line (*in vitro*)/animal model (*in vivo*)] and thus determined whether these factors could serve as predictive factors/biomarkers for proliferation, invasion or metastasis and/or have diagnostic or prognostic value<sup>[7,8]</sup>. An increasing number of studies has revealed that antiangiogenic agents attack tumor ECs as their target instead of tumor cells themselves, which is the final goal of tumor dormancy therapy. Moreover, the therapeutic target of antiangiogenic agents is tumor ECs, which are more genetically stable, show increased homogeneity and have a lower alteration level; antiangiogenic drugs can interact with ECs directly, resulting in

higher potency, decreased drug resistance and fewer side effects<sup>[150]</sup>. We explored the combination of antiangiogenic drugs and cytotoxic anticancer (chemical) drugs to develop a highly effective strategy for the management of advanced GC<sup>[13-15]</sup>. Thus, antiangiogenic drugs might be valuable for the long-term management of tumor dormancy because they do not induce the development of antiangiogenic drug resistance, and these drugs present fewer side effects. A few recent clinical trials have revealed that antiangiogenic therapy could potentially extend the survival outcomes of advanced GC patients<sup>[109]</sup>.

## DISCUSSION

In assessing the effectiveness of antiangiogenesis therapy, a clinical phase III trial showed that only ramucirumab (an anti-VEGFR antibody) and apatinib (VEGFR TKI blocker) achieved positive results (Table 2). Although both ramucirumab and bevacizumab are anti-VEGF drugs, bevacizumab (AVAGAST, AVATAR, ST03, Ma *et al.*<sup>[116]</sup>) had no positive results on OS, while ramucirumab (REGARD, RAINBOW) was more effective targeted drug and exerted more positive results for OS in advanced GC. We suggested that this is because bevacizumab only binds to VEGF-A, whereas ramucirumab binds to VEGFR-2, which blocks more VEGFs. Therefore, ramucirumab could exert more effective antiangiogenic function due to the inhibition of more VEGF molecules. One possible reason is the differences in the targets of the antiangiogenic action. However, the differences in the ability of these two anti-VEGF drugs remain partially unknown. Furthermore, the different populations of GC patients might be another factor that affects the benefits of these drugs. In the AVAGAST and RAINBOW studies, the non-Asian subgroup (66.5%; RAINBOW) achieved a greater benefit in OS from antiangiogenic therapy than did the Asian subgroup (51%; AVAGAST). However, the effect of ramucirumab still lacks 1st-line chemotherapy evidence. The extent of the usefulness of ramucirumab still requires exploration in further trials in different ethnicities and upon delivery as a 1<sup>st</sup>-, 2<sup>nd</sup>- or 3<sup>rd</sup>-line chemotherapy. Additionally, in evaluating the safety of antiangiogenic therapy, most adverse events related to antiangiogenesis are tolerable and controllable, including hypertension, neutropenia and wound healing (Table 2). Conversely, the Cougar-02 trial, a Doc+best supportive care (BSC) study, has a similar result for OS as the REGARD trial and was more cost effective<sup>[151]</sup>. Finally, of the VEGFR TKIs, only apatinib in the phase III clinical trial showed extended PFS and OS in advanced GC patients. We recommend that chemotherapy in combination with ramucirumab (anti-VEGFR) and apatinib (VEGFR TKI) significantly improves the outcome in ORR, extended PFS, and OS in the management of advanced GC.

Here, this review only included phase III clinical trials published in English. Previous studies have found that the combination of antiangiogenic agents with chemotherapy may be beneficial for advanced GC in OS, but potential publication bias should be considered when construing these results. To reduce possible publication bias, we tried to search in multiple databases. Nevertheless, some restrictions were present in this systemic review and statistical analysis (*e.g.*, meta-analysis)<sup>[152,153]</sup> such as the small size of included studies, multiple drugs implemented and the high heterogeneity between different studies. Therefore, a larger cohort size, more standardized research and high statistical quality should be implemented in future studies to identify patients who would most likely benefit from antiangiogenic treatment. Thus, this review will provide basic (tumor angiogenesis) and clinical (antiangiogenic drugs) research for the survey of the management of GC treatments.

## FURTHER CHALLENGES OF ANTIANGIOGENIC THERAPY

Although several phase III clinical trials have reported positive results, new vessels in tumors have pleomorphic features, including heterogeneity, flexibility, penetrability, various vascular biomarkers, and turbulent blood flow with no lymphatic vessels, and these unusual features make the delivery of therapeutic drugs difficult. Hence, there remain several obstacles regarding the translation of antiangiogenic strategies from animal models to clinical trials<sup>[92,108,154]</sup>.

The current problems regarding preclinical to clinical trials and the future directions for antiangiogenic therapy are discussed below.

In preclinical trials, we usually perform experiments in animals with xenografts of various tumor cells, but these models cannot represent spontaneous and orthotopic human cancers, particularly highly metastatic tumors<sup>[155]</sup>. Therefore, antiangiogenic drugs are not effective for every organ in the body. Antiangiogenic drugs often yield

different results or side effects in preclinical and clinical trials.

In advanced GC, the tumor develops several ways of escaping treatment and rapidly activating angiogenic pathways. Ebos *et al*<sup>[156]</sup> reported that enhanced metastasis was treated with sunitinib in a mouse model. Another group found a similar result<sup>[157]</sup>. This may partly fail to translate to a survival benefit of antiangiogenic drugs in localized or nonmetastatic GC. Therefore, it is crucial to develop novel biomarkers that are able to predict the prognosis of antiangiogenic treatments for advanced GC. In clinical trials, to assess antiangiogenic therapies, newer imaging systems and/or substitute biomarkers should be established for monitoring tumor vessel functions. Antiangiogenic drugs induce tumor dormancy, which is different from the results of chemotherapy<sup>[155]</sup>.

The aims of managing GC are to reduce drug toxicity and adverse events and prolong survival. Therefore, the optimal biological dose and therapeutic schedule of antiangiogenic drugs should be established. Moreover, antiangiogenic drugs can be combined with chemotherapy and/or radiotherapy<sup>[149]</sup>.

According to previous studies, the clinical effect is quite different in individuals due to heterogeneity of the tumor. It is unclear which patients benefit most from angiogenesis inhibitors. The race/ethnicity of patients seems to influence the efficacy of antiangiogenic treatments on OS. The patients should be selected, and angiogenic factors should be detected before the administration of antiangiogenic drugs. Individual angiogenic profiling according to an individual's genetic background remain a problem that need to be addressed.

## REFERENCES

- 1 Crew KD, Neugut AI. Epidemiology of gastric cancer. *World J Gastroenterol* 2006; **12**: 354-362 [PMID: 16489633 DOI: 10.3748/wjg.v12.i3.354]
- 2 Wu CW, Hsiung CA, Lo SS, Hsieh MC, Chen JH, Li AF, Lui WY, Whang-Peng J. Nodal dissection for patients with gastric cancer: a randomised controlled trial. *Lancet Oncol* 2006; **7**: 309-315 [PMID: 16574546 DOI: 10.1016/S1470-2045(06)70623-4]
- 3 Wu CW, Lo SS, Shen KH, Hsieh MC, Lui WY, P'eng FK. Surgical mortality, survival, and quality of life after resection for gastric cancer in the elderly. *World J Surg* 2000; **24**: 465-472 [PMID: 10706921 DOI: 10.1007/s002689910074]
- 4 Dassen AE, Lemmens VE, van de Poll-Franse LV, Creemers GJ, Brenninkmeijer SJ, Lips DJ, Vd Wurff AA, Bosscha K, Coebergh JW. Trends in incidence, treatment and survival of gastric adenocarcinoma between 1990 and 2007: a population-based study in the Netherlands. *Eur J Cancer* 2010; **46**: 1101-1110 [PMID: 20219351 DOI: 10.1016/j.ejca.2010.02.013]
- 5 GASTRIC (Global Advanced/Adjuvant Stomach Tumor Research International Collaboration). Group Oba K, Paoletti X, Bang YJ, Bleiberg H, Burzykowski T, Fuse N, Michiels S, Morita S, Ohashi Y, Pignon JP, Rougier P, Sakamoto J, Sargent D, Sasako M, Shitara K, Tsuburaya A, Van Cutsem E, Buyse M. Role of chemotherapy for advanced/recurrent gastric cancer: an individual-patient-data meta-analysis. *Eur J Cancer* 2013; **49**: 1565-1577 [PMID: 23352439 DOI: 10.1016/j.ejca.2012.12.016]
- 6 Esteller M. Epigenetics in cancer. *N Engl J Med* 2008; **358**: 1148-1159 [PMID: 18337604 DOI: 10.1056/NEJMr072067]
- 7 Mbeunkui F, Johann DJ. Cancer and the tumor microenvironment: a review of an essential relationship. *Cancer Chemother Pharmacol* 2009; **63**: 571-582 [PMID: 19083000 DOI: 10.1007/s00280-008-0881-9]
- 8 Liotta LA, Kohn EC. The microenvironment of the tumour-host interface. *Nature* 2001; **411**: 375-379 [PMID: 11357145 DOI: 10.1038/35077241]
- 9 Finger EC, Giaccia AJ. Hypoxia, inflammation, and the tumor microenvironment in metastatic disease. *Cancer Metastasis Rev* 2010; **29**: 285-293 [PMID: 20393783 DOI: 10.1007/s10555-010-9224-5]
- 10 Balkwill F, Mantovani A. Inflammation and cancer: back to Virchow? *Lancet* 2001; **357**: 539-545 [PMID: 11229684 DOI: 10.1016/S0140-6736(00)04046-0]
- 11 Folkman J, Klagsbrun M. Angiogenic factors. *Science* 1987; **235**: 442-447 [PMID: 2432664 DOI: 10.1126/science.2432664]
- 12 Weidner N. Tumor angiogenesis: review of current applications in tumor prognostication. *Semin Diagn Pathol* 1993; **10**: 302-313 [PMID: 7511250]
- 13 Alsbati EA. Tumor dormancy: a review. *J Cancer Res Clin Oncol* 1979; **95**: 209-220 [PMID: 393706 DOI: 10.1007/BF00410641]
- 14 Bergers G, Benjamin LE. Tumorigenesis and the angiogenic switch. *Nat Rev Cancer* 2003; **3**: 401-410 [PMID: 12778130 DOI: 10.1038/nrc1093]
- 15 Folkman J. Tumor angiogenesis: therapeutic implications. *N Engl J Med* 1971; **285**: 1182-1186 [PMID: 4938153 DOI: 10.1056/NEJM197111182852108]
- 16 Bottaro DP, Liotta LA. Cancer: Out of air is not out of action. *Nature* 2003; **423**: 593-595 [PMID: 12789320 DOI: 10.1038/423593a]
- 17 Harris AL. Hypoxia--a key regulatory factor in tumour growth. *Nat Rev Cancer* 2002; **2**: 38-47 [PMID: 11902584 DOI: 10.1038/nrc704]
- 18 Semenza GL. HIF-1 and tumor progression: pathophysiology and therapeutics. *Trends Mol Med* 2002; **8**: S62-S67 [PMID: 11927290 DOI: 10.1016/S1471-4914(02)02317-1]
- 19 Zhong H, De Marzo AM, Laughner E, Lim M, Hilton DA, Zagzag D, Buechler P, Isaacs WB, Semenza GL, Simons JW. Overexpression of hypoxia-inducible factor 1alpha in common human cancers and their metastases. *Cancer Res* 1999; **59**: 5830-5835 [PMID: 10582706]
- 20 Ratcliffe PJ. HIF-1 and HIF-2: working alone or together in hypoxia? *J Clin Invest* 2007; **117**: 862-865 [PMID: 17404612 DOI: 10.1172/JCI1750]
- 21 Semenza GL. Targeting HIF-1 for cancer therapy. *Nat Rev Cancer* 2003; **3**: 721-732 [PMID: 13130303]



- DOI: [10.1038/nrc1187](https://doi.org/10.1038/nrc1187)
- 22 **Yeo EJ**, Chun YS, Cho YS, Kim J, Lee JC, Kim MS, Park JW. YC-1: a potential anticancer drug targeting hypoxia-inducible factor 1. *J Natl Cancer Inst* 2003; **95**: 516-525 [PMID: [12671019](https://pubmed.ncbi.nlm.nih.gov/12671019/) DOI: [10.1093/jnci/95.7.516](https://doi.org/10.1093/jnci/95.7.516)]
  - 23 **Stoeltzing O**, McCarty MF, Wey JS, Fan F, Liu W, Belcheva A, Bucana CD, Semenza GL, Ellis LM. Role of hypoxia-inducible factor 1alpha in gastric cancer cell growth, angiogenesis, and vessel maturation. *J Natl Cancer Inst* 2004; **96**: 946-956 [PMID: [15199114](https://pubmed.ncbi.nlm.nih.gov/15199114/) DOI: [10.1093/jnci/djh168](https://doi.org/10.1093/jnci/djh168)]
  - 24 **Obst B**, Wagner S, Sewing KF, Beil W. Helicobacter pylori causes DNA damage in gastric epithelial cells. *Carcinogenesis* 2000; **21**: 1111-1115 [PMID: [10836997](https://pubmed.ncbi.nlm.nih.gov/10836997/) DOI: [10.1093/carcin/21.5.111](https://doi.org/10.1093/carcin/21.5.111)]
  - 25 **Park JH**, Kim TY, Jong HS, Kim TY, Chun YS, Park JW, Lee CT, Jung HC, Kim NK, Bang YJ. Gastric epithelial reactive oxygen species prevent normoxic degradation of hypoxia-inducible factor-1alpha in gastric cancer cells. *Clin Cancer Res* 2003; **9**: 433-440 [PMID: [12538497](https://pubmed.ncbi.nlm.nih.gov/12538497/)]
  - 26 **Bose S**, Deininger M, Gora-Tybor J, Goldman JM, Melo JV. The presence of typical and atypical BCR-ABL fusion genes in leukocytes of normal individuals: biologic significance and implications for the assessment of minimal residual disease. *Blood* 1998; **92**: 3362-3367 [PMID: [9787174](https://pubmed.ncbi.nlm.nih.gov/9787174/)]
  - 27 **Adams RH**, Alitalo K. Molecular regulation of angiogenesis and lymphangiogenesis. *Nat Rev Mol Cell Biol* 2007; **8**: 464-478 [PMID: [17522591](https://pubmed.ncbi.nlm.nih.gov/17522591/) DOI: [10.1038/nrm2183](https://doi.org/10.1038/nrm2183)]
  - 28 **Carmeliet P**. Angiogenesis in health and disease. *Nat Med* 2003; **9**: 653-660 [PMID: [12778163](https://pubmed.ncbi.nlm.nih.gov/12778163/) DOI: [10.1038/nm0603-653](https://doi.org/10.1038/nm0603-653)]
  - 29 **Fong GH**, Rossant J, Gertsenstein M, Breitman ML. Role of the Flt-1 receptor tyrosine kinase in regulating the assembly of vascular endothelium. *Nature* 1995; **376**: 66-70 [PMID: [7596436](https://pubmed.ncbi.nlm.nih.gov/7596436/) DOI: [10.1038/376066a0](https://doi.org/10.1038/376066a0)]
  - 30 **Fong GH**, Zhang L, Bryce DM, Peng J. Increased hemangioblast commitment, not vascular disorganization, is the primary defect in flt-1 knock-out mice. *Development* 1999; **126**: 3015-3025 [PMID: [10357944](https://pubmed.ncbi.nlm.nih.gov/10357944/)]
  - 31 **Karar J**, Maity A. PI3K/AKT/mTOR Pathway in Angiogenesis. *Front Mol Neurosci* 2011; **4**: 51 [PMID: [22144946](https://pubmed.ncbi.nlm.nih.gov/22144946/) DOI: [10.3389/fnmol.2011.00051](https://doi.org/10.3389/fnmol.2011.00051)]
  - 32 **Bruick RK**, McKnight SL. A conserved family of prolyl-4-hydroxylases that modify HIF. *Science* 2001; **294**: 1337-1340 [PMID: [11598268](https://pubmed.ncbi.nlm.nih.gov/11598268/) DOI: [10.1126/science.1066373](https://doi.org/10.1126/science.1066373)]
  - 33 **Ruiz de Almodovar C**, Lambrechts D, Mazzone M, Carmeliet P. Role and therapeutic potential of VEGF in the nervous system. *Physiol Rev* 2009; **89**: 607-648 [PMID: [19342615](https://pubmed.ncbi.nlm.nih.gov/19342615/) DOI: [10.1152/physrev.00031.2008](https://doi.org/10.1152/physrev.00031.2008)]
  - 34 **Shalaby F**, Rossant J, Yamaguchi TP, Gertsenstein M, Wu XF, Breitman ML, Schuh AC. Failure of blood-island formation and vasculogenesis in Flk-1-deficient mice. *Nature* 1995; **376**: 62-66 [PMID: [7596435](https://pubmed.ncbi.nlm.nih.gov/7596435/) DOI: [10.1038/376062a0](https://doi.org/10.1038/376062a0)]
  - 35 **Carmeliet P**, Ferreira V, Breier G, Pollefeys T, Kieckens L, Gertsenstein M, Fahrig M, Vandenhoek A, Harpal K, Eberhardt C, Declercq C, Pawling J, Moons L, Collen D, Risau W, Nagy A. Abnormal blood vessel development and lethality in embryos lacking a single VEGF allele. *Nature* 1996; **380**: 435-439 [PMID: [8602241](https://pubmed.ncbi.nlm.nih.gov/8602241/) DOI: [10.1038/380435a0](https://doi.org/10.1038/380435a0)]
  - 36 **Ferrara N**, Carver-Moore K, Chen H, Dowd M, Lu L, O'Shea KS, Powell-Braxton L, Hillan KJ, Moore MW. Heterozygous embryonic lethality induced by targeted inactivation of the VEGF gene. *Nature* 1996; **380**: 439-442 [PMID: [8602242](https://pubmed.ncbi.nlm.nih.gov/8602242/) DOI: [10.1038/380439a0](https://doi.org/10.1038/380439a0)]
  - 37 **Shi J**, Wei PK. Interleukin-8: A potent promoter of angiogenesis in gastric cancer. *Oncol Lett* 2016; **11**: 1043-1050 [PMID: [26893688](https://pubmed.ncbi.nlm.nih.gov/26893688/) DOI: [10.3892/ol.2015.4035](https://doi.org/10.3892/ol.2015.4035)]
  - 38 **Xu WH**, Ge YL, Li Q, Zhang X, Duan JH. Inhibitory effect of vascular endothelial growth factors-targeted small interfering RNA on proliferation of gastric cancer cells. *World J Gastroenterol* 2007; **13**: 2044-2047 [PMID: [17465445](https://pubmed.ncbi.nlm.nih.gov/17465445/) DOI: [10.3748/wjg.v13.i14.2044](https://doi.org/10.3748/wjg.v13.i14.2044)]
  - 39 **Forsythe JA**, Jiang BH, Iyer NV, Agani F, Leung SW, Koos RD, Semenza GL. Activation of vascular endothelial growth factor gene transcription by hypoxia-inducible factor 1. *Mol Cell Biol* 1996; **16**: 4604-4613 [PMID: [8756616](https://pubmed.ncbi.nlm.nih.gov/8756616/) DOI: [10.1128/MCB.16.9.4604](https://doi.org/10.1128/MCB.16.9.4604)]
  - 40 **Ferrara N**, Gerber HP, LeCouter J. The biology of VEGF and its receptors. *Nat Med* 2003; **9**: 669-676 [PMID: [12778165](https://pubmed.ncbi.nlm.nih.gov/12778165/) DOI: [10.1038/nm0603-669](https://doi.org/10.1038/nm0603-669)]
  - 41 **Karayianakis AJ**, Syrigos KN, Polychronidis A, Zbar A, Kouraklis G, Simopoulos C, Karatzas G. Circulating VEGF levels in the serum of gastric cancer patients: correlation with pathological variables, patient survival, and tumor surgery. *Ann Surg* 2002; **236**: 37-42 [PMID: [12131083](https://pubmed.ncbi.nlm.nih.gov/12131083/) DOI: [10.1097/00000658-200207000-00007](https://doi.org/10.1097/00000658-200207000-00007)]
  - 42 **Kakeji Y**, Koga T, Sumiyoshi Y, Shibahara K, Oda S, Maehara Y, Sugimachi K. Clinical significance of vascular endothelial growth factor expression in gastric cancer. *J Exp Clin Cancer Res* 2002; **21**: 125-129 [PMID: [12071518](https://pubmed.ncbi.nlm.nih.gov/12071518/) DOI: [10.31021/jcro.20181111](https://doi.org/10.31021/jcro.20181111)]
  - 43 **Wang TB**, Wang J, Wei XQ, Wei B, Dong WG. Serum vascular endothelial growth factor-C combined with multi-detector CT in the preoperative diagnosis of lymph node metastasis of gastric cancer. *Asia Pac J Clin Oncol* 2012; **8**: 180-186 [PMID: [22524577](https://pubmed.ncbi.nlm.nih.gov/22524577/) DOI: [10.1111/j.1743-7563.2011.01490.x](https://doi.org/10.1111/j.1743-7563.2011.01490.x)]
  - 44 **Kikuchi S**, Obata Y, Yagyu K, Lin Y, Nakajima T, Kobayashi O, Kikuichi M, Ushijima R, Kurosawa M, Ueda J. Reduced serum vascular endothelial growth factor receptor-2 (sVEGFR-2) and sVEGFR-1 levels in gastric cancer patients. *Cancer Sci* 2011; **102**: 866-869 [PMID: [21219538](https://pubmed.ncbi.nlm.nih.gov/21219538/) DOI: [10.1111/j.1349-7006.2011.01860.x](https://doi.org/10.1111/j.1349-7006.2011.01860.x)]
  - 45 **Sheng SL**, Bao SH, Huang G, Wang LM. Development of time-resolved immunofluorometric assays for vascular endothelial growth factor and application on plasma of patients with gastric tumours. *Clin Exp Immunol* 2008; **151**: 459-466 [PMID: [18234057](https://pubmed.ncbi.nlm.nih.gov/18234057/) DOI: [10.1111/j.1365-2249.2007.03548.x](https://doi.org/10.1111/j.1365-2249.2007.03548.x)]
  - 46 **Vidal O**, Metges JP, Elizalde I, Valentini M, Volant A, Molina R, Castells A, Pera M. High preoperative serum vascular endothelial growth factor levels predict poor clinical outcome after curative resection of gastric cancer. *Br J Surg* 2009; **96**: 1443-1451 [PMID: [19918848](https://pubmed.ncbi.nlm.nih.gov/19918848/) DOI: [10.1002/bjs.6780](https://doi.org/10.1002/bjs.6780)]
  - 47 **Villarejo-Campos P**, Padilla-Valverde D, Martin RM, Menéndez-Sánchez P, Cubo-Cintas T, Bondia-Navarro JA, Fernández JM. Serum VEGF and VEGF-C values before surgery and after postoperative treatment in gastric cancer. *Clin Transl Oncol* 2013; **15**: 265-270 [PMID: [22855190](https://pubmed.ncbi.nlm.nih.gov/22855190/) DOI: [10.1007/s12094-012-0908-x](https://doi.org/10.1007/s12094-012-0908-x)]
  - 48 **Olsson AK**, Dimberg A, Kreuger J, Claesson-Welsh L. VEGF receptor signalling - in control of vascular function. *Nat Rev Mol Cell Biol* 2006; **7**: 359-371 [PMID: [16633338](https://pubmed.ncbi.nlm.nih.gov/16633338/) DOI: [10.1038/nrm1911](https://doi.org/10.1038/nrm1911)]
  - 49 **Akrami H**, Mahmoodi F, Havasi S, Sharifi A. PlGF knockdown inhibited tumor survival and migration in gastric cancer cell via PI3K/Akt and p38MAPK pathways. *Cell Biochem Funct* 2016; **34**: 173-180 [PMID: [26968576](https://pubmed.ncbi.nlm.nih.gov/26968576/) DOI: [10.1002/cbf.3176](https://doi.org/10.1002/cbf.3176)]

- 50 **Mahmoodi F**, Akrami H. PlGF Knockdown Decreases Tumorigenicity and Stemness Properties of Spheroid Body Cells Derived from Gastric Cancer Cells. *J Cell Biochem* 2017; **118**: 851-859 [PMID: 27735991 DOI: 10.1002/jcb.25762]
- 51 **Chen CN**, Hsieh FJ, Cheng YM, Cheng WF, Su YN, Chang KJ, Lee PH. The significance of placenta growth factor in angiogenesis and clinical outcome of human gastric cancer. *Cancer Lett* 2004; **213**: 73-82 [PMID: 15312686 DOI: 10.1016/j.canlet.2004.05.020]
- 52 **Liang G**, Liu Z, Wu J, Cai Y, Li X. Anticancer molecules targeting fibroblast growth factor receptors. *Trends Pharmacol Sci* 2012; **33**: 531-541 [PMID: 22884522 DOI: 10.1016/j.tips.2012.07.001]
- 53 **Forough R**, Weylie B, Patel C, Ambrus S, Singh US, Zhu J. Role of AKT/PKB signaling in fibroblast growth factor-1 (FGF-1)-induced angiogenesis in the chicken chorioallantoic membrane (CAM). *J Cell Biochem* 2005; **94**: 109-116 [PMID: 15517595 DOI: 10.1002/jcb.20274]
- 54 **Sahin F**, Celik HA, Aydin HH, Oktem G, Omay SB, Saydam G. The interaction between taxoids and serine/threonine protein phosphatase activities during taxan-induced apoptosis of HL 60 leukemic cells. *Hematology* 2008; **13**: 215-223 [PMID: 18796247 DOI: 10.1179/102453308X315997]
- 55 **Shibuya M**. Vascular endothelial growth factor-dependent and -independent regulation of angiogenesis. *BMB Rep* 2008; **41**: 278-286 [PMID: 18452647 DOI: 10.5483/BMBRep.2008.41.4.278]
- 56 **Battagay EJ**, Rupp J, Iruela-Arispe L, Sage EH, Pech M. PDGF-BB modulates endothelial proliferation and angiogenesis in vitro via PDGF beta-receptors. *J Cell Biol* 1994; **125**: 917-928 [PMID: 7514607 DOI: 10.1083/jcb.125.4.917]
- 57 **Xue Y**, Lim S, Yang Y, Wang Z, Jensen LD, Hedlund EM, Andersson P, Sasahara M, Larsson O, Galter D, Cao R, Hosaka K, Cao Y. PDGF-BB modulates hematopoiesis and tumor angiogenesis by inducing erythropoietin production in stromal cells. *Nat Med* 2011; **18**: 100-110 [PMID: 22138754 DOI: 10.1038/nm.2575]
- 58 **Ernst M**, Najdovska M, Grail D, Lundgren-May T, Buchert M, Tye H, Matthews VB, Armes J, Bhathal PS, Hughes NR, Marcusson EG, Karras JG, Na S, Sedgwick JD, Hertzog PJ, Jenkins BJ. STAT3 and STAT1 mediate IL-11-dependent and inflammation-associated gastric tumorigenesis in gp130 receptor mutant mice. *J Clin Invest* 2008; **118**: 1727-1738 [PMID: 18431520 DOI: 10.1172/JCI34944]
- 59 **Singh R**, Kim WJ, Kim PH, Hong HJ. Combined blockade of HER2 and VEGF exerts greater growth inhibition of HER2-overexpressing gastric cancer xenografts than individual blockade. *Exp Mol Med* 2013; **45**: e52 [PMID: 24176949 DOI: 10.1038/emm.2013.111]
- 60 **Laughner E**, Taghavi P, Chiles K, Mahon PC, Semenza GL. HER2 (neu) signaling increases the rate of hypoxia-inducible factor 1alpha (HIF-1alpha) synthesis: novel mechanism for HIF-1-mediated vascular endothelial growth factor expression. *Mol Cell Biol* 2001; **21**: 3995-4004 [PMID: 11359907 DOI: 10.1128/MCB.21.12.3995-4004.2001]
- 61 **Wen XF**, Yang G, Mao W, Thornton A, Liu J, Bast RC, Le XF. HER2 signaling modulates the equilibrium between pro- and antiangiogenic factors via distinct pathways: implications for HER2-targeted antibody therapy. *Oncogene* 2006; **25**: 6986-6996 [PMID: 16715132 DOI: 10.1038/sj.onc.1209685]
- 62 **Seidman AD**, Fournier MN, Esteve FJ, Tan L, Kaptain S, Bach A, Panageas KS, Arroyo C, Valero V, Currie V, Gilewski T, Theodoulou M, Moynahan ME, Moasser M, Sklarin N, Dickler M, D'Andrea G, Cristofanilli M, Rivera E, Hortobagyi GN, Norton L, Hudis CA. Weekly trastuzumab and paclitaxel therapy for metastatic breast cancer with analysis of efficacy by HER2 immunophenotype and gene amplification. *J Clin Oncol* 2001; **19**: 2587-2595 [PMID: 11352950 DOI: 10.1200/JCO.2001.19.10.2587]
- 63 **Augustin HG**, Koh GY, Thurston G, Alitalo K. Control of vascular morphogenesis and homeostasis through the angiopoietin-Tie system. *Nat Rev Mol Cell Biol* 2009; **10**: 165-177 [PMID: 19234476 DOI: 10.1038/nrm2639]
- 64 **Saharinen P**, Bry M, Alitalo K. How do angiopoietins Tie in with vascular endothelial growth factors? *Curr Opin Hematol* 2010; **17**: 198-205 [PMID: 20375888 DOI: 10.1097/MOH.0b013e3283386673]
- 65 **Davis S**, Aldrich TH, Jones PF, Acheson A, Compton DL, Jain V, Ryan TE, Bruno J, Radziejewski C, Maisonpierre PC, Yancopoulos GD. Isolation of angiopoietin-1, a ligand for the TIE2 receptor, by secretion-trap expression cloning. *Cell* 1996; **87**: 1161-1169 [PMID: 8980223 DOI: 10.1016/S0092-8674(00)81812-7]
- 66 **Maisonpierre PC**, Suri C, Jones PF, Bartunkova S, Wiegand SJ, Radziejewski C, Compton D, McClain J, Aldrich TH, Papadopoulos N, Daly TJ, Davis S, Sato TN, Yancopoulos GD. Angiopoietin-2, a natural antagonist for Tie2 that disrupts in vivo angiogenesis. *Science* 1997; **277**: 55-60 [PMID: 9204896 DOI: 10.1126/science.277.5322.55]
- 67 **Fagiani E**, Christofori G. Angiopoietins in angiogenesis. *Cancer Lett* 2013; **328**: 18-26 [PMID: 22922303 DOI: 10.1016/j.canlet.2012.08.018]
- 68 **Fukuhara S**, Sako K, Minami T, Noda K, Kim HZ, Kodama T, Shibuya M, Takakura N, Koh GY, Mochizuki N. Differential function of Tie2 at cell-cell contacts and cell-substratum contacts regulated by angiopoietin-1. *Nat Cell Biol* 2008; **10**: 513-526 [PMID: 18425120 DOI: 10.1038/ncb1714]
- 69 **Saharinen P**, Eklund L, Miettinen J, Wirkkala R, Anisimov A, Winderlich M, Nottebaum A, Vestweber D, Deutsch U, Koh GY, Olsen BR, Alitalo K. Angiopoietins assemble distinct Tie2 signalling complexes in endothelial cell-cell and cell-matrix contacts. *Nat Cell Biol* 2008; **10**: 527-537 [PMID: 18425119 DOI: 10.1038/ncb1715]
- 70 **Wang J**, Wu KC, Zhang DX, Fan DM. Antisense angiopoietin-1 inhibits tumorigenesis and angiogenesis of gastric cancer. *World J Gastroenterol* 2006; **12**: 2450-2454 [PMID: 16688843 DOI: 10.3748/wjg.v12.i15.2450]
- 71 **Chen Z**, Zhu S, Hong J, Soutto M, Peng D, Belkhir A, Xu Z, El-Rifai W. Gastric tumour-derived ANGPT2 regulation by DARPP-32 promotes angiogenesis. *Gut* 2016; **65**: 925-934 [PMID: 25779598 DOI: 10.1136/gutjnl-2014-308416]
- 72 **Ou XL**, Chen HJ, Sun WH, Hang C, Yang L, Guan YY, Yan F, Chen BA. Effects of angiopoietin-1 on attachment and metastasis of human gastric cancer cell line BGC-823. *World J Gastroenterol* 2009; **15**: 5432-5441 [PMID: 19916173 DOI: 10.3748/wjg.15.5432]
- 73 **Tang S**, Wang D, Zhang Q, Li L. miR-218 suppresses gastric cancer cell proliferation and invasion via regulation of angiopoietin-2. *Exp Ther Med* 2016; **12**: 3837-3842 [PMID: 28105117 DOI: 10.3892/etm.2016.3893]
- 74 **Blank S**, Deck C, Dreikhausen L, Weichert W, Giese N, Falk C, Schmidt T, Ott K. Angiogenic and growth factors in gastric cancer. *J Surg Res* 2015; **194**: 420-429 [PMID: 25577146 DOI: 10.1016/j.jss.2014.11.028]
- 75 **Dreikhausen L**, Blank S, Sisic L, Heger U, Weichert W, Jäger D, Bruckner T, Giese N, Grenacher L, Falk C, Ott K, Schmidt T. Association of angiogenic factors with prognosis in esophageal cancer. *BMC Cancer*

- 2015; **15**: 121 [PMID: 25885021 DOI: 10.1186/s12885-015-1120-5]
- 76 **Hacker UT**, Escalona-Espinosa L, Consalvo N, Goede V, Schiffrmann L, Scherer SJ, Hedge P, Van Cutsem E, Coutelle O, Büning H. Evaluation of Angiopoietin-2 as a biomarker in gastric cancer: results from the randomised phase III AVAGAST trial. *Br J Cancer* 2016; **114**: 855-862 [PMID: 27031850 DOI: 10.1038/bjc.2016.30]
  - 77 **Aktaş SH**, Akbulut Yazici HO, Zengin N, Akgün HN, Üstüner Z, İçli F. A new angiogenesis prognostic index with VEGFA, PlGF, and angiopoietin1 predicts survival in patients with advanced gastric cancer. *Turk J Med Sci* 2017; **47**: 399-406 [PMID: 28425270 DOI: 10.3906/sag-1509-80]
  - 78 **Wu X**, Yang T, Liu X, Guo JN, Xie T, Ding Y, Lin M, Yang H. IL-17 promotes tumor angiogenesis through Stat3 pathway mediated upregulation of VEGF in gastric cancer. *Tumour Biol* 2016; **37**: 5493-5501 [PMID: 26566627 DOI: 10.1007/s13277-015-4372-4]
  - 79 **Morris DR**, Ding Y, Ricks TK, Gullapalli A, Wolfe BL, Trejo J. Protease-activated receptor-2 is essential for factor VIIa and Xa-induced signaling, migration, and invasion of breast cancer cells. *Cancer Res* 2006; **66**: 307-314 [PMID: 16397244 DOI: 10.1158/0008-5472.CAN-05-1735]
  - 80 **Ammendola M**, Marech I, Sammarco G, Zuccalà V, Luposella M, Zizzo N, Patruno R, Crovace A, Ruggieri E, Zito AF, Gadaleta CD, Sacco R, Ranieri G. Infiltrating mast cells correlate with angiogenesis in bone metastases from gastric cancer patients. *Int J Mol Sci* 2015; **16**: 3237-3250 [PMID: 25648323 DOI: 10.3390/ijms16023237]
  - 81 **Ammendola M**, Sacco R, Zuccalà V, Luposella M, Patruno R, Gadaleta P, Zizzo N, Gadaleta CD, De Sarro G, Sammarco G, Oltean M, Ranieri G. Mast Cells Density Positive to Tryptase Correlate with Microvascular Density in both Primary Gastric Cancer Tissue and Loco-Regional Lymph Node Metastases from Patients That Have Undergone Radical Surgery. *Int J Mol Sci* 2016; **17**: E1905 [PMID: 27854307 DOI: 10.3390/ijms17111905]
  - 82 **Dormond O**, Foletti A, Paroz C, Rüegg C. NSAIDs inhibit alpha V beta 3 integrin-mediated and Cdc42/Rac-dependent endothelial-cell spreading, migration and angiogenesis. *Nat Med* 2001; **7**: 1041-1047 [PMID: 11533708 DOI: 10.1038/nm0901-1041]
  - 83 **Deissler HL**, Lang GE. [In vitro studies on the mechanism of action of VEGF and its inhibitors]. *Klin Monbl Augenheilkd* 2008; **225**: 623-628 [PMID: 18642204 DOI: 10.1055/s-2008-1027513]
  - 84 **Ziemssen F**, Sobolewska B, Deissler H, Deissler H. Safety of monoclonal antibodies and related therapeutic proteins for the treatment of neovascular macular degeneration: addressing outstanding issues. *Expert Opin Drug Saf* 2016; **15**: 75-87 [PMID: 26568279 DOI: 10.1517/14740338.2016.1121232]
  - 85 **Peters GJ**. Therapeutic potential of TAS-102 in the treatment of gastrointestinal malignancies. *Ther Adv Med Oncol* 2015; **7**: 340-356 [PMID: 26557901 DOI: 10.1177/1758834015603313]
  - 86 **Lv Y**, Song L, Chang L, Liu Y, Zhang X, Li Q, Zhou X, Liu W. Inhibitory effects of bevacizumab monoclonal antibodies in combination with chemotherapy in different time sequences on a human gastric carcinoma cell line. *Ir J Med Sci* 2017; **186**: 275-280 [PMID: 27351431 DOI: 10.1007/s11845-016-1471-1]
  - 87 **Yamashita-Kashima Y**, Fujimoto-Ouchi K, Yorozu K, Kurasawa M, Yanagisawa M, Yasuno H, Mori K. Biomarkers for antitumor activity of bevacizumab in gastric cancer models. *BMC Cancer* 2012; **12**: 37 [PMID: 22273502 DOI: 10.1186/1471-2407-12-37]
  - 88 **Ninomiya S**, Inomata M, Tajima M, Ali AT, Ueda Y, Shiraishi N, Kitano S. Effect of bevacizumab, a humanized monoclonal antibody to vascular endothelial growth factor, on peritoneal metastasis of MNK-45P human gastric cancer in mice. *J Surg Res* 2009; **154**: 196-202 [PMID: 19329124 DOI: 10.1016/j.jss.2008.08.017]
  - 89 **Imaizumi T**, Aoyagi K, Miyagi M, Shirouzu K. Suppressive effect of bevacizumab on peritoneal dissemination from gastric cancer in a peritoneal metastasis model. *Surg Today* 2010; **40**: 851-857 [PMID: 20740349 DOI: 10.1007/s00595-009-4154-y]
  - 90 **Abdel-Rahman O**, Fouad M. Bevacizumab-based combination therapy for advanced gastroenteropancreatic neuroendocrine neoplasms (GEP-NENs): a systematic review of the literature. *J Cancer Res Clin Oncol* 2015; **141**: 295-305 [PMID: 24990591 DOI: 10.1007/s00432-014-1757-5]
  - 91 **Pinto MP**, Owen GI, Retamal I, Garrido M. Angiogenesis inhibitors in early development for gastric cancer. *Expert Opin Investig Drugs* 2017; **26**: 1007-1017 [PMID: 28770623 DOI: 10.1080/13543784.2017.1361926]
  - 92 **Brown PD**. Ongoing trials with matrix metalloproteinase inhibitors. *Expert Opin Investig Drugs* 2000; **9**: 2167-2177 [PMID: 11060801 DOI: 10.1517/13543784.9.9.2167]
  - 93 **Xu RH**, Kalechman Y, Albeck M, Sredni B. The cytoprotective effect of the immunomodulator AS101 against hydrochloride induced gastric lesions. *Res Commun Mol Pathol Pharmacol* 1995; **87**: 4-20 [PMID: 7735728 DOI: 10.1038/nrd.2015.17]
  - 94 **Muehlbauer PM**. Anti-angiogenesis in cancer therapy. *Semin Oncol Nurs* 2003; **19**: 180-192 [PMID: 12962008 DOI: 10.1016/S0749-2081(03)00046-9]
  - 95 **Falcon BL**, Chintharlapalli S, Uhlik MT, Pytowski B. Antagonist antibodies to vascular endothelial growth factor receptor 2 (VEGFR-2) as anti-angiogenic agents. *Pharmacol Ther* 2016; **164**: 204-225 [PMID: 27288725 DOI: 10.1016/j.pharmthera.2016.06.001]
  - 96 **Arakawa Y**, Tamura M, Aiba K, Morikawa K, Aizawa D, Ikegami M, Yuda M, Nishikawa K. Significant response to ramucirumab monotherapy in chemotherapy-resistant recurrent alpha-fetoprotein-producing gastric cancer: A case report. *Oncol Lett* 2017; **14**: 3039-3042 [PMID: 28928842 DOI: 10.3892/ol.2017.6514]
  - 97 **Jung YD**, Mansfield PF, Akagi M, Takeda A, Liu W, Bucana CD, Hicklin DJ, Ellis LM. Effects of combination anti-vascular endothelial growth factor receptor and anti-epidermal growth factor receptor therapies on the growth of gastric cancer in a nude mouse model. *Eur J Cancer* 2002; **38**: 1133-1140 [PMID: 12008203 DOI: 10.1016/S0959-8049(02)00013-8]
  - 98 **Sun P**, Yu H, Zhang WQ, Hu M, Lv R. Lentivirus-mediated siRNA targeting VEGF inhibits gastric cancer growth in vivo. *Oncol Rep* 2012; **28**: 1687-1692 [PMID: 22895814 DOI: 10.3892/or.2012.1966]
  - 99 **Lin Y**, Zhai E, Liao B, Xu L, Zhang X, Peng S, He Y, Cai S, Zeng Z, Chen M. Autocrine VEGF signaling promotes cell proliferation through a PLC-dependent pathway and modulates Apatinib treatment efficacy in gastric cancer. *Oncotarget* 2017; **8**: 11990-12002 [PMID: 28061477 DOI: 10.18632/oncotarget.14467]
  - 100 **Li T**, Kang G, Wang T, Huang H. Tumor angiogenesis and anti-angiogenic gene therapy for cancer. *Oncol Lett* 2018; **16**: 687-702 [PMID: 29963134 DOI: 10.3892/ol.2018.8733]
  - 101 **Xu X**, Tang X, Wu X, Feng X. Biosynthesis of sorafenib coated graphene nanosheets for the treatment of gastric cancer in patients in nursing care. *J Photochem Photobiol B* 2019; **191**: 1-5 [PMID: 30557787 DOI: 10.1016/j.jphotobiol.2018.11.013]

- 102 **Yang F**, Li A, Liu H, Zhang H. Gastric cancer combination therapy: synthesis of a hyaluronic acid and cisplatin containing lipid prodrug coloaded with sorafenib in a nanoparticulate system to exhibit enhanced anticancer efficacy and reduced toxicity. *Drug Des Devel Ther* 2018; **12**: 3321-3333 [PMID: [30323564](#) DOI: [10.2147/DDDT.S176879](#)]
- 103 **Lyros O**, Mueller A, Heidel F, Schimanski CC, Gockel I, Galle PR, Lang H, Moehler M. Analysis of anti-proliferative and chemosensitizing effects of sunitinib on human esophagogastric cancer cells: Synergistic interaction with vandetanib via inhibition of multi-receptor tyrosine kinase pathways. *Int J Cancer* 2010; **127**: 1197-1208 [PMID: [20039326](#) DOI: [10.1002/ijc.25137](#)]
- 104 **Fuereder T**, Jaeger-Lansky A, Hoeflmayer D, Preusser M, Strommer S, Cejka D, Koehrer S, Crevenna R, Wachek V. mTOR inhibition by everolimus counteracts VEGF induction by sunitinib and improves anti-tumor activity against gastric cancer in vivo. *Cancer Lett* 2010; **296**: 249-256 [PMID: [20471160](#) DOI: [10.1016/j.canlet.2010.04.015](#)]
- 105 **Chen LT**, Oh DY, Ryu MH, Yeh KH, Yeo W, Carlesi R, Cheng R, Kim J, Orlando M, Kang YK. Anti-angiogenic Therapy in Patients with Advanced Gastric and Gastroesophageal Junction Cancer: A Systematic Review. *Cancer Res Treat* 2017; **49**: 851-868 [PMID: [28052652](#) DOI: [10.4143/crt.2016.176](#)]
- 106 **Kishida O**, Miyazaki Y, Murayama Y, Ogasa M, Miyazaki T, Yamamoto T, Watabe K, Tsutsui S, Kiyohara T, Shimomura I, Shinomura Y. Gefitinib (Iressa, ZD1839) inhibits SN38-triggered EGF signals and IL-8 production in gastric cancer cells. *Cancer Chemother Pharmacol* 2005; **55**: 584-594 [PMID: [15723219](#) DOI: [10.1007/s00280-004-0959-y](#)]
- 107 **Folkman J**. Fighting cancer by attacking its blood supply. *Sci Am* 1996; **275**: 150-154 [PMID: [8701285](#) DOI: [10.1038/scientificamerican0996-150](#)]
- 108 **Vecchione L**, Orditura M, Ciardiello F, De Vita F. Novel investigational drugs for gastric cancer. *Expert Opin Investig Drugs* 2009; **18**: 945-955 [PMID: [19466878](#) DOI: [10.1517/13543780902969455](#)]
- 109 **Xie L**, Ji T, Guo W. Anti-angiogenesis target therapy for advanced osteosarcoma (Review). *Oncol Rep* 2017; **38**: 625-636 [PMID: [28656259](#) DOI: [10.3892/or.2017.5735](#)]
- 110 **Presta M**, Dell'Era P, Mitola S, Moroni E, Ronca R, Rusnati M. Fibroblast growth factor/fibroblast growth factor receptor system in angiogenesis. *Cytokine Growth Factor Rev* 2005; **16**: 159-178 [PMID: [15863032](#) DOI: [10.1016/j.cytogfr.2005.01.004](#)]
- 111 **Folberg R**, Hendrix MJ, Maniotis AJ. Vasculogenic mimicry and tumor angiogenesis. *Am J Pathol* 2000; **156**: 361-381 [PMID: [10666364](#) DOI: [10.1016/S0002-9440\(10\)64739-6](#)]
- 112 **van Beijnum JR**, Nowak-Sliwinska P, Huijbers EJ, Thijssen VL, Griffioen AW. The great escape; the hallmarks of resistance to antiangiogenic therapy. *Pharmacol Rev* 2015; **67**: 441-461 [PMID: [25769965](#) DOI: [10.1124/pr.114.010215](#)]
- 113 **Loges S**, Schmidt T, Carmeliet P. Mechanisms of resistance to anti-angiogenic therapy and development of third-generation anti-angiogenic drug candidates. *Genes Cancer* 2010; **1**: 12-25 [PMID: [21779425](#) DOI: [10.1177/1947601909356574](#)]
- 114 **Ohtsu A**, Shah MA, Van Cutsem E, Rha SY, Sawaki A, Park SR, Lim HY, Yamada Y, Wu J, Langer B, Starnawski M, Kang YK. Bevacizumab in combination with chemotherapy as first-line therapy in advanced gastric cancer: a randomized, double-blind, placebo-controlled phase III study. *J Clin Oncol* 2011; **29**: 3968-3976 [PMID: [21844504](#) DOI: [10.1200/JCO.2011.36.2236](#)]
- 115 **Shen L**, Li J, Xu J, Pan H, Dai G, Qin S, Wang L, Wang J, Yang Z, Shu Y, Xu R, Chen L, Liu Y, Yu S, Bu L, Piao Y. Bevacizumab plus capecitabine and cisplatin in Chinese patients with inoperable locally advanced or metastatic gastric or gastroesophageal junction cancer: randomized, double-blind, phase III study (AVATAR study). *Gastric Cancer* 2015; **18**: 168-176 [PMID: [24557418](#) DOI: [10.1007/s10120-014-0351-5](#)]
- 116 **Ma J**, Yao S, Li XS, Kang HR, Yao FF, Du N. Neoadjuvant Therapy of DOF Regimen Plus Bevacizumab Can Increase Surgical Resection Rate in Locally Advanced Gastric Cancer: A Randomized, Controlled Study. *Medicine (Baltimore)* 2015; **94**: e1489 [PMID: [26496252](#) DOI: [10.1097/MD.0000000000001489](#)]
- 117 **Cunningham D**, Stenning SP, Smyth EC, Okines AF, Allum WH, Rowley S, Stevenson L, Grabsch HI, Alderson D, Crosby T, Griffin SM, Mansoor W, Coxon FY, Falk SJ, Darby S, Sumpter KA, Blazeby JM, Langley RE. Peri-operative chemotherapy with or without bevacizumab in operable oesophagogastric adenocarcinoma (UK Medical Research Council ST03): primary analysis results of a multicentre, open-label, randomised phase 2-3 trial. *Lancet Oncol* 2017; **18**: 357-370 [PMID: [28163000](#) DOI: [10.1016/S1470-2045\(17\)30043-8](#)]
- 118 **Fuchs CS**, Tomasek J, Yong CJ, Dumitru F, Passalacqua R, Goswami C, Safran H, Dos Santos LV, Aprile G, Ferry DR, Melichar B, Tehfe M, Topuzov E, Zalcberg JR, Chau I, Campbell W, Sivanandan C, Pikiel J, Koshiji M, Hsu Y, Liepa AM, Gao L, Schwartz JD, Tabernero J; REGARD Trial Investigators. Ramucirumab monotherapy for previously treated advanced gastric or gastro-oesophageal junction adenocarcinoma (REGARD): an international, randomised, multicentre, placebo-controlled, phase 3 trial. *Lancet* 2014; **383**: 31-39 [PMID: [24094768](#) DOI: [10.1016/S0140-6736\(13\)61719-5](#)]
- 119 **Wilke H**, Muro K, Van Cutsem E, Oh SC, Bodoky G, Shimada Y, Hironaka S, Sugimoto N, Lipatov O, Kim TY, Cunningham D, Rougier P, Komatsu Y, Ajani J, Emig M, Carlesi R, Ferry D, Chandrawansa K, Schwartz JD, Ohtsu A; RAINBOW Study Group. Ramucirumab plus paclitaxel versus placebo plus paclitaxel in patients with previously treated advanced gastric or gastro-oesophageal junction adenocarcinoma (RAINBOW): a double-blind, randomised phase 3 trial. *Lancet Oncol* 2014; **15**: 1224-1235 [PMID: [25240821](#) DOI: [10.1016/S1470-2045\(14\)70420-6](#)]
- 120 **Fuchs CS**, Shitara K, Di Bartolomeo M, Lonardi S, Al-Batran SE, Van Cutsem E, Ilson DH, Alsina M, Chau I, Lacy J, Ducreux M, Mendez GA, Alavez AM, Takahara D, Mansoor W, Enzinger PC, Gorbounova V, Wainberg ZA, Hegewisch-Becker S, Ferry D, Lin J, Carlesi R, Das M, Shah MA; RAINFALL Study Group. Ramucirumab with cisplatin and fluoropyrimidine as first-line therapy in metastatic gastric or junctional adenocarcinoma (RAINFALL): a double-blind, randomised, placebo-controlled, phase 3 trial. *Lancet Oncol* 2019; **20**: 420-435 [PMID: [30718072](#) DOI: [10.1016/S1470-2045\(18\)30791-5](#)]
- 121 **Li J**, Qin S, Xu J, Xiong J, Wu C, Bai Y, Liu W, Tong J, Liu Y, Xu R, Wang Z, Wang Q, Ouyang X, Yang Y, Ba Y, Liang J, Lin X, Luo D, Zheng R, Wang X, Sun G, Wang L, Zheng L, Guo H, Wu J, Xu N, Yang J, Zhang H, Cheng Y, Wang N, Chen L, Fan Z, Sun P, Yu H. Randomized, Double-Blind, Placebo-Controlled Phase III Trial of Apatinib in Patients With Chemotherapy-Refractory Advanced or Metastatic Adenocarcinoma of the Stomach or Gastroesophageal Junction. *J Clin Oncol* 2016; **34**: 1448-1454 [PMID: [26884585](#) DOI: [10.1200/JCO.2015.63.5995](#)]
- 122 **Jäger E**, Bernhard H, Klein O, Wächter B, Theiss F, Dippold W, Meyer zum Büschenfelde KH, Knuth A. Combination 5-fluorouracil (FU), folinic acid (FA), and alpha-interferon 2B in advanced gastric cancer: results of a phase II trial. *Ann Oncol* 1995; **6**: 153-156 [PMID: [7540418](#) DOI: [10.1093/oxfordjournals.annonc.a010000](#)]



- 10.1093/oxfordjournals.annonc.a059110]
- 123 **Al-Batran SE**, Ducreux M, Ohtsu A. mTOR as a therapeutic target in patients with gastric cancer. *Int J Cancer* 2012; **130**: 491-496 [PMID: 21898386 DOI: 10.1002/ijc.26396]
  - 124 **Pavlakakis N**, Sjoquist KM, Martin AJ, Tsoibanis E, Yip S, Kang YK, Bang YJ, Alcindor T, O'Callaghan CJ, Burnell MJ, Tebbutt NC, Rha SY, Lee J, Cho JY, Lipton LR, Wong M, Strickland A, Kim JW, Zalberg JR, Simes J, Goldstein D. Regorafenib for the Treatment of Advanced Gastric Cancer (INTEGRATE): A Multinational Placebo-Controlled Phase II Trial. *J Clin Oncol* 2016; **34**: 2728-2735 [PMID: 27325864 DOI: 10.1200/JCO.2015.65.1901]
  - 125 **Shah MA**, Wainberg ZA, Catenacci DV, Hochster HS, Ford J, Kunz P, Lee FC, Kallender H, Cecchi F, Rabe DC, Keer H, Martin AM, Liu Y, Gagnon R, Bonate P, Liu L, Gilmer T, Bottaro DP. Phase II study evaluating 2 dosing schedules of oral foretinib (GSK1363089), cMET/VEGFR2 inhibitor, in patients with metastatic gastric cancer. *PLoS One* 2013; **8**: e54014 [PMID: 23516391 DOI: 10.1371/journal.pone.0054014]
  - 126 **Shan F**, Miao R, Xue K, Li Z, Li Z, Bu Z, Wu A, Zhang L, Wu X, Zong X, Wang X, Li S, Ji X, Jia Z, Li Z, Ji J. Controlling angiogenesis in gastric cancer: A systematic review of anti-angiogenic trials. *Cancer Lett* 2016; **380**: 598-607 [PMID: 26724681 DOI: 10.1016/j.canlet.2015.12.023]
  - 127 **Bergers G**, Song S. The role of pericytes in blood-vessel formation and maintenance. *Neuro Oncol* 2005; **7**: 452-464 [PMID: 16212810 DOI: 10.1215/S1152851705000232]
  - 128 **Izzedine H**, Ederhy S, Goldwasser F, Soria JC, Milano G, Cohen A, Khayat D, Spano JP. Management of hypertension in angiogenesis inhibitor-treated patients. *Ann Oncol* 2009; **20**: 807-815 [PMID: 19150949 DOI: 10.1093/annonc/mdn713]
  - 129 **Liu SX**, Xia ZS, Zhong YQ. Gene therapy in pancreatic cancer. *World J Gastroenterol* 2014; **20**: 13343-13368 [PMID: 25309069 DOI: 10.3748/wjg.v20.i37.13343]
  - 130 **Ginn SL**, Alexander IE, Edelstein ML, Abedi MR, Wixon J. Gene therapy clinical trials worldwide to 2012 - an update. *J Gene Med* 2013; **15**: 65-77 [PMID: 23355455 DOI: 10.1002/jgm.2698]
  - 131 **Ortiz R**, Melguizo C, Prados J, Álvarez PJ, Caba O, Rodríguez-Serrano F, Hita F, Aránega A. New gene therapy strategies for cancer treatment: a review of recent patents. *Recent Pat Anticancer Drug Discov* 2012; **7**: 297-312 [PMID: 22339358 DOI: 10.2174/157489212801820093]
  - 132 **Cao S**, Cripps A, Wei MQ. New strategies for cancer gene therapy: progress and opportunities. *Clin Exp Pharmacol Physiol* 2010; **37**: 108-114 [PMID: 19671071 DOI: 10.1111/j.1440-1681.2009.05268.x]
  - 133 **Tseng SJ**, Liao ZX, Kao SH, Zeng YF, Huang KY, Li HJ, Yang CL, Deng YF, Huang CF, Yang SC, Yang PC, Kempson IM. Highly specific in vivo gene delivery for p53-mediated apoptosis and genetic photodynamic therapies of tumour. *Nat Commun* 2015; **6**: 6456 [PMID: 25739372 DOI: 10.1038/ncomms7456]
  - 134 **Tazawa H**, Kagawa S, Fujiwara T. Advances in adenovirus-mediated p53 cancer gene therapy. *Expert Opin Biol Ther* 2013; **13**: 1569-1583 [PMID: 24107178 DOI: 10.1517/14712598.2013.845662]
  - 135 **Prabha S**, Sharma B, Labhasetwar V. Inhibition of tumor angiogenesis and growth by nanoparticle-mediated p53 gene therapy in mice. *Cancer Gene Ther* 2012; **19**: 530-537 [PMID: 22595792 DOI: 10.1038/cgt.2012.26]
  - 136 **Teodoro JG**, Evans SK, Green MR. Inhibition of tumor angiogenesis by p53: a new role for the guardian of the genome. *J Mol Med (Berl)* 2007; **85**: 1175-1186 [PMID: 17589818 DOI: 10.1007/s00109-007-0221-2]
  - 137 **Zhang C**, Wang QT, Liu H, Zhang ZZ, Huang WL. Advancement and prospects of tumor gene therapy. *Chin J Cancer* 2011; **30**: 182-188 [PMID: 21352695 DOI: 10.5732/cjc.010.10074]
  - 138 **Allen JW**, Moon J, Redman M, Gadgeel SM, Kelly K, Mack PC, Saba HM, Mohamed MK, Jahanzeb M, Gandara DR. Southwest Oncology Group S0802: a randomized, phase II trial of weekly topotecan with and without ziv-aflibercept in patients with platinum-treated small-cell lung cancer. *J Clin Oncol* 2014; **32**: 2463-2470 [PMID: 25002722 DOI: 10.1200/JCO.2013.51.4109]
  - 139 **Siu LL**, Shapiro JD, Jonker DJ, Karapetis CS, Zalberg JR, Simes J, Couture F, Moore MJ, Price TJ, Siddiqui J, Nott LM, Charpentier D, Liauw W, Sawyer MB, Jefford M, Magoski NM, Haydon A, Walters I, Ringash J, Tu D, O'Callaghan CJ. Phase III randomized, placebo-controlled study of cetuximab plus brivanib alaninate versus cetuximab plus placebo in patients with metastatic, chemotherapy-refractory, wild-type K-RAS colorectal carcinoma: the NCIC Clinical Trials Group and AGITG CO.20 Trial. *J Clin Oncol* 2013; **31**: 2477-2484 [PMID: 23690424 DOI: 10.1200/JCO.2012.46.0543]
  - 140 **Lordick F**, Kang YK, Chung HC, Salman P, Oh SC, Bodoky G, Kurteva G, Volovat C, Moiseyenko VM, Gorbunova V, Park JO, Sawaki A, Celik I, Götte H, Melezinková H, Moehler M; Arbeitsgemeinschaft Internistische Onkologie and EXPAND Investigators. Capecitabine and cisplatin with or without cetuximab for patients with previously untreated advanced gastric cancer (EXPAND): a randomised, open-label phase 3 trial. *Lancet Oncol* 2013; **14**: 490-499 [PMID: 23594786 DOI: 10.1016/S1470-2045(13)70102-5]
  - 141 **Hitre E**, Budai B, Takácsi-Nagy Z, Rubovszky G, Tóth E, Remenár É, Polgár C, Láng I. Cetuximab and platinum-based chemoradio- or chemotherapy of patients with epidermal growth factor receptor expressing adenoid cystic carcinoma: a phase II trial. *Br J Cancer* 2013; **109**: 1117-1122 [PMID: 23942070 DOI: 10.1038/bjc.2013.468]
  - 142 **Österlund P**, Soveri LM, Isoniemi H, Poussa T, Alanko T, Bono P. Hypertension and overall survival in metastatic colorectal cancer patients treated with bevacizumab-containing chemotherapy. *Br J Cancer* 2011; **104**: 599-604 [PMID: 21304526 DOI: 10.1038/bjc.2011.2]
  - 143 **Tahover E**, Uziely B, Salah A, Temper M, Peretz T, Hubert A. Hypertension as a predictive biomarker in bevacizumab treatment for colorectal cancer patients. *Med Oncol* 2013; **30**: 327 [PMID: 23254964 DOI: 10.1007/s12032-012-0327-4]
  - 144 **Khoja L**, Kumaran G, Zee YK, Murukesh N, Swindell R, Saunders MP, Clamp AR, Valle JW, Wilson G, Jayson GC, Hasan J. Evaluation of hypertension and proteinuria as markers of efficacy in antiangiogenic therapy for metastatic colorectal cancer. *J Clin Gastroenterol* 2014; **48**: 430-434 [PMID: 24153157 DOI: 10.1097/MCG.0b013e3182a8804c]
  - 145 **Hwang JE**, Lee JH, Park MR, Kim DE, Bae WK, Shim HJ, Cho SH, Chung JJ. Blockade of VEGFR-1 and VEGFR-2 enhances paclitaxel sensitivity in gastric cancer cells. *Yonsei Med J* 2013; **54**: 374-380 [PMID: 23364970 DOI: 10.3349/ymj.2013.54.2.374]
  - 146 **Liu L**, Ning X, Sun L, Zhang H, Shi Y, Guo C, Han S, Liu J, Sun S, Han Z, Wu K, Fan D. Hypoxia-inducible factor-1 alpha contributes to hypoxia-induced chemoresistance in gastric cancer. *Cancer Sci* 2008; **99**: 121-128 [PMID: 17953712 DOI: 10.1111/j.1349-7006.2007.00643.x]
  - 147 **Zhao Q**, Li Y, Tan BB, Fan LQ, Yang PG, Tian Y. HIF-1 $\alpha$  Induces Multidrug Resistance in Gastric

- Cancer Cells by Inducing MiR-27a. *PLoS One* 2015; **10**: e0132746 [PMID: 26292288 DOI: 10.1371/journal.pone.0132746]
- 148 Rohwer N, Dame C, Haugstetter A, Wiedenmann B, Detjen K, Schmitt CA, Cramer T. Hypoxia-inducible factor 1alpha determines gastric cancer chemosensitivity via modulation of p53 and NF-kappaB. *PLoS One* 2010; **5**: e12038 [PMID: 20706634 DOI: 10.1371/journal.pone.0012038]
  - 149 Groenewald P, Bradshaw D, Neethling I, Martin LJ, Dempers J, Morden E, Zinyakatira N, Coetzee D. Linking mortality data improves vital statistics on cause of death of children under five years in the Western Cape Province of South Africa. *Trop Med Int Health* 2016; **21**: 114-121 [PMID: 26485307 DOI: 10.1111/tmi.12624]
  - 150 Kakeji Y, Maehara Y, Sumiyoshi Y, Oda S, Emi Y. Angiogenesis as a target for gastric cancer. *Surgery* 2002; **131**: S48-S54 [PMID: 11821787]
  - 151 Ford HE, Marshall A, Bridgewater JA, Janowitz T, Coxon FY, Wadsley J, Mansoor W, Fyfe D, Madhusudan S, Middleton GW, Swinson D, Falk S, Chau I, Cunningham D, Kareclas P, Cook N, Blazeby JM, Dunn JA; COUGAR-02 Investigators. Docetaxel versus active symptom control for refractory oesophagogastric adenocarcinoma (COUGAR-02): an open-label, phase 3 randomised controlled trial. *Lancet Oncol* 2014; **15**: 78-86 [PMID: 24332238 DOI: 10.1016/S1470-2045(13)70549-7]
  - 152 Lei X, Wang F, Ke Y, Wei D, Gu H, Zhang Z, Jiang L, Lv L, Lin J, Wang L. The role of antiangiogenic agents in the treatment of gastric cancer: A systematic review and meta-analysis. *Medicine (Baltimore)* 2017; **96**: e6301 [PMID: 28272258 DOI: 10.1097/MD.0000000000006301]
  - 153 Bai ZG, Zhang ZT. A systematic review and meta-analysis on the effect of angiogenesis blockade for the treatment of gastric cancer. *Onco Targets Ther* 2018; **11**: 7077-7087 [PMID: 30410364 DOI: 10.2147/OTT.S169484]
  - 154 Nelson NJ. Inhibitors of angiogenesis enter phase III testing. *J Natl Cancer Inst* 1998; **90**: 960-963 [PMID: 9665141 DOI: 10.1093/jnci/90.13.960a]
  - 155 Lu TH, Lee MC, Chou MC. Accuracy of cause-of-death coding in Taiwan: types of miscoding and effects on mortality statistics. *Int J Epidemiol* 2000; **29**: 336-343 [PMID: 10817134 DOI: 10.1093/ije/29.2.336]
  - 156 Ebos JM, Lee CR, Cruz-Munoz W, Bjarnason GA, Christensen JG, Kerbel RS. Accelerated metastasis after short-term treatment with a potent inhibitor of tumor angiogenesis. *Cancer Cell* 2009; **15**: 232-239 [PMID: 19249681 DOI: 10.1016/j.ccr.2009.01.021]
  - 157 Páez-Ribes M, Allen E, Hudock J, Takeda T, Okuyama H, Viñals F, Inoue M, Bergers G, Hanahan D, Casanovas O. Antiangiogenic therapy elicits malignant progression of tumors to increased local invasion and distant metastasis. *Cancer Cell* 2009; **15**: 220-231 [PMID: 19249680 DOI: 10.1016/j.ccr.2009.01.027]



# Multivariate analysis of metabolic parameters and optimization of antibody production using high cell density hybridoma in hollow fiber bioreactors

Chi-Hsien Liu · Yi-Xin Liu · Monika Kumari · Wei-Chi Wu

Received: 18 April 2019 / Accepted: 15 July 2019  
© Springer Nature B.V. 2019

## Abstract

**Objectives** The relationships of manipulation of culture temperature and medium circulation rate on the metabolic parameters were regressed by multiple linear regression analysis in hollow fiber bioreactors (HFB).

**Results** The high circulation rate could significantly enhance the oxygen consumption of the hybridoma cells and the medium's oxidation–reduction potential. A mildly hypothermic condition of 36 °C and a circulation rate of 182.5 mL/min could support the hybridoma had the maximal antibody titer of 60.75 µg/mL for 20 days. When the ammonium ion was 65 ppm or lactate close to 2.6 g/L, the medium was replaced to maintain the stable and healthy cells at

the high cell concentration of  $3.33 \times 10^8$ /mL for continuous antibody production. Two serum-free media could be successfully applied to this perfusion system and maintain hybridoma growth and antibody production.

**Conclusion** The single-use HFBs could provide the advantages including high cell density, low shear stress, and continuous antibody production.

**Keywords** Antibody · High cell density · Hollow fiber bioreactor · Perfusion

---

C.-H. Liu (✉) · M. Kumari  
Department of Chemical and Materials Engineering,  
Chang Gung University, 259, Wen-Hwa First Road,  
Kwei-Shan, Tao-Yuan 333, Taiwan, ROC  
e-mail: chl@mail.cgu.edu.tw

C.-H. Liu  
Research Center for Chinese Herbal Medicine and  
Research Center for Food and Cosmetic Safety, College  
of Human Ecology, Chang Gung University of Science  
and Technology, 261, Wen-Hwa First Road, Taoyuan,  
Taiwan, ROC

C.-H. Liu  
Department of Chemical Engineering, Ming Chi  
University of Technology, 84, Gung-Juan Road,  
New Taipei City, Taiwan, ROC

C.-H. Liu · W.-C. Wu  
Department of Ophthalmology, Chang Gung Memorial  
Hospital, 5, Fu-Hsing Street, Taoyuan, Taiwan, ROC

Y.-X. Liu  
Graduate Institute of Biomedical Engineering, Chang  
Gung University, 259, Wen-Hwa First Road, Kwei-Shan,  
Tao-Yuan 333, Taiwan, ROC

W.-C. Wu  
College of Medicine, Chang Gung University, 259, Wen-  
Hwa First Road, Taoyuan, Taiwan, ROC

## Introduction

Monoclonal antibodies (MAbs) account for important therapeutic proteins in the biopharmaceutical industry. Several strategies can improve the production yield of recombinant proteins by using genetic engineering, high-throughput screening, the optimization of culture medium, and the improvement of biochemical processes (Templeton and Young 2018). Traditionally, stirred-tank reactors have been explored for the continuous production of recombinant proteins (Donini and Marusic 2019). Hollow fiber bioreactors (HFBs) involve the retention of mammalian cells and the secreted protein within the extra-capillary space (ECS) while circulating the medium through the inside fiber continuously (Fig. 1a). The distinct characteristics of HFB include the ability to support high cell-density growth and to form a porous fiber supporting cell attachment, which is the most *in vivo*-like and tissue-like growth (Diban and Stamatialis 2014). The advantages of HFBs over suspension systems include: (1) no turbulence flow against cells, thereby reducing the damage of shear stress on cells (2) high cell density and concentrated MAb can be achieved, and (3) waste byproducts can be dialyzed away from cells in the ECS (Vermasvuori and Hurme 2011). High cell density in a perfusion culture can maintain the viable cells and elevate the volumetric MAb productivity (Sen and Roychoudhury 2013). The other benefits of disposable HFBs also include their high recovery efficiency, easy operation, and no need of bioreactor sterilization. In addition, the periodical withdraw of cells from the ECS enable the partial renewal of the cell population and prevent the accumulation of dead cells (Eghbali et al. 2016).

Manipulations of cultivation conditions have been reported to enhance the recombinant protein yield by affecting the cell growth and metabolism in the different culture systems (Liu et al. 2018b). For example, hypothermic culture conditions (30–36 °C) can induce a growth reduction in cells within the S or G1 phase during the cell cycle. In addition to a growth arrest-induced increase in specific productivity, cells under mild hypothermic conditions have other relevant advantages: extended culture durations and decreased O<sub>2</sub> demand during the culture (Sunley and Butler 2010). A decrease in the culture temperature resulted in a significant increase in MAb production using hybridoma (García Münzer et al. 2015) and

CHO cells (Kishishita et al. 2015). Mild hypothermia can enhance several recombinant proteins in CHO cell lines using fed-batch or perfusion cultures (Becerra et al. 2012). The effect of a low culture temperature on the productivity of recombinant proteins has been found to be cell line- or clonal-dependent (Sung et al. 2004). However, there are few studies related to the hypothermic effects on antibody production by the hybridoma using the HFB.

The medium perfusion can provide the nutrients continuously, remove the toxic byproducts, and maintain the stable environment in the HFB. Previously, attention has been given to analyzing the limiting nutrients or how the fluid flow distribution affects nutrients' availability in an HFB system (Yang et al. 2004; Eghbali et al. 2016). Very few papers discussed the influence of circulation rate on the metabolic characteristics and MAb production using the hybridoma culture in HFBs. Some important issues, like the membrane permeability and the crowding effects in the membrane bioreactors have not encountered in the low-density suspension cultures (Diban and Stamatialis 2014). These problems need more investigation to improve the MAb productivity using the HFB. The bioprocess complexity, difficulty of characterizing cultivation environment, the lack of direct relation to physiological mechanisms and different recombinant proteins make it difficult to conduct process parameter analysis (von Stosch et al. 2014). A robust statistical mode can help analyze the critical variables among the important process parameters to ensure the quality and productivity of recombinant proteins. Multivariate analysis can extract important information from cell culture processes and improve the quality and yield of MAb (Del Val et al. 2010). Various serum free media have been developed to enhance the performance of mammalian cells (Templeton and Young 2018). Many serum-free media containing their own proprietary composition are available now. We also compare the impact of a commercial and a published serum-free media on hybridoma growth and antibody production in the HFB in this study. The purpose of this study was to systematically investigate the critical process parameters and their interactions in HFBs under serum-free conditions in HFB for the MAb production by hybridoma cells. The influence of important operating parameters, such as the culture temperature and the medium circulation rate, on MAb production and cell



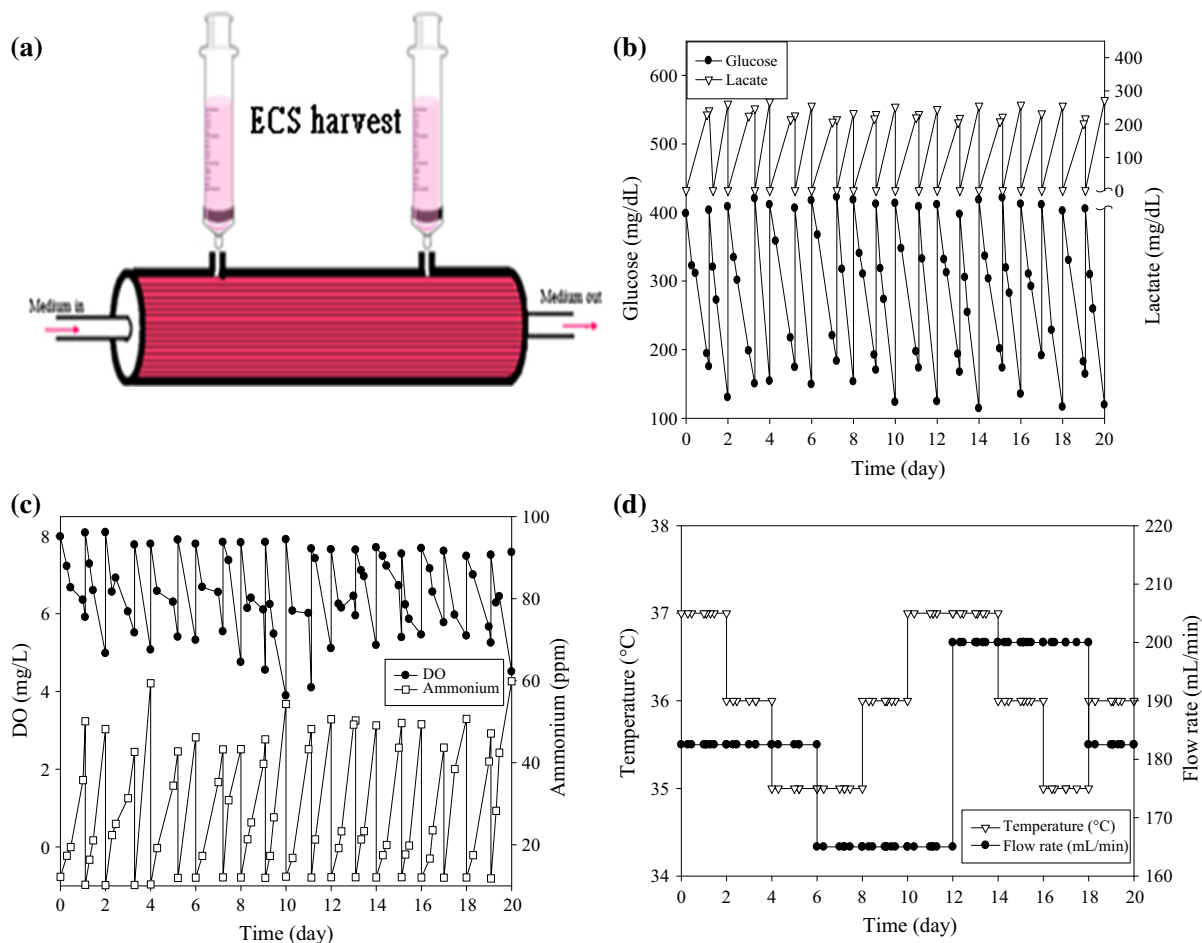


**Fig. 1** Hollow fiber bioreactor (a); glucose and lactate changes using the optimal SDM medium in HFB (b); DO and ammonium using the optimal SDM medium in HFB (c); the operation regime of temperature and circulation rate in HFB (d)

metabolism were statistically evaluated in an HFB system based on the factorial design. The monitoring parameters, including viable cell concentration, cellular morphology, lactate, ammonium production, oxidation–reduction potential (ORP) and glucose consumption, were correlated with the operating parameters using the first-order equations. Effects of the operating conditions on the antibody titer and cell metabolism were analyzed using multiple linear regression analysis.

## Materials and methods

### Cell line and cell culture

The hybridoma cell line (CRL-1754) from American Type Culture Collection (Manassas, VA, USA) was used in this study. These cells produce an MAb against the Fc fragment of human immunoglobulin G2. The cell line was maintained in a spinner flask using a chemically defined hybridoma medium (CD Hybridoma AGT, Thermo Fisher Scientific, Waltham, MA, USA) at 37 °C under a humidified atmosphere of 5% CO<sub>2</sub> and 95% air. The concentration of cells was determined using a Coulter Multisizer 3 (Beckman, Brea, CA, USA). For the analysis of viable cells, cells were harvested from the spinner flask (Bellco,

Vineland, NJ, USA) or an HFB. After mixing with Trypan blue (Sigma-Aldrich, St. Louis, MO, USA) for 5 min, the cell viability was then determined using a hemocytometer.

#### Culture media and devices

Ferric citrate, glutathione, glutamine, and ascorbic acid were purchased from Sigma-Aldrich (St. Louis, MO, USA). SFM4MAB medium and DMEM were purchased from Hyclone (Chicago, IL, USA). Meat peptone was purchased from Conda (Madrid, Spain) and the trace element solution from Corning (Tewksbury, MA, USA). The CDM-HD supplement and the HFB were purchased from Fibercell System (C5011, membrane MWCO: 20-kD, fiber surface area: 2100 cm<sup>2</sup>, Frederick, MD, USA). The fiber bundle retained the cells and their secreted antibody within the ECS, which had a volume of 15 mL. In addition, this disposable bioreactor has a silicone tubing for oxygenation, and its duet pump provides a flexible circulation rate to support nutrient exchange in the cartridges. A supplement of 7.7 µg/mL of ferric citrate (Sigma-Aldrich), 0.625 mg/mL of peptone, and 0.125% (v/v) of trace elements (Corning) were added in the 1:2 mixtures of SFM4MAB medium and DMEM to prepare the optimal SDM medium (Liu et al. 2018a). CDM-HD is a chemically defined, protein-free, and cGMP compliant serum replacement provided by Fibercell System. DMEM supplemented with 10% CDM-HD, termed CDMHD medium, was used in the HFB as a control.

#### Cell culture in spinner flasks and the HFB

The cells were cultured in the 50 mL optimal SDM medium using a 100 mL spinner flask at a 60-rpm rate for further inoculum into the HFB. A total of 10<sup>8</sup> cells were seeded into the ECS to establish a hybridoma culture. The operation of the HFB is based on the instructions in the Fibercell manual. Prior to cell inoculation, the bioreactor was aseptically circulated with phosphate-buffered saline and DMEM. The serum-free medium was circulated at a 150 mL/min rate between the intra-capillary space and the reservoir bottle. The monitoring of glucose and lactate in the reservoir was performed every 8 h using YSI 2300 Glucose Analyzer (Yellow Springs, OH, USA).

#### Operation of the HFB

Before the cell culture, a pre-wash step was carried out to remove the wetting agent from reactor and to equilibrate the system with growth medium and serum proteins. First, 300 mL of PBS was circulated through the HFB two times for 24 h each. Second, 200 mL of DMEM containing 10%v/v FBS was circulated in three cycles for 24 h each. These operations were carried out in a CO<sub>2</sub> incubator in an incubator containing 5% CO<sub>2</sub> and 95% Air at 37 °C temperature. The cells (10<sup>8</sup>) from the spinner flask were suspended in 15 ml of fresh serum-containing medium. The cell suspension was uniformly inoculated into the ECS by the suction and push of syringe. Initially, no circulation was provided to promote the settling of cells on the fiber bundle for 12 h in the incubator. Then, the medium circulation rate between the reservoir and bioreactor was gradually increased from an initial 20 to a final 180 mL/min to obtain the stable cell growth for the first 6 days after inoculation. After the cells in the bioreactor reached a steady state, 15 mL of the ECS content was homogeneously harvested using two syringes every 24 h at the specified culture temperature and pump rate. The specified culture condition was maintained for 48 h and 15-mL content was suctioned for analysis every 24 h. The consumption and production rates were calculated by the equation:

The rate = (measurement<sub>48 h</sub> – measurement<sub>24 h</sub>)/time

The fresh medium was replaced every day, and the spent medium in the reservoir was analyzed to obtain the metabolic parameters. The cells and MAb titer from the ECS content were monitored by inverted microscopy and an ELISA, respectively. In addition, MAb in the ECS withdraw was purified by the elution protocol in the application templates of ÄKTAprime with the aid of HiTrap Protein A column (GE, Logan, Utah, USA). The culture temperature and the circulation rate were changed every 48 h after the completion of the designed culture. The culture conditions were sequentially operated according to the conditions listed in Table 1. When the temperature of the incubator was changed, the incubator needed 0.5 h to reach the set temperature. Based on our results, the cells in the HFB system were stable after 12–24 h of the environment shift. Only an inoculum was applied

**Table 1** Effects of culture temperature and circulation rate on the measuring parameters in the hollow fiber bioreactor by the 2<sup>2</sup> factorial design

Trials Temperature (°C), circulation rate (mL/min)	Trial 1 37, 182.5	Trial 2 <sup>##</sup> 36, 182.5	Trial 3 35, 182.5	Trial 4 35, 165	Trial 5 36, 165
Glucose consumption (mg/dL/h)	12.17	13.08	13.63	12.75	12.96
<sup>a</sup> ΔLactate (mg/dL/day)	272.05	289.05	266.05	239.05	264.05
ΔAmmonium production (ppm/h)	2.18	2.52	1.78	1.63	2.01
ΔDO change (mg/L)	− 3.54	− 3.24	− 3.48	− 4.1	− 5.55
ΔpH (/day); ΔORP (mV/day)	− 1.06; − 57.4	− 1.06; − 56.8	− 0.92; − 46.3	− 1.19; − 55.8	− 1.34; − 81.5
ΔConductivity (mS/day)	10.07	10.34	9.78	14.81	12.44
Viable cells (10 <sup>8</sup> /mL) <sup>b</sup>	3.22	3.33	3.06	2.88	3.05
Predicted viable cells (10 <sup>8</sup> /mL)	3.19	3.311	3.065	2.846	3.102
MAB production (μg/mL)	58.84 ± 0.22 <sup>#</sup>	60.75 ± 0.27	56.67 ± 0.15 <sup>#</sup>	48.34 ± 0.29 <sup>#</sup>	50.00 ± 0.22 <sup>#</sup>
Predicted MAB (μg/mL)	58.8	59.97	57.22	47.89	50.6
Trials Temperature (°C), circulation rate (mL/min)	Trial 6 37, 165	Trial 7 37, 200	Trial 8 36, 200	Trial 9 35, 200	Trial 10 <sup>##</sup> 36, 182.5
Glucose consumption (mg/dL/h)	12.83	12.88	13.08	12.29	12.67
ΔLactate (mg/dL/day)	254.04	267.05	271.05	254.05	286.05
ΔAmmonium production (ppm/h)	1.81	1.58	1.80	1.61	2.285
ΔDO change (mg/L)	− 4.47	− 2.95	− 3.41	− 2.18	− 3.41
ΔpH (/day); ΔORP (mV/day)	− 1.13; − 62.26	− 0.86; − 48.00	− 0.92; − 51.30	− 0.59; − 36.80	− 1.05; − 56.7
ΔConductivity (mS/day)	11.61	8.22	9.78	8.17	11.61
Viable cells (10 <sup>8</sup> /mL) <sup>b</sup>	3.01	3.09	3.32	3.00	3.3
Predicted viable cells (10 <sup>8</sup> /mL)	2.99	3.126	3.258	3.022	3.311
MAB production (μg/mL)	49.54 ± 0.29 <sup>#</sup>	54.21 ± 0.18 <sup>#</sup>	55.61 ± 0.14 <sup>#</sup>	52.84 ± 0.22 <sup>#</sup>	59.95 ± 0.14
Predicted MAB (μg/mL)	49.39	54.39	55.52	52.73	59.97

<sup>a</sup>The definition of Δ = (measurement<sub>48 h</sub> − measurement<sub>24 h</sub>)/time<sup>b</sup>The volume was 20 mL<sup>#</sup>*p* < 0.01 compared to Trial 2 (36 °C, 182.5 mL/min) using the two-tailed Student *T* test (*n* = 3)<sup>##</sup>Trial 2 and Trial 10 were two repeats at the same condition

in the ECS at the starting for the whole experiment and no cells were reseeded into the HFB operation.

#### Analytical methods

The concentrations of glucose and lactate in the spent medium were measured using YSI 2300 STAT (YSI, Yellow Spring, OH, USA) after removing suspended cells by centrifugation at 1000 rpm for 5 min. The metabolic parameters of the hybridoma were analyzed by using the off-line probes, such as the pH probe (WTW, Weilheim, Germany), the conductivity probe (Eutech, Singapore), the oxidation reduction potential

probe (Sensorex, Garden Grove, CA, USA), the ammonium probe (Cole Parmer, Vernon Hills, IL, USA), and the dissolved oxygen (DO) probe (YSI, Yellow Spring, OH, USA). The MAb concentration was analyzed using an enzyme linked immunosorbent assay (ELISA). The 96-well plate (Rochester, NY, USA) was coated with the primary capture antibody against mouse immunoglobulin G (IgG, KPL 01-18-06, Gaithersburg, MD, USA) at room temperature for an overnight incubation. Then the plate was blocked by a blocking buffer (180 μL/well, 3 g skim milk powder and 5 g sucrose in 100 mL PBS). Diluted normal mouse IgG standard (SCBT, Santa Cruz, CA,

USA) and the diluted samples were added to the plate and incubated for 2 h at 37 °C. Then, a detection antibody conjugated with peroxidase (KPL 474-1806, Gaithersburg, MD, USA) was added and incubated for 2 h at 37 °C, followed by a reaction with TMB substrate solution. The reaction was stopped by adding 2 N sulfuric acid (50 µL/well), and the absorbance was measured at 450 nm with an ELISA reader (Molecular Device, Sunnyvale, CA, USA). All measurements were performed in triplicate. The absorbance at 450 nm was measured using a 96-well microplate reader (Molecular Device, Sunnyvale, CA, USA).

#### Polyacrylamide gel electrophoresis (PAGE) analysis

Acrylamide at 12% was used as the resolving gel, and 5.0% acrylamide (VWR, Radnor, PA, USA) was used to prepare the stacking gel. After the gel was completely gelled, the samples and marker (Protech, Taipei, Taiwan) were loaded into the wells. The electrophoresis equipment was Bio-Rad (Hercules, CA, USA) with a fixed voltage of 130 V in the 25 mM tris–glycine buffer (pH of 8.3). After 2 h, the gel was stained with 0.1% coomassie brilliant blue G-250 light for 30 min and was then de-stained with water overnight. The final gel was scanned by the scanner (Biorad, Hercules, CA, USA).

#### Experimental design and statistical analysis

The data from the factorial design were regressed and analyzed by running the procedure of response surface regression (RSREG) in SAS 9.4 software (Cary, NC, USA) and the Data Analysis Tool in Microsoft Excel, respectively. Three-dimensional response surfaces were generated by Sigmaplot (Systat, San Jose, CA, USA) based on the second-order equation. The culture temperature and circulation rate were chosen as the major operation factors for the optimization of MAb production by hybridoma cells in the biopreactor. According to the design of experiment (DoE, Table 1) rule, three temperature conditions (35, 36, 37 °C) and three circulation rates (165, 182.5, 200 mL/min) were designed to explore the operation ranges and find the optimal condition. The effects of the temperature and circulation rate on the cell concentration, antibody titer, glucose, lactate, ammonium, conductivity, pH, and DO were quantitatively analyzed using the linear

regression function in Microsoft Excel 2010. The parameter change per day is defined as the difference between the measurement 48 h and 24 h. Data were reported as means  $\pm$  standard deviations ( $n = 3$ ). The MAB production under different conditions was compared using the two-tailed Student *T* test.

## Results and discussion

### The effects of the culture temperature and the medium circulation rate in the high-density HFB

HFB systems introduce some unique fermentation topics for high cell-density and perfusion cultures that are distinct from suspended flasks and stirred tanks. The influence of the culture temperature and the medium circulation rate on hybridoma growth and antibody production in the HFB was investigated using the low-cost serum-free medium developed in our lab (Liu et al. 2018a). Culture temperature and the medium circulation rate were chosen as the operating variables since they have been reported to affect the cell growth and metabolism in different culture systems (Templeton and Young 2018). The other reasons include their easy implementation and low maintenance fee. The HFB results including the oxidation reduction potential, conductivity, pH, DO as well as the concentrations of glucose, lactate, ammonium, viable cells, cell size, and antibody titer are shown in Table 1. The quantitative relationships between two operating parameters (culture temperature and circulation rate) and the measuring parameters were quantitatively analyzed using polynomial first-order equations (Table 2). The trends of important parameters, such as glucose, lactate, ammonium, and DO during the cultivation are demonstrated in Fig. 1b, c. The rate of glucose consumption in the HFB was 2.92–3.67 g/L/day under the tested conditions. Different temperatures and circulation rates caused lactate production to fall within the range of 2.39–2.89 g/L/day (Table 1). The lactate concentration increased from 0 to 289 mg/dL (2.89 g/L) with an increase in culture time. In the HFB, the lactate concentration was slightly lower than that in prior research (3.0–3.2 g/L) on the low cell-density system (Mercille and Massie 1994). Compared with the low cell concentration status in the culture flask, the

**Table 2** Linear regression coefficients and their *p*-values of temperature and circulation rate on the cell performance of hollow fiber bioreactor

Coefficient	MAb ( $\mu\text{g/mL/day}$ )	$\Delta\text{DO}$ (mg/L)	$\Delta\text{pH}$ (/day)	Glucose consumption (mg/dL/h)	$\Delta\text{Ammonium}$ (ppm/h)	$\Delta\text{ORP}$ (mV/day)	$\Delta\text{Conductivity}$ (mS/day)	Cell concentration (/mL)	$\Delta\text{Lactate}$ (mg/dL/day)
Intercept	54.585 <sup>#</sup> ( $< 0.001$ )	- 3.633 <sup>#</sup> ( $< 0.001$ )	- 1.012 <sup>#</sup> ( $< 0.001$ )	12.833 <sup>#</sup> ( $< 0.001$ )	1.921 <sup>#</sup> ( $< 0.001$ )	- 55.286 <sup>#</sup> ( $< 0.001$ )	10.683 <sup>#</sup> ( $< 0.001$ )	$3.1 \times 10^{8\#}$ ( $< 0.001$ )	266.549 ( $< 0.001$ )
Temperature effect ( <i>p</i> -value)	0.790 (0.667)	- 0.2 (0.393)	- 0.058 (0.222)	- 0.132 (0.496)	0.091 (0.535)	- 4.793 (0.177)	- 0.477 (0.315)	$6.217 \times 10^6$ (0.340)	5.665 (0.408)
Circulation rate effect ( <i>p</i> -value)	2.463 (0.204)	0.93 <sup>#</sup> (0.004)	0.215 <sup>#</sup> (0.002)	- 0.048 (0.800)	- 0.076 (0.605)	10.577 <sup>#</sup> (0.013)	- 2.115 <sup>#</sup> (0.002)	$7.8 \times 10^6$ (0.242)	5.835 (0.395)

Performance = intercept + a  $\times$  temperature + b  $\times$  circulation rate, the value in parentheses was the *p*-value

<sup>#</sup>*p* < 0.01

oxygen and supply in the HFB was sufficient to maintain the regular metabolism of the high cell-density culture. The specific condition of temperature and circulation rate was maintained for 48 h and shifted to next operation using the regime shown in Fig. 1d. The trends of the DO and ammonium in the HFB medium are shown in Fig. 1c. DO, having a limiting solubility in the medium (Fontova et al. 2018), is supplied by air diffusion using the silicon tubing in the HFB. The tested circulation rates could maintain an oxygen concentration above 4 ppm for cell growth. The DO decreased steadily from 8 to 4 ppm every 24 h as the cells gradually grew. After withdrawing the cells in the ECS and replacing the medium, the DO repeatedly reached 8 ppm in this system. A culture temperature reduction resulted in a cellular metabolism reduction, bringing about a decrease in the oxygen requirement (Chen et al. 2004). In addition, increase in oxygen solubility in the medium was observed at lower temperatures. The oxygen supply was sufficient for the high-density cultures in our tested conditions. The ammonium accumulation in the medium ranged from 38 to 60 ppm within 24 h, corresponding to the rate of 1.58–2.52 ppm/h (Table 1). A high ammonium concentration in the culture medium has been reported to be toxic and inhibitory for mammalian cell growth (Legazpi et al. 2005). In the HFB, 60 ppm of ammonium in the medium did not show harmful effects on the cells. Ammonium and lactate in the medium were indicators for the medium's deterioration and waste accumulation. When the concentration of ammonium ion was close to 65 ppm or lactate close to 2.6 g/L, we replaced the medium to maintain the stable and healthy cells.

The quantitative relationships of the culture temperature and the circulation rate on the cell concentration, antibody titer, glucose, lactate, ammonium, conductivity, pH, and DO are shown in Table 2. The magnitude and sign of the linear regression constants can be used to identify the influence of the operation parameters on the measuring parameters, such as glucose consumption or antibody production. When the coefficient is relatively large, it has more significant effects on the response than a small coefficient. In addition, an operation variable having a positive coefficient can increase the response, and one having a negative coefficient can decrease the response when increasing the operation variable. For example, an

increase in the temperature and circulation rate would enhance the glucose consumption and lactate production since their regression coefficients are positive. The circulation rate had a significant impact on the oxygen consumption (or DO), pH, and ORP ( $p < 0.05$ ), as indicated in Table 2. The temperatures tested (35, 36, 37 °C) in the factorial experiments had minor impacts on the measuring parameters ( $p > 0.05$ ) in Table 2 using the linear regression model. However, low culture temperature ( $< 31$  °C) has been reported to be harmful to CHO cell growth (Coronel et al. 2016).

The ORP decreased from positive to negative when the culture duration increased. The consumption of the reducing substance and the accumulation of the oxidative metabolites from the cells contributed to the negative ORP in the spent medium after 24 h of cultivation. The ORP in the culture process has been verified as an indicator to monitor the metabolic flux distribution towards the desired MAb products (Higareda et al. 1997). Recently, an aeration strategy using the redox potential was developed for ethanol production in yeast fermentation (Liu et al. 2016). On-line measurements of ORP and oxygen uptake rate and their control algorithms have successfully reduced the accumulation of metabolic wastes and improved monoclonal antibody production in hybridoma batch cultures (Li et al. 2010). Several factors contribute to the oxidation reduction potential change, including the accumulation of lactate or ammonium, the depletion of glucose or glutamine, and intracellular metabolic changes in hybridoma cells (Higareda et al. 1997). The ORP decrease rate  $> 60$  mV/day could be an indicator for the good cell status in the HFB as indicated in Table 2.

The antibody and metabolites were sampled and analyzed for the ten trials. The titer of MAb ranged around 50–60 µg/mL when the culture temperature decreased from 37 to 35 °C (Table 1). The results indicate that the culture temperature in the HFB affected the hybridoma cells to produce antibody. The antibody production was increased when the culture temperature was reduced from 37 to 36 °C, proving that lowering the culture temperature helps to improve the accumulation of antibody. The hypothermic treatment also slightly influenced hybridoma's metabolism since lactate and ammonium generation as well as glucose and oxygen consumption were negatively affected. The results of Tables 1 and 2 are used to fit

the linear models of temperature and circulation rate to obtain the first-order equations in Table 2, which could provide the quantitative evaluation of the operation parameters. Some researchers also found that hypothermia benefitted the urokinase production in a high-density bioreactor (Khaparde and Roychoudhury 2012). However, a reduction of the culture temperature from 36 to 35 °C could not further enhance the MAb production in this HFB system. The specific MAb production rate and the titer in the optimal SDM medium under different culture temperatures are demonstrated in Fig. 2a, b. The cells in the low culture temperature had a higher specific MAb production rate than those in 37 °C. For example, the cells in 35 °C had a specific MAb production rate of 0.154, which was 30% higher than that (0.118 pg/cell/day) cultivated in 37 °C and the 200 mL/min circulation rate. The highest MAb titer among 10 trials was 60.75 µg/mL at 36 °C and 182.5 mL/min, which was quite close to the maximal point predicted by the second-order response model (Table 1). Importantly, the MAb titers in the nine conditions using two serum-free media were compared and their individual difference was significant as indicated in Fig. 2b, d.

The culture temperature affects the physiology and metabolism of mammalian cells (Zhang et al. 2015). Moreover, a decrease in the culture temperature results in a decrease in cellular metabolism, bringing about a decrease in the oxygen requirement (Coronel et al. 2016). In addition, a minor increase in oxygen solubility is expected at lower temperatures. Animal cells under mild hypothermic conditions (33–36 °C) have been found to induce a growth reduction in cells within the S or G1 phase of the cell cycle. In addition to a growth arrest-induced increase in specific productivity, the cultivation of cells under mild hypothermic conditions offers other relevant advantages: extended culture durations and decreased O<sub>2</sub> demand in a suspension-type culture (Sunley and Butler 2010). For example, a decrease in the culture temperature resulted in a significant increase in urokinase production using HT-1080 cells (Gramer et al. 2003). Mild hypothermic treatment combined with valeric acid can enhance productivity and a higher secretory capacity in a recombinant CHO cell line (Coronel et al. 2016). However, the effect of low culture temperature on specific productivity has been found to be cell line- or clonal-dependent (Sung et al. 2004). A mild



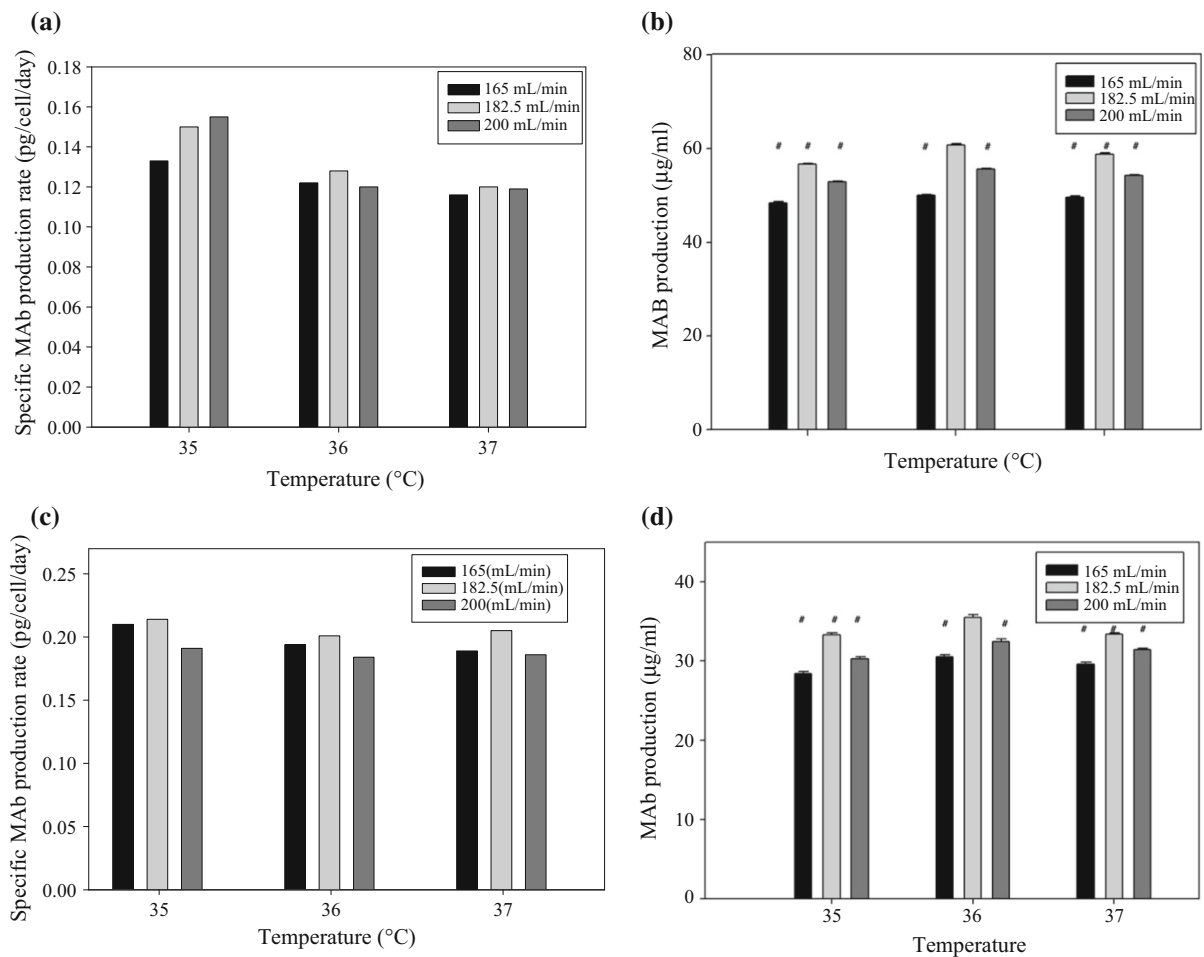


**Fig. 2** Effects of culture temperature and circulation rate on the specific MAb production rate (a) and antibody production (b) in the optimal SDM medium. The results of culture temperature and circulation rate on the specific MAb production rate (c) and

antibody production (d) in the CDMHD medium.  $^{\#}p < 0.01$  compared to Trial 2 (36 °C, 182.5 mL/min) using the two-tailed Student *T* test ( $n = 3$ )

hypothermic culture has been reported to increase the production of recombinant proteins in mammalian cells by inhibiting the progression of the cell cycle. This arrest increases the proportion of cells in the G1-phase of the cell cycle, and subsequently increases their specific productivity of the targeted protein through the up-regulation of family members of the cyclin-dependent kinase inhibitor (Sunley and Butler 2010). In addition, low temperature-induced cellular effects include increased phosphoglycerate kinase expression, extended culture durations, reduced overall nutrient uptake, improved protein sialylation, and a decreased sensitivity to pro-apoptotic agents (García Münzer et al. 2015).

Several mathematical models for nutrient transport in HFB equipped with different fiber materials have been used to understand and simulate the transport phenomena (De Napoli et al. 2014). The detailed analysis of nutrients and wastes metabolized by hybridoma under the hypothermic condition in the HFB is still under investigation. The medium circulation provides nutrients and oxygen and removes metabolic wastes including urea, carbon dioxide and lactate produced by the cells. There is a continuous exchange of oxygen and carbon dioxide between the medium in the silicone tubing and air in the incubator (Eisenstein 2006). The circulation rate affects the frequency of the exchange rate of the medium and gas.

The gross filtration rate between the 30-kD MWCO fiber has been estimated to be approximately 15 mL/(min cm<sup>2</sup> mmHg pressure) under the circulation rate of 165 mL/min (Cadwell 2004). Therefore, hybridoma growth and MAb productivity in an HFB device can affect the medium circulation rate. The effects of the medium circulation rate and culture temperature on MAb production are shown in Fig. 2b. An increase

in the medium circulation rate from 165 up to 182.5 mL/min increased MAb production. However, the MAb production of hybridoma reached a plateau when the circulation rate increased to 200 mL/min at three tested temperatures. In contrast, the increase in the circulation rate did not enhance the specific MAb production at 36 and 37 °C. The reasons the circulation rate affected the DO, pH, and oxidation reduction

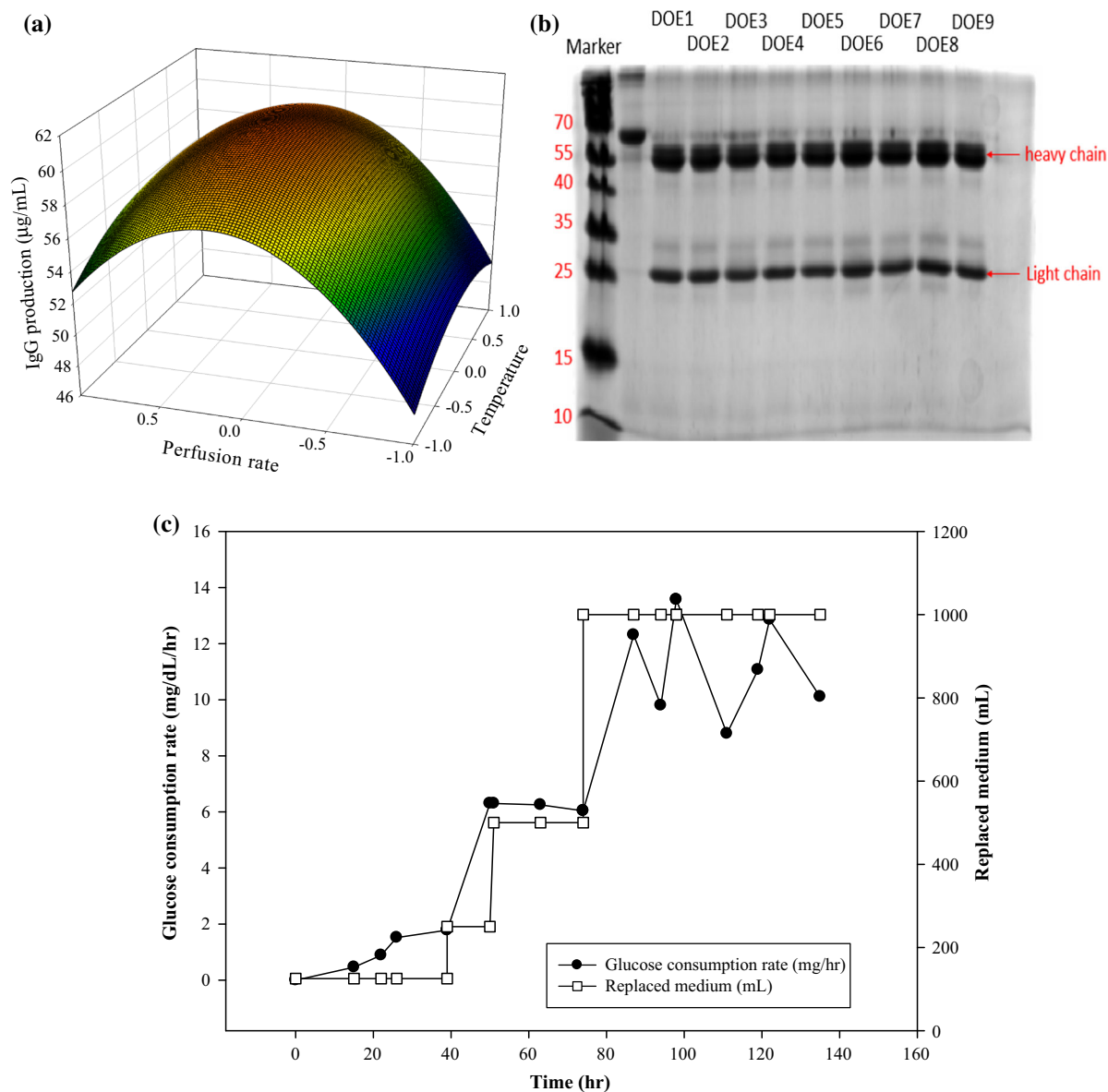


**Fig. 3** Response surface of temperature and circulation rate on MAb production in the HFB (a). SDS-PAGE analysis of MAb produced in hollow fiber bioreactor by hybridoma using the

optimal SDM medium (b). Glucose consumption rate and the medium volume in the HFB at 36 °C and 180 mL/min (c)



potential of the medium may be related to the greater oxygen supply at higher rates. The increase in the medium circulating rate also resulted in reduced conductivity, which related to the decreased number of ions and cations metabolized by the cells (Table 2). These linear equations provided the simple evaluation of the impact of the HFB conditions on the hybridoma. In our linear modes, the interaction of temperature and circulation rate on the metabolism of hybridoma in HFB could not be discussed. We will optimize the culture temperature and medium circulation rate on antibody production using the response surface model in the following section.

Trial 2 and Trial 10 in Table 1 were two repeats which were sequentially operated at the third and the 18th day using the condition of 36 °C and the circulation rate of 182.5 mL/min (Fig. 1d). The results from two distinct trials including glucose consumption, lactate production, and cell concentration were very similar. The respective MAb productions in two trials were  $60.75 \pm 0.27$  and  $59.05 \pm 0.14$  µg/mL as indicated in Table 1. The cells in the HFB remained in the steady state even after the different conditions within a 20-day period. In another HFB culture, the glucose consumption rate of the cells raised gradually from 2 to 12 mg/dL/h and the consumption was stable within 80–140 h at the condition of 36 °C and 180 mL/min circulation rate (Fig. 3c). The average of the seven consumption data during the 80–140 h was around 11.5 mg/dL/h which very close to the consumption rate of Trial 2 and Trial 10 in a 20-day culture (Table 1). These results indicated the cells maintained in the stable condition during the HFB culture. The similarity in the three experiments also indicated the repeatability of our HFB platform by using the following procedure. The cells and contents were suctioned and the whole medium was replaced for analysis every 24 h in a specified 48-h culture condition. A two-day period was satisfactory to obtain the characteristic data since the cells reached the steady state. A similar approach has been reported (Yang et al. 2004; Eghbali et al. 2016). The duration of one repeated culture was also 48 h for the immobilized cells in the fibrous matrix system. The authors also choose a single inoculation for a series of experiments to demonstrate the system's fermentation characteristics. Every 48 h, a new perfusion was restarted for the comparison after the immobilized system reaches the steady state. In our HFB system, the time needed for

reaching the new temperature and the new circulation rate was around 20 min.

### Optimization of hybridoma culture in the HFB

Traditionally, process optimization has been carried out by keeping an operation parameter as a constant and investigating another parameter. This technique needs many experiments, which leads to increases in time, the consumption of reagents, and materials (Yolmeh and Jafari 2017). To overcome this problem, the statistical design has been adapted herein to optimize the operation condition of an HFB in serum-free conditions. The full factorial design for the culture temperature and the circulation rate is shown in Table 1. The MAb production and cell growth in the factorial design data were further regressed by SAS 9.4 software to obtain the second-order polynomials (Eqs. 1 and 2). The response polynomial predicted that the MAb production was 60.27 µg/mL at the optimal condition of 36.2 °C and 185.65 mL/min. The real MAb titer was 60.39 µg/mL in the HFB, which was close to the prediction (60.27 µg/mL) using the response surface model. The F-value and its probability for the full quadratic equation for MAb production was 59.86 and 0.0008, respectively. The determination coefficient ( $R^2$ ) indicated that the second-order response surface of MAb production could explain 98.68% of the variability. The maximal titer of MAb production could be identified in the three-dimensional response surface plot in Fig. 3a around the coordinate position of (0.21, 0.18), which was equivalent to the real condition of 36.2 °C and 185.65 mL/min. Table 1 indicates that good agreement existed between the experimental growth (MAb) and the values predicted by the response models (Eqs. 1 and 2). These models could predict the MAb titer and cell density with prediction errors < 2%, as indicated in Table 1. However, the cell samples from the ECS may not be representative of the whole cell culture in HFB systems since there was poor mixing in the compact ECS. In addition, the HFB condition (36 °C and 182.5 mL/min) near the optimal operation had been repeated twice in trial 2 and 10 of Table 1 for antibody production. The antibody titers were 60.75 and 59.05 µg/mL, which also close to the model prediction. These results confirmed that the second-order model could describe the antibody production of hybridoma in the HFBs.

**Table 3** Effects of different serum-free CDMHD on hybridoma metabolisms in hollow fiber bioreactor

Parameter (°C, mL/min)	CDMHD		
	Trial 2 (36, 182.5)	Trial 5 (36, 165)	Trial 8 (36, 200)
Glucose consumption (mg/dL/h)	5.45	5.29	5.42
ΔAmmonium production (ppm/h)	0.84	0.65	0.79
ΔDO change (mg/L)	− 1.13	− 0.88	− 1.02
ΔpH (/day)	− 0.36	− 0.21	− 0.31
ΔORP (mV/day)	− 17.80	− 12.70	− 15.10
ΔConductivity (mS/day)	5.94	4.36	5.49
ΔLactate (mg/dL/day)	96.30	88.50	94.80
MAB production (μg/mL)	35.48 ± 0.38	30.51 ± 0.22 <sup>#</sup>	32.46 ± 0.22 <sup>#</sup>
Viable cells (/mL)	1.61 × 10 <sup>8</sup>	1.51 × 10 <sup>8</sup>	1.55 × 10 <sup>8</sup>
Specific MAB production (pg/cell/day)	0.22	0.20	0.21
Cell size (μm)	16.85	16.98	16.79

<sup>#</sup>*p* < 0.01 compared to Trial 2 (36 °C, 182.5 mL/min) using the two-tailed Student *T* test (*n* = 3)

$$\begin{aligned} \text{MAB production } (\mu\text{g/mL}) = & 59.97 + 0.79 \times X_1 \\ & + 2.46 \times X_2 - 1.82 \\ & \times X_3 - 6.77 \times X_2^2 \\ & + 0.04 \times X_1 \times X_2 \end{aligned} \quad (1)$$

$$\begin{aligned} \text{Viable cells } (\times 10^8/\text{mL}) = & 3.32 + 0.06 \times X_1 + 0.08 \\ & \times X_2 - 0.18 \times X_1^2 \\ & - 0.13 \times X_2^2 - 0.01 \\ & \times X_1 \times X_2 \end{aligned} \quad (2)$$

We further verified the quality of the antibody remaining in the ECS from different culture conditions. The PAGE results of the samples using PAGE are shown in Fig. 3b. The characteristic bands of the antibody's heavy and light chains appeared at the 25-kD and 50-kD positions, which were consistent with the literature results of the antibody production by hybridoma (Liu et al. 2007). Antibody quality can be substantially affected by process variables, such as glucose and nutrient concentrations. Our data demonstrated that not only can the antibody production in HFBs be stable, but the MAB can avoid degradation, like smearing bands on the PAGE gel. Additionally, the cell morphologies after cultivation in the HFB also indicated that most cells had good growth in the different culture conditions. Most remained round. No cell deformation was observed from the light microscopy. The diameter of cell spheroid distributed from 16.5 to 17.5 μm as indicated in Table 3. These data

indicated that the HFB was a safe and convenient device for high-density cultures and the production of antibodies. The operating parameters (temperature and circulation rate) did not deteriorate the process outputs, such as performance indicators and quality attributes. The response surface methodology could improve the antibody titer of an HFB system by adjusting the culture temperature and circulation rate. This technique could use a second-order equation to visualize the single and combined effects of the operating parameters on the responses, such as antibody titers and cell growth (Fig. 3a). In addition, this optimization strategy could reduce the number of experiments and could evaluate the interactive effects among the operation variables studied compared to the one-variable at-a-time method. Recently, the researchers described the effect of media composition upon glycosylation using the response surface methodology and successfully predicted the glycosylation affected by media (Grainger and James 2013). Our results also suggested that adopting a statistical analysis of culture conditions was useful to optimize the MAB production by hybridoma cells. The impact of another serum-free medium on hybridoma growth and antibody production in the HFB is investigated in the following section to explore the HFB's flexibility.

Effects of two serum-free media on the metabolism of hybridoma cells in the HFB

The complex nutrients of medium affect the hybridoma physiology, metabolism, growth, and MAB

production (Even et al. 2006). Recently, a serum-free medium has been developed for the hybridoma culture by our lab (Liu et al. 2018a). Another commercial serum-free medium, i.e. DMEM plus 10% CDM-HD (Fibercell) was termed CDMHD. The implement of another culture medium in HFB could explore the operation flexibility of the bioreactor. The operation regime of temperature and circulation rate using CDMHD in HFB is shown in Fig. 1d. The CDMHD was compared with our serum-free medium using three circulation rates at the temperature of 36 °C. The cells cultivated in the optimal SDM medium had approximately 1.7-fold MAb production compared to that in the CDMHD medium (Fig. 2c, d). All biological and chemical parameters including the cell concentration, antibody titer, glucose, lactate, ammonium, conductivity, pH, and DO in the CDMHD (Table 3) were lower than that in the optimal SDM medium (Table 1). This optimal medium containing three supplements (peptone, ferric citrate, and trace elements) in the basal medium (1:2 mixtures of SFM4MAB and DMEM) could support more cells in the bioreactor. The CDMHD medium does not provide the information of nutrient composition. The production of metabolic byproducts like ammonium and lactate by hybridoma in CDMHD was lower than those in the optimal medium. The cells cultivated in both media at the circulation rate of 182.5 mL/min had a higher antibody production than cells in other circulation rates. The specific MAb production of the hybridoma in the CDMHD medium was better than that in the optimal SDM medium. The specific antibody production rate was 0.214 pg/cell/day at 35 °C in the commercial CDM-HD medium, which was slightly higher than that (0.17 pg/cell/day) in the optimal SDM (Table 3). However, the two-fold higher cell population ( $3.33 \times 10^8/\text{mL}$ ) in the optimal SDM sustained higher MAb production than that in the CDM-HD medium ( $1.61 \times 10^8/\text{mL}$ ). The cells in the optimal SDM medium produced more antibody than those in the CDMHD medium. The higher MAb titer was attributed to better cell growth in the optimal SDM. The hybridoma cells grown in the two media had distinct performance in their glucose and oxygen consumption, lactate and ammonium production, and antibody production at tested circulation rates. Among the tested rates, the antibody production was still relatively high at a culture rate of 182.5 mL/min. The differences in the monitoring parameters in the two

culture media were mostly related with the cell concentration in the HFB. While the MAb specific production rate in the CDMHD medium was higher, the higher cell amount in the HFB led to better MAb production in the optimal SDM medium. The medium formulation can dramatically influence the cell metabolism and antibody yield in the HFB. The high-density and continuous culture technique has the potential to improve the bottlenecks of biologic manufacturing. HFBs may contribute to improving volumetric antibody productivity (Croughan et al. 2015). However, some problems have been reported for continuous operations, including the long-term operability and maintenance of sterility, poor short-term process flexibility, and the genetic instability of recombinant cells. Single-use HFB may provide some advantages, including reduced contamination risks of autoclaving reactors, low initial investment costs, low operating costs, and simple configuration. In contrast, the perfusion fermentation in a stirred tank bioreactor needs a spin filter for the separation of suspended cells or microcarriers with the culture medium (Yun et al. 2000). Many countries have imposed some bans on the *in vivo* ascites technique for MAb production using mice. Therefore, the HFB is a valuable alternative to murine ascites for laboratory-scale MAb production.

#### Comparison of antibody production in two systems

The hybridoma growth and antibody production in the agitated spinner flask and the HFB were evaluated using the Optimal SDM (Table 4). The immobilized cells in the HFB were 24-fold higher than the suspended cells in the flask. The IgG production in the HFB was 17-fold higher than that in the flask. In Table 4, the immobilized cells in the HFB were collected by repeatedly pipetting and there might be some cells remained in the ECS (Liu et al. 2018a). The specific MAb production in the agitated flask was slight higher than that in the immobilized HFB system. Basically, the batch operation in the spinner flask was distinct from the perfusion operation in HFB. The HFB platform could support higher cell density, easier operation, and lower shear-rate environment compared to the agitated system.

**Table 4** Comparison of antibody production in HFB and spinner flask

	Hollow fiber bioreactor	Spinner flask (Liu et al. 2018a)
MAB concentration ( $\mu\text{g/mL}$ )	$55.61 \pm 0.14$	$3.28 \pm 0.23^{\#}$
Total cells	$3.06 \times 10^9$	$1.25 \times 10^8$

The flow rate of HFB was 182.5 mL/min at 37 °C and the medium volume of spinner flask was 50 mL. n = 3

$^{\#}p < 0.01$  compared to HFB system using the two-tailed Student *T* test (n = 3)

## Conclusion

A high cell-density hybridoma culture in an HFB was successfully developed herein. The culture temperature and medium circulation rate affected the cell metabolism and antibody production of hybridoma cells. A mildly hypothermic condition of 36 °C and a circulation rate of 182.5 mL/min could support the maximal antibody titer of 60.75  $\mu\text{g/mL}$  in the HFB system. Two kinds of serum-free media could be successfully applied to this perfusion system and maintain hybridoma growth and antibody production. By monitoring the cell metabolic parameters, the HFB platform was proved to be stable under different operation conditions. The changes in the measuring parameters were directly related to cell metabolism and linear relationships between the cell concentration and antibody titer could be obtained. When the concentration of ammonium ion was close to 65 ppm or lactate close to 2.6 g/L, the medium was replaced to maintain the stable and healthy cells at the high cell concentration of  $3.33 \times 10^8/\text{mL}$  more than 20 days. Our results clearly indicated the HFB had the potential for high density culture and continuous antibody production.

**Acknowledgements** We express gratitude to Ministry of Science and Technology (MOST 106-2221-E-182-050, 108-2221-E-182-039), Chang Gung University (BMRP 758) and Chang Gung Memorial Hospital (CMRPD2G0282, 2H0071, 2H0072) for funding and supporting this research. We thank the valuable suggestions for bioreactor operation from Frank R. H. Wang, at United BioPharma, Hsinchu, Taiwan.

## Compliance with ethical standards

**Conflicts of interest** The authors declare that no conflicting financial interests exist.

## References

- Becerra S, Berrios J, Osses N, Altamirano C (2012) Exploring the effect of mild hypothermia on CHO cell productivity. *Biochem Eng J* 60:1–8
- Cadwell JJS (2004) New developments in hollow-fiber cell culture. *Am Biotechnol Lab* 22(8):14
- Chen ZL, Wu BC, Liu H, Liu XM, Huang PT (2004) Temperature shift as a process optimization step for the production of pro-urokinase by a recombinant Chinese hamster ovary cell line in high-density perfusion culture. *J Biosci Bioeng* 97:239–243
- Coronel J, Klausing S, Heinrich C, Noll T, Figueredo-Cardero A, Castilho LR (2016) Valeric acid supplementation combined to mild hypothermia increases productivity in CHO cell cultivations. *Biochem Eng J* 114:101–109
- Croughan MS, Konstantinov KB, Cooney C (2015) The future of industrial bioprocessing: batch or continuous? *Biotechnol Bioeng* 112(4):648–651
- De Napoli IE, Zanetti EM, Fragomeni G, Giuzio E, Audenino AL, Catapano G (2014) Transport modeling of convection-enhanced hollow fiber membrane bioreactors for therapeutic applications. *J Membr Sci* 471:347–361
- Del Val JJ, Kontoravdi C, Nagy JM (2010) Towards the implementation of quality by design to the production of therapeutic monoclonal antibodies with desired glycosylation patterns. *Biotechnol Prog* 26(6):1505–1527
- Diban N, Stamatiadis D (2014) Polymeric hollow fiber membranes for bioartificial organs and tissue engineering applications. *J Chem Technol Biotechnol* 89(5):633–643
- Donini M, Marusic C (2019) Current state-of-the-art in plant-based antibody production systems. *Biotechnol Lett* 41(3):335–346
- Eghbali H, Nava MM, Mohebbi-Kalhari D, Raimondi MT (2016) Hollow fiber bioreactor technology for tissue engineering applications. *Int J Artif Organs* 39(1):1–15
- Eisenstein M (2006) Thinking outside the dish. *Nat Methods* 3(12):1035–1043
- Even MS, Sandusky CB, Barnard ND (2006) Serum-free hybridoma culture: ethical, scientific and safety considerations. *Trends Biotechnol* 24(3):105–108
- Fontova A, Lecina M, López-Repullo J, Martínez-Monge I, Comas P, Bragós R, Cairó JJ (2018) A simplified implementation of the stationary liquid mass balance method for on-line OUR monitoring in animal cell cultures. *J Chem Technol Biotechnol* 93(6):1757–1766
- García Münzer DG, Ivarsson M, Usaku C, Habicher T, Soos M, Morbidelli M, Pistikopoulos EN, Mantalaris A (2015) An unstructured model of metabolic and temperature

- dependent cell cycle arrest in hybridoma batch and fed-batch cultures. *Biochem Eng J* 93:260–273
- Grainger RK, James DC (2013) CHO cell line specific prediction and control of recombinant monoclonal antibody n-glycosylation. *Biotechnol Bioeng* 110(11):2970–2983
- Gramer MJ, Maas J, Lieberman MM (2003) Use of hollow fiber systems for rapid and direct scale up of antibody production from hybridoma cell lines cultured in CL-1000 flasks using BD Cell MAb medium. *Cytotechnology* 42:155–162
- Higareda AE, Possani LD, Ramírez OT (1997) The use of culture redox potential and oxygen uptake rate for assessing glucose and glutamine depletion in hybridoma cultures. *Biotechnol Bioeng* 56:555–563
- Khaparde SS, Roychoudhury PK (2012) Effect of low culture temperature on urokinase production in hollow fiber reactor. *Appl Biochem Biotechnol* 168:1655–1663
- Kishishita S, Nishikawa T, Shinoda Y, Nagashima H, Okamoto H, Takuma S, Aoyagi H (2015) Effect of temperature shift on levels of acidic charge variants in IgG monoclonal antibodies in Chinese hamster ovary cell culture. *J Biosci Bioeng* 119(6):700–705
- Legazpi L, Díaz J, Laca A, Díaz M (2005) Kinetic analysis of hybridoma cell culture in a protein-free medium: substrate and agitation effects. *Biochem Eng J* 26(2–3):122–130
- Li F, Vijayasankaran N, Shen A, Kiss R, Amanullah A (2010) Cell culture processes for monoclonal antibody production. *mAbs* 2(5):466–479
- Liu H, Gaza-Bulsecu G, Chumsae C, Newby-Kew A (2007) Characterization of lower molecular weight artifact bands of recombinant monoclonal IgG1 antibodies on non-reducing SDS-PAGE. *Biotechnol Lett* 29(11):1611–1622
- Liu CG, Hao XM, Lin YH, Bai FW (2016) Redox potential driven aeration during very-high-gravity ethanol fermentation by using flocculating yeast. *Sci Rep* 6:25763
- Liu CH, Liu YX, Wu WC (2018a) Facile development of medium optimization for antibody production: implementation in spinner flask and hollow fiber reactor. *Cytotechnology* 70:1631–1642
- Liu M, Wang J, Tang H, Fan L, Zhao L, Wang HB, Zhou Y, Tan WS (2018b) Cell culture medium supplemented with taurine decreases basic charge variant levels of a monoclonal antibody. *Biotechnol Lett* 40(11–12):1487–1493
- Mercille S, Massie B (1994) Induction of apoptosis in nutrient-deprived cultures of hybridoma and myeloma cells. *Biotechnol Bioeng* 44:1140–1152
- Sen S, Roychoudhury PK (2013) Step-up/step-down perfusion approach for increased mAb 520C9 production by a hybridoma cell line. *Biotechnol Lett* 35(2):153–163
- Sung KY, Sun OH, Gyun ML (2004) Enhancing effect of low culture temperature on specific antibody productivity of recombinant Chinese hamster ovary cells: clonal variation. *Biotechnol Prog* 20(6):1683–1688
- Sunley K, Butler M (2010) Strategies for the enhancement of recombinant protein production from mammalian cells by growth arrest. *Biotechnol Adv* 28(3):385–394
- Templeton N, Young JD (2018) Biochemical and metabolic engineering approaches to enhance production of therapeutic proteins in animal cell cultures. *Biochem Eng J* 136:40–50
- Vermasvuori R, Hurme M (2011) Economic comparison of diagnostic antibody production in perfusion stirred tank and in hollow fiber bioreactor processes. *Biotechnol Prog* 27(6):1588–1598
- von Stosch M, Davy S, Francois K, Galvanauskas V, Hamelink JM, Luebbert A, Mayer M, Oliveira R, O’Kennedy R, Rice P, Glassey J (2014) Hybrid modeling for quality by design and PAT-benefits and challenges of applications in biopharmaceutical industry. *Biotechnol J* 9(6):719–726
- Yang ST, Luo J, Chen C (2004) A fibrous-bed bioreactor for continuous production of monoclonal antibody by hybridoma. *Adv Biochem Eng Biotechnol* 87:61–96
- Yolmeh M, Jafari SM (2017) Applications of response surface methodology in the food industry processes. *Food Bioprocess Technol* 10(3):413–433
- Yun JW, Lee SY, Choi BW, Oh HK, Kim SH, Byun TH, Park SY (2000) Continuous stable production of von Willebrand factor monoclonal antibody in spin filter bioreactor with bleeding technology. *Biotechnol Bioprocess Eng* 5(2):130–135
- Zhang X, Sun YT, Tang H, Fan L, Hu D, Liu J, Liu X, Tan WS (2015) Culture temperature modulates monoclonal antibody charge variation distribution in Chinese hamster ovary cell cultures. *Biotechnol Lett* 37(11):2151–2157

**Publisher’s Note** Springer Nature remains neutral with regard to jurisdictional claims in published maps and institutional affiliations.



Article

# Water-Soluble Fullerenol C<sub>60</sub>(OH)<sub>36</sub> toward Effective Anti-Air Pollution Induced by Urban Particulate Matter in HaCaT Cell

Chiang-Wen Lee <sup>1,2,3</sup>, Miao-Ching Chi <sup>1,4,5</sup>, Kuo-Ti Peng <sup>3,6</sup>, Yao-Chang Chiang <sup>1,3</sup> ,  
Lee-Fen Hsu <sup>1,4,7</sup>, Yi-Ling Yan <sup>1,8</sup>, Hsing-Yen Li <sup>8,9</sup>, Ming-Chun Chen <sup>8</sup>, I-Ta Lee <sup>10,\*</sup> and  
Chian-Hui Lai <sup>8,9,\*</sup>

- <sup>1</sup> Department of Nursing, Division of Basic Medical Sciences, and Chronic Diseases and Health Promotion Research Center, Chang Gung University of Science and Technology, Puzi City, Chiayi County 613, Taiwan
- <sup>2</sup> Research Center for Industry of Human Ecology and Research Center for Chinese Herbal Medicine, Chang Gung University of Science and Technology, Guishan District, Taoyuan City 333, Taiwan
- <sup>3</sup> Department of Orthopaedic Surgery, Chang Gung Memorial Hospital, Puzi City, Chiayi County 613, Taiwan
- <sup>4</sup> Department of Respiratory Care, Chang Gung University of Science and Technology, Puzi City, Chiayi County 613, Taiwan
- <sup>5</sup> Division of Pulmonary and Critical Care Medicine, Chiayi Chang Gung Memorial Hospital, Kaohsiung 833, Taiwan
- <sup>6</sup> College of Medicine, Chang Gung University, Guishan District, Taoyuan City 333, Taiwan
- <sup>7</sup> Division of Neurosurgery, Department of Surgery, Chang Gung Memorial Hospital, Puzi City, Chiayi County 613, Taiwan
- <sup>8</sup> Graduate Institute of Biomedical Engineering, National Chung Hsing University, Taichung 402, Taiwan
- <sup>9</sup> Department of Medicinal and Applied Chemistry, Kaohsiung Medical University, Kaohsiung 807, Taiwan
- <sup>10</sup> School of Dentistry, College of Oral Medicine, Taipei Medical University, Taipei 110, Taiwan
- \* Correspondence: itlee0128@tmu.edu.tw (I.-T.L.); chianhuilai@dragon.nchu.edu.tw (C.-H.L.);  
Tel.: +886-2-27361661 (ext. 5162) (I.-T.L.); +886-4-22840733 (ext. 634) (C.-H.L.)

Received: 17 July 2019; Accepted: 28 August 2019; Published: 30 August 2019



**Abstract:** Particulate matter (PM), a widespread air pollutant, consists of a complex mixture of solid and liquid particles suspended in air. Many diseases have been linked to PM exposure, which induces an imbalance in reactive oxygen species (ROS) generated in cells, and might result in skin diseases (such as aging and atopic dermatitis). New techniques involving nanomedicine and nano-delivery systems are being rapidly developed in the medicinal field. Fullerene, a kind of nanomaterial, acts as a super radical scavenger. Lower water solubility levels limit the bio-applications of fullerene. Hence, to improve the water solubility of fullerene, while retaining its radical scavenger functions, a fullerene derivative, fullerenol C<sub>60</sub>(OH)<sub>36</sub>, was synthesized, to examine its biofunctions in PM-exposed human keratinocyte (HaCaT) cells. The PM-induced increase in ROS levels and expression of phosphorylated mitogen-activated protein kinase and Akt could be inhibited via fullerenol pre-treatment. Furthermore, the expression of inflammation-related proteins, cyclooxygenase-2, heme oxygenase-1, and prostaglandin E2 was also suppressed. Fullerenol could preserve the impaired state of skin barrier proteins (filaggrin, involucrin, repetin, and loricrin), which was attributable to PM exposure. These results suggest that fullerenol could act against PM-induced cytotoxicity via ROS scavenging and anti-inflammatory mechanisms, and the maintenance of expression of barrier proteins, and is a potential candidate compound for the treatment of skin diseases.

**Keywords:** fullerenol; particulate matter; reactive oxygen species; human keratinocyte cell; antioxidant; anti-inflammation



## 1. Introduction

Exposure to air particulate matter (PMs) through inhalation is correlated with pulmonary dysfunction, cardiovascular disease, atherosclerosis, and hepatic fibrogenesis, and with a higher level of morbidity and mortality [1,2]. Cumulative data from epidemiological studies have shown that exposure to air pollutants could lead to an increase in cardiovascular ischemic events (out-of-hospital cardiac arrests and ischemic heart disease) and enhance atherosclerosis; their possible pathogeneses were also investigated [2–5]. PM exposure affected the functioning of pulmonary and cardiovascular systems, and is also associated with skin aging, skin cancer, and inflammatory responses to allergic skin conditions (atopic dermatitis, eczema, psoriasis, or acne) [6]. The possible pathological mechanisms for PM-induced skin diseases are linked to an increase in reactive oxygen species (ROS) level and inflammatory activity, and a loss of barrier proteins [7]. PMs are complex, heterogeneous mixtures of polyaromatic hydrocarbons, metals, organic toxins, and biological materials. In general, PMs can be grouped into four classes based on their size, as ultrafine particles ( $PM < 0.1 \mu m$ ), fine particles ( $PM < 2.5 \mu m$ ), coarse particles ( $PM 2.5\text{--}10 \mu m$ ), and thoracic particles ( $PM > 10 \mu m$ ) [4]. Among these air pollutant particles, the fine particles ( $PM_{2.5}$ ) have the longest atmospheric half-life of a few days to weeks [4]. PMs can induce the generation of ROS, which potentially triggers oxidative stress and subcellular organelle dysfunction in the cell, and triggers apoptosis by causing DNA damage or lipid peroxidation [8,9].  $PM_{2.5}$  induced endoplasmic reticulum stress, mitochondrial swelling, and autophagy, and caused apoptosis in the human keratinocyte (HaCaT) model and mouse skin tissue [8]. Previously, we had also studied PM-induced toxic effects that were attributable to inflammatory and oxidative stress mechanisms in vitro and in vivo [10].

Fullerene, a nanomaterial, has valuable applications in the biomedicine field. It has been used in skin whitening, sunscreen, or antiaging products in the dermatologic and cosmetic fields, because of its extremely high reactivity to radical species [11]. Since 1995, when the FDA first approved a nano-drug, nanomedicine has constantly revolutionized the treatment of several diseases [12–14]. Fullerene, first discovered in 1985, is a kind of carbon allotrope, and could form a hollow sphere, such as that observed in a soccer ball [15]. Fullerene can be best described as a polygonal structure with 60 carbon atoms that have 60 vertices and 32 faces, which are responsible for its stable configuration [16]. Fullerene is a super radical scavenger with a single  $C_{60}$  molecule that could reportedly include up to 34 methyl radicals onto itself [17]. Fullerene has biomedical functions, such as the induction of photo-induced cytotoxicity for DNA cleavage [18], and antioxidant, anticancer, and antimicrobial activities [19]. However, the poor water solubility of fullerene limits its bio-application; therefore, the water-soluble polyhydroxylated fullerene derivative, fullerenol  $C_{60}(OH)_{36}$ , was introduced in the current study, to perform a bioassay. Fullerenol can reduce the toxic effects of certain hazardous toxicants [20], infarct volume, and cerebral inflammation during ischemic stroke in normotensive and hypertensive rats [21]. Besides, fullerenol  $C_{60}(OH)_{36}$  can protect the human erythrocyte membrane against high-energy electrons [22]. The protective functions of fullerenol against PM-induced disease have not been studied yet.

We had previously developed both eupafolin [23] and eupafolin nanoparticle (NP) delivery systems [24] and a water-soluble trihydroxyisoflavone NP [25] system, to study their individual anti-oxidant and anti-inflammatory activities that prevented PM-induced skin inflammation. Our previous findings revealed that PM could mediate the AhR/p47 phox/NADPH oxidase pathway, and subsequently results in ERK1/2, p38/NF- $\kappa$ B and JNK/AP-1 activation. Finally, PM induces COX-2 protein expression and filaggrin downregulation. The upregulated expression of COX-2 and production of PGE2 might impair their ability to function as skin barriers [10]. PM could increase the level of oxidative stress to the cell and cause either serious irregularities in signal transduction or protein expression in cells; hence, because fullerene nanoparticles can act as an exceptional antioxidant; they have been applied in the dermatologic and cosmetic fields [11]. To continue our efforts to study the inhibition of PM-induced inflammation, we have tried to develop a water-soluble fullerene derivative, fullerenol  $C_{60}(OH)_{36}$ , as a new nanomedicine, and evaluated its anti-air pollution activity

on HaCaT cells. We hypothesize that fullereneol  $C_{60}(OH)_{36}$  might be used in cosmeceutical products or medicines that inhibit and prevent PM-induced skin injuries in the future. The levels of ROS, expression of phosphorylated mitogen-activated protein kinase, Akt, and inflammation-related proteins (cyclooxygenase-2, heme oxygenase-1, and prostaglandin E2) that were induced by PM were analyzed. Four specific skin barrier proteins (filaggrin, involucrin, repetin, and loricrin) were also studied.

## 2. Results

### 2.1. Synthesis and Characterization of Fullereneol $C_{60}(OH)_{36}$

Several methods can be used to synthesize fullereneols with different degrees of hydroxyl groups [26]. In this report, an alkaline reaction method was applied to synthesize fullereneol,  $C_{60}(OH)_{36}$  [21]. The fullerene  $C_{60}$  was first dissolved in toluene, after which aqueous NaOH and TBAH solutions were added to the reaction mixture (Figure 1a). After the removal of toluene, water was added and the reaction was allowed to occur for 18 h. The aqueous phase was then evaporated. The crude sample was formed as a brown sludge that became precipitated upon the addition of methanol. The precipitate was finally washed with methanol several times, to remove traces of TBAH and NaOH, to obtain  $C_{60}(OH)_{36}$ . The molecular weight of fullereneol  $C_{60}(OH)_{36}$  was confirmed by ESI-TOF MS.

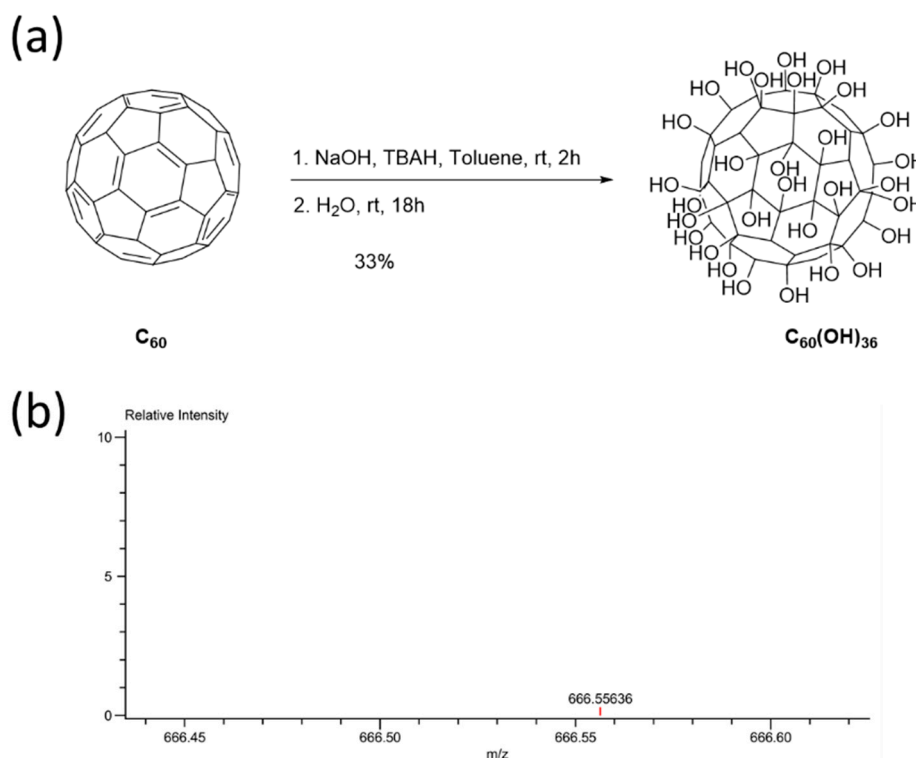


**Figure 1.** (a) Synthesis procedure for fullereneol  $C_{60}(OH)_{36}$ ; (b) ESI-TOF MS spectral data.

Fullereneol  $C_{60}(OH)_{36}$  was then characterized by fourier-transform infrared spectroscopy (FTIR), DLS, and TEM (Figure 2). The FTIR spectrum of fullereneol  $C_{60}(OH)_{36}$  and the starting material, i.e., fullerene  $C_{60}$ , are shown in Figure 2a. The FTIR spectrum of  $C_{60}(OH)_{36}$  (Figure 2a) indicated a broad single at around  $3400\text{ cm}^{-1}$ , at which typical O–H stretching occurred for  $C_{60}(OH)_{36}$ . The starting material, fullerene  $C_{60}$ , shows typical IR signals at  $\sim 1482$ ,  $\sim 1180$ ,  $\sim 575$ , and  $\sim 526\text{ cm}^{-1}$  [27]. The specific bands at  $1620$ ,  $1370$ , and  $1080\text{ cm}^{-1}$  are characteristic of C = C, C–O–H, and C–O absorption, respectively, on  $C_{60}(OH)_{36}$ . The hydrodynamic diameter of fullereneol  $C_{60}(OH)_{36}$  is  $283.5 \pm 28.0\text{ nm}$  (Figure 2b). The zeta potentials of fullerene  $C_{60}$  and fullereneol  $C_{60}(OH)_{36}$  in water are  $-45.7 \pm 5.4$  and  $-48.6 \pm 0.6$ , respectively (Figure 2c). The TEM images showed the fullereneol  $C_{60}(OH)_{36}$  particle morphology; its

size was ~20–30 nm (Figure 2d). Besides, as shown in Figure 2e, fullerene  $C_{60}$  is insoluble in water and forms a precipitate in the Eppendorf tube; in contrast, fulleranol  $C_{60}(OH)_{36}$  was completely suspended in the aqueous solution.

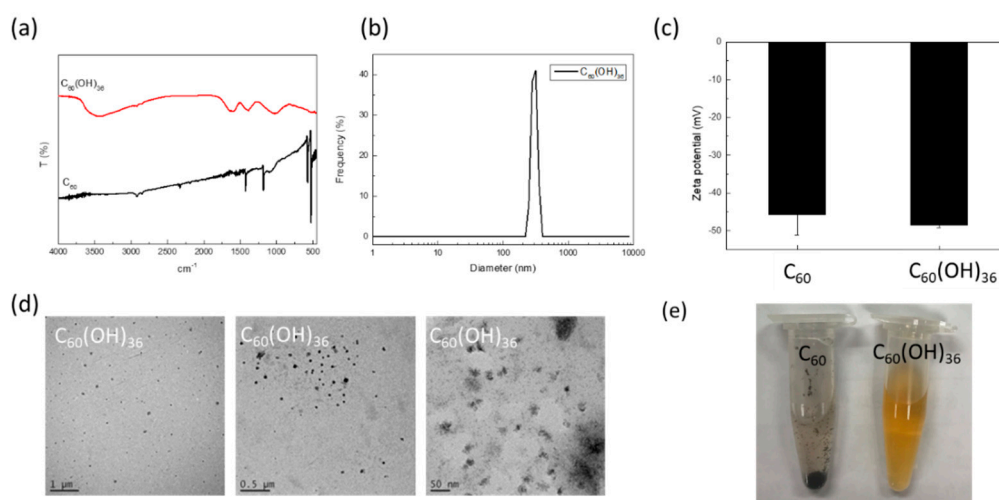


**Figure 2.** (a) FTIR, (b) DLS, (c) zeta-potential, and (d) TEM data; (e) images for fulleranol  $C_{60}(OH)_{36}$  or fullerene  $C_{60}$ , respectively.

## 2.2. Fulleranol $C_{60}(OH)_{36}$ Blocked PM-Induced Cell Apoptosis

Annexin V-fluorescein isothiocyanate (FITC)/propidium iodide staining was used to detect apoptosis at an early stage in HaCaT cells, using flow cytometry. Annexin V is a  $Ca^{2+}$ -dependent phospholipid-binding protein, which exhibits a high affinity towards phosphatidylserine, when exposed to the external cellular environment, at an early stage of apoptosis. Hence, annexin V could identify early stages of apoptosis more effectively than other assays that are based on nuclear changes (DNA fragmentation). Annexin V staining precedes the loss of membrane integrity, which also occurred after the later stages of cell death (apoptotic or necrotic processes). Therefore, propidium iodide is usually used in conjunction with Annexin V to identify intact cellular membranes. Hence, a combination of Annexin V and propidium iodide positive/negative signals could be used to identify early apoptosis, or the late stages of apoptosis and necrosis. In addition, Annexin V is commonly used for detecting apoptosis in the HaCaT cell [28,29]. As shown in Figure 3A, fulleranol ( $C_{60}(OH)_{36}$ ) and water non-soluble fullerene ( $C_{60}$ ) did not affect the early apoptosis of HaCaT cells, while PM could accelerate early apoptosis in HaCaT cells. Pre-treatment with 1  $\mu$ M of fulleranol ( $C_{60}(OH)_{36}$ ) for 1 h could partially but significantly suppress PM (SRM 1649b, 50  $\mu$ g/cm<sup>2</sup>)-triggered cell apoptosis, especially during early apoptosis, but could not do so when fullerene  $C_{60}$  was used (Figure 3B). Furthermore, the similar effects of fulleranol ( $C_{60}(OH)_{36}$ ) were obtained in the caspase-3 activities assay (Figure 3C,D). These results indicate that pre-treatment with fulleranol ( $C_{60}(OH)_{36}$ ) could partially suppress PM-induced apoptosis.

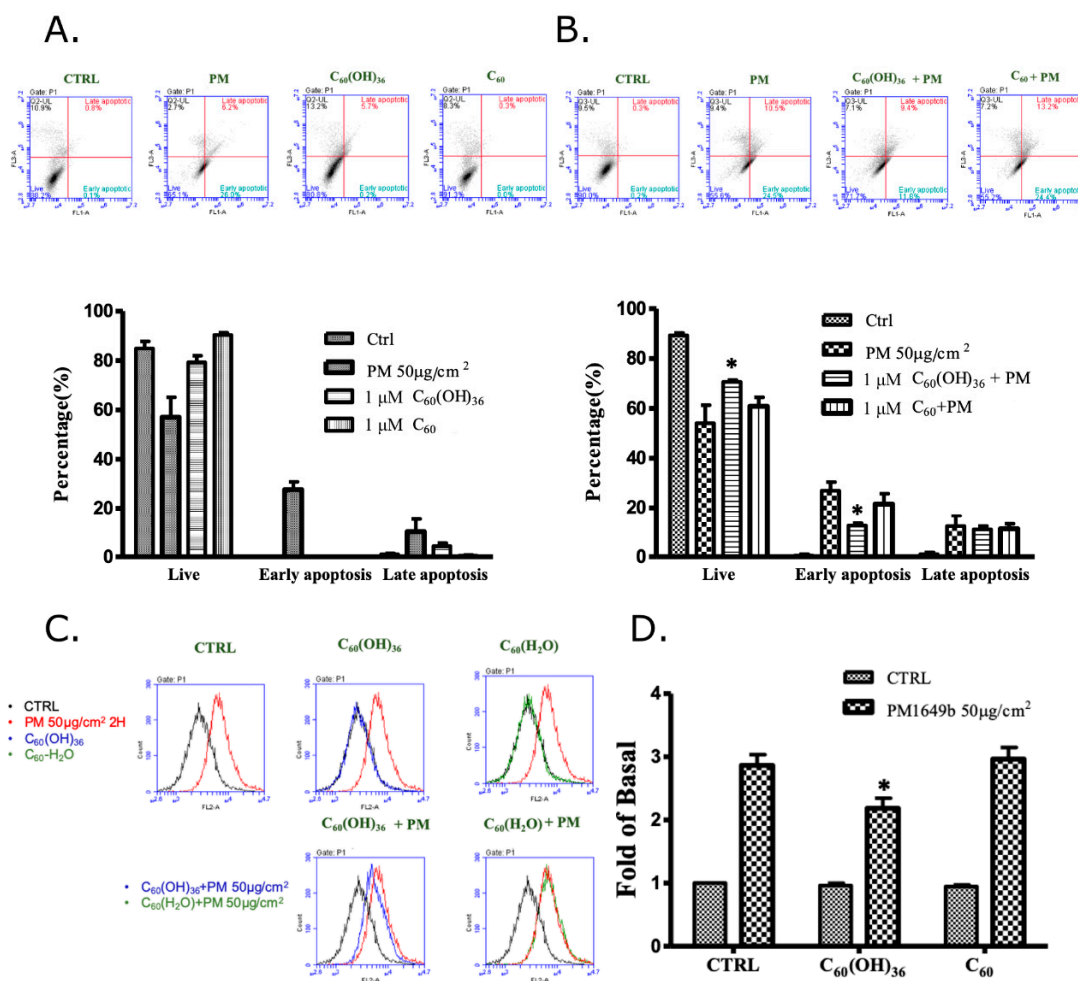


**Figure 3.** Effects of fullereneol ( $C_{60}(OH)_{36}$ ), fullerene ( $C_{60}$ ), and PM on cell apoptosis in human skin keratinocyte (HaCaT) cells. Cells were treated with (A) fullereneol ( $C_{60}(OH)_{36}$ ), fullerene ( $C_{60}$ ), or PM for 24 h, and pre-treated with (B) fullereneol ( $C_{60}(OH)_{36}$ ) and fullerene ( $C_{60}$ ) (1 µM) for 1 h; then, cells were treated with PM (50 µg/cm<sup>2</sup>) for another 24 h, and values were measured via flow cytometry by Annexin V-fluorescein isothiocyanate (FITC)/propidium iodide staining. (C) The raw data and (D) the calculated values of caspase-3 activity, which were measured by flow cytometry, were presented. The upper panel of (A,B) shows the raw flow cytometry data, and the lower right quadrant of each raw figure indicates the percentage of cells undergoing early apoptosis. The bar graphs illustrate the cumulative counts observed using the flow cytometer. All data are expressed as means ± SEM values from at least three individual experiments. \*  $p < 0.05$ , as compared to the values for the PM exposure group.

### 2.3. Fullereneol $C_{60}(OH)_{36}$ Suppressed PM-Triggered the Cellular and Mitochondrial Production of Reactive Oxygen Species

It is known that PM could increase ROS levels and subsequently cause diseases [5,10]. Moreover, a previous study has suggested that the presence of water-soluble fullerenes could enhance their ROS scavenging activity [30]. Hence, the effects of nanolization of fullereneol  $C_{60}(OH)_{36}$  on ROSs production were investigated. In the study, three ROS probes were used in a flow cytometry system, to detect the different types and locations of ROS within cells. H2DCFDA was majorly used to measure the activity of hydroxyl and peroxy groups. The CellROX Red dye does not bind to DNA; hence, it was localized in the cytoplasm. CellROX is weakly fluorescent, though it shows photostable fluorescence after ROS oxidation. Figure 4C shows that the presence of fullereneol  $C_{60}(OH)_{36}$  and fullerene  $C_{60}$  in water did not change the ROS levels, as compared to those of the control group, upon measuring a cellular

ROS determinant reagent, H2DCFDA. However, PM triggered a significant increase in the ROS level. Most importantly, fullereneol  $C_{60}(OH)_{36}$  could significantly inhibit PM-caused ROS production, though fullerene  $C_{60}$  in water could not do so. Similar results were obtained after cell staining with another cellular ROS staining reagent, CellROX (Figure 4F). However, our results showed that fullereneol  $C_{60}(OH)_{36}$  only partially suppressed the PM-induced increase in cellular ROS. Based on the detection ranges of assay kits, this might imply that other pathways, such as NO or CO pathways, influence ROS generation. ROS could be generated in cells as well as mitochondria. Hence, the mitochondrial ROS levels were then detected via flow cytometry and MitoSOX staining with similar fullereneol or fullerenes, and a PM-treated schedule for the cellular ROS assay. MitoSox is a red dye that is specifically sensitive to superoxides produced by mitochondria in live cells. As shown in Figure 5C, the ROS levels were increased by PM treatment, while the presence of fullereneol  $C_{60}(OH)_{36}$  or fullerene  $C_{60}$  in water did not affect ROS production in mitochondria, as compared to that for the control group. Moreover, fullereneol  $C_{60}(OH)_{36}$  (1  $\mu$ M) pre-treatment could suppress PM-triggered mitochondrial ROS generation in HaCaT cells. The results indicate that the PM-induced production of cellular and mitochondria ROS ( $H_2O_2$  and superoxide) could be prevented by pre-treatment with fullereneol  $C_{60}(OH)_{36}$ , but not with fullerene  $C_{60}$  in water.

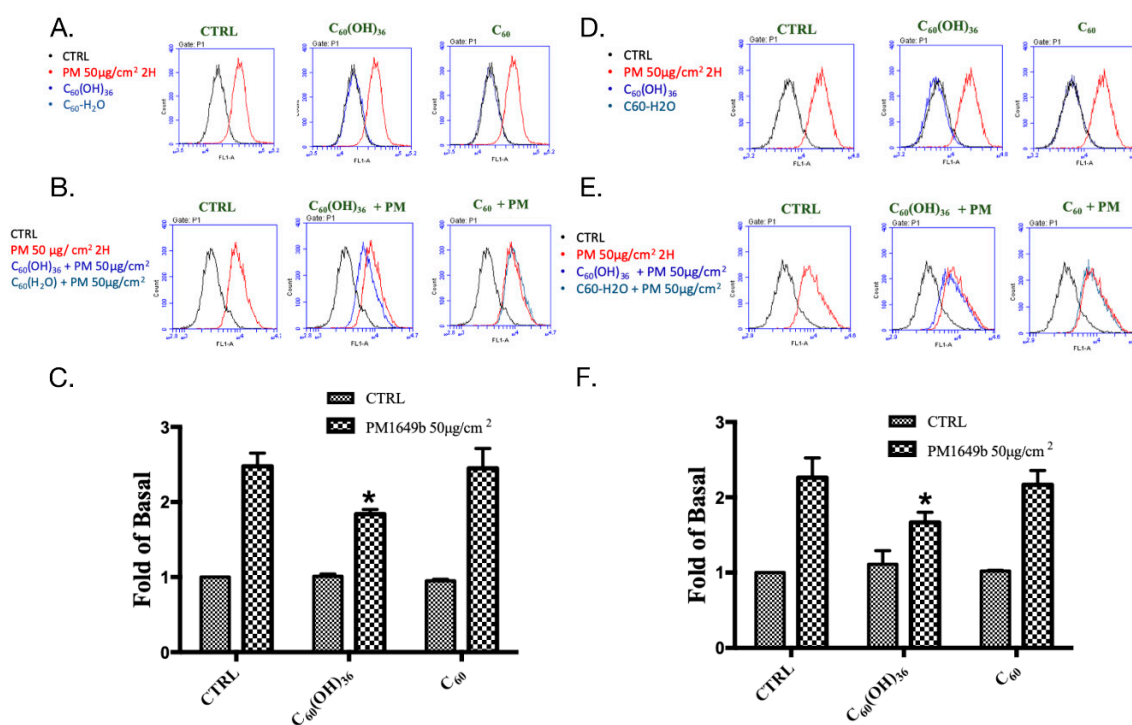


**Figure 4.** Cellular reactive oxygen species (ROS) production after treating HaCaT cells with fullereneol  $C_{60}(OH)_{36}$ , fullerene  $C_{60}$ , and PM. (A) Raw flow cytometry data obtained after H2DCFDA staining of cells treated with fullereneol  $C_{60}(OH)_{36}$ , fullerene  $C_{60}$ , or PM alone; (B) cells were treated with fullereneol  $C_{60}(OH)_{36}$  or fullerene  $C_{60}$  for 1 h and then administered PM (SRM 1649b, 50  $\mu$ g/cm<sup>2</sup>) for another 2 h. Signals were detected via H2DCFDA staining. (C) The bar graphs illustrate the cumulative counts of H2DCFDA flow cytometry results. (D) Raw flow cytometry data obtained after CellROX staining of cells treated with fullereneol  $C_{60}(OH)_{36}$ , fullerene  $C_{60}$ , or PM alone; (E) cells were treated with fullereneol  $C_{60}(OH)_{36}$  or fullerene  $C_{60}$  for 1 h and then administered PM for another 2 h. Signals were detected with CellROX staining. (F) The bar graphs illustrate the cumulative counts of CellROX flow cytometry results. All bar graph data were collected from at least three individual experiments and expressed as mean  $\pm$  SEM values. \*  $p < 0.05$ , as compared to the values for the PM exposure group.



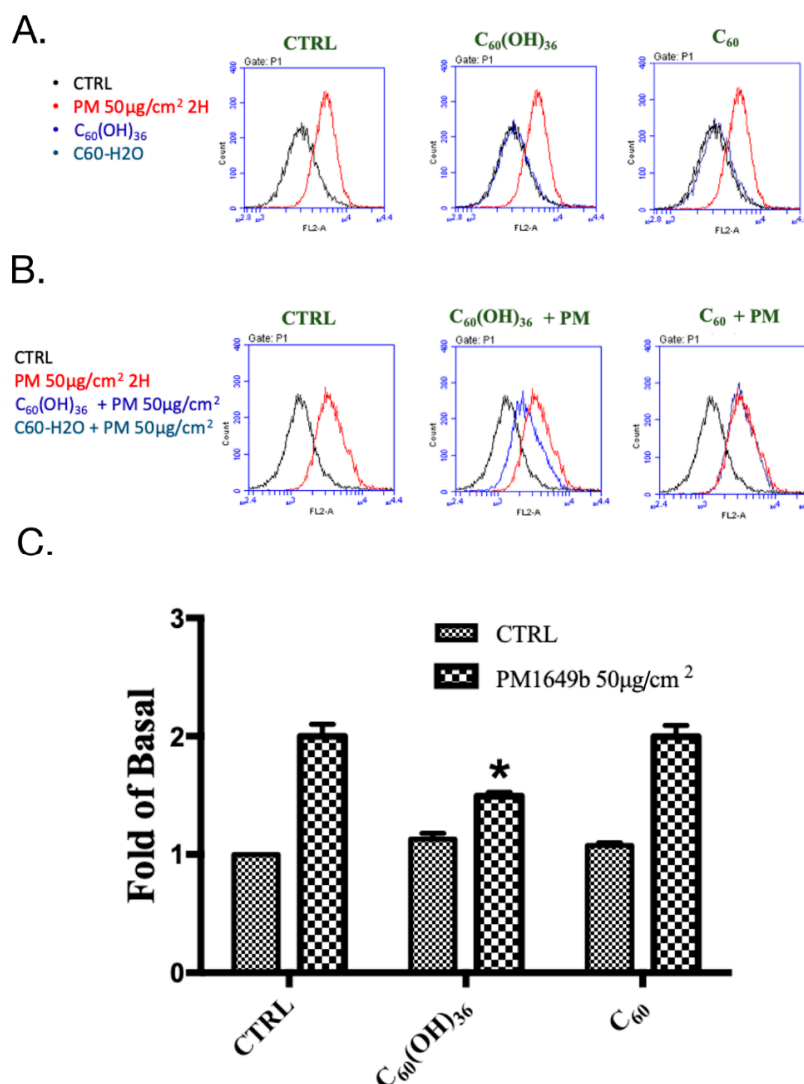


**Figure 5.** Effect of fullereneol  $\text{C}_{60}(\text{OH})_{36}$ , fullerene  $\text{C}_{60}$ , and PM on mitochondrial reactive oxygen species (ROS) production (determined by flow cytometry with MitoSOX staining) in HaCaT cells. (A) Raw flow cytometry data obtained along with MitoSOX staining data in cells treated with fullereneol  $\text{C}_{60}(\text{OH})_{36}$ , fullerene  $\text{C}_{60}$ , or PM alone. (B) Raw flow cytometry data obtained along with MitoSOX staining data in cells that received fullereneol  $\text{C}_{60}(\text{OH})_{36}$ , or fullerene  $\text{C}_{60}$  (1  $\mu\text{M}$ ) for 1 h, after which PM (SRM 1649b, 50  $\mu\text{g}/\text{cm}^2$ ) was administered for another 2 h. (C) The bar graph illustrates the cumulative counts of MitoSOX flow cytometry results. All bar graph data were collected from at least three individual experiments and expressed as mean  $\pm$  SEM values. \*  $p < 0.05$ , as compared to the values for the PM exposure group.

#### 2.4. Fullereneol $\text{C}_{60}(\text{OH})_{36}$ Reduced the PM-Induced Phosphorylation of Mitogen-Activated Protein Kinases (MAPKs) and AKT Proteins in HaCaT Cells

It has been demonstrated that mitogen-activated protein kinase (MAPK) and Akt (also called protein kinase B) levels could be regulated by ROS and could subsequently regulate various important cellular processes, such as transcription factor expression, cell proliferation, growth, and death [10,31]. Immunoblotting is a useful assay tool for the measurement of changes in protein expression levels. Hence, immunoblotting was used to determine the effects of fullereneol  $\text{C}_{60}(\text{OH})_{36}$  on PM-induced changes in expression levels of MAPK and Akt pathway proteins in HaCaT cells. As shown in Figure 6, the presence of fullereneol  $\text{C}_{60}(\text{OH})_{36}$  and fullerene  $\text{C}_{60}$  in water did not change the levels of total and phosphorylated proteins of extracellular signal-regulated kinases 1 and 2 (ERK, pp42 and pp44), P38,



c-Jun N-terminal kinase (JNK), and Akt. However, higher expression levels of phospho-ERK, P38, JNK, and Akt were observed after the treatment of cells with PM for another 6 h. Furthermore, the PM-induced expression of phosphorylated MAPK and Akt proteins was significantly suppressed by pre-treatment with 1  $\mu$ M of fullereneol  $C_{60}(OH)_{36}$ ; these effects were not observed with fullerene  $C_{60}$  dissolved in water.

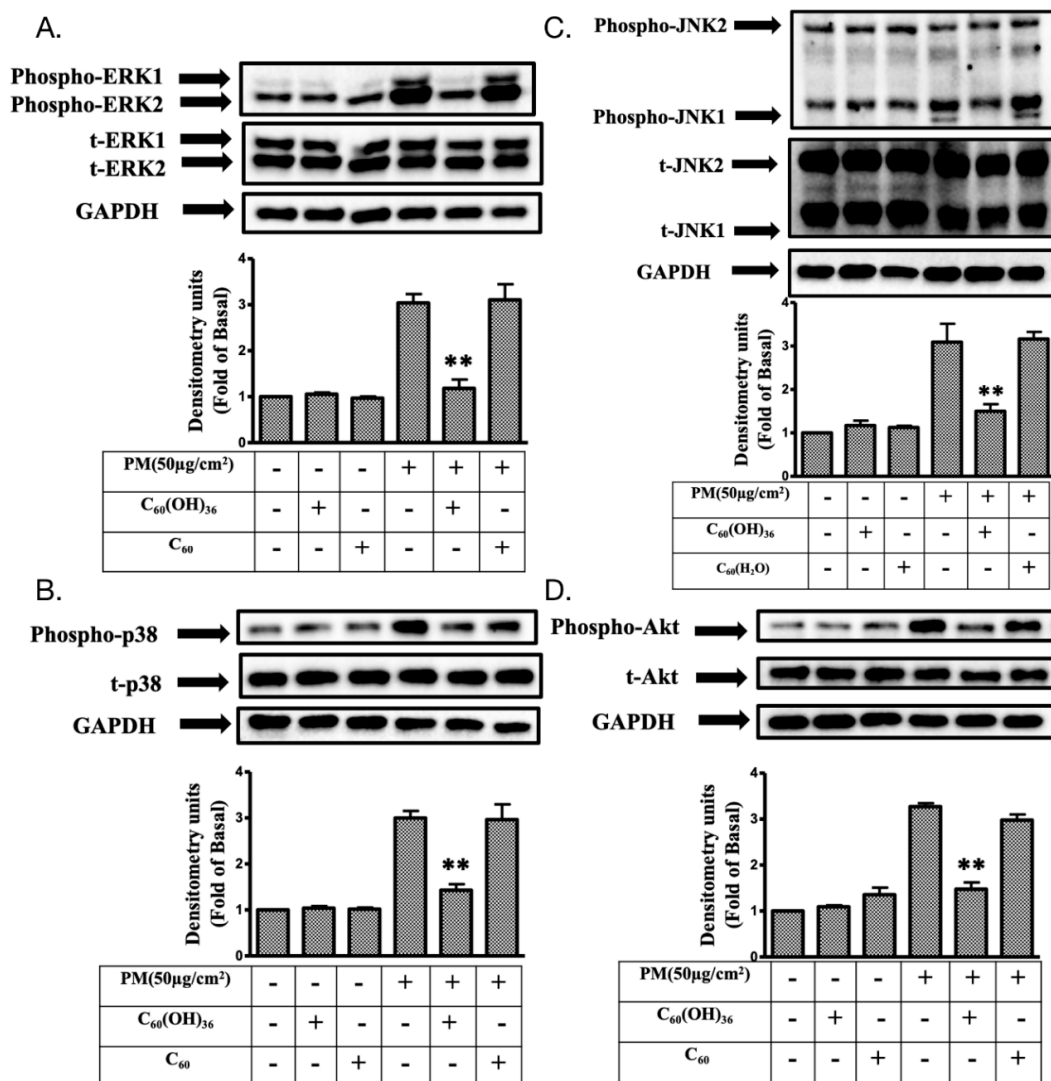


**Figure 6.** The changes in phosphorylated MAPK and Akt protein levels in fullereneol  $C_{60}(OH)_{36}$  and PM-treated HaCaT cells. The expression levels of different kinases, including (A) extracellular signal-regulated kinase (ERK, p42/p44), (B) P38, (C) c-Jun N-terminal kinase (JNK), and (D) Akt were measured by immunoblotting in the HaCaT cells with or without providing pre-treatment with 1  $\mu$ M of fullereneol  $C_{60}(OH)_{36}$  or fullerene  $C_{60}$  for 1 h and with PM (SRM 1649b, 50  $\mu$ g/cm<sup>2</sup>) for another 6 h. Glyceraldehyde 3-phosphate dehydrogenase (GAPDH) was used as a loading control. Blots were representative of three independent experiments, and the data were expressed as mean  $\pm$  SEM values. \*\*  $p < 0.01$ , as compared to the values for the PM exposure group.

### 2.5. Fullereneol $C_{60}(OH)_{36}$ Suppressed PM-Induced Inflammatory Protein Expression

Several inflammatory proteins could be induced by ROS, to cause cell or tissue injury, because of the effects of activation of cellular kinase pathways [10,32]. Here, various inflammatory proteins were selected for analysis via immunoblotting. The levels of cyclooxygenase-2 (COX-2), prostaglandin E2 (PGE2), intercellular adhesion molecular-1 (ICAM-1), heme oxygenase-1 (HO-1), cytosolic

phospholipase A2 (cPLA2), and metalloproteinase-9 (MMP-9) were detected after PM or fullerene treatment. As shown in Figure 7, the base levels of COX-2, ICAM-1, HO-1, cPLA2, MMP-9, and PGE2 were not changed after treatment with fullereneol C<sub>60</sub>(OH)<sub>36</sub> (1  $\mu$ M) or fullerene C<sub>60</sub> in water, as compared to the levels for the control group. Moreover, fullereneol C<sub>60</sub>(OH)<sub>36</sub> could significantly block PM-induced COX-2, ICAM-1, HO-1, cPLA2, and MMP-9 protein expression and PGE2 production, but these phenomena were not observed in the group treated with fullerene C<sub>60</sub> in water.

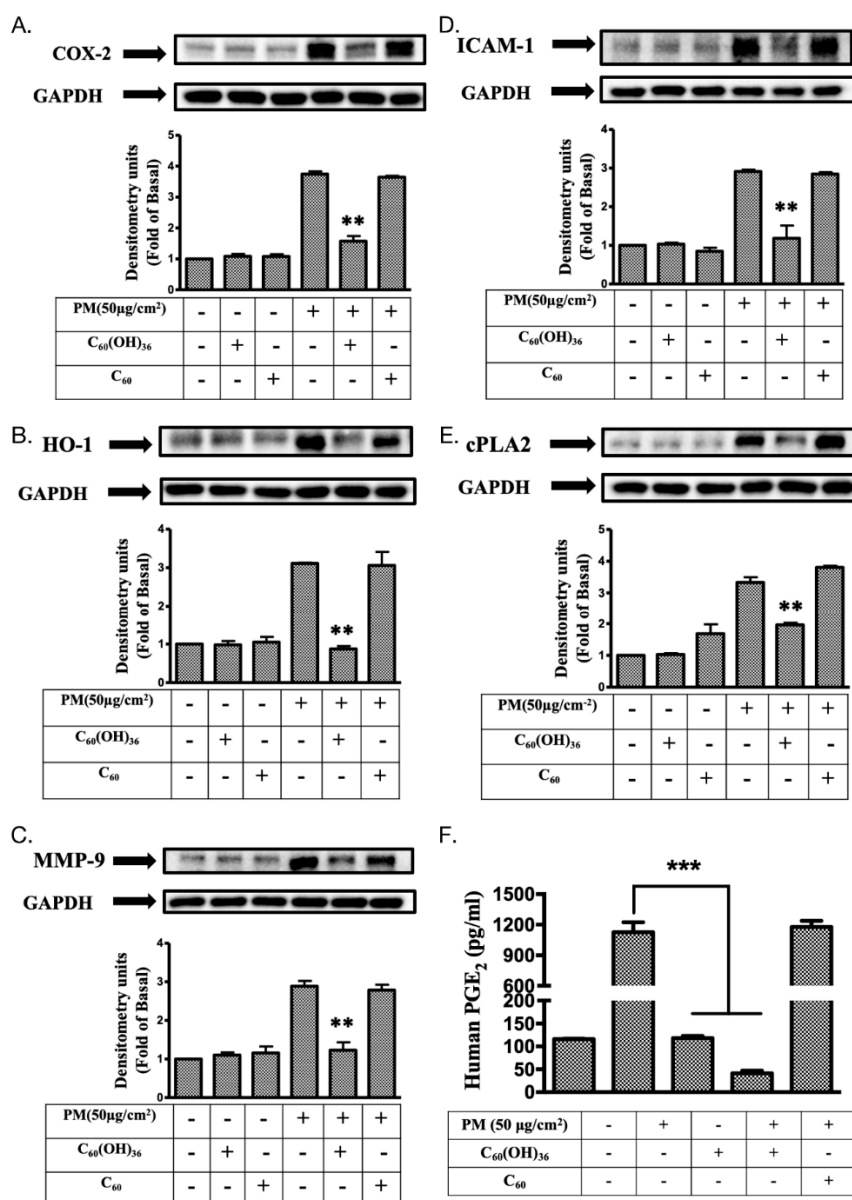


**Figure 7.** The changes in inflammation-related proteins in the fullereneol C<sub>60</sub>(OH)<sub>36</sub> and PM-treated HaCaT cells. The effects of inflammation-related proteins, including (A) cyclooxygenase-2 (COX-2), (B) intercellular adhesion molecular-1 (ICAM-1), (C) heme oxygenase-1 (HO-1), (D) cytosolic phospholipase A2 (cPLA2), and (E) metalloproteinase-9 (MMP-9) were measured by immunoblotting, and (F) prostaglandin E<sub>2</sub> (PGE<sub>2</sub>) levels were detected using an ELISA kit in HaCaT cells that did or did not receive pre-treatment with 1  $\mu$ M fullereneol C<sub>60</sub>(OH)<sub>36</sub> or fullerene C<sub>60</sub> dissolved in water for 1 h, followed by PM (SRM 1649b, 50  $\mu$ g/cm<sup>2</sup>) treatment for another 24 h. Glyceraldehyde 3-phosphate dehydrogenase (GAPDH) was used as a loading control during the immunoblotting process. Data were collected from at least three individual experiments and expressed as mean  $\pm$  SEM values. \*  $p < 0.01$ , as compared to the values for the PM exposure group.

## 2.6. Fullereneol $C_{60}(OH)_{36}$ Could Maintain the Levels of Proteins Exhibiting Protective Effects towards PM-Exposed Keratinocytes

Filaggrin, involucrin, repetin, and loricrin are known to act as barriers against damage caused by PM exposure in keratinocytes [10,33]. In the above experiments, we have suggested that fullereneol  $C_{60}(OH)_{36}$  could reduce the expression of proteins involved in inflammatory pathways via scavenging ROS production. We further investigated whether fullereneol  $C_{60}(OH)_{36}$  protected PM-exposed HaCaT cells from protein loss. The immunoblotting method was applied in this experiment. As shown in Figure 8, significant suppressive effects were observed on the PM-induced loss of filaggrin, involucrin, loricrin and repetin (at 24 h) after pre-treatment with 1  $\mu$ M fullereneol  $C_{60}(OH)_{36}$ , but these effects were not observed with water-dissolved fullerenes  $C_{60}$ . This indicates that fullereneol  $C_{60}(OH)_{36}$  could maintain the levels of proteins exhibiting protective effects towards PM-exposed keratinocytes and act against PM-induced skin aging.

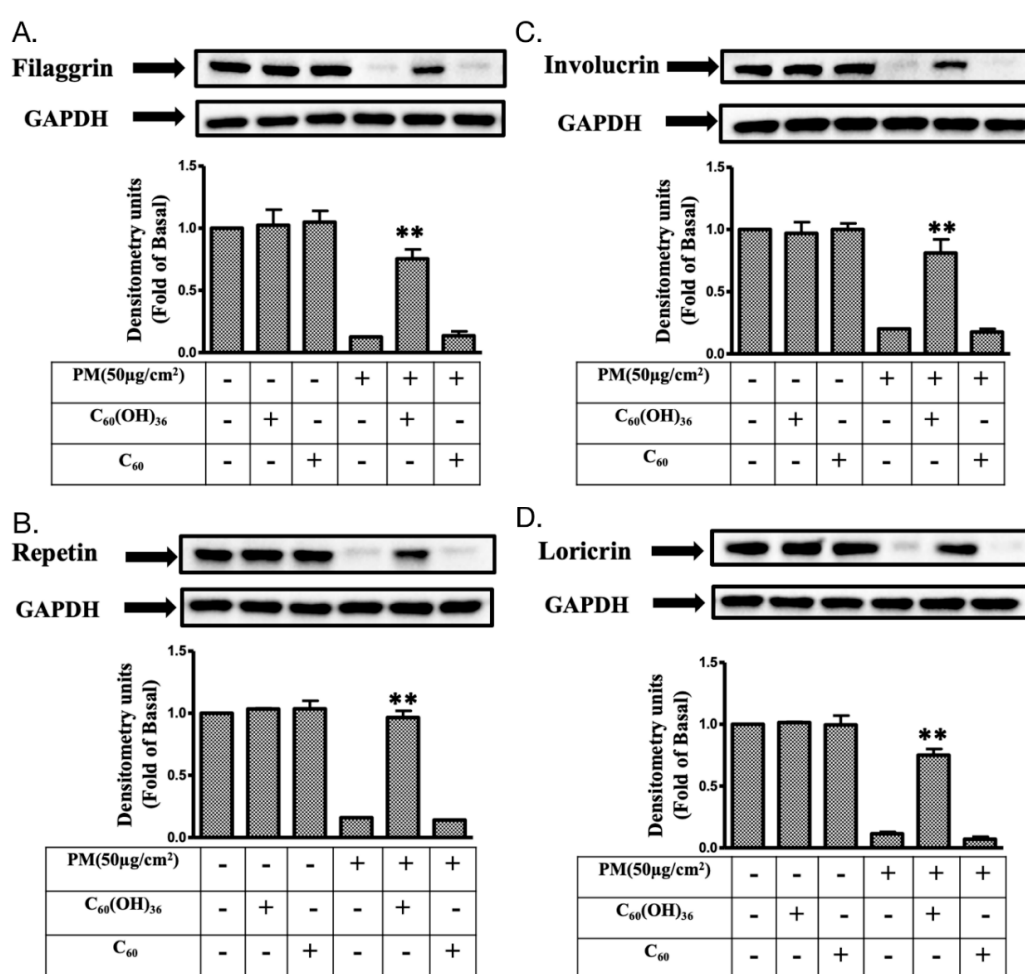


**Figure 8.** The expression levels of proteins exhibiting protective effects towards keratinocytes in fullereneol  $C_{60}(OH)_{36}$  and PM-treated HaCaT cells. The effects of proteins with protective effects, including (A) filaggrin, (B) repetin, (C) involucrin, and (D) loricrin, were measured by immunoblotting in HaCaT cells that did or did not receive pre-treatment with fullereneol  $C_{60}(OH)_{36}$  or fullerene  $C_{60}$  dissolved in water for 1 h and with PM (SRM 1649b, 50  $\mu$ g/cm<sup>2</sup>) for another 24 h. Glyceraldehyde 3-phosphate dehydrogenase (GAPDH) was used as a loading control. Blots were representative of three independent experiments, and data are expressed as mean  $\pm$  SEM values. \*  $p < 0.01$ , as compared to the values for the PM exposure group.

### 3. Discussion

Fullerene has been called a “radical sponge” because of its extremely high reactivity to radical species [11]. Because fullerene nanoparticles exhibit an exceptional antioxidant capacity, they have been applied in dermatologic and cosmetic fields [11]. In general, fullerene can be easily obtained in skin whitening, sunscreen, or antiaging products. However, the low water solubility of non-modified fullerene  $C_{60}$  limits its further use in bio-applications. Therefore, this study focuses on the synthesis of water-soluble fullerenes  $C_{60}(OH)_{36}$  and investigates the levels of inflammation and oxidative stress induced by them in response to PM exposure. Water-soluble fullerlenols  $C_{60}(OH)_{36}$  were synthesized according to a previously described procedure that was modified slightly (Figure 1) [27,34]. FTIR measurement (Figure 2a) showed that fullerlenol had been synthesized successfully, and that it had functional hydroxyl groups around  $3400\text{ cm}^{-1}$  that clearly differed from the fullerene signal. The DLS data (Figure 2b) provides the hydrodynamic diameter ranges of fullerlenol  $C_{60}(OH)_{36}$  in water. TEM images can complementarily estimate the sizes and further enable the particle morphology of fullerlenols  $C_{60}(OH)_{36}$  to be visualized (Figure 2d).

Fullerlenol can also show several antioxidant effects [27]. The antioxidant properties of fullerlenol were first described for an anti-ROS-induced injury of the hippocampus in vitro [35], in animal models of intestinal ischemia-reperfusion [36], and even in cases of transplantation [37]. Fullerlenol  $C_{60}(OH)_{36}$  can protect the human erythrocyte membrane against high-energy electrons [22].

The inhalation of ambient PM generated because of industrialization and urbanization has adverse effects on human health [38,39] and causes problems such as pulmonary dysfunction, cardiovascular disease, atherosclerosis, and hepatic fibrogenesis, which increases the morbidity and mortality [1,2]. PM affects the visceral dysfunctions; in addition, previous studies have suggested that an increase in the PM concentration was highly associated with the occurrence and progression of various skin diseases attributable to oxidative stress and the activation of inflammatory pathways [40]. Studies showed that PM can cause abnormal ROS production and accumulation [5,10]. ROS affects the physiological and pathological functions of cells, tissues, and even the entire organism [41–43]. ROS could facilitate the occurrence of several cellular activities, such as cell-signaling transduction, homeostasis regulation, and phagocytosis, after which ROS could be eliminated by the scavenging system (enzymes, superoxide dismutase, catalase, lactoperoxidase, glutathione peroxidase, and peroxiredoxin) of cells under physiological conditions [44,45]. Under pathological conditions, high levels of ROS that were difficult to eliminate were generated; they caused oxidative stress in cells. Subsequently, cellular biomacromolecules (lipids, sugars, proteins, and DNA) were oxidized by ROS; those of the secondary product generated by ROS might cause more harmful damage than that observed in the initially formed ROS. Hence, the aggravation and exacerbation of several diseases and phenomena, such as inflammation, neurodegeneration, aging, and cancer, were observed [45–49].

Small molecules, such as vitamin C,  $\alpha$ -tocopherol (vitamin E), and glutathione are well known as antioxidants that reportedly prevent PM-induced damage [50]. This implies that the addition of antioxidants into cells or organisms is advantageous, as they reduce the impact of PM on health. Fullerene is a stronger antioxidant with anti-aging properties. Recently, Baati et al. [51] showed that the repeated oral administration of fullerene (in olive oil) in rats doubled their lifespan without causing chronic toxicity. However, a lower water solubility limited the medical applications of fullerene. Hydroxylated fullerenes (fullerlenols) represent a major group of fullerene ( $C_{60}$ ) derivatives [52]. Although the hydroxylated form of fullerenes (fullerlenols) significantly differs from fullerenes ( $C_{60}$ ) with regard to water solubility, the adaptogenic and biophysical effects, including their interaction with mitochondria, are similar [52]. Moreover, the changes in the solubility and velocity of fullerlenols might affect their intra-membrane translocation; hence, their bio-activities/bio-functions are difficult to predict, specifically in complicated culture media or body fluids.

The Standard Reference Material® 1649b (SRM 1649b) has been certified by the National Institute of Standards and Technology for organic constituents (such as polycyclic aromatic hydrocarbons and polychlorinated biphenyl) and mimics the effects of damage attributable to urban dust on skin cells in

the current study. We used 1  $\mu\text{M}$  of fullereneol  $\text{C}_{60}(\text{OH})_{36}$  and non-water soluble  $\text{C}_{60}(\text{H}_2\text{O})$  to investigate and compare the levels of inflammation and oxidative stress induced by exposure to PM (1949b). We first demonstrated that fullereneol  $\text{C}_{60}(\text{OH})_{36}$  is partially responsible for the anti-PM-induced early apoptosis and cytotoxicity-linked generation of ROS and the activation of mitogen-activated protein kinase (MAPK) and Akt pathways in HaCaT cells. The HaCaT cell was first generated by Boukamp et al., [53] and is a useful and stable cell platform for disease research and medicine development [10,23,24,54]. The MAPK is a superfamily that includes ERKs, JNKs, and p38 kinases, the three main protein kinase families. Each of these has been shown to play important roles in various processes such as intracellular metabolism regulation, gene expression and integral activities, such as mitosis, differentiation, apoptosis, gene expression, and cellular responses to external stresses and disease [55]. Our previous studies have suggested that the PM-stimulated phosphorylation of ERK1/2, JNK1/2 and p38 was mediated by ROS in HaCaT cells, while the phosphorylation of ERK1/2 simultaneously played a necessary role in downstream p38 phosphorylation [10,24]. In general, the levels of ERK2 were higher than those of ERK1 due to the strong strength of their proximal promoter in most mammalian tissues [56]. Our findings also support this phenomenon. However, some studies have suggested that ERK1 and 2 may present different regulated patterns after stimulation and play different roles in some cells, under certain experimental conditions [56]; this phenomenon was not observed in our study. In general, JNK1 might act as a positive regulator, while JNK2 exhibits a negative or down-regulatory function under normal conditions in several cell and animal models, and during the proliferation of keratinocytes in mouse skin [57]. However, a previous study suggests that JNK2 might be more important than the JNK1 in skin diseases such as human squamous cell carcinoma [58]. Furthermore, JNK2<sup>-/-</sup> mice showed a greater resistance to chemically-induced skin cancer than JNK1<sup>-/-</sup> mice [59], which might imply that JNK2 is more sensitive to some chemical agents-induced skin damage, but the details need further investigation. In addition, the functions of Akt are associated with skin aging [60] and are also known to play a prominent role in the healing of wounds and tissue regeneration [61,62]. The thinning of the epidermal layer and delayed development of hair follicles were observed in Akt1-deficient mice [63]. The evidence described above indicates that both MAPK and Akt pathways are essential for maintaining the normal functions of skin cells and facilitate the resistance towards the impact of environmental toxins. Hence, the maintenance of MAPK and Akt expression within the physiological range is advantageous for maintaining skin health. In this study, the PM-triggered higher expression of MAPK and Akt activities could be brought to the normal range (as compared to control group) using pre-treated fullereneol  $\text{C}_{60}(\text{OH})_{36}$ , but this could not be achieved with  $\text{C}_{60}(\text{H}_2\text{O})$  (Figure 6); this finding supports our hypothesis.

The expression of various inflammatory proteins has been linked with ROS and downstream MAPK pathways in keratinocytes. Our previous study showed that PM-induced ROS triggered MAPK signal activation, which mediated the expression of COX-2/PGE2 and MMP-9 inflammatory proteins [24]. In addition, the levels of HO-1, ICAM-1, and cPLA2 were also increased because of ROS during inflammation in various types of cells [64–67]. The up-regulation of these inflammatory proteins might enable the cell to act against the impairments attributable to ROS generation. For example, oxidative or nitrosative stress-induced higher levels of HO-1 were observed to perform antioxidant and anti-inflammatory roles in cells [68–70]. In addition, ICAM-1 was highly expressed in epidermal keratinocytes exhibiting lymphoid infiltration and plays an important inflammatory role in transendothelial lymphocyte migration [71–73]. Moreover, cPLA2, an enzyme with an inflammatory role, could hydrolyze phospholipids, to produce arachidonic acid or lysophospholipids, which increase COX-2 expression [74,75]; the inhibition of cPLA2 could suppress inflammation in skin diseases [76,77]. The results of the current study revealed that the PM-triggered up-regulation of COX-2, HO-1, MMP-9, ICAM-1, cPLA2 expression and PGE2 production could be inhibited by pretreatment with fullereneol  $\text{C}_{60}(\text{OH})_{36}$ , but not with  $\text{C}_{60}(\text{H}_2\text{O})$  (Figure 7). The filaggrin, repetin, involucrin, and lorcrin present in keratinocytes have barrier/protective functions, such as the defense against external environmental pathogens and allergen entry or chemical damage, and decrease the level of water loss occurring from



the skin [78]. The maintenance of filaggrin, repetin, involucrin, and loricrin levels allows keratinocytes to resist PM-induced cell toxicity [10,33]. The expression of filaggrin is associated with the activation of the inflammatory pathway [79]. Our previous data showed that the increase in COX-2/PGE2 signals negatively regulated filaggrin expression after PM exposure [10]. Here, we further demonstrate the fact that fullereneol  $C_{60}(OH)_{36}$  can preserve the levels of these of barrier proteins in keratinocytes after PM exposure (Figure 8).

In conclusion, this is the first study in which fullereneol  $C_{60}(OH)_{36}$  reportedly exhibited protective effects against PM-induced oxidative stress and inflammation, and the impairment of barrier proteins and apoptosis, in HaCaT keratinocytes (Figure 9). In contrast, fullerene  $C_{60}$  did not exhibit similar effects after PM exposure; this might be attributable to their lower water-soluble properties. Fullereneol  $C_{60}(OH)_{36}$  could be valuable when used in cosmeceutical products and medicines that inhibit and prevent PM-induced skin injuries in the future.

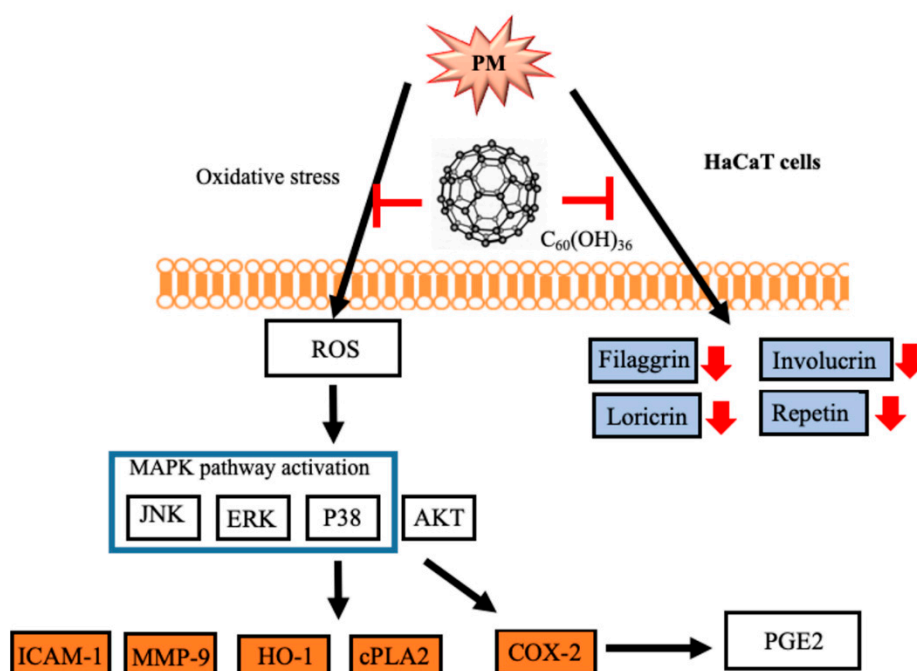


**Figure 9.** A diagram of the molecular mechanisms underlying the inhibition of PM-induced effects by fullereneols  $C_{60}(OH)_{36}$  in HaCaT cells. PM causes oxidation, inflammation, and barrier protein losses, which lead to cell toxicity. The levels of ROS were increased and triggered the activation of downstream MAPK and Akt pathways, and subsequently enhanced inflammatory protein (ICAM-1, COX-2, HO-1 and PGE2 etc.) expression. In addition, the loss of barrier proteins after PM exposure could be blocked by fullereneol  $C_{60}(OH)_{36}$  pre-treatment. This indicates that fullereneols  $C_{60}(OH)_{36}$  could act via ROS scavenger and anti-inflammatory mechanisms and the maintenance of expression of barrier proteins, to prevent PM-induced adverse effects in HaCaT cells.

#### 4. Materials and Methods

##### 4.1. Materials

PM (Standard Reference Material® 1649b, SRM-1649b) was obtained from the National Institute of Standards and Technology, Gaithersburg, MD, USA. HaCaT cells were purchased from AddexBio (San Diego, CA, USA). Fullerene, toluene (Tol), tetrabutyl-ammonium hydroxide (TBAH), sodium hydroxide (NaOH), and Sephadex LH-20 resin were purchased from Sigma-Aldrich. All chemicals used in bioassays were of the ACS reagent grade and were purchased from Sigma-Aldrich (St Louis, MO, USA). Buffers and solutions were prepared using Millipore water. The bicinchoninic acid (BCA) protein assay kit was purchased from Pierce (Rockford, IL, USA). Dulbecco's modified Eagle



(DMEM) medium was purchased from GIBCO, Grand Island, NY, USA. Fetal bovine serum (FBS) was obtained from Hazelton Products (Denver, PA, USA). Antibodies were purchased from different sources; total and phosphorylated p38, ERK 1/2, JNK1/2, and phospho-Akt were purchased from Cell Signaling Technology (Danvers, MA, USA); total-Akt and cPLA2 were purchased from Santa Cruz Biotechnology (Dallas, TX, USA); MMP-9, involucrin, and repetin were purchased from Proteintech Group Inc (Rosemont, IL, USA); HO-1 and COX-2 were obtained from Abcam (Cambridge, UK). We also purchased loricrin (Boster, Pleasanton, CA, USA), filaggrin (Genetex, Hsinchu, Taiwan), and GAPDH (Biogenesis, Boumemouth, UK), as well as an immunoblotting enhanced chemiluminescence (ECL) detection kit and Hyperfilms (purchased from GE Healthcare Biosciences, Buckinghamshire, UK).

#### 4.2. Thin-Layer Chromatography, Mass and Spectrometer Assay

Analytical thin-layer chromatography (TLC) was performed on precoated plates (Silica Gel 60, Merck). ESI ionization time-of-flight mass (ESI-TOF MS) spectral data were collected on a JMS-T100LP 4G(JEOL) using a mass spectrometer equipped with the ESI source, for detecting positive and negative ions. Typical measurement conditions used were as follows: needle voltage: 2000 kV, orifice 1 voltage: 300 V, ring lens voltage: 10 V, spray temperature: 250 °C. Fourier-transform infrared spectroscopy (FTIR) spectra were recorded using a Thermo Nicolet iS5 FTIR spectrometer.

#### 4.3. Transmission Electron Microscopy Assay

Transmission electron microscopy (TEM) was performed using a JEOL microscope (Model JEM-2100) operated at 200 keV, to characterize the sizes and dispersion of the glycofullerenes. A drop of fullerene solution (~1 µL) was placed on a carbon-coated 200-mesh copper grid. The grid was allowed to dry at room temperature for several hours and further dried under vacuum conditions overnight, prior to TEM analysis.

#### 4.4. Hydro-Diameter Size and Zeta Potential

The hydro-diameter size and zeta potential of fullerene particles were analyzed using a particle analyzer, using the dynamic light scattering (DLS) technique (Horiba, SZ-100V2, Japan) at 25 °C, at a laser angle of 90°. The samples were diluted with pure water. Each value was measured in triplicate.

#### 4.5. Synthesis of Fullerene $C_{60}(OH)_{36}$

Fullerene (80 mg, 0.11 mmol) was dissolved in toluene (60 mL), and aqueous NaOH (1 g/mL, 2 mL) and tetrabutylammonium hydroxide solution (TBAH, 1 mL, 40% in H<sub>2</sub>O) were added to this reaction mixture. The reaction mixture was stirred at room temperature in an open flask for 2 h. After the removal of toluene by decantation and concentration under reduced pressure, the brown sludge and remaining solution was stirred with additional water (10 mL), for another 18 h. An additional amount of water (20 mL) was added; the solution was filtered and concentrated. Then, water (5 mL) and MeOH (50 mL) were added to produce a brown precipitate. The precipitate was centrifuged and washed with MeOH (100 mL) and dried in vacuo to obtain fullerene 2 (48.8 mg, 33%). IR (neat): 3447 (O-H); HRMS (ESI): calculated for  $C_{60}H_{36}O_{36}$  [M + H]<sup>2+</sup>: 666.5533; found: 666.5564.

#### 4.6. Cell Culture Conditions

Human epidermal keratinocyte (HaCaT) cells were purchased from AddexBio (San Diego, CA, USA). Cells were cultured in the Dulbecco's Modified Eagle Medium (DMEM, Gibco, Grand Island, NY, USA) supplemented with 10% FBS (Hazelton Research Products, Denver, PA, USA) and 1% penicillin–streptomycin (Gibco, USA), and incubated at 37 °C in a humidified atmosphere containing 5% CO<sub>2</sub>/95% air. When cultures reached confluence, cells were treated with 0.05% (*w/v*) trypsin/0.53 mM EDTA for 5 min at 37 °C. The HaCaT keratinocyte cell line was seeded in a 12-well plate (2 × 10<sup>5</sup> per well) with 1 mL medium. The cell viability was also simultaneously tested using the

3-(4,5-Dimethylthiazol-2-yl)-2,5-diphenyltetrazolium bromide (MTT) assay, to ensure a survival rate of at least 90% with each passage. After cells were seeded for 24 h for stable, the medium was renewed before the followed experiments were performed. The cells obtained within passages 5 to 12 of HaCaT cells were used for preforming experiments.

#### 4.7. Cell Apoptosis Assay

The Annexin V-FITC/propidium iodide assay kit (Thermo Fisher Scientific, Waltham, MA, USA) and caspase-3 assay kit (Santa Cruz Biotechnology, Dallas, TX, USA) were utilized to analyze cell apoptosis by flow cytometry, according to the instructions provided in the manuals. Fullerene and fullerenol (1  $\mu$ M) were dissolved in pure water and pre-treated to HaCaT cells for 1 h; after treatment with PM (50  $\mu$ g/cm<sup>2</sup>) for another 24 h, cells were stained with Annexin V-FITC/propidium iodide or added caspase-3 antibody, as suggested in the manuals respectively, and then detected by flow cytometry (Accuri C6, BD Biosciences, San Jose, CA, USA). At least three independent experiments were repeated and data were collected.

#### 4.8. Cellular and Mitochondrial ROS Measurement

The cellular ROS levels were measured using the CellROX and 2', 7'-dichlorodihydrofluorescein diacetate (H2DCFDA) assays (Thermo Fisher Scientific, USA). Briefly, HaCaT cells were seeded onto 12-well plates ( $2 \times 10^5$  per well) and incubated for 24 h, to ensure that they were stable. Fullerene or fullerenol was added into cells for 1 h, and cells were treated with PM (50  $\mu$ g/cm<sup>2</sup>) for another 2 h. The fluorescence intensity of the cells was measured using flow cytometry (excitation/emission wavelength, 488/530 nm) after H2DCFDA or CellROX staining. In addition, MitoSOX<sup>TM</sup> (Molecular Probes, Eugene, OR, USA) was used for detecting the ROS level in the mitochondria using the same treatment schedule described above. The fluorescence intensity was measured at the excitation and emission wavelengths (488 and 585 nm, respectively) for flow cytometry. Experiments were repeated at least three times and the data were collected.

#### 4.9. Immunoblotting

HaCaT cells were seeded onto 12-well plates ( $2 \times 10^5$  per well) and incubated for 24 h for continued experiments. Fullerene or fullerenol (1  $\mu$ M) was added to cells for 1 h and then exposed to PM (50  $\mu$ g/cm<sup>2</sup>) for another 6 h (kinases) or 24 h (inflammatory- and protection-related proteins), respectively. Lysis buffer was used to lyse cells for protein extraction. Samples with equal amounts of proteins were separated through SDS-polyacrylamide gel electrophoresis (10%–12.5% polyacrylamide) and then transferred onto a polyvinylidene fluoride membrane (Millipore). The primary antibodies, total and phospho-p38, ERK, JNK, Akt, cPLA2, MMP-9, involucrin, repetin, HO-1, COX-2, loricrin, and filaggrin (the suppliers of antibodies have been indicated in 4.1 Materials) were utilized to measure the protein expression levels. The enhanced chemiluminescence (ECL) detection kit was used for measuring signals with a ChemiDoc<sup>TM</sup> XRS+ image system (Bio-Rad Laboratories, Hercules, CA, USA). The blots were then stripped and re-probed using anti-GAPDH for quantitative control analysis. Data were collected from at least three independent experiments exhibiting a similar pattern. The values were calculated from the collected blots and a figure with a closer pattern of statistical values was selected for presentation.

#### 4.10. Prostaglandin E2 (PGE2) Production Measurement

HaCaT cells were cultured in a 12-well plate for 24 h before the addition of fullerene or fullerenol (1  $\mu$ M). After they received treatment for 1 h, cells were exposed to PM for another 24 h. The medium was collected for further measuring PGE2 levels using the PGE2 enzyme immunoassay kit (Cayman Chemical, Ann Arbor, MI, USA), as per the manufacturer's instructions. Three independent experiments were performed and values were calculated.

#### 4.11. Statistical Analysis

All data were expressed as mean  $\pm$  SEM values and analyzed using GraphPad Prism software (v5, GraphPad, San Diego, CA, USA), with one-way ANOVA, followed by the post-hoc Tukey's multiple comparison (multiple groups) test. A  $p$  value  $< 0.05$  was considered significant.

**Author Contributions:** Conceptualization, C.-W.L., M.-C.C. (Miao-Ching Chi) and K.-T.P. and C.-H.L.; investigation, methodology and compound synthesis, M.-C.C. (Miao-Ching Chi), L.-F.H., Y.-L.Y., H.-Y.L., M.-C.C. (Ming-Chun Chen) and C.-H.L.; western blotting, flow, and oversaw analysis of the results, I.-T.L., Y.-C.C., Y.-L.Y. and C.-W.L.; writing—original draft preparation, M.-C.C. (Miao-Ching Chi), K.-T.P., Y.-C.C. and C.-H.L.; Writing—review and editing, C.-W.L., I.-T.L. and C.-H.L.; supervision, C.-W.L., I.-T.L. and C.-H.L.; project administration, C.-W.L. and C.-H.L.; All authors have read and approved the final manuscript.

**Funding:** We thank National Chung Hsing University and Ministry of Science and Technology of Taiwan for the financial support under contracts MOST 106-2320-B-255-001-, 106-2314-B-255-007-, 107-2113-M-005-014-, 108-2113-M-005-004-, Chang Gung University of Science Foundation (grants ZRRPF3J0081) and Chang Gung Medical Research Program Foundation (grants CMRPF6G0081).

**Conflicts of Interest:** The authors declare no conflict of interest and the funders had no role in the design of the study; in the collection, analyses, or interpretation of data; in the writing of the manuscript, or in the decision to publish the results.

#### Abbreviations

COX-2	Cyclooxygenase
cPLA2	Cytosolic phospholipases A2
ERK	Extracellular regulated protein kinase
FITC	Fluorescein isothiocyanate
GAPDH	Glyceraldehyde 3-phosphate dehydrogenase
HO-1	Heme oxygenase-1
ICAM-1	Intercellular adhesion molecular-1
JNK	c-Jun N-terminal kinase
MAPK	Mitogen-activated protein kinase
MMP-9	Metalloproteinase-9
PM	Particulate matter
PGE2	Prostaglandin E2
ROS	Reactive oxygen species

#### References

1. A Prüss-Ustün, J.W.; Corvalán, C.; Bos, R.; Neira, M. Preventing disease through healthy environments: A global assessment of the burden of disease from environmental risks. Available online: [https://www.who.int/quantifying\\_ehimpacts/publications/preventing-disease/en/](https://www.who.int/quantifying_ehimpacts/publications/preventing-disease/en/) (accessed on 2 May 2019).
2. Lawal, A.O. Air particulate matter induced oxidative stress and inflammation in cardiovascular disease and atherosclerosis: The role of Nrf2 and AhR-mediated pathways. *Toxicol. Lett.* **2017**, *270*, 88–95. [CrossRef] [PubMed]
3. Haikerwal, A.; Akram, M.; Monaco, A.D.; Smith, K.; Sim, M.R.; Meyer, M.; Tonkin, A.M.; Abramson, M.J.; Dennekamp, M. Impact of Fine Particulate Matter (PM<sub>2.5</sub>) Exposure during Wildfires on Cardiovascular Health Outcomes. *J. Am. Heart Assoc.* **2015**, *4*, e001653. [CrossRef] [PubMed]
4. Araujo, J.A.; Nel, A.E. Particulate matter and atherosclerosis: Role of particle size, composition and oxidative stress. *Part. Fibre Toxicol.* **2009**, *6*, 24. [CrossRef] [PubMed]
5. Rao, X.; Zhong, J.; Brook, R.D.; Rajagopalan, S. Effect of Particulate Matter Air Pollution on Cardiovascular Oxidative Stress Pathways. *Antioxid. Redox Signal.* **2018**, *28*, 797–818. [CrossRef] [PubMed]
6. Drakaki, E.; Dessinioti, C.; Antoniou, C.V. Air pollution and the skin. *Front. Environ. Sci.* **2014**, *2*. [CrossRef]
7. Parrado, C.; Mercado-Saenz, S.; Perez-Davo, A.; Gilaberte, Y.; Gonzalez, S.; Juarranz, A. Environmental Stressors on Skin Aging. Mechanistic Insights. *Front. Pharmacol.* **2019**, *10*. [CrossRef] [PubMed]
8. Piao, M.J.; Ahn, M.J.; Kang, K.A.; Ryu, Y.S.; Hyun, Y.J.; Shilnikova, K.; Zhen, A.X.; Jeong, J.W.; Choi, Y.H.; Kang, H.K.; et al. Particulate matter 2.5 damages skin cells by inducing oxidative stress, subcellular organelle dysfunction, and apoptosis. *Arch. Toxicol.* **2018**, *92*, 2077–2091. [CrossRef]

9. Park, J.; Park, E.H.; Schauer, J.J.; Yi, S.-M.; Heo, J. Reactive oxygen species (ROS) activity of ambient fine particles (PM<sub>2.5</sub>) measured in Seoul, Korea. *Environ. Int.* **2018**, *117*, 276–283. [[CrossRef](#)]
10. Lee, C.W.; Lin, Z.C.; Hu, S.C.; Chiang, Y.C.; Hsu, L.F.; Lin, Y.C.; Lee, I.T.; Tsai, M.H.; Fang, J.Y. Urban particulate matter down-regulates filaggrin via COX2 expression/PGE2 production leading to skin barrier dysfunction. *Sci. Rep.* **2016**, *6*, 27995. [[CrossRef](#)]
11. Mousavi, S.Z.; Nafisi, S.; Maibach, H.I. Fullerene nanoparticle in dermatological and cosmetic applications. *Nanomed. Nanotechnol. Biol. Med.* **2017**, *13*, 1071–1087. [[CrossRef](#)]
12. Lai, C.-H.; Lin, C.-Y.; Wu, H.-T.; Chan, H.-S.; Chuang, Y.-J.; Chen, C.-T.; Lin, C.-C. Galactose Encapsulated Multifunctional Nanoparticle for HepG2 Cell Internalization. *Adv. Funct. Mater.* **2010**, *20*, 3948–3958. [[CrossRef](#)]
13. Lai, C.-H.; Chang, T.-C.; Chuang, Y.-J.; Tzou, D.-L.; Lin, C.-C. Stepwise Orthogonal Click Chemistry toward Fabrication of Paclitaxel/Galactose Functionalized Fluorescent Nanoparticles for HepG2 Cell Targeting and Delivery. *Bioconjug. Chem.* **2013**, *24*, 1698–1709. [[CrossRef](#)] [[PubMed](#)]
14. Shi, J.; Kantoff, P.W.; Wooster, R.; Farokhzad, O.C. Cancer nanomedicine: Progress, challenges and opportunities. *Nat. Rev. Cancer* **2017**, *17*, 20–37. [[CrossRef](#)] [[PubMed](#)]
15. Kroto, H.W.; Heath, J.R.; O'Brien, S.C.; Curl, R.F.; Smalley, R.E. C<sub>60</sub>: Buckminsterfullerene. *Nature* **1985**, *318*, 162. [[CrossRef](#)]
16. Krätschmer, W.; Lamb, L.D.; Fostiropoulos, K.; Huffman, D.R. Solid C<sub>60</sub>: A new form of carbon. *Nature* **1990**, *347*, 354. [[CrossRef](#)]
17. Krusic, P.J.; Wasserman, E.; Keizer, P.N.; Morton, J.R.; Preston, K.F. Radical Reactions of C<sub>60</sub>. *Science* **1991**, *254*, 1183–1185. [[CrossRef](#)] [[PubMed](#)]
18. Tokuyama, H.; Yamago, S.; Nakamura, E.; Shiraki, T.; Sugiura, Y. Photoinduced biochemical activity of fullerene carboxylic acid. *J. Am. Chem. Soc.* **1993**, *115*, 7918–7919. [[CrossRef](#)]
19. Castro, E.; Hernandez Garcia, A.; Zavala, G.; Echegoyen, L. Fullerenes in Biology and Medicine. *J. Mater. Chem. B* **2017**, *5*, 6523–6535. [[CrossRef](#)] [[PubMed](#)]
20. Semenov, K.N.; Charykov, N.A.; Postnov, V.N.; Sharoyko, V.V.; Vorotyntsev, I.V.; Galagudza, M.M.; Murin, I.V. Fullerenols: Physicochemical properties and applications. *Prog. Solid State Chem.* **2016**, *44*, 59–74. [[CrossRef](#)]
21. Fluri, F.; Grünstein, D.; Cam, E.; Ungethuem, U.; Hatz, F.; Schäfer, J.; Samnick, S.; Israel, I.; Kleinschnitz, C.; Orts-Gil, G.; et al. Fullerenols and glucosamine fullerenes reduce infarct volume and cerebral inflammation after ischemic stroke in normotensive and hypertensive rats. *Exp. Neurol.* **2015**, *265*, 142–151. [[CrossRef](#)] [[PubMed](#)]
22. Grebowski, J.; Kazmierska, P.; Litwinienko, G.; Lankoff, A.; Wolszczak, M.; Krokosz, A. Fullereneol C<sub>60</sub>(OH)<sub>36</sub> protects human erythrocyte membrane against high-energy electrons. *Biochim. Biophys. Acta (Bba) - Biomembr.* **2018**, *1860*, 1528–1536. [[CrossRef](#)] [[PubMed](#)]
23. Lee, C.-W.; Lin, Z.-C.; Hsu, L.-F.; Fang, J.-Y.; Chiang, Y.-C.; Tsai, M.-H.; Lee, M.-H.; Li, S.-Y.; Hu, S.C.-S.; Lee, I.T.; et al. Eupafolin ameliorates COX-2 expression and PGE2 production in particulate pollutants-exposed human keratinocytes through ROS/MAPKs pathways. *J. Ethnopharmacol.* **2016**, *189*, 300–309. [[CrossRef](#)] [[PubMed](#)]
24. Lin, Z.C.; Lee, C.W.; Tsai, M.H.; Ko, H.H.; Fang, J.Y.; Chiang, Y.C.; Liang, C.J.; Hsu, L.F.; Hu, S.C.; Yen, F.L. Eupafolin nanoparticles protect HaCaT keratinocytes from particulate matter-induced inflammation and oxidative stress. *Int. J. Nanomed.* **2016**, *11*, 3907–3926. [[CrossRef](#)]
25. Huang, P.H.; Tseng, C.H.; Lin, C.Y.; Lee, C.W.; Yen, F.L. Preparation, characterizations and anti-pollutant activity of 7,3',4'-trihydroxyisoflavone nanoparticles in particulate matter-induced HaCaT keratinocytes. *Int. J. Nanomed.* **2018**, *13*, 3279–3293. [[CrossRef](#)] [[PubMed](#)]
26. Djordjevic, A.; Srdjenovic, B.; Seke, M.; Petrovic, D.; Injac, R.; Mrdjanovic, J. Review of Synthesis and Antioxidant Potential of Fullereneol Nanoparticles. *J. Nanomater.* **2015**, *2015*, 15. [[CrossRef](#)]
27. Roy, P.; Bag, S.; Chakraborty, D.; Dasgupta, S. Exploring the Inhibitory and Antioxidant Effects of Fullerene and Fullereneol on Ribonuclease A. *ACS Omega* **2018**, *3*, 12270–12283. [[CrossRef](#)] [[PubMed](#)]
28. Narayanapillai, S.; Agarwal, C.; Tilley, C.; Agarwal, R. Silibinin is a potent sensitizer of UVA radiation-induced oxidative stress and apoptosis in human keratinocyte HaCaT cells. *Photochem. Photobiol.* **2012**, *88*, 1135–1140. [[CrossRef](#)]

29. Fujisaki, H.; Futaki, S.; Yamada, M.; Sekiguchi, K.; Hayashi, T.; Ikejima, T.; Hattori, S. Respective optimal calcium concentrations for proliferation on type I collagen fibrils in two keratinocyte line cells, HaCaT and FEPE1L-8. *Regen. Ther.* **2018**, *8*, 73–79. [\[CrossRef\]](#)
30. Tzirakis, M.D.; Orfanopoulos, M. Radical Reactions of Fullerenes: From Synthetic Organic Chemistry to Materials Science and Biology. *Chem. Rev.* **2013**, *113*, 5262–5321. [\[CrossRef\]](#)
31. Son, Y.; Cheong, Y.K.; Kim, N.H.; Chung, H.T.; Kang, D.G.; Pae, H.O. Mitogen-Activated Protein Kinases and Reactive Oxygen Species: How Can ROS Activate MAPK Pathways? *J. Signal. Transduct.* **2011**, *2011*, 792639. [\[CrossRef\]](#)
32. Mittal, M.; Siddiqui, M.R.; Tran, K.; Reddy, S.P.; Malik, A.B. Reactive oxygen species in inflammation and tissue injury. *Antioxid. Redox Signal.* **2014**, *20*, 1126–1167. [\[CrossRef\]](#) [\[PubMed\]](#)
33. Li, Q.; Kang, Z.; Jiang, S.; Zhao, J.; Yan, S.; Xu, F.; Xu, J. Effects of Ambient Fine Particles PM2.5 on Human HaCaT Cells. *Int. J. Environ. Res. Public Health* **2017**, *14*. [\[CrossRef\]](#) [\[PubMed\]](#)
34. Kokubo, K.; Shirakawa, S.; Kobayashi, N.; Aoshima, H.; Oshima, T. Facile and scalable synthesis of a highly hydroxylated water-soluble fullereneol as a single nanoparticle. *Nano Res.* **2011**, *4*, 204–215. [\[CrossRef\]](#)
35. TSAI, M.-C.; CHEN, Y.H.; CHIANG, L.Y. Polyhydroxylated C<sub>60</sub>, Fullereneol, a Novel Free-radical Trapper, Prevented Hydrogen Peroxide- and Cumene Hydroperoxide-elicited Changes in Rat Hippocampus In-vitro. *J. Pharm. Pharmacol.* **1997**, *49*, 438–445. [\[CrossRef\]](#) [\[PubMed\]](#)
36. Lai, H.-S.; Chen, W.-J.; Chiang, L.-Y. Free Radical Scavenging Activity of Fullereneol on the Ischemia-reperfusion Intestine in Dogs. *World J. Surg.* **2000**, *24*, 450–454. [\[CrossRef\]](#) [\[PubMed\]](#)
37. Lai, H.S.; Chen, Y.; Chen, W.J.; Chang, K.J.; Chiang, L.Y. Free radical scavenging activity of fullereneol on grafts after small bowel transplantation in dogs. *Transplant. Proc.* **2000**, *32*, 1272–1274. [\[CrossRef\]](#)
38. Beelen, R.; Raaschou-Nielsen, O.; Stafoggia, M.; Andersen, Z.J.; Weinmayr, G.; Hoffmann, B.; Wolf, K.; Samoli, E.; Fischer, P.; Nieuwenhuijsen, M.; et al. Effects of long-term exposure to air pollution on natural-cause mortality: An analysis of 22 European cohorts within the multicentre ESCAPE project. *Lancet (Lond. Engl.)* **2014**, *383*, 785–795. [\[CrossRef\]](#)
39. Shah, A.S.; Langrish, J.P.; Nair, H.; McAllister, D.A.; Hunter, A.L.; Donaldson, K.; Newby, D.E.; Mills, N.L. Global association of air pollution and heart failure: A systematic review and meta-analysis. *Lancet (Lond. Engl.)* **2013**, *382*, 1039–1048. [\[CrossRef\]](#)
40. Kim, K.E.; Cho, D.; Park, H.J. Air pollution and skin diseases: Adverse effects of airborne particulate matter on various skin diseases. *Life Sci.* **2016**, *152*, 126–134. [\[CrossRef\]](#)
41. Brandes, R.P.; Weissmann, N.; Schroder, K. Nox family NADPH oxidases: Molecular mechanisms of activation. *Free Radic. Biol. Med.* **2014**, *76*, 208–226. [\[CrossRef\]](#)
42. Day, B.J. Antioxidant therapeutics: Pandora's box. *Free Radic. Biol. Med.* **2014**, *66*, 58–64. [\[CrossRef\]](#) [\[PubMed\]](#)
43. Singh, S.; Bocker, C.; Koppaka, V.; Chen, Y.; Jackson, B.C.; Matsumoto, A.; Thompson, D.C.; Vasiliou, V. Aldehyde dehydrogenases in cellular responses to oxidative/electrophilic stress. *Free Radic. Biol. Med.* **2013**, *56*, 89–101. [\[CrossRef\]](#) [\[PubMed\]](#)
44. Devasagayam, T.P.; Tilak, J.C.; Bloor, K.K.; Sane, K.S.; Ghaskadbi, S.S.; Lele, R.D. Free radicals and antioxidants in human health: Current status and future prospects. *J. Assoc. Phys. India* **2004**, *52*, 794–804.
45. Trachootham, D.; Alexandre, J.; Huang, P. Targeting cancer cells by ROS-mediated mechanisms: A radical therapeutic approach? *Nat. Rev. Drug Discov.* **2009**, *8*, 579–591. [\[CrossRef\]](#) [\[PubMed\]](#)
46. Farmer, E.E.; Mueller, M.J. ROS-mediated lipid peroxidation and RES-activated signaling. *Annu. Rev. Plant. Biol.* **2013**, *64*, 429–450. [\[CrossRef\]](#) [\[PubMed\]](#)
47. Radak, Z.; Zhao, Z.; Goto, S.; Koltai, E. Age-associated neurodegeneration and oxidative damage to lipids, proteins and DNA. *Mol. Asp. Med.* **2011**, *32*, 305–315. [\[CrossRef\]](#) [\[PubMed\]](#)
48. Zhang, W.; Xiao, S.; Ahn, D.U. Protein oxidation: Basic principles and implications for meat quality. *Crit. Rev. Food Sci. Nutr.* **2013**, *53*, 1191–1201. [\[CrossRef\]](#) [\[PubMed\]](#)
49. Schieber, M.; Chandel, N.S. ROS function in redox signaling and oxidative stress. *Curr. Biol.* **2014**, *24*, R453–R462. [\[CrossRef\]](#)
50. Whyand, T.; Hurst, J.R.; Beckles, M.; Caplin, M.E. Pollution and respiratory disease: Can diet or supplements help? A review. *Respir. Res.* **2018**, *19*, 79. [\[CrossRef\]](#)

51. Baati, T.; Bourasset, F.; Gharbi, N.; Njim, L.; Abderrabba, M.; Kerkeni, A.; Szwarc, H.; Moussa, F. The prolongation of the lifespan of rats by repeated oral administration of [60] fullerene. *Biomaterials* **2012**, *33*, 4936–4946. [\[CrossRef\]](#)
52. Galvan, Y.P.; Alperovich, I.; Zolotukhin, P.; Prazdnova, E.; Mazanko, M.; Belanova, A.; Chistyakov, V. Fullerenes as Anti-Aging Antioxidants. *Curr. Aging Sci.* **2017**, *10*, 56–67. [\[CrossRef\]](#) [\[PubMed\]](#)
53. Boukamp, P.; Petrussevska, R.T.; Breitkreutz, D.; Hornung, J.; Markham, A.; Fusenig, N.E. Normal keratinization in a spontaneously immortalized aneuploid human keratinocyte cell line. *J. Cell Biol.* **1988**, *106*, 761–771. [\[CrossRef\]](#) [\[PubMed\]](#)
54. Schoop, V.M.; Mirancea, N.; Fusenig, N.E. Epidermal organization and differentiation of HaCaT keratinocytes in organotypic coculture with human dermal fibroblasts. *J. Invest. Derm.* **1999**, *112*, 343–353. [\[CrossRef\]](#) [\[PubMed\]](#)
55. Cargnello, M.; Roux, P.P. Activation and function of the MAPKs and their substrates, the MAPK-activated protein kinases. *Microbiol. Mol. Biol. Rev.* **2011**, *75*, 50–83. [\[CrossRef\]](#) [\[PubMed\]](#)
56. Busca, R.; Pouyssegur, J.; Lenormand, P. ERK1 and ERK2 Map Kinases: Specific Roles or Functional Redundancy? *Front. Cell Dev. Biol.* **2016**, *4*, 53. [\[CrossRef\]](#) [\[PubMed\]](#)
57. Bode, A.M.; Dong, Z. The functional contrariety of JNK. *Mol. Carcinog.* **2007**, *46*, 591–598. [\[CrossRef\]](#) [\[PubMed\]](#)
58. Ke, H.; Harris, R.; Coloff, J.L.; Jin, J.Y.; Leshin, B.; Miliani de Marval, P.; Tao, S.; Rathmell, J.C.; Hall, R.P.; Zhang, J.Y. The c-Jun NH2-terminal kinase 2 plays a dominant role in human epidermal neoplasia. *Cancer Res.* **2010**, *70*, 3080–3088. [\[CrossRef\]](#) [\[PubMed\]](#)
59. Sabapathy, K.; Wagner, E.F. JNK2: A negative regulator of cellular proliferation. *Cell Cycle* **2004**, *3*, 1520–1523. [\[CrossRef\]](#) [\[PubMed\]](#)
60. Chen, H.; Wang, X.; Han, J.; Fan, Z.; Sadia, S.; Zhang, R.; Guo, Y.; Jiang, Y.; Wu, Y. AKT and its related molecular feature in aged mice skin. *PLoS ONE* **2017**, *12*, e0178969. [\[CrossRef\]](#) [\[PubMed\]](#)
61. Castilho, R.M.; Squarize, C.H.; Gutkind, J.S. Exploiting PI3K/mTOR signaling to accelerate epithelial wound healing. *Oral Dis.* **2013**, *19*, 551–558. [\[CrossRef\]](#) [\[PubMed\]](#)
62. Gao, Y.L.; Liu, C.S.; Zhao, R.; Wang, L.L.; Li, S.S.; Liu, M.; Zhang, M.; Jiang, S.K.; Tian, Z.L.; Wang, M.; et al. Effects of PI3K/Akt Pathway in Wound Healing Process of Mice Skin. *Fa Yi Xue Za Zhi* **2016**, *32*, 7–12. [\[PubMed\]](#)
63. Di-Poi, N.; Ng, C.Y.; Tan, N.S.; Yang, Z.; Hemmings, B.A.; Desvergne, B.; Michalik, L.; Wahli, W. Epithelium-mesenchyme interactions control the activity of peroxisome proliferator-activated receptor beta/delta during hair follicle development. *Mol. Cell Biol.* **2005**, *25*, 1696–1712. [\[CrossRef\]](#) [\[PubMed\]](#)
64. Paine, A.; Eiz-Vesper, B.; Blasczyk, R.; Immenschuh, S. Signaling to heme oxygenase-1 and its anti-inflammatory therapeutic potential. *Biochem. Pharm.* **2010**, *80*, 1895–1903. [\[CrossRef\]](#) [\[PubMed\]](#)
65. Cho, R.L.; Yang, C.C.; Lee, I.T.; Lin, C.C.; Chi, P.L.; Hsiao, L.D.; Yang, C.M. Lipopolysaccharide induces ICAM-1 expression via a c-Src/NADPH oxidase/ROS-dependent NF-kappaB pathway in human pulmonary alveolar epithelial cells. *Am. J. Physiol. Lung Cell Mol. Physiol.* **2016**, *310*, L639–L657. [\[CrossRef\]](#) [\[PubMed\]](#)
66. Lin, C.C.; Lin, W.N.; Cho, R.L.; Wang, C.Y.; Hsiao, L.D.; Yang, C.M. TNF-alpha-Induced cPLA2 Expression via NADPH Oxidase/Reactive Oxygen Species-Dependent NF-kappaB Cascade on Human Pulmonary Alveolar Epithelial Cells. *Front. Pharm.* **2016**, *7*, 447. [\[CrossRef\]](#)
67. Chuang, D.Y.; Simonyi, A.; Kotzbauer, P.T.; Gu, Z.; Sun, G.Y. Cytosolic phospholipase A2 plays a crucial role in ROS/NO signaling during microglial activation through the lipoxigenase pathway. *J. Neuroinflamm.* **2015**, *12*, 199. [\[CrossRef\]](#) [\[PubMed\]](#)
68. Vile, G.F.; Basu-Modak, S.; Waltner, C.; Tyrrell, R.M. Heme oxygenase 1 mediates an adaptive response to oxidative stress in human skin fibroblasts. *Proc. Natl. Acad. Sci. USA* **1994**, *91*, 2607–2610. [\[CrossRef\]](#) [\[PubMed\]](#)
69. Wu, M.L.; Ho, Y.C.; Lin, C.Y.; Yet, S.F. Heme oxygenase-1 in inflammation and cardiovascular disease. *Am. J. Cardiovasc. Dis.* **2011**, *1*, 150–158.
70. Turkseven, S.; Kruger, A.; Mingone, C.J.; Kaminski, P.; Inaba, M.; Rodella, L.F.; Ikehara, S.; Wolin, M.S.; Abraham, N.G. Antioxidant mechanism of heme oxygenase-1 involves an increase in superoxide dismutase and catalase in experimental diabetes. *Am. J. Physiol. Heart Circ. Physiol.* **2005**, *289*, H701–H707. [\[CrossRef\]](#)
71. Muller, W.A. Mechanisms of leukocyte transendothelial migration. *Annu. Rev. Pathol.* **2011**, *6*, 323–344. [\[CrossRef\]](#)



72. Viac, J.; Schmitt, D.; Claudy, A. Adhesion molecules and inflammatory dermatoses. *Allerg. Immunol. (Paris)* **1994**, *26*, 274–277. [[PubMed](#)]
73. Singer, K.H.; Tuck, D.T.; Sampson, H.A.; Hall, R.P. Epidermal keratinocytes express the adhesion molecule intercellular adhesion molecule-1 in inflammatory dermatoses. *J. Investig. Derm.* **1989**, *92*, 746–750. [[CrossRef](#)]
74. Murakami, M.; Kuwata, H.; Amakasu, Y.; Shimbara, S.; Nakatani, Y.; Atsumi, G.; Kudo, I. Prostaglandin E2 amplifies cytosolic phospholipase A2- and cyclooxygenase-2-dependent delayed prostaglandin E2 generation in mouse osteoblastic cells. Enhancement by secretory phospholipase A2. *J. Biol. Chem.* **1997**, *272*, 19891–19897. [[CrossRef](#)] [[PubMed](#)]
75. Lee, I.T.; Lee, C.W.; Tung, W.H.; Wang, S.W.; Lin, C.C.; Shu, J.C.; Yang, C.M. Cooperation of TLR2 with MyD88, PI3K, and Rac1 in lipoteichoic acid-induced cPLA2/COX-2-dependent airway inflammatory responses. *Am. J. Pathol.* **2010**, *176*, 1671–1684. [[CrossRef](#)] [[PubMed](#)]
76. Mruwat, R.; Cohen, Y.; Yedgar, S. Phospholipase A(2) inhibition as potential therapy for inflammatory skin diseases. *Immunotherapy* **2013**, *5*, 315–317. [[CrossRef](#)] [[PubMed](#)]
77. Soubhye, J.; van Antwerpen, P.; Dufrasne, F. Targeting Cytosolic Phospholipase A2alpha for Novel Anti-Inflammatory Agents. *Curr. Med. Chem.* **2018**, *25*, 2418–2447. [[CrossRef](#)] [[PubMed](#)]
78. Sandilands, A.; Sutherland, C.; Irvine, A.D.; McLean, W.H. Filaggrin in the frontline: Role in skin barrier function and disease. *J. Cell Sci.* **2009**, *122*, 1285–1294. [[CrossRef](#)] [[PubMed](#)]
79. Jin, S.H.; Choi, D.; Chun, Y.J.; Noh, M. Keratinocyte-derived IL-24 plays a role in the positive feedback regulation of epidermal inflammation in response to environmental and endogenous toxic stressors. *Toxicol. Appl. Pharmacol.* **2014**, *280*, 199–206. [[CrossRef](#)] [[PubMed](#)]



© 2019 by the authors. Licensee MDPI, Basel, Switzerland. This article is an open access article distributed under the terms and conditions of the Creative Commons Attribution (CC BY) license (<http://creativecommons.org/licenses/by/4.0/>).



Article

# Positive Effects of Ger-Gen-Chyn-Lian-Tang on Cholestatic Liver Fibrosis in Bile Duct Ligation-Challenged Mice

Zi-Yu Chang <sup>1,2,†</sup>, Chin-Chang Chen <sup>1,3,†</sup>, Hsuan-Miao Liu <sup>4</sup>, Yuan-Chieh Yeh <sup>1</sup>, Tung-Yi Lin <sup>1,4</sup> , Tzung-Yan Lee <sup>1,2,4,5,\*</sup> and Tse-Hung Huang <sup>1,3,4,5,6,7,\*</sup>

<sup>1</sup> Department of Traditional Chinese Medicine, Chang Gung Memorial Hospital, Keelung 204, Taiwan

<sup>2</sup> Institute of Traditional Medicine, School of Medicine, National Yang-Ming University, Taipei 112, Taiwan

<sup>3</sup> Research Center for Chinese Herbal Medicine, Chang Gung University of Science and Technology, Taoyuan 333, Taiwan

<sup>4</sup> Graduate Institute of Traditional Chinese Medicine, Chang Gung University, Taoyuan 333, Taiwan

<sup>5</sup> School of Traditional Chinese Medicine, Chang Gung University, Taoyuan 333, Taiwan

<sup>6</sup> School of Nursing, National Taipei University of Nursing and Health Sciences, Taipei 112, Taiwan

<sup>7</sup> Graduate Institute of Health Industry Technology, Chang Gung University of Science and Technology, Taoyuan 333, Taiwan

\* Correspondence: joyamen@mail.cgu.edu.tw (T.-Y.L.); huangtsehung@gmail.com (T.-H.H.)

† These authors contributed equally to this work.

Received: 5 July 2019; Accepted: 24 August 2019; Published: 26 August 2019



**Abstract:** The purpose of this study was to investigate whether Ger-Gen-Chyn-Lian-Tang (GGCLT) suppresses oxidative stress, inflammation, and angiogenesis during experimental liver fibrosis through the hypoxia-inducible factor-1 $\alpha$  (HIF-1 $\alpha$ )-mediated pathway. Male C57BL/6 mice were randomly assigned to a sham-control or bile duct ligation (BDL) group with or without treatment with GGCLT at 30, 100, and 300 mg/kg. Plasma alanine aminotransferase (ALT) levels were analyzed using a diagnostic kit. Liver histopathology and hepatic status parameters were measured. Compared to control mice, the BDL mice exhibited an enlargement in liver HIF-1 $\alpha$  levels, which was suppressed by 100 and 300 mg/kg GGCLT treatments (control: BDL: BDL + GGCLT-100: BDL + GGCLT-300 =  $0.95 \pm 0.07$ :  $1.95 \pm 0.12$ :  $1.43 \pm 0.05$ :  $1.12 \pm 0.10$  fold;  $p < 0.05$ ). GGCLT restrained the induction of hepatic hydroxyproline and malondialdehyde levels in the mice challenged with BDL, further increasing the hepatic glutathione levels. Furthermore, in response to increased hepatic inflammation and fibrogenesis, significant levels of ALT, nuclear factor kappa B, transforming growth factor- $\beta$ ,  $\alpha$ -smooth muscle actin, matrix metalloproteinase-2 (MMP-2), MMP-9, and procollagen-III were found in BDL mice, which were attenuated with GGCLT. In addition, GGCLT reduced the induction of angiogenesis in the liver after BDL by inhibiting vascular endothelial growth factor (VEGF) and VEGF receptors 1 and 2. In conclusion, the anti-liver fibrosis effect of GGCLT, which suppresses hepatic oxidative stress and angiogenesis, may be dependent on an HIF-1 $\alpha$ -mediated pathway.

**Keywords:** Ger-Gen-Chyn-Lian-Tang; liver fibrosis; HIF-1 $\alpha$ ; oxidative stress; angiogenesis

## 1. Introduction

Extracellular matrix (ECM) degradation, which disrupts the normal architecture of the liver, is a major characteristic in hepatic fibrosis, a common pathway to chronic liver disease [1,2]. It has been reported that fibrogenesis-mediated impaired blood supply induces a hypoxic microenvironment as a consequence of fibrosis, which leads to liver cirrhosis [3]. Previous evidence suggests that hypoxia promotes inflammation and fibrosis in the liver by the activation of hypoxia-inducible

factor-1 $\alpha$  (HIF-1 $\alpha$ ) and nuclear factor kappa B (NF- $\kappa$ B) under the regulation of fibrogenesis and angiogenesis [4,5]. Furthermore, hypoxic-induced generation of reactive oxygen species greatly aggravates inflammation [4], which promotes ECM deposition [6]. In addition, activated hepatic stellate cells (HSCs) and portal myofibroblasts stimulate angiogenesis by inducing vascular endothelial growth factor (VEGF) in the pathogenesis of liver fibrosis [7,8]. The HIF-1 protein complex is activated in response to a hypoxic microenvironment and acts as a vital transcriptional regulator by binding to nuclear hypoxia response elements. It is noteworthy that hypoxia contributes to organ fibrosis by causing epithelial-to-mesenchymal transition (EMT) in tubular epithelial cells via HIF-1 signaling [9]. Moreover, the transforming growth factor- $\beta$  (TGF- $\beta$ ) signal pathway also plays a vital role in HSC activation through the stimulation of HIF-1 $\alpha$  [10,11].

Bile duct ligation (BDL) is a surgical procedure in the common bile duct that is used to cause extrahepatic biliary obstruction, which mimics cholestatic liver damage. The process of BDL-induced liver cirrhosis is that it induces the rapid growth of biliary epithelial cells and oval cells, then causes bile ductular proliferation, cholestasis, and fibrosis, ultimately leading to secondary biliary cirrhosis [12–14]. Following this process, rodent models exhibit alterations of phagocytic, immune, and macrophage function, as well as neutrophil recruitment in the liver tissues [15–17]. In this regard, BDL in mice is a widespread model used to induce biliary inflammation, fibrosis and cholestatic liver injury [18]. In addition, persinusoidal and periportal fibrosis have both been reported to have fully developed on day 10 and day 20, respectively, after BDL surgery in mice [19]. Previously, Gabbiani and his colleagues suggested that a marked expansion of portal fibroblasts played an initiating role in the early development of liver fibrosis by rapidly inducing  $\alpha$ -smooth muscle actin ( $\alpha$ -SMA) expression and ECM deposition in BDL-challenged rats [20,21]. Furthermore, Moczydlowska et al. demonstrated that matrix metalloproteinase-2 (MMP-2) and MMP-9 were highly regulated and involved in the mechanism of liver fibrosis via upregulation of HIF-1 $\alpha$  and NF- $\kappa$ B transcriptional activation after BDL challenge [22]. a previous study indicated that HIF-1 $\alpha$  is activated in the livers of BDL-treated mice [23]. Of note, a large amount of nuclear HIF-1 $\alpha$  accumulated in bile obstruction- and periportal region-adjacent hepatocytes and macrophages in the early stage of BDL. Moreover, hypoxia induced the expression of VEGF in an in vitro study of rodent hepatocytes [24,25], and VEGF has been shown to stimulate the proliferation and chemoattraction of HSCs to promote liver fibrosis [26–28]. Additionally, both receptors between integrins and TGF- $\beta$  induce signaling that stimulate collagen biosynthesis and fibrotic generation [29].

Ger-Gen-Chyn-Lian-Tang (GGCLT), a standardized Chinese herbal medicine used in Taiwan, contains *Puerariae radix*, *Scutellariae radix*, *Coptidis rhizome*, and *Glycyrrhizae radix*. a previous study revealed that GGCLT treatment reduced progression of atherosclerosis in an apolipoprotein E<sup>-/-</sup> mouse model [30]. Meanwhile, our previous report suggested that GGCLT protected hepatic cells from thioacetamide-induced liver injury via the reduction of oxidative stress status [31]. It has been reported that puerarin, baicalin, berberine and glycyrrhiza are the effective constituents of *Puerariae radix*, *Scutellariae radix*, *Coptidis rhizoma* and *Glycyrrhizae radix*, respectively [32–35]. Previous studies have indicated that puerarin, baicalin, and berberine can suppress cell proliferation and angiogenesis in diabetic retinopathy, pulmonary hypertension and tumor-directed capillary formation, respectively, by downregulating HIF-1 expression [36–38]. a better understanding of the cellular and molecular mechanisms in liver fibrogenesis can be gained by using multiple experimental rodent model systems. Therefore, we investigated whether GGCLT suppresses the oxidative stress, inflammation, and angiogenesis underlying hypoxia during BDL-induced liver fibrosis in mice.

## 2. Results

### 2.1. GGCLT Treatment Effect on Liver Injury and Hepatic Oxidative Stress

At first, the four main index ingredients of our prepared GGCLT, specifically puerarin, baicalin, berberine and glycyrrhiza, were identified using high-performance liquid chromatography (HPLC), and are shown in Figure 1. As shown in Figure 2A, a large deposition of collagen fibers in perivenular

and periportal areas of the liver lobules was found in BDL-challenged mice. Subsequently, mice that received 300 mg/kg GGCLT showed a thinner septum of collagen, a decrease in inflammatory cells, and retained hepatic parenchyma more than the mice with BDL. In comparison with the sham-control group, a significant elevation of plasma alanine aminotransferase (ALT) levels and hepatic HIF-1 $\alpha$  mRNA expression occurred in the BDL mice, which was suppressed by GGCLT treatment, especially at doses of 100 and 300 mg/kg (Figure 2B,C). Moreover, the hydroxyproline and thiobarbituric acid reactive substances (TBARS) levels in the liver tissues were markedly increased in the BDL mice in comparison with the sham-control mice. Administration of GGCLT significantly attenuated the increase in hydroxyproline and TBARS in the BDL mice (Figure 3A,B). In addition, a significant decrease in hepatic glutathione (GSH) activity occurred after the BDL challenge; this effect was reversed by treatment with GGCLT at doses of 100 and 300 mg/kg (Figure 3C).

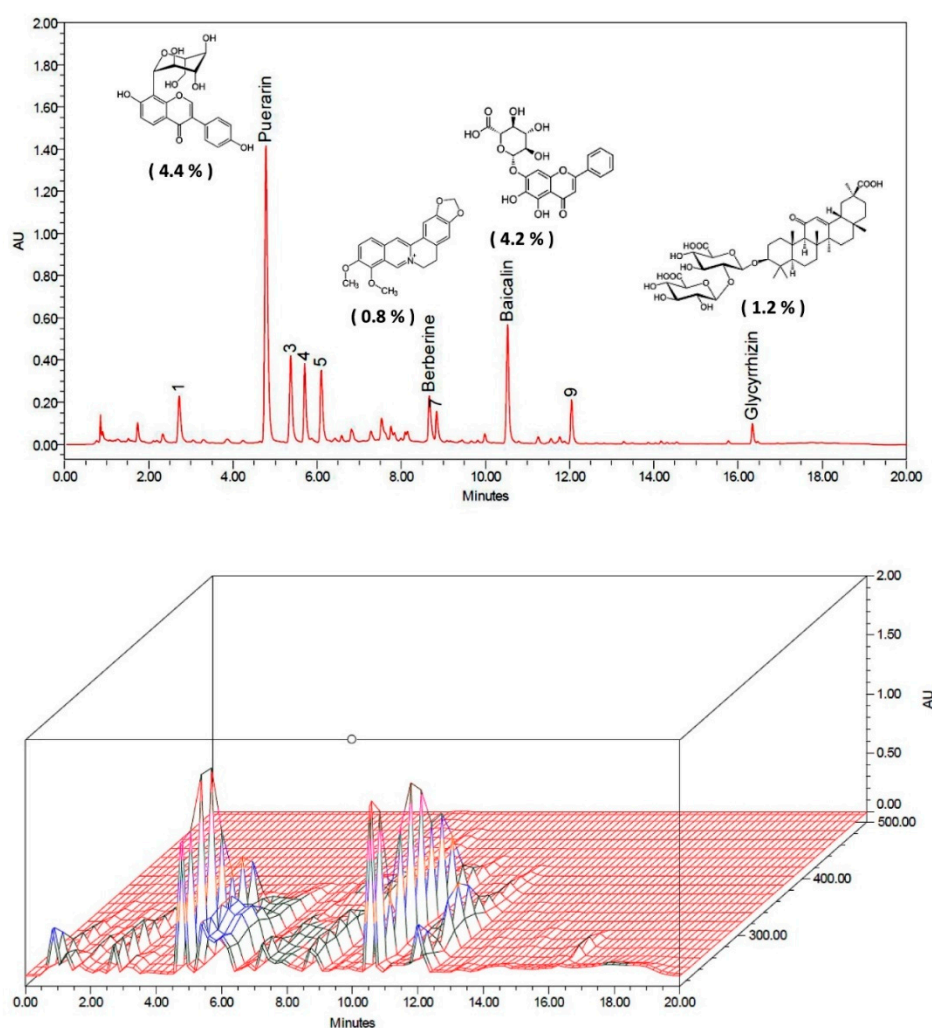


**Figure 1.** Chromatogram of Ger-Gen-Chyn-Lian-Tang (GGCLT) by high-performance liquid chromatography (HPLC) analysis. The upper panel shows the peaks, compound structure, and ingredient percentages of puerarin, baicalin, berberine, and glycyrrhiza, the four main index components of *Puerariae radix*, *Scutellariae radix*, *Coptidis rhizoma* and *Glycyrrhizae radix*, respectively. The lower panel shows the fingerprint of the three-dimensional structures of these four main index components, as determined by HPLC analysis.

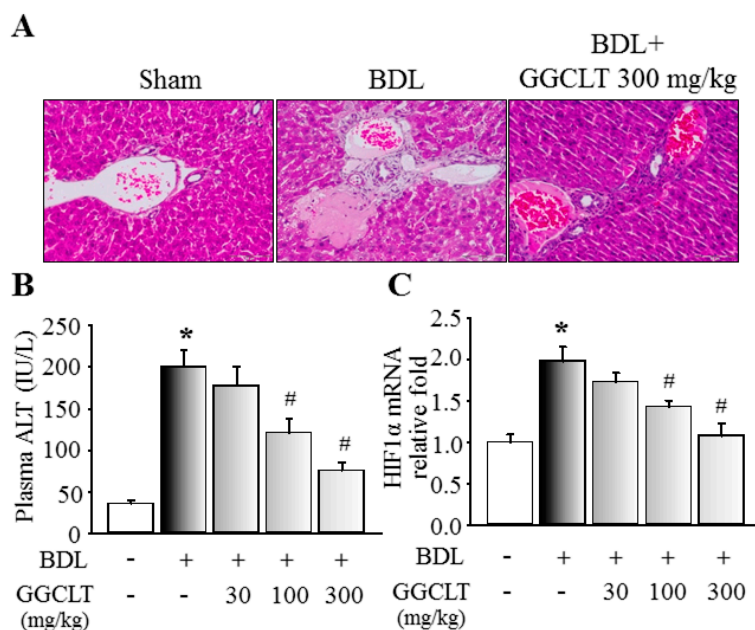


**Figure 2.** GGCLT-attenuated bile duct ligation (BDL)-induced liver injury in mice. **(A)** Representative histological results of liver tissue stained with hematoxylin and eosin from a sham-control mouse, a BDL mouse, and a BDL mouse treated with 300 mg/kg GGCLT (200× magnification); **(B)** plasma alanine aminotransferase (ALT) levels; and **(C)** hepatic hypoxia-inducible factor-1α (HIF-1α) mRNA levels. \*  $p < 0.05$  vs. sham-control mice ( $n = 6$ ), #  $p < 0.05$  vs. BDL mice ( $n = 8$ ).

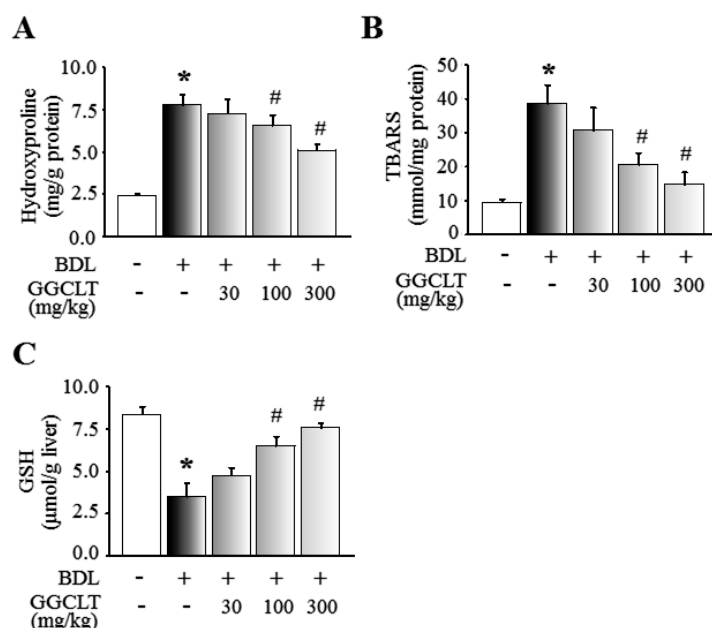


**Figure 3.** GGCLT reduced BDL-induced oxidative stress in the liver tissues of mice. **(A)** Hepatic hydroxyproline content; **(B)** hepatic lipid peroxidation represented by thiobarbituric acid reactive substances (TBARS); and **(C)** hepatic glutathione (GSH) levels. \*  $p < 0.05$  vs. sham-control mice ( $n = 6$ ); #  $p < 0.05$  vs. BDL mice ( $n = 8$ ).

## 2.2. GGCLT Treatment Effect on Fibrogenesis and Angiogenesis-Related Factors in the Liver

The results of Western blotting showed that hepatic levels of NF-κB, α-SMA, TGFβ-R1, and TGFβ-R2, four fibrogenesis-related factors, were obviously elevated to a greater extent in the BDL mice than in the sham-control mice. However, these effects were suppressed by 300 mg/kg

GGCLT administration (Figure 4). In parallel, the hepatic mRNA levels of TGF- $\beta$ , MMP-2, MMP-9, and procollagen-III were increased in the livers of the BDL mice and then decreased after treatment with GGCLT (Figure 5). GGCLT treatment also decreased the hepatic mRNA levels of VEGF, VEGFR1, and VEGFR2 in the BDL mice (Figure 6). GGCLT treatment suppressed the increase of HIF-1 $\alpha$  and fibrogenesis- and angiogenesis-related factors in the livers of BDL-challenged mice.

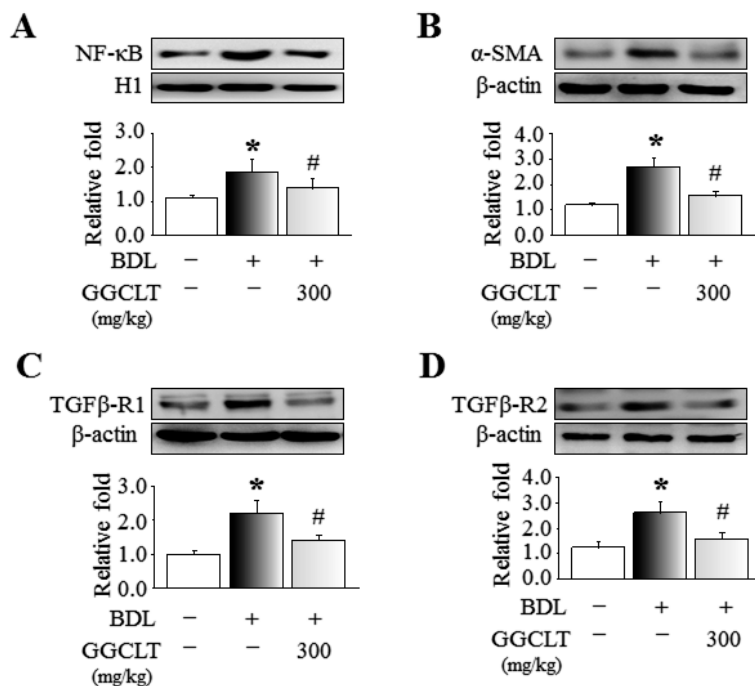


**Figure 4.** Western blot analysis of hepatic protein levels of (A) nuclear factor kappa B (NF- $\kappa$ B), (B)  $\alpha$ -smooth muscle actin ( $\alpha$ -SMA), (C) transforming growth factor- $\beta$  (TGF $\beta$ )-R1 and (D) TGF $\beta$ -R2 in the liver tissues of sham-control mice and BDL mice treated with or without 300 mg/kg GGCLT. The data presented are the mean  $\pm$  SEM from three independent measurements. \*  $p < 0.05$  vs. sham-control mice; #  $p < 0.05$  vs. BDL mice.

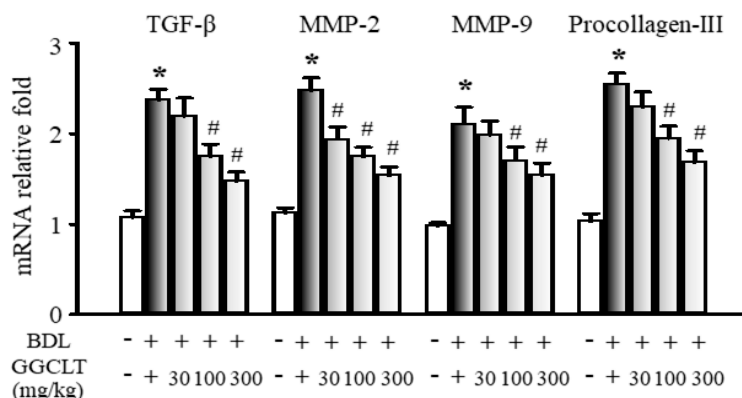


**Figure 5.** Effects of GGCLT on hepatic fibrotic signaling in BDL mice. The quantitative real-time PCR results show the mRNA levels of TGF- $\beta$ , matrix metalloproteinase-2 (MMP-2), MMP-9, and procollagen-III in the liver tissues. The data presented are the mean  $\pm$  SEM from three independent measurements. \*  $p < 0.05$  vs. sham-control mice; #  $p < 0.05$  vs. BDL mice.



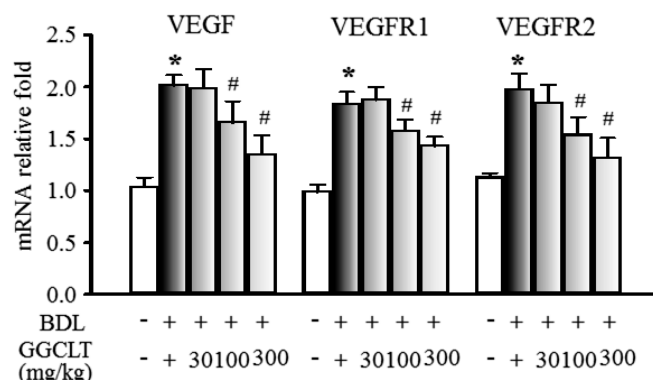


**Figure 6.** Effects of GGCLT on hepatic levels of HIF-1 $\alpha$  and angiogenesis-regulated factors in BDL mice. The quantitative real-time PCR results show the mRNA levels of vascular endothelial growth factor (VEGF), VEGFR1, and VEGFR2 in the liver tissues. The data presented are the mean  $\pm$  SEM from three independent measurements. \*  $p < 0.05$  vs. sham-control mice; #  $p < 0.05$  vs. BDL mice.

### 3. Discussion

Hypoxia-inducible factors are key mediators of fibrogenesis and angiogenesis in hypoxic liver cells. Therefore, a pharmaceutical strategy for liver fibrosis involving inhibition of the level of HIF-1 $\alpha$  may be beneficial for patients with liver disease. It has been reported that HIF-1 $\alpha$  is activated in mice with BDL-induced liver fibrosis [23]. Despite the relatively high mortality rates due to bile leakage and rupture of biliary cysts, BDL-induced liver fibrosis is still widely used in mice models. This is because of its advantage of more convenient manipulation on targeted gene knockouts, which is a powerful strategy to address genic disorders. Our findings demonstrated that GGCLT treatment improved liver fibrosis caused by BDL in mice, in part through a decrease in HIF-1 $\alpha$ -induced elevation of inflammation, oxidative stress, and angiogenesis-related factors.

Hydroxyproline serves as a marker of collagen deposition in liver fibrosis. According to a report by Moczydłowska et al., BDL results in the significant upregulation of hydroxyproline, HIF-1 $\alpha$ , TGF- $\beta$ , MMP-2, and MMP-9 in rats with liver fibrosis [22]. Moreover, Copple et al. suggested that HIF-1 $\alpha$  deficiency is responsible for the reduction of collagen deposition in the liver of mice after BDL challenge as it reduces hepatic  $\alpha$ -SMA and type I collagen expression [25]. It is noteworthy that the transcriptional activity of NF- $\kappa$ B is critical for HIF-1 $\alpha$  to contribute to hypoxic liver disease [4,39]. In the present study, we observed a significant reduction in plasma ALT levels, inflammatory cell infiltration, and hepatic levels of hydroxyproline, NF- $\kappa$ B,  $\alpha$ -SMA, TGF- $\beta$ , MMP-2 and MMP-9 in the BDL mice after treatment with 300 mg/kg of GGCLT. Therefore, for our BDL-challenge mouse model, we speculate that hepatic inflammatory cells may have triggered HSCs to produce a deposition of collagen by releasing profibrotic growth factors, thus causing liver fibrosis, and GGCLT diminished these phenomena. Meanwhile, we suggest that NF- $\kappa$ B plays an essential role in these mechanisms. Of note, portal fibroblasts have a dominant role—alongside HSCs—in early liver fibrogenesis in rats through their stimulation of  $\alpha$ -SMA levels and ECM deposition during the first 72 h after BDL challenge [20,21]. In addition, portal myofibroblasts promote angiogenic properties and vascular remodeling by increasing VEGFA and VEGFR2 levels, thereby underlying hepatic fibrosis formation [8]. However, there has been little exploration of the relationship between proliferation of portal fibroblasts and a hypoxic microenvironment (e.g., upregulation of HIF-1 $\alpha$ ) at the beginning of cholestatic liver fibrosis. Therefore, our future studies on whether GGCLT treatment could restrain expansion of portal fibroblasts and enhance HIF-1 $\alpha$  in the liver in the early stages after a BDL surgical procedure (e.g., 1 to 3 days) are warranted.

VEGF is a crucial angiogenic factor that enhances wound healing and tumor growth in hypoxia. It has distinctive binding specificities to VEGFR1 and VEGFR2, which are expressed in the vascular endothelium to mediate its biologic effects [40]. Moreover, VEGF and angiopoietin-1, produced by activated HSCs, have been shown to trigger angiogenesis in a murine model with

liver fibrosis or following exposure to leptin [41,42]. Based on our findings, we suggest that VEGF enhances angiogenesis through VEGFR-1 and VEGFR-2 in the BDL mouse model, in which GGCLT inhibited VEGF.

In rats, BDL increases oxidative stress in the liver, which is characterized by increases in hepatic lipid peroxidation and total nonprotein mixed disulfides, as well as a reduction in glutathione [43,44]. Of note, oxidative stress is a major feature of experimental models of fibrosis. Antioxidants have been proven to be partially effective in the treatment of fibrosis and cirrhosis [45]. In our study, the hepatic hydroxyproline and malondialdehyde levels were obviously increased in experimental cholestatic liver fibrosis, revealing increased oxidative stress. In contrast, BDL-challenged mice treated with GGCLT displayed a vigorous increase in the level of hepatic GSH. Thus, GGCLT may act as an antioxidant. GGCLT is widely reported to ameliorate gastrointestinal dysfunction and upregulate the immune response to combat inflammation, and it has been beneficial for the treatment of infectious diseases [46]. However, the mechanism underlying GGCLT's antifibrotic activity is still unclear. Based on our findings, we suggest that the possible mechanisms of the anti-liver fibrosis effect of GGCLT (i.e., suppression of hepatic oxidative stress and angiogenesis) may be dependent on an HIF-1 $\alpha$ -mediated pathway. As such, a schematic hypothesis of the anti-liver fibrosis effect of GGCLT is shown in Figure 7. Taken together, cholestatic cholangiopathy and liver fibrosis, which result from biliary duct obstruction, may manifest early in life and present a therapeutic challenge that necessitates surgical operation. According to the principles of treatment in traditional Chinese medicine (TCM), GGCLT aims to "clear heat and detoxify", and may be used to treat liver fibrosis. Therefore, we suggest GGCLT as a complementary therapeutic strategy in chronic liver disease for clinical practice.

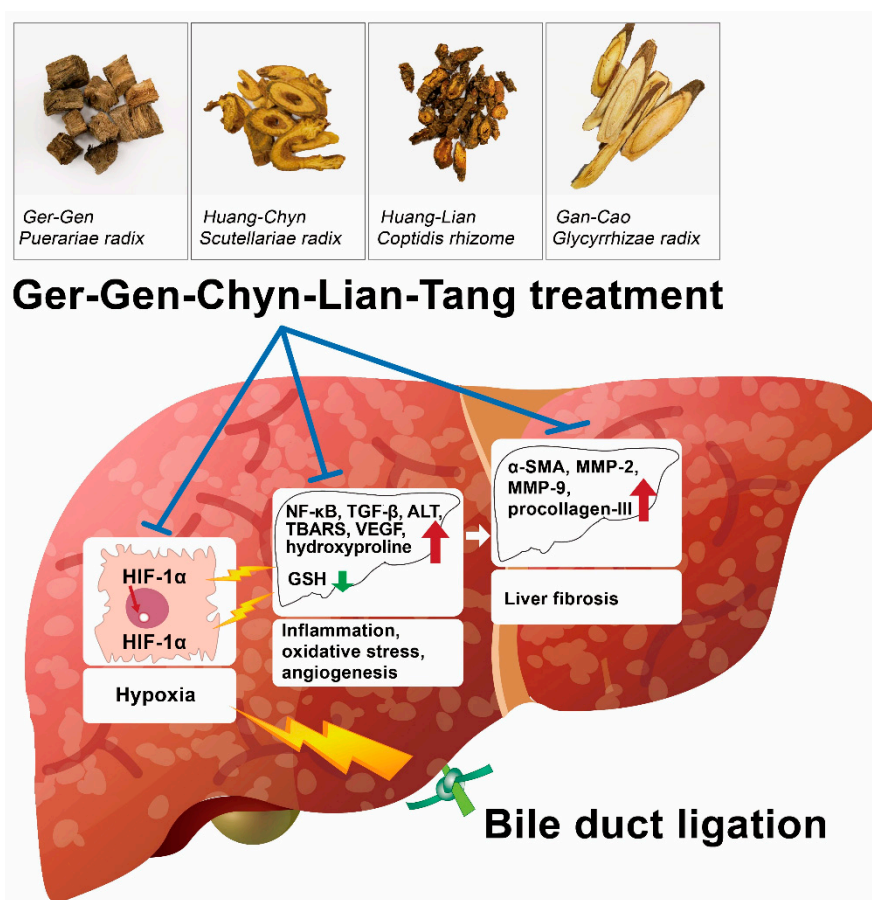


**Figure 7.** Schematic representative hypothesis of the use of GGCLT treatment to decrease inflammation, oxidative stress and angiogenesis, and further improve liver fibrosis in BDL-challenged mice in our study.

## 4. Materials and Methods

### 4.1. Preparation of GGCLT

The preparation and formula analysis of GGCLT were conducted according to our previous study [31]. Powdered constituents of GGCLT were mixed from the crude ingredients of *P. radix*, *S. radix*, *C. rhizome*, and *G. radix* at a ratio of 8:3:3:2 by weight. Firstly, the GGCLT power was boiled with dH<sub>2</sub>O at 80 °C for 2 h. The mixture was filtered and frozen at −80 °C to create a paste crystal residue, with an approximate yield of 12.5% (*w/w*). These contents were lyophilized at −20 °C. The dried compound was subsequently dissolved in dH<sub>2</sub>O before use.

### 4.2. Animals and Experimental Protocols

Male C57BL/6 mice (5–6 weeks old) were obtained from the National Laboratory Animal Center (Taipei, Taiwan) and were housed in a temperature-controlled chamber at 20 ± 2 °C under a 12 h light/dark cycle. Mice were randomly grouped and treated with either dH<sub>2</sub>O or GGCLT at the three doses of 30, 100, and 300 mg/kg body weight. Treatment was administered via gastric gavage, occurring once per day for 4 weeks. Hepatic fibrosis in mice was performed through a BDL procedure. In brief, mice were anaesthetized with inhalation of 4 vol% isoflurane in 100% oxygen at a flow rate of 4 L/min for execution of a ventral laparotomy. Subsequently, the common bile duct above the duodenum was ligated with 3-0 silk by two ligatures and sectioned between the ligatures. The midline abdominal incision was closed with catgut. The sham-control mice also underwent a laparotomy and manipulation of the common bile duct but without ligation. In addition, the sham-control mice were gavaged with an equal volume of dH<sub>2</sub>O. At the end of the procedure, the mice were anesthetized by CO<sub>2</sub> inhalation prior to decapitation. The plasma and liver tissues were collected for further analysis. All experimental animal protocols were approved by the Chang Gung Memorial Hospital Animal Care and Use Committee (IACUC No.2016060603) in accordance with the International Guidelines for Humane Animal Care and Use.

### 4.3. Analyses of Liver Histology, Cytokines, and Biochemicals

Liver hematoxylin and eosin staining was performed according to our previous protocol [31]. Plasma alanine aminotransferase was measured using a commercially available colorimetric kit (Randox Laboratories, Antrim, UK). The hepatic hydroxyproline content was determined according to previously published methods [31]. The production of thiobarbituric acid reactive substances (TBARS) was used to represent the amount of lipid peroxidation and was expressed as malondialdehyde equivalents. The amount of malondialdehyde was assessed by spectrophotometric measurement of the absorbance at 535 nm and 37 °C; the results are expressed as nmol/mg protein. The hepatic glutathione was analyzed colorimetrically using a commercially available assay kit (Cayman, MI, USA) in accordance with the manufacturer's instructions.

### 4.4. Quantitative Real-Time PCR

Total RNA was prepared using the guanidinium-phenol-chloroform method. Reverse transcription was performed using a RevertAid First Strand cDNA Synthesis Kit (Thermo Scientific, Waltham, MA, USA) in accordance with the manufacturer's protocol. Quantitative real-time PCR using the SYBR system was conducted on a LightCycler 1.5 apparatus (both from Roche Applied Science, Mannheim, Germany). The PCR reaction was performed under the following conditions: 95 °C for 10 min and then 45 cycles of 95 °C for 15 s, 57 °C for 30 s and 72 °C for 30 s. The real-time PCR data were normalized to glyceraldehyde 3-phosphate dehydrogenase (GAPDH) expression. The primer sequences are listed in Table 1.

**Table 1.** Primer sequences used for quantitative real-time PCR analysis.

Gene	Forward	Reverse
HIF-1 $\alpha$	TCAAGTCAGCAACGTGGAAG	TATCGAGGCTGTGTCGACTG
VEGF	GAGAGAGGCCGAAGTCCTTT	TTGGAACCGGCATCTTATC
VEGFR1	GAAGCGGTTACCTGGACTGAGACC	GGCTTTGCTGGGGGATTCTCTAA
VEGFR2	ACAGCAGTGGGATGGTCCTTGCA	AAACAGGAGGTGAGCTGCAGTGTGG
TGF- $\beta$	TGCCCTCTACAACCAACACAACCCG	AACTGCTCCACCTTGGGCTTGCAGC
MMP-2	GCTGATACTGACA CTGGTACTG	CAATCTTTTCTGGGAGCTC
MMP-9	CGTCGTGATCCCCACTTACT	AGAGTACTGCTTGCCAGGA
Procollagen-III	CCCCTGGTCCCTGCTGTGG	GAGGCCCGGCTGGAAAGAA
GAPDH	CCCTTCATTGACCTCAACTACATGG	CATGGTGGTGAAGACGCCAG

HIF-1 $\alpha$ , hypoxia-inducible factor-1 $\alpha$ ; VEGF, vascular endothelial growth factor; VEGFR1 and 2, vascular endothelial growth factor receptor 1 and 2; TGF- $\beta$ , transforming growth factor- $\beta$ ; MMP-2 and 9, matrix metalloproteinase-2 and 9.

#### 4.5. Western Blot Measurement

The liver tissue was lysed in 0.5 mL of CelLytic M lysis reagent (Sigma-Aldrich, St. Louis, MO, USA) with 1% phosphatase inhibitor cocktail and protease inhibitor cocktail and centrifuged at 13,000 $\times$  g for 30 min at 4 °C. The concentration of protein lysate was determined using the Bradford assay. In addition, the nuclear fraction was harvested using a nuclear extraction kit (Abcam, Cambridge, MA, USA) in accordance with the manufacturer's instructions. The cell lysates were separated using sodium dodecyl sulfate (SDS)-polyacrylamide gel electrophoresis and transferred onto polyvinylidene fluoride (PVDF) membranes, following incubation with primary antibodies against NF- $\kappa$ B,  $\alpha$ -SMA, TGF $\beta$ -R1, and TGF $\beta$ -R2 (all from Santa Cruz Biotechnology, Dallas, TX, USA). Finally, horseradish peroxidase-conjugated secondary antibodies were added, and the reaction was detected by electrochemiluminescence. The data were calibrated using H1 and  $\beta$ -actin as internal controls.

#### 4.6. Statistical Analysis

All samples for each experimental analysis were randomized. Data are expressed as a mean  $\pm$  SEM. Quantitative variables were compared using Student's *t*-tests. *p* < 0.05 was considered statistically significant.

**Author Contributions:** Z.-Y.C. and C.-C.C. executed the experiments and wrote the majority of the manuscript; H.-M.L. executed the experiments and wrote a small part of the manuscript; Y.-C.Y. and T.-Y.L. (Tung-Yi Lin) contributed to the data analysis and figures preparation; T.-Y.L. (Tzung-Yan Lee) and T.-H.H. provided the initial concept, arranged the study design and checked the final manuscript. All authors approved the manuscript.

**Funding:** This work was supported by grants from Chang Gung Memorial Hospital Research Foundation, Taiwan (CMRPG2F0141-2, CMRPG3A0661, CMRPG2B0281, CMRPG2D0091-3, CMRPG2C0291, and CMRPG2C0292) and the Ministry of Science and Technology, Taipei, Taiwan (MOST 105-2314-B-182A-133).

**Acknowledgments:** The authors thank the research assistants of high performance liquid chromatography by Chuang Song Zong Pharmaceutical Co., Ltd., especially Shu-Tuan Chiang for her technical assistance.

**Conflicts of Interest:** The authors declare no conflict of interest.

#### References

1. Friedman, S.L. Liver fibrosis—from bench to bedside. *J. Hepatol.* **2003**, *38*, S38–S53. [[CrossRef](#)]
2. Iredale, J.P. Models of liver fibrosis: Exploring the dynamic nature of inflammation and repair in a solid organ. *J. Clin. Invest.* **2007**, *117*, 539–548. [[CrossRef](#)] [[PubMed](#)]
3. Kim, K.R.; Moon, H.E.; Kim, K.W. Hypoxia-induced angiogenesis in human hepatocellular carcinoma. *J. Mol. Med.* **2002**, *80*, 703–714. [[CrossRef](#)] [[PubMed](#)]
4. Rosmorduc, O.; Housset, C. Hypoxia: a link between fibrogenesis, angiogenesis, and carcinogenesis in liver disease. *Semin. Liver Dis.* **2010**, *30*, 258–270. [[CrossRef](#)] [[PubMed](#)]
5. Bozova, S.; Elpek, G.O. Hypoxia-inducible factor-1 $\alpha$  expression in experimental cirrhosis: Correlation with vascular endothelial growth factor expression and angiogenesis. *Apmis* **2007**, *115*, 795–801. [[CrossRef](#)]

6. Cannito, S.; Novo, E.; Compagnone, A.; Valfre di Bonzo, L.; Busletta, C.; Zamara, E.; Paternostro, C.; Povero, D.; Bandino, A.; Bozzo, F.; et al. Redox mechanisms switch on hypoxia-dependent epithelial-mesenchymal transition in cancer cells. *Carcinogenesis* **2008**, *29*, 2267–2278. [[CrossRef](#)] [[PubMed](#)]
7. Thabut, D.; Shah, V. Intrahepatic angiogenesis and sinusoidal remodeling in chronic liver disease: New targets for the treatment of portal hypertension? *J. Hepatol.* **2010**, *53*, 976–980. [[CrossRef](#)]
8. Lemoine, S.; Cadoret, A.; Rautou, P.E.; El Mourabit, H.; Ratzu, V.; Corpechot, C.; Rey, C.; Bosselut, N.; Barbu, V.; Wendum, D. Portal myofibroblasts promote vascular remodeling underlying cirrhosis formation through the release of microparticles. *Hepatology* **2015**, *61*, 1041–1055. [[CrossRef](#)]
9. Higgins, D.F.; Kimura, K.; Bernhardt, W.M.; Shrimanker, N.; Akai, Y.; Hohenstein, B.; Saito, Y.; Johnson, R.S.; Kretzler, M.; Cohen, C.D.; et al. Hypoxia promotes fibrogenesis in vivo via HIF-1 stimulation of epithelial-to-mesenchymal transition. *J. Clin. Invest.* **2007**, *117*, 3810–3820. [[CrossRef](#)]
10. Shi, Y.F.; Fong, C.C.; Zhang, Q.; Cheung, P.Y.; Tzang, C.H.; Wu, R.S.; Yang, M. Hypoxia induces the activation of human hepatic stellate cells LX-2 through TGF-beta signaling pathway. *FEBS Lett.* **2007**, *581*, 203–210. [[CrossRef](#)]
11. Meurer, S.K.; Tihaa, L.; Borkham-Kamphorst, E.; Weiskirchen, R. Expression and functional analysis of endoglin in isolated liver cells and its involvement in fibrogenic Smad signalling. *Cell Signal.* **2011**, *23*, 683–699. [[CrossRef](#)]
12. Geerts, A.M.; Vanheule, E.; Praet, M.; Van Vlierberghe, H.; De Vos, M.; Colle, I. Comparison of three research models of portal hypertension in mice: macroscopic, histological and portal pressure evaluation. *Int. J. Exp. Pathol.* **2008**, *89*, 251–263. [[CrossRef](#)]
13. Kountouras, J.; Billing, B.H.; Scheuer, P.J. Prolonged bile duct obstruction: a new experimental model for cirrhosis in the rat. *Br. J. Exp. Pathol.* **1984**, *65*, 305–311.
14. Popov, Y.; Sverdlov, D.Y.; Bhaskar, K.R.; Sharma, A.K.; Millonig, G.; Patsenker, E.; Krahenbuhl, S.; Krahenbuhl, L.; Schuppan, D. Macrophage-mediated phagocytosis of apoptotic cholangiocytes contributes to reversal of experimental biliary fibrosis. *Am. J. Physiol. Gastrointest. Liver Physiol.* **2010**, *298*, G323–G334. [[CrossRef](#)]
15. Scott-Conner, C.E.; Grogan, J.B. The pathophysiology of biliary obstruction and its effect on phagocytic and immune function. *J. Surg. Res.* **1994**, *57*, 316–336. [[CrossRef](#)]
16. Minter, R.M.; Fan, M.H.; Sun, J.; Niederbichler, A.; Ipaktchi, K.; Arbabi, S.; Hemmila, M.R.; Remick, D.G.; Wang, S.C.; Su, G.L. Altered Kupffer cell function in biliary obstruction. *Surgery* **2005**, *138*, 236–245. [[CrossRef](#)]
17. Saito, J.M.; Maher, J.J. Bile duct ligation in rats induces biliary expression of cytokine-induced neutrophil chemoattractant. *Gastroenterology* **2000**, *118*, 1157–1168. [[CrossRef](#)]
18. Prado, I.B.; Santos, M.H.H.; Lopasso, F.P.; Iriya, K.; Laudanna, A.A. Cholestasis in a murine experimental model: lesions include hepatocyte ischemic necrosis. *Rev. Hosp. Clín.* **2003**, *58*, 27–32. [[CrossRef](#)]
19. Tag, C.G.; Sauer-Lehnen, S.; Weiskirchen, S.; Borkham-Kamphorst, E.; Tolba, R.H.; Tacke, F.; Weiskirchen, R. Bile duct ligation in mice: induction of inflammatory liver injury and fibrosis by obstructive cholestasis. *J. Vis. Exp.* **2015**, *96*, e52438. [[CrossRef](#)]
20. Tuchweber, B.; Desmouliere, A.; Bochaton-Piallat, M.-L.; Rubbia-Brandt, L.; Gabbiani, G. Proliferation and phenotypic modulation of portal fibroblasts in the early stages of cholestatic fibrosis in the rat. *Lab. Invest.* **1996**, *74*, 265–278.
21. Desmouliere, A.; Darby, I.; Costa, A.; Raccurt, M.; Tuchweber, B.; Sommer, P.; Gabbiani, G. Extracellular matrix deposition, lysyl oxidase expression, and myofibroblastic differentiation during the initial stages of cholestatic fibrosis in the rat. *Lab. Invest.* **1997**, *76*, 765–778.
22. Moczydlowska, J.; Mityk, W.; Hermanowicz, A.; Lebensztejn, D.M.; Palka, J.A.; Debek, W. HIF-1 alpha as a Key Factor in Bile Duct Ligation-Induced Liver Fibrosis in Rats. *J. Invest. Surg.* **2016**, *30*, 41–46. [[CrossRef](#)]
23. Moon, J.O.; Welch, T.P.; Gonzalez, F.J.; Copple, B.L. Reduced liver fibrosis in hypoxia-inducible factor-1alpha-deficient mice. *Am. J. Physiol. Gastrointest. Liver Physiol.* **2009**, *296*, G582–G592. [[CrossRef](#)]
24. Corpechot, C.; Barbu, V.; Wendum, D.; Kinnman, N.; Rey, C.; Poupon, R.; Housset, C.; Rosmorduc, O. Hypoxia-induced VEGF and collagen I expressions are associated with angiogenesis and fibrogenesis in experimental cirrhosis. *Hepatology* **2002**, *35*, 1010–1021. [[CrossRef](#)]
25. Copple, B.L.; Kaska, S.; Wentling, C. Hypoxia-inducible factor activation in myeloid cells contributes to the development of liver fibrosis in cholestatic mice. *J. Pharmacol. Exp. Ther.* **2012**, *341*, 307–316. [[CrossRef](#)]



26. Ankoma-Sey, V.; Matli, M.; Chang, K.B.; Lalazar, A.; Donner, D.B.; Wong, L.; Warren, R.S.; Friedman, S.L. Coordinated induction of VEGF receptors in mesenchymal cell types during rat hepatic wound healing. *Oncogene* **1998**, *17*, 115–121. [\[CrossRef\]](#)
27. Yoshiji, H.; Kuriyama, S.; Yoshii, J.; Ikenaka, Y.; Noguchi, R.; Hicklin, D.J.; Wu, Y.; Yanase, K.; Namisaki, T.; Yamazaki, M.; et al. Vascular endothelial growth factor and receptor interaction is a prerequisite for murine hepatic fibrogenesis. *Gut* **2003**, *52*, 1347–1354. [\[CrossRef\]](#)
28. Novo, E.; Cannito, S.; Zamara, E.; Valfre di Bonzo, L.; Caligiuri, A.; Cravanzola, C.; Compagnone, A.; Colombatto, S.; Marra, F.; Pinzani, M.; et al. Proangiogenic cytokines as hypoxia-dependent factors stimulating migration of human hepatic stellate cells. *Am. J. Pathol.* **2007**, *170*, 1942–1953. [\[CrossRef\]](#)
29. Margadant, C.; Sonnenberg, A. Integrin-TGF-beta crosstalk in fibrosis, cancer and wound healing. *EMBO Rep.* **2010**, *11*, 97–105. [\[CrossRef\]](#)
30. Ho, F.M.; Liao, Y.H.; Yang, A.J.; Lee Chao, P.D.; Hou, Y.C.; Huang, C.T.; Lin, S.R.; Lee, K.R.; Huang, K.C.; Lin, W.W. Anti-atherosclerotic action of Ger-Gen-Chyn-Lian-Tang and AMPK-dependent lipid lowering effect in hepatocytes. *J. Ethnopharmacol.* **2012**, *142*, 175–187. [\[CrossRef\]](#)
31. Chang, Z.Y.; Lee, T.Y.; Huang, T.H.; Wen, C.K.; Chien, R.N.; Chang, H.H. Hepatoprotective effects of Ger-Gen-Chyn-Lian-Tang in thioacetamide-induced fibrosis in mice. *J. Chin. Med. Assoc.* **2014**, *77*, 360–366. [\[CrossRef\]](#)
32. Guo, Z.; Jin, Q.; Fan, G.; Duan, Y.; Qin, C.; Wen, M. Microwave-assisted extraction of effective constituents from a Chinese herbal medicine Radix puerariae. *Analytica. Chimica. Acta.* **2001**, *436*, 41–47. [\[CrossRef\]](#)
33. Chen, G.; Zhang, H.; Ye, J. Determination of baicalein, baicalin and quercetin in Scutellariae Radix and its preparations by capillary electrophoresis with electrochemical detection. *Talanta* **2000**, *53*, 471–479. [\[CrossRef\]](#)
34. Kong, W.; Li, Z.; Xiao, X.; Zhao, Y. Quality control for Coptidis rhizoma through the determination of five alkaloids by HPLC–ELSD coupled with chemometrics. *Nat. Prod. Res.* **2010**, *24*, 1616–1629. [\[CrossRef\]](#)
35. Lin, Z.J.; Qiu, S.-X.; Wufuer, A.; Shum, L. Simultaneous determination of glycyrrhizin, a marker component in radix Glycyrrhizae, and its major metabolite glycyrrhetic acid in human plasma by LC–MS/MS. *J. Chromatogr. B* **2005**, *814*, 201–207. [\[CrossRef\]](#)
36. Teng, Y.; Cui, H.; Yang, M.; Song, H.; Zhang, Q.; Su, Y.; Zheng, J. Protective effect of puerarin on diabetic retinopathy in rats. *Mol. Biol. Rep.* **2009**, *36*, 1129. [\[CrossRef\]](#)
37. Zhang, L.; Pu, Z.; Wang, J.; Zhang, Z.; Hu, D.; Wang, J. Baicalin inhibits hypoxia-induced pulmonary artery smooth muscle cell proliferation via the AKT/HIF-1 $\alpha$ /p27-associated pathway. *Int. J. Mol. Sci.* **2014**, *15*, 8153–8168. [\[CrossRef\]](#)
38. Hamsa, T.; Kuttan, G. Antiangiogenic activity of berberine is mediated through the downregulation of hypoxia-inducible factor-1, VEGF, and proinflammatory mediators. *Drug Chem. Toxicol.* **2012**, *35*, 57–70. [\[CrossRef\]](#)
39. Abe, M.; Koga, H.; Yoshida, T.; Masuda, H.; Iwamoto, H.; Sakata, M.; Hanada, S.; Nakamura, T.; Taniguchi, E.; Kawaguchi, T.; et al. Hepatitis C virus core protein upregulates the expression of vascular endothelial growth factor via the nuclear factor-kappaB/hypoxia-inducible factor-1 $\alpha$  axis under hypoxic conditions. *Hepatol. Res.* **2012**, *42*, 591–600. [\[CrossRef\]](#)
40. Hicklin, D.J.; Ellis, L.M. Role of the vascular endothelial growth factor pathway in tumor growth and angiogenesis. *J. Clin. Oncol.* **2005**, *23*, 1011–1027. [\[CrossRef\]](#)
41. Taura, K.; De Minicis, S.; Seki, E.; Hatano, E.; Iwaisako, K.; Osterreicher, C.H.; Kodama, Y.; Miura, K.; Ikai, I.; Uemoto, S.; et al. Hepatic stellate cells secrete angiopoietin 1 that induces angiogenesis in liver fibrosis. *Gastroenterology* **2008**, *135*, 1729–1738. [\[CrossRef\]](#)
42. Aleffi, S.; Petrai, I.; Bertolani, C.; Parola, M.; Colombatto, S.; Novo, E.; Vizzutti, F.; Anania, F.A.; Milani, S.; Rombouts, K.; et al. Upregulation of proinflammatory and proangiogenic cytokines by leptin in human hepatic stellate cells. *Hepatology* **2005**, *42*, 1339–1348. [\[CrossRef\]](#)
43. Assimakopoulos, S.F.; Vagianos, C.E.; Patsoukis, N.; Georgiou, C.; Nikolopoulou, V.; Scopa, C.D. Evidence for intestinal oxidative stress in obstructive jaundice-induced gut barrier dysfunction in rats. *Acta. Physiol. Scand.* **2004**, *180*, 177–185. [\[CrossRef\]](#)
44. Assimakopoulos, S.F.; Scopa, C.D.; Zervoudakis, G.; Mylonas, P.G.; Georgiou, C.; Nikolopoulou, V.; Vagianos, C.E. Bombesin and neurotensin reduce endotoxemia, intestinal oxidative stress, and apoptosis in experimental obstructive jaundice. *Ann. Surg.* **2005**, *241*, 159–167.



45. Guimaraes, E.L.; Franceschi, M.F.; Grivicich, I.; Dal-Pizzol, F.; Moreira, J.C.; Guaragna, R.M.; Borojevic, R.; Margis, R.; Guma, F.C. Relationship between oxidative stress levels and activation state on a hepatic stellate cell line. *Liver Int.* **2006**, *26*, 477–485. [[CrossRef](#)]
46. Tong, L. Antipuretic, antimicrobic action of gegen qinlian tang. *Zhong Yao Tong Bao* **1987**, *12*, 49–50.



© 2019 by the authors. Licensee MDPI, Basel, Switzerland. This article is an open access article distributed under the terms and conditions of the Creative Commons Attribution (CC BY) license (<http://creativecommons.org/licenses/by/4.0/>).



## Research Paper

## A novel NOX2 inhibitor attenuates human neutrophil oxidative stress and ameliorates inflammatory arthritis in mice

Fu-Chao Liu<sup>a,b,1</sup>, Huang-Ping Yu<sup>a,b,1</sup>, Po-Jen Chen<sup>c,d,1</sup>, Hsuan-Wu Yang<sup>d,1</sup>, Shih-Hsin Chang<sup>d,e</sup>,  
Cherng-Chyi Tzeng<sup>f,g</sup>, Wei-Jen Cheng<sup>h,i</sup>, You-Ren Chen<sup>f,g</sup>, Yeh-Long Chen<sup>f,g,\*</sup>,  
Tsong-Long Hwang<sup>b,d,e,j,k,\*\*</sup>

<sup>a</sup> College of Medicine, Chang Gung University, Taoyuan, 333, Taiwan

<sup>b</sup> Department of Anesthesiology, Chang Gung Memorial Hospital, Taoyuan, 333, Taiwan

<sup>c</sup> Department of Cosmetic Science, Providence University, Taichung, 433, Taiwan

<sup>d</sup> Graduate Institute of Natural Products, College of Medicine, Chang Gung University, Taoyuan, 333, Taiwan

<sup>e</sup> Research Center for Chinese Herbal Medicine, Research Center for Food and Cosmetic Safety, and Graduate Institute of Health Industry Technology, College of Human Ecology, Chang Gung University of Science and Technology, Taoyuan, 333, Taiwan

<sup>f</sup> Department of Medicinal and Applied Chemistry, College of Life Science, Kaohsiung Medical University, Kaohsiung, 807, Taiwan

<sup>g</sup> Department of Medical Research, Kaohsiung Medical University-Hospital, Kaohsiung, 807, Taiwan

<sup>h</sup> Graduate Institute of Clinical Medicine, College of Medicine, Chang Gung University, Taoyuan, 333, Taiwan

<sup>i</sup> Department of Traditional Chinese Medicine, Center of Traditional Chinese Medicine, Chang Gung Memorial Hospital, Taoyuan, 333, Taiwan

<sup>j</sup> Chinese Herbal Medicine Research Team, Healthy Aging Research Center, Chang Gung University, Taoyuan, 333, Taiwan

<sup>k</sup> Department of Chemical Engineering, Ming Chi University of Technology, New Taipei City, 243, Taiwan



## ARTICLE INFO

## Keywords:

Inflammatory arthritis

CYR5099

NADPH oxidase 2

Neutrophil

Reactive oxygen species

## ABSTRACT

Neutrophil infiltration plays a significant pathological role in inflammatory diseases. NADPH oxidase type 2 (NOX2) is a respiratory burst oxidase that generates large amounts of superoxide anion ( $O_2^{\cdot-}$ ) and subsequent other reactive oxygen species (ROS). NOX2 is an emerging therapeutic target for treating neutrophilic inflammatory diseases. Herein, we show that 4-[(4-(dimethylamino)butoxy)imino]-1-methyl-1*H*-benzo[*f*]indol-9(4*H*)-one (CYR5099) acts as a NOX2 inhibitor and exerts a protective effect against complete Freund's adjuvant (CFA)-induced inflammatory arthritis in mice. CYR5099 restricted the production of  $O_2^{\cdot-}$  and ROS, but not the elastase release, in human neutrophils activated with various stimulators. The upstream signaling pathways of NOX2 were not inhibited by CYR5099. Significantly, CYR5099 inhibited NOX2 activity in activated human neutrophils and in reconstituted subcellular assays. In addition, CYR5099 reduced ROS production, neutrophil infiltration, and edema in CFA-induced arthritis in mice. Our findings suggest that CYR5099 is a NOX2 inhibitor and has therapeutic potential for treating neutrophil-dominant oxidative inflammatory disorders.

## 1. Introduction

Leukocytes are major immune cells in the human circulatory system. Neutrophils are the predominant leukocytes for defense against pathogen invasion [1,2]. However, neutrophils phagocytose pathogens and generate cytotoxic mediators that induce severe inflammatory responses [1,3]. Overproduction of superoxide anion ( $O_2^{\cdot-}$ ), a reactive oxygen species (ROS) precursor, from neutrophils can damage surrounding cells and result in inflammatory disorders and autoimmune diseases [3–5].

NADPH oxidase type 2 (NOX2) is composed of six subunits and responsible for  $O_2^{\cdot-}$  generation during respiratory burst. With stimulation, membrane-associated catalytic subunit, gp91<sup>phox</sup>, assembles with other subunits, p22<sup>phox</sup>, p47<sup>phox</sup>, p67<sup>phox</sup>, p40<sup>phox</sup>, and Rac2, to form active NADPH oxidase in neutrophils [5,6]. Prolonged and uncontrolled ROS generation by NOX2 is a crucial pathogenic factor in the pathogenesis of several inflammatory disorders and autoimmune diseases, such as arthritis, acute respiratory distress syndrome, or systemic lupus erythematosus [3,7–9]. Importantly, pharmacological inhibition or deficiency of NOX2 can restrict inflammatory responses and

\* Corresponding author. Department of Medicinal and Applied Chemistry, College of Life Science, Kaohsiung Medical University, Kaohsiung, 807, Taiwan.

\*\* Corresponding author. Graduate Institute of Natural Products, College of Medicine, Chang Gung University, Taoyuan, 333, Taiwan.

E-mail addresses: [yeloch@kmu.edu.tw](mailto:yeloch@kmu.edu.tw) (Y.-L. Chen), [ht@mail.cgu.edu.tw](mailto:ht@mail.cgu.edu.tw) (T.-L. Hwang).

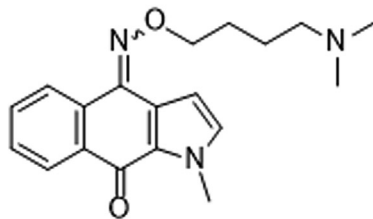
<sup>1</sup> These authors contributed equally to this work.

## Abbreviations

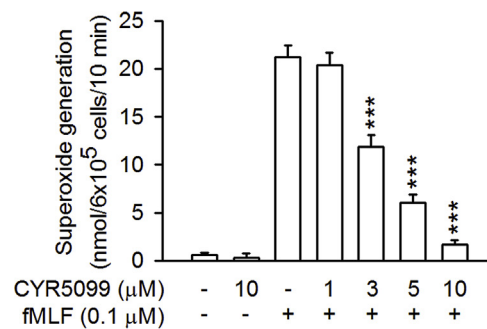
ABTS	2,2'-azino-bis(3-ethylbenzothiazoline-6-sulphonic acid)
CB	cytochalasin B
CFA	complete Freund's adjuvant
CYR5099	4-[(4-(dimethylamino)butoxy)imino]-1-methyl-1 <i>H</i> -benzo[ <i>f</i> ]indol-9(4 <i>H</i> )-one
DPI	diphenyleneiodonium
ERK	extracellular signal-regulated kinase
fMLF	<i>N</i> -formyl-L-methionyl-L-leucyl-L-phenylalanine
f-MMYALF	<i>N</i> -formyl-Met-Met-Tyr-Ala-Leu-Phe
FPR	formyl peptide receptor
GPCR	G protein-couple receptor
IC <sub>50</sub>	The half maximal inhibitory concentration

JNK	c-Jun <i>N</i> -terminal kinase
LDH	lactate dehydrogenase
LPS	lipopolysaccharide
<i>m</i> -3M3FBS	2,4,6-trimethyl- <i>N</i> -(meta-3-trifluoromethyl-phenyl)-benzenesulfonamide
MAPK	mitogen-activated protein kinase
MMK1	Leu-Glu-Ser-Ile-Phe-Arg-Ser-Leu-Leu-Phe-Arg-Val-Met
MPO	myeloperoxidase
NOX2	NADPH oxidase type 2
PKC	protein kinase C
PMA	phorbol-12-myristate-13-acetate
ROS	reactive oxygen species
WST-1	2-(4-iodophenyl)-3-(2,4-dinitrophenyl)-5-(2,4-disulphophenyl)-2 <i>H</i> -tetrazolium

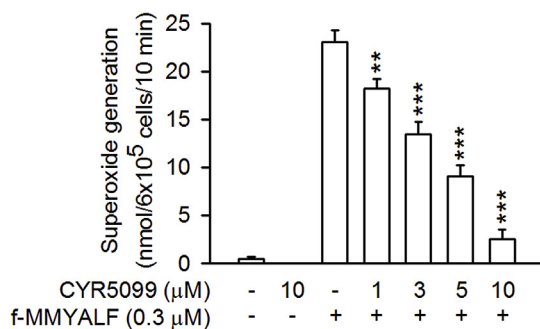
(A)



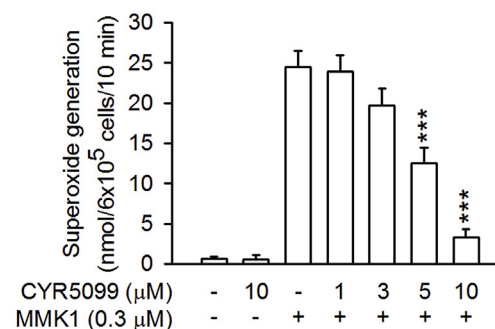
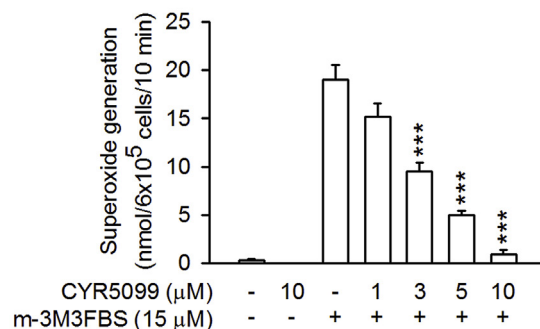
(B) fMLF



(C) f-MMYALF



(D) MMK1

(E) *m*-3M3FBS

(F) PMA

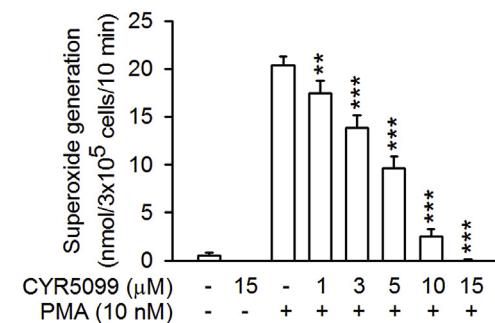


**Fig. 1.** CYR5099 inhibits superoxide anion generation in activated human neutrophils. (A) The chemical structure of CYR5099. Human neutrophils were incubated with DMSO (0.1%, as control) or CYR5099 (1–10 μM) for 5 min and then activated with (B) fMLF (0.1 μM)/CB (1 μg/ml), (C) f-MMYALF (0.3 μM) and CB (1 μg/ml), (D) MMK1 (0.3 μM)/CB (1 μg/ml), (E) *m*-3M3FBS (15 μM)/CB (1 μg/ml), or (F) PMA (10 nM). Ferricytochrome *c* reduction was monitored by a spectrophotometer at 550 nm. All data are expressed as mean ± S.E.M. (n = 6 or 8). \*\**p* < 0.01; \*\*\**p* < 0.001 compared with activator alone.

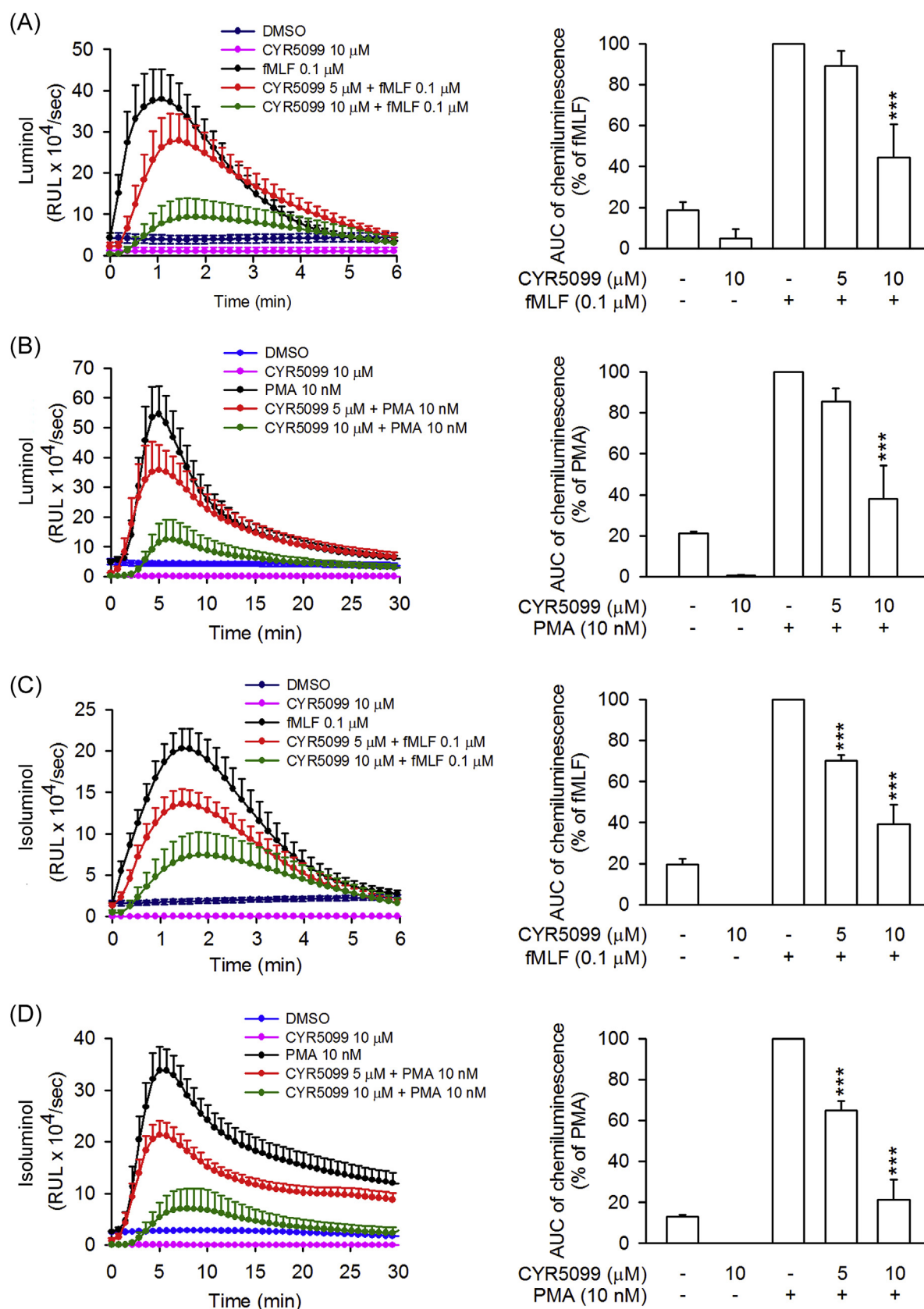


**Fig. 2.** CYR5099 inhibits total and extracellular ROS generation in activated human neutrophils. Human neutrophils were incubated with DMSO or CYR5099 (5 and 10  $\mu\text{M}$ ) for 5 min before stimulation with fMLF (0.1  $\mu\text{M}$ ) or PMA (10 nM). (A) Luminol was used to detect total ROS. (B) Isoluminol was used to detect extracellular ROS. Chemiluminescence levels were calculated and data are shown as the mean  $\pm$  S.E.M. ( $n = 5$ ). \*\*\* $p < 0.001$ .

oxidative stress accumulation [10]. Therefore, NOX2 is a promising therapeutic target for treating neutrophil-dominant inflammatory disorders.

Currently, only few drugs are used to inhibit neutrophil dysregulation during inflammation [11–13]. In a search for new anti-inflammatory agents, our laboratory established a platform for randomly screening small molecular compounds in activated human neutrophils. 4-[(4-(Dimethylamino)butoxy)imino]-1-methyl-1H-benzo[f]indol-9(4H)-one (CYR5099) (Fig. 1A), a newly synthesized derivative of benzo[f]indole-4,9-dione, was found to selectively inhibit  $O_2^{\cdot-}$  generation but not elastase release in activated human neutrophils. In this study, we identified that CYR5099 acts as a NOX2 inhibitor and effectively inhibits the production of  $O_2^{\cdot-}$  and ROS in activated human neutrophils. Therefore, we hypothesized that CYR5099 may have anti-inflammatory effects via inhibiting oxidative stress. Arthritis is a common inflammatory disease characterized by increased ROS and proinflammatory cytokines that cause joint pain, swelling, and stiffness. Excessive ROS generation, particularly via NOX2, contributes to joint inflammation and articular cartilage degradation [3,14]. Complete Freund's adjuvant (CFA) is a known potent inflammatory stimulus used in an experimental arthritis animal model [15–17]. CFA injection has been found to induce an increase of neutrophil infiltration in the arthritis synovium [17,18]. The present study aimed to investigate the effects and molecular action of CYR5099 in human neutrophils and its protective effect in a murine CFA-induced paw inflammation model.

## 2. Materials and methods

### 2.1. Reagents

CYR5099 was synthesized by Professors Cherng-Chyi Tzeng and Yeh-Long Chen, Department of Medicinal and Applied Chemistry, Kaohsiung Medical University, Taiwan, and described in Supplementary Fig. 1. Protease inhibitor cocktail tablet was obtained from Roche (Indianapolis, IN, USA). Dulbecco's Modified Eagle Medium (DMEM) and Hank's balanced salts solution (HBSS) were obtained from Gibco (Grand Island, NY, USA). Methoxysuccinyl-Ala-Ala-Pro-Val-p-nitroanilide and apocynin was obtained from Calbiochem (La Jolla, CA,

USA). Interleukin-8 (IL-8) was obtained from ProSpec (East Brunswick, NJ, USA). 8-Amino-5-chloro-2,3-dihydro-7-phenyl-pyrido[3,4-d]pyridazine sodium salt (L-012) and Leu-Glu-Ser-Ile-Phe-Arg-Ser-Leu-Leu-Phe-Arg-Val-Met (MMK-1) were obtained from Tocris Bioscience (Bristol, UK). Leukotriene B<sub>4</sub> (LTB<sub>4</sub>) was purchased from Enzo Life Science (Farmingdale, NY, USA). 2-(4-Iodophenyl)-3-(4-nitrophenyl)-5-(2,4-disulfophenyl)-2H-tetrazolium monosodium salt (WST-1) was obtained from Dojindo (Kunamoto, Japan). Fluo-3 acetomethoxyester (Fluo-3/AM) was obtained from Molecular Probes (Eugene, OR, USA). Anti-rabbit Oregon Green 488, dihydroethidine (HE), Hoechst 33342, and 1,1'-dioctadecyl-3,3,3',3'-tetramethylindocarbocyanine perchlorate (DiI) were purchased from Invitrogen (Carlsbad, CA, USA). Xanthine were obtained from Santa Cruz Biotechnology (Santa Cruz, CA, USA). The antibodies of p38, phospho-p38 (Thr180/Tyr182), JNK, phospho-JNK (Thr183/Tyr185), Akt (pan), phospho-Akt (Ser473), ERK, phospho-ERK (Thr202/Tyr204), and HRP-linked anti-rabbit IgG were purchased from Cell Signaling (Beverly, MA, USA). Anti-Ly6G antibody was purchased from eBiosciences (San Diego, CA, USA). Anti-myeloperoxidase (MPO) antibody was purchased from (Abcam, Cambridge, MA, USA). Immobilon™ Western chemiluminescence HRP substrate and Millicell® hanging cell culture inserts were obtained from Millipore Sigma (Billerica, MA, USA). Nitrocellulose membrane was obtained from PerkinElmer Inc. (Boston, MA, USA). 2,2'-Azino-bis (3-ethylbenzothiazoline-6-sulfonic acid) (ABTS), cytochalasin B (CB), diphenyleneiodonium (DPI), diphenyl-p-picrylhydrazyl (DPPH), ferricytochrome c, *N*-formyl-Met-Met-Tyr-Ala-Leu-Phe (f-MMYALF), *N*-formyl-Met-Leu-Phe (fMLF), lipopolysaccharide (LPS), *m*-3M3FBS, phorbol 12-myristate 13-acetate (PMA), platelet activating factor (PAF), zymosan A,  $\alpha$ -tocopherol, and xanthine oxidase (XO) were purchased from Sigma-Aldrich (St. Louis, MO, USA).

### 2.2. Isolation of human neutrophils

This study has been approved by the Institutional Review Board of Chang Gung Memorial Hospital (Registration number: IRB 100 1278C). Informed consent was written and obtained from healthy volunteer. Human neutrophils were isolated according to a standardized procedure: 3% (w/v) dextran sedimentation for 30 min, followed by gradient

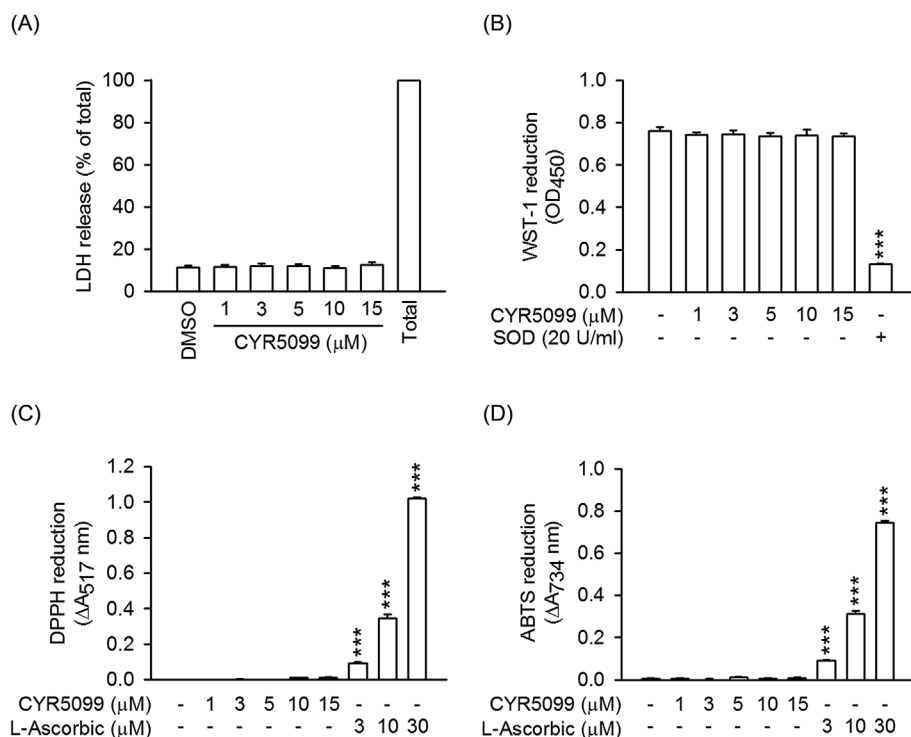


**Fig. 3. CYR5099 does not have cytotoxicity and radical-scavenging effects.** Human neutrophils were incubated with DMSO or CYR5099 (1–15 μM) for 15 min. (A) LDH release was expressed as percentage of enzyme liberated by incubation with 0.1% Triton X-100. (B) Reduction of WST-1 by xanthine/xanthine oxidase was measured spectrophotometrically at 450 nm. Superoxide dismutase (SOD) was used as positive control. (C) Reduction of DPPH and (D) ABTS was assayed spectrophotometrically at 517 and 734 nm, respectively. L-Ascorbic acid was used as positive control. All data are expressed as the mean ± S.E.M. (n = 3). \*\*\*p < 0.001 compared with DMSO.

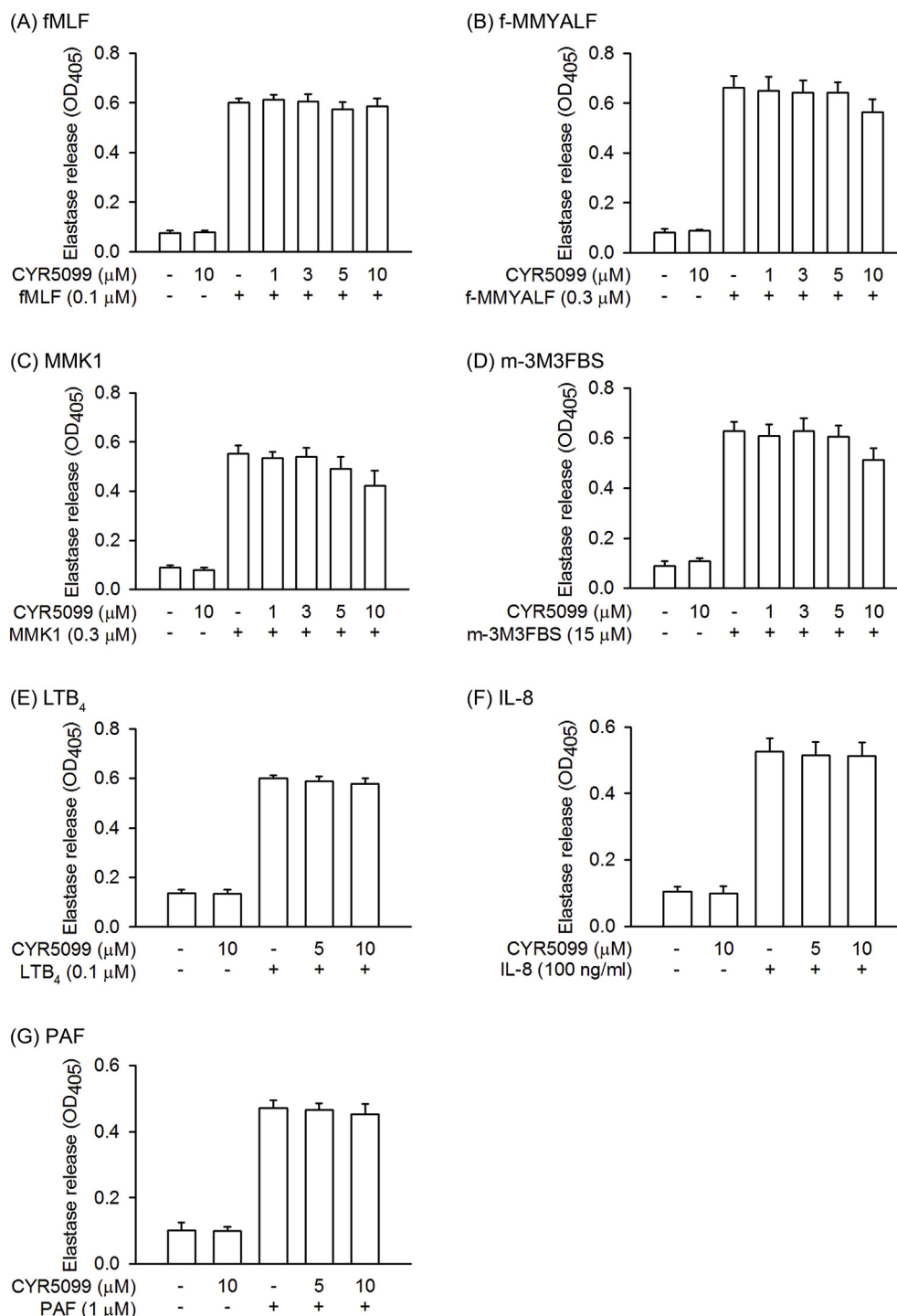


**Fig. 4.** CYR5099 does not affect elastase release in activated human neutrophils. Human neutrophils were incubated with DMSO or CYR5099 (1–10 μM) for 5 min, and then activated by (A) fMLF (0.1 μM)/CB (0.5 μg/ml), (B) f-MMYALF (0.3 μM)/CB (0.5 μg/ml), (C) MMK1 (0.3 μM)/CB (0.5 μg/ml), (D) m-3M3FBS (15 μM)/CB (0.5 μg/ml), (E) LTB<sub>4</sub> (0.1 μM)/CB (0.5 μg/ml), (F) IL-8 (100 ng/ml)/CB (2 μg/ml), or (G) PAF (1 μM)/CB (0.5 μg/ml). Elastase release was measured spectrophotometrically at 450 nm. All data are expressed as mean ± S.E.M. (n = 4 or 6).

centrifugation in Ficoll-Hypaque and hypotonic lysis of erythrocytes. Cell viability of the purified neutrophils was determined using a hemocytometer and the trypan blue-positive neutrophils were determined. Experiments were performed using neutrophils that were > 98% viable. Neutrophils were suspended and maintained in cold HBSS buffer (pH 7.4) without calcium [19].

### 2.3. Preparation of endothelial cell (ECs)

The murine brain microvascular ECs (bEnd.3) was obtained from the Bioresource Collection Center (Hsinchu, Taiwan). bEnd.3 were cultured in DMEM supplemented with 10% fetal bovine serum (FBS) containing antibiotics in a humidified atmosphere at 37 °C with 5% CO<sub>2</sub>. bEnd.3 were passaged every 3 days at 1 × 10<sup>5</sup> cells/ml after cells reached confluence [20].



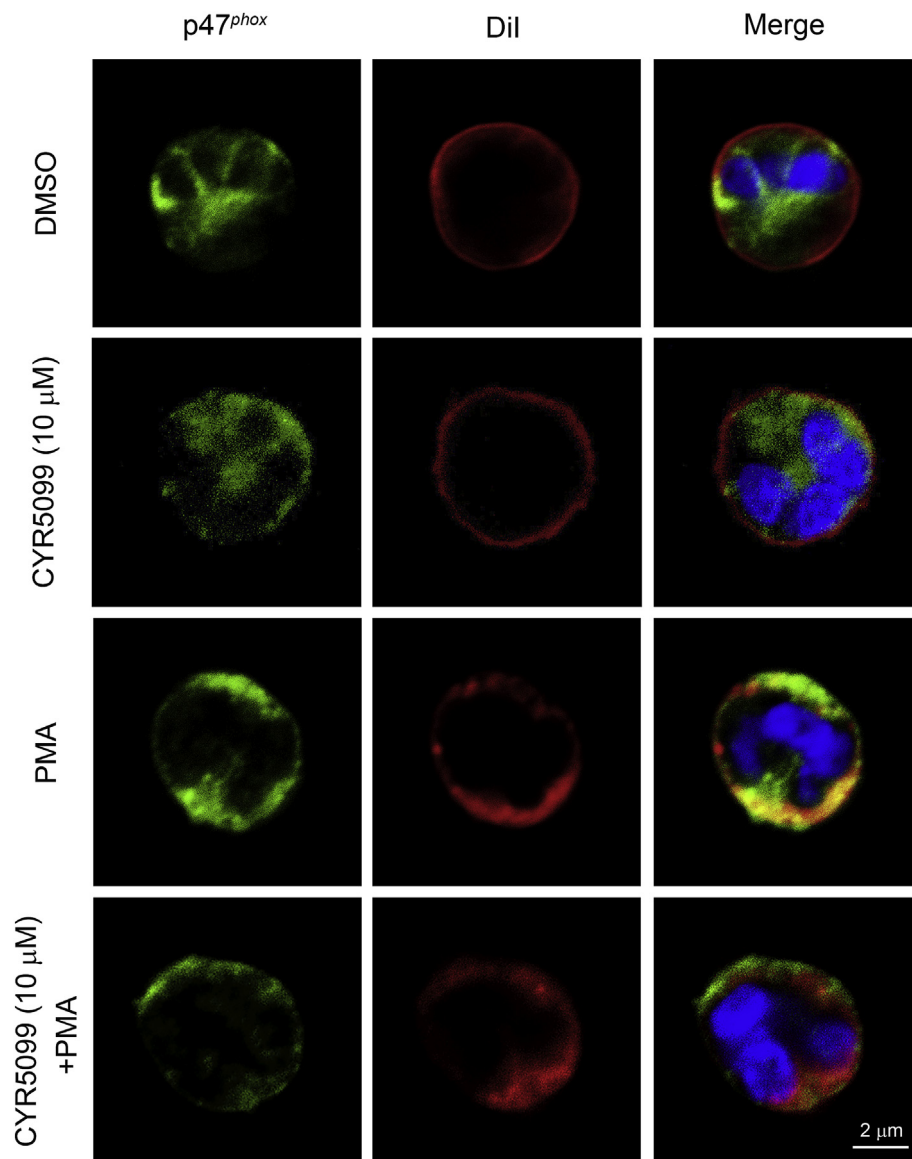


**Fig. 5.** CYR5099 does not inhibit p47<sup>phox</sup> translocation in human neutrophils. Human neutrophils were incubated with DMSO or CYR5099 (10  $\mu$ M) for 5 min, and then activated PMA (10 nM). Cells were fixed with 4% paraformaldehyde and stained with anti-p47<sup>phox</sup> antibody, DiI, and Hoechst 33342. p47<sup>phox</sup>, DiI, and Hoechst 33342 staining are shown in green, red, and blue, respectively. Co-distribution (orange) was determined by merging the green and red images. Scale bar: 2  $\mu$ m. (For interpretation of the references to color in this figure legend, the reader is referred to the Web version of this article.)

#### 2.4. Measurement of $O_2^{\cdot-}$ generation

Ferricytochrome *c* was used to measure the amount of  $O_2^{\cdot-}$  [21]. Human neutrophils ( $3 \times 10^5$  or  $6 \times 10^5$  cells/ml) were preincubated with 0.5 mg/ml (40.4  $\mu$ M) ferricytochrome *c* at 37  $^{\circ}$ C, and then incubated with DMSO or CYR5099 for 5 min before activation by fMLF (0.1  $\mu$ M), MMK1 (0.3  $\mu$ M), f-MMYALF (0.3  $\mu$ M), *m*-3M3FBS (15  $\mu$ M) or PMA (10 nM). CB (1  $\mu$ g/ml) was added to priming neutrophils before stimulators, except for PMA. CB converted neutrophils from phagocytic to secretory cells for facilitating respiratory burst and degranulation via disaggregation of intracellular actin network [22]. The absorbance was monitored continuously using a spectrophotometer at 550 nm.

Luminal or isoluminol enhanced chemiluminescence was used to assay total ROS or extracellular ROS, respectively [19]. Human neutrophils ( $7 \times 10^5$  cells/ml) were preincubated with 37.5  $\mu$ M luminol or isoluminol in the presence of 6 U/ml horseradish peroxidase at 37  $^{\circ}$ C, and then incubated with DMSO or CYR5099 for 5 min before activation.

#### 2.5. Analysis of elastase release

Human neutrophils ( $6 \times 10^5$  or  $1 \times 10^6$  cells/ml) were pre-incubated with methoxysuccinyl-Ala-Ala-Pro-Val-*p*-nitroanilide (elastase substrate, 100  $\mu$ M) at 37  $^{\circ}$ C, and then treated with DMSO or CYR5099 for 5 min before activation by fMLF (0.1  $\mu$ M), f-MMYALF (0.3  $\mu$ M), MMK1 (0.3  $\mu$ M), *m*-3M3FBS (15  $\mu$ M), LTB<sub>4</sub> (0.1  $\mu$ M), IL-8 (100 ng/ml) or PAF (1  $\mu$ M) in the presence of CB (0.5 or 2  $\mu$ g/ml). The absorbance was monitored continuously using a spectrophotometer at 405 nm [23].

#### 2.6. Detection of cytotoxicity

Lactate dehydrogenase (LDH) assay kit (Promega, Madison, WI, USA) was used to determine the cytotoxicity. Human neutrophils were treated with DMSO or CYR5099 for 15 min at 37  $^{\circ}$ C. Cell-free supernatants were collected and LDH was measured [24].

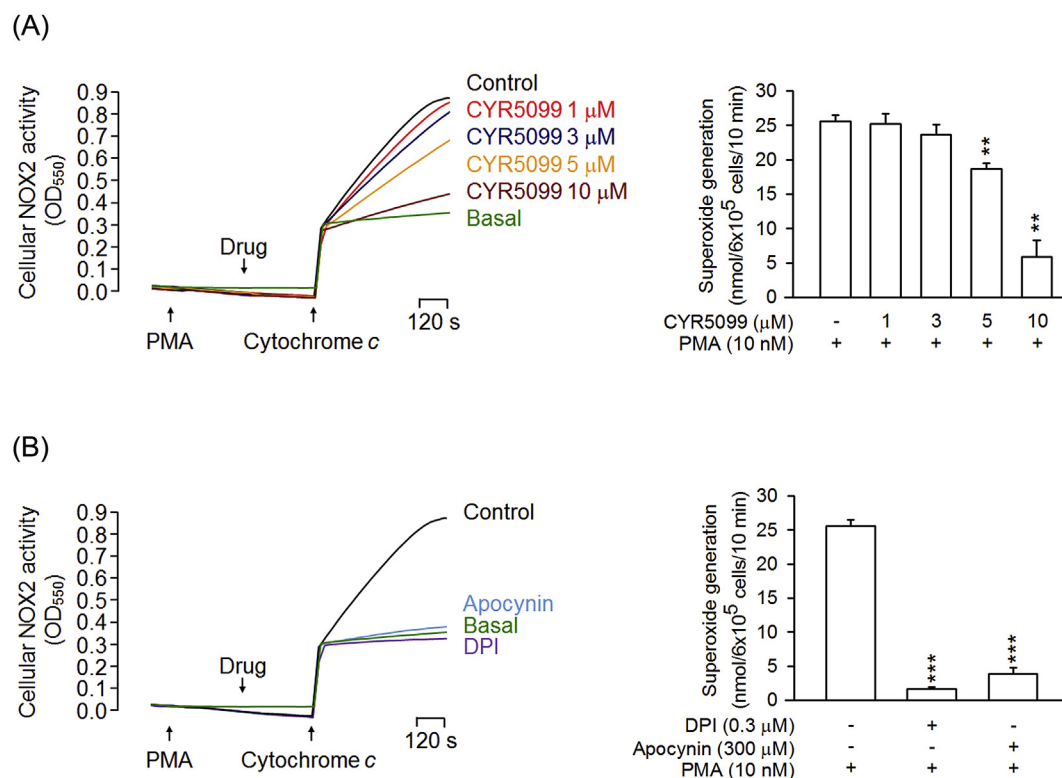


**Fig. 6. CYR5099 inhibits NOX2 activity in human neutrophils.** Human neutrophils were activated by PMA (10 nM) for 5 min, and then incubated with (A) CYR5099 (5099, 1–10 μM) or (B) DPI (0.3 μM) and apocynin (300 μM) for another 5 min. NOX2-mediated superoxide anion generation was measured by adding ferricytochrome c (0.5 mg/ml). All data are expressed as mean ± S.E.M. (n = 3) from. \*\**p* < 0.01; \*\*\**p* < 0.001 compared with PMA alone.

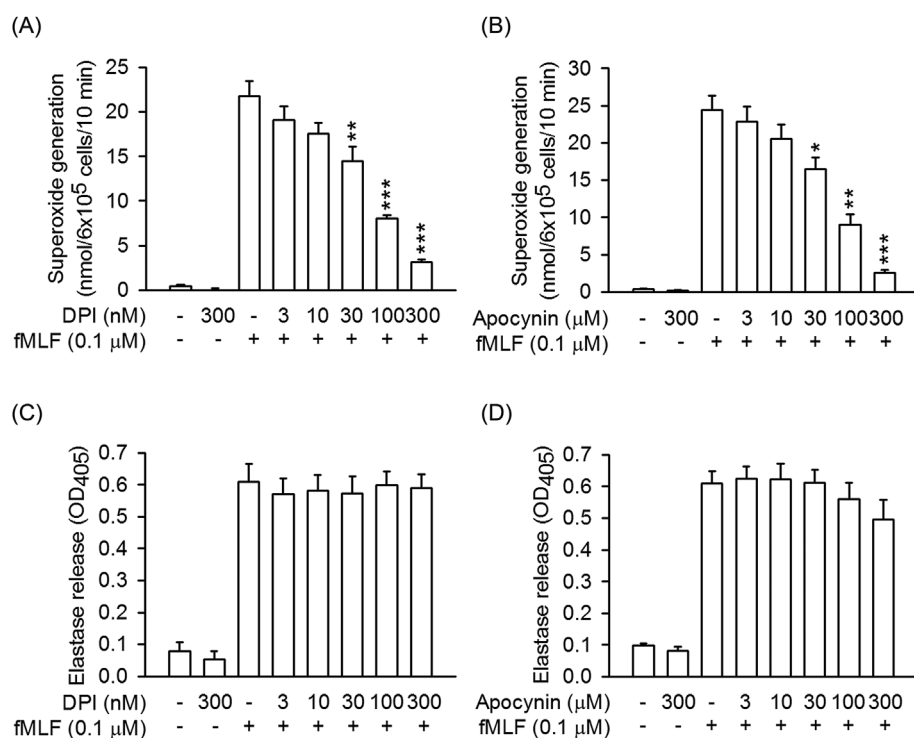


**Fig. 7. DPI and apocynin inhibit superoxide anion generation, but not elastase release, in activated human neutrophils.** Human neutrophils were incubated with DMSO, (A and C) DPI (3–300 nM), or (B and D) apocynin (3–300 μM) for 5 min, and then activated by fMLF/CB for another 10 min. (A and B) Superoxide anion and (C and D) elastase release were measured. All data are expressed as mean ± S.E.M. (n = 5). \**p* < 0.05; \*\**p* < 0.01; \*\*\**p* < 0.001 compared with fMLF alone.

## 2.7. O<sub>2</sub><sup>•−</sup> and free radical scavenging assay

The scavenging effects of CYR5099 on O<sub>2</sub><sup>•−</sup> or free radicals were determined in cell-free xanthine/xanthine oxidase (XO), DPPH, or ABTS assays [25].

## 2.8. NOX2 activity assay

Cellular NOX2 activity was measured in human neutrophils. Neutrophils (6 × 10<sup>5</sup> cells/ml) were preincubated with PMA (10 nM) at 37 °C for 5 min, and treated with DMSO, CYR5099 or NOX2 inhibitors

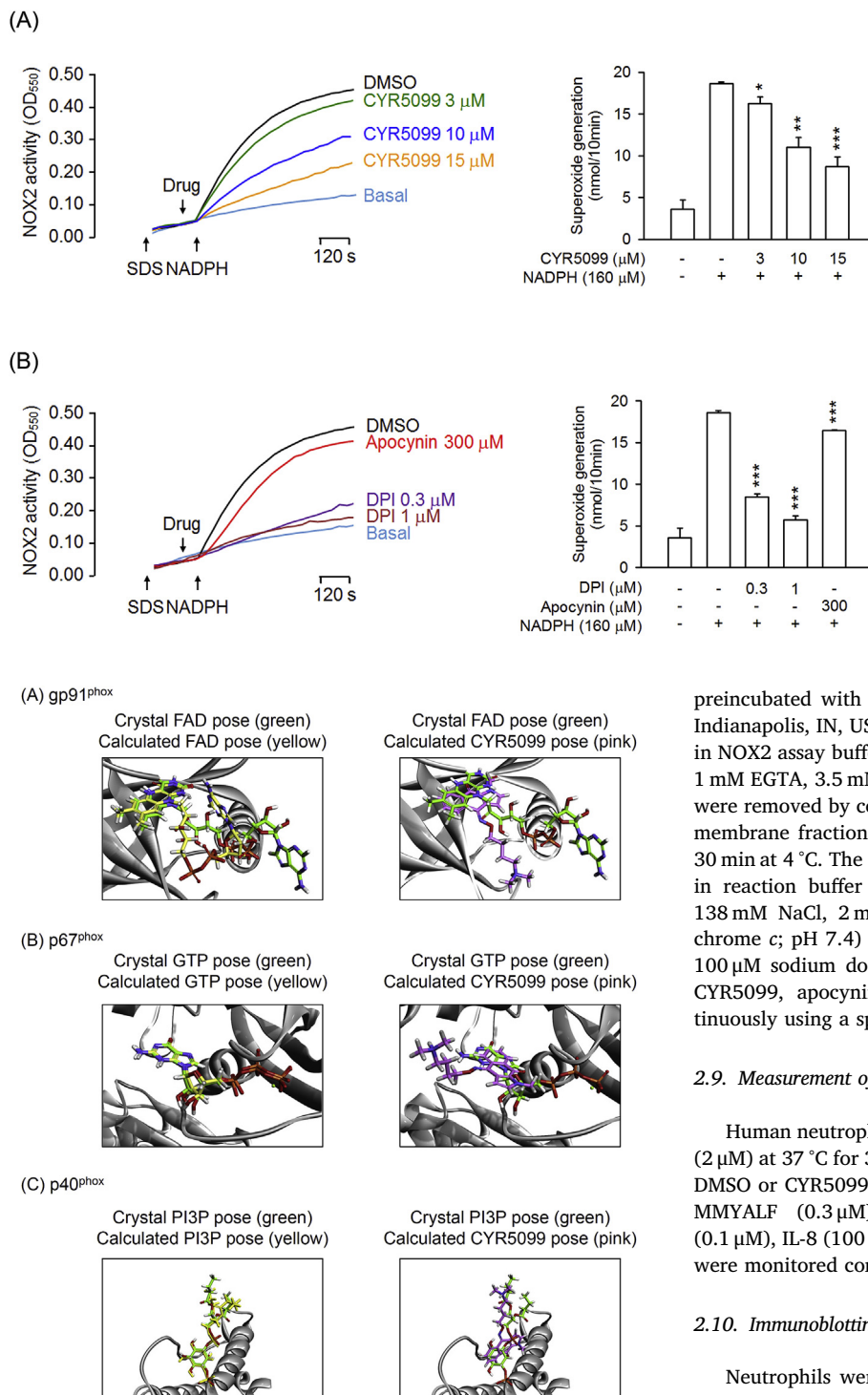


**Fig. 9.** CYR5099 is proposed to selectively bind to gp91<sup>phox</sup> *in vitro*. The crystal *in-situ* structures of (A) FAD-targeted gp91<sup>phox</sup>, (B) GTP-targeted p67<sup>phox</sup>, and (C) PI3P-targeted p40<sup>phox</sup> were adopted from PDB 5O0X, 1E96, and 1H6H, respectively (crystal pose; green color). The calculated *in-situ* structures of (A) FAD- and CYR5099-targeted gp91<sup>phox</sup>, (B) GTP- and CYR5099-targeted p67<sup>phox</sup>, and (C) PI3P- and CYR5099-targeted p40<sup>phox</sup> (calculated pose; yellow and pink color, respectively). (For interpretation of the references to color in this figure legend, the reader is referred to the Web version of this article.)

(apocynin and DPI) for 5 min. O<sub>2</sub><sup>•−</sup> generation by NOX2 was assayed by the addition of ferricytochrome *c* (0.5 mg/ml).

Subcellular NOX2 activity was also determined. Neutrophils were

**Fig. 8.** CYR5099 inhibits NOX2 activity. A mixture of cytosolic and membrane fractions from neutrophils was pretreated with SDS (100 μM) for 2 min, and then incubated with (A) CYR5099 (3, 10, and 15 μM) or (B) DPI (0.3 and 1 μM) and apocynin (300 μM). The reaction was initiated by adding NADPH (160 μM). All data are expressed as mean ± S.E.M. (n = 3). \**p* < 0.05; \*\**p* < 0.01; \*\*\**p* < 0.001 compared with control.

preincubated with protease inhibitor cocktail tablet (1/1000; Roche, Indianapolis, IN, USA) for 30 min at 4 °C, and then cells were sonicated in NOX2 assay buffer (pH 7.3; 100 mM KCl, 10 mM PIPES, 3 mM NaCl, 1 mM EGTA, 3.5 mM MgCl<sub>2</sub>, and 1 mM ATP). Nonruptured neutrophils were removed by centrifugation at 300 × *g* for 5 min. The cytosolic and membrane fractions were isolated by centrifugation at 14,000 × *g* for 30 min at 4 °C. The cytosol fraction and membrane fraction were mixed in reaction buffer (10 mM NaH<sub>2</sub>PO<sub>4</sub>/Na<sub>2</sub>HPO<sub>4</sub>·12H<sub>2</sub>O, 2.7 mM KCl, 138 mM NaCl, 2 mM MgCl<sub>2</sub>, 2 μM GTPγS, and 0.5 mg/ml ferricytochrome *c*; pH 7.4) at 30 °C. NOX2 was activated with the addition of 100 μM sodium dodecyl sulfate (SDS) before the addition of DMSO, CYR5099, apocynin, or DPI. The absorbance was monitored continuously using a spectrophotometer at 550 nm [21].

## 2.9. Measurement of intracellular calcium concentration ([Ca<sup>2+</sup>]<sub>i</sub>)

Human neutrophils (3 × 10<sup>6</sup> cells/ml) were labeled with fluo-3/AM (2 μM) at 37 °C for 35 min. Labeled neutrophils were preincubated with DMSO or CYR5099 for 5 min, and then activated by fMLF (0.1 μM), f-MYALF (0.3 μM), MMK1 (0.3 μM), *m*-3M3FBS (15 μM), LTB<sub>4</sub> (0.1 μM), IL-8 (100 ng/ml), or PAF (1 μM). The changes of fluorescence were monitored continuously using a spectrofluorometer [26].

## 2.10. Immunoblotting analysis

Neutrophils were treated with DMSO or CYR5099 for 5 min, and then activated with fMLF (0.1 μM)/CB (0.5 μg/ml) for 25 s. The reaction was stopped by the addition of sample buffer (62.5 mM pH 6.8 Tris-HCl, 4% sodium dodecyl sulfate (SDS), 5% β-mercaptoethanol, 0.0125% bromophenol blue, and 8.75% glycerol) at 100 °C for 15 min. Whole-cell lysates were obtained by centrifugation at 14,000 × *g* for 20 min at 4 °C. Phosphorylation of MAPKs and Akt was assayed by immunoblotting with the corresponding rabbit antibodies (1:2000) and HRP-linked anti-rabbit IgG antibodies (1:10000). The phosphorylated and total proteins were identified using enhanced chemiluminescence kits, and evaluated using a densitometer (UVP, Upland, CA, USA) [27].

## 2.11. Analysis of CD11b expression

Human neutrophils were pretreated with DMSO or CYR5099 for

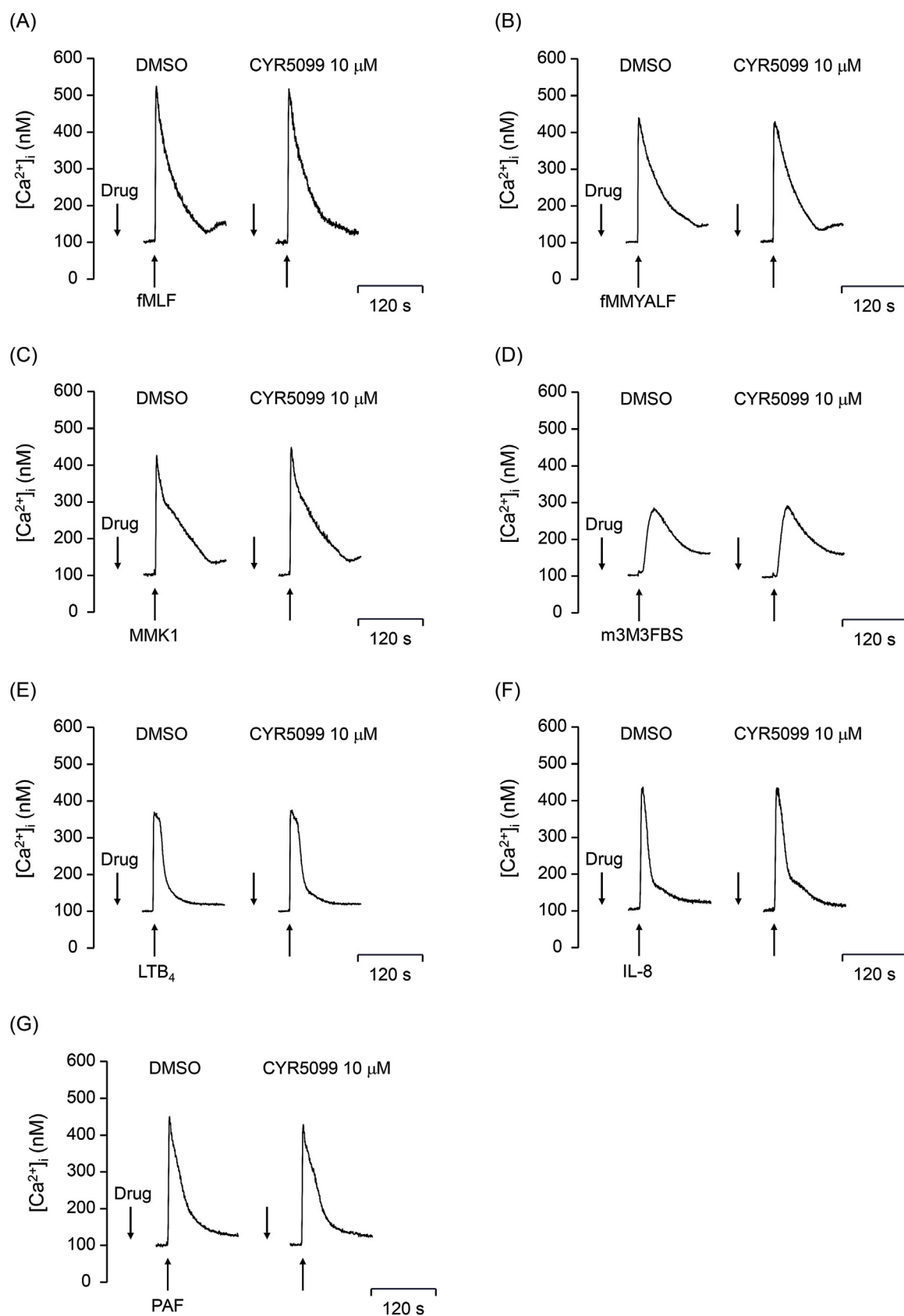


**Fig. 10. CYR5099 does not alter  $\text{Ca}^{2+}$  mobilization in activated human neutrophils.** Fluo-3-labeled human neutrophils were incubated with DMSO or CYR5099 (10  $\mu\text{M}$ ) for 5 min, and then activated by DMSO, (A) fMLF (0.1  $\mu\text{M}$ ), (B) f-MMYALF (0.3  $\mu\text{M}$ ), (C) MMK1 (0.3  $\mu\text{M}$ ), (D) m-3M3FBS (15  $\mu\text{M}$ ), (E)  $\text{LTB}_4$  (0.1  $\mu\text{M}$ ), (F) IL-8 (100 ng/ml), or (G) PAF (1  $\mu\text{M}$ ).  $\text{Ca}^{2+}$  mobilization was determined in real-time using a spectrofluorometer. Representative traces of  $\text{Ca}^{2+}$  mobilization are shown (n = 3 or 4).

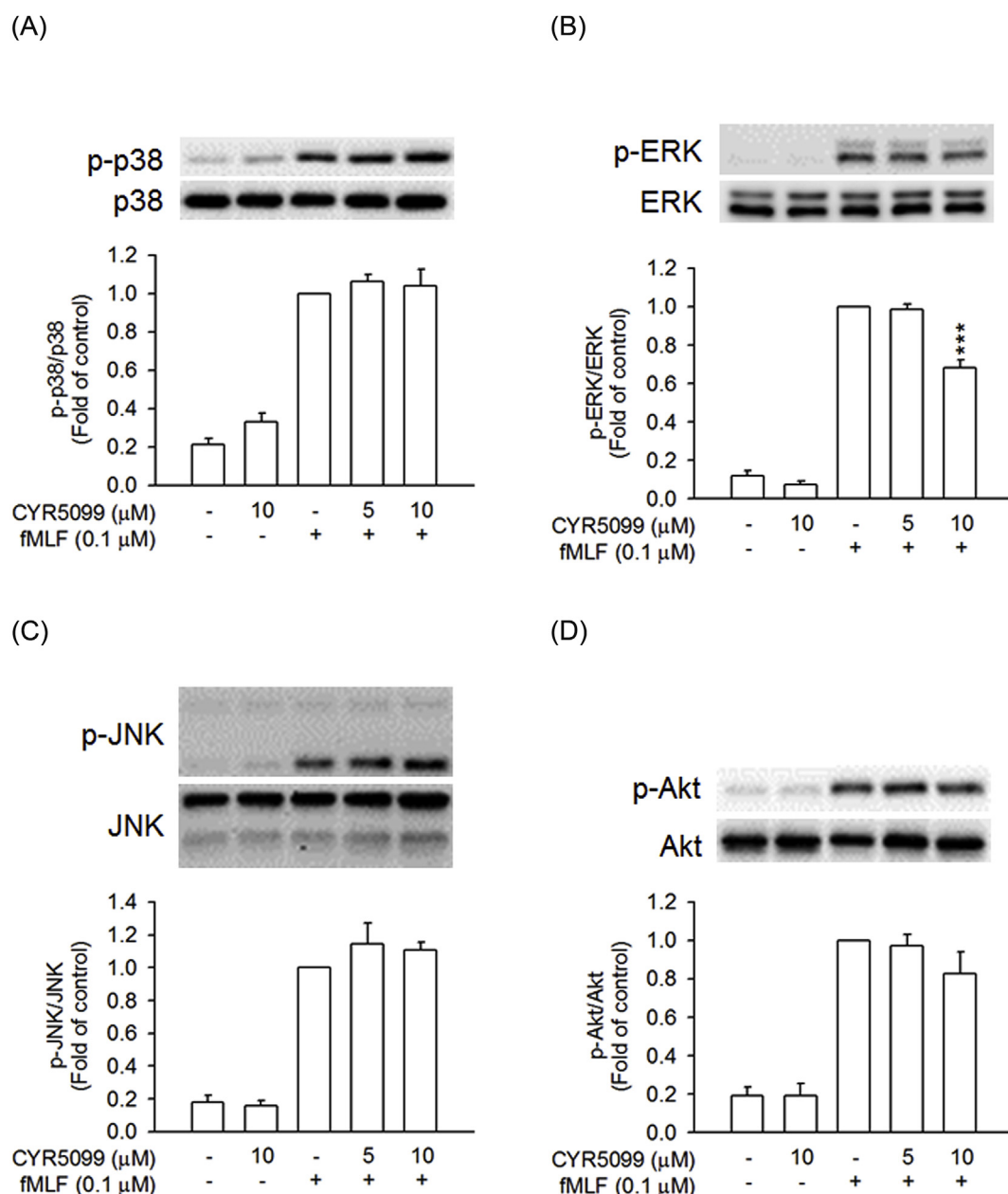


**Fig. 11.** Effects of CYR5099 on phosphorylation of MAPKs and Akt in fMLF-activated human neutrophils. Human neutrophils were incubated with DMSO or CYR5099 (5 and 10  $\mu$ M) for 5 min, and then activated by fMLF (0.1  $\mu$ M)/CB (0.5  $\mu$ g/ml) for 25 s. Phosphorylation of (A) p38, (B) ERK, (C) JNK, or (D) Akt was assayed by Western blot. All data are expressed as mean  $\pm$  S.E.M. ( $n = 3-4$ ). \*\*\* $p < 0.001$  compared with fMLF alone.

5 min and then activated by fMLF (0.1  $\mu$ M)/CB (0.5  $\mu$ g/ml) or PMA (10 nM) for another 5 min. After centrifugation at  $200 \times g$  for 8 min at 4  $^{\circ}$ C, cells were re-suspended in HBSS with 0.5% BSA and FITC-labeled anti-CD11b mouse monoclonal antibody (12.5  $\mu$ g/ml) for 90 min. CD11b expression was examined by flow cytometry [25].

## 2.12. Neutrophil adhesion detection

Human neutrophils were pre-incubated with Hoechst 33342 for 10 min and then centrifuged at  $200 \times g$  for 8 min to discard the supernatant. Hoechst 33342-labeled human neutrophils were treated with DMSO or CYR5099 for 5 min and then activated by fMLF (0.1  $\mu$ M)/CB (0.5  $\mu$ g/ml) for 10 min. Afterwards, cells were co-cultured with LPS (2  $\mu$ g/ml)-pretreated bEnd.3 cells for 15 min. Non-adherent neutrophils were removed by gentle washing with HBSS and neutrophils adhered to bEnd.3 were counted in 6 fields by microscopy [20,28].

## 2.13. Immunofluorescence staining

Human neutrophils were incubated on fibrinogen (1 mg/ml)-coated glass slides at 37  $^{\circ}$ C for 30 min, and then treated with DMSO or CYR5099 for 5 min before activating by PMA (10 nM) for an additional 5 min. Cells were fixed with 4% paraformaldehyde, washed three times with PBS, and permeabilized with 0.05% (w/v) Triton X-100. Afterwards, cells were soaked three times with 0.15 M glycine/PBS, and blocked with 5% goat serum for 1 h at 4  $^{\circ}$ C. Cells were incubated with anti-p47<sup>phox</sup> antibody (1:500) overnight at 4  $^{\circ}$ C, followed by incubation with secondary Oregon Green 488-conjugated anti-rabbit IgG antibody (1:1000) for 1 h. Cells were then washed with 0.15 M glycine/PBS and stained with Hoechst 33342 (1 ng/ml) and DiI (1 ng/ml) for 10 min at room temperature. Images were collected by Zeiss LSM 510 Meta confocal microscopy [24].



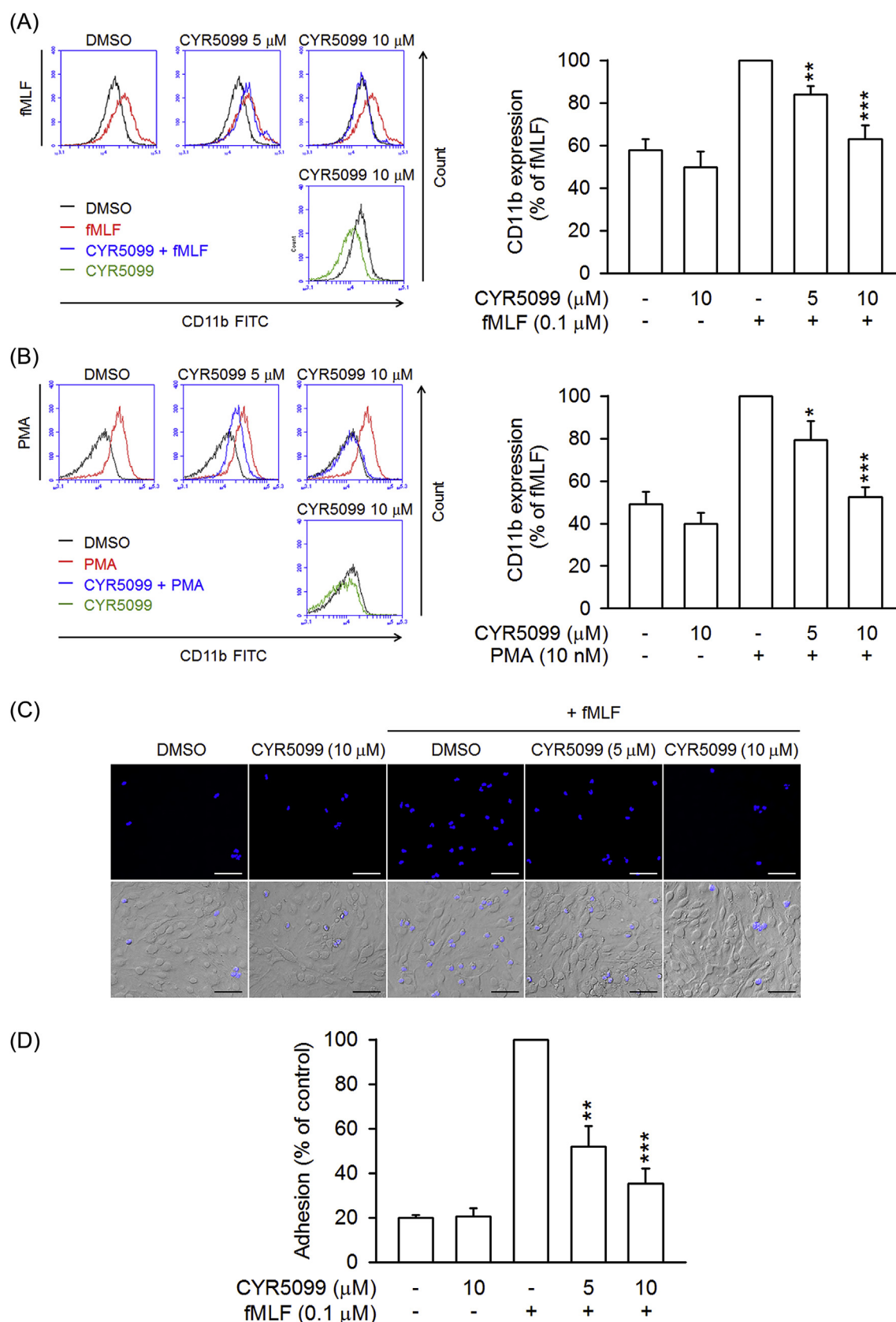


**Fig. 12. CYR5099 inhibits human neutrophil CD11b expression and adhesion.** Human neutrophils were incubated with DMSO or CYR5099 (5 and 10 μM) for 5 min, and then activated by (A) fMLF (0.1 μM)/CB (0.5 μg/ml) or (B) PMA (10 nM) for an additional 5 min. The fluorescent intensity was determined by FACS using FITC-labeled anti-CD11b antibody. Fluorescence intensities of CD11b are represented as mean ± S.E.M. (n = 6). (C) Hoechst 33342-labelled human neutrophils were incubated with DMSO or CYR5099 (5 and 10 μM), and activated by fMLF (0.1 μM)/CB (0.5 μg/ml). Drug-treated neutrophils were then co-incubated for 15 min with LPS-preincubated bEnd.3. Adherent neutrophils were detected by fluorescent microscopy. Bar = 100 μm. Representative images are shown. (D) Data from (C) are expressed as mean ± S.E.M. (n = 3). \**p* < 0.05; \*\**p* < 0.01; \*\*\**p* < 0.001 compared with fMLF or PMA alone.



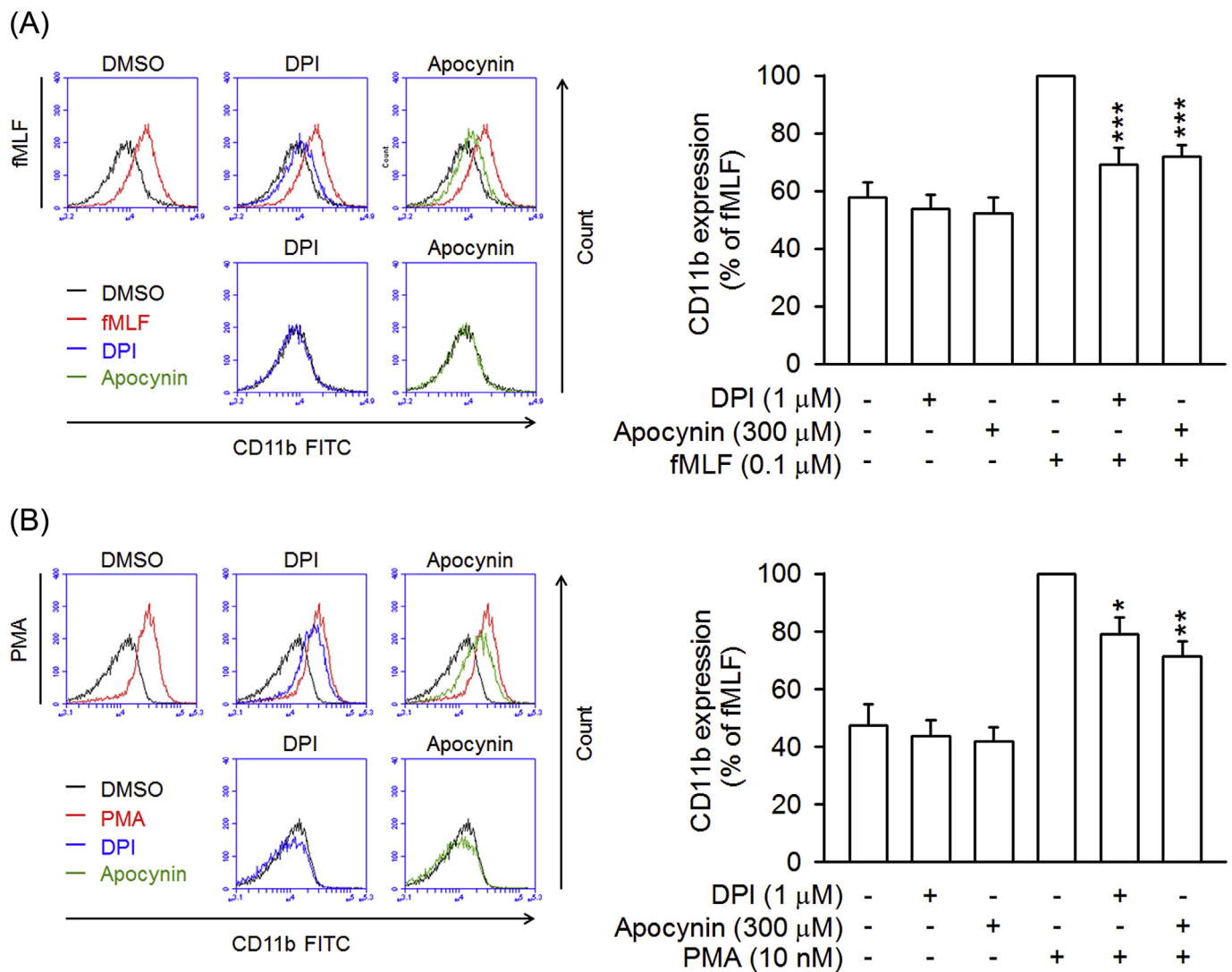


**Fig. 13. DPI and apocynin inhibits CD11b expression in activated human neutrophils.** Human neutrophils were incubated with DMSO, DPI (1  $\mu$ M), or apocynin (300  $\mu$ M) for 5 min, and then activated by (A) fMLF (0.1  $\mu$ M)/CB (0.5  $\mu$ g/ml) or (B) PMA (10 nM) for an additional 5 min. The fluorescent intensity was determined by FACS using FITC-labeled anti-CD11b antibody. Fluorescence intensities of CD11b are represented as mean  $\pm$  S.E.M. (n = 4 or 5). \* $p$  < 0.05; \*\* $p$  < 0.01; \*\*\* $p$  < 0.001 compared with fMLF or PMA alone.

#### 2.14. Protein preparation and molecular docking

The crystal structure of p67<sup>phox</sup> and p40<sup>phox</sup> were obtained from the Protein Data Bank (PDB; accession code: 1E96 and 1H6H, respectively). The remodeling structure of human gp91<sup>phox</sup> was superimposed from the C-terminal human gp91<sup>phox</sup> (PDB 3A1F) and FAD-binding region of *C. stagnale* NADPH oxidase (PDB 5O0X) using MODELLER (Supplementary Fig. 2). All structures were prepared to fix commonly problems and protonated at pH 7.4. The 2D structure of CYR5099 was sketched by BIOVIA draw and transfer to 3D coordinates using Catalyst.

CYR5099 was docked to gp91<sup>phox</sup>, p67<sup>phox</sup>, or p40<sup>phox</sup> protein using CDOCKER program (Dassault Systèmes BIOVIA, Discovery Studio Modeling Environment, Release 2019, San Diego: Dassault Systèmes, 2019). The conformational differences between crystal and calculated substrates were evaluated by RMSD value for each NOX2 subunit. CDOCKER interaction energy and binding energy ( $\Delta G_{\text{bind}}$ ) were employed to prioritize the potential target of CYR5099.

#### 2.15. Complete Freund's adjuvant (CFA)-induced paw inflammation

C57BL/6 male mice (7–8 weeks) were housed in an air-conditioned

room with 12 h light–dark cycle, and animal studies were conducted according to the guidelines and protocol approved by Institutional Animal Care and Use Committee at Chang Gung University, Taiwan (IACUC approval No. CGU14-150). Mice were injected subcutaneously with carprofen (5 mg/kg) as analgesia and then intraperitoneally with CYR5099 (10 or 25 mg/kg body weight) or an equal volume of 0.9% saline under anesthesia (Isoflurane). After 1 h, paw inflammation was induced by intraplantar injection of CFA (1.5 mg/kg body weight in right-rear foot) or 0.9% saline (left-rear foot; as control). The change in paw thickness (nm) was determined before (baseline) and after CFA/saline injection at the indicated times. After injection of CFA for 4 h, L-012 (25 mg/kg body weight) was intraperitoneally administered. ROS production was determined using a Xenogen IVIS100 imaging system (PerkinElmer, Waltham, MA, USA) under anesthesia (30 mg/kg Zoletil 50 and 6 mg/kg xylazine) [17,29]. CO<sub>2</sub> euthanasia was used to stop the experiments. The hind paws were removed, fixed using 10% neutral buffered formalin, and embedded in paraffin blocks before cutting into 5- $\mu$ m-thick sections. The staining of hematoxylin and eosin (H&E) and immunohistochemistry (Ly6G and MPO) was performed as previously described [17].

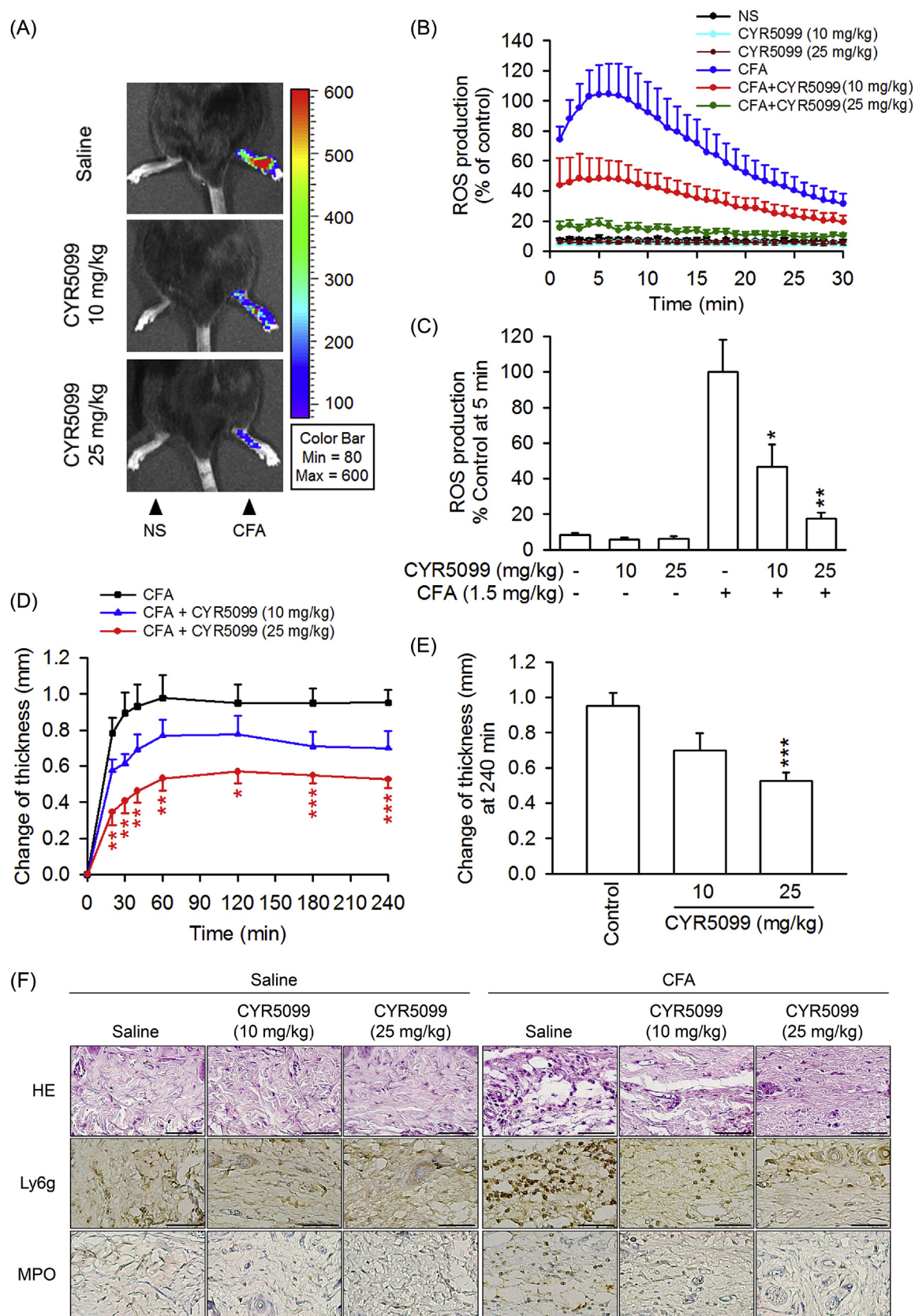


**Fig. 14.** CYR5099 ameliorates Freund's adjuvant (CFA)-induced paw injury in C57BL/6 mice. Mice were injected with CYR5099 (10 and 25 mg/kg body weight, intraperitoneally) or an equal volume of 0.9% saline for 1 h before injecting CFA (1.5 mg/kg body weight) into the intraplantar space in the hind paw. After CFA injection for 4 h, animals were administered L-012 (25 mg/kg body weight, intraperitoneally). (A) Representative chemiluminescent photos of paw edema are shown using a Xenogen IVIS 100 imaging system. (B) ROS generation from (A). (C) Peak ROS production was shown at 5 min after L-012 injection. (D) Paw thickness was measured with a digital Vernier caliper at the indicated times after CFA injection. (E) Paw edema was determined at 240 min after induction. (F) Representative staining photos of H&E, Ly6G, and MPO are shown. Bar = 50  $\mu$ m. All data are expressed as the mean  $\pm$  S.E.M (n = 6). \* $p$  < 0.5; \*\* $p$  < 0.01 compared with the CFA alone.

## 2.16. Statistical analysis

Statistical analyses were performed with SigmaPlot 8.02 (Systat Software, San Jose, CA, USA) and significance was calculated using Student's *t*-test. All data were normally distributed and expressed as the mean  $\pm$  standard error of the mean (S.E.M.). A value of  $p < 0.05$  was considered statistically significant.

## 3. Results

### 3.1. CYR5099 significantly decreases $O_2^{\cdot-}$ and ROS production, but not elastase release, in activated human neutrophils

To examine the anti-inflammatory effects of CYR5099 in human neutrophils, the  $O_2^{\cdot-}$  generation and ROS production were analyzed. CYR5099 dose-dependently (1–15  $\mu$ M) inhibited  $O_2^{\cdot-}$  generation in human neutrophils activated by fMLF (bacterial formyl peptide receptor (FPR)1 activator), f-MMYALF (mitochondrial FPR1 activator), MMK1 (FPR2 activator), *m*-3M3FBS (phospholipase C activator) and PMA (protein kinase C activator) (Fig. 1). The  $IC_{50}$  values of CYR5099 are  $3.27 \pm 0.03 \mu$ M for fMLF,  $3.77 \pm 0.79 \mu$ M for f-MMYALF,  $5.19 \pm 0.49 \mu$ M for MMK1,  $2.80 \pm 0.27 \mu$ M for *m*-3M3FBS, and  $4.74 \pm 0.51 \mu$ M for PMA. Using the specific 2-hydroxyethidium quantification assay to detect  $O_2^{\cdot-}$ , CYR5099 (1, 3, and 10  $\mu$ M) significantly inhibited the  $O_2^{\cdot-}$  generation in fMLF-activated human neutrophils (Supplementary Fig. 3). In addition, luminal and isoluminol-enhanced chemiluminescence assays indicated that CYR5099 significantly decreased total and extracellular ROS generation induced by fMLF and PMA (Fig. 2). CYR5099 also restricted total ROS production in human neutrophils stimulated by zymosan A, a pathogen prepared from *S. cerevisiae* (Supplementary Fig. 4). These results indicated that CYR5099 has anti-inflammatory effects through inhibiting human neutrophil oxidative stress. CYR5099 did not induce LDH release in human neutrophils, even in the presence of activators (fMLF or PMA), and it did not have  $O_2^{\cdot-}$  and free radicals-scavenging activity in cell-free xanthine/xanthine oxidase, DPPH, or ABTS assays (Fig. 3 and Supplementary Fig. 5), ruling out the anti-inflammatory effects were due to cytotoxicity or direct  $O_2^{\cdot-}$ -scavenging.

Elastase release is an important indicator of neutrophil degranulation. To determine whether CYR5099 has inhibitory effect on degranulation, elastase release was monitored. CYR5099 did not affect elastase release in human neutrophils activated by fMLF, f-MMYALF, MMK1, *m*-3M3FBS, LTB<sub>4</sub>, IL-8, and PAF (Fig. 4).

### 3.2. CYR5099 inhibits NOX2 activity

NOX2 activation is dependent on phosphorylation of p47<sup>phox</sup>, a cytosolic component of the enzyme. p47<sup>phox</sup> phosphorylation stimulates translocation of the cytosolic components to the membranes to induce NOX2 activation [30,31]. Our result indicated that CYR5099 failed to alter PMA-induced p47<sup>phox</sup> phosphorylation and translocation to membrane in human neutrophils (Fig. 5 and Supplementary Fig. 6), ruling out that the inhibition of  $O_2^{\cdot-}$  and ROS production by CYR5099 was through regulating NOX2 upstream pathways.

To further examine the inhibitory effect of CYR5099 on NOX2, cellular and subcellular NOX2 activities were measured. In the cellular system, CYR5099 inhibited NOX2-mediated  $O_2^{\cdot-}$  generation in PMA-preactivated human neutrophils (Fig. 6A). DPI and apocynin are two well-studied inhibitor of NOX2 [32]. In this study, DPI (0.3  $\mu$ M) and apocynin (300  $\mu$ M) were used as positive controls and showed significant inhibition (Fig. 6B). Furthermore, DPI (3–300 nM) and apocynin (3–300  $\mu$ M) inhibited  $O_2^{\cdot-}$  production, but not elastase release, in fMLF-activated human neutrophils (Fig. 7).

We suggest that CYR5099 may act as an inhibitor of NOX2. To identify this hypothesis, NOX2 activity assay was performed in subcellular experiments. Noticeably, our data showed that CYR5099 and

DPI reduced the NOX2 activity in SDS-reconstituted subcellular assay (Fig. 8). Therefore, CYR5099 is a new NOX2 inhibitor and can inhibit respiratory burst in human neutrophils. Interestingly, apocynin did not significantly inhibit subcellular NOX2 activity. A possible explanation is that apocynin is a prodrug. Apocynin requires MPO and H<sub>2</sub>O<sub>2</sub> to form an activate apocynin radical and dimer [33–36].

NOX2 is comprised of gp91<sup>phox</sup> (NOX2), p22<sup>phox</sup>, p47<sup>phox</sup>, p67<sup>phox</sup>, p40<sup>phox</sup>, and Rac2 in neutrophils [5,6]. The molecular docking of CYR5099 with NOX2 subunits was performed to determine how CYR5099 blocked the NOX2 activity. CDOCKER interaction energy and CHARMM forcefield were employed for the molecular dynamics scheme to dock ligands into a protein binding site. The crystal *in-situ* structures of FAD-targeted gp91<sup>phox</sup>, GTP-targeted p67<sup>phox</sup>, and phosphatidylinositol 3-phosphate (PI3P)-targeted p40<sup>phox</sup> were remodeled and modified from PDB 5O0X, 1E96, and 1H6H, respectively. The RMSD values between the crystal and calculated *in-situ* structures were estimated as 5.87 Å, 0.60 Å, and 1.96 Å, respectively. The CDOCKER energy values of calculated *in-situ* structures were 41.94, 169.50, and 131.31 –kcal/mol, respectively. Importantly, the CDOCKER energy values of CYR5099-targeted gp91<sup>phox</sup>, CYR5099-targeted p67<sup>phox</sup>, and CYR5099-targeted p40<sup>phox</sup> were 38.62, 27.38, and 10.21 –kcal/mol, respectively (Fig. 9). Based on molecular docking results, we suggest that CYR5099 may selectively target gp91<sup>phox</sup>, a specific subunit of NOX2.

To further examine the selectivity of CYR5099, we detected the ROS generation in HT-29 cells, which highly expressed NOX1 but not other NOX types [37,38]. DPI (0.3 and 3  $\mu$ M) and apocynin (10 and 30  $\mu$ M) but not CYR5099 (5 and 10  $\mu$ M) apparently inhibited NOX1-dependent ROS generation (Supplementary Fig. 7). Using neutrophil-like differentiated HL-60 (dHL-60) cells [39], both CYR5099 (5 and 10  $\mu$ M) and p47<sup>phox</sup> knockdown clearly inhibited the PMA-induced superoxide anion generation. Additionally, CYR5099 (5 and 10  $\mu$ M) failed to further repress the superoxide anion generation in p47<sup>phox</sup>-knockdown dHL-60 cells (Supplementary Fig. 8), suggesting that CYR5099 may be a selective inhibitor of NOX2.

### 3.3. CYR5099 does not significantly alter $Ca^{2+}$ mobilization and activity of MAPKs and Akt in human neutrophils

$Ca^{2+}$  signals play a key role in several neutrophil functions. To access whether CYR5099 influences  $Ca^{2+}$  signaling in activated human neutrophils, intracellular  $Ca^{2+}$  concentration ( $[Ca^{2+}]_i$ ) was measured. Our results showed that CYR5099 did not affect  $[Ca^{2+}]_i$  in human neutrophils activated by fMLF, f-MMYALF, MMK1, *m*-3M3FBS, LTB<sub>4</sub>, IL-8, or PAF (1  $\mu$ M) (Fig. 10).

Additionally, MAPKs and Akt play important roles in neutrophil inflammatory responses [17,19]. Treatment with fMLF caused rapid activation of p38 MAPK, ERK, JNK, and Akt in human neutrophils. CYR5099 did not affect the phosphorylation of p38 MAPK, JNK, and Akt. However, CYR5099 at high concentration of 10  $\mu$ M had a minor inhibitory effect on ERK phosphorylation (Fig. 11).

### 3.4. CYR5099 inhibits neutrophil CD11b expression and adhesion to ECs

CD11b/CD18 is an important integrin for neutrophil adhesion to endothelium [40]. Treatment with fMLF and PMA induced increases in CD11b expression in human neutrophils. CYR5099 significantly reduced fMLF and PMA-induced CD11b expression (Fig. 12A and B). Likewise, fMLF-induced human neutrophil adhesion to bEnd.3 was inhibited by CYR5099 (Fig. 12C and D). Both DPI and apocynin also showed significant inhibitory effects on CD11b expression (Fig. 13), suggesting that NOX2-mediated ROS may involve in integrin expression.

### 3.5. CYR5099 ameliorates CFA-induced arthritis inflammation

The *in vivo* effect of CYR5099 was investigated in CFA-induced



arthritis inflammation in mice. CFA treatment caused an increase in ROS generation and edema in mouse paw. The histology of paw sections showed that CFA induced neutrophil (Ly6G<sup>+</sup> and MPO<sup>+</sup>) infiltration and interstitial edema (Fig. 14). The intraperitoneal administration of CYR5099 (10 or 25 mg/kg body weight) resulted in a significant reduction of CFA-induced paw ROS production, neutrophil infiltration, and edema (Fig. 14).

#### 4. Discussion

NOX2, a respiratory burst oxidase, generates O<sub>2</sub><sup>•-</sup> in activated neutrophils [41,42]. Dysregulation of NOX2 plays a significant role in the development of neutrophil-dominated inflammatory diseases [3]. Therefore, NOX2 is a promising therapeutic target for oxidative stress-related inflammatory diseases. In the present study, we demonstrated that CYR5099, a new small molecule compound derived from benzo[f]indole-4,9-dione, reduces O<sub>2</sub><sup>•-</sup> production, ROS generation, and CD11b integrin expression in activated human neutrophils via inhibiting NOX2 activity. CYR5099 also showed therapeutic potential against CFA-induced inflammatory arthritis injury.

Neutrophils are essential innate immune cells. Neutrophils generate ROS by NOX2 which can kill pathogen [41–43]. However, large amounts of ROS can cause tissue damage and lead to inflammatory diseases, such as arthritis, psoriasis, and systemic lupus erythematosus [3,44–46]. In this study, we confirmed the anti-inflammatory properties of CYR5099 on reducing oxidative stress caused by activated human neutrophils. CYR5099 does-dependently attenuated O<sub>2</sub><sup>•-</sup> production and ROS generation in different activators-induced human neutrophils. Previous studies have shown that O<sub>2</sub><sup>•-</sup> generation in activated neutrophils could be controlled by direct scavenging or regulation of intracellular signaling pathways [47,48]. CYR5099 did not have an inhibitory effect on elastase release in human neutrophils, and it did not display direct O<sub>2</sub><sup>•-</sup> and free-radical scavenging ability in cell-free assays. These results suggested that CYR5099 selectively inhibited O<sub>2</sub><sup>•-</sup> production in activated human neutrophils via blocking NOX2 upstream signaling pathway or inhibiting NOX2 activity.

Ca<sup>2+</sup> is an important second messenger in controlling NOX2 activity [49,50]. Calcium signals in neutrophils are initiated by various membrane-associated receptors, such as G protein-coupled receptors (GPCRs), FcRs, and integrins. GPCR activation triggers intracellular signaling pathways, including conversion of phosphoinositol 4,5-bisphosphate to inositol 1,4,5-trisphosphate by phospholipase C [49–51]. CYR5099 did not affect intracellular Ca<sup>2+</sup> mobilization in human neutrophils activated with fMLF, MMK1, f-MMYALF, m-3M3FBS, IL-8, LTB<sub>4</sub>, and PAF. Thus, the anti-inflammatory effects of CYR5099 were not due to suppression of phospholipase C pathway and intracellular Ca<sup>2+</sup> mobilization. GPCR activation also stimulates MAPK and Akt phosphorylation, resulting in p47<sup>phox</sup> or p67<sup>phox</sup> phosphorylation, p47<sup>phox</sup>-p67<sup>phox</sup> complex formation, and subsequent activation of NOX2 to induce respiratory burst in neutrophils [52]. CYR5099 did not inhibit the phosphorylation of p38, JNK, and Akt. However, CYR5099 inhibited ERK phosphorylation by 31.6% in fMLF-activated human neutrophils. Previous studies have shown that ROS can induced ERK phosphorylation [53–55]. Therefore, reduction of ERK phosphorylation by CYR5099 may result from its inhibitory effect on ROS formation in activated human neutrophils.

Since CYR5099 did not block NOX2 upstream signaling pathways, we propose that CYR5099 is a direct NOX2 inhibitor. Consistent with our hypothesis, CYR5099 revealed significant inhibitory effects on NOX2-mediated O<sub>2</sub><sup>•-</sup> generation in PMA-preactivated human neutrophils and SDS-reconstructed subcellular system. p47<sup>phox</sup> phosphorylation plays a critical role in NOX2 activation [56–58]. The immunofluorescence and immunoblotting assay indicated that CYR5099 did not influence p47<sup>phox</sup> membrane translocation in activated human neutrophils. Apocynin and DPI, two well-known inhibitors of NOX2 [32], inhibited NOX2-mediated O<sub>2</sub><sup>•-</sup> generation in activated human

neutrophils. ROS can stimulate CD11b expression, which mediates neutrophil adhesion and migration [20,59]. Additionally, angiotensin II-induced T cells tissue homing is ameliorated in p47<sup>phox</sup>-deficient mice [60], suggesting that targeting NOX2 prevents immune cell infiltration. CYR5099 significantly inhibited CD11b expression in fMLF- or PMA-activated human neutrophils. The NOX2 inhibitors, DPI and apocynin, showed the same effects. CYR5099 is a NOX2 inhibitor that functions similar to DPI. The prodrug apocynin requires MPO and H<sub>2</sub>O<sub>2</sub> to form an activate NOX2 inhibitor [33–36]. We also noted that apocynin failed to inhibit NOX2-mediated O<sub>2</sub><sup>•-</sup> generation in SDS-reconstructed subcellular system.

Arthritis is a common health problem resulting from joint inflammation. The pathogenesis of arthritis involves ROS formation, immune cell infiltration, and synovial hyperplasia [61,62]. Previous studies have shown that the severity of arthritis correlates with ROS level and NOX2 overexpression in mice with hypoxic inflammatory arthritis [8]. Excessive ROS generation is also associated with synovial membrane inflammation, and NOX2-mediated ROS production contributes to osteoarthritic joint inflammation and articular cartilage degradation [63]. Our results showed that CYR5099 significantly reduced ROS level, neutrophil infiltration, and edema in CFA-induced paw inflammation in mice. Therefore, targeting NOX2 may have therapeutic potential in arthritis inflammation.

Direct inhibition of NOX2 activity could be dangerous. Chronic granulomatous disease patients, who have defects in O<sub>2</sub><sup>•-</sup>-generating NOX2, suffer from increased susceptibility for bacterial and fungal infections and also other disease conditions such as Crohn's disease and pancolitis [64,65]. Therefore, people should pay attention to the clinical use of NOX2 inhibitors. In this study, an acute inflammatory arthritis mouse model was used to examine the preclinical effect of CYR5099. Our results suggest that CYR5099 may be a lead compound for the development of NOX2 inhibitor to treat neutrophil-dominant acute oxidative inflammatory disorders.

#### 5. Conclusion

In summary, this is the first time to identify a novel small molecule CYR5099 to target NOX2 for restricting neutrophilic inflammation, including O<sub>2</sub><sup>•-</sup> production, ROS generation, CD11b integrin expression, and cell adhesion. Our *in vivo* study demonstrates that CYR5099 ameliorates neutrophil-mediated inflammatory arthritis. CYR5099 can be a lead compound for the development of NOX2 inhibitor to treat neutrophil-mediated inflammatory diseases.

#### Conflicts of interest

The authors declare that no competing interests exist.

#### Acknowledgements

This research was financial supported by the grants from the Ministry of Science and Technology (MOST 108-2320-B-126-001, MOST 106-2320-B-255-003-MY3, MOST 104-2320-B-255-004-MY3, MOST 105-2314-B-182A-012-MY3, MOST 107-2320-B-037-013 and MOST 105-2314-B-182A-137-MY3), Taiwan; Ministry of Education (EMRPD110441 and EMRPD110501), Taiwan; Chang Gung Memorial Hospital (CMRPG3H0811, CMRPF1F0061~3, CMRPF1G0241~3, CMRPG3E1552, CMRPG3G1601, CMRPG3F6221~3, and BMRP450), Taiwan. The funders had no role in study design, data collection and analysis, decision to publish, or preparation of the manuscript.

#### Appendix A. Supplementary data

Supplementary data to this article can be found online at <https://doi.org/10.1016/j.redox.2019.101273>.

## References

- [1] E. Kolaczowska, P. Kubes, Neutrophil recruitment and function in health and inflammation, *Nat. Rev. Immunol.* 13 (3) (2013) 159–175.
- [2] B. Amulic, C. Cazalet, G.L. Hayes, K.D. Metzler, A. Zychlinsky, Neutrophil function: from mechanisms to disease, *Annu. Rev. Immunol.* 30 (2012) 459–489.
- [3] L. Glennon-Alty, A.P. Hackett, E.A. Chapman, H.L. Wright, Neutrophils and redox stress in the pathogenesis of autoimmune disease, *Free Radic. Biol. Med.* 125 (2018) 25–35.
- [4] C.C. Winterbourn, A.J. Kettle, M.B. Hampton, Reactive oxygen species and neutrophil function, *Annu. Rev. Biochem.* 85 (2016) 765–792.
- [5] J. El-Benna, M. Hurtado-Nedelec, V. Marzaioli, J.C. Marie, M.A. Gougerot-Pocidalo, P.M. Dang, Priming of the neutrophil respiratory burst: role in host defense and inflammation, *Immunol. Rev.* 273 (1) (2016) 180–193.
- [6] S.A. Belambri, L. Rolas, H. Raad, M. Hurtado-Nedelec, P.M. Dang, J. El-Benna, NADPH oxidase activation in neutrophils: role of the Phosphorylation of its subunits, *Eur. J. Clin. Invest.* (2018) e12951.
- [7] M.H. Hoffmann, H.R. Griffiths, The dual role of ROS in autoimmune and inflammatory diseases: evidence from preclinical models, *Free Radic. Biol. Med.* 125 (2018) 62–71.
- [8] M. Biniecka, M. Connolly, W. Gao, C.T. Ng, E. Balogh, M. Gogarty, L. Santos, E. Murphy, D. Brayden, D.J. Veale, U. Fearon, Redox-mediated angiogenesis in the hypoxic joint of inflammatory arthritis, *Arthritis & rheumatology* 66 (12) (2014) 3300–3310.
- [9] K. Bernard, L. Hecker, T.R. Luckhardt, G. Cheng, V.J. Thannickal, NADPH oxidases in lung health and disease, *Antioxidants Redox Signal.* 20 (17) (2014) 2838–2853.
- [10] K. Hirano, W.S. Chen, A.L. Chueng, A.A. Dunne, T. Seredenina, A. Filipova, S. Ramachandran, A. Bridges, L. Chaudry, G. Pettman, C. Allan, S. Duncan, K.C. Lee, J. Lim, M.T. Ma, A.B. Ong, N.Y. Ye, S. Nasir, S. Mulyanidewi, C.C. Aw, P.P. Oon, S. Liao, D. Li, D.G. Johns, N.D. Miller, C.H. Davies, E.R. Browne, Y. Matsuoaka, D.W. Chen, V. Jaquet, A.R. Rutter, Discovery of GSK2795039, a novel small molecule NADPH oxidase 2 inhibitor, *Antioxidants Redox Signal.* 23 (5) (2015) 358–374.
- [11] F.C. Liu, H.P. Yu, C.Y. Lin, A.O. Elzoghby, T.L. Hwang, J.Y. Fang, Use of cilomilast-loaded phosphatidosomes to suppress neutrophilic inflammation for attenuating acute lung injury: the effect of nanovesicular surface charge, *J. Nanobiotechnol.* 16 (1) (2018) 35.
- [12] P.H. Schafer, A. Parton, A.K. Gandhi, L. Capone, M. Adams, L. Wu, J.B. Bartlett, M.A. Loveland, A. Gilhar, Y.F. Cheung, G.S. Baillie, M.D. Houslay, H.W. Man, G.W. Muller, D.I. Stirling, Apremilast, a cAMP phosphodiesterase-4 inhibitor, demonstrates anti-inflammatory activity in vitro and in a model of psoriasis, *Br. J. Pharmacol.* 159 (4) (2010) 842–855.
- [13] M.A. Gienbycz, S.K. Field, Roflumilast: first phosphodiesterase 4 inhibitor approved for treatment of COPD, *Drug Des. Dev. Ther.* 4 (2010) 147–158.
- [14] H.L. Wright, R.J. Moots, S.W. Edwards, The multifactorial role of neutrophils in rheumatoid arthritis, *Nat. Rev. Rheumatol.* 10 (10) (2014) 593–601.
- [15] R. Holmdahl, J.C. Lorentzen, S. Lu, P. Olofsson, L. Wester, J. Holmberg, U. Pettersson, Arthritis induced in rats with nonimmunogenic adjuvants as models for rheumatoid arthritis, *Immunol. Rev.* 184 (2001) 184–202.
- [16] M.F. Rossato, C. Hoffmeister, R. Tonello, A.P. de Oliveira Ferreira, J. Ferreira, Anti-inflammatory effects of vitamin E on adjuvant-induced arthritis in rats, *Inflammation* 38 (2) (2015) 606–615.
- [17] S.C. Yang, P.J. Chen, S.H. Chang, Y.T. Weng, F.R. Chang, K.Y. Chang, C.Y. Chen, T.I. Kao, T.L. Hwang, Luteolin attenuates neutrophil oxidative stress and inflammatory arthritis by inhibiting Raf1 activity, *Biochem. Pharmacol.* 154 (2018) 384–396.
- [18] J.I. Chung, S. Barua, B.H. Choi, B.H. Min, H.C. Han, E.J. Baik, Anti-inflammatory effect of low intensity ultrasound (LIUS) on complete Freund's adjuvant-induced arthritis synovium, *Osteoarthritis. Cartil.* 20 (4) (2012) 314–322.
- [19] S.C. Yang, S.H. Chang, P.W. Hsieh, Y.T. Huang, C.M. Ho, Y.F. Tsai, T.L. Hwang, Dipeptide HCH6-1 inhibits neutrophil activation and protects against acute lung injury by blocking FPR1, *Free Radic. Biol. Med.* 106 (2017) 254–269.
- [20] P.J. Chen, Y.L. Wang, L.M. Kuo, C.F. Lin, C.Y. Chen, Y.F. Tsai, J.J. Shen, T.L. Hwang, Honokiol suppresses TNF-alpha-induced neutrophil adhesion on cerebral endothelial cells by disrupting polyubiquitination and degradation of IkappaBalpha, *Sci. Rep.* 6 (2016) 26554.
- [21] T.L. Hwang, H.W. Hung, S.H. Kao, C.M. Teng, C.C. Wu, S.J. Cheng, Soluble guanylyl cyclase activator YC-1 inhibits human neutrophil functions through a cGMP-independent but cAMP-dependent pathway, *Mol. Pharmacol.* 64 (6) (2003) 1419–1427.
- [22] P.C. Braga, M. Dal Sasso, M. Culici, T. Bianchi, L. Bordoni, L. Marabini, Anti-inflammatory activity of thymol: inhibitory effect on the release of human neutrophil elastase, *Pharmacology* 77 (3) (2006) 130–136.
- [23] T.L. Hwang, Y.C. Su, H.L. Chang, Y.L. Leu, P.J. Chung, L.M. Kuo, Y.J. Chang, Suppression of superoxide anion and elastase release by C18 unsaturated fatty acids in human neutrophils, *J. Lipid Res.* 50 (7) (2009) 1395–1408.
- [24] T.L. Hwang, I.A. Aljuffali, C.F. Hung, C.H. Chen, J.Y. Fang, The impact of cationic solid lipid nanoparticles on human neutrophil activation and formation of neutrophil extracellular traps (NETs), *Chem. Biol. Interact.* 235 (2015) 106–114.
- [25] Y.F. Tsai, T.C. Chu, W.Y. Chang, Y.C. Wu, F.R. Chang, S.C. Yang, T.Y. Wu, Y.M. Hsu, C.Y. Chen, S.H. Chang, T.L. Hwang, 6-Hydroxy-5,7-dimethoxy-flavone suppresses the neutrophil respiratory burst via selective PDE4 inhibition to ameliorate acute lung injury, *Free Radic. Biol. Med.* 106 (2017) 379–392.
- [26] H.P. Yu, P.W. Hsieh, Y.J. Chang, P.J. Chung, L.M. Kuo, T.L. Hwang, DSM-RX78, a new phosphodiesterase inhibitor, suppresses superoxide anion production in activated human neutrophils and attenuates hemorrhagic shock-induced lung injury in rats, *Biochem. Pharmacol.* 78 (8) (2009) 983–992.
- [27] F.C. Liu, H.P. Yu, Y.T. Syu, J.Y. Fang, C.F. Lin, S.H. Chang, Y.T. Lee, T.L. Hwang, Honokiol suppresses formyl peptide-induced human neutrophil activation by blocking formyl peptide receptor 1, *Sci. Rep.* 7 (1) (2017) 6718.
- [28] I. Ginis, D.V. Faller, Protection from apoptosis in human neutrophils is determined by the surface of adhesion, *Am. J. Physiol.* 272 (1 Pt 1) (1997) C295–C309.
- [29] A. Kielland, T. Blom, K.S. Nandakumar, R. Holmdahl, R. Blomhoff, H. Carlsen, In vivo imaging of reactive oxygen and nitrogen species in inflammation using the luminescent probe L-012, *Free Radic. Biol. Med.* 47 (6) (2009) 760–766.
- [30] L. Fialkow, Y. Wang, G.P. Downey, Reactive oxygen and nitrogen species as signaling molecules regulating neutrophil function, *Free Radic. Biol. Med.* 42 (2) (2007) 153–164.
- [31] R. Takeya, H. Sumimoto, Regulation of novel superoxide-producing NAD(P)H oxidases, *Antioxidants Redox Signal.* 8 (9–10) (2006) 1523–1532.
- [32] S. Altenhofer, K.A. Radermacher, P.W. Kleikers, K. Winkler, H.H. Schmidt, Evolution of NADPH oxidase inhibitors: selectivity and mechanisms for target engagement, *Antioxidants Redox Signal.* 23 (5) (2015) 406–427.
- [33] M. Mora-Pale, S.J. Kwon, R.J. Linhardt, J.S. Dordick, Trimer hydroxylated quinone derived from apocynin targets cysteine residues of p47phox preventing the activation of human vascular NADPH oxidase, *Free Radic. Biol. Med.* 52 (5) (2012) 962–969.
- [34] J. Stefanska, R. Pawliczak, Apocynin: Molecular Aptitudes, Mediators of Inflammation 2008, (2008), p. 106507.
- [35] V.F. Ximenes, M.P. Kanegae, S.R. Rissato, M.S. Galhiane, The oxidation of apocynin catalyzed by myeloperoxidase: proposal for NADPH oxidase inhibition, *Arch. Biochem. Biophys.* 457 (2) (2007) 134–141.
- [36] J.M. Simons, B.A. Hart, T.R. Ip Vai Ching, H. Van Dijk, R.P. Labadie, Metabolic activation of natural phenols into selective oxidative burst agonists by activated human neutrophils, *Free Radic. Biol. Med.* 8 (3) (1990) 251–258.
- [37] D. Gianni, B. Bohl, S.A. Courtneidge, G.M. Bokoch, The involvement of the tyrosine kinase c-Src in the regulation of reactive oxygen species generation mediated by NADPH oxidase-1, *Mol. Biol. Cell* 19 (7) (2008) 2984–2994.
- [38] D. Gianni, N. Taulet, H. Zhang, C. DerMardirossian, J. Kister, L. Martinez, W.R. Roush, S.J. Brown, G.M. Bokoch, H. Rosen, A. novel and specific NADPH oxidase-1 (Nox1) small-molecule inhibitor blocks the formation of functional invadopodia in human colon cancer cells, *ACS Chem. Biol.* 5 (10) (2010) 981–993.
- [39] P.J. Chen, I.L. Ko, C.L. Lee, H.C. Hu, F.R. Chang, Y.C. Wu, Y.L. Leu, C.C. Wu, C.Y. Lin, C.Y. Pan, Y.F. Tsai, T.L. Hwang, Targeting allosteric site of AKT by 5,7-dimethoxy-1,4-phenanthrenequinone suppresses neutrophilic inflammation, *EBioMedicine* 40 (2019) 528–540.
- [40] L.C. Tajra, X. Martin, J. Margonari, N. Blanc-Brunat, M. Ishibashi, G. Vivier, J.P. Steghens, H. Kawashima, M. Miyasaka, J.M. Dubernard, J.P. Revillard, Antibody-induced modulation of the leukocyte CD11b integrin prevents mild but not major renal ischaemic injury, *Nephrol. Dial. Transplant.* 15 (10) (2000) 1556–1561.
- [41] B.M. Babior, J.D. Lambeth, W. Nauseef, The neutrophil NADPH oxidase, *Arch. Biochem. Biophys.* 397 (2) (2002) 342–344.
- [42] J. El-Benna, P.M. Dang, M.A. Gougerot-Pocidalo, J.C. Marie, F. Braut-Boucher, p47phox, the phagocyte NADPH oxidase/NOX2 organizer: structure, phosphorylation and implication in diseases, *Exp. Mol. Med.* 41 (4) (2009) 217–225.
- [43] B.H. Segal, M.J. Grimm, A.N. Khan, W. Han, T.S. Blackwell, Regulation of innate immunity by NADPH oxidase, *Free Radic. Biol. Med.* 53 (1) (2012) 72–80.
- [44] M. Mittal, M.R. Siddiqui, K. Tran, S.P. Reddy, A.B. Malik, Reactive oxygen species in inflammation and tissue injury, *Antioxidants Redox Signal.* 20 (7) (2014) 1126–1167.
- [45] J. El Benna, G. Hayem, P.M. Dang, M. Fay, S. Chollet-Martin, C. Elbim, O. Meyer, M.A. Gougerot-Pocidalo, NADPH oxidase priming and p47phox phosphorylation in neutrophils from synovial fluid of patients with rheumatoid arthritis and spondylarthropathy, *Inflammation* 26 (6) (2002) 273–278.
- [46] F.J. Bloomfield, M.M. Young, Enhanced chemiluminescence production by phagocytosing neutrophils in psoriasis, *Inflammation* 12 (2) (1988) 153–159.
- [47] N. Kitaoka, G. Liu, N. Masuoka, K. Yamashita, M. Manabe, H. Kodama, Effect of sulfur amino acids on stimulus-induced superoxide generation and translocation of p47phox and p67phox to cell membrane in human neutrophils and the scavenging of free radical, *Clinica chimica acta, Int. J. Clin. Chem.* 353 (1–2) (2005) 109–116.
- [48] S.C. Yang, P.J. Chung, C.M. Ho, C.Y. Kuo, M.F. Hung, Y.T. Huang, W.Y. Chang, Y.W. Chang, K.H. Chan, T.L. Hwang, Propofol inhibits superoxide production, elastase release, and chemotaxis in formyl peptide-activated human neutrophils by blocking formyl peptide receptor 1, *J. Immunol.* 190 (12) (2013) 6511–6519.
- [49] I. Migeotte, D. Communi, M. Parmentier, Formyl peptide receptors: a promiscuous subfamily of G protein-coupled receptors controlling immune responses, *Cytokine Growth Factor Rev.* 17 (6) (2006) 501–519.
- [50] M.C. Lavigne, P.M. Murphy, T.L. Leto, J.L. Gao, The N-formylpeptide receptor (FPR) and a second G(i)-coupled receptor mediate fMet-Leu-Phe-stimulated activation of NADPH oxidase in murine neutrophils, *Cell. Immunol.* 218 (1–2) (2002) 7–12.
- [51] M.D. Salmon, J. Ahluwalia, Pharmacology of receptor operated calcium entry in human neutrophils, *Int. Immunopharmacol.* 11 (2) (2011) 145–148.
- [52] Y. Lin, R. Jia, Y. Liu, Y. Gao, X. Zeng, J. Kou, B. Yu, Diosgenin inhibits superoxide generation in FMLP-activated mouse neutrophils via multiple pathways, *Free Radic. Res.* 48 (12) (2014) 1485–1493.
- [53] K. Ke, O.J. Sul, E.K. Choi, A.M. Safdar, E.S. Kim, H.S. Choi, Reactive oxygen species induce the association of SHP-1 with c-Src and the oxidation of both to enhance osteoclast survival, *Am. J. Physiol. Endocrinol. Metab.* 307 (1) (2014) 67–70.
- [54] R. Bhattacharyya A Fau - Chattopadhyay, S. Chattopadhyay R Fau - Mitra, S.E. Mitra S Fau - Crowe, S.E. Crowe, Oxidative stress: an essential factor in the


- pathogenesis of gastrointestinal mucosal diseases, *Physiol. Rev.* 94 (2) (2014) 329–354.
- [55] K. Traore, R. Sharma, R.K. Thimmulappa, W.H. Watson, S. Biswal, M.A. Trush, Redox-regulation of Erk1/2-directed phosphatase by reactive oxygen species: role in signaling TPA-induced growth arrest in ML-1 cells, *J. Cell. Physiol.* 216 (1) (2008) 276–285.
- [56] W. Liu, H. Wu, L. Chen, Y. Wen, X. Kong, W.Q. Gao, Park7 interacts with p47(phox) to direct NADPH oxidase-dependent ROS production and protect against sepsis, *Cell Res.* 25 (6) (2015) 691–706.
- [57] A. Aljada, H. Ghanim, P. Dandona, Translocation of p47phox and activation of NADPH oxidase in mononuclear cells, *Methods Mol. Biol.* 196 (2002) 99–103.
- [58] J. Renwick, E.P. Reeves, F.B. Wientjes, K. Kavanagh, Translocation of proteins homologous to human neutrophil p47phox and p67phox to the cell membrane in activated hemocytes of *Galleria mellonella*, *Dev. Comp. Immunol.* 31 (4) (2007) 347–359.
- [59] G. Svineng, O. Ravuri C Fau - Rikardsen, N.-E. Rikardsen O Fau - Huseby, J.-O. Huseby Ne Fau - Winberg, J.O. Winberg, The role of reactive oxygen species in integrin and matrix metalloproteinase expression and function, *Connect. Tissue Res.* 49 (3) (2008) 197–202.
- [60] T.J. Guzik, N.E. Hoch, K.A. Brown, L.A. McCann, A. Rahman, S. Dikalov, J. Goronzy, C. Weyand, D.G. Harrison, Role of the T cell in the genesis of angiotensin II induced hypertension and vascular dysfunction, *J. Exp. Med.* 204 (10) (2007) 2449–2460.
- [61] C.O. Bingham 3rd, The pathogenesis of rheumatoid arthritis: pivotal cytokines involved in bone degradation and inflammation, *J. Rheumatol. Suppl.* 65 (2002) 3–9.
- [62] P. Miossec, Update on interleukin-17: a role in the pathogenesis of inflammatory arthritis and implication for clinical practice, *RMD open* 3 (1) (2017) e000284.
- [63] D. Clavijo-Cornejo, K. Martinez-Flores, K. Silva-Luna, G.A. Martinez-Nava, J. Fernandez-Torres, Y. Zamudio-Cuevas, M. Guadalupe Santamaria-Olmedo, J. Granados-Montiel, C. Pineda, A. Lopez-Reyes, The Overexpression of NALP3 Inflammasome in Knee Osteoarthritis Is Associated with Synovial Membrane Prolidase and NADPH Oxidase 2, *Oxidative Medicine and Cellular Longevity* 2016, (2016), p. 1472567.
- [64] G. Aviello, U.G. Knaus, ROS in gastrointestinal inflammation: rescue or Sabotage? *Br. J. Pharmacol.* 174 (12) (2017) 1704–1718.
- [65] S. O'Neill, J. Brault, M.J. Stasia, U.G. Knaus, Genetic disorders coupled to ROS deficiency, *Redox Biol.* 6 (2015) 135–156.





Article

# Preparation of Gelatin and Gelatin/Hyaluronic Acid Cryogel Scaffolds for the 3D Culture of Mesothelial Cells and Mesothelium Tissue Regeneration

Hao-Hsi Kao <sup>1,2</sup>, Chang-Yi Kuo <sup>2</sup>, Kuo-Su Chen <sup>1,3</sup> and Jyh-Ping Chen <sup>2,4,5,6,\*</sup> 

<sup>1</sup> Division of Nephrology, Chang Gung Memorial Hospital, Keelung 20401, Taiwan; luhuichun@adm.cgmh.org.tw (H.-H.K.); cksdavid@cgmh.org.tw (K.-S.C.)

<sup>2</sup> Department of Chemical and Materials Engineering, Chang Gung University, Kwei-San, Taoyuan 33302, Taiwan; onesky1997@gmail.com

<sup>3</sup> School of Medicine, Chang Gung University, Kwei-San, Taoyuan 33303, Taiwan

<sup>4</sup> Department of Plastic and Reconstructive Surgery and Craniofacial Research Center, Chang Gung Memorial Hospital, Linkou, Kwei-San, Taoyuan 33305, Taiwan

<sup>5</sup> Research Center for Food and Cosmetic Safety and Research Center for Chinese Herbal Medicine, College of Human Ecology, Chang Gung University of Science and Technology, Taoyuan 33302, Taiwan

<sup>6</sup> Department of Materials Engineering, Ming Chi University of Technology, Tai-Shan, New Taipei City 24301, Taiwan

\* Correspondence: jpchen@mail.cgu.edu.tw; Tel.: +886-3-211-8800 (ext. 5298)

Received: 8 August 2019; Accepted: 7 September 2019; Published: 12 September 2019



**Abstract:** Mesothelial cells are specific epithelial cells that are lined in the serosal cavity and internal organs. Nonetheless, few studies have explored the possibility to culture mesothelial cells in a three-dimensional (3D) scaffold for tissue engineering applications. Towards this end, we fabricated macroporous scaffolds from gelatin and gelatin/hyaluronic acid (HA) by cryogelation, and elucidated the influence of HA on cryogel properties and the cellular phenotype of mesothelial cells cultured within the 3D scaffolds. The incorporation of HA was found not to significantly change the pore size, porosity, water uptake kinetics, and swelling ratios of the cryogel scaffolds, but led to a faster scaffold degradation in the collagenase solution. Adding 5% HA in the composite cryogels also decreased the ultimate compressive stress (strain) and toughness of the scaffold, but enhanced the elastic modulus. From the in vitro cell culture, rat mesothelial cells showed quantitative cell viability in gelatin (G) and gelatin/HA (GH) cryogels. Nonetheless, mesothelial cells cultured in GH cryogels showed a change in the cell morphology and cytoskeleton arrangement, reduced cell proliferation rate, and downregulation of the mesothelium specific marker gene expression. The production of key mesothelium proteins E-cadherin and calretinin were also reduced in the GH cryogels. Choosing the best G cryogels for in vivo studies, the cell/cryogel construct was used for the transplantation of allograft mesothelial cells for mesothelium reconstruction in rats. A mesothelium layer similar to the native mesothelium tissue could be obtained 21 days post-implantation, based on hematoxylin and eosin (H&E) and immunohistochemical staining.

**Keywords:** cryogel; scaffold; mesothelial cells; gelatin; hyaluronic acid; 3D cell culture; tissue engineering

## 1. Introduction

Mesothelial cells are specific epithelial cells that are lined in the serosal cavity (pleura, pericardium, and peritoneum) and internal organs. Their primary function is to provide a non-stick, frictionless protective barrier that facilitates the relative movement of tissues and organs within the serosal cavity [1]. The normal peritoneum is composed of a monolayer of mesothelial cells on the basement

membrane as mesothelium, and is supported by a thin layer of connective tissue containing cells, blood vessels, and lymphatic vessels. Significantly increasing abnormalities in the mesothelium could be observed for patients on peritoneal dialysis with the length of time on dialysis, where the mesothelial cells are separated from the basement membrane, and in some cases, completely disappear [2]. As the peritoneum consists only of the connective tissue under mesothelial cells, the loss of peritoneal mesothelial cells is deemed to be associated with the development of ultrafiltration failure after long-term peritoneal dialysis [3].

In tissue engineering, cells can be seeded onto a three-dimensional (3D) artificial structure, called a scaffold. The scaffold provides mechanical support primarily in the formation of tissue engineered cell/scaffold constructs, which could be subsequently implanted into a host with defective tissues [4]. The biodegradable scaffold should have open interconnected macroporous network to allow for unimpeded cell penetration and the transport of oxygen, waste products, and nutrients. The 3D scaffold could also act as an artificial extracellular matrix (ECM), and serves as a template to guide cell adhesion, proliferation, and tissue development.

The cryogelation process could fabricate 3D scaffolds with a macroporous structure and allow for effective control over the pore size using ice crystals as templates [5]. During the cryogelation process, a polymer precursor solution was mixed with a crosslinking agent and allowed to undergo consecutive freezing, chemical crosslinking, and thawing steps [6]. As the polymer solution is reacted at a subzero temperature, most of the solvent freezes into ice crystals so as to concentrate the reactants; the cross-linking reaction is therefore carried out at a high solute concentration in order to form a dense network structure that enhances the mechanical strength of the cryogel scaffold [7,8]. Therefore, as cryogels can withstand high levels of deformation, including tensile, compressive, or flexural strains [9], it could be suggested as a suitable scaffold for a mesothelial cell culture and be used in the repair of the mesothelium layer in the peritoneum. Indeed, as cryogels are endowed with important properties, like a highly porous structure, pore interconnectivity, mechanical stability and flexibility, and good swelling in an aqueous solution, they are applied as scaffolds in many tissue engineering applications [10–13].

As one of the chief components of the basal lamina, collagen contributes to cell proliferation and migration; in addition, it can facilitate the integration of mesothelium. Compared with collagen, gelatin is a partially degraded product from collagen, with a lower antigenicity. Gelatin is not only more cost-effective than collagen as a scaffold material, but also is similar to collagen, which contains the important arginine–glycine–aspartic acid (RGD) amino acid sequence needed to enhance cell attachment [14,15]. Therefore, gelatin has been used alone, or by blending with other natural or synthetic biomaterials to produce different types of structures, including microparticles, nanoparticles, electrospun nanofibers, and in-situ gelling scaffolds for different tissue engineering applications [16].

Hyaluronic acid (HA) is a naturally polysaccharide composed of repeating disaccharide units of N-acetyl-D-glucosamine and D-glucuronic acid, linked by alternating (1→3) and (1→4) linkages. As one of the important ECM components, HA can increase cell attachment and cell migration into a tissue engineering scaffold, because of its intrinsic swelling and high water-retention properties. Thus, HA has been used alone, or cross-linked with other biological materials, for use in tissue engineering, such as skin, fat, bone, and cartilage [17].

In view of the successful use of gelatin and HA-based scaffolds in many tissue engineering applications, we hypothesized that cryogel scaffolds fabricated from gelatin and gelatin/HA, whose microenvironment mimics that of mesothelium ECM, would be suitable for a 3D culture of mesothelial cells. The purpose of this study is therefore to first fabricate macroporous, flexible cryogel scaffolds based on gelatin, and to elucidate the influence of HA on the physico-chemical properties of the cryogel scaffold, followed by studying the cellular response of seeded mesothelial cells. After identifying the best cryogel scaffold from in vitro experiments, mesothelium regeneration in vivo is followed by implanting a cell/scaffold construct into a rat abdomen for treating the peritoneum defect.

## 2. Results and Discussion

### 2.1. Synthesis and Characterization of Gelatin (G) and Gelatin/Hyaluronic Acid (HA) Cryogels

A macroporous structure of a cryogel scaffold is important in order to allow for cell penetration into the scaffold, and not to inhibit the cell growth and ECM secretion of the seeded cells. The morphology of the cryogel scaffolds was examined by scanning electron microscopy (SEM), where both gelatin (G) and gelatin/hyaluronic acid (GH) cryogels revealed a highly porous structure with an interconnected open pore morphology (Figure 1A). The average pore size from the SEM observations was estimated to be  $88.3 \pm 20.7 \mu\text{m}$  and  $102.7 \pm 39.9$  for G and GH, respectively, with no significant difference found between them. The cryogel scaffolds also exhibited a similar porosity, close to ~90% (Figure 1B), which is considered to be beneficial for cell ingrowth and survival.

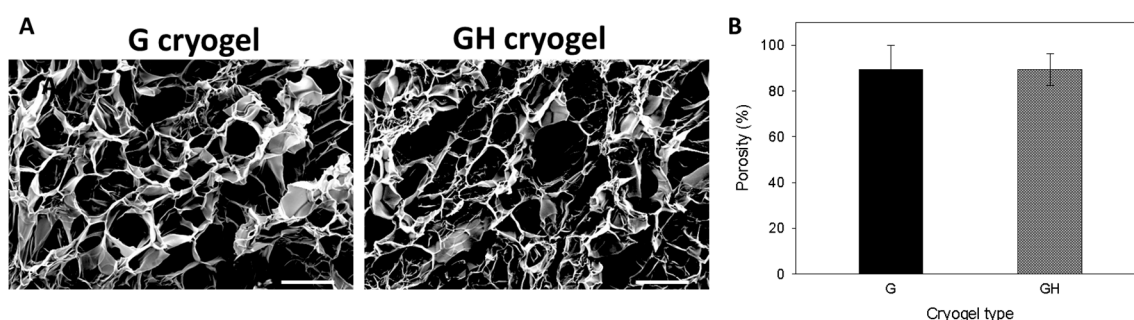


**Figure 1.** The SEM micrographs (A) and porosity (B) of gelatin (G) and gelatin/hyaluronic acid (GH) cryogels. Bar = 100  $\mu\text{m}$ .

The water uptake kinetics and swelling ratio of the cryogel scaffolds was determined in phosphate buffered saline (PBS). In both cryogels, most of the water absorption occurred within the first 20 min, and reached a constant value after 200 min (Figure 2A). The swelling ratio calculated from the equilibrium water uptake was higher for G ( $18.2 \pm 1.3$ ) than GH ( $16.1 \pm 1.9$ ), but there was no significant difference between them. The water uptake kinetics was analyzed, and the results verify the satisfactory prediction of water diffusion into cryogels, with the fitted parameters' ( $k$  and  $n$ ) values being 28.49 and 0.42 for G ( $r^2 = 0.998$ ), respectively, and 30.66 and 0.36 for GH ( $r^2 = 0.999$ ), respectively. The mechanism of water diffusion within cryogel scaffolds could be inferred from the values of  $n$  for the disk-shaped cryogel samples, to be a Fickian type diffusion with  $n \leq 0.5$  [18].

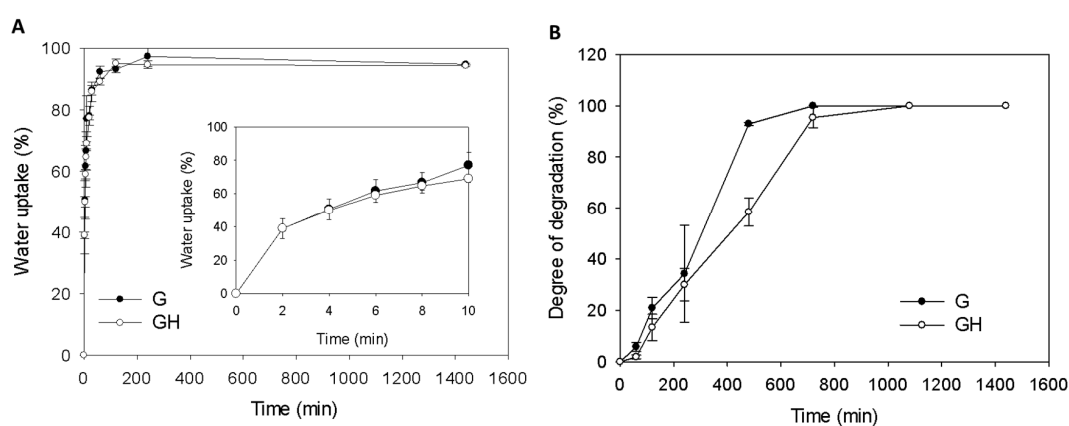


**Figure 2.** The water uptake kinetics in phosphate buffered saline (PBS) (A) and degradation kinetics in collagenase (B) of G and GH cryogels.

The degradation studies showed ~30% degradation in collagenase at 37 °C in 4 h, and quantitative degradation after 20 h (Figure 2B). That degradation of G was faster than GH in a collagenase solution (Figure 2B).

The compressive stress–strain behavior of cryogels was non-linear, without an obvious linear elastic region (Figure 3). The incorporation of HA significantly increased the elastic modulus and stiffness up to the failure point, but decreased the toughness (Table 1). There is also a significant difference in the ultimate stress and ultimate strain, with G exhibiting a higher compressive strain and withstanding higher stress at failure point than GH (Table 1).

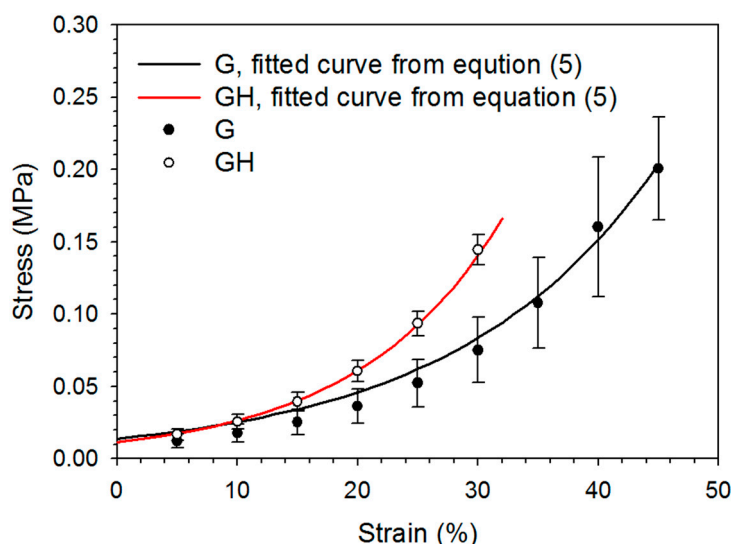


**Figure 3.** The typical compressive stress–strain curves of the G and GH cryogels. The lines are fitted curves from Equation (5).

**Table 1.** Mechanical properties of G and GH cryogels. Values are the mean  $\pm$  standard deviation (SD) of five independent measurements.

Mechanical Property	G	GH
Compressive elastic modulus at 10% strain (MPa)	0.15 $\pm$ 0.05	0.22 $\pm$ 0.03 *
Compressive elastic modulus at 20% strain (MPa)	0.31 $\pm$ 0.11	0.52 $\pm$ 0.04 *
Compressive elastic modulus at 30% strain (MPa)	0.64 $\pm$ 0.23	1.26 $\pm$ 0.16 *
Compressive strain to failure (%)	45.0 $\pm$ 4.9	32.8 $\pm$ 2.2 *
Compressive stress to failure (MPa)	0.21 $\pm$ 0.04	0.17 $\pm$ 0.02 *
Toughness (kJ/m <sup>3</sup> )	35.0 $\pm$ 2.6	22.5 $\pm$ 5.4 *
Compressive stiffness at 0.2 mm displacement (kN/m)	4.45 $\pm$ 1.55	6.51 $\pm$ 0.67 *
Compressive stiffness at 0.4 mm displacement (kN/m)	8.99 $\pm$ 3.08	14.54 $\pm$ 0.84 *
Compressive stiffness at 0.6 mm displacement (kN/m)	18.20 $\pm$ 6.19	32.63 $\pm$ 3.68 *

\*  $p < 0.05$  compared with G.

## 2.2. In Vitro Cell Culture

From the SEM observations of the cell-seeded cryogels, the mesothelial cells were mostly polygonal in shape, resembling a typical cobblestone pattern of mesothelial cells, on day three (Figure 4A). With the increase of culture time to seven days, the cells became more elongated, but the general phenotype remained. More cells, together with their secreted ECM, were also found to fill the pores within the cryogel scaffolds. Overall, the SEM images clearly supported the mesothelial characteristics of the seeded cells with a polygonal cell shape, with the microvilli visible on the surfaces of the cells. To further determine the cell proliferation, a cell number was compared between the G and GH cryogels, based on the DNA content per scaffold (Figure 4B). No significant difference in the DNA content was found on day three, and the mesothelial cells steadily proliferated up to day seven. Nonetheless,

the cell number in G was significantly higher than that in GH on days five and seven, indicating that the incorporation of HA in the cryogel formulation may adversely affect cell proliferation.

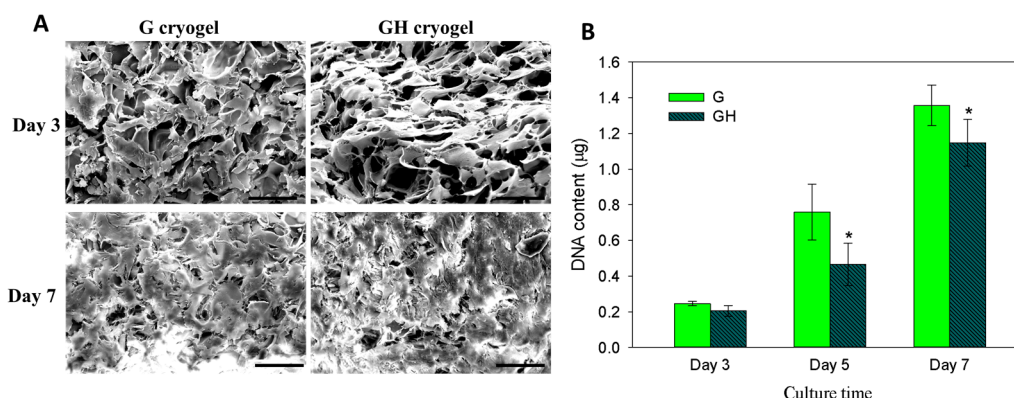


**Figure 4.** The cell morphology from SEM observation (A) and cell proliferation from DNA assays (B) of mesothelial cells cultured in G and GH cryogels. Bar = 50 μm. \*  $p < 0.05$  compared with G.

From the confocal microscopy analysis, the live/dead cell viability assays demonstrated a high cell viability in both cryogels, irrespective of culture time, with no dead cells (red) observed on days three and seven (Figure 5A). The top- and cross-section views indicated a good cell proliferation and penetration with a thick cell layer, increasing with the culture time, was found within the cryogel because of the macroporous nature of the scaffold. However, more live cells were observed on day seven in G, which is consistent with the DNA assays in Figure 4B. To reveal the cell morphology, the cell nucleus and cytoskeleton of the mesothelial cells cultured in the cryogels at the end of cultured period (seven days) were stained with rhodamine-phalloidin and Hoechst 33342, and were observed by confocal microscopy (Figure 5B). Although close to round shaped nuclei (blue) were observed for the mesothelial cells in both cryogels, there appeared to be a difference in the organization of the cellular cytoskeleton (red), with cells in the GH associated with more prominent, thick, actin-rich microfilaments that were arranged in stress fibers.

The gene expression of the mesothelial cell markers (*E-cadherin*, intercellular adhesion molecule (*ICAM-1*), *calretinin*, *cytokeratin-18*, vascular endothelial factor (*VEGF*), and *vimentin*) were detected using a quantitative real-time polymerase chain reaction (qRT-PCR) to compare the relative mRNA levels for the cells cultured in G and GH at different times after normalizing with glyceraldehyde 3-phosphate dehydrogenase (*GAPDH*; Figure 6). The expression of the *E-cadherin*, *ICAM-1*, and *calretinin* genes were significantly upregulated for the cells cultured in G over GH, regardless of the culture period, except for *E-cadherin* on day three. On the contrary, the *VEGF* and *vimentin* genes were significantly downregulated in G compared to GH on day three and day seven. Although the mesothelial cells in G showed a similar *cytokeratin-18* gene expression as GH on day seven, the relative mRNA value was also significantly lower on day three.

Immunofluorescence (IF) staining was used to reveal the production of the mesothelial marker proteins *E-cadherin* and *calretinin* on day seven, with cells identified from the nuclear staining (Figure 7). Consistent with the gene expression in Figure 6, the production of both *E-cadherin* and *calretinin* were more elevated in G than in GH. A semi-quantitative comparison of the protein production using PAX-it image analysis microscopy software (normalizing the area percentage of the green fluorescence with the number of nucleus in a single image) also indicated the dominance of G over GH in mesothelial marker protein production, as the value is 1.82 (G) and 1.58 (GH) for *calretinin*, and 1.30 (G) and 0.48 (GH) for *E-cadherin*.



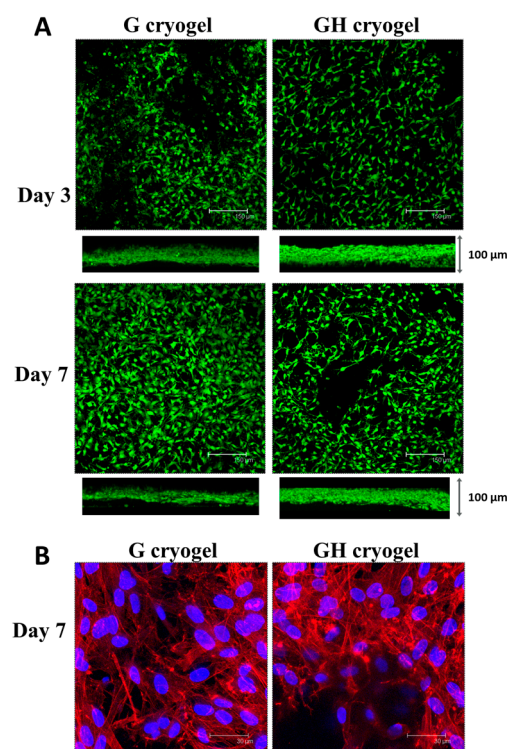


**Figure 5.** Confocal microscopy observation of mesothelial cells cultured in G and GH by live/dead (A) (bar = 150 μm) and nucleus/cytoskeleton staining (B) (bar = 30 μm). The live cells were stained green and the dead cells were stained red in (A), while the cell nuclei were stained blue by Hoechst 33342 and the actin cytoskeleton was stained red by rhodamine-phalloidin in (B). Both the merged top-view image and cross-sectional-view image are included in (A).

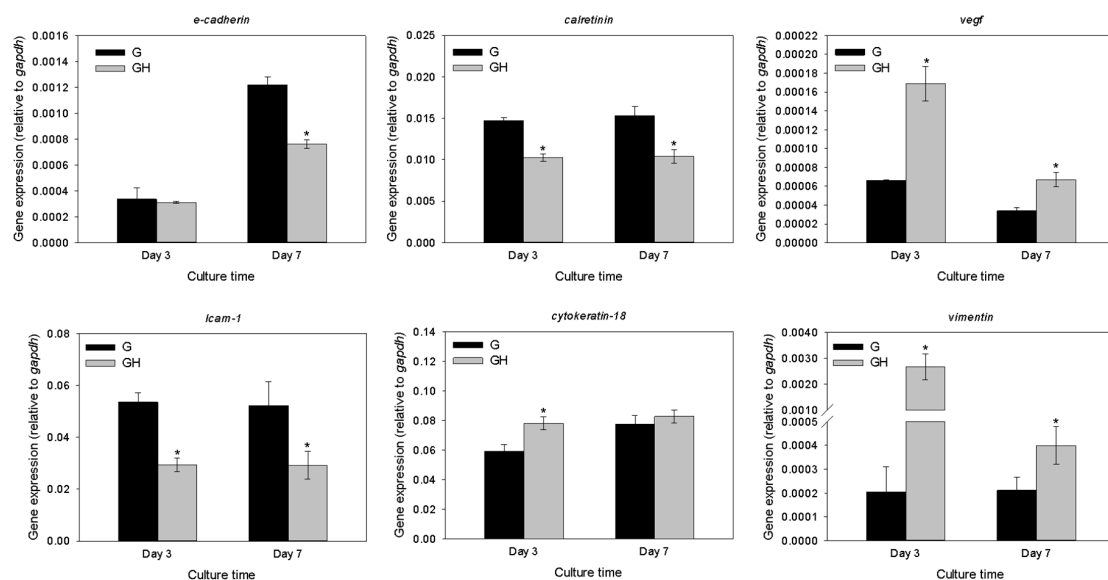


**Figure 6.** Gene expression of the mesothelial cells cultured in G and GH from a quantitative real-time polymerase chain reaction (qRT-PCR). \*  $p < 0.05$  compared with G.



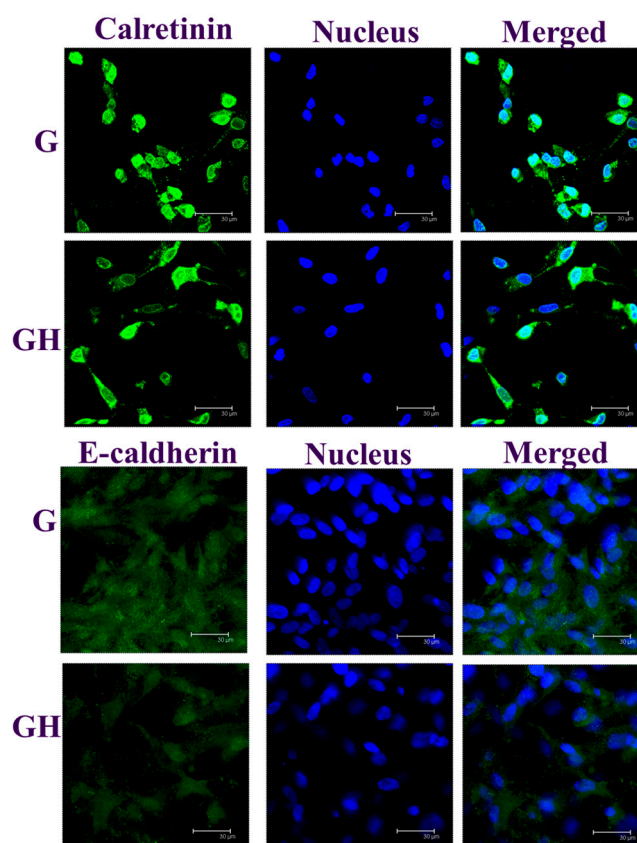


**Figure 7.** The immunofluorescence (IF) staining of calretinin and E-cadherin of the mesothelial cells cultured in G and GH for seven days. The protein was stained green by a fluorescein isothiocyanate (FITC)-conjugated secondary antibody, while the nuclei were stained blue by Hoechst 33342. Bar = 30  $\mu$ m.

### 2.3. In Vivo Studies

For the *in vivo* studies, rat parietal peritoneum was abraded to create a 10-mm diameter wound area, and was covered with a cell-scaffold construct (cultured *in vitro* for seven days beforehand) and examined 7- and 21-days post-implantation. During the course of the three-week *in vivo* animal experiment, we did not observe animal disability, infection, or death. One week after implantation, the cell/scaffold construct attached firmly to the defect (Figure 8). The scaffold was well recognized on the abdominal wall, and did not adhere to any internal organs. The formation of new tissues was scarce, and there was no ecchymosis around the scaffold, but local edema was noted. After three weeks, the construct became thinner around the edge because of biodegradation, but a thin layer of scaffold could still be identified attaching firmly to the abdominal wall, and free from adhesion with the surrounding tissues. The edges of the scaffold are smoother than before and edema is rare (Figure 8).

From the histological examination, the hematoxylin and eosin (H&E) staining showed polygonal-shaped mesothelial cells in the cryogel scaffold on day seven, which showed a typical cobblestone pattern (Figure 9). After 21 days, mesothelial-like squamous cells were observed on the surface of the cell-laden cryogel scaffold, which is similar to native peritoneum. The immunohistochemical (IHC) staining of E-cadherin and calretinin indicated that the key mesothelial marker proteins of the transplanted cells could be identified from the brown stained color, with an increasing staining intensity with the transplantation time. This indicates that the transplanted allografts could continuously secrete mesothelial cell marker proteins. Overall, the transplanted cell/cryogel scaffold revealed a close similarity pattern of cell morphology and stained protein intensity to those of native peritoneum on day 21.

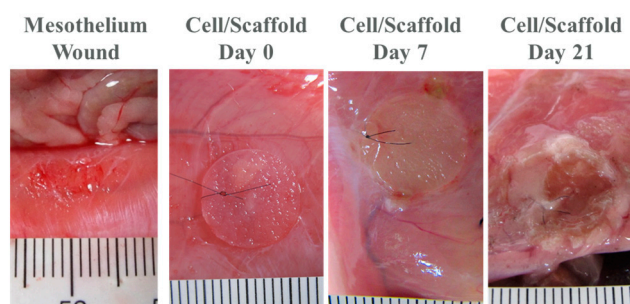


**Figure 8.** Gross view of the initial mesothelium wound and the transplanted cell/scaffold constructs at different time points post-implantation.

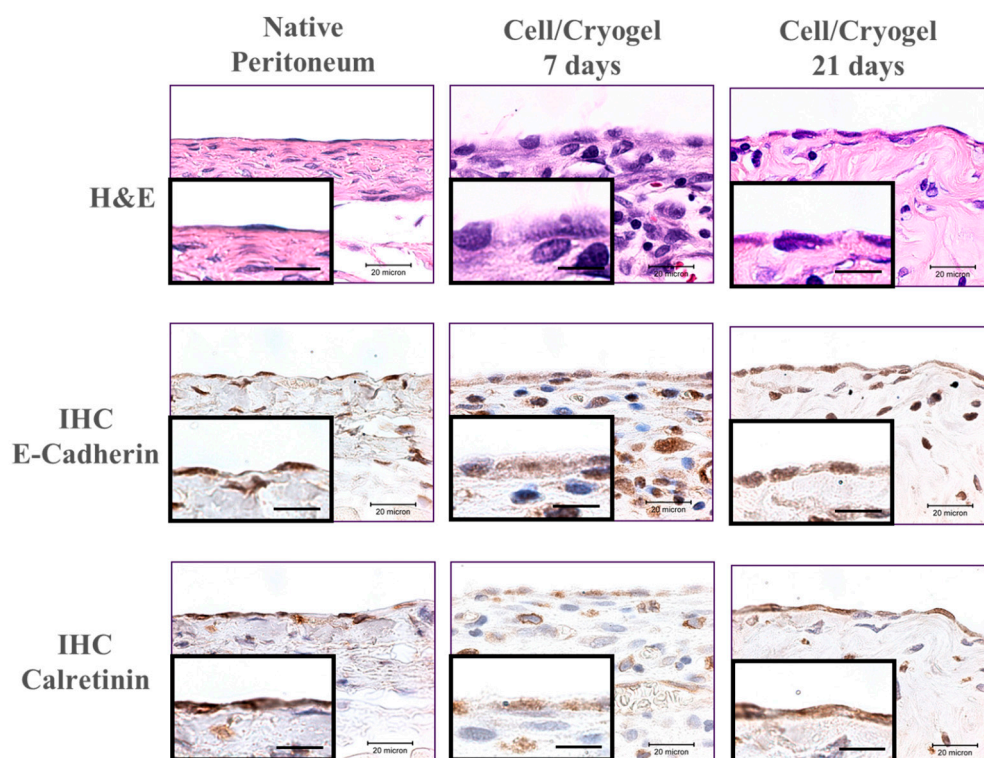


**Figure 9.** Hematoxylin and eosin (H&E) staining and immunohistochemical (IHC) staining of E-cadherin and calretinin of the cell/cryogel constructs 7- and 21-days post-implantation (bar = 20  $\mu$ m). Native peritoneum tissue was used for comparison. The inserts are enlarged views on the surface of the specimen (bar = 10  $\mu$ m).

### 3. Discussion

In the study, we used cryogelation to fabricate a 3D macroporous scaffold for the culture of mesothelial cells. The peritoneal membrane is composed of a single layer of flattened mesothelial cells that have some characteristics of epithelial cells, attaching to the surface of a thin layer of collagenous tissue [19]. In the past, mesothelial cells were generally cultured in a two-dimensional (2D) fashion on tissue culture polystyrene (TCPS) or on dishes coated with gelatin or collagen [20]. For the transplantation of mesothelial cells, the mesothelial cells were seeded onto the upper surface of an artificial connective tissue sheet consisting of fibroblasts and collagen [21], or on fibrin gel matrix [22]. A transplantable peritoneal cell sheet was also reported using the cell sheet engineering approach with a temperature-responsive culture system, using fetal liver mesothelial cells [23], or an upper monolayer of mesothelial cells and underlying multilayered fibroblasts [24]. To the best of our

knowledge, this study might be the first report of a 3D mesothelial cell culture in a cryogel scaffold for mesothelium tissue engineering.

For the preparation of the cryogel scaffolds, we used a non-toxic and biocompatible zero-length cross-linker, 1-ethyl-3-(3-dimethylaminopropyl) carbodiimide (EDC), to cross-link the adjacent gelatin/gelatin or gelatin/HA molecules, by forming covalent amide bonds [25]. During the fabrication of the GH cryogels, HA was first reacted with EDC to activate its carboxyl groups, and then the activated groups reacted with the primary amine group of the lysine residue in the gelatin. This method maximizes intermolecular cross-linking and minimizes intramolecular covalent bond formation within gelatin, and produces a robust cryogel with a high porosity.

Overall, gelatin and HA are good base materials in tissue engineering. The successful formation of intermolecular covalent linkages between gelatin–gelatin and gelatin–HA during cryogel fabrication could be justified from the macroporous structure after cryogelation at  $-17^{\circ}\text{C}$ , which promotes the formation of pores in micrometer scales from ice crystal growth within the gelling solution. The pore size may affect cell proliferation and growth. Previous studies have reported that a pore size ranging from 63–150  $\mu\text{m}$  was beneficial for the cell culture [26,27], while a higher than 80% porosity is expected to be beneficial for cell ingrowth and survival [11]. Therefore, both of our scaffolds were endowed with a suitable pore size and porosity for the 3D mesothelial cell culture (Figure 1A,B).

The water binding ability is an important feature for a tissue engineering scaffold, as the swelling increases the pore size to maximize the surface area/volume ratio, which facilitates the cell infiltration into the scaffolds during a 3D cell culture [28]. From Figure 2A, both cryogels are associated with very fast water uptake kinetics and a high swelling capacity, where the equilibrium swelling ratio is approaching 20. This rapid swelling behavior is a characteristic observed in response to porous and hydrophilic materials [27]. Also, because of the high porosity ( $\sim 90\%$ ) of the cryogel (Figure 1B), the swelling ratio did not change upon introducing the high-water absorbing HA in the cryogel. Judging from the Fickian diffusion mechanism of water during the cryogel swelling stage, no capillary effect was expected during the swelling step in the water, which could be correlated with the cryogel structure from the SEM observation (Figure 1A), where large pores free from long-aligned channels could be observed. This will allow for the unrestricted passage of water into the inner part of the cryogel during the swelling process.

The *in vitro* degradation of cryogels at  $37^{\circ}\text{C}$  in collagenase solutions could reveal the cryogel stability under physiologically-relevant conditions, as collagenase could specifically imitate the enzymatic response of the cryogel *in vivo*. Collagenase induces the proteolytic cleavage at the peptide bond between glycine and a neutral amino acid (X) in the Pro–X–Gly–Pro amino acid sequence that occurs frequently in gelatin. The degradation studies using collagenase thus mimic the possible deterioration of the cryogels *in vivo*, and the endorsed biodegradable scaffold is suitable as a cell carrier for mesothelial cells (Figure 2B). That the degradation studies show a faster degradation rate of G than GH correlates well with the replacement of 5% gelatin with HA in GH cryogel, as collagenase will only hydrolyze peptide bonds in gelatin. We also checked the degradation of cryogels in PBS at  $37^{\circ}\text{C}$ , where only 13% and 16% degradation rates were found for G and GH, respectively, after eight weeks. Therefore, we concluded that the cryogel scaffold should retain its structure during the *in vitro* cell culture, but it is biodegradable after implantation in order to fulfill the requirement of a tissue engineering scaffold. After cross-linking, the porosity, pore structure, and hydrophilic properties make both cryogels a suitable scaffold for the cell culture. The cryogels are also endowed with the proper mechanical properties for tissue engineering applications from compression testing (Figure 3). However, the G cryogel is more flexible and tough (Table 1). This feature is conducive to the environment of internal organ peristalsis when implanted in the abdominal cavity.

The mechanical testing of the mesothelium tissue is difficult, as it is a single layer of flattened cells, 2.5 to 3  $\mu\text{m}$  in thickness, which is difficult to remove intactly from the bottom layer of the fibrous connective tissue. Considering the mechanical properties of peritoneum tissue, the maximum stress and strain were shown to be 0.37 MPa and 26%, respectively, from tensile tests [29]. Also, using the

tensile tests, the ultimate stress of porcine peritoneum was reported to be from 0.525 to 0.579 MPa, and the modulus was from 0.09 to 1.01 MPa [30]. Using an atomic force microscope, the maximum Young's modulus value of the normal mouse peritoneum was 35.88 kPa [31]. The mechanical strength tensile testing showed that the bovine peritoneum/fascia had a 31% ultimate strain and 60.6 kN/m stiffness [32]. Overall, the mechanical properties of the cryogels (shown in Table 1) compared favorably with those of peritoneum tissue, considering the ultimate stress (strain), Young's modulus, and stiffness.

An analysis of the SEM images revealed that the mesothelial cells attached well to the walls of the inner pores within the scaffold, and produced abundant ECM during the 3D culture in cryogel (Figure 4A), while the live/dead staining also showed that the number of viable cells increased with time from both the top- and cross-sectional views (Figure 5A), indicating that the cryogel could maintain the cell viability and promote cell proliferation. In addition, the analysis showed that the cells proliferated along the 3D distribution of the pores. Mesothelial cells are peritoneal lining monolayer cells that have certain characteristics of epithelial cells and secrete various substances associated with peritoneal homeostasis [19]. Mesothelial cells are usually cultured on a 2D plane, but generally, solid organ cells are grown in a 3D manner. We can demonstrate that cryogel could be a suitable 3D scaffold for the attachment, proliferation, and maintenance of the phenotype of the mesothelial cells, with the configuration of cytoskeleton shown from rhodamine-phalloidin staining (Figure 5B).

Regardless of the species (human, rodent, rabbit, or horse) or anatomical origin, mesothelial cells constitute a uniform population that lines the internal organs and body walls in the peritoneum, pleura, and pericardium [33]. Although mesothelial cells are derived from mesoderm, they are very similar to simple epithelial cells; therefore, they express epithelial markers and can undergo an epithelial–mesenchymal transition (EMT), a transdifferentiation mechanism that induces the loss of their epithelial characteristics and the expression of the mesenchymal phenotype [34,35]. However, EMT in mesothelial cells is not just a pathological event. During development, mesothelial cells expressing membrane glycoprotein mesothelin (Msln) produce endothelial cells, fibroblasts, and smooth muscle in intra-abdominal organs, including in the lungs, liver, heart, and intestine [36–38]. This is consistent with previous studies, demonstrating that adipocytes and other mesenchymal lineages can be differentiated from mesothelial cells in a culture [39,40].

On the other hand, after reconstituting the intact mesothelium, these cells return to the epithelial-like phenotype [41,42]. From the cytoskeleton and live/dead staining, it can be seen that the performance of the mesothelial cells could be the same as that of the mesenchymal cells using a 3D culture in the cryogel scaffolds. When the mesothelial cells are removed and cultured, it will drive the performance of mesenchyme. The mesothelial cells have the potential to undergo 3D proliferation, and can be similar to the mesenchymal tissue proliferation. Therefore, the culture process will be different from that of normal epithelial cells, and there will still be ways to increase the growth in a 3D environment. The DNA content analysis also showed that the attached cell number in the scaffold increased with time. This means that the proliferation and growth of the mesothelial cells is feasible in cryogel. Concerning the cell proliferation rate, it was altered by the incorporation of HA into the cryogel from the DNA content comparison between G and GH (Figure 4B). One study indicated that soluble sodium hyaluronate could increase the proliferation rate of the attached human peritoneal mesothelial cells during the 2D cell culture [43]. The reduced cell proliferation could be associated with several mechanisms, including the ways HA interacts with mesothelial cells to affect its proliferation. HA might have effects on ECM synthesis or structuring [44]. HA might modulate the effects of the growth factors through regulating the surface receptor expression, or might modulate cell proliferation directly by a receptor-mediated pathway [45]. The presence of the CD44 receptor on the mesothelial cells also suggests that the binding of HA to the CD44 receptor may play a crucial role in the CD44-mediated cell–cell interactions, cell–matrix interactions, and in signal transduction [46].

The gene expressions of the mesothelial cells, including *E-cadherin*, *ICAM-1*, *calretinin* *cytokeratin-18*, *VEGF*, and *vimentin*, were detected using qRT-PCR (Figure 6). Mesothelial cells are unique in that they are derived from the mesoderm, and express mesenchymal intermediate filament vimentin



and desmin, which also express cytokeratin [47]. Cytokeratins are keratin proteins found in the cytoplasmic cytoskeleton of epithelial tissues. They are an important component of the intermediate filaments, and help the cells resist mechanical stress [48]. The expression of these cytokeratins in epithelial cells is highly specific to a particular organ or tissue. Vimentin plays an important role in maintaining the cellular structure of the organelles in the cytoplasm. It interacts with other structural proteins, such as microtubules, to make cells stiff and sturdy [49]. Vimentin is attached either laterally or terminally to the nucleus, endoplasmic reticulum, and mitochondria [49]. As an organizer of many key proteins, vimentin may be involved in cell signaling, migration, and attachment [50]. Vimentin is commonly used as a marker for mesenchymally-derived cells or cells undergoing EMT during normal development [51]. Mesothelial cells normally have a high keratin and a low vimentin content in vivo [52]. The *cytokeratin* expression was diminished and associated with an increment in the *vimentin* expression [53]. Many transforming epithelial cells also change their intermediate filaments from cytokeratin to vimentin, and the cytoskeletal transformation seems to be necessary for the beginning of the transformation process [54]. Comparing the gene expression patterns of *cytokeratin* and *vimentin*, *cytokeratin* was significantly more prominent than *vimentin* (Figure 6). This means that the characteristics of the epithelial cells continue to persist during cell division and proliferation during the 3D culture in cryogels. Nonetheless, the expression of *vimentin* was significantly up-regulated by the incorporation of HA in the cryogel, while the *cytokeratin* expression was largely maintained, which indicates that the G cryogel excels over GH in maintaining the phenotype of the seeded mesothelial cells (Figure 6).

Calretinin is a calcium-binding protein involved in calcium signaling, and is expressed in the mesothelial cells, in addition to certain neural tissues [55,56]. The exact function of calretinin is not well-defined, but it is thought to play a role in the cell cycle. Several immunohistochemical studies have suggested that it is a very useful marker for cells of the mesothelial lineage [57,58]. E-Cadherin is a calcium-dependent transmembrane epithelial protein that promotes intercellular adhesion [59]. The intercellular adhesion molecule E-cadherin appears to have a central role in the control of the epithelial-to-mesenchymal transition, as the loss of E-cadherin expression or function correlates with the ability of the epithelial cells to adopt a mesenchymal migratory and invasive phenotype [60]. Intercellular adhesion molecule-1 (ICAM-1, also called CD54) is localized to the plasma membrane and cytosol. Mesothelial cells characteristically express the adhesion molecule *ICAM-1*, whose expression is constitutive [61]. In addition, *ICAM-1* appears to be a potential marker that discriminates between mesothelial cells and fibroblasts [53]. The culture of mesothelial cells in the GH cryogel scaffold rendered the down-regulation of the mesothelium marker genes (*calretinin*, *E-cadherin*, and *ICAM1*; Figure 6). This underlines the use of G cryogels for the 3D culture of mesothelial cells in the persistence of epithelial cell characteristics during cell division and proliferation. Vascular endothelial growth factor (VEGF) is a potent proangiogenic factor involved in endothelial cell proliferation and vascular permeability [62]. However, VEGF is considered a main autocrine growth factor for mesothelial cells; an increase in its production might stimulate mesothelial cell growth [63]. It is reported that the mechanism underlying *VEGF* up-regulation in mesothelial cells is the EMT of these cells [64]. Furthermore, the local production of VEGF by transitional mesothelial cells appears to play an important role in the process leading to peritoneal angiogenesis [65]. The gene expression of *VEGF* was up-regulated in the presence of HA in the cryogel (Figure 6), indicating the maintenance of mesothelial cell characteristics in cryogels.

To confirm the gene expression patterns, the production of calretinin and E-cadherin was evaluated by IF staining, which could show the distribution and production of the proteins by seeded mesothelial cells within the cryogel scaffold (Figure 7). Specifically, abundant mesothelial-specific proteins could be identified to be lined along the cryogel pore wall, where mesothelial cells could be also identified from the nuclear staining. Consistent with the gene expression, the dominance of G over GH in the production of both proteins was confirmed from a semi-quantitative analysis with the normalized area percentage of the green fluorescence.

It has been reported that increased hyaluronan levels can induce EMT in mesothelial cells, which is essential for cell migration during wound healing and remesothelization [66]. HA fragments also possess proinflammatory properties that can activate the inflammatory cascade [67]. Therefore, mesothelial cells cultured in GH have a tendency to induce EMT, where the cell proliferation, protein expression, and gene expression were inferior to those in G. Based on studies where the G scaffolds are superior to the GH scaffolds for in vitro mesothelial cell cultures, we chose a G cryogel scaffold for the animal studies, and implanted a seven-day in vitro cultured cells/scaffold construct into the abdomen of a rat that was induced with a defective mesothelium. The scaffold retained its structure during the in vitro culture, but gradually degraded after 21 days post-implantation, with a discernible scaffold residue (Figure 8).

The mesothelial cells form a monolayer, known as the mesothelium, which lines the pleural, peritoneal, and pericardial cavities, with visceral and parietal surfaces covering the internal organs and body wall, respectively [33]. From the H&E staining, many inflammatory cells were found to infiltrate the scaffold, and were found within the scaffold on day seven because of the initial inflammatory response induced by foreign body reactions, which drastically decreased after 21 days (Figure 9). Most importantly, the uppermost layer of the cell/cryogel construct showed a mesothelial cell layer that closely resembles that in the native mesothelium from the close-up views in the inserts of each group on day 21. The IHC staining also endorsed the formation of a mesothelium layer similar to that of the native mesothelium on the top surface of the cell-scaffold construct, forming from the transplanted mesothelial cells that are associated with abundant key marker protein (calretinin and E-cadherin) secretion. Indeed, many inflammatory cells were noted on day seven, which disappeared on day 21 after the wounds healed. The uppermost layer of the scaffold was finally only covered with a monolayer of mesothelial cells when the scaffold was degrading. After 21 days post-implantation, the normal physiological manifestation of mesothelium was that the mesothelial cells at the visceral and parietal contact surfaces were monolayer distributed. As shown in Figure 9, the uppermost layer of the cell/scaffold is equivalent to the parietal peritoneum surface, and the mesothelial cells should not be distributed elsewhere, because they will not perform their normal physiological functions. It is expected that the new mesothelium will be remodelled, and a functional mesothelium developing from the allograft mesothelial cells will attach to the wound to repair the damaged mesothelium when the cryogel scaffold is completely degraded over times.

#### 4. Materials and Methods

##### 4.1. Materials

The ethyl-3-(3-dimethylaminopropyl) carbodiimide (EDC) was obtained from Acros Organics (Geel, Belgium). The gelatin (type A from porcine skin, 300 bloom) was purchased from Sigma-Aldrich (St Louis, MO, USA) and hyaluronic acid (sodium salt, average molecular weight =  $1.3 \times 10^6$  Da) were acquired from Bloomage Biotechnology (Jinan, China). HyClone Dulbecco's Modified Eagles Medium (DMEM) and fetal bovine serum (FBS) were used for the cell culture and were purchased from Thermo Fisher Scientific (Waltham, MA, USA). The rhodamine-phalloidin (tetramethylrhodamine B isothiocyanate-phalloidin, TRITC-phalloidin) and Hoechst 33342 for the actin cytoskeleton and nucleus staining were purchased from Life Technologies (Carlsbad, CA, USA).

##### 4.2. Preparation of Gelatin (G) and Gelatin-Hyaluronic Acid (GH) Scaffold by Cryogelation

Cryogels containing 5% gelatin and 5% gelatin/0.25% HA were prepared. The gelatin (10% *w/v*) and HA (0.5% *w/v*) solutions were prepared separately in a 0.1 M 2-(N-morpholino) ethanesulfonic acid (MES) buffer (pH 6.0). The gelatin solution was gently shaken in a 70 °C water bath until the gelatin flake was completely dissolved and cooled to room temperature. For the preparation of the gelatin (G) cryogel, 1 mL of a 10% gelatin solution was mixed with 1 mL of 4% 1-ethyl-3-(3-dimethylaminopropyl) carbodiimide (EDC) in a 0.1 M MES buffer (pH 6.0), in a 3 mL polypropylene syringe (inside diameter



= 8 mm). The mixture was stirred at a low speed for 5 s, and placed in a water bath filled with  $-17^{\circ}\text{C}$  ethanol. The whole mixing and transfer step was completed within 1 min. The syringe mold was incubated in the bath for 16 h so as to complete the cross-linking reaction, and was then completely thawed at room temperature. For the gelatin/hyaluronic acid (GH) cryogel, the EDC powder was dissolved in a 1 mL 0.5% *w/v* HA solution prepared in a MES buffer (pH 6.0) to a final concentration of 4%. The solution was mixed for 30 min at room temperature so as to activate the carboxyl groups of HA. The HA solution (1 mL) was then mixed with an equal volume of 10% *w/v* gelatin solution prepared in a MES buffer (pH 6) and placed in a 3 mL polypropylene syringe (inside diameter = 8 mm) syringe mold. The same cryogelation procedure was followed as for the G cryogel. After receding from the syringe, the cryogel was cut into disc-shaped scaffolds (1 mm thickness  $\times$  8 mm diameter) using a surgical blade, and was thoroughly washed with deionized water at room temperature in order to remove any residual reactants. The cryogel scaffolds were dehydrated in gradient alcohol, followed by critical point drying for storage. For the *in vivo* studies, a 5 mL polypropylene syringe (inside diameter = 12 mm) was used to prepare the disc-shaped scaffolds (1 mm thickness  $\times$  12 mm diameter) for implantation, following the same preparation condition described before.

#### 4.3. Characteristics of Cryogel

The microstructure of the scaffold of cryogel samples was examined with an S-3000N scanning electron microscope (SEM) from Hitachi (Tokyo, Japan), after gold sputter coating. The porosity of the cryogel was calculated using the ethanol displacement method [68]. To study *in vitro* degradation of cryogel, a collagenase (30 units/mL) solution was prepared in PBS (pH 7.4). The dry weight ( $W_1$ ) of the oven-dried cryogel samples were measured and placed in wells of a 24-well culture plate. Then, 2 mL of a collagenase solution was added to each well, and they were incubated at  $37^{\circ}\text{C}$ . The cryogel samples were retrieved at different time points from the well, were rinsed with distilled deionized water, and dried overnight in an oven at  $70^{\circ}\text{C}$  to a constant weight ( $W_2$ ). The degree of degradation was calculated from the following equation.

$$\text{Degree of degradation (\%)} = \frac{(W_1 - W_2)}{W_1} \times 100 \quad (1)$$

The water uptake and swelling of the cryogel scaffolds were studied in PBS (pH 7.4) following the gravimetric procedure. The cryogel samples were dried for 24 h at  $70^{\circ}\text{C}$  and were weighed ( $W_d$ ) [69]. The dried samples were immersed in PBS at room temperature, followed by retrieving the wet samples at different time points. The retrieved samples were gently shaken and blotted with tissue paper in order to remove any excess water from the surface, and the weight of the swollen gel samples ( $W_t$ ) were determined immediately. The equilibrium weight ( $W_{eq}$ ) of the swollen sample was obtained after being immersed in PBS for 24 h at room temperature, where no measurable weight increase could be observed. To determine the swelling kinetics, the water uptake was calculated at different time points using Equation (2).

$$\text{Water uptake (\%)} = \frac{W_t - W_d}{W_{eq}} \times 100 \quad (2)$$

To investigate the diffusion of water in the cryogels, the swelling kinetics were fitted to Equation (3) [18].

$$\frac{W_t - W_d}{W_{eq} - W_d} = kt^n \quad (3)$$

where  $k$  is a characteristic constant of the gel,  $t$  is time, and  $n$  is a characteristic exponent of the transport mode of water.

The swelling ratio was calculated from Equation (4).

$$\text{Swelling ratio} = \frac{W_t - W_d}{W_d} \quad (4)$$

To determine the mechanical properties of the cryogels, unconfined quasi-static compression tests using wet cryogel samples were performed. The samples were soaked in PBS for 24 h prior to testing, and the testing was carried out at 37 °C using an ElectroForce 5200 BioDynamic Test Instrument from TA Instruments (New Castle, DE, USA). A 250 N load cell was used to apply the compression load at a 0.05 mm/s crosshead speed. Based on the stress ( $\sigma$ ) vs strain ( $\epsilon$ ) curve of the load–deformation data subject to the uniaxial stress, the ultimate stress and ultimate strain at the failure point and compressive Young's (elastic) modulus were determined. To model the non-linear compressive behavior of a cryogel sample, Equation (5) was used to fit the  $\sigma$ – $\epsilon$  curve, up to failure [70].

$$\sigma = Ae^{(B\epsilon-1)} \quad (5)$$

where A and B are the fitted empirical parameters. The tangential Young's moduli (slope of the tangent to the  $\sigma$ – $\epsilon$  curve) at 10%, 20%, and 30% strains were calculated using Equation (5), while the toughness (compressive strain energy to failure) representing the energy required to deform the sample was obtained from the region under the curve.

#### 4.4. Culture of Mesothelial Cells in Cryogel Scaffolds

##### 4.4.1. Isolation and Harvest of Mesothelial Cells

To harvest the mesothelial cells from the lower abdomen of a Sprague-Dawley (SD) rat, the abdomen wall was pre-sterilized with a beta-iodine solution. The skin was picked up with forceps on the abdomen wall, and was gently cut with a blade to separate it from the peritoneum. The procedure was approved by the Institutional Animal Care and Use Committee of Chang Gung University (IACUC approval no. CGU106-045, approved on 6/9/2017), and followed the standards of the Association for Assessment and Accreditation of Laboratory Animal Care. The peritoneum was diced into pieces of a 2 × 2 cm<sup>2</sup> area using scissors, in a sterile procedure. The diced peritoneum sample was washed extensively with equal volumes of PBS, and the ECM was digested with 0.2% collagenase at 37 °C, and was shaken at 20 rpm for 30 min. The peritoneum was discarded and the liquid was filtered through a 70 µm pore-size filter to remove the debris. The enzyme activity was neutralized by adding 20 mL of a culture medium consisting of DMEM with 10% FBS, and centrifuged at 100× g for 5 min in order to obtain a high-density cell pellet. The supernatant was discarded, and the cell pellet was re-suspended in a culture medium and incubated at room temperature.

##### 4.4.2. In Vitro Cell Culture

Disc-shaped cryogel scaffolds (1 mm thickness × 8 mm diameter) were sterilized with 75% ethanol for 24 h, and rinsed two times with PBS before being placed in 24-well culture plates for cell seeding. An aliquot of a 10 µL cell suspension (10<sup>7</sup> cells/mL) was loaded onto the surface of the cryogel scaffold. The cell-seeded cryogels were incubated at 37 °C for 2 h so as to allow for cell adhesion, and were transferred to a new well, followed by adding 1 mL of a culture medium to each well. The cells were cultured at 37 °C in 5% CO<sub>2</sub>, with a medium change every three days.

##### 4.4.3. SEM Analysis

After three and seven days of the cell culture, the mesothelial cell/cryogel constructs were examined by SEM. The constructs were washed with PBS and the cells in the scaffold were fixed using 2.5% glutaraldehyde at room temperature for 3 h. All of the samples were washed another three times with PBS, and were treated with increasing concentrations of ethanol from 50% to 100%, and were dried in a critical point dryer. The completely dried samples were sputter coated with gold and mounted on a S-3000N SEM (Hitachi, Tokyo, Japan) in order to observe the cell morphology.

#### 4.4.4. DNA Quantification

The cell-seeded scaffolds were harvested at predetermined times, and were digested for 24 h in papain solutions (55 mM sodium citrate, 150 mM sodium chloride, 5 mM cysteine hydrochloride, 5 mM ethylenediaminetetraacetic acid (EDTA), and 0.2 mg/mL papain) at 60 °C to determine the DNA content. The DNA content was determined with Hoechst 33258 in an enzyme-linked immunosorbent assay (ELISA) reader (excitation = 360 nm; emission = 460 nm) [71].

#### 4.4.5. Live/Dead Staining

The live/dead viability/cytotoxicity kit was purchased from Molecular Probes Inc. (Eugene, OR, USA) and was used to qualitatively evaluate the cell viability. After being cultured for seven days in vitro, the cell-seeded scaffolds were washed with PBS and stained with 1 mL of a staining solution. The staining solution was prepared by diluting 3 µL of calcein AM and 5 µL of ethidium homodimer-1 (EthD-1) reagents in 10 mL of PBS at 37 °C for 15 min. The live and dead cells were stained green and red separately, with calcein AM and EthD-1, which could be imaged under a confocal laser scanning microscope (Leica TCS SP2, Leica Microsystems, Wetzlar, Germany) at an excitation/emission wavelength of 494/517 nm and 528/617 nm.

#### 4.4.6. Cell Cytoskeleton Staining

To assess the cytoskeletal structure of the mesothelial cells within the cryogels, the cell/scaffold constructs after the seven-day culture were fixed in 10% *w/v* formaldehyde in PBS for 30 min at room temperature. The sample was washed with PBS three times, and treated with 0.1% Triton X-100 in PBS for 10 min for the permeabilization of the cell membrane. The constructs were then immersed in 1 µg/mL rhodamine-phalloidin for 30 min in the dark, and were washed three times with PBS. The cell nuclei were counterstained with 10 µg/mL Hoechst 33342 in PBS for 30 min, and were immediately visualized for their cytoskeletal arrangements using a Leica TCS SP2 confocal laser scanning microscope. The F-actin cytoskeleton emits a red fluorescence and the nucleus is stained blue using an excitation/emission wavelength of 540/570 nm for the rhodamine-phalloidin and 350/461 nm for the Hoechst 33342.

#### 4.4.7. Quantitative Real-Time Polymerase Chain Reaction (qPCR)

The expression of the mesothelial marker genes was analyzed by a quantitative real-time polymerase chain reaction (qRT-PCR) using standard protocols of cDNA synthesis and RNA isolation. The total RNA from each sample was isolated using the TRIzol reagent, according to the standard protocol. The isolated RNA was dissolved in diethylpyrocarbonate (DEPC)-treated water, and the amount of RNA was determined by measuring the absorbance at 260 nm ( $OD_{260}$ ) with a NanoDrop 2000 spectrophotometer (Thermo Fisher Scientific, Waltham, MA, USA). The RNA quality was verified from  $OD_{260}/OD_{280}$  measurements. The cDNA was synthesized using a Maxime RT PreMix Kit, according to the standard procedures. Glyceraldehyde-3-phosphate dehydrogenase (*GAPDH*) acted as a housekeeping control. Amplification was conducted for 45 cycles in a PCR thermo cycler. Each cycle consisted of 10 min at 95 °C for denaturation; 30 s at 95 °C, as obtained from the melting curves for annealing; and 1 min at 60.9 °C (*calretinin*) or 67.1 °C (*cytokeratin-18*, *E-cadherin*, *GAPDH*, *ICAM-1*, *VEGF*, and *vimentin*) for extension. A MiniOpticon real-time PCR system (Bio-Rad CFD-3120, Bio-Rad, Hercules, CA, USA) was used for the qPCR measurements using the SYBR Green qPCR Supermixes. The primer sequences were *E-cadherin* (forward: 5' AAGGGCTTGGATTTTGAGG 3'; reverse: 5' AGATGGGGGCTTCATTCAC 3'), *ICAM-1* (forward: 5' GCCTGGGGTTGGAGACTAAC 3'; reverse: 5' CTGTCTTCCCAATGTCGCT 3'), *vimentin* (forward: 5' TGCCAACCGGAACAACGAT 3'; reverse: 5' AATTCTCTTCCATTTACGCATC 3'), *cytokeratin-18* (forward: 5' CAGATACAGGGTGCAGATGGAG 3'; reverse: 5' GGGCGTCGTTGAGACTGAAATC 3'), *calretinin* (forward: 5' TATCCAGCAGCTACACCTAC 3'; reverse: 5' GAGAGGTCTGGGAAGGAGTTTC

3'), *VEGF* (forward: 5' TGAGACCCTGGTGGACATCT 3'; reverse: 5' CTCCTATGTGCTGGCTTTGG 3'), and *GAPDH* (forward: 5' CACCATCTTCCAGGAGCGAG 3'; reverse: 5' GGCGGAGATGATGACCCTTT 3').

#### 4.4.8. Immunofluorescence (IF) Staining

For the immunofluorescence (IF) staining of E-cadherin and calretinin, the cell/cryogel constructs that were cultured for seven days were fixed with 10% *w/v* formaldehyde at 4 °C for 1 h. After fixation, the constructs were washed three times in PBS containing 0.1% Tween 20 (PBST) for 10 min. The non-specific binding sites were blocked with a Hyblock blocking buffer for 1 min, and washed three times in PBST for 30 min. An anti-calretinin (rabbit polyclonal, Thermo Fisher Scientific PA5-16681, 1:400 in PBST) or E-cadherin (rabbit polyclonal, Thermo Fisher Scientific PA5-32178, 1:500 in PBST) primary antibody was added and incubated overnight at 4 °C. The samples were washed three times in PBST for 10 min, and then incubated in a fluorescein isothiocyanate (FITC) AffiniPure goat anti-rabbit IgG (H+L) secondary antibody (Jackson Immuno Research Laboratories Inc., 111-095-003) for 1 h at 37 °C. After washing three times in PBST for 10 min, the construct was incubated for an additional 30 min at room temperature in 100 µg/mL Hoechst 33342 for nuclear staining, and washed three times in PBST for 15 min. The sample was observed by a confocal laser scanning microscope (Leica TCS SP8, Leica Microsystems, Wetzlar, Germany) at excitation/emission wavelengths of 490/525 nm for FITC, and 350/461 nm for Hoechst 33342. The PAX-it!™ image analysis software (version 7.8.1, MIS Inc., Villa Park, IL, USA) was used for the semi-quantitative evaluation of the E-cadherin and calretinin produced by the mesothelial cells.

#### 4.5. In Vivo Studies

The animal protocols were approved by the Institutional Animal Care and Use Committee of Chang Gung University (IACUC approval no. CGU106-045, approved on 6/9/2017). The male SD rats weighed between 300 to 380 g were used for the in vivo experiments. The rats underwent surgery during an inhalation induction of isoflurane anesthesia, then depilating the lower abdomen area. After the abdomens were cleaned with an alcohol and betadine solution, a C-shaped incision with a 5-cm diameter was made using sterile techniques for laparotomy. The parietal peritoneum was abraded with a sterile tooth brush for 100 strokes in order to create a 10-mm diameter wound area. After the abraded surface formation, the wound was covered with a cryogel (12 mm diameter × 1 mm thickness) seeded with  $3 \times 10^5$  mesothelial cells, which was cultured for seven days in vitro before implantation. The abdominal wall was closed using 3–0 nylon running suture, without creating any trauma on abdominal wall, and the skin incision was closed with a 3–0 nylon interrupted suture. The animals were sacrificed by CO<sub>2</sub> inhalation 7- and 21-days post-implantation. The abdominal cavities were opened in a U-shaped incision, and were examined from gross view observation. For the histological examination, the specimens were collected and fixed in a 10% buffered formaldehyde solution for 48 h, and were embedded into paraffin. The paraffin sections were cut at 5 µm and were subject to hematoxylin and eosin (H&E) stain for the histological evaluation. For the immunohistochemical (IHC) staining, the sections were deparaffinized and rehydrated. The sections were then washed three times in PBST for 5 min. The non-specific binding sites were blocked with hydrogen peroxide for 10 min, and the sections were washed three times in PBST for 5 min again. The sections were then incubated for an additional 60 min at room temperature in a rabbit anti-calretinin primary antibody (rabbit polyclonal, Thermo Fisher Scientific PA5-16681, 1:600 in PBST) or rabbit anti-E-cadherin primary antibody (rabbit polyclonal, Thermo Fisher Scientific PA5-32178, 1:800 in PBST), in a humid environment. The slides were washed in PBST for 5 min and were treated with an HRP Polymer Quanto (Thermo Fisher Scientific, Waltham, MA, USA) for 10 min, followed by a washing step for 5 min. The peroxidase activity was visualized using 3-diaminobenzidine (DAB) as the substrate, by incubation for 1 min. The sections were finally counterstained with hematoxylin for 30 s, and were observed under an inverted optical microscope.

#### 4.6. Statistical Analysis

All of the quantitative data were expressed as mean  $\pm$  standard deviation (SD), and the statistical analysis was performed by a one-way analysis of variance (ANOVA) least significant difference (LSD) test in order to determine the significant difference ( $p < 0.05$ ).

### 5. Conclusions

This study demonstrates the feasibility of a cryogel scaffold for a 3D culture of mesothelial cells. The incorporation of HA in gelatin-based cryogel was found to modulate the scaffold properties, in addition to influencing the cellular response of the seeded mesothelial cells. Although there was no change in the pore structure and water absorbing properties, GH showed a faster degradation in the collagenase solution and a higher elastic modulus than G cryogel. From the in vitro cell culture, the rat mesothelial cells proliferated well in the cryogel scaffolds, although the cells cultured in GH showed a change in the cell morphology, cytoskeleton arrangement, and proliferation rate. The mesothelial cells in the cryogels also have a good phenotypic expression from qRT-PCR, as well as IF staining results. Nonetheless, the downregulation of the mesothelium specific marker gene, together with the reduced production of the key mesothelium proteins, E-cadherin and calretinin, was noted for the GH compared with G cryogel. Taken together, the HA incorporation in the cryogel may have an adverse effect on the mesothelial cell behavior during the 3D in vitro cell culture, pointing out the choice of G cryogel as the scaffold for tissue engineering applications, where in vitro cultured cell/scaffold constructs were used for neo-mesothelium formation in vivo. In animal studies, the G cryogel could be shown to provide a good vehicle for delivering mesothelial cells from a rat mesothelium wound model. After implantation, the scaffold degraded gradually in concomitant with the remodeling of the mesothelial cells into a parietal mesothelium, similar to the native mesothelium from H&E and IHC staining. It is expected that the damaged mesothelium could be repaired after the cryogel is completely degraded and the neo-mesothelium tissue attaches to the wound.

**Author Contributions:** H.-H.K., C.-Y.K., and K.-S.C. conceived and designed the experiments; H.-H.K. and C.-Y.K. performed the experiments; H.-H.K., C.-Y.K., and J.-P.C. analyzed the data; H.-H.K. and J.-P.C. wrote the paper.

**Funding:** This research was funded by Chang Gung Memorial Hospital, Keelung, grant number CMRPG2G0251 and CMRPG2I0121.

**Acknowledgments:** The Microscope Core Laboratory in Chang Gung Memorial Hospital, Linkou, is acknowledged for the confocal microscopic analysis.

**Conflicts of Interest:** The authors declare no conflict of interest.

### References

1. Mutsaers, S.E. The mesothelial cell. *Int. J. Biochem. Cell Biol.* **2004**, *36*, 9–16. [[CrossRef](#)]
2. Yung, S.; Chan, T.M. Pathophysiological changes to the peritoneal membrane during PD-related peritonitis: The role of mesothelial cells. *Mediat. Inflamm.* **2012**, *2012*, 484167. [[CrossRef](#)] [[PubMed](#)]
3. Margetts, P.J.; Churchill, D.N. Acquired ultrafiltration dysfunction in peritoneal dialysis patients. *J. Am. Soc. Nephrol.* **2002**, *13*, 2787–2794.
4. O'Brien, F.J. Biomaterials & scaffolds for tissue engineering. *Mater. Today* **2011**, *14*, 88–95.
5. Bencherif, S.A.; Sands, R.W.; Bhatta, D.; Arany, P.; Verbeke, C.S.; Edwards, D.A.; Mooney, D.J. Injectable preformed scaffolds with shape-memory properties. *Proc. Natl. Acad. Sci. USA* **2012**, *109*, 19590–19595. [[CrossRef](#)] [[PubMed](#)]
6. Dainiak, M.B.; Kumar, A.; Galaev, I.Y.; Mattiasson, B. Detachment of affinity-captured bioparticles by elastic deformation of a macroporous hydrogel. *Proc. Natl. Acad. Sci. USA* **2006**, *103*, 849–854. [[CrossRef](#)]
7. Kumar, A.; Srivastava, A. Cell separation using cryogel-based affinity chromatography. *Nat. Protoc.* **2010**, *5*, 1737–1747. [[CrossRef](#)]
8. Lozinsky, V.I.; Plieva, F.M.; Galaev, I.Y.; Mattiasson, B. The potential of polymeric cryogels in bioseparation. *Bioseparation* **2001**, *10*, 163–188. [[CrossRef](#)] [[PubMed](#)]



9. Lozinsky, V.I.; Galaev, I.Y.; Plieva, F.M.; Savina, I.N.; Jungvid, H.; Mattiasson, B. Polymeric cryogels as promising materials of biotechnological interest. *Trends Biotechnol.* **2003**, *21*, 445–451. [\[CrossRef\]](#)
10. Hwang, Y.; Sangaj, N.; Varghese, S. Interconnected macroporous poly(ethylene glycol) cryogels as a cell scaffold for cartilage tissue engineering. *Tissue Eng. Part. A* **2010**, *16*, 3033–3041. [\[CrossRef\]](#)
11. Chang, K.H.; Liao, H.T.; Chen, J.P. Preparation and characterization of gelatin/hyaluronic acid cryogels for adipose tissue engineering: In vitro and in vivo studies. *Acta Biomater.* **2013**, *9*, 9012–9026. [\[CrossRef\]](#)
12. Sharma, A.; Bhat, S.; Nayak, V.; Kumar, A. Efficacy of supermacroporous poly(ethylene glycol)-gelatin cryogel matrix for soft tissue engineering applications. *Mater. Sci. Eng. CMater. Biol. Appl.* **2015**, *47*, 298–312. [\[CrossRef\]](#)
13. Liao, H.-T.; Shalumon, K.T.; Chang, K.-H.; Sheu, C.; Chen, J.-P. Investigation of synergistic effects of inductive and conductive factors in gelatin-based cryogels for bone tissue engineering. *J. Mater. Chem. B* **2016**, *4*, 1827–1841. [\[CrossRef\]](#)
14. Chang, C.H.; Liu, H.C.; Lin, C.C.; Chou, C.H.; Lin, F.H. Gelatin-chondroitin-hyaluronan tri-copolymer scaffold for cartilage tissue engineering. *Biomaterials* **2003**, *24*, 4853–4858. [\[CrossRef\]](#)
15. Yin, B.; Ma, P.; Chen, J.; Wang, H.; Wu, G.; Li, B.; Li, Q.; Huang, Z.; Qiu, G.; Wu, Z. Hybrid macro-porous titanium ornamented by degradable 3d gel/nha micro-scaffolds for bone tissue regeneration. *Int. J. Mol. Sci.* **2016**, *17*, 575. [\[CrossRef\]](#)
16. Echave, M.C.; Saenz del Burgo, L.; Pedraz, J.L.; Orive, G. Gelatin as biomaterial for tissue engineering. *Curr. Pharm. Des.* **2017**, *23*, 3567–3584. [\[CrossRef\]](#)
17. Borzacchiello, A.; Mayol, L.; Ramires, P.A.; Pastorello, A.; Di Bartolo, C.; Ambrosio, L.; Milella, E. Structural and rheological characterization of hyaluronic acid-based scaffolds for adipose tissue engineering. *Biomaterials* **2007**, *28*, 4399–4408. [\[CrossRef\]](#)
18. Khare, A.R.; Peppas, N.A. Swelling/deswelling of anionic copolymer gels. *Biomaterials* **1995**, *16*, 559–567. [\[CrossRef\]](#)
19. Brulez, H.F.; Verbrugh, H.A. First-line defense mechanisms in the peritoneal cavity during peritoneal dialysis. *Perit. Dial. Int.* **1995**, *15*, S24–S33.
20. Stylianou, E.; Jenner, L.A.; Davies, M.; Coles, G.A.; Williams, J.D. Isolation, culture and characterization of human peritoneal mesothelial cells. *Kidney Int.* **1990**, *37*, 1563–1570. [\[CrossRef\]](#)
21. Kuga, H.; Morisaki, T.; Nakamura, K.; Onishi, H.; Matsuda, T.; Sueishi, K.; Tanaka, M.; Katano, M. Construction of a transplantable tissue-engineered artificial peritoneum. *Eur. Surg. Res. Eur. Chir. Forsch. Rech. Chir. Eur.* **2004**, *36*, 323–330. [\[CrossRef\]](#)
22. Takazawa, R.; Yamato, M.; Kageyama, Y.; Okano, T.; Kihara, K. Mesothelial cell sheets cultured on fibrin gel prevent adhesion formation in an intestinal hernia model. *Tissue Eng.* **2005**, *11*, 618–625. [\[CrossRef\]](#)
23. Inagaki, N.F.; Inagaki, F.F.; Kokudo, N.; Miyajima, A. Cell-based therapy for preventing postoperative adhesion and promoting regeneration after hepatectomy. *J. Hepato-Biliary-Pancreat. Sci.* **2015**, *22*, 524–530. [\[CrossRef\]](#)
24. Kawanishi, K.; Yamato, M.; Sakiyama, R.; Okano, T.; Nitta, K. Peritoneal cell sheets composed of mesothelial cells and fibroblasts prevent intra-abdominal adhesion formation in a rat model. *Journal Tissue Eng. Regen. Med.* **2016**, *10*, 855–866. [\[CrossRef\]](#)
25. Tripathi, A.; Kumar, A. Multi-featured macroporous agarose-alginate cryogel: Synthesis and characterization for bioengineering applications. *Macromol. Biosci.* **2011**, *11*, 22–35. [\[CrossRef\]](#)
26. Zeltinger, J.; Sherwood, J.K.; Graham, D.A.; Mueller, R.; Griffith, L.G. Effect of pore size and void fraction on cellular adhesion, proliferation, and matrix deposition. *Tissue Eng.* **2001**, *7*, 557–572. [\[CrossRef\]](#)
27. Jain, E.; Srivastava, A.; Kumar, A. Macroporous interpenetrating cryogel network of poly(acrylonitrile) and gelatin for biomedical applications. *J. Mater. Sci. Mater. Med.* **2009**, *20*, S173–S179. [\[CrossRef\]](#)
28. Jayakumar, R.; Ramachandran, R.; Sudheesh Kumar, P.T.; Divyarani, V.V.; Srinivasan, S.; Chennazhi, K.P.; Tamura, H.; Nair, S.V. Fabrication of chitin-chitosan/nano ZrO<sub>2</sub> composite scaffolds for tissue engineering applications. *Int. J. Biol. Macromol.* **2011**, *49*, 274–280. [\[CrossRef\]](#)
29. Faturechi, R.; Karimi, A.; Hashemi, S.A.; Navidbakhsh, M. Mechanical characterization of peritoneum/fascia under uniaxial loading. *J. Biomater. Tissue Eng.* **2014**, *4*, 189–193. [\[CrossRef\]](#)
30. White, E.J.; Cunnane, E.M.; McMahon, M.; Walsh, M.T.; Coffey, J.C.; O'Sullivan, L. Mechanical characterisation of porcine non-intestinal colorectal tissues for innovation in surgical instrument design. *Proc. Inst. Mech. Eng. Part. H J. Eng. Med.* **2018**, *232*, 796–806. [\[CrossRef\]](#)

31. McKenzie, A.J.; Hicks, S.R.; Svec, K.V.; Naughton, H.; Edmunds, Z.L.; Howe, A.K. The mechanical microenvironment regulates ovarian cancer cell morphology, migration, and spheroid disaggregation. *Sci. Rep.* **2018**, *8*, 7228. [[CrossRef](#)]
32. Sarac, T.P.; Carnevale, K.; Smedira, N.; Tanquilut, E.; Augustinos, P.; Patel, A.; Naska, T.; Clair, D.; Ouriel, K. In vivo and mechanical properties of peritoneum/fascia as a novel arterial substitute. *J. Vasc. Surg.* **2005**, *41*, 490–497. [[CrossRef](#)]
33. Mutsaers, S.E. Mesothelial cells: Their structure, function and role in serosal repair. *Respirology* **2002**, *7*, 171–191. [[CrossRef](#)]
34. Mutsaers, S.E.; Wilkosz, S. Structure and function of mesothelial cells. *Cancer Treat. Res.* **2007**, *134*, 1–19.
35. Thiery, J.P.; Acloque, H.; Huang, R.Y.; Nieto, M.A. Epithelial-mesenchymal transitions in development and disease. *Cell* **2009**, *139*, 871–890. [[CrossRef](#)]
36. Asahina, K.; Zhou, B.; Pu, W.T.; Tsukamoto, H. Septum transversum-derived mesothelium gives rise to hepatic stellate cells and perivascular mesenchymal cells in developing mouse liver. *Hepatology* **2011**, *53*, 983–995. [[CrossRef](#)]
37. Que, J.; Wilm, B.; Hasegawa, H.; Wang, F.; Bader, D.; Hogan, B.L. Mesothelium contributes to vascular smooth muscle and mesenchyme during lung development. *Proc. Natl. Acad. Sci. USA* **2008**, *105*, 16626–16630. [[CrossRef](#)]
38. Rinkevich, Y.; Mori, T.; Sahoo, D.; Xu, P.X.; Bermingham, J.R., Jr.; Weissman, I.L. Identification and prospective isolation of a mesothelial precursor lineage giving rise to smooth muscle cells and fibroblasts for mammalian internal organs, and their vasculature. *Nat. Cell Biol.* **2012**, *14*, 1251–1260. [[CrossRef](#)]
39. Lachaud, C.C.; Pezzolla, D.; Dominguez-Rodriguez, A.; Smani, T.; Soria, B.; Hmadcha, A. Functional vascular smooth muscle-like cells derived from adult mouse uterine mesothelial cells. *PLoS ONE* **2013**, *8*, e55181. [[CrossRef](#)]
40. Lansley, S.M.; Searles, R.G.; Hoi, A.; Thomas, C.; Moneta, H.; Herrick, S.E.; Thompson, P.J.; Newman, M.; Sterrett, G.F.; Prele, C.M.; et al. Mesothelial cell differentiation into osteoblast- and adipocyte-like cells. *J. Cell. Mol. Med.* **2011**, *15*, 2095–2105. [[CrossRef](#)]
41. Foley-Comer, A.J.; Herrick, S.E.; Al-Mishlab, T.; Prele, C.M.; Laurent, G.J.; Mutsaers, S.E. Evidence for incorporation of free-floating mesothelial cells as a mechanism of serosal healing. *J. Cell Sci.* **2002**, *115*, 1383–1389.
42. Mutsaers, S.E.; Whitaker, D.; Papadimitriou, J.M. Stimulation of mesothelial cell proliferation by exudate macrophages enhances serosal wound healing in a murine model. *Am. J. Pathol.* **2002**, *160*, 681–692. [[CrossRef](#)]
43. Reijnen, M.M.; Falk, P.; van Goor, H.; Holmdahl, L. The antiadhesive agent sodium hyaluronate increases the proliferation rate of human peritoneal mesothelial cells. *Fertil. Steril.* **2000**, *74*, 146–151. [[CrossRef](#)]
44. Brecht, M.; Mayer, U.; Schlosser, E.; Prehm, P. Increased hyaluronate synthesis is required for fibroblast detachment and mitosis. *Biochem. J.* **1986**, *239*, 445–450. [[CrossRef](#)]
45. West, D.C.; Kumar, S. Hyaluronan and angiogenesis. *Ciba Found. Symp.* **1989**, *143*, 187–201.
46. Entwistle, J.; Hall, C.L.; Turley, E.A. HA receptors: Regulators of signalling to the cytoskeleton. *J. Cell. Biochem.* **1996**, *61*, 569–577. [[CrossRef](#)]
47. Ferrandez-Izquierdo, A.; Navarro-Fos, S.; Gonzalez-Devesa, M.; Gil-Benso, R.; Llombart-Bosch, A. Immunocytochemical typification of mesothelial cells in effusions: In vivo and in vitro models. *Diagn. Cytopathol.* **1994**, *10*, 256–262. [[CrossRef](#)]
48. Herrmann, H.; Bar, H.; Kreplak, L.; Strelkov, S.V.; Aebi, U. Intermediate filaments: From cell architecture to nanomechanics. *Nat. Rev. Mol. Cell Biol.* **2007**, *8*, 562–573. [[CrossRef](#)]
49. Goldman, R.D.; Khuon, S.; Chou, Y.H.; Opal, P.; Steinert, P.M. The function of intermediate filaments in cell shape and cytoskeletal integrity. *J. Cell Biol.* **1996**, *134*, 971–983. [[CrossRef](#)]
50. Ivaska, J.; Pallari, H.M.; Nevo, J.; Eriksson, J.E. Novel functions of vimentin in cell adhesion, migration, and signaling. *Exp. Cell Res.* **2007**, *313*, 2050–2062. [[CrossRef](#)]
51. Gong, L.; Zhao, H.; Wang, L.; Sun, B.; Yu, L.; Qi, X.; Zhou, X.; Zhang, L.; Guan, H.; Shao, S. Upregulation of annexin A5 affects the biological behaviors of lung squamous carcinoma cells in vitro. *Chin. Sci. Bull.* **2014**, *59*, 3610–3620. [[CrossRef](#)]
52. Graf, T.; Beug, H. Role of the v-erbA and v-erbB oncogenes of avian erythroblastosis virus in erythroid cell transformation. *Cell* **1983**, *34*, 7–9. [[CrossRef](#)]

53. Yanez-Mo, M.; Lara-Pezzi, E.; Selgas, R.; Ramirez-Huesca, M.; Dominguez-Jimenez, C.; Jimenez-Heffernan, J.A.; Aguilera, A.; Sanchez-Tomero, J.A.; Bajo, M.A.; Alvarez, V.; et al. Peritoneal dialysis and epithelial-to-mesenchymal transition of mesothelial cells. *N. Engl. J. Med.* **2003**, *348*, 403–413. [\[CrossRef\]](#)
54. Perez-Pomares, J.M.; Munoz-Chapuli, R. Epithelial-mesenchymal transitions: A mesodermal cell strategy for evolutive innovation in Metazoans. *Anat. Rec.* **2002**, *268*, 343–351. [\[CrossRef\]](#)
55. Gotzos, V.; Vogt, P.; Celio, M.R. The calcium binding protein calretinin is a selective marker for malignant pleural mesotheliomas of the epithelial type. *Pathol. Res. Pract.* **1996**, *192*, 137–147. [\[CrossRef\]](#)
56. Nagel, H.; Hemmerlein, B.; Ruschenburg, I.; Huppe, K.; Droese, M. The value of anti-calretinin antibody in the differential diagnosis of normal and reactive mesothelia versus metastatic tumors in effusion cytology. *Pathol. Res. Pract.* **1998**, *194*, 759–764. [\[CrossRef\]](#)
57. Doglioni, C.; Dei Tos, A.P.; Laurino, L.; Iuzzolino, P.; Chiarelli, C.; Celio, M.R.; Viale, G. Calretinin: A novel immunocytochemical marker for mesothelioma. *Am. J. Surg. Pathol.* **1996**, *20*, 1037–1046. [\[CrossRef\]](#)
58. Kitazume, H.; Kitamura, K.; Mukai, K.; Inayama, Y.; Kawano, N.; Nakamura, N.; Sano, J.; Mitsui, K.; Yoshida, S.; Nakatani, Y. Cytologic differential diagnosis among reactive mesothelial cells, malignant mesothelioma, and adenocarcinoma: Utility of combined E-cadherin and calretinin immunostaining. *Cancer* **2000**, *90*, 55–60. [\[CrossRef\]](#)
59. Perl, A.K.; Wilgenbus, P.; Dahl, U.; Semb, H.; Christofori, G. A causal role for E-cadherin in the transition from adenoma to carcinoma. *Nature* **1998**, *392*, 190–193. [\[CrossRef\]](#)
60. Takeichi, M. Morphogenetic roles of classic cadherins. *Curr. Opin. Cell Biol.* **1995**, *7*, 619–627. [\[CrossRef\]](#)
61. Suassuna, J.H.; Das Neves, F.C.; Hartley, R.B.; Ogg, C.S.; Cameron, J.S. Immunohistochemical studies of the peritoneal membrane and infiltrating cells in normal subjects and in patients on CAPD. *Kidney Int.* **1994**, *46*, 443–454. [\[CrossRef\]](#)
62. Ferrara, N.; Gerber, H.P.; LeCouter, J. The biology of VEGF and its receptors. *Nat. Med.* **2003**, *9*, 669–676. [\[CrossRef\]](#)
63. Romano, M.; Catalano, A.; Nutini, M.; D'Urbano, E.; Crescenzi, C.; Claria, J.; Libner, R.; Davi, G.; Procopio, A. 5-lipoxygenase regulates malignant mesothelial cell survival: Involvement of vascular endothelial growth factor. *FASEB J.* **2001**, *15*, 2326–2336. [\[CrossRef\]](#)
64. Aguilera, A.; Yanez-Mo, M.; Selgas, R.; Sanchez-Madrid, F.; Lopez-Cabrera, M. Epithelial to mesenchymal transition as a triggering factor of peritoneal membrane fibrosis and angiogenesis in peritoneal dialysis patients. *Curr. Opin. Investig. Drugs* **2005**, *6*, 262–268.
65. Selgas, R.; Bajo, A.; Jimenez-Heffernan, J.A.; Sanchez-Tomero, J.A.; Del Peso, G.; Aguilera, A.; Lopez-Cabrera, M. Epithelial-to-mesenchymal transition of the mesothelial cell—its role in the response of the peritoneum to dialysis. *Nephrol. Dial. Transplant.* **2006**, *21*, ii2–ii7. [\[CrossRef\]](#)
66. Yung, S.; Thomas, G.J.; Davies, M. Induction of hyaluronan metabolism after mechanical injury of human peritoneal mesothelial cells in vitro. *Kidney Int.* **2000**, *58*, 1953–1962. [\[CrossRef\]](#)
67. Yung, S.; Chan, T.M. Intrinsic cells: Mesothelial cells—central players in regulating inflammation and resolution. *Perit. Dial. Int.* **2009**, *29*, S21–S27.
68. Chen, C.H.; Kuo, C.Y.; Wang, Y.J.; Chen, J.P. Dual function of glucosamine in gelatin/hyaluronic acid cryogel to modulate scaffold mechanical properties and to maintain chondrogenic phenotype for cartilage tissue engineering. *Int. J. Mol. Sci.* **2016**, *17*, 1957. [\[CrossRef\]](#)
69. Xue, W.; Champ, S.; Huglin, M.B.; Jones, T.G.J. Rapid swelling and deswelling in cryogels of crosslinked poly(N-isopropylacrylamide-co-acrylic acid). *Eur. Polym. J.* **2004**, *40*, 467–476. [\[CrossRef\]](#)
70. Woo, S.L.Y.; Gomez, M.A.; Akeson, W.H. The Time and history-dependent viscoelastic properties of the canine medial collateral ligament. *J. Biomech. Eng.* **1981**, *103*, 293–298. [\[CrossRef\]](#)
71. Kim, Y.J.; Sah, R.L.; Doong, J.Y.; Grodzinsky, A.J. Fluorometric assay of DNA in cartilage explants using Hoechst 33258. *Anal. Biochem.* **1988**, *174*, 168–176. [\[CrossRef\]](#)



REVIEW



## Laser ablation and topical drug delivery: a review of recent advances

Chien-Yu Hsiao<sup>a,b,c</sup>, Shih-Chun Yang<sup>d</sup>, Ahmed Alalaiwe<sup>e</sup> and Jia-You Fang<sup>b,f,g</sup>

<sup>a</sup>Department of Nutrition and Health Sciences, Chang Gung University of Science and Technology, Taoyuan, Taiwan; <sup>b</sup>Research Center for Food and Cosmetic Safety and Research Center for Chinese Herbal Medicine, Chang Gung University of Science and Technology, Taoyuan, Taiwan; <sup>c</sup>Aesthetic Medical Center, Department of Dermatology, Chang Gung Memorial Hospital, Taoyuan, Taiwan; <sup>d</sup>Department of Cosmetic Science, Providence University, Taichung, Taiwan; <sup>e</sup>Department of Pharmaceutics, College of Pharmacy, Prince Sattam Bin Abdulaziz University, Al Kharj, Saudi Arabia; <sup>f</sup>Pharmaceutics Laboratory, Graduate Institute of Natural Products, Chang Gung University, Taoyuan, Taiwan; <sup>g</sup>Department of Anesthesiology, Chang Gung Memorial Hospital, Taoyuan, Taiwan

### ABSTRACT

**Introduction:** The ablative laser can be used as an effective approach for enhancing drug permeation via the skin. The enhancement mechanisms of laser-assisted drug permeation are the direct ablation of the superficial skin, optical breakdown by a photomechanical wave, and a photothermal effect.

**Areas covered:** This review describes the development of laser-assisted drug delivery in the recent 5 years. This review systematically introduces the concepts and enhancement mechanisms of the technique, highlighting the potential of the laser approach for increasing drug absorption via the skin. A recent advance of this approach is the use of fractional laser offering limited skin damage and short recovery time. Another sign of progress regarding laser-assisted drug delivery in the recent 5 years is the clinical trials for treating various dermatological disorders.

**Expert opinion:** The potential use of the laser-assisted approach affords a novel treatment for topical drug application with significant efficacy. Although many clinical studies have been performed, further studies using a large group for patients are needed to confirm and clarify the findings in the in vitro or animal experiments. The laser-assisted delivery should be optimized to achieve skin targeting without the risk of diffusion into circulation.

### ARTICLE HISTORY

Received 19 May 2019  
Accepted 25 July 2019

### KEYWORDS

Laser; Topical delivery; Skin; Skin resurfacing; Fractional ablation

## 1. Introduction

Skin disorder is a commonly found human illness, affecting about 70% of the population worldwide. It is the fourth leading cause of disability in the world [1]. For the management of skin diseases by drug therapy, topical administration offers an appealing method for direct nidus targeting, limitation of systemic toxicity, and noninvasive application [2]. Nevertheless, the skin delivery of drugs is usually challenging because of the outer barrier of the skin. This barrier includes the stratum corneum (SC) and tight junction (TJ) [3]. SC, in particular, presents rigid resistance to the topical delivery of drugs. Successful skin delivery of drugs necessitates distinct characteristics regarding molecular size and physicochemical properties. The ideal physicochemical characters for facile skin absorption of the permeants should be low molecular weight of <500 g/mol, moderate lipophilicity (partition coefficient  $\log P = 2 \sim 3$ ), adequate solubility in both water and oil, as well as low melting point [4]. SC is rather impermeable to hydrophilic and macromolecular drugs due to the unfavorable physicochemical properties. Enhancement strategies are necessary to overcome the cutaneous barrier function in order to ameliorate the topical permeation of hydrophilic drugs and macromolecules. The enhancement approaches can be divided into chemical and physical techniques [5]. The chemical strategy includes permeation enhancers, prodrugs, and nanoparticle inclusion. The physical methods for permeation enhancement

include tape stripping, iontophoresis, electroporation, and sonophoresis. Recently, attention has focused on physical ablation techniques, such as microneedles, radiofrequency, microdermabrasion, and laser to remove some SC or epidermal layers for elevating drug absorption [6]. Among these, laser-assisted drug permeation has gained much attention in the pharmaceutical and dermatological fields.

The term laser is an abbreviation of light amplification by stimulated emission of radiation. Laser is a modality producing an intense beam of coherent monochromatic radiation by photon emission stimulation from excited molecules or atoms. The first laser device was developed in 1955 by Dr. Theodore Maiman at Hughes Research Laboratories [7]. The first experience of employing laser for medicinal practice was the use of a ruby laser in tattoo removal by Dr. Leon Goldman [8]. Over the last few decades, lasers have largely been used in dermatology for treating wrinkling, photoaging, hyperpigmentation, actinic keratosis, and scars. The laser is also useful to treat cancers in the presence of photothermal effect. For instance, the near infrared laser in combination with photothermal agents can be applied to deliver anticancer drugs for tumor inhibition [9–11]. The concept of laser-assisted drug transport is based on the reversible ablation or disruption of skin by irradiation to increase skin absorption of the drugs and allow deeper penetration. The first approval of



**Article highlights**

- This review describes recent development in skin drug absorption using laser ablation.
- Fractional laser is a mainstream tool for laser-assisted drug delivery in recent 5 years because of faster recovery time and less damage to skin compared to conventional laser.
- Er:YAG and CO<sub>2</sub> laser modalities are a center of attention in the assistance of drug permeation via skin.
- The hydrophilic and macromolecular drugs are feasible for laser-assisted delivery to achieve a great enhancement of absorption.
- More results in clinical studies will encourage future application of laser-mediated drug therapy in dermatology.

This box summarizes key points contained in the article.

laser-assisted skin delivery was reported by Jacques et al. in 1987 [12]. In that paper, an excimer laser (193 nm) was used to ablate SC from *in vitro* human skin. The laser fluence at 70 mJ/cm<sup>2</sup> produced a 124-fold enhancement of tritiated water permeation, which is similar to that obtained after SC stripping or epidermal removal by mild heat treatment. Since then, some research groups put their efforts into studying drug absorption enhancement by a variety of laser modalities.

Drug permeation enhancement by lasers allows for more efficacious therapy than passive delivery. The treatment duration of the therapy is possibly shortened. In addition, the applied drug dose can be lowered with less adverse effects. As compared to the other ablation techniques, the laser is capable of controlling the etched depth by energy adjustment in a precise way. Moreover, the skin is exposed by the laser in a non-contact fashion, minimizing the contamination or infection risk [13]. No bio-hazardous waste is produced after the laser application. Laser ablation even sterilizes the entrance to the created pores. Since the superficial ablation of SC or upper epidermis is enough to generate a significant increase in skin absorption, the fluence used for laser-assisted delivery is much lower than that used for cosmetic dermatology or rejuvenation [14], assuring the safe use of the laser for drug permeation aid. Laser ablation for drug permeation enhancement has conventionally been utilized in a continuous mode to create full surface ablation. In the past decade, the fractional laser procedure was developed to replace the full surface resurfacing in laser-assisted drug delivery. Fractional laser generates microchannels in the skin with regularly spaced arrays, which serve as reservoirs of topically applied drugs. The abundant uptake of the drugs in the microscopic treatment zones (MTZs) has led to diffusion into deeper skin strata [15]. The nonablative fractional laser was first introduced in 2004 by Manstein et al. [16]. The fractional laser with the wavelength of 1500 nm produced MTZs by a photothermolysis mechanism. In 2007, the first ablative fractional laser was developed for resurfacing with the aims of fewer side effects and a reduced post-treatment recovery phase [17]. Only a small part of skin surface is exposed to the fractional laser beam to create microscopic channels surrounded by undamaged normal tissue. The untreated tissue acts as a reservoir of healing, allowing faster re-epithelialization and skin barrier restoration as compared to the traditional laser treatment. Previous studies [18,19] reported a complete re-epithelialization of 12 ~ 24 h by

fractional laser as compared to 3 ~ 4 days by full ablation laser. However, fractional laser was generally less effective in facilitating drug permeation via the skin than conventional laser because of partial ablation of the drug diffusion area exposed with the irradiation.

After incubation of the research on laser-assisted drug permeation since 1987, a recent advance in this approach is evident in the performance of clinical trials. A long-term accumulation of the knowledge about laser-assisted drug delivery in the *in vitro* and animal studies has led to the further application on humans. With the optimization of laser modality, pulse duration, pulse number, and laser fluence for drug permeation enhancement in the animal model, these experiences are advantageous in providing feasible setup in clinical investigations. With the evolution of topical drug application, the investigation into laser-mediated drug delivery is expected to change the landscape of dermatological therapy. In this review, we highlight recent advances in laser application for drug delivery into the skin. We focus on the reports on laser-based drug delivery during the past 5 years (2014 until the present). The promising perspective in this emerging application is also discussed in the text.

## 2. Laser modalities for drug permeation enhancement

The techniques in the field of laser-activated drug permeation are classified as full ablation and fractional ablation. Besides the ablative mechanism for promoting drug absorption, non-ablative laser has also proven to be helpful for improving skin delivery. The laser modalities employing superficial skin ablation as the drug permeation enhancement mechanism include excimer (193 nm), Nd:YAG (355, 532, 1064, or 1320 nm), Er:YAG (2940 nm), and CO<sub>2</sub> lasers (10,600 nm). Er:YAG and CO<sub>2</sub> lasers are the most popular current modalities for laser-based drug delivery [20]. Both ablative lasers cause skin resurfacing based on the high absorption by water in biological tissues and the bulk heating for the elimination of epidermal or dermal layers. The water absorption characteristic of Er:YAG laser is greater than that of CO<sub>2</sub> laser by 10-fold [21]. The high water absorption by Er:YAG laser leads to a shallow ablation depth with minimal thermal damage. This unique property makes Er:YAG laser perfect for controlling SC removal. The Er:YAG laser is largely used in cosmetic skin resurfacing for treating wrinkling, aging skin, scar, actinic keratosis, rhytide, and melasma [22,23]. The CO<sub>2</sub> laser generates skin tissue vaporization via instant water heating. The residual thermal effect creates skin coagulation for the purpose of cosmetic rejuvenation. The CO<sub>2</sub> laser is effective in treating photoaged skin, rhytide, scar, and nigricans in clinical dermatology [24,25]. The etched depth by CO<sub>2</sub> laser is basically less than that of the Er:YAG laser. There is little experience in using an excimer laser for enhancing drug permeation as investigation into laser-assisted drug delivery is at the very beginning [12].

The excimer laser is clinically used with verified efficacy in treating psoriasis, vitiligo, atopic dermatitis, alopecia areata, allergic rhinitis, and folliculitis [26]. Partial ablation of the SC is achieved with the excimer laser in the presence of inertial confinement provided by the layer of water, confirming



a photoacoustic disruption of the skin [27]. The Nd:YAG laser is another ablative modality with the capability of skin resurfacing for assisting drug absorption. The irradiation can increase the skin temperature to loosen SC keratin, resulting in the fragile and exfoliative corneocytes [28]. The Nd:YAG laser is widely used for treating vascular lesion, hyperpigmentation, tattoo, and wrinkling under aesthetic consideration [29]. Fractional ablative lasers represent a novel device with improved safety and recovery duration compared with traditional laser resurfacing [30]. The most commonly used fractional lasers are Er:YAG and CO<sub>2</sub> lasers. Both fractional lasers evaporate skin tissue and create MTZs consisting of vertical microchannel arrays as the penetration pathways of the drugs. The modulation of microspot size and density of the fractional laser beam is favorable for adjusting the resurfacing area, followed by the controllable drug transport into the laser-treated skin. The other fractional laser parameters, such as fluence and pulse duration, can govern the enhancement level of drug permeation.

There are some doubts about the use of ablative laser for resurfacing or drug absorption since this technique may produce undesired residual thermal effects such as prolonged erythema, oozing, and swelling. Compared to fractional ablative laser, the nonablative fractional laser has shorter recovery time to intact status [31]. A previous report [32] confirmed less barrier dysfunction and redness after nonablative laser exposure than ablative irradiation. Nonablative laser, such as ruby (694 nm), Er-doped fiber (1410 nm), and Er:glass (1540 nm), modalities generate heat within the dermal layers without the removal of overlying skin surface, based on the selective photothermolysis of the applied wavelengths to match the absorption properties of chromophores such as water, melanin, or hemoglobin [20]. The maintenance of partial barrier quality by nonablative laser is favorable for impeding pathogen or toxic invasion. The nonablative fractional laser creates thermal injury to produce MTZs, which have a loosening

structure allowing the entrance of drugs. Photomechanical wave generated by nonablative laser is another mechanism explaining the enhanced drug transport [33]. The photomechanical wave is a unipolar and compressive wave causing the lacunar space expansion within the highly tortuous intercellular domains, resulting in the establishment of transient channels in the SC lipids [34]. Nonablative laser management produces controlled disruption in the lower skin strata to improve photodamaged skin and acne scar in cosmetic dermatology. The interactions between the skin structure and various laser types are illustrated in Figure 1. The wavelengths of various lasers used for assisting drug delivery are summarized in Table 1.

### 3. The mechanisms of laser-assisted drug permeation

The lasers deploy determined wavelengths of irradiation to selectively damage the specific chromophores in the skin. This ablation in skin significantly diminishes the barrier function, resulting in the possibility of facilitating drug permeation into or across the skin. The ablative lasers commonly used for drug-assisted absorption are the Er:YAG and CO<sub>2</sub> lasers. Both lasers possess the requisite wavelengths for water targeting. Thus, the water-containing SC and epidermis can be deteriorated. Currently, the fractional modality of the lasers is a popular application of laser-assisted drug diffusion into/across the skin. The fractional lasers create microchannels which function as pathways for drug delivery. The intact skin area surrounding the microchannels serves as the reservoir of stem cells so that growth factors and activated immune cells can quickly migrate to the MTZs for rapid wound healing [35]. The parameters of the technical specification in terms of laser energy, pulse duration, spot diameter, spot density, and ablation area govern the interaction between the laser and skin tissue. Drug permeation is subsequently modulated with different levels of

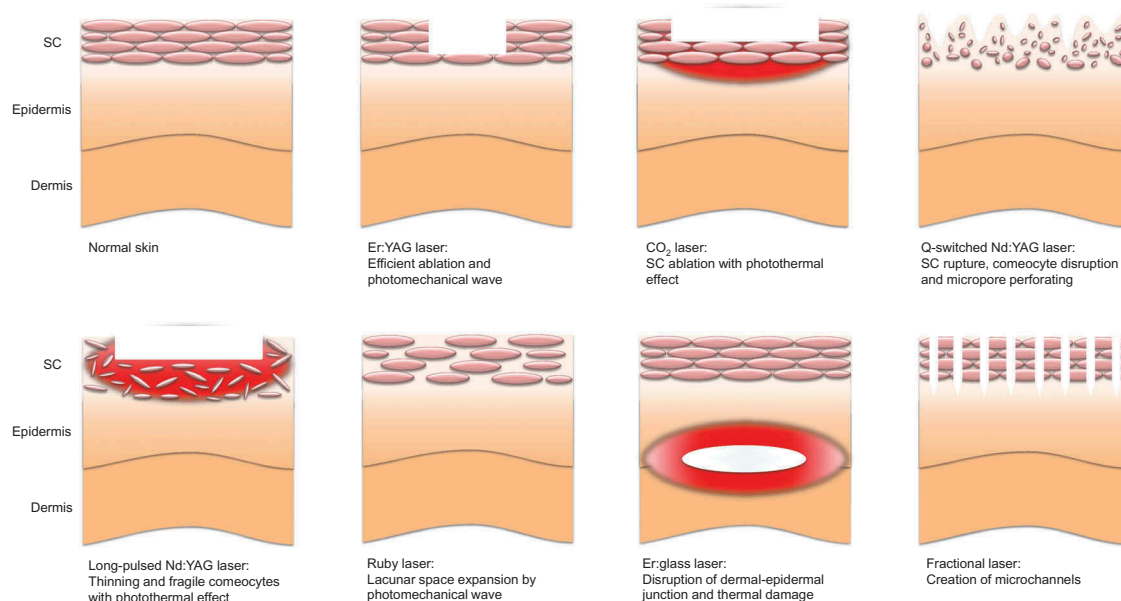


Figure 1. The impact of different laser types on interaction to skin structure.

**Table 1.** The wavelengths of various laser types.

Laser type	Wavelength (nm)
Excimer	193 or 308
Femtosecond fiber laser	532
Ruby	694
Er-doped fiber	1410
Er:glass	1540
Er:YAG	2940
Nd:YAG	355, 532, 1064, or 1320
CO <sub>2</sub>	10,600

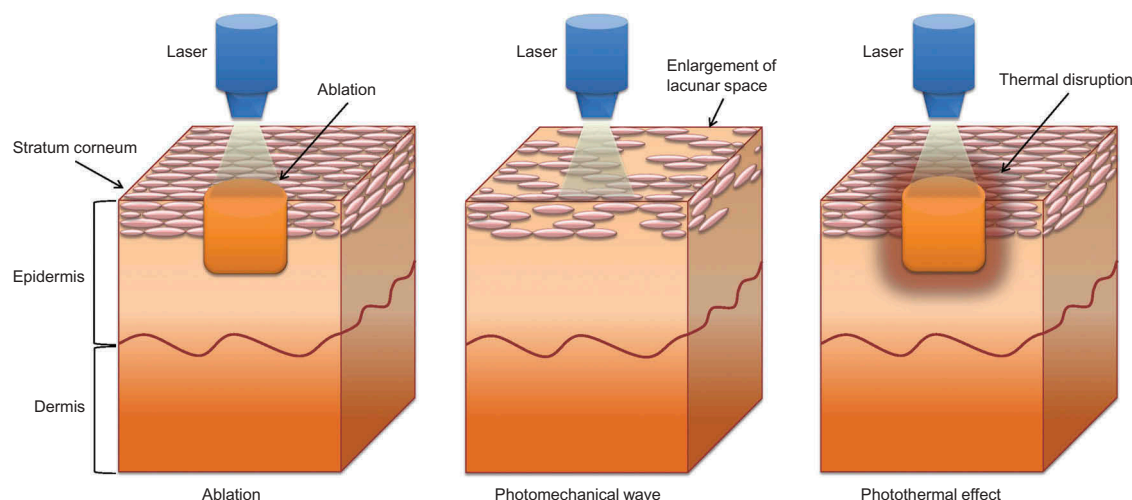
laser-skin interaction. The impact of fractional laser on skin structure can be examined histologically under light microscopy or electron microscopy. The fractional laser is topically applied onto the skin in precise alignment with the MTZs in the skin. The ablation depth of the fractional laser can penetrate the SC to reach the upper dermis, depending on the laser fluence used. The created pores usually show a cylindrical shape on the disrupted SC or viable skin. The diameter of the microchannels basically approximates the irradiated spot size of the fractional laser. The fractional Er:YAG laser with low fluence removes the SC but leaves the viable skin intact [36]. The SC still adheres to the skin surface adjacent to the MTZs. The MTZs are lined by the thermal coagulation region; coagulation results from the collateral deposition of heat into the surrounding skin region after the vaporization of the microchannels in the skin [37].

Because of the specific characteristic of the Er:YAG laser, the coagulation layer around the MTZs exists but is thin. The fractional CO<sub>2</sub> laser generates a greater coagulation zone, which is 3 ~ 4 times thicker than the zone created by the fractional Er:YAG laser [38]. The en face view of the fractional CO<sub>2</sub> laser-irradiated skin usually exhibits an array of dark-colored micropores because of the heat effect. The fractional CO<sub>2</sub> laser irradiation results in the creation of cylindrical ablation of both the SC and epidermis. The ablated holes are surrounded by the thermal coagulation zone. The spherical-shaped micropores are immediately enclosed by elevated edges after irradiation, indicating thermal coagulation development. The laser-treated skin sample reveals the symptom of inflammation as indicated by the immune-cell infiltration in

the dermis [39]. The fractional nonablative laser is also responsible for the enhancement of drug absorption. For example, the Er:glass laser creates an array of microchannels with clear, uniform, and reproducible morphology [40]. The Er:glass laser results in the creation of cone-shaped coagulation within the viable skin. Following irradiation by the fractional Er:glass laser, the histology reveals well-delineated fractional columns of thermal damage in the dermis, as discerned by intact surrounding tissue. There is isolated disruption in the dermal-epidermal junction (DEJ) of each microcolumn. The SC of the Er:glass laser-treated MTZs remains anatomically intact with a small loss of cohesion; the histological change elicited by fractional Er:glass laser is beneficial in increasing drug penetration.

There are three mechanisms involved in the laser-skin interaction for the elevation of drug delivery: direct ablation, photomechanical wave, and photothermal effect (Figure 2) [41]. The fractional ablation breaks the skin barrier through micropore formation. The administered drug molecules are then released from the vehicle for delivery into the microchannels. The drugs largely accumulate in the microchannels to generate a reservoir for further diffusion. The increased diffusion area by the microchannel formation makes permeation more efficient. The vertical diffusion of the drugs reaches deeper skin strata. This delivery to deeper skin layers leads to enhanced therapeutic capability. Besides the vertical diffusion, the drugs may diffuse into surrounding tissue by a lateral pathway. Photomechanical wave is a unipolar compressive wave produced by laser. This wave can transiently permeabilize the superficial skin without the SC ablation [42]. Intracellular lipid disruption and lacunar space extension produced by photomechanical wave allows drug delivery into the deeper cutaneous layers. The laser intensity absorbed by the water can be converted into heat. This phenomenon is especially significant for the CO<sub>2</sub> laser [43]. The photothermal effect damages the skin barrier property for facile drug penetration into the skin.

The thermal effect of the laser also contributes to the skin denaturation and coagulation. The coagulation zone in the MTZs is an assembly of thermally damaged cells affected by

**Figure 2.** The possible mechanisms of laser for enhancing drug delivery via skin.

the laser irradiation. The constituents of coagulation are mainly the platelets and fibrin fibers. The matrix serves as a protective shield against pathogenic microbes [44]. This thermal denaturation in the rim of the MTZs is found to hinder the passage of drugs, especially the hydrophilic small molecules [45]. The lateral partitioning of the drugs into the carbonization layers of the coagulation zone can be retarded. Not only the ablative laser but also the nonablative laser creates the coagulation zone in the micropores. The nonablative laser emits the wavelengths to stimulate the remodeling of collagen. The coagulated column of collagen is found in nonablative laser-treated skin without the ablation effect [46]. The scheme of the possible pathways and processes for laser-assisted drug absorption into skin is shown in Figure 3.

## 4. Animal and in vitro studies

### 4.1. Er:YAG laser

Irradiation of the Er:YAG laser with a wavelength of 2940 nm is highly absorbed by water in the skin. The laser beam generates a minimal thermal effect and coagulation zone. Because of the characteristics of superficial ablation of SC and epidermis, this technique is practical for improving drug permeation, especially the hydrophilic and macromolecular permeants. Ingenol mebutate is a topically applied drug approved for actinic keratosis management. The limited penetration to deeper skin strata has restrained the therapeutic outcome [47]. Erlendsson et al. [48] investigated the usefulness of the fractional Er:YAG laser for improving ingenol permeation. The Er:YAG laser generated intraepidermal (66  $\mu\text{m}$  depth) and intradermal (570  $\mu\text{m}$  depth) MTZs in pigskin. Ingenol transport to receptor compartment of in vitro Franz cell was increased from 0 ng in intact skin to 547 and 677 ng after intraepidermal and intradermal ablation, respectively. The MTZ densities of 0.5%, 1%, 2.5%, 5%, and 10.5% elevated dermal uptake by 1.6-,

2.1-, 3.1-, 3.4-, and 3.9-fold, respectively, as compared to untreated control.

Methotrexate is a hydrophilic small molecule with an unsatisfactory skin permeation to achieve chemopreventive and anti-inflammatory activities [49]. Some investigations were conducted to use fractional Er:YAG laser ablation for enhancing methotrexate absorption. Taudorf et al. [50] determined cutaneous biodistribution of methotrexate after the exposure of fractional laser at 256 mJ/MTZ and 2.4% density. The creation of MTZ increased methotrexate transport via the cone-shaped MTZs with a 690- $\mu\text{m}$  depth and 47- $\mu\text{m}$  coagulation thickness. The laser extended methotrexate deposition in pigskin from 0.30 to 3.08 mg/cm<sup>3</sup>. The fluorescence intensity of laser-assisted methotrexate was increased in the coagulation zone and thermally unaffected tissue by 5- and 13-fold compared with untreated group, respectively, indicating the radial diffusion of the drug from MTZs. Taudorf et al. [51] further explored the effect of ablation depth on laser-facilitated methotrexate delivery. The MTZs were created to reach the depth of the epidermis (11 mJ/MTZ), upper dermis (26 mJ/MTZ), and middle dermis (256 mJ/MTZ). Methotrexate deposition in pigskin was promoted to 6-, 9-, and 11-fold by the ablation to these three depths, respectively. The fluorescence microscopy demonstrated the methotrexate diffusion from coagulation zone into surrounding tissue. Nguyen and Banga [52] employed a fractional Er:YAG laser (PLEASE®) to raise methotrexate permeation via dermatomed pig ear and cadaver human skins at the fluence and density of 34.1 J/cm<sup>2</sup> and 10%, respectively. The ablation depth of the micropores was about 120  $\mu\text{m}$ . The MTZs remained open for a period of 72 h. The microneedle-assisted drug permeation was conducted for comparison. The in vitro Franz cell study showed that the ablative laser offered 9- and 55-fold increase of methotrexate permeation than microneedles in pig and human skin, respectively.

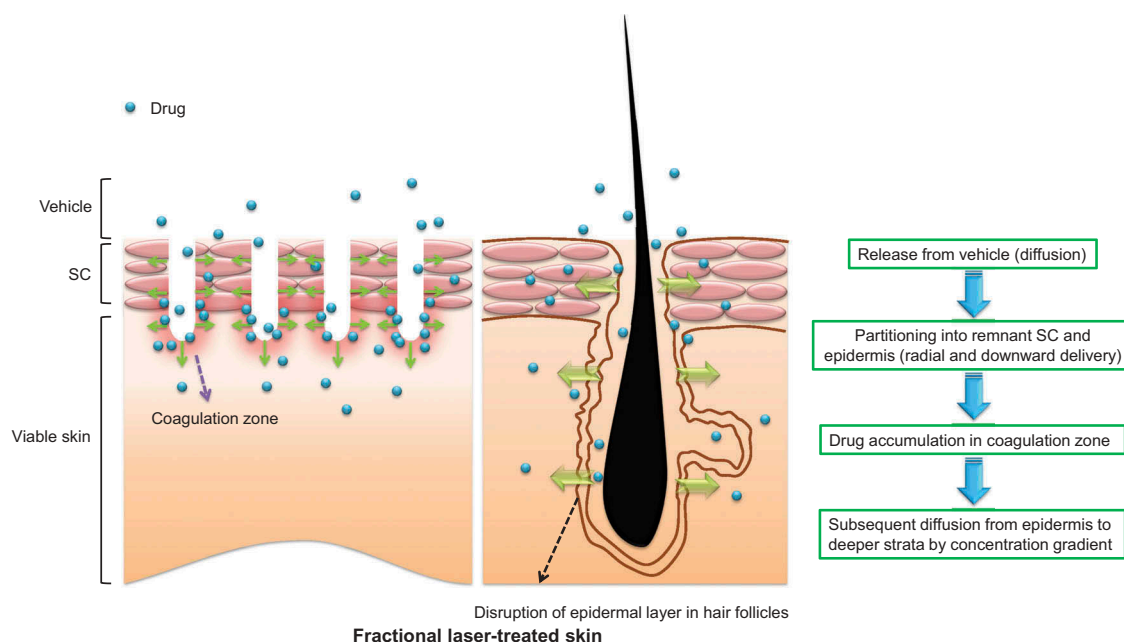


Figure 3. The possible pathways of fractional laser-assisted drug delivery.

The fractional PLEASE® laser system was also applied to facilitate 3-fluoroamphetamine delivery through cadaver human skin [53]. The indication of this dopamine/norepinephrine releaser is the treatment of cocaine dependency and cocaine-use disorder [54]. The laser produced microchannels with the depth and diameter of 250 and 274  $\mu\text{m}$ , respectively. The permeation of 3-fluoroamphetamine through laser-ablated skin was 523  $\mu\text{g}/\text{cm}^2$ , which was 508 times that of passive permeation. Lee et al. found that the Er:YAG laser could increase the follicular uptake of antialopeia drugs [55]. The laser ablation with the depths of 6 and 10  $\mu\text{m}$  in pigskin enhanced minoxidil deposition from 1.0 (passive delivery) to 9.0 and 6.7  $\mu\text{g}/\text{g}$ , respectively. In the case of diphencyprone, the skin deposition was increased from 11.4 to 20.4 and 18.4  $\mu\text{g}/\text{g}$  after the 6- and 10- $\mu\text{m}$  ablation, respectively. The laser raised diphencyprone uptake in hair follicles sixfold compared to passive control. The confocal imaging confirmed the large distribution of the dye in follicles after laser irradiation. The results indicate that the Er:YAG laser was also functional to propagate the ablation effect into the epidermal layer of hair follicles for increasing antialopeia drug targeting.

In addition to the small molecules described above, the Er:YAG laser is useful for promoting macromolecule delivery into/ across the skin. The skin penetration of the macromolecules is always difficult due to their large size and hydrophilic nature. Zorec et al. [56] studied whether the fractional Er:YAG laser could promote skin delivery of fluorescein isothiocyanate (FITC)-conjugated dextran (FD) as the model macromolecule. FD permeation through dermatomed pig ear skin treated with the laser increased following the decrease in molecular size (4 kDa > 10 kDa > 20 kDa). The longer laser pulse (250  $\mu\text{s}$ ) achieved a more significant thermal coagulation zone than the shorter pulse (50 and 100  $\mu\text{s}$ ). The FD partitioning into skin tissue becomes more difficult with greater thermal disruption, demonstrating the barrier property of coagulation for drug diffusion. Immunoglobulin E (IgE)-mediated allergic asthma can be treated by allergen-specific immunotherapy; however, there is a high risk of anaphylaxis by subcutaneous immunotherapy [57]. Epicutaneous immunotherapy presents a choice to avoid anaphylaxis. Kumar et al. [58] developed laser-assisted epicutaneous immunotherapy for delivering powdered allergen and adjuvants. The fluence of PLEASE® at 2.8  $\text{J}/\text{cm}^2$  created the MTZ size of 20 ~ 30  $\mu\text{m}$  in depth and 50 ~ 75  $\mu\text{m}$  in diameter. The topical application of the allergen (ovalbumin) patch on the laser-treated skin led to a great degree of skin permeation while reducing allergen leakage into circulation compared with subcutaneous immunotherapy

by 5–6-fold. The laser-assisted delivery contributed to about 1% ovalbumin-loaded cells in draining mouse inguinal lymph node. This level was 45-fold higher than the topical administration via intact skin. Human growth hormone is a protein used to treat Turner syndrome, renal insufficiency, and toddler growth disorder via injection routes. The compliance of the patients, especially children, is low due to the invasive administration and pain sensation. Topical delivery may be an alternative way for growth hormone delivery if the skin barrier function can be overcome [59]. Transdermal delivery of human growth hormone was investigated under the assistance of Er:YAG laser [60]. The laser condition was variable in fluencies (34.1, 45.4, and 68.1  $\text{J}/\text{cm}^2$ ) and MTZ density (5%, 10%, and 15%). The ablative depth of the micropores in pig ear skin was 140, 170, and 250  $\mu\text{m}$  for the fluence of 34.1, 45.4, and 68.1  $\text{J}/\text{cm}^2$ , respectively. The fluence of 68.1  $\text{J}/\text{cm}^2$  revealed the highest growth hormone amount in Franz cell receptor of 77.1  $\mu\text{g}/\text{cm}^2$ . The permeated amount increased from 7.1 to 95.9  $\mu\text{g}/\text{cm}^2$ , following the increase in micropore density from 5% to 15%.

Er:YAG laser-induced microjet injection is a novel approach for drug permeation enhancement. The Er:YAG laser displays the highest absorption coefficient in water. The mechanism of microjet injection is the division of the laser light into two parts: one for ablating a targeted spot on skin and the other for driving the injector for fast microjet ejection into the pre-ablated spot. Jang et al. [61] used an Er:YAG laser with a 250- $\mu\text{s}$  pulse duration to produce a microjet that was ejected at 50 m/s in air. The thermal damage to human growth hormone was evaluated after microjet driving. The results exhibited no thermal damage associated with the laser-induced microjet, indicating the possibility of employing this technique for drug delivery without the concern of drug degradation. Jang et al. [62] further examined the FITC biodistribution in abdominal pigskin after laser-induced microjet injection. The confocal imaging showed a maximum depth of FITC delivery to 350  $\mu\text{m}$  by microjet alone. The combination of microjet and laser ablation led to a greater FITC staining depth of 417  $\mu\text{m}$ , demonstrating better delivery of the combined tissue ablation and microjet injection. Table 2 summarizes the laser fluence, drug, and animal model for Er:YAG laser-assisted drug delivery.

## 4.2. CO<sub>2</sub> laser

Similar to the Er:YAG laser, the CO<sub>2</sub> laser enhances drug absorption due to the capability of superficial ablation on skin. The

**Table 2.** Er:YAG laser as an enhancement approach for assisting drug delivery in animal or in vitro experiments.

Laser fluence	Drug	Animal or skin type	In vitro or in vivo	Reference
11.2 ~ 128 mJ/MTZ	Ingenol mebutate	Pigskin	In vitro	Erlendsson et al. [48]
256 mJ/MTZ	Methotrexate	Pigskin	In vitro	Taudorf et al. [50]
11 ~ 256 mJ/MTZ	Methotrexate	Pigskin	In vitro	Taudorf et al. [51]
34.1 $\text{J}/\text{cm}^2$	Methotrexate	Pig ear and cadaver human skins	In vitro	Nguyen and Banga [52]
41.5 $\text{J}/\text{cm}^2$	3-Fluoroamphetamine	Cadaver human skin	In vitro	Puri et al. [53]
1.5 and 2.5 $\text{J}/\text{cm}^2$	Minoxidil and diphencyprone	Nude mouse and pigskins	In vitro and in vivo	Lee et al. [55]
7.1 ~ 33.6 $\text{J}/\text{cm}^2$	FITC-conjugated dextran	Pig ear skin	In vitro	Zorec et al. [56]
2.8 $\text{J}/\text{cm}^2$	ovalbumin	Balb/c mouse	In vivo	Kumar et al. [58]
34.1, 45.4, and 68.1 $\text{J}/\text{cm}^2$	Human growth hormone	Pig ear skin	In vitro	Song et al. [60]
87 $\text{J}/\text{cm}^2$	FITC	Pig abdominal skin	In vitro	Jang et al. [62]

FITC, Fluorescein isothiocyanate; MTZ, microscopic treatment zone.



difference between the two modalities is the more significant thermal effect of the CO<sub>2</sub> laser compared to the Er:YAG laser. Based on the ablative effect of the CO<sub>2</sub> laser, Hsiao et al. [63] examined tranexamic acid absorption via pigskin with irradiation via conventional and fractional CO<sub>2</sub> lasers. Tranexamic acid is a skin whitener with a hydrophilic characteristic. The long-term use for melasma treatment is necessary for this agent [64]. The flux of tranexamic acid across intact skin was 0.9 µg/cm<sup>2</sup>/h. The flux was increased to 40.6 and 21.8 µg/cm<sup>2</sup>/h by conventional and fractional CO<sub>2</sub> laser, respectively. The complete SC ablation by conventional laser contributed to the greater flux than fractional laser with partial ablation. 5-fluorouracil (5-FU) is an anticancer drug for treating skin malignancy and actinic keratosis. The hydrophilic nature of this drug has led to the difficulty to penetrate through thick or deeper skin lesion [65]. In vitro pigskin underwent fractional CO<sub>2</sub> laser exposure to produce MTZs reaching DEJ, upper dermis, or middle dermis for 5-FU permeation enhancement [66]. The laser increased 5-FU deposition from 0.1 (intact skin) to 2.3, 4.1, and 4.7 mg/cm<sup>3</sup> by the ablation depth to DEJ, upper dermis, and middle dermis, respectively. The results of biodistribution demonstrated the enhancement ratio of 36, 51, and 82 in the cutaneous depth of 100, 500, and 1500 µm, respectively, after the irradiation to middle dermis. Combined with chemotherapy, it represents the advantages of increasing therapeutic efficacy and minimizing drug resistance. Wenande et al. [67] further examined the synergic 5-FU and cisplatin permeation with exposure to the fractional CO<sub>2</sub> laser. Compared to the transepidermal water loss (TEWL) of intact pigskin (7.3 g/m<sup>2</sup>/h), laser-treated skin exhibited a TEWL value of 15.8 g/m<sup>2</sup>/h, suggesting the reduced skin barrier function by the laser. The laser provided quick absorption of 5-FU to reach a peak deposition within 1 h. The 5-FU deposition into deeper skin strata was increased fivefold after laser treatment. The enhancement of cisplatin deposition by the laser was 12-fold. The in vivo study demonstrated less epidermal proliferation and higher apoptosis in the laser-treated skin than intact skin.

Both 5-aminolevulinic acid (ALA) and methyl ALA are porphyrin precursors for photodynamic therapy (PDT), which is well established to treat Bowen's disease, basal cell carcinoma (BCC), and actinic keratosis [68]. The hydrophilic feature of ALA makes this drug a good candidate for laser-assisted delivery. Haedersdal et al. [69] tested the feasibility of fractional CO<sub>2</sub> laser for promoting ALA and methyl ALA biodistribution. The fluorescence microscopy illustrated a stronger intensity of methyl ALA (21.1 a.u.) than ALA (7.7 a.u.) distributed in intact pigskin. Methyl ALA expressed higher porphyrin fluorescence than ALA in laser-treated skin (26.4 vs. 14.1 a.u.). On the other hand, ALA uptake in hair follicles was greater than methyl ALA uptake after laser treatment (46.7 vs. 35.3 a.u.). The same as Er:YAG laser, the CO<sub>2</sub> modality can augment the drug accumulation in hair follicles. The cutaneous delivery of a drug largely depends on the selection of vehicles. The vehicle can influence the drug release, portioning to SC, and skin structure. Lee et al. [70] elucidated the effect of vehicles on CO<sub>2</sub> laser-assisted permeation of ALA and imiquimod as the hydrophilic and lipophilic model drugs, respectively. The vehicles used included water, polyethylene glycol 400 (PEG400), and propylene glycol (PG). ALA permeation from water, PEG400, and PG with the laser was

641-, 445-, and 104-fold greater than passive delivery. A similar trend was observed for lipophilic imiquimod, demonstrating that polar vehicles, such as water and PEG400, revealed superior laser-assisted delivery than less-polar vehicle. Diffusion of cosolvent into ablative skin and the partitioning between vehicle and skin was the factors predominating drug release from the vehicle to the ablative skin. Vismodegib as a hedgehog inhibitor is applicable for treating BCC. The inclusion of drugs into microemulsion is suitable for achieving increased skin absorption and controlled release [71]. Olsen et al. [72] used microemulsion as the vehicle of vismodegib to examine the CO<sub>2</sub> laser-mediated absorption. The microemulsion alone caused greater vismodegib concentration in skin as compared to ethanol. The highest skin deposition was found in the group of combined microemulsion and laser ablation after 24-h delivery, with an eightfold increase compared with ethanol alone. Banzhaf et al. [73] investigated the influence of CO<sub>2</sub> laser-generated coagulation on the cutaneous absorption of sodium fluorescein. After laser exposure on human abdominal skin, coagulation was found from skin surface to a depth of about 50 µm. Sodium fluorescein quickly accumulated with the coagulation zone with a higher fluorescence signal than the surrounding tissue. The fluorescence intensity increased from 21 a.u. to 42 a.u. after a 4-h application. The depth of sodium fluorescein signal could reach a depth of 160 µm in the coagulation zone and surrounding tissue. The results manifested that the coagulation zone was a reservoir for hydrophilic permeant to achieve a sustained release.

The CO<sub>2</sub> laser is also capable of inducing the skin permeation of macromolecules such as siRNA, vaccine, and protein. RNA interference is a therapy of siRNA delivery for silencing specific genes. Some evidences show that RNA interference has the potential to treat some skin diseases, including neoplasm, pachyonychia congenital, psoriasis, atopic dermatitis, and epidermolysis bullosa [74]. The clinical translation of siRNA therapy for cutaneous disorder management is always difficult due to the SC barrier [75]. Lee et al. [76] compared the skin permeation of siRNA mediated by fractional CO<sub>2</sub> and Er:YAG lasers. The CO<sub>2</sub> and Er:YAG lasers created MTZs with diameters of 120 and 250 µm, respectively. The TJ marker claudin-1 was absent in and around the micropores, suggesting a loss of epidermal barrier function. The respective siRNA flux mediated by CO<sub>2</sub> and Er:YAG lasers was 12- and 11-fold superior to the passive control. There was a broad distribution of fluorescein-conjugated siRNA throughout the epidermis by the irradiation of both lasers. Appendageal pathway is vital as a delivery route for topically applied macromolecules [77]. The fluorescence microscopy illustrated that hair follicles were important accumulation regions for laser-mediated siRNA delivery.

Epidermal powder delivery is based on the creation of MTZs by fractional laser, followed by topical administration of a powder drug-coated array patch [78]. Interstitial fluid is anticipated to be drawn into the microchannels for dissolving the drug powders. This technique was used to enhance skin delivery of antigen ovalbumin as a model vaccine [79]. The fractional CO<sub>2</sub> laser produced MTZs with a diameter of 80 ~ 100 µm at a fluence of 2.5 mJ. More than 80% ovalbumin was delivered into laser-treated skin within 1 h as compared to less than 10% by passive delivery. The anti-ovalbumin antibody



titer in mouse after laser exposure was comparable to titer by intradermal injection. This enhancement effect by the laser was even better than the tape stripping. The local irritation reaction induced by intradermal route was absent in the case of laser-assisted vaccine delivery. A fast infusion of interstitial fluid into MTZs may compromise the filling of drug vehicle into the pores. In order to secure the filling of drug medium into MTZs, Erlendsson et al. [80] actively filled MTZs by pressure, vacuum, and pressure (PVP) for mobilizing tissue fluid and filling the microchannels with the delivered permeants. Passive filling without PVP left a majority of MTZs empty of 56%, leading to an inhomogeneous distribution of PEG400 in dermis after CO<sub>2</sub> laser exposure. Active filling by PVP led to the reduction of empty (6%). A sixfold increase of PEG400 deposition was detected by active filling. Haak et al. [81] found that coagulation thickness induced by fractional CO<sub>2</sub> laser largely affected pigskin distribution of fluorescent-labeled PEG with the molecular weights between 350 and 5000 g/mol. A thin coagulation of 20 µm showed greater fluorescence intensity in skin as compared to thick coagulation (80 µm). The PEG level in dermis with 20-µm coagulation was higher than that of 20-µm coagulation and microneedle perforation (without coagulation), indicating the benefit of a small amount of thermal coagulation for macromolecule penetration. Lee et al. [82] studied the effect of post-irradiation recovery time on FD permeation in nude mouse. TEWL exhibited the restoration of barrier function within 16 h after CO<sub>2</sub> laser irradiation; however, the microscopy showed that MTZs were progressively closed during the recovery but had not totally closed at 16 h. The measurement of TJ-related proteins revealed that filaggrin and integrin β1 were not recovered to the normal baseline within 16 h. FD deposition peaked at 1 h post-irradiation. The FD flux across laser-treated skin was even increased following the increase of recovery time, possibly due to the subsequent inflammation to disrupt TJ barrier.

The same as macromolecules, nanoparticles have a larger size as compared to small molecules. Except the large size, the inclusion of the drugs into nanoparticles such as liposomes is advantageous to enhance the permeation via the SC lipid affinity, facile follicular uptake, and formation of occlusive layer on skin surface [83]. Fujimoto et al. [84] combined liposomes and fractional CO<sub>2</sub> laser for facilitating ovalbumin delivery. The vesicle diameter of

the ovalbumin-loaded liposomes was 324 nm. The macrophage internalization of the liposomes was 10-fold greater than the solution type. Laser treatment elevated ovalbumin permeation from 4 to 40% in an energy-dependent manner. Fujimoto et al. [85] further developed temperature-sensitive liposomes for laser-assisted ovalbumin delivery. The liposomes were prepared using a thermosensitive polymer derived from poly-*N*-isopropylacrylamide. The heat-responsive liposomes could trigger drug release above body temperature (37°C). The ovalbumin permeation percentage via intact and laser-treated hairless mouse skin was about 10% and 40% at 45°C, respectively. Ovalbumin penetrated deeper into laser-treated skin at 45°C than the diffusion at 37°C. Table 3 summarizes the laser fluence, drug, and animal model for CO<sub>2</sub> laser-assisted drug delivery.

#### 4.3. The other laser modalities

The Nd:YAG laser is an ablative modality with the ability to disrupt corneocytes and attenuate SC thickness for promoting drug transport [86]. Fractional Nd:YAG laser is also effective in perforating the nails [87]. A combination of Nd:YAG laser irradiation on nail and the subsequent drug application may be beneficial to deliver drugs into the skin under the nail. The femtosecond fractional Nd:YAG skin ablated the nail for caffeine transport into the skin beneath the nail plate [88]. The cumulative penetration of caffeine across intact human nail was <100 µg within 72 h. The entire poration by the laser induced an increased total caffeine permeation by approximately 100-fold. Garvie-Cook et al. [89] employed a femtosecond fiber laser with a wavelength of 532 nm to assist in vitro caffeine absorption. This laser could create micropores with minimal tissue coagulation according to the data of Raman spectroscopy. The pore depth was 33 µm with a diameter of 31 µm at a pulse power of 0.05 W. A sevenfold increase in caffeine permeation was detected after the laser exposure. A higher power of 0.3 W enhanced a caffeine permeation by 18-fold as compared to the untreated control.

The nonablative laser induces thermal damage on skin without the tissue ablation. The SC basically remains intact to preserve barrier performance. Lee et al. [90] explored the safety and permeation enhancement efficiency of a nonablative fractional Er:glass laser. The diameter and depth of the laser-produced microdots were 350 and 200 µm, respectively. Some vacuoles

**Table 3.** CO<sub>2</sub> laser as an enhancement approach for assisting drug delivery in animal or in vitro experiments.

Laser fluence	Drug	Animal or skin type	In vitro or in vivo	Reference
5 ~ 11 W	Tranexamic acid	Pigskin	In vitro	Hsiao et al. [63]
5, 15, and 25 mJ/pulse	5-FU	Pigskin	In vitro	Wenande et al. [66]
50 mJ/pulse	5-FU and cisplatin	Yorkshire pig	In vitro and in vivo	Wenande et al. [67]
91.6 mJ/pulse	ALA and methyl ALA	Yorkshire pig	In vivo	Haedersdal et al. [69]
2 and 4 mJ/pulse	ALA and imiquimod	Nude mouse	In vitro and in vivo	Lee et al. [70]
80 mJ/pulse	Vismodegib	Pigskin	In vitro	Olsen et al. [72]
15 mJ/pulse	Sodium fluorescein	Human abdominl skin	In vitro	Banzhaf et al. [73]
2 and 4 mJ/pulse	siRNA	Nude mouse	In vitro and in vivo	Lee et al. [76]
5 mJ/pulse	Ovalbumin	Balb/c mouse and pigskins	In vitro and in vivo	Chen et al. [79]
18 and 131 mJ/pulse	PEG400	Pigskin	In vitro	Erlendsson et al. [80]
Unknown	PEG350, PEG1000, and PEG5000	Pigskin	In vitro	Haak et al. [81]
4 mJ/pulse	FITC-conjugated dextran	Nude mouse	In vitro and in vivo	Lee et al. [82]
10, 20, and 30 W	Ovalbumin	Micropigskin	In vitro	Fujimoto et al. [84]
12 mJ/pulse	Ovalbumin	Hairless mouse and micropigskins	In vitro	Fujimoto et al. [85]

ALA, 5-aminolevulinic acid; 5-FU, 5-fluorouracil; MTZ, microscopic treatment zone; PEG400, polyethylene glycol 400; siRNA, small interfering RNA.

were observed in DEJ after laser treatment. The laser exposure caused no skin infection of *Staphylococcus aureus* and *Pseudomonas aeruginosa*, suggesting the maintenance of the barrier function. The cutaneous permeation of ALA and peptide was respectively 1200- and 10-fold higher by laser assistance as compared to the untreated group. The confocal microscopy of the laser-treated skin displayed both perpendicular and lateral drug diffusion via the microdots. Lee et al. [91] compared the enhancement of peptide permeation by nonablative Er:glass and ablative Er:YAG lasers. SC-stripped, psoriasis-like, and atopic dermatitis-like skins were used as the diseased skins. Stripping enhanced peptide flux through pigskin by sevenfold as compared to healthy skin. A further 12-fold increase of flux was shown after Er:YAG laser treatment on SC-stripped skin. On the other hand, the Er:glass laser did not further enhance the flux across stripped skin. A similar tendency was observed in the psoriasis-like skin. However, the Er:glass laser could increase peptide flux via dermatitis-like skin by 2.6-fold compared with the absence of laser irradiation. Ganti and Banga [92] investigated the use of a nonablative Er-doped fiber laser at 1410 nm for enhancing transdermal absorption of diclofenac and sumatriptan. Both drugs are prescribed to alleviate the symptoms associated with migraine. Fractional Er-doped fiber laser targets the water in dermis inducing photothermolysis with the preservation of superficial skin structure. There are coagulation zone and denatured proteins in the MTZs. The reduction of electrical resistance of the dermatomed human skin demonstrated a loss of barrier function by this nonablative laser. The laser increased diclofenac flux from 72.6 (intact skin) to 575.7  $\mu\text{g}/\text{cm}^2$ . In the case of sumatriptan, the laser-assisted flux was 498.3  $\mu\text{g}/\text{cm}^2$ , 22-fold the untreated skin (22.8  $\mu\text{g}/\text{cm}^2$ ).

## 5. Clinical studies

### 5.1. Er:YAG laser

The laser-assisted delivery for treating skin disorders has been clinically applied in the last decades [93]. In the recent 5 years, the concept of a fractional laser has reflected clinical progress in the laser-mediated drug permeation for attaining effective therapy and safe use. The ablative fractional Er:YAG laser causes limited thermal damage on skin, providing safe intervention with satisfactory patient compliance. Togsverd-Bo et al. [94] evaluated fractional Er:YAG laser-assisted daylight PDT using methyl ALA as the drug in organ transplantation patients with actinic keratosis. The lesion was divided into four treatments: laser+daylight PDT, daylight PDT, conventional PDT, and laser alone. Sixteen patients were enrolled in this study. The results revealed that the complete response rate was 74% for the combined laser and daylight PDT after a 3-month therapy. This rate was higher than that of daylight PDT (46%), conventional PDT (50%), and laser only (5%). The laser exposure caused no pain in 11 patients, whereas minimal to moderate pain was reported in five patients.

Ko et al. [95] assessed the effect of Er:YAG laser-assisted PDT on facial actinic keratosis. This was a prospective randomized non-blind study with 45 patients. The complete response rate of the laser-assisted PDT (87%) was higher than that without laser (61%). The recurrence percentage of lesion was 10% for the

combined laser and PDT. This level was significantly lower than that of the control group (27%). The main side effects of laser-assisted PDT were a burning sensation, pruritus, and edema. Nevertheless, most of the side effects were mild and well tolerated. The treatment of facial and scalp actinic keratosis by laser-assisted PDT with short incubation time (2 and 3 h) was compared with conventional PDT [96]. The prospective randomized trial enrolled 93 patients. After a 3-month treatment, the complete response rate of combined laser and PDT (92%) was greater than that of PDT alone (66%) with 3-h incubation. This efficacy could be prolonged at 12-month follow-up. The recurrence rates of laser-assisted PDT and conventional PDT were 8% and 22%, respectively. Actinic cheilitis is a keratinocyte neoplasm found in the lip because of excessive ultraviolet exposure [97]. It is an advanced manifestation of squamous cell carcinoma (SCC). A prospective, randomized, comparative trial was conducted to compare the efficacy of Er:YAG laser-assisted PDT and standard PDT on actinic cheilitis amelioration [98]. At a 3-month follow-up of PDT, the assistance of the laser resulted in a complete response rate of 92%. The 12-month follow-up showed a response rate of 85%. These values were significantly higher than those of conventional PDT. All the patients experienced mild to moderate pain, with no difference between the groups with and without fractional laser application. PDT is also approved to treat Bowen's disease. The same as actinic cheilitis, Bowen's disease is a precancerous skin lesion of SCC [99]. Twenty-one patients with Bowen's disease were involved in a clinical study for checking the therapeutic outcome of Er:YAG laser-assisted PDT [100]. The intervention of laser induced a high complete response rate of 94%, which was greater than the response by standard PDT (73%). The recurrence percentages by PDT with and without laser were 7% and 32%, respectively. The visual analog scale (VAS) score for estimating pain sensation was comparable for laser-assisted PDT (4.86) and PDT alone (4.30). No significant difference was observed between the two groups in terms of cosmetic appearance and safety.

Braun et al. [101] presented a case report about the use of Er:YAG laser-assisted ingenol mebutate delivery for treating multiple actinic keratosis. A 68-year-old patient received laser irradiation at 63 J/cm<sup>2</sup> followed by topical administration of ingenol mebutate (0.015%). The clinical observation showed that the laser promoted an inflammatory response of the drug with tolerable side effects. Keloid is a cutaneous skin disorder resulting from the overgrowth of dense fibrous tissue after injury or surgery. This disease is difficult to eradicate and has high recurrence rates [102]. To increase the therapeutic efficacy against resistant keloid, fractional laser-mediated beta-methasone delivery was applied on 23 patients [103]. The laser-assisted therapy demonstrated a median percentage of improvement of 50%. The median satisfaction rate was 70%. Although no control group was used for comparison, the recurrence after laser intervention was believed to be low (22%). The Er:YAG laser-assisted drug absorption was also helpful in improving recalcitrant psoriatic lesion [104]. Five patients were given laser with the following calcipotriol ointment application. The psoriasis area severity index (PASI) score of the patients was 10 ~ 11 before therapy. This score could be reduced to 4 ~ 5 after calcipotriol treatment. A further reduction to 2 ~ 3 resulted with the intervention of laser exposure.

The side effect of the laser treatment was limited to hyperpigmentation, and this adverse effect could disappear after 3 months. The laser fluence used, patient number, drug applied, and the targeted disease of the Er:YAG laser-assisted delivery are shown in Table 4.

### 5.2. CO<sub>2</sub> laser

The fractional CO<sub>2</sub> laser is also popular for use in laser-assisted drug delivery in clinical trials. In addition to the application in patients, the utility of the CO<sub>2</sub> laser for facilitating drug permeation was examined in healthy volunteers. Eleven healthy subjects were registered to test the usefulness of the CO<sub>2</sub> laser for the enhancement of sodium fluorescein permeation monitored by fluorescence photography [105]. The fluorescence intensity of sodium fluorescein in laser-irradiated skin was 1947 a.u., which was stronger than that in the intact skin (1004 a.u.). The intensity of laser-assisted sodium fluorescein peaked at 30 min after laser exposure. The intensity gradually faded after 30 min. The fluorescence signal of laser-assisted delivery approximated that of intact skin at 24 ~ 48 h post-irradiation. The TEWL confirmed the recovery of cutaneous barrier function to baseline control at 24 ~ 48 h post-treatment. Waibel et al. et al. [106] examined whether laser-assisted absorption of vitamin C, vitamin E, and ferulic acid from serum formulation could improve wound healing caused by laser resurfacing. Fifteen healthy volunteers were treated with the serum on one side of their face and a control vehicle on the other side after laser ablation. The clinical observation demonstrated decreased edema and erythema by serum application on laser-treated skin. The expression of fibroblast growth factor in skin was significantly increased on the laser-treated skin with serum administration, in comparison with the vehicle control.

Topical anesthetics need prolonged occlusion to achieve pain control. Ablative laser treatment can increase skin delivery of the anesthetics to accelerate pain reduction. Meesters et al. [107] assessed the effect of fractional CO<sub>2</sub> laser-mediated delivery of anesthetics by VAS scoring after pain stimulus through high-fluence laser (35 mJ/pulse). The topical application of articain+epinephrine showed a median VAS score of 4.55 in 10 healthy volunteers. The score was reduced to 2.35 with the intervention of CO<sub>2</sub> laser. This anesthesia could be obtained within 10 min post-administration. In the groups receiving topically applied EMLA cream (lidocaine+prilocaine), the laser diminished the median VAS score to 3.15. Meesters et al. [108] further compared the impact of fractional CO<sub>2</sub> and Er:YAG laser (PLEASE®) on the permeation enhancement of articain+epinephrine. The VAS score was 4.50 for the subjects

without anesthesia. The VAS value was reduced to 0.5 and 0.43 by CO<sub>2</sub> and Er:YAG laser-assisted articain+epinephrine application, respectively. The occlusion time for achieving this reduction was 15 min. Sonophoresis is a physical approach to enhance drug permeation via skin. The absorption enhancement mechanism of sonophoresis is the generation of a thermal effect by ultrasound pressure wave to disrupt the cutaneous barrier [109]. Choi et al. [110] analyzed the absorption of ALA into the skin assisted by the combination of fractional CO<sub>2</sub> laser and sonophoresis in healthy men. Application of the laser contributed to higher fluorescence intensity than passive permeation by about twofold at 2- and 3-h post-irradiation. The incorporation of sonophoresis did not further increase the intensity of laser-assisted delivery, perhaps due to the excessive thermal effect propagated by the ultrasound impeding ALA penetration. The thermal coagulation zone is expected to retard drug diffusion. Trelles et al. [111] combined CO<sub>2</sub> laser and sonophoresis for topical delivery of cosmeceuticals in patients with facial aging. The ingredients of the serum cosmeceuticals (PixelTreatSR®) included hydrating components, moisturizers, oligopeptides, vitamins, and lipids. The 6-point global aesthetic improvement scale (0-5GAIS) was used to rate the aesthetic change. The mean 0-5GAIS of the laser-assisted delivery after 6-month therapy was 3.44, indicating an improvement average of 69%. The intervention of ultrasound in laser-assisted permeation resulted a 0-5GAIS of 3.96, representing an overall improvement of 79%. The majority of the patients (86%) expressed satisfied or very satisfied results without unexpected side effects.

Fractional CO<sub>2</sub> laser-assisted PDT was beneficial for the inhibition of actinic keratosis or skin carcinoma in some trials. Song et al. [112] investigated whether CO<sub>2</sub> laser ablation could shorten the incubation time of methyl ALA administration for attaining therapeutic efficiency against actinic keratosis. The intervention of the laser halved the incubation time from 3 to 1.5 h. The clearance rate for conventional PDT with a 3-h incubation was 65%, which was comparable to the value of laser-assisted PDT with a 1.5-h incubation (71%). The pain raised by the laser irradiation was tolerable with no signs of oozing, bleeding, and hyperpigmentation. Three patients bearing scalp actinic keratosis were treated with CO<sub>2</sub> laser to deliver topically applied ingenol mebutate [113]. After 8 weeks, the clearance rates of the laser-facilitated therapy ranged between 62.5% and 100%. The levels were higher than the clearance of passive delivery (50%~60%). Each patient reported no difference in pain between the two treatments. A total of 32 BCC patients were enrolled to test the

Table 4. Er:YAG laser as an enhancement approach for assisting drug delivery in clinical trials.

Laser fluence or ablation depth	Patient number	Drug	Disease	Reference
2.3 mJ/pulse	16	Methyl ALA	Organ transplant patients with actinic keratosis	Togsverd-Bo et al. [94]
300 ~ 550 µm depth	45	Methyl ALA	Facial actinic keratosis	Ko et al. [95]
300 ~ 550 µm depth	93	Methyl ALA	Facial and scalp actinic keratosis	Choi et al. [96]
300 µm depth	33	Methyl ALA	Actinic cheilitis	Choi et al. [98]
550 ~ 600 µm depth	21	Methyl ALA	Bowen's disease	Ko et al. [100]
180 J/cm <sup>2</sup>	23	Betamethasone	Keloid	Braun et al. [101]
100 µm depth	5	Calcipotriol	Psoriasis	Cavalié et al. [103]
				Li et al. [104]

ALA, 5-aminolevulinic acid.

efficacy and safety of CO<sub>2</sub> laser-assisted PDT [114]. The cure rate by clinical observation was 100% and 88% for the PDT treatment with and without laser at 3 months, respectively. A decreased recurrence was demonstrated by laser-mediated PDT (19%) as compared to traditional PDT (44%) after 12 months. The fluorescence in the laser-treated skin tended to reach a greater amount (12.3 a.u.) than intact skin (9.3 a.u.) at the second treatment sessions. 5-FU was utilized to treat superficial BCC and SCC with the incorporation of fractional laser in 28 patients [115]. A 10-mJ laser irradiation was treated on the lesional area followed by topical 5-FU application (5%) for 7 days. The histological clearance was 71% and 100% for BCC and SCC, respectively. The local irritation was tolerated by the patients. All the patients recorded the treatment as easy or very easy. Topical delivery of 5-FU was enhanced by fractional laser for the therapy to treat cicatricial ectropion and periocular scarring [116]. Cicatricial ectropion in the lower eyelid occurs following loss of skin secondary to thermal burn, surgical trauma, and chronic actinic skin damage [117]. Periocular scar can produce functional abnormality in the form of cicatricial ectropion. Intradermal 5-FU injection is an option to treat both diseases, but the invasive approach and difficulty to disperse uniformly in the lesion have limited its use. Six patients received laser-mediated 5-FU delivery via the topical route to examine the aesthetic improvement. The corneal fluorescein staining exhibited an average improvement of 6.0 on a 20-point scale after laser application. The dry eye symptom calculated by ocular surface disease index score showed a mean improvement of 14.5 on a 100-point scale. All the patients reported a significant cosmetic improvement, based on self-assessment.

Infantile hemangioma (IH) is a benign vascular neoplasm in infancy showing clinical course marked by early proliferation. Topical timolol is effective in treating superficial IH but fails to reveal the effect on deep IH [118]. Nine patients aged less than 6 months were enrolled to perform laser-assisted timolol absorption for treating deep IH [119]. Four patients experienced excellent regression, while the other patients demonstrated moderate to good response. The hemangioma activity score declined from 4.1 at baseline to 1.7 at one week post-treatment. No systemic complications or adverse effects on skin were found for each patient. The barrier function of skin limits topical drug therapy against vitiligo due to the failure of drugs reaching the epidermis where the melanocytes reside [120]. Topical tacrolimus delivery was improved by CO<sub>2</sub> laser in 45 vitiligo patients [121]. The laser treatment showed a healing rate of skin defect of 51%, whereas the healing rate for the control group without laser was only 20%; 52 of 65 skin defects revealed repigmentation after laser treatment. This percentage was higher than that of the control (44/80). Sobhi et al. [122] determined the effect of fractional laser on steroid and vitamin C absorption for treating macular amyloidosis (MA). MA is lace-like reddish-brown stains found on the upper back, chest, and extremities [123]. The treatments were divided into laser alone, laser+betamethasone, and laser+vitamin C. The laser-assisted betamethasone delivery represented the greatest pigmentation score improvement of 70%, followed by laser-assisted vitamin C (60%) and laser

only (30%). The amyloid deposits were decreased by 79% in the betamethasone group. No patients suffered from ulceration and pain sensation.

The difficulty of macromolecule penetration via intact skin can be overcome by CO<sub>2</sub> laser ablation with some evidences in clinical studies. Platelet-rich plasma (PRP) is the concentrated human platelets in a small amount of plasma; it is effective for wound healing [124]. Gawdat et al. [125] conducted a clinical trial involving laser-facilitated PRP delivery to treat atrophic acne scar. Fractional CO<sub>2</sub> laser alone is also useful to diminish acne scar. The results of this prospective, randomized, comparative, single-blind trial showed 60% excellent response in the group of combined laser and PRP. Laser alone achieved excellent response of 27%. Although the intradermal PRP showed greater improvement than laser-assisted PRP, a lower pain sensation was recorded by the topical application. Another case of laser-assisted macromolecule delivery is the use of botulinum toxin for treating periorbital wrinkle [126]. Injection of botulinum neurotoxin is increasingly employed to reduce wrinkling for the aim of rejuvenation [127]. Topical botulinum toxin application provides a noninvasive approach to deliver this macromolecule if the skin barrier for permeation can be resolved. The fractional laser allowed a superficial ablation with a depth of about 50 µm. A greater degree of improvement was estimated for the laser-assisted botulinum toxin permeation than for the laser treatment only. Subject satisfaction was also higher in the group receiving laser-assisted delivery and without side effects. Fractional CO<sub>2</sub> laser was also employed to ablate the toenail for applying amorolfine to eradicate fungi [128]. Among the 24 patients, 92% demonstrated a clinical response and 50% showed a complete response. Only two patients (8%) exhibited no amelioration after laser intervention. No recurrence was found during 3 months. The infected region after the treatment was decreased to 19% as compared to the baseline. The laser fluence used, patient number, drug applied, and the targeted disease of the CO<sub>2</sub> laser-assisted delivery are shown in Table 5.

### 5.3. Nonablative laser

There was only one case for investigating the effect of nonablative laser on drug absorption in clinical trial. The dorsal area of 10 healthy male subjects was treated by the fractional Er:glass laser at 20 or 50 mJ, and then topically applied ALA with the incubation time of 0.5, 1, or 3 h [129]. Fluorescence photography showed that the irradiation by the laser significantly enhanced the fluorescence signal in the skin compared with the control. The intensity was increased following the increased incubation time. A minimal skin barrier disruption was achieved by this nonablative laser.

## 6. Conclusion

The rapid development of fractional ablative laser, together with the faster recovery to normal skin than conventional laser, makes the investigators convinced that laser-assisted drug absorption will gain prominent attention in drug delivery technology and clinical dermatology. Very low laser fluence is necessary for ablating the SC without affecting the structures of viable skin, and assuring a fast recovery to healthy status.



**Table 5.** CO<sub>2</sub> laser as an enhancement approach for assisting drug delivery in clinical trials.

Laser fluence	Patient or subject number	Drug	Disease	Reference
15 mJ/pulse	11	Sodium fluorescein	None	Banzhaf et al. [105]
90 ~ 125 mJ/pulse	15	Vitamin C, vitamin E, and ferulic acid	None	Waibel et al. et al. [106]
2.5 mJ/pulse	10	Articain, epinephrine, lidocaine, and prilocaine	None	Meesters et al. [107]
2.5 mJ/pulse	15	Articain and epinephrine	None	Meesters et al. [108]
10 and 20 mJ/pulse	10	ALA	None	Choi et al. [110]
50 ~ 70 mJ/pulse	14	Oligopeptides and vitamins	Facial aging	Trelles et al. [111]
50 mJ/pulse	46	Methyl ALA	Actinic keratosis	Song et al. [112]
10 mJ/pulse	3	Ingenol mebutate	Actinic keratosis	Karmisholt and Haedersdal [113]
40 mJ/pulse	32	Methyl ALA	BCC	Haak et al. [114]
10 mJ/pulse	28	5-FU	BCC and SCC	Nguyen et al. [115]
Unknown	6	5-FU	Cicatricial ectropion and periocular scarring	Lee et al. [116]
25 ~ 30 mJ/pulse	9	Timolol	Infantile hemangioma	Ma et al. [119]
10 mJ/cm <sup>2</sup>	45	Tacrolimus	Vitiligo	Chen et al. [121]
18 W	10	Betamethasone and vitamin C	Macular amyloidosis	Sobhi et al. [122]
15 W	30	PRP	Atrophic acne scar	Gawdat et al. [125]
100 mJ/pulse	10	Botulinum toxin A	Periorbital wrinkle	Mahmoud et al. [126]
160 mJ/pulse	24	Amorolfine	Onychomycosis	Lim et al. [128]

5-FU, 5-fluorouracil; ALA, 5-aminolevulinic acid; BCC, basal cell carcinoma; PRP, platelet-rich plasma; SCC, squamous cell carcinoma.

Lasers can irradiate the SC using non-contact behavior, bypassing the risk of cross-contamination. Another benefit of laser-assisted drug delivery is the very short time required for an operation within nano- or microseconds. The application of topical drug delivery via skin is usually restrained to lipophilic permeants which can facily pass across lipid bilayers of SC to reach therapeutic concentration. The skin penetration of hydrophilic and macromolecular drugs is limited. The potential of combination approach with topical drug delivery and laser ablation leads to augmented application of a variety of drugs for noninvasive topical administration. The optimization of laser parameters is crucial to achieve the maximum enhancement of drug transport. Laser type, laser fluence, MTZ density, and pore radius are the key parameters governing drug permeation. In addition, the laser-assisted drug delivery largely depends on the physicochemical characteristics of the drugs, such as molecular weight, lipophilicity, ionization, and steric structure. This potential use of the laser affords a novel strategy for cutaneous application with significant efficacy. This treatment modality deserves further exploration to maximize its advantages.

## 7. Expert opinion

Increasing attention has been paid to laser ablation approaches for enhancing drug delivery topically. The current problem of the limited skin permeation of some drugs, especially hydrophilic molecules, and macromolecules, can be resolved by laser assistance. This efficacy results in the more extensive application of topical administration. The therapeutic efficiency of dermatological diseases is expected to be improved since the laser can significantly increase drug accumulation in skin. Most of the studies involving laser-assisted drug delivery focus on the *in vitro* or animal platform. Healthy or intact skin is frequently employed as the permeation barrier for evaluating the effect of laser irradiation on drug

absorption. However, most of the patients who need the intervention of laser-assisted delivery possess lesional skin with defective barrier function. The permeation enhancement by the laser can be reduced in diseased skin. How the laser is still effective in the drug permeation enhancement on diseased skin should be understood in the near future. Of course, many clinical trials prove the impact of laser-assisted drug delivery on the management of skin disorders. Nevertheless, some clinical studies lack the proper control group. The patient number is always low (<100). Conscientious design of clinical trials is urgent in the future for confirming the effect of laser-assisted drug application. Fractional ablation by the laser has remained popular in the recent 5 years in clinical dermatology and aesthetics. The performance of basic and clinical studies on fractional laser-facilitated drug absorption has accumulated many experiences and much knowledge in permeation enhancement approaches. The advance of the fractional laser also drives the wide application of other physical enhancement techniques related to the fractional concept. These include microneedle, radiofrequency, and thermo-mechanical action technology.

The use of a large and expensive device is a concern for the application of laser-mediated drug application. The large dimension of the laser is only suitable for inpatients, and not outpatients, for routine use. This inconvenience has led to the lack of general use of laser-assisted drug delivery in clinics. The development of a portable device is in progress and demonstrates some successful results; however, the visibility of the small devices is still few in number. Further effort is necessary to develop the small device for convenient application with the collaboration of the experts in biomedical engineering and mechanical engineering. The applications of a nonablative laser for drug delivery enhancement are still few in the clinical studies. The superiority of the nonablative laser is evident in the less damage to superficial skin layer. More clinical trials for testing the nonablative laser-facilitated drug absorption are



anticipated. The promotion of drug transport into the laser-irradiated skin raises the concern of possible diffusion into circulation; systemic absorption may lead to potential toxicity. Another issue for the future investigation is the exploration of drug targeting into the skin to obtain efficient therapy without adverse effects. The final suggestion for the investigators and physicians with interest in laser-assisted drug delivery is the understanding of the entire concept and knowledge of physical details of the laser and biological details of drug permeation in order to achieve a satisfactory outcome with minimal risk. The cellular and molecular aspects of the action mode of laser-assisted drug permeation are still unclear. Further effort is needed to elucidate the insight involved in the microscopic or molecular change of SC, TJ, and keratinocytes through the irradiation of ablative lasers.

## Funding

This study was supported by the Ministry of Science and Technology, Taiwan (MOST-107-2320-B-182-016-MY3) Chang Gung Memorial Hospital, Linkou (CMRPD1G0411-2).

## Declaration of interest

The authors have no relevant affiliations or financial involvement with any organization or entity with a financial interest in or financial conflict with the subject matter or materials discussed in the manuscript. This includes employment, consultancies, honoraria, stock ownership or options, expert testimony, grants or patents received or pending, or royalties.

## Reviewer disclosures

Peer reviewers on this manuscript have no relevant financial or other relationships to disclose.

## References

Papers of special note have been highlighted as either of interest (\*) or of considerable interest (\*\*) to readers.

- Karimkhani C, Dellavalle RP, Coffeng LE, et al. Global skin disease morbidity and mortality: an update from the global burden of disease study 2013. *JAMA Dermatol.* **2017**;153:406–412.
- Abd E, Roberts MS, Grice JE. A comparison of the penetration and permeation of caffeine into and through human epidermis after application in various vesicle formulations. *Skin Pharmacol Physiol.* **2016**;29:24–30.
- Chuang SY, Lin YK, Lin CF, et al. Elucidating the skin delivery of aglycone and glycoside flavonoids: how the structures affect cutaneous absorption. *Nutrients.* **2017**;9:1304.
- Rzhevskiy AS, Guy RH, Anissimov YG. Modelling drug flux through microporated skin. *J Control Release.* **2016**;241:194–199.
- Iqbal B, Ali J, Baboota S. Recent advances and development in epidermal and dermal drug deposition enhancement technology. *Int J Dermatol.* **2018**;57:646–660.
- A complete introduction of drug permeation enhancement approaches.**
- Aljuffali IA, Lin CF, Fang JY. Skin ablation by physical techniques for enhancing dermal/transdermal drug delivery. *J Drug Deliv Sci Technol.* **2014**;24:277–287.
- Spyropoulos B. 50 years LASERS: in vitro diagnostics, clinical applications and perspectives. *Clin Lab.* **2011**;57:131–142.
- The overview of laser application on medicine.**

- Straight RC. Leon Goldman: dermatologist & surgeon; pioneer and leader in laser surgery and medicine (1905–1997). *Lasers Surg Med.* **2016**;48:911.
- Yuan A, Huan W, Liu X, et al. NIR light-activated drug release for synergetic chemo-photothermal therapy. *Mol Pharm.* **2017**;14:242–251.
- Zhang H, Zhang X, Zhu X, et al. NIR light-induced tumor phototherapy using photo-stable ICG delivery system based on inorganic hybrid. *Nanomedicine.* **2018**;14:73–84.
- Manivasagan P, Jun SW, Nguyen VT, et al. A multifunctional near-infrared laser-triggered drug delivery system using folic acid conjugated chitosan oligosaccharide encapsulated gold nanorods for targeted chemo-photothermal therapy. *J Mater Chem B.* **2019**;7:3811.
- Jacques SL, McAuliffe DJ, Blank IH, et al. Controlled removal of human stratum corneum by pulsed laser. *J Invest Dermatol.* **1987**;88:88–93.
- The earliest concept of laser-assisted drug delivery.**
- Chen X, Shah D, Kosiratna G, et al. Facilitation of transcutaneous drug delivery and vaccine immunization by a safe laser technology. *J Control Release.* **2012**;159:43–51.
- Waibel JS, Rudnick A, Shagalov DR, et al. Update of ablative fractionated lasers to enhance cutaneous topical drug delivery. *Adv Ther.* **2017**;34:1840–1849.
- Zaleski-Larsen LA, Fabbri SG. Laser-assisted drug delivery. *Dermatol Surg.* **2016**;42:919–931.
- Manstein D, Herron GS, Sink RK, et al. Fractional photothermolysis: a new concept for cutaneous remodeling using microscopic patterns of thermal injury. *Lasers Surg Med.* **2004**;34:426–438.
- Hantash BM, Bedi VP, Kapadia B, et al. In vivo histological evaluation of a novel ablative fractional resurfacing device. *Lasers Surg Med.* **2007**;39:96–107.
- Lee WR, Shen SC, Al-Suwayeh SA, et al. Laser-assisted topical drug delivery by using a low-fluence fractional laser: imiquimod and macromolecules. *J Control Release.* **2011**;153:240–248.
- Lee WR, Shen SC, Al-Suwayeh SA, et al. Skin permeation of small-molecule drugs, macromolecules, and nanoparticles mediated by a fractional carbon dioxide laser: the role of hair follicles. *Pharm Res.* **2013**;30:792–802.
- Paasch U, Haedersdal M. Laser systems for ablative fractional resurfacing. *Expert Rev Med Devices.* **2011**;8:67–83.
- The introduction of the lasers with the capability of superficial skin ablation.**
- Osman MAR, Kassab AN. Carbon dioxide laser versus erbium: yAGlaser in treatment of epidermal verrucous nevus: a comparative randomized clinical study. *J Dermatol Treat.* **2017**;28:452–457.
- Worley B, Cohen JL. Combination ablative approach to laser therapy in advanced aging of the face. *J Drugs Dermatol.* **2018**;17:796–799.
- Sannic K, Afroz PN, Burns AJ. Long-term assessment of perioral rhytide correction with erbium: yAGlaser resurfacing. *Plast Reconstr Surg.* **2019**;143:64–74.
- Datz E, Schönberger C, Zeman F, et al. Fractional carbon dioxide laser resurfacing of skin grafts: long-term results of a prospective, randomized, split-scar, evaluator-blinded study. *Lasers Surg Med.* **2018**;50:1010–1016.
- Zaki NS, Hilal RF, Essam RM. Comparative study using fractional carbon dioxide laser versus glycolic acid peel in treatment of pseudo-acanthosis nigricans. *Lasers Med Sci.* **2018**;33:1485–1491.
- Mehraban S, Feily A. 308 nm excimer laser in dermatology. *J Lasers Med Sci.* **2014**;5:8–12.
- Yashima Y, McAuliffe DJ, Jacques SL, et al. Laser-induced photo-acoustic injury of skin: effect of inertial confinement. *Lasers Surg Med.* **1991**;11:62–68.
- Liu C, Zhang J, Yue Y, et al. 1064 nm-Nd: yAGlasers with different output modes enhancing transdermal delivery: physical and physiological mechanisms. *J Biomed Opt.* **2013**;18:61228.
- Hsieh MC, Wu YC, Huang SH, et al. A single-center, randomized, double-blind, placebo-controlled clinical trial of the effectiveness of ANT1 soybean extract cream on skin recovery after Nd: yAGlaser treatment. *Ann Plast Surg.* **2018**;80(Suppl 1):S26–9.

30. Kim HJ, Hong ES, Cho SH, et al. Fractional carbon dioxide laser as an "add-on" treatment for vitiligo: a meta-analysis with systematic review. *Acta Derm Venereol.* **2018**;98:180–184.
31. Carniol PJ, Hamilton MM, Carniol ET. Current status of fractional laser resurfacing. *JAMA Facial Plast Surg.* **2015**;17:360–366.
- **The updated review about fractional lasers used in clinical dermatology.**
32. Kim JM, Kim WI, Ko HC, et al. Epidermal barrier function changes after ablative and non-ablative fractional laser administration. *J Eur Acad Dermatol Venereol.* **2017**;31:e83–5.
- **The comparison of barrier function reduction between ablative and nonablative lasers.**
33. Lee S, McAuliffe DJ, Flotte TJ, et al. Photomechanical transdermal delivery: the effect of laser confinement. *Lasers Surg Med.* **2001**;28:344–347.
34. Lee WR, Shen SC, Zhuo RZ, et al. Enhancement of topical small interfering RNA delivery and expression by low-fluence erbium: yAGlaser pretreatment of skin. *Hum Gene Ther.* **2009**;20:580–588.
35. Ali FR, Al-Niaimi F. Laser-assisted drug delivery in dermatology: from animal models to clinical practice. *Lasers Med Sci.* **2016**;31:373–381.
36. Lee WR, Shen SC, Pai MH, et al. Fractional laser as a tool to enhance the skin permeation of 5-aminolevulinic acid with minimal skin disruption: a comparison with conventional erbium: yAGlaser. *J Control Release.* **2010**;145:124–133.
37. Tanghetti E, Mirkov M, Sierra RA. Delivery of light to the skin through ablated conduits. *Lasers Surg Med.* **2017**;49:69–77.
38. Farkas JP, Richardson JA, Burrus CF, et al. In vivo histopathologic comparison of the acute injury following treatment with five fractional ablative laser devices. *Aesthet Surg J.* **2010**;30:457–464.
39. Chen WY, Fang CL, Al-Suwayeh SA, et al. Risk assessment of excess drug and sunscreen absorption via skin with ablative fractional laser resurfacing: optimization of the applied dose for postoperative care. *Lasers Med Sci.* **2013**;28:1363–1374.
40. Shin MK, Choi JH, Ahn SB, et al. Histologic comparison of microscopic treatment zones induced by fractional lasers and radiofrequency. *J Cosmet Laser Ther.* **2014**;16:317–323.
- **The skin histology after fractional laser irradiation.**
41. Lin CH, Aljuffali IA, Fang JY. Lasers as an approach for promoting drug delivery via skin. *Expert Opin Drug Deliv.* **2014**;11:599–614.
42. Wong TW. Electrical, magnetic, photomechanical and cavitation waves to overcome skin barrier for transdermal drug delivery. *J Control Release.* **2014**;193:257–269.
43. Baleg SM, Bidin N, Suan LP, et al. The effect of CO<sub>2</sub> laser treatment on skin tissue. *J Cosmet Dermatol.* **2015**;14:246–253.
44. Minutti CM, Knipper JA, Allen JE, et al. Tissue-specific contribution of macrophages to wound healing. *Semin Cell Dev Biol.* **2017**;61:3–11.
45. Oni G, Brown SA, Kenkel JM. Can fractional lasers enhance transdermal absorption of topical lidocaine in an in vivo animal model? *Lasers Surg Med.* **2012**;44:168–174.
46. Borges J, Manela-Azulay M, Cuzzi T. Photoaging and the clinical utility of fractional laser. *Clin Cosmet Invest Dermatol.* **2016**;9:107–114.
47. Siller G, Rosen R, Freeman M, et al. PEP005 (ingenol mebutate) gel for the topical treatment of superficial basal cell carcinoma: results of a randomized phase IIa trial. *Australas J Dermatol.* **2010**;51:99–105.
48. Erlendsson AM, Taudorf EH, Eriksson AH, et al. Ablative fractional laser alters biodistribution of ingenol mebutate in the skin. *Arch Dermatol Res.* **2015**;307:515–522.
49. Prasad R, Koul V. Transdermal delivery of methotrexate: past, present and future prospects. *Ther Deliv.* **2012**;3:315–325.
50. Taudorf EH, Lerche CM, Vissing AC, et al. Topically applied methotrexate is rapidly delivered into skin by fractional laser ablation. *Expert Opin Drug Deliv.* **2015**;12:1059–1069.
51. Taudorf EH, Lerche CM, Erlendsson AM, et al. Fractional laser-assisted drug delivery: laser channel depth influences biodistribution and skin deposition of methotrexate. *Lasers Surg Med.* **2016**;48:519–529.
52. Nguyen HX, Banga AK. Delivery of methotrexate and characterization of skin treated by fabricated PLGA microneedles and fractional ablative laser. *Pharm Res.* **2018**;35:68.
53. Puri A, Murnane KS, Blough BE, et al. Effects of chemical and physical enhancement techniques on transdermal delivery of 3-fluoroamphetamine hydrochloride. *Int J Pharm.* **2017**;528:452–462.
54. Negus SS, Henningfield J. Agonist medications for the treatment of cocaine use disorder. *Neuropsychopharmacology.* **2015**;40:1815–1825.
55. Lee WR, Shen SC, Aljuffali IA, et al. Erbium-yttrium-aluminum-garnet laser irradiation ameliorates skin permeation and the follicular delivery of antialopeia drugs. *J Pharm Sci.* **2014**;103:3542–3552.
- **The ablative laser can increase drug targeting to hair follicles.**
56. Zorec B, Škrabelj D, Marincek M, et al. The effect of pulse duration, power and energy of fractional Er: yAGlaser for transdermal delivery of differently sized FITC dextrans. *Int J Pharm.* **2017**;516:204–213.
57. Castells M. Diagnosis and management of anaphylaxis in precision medicine. *J Allergy Clin Immunol.* **2017**;140:321–333.
58. Kumar MNK, Zhou C, Wu MX. Laser-facilitated epicutaneous immunotherapy to IgE-mediated allergy. *J Control Release.* **2016**;235:82–90.
59. Lee JW, Choi SO, Felner EI, et al. Dissolving microneedle patch for transdermal delivery of human growth hormone. *Small.* **2011**;7:531–539.
60. Song Y, Hemmady K, Puri A, et al. Transdermal delivery of human growth hormone via laser-generated micropores. *Drug Deliv Transl Res.* **2018**;8:450–460.
61. Jang HJ, Yu H, Lee S, et al. Towards clinical use of a laser-induced microjet system aimed at reliable and safe drug delivery. *J Biomed Opt.* **2014**;19:058001.
62. Jang HJ, Hur E, Kim Y, et al. Laser-induced microjet injection into preablated skin for more effective transdermal drug delivery. *J Biomed Opt.* **2014**;19:118002.
63. Hsiao CY, Sung HC, Hu S, et al. Fractional CO<sub>2</sub> laser treatment to enhance skin permeation of tranexamic acid with minimal skin disruption. *Dermatology.* **2015**;230:269–275.
64. Perper M, Eber AE, Fayne R, et al. Tranexamic acid in the treatment of melasma: a review of the literature. *Am J Clin Dermatol.* **2017**;18:373–381.
65. Naguib YW, Kumar A, Cui Z. The effect of microneedles on the skin permeability and antitumor activity of topical 5-fluorouracil. *Acta Pharm Sin B.* **2014**;4:94–99.
66. Wenande E, Olesen UH, Nielsen MM, et al. Fractional laser-assisted topical delivery leads to enhanced, accelerated and deeper cutaneous 5-fluorouracil uptake. *Expert Opin Drug Deliv.* **2017**;14:307–317.
67. Wenande E, Tam J, Bhayana B, et al. Laser-assisted delivery of synergistic combination chemotherapy in in vivo skin. *J Control Release.* **2018**;275:242–253.
68. Zhang LW, Fang YP, Fang JY. Enhancement techniques for improving 5-aminolevulinic acid delivery through the skin. *Dermatol Sin.* **2011**;29:1–7.
- **The review of enhancement approaches for photodynamic therapy.**
69. Haedersdal M, Sakamoto FH, Farinelli WA, et al. Pretreatment with ablative fractional laser changes kinetics and biodistribution of topical 5-aminolevulinic acid (ALA) and methyl aminolevulinic acid (MAL). *Lasers Surg Med.* **2014**;46:462–469.
70. Lee WR, Shen SC, Aljuffali IA, et al. Impact of different vehicles for laser-assisted drug permeation via skin: full-surface versus fractional ablation. *Pharm Res.* **2014**;31:382–393.
71. Nastiti CMRR, Ponto T, Abd E, et al. Topical nano and microemulsions for skin delivery. *Pharmaceutics.* **2017**;9:E37.
72. Olesen UH, Clergeaud G, Lerche CM, et al. Topical delivery of vismodegib using ablative fractional laser and micro-emulsion formulation in vitro. *Lasers Surg Med.* **2019**;51:79–87.
73. Banzhaf CA, Lin LL, Dang N, et al. The fractional laser-induced coagulation zone characterized over time by laser scanning confocal microscopy? A proof of concept study. *Lasers Surg Med.* **2018**;50:70–77.

74. Aljuffali IA, Lin YK, Fang JY. Noninvasive approach for enhancing small interfering RNA delivery percutaneously. *Expert Opin Drug Deliv*. 2016;13:265–280.
75. Lee WR, Shen SC, Sun CK, et al. Fractional thermolysis by bipolar radiofrequency facilitates cutaneous delivery of peptide and siRNA with minor loss of barrier function. *Pharm Res*. 2015;32:1704–1713.
76. Lee WR, Shen SC, Chen WY, et al. Noninvasive delivery of siRNA and plasmid DNA into skin by fractional ablation: erbium: yAGlaser versus CO<sub>2</sub> laser. *Eur J Pharm Biopharm*. 2014;86:315–323.
77. Inacio R, Poland S, Cai XJ, et al. The application of local hypobaric pressure? A novel means to enhance macromolecule entry into the skin. *J Control Release*. 2016;226:66–76.
78. Cao Y, Kakar P, Hossen MN, et al. Sustained epidermal powder drug delivery via skin microchannels. *J Control Release*. 2017;249:94–102.
79. Chen X, Kositratna G, Zhou C, et al. Micro-fractional epidermal powder delivery for improved skin vaccination. *J Control Release*. 2014;192:310–316.
- **Laser approach for promoting cutaneous vaccination.**
80. Erlendsson AM, Doukas AG, Farinelli WA, et al. Fractional laser-assisted drug delivery: active filling of laser channels with pressure and vacuum alteration. *Lasers Surg Med*. 2016;48:116–124.
81. Haak CS, Hannibal J, Paasch U, et al. Laser-induced thermal coagulation enhances skin uptake of topically applied compounds. *Lasers Surg Med*. 2017;49:582–591.
- **The impact of laser-induced coagulation on topical drug delivery.**
82. Lee WR, Hsiao CY, Huang TH, et al. Post-irradiation recovery time strongly influences fractional laser-facilitated skin absorption. *Int J Pharm*. 2019;564:48–58.
83. Carita AC, Eloy JO, Chorilli M, et al. Recent advances and perspectives in liposomes for cutaneous drug delivery. *Curr Med Chem*. 2018;25:606–635.
84. Fujimoto T, Wang J, Baba K, et al. Transcutaneous drug delivery by liposomes using fractional laser technology. *Lasers Surg Med*. 2017;49:525–532.
85. Fujimoto T, Ito M, Ito S, et al. Fractional laser-assisted percutaneous drug delivery via temperature-responsive liposomes. *J Biomater Sci Polym Ed*. 2017;28:679–689.
86. Gómez C, Á C, García-Moreno I, et al. Skin laser treatments enhancing transdermal delivery of ALA. *J Pharm Sci*. 2011;100:223–231.
87. Kartal SP, Canpolat F, Gonul M, et al. Long-pulsed Nd: yAGlaser treatment for nail psoriasis. *Dermatol Surg*. 2018;44:227–233.
88. Vanstone S, Cordery SF, Stone JM, et al. Precise laser poration to control drug delivery into and through human nail. *J Control Release*. 2017;268:72–77.
- **Laser-assisted drug delivery applied for permeation through nail.**
89. Garvie-Cook H, Stone JM, Yu F, et al. Femtosecond pulsed laser ablation to enhance drug delivery across the skin. *J Biophotonics*. 2016;9:144–154.
90. Lee WR, Shen SC, Aljuffali IA, et al. Non-ablative fractional laser assists cutaneous delivery of small- and macro-molecules with minimal bacterial infection risk. *Eur J Pharm Sci*. 2016;92:1–10.
91. Lee WR, Shen SC, Sung CT, et al. Is the fractional laser still effective in assisting cutaneous macromolecule delivery in barrier-deficient skin? Psoriasis and atopic dermatitis as the disease models. *Pharm Res*. 2018;35:128.
- **The use of diseased skin for evaluating laser-assisted drug delivery.**
92. Ganti SS, Banga AK. Non-ablative fractional laser to facilitate transdermal delivery. *J Pharm Sci*. 2016;105:3324–3332.
93. Haedersdal M, Erlendsson AM, Paasch U, et al. Translational medicine in the field of ablative fractional laser (AFXL)-assisted drug delivery: a critical review from basics to current clinical status. *J Am Acad Dermatol*. 2016;74:981–1004.
94. Togsverd-Bo K, Lei U, Erlendsson AM, et al. Combination of ablative fractional laser and daylight-mediated photodynamic therapy for actinic keratosis in organ transplant recipients? A randomized controlled trial. *Br J Dermatol*. 2015;172:467–474.
95. Ko DY, Jeon SY, Kim KH, et al. Fractional erbium: YAG laser-assisted photodynamic therapy for facial actinic keratoses: a randomized, comparative, prospective study. *J Eur Acad Dermatol Venereol*. 2014;28:1529–1539.
96. Choi SH, Kim KH, Song KH. Efficacy of ablative fractional laser-assisted photodynamic therapy with short-incubation time for the treatment of facial and scalp actinic keratosis: 12-month follow-up results of a randomized, prospective, comparative trial. *J Eur Acad Dermatol Venereol*. 2015;29:1598–1605.
97. Carvalho MV, de Moraes SLD, Lemos CAA, et al. Surgical versus non-surgical treatment of actinic cheilitis: a systematic review and meta-analysis. *Oral Dis*. 2019;25:972–981.
98. Choi SH, Kim KH, Song KH. Efficacy of ablative fractional laser-assisted photodynamic therapy for the treatment of actinic cheilitis: 12-month follow-up results of a prospective, randomized, comparative trial. *Br J Dermatol*. 2015;173:184–191.
99. Bath-Hextall FJ, Matin RN, Wilkinson D, et al. Interventions for cutaneous Bowen's disease. *Cochrane Database Syst Rev*. 2013;6:CD007281.
100. Ko DY, Kim KH, Song KH. A randomized trial comparing methyl aminolaevulinate photodynamic therapy with and without Er: yAGlaser fractional laser treatment in Asian patients with lower extremity Bowen disease: results from a 12-month follow-up. *Br J Dermatol*. 2014;170:165–172.
101. Braun SA, Hevezi P, Homey B, et al. Laser-assisted drug delivery: enhanced response to ingenol mebutate after ablative fractional laser treatment. *J Am Acad Dermatol*. 2015;72:364–365.
102. Lee HJ, Jang YJ. Recent understandings of biology, prophylaxis and treatment strategies for hypertrophic scars and keloids. *Int J Mol Sci*. 2018;19:711.
103. Cavalié M, Sillard L, Montaudie H, et al. Treatment of keloids with laser-assisted topical steroid delivery: a retrospective study of 23 cases. *Dermatol Ther*. 2015;28:74–78.
104. Li R, Zhou J, Su H, et al. 2940-nm Er: yAG fractional laser enhanced the effect of topical drug for psoriasis. *Lasers Med Sci*. 2017;32:1393–1397.
105. Banzhaf CA, Thaysen-Petersen D, Bay C, et al. Fractional laser-assisted drug uptake: impact of time-related topical application to achieve enhanced delivery. *Lasers Surg Med*. 2017;49:348–354.
106. Waibel JS, Mi QS, Ozog D, et al. Laser-assisted delivery of vitamin C, vitamin E, and ferulic acid formula serum decreases fractional laser postoperative recovery by increased beta fibroblast growth factor expression. *Lasers Surg Med*. 2016;48:238–244.
107. Meesters AA, Bakker MM, de Rie MA, et al. Fractional CO<sub>2</sub> laser assisted delivery of topical anesthetics: a randomized controlled pilot study. *Lasers Surg Med*. 2016;48:208–211.
108. Meesters AA, Nieboer MJ, Kezic S, et al. Parameters in fractional laser assisted delivery of topical anesthetics: role of laser type and laser settings. *Lasers Surg Med*. 2018;50:813–818.
109. Seah BC, Teo BM. Recent advances in ultrasound-based transdermal drug delivery. *Int J Nanomed*. 2018;13:7749–7763.
110. Choi JH, Shin EJ, Jeong KH, et al. Comparative analysis of the effects of CO<sub>2</sub> fractional laser and sonophoresis on human skin penetration with 5-aminolevulinic acid. *Lasers Med Sci*. 2017;32:1895–1900.
111. Trelles MA, Leclère FM, Martínez-Carpio PA. Fractional carbon dioxide laser and acoustic-pressure ultrasound for transepidermal delivery of cosmeceuticals: a novel method of facial rejuvenation. *Aesth Plast Surg*. 2013;37:965–972.
- **The combination of laser and sonophoresis for drug permeation enhancement.**
112. Song HS, Jung SE, Jang YH, et al. Fractional carbon dioxide laser-assisted photodynamic therapy for patients with actinic keratosis. *Photodermatol Photoimmunol Photomed*. 2015;31:296–301.
113. Karmisholt KE, Haedersdal M. Ablative fractional laser intensifies treatment outcome of scalp actinic keratoses with ingenol mebutate: a case report. *Eur Acad Dermatol Venereol*. 2016;30:854–855.
114. Haak CS, Togsverd-Bo K, Thaysen-Petersen D, et al. Fractional laser-mediated photodynamic therapy of high-risk basal cell

- carcinomas? A randomized clinical trial. *Br J Dermatol*. 2015;172:215–222.
115. Nguyen BT, Gan SD, Konnikov N, et al. Treatment of superficial basal cell carcinoma and squamous cell carcinoma in situ on the trunk and extremities with ablative fractional laser-assisted delivery of topical fluorouracil. *J Am Acad Dermatol*. 2015;72:558–560.
  116. Lee BW, Levitt AE, Erickson BP, et al. Ablative fractional laser resurfacing with laser-assisted delivery of 5-fluorouracil for the treatment of cicatricial ectropion and periocular scarring. *Ophthalmic Plast Reconstr Surg*. 2018;34:274–279.
  117. McKelvie J, Papchenko T, Carroll S, et al. Cicatricial ectropion surgery: a prospective study of long-term symptom control, patient satisfaction and anatomical success. *Clin Exp Ophthalmol*. 2018;46:1002–1007.
  118. Harter N, Mancini AJ. Diagnosis and management of infantile hemangiomas in the neonate. *Pediatr Clin North Am*. 2019;66:437–459.
  119. Ma G, Wu P, Lin X, et al. Fractional carbon dioxide laser-assisted drug delivery of topical timolol solution for the treatment of deep infantile hemangioma: a pilot study. *Pediatr Dermatol*. 2014;31:286–291.
  120. Iriarte C, Awosika O, Rengifo-Pardo M, et al. Review of applications of microneedling in dermatology. *Clin Cosmet Invest Dermatol*. 2017;10:289–298.
  121. Chen W, Zhou Y, Huang FR, et al. Preliminary study on the treatment of vitiligo with carbon dioxide fractional laser together with tacrolimus. *Lasers Surg Med*. 2018;50:829–836.
  122. Sobhi RM, Sharaoui I, El Nabrawy EA, et al. Comparative study of fractional CO<sub>2</sub> laser and fractional CO<sub>2</sub> laser-assisted drug delivery of topical steroid and topical vitamin C in macular amyloidosis. *Lasers Med Sci*. 2018;33:909–916.
  123. Weidner T, Illing T, Elsner P. Primary localized cutaneous amyloidosis: a systematic treatment review. *Am J Clin Dermatol*. 2017;18:629–642.
  124. Zhang M, Park G, Zhou B, et al. Applications and efficacy of platelet-rich plasma in dermatology: a clinical review. *J Cosmet Dermatol*. 2018;17:660–665.
  125. Gawdat HI, Hegazy RA, Fawzy MM, et al. Autologous platelet rich plasma: topical versus intradermal after fractional ablative carbon dioxide laser treatment of atrophic acne scars. *Dermatol Surg*. 2014;40:152–161.
  126. Mahmoud BH, Burnett C, Ozog D. Prospective randomized controlled study to determine the effect of topical application of botulinum toxin A for crow's feet after treatment with ablative fractional CO<sub>2</sub> laser. *Dermatol Surg*. 2015;41(Suppl 1):S75–81.
  127. Gart MS, Gutowski KA. Overview of botulinum toxins for aesthetic uses. *Clin Plast Surg*. 2016;43:459–471.
  128. Lim EH, Kim HR, Park YO, et al. Toenail onychomycosis treated with a fractional carbon-dioxide laser and topical antifungal cream. *J Am Acad Dermatol*. 2014;70:918–923.
  129. Lim HK, Jeong KH, Kim NI, et al. Nonablative fractional laser as a tool to facilitate skin penetration of 5-aminolaevulinic acid with minimal skin disruption: a preliminary study. *Br J Dermatol*. 2014;170:1336–1340.





Article

# Characterization of Fibrinogen as a Key Modulator in Patients with Wilson's Diseases with Functional Proteomic Tools

Pei-Wen Wang <sup>1</sup>, Tung-Yi Lin <sup>2</sup> , Yu-Chiang Hung <sup>3</sup>, Wen-Neng Chang <sup>4</sup>, Pei-Ming Yang <sup>5,6</sup> , Mu-Hong Chen <sup>7,8</sup>, Chau-Ting Yeh <sup>9</sup> and Tai-Long Pan <sup>9,10,11,12,\*</sup>

<sup>1</sup> Department of Medical Research, China Medical University Hospital, China Medical University, Taichung 40447, Taiwan; pwwang5105@hotmail.com

<sup>2</sup> Department of Traditional Chinese Medicine, Chang Gung Memorial Hospital, Keelung 20401, Taiwan; tungyi30@cgmh.org.tw

<sup>3</sup> Department of Chinese Medicine, College of Medicine, Kaohsiung Chang Gung Memorial Hospital and Chang Gung University, Kaohsiung 83301, Taiwan; e120845@cgmh.org.tw

<sup>4</sup> Departments of Neurology, College of Medicine, Kaohsiung Chang Gung Memorial Hospital and Chang Gung University, Kaohsiung 83301, Taiwan; cwenneng@ms19.hinet.net

<sup>5</sup> TMU Research Center of Cancer Translational Medicine, Taipei Medical University, Taipei 11042, Taiwan; yangpm@tmu.edu.tw

<sup>6</sup> Graduate Institute of Cancer Biology and Drug Discovery, College of Medical Science and Technology, Taipei Medical University, Taipei 11042, Taiwan

<sup>7</sup> Department of Psychiatry, Taipei Veterans General Hospital, Taipei 11217, Taiwan; kremer7119@gmail.com

<sup>8</sup> Department of Psychiatry, College of Medicine, National Yang-Ming University, Taipei 11221, Taiwan

<sup>9</sup> Liver Research Center, Chang Gung Memorial Hospital, Taoyuan 33375, Taiwan; chautingy@gmail.com

<sup>10</sup> School of Traditional Chinese Medicine, Chang Gung University, Taoyuan 33302, Taiwan

<sup>11</sup> Chinese Herbal Medicine Research Team, Healthy Aging Research Center, Chang Gung University, Taoyuan 33302, Taiwan

<sup>12</sup> Research Center for Chinese Herbal Medicine and Research Center for Food and Cosmetic Safety, College of Human Ecology, Chang Gung University of Science and Technology, Taoyuan 33303, Taiwan

\* Correspondence: pan@mail.cgu.edu.tw; Tel.: +886-3-211-8800 (ext. 5105)

Received: 12 August 2019; Accepted: 12 September 2019; Published: 12 September 2019



**Abstract:** Wilson's disease (WD) is an autosomal recessive disorder of copper metabolism caused by defects in the ATPase gene (ATP7B). The various clinical features result from the massive accumulation of copper in the liver, cornea and basal ganglia. Although WD can be effectively treated with proper medicine, this disease is difficult to clearly diagnose due to its indefinite symptoms. In the current study, we achieved a positive correlation between clinical symptoms and the enzymatic activity of ceruloplasmin in WD patients. Furthermore, proteome profiles of plasma as well as network analysis demonstrated that fibrinogen is a critical indicator which is significantly unregulated in WD subjects in comparison to healthy donors and closely linked to pathogenesis of WD. Here, we applied 2DE-immunoblots and immunohistochemistry to verify the protein level and localization in situ. The enhanced expression of fibrinogen in the plasma of WD subjects with respect to that of healthy controls and patients with distinct disorders was also confirmed by utilizing clinical samples. As expected, application of high dose of copper induced expression of fibrinogen, while knockdown of ceruloplasmin also resulted in upregulation of fibrinogen as well as elimination of superoxide dismutase (SOD), leading to increased oxidative stress in cells. In summary, the liver injury or oxidative stress induced by the progression of WD may account for the obvious increase of fibrinogen, which in turn triggers inflammatory responses and interferes coagulation cascades; this finding sheds light on the early detection and diagnosis of WD.

**Keywords:** Wilson's disease; ceruloplasmin; oxidative stress; fibrinogen; network analysis



## 1. Introduction

Wilson's disease (WD) is hereditary and affects approximately one in 30,000 individuals worldwide, with exceptions found in specific subgroups with consanguinity [1]. The biochemical defect that causes WD is a deficiency of gene, encoding a copper transporting p-type ATPase (ATP7B), located on chromosome 13. Over hundred mutations of ATP7B, including point mutations, deletions and frame-shift, have been reported in patients with WD. Most patients have two different mutations of the gene on each allele encoding the WD gene, called compound heterozygotes [2,3]. This protein product is similar to other ATP-dependent transporters for heavy metals, which is mainly expressed in the liver and mediates copper homeostasis in liver cells.

Copper is an essential trace metal for living systems, however, cellular copper in excess of the needed quantity leads to oxidative stress and toxic effects [4,5]. Patients with WD are characterized by excessive accumulation of hepatic copper and a significant decrease in the plasma concentration of ceruloplasmin, thus suggesting reduced biliary excretion of copper and disturbed incorporation of copper during the biosynthesis of ceruloplasmin (CP) [5,6]. Affected patients usually present liver diseases such as inflammation, cirrhosis or fulminant liver failure. Neuropsychiatric symptoms are common in adults with WD, including movement disorder, tremor, incoordination and dystonia as the results of copper accumulation in the basal ganglia and brain. Besides, patients cannot always fully recover from toxic levels of copper resulting in permanent liver or neurological deficits because of irreversible tissue damage [7,8].

The therapeutic outcome of WD depends upon precise diagnosis and recognition. The presence of various clinical symptoms and difference in age at onset in WD highlight the problem of delaying the time for appropriate treatment leading to severe complications [6,9]. According to previous reports, serum ceruloplasmin measurement is an unreliable diagnostic indicator in patients with liver disease and those who were taking chelation therapy, showing a positive predictive value of only about 5% [10]. In this regard, the generally utilized clinical and laboratory parameters are insufficient to exclude the diagnosis of WD in patients with liver disease of unknown origin. Then we establish a simple and direct biomarker to effectively distinguish WD from other similar diseases, except for the evaluation of ceruloplasmin oxidase activity in the first place.

Fibrinogen is the key coagulation protein and an important determinant of blood viscosity as well as platelet aggregation. In addition, fibrinogen levels were correlated with established risk factors of different chronic diseases including coronary heart disease (CHD), stroke and other vascular problems [11]. There are several mechanisms by which fibrinogen may increase cardiovascular risk. Fibrinogen could bind specifically to activate platelets, leading to platelet aggregation and increased fibrinogen levels may promote fibrin formation. Furthermore, it is also an acute-phase reactant that is increased in inflammatory states [12]. In this regard, measurement of fibrinogen may help in disease prediction or prevention.

Genetic mutational analysis for index cases remains difficult as there are numerous mutations scattered throughout the coding region of the gene within 21 exons [13]. In contrast to the analysis of a selected single parameter, proteomic analysis allows a comprehensive evaluation of hundreds of proteins in parallel [14]. Another reason for focusing on the analysis of protein is that gene sequence does not completely describe the post-translation modification which may be essential for protein function and activity [15]. The proteomic technology comprises a plethora of techniques to resolve two-dimensional electrophoresis (2-DE), quantitate (scanner with software), identify and characterize proteins (sequencing and mass spectrometry), as well as to map information (bioinformatics). In the current study, functional proteome tools were applied to plasma protein analysis related to clinical representations of WD patients.

Since WD patients may present with a variety of clinical characteristics and laboratory alterations, a multidisciplinary approach is necessary. The subjects of WD diagnosed by clinical findings exhibited the obvious decrease in oxidase activity of ceruloplasmin with enzymatic assay. We also presented a 2-DE protein map of plasma from the WD patients and normal controls to develop possible diagnostic markers. According to the results of alignment with protein database, fibrinogen, which may be associated with pathologic processes of liver cirrhosis in WD was characterized and further validated with 2D-immunoblots, immunohistochemistry and analysis of clinical samples. This study aimed at targeting changes in plasma protein profile by proteomic tool to reveal the biological function of plasma protein which may be involved in WD pathology. These proteins might shed light on developing a high throughput screen for potential WD subjects and facilitate diagnosis in this complex disease.

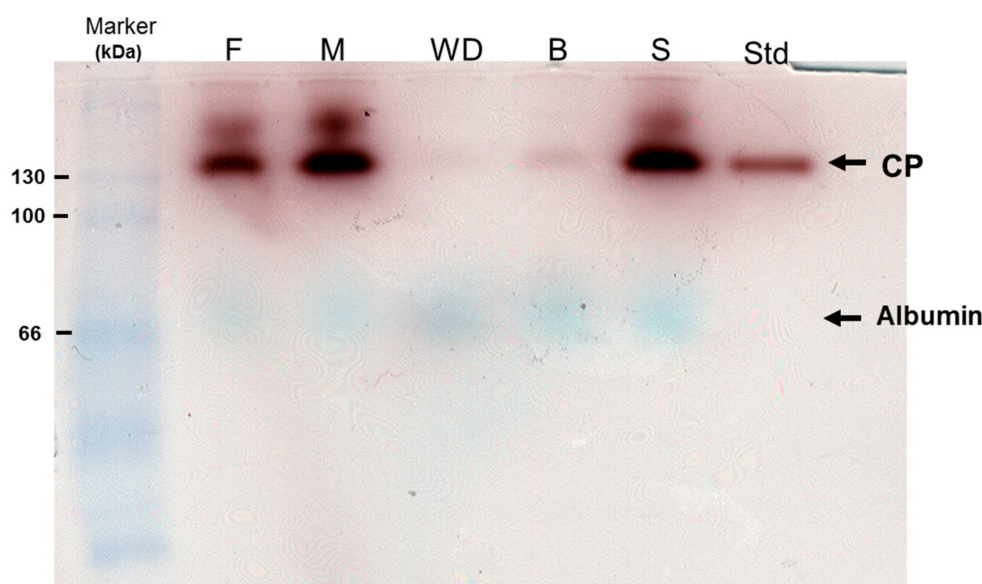
## 2. Results

### 2.1. Enzymatic Analysis of Ceruloplasmin Activity and Evaluation of Protein Carbonylation

Oxidase activity of ceruloplasmin within plasma collected from asymptomatic control (B,S), two parents (F,M) and homozygous WD patient (WD) was assayed simultaneously (Figure 1A). Commercial ceruloplasmin (Std) was used as the standard with 130 kDa in molecular weight. After quantitative analysis divided by internal control (albumin), the enzymatic activity attained to almost 100% in the plasma of sample S; it showed significant decrease by 95% in sample WD and 90% in sample B.

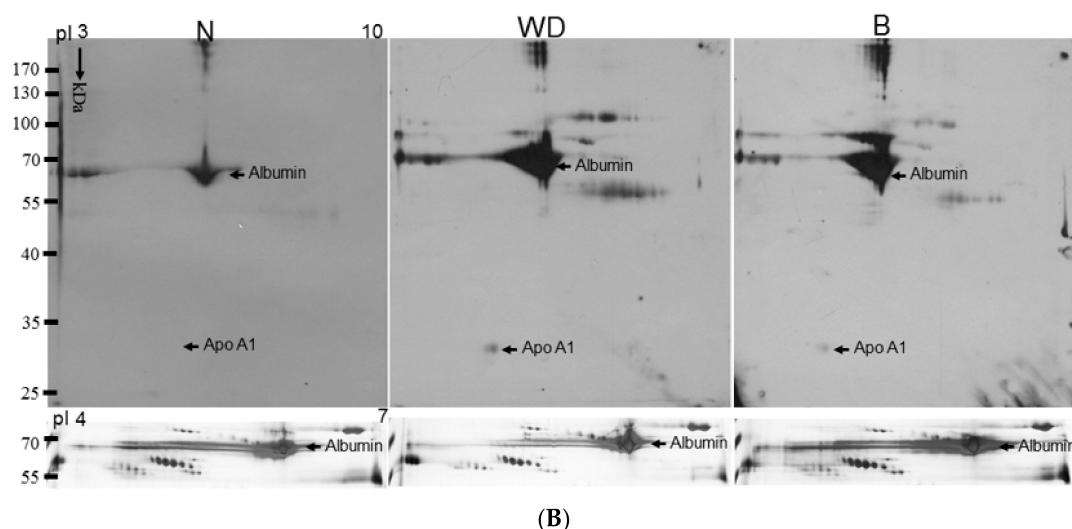
About 20% and 5% reduction of activity were observed in both F and M, respectively, who were considered as heterozygous carriers. Novel WD patient (B) was first identified and introduced to an early regimen because of our findings from this experiment.

Figure 1B shows that protein carbonylation was significantly induced in patients WD and B compared to the control (N) samples. These results implied that high dose of oxidative stress was induced and directly promoted protein oxidation in WD subjects.



(A)

Figure 1. Cont.



**Figure 1.** (A) In situ oxidase activity of ceruloplasmin oxidase among health donor, heterozygous carriers and homozygous WD patients. The patient (WD) had been undergoing therapy while S and B were diagnosed as health individuals and asymptomatic subjects; however, B started onset six month later. Two paternal samples referred to as F and M, respectively. Marker: protein marker, Std: commercial ceruloplasmin as standard. Albumin is naturally presented as the blue bands after conducting the assay. (B) Levels of protein carbonylation. Significantly increased expression of carbonylated proteins were observed in the samples of WD and B compared to the control. Albumin in the lower panels was utilized as a loading control.

## 2.2. Identification of WD-Associated Proteins by Proteomics Analysis

In order to screen the potential biomarkers associated with WD, 200  $\mu$ g of plasma from each control and the WD patient were separated by 2-DE with pH value from 3 to 10 and visualized by silver stain (Figure 2 upper panels). Some protein spots were presented clearly after removing the albumin (Figure 2 lower panels).

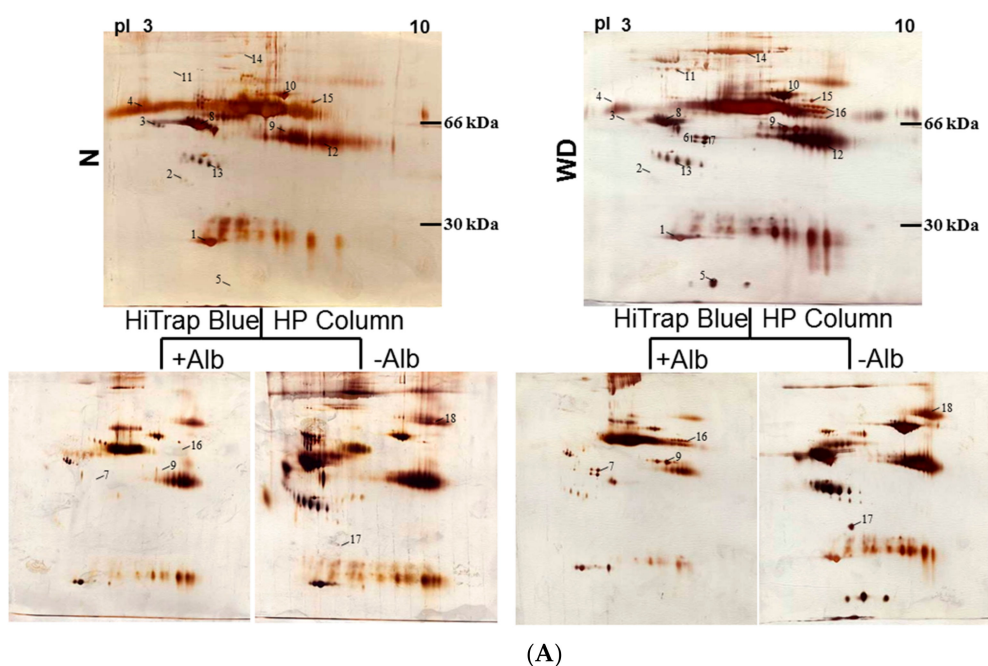
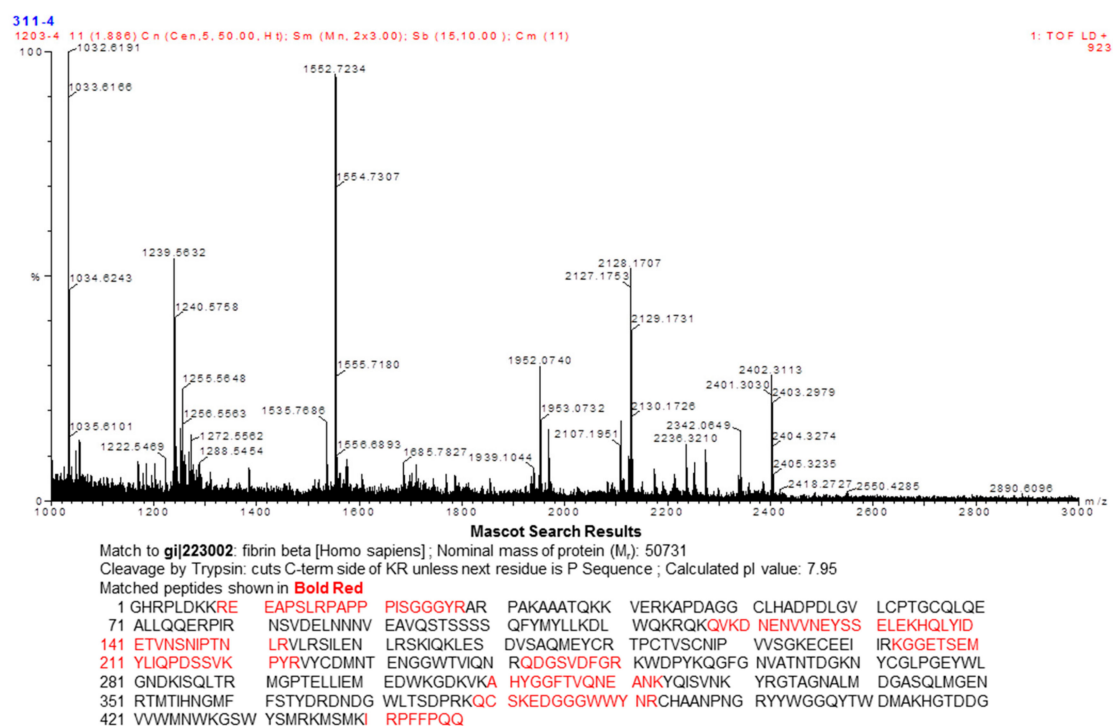
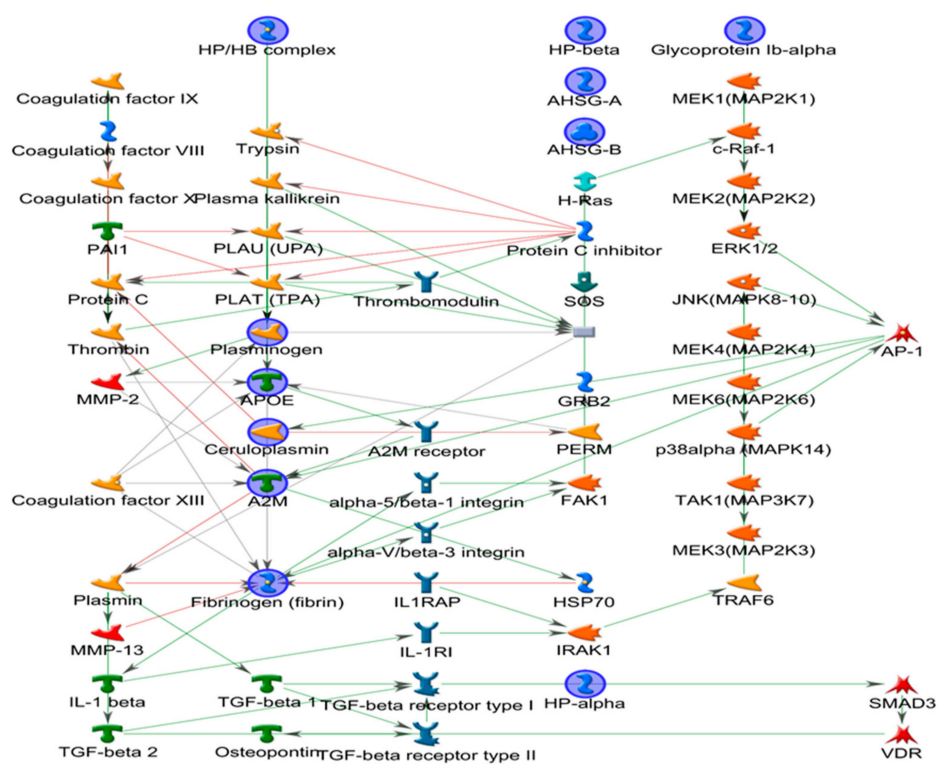


**Figure 2.** Cont.



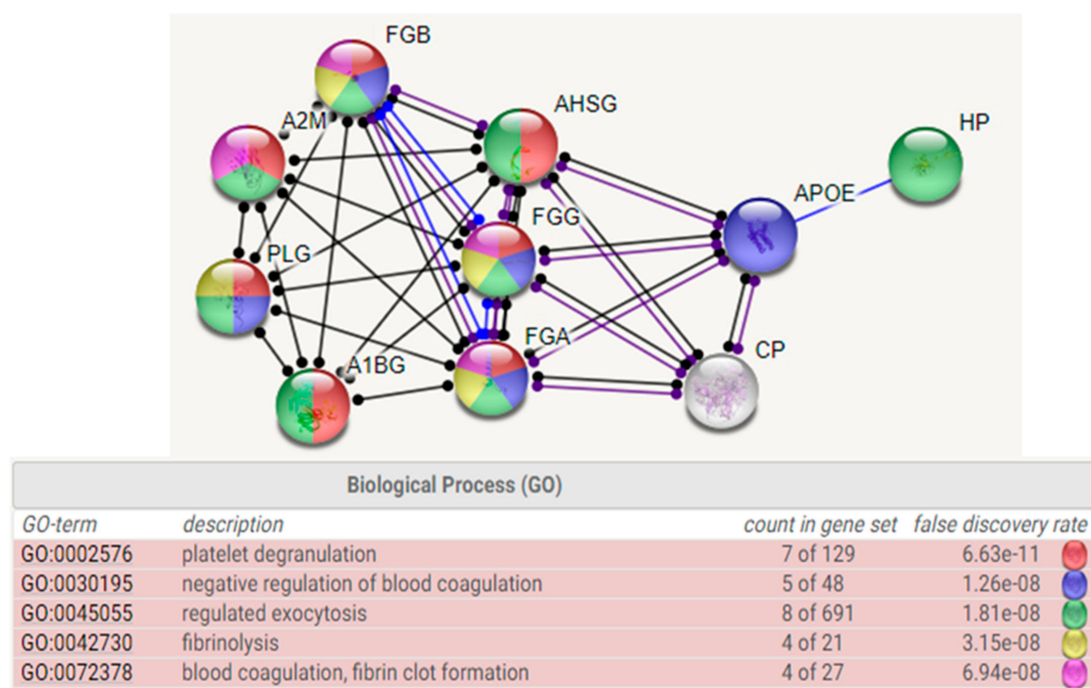
(B)



(C)

Figure 2. Cont.





(D)

**Figure 2.** (A) Silver-stained 2-DE patterns of plasma and plasma depleted of albumin. N: health donor; WD: Wilson's disease patients. Most albumins in plasma samples from health donor and WD were removed by using a Millipore Montage Albumin Deplete kit. The protein spots with significantly increasing intensity were labeled as Arabic numerals. Of these thirty one spots, 4 spots which appeared in normal samples were expressed in high level. Conversely, the other 14 spots were found in more abundant quantity for WD samples. (B) Peptide mass fingerprints of human fibrinogen  $\beta$  chain by. After 2-DE separation, spots was digested with trypsin and applied to MALDI-TOF mass spectrum which marked 9 in Table 1. By mean of Mascort software, 13 peptides with  $m/z$  values could be matched to accession number from Swiss-Prot database. Matched peptides showed with underline within the internal amino acid sequence of fibrinogen  $\beta$  chain. (C) Biological network analyses of differentially expressed proteins using MetaCore™ mapping tools. Nodes represent proteins and lines between the nodes indicate direct protein–protein interactions. The various proteins on this map are indicated by different symbols representing the functional class of the proteins. (D) Top-ranked pathways from the GeneGo MetaCore pathway analysis. Pathways were ranked according to  $p$  values.

Using a Nonlinear Progenesis computerized program, a total of 18 protein spots with significant difference between normal controls and WD patients were counted. Of these proteins, four spots appearing in the control samples markedly increased in volume, whereas another 14 spots were found in more abundant quantity for WD samples. As shown in Figure 2A, these protein spots were subsequently identified by peptide mass fingerprinting (PMF) and aligned with the protein sequence in the database as listed in Table 1. Among the identified proteins, two spots (spots 6,7) covering the fibrinogen-gamma family, the protein spots (spots 16) belonging to the fibrinogen- $\alpha$  group and fibrinogen- $\beta$  chain (spot 9) were also found. Numerous Apo-family protein spots such as Apo A1, Apo J and Apo E, and acute phase proteins which include  $\alpha$ 2-macroglobulin and haptoglobin  $\alpha/\beta$  chain were explored by this method. At the same time, some proteins considered to relate to the etiology of WD, including antithrombin, complement C3, serotransferrin and other binding proteins were confirmed as well. MS analysis was used to unambiguously identify human fibrinogen as presented in Figure 2B.



**Table 1.** List of identified protein spots.

Spot No.	Protein Name	Accession number	Score (Coverage)	Mw (kDa)/pI	Function
1	Apo A1	P02647	215 (61%)	30.76/5.56	Participates in the reverse transport of cholesterol from tissues to the liver for excretion by promoting cholesterol efflux from tissues and by acting as a cofactor for the lecithin cholesterol acyltransferase (LCAT).
2	Apo J (clusterin)	P10909	38 (19%)	49.34/6.27	Prevents stress-induced aggregation of blood plasma proteins.
3	$\alpha$ 2-HS-glycoprotein	P02765	72 (28%)	40.10/5.43	Promotes endocytosis, possesses opsonic properties and influences the mineral phase of bone. Shows affinity for calcium and barium ions.
4	$\alpha$ 1-B-glycoprotein	P04219	130 (43%)	54.81/5.65	
5	Haptoglobin $\alpha$ chain	P00738	80 (51%)	13.74/6.10	Haptoglobin also acts as an antioxidant, has antibacterial activity, and plays a role in modulating many aspects of the acute phase response.
6	Fibrinogen- $\gamma$ -A chain	P02679	158 (58%)	50.82/5.70	Together with fibrinogen- $\alpha$ (FGA) and fibrinogen- $\beta$ (FGB), polymerizes to form an insoluble fibrin matrix.
7	Fibrinogen- $\gamma$ -B chain	P02679	156 (56%)	52.11/5.37	Together with fibrinogen- $\alpha$ (FGA) and fibrinogen- $\beta$ (FGB), polymerizes to form an insoluble fibrin matrix.
8	antithrombin	P01008	182 (58%)	53.04/6.32	Most important serine protease inhibitor in plasma that regulates the blood coagulation cascade. AT-III inhibits thrombin, matriptase-3/TMPRSS7, as well as factors IXa, Xa and XIa.
9	Fibrinogen-	P02675	225 (62%)	56.58/8.54	Cleaved by the protease thrombin to yield monomers which, together with fibrinogen- $\alpha$ (FGA) and fibrinogen- $\gamma$ (FGG), polymerize to form an insoluble fibrin matrix. Fibrin deposition is also associated with infection, where it protects against IFNG-mediated hemorrhage.
10	Serotransferrin	P02787	93 (37%)	74.28/6.63	Transferrins are iron binding transport proteins which can bind two $\text{Fe}^{3+}$ ions in association with the binding of an anion, usually bicarbonate.
11	$\alpha$ 1-antiproteinase	P01009	148 (47%)	46.88/5.37	Inhibitor of serine proteases. Its primary target is elastase, but it also has a moderate affinity for plasmin and thrombin.
12	Immunoglobulin $\alpha$ 2 heavy chain	P01876	133 (37%)	54.82/6.02	Constant region of immunoglobulin heavy chains. Immunoglobulins, also known as antibodies, are membrane-bound or secreted glycoproteins produced by B lymphocytes.
13	Haptoglobin $\beta$ chain	P00738	126 (46%)	38.87/6.26	Haptoglobin captures, and combines with free plasma hemoglobin to allow hepatic recycling of heme iron and to prevent kidney damage.
14	$\alpha$ 2-microglobulin	P01023	172 (25%)	164.6/6.00	Is able to inhibit all four classes of proteinases by a unique 'trapping' mechanism.
15	Complement C3	P01024	107 (24%)	188.57/6.02	C3 plays a central role in the activation of the complement system.
16	Fibrinogen- $\alpha$	P02671	127 (38%)	94.97/5.70	Cleaved by the protease thrombin to yield monomers which, together with fibrinogen- $\beta$ (FGB) and fibrinogen- $\gamma$ (FGG), polymerize to form an insoluble fibrin matrix.
17	ApoE	P02649	82 (43%)	36.15/5.65	APOE is an apolipoprotein, a protein associating with lipid particles, that mainly functions in lipoprotein-mediated lipid transport between organs via the plasma and interstitial fluids
18	Plasminogen	P00747	72 (23%)	90.57/7.04	Plasmin dissolves the fibrin of blood clots and acts as a proteolytic factor in a variety of other processes including embryonic development, tissue remodeling, tumor invasion, and inflammation.

Database: NCBIprot 20180429 (152462470 sequences; 55858910152 residues).

### 2.3. Biological Network Analysis

To further elucidate the relationship of the differentially expressed proteins revealed by the 2-DE analysis and their significance in the mechanisms associated with the WD etiology, proteins were analyzed by applying the MetaCore™ software. The algorithm builds biological networks from an uploaded protein list and assigns a biological process to each network which was generated using the shortest-path algorithm to map interactions among proteins identified from the plasma samples. Map Editor was used to build the network based on key proteins which were up- or downregulated in the network. Highlighted lines represent specific, designated pathways. Background lines represent secondary, related biological pathways (Figure 2C). As shown in Figure 2D, protein-protein interaction networks indicated that proteins differentially expressed were primarily related to coagulation system. The following statistically significant networks: platelet degranulation ( $6.63 \times 10^{-11}$ ), negative regulation of blood coagulation ( $1.26 \times 10^{-8}$ ), regulated exocytosis ( $1.81 \times 10^{-8}$ ), fibrinolysis ( $3.15 \times 10^{-8}$ ) and blood coagulation ( $6.94 \times 10^{-8}$ ). Based on this network, we found that change of fibrinogen caused by WD might be strongly correlated with coagulation system.

### 2.4. Fibrinogen Level Was Detected by 2DE-Immunoblots

According to the results from the proteome alternation profiles, we suggest that fibrinogen may be an important index in plasma of WD patients due to hepatic injury, as it was dominant in the Taiwan WD patients. To directly indicate the presence of fibrinogen, we analyzed sera samples from normal controls and WD patients by using 2D-immunoblots. There were seven spots of fibrinogen subunits including fibrinogen  $\alpha$ ,  $\beta$ ,  $\gamma$  chain significantly increased in WD patient while these proteins were expressed in negligible quantity or absent for normal controls (Figure 3A).

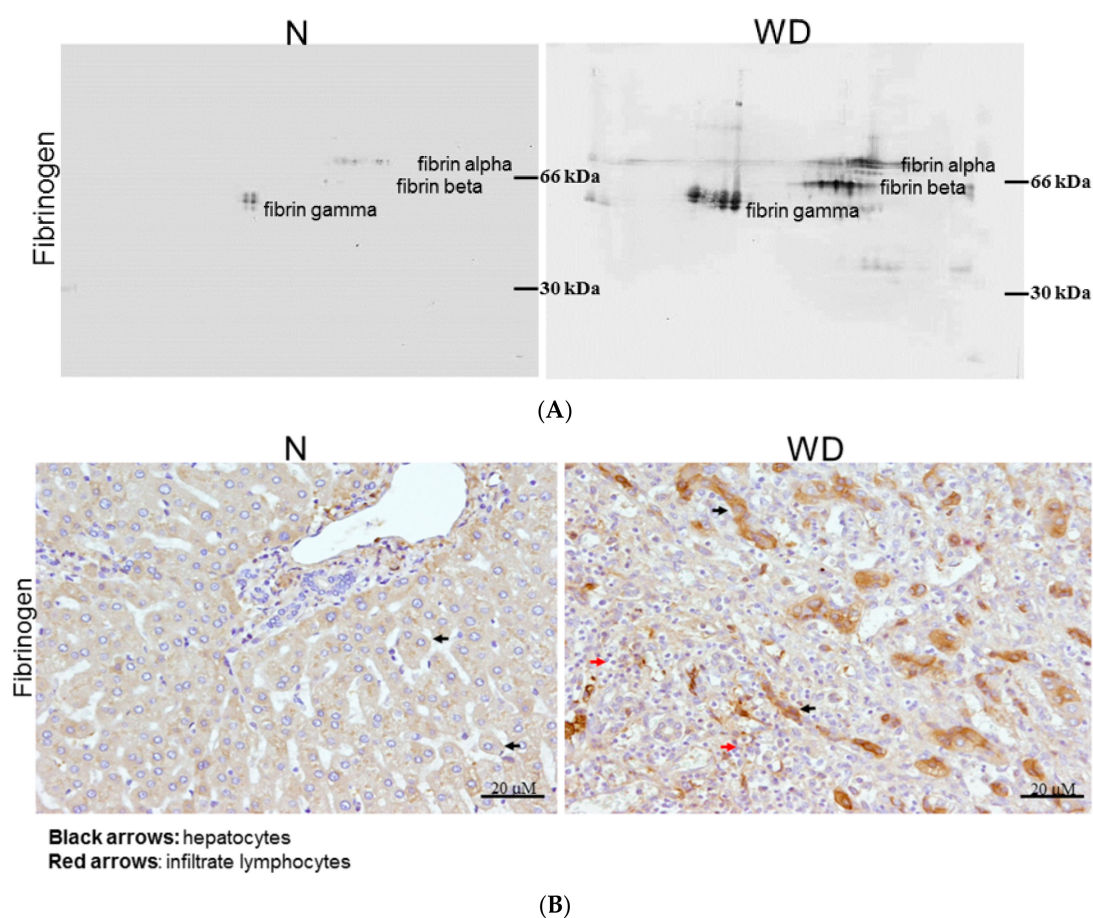
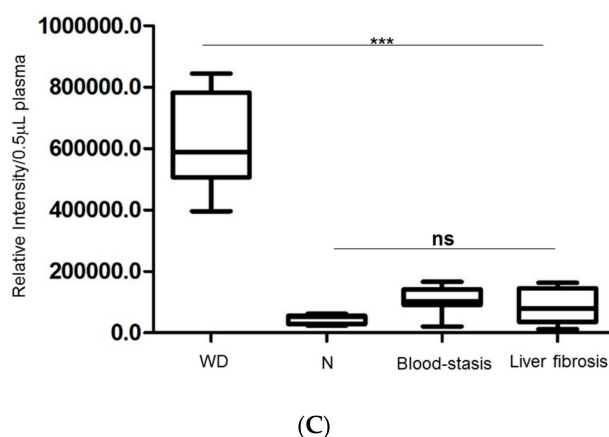


Figure 3. Cont.



**Figure 3.** (A) Compares the expression of fibrinogen in plasma between normal (N) and WD patient by immunoblots. 2-DE western blot shows the different type of fibrinogen ( $\alpha$ ,  $\beta$  and  $\gamma$ ) with a specific reactive antihuman antibody. (B) Immunohistochemical analysis of fibrinogen in the normal part of liver (N) and WD cirrhotic liver are observed under microscope. The hepatocytes were showing obvious staining of fibrinogen in WD patients as black arrows indicate while great amount of inflammatory cells were observed in WD samples as demonstrated by red arrows. However, faint staining of fibrinogen in hepatocytes was found in normal liver sample. (C) Changes of fibrinogen level in plasma from clinical subjects with WD, blood-stasis, hepatic fibrosis and healthy donors. Each sample was analyzed in triplicate with specific antibody of fibrinogen in dot blot assay. These results were analyzed statistically by two-way ANOVA and fibrinogen significantly expressed in patients' plasma with Wilson's disease (\*\* $p < 0.0001$ ).

### 2.5. Evaluating Fibrinogen Expression in Liver Tissue by Immunohistochemistry

As shown in Figure 3B, fibrinogen distribution in the liver was quite different between normal and WD patients under immunohistochemical assay. We observed that fibrinogen in normal liver was faint staining and localized on the cytoplasm of hepatocytes (Figure 3B; left). Alternatively, the fibrinogen staining became condensed in the perisinusoidal space of the periportal region and cytosol of hepatocytes (Figure 3B; right), which dramatically increased in quantity on WD specimens. The results demonstrated coordinate tendency as in proteomic profiles and western blotting analysis.

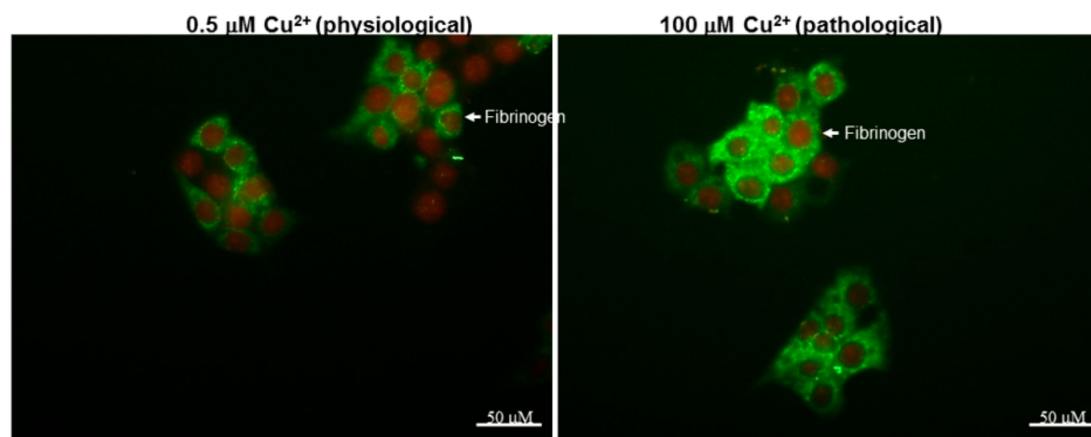
### 2.6. Estimation of Fibrinogen Expression in Healthy Controls, Patients with WD and Liver Fibrosis and Blood-Stasis Subjects

Although fibrinogen could be suggested as a potential indicator or biomarker in WD detection, it might also increase in patients with cardiovascular diseases. In order to examine its specific merit, we applied dot-blotting analysis to normal controls, patients with WD and liver fibrosis, and blood-stasis syndrome subjects characterized by a traditional Chinese medical doctor. The levels of fibrinogen were remarkably upregulated (~20-fold) in WD patients compared to healthy donors, patients with liver fibrosis and blood-stasis syndrome (Figure 3C). Based on the above data, we propose that fibrinogen could be feasible in WD diagnosis due to its high specificity.

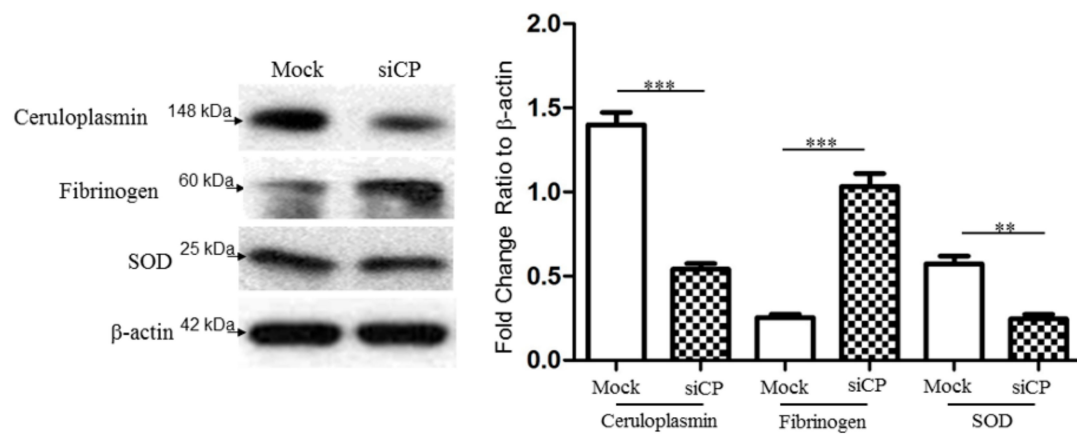
### 2.7. Characterize the Interplay between Ceruloplasmin and Fibrinogen with Cell Model

To further ascertain the effect of copper and fibrinogen upon hepatic cells, HepG2 cells were exposed to 0.5 and 100  $\mu$ M copper. As shown in Figure 4A, exogenous administration of high dose of copper markedly increased in fibrinogen level with respect to the sample treated with low dose of copper. Meanwhile, we have utilized ceruloplasmin RNA interference (siCP) to verify the modulation of fibrinogen level and oxidative status in a cell model. Silence of ceruloplasmin significantly enhanced the level of fibrinogen and attenuated antioxidant enzyme protein such as SOD (Figure 4B). Furthermore, increased levels of carbonylated proteins were observed in HepG2 cells transfected with siCP compared

to mock-control cells, indicating that the oxidative processes may be initiated under ceruloplasmin suppression (Figure 4C).



(A)



(B)

Figure 4. Cont.

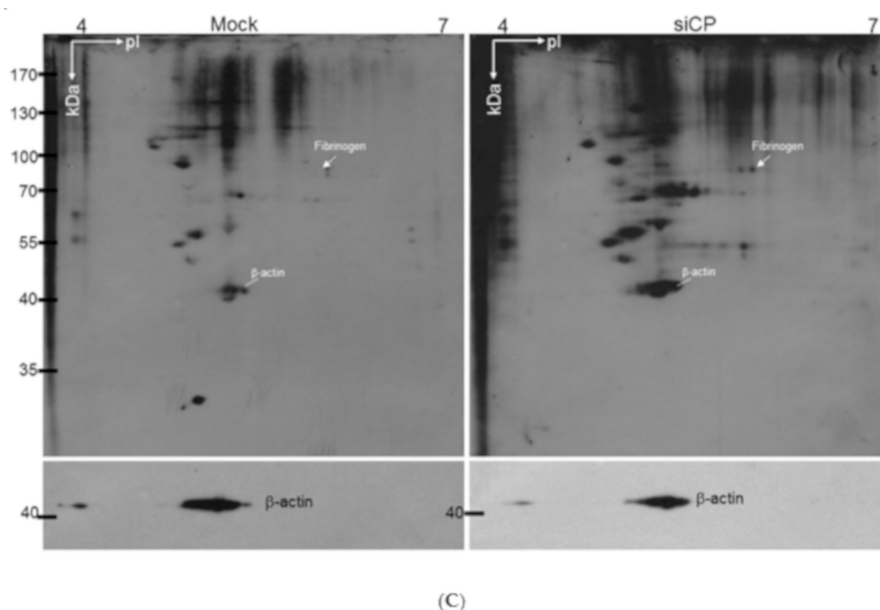


**Figure 4.** (A) Effects of exogenous copper upon changes in the fibrinogen expression of HepG2 cells. After HepG2 cells had been treated with 0.5 and 100  $\mu$ M copper, the intracellular localizations and level of fibrinogen (green) and nucleus (red) were examined by immunofluorescence microscopy. (B) Silence of ceruloplasmin (siCp) treatment induced the protein expression of fibrinogen, while the significant reduction in protein level for SOD was observed under siCp applications.  $\beta$ -actin was used as a loading control. Quantification of the result was presented as the bar diagram and the results represent the mean  $\pm$  SD of three independent experiments (\*\* $p < 0.0001$ ; \*\*  $p < 0.001$ ). (C) Levels of protein carbonylation. Significantly increased expression of carbonylated proteins were observed in the ceruloplasmin-silenced group (siCp) compared to the control (Mock).  $\beta$ -actin performed by Western blot analysis was utilized as the loading control and the individual carbonylated proteins separated by 2-DE analysis then could be normalized to the intensity of the  $\beta$ -actin protein for determining the protein oxidation levels.

### 3. Discussion

The main clinical challenge in the diagnosis of WD is how to characterize this disease earlier and easier by non-invasive method. In current studies, we integrated both ceruloplasmin oxidase activity and proteomics tool, providing evidence for a strategy to screen WD patients effectively whereby only a small amount of plasma is required. Although the serum concentration of ceruloplasmin has been considered as a useful indicator for WD diagnosis, recent studies have demonstrated that immunologic assay of ceruloplasmin may be erroneously estimated because the total amount of ceruloplasmin protein does not reflect ceruloplasmin enzyme activity in the plasma [16,17]. Herein, oxidative function of plasma holoceruloplasmin will be measured via *p*-phenylenediamine oxidation under non-reducing conditions, which is useful for early diagnosis of typically homozygous WD patients and for heterozygous subjects with minor symptoms. Previous experiments on copper depletion in humans suggest that specific enzymatic activity may be a more sensitive indicator of copper accumulation [18,19]. This result supports our hypothesis that measuring enzymatic activity of ceruloplasmin is more accurate and precise than ceruloplasmin concentration assay.

Currently, there are no effective biomarkers or methods available for screening WD, which can lead to neurological disabilities and/or liver cirrhosis. In addition to the measurement of copper accumulation in the liver tissue and ceruloplasmin oxidase activity in plasma, there is still an urgent need to identify other novel biomarkers for improvement in early WD diagnosis [20]. We noted that plasma protein usually reflects physiological changes and is easy to collect. It is reasonable to seek potential diagnostic biomarkers via plasma analysis [21]. In order to comprehensively characterize alterations of the composition in plasma protein occurring to patients with WD, we used 2-DE and



MALDI-TOF mass spectrometry to analyze protein profiles herein. From the comparative expression pattern of protein, most meaningful differences of protein between normal controls and WD patients were associated with the hepatic damage.

Fibrinogen, in particular, was found to be abundant in the plasma among all WD patients. It is composed of three structurally different subunits:  $\alpha$ ,  $\beta$ , and  $\gamma$  chains. In a variety of species, including rodents and human, the  $\gamma$  chain exists in two different forms, called  $\gamma$ -A and  $\gamma$ -B. The  $\gamma$  chain of human fibrinogen has been demonstrated as indicative of tumor-associated fibrin deposition and fibrinolysis [22–24]. Interestingly, the relative enrichment with the uploaded data in the bioinformatics experiment indicated that low plasma level of ceruloplasmin has been majorly responsible for the changes in coagulation pathway, resulting in impaired liver function on coagulation [25]. On the other hand, excessive copper accumulating in WD patients destroys the function of fibrinogen and leads to the damage to various organs such as liver and brain. In addition, the network analysis verified that induced fibrinogen is mediated via ROS-ERK1/2/p38/AP-1 signaling pathway. This finding provides an evidence for pro-inflammatory effect of fibrinogen, implying subsequent system injury in WD patients [26]. We also observed significant expression of fibrinogen in liver of WD patients and severe infiltration of lymphocytes through an immunohistochemistry experiment, suggesting the roles of fibrinogen in inducing inflammatory responses (Figure 3B, red arrows). To assess the potent of fibrinogen as a biomarker in early and precise diagnosis of WD, the blood samples obtained from WD patients, liver fibrosis, blood-stasis victims and normal control were applied for evaluation of fibrinogen expression. We found that the plasma content of fibrinogen in subjects with WD is significantly higher than it is in hepatic fibrosis, blood-stasis and normal ones, suggesting fibrinogen may be considered a potential parameter in WD diagnosis.

Biological systems are continuously exposed to reactive oxygen species (ROS) like in the disturbance of copper metabolism in WD subjects [27–29]. High doses of ROS determine oxidative stress responsible for serious metabolic dysfunctions and damage to the structures of biological macromolecules such as proteins [30]. Protein carbonylation is considered as a hallmark of oxidative stress [31,32]. The view of 2DE-oxyblots showed that the extent of oxidation in proteins was dramatically upregulated in the case of WD patients compared to the normal control, implying that oxidative stress caused by WD progression would result in increased ROS generation and reduced antioxidant capacity, which caused a visible deterioration in liver and neuron system [33–35]. The accumulation of hepatic copper and abrogation of ceruloplasmin synthesis caused by impairment of ATP7B-mediated intracellular copper transport were further simulated by cellular experiments. Our results indicated that high dose copper would induce overproduction of fibrinogen and ceruloplasmin diminution mediated by siRNAs significantly promoted oxidative stress by downregulating the SOD level [36]. These findings highlight the unique properties of fibrinogen in cellular targets and signal transduction pathways related to WD development.

Up to now, no single diagnostic test can exclude or confirm WD with 100% certainty. The prognosis for survival in the majority of WD patients is favorable if they could be provided accurate therapy before complications resulting from copper deficiency. In this paper, we combined two methods: ceruloplasmin oxidase activity and fibrinogen level for achieving an early and rapid diagnosis in WD for the first time.

#### 4. Conclusions

In summary, decreased expression and impaired function of ceruloplasmin in WD patients could bring about copper accumulation and subsequent oxidative stress, which consecutively induces expression of fibrinogen and elicits inflammatory responses as well as dysregulation of coagulation cascades (Figure 5).

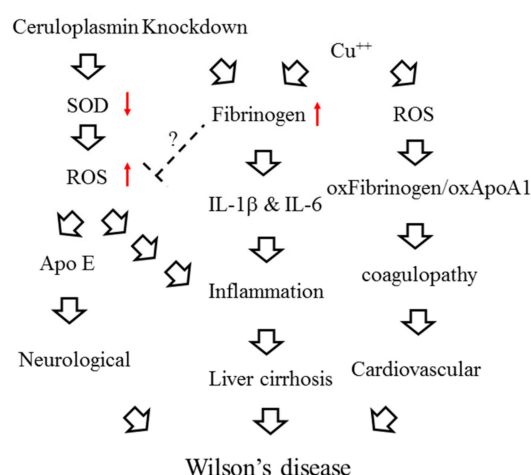


**Figure 5.** Schematic diagram of the interactions between ceruloplasmin, fibrinogen and oxidative stress. The red arrow up means increase and the red arrow down indicates decrease.

## 5. Materials and Methods

### 5.1. Subjects

All clinical data of WD patients were provided by Wen-Neng Chang. The Committee on Research Involving Human Subjects of the Chang Gung Memorial Hospital in Kaohsiung, Taiwan, approved this study. Informed consent was obtained from all subjects in this study. The clinical samples belong to the same family which is including of two parents (F,M), brother and sister (B,S) and homozygous WD patient (WD). Of note, subject B without WD symptoms starts onset six month later after conducting experiment while F, M and S are asymptomatic. Plasma from patients and healthy volunteers was collected, aliquots and storage at  $-80^{\circ}\text{C}$  until assayed.

### 5.2. In Situ Oxidase Activity of Ceruloplasmin

Plasma (5  $\mu\text{L}$ ) was mixed with Laemmli sample buffer lacking DTE, and was separated without prior heating by SDS-PAGE. The gel was then equilibrated with 50 vol. of 0.05% Triton X-100 in 10% (wt/vol) glycerol, soaked for an equal time in 5 vol. of 3 mM *p*-phenylenediamine dihydrochloride/100 mM sodium acetate, pH 5.7, 1 mM  $\text{NaN}_3$ , and air-dried in the dark at room temperature for 24 h [37]. Albumin present in the plasma samples will be presented as a blue color under the above treatment.

### 5.3. Two-Dimensional Polyacrylamide Gel Electrophoresis (2-DE)

Approximately 200  $\mu\text{g}$  of plasma were solubilized in the rehydration buffer containing 8 M urea, 2% CHAPS, 0.002% bromophenol blue, 2% IPG buffer pH 3–10 and 65 mM DTE. The samples were then separated by the Immobiline Drystrip on the IPGphor III System (GE Healthcare, Göteborg, Sweden) for the first dimension. The 2-DE was carried out on 10% acrylamide gels at 30 mA/gel [38]. All gels were visualized by silver staining and then scanned using an Imagescanner (GE Healthcare, Göteborg, Sweden). All experiments were repeated three times to confirm the reproducibility.

### 5.4. Albumin Removal

The protocol was followed as described in the Montage Albumin Deplete Kit user guide (Merck Millipore, Burlington, MA, USA). Flow-through contained the albumin-depleted plasma fraction. Albumin was recovered from the column with 2-DE rehydrated buffer. Both fractions were further analyzed by 2-DE platform.

### 5.5. Tryptic In-Gel Digestion of Proteins & MALDI-TOF Mass Spectrometry

Protein spots of interest were excised and in-gel digested with trypsin as previously described [39]. Briefly, tryptic peptides were acidified with 0.5% TFA and loaded onto an MTP AnchorChip™ 600/384 TF (Bruker-Daltonik, Bremen, Germany). The MS analysis was performed on an Ultraflex™ MALDI-TOF mass spectrometer (Bruker-Daltonik, Bremen, Germany) and the monoisotopic peptide masses were applied for database searches with the MASCOT search engine [<http://www.matrixscience.com>].

### 5.6. Biological Network Analysis Using Metacore™

Applied MetaCore™ software (vers. 5.2 build 17389, GeneGo, St. Joseph, MI, USA) was utilized to explore ontological classes and associated pathways which were denoted for the protein targets characterized by the mass fingerprint [39].

### 5.7. D-Oxyblot and 2D-Immunoblots

Following IEF, IPG strips were incubated in 2N HCl with 10 mM DNPH at 25 °C for 20 min. Next, samples were washed with 2M Tris-Base/30% glycerol for 15 min and the protein was separated according to molecular weight as described above. The 2-DE gels were then transferred to a PVDF membrane which was incubated overnight at 4 °C with the primary antibody for DNPH (Molecular Probes, Eugene, Oregon, USA) or fibrinogen (DAKO, Santa Clara, CA, USA). The blots were washed and incubated with goat anti-rabbit IgG conjugated HRP for 2 h. Enhanced chemiluminescence (Millipore, Burlington, MA, USA) was applied for detection [40].

### 5.8. Immunohistochemistry

Paraffin-embedded tissue blocks were sectioned in 2-μm slices and placed on slides coated with poly-L-lysine. IHC with a fibrinogen (1:400-diluted in phosphate-buffered saline) was applied to sections as previously described [39]. Thereafter, sections were counter-stained with Mayer's hematoxylin for 2 min, and slides were mounted with mounting medium and evaluated under a light microscope (BX51, Olympus, Tokyo, Japan). Digital photomicrographs were then processed with DP-72 (Olympus).

### 5.9. Analysis of Plasma Fibrinogen in Clinical Samples

Blood samples from 10 healthy volunteers, patients with WD, blood-stasis syndrome and hepatic fibrosis were collected. 0.5 μL of plasma was spotted onto pieces of nitrocellulose paper (Millipore, Burlington, MA, USA) and allowed to dry under room temperature. Paper was then incubated in anti-fibrinogen antibody for 1 h at RT. After three washes with TBST, anti-rabbit IgG conjugated AP was applied to react further for 1 h at RT. After washing as before and rinse with ddH<sub>2</sub>O, paper was developed using NBT/BCIP for 5 min [41]. The target dots were scanned, analyzed and quantified using GeneTools software (version 4.03, Syngene, Cambridge, UK). All experiments were repeated more than twice.

### 5.10. Immunofluorescence

HepG2 cells were treated with copper (0.5 and 100 μM) for 24 h, and were then fixed in ice-cold methanol for 10 min at 4 °C. After washing in PBS, cells were permeabilized with 0.1% Triton-X100 in PBS for 10 min at room temperature. Cells were then incubated with primary antibodies against fibrinogen and rinsed three times in PBS. Cells were subsequently exposed to a Fluorescein-5-Isothiocyanate conjugated secondary antibody (Santa Cruz Biotechnology, Dallas, TX, USA). After incubation, cells were rinsed in PBS three times and nuclei were counterstained with propidium iodide (Sigma-Aldrich, St. Louis, MO, USA) for 1 min. After washing three times, the cells were maintained with mounting medium and observed by Olympus IX71 fluorescence microscope (Olympus, Tokyo, Japan) under a DP72 PhotoImage system (Olympus, Tokyo, Japan) [39].

### 5.11. siRNA Administration

$6 \times 10^5$  cells/dish HepG2 cells were cultured with antibiotic-free medium for 6 h and transfected with a mixture containing either 0.5  $\mu$ g/well scrambled siRNA (mock) or a mixture of three ceruloplasmin siRNAs (smart pool; Invitrogen, Waltham, MA, USA), Opti-MEM, 8  $\mu$ L/well Lipofectamine 2000 (Invitrogen). The cells were harvested and subjected to following experiments after 48 h post-transfection.

### 5.12. Western Blot Analysis

The protein obtained from the various experiments was isolated using  $1 \times$  cell lysis buffer (Cell Signaling, Danvers, MA, USA) and the concentration was determined with the Bradford Protein Assay Kit (AMRESCO, Solon, OH, USA). Protein lysates were then investigated by Western blot analyses as previously described [39,42]. The specific antibodies used in the current study were listed as follows: CP (abcam, Cambridge, UK), Fibrinogen, SOD and  $\beta$ -actin. The band intensity was quantified by using GeneTools software and the level of  $\beta$ -actin was performed as internal control.

### 5.13. Statistical Analysis

All values were presented as the mean  $\pm$  SD. Statistical analysis of the mean values was carried out with the ANOVA test using the SPSS software (version 12.0, SPSS, Chicago, IL, USA). Differences were considered significant at  $p < 0.001$ . Data was confirmed through three repetitions.

**Author Contributions:** P.-W.W., T.-L.P. designed the protocol and prepared the manuscript, P.-W.W., T.-Y.L., Y.-C.H., W.-N.C., P.-M.Y., C.-T.Y., T.-L.P. helped conduct the experiment, M.-H.C. helped to conduct the statistical analysis and T.-L.P. was in charge of the whole experiment conduction and proofreading of the manuscript.

**Funding:** This work was supported by a grant from the Ministry of Science and Technology for Tai-Long Pan (MOST105-2320-B-182-007-MY3) and for Pei-Wen Wang (MOST108-2320-B-182-039-006), Chang Gung Memorial Hospital (CRRPD1F0061~3, BMRP445) and Chang Gung University (EMRPD1I0441), Taiwan.

**Conflicts of Interest:** The authors declare no conflicts of interest.

### Abbreviations

WD	Wilson's disease
DNPH	2,4-Dinitrophenylhydrazine
MALDI-TOF-MS	Matrix-Assisted Laser Desorption/ Ionization Time of Flight Mass Spectrometry
SOD	Superoxide dismutase
2-DE	Two-dimensional electrophoresis
CP	Ceruloplasmin
PMF	Peptide mass fingerprinting
ROS	Reactive oxygen species
IPG	Immobilized pH gradient
IHC	Immunohistochemistry
NBT	p-Nitrobluetetrazolium chloride
BCIP	5-Bromo-4-chloro-3-indolyl phosphate
DTE	Dithioerythritol
SDS-PAGE	Sodium dodecyl sulfate-polyacrylamide gel electrophoresis.

### References

1. Dziezyc, K.; Litwin, T.; Chabik, G.; Gramza, K.; Czlonkowska, A. Families with Wilson's disease in subsequent generations: Clinical and genetic analysis. *Mov. Disord.* **2014**, *29*, 1828–1832. [[CrossRef](#)] [[PubMed](#)]
2. Medici, V.; Weiss, K.H. Genetic and environmental modifiers of Wilson disease. *Handb. Clin. Neurol.* **2017**, *142*, 35–41. [[PubMed](#)]
3. Kluska, A.; Kulecka, M.; Litwin, T.; Dziezyc, K.; Balabas, A.; Piatkowska, M.; Paziewska, A.; Dabrowska, M.; Mikula, M.; Kaminska, D.; et al. Whole-exome sequencing identifies novel pathogenic variants across the ATP7B gene and some modifiers of Wilson's disease phenotype. *Liver Int.* **2019**, *39*, 177–186. [[CrossRef](#)] [[PubMed](#)]

4. Bhattacharjee, A.; Chakraborty, K.; Shukla, A. Cellular copper homeostasis: Current concepts on its interplay with glutathione homeostasis and its implication in physiology and human diseases. *Metallomics* **2017**, *9*, 1376–1388. [[CrossRef](#)] [[PubMed](#)]
5. Bandmann, O.; Weiss, K.H.; Kaler, S.G. Wilson's disease and other neurological copper disorders. *Lancet Neurol.* **2015**, *14*, 103–113. [[CrossRef](#)]
6. Roberts, E.A. Update on the Diagnosis and Management of Wilson Disease. *Curr. Gastroenterol. Rep.* **2018**, *20*, 56. [[CrossRef](#)]
7. Wu, F.; Wang, J.; Pu, C.; Qiao, L.; Jiang, C. Wilson's disease: A comprehensive review of the molecular mechanisms. *Int. J. Mol. Sci.* **2015**, *16*, 6419–6431. [[CrossRef](#)]
8. Hordyjewska, A.; Popiolek, L.; Kocot, J. The many “faces” of copper in medicine and treatment. *Biometals* **2014**, *27*, 611–621. [[CrossRef](#)]
9. Lorincz, M.T. Recognition and treatment of neurologic Wilson's disease. *Semin. Neurol.* **2012**, *32*, 538–543. [[CrossRef](#)]
10. Macintyre, G.; Gutfreund, K.S.; Martin, W.R.; Camicioli, R.; Cox, D.W. Value of an enzymatic assay for the determination of serum ceruloplasmin. *J. Lab. Clin. Med.* **2004**, *144*, 294–301. [[CrossRef](#)]
11. Danesh, J.; Lewington, S.; Thompson, S.G.; Lowe, G.D.; Collins, R.; Kostis, J.B.; Wilson, A.C.; Folsom, A.R.; Wu, K.; Benderly, M.; et al. Plasma fibrinogen level and the risk of major cardiovascular diseases and nonvascular mortality: An individual participant meta-analysis. *JAMA* **2005**, *294*, 1799–1809. [[PubMed](#)]
12. Stec, J.J.; Silbershatz, H.; Tofler, G.H.; Matheney, T.H.; Sutherland, P.; Lipinska, I.; Massaro, J.M.; Wilson, P.F.; Muller, J.E.; D'Agostino, R.B., Sr. Association of fibrinogen with cardiovascular risk factors and cardiovascular disease in the Framingham Offspring Population. *Circulation* **2000**, *102*, 1634–1638. [[CrossRef](#)] [[PubMed](#)]
13. Ferenci, P. Regional distribution of mutations of the ATP7B gene in patients with Wilson disease: Impact on genetic testing. *Hum. Genet.* **2006**, *120*, 151–159. [[CrossRef](#)] [[PubMed](#)]
14. Greco, V.; Piras, C.; Pieroni, L.; Urbani, A. Direct Assessment of Plasma/Serum Sample Quality for Proteomics Biomarker Investigation. *Methods Mol. Biol.* **2017**, *1619*, 3–21. [[PubMed](#)]
15. Gallart-Palau, X.; Serra, A.; Sze, S.K. Uncovering Neurodegenerative Protein Modifications via Proteomic Profiling. *Int. Rev. Neurobiol.* **2015**, *121*, 87–116. [[PubMed](#)]
16. Cauza, E.; Maier-Dobersberger, T.; Polli, C.; Kaserer, K.; Kramer, L.; Ferenci, P. Screening for Wilson's disease in patients with liver diseases by serum ceruloplasmin. *J. Hepatol.* **1997**, *27*, 358–362. [[CrossRef](#)]
17. Xu, R.; Jiang, Y.F.; Zhang, Y.H.; Yang, X. The optimal threshold of serum ceruloplasmin in the diagnosis of Wilson's disease: A large hospital-based study. *PLoS ONE* **2018**, *13*, e0190887. [[CrossRef](#)] [[PubMed](#)]
18. Vassiliev, V.B.; Kachurin, A.M.; Beltramini, M.; Rocco, G.P.; Salvato, B.; Gaitskhoki, V.S. Copper depletion/repletion of human ceruloplasmin is followed by the changes in its spectral features and functional properties. *J. Inorg. Biochem.* **1997**, *65*, 167–174. [[CrossRef](#)]
19. Merle, U.; Eisenbach, C.; Weiss, K.H.; Tuma, S.; Stremmel, W. Serum ceruloplasmin oxidase activity is a sensitive and highly specific diagnostic marker for Wilson's disease. *J. Hepatol.* **2009**, *51*, 925–930. [[CrossRef](#)]
20. Hahn, S.H. Population screening for Wilson's disease. *Ann. NY Acad. Sci.* **2014**, *1315*, 64–69. [[CrossRef](#)]
21. Geyer, P.E.; Kulak, N.A.; Pichler, G.; Holdt, L.M.; Teupser, D.; Mann, M. Plasma Proteome Profiling to Assess Human Health and Disease. *Cell Syst.* **2016**, *2*, 185–195. [[CrossRef](#)] [[PubMed](#)]
22. Litvinov, R.I.; Weisel, J.W. What Is the Biological and Clinical Relevance of Fibrin? *Semin Thromb. Hemost.* **2016**, *42*, 333–343. [[CrossRef](#)] [[PubMed](#)]
23. Lin, Y.; Liu, Z.; Qiu, Y.; Zhang, J.; Wu, H.; Liang, R.; Chen, G.; Qin, G.; Li, Y.; Zou, D. Clinical significance of plasma D-dimer and fibrinogen in digestive cancer: A systematic review and meta-analysis. *Eur. J. Surg. Oncol.* **2018**, *44*, 1494–1503. [[CrossRef](#)] [[PubMed](#)]
24. Pieters, M.; Wolberg, A.S. Fibrinogen and fibrin: An illustrated review. *Res. Pract. Thromb. Haemost.* **2019**, *3*, 161–172. [[CrossRef](#)] [[PubMed](#)]
25. Schaefer, M.; Weber, L.; Gotthardt, D.; Seessle, J.; Stremmel, W.; Pfeifferberger, J.; Weiss, K.H. Coagulation Parameters in Wilson Disease. *J. Gastrointest. Liver Dis.* **2015**, *24*, 183–188.
26. Davalos, D.; Akassoglou, K. Fibrinogen as a key regulator of inflammation in disease. *Semin Immunopathol.* **2012**, *34*, 43–62. [[CrossRef](#)]
27. Zischka, H.; Lichtmannegger, J. Pathological mitochondrial copper overload in livers of Wilson's disease patients and related animal models. *Ann. NY Acad. Sci.* **2014**, *1315*, 6–15. [[CrossRef](#)] [[PubMed](#)]



28. Clayton, P.T. Inherited disorders of transition metal metabolism: An update. *J. Inherit. Metab. Dis.* **2017**, *40*, 519–529. [[CrossRef](#)]
29. Yu, Y.; Guerrero, C.R.; Liu, S.; Amato, N.J.; Sharma, Y.; Gupta, S.; Wang, Y. Comprehensive Assessment of Oxidatively Induced Modifications of DNA in a Rat Model of Human Wilson's Disease. *Mol. Cell Proteom.* **2016**, *15*, 810–817. [[CrossRef](#)]
30. Rosenfeld, M.A.; Vasilyeva, A.D.; Yurina, L.V.; Bychkova, A.V. Oxidation of proteins: Is it a programmed process? *Free Radic. Res.* **2018**, *52*, 14–38. [[CrossRef](#)]
31. Fedorova, M.; Bollineni, R.C.; Hoffmann, R. Protein carbonylation as a major hallmark of oxidative damage: Update of analytical strategies. *Mass. Spectrom. Rev.* **2014**, *33*, 79–97. [[CrossRef](#)] [[PubMed](#)]
32. Baraibar, M.A.; Friguet, B. Oxidative proteome modifications target specific cellular pathways during oxidative stress, cellular senescence and aging. *Exp. Gerontol.* **2013**, *48*, 620–625. [[CrossRef](#)] [[PubMed](#)]
33. Scheiber, I.F.; Brůha, R.; Dušek, P. Pathogenesis of Wilson disease. *Handb. Clin. Neurol.* **2017**, *142*, 43–55. [[PubMed](#)]
34. Scheiber, I.F.; Mercer, J.F.; Dringen, R. Metabolism and functions of copper in brain. *Prog. Neurobiol.* **2014**, *116*, 33–57. [[CrossRef](#)] [[PubMed](#)]
35. Boukhenouna, S.; Wilson, M.A.; Bahmed, K.; Kosmider, B. Reactive Oxygen Species in Chronic Obstructive Pulmonary Disease. *Oxid. Med. Cell Longev.* **2018**, *2018*, 5730395. [[CrossRef](#)] [[PubMed](#)]
36. Fukai, T.; Ushio-Fukai, M. Superoxide dismutases: Role in redox signaling, vascular function, and diseases. *Antioxid. Redox Signal.* **2011**, *15*, 1583–1606. [[CrossRef](#)] [[PubMed](#)]
37. Levin, L.A. Ceruloplasmin detection by SDS-PAGE, immunoblotting, and in situ oxidase activity. *Methods Mol. Biol.* **2002**, *186*, 265–271.
38. Wang, P.W.; Chang, W.N.; Lu, C.H.; Chao, D.; Schrag, C.; Pan, T.L. New insights into the pathological mechanisms of cerebrotendinous xanthomatosis in the Taiwanese using genomic and proteomic tools. *Proteomics* **2006**, *6*, 1029–1037. [[CrossRef](#)]
39. Pan, T.L.; Wang, P.W.; Huang, C.C.; Yeh, C.T.; Hu, T.H.; Yu, J.S. Network analysis and proteomic identification of vimentin as a key regulator associated with invasion and metastasis in human hepatocellular carcinoma cells. *J. Proteomics* **2012**, *75*, 4676–4692. [[CrossRef](#)]
40. Wang, P.W.; Wu, T.H.; Pan, T.L.; Chen, M.H.; Goto, S.; Chen, C.L. Integrated Proteome and Cytokine Profiles Reveal Ceruloplasmin Eliciting Liver Allograft Tolerance via Antioxidant Cascades. *Front. Immunol.* **2018**, *9*, 2216. [[CrossRef](#)]
41. Pan, T.L.; Goto, S.; Lin, Y.C.; Lord, R.; Chiang, K.C.; Lai, C.Y.; Chen, Y.S.; Eng, H.L.; Cheng, Y.F.; Tatsuma, T.; et al. The fas and fas ligand pathways in liver allograft tolerance. *Clin. Exp. Immunol.* **1999**, *118*, 180–187. [[CrossRef](#)]
42. Pan, T.L.; Wang, P.W.; Leu, Y.L.; Wu, T.H.; Wu, T.S. Inhibitory effects of *Scutellaria baicalensis* extract on hepatic stellate cells through inducing G2/M cell cycle arrest and activating ERK-dependent apoptosis via Bax and caspase pathway. *J. Ethnopharmacol.* **2012**, *139*, 829–837. [[CrossRef](#)]



© 2019 by the authors. Licensee MDPI, Basel, Switzerland. This article is an open access article distributed under the terms and conditions of the Creative Commons Attribution (CC BY) license (<http://creativecommons.org/licenses/by/4.0/>).

REVIEW

Open Access



# Antivirals and vaccines for Enterovirus A71

Jing-Yi Lin<sup>1†</sup>, Yu-An Kung<sup>2†</sup> and Shin-Ru Shih<sup>2,3,4,5\*</sup>

## Abstract

Enterovirus A71 (EV-A71) is an important emerging virus posing a threat to children under five years old. EV-A71 infection in infants or young children can cause hand-foot-and-mouth disease, herpangina, or severe neurological complications. However, there are still no effective antivirals for treatment of these infections. In this review, we summarize the antiviral compounds developed to date based on various targets of the EV-A71 life cycle. Moreover, development of a vaccine would be the most effective approach to prevent EV-A71 infection. Therefore, we also summarize the development and clinical progress of various candidate EV-A71 vaccines, including inactivated whole virus, recombinant VP1 protein, synthetic peptides, viral-like particles, and live attenuated vaccines.

**Keywords:** Enterovirus A71, Antivirals, Vaccines

## Background

Enterovirus A71 (EV-A71), a positive-strand RNA virus of the family *Picornaviridae*, represents a persistent global health problem and has caused large outbreaks in the Asia-Pacific region in recent years [1]. Infection by EV-A71 can result in hand-foot-and-mouth disease (HFMD) and herpangina. Children under five years old are particularly susceptible to the most severe forms of EV-A71-associated neurological complications, including aseptic meningitis, brainstem and/or cerebellar encephalitis, myocarditis, acute flaccid paralysis, and rapid fatal pulmonary edema and hemorrhage [2]. Owing to the lack of effective drugs for inhibiting EV-A71 infection, supportive therapy remains the primary means of managing severe cases. Nevertheless, there has been substantial progress in identifying candidate targets for anti-viral drugs and vaccines.

The enterovirus genome encodes four structural capsid proteins (VP1, VP2, VP3, and VP4) that facilitate the cellular entry and delivery of the viral genome into the cytosol of the host cell, and seven non-structural proteins (2A<sup>pro</sup>, 2B, 2C, 3A, 3B, 3C<sup>pro</sup>, and 3D<sup>pol</sup>) that mediate viral RNA replication [3]. Antiviral therapy and

vaccines can have a variety of mechanisms of action and each step of the virus replication cycle can be targeted. Here, we summarize these recent advances and some of the key compounds showing potential for new therapeutic strategies in the development of vaccine and antiviral compounds that target the life cycle of EV-A71, and discuss the prospects and challenges in this field.

## Inhibitors of the EV-A71 life cycle

### Capsid inhibitors

The first step in successful viral infection is receptor binding, and the capsid protein VP1 is involved in the recognition of EV-A71 receptors on the surface of host cells. Numerous viral receptors that are responsible for the entry of EV-A71 into host cells have been characterized, including human scavenger receptor class B member 2 (hSCARB2) [4], human P-selectin glycoprotein ligand 1 (PSGL-1) [5], annexin A2 (Anx2) [6], heparan sulfate [7], sialylated glycan [8], and dendritic cell-specific intercellular adhesion molecule-3 grabbing nonintegrin (DC-SIGN) [9]. Various approaches have been proposed for the discovery of antivirals targeting EV-A71 host receptor binding.

Antibodies against SCARB2, PSGL-1, and DC-SIGN effectively inhibited EV-A71 infection in a dose-dependent manner [4, 5, 10, 11]. EV-A71 VP1 inhibitors were the first candidates proposed for developing antivirals against viral infection. To date, pleconaril and vapendavir have been identified to bind to the viral capsid and thus inhibit EV-A71 infection [12]. Moreover, the capsid binder pyridyl imidazolidinone showed

\* Correspondence: [srshih@mail.cgu.edu.tw](mailto:srshih@mail.cgu.edu.tw)

<sup>†</sup>Jing-Yi Lin and Yu-An Kung contributed equally, thus sharing first authorship.

<sup>2</sup>Research Center for Emerging Viral Infections, College of Medicine, Chang Gung University, Taoyuan, Taiwan

<sup>3</sup>Department of Medical Biotechnology and Laboratory Science, College of Medicine, Chang Gung University, Taoyuan, Taiwan

Full list of author information is available at the end of the article



notable potency against EV-A71 infection in several consecutive studies [13–15]. Pyridyl imidazolidinone fits into the viral hydrophobic pocket of VP1 to inhibit viral infection [16, 17]. In addition, an imidazolidinone derivative (PR66) was found to inhibit EV-A71 infection by impeding the uncoating process via its interaction with the capsid protein VP1. PR66 could also protect against EV-A71-induced neurological symptoms in vivo by suppressing EV-A71 replication [18].

One compound (14) of aminopyridyl 1,2,5-thiadiazolidine 1,1-dioxides, which was capsid inhibitor, showed anti-EV-A71 infection effects ( $EC_{50} = 4$  nM) and exhibited good in vivo efficiency in an EV-A71-infected mouse model [19]. A sulfonated food azo dye, Brilliant Black BN (E151), was reported to inhibit EV-A71 infection by competing with EV71 attachment factors for viral binding, thereby blocking viral attachment/entry to host cells in vitro; moreover, in vivo studies demonstrated that daily administration of E151 at 200 mg/kg given in the initial four days of challenge protected AG129 mice challenged with a 10 of 50% lethal dose ( $LD_{50}$ ) of EV-A71 [20].

### 2A<sup>pro</sup> inhibitors

2A<sup>pro</sup> is enterovirus-encoded protease and is important for viral polyprotein processing [21, 22]. 2A<sup>pro</sup> could also cleave the host factor eIF4G1 to inhibit the cap-dependent translation of cellular mRNA. Falah and coworkers showed that a six-amino acid peptide (LVLQTM) exhibited antiviral potencies against EV-A71 in HeLa cells. This peptide bound to the 2A<sup>pro</sup> active site and inhibited eIF4G1 cleavage by 2A<sup>pro</sup> [23].

### 2B inhibitor

Viral protein 2B and its precursor 2BC have been suggested to be responsible for membranous alteration and inhibition of cellular protein secretion in infected cells [24, 25]. EV-A71 2B protein also induced cell apoptosis by modulating Bax protein activation [26]. Xie and colleagues reported that 4,4'-diisothiocyano-2,2'-stilbenedisulfonic acid (DIDS), which is a chloride-dependent current inhibitor, could prevent EV-A71 2B activity and lead to the inhibition of virus production in RD cells [27].

### 2C inhibitor

The 2C protein plays a role in viral replication complex formation and is involved in processing nucleoside triphosphatase activity and in the synthesis of RNA-negative strands [28, 29]. Two adenosine analogs, metrifudil and N6-benzyladenosine, have been demonstrated to interact with 2C protein to inhibit EV-A71 infection [30].

### 3A inhibitor

The 3A protein also plays a role in viral replication complex formation and inhibits cellular protein secretion. An enviroxime mimetic compound, AN-12-H5, was found to inhibit EV-A71 infection. Assays with resistant mutants have suggested that AN-12-H5 blocked replication by targeting 3A and also inhibited an early stage of infection by targeting VP1 and VP3 [31]. Another compound, GW5074, 3-(3,5-dibromo-4-hydroxybenzylidene-5-iodo-1,3-dihydro-indol-2-one), which is a Raf-1 inhibitor, has been demonstrated to target 3A to inhibit EV-A71 infection [30, 32].

### 3C<sup>pro</sup> inhibitor

The 3C protein acts as a protease to cleave viral polypeptides toward their conversion to mature viral proteins during viral infection, and is thus another useful target for antiviral therapy. The compound rupintrivir (also known as AG7088) inhibited EV-A71 3C protein by mimicking the substrate of the 3C protein in vitro and protected suckling mice from EV-A71-caused limb paralysis in vivo [33, 34]. On the other hand, a series of rupintrivir analogues have also been synthesized and more inhibited EV-A71 3C protease activity and viral growth than rupintrivir [35]. Another 3C protease inhibitor (SG85) also inhibited the replication of 21 EV-A71 strains [12].

Cyanohydrin (R)-1 is another potent inhibitor of EV-A71 3C<sup>pro</sup> but was unstable and showed potential toxicity. Modifying the labile cyanohydrin moiety led to the discovery of the 4-iminoxazolidin-2-one-based inhibitors 4e and 4g with potent inhibitory activity and significantly improved stability [36]. One small-molecule inhibitor, DC07090, inhibited EV-A71 replication with an  $EC_{50}$  value of  $22.09 \pm 1.07$   $\mu$ M by targeting 3C protease [37]. Luteoloside is a member of the flavonoids family that exhibits several bioactivities, including antimicrobial and anti-cancer activities, and was also shown to act as a 3C protease inhibitor of EV-A71 in vitro [38].

### 3D<sup>pol</sup> inhibitor

3D<sup>pol</sup> of EV-A71 is an RNA-dependent RNA polymerase that plays a role in viral RNA synthesis. DTriP-22 is a non-nucleoside analogue that was shown to inhibit EV-A71 infection by reducing the accumulation of viral RNA [39]. Aurintricarboxylic acid, a compound of a group of polyanionic compounds, could also prevent EV-A71 infection through interference with 3D<sup>pol</sup> in vitro [40]. As another antiviral strategy, monoclonal antibodies against EV-A71 3D<sup>pol</sup> were generated to inhibit polymerase activity and viral replication [41].

Apolipoprotein B messenger RNA-editing enzyme catalytic polypeptide-like 3G (APOBEC3G or A3G) can interact with viral 3D<sup>pol</sup> and viral RNA and can be

packaged into progeny virions to reduce the infectivity. APOBEC3G is also a mediator of the antiviral activity of IMB-Z, an *N*-phenylbenzamide derivative [42].

#### **Viral release inhibitor**

Retro-2<sup>cycl</sup> and Retro-2.1 are inhibitors of several pathogens specifically targeting intracellular vesicle transport, and also participate in EV-A71 life cycle processes, including progeny virus release in vitro. Administration of Retro-2<sup>cycl</sup> at 10 mg/kg significantly protected 90% of newborn mice from lethal EV-A71 challenge [43].

#### **Internal ribosome entry site (IRES) inhibitor**

The 5' untranslated region (UTR) of the EV-A71 genome is about 745 nucleotides long and highly structured, containing a cloverleaf-like structure that is critical for viral RNA synthesis and an IRES that is important for viral translation. Idarubicin (IDR) is an anthracycline compound and a USA Food and Drug Administration-approved anticancer drug. IDR inhibits EV-A71 through impaired binding between the EV-A71 IRES RNA and hnRNP A1, a known host IRES *trans*-acting factor [44].

#### **Other strategies targeting EV-A71**

##### **Ribavirin**

Ribavirin is a nucleotide analogue that can serve as a base analogue of either ATP or GTP, and was reported to reduce the EV-A71 titer in vitro. Ribavirin also significantly reduced the mortality, morbidity, and subsequent paralysis sequelae in EV-A71-infected mice [45, 46].

##### **RNA interference**

RNA interference, a native and specific post-transcriptional gene silencing mechanism, has also been exploited as another antiviral tool against EV-A71 infection in vitro and in vivo. Short hairpin RNA (shRNA) expression plasmids or small interfering RNAs (siRNAs) that specifically targeted viral genome to inhibit viral protein expression and viral infection [47–52].

##### **MicroRNA (miRNA)**

MiRNAs are approximately 19–24-nucleotide-long non-coding RNAs that post-transcriptionally repress gene expression by targeting mRNAs, and play a pivotal role in the complicated interaction networks between viruses and their hosts. MiRNAs regulate viral replication through multiple mechanisms. For example, miR-9-5p was shown to exert an anti-EV-A71 effect in cells and in a mouse model via mediating the nuclear factor-kappa B (NF-κB) activity of the RIG-I signaling pathway [53]. In addition, miR-2911 inhibited EV-A71 replication via targeting the VP1 gene [54]. MiR-23b could also inhibit EV-A71 replication through downregulation of EV-A71 VP1 protein [55]. Overexpression of miR-16-5p enhanced

EV-A71-induced apoptosis and inhibited viral replication [56]. MiR-134 inhibited both EV-A71 and poliovirus infection [57], and miR-27a suppressed EV-A71 replication by directly targeting the epidermal growth factor receptor gene [58]. The human miRNA hsa-miR-296-5p suppressed EV-A71 replication by targeting the viral genome located in the regions of nt 2115 to 2135 and nt 2896 to 2920 (strain BrCr) [59]. These studies provide novel mechanisms for the miRNA-mediated regulation of EV-A71 in host cells, suggesting a novel approach in combating infection and in the development of antiviral strategies.

#### **Heparan sulfate (HS) mimetics**

HS is present in the extracellular matrix, on cell surfaces, and in the intracellular granule secretions of all types of animal tissues. HS mimetics are a group of soluble synthetic or semi-synthetic compounds that are structurally related to cellular HS, and can stimulate the functions of cell-surface HS. HS is also a receptor of EV-A71. HS mimetics exhibited anti-EV-A71 activity at less than 250 mg/ml in Vero cells [60].

#### **Signal pathway targets**

GS-9620, a potent and selective agonist of Toll-like receptor 7, could inhibit EV-A71 replication mainly through the NF-κB and PI3K-AKT signaling pathways [61]. Berberine inhibited EV-A71 replication by down-regulating autophagy and the MEK/ERK signaling pathway [62]. Isochlorogenic acid C showed antioxidant activity and prevented EV-A71 infection by modulating the redox homeostasis of glutathione [63].

#### **Development of an EV-A71 vaccine**

##### **Inactivated whole EV-A71 vaccine**

Vaccination is considered to be one of the most effective ways to protect against virus infection. Although there are many different approaches available for developing EV-A71 vaccines, including inactivating the whole virus, a live attenuated virus, virus-like particles (VLPs), recombinant subunits, and synthetic peptides, currently, only an inactivated whole virus vaccine for EV-A71 is the only candidate that has proceeded to a completed human clinical trial. To date, inactivated whole EV-A71 vaccines have been established in Taiwan, China, and Singapore. Three vaccine organizations, including Beijing Vigoo Biological Co., Ltd. (Vigoo), Sinovac Biotech Co., Ltd. (Sinovac), and the Chinese Academy of Medical Sciences (CAMS) in China completed EV-A71 vaccine phase III clinical trials in 2013 and received a license for their administration that was approved by China's Food and Drug Administration in 2015 [64, 65].

These three vaccine organizations in China used different technologies to develop an EV-A71 vaccine. CAMS used KMB-17 human diploid cells as a cell bank



that were cultured using a cell factory, whereas Vigoo and Sinovac used Vero cells to amplify EV-A71 with a microcarrier bioreactor and a cell factory, respectively. All organizations selected the EV-A71 C4 subgenotype as a virus seed for vaccine development, which is the most prevalent genotype circulating in China, although they each used a different virus strain: CAMS chose the EV-A71 FY-23 strain, Vigoo chose the FY7VP5 strain, and Sinovac chose the H07 strain. The three organizations began their phase I clinical trials in 2010 to 2011, and completed their phase III clinical trials in 2013. In the Vigoo phase III clinical trial, a total of 10,245 participants aged 6–35 months randomly received a 320 U (EV-A71 antigen unit) alum-adjuvant vaccine (5120 participants) or a placebo control (5125 participants) at days 0 and 28, and were then followed-up for 1 [66] and 2 years [67] ([ClinicalTrials.gov](#), number NCT01508247). The efficacy of the Vigoo EV-A71 vaccine against EV-A71-associated HFMD was 90%, and that against other EV-A71-associated diseases was 80.4% during the 1-year surveillance period. In addition, the vaccine efficacy against EV-A71-associated HFMD was 100% during the second year, and no serious adverse events were reported. Thus, Vigoo claimed that their EV-A71 vaccine is safe and had good efficacy for protecting against EV-A71-associated HFMD in children. Sinovac also conducted a follow-up study for 1 and 2 years [68, 69] in which a total of 10,077 participants aged 6–35 months were assigned to two groups receiving 400 U of the alum-adjuvant Sinovac EV-A71 vaccine or a placebo control at days 0 and 28 ([ClinicalTrials.gov](#), number NCT01507857). During the 1-year surveillance period, the vaccine efficacy was 94.8% against EV-A71-associated HFMD or herpangina, and was 100% against EV-A71-associated HFMD with neurological complications. Given this success, they extended their study to follow-up the vaccine efficacy for another 12 months [69], and reported a vaccine efficacy of 95.1% for the second year; the overall efficacy of the Sinovac EV-A71 vaccine against EV-A71-associated HFMD was 94.7% [68]. Recently, a five-year follow-up study also indicated that the Sinovac EV-A71 vaccine showed long-term immunity persistence [70]. In the phase III clinical trial of the CAMS EV-A71 vaccine, 12,000 children of 6–71 months of age were assigned (at a 1:1 ratio) to receive 100 U of the alum-adjuvant vaccine or placebo control ([ClinicalTrials.gov](#) number, NCT01569581). The vaccine efficacy against EV-A71-associated HFMD was 97.4% [71]. However, both the Sinovac and CAMS EV-A71 vaccines showed no efficacy against HFMD caused by coxsackievirus A16 (CV-A16), demonstrating their specificity [68, 71].

In contrast to these three organizations in China, the National Health Research Institutes (NHRI) in Taiwan used the EV-A71 clinical isolate E59 strain (B4 subgenotype) as a

virus seed, which was grown in Vero cells cultured with roller-bottle technology. This strain was chosen for producing the EV-A71 inactivated vaccine because of its confirmed genetic stability over several passages and its ability to grow well in Vero cells [72]. The phase I clinical trial of the NHRI was completed in 2012 ([ClinicalTrials.gov](#) number, NCT01268787). Sixty healthy adults aged 20–60 years randomly received two intramuscular doses of either 5 µg of EV71 antigen with 150 µg of aluminum adjuvant or 10 µg of EV71 antigen with 300 µg of aluminum adjuvant, 21 days apart. The immunogenicity results indicated that the EV-A71 vaccine produced from the NHRI was safe and immunogenic in healthy adults [73]. Moreover, over 85% of the participants developed a strong cross-neutralizing antibody response against subgenotypes B1, B5, and C4a; however, only 20% of the participants developed a weak cross-neutralizing antibody response against subgenotype C4b and CV-A16 [74]. Two organizations of Taiwan, Enimmune Corp. and Medigen Vaccinology Corp., continue to evaluate the safety and immunogenicity of the E59 strain EV-A71 vaccine in phase II clinical trials ([ClinicalTrials.gov](#) number, NCT02777411, NCT03268083 and NCT02200237). In the clinical trial of Medigen Vaccinology Corp., a total of 365 infants or children aged 2 months to 11 years received different doses (low, mid, or high) of alum-adjuvant EV-A71 vaccine or the placebo control in a double-blind and randomized design ([ClinicalTrials.gov](#) number, NCT02200237). No vaccine-related serious adverse events were reported in this trial. In addition, the EV-A71 vaccine could elicit an immune response against not only subgenotype B4 but also B5, C4a, C4b, and C5. The EV-A71 vaccine also showed persistence for 2 years [75]. Based on these findings, Medigen Vaccinology Corp. is initiating a phase III clinical trial ([ClinicalTrials.gov](#) number, NCT03865238) in 2019, which is expected to be completed in 2022.

In Singapore, Inviragen Inc. (Takeda Pharmaceuticals International, Inc.) completed a phase I clinical trial of an EV-A71 vaccine in April 2012 ([ClinicalTrials.gov](#) number, NCT01376479). In contrast to the organizations of China and Taiwan, Inviragen used the B3 subgenotype as the virus seed for EV-A71 vaccine production, which was named INV21. A total of 36 adults aged 21–45 years received two doses (low or high) of INV21 or placebo control 28 days apart. Inviragen claimed that INV21 induced a high immune response against HFMD caused by EV-A71. However, there has been no further clinical trial conducted in Singapore recently.

#### Recombinant VP1 vaccine

VP1 is not only a structural protein of EV-A71 but also exhibits strong antigenicity. Accordingly, several research groups have adopted various strategies to express EV-A71 VP1. Wu et al. [76] produced recombinant VP1



proteins of EV-A71 expressed by *Escherichia coli* (*E. coli*). The purified VP1 proteins were then injected into adult female mice through an intraperitoneal route. Although the VP1 subunit vaccine could protect suckling mice against a lower challenge dose of EV-A71 (230 LD<sub>50</sub> virus/mouse), the inactivated EV-A71 vaccine still elicited a greater immune response than the VP1 subunit vaccine and protected suckling mice against a lethal dose (2300 LD<sub>50</sub> virus/mouse) of EV-A71. Zhou et al. [77] also expressed recombinant VP1 protein in *E. coli*, and then vaccinated rabbits with the purified VP1 protein or heat-inactivated EV-A71 virus, which elicited comparable humoral and cellular immune responses. Moreover, maternal antibodies protect newborn mice against EV-A71 challenge. EV-A71-specific antibodies of immunized mice were elicited by purified recombinant baculovirus expressing VP1. In addition, the antisera exhibited cross-neutralization activities against different subgenotypes of EV-A71 [78]. Wang et al. [79] generated an HIV-gag-based VLP as a carrier to express EV-A71 VP1 protein, which provided passive protection of newborn mice against EV-A71 infection.

VP1 protein has also been developed as an antigen for oral vaccine development. Adult female BALB/c mice were orally immunized with transgenic tomato fruit expressing VP1 protein [80], attenuated *Salmonella enterica* serovar Typhimurium expressing VP1 [81], VP1-expressing *Bifidobacterium longum* [82], surface-displayed VP1 *Saccharomyces cerevisiae* [83], or recombinant *Lactococcus lactis* expressing secretory VP1 [84]. All of these VP1-expressing vaccines elicited immune responses by oral immunization and could protect newborn mice against EV-A71 infection. Chen et al. [85] generated a transgenic mouse that can express VP1 and secrete into their milk, which could protect suckling mice against EV-A71 challenge. However, the recombinant VP1 proteins generally exhibited lower protective efficacy in mice compared to the inactivated EV-A71 virus.

### Synthetic peptide vaccines

Synthetic peptides have also been tested as an alternative strategy to develop EV-A71 vaccines, which are considered to be safe and efficacious for multivalent vaccines development. The majority of research related to antigen peptides has focused on mapping EV-A71 structural proteins (VP1, VP2, VP3, and VP4). Initially, Foo et al. [86] found that two peptides, SP55 (amino acids 163–177 of VP1) and SP70 (amino acids 208–222 of VP1), could elicit neutralizing antibodies against EV-A71. SP70 elicited a higher titer of neutralizing antibody (1:32) than the neutralizing antibody of SP55 (1:8); however, antisera from heat-inactivated EV-A71-immunized mice elicited the highest neutralization titer of 1:128 [86]. Moreover, Foo et al. [87] found that anti-SP70 antisera passively

protected suckling mice against both homologous and heterologous EV-A71 strains. In another strategy, six synthetic peptides (P<sub>70–159</sub> in VP2, P<sub>140–249</sub> in VP2, P<sub>324–443</sub> in VP2, and P<sub>746–876</sub> in VP1) were combined, which induced the antisera and passively protected newborn mice against EV-A71 infection [88]. The synthetic peptide VP2–28 (amino acids 136–150 of VP2) showed cross-neutralizing activity against EV-A71 and can bind to the anti-EV-A71 monoclonal antibody MAB979 [89]. Xu et al. [90] generated a fusion protein with hepatitis B virus core protein (HBc) and VP2 epitope corresponding to amino acids 141–155 of VP2, named HBc-VP2 (aa141–155), which induced cross-neutralizing EV-A71 antibodies, and the anti-sera from HBc-VP2 (aa141–155) immunized mice protected newborn mice from EV-A71 infection. Huo et al. [91] used the same strategy to display EV-A71 epitopes (SP70, amino acids 208–222 of VP1) and CV-A16 (PEP91, amino acids 271–285 of VP1) using HBc as a carrier protein. The chimeric VLP expressing SP70 and PEP91 epitopes induced an immune response and protected suckling mice against both EV-A71 and CV-A16 infection. Aw-Yong et al. [92] sought to comprehensively map the potential synthetic peptides within the structural and non-structural proteins of EV-A71. A total of 63 synthetic peptides were synthesized and used for characterization of EV-A71 B-cell linear epitopes. Among these, synthetic peptide PEP27 (VP1 residues 142–156) was recognized as an EV-A71 IgM-specific immunodominant epitope; moreover, synthetic peptide PEP23 (VP1 residues 41–55) was identified as an EV-A71 IgG cross-reactive immunodominant epitope. Jiang et al. [93] utilized the norovirus P protein as a carrier for delivery of the EV-A71 epitope, which is the 71–6 epitope spanning amino acids 176–190 of VP3. Sera from mice immunized with chimeric P protein displaying the 71–6 epitope protected suckling mice against a lethal dose of EV-A71 challenge.

### VLP-based vaccines

VLPs have been applied in the production of other viral vaccines such as hepatitis B virus and human papillomavirus, and could also be a suitable choice for EV-A71 vaccine development. The morphological characteristic and antigenicity of VLPs are similar to those of the naïve virus. Moreover, VLPs are associated with greater safety because they lack the viral genome and thus cannot replicate in the host. However, VLPs can still effectively elicit innate and adaptive immunity.

The baculovirus expression system has been widely used for VLP production. A recombinant baculovirus co-expressing the P1 region and the viral protease 3CD of EV-A71 with different promoters was infected to insect cells for VLPs production (subgenotype C2, *neu* strain) [94, 95]. The viral protease 3CD can cleave the

P1 region of structural proteins [VP0 (VP4 and VP2), VP3, and VP1], which is important to constitute the virus capsid. However, this VLP production method suffers from low yields and excessive VLP degradation. Several factors influencing the expression yields of VLP, including the control of various promoters, insect cell types, and incubation time. After researchers serially modified the system for the construction of recombinant baculoviruses, the yield of EV-A71 VLPs improved [96]. EV-A71 VLPs elicited humoral and cellular immune responses in immunized mice, and vaccination of female mice with VLPs, protected the neonatal mice from a lethal dose of EV-A71 challenge [97]. In another study, Macaque monkeys were vaccinated with EV-A71 VLPs produced from baculovirus, which elicited immune responses [98]. In addition to the baculovirus expression system, EV-A71 VLP also can be generated in yeast such as *Saccharomyces cerevisiae* or *Pichia pastoris*, which showed protective efficacy against EV-A71 challenge in mice. In addition, maternal immunization with VLPs could also protect neonate mice against lethal EV-A71 challenge [96, 99].

Chimeric VLPs, including adenovirus or varicella-zoster virus-based VLPs, have also been applied to co-express the P1 and 3CD regions of EV-A71, which could both induce an EV-A71-specific immune response and neutralization antibodies in vaccinated mice, and exhibited protective efficacy against EV-A71 infection [100, 101].

### Live-attenuated vaccines

According to the experience in developing the poliovirus Sabin vaccine, and the numerous advantages of live-attenuated vaccines, including elicitation of long-lasting immunity and cost-effective production, researchers have continued to investigate potential candidates for an EV-A71 live-attenuated vaccine. EV-A71(S1-3') was derived from the prototype EV-A71(BrCr) strain. Five cynomolgus monkeys were inoculated with EV-A71 (S1-3') via an intravenous route, followed by challenge with a lethal dose of EV-A71(BrCr-TR), demonstrating induction of an efficient immune response, and the sera showed neutralization activity against EV-A71(BrCr-TR) (subgenotype A) and other subgenotypes, including B1, B4, C2, and C4. However, EV71(S1-3') caused tremor in the inoculated monkeys, and the virus was isolated from the lumbar spinal cord of inoculated monkeys on days 4 or 10 post-inoculation [102]. Therefore, the safety issue of live-attenuated vaccine remains a concern.

Because the detailed molecular pathogenic mechanism of EV-A71 infection remains unexplored, the virulence determinants of EV-A71 are still being investigated. The amino acid residue 145 in VP1 is considered to be an important factor for EV-A71 virulence and receptor attachment [103, 104]. Mutation of a single amino acid,

glutamine (Q) to glutamic acid (E), at residue 145 of VP1 in the subgenotype C4 of EV-A71 was used to generate a mouse-virulent EV-A71 strain [105]. Viruses harboring the VP1-145E mutation could also induce neurological symptoms in cynomolgus monkeys; therefore, VP1-145E viruses are more virulent than VP1-145G viruses in cynomolgus monkeys [103]. The nucleotide 158 in the stem loop II region of the EV-A71 5' UTR play a pivotal role in EV-A71 virulence. The nucleotide substitution of C158U reduced the translation activity of EV-A71, and attenuated EV-A71 virulence in a mouse model [106].

Moreover, the nucleotide substitutions of G64R, G64T, and S264L in EV-A71 3D polymerase were shown to contribute to EV-A71 replication fidelity. Enhancement of the fidelity of 3D polymerase can improve the stability and safety of live-attenuated vaccines [107]. Another study also indicated that EV-A71 with the RdRp-G64R and RdRp-L123F mutations attenuated the virulence of the virus in an AG129 mouse model [108]. Yee et al. [109] constructed an miRNA-based EV-A71 vaccine strain, pIY, which carried let-7a and miR-124a target genes. They found that the viral yield of the pIY strain was much lower than that of the EV-A71 wild-type B4 strain 41 in SHY-5Y cells. Moreover, the pIY strain could still protect mice against EV-A71 in a mouse-adapted strain challenge.

In recent years, a new combination strategy of codon deoptimization and synthetic virus production has emerged for vaccine development. Tsai et al. [110] found that rgEV-A71-CD-HF, a virus with a deoptimized VP1 codon, and a high-fidelity virus with nucleotide substitutions of G64R and L123F in 3D polymerase showed less virulence in a mouse model.

### Mucosal vaccines

The mucosal immune response, which is effectively induced by the administration of a vaccine onto the mucosal surface, is the first line of defense against pathogen invasion. Several mucosal vaccines have been licensed for use in humans, such as oral vaccines against poliovirus, rotavirus, *Vibrio cholera*, and *Salmonella* Typhi, and an intranasal vaccine against influenza virus. The advantages of mucosal vaccines are that they are good inducers of mucosal and systematic immunity, and the needle-free administration is more acceptable for infants and young children [111, 112]. Although the poliovirus Sabin vaccine is a successful example of a mucosal vaccine, the safety issue of live-attenuated vaccine remains a concern. To date, there have been few studies focused on development of a mucosal vaccine for EV-A71. As summarized above, several studies involved immunizing mice with recombinant VP1 protein by an oral route [80–84]; however, these vaccines are still at the

preclinical stage of research and validation. Recently, Lin et al. [113] found that the titers of EV-A71-specific IgG and IgA, T-cell proliferative response, and interleukin-17 secretion were increased in a group of BALB/c mice immunized with a CpG-adjuvanted inactivated EV-A71 vaccine via an intranasal route. In addition, this vaccine could also protect human scavenger receptor class B, member 2 transgenic (hSCARB2-Tg) mice against lethal EV-A71 challenge. Although a mucosal vaccine seems to be another good choice for EV-A71 vaccine development, there are still some challenges in mucosal vaccine design to overcome, including how to effectively breach the epithelial barrier, and the relatively large amounts of vaccine needed for mucosal immunization.

## Conclusions and prospects

EV-A71 is one of the most pathogenic enteroviruses infecting humans, with many outbreaks occurring worldwide causes a wide range of human diseases. However, there is still no clinically approved antiviral drug available for the prevention and treatment of the EV-A71 infection. Although the development of antiviral therapy and vaccine represents a major challenge, the progress made so far in understanding the viral replication mechanism has provided novel targets for antiviral therapy and the characterization of compounds with antiviral activity. The development of pan-enteroviruses vaccine and anti-viral drugs is an important and achievable goal in the future.

## Abbreviations

5' UTR: 5' untranslated region; Anx2: Annexin A2; APOBEC3G or A3G: Apolipoprotein B messenger RNA-editing enzyme catalytic polypeptide-like 3G; CAMS: Chinese Academy of Medical Sciences; CV-A16: Coxsackievirus A16; DC-SIGN: Dendritic cell-specific intercellular adhesion molecule-3 grabbing nonintegrin; DIDS: 4,4'-diisothiocyano-2,2'-stilbenedisulfonic acid; *E. coli*: *Escherichia coli*; EV-A71: Enterovirus A71; HFMD: Hand-foot-and-mouth disease; HS: Heparan sulfate; IDR: Idarubicin; IRES: Internal ribosome entry site; NF-κB: Nuclear factor-kappa B; NHRI: National Health Research Institutes; PSGL-1: P-selectin glycoprotein ligand 1; SCARB2: Scavenger receptor class B member 2; Sinovac: Sinovac Biotech Co., Ltd; Vigoo: Beijing Vigoo Biological Co., Ltd; VLP: Virus-like particle

## Acknowledgements

Not applicable.

## Authors' contributions

J.-Y.L. and Y.-A.K. conducted literature research, and contributed in writing the manuscript. S.-R.S. designed, organized and edited the manuscript for submission. All authors read and approved the final manuscript.

## Funding

This work was financially supported by the Research Center for Emerging Viral Infections from The Featured Areas Research Center Program within the framework of the Higher Education Sprout Project by the Ministry of Education (MOE) in Taiwan and the Ministry of Science and Technology (MOST), Taiwan (MOST 108-3017-F-182-001).

## Availability of data and materials

Not applicable.

## Ethics approval and consent to participate

Not applicable.

## Consent for publication

Not applicable.

## Competing interests

The authors declare that they have no competing interests.

## Author details

<sup>1</sup>Department of Clinical Laboratory Sciences and Medical Biotechnology, College of Medicine, National Taiwan University, Taipei City, Taiwan. <sup>2</sup>Research Center for Emerging Viral Infections, College of Medicine, Chang Gung University, Taoyuan, Taiwan. <sup>3</sup>Department of Medical Biotechnology and Laboratory Science, College of Medicine, Chang Gung University, Taoyuan, Taiwan. <sup>4</sup>Department of Laboratory Medicine, Linkou Chang Gung Memorial Hospital, Taoyuan, Taiwan. <sup>5</sup>Research Center for Chinese Herbal Medicine, Research Center for Food and Cosmetic Safety, and Graduate Institute of Health Industry Technology, College of Human Ecology, Chang Gung University of Science and Technology, Taoyuan, Taiwan.

Received: 27 June 2019 Accepted: 23 August 2019

Published online: 03 September 2019

## References

- Huang PN, Shih SR. Update on enterovirus 71 infection. *Curr Opin Virol*. 2014;5:98–104.
- McMinn PC. An overview of the evolution of enterovirus 71 and its clinical and public health significance. *FEMS Microbiol Rev*. 2002;26(1):91–107.
- Bedard KM, Semler BL. Regulation of picornavirus gene expression. *Microbes Infect*. 2004;6(7):702–13.
- Yamayoshi S, Yamashita Y, Li J, Hanagata N, Minowa T, Takemura T, Koike S. Scavenger receptor B2 is a cellular receptor for enterovirus 71. *Nat Med*. 2009;15(7):798–801.
- Nishimura Y, Shimojima M, Tano Y, Miyamura T, Wakita T, Shimizu H. Human P-selectin glycoprotein ligand-1 is a functional receptor for enterovirus 71. *Nat Med*. 2009;15(7):794–7.
- Yang SL, Chou YT, Wu CN, Ho MS. Annexin II binds to capsid protein VP1 of enterovirus 71 and enhances viral infectivity. *J Virol*. 2011;85(22):11809–20.
- Tan CW, Poh CL, Sam IC, Chan YF. Enterovirus 71 uses cell surface heparan sulfate glycosaminoglycan as an attachment receptor. *J Virol*. 2013;87(1):611–20.
- Yang B, Chuang H, Yang KD. Sialylated glycans as receptor and inhibitor of enterovirus 71 infection to DLD-1 intestinal cells. *Virol J*. 2009;6:141.
- Ren XX, Ma L, Liu QW, Li C, Huang Z, Wu L, Xiong SD, Wang JH, Wang HB. The molecule of DC-SIGN captures enterovirus 71 and confers dendritic cell-mediated viral trans-infection. *Virol J*. 2014;11:47.
- He QQ, Ren S, Xia ZC, Cheng ZK, Peng NF, Zhu Y. Fibronectin Facilitates Enterovirus 71 Infection by Mediating Viral Entry. *J Virol*. 2018;92(9).
- Lin JY, Chen TC, Weng KF, Chang SC, Chen LL, Shih SR. Viral and host proteins involved in picornavirus life cycle. *J Biomed Sci*. 2009;16:103.
- Tijssma A, Franco D, Tucker S, Hilgenfeld R, Froeyen M, Leyssen P, Neyts J. The capsid binder Vapendavir and the novel protease inhibitor SG85 inhibit enterovirus 71 replication. *Antimicrob Agents Chemother*. 2014;58(11):6990–2.
- Chang CS, Lin YT, Shih SR, Lee CC, Lee YC, Tai CL, Tseng SN, Chern JH. Design, synthesis, and antipicornavirus activity of 1-[5-(4-arylphenoxy)alkyl]-3-pyridin-4-ylimidazolidin-2-one derivatives. *J Med Chem*. 2005;48(10):3522–35.
- Chern JH, Lee CC, Chang CS, Lee YC, Tai CL, Lin YT, Shia KS, Lee CY, Shih SR. Synthesis and antienteroviral activity of a series of novel, oxime ether-containing pyridyl imidazolidinones. *Bioorg Med Chem Lett*. 2004;14(20):5051–6.
- Shia KS, Li WT, Chang CM, Hsu MC, Chern JH, Leong MK, Tseng SN, Lee CC, Lee YC, Chen SJ, Peng KC, Tseng HY, Chang YL, Tai CL, Shih SR. Design, synthesis, and structure-activity relationship of pyridyl imidazolidinones: a novel class of potent and selective human enterovirus 71 inhibitors. *J Med Chem*. 2002;45(8):1644–55.
- Chen TC, Liu SC, Huang PN, Chang HY, Chern JH, Shih SR. Antiviral activity of pyridyl imidazolidinones against enterovirus 71 variants. *J Biomed Sci*. 2008;15(3):291–300.
- Shih SR, Tsai MC, Tseng SN, Won KF, Shia KS, Li WT, Chern JH, Chen GW, Lee CC, Lee YC, Peng KC, Chao YS. Mutation in enterovirus 71 capsid protein VP1 confers resistance to the inhibitory effects of pyridyl imidazolidinone. *Antimicrob Agents Chemother*. 2004;48(9):3523–9.

18. Ho JY, Chern JH, Hsieh CF, Liu ST, Liu CJ, Wang YS, Kuo TW, Hsu SJ, Yeh TK, Shih SR, Hsieh PW, Chiu CH, Horng JT. In vitro and in vivo studies of a potent capsid-binding inhibitor of enterovirus 71. *J Antimicrob Chemother*. 2016;71(7):1922–32.
19. Li P, Yu J, Hao F, He H, Shi X, Hu J, Wang L, Du C, Zhang X, Sun Y, Lin F, Gu Z, Xu D, Chen X, Shen L, Hu G, Li J, Chen S, Xiao W, Wang Z, Guo Q, Chang X, Tian X, Lin T. Discovery of potent EV71 capsid inhibitors for treatment of HFMD. *ACS Med Chem Lett*. 2017;8(8):841–6.
20. Meng T, Jia Q, Wong SM, Chua KB. In vitro and in vivo inhibition of infectivity of human Enterovirus 71 by a sulfonated food azo dye, Brilliant Black BN. *J Virol*. 2019.
21. Krausslich HG, Nicklin MJ, Lee CK, Wimmer E. Polyprotein processing in picornavirus replication. *Biochimie*. 1988;70(1):119–30.
22. Laitinen OH, Svedin E, Kapell S, Nurminen A, Hytonen VP, Flodstrom-Tullberg M. Enteroviral proteases: structure, host interactions and pathogenicity. *Rev Med Virol*. 2016;26(4):251–67.
23. Falah N, Montserret R, Lelogeais V, Schuffenecker I, Lina B, Cortay JC, Violot S. Blocking human enterovirus 71 replication by targeting viral 2A protease. *J Antimicrob Chemother*. 2012;67(12):2865–9.
24. Aldabe R, Barco A, Carrasco L. Membrane permeabilization by poliovirus proteins 2B and 2BC. *J Biol Chem*. 1996;271(38):23134–7.
25. Barco A, Carrasco L. A human virus protein, poliovirus protein 2BC, induces membrane proliferation and blocks the exocytic pathway in the yeast *Saccharomyces cerevisiae*. *EMBO J*. 1995;14(14):3349–64.
26. Cong H, Du N, Yang Y, Song L, Zhang W, Tien P. Enterovirus 71 2B induces cell apoptosis by directly inducing the conformational activation of the Proapoptotic protein Bax. *J Virol*. 2016;90(21):9862–77.
27. Xie S, Wang K, Yu W, Lu W, Xu K, Wang J, Ye B, Schwarz W, Jin Q, Sun B. DIDS blocks a chloride-dependent current that is mediated by the 2B protein of enterovirus 71. *Cell Res*. 2011;21(8):1271–5.
28. Banerjee R, Echeverri A, Dasgupta A. Poliovirus-encoded 2C polypeptide specifically binds to the 3'-terminal sequences of viral negative-strand RNA. *J Virol*. 1997;71(12):9570–8.
29. Rodriguez PL, Carrasco L. Poliovirus protein 2C has ATPase and GTPase activities. *J Biol Chem*. 1993;268(11):8105–10.
30. Arita M, Wakita T, Shimizu H. Characterization of pharmacologically active compounds that inhibit poliovirus and enterovirus 71 infectivity. *J Gen Virol*. 2008;89(Pt 10):2518–30.
31. Arita M, Takebe Y, Wakita T, Shimizu H. A bifunctional anti-enterovirus compound that inhibits replication and the early stage of enterovirus 71 infection. *J Gen Virol*. 2010;91(Pt 11):2734–44.
32. Arita M, Wakita T, Shimizu H. Cellular kinase inhibitors that suppress enterovirus replication have a conserved target in viral protein 3A similar to that of enviroxime. *J Gen Virol*. 2009;90(Pt 8):1869–79.
33. Kuo CJ, Shie JJ, Fang JM, Yen GR, Hsu JT, Liu HG, Tseng SN, Chang SC, Lee CY, Shih SR, Liang PH. Design, synthesis, and evaluation of 3C protease inhibitors as anti-enterovirus 71 agents. *Bioorg Med Chem*. 2008;16(15):7388–98.
34. Zhang X, Song Z, Qin B, Zhang X, Chen L, Hu Y, Yuan Z. Rupintrivir is a promising candidate for treating severe cases of enterovirus-71 infection: evaluation of antiviral efficacy in a murine infection model. *Antivir Res*. 2013;97(3):264–9.
35. Tan YW, Ang MJ, Lau QY, Poulsen A, Ng FM, Then SW, Peng J, Hill J, Hong WJ, Chia CS, Chu JJ. Antiviral activities of peptide-based covalent inhibitors of the Enterovirus 71 3C protease. *Sci Rep*. 2016;6:33663.
36. Ma Y, Shang C, Yang P, Li L, Zhai Y, Yin Z, Wang B, Shang L. 4-Iminoazolidin-2-one as a Bioisostere of the cyanohydrin moiety: inhibitors of Enterovirus 71 3C protease. *J Med Chem*. 2018;61(22):10333–9.
37. Ma GH, Ye Y, Zhang D, Xu X, Si P, Peng JL, Xiao YL, Cao RY, Yin YL, Chen J, Zhao LX, Zhou Y, Zhong W, Liu H, Luo XM, Chen LL, Shen X. Identification and biochemical characterization of DC07090 as a novel potent small molecule inhibitor against human enterovirus 71 3C protease by structure-based virtual screening. *Eur J Med Chem*. 2016;124:981–91.
38. Cao Z, Ding Y, Ke Z, Cao L, Li N, Ding G, Wang Z, Xiao W. Luteoloside acts as 3C protease inhibitor of Enterovirus 71 in vitro. *PLoS One*. 2016;11(2):e0148693.
39. Chen TC, Chang HY, Lin PF, Chern JH, Hsu JT, Chang CY, Shih SR. Novel antiviral agent DTriP-22 targets RNA-dependent RNA polymerase of enterovirus 71. *Antimicrob Agents Chemother*. 2009;53(7):2740–7.
40. Hung HC, Chen TC, Fang MY, Yen KJ, Shih SR, Hsu JT, Tseng CP. Inhibition of enterovirus 71 replication and the viral 3D polymerase by aurintricarboxylic acid. *J Antimicrob Chemother*. 2010;65(4):676–83.
41. Li Y, Yu J, Qi X, Yan H. Monoclonal antibody against EV71 3D(pol) inhibits the polymerase activity of RdRp and virus replication. *BMC Immunol*. 2019;20(1):6.
42. Wang H, Zhong M, Li Y, Li K, Wu S, Guo T, Cen S, Jiang J, Li Z, Li Y. APOBEC3G is a restriction factor of EV71 and mediator of IMB-Z antiviral activity. *Antivir Res*. 2019;165:23–33.
43. Dai W, Wu Y, Bi J, Lu X, Hou A, Zhou Y, Sun B, Kong W, Barbier J, Cintrat JC, Gao F, Gillet D, Su W, And Jiang C. antiviral effects of Retro-2(cycl) and Retro-2.1 against Enterovirus 71 in vitro and in vivo. *Antivir Res*. 2017;144:311–21.
44. Hou HY, Lu WW, Wu KY, Lin CW, Kung SH. Idarubicin is a broad-spectrum enterovirus replication inhibitor that selectively targets the virus internal ribosomal entry site. *J Gen Virol*. 2016;97(5):1122–33.
45. Li ZH, Li CM, Ling P, Shen FH, Chen SH, Liu CC, Yu CK, Chen SH. Ribavirin reduces mortality in enterovirus 71-infected mice by decreasing viral replication. *J Infect Dis*. 2008;197(6):854–7.
46. Zhang G, Zhou F, Gu B, Ding C, Feng D, Xie F, Wang J, Zhang C, Cao Q, Deng Y, Hu W, Yao K. In vitro and in vivo evaluation of ribavirin and pleconaril antiviral activity against enterovirus 71 infection. *Arch Virol*. 2012;157(4):669–79.
47. Deng JX, Nie XJ, Lei YF, Ma CF, Xu DL, Li B, Xu ZK, Zhang GC. The highly conserved 5' untranslated region as an effective target towards the inhibition of Enterovirus 71 replication by unmodified and appropriate 2'-modified siRNAs. *J Biomed Sci*. 2012;19:73.
48. Liu H, Qin Y, Kong Z, Shao Q, Su Z, Wang S, Chen J. siRNA Targeting the 2Apro Genomic Region Prevents Enterovirus 71 Replication In Vitro. *PLoS One*. 2016;11(2):e0149470.
49. Lu WW, Hsu YY, Yang JY, Kung SH. Selective inhibition of enterovirus 71 replication by short hairpin RNAs. *Biochem Biophys Res Commun*. 2004;325(2):494–9.
50. Sim AC, Luhur A, Tan TM, Chow VT, Poh CL. RNA interference against enterovirus 71 infection. *Virology*. 2005;341(1):72–9.
51. Tan EL, Tan TM, Chow VT, Poh CL. Enhanced potency and efficacy of 29-mer shRNAs in inhibition of Enterovirus 71. *Antivir Res*. 2007;74(1):9–15.
52. Tan EL, Tan TM, Tak Kwong Chow V, Poh CL. Inhibition of enterovirus 71 in virus-infected mice by RNA interference. *Mol Ther*. 2007;15(11):1931–8.
53. Li B, Zheng J. MicroR-9-5p suppresses EV71 replication through targeting Nfkapb of the RIG-I-mediated innate immune response. *FEBS Open Bio*. 2018;8(9):1457–70.
54. Li X, Huang Y, Sun M, Ji H, Dou H, Hu J, Yan Y, Wang X, Chen L. Honeysuckle-encoded microRNA2911 inhibits Enterovirus 71 replication via targeting VP1 gene. *Antivir Res*. 2018;152:117–23.
55. Wen BP, Dai HJ, Yang YH, Zhuang Y, Sheng R. MicroRNA-23b inhibits enterovirus 71 replication through downregulation of EV71 VP1 protein. *Intervirology*. 2013;56(3):195–200.
56. Zheng C, Zheng Z, Sun J, Zhang Y, Wei C, Ke X, Liu Y, Deng L, Wang H. MiR-16-5p mediates a positive feedback loop in EV71-induced apoptosis and suppresses virus replication. *Sci Rep*. 2017;7(1):16422.
57. Orr-Burks NL, Shim BS, Wu W, Bakre AA, Karpilow J, Tripp RA. MicroRNA screening identifies miR-134 as a regulator of poliovirus and enterovirus 71 infection. *Sci Data*. 2017;4:170023.
58. Zhang L, Chen X, Shi Y, Zhou B, Du C, Liu Y, Han S, Yin J, Peng B, He X, Liu W. miR-27a suppresses EV71 replication by directly targeting EGFR. *Virus Genes*. 2014;49(3):373–82.
59. Zheng Z, Ke X, Wang M, He S, Li Q, Zheng C, Zhang Z, Liu Y, Wang H. Human microRNA hsa-miR-296-5p suppresses enterovirus 71 replication by targeting the viral genome. *J Virol*. 2013;87(10):5645–56.
60. Pourianfar HR, Poh CL, Fecondo J, Grollo L. In vitro evaluation of the antiviral activity of heparan sulfate mimetic compounds against Enterovirus 71. *Virus Res*. 2012;169(1):22–9.
61. Chen J, Zhang C, Zhou Y, Zhang X, Shen C, Ye X, Jiang W, Huang Z, Cong Y. A 3.0-Angstrom Resolution Cryo-Electron Microscopy Structure and Antigenic Sites of Coxsackievirus A6-Like Particles. *J Virol*. 2018;92(2).
62. Wang H, Li K, Ma L, Wu S, Hu J, Yan H, Jiang J, Li Y. Berberine inhibits enterovirus 71 replication by downregulating the MEK/ERK signaling pathway and autophagy. *Virol J*. 2017;14(1):2.
63. Cao Z, Ding Y, Cao L, Ding G, Wang Z, Xiao W. Isochlorogenic acid C prevents enterovirus 71 infection via modulating redox homeostasis of glutathione. *Sci Rep*. 2017;7(1):16278.
64. Mao Q, Wang Y, Bian L, Xu M, Liang Z. EV-A71 vaccine licensure: a first step for multivalent enterovirus vaccine to control HFMD and other severe diseases. *Emerg Microbes Infect*. 2016;5(7):e75.
65. Mao QY, Wang Y, Bian L, Xu M, Liang Z. EV71 vaccine, a new tool to control outbreaks of hand, foot and mouth disease (HFMD). *Expert Rev Vaccines*. 2016;15(5):599–606.



66. Zhu FC, Meng FY, Li JX, Li XL, Mao QY, Tao H, Zhang YT, Yao X, Chu K, Chen QH, Hu YM, Wu X, Liu P, Zhu LY, Gao F, Jin H, Chen YJ, Dong YY, Liang YC, Shi NM, Ge HM, Liu L, Chen SG, Ai X, Zhang ZY, Ji YG, Luo FJ, Chen XQ, Zhang Y, Zhu LW, Liang ZL, Shen XL. Efficacy, safety, and immunology of an inactivated alum-adjuvant enterovirus 71 vaccine in children in China: a multicentre, randomised, double-blind, placebo-controlled, phase 3 trial. *Lancet*. 2013;381(9882):2024–32.
67. Wei M, Meng F, Wang S, Li J, Zhang Y, Mao Q, Hu Y, Liu P, Shi N, Tao H, Chu K, Wang Y, Liang Z, Li X, Zhu F. 2-year efficacy, immunogenicity, and safety of Vigoo Enterovirus 71 vaccine in healthy Chinese children: a randomized open-label study. *J Infect Dis*. 2017;215(1):56–63.
68. Li JX, Song YF, Wang L, Zhang XF, Hu YS, Hu YM, Xia JL, Li J, Zhu FC. Two-year efficacy and immunogenicity of Sinovac Enterovirus 71 vaccine against hand, foot and mouth disease in children. *Expert Rev Vaccines*. 2016;15(1):129–37.
69. Zhu F, Xu W, Xia J, Liang Z, Liu Y, Zhang X, Tan X, Wang L, Mao Q, Wu J, Hu Y, Ji T, Song L, Liang Q, Zhang B, Gao Q, Li J, Wang S, Hu Y, Gu S, Zhang J, Yao G, Gu J, Wang X, Zhou Y, Chen C, Zhang M, Cao M, Wang J, Wang H, Wang N. Efficacy, safety, and immunogenicity of an enterovirus 71 vaccine in China. *N Engl J Med*. 2014;370(9):818–28.
70. Hu Y, Zeng G, Chu K, Zhang J, Han W, Zhang Y, Li J, Zhu F. Five-year immunity persistence following immunization with inactivated enterovirus 71 type (EV71) vaccine in healthy children: a further observation. *Hum Vaccin Immunother*. 2018;14(6):1517–23.
71. Li R, Liu L, Mo Z, Wang X, Xia J, Liang Z, Zhang Y, Li Y, Mao Q, Wang J, Jiang L, Dong C, Che Y, Huang T, Jiang Z, Xie Z, Wang L, Liao Y, Liang Y, Nong Y, Liu J, Zhao H, Na R, Guo L, Pu J, Yang E, Sun L, Cui P, Shi H, Wang J, Li Q. An inactivated enterovirus 71 vaccine in healthy children. *N Engl J Med*. 2014;370(9):829–37.
72. Chang JY, Chang CP, Tsai HH, Lee CD, Lian WC, Ih JS, Sai IH, Liu CC, Chou AH, Lu YJ, Chen CY, Lee PH, Chiang JR, Chong PC. Selection and characterization of vaccine strain for Enterovirus 71 vaccine development. *Vaccine*. 2012;30(4):703–11.
73. Cheng A, Fung CP, Liu CC, Lin YT, Tsai HY, Chang SC, Chou AH, Chang JY, Jiang RH, Hsieh YC, Su IJ, Chong PC, Hsieh SM. A phase I, randomized, open-label study to evaluate the safety and immunogenicity of an enterovirus 71 vaccine. *Vaccine*. 2013;31(20):2471–6.
74. Chou AH, Liu CC, Chang JY, Jiang R, Hsieh YC, Tsao A, Wu CL, Huang JL, Fung CP, Hsieh SM, Wang YF, Wang JR, Hu MH, Chiang JR, Su IJ, Chong PC. Formalin-inactivated EV71 vaccine candidate induced cross-neutralizing antibody against subgenotypes B1, B4, B5 and C4A in adult volunteers. *PLoS One*. 2013;8(11):e79783.
75. Huang LM, Chiu CH, Chiu NC, Lin CY, Li MT, Kuo TY, Weng YJ, Hsieh EF, Tai IC. Immunogenicity, safety, cross-reaction, and immune persistence of an inactivated enterovirus A71 vaccine in children aged from two months to 11 years in Taiwan. *Vaccine*. 2019;37(13):1827–35.
76. Wu CN, Lin YC, Fann C, Liao NS, Shih SR, Ho MS. Protection against lethal enterovirus 71 infection in newborn mice by passive immunization with subunit VP1 vaccines and inactivated virus. *Vaccine*. 2001;20(5–6):895–904.
77. Zhou SL, Ying XL, Han X, Sun XX, Jin Q, Yang F. Characterization of the enterovirus 71 VP1 protein as a vaccine candidate. *J Med Virol*. 2015;87(2):256–62.
78. Meng T, Kolpe AB, Kiener TK, Chow VT, Kwang J. Display of VP1 on the surface of baculovirus and its immunogenicity against heterologous human enterovirus 71 strains in mice. *PLoS One*. 2011;6(7):e21757.
79. Wang X, Dong K, Long M, Lin F, Gao Z, Wang L, Zhang X, Chen X, Dai Y, Wang H, Zhang H. Induction of a high-titered antibody response using HIV gag-EV71 VP1-based virus-like particles with the capacity to protect newborn mice challenged with a lethal dose of enterovirus 71. *Arch Virol*. 2018;163(7):1851–61.
80. Chen HF, Chang MH, Chiang BL, Jeng ST. Oral immunization of mice using transgenic tomato fruit expressing VP1 protein from enterovirus 71. *Vaccine*. 2006;24(15):2944–51.
81. Chiu CH, Chu C, He CC, Lin TY. Protection of neonatal mice from lethal enterovirus 71 infection by maternal immunization with attenuated *Salmonella enterica* serovar typhimurium expressing VP1 of enterovirus 71. *Microbes Infect*. 2006;8(7):1671–8.
82. Yu Z, Huang Z, Sao C, Huang Y, Zhang F, Ma G, Chen Z, Zeng Z, Qiwen D, Zeng W. Oral immunization of mice using *Bifidobacterium longum* expressing VP1 protein from enterovirus 71. *Arch Virol*. 2013;158(5):1071–7.
83. Zhang C, Wang Y, Ma S, Li L, Chen L, Yan H, Peng T. Human Enterovirus 71 protein displayed on the surface of *Saccharomyces cerevisiae* as an Oral vaccine. *Viral Immunol*. 2016;29(5):288–95.
84. Xu P, Wang Y, Tao L, Wu X, Wu W. Recombinant *Lactococcus lactis* secreting viral protein 1 of enterovirus 71 and its immunogenicity in mice. *Biotechnol Lett*. 2019;41(6–7):867–72.
85. Chen HL, Huang JY, Chu TW, Tsai TC, Hung CM, Lin CC, Liu FC, Wang LC, Chen YJ, Lin MF, Chen CM. Expression of VP1 protein in the milk of transgenic mice: a potential oral vaccine protects against enterovirus 71 infection. *Vaccine*. 2008;26(23):2882–9.
86. Foo DG, Alonso S, Phoon MC, Ramachandran NP, Chow VT, Poh CL. Identification of neutralizing linear epitopes from the VP1 capsid protein of Enterovirus 71 using synthetic peptides. *Virus Res*. 2007;125(1):61–8.
87. Foo DG, Alonso S, Chow VT, Poh CL. Passive protection against lethal enterovirus 71 infection in newborn mice by neutralizing antibodies elicited by a synthetic peptide. *Microbes Infect*. 2007;9(11):1299–306.
88. Liu JN, Wang W, Duo JY, Hao Y, Ma CM, Li WB, Lin SZ, Gao XZ, Liu XL, Xu YF, Xu WB, Qin C, Zhang LF. Combined peptides of human enterovirus 71 protect against virus infection in mice. *Vaccine*. 2010;28(46):7444–51.
89. Liu CC, Chou AH, Lien SP, Lin HY, Liu SJ, Chang JY, Guo MS, Chow YH, Yang WS, Chang KH, Sia C, Chong P. Identification and characterization of a cross-neutralization epitope of Enterovirus 71. *Vaccine*. 2011;29(26):4362–72.
90. Xu L, He D, Li Z, Zheng J, Yang L, Yu M, Yu H, Chen Y, Que Y, Shih JW, Liu G, Zhang J, Zhao Q, Cheng T, Xia N. Protection against lethal enterovirus 71 challenge in mice by a recombinant vaccine candidate containing a broadly cross-neutralizing epitope within the VP2 EF loop. *Theranostics*. 2014;4(5):498–513.
91. Huo C, Yang J, Lei L, Qiao L, Xin J, Pan Z. Hepatitis B virus core particles containing multiple epitopes confer protection against enterovirus 71 and coxsackievirus A16 infection in mice. *Vaccine*. 2017;35(52):7322–30.
92. Aw-Yong KL, Sam IC, Koh MT, Chan YF. Immunodominant IgM and IgG epitopes recognized by antibodies induced in Enterovirus A71-associated hand, foot and mouth disease patients. *PLoS One*. 2016;11(11):e0165659.
93. Jiang L, Fan R, Sun S, Fan P, Su W, Zhou Y, Gao F, Xu F, Kong W, Jiang C. A new EV71 VP3 epitope in norovirus P particle vector displays neutralizing activity and protection in vivo in mice. *Vaccine*. 2015;33(48):6596–603.
94. Chung YC, Huang JH, Lai CW, Sheng HC, Shih SR, Ho MS, Hu YC. Expression, purification and characterization of enterovirus-71 virus-like particles. *World J Gastroenterol*. 2006;12(6):921–7.
95. Hu YC, Hsu JT, Huang JH, Ho MS, Ho YC. Formation of enterovirus-like particle aggregates by recombinant baculoviruses co-expressing P1 and 3CD in insect cells. *Biotechnol Lett*. 2003;25(12):919–25.
96. Zhang C, Ku Z, Liu Q, Wang X, Chen T, Ye X, Li D, Jin X, Huang Z. High-yield production of recombinant virus-like particles of enterovirus 71 in *Pichia pastoris* and their protective efficacy against oral viral challenge in mice. *Vaccine*. 2015;33(20):2335–41.
97. Chung YC, Ho MS, Wu JC, Chen WJ, Huang JH, Chou ST, Hu YC. Immunization with virus-like particles of enterovirus 71 elicits potent immune responses and protects mice against lethal challenge. *Vaccine*. 2008;26(15):1855–62.
98. Lin YL, Yu CI, Hu YC, Tsai TJ, Kuo YC, Chi WK, Lin AN, Chiang BL. Enterovirus type 71 neutralizing antibodies in the serum of macaque monkeys immunized with EV71 virus-like particles. *Vaccine*. 2012;30(7):1305–12.
99. Li HY, Han JF, Qin CF, Chen R. Virus-like particles for enterovirus 71 produced from *Saccharomyces cerevisiae* potently elicits protective immune responses in mice. *Vaccine*. 2013;31(32):3281–7.
100. Tsou YL, Lin YW, Shao HY, Yu SL, Wu SR, Lin HY, Liu CC, Huang C, Chong P, Chow YH. Recombinant adeno-vaccine expressing enterovirus 71-like particles against hand, foot, and mouth disease. *PLoS Negl Trop Dis*. 2015;9(4):e0003692.
101. Yan Q, Wu L, Chen L, Qin Y, Pan Z, Chen M. Vesicular stomatitis virus-based vaccines expressing EV71 virus-like particles elicit strong immune responses and protect newborn mice from lethal challenges. *Vaccine*. 2016;34(35):4196–204.
102. Arita M, Nagata N, Iwata N, Ami Y, Suzuki Y, Mizuta K, Iwasaki T, Sata T, Wakita T, Shimizu H. An attenuated strain of enterovirus 71 belonging to genotype a showed a broad spectrum of antigenicity with attenuated neurovirulence in cynomolgus monkeys. *J Virol*. 2007;81(17):9386–95.
103. Fujii K, Sudaka Y, Takashino A, Kobayashi K, Kataoka C, Suzuki T, Iwata-Yoshikawa N, Kotani O, Ami Y, Shimizu H, Nagata N, Mizuta K, Matsuzaki Y, Koike S. VP1 Amino Acid Residue 145 of Enterovirus 71 Is a Key Residue for Its Receptor Attachment and Resistance to Neutralizing Antibody during Cynomolgus Monkey Infection. *J Virol*. 2018;92(15).
104. Nishimura Y, Lee H, Hafenstein S, Kataoka C, Wakita T, Bergelson JM, Shimizu H. Enterovirus 71 binding to PSGL-1 on leukocytes: VP1-145 acts as a molecular switch to control receptor interaction. *PLoS Pathog*. 2013;9(7):e1003511.



105. Zaini Z, McMinn P. A single mutation in capsid protein VP1 (Q145E) of a genogroup C4 strain of human enterovirus 71 generates a mouse-virulent phenotype. *J Gen Virol*. 2012;93(Pt 9):1935–40.
106. Yeh MT, Wang SW, Yu CK, Lin KH, Lei HY, Su IJ, Wang JR. A single nucleotide in stem loop II of 5'-untranslated region contributes to virulence of enterovirus 71 in mice. *PLoS One*. 2011;6(11):e27082.
107. Sadeghipour S, Bek EJ, McMinn PC. Ribavirin-resistant mutants of human enterovirus 71 express a high replication fidelity phenotype during growth in cell culture. *J Virol*. 2013;87(3):1759–69.
108. Meng T, Kwang J. Attenuation of human enterovirus 71 high-replication-fidelity variants in AG129 mice. *J Virol*. 2014;88(10):5803–15.
109. Yee PTI, Tan SH, Ong KC, Tan KO, Wong KT, Hassan SS, Poh CL. Development of live attenuated Enterovirus 71 vaccine strains that confer protection against lethal challenge in mice. *Sci Rep*. 2019;9(1):4805.
110. Tsai YH, Huang SW, Hsieh WS, Cheng CK, Chang CF, Wang YF, Wang JR. Enterovirus A71 Containing Codon-Deoptimized VP1 and High-Fidelity Polymerase as Next-Generation Vaccine Candidate. *J Virol*. 2019;93(13).
111. Kim SH, Jang YS. The development of mucosal vaccines for both mucosal and systemic immune induction and the roles played by adjuvants. *Clin Exp Vaccine Res*. 2017;6(1):15–21.
112. Miquel-Clopes A, Bentley EG, Stewart JP, Carding SR. Mucosal vaccines and technology. *Clin Exp Immunol*. 2019;196(2):205–14.
113. Lin YL, Chow YH, Huang LM, Hsieh SM, Cheng PY, Hu KC, Chiang BL. A CpG-adjuvanted intranasal enterovirus 71 vaccine elicits mucosal and systemic immune responses and protects human SCARB2-transgenic mice against lethal challenge. *Sci Rep*. 2018;8(1):10713.

## Publisher's Note

Springer Nature remains neutral with regard to jurisdictional claims in published maps and institutional affiliations.

**Ready to submit your research? Choose BMC and benefit from:**

- fast, convenient online submission
- thorough peer review by experienced researchers in your field
- rapid publication on acceptance
- support for research data, including large and complex data types
- gold Open Access which fosters wider collaboration and increased citations
- maximum visibility for your research: over 100M website views per year

**At BMC, research is always in progress.**

Learn more [biomedcentral.com/submissions](https://biomedcentral.com/submissions)



# Novel Role for miR-1290 in Host Species Specificity of Influenza A Virus

Sheng-Yu Huang,<sup>1,2</sup> Chih-Heng Huang,<sup>2,3,4</sup> Chi-Jene Chen,<sup>2</sup> Ting-Wen Chen,<sup>5,6</sup> Chun-Yuan Lin,<sup>2,7</sup> Yueh-Te Lin,<sup>2,7,8</sup> Shu-Ming Kuo,<sup>2</sup> Chung-Guei Huang,<sup>1,2,8,9</sup> Li-Ang Lee,<sup>10,11</sup> Yi-Hsiang Chen,<sup>1,2</sup> Mei-Feng Chen,<sup>2</sup> Rei-Lin Kuo,<sup>1,2,8,12</sup> and Shin-Ru Shih<sup>2,8,9,13,14,15</sup>

<sup>1</sup>Graduate Institute of Biomedical Science, Division of Biotechnology, College of Medicine, Chang Gung University, Taoyuan 33302, Taiwan; <sup>2</sup>Research Center for Emerging Viral Infections, College of Medicine, Chang Gung University, Taoyuan 33302, Taiwan; <sup>3</sup>The Institute of Microbiology and Immunology, National Defense Medical Center, Taipei 11490, Taiwan; <sup>4</sup>The Institute of Preventive Medicine, National Defense Medical Center, Taipei 11490, Taiwan; <sup>5</sup>Institute of Bioinformatics and Systems Biology, National Chiao Tung University, Hsinchu 30068, Taiwan; <sup>6</sup>Department of Biological Science and Technology, National Chiao Tung University, Hsinchu, 30068, Taiwan; <sup>7</sup>Department of Computer Science and Information Engineering, College of Engineering, Chang Gung University, Taoyuan 33302, Taiwan; <sup>8</sup>Department of Medical Biotechnology and Laboratory Science, College of Medicine, Chang Gung University, Taoyuan 33302, Taiwan; <sup>9</sup>Department of Laboratory Medicine, Linkou Chang Gung Memorial Hospital, Taoyuan 33305, Taiwan; <sup>10</sup>Department of Otorhinolaryngology-Head and Neck Surgery, Linkou Chang Gung Memorial Hospital, Taoyuan 33305, Taiwan; <sup>11</sup>Faculty of Medicine, College of Medicine, Chang Gung University, Taoyuan 33302, Taiwan; <sup>12</sup>Department of Pediatrics, Linkou Chang Gung Memorial Hospital, Taoyuan 33302, Taiwan; <sup>13</sup>Research Center for Chinese Herbal Medicine, College of Human Ecology, Chang Gung University of Science and Technology, Taoyuan 33303, Taiwan; <sup>14</sup>Research Center for Food and Cosmetic Safety, College of Human Ecology, Chang Gung University of Science and Technology, Taoyuan 33303, Taiwan; <sup>15</sup>Graduate Institute of Health Industry Technology, College of Human Ecology, Chang Gung University of Science and Technology, Taoyuan 33303, Taiwan

**The role of microRNA (miRNA) in influenza A virus (IAV) host species specificity is not well understood as yet. Here, we show that a host miRNA, miR-1290, is induced through the extracellular signal-regulated kinase (ERK) pathway upon IAV infection and is associated with increased viral titers in human cells and ferret animal models. miR-1290 was observed to target and reduce expression of the host vimentin gene. Vimentin binds with the PB2 subunit of influenza A virus ribonucleoprotein (vRNP), and knockdown of vimentin expression significantly increased vRNP nuclear retention and viral polymerase activity. Interestingly, miR-1290 was not detected in either chicken cells or mouse animal models, and the 3' UTR of the chicken vimentin gene contains no binding site for miR-1290. These findings point to a host species-specific mechanism by which IAV upregulates miR-1290 to disrupt vimentin expression and retain vRNP in the nucleus, thereby enhancing viral polymerase activity and viral replication.**

## INTRODUCTION

The vast reservoir of influenza A virus (IAV) in aquatic birds serves as a genetic base that facilitates virus reassortment and antigenic shifts, some of which may confer on IAV strains the ability to cross species barriers and infect humans. Avian influenza A virus (AIV) typically does not replicate efficiently or cause disease in humans<sup>1</sup> because of differences in receptor binding affinity, thereby limiting virus host range.<sup>2</sup> Furthermore, the poor polymerase activity of AIV in human cells constitutes another major barrier that must be overcome for successful infection. The IAV viral ribonucleoprotein (vRNP) is known to harbor numerous host-determinant amino acid signatures,<sup>3</sup> which, when changed, can affect viral replication efficiency in different hosts.

For example, a change from glutamate to lysine for amino acid residue 627 (E627K) in the PB2 subunit (PB2 K627-type) of an AIV vRNP is known to enhance polymerase activity, virus replication, viral transmission, and even pathogenicity and mortality in mammals.<sup>4–7</sup> Conversely, IAVs with an engineered PB2 E627-type vRNP demonstrate reduced polymerase activity in mammalian systems.<sup>8,9</sup> Statistical analysis indicates that most human IAVs are of the PB2 K627-type, whereas most AIVs are of the PB2 E627-type.<sup>4,10</sup> Our previous research also found that a host species-specific factor in humans, TUFM, exhibits stronger binding affinity with PB2<sub>627</sub>E than with PB2<sub>627</sub>K and can inhibit the replication of PB2 E627-type but not PB2 K627-type IAVs in human cells.<sup>11</sup> There is compelling evidence to show that AIV adaptation to humans is dependent on such mutations in the polymerase subunits (PB1, PB2, and PA) or viral nucleocapsid protein (NP), which can enhance interaction with mammalian-specific factors to enable efficient viral replication.<sup>12</sup> A better understanding of host species-specific factors that affect IAV replication is therefore important for the study of virus transmission and infectivity, but current research is centered on proteins, and little information is available regarding other types of regulatory factors.

MicroRNA (miRNA) is a short, noncoding RNA molecule that is believed to regulate at least 30% of cellular gene expression.<sup>13,14</sup>

Received 11 February 2019; accepted 29 April 2019;  
<https://doi.org/10.1016/j.omtn.2019.04.028>.

**Correspondence:** Shin-Ru Shih, PhD, Research Center for Emerging Viral Infections, College of Medicine, College of Medicine, Chang Gung University, Taoyuan 33302, Taiwan  
**E-mail:** [srshih@mail.cgu.edu.tw](mailto:srshih@mail.cgu.edu.tw)



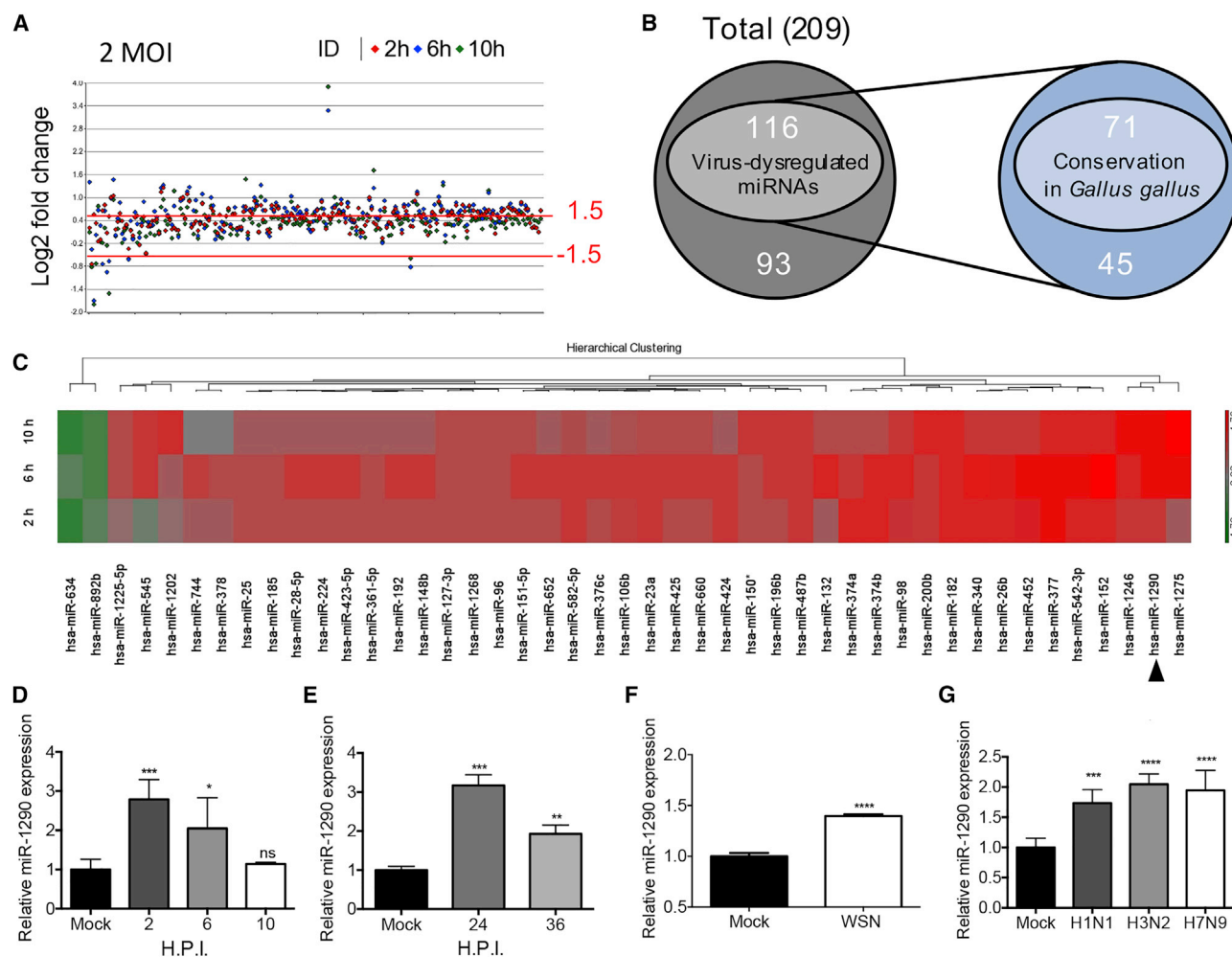


**Figure 1. Dysregulation of Host Species-Specific miR-1290 Expression in IAV-Infected Human Cells**

(A) A miRNA microarray analysis was performed using RNA extracts from WSN-infected A549 cells at 2, 6, and 10 h after infection with an MOI of 2 ( $n = 1$  for each time point). The scatterplot indicates the relative expression of each identified miRNA in the WSN-infected samples, as compared with the mock-infected samples at the stated time points after infection. The y axis represents the log<sub>2</sub>-fold change of miRNA expression in the WSN-infected samples relative to the mock-infected samples. (B) A Venn diagram depicting the conservation of dysregulated miRNAs in *Gallus gallus*, analyzed by the microRNAviewer.<sup>31</sup> Dysregulation was determined by a threshold of a 1.5-fold change in expression relative to mock-infected controls. (C) Key miRNA expression patterns in WSN-infected A549 cells at various time points after infection. The columns correspond to expression patterns of dysregulated miRNAs relative to mock-infected samples at 2, 6, and 10 h after infection. The red and green colors respectively indicate upregulation and downregulation. MiR-1290 expression was validated in A549 cells infected with WSN (D) in a single-cycle infection at an MOI of 2 and (E) in multiple cycle infections at an MOI of 0.001. (F) Comparison of miR-1290 expression in human bronchial epithelial (NHBE) cells that were mock infected or infected with WSN at an MOI of 0.001 for 24 h. (G) Validation of miR-1290 expression in A549 cells infected with WSN (H1N1), H3N2, or H7N9 at an MOI of 0.01 for 48 h. U6 was used as an internal control, and each sample was normalized with a mock control. (D and E) Experiments were performed in triplicate and repeated at least three times. Data are presented as mean values  $\pm$  SD from one representative experiment. ( $n \geq 3$  for each sample). Error bars represent SD derived from three independent experiments. Statistical significance was determined by conducting an unpaired t test (\* $p < 0.05$ ; \*\* $p < 0.01$ ; \*\*\* $p < 0.005$ ; \*\*\*\* $p < 0.001$ ; ns, nonsignificant). H.P.I., hours post infection.

Individual miRNA can repress the expression of hundreds to thousands of genes through partial recognition of binding sites in the 3' UTR of target genes.<sup>15</sup> Furthermore, it is now known that miRNA is involved in the replication process of both DNA and RNA viruses,<sup>16,17</sup> and recent studies have reported on host miRNAs that can regulate IAV replication.<sup>18–21</sup> Because virus replication usually involves multiple factors,<sup>22,23</sup> miRNAs with multi-targeting capability

may serve as a more efficient and effective focus for novel antiviral drugs; moreover, it is relatively easier to develop complementary-sequence-based treatments against miRNA, as compared to protein-targeting therapies. The first miRNA-based antiviral therapy, miravirsin, is already in phase II clinical trials for the treatment of chronic hepatitis C infection.<sup>24</sup> However, current research has not specifically examined the role of miRNA in host species specificity.

Here, we identified a novel role for miR-1290, a host miRNA found in human and ferret lung cells, but not in mouse or chicken cells. Previously, miR-1290 expression has been reported to be upregulated in non-small cell lung cancer (NSCLC),<sup>25</sup> and miR-1290 has been implicated as a driver of invasiveness and proliferation in NSCLC<sup>26–28</sup> and lung adenocarcinoma.<sup>29</sup> We found that an IAV can upregulate miR-1290 expression to enhance IAV replication. When miR-1290 function was inhibited by a miR-1290 antagonist, LNA-1290, viral titers of the IAV decreased significantly in both human cells and ferret animal models. We further observed that miR-1290 can target the vimentin gene to reduce its expression. Nuclear levels of the IAV NP subunit were shown to rise in vimentin knockdown cells, and this led to significantly increased vRNP polymerase activity. Interestingly, the 3' UTR of the chicken vimentin gene did not contain any binding site for miR-1290. These findings point to a host species-specific mechanism in which the IAV upregulates miR-1290 to interfere with vimentin expression and increase the vRNP in the host nucleus, thereby enhancing polymerase activity and viral replication.

## RESULTS

### Dysregulation of miR-1290 Expression Observed in IAV-Infected Human Cells

To identify miRNAs affected by IAV infection, we systematically performed miRNA microarray analysis of a human alveolar adenocarcinoma cell line, A549, which was infected with a common laboratory strain of influenza A/WSN/33(H1N1) virus (WSN). We compared miRNA expression profiles in A549 cells infected with WSN for 2, 6, and 10 h at an MOI of 2. Among 955 miRNAs on the microarray, 209 were detected in all three infected A549 samples, but most expression changes were less than 1.5-fold higher or lower when compared with analysis results from mock-infected A549 cells (Figure 1A), which is consistent with a previous report.<sup>30</sup> Therefore, we established a 1.5-fold expression change as a screening threshold. Further screening revealed 116 miRNAs that underwent 1.5-fold or greater expression changes at any time point following WSN infection (Figure 1B). To identify host species-specific miRNA not conserved in *Gallus* (chicken), we used microRNAviewer<sup>31</sup> to search for human miRNA without avian homology and subsequently found 45 miRNAs that fit this condition (Figure 1B). Comparative analysis of their expression patterns at different time points after WSN infection, using a clustered heatmap (Figure 1C), revealed that miR-1290 was strongly upregulated. We used stem-loop real-time PCR to validate miR-1290 upregulation following WSN infection and observed that for a single-cycle infection, miR-1290 expression increased by 2.8-, 2.1-, and 1.3-fold over uninfected cells at 2, 6, and 10 h after infection, respectively (Figure 1D). Moreover, for multiple-cycle infections, miR-1290 expression levels rose by 3.2- and 1.9-fold over uninfected cells at 24 and 36 h after infection, respectively (Figure 1E). To dispel concerns regarding whether such upregulation takes place only in immortalized cell lines, we repeated these experiments in normal human bronchial epithelial (NHBE) cells challenged with WSN. The results showed that miR-1290 exhibited a 1.5-fold increase in expression levels after WSN infection (Figure 1F). We proceeded to examine whether other IAV strains were similarly capable of upregu-

lating miR-1290 expression, and our results demonstrated that levels of miR-1290 also rose significantly in cells infected with H3N2 or emerging AIV (H7N9) viruses (Figure 1G). Previous research has reported that miR-1290 is specific to humans and great apes<sup>32</sup> and that it is not detectable in mouse cells by *in situ* hybridization (ISH). We also used the University of California, Santa Cruz (UCSC), Genome Browser to align the miR-1290 precursor sequence across 100 vertebrate genomes and confirmed that this sequence was indeed strongly conserved across several higher primate species (Figure S1). However, to the best of our knowledge, the role of miR-1290 in IAV replication has not been reported.

### miR-1290 Inhibition Disrupted IAV Replication in Human Cells and Ferrets

To further elucidate the functional impact of miR-1290 on IAV replication, we transfected a miR-1290 antagonist, LNA-1290, into A549 cells and then challenged the transfected cells with WSN virus. Real-time PCR results revealed that miR-1290 levels in transfected cells at the final post-infection time point that was tracked were about 38% that of the negative control (Figure 2A, left panel), LNA-NC, whose sequence has no homology to any known human, mouse, or rat miRNA or mRNA sequence. Corresponding viral titers examined at different time points after infection by plaque assay subsequently showed that viral titers were respectively 40% and 15% that of the negative control (LNA-NC) at 48 and 72 h after infection (Figure 2A, right panel). However, when a miR-1290 mimic alone was overexpressed in cells, at the final post-infection time point that was tracked, miR-1290 levels were upregulated 5.3-fold compared to the negative control (miR-NC; Figure 2B, left panel), and viral titers were subsequently found to be 3.8- and 1.3-fold higher than those observed in the miR-NC negative control at 48 and 72 h after infection, respectively (Figure 2B, right panel). The miR-NC negative control is a random-sequence miRNA mimic molecule that has been extensively tested in human cell lines and tissues and has been validated to have no identifiable effects on any known miRNA function. To confirm the specificity of this effect by miR-1290 on viral replication, we designed a seed sequence mutant miR-1290 mimic (sm-miR-1290) as a specific negative control. The seed sequence of the sm-miR-1290 mimic was designed to be the reverse complement of the miR-1290 sequence. Subsequent experimental results also showed that viral titers in miR-1290 overexpressed cells were 5.7- and 2.7-fold higher than this specific sm-miR-1290 negative control at 48 and 72 h after infection, respectively. We confirmed by MTT cell viability assay that both LNA-1290 and the miR-1290 mimic did not induce cell toxicity at concentrations up to 100 nM (Figure S2).

We further sought to ascertain whether LNA-1290 is capable of inhibiting IAV replication in an animal model. Although miR-1290 was previously reported to be specific to humans and great apes<sup>32</sup> and this was corroborated by our own genome alignment analysis (Figure S1), we nevertheless measured basal levels of miR-1290 in a variety of animal lung tissues. MiR-1290 was indeed undetectable in mouse and chicken lung tissue, but was detected in human and ferret (*Mustela putorius furo*) lung tissue (Figure 2C). Although a BLAST

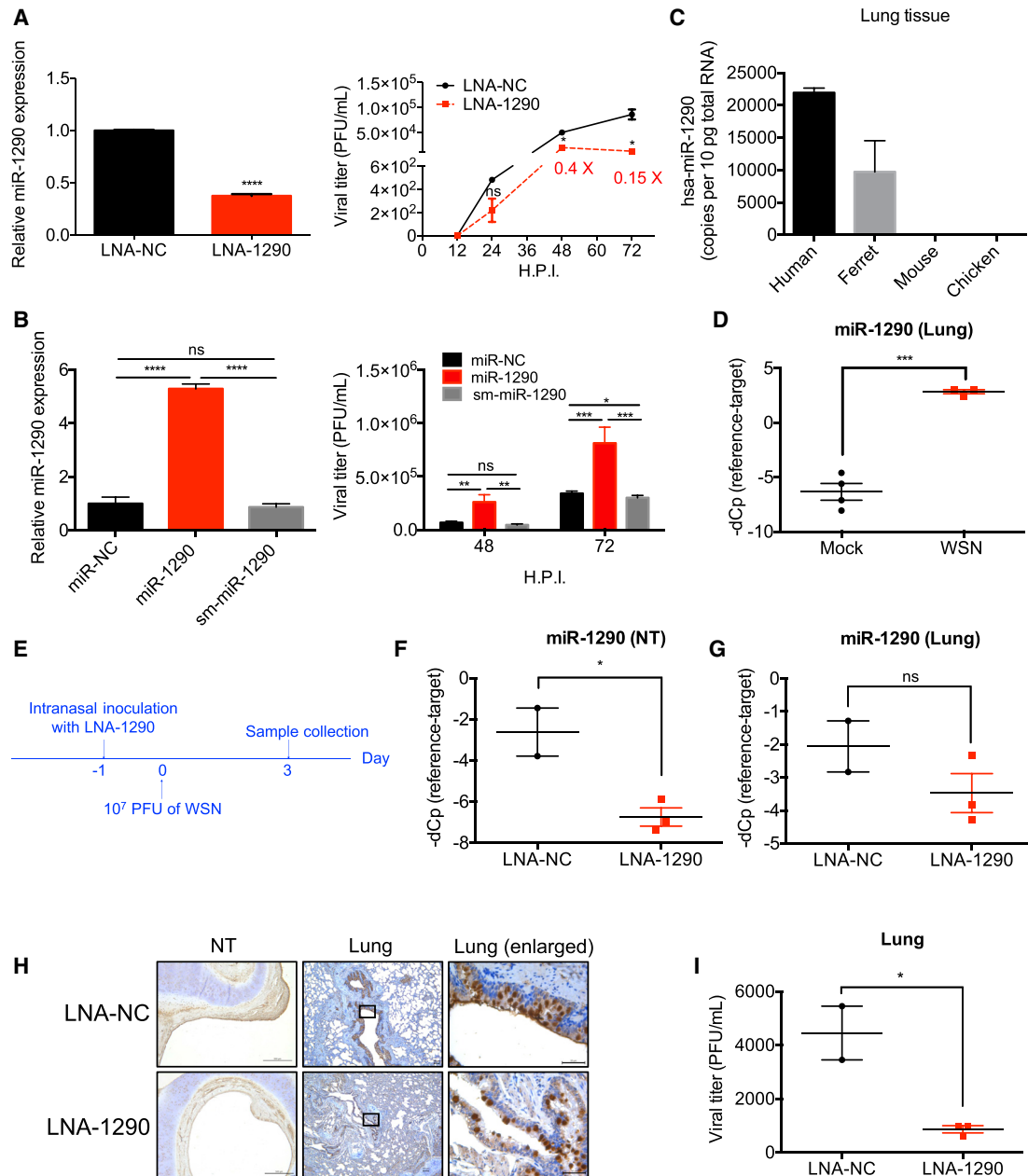


**Figure 2. Inhibition of miR-1290 Reduced IAV Viral Titers in Human Cells and Ferret Models**

(A and B) Comparison of miR-1290 expression levels and viral titers in (A) human A549 cells treated with a miR-1290 antagonist (LNA-1290) or a negative control (LNA-NC) or (B) human A549 cells treated with a miR-1290 mimic (miR-1290), a seed sequence mutant miR-1290 mimic (sm-miR-1290) that serves as a specific negative control, or a negative control miRNA (miR-NC). qPCR experiments (A) were performed in triplicate and repeated at least three times; for viral titer titration (B), experiments were performed in duplicate and repeated at least three times, and data are presented as mean values  $\pm$  SD from one representative experiment. (C) Detected expression levels of miR-1290 in human, ferret, mouse, and chicken lung tissue. Error bars represent the SD of mean values ( $n = 3$ ). (D) Real-time qPCR assessment of miR-1290 expression in mock-infected (MOCK) or WSN-infected (WSN) ferret lung tissue. (E) Schematic of the experimental setup for analysis of the relationship between miR-1290 expression and WSN viral titers in ferret models. (F) Nasal turbinate (NT) and (G) lung tissue (Lung) miR-1290 expression levels for ferrets treated with a miR-1290 antagonist (LNA-1290) or a negative control (LNA-NC). (H) Representative immunohistochemical (IHC) staining results for IAV viral proteins in the nasal turbinate (NT) or lung tissue (Lung) derived from ferrets treated with LNA-1290 or LNA-NC ( $\times 5$  magnification,  $\times 40$  magnification for the enlarged panel). (I) Viral titers in the lung tissue were detected with a plaque assay. (D, F, G, and I) Two independent experiments were conducted, and data were pooled from both experiments and are presented as mean values  $\pm$  SEM. Statistical significance was determined by conducting an unpaired t test (\* $p < 0.05$ ; \*\* $p < 0.01$ ; \*\*\* $p < 0.005$ ; ns, nonsignificant). H.P.I., hours post infection.



search produced no alignment with the miR-1290 sequence in the MusPutFur1.0 draft genome downloaded from Ensembl, we suspect that this may be due to the incompleteness of the ferret genome sequence currently available. MiR-1290 expression in ferret lung tissue was confirmed by real-time PCR, and sequencing results of the PCR product revealed an exact 100% match between ferret and human miR-1290. Considering that ferrets are an excellent mammalian model with a detailed record of use in studying the pathogenicity and transmissibility of human and avian IAV and can reflect many characteristics of IAV infection,<sup>33</sup> we elected to use ferrets to assess the effect of miR-1290 on IAV replication. We found that, at baseline, miR-1290 expression in ferret lung tissue was about half that in human cells, but miR-1290 levels similarly increased significantly after WSN infection, as compared with mock-infected controls (Figure 2D). We then treated ferrets intranasally with LNA-1290 1 day prior to WSN inoculation and collected tissue samples at 3 days after infection for analysis (Figure 2E). Real-time PCR results showed that miR-1290 expression decreased in the nasal turbinate (NT) and lung tissue of ferrets treated with LNA-1290, as compared to the negative controls (Figures 2F and 2G); viral protein levels (Figure 2H) and viral titers (Figure 2I) also fell in LNA-1290-treated ferrets compared to the negative controls. These results provide confirmation in an animal model that LNA-1290 can affect both viral protein levels and viral titers by inhibiting miR-1290 expression.

#### IAV-Enhanced miR-1290 Expression Downregulates Vimentin Expression

To better understand how miR-1290 acts to affect IAV replication, we designed a screening pipeline (Figure 3A) to investigate 62 potential target genes of miR-1290 that are important for IAV replication and are downregulated in response to IAV infection (Table S1). Screening results revealed that protein levels of vimentin were downregulated in miR-1290-overexpressing cells, but not in the negative controls (Figure 3B). To ensure that the regulation of miR-1290 on vimentin expression was not an artifact created by the miR-1290 mimic, the sm-miR-1290-specific negative control was used (Figure 3C, upper panel), and subsequent results showed that both mRNA and protein levels of vimentin were not downregulated in sm-miR-1290-overexpressing cells, as with the previous negative controls (Figure 3B) used. To verify the direct regulation specificity at the binding site between miR-1290 and the 3' UTR of vimentin, we proceeded to construct a luciferase reporter vector containing the 3' UTR from the human vimentin gene (*huVIM*), with the miR-1290 binding site located in this region included in either wild-type (*huVIM*-3' UTR) or mutant (*mut-huVIM*-3' UTR) form (Figure 3C). The reporter vector was co-transfected with miR-1290 into A549 cells, and reduced luciferase activity was observed in comparison to the negative controls or the sm-miR-1290-specific negative control in cells transfected with the wild-type *huVIM*-3' UTR-containing vector (Figure 3C). By contrast, in cells transfected with the mutant *mut-huVIM*-3' UTR-containing vector, for which the miR-1290 binding site is mutated, luciferase activity did not change in response to the increased miR-1290 levels (Figure 3C). These results indicate that

miR-1290 can downregulate vimentin expression via binding to a specific site in the 3' UTR of the human vimentin gene.

Downregulation of vimentin mRNA and protein levels was also observed in WSN-infected A549 cells (Figure 3D), and to confirm that this downregulation was indeed affected by miR-1290, instead of an IAV-induced transcription shutoff mechanism, we co-transfected cells with the wild-type *huVIM*-3' UTR luciferase reporter vector, and either LNA-1290 or a negative control (LNA-NC). Following WSN infection, luciferase activity significantly decreased in cells transfected with LNA-NC, but remained comparable in LNA-1290-transfected cells, or even increased after infection (Figure 3E), indicating that LNA-1290 can block the inhibitory effect of miR-1290 on vimentin expression. We repeated this experiment in ferrets and observed that mRNA expression of the ferret vimentin gene (*feVIM*), which also contains a miR-1290 binding site in the 3' UTR, similarly remained stable in LNA-1290-treated ferrets, as opposed to those treated with LNA-NC (Figure 3F).

#### Host Species-Specific miR-1290 Vimentin Regulation Is Absent in Chicken Cells

Vimentin is a highly conserved cytoskeleton protein, with 83.7% nucleotide similarity between the human and chicken vimentin coding sequence (CDS), and 74.6% similarity in the 3' UTR. However, we did not observe any change in chicken vimentin mRNA levels in response to infection with IAV (Figure 4A). Upon analysis of the 3' UTR of the chicken vimentin gene, we observed that there was no miR-1290 binding site (Figure 4B); however, to confirm the effects of miR-1290 on *chVIM*-3' UTR, we also constructed luciferase reporter vectors containing either the wild-type chicken vimentin 3' UTR sequence (*chVIM*-3' UTR) or a mutated sequence that contained a miR-1290 binding site (*mut-chVIM*-3' UTR). Overexpression of miR-1290, sm-miR-1290, or a negative control miRNA in chicken cells transfected with a luciferase reporter vector containing the wild-type *chVIM*-3' UTR did not lead to any differences in luciferase expression, but overexpression of miR-1290 in chicken cells transfected with a luciferase reporter vector containing the *mut-chVIM*-3' UTR led to a significant decrease in luciferase expression, as compared with the sm-miR-1290-specific negative control or previous miRNA negative controls (Figure 4B). These results confirm that miR-1290 can affect chicken vimentin expression if a binding site on the *chVIM*-3' UTR is present, and the failure of miR-1290 to induce expression changes in the wild-type chicken vimentin gene indicates that such a binding site is likely not present in chickens, which also do not express miR-1290. We proceeded to transfect luciferase reporter vectors containing either *huVIM*-3' UTR or *chVIM*-3' UTR into A549 or DF-1 chicken fibroblast cells, after which cells were infected with WSN for 2, 6, or 10 h at an MOI of 2. Compared with mock-infected A549 cells, luciferase activity in cells transfected with *huVIM*-3' UTR-containing vector decreased after infection; however, luciferase activity in DF-1 cells transfected with *chVIM*-3' UTR-containing vector remained comparable to mock-infected controls, or even increased after infection

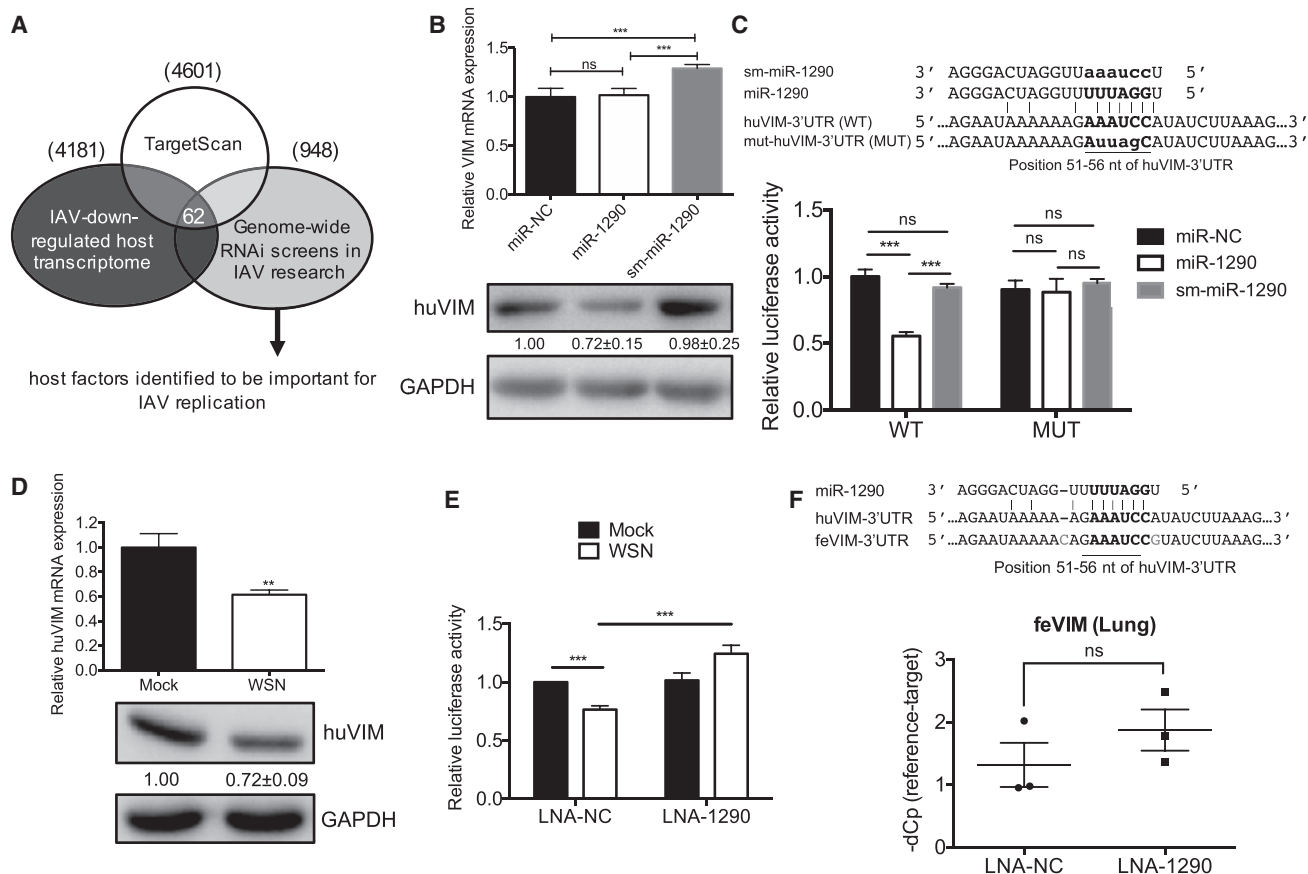


**Figure 3. IAV Upregulation of miR-1290 Expression Downregulates Vimentin Expression**

(A) Screening strategy used to identify miR-1290 target genes. (B) Expression levels of human vimentin gene (huVIM) mRNA and vimentin protein in miR-1290 mimic-overexpressing A549 cells. (C) The effect of miR-1290 on the luciferase activity of reporter vectors with wild-type (WT) or mutant (MUT) huVIM-3' UTR. The putative miR-1290-binding site is located at nt 51–56 of the huVIM 3' UTR (downstream; the first nucleotide following the stop codon is designated as +1) and is denoted in bold uppercase letters; the bold lowercase letters indicate the nucleic acid substitutions in the mutated version (mut-huVIM-3' UTR) of the miR-1290 binding site. (D) Real-time qPCR results for huVIM mRNA expression and western blotting results for vimentin expression in A549 cells mock-infected or infected with WSN at an MOI of 2 for 6 h. Glyceraldehyde 3-phosphate dehydrogenase (GAPDH) was used as an internal control in western blotting. (E) Comparison of luciferase activity with wild-type huVIM-3' UTR in mock- or WSN-infected A549 cells treated with a miR-1290 antagonist (LNA-1290) or control (LNA-NC). (F) Real-time qPCR results for the ferret vimentin gene (feVIM) mRNA expression in WSN-infected lung tissue treated with either LNA-1290 or LNA-NC. The putative miR-1290 binding site in the feVIM-3' UTR is marked in bold uppercase letters and compared with the huVIM-3' UTR. (B–E) Experiments were performed in triplicate and repeated at least three times. Data are presented as mean values ± SD from one representative experiment. (F) Two independent experiments were conducted, and data were pooled and are presented as mean values ± SD. Statistical significance was determined by conducting an unpaired t test (\*\*p < 0.01; \*\*\*p < 0.005; ns, nonsignificant).

(Figure 4C). This indicates that IAV-induced downregulation of vimentin is likely a host species-specific mechanism.

#### Vimentin Knockdown Enhances Viral Polymerase Activity by Disrupting vRNP Distribution

Previous studies have shown that vimentin can associate with IAV vRNP,<sup>34,35</sup> and we therefore conducted an immunoprecipitation (IP) assay to assess the binding affinity of vimentin with the PB1, PB2, PA, and NP subunits of vRNP. IP results from cells transfected with FLAG-tagged vimentin and the respective vectors expressing each vRNP subunit revealed that only the PB2 subunit was pulled down by an anti-FLAG antibody (Figure 5A); however, when

FLAG-tagged vimentin was overexpressed in IAV-infected cells, the PB2, PB1, PA, and NP subunits were all pulled down by an anti-FLAG antibody (Figure 5B), indicating that vimentin can interact with vRNP through binding with the PB2 subunit. A non-vRNP protein, NS1, was used as the negative control to demonstrate the binding specificity between vimentin and the vRNP subunits (Figure 5B). We observed through confocal microscopy that NP and vimentin were colocalized around the nucleus (Figure 5C) and therefore hypothesized that the interaction between vimentin and vRNP affects vRNP translocation. To ascertain this, we co-expressed vimentin small interfering RNA (siRNA) or NC siRNA, and an IAV mini-genome in A549 cells and subsequently analyzed vRNP subunit distribution

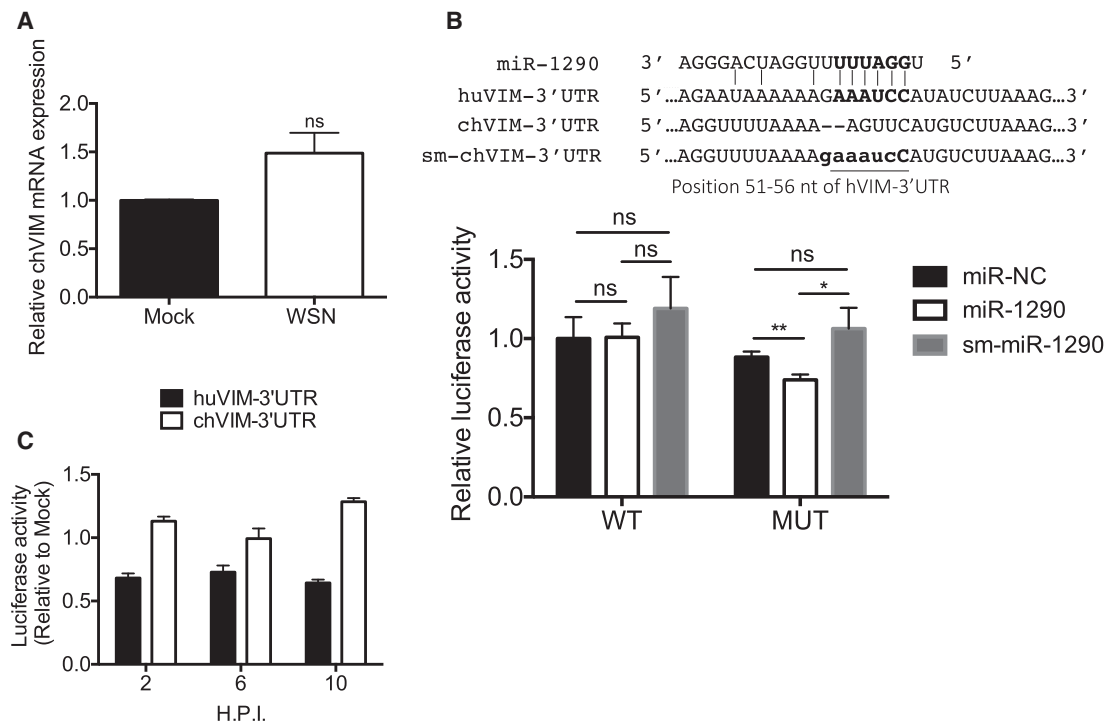


**Figure 4. MiR-1290 Regulation of Vimentin was Undetectable in *Gallus gallus***

(A) Comparison of chVIM mRNA expression in chicken DF-1 cells infected with WSN at an MOI of 2 for 2 h (WSN) or mock-infected (MOCK). (B) The effect of miR-1290 on luciferase activity exhibited by reporter vectors with chicken VIM-3' UTR (chVIM-3' UTR) or mutant (MUT) chVIM-3' UTR. (C) The effect of virus infections on the expression of luciferase activity with huVIM-3' UTR or chVIM-3' UTR assessed in WSN-infected A549 cells and WSN-infected DF-1 cells, respectively. Experiments were repeated at least three times, and data are presented as mean values  $\pm$  SD from one representative experiment. Statistical significance was determined by conducting an unpaired t test (\* $p < 0.05$ ; \*\* $p < 0.01$ ; ns, nonsignificant). H.P.I., hours post infection.

in fractionated cell lysates (Figure 5D). We found that the ratio of NP subunit in the nuclear fraction of vimentin knockdown cells was higher than that in the NC siRNA. As the NP protein is one of the subunits of vRNP polymerase, to observe whether viral polymerase activity changes in vimentin knockdown cells, we co-expressed vector control (VC) or vimentin, vimentin siRNA or NC siRNA, and an IAV mini-genome in HEK293T cells to assess the impact of vimentin on vRNP activity. The results showed that vRNP activity rose in vimentin knockdown cells compared with NC siRNA controls, but when vimentin was overexpressed, no significant differences were observed in vRNP activity between cells transfected with vimentin siRNA and NC siRNA (Figure 5E). These findings suggest that vimentin may be involved in vRNP translocation, and knockdown of vimentin expression may lead to increased vRNP in the host cell nucleus, thereby enhancing viral polymerase activity.

#### Influenza A Virus Induces miR-1290 Expression via ERK Pathway Activation

We observed that WSN infection elevated miR-1290 expression starting from 2 h after infection, during an early stage of the viral replication cycle (Figure 1D). To explore the underlying mechanism(s), we proceeded to infect A549 cells with wild-type (WT) or UV-inactivated WSN vi-

rus. Subsequent results showed that UV-inactivated WSN virus still increased miR-1290 levels (Figure 6A), thereby indicating that IAV-induced increases in miR-1290 expression are independent of viral RNA replication. Processes upstream of viral RNA replication, such as viral endosome uncoating or viral attachment, may also be involved in miR-1290 induction, and to understand whether the endosome-uncoated-vRNP complex is sufficient for miR-1290 induction, we treated cells with ammonium chloride ( $\text{NH}_4\text{Cl}$ ) to prevent endosome fusion. Results showed that miR-1290 expression still increased in cells treated with either  $\text{NH}_4\text{Cl}$  or double-distilled water ( $\text{ddH}_2\text{O}$ ) after virus infection, compared with mock-infected controls (Figure 6B). We further examined whether IAV-induced miR-1290 expression may occur at viral attachment, as previous studies have shown that IAV can activate the Raf/MEK/ERK signaling cascade in the early stages of viral infection.<sup>36</sup> We subsequently detected ERK activation at 30 min after viral infection (Figure 6C). It has been reported that the ERK1/2 can phosphorylate the transcription factor, Elk, to activate miR-1290 expression.<sup>37</sup> Therefore, we hypothesized that IAV attachment to host cells may activate the ERK pathway to promote miR-1290 transcription, and to confirm this, we assessed the expression of miR-1290 in cells treated with 12-O-tetradecanoylphorbol 13-acetate (TPA), an ERK activator. We found that p-ERK1/2 (phosphorylated ERK) was activated in

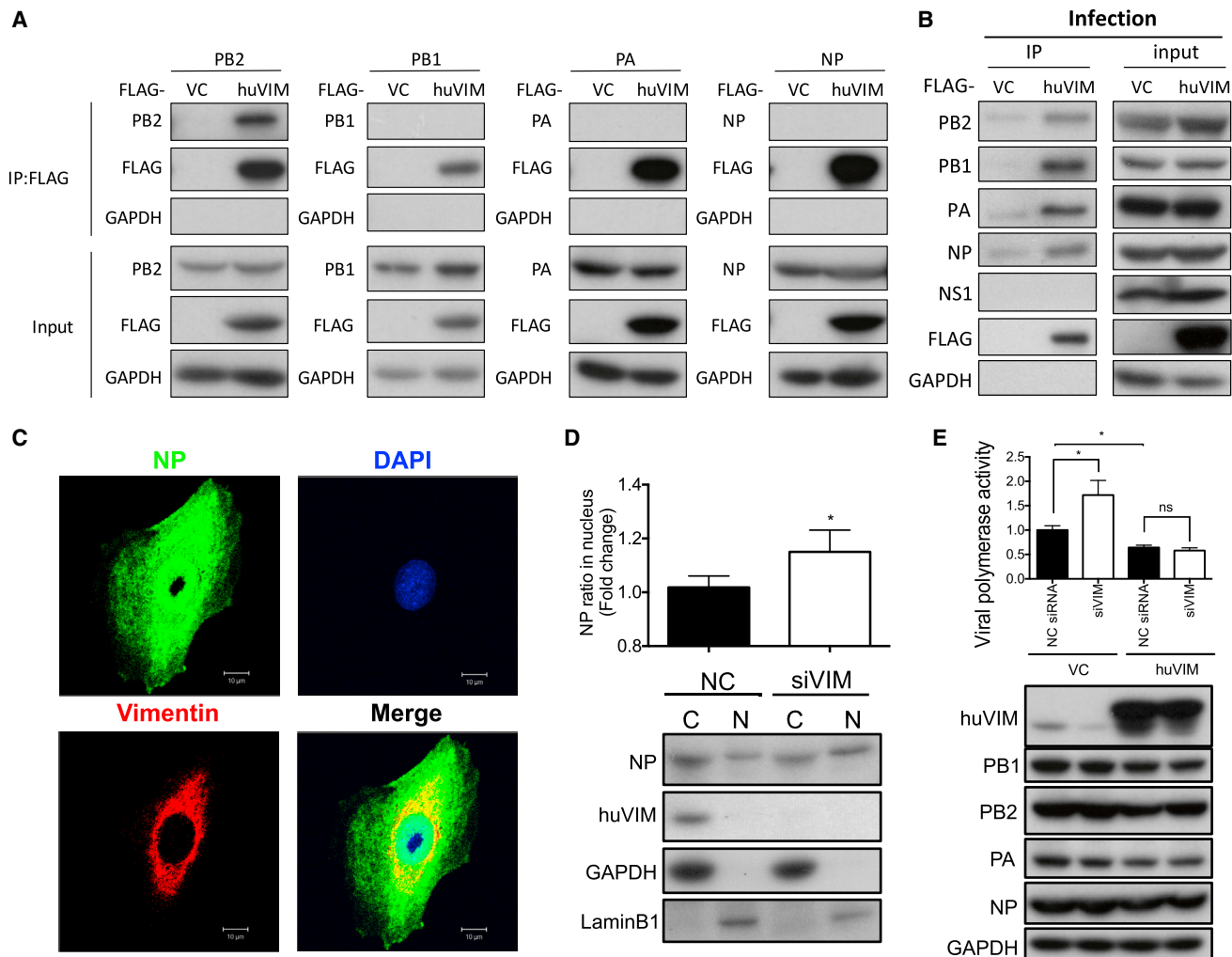


**Figure 5. Vimentin Knockdown Enhances Viral Polymerase Activity by Disrupting vRNP Translocation**

(A) HEK293T cells were co-transfected with constructs expressing PB2, PB1, PA, or NP, together with FLAG-tagged huVIM (huVIM) or vector control (VC). Immunoprecipitation was conducted with anti-FLAG antibodies, and precipitated proteins were detected by western blot, using the antibodies indicated at the left of each column. GAPDH was used as the control. (B) HEK293T cells infected with WSN at an MOI of 0.01 for 24 h were transfected with FLAG-tagged huVIM or VC. Immunoprecipitation was conducted with anti-FLAG antibodies, and precipitated proteins were detected by western blot, using the antibodies indicated at left. (C) Distribution of NP and vimentin in A549 cells infected with WSN at an MOI of 0.01 for 48 h after infection, using antibodies directed against vimentin (red) and NP (green). (A–C) Experiments were performed at least three times. Data are presented from one representative experiment. (D) A549 cells were co-transfected with negative control siRNA (NC siRNA) or vimentin siRNA (siVIM), as well as a WSN mini-replicon. Fractionated lysates were analyzed by western blot for detection of NP, vimentin, and the subcellular markers GAPDH and LaminB1. Quantitative results are presented as mean values  $\pm$  SD from three independent experiments. (E) Viral polymerase activity in HEK293T cells transfected with vector control (VC) and treated with control siRNA (NC siRNA) or vimentin siRNA (siVIM) to induce vimentin knockdown, compared with HEK293T cells transfected with huVIM to rescue vimentin expression. The antibodies listed at left were used in western blotting of cell lysates. Luciferase activity assays were repeated at least three times, and data are presented as mean values  $\pm$  SD from one representative experiment. Western blotting was performed at least three times. Data are presented from one representative experiment. Statistical significance was determined by conducting an unpaired t test (\* $p < 0.05$ ; \*\* $p < 0.01$ ; ns, nonsignificant). Non-structural viral protein NS1, which primarily functions to disrupt interferon production, was used as the negative control.

TPA-treated cells, and miR-1290 expression was also higher in TPA-treated cells than in DMSO-treated cells (Figure 6D), suggesting that IAV can activate ERK immediately after viral attachment to promote miR-1290 expression. In addition to WSN, we found that the PR8, pdmH1N1, and H3N2 viral strains promoted ERK activation (Figure 6E), and elevated miR-1290 expression was also detected after infec-

tion with these strains (Figure 6F), indicating that other IAV strains can also promote miR-1290 expression through ERK pathway activation.

## DISCUSSION

Here, we identified an interesting host species-specific mechanism by which IAV exploits the miR-1290-vimentin regulation axis to

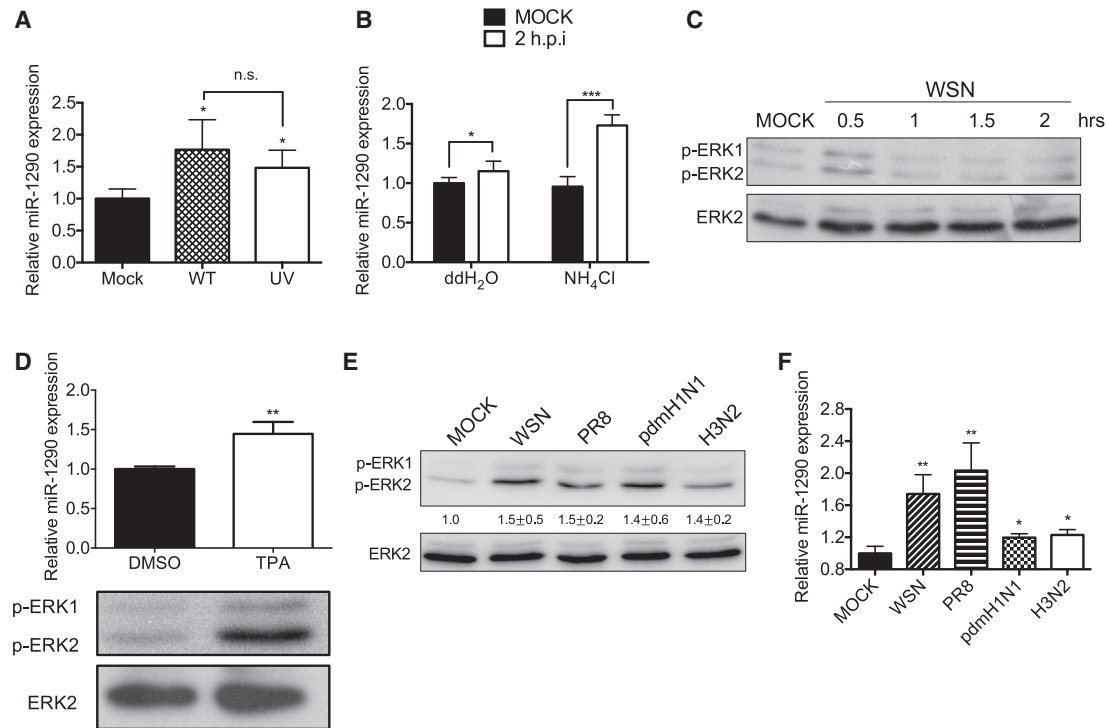


**Figure 6. IAV Induces miR-1290 Expression by Activation of the ERK Pathway**

(A) Comparison of miR-1290 expression in A549 cells infected with either WSN (wild type) or UV-inactivated WSN (UV) at an MOI of 2 for 2 h. (B) Comparison of miR-1290 expression in mock-infected or WSN-infected A549 cells treated with either ddH<sub>2</sub>O or NH<sub>4</sub>Cl. (A and B) Experiments were performed in triplicate and repeated at least three times. Data are presented as mean values  $\pm$  SD from one representative experiment. (C) Validation of ERK phosphorylation in WSN-infected A549 cells. A549 cells were infected at an MOI of 5. Experiments were performed at least three times. Data are presented from one representative experiment. (D) Comparison of miR-1290 expression in DMSO- or TPA-treated A549 cells. qPCR was performed in triplicate and repeated at least three times. Data are presented as mean values  $\pm$  SD from one representative experiment. Western blotting was performed at least three times. Data are presented from one representative experiment. (E) Validation of ERK phosphorylation in A549 cells infected with different IAV strains. A549 cells were infected at an MOI of 5 for 0.5 h. Western blotting was performed at least three times. Data are presented from one representative experiment. (F) Comparison of miR-1290 expression in A549 cells infected with different IAV strains at an MOI of 5 for 2 h. Experiments were performed in triplicate and repeated at least three times. Data are presented as mean values  $\pm$  SD from one representative experiment. (C–E) After western blot analysis, ERK activation was analyzed with a monoclonal antibody specific to phosphorylated ERK (p-ERK). Loading levels were controlled with a polyclonal antibody against ERK2. U6 was used as an internal control, and each sample was normalized with a mock control. Error bars represent the SD derived from three independent experiments. Statistical significance was determined by conducting an unpaired t test (\*p < 0.05; \*\*p < 0.01; \*\*\*p < 0.005; \*\*\*\*p < 0.001; ns, nonsignificant). H.P.I., hours post infection.

promote viral replication in human lung cells and a ferret animal model. This process was not found in chicken or mouse cells, and, as more research and genome sequence data become available, the role of miR-1290 in IAV host species specificity may become clearer, as with the underlying evolutionary processes involved.

An earlier analysis of serum miRNA from patients infected with emerging AIV H7N9 found that miR-1290 was upregulated during infection,<sup>38</sup> and in this study, we showed that IAV infection upregulates miR-1290 expression, the result of which can benefit vRNP nuclear increase and viral replication. Interestingly, miR-1290 is located in the first intron of the *ALDH4A1* gene, and both miR-1290 and the *ALDH4A1* gene product are transcribed by the same promoter. It has been reported that *ALDH4A1* is a p53-inducible gene that is protective against cellular stresses,<sup>39</sup> but it is not yet known whether *ALDH4A1* also plays a role in IAV infection and host species specificity. However, previous research

on miR-1290 has mostly centered on its role in promoting cell proliferation and invasiveness of lung cancer,<sup>26–29</sup> and cellular and animal studies have shown that inhibition of miR-1290 can decrease tumor cell invasiveness and arrest xenograft tumor growth.<sup>27,28</sup> Considering that miR-1290 has been reported to be upregulated in NSCLC,<sup>26</sup> lung adenocarcinoma,<sup>29</sup> and other tumors, together with the fact that cancer patients appear to be at increased risk of influenza complications, further research into the impact of miR-1290 on IAV proliferation and virulence in patients with miR-1290-upregulated tumors may be warranted. The clinical effects of novel miR-1290 inhibitors, such as the LNA-1290 inhibitor described in this study, may also be worth additional investigation in both influenza and cancer.

Previous studies have also observed vimentin mRNA degradation<sup>40</sup> and structural alteration<sup>41,42</sup> during IAV infection. Interestingly, vimentin was shown to immunoprecipitate with vRNP in an earlier



study,<sup>34</sup> and a recent study reported that vimentin can facilitate endosome trafficking and acidification to play a critical role in IAV H5N1 infection.<sup>43</sup> In this study, we showed that vimentin expression is downregulated by IAV-induced miR-1290, and this leads to the nuclear enrichment of vRNP components (Figures 5C and 5D). We speculated that vimentin may interfere with vRNP import into the host cell nucleus and/or delay vRNP export from the host cell nucleus, possibly through the interaction between vimentin and vRNP that is mediated by PB2 binding. Therefore, knockdown of vimentin would reduce interference with vRNP transport, and the vRNP complex could be better retained in the nucleus during the late stage of viral replication, resulting in increased IAV vRNP activity (Figure 5E). These results do not preclude the possibility that vimentin may take on various roles at different stages of IAV infection.

Considering that the infectivity and replicative ability of IAV can differ greatly between species, it is therefore important to study the factors influencing host species specificity, particularly those with respect to humans. A robust animal model is needed to conduct such studies, and to date, mouse models have been widely employed to study the pathology of IAV. However, there are many differences between humans and mice, and mouse models may not be able to accurately reflect the human response. Our findings regarding miR-1290 represents one example of the differences between humans and mice: bioinformatic analysis (Figure S1) and real-time PCR analysis (Figure 2C) have shown that the precursor sequence of miR-1290 is absent in the mouse genome. Yelamanchili et al.<sup>32</sup> also verified that miR-1290 could not be detected in mouse cell lines by ISH analysis. Even though the convenience and low cost of mouse models represents a major advantage, it is possible that the use of such models may cause a promising anti-IAV therapy to be overlooked or discarded before clinical testing because of poor performance in mice. Our results suggest that ferret models may serve as an alternative or possibly better choice for studying the interaction of host factors with IAV, although further studies are likely to be needed to corroborate this.

Recently approved anti-IAV therapies primarily target viral proteins and can be broadly divided into two categories: neuraminidase inhibitors and M2 inhibitors. However, because of the high mutation rate<sup>44,45</sup> and reassortment capability of IAV,<sup>46–48</sup> drug resistance is a major issue that limits the application of these antiviral drugs.<sup>49,50</sup> Novel anti-viral drugs targeting host species-specific factors may represent a solution to this problem, but other side effects may emerge from these treatments, and thus more evidence regarding the use of such strategies will be needed. In this study, we observed that miR-1290 expression is enhanced upon IAV infection, and therefore we used a specific antagonist, LNA-1290, to target and block IAV-enhanced expression of miR-1290. This strategy merely reduces miR-1290 to normal pre-infection levels, and thus carries a reduced risk of side effects. We further found that intranasally applied LNA-1290 can effectively reduce IAV-induced miR-1290 overexpression in a ferret animal model, resulting in decreased viral protein levels and viral titers. These results suggest that further exploration of a therapeutic role for LNA-1290 may be worthwhile in the future.

In conclusion, our findings point to a host species-specific mechanism by which IAV utilizes miR-1290 to increase vRNP in the nucleus, thereby enhancing viral polymerase activity and viral replication. This mechanism was observed in both human cells and ferret animal models; however, miR-1290 regulation of vimentin expression was not observed in chicken cells or mouse animal models, and the 3' UTR of the chicken vimentin gene did not contain a miR-1290 binding site. Intranasal administration of a miR-1290 antagonist, LNA-1290, subsequently reduced viral protein levels and viral titers in ferrets, suggesting that this mechanism may serve as a viable target for the future development of novel antiviral therapies. These results may also have implications for understanding how viruses can cross the species barrier and adapt to different hosts.

## MATERIALS AND METHODS

### Ethics Statement

The research ethics of this study were reviewed and approved by the Institutional Review Board at the Chang Gung Medical Foundation, Taoyuan, Taiwan (Approval Notices 102-4819B and 104-9560C).

### Antibodies

Anti-phosphorylated-ERK (1:2,000 dilution, CST9106; Cell Signaling Technology, Danvers, MA, USA), anti-total-ERK2 (1:2,000 dilution, GTX113094; GeneTex, Irvine, CA, USA), anti-vimentin (1:1,000 dilution, sc-6260; Santa Cruz Biotechnology, Santa Cruz, CA, USA), anti-glyceraldehyde 3-phosphate dehydrogenase (GAPDH; 1:5,000 dilution, GTX100118; GeneTex), anti-actin (1:10,000 dilution, MAB1501; Millipore, Burlington, MA, USA), anti-LaminB1 (1:3,000 dilution, ab16048; Abcam, Cambridge, UK), and anti-NP (1:10,000 dilution for western blotting; 1:2,000 dilution for immunofluorescence, produced in our laboratory) antibodies were used in western blotting. Anti-influenza A (1:1,000 dilution, AB1074; Millipore) antibody was used in IHC staining.

### Cells

HEK293T cells (ATCC CRL-11268), chicken fibroblast DF-1 cells (ATCC CRL-12203), and Madin-Darby canine kidney (MDCK) cells (ATCC CCL-34) were grown in DMEM (Gibco, Grand Island, NY, USA) containing 10% fetal bovine serum (FBS; Gibco). Human type II alveolar epithelial A549 cells (ATCC CCL-185) were maintained in minimum essential medium (MEM; Gibco) containing 10% FBS. NHBE cells (ATCC PCS-300-010) were grown in bronchial epithelial cell growth medium (BEGM; Lonza, Walkersville, MD, USA) containing growth factors, cytokines, and supplements. All cells were cultured at 37°C with 5% CO<sub>2</sub>.

### Viruses

The A/Taiwan/4-CGMH2/2014 (H7N9) virus was derived from Chang Gung Memorial Hospital, and the amplification and manipulation of the H7N9 virus was conducted in an accredited P3 laboratory at Chang Gung Memorial Hospital. The Pol I and Pol II plasmids of WSN virus and plasmids of A/PR8/34 were kindly provided by Dr. Robert G. Webster of the Department of Infectious Diseases, St. Jude Children's Research Hospital, Memphis, TN, USA. The whole

genome of the A/TW/3446/02 (H3N2) virus and swine-origin influenza A/Taiwan/126/2009(pdmH1N1) virus was isolated from Chang Gung Memorial Hospital and was cloned into the pHW2000 vector, as described previously.<sup>51</sup> The recombinant viruses were generated using 12-plasmid-based (WSN) or 8-plasmid-based (H3N2 and pdmH1N1) reverse genetic systems.<sup>52,53</sup>

### miRNA Microarray Analysis

miRNA expression in human A549 cells was assessed with the Agilent Human miRNA Oligo Microarray R12 (Agilent Technologies), which contains probes for 866 human and 89 viral miRNAs. Signals from microarrays were analyzed with GeneSpring software version 7.3.1 (Agilent Technologies), and only miRNAs with detected flag values labeled as present were used for further analysis. Changes in miRNA expression between experimental and control samples were calculated using Partek software (Partek, St. Louis, MO, USA). The threshold used to select differentially expressed miRNAs was a greater than 1.5-fold increase or decrease in expression over controls. The data have been submitted to the NCBI GEO: GSE115069 (<https://www.ncbi.nlm.nih.gov/geo/>).

### Real-Time Quantification of miRNA Expression by Stem-Loop RT-PCR

To synthesize cDNA from mRNA, corresponding miRNA-specific stem-loop RT primers (Table S2) and ReverTra Ace RT (Toyobo, Osaka, Japan) were used, and real-time PCR was performed using KAPA SYBR FAST qPCR Kits (Kapa Biosystems, Wilmington, MA, USA) with the corresponding primers (Table S2) on a LightCycler 480 Real-Time PCR System (Roche Applied Science, Mannheim, Germany). The specificity of the SYBR Green PCR signal was confirmed by melting-curve analysis. The PCR reaction mixture (10  $\mu$ L) consisted of 5  $\mu$ L of KAPA SYBR FAST qPCR solution, 3  $\mu$ L of miRNA-specific anti-sense primer (Table S2), 1  $\mu$ L of universal sense primers, and 1  $\mu$ L of 20-fold-diluted miRNA cDNA. Cycling conditions were 95°C for 5 min, followed by 40 cycles at 95°C for 15 s, then 63°C for 32 s, and 40°C for 20 s. U6 was used as an endogenous control for normalization. Data were analyzed using the  $2^{-\Delta\Delta C_t}$  method.<sup>54</sup>

### Anti-miR and Mimic to miR-1290

To assess the cellular function of miR-1290, we used an anti-sense approach to inhibit miR-1290 function, and transfected cells with a miR-1290 mimic to increase miR-1290 expression. For these experiments, A549 cells were grown to 70% confluence and treated with anti-miR-1290 (Exiqon, Vedbaek, Denmark) or miR-1290 precursor (Ambion) using Lipofectamine 2000 (Invitrogen) according to the manufacturer's instructions.

### Effect of LNA-1290 on WSN Viral Replication in Ferrets

Eight female healthy ferrets (*Mustela putorius furo*: outbred) of approximately 12 months of age, with body weights between 700 and 1,100 g and confirmed to be seronegative for antibodies against Aleutian disease virus, circulating seasonal influenza viruses, and A/WSN/33 by hemagglutination inhibition (HI) assays, were purchased

from a commercial breeder. The ferrets were anesthetized by intramuscular injection (i.m.) in the hind legs with a Zoletil-xylazine cocktail prior to the administration of LNA-1290 and virus. We dissolved the lyophilized LNA-1290 (Exiqon) in Tris-EDTA (pH 8.0) to a stock concentration of 20 mg/mL, and mixed 2 mg LNA-1290 or LNA-NC control with 150  $\mu$ L TransIT-TKO (Mirus Bio, Madison, WI, USA) transfection reagent and 100  $\mu$ L Opti-MEM (Gibco) for each ferret. The 1 mg/kg LNA-NC or LNA-1290 complex was intranasally administered to four ferrets each, at 1 day before virus challenge. The trachea was inoculated with WSN at a dose of  $10^7$  plaque-forming units (PFU) in 1 mL PBS. At 3 days after infection, nasal turbinate and lung tissue were collected for further analysis.

### Prediction of miR-1290 Target Genes

TargetScan was used to predict miR-1290 target genes, as described in previous research.<sup>55</sup> As mRNA destabilization is one of the effects that miRNA can exert on target genes, the IAV-downregulated host transcriptome was analyzed using the HumanHT-12 v4 Expression BeadChip Kit (Illumina, San Diego, CA, USA), as described in previous research.<sup>56</sup> The data were normalized, and calculation of the false discovery rate (FDR) was performed with Beadstudio 2.0 software (Illumina), using a customized algorithm. The genes that crossed the threshold of detection with  $p$  value  $\leq 0.05$ , and which had a differential score  $p$  value  $\leq 0.05$ , were considered to be differentially expressed. In addition, 948 host genes derived from RNAi-based screening assays have already been reported in the literature to be important for IAV replication.<sup>22,23,35,57–60</sup> Based on the integration of TargetScan predictions, IAV-downregulated transcriptome analysis results, and literature searches, 62 potential target genes were identified (Table S1). Among these, genes that were reported as part of the IAV vRNP interactome,<sup>3,34,61–63</sup> and for which antibodies were available in our laboratory, were subsequently selected for further study.

### Luciferase Reporter Assay

For the luciferase reporter assay, the CDS of huVIM-3' UTR and chVIM-3' UTR derived from A549 and DF-1 cells, respectively, were cloned into the pMIR-reporter vector. huVIM-3' UTR containing a mutant miR-1290 binding site (mut-huVIM-3' UTR) or chicken VIM-3' UTR containing a miR-1290 binding site (mut-chVIM-3' UTR) was mutated from wild-type huVIM-3' UTR or chVIM-3' UTR by two-step RT-PCR (2 $\times$  SuperRed PCR Master Mix with loading dye; BioTools, Taipei, Taiwan). At 24 or 48 h after cotransfection, the dual-luciferase-expressing cells were lysed with 50  $\mu$ L passive lysis buffer (Promega, Madison, WI, USA), and firefly and *Renilla* luciferase bioluminescence was measured with a Dual-Luciferase Reporter Assay with GloMax-Multi Detection System (Promega). *Renilla* luciferase was used as an internal control.

### FLAG-IP

To assess whether vimentin interacts with the IAV viral components NP, PB1, PB2, and PA (Figure 5A), HEK293T cells were respectively cotransfected with pcDNA3-PB1, pcDNA3-PB2, pcDNA3-PA, or pcDNA3-NP, and plasmids expressing FLAG-tagged human

vimentin (pFLAG-CMV2-huVIM) or a vector control (pFLAG-CMV2). After 48 h of transfection, cell lysates were collected with a FLAG Immunoprecipitation Kit (Sigma, St. Louis, MO, USA), and IP was performed using ANTI-FLAG M2 affinity gels (Sigma) and eluted using a FLAG peptide (Sigma), according to the manufacturer's protocol. Before the final wash, samples were incubated with 50 ng/ $\mu$ L RNaseA on ice for 30 min. The amount of input was 5% of the total IP lysates. To assess the interaction between vimentin with PB1, PB2, PA, or NP in a viral infection system (Figure 5B), HEK293T cells were transfected with plasmids expressing FLAG-tagged human vimentin (pFLAG-CMV2-huVIM) or a vector control (pFLAG-CMV2). After 24 h of transfection, the cells were infected with WSN at an MOI of 0.01 for 24 h. After 24 h of infection, cell lysates were collected and processed as described above, and the amount of input was 5% of the total IP lysates.

#### IFA and Confocal Microscopy

A549 cells were infected with WSN at an MOI of 0.01 for 48 h. At specific time points after infection, cells were fixed, permeabilized, stained, and analyzed as described in our previous study.<sup>11</sup>

#### Subcellular Protein Fractionation of A549 Cells Subjected to Vimentin Knockdown

A549 cells were respectively cotransfected with pcDNA3-PB1, pcDNA3-PB2, pcDNA3-PA, or pcDNA3-NP, and pol I-WSN-NS non-coding region minigenome reporter, using X-tremeGENE HP DNA Transfection Reagent (Sigma), as well as 20 nM of VIM siRNA (4390824, Silencer Select siRNAs; Thermo Fisher Scientific) or control siRNA (4390843, Silencer Negative Control No. 1 siRNA; Thermo Fisher Scientific), using Lipofectamine RNAiMAX (Invitrogen) transfection reagent according to the manufacturer's instructions. At 48 h after transfection, the cells were harvested and fractionated according to the experimental procedures described in the handbook provided along with the NE-PER Nuclear and Cytoplasmic Extraction Reagents (78833; Thermo Fisher Scientific). Approximately 60  $\mu$ g of protein lysate from the cytosol fraction and lysate from the nuclear fraction at half the volume of the cytosol fraction were further used to analyze the expression of NP, vimentin, LaminB1, and GAPDH, using western blotting.

#### Assessing the Effect of Vimentin on vRNP Polymerase Activity

For the viral polymerase activity assay, pPolI-Luc was kindly provided by Dr. Michael M. C. Lai of the Institute of Molecular Biology, Academia Sinica, Taiwan; plasmids pcDNA-3-PB1, pcDNA-3-PB2, pcDNA-3-PA, and pcDNA-3-NP were kindly provided by Dr. Robert G. Webster of the Department of Infectious Diseases, St. Jude Children's Research Hospital, Memphis TN, USA.

To assess the effect of vimentin on IAV viral polymerase activity, HEK293T cells were cotransfected with pcDNA3-PB1, pcDNA3-PB2, pcDNA3-PA, or pcDNA3-NP, as well as pol I-WSN-NS non-coding region minigenome reporter and *Renilla* luciferase expression plasmid (pRL-TK, internal control), using Lipofectamine 2000 (Invitrogen) transfection reagent. For vimentin overexpression exper-

iments, HEK293T cells were transfected with pFLAG-CMV-2-VIM or pFLAG-CMV-2 (vector control), using Lipofectamine 2000 (Invitrogen) transfection reagent. In vimentin knock-down experiments, HEK293T cells were transfected with 80 nM of VIM siRNA (4390824, Silencer Select siRNAs; Thermo Fisher Scientific, Waltham, MA, USA) or control siRNA (4390843, Silencer Negative Control No. 1 siRNA; Thermo Fisher Scientific), using Lipofectamine RNAiMAX (Invitrogen) transfection reagent, according to the manufacturer's instructions. At 48 h after transfection, cells were lysed with 250  $\mu$ L passive lysis buffer (Promega), and firefly and *Renilla* luciferase bioluminescence was measured with the Dual-Luciferase Reporter Assay with GloMax-Multi Detection System (Promega). The protein expression of vRNP components and vimentin was analyzed by western blotting.

#### Expression of miR-1290 in Virus-Infected Cells Treated with NH<sub>4</sub>Cl

A549 cells were pretreated with 40 mM NH<sub>4</sub>Cl in serum-free MEM for 30 min before virus absorption. The cells were infected with WSN at an MOI of 2 in 40 mM NH<sub>4</sub>Cl containing serum-free MEM for 2 h. After 2 h, cells were collected to measure miR-1290 expression using quantitative real-time PCR.

#### Expression of miR-1290 in Cells Treated with the ERK Activator TPA

A549 cells were treated with 100 ng/ $\mu$ L TPA in serum-free MEM for 30 min. After 30 min, cells were collected to measure miR-1290 expression, as well as the expression of p-ERK and total ERK, using quantitative real-time PCR and western blotting, respectively.

#### Statistical Analysis

The statistical analysis methods used to assess and present the results for each set of experiments are described in the figure legends.

#### Data and Materials Availability

Data have been submitted to the NCBI GEO: GSE115069 (<https://www.ncbi.nlm.nih.gov/geo/>).

#### SUPPLEMENTAL INFORMATION

Supplemental Information can be found online at <https://doi.org/10.1016/j.omtn.2019.04.028>.

#### AUTHOR CONTRIBUTIONS

S.-Y.H., C.-J.C., and S.-R.S. conceived and designed the study; S.-Y.H., C.-H.H., C.-J.C., Y.-T.L., S.-M.K., C.-G.H., L.-A.L., Y.-H.C., R.-L.K., and M.-F.C. conducted the experiments; T.-W.C. and C.-Y.L. analyzed the data; S.-Y.H. drafted the paper; and S.-Y.H. and S.-R.S. revised the paper. All authors have read and approved the paper.

#### CONFLICTS OF INTEREST

Part of the findings in this study were used to support an application for a United States patent, which was subsequently granted on January 31, 2017 (Patent No. US 9,556,436 B2, with S.-R.S., C.-J.C., and S.-Y.H. as the Inventors, and Chang Gung University as the Assignee). The authors report no other competing interests.

## ACKNOWLEDGMENTS

We would like to thank Dr. Robert G. Webster and Dr. Michael M. C. Lai for generously providing plasmids and Li-Zheng Tarn, DVM, for assistance with the animal work. We also thank Dr. Sung-Liang Yu, Dr. Jim-Tong Horng, and Dr. Bertrand Tan for helpful discussions related to this study. This study was supported by the Ministry of Science and Technology of Taiwan (MOST 104-2320-B-182-026-MY3 to S.-R. S.; and MOST 104-2321-B-016-002 and MOST 103-2321-B-016-006 to C.-H. H.) and Chang Gung Memorial Hospital (BMRP367 to S.-R. S.). This work was financially supported by the Research Center for Emerging Viral Infections from The Featured Areas Research Center Program within the framework of the Higher Education Sprout Project by the Ministry of Education (MOE) in Taiwan and the Ministry of Science and Technology (MOST), Taiwan (MOST 108-3017-F-182-001). The funders had no role in the study design, data collection and interpretation, or the decision to submit the study results for publication.

## REFERENCES

- Beare, A.S., and Webster, R.G. (1991). Replication of avian influenza viruses in humans. *Arch. Virol.* 119, 37–42.
- Suzuki, Y., Ito, T., Suzuki, T., Holland, R.E., Jr., Chambers, T.M., Kiso, M., Ishida, H., and Kawaoka, Y. (2000). Sialic acid species as a determinant of the host range of influenza A viruses. *J. Virol.* 74, 11825–11831.
- Naffakh, N., Tomoiu, A., Rameix-Welti, M.A., and van der Werf, S. (2008). Host restriction of avian influenza viruses at the level of the ribonucleoproteins. *Annu. Rev. Microbiol.* 62, 403–424.
- Subbarao, E.K., London, W., and Murphy, B.R. (1993). A single amino acid in the PB2 gene of influenza A virus is a determinant of host range. *J. Virol.* 67, 1761–1764.
- Steel, J., Lowen, A.C., Mubareka, S., and Palese, P. (2009). Transmission of influenza virus in a mammalian host is increased by PB2 amino acids 627K or 627E/701N. *PLoS Pathog.* 5, e1000252.
- Fornek, J.L., Gillim-Ross, L., Santos, C., Carter, V., Ward, J.M., Cheng, L.I., Proll, S., Katze, M.G., and Subbarao, K. (2009). A single-amino-acid substitution in a polymerase protein of an H5N1 influenza virus is associated with systemic infection and impaired T-cell activation in mice. *J. Virol.* 83, 11102–11115.
- Li, J., Ishaq, M., Prudence, M., Xi, X., Hu, T., Liu, Q., and Guo, D. (2009). Single mutation at the amino acid position 627 of PB2 that leads to increased virulence of an H5N1 avian influenza virus during adaptation in mice can be compensated by multiple mutations at other sites of PB2. *Virus Res.* 144, 123–129.
- Mehle, A., and Doudna, J.A. (2008). An inhibitory activity in human cells restricts the function of an avian-like influenza virus polymerase. *Cell Host Microbe* 4, 111–122.
- Moncorgé, O., Mura, M., and Barclay, W.S. (2010). Evidence for avian and human host cell factors that affect the activity of influenza virus polymerase. *J. Virol.* 84, 9978–9986.
- Chen, G.W., Chang, S.C., Mok, C.K., Lo, Y.L., Kung, Y.N., Huang, J.H., Shih, Y.H., Wang, J.Y., Chiang, C., Chen, C.J., and Shih, S.R. (2006). Genomic signatures of human versus avian influenza A viruses. *Emerg. Infect. Dis.* 12, 1353–1360.
- Kuo, S.M., Chen, C.J., Chang, S.C., Liu, T.J., Chen, Y.H., Huang, S.Y., and Shih, S.R. (2017). Inhibition of avian influenza A virus replication in human cells by host restriction factor tufm is correlated with autophagy. *MBio* 8, e00481-17.
- Mänz, B., Schwemmler, M., and Brunotte, L. (2013). Adaptation of avian influenza A virus polymerase in mammals to overcome the host species barrier. *J. Virol.* 87, 7200–7209.
- Lewis, B.P., Burge, C.B., and Bartel, D.P. (2005). Conserved seed pairing, often flanked by adenosines, indicates that thousands of human genes are microRNA targets. *Cell* 120, 15–20.
- Friedman, R.C., Farh, K.K., Burge, C.B., and Bartel, D.P. (2009). Most mammalian mRNAs are conserved targets of microRNAs. *Genome Res.* 19, 92–105.
- Huntzinger, E., and Izaurralde, E. (2011). Gene silencing by microRNAs: contributions of translational repression and mRNA decay. *Nat. Rev. Genet.* 12, 99–110.
- Voinnet, O. (2005). Induction and suppression of RNA silencing: insights from viral infections. *Nat. Rev. Genet.* 6, 206–220.
- Gottwein, E., and Cullen, B.R. (2008). Viral and cellular microRNAs as determinants of viral pathogenesis and immunity. *Cell Host Microbe* 3, 375–387.
- Bakre, A., Andersen, L.E., Meliopoulos, V., Coleman, K., Yan, X., Brooks, P., Crabtree, J., Tompkins, S.M., and Tripp, R.A. (2013). Identification of host kinase genes required for influenza virus replication and the regulatory role of microRNAs. *PLoS ONE* 8, e66796.
- Othumpangat, S., Noti, J.D., and Beezhold, D.H. (2014). Lung epithelial cells resist influenza A infection by inducing the expression of cytochrome c oxidase VIc which is modulated by miRNA 4276. *Virology* 468–470, 256–264.
- Khongnomnan, K., Makkoch, J., Poomipak, W., Poovorawan, Y., and Payungporn, S. (2015). Human miR-3145 inhibits influenza A viruses replication by targeting and silencing viral PB1 gene. *Exp. Biol. Med.* (Maywood) 240, 1630–1639.
- Loveday, E.K., Diederich, S., Pasick, J., and Jean, F. (2015). Human microRNA-24 modulates highly pathogenic avian-origin H5N1 influenza A virus infection in A549 cells by targeting secretory pathway furin. *J. Gen. Virol.* 96, 30–39.
- Karlas, A., Machuy, N., Shin, Y., Pleissner, K.P., Artarini, A., Heuer, D., Becker, D., Khalil, H., Ogilvie, L.A., Hess, S., et al. (2010). Genome-wide RNAi screen identifies human host factors crucial for influenza virus replication. *Nature* 463, 818–822.
- König, R., Stertz, S., Zhou, Y., Inoue, A., Hoffmann, H.H., Bhattacharyya, S., Alamares, J.G., Tscherne, D.M., Ortigoza, M.B., Liang, Y., et al. (2010). Human host factors required for influenza virus replication. *Nature* 463, 813–817.
- Gebert, L.F.R., Rebhan, M.A.E., Crivelli, S.E.M., Denzler, R., Stoffel, M., and Hall, J. (2014). Miravirsen (SPC3649) can inhibit the biogenesis of miR-122. *Nucleic Acids Res.* 42, 609–621.
- Yang, C., Sun, C., Liang, X., Xie, S., Huang, J., and Li, D. (2016). Integrative analysis of microRNA and mRNA expression profiles in non-small-cell lung cancer. *Cancer Gene Ther.* 23, 90–97.
- Mo, D., Gu, B., Gong, X., Wu, L., Wang, H., Jiang, Y., Zhang, B., Zhang, M., Zhang, Y., Xu, J., and Pan, S. (2015). miR-1290 is a potential prognostic biomarker in non-small cell lung cancer. *J. Thorac. Dis.* 7, 1570–1579.
- Kim, G., An, H.J., Lee, M.J., Song, J.Y., Jeong, J.Y., Lee, J.H., and Jeong, H.C. (2016). Hsa-miR-1246 and hsa-miR-1290 are associated with stemness and invasiveness of non-small cell lung cancer. *Lung Cancer* 91, 15–22.
- Zhang, W.C., Chin, T.M., Yang, H., Nga, M.E., Lunny, D.P., Lim, E.K., Sun, L.L., Pang, Y.H., Leow, Y.N., Malusay, S.R., et al. (2016). Tumour-initiating cell-specific miR-1246 and miR-1290 expression converge to promote non-small cell lung cancer progression. *Nat. Commun.* 7, 11702.
- Xiao, X., Yang, D., Gong, X., Mo, D., Pan, S., and Xu, J. (2018). miR-1290 promotes lung adenocarcinoma cell proliferation and invasion by targeting SOCS4. *Oncotarget* 9, 11977–11988.
- Bugge, W.A., Krause, K.E., and Horvath, C.M. (2013). Small RNA profiling of influenza A virus-infected cells identifies miR-449b as a regulator of histone deacetylase 1 and interferon beta. *PLoS ONE* 8, e76560.
- Kiezun, A., Artzi, S., Modai, S., Volk, N., Isakov, O., and Shomron, N. (2012). miRviewer: a multispecies microRNA homologous viewer. *BMC Res. Notes* 5, 92.
- Yelamanchili, S.V., Morsey, B., Harrison, E.B., Rennard, D.A., Emanuel, K., Thapa, I., Bastola, D.R., and Fox, H.S. (2014). The evolutionary young miR-1290 favors mitotic exit and differentiation of human neural progenitors through altering the cell cycle proteins. *Cell Death Dis.* 5, e982.
- Oh, D.Y., and Hurt, A.C. (2016). Using the ferret as an animal model for investigating influenza antiviral effectiveness. *Front. Microbiol.* 7, 80.
- Mayer, D., Molawi, K., Martínez-Sobrido, L., Ghanem, A., Thomas, S., Baginsky, S., Grossmann, J., García-Sastre, A., and Schwemmler, M. (2007). Identification of cellular interaction partners of the influenza virus ribonucleoprotein complex and polymerase complex using proteomic-based approaches. *J. Proteome Res.* 6, 672–682.
- Watanabe, T., Kawakami, E., Shoemaker, J.E., Lopes, T.J., Matsuoka, Y., Tomita, Y., Kozuka-Hata, H., Gorai, T., Kuwahara, T., Takeda, E., et al. (2014). Influenza virus-



- host interactome screen as a platform for antiviral drug development. *Cell Host Microbe* 16, 795–805.
36. Marjuki, H., Gornitzky, A., Marathe, B.M., Ilyushina, N.A., Aldridge, J.R., Desai, G., Webby, R.J., and Webster, R.G. (2011). Influenza A virus-induced early activation of ERK and PI3K mediates V-ATPase-dependent intracellular pH change required for fusion. *Cell. Microbiol.* 13, 587–601.
37. Zhu, Y., Jiang, Q., Lou, X., Ji, X., Wen, Z., Wu, J., Tao, H., Jiang, T., He, W., Wang, C., et al. (2012). MicroRNAs up-regulated by CagA of *Helicobacter pylori* induce intestinal metaplasia of gastric epithelial cells. *PLoS ONE* 7, e35147.
38. Zhu, Z., Qi, Y., Ge, A., Zhu, Y., Xu, K., Ji, H., Shi, Z., Cui, L., and Zhou, M. (2014). Comprehensive characterization of serum microRNA profile in response to the emerging avian influenza A (H7N9) virus infection in humans. *Viruses* 6, 1525–1539.
39. Yoon, K.A., Nakamura, Y., and Arakawa, H. (2004). Identification of ALDH4 as a p53-inducible gene and its protective role in cellular stresses. *J. Hum. Genet.* 49, 134–140.
40. Beloso, A., Martínez, C., Valcárcel, J., Santarén, J.F., and Ortín, J. (1992). Degradation of cellular mRNA during influenza virus infection: its possible role in protein synthesis shutoff. *J. Gen. Virol.* 73, 575–581.
41. Wheeler, J.G., Winkler, L.S., Seeds, M., Bass, D., and Abramson, J.S. (1990). Influenza A virus alters structural and biochemical functions of the neutrophil cytoskeleton. *J. Leukoc. Biol.* 47, 332–343.
42. Arcangeletti, M.C., Pinardi, F., Missorini, S., De Conto, F., Conti, G., Portincasa, P., Scherrer, K., and Chezzi, C. (1997). Modification of cytoskeleton and prosome networks in relation to protein synthesis in influenza A virus-infected LLC-MK2 cells. *Virus Res.* 51, 19–34.
43. Wu, W., and Panté, N. (2016). Vimentin plays a role in the release of the influenza A viral genome from endosomes. *Virology* 497, 41–52.
44. Parvin, J.D., Moscona, A., Pan, W.T., Leider, J.M., and Palese, P. (1986). Measurement of the mutation rates of animal viruses: influenza A virus and poliovirus type 1. *J. Virol.* 59, 377–383.
45. Nobusawa, E., and Sato, K. (2006). Comparison of the mutation rates of human influenza A and B viruses. *J. Virol.* 80, 3675–3678.
46. Castrucci, M.R., Donatelli, I., Sidoli, L., Barigazzi, G., Kawaoka, Y., and Webster, R.G. (1993). Genetic reassortment between avian and human influenza A viruses in Italian pigs. *Virology* 193, 503–506.
47. Zhou, N.N., Senne, D.A., Landgraf, J.S., Swenson, S.L., Erickson, G., Rossow, K., Liu, L., Yoon, K.J., Krauss, S., and Webster, R.G. (1999). Genetic reassortment of avian, swine, and human influenza A viruses in American pigs. *J. Virol.* 73, 8851–8856.
48. Lu, L., Lycett, S.J., and Leigh Brown, A.J. (2014). Reassortment patterns of avian influenza virus internal segments among different subtypes. *BMC Evol. Biol.* 14, 16.
49. Kelso, A., and Hurt, A.C. (2012). The ongoing battle against influenza: Drug-resistant influenza viruses: why fitness matters. *Nat. Med.* 18, 1470–1471.
50. Hayden, F.G., and de Jong, M.D. (2011). Emerging influenza antiviral resistance threats. *J. Infect. Dis.* 203, 6–10.
51. Neumann, G., Watanabe, T., Ito, H., Watanabe, S., Goto, H., Gao, P., Hughes, M., Perez, D.R., Donis, R., Hoffmann, E., et al. (1999). Generation of influenza A viruses entirely from cloned cDNAs. *Proc. Natl. Acad. Sci. USA* 96, 9345–9350.
52. Hoffmann, E., Neumann, G., Kawaoka, Y., Hobom, G., and Webster, R.G. (2000). A DNA transfection system for generation of influenza A virus from eight plasmids. *Proc. Natl. Acad. Sci. USA* 97, 6108–6113.
53. Hoffmann, E., and Webster, R.G. (2000). Unidirectional RNA polymerase I-polymerase II transcription system for the generation of influenza A virus from eight plasmids. *J. Gen. Virol.* 81, 2843–2847.
54. Chhabra, R., Dubey, R., and Saini, N. (2011). Gene expression profiling indicate role of ER stress in miR-23a~27a~24-2 cluster induced apoptosis in HEK293T cells. *RNA Biol.* 8, 648–664.
55. Agarwal, V., Bell, G.W., Nam, J.W., and Bartel, D.P. (2015). Predicting effective microRNA target sites in mammalian mRNAs. *eLife* 4, e05005.
56. Hao, L., Sakurai, A., Watanabe, T., Sorensen, E., Nidom, C.A., Newton, M.A., Ahlquist, P., and Kawaoka, Y. (2008). Drosophila RNAi screen identifies host genes important for influenza virus replication. *Nature* 454, 890–893.
57. Brass, A.L., Huang, I.C., Benita, Y., John, S.P., Krishnan, M.N., Feeley, E.M., Ryan, B.J., Weyer, J.L., van der Weyden, L., Fikrig, E., et al. (2009). The IFITM proteins mediate cellular resistance to influenza A H1N1 virus, West Nile virus, and dengue virus. *Cell* 139, 1243–1254.
58. Shapira, S.D., Gat-Viks, I., Shum, B.O., Dricot, A., de Grace, M.M., Wu, L., Gupta, P.B., Hao, T., Silver, S.J., Root, D.E., et al. (2009). A physical and regulatory map of host-influenza interactions reveals pathways in H1N1 infection. *Cell* 139, 1255–1267.
59. Su, W.C., Chen, Y.C., Tseng, C.H., Hsu, P.W., Tung, K.F., Jeng, K.S., and Lai, M.M. (2013). Pooled RNAi screen identifies ubiquitin ligase Itch as crucial for influenza A virus release from the endosome during virus entry. *Proc. Natl. Acad. Sci. USA* 110, 17516–17521.
60. Cheng, Q., Pappas, V., Hallmann, A., and Miller, S.M. (2005). Hsp70A and GlcA interact as partner chaperones to regulate asymmetric division in *Volvex*. *Dev. Biol.* 286, 537–548.
61. Dyer, M.D., Murali, T.M., and Sobral, B.W. (2008). The landscape of human proteins interacting with viruses and other pathogens. *PLoS Pathog.* 4, e32.
62. Nagata, K., Kawaguchi, A., and Naito, T. (2008). Host factors for replication and transcription of the influenza virus genome. *Rev. Med. Virol.* 18, 247–260.
63. Li, Y., Anderson, D.H., Liu, Q., and Zhou, Y. (2008). Mechanism of influenza A virus NS1 protein interaction with the p85 $\beta$ , but not the p85 $\alpha$ , subunit of phosphatidylinositol 3-kinase (PI3K) and up-regulation of PI3K activity. *J. Biol. Chem.* 283, 23397–23409.



Review

# The Redox Role of G6PD in Cell Growth, Cell Death, and Cancer

Hung-Chi Yang <sup>1,\*†</sup>, Yi-Hsuan Wu <sup>2,†</sup>, Wei-Chen Yen <sup>3,4</sup>, Hui-Ya Liu <sup>4</sup>,  
Tsong-Long Hwang <sup>5,6,7,8,9,10</sup> , Arnold Stern <sup>11</sup> and Daniel Tsun-Yee Chiu <sup>4,10,12,13,\*</sup>

<sup>1</sup> Department of Medical Laboratory Science and Biotechnology, Yuanpei University of Medical Technology, Hsinchu 30041, Taiwan

<sup>2</sup> Research Center for Chinese Herbal Medicine, College of Human Ecology, Chang Gung University of Science and Technology, Taoyuan 33043, Taiwan

<sup>3</sup> Graduate Institute of Biomedical Sciences, College of Medicine, Chang Gung University, Taoyuan 33043, Taiwan

<sup>4</sup> Department of Medical Biotechnology and Laboratory Sciences, College of Medicine, Chang Gung University, Taoyuan 33043, Taiwan

<sup>5</sup> Research Center for Food and Cosmetic Safety, College of Human Ecology, Chang Gung University of Science and Technology, Taoyuan 33043, Taiwan

<sup>6</sup> Graduate Institute of Natural Products, College of Medicine, Chang Gung University, Taoyuan 33043, Taiwan

<sup>7</sup> Chinese Herbal Medicine Research Team, Healthy Aging Research Center, Chang Gung University, Taoyuan 33043, Taiwan

<sup>8</sup> Department of Anaesthesiology, Chang Gung Memorial Hospital, Taoyuan 33043, Taiwan

<sup>9</sup> Department of Chemical Engineering, Ming Chi University of Technology, New Taipei City 24301, Taiwan

<sup>10</sup> Research Center for Chinese Herbal Medicine, Graduate Institute of Health Industry Technology, College of Human Ecology, Chang Gung University of Science and Technology, Taoyuan 33043, Taiwan

<sup>11</sup> School of Medicine, New York University, New York, NY 10016, USA

<sup>12</sup> Department of Pediatric Hematology/Oncology, Linkou Chang Gung Memorial Hospital, Taoyuan 33043, Taiwan

<sup>13</sup> Healthy Aging Research Center, Chang Gung University, Taoyuan 33043, Taiwan

\* Correspondence: hcyang@mail.ypu.edu.tw (H.-C.Y.); dtychiu@mail.cgu.edu.tw (D.T.-Y.C.); Tel.: +886-3-6108175 (H.-C.Y.); +886-3-2118800 (ext. 5097) (D.T.-Y.C.); Fax: +886-3-6102327 (H.-C.Y.); +886-3-2118540 (D.T.-Y.C.)

† These authors contributed equally to this work.

Received: 20 August 2019; Accepted: 7 September 2019; Published: 8 September 2019



**Abstract:** The generation of reducing equivalent NADPH via glucose-6-phosphate dehydrogenase (G6PD) is critical for the maintenance of redox homeostasis and reductive biosynthesis in cells. NADPH also plays key roles in cellular processes mediated by redox signaling. Insufficient G6PD activity predisposes cells to growth retardation and demise. Severely lacking G6PD impairs embryonic development and delays organismal growth. Altered G6PD activity is associated with pathophysiology, such as autophagy, insulin resistance, infection, inflammation, as well as diabetes and hypertension. Aberrant activation of G6PD leads to enhanced cell proliferation and adaptation in many types of cancers. The present review aims to update the existing knowledge concerning G6PD and emphasizes how G6PD modulates redox signaling and affects cell survival and demise, particularly in diseases such as cancer. Exploiting G6PD as a potential drug target against cancer is also discussed.

**Keywords:** G6PD; redox signaling; cell growth; cell death; cancer

## 1. Introduction

The central roles of glucose-6-phosphate dehydrogenase (G6PD) are the production of ribose and the reducing equivalent nicotinamide adenine dinucleotide phosphate (NADPH) via the pentose phosphate pathway (PPP). Both products are vital for the synthesis of many biological building blocks, such as nucleic and fatty acids. It has long been known that NADPH is extremely important in the maintenance of antioxidant defenses [1]. A preponderance of evidence has emerged recently to indicate that NADPH also serves as a pro-oxidant to generate reactive oxygen species (ROS) and reactive nitrogen species (RNS) as signal molecules for promoting cellular processes, such as cell growth. Clinically, G6PD deficiency is the most pervasive X-linked enzymopathy in the world. G6PD-deficient individuals tend to suffer from red cell disorders, including jaundice and drug- or infection-induced hemolytic anemia. These disorders are mostly due to a point mutation in G6PD [2]. Severe G6PD deficiency is intolerant for growth and development in animal models [3–8], while a modest increase of G6PD promotes a healthy lifespan [9].

Many excellent reviews have discussed the pro-survival role of G6PD [10–15]. How G6PD as a part of PPP affects cells, including cancer cell growth and death, has not been clearly defined. G6PD enhances tumor growth by maintaining intracellular redox homeostasis [16]. G6PD activity is increased in several types of cancers, including bladder, breast, endometrial, esophageal, prostate, gastric, renal, hepatic, colorectal, cervical, lung, and ovarian cancers, glioblastomas and leukemia, as well as gliomas [17–58]. The current review provides an update of the existing knowledge concerning G6PD and focuses on how G6PD is involved in redox signaling and how it affects cell survival and death, particularly in diseases such as cancer. Exploiting G6PD as a potential drug target against cancer is also discussed.

## 2. G6PD and Cellular Signaling with Emphasis on Redox Signaling

### 2.1. The Relationship between G6PD and Reactive Species (RS)

The production of superoxide by NADPH oxidase (NOX) and nitric oxide (NO) by NO synthase (NOS) is NADPH-dependent [59]. PPP is the major pathway for NADPH generation. Oxidative stress is considered a risk factor for aging and chronic diseases [60,61]. Low molecular weight signaling molecules play an important role in human health and disease. They are highly reactive and easily diffusible molecules that include ROS, RNS, reactive sulfur species (RSS), carbon monoxide, ammonia, and methane [59,62–65]. Questions of whether or not G6PD status affects the production of ROS, RNS, and RSS and how G6PD regulates the downstream redox signaling pathways, as well as its impact on human health and diseases, are of great interest.

Intracellular RS production is regulated by enzymatic reactions, which can subsequently affect the function and structure of proteins as well as the transcription of genes by modification of cysteines [66,67]. However, excess RS also contributes to the development of chronic diseases by attacking cellular components, such as proteins, lipids, and nucleic acids, leading to cellular dysfunction [68]. NO is a radical as well as an effector and messenger. Interaction between NO and ROS generates RNS. Both ROS and RNS can react with cysteine thiols to form RSS [69]. Hydrogen sulfide (H<sub>2</sub>S) has been initially considered as an environmental toxin through inhibition of mitochondrial respiration [62]. Endogenous H<sub>2</sub>S plays a role in diverse biochemical pathways governing signal transduction, bioenergetics, and lifespan [63,70]. Bacterial H<sub>2</sub>S is considered as a protective factor conferring antibiotic resistance and is involved in the host immune response [64]. The inhalation of H<sub>2</sub>S by mice causes hibernation-like behavior associated with reduced body temperature and metabolism [71].

Due to the complex interaction of signaling molecules and downstream effectors, the reactive species interactome (RSI) has been introduced as an integrative concept to delineate the complexity of the multiple level redox regulation system [65]. In response to various stress and environmental cues, the RSI increases fitness and flexibility at cell, tissue, and organismal level through rapid sensing and

adjustment. Full understanding of the mechanistic action of the RSI opens the opportunity to appreciate redox biology in human health and disease as well as providing novel strategies of prevention or intervention for precision medicine.

## 2.2. The Interaction between G6PD Status and Reactive Species

Human G6PD-deficient granulocytes exhibit impairment of hydrogen peroxide and superoxide production [72]. Similar to the finding in cells, lower superoxide release, and reduced atherosclerotic lesions have been observed in G6PD-deficient mice crossbred with ApoE null hemizygous mice [73]. G6PD-derived NADPH is responsible for superoxide production as found in a pacing-induced heart failure canine model [74]. The ventricular tissue homogenates show an increase in NADPH, superoxide, and G6PD activity. Treatment with a NOX inhibitor gp91(ds-tat) or a G6PD inhibitor, 6-aminonicotinamide (6-AN), significantly reduces superoxide generation in the failing heart homogenates. The upregulation of myocardial G6PD provides sufficient NADPH and fuels the superoxide-producing enzymes, suggesting a redox role for G6PD in the pathogenesis of heart disease [74]. G6PD regulates nuclear superoxide production by cooperating with NOX4 in the hepatocytes, where G6PD and NOX4 are co-localized in the nucleus [75]. The close relationship between G6PD and NOX4 maintains ROS homeostasis and promotes downstream redox signaling, including STAT3, c-SRC and SHP2, in melanoma cells [16]. Overexpression of G6PD in bovine aortic endothelial cells (BAECs) diminishes ROS accumulation following exposure to hydrogen peroxide, TNF- $\alpha$  or xanthine oxidase. Upregulation of G6PD in BAECs maintains the reduced form of glutathione [76].

NO generation can be stimulated by cytokines and NO donors [77,78]. NO affects cell survival, the immune response, insulin signaling, and stress disorders and provides vascular and neural protection [72,76,79–84]. NO production is dependent on G6PD status [10]. Increased levels of NO and G6PD have been found in the saliva of refugees suffering from stress and anxiety [80]. Upon lipopolysaccharide (LPS) or 12-myristate 13-acetate (PMA) stimulation, human granulocytes produce nitrite (derived from NO). Human granulocytes lacking G6PD fail to generate NO in the presence of LPS or PMA [72]. The cytokine IL-1 $\beta$  enhances inducible nitric oxide synthase (iNOS) expression and NO production in pancreatic islet cells causing cell death and disruption of insulin secretion. IL-1 $\beta$  upregulates G6PD activity and reduces cyclic adenosine monophosphate (cAMP) levels. 8-bromo-cAMP, an activator of cAMP-dependent protein kinase, increases G6PD activity, while a protein kinase A (PKA) inhibitor decreases G6PD activity [79].

G6PD status is positively correlated with NO production. Suppression of G6PD by the biochemical inhibitor dehydroepiandrosterone (DHEA) or an antisense oligonucleotide reduces the IL-1 $\beta$ -induced NO level, indicating that cAMP-dependent PKA enhances G6PD status stimulated by IL-1 $\beta$ -derived NO. Sodium nitroprusside, an NO donor, stimulates cell growth in G6PD-normal fibroblasts but induces apoptosis in G6PD-deficient fibroblasts [81]. Treatment with Trolox, an antioxidant, or ectopic expression of G6PD reverses NO-induced apoptosis in G6PD-deficient fibroblasts, suggesting a pro-survival role for G6PD. Reduced G6PD activity in endothelial cells is associated with elevated ROS and decreased NO bioavailability [82]. Overexpression of G6PD in BAECs treated with bradykinin also enhances cGMP and NOS activity. This results in an increase in bioavailable NO [76].

NO availability is essential for the regulation of leukocyte adhesion in the endothelium [85]. G6PD-deficient endothelial cells display lower level of endothelial nitric oxide synthase (eNOS), NO, and glutathione (GSH). Treatment of G6PD-deficient endothelial cells with high concentrations of glucose as a pro-atherosclerotic stimulus upregulates ICAM-1 and VCAM-1, as well as the oxidant markers, ROS, NOX4, and iNOS. By contrast, l-cysteine (a GSH precursor) attenuates these oxidative markers, suggesting that G6PD and GSH play a role in endothelial cell protection associated with NO availability [85]. LPS increases the mRNA expression of G6PD and glucose utilization of the PPP independent of iNOS in cultured rat astrocytes, while inhibition of NF- $\kappa$ B blocks the expression of G6PD and iNOS [83]. Inhibition of G6PD in rat astrocytes by DHEA prevents PPP activity and lowers

NADPH and the GSH/ glutathione disulfide (GSSG) ratio. The alteration of the GSH/GSSG ratio due to DHEA can be reversed by an iNOS inhibitor (AMT). These observations indicate that G6PD protects astrocytes from NO-mediated cell damage.

Peroxynitrite is an NO-derived neurotoxin [86,87]. It rapidly increases the activity of the PPP in neurons and astrocytes in primary culture, which leads to an increase in NADPH [84]. NO causes glutathione oxidation, NADPH consumption, and apoptosis in neurons but not astrocytes. Peroxynitrite treatment can counteract the effect caused by NO in neurons. Both endogenous and exogenous peroxynitrite induces G6PD activity in PC12 cells. Overexpression of G6PD confers resistance to NO-mediated apoptosis, while G6PD knockdown exacerbates cellular injury. Taken together, the cross-talk between G6PD and NO is crucial for cell protection.

H<sub>2</sub>S, an endogenous gasotransmitter, is involved in many biological functions, including neuronal regulation [88], smooth muscle relaxation [89], vascular relaxation and blood pressure regulation [90], inflammation [91,92], cell death signaling [93], and metabolism [71,94,95]. Overstimulation of the  $\beta$ -adrenergic receptor ( $\beta$ -AR) by isoproterenol in hypertrophic cardiomyocytes rapidly reduces the endogenous H<sub>2</sub>S level. Treatment with the H<sub>2</sub>S agonist (NaHS or norepinephrine) to augment H<sub>2</sub>S production suppresses the hypertrophy stimulated by the  $\beta$ -AR in cardiomyocytes [96]. Rats with transverse aortic constriction have approximately half the H<sub>2</sub>S level compared to normal rats [96]. Treatment of NaHS enhances G6PD activity, while the G6PD inhibitor (6-AN or DHEA) decreases hypertrophic responses in cardiomyocytes.  $\beta$ -AR upregulates G6PD expression and activity in rats [96].  $\beta$ -AR reduces cardiac p53, which negatively regulates G6PD by preventing G6PD dimerization [48]. G6PD inhibitors (either 6-AN or DHEA) reverse the  $\beta$ -AR-induced effect in rats with cardiac hypertrophy. Enhancing G6PD activity directly or inhibiting G6PD activity by p53 indicates that G6PD plays a critical role in mediating cardiac function regulated by H<sub>2</sub>S. Global transcriptome analysis reveals that H<sub>2</sub>S modulates an integrated metabolic network regulating cellular redox homeostasis. Consistent with these findings, several common biological processes emerging from the transcriptome data show that G6PD is a critical node modulating the effects among metabolic processes downstream of H<sub>2</sub>S [96].

Carbon monoxide (CO) is also a gaseous signaling molecule produced in humans. The major roles of CO are the modulation of the cardiovascular system, inhibition of platelet aggregation and adhesion, and neuronal development [97]. Like NO and H<sub>2</sub>S, CO is antiapoptotic, anti-inflammatory, and vasodilatory. It also promotes vascular growth [98–100]. The abnormal metabolism of CO has been associated with diseases, including heart failure, hypertension, inflammation, and neurodegeneration [101,102]. Since CO is produced from hemoglobin by heme oxygenase 1 and 2, it can be used as an index of heme catabolism [103]. Endogenous CO is increased in G6PD-deficient neonates with hyperbilirubinemia. CO may have a role in promoting neuronal differentiation, as the CO-releasing molecule (CORM-A1) enhances neuronal differentiation in neuroblastomas [104]. The PPP pathway in neuroblastomas is upregulated by CO, including 6-phosphogluconate dehydrogenase (PGDH) from the oxidative branch of the PPP and transketolase (TKT) from the non-oxidative branch of the PPP. The concentration and activity of G6PD are also increased. Knockdown of G6PD reverses the effect of neuronal differentiation induced by CO [104]. This finding is indicative of a protective role of G6PD in the modulation of CO-induced neuronal development.

### 2.3. The Redox Role of G6PD in Pathophysiology

Altered G6PD status is implicated in many cellular pathophysiological processes and diseases, including hypoxia, inflammation, microbial infection, sepsis, pulmonary vessel dilation, diabetes, hypertension, kidney disease, and brain injuries [24,30,105–126]. The PPP and glutathione-associated metabolic pathways are major antioxidant defense systems in cells. The regulation of these enzymes profoundly affects the development and clinical outcome of diseases.

One of the pro-inflammatory conditions leading to vascular injuries is hyperglycemia. The pro-inflammatory cytokine IL-1 $\beta$  primes high glucose-induced vascular inflammation. In human aortic smooth muscle cells (HASMC), surplus glucose uptake can be activated by IL-1 $\beta$  [105].

Upregulation of the glucose transporter, GLUT-1 or downregulation of mitochondrial respiration alone is insufficient for stimulating the inflammatory response. IL-1 $\beta$  activates the PPP, where excess glucose reroutes to this pathway. This in turn overactivates NOX, which produces superoxide and its reaction with neighboring molecules such as NO, resulting in the production of free radicals that stimulate a downstream inflammatory signaling pathway that leads to endothelial dysfunction [105]. Chronic inflammation in adipose tissue is implicated in insulin resistance found in obesity [117]. Downregulation of G6PD, 6-phosphogluconate dehydrogenase (6PGD) and glutathione-S-transferase (GST) is found in the liver of aged and streptozotocin-induced diabetic rats [106]. The antioxidant, SMe1EC2, increases the G6PD activity but not 6PGD and GST in diabetic rats. SMe1EC2 can also enhance G6PD activity in the lung and heart of aged diabetic rats. These findings suggest that diabetes-induced glucotoxicity can be affected by modulating the activity of redox enzymes [24].

Diabetes is a condition that impairs the body's ability to process blood glucose, including type 1, type 2, and gestational diabetes. G6PD deficiency could be a risk factor for diabetes. Impaired G6PD activity by high glucose concentrations in endothelial and kidney cells is associated with increased ROS production and decreased cell survival [127]. A decrease in G6PD expression and activity induced by ubiquitination and an increase in ROS in podocytes occurs at high glucose concentrations [128]. Hyperglycemia in obese mice results in increased oxidative stress in vascular endothelial cells and causes cardiovascular complications [129]. Smaller islets and impaired glucose tolerance are observed in G6PD-deficient mice [127]. Abnormal G6PD status mediates insulin resistance through oxidative stress in adipose tissue found in obese mice [118,119]. Upregulation of G6PD occurs in pancreatic  $\beta$ -cells in diabetic murine models [120]. Bone marrow transplantation from G6PD-deficient mice to wild-type mice reduces obesity-induced inflammation in adipose tissue and improves insulin resistance [107]. Overexpression of G6PD enhances ROS production and prooxidant enzymes, including iNOS and NOX [120].

ROS accumulation and  $\beta$ -cell apoptosis are indicative of the development of type 2 diabetes [130,131]. In high-fat-diet (HFD)-induced obesity, G6PD-deficient mice have decreased insulin and Homeostatic Model Assessment for Insulin Resistance (HOMA-IR) index [107]. These G6PD-deficient mice exhibit glucose and insulin tolerance as well as reduced insulin signaling, suggesting that G6PD deficiency is associated with an improvement in insulin resistance. Downregulation of NOX and upregulation of antioxidant genes, including catalase and glutathione peroxidase (GPx), are observed in G6PD-deficient mice. Although HFD-induced adiposity and fatty liver are not alleviated, the pro-inflammatory macrophages and cytokines are reduced in the G6PD-deficient mice. G6PD-deficient macrophages have decreased phosphorylation of MAPK, nuclear translocation of NF- $\kappa$ B, pro-inflammatory cytokines, and ROS accumulation. These events lead to enhanced insulin sensitivity in G6PD-deficient adipocytes and hepatocytes. Aberrant G6PD status in lipid-overload hepatocytes is associated with impaired pro-inflammatory cytokines via NF- $\kappa$ B and oxidative stress [117]. However, in some diseases with highly inflammasome activation, such as systemic lupus erythematosus, G6PD is upregulated (from array data GDS4185).

Microbial infection in G6PD-deficient patients is mainly related to hemolytic anemia caused by plasmodia or viruses [132–135]. Lack of G6PD activity is a risk factor for neonatal sepsis in males [108]. Sepsis-induced systemic inflammation and direct pulmonary injury cause acute lung injury (ALI) [136]. In airway epithelial cells (AECs), ALI can induce G6PD activity with the concomitant increase of ROS, nitrotyrosine, and NOX2 [110]. A G6PD inhibitor 6-AN suppresses airway inflammation in AECs induced by LPS and the ROS derived from NOX2, as well as increasing glutathione reductase activity. G6PD-knockdown A549 lung carcinoma cells are sensitive to staphylococcal infection, leading to apoptosis and ROS accumulation [109]. G6PD-deficient cells are susceptible to corona virus infection through inflammation and NF- $\kappa$ B signaling [111–113]. G6PD-deficient monocytes are more sensitive to infection by the dengue virus and have redox imbalance compared to matched control monocytes [115,116]. G6PD is highly expressed in human liver infected by the Hepatitis B virus (HBV) and HBV-associated cancer. G6PD activity can be stimulated by Hepatitis B virus X protein (HBx)



mediated by the activation of the transcription factor, Nrf2 [30]. Low G6PD activity in children following acute hepatitis infection may cause high morbidity [114]. Mild hepatic encephalopathy (MHE) is a hallmark of chronic liver failure (CLF). The upregulation of G6PD and nNOS in MHE suggests that there is a role for NO in its pathogenesis [123]. Increased level of nNOS and NO is associated with increased activity of NADPH diaphorase in the cerebellum of CLF rats, where overactivation of G6PD is observed [123].

NADPH oxidation can regulate vascular muscle relaxation [137]. Dimerization of the 1 $\alpha$  form of protein kinase G (PKG1 $\alpha$ ) induced by thiol oxidation contributes to the relaxation of isolated endothelium-removed bovine pulmonary arteries (BPA) to peroxide and responses to hypoxia [122]. G6PD inhibitors 6-AN and epiandrosterone are associated with enhanced PKG1 $\alpha$ . An siRNA against G6PD increases PKG1 $\alpha$  dimerization in BPA. Hence, reduced G6PD activity is associated with vasodilation, which may be beneficial in ameliorating pulmonary hypertension [121]. In addition, hypoxia activates G6PD and causes proliferation of the pulmonary artery smooth muscle (PASM) cell by increasing Sp1 and hypoxia-inducible factor 1 $\alpha$  (HIF-1 $\alpha$ ), which synthesize less contractile (myocardin and SM22 $\alpha$ ) and more proliferative (cyclin A and phospho-histone H3) proteins. Consequently, G6PD overactivation contributes to remodeling of pulmonary arterial and development of pulmonary hypertension [138].

### 3. The Role of G6PD in Cell Growth and Development

G6PD is an archetypical housekeeping enzyme for maintaining growth and development. Diminished G6PD activity or a dysfunctional PPP prevents normal cell proliferation [52,139–141] as well as embryonic and organismal development [3–8,142]. Aberrant activation of the PPP or G6PD is associated with tumorigenesis [21,23,25,27,29,32,42,44,45,47,49,52–54,57,58,141,143–149]. Rapidly growing cancer cells have evolved myriad mechanisms to activate G6PD for supporting the cellular requirements for NADPH production and fatty acid and nucleic acid synthesis. For example, activation of pro-oncogenic pathways enhances G6PD activity, including Ras, Src, and PI3K/Akt [16,37,150,151]. NAD-dependent deacetylase Sirtuin 2, encoded by the SIRT2 gene, promotes NADPH production and leukemia cell growth through deacetylating G6PD [57]. Heat shock protein 27 (HSP27 or HSPB1) enhances the binding between G6PD and SIRT2, leading to deacetylation and activation of G6PD. HSPB1 activates G6PD through SIRT2 to sustain cellular NADPH and pentose production in glioma cells [152]. SIRT5 desuccinylates and deglutarylates isocitrate dehydrogenase 2 (IDH2) and G6PD, respectively, and thus activates both NADPH-producing enzymes and confers resistance to oxidative stress [153].

Signaling pathways governing cancer cell survival associated with G6PD status are discussed in this review, including signal transducers and activators of transcription (STAT), Wnt/ $\beta$ -catenin, AMP-activated protein kinase (AMPK), p21-activated kinases (PAK), as well as others listed in Tables 1 and 2.

**Table 1.** The effects of upregulated glucose-6-phosphate dehydrogenase (G6PD) in cells.

Cancer Type	Effects of G6PD Activation	Mechanism	Reference
Breast	Enhanced proliferation and migration	Nrf2 upregulates Notch1 and HES-1 (proliferation) via G6PD/HIF-1 and regulates EMT (migration)	[44]
	Increased glucose uptake and NADPH production	Histone deacetylase inhibitor reprograms metabolism by upregulating G6PD	[32]
	Elevated NADPH, Reduced ROS	Overexpression of Histone H3K36 methyltransferase (NSD2) methylates the promoters and upregulates hexokinase 2 (HK2) and G6PD	[54]

Table 1. Cont.

Cancer Type	Effects of G6PD Activation	Mechanism	Reference
Leukemia	Enhanced cell proliferation and colony formation, lipid synthesis, and NADPH level	Deacetylation of G6PD by SIRT2	[57]
Lung	Increased glucose flux through PPP, Enhanced tumor growth as well as production of nucleotide, lipid and reducing equivalents	Glycosylation (O-GlcNAcylation) of G6PD	[45]
Ovarian	Cancer progression and carcinogenicity	Exosomes	[145]
Renal	Increased cell proliferation, altered cell cycle, increased ROS production	Activation of NOX4 leads to increased p-STAT3 and CyclinD1	[146]
Glioma	Increased cell proliferation, reduced DNA damage	Hsp27 (HSPB1) promotes the interaction between G6PD and SirT2	[152]
Multiple cancers	Cell cycle progression and cell proliferation	Phosphorylation of G6PD by Polo-like kinase 1(Plk1)	[49]

Table 2. The effects of downregulated G6PD in cells.

Cancer Type	Effects of G6PD Deficiency	Mechanism	Reference
Bladder	Reduced cell viability and growth, increased apoptosis	Increased ROS accumulation. Suppression of AKT	[42]
Breast	Reduced cell proliferation, cell survival, increased ROS, decreased ribose (in combination with TKT deficiency)	Increased glycolytic flux and glutamine intake. Decreased lipid synthesis	[25]
	Increased autophagosome, impairment of autophagy flux, increased lapatinib-induced cytotoxicity	Induced endoplasmic reticulum stress	[26]
Cervical	Inhibition of viability, decreased migration and proliferation, abnormal cytoskeleton reorganization	Increased ROS induces apoptosis	[20]
	Reduced cell proliferation	miR-206 targets 3'UTR of G6PD	[40]
	Inhibition of proliferation, promotion of apoptosis, reduced xenograft tumor growth in nude mice	miR-1 suppresses G6PD activity	[41]
Colon	High NADP, inhibition of dihydrofolate reductase (DHFR), impairment of folate-mediated biosynthesis	Induced ME1 and IDH1 compensation	[43]
Colorectal	Decreased synthesis of ribose and NADPH	Acetylation of G6PD at catalytic site by aspirin	[18]
Hepatocellular	Suppressed PPP flux, DNA synthesis, and cell growth	Bcl-2 associated athanogene (BAG3) suppresses dimerization and activity of G6PD	[154]
	Reduced G6PD activity	miR-1, miR-122 repress G6PD expression	[55]
Leukemia	Increased cytotoxicity, sensitivity to chemotherapy	Overactivation of TORC1	[31]
Lung epithelial	Induction of apoptosis, generation of ROS	Activation of TRAIL, FAS, TNF- $\alpha$ receptors, caspase3/9 by phytol	[155]
Melanoma	Cell cycle arrest, blockade of cell proliferation	Downregulation of cyclin D1 and CDK4, upregulation of p53 and p21	[16]
Pituitary	Inhibition of growth, Reduction of NADPH, Reduction of glycolysis	Upregulation miR-1 inhibits G6PD	[19]
Multiple cancers	Reduction of ribonucleotide and GSH and cell proliferation	Phase 2 drug (RRx-001) downregulates G6PD	[56]

### 3.1. Cyclin and STAT3/5

Signal transducer and activator of transcription (STAT) proteins are transcription factors involved in immunity and cellular proliferation, apoptosis, and differentiation. Misregulation of STATs causes cellular transformation and tumorigenesis by compromising immune surveillance. STAT proteins are constitutively active and enhance the expression of pro-survival and pro-growth genes [156]. Although they do not directly contribute to the regulation of DNA repair and the cell cycle checkpoint, they facilitate oncogenesis through their close relationship with apoptosis, angiogenesis, and the growth factor signaling pathways [157].

In melanoma cells, STAT3 and STAT5 are highly activated. Knockdown of G6PD in melanoma cell lines leads to the reduction of phosphorylated STAT5 [157]. Overexpression of G6PD in human melanoma cells enhances phosphorylated STAT5. Likewise, phosphorylated STAT3 is modulated by G6PD status [157]. These findings indicate that G6PD has an important role in oncogenesis mediated by STAT3 and STAT5. However, the detailed mechanism between G6PD status and STAT3/5 activity remains unclear. Using a melanoma cell line xenograft nude mouse model, mice injected with wild-type G6PD cells display faster tumor formation and larger tumor size than those mice with G6PD-deficient cells [158]. Tumors of wild-type G6PD cells are more aggressively malignant compared to G6PD-deficient cells. These observations suggest that G6PD status is vital to melanoma proliferation and differentiation.

G6PD status in melanoma cells is positively correlated with the expression of the cell cycle proteins, including cyclin D1 and cyclin E [158]. S100A4, a calcium binding protein that binds to p53, is involved in cancer growth, invasion and metastasis [159]. As both proteins are elevated in melanoma cells, it has been proposed that G6PD modulates p53 activity, thereby affecting melanoma cell growth and metastases through its influence on S100A4 [157]. G6PD status is also correlated with apoptosis inhibitory factors. In G6PD-deficient melanoma cells, the expression of Bcl-2 and Bcl-xL is significantly reduced. Fas, a death domain-containing protein regulating programmed cell death, is highly expressed in G6PD-deficient melanoma cells [160]. The protein expression of the STAT3/5 ratio and the phosphorylated STAT3/5 ratio are decreased in G6PD-deficient melanoma cells. Lack of G6PD in mice melanoma cells enhances apoptosis by upregulating Fas and downregulating Bcl-2 and Bcl-xL [158]. Taken together, G6PD status is linked to cell proliferation and cellular malignancy, possibly through the STAT3/5 ratio, in mice melanoma cells.

### 3.2. ID1/c-Myc/Wnt/ $\beta$ -Catenin

The potential oncogene ID1 is found in several cancers in humans, including breast, kidney, pancreas, and prostate cancers [161–163]. ID1, an inhibitor of differentiation and DNA binding-1, is a member of the helix–loop–helix of transcription factors. Cellular ID1 is involved in delaying replicative senescence, inhibition of differentiation, enhancement of proliferation, invasion, immortalization, and metastases [164]. ID1 confers chemotherapy and radiotherapy resistance in breast, colorectal, esophageal, lung, and pancreatic cancers [165,166]. Elevated ID1 is correlated with a poor clinical outcome which includes shorter survival or resistance to therapies in breast, cervical, and non-small cell lung cancers [167–169]. Knockdown of ID1 in oxaliplatin-resistant hepatocellular carcinoma (HCC) cells reduces proliferation and induces apoptosis [33]. Consistent with the in vitro findings, silencing ID1 reduces the size and growth of tumor xenografts in nude mice. These tumors have a lower level of proliferation and a higher level of apoptosis. Silencing ID1 in HCC cells results in a decrease of G6PD activity, NADPH, and an increase in ROS. Transfection of G6PD into ID1-knockdown HCC cells reverses these findings and induces oxaliplatin resistance [33]. These results suggest that the malignancy and chemoresistance of HCC cells induced by ID1 are mediated by the activation of the PPP via G6PD.

The fact that ID1 silencing in HCC cells suppresses G6PD promoter activity facilitates the identification of c-Myc binding sites in the G6PD promoter sequence. The oncogene c-Myc is essential for the regulation of tumor cell cycle progression and metabolic adaptation. c-Myc regulates many

genes that are involved in energy and glucose metabolism [170–172]. Transfection of c-Myc rescues the deficiency in ID1-knockdown in HCC cells. Pathway analysis indicates that ID1 activates c-Myc through Wnt/ $\beta$ -catenin. Activation of c-Myc through Wnt/ $\beta$ -catenin by ID1 is followed by the transcription of G6PD, thereby switching on the PPP, and consequently conferring HCC cells with chemoresistance to oxaliplatin [161].

### 3.3. AMPK

AMP-activated protein kinase (AMPK), ubiquitous in eukaryotes, is a heterotrimeric protein complex. It contains a protein kinase domain ( $\alpha$  subunit), a glycogen binding domain ( $\beta$  subunit), and four cystathionine- $\beta$ -synthase domains ( $\gamma$  subunit) [173]. A main function of AMPK is the monitoring of intracellular ATP fluctuations and the balancing of ATP levels by phosphorylation of downstream substrates. AMPK regulates cell growth and reprograms metabolism through transcription and by interacting with metabolic enzymes, including acetyl-CoA carboxylase (ACC), HMG-CoA reductase, and G6PD [174].

Reprogramming of energy metabolism is closely linked to metastases in tumor cells [175,176]. During metastases, reprogramming of glycolysis and the acidic environment enhance angiogenesis [177]. Increased carbon flux through the PPP enhances tumor cell malignancy and aggressiveness [178]. Attachment to the extracellular matrix (ECM) is critical for growth and differentiation of normal epithelial cells [179]. Upon detachment from the ECM, cells undergo apoptosis, known as anoikis [180]. Cancer cells need to adapt to the absence of the ECM in the circulation during metastases. Such a phenomenon is known as anchorage-independent growth. During this process, multiple survival-related cellular and molecular changes confer anoikis resistance in cancer cells.

Anchorage-independent growth is found in human breast cancer cells [51]. Compared to adhered breast cancer cells, detached cells display elevated ROS. Suppression of G6PD further increases the ROS level, suggesting that G6PD regulates intracellular ROS. The detached breast cancer cells compared to the adhered breast cancer cells have reduced glucose uptake, lactic acid, and ATP, indicating a reduction in glycolysis. Fatty acid oxidation (FAO) enzymes, including phospho-ACC and palmitoyl-transferase-1, as well as G6PD are upregulated in the detached cells. Inhibition with a newly synthesized flavonoid GL-V9 shows that FAO, not glycolysis, is the main source of ATP upon detachment. These findings suggest that during anoikis, detached cells shift glycolysis to the PPP in order to maintain redox homeostasis, while fatty acid oxidation is enhanced to support ATP. GL-V9 inhibits anchorage-independent growth through an increase in ROS. The mechanism involves the disruption of the balance between the PPP and FAO and the induction of glycolipid reprogramming. Activation of AMPK increases p-ACC and CPT1A. GL-V9 downregulates G6PD mRNA and its protein level through AMPK. Taken together, AMPK is activated by a flavonoid, causing a decrease in the PPP and FAO reprogramming and an increase in ROS. This results in the inhibition of anchorage-independent growth in breast cancer cells [51].

### 3.4. PAK4/Mdm2/E3/p53

The tumor suppressor p53 is a highly mutated gene in human cancers. p53 interacts with G6PD and regulates its function by preventing G6PD dimerization. Mutants of p53 in tumors lack G6PD-inhibitory activity [48]. Maintaining p53 activation is important for regulating cellular glucose consumption and biosynthesis via G6PD modulation. This suggests that other G6PD-interacting proteins can be used in cancers with p53 mutations. Members of the p21-activated kinases (PAKs) are serine/threonine protein kinases. The role of PAKs includes cell survival, cytoskeletal reorganization, gene transcription, and cell transformation. Overexpression of PAKs is commonly found in cancers [181–184]. The group II PAK4 is associated with tumorigenesis and progression. Although PAK1 is a regulator of glucose metabolism [185], it is not known if glucose metabolism is regulated by PAK4 in tumorigenesis.

PAK4 promotes lipid biosynthesis in colon cancer cells. Overexpression of PAK4 in colon cancer cells enhances glucose and NADPH production [186]. Elevation of G6PD activity is associated with

PAK4 overexpression, while PAK4 knockdown reduces G6PD activity. DHEA decreases glucose consumption and NADPH. These findings indicate that PAK4-induced glucose consumption and NADPH production is mediated by enhanced G6PD activity. The close relationship between PAK4 and G6PD is supported by the fact that PAK4 binds to G6PD and the complex is co-localized in the cytoplasm. p53 is a downstream protein of PAK4 [48,187]. In vitro translated p53 binds to PAK4, suggesting that p53 interacts with PAK4. Silencing of PAK4 enhances p53 protein expression, indicating that PAK4 causes p53 degradation.

The ubiquitin proteasome pathway modulates p53 degradation [188]. PAK4 knockdown impairs p53 ubiquitination. Murine double minute 2 (Mdm2), a p53 antagonist, suppresses p53 activity by two mechanisms: inhibition of p53 transcriptional activity by direct binding and enhancement of p53 degradation through the Mdm2 component, E3 ligase [189]. PAK4 interacts with Mdm2, while PAK4 knockdown reduces the level of Mdm2. PAK4 facilitates the binding of Mdm2 and p53. These findings indicate that the enhanced interaction of Mdm2 and p53 caused by PAK4 can promote ubiquitin-mediated p53 degradation. In the absence of p53, PAK4 fails to affect glucose consumption and NADPH. PAK4 status in colon tissue from patients with colon cancer is positively correlated with the level of G6PD. This is in accord with the fact that PAK4 upregulates G6PD activity. Histological scoring shows that elevated PAK4 and G6PD is significantly linked to poor pathological tumor-node metastases (pTNM) [186].

#### 4. The Role of G6PD in Cell Death

Dying cells engage in a reversible process until a first irreversible phase is trespassed, such as caspase activation, complete permeabilization of the mitochondrial outer membrane or exposure of phosphatidylserine (PS) sending the “eat me” signal to neighboring cells [190]. The concept of the restriction point concerning cell death has yet to be specifically defined, and different types of cell death may occur at the same time. There are several types of cell death, such as regulated cell death (RCD), accidental cell death, and necroptosis, depending on different characteristics and criteria. Cells can readily switch from one type of cell death to another [191].

Based on the distinct cellular morphology, there are three major types of cell death, including type I (apoptosis), type II (autophagy), and type III (necrosis) [191,192]. Downregulation of G6PD impairs most cellular functions, especially regarding cell survival [1]. The major function of G6PD is the maintenance of cellular redox homeostasis by regenerating NADPH. A deficiency of G6PD makes cells more susceptible to stress by increasing oxidative damage [193]. G6PD-depleted embryos show more oxidative damage after the establishment of the blood circulation [3]. These studies indicate the importance of the antioxidant function of G6PD in growth and development [194].

##### 4.1. Apoptosis

Apoptosis (extrinsic apoptosis) is the most common cell death caused by G6PD inhibition. G6PD deficiency enhances cellular oxidative stress and apoptosis that can be inhibited by free radical scavengers [195]. In erythrocytes, G6PD is the predominant enzyme for the production of NADPH against oxidative damage. Erythrocyte suicide, known as eryptosis, causes cell shrinkage, membrane blebbing, protease activation, and phosphatidylserine migration to the outer membrane leaflet [196,197]. In nucleated cells, G6PD inhibition induces apoptosis and suppresses cellular proliferation [127,198], especially in cells undergoing oxidative stress [4,199]. Increased glucose levels impair G6PD activity and result in apoptosis in kidney podocytes mediated by ubiquitination of G6PD at K366 and K403 [128]. The Von Hippel–Lindau (VHL) protein, a subunit of E3 ubiquitin ligase, binds to G6PD and undergoes ubiquitination in kidney podocytes. The ubiquitinated G6PD protein is degraded by the ubiquitin proteasome pathway, and cellular redox homeostasis becomes unbalanced by the increased oxidative stress [128].



## 4.2. Autophagy

Autophagy is a different programmed cell death characterized by large-scale vacuolization of the cytoplasm in a caspase-independent manner [200]. The autophagy–lysosomal pathway is a major pathway for removing damaged macromolecules and organelles [201]. Autophagic pathways can be stimulated by a number of events, such as exposure to pathogens and oxidative stress. Autophagy is modulated by redox homeostasis and glucose metabolism [202]. G6PD status can affect autophagy [26]. G6PD inhibition by polydatin induces endoplasmic reticulum stress and deregulates autophagy flux in cancer cells. Autophagosome formation is increased by polydatin. G6PD inhibition synergistically increases the cytotoxic effect of lapatinib in cancer cells, which can be abolished upon autophagy inhibition [26].

## 4.3. Necrosis and NETotic Cell Death

Necrosis is a premature cell death induced by injuries, including toxins, trauma or infections. Cells undergoing necrosis show swelling, cell membrane rupture, and expulsion of cell contents to nearby cells [203]. G6PD deficiency predisposes cells to the risk of viral and bacterial infections [109, 111, 116, 204] followed by necrotic cell death. Pretreatment with antioxidant N-acetylcysteine (NAC) confers resistance to infection of G6PD-deficient cells [204]. NETotic cell death is another form of cell death in neutrophils by producing neutrophil extracellular traps (NETs). It is considered as regulated form of necrosis [205]. The function of NETs is to trap bacteria and kill them by protruding filaments consisting of fragmented chromatin and antimicrobial peptides [206]. NETotic cell death is regulated by NOX activity [207]. Severe G6PD deficiency increases the susceptibility to infection by the absence of NETotic cell death [208].

## 5. Strategies to Suppress G6PD

The modulation of G6PD status can be achieved by biochemical inhibitors or molecular technologies. These approaches are discussed in this section as well as listed in Table 3.

**Table 3.** Strategies of G6PD inhibition.

Status	Mechanism	Reference
High glucose	Ubiquitination and degradation of G6PD	[128]
G6PD inhibitors		
DHEA	Uncompetitive inhibitor of G6PD	[20,209]
6-AN	Competitive inhibitor of G6PD	[42]
Polydatin	Inhibition of G6PD activity	[210]
Zoledronic acid	Inhibition of G6PD activity	[211]
Metabolic switch	From PPP to glycolysis	[31,211,212]
Noncoding RNA regulation	Direct target to G6PD mRNA or target to G6PD mRNA's 3'-UTR	[7,41,55,213,214]
TERT regulation	Inhibition of hTERT decrease G6PD expression	[215]
Protein-protein interaction	BAG3 directly interacts with G6PD	[48,154]

### 5.1. Biochemical Inhibitors

#### 5.1.1. Dehydroepiandrosterone

Dehydroepiandrosterone (DHEA) is an adrenal steroid whose biological role is not fully understood. G6PD can be inhibited by 17- and 20-ketosteroids [216]. DHEA is a potent noncompetitive inhibitor of mammalian G6PD. It decreases cellular NADPH levels and NADPH-dependent ROS production. The detailed mechanism of noncompetitive inhibition is with respect to both G6P and NADP<sup>+</sup>, where DHEA binds to the enzyme–coenzyme–substrate ternary complex [209]. DHEA has been widely used as a G6PD inhibitor to suppress the PPP in cancer cells [20,217].

### 5.1.2. 6-Aminonicotinamide

Structurally similar to NADP, 6-Aminonicotinamide (6-AN) is an inhibitor of 6-phosphogluconate dehydrogenase. 6-AN is a competitive inhibitor of G6PD [218]. 6-AN also inhibits oxidoreductase and, in turn, the malic enzyme reaction [219].

### 5.1.3. Polydatin

Polydatin (3,4',5-trihydroxystilbene-3- $\beta$ -d-glucoside (PD)), also named piceid, is a natural monocrystalline compound found in *Polygonum cuspidatum* (Polygonaceae) and other plants, such as grapes and peanuts [220]. PD is a glucoside of resveratrol. It has several biological effects, such as induction of apoptosis in cancer cells. PD inhibits G6PD activity and stimulates the generation of cellular ROS by increasing endoplasmic reticulum stress [210]. PD causes cell cycle arrest in the S phase, inducing about 50% apoptosis and inhibiting about 60% invasion. Currently, there is no specific G6PD or PPP inhibitors available in clinical trial. A phase II clinical trial shows PD is well tolerated in humans. It also limits cancer growth and metastatic spread in mice models of oral cancer [210].

### 5.1.4. Zoledronic Acid

Zoledronic acid (ZA), also known as zoledronate, is currently a standard medication used to treat bone diseases, such as bone metastases and osteoporosis. ZA inhibits cell proliferation by decreasing the expression of G6PD in bladder cancer cells [211]. The stability of TAp73, the activator of G6PD, is decreased in ZA-treated bladder cancer cells through inhibition of Ras activity. This suggests that ZA can inhibit TAp73 stability and decrease G6PD activity via blocking Ras signaling in bladder cancer cells.

## 5.2. Noncoding RNA Regulation

### 5.2.1. Small Interfering RNA

Small interfering RNA (siRNA) is a class of double-stranded RNA molecules with 20–25 base pairs in length. It mediates the interference of gene expression by its complementary nucleotide sequences to degrade mRNA. Due to the polymorphism of target genes, the specific sequence complementary to target genes needs to be carefully considered. Many studies on G6PD use siRNA to knockdown G6PD and investigate its role in cell lines. The human G6PD gene has more than 400 biochemical variants worldwide [221]. In this regard, the genetic polymorphism of G6PD needs to be considered for knocking down G6PD expression.

### 5.2.2. Long Noncoding RNA

The genome sequences which do not encode proteins with lengths exceeding 200 nucleotides are usually transcribed into long noncoding RNA (lncRNA). LncRNAs play an important role in disease progression. Growth arrest-specific transcript 5 (GAS5), a lncRNA, has been identified in the dysregulation of the cell cycle in several cancers [222–224]. Melanoma samples from patients show significantly reduced GAS5 expression in advanced disease, such as larger tumor size and a high incidence of metastases [213]. GAS5 knockdown increases melanoma cell proliferation by inducing Cyclin D1, CDK4, and p27 expression and inhibiting apoptosis via increasing Bcl-2 expression. The use of RNA co-immunoprecipitation reveals that GAS5 interacts with G6PD. This results in inhibition of G6PD and NOX activity leading to a decrease in superoxide and NADP<sup>+</sup>. These data suggest that GAS5 could regulate cellular redox balance by directly interacting with G6PD.

### 5.2.3. MicroRNA

MicroRNA (miRNA) are small noncoding RNA molecules that inhibit gene expression via base-pairing with complementary sequences within mRNA molecules. MiR-1, which belongs to the

miR-1/206 family, is involved in heart diseases such as myocardial hypertrophy and infarction [225,226]. High concentrations of glucose lead to significant upregulation of miR-1 and miR-206 in cardiomyocytes. This results in an acceleration of glucose-mediated apoptosis [214]. In cardiovascular diseases, the upregulation of miR-1 increases cellular oxidative stress by downregulating superoxide dismutase 1 and G6PD protein expression [227]. miR-1 is involved in the regulation of G6PD expression through targeting the 3' UTR sequence [41,227,228]. This indicates that the inhibition of G6PD by high glucose concentrations may be due to the upregulation of miR-1. Another miRNA candidate of G6PD inhibition is miR-122, which is the liver-specific miRNA. MiR-122 decreases G6PD expression by directly interacting with its 3'UTR as determined by the luciferase reporter assay. Ectopic expression of miR-122 decreases G6PD expression in hepatocellular carcinoma cells and HepG2 cells [55]. These data indicate that miR-1 and miR-122 regulate the PPP by inhibiting G6PD.

### 5.3. Other Approaches

#### 5.3.1. TERT Regulation

Telomerase is a ribonucleoprotein with three components, including a human telomerase RNA subunit, a telomerase-associated protein, and a human telomerase reverse transcriptase (hTERT). Its main function is to insert a telomere repeat sequence at the 3' end of telomeres [215]. The maintenance of telomeres supports long-term cellular growth [229]. Active telomerase is commonly observed in stem cells and human cancers [230]. In glioma cells, costunolide treatment inhibits hTERT activity and induces cell apoptosis by an ROS-dependent pathway. hTERT inhibition by costunolide, or by molecular technologies, such as siRNA or dominant-negative hTERT, attenuates G6PD expression [215]. This indicates that there is a possible role for G6PD in the Nrf2-TERT loop for maintaining the oxidative defense responses in astrocytes or glial cells.

#### 5.3.2. Protein-Protein Interactions

The Bcl-2 associated athanogene 3 (BAG3) protein is involved in several cellular functions, such as autophagy, cell cycle regulation, cellular development, and pathogen replication [231,232]. In addition to the interaction with the ATPase domain of Hsc/Hsp70 family, it also contains multiple protein-binding motifs interacting with chaperons. In hepatocellular carcinoma cell models, BAG3 protein directly interacts with G6PD by inhibiting G6PD dimerization and activity. Such an interaction decreases the PPP flux and cell growth without altering cellular NADPH. BAG3 protein directly binds to G6PD to exert the tumor suppressor-like function in HCCs [154].

### 5.4. G6PD as the Basis for Therapeutic Approaches

Several G6PD inhibitors induce apoptosis in tumor cells. In noncoding RNA regulation, RNA-based therapeutics might be a reasonable approach in cancer therapy. Although there has been some success with preclinical studies utilizing RNA-based therapy, few have proceeded to clinical trials [233]. The challenges for RNA-based therapeutics include an off-target effect, target gene polymorphisms, and ineffective delivery systems to the site of interest [234].

6-AN is used for chemotherapy in various cancers, but the treatment is always associated with severe nerve damage [235]. Clinical trials with DHEA have been unsuccessful because of the need for high oral doses and the conversion of DHEA into other active forms [11]. Although PD and ZA have been used in clinical trials for the treatment of irritable bowel syndrome [234] and Paget's disease of bone, respectively, the detail mechanism of G6PD inhibition of PD and ZA requires further elucidation.

Since G6PD is a biomarker and G6PD inhibition has potential as a therapy for cancer, a promising series of recently developed inhibitors could be designed according to their interaction. Using the backbone of the inhibitor to develop a novel and powerful G6PD inhibitor has become an important issue in cancer therapeutics. Computational methods have been used to analyze the binding structures and free energies of G6PD for designing potential DHEA derivatives [236]. This establishes valuable insights

into detailed enzyme-inhibitor binding. Such *in silico* findings can provide a new understanding for the possible design of potent G6PD inhibitors for the treatment of diseases.

## 6. G6PD/PPP as an Anticancer Target

Tumorigenesis is a dynamic and complex process, in which each state of the tumor development is closely connected. A dynamic change in glucose metabolism is a feature of cancer cells. The Warburg effect is characterized by the fact that cancer cells favor glycolysis with increased lactate production even in the presence of oxygen rather than the oxidative phosphorylation pathway, which is the preference of most other cells of the body [237]. The metabolic switch is known as the Warburg effect and is responsible for promoting the synthesis of essential cellular components in rapidly-proliferating cancer cells. The metabolic switch affects cancer cells and other immune cells, such as macrophages, T lymphocytes, and myeloid-derived suppressor cells (MDSCs) [238]. Targeting metabolic switches or metabolism-regulated signaling pathways in tumor development can be a potential strategy for anticancer treatment, or in combination with immunotherapies.

The metabolic switch plays an important role in tumor growth, including immune escape, tumor progression, and resistance to chemotherapy. Activation of G6PD is the first line response against oxidative stress in cancer cells [239]. Cancer cells obtained from thoracic esophageal squamous cell carcinoma patients utilize the PPP in order to meet the need for rapid growth and for developing resistance to chemotherapy [38,240,241]. Oxidation of G6PD, post-translational modification or allosteric interactions are the direct result of inhibition by NADPH during acute stress-induced glucose rerouting [242,243]. This may explain why G6PD is important in redox-sensitive metabolism and is required in rapidly proliferating cells. In bladder cancer cell metabolism, increased expression of G6PD and fatty acid synthase are observed. This favors increased metabolism of glucose by the PPP and increased fatty-acid synthesis [37]. PPP hyperactivation may act procarcinogenically in bladder cancer cells [211]. Mitigation of the Ras-TAp73-G6PD pathway by ZA results in the inhibition of G6PD, leading to retardation of bladder cancer cell proliferation. This indicates that the Ras-TAp73-G6PD pathway may be the target for G6PD inhibition. Metabolic analysis of acute myeloid leukemia (AML) cells has revealed that the PPP acts as an important pro-survival pathway by increasing mTORC1 activity [31]. Overexpression of G6PD correlates with an adverse prognosis and has been pinpointed as a new biomarker in AML as determined by analysis of the cancer genome atlas AML database. G6PD inhibition induces *in vitro* and *in vivo* chemotherapeutic cytotoxicity in AML cells, demonstrating that high mTORC1 expression may be a target for G6PD inhibition. Unlike in cancer cell studies, the metabolic switch is also important in neuronal development [244]. Cdh1 is involved in regulating neuronal survival, especially in volatile anesthetic-induced neuronal apoptosis. Prolonged sevoflurane anesthesia significantly decreases Cdh1 and results in a glucose metabolism shift from the PPP to neuronal glycolysis, leading to higher susceptibility to oxidative stress in the brain. This indicates that Cdh1 may be a novel target for glucose metabolic reprogramming.

Mutations of FMS-like tyrosine kinase 3 (FLT3) are often observed in acute myeloid leukemia (AML). This is most likely why FLT3 inhibitors ultimately fail to achieve long-term remission. Ataxia telangiectasia mutated (ATM) is identified as the reason for resistance to FLT3 inhibitor therapy as found by a genome-wide RNAi-based screen. Inactivating ATM or its downstream effector G6PD sensitizes AML cells to FLT3 inhibitor-induced apoptosis [245]. These studies indicate that G6PD plays an important role in cancer metabolism. Its key role in cancer promotes cell proliferation and antioxidation. The use of a G6PD inhibitor increases cancer cell death. This could be a strategy for combining with other cancer therapies, such as radiotherapy, chemotherapy, and immunotherapy.

The upregulation of the PPP in cancer cells makes it a potential target for cancer therapy. A major characteristic of cancer cells in coordinating glucose utilization in response to cell physiology is the reprogramming of glucose metabolism. The rerouting of glucose to the PPP produces high levels of NADPH to counteract the ROS, while providing nucleotides for DNA synthesis. These activities confer resistance to elevated ROS and DNA damage. Increased PPP activity induces high levels of

ROS. This is counteracted by an adaptive response that is found with the use of chemotherapeutic agents [26,32,246], radiation [247–250], and oxidative agents [28,239,251]. Drug-resistant cancer cell lines display increased G6PD activity and increased intracellular glutathione concentrations indicative of oxidative PPP. Enhanced non-oxidative PPP is linked to the resistance of DNA-damaging drugs, like 5-fluorouracil (5-FU) [252]. Elevated TKT is detected in colon cancer cells. Although increased PPP is a weapon used by drug-resistant cancer cells, modulation of the PPP status can serve as a strategy for sensitizing cancer cells to therapies. Doxorubicin, a member of the anthracyclines, is used in chemotherapy. It is metabolized by cytochrome p450 and causes cytotoxicity by producing ROS [253]. Reduced G6PD activity has been found in doxorubicin-resistant breast cancer cells. Stimulation of the PPP may sensitize cancer cells to doxorubicin. Treatment of breast cancer cell lines with l-arginine in combination with 5-FU enhances apoptosis and decreases metastases by targeting G6PD [36]. 6-AN, is cytotoxic in acute myeloid leukemia cells and sensitizes these cells to chemotherapy [31]. Inhibiting G6PD in breast cancer cells synergistically enhances the anti-HER2 tyrosine kinase inhibitor-induced cytotoxic effect [26].

Such metabolism-based therapeutic strategies might be a solution for impeding rapid growth and metastases as well as cancer cell heterogeneity in cancer stem cells [144,254,255]. The activity and localization of G6PD are regulated by several proteins, including STAT, ID1, p53, BAG3, PAK4, HGF, and AMPK [33,48,51,154,186]. Disrupting the interaction between G6PD and these proteins can inhibit the reprogramming of glucose toward the PPP and impair the biosynthesis of the building blocks of cancer cells associated with a decrease in intracellular NADPH. This can be another potential therapeutic strategy to thwart rapidly growing cancer cells.

## 7. Conclusions

The main function of G6PD is to provide sufficient reducing power to support growth and maintain redox homeostasis. Studies regarding G6PD deficiency have traditionally focused on red cell disorders. Current studies on nucleated cells reveal that G6PD participates in a variety of cellular processes via redox signaling. A close relationship exists between G6PD-derived NADPH and reactive species. In particular, NOX and NOS are two major NADPH-dependent enzymes that generate reactive species involved in cellular signaling. Altered redox homeostasis in G6PD-deficient cells leads to impaired antioxidant defenses and cellular signaling. G6PD deficiency is associated with a myriad of pathological events and diseases.

G6PD is critical in signaling for governing cell growth and cell death. Aberrant activation of G6PD is linked to tumorigenesis and malignancy in rapidly growing cancer cells. This raises the possibility of whether or not G6PD can serve as a therapeutic target concomitant with existing anticancer drug to tackle cancer resistance [256]. Approaches with chemical or molecular inhibitors of G6PD have been used widely. Novel methods of inhibiting the action of G6PD through modulating the metabolic switch, redox homeostasis, and protein–protein interactions are of great interest in thwarting rapid growth, metastasis, and heterogeneity of cancer cells.

**Author Contributions:** Conceptualization, H.-C.Y., Y.-H.W., A.S., T.-L.H., and D.T.-Y.C.; Resources, H.-C.Y. and Y.-H.W.; Writing—Original Draft Preparation, H.-C.Y. and Y.-H.W.; Writing—Review and Editing, H.-C.Y., Y.-H.W., A.S., and W.-C.Y.; Supervision, A.S. and D.T.-Y.C.; Project Administration, H.-Y.L.; Funding Acquisition, H.-C.Y., T.-L.H., and D.T.-Y.C.

**Funding:** This research was funded by the Ministry of Science and Technology, Taiwan (MOST107-2320-B-264-001-MY2 to HCY, MOST107-2320-B-182-013 to D.T.Y.C., MOST106-2320-B-255-003-MY3 and MOST107-2320-B-255-003 to T.L.H.), Chang Gung Medical Research Foundation (MRP450, CMRPF1G0241, CMRPF1G0242, CMRPF1G0243, CMRPF1F0132, CMRPF1H0051, CMRPF1H0052, CMRPF1I0041, and ZRRPF3H0131 to T.L.H.) and Chang Gung Memorial Hospital (BMRP098 and CMRPD1I0121 to D.T.Y.C.).

**Conflicts of Interest:** The authors declare no conflict of interest.



## References

- Yang, H.C.; Wu, Y.H.; Liu, H.Y.; Stern, A.; Chiu, D.T. What has passed is prolog: New cellular and physiological roles of G6PD. *Free Radic Res.* **2016**, *50*, 1047–1064. [\[CrossRef\]](#) [\[PubMed\]](#)
- Beutler, E. G6PD deficiency. *Blood* **1994**, *84*, 3613–3636. [\[PubMed\]](#)
- Longo, L.; Vanegas, O.C.; Patel, M.; Rosti, V.; Li, H.; Waka, J.; Merghoub, T.; Pandolfi, P.P.; Notaro, R.; Manova, K.; et al. Maternally transmitted severe glucose 6-phosphate dehydrogenase deficiency is an embryonic lethal. *EMBO J.* **2002**, *21*, 4229–4239. [\[CrossRef\]](#) [\[PubMed\]](#)
- Yang, H.C.; Chen, T.L.; Wu, Y.H.; Cheng, K.P.; Lin, Y.H.; Cheng, M.L.; Ho, H.Y.; Lo, S.J.; Chiu, D.T. Glucose 6-phosphate dehydrogenase deficiency enhances germ cell apoptosis and causes defective embryogenesis in *Caenorhabditis elegans*. *Cell Death Dis.* **2013**, *4*, e616. [\[CrossRef\]](#) [\[PubMed\]](#)
- Chen, T.L.; Yang, H.C.; Hung, C.Y.; Ou, M.H.; Pan, Y.Y.; Cheng, M.L.; Stern, A.; Lo, S.J.; Chiu, D.T. Impaired embryonic development in glucose-6-phosphate dehydrogenase-deficient *Caenorhabditis elegans* due to abnormal redox homeostasis induced activation of calcium-independent phospholipase and alteration of glycerophospholipid metabolism. *Cell Death Dis.* **2017**, *8*, e2545. [\[CrossRef\]](#)
- Yang, H.C.; Yu, H.; Liu, Y.C.; Chen, T.L.; Stern, A.; Lo, S.J.; Chiu, D.T. IDH-1 deficiency induces growth defects and metabolic alterations in GSPD-1-deficient *Caenorhabditis elegans*. *J. Mol. Med. (Berl)* **2019**, *97*, 385–396. [\[CrossRef\]](#) [\[PubMed\]](#)
- Wu, Y.H.; Lee, Y.H.; Shih, H.Y.; Chen, S.H.; Cheng, Y.C.; Tsun-Yee Chiu, D. Glucose-6-phosphate dehydrogenase is indispensable in embryonic development by modulation of epithelial-mesenchymal transition via the NOX/Smad3/miR-200b axis. *Cell Death Dis.* **2018**, *9*, 10. [\[CrossRef\]](#)
- Xia, H.; Li, L.; Zhou, Y.; Ren, P.; He, Z.; Shu, L. [Expression of g6pd gene in wild type zebrafish embryos of early development]. *Zhejiang Da Xue Xue Bao Yi Xue Ban* **2018**, *47*, 57–63.
- Nobrega-Pereira, S.; Fernandez-Marcos, P.J.; Brioché, T.; Gomez-Cabrera, M.C.; Salvador-Pascual, A.; Flores, J.M.; Vina, J.; Serrano, M. G6PD protects from oxidative damage and improves healthspan in mice. *Nat. Commun.* **2016**, *7*, 10894. [\[CrossRef\]](#)
- Stanton, R.C. Glucose-6-phosphate dehydrogenase, NADPH, and cell survival. *IUBMB Life* **2012**, *64*, 362–369. [\[CrossRef\]](#)
- Zhang, C.; Zhang, Z.; Zhu, Y.; Qin, S. Glucose-6-phosphate dehydrogenase: A biomarker and potential therapeutic target for cancer. *Anticancer Agents Med. Chem.* **2014**, *14*, 280–289. [\[CrossRef\]](#) [\[PubMed\]](#)
- Barcia-Vieitez, R.; Ramos-Martinez, J.I. The regulation of the oxidative phase of the pentose phosphate pathway: New answers to old problems. *IUBMB Life* **2014**, *66*, 775–779. [\[CrossRef\]](#) [\[PubMed\]](#)
- Villa, E.; Ricci, J.E. How does metabolism affect cell death in cancer? *FEBS J.* **2016**, *283*, 2653–2660. [\[CrossRef\]](#) [\[PubMed\]](#)
- Assi, M. The differential role of reactive oxygen species in early and late stages of cancer. *Am. J. Physiol. Regul. Integr. Comp. Physiol.* **2017**, *313*, R646–R653. [\[CrossRef\]](#) [\[PubMed\]](#)
- Sun, L.; Suo, C.; Li, S.T.; Zhang, H.; Gao, P. Metabolic reprogramming for cancer cells and their microenvironment: Beyond the Warburg Effect. *Biochim. Biophys. Acta Rev. Cancer* **2018**, *1870*, 51–66. [\[CrossRef\]](#)
- Cai, T.; Kuang, Y.; Zhang, C.; Zhang, Z.; Chen, L.; Li, B.; Li, Y.; Wang, Y.; Yang, H.; Han, Q.; et al. Glucose-6-phosphate dehydrogenase and NADPH oxidase 4 control STAT3 activity in melanoma cells through a pathway involving reactive oxygen species, c-SRC and SHP2. *Am. J. Cancer Res.* **2015**, *5*, 1610–1620. [\[PubMed\]](#)
- Dong, T.; Kang, X.; Liu, Z.; Zhao, S.; Ma, W.; Xuan, Q.; Liu, H.; Wang, Z.; Zhang, Q. Altered glycometabolism affects both clinical features and prognosis of triple-negative and neoadjuvant chemotherapy-treated breast cancer. *Tumor Biol.* **2016**, *37*, 8159–8168. [\[CrossRef\]](#)
- Ai, G.; Dachineni, R.; Kumar, D.R.; Alfonso, L.F.; Marimuthu, S.; Bhat, G.J. Aspirin inhibits glucose6phosphate dehydrogenase activity in HCT 116 cells through acetylation: Identification of aspirin-acetylated sites. *Mol. Med. Rep.* **2016**, *14*, 1726–1732. [\[CrossRef\]](#)
- He, C.; Yang, J.; Ding, J.; Li, S.; Wu, H.; Xiong, Y.; Zhou, F.; Jiang, Y.; Teng, L.; Yang, J. Downregulation of glucose6phosphate dehydrogenase by microRNA1 inhibits the growth of pituitary tumor cells. *Oncol. Rep.* **2018**, *40*, 3533–3542. [\[CrossRef\]](#)

20. Fang, Z.; Jiang, C.; Feng, Y.; Chen, R.; Lin, X.; Zhang, Z.; Han, L.; Chen, X.; Li, H.; Guo, Y.; et al. Effects of G6PD activity inhibition on the viability, ROS generation and mechanical properties of cervical cancer cells. *Biochim. Biophys. Acta* **2016**, *1863*, 2245–2254. [[CrossRef](#)]
21. Hu, T.; Li, Y.S.; Chen, B.; Chang, Y.F.; Liu, G.C.; Hong, Y.; Chen, H.L.; Xiyang, Y.B. Elevated glucose-6-phosphate dehydrogenase expression in the cervical cancer cases is associated with the cancerigenic event of high-risk human papillomaviruses. *Exp. Biol. Med. (Maywood)* **2015**, *240*, 1287–1297. [[CrossRef](#)] [[PubMed](#)]
22. Nna, E.; Tothill, I.E.; Ludeman, L.; Bailey, T. Endogenous control genes in prostate cells: Evaluation of gene expression using ‘real-time’ quantitative polymerase chain reaction. *Med. Princ. Pract.* **2010**, *19*, 433–439. [[CrossRef](#)] [[PubMed](#)]
23. Yang, C.A.; Huang, H.Y.; Lin, C.L.; Chang, J.G. G6PD as a predictive marker for glioma risk, prognosis and chemosensitivity. *J. Neurooncol.* **2018**, *139*, 661–670. [[CrossRef](#)] [[PubMed](#)]
24. Spencer, N.Y.; Stanton, R.C. Glucose 6-phosphate dehydrogenase and the kidney. *Curr. Opin. Nephrol. Hypertens* **2017**, *26*, 43–49. [[CrossRef](#)]
25. Benito, A.; Polat, I.H.; Noe, V.; Ciudad, C.J.; Marin, S.; Cascante, M. Glucose-6-phosphate dehydrogenase and transketolase modulate breast cancer cell metabolic reprogramming and correlate with poor patient outcome. *Oncotarget* **2017**, *8*, 106693–106706. [[CrossRef](#)] [[PubMed](#)]
26. Mele, L.; la Noce, M.; Paino, F.; Regad, T.; Wagner, S.; Liccardo, D.; Papaccio, G.; Lombardi, A.; Caraglia, M.; Tirino, V.; et al. Glucose-6-phosphate dehydrogenase blockade potentiates tyrosine kinase inhibitor effect on breast cancer cells through autophagy perturbation. *J. Exp. Clin. Cancer Res.* **2019**, *38*, 160. [[CrossRef](#)] [[PubMed](#)]
27. Dore, M.P.; Davoli, A.; Longo, N.; Marras, G.; Pes, G.M. Glucose-6-phosphate dehydrogenase deficiency and risk of colorectal cancer in Northern Sardinia: A retrospective observational study. *Medicine (Baltim.)* **2016**, *95*, e5254. [[CrossRef](#)]
28. Zhang, Z.Z.; Lee, E.E.; Sudderth, J.; Yue, Y.; Zia, A.; Glass, D.; Deberardinis, R.J.; Wang, R.C. Glutathione Depletion, Pentose Phosphate Pathway Activation, and Hemolysis in Erythrocytes Protecting Cancer Cells from Vitamin C-induced Oxidative Stress. *J. Biol. Chem.* **2016**, *291*, 22861–22867. [[CrossRef](#)]
29. Kathagen-Buhmann, A.; Schulte, A.; Weller, J.; Holz, M.; Herold-Mende, C.; Glass, R.; Lamszus, K. Glycolysis and the pentose phosphate pathway are differentially associated with the dichotomous regulation of glioblastoma cell migration versus proliferation. *Neuro Oncol.* **2016**, *18*, 1219–1229. [[CrossRef](#)]
30. Liu, B.; Fang, M.; He, Z.; Cui, D.; Jia, S.; Lin, X.; Xu, X.; Zhou, T.; Liu, W. Hepatitis B virus stimulates G6PD expression through HBx-mediated Nrf2 activation. *Cell Death Dis.* **2015**, *6*, e1980. [[CrossRef](#)]
31. Poulain, L.; Sujobert, P.; Zylbersztejn, F.; Barreau, S.; Stuardi, L.; Lambert, M.; Palama, T.L.; Chesnais, V.; Birsén, R.; Vergez, F.; et al. High mTORC1 activity drives glycolysis addiction and sensitivity to G6PD inhibition in acute myeloid leukemia cells. *Leukemia* **2017**, *31*, 2326–2335. [[CrossRef](#)] [[PubMed](#)]
32. Debeb, B.G.; Lacerda, L.; Larson, R.; Wolfe, A.R.; Krishnamurthy, S.; Reuben, J.M.; Ueno, N.T.; Gilcrease, M.; Woodward, W.A. Histone deacetylase inhibitor-induced cancer stem cells exhibit high pentose phosphate pathway metabolism. *Oncotarget* **2016**, *7*, 28329–28339. [[CrossRef](#)] [[PubMed](#)]
33. Yin, X.; Tang, B.; Li, J.H.; Wang, Y.; Zhang, L.; Xie, X.Y.; Zhang, B.H.; Qiu, S.J.; Wu, W.Z.; Ren, Z.G. ID1 promotes hepatocellular carcinoma proliferation and confers chemoresistance to oxaliplatin by activating pentose phosphate pathway. *J. Exp. Clin. Cancer Res.* **2017**, *36*, 166. [[CrossRef](#)] [[PubMed](#)]
34. Ohl, F.; Jung, M.; Radonic, A.; Sachs, M.; Loening, S.A.; Jung, K. Identification and validation of suitable endogenous reference genes for gene expression studies of human bladder cancer. *J. Urol.* **2006**, *175*, 1915–1920. [[CrossRef](#)]
35. Chen, Y.; Xu, Q.; Ji, D.; Wei, Y.; Chen, H.; Li, T.; Wan, B.; Yuan, L.; Huang, R.; Chen, G. Inhibition of pentose phosphate pathway suppresses acute myelogenous leukemia. *Tumor Biol.* **2016**, *37*, 6027–6034. [[CrossRef](#)]
36. Jahani, M.; Azadbakht, M.; Norooznezhad, F.; Mansouri, K. L-arginine alters the effect of 5-fluorouracil on breast cancer cells in favor of apoptosis. *Biomed. Pharm.* **2017**, *88*, 114–123. [[CrossRef](#)]
37. Massari, F.; Ciccarese, C.; Santoni, M.; Iacovelli, R.; Mazzucchelli, R.; Piva, F.; Scarpelli, M.; Berardi, R.; Tortora, G.; Lopez-Beltran, A.; et al. Metabolic phenotype of bladder cancer. *Cancer Treat. Rev.* **2016**, *45*, 46–57. [[CrossRef](#)]

38. Lucarelli, G.; Galleggiante, V.; Rutigliano, M.; Sanguedolce, F.; Cagiano, S.; Bufo, P.; Lastilla, G.; Maiorano, E.; Ribatti, D.; Giglio, A.; et al. Metabolomic profile of glycolysis and the pentose phosphate pathway identifies the central role of glucose-6-phosphate dehydrogenase in clear cell-renal cell carcinoma. *Oncotarget* **2015**, *6*, 13371–13386. [[CrossRef](#)]
39. Langbein, S.; Frederiks, W.M.; zur Hausen, A.; Popa, J.; Lehmann, J.; Weiss, C.; Alken, P.; Coy, J.F. Metastasis is promoted by a bioenergetic switch: New targets for progressive renal cell cancer. *Int. J. Cancer* **2008**, *122*, 2422–2428. [[CrossRef](#)]
40. Cui, J.; Pan, Y.; Wang, J.; Liu, Y.; Wang, H.; Li, H. MicroRNA-206 suppresses proliferation and predicts poor prognosis of HR-HPV-positive cervical cancer cells by targeting G6PD. *Oncol. Lett.* **2018**, *16*, 5946–5952. [[CrossRef](#)]
41. Hu, T.; Chang, Y.F.; Xiao, Z.; Mao, R.; Tong, J.; Chen, B.; Liu, G.C.; Hong, Y.; Chen, H.L.; Kong, S.Y.; et al. miR-1 inhibits progression of high-risk papillomavirus-associated human cervical cancer by targeting G6PD. *Oncotarget* **2016**, *7*, 86103–86116. [[CrossRef](#)] [[PubMed](#)]
42. Chen, X.; Xu, Z.; Zhu, Z.; Chen, A.; Fu, G.; Wang, Y.; Pan, H.; Jin, B. Modulation of G6PD affects bladder cancer via ROS accumulation and the AKT pathway in vitro. *Int. J. Oncol.* **2018**, *53*, 1703–1712. [[CrossRef](#)] [[PubMed](#)]
43. Chen, L.; Zhang, Z.; Hoshino, A.; Zheng, H.D.; Morley, M.; Arany, Z.; Rabinowitz, J.D. NADPH production by the oxidative pentose-phosphate pathway supports folate metabolism. *Nat. Metab.* **2019**, *1*, 404–415. [[CrossRef](#)] [[PubMed](#)]
44. Zhang, H.S.; Zhang, Z.G.; Du, G.Y.; Sun, H.L.; Liu, H.Y.; Zhou, Z.; Gou, X.M.; Wu, X.H.; Yu, X.Y.; Huang, Y.H. Nrf2 promotes breast cancer cell migration via up-regulation of G6PD/HIF-1 $\alpha$ /Notch1 axis. *J. Cell. Mol. Med.* **2019**, *23*, 3451–3463. [[CrossRef](#)] [[PubMed](#)]
45. Rao, X.; Duan, X.; Mao, W.; Li, X.; Li, Z.; Li, Q.; Zheng, Z.; Xu, H.; Chen, M.; Wang, P.G.; et al. O-GlcNAcylation of G6PD promotes the pentose phosphate pathway and tumor growth. *Nat. Commun.* **2015**, *6*, 8468. [[CrossRef](#)] [[PubMed](#)]
46. Wang, J.; Yuan, W.; Chen, Z.; Wu, S.; Chen, J.; Ge, J.; Hou, F.; Chen, Z. Overexpression of G6PD is associated with poor clinical outcome in gastric cancer. *Tumor Biol.* **2012**, *33*, 95–101. [[CrossRef](#)] [[PubMed](#)]
47. Zhang, Q.; Yi, X.; Yang, Z.; Han, Q.; Di, X.; Chen, F.; Wang, Y.; Yi, Z.; Kuang, Y.; Zhu, Y. Overexpression of G6PD Represents a Potential Prognostic Factor in Clear Cell Renal Cell Carcinoma. *J. Cancer* **2017**, *8*, 665–673. [[CrossRef](#)]
48. Jiang, P.; Du, W.; Wang, X.; Mancuso, A.; Gao, X.; Wu, M.; Yang, X. p53 regulates biosynthesis through direct inactivation of glucose-6-phosphate dehydrogenase. *Nat. Cell Biol.* **2011**, *13*, 310–316. [[CrossRef](#)]
49. Ma, X.; Wang, L.; Huang, D.; Li, Y.; Yang, D.; Li, T.; Li, F.; Sun, L.; Wei, H.; He, K.; et al. Polo-like kinase 1 coordinates biosynthesis during cell cycle progression by directly activating pentose phosphate pathway. *Nat. Commun.* **2017**, *8*, 1506. [[CrossRef](#)]
50. Van Driel, B.E.; Valet, G.K.; Lyon, H.; Hansen, U.; Song, J.Y.; Van Noorden, C.J. Prognostic estimation of survival of colorectal cancer patients with the quantitative histochemical assay of G6PDH activity and the multiparameter classification program CLASSIF1. *Cytometry* **1999**, *38*, 176–183. [[CrossRef](#)]
51. Yang, L.; He, Z.; Yao, J.; Tan, R.; Zhu, Y.; Li, Z.; Guo, Q.; Wei, L. Regulation of AMPK-related glycolipid metabolism imbalances redox homeostasis and inhibits anchorage independent growth in human breast cancer cells. *Redox Biol.* **2018**, *17*, 180–191. [[CrossRef](#)] [[PubMed](#)]
52. Tsouko, E.; Khan, A.S.; White, M.A.; Han, J.J.; Shi, Y.; Merchant, F.A.; Sharpe, M.A.; Xin, L.; Frigo, D.E. Regulation of the pentose phosphate pathway by an androgen receptor-mTOR-mediated mechanism and its role in prostate cancer cell growth. *Oncogenesis* **2014**, *3*, e103. [[CrossRef](#)] [[PubMed](#)]
53. Frederiks, W.M.; Bosch, K.S.; Hoebe, K.A.; van Marle, J.; Langbein, S. Renal cell carcinoma and oxidative stress: The lack of peroxisomes. *Acta Histochem.* **2010**, *112*, 364–371. [[CrossRef](#)] [[PubMed](#)]
54. Wang, J.; Duan, Z.; Nugent, Z.; Zou, J.X.; Borowsky, A.D.; Zhang, Y.; Tepper, C.G.; Li, J.J.; Fiehn, O.; Xu, J.; et al. Reprogramming metabolism by histone methyltransferase NSD2 drives endocrine resistance via coordinated activation of pentose phosphate pathway enzymes. *Cancer Lett.* **2016**, *378*, 69–79. [[CrossRef](#)] [[PubMed](#)]
55. Barajas, J.M.; Reyes, R.; Guerrero, M.J.; Jacob, S.T.; Motiwala, T.; Ghoshal, K. The role of miR-122 in the dysregulation of glucose-6-phosphate dehydrogenase (G6PD) expression in hepatocellular cancer. *Sci. Rep.* **2018**, *8*, 9105. [[CrossRef](#)] [[PubMed](#)]

56. Oronsky, B.; Scicinski, J.; Reid, T.; Oronsky, A.; Carter, C.; Oronsky, N.; Cabrales, P. RRx-001, a novel clinical-stage chemosensitizer, radiosensitizer, and immunosensitizer, inhibits glucose 6-phosphate dehydrogenase in human tumor cells. *Discov. Med.* **2016**, *21*, 251–265. [[PubMed](#)]
57. Xu, S.N.; Wang, T.S.; Li, X.; Wang, Y.P. SIRT2 activates G6PD to enhance NADPH production and promote leukaemia cell proliferation. *Sci. Rep.* **2016**, *6*, 32734. [[CrossRef](#)]
58. Wu, S.; Wang, H.; Li, Y.; Xie, Y.; Huang, C.; Zhao, H.; Miyagishi, M.; Kasim, V. Transcription Factor YY1 Promotes Cell Proliferation by Directly Activating the Pentose Phosphate Pathway. *Cancer Res.* **2018**, *78*, 4549–4562. [[CrossRef](#)]
59. Yang, H.C.; Cheng, M.L.; Ho, H.Y.; Chiu, D.T. The microbicidal and cyto regulatory roles of NADPH oxidases. *Microbes Infect.* **2011**, *13*, 109–120. [[CrossRef](#)]
60. El Assar, M.; Angulo, J.; Rodriguez-Manas, L. Oxidative stress and vascular inflammation in aging. *Free Radic. Biol. Med.* **2013**, *65*, 380–401. [[CrossRef](#)]
61. Shaw, P.X.; Stiles, T.; Douglas, C.; Ho, D.; Fan, W.; Du, H.; Xiao, X. Oxidative stress, innate immunity, and age-related macular degeneration. *Aims Mol. Sci.* **2016**, *3*, 196–221. [[CrossRef](#)]
62. Szabo, C. A timeline of hydrogen sulfide (H<sub>2</sub>S) research: From environmental toxin to biological mediator. *Biochem. Pharm.* **2018**, *149*, 5–19. [[CrossRef](#)] [[PubMed](#)]
63. Paul, B.D.; Snyder, S.H. H<sub>2</sub>S: A Novel Gasotransmitter that Signals by Sulfhydration. *Trends Biochem. Sci.* **2015**, *40*, 687–700. [[CrossRef](#)] [[PubMed](#)]
64. Yuan, S.; Shen, X.; Kevil, C.G. Beyond a Gasotransmitter: Hydrogen Sulfide and Polysulfide in Cardiovascular Health and Immune Response. *Antioxid. Redox Signal.* **2017**, *27*, 634–653. [[CrossRef](#)]
65. Cortese-Krott, M.M.; Koning, A.; Kuhnle, G.G.C.; Nagy, P.; Bianco, C.L.; Pasch, A.; Wink, D.A.; Fukuto, J.M.; Jackson, A.A.; van Goor, H.; et al. The Reactive Species Interactome: Evolutionary Emergence, Biological Significance, and Opportunities for Redox Metabolomics and Personalized Medicine. *Antioxid. Redox Signal.* **2017**, *27*, 684–712. [[CrossRef](#)]
66. Hopkins, B.L.; Neumann, C.A. Redoxins as gatekeepers of the transcriptional oxidative stress response. *Redox Biol.* **2019**, *21*, 101104. [[CrossRef](#)] [[PubMed](#)]
67. Balsera, M.; Buchanan, B.B. Evolution of the thioredoxin system as a step enabling adaptation to oxidative stress. *Free Radic Biol. Med.* **2019**. [[CrossRef](#)]
68. Vona, R.; Gambardella, L.; Cittadini, C.; Straface, E.; Pietraforte, D. Biomarkers of Oxidative Stress in Metabolic Syndrome and Associated Diseases. *Oxid. Med. Cell Longev.* **2019**, *2019*, 8267234. [[CrossRef](#)]
69. Williams, E.; Whiteman, M.; Wood, M.E.; Wilson, I.D.; Ladomery, M.R.; Allainguillaume, J.; Teklic, T.; Lisjak, M.; Hancock, J.T. Investigating ROS, RNS, and H<sub>2</sub>S-Sensitive Signaling Proteins. *Methods Mol. Biol.* **2019**, *1990*, 27–42. [[CrossRef](#)]
70. Miller, D.L. Hydrogen sulfide increases thermotolerance and lifespan in *Caenorhabditis elegans*. *Proc. Natl. Acad. Sci. USA* **2007**, *104*, 20618–20622. [[CrossRef](#)]
71. Blackstone, E.; Morrison, M.; Roth, M.B. H<sub>2</sub>S induces a suspended animation-like state in mice. *Science* **2005**, *308*, 518. [[CrossRef](#)] [[PubMed](#)]
72. Tsai, K.J.; Hung, I.J.; Chow, C.K.; Stern, A.; Chao, S.S.; Chiu, D.T. Impaired production of nitric oxide, superoxide, and hydrogen peroxide in glucose 6-phosphate-dehydrogenase-deficient granulocytes. *FEBS Lett.* **1998**, *436*, 411–414. [[CrossRef](#)]
73. Matsui, R.; Xu, S.; Maitland, K.A.; Mastroianni, R.; Leopold, J.A.; Handy, D.E.; Loscalzo, J.; Cohen, R.A. Glucose-6-phosphate dehydrogenase deficiency decreases vascular superoxide and atherosclerotic lesions in apolipoprotein E(-/-) mice. *Arter. Thromb. Vasc. Biol.* **2006**, *26*, 910–916. [[CrossRef](#)] [[PubMed](#)]
74. Gupte, S.A.; Levine, R.J.; Gupte, R.S.; Young, M.E.; Lionetti, V.; Labinskyy, V.; Floyd, B.C.; Ojaimi, C.; Bellomo, M.; Wolin, M.S.; et al. Glucose-6-phosphate dehydrogenase-derived NADPH fuels superoxide production in the failing heart. *J. Mol. Cell Cardiol.* **2006**, *41*, 340–349. [[CrossRef](#)] [[PubMed](#)]
75. Spencer, N.Y.; Yan, Z.; Boudreau, R.L.; Zhang, Y.; Luo, M.; Li, Q.; Tian, X.; Shah, A.M.; Davidsson, R.L.; Davidson, B.; et al. Control of hepatic nuclear superoxide production by glucose 6-phosphate dehydrogenase and NADPH oxidase-4. *J. Biol. Chem.* **2011**, *286*, 8977–8987. [[CrossRef](#)] [[PubMed](#)]
76. Leopold, J.A.; Zhang, Y.Y.; Scribner, A.W.; Stanton, R.C.; Loscalzo, J. Glucose-6-phosphate dehydrogenase overexpression decreases endothelial cell oxidant stress and increases bioavailable nitric oxide. *Arter. Thromb. Vasc. Biol.* **2003**, *23*, 411–417. [[CrossRef](#)] [[PubMed](#)]



77. Santana, A.P.; Tavares, B.M.; Lucetti, L.T.; Gouveia, F.S., Jr.; Ribeiro, R.A.; Soares, P.M.; Sousa, E.H.; Lopes, L.G.; Medeiros, J.V.; Souza, M.H. The nitric oxide donor cis-[Ru(bpy)<sub>2</sub>(SO<sub>3</sub>)NO](PF<sub>6</sub>) increases gastric mucosa protection in mice—involvement of the soluble guanylate cyclase/K(ATP) pathway. *Nitric Oxide* **2015**, *45*, 35–42. [[CrossRef](#)] [[PubMed](#)]
78. Yang, F.; Li, Y.; Wu, T.; Na, N.; Zhao, Y.; Li, W.; Han, C.; Zhang, L.; Lu, J.; Zhao, Y. TNF $\alpha$ -induced M-MDSCs promote transplant immune tolerance via nitric oxide. *J. Mol. Med. (Berl)* **2016**, *94*, 911–920. [[CrossRef](#)]
79. Guo, L.; Zhang, Z.; Green, K.; Stanton, R.C. Suppression of interleukin-1 beta-induced nitric oxide production in RINm5F cells by inhibition of glucose-6-phosphate dehydrogenase. *Biochemistry* **2002**, *41*, 14726–14733. [[CrossRef](#)]
80. Gammoh, O.S.; Al-Smadi, A.; Al-Awaida, W.; Badr, M.M.; Qinna, N.A. Increased Salivary Nitric Oxide and G6PD Activity in Refugees with Anxiety and Stress. *Stress Health* **2016**, *32*, 435–440. [[CrossRef](#)]
81. Cheng, M.L.; Ho, H.Y.; Liang, C.M.; Chou, Y.H.; Stern, A.; Lu, F.J.; Chiu, D.T. Cellular glucose-6-phosphate dehydrogenase (G6PD) status modulates the effects of nitric oxide (NO) on human foreskin fibroblasts. *FEBS Lett.* **2000**, *475*, 257–262. [[CrossRef](#)]
82. Leopold, J.A.; Cap, A.; Scribner, A.W.; Stanton, R.C.; Loscalzo, J. Glucose-6-phosphate dehydrogenase deficiency promotes endothelial oxidant stress and decreases endothelial nitric oxide bioavailability. *FASEB J.* **2001**, *15*, 1771–1773. [[CrossRef](#)] [[PubMed](#)]
83. Garcia-Nogales, P.; Almeida, A.; Fernandez, E.; Medina, J.M.; Bolanos, J.P. Induction of glucose-6-phosphate dehydrogenase by lipopolysaccharide contributes to preventing nitric oxide-mediated glutathione depletion in cultured rat astrocytes. *J. Neurochem.* **1999**, *72*, 1750–1758. [[CrossRef](#)] [[PubMed](#)]
84. Garcia-Nogales, P.; Almeida, A.; Bolanos, J.P. Peroxynitrite protects neurons against nitric oxide-mediated apoptosis. A key role for glucose-6-phosphate dehydrogenase activity in neuroprotection. *J. Biol. Chem.* **2003**, *278*, 864–874. [[CrossRef](#)] [[PubMed](#)]
85. Parsanathan, R.; Jain, S.K. Glucose-6-phosphate dehydrogenase deficiency increases cell adhesion molecules and activates human monocyte-endothelial cell adhesion: Protective role of l-cysteine. *Arch. Biochem. Biophys.* **2019**, *663*, 11–21. [[CrossRef](#)]
86. Schulz, J.B.; Matthews, R.T.; Beal, M.F. Role of nitric oxide in neurodegenerative diseases. *Curr. Opin. Neurol.* **1995**, *8*, 480–486. [[CrossRef](#)] [[PubMed](#)]
87. Segura Aguilar, J.; Kostrzewa, R.M. Neurotoxins and neurotoxic species implicated in neurodegeneration. *Neurotox Res.* **2004**, *6*, 615–630. [[CrossRef](#)]
88. Abe, K.; Kimura, H. The possible role of hydrogen sulfide as an endogenous neuromodulator. *J. Neurosci.* **1996**, *16*, 1066–1071. [[CrossRef](#)]
89. Hosoki, R.; Matsuki, N.; Kimura, H. The possible role of hydrogen sulfide as an endogenous smooth muscle relaxant in synergy with nitric oxide. *Biochem. Biophys. Res. Commun.* **1997**, *237*, 527–531. [[CrossRef](#)]
90. Yang, G.; Wu, L.; Jiang, B.; Yang, W.; Qi, J.; Cao, K.; Meng, Q.; Mustafa, A.K.; Mu, W.; Zhang, S.; et al. H<sub>2</sub>S as a physiologic vasorelaxant: Hypertension in mice with deletion of cystathionine gamma-lyase. *Science* **2008**, *322*, 587–590. [[CrossRef](#)]
91. Li, L.; Bhatia, M.; Zhu, Y.Z.; Zhu, Y.C.; Ramnath, R.D.; Wang, Z.J.; Anuar, F.B.; Whiteman, M.; Salto-Tellez, M.; Moore, P.K. Hydrogen sulfide is a novel mediator of lipopolysaccharide-induced inflammation in the mouse. *FASEB J.* **2005**, *19*, 1196–1198. [[CrossRef](#)] [[PubMed](#)]
92. Zano, R.C.; Brancalione, V.; Distrutti, E.; Fiorucci, S.; Cirino, G.; Wallace, J.L. Hydrogen sulfide is an endogenous modulator of leukocyte-mediated inflammation. *FASEB J.* **2006**, *20*, 2118–2120. [[CrossRef](#)] [[PubMed](#)]
93. Sen, N.; Paul, B.D.; Gadalla, M.M.; Mustafa, A.K.; Sen, T.; Xu, R.; Kim, S.; Snyder, S.H. Hydrogen sulfide-linked sulfhydration of NF- $\kappa$ B mediates its antiapoptotic actions. *Mol. Cell* **2012**, *45*, 13–24. [[CrossRef](#)] [[PubMed](#)]
94. Hine, C.; Harputlugil, E.; Zhang, Y.; Ruckenstein, C.; Lee, B.C.; Brace, L.; Longchamp, A.; Trevino-Villarreal, J.H.; Mejia, P.; Ozaki, C.K.; et al. Endogenous hydrogen sulfide production is essential for dietary restriction benefits. *Cell* **2015**, *160*, 132–144. [[CrossRef](#)] [[PubMed](#)]
95. Szabo, C.; Coletta, C.; Chao, C.; Modis, K.; Szczesny, B.; Papapetropoulos, A.; Hellmich, M.R. Tumor-derived hydrogen sulfide, produced by cystathionine-beta-synthase, stimulates bioenergetics, cell proliferation, and angiogenesis in colon cancer. *Proc. Natl. Acad. Sci. USA* **2013**, *110*, 12474–12479. [[CrossRef](#)] [[PubMed](#)]



96. Chhabra, A.; Mishra, S.; Kumar, G.; Gupta, A.; Keshri, G.K.; Bharti, B.; Meena, R.N.; Prabhakar, A.K.; Singh, D.K.; Bhargava, K.; et al. Glucose-6-phosphate dehydrogenase is critical for suppression of cardiac hypertrophy by H<sub>2</sub>S. *Cell Death Discov.* **2018**, *4*, 6. [[CrossRef](#)] [[PubMed](#)]
97. Li, L.; Hsu, A.; Moore, P.K. Actions and interactions of nitric oxide, carbon monoxide and hydrogen sulphide in the cardiovascular system and in inflammation—a tale of three gases! *Pharmacol. Ther.* **2009**, *123*, 386–400. [[CrossRef](#)]
98. Kim, D.S.; Song, L.; Wang, J.; Wu, H.; Gou, W.; Cui, W.; Kim, J.S.; Wang, H. Carbon Monoxide Inhibits Islet Apoptosis via Induction of Autophagy. *Antioxid. Redox Signal.* **2018**, *28*, 1309–1322. [[CrossRef](#)]
99. Murphy, P.B.; Bihari, A.; Parry, N.G.; Ball, I.; Leslie, K.; Vogt, K.; Lawendy, A.R. Carbon monoxide and hydrogen sulphide reduce reperfusion injury in abdominal compartment syndrome. *J. Surg. Res.* **2018**, *222*, 17–25. [[CrossRef](#)]
100. Correa-Costa, M.; Gallo, D.; Csizmadia, E.; Gomperts, E.; Lieberum, J.L.; Hauser, C.J.; Ji, X.; Wang, B.; Camara, N.O.S.; Robson, S.C.; et al. Carbon monoxide protects the kidney through the central circadian clock and CD39. *Proc. Natl. Acad. Sci. USA* **2018**, *115*, E2302–E2310. [[CrossRef](#)]
101. Kim, H.J.; Joe, Y.; Chen, Y.; Park, G.H.; Kim, U.H.; Chung, H.T. Carbon monoxide attenuates amyloidogenesis via down-regulation of NF-kappaB-mediated BACE1 gene expression. *Aging Cell* **2019**, *18*, e12864. [[CrossRef](#)]
102. Ryter, S.W.; Ma, K.C.; Choi, A.M.K. Carbon monoxide in lung cell physiology and disease. *Am. J. Physiol. Cell Physiol.* **2018**, *314*, C211–C227. [[CrossRef](#)] [[PubMed](#)]
103. Kaplan, M.; Wong, R.J.; Stevenson, D.K. Hemolysis and Glucose-6-Phosphate Dehydrogenase Deficiency-Related Neonatal Hyperbilirubinemia. *Neonatology* **2018**, *114*, 223–225. [[CrossRef](#)] [[PubMed](#)]
104. Almeida, A.S.; Soares, N.L.; Sequeira, C.O.; Pereira, S.A.; Sonnewald, U.; Vieira, H.L.A. Improvement of neuronal differentiation by carbon monoxide: Role of pentose phosphate pathway. *Redox Biol.* **2018**, *17*, 338–347. [[CrossRef](#)] [[PubMed](#)]
105. Peiro, C.; Romacho, T.; Azcutia, V.; Villalobos, L.; Fernandez, E.; Bolanos, J.P.; Moncada, S.; Sanchez-Ferrer, C.F. Inflammation, glucose, and vascular cell damage: The role of the pentose phosphate pathway. *Cardiovasc. Diabetol.* **2016**, *15*, 82. [[CrossRef](#)] [[PubMed](#)]
106. Ulusu, N.N.; Gok, M.; Sayin Sakul, A.A.; Ari, N.; Stefek, M.; Karasu, C.; The, A.S.G. Antioxidant SMe1EC2 modulates pentose phosphate pathway and glutathione-dependent enzyme activities in tissues of aged diabetic rats. *Interdiscip. Toxicol.* **2017**, *10*, 148–154. [[CrossRef](#)] [[PubMed](#)]
107. Ham, M.; Choe, S.S.; Shin, K.C.; Choi, G.; Kim, J.W.; Noh, J.R.; Kim, Y.H.; Ryu, J.W.; Yoon, K.H.; Lee, C.H.; et al. Glucose-6-Phosphate Dehydrogenase Deficiency Improves Insulin Resistance With Reduced Adipose Tissue Inflammation in Obesity. *Diabetes* **2016**, *65*, 2624–2638. [[CrossRef](#)] [[PubMed](#)]
108. Rostami-Far, Z.; Ghadiri, K.; Rostami-Far, M.; Shaveisi-Zadeh, F.; Amiri, A.; Rahimian Zarif, B. Glucose-6-phosphate dehydrogenase deficiency (G6PD) as a risk factor of male neonatal sepsis. *J. Med. Life* **2016**, *9*, 34–38. [[PubMed](#)]
109. Hsieh, Y.T.; Lin, M.H.; Ho, H.Y.; Chen, L.C.; Chen, C.C.; Shu, J.C. Glucose-6-phosphate dehydrogenase (G6PD)-deficient epithelial cells are less tolerant to infection by *Staphylococcus aureus*. *PLoS ONE* **2013**, *8*, e79566. [[CrossRef](#)]
110. Nadeem, A.; Al-Harbi, N.O.; Ahmad, S.F.; Ibrahim, K.E.; Siddiqui, N.; Al-Harbi, M.M. Glucose-6-phosphate dehydrogenase inhibition attenuates acute lung injury through reduction in NADPH oxidase-derived reactive oxygen species. *Clin. Exp. Immunol.* **2018**, *191*, 279–287. [[CrossRef](#)]
111. Wu, Y.H.; Tseng, C.P.; Cheng, M.L.; Ho, H.Y.; Shih, S.R.; Chiu, D.T. Glucose-6-phosphate dehydrogenase deficiency enhances human coronavirus 229E infection. *J. Infect. Dis.* **2008**, *197*, 812–816. [[CrossRef](#)] [[PubMed](#)]
112. Wu, Y.H.; Chiu, D.T.; Lin, H.R.; Tang, H.Y.; Cheng, M.L.; Ho, H.Y. Glucose-6-Phosphate Dehydrogenase Enhances Antiviral Response through Downregulation of NADPH Sensor HSCARG and Upregulation of NF-kappaB Signaling. *Viruses* **2015**, *7*, 6689–6706. [[CrossRef](#)] [[PubMed](#)]
113. Lin, H.R.; Wu, Y.H.; Yen, W.C.; Yang, C.M.; Chiu, D.T. Diminished COX-2/PGE2-Mediated Antiviral Response Due to Impaired NOX/MAPK Signaling in G6PD-Knockdown Lung Epithelial Cells. *PLoS ONE* **2016**, *11*, e0153462. [[CrossRef](#)] [[PubMed](#)]
114. Choudhry, V.P.; Bagga, A.; Desai, N. Increased morbidity following acute viral hepatitis in children with glucose-6-phosphate dehydrogenase deficiency. *J. Trop. Pediatr.* **1992**, *38*, 139–140. [[CrossRef](#)]

115. Al-Alimi, A.A.; Ali, S.A.; Al-Hassan, F.M.; Idris, F.M.; Teow, S.Y.; Mohd Yusoff, N. Dengue virus type 2 (DENV2)-induced oxidative responses in monocytes from glucose-6-phosphate dehydrogenase (G6PD)-deficient and G6PD normal subjects. *PLoS Negl. Trop. Dis.* **2014**, *8*, e2711. [[CrossRef](#)] [[PubMed](#)]
116. Chao, Y.C.; Huang, C.S.; Lee, C.N.; Chang, S.Y.; King, C.C.; Kao, C.L. Higher infection of dengue virus serotype 2 in human monocytes of patients with G6PD deficiency. *PLoS ONE* **2008**, *3*, e1557. [[CrossRef](#)]
117. Yang, H.C.; Cheng, M.L.; Hua, Y.S.; Wu, Y.H.; Lin, H.R.; Liu, H.Y.; Ho, H.Y.; Chiu, D.T. Glucose 6-phosphate dehydrogenase knockdown enhances IL-8 expression in HepG2 cells via oxidative stress and NF-kappaB signaling pathway. *J. Inflamm. (Lond.)* **2015**, *12*, 34. [[CrossRef](#)]
118. Park, Y.J.; Choe, S.S.; Sohn, J.H.; Kim, J.B. The role of glucose-6-phosphate dehydrogenase in adipose tissue inflammation in obesity. *Adipocyte* **2017**, *6*, 147–153. [[CrossRef](#)]
119. Ham, M.; Lee, J.W.; Choi, A.H.; Jang, H.; Choi, G.; Park, J.; Kozuka, C.; Sears, D.D.; Masuzaki, H.; Kim, J.B. Macrophage glucose-6-phosphate dehydrogenase stimulates proinflammatory responses with oxidative stress. *Mol. Cell Biol.* **2013**, *33*, 2425–2435. [[CrossRef](#)]
120. Lee, J.W.; Choi, A.H.; Ham, M.; Kim, J.W.; Choe, S.S.; Park, J.; Lee, G.Y.; Yoon, K.H.; Kim, J.B. G6PD up-regulation promotes pancreatic beta-cell dysfunction. *Endocrinology* **2011**, *152*, 793–803. [[CrossRef](#)]
121. Patel, D.; Kandhi, S.; Kelly, M.; Neo, B.H.; Wolin, M.S. Dehydroepiandrosterone promotes pulmonary artery relaxation by NADPH oxidation-elicited subunit dimerization of protein kinase G 1alpha. *Am. J. Physiol. Lung Cell Mol. Physiol.* **2014**, *306*, L383–L391. [[CrossRef](#)] [[PubMed](#)]
122. Neo, B.H.; Patel, D.; Kandhi, S.; Wolin, M.S. Roles for cytosolic NADPH redox in regulating pulmonary artery relaxation by thiol oxidation-elicited subunit dimerization of protein kinase G1alpha. *Am. J. Physiol. Heart Circ. Physiol.* **2013**, *305*, H330–H343. [[CrossRef](#)] [[PubMed](#)]
123. Singh, S.; Trigun, S.K. Activation of neuronal nitric oxide synthase in cerebellum of chronic hepatic encephalopathy rats is associated with up-regulation of NADPH-producing pathway. *Cerebellum* **2010**, *9*, 384–397. [[CrossRef](#)] [[PubMed](#)]
124. Borges, C.G.; Canani, C.R.; Fernandes, C.G.; Zanatta, A.; Seminotti, B.; Ribeiro, C.A.; Leipnitz, G.; Vargas, C.R.; Wajner, M. Reactive nitrogen species mediate oxidative stress and astrogliosis provoked by in vivo administration of phytanic acid in cerebellum of adolescent rats: A potential contributing pathomechanism of cerebellar injury in peroxisomal disorders. *Neuroscience* **2015**, *304*, 122–132. [[CrossRef](#)] [[PubMed](#)]
125. Wan, G.H.; Tsai, S.C.; Chiu, D.T. Decreased blood activity of glucose-6-phosphate dehydrogenase associates with increased risk for diabetes mellitus. *Endocrine* **2002**, *19*, 191–195. [[CrossRef](#)]
126. Gaskin, R.S.; Estwick, D.; Peddi, R. G6PD deficiency: Its role in the high prevalence of hypertension and diabetes mellitus. *Ethn. Dis.* **2001**, *11*, 749–754.
127. Zhang, Z.; Liew, C.W.; Handy, D.E.; Zhang, Y.; Leopold, J.A.; Hu, J.; Guo, L.; Kulkarni, R.N.; Loscalzo, J.; Stanton, R.C. High glucose inhibits glucose-6-phosphate dehydrogenase, leading to increased oxidative stress and beta-cell apoptosis. *FASEB J.* **2010**, *24*, 1497–1505. [[CrossRef](#)] [[PubMed](#)]
128. Wang, M.; Hu, J.; Yan, L.; Yang, Y.; He, M.; Wu, M.; Li, Q.; Gong, W.; Yang, Y.; Wang, Y.; et al. High glucose-induced ubiquitination of G6PD leads to the injury of podocytes. *FASEB J.* **2019**, *33*, 6296–6310. [[CrossRef](#)]
129. Zhang, W.; Ni, C.; Sheng, J.; Hua, Y.; Ma, J.; Wang, L.; Zhao, Y.; Xing, Y. TLQP-21 protects human umbilical vein endothelial cells against high-glucose-induced apoptosis by increasing G6PD expression. *PLoS ONE* **2013**, *8*, e79760. [[CrossRef](#)]
130. Yang, H.; Jin, X.; Kei Lam, C.W.; Yan, S.K. Oxidative stress and diabetes mellitus. *Clin. Chem. Lab. Med.* **2011**, *49*, 1773–1782. [[CrossRef](#)]
131. Leibowitz, G.; Bachar, E.; Shaked, M.; Sinai, A.; Ketzinel-Gilad, M.; Cerasi, E.; Kaiser, N. Glucose regulation of beta-cell stress in type 2 diabetes. *Diabetes Obes. Metab.* **2010**, *12*, 66–75. [[CrossRef](#)] [[PubMed](#)]
132. Tomar, L.R.; Aggarwal, A.; Jain, P.; Rajpal, S.; Agarwal, M.P. Acute viral hepatitis E presenting with haemolytic anaemia and acute renal failure in a patient with glucose-6-phosphate dehydrogenase deficiency. *Trop. Dr.* **2015**, *45*, 245–246. [[CrossRef](#)] [[PubMed](#)]
133. Ozbay Hosnut, F.; Ozcay, F.; Selda Bayrakci, U.; Avci, Z.; Ozbek, N. Etiology of hemolysis in two patients with hepatitis A infection: Glucose-6-phosphate dehydrogenase deficiency or autoimmune hemolytic anemia. *Eur. J. Pediatr.* **2008**, *167*, 1435–1439. [[CrossRef](#)] [[PubMed](#)]

134. Araujo, T.; Katiyar, V.; Gonzales Zamora, J.A. Acute Retroviral Syndrome Presenting with Hemolytic Anemia Induced by G6PD Deficiency. *Trop. Med. Infect. Dis.* **2018**, *4*, 6. [\[CrossRef\]](#) [\[PubMed\]](#)
135. Mbanefo, E.C.; Ahmed, A.M.; Titouna, A.; Elmaraezy, A.; Trang, N.T.; Phuoc Long, N.; Hoang Anh, N.; Diem Nghi, T.; The Hung, B.; Van Hieu, M.; et al. Association of glucose-6-phosphate dehydrogenase deficiency and malaria: A systematic review and meta-analysis. *Sci. Rep.* **2017**, *7*, 45963. [\[CrossRef\]](#) [\[PubMed\]](#)
136. Nadeem, A.; Siddiqui, N.; Al-Harbi, N.O.; Attia, S.M.; AlSharari, S.D.; Ahmad, S.F. Acute lung injury leads to depression-like symptoms through upregulation of neutrophilic and neuronal NADPH oxidase signaling in a murine model. *Int. Immunopharmacol.* **2017**, *47*, 218–226. [\[CrossRef\]](#)
137. Neo, B.H.; Kandhi, S.; Wolin, M.S. Roles for redox mechanisms controlling protein kinase G in pulmonary and coronary artery responses to hypoxia. *Am. J. Physiol. Heart Circ. Physiol.* **2011**, *301*, H2295–H2304. [\[CrossRef\]](#)
138. Chettimada, S.; Gupte, R.; Rawat, D.; Gebb, S.A.; McMurtry, I.F.; Gupte, S.A. Hypoxia-induced glucose-6-phosphate dehydrogenase overexpression and -activation in pulmonary artery smooth muscle cells: Implication in pulmonary hypertension. *Am. J. Physiol. Lung Cell Mol. Physiol.* **2015**, *308*, L287–L300. [\[CrossRef\]](#)
139. Tian, W.N.; Braunstein, L.D.; Pang, J.; Stuhlmeier, K.M.; Xi, Q.C.; Tian, X.; Stanton, R.C. Importance of glucose-6-phosphate dehydrogenase activity for cell growth. *J. Biol. Chem.* **1998**, *273*, 10609–10617. [\[CrossRef\]](#)
140. Li, D.; Zhu, Y.; Tang, Q.; Lu, H.; Li, H.; Yang, Y.; Li, Z.; Tong, S. A new G6PD knockdown tumor-cell line with reduced proliferation and increased susceptibility to oxidative stress. *Cancer Biother. Radiopharm.* **2009**, *24*, 81–90. [\[CrossRef\]](#)
141. Lin, R.; Elf, S.; Shan, C.; Kang, H.B.; Ji, Q.; Zhou, L.; Hitosugi, T.; Zhang, L.; Zhang, S.; Seo, J.H.; et al. 6-Phosphogluconate dehydrogenase links oxidative PPP, lipogenesis and tumour growth by inhibiting LKB1-AMPK signalling. *Nat. Cell Biol.* **2015**, *17*, 1484–1496. [\[CrossRef\]](#) [\[PubMed\]](#)
142. Paglialunga, F.; Fico, A.; Iaccarino, I.; Notaro, R.; Luzzatto, L.; Martini, G.; Filosa, S. G6PD is indispensable for erythropoiesis after the embryonic-adult hemoglobin switch. *Blood* **2004**, *104*, 3148–3152. [\[CrossRef\]](#) [\[PubMed\]](#)
143. Pu, H.; Zhang, Q.; Zhao, C.; Shi, L.; Wang, Y.; Wang, J.; Zhang, M. Overexpression of G6PD is associated with high risks of recurrent metastasis and poor progression-free survival in primary breast carcinoma. *World J. Surg. Oncol.* **2015**, *13*, 323. [\[CrossRef\]](#) [\[PubMed\]](#)
144. Elf, S.; Lin, R.; Xia, S.; Pan, Y.; Shan, C.; Wu, S.; Lonial, S.; Gaddh, M.; Arellano, M.L.; Khoury, H.J.; et al. Targeting 6-phosphogluconate dehydrogenase in the oxidative PPP sensitizes leukemia cells to antimalarial agent dihydroartemisinin. *Oncogene* **2017**, *36*, 254–262. [\[CrossRef\]](#) [\[PubMed\]](#)
145. Yi, H.; Zheng, X.; Song, J.; Shen, R.; Su, Y.; Lin, D. Exosomes mediated pentose phosphate pathway in ovarian cancer metastasis: A proteomics analysis. *Int J. Clin. Exp. Pathol.* **2015**, *8*, 15719–15728. [\[PubMed\]](#)
146. Zhang, Q.; Yang, Z.; Han, Q.; Bai, H.; Wang, Y.; Yi, X.; Yi, Z.; Yang, L.; Jiang, L.; Song, X.; et al. G6PD promotes renal cell carcinoma proliferation through positive feedback regulation of p-STAT3. *Oncotarget* **2017**, *8*, 109043–109060. [\[CrossRef\]](#)
147. Jonas, S.K.; Benedetto, C.; Flatman, A.; Hammond, R.H.; Micheletti, L.; Riley, C.; Riley, P.A.; Spargo, D.J.; Zonca, M.; Slater, T.F. Increased activity of 6-phosphogluconate dehydrogenase and glucose-6-phosphate dehydrogenase in purified cell suspensions and single cells from the uterine cervix in cervical intraepithelial neoplasia. *Br. J. Cancer* **1992**, *66*, 185–191. [\[CrossRef\]](#)
148. Sulis, E. G-6-P.D. deficiency and cancer. *Lancet* **1972**, *1*, 1185. [\[CrossRef\]](#)
149. Patra, K.C.; Hay, N. The pentose phosphate pathway and cancer. *Trends Biochem. Sci.* **2014**, *39*, 347–354. [\[CrossRef\]](#)
150. Pan, S.; World, C.J.; Kovacs, C.J.; Berk, B.C. Glucose 6-phosphate dehydrogenase is regulated through c-Src-mediated tyrosine phosphorylation in endothelial cells. *Arter. Thromb. Vasc. Biol.* **2009**, *29*, 895–901. [\[CrossRef\]](#)
151. Santana-Codina, N.; Roeth, A.A.; Zhang, Y.; Yang, A.; Mashadova, O.; Asara, J.M.; Wang, X.; Bronson, R.T.; Lyssiotis, C.A.; Ying, H.; et al. Oncogenic KRAS supports pancreatic cancer through regulation of nucleotide synthesis. *Nat. Commun.* **2018**, *9*, 4945. [\[CrossRef\]](#) [\[PubMed\]](#)
152. Ye, H.; Huang, H.; Cao, F.; Chen, M.; Zheng, X.; Zhan, R. HSPB1 Enhances SIRT2-Mediated G6PD Activation and Promotes Glioma Cell Proliferation. *PLoS ONE* **2016**, *11*, e0164285. [\[CrossRef\]](#) [\[PubMed\]](#)

153. Zhou, L.; Wang, F.; Sun, R.; Chen, X.; Zhang, M.; Xu, Q.; Wang, Y.; Wang, S.; Xiong, Y.; Guan, K.L.; et al. SIRT5 promotes IDH2 desuccinylation and G6PD deglutarylation to enhance cellular antioxidant defense. *EMBO Rep.* **2016**, *17*, 811–822. [[CrossRef](#)] [[PubMed](#)]
154. Kong, D.H.; Li, S.; Du, Z.X.; Liu, C.; Liu, B.Q.; Li, C.; Zong, Z.H.; Wang, H.Q. BAG3 elevation inhibits cell proliferation via direct interaction with G6PD in hepatocellular carcinomas. *Oncotarget* **2016**, *7*, 700–711. [[CrossRef](#)] [[PubMed](#)]
155. Thakor, P.; Subramanian, R.B.; Thakkar, S.S.; Ray, A.; Thakkar, V.R. Phytol induces ROS mediated apoptosis by induction of caspase 9 and 3 through activation of TRAIL, FAS and TNF receptors and inhibits tumor progression factor Glucose 6 phosphate dehydrogenase in lung carcinoma cell line (A549). *Biomed. Pharm.* **2017**, *92*, 491–500. [[CrossRef](#)] [[PubMed](#)]
156. Heppler, L.N.; Frank, D.A. Targeting Oncogenic Transcription Factors: Therapeutic Implications of Endogenous STAT Inhibitors. *Trends Cancer* **2017**, *3*, 816–827. [[CrossRef](#)]
157. Bromberg, J. Stat proteins and oncogenesis. *J. Clin. Investig.* **2002**, *109*, 1139–1142. [[CrossRef](#)]
158. Hu, T.; Zhang, C.; Tang, Q.; Su, Y.; Li, B.; Chen, L.; Zhang, Z.; Cai, T.; Zhu, Y. Variant G6PD levels promote tumor cell proliferation or apoptosis via the STAT3/5 pathway in the human melanoma xenograft mouse model. *BMC Cancer* **2013**, *13*, 251. [[CrossRef](#)]
159. Sherbet, G.V.; Lakshmi, M.S. S100A4 (MTS1) calcium binding protein in cancer growth, invasion and metastasis. *Anticancer Res.* **1998**, *18*, 2415–2421.
160. Meynier, S.; Rieux-Laucat, F. FAS and RAS related Apoptosis defects: From autoimmunity to leukemia. *Immunol. Rev.* **2019**, *287*, 50–61. [[CrossRef](#)]
161. Shin, D.H.; Park, J.H.; Lee, J.Y.; Won, H.Y.; Jang, K.S.; Min, K.W.; Jang, S.H.; Woo, J.K.; Oh, S.H.; Kong, G. Overexpression of Id1 in transgenic mice promotes mammary basal stem cell activity and breast tumorigenesis. *Oncotarget* **2015**, *6*, 17276–17290. [[CrossRef](#)] [[PubMed](#)]
162. Georgiadou, D.; Sergeantanis, T.N.; Sakellariou, S.; Filippakis, G.M.; Zagouri, F.; Vlachodimitropoulos, D.; Psaltopoulou, T.; Lazaris, A.C.; Patsouris, E.; Zografos, G.C. VEGF and Id-1 in pancreatic adenocarcinoma: Prognostic significance and impact on angiogenesis. *Eur. J. Surg. Oncol.* **2014**, *40*, 1331–1337. [[CrossRef](#)] [[PubMed](#)]
163. Forootan, S.S.; Wong, Y.C.; Dodson, A.; Wang, X.; Lin, K.; Smith, P.H.; Foster, C.S.; Ke, Y. Increased Id-1 expression is significantly associated with poor survival of patients with prostate cancer. *Hum. Pathol.* **2007**, *38*, 1321–1329. [[CrossRef](#)] [[PubMed](#)]
164. Perk, J.; Iavarone, A.; Benezra, R. Id family of helix-loop-helix proteins in cancer. *Nat. Rev. Cancer* **2005**, *5*, 603–614. [[CrossRef](#)] [[PubMed](#)]
165. Ponz-Sarvisé, M.; Nguewa, P.A.; Pajares, M.J.; Agorreta, J.; Lozano, M.D.; Redrado, M.; Pio, R.; Behrens, C.; Wistuba, I.I.; Garcia-Franco, C.E.; et al. Inhibitor of differentiation-1 as a novel prognostic factor in NSCLC patients with adenocarcinoma histology and its potential contribution to therapy resistance. *Clin. Cancer Res.* **2011**, *17*, 4155–4166. [[CrossRef](#)] [[PubMed](#)]
166. Zhao, Y.; Luo, A.; Li, S.; Zhang, W.; Chen, H.; Li, Y.; Ding, F.; Huang, F.; Liu, Z. Inhibitor of Differentiation/DNA Binding 1 (ID1) Inhibits Etoposide-induced Apoptosis in a c-Jun/c-Fos-dependent Manner. *J. Biol. Chem.* **2016**, *291*, 6831–6842. [[CrossRef](#)] [[PubMed](#)]
167. Castanon, E.; Bosch-Barrera, J.; Lopez, I.; Collado, V.; Moreno, M.; Lopez-Picazo, J.M.; Arbea, L.; Lozano, M.D.; Calvo, A.; Gil-Bazo, I. Id1 and Id3 co-expression correlates with clinical outcome in stage III-N2 non-small cell lung cancer patients treated with definitive chemoradiotherapy. *J. Transl. Med.* **2013**, *11*, 13. [[CrossRef](#)]
168. Schindl, M.; Oberhuber, G.; Obermair, A.; Schoppmann, S.F.; Karner, B.; Birner, P. Overexpression of Id-1 protein is a marker for unfavorable prognosis in early-stage cervical cancer. *Cancer Res.* **2001**, *61*, 5703–5706.
169. Wazir, U.; Jiang, W.G.; Sharma, A.K.; Newbold, R.F.; Mokbel, K. The mRNA expression of inhibitors of DNA binding-1 and -2 is associated with advanced tumour stage and adverse clinical outcome in human breast cancer. *Anticancer Res.* **2013**, *33*, 2179–2183.
170. Xiao, Z.D.; Han, L.; Lee, H.; Zhuang, L.; Zhang, Y.; Baddour, J.; Nagrath, D.; Wood, C.G.; Gu, J.; Wu, X.; et al. Energy stress-induced lncRNA FILNC1 represses c-Myc-mediated energy metabolism and inhibits renal tumor development. *Nat. Commun.* **2017**, *8*, 783. [[CrossRef](#)]
171. Ciribilli, Y.; Singh, P.; Inga, A.; Borlak, J. c-Myc targeted regulators of cell metabolism in a transgenic mouse model of papillary lung adenocarcinoma. *Oncotarget* **2016**, *7*, 65514–65539. [[CrossRef](#)] [[PubMed](#)]



172. Jain, S.; Wang, X.; Chang, C.C.; Ibarra-Drendall, C.; Wang, H.; Zhang, Q.; Brady, S.W.; Li, P.; Zhao, H.; Dobbs, J.; et al. Src Inhibition Blocks c-Myc Translation and Glucose Metabolism to Prevent the Development of Breast Cancer. *Cancer Res.* **2015**, *75*, 4863–4875. [[CrossRef](#)] [[PubMed](#)]
173. Hardie, D.G.; Schaffer, B.E.; Brunet, A. AMPK: An Energy-Sensing Pathway with Multiple Inputs and Outputs. *Trends Cell Biol.* **2016**, *26*, 190–201. [[CrossRef](#)] [[PubMed](#)]
174. Mihaylova, M.M.; Shaw, R.J. The AMPK signalling pathway coordinates cell growth, autophagy and metabolism. *Nat. Cell Biol.* **2011**, *13*, 1016–1023. [[CrossRef](#)] [[PubMed](#)]
175. Gandhi, N.; Das, G.M. Metabolic Reprogramming in Breast Cancer and Its Therapeutic Implications. *Cells* **2019**, *8*, 89. [[CrossRef](#)] [[PubMed](#)]
176. Hanahan, D.; Weinberg, R.A. Hallmarks of cancer: The next generation. *Cell* **2011**, *144*, 646–674. [[CrossRef](#)]
177. Oronsky, B.T.; Oronsky, N.; Fanger, G.R.; Parker, C.W.; Caroen, S.Z.; Lybeck, M.; Scicinski, J.J. Follow the ATP: Tumor energy production: A perspective. *Anticancer Agents Med. Chem.* **2014**, *14*, 1187–1198. [[CrossRef](#)]
178. Richardson, A.D.; Yang, C.; Osterman, A.; Smith, J.W. Central carbon metabolism in the progression of mammary carcinoma. *Breast Cancer Res. Treat.* **2008**, *110*, 297–307. [[CrossRef](#)]
179. Buchheit, C.L.; Weigel, K.J.; Schafer, Z.T. Cancer cell survival during detachment from the ECM: Multiple barriers to tumour progression. *Nat. Rev. Cancer* **2014**, *14*, 632–641. [[CrossRef](#)]
180. Haun, F.; Neumann, S.; Peintner, L.; Wieland, K.; Habicht, J.; Schwan, C.; Ostevold, K.; Koczorowska, M.M.; Biniossek, M.; Kist, M.; et al. Identification of a novel anoikis signalling pathway using the fungal virulence factor gliotoxin. *Nat. Commun.* **2018**, *9*, 3524. [[CrossRef](#)]
181. Dummmler, B.; Ohshiro, K.; Kumar, R.; Field, J. Pak protein kinases and their role in cancer. *Cancer Metastasis Rev.* **2009**, *28*, 51–63. [[CrossRef](#)] [[PubMed](#)]
182. Radu, M.; Semenova, G.; Kosoff, R.; Chernoff, J. PAK signalling during the development and progression of cancer. *Nat. Rev. Cancer* **2014**, *14*, 13–25. [[CrossRef](#)] [[PubMed](#)]
183. Thillai, K.; Lam, H.; Sarker, D.; Wells, C.M. Deciphering the link between PI3K and PAK: An opportunity to target key pathways in pancreatic cancer? *Oncotarget* **2017**, *8*, 14173–14191. [[CrossRef](#)] [[PubMed](#)]
184. Ye, D.Z.; Field, J. PAK signaling in cancer. *Cell Logist.* **2012**, *2*, 105–116. [[CrossRef](#)] [[PubMed](#)]
185. Wang, Z.; Oh, E.; Clapp, D.W.; Chernoff, J.; Thurmond, D.C. Inhibition or ablation of p21-activated kinase (PAK1) disrupts glucose homeostatic mechanisms in vivo. *J. Biol. Chem.* **2011**, *286*, 41359–41367. [[CrossRef](#)] [[PubMed](#)]
186. Zhang, X.; Zhang, X.; Li, Y. PAK4 regulates G6PD activity by p53 degradation involving colon cancer cell growth. *Cell Death Dis.* **2017**, *8*, e2820. [[CrossRef](#)] [[PubMed](#)]
187. Murray, B.W.; Guo, C.; Piraino, J.; Westwick, J.K.; Zhang, C.; Lamerdin, J.; Dagostino, E.; Knighton, D.; Loi, C.M.; Zager, M.; et al. Small-molecule p21-activated kinase inhibitor PF-3758309 is a potent inhibitor of oncogenic signaling and tumor growth. *Proc. Natl. Acad. Sci. USA* **2010**, *107*, 9446–9451. [[CrossRef](#)] [[PubMed](#)]
188. Pant, V.; Lozano, G. Limiting the power of p53 through the ubiquitin proteasome pathway. *Genes Dev.* **2014**, *28*, 1739–1751. [[CrossRef](#)] [[PubMed](#)]
189. Wei, J.; Yang, Y.; Lu, M.; Xu, L.; Liu, F.; Yuan, Z.; Bao, Q.; Jiang, Z.; Xu, X.; Guo, X.; et al. Escape, or Vanish: Control the Fate of p53 through MDM2-Mediated Ubiquitination. *Anticancer Agents Med. Chem.* **2015**, *16*, 174–189. [[CrossRef](#)] [[PubMed](#)]
190. Kroemer, G.; Galluzzi, L.; Vandenabeele, P.; Abrams, J.; Alnemri, E.S.; Baehrecke, E.H.; Blagosklonny, M.V.; El-Deiry, W.S.; Golstein, P.; Green, D.R.; et al. Classification of cell death: Recommendations of the Nomenclature Committee on Cell Death 2009. *Cell Death Differ.* **2009**, *16*, 3–11. [[CrossRef](#)]
191. Galluzzi, L.; Vitale, I.; Aaronson, S.A.; Abrams, J.M.; Adam, D.; Agostinis, P.; Alnemri, E.S.; Altucci, L.; Amelio, I.; Andrews, D.W.; et al. Molecular mechanisms of cell death: Recommendations of the Nomenclature Committee on Cell Death 2018. *Cell Death Differ.* **2018**, *25*, 486–541. [[CrossRef](#)] [[PubMed](#)]
192. Green, D.R.; Llamby, F. Cell Death Signaling. *Cold Spring Harb. Perspect. Biol.* **2015**, *7*. [[CrossRef](#)] [[PubMed](#)]
193. Calabro, V.; Mason, P.J.; Filosa, S.; Civitelli, D.; Cittadella, R.; Tagarelli, A.; Martini, G.; Brancati, C.; Luzzatto, L. Genetic heterogeneity of glucose-6-phosphate dehydrogenase deficiency revealed by single-strand conformation and sequence analysis. *Am. J. Hum. Genet.* **1993**, *52*, 527–536. [[PubMed](#)]
194. Ho, H.Y.; Cheng, M.L.; Chiu, D.T. Glucose-6-phosphate dehydrogenase—from oxidative stress to cellular functions and degenerative diseases. *Redox Rep.* **2007**, *12*, 109–118. [[CrossRef](#)]



195. Shan, F.; Yang, R.; Ji, T.; Jiao, F. Vitamin C Inhibits Aggravated Eryptosis by Hydrogen Peroxide in Glucose-6-Phosphated Dehydrogenase Deficiency. *Cell Physiol. Biochem.* **2016**, *39*, 1453–1462. [[CrossRef](#)] [[PubMed](#)]
196. Qasim, N.; Mahmood, R. Diminution of Oxidative Damage to Human Erythrocytes and Lymphocytes by Creatine: Possible Role of Creatine in Blood. *PLoS ONE* **2015**, *10*, e0141975. [[CrossRef](#)] [[PubMed](#)]
197. Lang, F.; Abed, M.; Lang, E.; Foller, M. Oxidative stress and suicidal erythrocyte death. *Antioxid. Redox Signal.* **2014**, *21*, 138–153. [[CrossRef](#)] [[PubMed](#)]
198. Xu, Y.; Zhang, Z.; Hu, J.; Stillman, I.E.; Leopold, J.A.; Handy, D.E.; Loscalzo, J.; Stanton, R.C. Glucose-6-phosphate dehydrogenase-deficient mice have increased renal oxidative stress and increased albuminuria. *FASEB J.* **2010**, *24*, 609–616. [[CrossRef](#)] [[PubMed](#)]
199. Lin, C.J.; Ho, H.Y.; Cheng, M.L.; You, T.H.; Yu, J.S.; Chiu, D.T. Impaired dephosphorylation renders G6PD-knockdown HepG2 cells more susceptible to H<sub>2</sub>O<sub>2</sub>-induced apoptosis. *Free Radic Biol. Med.* **2010**, *49*, 361–373. [[CrossRef](#)] [[PubMed](#)]
200. Kroemer, G.; Levine, B. Autophagic cell death: The story of a misnomer. *Nat. Rev. Mol. Cell Biol.* **2008**, *9*, 1004–1010. [[CrossRef](#)]
201. Dodson, M.; Darley-USmar, V.; Zhang, J. Cellular metabolic and autophagic pathways: Traffic control by redox signaling. *Free Radic Biol. Med.* **2013**, *63*, 207–221. [[CrossRef](#)] [[PubMed](#)]
202. Jenwitheesuk, A.; Nopparat, C.; Mukda, S.; Wongchitrat, P.; Govitrapong, P. Melatonin regulates aging and neurodegeneration through energy metabolism, epigenetics, autophagy and circadian rhythm pathways. *Int. J. Mol. Sci.* **2014**, *15*, 16848–16884. [[CrossRef](#)] [[PubMed](#)]
203. Nikolettou, V.; Markaki, M.; Palikaras, K.; Tavernarakis, N. Crosstalk between apoptosis, necrosis and autophagy. *Biochim. Biophys. Acta* **2013**, *1833*, 3448–3459. [[CrossRef](#)] [[PubMed](#)]
204. Ho, H.Y.; Cheng, M.L.; Weng, S.F.; Chang, L.; Yeh, T.T.; Shih, S.R.; Chiu, D.T. Glucose-6-phosphate dehydrogenase deficiency enhances enterovirus 71 infection. *J. Gen. Virol.* **2008**, *89*, 2080–2089. [[CrossRef](#)] [[PubMed](#)]
205. Khan, M.A.; Palaniyar, N. Transcriptional firing helps to drive NETosis. *Sci. Rep.* **2017**, *7*, 41749. [[CrossRef](#)] [[PubMed](#)]
206. Remijsen, Q.; Vanden Berghe, T.; Wirawan, E.; Asselbergh, B.; Parthoens, E.; De Rycke, R.; Noppen, S.; Delforge, M.; Willems, J.; Vandenabeele, P. Neutrophil extracellular trap cell death requires both autophagy and superoxide generation. *Cell Res.* **2011**, *21*, 290–304. [[CrossRef](#)]
207. Cheng, M.L.; Ho, H.Y.; Lin, H.Y.; Lai, Y.C.; Chiu, D.T. Effective NET formation in neutrophils from individuals with G6PD Taiwan-Hakka is associated with enhanced NADP(+) biosynthesis. *Free Radic Res.* **2013**, *47*, 699–709. [[CrossRef](#)] [[PubMed](#)]
208. Siler, U.; Romao, S.; Tejera, E.; Pastukhov, O.; Kuzmenko, E.; Valencia, R.G.; Meda Spaccamela, V.; Belohradsky, B.H.; Speer, O.; Schmugge, M.; et al. Severe glucose-6-phosphate dehydrogenase deficiency leads to susceptibility to infection and absent NETosis. *J. Allergy Clin. Immunol.* **2017**, *139*, 212–219 e213. [[CrossRef](#)]
209. Gordon, G.; Mackow, M.C.; Levy, H.R. On the mechanism of interaction of steroids with human glucose 6-phosphate dehydrogenase. *Arch. Biochem. Biophys.* **1995**, *318*, 25–29. [[CrossRef](#)]
210. Mele, L.; Paino, F.; Papaccio, F.; Regad, T.; Boocock, D.; Stiuso, P.; Lombardi, A.; Liccardo, D.; Aquino, G.; Barbieri, A.; et al. A new inhibitor of glucose-6-phosphate dehydrogenase blocks pentose phosphate pathway and suppresses malignant proliferation and metastasis in vivo. *Cell Death Dis.* **2018**, *9*, 572. [[CrossRef](#)]
211. Wang, X.; Wu, G.; Cao, G.; Yang, L.; Xu, H.; Huang, J.; Hou, J. Zoledronic acid inhibits the pentose phosphate pathway through attenuating the Ras-TAp73-G6PD axis in bladder cancer cells. *Mol. Med. Rep.* **2015**, *12*, 4620–4625. [[CrossRef](#)] [[PubMed](#)]
212. Li, Z.; Zhang, B.; Yao, W.; Zhang, C.; Wan, L.; Zhang, Y. APC-Cdh1 Regulates Neuronal Apoptosis Through Modulating Glycolysis and Pentose-Phosphate Pathway After Oxygen-Glucose Deprivation and Reperfusion. *Cell Mol. Neurobiol.* **2019**, *39*, 123–135. [[CrossRef](#)] [[PubMed](#)]
213. Chen, L.; Yang, H.; Yi, Z.; Jiang, L.; Li, Y.; Han, Q.; Yang, Y.; Zhang, Q.; Yang, Z.; Kuang, Y.; et al. LncRNA GAS5 regulates redox balance and dysregulates the cell cycle and apoptosis in malignant melanoma cells. *J. Cancer Res. Clin. Oncol.* **2019**, *145*, 637–652. [[CrossRef](#)] [[PubMed](#)]

214. Shan, Z.X.; Lin, Q.X.; Deng, C.Y.; Zhu, J.N.; Mai, L.P.; Liu, J.L.; Fu, Y.H.; Liu, X.Y.; Li, Y.X.; Zhang, Y.Y.; et al. miR-1/miR-206 regulate Hsp60 expression contributing to glucose-mediated apoptosis in cardiomyocytes. *FEBS Lett.* **2010**, *584*, 3592–3600. [[CrossRef](#)] [[PubMed](#)]
215. Ahmad, F.; Dixit, D.; Sharma, V.; Kumar, A.; Joshi, S.D.; Sarkar, C.; Sen, E. Nrf2-driven TERT regulates pentose phosphate pathway in glioblastoma. *Cell Death Dis.* **2016**, *7*, e2213. [[CrossRef](#)] [[PubMed](#)]
216. Levy, H.R. Glucose-6-phosphate dehydrogenases. *Adv. Enzym. Relat. Areas Mol. Biol.* **1979**, *48*, 97–192.
217. Hamilton, N.M.; Dawson, M.; Fairweather, E.E.; Hamilton, N.S.; Hitchin, J.R.; James, D.I.; Jones, S.D.; Jordan, A.M.; Lyons, A.J.; Small, H.F.; et al. Novel steroid inhibitors of glucose 6-phosphate dehydrogenase. *J. Med. Chem.* **2012**, *55*, 4431–4445. [[CrossRef](#)] [[PubMed](#)]
218. Kohler, E.; Barrach, H.; Neubert, D. Inhibition of NADP dependent oxidoreductases by the 6-aminonicotinamide analogue of NADP. *FEBS Lett.* **1970**, *6*, 225–228. [[CrossRef](#)]
219. Sharma, P.K.; Bhardwaj, R.; Dwarakanath, B.S.; Varshney, R. Metabolic oxidative stress induced by a combination of 2-DG and 6-AN enhances radiation damage selectively in malignant cells via non-coordinated expression of antioxidant enzymes. *Cancer Lett.* **2010**, *295*, 154–166. [[CrossRef](#)]
220. Du, Q.H.; Peng, C.; Zhang, H. Polydatin: A review of pharmacology and pharmacokinetics. *Pharm. Biol.* **2013**, *51*, 1347–1354. [[CrossRef](#)]
221. Youngster, I.; Arcavi, L.; Schechmaster, R.; Akayzen, Y.; Popliski, H.; Shimonov, J.; Beig, S.; Berkovitch, M. Medications and glucose-6-phosphate dehydrogenase deficiency: An evidence-based review. *Drug Saf.* **2010**, *33*, 713–726. [[CrossRef](#)] [[PubMed](#)]
222. Romanuik, T.L.; Wang, G.; Morozova, O.; Delaney, A.; Marra, M.A.; Sadar, M.D. LNCaP Atlas: Gene expression associated with in vivo progression to castration-recurrent prostate cancer. *BMC Med. Genom.* **2010**, *3*, 43. [[CrossRef](#)] [[PubMed](#)]
223. Zhang, Z.; Zhu, Z.; Watabe, K.; Zhang, X.; Bai, C.; Xu, M.; Wu, F.; Mo, Y.Y. Negative regulation of lncRNA GAS5 by miR-21. *Cell Death Differ.* **2013**, *20*, 1558–1568. [[CrossRef](#)] [[PubMed](#)]
224. Shi, X.; Sun, M.; Liu, H.; Yao, Y.; Kong, R.; Chen, F.; Song, Y. A critical role for the long non-coding RNA GAS5 in proliferation and apoptosis in non-small-cell lung cancer. *Mol. Carcinog.* **2015**, *54* (Suppl. 1), E1–E12. [[CrossRef](#)]
225. Chen, J.F.; Tao, Y.; Li, J.; Deng, Z.; Yan, Z.; Xiao, X.; Wang, D.Z. microRNA-1 and microRNA-206 regulate skeletal muscle satellite cell proliferation and differentiation by repressing Pax7. *J. Cell Biol.* **2010**, *190*, 867–879. [[CrossRef](#)] [[PubMed](#)]
226. Townley-Tilson, W.H.; Callis, T.E.; Wang, D. MicroRNAs 1, 133, and 206: Critical factors of skeletal and cardiac muscle development, function, and disease. *Int. J. Biochem. Cell Biol.* **2010**, *42*, 1252–1255. [[CrossRef](#)] [[PubMed](#)]
227. Wang, L.; Yuan, Y.; Li, J.; Ren, H.; Cai, Q.; Chen, X.; Liang, H.; Shan, H.; Fu, Z.D.; Gao, X.; et al. MicroRNA-1 aggravates cardiac oxidative stress by post-transcriptional modification of the antioxidant network. *Cell Stress Chaperones* **2015**, *20*, 411–420. [[CrossRef](#)] [[PubMed](#)]
228. Cacchiarelli, D.; Martone, J.; Girardi, E.; Cesana, M.; Incitti, T.; Morlando, M.; Nicoletti, C.; Santini, T.; Sthandier, O.; Barberi, L.; et al. MicroRNAs involved in molecular circuitries relevant for the Duchenne muscular dystrophy pathogenesis are controlled by the dystrophin/nNOS pathway. *Cell Metab.* **2010**, *12*, 341–351. [[CrossRef](#)] [[PubMed](#)]
229. Bodnar, A.G.; Ouellette, M.; Frolkis, M.; Holt, S.E.; Chiu, C.P.; Morin, G.B.; Harley, C.B.; Shay, J.W.; Lichtsteiner, S.; Wright, W.E. Extension of life-span by introduction of telomerase into normal human cells. *Science* **1998**, *279*, 349–352. [[CrossRef](#)]
230. Kim, N.W.; Piatyszek, M.A.; Prowse, K.R.; Harley, C.B.; West, M.D.; Ho, P.L.; Coviello, G.M.; Wright, W.E.; Weinrich, S.L.; Shay, J.W. Specific association of human telomerase activity with immortal cells and cancer. *Science* **1994**, *266*, 2011–2015. [[CrossRef](#)] [[PubMed](#)]
231. Behl, C. BAG3 and friends: Co-chaperones in selective autophagy during aging and disease. *Autophagy* **2011**, *7*, 795–798. [[CrossRef](#)] [[PubMed](#)]
232. Rosati, A.; Graziano, V.; De Laurenzi, V.; Pascale, M.; Turco, M.C. BAG3: A multifaceted protein that regulates major cell pathways. *Cell Death Dis.* **2011**, *2*, e141. [[CrossRef](#)] [[PubMed](#)]
233. Burnett, J.C.; Rossi, J.J. RNA-based therapeutics: Current progress and future prospects. *Chem. Biol.* **2012**, *19*, 60–71. [[CrossRef](#)] [[PubMed](#)]

234. Juliano, R.L. The delivery of therapeutic oligonucleotides. *Nucleic Acids Res.* **2016**, *44*, 6518–6548. [[CrossRef](#)] [[PubMed](#)]
235. Gupte, S.A. Glucose-6-phosphate dehydrogenase: A novel therapeutic target in cardiovascular diseases. *Curr. Opin. Investig. Drugs* **2008**, *9*, 993–1000. [[PubMed](#)]
236. Zhao, Z.B.; Liu, Y.; Yao, Y. Computational determination of binding structures and free energies of glucose 6-phosphate dehydrogenase with novel steroid inhibitors. *J. Mol. Graph. Model.* **2014**, *51*, 168–172. [[CrossRef](#)] [[PubMed](#)]
237. Alfarouk, K.O.; Verduzco, D.; Rauch, C.; Muddathir, A.K.; Bashir, A.H.; Elhassan, G.O.; Ibrahim, M.E.; Orozco, J.D.; Cardone, R.A.; Reshkin, S.J.; et al. Erratum: Glycolysis, tumor metabolism, cancer growth and dissemination. A new pH-based etiopathogenic perspective and therapeutic approach to an old cancer question. *Oncoscience* **2015**, *2*, 317. [[CrossRef](#)] [[PubMed](#)]
238. Wegiel, B.; Vuerich, M.; Daneshmandi, S.; Seth, P. Metabolic Switch in the Tumor Microenvironment Determines Immune Responses to Anti-cancer Therapy. *Front. Oncol.* **2018**, *8*, 284. [[CrossRef](#)] [[PubMed](#)]
239. Kuehne, A.; Emmert, H.; Soehle, J.; Winnefeld, M.; Fischer, F.; Wenck, H.; Gallinat, S.; Terstegen, L.; Lucius, R.; Hildebrand, J.; et al. Acute Activation of Oxidative Pentose Phosphate Pathway as First-Line Response to Oxidative Stress in Human Skin Cells. *Mol. Cell* **2015**, *59*, 359–371. [[CrossRef](#)]
240. Fukuda, S.; Miyata, H.; Miyazaki, Y.; Makino, T.; Takahashi, T.; Kurokawa, Y.; Yamasaki, M.; Nakajima, K.; Takiguchi, S.; Mori, M.; et al. Pyruvate Kinase M2 Modulates Esophageal Squamous Cell Carcinoma Chemotherapy Response by Regulating the Pentose Phosphate Pathway. *Ann. Surg. Oncol.* **2015**, *22* (Suppl. 3), S1461–S1468. [[CrossRef](#)]
241. Du, W.; Jiang, P.; Mancuso, A.; Stonestrom, A.; Brewer, M.D.; Minn, A.J.; Mak, T.W.; Wu, M.; Yang, X. TAp73 enhances the pentose phosphate pathway and supports cell proliferation. *Nat. Cell Biol.* **2013**, *15*, 991–1000. [[CrossRef](#)] [[PubMed](#)]
242. Ozer, N.; Aksoy, Y.; Ogun, I.H. Kinetic properties of human placental glucose-6-phosphate dehydrogenase. *Int. J. Biochem. Cell Biol.* **2001**, *33*, 221–226. [[CrossRef](#)]
243. Cho, S.W.; Joshi, J.G. Characterization of glucose-6-phosphate dehydrogenase isozymes from human and pig brain. *Neuroscience* **1990**, *38*, 819–828. [[CrossRef](#)]
244. Liu, B.; Bai, W.; Ou, G.; Zhang, J. Cdh1-Mediated Metabolic Switch from Pentose Phosphate Pathway to Glycolysis Contributes to Sevoflurane-Induced Neuronal Apoptosis in Developing Brain. *ACS Chem. Neurosci.* **2019**, *10*, 2332–2344. [[CrossRef](#)] [[PubMed](#)]
245. Gregory, M.A.; D'Alessandro, A.; Alvarez-Calderon, F.; Kim, J.; Nemkov, T.; Adane, B.; Rozhok, A.I.; Kumar, A.; Kumar, V.; Pollyea, D.A.; et al. ATM/G6PD-driven redox metabolism promotes FLT3 inhibitor resistance in acute myeloid leukemia. *Proc. Natl. Acad. Sci. USA* **2016**, *113*, E6669–E6678. [[CrossRef](#)] [[PubMed](#)]
246. Yeh, G.C.; Occhipinti, S.J.; Cowan, K.H.; Chabner, B.A.; Myers, C.E. Adriamycin resistance in human tumor cells associated with marked alteration in the regulation of the hexose monophosphate shunt and its response to oxidant stress. *Cancer Res.* **1987**, *47*, 5994–5999. [[PubMed](#)]
247. Biaglow, J.E.; Ayene, I.S.; Koch, C.J.; Donahue, J.; Stamato, T.D.; Mieyal, J.J.; Tuttle, S.W. Radiation response of cells during altered protein thiol redox. *Radiat. Res.* **2003**, *159*, 484–494. [[CrossRef](#)]
248. Tuttle, S.; Stamato, T.; Perez, M.L.; Biaglow, J. Glucose-6-phosphate dehydrogenase and the oxidative pentose phosphate cycle protect cells against apoptosis induced by low doses of ionizing radiation. *Radiat. Res.* **2000**, *153*, 781–787. [[CrossRef](#)]
249. Liu, R.; Li, W.; Tao, B.; Wang, X.; Yang, Z.; Zhang, Y.; Wang, C.; Liu, R.; Gao, H.; Liang, J.; et al. Tyrosine phosphorylation activates 6-phosphogluconate dehydrogenase and promotes tumor growth and radiation resistance. *Nat. Commun.* **2019**, *10*, 991. [[CrossRef](#)]
250. Heller, S.; Maurer, G.D.; Wanka, C.; Hofmann, U.; Luger, A.L.; Bruns, I.; Steinbach, J.P.; Rieger, J. Gene Suppression of Transketolase-Like Protein 1 (TKTL1) Sensitizes Glioma Cells to Hypoxia and Ionizing Radiation. *Int. J. Mol. Sci.* **2018**, *19*, 2168. [[CrossRef](#)]
251. Chen, C.; Mei, Q.; Wang, L.; Feng, X.; Tao, X.; Qiu, C.; Zhu, J. TIGAR suppresses seizures induced by kainic acid through inhibiting oxidative stress and neuronal apoptosis. *Biochem. Biophys. Res. Commun.* **2019**. [[CrossRef](#)] [[PubMed](#)]

- 252. Shin, Y.K.; Yoo, B.C.; Hong, Y.S.; Chang, H.J.; Jung, K.H.; Jeong, S.Y.; Park, J.G. Upregulation of glycolytic enzymes in proteins secreted from human colon cancer cells with 5-fluorouracil resistance. *Electrophoresis* **2009**, *30*, 2182–2192. [[CrossRef](#)] [[PubMed](#)]
- 253. Bachur, N.R.; Gordon, S.L.; Gee, M.V.; Kon, H. NADPH cytochrome P-450 reductase activation of quinone anticancer agents to free radicals. *Proc. Natl. Acad. Sci. USA* **1979**, *76*, 954–957. [[CrossRef](#)] [[PubMed](#)]
- 254. Jagust, P.; de Luxan-Delgado, B.; Parejo-Alonso, B.; Sancho, P. Metabolism-Based Therapeutic Strategies Targeting Cancer Stem Cells. *Front. Pharm.* **2019**, *10*, 203. [[CrossRef](#)] [[PubMed](#)]
- 255. Xu, I.M.; Lai, R.K.; Lin, S.H.; Tse, A.P.; Chiu, D.K.; Koh, H.Y.; Law, C.T.; Wong, C.M.; Cai, Z.; Wong, C.C.; et al. Transketolase counteracts oxidative stress to drive cancer development. *Proc. Natl. Acad. Sci. USA* **2016**, *113*, E725–E734. [[CrossRef](#)]
- 256. Hong, W.; Cai, P.; Xu, C.; Cao, D.; Yu, W.; Zhao, Z.; Huang, M.; Jin, J. Inhibition of Glucose-6-Phosphate Dehydrogenase Reverses Cisplatin Resistance in Lung Cancer Cells via the Redox System. *Front. Pharm.* **2018**, *9*, 43. [[CrossRef](#)] [[PubMed](#)]



© 2019 by the authors. Licensee MDPI, Basel, Switzerland. This article is an open access article distributed under the terms and conditions of the Creative Commons Attribution (CC BY) license (<http://creativecommons.org/licenses/by/4.0/>).

## Original Article

**Cite this article:** Chen M-H *et al.* (2018). Risk and coaggregation of major psychiatric disorders among first-degree relatives of patients with bipolar disorder: a nationwide population-based study. *Psychological Medicine* 1–8. <https://doi.org/10.1017/S003329171800332X>

Received: 20 May 2018

Revised: 11 October 2018

Accepted: 15 October 2018

### Key words:

ADHD; ASD; bipolar disorder; familial co-aggregation; first-degree relatives; MDD; schizophrenia

### Author for correspondence:

Ya-Mei Bai, E-mail: [yumbi@mail2000.com.tw](mailto:yumbi@mail2000.com.tw)  
and Tung-Ping Su, E-mail: [tomsu0402@gmail.com](mailto:tomsu0402@gmail.com)

# Risk and coaggregation of major psychiatric disorders among first-degree relatives of patients with bipolar disorder: a nationwide population-based study

Mu-Hong Chen<sup>1,2</sup>, Ju-Wei Hsu<sup>1,2</sup>, Kei-Lin Huang<sup>1,2</sup>, Tung-Ping Su<sup>1,2,3</sup>,  
Cheng-Ta Li<sup>1,2</sup>, Wei-Chen Lin<sup>1,2</sup>, Shih-Jen Tsai<sup>1,2</sup>, Chih-Ming Cheng<sup>1,2</sup>,  
Wen-Han Chang<sup>1</sup>, Tai-Long Pan<sup>4,5,6</sup>, Tzeng-Ji Chen<sup>7,8</sup> and Ya-Mei Bai<sup>1,2</sup>

<sup>1</sup>Department of Psychiatry, Taipei Veterans General Hospital, Taipei, Taiwan; <sup>2</sup>Division of Psychiatry, School of Medicine, National Yang-Ming University, Taipei, Taiwan; <sup>3</sup>Department of Psychiatry, Cheng Hsin General Hospital, Taipei, Taiwan; <sup>4</sup>School of Traditional Chinese Medicine, Chang Gung University, Taoyuan, Taiwan; <sup>5</sup>Liver Research Center, Chang Gung Memorial Hospital, Taoyuan, Taiwan; <sup>6</sup>Research Center for Chinese Herbal Medicine and Research Center for Food and Cosmetic Safety, College of Human Ecology, Chang Gung University of Science and Technology, Taoyuan, Taiwan; <sup>7</sup>Department of Family Medicine, Taipei Veterans General Hospital, Taipei, Taiwan and <sup>8</sup>Institute of Hospital and Health Care Administration, National Yang-Ming University, Taipei, Taiwan

## Abstract

**Background.** Bipolar disorder is a highly heritable mental illness that transmits intergeneratively. Previous studies supported that first-degree relatives (FDRs), such as parents, offspring, and siblings, of patients with bipolar disorder, had a higher risk of bipolar disorder. However, whether FDRs of bipolar patients have an increased risk of schizophrenia, major depressive disorder (MDD), autism spectrum disorder (ASD), and attention deficit hyperactivity disorder (ADHD) remains unclear.

**Methods.** Among the entire population in Taiwan, 87 639 patients with bipolar disorder and 188 290 FDRs of patients with bipolar disorder were identified in our study. The relative risks (RRs) of major psychiatric disorders were assessed among FDRs of patients with bipolar disorder.

**Results.** FDRs of patients with bipolar disorder were more likely to have a higher risk of major psychiatric disorders, including bipolar disorder (RR 6.12, 95% confidence interval (CI) 5.95–6.30), MDD (RR 2.89, 95% CI 2.82–2.96), schizophrenia (RR 2.64, 95% CI 2.55–2.73), ADHD (RR 2.21, 95% CI 2.13–2.30), and ASD (RR 2.10, 95% CI 1.92–2.29), than the total population did. These increased risks for major psychiatric disorders were consistent across different familial kinships, such as parents, offspring, siblings, and twins. A dose-dependent relationship was also found between risk of each major psychiatric disorder and numbers of bipolar patients.

**Conclusions.** Our study was the first study to support the familial coaggregation of bipolar disorder with other major psychiatric disorders, including schizophrenia, MDD, ADHD, and ASD, in a Taiwanese (non-Caucasian) population. Given the elevated risks of major psychiatric disorders, the public health government should pay more attention to the mental health of FDRs of patients with bipolar disorder.

Bipolar disorder is a recurrent chronic severe mental disorder characterized by alternative episodes of mania/hypomania and depression. It affects more than 2% of the world's population regardless of nationality, ethnic origin, or socioeconomic status. Bipolar disorder is one of the main causes of disability, particularly among young people. Bipolar disorder accounts for approximately 7% of disability-adjusted life years caused by mental and substance use disorders. Bipolar disorder leads to cognitive and functional impairment and increased mortality, in particularly through suicide (Muller-Oerlinghausen *et al.*, 2002; Grande *et al.*, 2016; Blanco *et al.*, 2017).

Bipolar disorder is a highly heritable mental illness that transmits intergeneratively and is commonly clustered within families. Lin *et al.* evaluated a total of 211 families with 1856 individuals who were ascertained through patients with bipolar disorder and showed that individuals from a family with a bipolar proband were more likely to develop bipolar disorder than others [odds ratio (OR) 4.53, 95% confidence interval (CI) 3.09–6.64] (Lin *et al.*, 2006). Song *et al.*, found that the relative risks (RRs) for first-degree relatives (FDRs) of bipolar patients were 5.8–7.9 across different kinships (parents, offspring, and siblings) (Song *et al.*, 2015). They further demonstrated that the siblings of individuals with bipolar disorder had higher risks of schizophrenia (RR 2.8, 95% CI 2.5–3.0), major depressive disorder (MDD, RR 2.1, 95% CI 2.0–2.2), attention deficit hyperactivity disorder (ADHD, RR 2.4, 95% CI 2.1–2.7),



and autism spectrum disorder (ASD, RR 2.6, 95% CI 2.3–3.0) (Song *et al.*, 2015). Axelson *et al.* followed the offspring, aged 6–18 years, of parents with bipolar disorder and the age-, sex-, and neighborhood-matched offspring of community parents without bipolar disorder. They revealed that compared with community offspring, the offspring of parents with bipolar disorder had significantly higher rates of manic/mixed/hypomanic episodes (9.2% *v.* 0.8%,  $p < 0.001$ ) and MDD (32.0% *v.* 14.9%,  $p < 0.001$ ), and they also had a higher rate of ADHD (30.7% *v.* 18.1%,  $p = 0.01$ ) (Axelson *et al.*, 2015). A 12-year follow-up study revealed that 72% of the bipolar offspring developed a lifetime DSM-IV axis I disorder, 54% an affective disorder, and 13% bipolar spectrum disorder (Mesman *et al.*, 2013). A meta-analysis of 33 studies with 3863 offspring of parents with severe mental illness (schizophrenia, bipolar disorder or MDD) and 3158 control offspring, and found that offspring of parents with severe mental illness were at increased risk for a range of psychiatric disorders (schizophrenia, bipolar disorder, depression, anxiety, substance use disorder, ADHD) and one third of them may develop a severe mental illness by early adulthood (Rasic *et al.*, 2014).

However, several previous epidemiological studies failed to find the cross-transmission of bipolar disorder with other psychiatric disorders, including schizophrenia and MDD (Maier *et al.*, 1993; McGuffin *et al.*, 2003; Merikangas *et al.*, 2012; Merikangas *et al.*, 2014; Vandeley *et al.*, 2014). Vandeley *et al.* analyzed a sample of 293 patients with schizophrenia, bipolar disorder or MDD, 110 controls, and 1734 adult FDRs. Among them, probands with schizophrenia, bipolar disorder or MDD and controls did not differ in age and sex; relatives of probands with schizophrenia, bipolar disorder or MDD and controls also did not differ in age and sex. They determined no evidence for cross-transmission of mania and major depressive episodes (OR 0.7, CI 0.5–1.1) and psychosis and mania (OR 1.0, CI 0.4–2.7) (Vandeley *et al.*, 2014). Maier *et al.* supported an independent transmission of schizophrenia and bipolar disorder (Maier *et al.*, 1993). Merikangas *et al.* further suggested no significant cross-aggregation between affective disorder subtypes suggesting that the familial transmission of manic and major depressive episodes was independent (Merikangas *et al.*, 2014). A twin study analyzed the data from 30 monozygotic and 37 dizygotic twin pairs in which the proband had bipolar disorder and 68 monozygotic and 109 dizygotic twin pairs in which the proband had MDD and found that approximately 71% of the genetic variance for mania was not shared with depression (McGuffin *et al.*, 2003). Whether bipolar disorder would be co-aggregated with other psychiatric disorders, such as schizophrenia and MDD, required further investigation.

From the genetic view of co-aggregation of major psychiatric disorders, a genome-wide association study (GWAS), which was composed of 33 332 patients and 27 888 controls of European ancestry, reported that five major psychiatric disorders – namely schizophrenia, bipolar disorder, MDD, ASD, and ADHD – may share common genes (Cross-Disorder Group of the Psychiatric Genomics Consortium, 2013b). Cross-Disorder Group of the Psychiatric Genomics Consortium further reported that the genetic correlation calculated using common single-nucleotide polymorphisms (SNPs) was high between schizophrenia and bipolar disorder [ $0.68 \pm 0.04$  standard error (S.E.),  $p < 10^{-16}$ ] and moderate between bipolar disorder and MDD ( $0.47 \pm 0.06$  S.E.,  $p = 1.5 \times 10^{-14}$ ) (Cross-Disorder Group of the Psychiatric Genomics Consortium, 2013a). However, the aforementioned studies have only been conducted in the Caucasian population, and most of

them focused on the offspring and siblings of bipolar patients; it is difficult to generalize these findings to other ethnicities, such as Asians, and to other kinships, such as parents of bipolar disorder patients.

In our study, using the Taiwan National Health Insurance Research Database (NHIRD), which contains the claims data of the entire Taiwan population ( $n > 2\,300\,000$ ), we investigated the risks of schizophrenia, bipolar disorder, MDD, ADHD, and ASD among the FDRs of patients with bipolar disorder, including their parents, offspring, siblings, and twins. We hypothesized that the FDRs of patients with bipolar disorder are more likely to have the aforementioned five major psychiatric disorders than those without bipolar patients, and we also hypothesized that a dose-dependent relationship exists between the risks of the five major psychiatric disorders and the numbers of bipolar patients in a family.

## Methods

### Data source

Taiwan's National Health Insurance (NHI), a mandatory universal health insurance program, was implemented in 1995 and offers comprehensive medical care coverage to all Taiwanese residents. The National Health Research Institute (NHRI) is in charge of the entire insurance claims database, namely the NHIRD, which consists of healthcare data from >99% of the entire Taiwan population. The NHRI audits and releases the NHIRD for scientific and study purposes. Claims data of subjects included in the NHIRD are anonymous to maintain individual privacy. Comprehensive information on insured subjects is included in the database, including demographic data, dates of clinical visits, and disease diagnoses. Using a unique personal identification number assigned to each resident in Taiwan, all of the information were linked together. Following Kuo *et al.*'s and Cheng *et al.*'s method, the recorded family kinships in the NHIRD were used for genealogy reconstruction (Kuo *et al.*, 2015; Cheng *et al.*, 2018). The diagnostic codes used were based on the International Classification of Diseases, 9th Revision, Clinical Modification (ICD-9-CM). The NHIRD has been used extensively in many epidemiologic studies in Taiwan (Chen *et al.*, 2013; Chen *et al.*, 2016; Chen *et al.*, 2018; Cheng *et al.*, 2018). Taipei Veterans General Hospital institutional review board approved this study.

### Inclusion criteria and disease classifications

All individuals with bipolar disorder (ICD-9-CM codes: 296 except 296.2, 296.3, 296.9, and 296.82) given by board-certified psychiatrists were identified between 2001 and 2011 as the bipolar patients. FDRs of bipolar patients, including parents, offspring, and siblings, were assessed for the presence or absence of major psychiatric disorders. Major psychiatric disorders included ASD (ICD-9-CM code: 299), ADHD (ICD-9-CM code: 314), schizophrenia (ICD-9-CM code: 295), bipolar disorder, and MDD (ICD-9-CM codes: 296.2 and 296.3). All psychiatric disorders were diagnosed at least twice by board-certified psychiatrists based on their clinical judgement and diagnostic interviews.

### Statistical analysis

We used independent *t* tests for continuous variables and Pearson's  $\chi^2$  tests for nominal variables to assess the differences

between the FDRs of patients with bipolar disorder and the total population. The relative risks (RRs) and 95% CIs of five major psychiatric disorders (ASD, ADHD, schizophrenia, bipolar disorder, and MDD) were calculated among FDRs of patients with bipolar disorder compared with the total population after adjusting for demographic data (age, sex, residence, and income). Age, sex, income, residence significantly differed between FDRs of patients with bipolar disorder and the total population. Clustering effect from the measurements taken on multiple subjects within one family may exist in our study. In order to manage the clustering effect, modified Poisson regression analysis with the robust variance estimation was an appropriate method for estimating the RRs in the clustered data (Zou, 2004; Yelland *et al.*, 2011). The modified Poisson regression uses a log link and has the equation:  $\log(\pi_i) = \beta_0 + \beta_1 X_{1i} + \beta_2 X_{2i} + \dots + \beta_k X_{ki}$ , where  $\pi_i$  is the probability of experiencing the outcome of interest for subject  $i$ , and  $X_{1i}, X_{2i}, \dots, X_{ki}$  are predictor variables. However, the modified Poisson regression applies a Poisson distribution to the data, which produces consistent estimates of the parameters in the above equation but inconsistent variances, since the variance under a Poisson model is larger than the variance under a binomial model unless the outcome is rare. Robust variance estimation is therefore used to avoid overestimating standard errors of parameter estimates (Zou, 2004; Yelland *et al.*, 2011). We further assessed the dose-dependent relationship between the risks of major psychiatric disorders and the numbers of bipolar patients (1 or  $\geq 2$ ) among FDRs of patients with bipolar disorder. Finally, stratified by different familial kinships (parents, offspring, siblings, and twins), the RRs and 95% CIs of five major psychiatric disorders (ASD, ADHD, schizophrenia, bipolar disorder, and MDD) were calculated between FDRs with or without bipolar patients. All tests were two-tailed and result with  $p < 0.05$  were considered statistically significant. All statistical analyses were performed using SPSS Version 21.0 for Windows (IBM, Armonk, NY, USA) and SAS Version 9.2 (SAS Institute, Cary, NC, USA).

## Results

Among the entire population in Taiwan, 72 573 patients with bipolar disorder and 188 290 FDRs of patients with bipolar disorder were identified in our study (Table 1). FDRs of bipolar patients had a higher prevalence of schizophrenia (1.67% *v.* 0.65%,  $p < 0.001$ ), bipolar disorder (2.51% *v.* 0.42%,  $p < 0.001$ ), MDD (3.75% *v.* 1.40%,  $p < 0.001$ ), ASD (0.26% *v.* 0.12%,  $p < 0.001$ ), and ADHD (1.46% *v.* 0.65%,  $p < 0.001$ ) compared with the total population (Table 2). FDRs of patients with bipolar disorder were more likely to have a higher risk of major psychiatric disorders, including bipolar disorder (RR 6.12, 95% CI 5.95–6.30), MDD (RR 2.89, 95% CI 2.82–2.96), schizophrenia (RR 2.64, 95% CI 2.55–2.73), ADHD (RR 2.21, 95% CI 2.13–2.30), and ASD (RR 2.10, 95% CI 1.92–2.29), than the total population did after adjusting for demographic data (Table 2). In addition, a dose-dependent association was found between risk of each major psychiatric disorder, including bipolar disorder (1: RR 6.10, 95% CI 5.92–6.29;  $\geq 2$ : 29.10, 95% CI 25.87–32.7), MDD (RR 2.88, 95% CI 2.81–2.94; RR 7.71, 95% CI 6.75–8.81), schizophrenia (RR 2.59, 95% CI 2.50–2.69; RR 8.78, 95% CI 7.41–10.39), ADHD (RR 2.22, 95% CI 2.14–2.31; RR 3.47, 95% CI 2.67–4.49), and ASD (RR 2.04, 95% CI 1.87–2.24; RR 7.11, 95% CI 4.72–10.70), and the numbers of bipolar patients (Table 3).

Figure 1 reported the risks of five major psychiatric disorders among FDRs (parents, offspring, siblings, and twins) of patients

with bipolar disorder. The parents, the offspring, the siblings, and the twins of patients with bipolar disorder had an increased risk (RR, 95% CI) of each major psychiatric disorders, including bipolar disorder (parents of patients with bipolar disorder: 6.69, 6.37–7.02; offspring: 6.38, 6.06–6.71; siblings: 7.26, 6.91–7.63; twins: 41.86, 32.78–53.5), schizophrenia (parents: 3.31, 3.13–3.51; offspring: 3.19, 2.97–3.43; siblings: 3.89, 3.68–4.12; twins: 16.93, 12.56–22.8), MDD (parents: 3.00, 2.87–3.13; offspring: 2.79, 2.69–2.89; siblings: 3.31, 3.17–3.46; twins: 8.12, 5.90–11.17), ADHD (parents: 2.30, 2.21–2.40; offspring: 2.87, 2.06–3.99; siblings: 1.81, 1.67–1.96; twins: 5.26, 3.42–8.09), and ASD (parents: 1.96, 1.75–2.18; offspring: 6.77, 2.98–15.4; siblings: 2.51, 2.14–2.94; twins: 18.83, 11.01–32.2), compared with FDRs without bipolar disorder patients (Fig. 1, online Supplementary Tables S1–S5).

## Discussion

Our results supported the study hypotheses that the FDRs, including parents, offspring, siblings, and twins, of patients with bipolar disorder have increased risks of being diagnosed with schizophrenia, bipolar disorder, MDD, ADHD, and ASD. The co-twins of patients with bipolar disorder had the highest risks of those five major psychiatric disorders. A dose-dependent relationship was found between the risks of the five major psychiatric disorders and the numbers of bipolar patients. In addition, the coaggregation risk of bipolar disorder was highest with bipolar disorder, followed by MDD, schizophrenia, ADHD, and ASD.

As mentioned in the Introduction section, the offspring and siblings of patients with bipolar disorder are more likely to have bipolar disorder and other major psychiatric disorders, including schizophrenia, MDD, and ADHD (Birmaher *et al.*, 2009; Birmaher *et al.*, 2010; Axelson *et al.*, 2015; Song *et al.*, 2015). The Pittsburgh Bipolar Offspring Study evaluated the lifetime prevalence of psychiatric disorders in the preschool- and school-aged offspring of parents with bipolar disorders and found that the offspring of parents with bipolar disorder had elevated risks of bipolar disorder (OR 13.4, 95% CI 2.9–61.6), depressive disorder (OR 2.1, 95% CI 0.9–4.9), and ADHD (OR 3.5, 95% CI 1.1–11.4) (Birmaher *et al.*, 2009; Birmaher *et al.*, 2010). A study examining Swedish families demonstrated that the siblings of patients with bipolar disorder had increased risks of schizophrenia, bipolar disorder, MDD, ADHD, and ASD (Song *et al.*, 2015). The findings of the present study are consistent with the previous findings of the association between parental bipolar disorders and bipolar disorder, MDD, and ADHD in offspring. Furthermore, we found that the offspring, both sons and daughters, of parents with bipolar disorder had higher risks of schizophrenia and ASD than those without parents having bipolar disorder. Regarding the risks of major psychiatric disorders among the siblings of patients with bipolar disorder, we demonstrated that the co-twins of patients with bipolar disorder had the highest risks of schizophrenia, bipolar disorder, MDD, ADHD, and ASD. A few studies have investigated the risk of psychiatric disorders, except for bipolar disorder, among the parents of patients with bipolar disorder (Sucksdorff *et al.*, 2014; Song *et al.*, 2015). Sucksdorff *et al.* assessed 1861 patients with bipolar disorder aged up to 25 years, 3643 matched controls, and their parents, and revealed that the parental psychiatric diagnoses of bipolar disorder [OR (maternal): 5.2, 95% CI 2.52–10.62; OR (paternal): 8.1, 95% CI 3.77–17.26] and schizophrenia [OR (maternal): 3.1, 95% CI 1.69–5.84; OR (paternal): 4.5, 95% CI

**Table 1.** Demographic characteristics among FDRs of patients with bipolar disorder and the total population

No. (%)	Female				Male				Total			
	Patients with bipolar disorder	FDRs of patients with bipolar disorder	Total Population	<i>p</i> value	Patients with bipolar disorder	FDRs of patients with bipolar disorder	Total Population	<i>p</i> value	Patients with bipolar disorder	FDRs of patients with bipolar disorder	Total Population	<i>p</i> value
Age, mean (s.d.)	41.32 (15.27)	34.6 (18.3)	38.1 (20.6)	<b>&lt;0.001</b>	40.61 (15.65)	34.9 (19.0)	37.5 (20.8)	<b>&lt;0.001</b>	41.01 (15.44)	34.8 (18.7)	37.8 (20.7)	<b>&lt;0.001</b>
Sex ( <i>n</i> , %)												<b>&lt;0.001</b>
Male	–	–	–		31 907 (100)	93 898 (100)	11 413 781 (100)		31 907 (44.0)	93 898 (49.9)	11 413 781 (49.3)	
Female	40 666 (100)	94 392 (100)	11 755 970 (100)		–	–	–		40 666 (56.0)	94 392 (50.1)	11 755 970 (50.7)	
Monthly Income				<b>&lt;0.001</b>				<b>&lt;0.001</b>				<b>&lt;0.001</b>
0–500 USDs	28 829 (71.8)	69 866 (74.0)	7 678 667 (65.3)		21 115 (66.1)	66 136 (70.4)	7 012 061 (61.4)		49 944 (68.8)	136 002 (72.2)	14 690 728 (63.4)	
501–800 USDs	9091 (22.4)	15 982 (16.9)	2 958 248 (25.2)		7331 (23.0)	15 562 (16.6)	2 657 690 (23.3)		16 422 (22.6)	31 544 (16.8)	5 615 938 (24.2)	
≥801 USDs	2746 (6.8)	85 44 (9.1)	1 119 055 (9.5)		3461 (10.9)	12 200 (13.0)	1 744 030 (15.3)		6207 (8.6)	20 744 (11.0)	2 863 085 (12.4)	
Residence				<b>&lt;0.001</b>				<b>&lt;0.001</b>				<b>&lt;0.001</b>
1 (urbanized)	15 496 (38.2)	35 886 (38.0)	4 123 979 (35.1)		11 062 (34.5)	32 713 (34.8)	3 734 313 (32.7)		26 558 (36.6)	68 599 (36.4)	7 858 292 (33.9)	
2	13 133 (32.3)	30 002 (31.8)	3 608 434 (30.7)		10 003 (31.4)	30 562 (32.6)	3 532 823 (31.0)		23 136 (31.9)	60 564 (32.2)	7 141 257 (30.8)	
3	5017 (12.3)	12 306 (13.0)	1 746 289 (14.9)		4164 (13.1)	13 169 (14.0)	1 864 605 (16.3)		9181 (12.7)	25 475 (13.5)	3 610 894 (15.6)	
4	4725 (11.6)	10 850 (11.5)	1 411 297 (12.0)		4354 (13.7)	11 537 (12.3)	1 410 872 (12.4)		9079 (12.5)	22 387 (11.9)	2 822 169 (12.2)	
5 (rural)	2295 (5.6)	53 48 (5.7)	865 971 (7.4)		2324 (7.3)	5917 (6.3)	871 168 (7.6)		4619 (6.4)	11 265 (6.0)	1 737 139 (7.5)	

FDRs, first-degree relatives; s.d., standard deviation; USD, US dollar; RR, relative risk; CI, confidence interval.

1 US dollar (USD) = 31.63 New Taiwan Dollar.

Bold type indicates the statistical significance.

**Table 2.** Relative risks of major psychiatric disorders among FDRs of patients with bipolar disorder and the total population

Major psychiatric disorder (n, %)	Female			Male			Total		
	FDRs	Total Population	RR (95% CI)	FDRs	Total Population	RR (95% CI)	FDRs	Total Population	RR (95% CI)
ASD	110 (0.12)	4828 (0.04)	<b>2.56 (2.12–3.10)</b>	375 (0.40)	22 063 (0.19)	<b>2.00 (1.80–2.21)</b>	485 (0.26)	26 891 (0.12)	<b>2.10 (1.92–2.29)</b>
ADHD	700 (0.74)	32 612 (0.28)	<b>2.56 (2.38–2.76)</b>	2050 (2.18)	117 741 (1.03)	<b>2.11 (2.02–2.21)</b>	2750 (1.46)	150 353 (0.65)	<b>2.21 (2.13–2.30)</b>
Schizophrenia	1507 (1.60)	72 478 (0.62)	<b>2.71 (2.57–2.85)</b>	1643 (1.75)	78 558 (0.69)	<b>2.58 (2.46–2.71)</b>	3150 (1.67)	151 036 (0.65)	<b>2.64 (2.55–2.73)</b>
Bipolar disorder	2640 (2.80)	56 018 (0.48)	<b>6.07 (5.84–6.31)</b>	2084 (2.22)	41 731 (0.37)	<b>6.18 (5.92–6.46)</b>	4724 (2.51)	97 749 (0.42)	<b>6.12 (5.95–6.30)</b>
MDD	4486 (4.75)	210 727 (1.79)	<b>2.89 (2.81–2.98)</b>	2574 (2.74)	114 265 (1.00)	<b>2.88 (2.77–3.00)</b>	7060 (3.75)	324 992 (1.40)	<b>2.89 (2.82–2.96)</b>

FDRs, first-degree relatives; RR, relative risk; CI, confidence interval; ASD, autism spectrum disorder; ADHD, attention deficit hyperactivity disorder; MDD, Major depressive disorder. Bold type indicates the statistical significance.

1.97–10.27] were associated with bipolar disorder in offspring (Sucksdorff *et al.*, 2014). In addition to parental schizophrenia and bipolar disorder, we found that both fathers and mothers of patients with bipolar disorder were likely to have MDD and ADHD, and the mothers of patients with bipolar disorder additionally had a higher risk of ASD. On the basis of the aforementioned evidence, we can conclude bipolar disorder coaggregates with other major psychiatric disorders, including schizophrenia, MDD, ADHD, and ASD, within families.

Increasing evidence supports that schizophrenia, bipolar disorder, MDD, ASD, and ADHD may share some common genes and underlying pathophysiology in the neurodevelopmental process. To examine this shared genetic etiology, the Cross-Disorder Group of the Psychiatric Genomics Consortium analyzed genome-wide single-nucleotide polymorphism (SNP) data for schizophrenia, bipolar disorder, MDD, ASD, and ADHD in 33 332 patients and 27 888 controls of European ancestry and reported that SNPs at four loci exceeded the cutoff value for genome-wide significance in the analysis (Cross-Disorder Group of the Psychiatric Genomics Consortium, 2013b). Furthermore, they reported that SNPs explained 17–29% of the variance in liability and revealed that the genetic correlation, which was calculated using common SNPs, was high between bipolar disorder and schizophrenia ( $0.68 \pm 0.04$  s.e.,  $p < 10^{-16}$ ), moderate between bipolar disorder and MDD ( $0.47 \pm 0.06$  s.e.,  $p = 1.5 \times 10^{-14}$ ), and low between bipolar disorder and ADHD ( $0.05 \pm 0.05$  s.e.,  $p = 0.31$ ) and ASD ( $0.04 \pm 0.06$  s.e.,  $p = 0.53$ ) (Cross-Disorder Group of the Psychiatric Genomics Consortium, 2013a). This GWAS provided convincing evidence that specific genes shared by major psychiatric disorders are hereditary in a family and result in the highly variable endophenotypes of psychiatric disorders. Our findings supported the results of the GWAS, which reported a significant coaggregation of bipolar disorder with schizophrenia and MDD. However, we also indicated a significant coaggregation of bipolar disorder with ADHD and ASD, but only a low genetic association was noted in the GWAS. Establishing the differences between the genetic level and the clinical or psychopathological level requires further investigation.

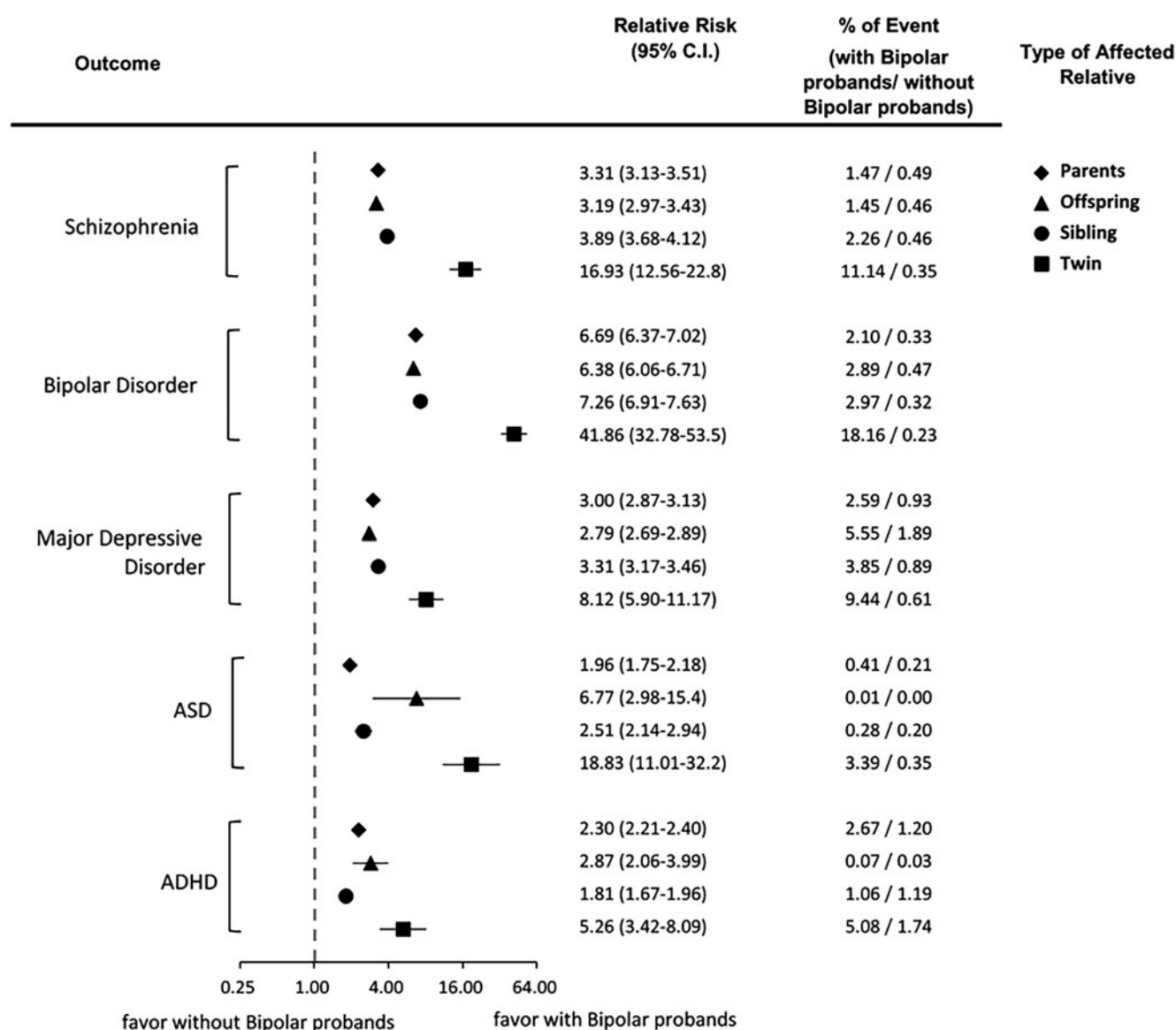
This study has several limitations. First, the prevalence of major psychiatric disorders may be underestimated because only those who sought medical consultation and help are identified in the database. However, medical services are easily accessible in Taiwan because of the high coverage and affordability of Taiwan NHI. In addition, in our study, the diagnoses of major psychiatric disorders were made by board-certificated psychiatrists, yielding higher diagnostic validity. In our study, prevalence estimates calculated for the disorders in the total population were considerably lower than those found in the majority of population-based studies in the USA and in Europe. The much lower prevalence of bipolar disorder and MDD in Taiwanese population was reported in the previous cross-national study (Weissman *et al.*, 1996). The reasons for the low prevalence of psychiatric disorders, such as bipolar disorder and MDD, required further investigation. Second, in our study, we defined twins as those with the same birthdate and the same mother in the database; thus, homozygotes or heterozygotes could not be differentiated because homozygote or heterozygote state would not be recorded in NHIRD. Based on the concept of genetics, the homozygote sibling of a twin with bipolar disorder should exhibit the higher likelihood of having major psychiatric disorders than the heterozygote sibling of a twin with bipolar disorder. Additional clinical twin-based studies are required to validate our findings



**Table 3.** The dose-dependent relationship between the risks of major psychiatric disorders and the numbers of bipolar patients among FDRs of patients with bipolar disorder

	ASD	ADHD	Schizophrenia	Bipolar disorder	MDD
Numbers of bipolar patients	RR (95% CI)	RR (95% CI)	RR (95% CI)	RR (95% CI)	RR (95% CI)
0	1.00 (reference)	1.00 (reference)	1.00 (reference)	1.00 (reference)	1.00 (reference)
1	<b>2.04 (1.87–2.24)</b>	<b>2.22 (2.14–2.31)</b>	<b>2.59 (2.50–2.69)</b>	<b>6.10 (5.92–6.29)</b>	<b>2.88 (2.81–2.94)</b>
≥2	<b>7.11 (4.72–10.7)</b>	<b>3.47 (2.67–4.49)</b>	<b>8.78 (7.41–10.39)</b>	<b>29.1 (25.87–32.7)</b>	<b>7.71 (6.75–8.81)</b>
<i>p</i> for trend	<b>&lt;0.001</b>	<b>&lt;0.001</b>	<b>&lt;0.001</b>	<b>&lt;0.001</b>	<b>&lt;0.001</b>

FDRs, first-degree relatives; RR, relative risk; CI, confidence interval; ASD, autism spectrum disorder; ADHD, attention deficit hyperactivity disorder; MDD, Major depressive disorder. Bold type indicates the statistical significance.

**Fig. 1.** Relative risks for major psychiatric disorder among FDRs of patients with bipolar disorder by different kinships.


and further inference. In addition, some other factors, such as education level and environmental factors, are not available in the Taiwan NHIRD. Without this information, we cannot assess their impact. Third, because the specific diagnostic code of bipolar II disorder is not available in the ICD-9-code system in Taiwan

NHIRD, we were unable to differentiate between bipolar I disorder and bipolar II disorder in the current study. Some previous studies suggested that bipolar I disorder and bipolar II disorder may display different familial aggregation patterns; bipolar I disorder is highly heritable and bipolar II disorder is not



(Merikangas *et al.*, 2014; Vandeley *et al.*, 2014). Further study would be necessary to elucidate the possible different familial coaggregation patterns of bipolar I disorder and bipolar II disorder with other psychiatric disorders. Fourth, we only focused on the familial coaggregation of bipolar disorder with schizophrenia, MDD, ASD, and ADHD in our study. Whether bipolar disorder may be co-aggregated with other psychiatric disorders, such as anxiety disorders, required further investigation. Fifth, because something is shown to be familial may not mean that this is necessarily a genetic relationship. Many other dynamics, such as shared environment factors, are potentially conveyed in families over and above shared genes. Further studies would be necessary to elucidate non-genetic factors in the familial coaggregation of bipolar disorder with other major psychiatric disorders.

In conclusion, the FDRs, including parents, offspring, siblings, and twins, of patients with bipolar disorder have a higher likelihood of schizophrenia, bipolar disorder, MDD, ADHD, and ASD after adjustment for demographic data. The association between the risk of each major psychiatric disorder and the numbers of bipolar patients is dose-dependent. Our findings indicated a coaggregation of bipolar disorder with other major psychiatric disorders in a family and were consistent with the GWAS results that schizophrenia, bipolar disorder, MDD, ADHD, and ASD share common genes. Furthermore, given the increased risks of major psychiatric disorders, our results encourage clinicians and state mental health institutions to pay more attention to the mental health of the FDRs of patients with bipolar disorder. Early identification of the risk of mental illnesses would be helpful for early prevention and intervention among the FDRs of patients with bipolar disorder.

**Author ORCIDs.**  Mu-Hong Chen 0000-0001-6516-1073.

**Supplementary material.** The supplementary material for this article can be found at <https://doi.org/10.1017/S003329171800332X>.

**Acknowledgements.** We thank Mr I-Fan Hu for his friendship and support. We thank Dr MHC, Dr TPS, and Dr YMB, who designed the study and wrote the protocol, Dr MHC, who wrote the manuscripts, Dr SJT, Dr JWH, Dr KLH, Dr CMC, Dr CTL, Prof TLP, Prof PWW, and Dr WCL, who assisted with the literature review, and preparation and proof-reading of the manuscript, and Dr YMB, Dr TJC, Miss WHC, and Dr MHC, who performed the statistical analysis and provided the advice on statistical analysis. All authors have no financial relationships relevant to this article to disclose. The study was supported by grant from Taipei Veterans General Hospital (V103E10-001, V104E10-002, V105E10-001-MY2-1, V105A-049, V106B-020, V107B-010, V107C-181) and Ministry of Science and Technology, Taiwan (107-2314-B-075-063-MY3). The funding source had no role in any process of our study.

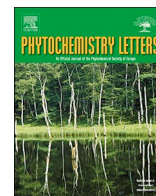
**Author contributions.** Dr Mu-Hong Chen, Dr Tung-Ping Su, and Dr Ya-Mei Bai designed the study and wrote the protocol. Dr Mu-Hong Chen wrote the manuscripts; Dr Ju-Wei Hsu, Dr Kai-Lin Huang, Dr Shih-Jen Tsai, Dr Cheng-Ta Li, Dr Chih-Ming Cheng, Prof Tai-Long Pan, Prof Pei-Wen Wang, and Dr Wei-Chen Lin assisted with the literature reviews, and preparation and proof-reading of the manuscript; Dr Ya-Mei Bai, Dr Tzeng-Ji Chen, Miss Wen-Han Chang, and Dr Mu-Hong Chen performed the statistical analysis and provided the advice on statistical analysis.

**Conflict of interest.** No conflict of interest.

## References

- Axelson D, Goldstein B, Goldstein T, Monk K, Yu H, Hickey MB, Sakolsky D, Diler R, Hafeman D, Merranko J, Iyengar S, Brent D, Kupfer D and Birmaher B (2015) Diagnostic precursors to bipolar disorder in offspring of parents with bipolar disorder: a longitudinal study. *American Journal of Psychiatry* 172, 638–646.
- Birmaher B, Axelson D, Monk K, Kalas C, Goldstein B, Hickey MB, Obreja M, Ehmann M, Iyengar S, Shamseddeen W, Kupfer D and Brent D (2009) Lifetime psychiatric disorders in school-aged offspring of parents with bipolar disorder: the Pittsburgh Bipolar Offspring study. *Archives of General Psychiatry* 66, 287–296.
- Birmaher B, Axelson D, Goldstein B, Monk K, Kalas C, Obreja M, Hickey MB, Iyengar S, Brent D, Shamseddeen W, Diler R and Kupfer D (2010) Psychiatric disorders in preschool offspring of parents with bipolar disorder: the Pittsburgh Bipolar Offspring Study (BIOS). *American Journal of Psychiatry* 167, 321–330.
- Blanco C, Compton WM, Saha TD, Goldstein BI, Ruan WJ, Huang B and Grant BF (2017) Epidemiology of DSM-5 bipolar I disorder: results from the national epidemiologic survey on alcohol and related conditions - III. *Journal of Psychiatric Research* 84, 310–317.
- Chen MH, Su TP, Chen YS, Hsu JW, Huang KL, Chang WH and Bai YM (2013) Attention deficit hyperactivity disorder, tic disorder, and allergy: is there a link? A nationwide population-based study. *Journal of Child Psychology Psychiatry* 54, 545–551.
- Chen MH, Pan TL, Hsu JW, Huang KL, Su TP, Li CT, Lin WC, Tsai SJ, Chang WH, Chen TJ and Bai YM (2016) Attention-deficit hyperactivity disorder comorbidity and antidepressant resistance among patients with major depression: a nationwide longitudinal study. *European Neuropsychopharmacology* 26, 1760–1767.
- Chen MH, Hsu JW, Huang KL, Bai YM, Ko NY, Su TP, Li CT, Lin WC, Tsai SJ, Pan TL, Chang WH and Chen TJ (2018) Sexually transmitted infection among adolescents and young adults with attention-deficit/hyperactivity disorder: a nationwide longitudinal study. *Journal of the American Academy of Child and Adolescent Psychiatry* 57, 48–53.
- Cheng CM, Chang WH, Chen MH, Tsai CF, Su TP, Li CT, Tsai SJ, Hsu JW, Huang KL, Lin WC, Chen TJ and Bai YM (2018) Co-aggregation of major psychiatric disorders in individuals with first-degree relatives with schizophrenia: a nationwide population-based study. *Molecular Psychiatry* 23, 1756–1763.
- Cross-Disorder Group of the Psychiatric Genomics Consortium (2013a) Genetic relationship between five psychiatric disorders estimated from genome-wide SNPs. *Nature Genetics* 45, 984–994.
- Cross-Disorder Group of the Psychiatric Genomics Consortium (2013b) Identification of risk loci with shared effects on five major psychiatric disorders: a genome-wide analysis. *Lancet* 381, 1371–1379.
- Grande I, Berk M, Birmaher B and Vieta E (2016) Bipolar disorder. *Lancet* 387, 1561–1572.
- Kuo CF, Grainge MJ, Valdes AM, See LC, Luo SF, Yu KH, Zhang W and Doherty M (2015) Familial aggregation of systemic lupus erythematosus and coaggregation of autoimmune diseases in affected families. *JAMA Internal Medicine* 175, 1518–1526.
- Lin PI, McInnis MG, Potash JB, Willour V, MacKinnon DF, DePaulo JR and Zandi PP (2006) Clinical correlates and familial aggregation of age at onset in bipolar disorder. *American Journal of Psychiatry* 163, 240–246.
- Maier W, Lichtermann D, Minges J, Hallmayer J, Heun R, Benkert O and Levinson DF (1993) Continuity and discontinuity of affective disorders and schizophrenia. Results of a controlled family study. *Archives of General Psychiatry* 50, 871–883.
- McGuffin P, Rijdsdijk F, Andrew M, Sham P, Katz R and Cardno A (2003) The heritability of bipolar affective disorder and the genetic relationship to unipolar depression. *Archives of General Psychiatry* 60, 497–502.
- Merikangas KR, Cui L, Kattan G, Carlson GA, Youngstrom EA and Angst J (2012) Mania with and without depression in a community sample of US adolescents. *Archives of General Psychiatry* 69, 943–951.
- Merikangas KR, Cui L, Heaton L, Nakamura E, Roca C, Ding J, Qin H, Guo W, Shugart YY, Zarate C and Angst J (2014) Independence of familial transmission of mania and depression: results of the NIMH family study of affective spectrum disorders. *Molecular Psychiatry* 19, 214–219.
- Mesman E, Nolen WA, Reichart CG, Wals M and Hillegers MH (2013) The Dutch bipolar offspring study: 12-year follow-up. *American Journal of Psychiatry* 170, 542–549.

- Muller-Oerlinghausen B, Berghofer A and Bauer M** (2002) Bipolar disorder. *Lancet* **359**, 241–247.
- Rasic D, Hajek T, Alda M and Uher R** (2014) Risk of mental illness in offspring of parents with schizophrenia, bipolar disorder, and major depressive disorder: a meta-analysis of family high-risk studies. *Schizophrenia Bulletin* **40**, 28–38.
- Song J, Bergen SE, Kuja-Halkola R, Larsson H, Landen M and Lichtenstein P** (2015) Bipolar disorder and its relation to major psychiatric disorders: a family-based study in the Swedish population. *Bipolar Disorders* **17**, 184–193.
- Sucksdorff D, Chudal R, Suominen A, Jokiranta E, Brown AS and Sourander A** (2014) Bipolar disorder and parental psychopathology. *Social Psychiatry and Psychiatric Epidemiology* **49**, 1973–1984.
- Vandeleur CL, Merikangas KR, Strippoli MP, Castelao E and Preisig M** (2014) Specificity of psychosis, mania and major depression in a contemporary family study. *Molecular Psychiatry* **19**, 209–213.
- Weissman MM, Bland RC, Canino GJ, Faravelli C, Greenwald S, Hwu HG, Joyce PR, Karam EG, Lee CK, Lellouch J, Lepine JP, Newman SC, Rubio-Stipec M, Wells JE, Wickramaratne PJ, Wittchen H and Yeh EK** (1996) Cross-national epidemiology of major depression and bipolar disorder. *JAMA* **276**, 293–299.
- Yelland LN, Salter AB and Ryan P** (2011) Performance of the modified Poisson regression approach for estimating relative risks from clustered prospective data. *American Journal of Epidemiology* **174**, 984–992.
- Zou G** (2004) A modified Poisson regression approach to prospective studies with binary data. *American Journal of Epidemiology* **159**, 702–706.

New bioactive  $\Delta^{11(17)}$ -furano-eunicellins from an octocoral *Cladiella* sp.Ying-Fa Chen<sup>a,b</sup>, Wu-Fu Chen<sup>c,d</sup>, Zhi-Hong Wen<sup>d</sup>, Tsong-Long Hwang<sup>e,f,g,h,\*\*\*</sup>, Zhi-Jun Zhang<sup>i,j,\*\*</sup>, Ping-Jyun Sung<sup>d,i,j,k,l,\*</sup><sup>a</sup> Department of Neurology, Chang Gung Memorial Hospital and Chang Gung University College of Medicine, Kaohsiung 83301, Taiwan<sup>b</sup> Center for Parkinson's Disease, Kaohsiung Chang Gung Memorial Hospital and Chang Gung University College of Medicine, Kaohsiung 83301, Taiwan<sup>c</sup> Department of Neurosurgery, Kaohsiung Chang Gung Memorial Hospital and Chang Gung University College of Medicine, Kaohsiung 83301, Taiwan<sup>d</sup> Department of Marine Biotechnology and Resources, National Sun Yat-sen University, Kaohsiung 80424, Taiwan<sup>e</sup> Research Center for Chinese Herbal Medicine, Research Center for Food and Cosmetic Safety, Graduate Institute of Healthy Industry Technology, College of Human Ecology, Chang Gung University of Science and Technology, Taoyuan 33303, Taiwan<sup>f</sup> Graduate Institute of Natural Products, College of Medicine, Chang Gung University, Taoyuan 33302, Taiwan<sup>g</sup> Chinese Herbal Medicine Research Team, Healthy Aging Research Center, Chang Gung University, Taoyuan 33302, Taiwan<sup>h</sup> Department of Anaesthesiology, Chang Gung Memorial Hospital, Taoyuan 33305, Taiwan<sup>i</sup> Graduate Institute of Marine Biology, National Dong Hwa University, Pingtung 94450, Taiwan<sup>j</sup> National Museum of Marine Biology and Aquarium, Pingtung 94450, Taiwan<sup>k</sup> Chinese Medicine Research and Development Center, China Medical University Hospital, Taichung 40447, Taiwan<sup>l</sup> Graduate Institute of Natural Products, Kaohsiung Medical University, Kaohsiung 80708, Taiwan

## ARTICLE INFO

## Keywords:

*Cladiella*

Cladieunicellin

Sclerophytin

Elastase

Superoxide anion

Cytotoxicity

## ABSTRACT

A new eunicellin diterpenoid, cladieunicellin U (1), along with a new natural eunicellin, cladieunicellin V (2), and two known analogues, sclerophytins A (3) and B (4), were obtained from an octocoral identified as *Cladiella* sp. The structures, including the absolute configurations, of eunicellins 1–4 were elucidated by using spectroscopic methods and compared with the spectroscopic and physical data reported in the literature. Eunicellins 1, 3 and 4 decreased the release of elastase, while eunicellins 2 and 4 showed inhibitory effects in terms of the generation of superoxide anions by human neutrophils. Eunicellins 1 and 4 were found to show moderate cytotoxicity toward the leukemia K562 cells ( $IC_{50}$  = 12.8, 11.4  $\mu$ g/mL, respectively) and 2 exhibited moderate cytotoxicity toward the leukemia MOLT-4 cells ( $IC_{50}$  = 18.8  $\mu$ g/mL).

## 1. Introduction

Since the first structure elucidation of an eunicellin-based diterpenoid (2,11-cyclized cembranoid), eunicellin, from the gorgonian coral *Eunicella stricta*, in 1968, by a single-crystal X-ray diffraction analysis of its brominated derivative (Kennard et al., 1968), a series of compounds of this group has been prepared from various octocorals belonging to the genus *Cladiella* (family Alcyoniidae) (Radhika, 2006), with complex structures and interesting bioactivities. During the course of our research on new natural metabolites from the marine invertebrates distributed in the waters of Taiwan, at the intersection of the Kuroshio current and the South China Sea surface current, a series of eunicellin-based diterpenoids, isolated from various octocorals belonging to the genus *Cladiella* were proven to possess various interesting bioactivities

(Chen et al., 2013, 2014a,b; Peng et al., 2016; Shih et al., 2013; Zhang et al., 2019). Recently, we have focused our studies on a species of octocoral identified as *Cladiella* sp. collected on the Penghu Archipelago, Taiwan. From the results of our studies on this species, we report the isolation, structural determination, and bioactivity of a new eunicellin, cladieunicellin U (1), a new natural eunicellin, cladieunicellin V (2), along with two known metabolites, sclerophytins A (3) and B (4) (Fig. 1) (Bernardelli et al., 2001; Friedrich et al., 2000; Friedrich and Paquette, 2002; Paquette et al., 2000; Sharma and Alam, 1988).

## 2. Results and discussion

Cladieunicellin U (1) was found to have the molecular formula  $C_{36}H_{64}O_5$  and five degrees of unsaturation, as indicated from the

\* Corresponding author at: National Museum of Marine Biology and Aquarium, Pingtung 94450, Taiwan.

\*\* Corresponding author at: Graduate Institute of Marine Biology, National Dong Hwa University, Pingtung 94450, Taiwan.

\*\*\* Corresponding author at: Research Center for Chinese Herbal Medicine, Research Center for Food and Cosmetic Safety, Graduate Institute of Health Industry Technology, College of Human Ecology, Chang Gung University of Science and Technology, Taoyuan 33303, Taiwan.

E-mail addresses: [htl@mail.cgu.edu.tw](mailto:htl@mail.cgu.edu.tw) (T.-L. Hwang), [goldchain116@gmail.com](mailto:goldchain116@gmail.com) (Z.-J. Zhang), [pjsung@nmba.gov.tw](mailto:pjsung@nmba.gov.tw) (P.-J. Sung).<https://doi.org/10.1016/j.phytol.2019.07.002>

Received 26 May 2019; Received in revised form 2 July 2019; Accepted 4 July 2019

Available online 12 July 2019

1874-3900/© 2019 Phytochemical Society of Europe. Published by Elsevier Ltd. All rights reserved.

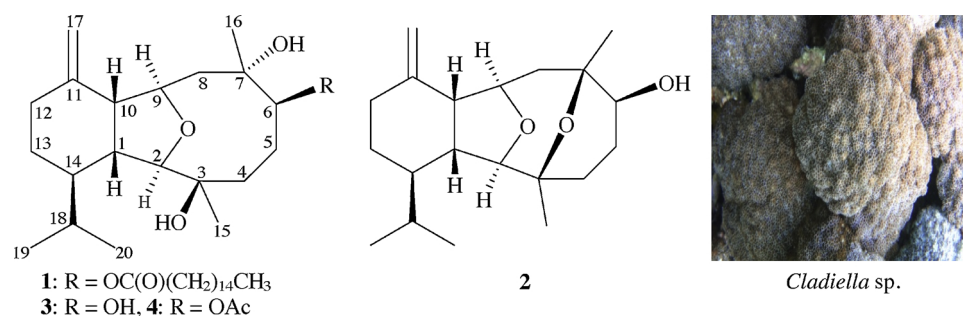


Fig. 1. Structures of cladieunicellins U (1), V (2) and sclerophytins A (3), B (4) and a picture of octocoral *Cladiella* sp.

Table 1

<sup>1</sup>H (400 MHz, CDCl<sub>3</sub>) and <sup>13</sup>C (100 MHz, CDCl<sub>3</sub>) NMR, COSY, HMBC data for 1.

Position	δ <sub>H</sub> (J in Hz)	δ <sub>C</sub> , type	COSY	HMBC
1	2.11 m	45.6, CH	H-10, H-14	C-3, C-9, C-14
2	3.68 s	90.6, CH	–	C-1, C-3, C-9, C-10, C-14, C-15
3		75.0, C		
4α/β	2.13 m; 1.70 m	39.9, CH <sub>2</sub>	H <sub>2</sub> -5	C-2, C-3, C-5, C-6
5α/β	1.39 m; 2.09 m	28.2, CH <sub>2</sub>	H <sub>2</sub> -4, H-6	C-3, C-4, C-6
6	5.62 d (4.4)	84.9, CH	H-5β	C-4, C-5, C-7, C-16
7		76.0, C		
8α	1.76 dd (14.8, 4.0)	45.4, CH <sub>2</sub>	H-8β, H-9	C-6, C-7, C-16
β	2.26 dd (14.8, 10.8)		H-8α, H-9	C-9, C-10
9	4.13 ddd (10.8, 7.2, 4.0)	78.1, CH	H <sub>2</sub> -8, H-10	C-11
10	3.02 dd (7.6, 7.2)	53.3, CH	H-1, H-9	C-1, C-9, C-11, C-12, C-14, C-17
11		148.0, C		
12α/β	2.04 m; 2.23 m	31.7, CH <sub>2</sub>	H <sub>2</sub> -13	C-10
13α/β	1.00 m; 1.73 m	24.9, CH <sub>2</sub>	H <sub>2</sub> -12	C-14
14	1.30 m	43.6, CH	H-1, H <sub>2</sub> -13, H-18	C-18
15	1.14 s	30.3, CH <sub>3</sub>		C-2, C-3, C-4
16	1.22 s	23.9, CH <sub>3</sub>		C-6, C-7, C-8
17a/b	4.65 br s; 4.62 br s	109.4, CH <sub>2</sub>		C-10, C-12
18	1.74 m	29.1, CH	H-14, H <sub>3</sub> -19, H <sub>3</sub> -20	C-19, C-20
19	0.96 d (6.8)	22.0, CH <sub>3</sub>	H-18	C-14, C-18, C-20
20	0.78 d (6.8)	15.6, CH <sub>3</sub>	H-18	C-14, C-18, C-19

HRESIMS at *m/z* 599.46479 (calcd for C<sub>36</sub>H<sub>64</sub>O<sub>5</sub> + Na, 599.46460). The diterpenoid structure of 1 was directly inferred from its <sup>13</sup>C NMR spectra (Table 1), where it indicated that there were 20 carbon signals in total after subtraction of the 16 carbons ascribed to a palmitate group. Comparison of the <sup>13</sup>C and DEPT data with the molecular formula indicated that there must be two exchangeable protons, requiring the presence of two hydroxy groups. This deduction was supported by a broad absorption in the IR spectrum at 3438 cm<sup>-1</sup>. The <sup>13</sup>C NMR data confirmed the presence of 36 signals, characterized by DEPT spectra as 5 methyls, 19 sp<sup>3</sup>–CH<sub>2</sub>, 7 sp<sup>3</sup>–CH (including 3 oxymethines), 2 sp<sup>3</sup> oxygenated quaternary carbons, 1 sp<sup>2</sup> methylene, 1 sp<sup>2</sup> quaternary carbon and 1 sp<sup>2</sup> carbonyl. Based on the <sup>1</sup>H and <sup>13</sup>C NMR data (Table 1), 1 was determined to possess an exocyclic carbon-carbon double bond (δ<sub>H</sub> 4.65, 1H, br s; 4.62, 1H, br s, H<sub>2</sub>-17; δ<sub>C</sub> 148.0, C-11; 109.4, CH<sub>2</sub>-17). An ester carbonyl carbon (δ<sub>C</sub> 174.7) was HMBC correlated by the methylene protons (δ<sub>H</sub> 2.32, 2H, t, *J* = 7.6 Hz) of a long-chain ester unit, and the long-chain ester was found to be palmitate. In the <sup>1</sup>H NMR spectrum, two doublets at δ<sub>H</sub> 0.96 and 0.78 (each 3H, d, *J* = 6.8 Hz, H<sub>3</sub>-19 and H<sub>3</sub>-20) were indicative of the two methyls of an isopropyl group. Two tertiary methyl groups bonded to oxygenated carbons were evident from the singlet signals at δ<sub>H</sub> 1.22 (3H, s, H<sub>3</sub>-16) and 1.14 (3H, s, H<sub>3</sub>-15). Thus, in light of the <sup>1</sup>H and <sup>13</sup>C NMR data

combined with the degrees of unsaturation, 1 was determined as a tricyclic eunicellin diterpene.

The <sup>1</sup>H NMR coupling information in the COSY spectrum of 1 enabled the determination of the proton sequences between H<sub>2</sub>-4/H<sub>2</sub>-5/H-6, H<sub>2</sub>-8/H-9/H-10/H-1/H-14/H<sub>2</sub>-13/H<sub>2</sub>-12 and H-14/H<sub>3</sub>-18/H<sub>3</sub>-20 (H<sub>3</sub>-20) (Table 1). These data, together with the key HMBC from H-1, H-2, H-4α, H-5β, H<sub>3</sub>-15 to C-3; H-6, H-8α, H<sub>3</sub>-16 to C-7; and H-9, H-10 to C-11, permitted elucidation of the carbon skeleton (Table 1). An exocyclic carbon-carbon double bond at C-11 was confirmed by the HMBC from H<sub>2</sub>-17 to C-10, C-12; and H-10 to C-17. In the HSQC spectrum, an oxymethine carbon (δ<sub>C</sub> 84.9) correlated with a methine proton (δ<sub>H</sub> 5.62), and this proton had a <sup>3</sup>*J*-correlation with H-5β (δ<sub>H</sub> 2.09) in COSY spectrum, <sup>2</sup>*J*-correlations with C-5 and C-7, and <sup>3</sup>*J*-correlations with C-4 and C-16, respectively, in HMBC spectrum. It thus confirmed the existence of a palmitate at C-6, although no HMBC was observed between H-6 and the palmitate carbonyl. Furthermore, an HMBC from H-2 (δ<sub>H</sub> 3.68) to an oxygen-containing methine at δ<sub>C</sub> 78.1 (CH-9) suggested the presence of a C-2/9 ether linkage in 1 for forming a tetrahydrofuran ring located between C-2 and C-9.

Based on NOESY correlations and further information provided by MM2 force field calculations (Allinger, 1977), the relative stereochemistry of 1 with a stable conformation is shown in Fig. 2. When H-1 is β-oriented, correlations from H-1 to H-10 and H<sub>3</sub>-20 were observed, suggesting that H-1, H-10 and the isopropyl groups were on the β-face. A lack of constant coupling was detected between H-1 and H-2, indicating that H-2 should be α-oriented. H<sub>3</sub>-15 showed a correlation with H-2, suggested the β-orientation of the hydroxy group at C-3. No correlation was found between H-9 and H-10, suggesting that H-9 was α-oriented. A correlation from H-10 to H-8 (δ<sub>H</sub> 2.26) suggested that this

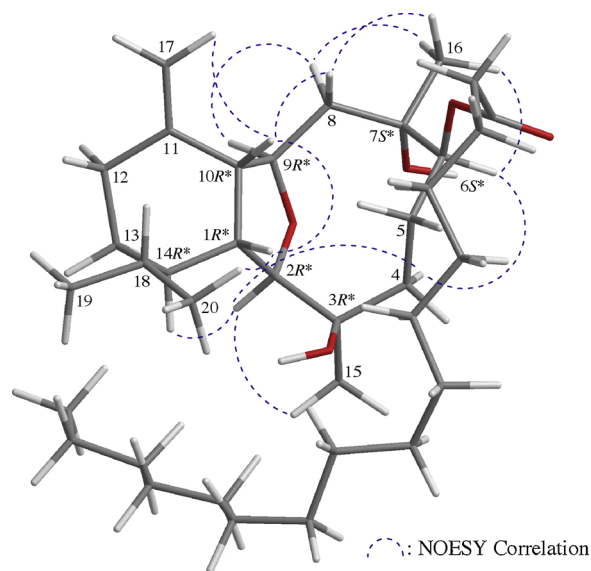


Fig. 2. Selected protons with key NOESY correlations of 1.



**Table 2**<sup>1</sup>H (400 MHz, CDCl<sub>3</sub>) and <sup>13</sup>C (100 MHz, CDCl<sub>3</sub>) NMR, COSY, HMBC data for **2**.

Position	$\delta_{\text{H}}$ (J in Hz)	$\delta_{\text{C}}$ , Mult.	COSY	HMBC
1	2.27 dd (11.2, 6.8)	44.9, CH	H-10, H-14	C-3, C-9, C-10, C-14, C-18
2	3.62 s	93.9, CH	–	C-3, C-4, C-9, C-10, C-14
3		76.0, C		
4 $\alpha$	1.65 m	29.1, CH <sub>2</sub>	H <sub>2</sub> -5	C-2, C-3, C-5, C-6
$\beta$	1.78 ddd (14.0, 13.2, 5.2)			C-2, C-3, C-5, C-6, C-15
5 $\alpha$	2.71 dddd (14.4, 14.0, 6.4, 2.4) 1.69 m	24.6, CH <sub>2</sub>	H <sub>2</sub> -4, H-6	C-4
$\beta$				C-7
6	3.29 br s	71.8, CH	H <sub>2</sub> -5	–
7		76.8, C		
8 $\alpha$	2.05 dd (14.4, 4.8)	44.4, CH <sub>2</sub>	H-9	C-6, C-7, C-9, C-10, C-16
$\beta$	1.93 dd (14.4, 1.6)			C-6, C-7, C-9, C-10, C-16
9	3.95 ddd (6.4, 4.8, 1.6)	82.2, CH	H <sub>2</sub> -8, H-10	C-2, C-7, C-10, C-11
10	3.47 dd (6.8, 6.4)	49.6, CH	H-1, H-9	C-1, C-2, C-9, C-11, C-12, C-14, C-17
11		149.3, C		
12 $\alpha$ / $\beta$	1.96 m; 2.25 m	31.3, CH <sub>2</sub>	H <sub>2</sub> -13	C-10, C-11, C-14
13 $\alpha$ / $\beta$	0.95 m; 1.69 m	24.5, CH <sub>2</sub>	H <sub>2</sub> -12, H-14	C-1, C-11, C-12, C-14
14	1.23 m	43.8, CH	H-1, H <sub>2</sub> -13, H-18	–
15	1.12 s	27.6, CH <sub>3</sub>		C-2, C-3, C-4
16	1.35 s	30.9, CH <sub>3</sub>		C-6, C-7, C-8
17a/b	4.67 s; 4.66 s	108.7, CH <sub>2</sub>		C-10, C-11, C-12
18	1.25 m	29.5, CH	H-14, H <sub>3</sub> -19, H <sub>3</sub> -20	–
19	0.95 d (6.8)	21.9, CH <sub>3</sub>	H-18	C-14, C-18, C-20
20	0.78 d (6.8)	15.8, CH <sub>3</sub>	H-18	C-14, C-18, C-19

proton is  $\beta$ , and the proton at  $\delta_{\text{H}}$  1.76 is  $8\alpha$ . Additionally, the proton signal of a methyl group displayed NOESY correlations with both H- $8\alpha$ / $\beta$ , which indicated that the Me-16 at C-7 was  $\beta$ -oriented. As one of the C-4 methylene ( $\delta_{\text{H}}$  2.13) exhibited a correlation to H-2, suggesting the  $\alpha$ -orientation of this proton by modeling study and the other was assigned as H-4 $\beta$  ( $\delta_{\text{H}}$  1.70). H-6 displayed correlations with H-4 $\alpha$  and H<sub>3</sub>-16, but not with either H- $8\alpha$ / $\beta$ , demonstrating the  $\beta$ -orientation of the palmitate group at C-6. The aforementioned results enabled establishment of the relative configuration of **1**, and therefore its stereogenic carbons were assigned as 1*R*\*,2*R*\*,3*R*\*,6*S*\*,7*S*\*,9*R*\*,10*R*\*,14*R*\*.

Compound **2** was isolated as an amorphous powder that showed a pseudomolecular ion  $[\text{M} + \text{Na}]^+$  at  $m/z$  343.22435 in HRESIMS analysis. The results revealed that **2** had a molecular formula of C<sub>20</sub>H<sub>32</sub>O<sub>3</sub> (calcd for C<sub>20</sub>H<sub>32</sub>O<sub>3</sub> + Na, 343.22437), with five degrees of unsaturation. IR spectrum analysis showed that this compound had a broad absorption peak at 3356 cm<sup>−1</sup>, suggesting that the structure of **2** included a hydroxy group. The <sup>13</sup>C and DEPT spectra revealed that compound **2** had 20 carbons, including 4 methyls, 5 sp<sup>3</sup> methylenes, 7 sp<sup>3</sup> methines (including 3 oxymethines), 2 sp<sup>3</sup> oxygenated quaternary carbons, 1 sp<sup>2</sup> methylene and 1 sp<sup>2</sup> quaternary carbon (Table 2). Therefore, according to the aforementioned data, one degree of unsaturation was accounted for, and **2** was identified as having four rings. From the COSY spectrum (Table 2), it was possible to differentiate the separate systems of H<sub>2</sub>-4/H<sub>2</sub>-5/H-6, H<sub>2</sub>-8/H-9/H-10/H-1/H-14/H<sub>2</sub>-13/H<sub>2</sub>-12 and H-14/H-18/ H<sub>3</sub>-19 (H<sub>3</sub>-20). Together with results of key HMBC from protons to quaternary carbons, such as H-1, H-2, H<sub>2</sub>-4, H<sub>3</sub>-15 to C-3; H-5 $\beta$ , H<sub>2</sub>-8, H-9, H<sub>3</sub>-16 to C-7; and H-9, H-10, H-12 $\beta$ , H<sub>2</sub>-13, H<sub>2</sub>-17 to C-11 (Table 2), the data confirmed the main carbon skeleton of **2**.

In a previous study, eunicellin **2** was reported and named as sclerophytin A (Sharma and Alam, 1988). However, by comparison of the NMR data of **2** with those of sclerophytin A, we found that the NMR data for sclerophytin A reported by Sharma and Alam (1988) differed significantly from that of **2** reported in our studies. In fact, the structure of sclerophytin A reported by Sharma and Alam (Sharma and Alam, 1988) is the hydrolytic product of **2** as shown with the structure **3**, while compound **3** has also been obtained in this study (Fig. 1). The structure of **2** was confirmed by comparing the spectroscopic and physical data with those of the product **2** synthesized by Paquette's group. By comparison of the rotation value of **2** ( $[\alpha]_{\text{D}}^{20}$  5(20),

$\text{CHCl}_3$ ) with that of synthetic product **2** ( $[\alpha]_{\text{D}}^{20}$  5(20),  $\text{CHCl}_3$ ) (Bernardelli et al., 2001; Paquette et al., 2002), the absolute configuration for the stereogenic carbons of **2** were determined as 1*R*,2*R*,3*R*,6*S*,7*R*,9*R*,10*R*,14*R*.

As **1** (cladieunicellin U) was isolated along with **2** from the same organism, it is reasonable on biogenetic grounds to assume that **1** has the same absolute configuration as **2**. Therefore, based on above findings, the configurations of the stereogenic centers of **1** were elucidated as 1*R*,2*R*,3*R*,6*S*,7*S*, 9*R*,10*R*,14*R*. On the other hand, to the best of our knowledge, there has been no report of eunicellin **2** being obtained from any natural sources, and this result proves that the setting of two oxygen bridges with the fused cyclodecanol B ring is a nature's way (Paquette et al., 2000). In order to avoid confusion, we suggested that eunicellin **2** be named as cladieunicellin V in future studies. Moreover, two known eunicellins were also isolated and identified as sclerophytin A (**3**) and sclerophytin B (**4**), by comparison with the spectroscopic and physical data reported in the literature (Bernardelli et al., 2001; Friedrich et al., 2000; Friedrich and Paquette, 2002; Paquette et al., 2000; Sharma and Alam, 1988).

In *in vitro* anti-inflammatory activity assay, it was found that eunicellins **1**, **3** and **4** showed inhibitory effects on the release of elastase, a marker of inflammation (inhibition rates = 12.01 ± 4.53, 11.35 ± 5.04 and 16.37 ± 8.14%, respectively), and eunicellins **2** and **4** showed 13.43 ± 1.57 and 28.12 ± 3.61% inhibitory effects on human neutrophils in terms of the generation of superoxide anions by human neutrophils, respectively, at a concentration of 10  $\mu\text{M}$ . In addition, the cytotoxicity of eunicellins **1–4** against K-562 (human chronic myelogenous leukemia) and MOLT-4 (human acute lymphoblastic leukemia) tumor cells shown in Table 3. Eunicellins **1** and **4** were found

**Table 3**Cytotoxic data of eunicellins **1–4**.

Cell lines IC <sub>50</sub> ( $\mu\text{g/mL}$ )	Compounds				
	1	2	3	4	Doxorubicin <sup>a</sup>
K-562	12.76	> 20	> 20	11.39	0.23
MOLT-4	> 20	18.83	> 20	> 20	0.01

<sup>a</sup> Doxorubicin was used as a positive control.



to show moderate cytotoxicity toward K562 cells and **2** exhibited moderate cytotoxicity toward MOLT-4 cells.

### 3. Experimental

#### 3.1. General

The Jeol NMR spectrometer (model ECZ400S) was used to record the spectra with the solvent peak of  $\text{CHCl}_3$  ( $\delta_{\text{H}}$  7.26 ppm) and  $\text{CDCl}_3$  ( $\delta_{\text{C}}$  77.1 ppm) as internal references for  $^1\text{H}$  NMR and  $^{13}\text{C}$  NMR, respectively. ESIMS and HRESIMS were obtained from the Bruker mass spectrometer with 7 T magnets (model: Solarix FTMS system). Column chromatography, IR spectra and optical rotation were performed according to our earlier research (Zhang et al., 2019).

#### 3.2. Animal material

Specimens of *Cladiella* sp. (Bayer, 1981) used for this study were collected in the Penghu Archipelago waters, Taiwan, in May 2017. A voucher specimen was deposited in the National Museum of Marine Biology and Aquarium (NMMBA) (voucher no.: NMMBA-TWSC-17032), Taiwan.

#### 3.3. Extraction and isolation

The freeze-dried and sliced bodies (wet/dry weight = 570.3/202.8 g) of the coral specimen were prepared and extracted with a 1:1 mixture of MeOH and  $\text{CH}_2\text{Cl}_2$  to give 25.8 g of crude extract which was partitioned between EtOAc and  $\text{H}_2\text{O}$  to obtain 16.8 g of the EtOAc extract. The EtOAc extract was eluted on silica gel column with gradients of n-hexane/EtOAc (100% n-hexane–100% EtOAc, stepwise), to furnish 16 fractions (fractions: A – P). Fractions E – I were combined and further chromatographed on silica gel column and eluted with gradients of n-hexane/EtOAc (50:1 – 100% EtOAc, stepwise) to afford 31 sub-fractions (fractions: E1 – E31). Afterward, fraction E11 was purified by normal-phase HPLC (NP-HPLC) using a mixture of n-hexane,  $\text{Me}_2\text{CO}$  and EtOAc (with volume:volume:volume = 16:1:2.5; at a flow rate = 2.0 mL/min) to afford **2** (3.9 mg). Fractions E18 and E19 were combined and separated by NP-HPLC using a mixture of n-hexane,  $\text{Me}_2\text{CO}$  and EtOAc (9:0.5:2.5) as solvent to obtain 8 subfractions (fractions: E18A – E18H). Then, fraction E18A was further separated by NP-HPLC using a mixture of n-hexane,  $\text{Me}_2\text{CO}$  and EtOAc (with volume:volume:volume = 21:0.5:2.5; at a flow rate = 2.0 mL/min) to afford **1** (1.5 mg). Fraction M was separated by NP-HPLC using a mixture of n-hexane and  $\text{Me}_2\text{CO}$  (with volume: volume = 3:1; at a flow rate = 4.0 mL/min) to afford **3** (16.6 mg). Fraction N was separated by NP-HPLC using a mixture of n-hexane and  $\text{Me}_2\text{CO}$  (with volume:volume = 2:1; at a flow rate = 4.0 mL/min) to afford **4** (1.2 mg).

#### 3.4. Cladieunicellin U (**1**)

Amorphous powder;  $[\alpha]_{\text{D}} -7$  (c 0.06,  $\text{CHCl}_3$ ), IR (neat)  $\nu_{\text{max}}$  3438, 1720  $\text{cm}^{-1}$ ;  $^1\text{H}$  and  $^{13}\text{C}$  NMR data, see Table 1. ESIMS:  $m/z$  599  $[\text{M} + \text{Na}]^+$ , HRESIMS:  $m/z$  599.46479 (calcd for  $\text{C}_{36}\text{H}_{64}\text{O}_5 + \text{Na}$ , 599.46460).

#### 3.5. Cladieunicellin V (**2**)

Amorphous powder;  $[\alpha]_{\text{D}} -5$  (c 0.15,  $\text{CHCl}_3$ ), IR (neat)  $\nu_{\text{max}}$  3356  $\text{cm}^{-1}$ ;  $^1\text{H}$  and  $^{13}\text{C}$  NMR data, see Table 2. ESIMS:  $m/z$  343  $[\text{M} + \text{Na}]^+$ , HRESIMS:  $m/z$  343.22435 (calcd for  $\text{C}_{20}\text{H}_{32}\text{O}_3 + \text{Na}$ , 343.22437).

#### 3.6. Sclerophytin A (**3**)

Amorphous powder;  $[\alpha]_{\text{D}} -3$  (c 0.83,  $\text{CHCl}_3$ ), IR (neat)  $\nu_{\text{max}}$

3391  $\text{cm}^{-1}$ ;  $^1\text{H}$  and  $^{13}\text{C}$  NMR data were found to be in absolute agreement with previous studies (Friedrich et al., 2000; Friedrich and Paquette, 2002; Paquette et al., 2000; Sharma and Alam, 1988). ESIMS:  $m/z$  361  $[\text{M} + \text{Na}]^+$ .

#### 3.7. Sclerophytin B (**4**)

Colorless oil;  $[\alpha]_{\text{D}} -10$  (c 0.06,  $\text{CHCl}_3$ ), IR (neat)  $\nu_{\text{max}}$  3461  $\text{cm}^{-1}$ ;  $^1\text{H}$  and  $^{13}\text{C}$  NMR data were found to be in absolute agreement with previous studies (Friedrich et al., 2000; Friedrich and Paquette, 2002; Paquette et al., 2000; Sharma and Alam, 1988). ESIMS:  $m/z$  403  $[\text{M} + \text{Na}]^+$ .

#### 3.8. Molecular mechanics calculations

The molecular models were generated by implementing the MM2 force field (Allinger, 1977) in ChemBio 3D Ultra software (ver. 12.0) which was created by CambridgeSoft (PerkinElmer, Cambridge, MA, USA).

#### 3.9. Superoxide anion generation and elastase release by human neutrophils

Human neutrophils were obtained by means of dextran sedimentation and Ficoll centrifugation. Measurements of elastase release and superoxide anion generation were carried out according to previously described procedures (Hwang et al., 2010; Yu et al., 2011). Briefly, superoxide anion production was assayed by monitoring the superoxide dismutase-inhibitable reduction of ferricytochrome c. Elastase release experiments were performed using MeO-Suc-Ala-Ala-Pro-Valp-nitroanilide as the elastase substrate.

#### 3.10. MTT antiproliferation assay

K-562 and MOLT-4 cells were obtained from the American Type Culture Collection (ATCC; Manassas, VA, USA). Cells were maintained in RPMI 1640 medium supplemented with 10% fetal calf serum, 2 mM glutamine, and antibiotics (100 units/mL penicillin and 100  $\mu\text{g}/\text{mL}$  streptomycin) at 37 °C in a humidified atmosphere of 5%  $\text{CO}_2$ . Cells were seeded at  $4 \times 10^4$  per well in 96-well culture plates before treatment with different concentrations of the tested compounds. The compounds were dissolved in DMSO and further used with concentrations of 1.25, 2.5, 5, 10 and 20  $\mu\text{g}/\text{mL}$  in the *in vitro* experiment. After treatment for 72 h, the cytotoxicity of the tested compounds was determined using a MTT cell proliferation assay. The MTT is reduced by the mitochondrial dehydrogenases of viable cells to a purple formazan product. The MTT-formazan product was dissolved in DMSO. Light absorbance values ( $\text{OD} = \text{OD}_{570} - \text{OD}_{620}$ ) were recorded at wavelengths of 570 and 620 nm using an ELISA reader to calculate the concentration that caused 50% inhibition ( $\text{IC}_{50}$ ), i.e., the cell concentration at which the light absorbance value of the experiment group was half that of the control group. These results were expressed as a percentage of the control  $\pm$  SD established from  $n = 4$  wells per one experiment from three separate experiments (Alley et al., 1988; Scudiero et al., 1988).

### Acknowledgments

This research was supported by grants from the National Museum of Marine Biology and Aquarium; and the Ministry of Science and Technology, Taiwan (Grant Nos: MOST 104-2320-B-291-001-MY3 and 107-2320-B-291-001-MY3) awarded to Ping-Jyun Sung.

### Appendix A. Supplementary data

Supplementary material related to this article can be found, in the online version, at doi:<https://doi.org/10.1016/j.phytol.2019.07.002>.

## References

- Alley, M.C., Scudiero, D.A., Monks, A., Hursey, M.L., Czerwinski, M.J., Fine, D.L., Abbott, B.J., Mayo, J.G., Shoemaker, R.H., Boyd, M.R., 1988. Feasibility of drug screening with panels of human tumor cell lines using a microculture tetrazolium assay. *Cancer Res.* 48, 589–601.
- Allinger, N.L., 1977. Conformational analysis. 130. MM2. A hydrocarbon force field utilizing  $V_1$  and  $V_2$  torsional terms. *J. Am. Chem. Soc.* 99, 8127–8134.
- Bayer, F.M., 1981. Key to the genera of octocorallia exclusive of Pennatulacea (Coelenterata: Anthozoa), with diagnoses of new taxa. *Proc. Biol. Soc. Wash.* 94, 902–947.
- Bernardelli, P., Moradei, O.M., Friedrich, D., Yang, J., Gallou, F., Dyck, B.P., Doskotch, R.W., Lange, T., Paquette, L.A., 2001. Total asymmetric synthesis of the putative structure of the cytotoxic diterpenoid (–)-sclerophytin A and of the authentic natural sclerophytins A and B. *J. Am. Chem. Soc.* 123, 9021–9032.
- Chen, T.-H., Lu, M.-C., Chang, Y.-C., Su, Y.-D., Chen, Y.-H., Lin, N.-C., Fang, L.-S., Wu, Y.-C., Sung, P.-J., 2013. Discovery of new eunicellin-based diterpenoids from a Formosan soft coral *Cladiella* sp. *Mar. Drugs* 11, 4585–4593.
- Chen, T.-H., Chen, W.-F., Wen, Z.-H., Lu, M.-C., Wang, W.-H., Li, J.-J., Wu, Y.-C., Sung, P.-J., 2014a. Cladieunicellins M–Q, new eunicellins from *Cladiella* sp. *Mar. Drugs* 12, 2144–2155.
- Chen, T.-H., Cheng, C.-H., Chen, Y.-H., Lu, M.-C., Fang, L.-S., Chen, W.-F., Wen, Z.-H., Wang, W.-H., Wu, Y.-C., Sung, P.-J., 2014b. Cladieunicellin J, a new hydroperoxyeunicellin from *Cladiella* sp. *Nat. Prod. Commun.* 9, 613–614.
- Friedrich, D., Doskotch, R.W., Paquette, L.A., 2000. Revised constitution of sclerophytins A and B. *Org. Lett.* 2, 1879–1882.
- Friedrich, D., Paquette, L.A., 2002. Structural and stereochemical reassessment of sclerophytin-type diterpenes. *J. Nat. Prod.* 65, 126–130.
- Hwang, T.-L., Wang, C.-C., Kuo, Y.-H., Huang, H.-C., Wu, Y.-C., Kuo, L.-M., Wu, Y.-H., 2010. The hederagenin saponin SMG-1 is a natural FMLP receptor inhibitor that suppresses human neutrophil activation. *Biochem. Pharmacol.* 80, 1190–1200.
- Kennard, O., Watson, D.G., Riva di Sanseverino, L., Tursch, B., Bosmans, R., Djerassi, C., 1968. Chemical studies of marine invertebrates. IV. Terpenoids LXII. Eunicellin, a diterpenoid of the gorgonian *Eunicella stricta*. X-ray diffraction analysis of eunicellin dibromide. *Tetrahedron Lett.* 9, 2879–2884.
- Paquette, L.A., Moradei, O.M., Bernardelli, P., Lange, T., 2000. Synthesis of the alleged structure of sclerophytin A: the setting of two oxygen bridges within the fused cyclodecanol B ring is not nature's way. *Org. Lett.* 2, 1875–1878.
- Peng, K.-Y., Chen, N.-F., Chen, Z.-C., Tsui, K.-H., Wen, Z.-H., Su, Y.-D., Chang, Y.-C., Chen, Y.-H., Lu, M.-C., Fang, L.-S., Chen, J.-J., Wu, T.-Y., Wu, Y.-C., Sung, P.-J., 2016. Cladieunicellins R and S, new eunicellins from the Formosan octocoral *Cladiella tuberculosa*. *Tetrahedron Lett.* 57, 4239–4242.
- Radhika, P., 2006. Chemical constituents and biological activities of the soft corals of genus *Cladiella*: a review. *Biochem. Syst. Ecol.* 34, 781–789.
- Scudiero, D.A., Shoemaker, R.H., Paull, K.D., Monks, A., Tierney, S., Nofziger, T.H., Currens, M.J., Seniff, D., Boyd, M.R., 1988. Evaluation of a soluble tetrazolium/formazan assay for cell growth and drug sensitivity in culture using human and other tumor cell lines. *Cancer Res.* 48, 4827–4833.
- Sharma, P., Alam, M., 1988. Sclerophytins A and B. Isolation and structures of novel cytotoxic diterpenes from the marine coral *Sclerophyllum capitalis*. *J. Chem. Soc. Perkin Trans. I* 2537–2540.
- Shih, F.-Y., Chen, T.-H., Lu, M.-C., Chen, W.-F., Wen, Z.-H., Kuo, Y.-H., Sung, P.-J., 2013. Cladieunicellins K and L, new eunicellin-based diterpenoids from an octocoral *Cladiella* sp. *Int. J. Mol. Sci.* 14, 21781–21789.
- Yu, H.-P., Hsieh, P.-W., Chang, Y.-J., Chung, P.-J., Kuo, L.-M., Hwang, T.-L., 2011. 2-(2-Fluorobenzamido)-benzoate ethyl ester (EFB-1) inhibits superoxide production by human neutrophils and attenuates hemorrhagic shock-induced organ dysfunction in rats. *Free Radic. Biol. Med.* 50, 1737–1748.
- Zhang, Z.-J., Peng, B.-R., Hu, C.-C., Lin, N.-C., Yao, J.-W., Lu, M.-C., Wen, Z.-H., Wu, Y.-C., Sung, P.-J., 2019. Cladieunicellin T, a new eunicellin-based diterpenoid produced by the octocoral *Cladiella* sp. *Nat. Prod. Commun.* 14, 101–102.

Article

# Characterization of the Roles of Vimentin in Regulating the Proliferation and Migration of HSCs during Hepatic Fibrogenesis

Pei-Wen Wang <sup>1</sup>, Tung-Ho Wu <sup>2</sup>, Tung-Yi Lin <sup>3,4</sup> , Mu-Hong Chen <sup>5,6</sup>, Chau-Ting Yeh <sup>7</sup> and Tai-Long Pan <sup>4,7,8,9,\*</sup> 

<sup>1</sup> Department of Medical Research, China Medical University Hospital, China Medical University, Taichung 40447, Taiwan; pwwang5105@hotmail.com

<sup>2</sup> Division of Cardiovascular Surgery, Veterans General Hospital, Kaohsiung 81362, Taiwan; thwu@vghks.gov.tw

<sup>3</sup> Department of Chinese Medicine, Chang Gung Memorial Hospital, Keelung 20401, Taiwan; tungyi30@cgmh.org.tw

<sup>4</sup> School of Traditional Chinese Medicine, Chang Gung University, Taoyuan 33302, Taiwan

<sup>5</sup> Department of Psychiatry, Taipei Veterans General Hospital, Taipei 11217, Taiwan; kremer7119@gmail.com

<sup>6</sup> Department of Psychiatry, College of Medicine, National Yang-Ming University, Taipei 11221, Taiwan

<sup>7</sup> Liver Research Center, Chang Gung Memorial Hospital, Taoyuan 33375, Taiwan; chautingy@gmail.com

<sup>8</sup> Chinese Herbal Medicine Research Team, Healthy Aging Research Center, Chang Gung University, Taoyuan 33302, Taiwan

<sup>9</sup> Research Center for Chinese Herbal Medicine and Research Center for Food and Cosmetic Safety, College of Human Ecology, Chang Gung University of Science and Technology, Taoyuan 33303, Taiwan

\* Correspondence: pan@mail.cgu.edu.tw; Tel.: +886-3-211-8800 (ext. 5105); +886-3-211-8700

Received: 30 August 2019; Accepted: 29 September 2019; Published: 1 October 2019



**Abstract:** The activation of hepatic stellate cells (HSCs) manifested as proliferation and migration is the pivotal event involved in liver fibrogenesis. The vimentin network, an intermediate filament (IF) system, is one of the critical cascades by which the cell morphology, growth, and motility are modulated. However, the vimentin-mediated cytoskeletal cross talk, as well as the signaling transduction, which further coordinates the cellular responses during hepatic fibrogenesis, is poorly understood. In the current study, both messenger RNA (mRNA) and the vimentin protein were significantly increased in a time-dependent manner in the dimethylnitrosamine (DMN)-exposed liver. In particular, vimentin was highly expressed in the activated HSCs. Again, the overexpressed vimentin was observed in the plasma samples derived from patients with hepatic fibrosis/cirrhosis, suggesting that vimentin may be a key factor in regulating the progression of liver fibrosis. Meanwhile, vimentin knockdown suppressed the migratory propensity, provoked morphological changes, and disturbed the focal adhesions in the HSCs due to the breakdown of associated cytoskeletal proteins. Western blotting showed that vimentin deletion inhibited proliferating cell nuclear antigen (PCNA) and arrested the Rho GTPase family, thereby impairing the HSCs' growth as well as motility. The phosphorylated extracellular-signal regulated kinase (ERK) and AKT signals were also notably reduced in response to the silence of vimentin. Inhibitors of selected signaling pathways suppressed the migration and differentiation of activated HSCs by regulating specific serine phosphorylated sites on vimentin. Taken together, these findings revealed a novel mechanism of vimentin through which various signaling pathways controlled the proliferation, differentiation, and movement of the HSCs via the ERK/AKT and Rho cascades.

**Keywords:** hepatic stellate cells; hepatic fibrosis; vimentin; Rho; ERK; AKT

## 1. Introduction

Hepatic fibrosis, the hallmark feature related to the failure of liver function, is characterized by the excessive deposition of extracellular matrix (ECM) proteins. Ongoing fibrosis may result in irreversible cirrhosis and an increased risk of hepatoma [1–4]. Currently, liver fibrogenesis has become an important public health issue worldwide due to the high prevalence of chronic liver diseases [5–7]. In this regard, anti-fibrotic administration should be urgently developed to control or even inhibit disease progression.

Hepatic stellate cells (HSCs), located in the space between the hepatocytes and the sinusoidal endothelium, play a critical role during the progression of liver fibrosis. Specific cytokines and molecules such as transforming growth factor- $\beta$ 1 (TGF- $\beta$ 1) and platelet-derived growth factor (PDGF) stimulate the HSCs to undertake the phenotypic switch from quiescent retinoid-storing cells to proliferative and fibrogenic cells, which are thought to play a key role in fibrosis of the liver [8–10]. Therefore, the suppression of cell growth and the migration of HSCs may be a promising strategy for reversing early fibrosis, although the intracellular signals regulating the changes in HSCs remain unclear.

One of the earliest events associated with HSC activation is cytoskeleton remodeling, which contributes to cell division and movement [11,12]. Coordinated movement is the result of the ability of a cell to spread protrusions and form adhesions at the leading edge, translocate the cell body, and eventually disconnect from the substrate. Of note, vimentin, a member of the intermediate filament (IF) protein family, helps to stabilize focal adhesion, which governs cell migration. It also performs as a signal transducer from the ECM to the nuclei [13,14]. Moreover, vimentin has a great number of phosphorylation sites that influence the assembly status and the architecture of the cellular filaments. The vimentin network recruits rapid phosphorylation and dephosphorylation that regulate integrin-mediated cell adhesion and facilitate directional cell motility [15,16]. In keeping with such roles, identification of the coordinated proteins and molecules modulated by vimentin might reveal the IF-mediated cytoskeleton cross talk associated with liver fibrosis.

Significant evidence has shown that HSC migration is essential for liver fibrogenesis and that preventing the cell migration could notably suppress the disease progression [17]. Activation-related morphological changes and migration in the HSCs are induced by liver injury, although the associated signaling mechanisms are still unclear. The Rho GTPase family of proteins, including Cdc42, RhoA/B/C, and Rac1, trigger and control specific signal transduction pathways that initiate and regulate cytoskeletal dynamics, cell proliferation, and cell movement via the activation of the PAK serine/threonine kinases [18,19]. Herein, we investigated how Rho proteins and their signaling pathways or the vimentin-mediated regulation of downstream cascades are involved in the pathological remodeling of HSCs.

Through our research to better understand the regulatory mechanisms of HSC migration in liver fibrogenesis, we verified the hypothesis that vimentin may influence cytoskeletal reorganization and cell migration in HSCs through Rho GTPase signaling, particularly RhoA.

## 2. Material and Methods

### 2.1. Materials

Specific antibodies to GAPDH, vimentin, PCNA, collagen I, filamin, vinculin, and talin were purchased from Santa Cruz Biotech (Dallas, TX, USA). Polyclonal antibodies to PPAR $\gamma$ ,  $\alpha$ -SM-actin, and  $\beta$ -actin were obtained from abcam (Cambridge, UK). Polyclonal antibodies to Rho A, Rho B, Rho C, Rac1/2/3, Cdc42, phospho-Rac1/cdc42, AKT, phospho-AKT, ERK, phospho-ERK, phospho-Vimentin<sup>Ser39</sup>, phospho-Vimentin<sup>Ser56</sup> and phospho-Vimentin<sup>Ser83</sup> were purchased from Cell Signaling (Danvers, MA, USA). U0126, Y27632, LY294002 was obtained from Cayman Chemical (Ann Arbor, Michigan, USA). DMN was purchased from Sigma-Aldrich (St. Louis, MO, USA).

## 2.2. Animals

Male Wistar rats weighing 200–225 g were purchased from Lasco Co. (Taipei, Taiwan) and were randomly divided into two groups of six each [control (saline treated) and DMN treated]. In the DMN-induced fibrosis group, rats were injected intraperitoneally with DMN (10 mg/kg body weight; Sigma) for three consecutive days per week for four weeks [20,21]. The control group was applied with only saline. At the end of the fourth week, all of the rats were sacrificed. The liver tissues were excised and the specimens were immediately fixed in 10% neutral buffered formaldehyde for pathological and immunohistochemical studies. The Committee on Research Involving Animal Subjects of the Chang Gung University, Taiwan, has approved the study.

## 2.3. Analysis of Transcripts of $\alpha$ -SMA, Vimentin, and Procollagen Genes

Total RNA was isolated from liver tissue, and single-stranded cDNA synthesis was performed on 10  $\mu$ g of total RNA by a complementary DNA synthesis system for the RT-PCR according to the manufacturer's instructions (Invitrogen, Waltham, MA, USA). The primers utilized for the PCR experiments are listed in the following.  $\alpha$ -SMA: 5'-TTCGTTACTACTGCTGAGCGTGAGA-3', 5'-AAAGATGGCTGGAAGAGGGTC-3'; vimentin: 5'-ATGGCTGCCAAAGTGTT-3', 5'-CTGGGGGAGCTGGAGG-3'; Col I: 5'-TACTACCGGGCCGATGATGC-3', 5'-TCCTTG GGGTTCGGGCTGATGTA-3'; Col III: 5'-CCCCTGGTCCCTGCTGTGG-3', 5'-GAGGCCCGGCTGGAAAGAA-3';  $\beta$ -actin: 5'-TGTTACCAACTGGGACGACA-3', 5'-CTCTCAGCTGTGGTGGTGAA-3' [21,22]. The condition consisted of denaturing at 94 °C for 1 min, annealing at 53 °C for 1.5 min, and extending at 72 °C for 2.5 min. Each PCR product was resolved on a 1.5% agarose gel incorporated with ethidium bromide. Transcript intensities were revealed as digitalized images using a high-resolution scanner (Syngene, Cambridge, UK). The  $\beta$ -actin transcript was used as a loading control to normalize the concentration of cDNA in each sample. Take a ratio of a net band value over the net loading control of that lane after background subtraction for quantification.

## 2.4. Western Blot Analysis

Equal amount of lysated protein was separated on 6%, 12% or 15% denatured gels, respectively and transferred to membranes. Next, the blots were incubated with specific primary antibody overnight at 4 °C after blocking and further incubated with a peroxidase-labeled anti-mice or -rabbit IgG for 2 h. After washing with TBST several times, enhanced chemiluminescence (PerkinElmer, Waltham, MA, USA) was used for signal detection. The band intensity was quantified using GeneTools Image Software (version 4.03, Syngene). GAPDH and  $\beta$ -actin were used as the loading controls [20]. Take a ratio of a net band value over the net loading control of that lane after background subtraction for quantification.

## 2.5. Histology and Immunohistochemistry

The liver tissue fixed by 5% neutral buffered formalin was immersed in paraffin and then sliced into 5  $\mu$ m sections. The sample slices were stained with hematoxylin–eosin (H/E) and Masson's trichrome (MT) for a histological assessment. Immunohistochemistry with vimentin was applied to specimens as previously described [20,23]. The histological changes were observed by using optical microscopy (Olympus BX51, Tokyo, Japan) in non-consecutive, randomly chosen 400 $\times$  histological fields. The digital photomicrographs were then processed with DP-72.

## 2.6. Clinical Cases

To reveal the clinicopathological significance and relevance of vimentin expression in hepatic fibrosis, we have applied a separate cohort of 55 subjects (22 controls and 33 patients with liver fibrosis) under approval of Institutional Review Board, Chang Gung Memorial Hospital, Taiwan, plasma samples were retrospectively retrieved from the serum bank, Liver Research Center, Chang Gung



Memorial Hospital for a study attempting to correlated biochemistry, tissue histology, and harmonic microscopy characteristics for liver fibrosis in hepatitis B patients. All patients included had previously received liver biopsy for evaluation of hepatitis activities and liver fibrosis which is classified by “ISHAK” score [24]. The protein amount was determined and normalized by using the Bradford Protein Assay Kit (AMRESCO, Solon, OH, USA). Western blotting assays were conducted and quantified with GeneTools Image Software (version 4.03, Syngene). All experiments were technically repeated three times.

### 2.7. Cell Culture

The immortalized rat myofibroblast cell line HSC-T6 was a kind gift of Dr. Scott L. Friedman (Mount Sinai School of Medicine, New York, NY, USA). The HSC-T6 cells were maintained in DMEM medium containing 10% FBS at 37 °C in a humidified atmosphere of 5% CO<sub>2</sub>.

### 2.8. Gene Silencing by Small Interfering RNA

HSC-T6 cells were plated onto six-well plates ( $1 \times 10^5$  cells/well), maintained in antibiotic-free medium for 24 h, and transfected with a mixture containing Opti-MEM, 8 µL/well Lipofectamine 2000 (Invitrogen), and either 0.5 µg/well scrambled siRNA (mock) or a vimentin siRNAs (smart pool; Invitrogen) for 6 h [25,26]. The sequences of these siRNAs are available from the manufacturer. After another 48 h culture with DMEM medium containing 10% FBS under transfection, cells were evaluated by the Wound-migration assay, Immunofluorescence and Western blot. Determination of cell proliferation and apoptosis by the flow cytometry and western blot was described previously [26].

### 2.9. Wound-Migration Assay

A wound-migration assay was performed as described by Van Lonkhuyzen et al. with slight modifications [27]. HSC-T6 cells transfected with or without siVIM were grown in 35-mm culture dishes to 95% confluence. A wound was formed using a 200 µL pipette tip to clear the cell monolayer, and the boundary of the wound was marked. Cells were then washed three times with PBS and incubated for 24 h at 37 °C under a 5% CO<sub>2</sub> atmosphere. After incubation, cell migration was measured by counting the number of cells that migrated into the clear space using an Olympus microscope (IX71) at 20× fitted with an ocular grid. Results presented are the mean of four random fields of wounds sampled from three independent experiments. The areas of cell migration were determined by dividing the mean number of cells that moved from the edge to the wounded area by cells that moved from the edge in the control culture.

### 2.10. Immunofluorescence

HSC-T6 cells (mock or siVIM) were fixed in ice-cold methanol for 10 min at 4 °C. After washing in PBS, cells were permeabilized with 0.1% Triton-X100 in PBS for 10 min. After blocking with 1% BSA in PBS, cells were then incubated with primary antibodies and rinsed three times in PBS. The cells were subsequently exposed to a rhodamine conjugated secondary antibody. After incubation, cells were rinsed in PBS three times and nuclei were counterstained with DAPI for 1 min. After washing three times, the cells were maintained with mounting medium and observed by Olympus IX71 fluorescence microscope with DP72 PhotoImage system [25].

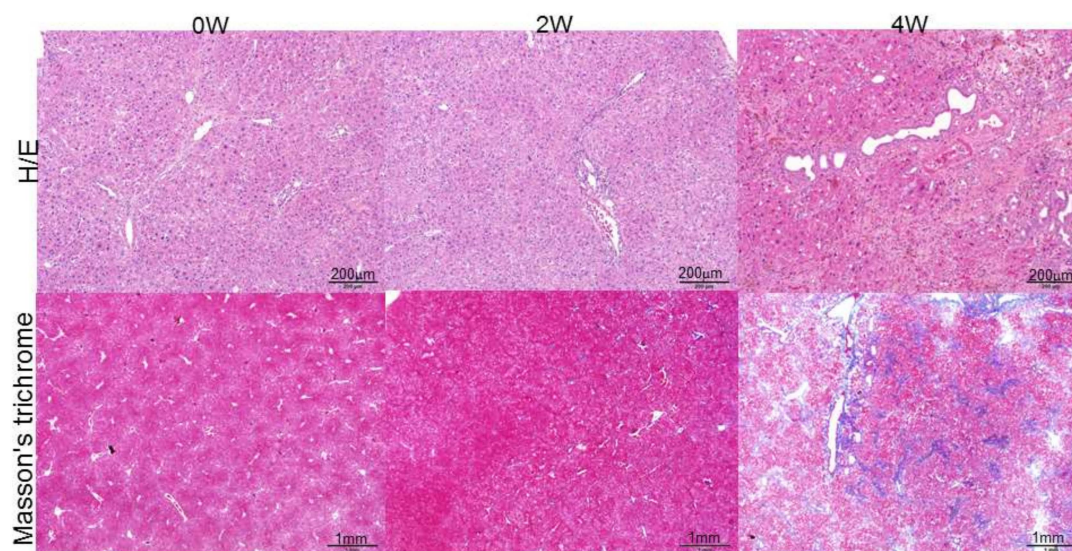
### 2.11. Statistical Analysis

The statistical analysis of the mean values was carried out with the ANOVA followed by Bonferroni post-hoc analysis to reveal what pairs of group means show differences with Prism software (v5.0, Prism GraphPad, San Diego, CA, USA). Bar charts are presented as the mean ± SD and *p* values from the post-hoc tests are included in the text and figure legends as conducting paired comparisons.

### 3. Results

#### 3.1. Liver Pathological Changes and Vimentin Expression Induced by DMN Administration

As shown in the upper panels of Figure 1A, with the use of hematoxylin–eosin (H/E) staining, the control sample showed intact lobular architecture, whereas the application of dimethylnitrosamine (DMN) for two weeks caused necrosis of the hepatocytes, inflammatory infiltration, and early liver fibrogenesis. Four-week exposure to DMN resulted in severe hepatic injury, which manifested as marked fibrosis with a huge amount of accumulated collagen. Masson's trichrome stain demonstrated that DMN at four weeks induced severe liver fibrosis where a large amount of collagen was accumulated (Figure 1A, lower panels) with respect to the control sample. Semi-quantification of RNA expression analysis also indicated that the mRNA expression of  $\alpha$ -smooth muscle actin ( $\alpha$ -SMA), collagen proteins such as collagen type I (COL I) and collagen type III (COL III), and vimentin was increased in a time-dependent manner after DMN treatment (Figure 1B). Consistent with the transcription results, the protein levels were gradually enhanced from week zero to week four following DMN administration (Figure 1C), which explains the development of hepatic fibrogenesis. Previous reports have shown that DMN would stimulate quiescent HSCs into proliferating myofibroblast-like cells, subsequently leading to liver fibrogenesis [20,28]. In the current study, histological changes in the liver tissue of rats were evaluated. Well-developed hepatocytes arranged in an orderly manner were identified in the normal control, and HSCs exhibited a dendrite-like shape encircling the sinusoids. Conversely, DMN applied samples showed serious hepatic injury characterized as activation of HSCs with extensive cytoplasmic fibers, massive necrosis of the hepatocytes, and inflammatory infiltration. Meanwhile, the location of vimentin was also confirmed by using immunohistochemistry, and a strong vimentin signal was predominantly detected in activated HSCs in the presence of DMN, suggesting the strong role of vimentin in directing the activation of HSCs (Figure 1D).



(A)

Figure 1. Cont.

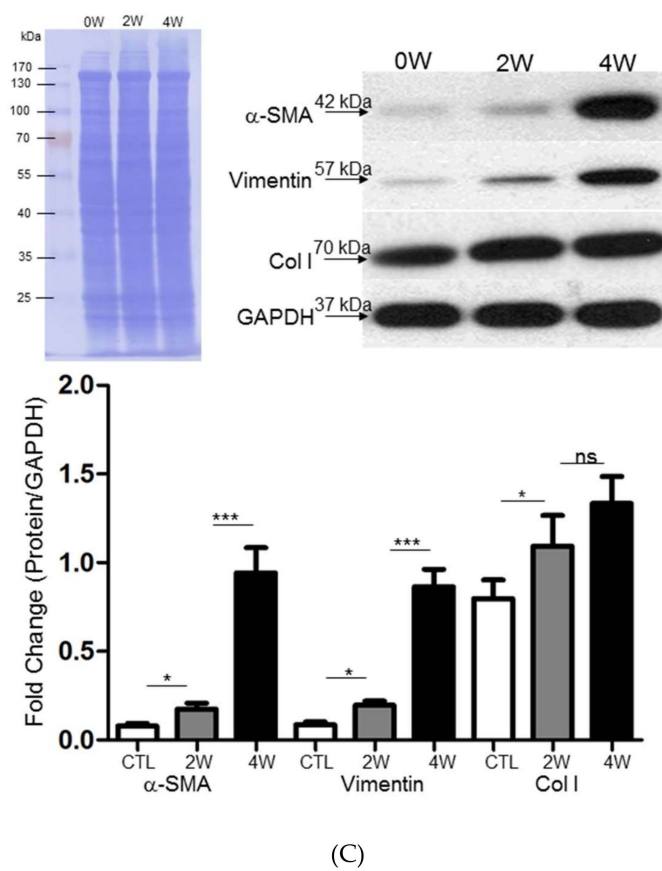
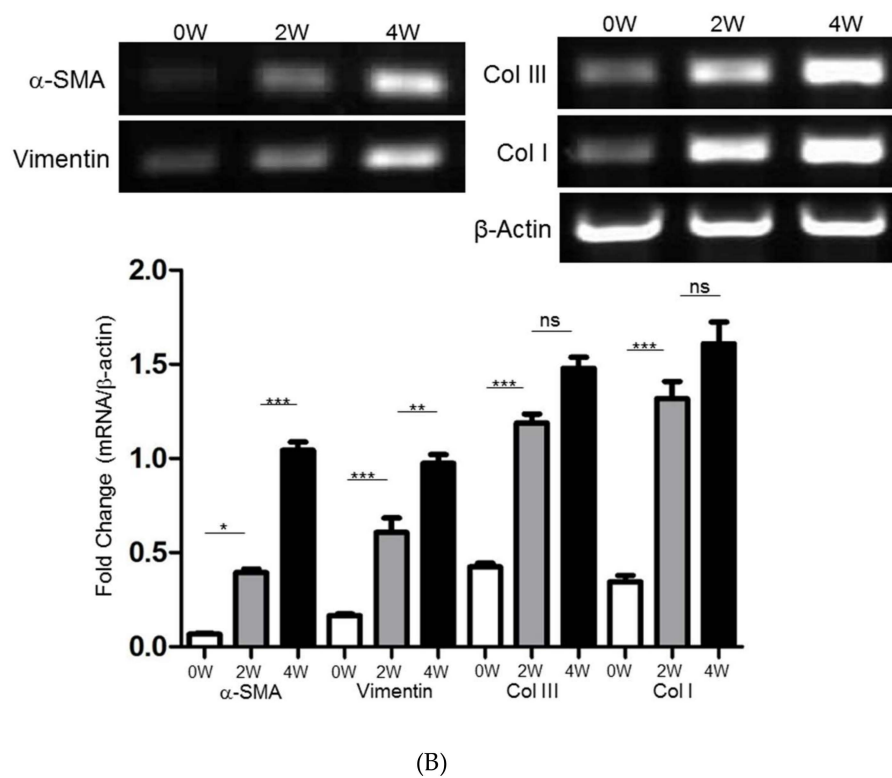
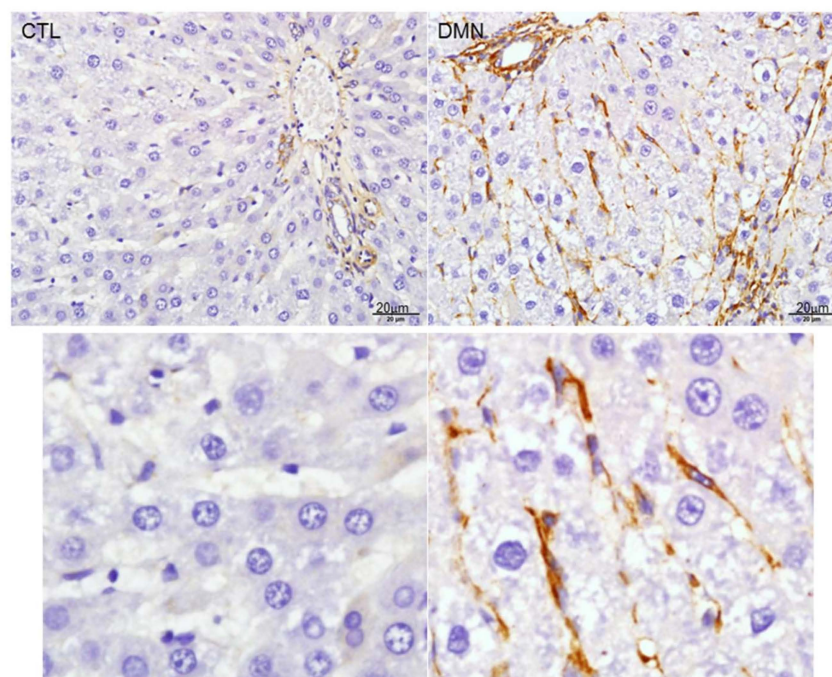


Figure 1. Cont.



(D)

**Figure 1.** (A) Histologic examination of rat liver at zero week (0W), two weeks (2W), and four weeks (4W). Upper panels: Hematoxylin–eosin (H/E) staining indicated necrosis of hepatocytes and infiltrated lymphocytes. Lower panels: Masson’s trichrome staining of rat liver tissues. The images indicated accumulation of collagen around portal tracts as blue images. (B) Validation of  $\alpha$ -smooth muscle actin ( $\alpha$ -SMA), vimentin, collagen type III (Col III), and collagen type I (Col I) expression by RT-PCR after treatment of dimethylnitrosamine (DMN).  $\beta$ -Actin was used as an internal control. The quantified results were indicated by the bar chart and represent the mean  $\pm$  SD of three independent experiments (\*  $p < 0.05$ , \*\*  $p < 0.01$ , \*\*\*  $p < 0.001$ , ns: no significance). (C) Confirmation of change in extracellular matrix (ECM) protein level after DMN application. Protein expression of  $\alpha$ -SMA, vimentin, and Col I was assessed by a Western blot analysis. Glyceraldehyde-3-phosphate dehydrogenase (GAPDH) was used as an internal control. Polyvinylidene difluoride (PVDF) membrane stained with Coomassie blue R-250 was utilized to perform loading amount of proteins. The quantified results were presented by the bar chart (\*  $p < 0.05$ , \*\*\*  $p < 0.001$ , ns: no significance.). The results are representative of the rats used in each group ( $n = 6$ ). (D) Immunohistochemical study of vimentin expression in representative liver tissues obtained from samples treated with or without DMN at four weeks (4W). The regions with differently expressed vimentin were shown by brown color. The lower panels presented the zoom figures.

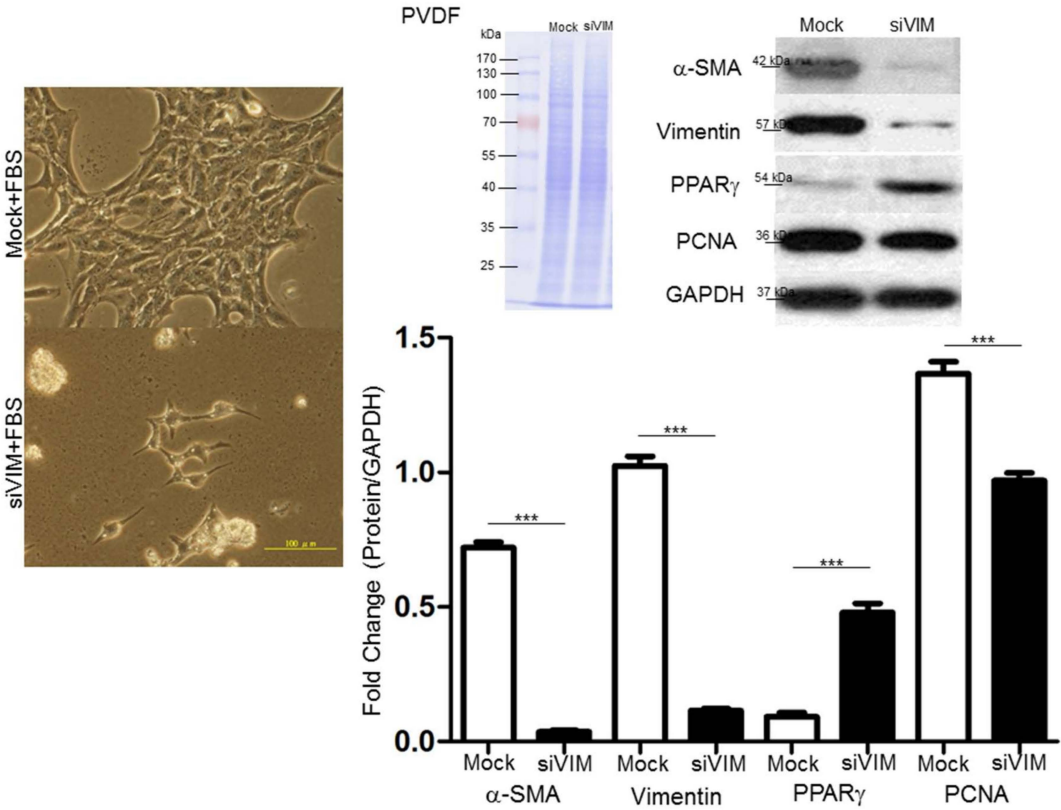
### 3.2. Plasma Levels of Vimentin between Control and Patients with Hepatic Fibrosis/Cirrhosis

To further verify the role of vimentin in the progression of hepatic fibrosis, we evaluated the levels of vimentin in the clinical plasma specimens obtained from the healthy controls and from subjects with liver fibrosis/cirrhosis. Not surprisingly, the level of vimentin in the patient sample was significantly upregulated compared with that in the control group ( $p < 0.001$ ) as shown in Figure 2, implying that vimentin may be a potential modulator in hepatic fibrosis.

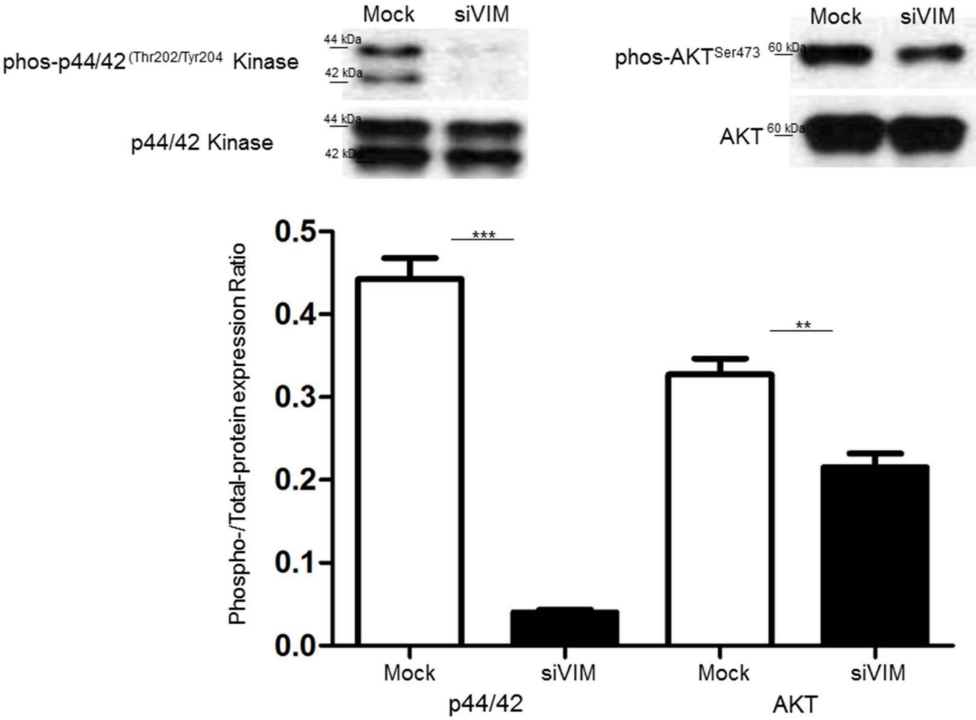






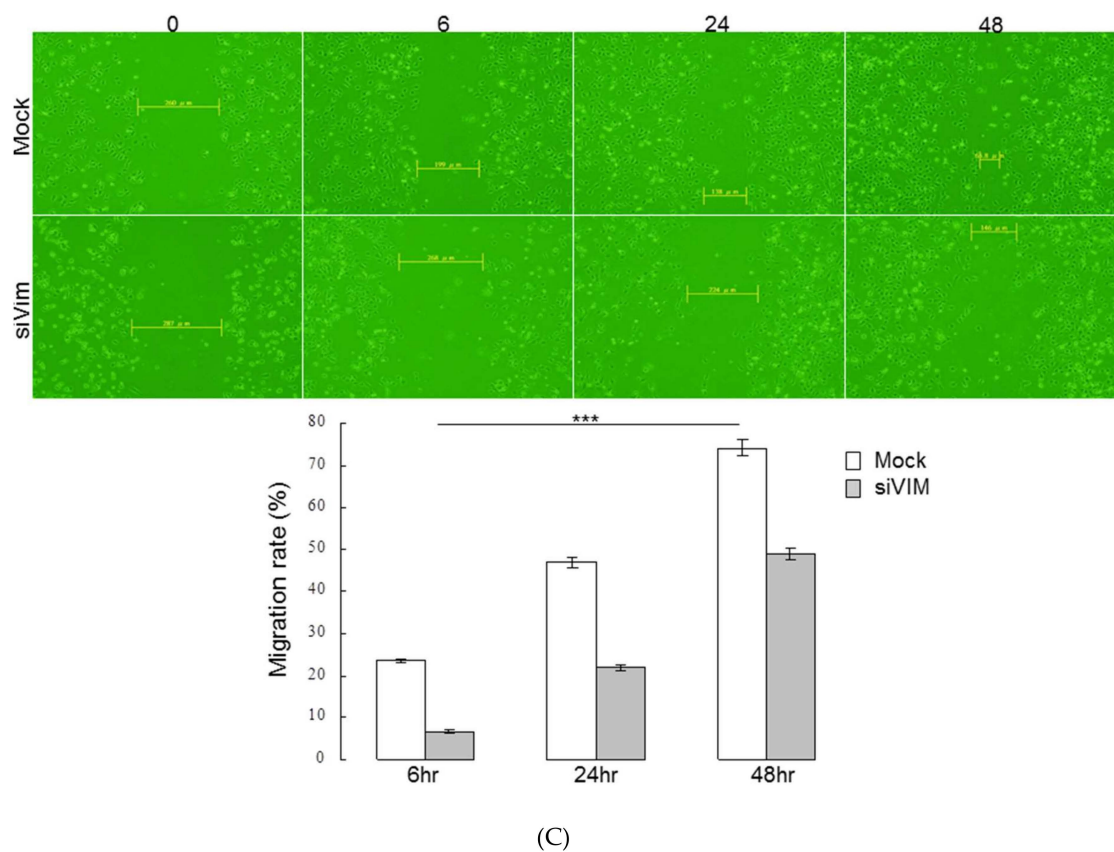


(A)

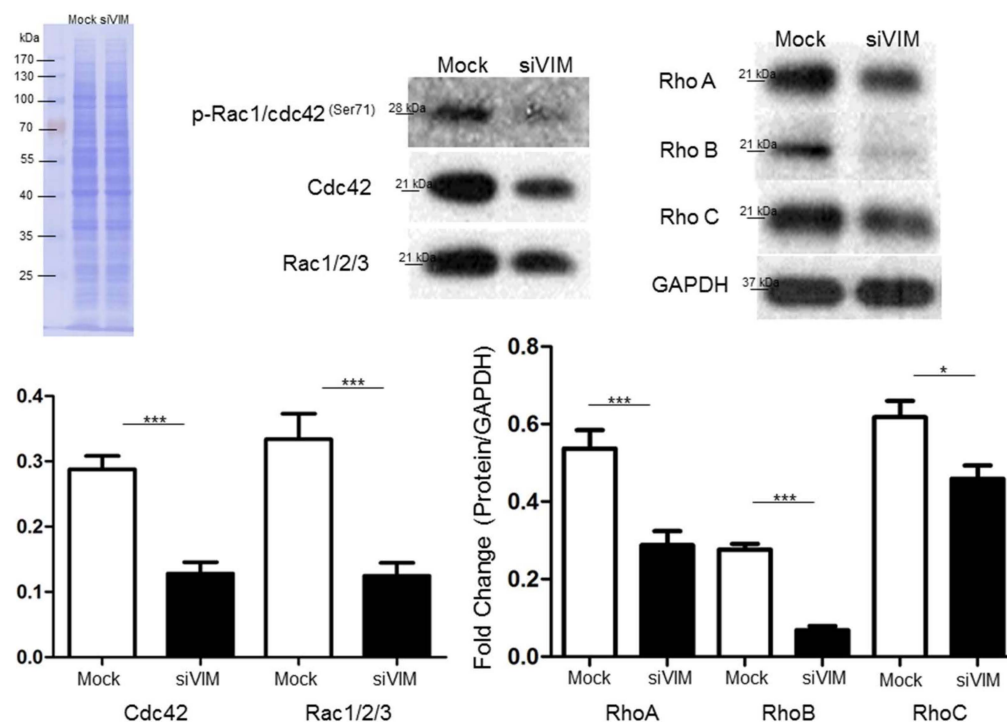


(B)

Figure 3. Cont.



(C)



(D)

**Figure 3.** (A) Validation of  $\alpha$ -SMA, vimentin, peroxisome proliferator activated receptor- $\gamma$  (PPAR $\gamma$ ) and proliferating cell nuclear antigen (PCNA) expression in hepatic stellate cell (HSC-T6 cells) applied with vimentin with RNA silencing (siVIM) or without (Mock) siVIM by Western blotting. GAPDH was used as an internal control. PVDF membrane stained with Coomassie blue R-250 was utilized to perform

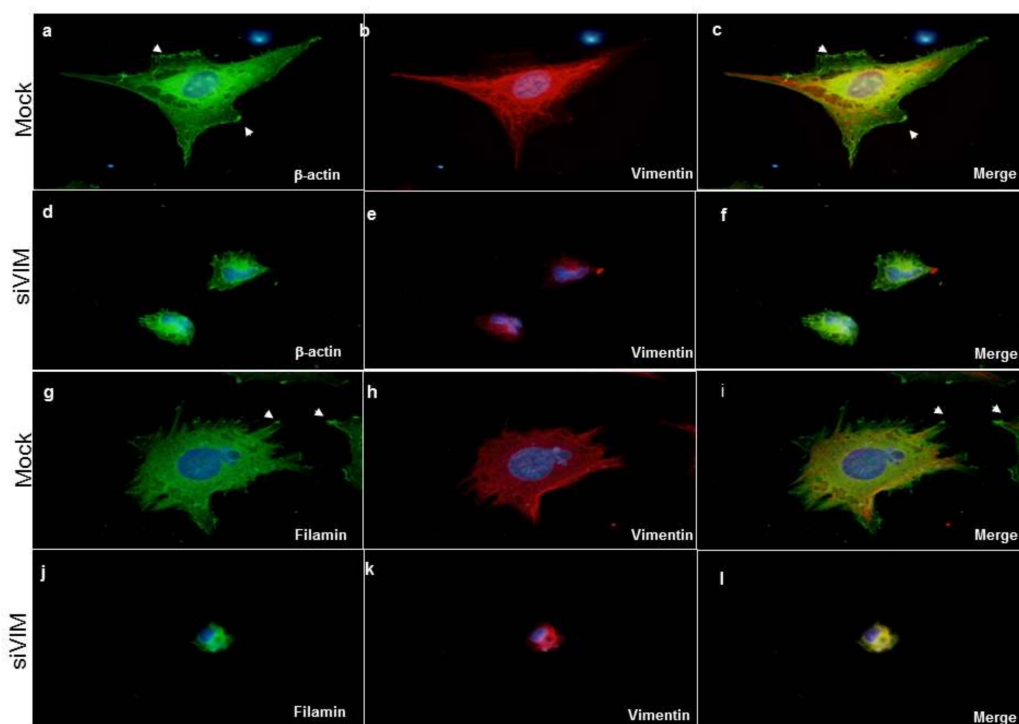
loading amount of proteins. The quantified results were indicated by the bar chart and represented the mean  $\pm$  SD of three independent experiments ( $*** p < 0.001$ ). Morphological changes of HSC-T6 cells with or without siVIM transfection by optical microscopy were demonstrated as the left figures. (B) Western blot analysis for phosphorylation and total protein levels of mitogen-activated protein kinases (MAPK) and protein kinase B (AKT) in HSC-T6 cells after administrating with or without siVIM. The quantification of phosphorylation in each lane was normalized by total protein levels ( $** p < 0.01$ ,  $*** p < 0.001$ ). (C) Knockdown of vimentin retarded wound closure. Representative phase-contrast micrographs of closure of scratch-wounded confluent cultures of mock- or siVIM-transfected HSC-T6 cells at a time point immediately after wounding and 24 h post-wounding. The migration rate was calculated by the percentage (%) and indicated with the bar chart ( $*** p < 0.001$ ). (D) Western blot analysis for phosphorylation and total protein levels of Cdc42, Rac1/2/3, and Rho A/B/C in HSC-T6 cells after administrating with or without siVIM. The quantification of phosphorylation in each lane was normalized by total protein levels. GAPDH was used as an internal control. The quantified results were indicated by the bar chart and represented the mean  $\pm$  SD of three independent experiments ( $* p < 0.05$ ,  $*** p < 0.001$ ).

### 3.4. Verification of Vimentin-Dependent Regulation of Cytoskeletal Proteins

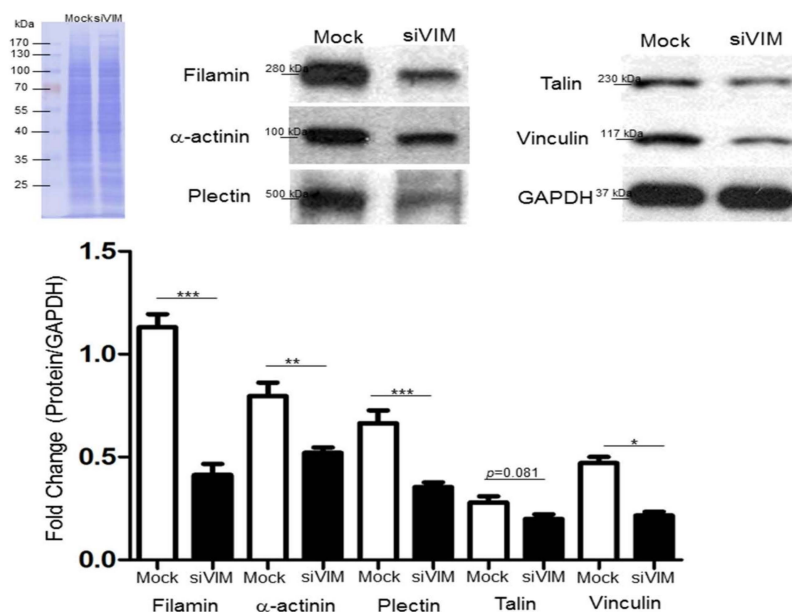
Next, we observed that vimentin was highly expressed at the leading edge of migrating cells and the vimentin-based scaffolding protein recruited other cytoskeletons such as actin to stabilize the structure required for HSC migration as well as related signaling transduction. Diminishment of vimentin by siVIM entirely abrogated the cytoskeletal restructuring and reorganization, leading to the cells' deficiency in protrusion, migratory property, and various processes during HSC activation. In addition, vimentin knockdown also interfered with the complete architecture of the focal adhesion complex involved in binding cells to the extracellular matrix (ECM). As expected, siVIM destroyed the whole constitution of the focal adhesion complex, suggesting the central role of vimentin in HSCs' architecture maintenance, contraction, and movement (Figure 4A). The aforementioned results supported the idea that vimentin should be involved in cell migration as an organizer and might also subsequently modulate other cytoskeletal proteins. Western blot analysis showed notable decreases in the levels of filamin A,  $\alpha$ -actinin, plectin, talin, and vinculin compared to the control (Figure 4B), implying that siVIM may inhibit cell invasion by undermining the expression and reorganization of various cytoskeletal proteins. The loading control for Western blot analysis indicated that an equal amount of protein was applied.

### 3.5. Intracellular Signaling of ERK, AKT and Rho Affecting HSC Proliferation and Motility

To extend the details in the activation of relevant pathways and subsequent HSCs' activation, inhibitors of ERK, PI3K/AKT, and Rho were applied. The inactivation of the ERK signal strongly suppressed the expression of p-p44/42<sup>Thr202/Tyr204</sup> MAP kinase without affecting the PI3K/AKT and Rho cascades. On the other hand, the specific Rho inhibitor not only inhibited the level of correlated components such as p-Rac1/cdc42<sup>Ser71</sup> but also significantly downregulated the expression of p-AKT<sup>Ser473</sup>, indicating that Rho/ROCK signaling plays an important role in AKT activation. Current studies have shown that PI3K/AKT contributed to cell growth and migration. AKT inhibitor treatment resulted in the blockage of p-AKT<sup>Ser473</sup> and simultaneously decreased p-p44/42<sup>Thr202/Tyr204</sup> MAP kinase (Figure 5A). The level of the phosphorylated signal was quantitated and normalized with respect to the intensities of the corresponding total protein (Figure 5B).



(A)

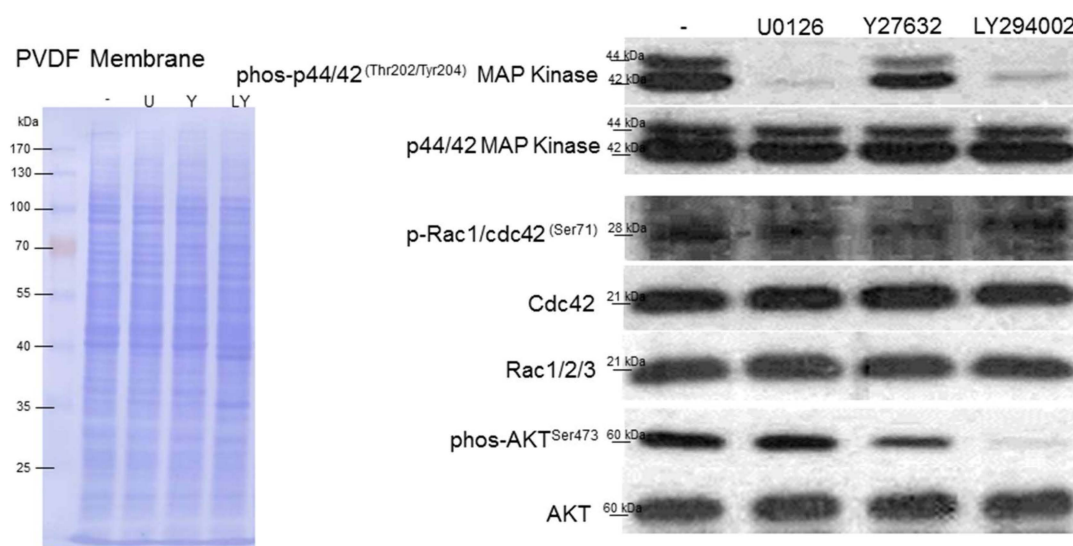


(B)

**Figure 4.** (A) Changes in architecture of hepatic stellate cells (HSCs) with or without siVIM transfection by immunofluorescence microscopy. Images of cells showed that vimentin knockdown caused the loss of actin stress fibers and disturbance of actin polymerization (**d,e,f**) compared to the mock samples (**a,b,c**) as indicated by arrows. The structure of local adhesion points which are constituted by filamin was destroyed in the presence of siVIM (**j,k,l**) with respect to the control (**g,h,i**). (B) Validation of changes in protein expression after treatment of RNA interference-mediated vimentin silencing. Protein levels of filamin,  $\alpha$ -actinin, plectin, talin, and vinculin were assessed by a Western blot analysis. GAPDH was used as an internal control. The quantitative results were demonstrated as a bar chart (\*  $p < 0.05$ , \*\*  $p < 0.01$ , \*\*\*  $p < 0.001$ ).

### 3.6. Interplays among ERK, AKT, and Rho Signaling Pathways and Different Vimentin Phosphorylated Sites

The phosphorylation of various vimentin sites is known to regulate their organization and function while the phosphorylation events are closely connected to the cellular processes, including proliferation and differentiation. To comprehensively explore the interaction among specific signaling pathways and phosphorylated sites of vimentin, the expression of p-VIM<sup>Ser39</sup>, p-VIM<sup>Ser56</sup> and p-VIM<sup>Ser83</sup> was detected under the administration of inhibitors of ERK, AKT, and Rho. Blocking ERK1/2 signaling using U0126 impaired the phosphorylation of p-VIM<sup>Ser56</sup> while the Rho inhibitor, Y27632, particularly inhibited phosphorylation on VIM<sup>Ser39</sup>. At the same time, p-VIM<sup>Ser83</sup> was significantly suppressed by the AKT inhibitor (Figure 5C). We also observed that the diminishment of different signaling pathways by inhibitors would notably change the morphology and differentiated status of HSCs. U0126 attenuated the cell proliferation and the Rho inhibitor altered the phenotype of the stress fiber in the HSCs. Interestingly, AKT suppression resulted in the overproduction of PPAR $\gamma$  and the morphology has transformed to “lipid-storing” cells in the presence of the AKT inhibitor (Figure 5D). These data reveal an integrative mechanism by which the cross talk between signaling cascades and the vimentin network may regulate the activation of the HSCs.



(A)

Figure 5. Cont.



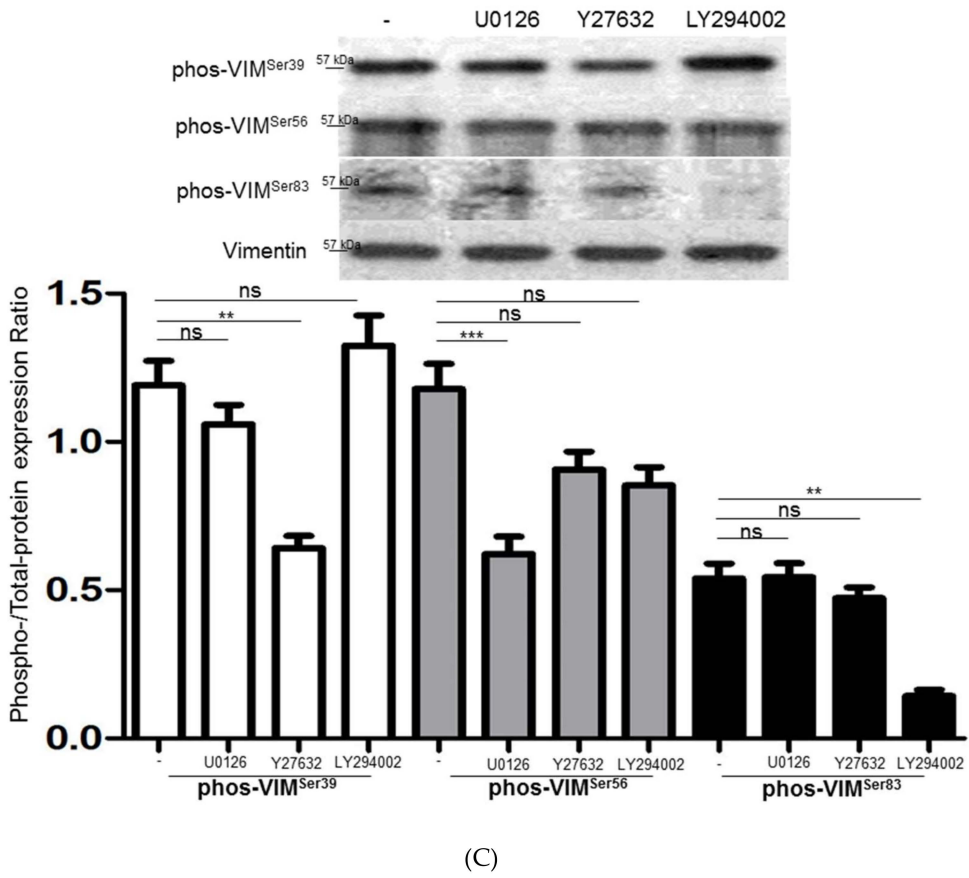
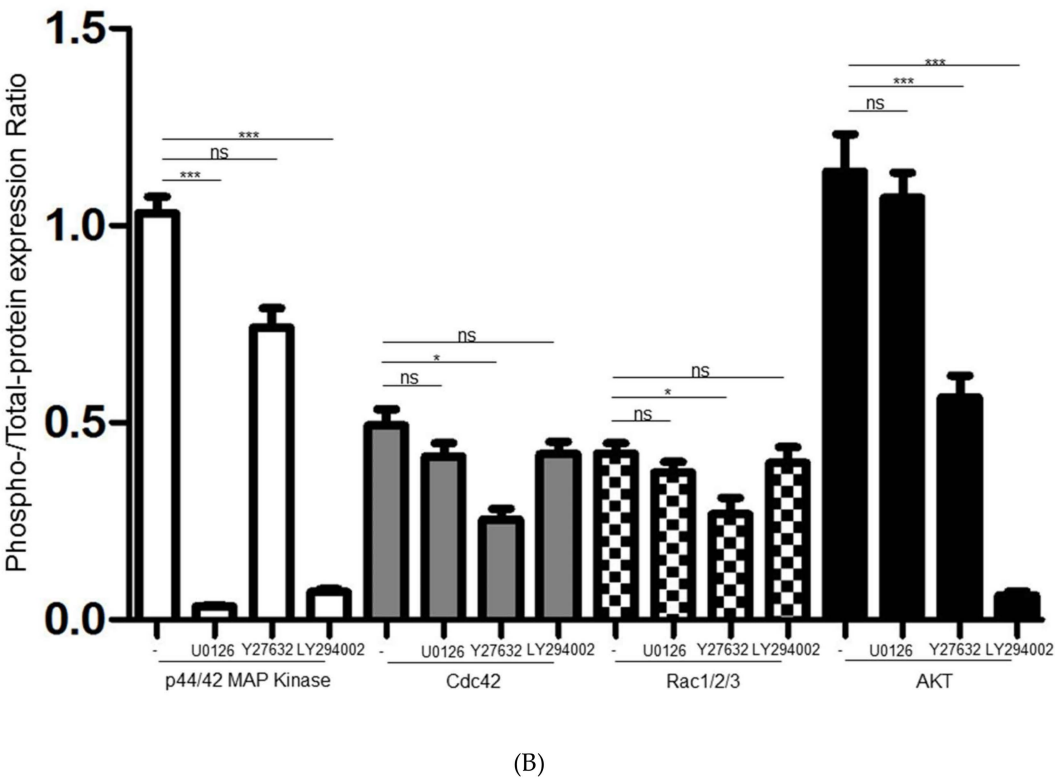
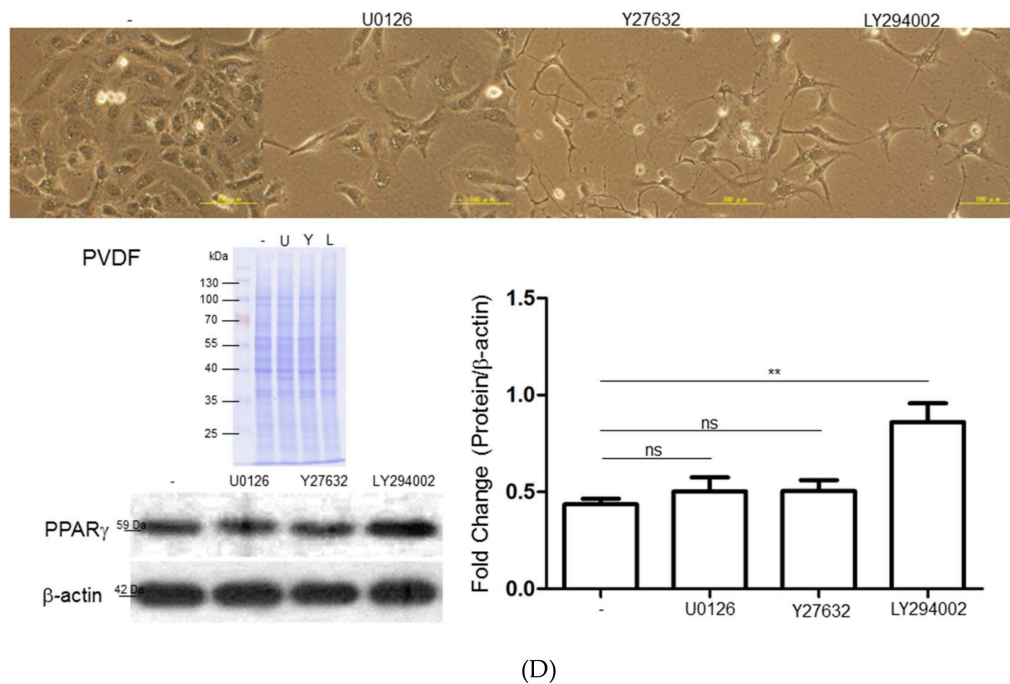


Figure 5. Cont.



**Figure 5.** (A) Western blot analysis for phosphorylation and total protein levels of ERK1/2, Cdc42, Rac1/2/3, and AKT with application of different inhibitors including U0126, Y27632, and LY294002. PVDF membrane stained with Coomassie blue R-250 was utilized to perform loading amount of proteins. (B) The phosphorylation levels were normalized by total protein levels and the corresponding results represented the mean  $\pm$  SD of three independent experiments (\* $p$  < 0.05, \*\*\* $p$  < 0.001, ns = no significance). (C) The expressed levels of various phosphorylated sites of vimentin were modulated under treatment of specific inhibitors such as U0126, Y27632, and LY294002. The quantified results were indicated by the bar chart and represented the mean  $\pm$  SD of three independent experiments (\*\* $p$  < 0.01, \*\*\* $p$  < 0.001, ns = no significance). (D) Upper panels: The morphological alteration of HSC-T6 cells treated with various inhibitors including U0126, Y27632, and LY294002. The scale bar is 100  $\mu$ m. Lower panels: The changes of PPAR $\gamma$  under exposure of different inhibitors were evaluated by Western blot analysis. The intensity of the signals was quantitated by normalizing with respect to  $\beta$ -actin used as internal controls. The quantified results were indicated by the bar chart and represented the mean  $\pm$  SD of three independent experiments (\*\* $p$  < 0.01, ns = no significance).

#### 4. Discussion

HSCs exhibit activation that transforms the quiescent cells into proliferative, fibrogenic, and contractile myofibroblasts during liver fibrogenesis [30,31]. However, the intracellular signaling pathways governing activation-mediated changes in the HSCs' morphology and motility are still unclear. Several studies have shown that the cytoskeletal system, including actin, microtubules, and IF protein such as vimentin, which is considered a hallmark of EMT, closely correlates with cell shape and motile behavior [32,33]. In the current study, vimentin was recognized as the key target for coordinating cell growth and migration during the activation of the HSCs.

The hepatic carcinogenic and mutagenic properties of DMN resulted in some liver pathological characteristics such as liver fibrogenesis and lymphocyte infiltration in a rat model [20,34]. Meanwhile, the gene and protein levels of the fibrotic markers, including  $\alpha$ -SMA, vimentin, and collagen, were simultaneously increased along with the progression of hepatic fibrogenesis. Interestingly, vimentin was chiefly observed in the activated HSCs caused by DMN application, suggesting the pivotal role of vimentin in the changes in cell shape, adhesion, and migration that occur during HSC activation. On the other hand, in areas of non-fibrotic liver tissue, vimentin immunoreactivity was almost negative. Again, our results also showed that vimentin was significantly upregulated in the plasma samples obtained from patients with liver fibrosis or cirrhosis compared to those in the control group ( $p$  < 0.001).

Current studies have revealed that vimentin is not only a feasible marker of epithelial to mesenchymal transition (EMT), but it also performs as a fundamental cytoskeletal protein and integrates external stimuli according to its dynamic property. In this regard, overproduction of vimentin may function as a structural scaffold and signaling system for HSC stimulation.

To further determine the functional roles of vimentin in modulating HSC activation, vimentin depletion with siRNAs was applied. Our results revealed that vimentin knockdown resulted in significant inhibition of PCNA and an increase of PPAR $\gamma$ , suggesting that vimentin would stimulate the proliferation and transdifferentiation of HSCs. In addition, the invasive and migratory abilities of HSCs were suppressed after siVIM application, indicating that HSC movement is clearly dependent upon the vimentin network. Moreover, the ablation of vimentin also impaired the HSCs' contractile capacities. This correlated with our findings that vimentin-negative cells showed reduced stress fiber and aberrant filopodia in migrating HSCs. In addition, we also detected that the loss of the functional vimentin network caused the breakdown of the focal adhesion that couples the ECM to the actin cytoskeleton during cell migration. The Western blot experiments indicated that the ablation of vimentin caused marked reductions in cytoskeletal proteins including filamin,  $\alpha$ -actinin, plectin, talin, and vinculin. Vimentin and actin are associated with integrins, through which the cytoskeletal proteins such as vinculin and plectin are recruited to induce Rho activity and act as a scaffold for proteins associated with the AMP-activated protein kinase signaling pathways [14,35–38]. Accordingly, our results also showed that vimentin deletion led to a great reduction in the activity of phos-p44/42<sup>Thr202/Tyr204</sup> kinase and the Rho signaling pathway. These observations emphasize the critical role of vimentin in HSC proliferation and motility.

The activation of quiescent HSC is a complex process comprising cell proliferation, transformation, movement, and ECM production, with each of these steps being triggered by various signaling pathways [10,39]. Additionally, many reports have shown that the vimentin assembly and functions are regulated by phosphorylation, and multiple phosphorylation sites have been identified on vimentin [16,40,41]. In this regard, we utilized inhibitors against specific signaling cascades to delineate the interaction as well as the regulation between vimentin and the intracellular signaling pathways. Using an inhibitor on ERK, we demonstrated that the ERK signaling pathway might be significantly involved in controlling the proliferative response of HSCs without affecting the Rho and AKT cascades via modulating p-VIM<sup>Ser56</sup>, whereas AKT blocking significantly suppressed both the ERK and AKT pathways, which subsequently induced the expression of PPAR $\gamma$ . Similarly, we observed that the treatment of the AKT inhibitor induced the activated HSC to acquire certain properties as a “fat-storing” cell [42,43], indicating that aberrant AKT signaling could regulate the differentiated status of HSCs through inhibiting cell proliferation and reverse HSC activation at the same time. Western blotting results also showed that inhibited AKT mediated by an inhibitor could downregulate the level of p-VIM<sup>Ser83</sup>.

Vimentin's enhancement of cell migration included the formation of a leading edge, lamellipodia extension, adhesion, and retraction of the trailing edge [44,45]. Cdc42 and Rac1 belonging to the Rho network are considered to be connected to the mobile ability of HSCs [46–48]. Furthermore, little is known about the relationship between the Rho signal and the specific sites of vimentin phosphorylation. Hence, a Rho inhibitor was applied. The results demonstrated that both the Rho and PI3K/AKT cascades were significantly arrested through the changing phosphorylation of VIM<sup>Ser39</sup>, which has been proven to induce vimentin filament reassembly and retraction in cells for serine phosphorylation on vimentin. It can be assumed that the upstream inhibition of Rho caused a serine phosphorylation-dependent collapse of the vimentin network, thereby disrupting the HSCs' migration and liver fibrogenesis. This conclusion was consistent with the observation that the Rho inhibitor resulted in the generation of non-phosphorylated vimentin and displayed extensive filamentous distribution.

## 5. Conclusions

In the current research, we have provided evidence that vimentin is the key factor in HSC activation due to its regulatory function in cell proliferation and motility. The ERK pathway is connected to HSC

growth through the phosphorylation of VIM<sup>Ser56</sup>. Rho signaling is closely associated with migration and vimentin assembly via the phosphorylation of VIM<sup>Ser39</sup>, and the AKT signaling cascade is linked to HSC transformation by phosphorylation on VIM<sup>Ser83</sup> (Figure 6). Vimentin also provides a major architecture for maintaining the stability of cytoskeletal proteins, which is essential for modulating the biological functions of HSCs. Our findings provide a better understanding of the intracellular signaling pathways and possible mechanisms behind the activation of HSCs. Interventions targeted at blocking the effects of these critical molecules may offer a therapeutic strategy for treating hepatic fibrosis.

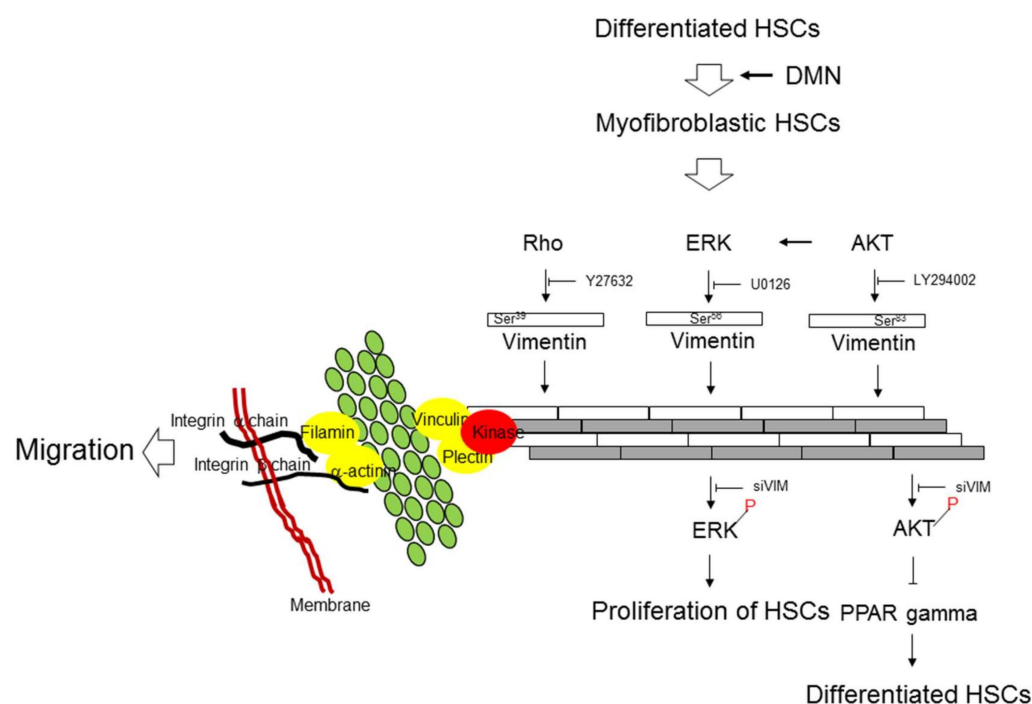


**Figure 6.** Schematic diagram indicates that the interaction between vimentin and specific signaling pathways are critically modulating the proliferation, differentiation, and migration of HSCs during liver fibrosis through the particular phosphorylated sites of vimentin.

**Supplementary Materials:** The following are available online at <http://www.mdpi.com/2073-4409/8/10/1184/s1>, Figures S1 and S2.

**Author Contributions:** P.-W.W. and T.-L.P. designed the protocol and prepared the manuscript; P.-W.W., T.-H.W., T.-Y.L., and T.-L.P. conducted the experiments; M.-H.C. evaluated the statistical analysis, and C.-T.Y. supervised the clinical study and revised the manuscript.

**Funding:** This work was supported by a grant from the Ministry of Science and Technology for Tai-Long Pan (MOST105-2320-B-182-007-MY3) and for Pei-Wen Wang (MOST 108-2320-B-182-039-006), Chang Gung Memorial Hospital (CRRPD1F0061~3, BMRP445), Taiwan.

**Conflicts of Interest:** The authors declare no conflict of interest.

## Abbreviations

$\alpha$ -SMA:  $\alpha$ -smooth muscle actin; BSA: Bovine serum albumin; Col I: Collagen type I; Col III: Collagen type III; DAPI: 4,6-diamidino-2-phenylindole; DMN: Dimethylnitrosamine; ECM: Extracellular matrix; EMT: Epithelial to Mesenchymal Transition; ERK: Extracellular-signal regulated kinase; FBS: Fetal bovine serum; GAPDH: Glyceraldehyde-3-phosphate dehydrogenase; HSCs: Hepatic stellate cells; IF: Intermediate filament; H/E: Hematoxylin–eosin; MT: Masson’s trichrome; PAKs: P21-activated kinases; PBS: Phosphate-Buffered Saline; PCNA: Proliferating cell nuclear antigen; PDGF: Platelet-derived growth factor; PPAR $\gamma$ : Peroxisome proliferator activated receptor- $\gamma$ ; RT-PCR: Reverse transcription- polymerase chain reaction; siVIM: Knockdown of vimentin with RNA silencing; TBST: Tris-buffered saline-Tween 20; TGF- $\beta$ 1: Transforming growth factor- $\beta$ 1.

## References

1. Bataller, R.; Brenner, D.A. Liver fibrosis. *J. Clin. Invest.* **2005**, *115*, 209–218. [\[CrossRef\]](#) [\[PubMed\]](#)
2. Lim, Y.S.; Kim, W.R. The global impact of hepatic fibrosis and end-stage liver disease. *Clin. Liver Dis.* **2008**, *12*, 733–746. [\[CrossRef\]](#) [\[PubMed\]](#)
3. Zhang, D.Y.; Friedman, S.L. Fibrosis-dependent mechanisms of hepatocarcinogenesis. *Hepatology* **2012**, *56*, 769–775. [\[CrossRef\]](#) [\[PubMed\]](#)
4. Baglieri, J.; Brenner, D.A.; Kisseleva, T. The Role of Fibrosis and Liver-Associated Fibroblasts in the Pathogenesis of Hepatocellular Carcinoma. *Int. J. Mol. Sci.* **2019**, *20*, 1723. [\[CrossRef\]](#) [\[PubMed\]](#)
5. Carloni, V.; Luong, T.V.; Rombouts, K. Hepatic stellate cells and extracellular matrix in hepatocellular carcinoma: more complicated than ever. *Liver Int.* **2014**, *34*, 834–843. [\[CrossRef\]](#) [\[PubMed\]](#)
6. Wong, G.L. Prediction of fibrosis progression in chronic viral hepatitis. *Clin. Mol. Hepatol.* **2014**, *20*, 228–236. [\[CrossRef\]](#) [\[PubMed\]](#)
7. Neuschwander-Tetri, B.A. Non-alcoholic fatty liver disease. *BMC Med.* **2017**, *15*, 45. [\[CrossRef\]](#)
8. Higashi, T.; Friedman, S.L.; Hoshida, Y. Hepatic stellate cells as key target in liver fibrosis. *Adv. Drug Deliv. Rev.* **2017**, *121*, 27–42. [\[CrossRef\]](#)
9. Tacke, F.; Trautwein, C. Mechanisms of liver fibrosis resolution. *J. Hepatol.* **2015**, *63*, 1038–1039. [\[CrossRef\]](#)
10. Tsuchida, T.; Friedman, S.L. Mechanisms of hepatic stellate cell activation. *Nat. Rev. Gastroenterol. Hepatol.* **2017**, *14*, 397–411. [\[CrossRef\]](#)
11. Wang, X.M.; Yu, D.M.; McCaughan, G.W.; Gorrell, M.D. Fibroblast activation protein increases apoptosis, cell adhesion, and migration by the LX-2 human stellate cell line. *Hepatology* **2005**, *42*, 935–945. [\[CrossRef\]](#) [\[PubMed\]](#)
12. Kim, J.; Jung, Y. Thymosin Beta 4 Is a Potential Regulator of Hepatic Stellate Cells. *Vitam. Horm.* **2016**, *102*, 121–149. [\[PubMed\]](#)
13. Lowery, J.; Kuczmarski, E.R.; Herrmann, H.; Goldman, R.D. Intermediate Filaments Play a Pivotal Role in Regulating Cell Architecture and Function. *J. Biol. Chem.* **2015**, *290*, 17145–17153. [\[CrossRef\]](#) [\[PubMed\]](#)
14. Tang, L.; Dai, F.; Liu, Y.; Yu, X.; Huang, C.; Wang, Y.; Yao, W. RhoA/ROCK signaling regulates smooth muscle phenotypic modulation and vascular remodeling via the JNK pathway and vimentin cytoskeleton. *Pharmacol. Res.* **2018**, *133*, 201–212. [\[CrossRef\]](#) [\[PubMed\]](#)
15. Dave, J.M.; Bayless, K.J. Vimentin as an integral regulator of cell adhesion and endothelial sprouting. *Microcirculation* **2014**, *21*, 333–344. [\[CrossRef\]](#) [\[PubMed\]](#)
16. Ivaska, J.; Pallari, H.M.; Nevo, J.; Eriksson, J.E. Novel functions of vimentin in cell adhesion, migration, and signaling. *Exp. Cell Res.* **2007**, *313*, 2050–2062. [\[CrossRef\]](#)
17. Greuter, T.; Shah, V.H. Hepatic sinusoids in liver injury, inflammation, and fibrosis: new pathophysiological insights. *J. Gastroenterol.* **2016**, *51*, 511–519. [\[CrossRef\]](#) [\[PubMed\]](#)
18. Wittmann, T.; Bokoch, G.M.; Waterman-Storer, C.M. Regulation of leading edge microtubule and actin dynamics downstream of Rac1. *J. Cell Biol.* **2003**, *161*, 845–851. [\[CrossRef\]](#)
19. Byrne, K.M.; Monsefi, N.; Dawson, J.C.; Degasperis, A.; Bukowski-Wills, J.C.; Volinsky, N.; Dobrzyński, M.; Birtwistle, M.R.; Tsyganov, M.A.; Kiyatkin, A.; et al. Bistability in the Rac1, PAK, and RhoA Signaling Network Drives Actin Cytoskeleton Dynamics and Cell Motility Switches. *Cell Syst.* **2016**, *2*, 38–48. [\[CrossRef\]](#)
20. Pan, T.L.; Wang, P.W.; Leu, Y.L.; Wu, T.H.; Wu, T.S. Inhibitory effects of Scutellaria baicalensis extract on hepatic stellate cells through inducing G2/M cell cycle arrest and activating ERK-dependent apoptosis via Bax and caspase pathway. *J. Ethnopharmacol.* **2012**, *139*, 829–837. [\[CrossRef\]](#)
21. Hsu, Y.C.; Chiu, Y.T.; Lee, C.Y.; Lin, Y.L.; Huang, Y.T. Increases in fibrosis-related gene transcripts in livers of dimethylnitrosamine-intoxicated rats. *J. Biomed. Sci.* **2004**, *11*, 408–417. [\[CrossRef\]](#) [\[PubMed\]](#)
22. Fang, J.Y.; Wu, T.H.; Huang, C.H.; Wang, P.W.; Chen, C.C.; Wu, Y.C.; Pan, T.L. Proteomics reveals plasma profiles for monitoring the toxicity caused by chromium compounds. *Clin. Chim. Acta.* **2013**, *423*, 23–31. [\[CrossRef\]](#) [\[PubMed\]](#)
23. Pan, T.L.; Wang, P.W.; Huang, C.H.; Leu, Y.L.; Wu, T.H.; Wu, Y.R.; You, J.S. Herbal formula, Scutellariae radix and Rhei rhizoma attenuate dimethylnitrosamine-induced liver fibrosis in a rat model. *Sci. Rep.* **2015**, *5*, 11734. [\[CrossRef\]](#)



24. Hsu, C.W.; Liang, K.H.; Huang, S.F.; Tsao, K.C.; Yeh, C.T. Development of a non-invasive fibrosis test for chronic hepatitis B patients and comparison with other unpatented scores. *BMC Res. Notes* **2013**, *6*, 212. [[CrossRef](#)] [[PubMed](#)]
25. Pan, T.L.; Wang, P.W.; Huang, C.C.; Yeh, C.T.; Hu, T.H.; Yu, J.S. Network analysis and proteomic identification of vimentin as a key regulator associated with invasion and metastasis in human hepatocellular carcinoma cells. *J. Proteomics*. **2012**, *75*, 4676–4692. [[CrossRef](#)] [[PubMed](#)]
26. Pan, T.L.; Wang, P.W. Explore the Molecular Mechanism of Apoptosis Induced by Tanshinone IIA on Activated Rat Hepatic Stellate Cells. *Evid. Based Complement. Alternat. Med.* **2012**, *2012*, 15. [[CrossRef](#)]
27. Van Lonkhuyzen, D.R.; Hollier, B.G.; Shooter, G.K.; Leavesley, D.I.; Upton, Z. Chimeric vitronectin:insulin-like growth factor proteins enhance cell growth and migration through co-activation of receptors. *Growth Factors*. **2007**, *25*, 295–308. [[CrossRef](#)]
28. George, J.; Tsuchishima, M.; Tsutsumi, M. Molecular mechanisms in the pathogenesis of N-nitrosodimethylamine induced hepatic fibrosis. *Cell Death Dis.* **2019**, *10*, 18. [[CrossRef](#)]
29. Tsukamoto, H.; Zhu, N.L.; Wang, J.; Asahina, K.; Machida, K. Morphogens and hepatic stellate cell fate regulation in chronic liver disease. *J. Gastroenterol. Hepatol.* **2012**, *27*, 94–98. [[CrossRef](#)]
30. Kisseleva, T. The origin of fibrogenic myofibroblasts in fibrotic liver. *Hepatology* **2017**, *65*, 1039–1043. [[CrossRef](#)]
31. Novo, E.; Cannito, S.; Morello, E.; Paternostro, C.; Bocca, C.; Miglietta, A.; Parola, M. Hepatic myofibroblasts and fibrogenic progression of chronic liver diseases. *Histol. Histopathol.* **2015**, *30*, 1011–1132. [[PubMed](#)]
32. Bernal, S.D.; Stahel, R.A. Cytoskeleton-associated proteins: their role as cellular integrators in the neoplastic process. *Crit. Rev. Oncol. Hematol.* **1985**, *3*, 191–204. [[CrossRef](#)]
33. Hohmann, T.; Dehghani, F. The Cytoskeleton-A Complex Interacting Meshwork. *Cells* **2019**, *8*, 362. [[CrossRef](#)] [[PubMed](#)]
34. Yanguas, S.C.; Cogliati, B.; Willebrords, J.; Maes, M.; Colle, I.; van den Bossche, B.; de Oliveira, C.P.M.S.; Andraus, W.; Alves, V.A.F.; Leclercq, I.; et al. Experimental models of liver fibrosis. *Arch. Toxicol* **2016**, *90*, 1025–1048. [[CrossRef](#)] [[PubMed](#)]
35. Kim, H.; Nakamura, F.; Lee, W.; Shifrin, Y.; Arora, P.; McCulloch, C.A. Filamin A is required for vimentin-mediated cell adhesion and spreading. *Am. J. Physiol. Cell Physiol.* **2010**, *298*, C221–C236. [[CrossRef](#)] [[PubMed](#)]
36. Kajita, M.; Sugimura, K.; Ohoka, A.; Burden, J.; Suganuma, H.; Ikegawa, M.; Shimada, T.; Kitamura, T.; Shindoh, M.; Ishikawa, S.; et al. Filamin acts as a key regulator in epithelial defence against transformed cells. *Nat. Commun.* **2014**, *5*, 4428. [[CrossRef](#)]
37. Jiu, Y.; Peränen, J.; Schaible, N.; Cheng, F.; Eriksson, J.E.; Krishnan, R.; Lappalainen, P. Vimentin intermediate filaments control actin stress fiber assembly through GEF-H1 and RhoA. *J. Cell Sci.* **2017**, *130*, 892–902. [[CrossRef](#)]
38. Ehrenreiter, K.; Piazzolla, D.; Velamoor, V.; Sobczak, I.; Small, J.V.; Takeda, J.; Leung, T.; Baccarini, M. Raf-1 regulates Rho signaling and cell migration. *J. Cell Biol.* **2005**, *168*, 955–964. [[CrossRef](#)]
39. Puche, J.E.; Saiman, Y.; Friedman, S.L. Hepatic stellate cells and liver fibrosis. *Compr. Physiol.* **2013**, *3*, 1473–1492.
40. Tang, D.D.; Gerlach, B.D. The roles and regulation of the actin cytoskeleton, intermediate filaments and microtubules in smooth muscle cell migration. *Respir. Res.* **2017**, *18*, 54. [[CrossRef](#)]
41. Sihag, R.K.; Inagaki, M.; Yamaguchi, T.; Shea, T.B.; Pant, H.C. Role of phosphorylation on the structural dynamics and function of types III and IV intermediate filaments. *Exp. Cell Res.* **2007**, *313*, 2098–2109. [[CrossRef](#)] [[PubMed](#)]
42. Tsukamoto, H. Fat paradox in liver disease. *Keio. J. Med.* **2005**, *54*, 190–192. [[CrossRef](#)] [[PubMed](#)]
43. Koo, J.B.; Nam, M.O.; Jung, Y.; Yoo, J.; Kim, D.H.; Kim, G.; Shin, S.J.; Lee, K.M.; Hahm, K.B.; Kim, J.W.; et al. Anti-fibrogenic effect of PPAR- $\gamma$  agonists in human intestinal myofibroblasts. *BMC Gastroenterol.* **2017**, *17*, 73. [[CrossRef](#)] [[PubMed](#)]
44. Menko, A.S.; Bleaken, B.M.; Libowitz, A.A.; Zhang, L.; Stepp, M.A.; Walker, J.L. A central role for vimentin in regulating repair function during healing of the lens epithelium. *Mol. Biol. Cell.* **2014**, *25*, 776–790. [[CrossRef](#)] [[PubMed](#)]
45. Schoumacher, M.; Goldman, R.D.; Louvard, D.; Vignjevic, D.M. Actin, microtubules, and vimentin intermediate filaments cooperate for elongation of invadopodia. *J. Cell Biol.* **2010**, *189*, 541–556. [[CrossRef](#)] [[PubMed](#)]

46. Li, L.; Wang, J.Y.; Yang, C.Q.; Jiang, W. Effect of RhoA on transforming growth factor  $\beta$ 1-induced rat hepatic stellate cell migration. *Liver Int.* **2012**, *32*, 1093–1102. [[CrossRef](#)] [[PubMed](#)]
47. Van Beuge, M.M.; Prakash, J.; Lacombe, M.; Gosens, R.; Post, E.; Reker-Smit, C.; Beljaars, L.; Poelstra, K. Reduction of fibrogenesis by selective delivery of a Rho kinase inhibitor to hepatic stellate cells in mice. *J. Pharmacol. Exp. Ther.* **2011**, *337*, 628–635. [[CrossRef](#)]
48. Iwamoto, H.; Nakamuta, M.; Tada, S.; Sugimoto, R.; Enjoji, M.; Nawata, H. A p160ROCK-specific inhibitor, Y-27632, attenuates rat hepatic stellate cell growth. *J. Hepatol.* **2000**, *32*, 762–770. [[CrossRef](#)]



© 2019 by the authors. Licensee MDPI, Basel, Switzerland. This article is an open access article distributed under the terms and conditions of the Creative Commons Attribution (CC BY) license (<http://creativecommons.org/licenses/by/4.0/>).



# Thermosensitive magnetic liposomes for alternating magnetic field-inducible drug delivery in dual targeted brain tumor chemotherapy

Yu-Jen Lu<sup>a,b,1</sup>, Er-Yuan Chuang<sup>c,1</sup>, Yu-Hsin Cheng<sup>a</sup>, Anilkumar T.S.<sup>a</sup>, Huai-An Chen<sup>a</sup>, Jyh-Ping Chen<sup>a,d,e,f,\*</sup>

<sup>a</sup> Department of Chemical and Materials Engineering, Chang Gung University, Kwei-San, Taoyuan 33302, Taiwan, ROC

<sup>b</sup> Department of Neurosurgery, Chang Gung Memorial Hospital, Kwei-San, Taoyuan 33305, Taiwan, ROC

<sup>c</sup> Graduate Institute of Biomedical Materials and Tissue Engineering, International PhD Program in Biomedical Engineering and Translational Therapies, College of Biomedical Engineering, Taipei Medical University, Taipei 11031, Taiwan, ROC

<sup>d</sup> Department of Plastic and Reconstructive Surgery and Craniofacial Research Center, Chang Gung Memorial Hospital, Kwei-San, Taoyuan 33305, Taiwan, ROC

<sup>e</sup> Research Center for Food and Cosmetic Safety, Research Center for Chinese Herbal Medicine, Chang Gung University of Science and Technology, Kwei-San, Taoyuan 33302, Taiwan, ROC

<sup>f</sup> Department of Materials Engineering, Ming Chi University of Technology, Tai-Shan, New Taipei City 24301, Taiwan, ROC

## HIGHLIGHTS

- Thermosensitive liposomes co-encapsulate magnetic nanoparticles and Camptosar.
- Conjugating Cetuximab to liposome surface enables dual targeted drug delivery.
- An alternating magnetic field controls drug release by magneto-thermal effects.
- Targeted and controlled drug delivery enhance cytotoxicity toward U87 glioma cells.
- *In vivo* therapeutic efficacy is confirmed from xenograft brain tumor model.

## ARTICLE INFO

### Keywords:

Magnetic liposome  
Thermo-sensitive  
Drug delivery  
Alternating magnetic field  
CPT-11  
Cetuximab

## ABSTRACT

The nonspecific distribution and non-targeted heating of chemotherapeutic agents in the human body commonly produce adverse side effects during brain cancer management. Even though an external magnetic field can partially gather extracellular magnetic drug carriers near brain tumor, magnetic guidance alone still cannot precisely identify and target either tumors or healthy tissues due to a lack of selectivity. In this study, we successfully developed thermal and magnetic dual-responsive thermosensitive magnetic liposomes (TML), which co-encapsulates Camptosar (CPT-11) and citric acid-coated magnetic  $\text{Fe}_3\text{O}_4$  nanoparticles within the aqueous core and surface-conjugated with Cetuximab (CET) for recognizing over-expressed epidermal growth factor receptors on cancer cell surface. This drug carrier system can control the release of encapsulated drug when exposed to a high-frequency alternating magnetic field (AMF) that elevates the temperature of the liposomal membrane and triggers drug release from TML after their selective endocytosis by cancer cells. By detailed characterizing the physico-chemical and biological properties of liposomes, we demonstrated the liposomal formulation is with high biocompatibility and showed no hemolysis *in vitro*. Enhanced intracellular uptake of TML-CPT-11-CET by human primary glioblastoma cells (U87) also supported targeted delivery through CET-mediated endocytosis. The treatment of TML-CPT-11-CET solutions by AMF *in vitro* showed rise in solution temperature and enhanced drug release, which enhanced cytotoxicity of CPT-11 toward U87 through cell apoptosis as revealed from flow cytometry analysis of apoptotic cells and Western blot studies of marker proteins. Finally, the *in vivo* therapeutic efficacy was demonstrated in mice orthotopic xenograft brain tumor model from IVIS and PET/MRI studies.

\* Corresponding author at: Department of Chemical and Materials Engineering, Chang Gung University, Kwei-San, Taoyuan 33302, Taiwan, ROC.  
E-mail address: [jpchen@mail.cgu.edu.tw](mailto:jpchen@mail.cgu.edu.tw) (J.-P. Chen).

<sup>1</sup> Y.J. Lu and E.Y. Chuang contributed equally to this work.

## 1. Introduction

Brain tumor is abnormal growth of cells in the brain or inside the skull. A high overall mortality rate would result from the prevalence of vigorous tumor types, such as glioblastoma multiforme, the most common brain cancer. Approximately 14% of new cases of brain tumors are diagnosed in persons under 20 years old. Treatment is challenging because it affects our most vital organ. Chemotherapy is commonly used in patients with high-grade brain cancer. Irinotecan, sold under the brand name Camptosar (CPT-11), can be used as a brain cancer medication [1–3]. However, different mechanisms in cancer cells, including multidrug resistance that confers resistance to one or more chemotherapeutics, hinder the efficacy of chemotherapy [4]. In current cancer therapies, an important problem in the treatment of cancer is in short of selective targeting, which can damage healthy tissues while only killing cancer cells minimally [5]. Therefore, innovative targeting strategies designed to increase cancer selectivity while preventing or minimizing accumulation in healthy tissues are needed [5–7].

Accumulation of a drug within the brain tumor environment can be achieved by external magnetic field-induced guidance technology where an external magnetic field placed near the brain tumor attracts a magnetic-fluid-loaded liposomal system after intravenous administration [8]. Magnetic liposomes have multifunctional applications, including providing image contrast during magnetic resonance imaging (MRI) [9]. Magnetic nanoparticles (MNP) loaded into thermosensitive liposomes can be used to transform electromagnetic energy from an external high-frequency field into a source of heat [10]. As well known, this ability to create heat under this proposed alternating magnetic field (AMF) makes magnetic nanomaterials a supreme heat source for biomedical uses such as cancer thermo-ablative treatment and remote control of drug release [11]. However, such thermally triggered, magnetically targeted drug-release systems are limited by inadequate magnetic gradients including the distance between the magnet and the actual target site [12]. Indeed, although externally-guided magnetic nanocarriers can partially bypass the reticuloendothelial system, they are still lacking a ‘smart’ selectivity for tumor tissues [13].

The anti-epidermal growth factor receptor (EGFR) monoclonal antibody, Cetuximab (CET), specifically binds the EGFR with a high affinity. The EGFR is concomitantly over-expressed by most brain tumors, but not by normal tissues, which explains why CET was developed specifically for brain tumor targeting [14]. As reported before, ligand-mediated targeting was bio-engineered to improve both biodistribution and tumor accumulation of chemotherapeutic nanodrugs, which resulted in higher therapeutic efficacy [15]. In addition, a targeted nanomedicine approach will be devoid of a self-propulsion ability that relies solely on passive enhanced permeability and retention (EPR)-mediated extravasation for transportation to and accumulation within the targeted tumor tissue, which was identified as a serious disadvantage [16].

Considering the limits exhibited by such a passive targeting strategy, numerous efforts have been made to develop multifunctional targeting strategy platforms [17]. In this study, we engineered a multifunctional drug delivery system for the treatment of brain cancer by combining magnetic features with ligand-mediated and thermal-triggered drug release features. The resulting nanocarrier is comprised of CET-conjugated thermosensitive magnetic liposomes (TML) entrapping CPT-11 and citric acid-coated  $\text{Fe}_3\text{O}_4$  magnetic nanoparticles (CMNP) (TML-CPT-11-CET) with dual targeting and magnetic heating-controllable drug release when CPT-11 was triggered release from the liposomal carrier under the influence of an AMF. The optimal formulation was evaluated by formulating a suitable encapsulation and loading efficiency of CPT-11 and CMNP. Intracellular trafficking of test formulations was observed using confocal laser scanning microscopy (CLSM). The *in vitro* anticancer efficacy of the test formulations was determined by measuring the apoptosis markers, phosphorylated extracellular signal-regulated kinases (phospho-ERK) and caspase-3,

extracted from treated cancer cells. Blood compatibility was assessed by evaluating if hemolysis occurred when the tested material was in contact with diluted red blood cells. Finally, *in vivo* antitumor efficacy was studied in a brain tumor-bearing mouse model using *in vivo* imaging system (IVIS) observations. PET/MRI was used to non-invasively assess anti-tumor activity of TMLs-CPT-11-CET.

## 2. Experimental section

### 2.1. Materials

All chemicals and reagents used were of analytical grade and purchased from Sigma-Aldrich (St. Louis, MO, USA) unless stated otherwise. Cell culture reagents were purchased from Life Technologies (Carlsbad, CA, USA).

### 2.2. Preparation of liposomal formulations

Magnetic nanoparticles (MNP) were prepared by chemical co-precipitation method [18]. Briefly, the mixture of  $\text{FeCl}_3 \cdot 6\text{H}_2\text{O}$  (4.75 g) with  $\text{FeCl}_2 \cdot 4\text{H}_2\text{O}$  (1.75 g) in deionized distilled (DDI) water (80 ml) was slowly increased to 60 °C in a reflux condition under a nitrogen atmosphere and then was slowly added  $\text{NH}_4\text{OH}$  (7.5 ml) and reacted for 30 min. To stabilize MNP, the surface of the MNP was modified by citrate ions to obtain citric acid-coated magnetic nanoparticles (CMNP) containing surface carboxylate groups [18]. Briefly, 2 ml of 0.5 g/ml citric acid was added to the above mixture of MNPs and reacted at 90 °C for 90 min. A hollow fiber filter was used for purification and 20 mg/ml CMNP in DDI water was stored at 4 °C for subsequent use.

Next, thermosensitive liposomes (TLs) were prepared by a thin-film hydration method and used to encapsulate CMNP and CPT-11 (TML-CPT-11). Ninety mol% dipalmitoylphosphatidylcholine (DPPC, Avanti), 5 mol% cholesterol, and 5 mol% 1,2-distearoyl-*sn*-glycero-3-phosphoethanolamine-N-[amino(polyethylene glycol)-2000] (DSPE-PEG<sub>2000</sub>-NH<sub>2</sub>, NOF) were mixed within 1 ml of chloroform/methanol (2:1 v/v) into a round-bottomed flask. The suspension was evaporated under a stream of nitrogen to generate a thin lipid film, and the dried lipid film was kept in a vacuum chamber overnight. TMLs were prepared by adding 1 ml of citric acid buffer (500 mM) containing suitable amount of CMNPs to the thin lipid film, followed by sonication and extrusion (200 nm polycarbonate filters) to reduce size. To encapsulate CPT-11 in TML (TML-CPT-11), the TML solution prepared above (1 ml) was mixed with 0.54 ml NaCl (1 M) and 0.1 ml CPT-11 by vortex and incubated at 45 °C for 20 min. The solution went through 5 freeze-thawing cycles in liquid nitrogen (1 min freezing/10 min thawing). Finally, excess impurities were removed by centrifugation at 30,000 g for 30 min.

To conjugate CET onto TML-CPT-11 (TML-CPT-11-CET), amine groups of DSPE-PEG-NH<sub>2</sub> on TML-CPT-11 surface were reacted with activated CET containing aldehyde groups. For this purpose, CET was first dissolved in DDI water (5 mg/ml, 0.8 ml) and oxidized by  $\text{NaIO}_4$  (0.2 ml, 0.1 M) for 20 min for opening of saccharide rings between vicinal diols to leave two aldehyde groups for spontaneous reaction with the amine groups. The solution was passed through a PV-10 desalting column (GE Healthcare, Milwaukee, WI, USA) to obtain purified CET-CHO. Next, purified CET-CHO (40  $\mu\text{l}$  in 0.2 M sodium carbonate buffer at pH 9.5) was reacted with TML-CPT-11 (5 mg/ml, 0.5 ml) in sodium carbonate buffer (pH 9.5) for 5 min, followed by stabilizing the covalent bonds with  $\text{NaBH}_4$  for 1 h. For this purpose, 50  $\mu\text{l}$  above mixture was placed into 1 ml  $\text{NaBH}_4$  (4 mg/ml) and stirred for 1 h at 4 °C, followed by centrifugation (30,000 g, 30 min). The amount of CMNP and CPT-11 entrapped in liposomes was measured by inductively coupled plasma optical emission spectrometry (ICP-OES, Varian 710-ES) and high performance liquid chromatography (HPLC, JASCO LC-4000 HPLC system), respectively, after breaking liposomes with Triton-100 [19,20]. The loading efficiency of CPT-11 in TML-CPT-

11 (%) is weight of encapsulated CPT-11  $\div$  weight of liposomes  $\times$  100, while the encapsulation efficiency of CPT-11 in TML-CPT-11 (%) is weight of encapsulated CPT-11  $\div$  weight of CPT-11 initially added  $\times$  100.

The CET concentration of the supernatant was quantified using the BCA protein assays kit (Bio-Rad) to calculate the amount of CET conjugated to TML-CPT11-CET. To visualize TML or TML-CET, 4.2  $\mu$ mol of 5(6)-carboxyfluorescein N-hydroxysuccinimide (NHS) ester (Nanocs Inc., New York, NY) was reacted with 100  $\mu$ g TML or TML-CET in 1 ml of 0.01 M pH 7.4 phosphate buffers for 1 h at room temperature to conjugate the NHS group with residual amine groups on liposome surface. After centrifugation at 30,000 g for 30 min, fluorescently labelled TML or TML-CET (TML-carboxyfluorescein or TML-CET-carboxyfluorescein) was obtained [21].

### 2.3. Characteristics of liposomal formulations

For Fourier transform infrared (FTIR) spectroscopy, the samples were analyzed with a Bruker TENSOR II Spectrometer (Bruker Optics, Inc., Billerica, MA) after blending with KBr from 400 to 4000  $\text{cm}^{-1}$  with a resolution of 4  $\text{cm}^{-1}$  at a scanning rate of 2.5 mm/s. The stability of liposomes was determined from the optical density (OD) values of liposomal solutions in phosphate buffered saline (PBS) at 2 mg/ml for up to 3 days. The morphology and particle size of CMNPs were observed by transmission electron microscopy (TEM) (JEOL JEM-2000 EX II, Tokyo, Japan) at an acceleration voltage of 100 kV while TML morphology was determined by cryo-TEM (JEOL JEM-1400, Tokyo, Japan) at  $-170^\circ\text{C}$  and 120 kV. For differential scanning calorimetry (DSC) analysis, 5  $\mu$ l of hydrated lipid (DPPC) or TML was put into a DSC aluminum pan and subjected to analysis (Q20 DSC, TA Instruments, New Castle, DE) under 30 ml/min nitrogen. The heating and cooling rate employed was  $5^\circ\text{C}/\text{min}$  over a temperature range from  $20^\circ\text{C}$  to  $60^\circ\text{C}$ . For X-ray diffraction (XRD) analysis, a D2 Phaser X-ray powder diffractometer (Bruker, WI) was used for scanning from  $25^\circ$  to  $70^\circ$  ( $2\theta$ ) with Cu K $\alpha$  radiation. The step size was  $0.05^\circ$  ( $2\theta$  value) per second. The phases were compared with the JCPDS database. For thermogravimetric analysis (TGA), a powder sample ( $\sim 10$  mg) was subject to TGA in a nitrogen atmosphere up to  $550^\circ\text{C}$  with a heating rate of  $10^\circ\text{C}/\text{min}$  using TGA2050 (TA Instruments, New Castle, DE). The magnetization curves of samples were obtained by using a superconducting quantum interference device (SQUID) magnetometer (MPMS XL-7, Quantum Design, San Diego, CA) at  $25^\circ\text{C}$  from  $-1000$  to  $10,000$  Gauss magnetic field. The particles size, polydispersity (PDI) and zeta potential of liposome preparations were determined by dynamic light scattering (DLS) using a Nano ZA90 Zetasizer (Malvern Instruments Ltd., Worcestershire, UK) at  $25^\circ\text{C}$ . Particles dispersions were diluted with DDI water for measurements.

The *in vitro* drug release profiles of CPT-11 from TML-CPT-11-CET (5 mg/ml) were investigated in 1 ml of phosphate buffered saline (PBS) at  $37$  or  $43^\circ\text{C}$  in dark. After shaken at 120 rpm for a specific time, the solution was centrifuged at 30,000 g for 30 min and the whole supernatant was removed for measuring the concentration of CPT-11 by high performance liquid chromatography using a 250 mm  $\times$  4.6 mm Eclipse XDB-C18 reverse phase column. The flow rate of mobile phase (40% 0.01 M pH 4 phosphate buffer + 60% acetonitrile) was 1 ml/min and detection was at 370 nm. After replenished with fresh PBS, the drug release experiment continued for calculating the cumulative drug release. As CMNP in TMLs could significantly elevate the temperature of TMLs after exposure to a high-frequency AMF, triggered release of CPT-11 from TML-CPT-11-CET in the presence of a AMF was also tested [22]. The TML-CPT-11-CET solution prepared in PBS (1 ml, 5 mg/ml) was placed in an Eppendorf tube and subject to AMF treatment in a 3.2-cm inner diameter coil at 60 A and 96 kHz to generate a heat source to loosen the liposomal structure and trigger drug release. The cumulative drug release with or without AMF treatment was calculated following the same procedure as described above. The temperature profile of the

TML-CPT-11-CET solution with or without AMF treatment was monitored from thermal images captured with a thermal camera (InfReC Thermo GEAR G100EX, Nippon Avionics Co., Tokyo, Japan) from the bottom of the tube.

### 2.4. In vitro cell culture studies

U-87 human primary glioblastoma cell line was obtained from American Type Culture Collection (ATCC HTB1, Manassas, VA, USA) and modified by lentiviral infection for stable expression of firefly luciferase to enable *in vivo* bioluminescence imaging [23]. The cell culture medium contained Dulbecco's Modified Eagle's Medium (DMEM) supplemented with 10% fetal bovine serum (FBS) and 1% penicillin/streptomycin. To monitor intracellular uptake of nanocarriers, U87 cells were seeded in a 6-well plate ( $10^5$  cells/well) and incubated for 24 h at  $37^\circ\text{C}$  in a humidified 5%  $\text{CO}_2$  incubator. After washing 3 times with sterilized PBS, 1 ml of TML-carboxyfluorescein or TML-CET-carboxyfluorescein (100  $\mu$ g/ml) in cell culture medium was added to each well and the plate was incubated for 3 h. Treated cells were washed twice with PBS before being fixed in 4% paraformaldehyde. The fixed cells were stained for cytoskeleton with Rhodamine-Phalloidin (red fluorescence) for 30 min and counter stained for cell nucleus with 4',6-diamidino-2-phenylindole (DAPI) (blue fluorescence) for 5 min before being observed by confocal laser scanning microscope (CLSM, Bio-Rad Radiance 2100MP). Possible fluorescence signals from extracellular fluorescein-labeled liposomes bound to the surface of U87 cells were quenched by trypan blue dye solution for 15 min. Identifications of nanocarriers were made possible by the green fluorescence signals from fluorescein-labeled liposomes. The excitation and emission wavelength for CLSM observation was at R/G/B = 543 nm/488 nm/364 nm and R/G/B = 550–650 nm/500–550 nm/407–482 nm, respectively. To study ligand-mediated intracellular uptake of TML-CET by binding to EGFR on U87 surface, CET blocking was carried out by treating U87 cells with 1 mg/ml CET solution for 1 h before adding TML-CET-carboxyfluorescein for CLSM observation.

To elucidate the cytotoxicity of tested samples, U87 cells were seed in a 96-well cell culture plate at a seeding density of  $2.5 \times 10^3$  cell/well and cultured for 24 h at  $37^\circ\text{C}$  in a humidified 5%  $\text{CO}_2$  incubator. After removing the culture medium, 100  $\mu$ l of test sample was added and cultured at  $37^\circ\text{C}$  (or  $43^\circ\text{C}$ ) for another 24 h. The MTS assay (Celltiter 96 $^\circ$  Aqueous One Solution Cell Proliferation Assay Kits (Promega) was then performed to measure the relative cell viability (normalized to pure cell culture medium). To study the cytotoxicity in the presence of AMF, U87 cells were seeded in a 24-well cell culture plate at a seeding density of  $1 \times 10^4$  cell/well and cultured for 24 h at  $37^\circ\text{C}$  in a humidified 5%  $\text{CO}_2$  incubator. After removing the culture medium, 500  $\mu$ l of test sample (containing 10  $\mu$ g/ml CPT-11) was added and cultured at  $37^\circ\text{C}$  for 3 h. The cells were detached from the well by treating with 1 ml of 0.1% trypsin/EDTA and placed in a 2 ml Eppendorf tubes for subsequent AMF treatment with a 3.2-cm diameter inner coil at 60 A and 96 kHz for 10 min. The same procedure was followed for the group without AMF treatment by not placing the tube in the AMF coil. The cells were transferred back to a new 24-well culture plate and cultured with culture medium for 24 h at  $37^\circ\text{C}$  in a humidified 5%  $\text{CO}_2$  incubator before determining the relative cell viability (normalized to pure cell culture medium) by the MTS assay. To study the apoptotic mechanism, cells was detached by adding 1 ml trypsin/EDTA (0.05%) and the detached cell suspension was reacted with FITC-Annexin V for 30 min and then with PI for flow cytometry analysis using FACSaria III (BD Bioscience).

To study the molecular anticancer mechanism, U87 cells were treated with test formulations and evaluated for anticancer efficacy using two cellular apoptosis markers (caspase-3 and phospho-ERK) [24,25] by Western immunoblot analysis. U87 cells ( $2 \times 10^6$ ) were seeded in a T-75 flask. After cultured for 12 h, the cells were exposed to test samples (containing 10  $\mu$ g/ml CPT-11) for 24 h at  $37^\circ\text{C}$  (or  $43^\circ\text{C}$ ).



After washing with PBS and harvesting with 0.05% trypsin/EDTA, U87 cells were treated with  $1 \times$  RIPA lysis buffer containing protease inhibitor cocktail (Thermo Fisher Scientific) for 30 min on ice to extract total protein. After centrifugation to remove cell debris, the supernatant was recovered and the protein concentration was determined by BCA protein assays. The protein was heat-denatured at 95 °C for 10 min in sample buffer and an aliquot of cell lysates ( $\sim 25$   $\mu$ g total protein/lane) was separated by sodium dodecyl sulfate polyacrylamide gel electrophoresis at 50 V for 30 min and then at 110 V for additional 2 h. The gels were transferred to polyvinylidene fluoride membrane, blocked with 5% fat-free milk for 1 h for nonspecific binding and blotted with anti-caspase 3 (Gene Tex GTX110543, rabbit anti-caspase 3 antibody, 1:1000), anti-phospho-ERK (Thermo Fisher Scientific MA5-15173, rabbit anti-phospho-ERK1/ERK2 (Thr202, Tyr204) monoclonal antibody, 1:1000) and anti- $\beta$ -actin (Sigma-Aldrich A2066, rabbit anti- $\beta$ -actin antibody, 1:10000) primary antibodies for 12 h at 4 °C. After probing with horseradish peroxidase-conjugated secondary antibodies (Sigma-Aldrich A0543 anti-rabbit IgG-HRP, 1:10000) and color development with ECL Western blotting substrate, the immune complexes were detected using a MultiGel-21 image system (Top Bio Co., Taiwan) and densitometric analysis of specific bands was performed using the ImageJ software (National Institute of Health, Bethesda, MD, USA).

## 2.5. *In vitro* hemolysis study

In the hemolysis assay, red blood cells (RBCs) from SD rats were separated from the plasma by centrifugation at 3000 g and diluted ten times with PBS. Test materials prepared in PBS were co-incubated with diluted RBCs for 2 h at 37 °C with gentle mixing [26]. Following centrifugation at 3000 g to sediment intact RBCs, the amount of released hemoglobin was determined using a UV–VIS spectrophotometer and the optical density (OD) values were determined from 500 to 600 nm for comparison with the negative control (PBS) or the positive control (DDI water).

## 2.6. Orthotopic xenograft brain tumor mouse model

Balb/c nude mice (6–8 weeks old) were purchased from the BioLASCO (Taipei, Taiwan). The Institutional Animal Care and Use Committee of Chang Gung University approved the study protocol. Using a 26-gauge needle, 100  $\mu$ l of cell culture medium containing  $1 \times 10^6$  U87 cells was administered intracranially in the right intracranial region of each mouse to a 3-mm depth. Mice bearing U87 tumors were used for *in vivo* evaluation of temperature profiles after AMF treatment and antitumor efficacy when the average bioluminescence imaging (BLI) intensity of tumors reached  $\sim 1 \times 10^7$  (11 days post-implantation).

## 2.7. *In vivo* temperature profiles induced by AMF

Eleven days post-implantation, tumor-bearing mice were used for *in vivo* evaluation of AMF treatment effect by determining the temperature profile in the tumor area. Each tumor-bearing mouse was injected with 200  $\mu$ l of saline (control) or TML-CPT-11-CET (30 mg/kg CPT-11) through the tail vein and subjected to magnetic guidance for 30 min with a magnet, followed by AMF treatment up to 15 min in a 3.2-cm inner diameter coil at 60 A and 96 kHz. The temperature profile around the tumor area was determined from thermal images captured with an infrared (IR) thermal camera (InfReC Thermo GEAR G100EX, Nippon Avionics Co., Tokyo, Japan) at different AMF treatment times.

## 2.8. *In vivo* antitumor efficacy

The tumor-bearing mice were randomly divided into seven groups ( $n = 6$ ) and each mouse was subject to intravenous (IV) injection of 200  $\mu$ l of test sample through the tail vein on day 11. The study groups

include: 1, saline (control); 2, CPT-11 (30 mg/kg); 3, TML-CET; 4, TML-CPT-11 (30 mg/kg CPT-11); 5, TML-CPT11-CET (30 mg/kg CPT-11); 6, TML-CPT11-CET (30 mg/kg CPT-11) with magnetic guidance for 30 min with a magnet; 7, TML-CPT-11-CET (30 mg/kg CPT-11) with magnetic guidance for 30 min with a magnet followed by AMF treatment (60 A and 96 kHz in a 3.2-cm inner diameter coil) for 15 min. The same treatment was given on day 14 and 17 post-implantation of U87 cells for each group.

On day 21 post-implantation of U87 cells, the mice were anesthetized with 1% isoflurane followed by injection of 200  $\mu$ l of D-luciferin solution intraperitoneally at a dose of 150 mg luciferin/kg body weight. The bioluminescence imaging (BLI) was performed using noninvasive *in vivo* imaging system (IVIS) (Xenogen IVIS-200, Caliper Life Sciences, Hopkinton, MA, USA) to determine the peak bioluminescence. The BLI intensity was determined by measuring the total bioluminescent signal intensity in the tumor and quantified with the Living Image® 4.0 software (PerkinElmer, Waltham, MA, USA). The BLI standardization was calculated from the total bioluminescent signal intensity at day 21 after normalized with the total signal intensity when treatment started (day 11) [27].

The survival experiment was done on a separate group of animals as the process of transporting and anesthetizing the mice for bioluminescence imaging may have a significant negative effect on mouse survival regardless of treatment strategy. The intracranial tumor establishment, tumor growth and treatments were the same as described previously ( $n = 9$  to 11). All mice used for therapy evaluation were observed daily and euthanized after they reached a moribund condition as body weight loss more than 25% of initial measurement, hunched back, hemiparesis or seizure.

## 2.9. *In vivo* PET/MRI study

The relaxivity of magnetic resonance imaging (MRI) was obtained by a Siemens 3.0 Tesla scanner (Magnetom Trio, Siemens, Munich, Germany) with a wrist coil. Test mice were given Gd-DTPA (300  $\mu$ l; OMNISCAN®, Nycomed Imaging, Oslo, Norway) before the study. Test mice were treated with TML-CET (control group) and TML-CPT-11-CET with magnetic guidance plus AMF treatment (treatment group) as described above. Test animals were anesthetized under isoflurane inhalant during the MRI examination on day 14, 17 and 21. Imaging parameters used for the T1\* sequence were as follows: (gradient echo, TR/TE: 230/3.81 ms, flip angle: 70, and slice thickness: 0.5 mm). For the positron emission tomography (PET) study, mice used in the MRI study were then anesthetized under isoflurane (2% in 100% O<sub>2</sub>), before approximately 12 MBq of 2-deoxy-2-[fluorine-18]fluoro-D-glucose (<sup>18</sup>F-FDG) in 100  $\mu$ l of saline was injected into a tail vein. Visual image acquisition using a PET scanner was conducted after <sup>18</sup>F-FDG administration (Siemens Medical Solutions, Knoxville, TN, USA).

## 2.10. Statistical analysis

All results are presented as the mean  $\pm$  standard deviation (SD). To compare means of pairs of groups, Student's *t*-test was used. Differences were considered to be significant at  $p < 0.05$ .

# 3. Results and discussion

## 3.1. Characteristics of the liposomal formulations

As smart formulations of active substances are a crucial step in drug discovery and development, we started by finding an optimal formulation of CPT-11 in TML-CPT-11. The loading and encapsulation efficiency of CPT-11 in TML-CPT-11 was reported in Fig. 1a when different CPT-11 concentration was used for drug loading with 0.05 mg/ml CMNP. Using a higher drug concentration, the drug loading efficiency (percentage of CPT-11 in TML-CPT-11) increased from

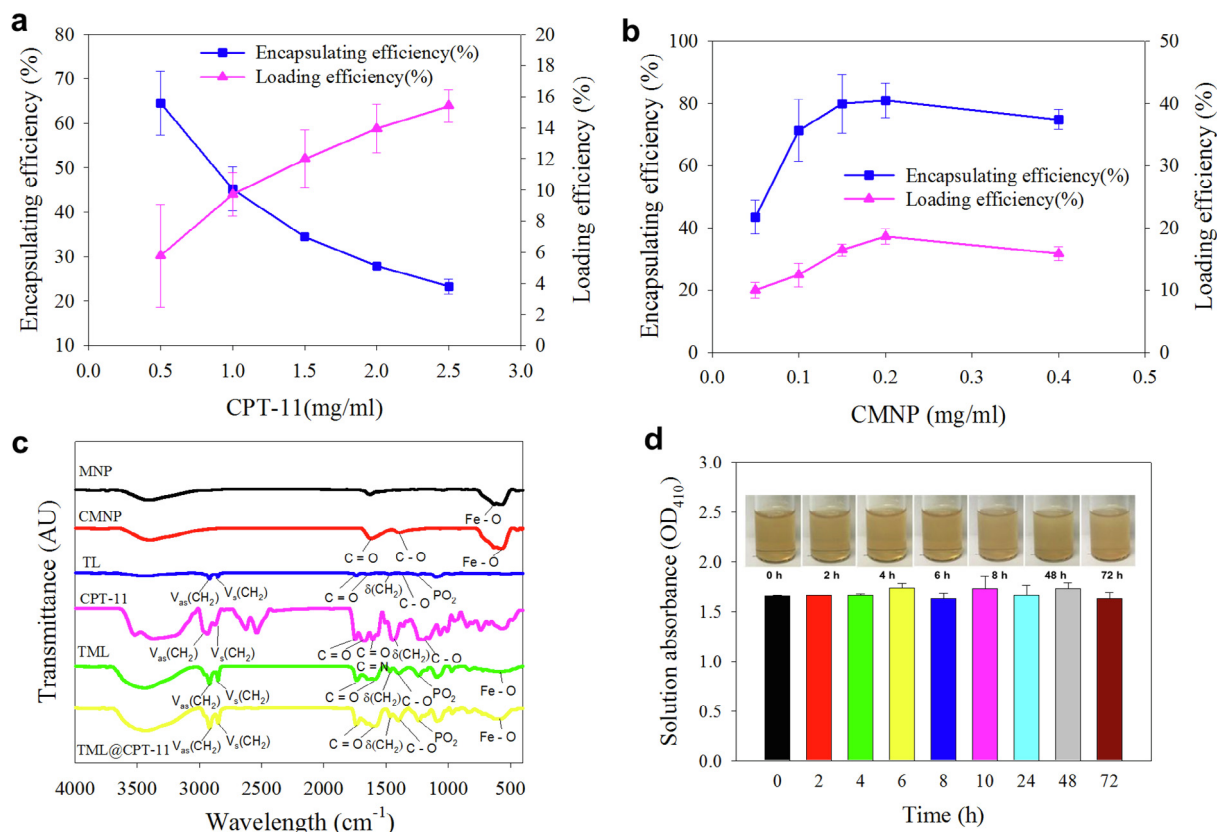


**Fig. 1.** (a) The effects of CPT-11 concentration on encapsulation efficiency and loading efficiency of CPT-11 in CPT-11 encapsulated thermosensitive magnetic liposome (TML-CPT-11) with 0.05 mg/ml citric acid-coated magnetic particles (CMNP). (b) The effects of CMNP concentration on encapsulation efficiency and loading efficiency of CPT-11 in TML-CPT-11 with 1 mg/ml CPT-11. (c) Characterization of Fe<sub>3</sub>O<sub>4</sub> magnetic nanoparticles (MNP), CMNP, thermosensitive liposome (TL), CPT-11, thermosensitive magnetic liposome (TML) and TML-CPT-11 by Fourier transform infrared (FTIR) spectroscopy. (d) The suspension stability of TML-CPT-11-CET (2 mg/mL) in PBS from gross view and by measuring solution absorbance at 410 nm.

5.77% ± 3.3% to 15.4% ± 1.0%. Nonetheless, the encapsulation efficiency (percentage of initial amount of CPT-11 loaded in liposomes) decreased from 64.6% ± 7.2% to 23.3% ± 1.6%. Therefore, a dramatic increase in drug loading efficiency resulted in a detrimental decrease in the encapsulation efficiency. To get a suitable formulation, an ideal tradeoff between the drug loading efficiency and encapsulation efficiency was thus calculated, leading us to select an optimal, economical concentration of 1 mg/ml CPT-11, which provided 9.7% ± 1.4% loading efficiency and 45.2% ± 5.0% encapsulation efficacy. Similarly, Fig. 1b shows that the encapsulation of CPT-11 in TML-CPT-11-CET could be obtained at 0.2 mg/ml CMNP with 1 mg/ml CPT-11, which provided the maximal loading efficiency (18.6% ± 1.3%) and encapsulation efficacy (81.0% ± 5.5%) simultaneously. Although some CPT-11 might be leaching out during the step when CET was conjugated to TML-CPT-11, we confirmed the loading efficiency of CPT-11 in TML-CPT-11-CET was similar to TML-CPT-11 at 18.1%. This preparation was used in the following studies.

The FTIR spectra in Fig. 1c further confirmed successful preparation of TML and TML-CPT-11. For MNP, the presence of Fe<sub>3</sub>O<sub>4</sub> could be confirmed by the strong absorption band at 571 cm<sup>-1</sup>, which corresponds to the Fe–O bond in the nanoparticles. The characteristic peaks of CMNP at 1387 and 1645 cm<sup>-1</sup>, corresponding to the symmetric vibration and asymmetric stretching of C–O from –COOH group and C=O from –COOH provides a direct evidence to support that citric acid was successfully coated onto the MNP surface. Furthermore, TML and TML-CPT-11 showed the Fe–O characteristic peak of CMNP at 575 cm<sup>-1</sup> in addition to the characteristic peaks of TL, liposomes of the same composition as TML but without CMNP, at 1242 cm<sup>-1</sup> (–PO<sub>2</sub>), 1471 cm<sup>-1</sup> δ(CH<sub>2</sub>), 2849 cm<sup>-1</sup> ν<sub>s</sub>(CH<sub>2</sub>) and 2926 cm<sup>-1</sup> ν<sub>as</sub>(CH<sub>2</sub>). Since nanoparticles are intended to be used for *in vivo* treatments, it is important to

clarify their suspension stability [28]. We therefore tested the dynamic stability of TML-CPT-11-CET in PBS. Fig. 1d shows that the TML-CPT-11-CET formed a well-dispersed solution for at least 72 h without visible precipitation and change in solution absorbance under physiological conditions, suggesting its suitability for intravenous administration. The stability of TML-CPT-11-CET was also confirmed in serum (Fig. S1, Supplementary material).

The amount of CET in TML-CPT-11-CET was estimated to be 87.1 ± 2.3 μg/mg from protein assays. The CET graft rate in this drug delivery system was calculated to be 16%. From DLS analysis in Fig. 2a, TML-CPT11-CET showed sharp particle size distribution with average particle size of 193.7 ± 2.3 nm, which was significant different from TMLs (147.8 ± 5.3 nm) and TML-CPT-11 (154.3 ± 2.3 nm). The polydispersity index (PDI) values were 0.16 ± 0.04, 0.14 ± 0.02 and 0.22 ± 0.01 for TML, TML-CPT-11 and TML-CPT-11-CET, respectively. The zeta potential of CMNP was –43.6 ± 1.6 mV due to the negatively charged carboxylate groups. The zeta potential changed to –1.23 ± 0.10 mV, 1.29 ± 0.26 mV and 2.3 ± 0.1 mV for TML, TML-CPT-11 and TML-CPT-11-CET, respectively, indicating successful encapsulation of CMNPs in TML and conjugation of CET onto TML-CPT-11 surface due to the slight positive charge of CET (isoelectric point = 8.5) [29]. The structure of TML characterized by cryo-TEM showed spherical morphology with ~150 nm size, which is consistent with that from DLS analysis, with few discrete CMNP in the aqueous core and enclosed within a lipid bilayer (Fig. 2b). The DSC calorimetric profiles of DPPC showed two characteristic peaks, a broader and lower peak at 36.5 °C and a sharp and higher one at 41.9 °C (Fig. 2c). The first peak could be attributed to a low enthalpy transition due to mobility of the choline polar head of DPPC; in contrast, the second peak indicated the main enthalpy transition arising from the mobility of the alkyl chains in

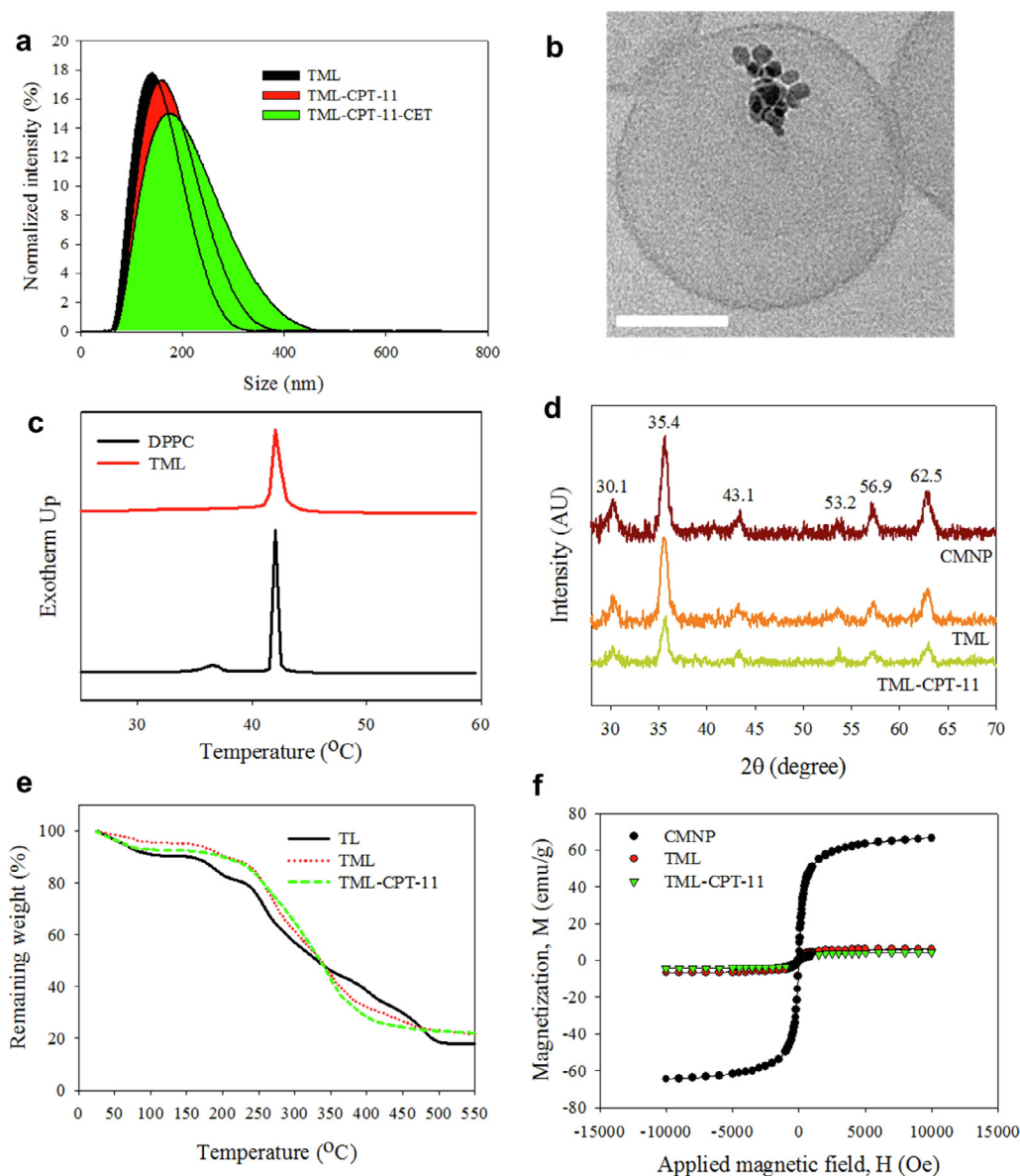


**Fig. 2.** (a) Particle size distribution curves of TML, TML-CPT-11 and TML-CPT-11-CET. (b) The structure of TML by cryo-TEM analysis (bar = 50 nm). (c) The differential scanning calorimetry (DSC) thermograms of dipalmitoylphosphatidylcholine (DPPC) lipid and thermosensitive magnetic liposomes (TML). (d) Characterization of CMNP, TML and TML-CPT-11 by X-ray diffraction (XRD) patterns. (e) Thermogravimetric analysis (TGA) of thermosensitive liposomes (TL), TML and TML-CPT-11. (f) The superconducting quantum interference device (SQUID) magnetization curves of CMNP, TML and TML-CPT-11.

the lipid [30]. The thermosensitive nature of TMLs could be revealed from its major peak temperature shown at 42.1 °C, which is similar to DPPC but increased slightly originating from the 5 mol% cholesterol present in the lipid bilayer [31]. The disappearance of the pre-transition peak in TML may be due to the influence of cholesterol in the liposomes.

The XRD patterns of CMNPs, TML and TML-CPT-11 are illustrated in Fig. 2d. All samples showed six diffraction peaks at  $2\theta = 30.1^\circ$ ,  $35.4^\circ$ ,  $43.1^\circ$ ,  $53.2^\circ$ ,  $56.9^\circ$ , and  $62.5^\circ$ , representing (2 2 0), (3 1 1), (4 0 0), (4 2 2), (5 1 1), and (4 4 0) indices, respectively, which is consistent with the crystal structure of magnetite (JCPDS card number 19-0629). In addition, the average grain sizes of magnetite calculated from the Debye-Scherrer equation by the highest diffraction peak at  $2\theta = 35.4^\circ$  were similar at 10.5 nm, 10.3 nm and 10.4 nm for CMNP, TML and TML-CPT-11, respectively. From the TGA curves shown in Fig. 2e, all samples showed small weight losses initially below 200 °C as adsorbed  $\text{CO}_2$  and water decomposed. At temperatures above 200 °C, TML and TML-CPT-11 showed similar but distinct decomposition behavior from

TL (prepared with the same composition as TML but without CMNP) due to the decomposition of lipids. The weight percentage of CMNP in TML (TML-CPT-11) could be calculated to be 4.7% (4.6%) from the difference of remaining weight between TML (TML-CPT-11) and TL at 550 °C. These values correlated well with those from ICP-OES measurements at 4.6% (4.2%). The results of SQUID analysis at room temperature indicate a saturation magnetization value of 6.2 emu/g for TML and 4.3 emu/g for TML-CPT-11, which is lower than that of CMNP (66.6 emu/g) (Fig. 2f). It is foreseeable that the saturation magnetization would be greatly diminished in TML and TML-CPT-11 due to the diamagnetic contribution of the lipid bilayer surrounding the magnetite in addition to the low weight percentage of CMNP in TML and TML-CPT-11. The superparamagnetism behavior observed from the magnetization curve, where both remanence and coercive force were close to zero, endowed the possibility to use TML-CPT-11 for magnetic targeted delivery for drugs [32].

### 3.2. Intracellular uptake

Ligand-decorated liposomes, which are specific for cancer cell surface receptors, are gaining importance for drug delivery, considering that their involvement in cellular uptake mechanisms can amplify therapeutic responses. A novel approach for targeting toward over-expressed cell surface receptors on cancer cells is through the use of antibodies or receptor-specific ligands [33]. Indeed, active targeting *via* cell-surface receptors has been widely explored in cancer therapeutics since many cancer cell types exhibit upregulation of tumor-specific receptors. For instance, EGFR is highly over-expressed in many tumor cell types, including brain cancer, in response to their increased metabolic demands. In this case, we expected that the designed carrier system after CET conjugation would be able to selectively bind onto the surface of U87 glioblastoma cell line (with rich EGFR) and thus facilitate cellular trafficking through ligand-mediated endocytosis for enhanced therapeutic effects [34]. To prove this hypothesis, confluent U87 cells attached to 6-well tissue culture plates were first treated with CET to occupy and block their cell surface EGFR as a control. After treatment with fluorescent TML-CET, the control group showed limited TML-CET fluorescence signals through CLSM, suggesting that pre-treatment with CET saturated the EGFR on the plasma membrane, rendering them inaccessible to TML-CET (Fig. 3). Thus, CET may promote high-affinity specific binding of test liposomes to EGFR, thereby enhancing their subsequent cellular uptake *via* an endocytosis pathway. Conversely, without prior EGFR blocking, the group treated with TML-CET showed increased fluorescence, revealing a considerably stronger cellular uptake necessary to enhance intracellular internalization. In comparison, when U87 cells were treated with fluorescent TML, only limited cellular internalization at the end of the same incubation period could be observed. Flow cytometry analysis further reveals of the effects of CET conjugation on intracellular uptake through analysis of CPT-11 accumulation in U87 (Fig. S3, Supplementary material) and intracellular uptake rate of TML-CET (Fig. S4, Supplementary material).

### 3.3. *In vitro* drug release

A potential active targeting strategy that utilizes subtle pathological

changes in the tumor microenvironment should be thoughtfully engineered to improve the efficiency of liposomal drug release [35]. Ideally, stimulus sensitivity should be responsive to certain features of the tumor microenvironment, including a lower pH, a higher temperature, and overexpression of several proteolytic enzymes or proteins [36]. Stimulus-sensitive liposomes maintain their structure and physical properties when in the circulation. However, they are engineered to sense rapid changes (disruption, permeability and transformation) that trigger drug release when subjected to a particular tumor microenvironment. These stimuli can be external magnetic fields, ultrasound, or light, to trigger the release of a drug by the test liposome close to tumor tissues.

Thermosensitive liposomes (TL) can be formulated from thermosensitive lipids or polymers with a low phase transition temperature. Once a heat source provided to increase the environmental temperature exceeds the transition temperature of TL, the structure of the TL is transformed and is disrupted to release the drug. For example, heat (above 40 °C) provided by AMF can cause transformation of TL as DPPC in the liposomal ingredients has a transition temperature of 41.9 °C (Fig. 2c). As shown in Fig. 4a, only ~22% CPT-11 was released from TML-CPT-11-CET after 30 min incubation at 37 °C whereas 58% drug was released after 24 h. In contrast, burst release of CPT-11 from TML-CPT-11-CET was observed immediately following an increase in the environmental temperature to 43 °C with quantitative recovery of CPT-11 in the release medium after 1 h. Further drug release experiments were carried out under AMF treatment, which induced magnetic thermal effects for thermo-responsive drug release to simulate *in vivo* drug release. As shown in Fig. 4b, ~19% CPT-11 was released after 15 min in the absence AMF, in contrast to a plateaued ~97% drug release in the presence of AMF. The *in vitro* photothermal effects of TML-CPT-11-CET with AMF treatment was monitored using an infrared thermal camera (Fig. 4c) with peak solution temperatures acquired from the images as a function of AMF treatment time shown in Fig. 4d. There was no obvious temperature change observed when PBS was exposed to AMF for 30 min. In comparison, under the same condition but with AMF treatment, the solution temperature reached 42.7 °C and 45.5 °C in 15 min and 30 min, respectively, which is consistent with the AMF-dependent CPT-11 drug release profile in Fig. 4b. These

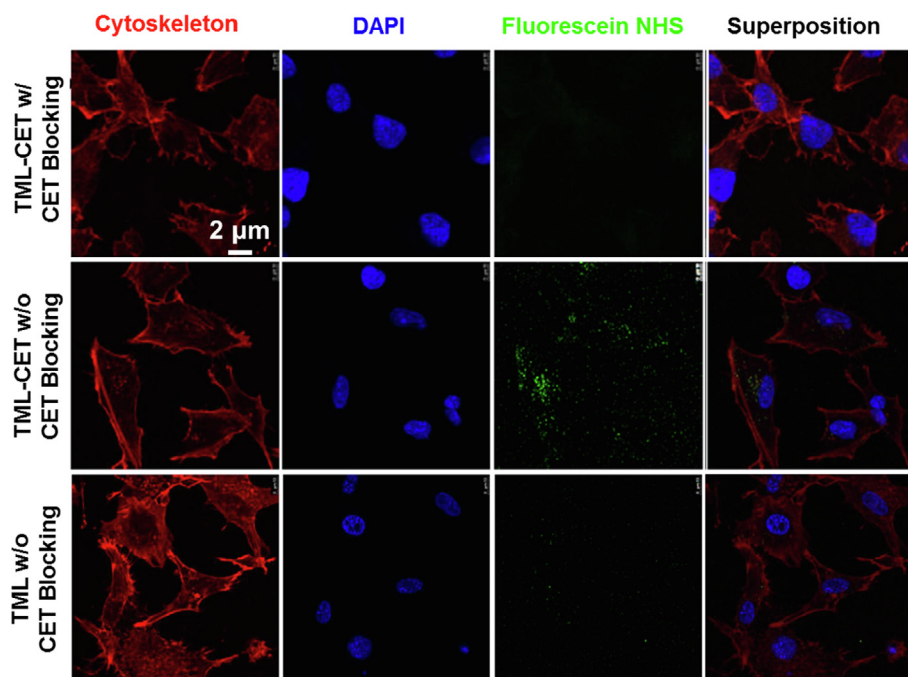
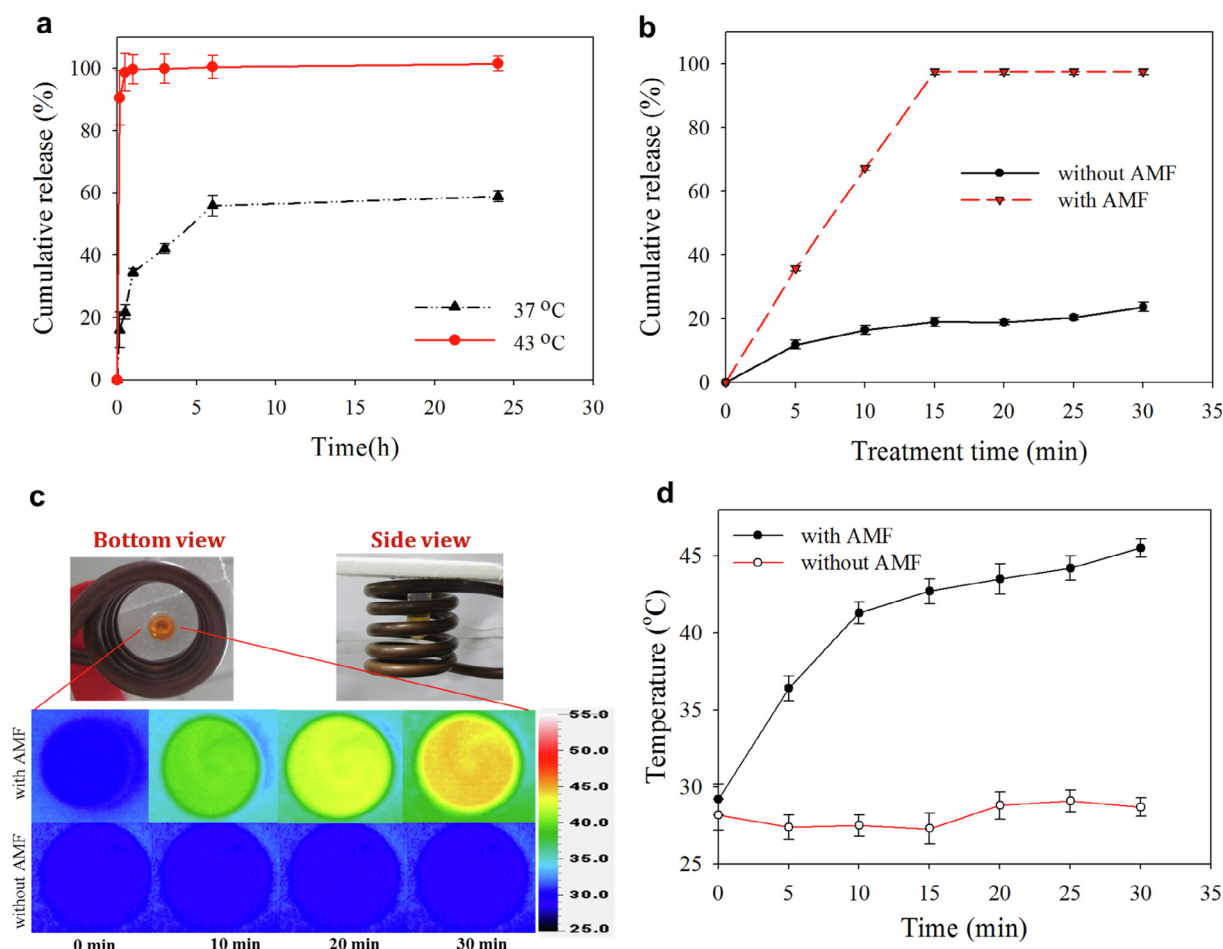


Fig. 3. CLSM observation of the intracellular uptake of fluorescein-labeled TML and TML-CET after incubation with U87 cells with (w) or without (w/o) CET blocking. DAPI: 4',6-diamidino-2-phenylindole; CET: Cetuximab.





**Fig. 4.** Cumulative release profiles of CPT-11 from TML-CPT-11-CET in 37 °C and 43 °C water bath (a) and with and without alternating magnetic field (AMF) treatment (b). The setup for AMF treatment of TML-CPT-11-CET solution and temperature profile images captured with an infrared thermal camera with and without AMF treatment are shown in (c) and the peak temperature profiles are shown in (d).

experimental results revealed that TML-CPT-11-CET would experience a unique and quick AMF-induced temperature alteration that created penetrable defects for CPT-11 in the lipid bilayers of TML-CPT-11-CET, ultimately leading to a swift local release of the entrapped drug. The limited drug release at 37 °C could facilitate a CPT-11 concentration within the therapeutic window being provided after IV-injected TML-CPT-11-CET was effectively transported to the tumor site *in vivo* through the dual targeting mechanism, followed by intracellular uptake by cancer cells and efficient triggered release of CPT-11 when treated by AMF.

### 3.4. Cell cytotoxicity and apoptosis

Once confirming the cellular internalization characteristic, the cytotoxicity was then studied. Due to the multiple functions of the developed liposomes, we sought to clarify both drug cytotoxic efficacy and mechanism. The methanethiosulfonate (MTS) reagent was used to evaluate cell viability in different formulations and under different conditions. From Fig. 5a, we could first confirm that TML to be biocompatible at concentration as high as 1 mg/ml in cell culture medium with relative cell viability (compared to culture medium) higher than 86%. The cytotoxicity of TML was also tested in PC12 neuronal cell line and no cytotoxicity was found up to 100 µg/ml (Fig. S5, Supplementary material). The results of drug cytotoxicity show that CPT-11 can facilitate the most toxic effect toward U87 at 37 °C and with the lowest IC<sub>50</sub> (16.0 µg/ml), in comparison with 51.0 µg/ml and 38.5 µg/ml for TML-CPT11 and TML-CPT11-CET, respectively (Fig. 5b). That only less than

60% of loaded CPT-11 in liposomes could be released after the extended incubation period at 37 °C (Fig. 4a) coincides with the observed increasing trend of IC<sub>50</sub> value when TML-CPT-11 or TML-CPT11-CET was used for CPT-11 delivery. Nonetheless, a lower IC<sub>50</sub> value was observed for TML-CPT11-CET than TML-CPT11, which endorses the enhanced intracellular uptake of TML-CPT11-CET (Fig. 3) as mediated by CET/EGFR interaction to upregulate the cytotoxicity of TML-CPT11-CET toward U87.

To further study the temperature effect, the cytotoxicity of CPT-11, TML-CPT-11 and TML-CPT-11-CET toward U87 at the same drug concentration (10 µg/ml) were evaluated below (37 °C) and above (43 °C) the transition temperature of the thermosensitive lipid (DPPC) in the liposomes. The cytotoxicity results show that cell viability of the CPT-11 group at 37 °C and 43 °C were not significantly different (Fig. 5c). However, the cell viability of the TML-CPT-11 group was reduced from ~80% (37 °C) to ~40% (43 °C), revealing enhanced CPT-11 cytotoxicity at a higher temperature due to increased intracellular drug concentration after CPT-11 was thermally triggered release from TML-CPT-11. Moreover, TML-CPT11-CET caused the lowest cell viability at 43 °C compared to CPT-11 and TML-CPT11. Additional experiments with AMF also revealed AMF-induced thermo-responsive drug release showed concerted cytotoxicity toward U87 with CET-targeting as TML-CPT-11-CET with AMF showing the least cell viability (Fig. 5d). Taken together, we could confirm the role of CET ligand plays in assisting the cellular internalization of TML-CPT-11-CET by U87 when CET was recognized by EGFR on glioma cell surface. After intracellular triggered release of toxic CPT-11 at 43 °C or in the presence of AMF, enhanced



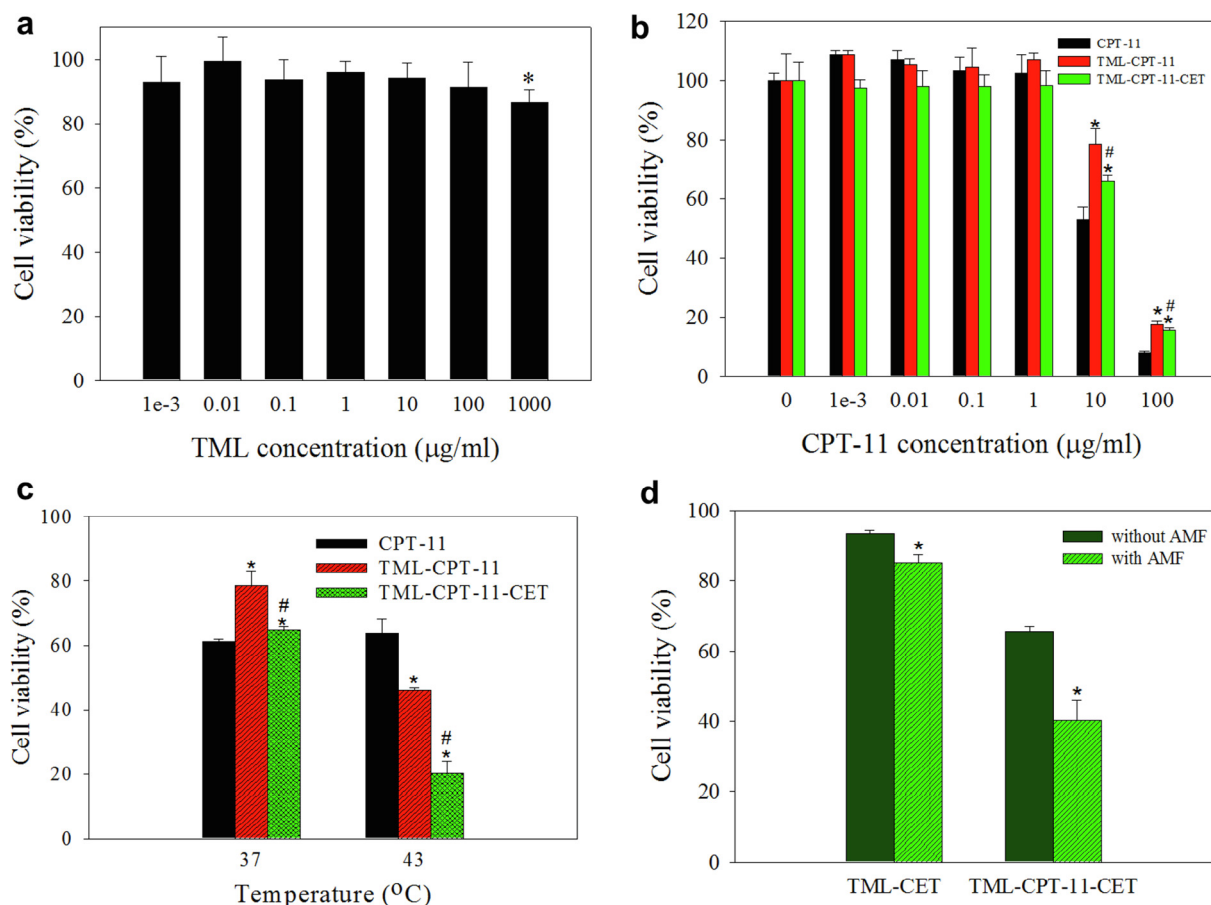


**Fig. 5.** The biocompatibility of TML ( $p < 0.05$  compared with culture medium) (a) and cytotoxicity of CPT-11 with different formulations (b) toward U87 cells. (c) The temperature-dependent cytotoxicity with different formulations at 10  $\mu\text{g/ml}$  CPT-11 toward U87 cells.  $*p < 0.05$  compared with CPT-11,  $\#p < 0.05$  compared with TML-CPT-11. (d) The AMF-dependent cytotoxicity with different formulations at 10  $\mu\text{g/ml}$  CPT-11 toward U87 cells.  $*p < 0.05$ .

cytotoxicity toward cancer cells would suggest TML-CPT-11-CET to be an effective platform for cancer therapy.

To confirm the AMF-dependent cytotoxicity of TML-CPT-11-CET, Annexin V/PI staining assays was performed by quantifying the percentage of live, early apoptotic, late apoptotic or necrotic cells by flow cytometry according to differences in plasma membrane integrity and permeability (Fig. 6). The controls without any treatment showed similar apoptosis rate irrespective of AMF treatment. Incubating U87 cells with TML-CPT-11-CET with AMF treatment revealed remarkably lower cell survival than without AMF treatment. Indeed, the apoptotic ratio was 30.7% with AMF compared to 13.2% without AMF, confirming the temperature-responsive drug release shown from previous results. It should be interesting to note that the necrotic cell ratio increased to 21.2% by combining AMF with TML-CPT-11-CET in comparison to only 8.2% for TML-CPT-11-CET alone. We ascribed this effect to magnetic hyperthermia as AMF was shown to induce hyperthermia of a TML-CPT-11-CET solution *in vitro* in Fig. 4d, which is consistent with a previous finding that magnetic hyperthermia led to necrotic cell death [37]. Indeed, the higher apoptotic and necrotic ratio will lead to the least live cancer cells, which suggested a combined magnetic hyperthermia/chemotherapy cancer therapy [38], by combining magneto-thermal heating of CMNP in TML and heat-triggered drug release from TML. The successful implementation of such approach will rely on efficient targeting of TML-CPT-11-CET to the tumor region through guidance of a magnet and CET-mediated active targeting of TML-CPT-11-CET to the EGFR over-expressed U87 glioma cells to prevent normal cells from being affected by focused thermal injury. After guiding TML-CPT-11-CET to U87 glioma with an external magnetic field, the drug-loaded nanocarrier could preferentially enters cancer cells by

endocytosis due to CET/EGFR interaction, after which an AMF could be used for heat-triggered intracellular drug release and hyperthermia to enhance cytotoxicity toward U87.

A key event in cell apoptosis is the activation of caspase-3, a reliable indicator of apoptosis [39]. In addition, a signaling pathway involving the activation of ERK protein is related to markedly increase of the phosphorylation level of ERK and apoptosis of cancer cells [40,41]. Thus, along with the cytotoxicity study, intracellular caspase-3 and phospho-ERK proteins were extracted from U87 cells that were treated with different formulations for quantitative evaluation of the *in vitro* anticancer mechanism. As shown from Fig. 7, cells treated with TML-CET showed almost no phospho-ERK protein expression, endorsing the biocompatibility of TML with U87 as reported in Fig. 5a. The TML-CPT-11-CET (43 °C) and TML-CPT-11 (43 °C) groups revealed significantly higher phospho-ERK protein production than their corresponding group at 37 °C. This indicates that the liposomes attenuate the cytotoxic effect of CPT-11 on U87 cancer cells, which is also consistent with the MTS cell cytotoxicity results shown in Fig. 5. We thus conclude that TML-CPT-11-CET (43 °C) would increase ER stress and lead to cell apoptosis, as revealed from the highest phospho-ERK protein concentration among all liposomal groups in Fig. 7. The same results were also observed with caspase-3, confirming the apoptotic mechanism of CPT-11. Taken together, the highest phospho-ERK and caspase-3 protein production when U87 cells were treated by TML-CPT-11-CET at 43 °C strongly support the CET/EGFR targeting efficacy and the thermally attenuated CPT-11 release from TML-CPT-11-CET.

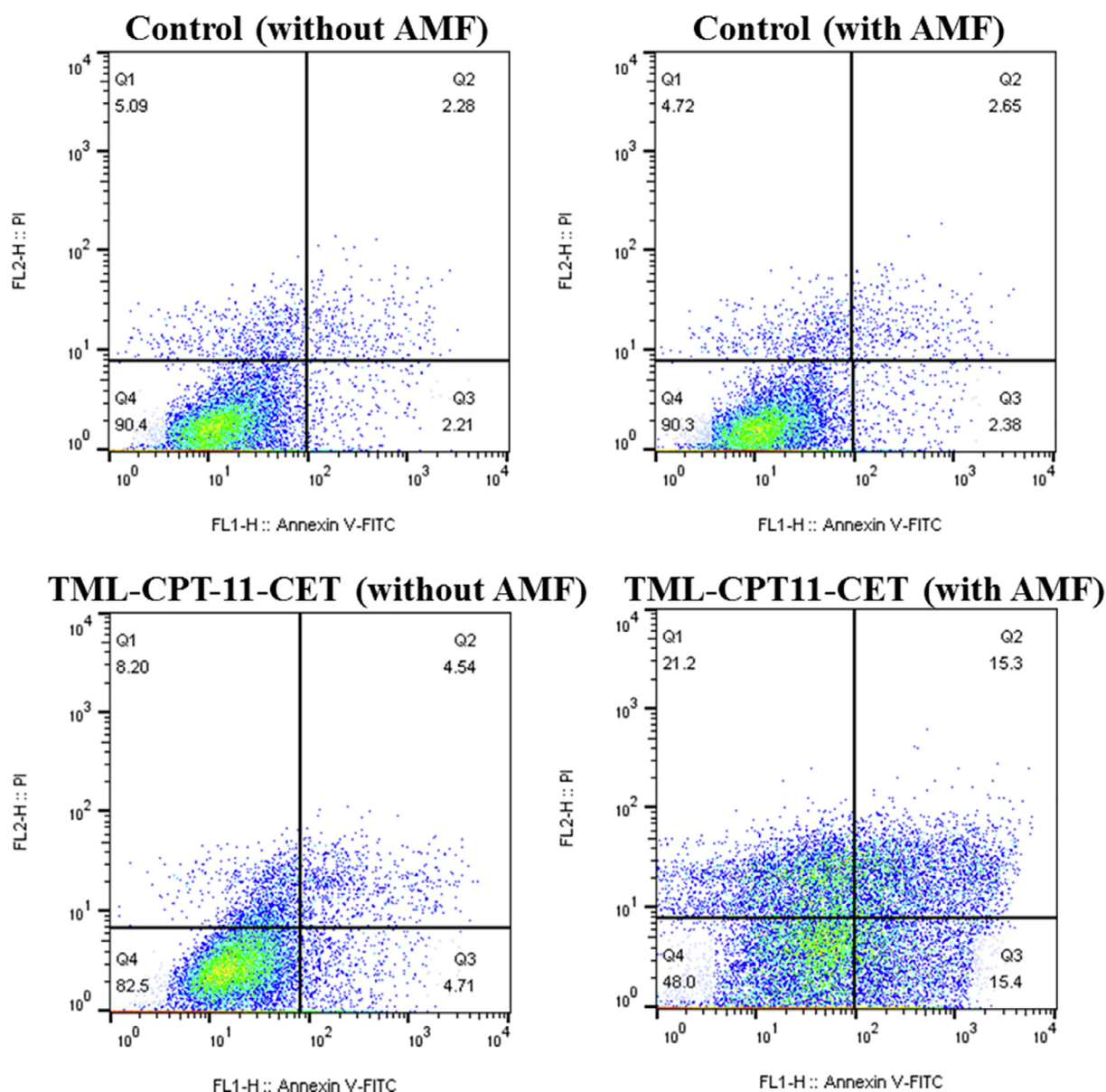


Fig. 6. The flow cytometer analysis of the AMF-dependent apoptosis of U87 cells by Annexin V-FITC/PI staining (Q1: necrotic; Q2: late apoptotic; Q3: early apoptotic; Q4: live) after 24 h incubation with TML-CPT-11-CET. The concentration of CPT-11 was at 10  $\mu$ g/ml.

### 3.5. *In vitro* hemolysis study

Hemolysis may occur *in vivo* as a result of intravascular administration of developed nanocarriers. Hemolysis would result in jaundice, anemia and other pathological and deteriorating conditions. Investigating the hemolytic potentiality of any administered anticancer agent is thus essential before conducting preclinical or clinical trials [42]. Engineered liposomes, or any other nanoscale sized drug carriers may affect erythrocytes and lead to RBC membrane instability or even rupture [43]. Thus, it is important to identify the hemolytic response. To investigate whether our TML might induce hemolysis, we mixed different concentrations of TML with prepared rat RBC samples (water as a positive hemolysis control and PBS as a negative hemolysis control). Results of blood compatibility tests confirmed that TML-treated samples show undetectable optical density (OD) readings with UV–VIS spectrophotometric analysis from 500 to 600 nm within the concentration of 150–1200  $\mu$ g/ml TML prepared in PBS, which is similar to PBS alone (Fig. 8). As TML-CPT11-CET could carry sufficient CPT-11 for cancer treatment within this concentration range without harming RBC

during circulation, it could be suggested for animal experiments. We thus follow up with *in vivo* experiment with xenogenic tumor models in nude mice *via* intravascular (IV) administration of TML-CPT-11-CET.

### 3.6. *In vivo* antitumor efficacy

The xenograft brain tumor mouse model was first used for confirmation of magnetic targeting and stability of TML-CPT-11-CET *in vivo* (Fig. S6, Supplementary material). The magneto-thermal effect of TML-CPT-11-CET after AMF treatment was shown from thermal images in Fig. 9a. From the peak temperature profile shown in Fig. 9b, there was only slight change of temperature (4  $^{\circ}$ C) 15 min after AMF treatment for the control group (injected with saline). In the group injected with TML-CPT-11-CET, there was a rapid temperature increase of 5.8  $^{\circ}$ C after 5 min AMF treatment and the temperature reached 43.5  $^{\circ}$ C after 15 min AMF treatment. This magnetic heating due to AMF is expected to trigger release of CPT-11 from TML-CPT-11-CET for enhanced cytotoxicity toward U87 tumor cells.

Bioluminescence imaging (BLI) through an *in vivo* imaging system

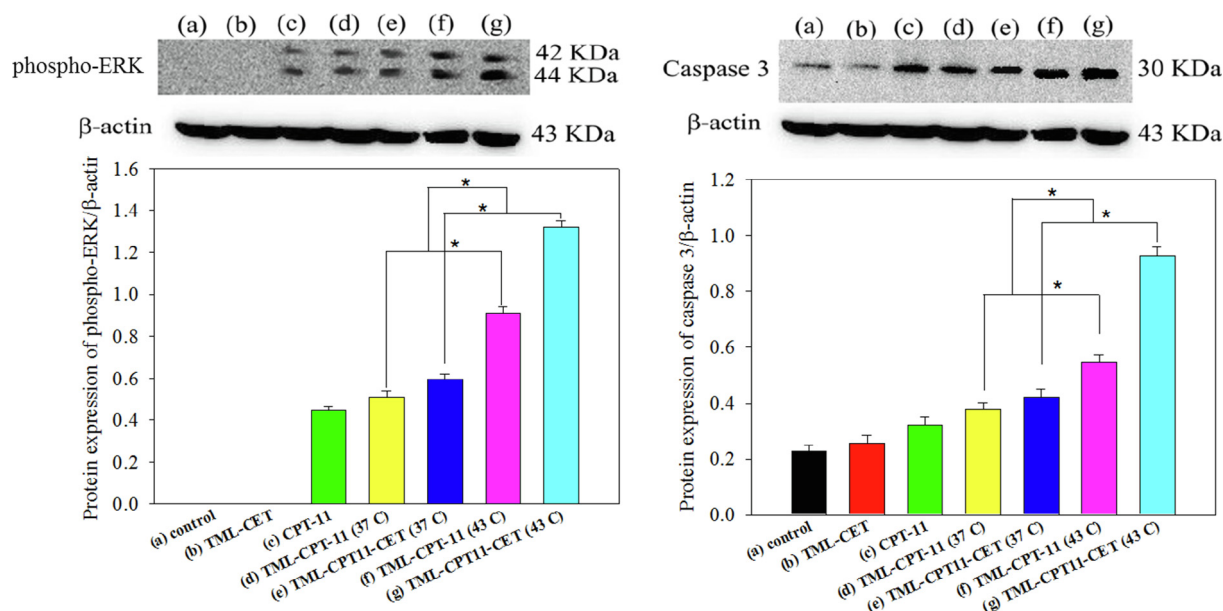


**Fig. 7.** The relative protein expression of caspase-3 and phosphorylated extracellular signal-regulated kinase (phospho-ERK) apoptotic markers in U87 cells subjected to treatment with different formulations at different temperatures. \* $p < 0.05$ .

(IVIS) allows the real-time, repeatable, high-sensitivity *in vivo* monitoring of tumor growth in experimental animals. This is especially applicable to intracranial tumors in animal models [44]. Compared to fluorescence, BLI exhibits minimal background signals from animal tissues and can detect relatively weak signals at high resolution compared to the background. BLI was suggested as a gold standard to evaluate the preclinical efficacy of drug candidates for brain tumor therapy [45]. After implanting  $1 \times 10^6$  U87 glioma cells in the right hemisphere claustrum of a nude, treatment started on day 11 when the average BLI intensity value reached  $\sim 1 \times 10^7$ . As expected, an increasing trend in antitumor efficacy was observed after treating tumor-bearing mice with different formulations as follows, control, CPT-11; TML-CET; TML-CPT-11; TML-CPT-11-CET; TML-CPT-11-CET with magnetic guidance; TML-CPT-11-CET with magnetic guidance plus AMF treatment (Fig. 10a). All BLI values were standardized to baseline BLI values when treatment started for each group and shown in Fig. 10b. The analysis of standardized BLI values revealed that all

animals treated with TML-CPT-11 and TML-CPT-11-CET (irrespective of magnetic guidance and AMF treatment), but not CPT-11, showed remarkable treatment benefits over control with significant difference in BLI signal intensity ( $p < 0.05$ ). The standardized BLI values of all TML-CPT-11-CET groups are also significant different from that of TML-CET (vehicle). Further analysis showed that the standardized BLI signal intensity of TML-CPT-11 was similar to that of free CPT-11 but was more consistent possibly due to the enhanced permeability effect. Indeed, CET conjugation and magnetic guidance enhance the treatment efficacy as the TML-CPT-11-CET with magnetic guidance group showed significantly lower BLI signal intensity in comparison with TML-CPT-11. Most importantly, the TML-CPT-11-CET with magnetic guidance plus AMF treatment group revealed significantly lower standardized BLI values and greater anti-tumor efficacy than all drug-carrying liposomal groups ( $p < 0.05$ ). This enhanced anti-tumor efficacy could be ascribed to triggered release of CPT-11 from TML-CPT-11-CET with the magneto-thermal effect as revealed from the *in vivo* temperature

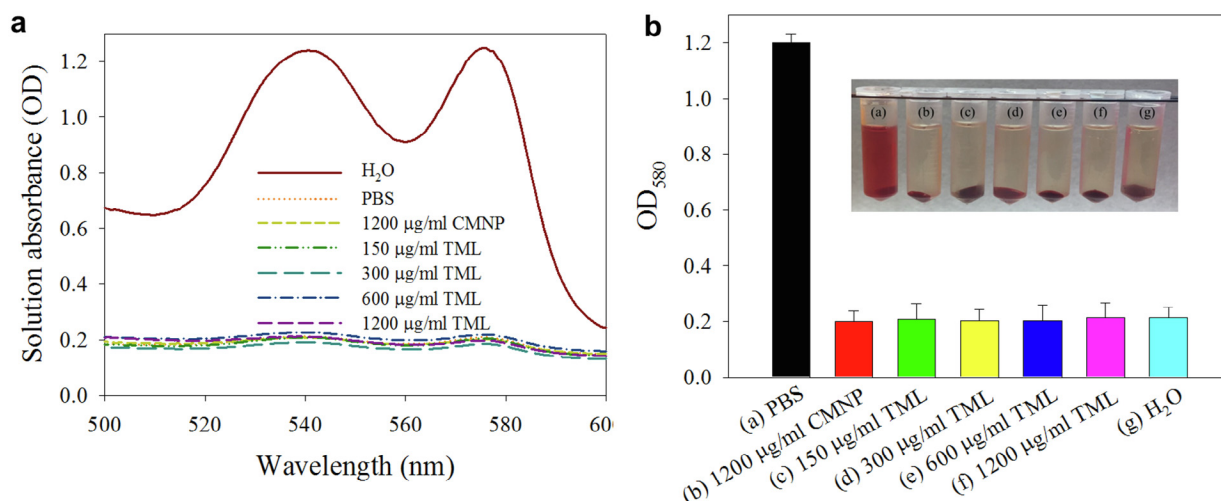


**Fig. 8.** *In vitro* hemolysis results of test formulations after incubation with diluted red blood cells. The hematological compatibility was determined from the absorption spectra of the supernatant after incubation for 2 h for hemolytic assay (a) and the optical density at 580 nm (OD<sub>580</sub>) of the supernatant was shown in (b) with the insert showing the gross view of samples visualized with a high-resolution camera. (For interpretation of the references to color in this figure legend, the reader is referred to the web version of this article.)



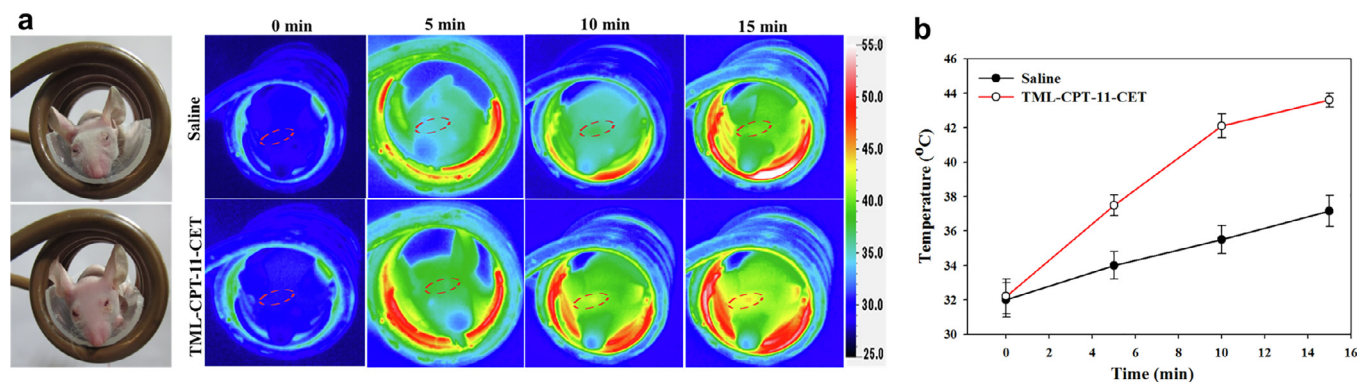


**Fig. 9.** *In vivo* magneto-thermal effects after injection of 200  $\mu$ l of saline or TML-CPT-11-CET intravenously to tumor-bearing mice, magnetic guidance for 30 min and AMF treatment for different times. (a) Gross views of mice in the AMF coil, and IR thermal images showing the temperature changes in tumor areas of mice at different AMF treatment times. The red circles indicate the tumor areas subject to analysis. (b) Peak temperature profiles of tumors at different AMF treatment times. Data are presented as mean  $\pm$  SD ( $n = 5$ ). (For interpretation of the references to color in this figure legend, the reader is referred to the web version of this article.)

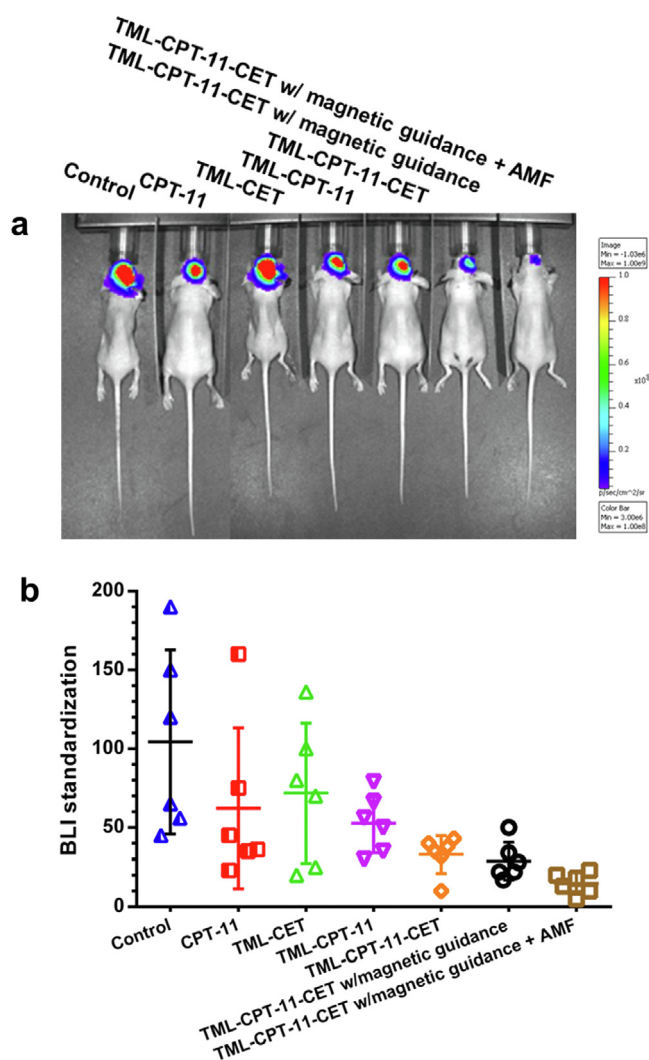


**Fig. 10.** The bioluminescence imaging (BLI) of intracranially implanted U87 cells in the right intracranial region of each mouse. (a) Representative BLI obtained by *in vivo* imaging system (IVIS) on day 21. (b) Plot of the relative BLI signal intensity on day 21 for each group ( $n = 6$ , mean  $\pm$  SD). The BLI standardization was calculated from the total bioluminescent signal intensity on day 21 normalized by the total bioluminescent signal intensity at baseline (day 11) when treatment started. The CPT-11 dosage was fixed at 30 mg/kg body weight.

elevation when TML-CPT-11-CET was injected to the tumor-bearing mice and treated with AMF. We thus confirmed that IV administration of TML-CPT-11-CET followed by magnetic guidance and AMF treatment resulted in the lowest BLI elevation compared with all groups received sample administration via the tail vein, suggesting a significantly greater reduction in tumor size as measured by BLI standardization.

Other than IVIS, the *in vivo* antitumor efficacy was also evaluated from the survival rate of mice after different treatments in a separate group of mice (Fig. 11). The median survival times of control and TML-CET were 20 and 21 days, respectively, with no animals survived beyond 22 days. CPT-11 slightly increased median survival time to 22 days. For CPT-11 loaded liposomes, TML-CPT-11 and TML-CPT-11-CET groups showed median survival times of 27 and 28 days, respectively. The median survival increased to 30 days with magnetic guidance, which further increased to 33.5 days when augmented with AMF treatment. The efficacy of different treatments from survival rate was consistent with those from IVIS (Fig. 10).

### 3.7. PET/MRI for tumor activity evaluation

To determine if the antitumor effects of the best treatment group shown in Fig. 10 (TML-CPT-11-CET with magnetic guidance plus AMF treatment group) as observed in the IVIS system could be translated clinically, we performed PET/MRI to evaluate our mouse intracranial glioma xenograft model. Our initial PET/MRI analysis non-invasively addressed the antitumor activity of TML-CPT-11-CET administered systemically via intravascular injection into nude mice. As anticipated, MRI results showed that U87 intracranial tumors responded to treatment with TML-CPT-11-CET, which was administered starting from day 11 and subsequently on day 14 and 17, delaying the tumor growth compared to mice treated with the vehicle (TML-CET) only (Fig. 12). The tumor sizes measured based on MRI results were 29.1 mm<sup>3</sup>, 105.9 mm<sup>3</sup> and 109.5 mm<sup>3</sup> at day 14, 17 and 21, respectively, for the control group (TML-CET). In contrast, the tumor sizes shrank markedly to 1.9 mm<sup>3</sup>, 27.1 mm<sup>3</sup> and 76.3 mm<sup>3</sup> at the same time point for animals in the treatment group. The PET/MRI also provided information on the precise size of tumors, anatomic location with peripheral brain parenchyma, and tumor cell proliferation activity. F-18 39-deoxy-39-fluorothymidine (F-18 FLT) was used as a tumor proliferation biotracer. Significant differences in tumor enlargement were identified in the control (TML-CET) versus the treatment (TML-CPT-11-CET) group after three treatments (day 11, 14 and 17) of U87 primary xenograft glioma tumors. The tumor had enlarged much earlier (second period) with more obvious central necrosis. The magnetic liposomes also penetrated more easily towards its center to produce a dark contrast due to encapsulated CMNP in liposomes from MRI images. Conversely, the tumor treated with TML-CPT-11-CET grew more slowly; even though it

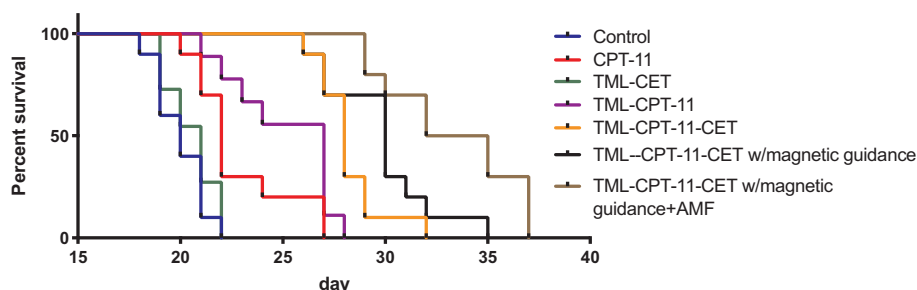


**Fig. 11.** The survival curves of nude mice with intracranially implanted U87 cells in the right intracranial region. All mice were observed daily and euthanized after they reached a moribund condition as body weight loss more than 25% of initial measurement, hunched back, hemiparesis or seizure ( $n = 9$  to 11).

grew to the last period. Overall, the F-18 FLT revealed much lower cell proliferation activity of tumor cells in the treatment group with TML-CPT-11-CET than in the control group with TML-CET.

Brain MRI is the gold standard for evaluating the anatomic location and three-dimensional (3D) structure of gliomas. It is a quick and reliable method to localize a tumor region or its invasion. However, without serial follow-up, tumor growth rate is difficult to predict while tumor activity is difficult to evaluate. Additionally, PET tracer is a niche application in oncology diagnosis as brain tumors typically have elevated proliferation rates. Thus, this diagnostic technology can be used to evaluate therapeutic effect. Several agents targeting increased metabolic activity and the DNA synthesis pathway were developed to target proliferation in many cancers. F-18 39-deoxy-39-fluorothymidine (F-18 FLT) gained attention as a cell proliferation biomarker due to its relationship with thymidine kinase 1 that sequesters FLT for phosphorylation. Thymidine kinase 1 is a key enzyme because it is hyper-expressed in multiplying tumor cells in brain, breast and lung tumors. Thus, F-18 FLT is very successful as a bio-tracer targeting cell proliferation marker, which clearly marks tumor proliferation. As shown in Fig. 12, the TML-CPT-11-CET-treated region of the brain tumor shrank along with the tested formulation accumulating in the tumor center. Therefore, nanocarrier-based drug delivery to the brain can be used as effective localized therapy for diseases such as brain tumors [46]. The precise location of tumor tissues can be marked in advance on the 3D MRI/PET panel to assist subsequent treatments. Accordingly, the TML-

CPT-11-CET developed in this study is magnetically responsive and can be visualized using MRI/PET imaging with non-invasive guidance for effective adjuvant therapy.

#### 4. Conclusions

Our work has led to the development of dual-targeted TMLs for antitumor drug (CPT-11) delivery in the treatment of brain tumors. CMNP and CPT-11 are loaded into liposomes and the nanocarrier was modified with CET to recognize the EGFR that is highly expressed on the surface of brain tumor cells. Using U87 cells, dual targeted delivery of CPT-11 followed by thermo-responsive drug release with AMF was demonstrated to increase the antitumor efficacy of the nanodrug. Finally, the therapeutic efficacy was confirmed in an orthotopic xenograft brain tumor mouse model. In the future, this developed nanoformulation would be evaluated for the safety profile via intravenous administration at the efficacious dose and planned for future study with large animals.

#### Acknowledgments

The authors would like to thank the Ministry of Science and Technology of Taiwan (ROC) (MOST106-2221-E-182-056-MY3 and MOST105-2314-B-182-073-MY2) and Chang Gung Memorial Hospital (CMRPD2G0081, CMRPD2G0082 and BMRP249) for financially

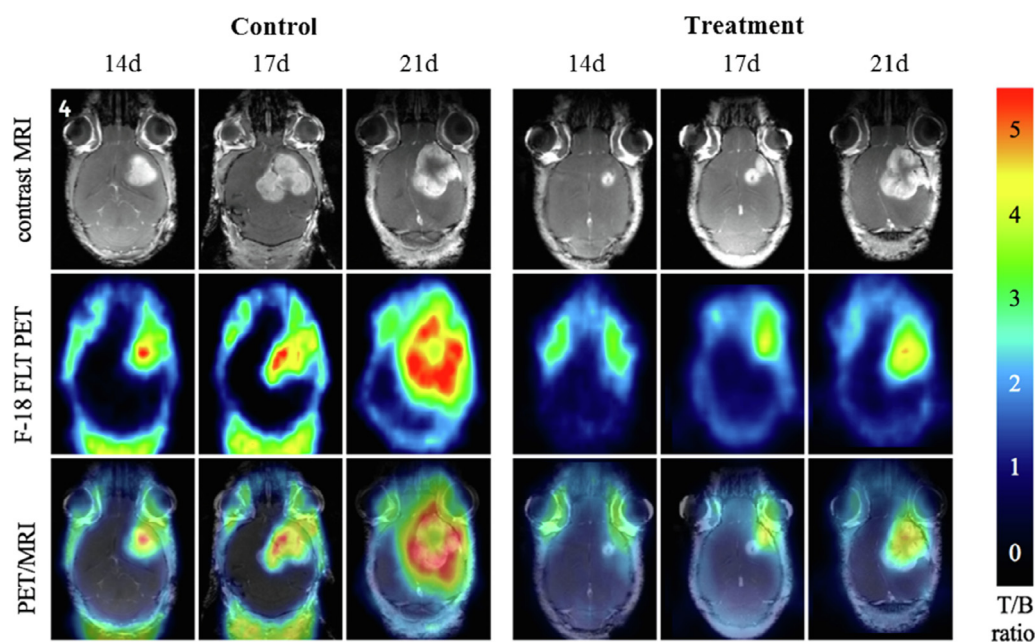


**Fig. 12.** Evaluation of antitumor efficacy using PET/MRI analysis. Results are shown for tumor-bearing nude mice in the control group (TML-CET) and the treatment group (TML-CPT-11-CET with magnetic guidance plus AMF treatment) at day 14 (14d), day 17 (17d) and day 21 (21d) post-implantation of U87 cells.



supporting this research. The MRI/PET imaging studies were carried out with the help of the Center of Advanced Molecular Imaging and Translation, Chang Gung Memorial Hospital, Linkou, Taiwan.

## Appendix A. Supplementary data

Supplementary data to this article can be found online at <https://doi.org/10.1016/j.cej.2019.05.055>.


## References

- [1] H.S. Friedman, M.D. Prados, P.Y. Wen, T. Mikkelsen, D. Schiff, L.E. Abrey, W.A. Yung, N. Paleologos, M.K. Nicholas, R. Jensen, Bevacizumab alone and in combination with irinotecan in recurrent glioblastoma, *J. Clin. Oncol.* 27 (2009) 4733–4740.
- [2] J.J. Vredenburg, A. Desjardins, J.E. Herndon, J. Marcello, D.A. Reardon, J.A. Quinn, J.N. Rich, S. Sathornsumetee, S. Gururangan, J. Sampson, Bevacizumab plus irinotecan in recurrent glioblastoma multiforme, *J. Clin. Oncol.* 25 (2007) 4722–4729.
- [3] M.D. Prados, K. Lamborn, W. Yung, K. Jaeckle, H.I. Robins, M. Mehta, H.A. Fine, P.Y. Wen, T. Cloughesy, S. Chang, A phase 2 trial of irinotecan (CPT-11) in patients with recurrent malignant glioma: a North American Brain Tumor Consortium study, *Neuro-Oncol.* 8 (2006) 189–193.
- [4] R. Krishna, L.D. Mayer, Multidrug resistance (MDR) in cancer: mechanisms, reversal using modulators of MDR and the role of MDR modulators in influencing the pharmacokinetics of anticancer drugs, *Eur. J. Pharm. Sci.* 11 (2000) 265–283.
- [5] R.M. Schiffer, A. Ansari, J. Xu, Q. Zhou, G. Tang, G. Storm, G. Molema, P.Y. Lu, P.V. Scaria, M.C. Woodle, Cancer siRNA therapy by tumor selective delivery with ligand-targeted sterically stabilized nanoparticle, *Nucl. Acids Res.* 32 (2004) e149–e149.
- [6] W.R. Wilson, M.P. Hay, Targeting hypoxia in cancer therapy, *Nat. Rev. Cancer* 11 (2011) 393–410.
- [7] W. Zhu, L. Zhang, Z. Yang, P. Liu, J. Wang, J. Cao, A. Shen, Z. Xu, J. Wang, An efficient tumor-inducible nanotheranostics for magnetic resonance imaging and enhanced photodynamic therapy, *Chem. Eng. J.* 358 (2019) 969–979.
- [8] C. Wilhelm, F. Gazeau, J.-C. Bacri, Magnetophoresis and ferromagnetic resonance of magnetically labeled cells, *Eur. Biophys. J.* 31 (2002) 118–125.
- [9] S. Ogawa, T.-M. Lee, A.R. Kay, D.W. Tank, Brain magnetic resonance imaging with contrast dependent on blood oxygenation, *Proc. Natl. Acad. Sci.* 87 (1990) 9868–9872.
- [10] T.-Y. Liu, S.-H. Hu, K.-H. Liu, R.-S. Shaiu, D.-M. Liu, S.-Y. Chen, Instantaneous drug delivery of magnetic/thermally sensitive nanospheres by a high-frequency magnetic field, *Langmuir* 24 (2008) 13306–13311.
- [11] S. Tong, C.A. Quinto, L. Zhang, P. Mohindra, G. Bao, Size-dependent heating of magnetic iron oxide nanoparticles, *ACS Nano* 11 (2017) 6808–6816.
- [12] N. Schleich, F. Danhier, V. Préat, Iron oxide-loaded nanotheranostics: major obstacles to in vivo studies and clinical translation, *J. Control. Release* 198 (2015) 35–54.
- [13] Y.-J. Lu, P.-Y. Lin, P.-H. Huang, C.-Y. Kuo, K.-T. Shalumon, M.-Y. Chen, J.-P. Chen, Magnetic graphene oxide for dual targeted delivery of doxorubicin and photothermal therapy, *Nanomaterials* 8 (2018) 193.
- [14] T.E. Taylor, F.B. Furnari, W.K. Cavenee, Targeting EGFR for treatment of glioblastoma: molecular basis to overcome resistance, *Curr. Cancer Drug Targets* 12 (2012) 197–209.
- [15] D. Rafael, F. Martínez, F. Andrade, J. Seras-Franzoso, N. Garcia-Aranda, P. Gener, J. Sayós, D. Arango, I. Abasolo, S. Schwartz, Efficient EGFR mediated siRNA delivery to breast cancer cells by Cetuximab functionalized Pluronic® F127/Gelatin, *Chem. Eng. J.* 340 (2018) 81–93.
- [16] A.R. Chowdhuri, D. Laha, S. Chandra, P. Karmakar, S.K. Sahu, Synthesis of multifunctional upconversion NMOFs for targeted antitumor drug delivery and imaging in triple negative breast cancer cells, *Chem. Eng. J.* 319 (2017) 200–211.
- [17] D. Rosenblum, N. Joshi, W. Tao, J.M. Karp, D. Peer, Progress and challenges towards targeted delivery of cancer therapeutics, *Nat. Commun.* 9 (2018) 1410.
- [18] H.-L. Hsu, J.-P. Chen, Preparation of thermosensitive magnetic liposome encapsulated recombinant tissue plasminogen activator for targeted thrombolysis, *J. Magn. Magn. Mater.* 427 (2017) 188–194.
- [19] M. Faraji, Y. Yamini, A. Saleh, M. Rezaee, M. Ghambarian, R. Hassani, A nanoparticle-based solid-phase extraction procedure followed by flow injection inductively coupled plasma-optical emission spectrometry to determine some heavy metal ions in water samples, *Anal. Chim. Acta* 659 (2010) 172–177.
- [20] N. Kaneda, H. Nagata, T. Furuta, T. Yokokura, Metabolism and pharmacokinetics of the camptothecin analogue CPT-11 in the mouse, *Cancer Res.* 50 (1990) 1715–1720.
- [21] E. Terpetschnig, H. Szmanski, A. Ozinskas, J.R. Lakowicz, Synthesis of squaraine-N-hydroxysuccinimide esters and their biological application as long-wavelength fluorescent labels, *Anal. Biochem.* 217 (1994) 197–204.
- [22] P.P. Deshpande, S. Biswas, V.P. Torchilin, Current trends in the use of liposomes for tumor targeting, *Nanomedicine* 8 (2013) 1509–1528.
- [23] E.B. Dinca, J.N. Sarkaria, M.A. Schroeder, B.L. Carlson, R. Voicu, N. Gupta, M.S. Berger, C.D. James, Bioluminescence monitoring of intracranial glioblastoma xenograft: response to primary and salvage temozolomide therapy, *J. Neurosurg.* 107 (2007) 610–616.
- [24] V. Gurtu, S.R. Kain, G. Zhang, Fluorometric and colorimetric detection of caspase activity associated with apoptosis, *Anal. Biochem.* 251 (1997) 98–102.
- [25] J. Liu, W. Mao, B. Ding, C.S. Liang, ERKs/p53 signal transduction pathway is involved in doxorubicin-induced apoptosis in H9c2 cells and cardiomyocytes, *Am. J. Physiol. – Heart Circulatory Physiol.* 295 (2008) H1956–H1965.
- [26] Y.-S. Lin, C.L. Haynes, Impacts of mesoporous silica nanoparticle size, pore ordering, and pore integrity on hemolytic activity, *J. Am. Chem. Soc.* 132 (2010) 4834–4842.
- [27] P. Pellegatti, L. Raffaghello, G. Bianchi, F. Piccardi, V. Pistoia, F. Di Virgilio, Increased level of extracellular ATP at tumor sites: in vivo imaging with plasma membrane luciferase, *PLoS ONE* 3 (2008) e2599.
- [28] G.P. Narayan, K. Anoop, S.K. Das, Mechanism of enhancement/deterioration of boiling heat transfer using stable nanoparticle suspensions over vertical tubes, *J. Appl. Phys.* 102 (2007) 074317.
- [29] S.H. Tseng, M.Y. Chou, I.M. Chu, Cetuximab-conjugated iron oxide nanoparticles for cancer imaging and therapy, *Int. J. Nanomed.* 10 (2015) 3663–3685.
- [30] K. Gardikis, S. Hatziantoniou, K. Viras, C. Demetrios, Effect of a bioactive curcumin derivative on DPPC membrane: a DSC and Raman spectroscopy study, *Thermochim. Acta* 447 (2006) 1–4.
- [31] J. Sabin, G. Prieto, J. Estelrich, F. Sarmiento, M. Costas, Insertion of semifluorinated diblocks on DMPC and DPPC liposomes. Influence on the gel and liquid states of the bilayer, *J. Colloid Interface Sci.* 348 (2010) 388–392.
- [32] T. Neuberger, B. Schöpf, H. Hofmann, M. Hofmann, B. von Rechenberg, Superparamagnetic nanoparticles for biomedical applications: Possibilities and limitations of a new drug delivery system, *J. Magn. Magn. Mater.* 293 (2005) 483–496.
- [33] N. Karra, S. Benita, The ligand nanoparticle conjugation approach for targeted cancer therapy, *Curr. Drug Metab.* 13 (2012) 22–41.
- [34] D. Peng, Z. Fan, Y. Lu, T. DeBlasio, H. Scher, J. Mendelsohn, Anti-epidermal growth factor receptor monoclonal antibody 225 up-regulates p27KIP1 and induces G1 arrest in prostatic cancer cell line DU145, *Cancer Res.* 56 (1996) 3666–3669.
- [35] E.-Y. Chuang, C.-C. Lin, K.-J. Chen, D.-H. Wan, K.-J. Lin, Y.-C. Ho, P.-Y. Lin, H.-W. Sung, A FRET-guided, NIR-responsive bubble-generating liposomal system for in vivo targeted therapy with spatially and temporally precise controlled release, *Biomaterials* 93 (2016) 48–59.
- [36] A. Shah, M.S. Malik, G.S. Khan, E. Nosheen, F.J. Iftikhar, F.A. Khan, S.S. Shukla, M.S. Akhter, H.-B. Kraatz, T.M. Aminabhavi, Stimuli-responsive peptide-based biomaterials as drug delivery systems, *Chem. Eng. J.* 353 (2018) 559–583.
- [37] K. Tanaka, A. Ito, T. Kobayashi, T. Kawamura, S. Shimada, K. Matsumoto, T. Saida, H. Honda, Intratumoral injection of immature dendritic cells enhances antitumor effect of hyperthermia using magnetic nanoparticles, *Int. J. Cancer* 116 (2005) 624–633.
- [38] S. Kossatz, J. Grandke, P. Couleaud, A. Latorre, A. Aires, K. Crosbie-Staunton, R. Ludwig, H. Dähling, V. Ettelt, A. Lazaro-Carrillo, M. Calero, M. Sader, J. Courtney, Y. Volkov, A. Prina-Mello, A. Villanueva, Á. Somoza, A.L. Cortajarena, R. Miranda, I. Hilger, Efficient treatment of breast cancer xenografts with multifunctionalized iron oxide nanoparticles combining magnetic hyperthermia and anti-cancer drug delivery, *Breast Cancer Res.* 17 (2015) 66.
- [39] J. Jeruc, A. Vizjak, B. Rozman, D. Ferluga, Immunohistochemical expression of activated caspase-3 as a marker of apoptosis in glomeruli of human lupus nephritis, *Am. J. Kidney Dis.* 48 (2006) 410–418.
- [40] Z. Qi, L. Yin, Y. Xu, F. Wang, Pegylated liposomal paclitaxel induces ovarian cancer cell apoptosis via TNF induced ERK/AKT signaling pathway, *Mol. Med. Rep.* 17 (2018) 7497–7504.
- [41] S. Cagnol, J.C. Chambard, ERK and cell death: mechanisms of ERK-induced cell death-apoptosis, autophagy and senescence, *FEBS J.* 277 (2010) 2–21.
- [42] S. Mourtas, G.P. Michanetzis, Y.F. Missirlis, S.G. Antimisiris, Haemolytic activity of liposomes: effect of vesicle size, lipid concentration and polyethylene glycol-lipid or arsonolipid incorporation, *J. Biomed. Nanotechnol.* 5 (2009) 409–415.
- [43] M.A. Dobrovolskaia, J.D. Clogston, B.W. Neun, J.B. Hall, A.K. Patri, S.E. McNeil, Method for analysis of nanoparticle hemolytic properties in vitro, *Nano Lett.* 8 (2008) 2180–2187.
- [44] D.M. Close, T. Xu, G.S. Saylor, S. Ripp, In vivo bioluminescent imaging (BLI): noninvasive visualization and interrogation of biological processes in living animals, *Sensors* 11 (2010) 180–206.
- [45] S.C. Jost, L. Collins, S. Travers, D. Pivnicka-Worms, J.R. Garbow, Measuring brain tumor growth: combined bioluminescence imaging-magnetic resonance imaging strategy, *Mol. Imaging* 8 (2009) 245–253.
- [46] E. Allard, C. Passirani, J.-P. Benoit, Convection-enhanced delivery of nanocarriers for the treatment of brain tumors, *Biomaterials* 30 (2009) 2302–2318.



Review

# Roles of Thyroid Hormone-Associated microRNAs Affecting Oxidative Stress in Human Hepatocellular Carcinoma

Po-Shuan Huang <sup>1,2</sup>, Chia-Siu Wang <sup>3</sup>, Chau-Ting Yeh <sup>4</sup> and Kwang-Huei Lin <sup>1,2,4,5,\*</sup> 

<sup>1</sup> Department of Biochemistry, College of Medicine, Chang-Gung University, Taoyuan 33302, Taiwan; leo\_6813@msn.com

<sup>2</sup> Department of Biomedical Sciences, College of Medicine, Chang-Gung University, Taoyuan 33302, Taiwan

<sup>3</sup> Department of General Surgery, Chang Gung Memorial Hospital, Chiayi 61363, Taiwan; wangcs@cgmh.org.tw

<sup>4</sup> Liver Research Center, Chang Gung Memorial Hospital, Linkou, Taoyuan 33302, Taiwan; chauting@adm.cgmh.org.tw

<sup>5</sup> Research Center for Chinese Herbal Medicine, College of Human Ecology, Chang Gung University of Science and Technology, Taoyuan 33302, Taiwan

\* Correspondence: khlin@mail.cgu.edu.tw; Tel.: +88-63-211-8263

Received: 26 September 2019; Accepted: 18 October 2019; Published: 21 October 2019



**Abstract:** Oxidative stress occurs as a result of imbalance between the generation of reactive oxygen species (ROS) and antioxidant genes in cells, causing damage to lipids, proteins, and DNA. Accumulating damage of cellular components can trigger various diseases, including metabolic syndrome and cancer. Over the past few years, the physiological significance of microRNAs (miRNA) in cancer has been a focus of comprehensive research. In view of the extensive level of miRNA interference in biological processes, the roles of miRNAs in oxidative stress and their relevance in physiological processes have recently become a subject of interest. In-depth research is underway to specifically address the direct or indirect relationships of oxidative stress-induced miRNAs in liver cancer and the potential involvement of the thyroid hormone in these processes. While studies on thyroid hormone in liver cancer are abundantly documented, no conclusive information on the potential relationships among thyroid hormone, specific miRNAs, and oxidative stress in liver cancer is available. In this review, we discuss the effects of thyroid hormone on oxidative stress-related miRNAs that potentially have a positive or negative impact on liver cancer. Additionally, supporting evidence from clinical and animal experiments is provided.

**Keywords:** oxidative stress; microRNA; thyroid hormone; liver cancer

## 1. Introduction

Hepatocellular carcinoma (HCC) is an inflammation-related cancer, with the majority of cases occurring in the context of hepatic injury and inflammation [1]. The risk factors correlated with HCC include chronic inflammation due to viral infection (such as hepatitis B virus (HBV) and hepatitis C virus (HCV)), excessive intake of alcohol, metabolic disease, non-alcoholic steatohepatitis (NASH), bacterial infection, type 2 diabetes, smoking, and chemical exposure [2]. Both HCC and the associated risk factors are significantly correlated with oxidative stress. Oxidative stress occurs when excessive production of reactive oxygen species (ROS) overpowers intrinsic antioxidant defense mechanisms. Accumulating levels of ROS can cause extensive damage to biological molecules, leading to cell injury, loss of function, development of cancer, and even death [3]. Therefore, elucidation of the relationship between oxidative stress and cancer is of clinical importance. Among the potential mechanisms

involved in carcinogenesis, the pathways triggered by oxidative stress-induced microRNAs (miRNA) have been widely investigated. MiRNAs are small endogenous non-coding RNA molecules that regulate multiple gene expression at the post-transcriptional level. These molecules suppress messenger RNA through binding to stretches of complementary sequences [4,5]. The potential associations of miRNAs with human disease are widely documented. As crucial regulators of gene expression, miRNAs thus present promising candidates for biomarkers and treatment strategies.

Thyroid hormones play major roles in cell growth, development, and metabolism. Considerable research supports a relationship between the thyroid hormone and pathophysiology of various cancer types. Thyroid hormones exert their effects on cancer cells through either genomic or non-genomic pathways and their dysregulation has significant effects on cancer development and progression. Hypothyroidism is reported to contribute to liver carcinogenesis [6]. Notably, both hyperthyroidism and hypothyroidism appear to be associated with oxidative stress in animal and human diseases, indicating involvement of the thyroid hormone in disease progression [7]. Preliminary data from recent studies focusing on the potential relationship between miRNAs associated with oxidative stress and dysregulation of thyroid hormone in liver cancer progression are comprehensively summarized in the current review.

## 2. Effect of Thyroid Hormone on the Role of Oxidative Stress-Related microRNAs in Liver

### 2.1. Oxidative Stress Promotes HCC Progression

Liver cancer is the second leading cause of cancer-related deaths worldwide. Hepatocellular carcinoma (HCC), a type of inflammation-related cancer with >90% cases associated with hepatic injury and inflammation, is the most common primary malignant tumor type [8]. The incidence of HCC is highly correlated with inflammatory risk factors, such as hepatitis B virus (HBV), hepatitis C virus (HCV), liver disease (non-alcoholic fatty liver disease/non-alcoholic steatohepatitis), habitual drinking (high alcohol exposure), obesity, type 2 diabetes (T2D), and aflatoxin exposure [9–12].

Oxidative stress additionally plays an important role in HCC development. Excess ROS levels induce liver DNA injury, in turn leading to increased fatty liver, hepatitis B/C, liver cirrhosis, and consequently, HCC [13]. Oxidative stress is defined as an imbalance between production of reactive oxygen species (ROS) and antioxidant capacity of the cell, which causes damage to biomolecules, such as DNA, lipids, and proteins [14].

ROS simultaneously affect a series of signaling cascades and mediate the regulation of several transcription factors that control the expression of various genes involved in cell survival, proliferation, invasion, and metastasis [15–19]. Common ROS species include superoxide anion ( $O_2^{\cdot-}$ ), hydrogen peroxide ( $H_2O_2$ ), hydroxyl radical ( $OH^{\cdot}$ ), singlet oxygen ( $^1O_2$ ), and ozone ( $O_3$ ) [20,21]. Reactive species induce nicks in DNA and failure in mechanisms to repair DNA damage that lead to HCC.

ROS can react with cellular biomolecules, yielding oxidatively modified DNA products that eventually induce cell damage and death. For instance, protein carbonyl and 8-hydroxydeoxyguanosine (8-OHdG), the well-known oxidatively modified molecular products of proteins and DNA, are associated with poor survival in HCC patients [16].

The inflammation risk factors, HCV and HBV infection, cause malignant degeneration by induction of oxidative stress that is critical in HCC. Oxidative stress is present to a greater degree in HCV infection than other inflammatory liver diseases and proposed as a major mechanism of liver injury in patients with chronic hepatitis C [22]. The core protein of HCV, which induces excess ROS production through adjustment of mitochondrial electron transport and mitochondria, is a primary target of ROS. Therefore, damage to mitochondria via ROS induced by HCV presents a potential mechanism underlying the development of HCC [23].

In addition to HCV, HBV infection markedly increases the risk of development of HCC. Among the viral proteins, HBV encoding HBV X protein (HBx) appears to have the greatest oncogenic potential in HCC. Similar to HCV core protein, HBx is associated with mitochondria, leading to augmented ROS

production and induction of oxidative stress in hepatocytes [24]. The key mechanisms used by HBx, such as inhibition of high-mobility group protein box1 (HMGB1) expression and generation of ROS via the NF- $\kappa$ B signaling pathway, are discussed in an earlier report [25].

Non-alcoholic fatty liver disease (NAFLD) is a complex disorder characterized by excessive lipid accumulation in the liver, controlled by multiple metabolic factors, that is often diagnosed in conjunction with obesity, type 2 diabetes (T2D), and hyperlipemia [26]. Among the numerous mechanisms underlying NAFLD pathogenesis, redox imbalance is suggested to be the most significantly correlated factor to HCC progression. In addition, conditions such as metabolic oxidative stress, cell autophagy, and inflammation induce more severe nonalcoholic steatohepatitis (NASH) progression [26]. In patients with NASH, the activities of mitochondrial respiratory chain complexes are decreased in liver tissue, resulting in reduced glutathione expression and consequent activation of the c-Jun N-terminal kinase (JNK)/c-Jun signaling pathway by oxidative stress that induces cell death in steatotic liver [27].

The issue of whether risk factors directly induce or are subject to oxidative stress to increase their effects remains to be established. However, the findings to date suggest that oxidative stress exerts harmful effects on liver cells through inducing lesions. Elucidation of the underlying mechanisms should facilitate the development of effective strategies to manage HCC.

## 2.2. Roles of microRNAs Correlated with Oxidative Stress in HCC

MicroRNAs (miRNAs) are small non-coding RNA molecules that regulate >70% human genes at the post-transcriptional level. The average miRNA length is ~21–23 nucleotides. DNA sequences are transcribed into primary miRNAs (pri-miRNA) and processed into precursor miRNAs (pre-miRNA) in the nucleus and mature miRNAs in the cytoplasm. In most cases, miRNAs interact with a specific sequence at the 3' untranslated region (UTR) of target mRNAs to induce translational repression via post-transcriptional regulation of cleavage or simply suppressing translation [28,29].

Accumulating studies support the importance of a series of oxidative stress-induced miRNAs in progression of carcinogenesis (Table 1). For instance, using the robust rank aggregation (RRA) method, miR-34a-5p, miR-1915-3p, miR-638, and miR-150-3p were shown to be upregulated under conditions of H<sub>2</sub>O<sub>2</sub> treatment as oxidative stress-responsive miRNAs in HCC cell lines [30]. The functions of these four miRNAs were further predicted using the TargetScan web tool and Gene Ontology (GO) pathway enrichment analysis. All four miRNAs were closely related to anti-apoptosis pathways and p53 signaling, clearly demonstrating a significant association between the p53 pathway and oxidative stress [31].

The importance of miRNAs in progression of chronic liver diseases to HCC is recognized. MiRNAs act as key mediators in the development of a number of cancer types owing to their involvement in inflammation and oncogenesis processes. Several miRNAs showing altered expression patterns in HCC and oxidative damage have been identified, including miRNA-92, miRNA-145, miRNA-199a, miRNA-199b, miRNA-195, and miRNA-122a [27].

In recent years, several miRNAs have been extensively investigated and their functions in association with oxidative stress determined. MiR-26a is reported to play a dual role in HCC. Considerable research has confirmed its activity as a tumor suppressor in HCC that inhibits proliferation, migration, and invasion by targeting F-box protein 11 (FBXO11), an E3 ubiquitin ligase, and type II methyltransferase [47,48]. DNA methyltransferase 3b (DNMT3B) is another direct target of miR-26a. Inhibition of DNMT3B associated with miR-26a upregulation led to a similar tumor suppressor effect in HCC cells [49]. In contrast, other studies suggest that miR-26a has potential oncogenic function in HCC. For instance, therapeutic miR-26a delivery suppresses tumorigenesis in an animal liver cancer model while other studies demonstrated that miR-26a expression promotes HCC cell migration and invasion in vivo. Another earlier in-depth study reported that miR-26a promotes cell migration and invasion by inhibiting the phosphatase prime time entertainment network (PTEN) [50,51]. Based on the metabolic perspective, increasing free fatty acid (FFA) supply into liver cells caused oxidative stress by ROS and lipid peroxidation generated during the metabolism of these accumulating fatty acids [52]. Recently, regulatory and protective roles of miR-26a on lipid metabolism and progression of NAFLD in human HepG2 cells loaded with FFA have



been demonstrated. Upregulation of miR-26a resulted in the downregulation of triglyceride (TG), total cholesterol (TCL), and malondialdehyde (MDA) through modulation of mRNA levels of genes involved in lipid homeostasis, ER stress, inflammation, and fibrogenesis [36]. Additionally, miR-26a targets different metabolic relative genes involved in fatty acid and cholesterol metabolism and insulin signaling, such as ACSL3, ACSL4, PKC $\delta$ , PKC $\theta$ , GSK3 $\beta$ , and SERBF1, suggesting a crucial role in preventing development of metabolic disease [53]. Notably, these liver-related lipid metabolism abnormalities are strongly associated with oxidative stress in liver cells [54,55].

**Table 1.** Oxidation stress-related microRNAs.

microRNA	Correlative with Oxidative Stress	Ref.
miR-34a-5p miR-1915-3p miR-638 miR-150-3p	Associated with oxidative stress-related apoptosis	[30]
miR-92	Correlated positively with telomerase activity, 8-OHdG Target to anti-oxidative gene Sirt1	[32]
miR-199a/b	Prevents the liver cell oxidative stress induced by bile acid Target to Sirt1	[33]
miR-122	Correlative with HCV/ HBV infection Positive association with antioxidant enzyme NQO1	[34] [35]
miR-26a	Affecting liver lipid metabolism	[36]
miR-155	Affecting liver lipid metabolism	[37]
miR-214	Associated with oxidative stress-related apoptosis Target to ATF4 and EZH2	[38] [39]
miR-200	Target to p38 $\alpha$ and repression anti-oxidative gene Nrf2	[40]
miR-181	Target to Sirt1 and impair insulin sensitivity	[41]
miR-128	Target to DJ-1 Target to Sirt1	[42] [43]
miR-29a/c	Controls the hepatic lipogenic process	[44]
miR-21	Leading to mitochondrial ROS accumulation	[45]
miR-196	Downregulates Bach1, and inhibition of HCV expression	[46]

\* Potential functions of miRNAs related to oxidative stress.

MiR-155 acts as a multifunctional oncogenic miRNA in different human cancer types, including breast, pancreatic, and liver cancer [56–58]. The miRNA promotes proliferation, invasion, and migration in HCC by directly targeting and inhibiting PTEN. The negative correlation between miR-155 and PTEN is significantly associated with TNM stage in HCC [56]. MiR-155 additionally inhibits Forkhead box O3 (FoxO3a) expression to suppress downstream apoptotic gene B-cell lymphoma-2 (Bcl-2)-interacting mediator of cell death (BIM) and suppresses cleavage of caspase-3 and caspase-9, consequently inhibiting HCC cell apoptosis and facilitating proliferation [59]. Furthermore, high expression of miR-155 is associated with poor survival, and in combination with Alpha-fetoprotein (AFP) shows higher sensitivity and specificity as a biomarker panel for diagnosis of HCC, compared with a single marker [60]. However, conflicting results on the role of miR-155 in lipid metabolism have been reported to date. Suppression of miR-155 in peripheral blood may be utilized as a novel biomarker for NAFLD screening. The transcription factor, Liver X Receptor  $\alpha$  (LXR $\alpha$ ), that interacts with the promoter region of sterol regulatory element-binding protein (SREBP)-1c, has been identified as a direct target of miR-155 [37,61]. Other studies have highlighted a reduction in alcohol-induced fat accumulation in miR-155 knockout mice, associated with increased Peroxisome proliferator-activated receptor response element (PPRE) binding to the miR-155 target gene, Peroxisome proliferator-activated receptor (PPAR) $\alpha$  [62]. However, further studies are required to confirm the finding that miR-155 participates in lipid accumulation in liver, inducing generation of oxidative stress.



### 2.3. Role of Thyroid Hormone and Its Receptor in HCC

Thyroid hormone, 3,3',5-tri-iodo-L-thyronine (T3), is a key mediator of multiple physiological processes, including cell development, differentiation, metabolism, and growth [38]. The pituitary gland secretes thyrotropin, which influences the thyroid gland to synthesize thyroid hormone mainly precursor T4. T4 moves across the cell membrane of responsive cells by specific transporters, including the monocarboxylate anion transporters 8 and 10 (MCT8 and MCT10), and is converted to the active T3 by type I 5'-deiodinase (DIO) 1 and 2, leading to increased levels of T3 [63]. T3 controls metabolic activities related to anabolism or catabolism, including carbohydrates, proteins, lipids, and damaged organelles in cells to maintain homeostasis under different physiological conditions [24]. To implement genomic effects, cytoplasmic T3 translocates to the nucleus and binds to specific high-affinity thyroid hormone receptors (TR) associated with thyroid hormone response elements (TRE) on DNA, thereby affecting transcriptional levels of downstream genes [14]. Typical TREs within promoter regions of downstream genes contain two half-site sequences (A/G)GGT(C/A/G)A in palindromic (Pal), direct repeat (DR), or inverted repeat arrangements (IP) recognized by TR. TRs bind to their respective TREs as monomers, homodimers, or heterodimers with retinoid X receptors (RXR). TRs usually form heterodimers with the RXR to interact with TREs within the promoter regions of target genes. Human TRs are encoded by two distinct genes, THRA (TR $\alpha$ ) and THRB (TR $\beta$ ), located on human chromosomes 17 and 3 [64]. Different TRs are composed of similar domains, including amino-terminal A/B domain to recruit regulatory proteins; central DNA-binding domain (DBD), or C region, which displays high affinity for DNA sequences of TREs; linker D region, which is necessary for nuclear translocation of the receptor; and carboxy-terminal ligand-binding domain (LBD), which interact with thyroid hormones [63,65]. In humans, TR $\beta$ /T3 regulates the metabolic activity of body and it is the major receptor isoform expressed in liver; in contrast, TR $\alpha$  is expressed mainly in the heart, skeletal muscle, adipose tissues, and specifically mediates adaptive thermogenesis [66].

Owing to its critical regulatory function in cellular homeostasis, imbalance of thyroid hormone in the body is highly associated with multiple chronic diseases including obesity, diabetes, cardiovascular, and liver disorders. The liver is the most important thyroid hormone target organ associated with cellular metabolic functions, such as hepatic fatty acid and cholesterol synthesis and metabolism. Hypothyroidism has been associated with increased serum expression of triglycerides and cholesterol as well as hypercholesterolemia or non-alcoholic fatty liver disease (NAFLD) [24,67]. Prevention of cardiovascular disease occurrence is important in patients with low-serum high-density lipoprotein cholesterol (HDL-C) due to thyroid dysfunction [68].

In addition to its effects on metabolism, thyroid hormone suppresses HCC development by protecting hepatocytes from HBx-induced damage through regulating mitochondrial quality control to suppress HBx protein stability. Mitochondrial quality maintenance by T3 prevents HBx-induced hepatocarcinogenesis and attenuates HCC progression [25,69]. In an earlier study, liver disease patients diagnosed with hepatic cirrhosis triggered by hepatitis B or C were screened for thyroid function status. The T3 levels of patients were lower than the normal range, suggesting that the serum T3 concentration is a good index of hepatic function, decreasing the severity of liver damage [70].

Several studies have demonstrated that treatment with T3 analogs can prevent hepatic steatosis and hepatitis. The thyroid hormone has potential therapeutic applications in hepatitis B and C, and T3 analogs may be effectively used as an alternative strategy to prevent HCC [71].

### 2.4. Thyroid Hormone Induces an Anti-Oxidative Stress Effect in Hepatocytes Mediated by microRNAs

Hypermetabolic effects of thyroid hormones as the major endocrine regulators of metabolic rate are well documented. Thyroid hormones have a profound impact on mitochondria, the organelles predominantly responsible for cellular energy metabolism, and are correlated with O<sub>2</sub> consumption and consequent ROS generation [72]. Effects of thyroid hormone on redox signaling to protect cellular function are documented. The pathways affected by thyroid hormone generally fall into two broad categories: Genomic and non-genomic. ROS production leads to activation of the redox-sensitive

transcription factors nuclear factor- $\kappa$ B (NF- $\kappa$ B), signal transducer and activator of transcription 3 (STAT3), signal transducer and activator of transcription 1 (STAT1), and nuclear factor erythroid 2-related factor 2 (Nrf2), promoting cell protection and survival mechanisms. Functions of the thyroid hormone include enhancement of homeostatic potential, through induction of antioxidant, anti-apoptotic, and anti-inflammatory gene expression, and higher detoxification capabilities and energy supply through AMP-activated protein kinase (AMPK) upregulation [73]. Thyroid hormone additionally regulates miRNAs that promote antioxidant capacity in the liver to prevent HCC progression.

In a previous study, our group used qRT-PCR array to explore the expression patterns of different miRNAs regulated by thyroid hormone (Tables 2 and 3) [38,74–76]. The functions of potentially important thyroid hormone-regulated miRNAs in HCC and their correlation with oxidative stress are further discussed below.

**Table 2.** MicroRNAs positively associated with thyroid hormones in HepG2 liver cancer cell lines.

miRNAs Positively Affected by Thyroid Hormones *								
TH/microRNAs	HepG2-TR $\alpha$ 1				HepG2-TR $\beta$ 1			
	MicroRNA	Fold	HCC/ROS Ref.	TH	MicroRNA	Fold	HCC/ROS Ref.	TH
Three times repetitive experiments	miR-122	10.54	[35,77]	[78]	miR-29c	4.21	[44,79]	
	miR-152	3.42			miR-214	3.50	[38,80,81]	[38]
	miR-139-5p	10.38			miR-202	2.41		
	miR-128a	71.90	[43]					
	miR-139-3p	3.85						
	miR-548d-3p	3.09						
	miR-140-3p	2.77						
Two times repetitive experiments	miR-143	6.20			miR-193b	2.99		
	miR-210	5.22			miR-139-5p	3.12		
	miR-365	5.53			miR-210	2.52		
	miR-135b	4.38			miR-323-3p	4.12		
	miR-148a	5.16			miR-22	2.54		
	miR-193b	3.30			miR-29a	2.18	[44,82]	
	miR-125a-3p	2.92			miR-29b-1 *	3.30		
	miR-29a	3.15	[44,82]		miR-193a-3p	3.34		
	miR-24	2.40	[83]	[78]	miR-139-3p	2.22		
	miR-372	3.57			miR-510	2.32		[75,78]
	miR-372	5.07			miR-21 *	2.22	[45,84–86]	
	miR-188-3p	3.05						
	miR-100	4.11						
	miR-126	2.35						
	miR-21	3.30	[45,84–86]	[75,78]				

\* HepG2 hepatoma cell lines overexpressing TR $\alpha$ 1 or TR $\beta$ 1 were treated with thyroid hormone (T3; 20 nM). After 24 h, qRT-PCR array analysis of microRNA (miRNA) expression was performed. The specified miRNAs were positively affected (>2-fold) upon thyroid hormone stimulation and selected candidates were identified from at least two times repetitive experiments. The references are to indicate oxidative stress (HCC/ROS) or thyroid hormone (TH) related miRNAs in liver cancer.

**Table 3.** MicroRNAs negativity associated with thyroid hormones in HepG2 liver cancer cell lines.

miRNAs Negativity Affected by Thyroid Hormones *								
HepG2-TR $\alpha$ 1				HepG2-TR $\beta$ 1				
TH/microRNAs	MicroRNA	Fold	HCC/ROS Ref.	TH	MicroRNA	Fold	HCC/ROS Ref.	TH
Three times repetitive experiments	miR-184	0.22			miR-455-3p	0.22		
	miR-455-3p	0.12			miR-148a	0.36		
	miR-499-3p	0.20			miR-425 *	0.24		
	miR-221	0.33			miR-187	0.27		
	miR-181b	0.30	[87]		miR-429	0.41		
	miR-130b	0.34		[76]				
	miR-149	0.35						
Two times repetitive experiments	miR-17	0.34	[85]	[74]				
	miR-425 *	0.22			miR-106a	0.23		
	miR-20a	0.31			miR-199a-5p	0.22	[33,87,88]	[38]
	miR-377	0.42			miR-548d-5p	0.24		
	miR-15b	0.43			miR-146a	0.31		
	miR-516a-5p	0.29			miR-221	0.27		
	miR-652	0.49			miR-30a *	0.35		
	miR-550	0.26			miR-499-3p	0.32		
	miR-18a	0.23			miR-888	0.27		
	miR-106a	0.28			miR-100	0.33		
	miR-628-3p	0.34			miR-339-3p	0.45		
	miR-146a	0.36			miR-18a	0.39		
	miR-181c	0.41	[87]		miR-18b	0.24		
	miR-92a	0.36	[32,89,90]		miR-10a	0.25		
	miR-106b	0.38			miR-421	0.30		
	miR-487b	0.35			miR-525-3p	0.41	[74,85]	
	miR-570	0.40			miR-17	0.37	[85,90]	[74]
	let-7d	0.44			miR-542-5p	0.33	[46,85]	
	miR-15b *	0.44			miR-196a *	0.42	[46]	
					miR-196b	0.46		
					miR-19a	0.46	[87]	
					miR-181d	0.32		
					miR-20b	0.40		

\* HepG2 hepatoma cell lines overexpressing TR $\alpha$ 1 or TR $\beta$ 1 were treated with thyroid hormone (T3; 20 nM). After 24 h, qRT-PCR array analysis of microRNA (miRNA) expression was performed. The specified miRNAs were negatively affected (<0.5-fold) upon thyroid hormone stimulation and selected candidates were identified from at least two times repetitive experiments. The references are to indicate oxidative stress (HCC/ROS) or thyroid hormone (TH)-related miRNAs in liver cancer.

MiR-214 is dysregulated in many human cancer types including cervical, prostate, and ovarian cancer [91–93]. In HCC, miR-214 acts as a tumor suppressor and is used as a potential prognostic marker for overall survival [94,95]. Earlier studies indicate that miR-214 plays a tumor suppressor role by inhibiting proliferation and migration of HCC cells through targeting pyruvate dehydrogenase kinase 2 (PDK2) and plant homeodomain finger protein 6 (PHF6) [80]. Forkhead box protein M1 (FoxM1) is an important transcription factor in the progression of HCC. Direct targeting and downregulation of FoxM1 mRNA by miR-214 inhibits proliferation, migration, and invasion of HCC [81]. In the clinic, miR-214 downregulation is positively associated with higher tumor recurrence and poorer clinical outcomes. Ectopically expressed miR-214 inhibits xenograft tumor growth and microvasculature of tumors and their surrounding tissues via targeting and suppressing its downstream target gene, hepatoma-derived growth factor (HDGF) [94].

Several oncogenic long non-coding RNAs (lncRNA) are correlated with miR-214. Among these, myocardial infarction-associated transcript (MIAT) regulates proliferation and invasion of HCC cells via sponging miR-214 [96]. Plasmacytoma variant translocation 1 (PVT1) lncRNA is increased in HCC tissues and associated with tumor size, histological differentiation grade, and advanced TNM stage. PVT1 has been shown to promote proliferation and invasion of HCC via inhibition of miR-214 expression by interacting with enhancer of zeste homolog 2 (EZH2) [97].

MiR-214 is upregulated by the thyroid hormone through direct interactions with its receptor in the promoter region, leading to repression of the target oncogene, PIM-1, and in turn, suppression of HCC cell proliferation and inhibition of tumor formation [38]. Diethylnitrosamine (DEN) is a typical chemical carcinogen with the potential to cause tumors in multiple organs, such as liver, skin, gastrointestinal tract, and the respiratory system. This significant environmental carcinogen triggers ROS production, resulting in oxidative stress and cellular injury. DEN is considered a complete hepatocarcinogen [98–100]. As highlighted previously, thyroid hormone promotes selective autophagy via induction of the death-associated protein kinase 2-Sequestosome 1 (DAPK2-SQSTM1) pathway, thus protecting against DEN-induced carcinogenesis in hepatocytes [101]. Notably, thyroid hormone additionally plays a protective role against DEN-induced HCC through upregulation of miR-214 [38].

Thyroid hormone is a human hormone that mediates the cell differentiation and metabolism and acts as an anti-apoptosis factor upon challenge of thyroid hormone receptor expression in HCC cells with cancer therapy drugs, such as cisplatin, doxorubicin, and tumor necrosis factor-related apoptosis-inducing ligand (TRAIL). Doxorubicin (Dox), a DNA topoisomerase II inhibitor, belongs to the anthracycline anticancer drug family [102]. Dox is widely used to treat lymphoma breast, head-and-neck, prostate, and liver cancers [103–106]. Dox induces pathogenic mechanisms including apoptosis, oxidative stress, and inflammation, through formation of ROS, reduces anti-oxidative defense, and stabilizes mitochondrial damage [107–109]. Thyroid hormone and its receptor signaling pathway promote chemotherapeutic resistance through negatively regulating the pro-apoptotic protein, BCL2-like 11 (BCL2L1/Bim), resulting in Dox-induced metastasis of chemotherapy-resistant HCC cells [110].

In addition, HCV infection promotes mitochondrion-mediated apoptosis through stimulating the upstream ROS/JNK signaling pathway to affect Bax-triggered mechanisms. In brief, HCV-induced ROS/JNK signaling transcriptionally activates Bim expression, which leads to Bax activation and apoptosis induction [111]. Bim is a direct target gene of miR-214 in nasopharyngeal carcinoma (NPC) and other tissues [112–114]. One possibility is that the thyroid hormone induces miR-214 to suppress Bim expression through negatively regulating the transcription factor Forkhead box protein O1 (FoxO1) to avoid liver cell apoptosis and ROS-induced stress [110]. In addition to miR-214, there are many miRNAs that have the potential to affect the apoptosis of liver cancer cells, such as miR-155, miR-4417, miR-199a, and miR-122 [59,77,115,116]. Among them, the expression levels of miR-199a and miR-122 are associated with thyroid hormone and oxidative stress (Tables 2 and 3) [27]. Previous studies have indicated that Dauricine (Dau) is a natural alkaloid, which promoted apoptosis of HCC cells induced by chemotherapeutic reagents. Dau stimulates the expression of miR-199a and results in inhibition of the target gene hexokinase 2 (HK2) and pyruvate kinase M2 (PKM2), resulting in sensitivity to chemotherapeutic reagents, including Cisplatin, Sorafenib, and Isoliquiritigenin in HCC cells [116]. However, thyroid hormones, which are inversely related to miR-199a, may also involve in this action of apoptosis. Interestingly, in addition to the target gene of miR-199a, PKM2, which is strongly associated with apoptosis, is also affected by miR-4417 and miR-122 in liver cancer cells [77,115].

Gemcitabine (GEM) is a commonly used chemotherapeutic agent for HCC that uses oxidative stress induction as a common effector pathway. Overexpression of mitochondrial uncoupling protein 2 (UCP2) causes resistance to GEM. GEM administered alone or in combination with oxaliplatin renders minimal survival benefits to HCC patients. The tumor suppressor activity of miR-214 is activated through targeting UCP2, which may solve the problem of GEM efficacy [117,118]. Combined usage of thyroid hormone combined with GEM could provide new insights into strategies to treat liver cancer based on this novel mechanism of action.

MiR-214 protects red blood cells against oxidative stress by targeting activating transcription factor 4 (ATF4) and enhancer of zeste homolog 2 (EZH2) [39]. Direct targeting of the transcriptional factor, ATF4, by miR-214, attenuates stress responses. Suppression of miR-214 leads to enhanced ATF4 translation and consequently, upregulation of ATF4 protein. Additionally, miRNA-214 is reported to reduce oxidative stress in diabetic nephropathy mediated the ROS/Akt/mTOR signaling pathway [119]. An earlier study by Liu et al. [120] showed that miR-424 inhibits oxidative stress and protects against transient cerebral ischemia injury.

MiR-122 plays a complex role in HBV and HCV infection [34,121,122]. MiR-122 is a liver-specific miRNA that acts as a host factor to increase the abundance of HCV RNA by stabilizing the positive strand of HCV RNA genome and promotes HCV synthesis by binding two sites near the HCV 5' end and associating with Ago2 [34,123–125]. In contrast to its role in HCV infection in HCC, miRNA-122 is significantly downregulated in patients with HBV infection [126,127]. Adenosine deaminases act on RNA-1 (ADAR1), an important gene involved in adenosine to inosine RNA editing and miRNA processing. ADAR1 also plays an anti-viral role against HBV infection by increasing the miRNA-122 level in hepatocytes [128]. In terms of the role of miR-122 in carcinogenesis, this liver-specific miRNA is reported to be dramatically downregulated in most HCCs. The tumor suppressor role of miR-122 in HCC is exerted by targeting the genes involved in cell proliferation, differentiation, apoptosis, and angiogenesis, and its expression is inversely associated with poor prognosis and metastasis [129]. Many studies have demonstrated that miR-122 acts as an important tumor suppressor through regulating different target genes including WNT1, Cyclin G1, MDR, ADAM17, CUTL1, and AKT3 in HCC [130,131]. Associations of miR-122 expressed in liver and anti-oxidant genes, such as heme oxygenase 1 (HMOX-1), NAD(P)H, quinone oxidoreductase-1 (NQO1), and growth factor erv1-like (GFER1) in liver tissue specimens obtained from patients with chronic hepatitis B, have been uncovered. A significant positive association between expression of NQO1 and miR-122 was determined [35]. NQO1 is a multifunctional antioxidant enzyme and exceptionally versatile cytoprotective agent that regulates the proteasomal degradation of specific antioxidant proteins, such as nuclear factor erythroid 2-like 2 (Nrf2) [132], one of the major mediators of inflammation and a transcription factor. Nrf2 promotes the expression of antioxidant as well as cytoprotective genes, resulting in anti-inflammatory effects [133].

Perfluorooctanesulfonate (PFOS) has been widely used in commercial applications as a surfactant and stain repellent. PFOS has been shown to cause liver damage (including liver tumors) in experimental animals through interactions with peroxisome proliferator-activated receptor  $\alpha$  (PPAR $\alpha$ ) and constitutive androstane receptor (CAR)/pregnane X receptor (PXR). Further studies have highlighted the ability of PFOS to disrupt thyroid function and induce thyroid hormone alterations, leading to hypothyroxinemia [78,134]. Assessment of changes in miRNA levels in rats with PFOS-induced hypothyroxinemia revealed that three members of the miR-200 family were the most significantly increased while miR-122 and miR-21 showed the greatest decrease in expression. Moreover, expression of the miR-23b/27b/24 cluster was decreased in PFOS-treated animals [78]. Consistently, experiments by our group demonstrated upregulation of miR-122, miR-21, and miR-24 by thyroid hormone treatment in HCC cells (Table 2).

Among the miRNAs affected by thyroid hormone, members of the miR-200 family were markedly enhanced in hepatic cells following hydrogen peroxide (H<sub>2</sub>O<sub>2</sub>) treatment. Among these, miR-200-3p modulates the H<sub>2</sub>O<sub>2</sub>-mediated oxidative stress response by targeting mitogen-activated protein kinase 14 (p38 $\alpha$ ). p38 $\alpha$  acts as a stress-activated protein kinase that negatively regulates tumorigenesis by acting on cell apoptosis, survival, and stress response. p38 $\alpha$  inhibition leads to increased ROS levels in liver cells through repression of Nrf2, a master regulator of antioxidant and detoxifying genes [40]. These results support a hepatoprotective role of thyroid hormone through effects on the pathway of oxidative stress-induced miR-200 to repress p38 $\alpha$  and Nrf2.

MiR-92a is highly expressed and specifically altered in HBV/HCV-related HCC [135,136]. This miRNA plays a critical role in HCC proliferation and invasion and could serve as a novel



therapeutic target via repression of Forkhead Box A2 (FOXA2) [137,138]. Clinical association analysis revealed a correlation of high expression of miR-92a with poor prognostic characteristics of HCC. Diagnostic efficacy of a combination of miR-92a and AFP was powerful for HCC, in particular screening of early tumor and low-level AFP patients [139]. A combination of the tumor suppressor gene phosphatase and tensin homolog (PTEN) and miR-92a also provided significant clinical value for early diagnosis and prognosis of HCC based on their significant negative correlation in HCC and para-cancerous tissue [140]. MiR-92a has been shown to promote tumor growth of HCC by targeting F-box and WD repeat domain-containing 7 (FBXW7) and may serve as a novel prognostic biomarker and therapeutic target [141]. ROS trigger DNA oxidation leading to multiple modifications in DNA bases, among which 8-OHdG is the most frequent [142]. 8-OHdG induces point mutations in DNA strands and accumulates in DNA to cause mispairing, resulting in mutagenic and potentially carcinogenic activity. HCC tissues are frequently characterized by increased oxidative damage, which contributes to acceleration of telomere shortening and telomerase activation in cancer cells. The telomere acts as a protective cap at the ends of chromosomes and telomere shortening promotes chromosomal instability [143,144]. Oncogenic miR-92a expression is significantly correlated with telomerase activity and 8-OHdG levels in HCC tissues, indicating a link with ROS-mediated oxidative DNA damage [32]. The pre-mRNA-splicing factor, SLU7, is essential for HCC cell viability. SLU7 expression is reduced in HCC cells, and its depletion triggers autophagy-related cellular apoptosis in association with generation of ROS. Low expression of SLU7 leads to altered splicing of the C13orf25 primary transcript and reduced expression of its miR-17-92a constituents, leading to upregulation of its target genes, CDKN1A (P21) and BCL2L11 (BIM), and mediators of pro-survival and tumorigenic activities [90]. Previous studies have shown that miR-92a and its cluster miR-17, miR-18a, and paralog, miR-20b, are downregulated by the thyroid hormone in HCC cells (Table 3). MiR-92 also plays a key regulatory role in neovascularization and is predicted to target Sirtuin-1 (Sirt1) [89], a NAD<sup>+</sup>-dependent deacetylase with potential anti-oxidative stress activity in vascular endothelial cells. The mechanisms underlying the protective effects involve Sirt1/FOXOs, Sirt1/NF- $\kappa$ B, Sirt1/NOX, Sirt1/SOD, and Sirt1/eNOS pathways [145]. Several other miRNAs, such as miR-181, miR-138, and miR-199, suppress Sirt1 in different cells/tissue types. Among these, miRNA-181 is upregulated under conditions of a high-fat diet and is reported to suppress Sirt1 and impair insulin sensitivity in liver [41,87]. Similar results have been reported for miR-200 and miR-199 in the DEN model [88]. Data from our qRT-PCR array disclosed downregulation of miR-181 and miR-199 by thyroid hormone (Table 3) [38]. Notably, miR-181 is inversely correlated with TR $\beta$ 1 in human cirrhotic peritumoral tissue, compared to normal liver [146]. These findings support the theory that thyroid hormone decreases oxidative stress via repression of miR-181 and miR-199 to increase the target gene Sirt1 expression in liver.

MiR-206 is downregulated during tumorigenesis and plays an important role in modulating the growth of multiple HCC cells via targeting cyclin-dependent kinase 9 (CDK9), which stimulates the production of abundant prosurvival proteins, leading to impaired cancer cell apoptosis [147]. Overexpression of miR-206 has been shown to inhibit proliferation, invasion, and migration of the HCC cell lines HepG2 and Huh7. Conversely, inhibition of miR-206 enhances expression of protein tyrosine phosphatase 1B (PTP1B) that plays an oncogenic role in HCC, in HepG2, and Huh7 cells [148]. MiR-206 also directly targets the c-Met gene for silencing and restoration of c-Met expression reverses the inhibitory effect of miR-206 on HCC [149]. Nrf2, involved in cellular antioxidant defense systems, protects against excessive ROS damage to macromolecules and consequent senescence and apoptosis. Upregulation of Nrf2-dependent antioxidant and metabolic genes and significantly reduced miR-1 and miR-206 expression in lung tumors are associated with reduced survival in patients with lung adenocarcinoma [150]. MiR-206 is involved in thyroid hormone-mediated regulation of lipid metabolism in HepG2 cells, and its expression is suppressed in patients with hyperthyroidism, indicating a role in thyroid hormone-induced disorders of lipid metabolism in the liver [151].

### 2.5. Thyroid Hormone Promotes Oxidative Stress in Hepatocytes by Regulating microRNAs

Thyroid hormone not only regulates miRNAs to prevent oxidative stress in hepatocytes, but also exerts effects on miRNAs that result in increased oxidative stress-induced damage to liver. Below, we have discussed a few examples of miRNAs positively correlated with oxidative stress and regulated by thyroid hormone.

MiR-128 is downregulated in HCC and suppresses cell proliferation through inducing G1 phase cell arrest via regulating phosphoinositide 3 kinase regulatory subunit 1 (PIK3R1) expression, which inhibits the phosphatidylinositol 3-kinase (PI3K)/AKT signal pathway [152]. In addition, miR-128 significantly inhibits HCC cell metastasis and stem-cell like properties through direct targeting of integrin alpha 2 (ITGA2) and integrin alpha 5 (ITGA5) [153]. Parkinson disease protein 7 (PARK7/ DJ-1) expression is elevated in various tumors and related to the survival of tumor cells under adverse stimuli, including oxidative stress. DJ-1, also known as Parkinson's disease-associated protein (PDAP), performs multiple functions, including cysteine protease, anti-oxidative stress reaction, and tumorigenesis activities [154,155]. MiR-128 is downregulated and negatively correlated with DJ-1, which is a direct target of the miRNA, in HCC cells [42]. Dox also markedly upregulates miR-128 and downregulates Sirt1 expression by direct targeting and affecting the expression of other antioxidant proteins, such as Nrf2, Keap1, Sirt3, NQO1, and HO-1, leading to excessive oxidative stress in liver [43]. In our qRT-PCR array, the tumor suppressor, miR-128, was upregulated by thyroid hormone, suggesting a correlation between thyroid hormone and miR-128-affected antioxidant genes, such as Sirt1 (Table 2).

According to our qRT-PCR data, thyroid hormone enhances miR-128 to suppress Sirt1 expression in liver. MiR-29a and miR-29c are also upregulated by the thyroid hormone and associated with Sirt1 expression (Table 2). Previous experiments have shown that miR-29 controls the hepatic lipogenic process through regulation of anti-lipogenic transcription factor aryl hydrocarbon receptor (AHR) and Sirt1 in liver [44]. MiR-29a suppresses cell proliferation through direct targeting of Sirt1 in HCC [82]. PU box binding protein (PU.1) is a critical transcription factor involved in many pathological processes. In PU.1-deficient mice, miR-34a and miR-29c are highly expressed and regulate Sirt1 expression in hepatic stellate cells to resistant hepatic fibrosis [79]. The data suggest that the thyroid hormone may suppresses the anti-oxidative stress reaction by miR-128, miR-29, miR-29a, and miR-29c to direct targeting Sirt1 and indirect effect other anti-oxidative stress genes expression.

In HCC cells and tissues, miR-21 is upregulated and positively associated with cell migration and invasion abilities. Krueppel-like factor 5 (KLF5) acts as a tumor inhibitor in some cancer types. In an earlier study, KLF5 expression was inhibited through direct targeting by miR-21, leading to the induction of migratory and invasive abilities in HCC [156]. Betulinic acid (BA) is a pentacyclic triterpene that possesses potential pro-apoptotic activities through increasing mitochondrial ROS generation. Mitochondrial dysfunction activates the molecular apoptotic events leading to cell death in HCC. BA suppresses superoxide dismutase 2 (Sod2) expression through upregulation of miR-21, leading to mitochondrial ROS accumulation and apoptosis in HCC [45]. MiR-21 is reported to be activated via thyroid hormone-receptor interactions at the native TRE site in the promoter region [75]. The thyroid hormone may thus have a similar function as BA in increasing mitochondrial ROS generation and mitochondrial dysfunction through miR-21 expression in HCC.

MiR-196 is readily released in body fluids and blood during HBV/HCV-associated hepatitis as well as metabolic, alcohol-associated, drug-induced, and autoimmune hepatitis. Liver-specific miR-196 is a potential indicator of liver injury (mainly apoptosis, necrosis, and necroptosis) or hepatitis, showing variable expression during acute/fulminant, chronic, liver fibrosis/cirrhosis, and HCC [157]. Bach1, a basic leucine-zipper mammalian transcriptional repressor, negatively regulates HMOX1, a key cytoprotective enzyme with antioxidant and anti-inflammatory activities. MiR-196 significantly downregulates Bach1, leading to upregulation of HMOX1 gene expression and inhibition of HCV expression, further affecting oxidative stress and liver injury induced by HCV [46]. Data from our qRT-PCR experiments suggest that miR-196 is a potential oncogenic miRNA downregulated by thyroid hormone (Table 3).

MiR-199 family members (miR-199a/b-5p) are downregulated in HCC. Notably, the lower expression of miR-199a is also associated with poorer overall survival of HCC patients. MiR-199a overexpression in HCC cell lines is reported to inhibit cell proliferation, migration, and invasion. The miR199a family suppresses Rho-associated coiled-coil kinase 1 (ROCK1) post-transcriptionally to inhibit PI3K/Akt signaling, which is necessary for HCC proliferation and metastasis [158]. Moreover, miR-199 targets and negatively regulates X-box binding protein 1 (XBP1) and affects cyclin D, which is associated with cell cycle regulation in HCC cells [159]. Bile salts retained within the liver play a major role in liver injury during cholestasis and trigger cellular stress events, including protein misfolding, DNA damage, endoplasmic reticulum (ER) stress, and oxidative stress, that may result in cell death and pathogenesis of several liver diseases [160]. Another study reported elevated miR-199a-5p levels in bile acid-stimulated cultured hepatocytes of liver from bile duct-ligated mice. Elevated miR-199-5p disrupted sustained ER stress and prevented hepatocytes from undergoing bile acid-induced cell death, supporting the potential of this miRNA as a target for clinical approaches aiming to protect against liver toxicity from bile salts in hepatocytes [33]. Analysis of the association between thyroid hormone and miR-199 unexpectedly revealed a negative correlation between the two molecules. MiR-199/miR-214 are clustered and located on opposite strands of the *Dynamin3* gene (*DNM3*). Under most conditions, while clusters have the same performance, but the thyroid hormone exerts differential effects on the two molecules, which seems to be due to the existence between miR-199 and miR-214 additional positivity TRE affecting miR-214 [38].

### 3. Discussion

The specific roles of thyroid hormone in different human cancer types are controversial. A number of investigators have reported that thyroid hormone promotes development of various cancers, whereas others suggest a tumor suppressor role [161–164]. Accumulating evidence from animal models and epidemiologic studies indicate an association between higher thyroid hormone levels and prevention of liver diseases, supporting the suppressor role of thyroid hormone and its receptor in HCC [25,38,164–166]. Moreover, clinical findings support a positive correlation between hypothyroidism and HCC development [167–169]. Oxidative stress-induced liver inflammation is the most important factor for HCC progression [1,170]. Oxidative stress is also related to thyroid hormone derangement, with the hormone reported to influence the antioxidant level or generation of ROS. Hyperthyroidism and hypothyroidism have been shown to be associated with oxidative stress in acute and chronic nonthyroidal illness syndrome (NTIS) [171,172].

In this report, we have discussed the involvement of a range of miRNAs in correlation with thyroid hormone and oxidative stress in HCC. Inconsistent results have been obtained from multiple studies on the role of the thyroid hormone in multiple cancer types. Based on the collective findings, thyroid hormone clearly regulates the expression of different miRNAs either directly or indirectly to affect oxidative stress (HCV/HBV-induced or DEN, Dox-induced) in liver. As shown in Figure 1, thyroid hormones can influence oxidative stress-induced hepatocarcinogenesis mediated by miRNAs, specifically, via upregulating miR-214, miR-122, and miR-206 in HCC. Several other studies indicate these miRNAs act as tumor suppressors in HCC. Simultaneously, these miRNAs regulate different oxidative stress-related genes that participate in liver cell antioxidant capacity, including Bim, NQO1, and Nrf2. A number of oncogenic miRNAs have been shown to be downregulated by thyroid hormone in HCC, including miR-200, miR-92a, and miR-181. Their target genes, p38 $\alpha$ , 8-OHdG, and Sirt1, participate in oxidative stress. Multiple studies have shown that thyroid hormones participate in the regulation of miRNA expression to prevent excessive generation of ROS (miR-122, miR-200, miR-206) and reduce DNA damage (miR-214, miR-92a, miR-181) in hepatocytes.

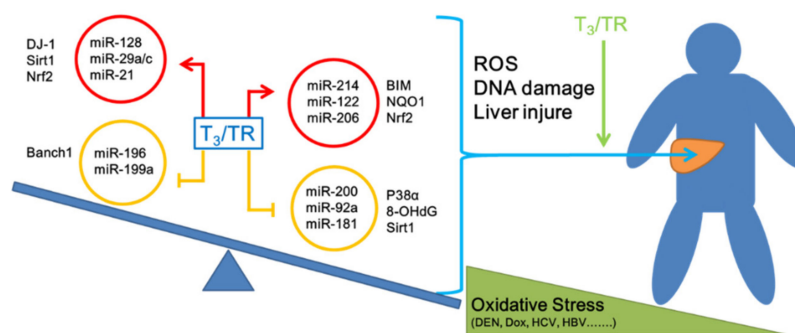


**Figure 1.** Thyroid hormones affect oxidative stress-induced hepatocarcinogenesis through effects on miRNAs. Oxidative stress is a risk factor associated with liver cancer. Among them, miRNAs strongly related to physiological significance are also involved. We analyzed the associations of thyroid hormones with oxidative stress and miRNAs in liver cells. While miRNAs related to promotion of resistance to oxidative stress were also affected by thyroid hormones, based on empirical evidence from other experimental animal and clinical studies, we believe that thyroid hormone plays a largely hepatoprotective role under conditions of oxidative stress. (The red arrow is a positive association, the yellow T bar is a negative association, blue arrow indicates the miRNAs affected liver genes, and green arrow is thyroid hormone associated-miRNAs affected liver genes)

Conversely, an oncogenic role of thyroid hormone in HCC has been reported by other investigators [14,173]. The thyroid hormone is reported to induce oxidative stress through enhancing the expression of different miRNAs in liver, such as miR-128, miR-29a/c, and miR-21, which directly regulate anti-oxidant genes, such as DJ-1, Sirt1, and Bach1, or affect related antioxidant genes, including Nrf2, Keap1, Sirt3, NQO1, and HO-1.

The role of thyroid hormone in various human organs is complex, especially under conditions of oxidative stress. In patients with hypothyroidism, high plasma levels of NO and malondialdehyde (MDA), a marker of oxidative stress, were measured in hepatic vein, along with lower activity of paraoxonase-1 (PON-1), a liver enzyme with antioxidant features. Data from this study further indicated that increased oxidative stress in hypothyroidism is primarily attributed not only to a decrease in antioxidant levels, but also effects on lipid metabolism [174,175]. The collective evidence suggests that thyroid hormone has potential antioxidant activity, at least in the liver [7,73]. The same findings were reported in experimental animals. Thyroid hormone signaling was altered following stimulation with various stress signals and played a crucial role in response to stress, post-stress recovery, and tissue repair by reducing the inflammatory response associated with NF- $\kappa$ B and STAT3 activation as well as the acute phase response [176–178]. Hepatic autophagy regulates lipid metabolism through elimination of triglyceride accumulation in liver, prevents the development of steatosis, and reduces oxidative stress [179]. Mitochondrial balance is a precisely regulated process that influences cellular homeostasis. Since activation of hepatic mitophagy eliminates the lipid content and oxidative stress, its dysregulation is implicated in progression of NAFLD. Dysregulation of autophagy and defective mitochondrial homeostasis contribute to hepatocyte injury and liver-related diseases [180]. In a murine model, disruption of thyroid hormone production led to a marked increase in progression of DEN-induced HCC. DEN triggers generation of ROS, resulting in oxidative stress and cellular injury, and consequently, progression of HCC. Data from this model indicate that thyroid hormone promotes autophagy via induction of the DAPK2-SQSTM1 cascade, thus protecting hepatocytes from DEN-induced hepatotoxicity or carcinogenesis. Furthermore, thyroid hormone is reported to participate in regulation of lipid metabolism through a chromosome 19 open reading frame 80 (C19orf80)-activated autophagic process in HCC [99,101,181].

Although the role of thyroid hormone in relation to oxidative stress in HCC remains a controversial issue, abundant reports support antioxidant over pro-oxidant activity, which prevents induction of liver cancer progression by oxidative stress in hepatocytes. This situation is similar to that of the



antioxidant genes Sirt1 and Nrf2. Sirt1 and Nrf2 are oppositely regulated by thyroid hormone in association with different miRNAs. However, the majority of reports indicate that the thyroid hormone activates Sirt1 [182,183]. Moreover, the thyroid hormone positively affects FOXO1 in addition to Sirt1 to stimulate genes that enhance the autophagic process [184–187]. Several animal studies have provided evidence to support a positive association of thyroid hormone with Nrf2, a key redox-sensitive transcription factor of antioxidant genes, in the liver. Thyroid hormone not only upregulates Nrf2, but also promotes antioxidant gene expression, since Nrf2 translocates from the cytosol to nucleus, mediating hepatic cytoprotection [188–191].

In this review, we have discussed several miRNAs associated with oxidative stress in HCC. Importantly, the relationships among miRNAs, thyroid hormone, and oxidative stress have been comprehensively explored. Despite conflicting results in the literature, thyroid hormone is considered a protective factor overall in hepatocytes. Thyroid hormone may aid in maintaining the normal environment of hepatocytes through effects on lipid metabolism and mitochondrial activity. Moreover, thyroid hormone protects against liver injury by reducing oxidative stress induced by harmful chemicals or HBV/HCV. Further studies should focus on the development of thyroid hormone analogs beneficial for human health.

**Author Contributions:** Conceptualization, P.-S.H. and K.-H.L.; investigation, P.-S.H.; writing—original draft preparation, P.-S.H.; writing—review and editing, K.-H.L.; visualization, supervision, C.-T.Y.; K.-H.L.; funding acquisition, C.-S.W. and K.-H.L.

**Funding:** This research was funded by grants from Chang Gung Memorial Hospital, Taoyuan, Taiwan (CMRPD1J0051, CMRPD1H0631 to K. H. Lin; CMRPG6F0621, CMRPG6F0622, CMRPG6F0623 to C. S. Wang) and from the Ministry of Science and Technology of the Republic of China (MOST 106-2320-B-182-031-MY3 and 106-2320-B-182-032-MY3 to K.H. Lin). And The APC was funded by Chang Gung Memorial Hospital, Taoyuan, Taiwan.

**Conflicts of Interest:** The authors declare no conflict of interest. The funders had no role in the design of the study; in the collection, analyses, or interpretation of data; in the writing of the manuscript, or in the decision to publish the results.

## References

1. Bishayee, A. The role of inflammation and liver cancer. *Adv. Exp. Med. Biol.* **2014**, *816*, 401–435. [PubMed]
2. Balogh, J.; Victor, D., 3rd; Asham, E.H.; Burroughs, S.G.; Boktour, M.; Saharia, A.; Li, X.; Ghobrial, R.M.; Monsour, H.P., Jr. Hepatocellular carcinoma: A review. *J. Hepatocell. Carcinoma* **2016**, *3*, 41–53. [CrossRef] [PubMed]
3. Burton, G.J.; Jauniaux, E. Oxidative stress. *Best Pract. Research. Clin. Obstet. Gynaecol.* **2011**, *25*, 287–299. [CrossRef]
4. Lu, T.X.; Rothenberg, M.E. MicroRNA. *J. Allergy Clin. Immunol.* **2018**, *141*, 1202–1207. [CrossRef] [PubMed]
5. Mohr, A.M.; Mott, J.L. Overview of microRNA biology. *Semin. Liver Dis.* **2015**, *35*, 3–11. [CrossRef] [PubMed]
6. Krashin, E.; Piekietko-Witkowska, A.; Ellis, M.; Ashur-Fabian, O. Thyroid Hormones and Cancer: A Comprehensive Review of Preclinical and Clinical Studies. *Front. Endocrinol.* **2019**, *10*, 59. [CrossRef]
7. Mancini, A.; Di Segni, C.; Raimondo, S.; Olivieri, G.; Silvestrini, A.; Meucci, E.; Curro, D. Thyroid Hormones, Oxidative Stress, and Inflammation. *Mediat. Inflamm.* **2016**, *2016*, 6757154. [CrossRef]
8. Kim, B.Y.; Cho, M.H.; Kim, K.J.; Cho, K.J.; Kim, S.W.; Kim, H.S.; Jung, W.W.; Lee, B.H.; Lee, B.H.; Lee, S.G. Effects of PRELI in Oxidative-Stressed HepG2 Cells. *Ann. Clin. Lab. Sci.* **2015**, *45*, 419–425.
9. Huang, F.Y.; Wong, D.K.; Tsui, V.W.; Seto, W.K.; Mak, L.Y.; Cheung, T.T.; Lai, K.K.; Yuen, M.F. Targeted genomic profiling identifies frequent deleterious mutations in FAT4 and TP53 genes in HBV-associated hepatocellular carcinoma. *BMC Cancer* **2019**, *19*, 789. [CrossRef]
10. Feld, J. Update on the Risk of Primary and Recurrent HCC With the Use of DAA Therapy for HCV Infection. *Gastroenterol. Hepatol.* **2019**, *15*, 303–306.
11. Vandenbulcke, H.; Moreno, C.; Colle, I.; Knebel, J.F.; Francque, S.; Serste, T.; George, C.; de Galocsy, C.; Laleman, W.; Delwaide, J.; et al. Alcohol intake increases the risk of HCC in hepatitis C virus-related compensated cirrhosis: A prospective study. *J. Hepatol.* **2016**, *65*, 543–551. [CrossRef] [PubMed]



12. Yang, J.D.; Ahmed, F.; Mara, K.C.; Addissie, B.D.; Allen, A.M.; Gores, G.J.; Roberts, L.R. Diabetes is Associated with Increased Risk of Hepatocellular Carcinoma in Cirrhosis Patients with Nonalcoholic Fatty Liver Disease. *Hepatology* **2019**. [[CrossRef](#)] [[PubMed](#)]
13. Bartsch, H.; Nair, J. Chronic inflammation and oxidative stress in the genesis and perpetuation of cancer: Role of lipid peroxidation, DNA damage, and repair. *Langenbeck's Arch. Surg.* **2006**, *391*, 499–510. [[CrossRef](#)] [[PubMed](#)]
14. Chen, C.Y.; Wu, S.M.; Lin, Y.H.; Chi, H.C.; Lin, S.L.; Yeh, C.T.; Chuang, W.Y.; Lin, K.H. Induction of nuclear protein-1 by thyroid hormone enhances platelet-derived growth factor A mediated angiogenesis in liver cancer. *Theranostics* **2019**, *9*, 2361–2379. [[CrossRef](#)] [[PubMed](#)]
15. Fu, Y.; Chung, F.L. Oxidative stress and hepatocarcinogenesis. *Hepatoma Res.* **2018**, *4*, 39. [[CrossRef](#)] [[PubMed](#)]
16. Ma-On, C.; Sanpavat, A.; Whongsiri, P.; Suwannasin, S.; Hirankarn, N.; Tangkijvanich, P.; Boonla, C. Oxidative stress indicated by elevated expression of Nrf2 and 8-OHdG promotes hepatocellular carcinoma progression. *Med. Oncol.* **2017**, *34*, 57. [[CrossRef](#)]
17. Bisht, S.; Dada, R. Oxidative stress: Major executioner in disease pathology, role in sperm DNA damage and preventive strategies. *Front. Biosci.* **2017**, *9*, 420–447.
18. Veskoukis, A.S.; Tsatsakis, A.M.; Kouretas, D. Dietary oxidative stress and antioxidant defense with an emphasis on plant extract administration. *Cell Stress Chaperones* **2012**, *17*, 11–21. [[CrossRef](#)]
19. Fu, N.; Yao, H.; Nan, Y.; Qiao, L. Role of Oxidative Stress in Hepatitis C Virus Induced Hepatocellular Carcinoma. *Curr. Cancer Drug Targets* **2017**, *17*, 498–504. [[CrossRef](#)]
20. Marra, M.; Sordelli, I.M.; Lombardi, A.; Lamberti, M.; Tarantino, L.; Giudice, A.; Stiuso, P.; Abbruzzese, A.; Sperlongano, R.; Accardo, M.; et al. Molecular targets and oxidative stress biomarkers in hepatocellular carcinoma: An overview. *J. Transl. Med.* **2011**, *9*, 171. [[CrossRef](#)]
21. Simic, M.G.; Bergtold, D.S.; Karam, L.R. Generation of oxy radicals in biosystems. *Mutat. Res.* **1989**, *214*, 3–12. [[CrossRef](#)]
22. Fujita, N.; Sugimoto, R.; Ma, N.; Tanaka, H.; Iwasa, M.; Kobayashi, Y.; Kawanishi, S.; Watanabe, S.; Kaito, M.; Takei, Y. Comparison of hepatic oxidative DNA damage in patients with chronic hepatitis B and C. *J. Viral Hepat.* **2008**, *15*, 498–507. [[CrossRef](#)] [[PubMed](#)]
23. Hino, K.; Nishina, S.; Sasaki, K.; Hara, Y. Mitochondrial damage and iron metabolic dysregulation in hepatitis C virus infection. *Free Radic. Biol. Med.* **2019**, *133*, 193–199. [[CrossRef](#)] [[PubMed](#)]
24. Sinha, R.A.; Singh, B.K.; Yen, P.M. Direct effects of thyroid hormones on hepatic lipid metabolism. *Nature reviews. Endocrinology* **2018**, *14*, 259–269.
25. Chi, H.C.; Chen, S.L.; Lin, S.L.; Tsai, C.Y.; Chuang, W.Y.; Lin, Y.H.; Huang, Y.H.; Tsai, M.M.; Yeh, C.T.; Lin, K.H. Thyroid hormone protects hepatocytes from HBx-induced carcinogenesis by enhancing mitochondrial turnover. *Oncogene* **2017**, *36*, 5274–5284. [[CrossRef](#)]
26. Spahis, S.; Delvin, E.; Borys, J.M.; Levy, E. Oxidative Stress as a Critical Factor in Nonalcoholic Fatty Liver Disease Pathogenesis. *Antioxid. Redox Signal.* **2017**, *26*, 519–541. [[CrossRef](#)]
27. Cardin, R.; Piciocchi, M.; Bortolami, M.; Kotsafti, A.; Barzon, L.; Lavezzo, E.; Sinigaglia, A.; Rodriguez-Castro, K.I.; Rugge, M.; Farinati, F. Oxidative damage in the progression of chronic liver disease to hepatocellular carcinoma: An intricate pathway. *World J. Gastroenterol.* **2014**, *20*, 3078–3086. [[CrossRef](#)]
28. Cai, Y.; Yu, X.; Hu, S.; Yu, J. A brief review on the mechanisms of miRNA regulation. *Genom. Proteom. Bioinform.* **2009**, *7*, 147–154. [[CrossRef](#)]
29. O'Brien, J.; Hayder, H.; Zayed, Y.; Peng, C. Overview of MicroRNA Biogenesis, Mechanisms of Actions, and Circulation. *Front. Endocrinol.* **2018**, *9*, 402. [[CrossRef](#)]
30. Wan, Y.; Cui, R.; Gu, J.; Zhang, X.; Xiang, X.; Liu, C.; Qu, K.; Lin, T. Identification of Four Oxidative Stress-Responsive MicroRNAs, miR-34a-5p, miR-1915-3p, miR-638, and miR-150-3p, in Hepatocellular Carcinoma. *Oxidative Med. Cell. Longev.* **2017**, *2017*, 5189138. [[CrossRef](#)]
31. Tian, Y.; Kuo, C.F.; Sir, D.; Wang, L.; Govindarajan, S.; Petrovic, L.M.; Ou, J.H. Autophagy inhibits oxidative stress and tumor suppressors to exert its dual effect on hepatocarcinogenesis. *Cell Death Differ.* **2015**, *22*, 1025–1034. [[CrossRef](#)]

32. Cardin, R.; Piciocchi, M.; Sinigaglia, A.; Lavezzo, E.; Bortolami, M.; Kotsafti, A.; Cillo, U.; Zanusi, G.; Mescoli, C.; Rugge, M.; et al. Oxidative DNA damage correlates with cell immortalization and miR-92 expression in hepatocellular carcinoma. *BMC Cancer* **2012**, *12*, 177. [[CrossRef](#)]
33. Dai, B.H.; Geng, L.; Wang, Y.; Sui, C.J.; Xie, F.; Shen, R.X.; Shen, W.F.; Yang, J.M. microRNA-199a-5p protects hepatocytes from bile acid-induced sustained endoplasmic reticulum stress. *Cell Death Dis.* **2013**, *4*, e604. [[CrossRef](#)] [[PubMed](#)]
34. Sendi, H. Dual Role of miR-122 in Molecular Pathogenesis of Viral Hepatitis. *Hepat. Mon.* **2012**, *12*, 312–314. [[CrossRef](#)]
35. Wojcik, K.; Piekarska, A.; Szymanska, B.; Jablonowska, E. Hepatic expression of miR-122 and antioxidant genes in patients with chronic hepatitis B. *Acta Biochim. Pol.* **2016**, *63*, 527–531. [[CrossRef](#)] [[PubMed](#)]
36. Ali, O.; Darwish, H.A.; Eldeib, K.M.; Abdel Azim, S.A. miR-26a Potentially Contributes to the Regulation of Fatty Acid and Sterol Metabolism In Vitro Human HepG2 Cell Model of Nonalcoholic Fatty Liver Disease. *Oxidative Med. Cell. Longev.* **2018**, *2018*, 8515343. [[CrossRef](#)] [[PubMed](#)]
37. Wang, L.; Zhang, N.; Wang, Z.; Ai, D.M.; Cao, Z.Y.; Pan, H.P. Decreased MiR-155 Level in the Peripheral Blood of Non-Alcoholic Fatty Liver Disease Patients may Serve as a Biomarker and may Influence LXN Activity. *Cell. Physiol. Biochem.* **2016**, *39*, 2239–2248. [[CrossRef](#)]
38. Huang, P.S.; Lin, Y.H.; Chi, H.C.; Chen, P.Y.; Huang, Y.H.; Yeh, C.T.; Wang, C.S.; Lin, K.H. Thyroid hormone inhibits growth of hepatoma cells through induction of miR-214. *Sci. Rep.* **2017**, *7*, 14868. [[CrossRef](#)]
39. Gao, M.; Liu, Y.; Chen, Y.; Yin, C.; Chen, J.J.; Liu, S. miR-214 protects erythroid cells against oxidative stress by targeting ATF4 and EZH2. *Free Radic. Biol. Med.* **2016**, *92*, 39–49. [[CrossRef](#)]
40. Xiao, Y.; Yan, W.; Lu, L.; Wang, Y.; Lu, W.; Cao, Y.; Cai, W. p38/p53/miR-200a-3p feedback loop promotes oxidative stress-mediated liver cell death. *Cell Cycle* **2015**, *14*, 1548–1558. [[CrossRef](#)]
41. Zhou, B.; Li, C.; Qi, W.; Zhang, Y.; Zhang, F.; Wu, J.X.; Hu, Y.N.; Wu, D.M.; Liu, Y.; Yan, T.T.; et al. Downregulation of miR-181a upregulates sirtuin-1 (SIRT1) and improves hepatic insulin sensitivity. *Diabetologia* **2012**, *55*, 2032–2043. [[CrossRef](#)] [[PubMed](#)]
42. Guo, X.L.; Wang, H.B.; Yong, J.K.; Zhong, J.; Li, Q.H. MiR-128-3p overexpression sensitizes hepatocellular carcinoma cells to sorafenib induced apoptosis through regulating DJ-1. *Eur. Rev. Med Pharmacol. Sci.* **2018**, *22*, 6667–6677. [[PubMed](#)]
43. Zhao, X.; Jin, Y.; Li, L.; Xu, L.; Tang, Z.; Qi, Y.; Yin, L.; Peng, J. MicroRNA-128-3p aggravates doxorubicin-induced liver injury by promoting oxidative stress via targeting Sirtuin-1. *Pharmacol. Res.* **2019**, *146*, 104276. [[CrossRef](#)] [[PubMed](#)]
44. Kurtz, C.L.; Fannin, E.E.; Toth, C.L.; Pearson, D.S.; Vickers, K.C.; Sethupathy, P. Inhibition of miR-29 has a significant lipid-lowering benefit through suppression of lipogenic programs in liver. *Sci. Rep.* **2015**, *5*, 12911. [[CrossRef](#)] [[PubMed](#)]
45. Yang, J.; Qiu, B.; Li, X.; Zhang, H.; Liu, W. p53-p66(shc)/miR-21-Sod2 signaling is critical for the inhibitory effect of betulinic acid on hepatocellular carcinoma. *Toxicol. Lett.* **2015**, *238*, 1–10. [[CrossRef](#)] [[PubMed](#)]
46. Hou, W.; Tian, Q.; Zheng, J.; Bonkovsky, H.L. MicroRNA-196 represses Bach1 protein and hepatitis C virus gene expression in human hepatoma cells expressing hepatitis C viral proteins. *Hepatology* **2010**, *51*, 1494–1504. [[CrossRef](#)] [[PubMed](#)]
47. Ma, Y.; Deng, F.; Li, P.; Chen, G.; Tao, Y.; Wang, H. The tumor suppressive miR-26a regulation of FBXO11 inhibits proliferation, migration and invasion of hepatocellular carcinoma cells. *Biomed. Pharmacother.* **2018**, *101*, 648–655.
48. Liang, L.; Zeng, J.H.; Wang, J.Y.; He, R.Q.; Ma, J.; Chen, G.; Cai, X.Y.; Hu, X.H. Down-regulation of miR-26a-5p in hepatocellular carcinoma: A qRT-PCR and bioinformatics study. *Pathol. Res. Pract.* **2017**, *213*, 1494–1509. [[CrossRef](#)]
49. Li, Y.; Ren, M.; Zhao, Y.; Lu, X.; Wang, M.; Hu, J.; Lu, G.; He, S. MicroRNA-26a inhibits proliferation and metastasis of human hepatocellular carcinoma by regulating DNMT3B-MEG3 axis. *Oncol. Rep.* **2017**, *37*, 3527–3535. [[CrossRef](#)]
50. Zhao, W.T.; Lin, X.L.; Liu, Y.; Han, L.X.; Li, J.; Lin, T.Y.; Shi, J.W.; Wang, S.C.; Lian, M.; Chen, H.W.; et al. miR-26a promotes hepatocellular carcinoma invasion and metastasis by inhibiting PTEN and inhibits cell growth by repressing EZH2. *Lab. Investig.* **2019**, *99*, 1484–1500. [[CrossRef](#)]
51. Zhang, L.; Hu, J.; Hao, M.; Bu, L. Long noncoding RNA Linc01296 promotes hepatocellular carcinoma development through regulation of the miR-26a/PTEN axis. *Biol. Chem.* **2019**. [[CrossRef](#)] [[PubMed](#)]

52. Koek, G.H.; Liedorp, P.R.; Bast, A. The role of oxidative stress in non-alcoholic steatohepatitis. *Clin. Chim. Acta* **2011**, *412*, 1297–1305. [\[CrossRef\]](#) [\[PubMed\]](#)
53. Fu, X.; Dong, B.; Tian, Y.; Lefebvre, P.; Meng, Z.; Wang, X.; Pattou, F.; Han, W.; Wang, X.; Lou, F.; et al. MicroRNA-26a regulates insulin sensitivity and metabolism of glucose and lipids. *J. Clin. Investig.* **2015**, *125*, 2497–2509. [\[CrossRef\]](#)
54. Greene, M.W.; Burrington, C.M.; Lynch, D.T.; Davenport, S.K.; Johnson, A.K.; Horsman, M.J.; Chowdhry, S.; Zhang, J.; Sparks, J.D.; Tirrell, P.C. Lipid metabolism, oxidative stress and cell death are regulated by PKC delta in a dietary model of nonalcoholic steatohepatitis. *PLoS ONE* **2014**, *9*, e85848. [\[CrossRef\]](#)
55. Chen, Q.; Tang, L.; Xin, G.; Li, S.; Ma, L.; Xu, Y.; Zhuang, M.; Xiong, Q.; Wei, Z.; Xing, Z.; et al. Oxidative stress mediated by lipid metabolism contributes to high glucose-induced senescence in retinal pigment epithelium. *Free Radic. Biol. Med.* **2019**, *130*, 48–58. [\[CrossRef\]](#) [\[PubMed\]](#)
56. Fu, X.; Wen, H.; Jing, L.; Yang, Y.; Wang, W.; Liang, X.; Nan, K.; Yao, Y.; Tian, T. MicroRNA-155-5p promotes hepatocellular carcinoma progression by suppressing PTEN through the PI3K/Akt pathway. *Cancer Sci.* **2017**, *108*, 620–631. [\[CrossRef\]](#)
57. Liu, J.H.; Yang, Y.; Song, Q.; Li, J.B. MicroRNA-155 regulates the proliferation and metastasis of human breast cancers by targeting MAPK7. *J. B. U.* **2019**, *24*, 1075–1080.
58. Wang, J.; Guo, J.; Fan, H. MiR-155 regulates the proliferation and apoptosis of pancreatic cancer cells through targeting SOCS3. *Eur. Rev. Med. Pharmacol. Sci.* **2019**, *23*, 5168–5175.
59. Liao, W.W.; Zhang, C.; Liu, F.R.; Wang, W.J. Effects of miR-155 on proliferation and apoptosis by regulating FoxO3a/BIM in liver cancer cell line HCCLM3. *Eur. Rev. Med. Pharmacol. Sci.* **2018**, *22*, 1277–1285.
60. Ning, S.; Liu, H.; Gao, B.; Wei, W.; Yang, A.; Li, J.; Zhang, L. miR-155, miR-96 and miR-99a as potential diagnostic and prognostic tools for the clinical management of hepatocellular carcinoma. *Oncol. Lett.* **2019**, *18*, 3381–3387. [\[CrossRef\]](#)
61. Csak, T.; Bala, S.; Lippai, D.; Kodys, K.; Catalano, D.; Iracheta-Vellve, A.; Szabo, G. MicroRNA-155 Deficiency Attenuates Liver Steatosis and Fibrosis without Reducing Inflammation in a Mouse Model of Steatohepatitis. *PLoS ONE* **2015**, *10*, e0129251. [\[CrossRef\]](#)
62. Bala, S.; Csak, T.; Saha, B.; Zatsiorsky, J.; Kodys, K.; Catalano, D.; Satishchandran, A.; Szabo, G. The pro-inflammatory effects of miR-155 promote liver fibrosis and alcohol-induced steatohepatitis. *J. Hepatol.* **2016**, *64*, 1378–1387. [\[CrossRef\]](#) [\[PubMed\]](#)
63. Perra, A.; Plateroti, M.; Columbano, A. T3/TRs axis in hepatocellular carcinoma: New concepts for an old pair. *Endocr. Relat. Cancer* **2016**, *23*, R353–R369. [\[CrossRef\]](#) [\[PubMed\]](#)
64. Wu, S.M.; Cheng, W.L.; Lin, C.D.; Lin, K.H. Thyroid hormone actions in liver cancer. *Cell. Mol. Life Sci.* **2013**, *70*, 1915–1936. [\[CrossRef\]](#) [\[PubMed\]](#)
65. Liu, Y.C.; Yeh, C.T.; Lin, K.H. Molecular Functions of Thyroid Hormone Signaling in Regulation of Cancer Progression and Anti-Apoptosis. *Int. J. Mol. Sci.* **2019**, *20*, 4986. [\[CrossRef\]](#)
66. Manka, P.; Coombes, J.D.; Boosman, R.; Gauthier, K.; Papa, S.; Syn, W.K. Thyroid hormone in the regulation of hepatocellular carcinoma and its microenvironment. *Cancer Lett.* **2018**, *419*, 175–186. [\[CrossRef\]](#)
67. Chi, H.C.; Tsai, C.Y.; Tsai, M.M.; Yeh, C.T.; Lin, K.H. Molecular functions and clinical impact of thyroid hormone-triggered autophagy in liver-related diseases. *J. Biomed. Sci.* **2019**, *26*, 24. [\[CrossRef\]](#)
68. Huang, F.; Wu, L.; Qiu, Y.; Bu, K.; Huang, H.; Li, B. The role of free triiodothyronine in high-density lipoprotein cholesterol metabolism. *Medicine* **2019**, *98*, e17016. [\[CrossRef\]](#)
69. Orsagova, I.; RoZnovsky, L.; Petrousova, L.; Konecna, M.; Kabieszova, L.; Safarcik, K.; Kloudova, A. Thyroid dysfunction during interferon alpha therapy for chronic hepatitis B and C—Twenty years of experience. *Klin. Mikrobiol. A Infekcni Lek.* **2014**, *20*, 92–97.
70. Mansour-Ghanaei, F.; Mehrdad, M.; Mortazavi, S.; Joukar, F.; Khak, M.; Atrkar-Roushan, Z. Decreased serum total T3 level in hepatitis B and C related cirrhosis by severity of liver damage. *Ann. Hepatol.* **2012**, *11*, 667–671. [\[CrossRef\]](#)
71. Chi, H.C.; Chen, C.Y.; Tsai, M.M.; Tsai, C.Y.; Lin, K.H. Molecular functions of thyroid hormones and their clinical significance in liver-related diseases. *Biomed. Res. Int.* **2013**, *2013*, 601361. [\[CrossRef\]](#) [\[PubMed\]](#)
72. Lanni, A.; Moreno, M.; Goglia, F. Mitochondrial Actions of Thyroid Hormone. *Compr. Physiol.* **2016**, *6*, 1591–1607. [\[PubMed\]](#)
73. Videla, L.A.; Fernandez, V.; Cornejo, P.; Vargas, R.; Castillo, I. Thyroid hormone in the frontier of cell protection, survival and functional recovery. *Expert Rev. Mol. Med.* **2015**, *17*, e10. [\[CrossRef\]](#) [\[PubMed\]](#)

74. Lin, Y.H.; Liao, C.J.; Huang, Y.H.; Wu, M.H.; Chi, H.C.; Wu, S.M.; Chen, C.Y.; Tseng, Y.H.; Tsai, C.Y.; Chung, I.H.; et al. Thyroid hormone receptor represses miR-17 expression to enhance tumor metastasis in human hepatoma cells. *Oncogene* **2013**, *32*, 4509–4518. [\[CrossRef\]](#)
75. Huang, Y.H.; Lin, Y.H.; Chi, H.C.; Liao, C.H.; Liao, C.J.; Wu, S.M.; Chen, C.Y.; Tseng, Y.H.; Tsai, C.Y.; Lin, S.Y.; et al. Thyroid hormone regulation of miR-21 enhances migration and invasion of hepatoma. *Cancer Res.* **2013**, *73*, 2505–2517. [\[CrossRef\]](#)
76. Lin, Y.H.; Wu, M.H.; Liao, C.J.; Huang, Y.H.; Chi, H.C.; Wu, S.M.; Chen, C.Y.; Tseng, Y.H.; Tsai, C.Y.; Chung, I.H.; et al. Repression of microRNA-130b by thyroid hormone enhances cell motility. *J. Hepatol.* **2015**, *62*, 1328–1340. [\[CrossRef\]](#)
77. Xu, Q.; Zhang, M.; Tu, J.; Pang, L.; Cai, W.; Liu, X. MicroRNA-122 affects cell aggressiveness and apoptosis by targeting PKM2 in human hepatocellular carcinoma. *Oncol. Rep.* **2015**, *34*, 2054–2064. [\[CrossRef\]](#)
78. Dong, H.; Curran, I.; Williams, A.; Bondy, G.; Yauk, C.L.; Wade, M.G. Hepatic miRNA profiles and thyroid hormone homeostasis in rats exposed to dietary potassium perfluorooctanesulfonate (PFOS). *Environ. Toxicol. Pharmacol.* **2016**, *41*, 201–210. [\[CrossRef\]](#)
79. Liu, Q.; Zhang, Y.; Yang, S.; Wu, Y.; Wang, J.; Yu, W.; Liu, Y. PU.1-deficient mice are resistant to thioacetamide-induced hepatic fibrosis: PU.1 finely regulates Sirt1 expression via transcriptional promotion of miR-34a and miR-29c in hepatic stellate cells. *Biosci. Rep.* **2017**, *37*. [\[CrossRef\]](#)
80. Yu, Q.; Zhou, J.; Jian, Y.; Xiu, Z.; Xiang, L.; Yang, D.; Zeng, W. MicroRNA-214 suppresses cell proliferation and migration and cell metabolism by targeting PDK2 and PHF6 in hepatocellular carcinoma. *Cell Biol. Int.* **2019**. [\[CrossRef\]](#)
81. Tian, C.; Wu, H.; Li, C.; Tian, X.; Sun, Y.; Liu, E.; Liao, X.; Song, W. Downregulation of FoxM1 by miR-214 inhibits proliferation and migration in hepatocellular carcinoma. *Gene Ther.* **2018**, *25*, 312–319. [\[CrossRef\]](#) [\[PubMed\]](#)
82. Zhang, Y.; Yang, L.; Wang, S.; Liu, Z.; Xiu, M. MiR-29a suppresses cell proliferation by targeting SIRT1 in hepatocellular carcinoma. *Cancer Biomark.* **2018**, *22*, 151–159. [\[CrossRef\]](#) [\[PubMed\]](#)
83. Fan, J.C.; Zeng, F.; Le, Y.G.; Xin, L. LncRNA CASC2 inhibited the viability and induced the apoptosis of hepatocellular carcinoma cells through regulating miR-24-3p. *J. Cell. Biochem.* **2018**, *119*, 6391–6397. [\[CrossRef\]](#) [\[PubMed\]](#)
84. Jiang, J.; Yang, P.; Guo, Z.; Yang, R.; Yang, H.; Yang, F.; Li, L.; Xiang, B. Overexpression of microRNA-21 strengthens stem cell-like characteristics in a hepatocellular carcinoma cell line. *World J. Surg. Oncol.* **2016**, *14*, 278. [\[CrossRef\]](#) [\[PubMed\]](#)
85. Zhang, J.; Wang, Y.; Zhen, P.; Luo, X.; Zhang, C.; Zhou, L.; Lu, Y.; Yang, Y.; Zhang, W.; Wan, J. Genome-wide analysis of miRNA signature differentially expressed in doxorubicin-resistant and parental human hepatocellular carcinoma cell lines. *PLoS ONE* **2013**, *8*, e54111. [\[CrossRef\]](#) [\[PubMed\]](#)
86. Rodrigues, P.M.; Rodrigues, C.M.P.; Castro, R.E. Modulation of liver steatosis by miR-21/PPARalpha. *Cell Death Discov.* **2018**, *4*, 9. [\[CrossRef\]](#) [\[PubMed\]](#)
87. Chen, Z.; Shentu, T.P.; Wen, L.; Johnson, D.A.; Shyy, J.Y. Regulation of SIRT1 by oxidative stress-responsive miRNAs and a systematic approach to identify its role in the endothelium. *Antioxid. Redox Signal.* **2013**, *19*, 1522–1538. [\[CrossRef\]](#)
88. Tang, Q.; Wang, Q.; Zhang, Q.; Lin, S.Y.; Zhu, Y.; Yang, X.; Guo, A.Y. Gene expression, regulation of DEN and HBx induced HCC mice models and comparisons of tumor, para-tumor and normal tissues. *BMC Cancer* **2017**, *17*, 862. [\[CrossRef\]](#)
89. Bonauer, A.; Carmona, G.; Iwasaki, M.; Mione, M.; Koyanagi, M.; Fischer, A.; Burchfield, J.; Fox, H.; Doebele, C.; Ohtani, K.; et al. MicroRNA-92a controls angiogenesis and functional recovery of ischemic tissues in mice. *Science* **2009**, *324*, 1710–1713. [\[CrossRef\]](#)
90. Urtasun, R.; Elizalde, M.; Azkona, M.; Latasa, M.U.; Garcia-Irigoyen, O.; Uriarte, I.; Fernandez-Barrena, M.G.; Vicent, S.; Alonso, M.M.; Muntane, J.; et al. Splicing regulator SLU7 preserves survival of hepatocellular carcinoma cells and other solid tumors via oncogenic miR-17-92 cluster expression. *Oncogene* **2016**, *35*, 4719–4729. [\[CrossRef\]](#)
91. Peng, R.; Men, J.; Ma, R.; Wang, Q.; Wang, Y.; Sun, Y.; Ren, J. miR-214 down-regulates ARL2 and suppresses growth and invasion of cervical cancer cells. *Biochem. Biophys. Res. Commun.* **2017**, *484*, 623–630. [\[CrossRef\]](#) [\[PubMed\]](#)



92. Zheng, C.; Guo, K.; Chen, B.; Wen, Y.; Xu, Y. miR-214-5p inhibits human prostate cancer proliferation and migration through regulating CRMP5. *Cancer Biomark.* **2019**. [[CrossRef](#)] [[PubMed](#)]
93. Liu, Y.; Zhou, H.; Ma, L.; Hou, Y.; Pan, J.; Sun, C.; Yang, Y.; Zhang, J. MiR-214 suppressed ovarian cancer and negatively regulated semaphorin 4D. *Tumour Biol.* **2016**, *37*, 8239–8248. [[CrossRef](#)] [[PubMed](#)]
94. Shih, T.C.; Tien, Y.J.; Wen, C.J.; Yeh, T.S.; Yu, M.C.; Huang, C.H.; Lee, Y.S.; Yen, T.C.; Hsieh, S.Y. MicroRNA-214 downregulation contributes to tumor angiogenesis by inducing secretion of the hepatoma-derived growth factor in human hepatoma. *J. Hepatol.* **2012**, *57*, 584–591. [[CrossRef](#)] [[PubMed](#)]
95. Jin, Y.; Wong, Y.S.; Goh, B.K.P.; Chan, C.Y.; Cheow, P.C.; Chow, P.K.H.; Lim, T.K.H.; Goh, G.B.B.; Krishnamoorthy, T.L.; Kumar, R.; et al. Circulating microRNAs as Potential Diagnostic and Prognostic Biomarkers in Hepatocellular Carcinoma. *Sci. Rep.* **2019**, *9*, 10464. [[CrossRef](#)] [[PubMed](#)]
96. Huang, X.; Gao, Y.; Qin, J.; Lu, S. lncRNA MIAT promotes proliferation and invasion of HCC cells via sponging miR-214. *Am. J. Physiol. Gastrointest. Liver Physiol.* **2018**, *314*, G559–G565. [[CrossRef](#)]
97. Gou, X.; Zhao, X.; Wang, Z. Long noncoding RNA PVT1 promotes hepatocellular carcinoma progression through regulating miR-214. *Cancer Biomark.* **2017**, *20*, 511–519. [[CrossRef](#)]
98. Park, D.H.; Shin, J.W.; Park, S.K.; Seo, J.N.; Li, L.; Jang, J.J.; Lee, M.J. Diethylnitrosamine (DEN) induces irreversible hepatocellular carcinogenesis through overexpression of G1/S-phase regulatory proteins in rat. *Toxicol. Lett.* **2009**, *191*, 321–326. [[CrossRef](#)]
99. Zhou, F.; Shen, T.; Duan, T.; Xu, Y.Y.; Khor, S.C.; Li, J.; Ge, J.; Zheng, Y.F.; Hsu, S.; De Stefano, J.; et al. Antioxidant effects of lipophilic tea polyphenols on diethylnitrosamine/phenobarbital-induced hepatocarcinogenesis in rats. *In Vivo* **2014**, *28*, 495–503.
100. Unsal, V.; Belge-Kurutas, E. Experimental Hepatic Carcinogenesis: Oxidative Stress and Natural Antioxidants. *Maced. J. Med. Sci.* **2017**, *5*, 686–691. [[CrossRef](#)]
101. Chi, H.C.; Chen, S.L.; Tsai, C.Y.; Chuang, W.Y.; Huang, Y.H.; Tsai, M.M.; Wu, S.M.; Sun, C.P.; Yeh, C.T.; Lin, K.H. Thyroid hormone suppresses hepatocarcinogenesis via DAPK2 and SQSTM1-dependent selective autophagy. *Autophagy* **2016**, *12*, 2271–2285. [[CrossRef](#)] [[PubMed](#)]
102. Chen, C.; Lu, L.; Yan, S.; Yi, H.; Yao, H.; Wu, D.; He, G.; Tao, X.; Deng, X. Autophagy and doxorubicin resistance in cancer. *Anti-Cancer Drugs* **2018**, *29*, 1–9. [[CrossRef](#)] [[PubMed](#)]
103. Ozlu, B.; Kabay, G.; Bocek, I.; Yilmaz, M.; Piskin, A.K.; Shim, B.S.; Mutlu, M. Controlled release of doxorubicin from polyethylene glycol functionalized melanin nanoparticles for breast cancer therapy: Part I. Production and drug release performance of the melanin nanoparticles. *Int. J. Pharm.* **2019**, *570*, 118613. [[CrossRef](#)] [[PubMed](#)]
104. Damiani, V.; Falvo, E.; Fracasso, G.; Federici, L.; Pitea, M.; De Laurenzi, V.; Sala, G.; Ceci, P. Therapeutic Efficacy of the Novel Stimuli-Sensitive Nano-Ferritins Containing Doxorubicin in a Head and Neck Cancer Model. *Int. J. Mol. Sci.* **2017**, *18*, 1555. [[CrossRef](#)] [[PubMed](#)]
105. Zheng, F.M.; Chen, W.B.; Qin, T.; Lv, L.N.; Feng, B.; Lu, Y.L.; Li, Z.Q.; Wang, X.C.; Tao, L.J.; Li, H.W.; et al. ACOX1 destabilizes p73 to suppress intrinsic apoptosis pathway and regulates sensitivity to doxorubicin in lymphoma cells. *BMB Rep.* **2019**, *52*, 566–571. [[CrossRef](#)] [[PubMed](#)]
106. Fang, Y.; Yang, W.; Cheng, L.; Meng, F.; Zhang, J.; Zhong, Z. EGFR-targeted multifunctional polymersomal doxorubicin induces selective and potent suppression of orthotopic human liver cancer in vivo. *Acta Biomater.* **2017**, *64*, 323–333. [[CrossRef](#)]
107. Akolkar, G.; da Silva Dias, D.; Ayyappan, P.; Bagchi, A.K.; Jassal, D.S.; Salemi, V.M.C.; Irigoyen, M.C.; De Angelis, K.; Singal, P.K. Vitamin C mitigates oxidative/nitrosative stress and inflammation in doxorubicin-induced cardiomyopathy. *Am. J. Physiol. Heart Circ. Physiol.* **2017**, *313*, H795–H809. [[CrossRef](#)]
108. Abdel-Daim, M.M.; Kilany, O.E.; Khalifa, H.A.; Ahmed, A.A.M. Allicin ameliorates doxorubicin-induced cardiotoxicity in rats via suppression of oxidative stress, inflammation and apoptosis. *Cancer Chemother. Pharmacol.* **2017**, *80*, 745–753. [[CrossRef](#)]
109. Govender, J.; Loos, B.; Marais, E.; Engelbrecht, A.M. Mitochondrial catastrophe during doxorubicin-induced cardiotoxicity: A review of the protective role of melatonin. *J. Pineal Res.* **2014**, *57*, 367–380. [[CrossRef](#)]
110. Chi, H.C.; Chen, S.L.; Cheng, Y.H.; Lin, T.K.; Tsai, C.Y.; Tsai, M.M.; Lin, Y.H.; Huang, Y.H.; Lin, K.H. Chemotherapy resistance and metastasis-promoting effects of thyroid hormone in hepatocarcinoma cells are mediated by suppression of FoxO1 and Bim pathway. *Cell Death Dis.* **2016**, *7*, e2324. [[CrossRef](#)]



111. Deng, L.; Chen, M.; Tanaka, M.; Ku, Y.; Itoh, T.; Shoji, I.; Hotta, H. HCV upregulates Bim through the ROS/JNK signalling pathway, leading to Bax-mediated apoptosis. *J. Gen. Virol.* **2015**, *96*, 2670–2683. [[CrossRef](#)] [[PubMed](#)]
112. Zhang, Z.C.; Li, Y.Y.; Wang, H.Y.; Fu, S.; Wang, X.P.; Zeng, M.S.; Zeng, Y.X.; Shao, J.Y. Knockdown of miR-214 promotes apoptosis and inhibits cell proliferation in nasopharyngeal carcinoma. *PLoS ONE* **2014**, *9*, e86149. [[CrossRef](#)] [[PubMed](#)]
113. Aurora, A.B.; Mahmoud, A.I.; Luo, X.; Johnson, B.A.; van Rooij, E.; Matsuzaki, S.; Humphries, K.M.; Hill, J.A.; Bassel-Duby, R.; Sadek, H.A.; et al. MicroRNA-214 protects the mouse heart from ischemic injury by controlling Ca(2)(+) overload and cell death. *J. Clin. Investig.* **2012**, *122*, 1222–1232. [[CrossRef](#)] [[PubMed](#)]
114. Wang, X.; Ha, T.; Hu, Y.; Lu, C.; Liu, L.; Zhang, X.; Kao, R.; Kalbfleisch, J.; Williams, D.; Li, C. MicroRNA-214 protects against hypoxia/reoxygenation induced cell damage and myocardial ischemia/reperfusion injury via suppression of PTEN and Bim1 expression. *Oncotarget* **2016**, *7*, 86926–86936. [[CrossRef](#)] [[PubMed](#)]
115. Song, L.; Zhang, W.; Chang, Z.; Pan, Y.; Zong, H.; Fan, Q.; Wang, L. miR-4417 Targets Tripartite Motif-Containing 35 (TRIM35) and Regulates Pyruvate Kinase Muscle 2 (PKM2) Phosphorylation to Promote Proliferation and Suppress Apoptosis in Hepatocellular Carcinoma Cells. *Med. Sci. Monit.* **2017**, *23*, 1741–1750. [[CrossRef](#)]
116. Li, W.; Qiu, Y.; Hao, J.; Zhao, C.; Deng, X.; Shu, G. Dauricine upregulates the chemosensitivity of hepatocellular carcinoma cells: Role of repressing glycolysis via miR-199a:HK2/PKM2 modulation. *Food Chem. Toxicol.* **2018**, *121*, 156–165. [[CrossRef](#)]
117. Yu, G.; Wang, J.; Xu, K.; Dong, J. Dynamic regulation of uncoupling protein 2 expression by microRNA-214 in hepatocellular carcinoma. *Biosci. Rep.* **2016**, *36*, e0035. [[CrossRef](#)]
118. Yokoyama, C.; Sueyoshi, Y.; Ema, M.; Mori, Y.; Takaishi, K.; Hisatomi, H. Induction of oxidative stress by anticancer drugs in the presence and absence of cells. *Oncol. Lett.* **2017**, *14*, 6066–6070. [[CrossRef](#)]
119. Yang, S.; Fei, X.; Lu, Y.; Xu, B.; Ma, Y.; Wan, H. miRNA-214 suppresses oxidative stress in diabetic nephropathy via the ROS/Akt/mTOR signaling pathway and uncoupling protein 2. *Exp. Ther. Med.* **2019**, *17*, 3530–3538. [[CrossRef](#)]
120. Liu, P.; Zhao, H.; Wang, R.; Wang, P.; Tao, Z.; Gao, L.; Yan, F.; Liu, X.; Yu, S.; Ji, X.; et al. MicroRNA-424 protects against focal cerebral ischemia and reperfusion injury in mice by suppressing oxidative stress. *Stroke* **2015**, *46*, 513–519. [[CrossRef](#)]
121. Henke, J.I.; Goergen, D.; Zheng, J.; Song, Y.; Schuttler, C.G.; Fehr, C.; Junemann, C.; Niepmann, M. microRNA-122 stimulates translation of hepatitis C virus RNA. *EMBO J.* **2008**, *27*, 3300–3310. [[CrossRef](#)] [[PubMed](#)]
122. Nabih, H.K. The Significance of HCV Viral Load in the Incidence of HCC: A Correlation Between Mir-122 and CCL2. *J. Gastrointest. Cancer* **2019**. [[CrossRef](#)] [[PubMed](#)]
123. Jopling, C.L. Regulation of hepatitis C virus by microRNA-122. *Biochem. Soc. Trans.* **2008**, *36*, 1220–1223. [[CrossRef](#)] [[PubMed](#)]
124. Li, Y.; Wang, L.; Rivera-Serrano, E.E.; Chen, X.; Lemon, S.M. TNRC6 proteins modulate hepatitis C virus replication by spatially regulating the binding of miR-122/Ago2 complexes to viral RNA. *Nucleic Acids Res.* **2019**, *47*, 6411–6424. [[CrossRef](#)] [[PubMed](#)]
125. Chahal, J.; Gebert, L.F.R.; Gan, H.H.; Camacho, E.; Gunsalus, K.C.; MacRae, I.J.; Sagan, S.M. miR-122 and Ago interactions with the HCV genome alter the structure of the viral 5' terminus. *Nucleic Acids Res.* **2019**, *47*, 5307–5324. [[CrossRef](#)]
126. Mahmoudian-Sani, M.R.; Asgharzade, S.; Alghasi, A.; Saeedi-Boroujeni, A.; Adnani Sadati, S.J.; Moradi, M.T. MicroRNA-122 in patients with hepatitis B and hepatitis B virus-associated hepatocellular carcinoma. *J. Gastrointest. Oncol.* **2019**, *10*, 789–796. [[CrossRef](#)]
127. Rana, M.A.; Ijaz, B.; Daud, M.; Tariq, S.; Nadeem, T.; Husnain, T. Interplay of Wnt beta-catenin pathway and miRNAs in HBV pathogenesis leading to HCC. *Clin. Res. Hepatol. Gastroenterol.* **2019**, *43*, 373–386. [[CrossRef](#)]
128. Liu, G.; Ma, X.; Wang, Z.; Wakae, K.; Yuan, Y.; He, Z.; Yoshiyama, H.; Iizasa, H.; Zhang, H.; Matsuda, M.; et al. Adenosine deaminase acting on RNA-1 (ADAR1) inhibits HBV replication by enhancing microRNA-122 processing. *J. Biol. Chem.* **2019**, *294*, 14043–14054. [[CrossRef](#)]
129. He, J.; Zhao, K.; Zheng, L.; Xu, Z.; Gong, W.; Chen, S.; Shen, X.; Huang, G.; Gao, M.; Zeng, Y.; et al. Upregulation of microRNA-122 by farnesoid X receptor suppresses the growth of hepatocellular carcinoma cells. *Mol. Cancer* **2015**, *14*, 163. [[CrossRef](#)]

130. Nassirpour, R.; Mehta, P.P.; Yin, M.J. miR-122 regulates tumorigenesis in hepatocellular carcinoma by targeting AKT3. *PLoS ONE* **2013**, *8*, e79655. [[CrossRef](#)]
131. Ahsani, Z.; Mohammadi-Yeganeh, S.; Kia, V.; Karimkhanloo, H.; Zarghami, N.; Paryan, M. WNT1 Gene from WNT Signaling Pathway Is a Direct Target of miR-122 in Hepatocellular Carcinoma. *Appl. Biochem. Biotechnol.* **2017**, *181*, 884–897. [[CrossRef](#)]
132. Dinkova-Kostova, A.T.; Talalay, P. NAD(P)H:quinone acceptor oxidoreductase 1 (NQO1), a multifunctional antioxidant enzyme and exceptionally versatile cytoprotector. *Arch. Biochem. Biophys.* **2010**, *501*, 116–123. [[CrossRef](#)]
133. Vomund, S.; Schafer, A.; Parnham, M.J.; Brune, B.; von Knethen, A. Nrf2, the Master Regulator of Anti-Oxidative Responses. *Int. J. Mol. Sci.* **2017**, *18*, 2772. [[CrossRef](#)]
134. Yu, W.G.; Liu, W.; Jin, Y.H. Effects of perfluorooctane sulfonate on rat thyroid hormone biosynthesis and metabolism. *Environ. Toxicol. Chem.* **2009**, *28*, 990–996. [[CrossRef](#)]
135. Wang, G.; Dong, F.; Xu, Z.; Sharma, S.; Hu, X.; Chen, D.; Zhang, L.; Zhang, J.; Dong, Q. MicroRNA profile in HBV-induced infection and hepatocellular carcinoma. *BMC Cancer* **2017**, *17*, 805. [[CrossRef](#)]
136. Sadri Nahand, J.; Bokharaei-Salim, F.; Salmaninejad, A.; Nesaee, A.; Mohajeri, F.; Moshtazan, A.; Tabibzadeh, A.; Karimzadeh, M.; Moghoofei, M.; Marjani, A.; et al. microRNAs: Key players in virus-associated hepatocellular carcinoma. *J. Cell. Physiol.* **2019**, *234*, 12188–12225. [[CrossRef](#)]
137. Shigoka, M.; Tsuchida, A.; Matsudo, T.; Nagakawa, Y.; Saito, H.; Suzuki, Y.; Aoki, T.; Murakami, Y.; Toyoda, H.; Kumada, T.; et al. Dereglulation of miR-92a expression is implicated in hepatocellular carcinoma development. *Pathol. Int.* **2010**, *60*, 351–357. [[CrossRef](#)]
138. Wang, L.; Wu, J.; Xie, C. miR-92a promotes hepatocellular carcinoma cells proliferation and invasion by FOXA2 targeting. *Iran. J. Basic Med. Sci.* **2017**, *20*, 783–790.
139. Zhang, Y.; Li, T.; Qiu, Y.; Zhang, T.; Guo, P.; Ma, X.; Wei, Q.; Han, L. Serum microRNA panel for early diagnosis of the onset of hepatocellular carcinoma. *Medicine* **2017**, *96*, e5642. [[CrossRef](#)]
140. Zhao, B.; Zhu, Y.; Cui, K.; Gao, J.; Yu, F.; Chen, L.; Li, S. Expression and significance of PTEN and miR-92 in hepatocellular carcinoma. *Mol. Med. Rep.* **2013**, *7*, 1413–1416. [[CrossRef](#)]
141. Yang, W.; Dou, C.; Wang, Y.; Jia, Y.; Li, C.; Zheng, X.; Tu, K. MicroRNA-92a contributes to tumor growth of human hepatocellular carcinoma by targeting FBXW7. *Oncol. Rep.* **2015**, *34*, 2576–2584. [[CrossRef](#)]
142. Ock, C.Y.; Kim, E.H.; Choi, D.J.; Lee, H.J.; Hahm, K.B.; Chung, M.H. 8-Hydroxydeoxyguanosine: Not mere biomarker for oxidative stress, but remedy for oxidative stress-implicated gastrointestinal diseases. *World J. Gastroenterol.* **2012**, *18*, 302–308. [[CrossRef](#)]
143. Liu, D.Y.; Peng, Z.H.; Qiu, G.Q.; Zhou, C.Z. Expression of telomerase activity and oxidative stress in human hepatocellular carcinoma with cirrhosis. *World J. Gastroenterol.* **2003**, *9*, 1859–1862. [[CrossRef](#)]
144. Saini, N.; Srinivasan, R.; Chawla, Y.; Sharma, S.; Chakraborti, A.; Rajwanshi, A. Telomerase activity, telomere length and human telomerase reverse transcriptase expression in hepatocellular carcinoma is independent of hepatitis virus status. *Liver Int.* **2009**, *29*, 1162–1170. [[CrossRef](#)]
145. Zhang, W.; Huang, Q.; Zeng, Z.; Wu, J.; Zhang, Y.; Chen, Z. Sirt1 Inhibits Oxidative Stress in Vascular Endothelial Cells. *Oxidative Med. Cell. Longev.* **2017**, *2017*, 7543973. [[CrossRef](#)]
146. Frau, C.; Loi, R.; Petrelli, A.; Perra, A.; Menegon, S.; Kowalik, M.A.; Pinna, S.; Leoni, V.P.; Fornari, F.; Gramantieri, L.; et al. Local hypothyroidism favors the progression of preneoplastic lesions to hepatocellular carcinoma in rats. *Hepatology* **2015**, *61*, 249–259. [[CrossRef](#)]
147. Pang, C.; Huang, G.; Luo, K.; Dong, Y.; He, F.; Du, G.; Xiao, M.; Cai, W. miR-206 inhibits the growth of hepatocellular carcinoma cells via targeting CDK9. *Cancer Med.* **2017**, *6*, 2398–2409. [[CrossRef](#)]
148. Yang, Q.; Zhang, L.; Zhong, Y.; Lai, L.; Li, X. miR-206 inhibits cell proliferation, invasion, and migration by down-regulating PTP1B in hepatocellular carcinoma. *Biosci. Rep.* **2019**, *39*. [[CrossRef](#)]
149. Wang, Y.; Tai, Q.; Zhang, J.; Kang, J.; Gao, F.; Zhong, F.; Cai, L.; Fang, F.; Gao, Y. MiRNA-206 inhibits hepatocellular carcinoma cell proliferation and migration but promotes apoptosis by modulating cMET expression. *Acta Biochim. Et Biophys. Sin.* **2019**, *51*, 243–253. [[CrossRef](#)]
150. Singh, A.; Happel, C.; Manna, S.K.; Acquaah-Mensah, G.; Carrerero, J.; Kumar, S.; Nasipuri, P.; Krausz, K.W.; Wakabayashi, N.; Dewi, R.; et al. Transcription factor NRF2 regulates miR-1 and miR-206 to drive tumorigenesis. *J. Clin. Investig.* **2013**, *123*, 2921–2934. [[CrossRef](#)]

151. Zheng, Y.; Zhao, C.; Zhang, N.; Kang, W.; Lu, R.; Wu, H.; Geng, Y.; Zhao, Y.; Xu, X. Serum microRNA miR-206 is decreased in hyperthyroidism and mediates thyroid hormone regulation of lipid metabolism in HepG2 human hepatoblastoma cells. *Mol. Med. Rep.* **2018**, *17*, 5635–5641. [[CrossRef](#)]
152. Huang, C.Y.; Huang, X.P.; Zhu, J.Y.; Chen, Z.G.; Li, X.J.; Zhang, X.H.; Huang, S.; He, J.B.; Lian, F.; Zhao, Y.N.; et al. miR-128-3p suppresses hepatocellular carcinoma proliferation by regulating PIK3R1 and is correlated with the prognosis of HCC patients. *Oncol. Rep.* **2015**, *33*, 2889–2898. [[CrossRef](#)]
153. Zhao, X.; Wu, Y.; Lv, Z. miR-128 modulates hepatocellular carcinoma by inhibition of ITGA2 and ITGA5 expression. *Am. J. Transl. Res.* **2015**, *7*, 1564–1573.
154. Lee, D.Y.; Kim, H.S.; Won, K.J.; Lee, K.P.; Jung, S.H.; Park, E.S.; Choi, W.S.; Lee, H.M.; Kim, B. DJ-1 regulates the expression of renal (pro)renin receptor via reactive oxygen species-mediated epigenetic modification. *Biochim. Et Biophys. Acta* **2015**, *1850*, 426–434. [[CrossRef](#)]
155. Bonilha, V.L.; Bell, B.A.; Rayborn, M.E.; Yang, X.; Kaul, C.; Grossman, G.H.; Samuels, I.S.; Hollyfield, J.G.; Xie, C.; Cai, H.; et al. Loss of DJ-1 elicits retinal abnormalities, visual dysfunction, and increased oxidative stress in mice. *Exp. Eye Res.* **2015**, *139*, 22–36. [[CrossRef](#)]
156. Wang, J.; Chu, Y.; Xu, M.; Zhang, X.; Zhou, Y.; Xu, M. miR-21 promotes cell migration and invasion of hepatocellular carcinoma by targeting KLF5. *Oncol. Lett.* **2019**, *17*, 2221–2227. [[CrossRef](#)]
157. Musaddaq, G.; Shahzad, N.; Ashraf, M.A.; Arshad, M.I. Circulating liver-specific microRNAs as noninvasive diagnostic biomarkers of hepatic diseases in human. *Biomarkers* **2019**, *24*, 103–109. [[CrossRef](#)]
158. Zhan, Y.; Zheng, N.; Teng, F.; Bao, L.; Liu, F.; Zhang, M.; Guo, M.; Guo, W.; Ding, G.; Wang, Q. MiR-199a/b-5p inhibits hepatocellular carcinoma progression by post-transcriptionally suppressing ROCK1. *Oncotarget* **2017**, *8*, 67169–67180. [[CrossRef](#)]
159. Lou, Z.; Gong, Y.Q.; Zhou, X.; Hu, G.H. Low expression of miR-199 in hepatocellular carcinoma contributes to tumor cell hyper-proliferation by negatively suppressing XBP1. *Oncol. Lett.* **2018**, *16*, 6531–6539. [[CrossRef](#)]
160. Bernstein, H.; Payne, C.M.; Bernstein, C.; Schneider, J.; Beard, S.E.; Crowley, C.L. Activation of the promoters of genes associated with DNA damage, oxidative stress, ER stress and protein misfolding by the bile salt, deoxycholate. *Toxicol. Lett.* **1999**, *108*, 37–46. [[CrossRef](#)]
161. Silva, T.M.; Moretto, F.C.F.; Sibio, M.T.; Goncalves, B.M.; Oliveira, M.; Olimpio, R.M.C.; Oliveira, D.A.M.; Costa, S.M.B.; Depra, I.C.; Namba, V.; et al. Triiodothyronine (T3) upregulates the expression of proto-oncogene TGFA independent of MAPK/ERK pathway activation in the human breast adenocarcinoma cell line, MCF7. *Arch. Endocrinol. Metab.* **2019**, *63*, 142–147. [[CrossRef](#)]
162. Cicatiello, A.G.; Ambrosio, R.; Dentice, M. Thyroid hormone promotes differentiation of colon cancer stem cells. *Mol. Cell. Endocrinol.* **2017**, *459*, 84–89. [[CrossRef](#)]
163. Latteyer, S.; Christoph, S.; Theurer, S.; Hones, G.S.; Schmid, K.W.; Fuehrer, D.; Moeller, L.C. Thyroxine promotes lung cancer growth in an orthotopic mouse model. *Endocr. Relat. Cancer* **2019**. [[CrossRef](#)]
164. Lin, Y.H.; Wu, M.H.; Huang, Y.H.; Yeh, C.T.; Chi, H.C.; Tsai, C.Y.; Chuang, W.Y.; Yu, C.J.; Chung, I.H.; Chen, C.Y.; et al. Thyroid hormone negatively regulates tumorigenesis through suppression of BC200. *Endocr. Relat. Cancer* **2018**, *25*, 967–979. [[CrossRef](#)]
165. Sap, J.; Munoz, A.; Damm, K.; Goldberg, Y.; Ghysdael, J.; Leutz, A.; Beug, H.; Vennstrom, B. The c-erb-A protein is a high-affinity receptor for thyroid hormone. *Nature* **1986**, *324*, 635–640. [[CrossRef](#)]
166. Barlow, C.; Meister, B.; Lardelli, M.; Lendahl, U.; Vennstrom, B. Thyroid abnormalities and hepatocellular carcinoma in mice transgenic for v-erbA. *EMBO J.* **1994**, *13*, 4241–4250. [[CrossRef](#)]
167. Kabir, A. Decreased serum total T3 level in hepatitis B and C related cirrhosis by severity of liver damage. *Ann. Hepatol.* **2013**, *12*, 506–507. [[CrossRef](#)]
168. Hassan, M.M.; Kaseb, A.; Li, D.; Patt, Y.Z.; Vauthey, J.N.; Thomas, M.B.; Curley, S.A.; Spitz, M.R.; Sherman, S.I.; Abdalla, E.K.; et al. Association between hypothyroidism and hepatocellular carcinoma: A case-control study in the United States. *Hepatology* **2009**, *49*, 1563–1570. [[CrossRef](#)]
169. Reddy, A.; Dash, C.; Leerapun, A.; Mettler, T.A.; Stadheim, L.M.; Lazaridis, K.N.; Roberts, R.O.; Roberts, L.R. Hypothyroidism: A possible risk factor for liver cancer in patients with no known underlying cause of liver disease. *Clin. Gastroenterol. Hepatol.* **2007**, *5*, 118–123. [[CrossRef](#)]
170. Yu, L.X.; Ling, Y.; Wang, H.Y. Role of nonresolving inflammation in hepatocellular carcinoma development and progression. *Npj Precis. Oncol.* **2018**, *2*, 6. [[CrossRef](#)]
171. Adler, S.M.; Wartofsky, L. The nonthyroidal illness syndrome. *Endocrinol. Metab. Clin. North Am.* **2007**, *36*, 657–672. [[CrossRef](#)]

172. De Groot, L.J. Non-thyroidal illness syndrome is a manifestation of hypothalamic-pituitary dysfunction, and in view of current evidence, should be treated with appropriate replacement therapies. *Crit. Care Clin.* **2006**, *22*, 57–86. [[CrossRef](#)]
173. Lin, S.L.; Wu, S.M.; Chung, I.H.; Lin, Y.H.; Chen, C.Y.; Chi, H.C.; Lin, T.K.; Yeh, C.T.; Lin, K.H. Stimulation of Interferon-Stimulated Gene 20 by Thyroid Hormone Enhances Angiogenesis in Liver Cancer. *Neoplasia* **2018**, *20*, 57–68. [[CrossRef](#)]
174. Baskol, G.; Atmaca, H.; Tanriverdi, F.; Baskol, M.; Kocer, D.; Bayram, F. Oxidative stress and enzymatic antioxidant status in patients with hypothyroidism before and after treatment. *Exp. Clin. Endocrinol. Diabetes* **2007**, *115*, 522–526. [[CrossRef](#)]
175. Haribabu, A.; Reddy, V.S.; Pallavi, C.; Bitla, A.R.; Sachan, A.; Pullaiah, P.; Suresh, V.; Rao, P.V.; Suchitra, M.M. Evaluation of protein oxidation and its association with lipid peroxidation and thyrotropin levels in overt and subclinical hypothyroidism. *Endocrine* **2013**, *44*, 152–157. [[CrossRef](#)]
176. Mourouzis, I.; Politi, E.; Pantos, C. Thyroid hormone and tissue repair: New tricks for an old hormone? *J. Thyroid Res.* **2013**, *2013*, 312104. [[CrossRef](#)]
177. D’Espessailles, A.; Dossi, C.; Intriago, G.; Leiva, P.; Romanque, P. Hormonal pretreatment preserves liver regenerative capacity and minimizes inflammation after partial hepatectomy. *Ann. Hepatol.* **2013**, *12*, 881–891. [[CrossRef](#)]
178. Fernandez, V.; Castillo, I.; Tapia, G.; Romanque, P.; Uribe-Echevarria, S.; Uribe, M.; Cartier-Ugarte, D.; Santander, G.; Vial, M.T.; Videla, L.A. Thyroid hormone preconditioning: Protection against ischemia-reperfusion liver injury in the rat. *Hepatology* **2007**, *45*, 170–177. [[CrossRef](#)]
179. Singh, R.; Kaushik, S.; Wang, Y.; Xiang, Y.; Novak, I.; Komatsu, M.; Tanaka, K.; Cuervo, A.M.; Czaja, M.J. Autophagy regulates lipid metabolism. *Nature* **2009**, *458*, 1131–1135. [[CrossRef](#)]
180. Ueno, T.; Komatsu, M. Autophagy in the liver: Functions in health and disease. *Nat. Reviews. Gastroenterol. Hepatol.* **2017**, *14*, 170–184. [[CrossRef](#)]
181. Tseng, Y.H.; Ke, P.Y.; Liao, C.J.; Wu, S.M.; Chi, H.C.; Tsai, C.Y.; Chen, C.Y.; Lin, Y.H.; Lin, K.H. Chromosome 19 open reading frame 80 is upregulated by thyroid hormone and modulates autophagy and lipid metabolism. *Autophagy* **2014**, *10*, 20–31. [[CrossRef](#)]
182. Vargas, R.; Riquelme, B.; Fernandez, J.; Alvarez, D.; Perez, I.F.; Cornejo, P.; Fernandez, V.; Videla, L.A. Docosahexaenoic acid-thyroid hormone combined protocol as a novel approach to metabolic stress disorders: Relation to mitochondrial adaptation via liver PGC-1 $\alpha$  and sirtuin1 activation. *BioFactors* **2019**, *45*, 271–278. [[CrossRef](#)]
183. El Agaty, S.M. Triiodothyronine improves age-induced glucose intolerance and increases the expression of sirtuin-1 and glucose transporter-4 in skeletal muscle of aged rats. *Gen. Physiol. Biophys.* **2018**, *37*, 677–686.
184. Singh, B.K.; Sinha, R.A.; Ohba, K.; Yen, P.M. Role of thyroid hormone in hepatic gene regulation, chromatin remodeling, and autophagy. *Mol. Cell. Endocrinol.* **2017**, *458*, 160–168. [[CrossRef](#)]
185. Singh, B.K.; Sinha, R.A.; Zhou, J.; Tripathi, M.; Ohba, K.; Wang, M.E.; Astapova, I.; Ghosh, S.; Hollenberg, A.N.; Gauthier, K.; et al. Hepatic FOXO1 Target Genes Are Co-regulated by Thyroid Hormone via RICTOR Protein Deacetylation and MTORC2-AKT Protein Inhibition. *J. Biol. Chem.* **2016**, *291*, 198–214. [[CrossRef](#)]
186. Sinha, R.A.; Singh, B.K.; Zhou, J.; Wu, Y.; Farah, B.L.; Ohba, K.; Lesmana, R.; Gooding, J.; Bay, B.H.; Yen, P.M. Thyroid hormone induction of mitochondrial activity is coupled to mitophagy via ROS-AMPK-ULK1 signaling. *Autophagy* **2015**, *11*, 1341–1357. [[CrossRef](#)]
187. Webb, A.E.; Brunet, A. FOXO transcription factors: Key regulators of cellular quality control. *Trends Biochem. Sci.* **2014**, *39*, 159–169. [[CrossRef](#)]
188. Videla, L.A.; Cornejo, P.; Romanque, P.; Santibanez, C.; Castillo, I.; Vargas, R. Thyroid hormone-induced cytosol-to-nuclear translocation of rat liver Nrf2 is dependent on Kupffer cell functioning. *Sci. World J.* **2012**, *2012*, 301494. [[CrossRef](#)]
189. Cornejo, P.; Vargas, R.; Videla, L.A. Nrf2-regulated phase-II detoxification enzymes and phase-III transporters are induced by thyroid hormone in rat liver. *BioFactors* **2013**, *39*, 514–521. [[CrossRef](#)]

190. Romanque, P.; Cornejo, P.; Valdes, S.; Videla, L.A. Thyroid hormone administration induces rat liver Nrf2 activation: Suppression by N-acetylcysteine pretreatment. *Thyroid* **2011**, *21*, 655–662. [[CrossRef](#)]
191. Li, N.; Alam, J.; Venkatesan, M.I.; Eiguren-Fernandez, A.; Schmitz, D.; Di Stefano, E.; Slaughter, N.; Killeen, E.; Wang, X.; Huang, A.; et al. Nrf2 is a key transcription factor that regulates antioxidant defense in macrophages and epithelial cells: Protecting against the proinflammatory and oxidizing effects of diesel exhaust chemicals. *J. Immunol.* **2004**, *173*, 3467–3481. [[CrossRef](#)]



© 2019 by the authors. Licensee MDPI, Basel, Switzerland. This article is an open access article distributed under the terms and conditions of the Creative Commons Attribution (CC BY) license (<http://creativecommons.org/licenses/by/4.0/>).





Article

# Ibuprofen-Loaded Hyaluronic Acid Nanofibrous Membranes for Prevention of Postoperative Tendon Adhesion through Reduction of Inflammation

Chien-Tzung Chen <sup>1,2,†</sup>, Chih-Hao Chen <sup>1,3,†</sup> , Chialin Sheu <sup>3</sup> and Jyh-Ping Chen <sup>1,3,4,5,\*</sup>

<sup>1</sup> Department of Plastic and Reconstructive Surgery and Craniofacial Research Center, Chang Gung Memorial Hospital at Linkou, Chang Gung University, College of Medicine, Kwei-San, Taoyuan 33305, Taiwan; ctchenap@cgmh.org.tw (C.-T.C.); chchen5027@gmail.com (C.-H.C.)

<sup>2</sup> Department of Plastic and Reconstructive Surgery, Chang Gung Memorial Hospital at Keelung, Chang Gung University, College of Medicine, Keelung 20401, Taiwan

<sup>3</sup> Department of Chemical and Materials Engineering, Chang Gung University, Kwei-San, Taoyuan 33302, Taiwan; chialinsheu@gmail.com

<sup>4</sup> Research Center for Food and Cosmetic Safety, Research Center for Chinese Herbal Medicine, College of Human Ecology, Chang Gung University of Science and Technology, Taoyuan 33302, Taiwan

<sup>5</sup> Department of Materials Engineering, Ming Chi University of Technology, Tai-Shan, New Taipei City 24301, Taiwan

\* Correspondence: jpchen@mail.cgu.edu.tw; Tel.: +886-3-211-8800 (ext. 5298)

† These authors contributed equally to this paper.

Received: 9 July 2019; Accepted: 8 October 2019; Published: 11 October 2019



**Abstract:** A desirable multi-functional nanofibrous membrane (NFM) for prevention of postoperative tendon adhesion should be endowed with abilities to prevent fibroblast attachment and penetration and exert anti-inflammation effects. To meet this need, hyaluronic acid (HA)/ibuprofen (IBU) (HAI) NFMs were prepared by electrospinning, followed by dual ionic crosslinking with FeCl<sub>3</sub> (HAIF NFMs) and covalent crosslinking with 1,4-butanediol diglycidyl ether (BDDE) to produce HAIFB NFMs. It is expected that the multi-functional NFMs will act as a physical barrier to prevent fibroblast penetration, HA will reduce fibroblast attachment and impart a lubrication effect for tendon gliding, while IBU will function as an anti-inflammation drug. For this purpose, we successfully fabricated HAIFB NFMs containing 20% (HAI20FB), 30% (HAI30FB), and 40% (HAI40FB) IBU and characterized their physico-chemical properties by scanning electron microscopy, Fourier transformed infrared spectroscopy, thermal gravimetric analysis, and mechanical testing. In vitro cell culture studies revealed that all NFMs except HAI40FB possessed excellent effects in preventing fibroblast attachment and penetration while preserving high biocompatibility without influencing cell proliferation. Although showing significant improvement in mechanical properties over other NFMs, the HAI40FB NFM exhibited cytotoxicity towards fibroblasts due to the higher percentage and concentration of IBU released from the membrane. In vivo studies in a rabbit flexor tendon rupture model demonstrated the efficacy of IBU-loaded NFMs (HAI30FB) over Septrafilm® and NFMs without IBU (HAFB) in reducing local inflammation and preventing tendon adhesion based on gross observation, histological analyses, and biomechanical functional assays. We concluded that an HAI30FB NFM will act as a multi-functional barrier membrane to prevent peritendinous adhesion after tendon surgery.

**Keywords:** nanofiber; ibuprofen; hyaluronic acid; post-operative adhesion; electrospinning; inflammation

## 1. Introduction

The limitation of hand function caused by postoperative tendon adhesion is mainly attributed to tendons adhering to surrounding tissues during the healing process, thereby limiting joint mobility [1]. Currently available anti-adhesion devices still exhibit certain problems. Seprafilm® is an anti-adhesion membrane comprising hydrophilic hyaluronic acid (HA) and carboxymethyl cellulose. To prevent post-surgical adhesion after tendon surgery, Seprafilm® shows some disadvantageous such as limited flexibility, poor handling capability, easily breaking into pieces, and a fast degradation rate [2,3]. SurgiWrap® is a membrane that mainly comprises polylactic acid (PLA), which does not easily curl over to cover the whole surgical site. Furthermore, SurgiWrap® is brittle due to the fact of its hydrophobic and nonporous natures, which also hinders nutrient exchanges in a surgical site with limited blood supply, such as during tendon repair operation, affecting postoperative healing [4]. Considering that an ideal anti-adhesion device requires properties such as mimicking the native tendon sheath, a nanofibrous membrane (NFM) obtained through electrospinning is expected to structurally serve as a tendon sheath to effectively separate damaged tendon tissue from surrounding tissues [5]. With the high porosity, suitable pore size, and excellent permeability associated with an NFM, it can also effectively prevent the penetration of fibroblasts without simultaneously compromising nutrient/waste exchanges [6].

Previous studies on anti-adhesion membranes to prevent tendon adhesion were mainly focused on electrospun nanofibers of HA-grafted poly(caprolactone) (PCL), poly(ethylene glycol) (PEG) blending with PCL, HA-loaded PCL, ibuprofen-loaded poly(lactic acid) (PLA), and ibuprofen-loaded PLA-PEG copolymer [6–10]. Incorporation of ibuprofen (IBU) in biodegradable electrospun NFMs is expected to inhibit inflammation [11]. With the anti-inflammatory property from IBU, a drug-loaded barrier membrane could augment its anti-adhesion efficacy just as nonsteroidal anti-inflammatory drugs (NSAIDs) such as IBU were reported to reduce flexion tendon adhesion [12,13]. Indeed, existing studies using nanomaterials for anti-adhesion purpose are based on biodegradable materials combined with other bioactive agents for better anti-adhesion outcomes [14,15]. For this purpose, anti-adhesion NFMs with multiple functions through combining with gene therapy or drugs conducive to healing should be developed [16–18]. In addition, as clinical Good Manufacture Practice (GMP)-grade electrospinning machines are already available commercially, the possibility of clinical applications of NFMs for anti-adhesion purposes may increase in the future [19].

Hyaluronic acid is a component of the extracellular matrix and is also present in the synovial fluid, making it biodegradable and biocompatible [20,21]. The main disadvantages of anti-adhesion products containing HA are their poor mechanical properties and fast degradation rates [22]. Poly(ethylene glycol) (PEG) (or poly(ethylene oxide), PEO) has favorable biocompatibility, as well as anti-adhesive, non-toxic, and anti-protein adsorption properties. Although the main mechanism of anti-adhesion property has yet to be clarified, the anti-protein adsorption mechanism of PEG is believed to be related to the exclusion effect of larger molecules in addition to favorable hydrophilicity [23–26]. Ibuprofen is a nonsteroidal drug with anti-inflammatory properties. Its absorption rate is not affected by age and it is metabolized in the liver with approximately 90% of metabolites being excreted through the urine [27,28]. This study aims to use iron ions ( $\text{Fe}^{3+}$ ) and 1,4-butanediol diglycidyl ether (BDDE) to prepare dual crosslinked IBU-loaded HA NFMs that could effectively prolong the degradation time and reduce cell attachment and penetration. It is expected that the drug-loaded NFMs may achieve better postoperative anti-adhesion effects from controlled released of IBU to reduce inflammatory reactions at the surgical site.

## 2. Results and Discussion

### 2.1. Characteristics of the NFMs

As shown in Figure 1, SEM images revealed that electrospinning and dual crosslinking post-treatment could successfully prepare continuous IBU-loaded HAIFB nanofibers containing

20, 30 or 40% IBU [29]. The average fiber diameter increased with IBU, which were  $0.52 \pm 0.16 \mu\text{m}$ ,  $0.58 \pm 0.17 \mu\text{m}$ , and  $0.63 \pm 0.21 \mu\text{m}$  for HAI20FB, HAI30FB, and HAI40FB, respectively. Nonetheless, no significant difference in fiber diameter was found among all NFMs.

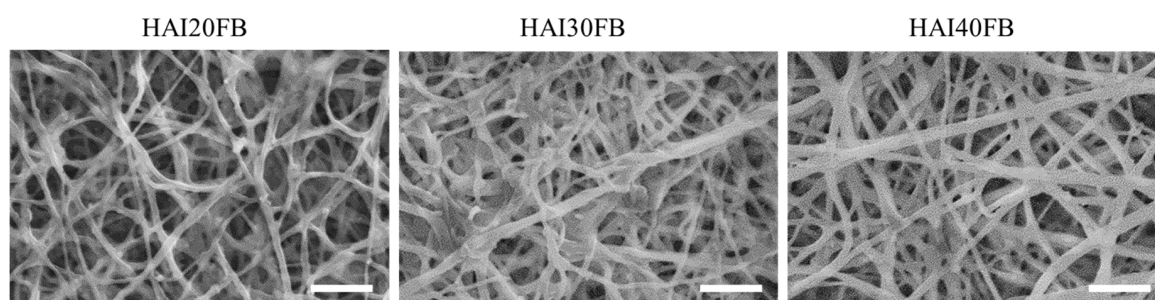


**Figure 1.** The SEM micrographs of HAI20FB, HAI30FB, and HAI40FB nanofibrous membranes (NFMs). Bar = 10  $\mu\text{m}$ . HAIFB nanofibers containing 20, 30 or 40% IBU become HAI20FB, HAI30FB and HAI40FB NFMs, respectively.

The thermal properties of HAI20FB, HAI30FB, and HAI40FB NFMs were analyzed from the TGA and DTG curves in Figure 2. The TGA curves indicated substantial weight loss for all NFMs when temperature was increased to 600  $^{\circ}\text{C}$ , with the initial weight loss before 100  $^{\circ}\text{C}$  likely due to the water bound to HA. The thermal decomposition started at  $\sim 210^{\circ}\text{C}$  and gave rise to 31.0% residual weight for HA. In contrast, the onset of weight loss for IBU started earlier at  $\sim 130^{\circ}\text{C}$  with  $\sim 0\%$  residual weight (Figure 2A) [30]. A broad DTG peak with a peak decomposition temperature occurring at  $\sim 220^{\circ}\text{C}$  was observed for IBU, while HA gave a sharper DTG peak with the maximum weight loss being observed at  $\sim 231^{\circ}\text{C}$  (Figure 2B). For NFMs, similar decomposition curves were observed from TGA, but the remaining weight at 600  $^{\circ}\text{C}$  decreased with higher IBU loading in the NFMs (Figure 2C). This trend could be explained from Figure 2A as IBU, but not HA, can be completely decomposed at higher temperatures. The DTG curves for NFMs showed a broad decomposition peak temperature due to the similarity of the peak temperatures of HA and IBU (Figure 2B) with a shoulder around 210  $^{\circ}\text{C}$  (Figure 2D). By increasing IBU content, this shoulder in the DTG curves diminished to result in only one discernible peak for HAI40FB.

From Figure 3A, the FTIR analysis of NFMs confirmed successful chemical crosslinking of HA by BDDE, where the peak observed at  $1253\text{ cm}^{-1}$  corresponded to the newly generated C–O in ether or ester from the carboxyl groups and hydroxyl groups of HA [31]. The presence of IBU in the NFMs could be inferred from the appearance of peaks assigned to IBU in all HAIFB NFMs. The peak at  $518\text{ cm}^{-1}$  denotes the aromatic C–H deformation of IBU whereas peaks at 777, 866, and  $1421\text{ cm}^{-1}$  could be assigned to the  $\text{CH}_2$ , CH, and CH–CO groups, respectively [32].

From mechanical testing, the NFMs showed typical stress–strain curves, as seen in Figure 3B, which indicated the ultimate tensile stress and tensile strain increased with increasing IBU loading in the membrane. Indeed, the ultimate stress (strain) of HAI40FB was 2.3 (1.5) times that of HAI20FB (Table 1). Similarly, the Young’s modulus also increased with IBU loading, with HAI40FB showing a significantly higher modulus than HAI20FB and HAI30FB. Without a significant increase in the fiber diameter with increasing IBU loading (Figure 1), the increase in the Young’s modulus and tensile stress may be related to more interactions between IBU and HA polymer chains, which could stabilize the crosslinked polymer networks [33]. Overall, the superior stretching capability and breaking strength will undoubtedly facilitate the application of the IBU-loaded NFMs to the curved and limited space around the operation site after tendon surgery.

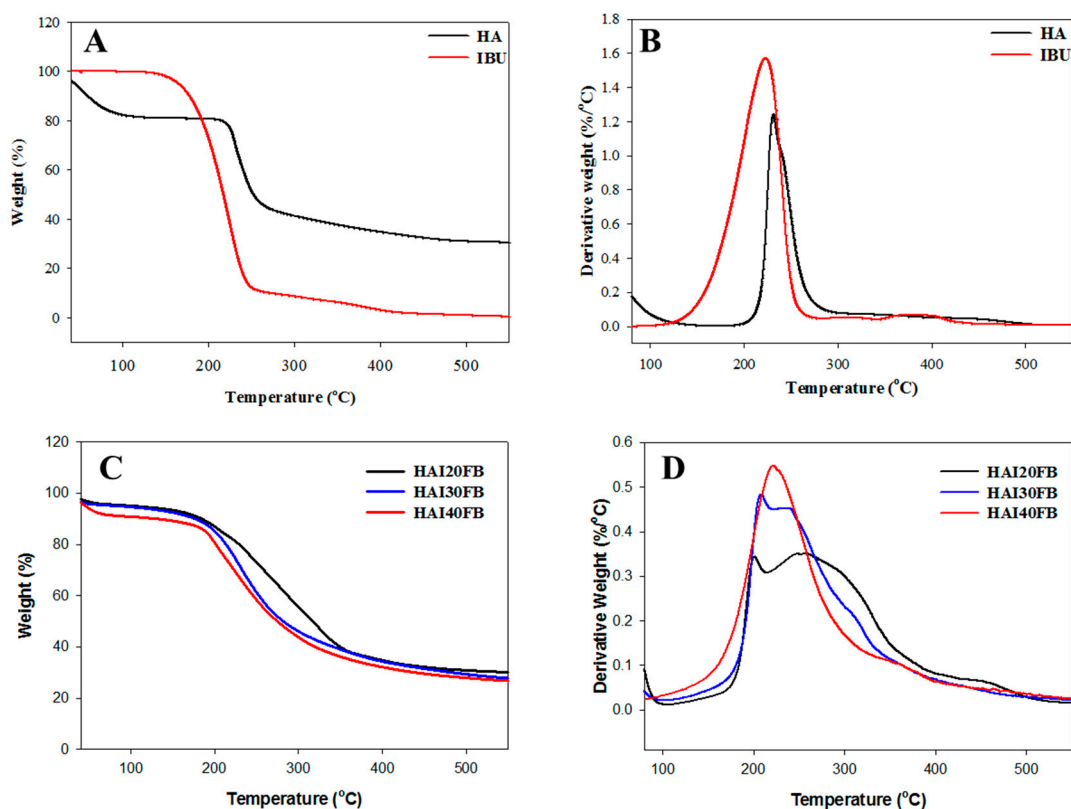


**Figure 2.** The TGA (A,C) and DTG (B,D) curves of hyaluronic acid (HA) and ibuprofen (IBU) (A,B) and HAI20FB, HAI30FB and HAI40FB NFMs (C,D).

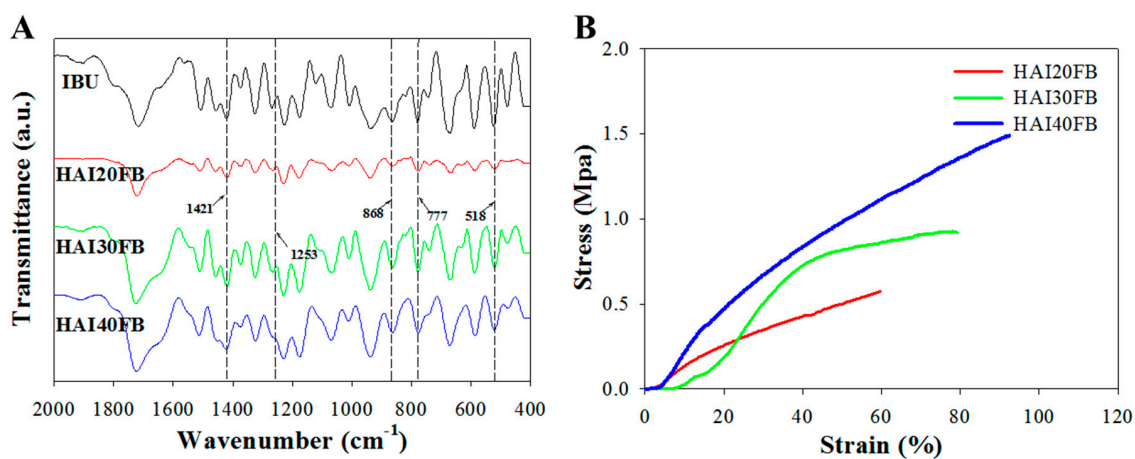


**Figure 3.** The FTIR spectra (A) and typical stress–strain curves (B) of the HAI20FB, HAI30FB, and HAI40FB NFMs.

**Table 1.** The ultimate tensile stress, ultimate tensile strain, and Young’s modulus of HAIFB NFMs with 20% (HAI20FB), 30% (HAI30FB), and 40% IBU (HAI40FB) loading.

Membrane	Ultimate Stress (MPa)	Ultimate Strain (%)	Young’s Modulus
HAI20FB	0.63 ± 0.53	61.46 ± 11.42	9.42 ± 0.83
HAI30FB	0.94 ± 0.89 *	81.22 ± 8.23 *	10.57 ± 0.84
HAI40FB	1.43 ± 0.13 *,#	90.11 ± 8.75 *,#	14.16 ± 1.25 *,#

\*  $p < 0.05$  compared with HAI20FB, #  $p < 0.05$  compared with HAI30FB.

## 2.2. Release of IBU from NFMs

As shown in Figure 4A, the released IBU weight from the NFMs correlated with its loading percentage in the membranes. The released drug content diminished rapidly with time but continuous drug release could still be observed up to 21 days. The cumulative drug release showed a 55%, 59%, and 65% drug release percentage for HAI20FB, HAI30FB, and HAI40FB on day 7, respectively, which increased gradually to 59%, 62%, and 71% on day 21 (Figure 4B). Nonetheless, sustained release of IBU from all NFMs was observed during the first 24 h with 40%–60% of drug release after 24 h (Figure 4B, insert). In this study, the IBU-loaded NFM was prepared by crosslinking HA with BDDE from reaction of the carboxyl or hydroxyl groups of HA with the end groups of BDDE in ethanol. As IBU is a monocarboxylic acid, we cannot rule out the possibility that IBU could be covalently bound to the NFM during crosslinking. Therefore, we did not extract all IBU from the fibers to obtain the real content in the formulations but used the amount of IBU fed to the system upon preparation for calculation of the cumulative drug release in Figure 4B. The HAI40FB NFM therefore provided the fastest IBU drug release rate and the highest drug concentration for anti-inflammation efficacy. It should be noted that the burst drug release profile with massive release within a week will be critical to inhibit tissue adhesion [34], which is caused by an inflammatory response during the early stage of the tendon healing process. The fast release of IBU from the implanted NFMs may also contribute to alleviate the associated pain after tendon surgery [35].

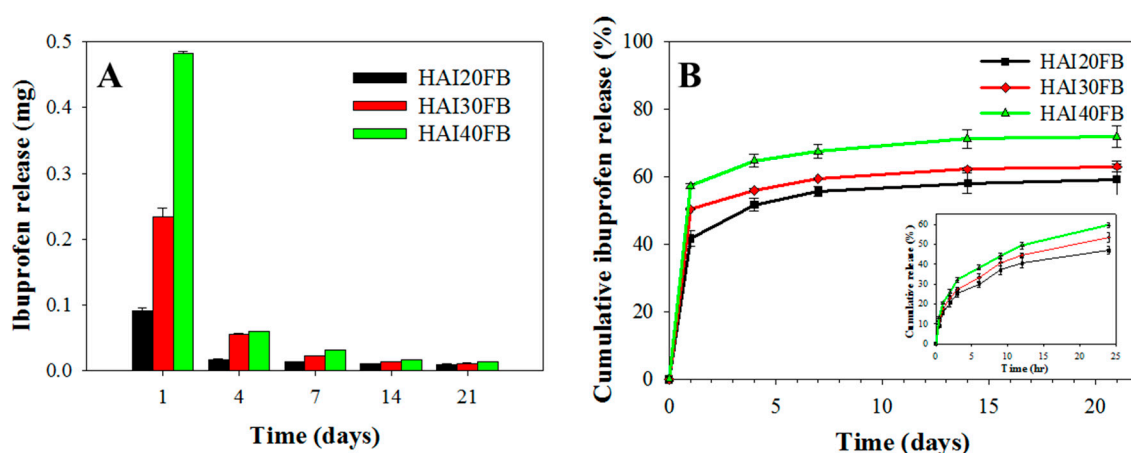


**Figure 4.** The released weight (A) and cumulative release percentage (B) of IBU from HAI20FB, HAI30FB, and HAI40FB NFMs. The insert in (B) is the release percentage of IBU within 24 h.

## 2.3. In Vitro Cell Culture

### 2.3.1. Cytotoxicity of NFMs

As constituents of NFMs such as IBU or HA may have cytotoxic effect, the cytotoxicity of IBU-loaded NFMs was evaluated following the ISO standards after extracting the NFMs for 24 h with cell culture medium. The relative cell viability was based on the solution absorbance from the 3-(4,5-dimethylthiazol-2-yl)-5-(3-carboxymethoxyphenyl)-2-(4-sulfophenyl)-2H-tetrazolium (MTS) assay after normalizing with that of fresh culture medium (control) (Figure 5). The relative cell viability of HAI20FB and HAI30FB, but not HAI40FB, was not significantly different from the control on day 1. On day 4, the relative viability of cells grown in HAI40FB extract was significantly less than all other groups and decreased from 77% to 50%, while still no significant difference was found for other NFMs from the control. The cytotoxicity found for HAI40FB was in line with the faster IBU release rate and the higher concentration of released IBU at high IBU-loading shown in Figure 4. Indeed, previous reports indicated cell viability in the presence of IBU may depend on drug dosage and a higher concentration of IBU resulted in substantial cytotoxicity in vitro [36,37]. These results indicated that IBU may lead



to toxic reactions in fibroblasts if in excess [38,39]. The consideration of NFM cytotoxicity pointed toward the choice of HAI30FB NFM to prevent tendon adhesion in vivo, which is biocompatible with the highest IBU loading.

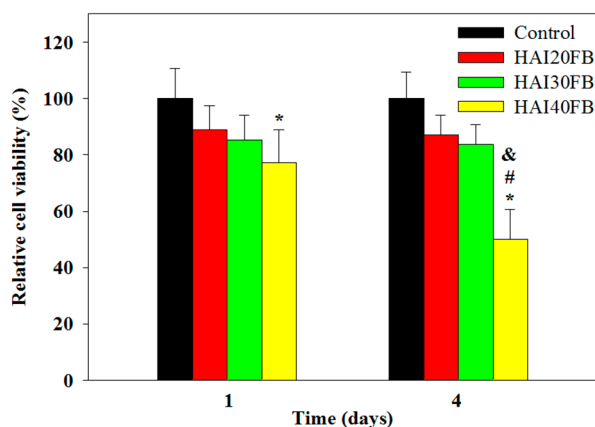


**Figure 5.** Cytotoxicity of NFMs by culture 3T3 fibroblasts with 24 h extracts (in cell culture medium) of HAI20FB, HAI30FB, and HAI40FB NFMs for 1 and 4 days. The relative cell viability was normalized with cells cultured in fresh cell culture medium (control), which was taken as 100%. \*  $p < 0.05$  compared with control; #  $p < 0.05$  compared with HAI20FB; &  $p < 0.05$  compared with HAI30FB.

### 2.3.2. Penetration of Cells through NFMs

As exogenous healing occurred before endogenous healing after tendon surgery, tendon adhesion is likely to happen if no barrier is used to prevent the peripheral fibroblasts from invading. Considering the role of fibroblasts in adhesion formation, the design of an NFM should also consider the migration and penetration of fibroblasts through the barrier membrane at the surgical site. Toward this end, we studied 3T3 fibroblast cell penetration through an NFM using gradient serum concentration to drive cell migration. The control group without an NFM in a cell insert was compared with the NFM group where an NFM was closely fitted to the bottom of the cell insert. As the difference in serum concentrations among compartments in the culture chamber forced cell penetration through the cell inset, the extent of cell migration to the bottom chamber could be observed by an optical microscopy (Figure 6A). The microscopic observation of cells on the surface of the lower chamber revealed few cells could be seen in the NFM groups, while abundant cells were found in the control group. Follow-up experiments to quantify the viable cell number collected in the bottom chamber indicated the penetrated cell numbers were 0.10, 0.12, 0.14, and  $0.87 \times 10^4$  cells for HAI20FB, HAI30FB, HAI40FB, and the control groups, respectively (Figure 6B). Therefore, all NFMs could significantly reduce the number of cells that penetrated the membrane. That the number of cells which penetrated through the NFM was drastically different from and in the range of 11–16% of the control group indicated that the membrane could effectively block cell penetration. This drastic reduction in the number of cells that penetrated an NFM in vitro also suggested its efficacy to prevent tendon adhesion in vivo due to the extrinsic fibroblastic cells. Indeed, the dense fiber morphology and the macroporous structure of the NFM shown in Figure 1 facilitates its use as a physical barrier to prevent postoperative adhesion [40]. That the number of penetrated cells of HAI40FB was significantly higher than HAI20FB may be due to the difference in pore sizes of the membrane [41].

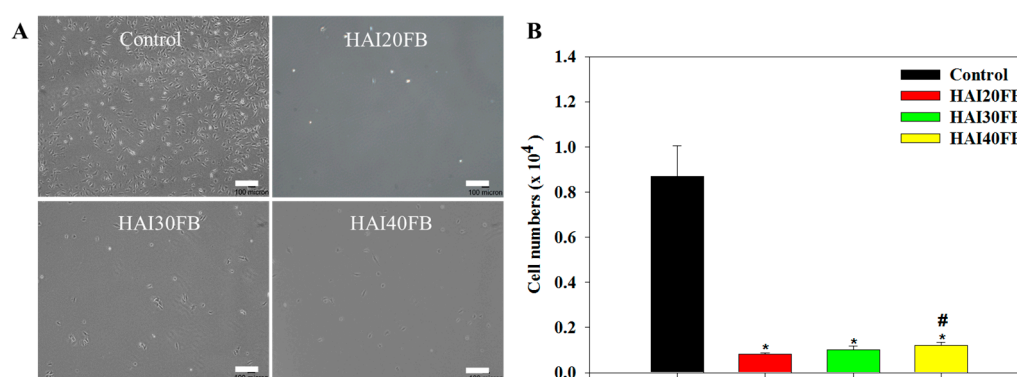


**Figure 6.** Migration of 3T3 fibroblasts through the control (no NFMs), HAI20FB, HAI30FB or HAI40FB NFMs in 24 h via optical microscopic observation of penetrated cells (A) and an assay of penetrated cell numbers (B). Bar = 100 µm. \*  $p < 0.05$  compared with control; #  $p < 0.05$  compared with HAI20FB.

### 2.3.3. Cell Attachment to NFMs

As fibroblast attachment is the first event responsible for adhesion formation, the adherence of fibroblasts to and cell proliferation on NFMs was compared with the control (TCPS) by seeding 3T3 cells directly on the membrane surface. The cell number after being cultured for 1 and 7 days was determined from DNA assays and shown in Figure 7A. The number of adhered cells on the TCPS (control) on day 1 was significantly higher than those on NFMs—up to 16.7 times, demonstrating that the membrane can effectively prevent cell attachment. There was no statistical difference between HAI20FB and HAI30FB, but HAI40FB showed a significantly lower adhered cell number. The drastic reduction of cell attachment to all NFMs on day 1 endorses the beneficial effects of IBU-loaded NFMs to reduce fibroblast adherence. During the process of adhesion formation, the deposition of fibroblasts and macrophages in the matrix led to the development of a fibrous band [42]. Therefore, as a critical step in adhesion formation, the examination of whether an NFM can reduce deposition of fibroblasts in vitro is important. All NFMs were observed to virtually eliminate fibroblast adherence and reduce the attached cell number by more than 90%, which strongly suggests an NFM can function in vivo to block fibroblast attachment to the injured surface, thus interrupting fibrin matrix formation that leads to adhesion formation [43]. We postulate the drastic drop in the number of adhered cells on NFMs may be correlated with the combined effect of IBU and HA in the membranes. Previously, dermal fibroblasts were found to show less attachment to HA-modified surfaces, which was explained based on the influence through the HA receptor CD44 [44]. By grafting HA to PCL NFMs, we also found less fibroblast adhesion compared to unmodified membrane surfaces [7]. Nonetheless, the significant reduction in the cell number for HAI40FB among all IBU-loaded NFMs may imply that the dosage of IBU influences cell adhesion as well, since a previous report suggested that IBU dosage directly leads to inhibition of cell adhesion [45].

Following the same trend as day 1, the TCPS group showed a distinctively higher cell number for all NFMs on day 7, while the HAI40FB NFM showed the minimum compared to all other groups. To compare the cell proliferation rate, the mean increase in cell number from day 1 to day 7 were calculated to be 1.69, 1.23, 1.19, and 0.74 for control (TCPS), HAI20FB, HAI30FB, and HAI40FB, respectively. The reduction in cell proliferation rate may be mainly due to the action of HA, which can inhibit the growth of fibroblasts [46]. Nonetheless, loading more IBU in NFMs (as for HAI40FB) may further induce cytotoxicity, which even reduces the cell number on day 7 from day 1. Taken together, increasing IBU loading in the membrane will influence cell proliferation, as evidenced from the reduced cell proliferation rate. Therefore, loading IBU up to 30% may be deemed as an optimized drug loading concentration without influencing the barrier and anti-adherence effects towards fibroblasts, which is expected to lead to successful tendon anti-adhesion in vivo.

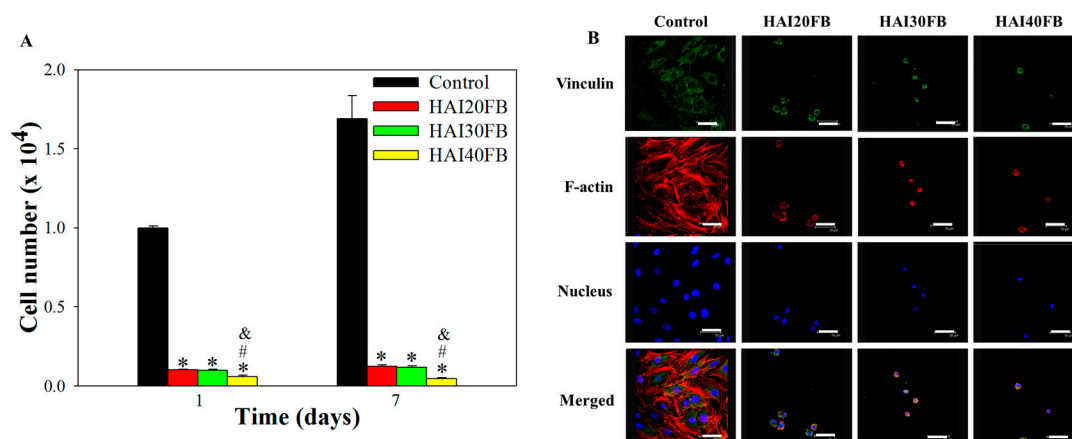


**Figure 7.** (A) Attachment and proliferation of 3T3 fibroblasts on TCPS (control) and HAI20FB, HAI30FB, and HAI40FB NFMs from assays of DNA contents. (B) The cytoskeletal arrangement and focal adhesion protein expression of 3T3 fibroblasts after cell seeding for 24 h were determined by actin cytoskeleton and vinculin staining and observed by confocal microscopy. Vinculin focal adhesion, actin cytoskeleton, and cell nucleus are shown in green, red, and blue, respectively. Bar = 50 mm. \*  $p < 0.05$  compared with control; #  $p < 0.05$  compared with HAI20FB; &  $p < 0.05$  compared with HAI30FB.

Follow-up study to validate the molecular mechanism responsible for reduced cell attachment was carried out by examining the expression of a focal adhesion protein (vinculin) and cytoskeletal actin distribution in 3T3 fibroblasts under a confocal microscope (Figure 7B). The protein vinculin was labelled in green to visualize focal adhesion; the red F-actin protein was stained in red to confirm cytoskeletal arrangement; the cell nucleus was counterstained in blue. In the control group, fibroblasts attached to the TCPS surface exhibited a nearly flattened and spread morphology with a well-distributed fibrous F-actin cytoskeleton 24 h after cell seeding, while enhanced vinculin expression indicated increased cellular spreading. In comparison, cells attached to all NFMs showed restricted cytoskeletal distribution and minimal vinculin expression revealed from the rounded morphology. The circular shape of the cell indicated that the cell had extended to induce adhesion to a substrate. All NFMs showed similar cell spreading and cytoskeletal distribution characteristics with adhered cells, endorsing excellent cell adhesion inhibition behavior exerted by the membrane as shown from the quantitative cell attachment results in Figure 7A. Fewer cells were also found for the HAI40FB group compared to other NFMs, as seen in Figure 7A. Our previous results also supported reduced fibroblast adhesion to NFMs containing HA [47]. The cell penetration and attachment study thus confirmed the applicability of IBU-loaded NFMs for post-surgical anti-adhesion, other than HAI40FB due to the fact of its cytotoxicity. We therefore chose an NFM with the next highest IBU content (i.e., HAI30FB) for subsequent in vivo studies.

## 2.4. In Vivo Studies

### 2.4.1. Gross Observation

From in vivo experiments, all animals were euthanized 3 weeks post-operation and gross view was adopted to observe tissue adhesion around the tendon repair site (Figure 8A–D). The animal study was divided into four groups, an untreated control group and three treatment groups using Seprafilm<sup>®</sup>, HAFB (without IBU) or HAIFB (with IBU, HAI30FB). The initial 3 week period was used for evaluation, as clinical rehabilitation in tendon healing is initiated and more critical during the early stage [34]. In the HAIFB group—NFMs with 30% IBU—the repaired tendon did not show adhesion with the surrounding tissues to exhibit a smooth morphology (Figure 8D). In comparison, tight peritendinous adhesions were noted at the repair site with the surrounding tissues in the untreated control group and strong force was required to separate them (Figure 8A). Moreover, the group treated with Seprafilm<sup>®</sup> (Figure 8B) and

HAFB (Figure 8C) showed some loose fibrous tissue connected to the tendon; therefore, considerable strength was still required to separate them from the surrounding tissues. Although moderate to mild tissue bridging was observed and adhesions could be removed by blunt dissection in both groups, the HAFB group showed relatively thinner adhesion bands. Based on gross observation, the extent of peritendinous adhesion was further evaluated and compared among four groups. The extent of tissue adhesion was graded into four categories with scores from 0 (no adhesion) to 3 (severe adhesion). The average adhesion scores of the control group, the group treated with Seprafilm®, HAFB, and HAI30FB were 2.67, 1.00, 0.83, and 0.17, respectively. The control group demonstrated the highest score, indicating the most severe adhesion. The HAI30FB group exhibited the lowest score, indicating its efficacy in preventing postoperative tendon adhesion (Figure 8D).

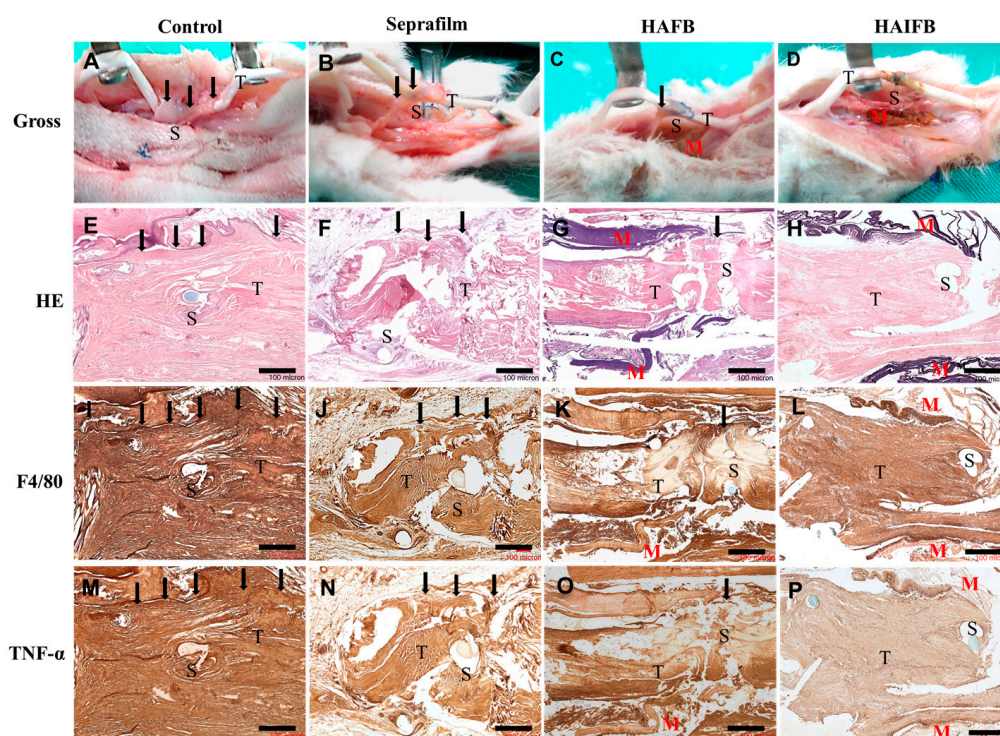


**Figure 8.** Gross view (A–D), H&E (E–H), F4/80 (I–L), and TNF- $\alpha$  (M–P) stainings of tissue sections of the repaired flexor digitorum profundus (FDP) tendons of the untreated control group and the experimental groups treated with Seprafilm®, HAFB, and HAIFB 3 weeks post-operation. Bar = 100  $\mu$ m. T: tendon; S: suture; M: membrane; black arrows: sites where adhesion occurred.

#### 2.4.2. Histological Staining

Histological analysis was performed to evaluate adhesion formation and inflammation around treated tendons by staining tissue slices with H&E and IHC staining of TNF- $\alpha$  and F4/80 (Figure 8E–P). In the control group, tendons were found to have tight adhesion to the surrounding tissues (Figure 8E) [48]. In the experimental groups treated with Seprafilm® (Figure 8F) and HAFB (Figure 8G), a slight to moderate adhesion of the tendon to the surrounding tissues occurred [6]. In contrast, the HAIFB group displayed no adhesions between the surrounding tissues and the repaired tendon (Figure 8H). Unlike Seprafilm®, the NFMs displayed more physical stability in vivo as membrane remnants (indicated by M) could still be observed after 3 weeks. This provided the membrane with a continuous barrier effect to effectively prevent fibroblast invasion and adhesion formation with the surrounding tissues post-surgically.



The F4/80 is one of the surface receptors on macrophages, and when the tissue is injured, it is accompanied by an inflammatory reaction that causes macrophages to accumulate at the site of injury. The number of macrophages is tantamount to the expression of their surface receptors, which affects the F4/80 staining intensity [49]. From a microscopic point of view, the control group had the darkest F4/80 stained color, indicating the most serious inflammatory reaction (Figure 8I). Furthermore, the colors of the groups treated with Seprafilm® (Figure 8J) and HAFB (Figure 8K) were observed to be darker than HAIFB (Figure 8L) in the vicinity of the wound, suggesting the number of macrophages was lowered by incorporating IBU in the NFM. This implies IBU released from the HAIFB NFM could inhibit the inflammatory reaction, thereby reducing the number of macrophages that accumulate at the tendon repair site. This observation undoubtedly endorsed that the anti-inflammatory action of HAIFB NFM during tendon healing may be correlated with its efficacy to prevent tendon adhesion [50].

Tumor necrosis factor alpha (TNF- $\alpha$ ) is released by macrophages and activates proteins that stop apoptosis and promote cell proliferation and inflammation [51]; therefore, it is considered a critical factor in inflammatory responses. Tendon repair sites or adhesions all exhibited denser staining intensity for TNF- $\alpha$  in the control group (Figure 8M). This is because inflammation occurred at the site of injury, resulting in a larger aggregation of macrophages that release TNF- $\alpha$ , resulting in a darker color. The groups treated with Seprafilm® and HAFB had the second darkest color (Figure 8N,O), indicating a notable inflammatory response [52]. Finally, the group treated with HAIFB had the lightest color (Figure 8P), confirming the membrane containing 30% IBU can reduce inflammation through drug release and simultaneously reduce the number of macrophages aggregated near the injured site [53].

#### 2.4.3. Evaluation of Tendon Adhesion by Biomechanical Evaluation

Through biomechanical evaluation, including range-of-motion, gliding excursion, and pull-out force of the FDP tendons, the anti-adhesion efficacy *in vivo* was further analyzed quantitatively (Figure 9). The evaluated proximal interphalangeal (PIP) and distal interphalangeal (DIP) joint angles are physiologically relevant for assessing the range-of-motion of the joint and providing meaningful comparison regarding the seriousness of adhesion formation after different treatments. Compared with the control group, the joint flexion DIP angle of the HAIFB group increased to the value of the normal FDP tendon (dotted line) and showed statistical improvement compared with the control group 3 weeks post-operation (Figure 9A). Although an increasing trend of DIP angles were found for Seprafilm® and HAFB groups, they fell short of the normal FDP tendon value and only the HAFB group showed statistical improvement of DIP angle from the control group. Similar to the trend observed for the DIP angle, the PIP angle of the HAIFB group was the highest, crossing the normal tendon angle value and significantly higher than all other groups. Indeed, the overall trend of average joint angles indicated tendons treated with HAIFB will display better range-of-motion than HAFB, which was further better than Seprafilm® and the control. The higher DIP and PIP angle values, which were close to those of the normal tendon, indicated the recovery of range-of-motion for the injured tendon 3 weeks after treatment with HAIFB, which could prevent post-surgical peritendinous adhesion *in vivo* [54,55].



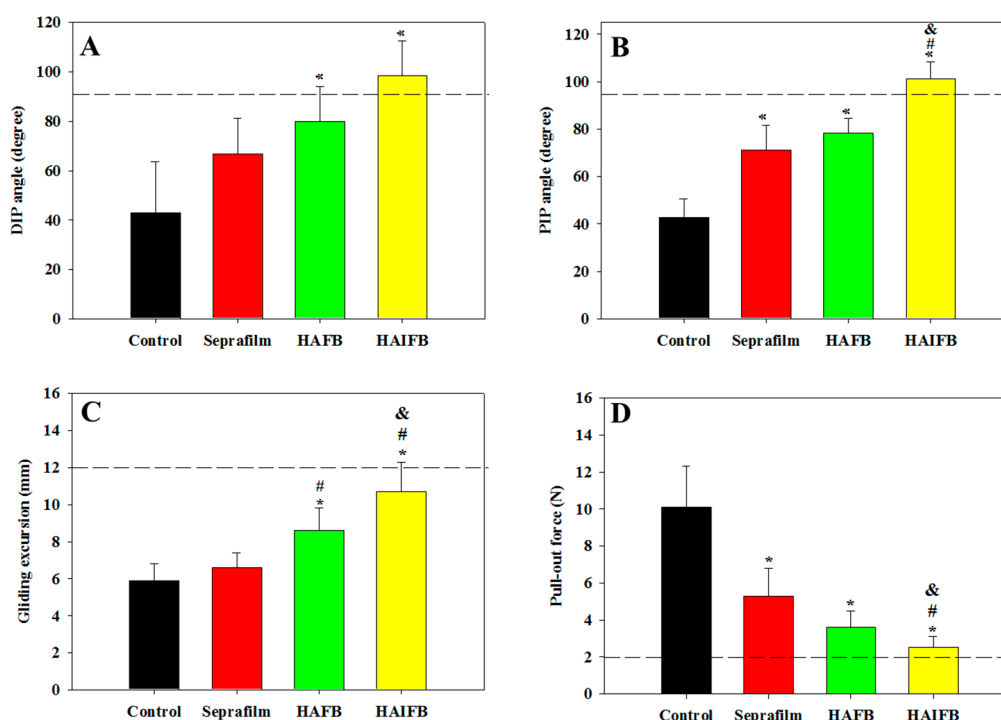


**Figure 9.** Evaluation of peritendinous adhesions from the distal interphalangeal (DIP) joint flexion angle (A), proximal interphalangeal (PIP) joint flexion angle (B), tendon gliding excursion (C), and pull-out force (D) 3 weeks post-operation. The dotted line represents the average value of the normal FDP tendon. \*  $p < 0.05$  compared with control, #  $p < 0.05$  compared with Seprafilm®, &  $p < 0.05$  compared with HAFB ( $n = 6$  for each group).

From the tendon gliding experiment, the gliding excursion distance revealed the same trend as the joint range-of-motion DIP and PIP angles in Figure 9A,B, i.e., HAIFB showed the least adhesion with the highest excursion, followed by HAFB and Seprafilm®, while the control was the most adhesive with the least excursion distance (Figure 9C). The gliding distance of HAFB was significantly higher than the control and Seprafilm®, with no difference among the two. Therefore, the tendon gliding experiment clearly indicated that the gliding excursion of the HAIFB group was significantly higher than the other groups and similar to the normal tendon. Since adhesion severity could be judged from the difference in the gliding displacement value, the excursion distance from the tendon gliding experiments further demonstrated the efficacy of IBU-loaded NFMs (HAIFB) in preventing peritendinous adhesion.

The pull-out force, which is defined as the required force to completely remove the FDP tendon from the tendon sheath by pulling, was also determined. As more severe adhesion will lead to higher pull-out force, it showed a reverse trend from previous range-of-motion biomechanical tests, with the untreated control group requiring the maximum force (10.1 N) to remove the FDP tendon from the tendon sheath due to the fact of severe adhesion (Figure 9D). The tendon treated with Seprafilm® needed the second largest pull-out force (5.3 N), while the HAFB group required 3.6 N to remove the tendon from the sheath. In accordance with previous anti-adhesion biomechanical testing, a repaired tendon covered with HAIFB showed the least adhesion judging from its minimum pull-out force (2.5 N), which was significantly lower than all other groups and approached that of a normal tendon (dotted line) [6].

Taken together, the biomechanical evaluation indicated that the repaired tendon wrapped with the HAIFB NFM post-surgically will result in the most favorable anti-adhesion outcome with following anti-adhesion efficacy HAIFB > HAFB > Seprafilm® > control. This is consistent with the gross observation and H&E staining results shown in Figure 8A–H. As a less inflammatory response of the healed tendon at the surgical site was found for IBU-loaded HAIFB NFMs from F4/80 and TNF- $\alpha$  IHC

staining (Figure 8L,P), we successfully correlated its preference over NFMs without IBU (HAIFB) to lower tendon adhesion with smaller pull-out force, higher DIP/PIP angles, and higher gliding excursion from biomechanical testing (Figure 9). This improvement in anti-adhesion efficacy should be offered from the prompt release of IBU from HAI30FB NFMs (Figure 4) without eliciting cytotoxicity (Figure 5).

### 3. Materials and Methods

#### 3.1. Materials

Hyaluronic acid (HA; sodium hyaluronate; average molecular weight =  $1.3 \times 10^6$  Da; range of molecular weights =  $0.8\text{--}1.5 \times 10^6$  Da) was purchased from Shandong Freda Biochem (Jinan, China); ibuprofen (IBU), poly(ethylene oxide) (PEO; average molecular weight =  $2.0 \times 10^6$  Da; viscosity = 2000–4000 cP for 2% solution in water at 25 °C), iron (III) chloride ( $\text{FeCl}_3$ ) hexahydrate, and 1,4-butanediol diglycidyl ether (BDDE) were purchased from Sigma–Aldrich (St. Louis, MO, USA). Antibiotics and trypsin-EDTA were obtained from Thermo Fisher Scientific (Waltham, MA, USA). CellTiter 96® AQueous One solution was purchased from Promega (Madison, WI, USA). Dulbecco's modified Eagle's medium (DMEM) and fetal bovine serum (FBS) were obtained from Life Technologies (Carlsbad, CA, USA). The actin cytoskeleton and focal adhesion staining kit (FAK100) was purchased from Millipore (Bedford, MA, USA).

#### 3.2. Fabrication of Nanofibrous Membranes (NFMs)

The HA/IBU/PEO solutions were prepared separately by mixing 0.0563 g, 0.0964 g, and 0.1500 g of IBU with 0.175 g of HA and 0.050 g of PEO in 10 mL of formic acid solution to obtain 20%, 30%, and 40% (*w/w*) IBU polymer solutions for preparation of HAI20, HAI30, and HAI40 NFMs. An electrospinning setup was used, comprising a 23 gauge stainless-steel needle, a 5 mL glass syringe, and a syringe pump (KD Scientific, Holliston, MA, USA). The syringe delivered the polymer solution at 1 mL/h by connecting with a high-voltage DC power supply (Glassman High Voltage Inc., High Bridge, NJ, USA) to the needle tip, which provided a 20 kV voltage. An NFM with an approximate thickness of 200  $\mu\text{m}$  was collected on a grounded aluminum target that was placed 15 cm away from the needle tip. To prepare the iron ion-crosslinked NFMs, the solution immersion method was used with some modification [56]. Briefly, a 6 cm  $\times$  5 cm HAI20, HAI30 or HAI40 NFM was immersed in a 30% (*w/w*)  $\text{FeCl}_3$  solution in anhydrous ethanol in a 10 cm diameter Petri dish and shaken at 30 rpm for 24 h to obtain HAI20F, HAI30F and HAI40F NFMs. Each membrane was washed with 10 mL of anhydrous ethanol twice to remove residual  $\text{Fe}^{3+}$  ions and vacuum dried for 24 h to get ionically crosslinked HAIF NFMs with different IBU contents. The ionically crosslinked HAI20F, HAI30F, and HAI40F NFMs were further separately reacted with 10% (*w/w*) of BDDE in anhydrous ethanol in a 10 cm Petri dish and shaken at 30 rpm for 24 h to produce HAI20FB, HAI30FB, and HAI40FB NFMs. The membrane was washed with 10 mL of anhydrous ethanol twice to remove residual BDDE and vacuum dried for 24 h to get dual crosslinked HAIFB NFMs. For comparison, HAIFB NFMs were prepared following the same procedure but using HA/PEO solutions without IBU.

#### 3.3. Characteristics of Nanofibrous Membranes (NFMs)

The surface morphology of HAIFB NFMs was observed using a scanning electron microscope (SEM, Hitachi S3000N, Tokyo, Japan). At least 100 fibers randomly chosen from 10 images were used to measure the fiber diameter with the ImageJ software. The thermal properties of the NFMs were evaluated using thermogravimetric analysis (TGA) and derivative thermogravimetry (DTG) (TGA 2050, TA Instruments, New Castle, DE, USA) up to 600 °C at a heating rate of 10 °C/min. For mechanical properties, a material testing machine (Tinius Olsen H1KT, Horsham, PA, USA) equipped with a 10 N load cell was used to measure the uniaxial tensile properties of NFMs by operating at 5 mm/min elongation rate. A 1 cm  $\times$  5 cm test membrane sample was vertically mounted on two mechanical gripping units at each end, leaving a 3 cm gauge length for mechanical loading. The ultimate

tensile stress, ultimate tensile strain, and Young's modulus were obtained from the stress–strain curve. Chemical analysis was performed using attenuated total reflection Fourier transform infrared (ATR-FTIR) spectroscopy from 400 to 4000  $\text{cm}^{-1}$  with 2  $\text{cm}^{-1}$  resolution using a Horiba FT-730 spectrometer (Kyoto, Japan) and recorded as transmittance versus wavenumber. To determine the release of IBU, the NFMs were punched into disc-shaped membranes (1.5 cm in diameter) and sterilized by UV exposure for 2 h in an UVP CL-1000 Crosslinker at 0.1  $\text{J}/\text{cm}^2$  for 2 h. Sterilized NFMs were immersed in 4 mL of phosphate buffered saline (PBS, pH = 7.4) in a vial and placed in a shaking incubator at 37 °C. After a fixed time, the whole solution was removed from the vial, followed by replenishing with 4 mL of PBS to the vial to continue the drug release experiments. To measure IBU concentration in the solution, high-performance liquid chromatography (HPLC) was used with a Hypersil™ ODS C18 column (5  $\mu\text{m}$ ) using 55%/45% methanol/water as the mobile phase at 1 mL/min flow rate and detected with an UV detector at 254 nm. The percentage of released IBU was calculated based on the amount of IBU used in preparing the NFM and presented in terms of cumulative release percentage from cumulative amount of released IBU.

### 3.4. In Vitro Cell Culture Studies

#### 3.4.1. Cell Penetration through NFMs

The NIH/3T3 mouse embryonic fibroblast cells (3T3) (ATCC CRL1658) were purchased from American Type Culture Collection (Manassas, VA, USA). The barrier effect of HAIFB NFMs was evaluated using the cell penetration test developed previously in our group [47]. The 3T3 cells were cultured in a double chamber dish containing DMEM with 2% or 10% FBS and divided with a porous membrane (Transwell cell culture insert). The concentration of FBS was 2% in the upper chamber and 10% in the lower chamber. An NFM was placed at the bottom of the cell insert and the 3T3 cells were inoculated at a density of  $1 \times 10^5$  per well in the upper chamber. Control experiments were conducted without placing an NFM at the bottom of the cell culture insert. To estimate the number of viable cells penetrated into the lower chamber after 24 h, an MTS cell viability assay with the CellTiter 96® AQueous One solution was used, which contains a novel tetrazolium salt to interact with metabolically active cells and produce a soluble formazan dye for detection at 492 nm. The optical density value ( $\text{OD}_{492}$ ) was determined using an ELISA plate reader (BioTek Synergy HT, Winooski, VT, USA) and converted to viable cell numbers using a standard curve. Qualitative evaluation of penetrated cells was also verified by observing the lower chamber surface under an inverted microscope (Olympus IX71, Tokyo, Japan).

#### 3.4.2. Cell Attachment and Proliferation

The NFMs were cut into 1.5 cm disc-shaped membranes and sterilized by UV light exposure for 2 h before use. The NFMs were placed in a 24 well culture plate, seeding with 0.2 mL of 3T3 cell suspension at a seeding density of  $1 \times 10^4$  cells per well and incubating at 37 °C for 4 h for cell adhesion. Subsequently, 1.5 mL of cell culture medium (DMEM containing 10% (*v/v*) FBS and 1% (*v/v*) antibiotic-antimycotic) was added to each well and maintained at 37 °C in a humidified 5%  $\text{CO}_2$  incubator. The number of cells attached to an NFM was determined on day 1 and 7 from DNA assays using Hoechst 33258. Cells cultured on tissue culture polystyrene (TCPS) surface were used for comparison.

#### 3.4.3. Cytoskeleton and Focal Adhesion Analyses by Confocal Microscopy

The cytoskeletal arrangement and focal adhesion of attached 3T3 cells on NFM were analyzed using an actin cytoskeleton/focal adhesion staining kit. After cultured in cell culture medium for 1 day, the cells were washed in PBS and fixed in 4% paraformaldehyde solution for 20 min. Further treatment with 0.1% Triton X-100 for 10 min at room temperature was used to permeabilize the cells. For cell staining, the cells were incubated with tetramethylrhodamine (TRITC)-conjugated phalloidin for 30 min for actin filaments, mouse anti-vinculin primary antibody (1 h), and fluorescein isothiocyanate

(FITC) AffiniPure goat anti-mouse IgG secondary antibody (1 h) for vinculin focal adhesion protein. Next, 4', 6-diamidino-2-phenylindole (DAPI) was used to stain the nucleus for 5 min. A confocal laser scanning microscope (Zeiss LSM 510 Meta, Oberkochen, Germany) was used to visualize the fluorescence signal at excitation/emission wavelength of 540 nm/545 nm (red), 340 nm/488 nm (blue), and 528 nm/617 nm (green), which represent the stained actin cytoskeleton, nucleus, and vinculin, respectively. Cells cultured on TCPS were used as control for comparison.

### 3.5. Animal Studies

#### 3.5.1. Flexor Tendon Adhesion Animal Model

The animal study was approved by the Institutional Animal Care and Use Committee (IACUC) of Chang Gung University (IACUC Approval No.: CGU14-078, approved on 9/22/2014). New Zealand white rabbits (12 weeks) were purchased from the National Laboratory Animal Breeding and Research Center (Taipei, Taiwan). The skin of the hindpaw was shaved and sterilized after the induction of general anesthesia through intramuscular injections of xylazine (6.7 mg/kg body weight) and ketamine (33.3 mg/kg body weight). The zone-II flexor tendons of the second and third digits from each hindpaw of the rabbits were released from the tendon sheath. The flexor digitorum superficialis (FDS) tendons were removed first and the flexor digitorum profundus (FDP) tendons were cut completely with a scalpel, just distal to the chiasm and proximal to the vincula. The FDP tendons were repaired with modified Kessler core suture technique using 5-0 braided polyester sutures. The animals were randomly divided into four groups (control, Seprafilm<sup>®</sup>, HAFB NFMs, and HAI30FB NFMs). All NFMs were sterilized with ethylene oxide before use. For each experimental group, a 10 mm × 12 mm piece of Seprafilm<sup>®</sup>, HAFB or HAI30FB was wrapped around the tendon repair site, whereas PBS solution was poured on the tendon repair surface in the control group. The skin was closed with 5-0 Nylon sutures and the operated leg was immobilized in a cast to limit interphalangeal joint movements. The animals were allowed unrestricted activity and received food and water ad libitum. After three weeks, animals from each group were euthanized using lethal doses of pentobarbital (0.5 g/kg body weight) and the toes were transected at the metatarsophalangeal joints. The skin incisions were reopened through the original suture line and the digits were randomly assigned for evaluation of peritendinous adhesions. Assessments were performed through gross evaluation, histological analysis, range-of-motion (flexion angle) of the distal interphalangeal (DIP) and proximal interphalangeal (PIP) joints, tendon gliding excursion (distance), and tendon pull-out force [24].

#### 3.5.2. Gross Observation

A midline incision was made at the plantar side of the experimental toe to expose the repaired FDP tendon. A macroscopic adhesion grading system was implemented to estimate the severity of adhesion around the repaired tendon by two surgeons who were blinded to the groups. The grading system was as follows: grade 0, no marked adhesion; grade 1, filmy adhesion that could be readily separated using blunt dissection; grade 2, mild adhesion; grade 3, severe adhesion [25,26].

#### 3.5.3. Histological Evaluation

The second and third digits of the rabbits were harvested for histological evaluations. Subsequently, the specimens were fixed in 10% formaldehyde in PBS, sectioned into 5 µm slices and stained with hematoxylin and eosin (H&E) using standard protocols. For immunohistochemical (IHC) staining of F4/80 and tumor necrosis factor alpha (TNF-α), mouse anti-TNF-α (Novus NBP2-34301, Centennial, CO, USA) and rabbit anti-F4/80 antibody (Abcam ab240946, Cambridge, UK) were used as the primary antibody. The ImmPRESS Excel Amplified HRP Polymer Staining Kit (Thermo Fisher Scientific, Waltham, MA, USA) containing the goat anti-mouse IgG or goat anti-rabbit IgG Amplifier Antibody, the ImmPRESS Excel Amplified HRP Polymer Reagent (anti-goat IgG), and the ImmPACT DAB EqV Substrate was used. The stained sections were examined under an Olympus IX-71 inverted microscope.

### 3.5.4. Biomechanical Evaluation

A range-of-motion test of toe joint flexion and the length of FDP tendon gliding distance were performed by transecting the sample at the same point at the proximal metacarpal level, suturing to a cable, and connecting to a load transducer of a custom-made range-of-motion device. The metatarsophalangeal joint was fixed by inserting a wire longitudinally through the metatarsal and the proximal phalanx. The proximal, middle, and distal phalanges were fixed to T-shaped pins containing two reflective markers. Subsequently, the prepared digit was mounted on the range-of-motion device by fixing the proximal wire to a non-slip clamp. A 50 g weight was attached to the extensor tendon to apply an initial tension and ensure full extension of the digit. The actuator pulled the tendon slowly at a rate of 3 mm/s to cause digital flexion (angular range of motion). The angle measured between the distal and middle phalanges determined the DIP joint flexion, and the angle between the middle and proximal phalanges determined the PIP joint flexion [27]. For the functional evaluation based on tendon gliding excursion, two metal pins were inserted through the proximal phalanx to fix the digits to a table, and then traction was applied to the tendon, thus flexion of the distal joints could easily be performed. The FDP tendon was exposed by removing the skin, subcutaneous tissue, and the other flexor tendons. The tendon sheath and FDP tendon were marked at the exit from the sheath, and a counterweight from the distal phalanx was applied to fully extend the interphalangeal joints. A constant force of 1 N was applied to pull the FDP tendon out of the sheath tunnel, and the distance after pulling was measured with a micrometer caliper. This tendon gliding distance was recorded as the gliding excursion of the FDP tendon. To evaluate peritendinous adhesions, the pull-out force was measured using a material testing machine (Tinius Olsen H1KT, Horsham, PA, USA) with a 50 N load cell. The digit was amputated through the metatarsophalangeal joint, leaving a 2 cm tail FDP tendon firmly fixed at the bottom by a custom-made static clamp. The distal digit was attached to the hook through a hole drilled in the distal phalanx and connected through a steel hook to the top crosshead. The FDP tendon was pulled at a rate of 5 mm/min and, ultimately, the movement of the crosshead pulled the tendon out of the tendon sheath. The pull-out force (N) was calculated by measuring the maximum force necessary to pull the tendon out of the tendon sheath.

### 3.6. Statistical Analysis

The results are expressed as mean  $\pm$  standard deviation. SPSS 10.0 (Chicago, IL, USA) was used to analyze the data with a one-way analysis of variance (ANOVA) with  $p < 0.05$  being considered significant.

## 4. Conclusions

In this study, electrospinning was used successfully to prepare NFMs loaded with 20 to 40% IBU (HAIFB) for controlled release of the anti-inflammatory drug in reducing postoperative tendon inflammation and preventing tendon adhesion. The microporous structure and excellent mechanical properties of the NFM enables proper tendon healing while providing a powerful physical barrier to prevent postoperative fibroblastic penetration, which leads to tissue adhesion. The different loading content of IBU did not change the macroporous nature of the NFMs, which contained nanofibers with similar fiber diameter and physico-chemical properties. However, higher IBU loading improved the mechanical properties of the NFMs, with higher ultimate stress (strain) and modulus. From in vitro cell culture experiments with fibroblasts, HAIFB NFMs could prevent cell attachment and penetration, which in turn could reduce the formation of tissue adhesions in vivo. Nonetheless, IBU loading above 30% induced cytotoxicity stemming from a higher concentration of released IBU. From an in vivo study using a rabbit flexor tendon rupture animal model, we confirmed that IBU-loaded HAIFB NFMs (HAI30FB) are an ideal physical barrier membrane to simultaneously inhibit inflammation and tendon adhesion formation. The HAI30FB membrane exhibited excellent anti-adhesion efficacy over



Septrafilm® and non-IBU-loaded NFMs (HAFB) from gross observations, histological analyses, and biomechanical testing evaluations.

**Author Contributions:** C.-T.C., C.-H.C. and J.-P.C. conceived and designed the experiments; C.-H.C. and C.S. performed the experiments; C.-T.C., C.-H.C., C.S. and J.-P.C. analyzed the data; C.-H.C. and J.-P.C. wrote the paper.

**Acknowledgments:** We would like to express our appreciation for the financial support provided by Chang Gung Memorial Hospital (CMRPG2D0433, CMRPG3D0233, BMRP249) and the Ministry of Science and Technology, Taiwan, ROC (MOST103-2321-B-182-017). The Microscope Core Laboratory in Chang Gung Memorial Hospital, Linkou is acknowledged for the confocal microscopic analysis.

**Conflicts of Interest:** The authors declare no conflict of interest.

## Abbreviations

ATR-FTIR	Attenuated total reflection Fourier-transform infrared
BDDE	1,4-butanediol diglycidyl
DMEM	Dulbecco's modified Eagle medium
DTG	Derivative thermogravimetry
DAPI	4',6-diamidino-2-phenylindole
DIP	Distal interphalangeal
ELISA	Enzyme-linked immunosorbent assay
FDP	Flexor digitorum profundus
FDS	Flexor digitorum superficialis
FBS	Fetal bovine serum
FITC	Fluorescein isothiocyanate
GMP	Good manufacturing practice
HA	Hyaluronic acid
H&E	Hematoxylin and eosin
IBU	Ibuprofen
IHC	Immunohistochemical
NFM	Nanofibrous membrane
NSAIDs	Nonsteroidal anti-inflammatory drugs
OD	Optical density
PBS	Phosphate buffered saline
PCL	Poly(caprolactone)
PEG	Poly(ethylene glycol)
PEO	Poly(ethylene oxide)
PLA	Poly(lactic acid)
PIP	Proximal interphalangeal
PIP	Proximal interphalangeal
SEM	Scanning electron microscopy
TGA	Thermogravimetric analysis
TCPS	Tissue culture polystyrene
TNF- $\alpha$	Tumor necrosis factor alpha

## References

1. Bolgen, N.; Vargel, I.; Korkusuz, P.; Menciloglu, Y.Z.; Piskin, E. In vivo performance of antibiotic embedded electrospun PCL membranes for prevention of abdominal adhesions. *J. Biomed. Mater. Res. B Appl. Biomater.* **2007**, *81*, 530–543. [[CrossRef](#)] [[PubMed](#)]
2. Diamond, M.P.; Burns, E.L.; Accomando, B.; Mian, S.; Holmdahl, L. Septrafilm®adhesion barrier: (1) a review of preclinical, animal, and human investigational studies. *Gynecol. Surg.* **2012**, *9*, 237–245. [[CrossRef](#)] [[PubMed](#)]

3. Hwang, H.; An, M.; Ha, T.; Kim, K.; Kim, T.; Choi, C.; Hong, K.; Jung, S.; Kim, S.-H.; Rho, K.; et al. All the commercially available adhesion barriers have the same effect on adhesion prophylaxis? A comparison of barrier agents using a newly developed, severe intra-abdominal adhesion model. *Int. J. Colorectal Dis.* **2013**, *28*, 1117–1125. [[CrossRef](#)] [[PubMed](#)]
4. Gruber-Blum, S.; Petter-Puchner, A.H.; Brand, J.; Fortelny, R.H.; Walder, N.; Oehlinger, W.; Koenig, F.; Redl, H. Comparison of three separate antiadhesive barriers for intraperitoneal onlay mesh hernia repair in an experimental model. *Br. J. Surg.* **2011**, *98*, 442–449. [[CrossRef](#)]
5. Shalumon, K.T.; Sheu, C.; Chen, C.-H.; Chen, S.-H.; Jose, G.; Kuo, C.-Y.; Chen, J.-P. Multi-functional electrospun antibacterial core-shell nanofibrous membranes for prolonged prevention of post-surgical tendon adhesion and inflammation. *Acta Biomater.* **2018**, *72*, 121–136. [[CrossRef](#)] [[PubMed](#)]
6. Chen, C.-H.; Chen, S.-H.; Shalumon, K.T.; Chen, J.-P. Prevention of peritendinous adhesions with electrospun polyethylene glycol/polycaprolactone nanofibrous membranes. *Colloids Surf. B Biointerfaces* **2015**, *133*, 221–230. [[CrossRef](#)] [[PubMed](#)]
7. Chen, S.-H.; Chen, C.-H.; Shalumon, K.T.; Chen, J.-P. Preparation and characterization of antiadhesion barrier film from hyaluronic acid-grafted electrospun poly(caprolactone) nanofibrous membranes for prevention of flexor tendon postoperative peritendinous adhesion. *Int. J. Nanomed.* **2014**, *9*, 4079–4092. [[CrossRef](#)] [[PubMed](#)]
8. Liu, S.; Zhao, J.; Ruan, H.; Tang, T.; Liu, G.; Yu, D.; Cui, W.; Fan, C. Biomimetic sheath membrane via electrospinning for antiadhesion of repaired tendon. *Biomacromolecules* **2012**, *13*, 3611–3619. [[CrossRef](#)] [[PubMed](#)]
9. Hu, C.; Liu, S.; Zhang, Y.; Li, B.; Yang, H.; Fan, C.; Cui, W. Long-term drug release from electrospun fibers for in vivo inflammation prevention in the prevention of peritendinous adhesions. *Acta Biomater.* **2013**, *9*, 7381–7388. [[CrossRef](#)] [[PubMed](#)]
10. Liu, S.; Hu, C.; Li, F.; Li, X.-j.; Cui, W.; Fan, C. Prevention of peritendinous adhesions with electrospun ibuprofen-loaded poly (l-lactic acid)-polyethylene glycol fibrous membranes. *Tissue Eng. A* **2012**, *19*, 529–537. [[CrossRef](#)] [[PubMed](#)]
11. James, R.; Kesturu, G.; Balian, G.; Chhabra, A.B. Tendon: Biology, biomechanics, repair, growth factors, and evolving treatment options. *J. Hand Surg.* **2008**, *33*, 102–112. [[CrossRef](#)] [[PubMed](#)]
12. Kulick, M.I.; Smith, S.; Hadler, K. Oral ibuprofen: Evaluation of its effect on peritendinous adhesions and the breaking strength of a tenorrhaphy. *J. Hand Surg.* **1986**, *11*, 110–120. [[CrossRef](#)]
13. Rouhani, A.; Tabrizi, A.; Ghavidel, E. Effects of non-steroidal anti-inflammatory drugs on flexor tendon rehabilitation after repair. *Arch. Bone Jt. Surg.* **2013**, *1*, 28–30. [[PubMed](#)]
14. Chen, S.; Wang, G.; Wu, T.; Zhao, X.; Liu, S.; Li, G.; Cui, W.; Fan, C. Silver nanoparticles/ibuprofen-loaded poly(l-lactide) fibrous membrane: Anti-infection and anti-adhesion effects. *Int. J. Mol. Sci.* **2014**, *15*, 14014–14025. [[CrossRef](#)]
15. Zhang, W.; Li, X.; Franchini, M.C.; Xu, K.; Locatelli, E.; Martin, R.C.; Monaco, I.; Li, Y.; Cui, S. Controlled release of curcumin from curcumin-loaded nanomicelles to prevent peritendinous adhesion during Achilles tendon healing in rats. *Int. J. Nanomed.* **2016**, *11*, 2873–2881.
16. Lee, S.; Jin, G.; Jang, J.-H. Electrospun nanofibers as versatile interfaces for efficient gene delivery. *J. Biol. Eng.* **2014**, *8*, 30. [[CrossRef](#)] [[PubMed](#)]
17. Nguyen, L.H.; Gao, M.; Lin, J.; Wu, W.; Wang, J.; Chew, S.Y. Three-dimensional aligned nanofibers-hydrogel scaffold for controlled non-viral drug/gene delivery to direct axon regeneration in spinal cord injury treatment. *Sci. Rep.* **2017**, *7*, 42212. [[CrossRef](#)]
18. Nagarajan, S.; Bechelany, M.; Kalkura, N.S.; Miele, P.; Bohatier, C.P.; Balme, S. Electrospun nanofibers for drug delivery in regenerative medicine. In *Applications of Targeted Nano Drugs and Delivery Systems*; Elsevier: Amsterdam, The Netherlands, 2019; pp. 595–625.
19. Figueroa-Lopez, K.; Castro-Mayorga, J.; Andrade-Mahecha, M.; Cabedo, L.; Lagaron, J. Antibacterial and barrier properties of gelatin coated by electrospun polycaprolactone ultrathin fibers containing black pepper oleoresin of interest in active food biopackaging applications. *Nanomaterials* **2018**, *8*, 199. [[CrossRef](#)]
20. Swann, D.A.; Radin, E.L.; Nazimiec, M.; Weissner, P.A.; Curran, N.; Lewinnek, G. Role of hyaluronic acid in joint lubrication. *Ann. Rheum. Dis.* **1974**, *33*, 318–326. [[CrossRef](#)]

21. Galandáková, A.; Ulrichová, J.; Langová, K.; Hanáková, A.; Vrbka, M.; Hartl, M.; Gallo, J. Characteristics of synovial fluid required for optimization of lubrication fluid for biotribological experiments. *J. Biomed. Mater. Res. B Appl. Biomater.* **2016**, *105*, 1422–1431. [[CrossRef](#)]
22. Diamond, M.P.; Burns, E.L.; Accomando, B.; Mian, S.; Holmdahl, L. Septrafilm adhesion barrier: (2) a review of the clinical literature on intraabdominal use. *Gynecol. Surg.* **2012**, *9*, 247–257. [[CrossRef](#)] [[PubMed](#)]
23. Lee, J.H.; Go, A.K.; Oh, S.H.; Lee, K.E.; Yuk, S.H. Tissue anti-adhesion potential of ibuprofen-loaded PLLA-PEG diblock copolymer films. *Biomaterials* **2005**, *26*, 671–678. [[CrossRef](#)] [[PubMed](#)]
24. Yeo, Y.; Kohane, D.S. Polymers in the prevention of peritoneal adhesions. *Eur. J. Pharm. Biopharm.* **2008**, *68*, 57–66. [[CrossRef](#)] [[PubMed](#)]
25. Zhang, Z.; Ni, J.; Chen, L.; Yu, L.; Xu, J.; Ding, J. Biodegradable and thermoreversible PCLA-PEG-PCLA hydrogel as a barrier for prevention of post-operative adhesion. *Biomaterials* **2011**, *32*, 4725–4736. [[CrossRef](#)] [[PubMed](#)]
26. Yamaoka, T.; Njatawidjaja, E.; Kasai, A.; Agudelo, C.A.; Ehashi, T.; Kakinoki, S.; Kato, S.; Mahara, A. Elastic/adhesive double-layered PLA-PEG multiblock copolymer membranes for postoperative adhesion prevention. *Polym. Degrad. Stab.* **2013**, *98*, 2168–2176. [[CrossRef](#)]
27. Angajala, K.K.; Vianala, S.; Macha, R.; Raghavender, M.; Thupurani, M.K.; Pathi, P.J. Synthesis, anti-inflammatory, bactericidal activities and docking studies of novel 1,2,3-triazoles derived from ibuprofen using click chemistry. *SpringerPlus* **2016**, *5*, 423. [[CrossRef](#)] [[PubMed](#)]
28. Tan, S.C.; Patel, B.K.; Jackson, S.H.D.; Swift, C.G.; Hutt, A.J. Influence of age on the enantiomeric disposition of ibuprofen in healthy volunteers. *Br. J. Clin. Pharmacol.* **2003**, *55*, 579–587. [[CrossRef](#)]
29. Tran, T.; Hernandez, M.; Patel, D.; Burns, E.; Peterman, V.; Wu, J. Controllable and switchable drug delivery of ibuprofen from temperature responsive composite nanofibers. *Nano Converg.* **2015**, *2*, 15. [[CrossRef](#)]
30. Lewandowska, K.; Sionkowska, A.; Grabska, S.; Kaczmarek, B. Surface and thermal properties of collagen/hyaluronic acid blends containing chitosan. *Int. J. Biol. Macromol.* **2016**, *92*, 371–376. [[CrossRef](#)]
31. Sheu, C.; Shalumon, K.T.; Chen, C.-H.; Kuo, C.-Y.; Fong, Y.T.; Chen, J.-P. Dual crosslinked hyaluronic acid nanofibrous membranes for prolonged prevention of post-surgical peritoneal adhesion. *J. Mater. Chem. B* **2016**, *4*, 6680–6693. [[CrossRef](#)]
32. Ofokansi, K.C.; Kenechukwu, F.C.; Ezugwu, R.O.; Attama, A.A. Improved dissolution and anti-inflammatory activity of ibuprofen-polyethylene glycol 8000 solid dispersion systems. *Int. J. Pharm. Investig.* **2016**, *6*, 139–147. [[PubMed](#)]
33. Chevalier, E.; Viana, M.; Cazalbou, S.; Makein, L.; Dubois, J.; Chulia, D. Ibuprofen-loaded calcium phosphate granules: Combination of innovative characterization methods to relate mechanical strength to drug location. *Acta Biomater.* **2010**, *6*, 266–274. [[CrossRef](#)] [[PubMed](#)]
34. Docheva, D.; Müller, S.A.; Majewski, M.; Evans, C.H. Biologics for tendon repair. *Adv. Drug Deliv. Rev.* **2015**, *84*, 222–239. [[CrossRef](#)] [[PubMed](#)]
35. Brain, P.; Leyva, R.; Doyle, G.; Kellstein, D. Onset of analgesia and efficacy of ibuprofen sodium in postsurgical dental pain: A randomized, placebo-controlled study versus standard ibuprofen. *Clin. J. Pain* **2015**, *31*, 444–450. [[CrossRef](#)] [[PubMed](#)]
36. Manrique-Moreno, M.; Villena, F.; Sotomayor, C.P.; Edwards, A.M.; Muñoz, M.A.; Garidel, P.; Suwalsky, M. Human cells and cell membrane molecular models are affected in vitro by the nonsteroidal anti-inflammatory drug ibuprofen. *Biochim. Biophys. Acta Biomembr.* **2011**, *1808*, 2656–2664. [[CrossRef](#)] [[PubMed](#)]
37. Koga, T.; Fujiwara, R.; Nakajima, M.; Yokoi, T. Toxicological evaluation of acyl glucuronides of nonsteroidal anti-inflammatory drugs using human embryonic kidney 293 cells stably expressing human UDP-glucuronosyltransferase and human hepatocytes. *Drug Metab. Dispos* **2011**, *39*, 54–60. [[CrossRef](#)] [[PubMed](#)]
38. Aghaei, H.; Nourbakhsh, A.A.; Karbasi, S.; JavadKalbasi, R.; Rafienia, M.; Nourbakhsh, N.; Bonakdar, S.; Mackenzie, K.J.D. Investigation on bioactivity and cytotoxicity of mesoporous nano-composite MCM-48/hydroxyapatite for ibuprofen drug delivery. *Ceramics Int.* **2014**, *40*, 7355–7362. [[CrossRef](#)]
39. Pozzi, A.; Gallelli, L. Pain management for dentists: The role of ibuprofen. *Ann. Stomatol.* **2011**, *2*, 3–24.
40. Chen, S.H.; Chou, P.Y.; Chen, Z.Y.; Lin, F.H. Electrospun water-borne polyurethane nanofibrous membrane as a barrier for preventing postoperative peritendinous adhesion. *Int. J. Mol. Sci.* **2019**, *20*, 1625. [[CrossRef](#)]

41. Ishiyama, N.; Moro, T.; Ohe, T.; Miura, T.; Ishihara, K.; Konno, T.; Ohyama, T.; Kimura, M.; Kyomoto, M.; Saito, T.; et al. Reduction of peritendinous adhesions by hydrogel containing biocompatible phospholipid polymer mpc for tendon repair. *J. Bone Joint Surg.* **2011**, *93*, 142–149. [\[CrossRef\]](#)
42. diZerega, G.S. Contemporary adhesion prevention. *Fertil. Steril.* **1994**, *61*, 219–235. [\[CrossRef\]](#)
43. Hellebrekers, B.W.; Kooistra, T. Pathogenesis of postoperative adhesion formation. *Br. J. Surg.* **2011**, *98*, 1503–1516. [\[CrossRef\]](#) [\[PubMed\]](#)
44. Köwitsch, A.; Yang, Y.; Ma, N.; Kuntsche, J.; Mäder, K.; Groth, T. Bioactivity of immobilized hyaluronic acid derivatives regarding protein adsorption and cell adhesion. *Biotechnol. Appl. Biochem.* **2011**, *58*, 376–389. [\[CrossRef\]](#)
45. Tsai, W.-C.; Tang, F.-T.; Hsu, C.-C.; Hsu, Y.-H.; Pang, J.-H.S.; Shiue, C.-C. Ibuprofen inhibition of tendon cell proliferation and upregulation of the cyclin kinase inhibitor p21cip1. *J. Orthop. Res.* **2004**, *22*, 586–591. [\[CrossRef\]](#) [\[PubMed\]](#)
46. Yagi, M.; Sato, N.; Mitsui, Y.; Gotoh, M.; Hamada, T.; Nagata, K. Hyaluronan modulates proliferation and migration of rabbit fibroblasts derived from flexor tendon epitenon and endotenon. *J. Hand Surg.* **2010**, *35*, 791–796. [\[CrossRef\]](#) [\[PubMed\]](#)
47. Chen, C.-H.; Chen, S.-H.; Shalumon, K.T.; Chen, J.-P. Dual functional core–sheath electrospun hyaluronic acid/polycaprolactone nanofibrous membranes embedded with silver nanoparticles for prevention of peritendinous adhesion. *Acta Biomater.* **2015**, *26*, 225–235. [\[CrossRef\]](#) [\[PubMed\]](#)
48. Meier Bürgisser, G.; Calcagni, M.; Bachmann, E.; Fessel, G.; Snedeker, J.G.; Giovanoli, P.; Buschmann, J. Rabbit achilles tendon full transection model–wound healing, adhesion formation and biomechanics at 3, 6 and 12 weeks post-surgery. *Biol. Open* **2016**, *5*, 1324–1333. [\[CrossRef\]](#) [\[PubMed\]](#)
49. Kwan, K.H.L.; Yeung, K.W.K.; Liu, X.; Wong, K.K.Y.; Shum, H.C.; Lam, Y.W.; Cheng, S.H.; Cheung, K.M.C.; To, M.K.T. Silver nanoparticles alter proteoglycan expression in the promotion of tendon repair. *Nanomed. Nanotechnol.* **2014**, *10*, 1375–1383. [\[CrossRef\]](#)
50. Tan, V.; Nourbakhsh, A.; Capo, J.; Cottrell, J.A.; Meyenhofer, M.; O'Connor, J.P. Effects of nonsteroidal anti-inflammatory drugs on flexor tendon adhesion. *J. Hand Surg.* **2010**, *35*, 941–947. [\[CrossRef\]](#)
51. Parameswaran, N.; Patial, S. Tumor necrosis factor- $\alpha$  signaling in macrophages. *Crit. Rev. Eukaryot. Gene Expr.* **2010**, *20*, 87–103. [\[CrossRef\]](#)
52. Dinarvand, P.; Hassanian, S.M.; Weiler, H.; Rezaie, A.R. Intraperitoneal administration of activated protein c prevents postsurgical adhesion band formation. *Blood* **2015**, *125*, 1339–1348. [\[CrossRef\]](#) [\[PubMed\]](#)
53. Donlin, L.T.; Jayatilleke, A.; Giannopoulou, E.G.; Kalliolias, G.D.; Ivashkiv, L.B. Modulation of TNF-induced macrophage polarization by synovial fibroblasts. *J. Immunol.* **2014**, *193*, 2373–2383. [\[CrossRef\]](#) [\[PubMed\]](#)
54. Chang, J.; Thunder, R.; Most, D.; Longaker, M.T.; Lineaweaver, W.C. Studies in flexor tendon wound healing: Neutralizing antibody to TGF- $\beta$ 1 increases postoperative range of motion. *Plast. Reconstr. Surg.* **2000**, *105*, 148–155. [\[CrossRef\]](#) [\[PubMed\]](#)
55. Namba, J.; Shimada, K.; Saito, M.; Murase, T.; Yamada, H.; Yoshikawa, H. Modulation of peritendinous adhesion formation by alginate solution in a rabbit flexor tendon model. *J. Biomed. Mater. Res. B Appl. Biomater.* **2007**, *80*, 273–279. [\[CrossRef\]](#)
56. Vorvolakos, K.; Isayeva, I.S.; Do Luu, H.-M.; Patwardhan, D.V.; Pollack, S.K. Ionically cross-linked hyaluronic acid: Wetting, lubrication, and viscoelasticity of a modified adhesion barrier gel. *Med. Devices (Auckl.)* **2011**, *4*, 1. [\[CrossRef\]](#) [\[PubMed\]](#)



© 2019 by the authors. Licensee MDPI, Basel, Switzerland. This article is an open access article distributed under the terms and conditions of the Creative Commons Attribution (CC BY) license (<http://creativecommons.org/licenses/by/4.0/>).



Review

# Molecular Functions of Thyroid Hormone Signaling in Regulation of Cancer Progression and Anti-Apoptosis

Yu-Chin Liu <sup>1,2</sup>, Chau-Ting Yeh <sup>3</sup> and Kwang-Huei Lin <sup>1,2,3,4,\*</sup>

<sup>1</sup> Department of Biochemistry, College of Medicine, Chang-Gung University, Taoyuan 333, Taiwan; k1506820@gmail.com

<sup>2</sup> Department of Biomedical Sciences, College of Medicine, Chang-Gung University, Taoyuan 333, Taiwan

<sup>3</sup> Liver Research Center, Chang Gung Memorial Hospital, Taoyuan 333, Taiwan; chauting@adm.cgmh.org.tw

<sup>4</sup> Research Center for Chinese Herbal Medicine, College of Human Ecology, Chang Gung University of Science and Technology, Taoyuan 333, Taiwan

\* Correspondence: khlin@mail.cgu.edu.tw; Tel./Fax: +886-3-2118263

Received: 31 August 2019; Accepted: 5 October 2019; Published: 9 October 2019



**Abstract:** Several physiological processes, including cellular growth, embryonic development, differentiation, metabolism and proliferation, are modulated by genomic and nongenomic actions of thyroid hormones (TH). Several intracellular and extracellular candidate proteins are regulated by THs. 3,3,5-Triiodo-L-thyronine (T<sub>3</sub>) can interact with nuclear thyroid hormone receptors (TR) to modulate transcriptional activities via thyroid hormone response elements (TRE) in the regulatory regions of target genes or bind receptor molecules showing no structural homology to TRs, such as the cell surface receptor site on integrin  $\alpha v \beta 3$ . Additionally, L-thyroxine (T<sub>4</sub>) binding to integrin  $\alpha v \beta 3$  is reported to induce gene expression through initiating non-genomic actions, further influencing angiogenesis and cell proliferation. Notably, thyroid hormones not only regulate the physiological processes of normal cells but also stimulate cancer cell proliferation via dysregulation of molecular and signaling pathways. Clinical hypothyroidism is associated with delayed cancer growth. Conversely, hyperthyroidism is correlated with cancer prevalence in various tumor types, including breast, thyroid, lung, brain, liver and colorectal cancer. In specific types of cancer, both nuclear thyroid hormone receptor isoforms and those on the extracellular domain of integrin  $\alpha v \beta 3$  are high risk factors and considered potential therapeutic targets. In addition, thyroid hormone analogs showing substantial thyromimetic activity, including triiodothyroacetic acid (Triac), an acetic acid metabolite of T<sub>3</sub>, and tetraiodothyroacetic acid (Tetrac), a derivative of T<sub>4</sub>, have been shown to reduce risk of cancer progression, enhance therapeutic effects and suppress cancer recurrence. Here, we have reviewed recent studies focusing on the roles of THs and TRs in five cancer types and further discussed the potential therapeutic applications and underlying molecular mechanisms of THs.

**Keywords:** thyroid hormone; thyroid hormone receptor; 3,3,5-triiodo-L-thyronine (T<sub>3</sub>), L-thyroxine (T<sub>4</sub>), cancer proliferation

## 1. Introduction

Thyroid hormone (TH) in adults is necessary for the regulation of multiple physiological effects, such as cell growth, structure, and metabolism [1]. The main thyroid hormones produced by the thyroid gland are thyroxine (T<sub>4</sub>), 3,5,3'-triiodothyronine (T<sub>3</sub>), and reverse 3,5,3'-triiodothyronine (rT<sub>3</sub>), which are controlled by thyroid-stimulating hormone (TSH). Under physiological conditions, both T<sub>4</sub> and T<sub>3</sub> are secreted into the bloodstream by the thyroid gland [2]. THs circulating in the body exert metabolic effects on multiple organs, including heart, bone, brain, liver, thyroid, kidney



and skeletal muscle [2]. The actions of thyroid hormone are classified into two main mechanisms: (1) A non-genomic effect initiated at the plasma membrane that regulates downstream gene expression via integrin  $\alpha v\beta 3$ ; and (2) transcriptional activity induced by interactions with nuclear thyroid hormone receptor proteins and further binding to thyroid hormone response elements of specific downstream genes. The  $\alpha v\beta 3$  isoform of integrin is a heterodimeric structure at the plasma membrane capable of interacting with a large number of extracellular matrix (ECM) proteins as ligands for activating downstream signal pathways [3]. In addition, the protein structure of thyroid hormone receptor is similar to nucleus receptor superfamily and acts as a sequence-specific ligand-dependent transcription factor that mediates several downstream effects of THs on activation or repression of target genes [4]. The above actions generated through either non-genomic or genomic effects overlap in the nucleus. Thyroid hormone activity is beneficial for normal cell development. However, when both the levels of THs and thyroid hormone receptors in the body are out of control, it causes multiple diseases, including cardiovascular disease, diabetes mellitus and chronic liver disease [5]. Earlier studies by our group and other investigators conducted to clarify the significance of thyroid hormone in cells and tissues have revealed activity in regulation of proliferation of both tumor and nonmalignant cells. The current review focuses on the potential association between thyroid hormones and progression of different cancer types.

## 2. Thyroid Hormone Effects via Interactions with the Thyroid Hormone Receptor

### 2.1. Thyroid Hormone

The thyroid hormone system starts from the hypothalamus, where thyrotropin-releasing hormone (TRH) is synthesized and released from the periventricular nucleus (PVN). TRH binding to its receptor on the thyrotroph of the anterior pituitary gland stimulates proliferation, synthesis and secretion of thyroid stimulating hormone (TSH). TSH subsequently interacts with the TSH receptor (TSHR) on individual thyroid follicular cells of the thyroid gland to stimulate synthesis and release of thyroid hormones L-thyroxine ( $T_4$ ) and 3,3,5-triiodo-L-thyronine ( $T_3$ ) [6]. In addition, thyroglobulin, a dimeric protein, is synthesized in the rough endoplasmic reticulum of thyroid follicular cells and secreted to enter the follicular colloid via exocytosis. Simultaneously, iodide ( $I^-$ ) is transported to thyroid follicular cells via sodium-iodide (Na/I) symporter pump activity and enters thyroid follicular cells from the cytoplasm in a pendrin-dependent manner. One of the enzymes in the follicular colloid, thyroid peroxidase, catalyzes iodide ( $I^-$ ) oxidization to iodine ( $I^0$ ). Iodine ( $I^0$ ) iodinates thyroglobulin and conjugates with the protein chain of tyrosyl residues. Subsequently, thyroglobulin re-enters thyroid follicular cells via endocytosis and undergoes proteolysis via actions of various proteases to liberate thyroxine ( $T_4$ ) and 3,3,5-triiodo-L-thyronine ( $T_3$ ). Efflux of  $T_4$  and  $T_3$  from thyroid follicular cells to various target cells is achieved through specific membrane transporter proteins [7], such as monocarboxylate transporter (MCT) 8 and 10 [8,9], the organic anion transporter protein-1c1 (OATP1c1), and nonspecific L-type amino acid transporters 1 and 2 (LAT1, LAT2) [10]. However, earlier studies indicate that euthyroid status in blood with circulating  $T_4$  and  $T_3$  is controlled by a negative feedback loop mediated by the hypothalamus-pituitary-thyroid (HPT) set axis [11].

### 2.2. Thyroid Hormone Receptor

Circulating THs interact with thyroid hormone receptors to promote downstream signaling pathways and activate transcription factors. Thyroid hormone receptors (TR) including  $TR\alpha$  and  $TR\beta$  contain several domains, specifically, amino terminal A/B that may function as a gene enhancer, DNA-binding domain (DBD), hinge region containing the nuclear localization signal and carboxy-terminal ligand-binding domain that binds  $T_3$  (Figure 1). These receptors display protein structures similar to most nuclear receptors and each domain performs specific functions [4,12–15]. In particular, the amino-terminal A/B of thyroid hormone receptors ( $TR\beta 1$  and  $TR\beta 2$ ) is generated from a signaling gene via alternative splicing or usage of alternative promoters [16]. The four major

TR isoforms, TR $\alpha$ 1, TR $\alpha$ 2, TR $\beta$ 1, and TR $\beta$ 2, are produced by *c-erbA $\alpha$*  and *c-erbA $\beta$*  genes. Their human homologs are designated THRA and THRB. The *c-erbA $\alpha$*  gene located on chromosome 17 encodes two different TR $\alpha$  isoforms. One is functional TH-binding TR $\alpha$ 1 and the other is a dominant-negative splice variant, TR $\alpha$ 2, lacking TH binding activity [17]. TR $\alpha$ 2 is unique in consideration of its lack of binding to THs while interacting with DNA, and its precise function is unclear at present. The *c-erbA $\beta$*  gene located on chromosome 3 encodes two isoforms, TR $\beta$ 1 and TR $\beta$ 2, that participate in TH binding and are widely distributed in a tissue-specific manner. TR $\alpha$ 1 and TR $\alpha$ 2 are expressed in the kidney, skeletal muscle, lungs, heart, and testes, with particularly high levels detected in the brain [18]. TR $\beta$ 1 expression is significant in brain, thyroid, liver, and kidney while the TR $\beta$ 2 isoform is specifically expressed in the anterior pituitary, hypothalamus, and developing brain [12,19–21] (Figure 1).

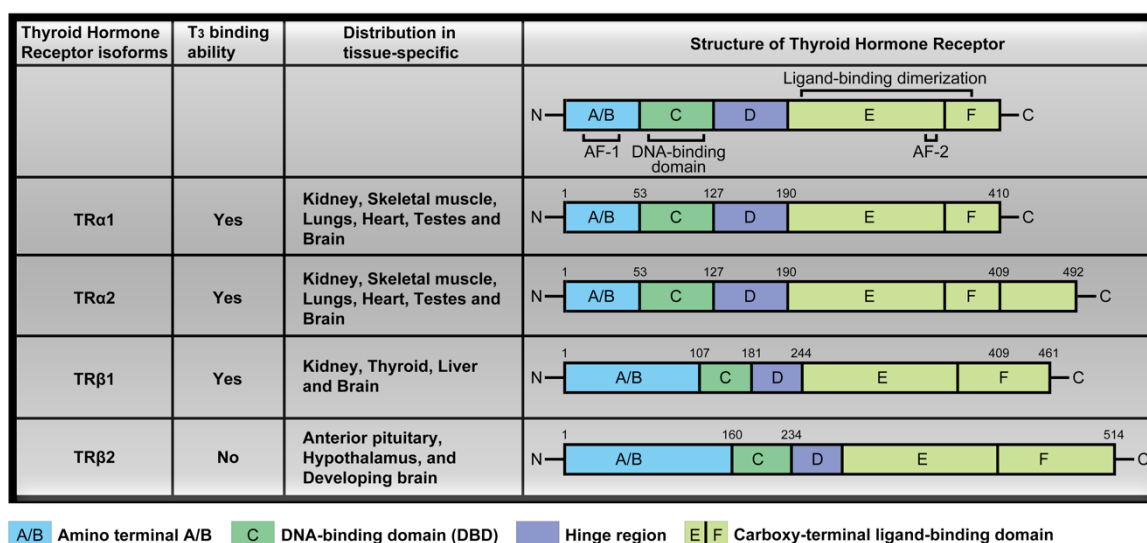


**Figure 1.** TR isoforms and structure distribution. Thyroid hormone receptors (TR) contain several domains, specifically, amino terminal A/B that may function as a gene enhancer, DNA-binding domain (DBD), hinge region containing the nuclear localization signal and carboxy-terminal ligand-binding domain that binds 3,3,5-Triiodo-L-thyronine (T<sub>3</sub>). The four major TR isoforms, TR $\alpha$ 1, TR $\alpha$ 2, TR $\beta$ 1, and TR $\beta$ 2. TH binding are widely distributed in a tissue-specific manner, for example, TR $\alpha$ 1 and TR $\alpha$ 2 are expressed in the kidney, skeletal muscle, lungs, heart, and testes, with particularly high levels detected in the brain. Table 1. expression is significant in brain, thyroid, liver, and kidney while the TR $\beta$ 2 isoform is specifically expressed in the anterior pituitary, hypothalamus, and developing brain.

Interestingly, TR $\alpha$ 1, TR $\alpha$ 2 and TR $\beta$ 1 are overexpressed in various tissues in the human body excepting the liver, the major TH target organ [17]. Additionally, TRs regulate transcriptional activity through associating with other nuclear receptors such as retinoid X receptor (RXR), retinoic acid receptor subtypes, and vitamin D receptor (VDR), which are homo or heterodimers (Figure 2A). TRs/RXR belong to non-permissive heterodimers that can be activated transcriptionally by TRs ligand but not by RXR ligand alone (Figure 2A). In particular, RXR forms a heterodimer with TRs that influence downstream target gene expression by binding to specific DNA sequences located in regulatory regions known as thyroid hormone elements (TRE) [22–24]. TREs within the promoter region contain individual DNA sequences (A/G)GGT(C/A/G)A, designated “half-sites”, that are recognized by TRs. The half-site sequences in TREs incorporate palindromic (Pal), direct repeat (DR) and inverted repeat arrangements (IP) [15] (Figure 2B). In the absence of thyroid hormone in cells, TRs interacting with TREs do not influence gene expression. TRs enter the nucleus and bind to DNA until arrival of the thyroid hormone.

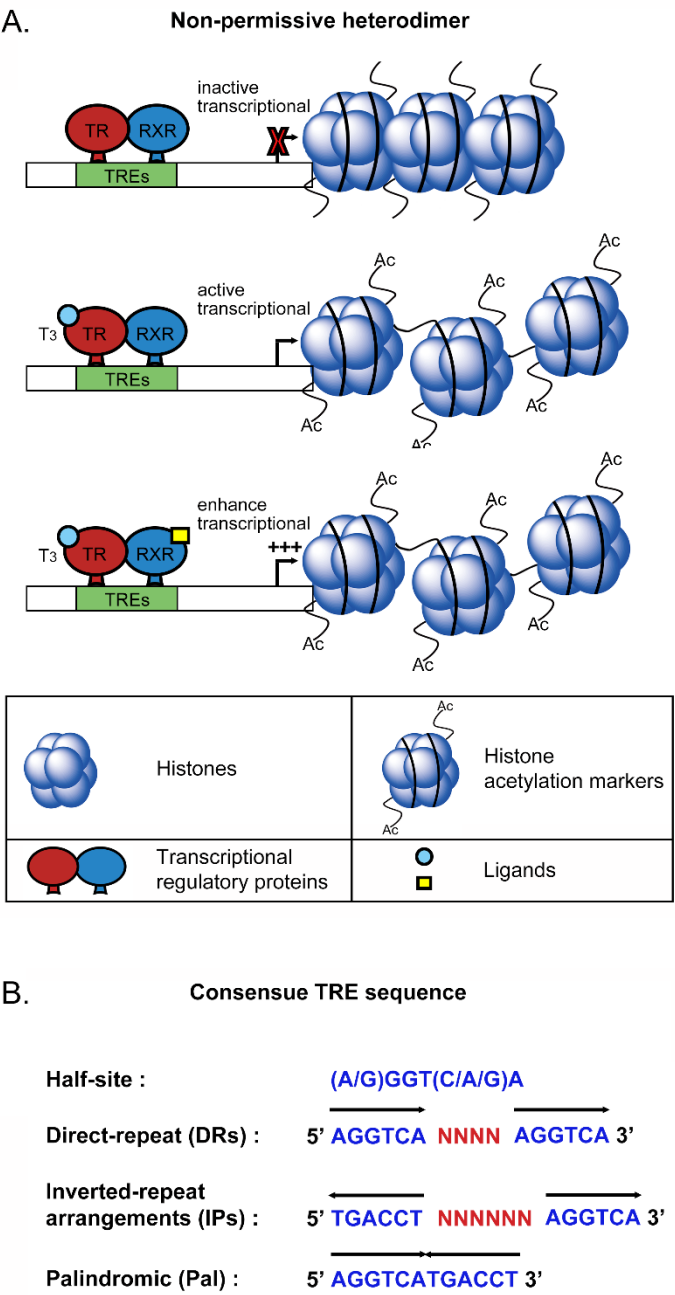


**Figure 2.** Schematic representation of TRs/RXR non-permissive heterodimers and consensus TRE half-sites. **(A)** TRs/RXR belong to non-permissive heterodimers that can be activated transcriptionally by TRs ligand but not by RXR ligand alone. Moreover, TRs/RXR can enhance the transcriptional response by binding of the RXR ligand and TRs ligand. **(B)** TREs within the promoter region contain individual DNA sequences (A/G)GGT(C/A/G)A, designated “half-sites”, that are recognized by TRs. The half-site sequences in TREs incorporate palindromic (Pal), direct repeat (DR) and inverted repeat arrangements (IP).

2.3. Nuclear Transcriptional Activity of Thyroid Hormone

Several recent studies have focused on transcriptional activation induced by TR binding to positive TRE sites. However, TRs play a dual modulatory role and can also repress gene expression in a ligand-dependent manner. TRs bind to their respective TREs as monomers, homodimers or heterodimers with retinoid X receptors (RXR). Heterodimers of TR/RXR contain LBDs that interact with T<sub>3</sub>. Additionally, DBD displays high affinity for DNA sequences of TREs [25]. TRs can

directly or indirectly associate with different molecular proteins (transcription factors, coactivators, transcription intermediary factors (TIF) and corepressors) to influence downstream target gene expression. Biochemical analyses have demonstrated that nuclear receptor corepressor (NCoR) and homolog, silencing mediator of retinoic and thyroid receptor (SMRT), are strongly associated with unliganded TR [26]. A number of studies suggest that the corepressor interacts with the TR homodimer but not monomer on DNA. Recruitment of NCoR and SMRT to the promoter via association with DBD of TR/RXR leads to strong repression of basal promoter activity of target genes. NCoR and SMRT are structurally and functionally similar. Both proteins contain three repressor domains (RD1, RD2, and RD3) and two receptor-interacting domains (RID). RD1 interacts with TBL1 and mSin3, which recruit class I deacetylases (HDAC1 and HDAC2). HDAC3 interacts directly with RD2. Moreover, class II deacetylases (HDAC4/5 and HDAC7) bind RD3 as a mediator for repressing downstream genes transcription. In other words, RD1, RD2 and RD3 domains of corepressors interact with different types of deacetylase and other proteins to form a large repressor complex that suppresses target gene transcription [27] (Figure 3A). Recent studies have shown strong links among histone acetylation, chromatin remodeling and gene regulation activities [28,29]. As specified above, NCoR and SMRT may function as corepressors via histone deacetylase activity for complex-mediated chromatin remodeling. HDACs and histone binding proteins RbAp46/48 associate with the homologs mSin3A and mSin3B. HDACs are recruited to target genes by associating with Sin3 protein that interacts with sequence-specific DNA binding factors [30] (Figure 3B). The mSin3-HDAC complex is highly abundant and stable, facilitating binding and recruitment by the nuclear receptor repressors NCoR and SMRT [31,32]. Specifically, HDACs interact with mSin3 for TR/RXR-mediated repression. The TR/RXR/mSin3 complexes are indirectly mediated by NCoR and SMRT, which function to link receptors to mSin3-HDAC complexes. NCoR and SMRT corepressors are reported to recruit class I deacetylases after interactions with adaptor mSin3 protein. However, biochemical research to date has failed to detect NCoR or SMRT in mSin3-HDAC complexes. Other class II histone deacetylases (HDAC4, HDAC5 and HDAC7) have been identified that associate with SMRT interacting-proteins and repress gene transcription (Figure 3B). Therefore, a single corepressor can mediate downstream target gene expression via class I HDAC complexes in a Sin3A-dependent manner or class II HDAC complexes in a Sin3A-independent manner. Furthermore, a novel SMRT-containing cellular complex incorporating HDAC3 and transducing beta-like protein 1 (TBL1), a protein that interacts with histone H3, has been identified (Figure 3B). In vivo, TBL1 is involved in a repressor complex that repression of gene transcription through is bridged to HDAC3 and further interactions with SMRT, and can potentiate repression via TR [33]. However, under TH presence conditions, the TR conformation is altered to allow dissociation of corepressors (NCoR or SMRT), subsequent recruitment of transcriptional coactivators and induction of target gene transcription. Multiprotein complexes designated 'TRAP' interact with TRs [34,35] (Figure 3B). Biochemical analyses have revealed binding of a series of proteins to TRs, the most abundant of those proteins are molecularly distinguished with a molecular mass of 140 or 160 kDa, designated p140 and p160 [34]. Steroid receptor coactivator 1 (SRC-1) is the first p160 family member identified as a coactivator and interacts with several nuclear receptors via C-terminal activation function-2 (AF-2) in the ligand binding domain (LBD), one of which is TR [36,37]. SRC-1 has been shown to enhance the transcriptional activity of a number of transcription factors [38]. SRC-1 and other SRC families of displaying coactivator structures contain a basic-helix-loop-helix (bHLH) and single-minded (PAS) domain, which interact with intermolecular or intramolecular substrates [39]. In addition, SRC-1 has a nuclear receptor interacting domain incorporating three LXXLL amino acid motifs, which are not only required for nuclear receptor binding but also recruit specificity to other proteins [40–42]. Another significant finding is that SRC-1 coactivators contain two activation domains in the C-terminal region, denoted AD1 and AD2. The stronger transactivation domain, AD1, interacts with co-integrator CREB binding protein (CBP) [43] and another weaker activation domain in the far C-terminal region while AD2 interacts with an arginine methyltransferase, CARM1 (Figure 3A). A number of studies suggest that the SRC family acts as a platform for recruitment of other proteins.

Histone acetyltransferase (HAT) activity is possessed by CREB-binding protein (CBP)/p300 and p300/CBP-associated factor (p/CAF), which modulate chromatin remodeling [44,45] via acetylation of histone H3 and H4 (Figure 3A,B). SRC-1 also plays a potential adapter role and is capable of interacting with specific basal transcription factors, such as TATA binding factor (TBP) and transcription factor IIB [46]. Multiprotein complexes known as TR-associated proteins (TRAP) have been identified that interact with TRs [34,35]. These complexes can indirectly interact with TRs in response to ligand binding via a receptor-interacting LXXLL motif in the p160 coactivator through TRAP 220 [47]. In a cell-free transcription system with chromatin templates, ligand activity of TRs is enhanced by the TRAP complex, as determined from studies on SRC-1 [48] (Figure 3B). Several investigations to date indicate that ligand-dependent transcriptional activity of TRs requires recruitment of p160-TRAP coactivator complexes but the function association between TRAP complexes and the p160/CBP/PCAF system is unclear. For example, both TRAPs and p160/CBP/PCAF interact with the same region of TRs but do not bind simultaneously, and the molecule that binds first is yet to be established.

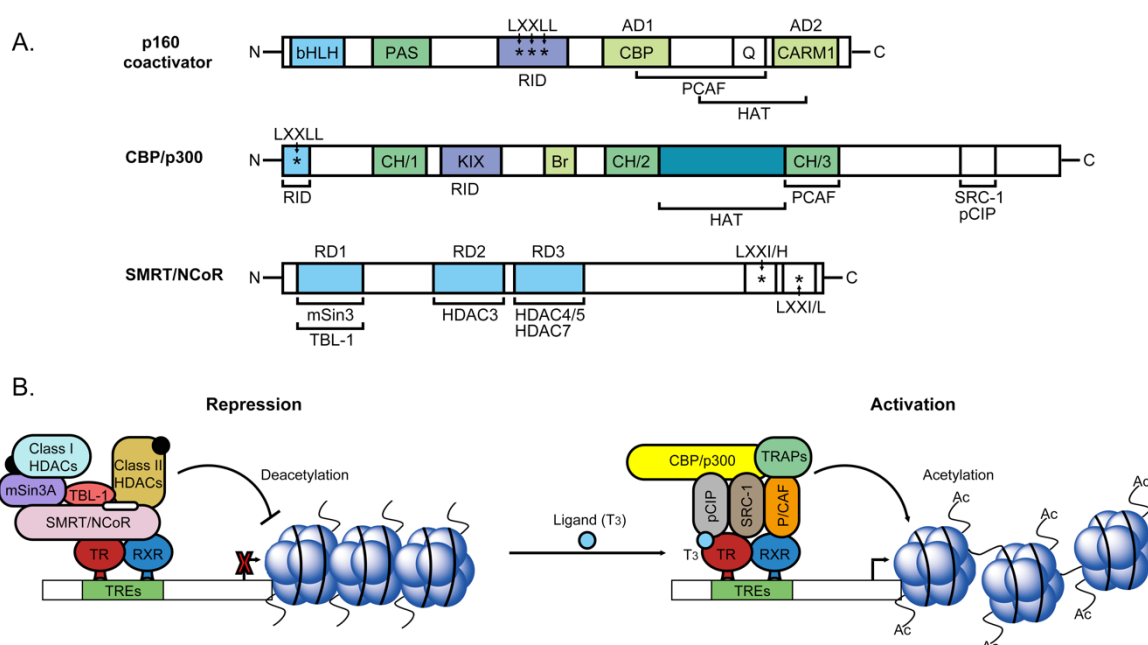


**Figure 3.** Schematic representation of the structure of receptor coactivators and corepressors and molecular action to regulation of genes transcription activity. (A) Biochemical analyses have revealed binding of a series of coactivators proteins to TRs, the most abundant of those proteins such as p160 family, and histone acetyltransferase (HAT), CREB-binding protein (CBP)/p300. Additionally, nuclear receptor corepressor (NCoR) and homolog, silencing mediator of retinoic and thyroid receptor (SMRT), are strongly associated with unliganded TR. (B) TRs repress gene expression in a ligand-dependent manner. TRs bind to their respective TREs with retinoid X receptors (RXR). Heterodimers of TR/RXR contain LBDs that interact with T<sub>3</sub>. Additionally, DBD displays high affinity for DNA sequences of TREs. TRs can directly or indirectly associate with different molecular proteins (transcription factors, coactivators, transcription intermediary factors (TIF) and corepressors) to influence downstream target gene expression.

#### 2.4. Non-Genomic Actions of Thyroid Hormone

The preliminary studies have revealed in the mitochondria and cytoskeleton that action of thyroid hormone that is not primarily involved in nuclear activities [49,50]. These actions are rapid in contrast to transcription and translation processes that occur over minutes or hours and are not exerted through gene transcription or protein synthesis, leading to coining of the term “non-genomic effects”. Non-genomic activity of the thyroid hormone in enucleate cells, plasma membrane and other cell fractions in vitro has been identified. According to these earlier studies, thyroid hormone receptors



on integrin  $\alpha v\beta 3$  are not homologous to nuclear thyroid hormone receptors. THs affect multiple physiological activities within the cell via interactions with integrin  $\alpha v\beta 3$  [51]. The integrin family has 24 structural proteins in the plasma membrane that essentially regulate cell–cell and cell–extracellular matrix (ECM) protein interactions [52].  $\alpha v\beta 3$ , one of the isoforms of integrin, is heterodimeric in structure and contains an Arg–Gly–Asp (RGD) recognition specific binding site for ECM proteins, such as osteopontin, fibronectin and vitronectin, for activation of intracellular signaling [52]. In other words, thyroid hormones bind the receptor near the RGD site of integrin  $\alpha v\beta 3$  that serves as a recognition and binding motif for ECM proteins [53]. Upon interaction of integrin  $\alpha v\beta 3$  with THs ( $T_3$  and  $T_4$ ), mitogen-activated protein kinase/extracellular signal-regulated kinase (MAPK/ERK 1/2) pathways are activated that regulate multiple cellular physiological processes [51] (Figure 4A). Integrin  $\alpha v\beta 3$  contains two binding domains: (1) S1 that specifically recognizes  $T_3$  and activates the phosphatidylinositol 3-kinase (PI3K)/Akt/protein kinase B (PKB) pathway via stimulation of Src kinase (Figure 4B) and (2) S2 that binds both  $T_3$  and  $T_4$ , leading to regulation of MAPK/ERK1/2 (Figure 4A).  $T_4$  has high affinity for the S2 domain while both S1 and S2 domains interact with  $T_3$ . In addition, the two binding domains mediate distinct downstream effects. For instance, Src kinase and PI3K pathways are activated by  $T_3$  binding to the S1 domain, leading to direct trafficking of  $TR\alpha 1$  from the cytoplasm to the nucleus and transcriptional activity of the target gene, *HIF1A* (Figure 4B). The S2 domain stimulates activation of MAPK/ERK1/2 via phospholipase C (PLC) and protein kinase  $C\alpha$  ( $PKC\alpha$ ), promoting phosphorylation of nucleoproteins TRP1, ERM, STAT1 and p35 [54,55] and modulation of intracellular protein trafficking of estrogen receptor  $\alpha$  ( $ER\alpha$ ) and nuclear uptake of  $TR\beta$  from the cytoplasm [56,57] (Figure 4A). Notably, estrogen receptor  $\alpha$  ( $ER\alpha$ ) in this pathway is phosphorylated, suggestive of crosslinking between thyroid and steroid hormone pathways [58]. These represent two of the five mechanisms underlying the non-genomic action of thyroid hormone. In the cytoplasm, the PI3K pathway is rapidly activated via  $T_3$  interactions with  $TR\beta 1$  and initiates downstream target gene transcription (Figure 4C). Interactions of  $T_3$ -liganded  $TR\beta 1$  with the regulatory p85 $\alpha$  subunit of PI3K that induces downstream AKT phosphorylation lead to subsequent phosphorylation of mTOR and further activation of mTOR-p70S6K along with a series of downstream target genes in the nucleus, such as hypoxia inducible factor-1 $\alpha$  (HIF-1 $\alpha$ ), glucose transporter 1 (GLUT1), platelet-type phosphofructokinase (PFKP) and monocarboxylate transporter 4 (MCT 4) [59–61] (Figure 4C). Additionally, at the plasma membrane,  $T_3$  interacts with truncated  $TR\alpha 1$  (p30  $TR\alpha 1$ ), and binding of PI3K to p85 $\alpha$  inactivates transcription of downstream genes. However, the  $T_3$ -liganded  $TR\alpha 1$  complex activates a series of signal transduction proteins (PKGII and ERK) and nitric oxide synthase (NOS) (Figure 4D). Additionally,  $T_3$  interactions with  $TR\beta 1$  are reported to modulate Na, K-ATPase activity via activation of both MAPK/ERK 1/2 and PI3K pathways (Figure 4C,E). However, only  $T_3$ -liganded  $TR\beta 1$  stimulates MAPK/ERK 1/2 activity, which activates the sodium proton exchanger ( $Na^+/H^+$ ) in the plasma membrane [57,62] (Figure 4E).

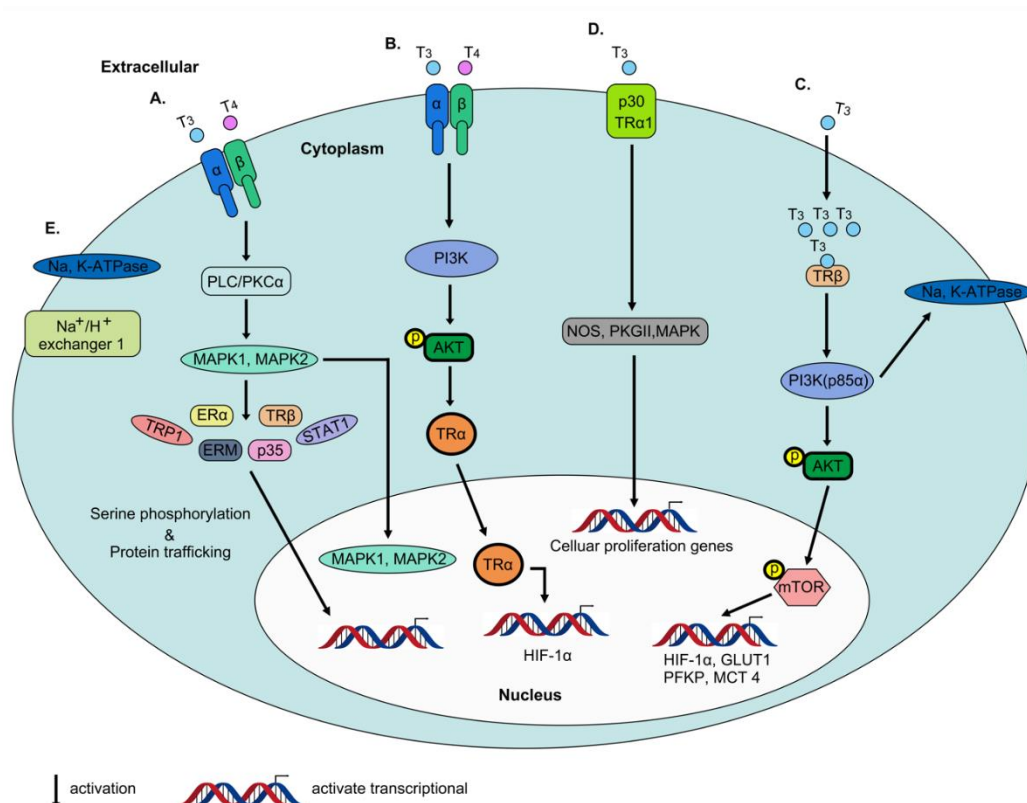


**Figure 4.** Non-genomic actions of thyroid hormone. THs affect multiple physiological activities within the cell via interactions with integrin  $\alpha\beta3$ . (A)  $\alpha\beta3$  that binds both  $T_3$  and  $T_4$ , leading to regulation of MAPK/ERK1/2 via PLC and PKC $\alpha$ , promoting phosphorylation of nucleoproteins TRP1, ERM, STAT1 and p35 and modulation of intracellular protein trafficking of ER $\alpha$  and nuclear uptake of TR $\beta$  from the cytoplasm. (B)  $\alpha\beta3$  that specifically recognizes  $T_3$  and activates the PI3K/Akt/PKB pathway via stimulation of Src kinase, leading to direct trafficking of TR $\alpha$ 1 from the cytoplasm to the nucleus and transcriptional activity of the target gene, HIF-1 $\alpha$ . (C) In the cytoplasm, the PI3K pathway is rapidly activated via  $T_3$  interactions with TR $\beta$ 1 and initiates downstream target gene transcription including HIF-1 $\alpha$ , GLUT1, PFKP and MCT 4. (D) At the plasma membrane,  $T_3$  interacts with p30 TR $\alpha$ 1, and binding of PI3K to p85 $\alpha$  inactivates transcription of downstream genes. However, the  $T_3$ -liganded TR $\alpha$ 1 complex activates a series of signal transduction proteins (PKGII and ERK) and NOS. (E)  $T_3$ -liganded TR $\beta$ 1 stimulates MAPK/ERK 1/2 activity, which activates the sodium proton exchanger ( $Na^+/H^+$ ) in the plasma membrane.

### 3. Functional Significance of Thyroid Hormone and Receptors in Tumors

Under physiological conditions, thyroid hormone receptors control tumor cell proliferation and cancer cell defense pathways [54,59,63]. TRs are reported to exert tumor suppressor effects [64], with 96% nuclear TR $\beta$ 1 expression detected in the normal epithelium but lower frequency of expression in adenomas (~83%) and cancer (68%), which is significantly lower than that in normal tissue and adenoma). Consistently, another study demonstrated a tumor suppressor role of wild-type TR $\beta$ 1 in thyroid cancer [65–67], similar to that in other cancer types [67,68]. Conversely, abnormal expression or mutation of TR $\beta$ 1 has been shown to promote carcinogenesis [69]. Interestingly, clinical data on BRCA1-associated breast cancer suggest that TR $\beta$ 1 expression can extend the overall survival curve. However, wild-type TR $\alpha$  was positively associated with reduced five-year overall survival for five years [70]. Wild-type TR $\alpha$  plays a distinct role in cancer relative to TR $\beta$ 1, which TR $\alpha$  potentially influences tumorigenesis and hematogenous metastasis via association with *nm23* genes [64,70]. Additionally, TR $\alpha$  binding to  $T_3$  promotes gastrointestinal cancer development through directly modulating the transcriptional activity of  $\beta$ -catenin and affecting downstream signal transduction [71].

Thyrotropin, THs, integrin  $\alpha v \beta 3$  and deiodinases are involved in cancer proliferation along with TRs. Earlier studies suggest that altered TH status modulates cancer cell proliferation and tumor growth. For example, low expression of circulating thyrotropin releasing hormone (TRH) is associated with increased risk of lung, colon, prostate, and breast cancer [72]. Hyperthyroidism in rodents stimulates tumor transplant growth and metastasis, and conversely, hypothyroidism suppresses these effects [73]. Furthermore, both breast and prostate cancers at advanced clinical stages display high expression of THs. Spontaneous hypothyroidism may beneficially alter the course and aggressiveness of breast cancer [74]. Clearly, TH expression is correlated with cancer initiation. In the following section, the underlying mechanisms modulating proliferation and metastasis of different cancer types, including thyroid hormone effects, deiodinase activities and thyroid hormone receptors, are discussed (Table 1).

**Table 1.** Summary of the relevant molecular mechanism in different kinds of cancer via THs/TRs.

Cancer Types	Thyroxine	Binding Receptor	Molecular Mechanisms	Physiological Processes	Ref.
Breast cancer	T <sub>3</sub> , T <sub>4</sub>	$\alpha v \beta 3$	activation of MAPK/ERK1/2	proliferation↑	[58,75]
	T <sub>3</sub>	$\alpha v \beta 3$	downregulation of SMP30 gene	anti-cancer↑, apoptosis↑	[76]
	T <sub>3</sub>	TR $\beta$	downregulation of T1 gene	proliferation↓	[77]
	T <sub>3</sub>	TR $\beta$	inhibition of STAT5 signaling	development↓	[78]
	T <sub>3</sub>	TR $\beta$	downregulation of $\beta$ -catenin	prognosis↑	[70]
Thyroid cancer	T <sub>3</sub> , T <sub>4</sub>	$\alpha v \beta 3$	activation of MAPK/ERK1/2	proliferation↑, anti-apoptosis↑	[79]
	T <sub>3</sub>	TR $\beta \Delta$	activation of PI3K-Akt	metastatic↓, development↑	[80]
	T <sub>3</sub>	TR $\beta$	inhibition of PI3K-Akt increase p27 decrease cyclin D	tumor growth↑ proliferation↓	[80]
Lung cancer	T <sub>3</sub> , T <sub>4</sub>	$\alpha v \beta 3$	increase proliferating cell nuclear antigen (PCNA) induce ER $\alpha$ phosphorylation activation of MAPK/ERK1/2	proliferation↑	[81]
Brain tumor	T <sub>3</sub> , T <sub>4</sub>	$\alpha v \beta 3$	increase proliferating cell nuclear antigen (PCNA) activation of MAPK/ERK1/2	tumor growth↑	[57,82–84]
	T <sub>3</sub>	TR $\beta$	activation of PI3K-Akt upregulation of HIF-1 $\alpha$ gene	proliferation↑	[57]
	T <sub>3</sub>	TR $\alpha$	expression of TR $\alpha$ 1 and TR $\alpha$ 2	tumor grade↓, tumor malignancy↓	[85]
Liver cancer	T <sub>3</sub>	TR $\alpha$ , TR $\beta$	downregulation of CDK2, cyclin E, phosphorylation-Rb	proliferation↑	[86,87]
	T <sub>3</sub> , T <sub>4</sub>	$\alpha v \beta 3$	upregulation of p21 induction of DKK4 reduction of MMP2	cell invasion↓ metastatic↓	[88,89]
	T <sub>3</sub>	TR $\alpha \Delta$	downregulation of ELF2 dysregulation of follistatin, activin $\beta$ C, thrombomodulin, SIX1, Rasgrp3, Ndrp2	development↑, carcinogenesis↑	[90]
	T <sub>3</sub>	TR $\alpha$	upregulation of lipocalin 2	invasion↑, metastasis↑	[91]

Table 1. Cont.

Cancer Types	Thyroxine	Binding Receptor	Molecular Mechanisms	Physiological Processes	Ref.
Colorectal cancer	T <sub>4</sub>	TR $\alpha$ , TR $\beta$	activation of NF- $\kappa$ B	cancer stem like cell $\uparrow$	[92]
	T <sub>3</sub>	$\alpha$ v $\beta$ 3	activation of BM1 gene	drug resistance $\uparrow$	[93]
	T <sub>3</sub> , T <sub>4</sub>	TR $\alpha$	activation of ERK1/2/Akt	tumor growth $\uparrow$	
	T <sub>3</sub> , T <sub>4</sub>	TR $\alpha$	activation of MET/FAK	invasion $\uparrow$ , metastasis $\uparrow$	[94]
	T <sub>4</sub>	$\alpha$ v $\beta$ 3	increase proliferating cell nuclear antigen (PCNA), cyclin D1, c-myc	proliferation $\uparrow$	[95,96]
	T <sub>4</sub>	TR $\alpha$	activation of NF- $\kappa$ B	Tumor progression $\uparrow$ , metastasis $\uparrow$	[97]
	T <sub>3</sub>	TR $\alpha$ 1	activation of Frizzled-related protein, sFRP2 modulation of $\beta$ -catenin	proliferation $\uparrow$	[98]

### 3.1. Breast Cancer

Thyroid hormone activity is related to breast cancer. Hypothyroidism is associated with low incidence of breast cancer, and conversely, hyperthyroidism with high incidence and aggressiveness of breast cancer [99]. Statistical studies suggest that high T<sub>3</sub> levels in women are associated with increased overall risk and occurrence of breast cancer. A study on 1322 peri/postmenopausal women disclosed a significant direct correlation between T<sub>3</sub> level and breast cancer occurrence [100]. High T<sub>4</sub> and T<sub>3</sub> expression in the blood leads to subclinical hyperthyroidism in menopausal breast cancer patients [101]. On the other hand, the most frequent endocrine disorders are encountered in breast cancer. An earlier clinical study showed that among 844 breast cancer patients, 74 were hypothyroid and not only older but also diagnosed at an earlier stage than euthyroid patients [74]. Hypothyroidism is reported to promote breast cancer apoptosis and suppress mammary carcinogenesis through alterations in body composition, including leptin secretion and serum 17 $\beta$ -estradiol (E2) [102]. Additionally, hypothyroidism can decrease inherent drug resistance and induce chemotherapy sensitivity [103]. Evidence of overlap of both non-genomic and genomic actions of thyroid hormones (THs) in breast cancer cells and crosslinking with other hormones, such as estrogens and testosterone, has been uncovered. TH-induced phosphorylation of estrogen receptor  $\alpha$  (ER $\alpha$ ) at Ser-118 via activation of the MAPK/ERK 1/2 pathway promotes human breast cancer cell proliferation [58,75]. In human breast cell lines MCF-7 and T47D, both T<sub>4</sub> and T<sub>3</sub> promote cell proliferation in a dose-dependent manner [104–106]. Hyperthyroidism and hypothyroidism are correlated with the incidence of tumor induction and reduction and aggressiveness of breast cancer in female mice [99]. Interestingly, other reports support anticancer activity of THs, for instance, via downregulation of *SMP30* expression and induction of apoptosis in MCF-7 cells through T<sub>3</sub> [76]. Both T<sub>4</sub> and T<sub>3</sub> have been shown to regulate the breast cancer process. T<sub>4</sub> only appears to interact with cell surface receptors of the hormone whereas T<sub>3</sub> binds nuclear THRs via genomic activity as well as integrin  $\alpha$ v $\beta$ 3 in the cytoplasm [107]. As stated above, physiological free T<sub>4</sub> acts as a growth factor that influences cancer progression, anti-apoptosis and endothelial cell migration. The main function of T<sub>3</sub> is to promote breast cancer cell division [54,79,82,108,109]. *T1* gene overexpression in breast adenocarcinoma is induced by mitogens, serum, specific oncogenes and cytokines [77] and inhibited under conditions of high T<sub>3</sub> concentrations, leading to reduced breast cancer cell proliferation. In addition, T<sub>3</sub> suppresses STAT5-mediated regulation of downstream target gene expression by inhibiting STAT5 signaling, which can associate with TR $\beta$ 1 as a tumor suppressor protein and inhibit mammary hyperplasia development [78]. TR $\beta$ 1 has been shown to function as a tumor suppressor in a number of cancer types (including breast,

lung and thyroid cancer). In a xenograft mouse experiment, injection of MCF-7-Neo cells into athymic mice promoted rapid tumor development. Conversely, when MCF-7 TR $\beta$  was injected into athymic mice, tumor growth was inhibited through serum 17 $\beta$ -estradiol (E2) [78]. In nuclei of breast cancer cells, both TR $\beta$  and TR $\alpha$  proteins are expressed, with 74% of breast tumors highly expressing TR $\alpha$ 1 and 40% TR $\alpha$ 2. TR $\alpha$ 2 influences prognostic histopathological parameters in breast cancer patients, such as tumor size, axillary lymph node involvement, grading and hormone receptor status, leading to improvement of overall survival [110,111].

### 3.2. Thyroid Cancer

Three morphological subtypes (papillary thyroid carcinoma, follicular thyroid carcinoma (FTC) and anaplastic carcinoma) constitute 90% of all thyroid cancer types [112]. The majority of studies indicate that thyroid cancer is commonly associated with hyperthyroidism [4,113]. T<sub>4</sub> induces proliferation of most human carcinoma cells (including follicular and papillary thyroid carcinoma cell lines) through binding to cell surface receptors on integrin  $\alpha$ v $\beta$ 3. Interactions of T<sub>4</sub> with integrin  $\alpha$ v $\beta$ 3 lead to inhibition of p53-dependent apoptosis in tumor cells. Additionally, in differentiated thyroid carcinomas (DTC), TSH act as a growth factor predominantly through interactions with the thyrotropin receptor on papillary and follicular thyroid cancer cells. Thus, lowering or suppression of host TSH with exogenous T<sub>4</sub> can be applied for standardized primary treatment and long-term management of DTC. On the other hand, T<sub>4</sub> can also be used to suppress TSH in recurrent disease, supporting a critical role of T<sub>4</sub> in modulating DTC proliferation and recurrence via influencing TSH [114]. In vitro findings suggest that treatment with external THs enhances proliferation of human papillary and follicular thyroid cancer cells. Specifically, THs interact with plasma membrane integrin  $\alpha$ v $\beta$ 3, activating MAPK/ERK1/2 signaling and promoting papillary and follicular thyroid cancer cell proliferation and anti-apoptosis [79]. Additionally, experiments on a mouse model of thyroid carcinoma primary and metastatic lesions showed activation of PI3K-Akt signaling upon mutation of TR $\beta$ . Thyroid hormone  $\beta$  receptor (TR $\beta$ )PV/PV mice with knock-in mutant TR $\beta$  gene (TR $\beta$ PV mutant) spontaneously developed thyroid cancer and distant metastasis similar to human follicular thyroid cancer. Furthermore, in these spontaneous thyroid tumors, the ligand binding domain of TR interacted with PI3K regulatory subunit, p85 $\alpha$ , to a greater extent than wild-type TR $\beta$ . LY-294002 is a PI3K signaling specific inhibitor, which blocks rapamycin-p70(S6K) of Akt mammalian signaling, leading to both increased p27 and decreased cyclin D1, further inhibiting thyroid tumor growth and tumor cell proliferation. LY294002 treatment promotes thyroid tumor apoptosis by increasing caspase-3 expression and reducing phosphorylated BAD and suppresses thyroid cancer cell motility, thus influencing metastatic ability [80]. Data from this study suggest that mutation of TR $\beta$  plays a critical role in thyroid cancer development. In another study, a mouse model with dominant-negative mutant thyroid hormone receptor  $\beta$  (denoted PV) was generated. Reduced PI3K activation by T<sub>3</sub> in Thr $\beta$ (PV/PV) mice was observed, along with inability to bind to mutant TR $\beta$  under conditions of hypothyroidism [66]. The data suggest that thyroid gland carcinogenesis in Thr $\beta$ (PV/PV) mice is promoted by thyroid hormone via binding to cell surface integrin  $\alpha$ v $\beta$ 3 [66]. Deiodinase type 3 (DIO3, D3) that converts T<sub>4</sub> to T<sub>3</sub> is upregulated in the human PTC-derived cell line, K1, by transforming growth factor  $\beta$ 1 (TGF $\beta$ 1). Additionally, treatment with the inhibitors U0126 (ERK pathway) and SB203580 (p38 pathway) led to blockage of the MAPK pathway, and subsequent decrease in DIO3 mRNA and inhibition of DIO3 transcriptional induction via TGF $\beta$ 1, clearly suggesting that D3 is upregulated via MAPK signaling [115]. The collective findings indicate that D3 expression is positively correlated with thyroid tumor size and disease spread [115].

### 3.3. Lung Cancer

Around 60% of patients diagnosed with lung cancer present an advanced stage of disease that is too late for surgical treatment. Small-cell lung carcinoma is associated with symptoms of hyperthyroidism [116]. Lung cancer patients often present with non-thyroidal illness syndrome (NTIS) or sick euthyroid syndrome, characterized by alterations in circulating TH expression in acute or



chronic systemic disease. In NTIS patients, the circulating  $T_3$  level is decreased and  $T_4/T_3$  expression ratio significantly increased along with modest alterations in regulation of  $rT_3$ . Over a six-month observation period, mortality of lung cancer patients with low-level  $T_3$  was higher than that of lung cancer patients with normal  $T_3$  expression [117]. In NTIS patients with both small cell and non-small cell cancer,  $T_3$  was associated with disease stage and served as a poor prognostic factor [118]. In the human non-small cell cancer cell lines NCI-H522 and NCI-H510A,  $T_4$  induced a significant increase in proliferating cell nuclear antigen (PCNA) as well as high concentrations of  $T_3$  [81]. These experiments suggest that high expression of  $T_4$  in  $ER\alpha$ -positive lung cancer cells induces phosphorylation of  $ER\alpha$  and activation of ERK1/2, further enhancing PCNA expression and proliferative activity. The collective findings indicate that  $T_4$  is correlated with lung cancer through inducing hyperthyroidism, which may be a potential risk factor. In an animal model of Lewis lung carcinoma (3LL), cell growth progression is associated with reduced  $T_4$  and  $T_3$  levels. Subcutaneous injection with  $T_4$  induces a hyperthyroid stage and further increase in  $T_4$  and  $T_3$  levels associated with primary tumor growth and development of pulmonary metastases 3LL cells. However, the functional effect of  $T_3$  on 3LL cells is distinct from that of  $T_4$ , which induces significant inhibition of pulmonary metastases and prolongs mouse survival. Additionally, THs ( $T_4$  and  $T_3$ ) treatment promotes cytotoxicity against 3LL cells mediated by alveolar macrophages [119]. Alterations in THs expression influence against primary tumor formation and metastases of lung cancer in the natural host. In lung cancer, THs regulate tumor proliferation and activation of MAPK/ERK1/2 signaling via interactions with TRs on  $\alpha v \beta 3$  integrin. Around 61% of small-cell lung cancer (SCLC) and 48% of non-SCLC (NSCLC) cases lack TR $\beta 1$  expression. While TR $\beta 1$  mutations are not commonly observed in human cancers, aberrant TR $\beta 1$  through epigenetic regulation has been reported. Neither SCLC nor NSCLC cell lines display somatic mutations of TR $\beta 1$ . However, methylation of the TR $\beta 1$  promoter has been shown to induce significant loss of TR $\beta 1$  mRNA expression [120].

### 3.4. Brain Tumors

Clinical studies to date have reported extremely low survival rates of patients with glioblastoma multiforme (GBM), the most malignant brain tumor type, with the poorest prognosis. The hypothyroid overall survival rate is longer than that of euthyroid patients [73]. Experiments by another group demonstrated that THs stimulate glioblastoma cell proliferation. Similar to data obtained with other solid tumors, hypothyroidism is associated with improved duration of survival [82,83]. Studies on 230 patients with primary brain tumors showed that 27% had NTIS with high 5-year mortality and short overall survival [121,122]. Additionally, NTIS is a poor prognostic marker for patients undergoing brain tumor surgery.  $T_4$  can further stimulate glioblastoma growth through interactions with integrin  $\alpha v \beta 3$  in the cytoplasm [57,82–84]. Both  $T_4$  and  $T_3$  act as stimulators that induce proliferating cell nuclear antigen (PCNA) accumulation in glioma cells via activation of MAPK/ERK1/2.  $T_3$  induces PI3K activation, Src kinase and MAPK/ERK1/2 signaling in U-87MG cells. Stimulation of the PI3K pathway by  $T_3$  promotes TR $\beta$  translocation from the cytoplasm to nucleus and activation of HIF-1 $\alpha$  mRNA transcription [57]. Interestingly, TR $\alpha 1$  and TR $\alpha 2$  expression in human astrocytomas decrease while TR $\beta 1$  expression increases with grade of malignancy [85]. Additionally, in the human medulloblastoma cell line, HTB-185, increased TR $\alpha 2$  transcriptional activity is not accompanied by TR $\beta 2$  expression [123].

### 3.5. Liver Cancer

Hypothyroidism plays an important role in liver carcinogenesis. A previous study reported hypothyroidism over ten years in female patients with hepatocellular carcinoma, indicating a significant association of hypothyroidism with high risk of human hepatocellular carcinoma (HCC) in females independent of known risk factors [124]. Additional findings support the prevalence of hypothyroidism in HCC patients. The correlation between thyroid function and cancer risk in HCC is related to induction of TSH under the hypothyroid state. In HCC tissue, thyroid stimulating hormone receptor (TSHR) is overexpressed. Therefore, under a hypothyroid state, TSH secretion and synthesis are induced

in response to increased binding with highly expressed TSHR and promote HCC progression [125]. A number of studies have demonstrated that  $T_3$  in HCC downregulates oncogenic CDK2, cyclin E and phospho-Rb, upregulates the tumor suppressor p21 and further inhibits cancer cell proliferation [86,87]. Additionally,  $T_3$  inhibits cell invasion and metastatic potential via inducing DKK4 expression by reduction of matrix MMP2 and downregulation of the transcription factor ELF2 associated with tumor growth and cell proliferation [88,89]. In HCC tissue and HCC cell lines, both  $TR\alpha$  and  $TR\beta$  display high dominance of truncating and point mutations [126–128]. Interestingly, *v-erbA* is not only an oncogene but also translates to a mutant form of  $TR\alpha$ . Oncogene activity is possibly stimulated in hepatocytes via *v-erbA* dominant-negative activity on  $T_3$ -responsive genes [90]. The *v-erbA* dysregulated  $T_3$  responsive genes include follistatin, activin  $\beta C$ , thrombomodulin, *Six1*, *Rasgrp3* and *Ndr2*, which are involved in carcinogenesis leading to HCC development in a transgene mouse model [90]. An earlier study suggested that the *v-erbA* oncogene of avian erythroblastosis virus is devoid of ligand-binding ability. In transgenic mice expressing *v-erbA*, some abnormal physiological phenomena were observed, including breeding disorders, abnormal behavior, reduced adipose tissue, hypothyroidism with inappropriate TSH response and enlarged seminal vesicles. As stated above, earlier experiments supported the development of hepatocellular carcinoma in male animals via *v-erbA* modulation and further identified aberrant (or mutant) TR in correlation with carcinogenesis [129]. On the other hand,  $T_3$  is reported to be upregulated lipocalin 2 and promote HCC invasiveness by TRs. Additionally, in HCC patient samples, both lipocalin 2 and  $TR\alpha$  are overexpressed, which are correlated with cancer grade, stage and survival [91].  $T_4$  can activate NF- $\kappa B$ , which is required for THs to induce HCC self-renewal and increase cancer stem-like cells and drug resistance [92]. Finally, similar to other cancer types,  $T_3$  induces HCC growth by activating ERK1/2/Akt signaling via binding to integrin  $\alpha v \beta 3$  [93]. In mice, dependent on hyperthyroid conditions and expression of  $TR\alpha 1$  in HCC cells, HCC invasion and metastasis are promoted through mediation of MET/FAK pathways. Simultaneously, clinical researchers have further confirmed that in human HCC, tissue samples highly express  $TR\alpha 1$  in association with lower survival. To date, no significant correlation between  $TR\beta 1$  and HCC clinical tissue sample has been established. However, in other HCC specimens, decreased expression of TRs (including  $TR\alpha 1$ ) is reported, supporting a tumor suppressor role [94]. Thus,  $T_3$ /TR may play a dual role (either as an oncogene or tumor suppressor), depending on the molecular background and disease stage. However, this hypothesis remains to be tested.

### 3.6. Colorectal Cancer

Significant clinical research has focused on colon cancer in addition to breast, prostate and lung cancer types. The pathogenesis rate of colon cancer has been shown to be increased by thyrotropin [72]. Data from the Molecular Epidemiology of Colorectal Cancer (MECC) study in Israel indicate that treatment with L-thyroxine for five years can reduce the risk of large bowel cancer [130]. In another study, patients with colorectal cancer displayed reduced  $T_3$  levels in plasma associated with systemic metastases, implying that inhibition of thyroid hormone signaling further suppresses colorectal cancer invasiveness [131]. This effect may be specifically associated with NTIS. A number of studies propose a possible link between colorectal cancer and thyroid hormone disorders, considering circulation of thyroid hormones, thyrotropin levels and duration of thyroid disease. An earlier investigation showed increased  $rT_3$  levels in plasma in 24% of colorectal cancer cases and elevated  $rT_3/T_3$  ratio in patients with metastatic colorectal cancer [131]. In view of this finding, it is hypothesized that  $rT_3$  accumulates in metastatic colorectal cancer via deiodinase type 3 ( $D_3$ ) activity,  $D_3$  converts  $T_3$  to  $T_2$ , thus attenuating  $T_3$  action locally, and the  $T_4/T_3$  ratio is increased, supporting a critical role of thyroid hormone in modulating colorectal cancer metastasis. The mechanism underlying polypoid growth of colorectal cancer remains unclear but may be associated with trophic stimuli, such as thyroid hormones. Colorectal cancer has a high level of integrin  $\alpha v \beta 3$ -expressing tumor vasculature and is associated with significantly lower relapse-free and overall survival, compared to that of patients with low integrin  $\alpha v \beta 3$  levels in tumor vasculature [132]. Based on these observations, it is proposed

that thyroid hormones not only modulate colorectal cancer progression through cell surface integrin  $\alpha v \beta 3$  but also that integrin  $\alpha v \beta 3$  acts as a prognostic indicator of colon carcinoma [132]. Colorectal cancer proliferation is induced by  $T_4$  and thyroxine, both in vitro and in vivo, in a dose-dependent manner in HCT-116, HT-29 and Colo205 cell lines [95,96]. In addition, colorectal cancer progression is promoted through enhancing epithelial cell proliferation in the colon mucosa by  $T_4$  [133]. Treatment of thyroidectomized rats with  $T_4$  has been shown to enhance the number of cells per intestinal crypt, suggesting an important regulatory role in intestinal stem-progenitor cell proliferation. However,  $T_4$  only affects tumor cell proliferative activity and not the histological appearance of colorectal tumors and colon adenocarcinoma type and depth [134]. As stated above, deiodinase type 3 ( $D_3$ ) is also involved in colorectal cancer and reported to promote human colon adenoma and adenocarcinoma relative to healthy surrounding mucosa [97]. The  $\beta$ -catenin/T-cell factor complex activated in colorectal cancer stimulates  $D_3$  expression and  $T_3$ -induced colorectal cancer cell proliferation. However, in both xenograft mice and colon cancer cells, knockdown of  $\beta$ -catenin either led to reduced cell proliferation or enhanced cell differentiation. Overexpression of  $TR\alpha 1$  in intestinal cancers promotes hyperproliferation and accelerates the tumorigenic process both in vivo and in vitro [98]. Upon  $TR\alpha 1$  overexpression in  $Apc^+/1638N$  mice, tumor appearance, metastasis and intestinal cancer progression are observed. In  $Apc^+/1638N$  mice overexpressing vil- $TR\alpha 1$  (intestinal epithelium-targeted overexpression of  $TR\alpha 1$ ), the tumor development rate is higher than that in control  $Apc^+/1638N$  mice, suggesting that  $TR\alpha 1$  is also involved in tumorigenesis via activation of  $\beta$ -catenin [98]. Wild-type  $TR\alpha 1$  is beneficial for intestinal regeneration after  $\gamma$ -irradiation-induced DNA damage. However, mutation of  $TR\alpha 1$  via irradiation neither induces apoptosis nor reduces cell proliferation. An animal model with the  $TR\alpha 1$  mutation showed delayed p53 phosphorylation after induction of the DNA damage response. These experiments indicate that  $TR\alpha 1$  plays an important role in intestinal cancer progression via modulation of cell renewal and apoptosis after irradiation treatment and accumulation of DNA damage [135]. Additionally,  $T_3$  interacts with  $TR\alpha 1$  via activation of Frizzled-related protein, sFRP2, which directly modulates  $\beta$ -catenin expression, a major regulator of intestinal cell proliferation [71,136]. Other studies suggest that loss of  $TR\beta 1$  promotes malignant transformation of human colon tumors. Conversely, overexpression of  $TR\beta 1$  is associated with reduced invasive activity and consequent biopsies in patients with colorectal cancer [137].

### 3.7. Thyroid Hormone Is Anti-Apoptosis in Cancer Cells

Previous studies reported that thyroid hormone not only play a key role to promote cancer cells proliferation but also induces anti-apoptosis. In breast cancer, the transcription of the pro-apoptotic Bcl-2-associated death promoter (Bad) gene and X-linked inhibitor of apoptosis (XIAP) gene are downregulated by  $T_3$ . Additionally, both  $T_3$  and  $T_4$  not only decrease some of the pro-apoptosis markers including caspase-3, Bax but also increase expression of XIAP [63]. The action of  $T_3$  in the human glioblastoma U-87 MG cells accumulate hypoxia-inducible factor (HIF)-1 $\alpha$  mRNA (Figure 5A), which has anti-apoptosis function of gene, via activation of the PI3K pathway by  $\alpha v \beta 3$  [57]. Under the condition of  $T_3$ , the human kidney showed an increase in the myeloid cell leukemia-1 (MCL-1) transcription activity, which is an anti-apoptotic member of Bcl-2 family, via the presence of  $TR\beta$  to prevent the formation of channels to release mitochondrial cytochrome c and induce apoptosis [138]. As stated above, we know that most THs promote cancer progression via activation of the signal transduction pathway, one is the MAPK/ERK1/2. Therefore, an ERK1/2 inhibitor, PD98059, which inhibits cascade of MAPK/ERK1/2 signaling transduction and further blocks thyroid hormone-induced cell proliferation [139]. In addition, resveratrol can activate ERK1/2 and induce accumulation of nuclear cyclooxygenase (COX-2) via directing interaction with the integrin  $\alpha v \beta 3$  receptor to further induce phosphorylation of ERK1/2, which translocates into the cell nucleus and complexes with inducible COX-2 in resveratrol treatment cancer cells. Immediately, the induction of p53-Ser15 phosphorylation can promote downstream gene expression including c-fos, c-jun, and p21 gene expression, and further induce cancer cell apoptosis. However, the action of  $T_4$  prevents p53-Ser15 phosphorylation and blocks

induction cancer cell apoptosis [139]. These results strongly suggest that the thyroid hormone has anti-apoptosis function.

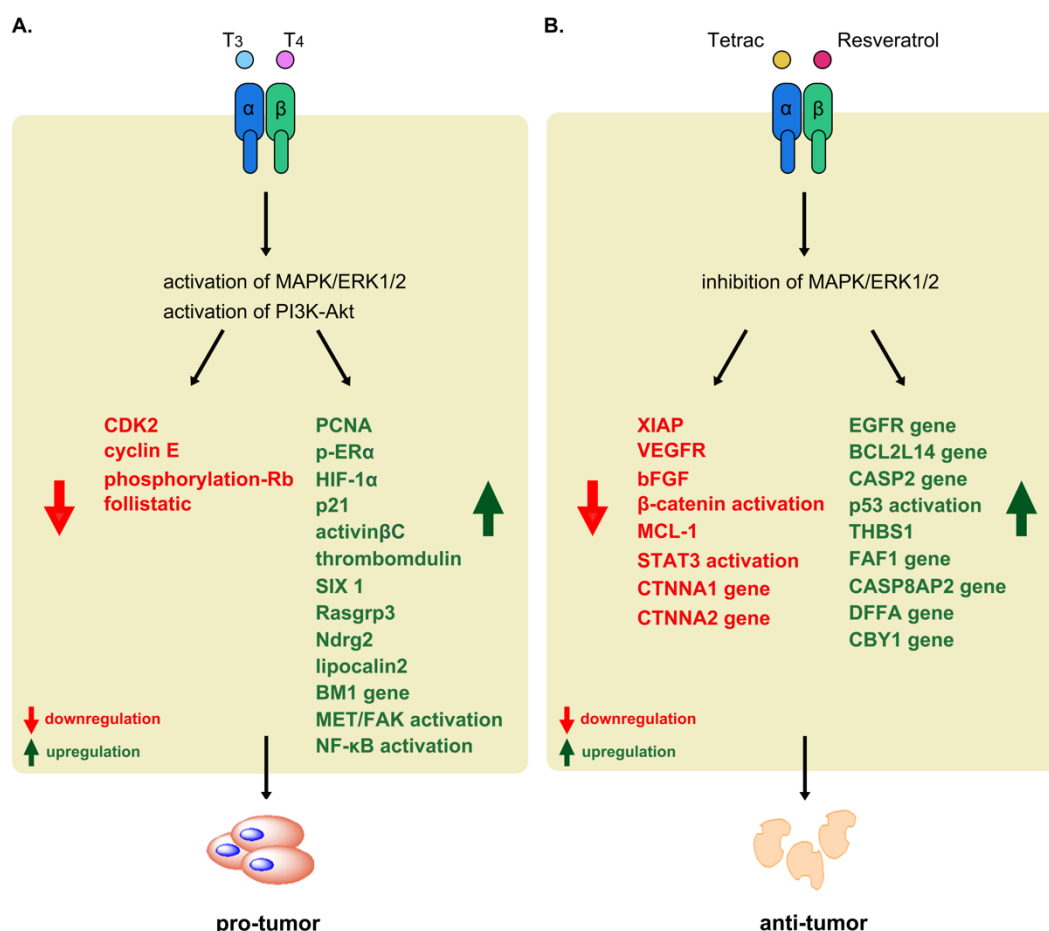


**Figure 5.** Non-genomic effects of pro-tumorigenic and anti-tumorigenic activities of thyroid hormones in tumor settings. (A)  $\alpha\beta3$  that binds both  $T_3$  and  $T_4$ , leading to activation of MAPK/ERK1/2 and PI3K-Akt, inducing of PCNA, HIF-1 $\alpha$ , P21, activin $\beta$ C, thrombomodulin, SIX1 Rasgrp3, Ndrgr2, lipocalin2 and BM1 gene expression to promote phosphorylation of ER $\alpha$ , and activation of MET/FAK, NF- $\kappa$ B, and downregulation of CDK2, cyclin E, phosphorylation of Rb and follistatin, respectively. (B) Tetrac can inhibit  $T_4$  and  $T_3$  interactions with the cell surface receptor site of integrin  $\alpha\beta3$  and blocks TH-mediated activation of MAPK/ERK1/2 by principal iodothyronines. Tetrac and resveratrol compete with the binding site on integrin  $\alpha\beta3$ , leading to blockage of cancer cell responses to TH, leading to upregulation of mRNA of EGFR, BCL2L14, CASP2, FAF1, CASP8AP2, DFFA, CBY1, p53 and TSBH1. Conversely, they downregulate CTNNA1, CTNNA2, XIAP, VEGFR, bFGF mRNA expression as well as inhibit  $\beta$ -catenin and STAT3 activation.

#### 4. TH Analogs Exert Anti-Proliferative Effects on Cancer Cells

Cancer cells display enhanced proliferation, reduced apoptosis and increased angiogenesis owing to both genomic and non-genomic actions of THs [140–142]. L-thyroxine ( $T_4$ ) is the primary thyroid hormone produced by the thyroid gland, which generates  $T_3$  via outer thyroid hormone ring deiodination at the 5' position of the diphenyl ether structure of iodothyronines [143]. An alanine side-chain modification of iodothyronine occurs at the cellular level to further generate tetraiodothyroacetic acid (Tetrac) and triiodothyroacetic acid (Triac), both of which have metabolic activities [144]. Accumulating studies have demonstrated the presence of a receptor that can bind thyroid hormone analogs on the plasma membrane of multiple cancer types and rapidly divide

endothelial cells [3,51,107], and focused on determining the functions of thyroid hormone analogs. TH derivatives have been effectively utilized to distinguish beneficial actions or deleterious effects of THs for potential therapeutic application [145–148].

#### 4.1. Tetraiodothyroacetic Acid (Tetrac)

Tetraiodothyroacetic acid (Tetrac) is an iodothyronine analog that inhibits  $T_4$  and  $T_3$  interactions with the cell surface receptor site of integrin  $\alpha v \beta 3$  and blocks TH-mediated activation of MAPK/ERK1/2 by principal iodothyronines. Tetrac competes with the binding site on integrin  $\alpha v \beta 3$ , leading to blockage of cancer cell responses to TH. In addition, in the absence of  $T_4$  and  $T_3$ , Tetrac can influence regulated coherent activities with induction of cell death, modulating the cancer cell survival pathway. Tetrac prevents the activity of  $T_4$ , thus restoring p53-dependent proapoptotic properties of cancer cells [79]. However, in the absence of  $T_4$ , Tetrac does not influence the activity of stilbene resveratrol, which initiates p53-dependent apoptosis through integrin  $\alpha v \beta 3$  in cancer cells [84]. Additionally, exposure of the estrogen receptor-negative human breast cancer cell line, MDA-MB-231, and medullary thyroid cancer cells, to unmodified Tetrac and nanoparticulate Tetrac (Nanotetrac), which is specifically covalently bound, revealed differential involvement in cancer survival and apoptosis pathways based on effects on gene transcription determined via microarray [149,150]. Tetrac treatment of MDA-MB-231 cells led to both downregulation of the apoptosis inhibitor, XIAP, and increased levels of the angiogenesis inhibitor, thrombospondin 1 (THBS1). On the other hand, Tetrac induced a significant increase in FAF1, CASP8AP2, DFFA, and CASP2 mRNA levels and inhibition of the angiogenic and metastatic effects of vascular endothelial growth factor (VEGFR) and basic fibroblast growth factor (bFGF) in cancer [151,152] (Figure 5B). Moreover, increased levels of CBY1, which inhibits  $\beta$ -catenin function in the nucleus, were observed in the presence of Tetrac [149,150]. Tetrac could directly modulate  $\beta$ -catenin abundance in the cell through downregulation of CTNNA1 and CTNNA2 mRNA (Figure 5B). According to a number of earlier studies,  $\beta$ -catenins are involved in cell-cell adhesion. However, mutation and overexpression of  $\beta$ -catenins occur in various cancer types, including colorectal carcinoma and breast and ovarian cancers [153,154]. In addition, mutation of one of the catenin genes, CTNNA1, which functions as a tumor suppressor in normal conditions, leads to susceptibility to gastrointestinal tract cancers [155], and mutation of the other catenin gene, CTNNA2, is associated with tumor invasiveness [156]. Nanotetrac is excluded from the cell interior, and inhibits cancer cell proliferation induced by thyroid hormone more effectively than unmodified Tetrac [63]. mRNA expression of anti-apoptotic MCL-1 is reduced and apoptosis-promoting CASP2, BCL2L14, and EGFR levels increased by Nanotetrac [63] (Figure 5B). In particular, Nanotetrac downregulates nine genes involved in the cell cycle, one of which is cyclin-dependent kinase gene, along with >20 oncogenes, including Ras family members [63,149]. Nanotetrac also influences tumor invasion, angiogenesis, and metastasis via regulation of matrix metalloproteinase-2 (MMP-2) whose major function is blockage of STAT3 activation by the thyroid hormone [157–159] (Figure 5B). The collective studies to date indicate that Tetrac modulates a series of genes involved in cancer cell proliferation, apoptosis and angiogenesis via inhibition of  $T_4$  and  $T_3$  actions on integrin  $\alpha v \beta 3$ .

#### 4.2. Triiodothyroacetic Acid (Triac)

Tetraiodothyroacetic acid (Tetrac) and 3,3',5-triiodothyroacetic acid (Triac), acetic acid analogs of THs, have similar structures with thyromimetic activity in the nucleus [160]. Earlier in vitro findings suggest that Triac binding affinity is better than that of  $T_3$  for both normal TR $\alpha$ 1 and TR $\beta$  (~three-fold) [161]. Studies on dominant-negative mutants of TR $\beta$  in cancer have confirmed that Triac is more powerful than  $T_3$ , i.e., Triac can overcome the dominant-negative effects of TR $\beta$  mutations [161]. Triac initiates apoptosis in human ovarian cancer cells via non-genomic actions through effects on integrin  $\alpha v \beta 3$  and does not influence mitochondria in tumor cells [162]. Nevertheless, the mechanisms by which Triac modulates genomic effects within cancer cells remain to be established. Triac does not interact with genetically modified TR $\beta$ . Genetically modified TR $\beta$  is trafficked between the



cytoplasm and nucleus in cancer cells in the presence or absence of T<sub>3</sub> and Triac; models can detect endocrine-disrupting chemicals (EDCs) that are a major health concern [163]. Long-term studies using non-cancer cells [164] have shown that Triac binds TR and can be used to clinically treat some forms of thyroid hormone resistance (THS) due to hypersecretion of TSH through elevating transport across the plasma membrane of normal cells [165–175]. However, the majority of findings to date suggest a significant reduction in basal TRH-stimulated TSH levels and serum-free T<sub>4</sub> and T<sub>3</sub> levels. In normal and hypothyroid patients, treatment with Triac led to inhibition of TSH synthesis and secretion without inducing changes in peripheral tissue metabolic effects, such as weight, heart rate, reflex time or serum concentrations of cholesterol or triglycerides [175]. Triac modulates normal growth and bone maturation in children with peripheral thyrotoxic features (pituitary RTH (PRT)) owing to genetic mutation of TR $\beta$  (TR $\beta$ 1) at exon 10 position 1642 (C to A) that generates the amino acid codon change, P453T. TR $\beta$ 1 mutation led to significantly reduced T<sub>3</sub> binding affinity. However, upon long-term treatment with Triac, normal heart rate, neurological and clinical signs were maintained in children. These findings suggest that administration of long-term Triac therapy in childhood is safe and efficacious for PRT [167]. However, no influence on thyroid hormone function after discontinuation of Triac was reported in a proportion of patients, leading to reservations on the specificity of the compound.

## 5. Conclusions

Interactions between nuclear receptors and corresponding ligands that elicit critical molecular pathways have been verified in both normal and cancer cells [4]. This review provides an overview on the individual mechanisms underlying physiological TH/TR-mediated regulation of different cancer types. TRs have been detected in the majority of organs. The mRNAs (THRA and THRB) of TRs generated via alternative splicing produce different isoforms that exert specific physiological effects on the organs [176–178]. Additionally, thyroid hormones and TRs play important regulatory roles in physiological processes via actions on intracellular and extracellular proteins and activate various genomic or non-genomic functions including cellular growth, embryonic development, differentiation, metabolism, and proliferation. In normal cells and tissues, both T<sub>4</sub> and T<sub>3</sub> modulate skeletal development, bone turnover and maintenance and metabolism of organs [2,143]. T<sub>4</sub> is a potent thyroid hormone with proliferation-enhancing activity in cancer cells that interacts with  $\alpha$ v $\beta$ 3 integrin, which may serve as a potential target for inhibition of cancer proliferation. T<sub>4</sub>- $\alpha$ v $\beta$ 3 inhibitors are not particularly efficacious and currently under preclinical analysis for treatment of a few cancer types. However, when disruption of TH signaling induces downstream target gene dysregulation or dysfunction, several organ diseases are initiated. Clinical researchers have suggested that TH/TRs promote proliferation of multiple cancer types including breast cancer, thyroid cancer, lung cancer, brain tumor, liver cancer, and colorectal cancer. In epidemiologic analyses, the risk of ovarian cancer development was shown to be almost double in patients with a history of hyperthyroidism. Moreover, risk was increased about two-fold for patients with pancreatic and prostate cancer with a history of hyperthyroidism. Both hyperthyroidism and hypothyroidism are known to influence the physiological processes underlying cancer. THs stimulate tumor growth and metastasis *in vivo* while hypothyroidism may be associated with inhibition of tumor proliferation and development. These findings collectively suggest that induction of hyperthyroidism is associated with progression of multiple cancer types. However, cancer progression pathways present considerable variability and complexity, and therefore, therapy utilizing THs/TRs continues to present several unknown challenges. Additionally, THs have not yet been established as a clinical risk factor or prognostic factor for cancer, partly due to their involvement in numerous physiological mechanisms, leading to conflicting experimental data over several years of research. The finding that different TR isoforms are involved in various tumor types and stages of development supports a dual role of TRs in human cancers, either as an oncogene or a tumor suppressor. However, this hypothesis remains to be investigated in detail. Further studies are required to establish the specific functions of TH/TR in cancers of different molecular backgrounds and stages.

**Author Contributions:** The conceptualization, Y.-C.L. and K.-H.L.; investigation, Y.-C.L.; writing—original draft preparation, Y.-C.L.; writing—review and editing, Y.-C.L. and K.-H.L.; visualization, Y.-C.L.; supervision, K.-H.L.; funding acquisition, C.-T.Y. and K.-H.L.

**Funding:** This research was funded by grants from Chang Gung Memorial Hospital, Taoyuan, Taiwan (CMRPD1G0421, CMRPD1G0422, CMRPD1G0423, CMRPD1J0051, NMRPD1G0941-1G0943, and NMRPD1G0951-1G0953 to K. H. Lin) and from the Ministry of Science and Technology of the Republic of China (MOST 106-2320-B-182-031-MY3 and 106-2320-B-182-032-MY3 to K.H. Lin). And The APC was funded by Chang Gung Memorial Hospital, Taoyuan, Taiwan.

**Conflicts of Interest:** The authors declare no conflict of interest.

## References

- Chi, H.C.; Chen, C.Y.; Tsai, M.M.; Tsai, C.Y.; Lin, K.H. Molecular functions of thyroid hormones and their clinical significance in liver-related diseases. *Biomed. Res. Int.* **2013**, *2013*, 601361. [\[CrossRef\]](#) [\[PubMed\]](#)
- Bassett, J.H.; Williams, G.R. Role of Thyroid Hormones in Skeletal Development and Bone Maintenance. *Endocr. Rev.* **2016**, *37*, 135–187. [\[CrossRef\]](#) [\[PubMed\]](#)
- Davis, P.J.; Goglia, F.; Leonard, J.L. Nongenomic actions of thyroid hormone. *Nat. Rev. Endocrinol.* **2016**, *12*, 111–121. [\[CrossRef\]](#) [\[PubMed\]](#)
- Aranda, A.; Pascual, A. Nuclear hormone receptors and gene expression. *Physiol. Rev.* **2001**, *81*, 1269–1304. [\[CrossRef\]](#) [\[PubMed\]](#)
- Chi, H.C.; Tsai, C.Y.; Tsai, M.M.; Yeh, C.T.; Lin, K.H. Molecular functions and clinical impact of thyroid hormone-triggered autophagy in liver-related diseases. *J. Biomed. Sci.* **2019**, *26*, 24. [\[CrossRef\]](#) [\[PubMed\]](#)
- Davies, T.F.; Ando, T.; Lin, R.Y.; Tomer, Y.; Latif, R. Thyrotropin receptor-associated diseases: from adenomata to Graves disease. *J. Clin. Invest.* **2005**, *115*, 1972–1983. [\[CrossRef\]](#) [\[PubMed\]](#)
- Visser, W.E.; Friesema, E.C.; Visser, T.J. Minireview: thyroid hormone transporters: the knowns and the unknowns. *Mol. Endocrinol.* **2011**, *25*, 1–14. [\[CrossRef\]](#) [\[PubMed\]](#)
- Brix, K.; Fuhrer, D.; Biebertmann, H. Molecules important for thyroid hormone synthesis and action - known facts and future perspectives. *Thyroid Res.* **2011**, *4* (Suppl 1), S9. [\[CrossRef\]](#)
- Friesema, E.C.; Jansen, J.; Jachtenberg, J.W.; Visser, W.E.; Kester, M.H.; Visser, T.J. Effective cellular uptake and efflux of thyroid hormone by human monocarboxylate transporter 10. *Mol. Endocrinol.* **2008**, *22*, 1357–1369. [\[CrossRef\]](#) [\[PubMed\]](#)
- Bernal, J. Thyroid hormone receptors in brain development and function. *Nat. Clin. Pract. Endocrinol. Metab.* **2007**, *3*, 249–259. [\[CrossRef\]](#)
- Bassett, J.H.; Williams, G.R. Critical role of the hypothalamic-pituitary-thyroid axis in bone. *Bone* **2008**, *43*, 418–426. [\[CrossRef\]](#) [\[PubMed\]](#)
- Cheng, S.Y. Multiple mechanisms for regulation of the transcriptional activity of thyroid hormone receptors. *Rev. Endocr. Metab. Disord.* **2000**, *1*, 9–18. [\[CrossRef\]](#) [\[PubMed\]](#)
- Larsen, P.R. Thyroid hormone analogs and metabolites: new applications for an old hormone? *Nat. Clin. Pract. Endocrinol. Metab.* **2009**, *5*, 1. [\[CrossRef\]](#) [\[PubMed\]](#)
- Oppenheimer, J.H.; Schwartz, H.L.; Surks, M.I. Nuclear binding capacity appears to limit the hepatic response to L-triiodothyronine (T3). *Endocr. Res. Commun.* **1975**, *2*, 309–325. [\[CrossRef\]](#) [\[PubMed\]](#)
- Yen, P.M. Physiological and molecular basis of thyroid hormone action. *Physiol. Rev.* **2001**, *81*, 1097–1142. [\[CrossRef\]](#) [\[PubMed\]](#)
- Shao, D.L.; Lazar, M.A. Modulating nuclear receptor function: may the phos be with you. *J. Clin. Investig.* **1999**, *103*, 1617–1618. [\[CrossRef\]](#) [\[PubMed\]](#)
- Mitsuhashi, T.; Tennyson, G.E.; Nikodem, V.M. Alternative splicing generates messages encoding rat c-erbA proteins that do not bind thyroid hormone. *Proc. Natl. Acad. Sci. USA* **1988**, *85*, 5804–5808. [\[CrossRef\]](#)
- Sakurai, A.; Nakai, A.; DeGroot, L.J. Expression of three forms of thyroid hormone receptor in human tissues. *Mol. Endocrinol.* **1989**, *3*, 392–399. [\[CrossRef\]](#)
- Jones, I.; Ng, L.; Liu, H.; Forrest, D. An intron control region differentially regulates expression of thyroid hormone receptor beta2 in the cochlea, pituitary, and cone photoreceptors. *Mol. Endocrinol.* **2007**, *21*, 1108–1119. [\[CrossRef\]](#)
- Williams, G.R. Cloning and characterization of two novel thyroid hormone receptor beta isoforms. *Mol. Cell Biol.* **2000**, *20*, 8329–8342. [\[CrossRef\]](#)

21. Ying, H.; Suzuki, H.; Zhao, L.; Willingham, M.C.; Meltzer, P.; Cheng, S.Y. Mutant thyroid hormone receptor beta represses the expression and transcriptional activity of peroxisome proliferator-activated receptor gamma during thyroid carcinogenesis. *Cancer Res.* **2003**, *63*, 5274–5280. [[PubMed](#)]
22. Pascual, A.; Aranda, A. Thyroid hormone receptors, cell growth and differentiation. *Biochim Biophys Acta* **2013**, *1830*, 3908–3916. [[CrossRef](#)] [[PubMed](#)]
23. Perlmann, T.; Rangarajan, P.N.; Umesono, K.; Evans, R.M. Determinants for selective RAR and TR recognition of direct repeat HREs. *Genes Dev.* **1993**, *7*, 1411–1422. [[CrossRef](#)]
24. Yen, P.M.; Ikeda, M.; Wilcox, E.C.; Brubaker, J.H.; Spanjaard, R.A.; Sugawara, A.; Chin, W.W. Half-site arrangement of hybrid glucocorticoid and thyroid hormone response elements specifies thyroid hormone receptor complex binding to DNA and transcriptional activity. *J. Biol. Chem.* **1994**, *269*, 12704–12709.
25. Mangelsdorf, D.J.; Evans, R.M. The RXR heterodimers and orphan receptors. *Cell* **1995**, *83*, 841–850. [[CrossRef](#)]
26. Horlein, A.J.; Naar, A.M.; Heinzel, T.; Torchia, J.; Gloss, B.; Kurokawa, R.; Ryan, A.; Kamei, Y.; Soderstrom, M.; Glass, C.K. Ligand-independent repression by the thyroid hormone receptor mediated by a nuclear receptor co-repressor. *Nature* **1995**, *377*, 397–404. [[CrossRef](#)] [[PubMed](#)]
27. Perissi, V.; Staszewski, L.M.; McInerney, E.M.; Kurokawa, R.; Krones, A.; Rose, D.W.; Lambert, M.H.; Milburn, M.V.; Glass, C.K.; Rosenfeld, M.G. Molecular determinants of nuclear receptor-corepressor interaction. *Genes Dev.* **1999**, *13*, 3198–3208. [[CrossRef](#)]
28. Struhl, K. Histone acetylation and transcriptional regulatory mechanisms. *Genes Dev.* **1998**, *12*, 599–606. [[CrossRef](#)]
29. Tyler, J.K.; Kadonaga, J.T. The "dark side" of chromatin remodeling: repressive effects on transcription. *Cell* **1999**, *99*, 443–446. [[CrossRef](#)]
30. Knoepfler, P.S.; Eisenman, R.N. Sin meets NuRD and other tails of repression. *Cell* **1999**, *99*, 447–450. [[CrossRef](#)]
31. Heinzel, T.; Lavinsky, R.M.; Mullen, T.M.; Soderstrom, M.; Laherty, C.D.; Torchia, J.; Yang, W.M.; Brard, G.; Ngo, S.D.; Davie, J.R.; et al. A complex containing N-CoR, mSin3 and histone deacetylase mediates transcriptional repression. *Nature* **1997**, *387*, 43–48. [[CrossRef](#)] [[PubMed](#)]
32. Nagy, L.; Kao, H.Y.; Chakravarti, D.; Lin, R.J.; Hassig, C.A.; Ayer, D.E.; Schreiber, S.L.; Evans, R.M. Nuclear receptor repression mediated by a complex containing SMRT, mSin3A, and histone deacetylase. *Cell* **1997**, *89*, 373–380. [[CrossRef](#)]
33. Guenther, M.G.; Lane, W.S.; Fischle, W.; Verdin, E.; Lazar, M.A.; Shiekhata, R. A core SMRT corepressor complex containing HDAC3 and TBL1, a WD40-repeat protein linked to deafness. *Genes Dev.* **2000**, *14*, 1048–1057. [[PubMed](#)]
34. Fondell, J.D.; Ge, H.; Roeder, R.G. Ligand induction of a transcriptionally active thyroid hormone receptor coactivator complex. *Proc. Natl. Acad. Sci. USA* **1996**, *93*, 8329–8333. [[CrossRef](#)] [[PubMed](#)]
35. Fondell, J.D.; Guermah, M.; Malik, S.; Roeder, R.G. Thyroid hormone receptor-associated proteins and general positive cofactors mediate thyroid hormone receptor function in the absence of the TATA box-binding protein-associated factors of TFIID. *Proc. Natl. Acad. Sci. USA* **1999**, *96*, 1959–1964. [[CrossRef](#)] [[PubMed](#)]
36. Chen, D.; Ma, H.; Hong, H.; Koh, S.S.; Huang, S.M.; Schurter, B.T.; Aswad, D.W.; Stallcup, M.R. Regulation of transcription by a protein methyltransferase. *Science* **1999**, *284*, 2174–2177. [[CrossRef](#)] [[PubMed](#)]
37. Onate, S.A.; Tsai, S.Y.; Tsai, M.J.; O'Malley, B.W. Sequence and characterization of a coactivator for the steroid hormone receptor superfamily. *Science* **1995**, *270*, 1354–1357. [[CrossRef](#)] [[PubMed](#)]
38. Webb, P.; Nguyen, P.; Shinsako, J.; Anderson, C.; Feng, W.; Nguyen, M.P.; Chen, D.; Huang, S.M.; Subramanian, S.; McKinerney, E.; et al. Estrogen receptor activation function 1 works by binding p160 coactivator proteins. *Mol. Endocrinol.* **1998**, *12*, 1605–1618. [[CrossRef](#)] [[PubMed](#)]
39. Leo, C.; Chen, J.D. The SRC family of nuclear receptor coactivators. *Gene* **2000**, *245*, 1–11. [[CrossRef](#)]
40. Heery, D.M.; Kalkhoven, E.; Hoare, S.; Parker, M.G. A signature motif in transcriptional co-activators mediates binding to nuclear receptors. *Nature* **1997**, *387*, 733–736. [[CrossRef](#)]
41. Leers, J.; Treuter, E.; Gustafsson, J.A. Mechanistic principles in NR box-dependent interaction between nuclear hormone receptors and the coactivator TIF2. *Mol. Cell. Biol.* **1998**, *18*, 6001–6013. [[CrossRef](#)] [[PubMed](#)]

42. McNerney, E.M.; Rose, D.W.; Flynn, S.E.; Westin, S.; Mullen, T.M.; Krones, A.; Inostroza, J.; Torchia, J.; Nolte, R.T.; Assa-Munt, N.; et al. Determinants of coactivator LXXLL motif specificity in nuclear receptor transcriptional activation. *Gene Dev.* **1998**, *12*, 3357–3368. [[CrossRef](#)] [[PubMed](#)]
43. Chen, X.Y.; Ferrington, D.A.; Bigelow, D.J.; Michaelis, E.K. Protein half-lives of two subunits of an NMDA receptor-like complex, the 71-kDa glutamate-binding and the 80-kDa CPP-binding protein. *Biochem. Biophys. Res. Co.* **1997**, *241*, 132–135. [[CrossRef](#)] [[PubMed](#)]
44. Kamei, Y.; Xu, L.; Heinzel, T.; Torchia, J.; Kurokawa, R.; Gloss, B.; Lin, S.C.; Heyman, R.A.; Rose, D.W.; Glass, C.K.; et al. A CBP integrator complex mediates transcriptional activation and AP-1 inhibition by nuclear receptors. *Cell* **1996**, *85*, 403–414. [[CrossRef](#)]
45. McKenna, N.J.; Nawaz, Z.; Tsai, S.Y.; Tsai, M.J.; O'Malley, B.W. Distinct steady-state nuclear receptor coregulator complexes exist in vivo. *Proc. Natl. Acad. Sci. USA* **1998**, *95*, 11697–11702. [[CrossRef](#)] [[PubMed](#)]
46. Takeshita, T.; Arita, T.; Asao, H.; Tanaka, N.; Higuchi, M.; Kuroda, H.; Kaneko, K.; Munakata, H.; Endo, Y.; Fujita, T.; et al. Cloning of a novel signal-transducing adaptor molecule containing an SH3 domain and ITAM. *Biochem. Biophys. Res. Co.* **1996**, *225*, 1035–1039. [[CrossRef](#)] [[PubMed](#)]
47. Rachez, C.; Gamble, M.; Chang, C.P.; Atkins, G.B.; Lazar, M.A.; Freedman, L.P. The DRIP complex and SRC-1/p160 coactivators share similar nuclear receptor binding determinants but constitute functionally distinct complexes. *Mol. Cell Biol.* **2000**, *20*, 2718–2726. [[CrossRef](#)]
48. Llopis, J.; Westin, S.; Ricote, M.; Wang, Z.; Cho, C.Y.; Kurokawa, R.; Mullen, T.M.; Rose, D.W.; Rosenfeld, M.G.; Tsien, R.Y.; et al. Ligand-dependent interactions of coactivators steroid receptor coactivator-1 and peroxisome proliferator-activated receptor binding protein with nuclear hormone receptors can be imaged in live cells and are required for transcription. *Proc. Natl. Acad. Sci. USA* **2000**, *97*, 4363–4368. [[CrossRef](#)]
49. Siegrist-Kaiser, C.A.; Juge-Aubry, C.; Tranter, M.P.; Ekenbarger, D.M.; Leonard, J.L. Thyroxine-dependent modulation of actin polymerization in cultured astrocytes. A novel, extranuclear action of thyroid hormone. *J. Biol. Chem.* **1990**, *265*, 5296–5302.
50. Sterling, K.; Brenner, M.A.; Sakurada, T. Rapid effect of triiodothyronine on the mitochondrial pathway in rat liver in vivo. *Science* **1980**, *210*, 340–342. [[CrossRef](#)]
51. Bergh, J.J.; Lin, H.Y.; Lansing, L.; Mohamed, S.N.; Davis, F.B.; Mousa, S.; Davis, P.J. Integrin  $\alpha$ V $\beta$ 3 contains a cell surface receptor site for thyroid hormone that is linked to activation of mitogen-activated protein kinase and induction of angiogenesis. *Endocrinology* **2005**, *146*, 2864–2871. [[CrossRef](#)] [[PubMed](#)]
52. Plow, E.F.; Haas, T.A.; Zhang, L.; Loftus, J.; Smith, J.W. Ligand binding to integrins. *J. Biol. Chem.* **2000**, *275*, 21785–21788. [[CrossRef](#)] [[PubMed](#)]
53. Lin, H.Y.; Cody, V.; Davis, F.B.; Hercbergs, A.A.; Luidens, M.K.; Mousa, S.A.; Davis, P.J. Identification and functions of the plasma membrane receptor for thyroid hormone analogues. *Discov. Med.* **2011**, *11*, 337–347. [[PubMed](#)]
54. Davis, P.J.; Davis, F.B.; Mousa, S.A.; Luidens, M.K.; Lin, H.Y. Membrane receptor for thyroid hormone: physiologic and pharmacologic implications. *Annu. Rev. Pharmacol. Toxicol.* **2011**, *51*, 99–115. [[CrossRef](#)] [[PubMed](#)]
55. Lin, H.Y.; Shih, A.; Davis, F.B.; Davis, P.J. Thyroid hormone promotes the phosphorylation of STAT3 and potentiates the action of epidermal growth factor in cultured cells. *Biochem. J.* **1999**, *338 Pt 2*, 427–432. [[CrossRef](#)]
56. Cao, H.J.; Lin, H.Y.; Luidens, M.K.; Davis, F.B.; Davis, P.J. Cytoplasm-to-nucleus shuttling of thyroid hormone receptor-beta1 (Trbeta1) is directed from a plasma membrane integrin receptor by thyroid hormone. *Endocr. Res.* **2009**, *34*, 31–42. [[CrossRef](#)] [[PubMed](#)]
57. Lin, H.Y.; Sun, M.; Tang, H.Y.; Lin, C.; Luidens, M.K.; Mousa, S.A.; Incerpi, S.; Drusano, G.L.; Davis, F.B.; Davis, P.J. L-Thyroxine vs. 3,5,3'-triiodo-L-thyronine and cell proliferation: activation of mitogen-activated protein kinase and phosphatidylinositol 3-kinase. *Am. J. Physiol. Cell Physiol.* **2009**, *296*, C980–C991. [[CrossRef](#)] [[PubMed](#)]
58. Davis, P.J.; Lin, H.Y.; Mousa, S.A.; Luidens, M.K.; Hercbergs, A.A.; Wehling, M.; Davis, F.B. Overlapping nongenomic and genomic actions of thyroid hormone and steroids. *Steroids* **2011**, *76*, 829–833. [[CrossRef](#)] [[PubMed](#)]
59. Cao, X.; Kambe, F.; Moeller, L.C.; Refetoff, S.; Seo, H. Thyroid hormone induces rapid activation of Akt/protein kinase B-mammalian target of rapamycin-p70S6K cascade through phosphatidylinositol 3-kinase in human fibroblasts. *Mol. Endocrinol.* **2005**, *19*, 102–112. [[CrossRef](#)] [[PubMed](#)]



60. Moeller, L.C.; Cao, X.; Dumitrescu, A.M.; Seo, H.; Refetoff, S. Thyroid hormone mediated changes in gene expression can be initiated by cytosolic action of the thyroid hormone receptor beta through the phosphatidylinositol 3-kinase pathway. *Nucl. Recept. Signal.* **2006**, *4*, e020. [[CrossRef](#)] [[PubMed](#)]
61. Moeller, L.C.; Dumitrescu, A.M.; Refetoff, S. Cytosolic action of thyroid hormone leads to induction of hypoxia-inducible factor-1alpha and glycolytic genes. *Mol. Endocrinol.* **2005**, *19*, 2955–2963. [[CrossRef](#)] [[PubMed](#)]
62. Bhargava, M.; Lei, J.; Ingbar, D.H. Nongenomic actions of L-thyroxine and 3,5,3'-triiodo-L-thyronine. Focus on “L-Thyroxine vs. 3,5,3'-triiodo-L-thyronine and cell proliferation: Activation of mitogen-activated protein kinase and phosphatidylinositol 3-kinase”. *Am. J. Physiol. Cell Physiol.* **2009**, *296*, C977–C979. [[CrossRef](#)] [[PubMed](#)]
63. Davis, P.J.; Glinesky, G.V.; Lin, H.Y.; Leith, J.T.; Hercbergs, A.; Tang, H.Y.; Ashur-Fabian, O.; Incerpi, S.; Mousa, S.A. Cancer Cell Gene Expression Modulated from Plasma Membrane Integrin alphavbeta3 by Thyroid Hormone and Nanoparticulate Tetrac. *Front. Endocrinol. (Lausanne)* **2014**, *5*, 240. [[CrossRef](#)] [[PubMed](#)]
64. Wang, C.S.; Lin, K.H.; Hsu, Y.C. Alterations of thyroid hormone receptor alpha gene: frequency and association with Nm23 protein expression and metastasis in gastric cancer. *Cancer Lett.* **2002**, *175*, 121–127. [[CrossRef](#)]
65. Lu, C.; Mishra, A.; Zhu, Y.J.; Meltzer, P.; Cheng, S.Y. Global expression profiling reveals gain-of-function oncogenic activity of a mutated thyroid hormone receptor in thyroid carcinogenesis. *Am. J. Cancer Res.* **2011**, *1*, 168–191. [[PubMed](#)]
66. Lu, C.; Zhu, X.; Willingham, M.C.; Cheng, S.Y. Activation of tumor cell proliferation by thyroid hormone in a mouse model of follicular thyroid carcinoma. *Oncogene* **2012**, *31*, 2007–2016. [[CrossRef](#)] [[PubMed](#)]
67. Park, J.W.; Zhao, L.; Cheng, S.Y. Inhibition of estrogen-dependent tumorigenesis by the thyroid hormone receptor beta in xenograft models. *Am. J. Cancer Res.* **2013**, *3*, 302–311.
68. Lin, K.H.; Zhu, X.G.; Shieh, H.Y.; Hsu, H.C.; Chen, S.T.; McPhie, P.; Cheng, S.Y. Identification of naturally occurring dominant negative mutants of thyroid hormone alpha 1 and beta 1 receptors in a human hepatocellular carcinoma cell line. *Endocrinology* **1996**, *137*, 4073–4081. [[CrossRef](#)]
69. Kamiya, Y.; Puzianowska-Kuznicka, M.; McPhie, P.; Nauman, J.; Cheng, S.Y.; Nauman, A. Expression of mutant thyroid hormone nuclear receptors is associated with human renal clear cell carcinoma. *Carcinogenesis* **2002**, *23*, 25–33. [[CrossRef](#)]
70. Heublein, S.; Mayr, D.; Meindl, A.; Angele, M.; Gallwas, J.; Jeschke, U.; Ditsch, N. Thyroid Hormone Receptors Predict Prognosis in BRCA1 Associated Breast Cancer in Opposing Ways. *PloS ONE* **2015**, *10*. [[CrossRef](#)]
71. Plateroti, M.; Kress, E.; Mori, J.I.; Samarut, J. Thyroid hormone receptor alpha1 directly controls transcription of the beta-catenin gene in intestinal epithelial cells. *Mol. Cell Biol.* **2006**, *26*, 3204–3214. [[CrossRef](#)] [[PubMed](#)]
72. Hellevik, A.I.; Asvold, B.O.; Bjoro, T.; Romundstad, P.R.; Nilsen, T.I.; Vatten, L.J. Thyroid function and cancer risk: a prospective population study. *Cancer Epidemiol. Biomarkers Prev.* **2009**, *18*, 570–574. [[CrossRef](#)] [[PubMed](#)]
73. Moeller, L.C.; Fuhrer, D. Thyroid hormone, thyroid hormone receptors, and cancer: a clinical perspective. *Endocr. Relat. Cancer* **2013**, *20*, R19–R29. [[CrossRef](#)] [[PubMed](#)]
74. Cristofanilli, M.; Yamamura, Y.; Kau, S.W.; Bevers, T.; Strom, S.; Patangan, M.; Hsu, L.; Krishnamurthy, S.; Theriault, R.L.; Hortobagyi, G.N. Thyroid hormone and breast carcinoma. Primary hypothyroidism is associated with a reduced incidence of primary breast carcinoma. *Cancer-Am. Cancer Soc.* **2005**, *103*, 1122–1128. [[CrossRef](#)]
75. Tang, H.Y.; Lin, H.Y.; Zhang, S.; Davis, F.B.; Davis, P.J. Thyroid hormone causes mitogen-activated protein kinase-dependent phosphorylation of the nuclear estrogen receptor. *Endocrinology* **2004**, *145*, 3265–3272. [[CrossRef](#)] [[PubMed](#)]
76. Sar, P.; Peter, R.; Rath, B.; Das Mohapatra, A.; Mishra, S.K. 3, 3'5 Triiodo L thyronine induces apoptosis in human breast cancer MCF-7 cells, repressing SMP30 expression through negative thyroid response elements. *PLoS ONE* **2011**, *6*, e20861. [[CrossRef](#)] [[PubMed](#)]
77. Gonzalez-Sancho, J.M.; Figueroa, A.; Lopez-Barahona, M.; Lopez, E.; Beug, H.; Munoz, A. Inhibition of proliferation and expression of T1 and cyclin D1 genes by thyroid hormone in mammary epithelial cells. *Mol. Carcinog.* **2002**, *34*, 25–34. [[CrossRef](#)] [[PubMed](#)]



78. Guigon, C.J.; Kim, D.W.; Willingham, M.C.; Cheng, S.Y. Mutation of thyroid hormone receptor-beta in mice predisposes to the development of mammary tumors. *Oncogene* **2011**, *30*, 3381–3390. [[CrossRef](#)]
79. Lin, H.Y.; Tang, H.Y.; Shih, A.; Keating, T.; Cao, G.; Davis, P.J.; Davis, F.B. Thyroid hormone is a MAPK-dependent growth factor for thyroid cancer cells and is anti-apoptotic. *Steroids* **2007**, *72*, 180–187. [[CrossRef](#)]
80. Furuya, F.; Lu, C.; Willingham, M.C.; Cheng, S.Y. Inhibition of phosphatidylinositol 3-kinase delays tumor progression and blocks metastatic spread in a mouse model of thyroid cancer. *Carcinogenesis* **2007**, *28*, 2451–2458. [[CrossRef](#)]
81. Meng, R.; Tang, H.Y.; Westfall, J.; London, D.; Cao, J.H.; Mousa, S.A.; Luidens, M.; Hercbergs, A.; Davis, F.B.; Davis, P.J.; et al. Crosstalk between integrin  $\alpha$ v $\beta$ 3 and estrogen receptor- $\alpha$  is involved in thyroid hormone-induced proliferation in human lung carcinoma cells. *PLoS ONE* **2011**, *6*, e27547. [[CrossRef](#)] [[PubMed](#)]
82. Davis, F.B.; Tang, H.Y.; Shih, A.; Keating, T.; Lansing, L.; Hercbergs, A.; Fenstermaker, R.A.; Mousa, A.; Mousa, S.A.; Davis, P.J.; et al. Acting via a cell surface receptor, thyroid hormone is a growth factor for glioma cells. *Cancer Res.* **2006**, *66*, 7270–7275. [[CrossRef](#)] [[PubMed](#)]
83. Hercbergs, A.; Johnson, R.E.; Ashur-Fabian, O.; Garfield, D.H.; Davis, P.J. Medically induced euthyroid hypothyroxinemia may extend survival in compassionate need cancer patients: an observational study. *Oncologist* **2015**, *20*, 72–76. [[CrossRef](#)] [[PubMed](#)]
84. Lin, H.Y.; Tang, H.Y.; Keating, T.; Wu, Y.H.; Shih, A.; Hammond, D.; Sun, M.; Hercbergs, A.; Davis, F.B.; Davis, P.J. Resveratrol is pro-apoptotic and thyroid hormone is anti-apoptotic in glioma cells: both actions are integrin and ERK mediated. *Carcinogenesis* **2008**, *29*, 62–69. [[CrossRef](#)] [[PubMed](#)]
85. Hwang, S.L.; Lin, C.L.; Lieu, A.S.; Hwang, Y.F.; Howng, S.L.; Hong, Y.R.; Chang, D.S.; Lee, K.S. The expression of thyroid hormone receptor isoforms in human astrocytomas. *Surg. Neurol.* **2008**, *70* (Suppl 1), S4–S8, discussion S1:8. [[CrossRef](#)] [[PubMed](#)]
86. Yen, C.C.; Huang, Y.H.; Liao, C.Y.; Liao, C.J.; Cheng, W.L.; Chen, W.J.; Lin, K.H. Mediation of the inhibitory effect of thyroid hormone on proliferation of hepatoma cells by transforming growth factor-beta. *J. Mol. Endocrinol.* **2006**, *36*, 9–21. [[CrossRef](#)] [[PubMed](#)]
87. Lin, Y.H.; Huang, Y.H.; Wu, M.H.; Wu, S.M.; Chi, H.C.; Liao, C.J.; Chen, C.Y.; Tseng, Y.H.; Tsai, C.Y.; Tsai, M.M.; et al. Thyroid hormone suppresses cell proliferation through endoglin-mediated promotion of p21 stability. *Oncogene* **2013**, *32*, 3904–3914. [[CrossRef](#)]
88. Mishkin, S.Y.; Pollack, R.; Yalovsky, M.A.; Morris, H.P.; Mishkin, S. Inhibition of local and metastatic hepatoma growth and prolongation of survival after induction of hypothyroidism. *Cancer Res.* **1981**, *41*, 3040–3045.
89. Chi, H.C.; Liao, C.H.; Huang, Y.H.; Wu, S.M.; Tsai, C.Y.; Liao, C.J.; Tseng, Y.H.; Lin, Y.H.; Chen, C.Y.; Chung, I.H.; et al. Thyroid hormone receptor inhibits hepatoma cell migration through transcriptional activation of Dickkopf 4. *Biochem. Biophys. Res. Commun.* **2013**, *439*, 60–65. [[CrossRef](#)]
90. Ventura-Holman, T.; Mamoon, A.; Subauste, M.C.; Subauste, J.S. The effect of oncoprotein v-erbA on thyroid hormone-regulated genes in hepatocytes and their potential role in hepatocellular carcinoma. *Mol. Biol. Rep.* **2011**, *38*, 1137–1144. [[CrossRef](#)]
91. Chung, I.H.; Chen, C.Y.; Lin, Y.H.; Chi, H.C.; Huang, Y.H.; Tai, P.J.; Liao, C.J.; Tsai, C.Y.; Lin, S.L.; Wu, M.H.; et al. Thyroid hormone-mediated regulation of lipocalin 2 through the Met/FAK pathway in liver cancer. *Oncotarget* **2015**, *6*, 15050–15064. [[CrossRef](#)] [[PubMed](#)]
92. Wang, T.; Xia, L.; Ma, S.; Qi, X.; Li, Q.; Xia, Y.; Tang, X.; Cui, D.; Wang, Z.; Chi, J.; et al. Hepatocellular carcinoma: thyroid hormone promotes tumorigenicity through inducing cancer stem-like cell self-renewal. *Sci. Rep.* **2016**, *6*, 25183. [[CrossRef](#)] [[PubMed](#)]
93. Gnoni, G.V.; Rochira, A.; Leone, A.; Damiano, F.; Marsigliante, S.; Siculella, L. 3,5,3'-triiodo-L-thyronine induces SREBP-1 expression by non-genomic actions in human HEP G2 cells. *J. Cell Physiol.* **2012**, *227*, 2388–2397. [[CrossRef](#)] [[PubMed](#)]
94. Liao, C.H.; Yeh, C.T.; Huang, Y.H.; Wu, S.M.; Chi, H.C.; Tsai, M.M.; Tsai, C.Y.; Liao, C.J.; Tseng, Y.H.; Lin, Y.H.; et al. Dickkopf 4 positively regulated by the thyroid hormone receptor suppresses cell invasion in human hepatoma cells. *Hepatology* **2012**, *55*, 910–920. [[CrossRef](#)] [[PubMed](#)]

95. Chin, Y.T.; Hsieh, M.T.; Yang, S.H.; Tsai, P.W.; Wang, S.H.; Wang, C.C.; Lee, Y.S.; Cheng, G.Y.; HuangFu, W.C.; London, D.; et al. Anti-proliferative and gene expression actions of resveratrol in breast cancer cells in vitro. *Oncotarget* **2014**, *5*, 12891–12907. [[CrossRef](#)] [[PubMed](#)]
96. Lee, Y.S.; Chin, Y.T.; Yang, Y.S.H.; Wei, P.L.; Wu, H.C.; Shih, A.; Lu, Y.T.; Pedersen, J.Z.; Incerpi, S.; Liu, L.F.; et al. The combination of tetraiodothyroacetic acid and cetuximab inhibits cell proliferation in colorectal cancers with different K-ras status. *Steroids* **2016**, *111*, 63–70. [[CrossRef](#)] [[PubMed](#)]
97. Dentice, M.; Luongo, C.; Ambrosio, R.; Sibilio, A.; Casillo, A.; Iaccarino, A.; Troncone, G.; Fenzi, G.; Larsen, P.R.; Salvatore, D. beta-Catenin regulates deiodinase levels and thyroid hormone signaling in colon cancer cells. *Gastroenterology* **2012**, *143*, 1037–1047. [[CrossRef](#)] [[PubMed](#)]
98. Kress, E.; Skah, S.; Sirakov, M.; Nadjar, J.; Gadot, N.; Scoazec, J.Y.; Samarut, J.; Plateroti, M. Cooperation between the thyroid hormone receptor TRalpha1 and the WNT pathway in the induction of intestinal tumorigenesis. *Gastroenterology* **2010**, *138*, 1863–1874. [[CrossRef](#)]
99. Glushakov, R.I.; Proshin, S.N.; Tapil'skaya, N.I. The incidence of breast tumor during experimental hyperthyroidism. *Bull. Exp. Biol. Med.* **2013**, *156*, 245–247. [[CrossRef](#)]
100. Conde, S.J.; Luvizotto Rde, A.; de Sibio, M.T.; Nogueira, C.R. Thyroid hormone status interferes with estrogen target gene expression in breast cancer samples in menopausal women. *ISRN Endocrinol.* **2014**, *2014*, 317398. [[CrossRef](#)] [[PubMed](#)]
101. Saraiva, P.P.; Figueiredo, N.B.; Padovani, C.R.; Brentani, M.M.; Nogueira, C.R. Profile of thyroid hormones in breast cancer patients. *Braz. J. Med. Biol. Res.* **2005**, *38*, 761–765. [[CrossRef](#)]
102. Lopez-Fontana, C.M.; Sasso, C.V.; Maselli, M.E.; Santiano, F.E.; Semino, S.N.; Cuello Carrion, F.D.; Jahn, G.A.; Caron, R.W. Experimental hypothyroidism increases apoptosis in dimethylbenzanthracene-induced mammary tumors. *Oncol. Rep.* **2013**, *30*, 1651–1660. [[CrossRef](#)]
103. Huang, J.; Jin, L.; Ji, G.; Xing, L.; Xu, C.; Xiong, X.; Li, H.; Wu, K.; Ren, G.; Kong, L. Implication from thyroid function decreasing during chemotherapy in breast cancer patients: chemosensitization role of triiodothyronine. *BMC Cancer* **2013**, *13*, 334. [[CrossRef](#)] [[PubMed](#)]
104. Dinda, S.; Sanchez, A.; Moudgil, V. Estrogen-like effects of thyroid hormone on the regulation of tumor suppressor proteins, p53 and retinoblastoma, in breast cancer cells. *Oncogene* **2002**, *21*, 761–768. [[CrossRef](#)] [[PubMed](#)]
105. Hall, L.C.; Salazar, E.P.; Kane, S.R.; Liu, N. Effects of thyroid hormones on human breast cancer cell proliferation. *J. Steroid Biochem. Mol. Biol.* **2008**, *109*, 57–66. [[CrossRef](#)] [[PubMed](#)]
106. Shao, Z.M.; Sheikh, M.S.; Rishi, A.K.; Dawson, M.I.; Li, X.S.; Wilber, J.F.; Feng, P.; Fontana, J.A. Thyroid hormone enhancement of estradiol stimulation of breast carcinoma proliferation. *Exp. Cell Res.* **1995**, *218*, 1–8. [[CrossRef](#)]
107. Cheng, S.Y.; Leonard, J.L.; Davis, P.J. Molecular aspects of thyroid hormone actions. *Endocr. Rev.* **2010**, *31*, 139–170. [[CrossRef](#)]
108. Davis, F.B.; Mousa, S.A.; O'Connor, L.; Mohamed, S.; Lin, H.Y.; Cao, H.J.; Davis, P.J. Proangiogenic action of thyroid hormone is fibroblast growth factor-dependent and is initiated at the cell surface. *Circ. Res.* **2004**, *94*, 1500–1506. [[CrossRef](#)]
109. Lombardi, A.; Moreno, M.; de Lange, P.; Iossa, S.; Busiello, R.A.; Goglia, F. Regulation of skeletal muscle mitochondrial activity by thyroid hormones: focus on the "old" triiodothyronine and the "emerging" 3,5-diiodothyronine. *Front. Physiol.* **2015**, *6*, 237. [[CrossRef](#)]
110. Ditsch, N.; Toth, B.; Himsl, I.; Lenhard, M.; Ochsenkuhn, R.; Friese, K.; Mayr, D.; Jeschke, U. Thyroid hormone receptor (TR)alpha and TRbeta expression in breast cancer. *Histol Histopathol* **2013**, *28*, 227–237. [[CrossRef](#)]
111. Jerzak, K.J.; Cockburn, J.; Pond, G.R.; Pritchard, K.I.; Narod, S.A.; Dhesy-Thind, S.K.; Bane, A. Thyroid hormone receptor alpha in breast cancer: prognostic and therapeutic implications. *Breast Cancer Res. Treat.* **2015**, *149*, 293–301. [[CrossRef](#)] [[PubMed](#)]
112. Zarebczan, B.; Chen, H. Multi-targeted approach in the treatment of thyroid cancer. *Minerva Chir.* **2010**, *65*, 59–69. [[PubMed](#)]
113. Ocak, S.; Akten, A.O.; Tez, M. Thyroid cancer in hyperthyroid patients: is it different clinical entity? *Endocr. Regul.* **2014**, *48*, 65–68. [[CrossRef](#)] [[PubMed](#)]
114. Davis, P.J.; Hercbergs, A.; Luidens, M.K.; Lin, H.Y. Recurrence of differentiated thyroid carcinoma during full TSH suppression: is the tumor now thyroid hormone dependent? *Horm. Cancer* **2015**, *6*, 7–12. [[CrossRef](#)] [[PubMed](#)]

115. Romitti, M.; Wajner, S.M.; Zennig, N.; Goemann, I.M.; Bueno, A.L.; Meyer, E.L.; Maia, A.L. Increased type 3 deiodinase expression in papillary thyroid carcinoma. *Thyroid* **2012**, *22*, 897–904. [\[CrossRef\]](#)
116. Faber, J.; Poulsen, S.; Iversen, P.; Kirkegaard, C. Thyroid hormone turnover in patients with small cell carcinoma of the lung. *Acta Endocrinol. (Copenh)* **1988**, *118*, 460–464. [\[CrossRef\]](#)
117. Ratcliffe, J.G.; Stack, B.H.; Burt, R.W.; Radcliffe, W.A.; Spilg, W.G.; Cuthbert, J.; Kennedy, R.S. Thyroid function in lung cancer. *Br. Med. J.* **1978**, *1*, 210–212. [\[CrossRef\]](#)
118. Yasar, Z.A.; Kirakli, C.; Yilmaz, U.; Ucar, Z.Z.; Talay, F. Can non-thyroid illness syndrome predict mortality in lung cancer patients? A prospective cohort study. *Horm. Cancer* **2014**, *5*, 240–246. [\[CrossRef\]](#)
119. Kinoshita, S.; Sone, S.; Yamashita, T.; Tsubura, E.; Ogura, T. Effects of experimental hyper- and hypothyroidism on natural defense activities against Lewis lung carcinoma and its spontaneous pulmonary metastases in C57BL/6 mice. *Tokushima J. Exp. Med.* **1991**, *38*, 25–35.
120. Iwasaki, Y.; Sunaga, N.; Tomizawa, Y.; Imai, H.; Iijima, H.; Yanagitani, N.; Horiguchi, K.; Yamada, M.; Mori, M. Epigenetic inactivation of the thyroid hormone receptor beta1 gene at 3p24.2 in lung cancer. *Ann. Surg. Oncol.* **2010**, *17*, 2222–2228. [\[CrossRef\]](#)
121. Bunevicius, A.; Deltuva, V.; Tamasauskas, S.; Tamasauskas, A.; Laws, E.R., Jr.; Bunevicius, R. Low triiodothyronine syndrome as a predictor of poor outcomes in patients undergoing brain tumor surgery: a pilot study: clinical article. *J. Neurosurg.* **2013**, *118*, 1279–1287. [\[CrossRef\]](#) [\[PubMed\]](#)
122. Bunevicius, A.; Deltuva, V.P.; Tamasauskas, S.; Smith, T.; Laws, E.R.; Bunevicius, R.; Iervasi, G.; Tamasauskas, A. Preoperative low tri-iodothyronine concentration is associated with worse health status and shorter five year survival of primary brain tumor patients. *Oncotarget* **2017**, *8*, 8648–8656. [\[CrossRef\]](#) [\[PubMed\]](#)
123. Monden, T.; Nakajima, Y.; Hashida, T.; Ishii, S.; Tomaru, T.; Shibusawa, N.; Hashimoto, K.; Satoh, T.; Yamada, M.; Mori, M.; et al. Expression of thyroid hormone receptor isoforms down-regulated by thyroid hormone in human medulloblastoma cells. *Endocr. J.* **2006**, *53*, 181–187. [\[CrossRef\]](#) [\[PubMed\]](#)
124. Hassan, M.M.; Kaseb, A.; Li, D.; Patt, Y.Z.; Vauthey, J.N.; Thomas, M.B.; Curley, S.A.; Spitz, M.R.; Sherman, S.I.; Abdalla, E.K.; et al. Association between hypothyroidism and hepatocellular carcinoma: a case-control study in the United States. *Hepatology* **2009**, *49*, 1563–1570. [\[CrossRef\]](#) [\[PubMed\]](#)
125. Shih, Y.L.; Huang, Y.H.; Lin, K.H.; Chu, Y.D.; Yeh, C.T. Identification of Functional Thyroid Stimulating Hormone Receptor and TSHR Gene Mutations in Hepatocellular Carcinoma. *Anticancer Res.* **2018**, *38*, 2793–2802. [\[CrossRef\]](#)
126. Chan, I.H.; Privalsky, M.L. Thyroid hormone receptors mutated in liver cancer function as distorted antimorphs. *Oncogene* **2006**, *25*, 3576–3588. [\[CrossRef\]](#) [\[PubMed\]](#)
127. Lin, K.H.; Shieh, H.Y.; Chen, S.L.; Hsu, H.C. Expression of mutant thyroid hormone nuclear receptors in human hepatocellular carcinoma cells. *Mol. Carcinog.* **1999**, *26*, 53–61. [\[CrossRef\]](#)
128. Lin, K.H.; Zhu, X.G.; Hsu, H.C.; Chen, S.L.; Shieh, H.Y.; Chen, S.T.; McPhie, P.; Cheng, S.Y. Dominant negative activity of mutant thyroid hormone alpha1 receptors from patients with hepatocellular carcinoma. *Endocrinology* **1997**, *138*, 5308–5315. [\[CrossRef\]](#) [\[PubMed\]](#)
129. Barlow, C.; Meister, B.; Lardelli, M.; Lendahl, U.; Vennstrom, B. Thyroid abnormalities and hepatocellular carcinoma in mice transgenic for v-erbA. *EMBO J.* **1994**, *13*, 4241–4250. [\[CrossRef\]](#)
130. Rennert, G.; Rennert, H.S.; Pinchev, M.; Gruber, S.B. A case-control study of levothyroxine and the risk of colorectal cancer. *J. Natl. Cancer Inst.* **2010**, *102*, 568–572. [\[CrossRef\]](#)
131. Rose, D.P.; Davis, T.E. Plasma thyronine levels in carcinoma of the breast and colon. *Arch. Intern. Med.* **1981**, *141*, 1161–1164. [\[CrossRef\]](#) [\[PubMed\]](#)
132. Vonlaufen, A.; Wiedle, G.; Borisch, B.; Birrer, S.; Luder, P.; Imhof, B.A. Integrin alpha(v)beta(3) expression in colon carcinoma correlates with survival. *Mod. Pathol.* **2001**, *14*, 1126–1132. [\[CrossRef\]](#) [\[PubMed\]](#)
133. Iishi, H.; Tatsuta, M.; Baba, M.; Okuda, S.; Taniguchi, H. Enhancement by thyroxine of experimental carcinogenesis induced in rat colon by azoxymethane. *Int. J. Cancer* **1992**, *50*, 974–976. [\[CrossRef\]](#) [\[PubMed\]](#)
134. Iishi, H.; Tatsuta, M.; Baba, M.; Taniguchi, H. Monoamine oxidase B inhibitor enhances experimental carcinogenesis in rat colon induced by azoxymethane. *Cancer Lett.* **1994**, *76*, 177–183. [\[CrossRef\]](#)
135. Kress, E.; Rezza, A.; Nadjar, J.; Samarut, J.; Plateroti, M. The thyroid hormone receptor-alpha (TRalpha) gene encoding TRalpha1 controls deoxyribonucleic acid damage-induced tissue repair. *Mol. Endocrinol.* **2008**, *22*, 47–55. [\[CrossRef\]](#)
136. Clevers, H. Wnt/beta-catenin signaling in development and disease. *Cell* **2006**, *127*, 469–480. [\[CrossRef\]](#)

137. Markowitz, S.; Haut, M.; Stellato, T.; Gerbic, C.; Molkentin, K. Expression of the ErbA-beta class of thyroid hormone receptors is selectively lost in human colon carcinoma. *J. Clin. Invest.* **1989**, *84*, 1683–1687. [[CrossRef](#)]
138. Pietrzak, M.; Puzianowska-Kuznicka, M. Triiodothyronine utilizes phosphatidylinositol 3-kinase pathway to activate anti-apoptotic myeloid cell leukemia-1. *J. Mol. Endocrinol.* **2008**, *41*, 177–186. [[CrossRef](#)]
139. Ho, Y.; Lin, Y.S.; Liu, H.L.; Shih, Y.J.; Lin, S.Y.; Shih, A.; Chin, Y.T.; Chen, Y.R.; Lin, H.Y.; Davis, P.J. Biological Mechanisms by Which Antiproliferative Actions of Resveratrol Are Minimized. *Nutrients* **2017**, *9*, 1046. [[CrossRef](#)]
140. Mousa, S.A.; Lin, H.Y.; Tang, H.Y.; Hercbergs, A.; Luidens, M.K.; Davis, P.J. Modulation of angiogenesis by thyroid hormone and hormone analogues: implications for cancer management. *Angiogenesis* **2014**, *17*, 463–469. [[CrossRef](#)]
141. Lin, H.Y.; Chin, Y.T.; Yang, Y.C.; Lai, H.Y.; Wang-Peng, J.; Liu, L.F.; Tang, H.Y.; Davis, P.J. Thyroid Hormone, Cancer, and Apoptosis. *Compr. Physiol.* **2016**, *6*, 1221–1237. [[CrossRef](#)] [[PubMed](#)]
142. Davis, P.J.; Sudha, T.; Lin, H.Y.; Mousa, S.A. Thyroid Hormone, Hormone Analogs, and Angiogenesis. *Compr. Physiol.* **2015**, *6*, 353–362. [[CrossRef](#)] [[PubMed](#)]
143. Peeters, R.P.; Visser, T.J. *Metabolism of Thyroid Hormone*, Feingold, K.R., Anawalt, B., Boyce, A., Chrousos, G., Dungan, K., Grossman, A., Hershman, J.M., Kaltsas, G., Koch, C., Kopp, P., et al., Eds.; South Dartmouth, MA, USA, 2000.
144. Senese, R.; Cioffi, F.; de Lange, P.; Goglia, F.; Lanni, A. Thyroid: biological actions of ‘nonclassical’ thyroid hormones. *J. Endocrinol.* **2014**, *221*, R1–R12. [[CrossRef](#)] [[PubMed](#)]
145. Moreno, M.; de Lange, P.; Lombardi, A.; Silvestri, E.; Lanni, A.; Goglia, F. Metabolic effects of thyroid hormone derivatives. *Thyroid* **2008**, *18*, 239–253. [[CrossRef](#)] [[PubMed](#)]
146. Brenta, G.; Danzi, S.; Klein, I. Potential therapeutic applications of thyroid hormone analogs. *Nat. Clin. Pract. Endocrinol. Metab.* **2007**, *3*, 632–640. [[CrossRef](#)]
147. Webb, P. Selective activators of thyroid hormone receptors. *Expert. Opin. Investig. Drugs* **2004**, *13*, 489–500. [[CrossRef](#)]
148. Baxter, J.D.; Webb, P. Thyroid hormone mimetics: potential applications in atherosclerosis, obesity and type 2 diabetes. *Nat. Rev. Drug Discov.* **2009**, *8*, 308–320. [[CrossRef](#)]
149. Glinskii, A.B.; Glinsky, G.V.; Lin, H.Y.; Tang, H.Y.; Sun, M.; Davis, F.B.; Luidens, M.K.; Mousa, S.A.; Hercbergs, A.H.; Davis, P.J. Modification of survival pathway gene expression in human breast cancer cells by tetraiodothyroacetic acid (tetrac). *Cell Cycle* **2009**, *8*, 3562–3570. [[CrossRef](#)]
150. Yalcin, M.; Dyskin, E.; Lansing, L.; Bharali, D.J.; Mousa, S.S.; Bridoux, A.; Hercbergs, A.H.; Lin, H.Y.; Davis, F.B.; Glinsky, G.V.; et al. Tetraiodothyroacetic acid (tetrac) and nanoparticulate tetrac arrest growth of medullary carcinoma of the thyroid. *J. Clin. Endocrinol. Metab.* **2010**, *95*, 1972–1980. [[CrossRef](#)]
151. Davidson, B.; Berner, A.; Nesland, J.M.; Risberg, B.; Berner, H.S.; Trope, C.G.; Kristensen, G.B.; Bryne, M.; Ann Florenes, V. E-cadherin and alpha-, beta-, and gamma-catenin protein expression is up-regulated in ovarian carcinoma cells in serous effusions. *J. Pathol.* **2000**, *192*, 460–469. [[CrossRef](#)]
152. Imai, T.; Horiuchi, A.; Shiozawa, T.; Osada, R.; Kikuchi, N.; Ohira, S.; Oka, K.; Konishi, I. Elevated expression of E-cadherin and alpha-, beta-, and gamma-catenins in metastatic lesions compared with primary epithelial ovarian carcinomas. *Hum. Pathol.* **2004**, *35*, 1469–1476. [[CrossRef](#)] [[PubMed](#)]
153. King, T.D.; Suto, M.J.; Li, Y. The Wnt/beta-catenin signaling pathway: a potential therapeutic target in the treatment of triple negative breast cancer. *J. Cell Biochem.* **2012**, *113*, 13–18. [[CrossRef](#)] [[PubMed](#)]
154. White, B.D.; Chien, A.J.; Dawson, D.W. Dysregulation of Wnt/beta-catenin signaling in gastrointestinal cancers. *Gastroenterology* **2012**, *142*, 219–232. [[CrossRef](#)] [[PubMed](#)]
155. Debruyne, P.; Vermeulen, S.; Mareel, M. The role of the E-cadherin/catenin complex in gastrointestinal cancer. *Acta Gastroenterol Belg* **1999**, *62*, 393–402. [[PubMed](#)]
156. Fanjul-Fernandez, M.; Quesada, V.; Cabanillas, R.; Cadinanos, J.; Fontanil, T.; Obaya, A.; Ramsay, A.J.; Llorente, J.L.; Astudillo, A.; Cal, S.; et al. Cell-cell adhesion genes CTNNA2 and CTNNA3 are tumour suppressors frequently mutated in laryngeal carcinomas. *Nat. Commun.* **2013**, *4*, 2531. [[CrossRef](#)] [[PubMed](#)]
157. Chen, R.N.; Huang, Y.H.; Lin, Y.C.; Yeh, C.T.; Liang, Y.; Chen, S.L.; Lin, K.H. Thyroid hormone promotes cell invasion through activation of furin expression in human hepatoma cell lines. *Endocrinology* **2008**, *149*, 3817–3831. [[CrossRef](#)] [[PubMed](#)]



158. de Franciscis, S.; Serra, R. Matrix metalloproteinases and endothelial dysfunction: The search for new prognostic markers and for new therapeutic targets for vascular wall imbalance. *Thromb. Res.* **2015**, *136*, 5–6. [[CrossRef](#)] [[PubMed](#)]
159. Xie, T.X.; Wei, D.; Liu, M.; Gao, A.C.; Ali-Osman, F.; Sawaya, R.; Huang, S. Stat3 activation regulates the expression of matrix metalloproteinase-2 and tumor invasion and metastasis. *Oncogene* **2004**, *23*, 3550–3560. [[CrossRef](#)]
160. Lu, C.; Cheng, S.Y. Extranuclear signaling of mutated thyroid hormone receptors in promoting metastatic spread in thyroid carcinogenesis. *Steroids* **2011**, *76*, 885–891. [[CrossRef](#)]
161. Takeda, T.; Suzuki, S.; Liu, R.T.; DeGroot, L.J. Triiodothyroacetic acid has unique potential for therapy of resistance to thyroid hormone. *J. Clin. Endocrinol. Metab.* **1995**, *80*, 2033–2040. [[CrossRef](#)]
162. Shinderman-Maman, E.; Cohen, K.; Moskovich, D.; Hercbergs, A.; Werner, H.; Davis, P.J.; Ellis, M.; Ashur-Fabian, O. Thyroid hormones derivatives reduce proliferation and induce cell death and DNA damage in ovarian cancer. *Sci. Rep.* **2017**, *7*, 16475. [[CrossRef](#)] [[PubMed](#)]
163. Stavreva, D.A.; Varticovski, L.; Levkova, L.; George, A.A.; Davis, L.; Pegoraro, G.; Blazer, V.; Iwanowicz, L.; Hager, G.L. Novel cell-based assay for detection of thyroid receptor beta-interacting environmental contaminants. *Toxicology* **2016**, *368–369*, 69–79. [[CrossRef](#)] [[PubMed](#)]
164. Groeneweg, S.; Peeters, R.P.; Visser, T.J.; Visser, W.E. Triiodothyroacetic acid in health and disease. *J. Endocrinol.* **2017**, *234*, R99–R121. [[CrossRef](#)] [[PubMed](#)]
165. Kunitake, J.M.; Hartman, N.; Henson, L.C.; Lieberman, J.; Williams, D.E.; Wong, M.; Hershman, J.M. 3,5,3'-triiodothyroacetic acid therapy for thyroid hormone resistance. *J. Clin. Endocrinol. Metab.* **1989**, *69*, 461–466. [[CrossRef](#)] [[PubMed](#)]
166. Dulgeroff, A.J.; Geffner, M.E.; Koyal, S.N.; Wong, M.; Hershman, J.M. Bromocriptine and Triac therapy for hyperthyroidism due to pituitary resistance to thyroid hormone. *J. Clin. Endocrinol. Metab.* **1992**, *75*, 1071–1075. [[CrossRef](#)] [[PubMed](#)]
167. Radetti, G.; Persani, L.; Molinaro, G.; Mannavola, D.; Cortelazzi, D.; Chatterjee, V.K.; Beck-Peccoz, P. Clinical and hormonal outcome after two years of triiodothyroacetic acid treatment in a child with thyroid hormone resistance. *Thyroid* **1997**, *7*, 775–778. [[CrossRef](#)]
168. Salmela, P.I.; Wide, L.; Juustila, H.; Ruokonen, A. Effects of thyroid hormones (T<sub>4</sub>, T<sub>3</sub>), bromocriptine and Triac on inappropriate TSH hypersecretion. *Clin. Endocrinol. (Oxf.)* **1988**, *28*, 497–507. [[CrossRef](#)]
169. Torre, P.; Bertoli, M.; Di Giovanni, S.; Scommegna, S.; Conte, C.; Novelli, G.; Cianfarani, S. Endocrine and neuropsychological assessment in a child with a novel mutation of thyroid hormone receptor: response to 12-month triiodothyroacetic acid (TRIAC) therapy. *J. Endocrinol. Invest.* **2005**, *28*, 657–662. [[CrossRef](#)]
170. Rivolta, C.M.; Mallea Gil, M.S.; Ballarino, C.; Ridruejo, M.C.; Miguel, C.M.; Gimenez, S.B.; Bernacchi, S.S.; Targovnik, H.M. A novel 1297-1304delGCCTGCCA mutation in the exon 10 of the thyroid hormone receptor beta gene causes resistance to thyroid hormone. *Mol. Diagn.* **2004**, *8*, 163–169.
171. Darendeliler, F.; Bas, F. Successful therapy with 3,5,3'-triiodothyroacetic acid (TRIAC) in pituitary resistance to thyroid hormone. *J. Pediatr. Endocrinol. Metab.* **1997**, *10*, 535–538. [[CrossRef](#)]
172. Beck-Peccoz, P.; Piscitelli, G.; Cattaneo, M.G.; Faglia, G. Successful treatment of hyperthyroidism due to nonneoplastic pituitary TSH hypersecretion with 3,5,3'-triiodothyroacetic acid (TRIAC). *J. Endocrinol. Invest.* **1983**, *6*, 217–223. [[CrossRef](#)] [[PubMed](#)]
173. Beck-Peccoz, P.; Mariotti, S.; Guillausseau, P.J.; Medri, G.; Piscitelli, G.; Bertoli, A.; Barbarino, A.; Rondena, M.; Chanson, P.; Pinchera, A. Treatment of hyperthyroidism due to inappropriate secretion of thyrotropin with the somatostatin analog SMS 201-995. *J. Clin. Endocrinol. Metab.* **1989**, *68*, 208–214. [[CrossRef](#)] [[PubMed](#)]
174. Lind, P.; Eber, O. Treatment of inappropriate TSH secretion with Triac. *Acta Med. Austriaca* **1986**, *13*, 13–16. [[PubMed](#)]
175. Medeiros-Neto, G.; Kallas, W.G.; Knobel, M.; Cavaliere, H.; Mattar, E. Triac (3,5,3'-triiodothyroacetic acid) partially inhibits the thyrotropin response to synthetic thyrotropin-releasing hormone in normal and thyroidectomized hypothyroid patients. *J. Clin. Endocrinol. Metab.* **1980**, *50*, 223–225. [[CrossRef](#)]
176. Falcone, M.; Miyamoto, T.; Fierro-Renoy, F.; Macchia, E.; DeGroot, L.J. Antipeptide polyclonal antibodies specifically recognize each human thyroid hormone receptor isoform. *Endocrinology* **1992**, *131*, 2419–2429. [[CrossRef](#)]



177. Hodin, R.A.; Lazar, M.A.; Chin, W.W. Differential and tissue-specific regulation of the multiple rat c-erbA messenger RNA species by thyroid hormone. *J. Clin. Invest.* **1990**, *85*, 101–105. [[CrossRef](#)]
178. Strait, K.A.; Schwartz, H.L.; Perez-Castillo, A.; Oppenheimer, J.H. Relationship of c-erbA mRNA content to tissue triiodothyronine nuclear binding capacity and function in developing and adult rats. *J. Biol. Chem.* **1990**, *265*, 10514–10521.



© 2019 by the authors. Licensee MDPI, Basel, Switzerland. This article is an open access article distributed under the terms and conditions of the Creative Commons Attribution (CC BY) license (<http://creativecommons.org/licenses/by/4.0/>).



# Neutrophils in Psoriasis

Chih-Chao Chiang<sup>1,2,3†</sup>, Wei-Jen Cheng<sup>1,4,5†</sup>, Michal Korinek<sup>6,7,8</sup>, Cheng-Yu Lin<sup>6</sup> and Tsong-Long Hwang<sup>4,6,7,9,10,11\*</sup>

<sup>1</sup> Graduate Institute of Clinical Medical Sciences, College of Medicine, Chang Gung University, Taoyuan, Taiwan, <sup>2</sup> Supervisor Board, Taoyuan Chinese Medicine Association, Taoyuan, Taiwan, <sup>3</sup> Puxin Fengze Chinese Medicine Clinic, Taoyuan, Taiwan, <sup>4</sup> School of Traditional Chinese Medicine, Chang Gung University, Taoyuan, Taiwan, <sup>5</sup> Center for Traditional Chinese Medicine, Chang Gung Memorial Hospital, Taoyuan, Taiwan, <sup>6</sup> Graduate Institute of Natural Products, College of Medicine, Chang Gung University, Taoyuan, Taiwan, <sup>7</sup> Research Center for Chinese Herbal Medicine, Research Center for Food and Cosmetic Safety, and Graduate Institute of Health Industry Technology, Chang Gung University of Science and Technology, Taoyuan, Taiwan, <sup>8</sup> Department of Biotechnology, College of Life Science, Kaohsiung Medical University, Kaohsiung, Taiwan, <sup>9</sup> Chinese Herbal Medicine Research Team, Healthy Aging Research Center, Chang Gung University, Taoyuan, Taiwan, <sup>10</sup> Department of Anesthesiology, Chang Gung Memorial Hospital, Taoyuan, Taiwan, <sup>11</sup> Department of Chemical Engineering, Ming Chi University of Technology, New Taipei City, Taiwan

## OPEN ACCESS

### Edited by:

Onur Boyman,  
University of Zurich, Switzerland

### Reviewed by:

Nicolas Gaudenzio,  
Institut National de la Santé et de la  
Recherche Médicale  
(INSERM), France  
Liv Eidsmo,  
Karolinska Institute (KI), Sweden

### \*Correspondence:

Tsong-Long Hwang  
htl@mail.cgu.edu.tw

<sup>†</sup>These authors have contributed  
equally to this work

### Specialty section:

This article was submitted to  
Inflammation,  
a section of the journal  
Frontiers in Immunology

**Received:** 18 April 2019

**Accepted:** 23 September 2019

**Published:** 09 October 2019

### Citation:

Chiang C-C, Cheng W-J, Korinek M,  
Lin C-Y and Hwang T-L (2019)  
Neutrophils in Psoriasis.  
Front. Immunol. 10:2376.  
doi: 10.3389/fimmu.2019.02376

Neutrophils are the most abundant innate immune cells. The pathogenic roles of neutrophils are related to chronic inflammation and autoimmune diseases. Psoriasis is a chronic systemic inflammatory disease affecting ~2–3% of the world population. The abundant presence of neutrophils in the psoriatic skin lesions serves as a typical histopathologic hallmark of psoriasis. Recent reports indicated that oxidative stress, granular components, and neutrophil extracellular traps from psoriatic neutrophils are related to the initial and maintenance phases of psoriasis. This review provides an overview on the recent (up to 2019) advances in understanding the role of neutrophils in the pathophysiology of psoriasis, including the effects of respiratory burst, degranulation, and neutrophil extracellular trap formation on psoriatic immunity and the clinical relationships.

**Keywords:** neutrophils, psoriasis, immunity, respiratory burst, degranulation, neutrophil extracellular traps

## INTRODUCTION

Neutrophils are the most abundant cells in innate immunity. The main offensive functions of neutrophils include respiratory burst accompanied by reactive oxygen species (ROS) generation, degranulation (release of granules), and the formation of neutrophil extracellular traps (NETs) (Figure 1) (1, 2). Neutrophils shape adaptive immunity because they communicate and interact with the antigen-presenting cells and lymphocytes at the sites of inflammation (3, 4). Recently great attention was brought to the role of neutrophils in the development and progression of autoimmune diseases such as psoriasis.

Psoriatic neutrophils produce augmented respiratory burst with an overt accumulation of oxidative stress involving complicated inflammatory pathways. Proteases released in the degranulation step by neutrophils, such as myeloperoxidase (MPO), neutrophil elastase (NE), proteinase 3, and cathepsin G, participate in the generation of ROS, proteolytical activation of inflammatory mediators, and formation of autoantigens in psoriasis. The complexity and prevalence of psoriasis among the population since antiquity encouraged scientists to study the etiology of the disease and its relation to the immune system and inflammatory responses. Elegant reviews described the role of inflammation and immune system in the development of psoriasis (5, 6), the importance of biologic therapies targeting systemic inflammation (7), the significance of

utilizing specific antibodies (8), the contribution of platelets to regulation of NET formation (9), the antimicrobial and pathogenetic roles of neutrophils in autoimmune, autoinflammatory, metabolic (10) and cardiovascular diseases (11). Also, recent books summarized the causes, symptoms, and treatment options of psoriasis (12–15).

However, the role of neutrophils in psoriasis was not deeply analyzed and summarized based on recent literature. Thus, in this work, we focus on summarizing recent findings on the main offensive features of neutrophils including respiratory burst, degranulation and NETs and their direct connection with development and progression of psoriasis (**Figure 2**). We hope that our work would provide a foundation for further studies to attenuate overstimulation of neutrophils in psoriasis and aid patients with a debilitating disease.

## PSORIASIS

Psoriasis affects ~2–3% of the world population (>125 million people). Psoriasis is a common, chronic, immune-mediated disease that is manifested mainly as skin lesions and extracutaneous comorbidities (16, 17). It is associated with systemic inflammation, similar to that observed in obesity, malignancy, psoriatic arthritis, cardiovascular disorders, chronic obstructive pulmonary diseases, type 2 diabetes mellitus, liver and renal diseases, and inflammatory bowel diseases (18–20). Psoriasis affects men and women equally and usually starts to be manifested at the age of 20 to 30, but children and teenagers can be also affected (21). Clinical types of psoriasis include psoriasis vulgaris, guttate psoriasis, inverse psoriasis, pustular psoriasis, and erythrodermic psoriasis (22). Typical skin manifestations of psoriasis include erythematous, indurated, and scaling plaques that are painful, itchy, and have a burning sensation (16, 23). Psoriasis decreases patients' quality of life due to unpleasant symptoms and related public stigma (24, 25). The unpleasant skin appearance contributes to reduced employment levels and thus, affects the financial status of patients (26). Depression and suicidal tendencies are also increased in patients with psoriasis (27, 28). Therefore, psoriasis results in long-term physical, psychological, and economic burden at both the individual and societal levels.

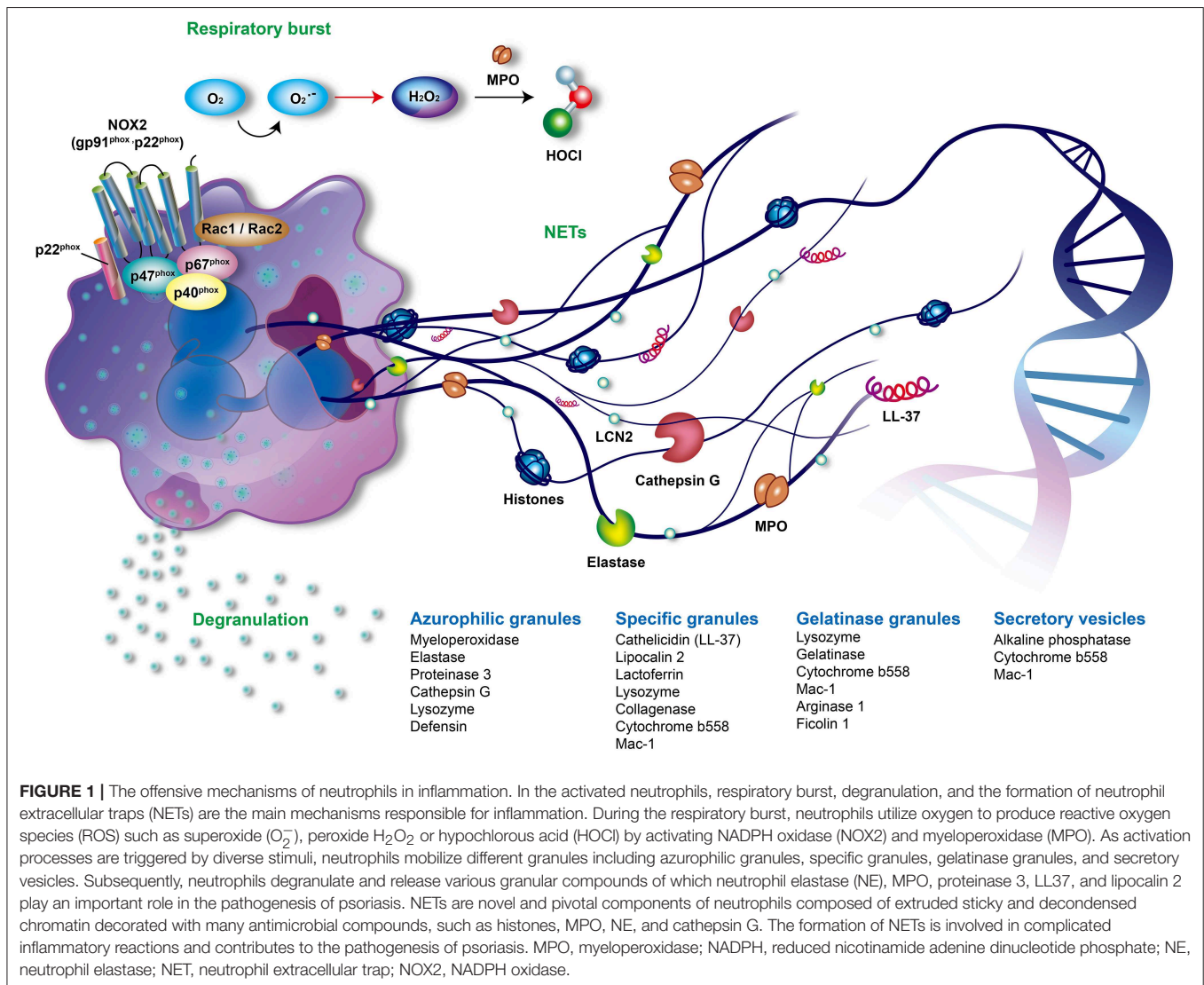
## NEUTROPHILS IN PSORIASIS

Psoriasis is an immunogenetic disease that is associated with the interactions between the innate and adaptive immune systems (29). The immunology disturbance in psoriasis is related to overstimulation of neutrophils, dendritic cells, T cells, keratinocytes, fibroblasts (6, 30), mast cells (31), and melanocytes (30, 32). Munro's microabscesses filled with neutrophils, which were first described in 1898, are considered as one of the major

histopathological hallmarks of psoriasis (33). Neutrophils are now thought to be regulators between the innate and adaptive immune systems (34, 35).

There is no cure for psoriasis, however the symptoms can be reduced either by avoiding triggers or by medications. Currently, the available treatments such as phototherapy, topical therapy (corticosteroids, vitamin D analogs), systemic therapy (methotrexate, apremilast, cyclosporin), and biological treatments offer a relieve for patients with different severity of psoriasis. However, the risk-benefit ratio must be well-considered on individual basis, particularly, considering the chronic course of the disease and limitations of the long-term use of certain drugs (16). Although T cell immunology-related treatments have emerged as attractive options for psoriasis, according to a systematic review of adherence and satisfaction to current treatment covering studies conducted in 2002 (36) or between beginning of 2009 and end of 2014 in European Union (37), psoriatic patients expressed only moderate satisfaction with the available treatments as evidenced by the poor adherence rates, in particular to topical treatments (36, 37). That might be the biggest motivating factor for the use of alternative treatment methods such as traditional Chinese medicine and herbs (*Scutellaria baicalensis*, *Zingiber officinale*, *Indigo naturalis*, *Mahonia aquifolium*, *Aloe vera*) (38), dietary supplements (fish oil, vitamin D) or other (39). Furthermore, the combination of certain alternative medicines with conventional drug therapies has been shown to improve the treatment efficacy, which points to the importance of evaluation of safety of combined treatments, education of doctors but also improvements in patient-doctor interactions (40). Indeed, modern biological therapies demonstrate improved safety and efficacy, as well as better satisfaction in patients, but belong to an expensive class of drugs, with limited availability (41). Biological therapies of psoriasis include monoclonal antibodies or inhibitors targeting tumor necrosis factor (TNF) $\alpha$  (infliximab, adalimumab; etanercept) (42–44), interleukin (IL)-23/IL-12 (ustekinumab) (42), IL-23 (guselkumab, tildrakizumab, risankizumab) (45, 46), or IL-17 (secukinumab, ixekizumab, brodalumab) (11, 47, 48). The available therapies indirectly affect the function and numbers of neutrophils. According to previous studies, the neutrophil-to-lymphocyte ratio (NLR) and platelet-to-lymphocyte ratio (PLR) are significantly increased in patients with psoriasis (49). While the elevated NLR and PLR values are particularly associated with psoriasis, they do not indicate the severity of the condition (50). The importance of NLR level in the progression of the disease was demonstrated by the reduction in NLR level following psoriasis treatment (51). That brings in question the effectiveness of certain treatments such as narrow-band ultraviolet B phototherapy which does not affect the increased level of NLR (52). Increased NLR and PLR levels emerged as unrecognized predictors of subclinical atherosclerosis in patients with psoriasis (53). The presence of excessive amount of neutrophils is characteristic for the generalized pustular psoriasis. Recent reports indicated that the depletion of neutrophils significantly relieves the symptoms of pustular psoriasis in patients that did not respond well to conventional treatments (54). Understanding the role of

**Abbreviations:** CCL, CC-chemokine ligand; CXCL, chemokine (C-X-C motif) ligand; IL, interleukin; IFN, interferon; LPS, lipopolysaccharide; mDCs, myeloid dendritic cells; MPO, myeloperoxidase; NET, neutrophil extracellular trap; NOX, NADPH oxidase; NE, neutrophil elastase; NLR, neutrophil-to-lymphocyte ratio; pDCs, plasmacytoid dendritic cells; PLR, platelet-to-lymphocyte ratio; Th, T helper cell; TLR, Toll-like receptor; TNE, tumor necrosis factor.



neutrophils in psoriasis attracted the attention of scientific community aiming to develop treatment protocols focusing on attenuating neutrophil overstimulation in this disease (55).

## RESPIRATORY BURST AND PSORIASIS

Circulating neutrophils are recruited to inflammatory sites following inflammatory signals. They are then activated to generate and release large amounts of ROS in a phenomenon known as respiratory burst. NADPH oxidase (NOX2) and MPO are two key enzymes that contribute to the respiratory burst (56, 57). NOX2 is composed of transmembrane cytochrome b558 (p22<sup>phox</sup> and gp91<sup>phox</sup>) and cytosolic subunits (p40<sup>phox</sup>, p47<sup>phox</sup>, p67<sup>phox</sup>, and Rac1/2). The assembled NOX2 complex, at the phagosomal and plasma membranes, is fully activated to generate superoxide anion ( $O_2^{\bullet -}$ ), which is the origin of various ROS produced by neutrophils. Superoxide ( $O_2^{\bullet -}$ ) is rapidly converted to hydrogen peroxide ( $H_2O_2$ ) by superoxide dismutase (SOD). MPO, a heme peroxidase enzyme which is

released in a process known as degranulation, utilizes  $H_2O_2$  to produce many secondary reactive products. These products include hypochlorous acid (HOCl), chloramines (R-NHCl), and hypothiocyanite (OSCN<sup>-</sup>), as well as organic radicals such as products of lipid peroxidation (Figure 1) (58, 59).

ROS production is an integral part of the antimicrobial activity of neutrophils. However, the overproduction or inadequate clearance of ROS can cause various oxidative stress-related dysfunctions. These include cell and tissue damage; peroxidation and modification of DNA, lipids, and proteins; autoimmune NET formation; and autoantibody generation (58, 60). Neutrophils obtained from patients with psoriasis were shown to possess increased MPO and NOX2 activities, and release more ROS compared with neutrophils from healthy individuals (61, 62). Keratinocytes and T cells in psoriatic lesions produce priming agents of neutrophils, which results in an augmented respiratory burst by neutrophils with the overproduction of ROS (63–66). Accumulation of oxidative radicals also contributes to the pathogenesis of psoriasis. In response to the overproduction of



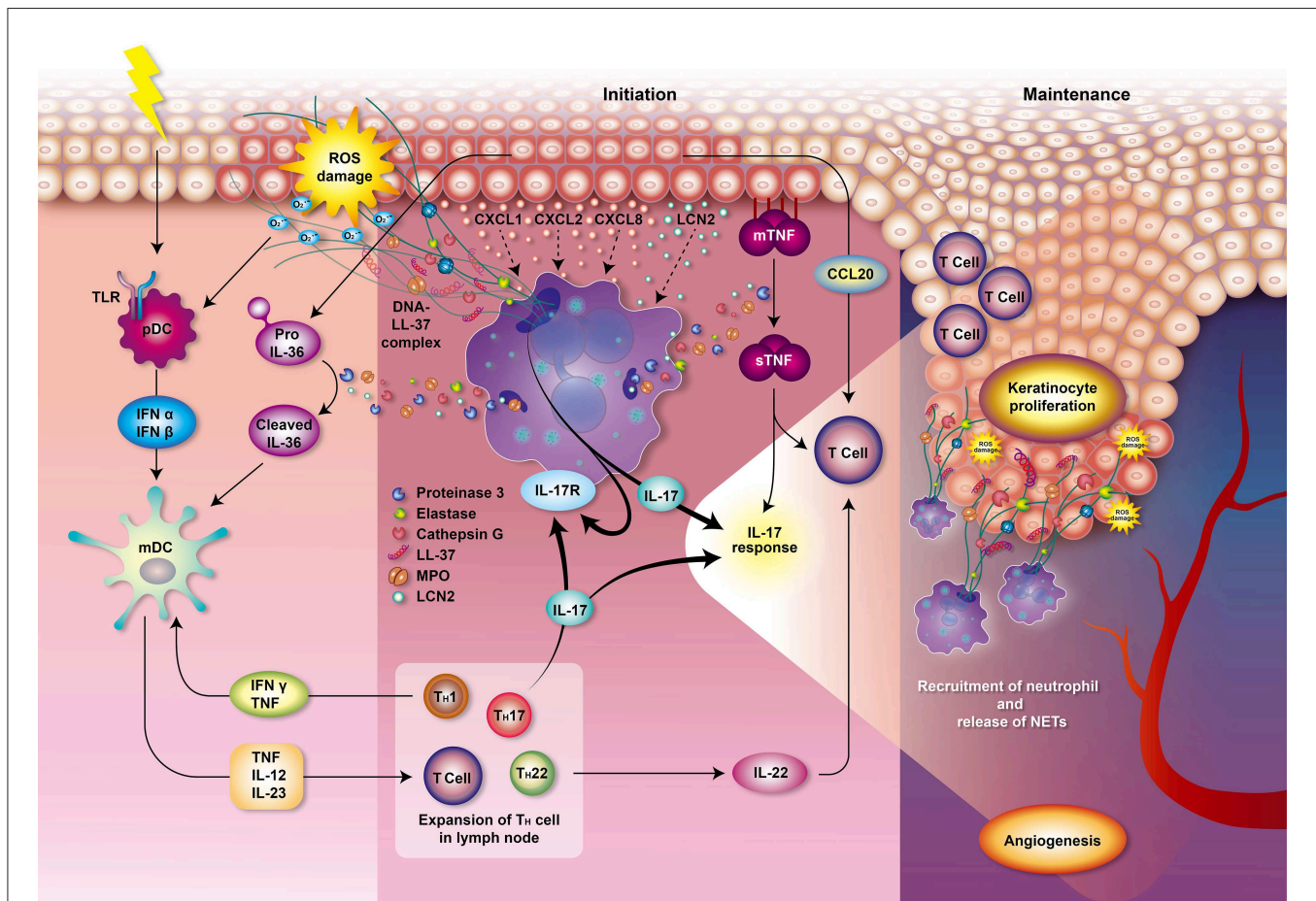


**FIGURE 2 |** Role of neutrophils in psoriasis. Various and diverse endogenous and exogenous impulses such as antigens, trauma, infection, or emotional stress can trigger the complex immune reactions leading to psoriasis. The interplay of neutrophils, dendritic cells, and T cells bridges the innate immune and adaptive immune systems. T cells and keratinocytes release chemokines, such as IL-17, CXCL1, CXCL2, and CXCL8, that mediate the recruitment of neutrophils. Circulating neutrophils migrate to the psoriatic lesions and induce respiratory burst, degranulation, and formation of NETs, thereby contributing to the immunopathogenesis of psoriasis which involves T cell imbalance, keratinocyte proliferation, angiogenesis, and auto-antigen formation. Neutrophils from patients with psoriasis have enhanced NOX2 and MPO activity and augmented respiratory burst. MPO also participates in generating oxidative stress and upregulating degranulation. The accumulated oxidative stress produced by neutrophils could stimulate the antigen-presenting cells pDCs via TLR receptors 7 and 9 which stimulate antigen-specific CD8+ T cells (memory T cells in dermis and naive T cells in lymph node) to release cytokines, chemokines, and other innate immune mediators. These T cells may also migrate to epidermis and trigger local inflammation and keratinocyte proliferation via MHC I receptor of keratinocytes. Production of IFN- $\alpha$  and IFN- $\beta$  by pDCs then stimulates mDCs to secrete pro-inflammatory mediators such as TNF, IL-12 and IL-23. Proteinase 3 released from neutrophils cleaves pro-IL-36 to activated IL-36 cytokine amplifying the response of mDCs. TNF, IL-12, and IL-23 play an important role in the initiation of the Th1, Th17, and Th22 cells immune response in lymph node, leading to a secretion of various cytokines and chemokines. IL-1 is further amplifying Th17 response while TNF and IFN- $\gamma$  is creating a back loop to mDCs activation. Th17 activation then leads to the production of IL-17 activating neutrophils and keratinocytes via IL-17 receptors which generates profound IL-17 response. Keratinocytes produce TNF and CCL20, a chemotactic for T cell and DCs. Neutrophils degranulate and release MPO, NE, proteinase 3, cathepsin G and lipocalin. Proteinase 3 cleaves and converts the resting TNF $\alpha$  located in membrane of epithelial cells (mTNF $\alpha$ ) to an activated state called soluble TNF $\alpha$  (sTNF $\alpha$ ). Proteinase 3 also contributes to the formation of the LL-37 which serves as autoantigen. The chromatin of NETs (DNA) combined with LL-37 have a profound role in the initiation and maintenance of immune response in psoriasis. NETs further supply IL-17 and induce Th17 cells to release more IL-17, which plays a decisive role in the maintenance of psoriasis. These processes participate in the psoriasis complex inflammatory reactions and lead to the escalation of local psoriatic tissue inflammation. IL-22 contributes to the formation of characteristic psoriatic skin lesions including epidermal hyperplasia and acanthosis (thickening of skin). The activation of the following transcription factors promote TNF and IL-17 production and formation of downstream amplification loops in psoriasis: the Janus kinase (JAK)-signal transducer and activator of transcription (STAT) family, nuclear factor- $\kappa$ B (NF- $\kappa$ B) and cyclic AMP. Furthermore, the activation of endothelial cells induces vascular proliferation, angiogenesis and the expression of adhesion molecules in the endothelium to recruit additional inflammatory cells into the skin such as mast cells and macrophages contributing to the pathogenesis of psoriasis. CCL, CC-chemokine ligand; CXCL, chemokine (C-X-C motif) ligand; IL, interleukin; IFN, interferon; MHC I, major histocompatibility complex class I; MPO, myeloperoxidase; NET, neutrophil extracellular trap; NOX, NADPH oxidase; NE, neutrophil elastase; pDCs, plasmacytoid dendritic cells; mDCs, myeloid dendritic cells; TLR, Toll-like receptor; TNF, tumor necrosis factor.

ROS, dendritic cells are stimulated to present antigens to the T cells which results in an imbalance of T helper cell (Th)1 and Th2 cells, stimulation of keratinocytes proliferation, and promotion of

angiogenesis (Figure 2). ROS then serve as the second messenger to activate mitogen-activated protein kinase (MAPK), nuclear factor-kappa B (NF- $\kappa$ B), or the Janus kinase-signal transducer



and activator of transcription proteins (JAK-STAT)-related inflammatory pathways (67, 68). Suppression of respiratory burst of neutrophils emerged as a plausible pathway of attenuating overly immune response associated with psoriatic symptoms.

## DEGRANULATION AND PSORIASIS

Neutrophils possess a multi-lobed nucleus, few mitochondria, and many specific storage organelles called granules. Granules are classified into azurophilic granules, specific granules, gelatinase granules, and secretory vesicles depending on their size, reaction with peroxidase-reactive dye, staining with 3,3'-diaminobenzidine, protein content, and tendency to mobilize (Figure 1) (69, 70). Azurophilic (peroxidase-positive or primary) granules are packed with MPO, bactericidal/permeability-increasing protein, defensins, lysozyme, and serine proteases, such as neutrophil elastase (NE), proteinase 3, and cathepsin G. Lysozyme is also found in specific and gelatinase granules (55). Specific (secondary) granules contain distinctive iron-binding glycoprotein lactoferrin, neutrophil gelatinase-associated lipocalin (NGAL, also called serum lipocalin-2, LCN2), collagenase, cytochrome b558, MAC-1 (CD11/CD18), and importantly, cathelicidins such as LL-37 (71). Cytochrome b558 and MAC-1 are also present in gelatinase granules and secretory vesicles (55). Gelatinase (tertiary) granules store gelatinase, lysozyme, arginase 1, and ficolin 1 (72). The secretory vesicles contain a characteristic alkaline phosphatase (57).

As activation processes of neutrophils are triggered by diverse stimuli such as bacterial or proinflammatory lipid mediators, neutrophils mobilize different granules and release the aforementioned granular components in a process known as degranulation or exocytosis (57). Degranulation is regulated by complicated control mechanisms, such as calcium signaling and actin remodeling (72–74). Azurophilic granules discharge toxic components into phagosomes and at inflammation sites. The secretion of specific and gelatinase granules promotes migration of neutrophils and the antimicrobial activity. The main purpose of releasing secretory vesicles is to facilitate neutrophils recruitment. Therefore, the degranulation process promotes firm adhesion, migration, respiratory burst, and successive NET formation of activated neutrophils (75). However, the dysregulation of neutrophil degranulation could damage tissues as observed in various diseases, such as hypoxia-related airway injury (76), severe pneumonia and chronic obstructive pulmonary diseases (77), atherosclerosis (78, 79), acute inflammatory liver injury (80), and rheumatoid arthritis (81, 82).

In psoriasis, MPO is significantly increased in skin plaques and is positively correlated with the severity of psoriasis (83). Serum MPO is also increased in patients with psoriasis, which may be related to recruited leukocytes in psoriatic skin lesions (84). MPO, the major enzymatic content of neutrophil granules, accounts for ~5% of the dry weight of the cell and represents the most toxic enzyme expressed by neutrophils (85). MPO is involved in the respiratory burst and can bind to CD11b/CD18 integrins, thereby contributing to the upregulation and augmentation of neutrophil degranulation

in psoriasis (86). Furthermore, the neutrophil granule-derived serine proteinases, such as NE, proteinase 3, and cathepsin G, can activate interleukin (IL)-36 cytokine and lead to the escalation of local psoriatic tissue inflammation (87, 88). Proteinase 3 cleaves and converts the resting TNF $\alpha$  located in membrane of epithelial cells (mTNF $\alpha$ ) to an activated state called soluble TNF $\alpha$  (sTNF $\alpha$ ), which participates in the psoriasis complex inflammatory reactions (Figure 2). Proteinase 3 also contributes to the formation of the LL-37, an antimicrobial peptide belonging to cathelicidin family of polypeptides (89, 90), which serves as autoantigen mediating immune response in psoriasis (33). Antimicrobial peptides, synthesized by various leukocytes and epithelial cells, act via DNA/RNA complexes binding Toll-like receptors (TLR) 7, 8, and 9 to facilitate skin inflammation (91, 92). In addition, NE proteolytically activates the epidermal growth factor receptor (EGFR) signaling pathway resulting in excessive keratinocyte proliferation in psoriasis (93). Thus, the inhibition of neutrophils degranulation process or some of the enzymes contributing to psoriasis (NE, MPO, proteinase 3) are feasible targets for alleviating psoriatic symptoms.

## NETS AND PSORIASIS

The process of forming neutrophil extracellular traps (NETs) was first reported in 2004 (94). NETs are composed of extruded sticky chromatin ornamented with many antimicrobial components including histones, MPO, NE, cathepsin G, high mobility group protein B1 (HMGB1) and antimicrobial peptides, such as LL-37 (Figure 1) (95). NETs can catch and destroy pathogens in order to prevent microbes from spreading (96). However, the dysregulated formation and clearance of NETs can result in many diseases. These include autoimmune diseases, such as systemic lupus erythematosus, anti-neutrophil cytoplasmic autoantibody (ANCA)-associated vasculitis, rheumatoid arthritis, gout (97), and autoimmune hepatitis (98); cardiovascular diseases, such as atherosclerosis, thrombosis, and abdominal aortic aneurysm (99–101); respiratory disorders inclusive of asthma, chronic obstructive pulmonary disease, cystic fibrosis, tuberculosis, bacterial and viral pneumonia, and transfusion-related acute lung injury (102, 103); digestive diseases, such as inflammatory bowel diseases, primary sclerosing cholangitis, primary biliary cholangitis (98); and cancer-related organ damage, metastasis, and thrombosis (9). Recently, a role of NETs in awakening of dormant cancer cells was discovered (104).

The process of NET formation is termed NETosis, which is subdivided into lytic NETosis and non-lytic NETosis. In lytic NETosis (also called suicidal NETosis), activated neutrophils generate NETs (it takes 2–4 h) and undergo a programmed cell death, which differs from necrosis, necroptosis, and apoptosis (105). Lytic NET formation is triggered by various stimuli undergoing different pathways. For instance, phorbol myristate acetate (PMA) increases cytosol calcium, activates protein kinase C (PKC)/Raf/MEK/ERK pathway, and induces NOX2 to generate ROS. ROS then acts as the second messenger to disintegrate the nuclear membrane and stimulate MPO to translocate NE to the nucleus where it causes proteolysis of histones and decondensation of chromatin. Afterward, peptidyl

arginine deiminase 4 (PAD4)-mediated hypercitrullination of histones allows decondensed chromatin, the main component of NETs, to be readily expelled from the cell nucleus. Finally, as the plasma membrane dissolves, the chromatin decorated with granular components is released as extracellular traps (106). Other pathways of lytic NETosis include stimulation by fungi (such as *Aspergillus* spp.) through Dectin 2 and complement receptor 3 (CR3) (107), LPS (lipopolysaccharide) under special conditions described later in detail (108) or by monosodium urate crystals via receptor-interacting serine/threonine-protein kinase 1 (RIPK1) and RIPK3 pathway (109). All of these pathways involve NOX2, MPO, and NE activation (105). Nevertheless, there are other stimulators of NETosis acting independently of NOX2 such as ionomycin, or immune complexes (110). Ionomycin induces NETs via small conductance calcium-activated potassium channel protein 3 (SK3) and protein kinase C  $\zeta$  (PKC $\zeta$ ), mitochondrial ROS (mitoROS), NE, and protein-arginine deiminase type 4 (PAD4) (111). Immune complexes related NETosis through Fc $\gamma$ RIIb are highly dependent on mitoROS (110, 112). The lytic-NETosis inducers such as PMA, ionomycin, or living bacteria were confirmed using a live imaging confocal microscopy, however, dead bacteria, LPS, glucose, or activated platelets alone failed to induce NETosis in the *in vitro* experiment (113). Such discrepancy might be due to variations in the experimental design of various studies.

On the other hand, non-lytic NETosis (also called vital NETosis) does not require neutrophils lysis or even the breach of the plasma membrane. Following the release of NETs, neutrophils are alive and keep their functions, such as chemotactic movement, phagocytotic ability, and respiratory burst power (98). This form of NETosis usually occurs early in infection by Gram-positive bacteria in human and mice. The process is very rapid (5–60 min to form NETs), requires both TLR 2 and complement-mediated opsonization, and is independent of NOX2 (114). Non-lytic NETosis can be induced by *Staphylococcus aureus* via a unique mechanism where the inner and outer nuclear membranes are separated, and the vesicles filled with nuclear DNA are extruded intact into the extracellular space where they rupture and release chromatin. Despite that this type of NETs keep a limited amount of proteolytic activity it is still able to kill *S. aureus* (115). Non-lytic NETosis can also be stimulated by *Candida albicans* via interaction with CR3 and fibronectin (116). Moreover, a special type of non-lytic NETosis, which releases mitochondrial DNA and is dependent on ROS, is stimulated by the granulocyte-macrophage colony-stimulating factor (GM-CSF) and LPS (10). Interestingly, *Leishmania* parasites induce both lytic and non-lytic NETosis (117). In that case, the chromatin decondensed by PAD4 is mixed with granular proteins and subsequently excreted with a minor nuclear envelope disruption and without cell membrane disorganization (10, 98). Delgado-Rizo et al. previously summarized the microbial inducers of NETs (10) but we would like to clarify the effect of LPS. Lipopolysaccharide (LPS) is an important component of the outer membrane of gram-negative bacteria known to trigger immune response (118). For a long time, it was unclear whether the direct interaction between LPS and neutrophils causes NETs release, because several reports showed LPS-induced lytic NET formation

(94, 119) while other not (113, 120). Recently, it has been shown that only species- and serotype-specific LPS is able to induce NETs by direct interaction with neutrophils. It was demonstrated that LPS has to be derived from specific bacterial strain of *Escherichia coli* (O128:B12) and *Pseudomonas aeruginosa* (serotype 10) and must be present at sufficient concentration (8 pg per neutrophil). The neutrophils then undergo a lytic-NETosis independent of TLR4. However, non-lytic NETosis is triggered when sufficient amount of LPS regardless of bacterial origin interacts with TLR4 of platelets (108). The process is followed by binding of platelets to the P-selectin glycoprotein ligand-1 (PSGL-1) of neutrophils, and the release of HMGB1 by platelets (9, 95). Moreover, there is a growing evidence of crucial role of the other endogenous and immune factors in the process of NET formation, such as presence of platelets (95, 120), glucose (10), or other effectors (121). To orchestrate inflammatory response, NETs in combination with LPS were shown to induce the production of IL-1 $\beta$  by J774 macrophages via the caspase-1 and caspase-8 pathways (122).

In patients with psoriasis, neutrophils are pre-activated and form NETs in psoriatic skin lesions (55, 123). NETs are increased in blood samples and correlate with the severity of psoriasis (124, 125). They create an extremely immunogenic environment and participate in the initial and maintenance phases of psoriasis (126, 127). NETs stimulate epidermis to release inflammatory cytokines via TLR4 and IL-36 receptor crosstalk (123). Various exogenous and endogenous stimuli and ROS generated by neutrophils initiate immune reaction leading to psoriasis which involves T cell imbalance, keratinocyte proliferation, angiogenesis, and auto-antigen formation (**Figure 2**). The chromatin of NETs in psoriasis plaques is accompanied with antimicrobial peptide LL-37 released by keratinocytes to stimulate the synthesis of inflammatory mediators including IFN- $\alpha$  and IFN- $\beta$  in plasmacytoid dendritic cells (pDCs) (16). Myeloid DCs (mDCs) are then activated to release many pro-inflammatory mediators, such as IL-6, IL-12, IL-23, and TNF $\alpha$  (91, 92), which play an important role in the initiation of the Th1, Th17, and Th22 cells immune response (16). Proteinase 3 released from neutrophils cleaves pro-IL-36 to activated IL-36 cytokine which is together with TNF and IFN- $\gamma$  amplifying the response of mDCs. Th17 activation then leads to the production of IL-17 activating neutrophils and keratinocytes via IL-17 receptors which generates profound IL-17 response (16). Secretory leukocyte protease inhibitor (SLPI), a component of NETs with an inhibitory function on NET formation, may bind to DNA and NE in psoriatic skin lesions and activate the pDCs to produce type 1 interferons (IFN- $\alpha$ , IFN- $\beta$ , etc.) which regulates autoimmunity in psoriasis (128–130). In addition, NETs allow the mDCs to readily sense the neutrophilic antigens and allow the T cells to be primed directly (45, 131, 132). Thus, NETs play an important role in the pathophysiology of psoriasis due to their link between the innate and adaptive immune systems. Psoriasis is accompanied with increased serum levels of TNF- $\alpha$ , interferon (IFN)- $\gamma$ , IL-1, IL-2, IL-4, IL-6, IL-8, IL-10, IL-12, IL-17, IL-18 (133), IL-22 (134), chemerin, resistin (135), lipocalin-2 (LCN2) (123), soluble E-selectin (sE-selectin) (136), complement 3 (137), and decreased levels of transforming growth factor-beta (TGF- $\beta$ ) and adiponectin (133). These cytokines may therefore serve as

potential biomarkers for psoriasis and treatment response in patients. According to a cross-sectional study, psoriasis patients had increased proinflammatory macrophage type 1 (IL-1, IL-6, TNF- $\alpha$ ), Th1 (IL-2, IL-12, IFN- $\gamma$ ), Th17 (IL-6, IL-17) but also anti-inflammatory Th2/T regulatory (Treg) (IL-4, IL-10) profiles which may be correlated to the severity of psoriasis (133). Among the important mediators in psoriasis, LCN2 acts as an antimicrobial protein as well as adipokine associated with obesity, insulin resistance, and atherosclerotic disease, and is also responsible for the activation of the immune system in response to inflammatory and toxic stimuli. Importantly, serum LCN2 levels are elevated in psoriatic patients (138) and correlate with the severity of itching and thus might be used as a clinical marker for itching in psoriasis (139). Not only granulocytes but also keratinocytes of epidermis secrete LCN2, which drives the chemotaxis of neutrophils and sustains NET formation, and thereby in turn maintains the psoriatic inflammation (123). The increased LCN2 blood levels were observed in patients with palmoplantar pustular psoriasis (140) as well as other chronic inflammatory skin diseases such as acne inversa (141) or atopic dermatitis (142). Wolk et al. reported a positive correlation between the LCN2 production and IL-1 $\beta$  levels in the epidermis, which was further enhanced by IL-17 and TNF- $\alpha$ , but not by IL-22. The contribution of LCN2 on skin neutrophil infiltration is apparent (141). In the clinical setting, tissue LCN2 was found to be also significantly higher in psoriasis, regardless of dyslipidemia, or metabolic disturbance in patients. But the LCN2 levels together with psoriasis area and severity index (PASI) score significantly dropped after NB-UVB treatment (143). The *in vivo* effects of LCN2 on topical imiquimod (IMQ)-induced psoriasis-like skin in BALB/c mice were evaluated by Hau group (138). In addition to markedly exacerbated erythema and scaling in IMQ-treated murine skin, LCN2 increased the mRNA expression of interleukin (IL)-17A, IL-17E, IL-22, IL-23, CC-chemokine ligand (CCL)20, TNF- $\alpha$ , chemokine (C-X-C motif) ligand (CXCL)1, CXCL2, LCN2, and S100A7 while it did not affect the mRNA levels of IFN- $\gamma$ , or CXCL10 in the skin. Similar effects were observed *in vitro* on human keratinocytes (138). The data suggest a link between NETs-related cytokines and Th-17 activation in psoriasis.

## NET-TH17 AXIS AND PSORIASIS

Psoriasis has been considered as a T-helper (Th)1/Th17-mediated, chronic inflammatory dermatosis with relation to metabolic syndromes (144). Apart from keratinocytes and T lymphocytes (145), neutrophils are one of the major cellular sources of IL-17 via NET formation in psoriasis (146), and also mast cells were reported to generate extracellular traps (147). NETs activation has been linked with Th17 responses in psoriasis and has drawn particular attention recently (148). In an experimental model, NETs induced the generation of CD3<sup>+</sup>CD4<sup>+</sup>IL-17<sup>+</sup> (Th17) cells from peripheral blood mononuclear cells, which requires monocyte and cell-to-cell contact. Th17 induction was enhanced by a psoriasis risk-associated variant in the TRAF3IP2 gene encoding the D10N variant of Act1 which serves as a key mediator of IL-17 signal transduction. That provides an evidence of genetic basis for the

enhanced IL-17 expression in psoriasis. IL-17-expressing T cells and neutrophils were suggested to have a cross-talk because IL-17-expressing T cells produce cytokines which promote the development, recruitment, and lifespan of neutrophils (149).

Although many immune diseases including psoriasis or atopic dermatitis have been traditionally classified as Th1/Th2 biphasic disorders, there is a growing evidence supporting a rather systemic activation of other multiple Th-cell subsets, such as Th17 cells producing IL-17 and IL-22 (**Figure 2**). Interestingly, in comparison with psoriasis, atopic dermatitis showed reduced genomic expression of IL-23, IL-17, IFN- $\gamma$ , and other innate defense genes (hBD2, elafin, LL-37) (150). Elevated IL-17 is detected in psoriatic skin lesions and in the blood (151). IL-17 mainly stimulates keratinocytes to produce neutrophil-tropic chemokines CXCL-1, CXCL-2, CXCL-8 (IL-8), and antimicrobial peptides, such as LL-37. IL-17 serves as an autocrine-amplifying mediator that is simultaneously involved in the recruitment, activation, and survival of neutrophils (6). There are several subtypes of IL-17 family cytokines binding to IL-17 receptors, namely IL-17A, IL-17B, IL-17C, IL-17D, IL-17E (also known as IL-25) and IL-17F (145). IL-17A from neutrophils stimulates keratinocytes to express CCL20, attracting Th17 cells with CCR6 expression to release IL-17A, and finally resulting in positive feedback and the development of the psoriatic lesions (8). IL-17C is a unique cytokine that is produced by keratinocytes and that is involved in such synergistic loops that may be responsible for amplifying the inflammation in both psoriasis and atopic dermatitis. This may ultimately lead to induction of S100As and other molecules that accompany epidermal hyperplasia. Thus, antagonism of IL-17C may be beneficial for psoriasis and atopic dermatitis treatment (152). IL-17E then recruits neutrophils by activating macrophages and contributes to the infiltration of psoriatic neutrophils (153). Besides other innate immune cells, neutrophils significantly contribute to IL-17-related immune regulations in psoriasis by employing several mechanisms including the formation of NETs (45). Moreover, IL-17 released by NETs leads to endothelial dysfunction in atherosclerosis and keratinocyte proliferation in psoriasis, which may explain why patients with psoriasis also suffer from increased risk of atherosclerosis (11). Anti-IL-17 drugs, such as secukinumab, clear the neutrophils in the epidermis and can be used to effectively treat psoriasis (48). The targeted biologic therapies are of great importance with regards to an increasing number of comorbidities associated with psoriasis together with its systemic inflammation nature indicating that these diseases are sharing some common pathological mechanisms (7). In summary, NETs were demonstrated as potential upstream drug targets for the treatment of psoriasis.

## CONCLUSION

Neutrophils in psoriasis are of interest, particularly, because of their crucial roles in the innate and adaptive immune system. The respiratory burst with ROS generation, degranulation, and formation of NETs are the main offensive functions of neutrophils and contribute to the immunopathogenesis of psoriasis. Recently, great attention was brought to the role of NETs in psoriasis because activated neutrophils producing



NETs are abundant in psoriatic skin plaques and pustules, as well as in the serum of patients with psoriasis. Overexpression of NETs leads to the activation of other cells releasing IL-17, which stimulates the synthesis of inflammatory mediators and in turn leads to auto-amplification of neutrophils. Therefore, further development of inhibitors and biologic drugs targeting overexpressed offensive features of neutrophils, i.e., respiratory burst, degranulation, and NET formation, is of great importance. We believe that the consideration of the role of neutrophil defense mechanisms in the pathogenesis of psoriasis offered in this review highlights the need to further investigate neutrophils for possible improvements of available treatments in the future.

## AUTHOR CONTRIBUTIONS

C-CC and W-JC wrote and revised the manuscript. MK consulted and revised the manuscript. C-YL drew the figures. T-LH initiated the concept and supervised the writing. All authors read and approved the final manuscript.

## REFERENCES

- Tecchio C, Cassatella MA. Neutrophil-derived chemokines on the road to immunity. *Semin Immunol.* (2016) 28:119–28. doi: 10.1016/j.smim.2016.04.003
- Nauseef WM, Borregaard N. Neutrophils at work. *Nat Immunol.* (2014) 15:602–11. doi: 10.1038/ni.2921
- Leliefeld PH, Koenderman L, Pillay J. How Neutrophils Shape Adaptive Immune Responses. *Front Immunol.* (2015) 6:471. doi: 10.3389/fimmu.2015.00471
- Rosales C, Lowell CA, Schnoor M, Uribe-Querol E. Neutrophils: Their Role in Innate and Adaptive Immunity 2017. *J Immunol Res.* (2017) 2017:9748345. doi: 10.1155/2017/9748345
- Georgescu SR, Tampa M, Caruntu C, Sarbu MI, Mitran CI, Mitran MI, et al. Advances in understanding the immunological pathways in psoriasis. *Int J Mol Sci.* (2019) 20:739. doi: 10.3390/ijms20030739
- Chiricozzi A, Romanelli P, Volpe E, Borsellino G, Romanelli M. Scanning the Immunopathogenesis of Psoriasis. *Int J Mol Sci.* (2018) 19:E179. doi: 10.3390/ijms19010179
- Korman NJ. Management of psoriasis as a systemic disease: What is the evidence? *Br J Dermatol.* (2019). doi: 10.1111/bjd.18245. [Epub ahead of print].
- Katayama H. Development of psoriasis by continuous neutrophil infiltration into the epidermis. *Exp Dermatol.* (2018) 27:1084–91. doi: 10.1111/exd.13746
- Cedervall J, Hamidi A, Olsson AK. Platelets, NETs and cancer. *Thromb Res.* (2018) 164(Suppl 1):S148–52. doi: 10.1016/j.thromres.2018.01.049
- Delgado-Rizo V, Martínez-Guzmán MA, Iñiguez-Gutierrez L, García-Orozco A, Alvarado-Navarro A, Fafutis-Morris M. Neutrophil extracellular traps and its implications in inflammation: an overview. *Front Immunol.* (2017) 8:81. doi: 10.3389/fimmu.2017.00081
- Sanda GE, Belur AD, Teague HL, Mehta NN. Emerging Associations Between Neutrophils, Atherosclerosis, and Psoriasis. *Curr Atheroscler Rep.* (2017) 19:53. doi: 10.1007/s11883-017-0692-8
- Bagchi D, Kundu-Raychaudhuri SK, Raychaudhuri SP. *Psoriasis and Psoriatic Arthritis: Pathophysiology, Therapeutic Intervention, and Complementary Medicine*. Portland, OR: CRC Press/Taylor & Francis Group (2018). p. 413.
- Menter A. RC. *Psoriasis*. 2nd ed. Portland, OR: CRC Press/Taylor & Francis Group (2017). p. 268
- Warren R. MA. *Handbook of Psoriasis and Psoriatic Arthritis*. Springer International Publishing (2016). p. 116.

## FUNDING

This review was supported by the grants from the Ministry of Science Technology (MOST 108-2320-B-255-003-MY3, MOST 106-2320-B-255-003-MY3, and MOST 104-2320-B-255-004-MY3), Ministry of Education (EMRPD1I0441), and Chang Gung Memorial Hospital (CMRPG5F0161 and BMRP450). The funding source had no role in this article.

## ACKNOWLEDGMENTS

We are grateful to Assoc. Prof. Mohamed El-Shazly for valuable comments and revision of the manuscript. Special thanks to Editage English Editorial Office, Taiwan for English editing. The authors wish to thank Miss Ingrid Kuo and the Center for Big Data Analytics and Statistics (Grant CLRP3 3D0045) at Chang Gung Memorial Hospital for creating the illustrations used herein.

- Adebajo A, Gladman DD, Mease PJ. *Psoriatic Arthritis and Psoriasis: Pathology and Clinical Aspects*. Springer International Publishing (2016). p. 316.
- Greb JE, Goldminz AM, Elder JT, Lebwohl MG, Gladman DD, Wu JJ, et al. Psoriasis. *Nat Rev Dis Primers.* (2016) 2:16082. doi: 10.1038/nrdp.2016.83
- Sticherling M. Psoriasis and autoimmunity. *Autoimmun Rev.* (2016) 15:1167–70. doi: 10.1016/j.autrev.2016.09.004
- Kaushik SB, Lebwohl MG. CME Part I Psoriasis: which therapy for which patient psoriasis comorbidities and preferred systemic agents. *J Am Acad Dermatol.* (2019) 80:27–40. doi: 10.1016/j.jaad.2018.06.057
- Geller S, Xu H, Lebwohl M, Nardone B, Lacouture ME, Kheterpal M. Malignancy risk and recurrence with psoriasis and its treatments: a concise update. *Am J Clin Dermatol.* (2018) 19:363–75. doi: 10.1007/s40257-017-0337-2
- Gelfand JM. Psoriasis, type 2 diabetes mellitus, and obesity: weighing the evidence. *JAMA Dermatol.* (2016) 152:753–4. doi: 10.1001/jamadermatol.2016.0670
- Armstrong AW. Psoriasis. *JAMA Dermatol.* (2017) 153:956. doi: 10.1001/jamadermatol.2017.2103
- Raychaudhuri SK, Mavarakis E, Raychaudhuri SP. Diagnosis and classification of psoriasis. *Autoimmun Rev.* (2014) 13:490–5. doi: 10.1016/j.autrev.2014.01.008
- Nestle FO, Kaplan DH, Barker J. Psoriasis. *N Engl J Med.* (2009) 361:496–509. doi: 10.1056/NEJMra0804595
- Vanderpuye-Orgle J, Zhao Y, Lu J, Shrestha A, Sexton A, Seabury S, et al. Evaluating the economic burden of psoriasis in the United States. *J Am Acad Dermatol.* (2015) 72:961–7.e5. doi: 10.1016/j.jaad.2015.02.1099
- Brezinski EA, Dhillon JS, Armstrong AW. Economic burden of psoriasis in the United States: a systematic review. *JAMA Dermatol.* (2015) 151:651–8. doi: 10.1001/jamadermatol.2014.3593
- Hawro T, Zalewska A, Hawro M, Kaszuba A, Krolukowska M, Maurer M. Impact of psoriasis severity on family income and quality of life. *J Eur Acad Dermatol Venerol.* (2015) 29:438–43. doi: 10.1111/jdv.12572
- Singh S, Taylor C, Kornmehl H, Armstrong AW. Psoriasis and suicidality: a systematic review and meta-analysis. *J Am Acad Dermatol.* (2017) 77:425–40.e2. doi: 10.1016/j.jaad.2017.05.019
- Dowlatsahi EA, Wakke M, Arends LR, Nijsten T. The prevalence and odds of depressive symptoms and clinical depression in psoriasis patients: a systematic review and meta-analysis. *J Invest Dermatol.* (2014) 134:1542–51. doi: 10.1038/jid.2013.508

29. Prinz JC. Autoimmune aspects of psoriasis: heritability and autoantigens. *Autoimmun Rev.* (2017) 16:970–9. doi: 10.1016/j.autrev.2017.07.011
30. Hwang ST, Nijsten T, Elder JT. Recent highlights in psoriasis research. *J Invest Dermatol.* (2017) 137:550–6. doi: 10.1016/j.jid.2016.11.007
31. Harvima IT, Nilsson G, Suttle MM, Naukkarinen A. Is there a role for mast cells in psoriasis? *Arch Dermatol Res.* (2008) 300:461–78. doi: 10.1007/s00403-008-0874-x
32. Prinz JC. Melanocytes: target cells of an HLA-C\*06:02-restricted autoimmune response in psoriasis. *J Invest Dermatol.* (2017) 137:2053–8. doi: 10.1016/j.jid.2017.05.023
33. Mrowietz U. Neutrophils' sexiness is independent of trendy fashion. *Exp Dermatol.* (2017) 26:312–3. doi: 10.1111/exd.13102
34. Mantovani A, Cassatella MA, Costantini C, Jaillon S. Neutrophils in the activation and regulation of innate and adaptive immunity. *Nat Rev Immunol.* (2011) 11:519–31. doi: 10.1038/nri3024
35. Jaillon S, Galdiero MR, Del Prete D, Cassatella MA, Garlanda C, Mantovani A. Neutrophils in innate and adaptive immunity. *Semin Immunopathol.* (2013) 35:377–94. doi: 10.1007/s00281-013-0374-8
36. Dubertret L, Mrowietz U, Ranki A, van de Kerkhof PC, Chimenti S, Lotti T, et al. European patient perspectives on the impact of psoriasis: the EUROSPO patient membership survey. *Br J Dermatol.* (2006) 155:729–36. doi: 10.1111/j.1365-2133.2006.07405.x
37. Belinchón I, Rivera R, Blanch C, Comellas M, Lizán L. Adherence, satisfaction and preferences for treatment in patients with psoriasis in the European Union: a systematic review of the literature. *Patient Prefer Adherence.* (2016) 10:2357–67. doi: 10.2147/PPA.S117006
38. Meng S, Lin Z, Wang Y, Wang Z, Li P, Zheng Y. Psoriasis therapy by Chinese medicine and modern agents. *Chin Med.* (2018) 13:16. doi: 10.1186/s13020-018-0174-0
39. Damevska K, Franca K, Lotti T, Nikolovska S, Pollozhani N. Complementary and integrative therapies for psoriasis: looking forward. *Dermatol Ther.* (2018) 31:e12627. doi: 10.1111/dth.12627
40. Talbott W, Duffy N. Complementary and alternative medicine for psoriasis: what the dermatologist needs to know. *Am J Clin Dermatol.* (2015) 16:147–65. doi: 10.1007/s40257-015-0128-6
41. Costanzo A, Malara G, Pelucchi C, Fatiga F, Barbera G, Franchi A, et al. Effectiveness end points in real-world studies on biological therapies in psoriasis: systematic review with focus on drug survival. *Dermatology.* (2018) 234:1–12. doi: 10.1159/000488586
42. Yamanaka K, Umezawa Y, Yamagiwa A, Saeki H, Kondo M, Gabazza EC, et al. Biologic therapy improves psoriasis by decreasing the activity of monocytes and neutrophils. *J Dermatol.* (2014) 41:679–85. doi: 10.1111/1346-8138.12560
43. de Groot M, Picavet DJ, van Kuijk AW, Tak PP, Bos JD, de Rie MA, et al. A prospective, randomized, placebo-controlled study to identify biomarkers associated with active treatment in psoriatic arthritis: effects of adalimumab treatment on lesional and nonlesional skin. *Dermatology.* (2012) 225:298–303. doi: 10.1159/000343290
44. Tan JK, Aphale A, Malaviya R, Sun Y, Gottlieb AB. Mechanisms of action of etanercept in psoriasis. *J Invest Dermatol Symp Proc.* (2007) 12:38–45. doi: 10.1038/sj.jidsymp.5650037
45. Schon MP, Erpenbeck L. The Interleukin-23/Interleukin-17 Axis Links Adaptive and Innate Immunity in Psoriasis. *Front Immunol.* (2018) 9:1323. doi: 10.3389/fimmu.2018.01323
46. Chen F, Cao A, Yao S, Evans-Marin HL, Liu H, Wu W, et al. mTOR Mediates IL-23 Induction of Neutrophil IL-17 and IL-22 Production. *J Immunol.* (2016) 196:4390–9. doi: 10.1097/01.ccm.0000508877.60312.7c
47. Liu L, Lu J, Allan BW, Tang Y, Tetreault J, Chow CK, et al. Generation and characterization of ixekizumab, a humanized monoclonal antibody that neutralizes interleukin-17A. *J Inflamm Res.* (2016) 9:39–50. doi: 10.2147/JIR.S100940
48. Reich K, Papp KA, Matheson RT, Tu JH, Bissonnette R, Bourcier M, et al. Evidence that a neutrophil-keratinocyte crosstalk is an early target of IL-17A inhibition in psoriasis. *Exp Dermatol.* (2015) 24:529–35. doi: 10.1111/exd.12710
49. Polat M, Bugdayci G, Kaya H, Oguzman H. Evaluation of neutrophil-to-lymphocyte ratio and platelet-to-lymphocyte ratio in Turkish patients with chronic plaque psoriasis. *Acta Dermatovenereol Alp Pannonica Adriat.* (2017) 26:97–100. doi: 10.15570/actaapa.2017.28
50. Paliogiannis P, Satta R, Deligia G, Farina G, Bassu S, Mangoni AA, et al. Associations between the neutrophil-to-lymphocyte and the platelet-to-lymphocyte ratios and the presence and severity of psoriasis: a systematic review and meta-analysis. *Clin Exp Med.* (2019) 19:37–45. doi: 10.1007/s10238-018-0538-x
51. Balevi A, Olmuscelik O, Ustuner P, Ozdemir M. Is there any correlation between red cell distribution width, mean platelet volume neutrophil count, lymphocyte count, and psoriasis area severity index in patients under treatment for psoriasis? *Acta Dermatovenereol Croat.* (2018) 26:199–205.
52. Ereğ Toprak A, Özlü E, Uzuncakmak TK, Yalcinkaya E, Sogut S, Karadag AS. Neutrophil/lymphocyte ratio, serum endocan, and nesfatin-1 levels in patients with psoriasis vulgaris undergoing phototherapy treatment. *Med Sci Monit.* (2016) 22:1232–7. doi: 10.12659/MSM.898240
53. Yurtdas M, Yaylali YT, Kaya Y, Ozdemir M, Ozkan I, Aladag N. Neutrophil-to-lymphocyte ratio may predict subclinical atherosclerosis in patients with psoriasis. *Echocardiography.* (2014) 31:1095–104. doi: 10.1111/echo.12511
54. Ikeda S, Takahashi H, Suga Y, Eto H, Etoh T, Okuma K, et al. Therapeutic depletion of myeloid lineage leukocytes in patients with generalized pustular psoriasis indicates a major role for neutrophils in the immunopathogenesis of psoriasis. *J Am Acad Dermatol.* (2013) 68:609–17. doi: 10.1016/j.jaad.2012.09.037
55. Schon MP, Broekaert SM, Erpenbeck L. Sexy again: the renaissance of neutrophils in psoriasis. *Exp Dermatol.* (2017) 26:305–11. doi: 10.1111/exd.13067
56. Belambri SA, Rolas L, Raad H, Hurtado-Nedelec M, Dang PM, El-Benna J. NADPH oxidase activation in neutrophils: role of the phosphorylation of its subunits. *Eur J Clin Invest.* (2018) 2:e12951. doi: 10.1111/eci.12951
57. Amulic B, Cazalet C, Hayes GL, Metzler KD, Zychlinsky A. Neutrophil function: from mechanisms to disease. *Annu Rev Immunol.* (2012) 30:459–89. doi: 10.1146/annurev-immunol-020711-074942
58. Glennon-Alty L, Hackett AP, Chapman EA, Wright HL. Neutrophils and redox stress in the pathogenesis of autoimmune disease. *Free Radic Biol Med.* (2018) 125:25–35. doi: 10.1016/j.freeradbiomed.2018.03.049
59. Winterbourn CC, Kettle AJ, Hampton MB. Reactive oxygen species and neutrophil function. *Annu Rev Biochem.* (2016) 85:765–92. doi: 10.1146/annurev-biochem-060815-014442
60. Hoffmann MH, Griffiths HR. The dual role of ROS in autoimmune and inflammatory diseases: Evidence from preclinical models. *Free Radic Biol Med.* (2018) 125:62–71. doi: 10.1016/j.freeradbiomed.2018.03.016
61. Bloomfield FJ, Young MM. Enhanced release of inflammatory mediators from lithium-stimulated neutrophils in psoriasis. *Br J Dermatol.* (1983) 109:9–13. doi: 10.1111/j.1365-2133.1983.tb03985.x
62. Bloomfield FJ, Young MM. Enhanced chemiluminescence production by phagocytosing neutrophils in psoriasis. *Inflammation.* (1988) 12:153–9. doi: 10.1007/BF00916398
63. Martin G, Guerard S, Fortin MM, Rusu D, Soucy J, Poubelle PE, et al. Pathological crosstalk *in vitro* between T lymphocytes and lesional keratinocytes in psoriasis: necessity of direct cell-to-cell contact. *Lab Invest.* (2012) 92:1058–70. doi: 10.1038/labinvest.2012.69
64. Vogt KL, Summers C, Chilvers ER, Condliffe AM. Priming and de-priming of neutrophil responses *in vitro* and *in vivo*. *Eur J Clin Invest.* (2018) 47:e12967. doi: 10.1111/eci.12967
65. Boehncke WH, Schon MP. Psoriasis. *Lancet.* (2015) 386:983–94. doi: 10.1016/S0140-6736(14)61909-7
66. Guerard S, Allaey I, Martin G, Pouliot R, Poubelle PE. Psoriatic keratinocytes prime neutrophils for an overproduction of superoxide anions. *Arch Dermatol Res.* (2013) 305:879–89. doi: 10.1007/s00403-013-1404-z
67. Lin X, Huang T. Oxidative stress in psoriasis and potential therapeutic use of antioxidants. *Free Radic Res.* (2016) 50:585–95. doi: 10.3109/10715762.2016.1162301
68. Lai R, Xian D, Xiong X, Yang L, Song J, Zhong J. Proanthocyanidins: novel treatment for psoriasis that reduces oxidative stress and modulates Th17 and Treg cells. *Redox Rep.* (2018) 23:130–5. doi: 10.1080/13510002.2018.1462027
69. Lacy P. Mechanisms of degranulation in neutrophils. *Allergy Asthma Clin Immunol.* (2006) 2:98–108. doi: 10.1186/1710-1492-2-3-98



70. Sheshachalam A, Srivastava N, Mitchell T, Lacy P, Eitzen G. Granule protein processing and regulated secretion in neutrophils. *Front Immunol.* (2014) 5:448. doi: 10.3389/fimmu.2014.00448
71. Kahlenberg JM, Kaplan MJ. Little peptide, big effects: the role of LL-37 in inflammation and autoimmune disease. *J Immunol.* (2013) 191:4895–901. doi: 10.4049/jimmunol.1302005
72. Cowland JB, Borregaard N. Granulopoiesis and granules of human neutrophils. *Immunol Rev.* (2016) 273:11–28. doi: 10.1111/immr.12440
73. Mitchell T, Lo A, Logan MR, Lacy P, Eitzen G. Primary granule exocytosis in human neutrophils is regulated by Rac-dependent actin remodeling. *Am J Physiol Cell Physiol.* (2008) 295:C1354–65. doi: 10.1152/ajpcell.00239.2008
74. Jog NR, Rane MJ, Lominadze G, Luerman GC, Ward RA, McLeish KR. The actin cytoskeleton regulates exocytosis of all neutrophil granule subsets. *Am J Physiol Cell Physiol.* (2007) 292:C1690–700. doi: 10.1152/ajpcell.00384.2006
75. Yin C, Heit B. Armed for destruction: formation, function and trafficking of neutrophil granules. *Cell Tissue Res.* (2018) 371:455–71. doi: 10.1007/s00441-017-2731-8
76. Hoenderdos K, Lodge KM, Hirst RA, Chen C, Palazzo SG, Emerenciana A, et al. Hypoxia upregulates neutrophil degranulation and potential for tissue injury. *Thorax.* (2016) 71:1030–8. doi: 10.1136/thoraxjnl-2015-207604
77. Polverino E, Rosales-Mayor E, Dale GE, Dembowski K, Torres A. The role of neutrophil elastase inhibitors in lung diseases. *Chest.* (2017) 152:249–62. doi: 10.1016/j.chest.2017.03.056
78. Chistiakov DA, Bobryshev YV, Orekhov AN. Neutrophil's weapons in atherosclerosis. *Exp Mol Pathol.* (2015) 99:663–71. doi: 10.1016/j.yexmp.2015.11.011
79. Sivalingam Z, Larsen SB, Grove EL, Hvas AM, Kristensen SD, Magnusson NE. Neutrophil gelatinase-associated lipocalin as a risk marker in cardiovascular disease. *Clin Chem Lab Med.* (2017) 56:5–18. doi: 10.1515/cclm-2017-0120
80. Ramaiah SK, Jaeschke H. Role of neutrophils in the pathogenesis of acute inflammatory liver injury. *Toxicol Pathol.* (2007) 35:757–66. doi: 10.1080/01926230701584163
81. Wright HL, Moots RJ, Bucknall RC, Edwards SW. Neutrophil function in inflammation and inflammatory diseases. *Rheumatology.* (2010) 49:1618–31. doi: 10.1093/rheumatology/keq045
82. Wright HL, Moots RJ, Edwards SW. The multifactorial role of neutrophils in rheumatoid arthritis. *Nat Rev Rheumatol.* (2014) 10:593–601. doi: 10.1038/nrrheum.2014.80
83. Dilek N, Dilek AR, Taskin Y, Erkinuresin T, Yalcin O, Saral Y. Contribution of myeloperoxidase and inducible nitric oxide synthase to pathogenesis of psoriasis. *Postepy Dermatol Alergol.* (2016) 33:435–9. doi: 10.5114/ada.2016.63882
84. Cao LY, Soler DC, Debanne SM, Grozdev I, Rodriguez ME, Feig RL, et al. Psoriasis and cardiovascular risk factors: increased serum myeloperoxidase and corresponding immunocellular overexpression by CD11b. (+) CD68. (+) macrophages in skin lesions. *Am J Transl Res.* (2013) 6:16–27.
85. Strzepa A, Pritchard KA, Dittel BN. Myeloperoxidase: a new player in autoimmunity. *Cell Immunol.* (2017) 317:1–8. doi: 10.1016/j.cellimm.2017.05.002
86. Lau D, Mollnau H, Eiserich JP, Freeman BA, Daiber A, Gehling UM, et al. Myeloperoxidase mediates neutrophil activation by association with CD11b/CD18 integrins. *Proc Natl Acad Sci USA.* (2005) 102:431–6. doi: 10.1073/pnas.0405193102
87. Guo J, Tu J, Hu Y, Song G, Yin Z. Cathepsin G cleaves and activates IL-36γ and promotes the inflammation of psoriasis. *Drug Des Devel Ther.* (2019) 13:581–8. doi: 10.2147/DDDT.S194765
88. Henry CM, Sullivan GP, Clancy DM, Afonina IS, Kulms D, Martin SJ. Neutrophil-derived proteases escalate inflammation through activation of IL-36 family cytokines. *Cell Rep.* (2016) 14:708–22. doi: 10.1016/j.celrep.2015.12.072
89. Xhindoli D, Pacor S, Benincasa M, Scocchi M, Gennaro R, Tossi A. The human cathelicidin LL-37–A pore-forming antibacterial peptide and host-cell modulator. *Biochim Biophys Acta.* (2016) 1858:546–66. doi: 10.1016/j.bbame.2015.11.003
90. Durr UH, Sudheendra US, Ramamoorthy A. LL-37, the only human member of the cathelicidin family of antimicrobial peptides. *Biochim Biophys Acta.* (2006) 1758:1408–25. doi: 10.1016/j.bbame.2006.03.030
91. Ganguly D, Chamilos G, Lande R, Gregorio J, Meller S, Facchinetti V, et al. Self-RNA-antimicrobial peptide complexes activate human dendritic cells through TLR7 and TLR8. *J Exp Med.* (2009) 206:1983–94. doi: 10.1084/jem.20090480
92. Lande R, Gregorio J, Facchinetti V, Chatterjee B, Wang YH, Homey B, et al. Plasmacytoid dendritic cells sense self-DNA coupled with antimicrobial peptide. *Nature.* (2007) 449:564–9. doi: 10.1038/nature06116
93. Meyer-Hoffert U, Wingerts Zahn J, Wiedow O. Human leukocyte elastase induces keratinocyte proliferation by epidermal growth factor receptor activation. *J Invest Dermatol.* (2004) 123:338–45. doi: 10.1111/j.0022-202X.2004.23202.x
94. Brinkmann V, Reichard U, Goosmann C, Fauler B, Uhlemann Y, Weiss DS, et al. Neutrophil extracellular traps kill bacteria. *Science.* (2004) 303:1532–5. doi: 10.1126/science.1092385
95. Kim SJ, Jenne CN. Role of platelets in neutrophil extracellular trap. (NET) production and tissue injury. *Semin Immunol.* (2016) 28:546–54. doi: 10.1016/j.smim.2016.10.013
96. Branzk N, Lubojemska A, Hardison SE, Wang Q, Gutierrez MG, Brown GD, et al. Neutrophils sense microbe size and selectively release neutrophil extracellular traps in response to large pathogens. *Nat Immunol.* (2014) 15:1017–25. doi: 10.1038/ni.2987
97. Apel F, Zychlinsky A, Kenny EF. The role of neutrophil extracellular traps in rheumatic diseases. *Nat Rev Rheumatol.* (2018) 14:467–75. doi: 10.1038/s41584-018-0039-z
98. Honda M, Kubes P. Neutrophils and neutrophil extracellular traps in the liver and gastrointestinal system. *Nat Rev Gastroenterol Hepatol.* (2018) 15:206–21. doi: 10.1038/nrgastro.2017.183
99. Fernandez-Ruiz I. Inflammation: NETs are involved in AAA. *Nat Rev Cardiol.* (2018) 15:257. doi: 10.1038/nrcardio.2018.28
100. Doring Y, Soehnlein O, Weber C. Neutrophil extracellular traps in atherosclerosis and atherothrombosis. *Circ Res.* (2017) 120:736–43. doi: 10.1161/CIRCRESAHA.116.309692
101. Dabrowska D, Jablonska E, Garley M, Sawicka-Powierza J, Nowak K. The Phenomenon of Neutrophil Extracellular Traps in Vascular Diseases. *Arch Immunol Ther Exp.* (2018) 66:273–81. doi: 10.1007/s00005-018-0505-y
102. Porto BN, Stein RT. Neutrophil extracellular traps in pulmonary diseases: too much of a good thing? *Front Immunol.* (2016) 7:311. doi: 10.3389/fimmu.2016.00311
103. Liu T, Wang FP, Wang G, Mao H. Role of neutrophil extracellular traps in asthma and chronic obstructive pulmonary disease. *Chin Med J.* (2017) 130:730–6. doi: 10.4103/0366-6999.201608
104. Albregues J, Shields MA, Ng D, Park CG, Ambrico A, Poindexter ME, et al. Neutrophil extracellular traps produced during inflammation awaken dormant cancer cells in mice. *Science.* (2018) 361:eaa04227. doi: 10.1126/science.aao4227
105. Kenny EF, Herzig A, Kruger R, Muth A, Mondal S, Thompson PR, et al. Diverse stimuli engage different neutrophil extracellular trap pathways. *Elife.* (2017) 6:e24437. doi: 10.7554/eLife.24437
106. Papayannopoulos V, Metzler KD, Hakkim A, Zychlinsky A. Neutrophil elastase and myeloperoxidase regulate the formation of neutrophil extracellular traps. *J Cell Biol.* (2010) 191:677–91. doi: 10.1083/jcb.201006052
107. Loures FV, Rohm M, Lee CK, Santos E, Wang JP, Specht CA, et al. Recognition of *Aspergillus fumigatus* hyphae by human plasmacytoid dendritic cells is mediated by dectin-2 and results in formation of extracellular traps. *PLoS Pathog.* (2015) 11:e1004643. doi: 10.1371/journal.ppat.1004643
108. Pieterse E, Rother N, Yanginlar C, Hilbrands LB, van der Vlag J. Neutrophils discriminate between lipopolysaccharides of different bacterial sources and selectively release neutrophil extracellular traps. *Front Immunol.* (2016) 7:484. doi: 10.3389/fimmu.2016.00484
109. Desai J, Kumar SV, Mulay SR, Konrad L, Romoli S, Schauer C, et al. PMA and crystal-induced neutrophil extracellular trap formation involves RIPK1-RIPK3-MLKL signaling. *Eur J Immunol.* (2016) 46:223–9. doi: 10.1002/eji.201545605
110. Papayannopoulos V. Neutrophil extracellular traps in immunity and disease. *Nat Rev Immunol.* (2018) 18:134–47. doi: 10.1038/nri.2017.105
111. Doua DN, Khan MA, Grasmann H, Palaniyar N. SK3 channel and mitochondrial ROS mediate NADPH oxidase-independent NETosis

- induced by calcium influx. *Proc Natl Acad Sci USA*. (2015) 112:2817–22. doi: 10.1073/pnas.1414055112
112. Behnen M, Leschczyk C, Moller S, Batel T, Klinger M, Solbach W, et al. Immobilized immune complexes induce neutrophil extracellular trap release by human neutrophil granulocytes via FcγRIIIB and Mac-1. *J Immunol*. (2014) 193:1954–65. doi: 10.4049/jimmunol.1400478
  113. Hoppenbrouwers T, Autar ASA, Sultan AR, Abraham TE, van Cappellen WA, Houtsmuller AB, et al. *In vitro* induction of NETosis: Comprehensive live imaging comparison and systematic review. *PLoS ONE*. (2017) 12:e0176472. doi: 10.1371/journal.pone.0176472
  114. Yipp BG, Petri B, Salina D, Jenne CN, Scott BN, Zbytniuk LD, et al. Infection-induced NETosis is a dynamic process involving neutrophil multitasking *in vivo*. *Nat Med*. (2012) 18:1386–93. doi: 10.1038/nm.2847
  115. Pilszczek FH, Salina D, Poon KK, Fahey C, Yipp BG, Sibley CD, et al. A novel mechanism of rapid nuclear neutrophil extracellular trap formation in response to *Staphylococcus aureus*. *J Immunol*. (2010) 185:7413–25. doi: 10.4049/jimmunol.1000675
  116. Byrd AS, O'Brien XM, Johnson CM, Lavigne LM, Reichner JS. An extracellular matrix-based mechanism of rapid neutrophil extracellular trap formation in response to *Candida albicans*. *J Immunol*. (2013) 190:4136–48. doi: 10.4049/jimmunol.1202671
  117. Rochael NC, Guimaraes-Costa AB, Nascimento MT, DeSouza-Vieira TS, Oliveira MP, Garcia e Souza LF, et al. Classical ROS-dependent and early/rapid ROS-independent release of neutrophil extracellular traps triggered by *Leishmania* parasites. *Sci Rep*. (2015) 5:18302. doi: 10.1038/srep18302
  118. Chandler CE, Ernst RK. Bacterial lipids: powerful modifiers of the innate immune response. *F1000Res*. (2017) 6:F1000. doi: 10.12688/f1000research.11388.1
  119. Petretto A, Bruschi M, Pratesi F, Croia C, Candiano G, Ghiggeri G, et al. Neutrophil extracellular traps (NET) induced by different stimuli: a comparative proteomic analysis. *PLoS ONE*. (2019) 14:e0218946. doi: 10.1371/journal.pone.0218946
  120. Clark SR, Ma AC, Tavener SA, McDonald B, Goodarzi Z, Kelly MM, et al. Platelet TLR4 activates neutrophil extracellular traps to ensnare bacteria in septic blood. *Nat Med*. (2007) 13:463–9. doi: 10.1038/nm1565
  121. Liu S, Su X, Pan P, Zhang L, Hu Y, Tan H, et al. Neutrophil extracellular traps are indirectly triggered by lipopolysaccharide and contribute to acute lung injury. *Sci Rep*. (2016) 6:37252. doi: 10.1038/srep37252
  122. Hu Z, Murakami T, Tamura H, Reich J, Kuwahara-Arai K, Iba T, et al. Neutrophil extracellular traps induce IL-1β production by macrophages in combination with lipopolysaccharide. *Int J Mol Med*. (2017) 39:549–58. doi: 10.3892/ijmm.2017.2870
  123. Shao S, Fang H, Dang E, Xue K, Zhang J, Li B, et al. Neutrophil extracellular traps promote inflammatory responses in psoriasis via activating epidermal TLR4/IL-36R crosstalk. *Front Immunol*. (2019) 10:746. doi: 10.3389/fimmu.2019.00746
  124. Hu SC, Yu HS, Yen FL, Lin CL, Chen GS, Lan CC. Neutrophil extracellular trap formation is increased in psoriasis and induces human β-defensin-2 production in epidermal keratinocytes. *Sci Rep*. (2016) 6:31119. doi: 10.1038/srep31119
  125. Lee KH, Kronbichler A, Park DD, Park Y, Moon H, Kim H, et al. Neutrophil extracellular traps (NETs) in autoimmune diseases: a comprehensive review. *Autoimmun Rev*. (2017) 16:1160–73. doi: 10.1016/j.autrev.2017.09.012
  126. Lowes MA, Suárez-Fariñas M, Krueger JG. Immunology of psoriasis. *Annu Rev Immunol*. (2014) 32:227–55. doi: 10.1146/annurev-immunol-032713-120225
  127. Pinegin B, Vorobjeva N, Pinegin V. Neutrophil extracellular traps and their role in the development of chronic inflammation and autoimmunity. *Autoimmun Rev*. (2015) 14:633–40. doi: 10.1016/j.autrev.2015.03.002
  128. Skrzeczynska-Moncznik J, Włodarczyk A, Zabieglo K, Kapinska-Mrowiecka M, Marewicz E, Dubin A, et al. Secretory leukocyte proteinase inhibitor-competent DNA deposits are potent stimulators of plasmacytoid dendritic cells: implication for psoriasis. *J Immunol*. (2012) 189:1611–7. doi: 10.4049/jimmunol.1103293
  129. Zabieglo K, Majewski P, Majchrzak-Gorecka M, Włodarczyk A, Grygier B, Zegar A, et al. The inhibitory effect of secretory leukocyte protease inhibitor (SLPI) on formation of neutrophil extracellular traps. *J Leukoc Biol*. (2015) 98:99–106. doi: 10.1189/jlb.4AB1114-543R
  130. Majewski P, Majchrzak-Gorecka M, Grygier B, Skrzeczynska-Moncznik J, Osiecka O, Cichy J. Inhibitors of serine proteases in regulating the production and function of neutrophil extracellular traps. *Front Immunol*. (2016) 7:261. doi: 10.3389/fimmu.2016.00261
  131. Tillack K, Breiden P, Martin R, Sospedra M. T lymphocyte priming by neutrophil extracellular traps links innate and adaptive immune responses. *J Immunol*. (2012) 188:3150–9. doi: 10.4049/jimmunol.1103414
  132. Sangaletti S, Tripodo C, Chiodoni C, Guarnotta C, Cappetti B, Casali P, et al. Neutrophil extracellular traps mediate transfer of cytoplasmic neutrophil antigens to myeloid dendritic cells toward ANCA induction and associated autoimmunity. *Blood*. (2012) 120:3007–18. doi: 10.1182/blood-2012-03-416156
  133. Cataldi C, Mari NL, Lozovoy MAB, Martins LMM, Reiche EMV, Maes M, et al. Proinflammatory and anti-inflammatory cytokine profiles in psoriasis: use as laboratory biomarkers and disease predictors. *Inflamm Res*. (2019) 68:557–67. doi: 10.1007/s00011-019-01238-8
  134. Murakami M, Hagforsen E, Morhenn V, Ishida-Yamamoto A, Iizuka H. Patients with palmoplantar pustulosis have increased IL-17 and IL-22 levels both in the lesion and serum. *Exp Dermatol*. (2011) 20:845–7. doi: 10.1111/j.1600-0625.2011.01325.x
  135. Gisondi P, Lora V, Bonauguri C, Russo A, Lippi G, Girolomoni G. Serum chemerin is increased in patients with chronic plaque psoriasis and normalizes following treatment with infliximab. *Br J Dermatol*. (2013) 168:749–55. doi: 10.1111/bjd.12118
  136. Shveta, Agarwal K, Ranchander, Agarwal S. Serum sE-selectin levels in newly diagnosed psoriasis patients and correlation with psoriasis area and severity index score. *J Clin Diagnost Res*. (2017) 11:EC09–12. doi: 10.7860/JCDR/2017/29957.10831
  137. Torres T, Bettencourt N, Mendonca D, Vasconcelos C, Silva BM, Selores M. Complement C3 as a marker of cardiometabolic risk in psoriasis. *Arch Dermatol Res*. (2014) 306:653–60. doi: 10.1007/s00403-014-1467-5
  138. Hau CS, Kanda N, Tada Y, Shibata S, Uozaki H, Fukusato T, et al. Lipocalin-2 exacerbates psoriasiform skin inflammation by augmenting T-helper 17 response. *J Dermatol*. (2016) 43:785–94. doi: 10.1111/1346-8138.13227
  139. Aizawa N, Ishiui Y, Tominaga M, Sakata S, Takahashi N, Yanaba K, et al. Relationship between the degrees of itch and serum lipocalin-2 levels in patients with psoriasis. *J Immunol Res*. (2019) 2019:8171373. doi: 10.1155/2019/8171373
  140. Wolk K, Frambach Y, Jacobi A, Wilschmann-Theis D, Philipp S, Witte-Handel E, et al. Increased levels of lipocalin 2 in palmoplantar pustular psoriasis. *J Dermatol Sci*. (2018) 90:68–74. doi: 10.1016/j.jdermsci.2017.12.018
  141. Wolk K, Wenzel J, Tsousi A, Witte-Handel E, Babel N, Zelenak C, et al. Lipocalin-2 is expressed by activated granulocytes and keratinocytes in affected skin and reflects disease activity in acne inversa/hidradenitis suppurativa. *Br J Dermatol*. (2017) 177:1385–93. doi: 10.1111/bjd.15424
  142. Esaki H, Brunner PM, Renert-Yuval Y, Czarnowicki T, Huynh T, Tran G, et al. Early-onset pediatric atopic dermatitis is TH2 but also TH17 polarized in skin. *J Allergy Clin Immunol*. (2016) 138:1639–51. doi: 10.1016/j.jid.2016.02.064
  143. Abdel Hay R, Samir N, Safwat M, Rashed L, Soliman M. Tissue lipocalin-2 in psoriasis: is it a marker of metabolic disturbance or a possible marker of therapeutic efficacy after narrow band ultraviolet B? *J Dermatolog Treat*. (2019) 17:1–5. doi: 10.1080/09546634.2019.1605141
  144. Cai Y, Fleming C, Yan J. New insights of T cells in the pathogenesis of psoriasis. *Cell Mol Immunol*. (2012) 9:302–9. doi: 10.1038/cmi.2012.15
  145. Brembilla NC, Senra L, Boehncke WH. The IL-17 family of cytokines in psoriasis: IL-17A and beyond. *Front Immunol*. (2018) 9:1682. doi: 10.3389/fimmu.2018.01682
  146. Blauvelt A, Chiricozzi A. The immunologic role of IL-17 in psoriasis and psoriatic arthritis pathogenesis. *Clin Rev Allergy Immunol*. (2018) 55:379–90. doi: 10.1007/s12016-018-8702-3

147. Lin AM. Mast cells and neutrophils release IL-17 through extracellular trap formation in psoriasis. *J Immunol.* (2011) 187:490–500. doi: 10.4049/jimmunol.1100123
148. Di Domizio J, Gilliet M. Psoriasis caught in the NET. *J Invest Dermatol.* (2019) 139:1426–9. doi: 10.1016/j.jid.2019.04.020
149. Lambert S, Hambro CA, Johnston A, Stuart PE, Tsoi LC, Nair RP, et al. Neutrophil extracellular traps induce human Th17 cells: effect of psoriasis-associated TRAF3IP2 genotype. *J Invest Dermatol.* (2019) 139:1245–53. doi: 10.1016/j.jid.2018.11.021
150. Guttman-Yassky E, Lowes MA, Fuentes-Duculan J, Zaba LC, Cardinale I, Nogales KE, et al. Low expression of the IL-23/Th17 pathway in atopic dermatitis compared to psoriasis. *J Immunol.* (2008) 181:7420–7. doi: 10.4049/jimmunol.181.10.7420
151. Chen K, Kolls JK. Interleukin-17A (IL17A). *Gene.* (2017) 614:8–14. doi: 10.1016/j.gene.2017.01.016
152. Guttman-Yassky E, Krueger JG. IL-17C: a unique epithelial cytokine with potential for targeting across the spectrum of atopic dermatitis and psoriasis. *J Invest Dermatol.* (2018) 138:1467–9. doi: 10.1016/j.jid.2018.02.037
153. Senra L, Mylonas A, Kavanagh RD, Fallon PG, Conrad C, Borowczyk-Michalowska J, et al. IL-17E (IL-25) Enhances innate immune responses during skin inflammation. *J Invest Dermatol.* (2019) 139:1732–42.e17. doi: 10.1016/j.jid.2019.01.021

**Conflict of Interest:** The authors declare that the research was conducted in the absence of any commercial or financial relationships that could be construed as a potential conflict of interest.

Copyright © 2019 Chiang, Cheng, Korinek, Lin and Hwang. This is an open-access article distributed under the terms of the Creative Commons Attribution License (CC BY). The use, distribution or reproduction in other forums is permitted, provided the original author(s) and the copyright owner(s) are credited and that the original publication in this journal is cited, in accordance with accepted academic practice. No use, distribution or reproduction is permitted which does not comply with these terms.



# Functional Change of Effector Tumor-Infiltrating CCR5<sup>+</sup>CD38<sup>+</sup>HLA-DR<sup>+</sup>CD8<sup>+</sup> T Cells in Glioma Microenvironment

## OPEN ACCESS

Pin-Yuan Chen<sup>1,2,3†</sup>, Caren Yu-Ju Wu<sup>2,4,5†</sup>, Jian-He Fang<sup>6</sup>, Hsiu-Chi Chen<sup>1</sup>, Li-Ying Feng<sup>1</sup>, Chung-Yin Huang<sup>1</sup>, Kuo-Chen Wei<sup>1,3</sup>, Jia-You Fang<sup>4,5,7,8\*</sup> and Chun-Yen Lin<sup>3,6\*</sup>

### Edited by:

Jose A. Garcia-Sanz,  
Spanish National Research Council  
(CSIC), Spain

### Reviewed by:

Volker Daniel,  
Heidelberg University  
Hospital, Germany  
Manisha Singh,  
University of Texas MD Anderson  
Cancer Center, United States

### \*Correspondence:

Jia-You Fang  
fajy@mail.cgu.edu.tw  
Chun-Yen Lin  
chunyenlin@gmail.com

<sup>†</sup>These authors have contributed  
equally to this work

### Specialty section:

This article was submitted to  
Cancer Immunity and Immunotherapy,  
a section of the journal  
Frontiers in Immunology

**Received:** 01 May 2019

**Accepted:** 24 September 2019

**Published:** 09 October 2019

### Citation:

Chen P-Y, Wu CY-J, Fang J-H,  
Chen H-C, Feng L-Y, Huang C-Y,  
Wei K-C, Fang J-Y and Lin C-Y (2019)  
Functional Change of  
Effector Tumor-Infiltrating  
CCR5<sup>+</sup>CD38<sup>+</sup>HLA-DR<sup>+</sup>CD8<sup>+</sup> T  
Cells in Glioma Microenvironment.  
Front. Immunol. 10:2395.  
doi: 10.3389/fimmu.2019.02395

<sup>1</sup> Department of Neurosurgery, Linkou Chang Gung Memorial Hospital, Taoyuan, Taiwan, <sup>2</sup> Department of Neurosurgery, Keelung Chang Gung Memorial Hospital, Keelung, Taiwan, <sup>3</sup> School of Medicine, Chang Gung University, Taoyuan, Taiwan, <sup>4</sup> Pharmaceuticals Laboratory, Graduate Institute of Natural Products, Chang Gung University, Taoyuan, Taiwan, <sup>5</sup> Graduate Institute of Biomedical Sciences, Chang Gung University, Taoyuan, Taiwan, <sup>6</sup> Department of Gastroenterology and Hepatology, Linkou Chang Gung Memorial Hospital, Taoyuan, Taiwan, <sup>7</sup> Research Center for Food and Cosmetic Safety, Research Center for Chinese Herbal Medicine, Chang Gung University of Science and Technology, Taoyuan, Taiwan, <sup>8</sup> Department of Anesthesiology, Linkou Chang Gung Memorial Hospital, Taoyuan, Taiwan

Human glioma facilitates an impaired anti-tumor immunity response, including defects in circulation of T lymphocytes. The level of CD8<sup>+</sup> T-cell activation acts as an immune regulator associated with disease progression. However, little is known about the characteristics of peripheral and tumor-infiltrating CD8<sup>+</sup> T cells in patients with glioma. In this study, we examined the level of CD8<sup>+</sup> T-cell activation in a group of 143 patients with glioma and determined that peripheral CD3<sup>+</sup> T cells decreased in accordance with disease severity. The patients' peripheral CD8<sup>+</sup> T-cell populations were similar to that of healthy donors, and a small amount of CD8<sup>+</sup> tumor-infiltrating lymphocytes was identified in glioma tissues. An increase in activated CD8<sup>+</sup> T cells, characterized as CD38<sup>+</sup>HLA-DR<sup>+</sup>, and their association with disease progression were identified in the patients' peripheral blood and glioma, and shown to display enriched CCR5<sup>+</sup> and TNFR2<sup>+</sup> expression levels. *Ex vivo* examination of CD38<sup>+</sup>HLA-DR<sup>+</sup>CD8<sup>+</sup> T cells indicated that this subset of cells displayed stronger secretion of IFN- $\gamma$  and IL-2 before and after a 6-h stimulation with phorbol 12-myristate 13-acetate (PMA) and ionomycin (ION) relative to healthy CD38<sup>+</sup>HLA-DR<sup>+</sup>CD8<sup>+</sup> T cells, indicating the functional feasibility of CD38<sup>+</sup>HLA-DR<sup>+</sup>CD8<sup>+</sup> T cells. Higher CCL5 protein and mRNA levels were identified in glioma tissues, which was consistent with the immunohistochemistry results revealing both CCL5 and CD38<sup>+</sup>HLA-DR<sup>+</sup>CD8<sup>+</sup> T cell expression. Patients' CCR5<sup>+</sup>CD38<sup>+</sup>HLA-DR<sup>+</sup>CD8<sup>+</sup> T cells were further validated and shown to display increases in CD45RA<sup>+</sup>CCR7<sup>-</sup> and T-bet<sup>+</sup> accompanied by substantial CD107-a, IFN- $\gamma$ , and Granzyme B levels in response to glioma cells.

**Keywords:** glioma, CD8, T cell, CCL5, CCR5



## INTRODUCTION

Gliomas are tumors that arise from glial precursor cells and include astrocytoma, oligodendroglioma, ependymoma, mixed glioma, and glioblastoma (GBM) (1), and their malignancy is graded as low grade (GI and GII) or high grade (GIII and GIV) (2). Amongst gliomas, glioblastoma multiforme (GBM; GIV) is the most lethal type of these malignant brain tumors with a median survival of 15 months despite multimodal therapies, including surgery followed by radiation and temozolomide therapy (2, 3). The recurrence of GBM usually takes place around the initial resected lesion (within 2 cm), which offsets the effects of standard therapeutic approaches on overall survival (2, 4). The immune response of patients with glioma are characterized by defects in circulating T-cell populations, poor tumor antigen-specific CD8<sup>+</sup> T-cell responses, and elevated programmed death 1 (PD-1) in CD8<sup>+</sup> T cells contributing to the poor prognosis of these patients (5–9). Previously, low tumor-infiltrating CD8<sup>+</sup> cells (CD8<sup>+</sup> TILs) were reported to associate with poor progression-free survival (PFS), defined as from the date of surgery to the first MRI-confirmed recurrence (10, 11).

The CD8<sup>+</sup> cytotoxic T cells are functional/effector cytotoxic T lymphocytes (CTLs) in which only 5–10% of the original burst size matures into long-lived protective memory CD8<sup>+</sup> T cells (12). In addition, autocrine IL-2 produced by CD8<sup>+</sup> T cells activated via interaction with APC pre-activated by CD4<sup>+</sup> T cells is important for the generation of competent CTLs (13). The presence of CD8<sup>+</sup> T cells was shown to reduce tumorigenicity when CD4<sup>+</sup> or NK<sup>+</sup> cell-depleted mice had been immunized with IL-7-producing glioma cells (14). In addition, local application of an AC133/CD133-specific T-cell-engaging antibody (a cancer stem cell marker) with human CD8<sup>+</sup> T cells has been shown to prevent tumor outgrowth of subcutaneous GBM xenografts (8). Recently, blockage of PD-1 using RMP1-14 (15) and IL-2-treated CD8<sup>+</sup> cells coinciding with IL-2R abundance have also been shown to consolidate CD8<sup>+</sup> T cells' functional viability (16). However, the mechanisms underlying this phenomenon along with the phenotypic presentation of the CD8<sup>+</sup> TILs are not clear.

Evidence has revealed that CD38 and HLA-DR are common effector T-cell activation markers that also associate with disease states, including autoimmune diseases, HIV, leukemia, and multiple myeloma (17–19). Expression of CD38 on tumor cells was indicated to serve as a negative prognostic marker implying disease severity and poor survival (20). The functional expression of CD38 and HLA-DR was reported to reflect infection status as it related to survival capacity in glioma (18, 19, 21, 22). Furthermore, Hua et al. (18) indicated that the increased expression of CD38<sup>+</sup>HLA-DR<sup>+</sup>CD8<sup>+</sup> HIV-specific T cells displayed a better survival capacity than the expression of CD38<sup>+</sup>HLA-DR<sup>+</sup>CD8<sup>+</sup> cells. In addition, the functional expression of C-C chemokine receptor 5 (CCR5) was demonstrated to be critical for effector CD8<sup>+</sup> T-cell migration to inflamed tissues, in which the production of INF- $\alpha$ , IL-2, and IFN- $\gamma$  were positive for CCR5 potentiation (23, 24). The association of increased CCR5 expression with

viral susceptibility and viral entry was evidenced in HIV and cytomegalovirus (CMV) studies (25, 26). As such, the current study sought to identify the basic immune functional capacity among patients with glioma for clinical reference. In addition, the role of the effector CD8<sup>+</sup> T cells in patients with glioma remains unclear. Therefore, we are interested in knowing whether the effector CD8<sup>+</sup> T cells are contributable toward glioma development and their role in tumor regression.

In the present study, we investigated the activation of the CD38<sup>+</sup>HLA-DR<sup>+</sup>CD8<sup>+</sup> subpopulation among total human CD8<sup>+</sup> cells along with their penetration into the tumor microenvironment in a large series of glioma samples. We demonstrated an association between increases of glioma CCL5 and CCR5<sup>+</sup>CD38<sup>+</sup>HLA-DR<sup>+</sup>CD8<sup>+</sup> TILs. In the presence of glioma cells, this CD8<sup>+</sup> T cell subset appears to facilitate the enhancement of effector molecules, including CD45RA<sup>+</sup>CCR7<sup>+</sup>, T-bet<sup>+</sup>, CD107a<sup>+</sup>, IFN- $\gamma$ <sup>+</sup>, and granzyme B<sup>+</sup>.

## MATERIALS AND METHODS

### Standard Protocol Approval, Registration, and Patient Consent

This study was approved by the Chang Gung Medical Foundation Institutional Review Board (No. 102-1096B) and in accordance with the Helsinki Declaration. Patients were recruited from the Department of Neurosurgery, Chang Gung Medical Foundation, Taiwan, between 2013 and 2016. All eligible patients were informed about the details of this study and provided a signed informed consent prior to study participation.

### Glioma Cell Culture

Human U87 glioblastoma cells were obtained from the American Type Culture Collection (ATCC, Manassas, VA). Cells were maintained in MEM supplemented with 10% FBS, 100 U/ml penicillin, and 100 mg/mL streptomycin. Cells were incubated at 37°C in a humidified incubator with an atmosphere of 5% CO<sub>2</sub> and 95% air.

### Preparation of Blood and Tumor Samples

Blood and freshly resected tumor materials were collected from the participants with primary glioma, who had been diagnosed histopathologically according to the current WHO criteria. Peripheral blood mononuclear cells (PBMCs) from healthy donors and patients with glioma were isolated by Ficoll density gradient centrifugation (Ficoll-Paque; GE Healthcare Life Sciences, Sweden) as described by Lefort and Kim (27). Tumor material was obtained from patients who had received surgical excision. Tissues were collected into medium (F12; Gibco, USA) containing 10% FBS and 5% P/S, and these were processed under sterile conditions as previously described (28). Briefly, tumor tissues were washed several times with PBS to remove the majority of erythrocytes. Tissues were cut into 1–2 mm pieces, digested with 0.05% trypsin for 40 min at 37°C, extensively filtered using a 70  $\mu$ m strainer, and then separated on Ficoll gradients to yield single cell-enriched preparations from tumor lysates, and characterized by staining of CD3,



CD8, CD38, HLA-DR, CCR5, and TNFR2 antibodies. CD8<sup>+</sup> T lymphocytes were negatively selected using a CD8 T-cell isolation kit (Miltenyi Biotec, USA) that non-CD8<sup>+</sup> cells including CD4<sup>+</sup>, CD15<sup>+</sup>, CD16<sup>+</sup>, CD19<sup>+</sup>, CD34<sup>+</sup>, CD36<sup>+</sup>, CD56<sup>+</sup>, CD123<sup>+</sup>, TCR  $\gamma/\delta$ <sup>+</sup>, and CD235a<sup>+</sup> cells are magnetically labeled, and depleted using magnetic separator. A purity of  $80 \pm 2\%$  was confirmed by flow cytometry analysis with anti-CD3-FITC and anti-CD8-PerCP antibodies for CD8<sup>+</sup> T lymphocytes, and there was an approximate 20% of cell debris (data not shown).

## Multiparameter Flow Cytometry Analysis

Four-color staining of lymphocytes was performed to determine the frequency and phenotype of lymphocytes among freshly isolated PBMCs from either healthy donors or patients as well as among TILs from patients. The following monoclonal antibodies (mAbs) were used: CD19-PerCP (#302228), CD56-APC (#555518), CD3-FITC (#555332), CD8-PerCP (#340693), CD8-FITC (#555366), CD45RA-FITC (#555488), CD38-FITC (#555459), CD38-APC (#555462), HLA-DR-APC (#559866), HLA-DR-BV421 (#307636), CCR5-FITC (#555992), CCR5-PE (#555993), TNFR2-PE (#FAB226P), IFN- $\gamma$ -PE (#559326), IL-2-PE (#559334), PD-1-PE (#129969), Tim-3-PE (#123109), CCR7-PE-Cy7 (#557648), T-bet-PerCP-Cy5.5 (#561316), CD107a-PE (#555801), and Granzyme B-PE (#561142) (BD Biosciences, USA). Lymphocytes were first stained at 4°C for 1 h with mAbs to cell surface markers. Each sample contained at least  $2 \times 10^6$  lymphocytes isolated from PBMCs or TILs. Expression of surface antigens was analyzed using a dual-laser fluorescence-activated cell sorting cytofluorimeter (FACSCalibur; FACSCanto<sup>TM</sup>II; BD Biosciences, USA) employing Cell-Quest software (BD Biosciences, USA).

## Intracellular Cytokine Production Assays

For intracellular IFN- $\gamma$  and IL-2 detection, lymphocyte and TIL suspensions were stimulated with phorbol 12-myristate 13-acetate (PMA; 50 ng/ml; Sigma-Aldrich, USA) plus ionomycin (ION; 1  $\mu$ g/ml; Sigma-Aldrich, USA) for 6 h. Cells were then stained with T-cell markers, further processed using a Fixation/Permeabilization kit (BD Bioscience, USA), and then labeled with a PE-conjugated IFN- $\gamma$  or IL-2 mAb (BD Biosciences, USA).

## Immunohistochemistry

Triple immunohistochemistry staining was used to assess the distribution of activated cytotoxic CD8 T cells. Briefly, brain sections were prepared for immunostaining via xylene treatment and gradual rehydration with 99–75% ethanol. Sections were blocked with 1% FBS for immunohistochemistry staining or 3% hydrogen peroxide for immunohistochemistry and then incubated with anti-CD8 (#ab17147; Abcam, USA), anti-CD38 (#ab108403; Abcam, USA), anti-HLA-DR (#17221-1-AP; Proteintech, USA), anti-PD-L1 (#13684; Cell Signaling, USA), or anti-CCL5 (#SC-1410; Santa Cruz, USA) overnight at 4°C in blocking solution. The sections were then incubated with fluorescent secondary antibodies or peroxidase-conjugated secondary antibodies for 1 h at room temperature

and subsequently stained using 3,3' diaminobenzidine and counterstained with hematoxylin. Slides were coverslipped using mounting medium (Histokitt, Germany). Images were captured with a 40x objective on a Nikon Eclipse E400 microscope using SPOT software (Nikon, Japan).

## Quantitative Real-Time PCR

Total RNA was extracted from both tumor and non-tumor biopsies using TRIzol reagent (Invitrogen, USA). First-strand cDNA was synthesized from 2  $\mu$ g total RNA with oligo(dT)<sub>20</sub> primers and reverse transcribed to cDNA using SuperScript III First-Strand Synthesis SuperMix (Invitrogen, USA). Real-time PCR was carried out using SYBR Green I Master Mix (Roche, USA). Amplification and detection of mRNA were performed using a LightCycler 480II system (Roche, USA) under the following conditions: 40 cycles at 95°C for 10 s and 60°C for 1 m. The threshold was set within the linear phase of the target gene amplification to calculate the cycle number at which point the transcript was detected as CT. The oligonucleotide primers used for real-time PCR were:

GAPDH: 5'-CTCAACTACATGGTCTACATGTTCCA-3' and 5'-CTTCCCATTTCTCAGCCTTGACT-3';

CCL5: 5'-GAGTATTTCTACACCAGTGGCAAG-3 and 5'-TCCCGAACCCATTTCTTCTCT-3'.

## Western Blotting

Glioma cells were co-cultured with CD8<sup>+</sup> T cells for 24 h using a transwell system, washed with PBS, and then lysed for 30 min on ice with RIPA lysis buffer (Thermo Fisher, MA). Protein samples were then separated by SDS-PAGEs and transferred to PVDF membranes. The membranes were blocked with 5% non-fat milk and then probed with primary antibodies against PD-L1 (Cell Signaling, MA) at 4°C overnight. After extensive washing, the membranes were incubated with secondary antibodies for 1 h at room temperature, and the blots were then visualized using Immobilon Western Chemiluminescent HRP Substrate (Millipore, MA) and Amersham Hyperfilm ECL (GE Healthcare, UK).

## Statistical Analysis

All results are expressed as means  $\pm$  SE of at least three independent experiments unless stated otherwise. Due to biosample availability, not every biosample contributed to every analysis. Statistical analyses were performed using a two-tailed Student's *t*-test to determine the statistical significance between the groups using SPSS Version 19 (IBM, USA). A *p* < 0.05 was considered significant.

## RESULTS

### Patients With Glioma Display a Decrement of Peripheral CD3<sup>+</sup> T Cells in Comparison to Healthy Donors

The baseline data for the 143 patients with glioma (mean age =  $52 \pm 14$ ) and 36 healthy donors (mean age =  $47 \pm 16$ ) are shown in **Table 1**. Patients were further characterized according to grade II (GII; *n* = 29), grade III (GIII; *n* =

**TABLE 1** | Study population of healthy donors ( $n = 36$ ) and patients with glioma ( $n = 143$ ).

Patient	Newly	Recurrent	Healthy Donor
N. (male/female)	72 (43/29)	71 (46/25)	36 (18/18)
Mean age (years)	50.3 $\pm$ 14	51.3 $\pm$ 12	46.2 $\pm$ 16
Grade II (n.)	17	12	–
Grade III (n.)	16	14	–
Grade IV (n.)	39	45	–

30), or grade IV (GIV;  $n = 84$ ). The independent sample  $t$ -test revealed no significant age difference between healthy donors (HD) and patients with glioma ( $t = -1.9$ ,  $p = 0.06$ ; **Supplementary Tables 1, 2**). Previously, immunological impairments were addressed in patients with malignant glioma with signature T-cell reduction (29, 30). We examined the proportion of the major components of lymphocytes among our patients and healthy donors using flow cytometry. Three-color staining of the surface antigens CD3, CD19, and CD56 against the lymphocyte population, representing T cells, B cells, and NK (natural killer) cells, was performed. The results revealed that the CD3<sup>+</sup> population was significantly lower in patient PBMCs (**Figures 1A,B**) compared to healthy donors (50.6  $\pm$  2% and 62.5  $\pm$  1%, respectively), especially in the high grade patient group (GII = 62.3  $\pm$  2%, GIII = 49.2  $\pm$  4%, and GIV = 47.0  $\pm$  3%; **Figures 1C,D**). On the other hand, the CD19<sup>+</sup> population in PBMCs was not significantly different between the patients and healthy donors, whereas the CD56<sup>+</sup> population was slightly higher in the patient PBMCs, especially in the GIII patient group (**Figure 1D**).

### Increased CD38<sup>+</sup>HLA-DR<sup>+</sup>CD8<sup>+</sup> T Cells and Accumulation in the Tumor Microenvironment in High-Grade Gliomas

The frequency of total CD8<sup>+</sup> cells in the patient PBMCs and TILs were evaluated. The results showed that the CD8<sup>+</sup> T population in the patient PBMCs was similar to that of the healthy donors (23.8  $\pm$  1% and 25.7  $\pm$  1%, respectively), whereas the presence of CD8<sup>+</sup> TILs (6.5  $\pm$  1%) was significantly lower in the glioma microenvironment compared to HD PBMCs (**Figures 2A,B**). In regard to the CD38<sup>+</sup>HLA-DR<sup>+</sup>CD8<sup>+</sup> and CD38<sup>+</sup>HLA-DR<sup>+</sup>CD8<sup>+</sup> T cells, the percentage of CD38<sup>+</sup>HLA-DR<sup>+</sup>CD8<sup>+</sup> T cells was lower in both the patient PBMCs and TILs compared to that in the PBMCs from healthy donors (7.8  $\pm$  1%, 14.1  $\pm$  5%, and 42.5  $\pm$  3%, respectively; **Figures 2C,D**). In contrast, the percentage of CD38<sup>+</sup>HLA-DR<sup>+</sup>CD8<sup>+</sup> cells was higher in the patient PBMCs and more prominent in the patient TILs than in the PBMCs from healthy donors (11.2  $\pm$  1%, 31.8  $\pm$  6%, and 6.1  $\pm$  1%; **Figures 2C,D**). Importantly, the percentage of CD38<sup>+</sup>HLA-DR<sup>+</sup>CD8<sup>+</sup> cells was significantly increased in patients with recurrent glioma (newly = 8.2  $\pm$  1%; recurrent = 12.5  $\pm$  2%; **Figure 2E**); high-grade glioma (GIII and/or GIV), both in the PBMCs (GII = 7.6  $\pm$  2%, GIII = 10.1  $\pm$  2%, and GIV = 12.9  $\pm$  2%; **Figure 2F**) and

TILs (GII = 2.0  $\pm$  1%, GIII = 24.5  $\pm$  4%, and GIV = 31.6  $\pm$  2%; **Figure 2G**).

### The Concurrent Expression of CCR5 and TNFR2 on CD38<sup>+</sup>HLA-DR<sup>+</sup>CD8<sup>+</sup> T Cells From Patient PBMCs and Tumors

The presentation of CCR5 and TNFR2 on CD38<sup>+</sup>HLA-DR<sup>+</sup>CD8<sup>+</sup> T cells was further examined. As expected, the CD38<sup>+</sup>HLA-DR<sup>+</sup>CD8<sup>+</sup> T cells from the patient PBMCs and tumors displayed significant upregulation of CCR5 compared to the healthy controls (34.7  $\pm$  5%, 51.0  $\pm$  3%, and 68.2  $\pm$  8%; **Figures 3A,B**). Interestingly, a remarkable reduction in the percentage of TNFR2 expression on CD38<sup>+</sup>HLA-DR<sup>+</sup>CD8<sup>+</sup> T cells in the patient PBMCs was observed, but this expression was increased in tumors. Further analysis on activated CCR5<sup>+</sup>CD38<sup>+</sup>HLA-DR<sup>+</sup>CD8<sup>+</sup> T cells revealed a grading increment on the average numbers of CCR5<sup>+</sup>CD38<sup>+</sup>HLA-DR<sup>+</sup>CD8<sup>+</sup> T cells presented in both patient PBMCs and tumors (**Figures 3C,D**).

### CD38<sup>+</sup>HLA-DR<sup>+</sup>CD8<sup>+</sup> T Cells From Patient PBMCs Produce IFN- $\gamma$ and IL-2 Upon Stimulation With PMA and ION

To further evaluate the T-cell activation capacity, we examined the intracellular production of IFN- $\gamma$  and IL-2 in CD8<sup>+</sup> T cells and CD38<sup>+</sup>HLA-DR<sup>+</sup>CD8<sup>+</sup> subsets from PBMCs. Cells were stimulated for 6 h with PMA (50 ng/ml) and ION (1  $\mu$ g/ml) prior to analysis. Increases in both IFN- $\gamma$  (HD = 0.4 to 5.5%,  $t = -3.4$ ,  $p < 0.01$ ; Patient = 0.7 to 4.6%,  $t = -2.1$ ,  $p < 0.05$ ; **Figures 4A,C**) and IL-2 (HD = 0.4 to 2.2%,  $t = -2.0$ ,  $p = 0.06$ ; Patient = 0.6 to 2.9%,  $t = -3.0$ ,  $p < 0.01$ ; **Figures 4E,G**) production were observed in total CD8<sup>+</sup> T cells after PMA/ION treatment, which does not elicit a significant between-group difference for IFN- $\gamma$  (HD = 5.46; Patient = 4.64,  $t = 0.34$ ,  $p = 0.73$ ) or IL-2 (HD = 2.21; Patient = 2.85,  $t = -0.54$ ,  $p = 0.59$ ) production. The baseline production of IFN- $\gamma$  (HD = 0.42; Patient = 0.71,  $t = -1.34$ ,  $p = 0.19$ ) and IL-2 (HD = 0.44; Patient = 0.59,  $t = -0.64$ ,  $p = 0.53$ ) in CD8<sup>+</sup> T cells was similar between the patients and healthy donors. Importantly, the baseline IFN- $\gamma$  (HD = 1.88; Patient = 12.71,  $t = -3.17$ ,  $p < 0.01$ ; **Figures 4B,D**) and IL-2 (HD = 1.84; Patient = 12.41,  $t = -2.99$ ,  $p < 0.01$ ; **Figures 4F,H**) production in patient CD38<sup>+</sup>HLA-DR<sup>+</sup>CD8<sup>+</sup> T cells was higher than in the healthy controls. The PMA/ION stimulation appeared to elicit a strong IFN- $\gamma$  (Patient = 14.7 to 42.3%,  $t = -3.0$ ,  $p < 0.01$ ; **Figures 4B,D**) and IL-2 (Patient = 12.4 to 36.2%,  $t = -2.34$ ,  $p < 0.05$ ; **Figures 4F,H**) production in patient CD38<sup>+</sup>HLA-DR<sup>+</sup>CD8<sup>+</sup> T cells. There was no significant difference in IFN- $\gamma$  (HD = 33.5; Patient = 42.3,  $t = -0.85$ ,  $p < 0.41$ ) or IL-2 (HD = 19.4; Patient = 36.2,  $t = -1.42$ ,  $p < 0.17$ ) production between healthy and patient CD38<sup>+</sup>HLA-DR<sup>+</sup>CD8<sup>+</sup> T cells after PMA/ION treatment. These results indicated that CD38<sup>+</sup>HLA-DR<sup>+</sup>CD8<sup>+</sup> T cells from the peripheral blood of patients were already activated as effector T cells and had the capacity to receive further induction similar to the rest of the CD8<sup>+</sup> cell population.

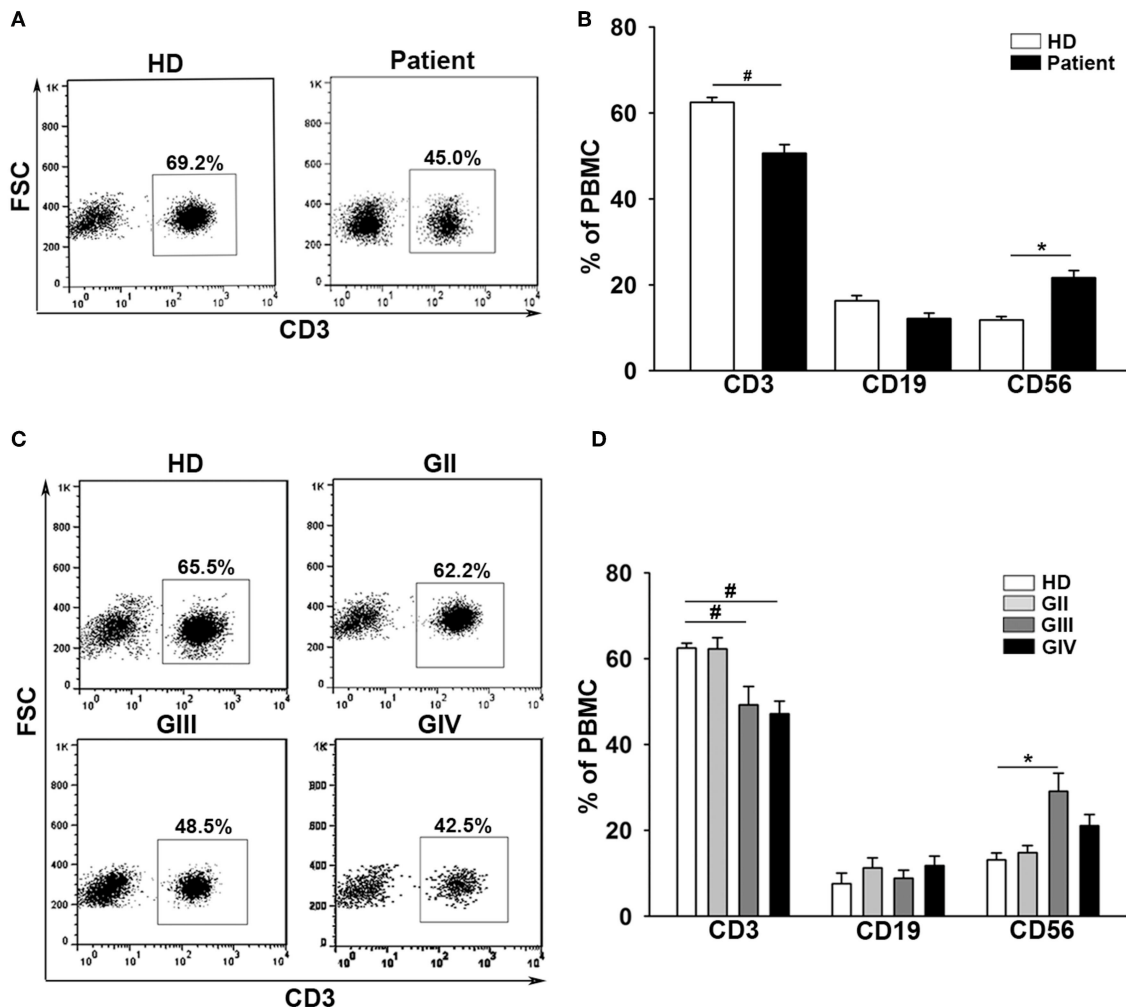


**FIGURE 1 |** Patients with glioma display a stepwise immune deficiency in accordance with the grade classification. **(A)** PBMCs from 31 healthy donors (HD) and 117 patients (Patient) were evaluated by flow cytometry for CD3, CD19, and CD56 after gating lymphocytes. **(B)** The percentages of CD3<sup>+</sup>, CD19<sup>+</sup>, and CD56<sup>+</sup> cells were quantified. **(C)** The expression of CD3<sup>+</sup> decreased in accordance with the grade. **(D)** Comparisons of the percentages of CD3<sup>+</sup>, CD19<sup>+</sup>, and CD56<sup>+</sup> cells across the grades are shown. Values shown are means  $\pm$  SEM (bars); \* $p$  < 0.05, # $p$  < 0.01 by Student's *t*-test.

## CCL5 and CD38<sup>+</sup>HLA-DR<sup>+</sup>CD8<sup>+</sup> T-Cell Presentation in Patient Tumor Tissues

The expression of CCL5, the ligand of CCR5, was significantly higher in the glioma microenvironment than in normal peripheral brain tissues, as shown in **Figure 5A**. Immunohistochemical staining of glioma samples from patients with GBM revealed that TILs were located in areas where CCL5 was abundantly expressed (**Figure 5B**). The presence of CD38<sup>+</sup>HLA-DR<sup>+</sup>CD8<sup>+</sup> T cells was also detected by triple fluorescent staining among these TILs in GBM and areas adjacent to blood vessels (**Figure 5C**). Increased PD-1 expression was observed more often in CD38<sup>+</sup>HLA-DR<sup>+</sup>CD8<sup>+</sup> T cells than in the rest of the other CD8<sup>+</sup> T cells obtained from the patient PBMCs and TILs (**Figure 5D**). We further validated the presence of CD8<sup>+</sup> T cells relative to glioma PD-L1 expression. To this end, CD8<sup>+</sup> T cells were isolated from PBMC of patients with

newly-diagnosed and recurrent glioma, and these cells appeared to reinforce PD-L1 protein expression after co-culture with glioma cells (**Supplementary Figure 1**). IHC results revealed PD-L1 expression in both newly-diagnosed (GII to GIV) and recurrent gliomas (GIV) in comparison with the tumor margins, which were shown to be PD-L1 negative (**Figure 5E**).

## Co-expression of Functional and Exhausted Molecules in CCR5<sup>+</sup>CD38<sup>+</sup>HLA-DR<sup>+</sup>CD8<sup>+</sup> T Cells in Response to Glioma

To elucidate the responsiveness of CCR5<sup>+</sup>CD38<sup>+</sup>HLA-DR<sup>+</sup>CD8<sup>+</sup> T cells toward glioma, CD8<sup>+</sup> T cells were isolated from HD or patient's PBMCs and then co-cultured with the U87 glioma cell line for 24 h. CD8<sup>+</sup> T cells in

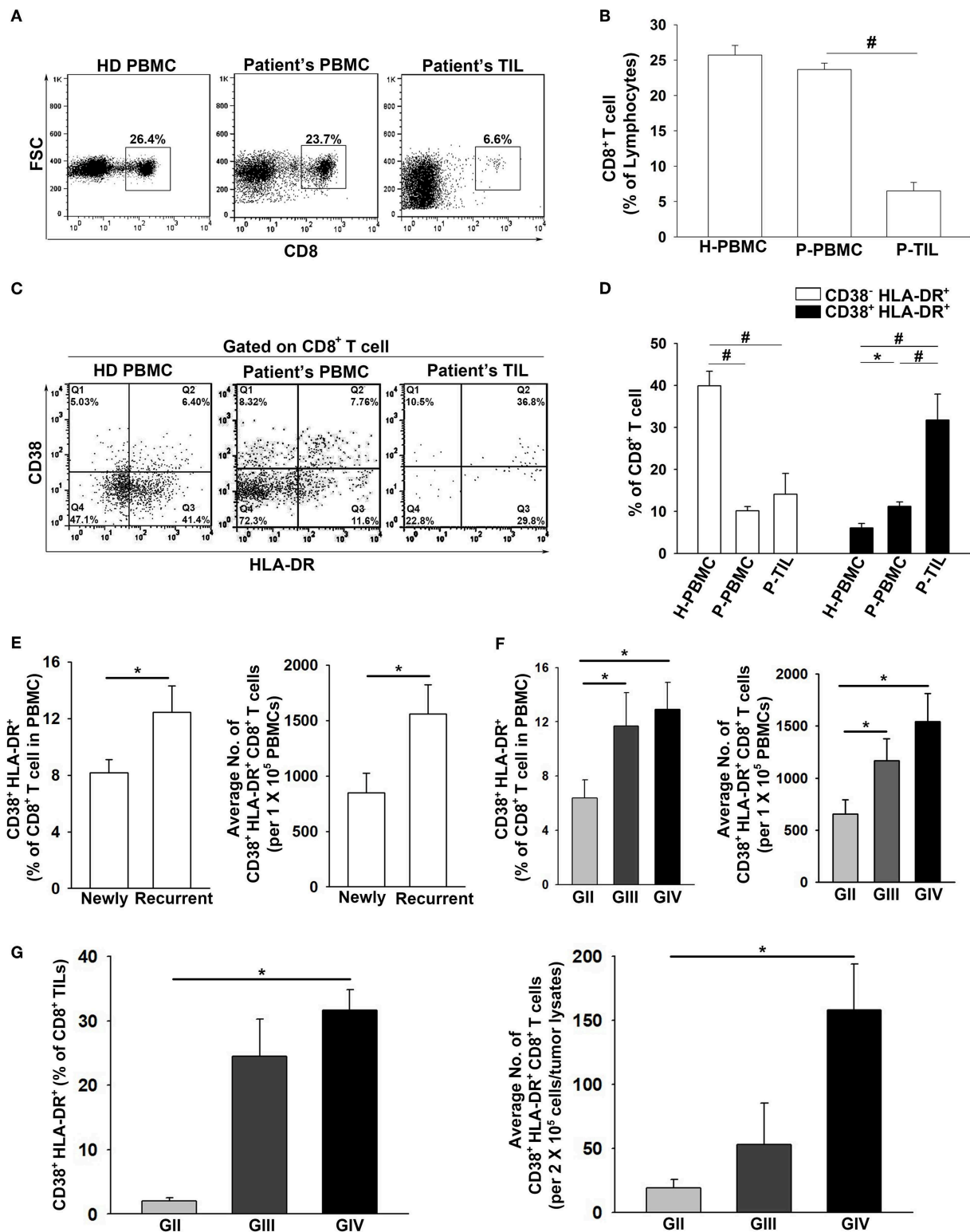
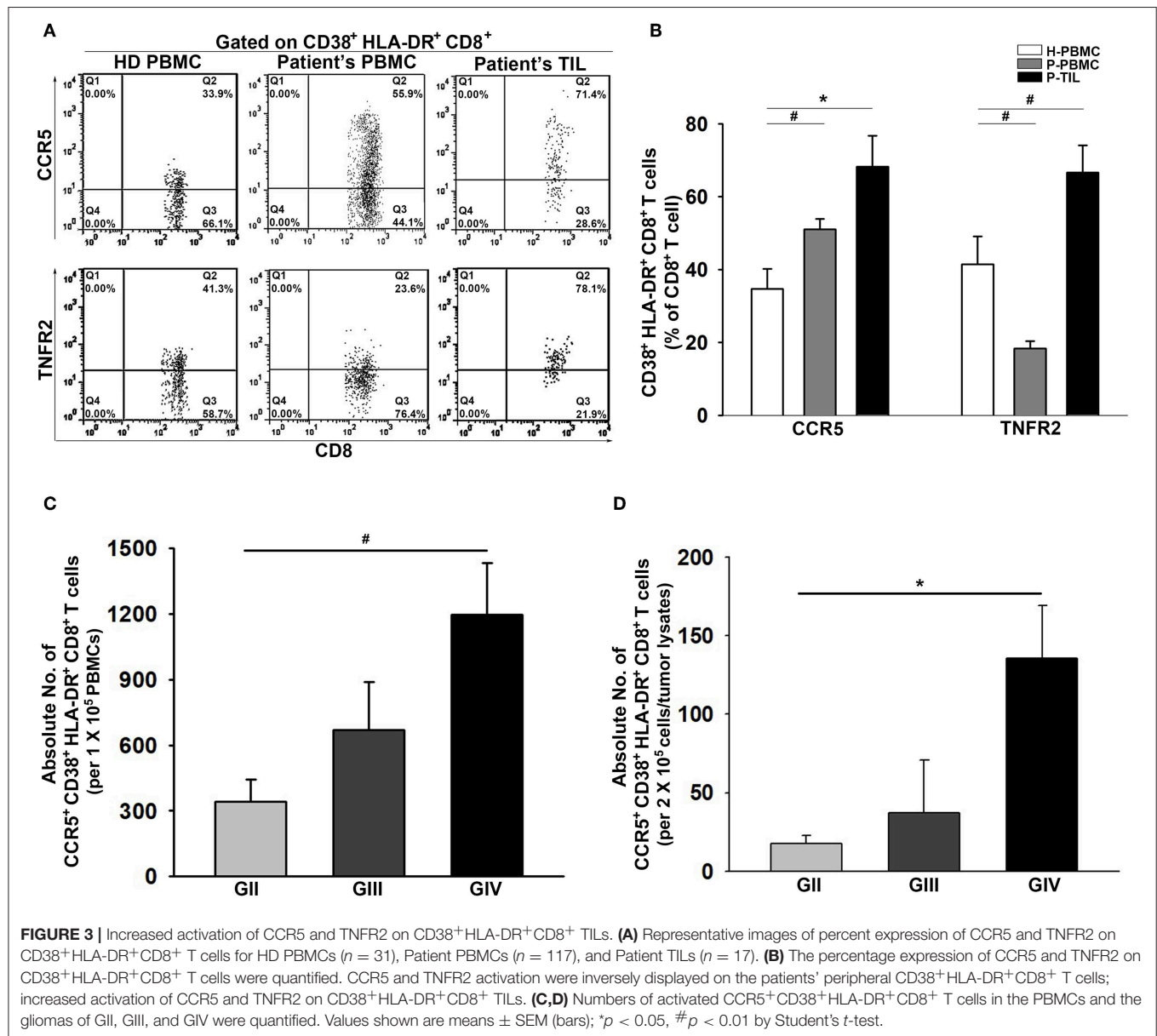


**FIGURE 2 |** Pronounced activation and penetration of CD38<sup>+</sup>HLA-DR<sup>+</sup>CD8<sup>+</sup> T cells in high-grade glioma. **(A,B)** The overall expression percentage of CD8<sup>+</sup> T cells was significantly lower in Patient TILs ( $n = 17$ ) than in Patient PBMCs ( $n = 117$ ) and healthy donors (HD PBMC;  $n = 31$ ). **(C,D)** The expression percentage of CD38<sup>-</sup>HLA-DR<sup>+</sup>CD8<sup>+</sup> cells was higher in HD PBMCs (H-PBMCs) than in Patient PBMCs (P-PBMCs) and TILs (P-TILs); profound CD38<sup>+</sup>HLA-DR<sup>+</sup>CD8<sup>+</sup> T-cell activation was observed in P-PBMCs and P-TILs. **(E)** The expression of CD38<sup>+</sup>HLA-DR<sup>+</sup>CD8<sup>+</sup> T cells in newly-diagnosed ( $n = 59$ ) and recurrent ( $n = 58$ ) patients. **(F)** The expression of CD38<sup>+</sup>HLA-DR<sup>+</sup>CD8<sup>+</sup> T cells in the PBMCs of GII ( $n = 22$ ), GIII ( $n = 17$ ), and GIV ( $n = 51$ ). **(G)** The expression of CD38<sup>+</sup>HLA-DR<sup>+</sup>CD8<sup>+</sup> TILs in the gliomas of GII ( $n = 3$ ), GIII ( $n = 5$ ), and GIV ( $n = 9$ ). Values shown are means  $\pm$  SEM (bars); \* $p < 0.05$ , # $p < 0.01$  by Student's  $t$ -test.





the supernatant were subjected to flow cytometry analysis, whereas U87 gliomas attached to the bottom of the wells were subjected to western blot analysis. Results of the flow cytometry analysis revealed an increase of TEMRA<sup>+</sup> (CD45RA<sup>+</sup>CCR7<sup>-</sup>) and T-bet<sup>+</sup> distributions in the CCR5<sup>+</sup>CD38<sup>+</sup>HLA-DR<sup>+</sup>CD8<sup>+</sup> T-cell subset after co-culture (Figures 6A–C). A significant increase in PD-1 expression was also observed in CCR5<sup>+</sup>CD38<sup>+</sup>HLA-DR<sup>+</sup>CD8<sup>+</sup> T cells prior to and after co-culture, whereas Tim-3 expression in CCR5<sup>+</sup>CD38<sup>+</sup>HLA-DR<sup>+</sup>CD8<sup>+</sup> T cells was not significantly increased after co-culture (Figure 6C). Several effector molecules, including CD107a, IFN- $\gamma$ , and Granzyme B, coincided significantly with CCR5<sup>+</sup>CD38<sup>+</sup>HLA-DR<sup>+</sup>CD8<sup>+</sup> T cells after contact with the U87 glioma cells (Figures 6D,E). Additionally, results of flow cytometry analysis showed that

CCR5<sup>+</sup>CD38<sup>+</sup>HLA-DR<sup>+</sup>CD8<sup>+</sup> T cells of HD were unresponsive toward the U87 cells, which ruled out the possibility of allograft rejection (Figures 6B,C,E).

## DISCUSSION

Suppression of adaptive immune activation can occur both systemically and locally in gliomas and other cancers such as melanoma (1, 31). Analysis from our patient group indicated that the reduced percentage of T cells in the peripheral blood was prominent and had a clear relation with disease severity. This phenomenon represents systemic immune modulation occurring in glioma. On the other hand, the presence of tumor-infiltrating effector CD8<sup>+</sup> T cells was determined in prior studies in human glioma and mouse models to be involved in



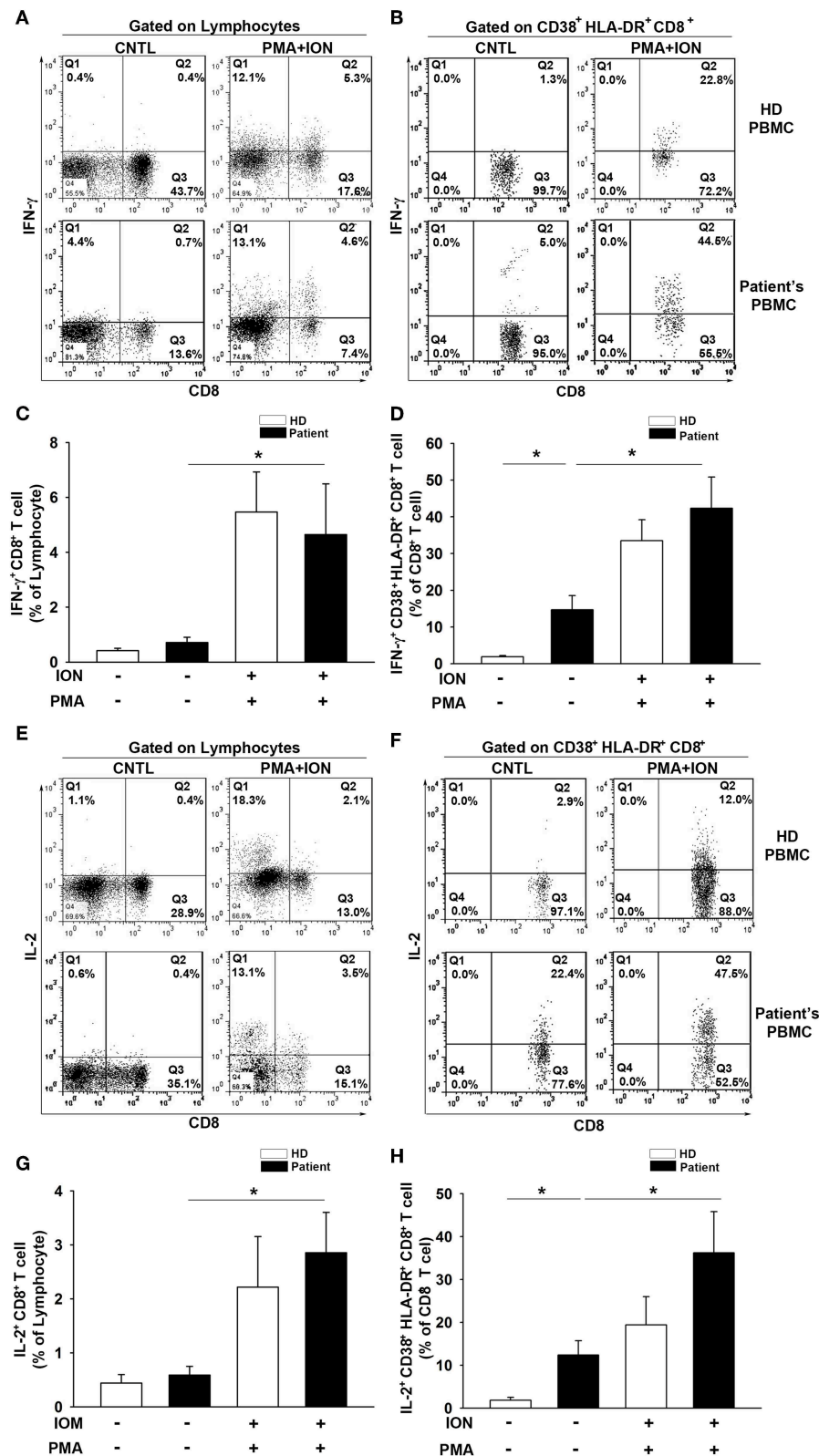


**FIGURE 4 |** IFN- $\gamma$  and IL-2 production by CD38<sup>+</sup>HLA-DR<sup>+</sup>CD8<sup>+</sup> T cells from patients with glioma is enhanced. **(A)** Lymphocytes were isolated from patient ( $n = 11$ ) and healthy donor ( $n = 10$ ) PBMCs and then cultured for 6 h with ION (1  $\mu$ g/ml) plus PMA (50  $\mu$ g/ml). Intracellular cytokine production in CD8<sup>+</sup> and CD38<sup>+</sup>HLA-DR<sup>+</sup>CD8<sup>+</sup> T cells was analyzed. Representative images of IFN- $\gamma$  production by CD8<sup>+</sup> T cells before and after ION/PMA stimulation. **(B)** Representative (Continued)

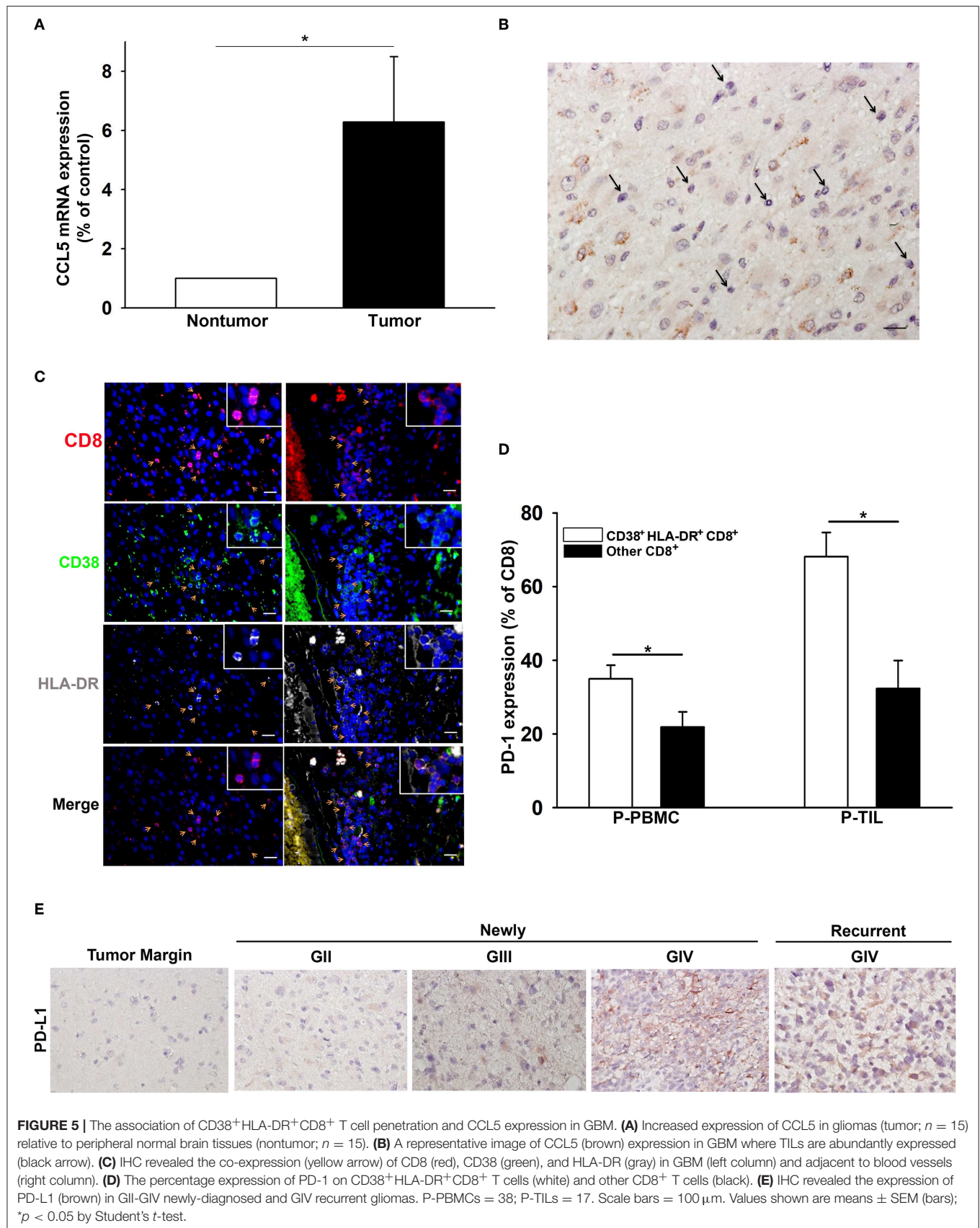
**FIGURE 4 |** images of IFN- $\gamma$  production by CD38<sup>+</sup>HLA-DR<sup>+</sup>CD8<sup>+</sup> T cells. **(C)** The percentage of IFN- $\gamma$  production was increased in patient CD8<sup>+</sup> T cells after ION/PMA stimulation. **(D)** The production percentage of IFN- $\gamma$  by CD38<sup>+</sup>HLA-DR<sup>+</sup>CD8<sup>+</sup> T cells was compared and analyzed before and after ION/PMA stimulation. **(E)** Representative images of intracellular IL-2 production by CD8<sup>+</sup> T cells before and after ION/PMA stimulation. **(F)** Representative images of intracellular IL-2 production by CD38<sup>+</sup>HLA-DR<sup>+</sup>CD8<sup>+</sup> T cells. **(G)** The percentage of IL-2 production by CD8<sup>+</sup> T cells after ION/PMA stimulation. **(H)** Baseline IL-2 production by CD38<sup>+</sup>HLA-DR<sup>+</sup>CD8<sup>+</sup> T cells was analyzed and compared after ION/PMA stimulation. CNTL = PBMCs without ION/PMA stimulation. Healthy donor = 10; patient = 11. Values shown are means  $\pm$  SEM (bars); \* $p$  < 0.05 by Student's  $t$ -test.

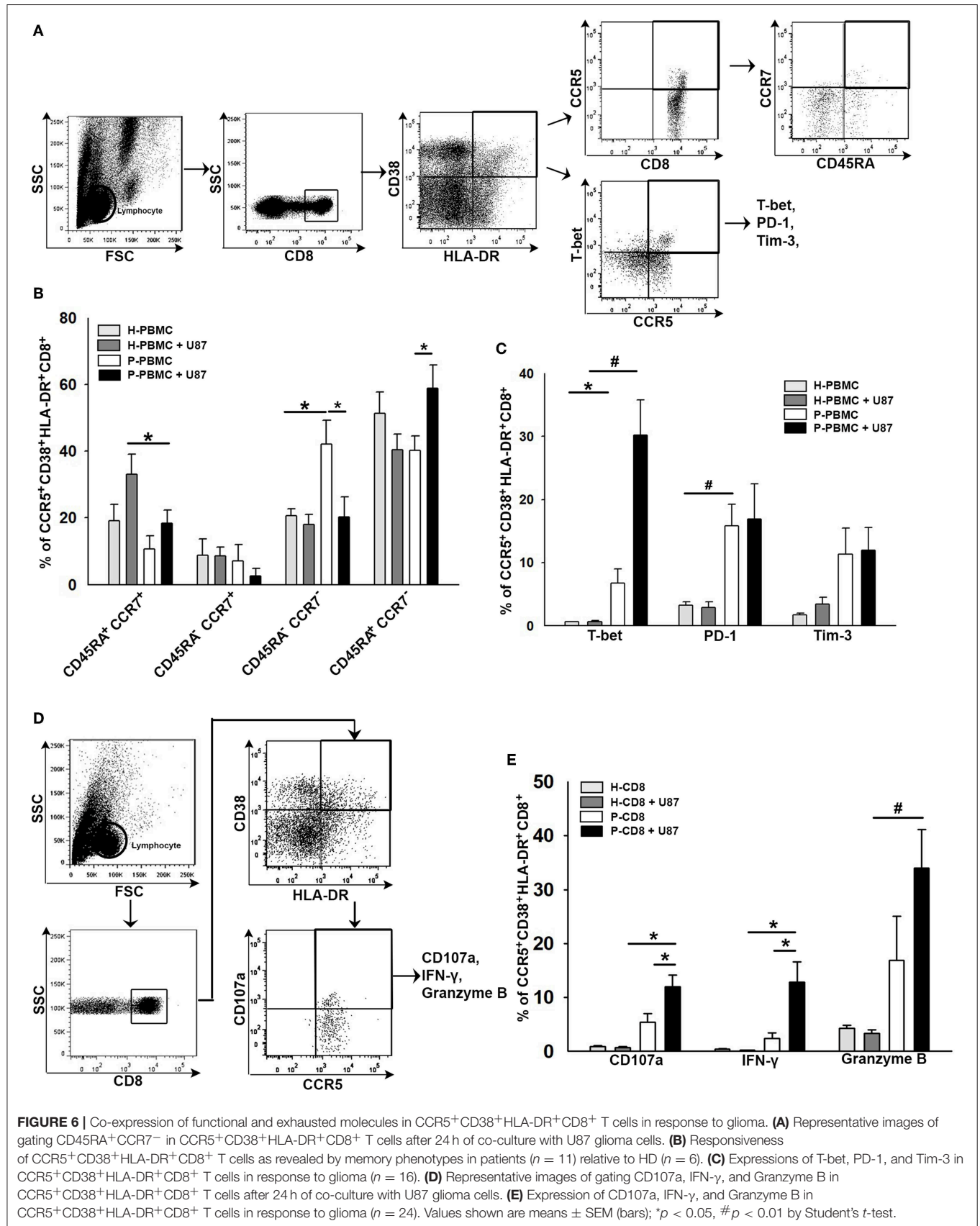
glioma eradication and to prompt certain anti-tumoral immune responses (8, 9, 32). The higher percentage of CD8<sup>+</sup> T cells and the ratio to CD4<sup>+</sup> T cells in TILs have been reported to be associated with a favorable prognosis in patients with glioma (11). However, the role of effector CD8 T cells in glioma is still obscure. Understanding whether a subset of effector CD8 T cells will infiltrate into tumors, their activity, and how they are suppressed might help identify immune-related therapeutic targets for intervention. The current study revealed that a subset of effector CD8<sup>+</sup> T cells characterized as CD38<sup>+</sup>HLA-DR<sup>+</sup>CD8<sup>+</sup> existed in both the peripheral blood and the tumor microenvironment, which indicated that the immune system of patients with glioma could recognize the tumor cells at an early stage. The high-grade gliomas appeared to generate a higher percentage of these cells, and these cells demonstrated increased infiltration into the tumors. Our data showed that the chemokine CCL5-CCR5 axis may be an important mechanism for attracting these effector T cells to the tumor microenvironment since tumor tissues expressed abundant CCL5 and T cells highly expressed CCR5. We also showed that CD38<sup>+</sup>HLA-DR<sup>+</sup>CD8<sup>+</sup> cells were still functional, as they could be activated *ex vivo*. In response to glioma, CCR5<sup>+</sup>CD38<sup>+</sup>HLA-DR<sup>+</sup>CD8<sup>+</sup> T cells were activated with a coinciding increase in TEMRA<sup>+</sup> (CD45RA<sup>+</sup>CCR7<sup>-</sup>). Increases of IFN- $\gamma$  and Granzyme B underlying CCR5<sup>+</sup>CD38<sup>+</sup>HLA-DR<sup>+</sup>CD8<sup>+</sup> T cell activation were observed after co-culturing with glioma cells. In addition, the CD38<sup>+</sup>HLA-DR<sup>+</sup>CD8<sup>+</sup> cells expressed higher levels of PD-1, and the presence of CD8<sup>+</sup> T cells indicated reinforcement of glioma PD-L1 expression, suggesting that the PD-1/PD-L1 loop may facilitate the maintenance of proper immune responses. As such, therapies that can modulate the immune check-point may rescue these cells and would have potential benefits in the treatment of glioma.

The percentage of CD38<sup>+</sup>HLA-DR<sup>+</sup>CD8<sup>+</sup> T-cell activation was significantly elevated in the circulating blood and tumors, indicating the active infiltration of these cells into the tumors. In addition, the elevated expression of CCL5 was also observed in patients with GBM, and this may be associated with an increased expression of CCR5 on CD38<sup>+</sup>HLA-DR<sup>+</sup>CD8<sup>+</sup> T cells. This is consistent with previous studies that have reported that the expression of CCR5 facilitates CD8<sup>+</sup> T-cell migration to damaged tissues (23, 33). The expression of CCR5 on CD8<sup>+</sup> T cells was determined to promote the M1 macrophage and T-helper cell immune response associated with  $\beta$  chemokines, including CCL5 (34, 35). Although previous studies have demonstrated that CCR5 expression is restricted to memory (CD28<sup>+</sup>CD45RA<sup>-</sup>) and effector (CD28<sup>-</sup>CD45RA<sup>-</sup> and CD28<sup>-</sup>CD45RA<sup>+</sup>) CD8<sup>+</sup> T cells (23), in this study we also demonstrated that CCR5

was distinctly expressed in the CD38<sup>+</sup>HLA-DR<sup>+</sup>CD8<sup>+</sup> T-cell population characterized as TEMRA<sup>+</sup> (CD45RA<sup>+</sup>CCR7<sup>-</sup>) from patients with glioma. In addition, expression of TNFR2<sup>+</sup> in the CD38<sup>+</sup>HLA-DR<sup>+</sup>CD8<sup>+</sup> T-cell population appeared to be tumor specific, as these cells were not significantly potentiated in the patient PBMCs. In addition, the regulation of CCR5 in human peripheral blood lymphocytes has been shown to be inversely regulated by TNF $\alpha$  via TNFR2 activation (33). Results have also revealed the tumor-specific activation of TNFR2 in CD38<sup>+</sup>HLA-DR<sup>+</sup>CD8<sup>+</sup> TILs. The regulation between CCR5 and TNFR2 appears to be consistent with past results as being inversely expressed in CD38<sup>+</sup>HLA-DR<sup>+</sup>CD8<sup>+</sup> T cells from patient PBMCs (Figures 3A,B). However, this reduction of TNFR2<sup>+</sup> on CD38<sup>+</sup>HLA-DR<sup>+</sup>CD8<sup>+</sup> T cells from patient PBMCs was not equally observed in CD38<sup>+</sup>HLA-DR<sup>+</sup>CD8<sup>+</sup> TILs, which displayed a marked increase in TNFR2<sup>+</sup> expression (Figures 3A,B). The activation of TNFR2 was previously indicated to initiate cell survival via the NF- $\kappa$ B pathway, which leads to the induction of anti-apoptotic factors such as BCL-2 (36). Moreover, TNFR2-deficient mice reveal significant tumor growth, and the presence of TNFR2 associates with the accumulation of CD8<sup>+</sup> TILs and CD8<sup>+</sup> T-cell IFN- $\gamma$  synthesis, suggesting TNFR2 potentiation on CD8<sup>+</sup> TILs has a role in anti-tumor activities (37, 38).

Accumulating evidence has indicated that the CCL5-CCR5 interaction facilitates cancer progression, including breast cancer, osteosarcoma, and colon cancer (39). Previously, CCL5 expression in human and murine colon cancers was demonstrated to enhance regulatory T cell (Treg) infiltration through CCR5 expression, which can initiate TGF- $\beta$ -dependent CD8<sup>+</sup> T-cell apoptosis (40). In the present study, we also found an elevation of CCL5 in the glioma microenvironment, which is in accordance with the infiltration of CD38<sup>+</sup>HLA-DR<sup>+</sup>CD8<sup>+</sup> TILs via CCR5 expression. However, it is unclear whether CCL5 in gliomas would also trigger similar Treg inhibition toward CD8<sup>+</sup> TILs, as we only found a negligible population (<2%) of Treg characterized as Foxp3<sup>+</sup> CD4<sup>+</sup> (data not shown). Several reports have also indicated that the expression of immune checkpoints, including Tim-3 and PD-1, render CD8<sup>+</sup> T cells exhausted, and PD-1 blockade can not only improve CD8<sup>+</sup> TIL activation and anti-tumor efficacy (41) but can also result in a CD8<sup>+</sup> T-cell-dependent survival benefit (42). Here, we have observed an increased expression of PD-1 on CD38<sup>+</sup>HLA-DR<sup>+</sup>CD8<sup>+</sup> cells relative to the rest of the CD8<sup>+</sup> cells, suggesting the possibility of CD38<sup>+</sup>HLA-DR<sup>+</sup>CD8<sup>+</sup> TIL exhaustion. Furthermore, the expression of CCR5 has been indicated as a co-factor for aiding virus entry (e.g., HIV and cytomegalovirus) into immune cells, and this can interrupt systematic immune coherence (43, 44). However,







whether or not elevated CCR5 expression in patients with glioma enforces susceptibility toward virus infection still requires further investigation.

The current study also revealed increased activation of effector CD38<sup>+</sup>HLA-DR<sup>+</sup>CD8<sup>+</sup> T cells accompanied by sustained IFN- $\gamma$  and IL-2 production, and these CD8<sup>+</sup> T-cell subsets were functionally capable after co-stimulation with PMA/ION. Accumulating evidence has indicated that cytokines, including IFN- $\gamma$  and IL-12, are essential for maximal effector CD8<sup>+</sup> T-cell accumulation and for sustaining effector differentiation (45, 46). It was shown that exposure of CD8<sup>+</sup> T cells to IL-12 and IFN- $\gamma$  maintains the surface expression of the IL-2 receptor, which prolongs the CD8<sup>+</sup> T-cell response to IL-2 and allows for sustained division of active CD8<sup>+</sup> T cells, resulting in greater expansion of antigen-specific cells (46). The peripheral cytotoxic CD8<sup>+</sup> T cells were shown to propagate a sustained basal level of IFN- $\gamma$  and IL-2 under disease states with heterogeneity effects in diseases and treatment results (47–49). In addition, IL-2 is thought to prompt effector T-cell differentiation (13). Our current results revealed that the basal levels of IFN- $\gamma$  and IL-2 were higher in the patient group, which may explain the hyperactivation of effector CD38<sup>+</sup>HLA-DR<sup>+</sup>CD8<sup>+</sup> T cells in these patients. The exact role of sustained basal production of IFN- $\gamma$  and IL-12 and its effect on antigen-specific cell expansion in patients with glioma remains unclear, but it may allow for persistent pathogen control. Our result also revealed that the lymphopenic state was notable in these patients. The relationship between lymphopenia and the burst activation of CD38<sup>+</sup>HLA-DR<sup>+</sup>CD8<sup>+</sup> T cells in high-grade glioma remains uncertain. Several reports have demonstrated that naïve T lymphocytes undergo rapid expansion during the lymphopenic state, requiring the engagement of MHCs and T cell receptors (TCR) (50, 51). The hyperexpansion of CD8<sup>+</sup> T cells driven by lymphopenia may transiently display effector functions prior to differentiation of memory-like T cells, which is coupled to the presence of CD44, CD122 (interleukin 2 receptor  $\beta$ ), and Ly6C to secrete IFN- $\gamma$  (52, 53).

In this present study, we demonstrated the functional expression of CCR5 on CD38<sup>+</sup>HLA-DR<sup>+</sup>CD8<sup>+</sup> T cells and the presence of CD45RA<sup>+</sup>CCR7<sup>−</sup> underlying CCR5<sup>+</sup>CD38<sup>+</sup>HLA-DR<sup>+</sup>CD8<sup>+</sup> T-cell activation in patients with glioma. The elevated TNFR2<sup>+</sup>CD38<sup>+</sup>HLA-DR<sup>+</sup>CD8<sup>+</sup> TILs indicated that TNFR2 might be involved in the anti-tumor response. Detection of CCL5 in GBM TILs suggested CCL5 might be one of the  $\beta$  chemokines that attract CD38<sup>+</sup>HLA-DR<sup>+</sup>CD8<sup>+</sup> TIL penetration. The PD-L1 expression level in GBM glioma appears to be preserved by the presence of CD8<sup>+</sup> T cells, which presumably limits the

effectiveness of CCR5<sup>+</sup>CD38<sup>+</sup>HLA-DR<sup>+</sup>CD8<sup>+</sup> TILs; therefore, the availability of CCR5<sup>+</sup>CD38<sup>+</sup>HLA-DR<sup>+</sup>CD8<sup>+</sup> T cells in term of numbers to initiate proper immune responses may also be violated and insufficient. As crucial central nervous system antigen-presenting cells, the effect of microglia on the propagation of CD38<sup>+</sup>HLA-DR<sup>+</sup>CD8<sup>+</sup> T cells may be a key factor that delineates the antigen-specific T-cell niche. Further studies of CCR5 on microglia will help to clarify the effect of CD38<sup>+</sup>HLA-DR<sup>+</sup>CD8<sup>+</sup> T cells on the anti-tumor response.

## DATA AVAILABILITY STATEMENT

The raw data supporting the conclusions of this manuscript will be made available by the authors, without undue reservation, to any qualified researcher.

## ETHICS STATEMENT

This study was approved by the Chang Gung Medical Foundation Institutional Review Board (No. 102-1096B) and in accordance with the Helsinki Declaration. Patients were recruited from the Department of Neurosurgery, Chang Gung Medical Foundation, Taiwan, between 2013 and 2016. All eligible patients were informed about the details of this study and provided a signed informed consent prior to study participation.

## AUTHOR CONTRIBUTIONS

CW, C-YL, J-YF, and P-YC were involved in the conception and design of the study. CW, H-CC, and L-YF performed the experiments. C-YL and J-HF provided technical support. CW, L-YF, C-YL, C-YH, and P-YC analyzed the data. K-CW and P-YC provided important materials. C-YL and J-YF critically revised the manuscript. CW and P-YC wrote the manuscript.

## FUNDING

This work was supported by grants from Chang Gung Memorial Hospital, Taiwan (CMRPG3D1343, CMRPG3F1731, and CMRPG3G0541) and the Ministry of Science and Technology, Taiwan (105-2314-B-182-007 and 108-2314-B-182A-052).

## SUPPLEMENTARY MATERIAL

The Supplementary Material for this article can be found online at: <https://www.frontiersin.org/articles/10.3389/fimmu.2019.02395/full#supplementary-material>

## REFERENCES

- Dunn GP, Rinne ML, Wykosky J, Genovese G, Quayle SN, Dunn IF, et al. Emerging insights into the molecular and cellular basis of glioblastoma. *Genes Dev.* (2012) 26:756–84. doi: 10.1101/gad.187922.112
- Arko L, Katsyiv I, Park GE, Luan WP, Park JK. Experimental approaches for the treatment of malignant gliomas. *Pharmacol Ther.* (2010) 128:1–36. doi: 10.1016/j.pharmthera.2010.04.015
- Uehara K, Sasayama T, Miyawaki D, Nishimura H, Yoshida K, Okamoto Y, et al. Patterns of failure after multimodal treatments for high-grade glioma: effectiveness of MIB-1 labeling index. *Radiat Oncol.* (2012) 7:104. doi: 10.1186/1748-717X-7-104
- Eljamel S, Petersen M, Valentine R, Buist R, Goodman C, Moseley H, et al. Comparison of intraoperative fluorescence and MRI image guided neuronavigation in malignant brain tumours, a prospective controlled

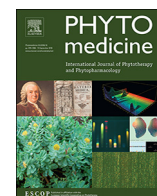


- study. *Photodiagn Photodyn Ther.* (2013) 10:356–61. doi: 10.1016/j.pdpdt.2013.03.006
5. Farmer JP, Antel JP, Freedman M, Cashman NR, Rode H, Villemure JG. Characterization of lymphoid cells isolated from human gliomas. *J Neurosurg.* (1989) 71:528–33. doi: 10.3171/jns.1989.71.4.0528
  6. El Andaloussi A, Lesniak MS. An increase in CD4<sup>+</sup>CD25<sup>+</sup>FOXP3<sup>+</sup> regulatory T cells in tumor-infiltrating lymphocytes of human glioblastoma multiforme. *Neurooncology.* (2006) 8:234–43. doi: 10.1215/15228517-2006-006
  7. Berghoff AS, Kiesel B, Widhalm G, Rajky O, Ricken G, Wohrer A, et al. Programmed death ligand 1 expression and tumor-infiltrating lymphocytes in glioblastoma. *Neurooncology.* (2015) 17:1064–75. doi: 10.1093/neuonc/nou307
  8. Prasad S, Gaedicke S, Machein M, Mittler G, Braun F, Hettich M, et al. Effective eradication of glioblastoma stem cells by local application of an AC133/CD133-specific T-cell-engaging antibody and CD8 T cells. *Cancer Res.* (2015) 75:2166–76. doi: 10.1158/0008-5472.CAN-14-2415
  9. Renner DN, Jin F, Litterman AJ, Balgeman AJ, Hanson LM, Gamez JD, et al. Effective treatment of established GL261 murine gliomas through picornavirus vaccination-enhanced tumor antigen-specific CD8<sup>+</sup> T cell responses. *PLoS ONE.* (2015) 10:e0125565. doi: 10.1371/journal.pone.0125565
  10. Mitchell DA, Fecci PE, Sampson JH. Immunotherapy of malignant brain tumors. *Immunol Rev.* (2008) 222:70–100. doi: 10.1111/j.1600-065X.2008.00603.x
  11. Han S, Zhang C, Li Q, Dong J, Liu Y, Huang Y, et al. Tumour-infiltrating CD4<sup>+</sup> and CD8<sup>+</sup> lymphocytes as predictors of clinical outcome in glioma. *Br J Cancer.* (2014) 110:2560–8. doi: 10.1038/bjc.2014.162
  12. Williams MA, Bevan MJ. Effector and memory CTL differentiation. *Annu Rev Immunol.* (2007) 25:171–92. doi: 10.1146/annurev.immunol.25.022106.141548
  13. Feau S, Arens R, Togher S, Schoenberger SP. Autocrine IL-2 is required for secondary population expansion of CD8<sup>+</sup> memory T cells. *Nat Immunol.* (2011) 12:908–13. doi: 10.1038/ni.2079
  14. Aoki T, Tashiro K, Miyatake S, Kinashi T, Nakano T, Oda Y, et al. Expression of murine interleukin 7 in a murine glioma cell line results in reduced tumorigenicity *in vivo*. *Proc Natl Acad Sci USA.* (1992) 89:3850–4. doi: 10.1073/pnas.89.9.3850
  15. Church SE, Jensen SM, Antony PA, Restifo NP, Fox BA. Tumor-specific CD4<sup>+</sup> T cells maintain effector and memory tumor-specific CD8<sup>+</sup> T cells. *Eur J Immunol.* (2014) 44:69–79. doi: 10.1002/eji.201343718
  16. Smith GA, Taunton J, Weiss A. IL-2Rbeta abundance differentially tunes IL-2 signaling dynamics in CD4<sup>+</sup> and CD8<sup>+</sup> T cells. *Sci Signal.* (2017) 10:eaan4931. doi: 10.1126/scisignal.aan4931
  17. Deaglio S, Vaisitti T, Aydin S, Ferrero E, Malavasi F. In-tandem insight from basic science combined with clinical research: CD38 as both marker and key component of the pathogenetic network underlying chronic lymphocytic leukemia. *Blood.* (2006) 108:1135–44. doi: 10.1182/blood-2006-01-013003
  18. Hua S, Lecoux C, Saez-Cirion A, Pancino G, Girault I, Versmisse P, et al. Potential role for HIV-specific CD38<sup>+</sup>/HLA-DR<sup>+</sup> CD8<sup>+</sup> T cells in viral suppression and cytotoxicity in HIV controllers. *PLoS ONE.* (2014) 9:e0101920. doi: 10.1371/journal.pone.0101920
  19. Wong SW, Comenzo RL. CD38 Monoclonal antibody therapies for multiple myeloma. *Clin Lymphoma Myeloma Leuk.* (2015) 15:635–45. doi: 10.1016/j.clml.2015.07.642
  20. Karan-Djurasevic T, Palibrk V, Zukic B, Spasovski V, Glumac I, Colovic M, et al. Expression of Bcl2L12 in chronic lymphocytic leukemia patients: association with clinical and molecular prognostic markers. *Med Oncol.* (2013) 30:405. doi: 10.1007/s12032-012-0405-7
  21. Malavasi F, Deaglio S, Funaro A, Ferrero E, Horenstein AL, Ortolan E, et al. Evolution and function of the ADP ribosyl cyclase/CD38 gene family in physiology and pathology. *Physiol Rev.* (2008) 88:841–86. doi: 10.1152/physrev.00035.2007
  22. Ma Y, Jiang J, Ying W. CD38 mediates the intracellular ATP levels and cell survival of C6 glioma cells. *Neuroreport.* (2014) 25:569–73. doi: 10.1097/WNR.000000000000139
  23. Fukada K, Sobao Y, Tomiyama H, Oka S, Takiguchi M. Functional expression of the chemokine receptor CCR5 on virus epitope-specific memory and effector CD8<sup>+</sup> T cells. *J Immunol.* (2002) 168:2225–32. doi: 10.4049/jimmunol.168.5.2225
  24. Palmer LA, Sale GE, Balogun JJ, Li D, Jones D, Molldrem JJ, et al. Chemokine receptor CCR5 mediates alloimmune responses in graft-versus-host disease. *Biol Blood Marrow Transplant.* (2010) 16:311–9. doi: 10.1016/j.bbmt.2009.12.002
  25. Wu L, Paxton WA, Kassam N, Ruffing N, Rottman JB, Sullivan N, et al. CCR5 levels and expression pattern correlate with infectability by macrophage-tropic HIV-1, *in vitro*. *J Exp Med.* (1997) 185:1681–91. doi: 10.1084/jem.185.9.1681
  26. Johnson EL, Howard CL, Thurman J, Pontiff K, Johnson ES, Chakraborty R. Cytomegalovirus upregulates expression of CCR5 in central memory cord blood mononuclear cells, which may facilitate *in utero* HIV type 1 transmission. *J Infect Dis.* (2015) 211:187–96. doi: 10.1093/infdis/jiu424
  27. Lefort CT, Kim M. Human T lymphocyte isolation, culture and analysis of migration *in vitro*. *J Vis Exp.* (2010) 40:2017. doi: 10.3791/2017
  28. Miescher S, Whiteside TL, de Tribolet N, von Flidner V. *In situ* characterization, clonogenic potential, and antitumor cytolytic activity of T lymphocytes infiltrating human brain cancers. *J Neurosurg.* (1988) 68:438–48. doi: 10.3171/jns.1988.68.3.0438
  29. Elliott LH, Brooks WH, Roszman TL. Activation of immunoregulatory lymphocytes obtained from patients with malignant gliomas. *J Neurosurg.* (1987) 67:231–6. doi: 10.3171/jns.1987.67.2.0231
  30. Wiencke JK, Accomando WP, Zheng S, Patoka J, Dou X, Phillips JJ, et al. Epigenetic biomarkers of T-cells in human glioma. *Epigenetics.* (2012) 7:1391–402. doi: 10.4161/epi.22675
  31. Vuletic A, Jovanic I, Jurisic V, Milovanovic Z, Nikolic S, Spurnic I, et al. Decreased interferon gamma production in CD3<sup>+</sup> and CD3<sup>+</sup>CD56<sup>+</sup> lymphocyte subsets in metastatic regional lymph nodes of melanoma patients. *Pathol Oncol Res.* (2015) 21:1109–14. doi: 10.1007/s12253-015-9938-3
  32. Domingues P, Gonzalez-Tablas M, Otero A, Pascual D, Miranda D, Ruiz L, et al. Tumor infiltrating immune cells in gliomas and meningiomas. *Brain Behav. Immun.* (2015) 53:1–15. doi: 10.1016/j.bbi.2015.07.019
  33. Hornung F, Scala G, Lenardo MJ. TNF-alpha-induced secretion of C-C chemokines modulates C-C chemokine receptor 5 expression on peripheral blood lymphocytes. *J Immunol.* (2000) 164:6180–7. doi: 10.4049/jimmunol.164.12.6180
  34. Sato W, Tomita A, Ichikawa D, Lin Y, Kishida H, Miyake S, et al. CCR2(+)CCR5(+) T cells produce matrix metalloproteinase-9 and osteopontin in the pathogenesis of multiple sclerosis. *J Immunol.* (2012) 189:5057–65. doi: 10.4049/jimmunol.1202026
  35. Li F, Cheng B, Cheng J, Wang D, Li H, He X. CCR5 blockade promotes M2 macrophage activation and improves locomotor recovery after spinal cord injury in mice. *Inflammation.* (2015) 38:126–33. doi: 10.1007/s10753-014-0014-z
  36. Brenner D, Blaser H, Mak TW. Regulation of tumour necrosis factor signalling: live or let die. *Nat Rev Immunol.* (2015) 15:362–74. doi: 10.1038/nri3834
  37. Bertrand F, Rochotte J, Colacios C, Montfort A, Tilkin-Mariame AF, Touriol C, et al. Blocking tumor necrosis factor alpha enhances CD8 T-cell-dependent immunity in experimental melanoma. *Cancer Res.* (2015) 75:2619–28. doi: 10.1158/0008-5472.CAN-14-2524
  38. Williams GS, Mistry B, Guillard S, Ulrichsen JC, Sandercock AM, Wang J, et al. Phenotypic screening reveals TNFR2 as a promising target for cancer immunotherapy. *Oncotarget.* (2016) 7:68278–91. doi: 10.18632/oncotarget.11943
  39. Aldinucci D, Colombatti A. The inflammatory chemokine CCL5 and cancer progression. *Mediators Inflamm.* (2014) 2014:292376. doi: 10.1155/2014/292376
  40. Chang LY, Lin YC, Mahalingam J, Huang CT, Chen TW, Kang CW, et al. Tumor-derived chemokine CCL5 enhances TGF-beta-mediated killing of CD8<sup>+</sup> T cells in colon cancer by T-regulatory cells. *Cancer Res.* (2012) 72:1092–102. doi: 10.1158/0008-5472.CAN-11-2493
  41. Speranza MC, Passaro C, Ricklefs F, Kasai K, Klein SR, Nakashima H, et al. Preclinical investigation of gene-mediated cytotoxic immunotherapy and checkpoint blockade in glioblastoma. *Neurooncology.* (2017) 20:225–35. doi: 10.1093/neuonc/now139

42. Antonios JP, Soto H, Everson RG, Orpilla J, Moughon D, Shin N, et al. PD-1 blockade enhances the vaccination-induced immune response in glioma. *JCI Insight*. (2016) 1:e87059. doi: 10.1172/jci.insight.87059
43. Berger EA, Murphy PM, Farber JM. Chemokine receptors as HIV-1 coreceptors: roles in viral entry, tropism, and disease. *Annu Rev Immunol*. (1999) 17:657–700. doi: 10.1146/annurev.immunol.17.1.657
44. Bongers G, Maussang D, Muniz LR, Noriega VM, Fraile-Ramos A, Barker N, et al. The cytomegalovirus-encoded chemokine receptor US28 promotes intestinal neoplasia in transgenic mice. *J Clin Invest*. (2010) 120:3969–78. doi: 10.1172/JCI42563
45. Curtsinger JM, Valenzuela JO, Agarwal P, Lins D, Mescher MF. Type I IFNs provide a third signal to CD8 T cells to stimulate clonal expansion and differentiation. *J Immunol*. (2005) 174:4465–9. doi: 10.4049/jimmunol.174.8.4465
46. Starbeck-Miller GR, Xue HH, Harty JT. IL-12 and type I interferon prolong the division of activated CD8 T cells by maintaining high-affinity IL-2 signaling *in vivo*. *J Exp Med*. (2014) 211:105–20. doi: 10.1084/jem.20130901
47. Berner B, Akca D, Jung T, Muller GA, Reuss-Borst MA. Analysis of Th1 and Th2 cytokines expressing CD4<sup>+</sup> and CD8<sup>+</sup> T cells in rheumatoid arthritis by flow cytometry. *J Rheumatol*. (2000) 27:1128–35.
48. Adams AB, Larsen CP, Pearson TC, Newell KA. The role of TNF receptor and TNF superfamily molecules in organ transplantation. *Am J Transpl*. (2002) 2:12–8. doi: 10.1034/j.1600-6143.2002.020104.x
49. Muraro E, Comaro E, Talamini R, Turchet E, Miolo G, Scalone S, et al. Improved Natural Killer cell activity and retained anti-tumor CD8(+) T cell responses contribute to the induction of a pathological complete response in HER2-positive breast cancer patients undergoing neoadjuvant chemotherapy. *J Transl Med*. (2015) 13:204. doi: 10.1186/s12967-015-0567-0
50. Ge Q, Rao VP, Cho BK, Eisen HN, Chen J. Dependence of lymphopenia-induced T cell proliferation on the abundance of peptide/ MHC epitopes and strength of their interaction with T cell receptors. *Proc Natl Acad Sci USA*. (2001) 98:1728–33. doi: 10.1073/pnas.98.4.1728
51. Long B, Wong CP, Wang Y, Tisch R. Lymphopenia-driven CD8(+) T cells are resistant to antigen-induced tolerance in NOD.scid mice. *Eur J Immunol*. (2006) 36:2003–12. doi: 10.1002/eji.200535717
52. Cho BK, Rao VP, Ge Q, Eisen HN, Chen J. Homeostasis-stimulated proliferation drives naive T cells to differentiate directly into memory T cells. *J Exp Med*. (2000) 192:549–56. doi: 10.1084/jem.192.4.549
53. Goldrath AW, Bogatzki LY, Bevan MJ. Naive T cells transiently acquire a memory-like phenotype during homeostasis-driven proliferation. *J Exp Med*. (2000) 192:557–64. doi: 10.1084/jem.192.4.557

**Conflict of Interest:** The authors declare that the research was conducted in the absence of any commercial or financial relationships that could be construed as a potential conflict of interest.

Copyright © 2019 Chen, Wu, Fang, Chen, Feng, Huang, Wei, Fang and Lin. This is an open-access article distributed under the terms of the Creative Commons Attribution License (CC BY). The use, distribution or reproduction in other forums is permitted, provided the original author(s) and the copyright owner(s) are credited and that the original publication in this journal is cited, in accordance with accepted academic practice. No use, distribution or reproduction is permitted which does not comply with these terms.



# High levels of EGFR prevent sulforaphane-induced reactive oxygen species-mediated apoptosis in non-small-cell lung cancer cells

Tong-Hong Wang<sup>a,b,1</sup>, Chin-Chuan Chen<sup>b,c,1</sup>, Kuo-Yen Huang<sup>a,d</sup>, Ya-Min Shih<sup>a</sup>, Chi-Yuan Chen<sup>a,b,\*</sup>

<sup>a</sup> Graduate Institute of Health Industry Technology and Research Center for Food and Cosmetic Safety, Research Center for Chinese Herbal Medicine, College of Human Ecology, Chang Gung University of Science and Technology, Tao-Yuan 333, Taiwan

<sup>b</sup> Tissue Bank, Chang Gung Memorial Hospital, Tao-Yuan 333, Taiwan

<sup>c</sup> Graduate Institute of Natural Products, Chang Gung University, Tao-Yuan 333, Taiwan

<sup>d</sup> Institute of Biomedical Sciences, Academia Sinica, Taipei 115, Taiwan

## ARTICLE INFO

**Keywords:**  
Sulforaphane  
NSCLC  
EGFR  
ROS  
DNA damage  
Apoptosis

## ABSTRACT

**Background:** Sulforaphane (SFN) has been shown to induce the production of reactive oxygen species (ROS) and inhibit epidermal growth factor receptor (EGFR)-mediated signaling in non-small-cell lung cancer (NSCLC). NSCLC cells harboring constitutively active EGFR mutations are more sensitive to SFN treatment than cells with wild-type EGFR, but whether NSCLC cells with high levels of EGFR expression are more resistant or sensitive to SFN treatment is not known.

**Study design:** We employed a pair of cell lines, CL1-0 and CL1-5, which have the same genetic background but different levels of EGFR expression, to examine the effects of high EGFR level in the sensitivity to SFN.

**Methods:** The effect of SFN on cell viability and tumorigenicity was examined by trypan blue dye-exclusion assay, clonogenic assays, flow cytometry, and immunoblotting *in vitro* as well as tumorigenicity study *in vivo*. ROS levels in cells were assessed by flow cytometry using the ROS-reactive fluorescent indicator CM-H2DCFDA. Knockdown of EGFR in CL1-5 cells was infected with an EGFR-targeting small hairpin (interfering) RNA (shRNA)-containing lentivirus.

**Results:** We present evidence that cells with high-level EGFR expression (CL1-5) are more resistant to SFN treatment than those with low-level expression (CL1-0). SFN treatment produced a similar increase in ROS and caused arrest of a cell population at S-phase accompanied by the induction of  $\gamma$ H2AX, a DNA damage-response marker, in both cell sublines. However, SFN induced apoptosis only in the high-EGFR-expressing CL1-0 subline. Pretreatment with the antioxidant N-acetyl-L-cysteine prevented SFN-induced apoptosis in CL1-0 cells and production of  $\gamma$ H2AX in both CL1-0 and CL1-5 cells. shRNA-mediated knockdown of EGFR in CL1-5 cells rendered the cells susceptible to SFN-induced apoptosis.

**Conclusion:** The cellular effects produced by SFN in NSCLC cells are largely mediated by SFN-induced production of ROS. Cells with higher levels of EGFR were more resistant to SFN treatment and showed resistance to SFN-induced apoptosis, suggesting that high EGFR levels protect cells from SFN-induced apoptosis. Despite this, we found that SFN retained the ability to inhibit the growth of NSCLC tumors with high-level EGFR expression *in vivo*.

## Introduction

Non-small-cell lung cancer (NSCLC) is the predominant type of lung cancer, which is the most common cause of cancer deaths worldwide (Siegel et al., 2015). Epidermal growth factor receptor (EGFR)-mediated signaling is the major driver of NSCLC (Pao and

Chmielecki, 2010), and EGFR is known to be highly expressed or mutated in about 60% of NSCLC patients (Sharma et al., 2007). Therefore, inhibition of EGFR signaling has been actively explored for its therapeutic potential against NSCLC. Targeted treatment using EGFR tyrosine kinase inhibitors (TKIs) has led to dramatic clinical improvement in NSCLC patients harboring EGFR mutations (Fukuoka et al., 2003).

**Abbreviations:** EGFR, epidermal growth factor receptor; NSCLC, non-small-cell lung cancer; ROS, reactive oxygen species; SFN, sulforaphane; TKIs, tyrosine kinase inhibitors

\* Corresponding author.

E-mail address: [cychen@mail.cgu.edu.tw](mailto:cychen@mail.cgu.edu.tw) (C.-Y. Chen).

<sup>1</sup> These authors contributed equally.

<https://doi.org/10.1016/j.phymed.2019.152926>

Received 4 December 2018; Received in revised form 7 April 2019; Accepted 8 April 2019

0944-7113/ © 2019 Elsevier GmbH. All rights reserved.

However, resistance to TKI treatment develops in most patients owing to the development of secondary mutations in EGFR (Pao and Chmielecki, 2010). Thus, new agents that can effectively counteract acquired TKI resistance are urgently needed.

The phytochemical sulforaphane (SFN), first identified in broccoli sprouts and present in high concentrations in most cruciferous vegetables (Whiteside et al., 2013), has been shown to modulate multiple targets involved in cancer development (Bayat Mokhtari et al., 2017). SFN activates different signaling pathways by inducing the production of reactive oxygen species (ROS), producing DNA damage, cell-cycle arrest, and/or cell death in many cancer cell lines (Choi et al., 2008; Clarke et al., 2011; Jo et al., 2014; Moon et al., 2009; Park et al., 2014; Singh et al., 2005; Wang et al., 2015; Wu et al., 2016). Depending on the cancer cell type studied, the effects of SFN can be very diverse and include inhibition of cell growth, invasion, and cell-cycle progression (Choi et al., 2008; Jo et al., 2014; Kim et al., 2006; Moon et al., 2009; Park et al., 2014; Singh et al., 2005; Wang et al., 2015; Wu et al., 2016). In addition, SFN has been shown to display differential cytotoxicity against prostate and breast cancer cell lines compared with normal prostate and mammary epithelial cells (Clarke et al., 2011; Telang et al., 2009). Thus, whereas SFN is known to induce the production of ROS, the basis for the differential inhibitory effects of SFN on different cell types remains poorly understood.

SFN has been demonstrated to be an anti-NSCLC agent (Jeong et al., 2017; Lin et al., 2017; Mi et al., 2007; Tripathi et al., 2015; Wang et al., 2017). In evaluating the potential of SFN to treat TKI-resistant NSCLC, we recently found that SFN inhibits EGFR expression and effectively inhibits the growth of EGFR-TKI-resistant NSCLC cells and tumors derived from them (Chen et al., 2015). Interestingly, the antitumor activity of SFN against TKI-resistant NSCLC cells harboring mutant EGFR was greater than that against wild-type EGFR NSCLC cells (Chen et al., 2015). This suggests the possibility that EGFR status in different cells may be a factor in governing the cell's sensitivity to SFN. Since more than 45% of NSCLCs exhibit EGFR overexpression (Herbst et al., 2008), it is important to know whether high levels of EGFR affect SFN sensitivity. Here, we examined whether ROS production is involved in the inhibition of EGFR signaling by SFN and whether the level of EGFR in NSCLC cells affects sensitivity to SFN.

## Materials and methods

### Compounds and antibodies

Antibodies against phospho-ATM, ATM, phospho-Chk1, Chk1,  $\gamma$ H2AX, LC3, and cleaved forms of PARP, caspase-7, and caspase-9 were purchased from Cell Signaling (Temecula, CA, USA). Antibodies against EGFR and  $\beta$ -actin were purchased from Santa Cruz Biotechnology (Santa Cruz, CA, USA). SFN (#S4441), N-acetyl-L-cysteine (NAC), hydrogen peroxide ( $H_2O_2$ ), and RNase A were purchased from Sigma (St. Louis, MO, USA). The purity of SFN was at least 90% as determined from high-performance liquid chromatography analysis. Gel electrophoresis reagents were from Bio-Rad (Berkeley, CA, USA).

### Cell lines and culture media

The human NSCLC cell lines CL1-0 and CL1-5, described previously (Chu et al., 1997), were kindly provided by Dr. Pan-Chyr Yang (National Taiwan University, Taipei, Taiwan). CL1-0 and CL1-5 cells were cultured in RPMI-1640 medium containing 10% fetal bovine serum (FBS), 100 U/ml penicillin, 100 U/ml streptomycin, and 2 mM sodium pyruvate. Culture media, chemical compounds, and FBS were purchased from Life Technologies (Grand Island, NY, USA).

### Assays for cell viability and clonogenic potential

Cell viability and clonogenic potential were assayed as described

previously (Chen et al., 2015).

### Flow cytometric analysis of the cell cycle

Cells were fixed in absolute ethanol at  $-20^\circ\text{C}$  for 4 h and resuspended in 1 ml of phosphate-buffered saline (PBS; pH 7.4) containing 20  $\mu\text{g/ml}$  RNase A. After incubating at  $37^\circ\text{C}$  for 30 min, the cells were treated with propidium iodide (100  $\mu\text{g/ml}$ ) at room temperature for 10 min in the dark. A total of 10,000 cells were analyzed by flow cytometry using a BD FACSCalibur system (Becton–Dickinson).

### Measurement of ROS generation

Cells were suspended in PBS containing 10  $\mu\text{M}$  CM- $H_2$ DCFDA (5-(and-6)-chloromethyl-2',7'-dichlorodihydrofluorescein diacetate) (#C6827; Invitrogen), a fluorescent reporter of ROS. After incubating at  $37^\circ\text{C}$  for 30 min in the dark, ROS levels in cells were assessed by flow cytometry using a FACSCalibur system.

### Western blotting, immunohistochemistry, and hematoxylin-eosin staining

Western blotting, immunohistochemistry, and hematoxylin and eosin staining were performed as described previously (Chen et al., 2013).

### Downregulation of EGFR by shRNAs

Lentiviruses containing small hairpin (interfering) RNAs (shRNAs) against EGFR (shEGFR-1, TRCN0000039634; shEGFR-2, TRCN0000121068) and pseudotyped lentivirus empty vector control (shV: pLKO TRC001) were obtained from the National RNAi Core Facility (Academia Sinica, Taipei, Taiwan). CL1-5 cells were infected with lentiviruses in the presence of polybrene at 6  $\mu\text{g/ml}$ . After 24 h of infection, cells were cultured in the presence of 0.75 mg/ml puromycin for 12 days, yielding pooled puromycin-resistant cells.

### Xenograft mouse model for studying the antitumor activity of SFN against CL1-5 cells in vivo

Male, 6-wk-old nude mice (BALB/c nu/nu; National Laboratory Animal Center, Taipei, Taiwan) were used as a xenograft mouse model to study the antitumor activity of SFN against CL1-5 cells. The xenograft mouse model was prepared by subcutaneously inoculating the right flank of nude mice with  $3 \times 10^6$  CL1-5 cells in 100  $\mu\text{l}$  of medium (Ho et al., 2015). Treatment was initiated when a tumors mass was detected in all nude mice ( $\sim 6$  days after tumor cell injection). Xenografted mice were randomized into three groups ( $n = 5/\text{group}$ ): (i) SFN only (50 mg/kg) (Wang et al., 2015), (ii) SFN plus NAC (10 mg/kg) (Liang and Zhang, 2016), and (iii) vehicle control (PBS). Drugs were administered intraperitoneally every 2 d (Wang et al., 2015). Tumor dimensions were measured using a caliper twice weekly, and tumor volume was calculated according to the formula  $\text{tumor width}^2 \times \text{length} \times 0.5$  (Wang et al., 2015). Animal experiments were performed according to an animal protocol approved by the Animal Care Ethics Commission of Chang Gung Memorial Hospital.

### Statistical analysis

The significance of differences between the two groups was assessed by Student's *t*-test using SPSS 16.0 and Excel 2007. *p* values  $< 0.05$  were considered statistically significant. The presented results are representative of three independent experiments that yielded similar results.



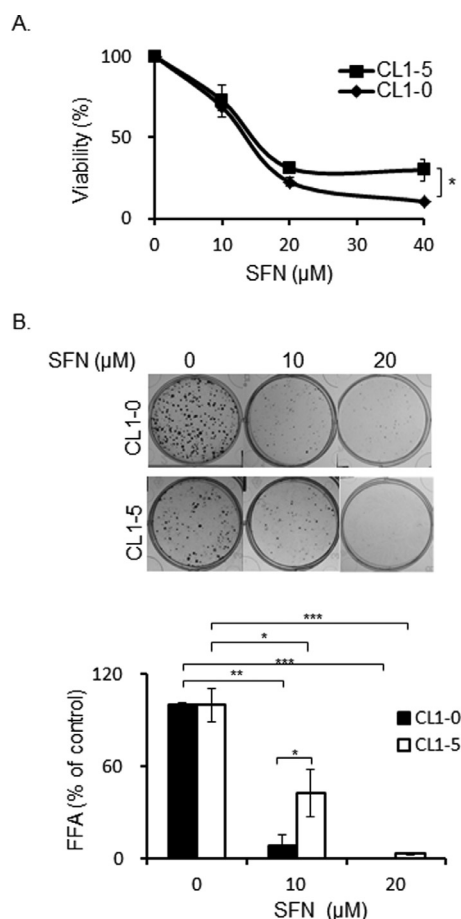


**Fig. 1.** Effects of SFN on the viability and clonogenic potential of CL1-0 and CL1-5 cells. (A) CL1-0 and CL1-5 cells were treated with different concentrations of SFN for 24 h. The viability of SFN-treated cells was determined by trypan blue dye-exclusion assay. (B) CL1-0 and CL1-5 cells were treated with SFN for 24 h and then cultured for an additional 6 days in the absence of drug. *Top panel:* Representative examples of focus formation by SFN-treated cells. *Bottom panel:* Relative focus-forming ability (FFA), expressed as means  $\pm$  SD from three independent experiments ( $p < 0.05$ ,  $p < 0.01$ , and  $p < 0.001$ ; unpaired *t*-tests).

## Results

### Effects of SFN on the viability and focus-forming potential of NSCLC cells with different levels of EGFR expression

To determine whether the level of EGFR plays a role in governing sensitivity to SFN, we performed a comparative study using CL1-0 and CL1-5 cells. CL1-5 is a highly invasive metastatic NSCLC cell line derived from CL1-0 cells (Chu et al., 1997). A previous study showed that CL1-5 cells express significantly higher levels of wild-type EGFR than CL1-0 cells (Chen et al., 2013). Because CL1-0 and CL1-5 cells have the same genetic background, this pair of cell lines is an ideal cell model for examining the role of EGFR expression level in the sensitivity to SFN.

We first assessed the cytotoxic effects of SFN in CL1-0 and CL1-5 cells using trypan blue dye-exclusion assay. As shown in Fig. 1A, SFN decreased the viability of both CL1-0 and CL1-5 cells in a concentration-dependent manner, although CL1-0 cells exhibited slightly higher sensitivity to SFN than CL1-5. Next, we examined the effects of SFN on clonogenic potential. As shown in Fig. 1B, SFN at a concentration of 20  $\mu$ M completely abrogated focus formation by both CL1-0 and CL1-5 cells. At 10  $\mu$ M, SFN significantly reduced focus-forming ability in both CL1-0 and CL1-5 cells. However, the inhibitory effect of 10  $\mu$ M SFN on clonogenic potential was significantly greater for CL1-0 cells than CL1-5

cells, results similar to those obtained in cytotoxicity assays shown above. These results indicate that CL1-5 cells are more resistant to SFN than CL1-0 cells.

### Effects of SFN on ROS generation and cell-cycle progression

To determine whether the sensitivity of NSCLC cells to SFN is related to SFN-induced production of ROS, we examined ROS production in SFN-treated CL1-0 and CL1-5 cells using the ROS-reactive fluorescent indicator, CM-H2DCFDA. After treating with 40  $\mu$ M SFN for 24 h, cells were incubated with CM-H2DCFDA, after which ROS production was determined by monitoring CM-H2DCFDA fluorescence using flow cytometry. As shown in Fig. 2A, ROS levels in SFN-treated CL1-0 and CL1-5 cells were increased  $\sim$ 1.6-fold compared with control cells. Pretreatment with the antioxidant NAC at 2 mM for 1 h essentially eliminated SFN-induced ROS production (Fig. 2A, right panel). It also reversed SFN-induced morphological alterations and loss of adherence in both CL1-0 and CL1-5 cells (Fig. 2B).

To elucidate the effects of SFN-induced ROS on cell-cycle progression, we exposed cells to SFN for 24 h, with or without pretreatment with 2 mM NAC for 1 h. Treated cells were then stained with propidium iodide and analyzed by flow cytometry. As shown in Fig. 2C, the percentage of cells in the sub-G1 region was substantially increased in SFN-treated CL1-0 cells in association with an increase in an S-phase-arrested cell population. Pretreatment of CL1-0 cells with NAC reversed the SFN-induced increase in the sub-G1 and S-phase populations. In SFN-treated CL1-5 cells, the population of cells arrested in the S-phase was increased, but there was no significant increase in the sub-G1 population. Pretreatment of CL1-5 cells with NAC reversed the SFN-induced increase in the S-phase population. Taken together, these results suggest that ROS play an important role in the cellular effects of SFN.

### Effects of SFN on apoptosis and DNA damage response in CL1-0 and CL1-5 NSCLC cells

Our analysis of the effects of SFN on cell-cycle progression (Fig. 2) revealed that SFN induced cell-cycle arrest at S-phase in both CL1-0 and CL1-5 cells but induced apoptosis only in CL1-0 cells, as evidenced by an increase in the sub-G1 population in SFN-treated CL1-0 cells. Because ROS can induce DNA damage by targeting nucleic acids (Matic, 2017), resulting in cell-cycle arrest at S-phase, we assessed DNA damage responses in SFN-treated cells. Cells were treated with SFN, and expression of  $\gamma$ H2AX, a DNA damage-response marker, was assessed by Western blotting. As shown in Fig. 3A,  $\gamma$ H2AX was highly induced by SFN in both CL1-0 and CL1-5 cells. In SFN-treated CL1-0 cells, this  $\gamma$ H2AX induction was not accompanied by activation of ATM (ataxia-telangiectasia mutated) or Chk1 (checkpoint kinase 1), downstream effectors in the DNA damage-response signaling cascade. In contrast, the induction of  $\gamma$ H2AX in SFN-treated CL1-5 cells was accompanied by activation of ATM and Chk1. To determine if SFN induces apoptosis and/or autophagy formation, we examined cells for activation of proapoptotic caspase markers and the expression of autophagy markers LC3-II by Western blotting. As shown in Fig. 3B, there was a dose-dependent increase of LC3-II in both of the SFN-treated CL1-0 and CL1-5 cells, indicating that SFN promoted autophagy induction in NSCLC cells. However, the induction of apoptosis as detected by cleaved (activated) caspase-9, caspase-7, and PARP was readily detected in SFN-treated CL1-0 cells but not in SFN-treated CL1-5 cells. These results are consistent with the results of our cell-cycle analysis (see Fig. 2), which showed that SFN induced apoptosis in CL1-0 cells but not in CL1-5 cells.

To determine whether ROS production is required for the different responses observed in CL1-0 and CL1-5 cells, we examined the effects of NAC pretreatment on the DNA damage response and apoptosis induction. As shown in Fig. 3C, scavenging of ROS with NAC significantly attenuated SFN-induced apoptosis in CL1-0 cells (Fig. 3C, upper panel) and the SFN-induced DNA damage response in CL1-5 cells (Fig. 3C,



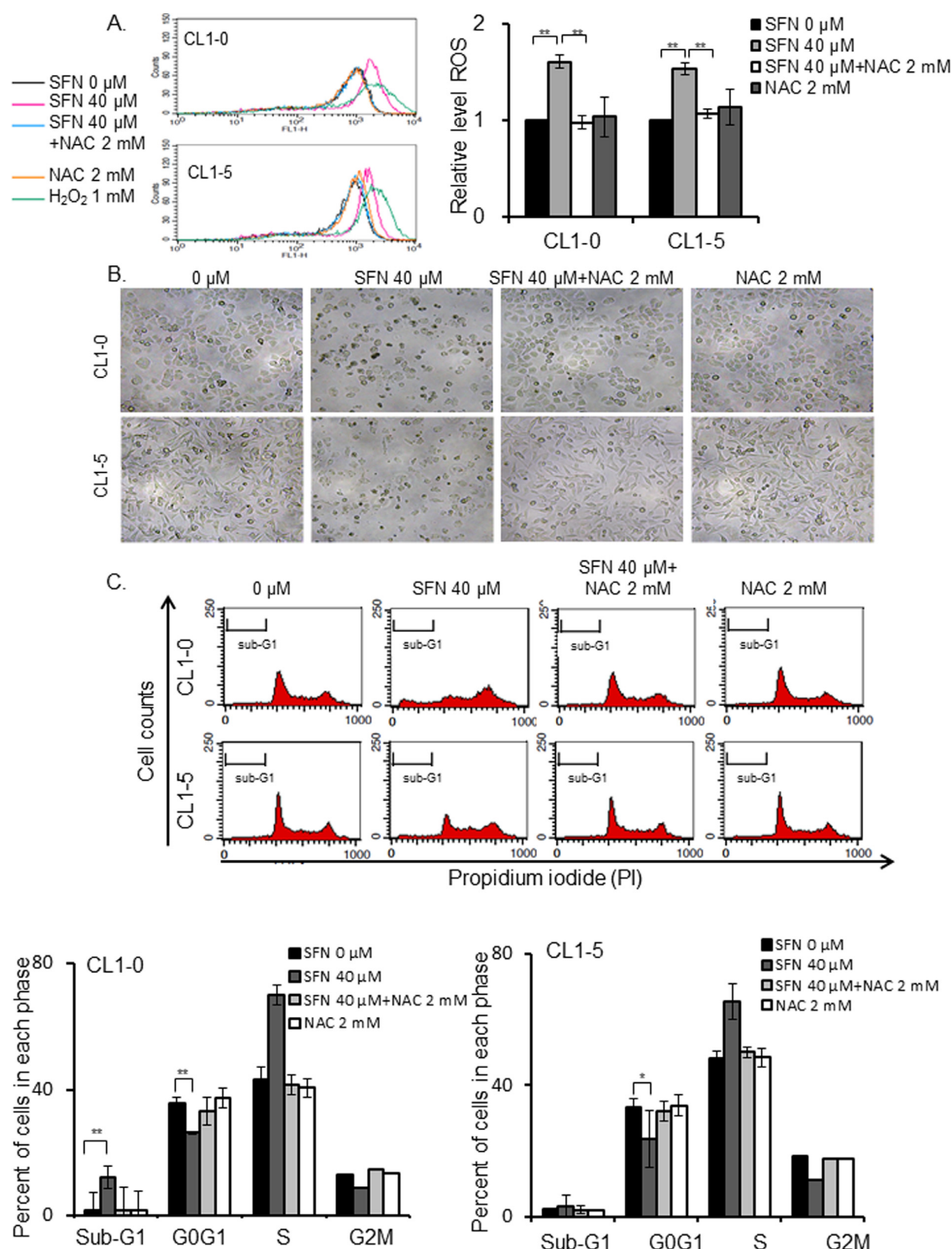


**Fig. 2.** Effects of SFN on ROS generation and cell-cycle progression. CL1-0 and CL1-5 cells were preincubated with or without 2 mM NAC for 1 h before exposure to 40  $\mu$ M SFN for 24 h. (A) ROS levels were determined by flow cytometry analysis of CM-H<sub>2</sub>DCFDA fluorescence in treated cells. Cells treated with 1 mM H<sub>2</sub>O<sub>2</sub> for 15 min served as a positive control. (B) Photomicrographs showing the morphology of treated cells. (C) The distribution of cells in a sub-G1 population and in different stages of the cell cycle was determined by flow cytometry analysis of cells stained with propidium iodide. *Top panel:* Representative flow cytometric results. *Bottom panel:* Results of three independent experiments, expressed as means  $\pm$  SD ( $p < 0.05$ ,  $p < 0.01$ , and  $p < 0.001$  vs. control).

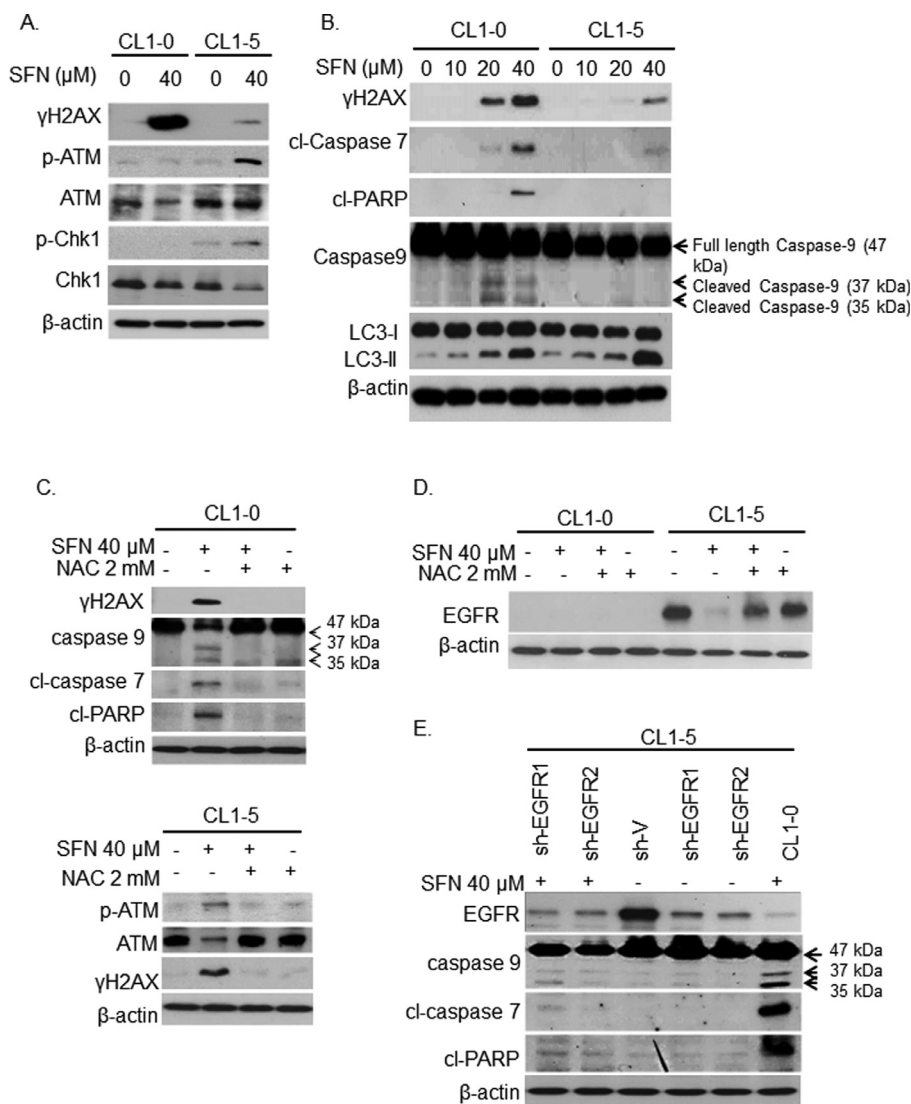


**Fig. 3.** Effects of SFN on apoptosis and DNA damage responses in CL1-0 and CL1-5 cells. (A) CL1-0 and CL1-5 cells were treated with 40  $\mu$ M SFN for 24 h. Cell lysates were collected and assayed for the expression of  $\gamma$ H2AX, phospho-ATM, ATM, phospho-Chk1, and Chk1 by Western blotting.  $\beta$ -actin served as a loading control. (B) CL1-0 and CL1-5 cells were treated with the indicated concentrations of SFN for 24 h. The expression levels of LC3-I, LC3-II,  $\gamma$ H2AX, cleaved forms of PARP (cl-PARP), caspase-7 (cl-caspase 7), and caspase-9 were determined by Western blotting.  $\beta$ -actin served as a loading control. (C) CL1-0 cells and CL1-5 cells were treated with 40  $\mu$ M SFN for 24 h, with or without pretreatment with 2 mM NAC for 1 h. The expression levels of  $\gamma$ H2AX, phospho-ATM, ATM, cl-PARP, cl-caspase 7, and caspase-9 were determined by Western blotting. (D) Downregulation of EGFR by SFN-induced ROS. CL1-0 and CL1-5 cells were treated with 40  $\mu$ M SFN for 24 h, with or without pretreatment with 2 mM NAC for 1 h. EGFR expression was semi-quantitatively determined by Western blotting.  $\beta$ -actin served as a loading control. (E). Pooled puromycin-resistant cells, obtained by infecting CL1-5 cells with sh-EGFR1 or sh-EGFR2 viruses followed by growth in puromycin-containing medium, were treated with 40  $\mu$ M SFN for 24 h; CL1-5 cells infected with pseudotyped lentivirus empty vector (sh-V) served as a control. Cell lysates were collected and assayed for the expression of EGFR and cl-PARP, cl-caspase-7, and caspase-9 by Western blotting. Data shown are from one of three experiments that yielded similar results.  $\beta$ -actin served as a loading control.

lower panel).

#### SFN induces apoptosis in EGFR-knockdown CL1-5 cells

SFN triggers apoptosis through downregulation of the EGFR protein in human gastric cancer (Mondal et al., 2016). Consistent with this, we recently showed that SFN promotes the proteasomal degradation of EGFR in NSCLC cells (Chen et al., 2015). As shown in Fig. 3D, SFN reduced EGFR expression in CL1-5 cells to a level that was still higher than that in untreated CL1-0 cells. Pretreatment of CL1-5 cells with NAC prevented SFN-induced downregulation of EGFR, suggesting the involvement of ROS in this process. To determine whether the failure of SFN to induce apoptosis in CL1-5 cells is attributable to the high level of EGFR, we examined the effects of downregulating EGFR in CL1-5 cells on the apoptotic response to SFN. To this end, CL1-5 cells were infected with an EGFR-targeting shRNA-containing lentivirus to knock down EGFR expression levels. As shown in Fig. 3E, shEGFR reduced the level of EGFR in CL1-5 cells to about 53% of that in control, infected with empty vector (sh-V) CL1-5 cells. Incubation of shEGFR-CL1-5 cells with SFN for 24 h induced a weak apoptotic response, as evidenced by the presence of cleaved forms of PARP and caspase-7 and -9. Therefore, high levels of EGFR expression appear to prevent SFN-induced, ROS-mediated apoptosis in NSCLC cells.

#### Effects of SFN on CL1-5 cell-derived tumors in vivo

To investigate the antitumor effects of SFN on high EGFR-expressing NSCLC tumor cells *in vivo*, we employed a xenograft animal model, prepared by injecting CL1-5 cells into the flanks of nude mice. After tumors had reached a size of approximately 5 mm<sup>3</sup> (6 days), mice were treated with SFN, with or without NAC treatment. As shown in Fig. 4A, SFN administration significantly inhibited tumor growth. This inhibitory effect was attenuated by co-treatment with NAC, suggesting the involvement of ROS generation in the anti-NSCLC effect of SFN *in vivo*. Under our experimental conditions, there was no noticeable change in the body weight of mice, suggesting the absence of overt drug toxicity (Fig. 4B). A histological analysis confirmed that the entire tumor consisted of NSCLC cells (Fig. 4C). Immunohistochemical staining of excised tumors revealed intense EGFR staining in untreated tumors and weak EGFR staining in SFN-treated tumors (Fig. 4D). Tumors excised from mice treated with both SFN and NAC showed increased staining of EGFR compared with tumors treated with SFN only. These results indicate that SFN exerts antitumor activity against NSCLC tumor cells that express high levels of EGFR *in vivo* and that SFN-induced ROS production is likely a major contributor to the *in vivo* antitumor activity of SFN.

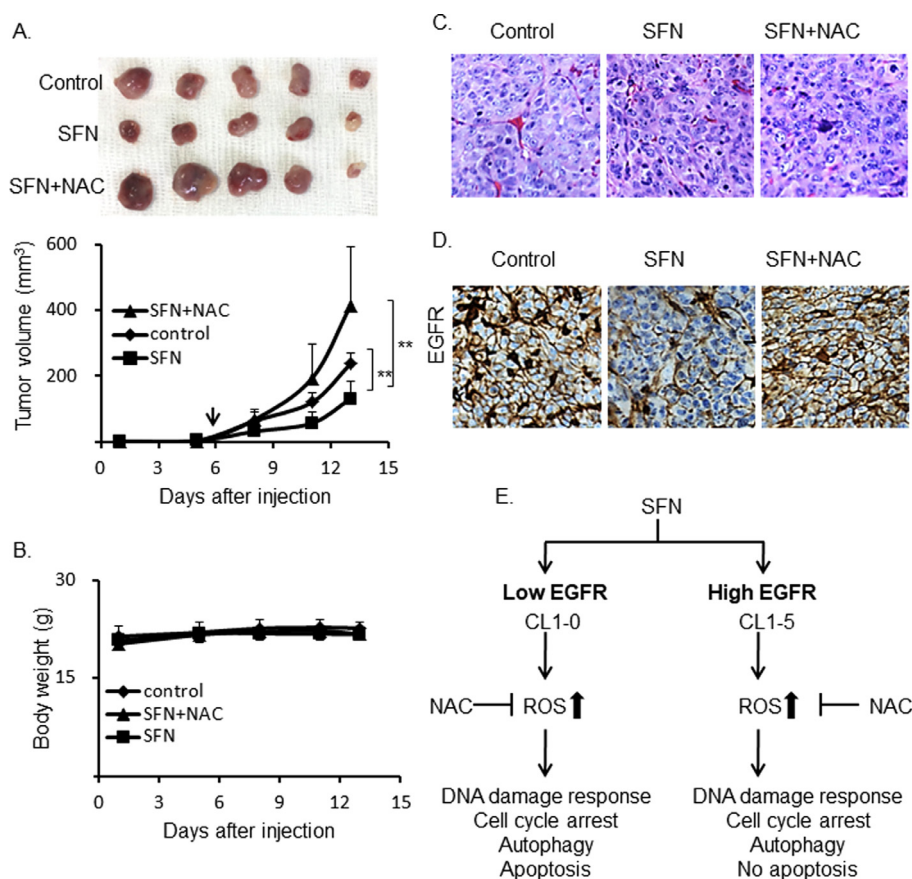


**Fig. 4.** SFN inhibits the growth of CL1-5 cell-derived tumors *in vivo*. CL1-5 cells were inoculated subcutaneously into the right flank of nude mice. Xenografted mice were treated with the indicated drugs beginning on day 6. (A) Effects of SFN alone and together with NAC on tumor growth. *Top panel*: Representative xenograft tumors excised from treated mice. (B) Effects of drug treatment on the body weights of mice. Data are presented as means  $\pm$  SD (\*\* $p \leq 0.01$ ; Student's *t*-test). (C) Hematoxylin and eosin-stained xenografted tumor tissues. (D) Immunohistochemical staining of EGFR. (E) Model for the effects of different EGFR expression in SFN-mediated cellular effects.

## Discussion

ROS generated by SFN target many signaling pathways involved in initiating cancer cell death (Sestili and Fimognari, 2015). For example, ROS have been shown to activate both intrinsic and extrinsic caspase cascades in prostate cancer cells (Singh et al., 2005), suppress Akt phosphorylation and telomerase activity in hepatocellular carcinoma Hep3B cells (Moon et al., 2010), induce mitotic arrest and apoptosis in human bladder cancer 5637 cells (Park et al., 2014), activate endoplasmic reticulum stress and the nuclear factor-E2-related factor-2 (Nrf2) signaling pathway in T24 human urinary bladder cancer cells (Jo et al., 2014), repress PI3K/Akt pathway activity in thyroid cancer cells (Wang et al., 2015), and inhibit TGF- $\beta$ -induced epithelial-mesenchymal transition and promote apoptosis in hepatocellular carcinoma cells (Wu et al., 2016). In the current study, we present evidence that the cellular effects produced by SFN in NSCLC cells, including cell-cycle arrest (Fig. 2), induction of DNA damage response and/or apoptosis, and downregulation of EGFR (Fig. 3), are largely attributable to SFN-induced production of ROS, since pretreatment with the ROS scavenger NAC prevented these cellular effects.

SFN has been shown to trigger apoptosis through downregulation of EGFR protein (Mondal et al., 2016). We have recently shown that SFN inhibits EGFR signaling by promoting proteasome-mediated degradation of EGFR in NSCLC (Chen et al., 2015). High-level induction of ROS has been shown to trigger the overoxidation and degradation of EGFR L858R T790M mutants and cause apoptosis in the TKI-resistant NSCLC cells that harbor these variants (Leung et al., 2016). Therefore, mutations in EGFR are among the factors governing the sensitivity of a cell to SFN. A related factor that may also affect a cell's sensitivity to SFN is the relative level of EGFR expression. In the current study, we employed a pair of cell lines that have the same genetic background but different degrees of EGFR expression to examine the effects of EGFR level on the sensitivity to SFN. We found that, whereas SFN induced a similar

increase in ROS production in both cell lines, high EGFR-expressing CL1-5 cells were more resistant to SFN treatment than low EGFR-expressing CL1-0 cells (Figs. 1 and 2). Moreover, whereas SFN induced DNA damage response, autophagy formation, and cell-cycle arrest in both cell lines, it induced apoptosis only in CL1-0 cells and not in CL1-5 cells (Figs. 2 and 3). The lack of apoptosis induction in cells with high-level EGFR expression is likely attributable to the abundance of EGFR. Although SFN treatment greatly decreased EGFR level, reducing it to about 66% of that in untreated controls, the residual level of EGFR was still higher than that in untreated CL1-0 cells (Fig. 3D). We postulated that the residual amount of undegraded EGFR in SFN-treated CL1-5 cells was sufficient to prevent the induction of apoptosis. Employing shRNA to downregulate EGFR in CL1-5 cells, we found that a weak apoptotic response could be detected in these EGFR-knockdown CL1-5 cells, suggesting that cells with a high level of EGFR resist SFN-induced apoptosis. Since the capability to repair DNA damage is known to depend on the EGFR expression and downstream pathways (Kriegs et al., 2010; Kryeziu et al., 2013; Myllynen et al., 2011), it is likely that cells with a high level of EGFR could perform greater repair of DNA damage and thus resist the induction of apoptosis.

Taken together with the observation that EGFR is overexpressed in more than 45% of NSCLC cases (Herbst et al., 2008), our current finding that NSCLC cells with high-level EGFR expression are more resistant to SFN treatment *in vitro* raised the question of whether SFN is capable of inhibiting the growth of high EGFR-expressing NSCLC tumors *in vivo*. Using a xenograft animal model, we showed that SFN could indeed inhibit the growth of CL1-5 cell-derived tumors *in vivo* (Fig. 4). Although SFN appeared to inhibit the growth of tumors derived from xenografted TKI-resistant NSCLC cells to a greater extent than that of tumors derived from xenografted EGFR-overexpressing NSCLC cells, it nonetheless showed good antitumor efficacy against EGFR-overexpressing NSCLC. We suggest that the appropriate combination of SFN with another EGFR-downregulating agent could greatly improve the



efficacy of SFN in the treatment of EGFR-overexpressing NSCLC.

In conclusion, we have shown that the cellular effects produced by SFN in NSCLC cells are largely mediated by SFN-induced production of ROS. Cells with higher levels of EGFR were more resistant to SFN treatment and showed resistance to SFN-induced apoptosis, suggesting that high EGFR levels protect cells from SFN-induced apoptosis (Fig. 4E).

## Conflict of interest

The authors state that they have no conflicts of interest.

## Acknowledgments

This work was supported by grants from Chang Gung Memorial Hospital (CMRPF1H0011 to C.Y. Chen), Chang Gung University of Science and Technology (ZRRPF3H0091 to C.Y. Chen), and the Ministry of Science and Technology of Taiwan (106-2320-B-255-006 to C.Y. Chen). The funders had no role in study design, data collection, data analysis, publication decisions, or manuscript preparation.

## References

- Bayat Mokhtari, R., Baluch, N., Homayouni, T.S., Morgatskaya, E., Kumar, S., Kazemi, P., Yeger, H., 2017. The role of Sulforaphane in cancer chemoprevention and health benefits: a mini-review. *J. Cell Commun. Signal.*
- Chen, C.Y., Jan, C.I., Lo, J.F., Yang, S.C., Chang, Y.L., Pan, S.H., Wang, W.L., Hong, T.M., Yang, P.C., 2013. Tidi-L inhibits EGFR signaling in lung adenocarcinoma by enhancing EGFR Ubiquitinylation and degradation. *Cancer Res.* 73, 4009–4019.
- Chen, C.Y., Yu, Z.Y., Chuang, Y.S., Huang, R.M., Wang, T.C., 2015. Sulforaphane attenuates EGFR signaling in NSCLC cells. *J. Biomed. Sci.* 22, 38.
- Choi, W.Y., Choi, B.T., Lee, W.H., Choi, Y.H., 2008. Sulforaphane generates reactive oxygen species leading to mitochondrial perturbation for apoptosis in human leukemia U937 cells. *Biomed. Pharmacother.* 62, 637–644.
- Chu, Y.W., Yang, P.C., Yang, S.C., Shyu, Y.C., Hendrix, M.J., Wu, R., Wu, C.W., 1997. Selection of invasive and metastatic subpopulations from a human lung adenocarcinoma cell line. *Am. J. Respir. Cell Mol. Biol.* 17, 353–360.
- Clarke, J.D., Hsu, A., Yu, Z., Dashwood, R.H., Ho, E., 2011. Differential effects of sulforaphane on histone deacetylases, cell cycle arrest and apoptosis in normal prostate cells versus hyperplastic and cancerous prostate cells. *Mol. Nutr. Food Res.* 55, 999–1009.
- Fukuoka, M., Yano, S., Giaccone, G., Tamura, T., Nakagawa, K., Douillard, J.Y., Nishiaki, Y., Vansteenkiste, J., Kudoh, S., Rischin, D., Eek, R., Horai, T., Noda, K., Takata, I., Smit, E., Averbuch, S., Macleod, A., Feyereislova, A., Dong, R.P., Baselga, J., 2003. Multi-institutional randomized phase II trial of gefitinib for previously treated patients with advanced non-small-cell lung cancer (The IDEAL 1 Trial) [corrected]. *J. Clin. Oncol.* 21, 2237–2246.
- Herbst, R.S., Heymach, J.V., Lippman, S.M., 2008. Lung cancer. *N. Engl. J. Med.* 359, 1367–1380.
- Ho, S.T., Tung, Y.T., Kuo, Y.H., Lin, C.C., Wu, J.H., 2015. Ferruginol inhibits non-small cell lung cancer growth by inducing caspase-associated apoptosis. *Integr. Cancer Ther.* 14, 86–97.
- Jeong, Y.J., Cho, H.J., Chung, F.L., Wang, X., Hoe, H.S., Park, K.K., Kim, C.H., Chang, H.W., Lee, S.R., Chang, Y.C., 2017. Isothiocyanates suppress the invasion and metastasis of tumors by targeting FAK/MMP-9 activity. *Oncotarget* 8, 63949–63962.
- Jo, G.H., Kim, G.Y., Kim, W.J., Park, K.Y., Choi, Y.H., 2014. Sulforaphane induces apoptosis in T24 human urinary bladder cancer cells through a reactive oxygen species-mediated mitochondrial pathway: the involvement of endoplasmic reticulum stress and the Nrf2 signaling pathway. *Int. J. Oncol.* 45, 1497–1506.
- Kim, H., Kim, E.H., Eom, Y.W., Kim, W.H., Kwon, T.K., Lee, S.J., Choi, K.S., 2006. Sulforaphane sensitizes tumor necrosis factor-related apoptosis-inducing ligand (TRAIL)-resistant hepatoma cells to TRAIL-induced apoptosis through reactive oxygen species-mediated up-regulation of DR5. *Cancer Res.* 66, 1740–1750.
- Kriegs, M., Kasten-Pisula, U., Rieckmann, T., Holst, K., Saker, J., Dahm-Daphi, J., Dikomey, E., 2010. The epidermal growth factor receptor modulates DNA double-strand break repair by regulating non-homologous end-joining. *DNA Repair (Amst.)* 9, 889–897.
- Kryeziu, K., Jungwirth, U., Hoda, M.A., Ferk, F., Knasmüller, S., Karnthaler-Benbakka, C., Kowol, C.R., Berger, W., Heffeter, P., 2013. Synergistic anticancer activity of arsenic trioxide with erlotinib is based on inhibition of EGFR-mediated DNA double-strand break repair. *Mol. Cancer Ther.* 12, 1073–1084.
- Leung, E.L., Fan, X.X., Wong, M.P., Jiang, Z.H., Liu, Z.Q., Yao, X.J., Lu, L.L., Zhou, Y.L., Yau, L.F., Tin, V.P., Liu, L., 2016. Targeting Tyrosine kinase inhibitor-resistant non-small cell lung cancer by inducing epidermal growth factor receptor degradation via methionine 790 oxidation. *Antioxidants Redox Signal.* 24, 263–279.
- Liang, L., Zhang, Z., 2016. Gambogic acid inhibits malignant melanoma cell proliferation through mitochondrial p66shc/ROS-p53/bax-mediated apoptosis. *Cell Physiol. Biochem.* 38, 1618–1630.
- Lin, K., Yang, R., Zheng, Z., Zhou, Y., Geng, Y., Hu, Y., Wu, S., Wu, W., 2017. Sulforaphane-cysteine-induced apoptosis via phosphorylated ERK1/2-mediated maspin pathway in human non-small cell lung cancer cells. *Cell Death Discov.* 3, 17025.
- Matic, I., 2017. The major contribution of the DNA damage-triggered reactive oxygen species production to cell death: implications for antimicrobial and cancer therapy. *Curr. Genetics.*
- Mi, L., Wang, X., Govind, S., Hood, B.L., Veenstra, T.D., Conrads, T.P., Saha, D.T., Goldman, R., Chung, F.L., 2007. The role of protein binding in induction of apoptosis by phenethyl isothiocyanate and sulforaphane in human non-small lung cancer cells. *Cancer Res.* 67, 6409–6416.
- Mondal, A., Biswas, R., Rhee, Y.H., Kim, J., Ahn, J.C., 2016. Sulforaphane promotes Bax/Bcl2, MAPK-dependent human gastric cancer AGS cells apoptosis and inhibits migration via EGFR, p-ERK1/2 down-regulation. *Gen. Physiol. Biophys.* 35, 25–34.
- Moon, D.O., Kang, S.H., Kim, K.C., Kim, M.O., Choi, Y.H., Kim, G.Y., 2010. Sulforaphane decreases viability and telomerase activity in hepatocellular carcinoma Hep3B cells through the reactive oxygen species-dependent pathway. *Cancer Lett.* 295, 260–266.
- Moon, D.O., Kim, M.O., Kang, S.H., Choi, Y.H., Kim, G.Y., 2009. Sulforaphane suppresses TNF-alpha-mediated activation of NF-kappaB and induces apoptosis through activation of reactive oxygen species-dependent caspase-3. *Cancer Lett.* 274, 132–142.
- Myllynen, L., Rieckmann, T., Dahm-Daphi, J., Kasten-Pisula, U., Petersen, C., Dikomey, E., Kriegs, M., 2011. In tumor cells regulation of DNA double strand break repair through EGF receptor involves both NHEJ and HR and is independent of p53 and K-Ras status. *Radiother. Oncol.* 101, 147–151.
- Pao, W., Chmielecki, J., 2010. Rational, biologically based treatment of EGFR-mutant non-small-cell lung cancer. *Nat. Rev. Cancer* 10, 760–774.
- Park, H.S., Han, M.H., Kim, G.Y., Moon, S.K., Kim, W.J., Hwang, H.J., Park, K.Y., Choi, Y.H., 2014. Sulforaphane induces reactive oxygen species-mediated mitotic arrest and subsequent apoptosis in human bladder cancer 5637 cells. *Food Chem. Toxicol.* 64, 157–165.
- Sestili, P., Fimognari, C., 2015. Cytotoxic and antitumor activity of sulforaphane: the role of reactive oxygen species. *Biomed. Res. Int.* 2015, 402386.
- Sharma, S.V., Bell, D.W., Settleman, J., Haber, D.A., 2007. Epidermal growth factor receptor mutations in lung cancer. *Nat. Rev. Cancer* 7, 169–181.
- Siegel, R.L., Miller, K.D., Jemal, A., 2015. Cancer statistics, 2015. *CA Cancer J. Clin.* 65, 5–29.
- Singh, S.V., Srivastava, S.K., Choi, S., Lew, K.L., Antosiewicz, J., Xiao, D., Zeng, Y., Watkins, S.C., Johnson, C.S., Trump, D.L., Lee, Y.J., Xiao, H., Herman-Antosiewicz, A., 2005. Sulforaphane-induced cell death in human prostate cancer cells is initiated by reactive oxygen species. *J. Biol. Chem.* 280, 19911–19924.
- Telang, U., Brazeau, D.A., Morris, M.E., 2009. Comparison of the effects of phenethyl isothiocyanate and sulforaphane on gene expression in breast cancer and normal mammary epithelial cells. *Exp. Biol. Med.* (Maywood) 234, 287–295.
- Tripathi, K., Hussein, U.K., Anupalli, R., Barnett, R., Bachaboina, L., Scalici, J., Rocconi, R.P., Owen, L.B., Piazza, G.A., Palle, K., 2015. Allyl isothiocyanate induces replication-associated DNA damage response in NSCLC cells and sensitizes to ionizing radiation. *Oncotarget* 6, 5237–5252.
- Wang, D.X., Zou, Y.J., Zhuang, X.B., Chen, S.X., Lin, Y., Li, W.L., Lin, J.J., Lin, Z.Q., 2017. Sulforaphane suppresses EMT and metastasis in human lung cancer through miR-616-5p-mediated GSK3beta/beta-catenin signaling pathways. *Acta Pharmacol. Sin.* 38, 241–251.
- Wang, L., Tian, Z., Yang, Q., Li, H., Guan, H., Shi, B., Hou, P., Ji, M., 2015. Sulforaphane inhibits thyroid cancer cell growth and invasiveness through the reactive oxygen species-dependent pathway. *Oncotarget* 6, 25917–25931.
- Whiteside, E.J., Seim, I., Pauli, J.P., O'Keeffe, A.J., Thomas, P.B., Carter, S.L., Walpole, C.M., Jung, J.N., Josh, P., Herington, A.C., Chopin, L.K., 2013. Identification of a long non-coding RNA gene, growth hormone secretagogue receptor opposite strand, which stimulates cell migration in non-small cell lung cancer cell lines. *Int. J. Oncol.* 43, 566–574.
- Wu, J., Han, J., Hou, B., Deng, C., Wu, H., Shen, L., 2016. Sulforaphane inhibits TGF-beta-induced epithelial-mesenchymal transition of hepatocellular carcinoma cells via the reactive oxygen species-dependent pathway. *Oncol. Rep.* 35, 2977–2983.

# Maslinic acid protects against obesity-induced nonalcoholic fatty liver disease in mice through regulation of the Sirt1/AMPK signaling pathway

Chian-Jiun Liou,<sup>\*,†,1</sup> Yi-Wen Dai,<sup>\*,†,1</sup> Chia-Ling Wang,<sup>‡</sup> Li-Wen Fang,<sup>§</sup> and Wen-Chung Huang<sup>†,‡,2</sup>

<sup>\*</sup>Division of Basic Medical Sciences, Department of Nursing, Research Center for Chinese Herbal Medicine, and <sup>†</sup>Research Center for Food and Cosmetic Safety, Graduate Institute of Health Industry Technology, College of Human Ecology, Chang Gung University of Science and Technology, Taoyuan City, Taiwan; <sup>‡</sup>Division of Allergy, Asthma, and Rheumatology, Department of Pediatrics, Chang Gung Memorial Hospital, Linkou, Taoyuan City, Taiwan; and <sup>§</sup>Department of Nutrition, I-Shou University, Kaohsiung City, Taiwan

**ABSTRACT:** Maslinic acid is a pentacyclic triterpenoid that is distributed in the peel of olives. Previous studies found that maslinic acid inhibited inflammatory response and antioxidant effects. We investigated whether maslinic acid ameliorates nonalcoholic fatty liver disease in mice with high-fat-diet (HFD)-induced obesity and evaluated the regulation of lipogenesis in hepatocytes. Male C57BL/6 mice fed a normal diet or HFD (60% fat, w/w) were tested for 16 wk. After the fourth week, mice were injected intraperitoneally with maslinic acid for 12 wk. In another experiment, HepG2 cells were treated with oleic acid to induce lipid accumulation or maslinic acid to evaluate lipogenesis. Maslinic acid significantly reduced body weight compared with HFD-fed mice. Maslinic acid reduced liver weight and liver lipid accumulation and improved hepatocyte steatosis. Furthermore, serum glucose, leptin, and free fatty acid concentrations significantly reduced, but the serum adiponectin concentration was higher, in the maslinic acid group than in the HFD group. In liver tissue, maslinic acid suppressed transcription factors involved in lipogenesis and increased adipose triglyceride lipase. *In vitro*, maslinic acid decreased lipogenesis by activating AMPK. These findings suggest that maslinic acid acts against hepatic steatosis by regulating enzyme activity involved in lipogenesis, lipolysis, and fatty acid oxidation in the liver.—Liou, C.-J., Dai, Y.-W., Wang, C.-L., Fang, L.-W., Huang, W.-C. Maslinic acid protects against obesity-induced nonalcoholic fatty liver disease in mice through regulation of the Sirt1/AMPK signaling pathway. FASEB J. 33, 000–000 (2019). www.fasebj.org

**KEY WORDS:** HepG2 • lipogenesis • lipolysis • hepatic steatosis

Obesity is a chronic inflammatory disease and is considered to be a major underlying factor in chronic diseases, including hypertension, hyperlipidemia, stroke, and diabetes (1). Many studies have also found that obesity can

induce abnormal lipid metabolism in the liver, developing into nonalcoholic fatty liver disease (NAFLD) (2). NAFLD is a complex chronic hepatitis involving multiple steps toward reduced liver function and metabolic disorders (3). Studies have demonstrated that initial symptoms of hepatic steatosis are characterized by an excessive accumulation of triglycerides in hepatocytes (2). If the patient does not properly maintain their weight and a balanced diet, the condition may gradually deteriorate and develop into nonalcoholic steatohepatitis, irreversible liver fibrosis, or cirrhosis, and, ultimately, hepatocellular carcinoma (3).

Excessive free fatty acids in the diet enter the liver for triglyceride and lipid synthesis, forming oil droplets and accumulating in the liver (4). These triglycerides can be stored as energy or are metabolized to produce energy to maintain the normal physiologic function of cells and tissues (5). However, obesity and being overweight are often accompanied by excessive triglyceride and cholesterol in the serum, causing cardiovascular diseases, and a large amount of free fatty acids that enter the liver and interfere with lipid storage and metabolism (6). Many studies have found that CCAAT/enhancer-binding protein (C/EBP),

**ABBREVIATIONS:** ACC, acetyl CoA carboxylase; AICAR, 5-aminoimidazole-4-carboxamide-1- $\beta$ -D-ribofuranoside; ALT, alanine aminotransferase; AST, aspartate aminotransferase; ATGL, adipose triglyceride lipase; Bodipy, boron-dipyrromethene; C/EBP, CCAAT/enhancer-binding protein; CPT-1, carnitine palmitoyltransferase 1; FAS, fatty acid synthase; H&E, hematoxylin and eosin; HFD, high-fat diet; HOMA-IR, Homeostatic Model Assessment of Insulin Resistance; HSL, hormone-sensitive lipase; NAFLD, nonalcoholic fatty liver disease; PAS, periodic acid-Schiff; PPAR, peroxisome proliferator-activated receptor; Sirt1, sirtuin 1; SREBP-1c, sterol regulatory element-binding protein 1c; TG, triglyceride; TC, total cholesterol

<sup>1</sup> These authors contributed equally to this work.

<sup>2</sup> Correspondence: Research Center for Food and Cosmetic Safety, Research Center for Chinese Herbal Medicine, Graduate Institute of Health Industry Technology, College of Human Ecology, Chang Gung University of Science and Technology, No. 261, Wenhua 1st Rd., Guishan District, Taoyuan City 33303, Taiwan. E-mail: wchuang@mail.cgu.edu.tw

doi: 10.1096/fj.201900413RRR

This article includes supplemental data. Please visit <http://www.fasebj.org> to obtain this information.



peroxisome proliferator-activated receptor (PPAR), and sterol regulatory element-binding protein 1c (SREBP-1c) are important transcription factors for regulating fatty acid synthase (FAS) gene expression and controlling the synthesis of fatty acid chains and lipid biosynthesis in the liver (7). Therefore, blocking transcription factors involved in lipogenesis could reduce triglyceride synthesis and ameliorate hepatic steatosis.

Improving lipolysis is also an effective strategy for improving lipid accumulation in fatty liver, but decomposition of triglycerides requires lipolytic enzymes, including adipose triglyceride lipase (ATGL) and hormone-sensitive lipase (HSL), resulting in free fatty acids and glycerol (8). Therefore, accelerating the decomposition of lipids could assist NAFLD in restoring normal liver function and improving lipid metabolism in the liver.

Sirtuin 1 (Sirt1) is a NAD<sup>+</sup>-dependent deacetylase that regulates intracellular NAD<sup>+</sup> levels to maintain energy balance. Sirt1 expression also induces AMPK phosphorylation to regulate lipid and glucose metabolism (9). AMPK phosphorylation could stimulate acetyl CoA carboxylase (ACC) phosphorylation, reducing lipid biosynthesis. Recent research found that the Sirt1/AMPK pathway is an important regulator sensor for energy balance (10). Excessive lipid accumulation in adipocytes and hepatocytes will suppress the activity of Sirt1 and reduce the energy regulation capacity of AMPK (11). Therefore, promoting Sirt1/AMPK pathway activity would contribute to a reduction in lipid accumulation and improve hepatic steatosis.

Maslinic acid (2 $\alpha$ ,3 $\beta$ -dihydroxiolean-12-en-28-oic acid) is a pentacyclic triterpenoid compound widely distributed

in the peel of olives, mustard, basil, and hawthorn (12). Previous studies have found that maslinic acid can inhibit inflammatory responses, with strong antitumor, antibacterial, and antioxidant effects (13–15). Maslinic acid has been found to increase glucose uptake and suppress lipid accumulation in 3T3-L1 adipocytes (16).

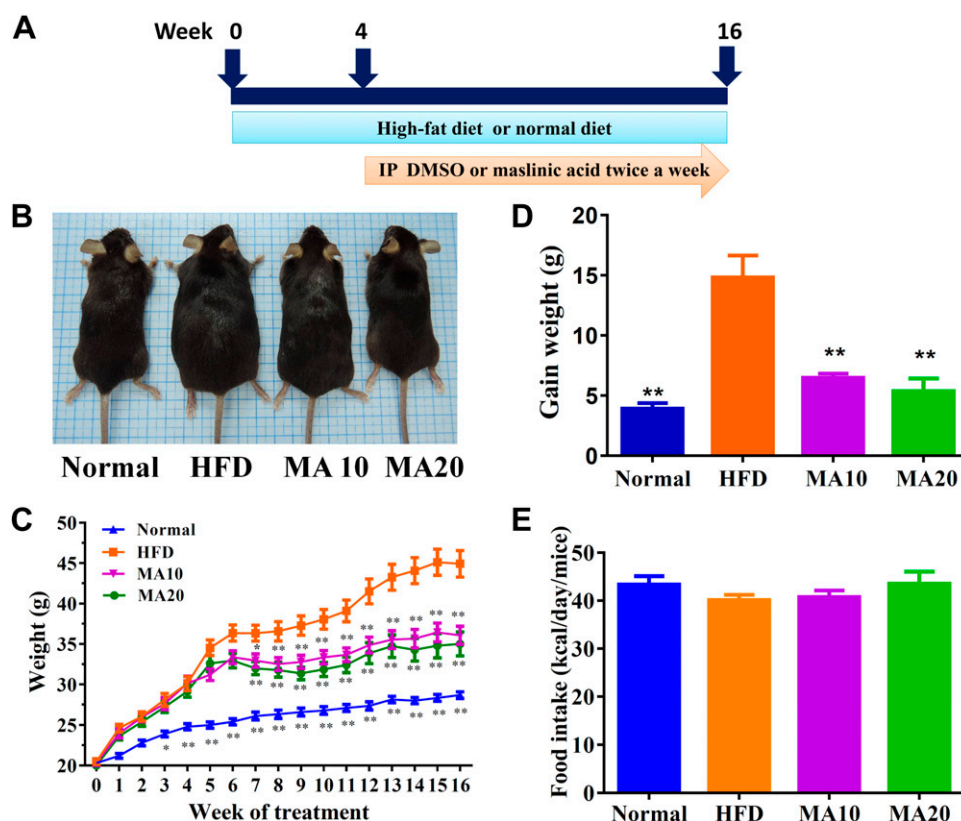
In the present study, we investigated whether maslinic acid modulates lipid metabolism and ameliorates NAFLD in high-fat-diet (HFD)-induced obese mice and regulates lipogenesis and lipolysis in HepG2 hepatocytes *in vitro*.

## MATERIALS AND METHODS

### Animals and treatments

Male C57BL/6 mice (4 wk old) were procured from the National Laboratory Animal Center (Taipei City, Taiwan). All mice were randomly divided into 4 groups of 12. The normal control group (N) was fed a standard chow diet and administered DMSO by intraperitoneal injection. The HFD control group (HFD) was fed an HFD containing 60% fat. The MA10 and MA20 groups were fed an HFD and administered 10 mg/kg and 20 mg/kg maslinic acid (purity  $\geq 98\%$ , MilliporeSigma, Burlington, MA, USA), respectively, by intraperitoneal injection. The HFD, MA10, and MA20 groups were fed the HFD for 4 wk and then treated with 50  $\mu$ l DMSO or maslinic acid (dissolved in DMSO) twice a week for the last 12 wk (Fig. 1A). Food intake was defined as the weight of consumed food (g)  $\times$  calories in the diet per day; dietary intake was monitored per day and body weight was recorded weekly. Animal experiments were approved by the Laboratory Animal Care Committee of Chang Gung University of Science and Technology (Institutional Animal Care and Use Committee Approval: 2016-023).

**Figure 1.** Maslinic acid reduced body weight in mice with HFD-induced obesity. A) Male mice were fed an HFD (containing 60% fat) for 16 wk and administered DMSO, 10 mg/kg maslinic acid (MA10), or 20 mg/kg maslinic acid (MA20) *via* intraperitoneal injection (I.P.) twice a week from wk 4 to 16. B) The appearance of the mice. C) Body weight was measured for 16 wk. D, E) Weight gain was measured in the last week (D), and food intake monitored each day (E). Data are presented as means  $\pm$  SEM;  $n = 12$ . \* $P < 0.05$ , \*\* $P < 0.01$  compared with HFD-induced obesity.



## Biochemical analysis

Mice were anesthetized with 4% isoflurane and blood sampled *via* the orbital vascular plexus. The blood was centrifuged at 6000 rpm for 5 min, and the serum to assay the levels of free fatty acids was collected using a Fatty Acid Quantitation Kit (MilliporeSigma) according to the manufacturer's protocol. The serum levels of HDL, LDL, total triglycerides (TGs), total cholesterol (TC), aspartate aminotransferase (AST), and alanine aminotransferase (ALT) were detected using a biochemical analyzer (Dri-Chem NX500; Fuji, Tokyo, Japan). In addition, the day before the end of the animal experiments, mice were unfed for 16 h and glucose was given by intraperitoneal injection to assay blood insulin levels using the Insulin Enzyme-Linked Immunosorbent Assay (EIA) Kit (Cayman Chemical Co., Ann Arbor, MI, USA) and blood glucose levels using a biochemical analyzer (Fuji; National Institutes of Health, Bethesda, MD, USA). Liver glycogen levels were detected using the Glycogen Assay Kit (Cayman Chemical Co.) based on the absorbance at 570 nm using a microplate reader (Multiskan FC; Thermo Fisher Scientific, Waltham, MA, USA).

## ELISA assay

Serum was assayed to detect TNF- $\alpha$ , leptin, and adiponectin levels using specific ELISA kits (R&D Systems, Minneapolis, MN, USA) according to the manufacturer's instructions. The value of absorbance was measured using a microplate reader (Multiskan FC) at 450 nm.

## Histologic analysis

Liver and adipose tissues were fixed with formalin and embedded in paraffin. All tissue samples were cut into 6- $\mu$ m sections and stained using hematoxylin and eosin (H&E) as previously described (17). In liver tissue, glycogen accumulation was detected by periodic acid-Schiff (PAS) staining (18). Biopsy specimens were inspected using a light microscope (Olympus, Tokyo, Japan), and the NAFLD score was evaluated as previously described (19).

## Immunohistochemical staining

Paraffin-embedded sections of liver tissues were incubated with primary antibody (1:50) overnight, followed by secondary antibody as previously described (20). The slides were treated with DAB substrate solution to detect carnitine palmitoyltransferase I (CPT-1), F4/80, FAS, and Sirt1 expression.

## Real-time PCR

Total RNA was extracted from liver tissues and cDNA synthesized using a cDNA Synthesis Kit (Thermo Fisher Scientific) as previously described (21). Specific gene expression was detected using fluorescently labeled SYBR Green and amplified using a spectrofluorometric thermal cycler (iCycler; Bio-Rad, Hercules, CA, USA).

The primers are provided in Table 1.

## Western blot analysis

Protein extracts were prepared using a Mammalian Cell Lysis Kit (MilliporeSigma) and the proteins separated by 8–10% SDS-PAGE as previously described (22). The proteins were transferred from the gels onto PVDF membrane, which was then incubated with specific primary antibodies overnight at 4°C, followed by secondary antibodies for 1 h at room temperature. Luminol/Enhancer solution (MilliporeSigma) was used to detect protein signals using the UVP BioSpectrum 600 system (Thermo Fisher Scientific). The specific primary antibodies were C/EBP- $\alpha$ , C/EBP- $\beta$ , PPAR- $\alpha$ , PPAR- $\gamma$ , ATGL, HSL, phosphorylated (p)HSL, ACC-1, pACC-1 (Abcam, Cambridge, MA, USA), CPT-1, CPT2, AMPK- $\alpha$ , pAMPK- $\alpha$ , Serbp-1c, FAS, Sirt1 (Cell Signaling Technology, Danvers, MA, USA), and  $\beta$ -actin (MilliporeSigma).

## Cell culture and induced fatty liver cells

The HepG2 hepatocyte cell line was purchased from the Bioresource Collection and Research Center (Hsinchu, Taiwan), and the cells were cultured in DMEM (Thermo Fisher Scientific) medium. For cell viability assays, maslinic acid was dissolved in DMSO, and in all cell experiments, <0.1% DMSO. HepG2 cells were treated with various concentrations of maslinic acid for 24 h to investigate cell viability using MTT solution (MilliporeSigma) as previously described (23). The culture medium was treated with 100% isopropanol to detect absorption, and cell viability was evaluated at 550 nm using a microtiter plate reader (Multiskan FC). For lipid accumulation in hepatocytes, HepG2 cells were plated on 6-well plates at a density of  $2 \times 10^4$  cells and incubated with oleic acid (0.5 mM) to stimulate lipid accumulation for 48 h. The cells were then left with vehicle (0.1% DMSO) or maslinic acid (6.25–50  $\mu$ M) for 24 h to investigate the molecular mechanism of lipid metabolism. In other cellular experiments, maslinic acid-treated HepG2 cells were treated with the AMPK activator 5-aminoimidazole-4-carboxamide-1- $\beta$ -D-ribofuranoside (AICAR; MilliporeSigma) or AMPK inhibitor compound C (MilliporeSigma) to investigate the molecular expression of lipid metabolism.

TABLE 1. Primers used for real-time PCR analysis of genes involved in lipogenesis and lipolysis

Gene	Sequence, 5'–3'	
	Forward	Reverse
PPAR- $\gamma$	GATGACAGCGACTTGGCAAT	TGTAGCAGGTTGTCTTGAATGT
C/EBP- $\beta$	GTCCAAACCAACCGCACAT	CAGAGGGAGAAGCAGAGAGTT
SREBP-1c	CTGTTGGTGCTCGTCTCTCT	TTGCGATGCCTCCAGAAGTA
FAS	ATCCTGGCTGACGAAGACTC	TGCTGCTGAGGTTGGAGAG
ATGL	GATTGCGAAGGTTGAACTGGAT	CTCAGGCGAGAGTGACATCT
HSL	CGGCGGCTGTCTAATGTCT	CGTTGGCTGGTGTCTCTGT
Sirt1	CGTCTTGTCCTCTAGTTCCTGT	GCCTCTCCGTATCATCTTCCA
CPT-1	GAGCCAGACCTTGAAGTAACG	GAGACAGACACCATCCAACAC
CPT-2	TTGACCACTGAGAACCAGAT	AGAGGCAGAAGACAGCAGAG
TNF- $\alpha$	GCACCACCATCAAGGACTC	AGGCAACCTGACCACTCTC
$\beta$ -actin	AAGACCTCTATGCCAACACAGT	AGCCAGAGCAGTAATCTCCTTC

## Effect of maslinic acid on hepatic lipid accumulation and lipoperoxidation

HepG2 cells were plated on a 6-well plate and incubated with oleic acid for 48 h. The cells were then treated with or without maslinic acid for 24 h. HepG2 cells were stained with the fluorescent probes boron-dipyrromethene (Bodipy) 493/503 and Bodipy 581/591 [ $^{11}\text{C}$ ] (Thermo Fisher Scientific) to detect lipid accumulation and lipoperoxidation, respectively, as previously described (24). Cell nuclei were stained with DAPI (MilliporeSigma). All cellular fluorescent images were observed using a fluorescence microscope (Olympus).

## Effect of maslinic acid on hepatic fatty acid uptake

HepG2 cells were incubated with 0.5 mM oleic acid for 48 h, and then the cells were treated with 50  $\mu\text{M}$  maslinic acid for 24 h. Next, cells were stained with the fluorescent probe Bodipy FL C12 (Thermo Fisher Scientific) to detect fatty acid uptake using a fluorescence microscope (Olympus).

## Oil Red O staining

HepG2 cells were plated on 6-well plates and incubated with oleic acid for 48 h. The cells were then treated with or without maslinic acid (0–50  $\mu\text{M}$ ) for 24 h. The plate was washed with PBS, and the cells were fixed with formalin and stained with Oil Red O to evaluate oil droplets as previously described (24). Oil droplet images were obtained using an inverted microscope (Olympus). Hepatocytes were treated with isopropanol to measure lipid accumulation using a microplate reader (Multiskan FC) at an absorbance of 490 nm.

## Statistical analysis

Statistical analyses were performed using 1-way ANOVA and a Dunnett *post hoc* test. Data are expressed as the mean  $\pm$  SEM of a minimum of 3 independent experiments. A value of  $P < 0.05$  was considered significant.

## RESULTS

### Maslinic acid reduced HFD-induced obesity in mice

Mice were divided into 6 groups (4 mice/group) and injected intraperitoneally with normal saline, DMSO, or various doses of maslinic acid, including 5, 10, 20, and 50 mg/kg for 14 consecutive days. We found 50 mg/kg maslinic acid has no toxins that affect the survival rate of mice (Supplemental Table S1). Hence, subsequent experiments used maslinic acid at 10 and 20 mg/kg for all animal experiments. Visual observation at the end of the animal experiments found that HFD mice were larger than normal mice. The MA20 and MA10 mice had lost significant body weight compared with the HFD mice in the last few weeks of the experiment ( $34.3 \pm 1.23$  and  $36.55 \pm 1.07$  vs.  $45.23 \pm 1.57$  g, respectively, both  $P < 0.01$ ; Fig. 1B, C). As maslinic acid was given for 12 wk, the weight gain in the MA groups was significantly less than that in the HFD group (MA10:  $6.49 \pm 0.94$  g, MA20:  $5.37 \pm 1.05$  g, HFD:  $14.28 \pm 1.81$  g;  $P < 0.01$ ; Fig. 1D). We also found that the

MA10 and MA20 groups did not have altered food intake compared with HFD mice (Fig. 1E).

### Maslinic acid attenuated the weight of adipose tissue in obese mice

Grossly, maslinic acid significantly reduced the epididymal (Fig. 2A, B) and inguinal (Fig. 2E, F) adipose tissue weight compared with HFD mice. Histologic staining and analysis of adipose tissue showed that maslinic acid significantly decreased adipocyte size in the epididymal (Fig. 2C, D) and inguinal (Fig. 2G, H) adipose tissue of mice treated with maslinic acid compared with HFD mice.

### Maslinic acid attenuated liver steatosis in obese mice

Grossly, the livers of the normal mice were dark brown-red, but the livers of the mice with HFD-induced obesity were lackluster and light yellow in color (Fig. 3A). Our results demonstrate that the dark brown-red color of the liver recovered in mice with HFD-induced obesity treated with maslinic acid. We also found that maslinic acid eliminated the liver weight compared with obese mice (Fig. 3B). H&E staining and analysis of liver tissue revealed fat vacuoles and lipid droplets in HFD mice, the number of which was significantly decreased in HFD mice treated with maslinic acid (Fig. 3C, D). Furthermore, HFD mice treated with maslinic acid had significantly reduced NAFLD scores compared with HFD mice (Fig. 3E).

Moreover, immunohistochemistry revealed a large amount of F4/80 (macrophage marker) in the livers of HFD mice compared with the N group. Maslinic acid could decrease macrophage infiltration in the livers of mice with HFD-induced obesity (Fig. 4A). Maslinic acid could suppress TNF- $\alpha$  gene expression of liver and epididymal adipose tissue compared with HFD mice (Fig. 4B, C). Maslinic acid also significantly decreased the levels of TNF- $\alpha$  in the serum of mice with HFD-induced obesity (Fig. 4D).

### Maslinic acid regulated adipogenesis in liver tissue

Maslinic acid suppressed the expression of transcription factors Srebp-1c, PPAR- $\gamma$ , C/EBP- $\beta$ , and FAS compared with the HFD group. Maslinic acid also enhanced ATGL and Sirt1 expression and the phosphorylation of AMPK compared with the HFD group. Moreover, when evaluating the fatty acid  $\beta$ -oxidation pathway in liver tissue, we found that administration of maslinic acid increased CPT-1 when compared with the HFD group (Fig. 5). Next, we evaluated the expression of genes involved in lipogenesis. Maslinic acid suppressed C/EBP- $\beta$ , PPAR- $\gamma$ , Srebp-1c, and FAS and increased ATGL, HSL, Sirt1, CPT-1, and CPT-2 expression compared with HFD mice (Fig. 6). PAS staining was performed to evaluate glycogen accumulation in hepatocytes, demonstrating that maslinic

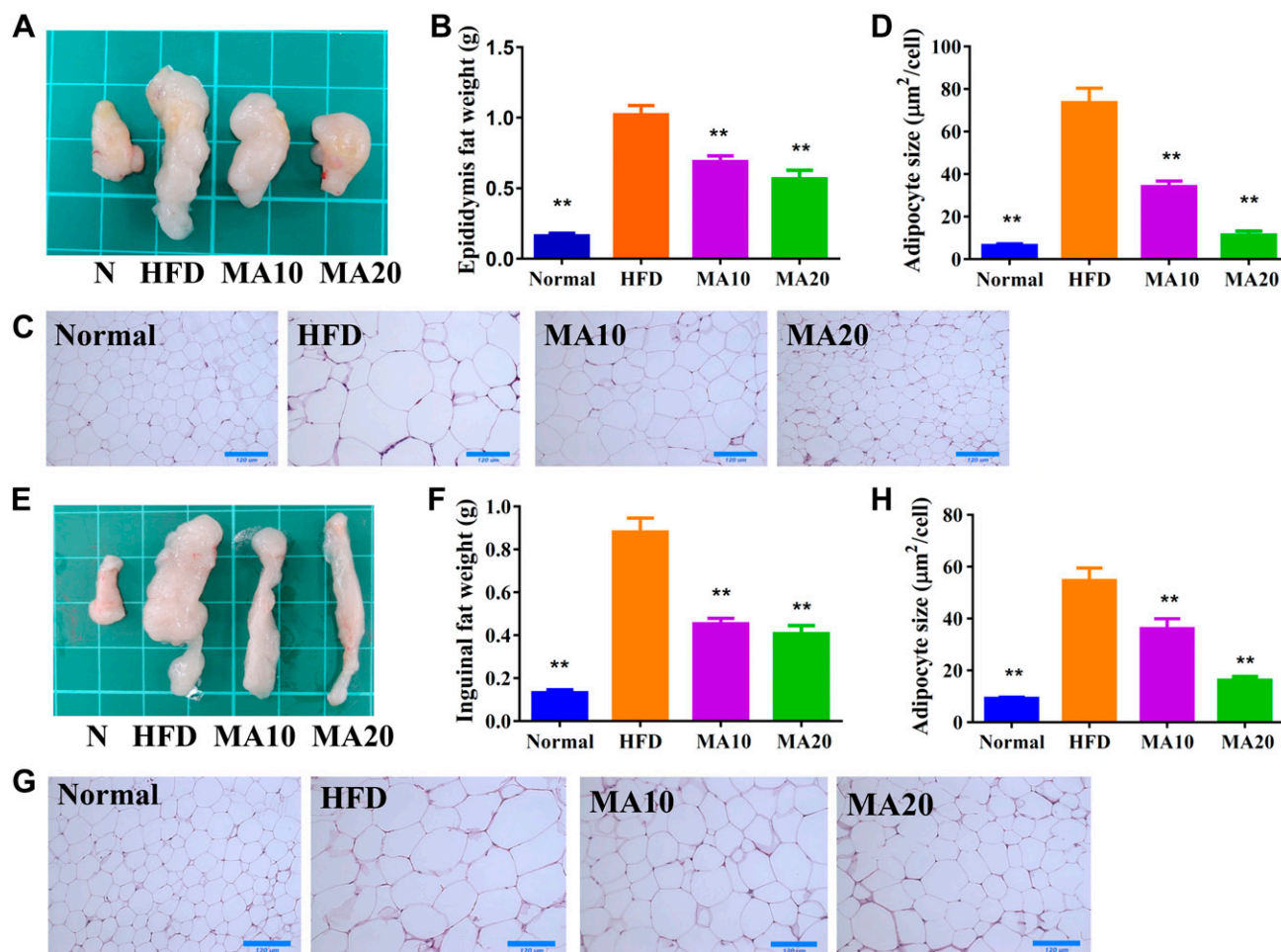


**Figure 2.** Maslinic acid (MA) reduced the epididymal and inguinal adipose tissue weight in HFD-induced obese mice. *A, B*) The appearance (*A*) and weight (*B*) of epididymal adipose tissue. *C*) HE staining of epididymal adipose tissue (original magnification,  $\times 200$ ). *D*) Adipocyte size in epididymal adipose tissue. *E, F*) The appearance (*E*) and weight (*F*) of inguinal adipose tissue. *G*) HE staining of inguinal adipose tissue (original magnification,  $\times 200$ ). *H*) Adipocyte size in inguinal adipose tissue. Data are presented as means  $\pm$  SEM;  $n = 12$ . \* $P < 0.05$ , \*\* $P < 0.01$  compared with HFD-induced obesity.

acid promoted glycogen accumulation compared with HFD-induced obesity (Fig. 7A). Moreover, maslinic acid recovered glycogen levels in the livers of mice with HFD-induced obesity (Fig. 7B) and reduced the TC and TG levels (Fig. 7D, E). Immunohistochemistry revealed a large amount of FAS and a small amount of CPT-1 and Sirt1 in the livers of HFD mice compared with the N group. In addition, maslinic acid significantly promoted CPT-1 and Sirt1 expression and decreased FAS production in the liver tissue compared with the HFD group (Fig. 7C).

### Effects of maslinic acid on serum lipid metabolism

Maslinic acid significantly decreased serum TG, TC, LDL, and free fatty acid levels and significantly increased HDL levels in HFD mice (Table 2). Furthermore, the administration of maslinic acid significantly inhibited the serum levels of insulin and glucose compared with the HFD group. Therefore, we calculated the Homeostatic Model Assessment of Insulin Resistance

(HOMA-IR) value to evaluate insulin resistance, and found that maslinic acid could significantly attenuate HOMA-IR for improved insulin resistance in HFD-induced obesity in mice (Table 2). Mice with HFD-induced obesity treated with maslinic acid also had significantly suppressed leptin and increased adiponectin expression in serum compared with HFD mice. Maslinic acid could improve NAFLD scores in mice with HFD-induced obesity and reduced the serum levels of ALT and AST, recovering liver function in mice with HFD-induced obesity (Table 2).

### Cell viability of maslinic acid in HepG2 cells

Next, we carefully studied whether maslinic acid can modulate lipid metabolism in HepG2 hepatocytes *in vitro*. First, cell viability was measured by the MTT assay. Oleic acid concentrations  $\leq 0.5$  mM did not significantly affect cell viability in HepG2 cells (Fig. 8A). No cell cytotoxicity was found at maslinic acid concentrations  $\leq 50$   $\mu$ M in HepG2 cells (Fig. 8B), and 0–50  $\mu$ M maslinic acid was used for all cell experiments.



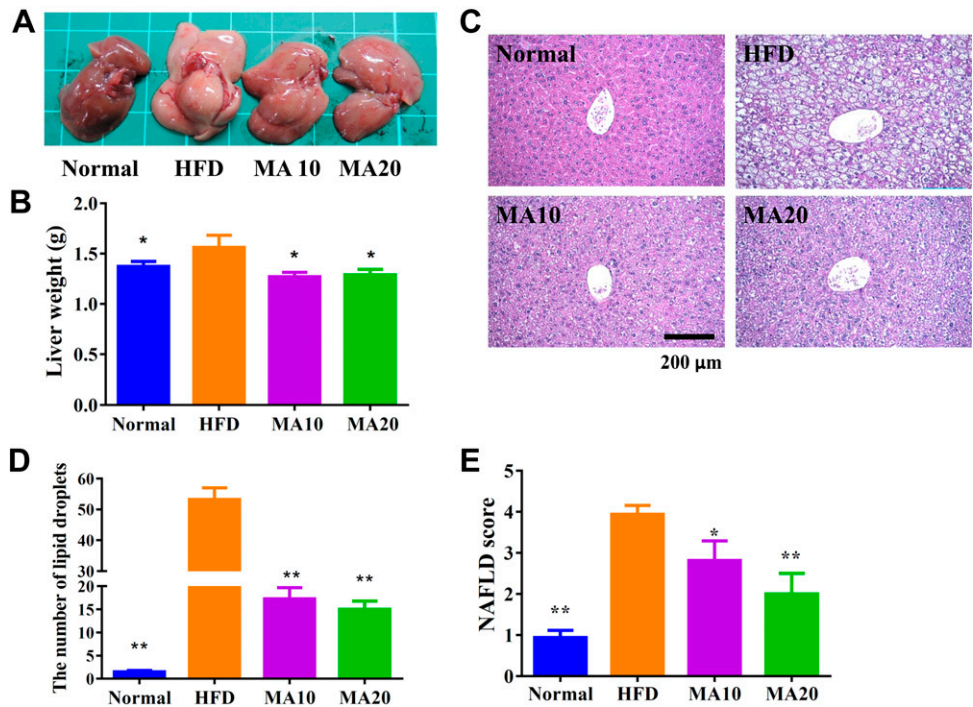


**Figure 3.** Maslinic acid (MA) ameliorated hepatic steatosis in HFD-induced obese mice. *A–C*) The appearance of the liver (*A*), liver weight (*B*), and HE staining of liver tissues (*C*) (original magnification,  $\times 200$ ). *D*) Calculated number of lipid droplets in liver tissue. *E*) NAFLD scores based on the evaluation of H&E staining of liver tissues. Data are presented as means  $\pm$  SEM;  $n = 12$ . \* $P < 0.05$ , \*\* $P < 0.01$  compared with HFD-induced obesity.

### Maslinic acid regulated lipid accumulation and lipoperoxidation in HepG2 cells

HepG2 cells were stimulated with oleic acid to induce lipid accumulation and treated with or without maslinic acid to evaluate lipid accumulation by Oil Red O staining. Maslinic acid reduced lipid droplets compared with oleic acid-induced hepatocytes (Fig. 8C). Next, hepatocytes were treated with isopropanol and lipid accumulation detected by recording the absorbance

at 490 nm. Maslinic acid significantly decreased lipid accumulation in oleic acid-incubated HepG2 cells (Fig. 8D). We also used fluorescent dye Bodipy 493/503 to detect lipid accumulation, showing that maslinic acid alleviated lipid droplets in a dose-dependent manner (Fig. 9A). Similarly, fluorescent dye Bodipy 581/591 [ $^{11}\text{C}$ ] was used to detect lipoperoxidation, showing that maslinic acid significantly reduces lipoperoxidation compared with oleic acid-induced HepG2 cells (Fig. 9A). Moreover, the Bodipy FL C12

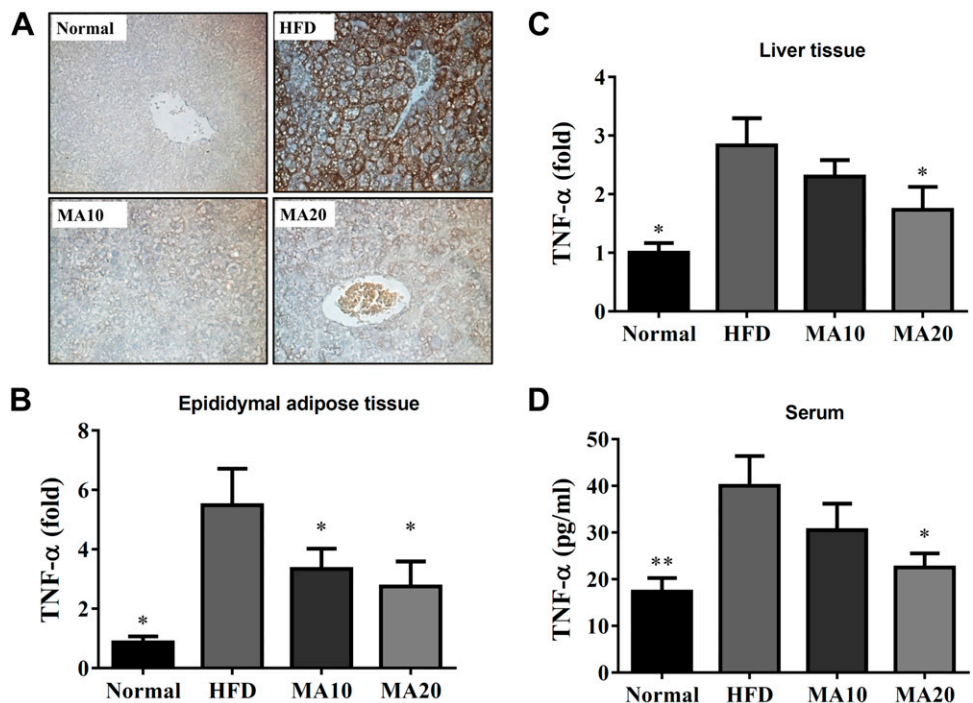


**Figure 4.** Effects of maslinic acid (MA) on inflammatory response in mouse. *A*) MA modulated F4/80 expression in the liver (brown color drop) by immunohistochemical staining. *B*, *C*) Gene expression levels of TNF- $\alpha$  in epididymal adipose tissue (*B*) and liver tissue (*C*) were determined using real-time PCR. *D*) MA modulated TNF- $\alpha$  levels in the serum. Three independent experiments were analyzed, and the data are presented as the means  $\pm$  SEM;  $n = 12$ . \* $P < 0.05$  compared with HFD-induced obesity.



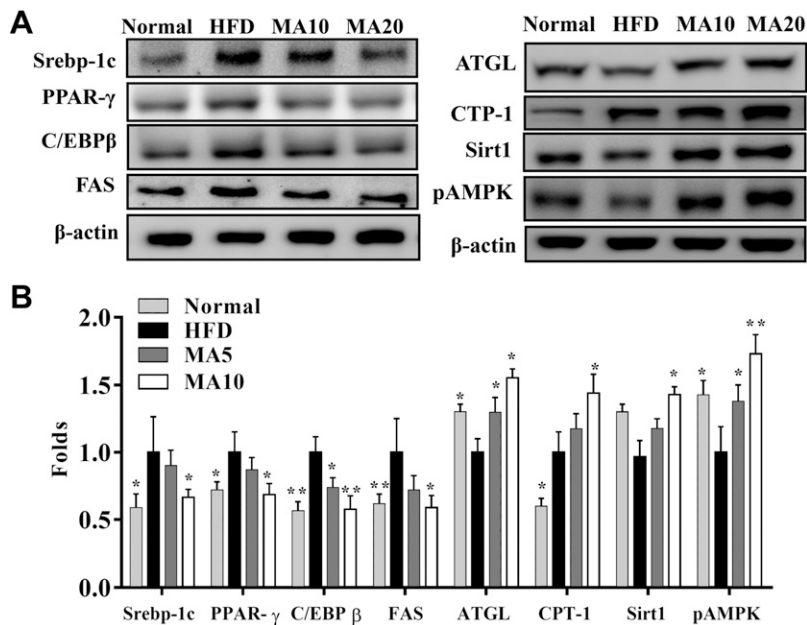


**Figure 5.** Effects of maslinic acid (MA) on lipid metabolism in mouse liver tissue. *A*) Expression of Srebp-1C, C/EBP-β, PPAR-γ, FAS, ATGL, CPT-1, Sirt1, and AMPK phosphorylation was detected by Western blot. *B*) The fold expression levels were measured relative to the expression of β-actin. Three independent experiments were analyzed, and the data are presented as the means ± SEM;  $n = 12$ . \* $P < 0.05$ , \*\* $P < 0.01$  compared with HFD-induced obesity.

fluorescent probe was used to assay fatty acid uptake, showing that HepG2 hepatocytes promote fatty acid uptake when the cells are incubated with oleic acid for 72 h. Interestingly, 50 μM maslinic acid clearly suppressed fatty acid uptake compared with the oleic acid group (Fig. 9B).

### Effect of maslinic acid on lipid metabolism in hepatocytes

Western blot demonstrated that maslinic acid decreased PPAR-γ, C/EBP-β, and Srebp-1c expression compared with oleic acid-treated HepG2 cells (Fig. 10A). Maslinic

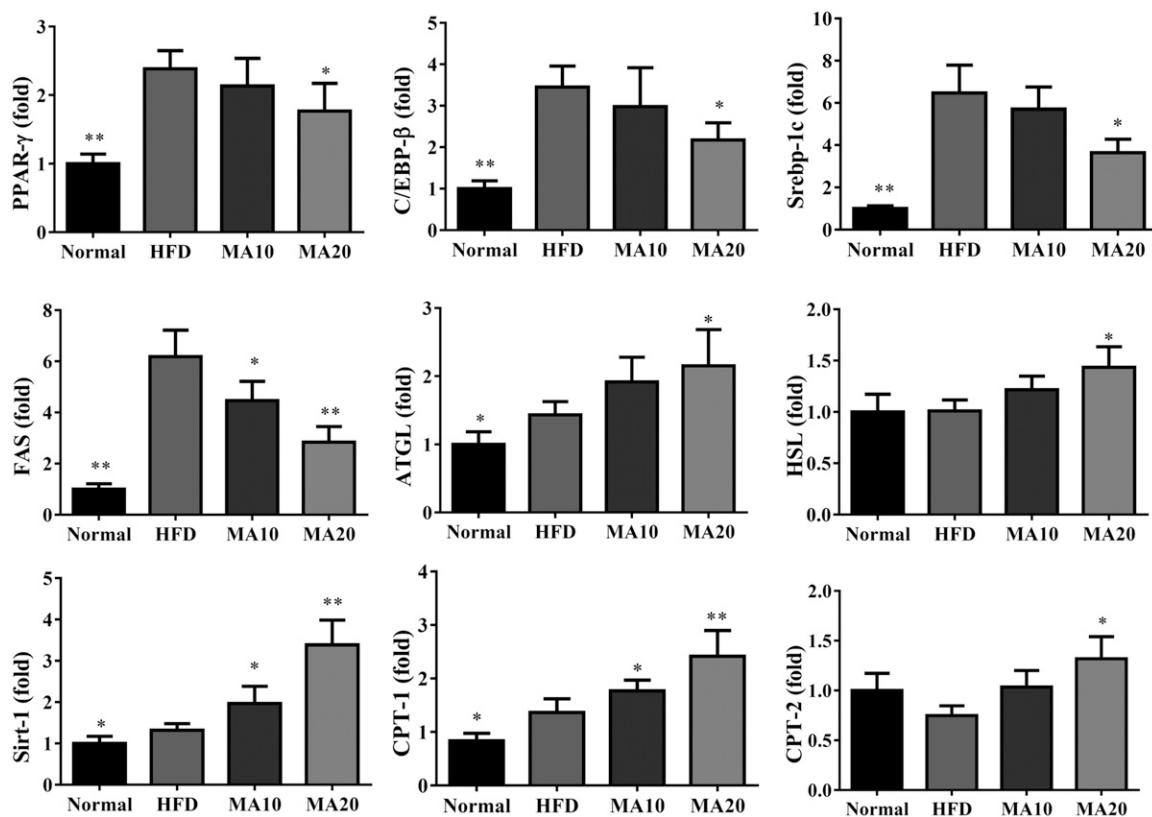


**Figure 6.** Maslinic acid (MA) modulated lipogenesis and lipolysis gene expression in liver tissue. Gene expression levels were determined using real-time PCR. Three independent experiments were analyzed, and the data are presented as the means ± SEM;  $n = 12$ . \* $P < 0.05$ , \*\* $P < 0.01$  compared with HFD-induced obesity.

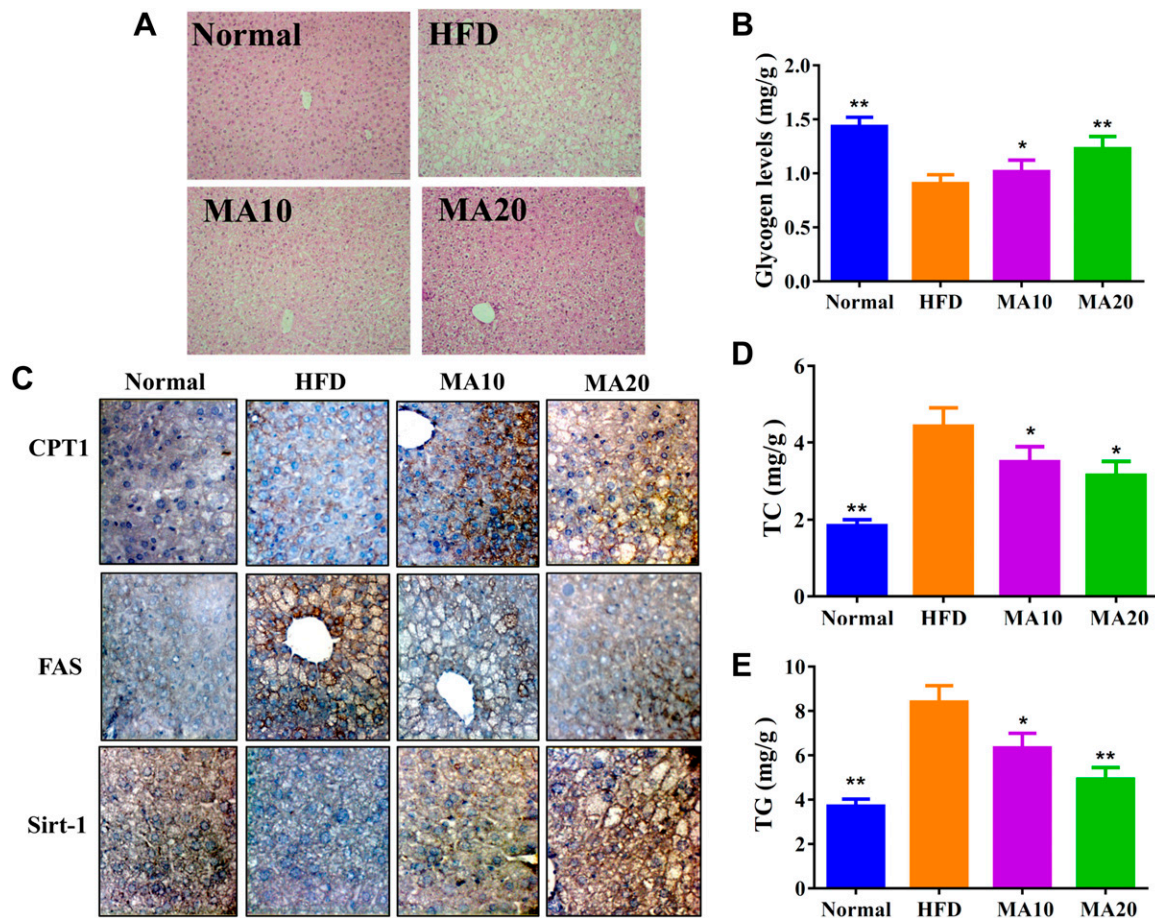


**Figure 7.** A) Maslinic acid (MA) modulated glycogen distribution based on PAS staining in the liver (original magnification,  $\times 200$ ). B) MA increased glycogen levels in liver tissue. C) MA modulated FAS, Sirt-1, and CPT-1 expression in the liver (brown color drop). D, E) MA modulated TC (D) and TG levels (E) in the liver tissue. Three independent experiments were analyzed, and the data are presented as the means  $\pm$  SEM;  $n = 12$ . \* $P < 0.05$ , \*\* $P < 0.01$  compared with HFD-induced obesity.

acid also increased phosphorylation of ACC and reduced FAS production in a concentration-dependent manner compared with oleic acid (Fig. 10B). Furthermore, maslinic acid significantly enhanced ATGL, phosphorylation of HSL, Sirt1, and phosphorylation of AMPK in a concentration-dependent manner compared with oleic acid (Fig. 10C, D). Interestingly, HepG2 cells treated with maslinic acid significantly increased PPAR- $\alpha$ , CPT-1, and CPT-2 expression compared with oleic acid-incubated

HepG2 cells (Fig. 10E). When oleic acid-induced HepG2 cells were cotreated with 50  $\mu$ M maslinic acid and compound C, maslinic acid restored Sirt1, pAMPK, pACC, and ATGL and significantly reduced FAS expression (Fig. 11A, B). Surprisingly, oleic acid-induced HepG2 cells cocultured with 50  $\mu$ M maslinic acid and AICAR demonstrated that maslinic acid promotes Sirt1, pAMPK, pACC, and ATGL and, more significantly, reduces FAS expression (Fig. 11C, D).

TABLE 2. Serum biochemical analysis

Variable	Normal	HFD	MA10	MA20
Glucose (mg/dl)	84.2 $\pm$ 15.1**	231.3 $\pm$ 22.8	156.5 $\pm$ 26.1*	101.3 $\pm$ 15.7**
Insulin (mg/dl)	61.6 $\pm$ 16.2**	230.9 $\pm$ 28.6	96.1 $\pm$ 16.8**	87.9 $\pm$ 21.6**
HOMA-IR	0.39 $\pm$ 0.11**	4.12 $\pm$ 0.61	1.12 $\pm$ 0.32**	0.67 $\pm$ 0.17**
TC (mg/dl)	85.67 $\pm$ 3.2**	227.01 $\pm$ 6.3	153.9 $\pm$ 5.2*	146.1 $\pm$ 6.9*
TG (mg/dl)	112.1 $\pm$ 2.7	109 $\pm$ 6.5	116 $\pm$ 7.6	115 $\pm$ 14.8
HDL-C (mg/dl)	78.1 $\pm$ 2.2*	51.3 $\pm$ 4.3	82.9 $\pm$ 8.4**	94.6 $\pm$ 7.6**
LDL-C (mg/dl)	34.6 $\pm$ 2.3**	133.8 $\pm$ 12.1	56.3 $\pm$ 4.8**	51.3 $\pm$ 3.2**
Free fatty acids (mM)	10.1 $\pm$ 0.7*	12.31 $\pm$ 0.9	10.6 $\pm$ 1.3*	11.3 $\pm$ 1.1*
AST (U/I)	81.6 $\pm$ 8.6**	132.1 $\pm$ 13.9	105.5 $\pm$ 12.4*	88.2 $\pm$ 12.4**
ALT (U/I)	42 $\pm$ 6.71**	77 $\pm$ 9.2	51.6 $\pm$ 11.8**	46.1 $\pm$ 10.5**
Leptin ( $\mu$ g/ml)	1.1 $\pm$ 0.2**	25.3 $\pm$ 2.5	10.9 $\pm$ 1.3**	10.7 $\pm$ 1.6**
Adiponectin ( $\mu$ g/ml)	2328.9 $\pm$ 68*	1974.7 $\pm$ 275.1	2386.5 $\pm$ 129.4*	2348.7 $\pm$ 88.7*

\* $P < 0.05$ , \*\* $P < 0.01$  compared with HFD-induced obese mice. Data are presented as means  $\pm$  SEM.

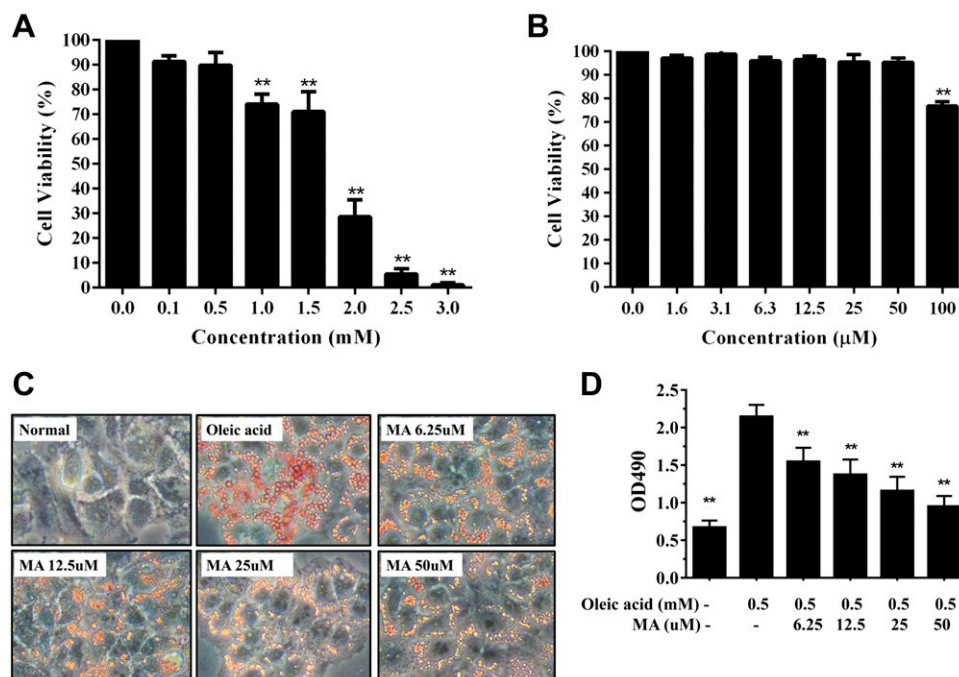


**Figure 8.** Maslinic acid (MA) reduced lipid accumulation in HepG2 cells. *A*) Cell viability of oleic acid in HepG2 cells. *B*) Cell viability of MA in HepG2 cells. *C*) Oil Red O staining revealed lipid accumulation. *D*) HepG2 cells were treated with isopropanol and lipid accumulation measured using the absorbance at ocular distance (OD) 490 nm. Three independent experiments were analyzed. Data represent the means  $\pm$  SEM. \*\* $P < 0.01$  compared with HepG2 cells treated with oleic acid.

## DISCUSSION

Fatty liver is defined as the accumulation of excess TGs in hepatocytes, with more than 5% of the liver's weight being fat or more than 10% fatty vacuoles in the liver tissue sections (25). Obesity and a diet high in fat and high in sugar will increase the lipid and carbohydrate metabolism

burden of the liver, causing the accumulation of excessive TGs in the liver and promoting the development of NAFLD (26). Therefore, limiting dietary intake and controlling weight will decrease hyperglycemia and hyperlipidemia and improve insulin resistance and NAFLD.

In recent years, many studies have found that plant extracts or pure compounds can reduce body weight and

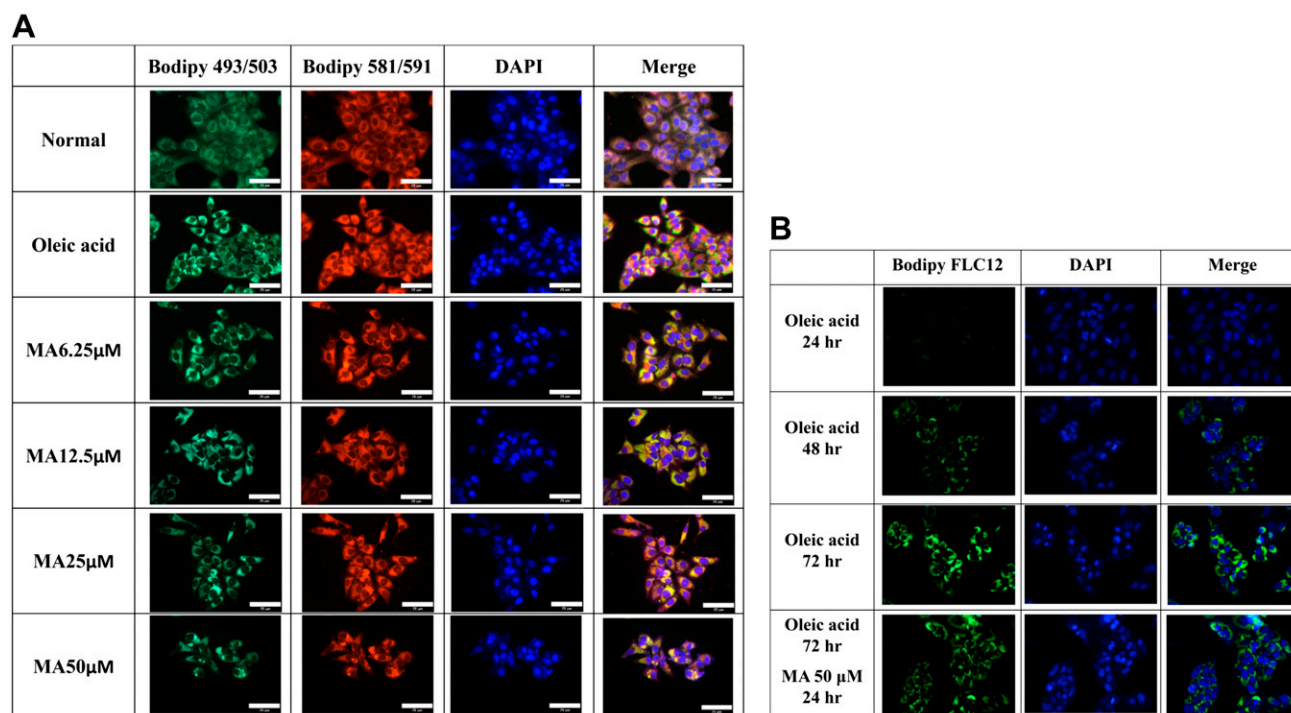
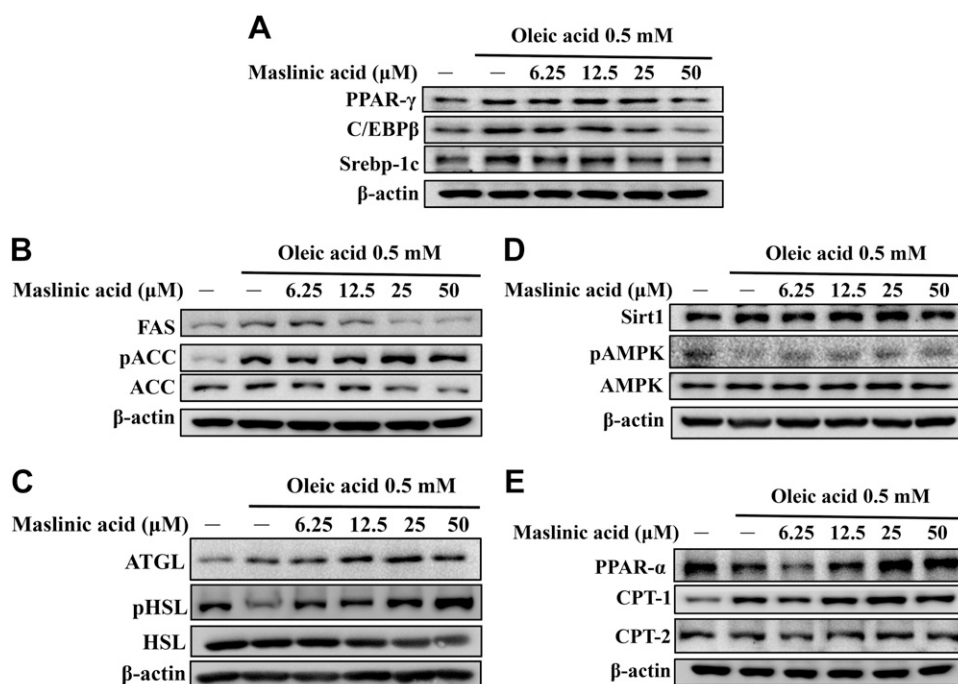


**Figure 9.** Maslinic acid (MA) reduced lipid accumulation, lipoperoxidation, and fatty acid uptake into HepG2 cells. *A*) The fluorescent dyes Bodipy 493/503 (green) and Bodipy 581/591 [ $^{11}\text{C}$ ] (red) were used to detect hepatic lipid droplets and hepatic lipoperoxidation, respectively, under a fluorescent microscope. *B*) Oleic acid-induced HepG2 cells treated with MA for 24 h before staining with the fluorescent probe Bodipy FL C12 (green). Three independent experiments were analyzed. Nuclei were stained with DAPI (blue).

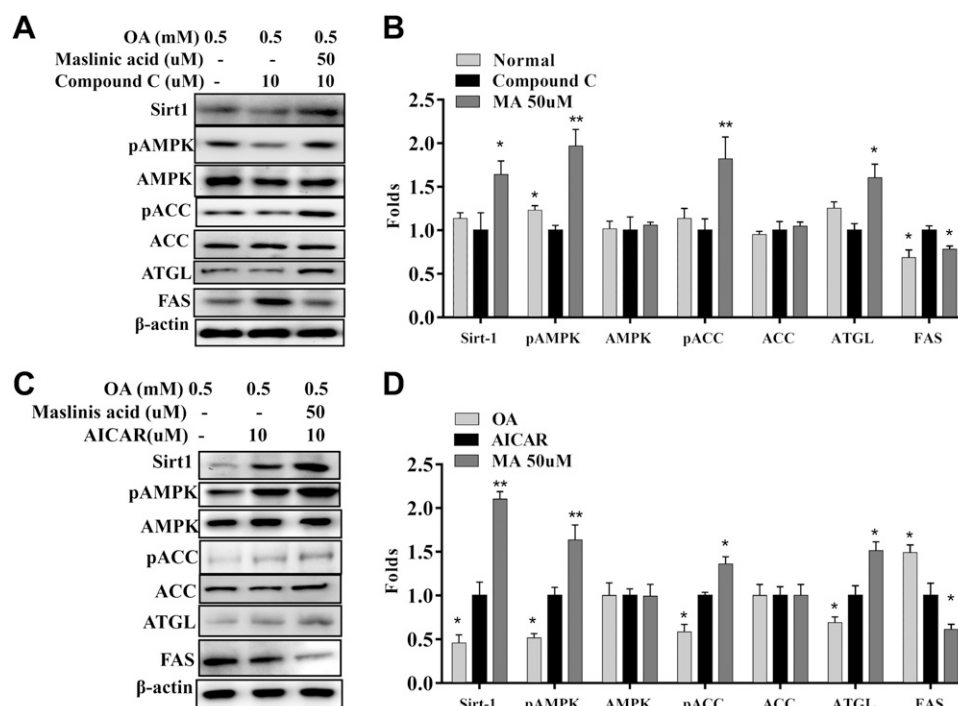
**Figure 10.** Effects of maslinic acid on lipid metabolism in HepG2 cells. The expression of transcription factors (A), lipogenesis (B), lipolysis (C), the Sirt1/AMPK pathway (D), and  $\beta$ -oxidation (E) were detected by Western blot. Three independent experiments were performed using  $\beta$ -actin as an internal control.



improve NAFLD (9, 27). In HFD-induced obese mice, fisetin, astaxanthin, and quercetin reduce body weight and hepatic metabolic damage by promoting Sirt1 and AMPK expression (19, 28, 29). Licochalcone A could ameliorate obesity and NAFLD *via* promotion of the Sirt-1/AMPK pathway in obese mice (30). Previous studies showed that oral administration of sulforaphane improved NAFLD *via* suppressed NLRP3 inflammasome signal in HFD-induced obese mice (31). Oral administration of resveratrol could decrease NAFLD severity in rats *via* improving inflammation,

oxidative stress, and lipogenesis (32, 33). In the current study, maslinic acid effectively reduced body weight and decreased epididymal and inguinal fat weight in HFD-induced obese mice. Maslinic acid also reduced liver weight, decreased lipid accumulation in the liver, and improved NAFLD in HFD-fed obese mice. We also confirmed that maslinic acid effectively inhibited lipogenesis and increased lipolysis and fatty acid  $\beta$ -oxidation by promoting the Sirt1/AMPK pathway in the liver. Our results demonstrate that maslinic acid could potentially ameliorate obesity and NAFLD.

**Figure 11.** Effects of maslinic acid on the AMPK/Sirt-1 pathway in HepG2 cells. A) HepG2 cells were treated with 0.5 mM oleic acid for 48 h, followed by 50  $\mu$ M maslinic acid with or without an AMPK inhibitor (compound C) for 24 h. B) The fold expression levels were measured relative to the expression of  $\beta$ -actin. Data are presented as means  $\pm$  SEM.  $*P < 0.05$ ,  $**P < 0.01$  compared with compound C treatment. C) HepG2 cells were treated with maslinic acid with or without an AMPK activator (AICAR) for 24 h. D) The fold expression levels were measured relative to the expression of  $\beta$ -actin. Three independent experiments were analyzed, and data are presented as the means  $\pm$  SEM.  $*P < 0.05$ ,  $**P < 0.01$  compared with the AICAR group.





Previous studies have shown that maslinic acid regulates the differentiation of 3T3-L1 adipocytes (16), and we supposed that maslinic acid would reduce body weight and NAFLD in mice. In the current study, maslinic acid effectively reduced the body weight, adipose tissue weight, and fat cell size in male C57BL/6 mice fed an HFD. Previous studies confirmed that adipose tissue from obese mice secretes excess leptin, which binds to the leptin receptors of hypothalamic neurons, reducing appetite and regulating body weight (34). Other studies have shown that quercetin improves obesity and insulin resistance by reducing serum leptin levels and increasing serum adiponectin levels in mice (35). We demonstrated no significant difference in the food intake between the groups. However, maslinic acid significantly reduced serum leptin and increased serum adiponectin levels, but it did not affect appetite or reduce body weight in mice. Glabridin, an AMPK activator, could reduce body weight, serum lipid levels, and hypoglycemic effects in streptozotocin-induced diabetic mice (36). Interestingly, we found that maslinic acid regulates fasting blood glucose and insulin levels. HFD mice have high HOMA-IR values and high risk factors for insulin resistance (37), and maslinic acid could significantly reduce HOMA-IR values. Therefore, maslinic acid could have a hypoglycemic effect, improving insulin resistance in obese mice by regulating the levels of leptin and adiponectin.

HFD-induced obese mice are not only suitable for observing the effects of obesity, but also for studying NAFLD. We found that HFD-induced obese mice have higher NAFLD scores, and obese mice treated with maslinic acid have reduced NAFLD scores. NAFLD scores are based on macrophage infiltration, fat vacuoles, and lobular inflammation in liver tissue (19). We found that maslinic acid significantly decreased fat vacuoles and lipid droplets, and macrophage infiltration in the livers of HFD-fed obese mice. Activated macrophage would release more proinflammatory cytokines to cause liver inflammation (9, 20). Maslinic acid inhibited TNF- $\alpha$  gene expression of liver and adipose tissue, and also significantly reduced TNF- $\alpha$  level in the serum of obese mice. Therefore, maslinic acid could reduce the inflammatory effects in obese mice.

During the formation of fatty liver cells and excess lipid accumulation in hepatocytes, lipid synthesis-related enzymes and transcription factors are activated, including FAS and Srebp-1c, PPAR- $\gamma$ , and C/EBP- $\beta$ , for enhanced fatty acid synthesis (38). The Sirt1/AMPK pathway is not activated in the liver tissue of Sirt1-deficient mice, and transcription factors involved in lipogenesis are not expressed in excess (9). Other studies have found that Srebp-1c regulates FAS expression to promote lipid synthesis in the livers of obese mice (7, 39). Sulforaphane regulates lipid metabolism in hepatic steatosis by regulating the Srebp1c/FAS pathways in mice (40). We found that maslinic acid reduces the expression of Srebp-1c, PPAR- $\gamma$ , C/EBP- $\beta$ , and FAS in liver tissue, reducing lipid accumulation in hepatocytes. We used Oil Red O stain and fluorescent staining to confirm that more oil droplets were distributed in oleic acid-induced hepatocytes, but maslinic acid reduced the oil droplet distribution in HepG2

cells *in vitro*. We also performed immunohistochemical staining to determine that maslinic acid reduces FAS distribution in liver tissue. In liver sections, HE staining showed that maslinic acid significantly improved the formation of fat vacuoles. Therefore, we demonstrated that maslinic acid inhibits transcription factors involved in lipid synthesis in the liver.

Uptake of free fatty acids by hepatocytes would initiate lipogenic transcription factors that activate FAS to increase TG synthesis, leading to fatty liver (38). The normal liver also transports synthetic TGs and lipoproteins into the blood to maintain physiologic functions (25). However, the uptake of excessive fatty acids would exert a metabolic burden on the liver and interfere with the lipid transport form. Therefore, high levels of TC and TGs were detected in the liver of HFD-induced obese mice, and high serum levels of TC, TGs, and LDL were measured, which affect the development of chronic cardiovascular diseases. Interestingly, maslinic acid significantly inhibited fatty acid uptake and decreased lipogenesis in oleic acid-induced HepG2 cells. We speculated that maslinic acid blocked fatty acid uptake in the liver by reducing lipogenesis. Therefore, HFD-induced obese mice treated with maslinic acid had reduced TC and TG levels in the liver compared with HFD-induced obese mice not treated with maslinic acid.

Accelerating lipid breakdown in liver cells can also prevent NAFLD. Previous studies have shown that sulforaphane and astaxanthin inhibit lipid synthesis and increase lipolysis in high glucose-induced fatty liver cells and improve lipolysis in the liver tissue of NAFLD mice (40, 41). Olive leaf extract could regulate lipid metabolism and promote lipolysis in obese rats (42). Our study demonstrated that maslinic acid has the ability to reduce body weight in obese mice and suppress adipose tissue weight and adipocyte size in inguinal and epididymal adipose tissue. Maslinic acid also promotes the phosphorylation of HSL and ATGL expression in oleic acid-induced hepatocytes and increases ATGL to accelerate lipolysis in the livers of obese mice. Previous studies have demonstrated that metformin increases ATGL, increasing lipolysis by activating AMPK phosphorylation (43). In the current study, maslinic acid could restore ATGL expression. We thought that maslinic acid increased lipolysis in fatty liver *via* regulated phosphorylation of HSL and ATGL and AMPK expression.

Previous studies have found that free fatty acids inhibit AMPK activation (44). Lipid accumulation in the liver and adipose tissue also inhibits AMPK activity and affects ACC expression, accelerating fatty acid synthesis, resulting in excessive accumulation of TGs in the liver, and inducing the development of NAFLD (44). Resveratrol is a Sirt1 enhancer that promotes the expression of Sirt1 and AMPK and reduces lipid accumulation in the livers of obese mice (45). Previous studies have found that metformin is a hypoglycemic drug that could regulate the metabolism of carbohydrates and lipids by activating AMPK phosphorylation (43). The current study found that maslinic acid can increase the expression of Sirt1 and pAMPK in oleic acid-induced HepG2 hepatocytes. AMPK phosphorylation would stimulate ACC phosphorylation, blocking FAS expression and reducing fatty acid synthesis (46). Our experimental results also confirmed that maslinic acid can increase ACC



phosphorylation and inhibit FAS production in oleic acid-induced HepG2 hepatocytes. In addition, maslinic acid cocultured with AMPK inhibitors has the ability to restore AMPK phosphorylation and inhibit FAS expression. Therefore, maslinic acid reduced lipid accumulation in the livers of obese mice by regulating the AMPK pathway.

In the liver, TGs could decompose to produce free fatty acids that require rapid breakdown by  $\beta$ -oxidation to produce energy or form bile acids and be excreted in the feces (2). Many studies have confirmed that AMPK and Sirt1 expression enhance CPT-1 expression, which converts long-chain fatty acyl-CoA to promote  $\beta$ -oxidation expression and increase fatty acid decomposition (11, 46). Maslinic acid significantly increased CPT1 expression in the livers of HFD-induced obese mice. Other studies have shown that quercetin enhances the expression of Sirt1/AMPK, thereby inhibiting ACC activity, and increases  $\beta$ -oxidation of lipolysis, improving NAFLD in HFD-fed mice (35, 47).

During the development of obesity and NAFLD, metabolic syndrome or insulin resistance often obstruct glucose transport into hepatocytes, adipocytes, and skeletal muscle cells (3). These insulin-resistant cells will use a lot of fatty acids to produce energy and promote free fatty acid levels in the serum for an aggravated chronic inflammatory response. More studies have demonstrated that hypoglycemic and hypolipidemic drugs could improve blood sugar and blood pressure and also relieve the effectiveness of fatty liver disease (43, 48). Other studies have shown that many purified plant compounds could improve insulin resistance and NAFLD (28, 41). In summary, we demonstrated that maslinic acid ameliorates hepatic steatosis, reduces adipose tissue weight and body weight, and significantly decreases lipid accumulation in the livers of obese mice by promoting the Sirt1/AMPK pathway. Therefore, maslinic acid has potential as a novel antiobesity agent for the treatment of NAFLD. **[F]**

## ACKNOWLEDGMENTS

This study was supported, in part, by grants from Chang Gung Memorial Hospital (CMRPF1H0022, CMRPF1G0232, and CMRPF1H0042) and the Ministry of Science and Technology in Taiwan (106-2320-B-255-007-MY3). The authors declare no conflicts of interest.

## AUTHOR CONTRIBUTIONS

C.-J. Liou, Y.-W. Dai, C.-L. Wang, and L.-W. Fang performed the experiments; C.-J. Liou, Y.-W. Dai, and W.-C. Huang designed the experiments; C.-J. Liou and W.-C. Huang drafted the manuscript; and Y.-W. Dai and C.-L. Wang performed the analysis and interpretation of data.

## REFERENCES

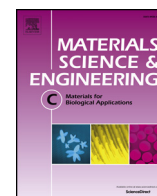
1. Sun, K., Kusminski, C. M., and Scherer, P. E. (2011) Adipose tissue remodeling and obesity. *J. Clin. Invest.* **121**, 2094–2101
2. Kitade, H., Chen, G., Ni, Y., and Ota, T. (2017) Nonalcoholic fatty liver disease and insulin resistance: new insights and potential new treatments. *Nutrients* **9**, E387

3. Hazlehurst, J. M., Woods, C., Marjot, T., Cobbold, J. F., and Tomlinson, J. W. (2016) Non-alcoholic fatty liver disease and diabetes. *Metabolism* **65**, 1096–1108
4. Zhu, Y., Liu, H., Zhang, M., and Guo, G. L. (2016) Fatty liver diseases, bile acids, and FXR. *Acta Pharm. Sin.* **B 6**, 409–412
5. Coppari, R., and Bjørbaek, C. (2012) Leptin revisited: its mechanism of action and potential for treating diabetes. *Nat. Rev. Drug Discov.* **11**, 692–708
6. Smith, M. M., and Minson, C. T. (2012) Obesity and adipokines: effects on sympathetic overactivity. *J. Physiol.* **590**, 1787–1801
7. Mota de Sá, P., Richard, A. J., Hang, H., and Stephens, J. M. (2017) Transcriptional regulation of adipogenesis. *Compr. Physiol.* **7**, 635–674
8. Saponaro, C., Gaggini, M., Carli, F., and Gastaldelli, A. (2015) The subtle balance between lipolysis and lipogenesis: a critical point in metabolic homeostasis. *Nutrients* **7**, 9453–9474
9. Zhang, Y., Geng, C., Liu, X., Li, M., Gao, M., Liu, X., Fang, F., and Chang, Y. (2016) Celastrol ameliorates liver metabolic damage caused by a high-fat diet through Sirt1. *Mol. Metab.* **6**, 138–147
10. Miller, R. A., and Birnbaum, M. J. (2010) An energetic tale of AMPK-independent effects of metformin. *J. Clin. Invest.* **120**, 2267–2270
11. Wu, L., Zhang, L., Li, B., Jiang, H., Duan, Y., Xie, Z., Shuai, L., Li, J., and Li, J. (2018) AMP-activated protein kinase (AMPK) regulates energy metabolism through modulating thermogenesis in adipose tissue. *Front. Physiol.* **9**, 122
12. Sánchez-González, M., Lozano-Mena, G., Juan, M. E., García-Granados, A., and Planas, J. M. (2013) Assessment of the safety of maslinic acid, a bioactive compound from *Olea europaea* L. *Mol. Nutr. Food Res.* **57**, 339–346
13. Fukumitsu, S., Villareal, M. O., Fujitsuka, T., Aida, K., and Isoda, H. (2016) Anti-inflammatory and anti-arthritis effects of pentacyclic triterpenoids maslinic acid through NF- $\kappa$ B inactivation. *Mol. Nutr. Food Res.* **60**, 399–409
14. Yang, Y. W., Tsai, C. W., Mong, M. C., and Yin, M. C. (2015) Maslinic acid protected PC12 cells differentiated by nerve growth factor against  $\beta$ -amyloid-induced apoptosis. *J. Agric. Food Chem.* **63**, 10243–10249
15. Qin, X., Qiu, C., and Zhao, L. (2014) Maslinic acid protects vascular smooth muscle cells from oxidative stress through Akt/Nrf2/HO-1 pathway. *Mol. Cell. Biochem.* **390**, 61–67
16. Pérez-Jiménez, A., Rufino-Palomares, E. E., Fernández-Gallego, N., Ortuño-Costela, M. C., Reyes-Zurita, F. J., Peragón, J., García-Salguero, L., Mokhtari, K., Medina, P. P., and Lupiáñez, J. A. (2016) Target molecules in 3T3-L1 adipocytes differentiation are regulated by maslinic acid, a natural triterpene from *Olea europaea*. *Phytomedicine* **23**, 1301–1311
17. Liou, C. J., Cheng, C. Y., Yeh, K. W., Wu, Y. H., and Huang, W. C. (2018) Protective effects of casticin from *Vitex trifolia* alleviate eosinophilic airway inflammation and oxidative stress in a murine asthma model. *Front. Pharmacol.* **9**, 635
18. Huang, W. C., Fang, L. W., and Liou, C. J. (2017) Phloretin attenuates allergic airway inflammation and oxidative stress in asthmatic mice. *Front. Immunol.* **8**, 134
19. Kleiner, D. E., Brunt, E. M., Van Natta, M., Behling, C., Contos, M. J., Cummings, O. W., Ferrell, L. D., Liu, Y. C., Torbenson, M. S., Unalp-Arida, A., Yeh, M., McCullough, A. J., and Sanyal, A. J.; Nonalcoholic Steatohepatitis Clinical Research Network. (2005) Design and validation of a histological scoring system for nonalcoholic fatty liver disease. *Hepatology* **41**, 1313–1321
20. Liou, C. J., and Huang, W. C. (2011) Dehydroepiandrosterone suppresses eosinophil infiltration and airway hyperresponsiveness via modulation of chemokines and Th2 cytokines in ovalbumin-sensitized mice. *J. Clin. Immunol.* **31**, 656–665
21. Liou, C. J., Wu, S. J., Chen, L. C., Yeh, K. W., Chen, C. Y., and Huang, W. C. (2017) Acacetin from traditionally used *Saussurea involucrelata* Kar. et Kir. suppressed adipogenesis in 3T3-L1 adipocytes and attenuated lipid accumulation in obese mice. *Front. Pharmacol.* **8**, 589
22. Huang, W. C., Su, H. H., Fang, L. W., Wu, S. J., and Liou, C. J. (2019) Licochalcone A inhibits cellular motility by suppressing E-cadherin and MAPK signaling in breast cancer. *Cells* **8**, 218
23. Huang, W. C., Chang, W. T., Wu, S. J., Xu, P. Y., Ting, N. C., and Liou, C. J. (2013) Phloretin and phlorizin promote lipolysis and inhibit inflammation in mouse 3T3-L1 cells and in macrophage-adipocyte co-cultures. *Mol. Nutr. Food Res.* **57**, 1803–1813
24. Chang, Y. H., Chen, Y. L., Huang, W. C., and Liou, C. J. (2018) Fucosanthin attenuates fatty acid-induced lipid accumulation in FL83B hepatocytes through regulated Sirt1/AMPK signaling pathway. *Biochem. Biophys. Res. Commun.* **495**, 197–203

25. Neuschwander-Tetri, B. A. (2017) Non-alcoholic fatty liver disease. *BMC Med.* **15**, 45
26. Li, M., Sharma, A., Yin, C., Tan, X., and Xiao, Y. (2017) Metformin ameliorates hepatic steatosis and improves the induction of autophagy in HFD-induced obese mice. *Mol. Med. Rep.* **16**, 680–686
27. Norris, G. H., and Blesso, C. N. (2017) Dietary sphingolipids: potential for management of dyslipidemia and nonalcoholic fatty liver disease. *Nutr. Rev.* **75**, 274–285
28. Liou, C. J., Wei, C. H., Chen, Y. L., Cheng, C. Y., Wang, C. L., and Huang, W. C. (2018) Fisetin protects against hepatic steatosis through regulation of the Sirt1/AMPK and fatty acid  $\beta$ -oxidation signaling pathway in high-fat diet-induced obese mice. *Cell. Physiol. Biochem.* **49**, 1870–1884
29. Liu, L., Gao, C., Yao, P., and Gong, Z. (2015) Quercetin alleviates high-fat diet-induced oxidized low-density lipoprotein accumulation in the liver: implication for autophagy regulation. *Biomed. Res. Int.* **2015**, 607531
30. Liou, C. J., Lee, Y. K., Ting, N. C., Chen, Y. L., Shen, S. C., Wu, S. J., and Huang, W. C. (2019) Protective effects of Licochalcone A ameliorates obesity and non-alcoholic fatty liver disease via promotion of the Sirt-1/AMPK pathway in mice fed a high-fat diet. *Cells* **8**, 447
31. Lei, P., Tian, S., Teng, C., Huang, L., Liu, X., Wang, J., Zhang, Y., Li, B., and Shan, Y. (2019) Sulforaphane improves lipid metabolism by enhancing mitochondrial function and biogenesis in vivo and in vitro. *Mol. Nutr. Food Res.* **63**, e1800795
32. Bujanda, L., Hijona, E., Larzabal, M., Beraza, M., Aldazabal, P., García-Urkia, N., Sarasqueta, C., Cosme, A., Irastorza, B., González, A., and Arenas, J. L., Jr. (2008) Resveratrol inhibits nonalcoholic fatty liver disease in rats. *BMC Gastroenterol.* **8**, 40
33. Zhu, W., Chen, S., Li, Z., Zhao, X., Li, W., Sun, Y., Zhang, Z., Ling, W., and Feng, X. (2014) Effects and mechanisms of resveratrol on the amelioration of oxidative stress and hepatic steatosis in KKAY mice. *Nutr. Metab. (Lond.)* **11**, 35
34. Cui, H., López, M., and Rahmouni, K. (2017) The cellular and molecular bases of leptin and ghrelin resistance in obesity. *Nat. Rev. Endocrinol.* **13**, 338–351
35. Kobori, M., Takahashi, Y., Sakurai, M., Akimoto, Y., Tsushida, T., Oike, H., and Ippoushi, K. (2016) Quercetin suppresses immune cell accumulation and improves mitochondrial gene expression in adipose tissue of diet-induced obese mice. *Mol. Nutr. Food Res.* **60**, 300–312
36. Lee, J. W., Choe, S. S., Jang, H., Kim, J., Jeong, H. W., Jo, H., Jeong, K. H., Tadi, S., Park, M. G., Kwak, T. H., Man Kim, J., Hyun, D. H., and Kim, J. B. (2012) AMPK activation with glabridin ameliorates adiposity and lipid dysregulation in obesity. *J. Lipid Res.* **53**, 1277–1286
37. Ippagunta, S. M., Kharitonov, A., Adams, A. C., and Hillgartner, F. B. (2018) Cholic acid supplementation of a high-fat obesogenic diet suppresses hepatic triacylglycerol accumulation in mice via a fibroblast growth factor 21-dependent mechanism. *J. Nutr.* **148**, 510–517
38. Wang, Y., Viscarra, J., Kim, S. J., and Sul, H. S. (2015) Transcriptional regulation of hepatic lipogenesis. *Nat. Rev. Mol. Cell Biol.* **16**, 678–689; erratum: 17, 64
39. Zhang, Y., Meng, T., Zuo, L., Bei, Y., Zhang, Q., Su, Z., Huang, Y., Pang, J., Xiang, Q., and Yang, H. (2017) Xylitol B attenuates fatty acid-induced lipid accumulation via the SREBP-1c pathway in NAFLD models. *Mar. Drugs* **15**, E163
40. Choi, K. M., Lee, Y. S., Kim, W., Kim, S. J., Shin, K. O., Yu, J. Y., Lee, M. K., Lee, Y. M., Hong, J. T., Yun, Y. P., and Yoo, H. S. (2014) Sulforaphane attenuates obesity by inhibiting adipogenesis and activating the AMPK pathway in obese mice. *J. Nutr. Biochem.* **25**, 201–207
41. Kim, B., Farruggia, C., Ku, C. S., Pham, T. X., Yang, Y., Bae, M., Wegner, C. J., Farrell, N. J., Harness, E., Park, Y. K., Koo, S. L., and Lee, J. Y. (2017) Astaxanthin inhibits inflammation and fibrosis in the liver and adipose tissue of mouse models of diet-induced obesity and nonalcoholic steatohepatitis. *J. Nutr. Biochem.* **43**, 27–35
42. Merola, N., Castillo, J., Benavente-García, O., Ros, G., and Nieto, G. (2017) The effect of consumption of citrus fruit and olive leaf extract on lipid metabolism. *Nutrients* **9**, E1062
43. Yang, S., Lv, Q., Luo, T., Liu, L., Gao, R., Chen, S., Ye, P., Cheng, Q., and Li, Q. (2013) Metformin inhibits expression and secretion of PEDF in adipocyte and hepatocyte via promoting AMPK phosphorylation. *Mediators Inflamm.* **2013**, 429207
44. Asrih, M., Montessuit, C., Philippe, J., and Jornayvaz, F. R. (2015) Free fatty acids impair FGF21 action in HepG2 cells. *Cell. Physiol. Biochem.* **37**, 1767–1778
45. Tian, Y., Ma, J., Wang, W., Zhang, L., Xu, J., Wang, K., and Li, D. (2016) Resveratrol supplement inhibited the NF- $\kappa$ B inflammation pathway through activating AMPK $\alpha$ -SIRT1 pathway in mice with fatty liver. *Mol. Cell. Biochem.* **422**, 75–84
46. López, M. (2018) Hypothalamic AMPK and energy balance. *Eur. J. Clin. Invest.* **48**, e12996
47. Pisonero-Vaquero, S., Martínez-Ferreras, Á., García-Mediavilla, M. V., Martínez-Flórez, S., Fernández, A., Benet, M., Olcoz, J. L., Jover, R., González-Gallego, J., and Sánchez-Campos, S. (2015) Quercetin ameliorates dysregulation of lipid metabolism genes via the PI3K/AKT pathway in a diet-induced mouse model of nonalcoholic fatty liver disease. *Mol. Nutr. Food Res.* **59**, 879–893
48. Shaw, R. J. (2013) Metformin trims fats to restore insulin sensitivity. *Nat. Med.* **19**, 1570–1572

Received for publication February 12, 2019.

Accepted for publication July 9, 2019.



# Rational design of gelatin/nanohydroxyapatite cryogel scaffolds for bone regeneration by introducing chemical and physical cues to enhance osteogenesis of bone marrow mesenchymal stem cells

K.T. Shalumon<sup>a,1</sup>, Han-Tsung Liao<sup>b,1</sup>, Chang-Yi Kuo<sup>a</sup>, Chak-Bor Wong<sup>c</sup>, Chien-Ju Li<sup>a</sup>, Mini P.A.<sup>d</sup>, Jyh-Ping Chen<sup>a,b,e,f,\*</sup>

<sup>a</sup> Department of Chemical and Materials Engineering, Chang Gung University, Kwei-San, Taoyuan 33302, Taiwan, ROC

<sup>b</sup> Department of Plastic and Reconstructive Surgery and Craniofacial Research Center, Chang Gung Memorial Hospital, Chang Gung University School of Medicine, Kwei-San, Taoyuan 33305, Taiwan, ROC

<sup>c</sup> Department of Orthopaedic Surgery, Chang Gung Memorial Hospital, Keelung 20401, Taiwan, ROC

<sup>d</sup> Department of Physics, St. Michael's College, Cherthala Alappuzha, Kerala 688539, India

<sup>e</sup> Research Center for Food and Cosmetic Safety, Research Center for Chinese Herbal Medicine, College of Human Ecology, Chang Gung University of Science and Technology, Taoyuan 33302, Taiwan, ROC

<sup>f</sup> Department of Materials Engineering, Ming Chi University of Technology, Tai-Shan, New Taipei City 24301, Taiwan, ROC

## ARTICLE INFO

### Keywords:

Cryogel  
Crosslinking agent  
Nanohydroxyapatite  
Gelatin  
Bone tissue engineering  
Dynamic culture

## ABSTRACT

Identification of key components in the chemical and physical milieu for directing osteogenesis is a requirement in the investigation of tissue engineering scaffolds for advancement of bone regeneration. In this study, we engineered different gelatin-based cryogels and studied the effect of nanohydroxyapatite (nHAP) and crosslinking agents on scaffold properties and its osteogenic response towards bone marrow stem cells (BMSCs). The cryogels examined are 5% gelatin and 5% gelatin/2.5% nHAP, crosslinked either with 1-ethyl-3-(3-dimethylaminopropyl)-carbodiimide (EDC) or glutaraldehyde (GA). We confirmed that nHAP or the crosslinking agent has no effects on scaffold pore size and porosity. Nonetheless, incorporation of nHAP increased mechanical strength, swelling ratio and degree of crosslinking, but decreased degradation rate. Cryogels crosslinked with EDC showed faster degradation and promoted osteogenic differentiation of BMSCs while those prepared from GA crosslinking promoted proliferation of BMSCs. Furthermore, osteogenic differentiation was always enhanced in the presence of nHAP irrespective of the culture medium (normal or osteogenic) used but osteogenic medium always provide a higher extent of osteogenic differentiation. Employing gelatin/nHAP cryogel crosslinked by EDC in a bioreactor for dynamic culture of BMSCs, cyclic compressive mechanical simulation was found to be beneficial for both cell proliferation and osteogenic differentiation. However, the optimum conditions for osteogenic differentiation and cell proliferation were found at 30% and 60% strain, respectively. We thus demonstrated that osteogenic differentiation of BMSCs could be tuned by taking advantages of chemical cues generated from scaffold chemistry or physical cues generated from dynamic cell culture *in vitro*. Furthermore, by combining the best cryogel preparation and *in vitro* cell culture condition for osteogenesis, we successfully employed *in vitro* cultured cryogel/BMSCs constructs for repair of rabbit critical-sized cranial bone defects.

## 1. Introduction

Gelatin is a heterogeneous mixture of water-soluble proteins produced by partial hydrolysis of collagen, which in many aspects is closely similar in chemical composition to collagen. In tissue engineering, scaffolds are designed to function as a temporary and artificial extracellular matrix (ECM) to support cell attachment and guide three-

dimensional (3D) tissue formation *in vivo* [1–3]. Being attractive in affordability, biodegradability and good biocompatibility, gelatin has been selected as a scaffolding material over the years to bypass the concerns of immunogenicity and pathogen transmission associated with collagen while still could mimic the biological ECM [4–7]. Bone tissue is a combination of ECM and cells with the composite ECM being mainly composed of nanofibrous collagen type I (COL I) and partially

\* Corresponding author at: Department of Chemical and Materials Engineering, Chang Gung University, Kwei-San, Taoyuan 33302, Taiwan, ROC.  
E-mail address: [jpchen@mail.cgu.edu.tw](mailto:jpchen@mail.cgu.edu.tw) (J.-P. Chen).

<sup>1</sup> K.T. Shalumon and Han-Tsung Liao contributed equally to this work.

<https://doi.org/10.1016/j.msec.2019.109855>

Received 13 March 2019; Received in revised form 20 May 2019; Accepted 1 June 2019

Available online 05 June 2019

0928-4931/ © 2019 Elsevier B.V. All rights reserved.

carbonated hydroxyapatite (HAP) [8]. Though it is one of the prime components of ECM, using HAP alone scaffold fabrication is limited due to the processing difficulty stemming from the brittle nature of HAP. In this aspect, the combination of HAP and gelatin in a single scaffold would therefore provide favorable properties from both HAP and gelatin [9].

Nanohydroxyapatite (nHAP) is similar to native HAP in bone with well-known biocompatibility and osteoconductive properties [10]. Many nHAP-based composite scaffolds fabricated from natural or synthetic polymers have been explored as bone graft substitutes for bone regeneration with improved bone properties [11]. nHAP can enhance cell-material interactions and the bioactivity of HAP-based synthetic grafts compared to larger size HAP particles [12]. Being a resource of free calcium, nHAP was reported to possess higher osteoconductivity than micro-sized HAP and to be suitable for the osteogenic process [13]. Additionally, nHAP has a positive effect on protein adhesion, cell adhesion, proliferation and osteointegration [14]. A 3D gelatin/chitosan scaffold embedded with nHAP with well-defined macropores was reported to mimic bone ECM and provide an ideal environment for bone regeneration from human induced pluripotent stem cells [15].

Cryogelation is a simple and effective method for producing macroporous scaffolds having controlled pore size [16]. This method allows effective control over the pore size using ice crystals as templates for producing macroporous scaffold structure. During the cryogelation process, a polymer solution was mixed with a crosslinking agent, which was allowed to undergo freezing, chemical crosslinking and subsequent thawing steps [17]. As the matrices are allowed to crosslink at sub-zero temperatures, the ice crystals formed within the scaffold act as porogen and result in interconnected pores within the gelled matrix after thawing. Considering various properties of cryogels such as their interconnected pores, elasticity, mechanical stability, reversibility and swelling ability, it would be suitable for tissue regeneration [18,19]. Nonetheless, stability of the cryogel scaffold still depends on the extent of crosslinking, nature of the crosslinking agent, and concentrations of the polymer solutions.

One of the challenges in the field of bone tissue engineering is the construction of comparable *in vitro* environments to native tissue for growing cells or tissues [20]. Essential to this paradigm are stimulating factors that promote the osteoinductive capacity of the scaffold, which include chemical and physical (electromagnetic and mechanical) stimuli [21]. Effects of chemical stimuli on bone formation using cryogel scaffolds have been studied before but not in the case of physical stimuli [22]. Using electromagnetic stimulation on mesenchymal stromal cells seeded in gelatin cryogels, Saino et al. reported enhanced cell proliferation and osteogenic differentiation and elevated production of bone marker proteins COL I, osteocalcin (OCN) and osteopontin (OPN) [23]. Gelatin cryogel seeded with human osteosarcoma cells in a bioreactor with electromagnetic stimulation resulted in more bone matrix production [24]. Studies using ultrasound on gelatin cryogels seeded with human osteosarcoma cells [25] and electric stimulation to composite cryogels seeded with C2C12 myoblasts also confirmed faster bone regeneration [26]. As one form of physical stimuli, mechanical stimulation has been used as a tool for promoting the development of a number of tissue types *in vitro*, including bone [27], cartilage [28], skeletal muscle [29], ligament and cardiac muscle [30].

The main goal of current study is to design 3D gelatin/nanohydroxyapatite (nHAP) cryogels and to test the hypothesis that mechanical stimulation in a bioreactor could promote osteogenic differentiation of bone marrow-derived stem cells (BMSCs) *in vitro*. For this purpose, factors pertaining to rational design of the cryogel scaffolds were studied, starting from a comprehensive evaluation of material characteristics to *in vivo* bone regeneration. The influence of nHAP and crosslinking agents, including glutaraldehyde (GA) and 1-ethyl-3-(3-dimethylaminopropyl)-carbodiimide (EDC), was verified through physico-chemical characterizations and cellular response of bone marrow stem cells (BMSCs) was evaluated *in vitro*. Although the combination of

nHAP and gelatin in a bone tissue engineering scaffold is well established, gelatin/nHAP cryogel was selected here due to its unique elastic property to provide facile dynamic mechanical compression towards differentiation of BMSCs and meaningful comparison of the regeneration potential in a stimuli-responsive mode. Using such *in-situ* stimulated *in vitro*-cultured scaffolds, the optimized cryogel/cell construct intended for bone tissue engineering was ultimately tested *in vivo* in a critical-sized rabbit cranial bone defect model.

## 2. Materials and methods

### 2.1. Materials

Glutaraldehyde (GA), 2-morpholinoethane sulfonic acid (MES), gelatin (type A from porcine skin, 300 bloom) and 2,4,6-trinitrobenzene sulfonic acid (TNBS) were purchased from Sigma-Aldrich. Fetal bovine serum (FBS) was obtained from HyClone. N-Hydroxysuccinimide (NHS) and 1-ethyl-3-(3-dimethylaminopropyl) carbodiimide (EDC) were procured from Acros. 6-Diamidino-2-phenylindole dihydrochloride (DAPI) and rhodamine phalloidin (phalloidin conjugated with tetramethylrhodamine isothiocyanate) were purchased from Life Technologies. Dulbecco's Modified Eagle Medium (DMEM) was obtained from Gibco.

### 2.2. Synthesis of nHAP

The nHAP was synthesized through chemical precipitation as reported in our previous study [31]. Briefly, 0.86 g of  $\text{CaHPO}_4 \cdot 2\text{H}_2\text{O}$  and 0.335 g of  $\text{CaCO}_3$  were gently mixed in a 2.5 M NaOH solution at 75 °C and further reacted for 1 h. After terminating the reaction in an ice bath, the solution was centrifuged and washed multiple times with double distilled water. The obtained slurry was dried at 70 °C for 24 h to obtain nHAP.

### 2.3. Preparation of gelatin and gelatin/nHAP composite cryogels

A gelatin solution with an initial concentration of 10%(w/w) was prepared in distilled deionized (DDI) water in a 70 °C water bath (solution A1). The crosslinking agent GA was prepared in DDI water with an initial concentration of 0.02 M (solution A2). Another gelatin solution with 10%(w/w) concentration was prepared similarly by dissolving gelatin flakes in MES buffer (pH = 6.5) (solution B1). The crosslinking agent EDC was prepared in MES buffer (pH = 6.5) at 0.02 M (solution B2). A solution was prepared at 70 °C by mixing equal volume of A1 and A2 or B1 and B2 solutions to crosslink 5% gelatin with 0.01 M GA in DDI water or with 0.01 M EDC in pH 6.5 MES buffer. In both cases, the pre-mixed solution was placed in an end-capped 3 ml plastic syringe (Terumo, inner diameter = 8.5 mm), followed by mixing with a home-made vibration-free overhead spindle stirrer. Stirring was maintained in such a way to avoid air bubble formation, which could lead to uneven pore formation in the cryogel. After closing the top end of the syringe mold with Parafilm Wrap (Cole-Parmer), the mold was immersed in a 95% ethanol bath at -16 °C in a freezer and crosslinked for 16 h to complete the cryogelation process. After completion of the reaction, the syringe mold was taken out of the bath and the gel was allowed to recede through the bottom cap after thawing. The gel was cut into cylindrical-shaped discs (8 mm diameter × 2 mm thickness). The unreacted aldehyde groups in GA-crosslinked cryogels were blocked after immersing the disc-shaped scaffolds with 0.01 M glycine in phosphate buffered saline (PBS) for 2 h. The prepared cryogels were washed with copious DDI water at 70 °C for 4 h to obtain macroporous cryogel scaffolds [32]. The preparation of gelatin/nHAP composite cryogels followed the same procedure but using solution A1 prepared in DDI water containing 10% gelatin/5% nHAP and solution B1 prepared in pH 6.5 MES buffer containing 10% gelatin/5% nHAP to obtain 5% gelatin/2.5% nHAP composite cryogels. Gelatin (gelatin/nHAP) cryogel

scaffolds synthesized using EDC and GA will be referred to as G-EDC (Gn-EDC) and G-GA (Gn-GA), respectively.

#### 2.4. Characterization of cryogels

The morphology of cryogel was characterized using scanning electron microscopy (SEM) (Hitachi S-3000N) whereas the elemental composition was estimated through energy dispersive X-ray spectroscopy (EDS) (Horiba EX-250). Chemical compositions were identified through Fourier-transform infrared spectroscopy (FTIR) (Horiba FT-730) from 400 to 4000  $\text{cm}^{-1}$  with 2  $\text{cm}^{-1} \text{s}^{-1}$  resolutions. The cryo-frozen samples were ground to fine powder in a mortar and mixed with dry KBr at 1:8 mass to make 1-cm diameter disc-shaped samples for FTIR analysis. X-ray diffraction (XRD) patterns of cryogels were recorded using a Siemens D5005 X-ray diffractometer having a CuK $\alpha$  source, a quartz monochromator and a goniometric plate at 2°  $\text{min}^{-1}$  from 10 to 60°. The spectra were recorded as intensity vs 2 $\theta$  value. Pore size was determined for a cryo-sectioned sample of 0.5 mm thickness by capillary flow porosimetry (PMI CFP-1100-AI, Porous Materials Inc.) with nitrogen gas from 0 to 5 psi and using ethanol as the wetting agent [33]. Porosity of the scaffold was determined using the ethanol displacement method [18]. The crosslinking density was evaluated by 2,4,6-trinitrobenzenesulfonic acid (TNBSA) assay after reacting free amino groups in a cryogel with TNBSA and a standard curve generated from glucosamine [34]. The degree of cross-linking (DC) was calculated from the amount of free amino groups in the sample after normalization with the mass of the sample,

$$\text{Degree of cross linking (\%)} = \left[ 1 - \frac{\left( \frac{\text{free amino groups}}{\text{mass}} \right)_c}{\left( \frac{\text{free amino groups}}{\text{mass}} \right)_{nc}} \right] \times 100 \quad (1)$$

where  $c$  and  $nc$  represent crosslinked and non-crosslinked samples, respectively.

The swelling ratios were evaluated through gravimetric procedure [18]. A dried cryogel sample was immersed in DDI water at room temperature for 24 h and the swelling ratio was calculated from the weight of the swollen sample after removing excess water from the sample,

$$\text{Swelling ratio} = (W_e - W_1)/W_1 \quad (2)$$

where  $W_e$  is the equilibrium mass of the wet cryogel and  $W_1$  is the mass of dry cryogel.

The degradation studies were performed in PBS or 0.01 mg/ml collagenase in PBS by calculating the degree of degradation.

$$\text{Degree of degradation (\%)} = \frac{(W_1 - W_2)}{W_1} \times 100 \quad (3)$$

where  $W_1$  is the mass of initial dry cryogel and  $W_2$  is the mass of dry cryogel after immersing in the solution for different time intervals.

The dynamic and quasi-static mechanical behavior of the cryogel scaffolds were evaluated through compression testing on wet cryogel samples (soaking in PBS for 24 h) using an ElectroForce® 5200 BioDynamic™ Test Instrument (Bose). A uniaxial stress was generated from a 250 N load cell with a cross-head speed of 0.02 mm/s to obtain the stress ( $\sigma$ ) vs strain ( $\epsilon$ ) curve. The point at which failure of the cryogel occurred determined the ultimate compressive strain and ultimate stress. A non-linear equation was used to curve-fit the stress-strain data up to failure [35].

$$\sigma = Ae^{(B\epsilon-1)} \quad (4)$$

with  $A$  and  $B$  being fitted constants. The elastic modulus at 30% strain was calculated using the non-linear elastic model. The toughness (compressive strain energy to failure) representing the necessary energy to deform a sample to failure was obtained from the area under the stress-strain curve.

The cyclic compression test was similarly performed by loading the sample to 30% strain for 1600 cycles at 1 Hz. Energy absorption in cryogel was derived from the stress-strain relation during repeated loading and unloading cycles, which showed a hysteresis loop. During the hysteresis cycle, the area bounded within the hysteresis loop by the loading and unloading curves gave the dissipation energy ( $\text{kJ/m}^3$ ) (energy absorbed due to the viscous properties of the cryogel). The percentage of energy dissipation (%) was calculated by dividing the dissipation energy with the area bounded between the loading curve and the horizontal axis, which represented the total energy applied during compression.

#### 2.5. In vitro cell culture

##### 2.5.1. Isolation and culture of BMSCs

Rabbit BMSCs were harvested and isolated according to standard procedures [22] and all experiments were approved by the Institutional Animal Care and Use Committee of Chang Gung University. Briefly, animals were anesthetized and 20 ml of bone marrow was drawn from a rabbit using a bone marrow aspiration needle fitted to a syringe containing 5 ml of heparin as an anticoagulant. Collected sample was diluted with an equal volume of PBS and centrifuged at 4 °C for 10 min at 1500 g. The supernatant was removed and the bottom layer was mixed with an equal volume of cell culture medium containing 20% FBS, 80% DMEM, 1% penicillin-streptomycin and 2  $\mu\text{g/ml}$  fibroblast growth factor-2 (FGF-2). Centrifugation was repeated at the same condition and the supernatant was removed. The bottom layer dark-red solution was added to a T-75 flask containing 10 ml of cell culture medium and kept in a CO $_2$  incubator maintained at 37 °C. The cells were further sub-cultured in multiple flasks and cells at passages 3 or 4 were used for all studies.

##### 2.5.2. Static cell culture

Disk-shaped crosslinked cryogel scaffolds (2 mm thickness  $\times$  8 mm diameter) were sterilized with 75% ethanol followed by UV exposure for 24 h and rinsed three times with PBS before being placed in a 24-well culture plate for cell seeding. An aliquot of 10  $\mu\text{l}$  cell suspension ( $2 \times 10^5$  BMSCs/ml) was seeded onto one side of the scaffold and incubated in a CO $_2$  incubator at 37 °C for 2 h, followed by seeding 10  $\mu\text{l}$  of the same cell suspension to the other side of the scaffold and incubated in a 37 °C CO $_2$  incubator for 2 h to allow cell adhesion. The cell-seeded scaffold was transferred to a new 24-well culture plate for separation from un-attached cells in the well. Cells culture in tissue culture polystyrene (TCPS) plates was taken as control. Both normal medium (NM) and osteogenic (OM) were employed for cell culture up to 28 days with medium change every three days. The NM consisted of 90% DMEM, 10% FBS and 1% penicillin-streptomycin whereas the OM was composed of 90% DMEM, 10% FBS, 1% penicillin-streptomycin, 0.1  $\mu\text{M}$  dexamethasone, 50  $\mu\text{M}$  L-ascorbic acid phosphate and 10 mM  $\beta$ -glycerolphosphate.

##### 2.5.3. Dynamic cell culture

For dynamic cell culture, a Gn-EDC cryogel scaffold was used following the same sterilization and cell seeding procedures as described for static cell culture. The cell-seeded scaffold was cultured under compressive mechanical stimulation for 14 days in an ElectroForce® 5200 BioDynamic™ bioreactor containing 150 ml NM at 30 or 60% compression strain, 1 Hz frequency and 1 h/day stimulation duration [36].

##### 2.5.4. DNA content and alkaline phosphatase (ALP) activity

The cell-seeded scaffold was removed from the culture plate and washed three times with PBS. For DNA content analysis, the scaffold was immersed in 1 ml digestion buffer solution (55 mM sodium citrate, 150 mM sodium chloride, 5 mM cysteine.HCl, 5 mM EDTA and 0.2 mg/ml papain) and shaken at 60 °C for 24 h. After centrifugation, 10  $\mu\text{l}$  of



the supernatant was mixed with 200  $\mu$ l bisBenzimide H 33258 solution (10 mg/ml) and the fluorescence intensity was determined at 365 nm excitation and 458 nm with an ELISA reader (Synergy HT, BioTek) [37].

For ALP activity, scaffolds were washed three times with PBS and immersed in 1 ml digestion buffer solution containing 55 mM sodium citrate, 150 mM sodium chloride, 5 mM cysteine HCl, 5 mM EDTA and 0.2 mg/ml of papain for 24 h at 60 °C. The solution was centrifuged and ALP activity in the supernatant solution was measured using an ALP kit (Sensolyte® pNPP ALP assay kit, AnaSpec, USA) at 405 nm using an ELISA reader and converted to mass using a standard curve. The specific ALP activity per cell basis was reported by normalizing the ALP mass with the DNA content (ng/ $\mu$ g).

#### 2.5.5. Scanning electron microscopy/energy dispersive X-ray spectroscopy (SEM/EDS) analysis

After washing with PBS for three times, cells in the scaffold were fixed using 2.5% glutaraldehyde at 37 °C for 2 h and post-fixed with 1% OsO<sub>4</sub> (in 0.1 M phosphate buffer) at 37 °C for 3 h. After another three times PBS washing, the scaffold was dehydrated in increasing concentrations (50, 70, 80, 90, 95, and 100%) of ethanol. After complete drying by a critical point dryer, the sample was sputter coated with gold. Cell morphology and mineral deposition were examined by a scanning electron microscope (Hitachi S-3000N SEM, Japan). Energy dispersive X-ray spectroscopy (EDS) analysis was used to confirm mineral deposition and determine the elemental atomic percentage in the mineral deposit (HORIBA EX-250 EDS).

#### 2.5.6. Live/dead and cytoskeleton staining

The qualitative evaluation of cell viability was assessed by a Live/Dead viability/cytotoxicity kit (Molecular Probes, USA). The scaffold was washed with PBS and stained with the Live/Dead staining solution containing 2  $\mu$ M calcein AM (for live cells) and 5  $\mu$ M ethidium homodimer-1 (EthD-1) (for dead cells) at 37 °C for 15 min. The morphology of cells was imaged under a Leica TCS SP2 confocal laser scanning microscope (excitation/emission 494/517 nm for live cells and 528/617 nm for dead cells).

For cytoskeletal staining, samples were fixed in 4%(w/v) paraformaldehyde in PBS for 30 min, followed by permeabilization in 0.1% Triton X-100 for 5 min. Before staining, the scaffold was washed with PBS and stained for actin cytoskeleton with 1% rhodamine phalloidin for 30 min in dark. After counter-stained with 0.1  $\mu$ g/ml DAPI for cell nucleus for 5 min, the cytoskeletal arrangement was immediately visualized using a confocal laser scanning microscope (Leica TCS SP2) at excitation/emission wavelengths of 540 nm/570 nm for rhodamine phalloidin and 340 nm/488 nm for DAPI.

#### 2.5.7. Immunofluorescence (IF) staining of COL I

Cells in the scaffolds were fixed in 4% paraformaldehyde in PBS for 30 min followed by PBST (PBS with 0.1% Tween 20) washing for 3 times, 15 min each. Nonspecific labeling was blocked with 1 ml of Hyblock 1-min Blocking Buffer (Goal Bio, Taiwan) and washed again with PBST. Collagen type I (COL I) primary antibody (1:200 in PBST, mouse monoclonal anti-COL I, Abcam, USA) was reacted with the sample for 24 h at 37 °C. Each sample was washed three times with PBST for 20 min each, followed by treating with Cy3-conjugated anti-mouse IgG secondary antibody (Jacksons Laboratories, USA) for 1 h at 37 °C. Another PBST washing was given prior to staining with 50  $\mu$ g/ml DAPI for 15 min for nucleus and the sample was observed by a confocal laser scanning microscope (Leica TCS SP8) at excitation/emission wavelengths of 554 nm/559–713 nm for Cy3 and 405 nm/410–476 nm for DAPI. The semi-quantitative evaluation of COL I by IF staining was done through PAX-it!™ image analysis software.

#### 2.5.8. Calcium and osteocalcin (OCN) quantification

Alizarin red S (ARS) was used to quantify the calcium ion content in mineralized ECM of BMSCs. The cell-seeded scaffold was removed from

a culture plate and washed 3 times with PBS. After fixing with 2.5% glutaraldehyde solution for 1 h at 37 °C, the samples were reacted with 1 ml of ARS solution (2%(w/v) ARS in water, pH 4.1–4.3) for 1 h at room temperature. After several washes with water to remove excess dye, the sample was incubated with 1 ml of 10% cetylpyridinium chloride (CPC) solution to elute the ARS-calcium ion chelated complex. The absorbance of the solution was read at 540 nm in an ELISA reader (OD<sub>540</sub>) and normalized with the DNA content.

The concentrations of OCN in cell-seeded scaffolds were determined by biochemical assays. Retrieved scaffolds were washed and immersed in digestion solution for 4 h (60 °C), followed by centrifugation to collect the supernatant. The OCN concentration was measured using a rabbit OCN ELISA kit (BlueGene Biotech., Shanghai, China) and quantified from a pre-determined standard curve.

#### 2.5.9. Quantitative real-time polymerase chain reaction (qPCR)

The expression of osteogenic differentiation marker genes COL I, ALP, OCN and OPN was examined using standard protocols of RNA isolation and cDNA synthesis. TRIzol (Invitrogen, USA) was used to isolate RNA and the solution was transferred to a 1.5 ml microcentrifuge tube. The tube was vortexed for 15–30 s after adding 200  $\mu$ l of chloroform to the cell suspension. The tube was placed in an ice bath for 5 min and centrifuged at 11000 rpm for 15 min. RNA was isolated from the supernatant layer and reacted with isopropanol in 1:1 ratio at –80 °C for 30 min. The supernatant was removed again and the solution was further centrifuged at 11000 rpm (4 °C) for 15 min. One milliliter of 75% ice cold ethanol was added and mixed at 4 °C for 10 min, followed by repeated centrifugation at 11000 rpm for 10 min each. The final supernatant solution was dried at room temperature and the RNA retrieved was dissolved in 30  $\mu$ l of DEPC-treated water (Invitrogen) at 55 °C for 15 min. The RNA obtained (1 mg) was reverse-transcribed into cDNA using SuperScript III RNase H (Invitrogen). Glyceraldehyde 3-phosphate dehydrogenase (GAPDH) was used as the housekeeping gene. A SYBR Green RT-PCR kit (SYBR Green I Supermix, Bio-Rad) was used for quantitative real-time PCR (qPCR) measurements using a Mini Option detection system (Bio-Rad CFD-3120). The primer sequences were COL I (forward: TTCTATTGGTCCCGTCGGT; reverse: GCTGAGT CTCAGGTCGCG-3), ALP (forward: ATGATTTCACCATTCTTAGTACTG; reverse: TCAGAACAGGACGCTCAGGGG), OCN (forward: GACACCAT GAGGACCTCTC; reverse: GCCTGGTAGTTGTTGTGAGC), OPN (forward: CACCATGAGAATCGCCGT; reverse: CGTGACTTTGGGTTTCTA CGC), GAPDH (GCTTTGCCCGCGATCTAATGTTT; reverse: GCCAAAT CCGTTCACCTCCGACCTT) [38].

#### 2.6. In vivo studies

A critical size calvarial bone defect model in rabbit was used to evaluate bone regeneration by implanting BMSCs/cryogel constructs in rabbit skull. Animal protocols were approved by the Institutional Animal Care and Use Committee of Chang Gung University. Male New Zealand white rabbits weighing 3–4 kg were selected for the study and were kept in a single room and fed dried diet and water *ad libitum*. An intramuscularly injection of Atropin (0.3 mg/kg) was given, followed by general anesthesia using a mixture of Zoletil 50 (18 mg/kg) and Rompun 20 (1 mg/kg). The scalp was sterilized with betadine solution and a longitudinal incision was induced to create sub-periosteal dissection to expose the skull bony area. A surgical trephine of 10-mm diameter created two circular defect sites at the calvarial bone of the rabbit and bony discs were removed. A Gn-EDC cryogel scaffold (2 mm thickness  $\times$  10 mm diameter) was seeded with  $1 \times 10^6$  BMSCs and dynamically cultured in an ElectroForce® 5200 BioDynamic™ bioreactor (with 150 ml NM) at 30% compression strain, 1 Hz frequency and 1 h/day stimulation duration for 14 days. The right defect created in the rabbit defect was filled with a cellular scaffold while an acellular cryogel was used to fill the left defect. Both defect sites were completely occupied by the samples and surgical sites were finally closed with 4-0

Ethicon sutures for post-operative care.

All animals were underwent computed tomography (CT) examination using a CT scanner (Somatom Sensation 16, Siemens) 1 and 8 weeks after implantation. The calvarial defect regeneration was analyzed by comparing both cellular and acellular sites, using OsiriX Image software (Pixmeo, Bernex, Switzerland) for 2D coronal and 3D views. All animals were euthanized at 16 weeks post-operation, using lethal doses of pentobarbital (0.5 g per kg body weight) and the implants were dissected out for gross evaluation. All samples were fixed in 10% formaldehyde, dehydrated and embedded in paraffin to make 10-mm slice sections. Samples were subjected to hematoxylin and eosin (H&E), Masson's trichrome and immunohistochemical (IHC) staining of COL I and OCN following standard protocols. Bone regeneration in cellular scaffolds in comparison with acellular ones was assessed by recording the images under an inverted optical microscope (Olympus IX-71).

## 2.7. Statistical analysis

All quantitative data were expressed as mean  $\pm$  standard deviation (SD) and one-way ANOVA LSD test was used to determine the significant difference.

## 3. Results and discussion

### 3.1. Characterization of cryogel scaffolds

#### 3.1.1. Physico-chemical properties

By combining ceramic nanoparticles (nHAP) with an organic polymer (gelatin), we aim to improve the osteo-inductive properties and mechanical properties of gelatin by designing a composite cryogel scaffold to enhance its applicability for bone tissue engineering [39]. As dominance of nHAP in the composite might lead to weakening of the scaffolds, we fixed the gelatin/nHAP mass ratio at 2/1 to study the effect of crosslinking agent on the properties of cryogels [22]. The optimum composition of gelatin/nHAP is expected to coincide with the slow degradation characteristics and mechanical properties requirement for a bone tissue engineering scaffold through chemical crosslinking of gelatin with EDC or GA. Considering the crosslinking agents for cryogel synthesis, GA is a longer crosslinker than EDC (a zero-length crosslinker) and has faster reaction kinetics [40]. However, GA was reported to cause local toxicity at the implantation site owing to the release of unreacted aldehydes [41].

From the SEM images, macroporous morphology with open interconnected pores with pore size ranging from 50 to 120  $\mu\text{m}$  was observed for cryogel scaffolds (Fig. 1). This pore size and pore morphology could meet the requirements for scaffolds intended for bone tissue engineering. From elemental analysis through EDS shown in inserts of Fig. 1, composite cryogels show strong Ca and P peaks with a Ca/P ratio value of 1.59 for Gn-EDC and 1.69 for Gn-GA. The Ca/P ratios are comparable to the theoretical value of HAP (1.67) and confirm the incorporation of nHAP in gelatin-based cryogel scaffolds.

Additional experiments with capillary flow porosimetry provided the average pore size of cryogel scaffolds (Table 1). The average pore size and porosity did not show significant dependence on the presence of nHAP or the type of crosslinking agent used (i.e. EDC or GA). In tissue engineering, an adequate porous structure of the scaffold is very important to allow cellular penetration into the construct. Apart from that, it is also necessary for waste and nutrient transports. Our experiments confirmed that the mean average pore size of all scaffolds is ideal for penetration and proliferation of BMSCs, while higher than 80% porosity is expected to be beneficial for cell ingrowth and survival [18].

The degree of crosslinking was above 80% for every scaffold and no significant difference was found when using different crosslinking agents. It should be noted that the degree of crosslinking was calculated based on the number of free amine groups in gelatin. The aldehyde group in GA will react with amino groups of lysyl and hydroxylysyl

residues in gelatin coupled with the release of a water molecule, after which imines (Schiff base intermediates) will be formed and react further to form larger crosslinked entities. In contrast, EDC as a zero-length crosslinker links amine and carboxyl groups of proteins by activating the carboxylic acid group of glutamic and aspartic amino acid of a protein molecule to form an amine-reactive O-acylisourea intermediate. Although EDC consumes only one amine group compared to GA that consumes two, it still efficiently crosslinked the matrix and showed high degree of crosslinking. This could be explained from the fact that the amount of glutamic and aspartic amino acid was reported to be 3.7 times that of lysine and hydroxylysine in porcine skin gelatin (12.81 vs. 3.46  $\mu\text{mol/g}$  ash-free protein) [42]. Nonetheless, there was significant decrease of degree of crosslinking when nHAP was added (Table 1). This should be due to the steric hindrance caused by entrapped nHAP, which might cause screening of the effective covalent crosslinking of gelatin macromolecules in a composite cryogel and lead to reduced crosslinking efficiency.

Swelling ratio in water is considered as an important feature to be evaluated for a scaffold designed for tissue engineering applications. Swelling will increase the pore size and the surface area to volume ratio of the scaffold and thereby facilitates the infiltration of cells into the 3D scaffold [43]. Moreover, since the gelatin scaffold is made up of crosslinked polymer chains embedded with ceramic constituents; its efficiency in water absorption would be a direct measure of pore-size mediated cellular infiltration as well as fluid absorption both *in vitro* and *in vivo*. The swelling behavior of scaffolds was measured through water immersion and the swelling ratio is shown in Table 1. Gelatin cryogel crosslinked with EDC had the highest swelling ratio among all scaffolds. Incorporation of nHAP led to significantly lower swelling ratio for both EDC and GA-crosslinked cryogels. However, unlike the insignificant effect of crosslinking agent on degree of crosslinking, the swelling ratio of GA-crosslinked cryogels were significantly lower than that of EDC-crosslinked cryogels for both G and Gn cryogels. We postulate that the difference in ionic carboxyl and amine groups in the crosslinked cryogel may play a role in influencing the swelling ratio, which might due to the different crosslinking mechanism between EDC and GA.

The *in vitro* degradation of cryogels in PBS and collagenase solutions at 37  $^{\circ}\text{C}$  is another important cryogel property, which determines the stability of a cryogel scaffold under physiological relevant conditions. PBS degradation is relevant due to the abundance of water in human body while collagenase specifically imitates enzymatic response of the cryogel *in vivo*. Collagenase is a protease that cleaves the bond between a neutral amino acid (X) and glycine in the sequence Pro-X-Gly-Pro, which is found abundantly in collagen and gelatin. The degradation studies using PBS and collagenase could thus mimic the possible deterioration of cryogels in aqueous solutions as well as *in vivo*. Compared to collagenase solutions, samples in PBS show much slower degradation rate as expected, with Gn-GA displayed the highest resistance to degradation (Fig. 2). All samples in PBS or collagenase show similar trends of degradation profiles with Gn > G, indicating faster hydrolysis rate of composite cryogels. The nHAP embedded in the crosslinked gelatin matrix in the composite cryogel may interrupt physical entanglements of gelatin polymer chains in the gel matrix and thereby lead to faster degradation rates in PBS and collagenase in accordance with lower values of degree of crosslinking (DC) in Table 1. Nonetheless, not in line with the trend observed for DC where insignificant difference was found using different crosslinking agents, EDC crosslinked cryogels showed much faster degradation rates compared to GA crosslinked ones (Fig. 2). This trend is consistent with a previous report using GA and EDC to crosslink electrospun collagen scaffolds, where collagen scaffolds treated with EDC were found to retain lower structural stability than GA [44]. Therefore, the degradation rates of cryogels calculated from weight loss should not be solely correlated to DC that measures the free amino groups. It may be related to the higher hydrolytic stability of imine linkages produced by GA crosslinking

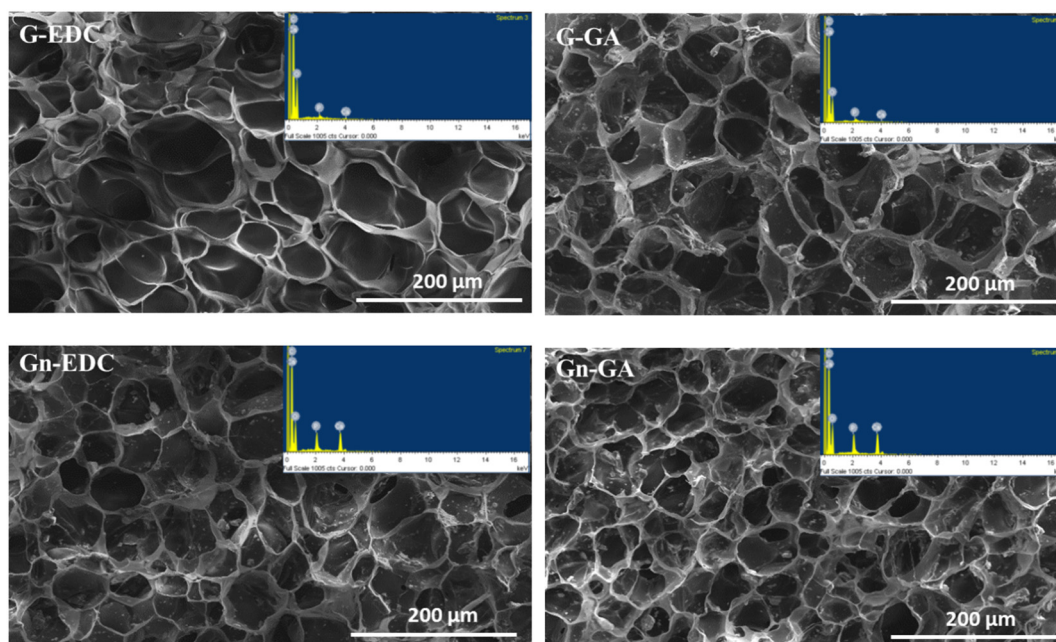


**Fig. 1.** Scanning electron microscope (SEM) images of gelatin (G) and gelatin/nanohydroxyapatite (Gn) cryogel prepared by using EDC or glutaraldehyde (GA) as the crosslinking agent (bar = 200  $\mu\text{m}$ ). The inserts are EDS spectra.

compared to the relatively more hydrophilic amide linkages by EDC crosslinking.

### 3.1.2. FTIR and XRD

FTIR was used to characterize the functional groups present in G and Gn cryogels to ensure the presence of nHAP in composite cryogels. As shown in Fig. 3A, pure gelatin shows characteristic amide I peak at  $1654\text{ cm}^{-1}$  and amide II peak at  $1517\text{ cm}^{-1}$ , which is consistent with the peaks observed in G and Gn. In a similar fashion, absorption bands of pure nHAP is correlated with its presence in Gn cryogels from the presence of carbonate peak at  $877\text{ cm}^{-1}$ , phosphate stretching vibrations at  $580$  and  $609\text{ cm}^{-1}$  and hydroxyl bands at  $1471$ ,  $1417$  and  $3429\text{ cm}^{-1}$  [45]. All results thus cross-confirm the presence of nHAP in composite gelatin cryogels.

In addition to FTIR, the presence of nHAP in composite cryogels was further examined through the identification of crystalline peaks of the ceramic counterpart by XRD analysis (Fig. 3B). The spectrum showed a semi-crystalline peak at  $21.5^\circ$  for gelatin, which was also displayed by G regardless of the crosslinking agent used. However, the intensity of the peak at  $21.5^\circ$  reduced to a minor broad distribution when gelatin was combined with nHAP to form composite cryogels [46]. Along with the minor gelatin peak, Gn cryogels showed all characteristic crystalline peaks assigned to nHAP at  $25.9^\circ$ ,  $32.2^\circ$ ,  $33.3^\circ$ ,  $34.2^\circ$ ,  $40.2^\circ$ ,  $46.9^\circ$ ,  $49.7^\circ$  and  $53.3^\circ$   $2\theta$  values. The reduction in the intensity of the gelatin peak in Gn cryogels is due to the screening effect from strong nHAP peaks, as mentioned in earlier literatures [45]. In short, the physico-chemical characterizations validate the formation of composite cryogel scaffolds through nHAP incorporation.

**Table 1**

The average pore size, porosity, degree of crosslinking (DC) and swelling ratio (SR) of cryogel scaffolds. Values are mean  $\pm$  SD of six independent measurements.

	EDC				GA			
	Pore size ( $\mu\text{m}$ )	Porosity (%)	DC (%)	SR	Pore size ( $\mu\text{m}$ )	Porosity (%)	DC (%)	SR
G	$55.0 \pm 4.7$	$87.9 \pm 2.4$	$87.7 \pm 0.3$	$10.6 \pm 0.6$	$58.3 \pm 5.0$	$85.8 \pm 1.2$	$88.6 \pm 0.3$	$7.2 \pm 0.1^{\#}$
Gn	$50.0 \pm 6.9$	$83.0 \pm 2.4$	$84.4 \pm 0.2^*$	$6.3 \pm 0.4^*$	$52.8 \pm 7.6$	$81.0 \pm 2.3$	$85.2 \pm 0.5^*$	$5.4 \pm 0.4^{*\#}$

\*  $p < 0.05$  compared with cryogels crosslinked with the same crosslinking agent but without nHAP.

$^{\#}$   $p < 0.05$  compared with cryogels of the same composition but crosslinked with different crosslinking agent.

### 3.1.3. Mechanical properties

As shown in Fig. 4A and B, compressive stress-strain curves of all cryogels could be fitted satisfactorily with the empirical non-linear model shown in Eq. (4). The elastic modulus calculated from the slope of the stress-strain curves at 30% strain, which represents the initial linear region, was found to be significantly increased using either GA as the crosslinking agent (i.e. G-GA > G-EDC, Gn-GA > Gn-EDC) or by incorporating nHAP (i.e. Gn-EDC > G-EDC, Gn-GA > G-GA) (Table 2). A similar trend was also observed for the ultimate strain, ultimate stress and toughness. Compared with the elastic moduli of gelatin cryogels embedded with HAP particles and crosslinked with oxidized dextran (18.5 kPa), our scaffolds are much stronger and is expected to be suitable for tissue-engineering of non-load-bearing bones such as in the craniofacial area [47]. Overall, the mechanical properties of Gn-GA were significantly better than those of other cryogels. This could be ascribed to the fact that nHAP are present in the cryogel strut, resulting in higher resistance to mechanical compression compared to the brittle nature of G samples. For cryogels crosslinked with different crosslinking agents, the higher network integration of GA-crosslinked cryogels is consistent with their slower degradation rates in both PBS and collagenase (Fig. 2).

The mechanical requirements of bone tissue engineering scaffolds are complex, where compressive, tensile and fatigue properties are all required for load bearing [48]. In general, bone tissue engineering scaffolds made from natural polymers (e.g. gelatin) have sub-optimal mechanical properties even after crosslinking [49]. Thus, they are insufficient to be used as a load-bearing scaffold for bone regeneration compared to metallic and ceramic materials. Combining natural



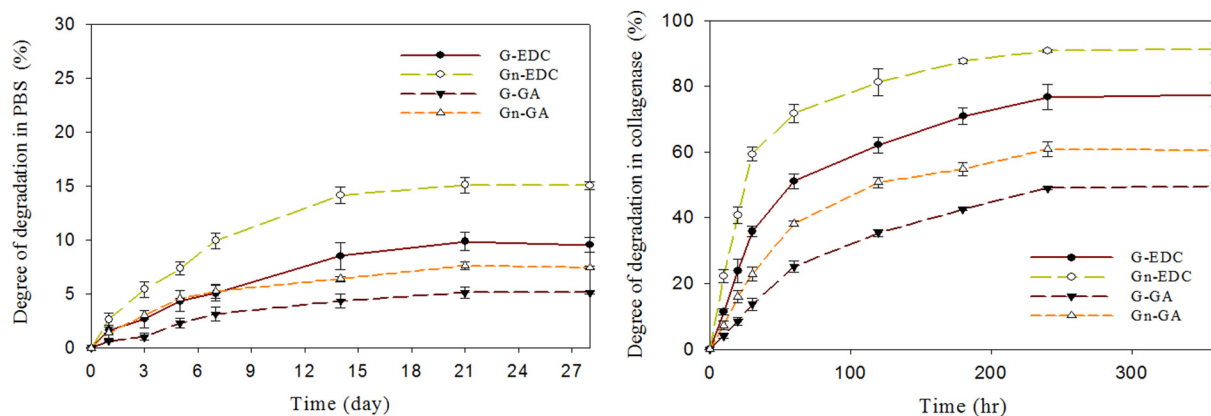


Fig. 2. Degradation of cryogels in PBS and collagenase solutions.

polymers with more robust materials such as bioceramics (e.g. nHAP) to create composite scaffolds may address these limitations. However, composite cryogels still lack mechanical strength to be evaluated for regeneration of segmental bone but could be considered for regeneration of calvarial or cancellous bones [50]. Indeed, due to the compliant mechanical properties of the G or Gn scaffolds, they are best suited for non-load-bearing indications such as craniofacial repair [51]. Nonetheless, as many bone fractures require fixation in combination with bone grafting, a compliant G or Gn scaffold could theoretically be applied in a load bearing application when combined with mechanical fixation [52]. Additionally, similar to formation of rigid bone from the soft cartilaginous callus during bone fracture healing, it is also possible that G or Gn scaffold could produce a graft that quickly fills the bone defect to supersede their poor mechanical properties for bone tissue engineering application.

From Fig. 5, the cyclic compression testing of cryogels at 30% strain and 1 Hz shows a hysteresis loop in the stress-strain curves of all cryogels. The dissipation energy is the amount of mechanical energy dissipated and could be calculated from the area enclosed in the hysteresis loop. From Table 2, the dissipation energy and the percentage of energy dissipation of G-EDC was not statistically different from that of G-GA. Nonetheless, Gn-GA displayed significantly higher dissipation energy and percentage of energy dissipation than G-GA and Gn-EDC, making it to dissipate the highest energy during compression and to perform better than other cryogels in terms of energy dissipation. Furthermore, cyclic compression loading-unloading curves during the first cycle and all subsequent cycles appeared to be reversible and reproducible, which endowed cryogels with an unique property to be fully recovered from compressive loading-unloading cycles without

causing permanent bond breakage even at 30% strain (Fig. 5). Indeed, the tough nature of a cryogel scaffold rendered the scaffold to absorb impacts without permanent damage and recover back to its original form even after experiencing large successive compressive force and deformation. That Gn-GA had the highest energy dissipation throughout the cyclic compressing is consistent with our previous study [53] as well as with other reported findings [54], where it was shown that under an identical dynamic compression, the dissipation energy of a scaffold crosslinked with higher amount of crosslinker or with a crosslinker that produces denser network will be much higher. Therefore, incorporation of nHAP in cryogels will have a positive impact on energy dissipation during cyclic compression, revealing the higher mechanical stability of the composite scaffolds in load bearing application. This unique feature contributes to the development of composite cryogels as tough scaffolds for bone tissue engineering, which can recover from large strains and absorb impacts without permanent damage. Most importantly, this property will facilitate dynamic cell culture using a cryogel scaffold when subject to cyclic compressive loading-unloading in a bioreactor. We will take advantage of this unique feature later in this study.

The superior recovery property of cryogel from large strains was further analyzed from the enclosed area of the hysteresis loops during the successive loading-unloading cycles at 30% maximum strain and the calculated dissipation energy during 100th, 200th, 400th 800th and 1600th cycles are compared in Fig. 6. The cryogels crosslinked by EDC (G-EDC and Gn-EDC) did not show significant difference in dissipation energy among all cycles. Nonetheless, cryogels crosslinked by GA (G-GA and Gn-GA) showed slightly but significantly lower dissipation energy during successive compression cycles, indicating EDC-

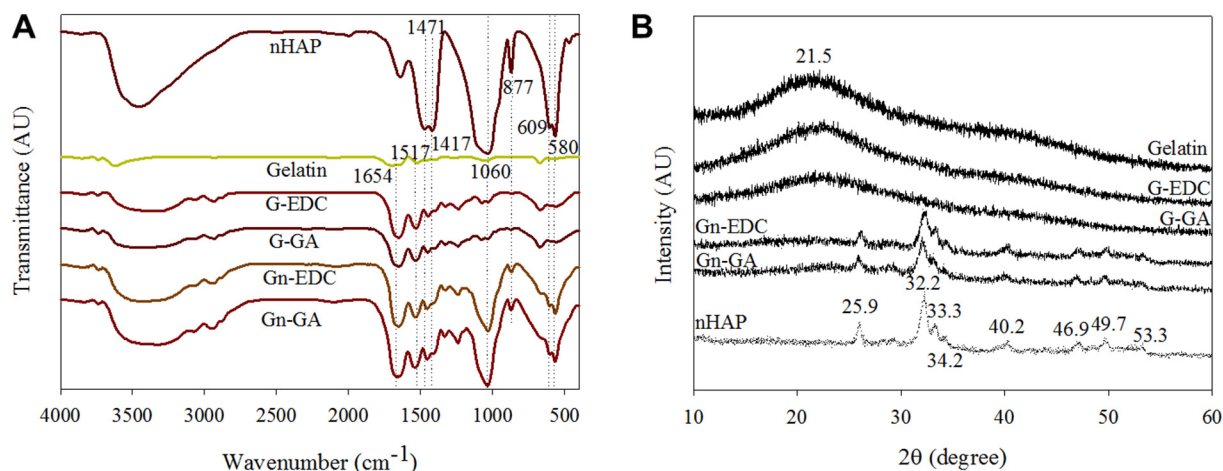


Fig. 3. The characterization of cryogels through FTIR (A) and XRD (B) analysis.

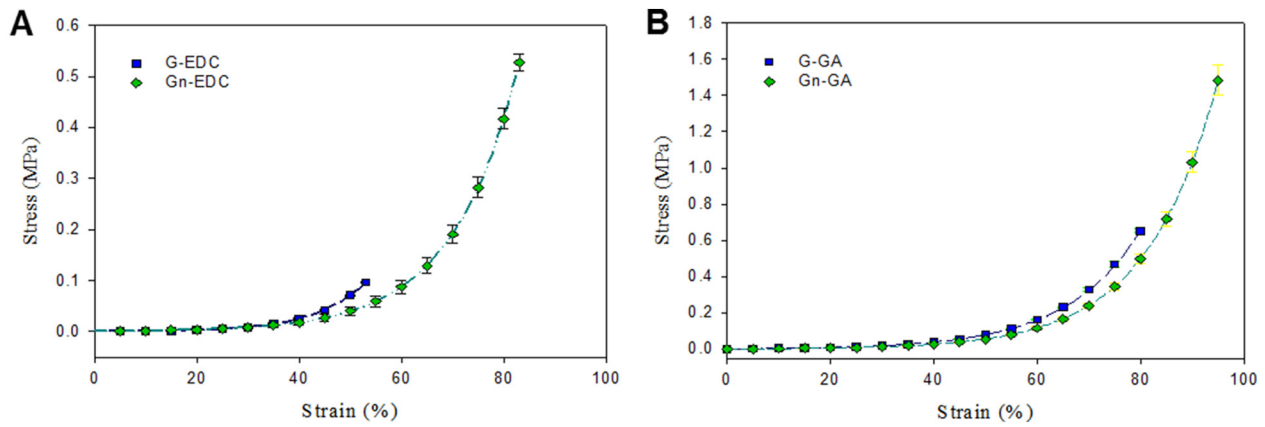


Fig. 4. The compressive stress-strain curves of G and Gn cryogels prepared through EDC (A) or GA crosslinking (B).

crosslinked gelatin network may be more stable in the presence of successive compressive force that may lead to irreversible breakage of bonds in the crosslinked polymer networks.

### 3.2. In vitro cell culture-static culture

#### 3.2.1. Cell proliferation and ALP activity

Since nHAP was reported to be a weak osteo-inductive material [55], we used normal medium (NM) as well as osteogenic medium (OM) to compare the *in vitro* cellular response of BMSCs in G and Gn cryogel scaffolds (Fig. 7A). In NM, the same cell number on day 0 (4 h) for all groups indicates excellent cell attachment efficiency in 3D cryogel scaffolds comparable to theoretically quantitative cell attachment on TCPS. This observation could be supported from similar pore size and pore structure among all cryogels in Fig. 1 and Table 1. Nonetheless, less DNA content was found for Gn cryogels compared to G cryogels and TCPS controls with TCPS groups consistently having higher cell numbers as culture time progresses, indicating BMSCs on TCPS or in G had higher cell proliferation rate than in Gn.

The effect of OM over NM in reducing the cell proliferation rate was further verified in Fig. 7A. Overall, the Gn groups exhibited the lowest cell proliferation rates among all groups in OM. Multiple rationales could be inferred by using OM for culture of BMSCs [56]. Nonetheless, the reduction of total DNA content in OM as well as the lower cell number in Gn inferred better osteogenic differentiation of BMSCs [57]. The influence of OM validates the effects of osteo-inducing factors in the medium on BMSCs, which could be further enhanced by using Gn cryogels by taking advantage of the osteoinductive properties of nHAP. The crosslinking agent also significantly affected cell proliferation rate; EDC-crosslinked cryogels always had lower cell number than GA-crosslinked ones, regardless of cryogel composition. Therefore, BMSCs cultured in Gn-EDC cryogels had the lowest cell numbers throughout the culture period. Overall, the cell proliferation studies suggest that by incorporating nHAP and using different crosslinking agents during cryogel preparation, chemical cues generated therewith will

synergistically influence the cellular response of seeded BMSCs.

The DNA content observed in different cryogels could be further correlated with the ALP activity of BMSCs (Fig. 7B). The ALP marker is used to identify the initiation of mineralization through nucleation of inorganic phosphates with  $\text{Ca}^{2+}$ , which results in calcification within local environment. The hydrolysis of phosphate esters by ALP leads to elevation of mineralization of ECM and regulation of downstream cell differentiation factors to initiate osteogenic differentiation [58]. Thus, ALP can be considered as an effective measurement tool for the differentiation of BMSCs into the osteogenic lineage. The normalized ALP activities of BMSCs cultured on TCPS and in cryogels are reported in Fig. 7B using NM or OM for cell culture. Even in NM, Gn cryogels exhibited higher ALP activities throughout the culture period; especially during the first 14 days. As shown from cell proliferation rates in Fig. 7A, Gn-EDC showed significant reduction in cell number compared with Gn-GA on day 7 and 14. This trend could be correlated well with concomitant higher ALP activities for Gn-EDC. Indeed, the ALP activity of Gn-EDC was 4.39, 3.70, 3.61, 1.84, 1.49 and 1.51 folds that of Gn-GA on day 0, 3, 7, 14, 21 and 28, respectively. A higher ALP value in the early period of cell-culture supports the osteogenic differentiation of BMSCs. In addition, the higher ALP activity of G-EDC (Gn-EDC) over G-GA (Gn-GA) reveals the advantage of using EDC for crosslinking gelatin cryogel scaffolds for differentiation of BMSCs towards the osteogenic lineage. When NM was replaced with OM, Gn cryogels displayed a drastic increase in ALP activity while G cryogels had comparable values. On day 14, Gn-EDC cryogel cultured in OM showed the highest ALP activity due to the synergistic effect of nHAP and the crosslinking agent as ALP is a characteristic early marker of osteogenesis [22].

#### 3.2.2. Cell morphology and mineralization

EDC and GA-crosslinked Gn cryogels cultured with BMSCs for 14 and 28 days in both NM and OM were assessed by SEM/EDS (Fig. 8). The process of mineralization of ECM due to of stem cell differentiation could be estimated both quantitatively and qualitatively. Inorganic calcium phosphate deposition occurs at the middle of the cell

Table 2

The mechanical properties of cryogel scaffolds. Values are mean  $\pm$  SD of six independent measurements.

	G-EDC	Gn-EDC	G-GA	Gn-GA
Elastic modulus @30% strain (kPa)	65.9 $\pm$ 15.4	94.1 $\pm$ 5.1*	95.2 $\pm$ 9.81 <sup>#</sup>	138.6 $\pm$ 2.7 <sup>*,#</sup>
Ultimate strain (%)	53.3 $\pm$ 0.6	83.3 $\pm$ 0.6*	80.3 $\pm$ 1.8 <sup>#</sup>	99.7 $\pm$ 0.6 <sup>*,#</sup>
Ultimate stress (kPa)	97.7 $\pm$ 3.2	523.8 $\pm$ 26.1*	700.9 $\pm$ 58.2 <sup>#</sup>	1941.0 $\pm$ 114.7 <sup>*,#</sup>
Toughness (kJ/m <sup>3</sup> )	9.8 $\pm$ 0.5	69.3 $\pm$ 5.8*	96.7 $\pm$ 10.4 <sup>#</sup>	286.2 $\pm$ 21.0 <sup>*,#</sup>
Initial dissipation energy (kJ/m <sup>3</sup> )	0.50 $\pm$ 0.02	0.58 $\pm$ 0.03*	0.52 $\pm$ 0.02	1.14 $\pm$ 0.01 <sup>*,#</sup>
Initial percentage of energy dissipation (%)	28.89 $\pm$ 3.97	30.66 $\pm$ 3.31*	32.08 $\pm$ 2.82	40.07 $\pm$ 1.81 <sup>*,#</sup>

\*  $p < 0.05$  compared with cryogels crosslinked with the same crosslinking agent but without nHAP.

<sup>#</sup>  $p < 0.05$  compared with cryogels of the same composition but crosslinked with different crosslinking agent.



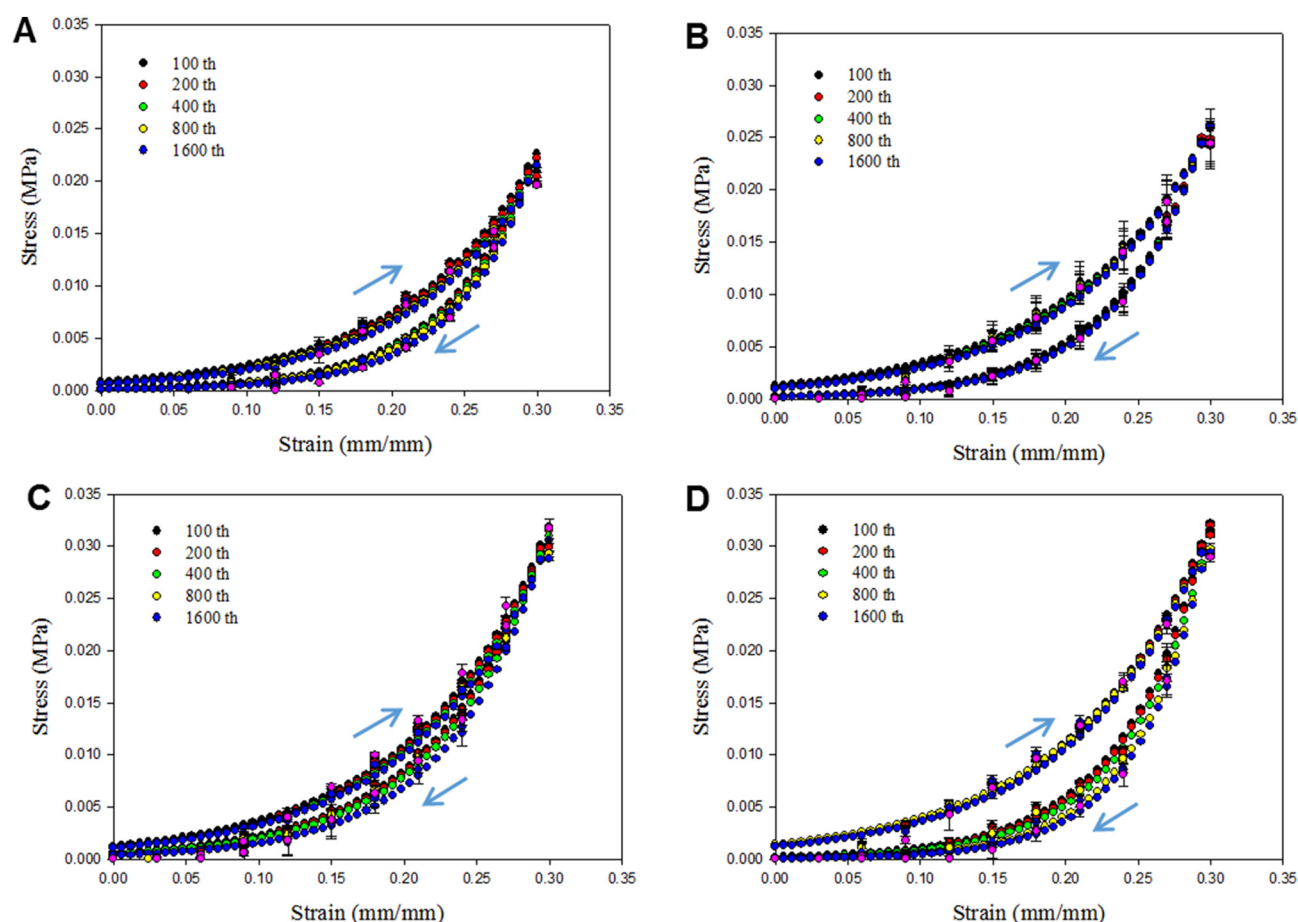


**Fig. 5.** The compressive loading-unloading hysteresis curves during 1600 successive compression to a maximum strain of 0.3 for G-EDC (A), Gn-EDC (B), G-GA (C) and Gn-GA (D) cryogels.

differentiation period and thus it could be considered as a proof of osteoblast formation [59]. The SEM observation could be taken as a qualitative tool for cell morphology and mineralization while EDS analysis is useful to determine the atomic percentages of elements present in the deposited mineral during osteogenic differentiation [60]. From Fig. 8, mineralized nodules were clearly visible within cryogels on day 14. In NM, cells in G cryogels displayed intermix of slightly rounded and spread cell morphology with visible porous cryogel background. Gn showed similar cell appearance, but the ECM appeared to be more mineralized judging from the white dots in the SEM images due to the osteoinductive nature of nHAP even without osteogenic

factors in NM (Fig. 8). These small white depositions observed in Gn are due to the early deposition of calcium phosphate in the form of hydroxyapatite.

Interestingly, all cryogels on day 28 had well spread cell morphology due to cell differentiation, which resulted in complete filling of 3D pores in a cryogel scaffold. A much thicker layer of BMSCs spreading in G should be due to the higher cell proliferation rate in G compared to Gn cryogels as shown before from DNA quantification. This was verifiable from more visible scaffold pores in Gn cryogels in the SEM images. The mineral deposition was much more pronounced in Gn than G on day 28 as mineral production is a late osteogenic differentiation

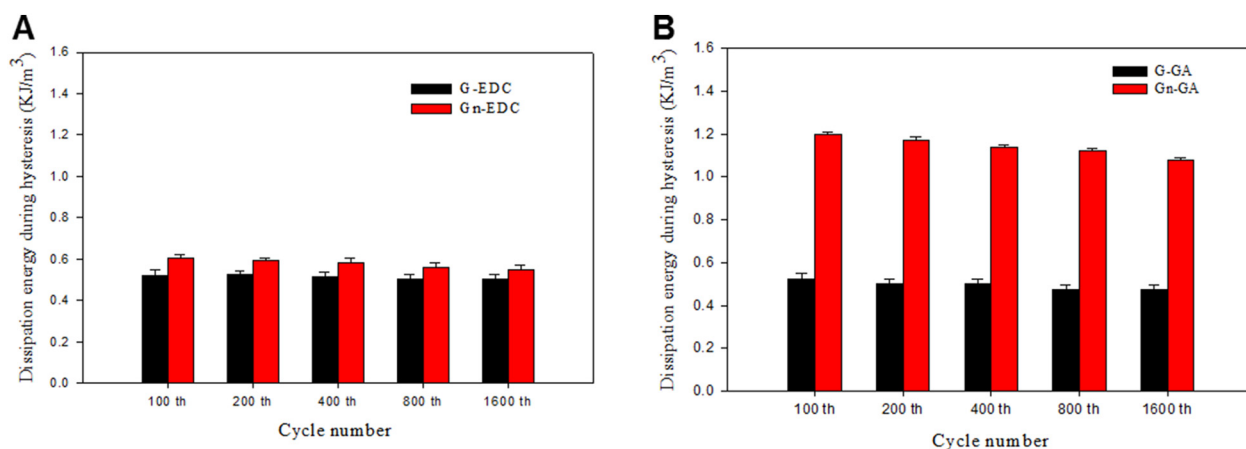


**Fig. 6.** Dissipation energy of EDC-crosslinked (A) and GA-crosslinked (B) cryogels during successive compression cycles.

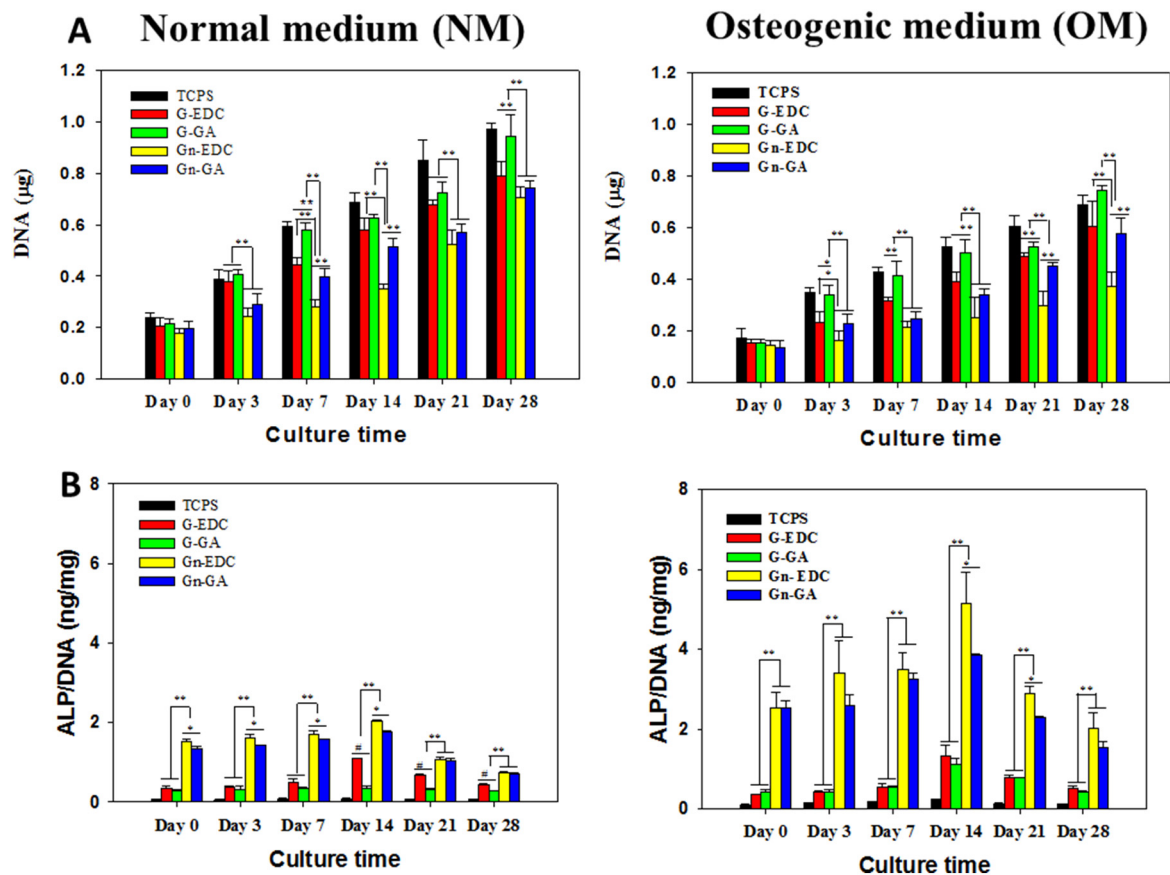


Fig. 7. The DNA content (A) and normalized alkaline phosphatase (ALP) activity when BMSCs (B) were cultured on TCPS and in different cryogels using normal medium (NM) and osteogenic medium (OM). \* $p < 0.05$ , \*\* $p < 0.01$ .

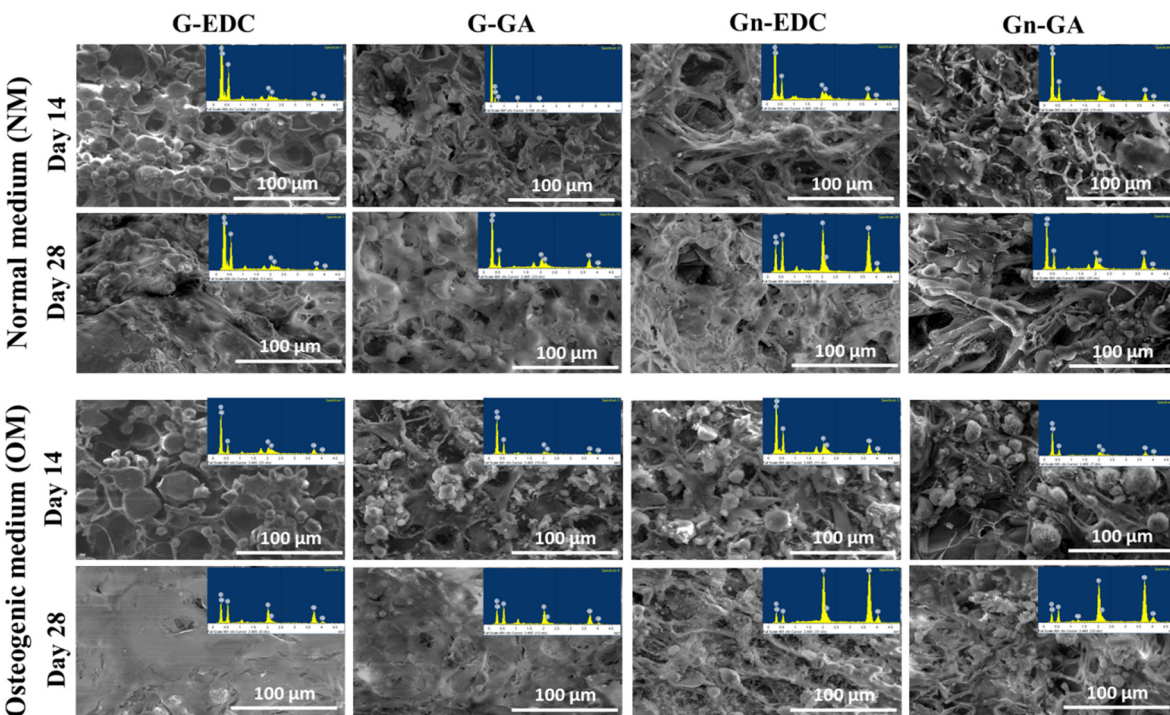


Fig. 8. Scanning electron microscopy/energy dispersive X-ray spectroscopy (SEM/EDS) analysis of the morphology and mineralization of BMSCs when cultured in different cryogels using normal medium (NM) and osteogenic medium (OM).

**Table 3**

The elemental composition analysis when BMSCs cultured in different cryogels for 14 and 28 days by SEM/EDS analysis.

Normal medium (NM)						Induction medium (OM)			
	Element	G-EDC	Gn-EDC	G-GA	Gn-GA	G-EDC	Gn-EDC	G-GA	Gn-GA
14 days	C	73.6%	76.1%	72.0%	75.1%	73.3%	72.11%	69.5%	67.1%
	O	25.3%	21.9%	27.4%	23.3%	24.1%	25.18%	29.4%	30.1%
	Ca	0.63%	1.20%	0.32%	0.99%	1.31%	1.73%	0.59%	1.59%
	P	0.52%	0.77%	0.26%	0.64%	1.26%	1.11%	0.52%	1.04%
	Ca/P ratio	1.21	1.56	1.23	1.55	1.04	1.56	1.13	1.53
28 days	C	55.9%	45.5%	72.8%	68.7%	53.8%	46.3%	49.3%	40.2%
	O	39.3%	43.2%	24.3%	26.8%	39.9%	27.6%	44%	38.0%
	Ca	2.49%	6.45%	1.66%	2.57%	3.33%	15.9%	3.44%	12.9%
	P	2.31%	4.84%	1.24%	1.89%	2.92%	10.17%	3.26%	8.41%
	Ca/P ratio	1.08	1.33	1.34	1.36	1.14	1.56	1.06	1.52

marker with the cell morphology to become more spread. Indeed, BMSCs tended to mineralize through differentiation than proliferation in Gn cryogels as shown from their elevated ALP activity in Fig. 7B. Similar to previous analysis, the synergistic effect on cell mineralization due to nHAP and OM is observed in all cryogel scaffolds. Taken together, both DNA and ALP quantification in Fig. 7 coincide with cell morphology and mineralization from SEM/EDS analysis in Fig. 8.

The quantitative estimation of mineralization through Ca/P atomic ratio was further confirmed through EDS (Table 3). The respective EDS spectrum detected the presence of C, O, Ca and P elements in the mineral deposits but with distinctive scaffold-dependent features. The highest levels of Ca and P were detected for Gn-EDC irrespective of culture medium used. The cortical bone contains calcium phosphate in the form of hydroxyapatite with an ideal Ca to P ratio of 1.67. Therefore, a similar ratio of mineral deposition is much preferable for ideal bone regeneration. The measured Ca/P ratios of G-EDC, G-GA, Gn-EDC and Gn-GA in NM were 1.21, 1.23, 1.56 and 1.55, respectively, while it were 1.04, 1.13, 1.56 and 1.53 in OM after 14 days. Irrespective of culture medium, all Gn cryogels had higher Ca/P ratios than G cryogels and approaching the ideal stoichiometric ratio of 1.67. A similar trend was observed on day 28, where G-EDC, G-GA, Gn-EDC and Gn-GA displayed respective Ca/P ratios of 1.08, 1.34, 1.33, 1.36 for NM and 1.14, 1.06, 1.56 and 1.52 for OM. A lower Ca/P ratio on day 28 may be due to leaching of  $\text{Ca}^{2+}$  ions from the cryogel surface during medium change. Nonetheless, the closer Ca/P ratio of Gn over G cryogels at both time points endorsed the suitability of Gn cryogels as bone tissue engineering scaffolds, with culture in OM could further accelerating the osteogenic differentiation of BMSCs.

### 3.2.3. Quantification of calcium and osteocalcin (OCN)

The calcium deposition observed in various cryogels was critically analyzed for the effect of nHAP, crosslinking agent and culture medium. Calcium deposition by BMSCs initiates at the later stages of the cell proliferation cycle and *in vitro* cell culture duration is much critical in the process of calcium deposition [61]. The calcium ions on cell surface attached to ARS when cryogels were stained with an ARS solution through a chelation process to form  $\text{ARS-Ca}^{2+}$ . In further treatment with CPC, the extracted  $\text{ARS-Ca}^{2+}$  complex in the extraction medium showed an absorbance value ( $\text{OD}_{540}$ ) to provide a direct estimation of the extent of mineralization after normalizing with the DNA content ( $\mu\text{g}$ ). The calcium quantification from mineralization of BMSCs in various cryogels on day 14, 21 or 28 demonstrates the influence of OM over NM in accelerating differentiation of BMSCs (Fig. 9A).

G-EDC and G-GA cryogels showed no significant difference in normalized calcium content throughout the culture period in NM and OM. Nonetheless, the calcium content of Gn-EDC was significantly higher than Gn-GA. Furthermore, the calcium content of Gn was also significantly elevated compared with G. Two scenarios could be suggested to be responsible for the difference in calcium deposition. One is the combined effect of incorporating nHAP and using EDC as the

crosslinking agent, which led to higher mineralization and calcium deposition. The other is the action of inductive factors in OM, which further enhanced the osteogenic differentiation of BMSCs. These are also in line with higher ALP activity (Fig. 7) and more mineral deposition from SEM/EDS (Fig. 8). Similar to previous assumptions, the calcium content measurement announced the superior performance of Gn-EDC cryogel over others as a scaffold for osteogenesis of BMSCs.

The protein concentration of OCN, a marker protein for the bone formation process, was shown in Fig. 9B. The normalized values of OCN on day 7 was similar in NM and OM with no significant difference among all cryogels. Longer durations to 14 and 28 days resulted in more OCN production with higher values in OM than NM. Gn-EDC supported the maximum OCN secretion from BMSCs on day 14 and 28 in both culture media. Similarly, Gn-GA had the second highest OCN, with substantial increase of normalized OCN values from day 7 to 28. Interestingly, Gn-EDC had higher OCN content than that of G-GA on day 14 in NM as well as on day 14 and 28 in OM, which could be correlated with the higher cell proliferation rate and lower cell differentiation rate of BMSCs in G-GA. Being a late stage marker during osteogenic differentiation of BMSCs [62], OCN quantification thus re-assures the advantage of Gn-EDC cryogel over other samples and declares the effect of nHAP-OM synergy in BMSC osteogenesis.

### 3.2.4. Osteogenic gene expression

A crucial evidence of BMSC differentiation is the identification of relevant osteogenic markers during *in vitro* cell culture. While undergoing differentiation, BMSCs undergo three different processes called proliferation, maturation and mineralization, which regulate the up-down expression of various marker genes during early, mid and later stages of cell differentiation [63]. Depending on the substrate and culture environments, the intensity and expression of each marker varies from one to another. ALP, COL I, OCN and OPN are considered the major osteogenic differentiation marker genes with ALP and COL I being the early differentiation markers while OCN and OPN expressed at mid-later stages of BMSC osteogenic differentiation [64].

The relative mRNA expressions of BMSCs in different cryogels in NM and OM are shown in Fig. 10. The ALP expression started to increase on day 3 and further elevated to reach a maximum on day 14 irrespective of culture medium. Similar to previous results, Gn-EDC had the highest ALP gene expression in both media while G-EDC is higher than G-GA but lower than Gn-GA. The ALP gene expression showed drastic down-regulation after day 14 and justified the bone regeneration pattern. Besides, all cryogels had higher relative ALP mRNA expression in OM than NM due to additional induction factors in the medium.

A similar trend followed in COL I expression, where Gn-EDC still dominated over other cryogels and OM resulted in the highest value as seen for ALP. Confirming the early stage marker, the relative mRNA expression of COL I also down-regulated drastically on day 21 and 28 in both culture media to validate the correct osteogenic differentiation

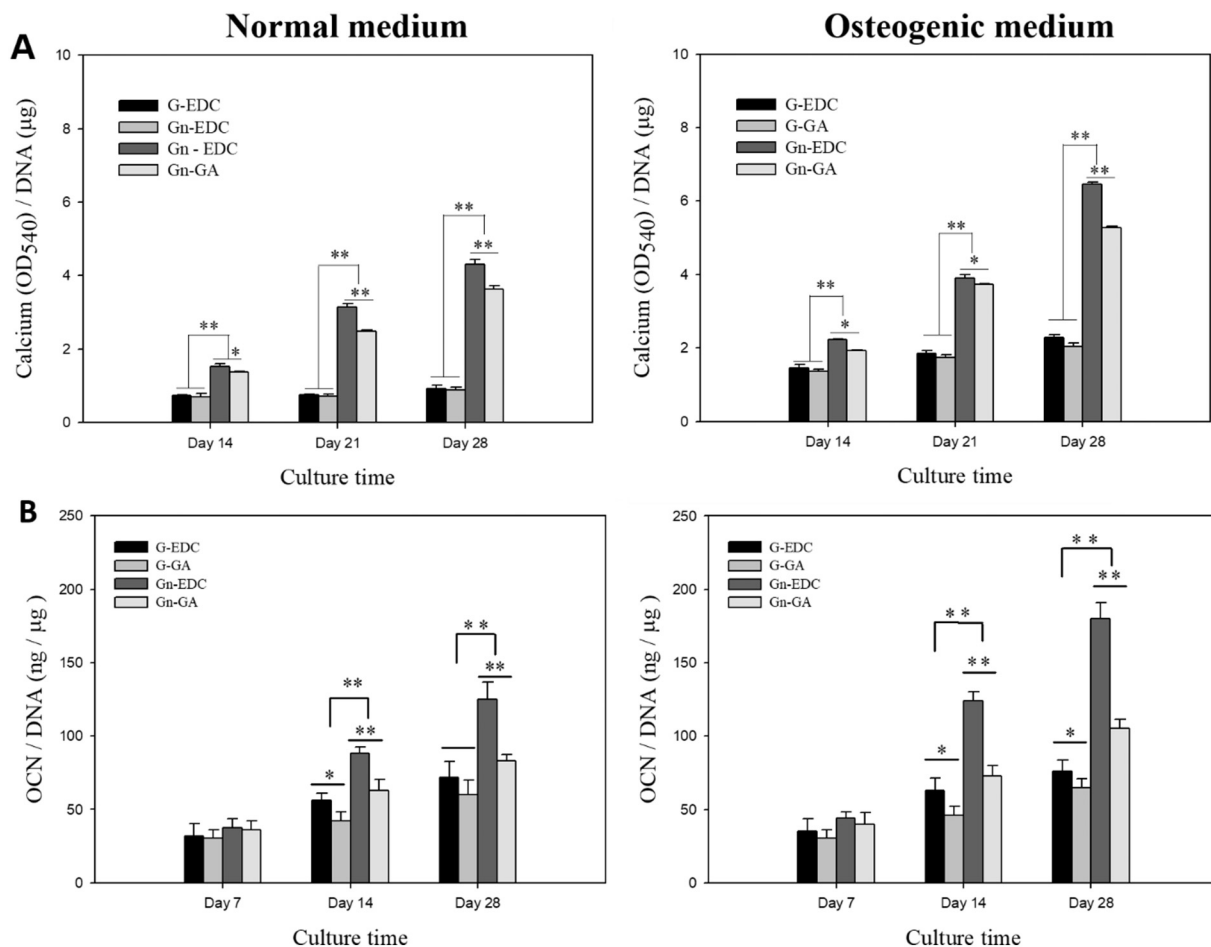


**Fig. 9.** The normalized calcium (A) and osteopontin (OCN) (B) content of BMSCs when cultured in different cryogels using normal medium and osteogenic medium. \* $p < 0.05$ , \*\* $p < 0.01$ .

pattern. In contrast, OCN and OPN illustrated a different gene expression trend as they belong to the mid-late stage markers. Unlike ALP and COL I, the relative mRNA expression of OCN and OPN were much lower on day 3 and 7 in NM and OM but displayed an exponential increase in later periods to reach the maximum on day 21 or 28. Considering Gn-EDC, the maximum mRNA expression of ALP in OM was 1.67 folds that in NM, while COL I, OCN and OPN were upregulated 1.35, 1.38 and 1.42 folds, respectively, taking 14 days as a reference point for ALP and COL I and 28 days for OCN and OPN. Overall, BMSCs in different cryogel scaffolds followed a pattern of osteogenic gene expression in the order of Gn-EDC > Gn-GA > G-EDC > G-GA, which is consistent with the quantitative results observed for ALP activity and calcium and OCN quantifications. Thus qPCR results thus validated the advantage of using Gn-EDC cryogel for faster differentiation of BMSCs to osteoblasts.

### 3.3. *In vitro* dynamic cell culture in a bioreactor

As Gn-EDC provides the best chemical cues for osteogenic differentiation of BMSCs, it was further explored to combine physical cues for osteogenesis through cyclic compression dynamic cell culture (30% and 60% strain) in a bioreactor, by taking advantage of its excellent elastic properties shown in Fig. 5. The effect of mechanical loading of cryogels towards the biological outcome was evaluated based on cell proliferation, ALP activity, mineralization, calcium content, cytoskeletal expression, immunofluorescence staining of COL I and gene expression. In bone tissue engineering, mechanical loading could be an important factor, as it is well known that bone functionally adapts to physical forces. Many reports including *in vivo* studies confirmed the importance

of mechano-sensitivity in modeling and remodeling processes of bone tissue, in the interaction between biomaterial and bone and in fracture healing [65,66]. Fig. 11A reveals the effect of dynamic culture and the extent of compression strain on cell proliferation. BMSCs cultured at 60% strain in dynamic culture showed the highest proliferation rate while 30% strain in dynamic culture resulted in the least cell growth. The cell proliferation rate could be inversely correlated with cell differentiation as shown in Fig. 11B. The highest ALP activity of 30% compressed Gn-EDC cryogel should be due to the effect of mechanical stimulation in NM without osteogenic factors, which serves as a physical cue for osteogenic differentiation. Interestingly, the ALP activity of the dynamic-60% group was much lower while cell proliferation was much higher than that of the static group. This may indicate an adverse effect of over-strained compression on BMSC differentiation during dynamic cell culture [67]. Indeed, the non-linear stress-strain curve of Gn-EDC cryogel under compression (Fig. 4A) indicated that 60% strain caused a shoot up in stress experienced by the cryogel. This may be one of the reasons that BMSCs react adversely to 60% strain rate and resulted in a lower ALP activity even than the static group. In a study reported by Kyung et al. [68], stimulation triggered by moderate 19.3% mechanical strain resulted in differentiation of pre-osteoblasts.

From SEM observations, BMSCs in dynamically cultured cryogel under 30% strain showed abundant mineral deposition while more spread cells covering up the pores could be observed in dynamically cultured cryogel under 60% strain (Fig. 11C). This is due to the combined effect of nHAP and mechanical stimulation to synergistically trigger BMSC differentiation. The effect of mechanical stimulation may be compared with the osteogenic induction factors in OM from the



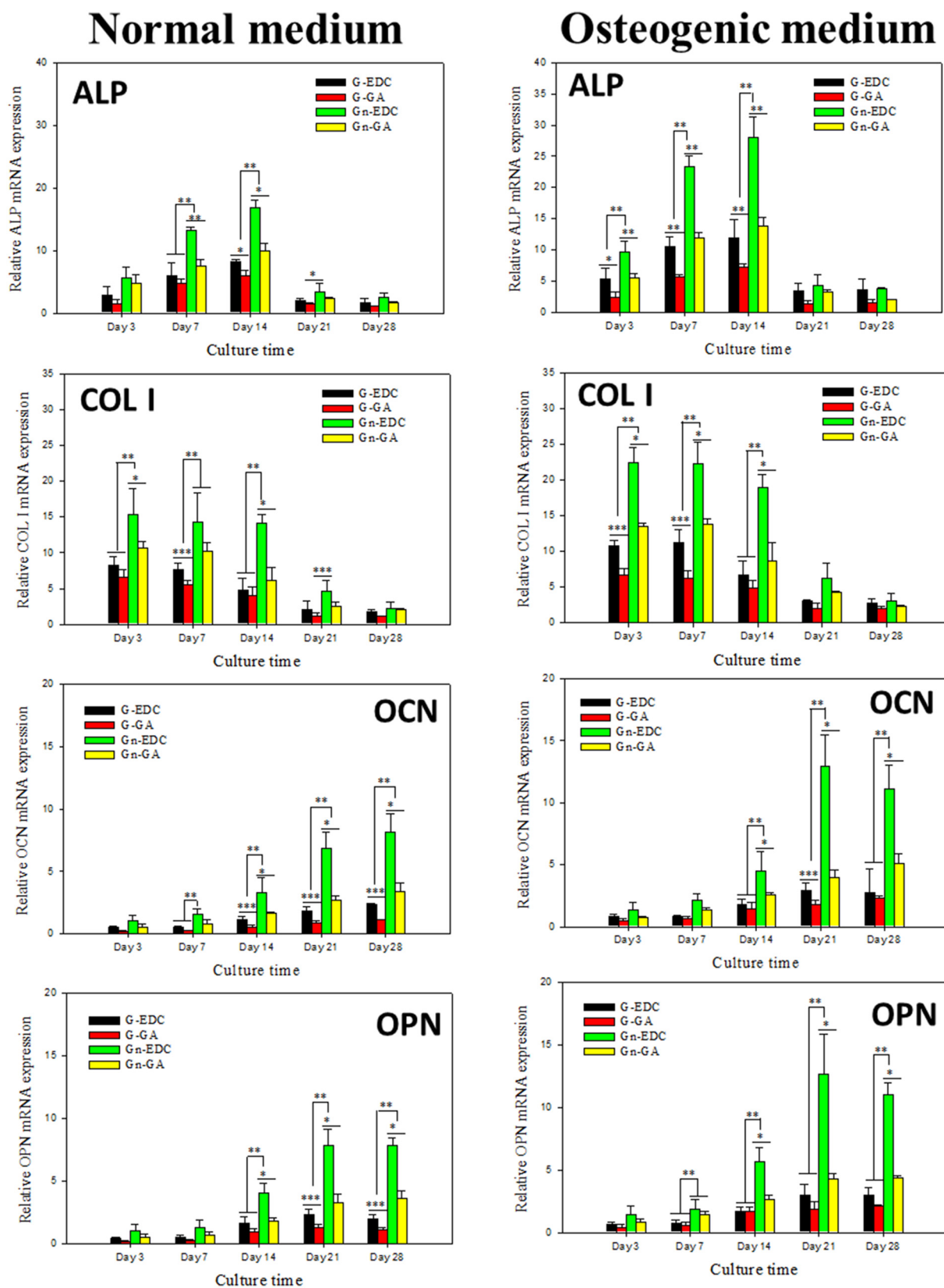


**Fig. 10.** The relative alkaline phosphatase (ALP), collagen type I (COL I), osteocalcin (OCN) and osteopontin (OPN) mRNA expression of BMSCs when cultured in different cryogels using normal medium and osteogenic medium. \* $p < 0.05$ , \*\* $p < 0.01$ .



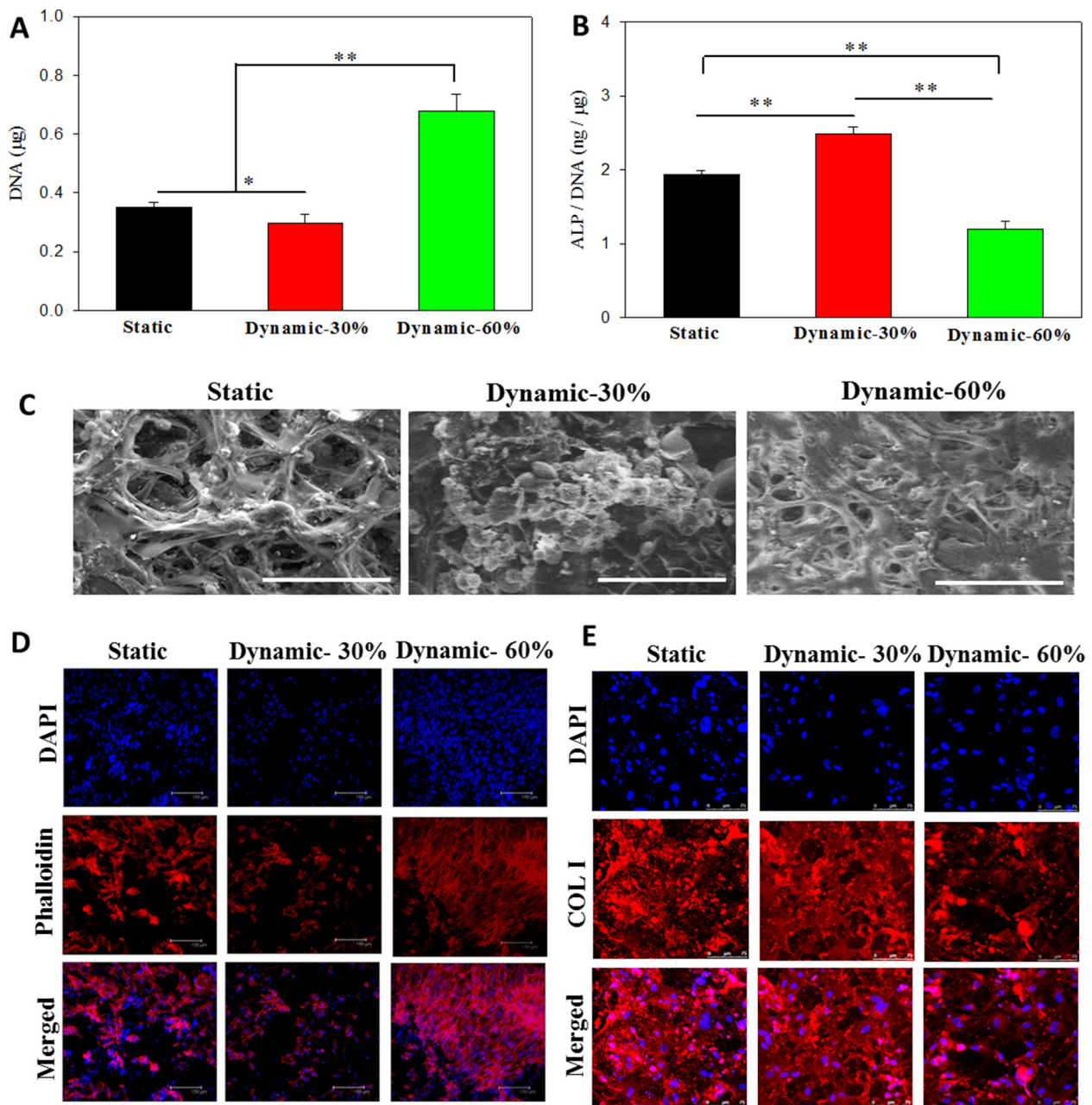


**Fig. 11.** DNA content (A), normalized alkaline phosphatase (ALP) activity (B), SEM/EDS analysis (C, bar = 100 µm), cytoskeletal actin staining by phalloidin conjugation (D, bar = 150 µm) and immunofluorescence staining of collagen type I (COL I) (E, bar = 75 µm) 14 days after static and dynamic culture (30% or 60% compression strain) of BMSCs in Gn-EDC cryogel in normal medium. \* $p < 0.05$ , \*\* $p < 0.01$ .

mineralization of BMSCs in Gn-EDC in Fig. 8. Nonetheless, higher mineral deposition in the dynamic-30% group confirms that mechanical stimulation could induce BMSCs towards the osteogenic lineage even in the absence of osteogenic induction factors [20]. ALP activity and cell mineralization thus reveal that under mechanical stimulation, NM could replace OM for efficient osteogenesis of BMSCs.

The morphology of BMSCs in Gn-EDC cryogel was further validated through staining of the actin cytoskeleton of adhered cells (Fig. 11D). A well-organized arrangement of the phalloidin-conjugated cytoskeleton was observed in static and dynamic-30% groups with DAPI staining confirming cell nuclei, where the anisotropic spreading of cells endorses normal cell spreading pattern. However, a totally different actin filament organization was observed in the dynamic-60% group with more elongated compressed cell spreading pattern. The higher DAPI-stained nuclear density observed in the dynamic-60% group also correlates

with its high cell proliferation rate from DNA quantification (Fig. 11A). Moreover, the merged images also disclose the spatial homogeneity of cellular distribution within the cryogel scaffolds, which is necessary for 3D cellular growth during tissue formation. The effects of cyclic compression on COL I protein production, which is the major protein component of the bone ECM, were further examined from immunofluorescence staining and confocal microscopy. As shown in Fig. 11E, the COL I secreted by BMSCs was stained red using Cy3-conjugated secondary antibody while the blue color was due to DAPI-stained nuclei. Uniform distribution of COL I was confirmed with the 60%-dynamic group showing relatively the lowest COL I fluorescence intensity. A semi-quantitative evaluation of COL I content was performed using an image analysis software (PAX-it!™) to compare the COL I content. For this purpose, the area percentages of red-stained COL I were normalized with the cell number from DAPI staining in each confocal

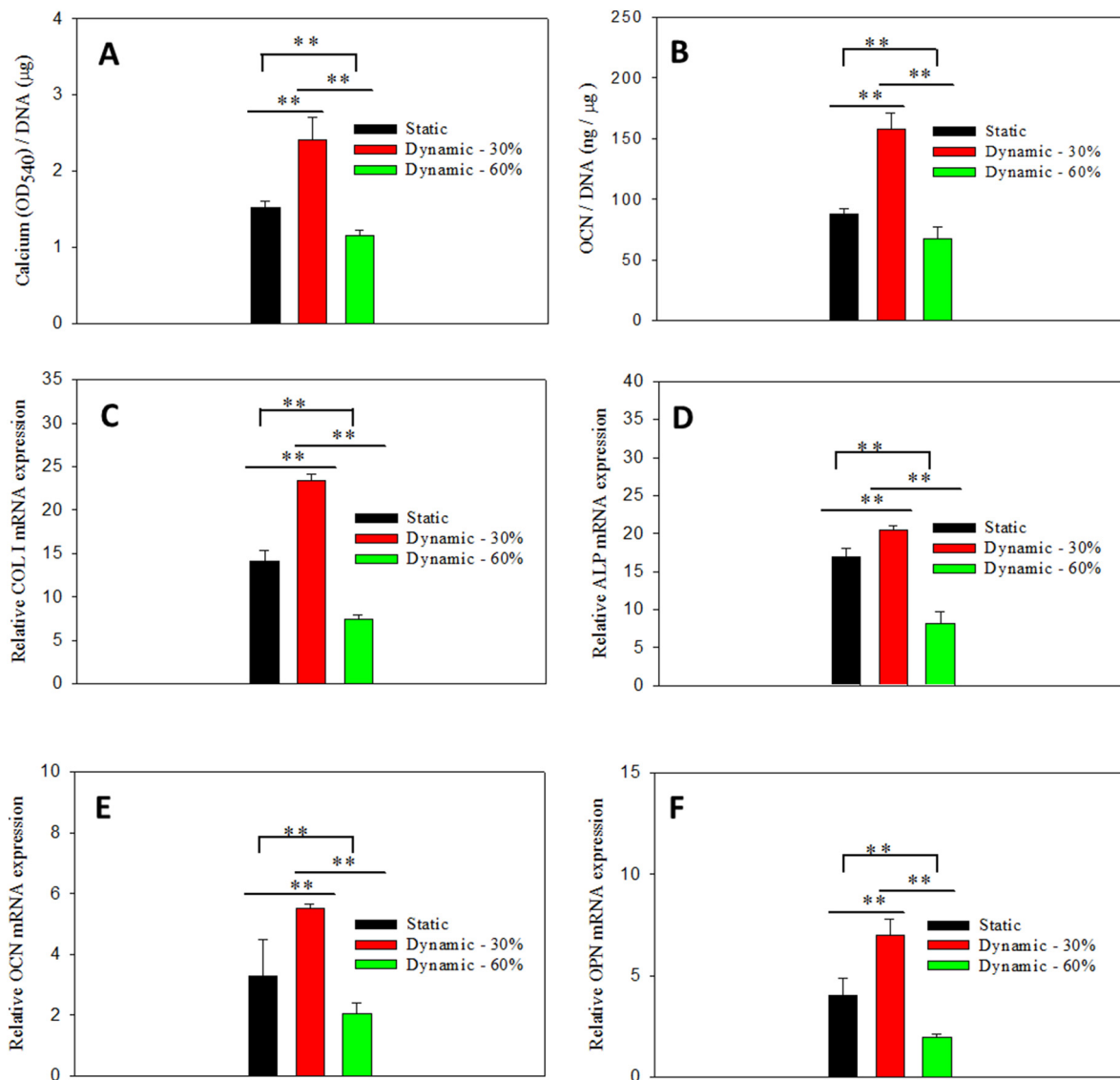


**Fig. 12.** Normalized calcium content (A), OCN content (B) and relative mRNA expression of COL I (C), ALP (D), OCN (E) and OPN (F) 14 days after static and dynamic culture (30% or 60% compression strain) of BMSCs in Gn-EDC cryogels. \*\* $p < 0.01$ .

image. The normalized COL I contents were 0.88, 1.36 and 0.28 for static, dynamic-30% and dynamic-60%, respectively. Similar to ALP production, static culture resulted in 3.1-fold specific COL I production over dynamic-60%, while dynamic-30% resulted in 4.9-fold specific COL I production over dynamic-60%. All results cross-confirm that dynamic culture with 30% strain offered the best culture condition for BMSC differentiation towards osteoblasts.

From Fig. 12A, the calcium content through static culture was compared with both dynamic cultured cryogels and the values after normalized to DNA content were reported in terms of optical density (OD<sub>540</sub>). Similar to previous results, 30% dynamic culture resulted in the highest calcium deposition while 60% the lowest. Specifically, the OD<sub>540</sub>/DNA value of the dynamic-30% group was 1.57 and 2.09 folds that of the static and dynamic-60% groups, confirming the advantage of a lower compression ratio towards cell differentiation. It is interesting to note that the mean normalized calcium content (OD<sub>540</sub>/μg) of Gn-EDC in OM with static culture was ~2.1 on day 14 (Fig. 9A). In comparison, dynamic culture in NM at 30% compression ratio was ~2.4 at the same time point. All findings extrapolating the dominance of low level dynamic compression of cryogels towards faster mineral deposition was further re-verified through OCN quantification (Fig. 12B).

Indeed, the trend of normalized OCN value was similar to that shown for calcium quantification in the order of dynamic-30% > static > dynamic-60%. All results are consistent with the lower cell proliferation rate and higher ALP production (Fig. 11A, B), higher mineral deposition from SEM/EDS images (Fig. 11C) as well as higher COL I production (Fig. 11E) observed earlier.

By assessing the expression of relevant osteogenic marker genes through q-PCR, the specific mRNA expression levels of COL I (Fig. 12C), ALP (Fig. 12D), OCN (Fig. 12E) and OPN (Fig. 12F) followed the same trend as observed for ALP activity, calcium deposition and OCN quantification with dynamic-30% > static > dynamic-60%. Being early and mid-stage differentiation genes, COL I and ALP had the highest expression values of 20.5 and 23.4, in comparison to 5.5 and 7.0 for the late expressing OCN and OPN in the dynamic-30% group on day 14. Those values could be compared with the relative mRNA expression levels of BMSCs in Gn-EDC under static culture in OM, which were 19.0, 28.0, 4.5 and 5.7 for COL I, ALP, OCN and OPN, respectively (Fig. 10). The similar gene expression patterns thus points out the fact that dynamic culture at 30% compression could induce osteogenic differentiation of BMSCs to the same extent as that induced by osteogenic factors in OM during static culture. Taken together, we concluded



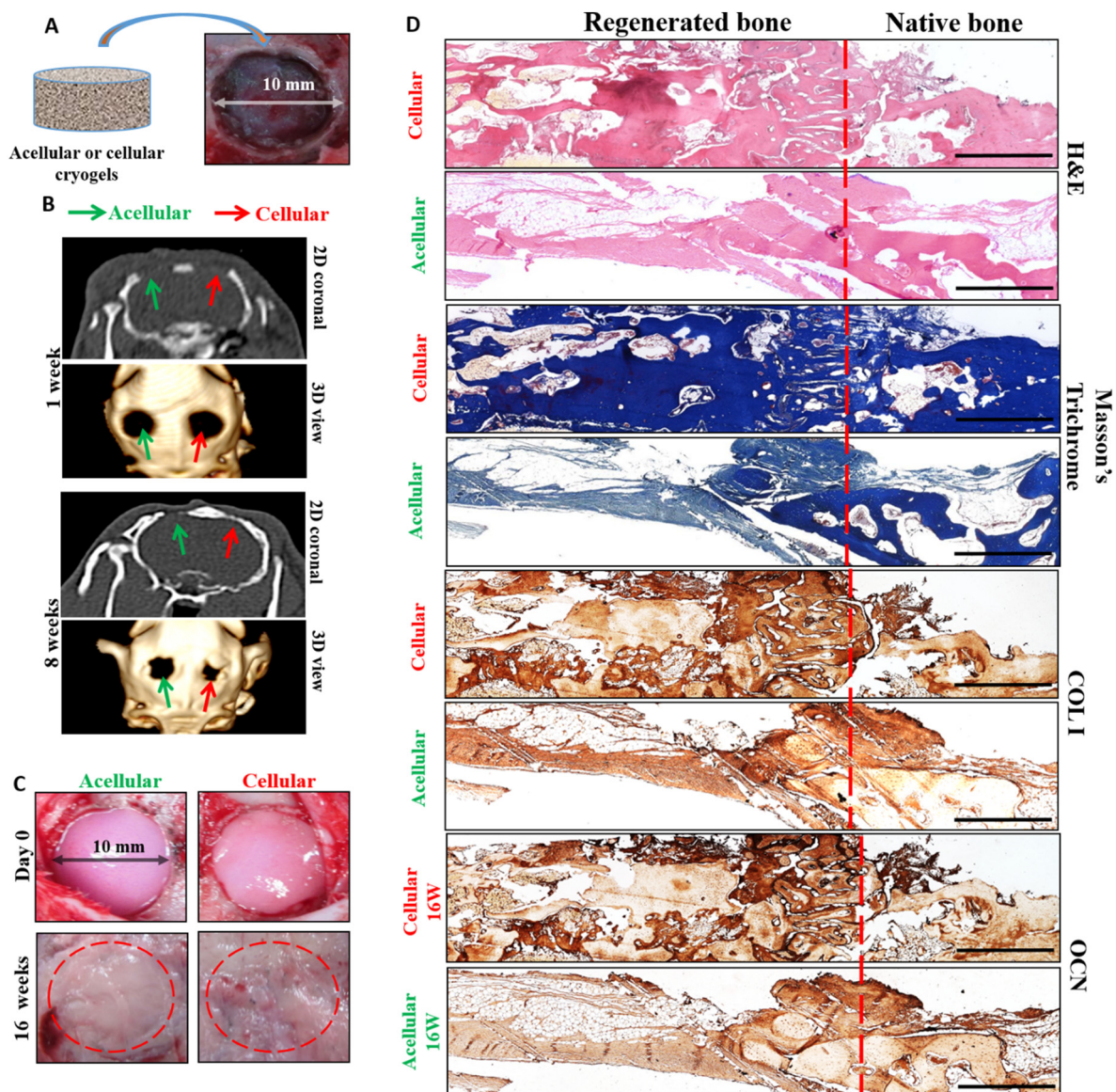


**Fig. 13.** (A) The schematic of acellular or cellular cryogel implantation in 10-mm rabbit cranial bone defect. (B) 2D coronal and 3D computed tomography (CT) images 1 and 8 weeks post-implantation of acellular or cellular cryogels. The green arrow denotes the defect site implanted with an acellular cryogel while the red arrow represents the site implanted with a cellular cryogel. (C) Gross views of cranial bone defect sites immediately after surgery and 16 weeks post-implantation. (D) Histological (H&E, Masson's trichrome) staining and immunohistochemical staining of COL I and OCN of the cellular and acellular samples 16 weeks post-implantation (bar = 500  $\mu$ m). (For interpretation of the references to color in this figure legend, the reader is referred to the web version of this article.)

that dynamic culture of BMSCs in Gn-EDC cryogels in a bioreactor with 30% compression strain provides effective physical cues for osteogenic differentiation of BMSCs.

### 3.4. In vivo animal studies

As *in vitro* dynamic cell culture experiments revealed the significance of mechanical stimulation in a bioreactor for osteogenic differentiation of BMSCs in Gn-EDC cryogels using NM, *in vivo* animal experiments followed to confirm the bone formation ability of *in vitro* cultured scaffold/cell constructs. Fig. 13A is the schematic of implantation of acellular or cellular cryogels in rabbit calvarial 10-mm critical size defects. The Gn-EDC/BMSCs constructs dynamically cultured at 30% strain in NM for 14 days were implanted in the right cranial bone defects (cellular) while blank Gn-EDC cryogels (acellular) were implanted in the left cranial bone defects for comparison.

All animals were allowed to undergo CT evaluation 1 and 8 weeks post-operation (Fig. 13B), where the top panel at each time point

displays the 2D coronal view while the bottom panel shows the 3D reconstructed image. The green arrow denotes the defect site implanted with an acellular cryogel while the red arrow represents the site implanted with a cellular cryogel in the CT images. No distinguishable difference between each defect site was observed from the CT images after 1 week as the broken white line in the 2D coronal view and the empty hole in the 3D CT image indicated no new bone formation at the defect sites for both groups. The CT image density of the acellular group scarcely increased after 8 weeks. In contrast, the image density of the cellular group elevated significantly and the broken white line from the 2D image or the empty hole from the 3D image was partially filled, indicating new bone formation. New bone tissue bridging the defect site to the surrounding bone was only observed for the cellular group in the 2D coronal view with the defect diameter shrinking to a much smaller size in the 3D view (Fig. 13B).

After anesthetization, all animals were euthanized for gross view observation and specimen were removed for histology 16 weeks post-implantation (Fig. 13C). From gross view, both implanted sites

appeared to be normal without swelling or necrosis while clinical complications like infection, wound breakdown or exudate were not observed. The acellular site appeared to be softer and whitish compared to the uniform hard nature of the cellular site (circled within red dotted lines). Slight red spots found within the cellular sample may be due to new blood vessel formation, which is beneficial for bone regeneration.

Histological evaluation of new bone formation and tissue development was further confirmed through H&E and Masson's trichrome staining and IHC staining of COL I and OCN (Fig. 13D). An average of eight images were recorded for each stained image and stitched together using a commercial software to show the repaired site and its surroundings to include both native bone and regenerated bone for comparison. The H&E staining showed drastic difference in cell number in the form of osteoblasts between cellular and acellular groups. For the cellular group, a uniform cellular distribution was observed throughout the regenerated area and the ECM was oriented in a native fashion indicating growth of bone tissue in the defect region. However, the acellular group had neither cell proliferation nor ECM deposition within the center, with cells found only in the marginal area due to cell migration from peripheral native bone.

Bone regeneration was further verified through Masson's trichrome staining. Osteoid, the un-mineralized organic portion of the bone matrix, will be secreted by osteoblasts during differentiation of BMSCs and embedded in the newly formed bone tissue matrix. Since mineralized osteoid will combine with adjacent bone cells and develop into new bone tissue, a blue staining through Masson's trichrome provides a good indication of new bone formation. As shown in Fig. 13D, the cellular group had deep blue-colored stains throughout the section and had no difference in intensity from surrounding native bone, which accounts for osteoid formation and bone regeneration. The acellular group revealed significantly lower level of staining intensity and the light blue color observed in the defect region close to the native bone should be due to post-operative osteoblast migration from the native tissue and thus accounts for the presence of few nuclei as observed from H&E stain. Although the color intensity in the native bone area of the acellular group was similar to that of the cellular group, the dominant white empty area in the defect region of the acellular group clearly implies the lack of regeneration in the absence of BMSCs. Indeed, the empty white region in the acellular group symbolizes the lack of regeneration while the dark blue color in the cellular group defines the presence of mature bone with the formation of new osteoid bodies.

It should be pointed out that although successful repair of rabbit critical-sized cranial bone defect was demonstrated using mechanically stimulated BMSCs in Gn-EDC cryogels, the bone regeneration effect may not be very high. We ascribe this limitation to the time of observation, which was only 8 weeks post-implantation. Besides, no osteogenic growth factor was incorporated in the scaffolds while the cell/scaffold construct was cultured *in vitro* dynamically in NM for 14 days before implantation. Despite the excellent biocompatibility and osteoconductivity of nHAP, Gn-EDC cryogels may not have high osteoinductivity for bone tissue engineering application [69]. Incorporation of osteoinductive materials in the composite cryogel should be an appealing strategy to enhance the osteogenic differentiation of seeded BMSCs [70]. We believe that higher bone regeneration ability could be accomplished by employing a longer implantation time (e.g. 16 weeks) or by introducing bone morphogenetic protein 2 (BMP-2) to the composite cryogel scaffolds as demonstrated from our previous study [22].

Other than confirmation of cellular distribution of differentiated BMSCs and the presence of newly formed bone tissue by H&E and Masson's trichrome staining, the presence of bone marker proteins in the ECM was confirmed by IHC staining of COL I and OCN (Fig. 13D). Positive staining of COL I and OCN could confirm bone regeneration through mid-later stage osteogenic differentiation. The brown color intensity in the tissue section of the cellular sample was much higher compared to the acellular sample, both for COL I and OCN. The uniform distribution of intense brown color throughout the cellular sample

confirms that BMSCs proliferated in a 3D fashion throughout the cryogel scaffold and differentiated into osteoblasts. The uniform cellular distribution and cell differentiation should have been achieved through the interconnected macro-porous structure of BMSC-seeded cryogels while the low intensity brown color with empty white background observed for the acellular cryogel proves the lack of bone formation in the absence of BMSCs. In short, both histology and IHC staining conclude the superior bone regeneration efficacy of mechanically stimulated BMSC-seeded Gn-EDC cryogels for effective bone replacement or repair.

#### 4. Conclusions

Cryogel scaffolds for bone tissue engineering applications could be prepared from 5% gelatin solution with or without replacing half gelatin with nHAP, using two different cross-linking agents (EDC and GA). SEM analysis confirmed the macroporous morphology with interconnected pores for all cryogels while FTIR, XRD and EDS revealed the presence of nHAP in composite cryogels. nHAP incorporation did not significantly influence the structure of the cryogels with ~80% porosity to be ideal for bone regeneration. G cryogels had significantly higher swelling ratios in water than Gn. Incorporation of nHAP in cryogels leads to faster *in vitro* degradation rates concomitant with lower degrees of crosslinking. Cryogels crosslinked with GA displayed higher degradation resistance and lesser swelling in water due to denser polymer network formation, which was also revealed from their better mechanical properties. Static *in vitro* culture confirmed the dominance of Gn-EDC cryogel cultured in OM towards BMSC differentiation. Gn-EDC seeded with BMSCs and cultured dynamically in a bioreactor with a moderate (30%) strain was the best culture condition for faster bone regeneration *in vitro*. This *in vitro* cultured cell/scaffold construct was useful for repair of rabbit cranial bone defect *in vivo* from CT and histology analysis. In short, our results first revealed change in physical properties due to nHAP-incorporation and the use of different cross-linking agents (EDC and GA), followed by revealing the dominance of EDC over GA on BMSC osteogenic differentiation. It further demonstrated enhanced osteogenesis efficacy of BMSCs in Gn-EDC cryogels through dynamic culture with a properly chosen mechanical stimulation condition in a bioreactor. Finally, such *in vitro*-cultured constructs could be useful for bone repair in an animal model. Therefore, by exploring chemical and physical cues offered by cryogels for bone regeneration using BMSCs *in vitro* and *in vivo*, this study could be taken as an ideal reference in process development of advanced biomaterials for bone tissue engineering.

#### Acknowledgements

This work was supported by Chang Gung Memorial Hospital (CMRPD3G0082, CRRPD2G0011, CRRPD2G0012, CRRPG3G0011, CRRPG3G0012, BMRP249) and Ministry of Science and Technology, Taiwan, ROC (MOST106-2314-B-182-013-MY2). The Microscope Core Laboratory, Chang Gung Memorial Hospital, Linkou is acknowledged for the expert technical assistance.

#### References

- [1] J.L. Drury, D.J. Mooney, Hydrogels for tissue engineering: scaffold design variables and applications, *Biomaterials* 24 (2003) 4337–4351.
- [2] M.P. Lutolf, J.A. Hubbell, Synthetic biomaterials as instructive extracellular microenvironments for morphogenesis in tissue engineering, *Nat. Biotechnol.* 23 (2005) 47–55.
- [3] G. Iviglia, C. Cassinelli, D. Bollati, F. Bairo, E. Torre, M. Morra, C. Vitale-Brovarone, Engineered porous scaffolds for periprosthetic infection prevention, *Mater. Sci. Eng. C* 68 (2016) 701–715.
- [4] K.Y. Lee, D.J. Mooney, Hydrogels for tissue engineering, *Chem. Rev.* 101 (2001) 1869–1880.
- [5] B. Balakrishnan, N. Joshi, A. Jayakrishnan, R. Banerjee, Self-crosslinked oxidized alginate/gelatin hydrogel as injectable, adhesive biomimetic scaffolds for cartilage



- regeneration, *Acta Biomater.* 10 (2014) 3650–3663.
- [6] S.A. Poursamar, J. Hatami, A.N. Lehner, C.L. da Silva, F.C. Ferreira, A.P.M. Antunes, Potential application of gelatin scaffolds prepared through in situ gas foaming in skin tissue engineering, *Int. J. Polym. Mater. Polym. Biomater.* 65 (2016) 315–322.
  - [7] X. Liu, L.A. Smith, J. Hu, P.X. Ma, Biomimetic nanofibrous gelatin/apatite composite scaffolds for bone tissue engineering, *Biomaterials* 30 (2009) 2252–2258.
  - [8] D.B. Burr, O. Akkus, Bone morphology and organization, in: D.B. Burr, M.R. Allen (Eds.), *Basic and Applied Bone Biology*, Academic Press, San Diego, 2014, pp. 3–25.
  - [9] H.-W. Kim, J.-H. Song, H.-E. Kim, Nanofiber generation of gelatin-hydroxyapatite biomimetics for guided tissue regeneration, *Adv. Func. Mater.* 15 (2005) 1988–1994.
  - [10] H. Kim, L. Che, Y. Ha, W. Ryu, Mechanically-reinforced electrospun composite silk fibroin nanofibers containing hydroxyapatite nanoparticles, *Mater. Sci. Eng. C* 40 (2014) 324–335.
  - [11] J. Venkatesan, S.K. Kim, Nano-hydroxyapatite composite biomaterials for bone tissue engineering - a review, *J. Biomed. Nanotechnol.* 10 (2014) 3124–3140.
  - [12] H. Zhou, J. Lee, Nanoscale hydroxyapatite particles for bone tissue engineering, *Acta Biomater.* 7 (2011) 2769–2781.
  - [13] E. Pepla, L.K. Besharat, G. Palaia, G. Tenore, G. Migliau, Nano-hydroxyapatite and its applications in preventive, restorative and regenerative dentistry: a review of literature, *Ann. Stomatol.* 5 (2014) 108–114.
  - [14] L. Meirelles, A. Arvidsson, M. Andersson, P. Kjellin, T. Albrektsson, A. Wennerberg, Nano hydroxyapatite structures influence early bone formation, *J. Biomed. Mater. Res. Part A* 87 (2008) 299–307.
  - [15] J. Ji, X. Tong, X. Huang, T. Wang, Z. Lin, Y. Cao, J. Zhang, L. Dong, H. Qin, Q. Hu, Sphere-shaped nano-hydroxyapatite/chitosan/gelatin 3D porous scaffolds increase proliferation and osteogenic differentiation of human induced pluripotent stem cells from gingival fibroblasts, *Biomed. Mater.* 10 (2015) 045005.
  - [16] S.A. Bencherif, T.M. Braschler, P. Renaud, Advances in the design of macroporous polymer scaffolds for potential applications in dentistry, *J. Periodontal Implant Sci.* 43 (2013) 251–261.
  - [17] Y. Privar, I. Malakhova, A. Pestov, A. Fedorets, Y. Azarova, S. Schwarz, S. Bratskaya, Polyethyleneimine cryogels for metal ions sorption, *Chem. Eng. J.* 334 (2018) 1392–1398.
  - [18] K.H. Chang, H.T. Liao, J.P. Chen, Preparation and characterization of gelatin/hyaluronic acid cryogels for adipose tissue engineering: in vitro and in vivo studies, *Acta Biomater.* 9 (2013) 9012–9026.
  - [19] A. Sharma, S. Bhat, V. Nayak, A. Kumar, Efficacy of supermacroporous poly(ethylene glycol)-gelatin cryogel matrix for soft tissue engineering applications, *Mater. Sci. Eng. C* 47 (2015) 298–312.
  - [20] J.R. Mauney, S. Sjöström, J. Blumberg, R. Horan, J.P. O'Leary, G. Vunjak-Novakovic, V. Volloch, D.L. Kaplan, Mechanical stimulation promotes osteogenic differentiation of human bone marrow stromal cells on 3-D partially demineralized bone scaffolds in vitro, *Calcified Tissue Int.* 74 (2004) 458–468.
  - [21] E.Y. Chao, N. Inoue, Biophysical stimulation of bone fracture repair, regeneration and remodeling, *Eur. Cells & Mater.* 6 (2003) 72–84.
  - [22] H.-T. Liao, K.T. Shalumon, K.-H. Chang, C. Sheu, J.-P. Chen, Investigation of synergistic effects of inductive and conductive factors in gelatin-based cryogels for bone tissue engineering, *J. Mater. Chem. B* 4 (2016) 1827–1841.
  - [23] E. Saino, L. Fassina, S. Van Vlierberghe, M.A. Avanzini, P. Dubrue, G. Magenes, L. Visai, F. Benazzo, Effects of electromagnetic stimulation on osteogenic differentiation of human mesenchymal stromal cells seeded onto gelatin cryogel, *Int. J. Immunopathology & Pharma* 24 (2011) 1–6.
  - [24] L. Fassina, E. Saino, L. Visai, J. Schelfhout, M. Dierick, L. Van Hoorbeke, P. Dubrue, F. Benazzo, G. Magenes, S. Van Vlierberghe, Electromagnetic stimulation to optimize the bone regeneration capacity of gelatin-based cryogels, *Int. J. Immunopathology & Pharma* 25 (2012) 165–174.
  - [25] L. Fassina, L. Visai, G. Magenes, J. Schelfhout, N. Bloise, F. Riva, C. Omes, M.A. Avanzini, M.G.C.D. Angelis, F. Benazzo, M. Dierick, L.V. Hoorbeke, P. Dubrue, S.V. Vlierberghe, Ultrasound stimulus to enhance the bone regeneration capability of gelatin cryogels, 2013 35th Annual International Conference of the IEEE Engineering in Medicine and Biology Society, 2013, pp. 846–849.
  - [26] R. Mishra, D.B. Raina, M. Pelkonen, L. Lidgren, M. Tagil, A. Kumar, Study of in vitro and in vivo bone formation in composite cryogels and the influence of electrical stimulation, *Int. J. Biol. Sci.* 11 (2015) 1325–1336.
  - [27] Y. Yang, J.L. Magnay, L. Cooling, H.A. El, Development of a 'mechano-active' scaffold for tissue engineering, *Biomaterials* 23 (2002) 2119–2126.
  - [28] T. Davissón, S. Kunig, A. Chen, R. Sah, A. Ratcliffe, Static and dynamic compression modulate matrix metabolism in tissue engineered cartilage, *J. Orthop. Res.* 20 (2002) 842–848.
  - [29] B.S. Kim, D.J. Mooney, Scaffolds for engineering smooth muscle under cyclic mechanical strain conditions, *J. Biomech. Eng.* 122 (2000) 210–215.
  - [30] W.H. Zimmermann, K. Schneiderbanger, P. Schubert, M. Didie, F. Munzel, J.F. Heubach, S. Kostin, W.L. Neuhuber, T. Eschenhagen, Tissue engineering of a differentiated cardiac muscle construct, *Circulation Res* 90 (2002) 223–230.
  - [31] W.-J. Shih, Y.-F. Chen, M.-C. Wang, M.-H. Hon, Crystal growth and morphology of the nano-sized hydroxyapatite powders synthesized from  $\text{CaHPO}_4 \cdot 2\text{H}_2\text{O}$  and  $\text{CaCO}_3$  by hydrolysis method, *J. Crystal Growth* 270 (2004) 211–218.
  - [32] K.S. Rho, L. Jeong, G. Lee, B.-M. Seo, Y.J. Park, S.-D. Hong, S. Roh, J.J. Cho, W.H. Park, B.-M. Min, Electrospinning of collagen nanofibers: effects on the behavior of normal human keratinocytes and early-stage wound healing, *Biomaterials* 27 (2006) 1452–1461.
  - [33] A. Jena, K. Gupta, Characterization of pore structure of filter media, *Fluid - Particle Sep. J.* 14 (2002) 227–241.
  - [34] A.F.S.A. Habeeb, Determination of free amino groups in proteins by trinitrobenzenesulfonic acid, *Anal. Biochem.* 14 (1966) 328–336.
  - [35] S.L.Y. Woo, M.A. Gomez, W.H. Akeson, The time and history-dependent viscoelastic properties of the canine medial collateral ligament, *J. Biomech. Eng.* 103 (1981) 293–298.
  - [36] C.H. Chen, C.Y. Kuo, J.P. Chen, Effect of cyclic dynamic compressive loading on chondrocytes and adipose-derived stem cells co-cultured in highly elastic cryogel scaffolds, *Int. J. Mol. Sci.* 19 (2018) 370.
  - [37] Y.-J. Kim, R.L.Y. Sah, J.-Y.H. Doong, A.J. Grodzinsky, Fluorometric assay of DNA in cartilage explants using Hoechst 33258, *Anal. Biochem.* 174 (1988) 168–176.
  - [38] G.J. Lai, K.T. Shalumon, S.H. Chen, J.P. Chen, Composite chitosan/silk fibroin nanofibers for modulation of osteogenic differentiation and proliferation of human mesenchymal stem cells, *Carbohydr. Polym.* 111 (2014) 288–297.
  - [39] G.M. Cunniffe, C.M. Curtin, E.M. Thompson, G.R. Dickson, F.J. O'Brien, Content-dependent osteogenic response of nanohydroxyapatite: an in vitro and in vivo assessment within collagen-based scaffolds, *Int. J. Mol. Sci.* 8 (2016) 23477–23488.
  - [40] Y.J. Hwang, J. Granelli, J. Lyubovitsky, Effects of zero-length and non-zero-length cross-linking reagents on the optical spectral properties and structures of collagen hydrogels, *Int. J. Mol. Sci.* 4 (2012) 261–267.
  - [41] C.P. Barnes, C.W. Pemble, D.D. Brand, D.G. Simpson, G.L. Bowlin, Cross-linking electrospun type II collagen tissue engineering scaffolds with carbodiimide in ethanol, *Tissue Eng.* 13 (2007) 1593–1605.
  - [42] J.E. Eastoe, The amino acid composition of mammalian collagen and gelatin, *Biochem. J.* 61 (1955) 589–600.
  - [43] S.N. Park, H.J. Lee, K.H. Lee, H. Suh, Biological characterization of EDC-crosslinked collagen-hyaluronic acid matrix in dermal tissue restoration, *Biomaterials* 24 (2003) 1631–1641.
  - [44] G.P. Huang, S. Shanmugasundaram, P. Masih, D. Pandya, S. Amara, G. Collins, T.L. Arinze, An investigation of common crosslinking agents on the stability of electrospun collagen scaffolds, *J. Biom. Mater. Res. Part A* 103 (2015) 762–771.
  - [45] J. Sundaram, T.D. Durance, R. Wang, Porous scaffold of gelatin-starch with nanohydroxyapatite composite processed via novel microwave vacuum drying, *Acta Biomater.* 4 (2008) 932–942.
  - [46] M. Peter, N. Ganesh, N. Selvamurugan, S.V. Nair, T. Furuike, H. Tamura, R. Jayakumar, Preparation and characterization of chitosan-gelatin/nanohydroxyapatite composite scaffolds for tissue engineering applications, *Carbohydr. Polym.* 80 (2010) 687–694.
  - [47] I. Inci, H. Kirsebom, I.Y. Galaev, B. Mattiasson, E. Piskin, Gelatin cryogels cross-linked with oxidized dextran and containing freshly formed hydroxyapatite as potential bone tissue-engineering scaffolds, *J. Tissue Eng. Regen. Med.* 7 (2013) 584–588.
  - [48] S.J. Hollister, W.L. Murphy, Scaffold translation: barriers between concept and clinic, *Tissue Engineering Part B* 17 (2011) 459–474.
  - [49] G. Turnbull, J. Clarke, F. Picard, P. Riches, L. Jia, F. Han, B. Li, W. Shu, 3D bioactive composite scaffolds for bone tissue engineering, *Bioact. Mater.* 3 (2018) 278–314.
  - [50] A.K. Shakyia, U. Kandam, Three-dimensional macroporous materials for tissue engineering of craniofacial bone, *Brit. J. Oral. Max. Sur.* 55 (2017) 875–891.
  - [51] K.R. Hixon, T. Lu, S.A. Sell, A comprehensive review of cryogels and their roles in tissue engineering applications, *Acta Biomater.* 62 (2017) 29–41.
  - [52] M.M. Villa, L. Wang, J. Huang, D.W. Rowe, M. Wei, Bone tissue engineering with a collagen-hydroxyapatite scaffold and culture expanded bone marrow stromal cells, *J. Biomed. Mater. Res. Part B* 103 (2015) 243–253.
  - [53] C.H. Chen, C.Y. Kuo, Y.J. Wang, J.P. Chen, Dual function of glucosamine in gelatin/hyaluronic acid cryogel to modulate scaffold mechanical properties and to maintain chondrogenic phenotype for cartilage tissue engineering, *Int. J. Mol. Sci.* 17 (2016) 1959.
  - [54] P. Abdel-Sayed, S.E. Darwiche, U. Kettenberger, D.P. Pioletti, The role of energy dissipation of polymeric scaffolds in the mechanobiological modulation of chondrogenic expression, *Biomaterials* 35 (2014) 1890–1897.
  - [55] E. Tsidis, A. Bhalla, Z. Ali, N. Gurav, M. Heliotis, S. Deb, L. DiSilvio, Enhancing the osteoinductive properties of hydroxyapatite by the addition of human mesenchymal stem cells, and recombinant human osteogenic protein-1 (BMP-7) in vitro, *Injury* 37 (Suppl. 3) (2006) S25–S32.
  - [56] I. Nishimura, R. Hisanaga, T. Sato, T. Arano, S. Nomoto, Y. Ikada, M. Yoshinari, Effect of osteogenic differentiation medium on proliferation and differentiation of human mesenchymal stem cells in three-dimensional culture with radial flow bioreactor, *Regen. Ther.* 2 (2015) 24–31.
  - [57] G.M. Boland, G. Perkins, D.J. Hall, R.S. Tuan, Wnt 3a promotes proliferation and suppresses osteogenic differentiation of adult human mesenchymal stem cells, *J. Cell. Biochem.* 93 (2004) 1210–1230.
  - [58] R.S. Siffert, The role of alkaline phosphatase in osteogenesis, *J. Exp. Med.* 93 (1951) 415–426.
  - [59] B.H. C., L.Q. C., L. Yanan, L. Hang, B.-S. Donna, L. Li, T.R. S., R.L. J., S.P. H., N.D. J., Osteoblast differentiation and bone matrix formation in vivo and in vitro, *Tissue Eng. Part B: Reviews* 23 (2017) 268–280.
  - [60] G. Toskas, C. Cherif, R.D. Hund, E. Laourine, B. Mahltig, A. Fahmi, C. Heinemann, T. Hanke, Chitosan(PEO)/silica hybrid nanofibers as a potential biomaterial for bone regeneration, *Carbohydr. Polym.* 94 (2013) 713–722.
  - [61] M. Ngiam, S. Liao, A.J. Patil, Z. Cheng, C.K. Chan, S. Ramakrishna, The fabrication of nano-hydroxyapatite on PLGA and PLGA/collagen nanofibrous composite scaffolds and their effects in osteoblastic behavior for bone tissue engineering, *Bone* 45 (2009) 4–16.
  - [62] S. Cremers, P. Garnerio, M.J. Seibel, Biochemical markers of bone metabolism, in: J.P. Bilezikian, L.G. Raisz, T.J. Martin (Eds.), *Principles of Bone Biology*, Third edition, Academic Press, San Diego, 2008, pp. 1857–1881.
  - [63] Y. Wang, Y. Wei, X. Zhang, M. Xu, F. Liu, Q. Ma, Q. Cai, X. Deng, PLGA/PDLLA core-shell microsphere sequential release system: preparation, characterization and promotion of bone regeneration in vitro and in vivo, *Chem. Eng. J.* 273



- (2015) 490–501.
- [64] A. Hughes, Analysis of gene expression in bone by quantitative RT/PCR, *Methods Mol. Biol.* 816 (2012) 261–275.
  - [65] A.E. Goodship, J.L. Cunningham, J. Kenwright, Strain rate and timing of stimulation in mechanical modulation of fracture healing, *Clin. Orthop. Relat. Res.* (1998) S105–S115.
  - [66] V.I. Sikavitsas, J.S. Temenoff, A.G. Mikos, Biomaterials and bone mechanotransduction, *Biomaterials* 22 (2001) 2581–2593.
  - [67] G. Bouet, D. Marchat, M. Cruel, L. Malaval, L. Vico, In vitro three-dimensional bone tissue models: from cells to controlled and dynamic environment, *Tissue Eng. Part B* 21 (2015) 133–156.
  - [68] K.S. Kang, S.-J. Lee, H. Lee, W. Moon, D.-W. Cho, Effects of combined mechanical stimulation on the proliferation and differentiation of pre-osteoblasts, *Exp. Mol. Med.* 43 (2011) 367.
  - [69] P. Habibovic, K. de Groot, Osteoinductive biomaterials—properties and relevance in bone repair, *J. Tissue Eng. Regen. Med.* 1 (2007) 25–32.
  - [70] G.E. Friedlaender, S. Lin, L.A. Solchaga, L.B. Snel, S.E. Lynch, The role of recombinant human platelet-derived growth factor-BB (rhPDGF-BB) in orthopaedic bone repair and regeneration, *Curr. Pharm. Des.* 19 (2013) 3384–3390.



# Cutaneous delivery of [1-(4-chloro-3-nitrobenzenesulfonyl)-1*H*-indol-3-yl]-methanol, an indole-3-carbinol derivative, mitigates psoriasiform lesion by blocking MAPK/NF- $\kappa$ B/AP-1 activation



Jing-Ru Weng<sup>a,b,c</sup>, Tse-Hung Huang<sup>d,e,f,g</sup>, Zih-Chan Lin<sup>h</sup>, Ahmed Alalaiwe<sup>i</sup>, Jia-You Fang<sup>j,k,l,\*</sup>

<sup>a</sup> Department of Marine Biotechnology and Resources, National Sun Yat-sen University, Kaohsiung, Taiwan

<sup>b</sup> Doctoral Degree Program in Marine Biotechnology, National Sun Yat-sen University, Kaohsiung, Taiwan

<sup>c</sup> Department of Medical Research, China Medical University Hospital, Taichung, Taiwan

<sup>d</sup> Department of Traditional Chinese Medicine, Chang Gung Memorial Hospital, Keelung, Taiwan

<sup>e</sup> School of Traditional Chinese Medicine, Chang Gung University, Kweishan, Taoyuan, Taiwan

<sup>f</sup> Graduate Institute of Health Industry Technology, Chang Gung University of Science and Technology, Kweishan, Taoyuan, Taiwan

<sup>g</sup> School of Nursing, National Taipei University of Nursing and Health Sciences, Taipei, Taiwan

<sup>h</sup> Graduate Institute of Biomedical Sciences, Chang Gung University, Kweishan, Taoyuan, Taiwan

<sup>i</sup> Department of Pharmaceutics, College of Pharmacy, Prince Sattam Bin Abdulaziz University, Al Kharj, Saudi Arabia

<sup>j</sup> Pharmaceutics Laboratory, Graduate Institute of Natural Products, Chang Gung University, Kweishan, Taoyuan, Taiwan

<sup>k</sup> Research Center for Food and Cosmetic Safety and Research Center for Chinese Herbal Medicine, Chang Gung University of Science and Technology, Kweishan, Taoyuan, Taiwan

<sup>l</sup> Department of Anesthesiology, Chang Gung Memorial Hospital, Kweishan, Taoyuan, Taiwan

## ARTICLE INFO

### Keywords:

[1-(4-chloro-3-nitrobenzenesulfonyl)-1*H*-indol-3-yl]-methanol  
Psoriasis  
Topical delivery  
Keratinocyte  
MAPK  
NF- $\kappa$ B

## ABSTRACT

[1-(4-chloro-3-nitrobenzenesulfonyl)-1*H*-indol-3-yl]-methanol (CIM) has been used as a bioactive agent for inhibiting tumor growth and angiogenesis via mitogen-activated protein kinase (MAPK) and NF- $\kappa$ B blocking. The present work was undertaken to investigate the potential of CIM against psoriasis using imiquimod (IMQ)-stimulated psoriasis-like mouse and in vitro HaCaT keratinocytes as the models. We demonstrated that topical CIM treatment reduced IMQ-activated scaling, erythema, and barrier dysfunction. This compound also restrained the recruitment of neutrophils. The cytokines, including TNF- $\alpha$ , IL-1 $\beta$ , IL-6, and IL-17 in psoriasiform skin, can be attenuated to normal baseline by CIM. Topically applied CIM can be easily delivered into skin based on the affinity with stratum corneum (SC) ceramides. IMQ intervention increased the permeability by 3-fold as compared to healthy skin. CIM ameliorated psoriatic lesion without incurring overt signs of irritation. Both TNF- $\alpha$  and IMQ were employed as the stimulators to activate HaCaT for reciprocal elucidation of the mechanism of action. CIM inhibited the overexpression of IL-1 $\beta$ , IL-6, and IL-24 in HaCaT. CIM exerted anti-inflammatory activity by suppressing the phosphorylation of NF- $\kappa$ B and activator protein-1 (AP-1) through MAPK pathways. Our results indicate that CIM has potential as the antipsoriatic molecule. The detailed signaling pathways still need further investigation.

## 1. Introduction

Psoriasis is a chronic autoimmune disorder manifested in the skin area. This disease basically affects 2~3% of the population [1]. Clinically, psoriasis is characterized by red plaques with silver multilayered

scales and a thickened epidermis. Pain, itching, and bleeding are commonly reported [2]. A high level of morbidity and reduced life quality are caused by psoriasis. The pathogenesis bases on keratinocyte hyperproliferation are associated with abnormal epidermis differentiation and cytokine infiltration by dendritic cells and T cells [3].

**Abbreviations:** AP-1, activator protein-1; CIM, [1-(4-chloro-3-nitrobenzenesulfonyl)-1*H*-indol-3-yl]-methanol; ERK, extracellular signal-regulated kinase; GAPDH, glyceraldehyde 3-phosphate dehydrogenase; HaCaT, immortalized human skin keratinocytes; H&E, hematoxylin and eosin; IL, interleukin; IMQ, imiquimod; JNK, c-Jun N-terminal kinase; Ly6G, lymphocyte antigen 6 complex locus G6D; MAPKs, mitogen-activated protein kinases; PASI, psoriasis area and severity index; SC, stratum corneum; TEWL, transepidermal water loss; TLR, Toll-like receptor; TNF- $\alpha$ , tumor necrosis factor- $\alpha$

\* Corresponding author at: Pharmaceutics Laboratory, Graduate Institute of Natural Products, Chang Gung University, 259 Wen-Hwa 1st Road, Kweishan, Taoyuan, 333, Taiwan

E-mail address: [fajy@mail.cgu.edu.tw](mailto:fajy@mail.cgu.edu.tw) (J.-Y. Fang).

<https://doi.org/10.1016/j.bioph.2019.109398>

Received 18 July 2019; Received in revised form 20 August 2019; Accepted 28 August 2019

0753-3322/© 2019 The Authors. Published by Elsevier Masson SAS. This is an open access article under the CC BY license (<http://creativecommons.org/licenses/by/4.0/>).

Besides the involvement of immune cells in psoriasis, keratinocytes are considered as an integral part of the resident immune system in skin due to their role as antigen presenting cells to induce innate immune mediators and sustain the chronic phase [4]. More than 90% of the cells in the epidermis are keratinocytes playing crucial roles in responding to environmental stimulation and inflammation. Keratinocytes are an important target for psoriasis management. Until now, the treatment for the complete resolution of psoriasis is still lacking because of the time-consuming treatment, inconvenient administration, and side effects [5]. It is necessary to develop novel treatments to achieve the aims of superior effectiveness and fewer adverse responses.

Indole-3-carbinol (I3C) is a natural compound, long investigated and found to exhibit chemopreventive and anticancer activities [6]. [1-(4-chloro-3-nitrobenzenesulfonyl)-1*H*-indol-3-yl]-methanol (CIM) is a novel derivative of I3C. This synthetic analog revealed 100-fold greater apoptosis against prostate tumor cells and higher chemical stability than I3C [7,8]. CIM is proved to block the NF- $\kappa$ B-mediated oncogenic pathways for inhibiting tumorigenesis and angiogenesis [9,10]. The activated NF- $\kappa$ B signaling is also important in the development of treatment for psoriasis. The modulation of NF- $\kappa$ B is a prominent target for antipsoriatic therapy [11]. Given that CIM has been reported to target NF- $\kappa$ B signaling, it is our purpose herein to explore the potential therapeutic value of CIM for ameliorating psoriasis. About 80% of psoriatic patients are recognized as mild-to-moderate [5]. Topical therapy is the first choice for the treatment of mild-to-moderate psoriasis. Although the use of injectable biologics is currently found to be very effective for psoriasis management, the possible risk of infection, generation of secondary autoimmune disorders, and resistance after initial improvement have limited their application [12]. We intended to employ topical administration for CIM delivery. In this study, Franz cell assembly was utilized to evaluate the skin absorption capability of CIM through psoriasiform and barrier-disrupted skins. The psoriasis-like plaque in the mouse was developed by imiquimod (IMQ), as described previously [13].

The expression of proinflammatory cytokines is promoted in the psoriatic lesion, leading to immune cell migration and keratinocyte proliferation. We examined the therapeutic activity of CIM by gross observation, histology, and the protein level of cytokines. The immune cells in concert with keratinocytes produced cytokines and chemokines, triggering the vicious cycle of inflammation. We determined the inhibition of CIM on TNF- $\alpha$ - or IMQ-induced production of cytokines, chemokines, mitogen-activated protein kinases (MAPKs), NF- $\kappa$ B, and activator protein-1 (AP-1) for exploring mechanism of action by using human keratinocytes (HaCaT) as the model cells. Both TNF- $\alpha$  and IMQ were used to activate keratinocytes since the two agents induced somewhat different signalings. This strategy was helpful to elucidate the therapeutic mechanisms of CIM.

## 2. Materials and methods

### 2.1. Animals

Male Balb/c mice and nude mice at 8 weeks of age were obtained from the National Laboratory Animal Center (Taipei, Taiwan). One-week-old specific-pathogen-free pigs were purchased from Pigmodel Animal Technology (Miaoli, Taiwan). All the experimental protocols used in this study were approved by the Institutional Animal Care and Use Committee of Chang Gung University.

### 2.2. Psoriasiform lesion induced by IMQ

The mouse back received a daily topical dose of IMQ cream (Aldara®, 3 M) at 62.5 mg for 5 days based on a previous study [13]. CIM was synthesized as described previously [7]. The structure of this compound is illustrated in Fig. 1a. The CIM treatment group was additionally pretreated with 10 mg/ml compound in PEG400/ethanol

(4:6, 100  $\mu$ l) before IMQ intervention. The gross observation of the skin surface with or without CIM treatment was accomplished using a handheld digital magnifier (Mini Scope-V, M&T Optics, Taipei, Taiwan). The level of erythema and transepidermal water loss (TEWL) was monitored using spectrophotometer (CD100, Yokogawa, Tokyo, Japan) and Tewameter (TM300, Courage and Khazaka, Köln, Germany), respectively. The Psoriasis Area and Severity Index (PASI) was employed to measure the severity grade on day 5.

### 2.3. Histology

The dorsal skin of the mice was excised after a 5-day IMQ treatment. The skin specimen was immersed in 10% formaldehyde and embedded in paraffin. The samples were cut into a thickness of 5  $\mu$ m for hematoxylin and eosin (H&E) staining. For immunohistochemical (IHC) staining, the skin sections were incubated with anti-Ki67 (the clone of antibody: SP6), anti-IL-6 (polyclone), anti-IL-17 (polyclone), or anti-Ly6G antibody (RB6-8C5) for 1 h, and subsequently incubated with biotinylated donkey anti-goat IgG for 20 min. Ly6G is a reliable biomarker to identify neutrophil infiltration in inflamed skin [14]. Photomicrographs were taken using Leica DMI8 microscopy.

### 2.4. Skin absorption

Franz cell was used to assess the cutaneous delivery of CIM into the skin. The mouse or pig skin was mounted between the donor and receptor with the stratum corneum (SC) facing the donor. The barrier-deficient skins, including IMQ treatment, SC stripping, lipid removal, and protein removal, were prepared according to a previous investigation [15]. The donor was filled with 0.5 ml of CIM in PEG400/pH 7.4 buffer (3:7, 1 mg/ml). The receptor medium was 30% ethanol in pH 7.4 phosphate buffer. The effective penetration area was 0.79 cm<sup>2</sup>. The stirring rate and receptor temperature were maintained at 600 rpm and 37 °C, respectively. The 300- $\mu$ l aliquot in the receptor was withdrawn at the determined intervals. At the end of experiment (24 h), the skin was removed to detect skin deposition of CIM, and then extracted by methanol in a homogenizer (MagNA Lyser, Roche). The homogenate was centrifuged at 10,000  $\times$  g for 10 min. The receptor medium and skin deposition of CIM were quantified by high performance liquid chromatography.

### 2.5. Molecular modeling

The structure of CIM was sketched by Discovery Studio® version 4.1 (Accelrys, San Diego, CA, USA) for obtaining Alog *P*, hydrogen-bond acceptor or -donor number, and total polarity surface. These data were useful to correlate with the skin permeation behavior. The superimposition of CIM with SC lipids was computed to visualize the conformation and ligand-binding interaction. The negative CDOCKER energy was calculated after conducting the docking simulation between CIM and lipids.

### 2.6. Skin tolerance

The safety of CIM application on skin was evaluated in healthy Balb/c mice. The PEG400/ethanol (4:6) containing CIM at 10 mg/ml was topically administered daily (0.6 ml) on the mouse back for 6 days. After removal of CIM vehicle, the treated skin was monitored by gross appearance, erythema, TEWL, and skin surface pH each day. The skin was excised for H&E observation after a 6-day treatment.

### 2.7. Cytotoxicity

HaCaT were cultured in DMEM supplemented with 10% fetal bovine serum and 1% penicillin-streptomycin in 5% CO<sub>2</sub> at 37 °C. After CIM incubation at different concentrations for 24 h, (3-(4,5-

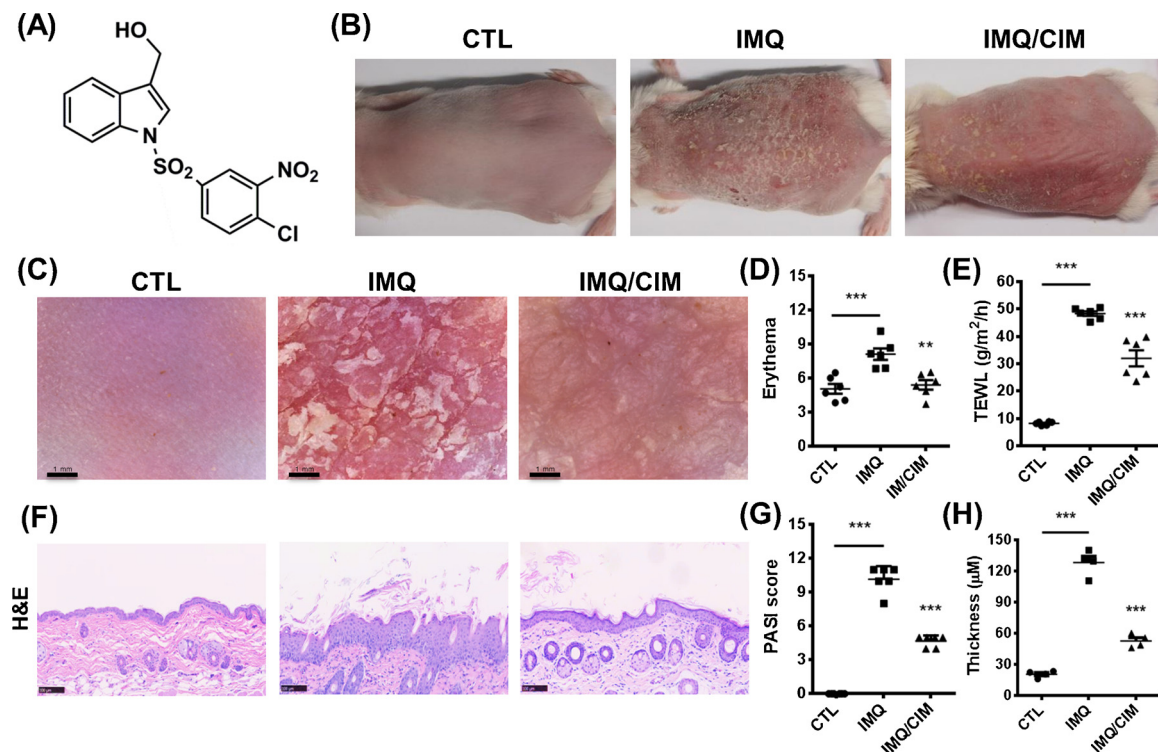


**Fig. 1.** CIM attenuates IMQ-induced mouse psoriatic lesion: (A) The chemical structure of CIM; (B) The gross images of mouse back skin were represented on day 5 by digital camera; (C) The close-up imaging by handheld digital microscopy; (D) Erythema measurement; (E) TEWL measurement; (F) Skin sections stained by H&E; (G) Quantification of mouse skin histology examined using PASI score; and (H) Epidermal thickness quantified from H&E staining. All data are expressed as the mean  $\pm$  SEM ( $n = 6$ ). \*\*\* $p < 0.001$ . The data of IMQ/CIM group are compared to the data of IMQ group to show the statistical result. CIM, [1-(4-chloro-3-nitrobenzenesulfonyl)-1H-indol-3-yl]-methanol; H&E, hematoxylin and eosin; IMQ, imiquimod; PASI, Psoriasis Area and Severity Index; TEWL, transepidermal water loss.

dimethylthiazol-2-yl)-2,5-diphenyltetrazolium bromide (MTT) solution (5 mg/ml) was incorporated into the plate for 4 h. The formazan precipitate was dissolved with DMSO. The plate was read by spectrophotometer at 550 nm for measuring the cell viability.

## 2.8. The activation of keratinocytes by $TNF-\alpha$ or IMQ

HaCaT cells were stimulated by  $TNF-\alpha$  (10 ng/ml) or IMQ (10  $\mu$ g/ml) to activate the inflammatory condition. CIM at concentrations of 1, 5, or 10  $\mu$ M was pretreated to the cells before 1 h of stimulation if necessary. After incubation with the stimulators for a determined duration, in the presence or absence of CIM, HaCaT was collected for further determination of proteins. The culture supernatant was harvested for analysis of cytokines and chemokines. The nuclear protein was collected for detecting phospho (p)-NF- $\kappa$ B, p-c-Jun, and p-c-Fos. The nuclear pellet was acquired by centrifugation at 400  $\times$ g and 4  $^{\circ}$ C for 5 min. After subsequent sonication, the nuclear protein was obtained by 8000  $\times$ g centrifugation for 10 min. The cells were pipetted into the lysis buffer to obtain IL-24 and p-MAPKs from the whole cell lysate for immunoblotting analysis.

## 2.9. Enzyme-linked immunosorbent assay (ELISA)

The cytokines and chemokines in the mouse skin or HaCaT were detected by ELISA approach. The extraction method of the skin was described previously [16]. The levels of  $TNF-\alpha$ , IL-1 $\beta$ , IL-6, IL-17A, IL-17E, and CXCL8 were measured using the commercial kits (BioLegend, San Diego, CA, USA) according to the manufacturer's instructions.

## 2.10. Western blotting

The separated proteins were transferred to nitrocellulose membrane

and probed with primary antibodies against IL-24 (the clone of antibody: C2C3), p-JNK (polyclone), p-ERK (polyclone), p-p38 (polyclone), p-NF- $\kappa$ B (93-H1), p-c-Jun (G-7), p-c-Fos (D-1), and GAPDH (0411) overnight at 4  $^{\circ}$ C. The membrane was washed three times and then incubated with anti-mouse horseradish peroxidase antibody for 1 h. The bound antibody was observed by enhanced chemiluminescence reagent. The level of proteins was quantified by the ratio of densitometric measurement of the indicated proteins to the corresponding standard (GAPDH).

## 2.11. Statistical analysis

The statistical difference in the data of the different treatment groups was analyzed using Kruskal-Wallis test. The post hoc test for checking individual differences was Dunn's test. The 0.05, 0.01, and 0.001 levels of probability were taken as statistically significant.

## 3. Results

### 3.1. Cutaneous CIM delivery for mitigating psoriasisiform lesion

A psoriasis-like skin model of mice was employed to evaluate the in vivo activity of topically applied CIM. The *en face* images of the mouse skin in gross and microscopic level are represented in Fig. 1b and c, respectively. IMQ treatment led to the observation of hyperplasia, erythema, and scaling. The mice dosed with CIM showed significant attenuation of these symptoms. CIM did not completely clear the hyperplasia and scales as compared with the healthy control. Erythema level was quantified by spectrophotometer, as shown in Fig. 1d. Treatment with CIM resulted in a suppression of erythema to the baseline control. TEWL, as an indicator of skin barrier function, showed a 5-fold increase in IMQ-treated skin compared to normal skin, as seen in Fig. 5e. The



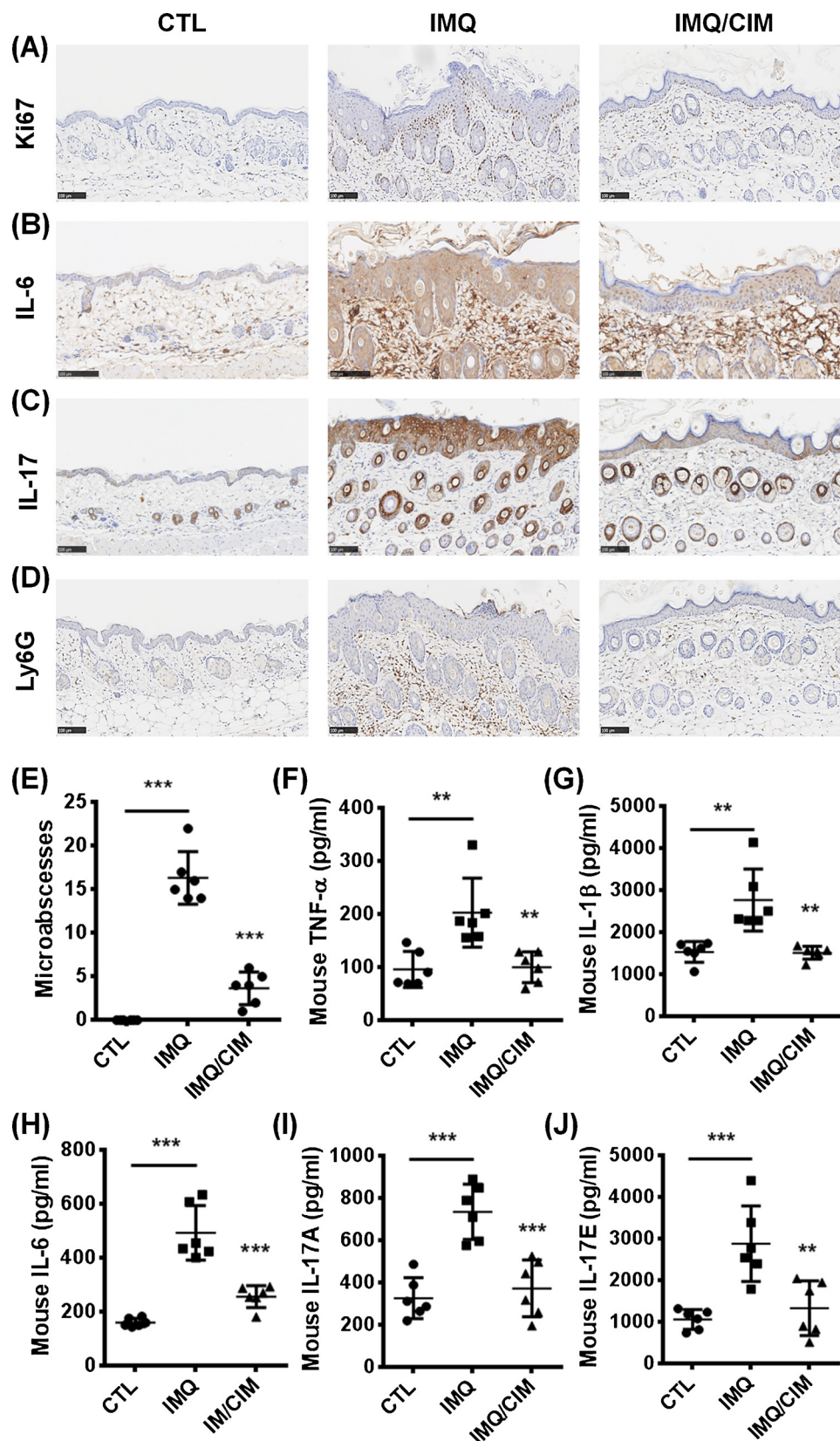


Fig. 2. CIM inhibits IMQ-induced mouse psoriatic skin inflammation based on IHC and cytokine assay: Skin sections were represented by IHC staining for (A) Ki67, (B) IL-6, (C) IL-17, and (D) Ly6G; (E) Total counts of abscesses; and the protein level of (F) TNF- $\alpha$ , (G) IL-1 $\beta$ , (H) IL-6, (I) IL-17A, and (J) IL-17E. All data are expressed as the mean  $\pm$  SEM (n = 6). \*\*p < 0.01, \*\*\*p < 0.001. The data of IMQ/CIM group are compared to the data of IMQ group to show the statistical result. CIM, [1-(4-chloro-3-nitrobenzenesulfonyl)-1H-indol-3-yl]-methanol; IHC, immunohistochemistry; IMQ, imiquimod; Ly6G, lymphocyte antigen 6 complex locus G6D.



application of CIM on psoriatic skin reduced TEWL from 48.5 to 37.0 g/m<sup>2</sup>/h. By contrast to the histology of healthy skin, as shown in Fig. 1f, the skin treated with IMQ exhibited the features of hyperkeratosis, elongated rete ridge, increased epidermis thickness, and inflammatory infiltrate in dermis, mimicking the phenotype of psoriasis in humans. The skin section from CIM-treated psoriasiform skin demonstrated a distinct inhibition in the severity of the lesion as compared to the vehicle control. The decrease of immune cell infiltration by CIM was notable. PASI was used for summing the severity of erythema, epidermal thickness, and scaling from histology. As depicted in Fig. 1g, topically applied CIM significantly inhibits average PASI by 50%. Keratinocyte proliferation led to the increase of epidermal thickness in IMQ-treated skin. The average epidermal thickness in the CIM-treated group (53.0 μm) measured from histology was decreased compared with 128.4 μm in the psoriasiform lesion with vehicle control (Fig. 1h).

We also observed the IHC staining of the mouse skin. The impact on keratinocyte hyperproliferation was analyzed using Ki67, a proliferation biomarker highly expressed in psoriatic plaque. Fig. 2a represents an extensive distribution of Ki67 throughout the basal layer following IMQ stimulation. Topically applied CIM produced a decrease in Ki67 staining. The expression of cytokines IL-6 and IL-17 was determined by IHC, as shown in Fig. 2b and c, respectively. Both cytokines were notably increased in epidermis by IMQ. By contrast, treatment with CIM markedly suppressed the expression of IL-6 and IL-17. The untreated healthy control was devoid of neutrophils, as shown in the left panel of Fig. 2d. A large infiltration of neutrophils in dermis was observed using Ly6G staining after IMQ treatment. Some neutrophils accumulated in the SC by IMQ intervention referred to Munro's microabscesses. The IHC staining of Ly6G demonstrated that CIM caused a significant decrease in neutrophil infiltration. As shown in Fig. 2e, the IMQ-induced microabscesses quantified from IHC were lessened by CIM application. The cytokine release in the skin was analyzed by ELISA. IMQ stimulation induced a 2-fold increase in TNF-α expression as revealed in Fig. 2f. The TNF-α level in psoriasiform skin could be inhibited to the baseline control by CIM. A similar tendency was detected for IL-1β, IL-6, IL-17A, and IL-17E as observed in Figs. 2g–j. Similar to the IHC results, the protein level of IL-6 and IL-17 induced by IMQ could be diminished by topical CIM.

### 3.2. CIM facilely penetrates the psoriasis-like skin

The success of topically applied drug development necessitates not only the recognition of pharmacological activity, but also the efficient delivery into the skin. We next inspected the skin absorption of CIM in pig and mouse skins for speculating on the capability of CIM delivery to cutaneous nidus. An in vitro permeation model is commonly used to assess skin absorption. In the present work, the cutaneous CIM transport was examined using in vitro Franz cells. The cumulative amount in receptor and CIM deposition in skin were examined. The cumulative amount predicts the possible delivery into deeper skin strata or systemic circulation. The skin deposition indicates the uptake within the skin. Fig. 3a shows the cumulative amount and skin deposition of CIM by using pig skin as the permeation barrier. The skins with different treatments were examined to elucidate the diffusion pathways of CIM. The SC removal evoked the cumulative amount by 29-fold compared to the intact skin. This was the greatest permeation among various skin types, followed by delipid, deprotein, and intact skins. CIM exhibited the intact skin deposition of 0.019 nmol/mg. The cutaneous deposition of the barrier-defective skins was comparable to that of intact skin. The tendency of cumulative amount across different mouse skin types was the same as that of pig skin, as shown in Fig. 3b. The cumulative amount across SC-stripped mouse skin was 2.6-fold greater than the intact control. The mouse skin deposition revealed a similar trend with cumulative amount, with SC-stripped skin showing the highest deposition. IMQ intervention resulted in the enhancement of CIM permeation by about 3-fold as compared to the healthy skin (Fig. 3c),

suggesting a barrier dysfunction of psoriasiform skin as proved by TEWL.

We applied molecular docking of CIM to analyze the possible interaction with SC lipids. The superimposition of CIM with the lipids, shown in Fig. 3d, indicates a possible affinity of CIM to the lipids, except for cholesterol. The in silico calculation of negative CDOCKER score is summarized in Fig. 3e. The greater value of the negative CDOCKER energy implies the higher interaction between the compound and lipids. Ceramides II, III, and VI are abundant in human SC. Ceramides and palmitic acid showed approximate affinity to CIM (−21.58 ~ −19.17). It may be difficult for CIM to interact with cholesterol and cholesteryl sulfate. The physicochemical parameters related to cutaneous absorption were obtained by the computation of molecular modeling, as exhibited in Fig. 3e.

### 3.3. CIM produces negligible irritation on skin

We attempted to determine whether topical CIM induced adverse effects on skin. The tolerance of CIM on healthy skin was conducted in Balb/c mice. Both the gross and close-up images of CIM-treated skin display the nearly normal appearance, as illustrated in Figs. 4a and b. As seen in Fig. 4c, the erythema quantification indicates a comparable level between the control and CIM-treated skins although, the rash is slightly larger for the CIM group. A significant elevation of TEWL was found after CIM application (Fig. 4d). The increase of 20% value of baseline control could be classified as very mild. The skin surface pH shows no change by a consecutive 6-day challenge (Fig. 4e). CIM-treated skin exhibits no significant histological change as compared to the vehicle control (Fig. 4f).

### 3.4. CIM inhibits TNF-α- or IMQ-induced cytokines in HaCaT

The cytotoxicity of CIM against HaCaT is shown in Fig. 5a. This compound did not cause a significant cell death up to a concentration of 10 μM, but the viability decreased by 37% at 50 μM. The non-cytotoxic doses of 1 ~ 10 μM were selected to study the anti-inflammatory effect on keratinocytes. The inflammatory condition of HaCaT was stimulated by TNF-α or IMQ. We performed ELISA assay to detect the effect of CIM on TNF-α- and IMQ-induced expression of cytokines and chemokines, as shown in Fig. 5b and c, respectively. TNF-α significantly increased the expression of IL-1β and IL-6. CIM treatment reduced TNF-α-induced enhancement of cytokine expression in a dose-dependent manner. Although the increased CXCL8 by TNF-α could be suppressed by CIM, this effect did not achieve statistical significance. In the case of IMQ activation (Fig. 5c), CIM at 10 μM completely inhibited IL-1β to the baseline. A dose dependence of IL-6 inhibition by CIM was found. IMQ did not promote CXCL8 level in HaCaT. The impact of CIM on IMQ-induced cytokines was similar to those observed in vivo. HaCaT was analyzed for IL-24 expression using Western blotting, as depicted in Fig. 5d. The uncut original blots in triplicate with the IL-24 bands highlighted are depicted in Supplementary Fig. 1. Incubation of CIM concentration-dependent suppressed TNF-α- and IMQ-induced IL-24 elevation.

Since CIM showed a suppressive impact on proinflammatory cytokines in keratinocytes, we investigated whether CIM could inhibit the phosphorylation of MAPKs. TNF-α or IMQ was treated with CIM for 15, 30, and 60 min. Maximum expression of p-JNK, p-ERK, and p-p38 was detected at 30 min in the case of TNF-α stimulation (Fig. 6a). The uncut original blots in triplicate with the MAPK bands highlighted are depicted in Supplementary Fig. 2. CIM could significantly reverse these increases, indicating the anti-inflammatory ability of CIM through the downregulation of MAPK signaling. Similar to TNF-α activation, a significant increase in the phosphorylation of MAPKs after IMQ treatment was observed, with a maximum at 30 min (Fig. 6b). CIM reduced IMQ-induced JNK and ERK phosphorylation but not p-p38.

Given that CIM regulated the MAPK pathways, we sought to estimate the possibility of MAPK involvement in the signaling of NF-κB and

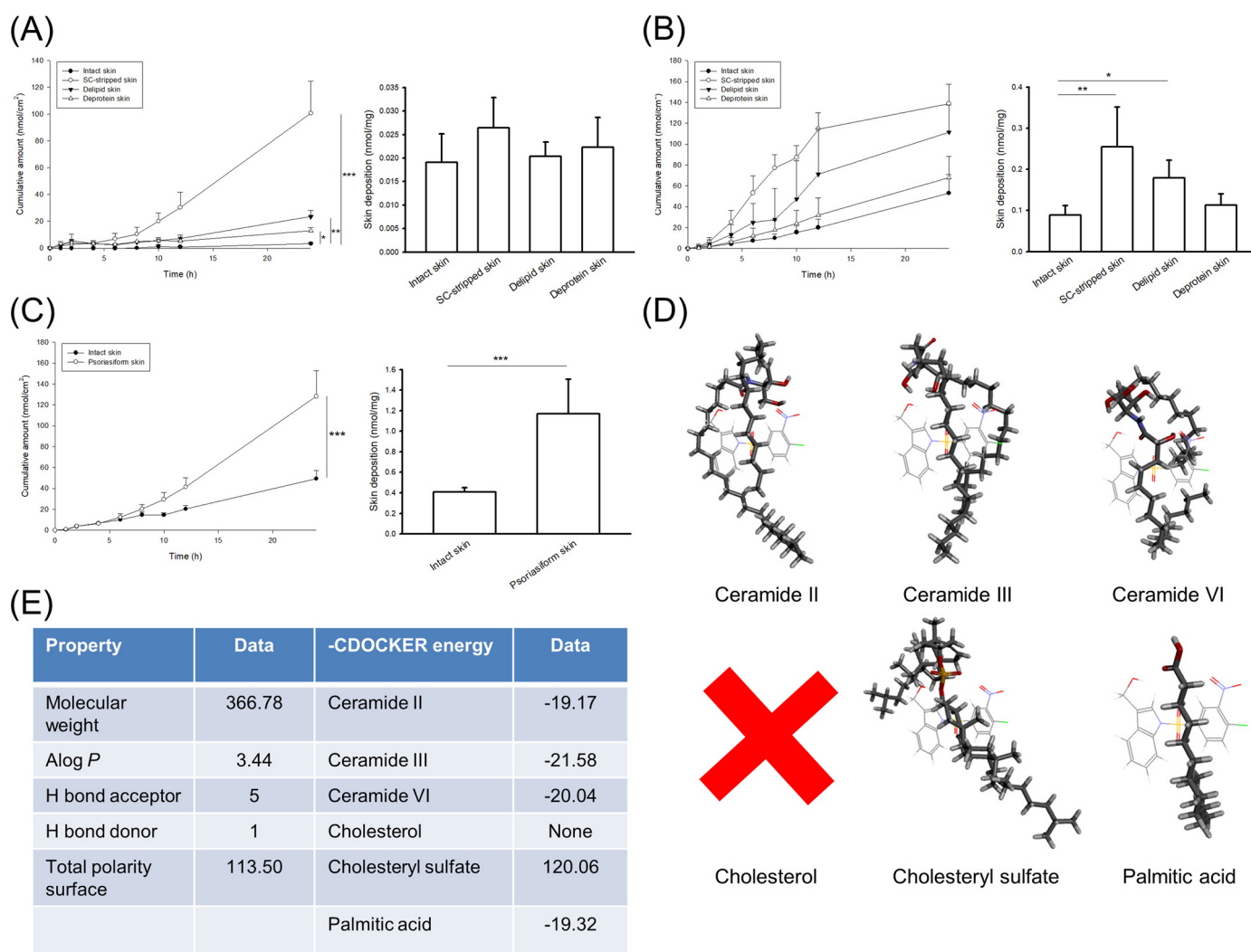


**Fig. 3.** In vitro cutaneous absorption of CIM indicates the facile permeation of this compound into/through pig and nude mouse skins: (A) Cumulative amount and skin deposition of CIM via pig skin with different treatments; (B) Cumulative amount and skin deposition of CIM via nude mouse skin with different treatments; (C) Cumulative amount and skin deposition of CIM via Balb/c mouse skin with and without IMQ intervention; (D) Superimposition of the computed poses for CIM with SC lipids; and (E) The summary of physicochemical parameters and negative CDocker energies of CIM. All data are expressed as the mean  $\pm$  SEM ( $n = 4$ ). \* $p < 0.05$ , \*\* $p < 0.01$ , \*\*\* $p < 0.001$ . CIM, [1-(4-chloro-3-nitrobenzenesulfonyl)-1*H*-indol-3-yl]-methanol; IMQ, imiquimod; SC, stratum corneum.

AP-1. We first examined the impact of CIM on NF- $\kappa$ B in TNF- $\alpha$ -stimulated cells, as shown in Fig. 7a. The p-NF- $\kappa$ B was dramatically increased in response to TNF- $\alpha$ . CIM at 10  $\mu$ M significantly ablated p-NF- $\kappa$ B in HaCaT. This compound also markedly reduced p-c-Jun and p-c-Fos expression by 53% and 51%, respectively, in TNF- $\alpha$ -stimulated HaCaT. As shown in Fig. 7b, p-NF- $\kappa$ B was increased 5-fold from the IMQ-treated cells. The stimulated expression of p-NF- $\kappa$ B was blocked by CIM, although this reduction level was minor than that in TNF- $\alpha$  activation. Contrary to TNF- $\alpha$ , p-AP-1 expression was not affected by IMQ treatment. This indicates that TNF- $\alpha$  and IMQ might govern somewhat different pathways for inducing HaCaT inflammation. The uncut original blots in triplicate with the bands highlighted are depicted in Supplementary Fig. 3.

#### 4. Discussion

As a synthetic compound, CIM regulated MAPK and NF- $\kappa$ B pathways to suppress carcinogenesis. MAPKs and NF- $\kappa$ B are also involved in cutaneous inflammation. In this study, we examined the therapeutic effect of topical CIM on psoriasis. Here we found that CIM could readily penetrate the skin to exert the bioactivity. After topical CIM delivery, the psoriasis-like lesion in mouse was markedly attenuated compared to the

vehicle control. The CIM-treated group demonstrated improved hyperplasia and inhibited inflammatory process in IMQ-treated skin. CIM significantly restrained TNF- $\alpha$ - and IMQ-induced production of the proinflammatory cytokines in keratinocytes. It also decreased the phosphorylation of MAPKs. Moreover, the activation of NF- $\kappa$ B translocation and AP-1 was impeded by CIM.

IMQ cream application on mouse skin induces the hyperplasia and inflammation which approximate the symptoms of human psoriasis. The phenotype of the IMQ-treated mouse skin demonstrates the similarity with the cytokine and chemokine pathways of human psoriasis; these include TNF- $\alpha$ , IL-1 $\beta$ , IL-6, and CXCL8 [17]. Our in vivo results indicate the effectiveness of CIM in suppressing cytokines in IMQ-treated skin. These cytokines are expressed in psoriasis to a high degree. Keratinocytes, dendritic cells, neutrophils, and T lymphocytes can be involved in the multiple feedback loops in IMQ-induced psoriasis-like lesion [18]. The change of keratinocytes is the initial detectable event after IMQ treatment [19]. IL-17 mainly produced by Th17 cells is demonstrated to enhance the expression of IL-6 in keratinocytes [20]. IL-6 has been recognized as a therapeutic target for psoriasis. IL-17 plays an essential role in recruiting neutrophils and inducing keratinocyte hyperproliferation. IL-17 is able to stimulate keratinocyte inflammasomes, resulting in the production of IL-1 $\beta$  [21]. All the cytokines mentioned

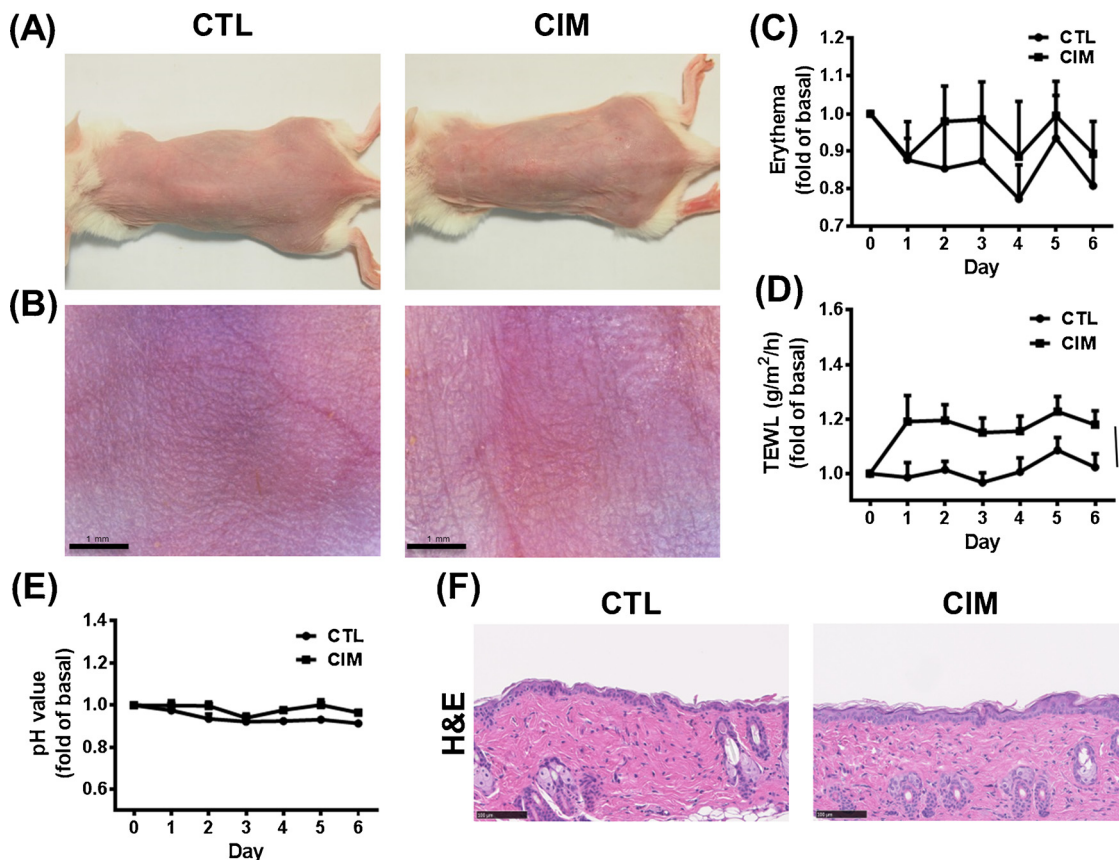


**Fig. 4.** In vivo skin tolerance examination after a 6-day application of topically applied CIM on Balb/c mice indicates that skin is tolerable to topically applied CIM with a minimal irritation: (A) The gross images of mouse back skin were represented on day 6 by digital camera; (B) the close-up imaging by handheld digital microscopy; (C) Erythema measurement; (D) TEWL measurement; (E) Skin surface pH value; and (F) Skin sections represented by H&E staining. All data are expressed as the mean  $\pm$  SEM (n = 6). \*p < 0.05. CIM, [1-(4-chloro-3-nitrobenzenesulfonyl)-1H-indol-3-yl]-methanol; H&E, hematoxylin and eosin; TEWL, transepidermal water loss.

above are upregulated in IMQ-treated skin, and can be restrained by topical CIM. Among the IL-17 family, IL-17A and IL-17E are predominantly produced by T cells and keratinocytes, respectively. IL-17A upregulates the inflammation-related genes in keratinocytes to increase the production of cytokines, including TNF- $\alpha$ , IL-1 $\beta$ , and IL-6 [22]. IL-17A can act synergistically with TNF- $\alpha$  to deteriorate psoriatic lesion, leading to the deficiency of skin barrier capacity [23]. IL-17E produced by keratinocytes also contributes to the barrier disruption [24]. The increased TEWL after IMQ treatment confirms this viewpoint. Our results indicate that CIM can inhibit TNF- $\alpha$ , IL-17A, and IL-17E to recover the skin barrier function.

The neutrophils are demonstrated to infiltrate the lesion of IMQ-treated skin, promoting the severity of the plaque. The generation of cytokines and chemokines by the stimulated keratinocytes acts as chemoattractants for neutrophil activation and migration [25]. The histological profiles of IMQ-treated skin reveal the formation of microabscesses, which are the clusters of neutrophils. Neutrophils are the dominant IL-17A-expressing cells in psoriatic skin [26]. IL-17 receptors are found in a variety of resident cells and immune cells, including keratinocytes and neutrophils [23]. Both cells can be activated to release IL-17 family; this can lead to the amplification of the local inflammation and the vicious cycle. Blocking IL-17 is considered important in the amelioration of psoriasis. The ability of topically applied CIM to inhibit IL-17A and IL-17E demonstrates the effect of suppressing keratinocyte and neutrophil activation for psoriasis mitigation. IL-1 $\beta$  and IL-6 function as the downstreams of IL-17A in exacerbating microabscess formation [27]. The IL-17 blocking by CIM led to the following inhibition of IL-1 $\beta$  and IL-6, as observed in our results, suggesting the possibility of CIM as effective therapy against psoriasis.

A prerequisite for a topically applied agent showing therapeutic potential is a vital permeation into the skin. Our data demonstrate the capability of CIM penetration into/across barrier-defective skins. These skin types are valid for exploring the penetration pathways of CIM. SC is a principal absorption barrier for CIM due to the large increase of permeation after removing SC. Permeation across SC can be divided into two compartments: intercellular lipid-rich and intracellular protein-rich pathways. CIM transport across delipid skin is higher than that across deprotein skin, signifying the preferred route of the lipophilic environment compared to the polar environment for CIM delivery. The physicochemical properties of a compound, such as molecular size, lipophilicity, hydrogen bonding, and polarity surface area are practical to explain the structure-permeation relationship. The facility of intercellular diffusion depends upon the partitioning from the vehicle to SC. Higher lipophilicity of the permeant generally causes greater permeation; however, the highly lipophilic permeant may remain in SC, retarding the further diffusion into viable epidermis/dermis [28]. An optimal log P, the indicator of lipophilicity, is important for skin absorption. The log P of CIM is 3.44. Riviere and Brooks [29] claimed a maximum permeation for the permeant with log P of 2~3, the value mimicking the lipophilicity of SC lipids. Yamaguchi et al. [30] suggested the hindrance of viable skin transport for the permeant with log P of > 2. Although the viable skin might contribute to a part of barrier for CIM, the log P of 3.44 still approximates the value of 2~3. The deficient barrier function of psoriasisform skin is also beneficial for the facile permeation of CIM. The log P of the clinically available anti-psoriatic drugs dithranol, calcipotriol, and tretinoin is 2.9, 4.7, and 5.6, respectively. CIM has superior topical application.

Although pig and mouse skins can be the alternatives for human

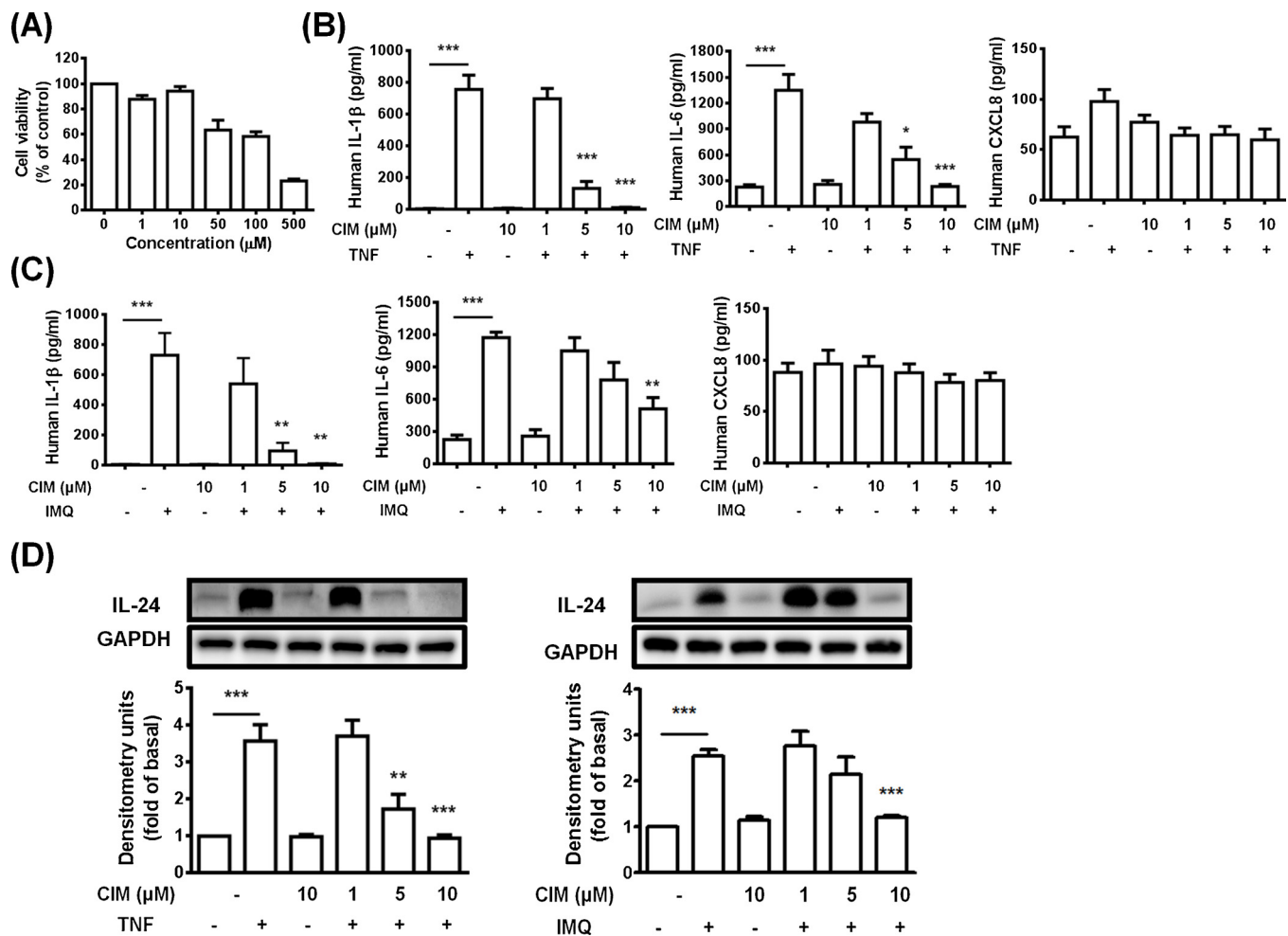


**Fig. 5.** CIM suppresses TNF- $\alpha$ - or IMQ-stimulated cytokines in HaCaT cells: (A) The cell viability measured by MTT assay; (B) IL-1 $\beta$ , IL-6, and CXCL8 in TNF- $\alpha$ -stimulated HaCaT measured by ELISA; (C) IL-1 $\beta$ , IL-6, and CXCL8 in IMQ- $\alpha$ -stimulated HaCaT measured by ELISA; and (D) IL-24 in TNF- $\alpha$ - or IMQ-stimulated HaCaT measured by Western blotting. All data are expressed as the mean  $\pm$  SEM ( $n = 4$ ). \* $p < 0.05$ , \*\* $p < 0.01$ , \*\*\* $p < 0.001$ . The data of IMQ/CIM group are compared to the data of IMQ group to show the statistical result. CIM, [1-(4-chloro-3-nitrobenzenesulfonyl)-1H-indol-3-yl]-methanol; ELISA, enzyme-linked immunosorbent assay; IMQ, imiquimod; MTT, (3-(4,5-dimethylthiazol-2-yl)-2,5-diphenyltetrazolium bromide; TNF- $\alpha$ , tumor necrosis factor- $\alpha$ .

skin in the Franz cell, the rodent or baby pig skin is much more permeable than human skin. The permeation of lipophilic permeant is highly affected by viable skin thickness [30]. The cumulative amount of CIM in receptors using animal skin as the barrier could be regarded as the CIM reservoir in human skin because of the thicker viable skin for humans. The large residence of CIM in psoriatic lesion (epidermis/dermis) is conceivable. The log  $P$  cannot solely explain the permeation behavior. The hydrogen bonding of the permeant impedes the transport across SC [31]. The number of hydrogen-bond acceptors and hydrogen-bond donor for CIM are 5 and 1, respectively. It is reported that hydrogen-bond acceptor is less important than hydrogen-bond donor in governing cutaneous permeation [30,32]. The facile absorption of CIM across the SC and into the epidermal nidus could be achieved because of the low hydrogen-bond donor number. The total polarity surface of CIM is 113.5, which is greater than that of dithranol (57.5), calcipotriol (60.7), and tretinoin (37.3). Although the high polarity surface is unfavorable for residence in SC lipids, the facile passage to viable skin can be predicted. The delivery into epidermis/dermis is the target for anti-psoriatic therapy. The low molecular weight ( $< 500$  g/mol) rendered CIM suitable to penetrate the skin barrier for topical application. The adverse effects to induce skin irritation can hinder the use of topical agents. CIM does not inflict the physiological and histological changes of the healthy skin over a 6-day period, except for a slight disturbance of the barrier function. We find that CIM is well tolerated in animal

experiments.

Even though psoriasis has been mainly considered as an immune cell-dependent disorder, it cannot be ignored that keratinocytes have a critical character in inducing the early pathogenesis and sustaining the prolonged phase of inflammation. Keratinocytes, being a crucial component triggering the onset of immune reaction, exert a potent role in initiating cutaneous inflammation. We employed HaCaT cells as a keratinocyte model to explore the effect of CIM on inflammation suppression, using both TNF- $\alpha$  and IMQ to stimulate HaCaT inflammation. To date, TNF- $\alpha$ -related signaling is regarded as particularly important in psoriasis [33]. Keratinocytes are the critical targets for TNF- $\alpha$  signaling in psoriasis. TNF- $\alpha$  is largely released by macrophages to induce the inflammatory process, resulting in psoriasis development [19]. The TNF receptor in keratinocytes mediates the TNF- $\alpha$  response through the activation of intracellular signaling cascades. TNF- $\alpha$  initiates the inflammatory and hyperproliferative signaling via MAPKs and NF- $\kappa$ B [34]. IMQ is the stimulator of psoriasis used in our *in vivo* study. Keratinocytes are the earliest cells that respond to IMQ [18]. The induction of psoriasisiform mouse skin by IMQ is mainly through the ligation of Toll-like receptor (TLR)7, which is highly expressed in dendritic cells and macrophages [19]. Since TLR7 is absent in HaCaT, the activation of this cell line by IMQ can be the adenosine receptor signaling [17]. IMQ causes the antagonism of the adenosine receptor to diminish anti-inflammatory cAMP in HaCaT, resulting in the



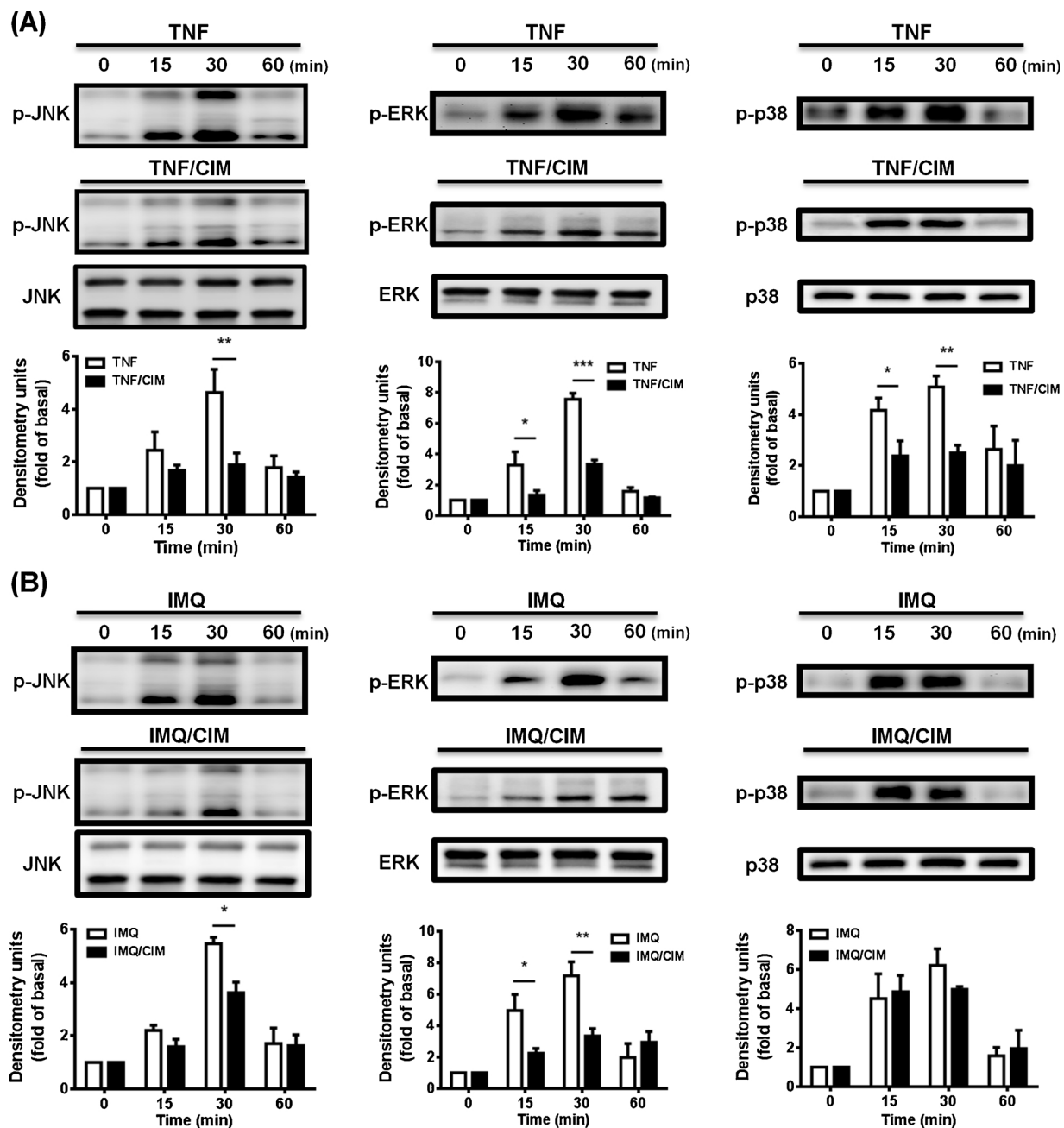


**Fig. 6.** CIM suppresses MAPK phosphorylation in TNF- $\alpha$ - or IMQ-stimulated HaCaT cells: (A) p-JNK, p-ERK, and p-p38 in TNF- $\alpha$ -stimulated HaCaT measured by Western blotting; and (B) p-JNK, p-ERK, and p-p38 in IMQ-stimulated HaCaT measured by Western blotting. All data are expressed as the mean  $\pm$  SEM ( $n = 3$ ). \* $p < 0.05$ , \*\* $p < 0.01$ , \*\*\* $p < 0.001$ . CIM, [1-(4-chloro-3-nitrobenzenesulfonyl)-1H-indol-3-yl]-methanol; IMQ, imiquimod; MAPK, mitogen-activated protein kinase; TNF- $\alpha$ , tumor necrosis factor- $\alpha$ .

upregulated expression of NF- $\kappa$ B and the downstream cytokines [16]. This signaling differs from that of TNF- $\alpha$ . The oxidative stress-related pathways are involved in the TNF- $\alpha$ -activated HaCaT [35]. The reactive oxygen species (ROS) is a primary cause of oxidative stress in psoriasis. The psoriatic keratinocytes display a complex etiology of inflammatory signaling. The exploration of the action mode of CIM by using both TNF- $\alpha$  and IMQ as the stimulators with somewhat different pathways was complementary to elucidate the mechanisms.

TNF- $\alpha$  and IMQ impel cytokine production in keratinocytes. These include IL-1 $\beta$  and IL-6, as reported previously [36]. For instance, keratinocyte inflammasome activation by IMQ leads to IL-1 $\beta$  release. IL-6 can be secreted by keratinocytes to evoke neutrophil infiltration [27]. Our data support the overexpression of IL-1 $\beta$  and IL-6 in HaCaT after stimulation, and this elevation could be suppressed by CIM. Another

observation is the significant inhibition of TNF- $\alpha$ - and IMQ-induced IL-24 by CIM. IL-24 is highly present in psoriatic keratinocytes. This cytokine is an upstream prompting inflammation after TNF- $\alpha$  stimulation [37]. IL-24 inhibition can upregulate filaggrin expression for the restoration of the barrier dysfunction in inflammation [38]. The recovery of TEWL in psoriasis-like skin by CIM confirms the role of IL-24. CXCL8 is a chemokine largely produced by keratinocytes in psoriasis evolution. This signaling peptide attracts neutrophils into the psoriatic lesion, deteriorating psoriasis [39]. We find that CXCL8 in HaCaT is not enhanced by TNF- $\alpha$  or IMQ in our case, although a slight but statistically insignificant increase of CXCL8 is observed in TNF- $\alpha$ -treated cells. This may suggest that the neutrophil recruitment in vivo was not governed by CXCL8 in keratinocytes. Further study is required to elucidate the possibility of neutrophil migration.



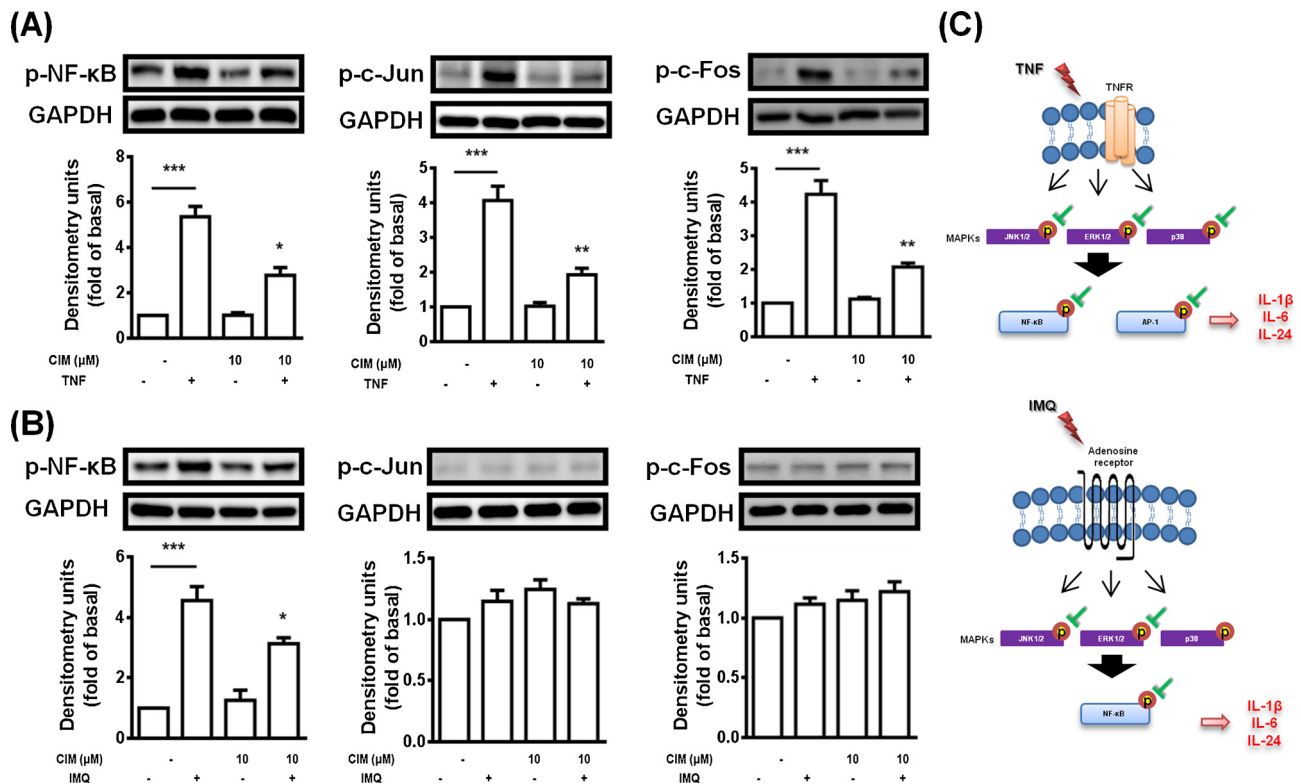


**Fig. 7.** CIM suppresses NF-κB and AP-1 phosphorylation in TNF-α- or IMQ-stimulated HaCaT cells: (A) NF-κB, c-Jun, and c-Fos in TNF-α-stimulated HaCaT measured by Western blotting; (B) NF-κB, c-Jun, and c-Fos in IMQ-stimulated HaCaT measured by Western blotting; and (C) The proposed mechanisms of the anti-psoriatic activity of CIM. All data are expressed as the mean  $\pm$  SEM ( $n = 3$ ). \* $p < 0.05$ , \*\* $p < 0.01$ , \*\*\* $p < 0.001$ . The data of IMQ/CIM group are compared to the data of IMQ group to show the statistical result. AP-1, activator protein-1; CIM, [1-(4-chloro-3-nitrobenzenesulfonyl)-1*H*-indol-3-yl]-methanol; IMQ, imiquimod.

MAPKs are known to play important roles on inflammatory signaling via cascades of phosphorylation, including keratinocyte proliferation and differentiation. The signaling of MAPKs is critical in TNF-α-activated pathways regulating the downstream effect in keratinocytes. The activation of p-JNK, p-ERK, and p-p38 is inhibited by CIM, indicating the possible molecular mechanisms of CIM action on MAPK regulation. On the other hand, CIM treatment decreases the phosphorylation of JNK and ERK, but not p38 in the case of IMQ activation. This demonstrates the higher efficiency of CIM for restraining MAPK phosphorylation stimulated by TNF-α than IMQ. The mechanisms underlying the suppression of MAPK pathways activated by TNF-α differ from those by IMQ. The suppression of JNK phosphorylation in TNF-α-activated keratinocytes increases the expression of filaggrin and lorcin, both of which are essential for maintaining the barrier function [22]. ERK-dependent IL-24 expression and ROS generation in keratinocytes are the early events contributing to psoriasis [37]. Since oxidative stress is related to TNF-α-activated inflammation, the implication is that CIM could be acting as an antioxidant agent to ameliorate psoriasis. The experimental results about MAPKs suggest that CIM could regulate keratinocyte proliferation, differentiation, and inflammation. A previous study [10] also revealed that CIM inhibited MAPKs to arrest the proliferation of umbilical vein endothelial cells.

MAPKs regulate the downstream signaling pathways in keratinocytes, including the transcription factors NF-κB and AP-1. Both transcription factors target genes coded for proinflammatory cytokines to exacerbate psoriasis involved in hyperproliferation and inflammation [40]. NF-κB phosphorylation is abundantly detected in the lesional skin of psoriasis. TNF-α can activate ROS-dependent NF-κB phosphorylation in keratinocytes [41]. The p-NF-κB is also promoted in IMQ-induced keratinocyte inflammation via the MAPK pathway [19,42]. CIM suppressed TNF-α- and IMQ-activated p-NF-κB, indicating antiproliferative and anti-inflammatory activities of CIM, since NF-κB is associated with

the regulation of proliferation [43]. Weng et al. [7,8,44] demonstrated that CIM blocks TNF-α-induced NF-κB-dependent transcription in cancer cells for preventing proliferation. Suppression of p-NF-κB in IMQ-exposed HaCaT can reduce the expression of IL-1β and IL-6 [17]. The NF-κB pathway can provide a key step in the antipsoriatic activity of CIM. Upon translocation to the keratinocyte nucleus in inflammation status, MAPKs activate transcription factors c-Jun and c-Fos, the main components of AP-1 [45]. The AP-1 phosphorylation elicited by TNF-α could be lessened by CIM at 10 μM, indicating its ability to regulate this transcription pathway. However, the AP-1 upregulation by IMQ is absent herein. This may suggest that the cAMP-dependent pathway was not related to AP-1. This result can explain the lack of CXCL8 upregulation by IMQ treatment since activated keratinocytes are shown to produce chemokines via AP-1 [27,46]. The downstream of the transcription factors is the production of cytokines to enhance epidermal hyperplasia and inflammation. Because of the capability of CIM to inhibit NF-κB and AP-1, the elevated cytokines are reduced to improve the severity of the psoriasisform lesion.

According to the mechanistic study, we propose that CIM suppressed the inflammation in keratinocytes for the amelioration of psoriasis-like plaque. The results suggest that CIM possesses multiple antipsoriatic mechanisms. CIM inhibited TNF-α- and IMQ-induced expression of proinflammatory cytokines through the suppression of JNK/ERK/p38 MAPKs and NF-κB phosphorylation in keratinocytes. We also verify that CIM could reduce MAPK phosphorylation to decrease p-AP-1 expression evoked by TNF-α. This effect is not found when using IMQ as the stimulator since IMQ does not elevate p-c-Jun and p-c-Fos. We propose that CIM might prohibit oxidative effect in TNF-α-stimulated keratinocytes. Given that the expression of cytokines is downstream of MAPKs and transcription factors, the further recruitment of immune cells such as neutrophils is prevented after topical CIM treatment. The capacity of CIM to target a broad spectrum of signaling pathways

underlies its anti-inflammatory effect against psoriasis. The possible mechanisms of action of CIM are illustrated in Fig. 7c.

The present work has some limitations. The IMQ-stimulated manifestation of psoriasis elapsed quickly. This model is useful for evaluating the preventive, but not therapeutic, benefit of the potential candidates [47]. There could be some differences between the pathogenesis and symptoms of experimental psoriasis and human psoriasis. It is suggested that a 75% reduction of PASI is adequate to efficiently ameliorate the signs and symptoms of psoriasis [5]. Our results demonstrate a 50% decline of PASI by topical CIM. Further optimization of applied dose, duration, or vehicle is needed to maximize the efficiency. We chiefly assess the cutaneous delivery of CIM by *in vitro* Franz cells. The use of excised skin *in vitro* may exert difference from *in vivo* or clinical condition. Although the pig and mouse skins can serve as alternative models for human skin, the experimental data could not directly mimic the absorption in human skin. Whether the results from animal skins can be correlated with human skin needs further clarification. Psoriasis is a complex disease concerning the cross-talk of a variety of cells. Besides the role of keratinocytes, the impact of CIM on immune cells activated by psoriasis should be investigated in the future.

## 5. Conclusions

Psoriasis is a chronic inflammatory cutaneous disease causing economic burden and psychological stress. It is urgent to develop a new therapy for efficient and safe application. The results of the present study demonstrate that CIM has the capability to ameliorate psoriasis-form lesion in IMQ-stimulated mice. We found that CIM suppressed cytokine expression through the inhibition of MAPKs, NF- $\kappa$ B, and AP-1. The underlying mechanisms may be associated with the anti-inflammatory and antioxidant activities of CIM. The advantages of topically applied CIM for treating psoriasis are the targeting of multiple signalings, facile absorption into the skin, and ease of manufacturing for scale up. This study offers the evidence and molecular mechanism of CIM for psoriasis treatment. This information is beneficial to the design and development of CIM as an antipsoriatic agent.

## Author contributions

J.-Y.F. designed the study. J.-R.W., T.-H.H., and Z.-C.L. performed the experiments. J.-R.W., Z.-C.L., and A.A. collected, analyzed, and interpreted the data. J.-R.W., and T.-H.H. prepared the manuscript. A.A. and J.-Y.F. revised the manuscript. All authors read and approved the final manuscript.

## Declaration of Competing Interest

The authors declare no competing financial interests.

## Acknowledgements

The authors are grateful for the financial support from Ministry of Science and Technology of Taiwan (MOST-107-2320-B-182-016-MY3) and Chang Gung Memorial Hospital (CMRPG2H0361-2).

## Appendix A. Supplementary data

Supplementary material related to this article can be found, in the online version, at doi:<https://doi.org/10.1016/j.biopha.2019.109398>.

## References

- [1] X.T. Lima, R. Minnillo, J.M. Spencer, A.B. Kimball, Psoriasis prevalence among the 2009 AAD national melanoma/skin cancer screening program participants, *J. Eur. Acad. Dermatol. Venereol.* 27 (2013) 680–685.
- [2] D.J. Pithadia, K.A. Reynolds, E.B. Lee, J.J. Wu, Psoriasis-associated cutaneous pain: etiology, assessment, impact, and management, *J. Dermatol. Treat.* 19 (2018) 1–6.
- [3] C. Conrad, M. Gilliet, Psoriasis: from pathogenesis to targeted therapies, *Clin. Rev. Allergy Immunol.* 54 (2018) 102–113.
- [4] C. Albanesi, S. Madonna, P. Gisondi, G. Girolomoni, The interplay between keratinocytes and immune cells in the pathogenesis of psoriasis, *Front. Immunol.* 9 (2018) 1549.
- [5] W.H. Boehncke, M.P. Schön, Psoriasis, *Lancet* 386 (2015) 983–994.
- [6] N. Fujioka, V. Fritz, P. Upadhyaya, F. Kassie, S.S. Hecht, Research on cruciferous vegetables, indole-3-carbinol, and cancer prevention: a tribute to Lee W. Wattenberg, *Mol. Nutr. Food Res.* 60 (2016) 1228–1238.
- [7] J.R. Weng, C.H. Tsai, S.K. Kulp, D. Wang, C.H. Lin, H.C. Yang, Y. Ma, A. Sargeant, C.F. Chiu, M.H. Tsai, C.S. Chen, A potent indole-3-carbinol-derived antitumor agent with pleiotropic effects on multiple signaling pathways in prostate cancer cells, *Cancer Res.* 67 (2007) 7815–7824.
- [8] J.R. Weng, C.H. Tsai, H.A. Omar, A.M. Sargeant, D. Wang, S.K. Kulp, C.L. Shapiro, C.S. Chen, OSU-A9, a potent indole-3-carbinol derivative, suppresses breast tumor growth by targeting the Akt-NF $\kappa$ B pathway and stress response signaling, *Carcinogenesis* 30 (2009) 1702–1709.
- [9] H.A. Omar, A.M. Sargeant, J.R. Weng, D. Wang, S.K. Kulp, T. Patel, C.S. Chen, Targeting of the Akt-nuclear factor- $\kappa$ B signaling network by [1-(4-chloro-3-nitrobenzenesulfonyl)-1H-indol-3-yl]-methanol (OSU-A9), a novel indole-3-carbinol derivative, in a mouse model of hepatocellular carcinoma, *Mol. Pharmacol.* 76 (2009) 957–968.
- [10] H.A. Omar, E.A. Arafa, S.A. Salama, H.H. Arab, C.H. Wu, J.R. Weng, OSU-A9 inhibits angiogenesis in human umbilical vein endothelial cells via disrupting Akt-NF $\kappa$ B and MAPK signaling pathways, *Toxicol. Appl. Pharmacol.* 272 (2013) 616–624.
- [11] A.M. Goldminz, S.C. Au, N. Kim, A.B. Gottlieb, P.F. Lizzul, NF $\kappa$ B: an essential transcription factor in psoriasis, *J. Dermatol. Sci.* 69 (2013) 89–94.
- [12] A. Di Cesare, M.C. Fargnoli, A. Marinucci, K. Peris, Rationale for the development of speckled hyperpigmentation in the areas of psoriatic plaques after treatment with biologic agents, *J. Invest. Dermatol.* 135 (2015) 318–320.
- [13] L. van der Fits, S. Mourits, J.S. Voerman, M. Kant, L. Boon, J.D. Laman, F. Cornelissen, A.M. Mus, E. Florencia, E.P. Prens, E. Lubberts, Imiquimod-induced psoriasis-like skin inflammation in mice is mediated via the IL-23/IL-17 axis, *J. Immunol.* 182 (2009) 5836–5845.
- [14] X. Guo, X. Fang, G. He, M.H. Zaman, X. Fei, W. Qiao, G.M. Deng, The role of neutrophils in skin damage induced by tissue-deposited lupus IgG, *Immunology* 154 (2018) 604–612.
- [15] S.Y. Chuang, Y.K. Lin, C.F. Lin, P.W. Wang, E.L. Chen, J.Y. Fang, Elucidating the skin delivery of aglycone and glycoside flavonoids: how the structures affect cutaneous absorption, *Nutrients* 9 (2017) 1304.
- [16] Z.C. Lin, P.W. Hsieh, T.L. Hwang, C.Y. Chen, C.T. Sung, J.Y. Fang, Topical application of anthranilate derivatives ameliorates psoriatic inflammation in a mouse model by inhibiting keratinocyte-derived chemokine expression and neutrophil infiltration, *FASEB J.* 32 (2018) 6783–6795.
- [17] M.P. Schön, M. Schön, Imiquimod: mode of action, *Br. J. Dermatol.* 157 (Suppl. 2) (2007) 8–13.
- [18] F. Rahmani, N. Rezaei, Therapeutic targeting of Toll-like receptors: a review of Toll-like receptors and their signaling pathways in psoriasis, *Expert Rev. Clin. Immunol.* 12 (2016) 1289–1298.
- [19] B. Flutter, F.O. Nestle, TLRs to cytokines: mechanistic insights from the imiquimod mouse of psoriasis, *Eur. J. Immunol.* 43 (2013) 3138–3146.
- [20] G. Monteleone, F. Pallone, T.T. MacDonald, S. Chimenti, A. Costanzo, Psoriasis: from pathogenesis to novel therapeutic approaches, *Clin. Sci.* 120 (2011) 1–11.
- [21] A. Balato, M. Schiattarella, S. Lembo, M. Matti, N. Prevete, N. Balato, F. Ayala, Interleukin-1 family members are enhanced in psoriasis and suppressed by vitamin D and retinoic acid, *Arch. Dermatol. Res.* 305 (2013) 255–262.
- [22] H.J. Li, N.L. Wu, G.A. Lee, C.F. Hung, The therapeutic potential and molecular mechanism of isoflavone extract against psoriasis, *Skin. Rep.* 8 (2018) 6335.
- [23] B.W. Kirkham, K. Kavanaugh, K. Reich, Interleukin-17A: a unique pathway in immune-mediated diseases: psoriasis, psoriatic arthritis and rheumatoid arthritis, *Immunology* 141 (2013) 133–142.
- [24] M. Deleuran, M. Hvid, K. Kemp, G.B. Christensen, B. Deleuran, C. Vestergaard, IL-25 induces both inflammation and skin barrier dysfunction in atopic dermatitis, *Chem. Immunol. Allergy* 96 (2012) 45–49.
- [25] W.H. Boehncke, N.C. Brembilla, Unmet needs in the field of psoriasis: pathogenesis and treatment, *Clin. Rev. Allergy Immunol.* 55 (2018) 295–311.
- [26] J.B. Golden, T.S. McCormick, N.L. Ward, IL-17 in psoriasis: implications for therapy and cardiovascular co-morbidities, *Cytokine* 62 (2013) 195–201.
- [27] A.L. Croxford, S. Karbach, F.C. Kurschus, S. Wörtge, A. Nikolaev, N. Yogeve, S. Klebow, R. Schüler, S. Reissig, C. Piotrowski, E. Brylla, I. Bechmann, J. Scheller, S. Rose-John, F.T. Wunderlich, T. Münzel, E. von Stebut, A. Waisman, IL-6 regulates neutrophil microabscess formation in IL-17A-driven psoriasisform lesions, *J. Invest. Dermatol.* 134 (2014) 728–735.
- [28] C.F. Lin, C.F. Hung, I.A. Aljuffali, Y.L. Huang, W.C. Liao, J.Y. Fang, Methylation and esterification of magnolol for ameliorating cutaneous targeting and therapeutic index by topical application, *Pharm. Res.* 33 (2016) 2152–2167.
- [29] J.E. Riviere, J.D. Brooks, Predicting skin permeability from complex chemical mixtures: dependency of quantitative structure permeation relationship on biology of skin model used, *Toxicol. Sci.* 119 (2011) 224–232.
- [30] K. Yamaguchi, T. Mitsui, Y. Aso, K. Sugibayashi, Structure-permeability relationship analysis of the permeation barrier properties of the stratum corneum and viable epidermis/dermis of rat skin, *J. Pharm. Sci.* 97 (2008) 4391–4403.
- [31] Q. Zhang, J.E. Grice, P. Li, O.G. Jepps, G.J. Wang, M.S. Roberts, Skin solubility determines maximum transepidermal flux for similar size molecules, *Pharm. Res.*

- 26 (2009) 1974–1985.
- [32] J. Grice, H.A.E. Benson, Analysing the skin barrier from down under, *Skin Pharmacol. Physiol.* 26 (2013) 254–262.
- [33] L. Grine, L. Dejager, C. Libert, R.E. Vandenbroucke, An inflammatory triangle in psoriasis: TNF, type I IFNs and IL-17, *Cytokine Growth Factor Rev.* 26 (2015) 25–33.
- [34] K. Urschel, I. Cicha, TNF- $\alpha$  in the cardiovascular system: from physiology to therapy, *Int. J. Interferon Cytokine Mediat. Res.* 7 (2015) 9–25.
- [35] Y. Jung, J.C. Kim, Y. Choi, S. Lee, K.S. Kang, Y.K. Kim, S.N. Kim, Eupatilin with PPAR $\alpha$  agonist effects inhibits TNF $\alpha$ -induced MMP signaling in HaCaT cells, *Biochem. Biophys. Res. Commun.* 493 (2017) 220–226.
- [36] A. Walter, M. Schäfer, V. Cecconi, C. Matter, M. Urošević-Maiwald, B. Belloni, N. Schönewolf, R. Dummer, W. Bloch, S. Werner, H.D. Beer, A. Knuth, M. van den Broek, Aldara activates TLR7-independent immune defense, *Nat. Commun.* 4 (2013) 1560.
- [37] S. Kumari, M.C. Bonnet, M.H. Ulvmar, K. Wolk, N. Karagianni, E. Witte, C. Uthoff-Hachenberg, J.C. Renauld, G. Kollias, R. Toftgard, R. Sabat, M. Pasparakis, I. Haase, Tumor necrosis factor receptor signaling in keratinocytes triggers interleukin-24-dependent psoriasis-like skin inflammation in mice, *Immunity* 39 (2013) 899–911.
- [38] Y. Mitamura, S. Nunomura, Y. Nanri, M. Ogawa, T. Yoshihara, M. Masuoka, G. Tsuji, T. Nakahara, A. Hashimoto-Hachiya, S.J. Conway, M. Furue, K. Izuhara, The IL-13/periostin/IL-24 pathway causes epidermal barrier dysfunction in allergic skin inflammation, *Allergy* 73 (2018) 1881–1891.
- [39] K. Takada, S. Komine-Aizawa, N. Hirohata, Q.D. Trinh, A. Nishina, H. Kimura, S. Hayakawa, Poly I:C induces collective migration of HaCaT keratinocytes via IL-8, *BMC Immunol.* 18 (2017) 19.
- [40] H. Li, H. Li, R. Huo, P. Wu, Z. Shen, H. Xu, B. Shen, N. Li, Cyr61/CCN1 induces CCL20 production by keratinocyte via activating p38 and JNK/AP-1 pathway in psoriasis, *J. Dermatol. Sci.* 88 (2017) 46–56.
- [41] W.C. Huang, Y.W. Dai, H.L. Peng, C.W. Kang, C.Y. Kuo, C.J. Liou, Phloretin ameliorates chemokines and ICAM-1 expression via blocking of the NF- $\kappa$ B pathway in the TNF- $\alpha$ -induced HaCaT human keratinocytes, *Int. Immunopharmacol.* 27 (2015) 32–37.
- [42] H. Chen, C. Lu, H. Liu, M. Wang, H. Zhao, Y. Yan, L. Han, Quercetin ameliorates imiquimod-induced psoriasis-like skin inflammation in mice via the NF- $\kappa$ B pathway, *Int. Immunopharmacol.* 48 (2017) 110–117.
- [43] J. An, Z. Li, Y. Dong, J. Ren, J. Huo, Amentoflavone protects against psoriasis-like skin lesion through suppression of NF- $\kappa$ B-mediated inflammation and keratinocyte proliferation, *Mol. Cell. Biochem.* 413 (2016) 87–95.
- [44] J.R. Weng, L.Y. Bai, H.A. Omar, A.M. Sargeant, C.T. Yeh, Y.Y. Chen, M.H. Tsai, C.F. Chiu, A novel indole-3-carbinol derivative inhibits the growth of human oral squamous cell carcinoma in vitro, *Oral Oncol.* 46 (2010) 748–754.
- [45] J.M. Kim, S.Y. Kim, E.M. Noh, H.K. Song, G.S. Lee, K.B. Kwon, Y.R. Lee, Reversine inhibits MMP-1 and MMP-3 expressions by suppressing of ROS/MAPK/AP-1 activation in UV-stimulated human keratinocytes and dermal fibroblasts, *Exp. Dermatol.* 27 (2018) 298–301.
- [46] S. Sano, K.S. Chan, S. Carbajal, J. Clifford, M. Peavey, K. Kiguchi, S. Itami, B.J. Nickoloff, J. DiGiovanni, Stat3 links activated keratinocytes and immunocytes required for development of psoriasis in a novel transgenic mouse model, *Nat. Med.* 11 (2005) 43–49.
- [47] J. Artym, M. Kocięba, E. Zaczynska, I. Kochanowska, M. Zimecki, W. Kałas, A. Fiedorowicz, A. Pawlak, L. Strzdała, M. Jeleń, B. Morak-Młodawska, K. Pluta, K. Kaleta-Kurawicz, J.P. Madej, P. Kuropka, J. Kuryszko, Topically applied azaphenothiazines inhibit experimental psoriasis in mice, *Int. Immunopharmacol.* 59 (2018) 276–286.



Article

# DEK Is a Potential Biomarker Associated with Malignant Phenotype in Gastric Cancer Tissues and Plasma

Kam-Fai Lee <sup>1,†</sup>, Ming-Ming Tsai <sup>2,3,4,†</sup> , Chung-Ying Tsai <sup>5,6,†</sup>, Chung-Guei Huang <sup>7,8</sup>, Yu-Hsiang Ou <sup>5,8</sup>, Ching-Chuan Hsieh <sup>4</sup>, Hsi-Lung Hsieh <sup>2,3,9</sup> , Chia-Siu Wang <sup>4,\*</sup> and Kwang-Huei Lin <sup>3,5,10,\*</sup>

- <sup>1</sup> Department of Pathology, Chang Gung Memorial Hospital, Chiayi 613, Taiwan; lkf2002@cgmh.org.tw
- <sup>2</sup> Department of Nursing, Division of Basic Medical Sciences, Chang-Gung University of Science and Technology, Taoyuan 333, Taiwan; mmtsai@mail.cgu.edu.tw (M.-M.T.); hlhsieh@gw.cgu.edu.tw (H.-L.H.)
- <sup>3</sup> Research Center for Chinese Herbal Medicine, College of Human Ecology, Chang Gung University of Science and Technology, Taoyuan 333, Taiwan
- <sup>4</sup> Department of General Surgery, Chang Gung Memorial Hospital, Chia-yi 613, Taiwan; p12155@cgmh.org.tw
- <sup>5</sup> Department of Biochemistry, College of Medicine, Chang-Gung University, Taoyuan 333, Taiwan; cytsai0616@cgmh.org.tw (C.-Y.T.); planet7668@hotmail.com (Y.-H.O.)
- <sup>6</sup> Kidney Research Center and Department of Nephrology, Chang Gung Memorial Hospital, Taoyuan 333, Taiwan
- <sup>7</sup> Department of Medical Biotechnology and Laboratory Science, and Graduate Institute of Biomedical Science, Chang Gung University, Taoyuan 333, Taiwan; joyce@adm.cgmh.org.tw
- <sup>8</sup> Department of Laboratory Medicine, Chang Gung Memorial Hospital, Linkou, Taoyuan 333, Taiwan
- <sup>9</sup> Department of Neurology, Chang Gung Memorial Hospital, Taoyuan 333, Taiwan
- <sup>10</sup> Liver Research Center, Chang Gung Memorial Hospital, Linkou, Taoyuan 333, Taiwan
- \* Correspondence: wangcs@cgmh.org.tw (C.-S.W.); khlin@mail.cgu.edu.tw (K.-H.L.); Tel/Fax: +886-3-2118263 (C.-S.W. & K.-H.L.)
- † These authors contributed equally to this work.

Received: 26 August 2019; Accepted: 9 November 2019; Published: 13 November 2019



**Abstract:** Gastric cancer (GC) is the second most widespread cause of cancer-related mortality worldwide. The discovery of novel biomarkers of oncoproteins can facilitate the development of therapeutic strategies for GC treatment. In this study, we identified novel biomarkers by integrating isobaric tags for relative and absolute quantitation (iTRAQ), a human plasma proteome database, and public Oncomine datasets to search for aberrantly expressed oncogene-associated proteins in GC tissues and plasma. One of the most significantly upregulated biomarkers, DEK, was selected and its expression validated. Our immunohistochemistry (IHC) ( $n = 92$ ) and quantitative real-time polymerase chain reaction (qRT-PCR) ( $n = 72$ ) analyses disclosed a marked increase in DEK expression in tumor tissue, compared with paired nontumor mucosa. Importantly, significantly higher preoperative plasma DEK levels were detected in GC patients than in healthy controls via enzyme-linked immunosorbent assay (ELISA). In clinicopathological analysis, higher expression of DEK in both tissue and plasma was significantly associated with advanced stage and poorer survival outcomes of GC patients. Data from receiver operating characteristic (ROC) curve analysis disclosed a better diagnostic accuracy of plasma DEK than carcinoembryonic antigen (CEA), carbohydrate antigen 19.9 (CA 19.9), and C-reactive protein (CRP), highlighting its potential as an effective plasma biomarker for GC. Plasma DEK is also more sensitive in tumor detection than the other three biomarkers. Knockdown of DEK resulted in inhibition of GC cell migration via a mechanism involving modulation of matrix metalloproteinase MMP-2/MMP-9 level and vice versa. Our results collectively support plasma DEK as a useful biomarker for making diagnosis and prognosis of GC patients.

**Keywords:** DEK; biomarker; gastric cancer; metastasis; prognosis; diagnosis

---

## 1. Introduction

Gastric cancer (GC) is the second most common cause of cancer-related death on a global scale [1]. The Department of Health of Taiwan reported GC as the seventh main cause of cancer-associated mortality in 2018 [2]. Despite recent improvements in diagnostic and therapeutic technologies, a large proportion of GC patients have poor survival, primarily because initial diagnosis is not made at the early stages. The recent advent of serum biomarkers offers a non-invasive and convenient method for diagnosis and monitoring of GC [3]. However, the currently available GC biomarkers, such as carcinoembryonic antigen (CEA) and carbohydrate antigen 19.9 (CA 19.9), have limited diagnostic sensitivity and specificity [4]. Previous studies by our group showed that higher serum C-reactive protein (CRP) levels are associated with advanced GC stages and poorer outcomes, suggesting that preoperative CRP may serve as a potential prognostic biomarker [5]. Suitable biomarkers with improved efficacy in monitoring disease progression should effectively facilitate earlier diagnosis and treatment of GC [6].

Proteomic approaches are powerful tools for biomarker identification in tissue specimens but not blood specimens of malignant tumors. Biomarkers for tumor screening are more easily detected in blood samples from patients, as proteins are secreted by or shed from tumor cells into the blood. The human plasma proteome database has been reported to assist as a reference platform for biomarker discovery [7]. However, problems remain regarding the depth to which these databases can be mined and the efficiency with which researchers can select useful candidates from the identified proteins. Here, we have presented a strategy to identify potential blood biomarkers overexpressed in GC tissue and secreted into peripheral blood. Oncomine (genomic) datasets (<https://www.oncomine.org>) were integrated with GC cDNA microarrays, and iTRAQ (proteomic) datasets as well as a human plasma proteome database (<http://www.plasmaproteomedatabase.org/>) to determine potential factors aberrantly regulated and secreted or released from GC tissues. Among the novel candidate proteins identified in our GC specimens, DEK was selected for further validation.

DEK is a well-known proto-oncogene found in a range of nuclear proteins involved in chromatin remodeling, transcriptional repression or activation, DNA damage repair, cell proliferation, and suppression of apoptotic pathways [8]. DEK overexpression has been documented in various human malignant tissues, including GC, pancreatic ductal adenocarcinoma, oral squamous cell carcinoma (OSCC), hepatocellular carcinoma (HCC), chronic lymphocytic leukemia (CLL), lung cancer, cervical cancer, breast cancer, melanoma, head-and-neck cancer, bladder cancer, retinoblastoma, T-cell large granular lymphocytic leukemia, colon cancer, prostate cancer, acute myeloid leukemia (AML), and malignant glioma melanoma [8–21]. Moreover, DEK has been detected extracellularly in the urine of patients with bladder cancer and shown to be released by activated macrophages in the hemopoietic system [11]. HepG2 cells are reported to secrete DEK peptide in conditioned media [22,23]. DEK can also be recognized by specific antibodies in autoimmune disease [24,25] or taken up as a functional exogenous protein by nearby cells, in turn stimulating chronic inflammation and inducing more proinflammatory factors that generate progressive tumor microenvironments [26]. In this study, the potential role of DEK as a biomarker in both blood and tissue specimens of GC patients was investigated.

## 2. Results

### 2.1. Identification and Validation Studies for DEK, a Potential Biomarker for GC

To accelerate the discovery of potential GC biomarkers, we used an omics approach including iTRAQ, Oncomine (<https://www.oncomine.org/resource/login.html>), and the Plasma Proteome



Database (<http://www.plasmaproteomedatabase.org/>) (Figure 1A). iTRAQ analyses revealed significant upregulation of oncogenic DEK in GC relative to paired normal tissues. The mean fold change in DEK expression in GC tissues was 1.94-fold higher than that in paired normal tissue in terms of relative expression (Table S1, Supplementary Materials). In addition, the evaluation of three public databases, specifically, the Oncomine public Chen, Cho, and DErrico Gastric datasets, consistently revealed significant overexpression of DEK in GC tissues relative to paired normal tissues (Figure S1, Supplementary Materials). Followed on the same selection criteria, DEK was worked further for verification in GC tissues and plasma specimens. In qRT-PCR analysis using 72 paired GC tissues, median DEK levels in normal and GC tissues ( $n = 72$ ) were  $-17.25$  and  $-16.22$  (interquartile range,  $-10.479/-29.943$  and  $-11.17/-24.971$ ), respectively, significantly elevated in GC compared with normal gastric mucosa ( $p = 0.0059$ ; Figure 1B). It is consistent with iTRAQ and public Oncomine data. The mean fold change in DEK expression in GC tissues was 14.87-fold ( $T > n = 47/72 = 65.28\%$ , range: 0.004–204.8) than that in matched nontumorous gastric mucosa (Figure 1C).

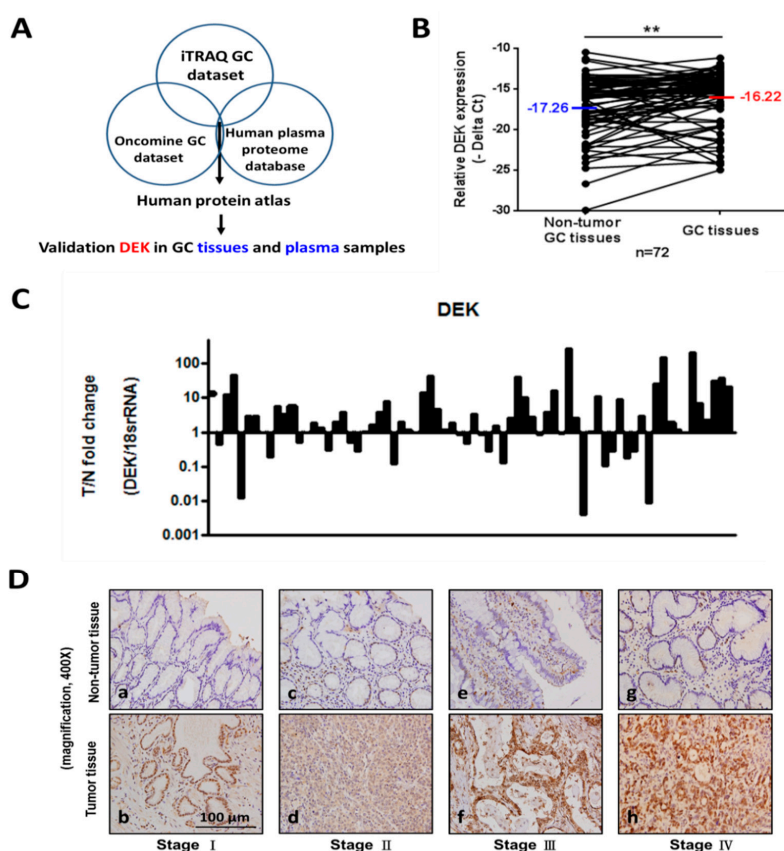


**Figure 1.** Identification and validation studies for DEK, a potential marker for gastric cancer (GC). (A) Identification of potential GC tissue/plasma biomarkers based on combined data from the iTRAQ GC dataset, Oncomine GC dataset, and human plasma proteome database. The strategy comprises genomic and proteomic profiling and subsequent validation in clinical specimens. (B) Relative expression levels of DEK in paired GC and adjacent normal tissues ( $n = 72$ ) determined via quantitative real-time polymerase chain reaction (qRT-PCR) and GAPDH normalization ( $p = 0.0059$ ) using paired sample  $t$ -tests. Error bars indicate standard deviations. (C) Distribution curves are shown as histograms for the same data. The DEK level was upregulated in GC tumors (T) relative to paired normal tissues ( $n$ ). (D) Immunohistochemistry (IHC) staining of GC tissues for DEK. Representative staining results from four pairs of GC (lower panel) and adjacent normal tissues (upper panel). Differentially expressed DEK levels in tumor cells are depicted at the top of the panel. The Mann–Whitney  $U$  test was used for comparison between the two groups (\*  $p < 0.01$ , \*\*  $p < 0.05$ , \*\*\*  $p < 0.001$ ).

## 2.2. Clinicopathologic Correlations of DEK in Gastric Tissues by IHC Study

DEK in gastric tissues was studied by IHC of the paraffin-fixed sections of gastrectomized specimens. Table 1 shows the correlation of tissue DEK with various clinicopathological characteristics in gastric tissues: gross type ( $p < 0.0001$ ), size ( $p < 0.0001$ ), depth of invasion ( $p < 0.0001$ ), serosal invasion ( $p < 0.0001$ ), lymph node status ( $p < 0.0001$ ), lymph node metastasis ( $p < 0.0001$ ), distant metastasis ( $p = 0.001$ ), pathological stage ( $p < 0.0001$ ), peritoneal seeding ( $p = 0.0312$ ), lymphatic invasion ( $p < 0.0001$ ), and perineural invasion ( $p = 0.0133$ ). DEK expressions were compared between GC and adjacent normal tissues from stages I to IV (Figure 1D). Notably, DEK expression displayed a stepwise increase parallel to GC progression from the early to late stages. The distributions of IHC scores were as follows: “++” (29/92; 31.5%) and “+++” (63/92; 68.5%) in GC tissues, and “+” (2/90; 2.2%) and “++” (88/90; 97.8%) in adjacent nontumor tissues (Table 2). This finding additionally showed that DEK is strongly upregulated in GC tissues and stepwise increased from early to advanced stages. The DEK expressions were divided into two groups based on IHC scoring: IHC-low (<51% of cells with positive staining, or < “+++”) and IHC-high ( $\geq 51\%$  of cells with positive staining, or  $\geq$  “+++”). The five-year survival rate of the low DEK expression group was significantly better than that of the high DEK expression group (81.7% vs. 40.0%, log-rank  $p = 0.0004$ ) (Figure 2A, Table 1), supporting a role of DEK as an oncoprotein during GC tumorigenesis. In view of these findings, we propose that DEK may serve as a novel prognostic factor influencing survival in GC patients.

**Table 1.** Clinicopathological correlations of DEK expression in cancer tissue and 5-year survival rate (S.R.) in 92 GC patients.

Characteristics	No.	High Expression <sup>a</sup> No. (%)	p-Value <sup>b</sup>	5-yr S.R. <sup>c</sup>	Log-Rank $p$ <sup>d</sup>
Age (yrs)					
<65	40	27 (67.5%)	1.000	51.6	0.5487
$\geq 65$	52	36 (69.2%)		55.4	
Gender					
Male	51	36 (70.6%)	0.6574	54.0	0.9059
Female	41	27 (65.9%)		53.4	
Location					
Upper third	21	14 (66.7%)	0.5558	57.4	0.9837 <sup>f</sup>
Middle third	21	12 (57.1%)		58.7	
Lower third	45	33 (73.3%)		56.1	
Whole	5	4 (80.0%)		0.0	
Gross type					
Localized	36	15 (41.7%)	<0.0001	82.1	<0.0001
Infiltrative	56	48 (85.7%)		34.5	
Size (maximal diameter)					
<5 cm	51	26 (51.0%)	<0.0001	77.2	<0.0001
$\geq 5$ cm	41	37 (90.2%)		20.3	
Histological type					
Intestinal	26	14 (53.8%)	0.0809	82.9	0.0011
Diffuse	66	49 (72.4%)		40.2	
Depth of invasion (pT)					
T1	19	2 (10.5%)	<0.0001	94.1	<0.0001
T2	13	9 (69.2%)		72.5	
T3	41	35 (85.4%)		42.7	
T4	19	17 (89.5%)		7.9	

Table 1. Cont.

Characteristics	No.	High Expression <sup>a</sup> No. (%)	p-Value <sup>b</sup>	5-yr S.R. <sup>c</sup>	Log-Rank p <sup>d</sup>
Serosal invasion					
No (T1, T2)	32	11 (34.4%)	<0.0001	85.9	<0.0001
Yes (T3, T4)	60	52 (86.7%)		31.9	
Lymph node status (pN)					
N0	30	9 (30.0%)	<0.0001	93.1	<0.0001
N1	34	28 (82.4%)		48.0	
N2	18	16 (88.9%)		17.1	
N3	10	10 (100.0%)		0.0	
Lymph node metastasis					
No	30	9 (30.0%)	<0.0001	93.1	<0.0001
Yes	62	54 (87.1%)		32.1	
Distant metastasis (pM)					
No	75	46 (61.3%)	0.0010	67.2	<0.0001
Yes	17	17 (100.0%)		0.0	
Pathological stage (pStage)					
Stage I	23	4 (17.4%)	<0.0001	100.0	<0.0001
Stage II	12	7 (58.3%)		68.8	
Stage III	37	33 (89.2%)		42.3	
Stage IV	20	9 (95.0%)		0.0	
Pathological stage					
Stage I, II	35	11 (31.4%)	<0.0001	90.1	<0.0001
Stage III, IV	57	52 (91.2%)		25.2	
Liver metastasis					
No	89	60 (67.4%)	0.5490	55.3	0.0030
Yes	3	3 (100.0%)		0.0	
Peritoneal seeding					
No	77	49 (63.6%)	0.0312	65.9	<0.0001
Yes	15	14 (93.3%)		0.0	
Vascular invasion					
No	68	45 (66.2%)	0.6099	64.7	0.0001
Yes	24	18 (75.0%)		19.9	
Lymphatic invasion					
No	38	17 (44.7%)	<0.0001	79.6	<0.0001
Yes	54	46 (85.2%)		35.7	
Perineural invasion					
No	52	30 (57.7%)	0.0133	68.8	0.0008
Yes	40	33 (82.5%)		32.4	
DEK <sup>(e)</sup> (IHC) expression					
Low	29			81.7	0.0004
High	63			40.0	

<sup>a</sup> High expression of DEK IHC staining: positive rate  $\geq 51\%$  of tumor cells. <sup>b</sup> Fisher's exact test (for two groups) or chi-squared test (for more than two groups). <sup>c</sup> Five-year survival rate. <sup>d</sup> Log-rank test. <sup>e</sup> "Low": positive staining rate  $< 51\%$  of tumor cells; "High": positive staining rate  $\geq 51\%$  of tumor cells. <sup>f</sup> If "whole" is not included.

**Table 2.** IHC scores for DEK expression in tumor tissues and adjacent nontumor tissues of the GC patients.

Tissues	No. Patients	DEK Staining Score <sup>a</sup> /No. Patients (%)			
		-	+	++	+++
Tumor	92	0	0	29 (31.5%)	63 (68.5%)
Adjacent mucosa	90	0	2 (2.2%)	88 (97.8%)	0

<sup>a</sup> IHC staining score: "-" ( $< 1\%$  positive cells); "+" (1%–10% positive cells); "++" (11%–50% positive cells); "+++" ( $\geq 51\%$  positive cells).

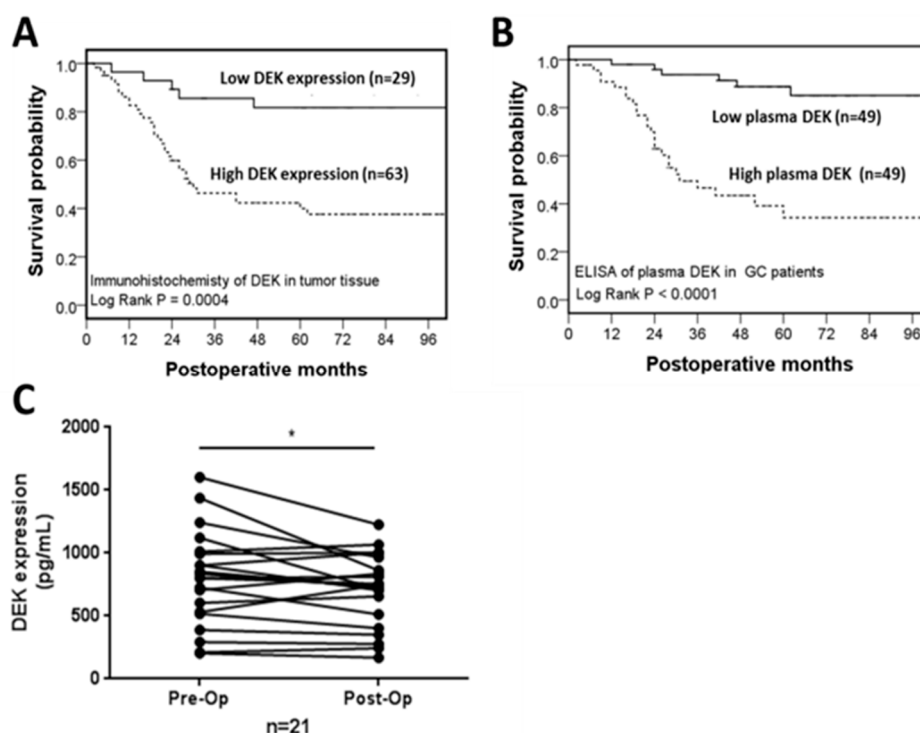


**Figure 2.** Kaplan–Meier survival curves of GC patients in two divided groups, high and low expressions, according to the IHC staining and plasma level in 98 GC patients. (A) DEK IHC staining in tumor tissues (positive stained cells: “<51%” vs. “≥51%”) (B) Plasma DEK level in GC patients (“<median” vs. “≥median”). (C) Plasma DEK level in 21 GC cases from the 98 original GC patients (paired pre- and postoperative samples), surgical removal of the tumor using paired sample *t*-tests.

### 2.3. Correlation of Plasma DEK with Clinicopathological Characteristic and Survival Outcome in GC Patients

A high expression of plasma DEK was significantly associated with the clinical and pathological characteristics of tumor progression, metastasis, or advanced stage of GC, manifested in the parameters: gross type, tumor size, histological type, depth of invasion, serosal invasion, lymph node metastasis, distant metastasis, pathological stage, liver metastasis, peritoneal seeding, vascular invasion, lymphatic invasion, and perineural invasion (Table 3). Figure 2B depicts the cumulative survival curves of the low and high plasma DEK expression groups, subdivided according to a median value of 734.0 pg/mL. The five-year survival rate of the low DEK expression group was significantly greater than that of the high expression group ( $p < 0.0001$ ; Figure 2B; Table 3). Multivariate analysis was further performed to determine the independent potential of plasma DEK for GC prognosis in association with significant clinicopathological parameters identified in the univariate analysis. It revealed plasma DEK emerged as an independent prognostic biomarker for GC ( $p = 0.035$ , HR = 3.061, 95% CI = 1.079–8.682; Table 4). We speculate that a larger GC tumor burden may promote the release of a greater amount of plasma DEK from cancer cells into the bloodstream, when the disease is in progression. Thus, plasma DEK level is elevated in parallel to both tumor stage and progression of GC.

In 21 available patients from the 98 original GC patients, plasma DEK was measured both before and after gastrectomy. Plasma DEK was significantly reduced in 13 patients after gastric resection ( $p = 0.0427$  by paired sample *t*-test) (Figure 2C).

**Table 3.** Correlation of clinicopathological characteristics and 5-year survival rates with plasma DEK expressions in 98 GC patients.

Clinicopathological Correlations				Univariate Analysis	
Characteristics	No.	Mean $\pm$ SE Plasma DEK (pg/mL) <sup>a</sup>	<i>p</i> <sup>b</sup>	5-yr S.R. <sup>c</sup>	Log-Rank <i>p</i> <sup>d</sup>
Age (yrs)					
<65	45	762.4 $\pm$ 79.1	0.4205	60.1	0.2335
$\geq$ 65	53	820.7 $\pm$ 69.3		67.2	
Gender					
Male	56	751.3 $\pm$ 61.5	0.5346	69.8	0.1061
Female	42	850.8 $\pm$ 88.6		56.4	
Location					
Upper third	21	816.2 $\pm$ 105.2	0.7472	54.6	0.3590 <sup>(f)</sup>
Middle third	23	795.1 $\pm$ 120.5		75.6	
Lower third	50	770.0 $\pm$ 71.6		68.7	
Whole	4	987.5 $\pm$ 283.4		0.0	
Gross type					
Localized	47	584.3 $\pm$ 78.1	<0.0001	86.4	<0.0001
Infiltrative	51	987.1 $\pm$ 58.0		42.7	
Size (maximal diameter)					
<5 cm	55	613.6 $\pm$ 57.3	<0.0001	84.8	<0.0001
$\geq$ 5 cm	43	1024.5 $\pm$ 81.2		34.3	
Histological type					
Intestinal	28	554.9 $\pm$ 72.4	0.0058	92.6	0.0016
Diffuse	70	889.5 $\pm$ 63.5		53.2	
Depth of invasion (pT)					
T1	24	311.4 $\pm$ 58.6	<0.0001	93.3	<0.0001
T2	17	774.2 $\pm$ 151.8		86.3	
T3	42	909.8 $\pm$ 61.1		58.0	
T4	15	1263.6 $\pm$ 136.6		0.0	
Serosal invasion					
No (T1, T2)	41	503.3 $\pm$ 76.9	<0.0001	90.5	<0.0001
Yes (T3, T4)	57	102.9 $\pm$ 56.2		42.1	
Lymph node status (pN)					
N0	37	505.8 $\pm$ 80.2	<0.0001	91.9	<0.0001
N1	36	893.9 $\pm$ 70.0		65.9	
N2	17	1065.1 $\pm$ 126.0		21.6	
N3	8	1100.1 $\pm$ 148.8		14.3	
Lymph node metastasis					
No	37	505.8 $\pm$ 80.2	<0.0001	91.9	0.0001
Yes	61	868.7 $\pm$ 57.7		46.3	
Distant metastasis (pM)					
No	81	674.7 $\pm$ 49.8	<0.0001	77.0	<0.0001
Yes	17	1362.1 $\pm$ 105.7		0.0	
Pathological stage (pStage)					
Stage I	30	375.2 $\pm$ 79.3	<0.0001	100.0	<0.0001
Stage II	12	752.4 $\pm$ 150.4		75.8	
Stage III	37	872.7 $\pm$ 44.5		54.0	
Stage IV	19	1327.8 $\pm$ 104.1		0.0	
Pathological stage					
Stage I, II	42	483.0 $\pm$ 75.0	<0.0001	92.6	<0.0001
Stage III, IV	56	1027.1 $\pm$ 53.9		35.6	
Liver metastasis					
No	97	968.1 $\pm$ 52.2	0.2095	64.9	0.0022
Yes	1	1354.1		0.0	
Peritoneal seeding					
No	83	717.4 $\pm$ 53.3	0.0006	74.0	<0.0001
Yes	15	1217.3 $\pm$ 123.9		14.3	
Vascular invasion					
No	71	678.8 $\pm$ 57.3	0.0003	75.0	0.0001
Yes	27	1096.5 $\pm$ 92.5		34.4	



Table 3. Cont.

Clinicopathological Correlations				Univariate Analysis	
Characteristics	No.	Mean $\pm$ SE Plasma DEK (pg/mL) <sup>a</sup>	$p^b$	5-yr S.R. <sup>c</sup>	Log-Rank $p^d$
Lymphatic invasion					
No	43	576.0 $\pm$ 71.3	0.0001	88.1	0.0001
Yes	55	964.2 $\pm$ 65.9		44.7	
Perineural invasion					
No	54	600.3 $\pm$ 64.4	<0.0001	80.7	0.0001
Yes	44	1031.5 $\pm$ 72.3		42.1	
DEK (Plasma)					
<median <sup>(e)</sup> (=734.0 pg/mL)	49			88.7	<0.0001
$\geq$ median	49			34.2	
CEA (Plasma)					
<median (=2.11 ng/mL)	49			57.1	0.1442
$\geq$ median	49			67.6	
CA19.9 (Plasma)					
<median (=9.91 U/mL)	49			70.2	0.3420
$\geq$ median	49			57.9	
CRP (Plasma)					
<median (=1.79 mg/L)	49			83.9	<0.0001
$\geq$ median	49			41.7	

<sup>a</sup> Plasma DEK (pg/mL) as the mean  $\pm$  SE by ELISA. <sup>b</sup> Mann–Whitney  $U$  test (for two groups) or Kruskal–Wallis test (for more than two groups). <sup>c</sup> Five-year survival rate. <sup>d</sup> Log-rank test. <sup>e</sup> = 50th percentile. <sup>f</sup> If “whole” not included.

**Table 4.** Multivariate survival analyses of various characteristics of 98 GC patients using a Cox regression model.

Characteristics	B <sup>a</sup>	SE <sup>b</sup>	Wald	HR <sup>c</sup>	95% CI <sup>d</sup>	P <sup>e</sup>
Histological type (intestinal/diffuse)	1.341	1.113	1.451	3.824	0.431–33.902	0.228
Gross type (localized/infiltrative)	0.442	0.661	0.446	1.555	0.425–5.687	0.504
Tumor size (<5 cm/ $\geq$ 5 cm)	0.644	0.653	0.974	1.905	0.530–6.851	0.324
Serosal invasion (no/yes)	−0.085	0.820	0.011	0.918	0.184–4.581	0.917
Lymph node metastasis (no/yes)	0.176	1.072	0.027	1.192	0.146–9.742	0.870
Distant metastasis (no/yes)	0.102	0.623	0.027	1.107	0.326–3.754	0.871
Liver metastasis (no/yes)	3.363	1.848	3.312	28.887	0.772–1081.15	0.069
Pathological stage (I, II/III, IV)	1.375	1.096	1.573	3.955	0.461–33.926	0.210
Peritoneal invasion (no/yes)	0.301	0.668	0.203	1.351	0.365–5.007	0.652
Vascular invasion (no/yes)	0.268	0.464	0.333	1.307	0.526–3.247	0.564
Lymphatic invasion (no/yes)	−0.040	0.717	0.003	0.961	0.236–3.920	0.956
Perineural invasion (no/yes)	0.265	0.506	0.274	1.303	0.484–3.511	0.601
CRP (<median/ $\geq$ median)	0.311	0.500	0.387	1.365	0.512–3.639	0.534
Plasma DEK level (<median/ $\geq$ median)	1.119	0.532	4.421	3.061	1.079–8.682	0.035

<sup>a</sup> B coefficient <sup>b</sup> Standard error <sup>c</sup> Hazard ratio <sup>d</sup> Confidence interval <sup>e</sup> Cox regression model.

#### 2.4. Plasma DEK as a Potential Diagnostic Biomarker in GC Patients

As shown in Figure 3A, plasma DEK levels of GC patients (mean = 786.14 pg/mL) were significantly higher than for healthy controls (mean = 345.81 pg/mL) ( $p < 0.0001$ ). Furthermore, for evaluating the diagnostic accuracy or discrimination between GC patients and healthy controls, ROC analysis of the four biomarkers were plotted. The areas under ROC curves (AUC) were calculated: 0.797 for DEK, 0.770 for CEA, 0.593 for CRP, and 0.555 for CA19.9 (Table 5; Figure 3B). AUC can provide a rough guide for classifying the accuracy of a diagnostic test in the traditional academic point system: 0.90–1.0

= excellent; 0.80–0.90 = good; 0.70–0.80 = fair; 0.60–0.70 = poor; 0.50–0.60 = fail [27]. Accordingly, both DEK and CEA would be classified as “fair”, whereas both CRP and CA19.9 would be “fail”. Pairwise comparison of AUCs between biomarkers revealed that both DEK and CEA are comparable in AUC ( $p = 0.5493$ ), and both are superior to CA19.9 ( $p < 0.0001$ ) and CRP ( $p < 0.0001$ ) in terms of diagnostic accuracy (Table 6). If plasma DEK was combined with CEA or CA19.9, the diagnostic accuracy could be upgraded (AUC = 0.855 and 0.802, respectively), from “fair” into the “good” category (AUC > 0.8); however, the improvement was not statistically significant from a single use of plasma DEK ( $p = 0.1483$ ,  $p = 0.9089$ , and  $p = 0.9819$ , respectively; Figure 3C, Tables S2 and S3).

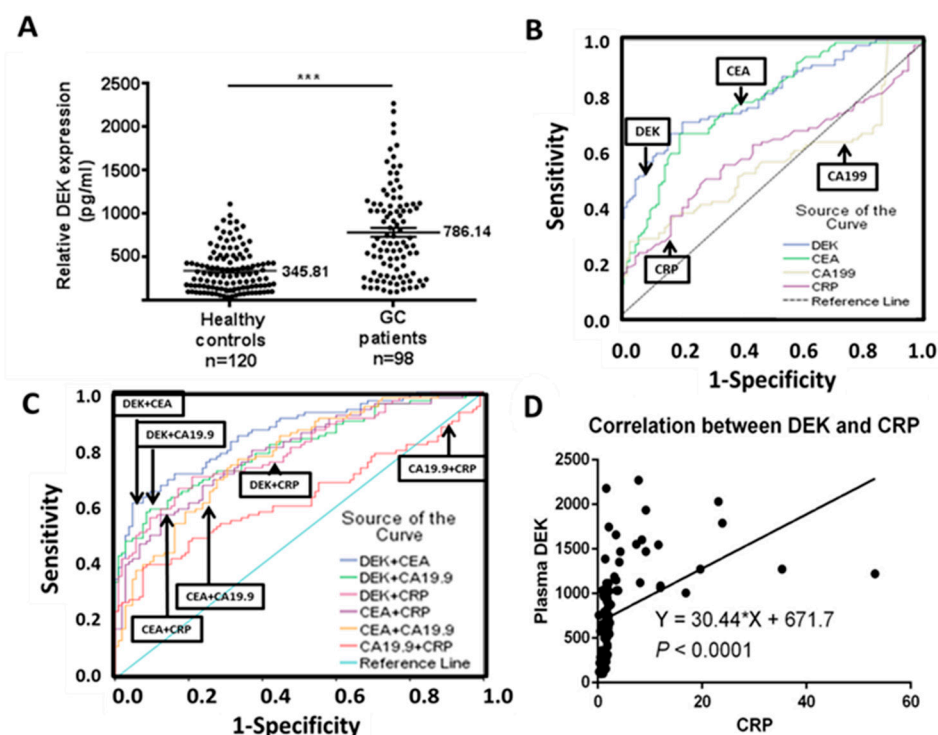


**Figure 3.** DEK levels in plasma from GC patients. (A) ELISA determination of plasma DEK levels in 120 healthy controls and 98 GC patients. (B) ROC curve analysis of DEK, CEA, and CA19.9 for discrimination between 98 GC patients and 120 healthy controls. AUC, area under the ROC curve. Logistic regression models were used for all pairwise comparisons. (C) ROC curve analysis of two combined in DEK, CEA, and CA19.9 for discrimination between 98 GC patients and 120 healthy controls. (D) Pearson’s correlation scatter plot of plasma DEK with plasma CRP in 98 GC patients ( $p < 0.0001$ ).

**Table 5.** The AUC, sensitivity and specificity of plasma DEK CEA, CA19.9, and CRP for diagnosis of GC, calculated from the ROC analysis.

Biomarkers	AUC <sup>a</sup>	SE <sup>b</sup>	<i>p</i> -Value <sup>c</sup>	Cut-Off Value	Sensitivity <sup>d</sup>	Specificity <sup>e</sup>
DEK	0.797	0.031	<0.001	484.22 pg/mL	70.4%	79.0%
CEA	0.770	0.033	<0.001	1.90 ng/mL	66.3%	80.0%
CA19.9	0.555	0.042	0.1726	23.57 U/mL	27.6%	95.8%
CRP	0.593	0.041	0.0228	1.81 mg/L	50.0%	74.2%

<sup>a</sup> AUC, area under the ROC curve. <sup>b</sup> SE, standard error. <sup>c</sup> Fisher’s exact test. A *p*-value > 0.05 was not significant. <sup>d</sup> Sensitivity indicates proportion of plasma-positive patients among cancer patients. <sup>e</sup> Specificity indicates proportion of cancer-free participants among plasma-negative participants.

**Table 6.** Pairwise comparisons (in *p*-values) of AUC, sensitivity, and specificity of biomarkers for GC, based on the ROC curves.

Biomarkers	AUC <sup>a</sup>	Sensitivity <sup>b</sup>	Specificity <sup>b</sup>
DEK vs. CEA	0.5493	0.5388	0.8573
DEK vs. CA19.9	<0.0001	<0.0001	0.0003
DEK vs. CRP	<0.0001	0.0035	0.4819
CEA vs. CA19.9	<0.0001	<0.0001	0.0004
CEA vs. CRP	0.0005	0.0205	0.3568
CA19.9 vs. CRP	0.4911	0.0013	<0.0001

<sup>a</sup> *p*-values by online calculator: “comparison of Two ROC Curves—VassarStats”. <sup>b</sup> *p*-values by chi-squared test.

The sensitivity and specificity that derived from the ROC analysis are also shown in Table 5. Plasma DEK has better sensitivity for GC diagnosis than the other three biomarkers ( $p < 0.0001$  for CA19.9 and  $p = 0.0205$  for CRP), but it was not significant for CEA ( $p = 0.5388$ ) (Tables 4 and 5). The specificity of plasma DEK was inferior to CA19.9 ( $p = 0.0003$ ), but it was not significantly different from CEA and CRP (Tables 5 and 6). However, if the cut-off values of the four biomarkers in ROC analysis were changed by using the upper limit (97.5 percentile) of reference ranges of the healthy controls to calculate the sensitivity, the upper limit of the reference range in our 120 healthy controls would be the following: 846.63 pg/mL for DEK, 3.65 ng/mL for CEA, 23.42 U/mL for CA19.9, and 3.62 mg/L for CRP, respectively, and the sensitivity of the plasma biomarkers would be changed accordingly as in Table 7. For GC diagnosis, the sensitivity of DEK was significantly superior to the other three biomarkers, CEA, CRP, and CA19.9 ( $p = 0.0063$ ,  $p = 0.0363$  and  $p = 0.0004$ , respectively, whereas the specificity of DEK did not differ significantly from the other three biomarkers (Table 8).

**Table 7.** Sensitivity and specificity for the diagnosis of GC among 98 GC patients and 120 healthy controls. The 97.5 percentile was set as the upper limit of the reference range of the healthy controls in calculating the sensitivity and specificity of each plasma biomarker.

Plasma Biomarkers	Upper Limit of Reference Range	Sensitivity	Specificity
DEK	846.63 pg/μL	42.9%	64.1%
CEA	3.65 ng/mL	23.5%	64.3%
CA19.9	23.42 U/mL	27.6%	61.6%
CRP	3.62 mg/L	18.4%	59.0%

**Table 8.** Pairwise comparisons (*p*-value <sup>a</sup>) of sensitivity of plasma biomarkers between plasma biomarkers in 98 GC patients, based on the cut-off point set at the upper limit (97.5 percentile) of reference ranges of the healthy controls.

Biomarkers	Sensitivity
DEK vs. CEA	0.0063
DEK vs. CA19.9	0.0363
DEK vs. CRP	0.0004
CEA vs. CRP	0.6250
CEA vs. CA19.9	0.4824
CRP vs. CA19.9	0.1742

<sup>a</sup> *p*-value by chi-squared test. Significant if  $<0.05$ .

Notably, a moderately positive correlation was evident between plasma DEK and CRP levels ( $r = 0.445$ ,  $p < 0.0001$ ; Figure 3D). Moreover, among the four plasma markers, both DEK and CRP had a prognostic effect on patients' survival in the univariate analysis (Table 3). CRP also had a higher sensitivity than CA19.9 in the ROC analysis ( $p = 0.0013$ ).

### 2.5. DEK Is Involved in the Invasive Ability of GC Cell Lines

To explore the potential role of DEK in GC cell invasion, cells were transfected with shDEK plasmid to eliminate endogenous DEK expression in AGS cell lines and the consequent effects on invasive activity assessed. In Western blot experiments, DEK protein levels were clearly reduced in AGS cells transfected with shDEK1 and shDEK2, compared with those transfected with shLuc control, as shown in Figure 4A, left. Notably, the invasion ability of DEK-knockdown AGS cell lines was reduced to 0.34- and 0.37-fold that of control GC cells, respectively (Figure 4B). To further establish whether overexpression of DEK conversely increases invasive ability, BGC and SGC cell lines were transfected with pcDNA3-DEK plasmid (Figure 4A, right). As shown in Figure 4C,D, overexpression of DEK promoted the invasive ability of BGC and SGC by 2.31- and 2.26-fold, respectively, compared to cells transfected with the pcDNA3 control vector.

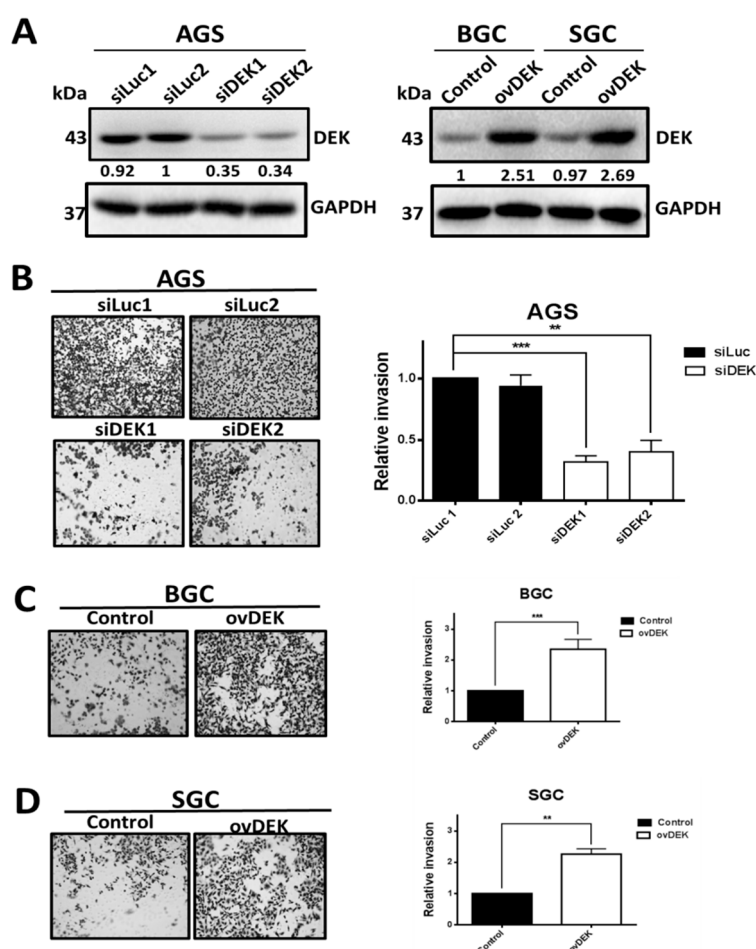


**Figure 4.** DEK contributes to the invasive ability of GC cells. (A) Knockdown of DEK inhibits the invasive ability of the AGS cell line. AGS cells were transfected with control and DEK siRNA, respectively. After two days, cell lysates were prepared and the extracted proteins (50 µg) analyzed via Western blot (left). Moreover, overexpression of DEK enhances the invasive abilities of BGC and SGC cells. The two GC cell lines were transfected with control pcDNA and pcDEK. After two days, cell lysates were prepared, and the extracted proteins (50 µg) analyzed via Western blot (right). (B) Invasion assay of GC cell lines. Representative microphotographs of filters obtained from the invasion assay are shown, along with quantitative analysis. (C,D) Invasion assay of cell lines as described in Materials and Methods. Representative microphotographs of filters obtained from the invasion assay are shown, along with quantitative analysis. Data are presented as mean values of cell counts obtained from three independent experiments. A *p*-value less than 0.05 indicates statistical significance according to the Mann–Whitney *U* test (\* *p* < 0.01, \*\* *p* < 0.05, \*\*\* *p* < 0.001).

### 2.6. DEK Promotes GC Cell Metastasis Mediated by MMP-2 and MMP-9

Overexpression of the oncogene DEK may induce an autocrine or paracrine mechanism through the release of several proinflammatory factors (IL-8, c-IAP2, MCP-1/CCL-2) during tumorigenesis and chronic inflammation [28]. Based on previous studies, we examined the interactions between DEK protein and other factors involved in the inflammatory pathway, including MMP-2, MMP-9, p53, VEGF, HIF-1 $\alpha$ , and RhoA. Notably, p53, VEGF, HIF-1 $\alpha$ , and RhoA levels in cell lines stably expressing DEK remained unchanged, as determined via Western blot (Figure S2), whereas MMP-2 and MMP-9 expression was significantly increased in AGS but decreased in BGC and SGC cell lines (Figure 5A). Gelatin zymography further showed that MMP-2 and MMP-9 level increased upon expression of DEK in AGS cells but decreased in BGC and SGC cells overexpressing DEK (Figure 5B). The collective results indicate that DEK participates in cell invasion during tumorigenesis of GC via a mechanism involving MMP-2 and MMP-9.

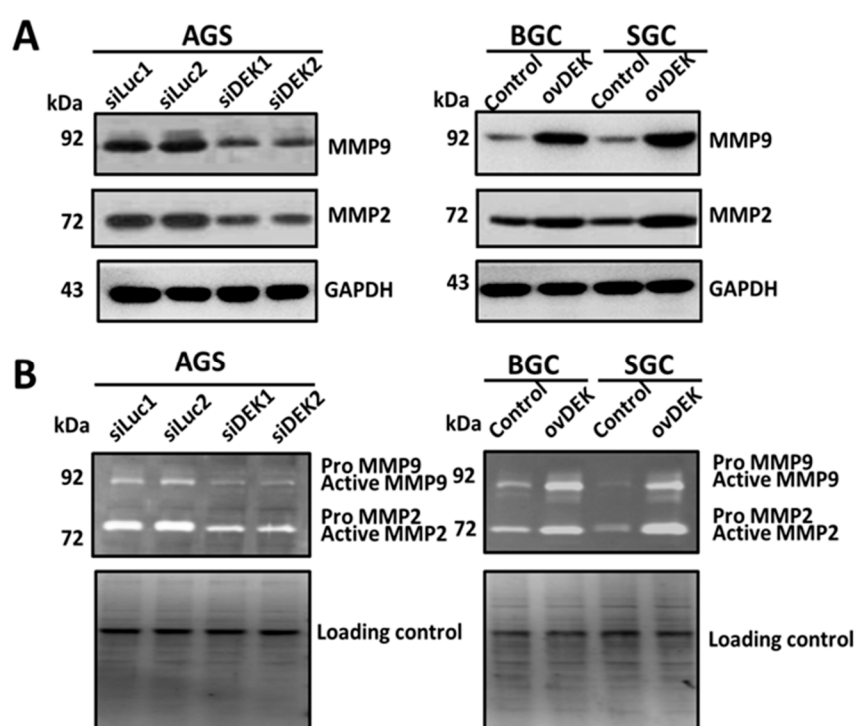


**Figure 5.** DEK induces MMP-9/MMP-2 level. (A) Total cell lysates from AGS, BGC, and SGC cells were analyzed via Western blot to detect MMPs. Actin served as an internal control. (B) Zymography revealing MMP-2 and MMP-9 expression in AGS, BGC, and SGC cells. Conditioned media from the three cell lines were assayed for MMP level as described in Materials and Methods. The electrophoretic positions of both proenzymes and active MMPs are shown.

### 3. Discussion

Detection of conventional serum tumor biomarkers (CEA, CA19.9, and CA72.4) is commonly applied for diagnosis and follow-up of GC [29]. The identification of novel biomarkers for GC is a feasible option to improve treatment outcomes [30]. Both genomic and proteomic approaches have recently been applied to understand global proteomic dynamics in tissue and plasma specimens. Importantly, research on the human plasma proteome database indicates that DEK is released into the blood, a common phenomenon in GC tissues, which further supports the theory that proteomics presents an efficient method to discover potentially useful biomarkers for GC.

In this study, plasma DEK (AUC = 0.797) displayed higher diagnostic accuracy than CEA (AUC = 0.770), CRP (AUC = 0.593), and CA19.9 (AUC = 0.555). Accordingly, the diagnostic accuracy



of DEK was classified as “fair”, a little below that required for a “good” grade ( $AUC > 0.8$ ) in ROC analysis highlighting the need for additional studies with larger sample sizes. Notably, plasma DEK combined with CEA could escalate the diagnostic accuracy into a good grade ( $AUC > 0.8$ ) (Figure 3C and Table S2). CEA and CA19.9 are the two most commonly used biomarkers of GC with reported sensitivity and specificity of  $\approx 30\%$  and  $72\%–95\%$ , respectively [4,31]. The sensitivity and specificity of plasma DEK in our series were  $42.9\%$  and  $64.1\%$ , respectively, based on the cut-off value ( $846.63 \text{ pg/mL}$ ) at the upper limit of reference range in our 120 healthy controls (Table 7). Plasma DEK would show a higher sensitivity than CEA, CA19.9, and CRP in the diagnosis of GC. Moreover, both CRP and DEK could be induced and secreted into the blood stream in response to inflammation [5,28,32]. Our data indicate a positive association between plasma DEK and CRP in GC patients. The superiority of plasma DEK over CEA, CA19.9, and CRP in diagnostic accuracy supports the clinical usefulness of plasma DEK in the detection of malignancy. DEK has been investigated as a potential tissue biomarker for many human cancers to date [16,28,33].

In this study, we selected DEK for the biological function study in GC, due to its upregulation in both tumor and blood stream. Furthermore, involvement of DEK in several signaling pathways, including p53, NF- $\kappa$ B, Wnt, mTOR, and Rho, has been reported [28,32,34,35], although the precise signaling mechanism underlying its expression remains to be established. DEK is actively secreted in both free form (non-classical) and exosome (classical) [8], which could be detectable in urine (bladder cancer) [11], plasma (oropharyngeal) [36], synovial fluid (juvenile idiopathic arthritis (JIA)) [26,37], and the HepG2 cell line (conditioned medium) [22,23]. Macrophages are not the only cells that secrete DEK in association with poor prognosis [26]. In vitro, DEK is polyADP-ribosylated and released into the extracellular space by apoptotic cells [38]. These results highlight a potential role of extracellular DEK in stimulating tumor-associated immunological responses and intracellular oncogenic activity in adjacent epithelial cells within the tumor microenvironment. To further confirm that DEK in plasma is of tumoral origin, a complex response process that transfers changes from tissue to the circulating system is essential. Accordingly, we compared plasma DEK before and after gastrectomy in a postoperative follow-up survey in 21 GC patients from the 98 original GC patients (Figure 2C). Plasma DEK level was significantly reduced in 13 patients ( $p = 0.0427$ , by paired sample  $t$ -test). These data suggest that plasma DEK may be tumor-derived and have the potential to be a novel biomarker for monitoring GC dynamics. However, immune cells in the tumor microenvironment may also affect plasma DEK concentrations through the bloodstream. DEK may mediate inflammation and immunity responses in tumor microenvironments. On the other hand, our data showed a positive correlation between intratumoral DEK staining scores and plasma DEK concentrations, suggesting that a large tumor burden promotes release of DEK from cancer cells. The implications of DEK activity in the context of tumorigenic microenvironments are poorly understood at present. Data from the current study provide potential insights that should aid in elucidating the mechanisms underlying regulation of GC tumorigenesis by DEK.

You et al. [39] demonstrated that the epithelial–mesenchymal transition (EMT) of colorectal carcinoma cells is partially mediated by DEK-regulated E-cadherin, vimentin, and matrix metalloproteinase (MMP-9). Another group showed that silencing of DEK led to downregulation of Wnt/ $\beta$ -catenin and MMP-9 in cervical cancer [13]. Experiments on a rat model by Sadeeshkumar et al. [40] additionally disclosed that DEK modulates the expression of key molecules that regulate apoptosis, inflammation, invasion, and angiogenesis (MMP-2/-9, VEGF). Furthermore, another group reported that microRNA-1292-5p directly targets DEK-mediated migration, invasion, and cell growth [41].

In summary, plasma DEK is superior to CEA, CA19.9, and CRP in terms of the sensitivity for the detection of GC. Its diagnostic accuracy ( $=0.797$ ) by ROC analysis is still not satisfactory for clinical practice, unless it can be classified into the “good” level ( $=0.800$ ). Nevertheless, it may serve as a novel biomarker effective for monitoring the progression or metastasis in GC patients. Further research,

preferably with the aid of large prospective studies, is warranted, before DEK can be clinically applied as a non-invasive screening marker and therapeutic target for GC.

#### 4. Materials and Methods

This study intended to identify useful biomarkers in both tumor tissues and peripheral bloods from 98 GC patients and 120 healthy controls.

##### 4.1. Clinical Specimens

The study was approved by the Institutional Review Board (IRB No. 103–7252B) of Chang Gung Memorial Hospital (CGMH). The specimens consisted of (1) fresh plasma from presurgical GC patients and healthy controls and (2) fresh stomach tissues surgically removed (gastrectomy) from GC patients. Both were frozen and stored in the Biobank of Chang Gung Memorial Hospital.

Whole blood of GC patients was withdrawn one day before surgery. Blood was centrifuged at 12,000 rpm for 15 min and isolated to collect plasma samples, which were frozen at  $-70^{\circ}\text{C}$  until use. All patients were pathologically diagnosed with gastric carcinoma and underwent gastric resection at CGMH of Chiayi. Tissue specimens were obtained from 92 patients (51 males and 41 females; median age of 67.5 years, range 28–84 years) who underwent surgery between 2001 and 2008.

Plasma specimens were obtained before surgery from 98 patients (58 males and 42 females; median age of 66.6 years, range 28–87 years) who also underwent gastrectomy between 2004 and 2012. The demographic characteristics of patients who contributed both tissue and plasma specimens are presented in Tables 1 and 3, respectively. Frozen plasma was additionally donated by 120 healthy control volunteers from the CGMH Healthcare Center (54 males and 66 females) between 2016 and 2017 for analysis. Further, plasma DEK was measured both before and after gastrectomy in 21 available patients from the 98 original GC patients (Figure 2C).

##### 4.2. Statistical Analysis

The Mann–Whitney *U* test (for two groups), the Kruskal–Wallis test (for more than two groups), or Fisher’s exact test was performed for between-group comparisons. The correlation between two paired variables was investigated using bivariate Pearson’s correlation coefficient. For determining prognostic significance, the cumulative 5-year survival rates of all GC patients were calculated using the log-rank test (excluding patients who died from diseases other than GC) to compare survival distribution of the groups. Cox’s proportional hazards model was applied as a multivariate analysis to identify independent predictors of survival. For diagnostic test evaluation, we applied SPSS software to plot receiver operating characteristic (ROC) curves that would generate an area under the curve (AUC) and its statistical significance. For combined ROC analysis, we applied the binary logistic regression to calculate the covariates for combined biomarkers according to their plasma levels, and then used the results as the probability to plot ROC curves [42]. Statistical analyses were performed using SPSS software (Version 19.0, SPSS Inc., Chicago, IL, USA). Data were considered statistically significant at *p*-values  $<0.05$ .

##### 4.3. Cell Culture

Human GC cell lines (AGS) obtained from the American Type Culture Collection (ATCC, CRL-1739, Manassas, WV, USA) as well as BGC and SGC (Xiamen, China) were incubated in Roswell Park Memorial Institute (RPMI) medium 1640 (Invitrogen, Waltham, MA, USA) with 10% fetal bovine serum (FBS) plus 100 IU/mL penicillin G and 100 mg/mL streptomycin sulfate (Sigma-Aldrich, St Louis, MO, USA) and nonessential amino acids (NEAA) at  $37^{\circ}\text{C}$  in 95% air and 5%  $\text{CO}_2$  [43].

#### 4.4. Measurement of CEA, CA19.9, and CRP Levels

Plasma CEA, CA19.9, and CRP levels were detected via fully automated electrochemistry luminescence immunity analyzer with the Roche Modular E170 platform (Roche Diagnostics, Mannheim, Germany) in the Department of Laboratory Medicine at CGMH [43].

#### 4.5. qRT-PCR

Total RNA was extracted via TRIzol reagent (Invitrogen, Carlsbad, CA, USA) from surgical specimens. The concentrations of all RNA samples were determined using a Colibri Microvolume Spectrometer (Pforzheim, Germany) [44]. To evaluate DEK mRNA expression in GC tissues, qRT-PCR was performed as described previously, using 18sRNA as an internal control for DEK [44,45]. Fluorescence emitted by SYBR Green was assayed using the ABI PRISM 7500 sequence detection system (Applied Biosystems, Warrington, UK). The primers used for RT-qPCR were as follows: DEK (forward, 5'-CAAAGCCTTCTGGCAAACCA-3', and reverse, 5'-CCTTGCCATTCCAGAACTGTTC-3') and human 18s rRNA (forward, 5'-CGAGCCGCTGGATACC-3', and reverse, 5'-CCTCAGTTCGAAACCAACAA-3').

#### 4.6. Western Blot

Total cell extracts were subjected to 12% SDS-PAGE and separated proteins transferred to polyvinylidene fluoride membrane. Western blot was performed using standard protocols described previously [46]. Rabbit anti-DEK, anti-E-cadherin, anti-vimentin, anti-MMP2, and anti-MMP9 antibodies were purchased from Proteintech (Chicago, IL, USA). Mouse anti-GAPDH antibody was obtained from Chemicon (Temecula, CA, USA).

#### 4.7. ELISA

Plasma DEK protein levels were measured using the Human Protein DEK ELISA Kit (MyBiosource, San Diego, CA, USA). All plasma samples were diluted 1:8 in sample dilution buffer, and various amounts of DEK recombinant protein added to the wells. Fluorescence intensity was measured at 450 nm using a SpectraMax M5 microplate reader (Molecular Devices, Sunnyvale, CA, USA).

#### 4.8. Overexpression/Depletion of DEK in GC Cell Lines

For overexpression purposes, DEK cDNA was amplified using RT-PCR and cloned into pcDNA3 [43]. Transfection of pcDNA3-ovDEK or pcDNA3-control vector into GC cell lines was performed using TurboFect Reagent (Invitrogen, Grand Island, NY, USA). After 24 h of incubation, cells were transferred to G418 medium for selection and cell lysates subjected to Western blot after two weeks to determine gene overexpression efficacy. Alternatively, DEK knockdown was performed with the aid of specific shRNA. Clones of DEK-targeting shRNA (shDEK1, TRCN0000235737; shDEK2, TRCN0000235740) and shRNA-Luc control were purchased from the National RNA Interference Core Facility (Academia Sinica, Taiwan). Transfection of shRNAs targeting endogenous DEK genes into GC cell lines was performed using TurboFect Reagent (Invitrogen, Grand Island, NY, USA). After 24 h of incubation, cells were selected in the presence of puromycin for two weeks of selection, followed by Western blot analysis of lysates to determine gene knockdown efficacy.

#### 4.9. In Vitro Invasion Assay

To assess the influence of DEK overexpression or depletion in GC cell lines on metastatic activity, the in vitro Transwell assay (Becton-Dickinson, Franklin Lakes, NJ, USA) was employed. After adjusting the density to  $1 \times 10^5$  cells/100  $\mu$ L serum-free RPMI, cells were added to the upper chamber and a Matrigel-coated (invasion assay) insert used to assess invasive capability, as described previously [46].

#### 4.10. Immunohistochemistry (IHC) and Scoring

Paraffin-embedded tissues (5 µm thick) were prepared for different GC tissue specimens and IHC performed to detect DEK (Epitomics, Burlingame, CA, USA; dilution 1:150), as described previously [47]. The intensity and percentage of staining of the entire tissue section per specimen (200× magnification) was evaluated. Samples with ≥51% positively or strongly stained tumor cells were denoted “High” and those showing positive staining for <51% tumor cells denoted “Low” in IHC analyses. Alternatively, IHC scores were assigned 0 (<1% positive cells), 1+ (1%–10% positive cells), 2+ (11%–50% positive cells) or 3+ (≥51% positive cells).

#### 4.11. Gelatin Zymography

Conditioned medium from various GC cell lines was harvested and concentrated in the absence of reducing agent, in keeping with a previously reported protocol [47].

**Supplementary Materials:** Supplementary Figure and Tables can be found at <http://www.mdpi.com/1422-0067/20/22/5689/s1>.

**Author Contributions:** C.-S.W. and M.-M.T. wrote the manuscript; K.-F.L., C.-Y.T., Y.-H.O., and C.-G.H. performed the experiments and analyzed data; C.-C.H. and H.-L.H. contributed to the supporting technology; K.-H.L. reviewed and revised the manuscript.

**Funding:** This work was supported by grants from the Chang Gung Medical Research Plan (CMRP), Taoyuan, Taiwan (CMRPF1G0011, CMRPF1G0251, CMRPF1I0031, CMRPG6F0621, CMRPG6F0622, CMRPG6F623), the Ministry of Science and Technology (MOST) of the Republic of China (MOST 105-2314-B-182A-044, MOST 106-2314-B-182A-130), and Chang Gung University of Science and Technology, Taoyuan, Taiwan (ZRRPF3J0081-7).

**Acknowledgments:** The authors wish to thank Q.X. Chen. and D.W. Zhou of Xiamen University (China) for providing the BGC and SGC cell lines.

**Conflicts of Interest:** The authors declare no conflict of interest. The funders had no role in the design of the study; in the collection, analyses, or interpretation of data; in the writing of the manuscript; or in the decision to publish the results.

#### Abbreviations

AUC	Area under the curve
CA 19.9	Carbohydrate antigen 19.9
CEA	Carcinoembryonic antigen
CGMH	Chang Gung Memorial Hospital
CI	Confidence interval
CRP	C-reactive protein
ELISA	Enzyme-linked immunosorbent assay
GC	Gastric cancer
<i>Hp</i>	<i>Helicobacter pylori</i>
HR	Hazard ratio
IHC	Immunohistochemistry
iTRAQ	Isobaric tags for relative and absolute quantitation
qRT-PCR	Quantitative real-time polymerase chain reaction
MMP	Matrix metalloproteinase
ROC	Receiver operating characteristic
TNM stage	Tumor–node–metastasis stage

#### References

1. Siegel, R.L.; Miller, K.D.; Jemal, A. Cancer Statistics, 2017. *CA A Cancer J. Clin.* **2017**, *67*, 7–30. [[CrossRef](#)] [[PubMed](#)]
2. Ministry of Health and Welfare, Taiwan. The Ten Leading Cause of Death 2018. Available online: <https://www.mohw.gov.tw/cp-16-48057-1.html> (accessed on 10 September 2019).

3. Chen, X.Z.; Zhang, W.H.; Yang, K.; Zhang, B.; Chen, Z.X.; Chen, J.P.; Zhou, Z.G.; Hu, J.K. Quantitative comparisons of summary receiver operating characteristics (sROC) curves among conventional serological tumor biomarkers for predicting gastric cancer in Chinese population. *Tumour Biol.* **2014**, *35*, 9015–9022. [[CrossRef](#)] [[PubMed](#)]
4. Marrelli, D.; Roviello, F.; De Stefano, A.; Farnetani, M.; Garosi, L.; Messano, A.; Pinto, E. Prognostic significance of CEA, CA 19-9 and CA 72-4 preoperative serum levels in gastric carcinoma. *Oncology* **1999**, *57*, 55–62. [[CrossRef](#)] [[PubMed](#)]
5. Chang, C.C.; Sun, C.F.; Pai, H.J.; Wang, W.K.; Hsieh, C.C.; Kuo, L.M.; Wang, C.S. Preoperative serum C-reactive protein and gastric cancer; clinical-pathological correlation and prognostic significance. *Chang. Gung Med. J.* **2010**, *33*, 301–312. [[PubMed](#)]
6. Wang, J.; Yu, J.C.; Kang, W.M.; Ma, Z.Q. Treatment strategy for early gastric cancer. *Surg. Oncol.* **2012**, *21*, 119–123. [[CrossRef](#)]
7. Nanjappa, V.; Thomas, J.K.; Marimuthu, A.; Muthusamy, B.; Radhakrishnan, A.; Sharma, R.; Ahmad Khan, A.; Balakrishnan, L.; Sahasrabudhe, N.A.; Kumar, S.; et al. Plasma Proteome Database as a resource for proteomics research: 2014 update. *Nucleic Acids Res.* **2014**, *42*, D959–D965. [[CrossRef](#)]
8. Broxmeyer, H.E.; Mor-Vaknin, N.; Kappes, F.; Legendre, M.; Saha, A.K.; Ou, X.; O’Leary, H.; Capitano, M.; Cooper, S.; Markovitz, D.M. Concise review: Role of DEK in stem/progenitor cell biology. *Stem Cells* **2013**, *31*, 1447–1453. [[CrossRef](#)]
9. Sun, J.; Bi, F.; Yang, Y.; Zhang, Y.; Jin, A.; Li, J.; Lin, Z. DEK protein overexpression predicts poor prognosis in pancreatic ductal adenocarcinoma. *Oncol. Rep.* **2017**, *37*, 857–864. [[CrossRef](#)]
10. Chen, X.; Wu, X.; Ouyang, W.; Gu, M.; Gao, Z.; Song, M.; Chen, Y.; Lin, Y.; Cao, Y.; Xiao, H. Novel ent-Kaurane Diterpenoid from *Rubus corchorifolius* L. f. Inhibits Human Colon Cancer Cell Growth via Inducing Cell Cycle Arrest and Apoptosis. *J. Agric. Food Chem.* **2017**, *65*, 1566–1573. [[CrossRef](#)]
11. Datta, A.; Adelson, M.E.; Mogilevkin, Y.; Mordechai, E.; Sidi, A.A.; Trama, J.P. Oncoprotein DEK as a tissue and urinary biomarker for bladder cancer. *BMC Cancer* **2011**, *11*, 234. [[CrossRef](#)]
12. Adams, A.K.; Hallenbeck, G.E.; Casper, K.A.; Patil, Y.J.; Wilson, K.M.; Kimple, R.J.; Lambert, P.F.; Witte, D.P.; Xiao, W.; Gillison, M.L.; et al. DEK promotes HPV-positive and -negative head and neck cancer cell proliferation. *Oncogene* **2015**, *34*, 868–877. [[CrossRef](#)] [[PubMed](#)]
13. Xu, X.; Zou, L.; Yao, Q.; Zhang, Y.; Gan, L.; Tang, L. Silencing DEK downregulates cervical cancer tumorigenesis and metastasis via the DEK/p-Ser9-GSK-3 $\beta$ /p-Tyr216-GSK-3 $\beta$ /beta-catenin axis. *Oncol. Rep.* **2017**, *38*, 1035–1042. [[CrossRef](#)] [[PubMed](#)]
14. Xu, Y.; Liang, Z.; Li, C.; Yang, Z.; Chen, L. LCMR1 interacts with DEK to suppress apoptosis in lung cancer cells. *Mol. Med. Rep.* **2017**, *16*, 4159–4164. [[CrossRef](#)] [[PubMed](#)]
15. Secchiero, P.; Voltan, R.; di Iasio, M.G.; Melloni, E.; Tiribelli, M.; Zauli, G. The oncogene DEK promotes leukemic cell survival and is downregulated by both Nutlin-3 and chlorambucil in B-chronic lymphocytic leukemic cells. *Clin. Cancer Res.* **2010**, *16*, 1824–1833. [[CrossRef](#)]
16. Piao, J.; Shang, Y.; Liu, S.; Piao, Y.; Cui, X.; Li, Y.; Lin, Z. High expression of DEK predicts poor prognosis of gastric adenocarcinoma. *Diagn. Pathol.* **2014**, *9*, 67. [[CrossRef](#)]
17. Yu, L.; Huang, X.; Zhang, W.; Zhao, H.; Wu, G.; Lv, F.; Shi, L.; Teng, Y. Critical role of DEK and its regulation in tumorigenesis and metastasis of hepatocellular carcinoma. *Oncotarget* **2016**, *7*, 26844–26855. [[CrossRef](#)]
18. Caliskaner, Z.O.; Cakar, T.; Ozcelik, E.; Ozdilek, A.; Kim, A.S.; Dogan, O.; Bosompem, A.; Grosveld, G.; Saka, B.; Kandilci, A. DEK protein level is a biomarker of CD138positive normal and malignant plasma cells. *PLoS ONE* **2017**, *12*, e0178025. [[CrossRef](#)]
19. Bub, C.B.; Torres, M.A.; Velloso, E.D.; Silveira, P.A.; Correia, R.P.; Bacal, N.S.; Manguiera, C.L.; Fernandes, J.F.; Odone Filho, V.; Hamerschlag, N.; et al. Eosinophil chimerism in the differential diagnosis between DEK-NUP214-positive acute myeloid leukaemia relapse and chronic graft-versus-host disease. *J. Clin. Pathol.* **2015**, *68*, 950–952.
20. Riveiro-Falkenbach, E.; Ruano, Y.; Garcia-Martin, R.M.; Lora, D.; Cifdaloz, M.; Acquadro, F.; Ballestin, C.; Ortiz-Romero, P.L.; Soengas, M.S.; Rodriguez-Peralto, J.L. DEK oncogene is overexpressed during melanoma progression. *Pigment Cell Melanoma Res.* **2017**, *30*, 194–202. [[CrossRef](#)]
21. Khodadoust, M.S.; Verhaegen, M.; Kappes, F.; Riveiro-Falkenbach, E.; Cigudosa, J.C.; Kim, D.S.; Chinnaiyan, A.M.; Markovitz, D.M.; Soengas, M.S. Melanoma proliferation and chemoresistance controlled by the DEK oncogene. *Cancer Res.* **2009**, *69*, 6405–6413. [[CrossRef](#)]



22. Choi, S.; Park, S.Y.; Jeong, J.; Cho, E.; Phark, S.; Lee, M.; Kwak, D.; Lim, J.Y.; Jung, W.W.; Sul, D. Identification of toxicological biomarkers of di(2-ethylhexyl) phthalate in proteins secreted by HepG2 cells using proteomic analysis. *Proteomics* **2010**, *10*, 1831–1846. [[CrossRef](#)] [[PubMed](#)]
23. Choi, S.; Park, S.Y.; Kwak, D.; Phark, S.; Lee, M.; Lim, J.Y.; Jung, W.W.; Sul, D. Proteomic analysis of proteins secreted by HepG2 cells treated with butyl benzyl phthalate. *J. Toxicol. Environ. Health Part A* **2010**, *73*, 1570–1585. [[CrossRef](#)] [[PubMed](#)]
24. Dong, X.; Michelis, M.A.; Wang, J.; Bose, R.; DeLange, T.; Reeves, W.H. Autoantibodies to DEK oncoprotein in a patient with systemic lupus erythematosus and sarcoidosis. *Arthritis Rheum.* **1998**, *41*, 1505–1510. [[CrossRef](#)]
25. Murray, K.J.; Szer, W.; Grom, A.A.; Donnelly, P.; Levinson, J.E.; Giannini, E.H.; Glass, D.N.; Szer, I.S. Antibodies to the 45 kDa DEK nuclear antigen in pauciarticular onset juvenile rheumatoid arthritis and iridocyclitis: Selective association with MHC gene. *J. Rheumatol.* **1997**, *24*, 560–567. [[PubMed](#)]
26. Mor-Vaknin, N.; Punturieri, A.; Sitwala, K.; Faulkner, N.; Legendre, M.; Khodadoust, M.S.; Kappes, F.; Ruth, J.H.; Koch, A.; Glass, D.; et al. The DEK nuclear autoantigen is a secreted chemotactic factor. *Mol. Cell. Biol.* **2006**, *26*, 9484–9496. [[CrossRef](#)]
27. Hoeboer, S.H.; van der Geest, P.J.; Nieboer, D.; Groeneveld, A.B. The diagnostic accuracy of procalcitonin for bacteraemia: A systematic review and meta-analysis. *Clin. Microbiol. Infect.* **2015**, *21*, 474–481. [[CrossRef](#)]
28. Pease, N.A.; Wise-Draper, T.; Privette Vinnedge, L. Dissecting the Potential Interplay of DEK Functions in Inflammation and Cancer. *J. Oncol.* **2015**, *2015*, 106517. [[CrossRef](#)]
29. Zheng, T.H.; Zhao, J.L.; Guleng, B. Advances in Molecular Biomarkers for Gastric Cancer. *Crit. Rev. Eukaryot. Gene Expr.* **2015**, *25*, 299–305. [[CrossRef](#)]
30. Huang, Z.; Ma, L.; Huang, C.; Li, Q.; Nice, E.C. Proteomic profiling of human plasma for cancer biomarker discovery. *Proteomics* **2017**, *17*, 1600240. [[CrossRef](#)]
31. Liang, Y.; Wang, W.; Fang, C.; Raj, S.S.; Hu, W.M.; Li, Q.W.; Zhou, Z.W. Clinical significance and diagnostic value of serum CEA, CA19-9 and CA72-4 in patients with gastric cancer. *Oncotarget* **2016**, *7*, 49565–49573. [[CrossRef](#)]
32. Liu, K.; Feng, T.; Liu, J.; Zhong, M.; Zhang, S. Silencing of the DEK gene induces apoptosis and senescence in CaSki cervical carcinoma cells via the up-regulation of NF-kappaB p65. *Biosci. Rep.* **2012**, *32*, 323–332. [[CrossRef](#)] [[PubMed](#)]
33. Sanden, C.; Gullberg, U. The DEK oncoprotein and its emerging roles in gene regulation. *Leukemia* **2015**, *29*, 1632–1636. [[CrossRef](#)] [[PubMed](#)]
34. Iannetti, A.; Ledoux, A.C.; Tudhope, S.J.; Sellier, H.; Zhao, B.; Mowla, S.; Moore, A.; Hummerich, H.; Gewurz, B.E.; Cockell, S.J.; et al. Regulation of p53 and Rb links the alternative NF-kappaB pathway to EZH2 expression and cell senescence. *PLoS Genet.* **2014**, *10*, e1004642. [[CrossRef](#)] [[PubMed](#)]
35. Wang, J.; Sun, L.; Yang, M.; Luo, W.; Gao, Y.; Liu, Z.; Qiu, X.; Wang, E. DEK depletion negatively regulates Rho/ROCK/MLC pathway in non-small cell lung cancer. *J. Histochem. Cytochem.* **2013**, *61*, 510–521. [[CrossRef](#)]
36. Wise-Draper, T.; Sendilnathan, A.; Palackdharry, S.; Pease, N.; Qualtieri, J.; Butler, R.; Sadraei, N.H.; Morris, J.C.; Patil, Y.; Wilson, K.; et al. Decreased plasma DEK Oncogene Levels Correlate with p16-Negative Disease and Advanced Tumor Stage in a Case-Control Study of Patients with Head and Neck Squamous Cell Carcinoma. *Transl. Oncol.* **2018**, *11*, 168–174. [[CrossRef](#)]
37. Mor-Vaknin, N.; Rivas, M.; Legendre, M.; Mohan, S.; Yuanfan, Y.; Mau, T.; Johnson, A.; Huang, B.; Zhao, L.; Kimura, Y.; et al. High levels of DEK autoantibodies in sera of polyarticular JIA patients and in early flare following cessation of anti-TNF therapy. *Arthritis Rheumatol.* **2017**, *70*, 594. [[CrossRef](#)]
38. Kappes, F.; Fahrner, J.; Khodadoust, M.S.; Tabbert, A.; Strasser, C.; Mor-Vaknin, N.; Moreno-Villanueva, M.; Burkle, A.; Markovitz, D.M.; Ferrando-May, E. DEK is a poly(ADP-ribose) acceptor in apoptosis and mediates resistance to genotoxic stress. *Mol. Cell. Biol.* **2008**, *28*, 3245–3257. [[CrossRef](#)]
39. You, S.; Guan, Y.; Li, W. Epithelial-mesenchymal transition in colorectal carcinoma cells is mediated by DEK/IMP3. *Mol. Med. Rep.* **2018**, *17*, 1065–1070.
40. Sadeeshkumar, V.; Duraikannu, A.; Ravichandran, S.; Kodisundaram, P.; Fredrick, W.S.; Gobalakrishnan, R. Modulatory efficacy of dieckol on xenobiotic-metabolizing enzymes, cell proliferation, apoptosis, invasion and angiogenesis during NDEA-induced rat hepatocarcinogenesis. *Mol. Cell. Biochem.* **2017**, *433*, 195–204. [[CrossRef](#)]

41. Hui, W.; Ma, X.; Zan, Y.; Song, L.; Zhang, S.; Dong, L. MicroRNA-1292-5p inhibits cell growth, migration and invasion of gastric carcinoma by targeting DEK. *Am. J. Cancer Res.* **2018**, *8*, 1228–1238.
42. McIntosh, M.W.; Drescher, C.; Karlan, B.; Scholler, N.; Urban, N.; Hellstrom, K.E.; Hellstrom, I. Combining CA 125 and SMR serum markers for diagnosis and early detection of ovarian carcinoma. *Gynecol. Oncol.* **2004**, *95*, 9–15. [[CrossRef](#)] [[PubMed](#)]
43. Tsai, M.M.; Wang, C.S.; Tsai, C.Y.; Chen, C.Y.; Chi, H.C.; Tseng, Y.H.; Chung, P.J.; Lin, Y.H.; Chung, I.H.; Lin, K.H. MicroRNA-196a/-196b promote cell metastasis via negative regulation of radixin in human gastric cancer. *Cancer Lett.* **2014**, *351*, 222–231. [[CrossRef](#)] [[PubMed](#)]
44. Cheng, W.L.; Tsai, M.M.; Tsai, C.Y.; Huang, Y.H.; Chen, C.Y.; Chi, H.C.; Tseng, Y.H.; Chao, I.W.; Lin, W.C.; Wu, S.M.; et al. Glyoxalase-I is a novel prognosis factor associated with gastric cancer progression. *PLoS ONE* **2012**, *7*, e34352. [[CrossRef](#)]
45. Tsai, M.M.; Lin, P.Y.; Cheng, W.L.; Tsai, C.Y.; Chi, H.C.; Chen, C.Y.; Tseng, Y.H.; Cheng, Y.F.; Chen, C.D.; Liang, Y.; et al. Overexpression of ADP-ribosylation factor 1 in human gastric carcinoma and its clinicopathological significance. *Cancer Sci.* **2012**, *103*, 1136–1144. [[CrossRef](#)] [[PubMed](#)]
46. Tsai, M.M.; Huang, H.W.; Wang, C.S.; Lee, K.F.; Tsai, C.Y.; Lu, P.H.; Chi, H.C.; Lin, Y.H.; Kuo, L.M.; Lin, K.H. MicroRNA-26b inhibits tumor metastasis by targeting the KPNA2/c-jun pathway in human gastric cancer. *Oncotarget* **2016**, *7*, 39511–39526. [[CrossRef](#)]
47. Chi, H.C.; Chen, S.L.; Liao, C.J.; Liao, C.H.; Tsai, M.M.; Lin, Y.H.; Huang, Y.H.; Yeh, C.T.; Wu, S.M.; Tseng, Y.H.; et al. Thyroid hormone receptors promote metastasis of human hepatoma cells via regulation of TRAIL. *Cell Death Differ.* **2012**, *19*, 1802–1814. [[CrossRef](#)]



© 2019 by the authors. Licensee MDPI, Basel, Switzerland. This article is an open access article distributed under the terms and conditions of the Creative Commons Attribution (CC BY) license (<http://creativecommons.org/licenses/by/4.0/>).



# Psorachromene Suppresses Oral Squamous Cell Carcinoma Progression by Inhibiting Long Non-coding RNA GAS5 Mediated Epithelial-Mesenchymal Transition

Tong-Hong Wang<sup>1,2,3†</sup>, Yann-Lii Leu<sup>4,5,6†</sup>, Chin-Chuan Chen<sup>1,4</sup>, Tzong-Ming Shieh<sup>7</sup>, Jang-Hau Lian<sup>8</sup> and Chi-Yuan Chen<sup>1,2\*</sup>

<sup>1</sup> Tissue Bank, Chang Gung Memorial Hospital, Tao-Yuan, Taiwan, <sup>2</sup> Research Center for Chinese Herbal Medicine, Graduate Institute of Health Industry Technology and Research Center for Food and Cosmetic Safety, College of Human Ecology, Chang Gung University of Science and Technology, Tao-Yuan, Taiwan, <sup>3</sup> Department of Hepato-Gastroenterology, Liver Research Center, Chang Gung Memorial Hospital, Tao-Yuan, Taiwan, <sup>4</sup> Graduate Institute of Natural Products, Chang Gung University, Tao-Yuan, Taiwan, <sup>5</sup> Chinese Herbal Medicine Research Team, Healthy Aging Research Center, Chang Gung University, Tao-Yuan, Taiwan, <sup>6</sup> Center for Traditional Chinese Medicine, Chang Gung Memorial Hospital, Tao-Yuan, Taiwan, <sup>7</sup> Department of Dental Hygiene, China Medical University, Taichung, Taiwan, <sup>8</sup> Genomic Medicine Core Laboratory, Chang Gung Memorial Hospital, Tao-Yuan, Taiwan

## OPEN ACCESS

### Edited by:

Cheng-Chia Yu,  
Chung Shan Medical  
University, Taiwan

### Reviewed by:

Yi Chiung Hsu,  
National Central University, Taiwan  
Hsifeng Tu,  
National Yang-Ming University, Taiwan

### \*Correspondence:

Chi-Yuan Chen  
d49417002@gmail.com

<sup>†</sup>These authors have contributed  
equally to this work

### Specialty section:

This article was submitted to  
Head and Neck Cancer,  
a section of the journal  
Frontiers in Oncology

**Received:** 23 August 2019

**Accepted:** 17 October 2019

**Published:** 05 November 2019

### Citation:

Wang T-H, Leu Y-L, Chen C-C,  
Shieh T-M, Lian J-H and Chen C-Y  
(2019) Psorachromene Suppresses  
Oral Squamous Cell Carcinoma  
Progression by Inhibiting Long  
Non-coding RNA GAS5 Mediated  
Epithelial-Mesenchymal Transition.  
Front. Oncol. 9:1168.  
doi: 10.3389/fonc.2019.01168

The extract of the seeds of *Psoralea corylifolia* Linn. (*P. corylifolia*) have been shown to display anti-tumor activity. However, the prospects of the active compounds from this plant in the treatment of oral squamous cell carcinoma (OSCC) remains unclear. In the present study, the antitumor effects of psorachromene, a flavonoid extracted from the seeds of *P. corylifolia*, were investigated using cells and animal models of OSCC; the downstream regulatory mechanisms were also elucidated. The results showed that psorachromene significantly repressed cell proliferation, migration, and invasiveness and increased the toxic effects of chemotherapeutic agents against OSCC cells. The repressive effects of psorachromene were attributable to the inhibition of EGFR-Slug signaling, and the induction of G2/M arrest and apoptosis in the OSCC cells. Additionally, we found that psorachromene induced the expression of tumor suppressor long non-coding ribonucleic acid (RNA) growth arrest-specific transcript 5 (GAS5) and the activation of its downstream anticancer mechanisms. Animal experiments also showed noticeable inhibition of tumor growth, without significant physiological toxicity. The findings indicate that psorachromene displays anti-tumor activity in OSCC, and warrants further investigation as a potential agent for clinical application.

**Keywords:** psorachromene, oral squamous cell carcinoma (OSCC), long non-coding RNA, growth arrest-specific transcript 5 (GAS5), epidermal growth factor receptor (EGFR)

## INTRODUCTION

Oral cancer is the eleventh most common malignancy worldwide (1). In Taiwan, more than 4,700 people are diagnosed with oral cancer each year, and ~2,200 people die from it. Among all types of oral cancer, oral squamous cell carcinoma (OSCC) is the most common, with an incidence of ~90% (2). Smoking, drinking alcohol, and chewing tobacco or betel seeds are risk factors for OSCC (3–5).

Currently, the mainstay treatment for OSCC is surgical resection, with adjuvant chemotherapy or radiotherapy (6, 7). In addition, epidermal growth factor receptor (EGFR) and cyclooxygenase-2 (COX-2) inhibitors are also used in the treatment of OSCC (8, 9). However, the benefits of these therapies remain sub-optimal, and their side effects have a considerable impact on patients' quality of life. Therefore, oral cancer research continues to focus on the development of effective new treatment methods with minimal side effects.

Cancer-causing gene mutations are one of the major causes of OSCC (10–12). Previous studies have shown that over 75% of OSCC shows epidermal growth factor receptor (EGFR; also known as ErbB1 or HER1) overexpression; EGFR expression has shown a significantly positive association with the degree of malignancy (13–15). Therefore, inhibiting the growth of cancer cells by EGFR signaling inhibition is one of the current treatment strategies for OSCC (16, 17). Various EGFR inhibitors including anti-EGFR monoclonal antibodies (cetuximab and panitumumab) and small-molecule EGFR tyrosine kinase inhibitors (gefitinib, afatinib, and erlotinib) have been developed, and have demonstrated efficacy in OSCC (16, 18–20). However, only the monoclonal antibody cetuximab is currently approved for the treatment of OSCC; it has demonstrated significant inhibition of the progress of OSCC, with extension of survival (21, 22). Unfortunately, for reasons that are not fully clear, only ~50% of patients respond to cetuximab (23, 24).

Traditional Chinese medicine (TCM) has long been used for the treatment of diseases in Asian countries (25, 26). Unlike Western medicine, TCM provides effective treatment options with relatively milder adverse effects (27–29). However, differences in the quality of TCM therapeutics and the levels of active ingredients usually result in variable therapeutic effects (30). In order to achieve more stable therapeutic effects, the active ingredients of many traditional Chinese medicinal materials have been purified and identified (31–33). The identified compounds can be used at lower doses with more specific therapeutic efficacy. Currently, many compounds extracted from TCM therapeutics, e.g., artemisinin, curcumin, resveratrol, and paclitaxel, which are used in the treatment of cancer have shown good efficacy (34–38). Among them, paclitaxel, camptothecin, and vinblastine, have also been approved for the treatment of various cancers, including lung cancer, liver cancer, and oral cancer (39).

*Psoralea corylifolia* L. is a TCM herb that is commonly used in Asian countries for the treatment of bacterial infections, inflammation, and cancer (40–44). *P. corylifolia* L. contains flavonoids such as bavachin, isobavachalcone, and neobavaisoflavone; polyphenols such as psoralidin, psoralen, and isopsoralen; and benzene ring compounds such as backuchiol; in addition, the herb has been found to have biological activity and various therapeutic effects (42). Psorachromene is an isoflavone component isolated from the fruit kernels of *P. corylifolia* L. (45). A few studies have investigated the mechanism of action of psorachromene. Recent reports indicate that psorachromene has anti-inflammatory effects that may inhibit inflammatory reactions caused by inducible NO synthase (iNOS) and cyclooxygenase (COX) expression induced by bacterial infection (46). However, there have been no studies on its anticancer

effects. In this study, we investigated the anticancer activity of psorachromene in oral cancer, and studied its downstream regulatory mechanisms.

## MATERIALS AND METHODS

### Cell Lines and Culture Media

SAS is a human tongue squamous cell carcinoma cell line from the Japanese Collection of Research Bioresources (Tokyo, Japan) (47). OECM1 is a Taiwanese human gingival squamous carcinoma cell line; its derivation has been described in a previous study (47). Both cell lines were cultured in Dulbecco's modified Eagle's medium (DMEM) containing 10% fetal bovine serum (FBS), 1.2 g/L sodium bicarbonate, 0.5 mM sodium pyruvate, and 2.5 mM L-glutamine. The culture media, FBS, and chemical compounds were purchased from Life Technologies (Grand Island, NY, USA). The cells were cultured at 37°C in a humidified 5% CO<sub>2</sub> incubator.

### Reagents and Antibodies

The crude materials of the *P. corylifolia* seed were purchased from Chuang Song Zong Pharmaceutical Co., Ltd (Kaohsiung, Taiwan). The dried seeds of *P. corylifolia* were infused in ethanol and were filtered to obtain the crude extract. The crude extract was partitioned in n-hexane/water (1:1). The n-hexane soluble extract was then fractionated by column chromatography on silica gel, eluting with n-hexane: ethylacetate to isolate psorachromene. The purity of psorachromene was determined by nuclear magnetic resonance analysis. Antibodies against vimentin, E-cadherin, slug, cleaved-PARP (cl-PARP, Asp214), and caspase 9 were obtained from Cell Signaling (Temecula, CA, USA). Antibodies against EGFR and  $\beta$ -actin were purchased from Santa Cruz Biotechnology (Santa Cruz, CA, USA). Prestained protein marker and TOOLS<sup>TM</sup> RNA extractor were purchased from BIONEER (New Taipei City, Taiwan). The cisplatin and doxorubicin were purchased from Sigma-Aldrich (St. Louis, MO, USA), and the reagents for gel electrophoresis were purchased from Bio-Rad (Berkeley, CA, USA).

### Cell Viability Assays

Cell viability was determined using the sulforhodamine B (SRB) assay by staining with trypan blue, as described previously (48, 49).

### Terminal Deoxynucleotidyl Transferase dUTP Nick End Labeling (TUNEL) Assay

The apoptotic status of the treated cells was determined using a DeadEnd<sup>TM</sup> Fluorometric TUNEL Assay Kit (Promega, Madison, WI) according to the manufacturers' protocol. In summary, the SAS cells were treated with psorachromene (50  $\mu$ M) for 24 h and were then subjected to a terminal deoxynucleotidyl transferase dUTP nick end labeling (TUNEL) assay. The apoptotic cells (DAPI and TUNEL double stained cells) were enumerated using a fluorescence microscope (magnification,  $\times 100$ ). Cells in five different microscopic fields/dish were analyzed for each experiment.

## Western Blotting

Cells were washed twice with phosphate-buffered saline (PBS), lysed in 200  $\mu$ L of RIPA lysis buffer (Biotools Co. Ltd., Taiwan) containing protease inhibitors, and incubated on ice for 10 min. The samples were then centrifuged at 12,000 rpm for 30 min at 4°C, and the protein-containing supernatants were collected. The protein concentrations were determined using the Bio-Rad protein assay, and western blotting was performed as described previously (49).

## Phenotypic Analysis for Clonogenic, Migration, and Invasion Ability

The clonogenic, migration, and invasion assays were performed as described previously (47).

## Cell-Cycle Analysis

Cells were trypsinized, washed twice, and incubated in PBS containing 0.12% Triton X-100, 0.12 mmol/L EDTA, and 100 mg/mL ribonuclease A. Propidium iodide (50  $\mu$ g/mL) was then added to each sample, and they were kept at 4°C for 20 min. Cell cycle distribution was then analyzed using flow cytometry (Beckman Coulter Epics Elite, Beckman, Inc.).

## Whole-Transcriptome Sequencing

RNA extraction and whole-transcriptome sequencing was performed as described in a previous study (25).

## Detection of lncRNA GAS5

RNA from the cells were isolated using a RNeasy mini kit (QIAGEN, Gaithersburg, MD, USA), according to the

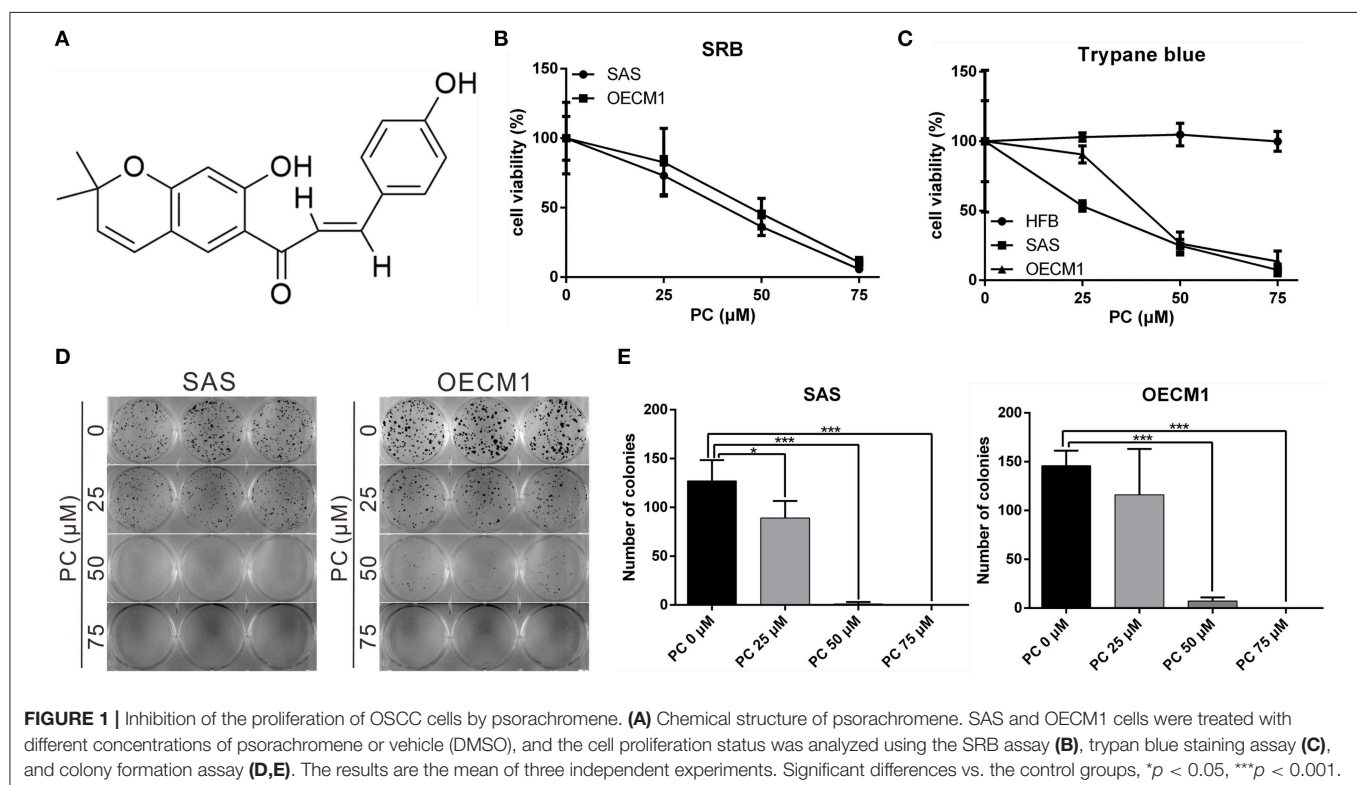
manufacturer's instructions. Two micrograms of RNA sample were subjected to reverse transcription (RT) using the reverse transcription kit (Applied Biosystems, Foster City, CA, USA). The expression of lncRNA GAS5 was detected by quantitative polymerase chain reaction (PCR) using the TaqMan gene expression assay (Applied Biosystems, Foster City, CA, USA), as described previously (50). Glyceraldehyde 3-phosphate dehydrogenase (GAPDH) was used as an internal control.

## RNA Interference (RNAi)

Human lncRNA GAS5 were downregulated using a mixture of four small interfering RNAs (siRNAs) (ON-TARGETplus SMARTpool; Dharmacon, Lafayette, CO) as previously described (50). In summary, the four siRNAs targeting lncRNA GAS5 (GenBank accession no. NR\_002578.2) covered the following: nucleotides 385-403 from the start codon (lncRNA GAS5-1: AGGCAGACCUGUUAUCCUA), nucleotides 248-266 (lncRNA GAS5-2: UGGAUGACUUGCUUGGGUA), nucleotides 567-585 (lncRNA GAS5-3: GAUGGAGUCUCAUGGCACA), and nucleotides 301-319 (lncRNA GAS5-4: AGGUAUGGAGAGUCGGCUU). Transfection was performed using the Dharmafect 1 transfection reagent (Dharmacon) according to the manufacturer's instructions.

## In vivo Tumor Xenograft Study

The *in vivo* antitumor activity of psorachromene against SAS cells was studied using 6-week-old nude BALB/c nu/nu male mice. SAS cells ( $5 \times 10^5$ ) were subcutaneously implanted in the right flank of the mice on day 0. The mice were then randomized





on day 7 into vehicle control and treatment groups of six animals each. Psorachromene and cisplatin were administered intraperitoneally thrice weekly, with 100  $\mu$ L of psorachromene (25 mg/kg of body weight), cisplatin (2 mg/kg), or an equal volume of dimethyl sulfoxide (DMSO), which served as a control. The tumor volume was evaluated every 2 days using calipers, based on the following formula: tumor volume = length  $\times$  width<sup>2</sup>/2. Their body weights and food consumption were also determined to evaluate apparent signs of toxicity. The tumor-bearing mice were weighed and sacrificed on day 22 for assaying the tumor biology. All animal experiments were performed in accordance with the guidelines for the Animal Care Ethics Commission of the Chang Gung Memorial Hospital, under an approved animal protocol (IACUC approval no. 2018031301).

## Immunohistochemistry

The tumors were fixed in formalin and embedded in paraffin. Consecutive 2- $\mu$ m-thick sections were obtained from the paraffin-embedded tissue blocks, and were floated onto glass slides. The slide-mounted tissue sections were subjected to immunohistochemical staining as described previously (51).

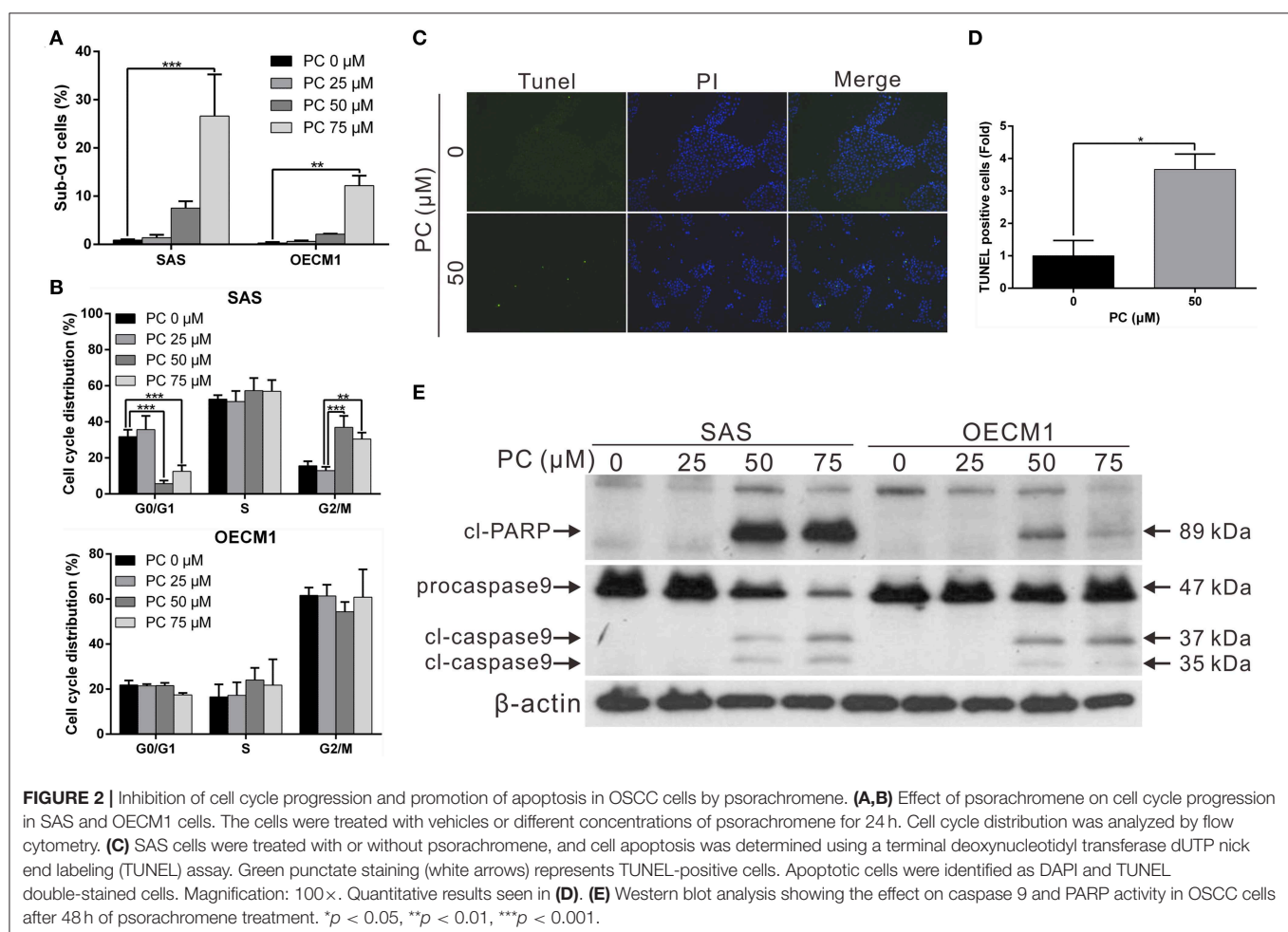
## Statistics

All data have been presented as means  $\pm$  standard deviations (SD). The Student's *t*-test was employed for comparison, and all analyses were performed using the Statistical Package for the Social Sciences version 12.0 (SPSS, Inc.). Differences between the variables were considered significant for *p*-values of  $> 0.05$ .

## RESULTS

### Psorachromene Inhibited the Growth of OSCC Cells and Promoted Their Apoptosis

Psorachromene is a flavonoid extracted from the seeds of *P. corylifolia* L. (Figure 1A). In this study, we treated OSCC cells and human fibroblast cell lines with different concentrations of psorachromene and analyzed the cell proliferation status using Sulforhodamine B (SRB) assay to determine whether psorachromene has inhibitory activity on OSCC. The results showed that psorachromene could significantly inhibit the growth of SAS and OECM1 cells starting from concentrations of 25  $\mu$ M; the inhibitory effect became more significant with increasing psorachromene concentrations (Figure 1B). Similar results were obtained on the trypan blue staining assay.



Psorachromene significantly inhibited the growth of SAS and OECM1 cells in a dose dependent manner. However, no inhibitory effect was observed on the growth of human fibroblast cell line HFB (Figure 1C). This indicated that psorachromene selectively inhibits the growth in OSCC cells without significant toxicity to normal cells. We also evaluated the impact of psorachromene on the colony forming ability of OSCC. The results showed significant inhibitory activity in a dose-dependent manner. At a concentration of 50  $\mu\text{M}$ , psorachromene inhibited the colony forming ability of OSCC cells by more than 90% (Figures 1D,E), confirming its inhibitory activity on the growth of OSCC cells.

To determine the mechanism of inhibition of OSCC, we further compared the cell cycle progression between cells treated and not treated with psorachromene. Those treated with psorachromene were found to have been arrested in the G2 phase, their numbers in the sub-G1 phase were significantly higher compared to the control group (Figures 2A,B). These findings suggested that psorachromene inhibits cell cycle progression and promotes cell apoptosis. The results of the TUNEL assay also demonstrated that the number of apoptotic cells in the psorachromene treatment group were significantly higher compared with the control group (Figures 2C,D). Furthermore, the results of western blotting analysis confirmed the activation of caspase-9 and the cleavage of poly (ADP-ribose) polymerases

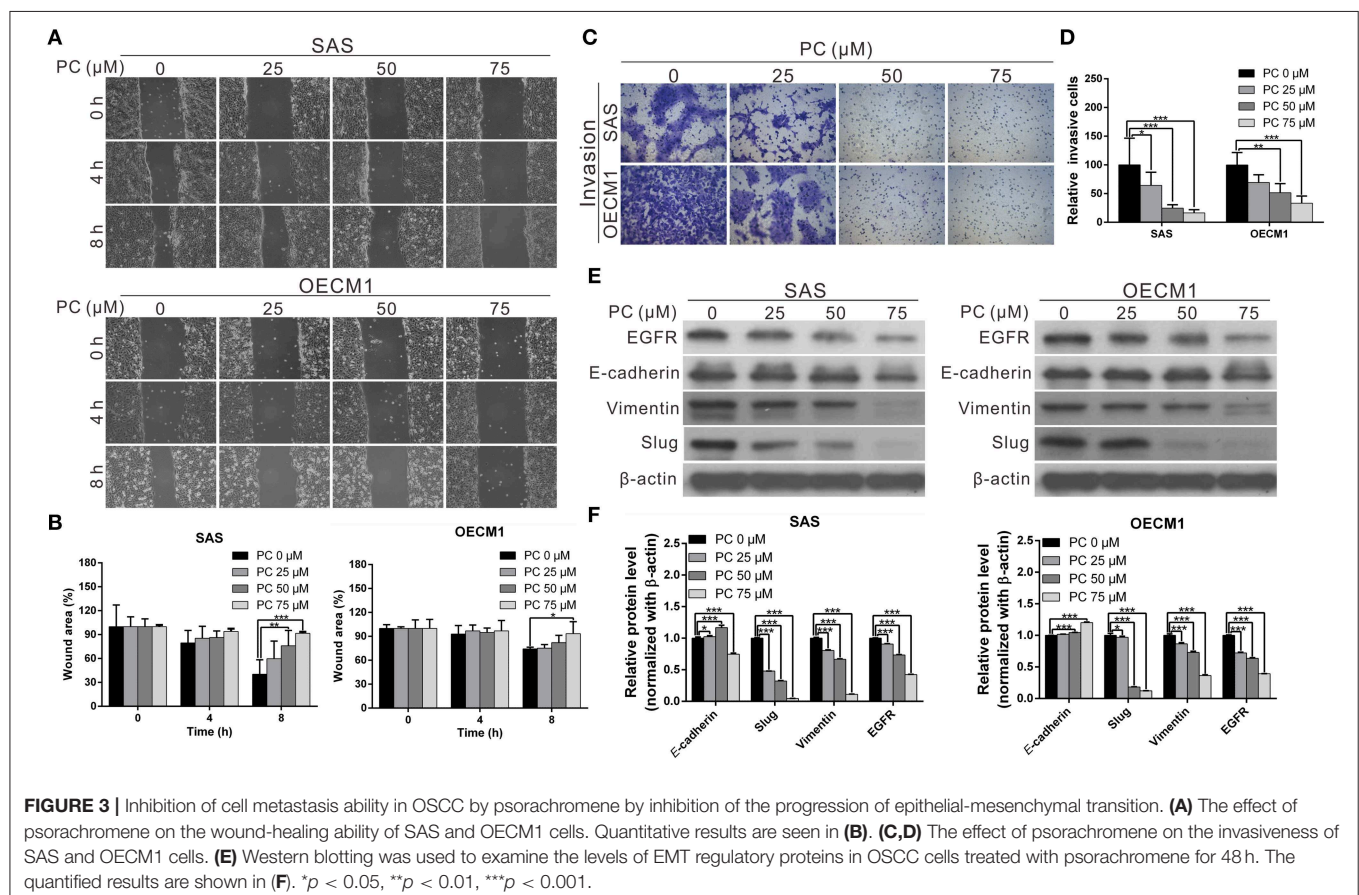
(PARPs) by psorachromene, indicating that it promotes cell apoptosis by activating apoptosis-related proteins (Figure 2E).

## Psorachromene Inhibits the Migration and Invasiveness of OSCC

Invasion and metastasis are the major contributors to the refractory nature of cancer. We conducted a wound-healing assay to evaluate whether psorachromene may affect cell migration; this was performed to further evaluate the potential of psorachromene in inhibiting metastasis and invasiveness in OSCC cells. The results showed that at a concentration of 25  $\mu\text{M}$ , psorachromene significantly inhibited cell migration ability, and the inhibitory effects increased with the concentration of psorachromene. At a concentration of 75  $\mu\text{M}$ , psorachromene inhibited the migration ability of SAS and OECM cells by 51.3 and 19.1%, respectively (Figures 3A,B). Furthermore, the invasion assay demonstrated that psorachromene may inhibit cell invasion by up to 83.7% at a concentration of 75  $\mu\text{M}$  (Figures 3C,D).

## Psorachromene Inhibits Epithelial-Mesenchymal Transition (EMT)

Epithelial-mesenchymal transition (EMT) is an important process in cancer cell metastasis, that weakens intercellular adhesions and facilitates metastasis. To determine whether



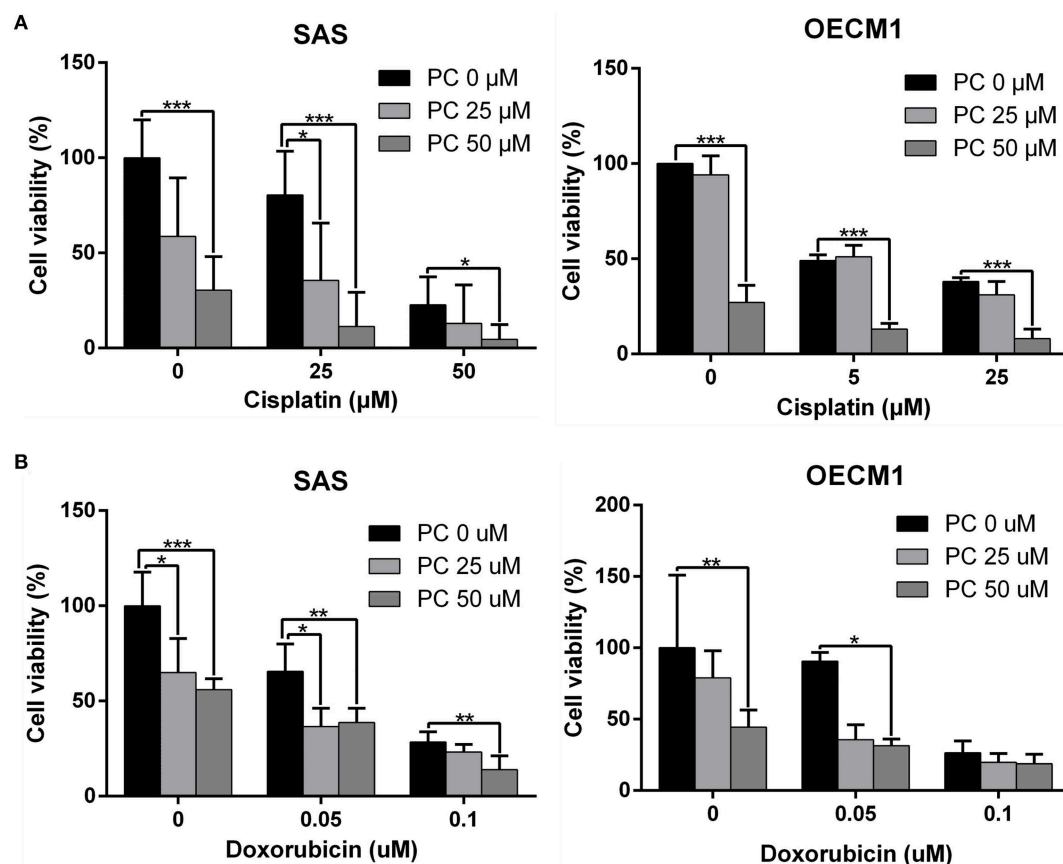


**FIGURE 4 |** Psorachromene combined with cisplatin and doxorubicin has additive effect. The effects of psorachromene combined with cisplatin and doxorubicin on proliferation of SAS (A) and OECM1 (B) cells. \* $p < 0.05$ , \*\* $p < 0.01$ , \*\*\* $p < 0.001$ . All experiments were performed in triplicate.

psorachromene regulates EMT when inhibiting OSCC migration and invasion abilities, we performed western blotting to analyze the effects of psorachromene on EMT associated proteins. The results indicated that the expression of EMT-promoting proteins such as vimentin and slug was significantly lower in psorachromene-treated cells compared with the control group. However, the expression of E-cadherin did not change significantly (Figures 3E,F), suggesting that psorachromene may inhibit OSCC migration and invasion by inhibiting EMT.

Slug is a downstream gene regulated by the EGFR signaling pathway. We also evaluated whether psorachromene affects EGFR expression, and found its expression in psorachromene-treated cells to be significantly lower compared to the control group (Figures 3E,F). The results indicated that psorachromene may inhibit the expression of slug, and the progression of EMT by downregulating EGFR expression.

### Psorachromene May Enhance the Therapeutic Effects of Cisplatin and Doxorubicin on OSCC

Cisplatin and doxorubicin are the commonly used chemotherapeutic drugs in the treatment of OSCC (52–54). In order to determine whether combining psorachromene

with these drugs may improve their therapeutic effects on OSCC, we administered psorachromene, cisplatin, and doxorubicin alone, or in combination to the OSCC cells; we also evaluated its inhibitory effects on the growth of these cells. Cisplatin and doxorubicin alone had an inhibitory effect on OSCC; however, combination with psorachromene significantly enhanced the inhibition of OSCC. Compared to cisplatin or doxorubicin alone, the combination with psorachromene enhanced the toxicity on OSCC cells by up to 3.3-fold (Figures 4A,B). The combination index also demonstrated the additive effect of psorachromene in combination with cisplatin and doxorubicin (Table 1).

### Psorachromene Inhibits Tumor Growth in Mice

The anticancer effects of psorachromene *in vivo* were verified using a mouse xenograft model; the effects of psorachromene on tumor growth in mice were similar to those of the cell experiments. The tumor growth rate was significantly reduced in mice treated with psorachromene. After 2 weeks of administering the drug, the tumor volume in the psorachromene-treated group was reduced by ~75.5% compared with the control group (Figures 5A,B), and the tumor inhibitory effect was equivalent to that of the cisplatin-treated group (84.6%).

In addition, there were no significant differences in body weight between the psorachromene-treated and control groups (Figure 5C), indicating that psorachromene may not have significant physiological toxicity.

In addition, we analyzed the expression of EGFR and EMT-related proteins including slug, vimentin, and E-cadherin in murine tumor tissues using immunohistochemical staining, and found that psorachromene may significantly inhibit the expression of EGFR and EMT-promoting proteins (Figure 5D). The results of this experiment were identical to those of cellular experiments, suggesting that psorachromene may inhibit EMT.

## Psorachromene May Inhibit the Activation of Signaling Pathways Associated With Cell Growth and Extracellular Structure Organization

To understand its anticancer mechanisms of action, we treated SAS and OECM1 cell lines with psorachromene, and performed whole-transcriptome sequencing to identify the genes and signaling pathways that may be regulated by psorachromene. Heatmap analysis showed that after psorachromene treatment, gene expression was significantly altered compared with the control group (Figure 6A). We further performed ingenuity pathway analysis, and found that psorachromene mainly regulates the LKB1 and ErbB/EGFR signaling pathways (Figure 6B), affects the energy metabolism of cells, and the composition and generation of the extracellular matrix, thereby inhibiting their growth and metastasis.

## Psorachromene Exerts Anticancer Effects by Inducing the Expression of Long Non-coding RNA GAS5

Previous studies have confirmed that long non-coding RNAs (lncRNAs) play an important role in cell physiological regulation, and drug responses. To understand the role of lncRNAs in the anti-OSCC mechanisms of action of psorachromene, we analyzed the previously-mentioned transcriptome sequencing data, and found that 12 lncRNAs demonstrated a higher than 2-fold change in expression after psorachromene treatment, compared to the control group (Figure 6C). Among these lncRNAs, growth arrest-specific transcript 5 (GAS5) has recently been discovered to suppress cancer. It has been shown to inhibit the growth and metastasis of OSCC by regulating the miR-21/PTEN axis. To confirm the regulatory relation between psorachromene and GAS5, we performed real-time reverse transcriptase-PCR to determine the expression of GAS5 in OSCC cells. The results indicated that the expression of GAS5 in SAS and OECM1 cells treated with psorachromene was significantly higher than that of the control group (Figure 6D); this indicates that psorachromene may inhibit the growth and metastasis of OSCC by inducing GAS5 mediated anticancer mechanisms.

We performed a rescue assay to further verify the mentioned conditions. The results showed that psorachromene significantly inhibited the growth and migration of OSCC cells. After silencing GAS5 expression, we found that the inhibitory

**TABLE 1 |** The combination index.

	PC ( $\mu$ M)	DOX ( $\mu$ M)	CI
SAS	25	0.05	0.68011
	25	0.1	0.50582
	50	0.05	1.04119
	50	0.1	0.84218
OECM1	25	0.05	0.79836
	25	0.1	1.18195
	50	0.05	1.51916
	50	0.1	1.84227
	PC ( $\mu$ M)	CIS ( $\mu$ M)	CI
SAS	25	25	0.99174
	25	50	0.63005
	50	25	0.96329
	50	50	0.75840
OECM1	25	5	1.93719
	25	25	0.84726
	50	5	0.84689
	50	25	0.76593

effects of psorachromene on OSCC cells were attenuated (Figures 7A–D); this indicated that the anti-OSCC action of psorachromene is partly achieved by regulating the lncRNA-GAS5 anticancer pathway.

## DISCUSSION

Psorachromene is a flavonoid component of *P. corylifolia* L., accounting for 0.0016% of the total extract from the seeds of *P. corylifolia* L (55). Current understanding on the biological functions of psorachromene is limited. Only a few studies have reported on its anti-inflammatory activity, which may inhibit inducible nitric oxide synthase (iNOS) and COX expression induced by lipopolysaccharide (LPS), thereby inhibiting inflammatory reaction (46). However, no studies have evaluated its anticancer effects. In this study, we investigated the inhibitory activity of psorachromene on OSCC, and found that it significantly inhibited the growth, migration, and invasiveness of OSCC cells, and suppressed EMT by inducing the expression of lncRNA-GAS5. The results of our animal experiments also showed that it may significantly inhibit the growth of tumor cells and the expression of EMT-associated proteins. To the best of our knowledge, this is the first study to demonstrate that psorachromene regulates lncRNAs to exert its antitumor effects.

Previous studies have shown that ~80% of OSCC over-express EGFR; this leads to uncontrolled cell growth and enhances the metastatic ability of the cells (13, 56). It also enhances the resistance of OSCC to chemotherapeutic drugs including, cisplatin, 5-fluorouracil (5FU), and doxorubicin (57–59). Previous studies have also confirmed that the use of the EGFR inhibitor gefitinib in combination with cisplatin enhanced the therapeutic effects of the latter on



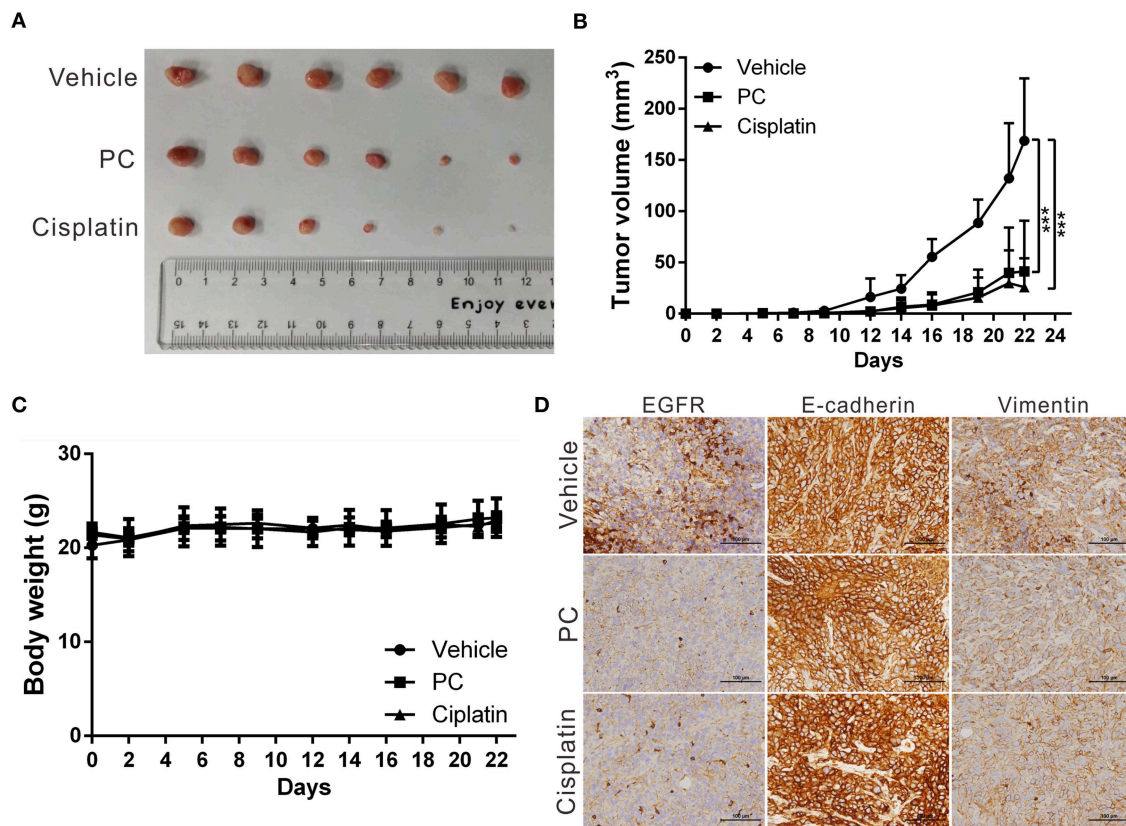


**FIGURE 5 |** Psorachromene inhibits tumor growth in mice. **(A)** A total of  $5 \times 10^6$  SAS cells were inoculated into nude mice ( $n = 6$ ). Representative images show the tumor xenografts at 3 weeks after implantation. Psorachromene significantly reduced tumor growth. **(B)** Tumor volumes were calculated every 3 days after injection. The volume of each tumor was calculated as follows: length  $\times$  width<sup>2</sup>  $\times$  0.5. Bars indicate S.D. \*\*\* $p < 0.001$ . **(C)** Body weights were calculated every 3 days after injection. **(D)** Immunohistochemical staining represents the effect of psorachromene on the expression of EGFR and EMT associated proteins in mice xenograft tumors. Magnification: 400 $\times$ .

OSCC (20). This study demonstrated similar results. In addition to the inhibition of EGFR expression, psorachromene has synergistic activity with cisplatin and doxorubicin in the treatment of OSCC, with no significant physiological toxicities. Therefore, psorachromene has considerable potential for use as a therapeutic adjuvant in the treatment of OSCC.

To identify the genes and anticancer signaling pathways that may be regulated by psorachromene, we performed whole-transcriptome sequencing that examined the gene expression profiling of psorachromene in treated and untreated cells. The results showed that psorachromene mainly regulates the expression of genes associated with cell growth, extracellular matrix composition, and inflammation, among others, thereby inhibiting the growth and metastasis of OSCC cells; this was consistent with the results observed on cell functional assay. The inhibitory effect of psorachromene on the Erb-1 pathway indicates that it has considerable potential in the treatment of cancers that overexpress EGFR (including cancers of the breast and liver); it may also synergize with other anticancer drugs to enhance their therapeutic efficacy.

This study revealed that psorachromene induces lncRNA-GAS5 expression, which is a known anticancer lncRNA, and participates in the regulation of many important physiological processes, including cell growth, apoptosis, cell cycle progression, and EMT (60, 61). The low expression of GAS5 is closely related to the poor prognosis and chemoresistance of many cancers (62–65). Overexpression of GAS5 could enhance the inhibitory effect of Gefitinib on EGFR phosphorylation and its downstream signaling activation, while enhancing the sensitivity of lung cancer cells to EGFR-TKI (66). In addition, the chemotherapeutic drug, Lapatinib, can also enhance the response of breast cancer cells to trastuzumab by inducing GAS5 expression (67). Some studies have also suggested that GAS5 is significantly downregulated in OSCC cells, and that GAS5 expression may inhibit the growth and metastasis of OSCC by regulating the miR-21/PTEN axis (68). In this study, we found that psorachromene may induce GAS5 expression. It is speculated that the inhibitory effects of psorachromene on OSCC are partly attributable to GAS5-mediated anticancer mechanisms. Moreover, this result also shows the potential of psorachromene as a



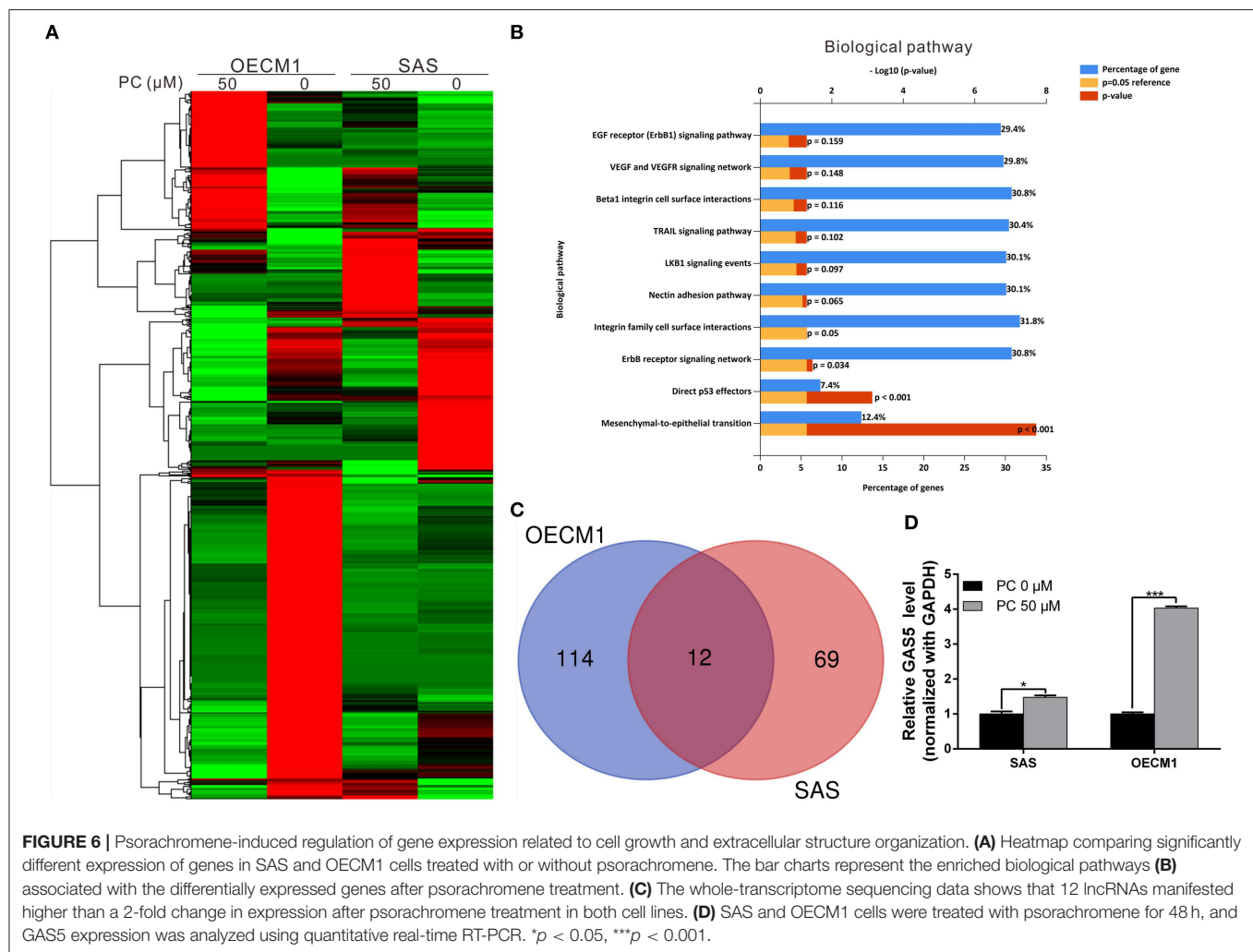


**FIGURE 6 |** Psorachromene-induced regulation of gene expression related to cell growth and extracellular structure organization. **(A)** Heatmap comparing significantly different expression of genes in SAS and OECM1 cells treated with or without psorachromene. The bar charts represent the enriched biological pathways **(B)** associated with the differentially expressed genes after psorachromene treatment. **(C)** The whole-transcriptome sequencing data shows that 12 lncRNAs manifested higher than a 2-fold change in expression after psorachromene treatment in both cell lines. **(D)** SAS and OECM1 cells were treated with psorachromene for 48 h, and GAS5 expression was analyzed using quantitative real-time RT-PCR. \* $p < 0.05$ , \*\*\* $p < 0.001$ .

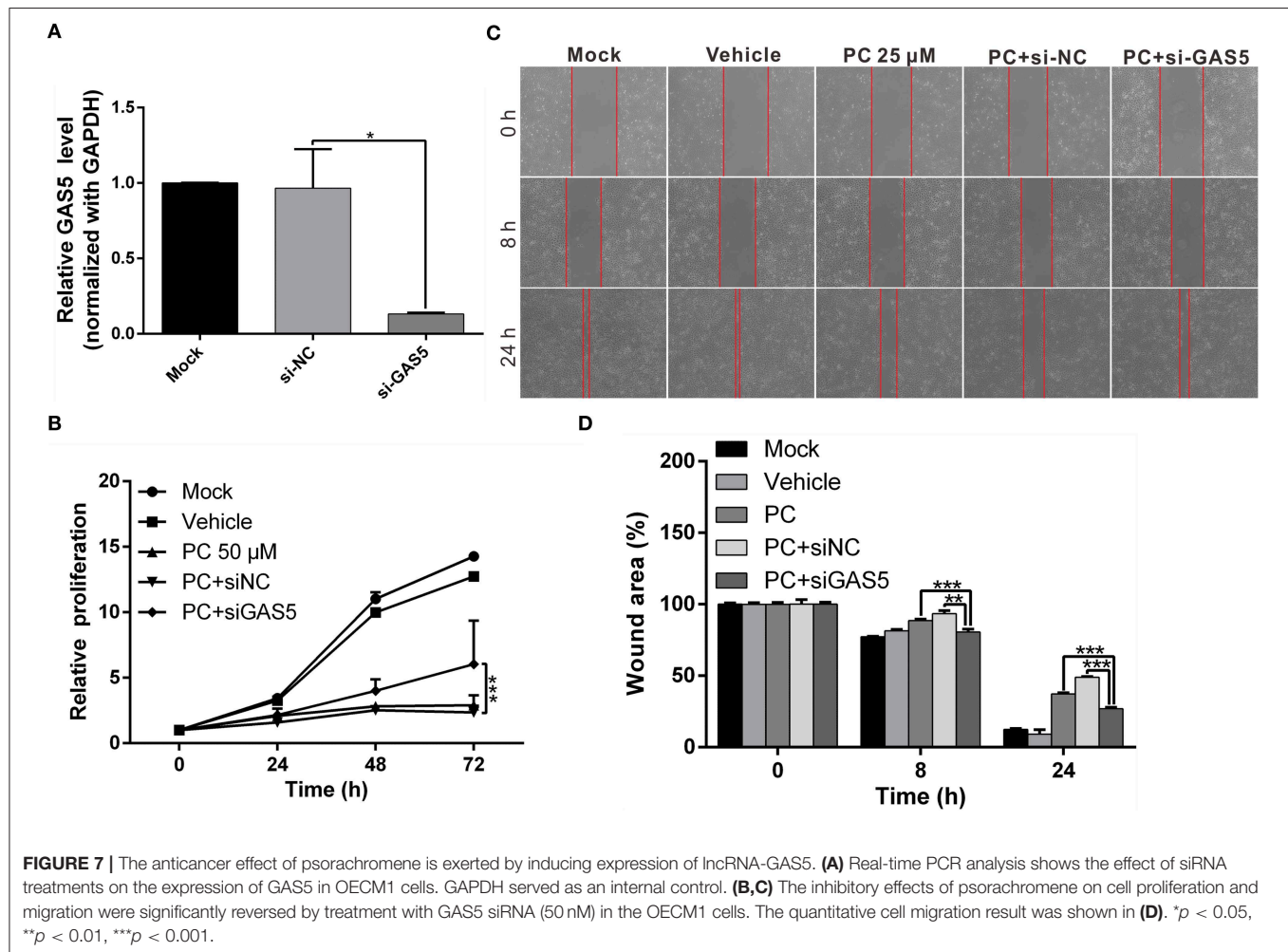
therapeutic adjuvant that enhances the sensitivity of cancer cells to chemotherapeutic drugs by inducing the expression of GAS5.

Previous studies have demonstrated that long non-coding RNAs are involved in the regulation of a wide range of gene expression or protein stability. However, recent studies have shown that GAS5 does not regulate EGFR expression (66). We speculate that psorachromene regulates GAS5 and EGFR expression through two independent mechanisms; however, the detailed regulatory mechanism is yet to be delineated. In addition, the results of whole-transcriptome sequencing analysis showed that numerous lncRNAs are also regulated by psorachromene; the role of these lncRNAs in the anticancer mechanisms of psorachromene warrant further research.

In cell cycle analysis related to psorachromene treatment, the distribution of cell cycle between SAS and OECM1 cells is quite different. The inhibitory effect of psorachromene on SAS cells is better than that of OECM1. We speculated that the anti-OSCC effect of psorachromene may be induced by specific receptors. The genetic background difference between

cells leads to the differences in receptor expression, which affect the anti-OSCC effect of psorachromene. However, the receptor that is targeted by psorachromene to achieve its anticancer mechanism and its detailed downstream regulation mechanism still need to be clarified to improve the clinical applicability of psorachromene.

The concentrations of psorachromene in *P. corylifolia* L. are not high; in addition, it has a simple structure. Therefore, psorachromene is mainly synthesized chemically for commercial formulations. Structural modifications may be introduced in the future to increase its anticancer activity and intracellular availability. In this study, we demonstrated the potential anticancer activity of psorachromene using cell and animal experiments; we also found that it affects certain relevant regulatory pathways. The small-molecule compounds that are commonly used in clinical practice only block specific carcinogenic pathways; in contrast, psorachromene has a wide range of targets. In addition, the animal experiments did not demonstrate significant differences in physiological toxicity compared to these molecules. In view of these findings, psorachromene holds



promise as a new therapeutic agent for OSCC. Further studies with larger sample sizes are needed to validate our findings.

## DATA AVAILABILITY STATEMENT

The data for this manuscript has been uploaded to: <https://www.ncbi.nlm.nih.gov/bioproject/PRJNA562818>.

## ETHICS STATEMENT

The animal study was reviewed and approved by Animal Care Ethics Commission of the Chang Gung Memorial Hospital (IACUC approval no. 2018031301).

## AUTHOR CONTRIBUTIONS

C-YC, T-HW, and Y-LL contributed to the conception and design of the study. C-YC, T-HW, Y-LL, C-CC, T-MS, and J-HL

performed the experiments and statistical analyses. T-HW and C-YC prepared the first draft of the manuscript. All authors contributed to manuscript revision and have read and approved the submitted version.

## FUNDING

This work was partially supported by the Ministry of Science and Technology, Taiwan (grant MOST 107-2314-B-182A-140-MY3) and the Chang Gung Medical Research Program of Taiwan (grant CMRPG3H1001 and CMRPF1H0012).

## ACKNOWLEDGMENTS

The authors would like to thank the staff of the Tissue Bank and Genomic Medicine Core Laboratory at the Chang Gung Memorial Hospital, Lin-Kou, Taiwan for the excellent tissue processing and data analysis support.

## REFERENCES

- Ghantous Y, Abu Elnaaj I. Global incidence and risk factors of oral cancer. *Harefuah*. (2017) 156:645–9.
- Bagan J, Sarrion G, Jimenez Y. Oral cancer: clinical features. *Oral Oncol*. (2010) 46:414–7. doi: 10.1016/j.oraloncology.2010.03.009
- Nagler R, Dayan D. The dual role of saliva in oral carcinogenesis. *Oncology*. (2006) 71:10–7. doi: 10.1159/000100445
- Chen YJ, Chang JT, Liao CT, Wang HM, Yen TC, Chiu CC, et al. Head and neck cancer in the betel quid chewing area: recent advances in molecular carcinogenesis. *Cancer Sci*. (2008) 99:1507–14. doi: 10.1111/j.1349-7006.2008.00863.x
- Zygiogianni AG, Kyrgias G, Karakitsos P, Psyrri A, Kouvaris J, Kelekis N, et al. Oral squamous cell cancer: early detection and the role of alcohol and smoking. *Head Neck Oncol*. (2011) 3:2. doi: 10.1186/1758-3284-3-2
- Huang SH, O'sullivan B. Oral cancer: current role of radiotherapy and chemotherapy. *Med Oral Patol Oral Cir Bucal*. (2013) 18:e233–40. doi: 10.4317/medoral.18772
- Gharat SA, Momin M, Bhavsar C. Oral squamous cell carcinoma: current treatment strategies and nanotechnology-based approaches for prevention and therapy. *Crit Rev Ther Drug Carrier Syst*. (2016) 33:363–400. doi: 10.1615/CritRevTherDrugCarrierSyst.2016016272
- Hamakawa H, Nakashiro K, Sumida T, Shintani S, Myers JN, Takes RP, et al. Basic evidence of molecular targeted therapy for oral cancer and salivary gland cancer. *Head Neck*. (2008) 30:800–9. doi: 10.1002/hed.20830
- Agnihotri NS, Astekar M. The role of novel prognostic markers PROX1 and FOXC2 in carcinogenesis of oral squamous cell carcinoma. *J Exp Ther Oncol*. (2018) 12:171–84.
- Choi S, Myers JN. Molecular pathogenesis of oral squamous cell carcinoma: implications for therapy. *J Dent Res*. (2008) 87:14–32. doi: 10.1177/154405910808700104
- Ramos-Garcia P, Ruiz-Avila I, Gil-Montoya JA, Ayen A, Gonzalez-Ruiz L, Navarro-Trivino FJ, et al. Relevance of chromosomal band 11q13 in oral carcinogenesis: an update of current knowledge. *Oral Oncol*. (2017) 72:7–16. doi: 10.1016/j.oraloncology.2017.04.016
- Lindemann A, Takahashi H, Patel AA, Osman AA, Myers JN. Targeting the DNA damage response in OSCC with TP53 mutations. *J Dent Res*. (2018) 97:635–44. doi: 10.1177/0022034518759068
- Kimura I, Kitahara H, Ooi K, Kato K, Noguchi N, Yoshizawa K, et al. Loss of epidermal growth factor receptor expression in oral squamous cell carcinoma is associated with invasiveness and epithelial-mesenchymal transition. *Oncol Lett*. (2016) 11:201–7. doi: 10.3892/ol.2015.3833
- Xie X, Wang Z, Chen F, Yuan Y, Wang J, Liu R, et al. Roles of FGFR in oral carcinogenesis. *Cell Prolif*. (2016) 49:261–9. doi: 10.1111/cpr.12260
- Huang SF, Chien HT, Cheng SD, Chuang WY, Liao CT, Wang HM. EGFR copy number alterations in primary tumors, metastatic lymph nodes, and recurrent and multiple primary tumors in oral cavity squamous cell carcinoma. *BMC Cancer*. (2017) 17:592. doi: 10.1186/s12885-017-3586-9
- Soria JC, Felip E, Cobo M, Lu S, Syrigos K, Lee KH, et al. Afatinib versus erlotinib as second-line treatment of patients with advanced squamous cell carcinoma of the lung (LUX-Lung 8): an open-label randomised controlled phase 3 trial. *Lancet Oncol*. (2015) 16:897–907. doi: 10.1016/S1470-2045(15)00006-6
- Fujiwara T, Eguchi T, Sogawa C, Ono K, Murakami J, Ibaragi S, et al. Carcinogenic epithelial-mesenchymal transition initiated by oral cancer exosomes is inhibited by anti-EGFR antibody cetuximab. *Oral Oncol*. (2018) 86:251–7. doi: 10.1016/j.oraloncology.2018.09.030
- Cohen RB. Current challenges and clinical investigations of epidermal growth factor receptor (EGFR)- and ErbB family-targeted agents in the treatment of head and neck squamous cell carcinoma (HNSCC). *Cancer Treat Rev*. (2014) 40:567–77. doi: 10.1016/j.ctrv.2013.10.002
- Brands RC, Muller-Richter UD, De Donno F, Seher A, Mutzbauer G, Linz C, et al. Co-treatment of wild-type EGFR head and neck cancer cell lines with afatinib and cisplatin. *Mol Med Rep*. (2016) 13:2338–44. doi: 10.3892/mmr.2016.4786
- Khalil A, Jameson MJ. The EGFR inhibitor gefitinib enhanced the response of human oral squamous cell carcinoma to cisplatin *in vitro*. *Drugs R D*. (2017) 17:545–55. doi: 10.1007/s40268-017-0204-x
- Rabinowits G, Haddad RI. Overcoming resistance to EGFR inhibitor in head and neck cancer: a review of the literature. *Oral Oncol*. (2012) 48:1085–9. doi: 10.1016/j.oraloncology.2012.06.016
- Lopez-Verdin S, Lavalle-Carrasco J, Carreon-Burciaga RG, Serafin-Higuera N, Molina-Frechero N, Gonzalez-Gonzalez R, et al. Molecular markers of anticancer drug resistance in head and neck squamous cell carcinoma: a literature review. *Cancers*. (2018) 10:E376. doi: 10.3390/cancers10100376
- Perri F, Longo F, Ionna F, Caponigro F. Recent results of cetuximab use in the treatment of squamous cell carcinoma of the head and neck. *Onco Targets Ther*. (2009) 2:243–50. doi: 10.2147/OTT.S6056
- Naruse T, Yanamoto S, Matsushita Y, Sakamoto Y, Morishita K, Ohba S, et al. Cetuximab for the treatment of locally advanced and recurrent/metastatic oral cancer: an investigation of distant metastasis. *Mol Clin Oncol*. (2016) 5:246–52. doi: 10.3892/mco.2016.928
- Chen CY, Chen CC, Shieh TM, Hsueh C, Wang SH, Leu YL, et al. Corylin suppresses hepatocellular carcinoma progression via the inhibition of epithelial-mesenchymal transition, mediated by long noncoding RNA GAS5. *Int J Mol Sci*. (2018) 19:E380. doi: 10.3390/ijms19020380
- An W, Lai H, Zhang Y, Liu M, Lin X, Cao S. Apoptotic pathway as the therapeutic target for anticancer traditional chinese medicines. *Front Pharmacol*. (2019) 10:758. doi: 10.3389/fphar.2019.00758
- He DY, Dai SM. Anti-inflammatory and immunomodulatory effects of paeonia lactiflora pall., a traditional chinese herbal medicine. *Front Pharmacol*. (2011) 2:10. doi: 10.3389/fphar.2011.00010
- Ji L, Tong X, Wang H, Tian H, Zhou H, Zhang L, et al. Efficacy and safety of traditional chinese medicine for diabetes: a double-blind, randomised, controlled trial. *PLoS ONE*. (2013) 8:e56703. doi: 10.1371/journal.pone.0056703
- Jiao L, Dong C, Liu J, Chen Z, Zhang L, Xu J, et al. Effects of Chinese medicine as adjunct medication for adjuvant chemotherapy treatments of non-small cell lung cancer patients. *Sci Rep*. (2017) 7:46524. doi: 10.1038/srep46524
- Zhang A, Sun H, Wang X. Potentiating therapeutic effects by enhancing synergism based on active constituents from traditional medicine. *Phytother Res*. (2014) 28:526–33. doi: 10.1002/ptr.5032
- Xu L, Zhao W, Wang D, Ma X. Chinese medicine in the battle against obesity and metabolic diseases. *Front Physiol*. (2018) 9:850. doi: 10.3389/fphys.2018.00850
- Jiang Z, Gao W, Huang L. Tanshinones, critical pharmacological components in *Salvia miltiorrhiza*. *Front Pharmacol*. (2019) 10:202. doi: 10.3389/fphar.2019.00202
- Zhu H, Liu C, Hou J, Long H, Wang B, Guo D, et al. Gastrodia elata blume polysaccharides: a review of their acquisition, analysis, modification, and pharmacological activities. *Molecules*. (2019) 24:E2436. doi: 10.3390/molecules24132436
- Ye MX, Li Y, Yin H, Zhang J. Curcumin: updated molecular mechanisms and intervention targets in human lung cancer. *Int J Mol Sci*. (2012) 13:3959–78. doi: 10.3390/ijms13033959
- Terlikowska KM, Witkowska AM, Zujko ME, Dobrzycka B, Terlikowski SJ. Potential application of curcumin and its analogues in the treatment strategy of patients with primary epithelial ovarian cancer. *Int J Mol Sci*. (2014) 15:21703–22. doi: 10.3390/ijms151221703
- Hong M, Tan HY, Li S, Cheung F, Wang N, Nagamatsu T, et al. Cancer stem cells: the potential targets of Chinese medicines and their active compounds. *Int J Mol Sci*. (2016) 17:E893. doi: 10.3390/ijms17060893
- Houh YK, Kim KE, Park S, Hur DY, Kim S, Kim D, et al. The effects of artemisinin on the cytolytic activity of natural killer (NK) cells. *Int J Mol Sci*. (2017) 18:E1600. doi: 10.3390/ijms18071600
- Slezakova S, Ruda-Kucerova J. Anticancer activity of artemisinin and its derivatives. *Anticancer Res*. (2017) 37:5995–6003. doi: 10.21873/anticancer.12046
- Cragg GM, Pezzuto JM. Natural products as a vital source for the discovery of cancer chemotherapeutic and chemopreventive agents. *Med Princ Pract*. (2016) 25(Suppl 2):41–59. doi: 10.1159/000443404
- Kim YJ, Lim HS, Lee J, Jeong SJ. Quantitative analysis of *Psoralea corylifolia* Linne and its neuroprotective and anti-neuroinflammatory effects in HT22 hippocampal cells and BV-2 microglia. *Molecules*. (2016) 21:E1076. doi: 10.3390/molecules21081076

41. Li CC, Wang TL, Zhang ZQ, Yang WQ, Wang YF, Chai X, et al. Phytochemical and pharmacological studies on the genus psoralea: a mini review. *Evid Based Complement Alternat Med.* (2016) 2016:8108643. doi: 10.1155/2016/8108643
42. Zhang X, Zhao W, Wang Y, Lu J, Chen X. The chemical constituents and bioactivities of *Psoralea corylifolia* Linn.: a review. *Am J Chin Med.* (2016) 44:35–60. doi: 10.1142/S0192415X16500038
43. Hung YL, Fang SH, Wang SC, Cheng WC, Liu PL, Su CC, et al. Corylin protects LPS-induced sepsis and attenuates LPS-induced inflammatory response. *Sci Rep.* (2017) 7:46299. doi: 10.1038/srep46299
44. Alam F, Khan GN, Asad M. *Psoralea corylifolia* L.: ethnobotanical, biological, and chemical aspects: a review. *Phytother Res.* (2018) 32:597–615. doi: 10.1002/ptr.6006
45. Choi YH, Yon GH, Hong KS, Yoo DS, Choi CW, Park WK, et al. *In vitro* BACE-1 inhibitory phenolic components from the seeds of *Psoralea corylifolia*. *Planta Med.* (2008) 74:1405–8. doi: 10.1055/s-2008-1081301
46. Kim DH, Li H, Han YE, Jeong JH, Lee HJ, Ryu JH. Modulation of inducible nitric oxide synthase expression in LPS-stimulated BV-2 microglia by prenylated chalcones from *Cullen corylifolium* (L.) medik. through Inhibition of I-kappaBalpha degradation. *Molecules.* (2018) 23:E109. doi: 10.3390/molecules23010109
47. Chen CY, Chiou SH, Huang CY, Jan CI, Lin SC, Hu WY, et al. Tid1 functions as a tumour suppressor in head and neck squamous cell carcinoma. *J Pathol.* (2009) 219:347–55. doi: 10.1002/path.2604
48. Chen CY, Yang SC, Lee KH, Yang X, Wei LY, Chow LP, et al. The antitumor agent PBT-1 directly targets HSP90 and hnRNP A2/B1 and inhibits lung adenocarcinoma growth and metastasis. *J Med Chem.* (2014) 57:677–85. doi: 10.1021/jm401686b
49. Chen CY, Jan CI, Pi WC, Wang WL, Yang PC, Wang TH, et al. Heterogeneous nuclear ribonucleoproteins A1 and A2 modulate expression of Tid1 isoforms and EGFR signaling in non-small cell lung cancer. *Oncotarget.* (2016) 7:16760–72. doi: 10.18632/oncotarget.7606
50. Wang TH, Chan CW, Fang JY, Shih YM, Liu YW, Wang TV, et al. 2-O-Methylmagnolol upregulates the long non-coding RNA, GAS5, and enhances apoptosis in skin cancer cells. *Cell Death Dis.* (2017) 8:e2638. doi: 10.1038/cddis.2017.66
51. Chen CC, Chen CY, Ueng SH, Hsueh C, Yeh CT, Ho JY, et al. Corylin increases the sensitivity of hepatocellular carcinoma cells to chemotherapy through long noncoding RNA RAD51-AS1-mediated inhibition of DNA repair. *Cell Death Dis.* (2018) 9:543. doi: 10.1038/s41419-018-0575-0
52. Chu Q, Amano O, Kanda Y, Kunii S, Wang Q, Sakagami H. Tumor-specific cytotoxicity and type of cell death induced by gefitinib in oral squamous cell carcinoma cell lines. *Anticancer Res.* (2009) 29:5023–31.
53. Sivanantham B, Sethuraman S, Krishnan UM. Combinatorial effects of curcumin with an anti-neoplastic agent on head and neck squamous cell carcinoma through the regulation of EGFR-ERK1/2 and apoptotic signaling pathways. *ACS Comb Sci.* (2016) 18:22–35. doi: 10.1021/acscmbosci.5b00043
54. Iocca O, Farcomeni A, Di Rocco A, Di Maio P, Golusinski P, Pardinas Lopez S, et al. Locally advanced squamous cell carcinoma of the head and neck: a systematic review and Bayesian network meta-analysis of the currently available treatment options. *Oral Oncol.* (2018) 80:40–51. doi: 10.1016/j.oraloncology.2018.03.001
55. Khushboo PS, Jadhav VM, Kadam VJ, Sathe NS. *Psoralea corylifolia* Linn.-“Kushtanashini.” *Pharmacogn Rev.* (2010) 4:69–76. doi: 10.4103/0973-7847.65331
56. Sarkis SA, Abdullah BH, Abdul Majeed BA, Talabani NG. Immunohistochemical expression of epidermal growth factor receptor (EGFR) in oral squamous cell carcinoma in relation to proliferation, apoptosis, angiogenesis and lymphangiogenesis. *Head Neck Oncol.* (2010) 2:13. doi: 10.1186/1758-3284-2-13
57. Yamano Y, Uzawa K, Saito K, Nakashima D, Kasamatsu A, Koike H, et al. Identification of cisplatin-resistance related genes in head and neck squamous cell carcinoma. *Int J Cancer.* (2010) 126:437–49. doi: 10.1002/ijc.24704
58. Celentano A, Mccullough M, Cirillo N. Glucocorticoids reduce chemotherapeutic effectiveness on OSCC cells via glucose-dependent mechanisms. *J Cell Physiol.* (2019) 234:2013–20. doi: 10.1002/jcp.27227
59. Maji S, Shriwas O, Samal SK, Priyadarshini M, Rath R, Panda S, et al. STAT3- and GSK3beta-mediated Mcl-1 regulation modulates TPF resistance in oral squamous cell carcinoma. *Carcinogenesis.* (2019) 40:173–83. doi: 10.1093/carcin/bgy135
60. Ma C, Shi X, Zhu Q, Li Q, Liu Y, Yao Y, et al. The growth arrest-specific transcript 5 (GAS5): a pivotal tumor suppressor long noncoding RNA in human cancers. *Tumour Biol.* (2016) 37:1437–44. doi: 10.1007/s13277-015-4521-9
61. Ghafouri-Fard S, Taheri M. Growth arrest specific transcript 5 in tumorigenesis process: an update on the expression pattern and genomic variants. *Biomed Pharmacother.* (2019) 112:108723. doi: 10.1016/j.biopha.2019.108723
62. Pickard MR, Williams GT. Regulation of apoptosis by long non-coding RNA GAS5 in breast cancer cells: implications for chemotherapy. *Breast Cancer Res Treat.* (2014) 145:359–70. doi: 10.1007/s10549-014-2974-y
63. Guo LJ, Zhang S, Gao B, Jiang Y, Zhang XH, Tian WG, et al. Low expression of long non-coding RNA GAS5 is associated with poor prognosis of patients with thyroid cancer. *Exp Mol Pathol.* (2017) 102:500–4. doi: 10.1016/j.yexmp.2017.05.008
64. Yang Y, Shen Z, Yan Y, Wang B, Zhang J, Shen C, et al. Long non-coding RNA GAS5 inhibits cell proliferation, induces G0/G1 arrest and apoptosis, and functions as a prognostic marker in colorectal cancer. *Oncol Lett.* (2017) 13:3151–8. doi: 10.3892/ol.2017.5841
65. Avgeris M, Tsilimantou A, Levis PK, Tokas T, Sideris DC, Stravodimos K, et al. Loss of GAS5 tumour suppressor lncRNA: an independent molecular cancer biomarker for short-term relapse and progression in bladder cancer patients. *Br J Cancer.* (2018) 119:1477–86. doi: 10.1038/s41416-018-0320-6
66. Dong S, Qu X, Li W, Zhong X, Li P, Yang S, et al. The long non-coding RNA, GAS5, enhances gefitinib-induced cell death in innate EGFR tyrosine kinase inhibitor-resistant lung adenocarcinoma cells with wide-type EGFR via downregulation of the IGF-1R expression. *J Hematol Oncol.* (2015) 8:43. doi: 10.1186/s13045-015-0140-6
67. Li W, Zhai L, Wang H, Liu C, Zhang J, Chen W, et al. Downregulation of LncRNA GAS5 causes trastuzumab resistance in breast cancer. *Oncotarget.* (2016) 7:27778–86. doi: 10.18632/oncotarget.8413
68. Zeng B, Li Y, Jiang F, Wei C, Chen G, Zhang W, et al. LncRNA GAS5 suppresses proliferation, migration, invasion, and epithelial-mesenchymal transition in oral squamous cell carcinoma by regulating the miR-21/PTEN axis. *Exp Cell Res.* (2019) 374:365–73. doi: 10.1016/j.yexcr.2018.12.014

**Conflict of Interest:** The authors declare that the research was conducted in the absence of any commercial or financial relationships that could be construed as a potential conflict of interest.

Copyright © 2019 Wang, Leu, Chen, Shieh, Lian and Chen. This is an open-access article distributed under the terms of the Creative Commons Attribution License (CC BY). The use, distribution or reproduction in other forums is permitted, provided the original author(s) and the copyright owner(s) are credited and that the original publication in this journal is cited, in accordance with accepted academic practice. No use, distribution or reproduction is permitted which does not comply with these terms.





## Original article

## Resveratrol suppresses neutrophil activation via inhibition of Src family kinases to attenuate lung injury

Yung-Fong Tsai<sup>a,b,1</sup>, Chun-Yu Chen<sup>a,b,1</sup>, Wen-Yi Chang<sup>a</sup>, Yu-Ting Syu<sup>a</sup>,  
Tsong-Long Hwang<sup>a,b,c,d,e,\*</sup><sup>a</sup> Graduate Institute of Natural Products, College of Medicine, Chang Gung University, Taoyuan, 333, Taiwan<sup>b</sup> Department of Anesthesiology, Chang Gung Memorial Hospital, Taoyuan, 333, Taiwan<sup>c</sup> Chinese Herbal Medicine Research Team, Healthy Aging Research Center, Chang Gung University, Taoyuan, 333, Taiwan<sup>d</sup> Research Center for Chinese Herbal Medicine, Research Center for Food and Cosmetic Safety, and Graduate Institute of Health Industry Technology, College of Human Ecology, Chang Gung University of Science and Technology, Taoyuan, 333, Taiwan<sup>e</sup> Department of Chemical Engineering, Ming Chi University of Technology, New Taipei City, 243, Taiwan

## ARTICLE INFO

## Keywords:

Resveratrol  
Superoxide anion  
Reactive oxygen species  
Lung injury  
Neutrophil  
Src family kinase

## ABSTRACT

The natural stilbenoid, Resveratrol (RSV; 3,5,4'-trihydroxystilbene) has been shown to have beneficial effects on inflammatory diseases as well as cancer, neurodegenerative diseases, and cardiovascular disorders. The underlying mechanism by which RSV affects neutrophil activation has yet to be fully elucidated. In this study, we tested the hypothesis that RSV modulates the inflammatory activities of formyl-Met-Leu-Phe-stimulated human neutrophils. We employed a well-established isolated-neutrophil model to investigate the effects of RSV on neutrophil functions and the underlying mechanism of signaling transduction. The lipopolysaccharide-induced ALI murine model was employed to evaluate the therapeutic effects of RSV. Experiment results demonstrate that RSV reduces respiratory burst, degranulation, integrin expression, and cell adhesion in activated neutrophils in dose-dependent manners. RSV inhibited phosphorylation of Src family kinases (SFKs) and reduced their enzymatic activities. Moreover, RSV and a selective inhibitor of SFKs (PP2) reduced the phosphorylation of Bruton's tyrosine kinase and Vav. These results indicated that the inhibitory effects of RSV are mediated through the inhibition of the SFKs-Btk-Vav pathway. This study also revealed that RSV attenuates endotoxin-induced lung injury. We surmise that the therapeutic effects of RSV on ALI may derive from its anti-neutrophilic inflammation function and free radical-scavenging effects.

## 1. Introduction

Resveratrol (RSV; 3,5,4'-trihydroxystilbene) is a natural stilbenoid found in a variety of foods, such as grapes, red wine, and berries. Studies have reported that RSV has beneficial effects on inflammatory diseases, neurodegenerative diseases, cardiovascular diseases, and cancer [1]. The positive effects of RSV can be primarily attributed to its anti-inflammatory and antioxidant properties. Moreover, it has also been associated with the regulation of various immune-associated cells and pathways. For example, RSV has been shown to inhibit cyclooxygenase activity both *in vitro* and *in vivo* [1,2], block NF-κB transcriptional activity [3,4], inhibit mitogen-activated protein kinase (MAPK) activity, decrease the production of nitric oxide, and also inhibit the production of pro-inflammatory cytokines [5–7] and matrix metalloproteinases [3,8,9]. In a previous study, we showed that

RSV attenuates cardiac injury in rats subjected to hemorrhagic shock via an Akt-dependent pathway [10]. RSV has also been reported to inhibit respiratory bursts in human neutrophils and nitric oxide production in macrophages [11]. Nevertheless, the underlying mechanisms by which RSV affects neutrophil activation have yet to be fully elucidated.

Researchers have developed numerous therapeutic strategies for the treatment of acute lung injury (ALI); however, it remains one of the most frequent cause of mortality among critically ill patients. A variety of etiologies can lead to ALI, including infection, sepsis, blood transfusion, hemorrhagic shock, burn injury, chemical inhalation, and ventilator-associated lung injury. The condition is characterized by severe inflammatory responses of the lung and infiltration of activated immune cells. Neutrophils, the most abundant professional phagocytes, make a major contribution to the process of ALI [12–15]. Activated

\* Corresponding author. Graduate Institute of Natural Products, College of Medicine, Chang Gung University, 259 Wenhwa 1st Road, Kweishan, Taoyuan, 333, Taiwan.

E-mail address: [htl@mail.cgu.edu.tw](mailto:htl@mail.cgu.edu.tw) (T.-L. Hwang).

<sup>1</sup> These authors contributed equally to this work.

<https://doi.org/10.1016/j.freeradbiomed.2019.09.021>

Received 9 August 2019; Received in revised form 18 September 2019; Accepted 20 September 2019

Available online 21 September 2019

0891-5849/© 2019 Elsevier Inc. All rights reserved.



neutrophils release high levels of superoxide anions, reactive oxygen species (ROS), and a variety of proteolytic enzymes, resulting in alveolar capillary barrier disruption and increased vascular permeability [12,15,16]. This makes neutrophils, in particular neutrophil elastases (NEs) and neutrophil extracellular traps (NETs), potential therapeutic targets in the treatment of ALI [13,17,18]. RSV produces a large number of anti-inflammatory effects; therefore, the potential therapeutic benefits of RSV as well as the mechanisms by which this stilbenoid affects ALI warrant careful evaluation [9].

Src family kinases (SFKs) are intracellular protein tyrosine kinases. Neutrophils mainly express three SFKs (Hck, Fgr, and Lyn) [19,20], which participate in transducing extracellular signals into the cell and regulating various neutrophil functions, such as recruitment to inflamed sites, adhesion to endothelium, degranulation, and ROS production [21–24]. The primary function of neutrophils is to fight against microorganism infections, which means that the most critical task performed by these cells is the recognition of pathogenic microbes. Formyl-Met-Leu-Phe (fMLF) is a formylated peptide produced by certain types of bacteria. It is recognized by neutrophils via formyl peptide receptors (FPR), which are responsible for recognizing chemoattractants and mediating neutrophil activation during inflammation. SFKs are indispensable in modulating FPR-mediated neutrophil activities [25,26]. Previous studies have demonstrated that SFKs mediate signaling transduction in fMLF-induced neutrophils and regulate downstream signals, such as JNK, p38 MAP kinases, and Vav-Rac-Pak [25,26]. In a recent study, we demonstrated that SFK inhibitors efficiently decrease a variety of neutrophil inflammatory responses triggered by fMLF [27]. This makes SFK a potential therapeutic target in the treatment of neutrophil-associated inflammation.

Herein, we hypothesize that RSV modulates the inflammatory activities of activated human neutrophils. We employed a well-established isolated-neutrophil model to investigate the effects of RSV on neutrophil functions, including superoxide anion release, elastase release, CD11b expression, and cell adhesion. We then sought to elucidate signaling transduction as well as the mechanisms by which RSV regulates neutrophil activity. Finally, we employed the lipopolysaccharide (LPS)-induced ALI murine model to evaluate the therapeutic effects of RSV.

## 2. Materials and Methods

### 2.1. Reagents

RSV (3,4',5-Trihydroxy-transstilbene, C<sub>14</sub>H<sub>12</sub>O<sub>3</sub>, MW: 228.24) was purchased from Sigma-Aldrich (St. Louis, MO, USA). The compound 2-(4-Iodophenyl)-3-(4-nitrophenyl)-5-(2,4-disulfophenyl)-2H-tetrazolium monosodium salt (WST-1) was purchased from Dojindo Molecular Technologies (Kumamoto, Japan). N-[2-[[3-(4-bromophenyl)-2-propenyl]amino]ethyl]-5-isouquinolinesulfonamide (H89) was purchased from Calbiochem (La Jolla, CA, USA). Purified neutrophil elastase was obtained from Enzo (Farmingdale, NY, USA). Dihydroethidium was purchased from Invitrogen (Eugene, OR, USA). Antibodies against SFK, phospho-SFK (Tyr416), Lyn, phospho-Lyn (Tyr396), Hck, phospho-Hck (Tyr410), phospho-Btk (Tyr223), phospho-Vav (Tyr174), and glyceraldehyde 3-phosphate dehydrogenase (GAPDH) were purchased from Cell Signaling (Beverly, MA, USA). Antibody against lymphocyte antigen 6 complex locus G6D (Ly6G) was purchased from Thermo Fisher Scientific (Waltham, MA, USA). Antibody against 4-hydroxynonenal (4-HNE) was purchased from Abcam (Cambridge, UK). All other reagents were purchased from Sigma-Aldrich (St. Louis, MO, USA).

### 2.2. Preparation of human neutrophils

All experiments in this study were conducted in accordance with a protocol approved by the Institutional Review Board at Chang Gung Memorial Hospital. After obtaining informed consent, heparinized venous blood samples were drawn from healthy donors (aged 20–30 years

old) who did not take any form of medication within one week prior to the sample collection day. Following dextran sedimentation, human neutrophils were isolated via centrifugation using Ficoll-Hypaque and hypotonically lysis of remaining erythrocytes. Neutrophils were suspended in cold Ca<sup>2+</sup>-free Hank's balanced salts solution (HBSS) [28].

### 2.3. Measurement of superoxide anion release

Superoxide anion released from human neutrophils were determined by measuring ferricytochrome *c* reduction. Isolated neutrophils ( $6 \times 10^5$  cells/mL) were suspended in HBSS containing 0.5 mg/mL cytochrome *c* and 1 mM Ca<sup>2+</sup> at 37 °C for 5 min. After pretreatment with DMSO (0.1%, as a control) or RSV (3–50 μM), the neutrophils were activated with fMLF (30 nM) and cytochalasin B (0.5 μg/mL) (fMLF/CB). Changes in absorbance that occurred at 550 nm were observed continuously using a double beam spectrophotometer (U-3010; Hitachi, Tokyo, Japan). Superoxide anion level was calculated using the methods described in previous report [27].

### 2.4. Assessment of elastase release

Degranulation of human neutrophils was determined by elastase release. Neutrophils ( $6 \times 10^5$  cells/mL) were mixed with an elastase substrate (MeO-Suc-Ala-Ala-Pro-Val-p-nitroanilide, 100 μM) at 37 °C for 5 min, and the cells were then stimulated with fMLF (30 nM)/CB (1 μg/mL). Changes in absorbance at 405 nm were continuously recorded using a spectrophotometer (U-3010; Hitachi) to evaluate elastase release.

### 2.5. Intracellular superoxide anion assessment

Human neutrophils ( $10^6$  cells/mL) were preincubated in HBSS containing 1 μM dihydroethidine at 37 °C for 10 min, and were then treated with RSV (3–50 μM) for another 5 min. Neutrophils were then stimulated using fMLF (30 nM)/CB (1 μg/mL) for 5 min. The reaction was terminated by adding ice-cold HBSS. Intracellular superoxide anion production was detected using flow cytometry.

### 2.6. Measurement of CD11b expression

Neutrophils ( $2.5 \times 10^6$  cells/mL) were preincubated with RSV, PP2, or LMF-A13 for 5 min and then stimulated with fMLF (30 nM)/CB (1 μg/mL) for 5 min. After centrifugation at 4 °C and discarded the supernatant, cells were resuspended in HBSS containing 0.5% bovine serum albumin for immunofluorescent staining using a FITC-labeled-anti-CD11b antibody (1 μg) for 90 min at 4 °C. The fluorescence intensity of FITC-labeled anti-CD11b was then monitored using flow cytometry.

### 2.7. Neutrophil adhesion assay

Hoechst 33342 (1 ng/mL)-stained human neutrophils were incubated with vehicle or RSV (3–50 μM) for 5 min, followed by activation with fMLF (30 nM)/CB (1 μg/mL) for 15 min. Meanwhile, endothelial cells were pretreated with LPS (2 μg/mL) for 4 h, and then co-incubated with previously labeled neutrophils ( $1 \times 10^5$  cells/mL) for 15 min. The non-adherent cells were removed by washing with RPMI medium, and the adherent neutrophils on endothelial cells were calculated by a motorized inverted microscope (IX81, Olympus, Japan). Six randomly areas (0.572 mm<sup>2</sup>) were selected for cell number counting with 10X objective setting.

### 2.8. Determination of superoxide-scavenging ability

A xanthine/xanthine oxidase (XO) cell-free system was used to assay the superoxide-scavenging function of RSV. Human neutrophils were incubated for 3 min in assay buffer containing Tris (50 mM, pH 7.4), XO (0.02 U/mL) and WST-1 (0.3 mM), in the presence or absence of RSV (10–50 μM). Following this, 0.1 mM xanthine was added to the buffer.

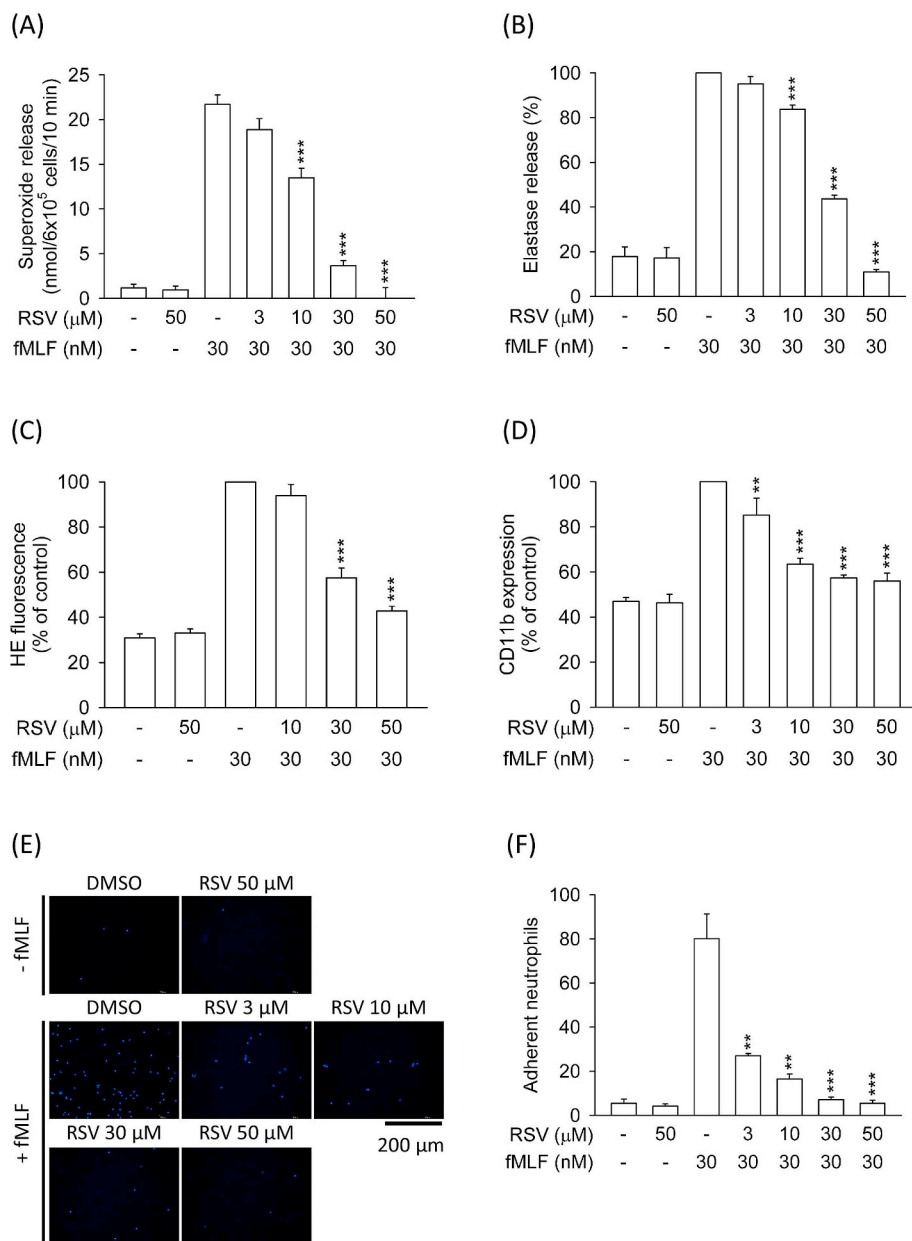


**Fig. 1.** RSV significantly inhibits superoxide anion release, elastase release, intracellular superoxide formation, CD11b expression, and cell adhesion in activated human neutrophils. Human neutrophils were incubated with DMSO (0.1%, as a control) or RSV (3–50 μM) for 5 min prior to cell activation. (A, B) The release of superoxide anion and elastase were respectively detected spectrophotometrically by using ferricytochrome c and elastase substrate (n = 6). (C) Hydroethidine-labeled neutrophils were stimulated using fMLF/CB for another 5 min. Intracellular superoxide levels were determined according to intracellular fluorescence intensity, as measured by flow cytometry (n = 7). (D) CD11b expression was induced by fMLF/CB for 5 min. The fluorescence intensity of FITC-labeled-anti-CD11b was monitored using flow cytometry (n = 8). (E, F) Hoechst 33342 (1 ng/mL)-stained neutrophils were incubated with RSV (3–50 μM) for 5 min, followed by activation with fMLF/CB for 15 min. The LPS-treated endothelial cells were co-incubated with previously labeled neutrophils for 15 min. The adherent neutrophils on endothelial cells were calculated by a motorized inverted microscope. All data are expressed as the mean ± SEM. \*\**p* < 0.01 and \*\*\**p* < 0.001 compared with the control.

Changes in absorbance resulting from superoxide-induced WST-1 reduction were monitored at 450 nm at 30 °C for a period of 10 min.

## 2.9. Measurement of lactate dehydrogenase (LDH) release

LDH release was quantified using a commercial LDH assay kit (Promega, Madison, WI, USA) in accordance with the manufacturer's instructions. Briefly, culture supernatants were collected from untreated neutrophils and from neutrophils that had been treated with RSV. LDH assay reagent was then added to the supernatants, and colorimetric signal was monitored and compared to total LDH release, which is determined the lysis of neutrophils with 0.1% Triton X-100 at 37 °C for 30 min.

## 2.10. Measurement of cyclic adenosine monophosphate (cAMP) concentration

An immunoassay kit (Amersham Biosciences, Buckinghamshire, UK) was used to determine the concentration of cellular cAMP. Following pretreatment with RSV (10–50 μM) or rolipram (3 μM) at 37 °C for

5 min, human neutrophils were activated using 30 nM fMLF for 1 min. Dodecyltrimethylammonium bromide (0.5%) was then added to stop the reaction. Following centrifugation, the supernatant was collected for the analysis of cAMP levels [29].

## 2.11. Immunoblotting

Following incubation with or without RSV (10–50 μM) at 37 °C for 5 min, human neutrophils were activated using fMLF (30 nM)/CB (1 μg/mL) for 30 s. Cells were then incubated in sample buffer (62.5 mM pH 6.8 Tris-HCl, 4% sodium dodecyl sulfate (SDS), 0.00125% bromophenol blue, 5% β-mercaptoethanol, 2.5 mM Na<sub>3</sub>VO<sub>4</sub>, 10 mM di-N-pentyl phthalate, and 8.75% glycerol) supplemented with protease inhibitors to obtain cell lysates. The lysates were heated for 15 min at 100 °C and centrifuged at 14,000 g at 4 °C for 20 min to obtain the supernatant, which was used for immunoblotting assays. Denatured proteins were separated using SDS-PAGE and blotted onto nitrocellulose membranes, which were subsequently blocked at room temperature for 1 h using a 0.1% Tween 20 solution containing 5% (w/v) non-fat milk. The target

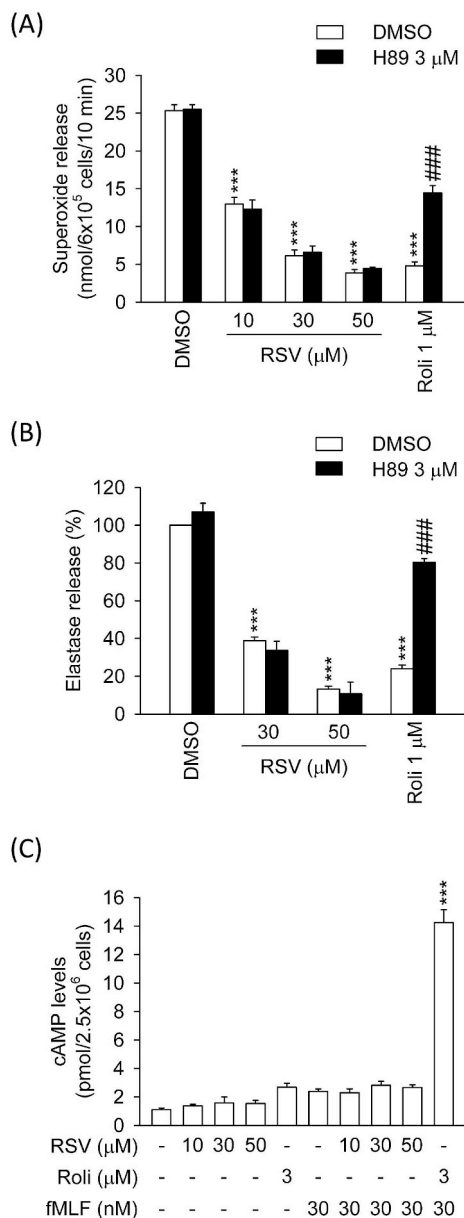


**Fig. 2.** The inhibitory effects of RSV are not mediated through an increased concentration of cAMP or the activity of PKA in activated neutrophils. Human neutrophils were preincubated with H89 (3 μM) for 5 min prior to the addition of RSV (10–50 μM), or rolipram (Roli, 1 μM). (A) Extracellular superoxide anion release was induced by fMLF/CB for 10 min and measured using SOD-inhibitable cytochrome c reduction (n = 10). (B) Elastase release was measured spectrophotometrically at 405 nm (n = 7). (C) Human neutrophils were pretreated with DMSO (0.1%, as a control), RSV (10–50 μM), or rolipram (Roli, 3 μM) for 5 min prior to activation with fMLF (30 nM) for 1 min. Concentrations of cAMP were assayed using commercial immunoassay kits (n = 6). All data are expressed as the mean ± SEM. \*\*\*p < 0.001 compared with the control, and ###p < 0.001 compared with the corresponding control.

protein was identified via immunoblotting at 4 °C overnight using the primary antibodies: anti-SFK, anti-phospho-SFK (Tyr416), anti-Lyn, anti-phospho-Lyn (Tyr396), anti-Hck, anti-phospho-Hck (Tyr410), anti-phospho-Btk (Tyr223), anti-phospho-Vav (Tyr174), and anti-GAPDH. Finally, the membrane was incubated in buffer containing peroxidase-labeled secondary anti-rabbit antibodies (Cell Signaling Technology, Beverly, MA). Blots were developed using an enhanced chemiluminescence system (Amersham Biosciences). Signal intensities were analyzed using a densitometer (UVP, Upland, CA), and the quantitative ratios of

all samples were normalized to the corresponding total protein or GAPDH.

## 2.12. Determination of enzymatic activities of SFKs

An enzymatic activity assay of SFKs was performed in a cell-free system. The recombinant SFKs, Src, Lyn, and Fgr, were purchased from Promega (Madison, WI, USA). Enzymatic activity of SFKs were determined by ADP-Glo™ kinase assay kit (Promega). Kinase assays were carried out in a reaction buffer containing tris-base (pH 7.5), MgCl<sub>2</sub> (20 mM), bovine serum albumin (0.1 mg/mL), dithiothreitol (50 μM), and MnCl<sub>2</sub> (2 mM). The kinase reaction was started by adding SFKs, substrate of SFKs, adenosine triphosphate (ATP, 50 μM), and RSV (30–100 μM) or PP2 (1 μM and 3 μM) into the buffer for 60 min. ADP-Glo™ reagent was then added to stop the kinase reaction and deplete the remaining ATP. The kinase detection reagent was added to convert ADP to ATP and introduce luciferase and luciferin to detect ATP. The luminescence was recorded with a microplate reader (Infinite 200 Pro; Tecan, Männedorf, Switzerland).

## 2.13. LPS-induced ALI and assay of pulmonary water content

Male C57BL/6 mice (8 wk old; Lasco, Taipei, Taiwan) were used for animal experiments performed in this study. Animals were maintained in the animal facility at Chang Gung University (CGU). All experiment protocols were approved by the Institutional Animal Care and Use Committee of CGU. Mice were randomly assigned to four groups: sham-operated mice pretreated with vehicle, sham-operated mice pretreated with RSV, ALI animals pretreated with vehicle, and ALI animals pretreated with RSV. Mice were intraperitoneally injected with or without 50 μL RSV (100 mg/kg) under anesthesia with 1% isoflurane. One hour after RSV administration, ALI was induced by instilling 50 μL of 3.2 mg/mL LPS (*Escherichia coli* serotype O55:B5) or normal saline (sham group) via a tracheostomy. Six hours after injury induction, the animals were re-anesthetized to obtain lung samples. Specifically, the left upper lobe was used for the analysis of lung water content, the right lower lobe was fixed in 10% formalin for histological examination, and the right upper lobe was used for myeloperoxidase (MPO) assays. Pulmonary tissue water content was defined as the wet/dry ratio. For this calculation, fresh lung sections were weighed, placed in a drying oven at 80 °C for 48 h, and the dried sections were then re-weighed [30].

## 2.14. Measurement of lung MPO activity

MPO activity can be used as a marker of neutrophil infiltration in the lungs of mice subjected to LPS-induced ALI. Lung samples were frozen in liquid nitrogen and stored at −70 °C until assays were performed. For assays, samples were thawed, immersed in phosphate buffer saline (PBS) containing hexadecyltrimethylammonium bromide (0.5%), and sonicated using a homogenizer. Following centrifugation, MPO activity was characterized by adding homogenates to phosphate buffer (pH 6.0) containing o-dianisidine hydrochloride (0.167 mg/mL) and hydrogen peroxide (0.0005%, Sigma). Light absorbance was monitored spectrophotometrically at 460 nm for 5 min. Final values of MPO activity were normalized to the corresponding protein concentration.

## 2.15. Histology and immunofluorescence staining of lungs

After being washed with PBS, fresh lung tissues were fixed in 10% formalin for 1 day. Samples were then dehydrated, embedded in 100% paraffin, sectioned using a microtome at 3 μm, and mounted on glass slides. Samples were then stained using hematoxylin and eosin. Images were obtained under a light microscope. For immunofluorescence staining, the sections were incubated with antibodies against Ly6G and 4-HNE at dilution of 1:200. The fluorescent-labeled secondary antibodies (Alexa Fluor 594 for Ly6G, and Alexa Fluor 488 for 4-HNE) were used at the dilution of 1:500. Fluorescence in slides was examined under an Olympus fluorescence microscope.

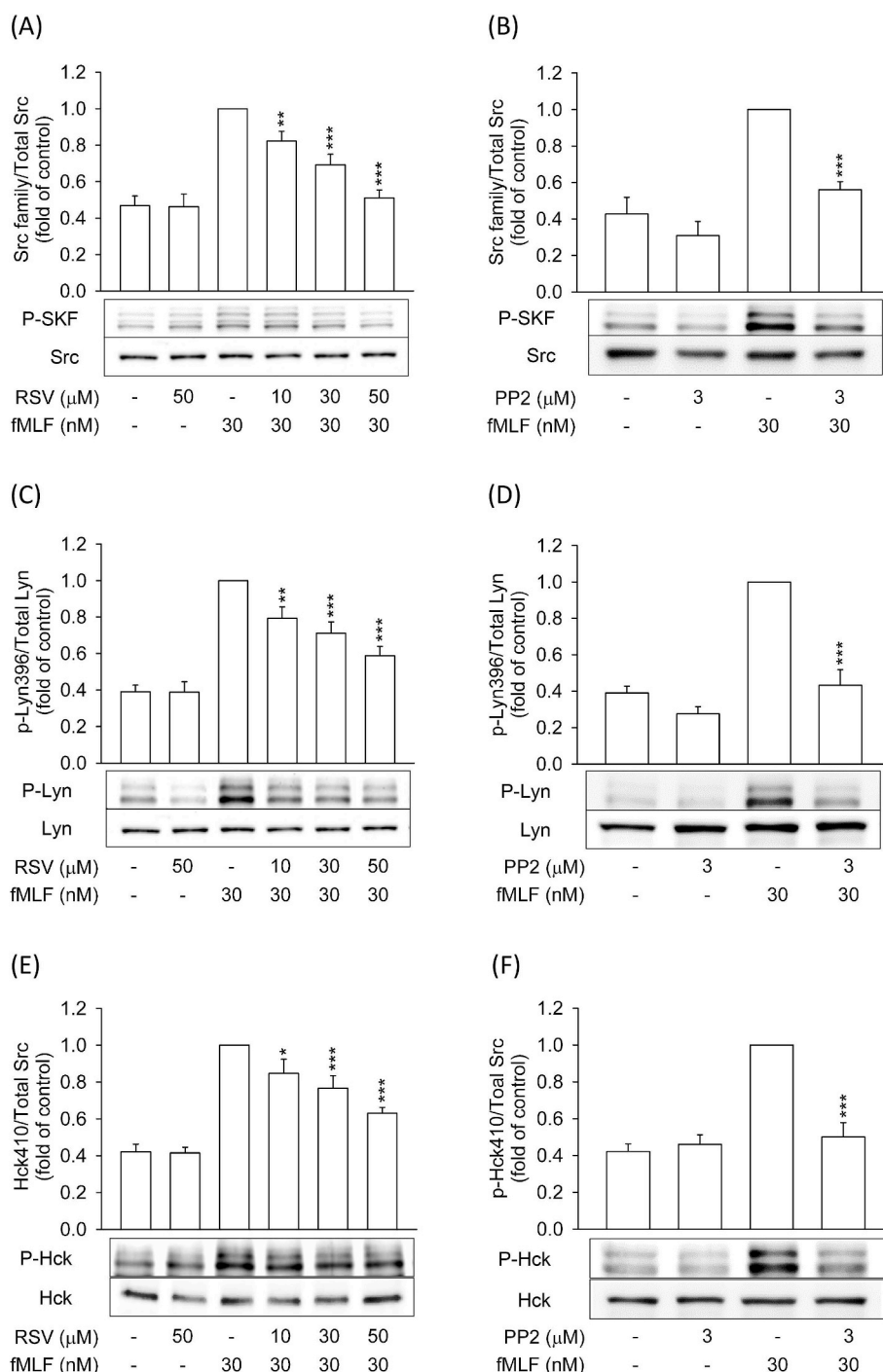


**Fig. 3. RSV attenuated the phosphorylation of SFKs in activated human neutrophils.** Human neutrophils were incubated with RSV (10–50 μM), or PP2 (SFK inhibitor, 3 μM) for 5 min prior to stimulation with or without fMLF (30 nM) for another 30 s. All Western blotting experiments were performed under the same conditions. After transferring the blots onto nitrocellulose membranes, we immediately cropped the targeted blots according to referenced indicator markers and then immunoblotted target proteins using their specific monoclonal antibodies. Images show the results of Western blot analysis using anti-phospho antibodies directed against (A, B) SFKs, (C, D) Lyn, and (E, F) Hck. Bands on the blots were analyzed using a densitometer, and the quantitative ratios in all samples were normalized to corresponding total protein values. All data are expressed as mean ± SEM (n = 9). \**p* < 0.05; \*\**p* < 0.01; and \*\*\**p* < 0.001 compared with the control.

## 2.16. Statistical analysis

For each group, the data are presented as mean ± SEM. Statistical analysis was performed using the Student's *t*-test with SigmaPlot (Systat Software, San Jose, CA). In examining differences among groups, a *p* value of < 0.05 was considered to be significant.

## 3. Results

### 3.1. RSV significantly inhibits superoxide anion release, elastase release, intracellular superoxide anion formation, CD11b expression and neutrophil adhesion in activated human neutrophils

We first analyzed the effects of RSV on human neutrophil effector

functions, including respiratory burst, degranulation, integrin expression, and cell adhesion. At IC<sub>50</sub> values of 13.99 ± 0.46 and 25.30 ± 1.09 μM, respectively, RSV (3–50 μM) was found to significantly inhibit the release of extracellular superoxide anion and elastase (Fig. 1A and B). RSV was also shown to diminish the fMLF-induced generation of intracellular superoxide anion and the expression of membrane CD11b (Fig. 1C and D). In addition, RSV decreased adhesion of neutrophils onto the surface of endothelial in a dose-dependent manner (Fig. 1E and F). LDH assays further confirmed that RSV (100 μM) did not induce cytotoxicity (Supp. 1A). In evaluating whether RSV has direct superoxide scavenging effects, we determined that RSV (10–50 μM) did not inhibit superoxide anion production in a cell-free xanthine/xanthine oxidase system (Supp. 1B).



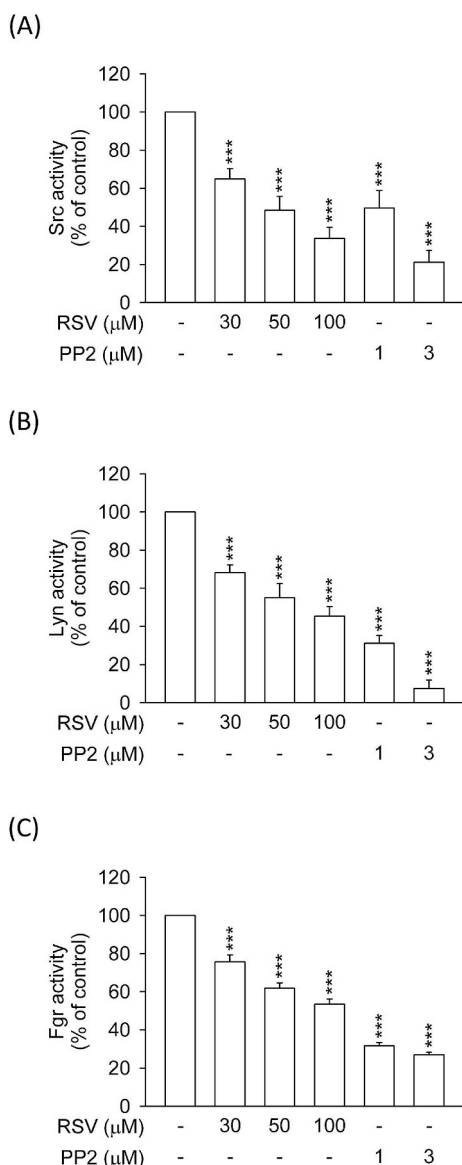


**Fig. 4. RSV inhibited the enzymatic activities of Src, Lyn, and Fgr.** An enzymatic activity assay of Src family kinases (SFKs) was performed in a cell-free system. The recombinant SFKs, Src, Lyn, and Fgr, were purchased from Promega (Madison, WI, USA). Enzymatic activity of SFKs were determined by ADP-Glo™ kinase assay kit (Promega). (A) Src (2 ng/mL), (B) Lyn (2 ng/mL), or (C) Fgr (2 ng/mL) was incubated with DMSO (0.1%, as a control), RSV (30–100  $\mu$ M), or PP2 (1 or 3  $\mu$ M) for 10 min, and then ATP/substrate was added to the mixture for 1 h before enzymatic activity was measured. The luminescence was recorded with a microplate reader (Infinite 200 Pro; Tecan, Männedorf, Switzerland). All data are expressed as mean  $\pm$  SEM (n = 6). \* $p$  < 0.05; \*\* $p$  < 0.01; and \*\*\* $p$  < 0.001 compared with the control.

### 3.2. The cAMP/protein kinase A (PKA) pathway is not involved in the inhibitory effects of RSV

Increased cAMP levels are known to activate cAMP dependent PKA signals and thereby negatively regulate neutrophil functions [31]. A PKA inhibitor, H89, was used to determine whether the cAMP/PKA pathway participates in the inhibitory effects of RSV. H89 (3  $\mu$ M) was shown to reverse the inhibitory effects of a PDE4 inhibitor, rolipram, but not the inhibitory effects of RSV (10–50  $\mu$ M) (Fig. 2A and B). Furthermore, the concentrations of cAMP that we observed indicates that RSV does not have an effect on cAMP levels (Fig. 2C). Based on these findings, we surmise that RSV does not mediate the cAMP/PKA pathway to inhibit neutrophil function.

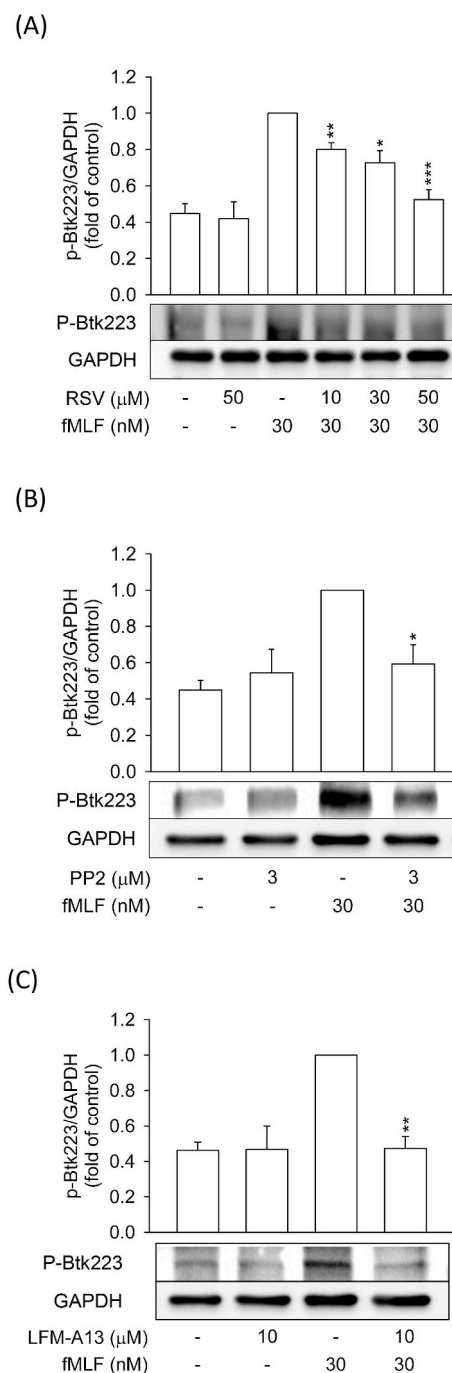


**Fig. 5. RSV, PP2, and LFM-A13 inhibited the phosphorylation of Btk in activated human neutrophils.** Human neutrophils were incubated with (A) RSV (10–50  $\mu$ M), (B) PP2 (3  $\mu$ M), or (C) LFM-A13 (10  $\mu$ M) for 5 min before stimulation with or without fMLF (30 nM) for another 30 s. The figure shows the results of Western blot analysis using anti-phospho antibodies directed against Btk223. Bands on the blots were analyzed using a densitometer, and the quantitative ratios in all samples were normalized to glyceraldehyde 3-phosphate dehydrogenase (GAPDH). All data are expressed as mean  $\pm$  SEM (n = 6). \* $p$  < 0.05, \*\* $p$  < 0.01 and \*\*\* $p$  < 0.001 compared with the control.

### 3.3. RSV inhibits the phosphorylation and enzymatic activities of SFKs

SFKs are tyrosine kinases which participate in signaling transduction of neutrophil activation [22,25]. By coupling with the  $G\alpha$  subunit of GPCR, SFKs function in a positive fashion to transduce downstream MAPK signals in leukocytes. To determine whether SFKs mediate the



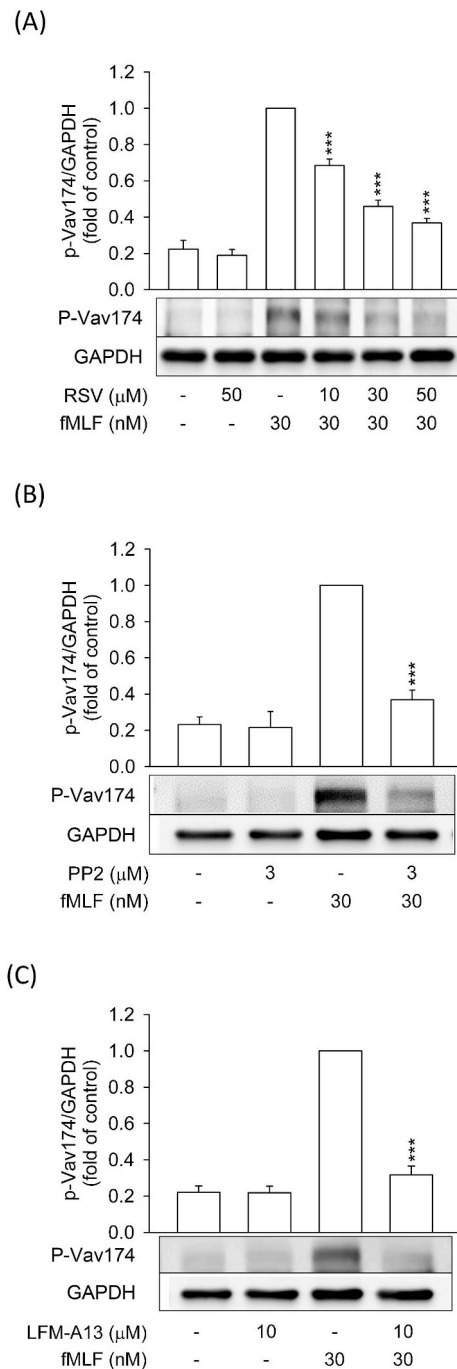


**Fig. 6.** RSV, PP2, and LFM-A13 inhibited the phosphorylation of Vav in activated human neutrophils. Human neutrophils were incubated with (A) RSV (10–50 μM), (B) PP2 (3 μM), or (C) LFM-A13 (10 μM) for 5 min before stimulation with or without fMLF (30 nM) for another 30 s. The images show the results of Western blot analysis using anti-phospho antibodies directed against Vav174. Bands on the blots were analyzed using a densitometer, and the quantitative ratios for all samples were normalized to the GAPDH. All data are expressed as mean ± SEM (n = 6). \*\*\*p < 0.001 compared with the control.

inhibitory function of RSV, we evaluated the phosphorylated forms of SFK (Tyr416), Lyn (Tyr396), and Hck (Tyr410) via Western blotting. Activating human neutrophils with fMLF led to the phosphorylation of SFK, Lyn, and Hck, whereas RSV (10–50 μM) inhibited kinase phosphorylation in a concentration-dependent manner (Fig. 3A, C, and 3E). PP2, a selective inhibitor of SFKs, was found to have effects similar to those of RSV (Fig. 3B, D, and 3F). We also performed *in vitro* assays to characterize the effects of RSV on kinase activity and determined that

RSV reduced the activity of SFKs (Fig. 4 and Supp. 2). PP2 was used as a positive control. These findings confirm that RSV directly inhibits the activities of SFKs.

#### 3.4. RSV inhibits the phosphorylation of Bruton's tyrosine kinase (Btk) and Vav

Btk is a member of the Tec family of cytoplasmic tyrosine kinases [32]. Btk activation is also involved in GPCR signaling transduced through the stimulation of human neutrophils by fMLF [33]. In the present study, RSV (10–50 μM), PP2 (SFK inhibitor, 3 μM), and LFM-A13 (Btk inhibitor, 10 μM) were shown to inhibit the phosphorylation of Btk in a dose dependent manner (Fig. 5). Vav proteins are guanine-nucleotide exchange factors associated with the RHO/RAC family of GTPases [34]. SFKs can trigger Vav phosphorylation and activation. In this study, RSV (10–50 μM), PP2 (3 μM), and LFM-A13 (10 μM), were shown to decrease Vav phosphorylation (Fig. 6).

#### 3.5. PP2 and LFM-A13 significantly suppress superoxide anion release, elastase release, intracellular ROS production, and CD11b expression in fMLF-activated human neutrophils

We further evaluated the effects of SFKs and Btk inhibitors on human neutrophil activation. PP2 (0.3 and 1 μM) and LFM-A13 (10 μM) were found to inhibit superoxide anion and elastase release in fMLF-activated human neutrophils (Fig. 7A and B). They also decreased the intracellular superoxide anion generation and CD11b expression induced by fMLF (Fig. 7C and D). These findings confirm that the inhibitory functions of RSV are mediated via SFK/Btk pathways.

#### 3.6. RSV alleviates LPS-induced ALI in mice

Intratracheal LPS elicited a major increase in pulmonary MPO activity in mice; these effects were attenuated when mice were treated intraperitoneally with RSV (100 mg/kg) (Fig. 8A). We evaluated the severity of pulmonary edema by calculating the wet/dry weight ratios of mouse lungs. The wet/dry weight ratios of lung samples from ALI mice were higher than those obtained from the sham group. Treatment with RSV significantly decreased these wet/dry weight ratios (Fig. 8B). In examining histopathologic features of lungs from the four groups (Fig. 8C), we observed marked inflammatory changes in the lung sections of ALI-treated mice, including pulmonary edema, congestion, hemorrhage, and alveolar wall thickening. RSV treatment was shown to alleviate the histopathologic features induced by LPS. Moreover, increased neutrophil infiltration and activation were observed in lungs of ALI mice, as evidenced by an increase in immunofluorescence of Ly6G and 4-HNE expression. Intraperitoneal administration of RSV effectively reduced the increase in pulmonary neutrophil infiltration and activation (Fig. 8C). Taken together, these findings demonstrate that RSV can alleviate LPS-induced lung injuries.

## 4. Discussion

A large body of experimental and clinical data have revealed that the dietary consumption of RSV (recognized as a potent anti-oxidant and free radical scavenger) [35] may have beneficial effects against inflammation-associated diseases, such as pulmonary system diseases [36], cardiovascular diseases [37], autoimmune diseases [38], and cancer [2,39]. Previous study has showed that RSV has significant inhibitory effect on various inflammatory functions of neutrophils [40]. However, the underlying mechanism remains largely obscure. In this study, we demonstrated that the neutrophil inhibitory effects are mediated through the inhibition of the SFKs-Btk-Vav pathway.

In this study, we determined that RSV reduces the generation and release of superoxide anion, which can be converted into a variety of

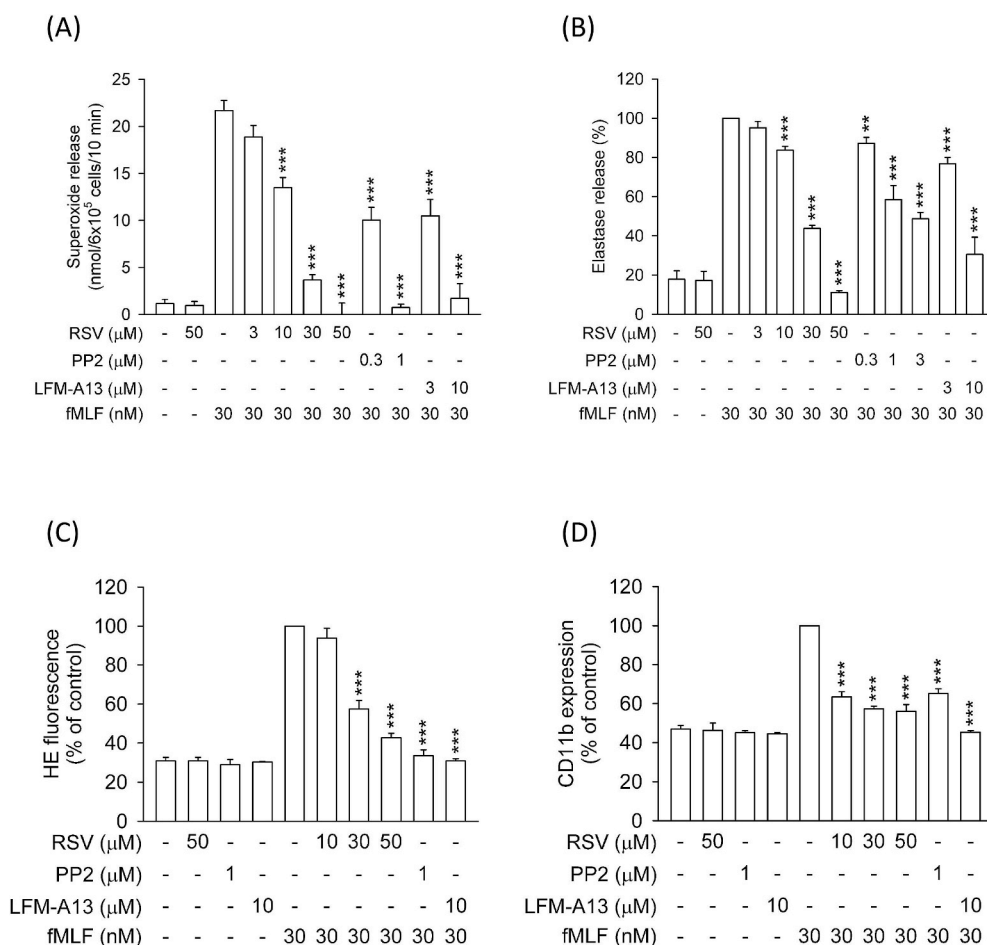


**Fig. 7.** RSV, PP2, and LFM-A13 significantly inhibited superoxide anion release, elastase release, intracellular superoxide formation, and CD11b expression in activated human neutrophils. Human neutrophils were incubated with RSV (3–50 μM), PP2 (0.3 or 1 μM), or (C) LFM-A13 (3 or 10 μM) for 5 min before cell activation. (A, B) Superoxide anion and elastase release were respectively detected spectrophotometrically using cytochrome *c* and elastase substrate (*n* = 8). (C) Intracellular superoxide was determined according to intracellular fluorescence intensity measured using flow cytometry. The expression of (D) CD11b (*n* = 7) was induced by fMLF/CB for 5 min. The fluorescence intensity of FITC-labeled-anti-CD11b was measured using flow cytometry. All data are expressed as the mean ± SEM (*n* = 8). \*\**p* < 0.01 and \*\*\**p* < 0.001 compared with the control.

other ROS in fMLF-induced human neutrophils. Previous studies have reported that RSV concentrations below 50 μM does not exhibit significant superoxide-scavenging effects [41]. Similarly, our experiment using a cell-free xanthine/xanthine oxidase system revealed that RSV (50 μM) does not scavenge superoxide anion. Thus, the effects of RSV against oxidative stress in human neutrophils can be attributed to the inhibition of signaling transduction, rather than superoxide scavenging.

Neutrophils contribute to inflammation and host defense. Formylpeptide receptors, which belong to the Gα<sub>i/o</sub> subfamily of GPCRs, are able to sense formylated peptides derived from bacteria and mitochondria, the presence of which implies bacterial invasion and tissue injury, respectively [42]. Activation of FPRs induces the dissociation of GPCR-specific Gα<sub>i</sub> from Gβγ subunits. Gα<sub>i</sub> inhibits adenylyl cyclase activity and in so doing reduces cytoplasmic cAMP levels. Increased intracellular cAMP levels trigger PKA activation, which negatively regulates neutrophil effector activities [31,43,44]. This means that the stimulation of FPRs evokes neutrophil effector activities via inhibition of the cAMP/PKA-dependent neutrophil inhibition pathway. Moreover, PDE4, which could be found in neutrophils can catalyze cAMP hydrolysis and has therefore been implicated in the regulation of intracellular cAMP levels. Various studies have revealed that PDE4 inhibitors can suppress neutrophil activation, ROS generation, and cell migration [45–47]. However, in the current research, RSV was shown not to affect intracellular cAMP levels. Moreover, one PKA inhibitor, H89, reversed the inhibitory effects of rolipram (a PDE4 inhibitor), but not the inhibitory effects of RSV. These findings indicate that the cAMP/PKA pathway is not associated with the RSV-mediated inhibition of fMLF-activated neutrophils.

We further examined the downstream signaling of GPCR to elucidate the mechanisms which underlie the anti-inflammatory effects of RSV in neutrophils. At present, there is a lack of direct evidence linking FPR to SFK activation [24]; however, some studies have revealed that the FPR-mediated activation of SFKs in neutrophils may occur parallel to other pathways, such as the PLC and PI3Kγ pathways [24,27]. Our immunoblotting assays revealed that RSV inhibited the phosphorylation of SFKs, Lyn, and Hck, and directly inhibited the enzymatic activities of Src and Lyn. Moreover, RSV and the SFK inhibitor PP2 were shown to reduce superoxide anion release, elastase release, and CD11b expression in fMLF-stimulated neutrophils. These results indicate that the mechanism by which RSV inhibited neutrophil-mediated inflammation was the suppression of SFK activity.

Btk belongs to the Tec family of cytoplasmic tyrosine kinases, and shares structural homologies with SFKs. SFKs have also been reported to mediate the phosphorylation of Btk [48,49]. Our results confirmed that Btk phosphorylation was suppressed by the SFK inhibitor, PP2, which suggests that Btk is a downstream kinase of SFKs. Moreover, RSV and the Btk inhibitor LFM-A13 were shown to reduce neutrophil activities induced by fMLF. These findings are consistent with those in a previous study [50], indicating that Btk plays a role in neutrophil activation. Furthermore, Vav proteins, the guanine-nucleotide exchange factors in the RHO/RAC family of GTPases [34], can be phosphorylated by SFKs and contribute to fMLF-induced neutrophil activation [24]. In the present study, we observed that an SFK inhibitor (PP2) and a Btk inhibitor (LFM-A13) both inhibited the phosphorylation of Vav. This indicates that SFKs and Btk are upstream modulators of Vav activation. LFM-A13 was also shown to

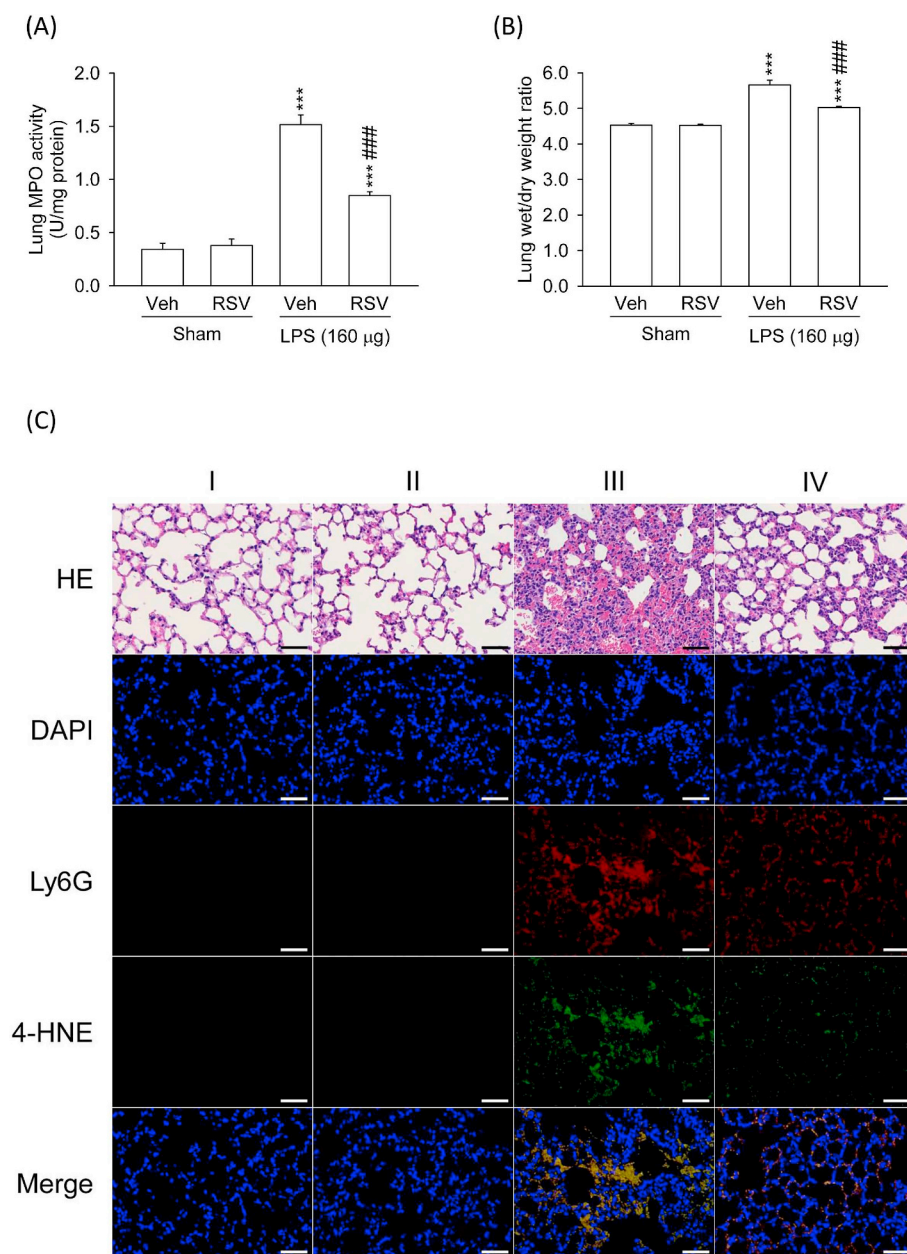


**Fig. 8. Effects of RSV on MPO activities, wet/dry weight ratios, histopathologic features, and neutrophil infiltration and activation of lungs in mice after LPS-induced ALI.** C57BL/6 mice were treated with RSV (100 mg/kg body weight, intraperitoneally) or an equal volume of vehicle. Six h after instilling LPS or 0.9% saline into the trachea, the mouse lungs were harvested for measurement of (A) MPO activity and (B) wet/dry weight ratios, as described in the Materials and Methods section. All data are expressed as the mean  $\pm$  SEM for the six mice in each group. <sup>\*\*\*</sup> $p < 0.001$  compared with the sham group; <sup>####</sup> $p < 0.001$  compared with the ALI + Veh group. (C) Representative photomicrographs of lungs from (I) sham-operated mice injected with vehicle, (II) sham-operated mice injected with RSV, (III) ALI animals injected with vehicle, and (IV) ALI animals injected with RSV. Mouse lungs were resected and subjected to hematoxylin and eosin (HE) staining as well as immunofluorescent detection for lymphocyte antigen 6 complex locus G6D (Ly6G) and 4-hydroxynonenal (4-HNE). The 4',6-diamidino-2-phenylindole (DAPI) stain was used for localizing nuclear DNA. RSV significantly attenuated pulmonary damage, neutrophil infiltration, and oxidative stress. Scale bar = 50  $\mu$ m.

significantly attenuate neutrophil activities stimulated by fMLF (Fig. 8). Taken together, these data provide evidence demonstrating that SFKs/Btk/Vav plays roles in fMLF-triggered neutrophil activation. Our findings also indicate that RSV inhibits neutrophil effector activities via the SFKs/Btk/Vav pathways.

Previous evidence from clinical and animal studies has revealed a strong link between neutrophil activation and ALI, indicating that neutrophils play a key role in the initiation, progression, and prognosis of ALI [12,51,52]. Neutrophil activation is indispensable to antimicrobial host defense systems; however, exaggerated inflammatory responses can result in tissue injury and increased permeability of the alveolar-capillary barrier by releasing cytotoxic agents, such as ROS, elastase, and cytokines. Studies in various fields have reported that RSV has positive regulatory effects on ALI [9]. In this study, we showed that RSV reduces neutrophil infiltration and pulmonary edema in mice with LPS-induced ALI. Another recent study provided

additional evidence that SFKs are implicated in neutrophil-associated oxidative stress and inflammation in ventilator-induced lung injuries [53]. Moreover, RSV has been shown to be a scavenger of many free radicals [54]. We proposed that the positive effect of RSV on ALI may attribute to its free radical scavenging ability and anti-neutrophil effects. Therefore, RSV could potentially be used as a novel therapeutic agent for the treatment of neutrophil-dominated inflammation and ALI.

## 5. Conclusion

RSV clearly reduces respiratory burst, degranulation, integrin expression, and cellular adhesion in activated neutrophils. These inhibitory effects are mediated through the inhibition of the SFKs-Btk-Vav pathway. Our current *in vivo* study revealed that RSV attenuates endotoxin-induced lung injury (Fig. 9). We therefore surmise that the



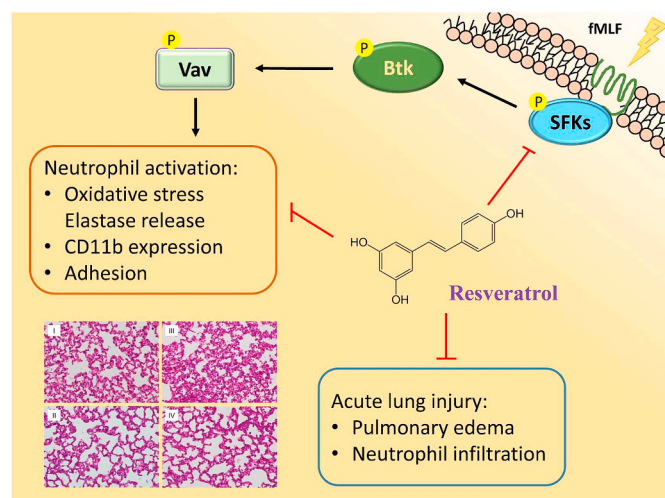


**Fig. 9.** RSV inhibits oxidative stress, elastase release, integrin expression, and cell adhesion in activated neutrophils and protects against LPS-induced ALI. RSV is a specific inhibitor of SFK. The anti-inflammatory effects of RSV are mediated through the inhibition of SFK activation in activated neutrophils. RSV ameliorated LPS-induced ALI in mice.

therapeutic effects of RSV on ALI may derive from its anti-neutrophilic inflammation function.

## Acknowledgments

**Funding:** This work was supported by the grants from the Ministry of Science Technology (MOST 107-2320-B-182A-008-MY3, MOST 106-2320-B-255-003-MY3, MOST 108-2320-B-255-003-MY3, MOST 106-2320-B-182A-002-MY2, and MOST 107-2320-B-182A-003), Ministry of Education (EMRPD1I0501 and EMRPD1I0441), and Chang Gung Memorial Hospital (CMRPG3J1001~3, CMRPF1J0051~3, CMRPF1G0241~3, BMRP450, and CMRPG3G1201), Taiwan.

## Appendix A. Supplementary data

Supplementary data to this article can be found online at <https://doi.org/10.1016/j.freeradbiomed.2019.09.021>.

## Abbreviations:

ALI	Acute lung injury
ATP	adenosine triphosphate
DMSO	Btk, Bruton's tyrosine kinase
cAMP	cyclic adenosine monophosphate Dimethyl sulfoxide
fMLF	Formyl-Met-Leu-Phe
FPR	formyl peptide receptor
GAPDH	glyceraldehyde 3-phosphate dehydrogenase
HBSS	Hank's balanced salts solution
LDH	lactate dehydrogenase
LPS	lipopolysaccharide
MAPK	mitogen-activated protein kinase
NE	neutrophil elastases
MPO	myeloperoxidase
NETs	neutrophil extracellular traps
PBS	phosphate buffer saline
PKA	protein kinase A
ROS	reactive oxygen species
RSV	Resveratrol
SDS	sodium dodecyl sulfate
SFKs	Src family kinases
XO	xanthine/xanthine oxidase

## References

- [1] M. Dvorakova, P. Landa, Anti-inflammatory activity of natural stilbenoids: a review, *Pharmacol. Res.* 124 (2017) 126–145.
- [2] T.A. Zykova, F. Zhu, X. Zhai, W.Y. Ma, S.P. Ermakova, K.W. Lee, A.M. Bode, Z. Dong, Resveratrol directly targets COX-2 to inhibit carcinogenesis, *Mol. Carcinog.* 47 (10) (2008) 797–805.
- [3] M. Shakibaei, C. Csaki, S. Nebrich, A. Mobasheri, Resveratrol suppresses interleukin-1 $\beta$ -induced inflammatory signaling and apoptosis in human articular chondrocytes: potential for use as a novel nutraceutical for the treatment of osteoarthritis, *Biochem. Pharmacol.* 76 (11) (2008) 1426–1439.
- [4] U.P. Singh, N.P. Singh, B. Singh, L.J. Hofseth, R.L. Price, M. Nagarkatti, P.S. Nagarkatti, Resveratrol (trans-3,5,4'-trihydroxystilbene) induces silent mating type information regulation-1 and down-regulates nuclear transcription factor-kappaB activation to abrogate dextran sulfate sodium-induced colitis, *J. Pharmacol. Exp. Ther.* 332 (3) (2010) 829–839.
- [5] A.R. Martin, I. Villegas, C. La Casa, C.A. de la Lastra, Resveratrol, a polyphenol found in grapes, suppresses oxidative damage and stimulates apoptosis during early colonic inflammation in rats, *Biochem. Pharmacol.* 67 (7) (2004) 1399–1410.
- [6] S. Sanchez-Fidalgo, A. Cardeno, I. Villegas, E. Talero, C.A. de la Lastra, Dietary supplementation of resveratrol attenuates chronic colonic inflammation in mice, *Eur. J. Pharmacol.* 633 (1–3) (2010) 78–84.
- [7] A.R. Martin, I. Villegas, M. Sanchez-Hidalgo, C.A. de la Lastra, The effects of resveratrol, a phytoalexin derived from red wines, on chronic inflammation induced in an experimentally induced colitis model, *Br. J. Pharmacol.* 147 (8) (2006) 873–885.
- [8] K.T. Wang, L.G. Chen, S.H. Tseng, J.S. Huang, M.S. Hsieh, C.C. Wang, Anti-inflammatory effects of resveratrol and oligostilbenes from *Vitis thunbergii* var. *taiwaniana* against lipopolysaccharide-induced arthritis, *J. Agric. Food Chem.* 59 (8) (2011) 3649–3656.
- [9] L.G. Wood, P.A. Wark, M.L. Garg, Antioxidant and anti-inflammatory effects of resveratrol in airway disease, *Antioxidants Redox Signal.* 13 (10) (2010) 1535–1548.
- [10] Y.F. Tsai, F.C. Liu, Y.T. Lau, H.P. Yu, Role of Akt-dependent pathway in resveratrol-mediated cardioprotection after trauma-hemorrhage, *J. Surg. Res.* 176 (1) (2012) 171–177.
- [11] R. Nosal, K. Drabikova, V. Jancinova, T. Perecko, G. Ambrozova, M. Ciz, A. Lojek, M. Pekarova, J. Smidrkal, J. Harmatha, On the molecular pharmacology of resveratrol on oxidative burst inhibition in professional phagocytes, *Oxid Med Cell Longev* 2014 (2014) 706269.
- [12] J. Grommes, O. Soehnlein, Contribution of Neutrophils to Acute Lung Injury, 17 (2011), pp. 293–307 3–4.
- [13] E. Polverino, E. Rosales-Mayor, G.E. Dale, K. Dembowsky, A. Torres, The role of neutrophil elastase inhibitors in lung diseases, *Chest* 152 (2) (2017) 249–262.
- [14] J.V. Camp, C.B. Jonsson, A role for neutrophils in viral respiratory disease, *Front. Immunol.* 8 (2017) 550.
- [15] C. Sharp, A.B. Millar, A.R. Medford, Advances in understanding of the pathogenesis of acute respiratory distress syndrome, *Respiration* 89 (5) (2015) 420–434.
- [16] P.A. Ward, Oxidative stress: acute and progressive lung injury, *Ann. N. Y. Acad. Sci.* 1203 (2010) 53–59.
- [17] Y.F. Tsai, T.L. Hwang, Neutrophil elastase inhibitors: a patent review and potential applications for inflammatory lung diseases (2010 - 2014), *Expert Opin. Ther. Pat.* 25 (10) (2015) 1145–1158.
- [18] M. Bosmann, P.A. Ward, Protein-based therapies for acute lung injury: targeting neutrophil extracellular traps, *Expert Opin. Ther. Targets* 18 (6) (2014) 703–714.
- [19] C.A. Lowell, Src-family kinases: rheostats of immune cell signaling, *Mol. Immunol.* 41 (6–7) (2004) 631–643.
- [20] H. Zhang, F. Meng, C.L. Chu, T. Takai, C.A. Lowell, The Src family kinases Hck and Fgr negatively regulate neutrophil and dendritic cell chemokine signaling via PIR-B, *Immunity* 22 (2) (2005) 235–246.
- [21] A. Zarbock, K. Ley, Protein tyrosine kinases in neutrophil activation and recruitment, *Arch. Biochem. Biophys.* 510 (2) (2011) 112–119.
- [22] L. Fumagalli, C.C. Campa, G. Germina, C.A. Lowell, E. Hirsch, G. Berton, Class I Phosphoinositide-3-Kinases and SRC Kinases Play a Nonredundant Role in Regulation of Adhesion-independent and -dependent Neutrophil Reactive Oxygen Species Generation, 190 (2013), pp. 3648–3660 7.
- [23] A. Baruzzi, E. Cavegion, G. Berton, Regulation of phagocyte migration and recruitment by Src-family kinases, *Cell. Mol. Life Sci.* 65 (14) (2008) 2175–2190.
- [24] K. Futosi, S. Fodor, A. Mocsai, Neutrophil cell surface receptors and their intracellular signal transduction pathways, *Int. Immunopharmacol.* 17 (3) (2013) 638–650.
- [25] L. Fumagalli, H. Zhang, A. Baruzzi, C.A. Lowell, G. Berton, The Src Family Kinases Hck and Fgr Regulate Neutrophil Responses to N-formyl-methionyl-leucyl-phenylalanine, 178 (2007), pp. 3874–3885 6.
- [26] A. Mocsai, Z. Jakus, T. Vantus, G. Berton, C.A. Lowell, E. Ligeti, Kinase pathways in chemoattractant-induced degranulation of Neutrophils: the role of P38 mitogen-activated protein kinase activated by Src family kinases, 164 (2000) 4321–4331 8.
- [27] C.Y. Chen, Y.L. Leu, Y. Fang, C.F. Lin, L.M. Kuo, W.C. Sung, Y.F. Tsai, P.J. Chung, M.C. Lee, Y.T. Kuo, H.W. Yang, T.L. Hwang, Anti-inflammatory effects of Perilla frutescens in activated human neutrophils through two independent pathways: Src family kinases and Calcium, *Sci. Rep.* 5 (2015) 18204.
- [28] H. Oh, B. Siano, S. Diamond, Neutrophil isolation protocol, *J. Vis. Exp.* 17 (2008).
- [29] C.Y. Chen, C.C. Liaw, Y.H. Chen, W.Y. Chang, P.J. Chung, T.L. Hwang, A novel immunomodulatory effect of ugonin U in human neutrophils via stimulation of phospholipase C, *Free Radic. Biol. Med.* 72 (2014) 222–231.

- [30] W. Tao, Y.S. Shu, Q.B. Miao, Y.B. Zhu, Attenuation of hyperoxia-induced lung injury in rats by adrenomedullin, *Inflammation* 35 (1) (2012) 150–157.
- [31] R. Anderson, A.J. Theron, C.M. Gravett, H.C. Steel, G.R. Tintinger, C. Feldman, Montelukast inhibits neutrophil pro-inflammatory activity by a cyclic AMP-dependent mechanism, *Br. J. Pharmacol.* 156 (1) (2009) 105–115.
- [32] A.J. Mohamed, L. Yu, C.M. Backesjo, L. Vargas, R. Faryal, A. Aints, B. Christensson, A. Berglof, M. Vihinen, B.F. Nore, C.I. Smith, Bruton's tyrosine kinase (Btk): function, regulation, and transformation with special emphasis on the PH domain, *Immunol. Rev.* 228 (1) (2009) 58–73.
- [33] G. Lachance, S. Levasseur, P.H. Naccache, Chemotactic factor-induced recruitment and activation of Tec family kinases in human neutrophils. Implication of phosphatidylinositol 3-kinases, *J. Biol. Chem.* 277 (24) (2002) 21537–21541.
- [34] M. Turner, D.D. Billadeau, VAV proteins as signal integrators for multi-subunit immune-recognition receptors, *Nat. Rev. Immunol.* 2 (7) (2002) 476–486.
- [35] N. Xia, A. Daiber, U. Forstermann, H. Li, Antioxidant effects of resveratrol in the cardiovascular system, *Br. J. Pharmacol.* 174 (12) (2017) 1633–1646.
- [36] X.D. Zhu, X.P. Lei, W.B. Dong, Resveratrol as a potential therapeutic drug for respiratory system diseases, *Drug Des. Dev. Ther.* 11 (2017) 3591–3598.
- [37] E. Fan, L. Zhang, S. Jiang, Y. Bai, Beneficial effects of resveratrol on atherosclerosis, *J. Med. Food* 11 (4) (2008) 610–614.
- [38] A.L.B. Oliveira, V.V.S. Monteiro, K.C. Navegantes-Lima, J.F. Reis, R.S. Gomes, D.V.S. Rodrigues, S.L.F. Gaspar, M.C. Monteiro, Resveratrol role in autoimmune disease-A mini-review, *Nutrients* 9 (12) (2017).
- [39] J.H. Ko, G. Sethi, J.Y. Um, M.K. Shanmugam, F. Arfuso, A.P. Kumar, A. Bishayee, K.S. Ahn, The role of resveratrol in cancer therapy, *Int. J. Mol. Sci.* 18 (12) (2017).
- [40] A. Cavallaro, T. Ainis, C. Bottari, V. Fimiani, Effect of resveratrol on some activities of isolated and in whole blood human neutrophils, *Physiol. Res.* 52 (5) (2003) 555–562.
- [41] Z. Jia, H. Zhu, B.R. Misra, J.E. Mahaney, Y. Li, H.P. Misra, EPR studies on the superoxide-scavenging capacity of the nutraceutical resveratrol, *Mol. Cell. Biochem.* 313 (1–2) (2008) 187–194.
- [42] H.Q. He, R.D. Ye, The Formyl Peptide Receptors: Diversity of Ligands and Mechanism for Recognition, 22 (2017) 3.
- [43] W. Zhu, Q. Jia, Y. Wang, Y. Zhang, M. Xia, The anthocyanin cyanidin-3-O-beta-glucoside, a flavonoid, increases hepatic glutathione synthesis and protects hepatocytes against reactive oxygen species during hyperglycemia: involvement of a cAMP-PKA-dependent signaling pathway, *Free Radic. Biol. Med.* 52 (2) (2012) 314–327.
- [44] T.L. Hwang, Y.L. Leu, S.H. Kao, M.C. Tang, H.L. Chang, Viscolin, a new chalcone from *Viscum coloratum*, inhibits human neutrophil superoxide anion and elastase release via a cAMP-dependent pathway, *Free Radic. Biol. Med.* 41 (9) (2006) 1433–1441.
- [45] C. Kroegel, M. Foerster, Phosphodiesterase-4 inhibitors as a novel approach for the treatment of respiratory disease: cilomilast, *Expert Opin. Investig. Drugs* 16 (1) (2007) 109–124.
- [46] M.J. Sanz, J. Cortijo, E.J. Morcillo, PDE4 inhibitors as new anti-inflammatory drugs: effects on cell trafficking and cell adhesion molecules expression, *Pharmacol. Ther.* 106 (3) (2005) 269–297.
- [47] Y.F. Tsai, T.C. Chu, W.Y. Chang, Y.C. Wu, F.R. Chang, S.C. Yang, T.Y. Wu, Y.M. Hsu, C.Y. Chen, S.H. Chang, T.L. Hwang, 6-Hydroxy-5,7-dimethoxy-flavone suppresses the neutrophil respiratory burst via selective PDE4 inhibition to ameliorate acute lung injury, *Free Radic. Biol. Med.* 106 (2017) 379–392.
- [48] D. Crosby, A.W. Poole, Interaction of Bruton's tyrosine kinase and protein kinase C $\theta$  in platelets. Cross-talk between tyrosine and serine/threonine kinases, *J. Biol. Chem.* 277 (12) (2002) 9958–9965.
- [49] M.I. Wahl, A.C. Fluckiger, R.M. Kato, H. Park, O.N. Witte, D.J. Rawlings, Phosphorylation of two regulatory tyrosine residues in the activation of Bruton's tyrosine kinase via alternative receptors, *Proc. Natl. Acad. Sci. U. S. A.* 94 (21) (1997) 11526–11533.
- [50] C. Gilbert, S. Levasseur, P. Desaulniers, A.A. Dusseault, N. Thibault, S.G. Bourgoin, P.H. Naccache, Chemotactic factor-induced recruitment and activation of Tec family kinases in human neutrophils. II. effects of LFM-A13, a specific Btk inhibitor, 170 (2003), pp. 5235–5243 10.
- [51] E. Abraham, A. Carmody, R. Shenkar, J. Arcaroli, Neutrophils as early immunologic effectors in hemorrhage- or endotoxemia-induced acute lung injury, *Am. J. Physiol. Lung Cell Mol. Physiol.* 279 (6) (2000) L1137–L1145.
- [52] P.J. Chen, I.L. Ko, C.L. Lee, H.C. Hu, F.R. Chang, Y.C. Wu, Y.L. Leu, C.C. Wu, C.Y. Lin, C.Y. Pan, Y.F. Tsai, T.L. Hwang, Targeting allosteric site of AKT by 5,7-dimethoxy-1,4-phenanthrenequinone suppresses neutrophilic inflammation, *EBioMedicine* 40 (2019) 528–540.
- [53] L.F. Li, C.S. Lee, Y.Y. Liu, C.H. Chang, C.W. Lin, L.C. Chiu, K.C. Kao, N.H. Chen, C.T. Yang, Activation of Src-dependent Smad3 signaling mediates the neutrophilic inflammation and oxidative stress in hyperoxia-augmented ventilator-induced lung injury, *Respir. Res.* 16 (2015) 112.
- [54] S. Bastianetto, C. Menard, R. Quirion, Neuroprotective action of resveratrol, *Biochim. Biophys. Acta* 1852 (6) (2015) 1195–1201.



OPEN

# NLRP3 inflammasome is attenuated in patients with *Mycobacterium avium* complex lung disease and correlated with decreased interleukin-1 $\beta$ response and host susceptibility

Ming-Fang Wu<sup>1,2</sup>, Chin-Chung Shu<sup>3,4</sup>, Jann-Yuan Wang<sup>3,4</sup>, Bo-Shiun Yan<sup>5</sup>, Hsin-Chih Lai<sup>6</sup>, Bor-Luen Chiang<sup>4,7</sup>, Lawrence Shih-Hsin Wu<sup>8</sup> & Chong-Jen Yu<sup>3,4</sup>

The incidence of nontuberculous mycobacteria lung disease (NTM-LD) is increasing in patients without human immunodeficiency virus. *Mycobacterium avium* complex (MAC) is one of the most common pathogenic species. The presence of MAC has a clinical relevance of around 35–42%, indicating the possibility of host susceptibility. Previous studies have shown that interleukin (IL)-1 $\beta$  and IL-1-receptor knock-out mice are susceptible to mycobacterial infections; however, the role of inflammasome-driven interleukin (IL)-1 $\beta$  has not been studied in MAC-LD. We enrolled patients with MAC-LD and healthy controls. Peripheral blood mononuclear cells (PBMCs), monocytes, and monocyte-derived macrophages were stimulated by MAC bacilli. The responses of interleukin (IL)-1 $\beta$  and the expression of inflammasome and toll-like receptors (TLRs) were measured. Single nucleotide polymorphisms (SNPs) were also examined for *NLRP3* and *TLR2* genes. In the patients with MAC-LD, the IL-1 $\beta$  responses decreased in PBMCs, monocytes, and macrophages assayed by MAC bacilli in comparison to the healthy controls. In addition, the level of caspase-1 after stimulation was lower in the MAC-LD group, although the mRNA level of IL-1 $\beta$  was not significantly lower. In surveying the activation of IL-1 $\beta$ , the MAC-LD group had an attenuated mRNA level of *NLRP3* but similar levels of *AIM2* and *ASC* compared with the controls. The SNPs rs3806268 and rs34298354 in *NLRP3* for females and rs3804100 in *TLR2* for males were associated with MAC-LD. In conclusion, our patients with MAC-LD had attenuated IL-1 $\beta$  production, which may have been due to lower activation of the *NLRP3*-caspase-1 axis. Two SNPs of *NLRP3* and one of *TLR2* were correlated with MAC-LD, possibly indicating host susceptibility.

Lung disease (LD) due to nontuberculous mycobacteria (NTM) has become an important clinical concern<sup>1</sup> because the incidence and prevalence of NTM-LD has increased over the last 10 years in patients without human immunodeficiency virus<sup>2,3</sup>. *Mycobacterium avium* complex (MAC) is the most common pathogenic species

<sup>1</sup>Institute of Statistical Sciences, Academia Sinica, Taipei, Taiwan. <sup>2</sup>Graduate Institute of Toxicology, College of Medicine, National Taiwan University, Taipei, Taiwan. <sup>3</sup>Department of Internal Medicine, National Taiwan University Hospital, Taipei, Taiwan. <sup>4</sup>College of Medicine, National Taiwan University, Taipei, Taiwan. <sup>5</sup>Institute of Biochemistry and Molecular Biology, College of Medicine, National Taiwan University, Taipei, Taiwan. <sup>6</sup>Department of Medical Biotechnology and Laboratory Science, College of Medicine, Chang Gung University, and Research Center for Chinese Herbal Medicine and Research Center for Food and Cosmetic Safety, College of Human Ecology, Chang Gung University of Science and Technology, Tao-Yuan, Taiwan. <sup>7</sup>Department of Pediatrics, National Taiwan University Hospital, Taipei, Taiwan. <sup>8</sup>Graduate Institute of Biomedical Sciences, China Medical University, Taichung, Taiwan. Ming-Fang Wu and Chin-Chung Shu contributed equally. Correspondence and requests for materials should be addressed to L.S.-H.W. (email: [lschwu@hotmail.com](mailto:lschwu@hotmail.com)) or C.-J.Y. (email: [jefferycjyu@ntu.edu.tw](mailto:jefferycjyu@ntu.edu.tw))

associated with NTM-LD in the USA and South East Asia<sup>2</sup>. The reasons for this increase are not clear; however, it could be related to the increase in patients with acquired compromised immunity and advances in mycobacterial culture techniques<sup>4–7</sup>.

Because MAC exists ubiquitously in the environment, the relevance of sputum growing NTM (the number of patients with true disease over the number of isolated patients) is around 35–42%<sup>8,9</sup>. This indicates host vulnerability; however, the mechanism for it is unknown. During MAC pulmonary infection, macrophages are the first-line defense. Once macrophages sense a variety of inflammatory stimuli, inflammasome receptors form an inflammasome structure and activate the pro-caspase-1 to produce active caspase-1 subunits, which can further process pre-interleukin(IL)-1 $\beta$  into the active cytokine form and induce specific cell death, called pyroptosis<sup>10,11</sup>. The production of IL-1 $\beta$  during a mycobacterial infection is important for successful host immune defense because IL-1 $\beta$  and IL-1-receptor knock-out mice are more susceptible to mycobacterial infections<sup>12–14</sup>.

Inflammasomes are multimeric protein complexes composed of receptors, adaptor proteins and pro-caspase-1, and they are mainly located in innate immune cells<sup>15,16</sup>. Of the inflammasome complexes, nucleotide-binding leucine-rich repeat containing receptor sensor molecule containing pyrin domain 3 (NLRP3) inflammasome is one of the most well reported, and the expression of NLRP3 will be up-regulated once exposed to danger signals or infectious reagents<sup>10,11</sup> and *Mycobacterium tuberculosis*<sup>17</sup>. The response of NLRP3 inflammasome in macrophages furtherly prevents mycobacterial infection<sup>12,18</sup>. However, the details of the inflammasome response have rarely been investigated in MAC-LD, especially with regards to the defense response and host susceptibility. Therefore, we conducted this study to investigate the role of the NLRP3 inflammasome-driven IL1 $\beta$  axis in MAC-LD.

## Materials and Methods

**Antibodies and reagents.** The antibodies for flow cytometry were anti-CD4-APC, anti-CD14-PerCP, and anti-IL-1 $\beta$ -FITC (Biolegend, CA, USA). Isotype-controlled mAbs were also purchased from Biolegend. Recombinant human macrophage colony stimulating factor (M-CSF) and the enzyme-linked immunosorbent assay (ELISA) kits for tumor necrosis factor-alpha (TNF- $\alpha$ ), IL-1 $\beta$ , and active caspase-1 were purchased from R&D Systems. All other chemical reagents, unless otherwise specified, were purchased from Sigma-Aldrich (St. Louis, Mo).

**Participant enrollment.** This prospective study was conducted at National Taiwan University Hospital in Taiwan from January 2015 to December 2017. The hospital's Research Ethics Committee approved the study (No. 201308008RINC), and all participants provided written informed consent. All methods were performed in accordance with the relevant ethic guidelines and regulations. Patients aged  $\geq 20$  years who had respiratory samples that were culture-positive for MAC were identified. Of these patients, we consecutively enrolled those with MAC-LD according to the ATS diagnostic guidelines<sup>1</sup>. Patients with human immunodeficiency virus (HIV) infection, those co-infected with non-MAC NTM-LD or tuberculosis, and those who had received chemotherapy in the preceding 3 months were excluded. Participants with sputum-negative mycobacterial cultures and normal chest radiographs were enrolled as the controls. All enrolled patients were Han-Taiwanese.

**PBMC and monocytes isolation and differentiation of macrophages.** Ten ml whole blood samples from the healthy controls and MAC-LD patients were collected. Peripheral blood mononuclear cells (PBMCs) were immediately collected using Ficoll-Paque PLUS (GE Healthcare). Human CD14<sup>+</sup> cells were purified from human PBMCs by high-gradient magnetic sorting (Miltenyi Biotec, Bergisch Gladbach, Germany). CD14<sup>+</sup> monocytes were cultured with 10 ng/ml M-CSF (R&D Systems, MN) for 7 days, and monocyte-derived macrophages (M-M $\phi$ ) were detached for 90 minutes using cell detachment solution (Accutase, Millipore, USA).

**MAC stimulation of cells.** *Mycobacterium avium* subspecies *avium* (ATCC 25291) was heated at 80 °C for 30 minutes for inactivation. The heat-killed MAC bacilli were used to stimulate PBMCs or macrophages in the indicated multiplicity of infection at a 1:100 ratio. Lipopolysaccharide (LPS, from *Escherichia coli* 0111: B4; Sigma-Aldrich, USA) was used as the paired positive control. At the indicated time points, the cells or supernatants were collected and further assayed for intracellular cytokine staining, real-time polymerase chain reaction (PCR) or ELISA for cytokine contents, respectively. For the cells used for intracellular staining, we added protein transport inhibitor (BD Bioscience, USA) for the second half of the co-culture.

**RNA isolation and quantitative PCR.** Total cellular RNA from M-M $\phi$  was isolated and first strand cDNA was synthesized. A real-time PCR with iQ SYBR Green Supermix (BIO-RAD, Singapore) was performed using a Bio-Rad MyiQ Single-Color Real-Time PCR Detection System (for details, please see Appendix S3). The mRNA expression level of each target gene was normalized to their respective GAPDH expression. The sequences of sense and anti-sense primers are shown in Table S1 in the Supplement File.

**Flow cytometry analysis.** To determine expressions of cell surface markers, cells were re-suspended in FACS buffer (1% FBS in PBS) and incubated with fluorochrome-conjugated antigen-specific mAbs at 4 °C for 30 minutes. To further measure the expression of intracellular cytokines, the cells were fixed and permeabilized using a FIX & PERM™ Cell Permeabilization kit (ThermoFisher Scientific Inc.) and incubated with fluorochrome-conjugated antibodies at 4 °C for 30 minutes. The cell samples were analyzed using FACSVerse (BD Biosciences, USA).

**Western blotting.** We prepared cell lysates of PBMC stimulated by dead MAC or infected by viable MAC for 24 hours by lysis buffer (RIPA Lysis Buffer, Millipore, USA) and proteinase inhibitor (Pierce

Protease and Phosphatase Inhibitor Mini Tablets, Thermo, USA). The IL-1 $\beta$  and pro-caspase-1 in cell lysates were detected by western blotting analysis (Mini-PROTEAN 3 CELL, Bio-Rad, USA). The blot was incubated with anti-IL-1 $\beta$  antibody (Clone: H-153, SANTA CRUZ BIOTECHNOLOGY, USA) or anti-caspase-1 antibody (Clone: D7F10, Rabbit mAb, Cell Signaling, USA), followed by Biotin-SP (long spacer) AffiniPure Goat Anti-Rabbit IgG (Jackson ImmunoResearch, USA) and then Peroxidase Streptavidin (Jackson ImmunoResearch, USA). For internal control (GAPDH), the membrane was further stripped for 10 minutes by stripping Buffer (GeneMarker, Taiwan) and reprobed with anti-GAPDH antibody (Clone 6C5, Millipore, Germany) and then HRP-conjugated goat anti-mouse IgG antibody (SANTA CRUZ BIOTECHNOLOGY, USA) subsequently.

**DNA extraction and single nucleotide polymorphism analysis.** DNA from the PBMCs of consecutively enrolled participants was extracted using a Quick-DNA Miniprep Kit (Zymo Research, CA, USA). Single nucleotide polymorphisms (SNPs) were selected from candidate genes, *AIM2* (absent in melanoma 2), *NLRP3* (nucleotide-binding leucine-rich repeat containing receptor sensor molecule containing pyrin domain 3) and *TLR2* (toll-like receptor 2) according to the study's findings. By the sample size of the present study, we finally examined SNPs in the exon location and minor allele frequency >1% (information from NCBI dbSNP). Three SNPs in *NLRP3* gene loci, namely, rs34298354, rs3806268 and rs7525979; three SNPs in *TLR2* gene loci, namely, rs3804099, rs3804100 and rs5743705; and one each in *caspase-1* (rs1792773) and *AIM2* (rs2276405) were selected to perform genotyping. We used the Agena MassARRAY platform with iPLEX chemistry (Agena, San Diego, CA) to investigate genotyping of the SNPs of interest. The Spectro-CHIPS were analyzed using a MassARRAY Analyzer 4, and the results were analyzed using clustering analysis with TYPER 4.0 software. The allele-specific diagnostic products had a unique molecular weight and were identified using matrix-assisted laser desorption ionization time-of-flight mass spectrometry.

**Statistical analysis.** All data are expressed as mean  $\pm$  standard error or number (%) and were evaluated using the Mann-Whitney *U* test or a paired *t*-test, where appropriate, and the chi-square test, respectively, from the PRISM software package (GraphPad). Odds ratios (ORs) were calculated by logistic regression. We adjusted the ORs of specific SNPs for MAC-LD by age, sex, smoking and underlying immunocompromised diseases. A two-tailed *p* value of <0.05 was considered to be significant.

**Ethics approval and consent to participate.** This prospective study was approved by National Taiwan University Hospital's Research Ethics Committee (No. 201308008RINC), and all participants provided written informed consent.

## Results

**Attenuated IL-1 $\beta$  production in the patients with MAC-LD.** To study whether MAC-LD infection leads to inflammasome activation in humans, we used MAC to stimulate the PBMCs from age- (42.2 vs 46.3 years, *p* = 0.251) and sex- (47% vs 33% male, *p* = 0.520) matched 20 healthy donors and 20 patients with MAC-LD, and found a strong inflammasome activation response with a higher IL-1 $\beta$  release in the healthy controls than in the patients with MAC-LD (290 pg/ml vs 162 pg/ml at MOI = 20; 360 pg/ml vs 178 pg/ml at MOI = 100, respectively). A borderline higher trend of IL-1 $\beta$  release was identified in the healthy controls after the LPS stimulation, a TLR4 agonist (*p* = 0.073) (Fig. 1A). They did not have underlying disease of malignancy or cirrhosis, and of the MAC-LD patients, 75% (*n* = 15) had the nodular-bronchiectasis pattern and 20%, the fibro-cavitary pattern. These results suggested that in contrast to healthy controls, a defective inflammasome platform exists in the PBMCs of patients with MAC-LD.

We then investigated the source of IL-1 $\beta$  in the circulation by detecting the expression of intracellular IL-1 $\beta$ . We found that MAC stimulation caused IL-1 $\beta$  synthesis in CD14<sup>+</sup> monocytes in both populations, but a lower IL-1 $\beta$  signal in the patients with MAC-LD than in the healthy controls (14.09% vs 2.23%, MOI = 100) (Fig. 1B, upper panel). We did not observe significant expression of IL-1 $\beta$  in CD4<sup>+</sup> T lymphocytes (Fig. 1B, lower panel). Our observations suggested that monocytes are the target cells in PBMCs for IL-1 $\beta$  synthesis and produced after MAC infection (Fig. 1A,B). The expression of IL-1 $\beta$  in CD14<sup>+</sup> monocytes was lower in the patients with MAC-LD than in the healthy controls after MAC stimulation (*p* < 0.05) and LPS treatment (*p* < 0.05, Fig. 1C). In addition to the synthesis and production of IL-1 $\beta$ , we detected the expression of active caspase-1 to identify the activation of inflammasome and observed a higher expression of active caspase-1 in the control group than in the patients (*p* < 0.05) (Fig. 1D).

As shown in Fig. 2, we performed the experiments of western blotting and showed intracellular mature IL-1 $\beta$  response by MAC stimulation, which was borderline attenuated in MAC-LD patients (median: 36.1 vs 8.8, *p* = 0.077 by dead MAC [*n* = 3 pairs]; 84.9 vs 19.2, *p* = 0.050 by viable MAC [*n* = 3 pairs]). The inactive form of IL-1 $\beta$  (pro-IL-1 $\beta$ ) was not significantly different (median: 42.5 vs 16.3, *p* = 0.400 by dead MAC [*n* = 3 pairs]; 50.0 vs 33.0, *p* = 0.686 by viable MAC [*n* = 3 pairs]). The intracellular inactive caspase-1 (pro-caspase-1) was similar between HC and MAC-LD patients after MAC bacilli stimulation (median: 1.34 vs 13.2, *p* = 0.686 by dead MAC [*n* = 3 pairs]; 1.61 vs 1.50, *p* = 1.000 by viable MAC [*n* = 3 pairs]) (Fig. 2). Our results suggested that MAC stimulation activated strong inflammasome activation signals in the controls, but that this response was attenuated in the patients with MAC-LD.

**IL-1 $\beta$  protein but not mRNA production was decreased in the monocyte-derived macrophages of the patients with MAC-LD.** When humans are infected with pathogens, macrophages act against locally invading pathogens in the lungs. Accordingly, we used the *in-vitro* monocyte/macrophage system and stimulated monocyte or M-M $\phi$  with MAC bacilli. Higher production of IL-1 $\beta$  (40 pg/ml vs 5 pg/ml, *p* < 0.05, from M-M $\phi$ )

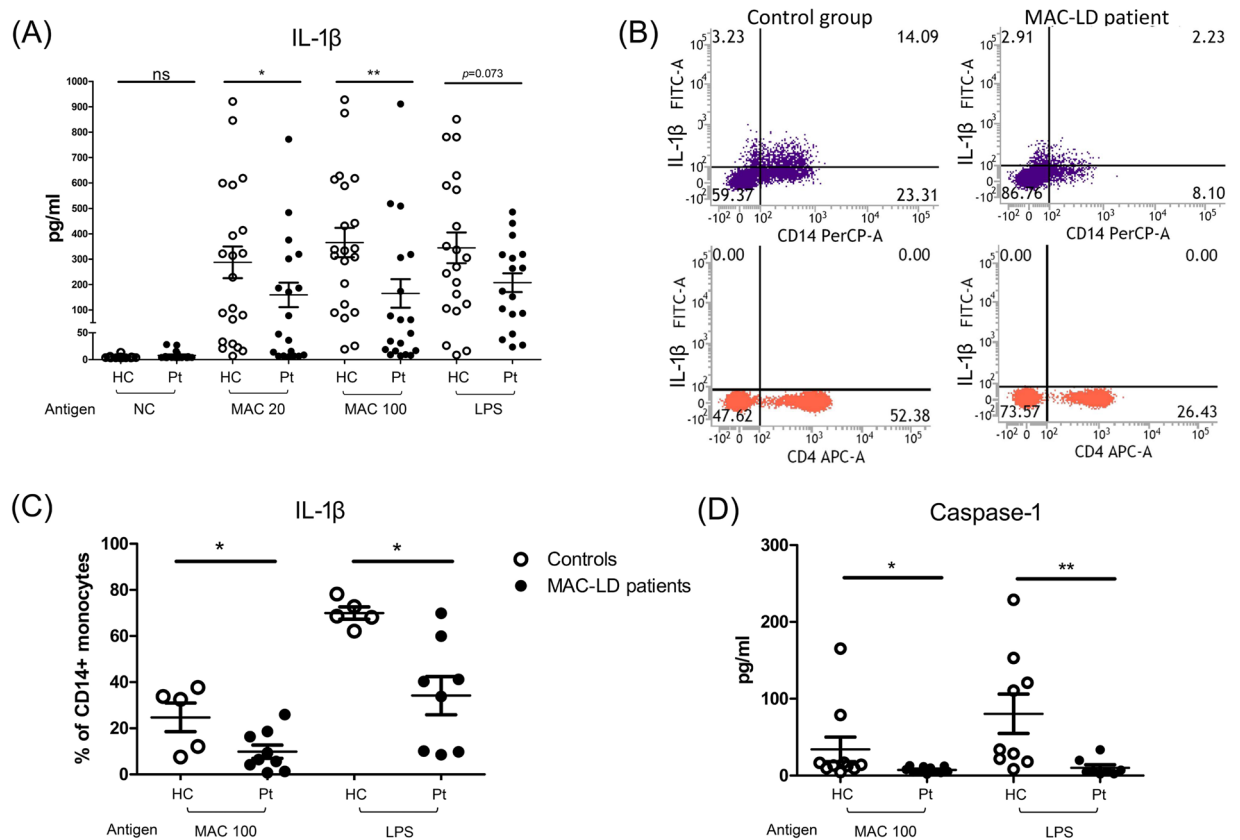


**Figure 1.** Interleukin 1 beta (IL-1 $\beta$ ) and active caspase-1 responses from peripheral blood mononuclear cells (PBMCs) were measured after stimulation with *Mycobacterium avium* complex (MAC) bacilli (multiplicity of infection [MOI] 20 and 100) and lipopolysaccharide (LPS) (5  $\mu$ g/ml) for 48 hours. **(A)** The levels of secreted IL-1 $\beta$  production from the PBMCs after the indicated stimulation were measured using enzyme-linked immunosorbent assay (ELISA). **(B)** Intracellular IL-1 $\beta$  in the assay was detected using flow cytometry. We discriminated the lymphocytes and monocytes by forward scatter and side scatter. The percentages of IL-1 $\beta$  in CD14+ cells (upper panel) and CD4+ cells (lower panel) were gating in monocyte and lymphocyte populations, respectively. **(C)** The levels of intracellular IL-1 $\beta$  expressed on CD14+ monocytes were pooled by dot plots. **(D)** The levels of active caspase-1 from PBMCs assayed after MAC stimulation were measured by ELISA. The data were compared using the Mann Whitney U test. The crossed lines are mean values and bars of standard errors. \*0.01  $\leq$  p < 0.05. \*\*0.001  $\leq$  p < 0.01. ns, not significant; HC, healthy controls; pt, patients.

(Fig. 3A, left panel), active caspase-1 (23.3 pg/ml vs 7.3 pg/ml, p = 0.005, from monocyte) (Fig. 3A, middle panel) and TNF- $\alpha$  (500 pg/ml vs 200 pg/ml, p < 0.05, from M-M $\phi$ ) (Fig. 3A, right panel) were induced from the healthy controls than from that derived from the patients with MAC-LD.

In addition to caspase-1 activation, IL-1 $\beta$  transcription is another key factor for successful IL-1 $\beta$  production<sup>10</sup>. We studied whether the priming signal for IL-1 $\beta$  RNA synthesis is defective in patients with MAC-LD. The results showed that there was no significant difference in IL-1 $\beta$  transcripts for both groups (controls vs MAC-LD group) after MAC stimulation (p = 0.364), indicating that the priming signals may be similar in both groups (Fig. 3B). In contrast, we observed a positive correlation between RNA transcripts and cytokines in TNF- $\alpha$  for both groups after MAC stimulation (Fig. 3A,B, right panel).

**Expressions of NLRP3 and TLR2 were lower in the patients with MAC-LD than in the healthy controls.** We determined the increase in expression of inflammasome receptors and adaptor proteins human M-M $\phi$ , which may have controlled the activation of inflammasomes after MAC stimulation. The increased in the expression of NLRP3 on M-M $\phi$  was greater in the control group than in the MAC-LD group after MAC stimulation, but there were no significant differences in other inflammasome receptors, including AIM2 and apoptosis-associated speck-like protein containing a CARD (ASC) between the two groups (Fig. 4). On the other hand, LPS stimulation led to insignificant differences in NLRP3 and AIM2 receptors between both groups. For TLR, the message RNA expression of TLR2 after MAC bacilli stimulation was lower in the MAC-LD group, whereas the level of TLR4 was similar (Fig. 4). The correlation was significant between mRNA expression of NLRP3 and the protein production of IL-1 $\beta$  from M-M $\phi$  stimulated by MAC bacilli (Pearson correlation: 0.368, p = 0.029).



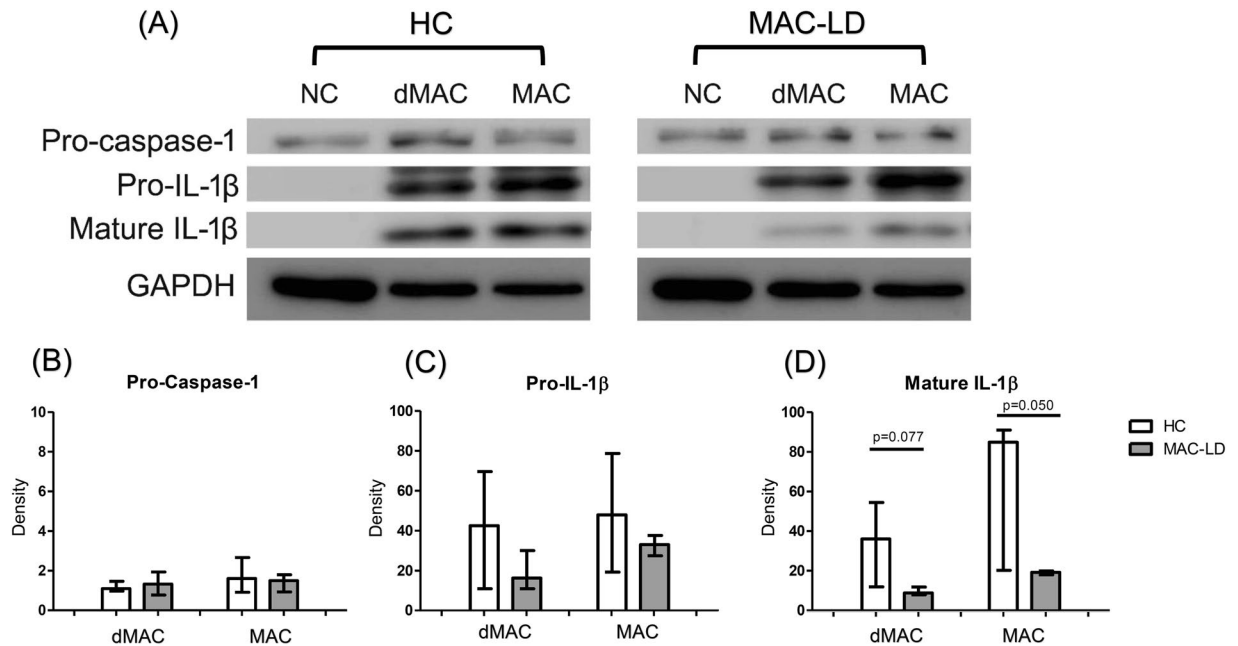


**Figure 2.** Intracellular protein of interleukin 1 beta (IL-1 $\beta$ ) and inactive caspase-1 responses from peripheral blood mononuclear cells (PBMCs) were measured by Western blotting after stimulation with dead *Mycobacterium avium* complex (dMAC) or infection by viable MAC (MAC) bacilli (multiplicity of infection: 100) for 24 hours. (A) Case demonstration and (B–D) bar charts for the protein levels of pro-caspase-1, pro-IL-1 $\beta$  and mature IL-1 $\beta$  by standardizing using individual internal control (GAPDH) and negative control. The data were compared using the Mann Whitney *U* test. The crossed lines are median values and bars of inter-quartile range. HC, healthy controls; LD, lung disease; NC, negative control. Full-length blot is presented in Supplementary Fig. S3.

**SNPs of *NLRP3* and *TLR2* genes were associated with MAC-LD.** As defective caspase-1 activation (Fig. 1D) and lower *NLRP3* and *TLR2* transcription (Fig. 4A) were found in the patients with MAC-LD, we tried to identify whether there was a differential SNP pattern for the genes that were correlated with reduced IL-1 $\beta$  production. We enrolled 106 patients with MAC-LD who were older ( $65.7 \pm 12.6$  vs  $57.1 \pm 15.3$  years,  $p < 0.001$ ) than the 119 controls, but they had a similar male proportion (40% vs 48%,  $p = 0.212$ ). There were no significant between-group differences regarding smoking status and underlying immunocompromised diseases including diabetes mellitus, cancer, and autoimmune disease (for details, please see Table S3 in the Supplement File). We analyzed three SNPs in *NLRP3* gene loci, namely, rs34298354, rs3806268 and rs7525979; three SNPs in *TLR2* gene loci, namely, rs3804099, rs3804100 and rs5743705; and one each in *caspase-1* (rs1792773) and *AIM2* (rs2276405) (Table 1). Among them, the pattern of GA in rs3806268, compared with GG and AA, was associated with MAC-LD ( $p = 0.022$ , Fisher's exact test). In logistic regression analysis, the crude odds ratio (OR) for MAC-LD was 1.782 (95% CI: 1.049–3.027,  $p = 0.033$ ), and the OR adjusted by age, sex, smoking, and underlying disease was 1.788 (95% CI: 1.022–3.130,  $p = 0.042$ ).

Furthermore, we investigated associations between interactions of genetic variants and sex. If we stratified the population by sex, the GA of rs3806268 ( $p = 0.041$ , Fisher's exact test) and CT in rs34298354 ( $p = 0.019$ ) were correlated with the disease in the female population. The crude OR of MAC-LD was 2.009 (95% CI: 0.981–4.115,  $p = 0.072$ ) and the adjusted OR was 1.945 (95% CI: 0.913–4.147,  $p = 0.085$ ) for GA of rs3806268. For CT in rs34298354, the crude and adjusted ORs were 8.571 (95% CI: 1.039–70.738,  $p = 0.033$ ) and 8.517 (95% CI: 1.010–71.838,  $p = 0.049$ ), respectively. With regards to the *TLR2* polymorphism, TT in rs3804100 favored MAC-LD with a crude OR of 2.750 (95% CI: 1.200–6.304,  $p = 0.025$ ) and an adjusted OR of 3.050 (95% CI: 1.218–7.638,  $p = 0.017$ ) in the male population. Taken together, these results suggest that *NLRP3* and *TLR2* polymorphisms may influence the genetic susceptibility to MAC-LD according to sex. The genetic variants of *AIM2* did not have any associations with MAC-LD.

For eighteen subjects, IL-1 $\beta$  ELISA and genotyping for genetic variants of *NLRP3*/*TLR2* were performed. Among them, the SNP rs34298354 in the *NLRP3* exon region showed significant association with IL-1 $\beta$  production in ten female subjects (Fig. 5A). For the SNP rs3806268 in *NLRP3* for all eighteen subjects (Fig. 5B) and rs3804100 in *TLR2* for eight male subjects (Fig. 5C), there were no significant associations with IL-1 $\beta$  response in PBMC stimulation.



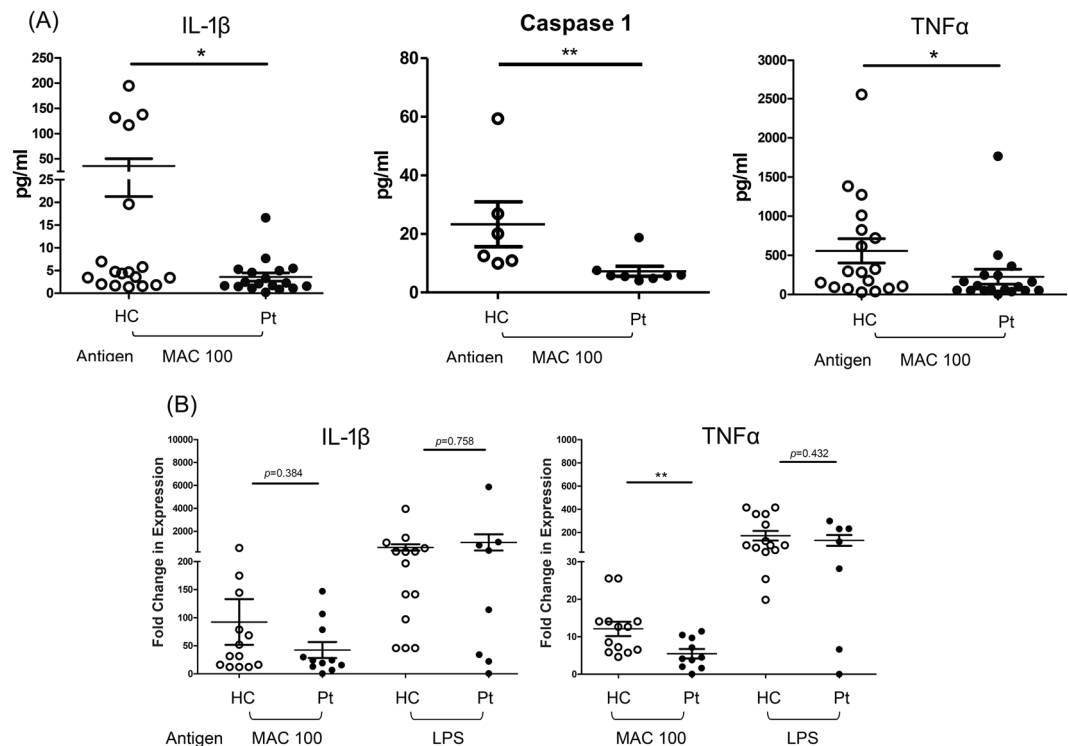


**Figure 3.** The responses of interleukin 1 beta (IL-1 $\beta$ ) and tumor necrosis factor-alpha (TNF- $\alpha$ ) were measured in assays of human blood monocyte or its derived macrophages with heat-killed *Mycobacterium avium* complex (MAC) (multiplicity of infection: 100) and lipopolysaccharide (LPS) (5  $\mu$ g/ml). (A) IL-1 $\beta$  and TNF- $\alpha$  in the reaction supernatant by monocyte derived macrophages and caspase-1 from reaction by monocyte, and (B) mRNA of cytokines response in cultured cells after stimulation for 24 hours and 6 hours, respectively. The Y axis of mRNA is fold-change compared to the negative controls. The data were compared using the Mann Whitney U test. The crossed lines are mean values and bars of standard errors. \*0.01  $\leq$  p < 0.05. \*\*0.001  $\leq$  p < 0.01. HC, healthy controls; pt, patients.

## Discussion

In the present study, the *in-vitro* response of IL-1 $\beta$  after MAC stimulation was decreased in the patients with MAC-LD compared to the healthy controls. The level of caspase-1 after the stimulation was lower in the patients with MAC-LD, but the mRNA expression of IL-1 $\beta$  was similar between the two groups. For the activation of inflammation, NLRP3 mRNA was attenuated in the patients, which correlated with lower IL-1 $\beta$  expression. For SNP analysis, the rs3806268 and rs34298354 SNPs in *NLRP3* and rs3804100 in *TLR2* were associated with MAC-LD. Among them, rs34298354 was directly associated with IL-1 $\beta$  response.

NLRP3 can respond to a range of intracellular damage or pathogen-derived ligands and then activate inflammasome assembly, thereby inducing the production of pro-inflammatory cytokines<sup>19</sup>. Mycobacteria infection initiates the NLRP3-dependent IL-1 $\beta$  axis<sup>20</sup>, which restricts the growth of mycobacteria<sup>18</sup>. To date, few studies have investigated the association between inflammasomes and MAC bacilli, which is one of the most common species involved in NTM-LD. We found that MAC bacilli could activate NLRP3 inflammasomes and downstream IL-1 $\beta$  production. However, the activations of NLRP3, caspase-1 and IL-1 $\beta$  were reduced in the patients with MAC-LD. This may indicate a susceptibility to MAC, although the detailed mechanism for the reduced response is unknown at present. A previous study suggested that *Mycobacterium tuberculosis* can suppress NLRP3-related innate immunity and favor evasion from macrophages<sup>21</sup>. The differences in the NLRP3-IL-1 $\beta$  axis between the patients with MAC-LD and controls suggested that the patients probably had immune vulnerability to MAC bacilli, leading to disease progression after exposure to environmental NTM<sup>22</sup>. However, the distributions of IL-1 $\beta$  were overlapped in the controls and patients (Figs 1A, 3A), and the higher trend in the controls was influenced by only a proportion of the subjects with higher expression. This finding indicates that the inflammasome influencing IL-1 $\beta$  exists in a proportion of MAC-LD patients but not in every patient.

In addition to a low response of NLRP3-dependent IL-1 $\beta$ , we also observed a low caspase-1 response in the MAC-LD group, suggesting that attenuated pyroptosis may exist in MAC-LD. Pyroptosis, a conserved program of inflammatory cell death<sup>23</sup>, is accompanied by caspase-1-dependent processing and activation of the inflammatory cytokine IL-1 $\beta$ <sup>24</sup>. With low pyroptosis, intracellular MAC bacilli may not be cleaned and then survive in macrophages<sup>25</sup>.

In the host genetic study, SNP analysis of the *NLRP3* and *TLR2* genes revealed that rs3806268, an SNP of *NLRP3*, had a GA variant associated with MAC-LD compared with a homo-dimer in the SNP locus. A CT variant

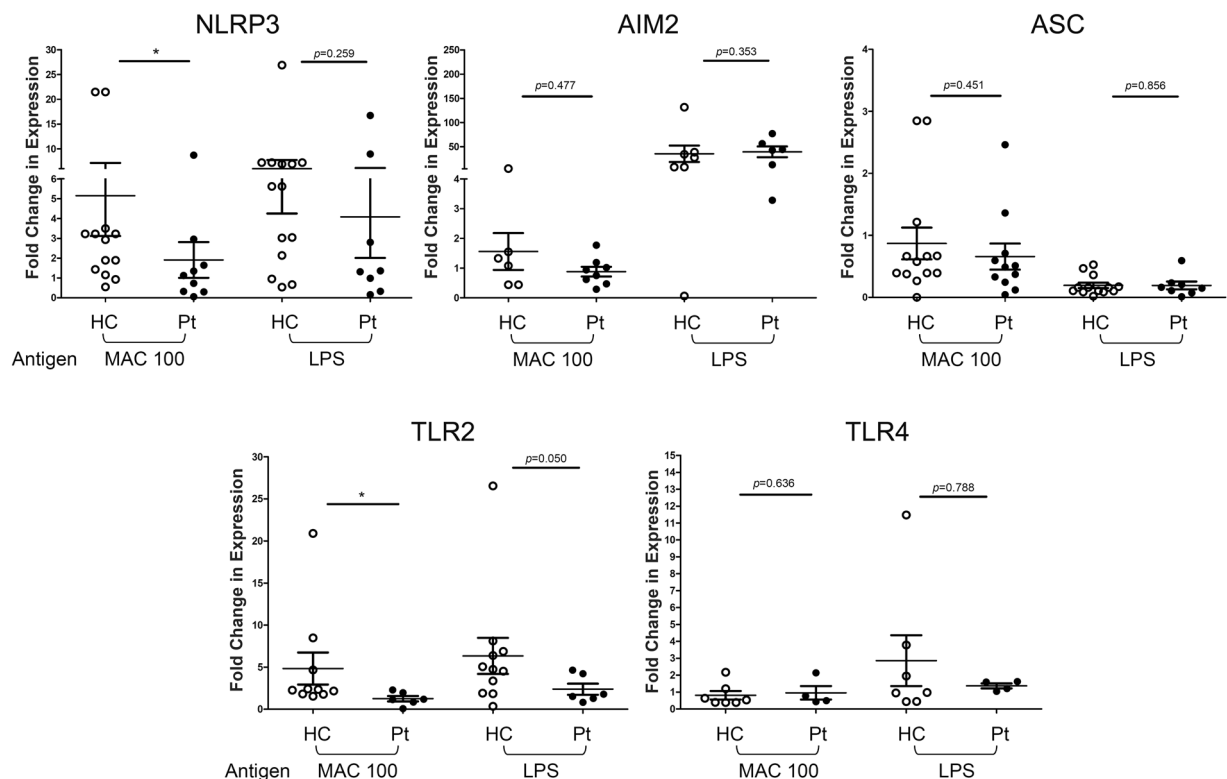


**Figure 4.** The mRNA levels of inflammasome receptors including NLRP3 and AIM2, adaptor protein-like ASC, and toll-like receptor 2 (TLR2) and TLR4 were measured in assays of human blood monocyte-derived macrophages with heat-killed *Mycobacterium avium* complex (MAC) (multiplicity of infection: 100) and lipopolysaccharide (LPS) (5  $\mu$ g/ml) for 6 hours. The data were compared using the Mann Whitney *U* test. The crossed lines are mean values and bars of standard errors. \* $0.01 \leq p < 0.05$ . \*\* $0.001 \leq p < 0.01$ . HC, healthy controls; pt, patients.

of rs34298354 in *NLRP3* was significantly associated with MAC-LD in the female subgroup. *NLRP3* gene polymorphisms have been associated with inflammation-related diseases such as inflammatory bowel disease<sup>26</sup>, juvenile idiopathic arthritis and type 2 diabetes<sup>27</sup>; however, few studies have investigated immune dysfunction. The association between SNPs of the *NLRP3* gene and MAC-LD in the females may indicate more direct evidence of host susceptibility to MAC bacilli. However, further studies are needed to investigate the dysfunction of the corresponding gene locus and the mechanism for the hypo-response of the *NLRP3* axis to MAC infection.

The SNP rs34298354 (C2054T) is exonic polymorphism of the *NLRP3* gene and is a silent polymorphism. The synonymous SNP is translated to the 436<sup>th</sup> amino acid in the *NLRP3* protein. Codon usage for the synonymous SNP rs34298354, with TCC changed to TCT (both encode serine), changes from 22% (frequency per thousand: 17.7) to 19% (frequency per thousand: 17.2; codon usage database: <https://www.kazusa.or.jp/codon/cgi-bin/showcodon.cgi?species=9606>). Previous reports of the Multidrug Resistance 1 (MDR1) gene indicated that silent polymorphism can change the substrate specificity<sup>28,29</sup>. The SNP rs34298354 in the *NLRP3* gene, associated with IL-1 $\beta$  production, may have a function like the MDR1 gene's silent polymorphism, but it needs to be further elucidated.

The trend of IL-1 $\beta$  mRNA was not significantly different between the control and patient groups, but TLR2 mRNA decreased significantly in the patient group compared with the controls. The possible explanations might be that IL-1 $\beta$  production could be regulated by many pathways<sup>13,30</sup> other than TLR2 signaling. The TLR2 mRNA in MAC-LD patients was significantly decreased, but possibly not enough to make IL-1 $\beta$  mRNA decrease significantly in a small case number. Other pathways were not studied in the present study and need to be investigated in the future.

The response of the mRNA of the TLR2 and TNF $\alpha$  axis to MAC was also impaired in the patients, which is consistent with previous reports<sup>31,32</sup>. Some gene polymorphisms of *TLR2* have been reported<sup>33,34</sup>, however, the current study is the first to report a correlation between a *TLR2* polymorphism and male MAC-LD. This finding suggests that multi-factorial predisposing factors cause MAC-LD, and that a different pathogenesis may exist in different genders.

There are several limitations to the present study. First, the case number was small and some significance may have been under-estimated. Second, the cases were enrolled in Taiwan, and the results may not be generalized to other ethnicities or areas.

SNP	Location	p value for HWE	Genotype	All			Male			Female		
				No.	% in with MAC-LD	p value	No.	% with MAC-LD	p value	No.	% with MAC-LD	p value
rs1792773	CARD17	0.4726	TT	41	21 (51)	0.831	20	10 (50)	0.546	21	11 (52)	0.741
	5' UTR		TC	120	56 (47)		49	18 (37)		71	38 (54)	
			CC	64	29 (45)		31	14 (45)		33	15 (46)	
rs2276405	AIM2	0.6921	TC	26	13 (50)	0.613	12	7 (58)	0.222	14	6 (43)	0.463
	Exonic stop gain		CC	198	93 (47)		88	35 (40)		110	58 (53)	
rs34298354	NLRP3	0.6985	CT	25	13 (56)	0.345	16	6 (38)	0.691	9	8 (89)	0.019
	Exonic synonymous		CC	200	92 (46)		84	36 (43)		116	56 (48)	
rs3806268	NLRP3	0.7203	AA	77	32 (42)	0.096	30	11 (37)	0.515	47	21 (45)	0.153
	Exonic		GA	104	57 (55)		48	23 (48)		56	34 (61)	
	synonymous		GG	44	17 (39)		22	8 (36)		22	9 (41)	
rs7525979	NLRP3	0.9995	CC	166	79 (48)	0.511	71	30 (42)	0.340	95	49 (52)	0.589
	Exonic		CT	54	24 (44)		25	9 (36)		29	15 (52)	
	synonymous		TT	4	3 (75)		4	3 (75)		0		
rs3804099	TLR2	0.6884	TT	106	54 (51)	0.582	47	24 (51)	0.088	59	30 (51)	0.094
	Exonic		TC	100	44 (44)		42	17 (41)		58	27 (47)	
	synonymous		CC	18	8 (44)		10	1 (10)		8	7 (88)	
rs3804100	TLR2	0.1096	CC	10	2 (20)	0.224	7	0	0.022	3	2 (67)	0.657
	Exonic		CT	97	45 (46)		40	14 (35)		57	31 (54)	
	synonymous		TT	117	59 (50)		52	28 (54)		65	31 (48)	
rs5743705	TLR2	0.6776	CT	25	13 (52)	0.603	11	5 (46)	0.806	14	8 (57)	0.637
	Exonic synonymous		CC	200	93 (47)		89	37 (42)		111	56 (51)	

**Table 1.** The analysis of single nucleotide polymorphisms (SNPs). Genotyping missing: 1 in rs2276405, 1 in rs3804100, 1 in rs3804099, 1 in rs7525979. Abbreviation: HWE, Hardy Weinberg Equilibrium.

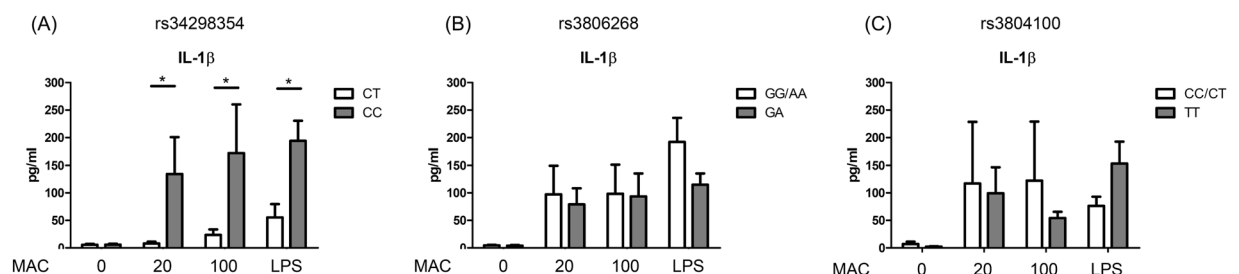


**Figure 5.** Under different patterns of single nucleotide polymorphisms, we measured and compared interleukin 1-beta (IL-1 $\beta$ ) responses from peripheral blood mononuclear cells (PBMCs) after stimulation with dead *Mycobacterium avium* complex (MAC) bacilli (multiplicity of infection [MOI] 20 and 100) and lipopolysaccharide (LPS) (5  $\mu$ g/ml) for 48 hours. The data were compared using the Mann Whitney U test. The crossed lines are mean values and bars of standard errors. \*0.01  $\leq$  p < 0.05.

## Conclusion

The responses of IL-1 $\beta$  in macrophages/monocytes were attenuated in the patients with MAC-LD. This may have been due to an impaired expression of NLRP3 inflammasome, which is responsible for the activation process of IL-1 $\beta$ . The gene polymorphisms of *NLRP3* and *TLR2* were correlated with MAC-LD, suggesting a possible host vulnerability. Further studies are needed to investigate the details of the impaired mechanism between gene polymorphisms and protein levels.

## Data Availability

The data of the present study will not be shared because no permission was granted by the Research Ethics Committee.

## References

- Griffith, D. E. *et al.* An official ATS/IDSA statement: diagnosis, treatment, and prevention of nontuberculous mycobacterial diseases. *Am J Respir Crit Care Med* **175**, 367–416 (2007).
- Lai, C. C. *et al.* Increasing incidence of nontuberculous mycobacteria, Taiwan, 2000–2008. *Emerg Infect Dis* **16**, 294–296 (2010).
- Field, S. K. & Cowie, R. L. Lung disease due to the more common nontuberculous mycobacteria. *Chest* **129**, 1653–1672 (2006).

4. Chetchotisakd, P. *et al.* Disseminated nontuberculous mycobacterial infection in patients who are not infected with HIV in Thailand. *Clin Infect Dis* **45**, 421–427 (2007).
5. Martin-Casabona, N. *et al.* Non-tuberculous mycobacteria: patterns of isolation. A multi-country retrospective survey. *Int J Tuberc Lung Dis* **8**, 1186–1193 (2004).
6. Shu, C. C. *et al.* Nontuberculous mycobacteria pulmonary infection in medical intensive care unit: the incidence, patient characteristics, and clinical significance. *Intensive Care Med* **34**, 2194–2201, <https://doi.org/10.1007/s00134-008-1221-6> (2008).
7. Donnabella, V., Salazar-Schicchi, J., Bonk, S., Hanna, B. & Rom, W. N. Increasing incidence of *Mycobacterium xenopi* at Bellevue hospital: An emerging pathogen or a product of improved laboratory methods? *Chest* **118**, 1365–1370 (2000).
8. Koh, W. J. *et al.* Clinical significance of nontuberculous mycobacteria isolated from respiratory specimens in Korea. *Chest* **129**, 341–348 (2006).
9. van Ingen, J. *et al.* Clinical relevance of non-tuberculous mycobacteria isolated in the Nijmegen-Arnhem region, The Netherlands. *Thorax* **64**, 502–506 (2009).
10. Sharma, D. & Kanneganti, T. D. The cell biology of inflammasomes: Mechanisms of inflammasome activation and regulation. *J Cell Biol* **213**, 617–629 (2016).
11. Awad, F. *et al.* Inflammasome biology, molecular pathology and therapeutic implications. *Pharmacol Ther* **187**, 133–149 (2018).
12. Briken, V., Ahlbrand, S. E. & Shah, S. Mycobacterium tuberculosis and the host cell inflammasome: a complex relationship. *Frontiers in cellular and infection microbiology* **3**, 62 (2013).
13. Mayer-Barber, K. D. *et al.* Caspase-1 independent IL-1 $\beta$  production is critical for host resistance to mycobacterium tuberculosis and does not require TLR signaling *in vivo*. *J Immunol* **184**, 3326–3330 (2010).
14. Mayer-Barber, K. D. *et al.* Innate and adaptive interferons suppress IL-1 $\alpha$  and IL-1 $\beta$  production by distinct pulmonary myeloid subsets during Mycobacterium tuberculosis infection. *Immunity* **35**, 1023–1034 (2011).
15. Awad, F. *et al.* Impact of human monocyte and macrophage polarization on NLR expression and NLRP3 inflammasome activation. *PLoS One* **12**, e0175336 (2017).
16. Bakele, M. *et al.* Localization and functionality of the inflammasome in neutrophils. *J Biol Chem* **289**, 5320–5329 (2014).
17. Lou, J., Wang, Y., Zhang, Z. & Qiu, W. MiR-20b inhibits mycobacterium tuberculosis induced inflammation in the lung of mice through targeting NLRP3. *Exp Cell Res* **358**, 120–128 (2017).
18. Chen, C. C. *et al.* Activation of an NLRP3 inflammasome restricts Mycobacterium kansasii infection. *PloS one* **7**, e36292 (2012).
19. Gross, O., Thomas, C. J., Guarda, G. & Tschopp, J. The inflammasome: an integrated view. *Immunol Rev* **243**, 136–151 (2011).
20. Dorhoi, A. *et al.* Activation of the NLRP3 inflammasome by Mycobacterium tuberculosis is uncoupled from susceptibility to active tuberculosis. *Eur J Immunol* **42**, 374–384 (2012).
21. Master, S. S. *et al.* Mycobacterium tuberculosis prevents inflammasome activation. *Cell Host Microbe* **3**, 224–232 (2008).
22. Chan, E. D. & Iseman, M. D. Underlying host risk factors for nontuberculous mycobacterial lung disease. *Seminars in respiratory and critical care medicine* **34**, 110–123 (2013).
23. Bergsbaken, T., Fink, S. L. & Cookson, B. T. Pyroptosis: host cell death and inflammation. *Nat Rev Microbiol* **7**, 99–109 (2009).
24. Fink, S. L. & Cookson, B. T. Caspase-1-dependent pore formation during pyroptosis leads to osmotic lysis of infected host macrophages. *Cell Microbiol* **8**, 1812–1825 (2006).
25. Jorgensen, I., Zhang, Y., Krantz, B. A. & Miao, E. A. Pyroptosis triggers pore-induced intracellular traps (PITs) that capture bacteria and lead to their clearance by efferocytosis. *J Exp Med* **213**, 2113–2128 (2016).
26. Zhang, H. X. *et al.* NLRP3 gene is associated with ulcerative colitis (UC), but not Crohn's disease (CD), in Chinese Han population. *Inflamm Res* **63**, 979–985 (2014).
27. Zheng, Y. *et al.* Variants of NLRP3 gene are associated with insulin resistance in Chinese Han population with type-2 diabetes. *Gene* **530**, 151–154 (2013).
28. Komar, A. A. Silent SNPs: impact on gene function and phenotype. *Pharmacogenomics* **8**, 1075–1080 (2007).
29. Kimchi-Sarfaty, C. *et al.* A “silent” polymorphism in the MDR1 gene changes substrate specificity. *Science* **315**, 525–528 (2007).
30. Zhu, Q. & Kanneganti, T. D. Cutting Edge: Distinct Regulatory Mechanisms Control Proinflammatory Cytokines IL-18 and IL-1 $\beta$ . *J Immunol* **198**, 4210–4215 (2017).
31. Shu, C. C. *et al.* Interleukin 23/interleukin 17 axis activated by Mycobacterium avium complex (MAC) is attenuated in patients with MAC-lung disease. *Tuberculosis (Edinb)* **110**, 7–14 (2018).
32. Ryu, Y. J. *et al.* Impaired expression of Toll-like receptor 2 in nontuberculous mycobacterial lung disease. *Eur Respir J* **30**, 736–742 (2007).
33. Pattabiraman, G., Panchal, R. & Medvedev, A. E. The R753Q polymorphism in Toll-like receptor 2 (TLR2) attenuates innate immune responses to mycobacteria and impairs MyD88 adapter recruitment to TLR2. *J Biol Chem* **292**, 10685–10695 (2017).
34. Yim, J. J., Kim, H. J., Kwon, O. J. & Koh, W. J. Association between microsatellite polymorphisms in intron II of the human Toll-like receptor 2 gene and nontuberculous mycobacterial lung disease in a Korean population. *Hum Immunol* **69**, 572–576 (2008).

## Acknowledgements

The authors thank the staff of the Seventh and Eighth Core Labs of the Department of Medical Research of National Taiwan University Hospital for their technical support. This study was supported in part by Grants from National Taiwan University Hospital (NTUH, 107-S3885) and the Ministry of Science and Technology Taiwan (MOST 104-2314-B-002-079-MY3; 107-2628-B-002-006). The funders had no role in study design, data collection and analysis, decision to publish, or preparation of the manuscript.

## Author Contributions

Dr. Shu C.C., Post-doc Wu M.F. and Prof. Wu L.S.H. conducted the experiments. Prof. Wang J.Y. and Dr Shu C.C. were involved in participant recruitment. Dr. Shu C.C., Post-doc Wu M.F. and Profs. Lai H.C., Yan B.S., Wang J.Y., Chiang B.L. and Wu L.S.H. contributed to data analysis and manuscript writing. Prof. Yu C.J. and Wu L.S.H. were responsible for the coordination.

## Additional Information

**Supplementary information** accompanies this paper at <https://doi.org/10.1038/s41598-019-47609-3>.

**Competing Interests:** The authors declare no competing interests.

**Publisher's note:** Springer Nature remains neutral with regard to jurisdictional claims in published maps and institutional affiliations.




**Open Access** This article is licensed under a Creative Commons Attribution 4.0 International License, which permits use, sharing, adaptation, distribution and reproduction in any medium or format, as long as you give appropriate credit to the original author(s) and the source, provide a link to the Creative Commons license, and indicate if changes were made. The images or other third party material in this article are included in the article's Creative Commons license, unless indicated otherwise in a credit line to the material. If material is not included in the article's Creative Commons license and your intended use is not permitted by statutory regulation or exceeds the permitted use, you will need to obtain permission directly from the copyright holder. To view a copy of this license, visit <http://creativecommons.org/licenses/by/4.0/>.

© The Author(s) 2019



## ORIGINAL ARTICLE

# In silico identification of thiostrepton as an inhibitor of cancer stem cell growth and an enhancer for chemotherapy in non-small-cell lung cancer

Tse-Hung Huang<sup>1,2,3,4,5</sup> | Alexander T. H. Wu<sup>6</sup> | Tai-Shan Cheng<sup>7</sup> | Kuan-Ting Lin<sup>8</sup> | Chia-Jou Lai<sup>7</sup> | Hao-Wen Hsieh<sup>9</sup> | Peter Mu-Hsin Chang<sup>10,11</sup> | Cheng-Wen Wu<sup>9,12</sup> | Chi-Ying F. Huang<sup>7,9,13</sup>  | Kuan-Yu Chen<sup>14</sup>

<sup>1</sup>Department of Traditional Chinese Medicine, Chang Gung Memorial Hospital, Keelung, Taiwan

<sup>2</sup>School of Traditional Chinese Medicine, Chang Gung University, Taoyuan, Taiwan

<sup>3</sup>School of Nursing, National Taipei University of Nursing and Health Sciences, Taipei, Taiwan

<sup>4</sup>Graduate Institute of Health Industry Technology, Chang Gung University of Science and Technology, Taoyuan, Taiwan

<sup>5</sup>Research Center for Chinese Herbal Medicine, Chang Gung University of Science and Technology, Taoyuan, Taiwan

<sup>6</sup>The Ph.D. Program for Translational Medicine, College of Medical Science and Technology, Taipei Medical University, Taipei, Taiwan

<sup>7</sup>Institute of Biopharmaceutical Sciences, National Yang-Ming University, Taipei, Taiwan

<sup>8</sup>Cold Spring Harbor Laboratory, Cold Spring Harbor, NY, USA

<sup>9</sup>Institute of Clinical Medicine, National Yang-Ming University, Taipei, Taiwan

<sup>10</sup>Department of Oncology, Taipei Veterans General Hospital, Taipei, Taiwan

<sup>11</sup>Faculty of Medicine, National Yang-Ming University, Taipei, Taiwan

<sup>12</sup>Institute of Biomedical Sciences, Academia Sinica, Taipei, Taiwan

<sup>13</sup>Department of Biochemistry, College of Medicine, Kaohsiung Medical University, Kaohsiung, Taiwan

<sup>14</sup>Division of Pulmonary Medicine, Department of Internal Medicine, National Taiwan University Hospital and College of Medicine, National Taiwan University, Taipei, Taiwan

## Correspondence

Kuan-Yu Chen, Division of Pulmonary Medicine, Department of Internal Medicine, National Taiwan University Hospital and College of Medicine, Taipei, National Taiwan University, No. 7, Chung-Shan South Road, Taipei 100, Taiwan.  
Email: tuff.chen@msa.hinet.net

Chi-Ying F. Huang, Institute of Biopharmaceutical Sciences, National Yang-Ming University, No. 155, Sec. 2, Linong St., Taipei 112, Taiwan.  
Email: cyhuang5@ym.edu.tw

## Funding information

Ministry of Science and Technology, Taiwan, Grant/Award Number: MOST106-2314-B-002-102-MY3, MOST107-2320-B-010-040-MY3 and

## Abstract

Cancer stem cells (CSCs) play an important role in cancer treatment resistance and disease progression. Identifying an effective anti-CSC agent may lead to improved disease control. We used CSC-associated gene signatures to identify drug candidates that may inhibit CSC growth by reversing the CSC gene signature. Thiostrepton, a natural cyclic oligopeptide antibiotic, was the top-ranked candidate. In non-small-cell lung cancer (NSCLC) cells, thiostrepton inhibited CSC growth in vitro and reduced protein expression of cancer stemness markers, including CD133, Nanog and Oct4A. In addition, metastasis-associated Src tyrosine kinase signalling, cell migration and epithelial-to-mesenchymal transition (EMT) were all inhibited by thiostrepton. Mechanistically, thiostrepton treatment led to elevated levels of tumour suppressor miR-98. Thiostrepton combined with gemcitabine synergistically suppressed NSCLC

Tse-Hung Huang, Alexander T. H. Wu, and Tai-Shan Cheng contributed equally to this study.

This is an open access article under the terms of the Creative Commons Attribution License, which permits use, distribution and reproduction in any medium, provided the original work is properly cited.

© 2019 The Authors. *Journal of Cellular and Molecular Medicine* published by John Wiley & Sons Ltd and Foundation for Cellular and Molecular Medicine.

MOST107-2320-B-182A-007-; Chang-Gung Memorial Hospital Research Foundation, Grant/Award Number: CMRPG2G0331 and CMRPG2G0332; Taipei Medical University, Grant/Award Number: 102CM-TMU-03; Veterans General Hospitals and University System of Taiwan Joint Research Program, Grant/Award Number: VGHUST108-G1-4-1; NYMU-FEMH Joint Research Program, Grant/Award Number: 106DN20

cell growth and induced apoptosis. The inhibition of NSCLC tumours and CSC growth by thiostrepton was also demonstrated in vivo. Our findings indicate that thiostrepton, an established drug identified in silico, is an inhibitor of CSC growth and a potential enhancer of chemotherapy in NSCLC.

#### KEYWORDS

cancer stem cell, epithelial-to-mesenchymal transition, miR-98, non-small-cell lung cancer, thiostrepton

## 1 | INTRODUCTION

Lung cancer is the leading cause of cancer-related death worldwide.<sup>1</sup> The five-year survival rate is approximately 18% for patients with lung cancer and 3.9% for those with advanced stages<sup>2</sup> of the disease, lower than the survival rates for colon (65%), female breast (90%) and prostate (99%) cancers.<sup>3</sup> Non-small-cell lung cancer (NSCLC) accounts for approximately 85% of all lung cancers. Chemotherapies, including pemetrexed or gemcitabine in combination with platinum, are frequently used as the first-line therapy for advanced NSCLC.<sup>4–6</sup> However, current chemotherapy regimens do not provide long-term disease control in most patients with NSCLC.<sup>7,8</sup> Those who receive chemotherapy eventually encounter drug resistance and disease progression.<sup>9,10</sup> Alternative therapeutic strategies are urgently needed.

Cancer stem cells (CSCs) play an important role in cancer recurrence, progression and drug resistance.<sup>11–13</sup> Lung CSCs were first identified as CD133<sup>+</sup> cells<sup>14</sup> and isolated in established NSCLC cell lines,<sup>15,16</sup> forming floating spheres in serum-free conditions. These CD133<sup>+</sup> lung cancer spheres exhibited self-renewal abilities, stress/drug resistance, epithelial-to-mesenchymal (EMT) potential and the ability to recapitulate tumour heterogeneity in vivo.<sup>14–18</sup> The drug resistance may be due to features related to the stem cell pathway, expression of high-level ATP-binding cassette transporters and specific surface biomarkers.<sup>19</sup> Identifying agents to eliminate CSCs has become an important issue for anti-cancer drug development.

Developing an entirely new drug is expensive and time-consuming. Drug repurposing offers an alternative strategy for anti-cancer drug development, which requires analysing biological and medical information for a huge number of drugs.<sup>20</sup> The Connectivity Map (CMap, <http://www.broad.mit.edu/cmap/>),<sup>21</sup> which stores expression profiles of diseases, genes and chemicals, provides a tool for making inferences based on a query and the internal profiles. We hypothesized that drugs with the ability to reverse the expression of CSC-like gene signatures may inhibit CSC growth and could prove beneficial in the treatment of lung cancer. We tested the top-ranked agent identified by CMap for reversing potential CSC gene signatures for anti-CSC abilities in vitro and in vivo. The synergistic effect of identified agents and existing chemotherapies on tumour growth inhibition was also examined.

Thiostrepton, a macrocyclic thiopeptide antibiotic, belongs to the thiopeptide family of highly modified macrocyclic peptides, which

are produced as secondary metabolites by actinomycetes of the genus *Streptomyces*.<sup>22</sup> Thiostrepton interacts directly with forkhead box M1 (FOXO1) and inhibits binding with genomic target sites.<sup>23</sup> Thiostrepton also inhibits growth and induces apoptosis in human cancer cells by inhibiting FOXO1 expression.<sup>24</sup> Based on CMap analysis, we identified thiostrepton as a candidate to be an anti-CSC agent. We also provided evidence that thiostrepton can suppress cancer cell proliferation, migration and CSC-like properties in vitro, as well as inhibit tumorigenesis in vivo. More importantly, thiostrepton combined with gemcitabine inhibited NSCLC cell growth synergistically. Collectively, our findings suggest thiostrepton can serve as an anti-CSC drug and play a beneficial role in lung cancer treatment.

## 2 | MATERIALS AND METHODS

### 2.1 | Cell lines and chemicals

A549, NCI-H441 and CL141 are lung adenocarcinoma cell lines with wild-type EGFR. CL152 is a lung squamous carcinoma cell line. H1299 is an NSCLC cell line, and H460 is large cell lung carcinoma cell line. A549-ON cells are A549 cells co-overexpressed Oct-4A and Nanog.<sup>25</sup> H460 cells were infected by a CD133 P1 promoter-driven GFP reporter lentivirus and cultured in RPMI-1640 supplemented with 10% foetal bovine serum (FBS) (GIBCO).<sup>26</sup> CD133<sup>+</sup>GFP<sup>+</sup>H460 cells were sorted by using a FACSria cell sorter (BD Biosciences). The other cell lines were maintained in RPMI medium and supplemented with 10% FBS (GIBCO), 2 mmol/L L-glutamine, 100 U/mL penicillin and 100 µg/mL streptomycin (GIBCO). For cell culture experiments, a 10 mmol/L thiostrepton stock solution was dissolved in dimethyl sulfoxide (DMSO; Sigma). Pemetrexed, gefitinib and gemcitabine were purchased from LC Laboratories, while thiostrepton and cisplatin were acquired from Sigma and Selleckchem, respectively.

### 2.2 | L1000 expression profiling

Gene expression profiles were obtained from cancer cells treated with perturbagens, including small molecules and Chinese herbal medicines, in triplicate for 6 hours, followed by L1000 expression profiling<sup>21,27</sup> by Genometry Inc. In brief, cells were lysed after 6 hours of treatment in triplicate, and mRNA transcripts from whole cell lysates were rapidly captured by oligo-dT. The cDNAs generated by reverse transcription from mRNA were amplified through

ligation-mediated polymerase chain reaction (PCR). The PCR amplicon was then hybridized to bar-coded Luminex beads to display the expression values of specific genes. The cDNA was annealed with specific probes for 978 landmark genes. A list of overexpressed and underexpressed probe sets was obtained using a *t* test rank order.

### 2.3 | Connectivity scoring by gene set enrichment analysis using CMap

Intensity values of gene expression profiles were first converted to robust *z*-scores using the *l1ktools* downloaded from the CMap/Library of Integrated Network-based Cellular Signatures (LINCS) project of the NIH Common Fund programme. Integrated Network-based Cellular Signatures has been replaced by the CLUE platform as of February, 2017. The new analytical tool can be accessed from <https://clue.io>. A Perl script was used to calculate the connectivity score for each gene expression profile against the anti-CSC or CSC gene signature.<sup>21</sup> The anti-CSC gene signature was identified using GEO2R for differentially expressed genes in the study of, for example, the Gene Expression Omnibus<sup>28</sup> gene signature GSE18150.<sup>29</sup>

The 11 641 profiles in our collection were ranked by connectivity scores and used as the input of the ranking matrix for gene set enrichment analysis (GSEA). Thiostrepton profiles (including repeats and treatments in different cancer cells) were grouped together and used as the input gene set for GSEA to map the ranking matrix and calculate the enrichment scores. Normalized enrichment scores were obtained from 1000 permutations of gene sets. Some of the gene signatures (eg GSE18931<sup>30</sup>) were obtained as CSC gene signatures. We scored the negative enrichment. Finally, for CMap/LINCS analysis, the query-gene signature was uploaded to LINCS Web Apps to obtain *score\_best4* scores of the perturbagens in the database.

### 2.4 | Colony formation assay

Non-small-cell lung cancer cells were seeded in 6-well plates at a density of 600 cells per well and cultured for 14 days. Thiostrepton was added 24 hours after seeding. The culture medium with thiostrepton was renewed every 4 days. Following the treatments, cells were washed with phosphate-buffered saline (PBS), and the colonies were fixed in a methanol-acetic acid fixing solution with a ratio of 3:1 and stained with 0.5% crystal violet solution in methanol. After carefully removing the crystal violet solution and rinsing with tap water, the colonies were counted manually. Each experiment was performed independently, in triplicate, at least twice.

### 2.5 | Cytotoxicity assay and drug combination analysis

Cells were seeded in 96-well plates at a density of 2000 cells per well in triplicate. The cells were treated with indicated agents for

48 hours on the second day to ensure adequate plating efficiency and cell vitality. Cells were treated with different concentrations of thiostrepton, pemetrexed, cisplatin, gemcitabine and gefitinib or a non-fixed-ratio combination of thiostrepton and one of the anti-cancer agents.

The cytotoxicity was assessed by using a sulforhodamine B (SRB) assay.<sup>31</sup> Briefly, the medium was discarded, and the adherent cells were fixed with 100  $\mu$ L of cold 10% trichloroacetic acid (w/v) in each well for 1 hour at 4°C. Cells were stained after fixing with 100  $\mu$ L/well of 0.4% (w/v, in 1% acetic acid) SRB solution for 30 minutes at room temperature and then washed five times with 1% acetic acid. After air-drying, 100  $\mu$ L of 10 mmol/L Tris base was added to each well and the absorbance was read at 546 nm. Cytotoxicity was defined as the percentage of cells in the drug-treated wells relative to the cell numbers in the solvent-only control (set to 100%). Each experiment was performed independently, in triplicate, at least twice, and the cytotoxicity was presented as the mean  $\pm$  standard deviation.

The synergy associated with inducing cytotoxicity among different drug combinations was evaluated by analysis of the median-dose effect and calculation of the combination index (CI) using commercially available software of Chou and Talalay software (CompuSyn).<sup>32,33</sup> According to the recommendations of this methodology, CI values of less or greater than 1 indicated synergism or antagonism, respectively. A value of 1 indicated an additive effect.

### 2.6 | Cell migration assay

Cell culture inserts (Millipore) were placed in 24-well plates. Serum-starved cells ( $2 \times 10^5$  cells) were seeded in the upper chambers of the transwell with 200  $\mu$ L of serum-free medium, in the presence of the vehicle (DMSO) or thiostrepton (5  $\mu$ mol/L). The lower chambers were filled with 750  $\mu$ L of medium containing 10% FBS as a chemo-attractant. After incubation for 16 hours, cells were fixed in 4% formaldehyde and stained with GEMSA (Sigma). After washing, the non-penetrating cells on the inner surfaces of the upper chambers were wiped off with cotton swabs. The penetrated cells were photographed and counted using a light microscope. Each assay was performed in triplicate.

### 2.7 | Immunoblotting

After treatments, cells were lysed in a lysis buffer. Total protein contents were isolated and subjected to SDS polyacrylamide gel electrophoresis and electro-transferred onto polyvinylidene fluoride membranes (Millipore). Immunoblotting was performed using primary antibodies, including  $\beta$ -catenin (Cell Signaling Technology), c-Myc (Cell Signaling Technology), CD44 (Cell Signaling Technology), CD133 (GeneTex), Oct-4A (GeneTex), Sox2 (Cell Signaling Technology), FOXM1 (Abcam), E-cadherin (Cell Signaling Technology), Src (Cell Signaling Technology), phosphorylated Src (Tyr416, Cell Signaling Technology), caspase-8 (Cell Signaling Technology), caspase-9 (Cell Signaling Technology), caspase-3 (Cell

Signaling Technology) and cleaved PARP (Cell Signaling Technology). GAPDH (Cell Signaling Technology),  $\alpha$ -tubulin (Cell Signaling Technology) or  $\beta$ -actin (GeneTex) acted as an internal control. Protein detection was performed by using an enhanced chemiluminescence (ECL™) method and the Luminescence Imaging System (LAS-4000™, Fuji Photo Film Co., Ltd).

## 2.8 | Assays for cancer stemness characteristics

The assay of ALDH1 activity is frequently used to define lung cancer stem cell populations.<sup>34</sup> Aldefluor assays were performed according to the manufacturer's guidelines (StemCell Technologies). Briefly, a single cell suspension obtained from cell cultures was incubated in Aldefluor assay buffer containing an ALDH substrate (bodipy-aminoacetaldehyde, BAAA) for 50 minutes at 37°C. As a negative control, a fraction of cells from each sample was incubated under identical conditions in the presence of an ALDH inhibitor (diethylaminobenzaldehyde, DEAB). Flow cytometry was used to detect the ALDH-positive cell population.

A tumour sphere formation assay was carried out to evaluate cancer stemness. Lung cancer cells were seeded in 6-well ultralow-attachment plates (Corning Inc) at a density of 2000 cells/mL in a serum-deprived culture medium consisting of DMEM/F12 supplemented with 1% N2 Supplement (GIBCO), 20 ng/mL basic fibroblast growth factor (Sigma), 20 ng/mL epidermal growth factor (GIBCO), 100 U/mL penicillin and 100 µg/mL streptomycin (GIBCO) at 37°C in a humidified atmosphere of 95% air and 5% CO<sub>2</sub>. Tumour spheres were counted after harvest using a Countess™ (GIBCO) automated cell counter.

## 2.9 | Quantitative PCR analyses and microRNA assays

All RNA-related experiments were performed by using kits purchased from QIAGEN (Taiwan) and following the instructions provided by the vendor. Total RNA was isolated, quantified and reverse transcribed into cDNA. The primers of different microRNAs tested in this study for microRNA quantitative real-time PCR assays were also purchased from QIAGEN. Up-regulation and down-regulation of miRNAs were performed by transfecting cells with miRNA precursors or anti-miRNAs, respectively. Fifty nanomoles of miScript mimic and inhibitors were transfected into lung cancer cells by using the lipofectamine 2000 reagent (Thermo Fisher Scientific). Total RNA and protein were isolated 48 hours after treatments to determine the effects on target-protein expression profiles.

## 2.10 | Examination of anti-lung cancer effects mediated by thiostrepton in vivo

The inhibitory effect of thiostrepton on tumour growth was evaluated by using a mouse subcutaneous tumour xenograft model. Human lung adenocarcinoma cells (NCI-H441, purchased from ATCC) were injected subcutaneously in the right flank of non-obese diabetic/severe

combined immunodeficient (NOD/SCID) mice (female, 4–6 weeks old) at 10<sup>6</sup> cells/injection. Once the tumour became palpable, the tumour-bearing mice were randomly assigned to a thiostrepton group (5 mg/kg, 5 days/wk, intraperitoneal injection) or a control group (DMSO vehicle). Over a period of 4 weeks, the tumour sizes in both groups were measured weekly with standard calipers. The in vivo tracking of tumour growth was then determined and presented as the fold change in tumour volume over time. All animal experiments were approved by the Taipei Medical University Animal Center (Protocol number: LAC-2013-0086). The animals were humanely killed by cervical dislocation to minimize the suffering. All tumour samples were harvested for further analyses.

## 3 | RESULTS

### 3.1 | Identification of thiostrepton as a potential anti-CSC agent using the Connectivity Map database

We compared 20 different published data sets (Table S1) and employed CSC-related gene expression profiles as inputs to query 11 641 L1000-based gene expression profiles. Thiostrepton was identified as a candidate that could significantly reverse lung cancer gene signatures (Figure 1A). As an example, GSE18150 was originally generated from cells treated with DZNep by disrupting *EZH2* and impairing CSC self-renewal.<sup>29</sup> Thiostrepton profiles, including treatments in different cancer cells in triplicate, were grouped together and used as the input gene set for GSEA to map the ranking matrix and calculate an enrichment score. The anti-CSC gene signature from GSE18150 and cancer cells treated with thiostrepton had a strong enrichment score in our 11 641 L1000 assays (normalized enrichment score = 1.914, *P*-value < .0001, Figure 1B). The majority of thiostrepton profiles had a positive connectivity score, and only a few had a score of zero. This indicated a strong positive connectivity between thiostrepton and the anti-CSC gene signature, meaning thiostrepton is a potential anti-CSC agent.

When the anti-CSC gene signature GSE18150 determined by GEO2R was used to query the CMap 2.0 (a database containing 6100 gene expression profiles), thiostrepton was ranked as the top candidate (enrichment score = 0.797, *P*-value < .001; Figure 1B). In results from the query of the LINCS database, which contained more than 1.3 million gene expression profiles, thiostrepton was ranked as the 22nd among drugs with positive similarity scores (score\_best4 = 97.368).

The human normal mammary stem cell (hNMSC) gene expression signature GSE18931, a CSC gene signature, can stratify biological and molecular features in tumours (Table S2). The degree of cells expressing hNMSC markers may reflect the CSC content of a tumour.<sup>30</sup> L1000 profiles with a negative connectivity score (normalized enrichment score = -2.0146; *P*-value < .0001; false discover rate < 0.0001) indicated that thiostrepton treatment may reverse gene signatures of GSE18931. Similarly, when GSE18931 was used to query the LINCS database, the results showed that thiostrepton had a score\_best4 of -93.176 among the compounds with negative

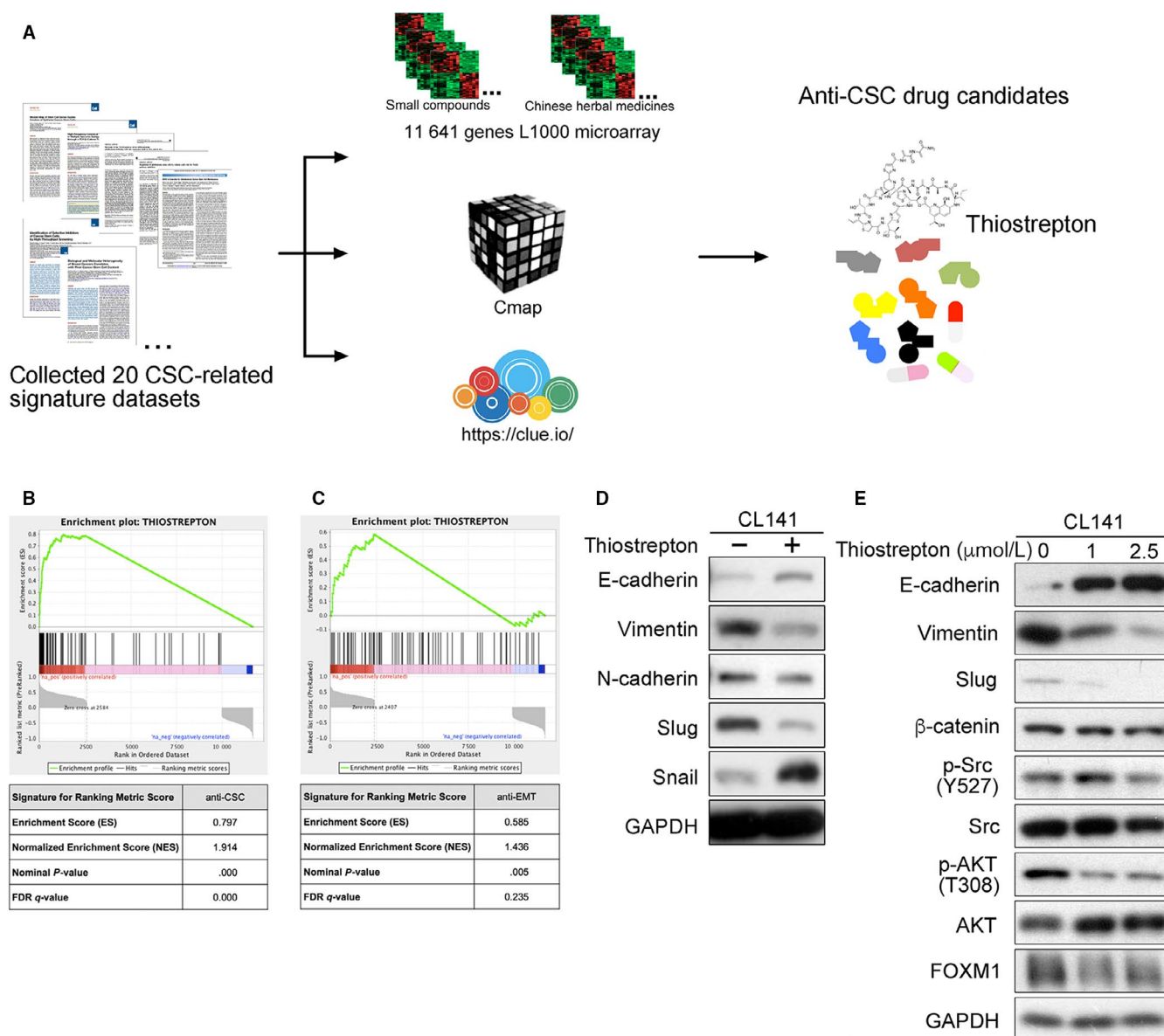


**FIGURE 1** Identification of thiostrepton as an anti-cancer stem cell agent using genomic approaches. A, Flowchart of array analysis and prediction of potential anti-CSC agents in NSCLC. B, Pre-ranked GSEA of 81 gene expression profiles of thiostrepton among the 11 641 L1000 gene expression profiles. The ranking metric scores were connectivity scores against the anti-CSC signature of DZNep (GSE18150). The hits (black vertical lines) are thiostrepton profiles. C, The anti-EMT signature (GSE17215) of salinomycin was used to generate connectivity scores for ranking metric scores. D, A Western blotting assay indicated that thiostrepton treatment (2.5 μmol/L) enhanced E-cadherin expression and reduced Slug expression in CL141 cells. E, Thiostrepton treatment reduced vimentin and Slug expression, inhibited Src and AKT activation and reduced FOXM1 expression in a dose-dependent manner in CL141 cells

similarity scores. This strong concordance across different perturbation databases indicated that thiostrepton is likely to have anti-CSC abilities.

In addition, our GSEA showed that thiostrepton has significant connectivity with the anti-EMT gene signature of salinomycin (GSE17215) with specific toxicity for epithelial CSCs<sup>35</sup> (normalized enrichment score = 1.436; *P*-value = .005, Figure 1C). Further validation was demonstrated by the up-regulated expression of E-cadherin and down-regulated expression of Slug and vimentin in thiostrepton-treated CL141 cells (Figure 1D). Moreover, treatment with thiostrepton not only distinctly reduced FOXM1 expression

but also reduced vimentin and Slug expression and inhibited Src and AKT activation in CL141 cells in a dose-dependent manner (Figure 1E).

### 3.2 | Thiostrepton suppresses NSCLC cell growth, clonogenicity and migration

Non-small-cell lung cancer cells were treated with thiostrepton. Figure 2A,B shows that thiostrepton suppressed cellular viability and colony-forming ability in a dose-dependent manner. The half-maximal inhibitory concentration (IC<sub>50</sub>) of thiostrepton



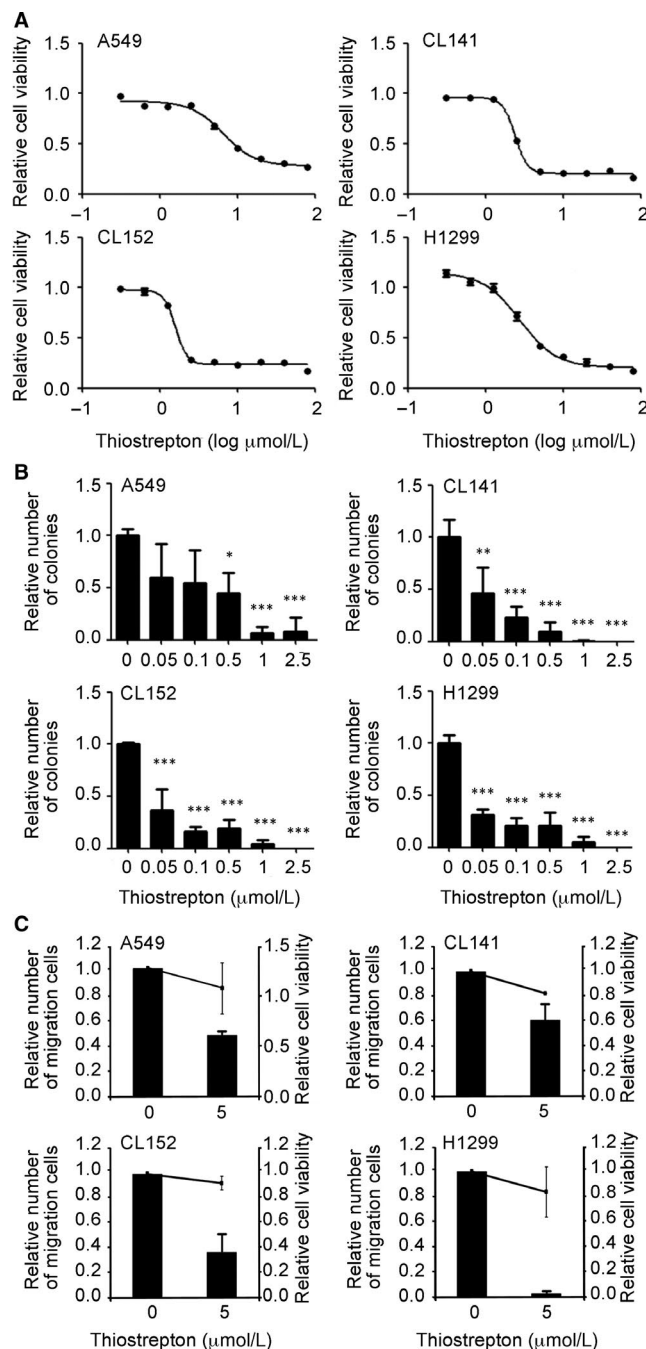


**FIGURE 2** Thiostrepton treatment suppresses NSCLC tumorigenesis. Thiostrepton treatment significantly suppressed NSCLC cell viability (A) and colony formation (B) in A549, H1299, CL141 and CL152 cells. C, Thiostrepton inhibited NSCLC cell migration. The bars indicate relative migratory ability (left y-axis), which is compared with the vehicle (control; 0). Relative cell viability (right y-axis) is indicated by solid lines. These data suggest that the decreased cell migration by thiostrepton was not associated with the reduction of cell viability.  $**P < .01$ ,  $***P < .001$

in the clonogenic assay was approximately  $0.05 \mu\text{mol/L}$ , which was distinctly lower than that of cytotoxic effects (Table S3). In addition, treatment with thiostrepton significantly reduced the migration capability of A549, CL141, CL152 and H1299 cells (Figure 2C).

A previous study demonstrated enhanced sphere-forming ability, cisplatin resistance and migration ability in  $\text{CD133}^+$  H460 cells.<sup>26</sup> To verify the potential anti-CSC effect of thiostrepton, we used H460 cells expressing GFP driven by a  $\text{CD133}$  promoter for cytotoxicity analysis. Both parental H460 and  $\text{CD133}^+$  H460 cells were then subjected to an SRB assay. We found that the  $\text{CD133}^+$  H460 cells ( $\text{IC}_{50} = 1.7 \mu\text{mol/L}$ ) were more sensitive to thiostrepton than the parental H460 cells ( $\text{IC}_{50} = 6.9 \mu\text{mol/L}$ ; Table S3).

### 3.3 | Thiostrepton suppresses CSC properties in NSCLC cells

For in vitro validation, tumour spheres of CL141 cells were generated under serum-free conditions and CSC properties were examined in these tumour spheres. By using an Aldefluor assay, we found CL141 tumour spheres were enriched with  $\text{ALDH1}^+$  cells (S: 1.2%) compared with their parental counterparts (P: 0.5%, Figure 3A), and the relative ALDH activity was significantly increased (Figure 3B). The expression of stem cell-related markers, including  $\text{CD44}$ , Oct-4A, Sox2 and c-Myc, was also up-regulated in CL141 tumour sphere cells (Figure 3C).

Thiostrepton treatment prominently suppressed CL141 tumour spheres formation in a dose-dependent manner (Figure 3D). This observation was supported by thiostrepton treatment in both parental cells and spheres. Treatment with thiostrepton reduced the expression of CSC markers, including  $\text{CD133}$ , Oct-4A and Nanog, as well as suppressed metastasis-associated Src signalling (Figure 3E).

Furthermore, a stable CSC-like A549-ON cells was used to validate the anti-CSC and anti-EMT ability of thiostrepton. Thiostrepton treatment significantly decreased expression of Oct-4A and Nanog and up-regulated expression of E-cadherin (Figure 3F), supporting the hypothesis that thiostrepton is a potential anti-CSC agent.

### 3.4 | Thiostrepton and gemcitabine synergistically suppresses NSCLC tumour sphere formation

Thiostrepton in combination with gemcitabine, cisplatin, pemetrexed or gefitinib reduced NSCLC cell viabilities synergistically (Figure 4A). The obtained average CI values from thiostrepton in combination with gemcitabine, gefitinib, cisplatin and pemetrexed were  $0.41 \pm 0.16$ ,  $0.80 \pm 0.19$ ,  $0.91 \pm 0.25$  and  $1.04 \pm 0.30$ , respectively. This indicates that thiostrepton plus gemcitabine showed the best synergistic effect among these combinations. In addition, the CI values in different ratios (1:1, 1:2, 1:4 and 1:8) all showed synergistic effects in the CL141, CL152 and H1299 cells (Figure 4B).

$\text{CD133}$  and Oct-4A, the CSC markers, have been suggested as protectors for cancer cells from apoptosis induced by chemotherapeutic agents.<sup>25,26,36</sup> Significantly increased apoptosis-related proteins—cleaved caspase-3 and cleaved PARP—were observed in cells treated with gemcitabine plus thiostrepton (Figure 4C). Apoptosis induced by gemcitabine plus thiostrepton was more significant compared with that induced by gemcitabine or thiostrepton alone (Figure 4C).

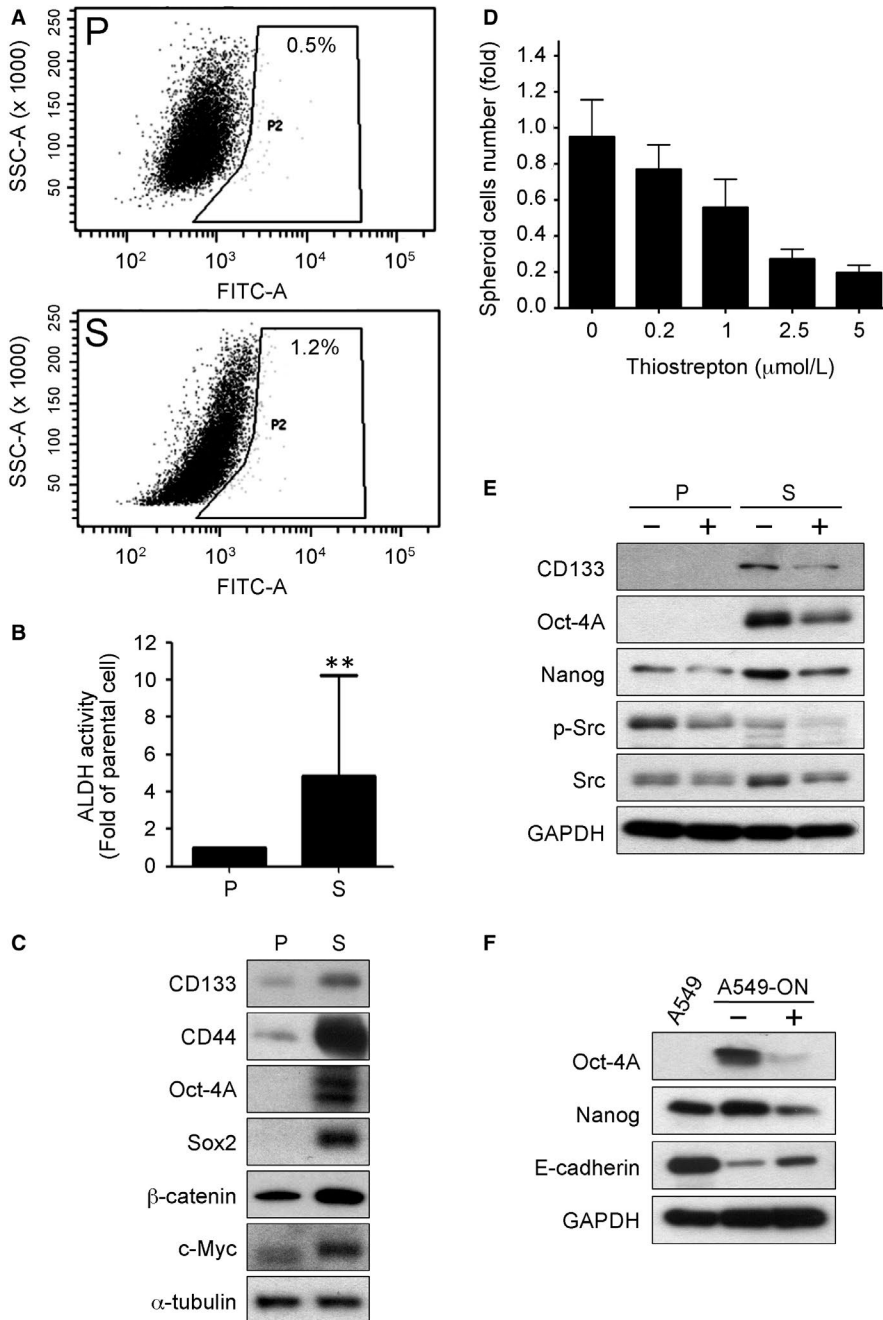


**FIGURE 3** Thiostrepton inhibits cancer stem cell properties. A, Flow cytometric analysis demonstrated that CL141 spheres (S) exhibited a higher percentage of ALDH1<sup>+</sup> cells compared with the CL141 parental cells (P). B, Quantitative presentation of the relative ALDH activity in CL141 spheres (S) compared with CL141 parental cells (P). C, Western blotting assay indicated that CL141 spheres (S) expressed a significantly higher level of CD133, CD44, Oct-4A and Sox2 (CSC markers) as well as  $\beta$ -catenin and c-Myc (oncogenic markers) compared with their parental counterparts (P). D, Thiostrepton suppressed tumour sphere formation in CL141 cells in a dose-dependent manner. E, Comparative western blotting assay of parental cells (P) and spheres (S) showed that thiostrepton treatment led to decreased expression of CD133, Oct-4A, Nanog (CSC markers) and metastasis-associated Src signalling. F, In the Oct-4A/Nanog overexpressing A549 (A549-ON) cells, thiostrepton treatment significantly decreased the expression of both cancer stem cell markers, Oct-4A and Nanog, and increased E-cadherin expression

Furthermore, the combination of thiostrepton and gemcitabine suppressed expression of stemness markers, such as Sox2,  $\beta$ -catenin and EMT transcription factor Slug in both CL141 and CL152 cells (Figure 4D), indicating that the combination of thiostrepton and gemcitabine suppresses stemness- and EMT-related profiles in both adenocarcinoma and squamous cell carcinoma cells. This finding suggests thiostrepton could reduce cancer stem-like cell populations and decrease the risk of distant metastasis.

We also characterized the combination treatment on CL141 parental cells and tumour spheres. Thiostrepton, with or without gemcitabine, was able to suppress CD133 expression, whereas gemcitabine treatment did not (Figure 4E). Importantly, CL141 spheres responded to a lower concentration of thiostrepton

(1  $\mu$ mol/L), as reflected by significantly decreased CD133 levels (Figure 4E). In the presence of thiostrepton, CL141 spheres also responded to gemcitabine at a lower concentration and underwent apoptotic cell death as reflected by the elevated level of cleavage of PARP.

### 3.5 | Thiostrepton inhibits NSCLC tumorigenesis and decreases the proportion of CSC in vivo

NOD/SCID mice that received daily thiostrepton treatment ( $n = 5$ ) exhibited a significantly slower tumour growth rate than mice receiving the vehicle treatment ( $n = 5$ ) at the fifth week,

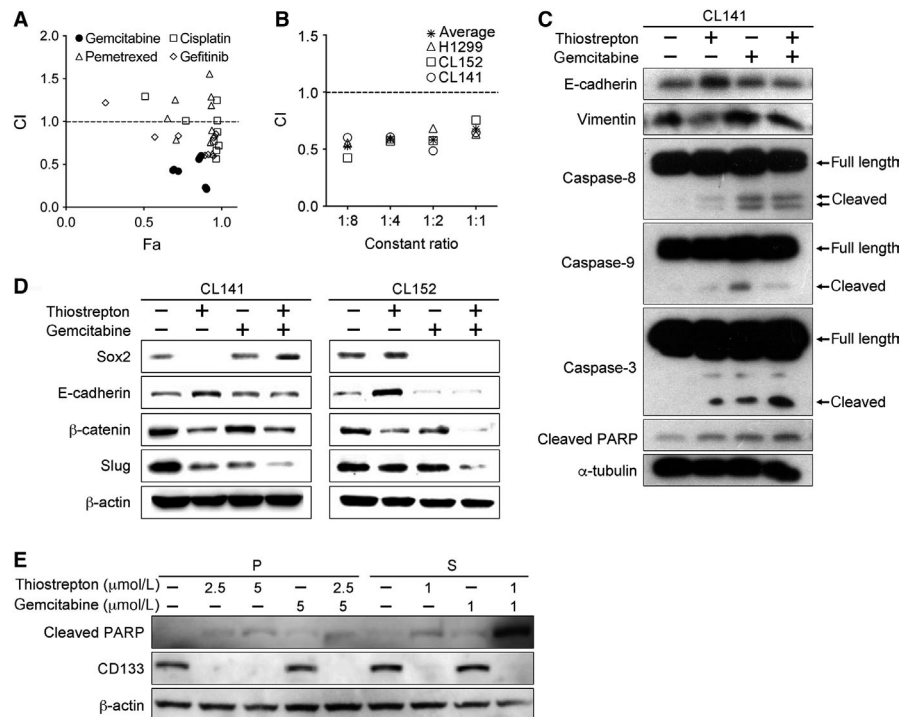


**FIGURE 4** Thiostrepton combined with anti-cancer drugs exhibits a synergistic effect on NSCLC growth. A, Fa-CI plot represents the CI values and the Fa (fraction affected, cytotoxic effect) at different concentrations of thiostrepton (1.25, 2.5, and 5 μmol/L) in combination with different chemotherapeutic drugs (pemetrexed, cisplatin, gemcitabine) or gefitinib (5, 10, and 20 μmol/L) for 48 h in CL152 cells. A combination of thiostrepton and gemcitabine showed the highest synergistic effect among the combinations. The data were analysed by CompuSyn software. B, Thiostrepton was combined with gemcitabine at different dosing ratios (1:1, 1:2, 1:4 or 1:8) in CL141, CL152 and H1299 cells. All combinations demonstrated synergistic anti-NSCLC effects. C, Western blotting assays for CL141 cells treated with thiostrepton and/or gemcitabine. The combination of thiostrepton and gemcitabine effectively reversed EMT and induced apoptosis. D, Comparative Western blotting assays of CL141 and CL152 cells with treatments of thiostrepton, gemcitabine, or thiostrepton plus gemcitabine. Thiostrepton treatment significantly suppressed the expression of β-catenin (stemness marker) and Slug (EMT marker). When combined with gemcitabine, the suppressive effect was more pronounced in CL152 cells. E, Western blotting assays of CL141 (P) and CL141 spheres (S) treated with thiostrepton and/or gemcitabine. The combination of thiostrepton and gemcitabine effectively suppressed the elevated CD133 expression in the CL141 spheres and induced the apoptotic marker-cleaved PARP

as demonstrated by approximately 2-fold smaller in tumour size (Figure 5A). The body weight of the mice did not change significantly during the treatment period (Figure 5B). Photographs of harvested tumour samples showed that thiostrepton treatment significantly suppressed tumour growth compared with control counterparts (Figure 5C). Further analysis of the tumour samples revealed that thiostrepton-treated tumours contained a significantly lower proportion of CD133<sup>+</sup> cells (5.6%) compared with those of the control group (16.1%) (Figure 5D).

### 3.6 | Thiostrepton treatment was associated with an increase in tumour suppressor miR-98

MicroRNAs have been extensively characterized and identified in lung cancer and reportedly to play an important promoter or suppressor role, depending on their target genes.<sup>37-39</sup> We examined a panel of microRNAs in response to thiostrepton treatment in CL141 cells, and the miR-98 level appeared to be elevated by approximately 1.5-fold (Figure 6A). By comparison, CL141 parental cells contained a significantly higher level of intrinsic miR-98 than their sphere

counterparts (Figure 6B). The level of miR-98 rose in the wake of thiostrepton treatment in both CL141 parental cells and spheres (Figure 6B).

By increasing miR-98 (mimic molecules) levels, Sox2, Oct-4A and β-catenin were suppressed in both CL141 and CL152 cells (Figure 6C). This was similar to the response to thiostrepton treatment in CL141 cells. Based on the decreased expression of Slug, EMT was considered reversed (Figure 6C). These findings suggest that the suppression of CSC characteristics and EMT by thiostrepton is through up-regulation of tumour suppressor miR-98.

## 4 | DISCUSSION

In this study, thiostrepton was identified as a potential drug for converting embryonic stem cell-like gene signatures to those of adult stem cell gene signatures. Through in vitro and in vivo experiments, we demonstrated that thiostrepton effectively inhibited lung CSC growth by the suppressing cancer stemness and expression of EMT genes. A combination of thiostrepton and gemcitabine synergistically

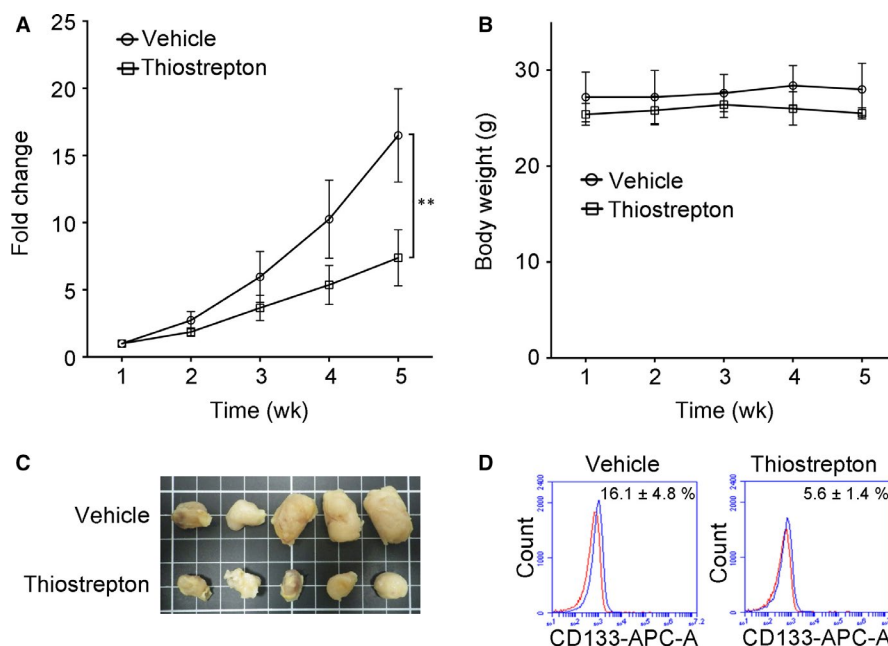


**FIGURE 5** In vivo evaluation of anti-NSCLC tumour growth effect of thiostrepton. A, H441 tumour-bearing NOD/SCID mice were used to evaluate the thiostrepton-mediated suppressive effect on tumour growth. Tumour burden (fold change in the tumour size) is plotted over time. The insert depicts photographs of the tumour samples collected. Thiostrepton treatment (5 mg/kg/d, 5 d/wk, intraperitoneal injection) inhibited H441 tumour growth compared with the vehicle control group after 4 wk of treatment.  $**P < .01$ . B, The treatment did not negatively affect the body weight of the animals during the experiment course. C, A photograph of tumours collected from mice in both thiostrepton-treated and vehicle control group. D, Flow cytometric analysis of tumours demonstrated that thiostrepton treatment significantly decreased the percentage of cells with stem cell marker CD133 expression (presented by the blue peak while the red peak indicates the isotype)

suppressed NSCLC cell growth. This exploratory methodology connecting disease, genes and chemical profiles represents an alternative approach to the development of novel therapeutic agents.

In tumour sphere assays, increased EMT potential and expression of CSC markers were showed in NSCLC cells. This finding is in agreement with the previously established hypothesis that enhanced EMT potential is positively associated with the generation of CSCs.<sup>25,40</sup> In addition, the well-established CSC marker, CD133, was shown to be associated with up-regulated expression of EMT-related genes, including Src and Slug.<sup>41,42</sup> A recent study reported that FOXM1 directly and constitutively activates Snail in lung adenocarcinoma, thereby promoting cancer metastasis.<sup>43</sup> Knockdown FOXM1 significantly suppressed EMT progression as well as tumour growth and metastasis.<sup>43</sup> However, we demonstrated that thiostrepton treatment did not inhibit Snail expression but strongly inhibited Slug expression in NSCLC cells. These findings indicate that the CD133/Src axis, in addition to FOXM1, is a potential therapeutic target for thiostrepton. Thiostrepton treatment not only inhibited CSC markers including CD133, Oct-4A and Sox2, but also restored E-cadherin expression, thereby reversing the EMT and generation of cancer spheres. This finding further supports an association between the EMT and CSC.

Ectopic expression of Oct4 and Nanog in lung cancer cells was associated with a significant increase in the percentage of CD133+ cell and mesenchymal cell populations, the ability to form tumour spheres and enhanced drug resistance.<sup>25</sup> To provide further support

the contention that thiostrepton is a potential anti-CSC agent, we utilized a cell model that A549 cells with overexpression of Oct-4A/Nanog exhibits enhanced CSC characteristics and EMT potential. Thiostrepton treatment not only significantly suppressed ectopic expression of both Nanog and Oct-4A in the A549-ON cells, but also markedly induced epithelial marker E-cadherin. These findings verify our bioinformatical prediction that thiostrepton treatment is associated with the reversal of CSC gene signatures, EMT status and CSC growth inhibition.

Thiostrepton reportedly enhances sensitivity to platinum in vitro and in vivo.<sup>44</sup> It has also been reported that cisplatin treatment significantly increases the proportion of CD133+ cells through the Notch signal pathway, and CD133+ cells are related to an increase in cross-drug resistance to paclitaxel and doxorubicin.<sup>26</sup> Therefore, the reduction in CD133+/Oct-4A+ cell populations in NSCLC by thiostrepton treatment (Figure 3) provides further support for a role for thiostrepton in combination with chemo- and/or target therapeutic agents in preventing drug resistance. Thiostrepton acted synergistically with gemcitabine to inhibit lung cancer cellular viability in this study.

The GSEA results of thiostrepton and thiostrepton plus gemcitabine with concomitant enrichment scores were related to GSE18931 (Table S2), which was evaluated for CSC gene signatures with impacts on clinical outcomes and the pathological features of cancer.<sup>30</sup> The gene signature of thiostrepton treatment with a positive enrichment score was also significantly related to GSE17215, an anti-CSC gene signature associated with EMT. Decreased CSCs

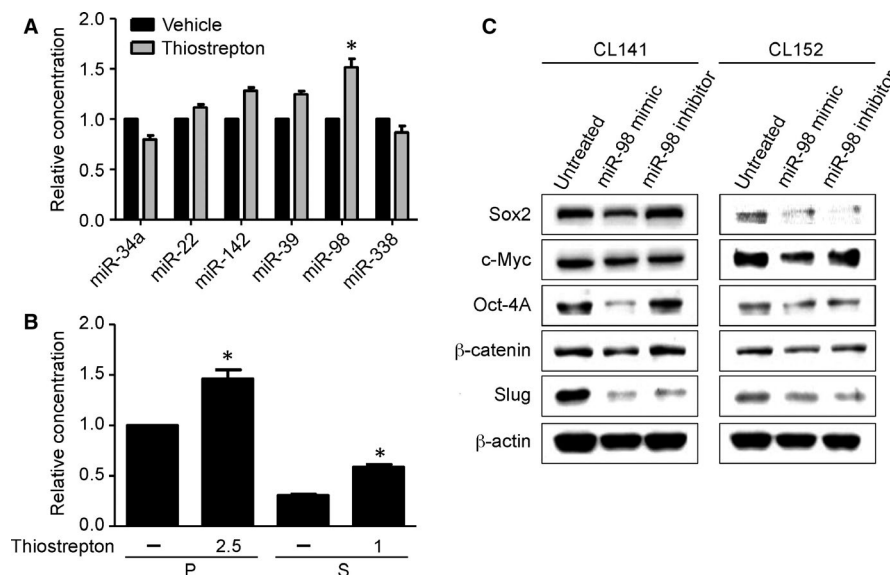


**FIGURE 6** Thiostrepton-mediated anti-lung CSC effect is associated with an elevated miR-98 level. A, A panel of microRNAs was examined in CL141 cells, and the miR-98 level was the most elevated after thiostrepton treatment. B, Comparative quantitative PCR analysis demonstrated that thiostrepton treatment induced elevation of miR-98 levels in both CL141 parental (P) and sphere (S) cells. \* $P < .05$  (C) Western blotting assays of miR-98-mediated effects in both CL141 and CL152 cells. Cancer stemness/EMT markers, including Sox2, Oct-4A and  $\beta$ -catenin, were significantly suppressed when miR-98 mimic was added. In contrast, when treated with miR-98 inhibitor, increases in Sox2 and Oct-4A expression were observed in CL141 cells

after drug treatment may prevent tumours from EMT. This finding provides evidence to link the CSC state with EMT. Thiostrepton may follow the same path as salinomycin in reverting M-type cells back to E-type cells.<sup>35</sup> Chemotherapy combined with thiostrepton may therefore be an alternative regimen to improve treatment effectiveness and prolong survival in patients with NSCLC.

Chemotherapy is still a major treatment option for lung squamous cell carcinoma. Thiostrepton in combination with gemcitabine significantly inhibited lung squamous cell carcinoma growth. However, cellular responses towards different treatment regimens varied between adenocarcinoma and squamous cell carcinoma cells. As shown in Figure 4D, thiostrepton alone significantly suppressed Sox2,  $\beta$ -catenin and Slug expression to a greater extent in CL141 cells than in CL152 cells. While gemcitabine treatment alone appeared to suppress Sox2 expression more significantly in CL152 cells, the suppressive effect of stemness and EMT was more pronounced (Figure 4D). Our previous study showed that thiostrepton can suppress colony and sphere formation and trigger apoptosis of colorectal cancer stem cells in HCT-15 and HT-29 cells as well as EMT and chemo-resistant clones derived from them.<sup>45</sup> These findings indicate that thiostrepton in combination with chemotherapies may improve treatment effectiveness in lung squamous cell carcinoma.

In this study, an increased level of miR-98 (a tumour suppressor) was observed in response to thiostrepton treatment. Because miR-98 is reportedly down-regulated in many cancer types, its targets, such as Myc, Kras and Wnt signalling, are generally oncogenic.<sup>46-48</sup> The exact targets for thiostrepton-induced miR-98 induction in NSCLC warrant further investigation.

In conclusion, thiostrepton was identified as a potential CSC inhibitor for lung cancer using an integrative bioinformatics and

pre-clinical approach. In combination with chemotherapeutic agents, especially gemcitabine, thiostrepton synergistically suppressed NSCLC growth and tumour spheres formation. An elevated miR-98 level was associated with thiostrepton treatment. These pre-clinical evidence warrants further clinical studies for thiostrepton in patients with NSCLC.

## ACKNOWLEDGEMENTS

This study was partially supported by grants from the Ministry of Science and Technology of Taiwan (MOST107-2320-B-182A-007-) and Chang-Gung Memorial Hospital Research Foundation (CMRPG2G0331 and CMRPG2G0332) to Tse-Hung Huang, by grant from 102CM-TMU-03 to Alexander T. H. Wu, by grants from the Ministry of Science and Technology of Taiwan (MOST107-2320-B-010-040-MY3), the Veterans General Hospitals and University System of Taiwan Joint Research Program (VGHUST108-G1-4-1) and NYMU-FEMH Joint Research Program (106DN20) to Chi-Ying F. Huang, and by grants from the Ministry of Science and Technology of Taiwan (MOST106-2314-B-002-102-MY3) to Kuan-Yu Chen.

## CONFLICT OF INTEREST

The authors have no conflict of interest.

## AUTHOR CONTRIBUTIONS

Tse-Hung Huang, Chi-Ying F. Huang and Kuan-Yu Chen designed research; Alexander T. H. Wu, Tai-Shan Cheng, Kuan-Ting Lin, Chia-Jou



Lai, Hao-Wen Hsieh and Peter Mu-Hsin Chang analysed data; Tse-Hung Huang, M. Alexander T. H. Wu, Tai-Shan Cheng, Kuan-Ting Lin, Chia-Jou Lai, Hao-Wen Hsieh and Peter Mu-Hsin Chang performed research; Tse-Hung Huang, Alexander T. H. Wu, Tai-Shan Cheng, Chi-Ying F. Huang and Kuan-Yu Chen wrote the paper; Tse-Hung Huang, Peter Mu-Hsin Chang and Cheng-Wen Wu contributed new reagents or analytic tools.

## DATA AVAILABILITY STATEMENT

The data sets generated and analysed during this study are available from the corresponding author on reasonable request.

## ORCID

Chi-Ying F. Huang  <https://orcid.org/0000-0003-4898-4937>

## REFERENCES

- Siegel R, Ma J, Zou Z, Jemal A. Cancer statistics, 2014. *CA: Cancer J Clin.* 2014;64(1):9-29.
- DeSantis CE, Lin CC, Mariotto AB, et al. Cancer treatment and survivorship statistics, 2014. *CA: Cancer J Clin.* 2014;64(4):252-271.
- Siegel RL, Miller KD, Jemal A. Cancer statistics, 2018. *CA Cancer J Clin.* 2018;68:7-30.
- Stinchcombe TE, Socinski MA. Current treatments for advanced stage non-small cell lung cancer. *Proc Am Thorac Soc.* 2009;6:233-241.
- Gronberg BH, Bremnes RM, Flotten O, et al. Phase III study by the Norwegian lung cancer study group: pemetrexed plus carboplatin compared with gemcitabine plus carboplatin as first-line chemotherapy in advanced non-small-cell lung cancer. *J Clin Oncol.* 2009;27:3217-3224.
- Sadowska AM, Nowe V, Janssens A, Boeykens E, De Backer WA, Germonpre PR. Customizing systemic therapy in patients with advanced non-small cell lung cancer. *Ther Adv Med Oncol.* 2011;3:207-218.
- Schiller JH, Harrington D, Belani CP, et al. Eastern cooperative oncology G. Comparison of four chemotherapy regimens for advanced non-small-cell lung cancer. *N Engl J Med.* 2002;346:92-98.
- Scagliotti GV, Parikh P, von Pawel J, et al. Phase III study comparing cisplatin plus gemcitabine with cisplatin plus pemetrexed in chemotherapy-naïve patients with advanced-stage non-small-cell lung cancer. *J Clin Oncol.* 2008;26:3543-3551.
- Galluzzi L, Vitale I, Michels J, et al. Systems biology of cisplatin resistance: past, present and future. *Cell Death Dis.* 2014;5:e1257.
- Shanker M, Willcutts D, Roth JA, Ramesh R. Drug resistance in lung cancer. *Lung Cancer (Auckl).* 2010;1:23-36.
- Bao S, Wu Q, McLendon RE, et al. Glioma stem cells promote radioresistance by preferential activation of the DNA damage response. *Nature.* 2006;444:756-760.
- Diehn M, Cho RW, Lobo NA, et al. Association of reactive oxygen species levels and radioresistance in cancer stem cells. *Nature.* 2009;458:780-783.
- Clevers H. The cancer stem cell: premises, promises and challenges. *Nat Med.* 2011;17:313-319.
- Eramo A, Lotti F, Sette G, et al. Identification and expansion of the tumorigenic lung cancer stem cell population. *Cell Death Differ.* 2008;15:504-514.
- Pirozzi G, Tirino V, Camerlingo R, et al. Epithelial to mesenchymal transition by TGFbeta-1 induction increases stemness characteristics in primary non small cell lung cancer cell line. *PLoS ONE.* 2011;6:e21548.
- Leung EL, Fiscus RR, Tung JW, et al. Non-small cell lung cancer cells expressing CD44 are enriched for stem cell-like properties. *PLoS ONE.* 2010;5:e14062.
- Wang P, Gao Q, Suo Z, et al. Identification and characterization of cells with cancer stem cell properties in human primary lung cancer cell lines. *PLoS ONE.* 2013;8:e57020.
- Wu Y, Wu PY. CD133 as a marker for cancer stem cells: progresses and concerns. *Stem Cells Dev.* 2009;18:1127-1134.
- Chen K, Huang YH, Chen JL. Understanding and targeting cancer stem cells: therapeutic implications and challenges. *Acta Pharmacol Sin.* 2013;34:732-740.
- Chen PC, Liu X, Lin Y. Drug repurposing in anticancer reagent development. *Comb Chem High Throughput Screening.* 2017;20(5):395-402.
- Lamb J, Crawford ED, Peck D, et al. The Connectivity Map: using gene-expression signatures to connect small molecules, genes, and disease. *Science.* 2006;313:1929-1935.
- Bagley MC, Dale JW, Merritt EA, Xiong X. Thiopeptide antibiotics. *Chem Rev.* 2005;105:685-714.
- Hegde NS, Sanders DA, Rodriguez R, Balasubramanian S. The transcription factor FOXM1 is a cellular target of the natural product thioestrepont. *Nature chemistry.* 2011;3:725-731.
- Bhat UG, Halasi M, Gartel AL. Thiazole antibiotics target FoxM1 and induce apoptosis in human cancer cells. *PLoS ONE.* 2009;4:e5592.
- Chiou SH, Wang ML, Chou YT, et al. Coexpression of Oct4 and Nanog enhances malignancy in lung adenocarcinoma by inducing cancer stem cell-like properties and epithelial-mesenchymal trans-differentiation. *Cancer Res.* 2010;70:10433-10444.
- Liu YP, Yang CJ, Huang MS, et al. Cisplatin selects for multidrug-resistant CD133+ cells in lung adenocarcinoma by activating Notch signaling. *Cancer Res.* 2013;73:406-416.
- Wawer MJ, Li K, Gustafsdottir SM, et al. Toward performance-diverse small-molecule libraries for cell-based phenotypic screening using multiplexed high-dimensional profiling. *Proc Natl Acad Sci USA.* 2014;111:10911-10916.
- George J, Lim JS, Jang SJ, et al. Comprehensive genomic profiles of small cell lung cancer. *Nature.* 2015;524:47-53.
- Suva ML, Riggi N, Janiszewska M, et al. EZH2 is essential for glioblastoma cancer stem cell maintenance. *Can Res.* 2009;69:9211-9218.
- Pece S, Tosoni D, Confalonieri S, et al. Biological and molecular heterogeneity of breast cancers correlates with their cancer stem cell content. *Cell.* 2010;140(1):62-73.
- Vichai V, Kirtikara K. Sulforhodamine B colorimetric assay for cytotoxicity screening. *Nat Protoc.* 2006;1:1112-1116.
- Chou TC, Talalay P. Quantitative analysis of dose-effect relationships: the combined effects of multiple drugs or enzyme inhibitors. *Adv Enzyme Regul.* 1984;22:27-55.
- Chou TC. Theoretical basis, experimental design, and computerized simulation of synergism and antagonism in drug combination studies. *Pharmacol Rev.* 2006;58:621-681.
- Ginestier C, Hur MH, Charafe-Jauffret E, et al. ALDH1 is a marker of normal and malignant human mammary stem cells and a predictor of poor clinical outcome. *Cell Stem Cell.* 2007;1:555-567.
- Gupta PB, Onder TT, Jiang G, et al. Identification of selective inhibitors of cancer stem cells by high-throughput screening. *Cell.* 2009;138:645-659.
- Safa AR. Resistance to cell death and its modulation in cancer stem cells. *Crit Rev Oncog.* 2016;21:203-219.
- Inamura K, Ishikawa Y. MicroRNA in lung cancer: novel biomarkers and potential tools for treatment. *J Clin Med.* 2016;5(3):36.
- Levy B, Hu ZI, Cordova KN, Close S, Lee K, Becker D. Clinical utility of liquid diagnostic platforms in non-small cell lung cancer. *Oncologist.* 2016;21:1121-1130.

39. Maltby S, Plank M, Tay HL, Collison A, Foster PS. Targeting MicroRNA function in respiratory diseases: mini-review. *Front Physiol.* 2016;7:21.
40. Mani SA, Guo W, Liao MJ, et al. The epithelial-mesenchymal transition generates cells with properties of stem cells. *Cell.* 2008;133:704-715.
41. Chen YS, Wu MJ, Huang CY, et al. CD133/Src axis mediates tumor initiating property and epithelial-mesenchymal transition of head and neck cancer. *PLoS ONE.* 2011;6:e28053.
42. Ding Q, Miyazaki Y, Tsukasa K, Matsubara S, Yoshimitsu M, Takao S. CD133 facilitates epithelial-mesenchymal transition through interaction with the ERK pathway in pancreatic cancer metastasis. *Mol Cancer.* 2014;13:15.
43. Wei P, Zhang N, Wang Y, et al. FOXM1 promotes lung adenocarcinoma invasion and metastasis by upregulating SNAIL. *Int J Biol Sci.* 2015;11:186-198.
44. Zhang X, Cheng L, Minn K, et al. Targeting of mutant p53-induced FoxM1 with thiostrepton induces cytotoxicity and enhances carboplatin sensitivity in cancer cells. *Oncotarget.* 2014;5:11365-11380.
45. Ju SY, Huang CY, Huang WC, Su Y. Identification of thiostrepton as a novel therapeutic agent that targets human colon cancer stem cells. *Cell Death Dis.* 2015;6:e1801.
46. Ni R, Huang Y, Wang J. miR-98 targets ITGB3 to inhibit proliferation, migration, and invasion of non-small-cell lung cancer. *Onco Targets Ther.* 2015;8:2689-2697.
47. Yang G, Zhang X, Shi J. MiR-98 inhibits cell proliferation and invasion of non-small cell carcinoma lung cancer by targeting PAK1. *Int J Clin Exp Med.* 2015;8:20135-20145.
48. Jiang P, Wu X, Wang X, Huang W, Feng Q. NEAT1 upregulates EGCG-induced CTR1 to enhance cisplatin sensitivity in lung cancer cells. *Oncotarget.* 2016;7(28):43337-43351.

## SUPPORTING INFORMATION

Additional supporting information may be found online in the Supporting Information section.

**How to cite this article:** Huang T-H, Wu ATH, Cheng T-S, et al. In silico identification of thiostrepton as an inhibitor of cancer stem cell growth and an enhancer for chemotherapy in non-small-cell lung cancer. *J Cell Mol Med.* 2019;23:8184-8195. <https://doi.org/10.1111/jcmm.14689>



# The effects of Jilin sika Deer's (*Cervus dybowskii*) tendon liquid supplementation on endurance drop jumps performance, biochemistry profile of free boxing players

I-Lin Wang (Ph.D.)<sup>a,1</sup>, Chien-Yu Hsiao<sup>b,c,d,1</sup>, Jiayu Shen<sup>a</sup>, Yanmei Wang<sup>e,f</sup>,  
Chi-Chang Huang (Ph.D.)<sup>g</sup>, Yi-Ming Chen (Ph.D.)<sup>a,\*</sup>

<sup>a</sup> Health Technology College, Jilin Sport University, Changchun, 130022, Jilin, China

<sup>b</sup> Department of Nutrition and Health Sciences, Chang Gung University of Science and Technology, Taoyuan, 33301, Taiwan

<sup>c</sup> Research Center for Industry of Human Ecology and Research Center for Chinese Herbal Medicine, College of Human Ecology, Chang Gung University of Science and Technology, Taoyuan, 33301, Taiwan

<sup>d</sup> Aesthetic Medical Center, Department of Dermatology, Chang Gung Memorial Hospital, Taoyuan, 33301, Taiwan

<sup>e</sup> Changchun Sci-Tech University, Changchun, 130600, Jilin, China

<sup>f</sup> Jilin Sino-ROK Institute of Animal Science, 130600, Jilin, China

<sup>g</sup> Graduate Institute of Sports Science, National Taiwan Sport University, Taoyuan, 33301, Taiwan

## ARTICLE INFO

### Keywords:

Tendon of deer liquid (TD)  
Maximal oxygen consumption  
Clinical biochemistry  
Drop vertical jumps (DVJs)  
Endurance exercise performance

## ABSTRACT

**Ethnopharmacological relevance:** Risk of anterior cruciate ligament is a persistent and severe problem in athletes owing to strenuous exercise-induced lower-body injury. Tendon of deer liquid (TD) a familiar traditional Chinese medicine, has been used for strengthening the bones and muscles.

**Aim of the study:** In this study, we seek to demonstrate the application of TD in improving endurance exercise performance and reducing the risk of endurance training injury for free boxing players.

**Materials and methods:** Sixteen male free boxing players were randomly assigned to the TD and placebo groups. Body composition, clinical biochemistry profiles, kinematic and physiology exercise tests were evaluated at 2 time points – pre-supplementation (pre-) and after 6 weeks post-supplementation (post-).

**Results:** TD group exhibited significant increase in levels of serum total protein (TP) compared to the placebo group after a 6-week supplementation. Following the treadmill test, serum glucose and maximal oxygen consumption (VO<sub>2</sub> max) levels were increased in the TD group. In the endurance test consisting of 200 counts of drop vertical jumps (DVJs), subjects in the TD group also showed an increase in vertical jump height and reduced risk of musculoskeletal system injuries.

**Conclusions:** TD supplementation leads to better physiological adaptation in free boxing players and has the potential for use as a nutrient supplement toward a variety of benefits for endurance athletes.

## 1. Introduction

Jilin Province is a major source of sika deers (*Cervus dybowskii*) in China. The domesticated sika deer population in China is approximately 550,000 with the Jilin Province accounting for more than 50% of the deer livestock industry (Qin et al., 2014). Sika deer is a northeastern subspecies mainly inhabiting the Changbai mountains of Jilin. Due to its markedly decreasing wild population, their capture from the wild

was previously prohibited. Subsequently, the breeding industry gradually developed and spread throughout Jilin (Wu et al., 2004). In the Compendium of Materia Medica, a Chinese herbology volume, the pilose antler of the sika deer has been recorded for use to treat many diseases (Tseng et al., 2012; Zhang et al., 2013). The use of the sika deer in many products and nutritional supplements gradually extended to its different parts including the antler tendon and blood (Cong et al., 2016; Prokopov et al., 2019; Tseng et al., 2012).

\* Corresponding author. Health Technology College, Jilin Sport University, No. 2476, Ziyouda Road, Nangan District, Changchun, 130022, Jilin, China, Tel. +8613843168711.

E-mail addresses: [ilin.wang@hotmail.com](mailto:ilin.wang@hotmail.com) (I.-L. Wang), [mozart@gw.cgust.edu.tw](mailto:mozart@gw.cgust.edu.tw) (C.-Y. Hsiao), [wjysjy51212@gmail.com](mailto:wjysjy51212@gmail.com) (J. Shen), [jyjszx@cstu.edu.cn](mailto:jyjszx@cstu.edu.cn) (Y. Wang), [john5523@ntsu.edu.tw](mailto:john5523@ntsu.edu.tw) (C.-C. Huang), [1021302@ntsu.edu.tw](mailto:1021302@ntsu.edu.tw) (Y.-M. Chen).

<sup>1</sup> These authors contributed equally to this work.

<https://doi.org/10.1016/j.jep.2019.112119>

Received 23 May 2019; Received in revised form 15 July 2019; Accepted 23 July 2019

Available online 31 July 2019

0378-8741/ © 2019 The Authors. Published by Elsevier B.V. This is an open access article under the CC BY-NC-ND license (<http://creativecommons.org/licenses/by-nc-nd/4.0/>).

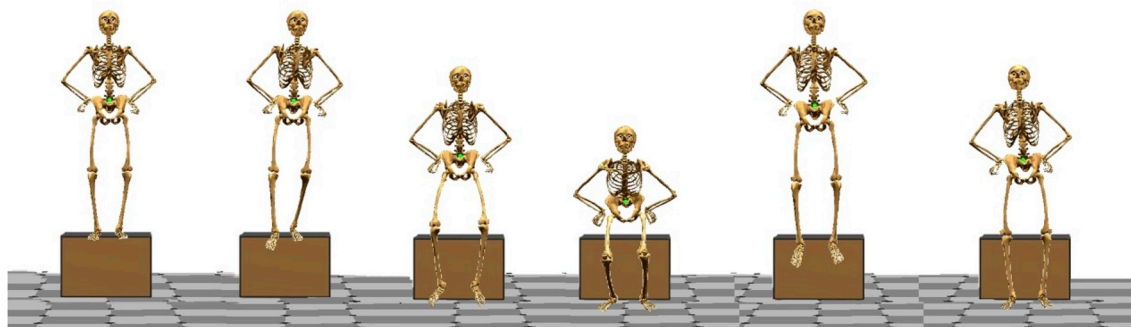


**Fig. 1.** Schematic of the study design on 200 counts of endurance drop vertical jumps (DVJs). Subjects were required to keep their hands on the hips and performed the DVJs by stepping off a raised platform onto two force platforms. They were instructed to perform the DVJs by stepping off a raised platform with their dominant leg sticking out from the platform and as soon as they touched the ground, to immediately perform a maximum vertical jump. A total of 200 counts of DVJs was performed for each subject.

Athletes are often interested in finding ways to be quicker, stronger and to improve their endurance. They often experiment on new training regimens and different food and/or beverage intake to improve performance (Momaya et al., 2015). Certain substances or drugs are termed ergogenic, i.e. they are able to enhance performance by improving exercise energy efficiency, strength, condition and endurance (Garthe and Maughan, 2018; Peeling et al., 2018). For centuries, dietary supplements that function as ergogenic aids have been used by athletes for a hosts of reasons, including to accelerate the exercise recovery, improve exercise performance, maintain health, and to compensate for diets that are inadequate in fulfilling the needs of an athlete (Knapik et al., 2016; Slesinski et al., 1995). For these reasons, animal food and beverage products e.g. chicken essence are popularly consumed amongst the adult Asian population, with their efficacy in exercise performance continually being studied (Huang et al., 2018; Huang et al., 2014).

In many old medicinal books and modern pharmacopeias for Traditional Chinese Medicine, deer tendon and other organs/tissues have been widely used as vitalising, tonifying, hemopoietic and strengthening agents for debilitated persons (Xu et al., 2018). However, to date, there has been very little scientific research on the deer tendon. A previous Chinese study (not listed on the Pubmed) investigated the composition of deer tendon and found that it has a higher mineral content than venison. Studies have also shown that collagen from the tendon of sika deer, a by-product of the meat industry, may be an important collagen source for use in the foods, cosmetics and medical fields (Nagai et al., 2012). In our previous study of animal study, we demonstrated that the pilose antler (*Cornu Cervi Pantotrichum*) could significantly increase exercise performance and mitigate the increase of physiological biomarkers induced by explosive exercise (Huang et al., 2014). Deer products may also contain other animal or plant materials (Zha et al., 2010). The use of tendon of deer (TD) in sports nutrition supplements warrants further investigations.

Although the Sika deer is one of best known Traditional Chinese Medicine, ecologists and conservation biologists pay little attention to the conservation and sustainable harvesting of the animals (Whiting et al., 2013). We need to adopt the necessary conservation measures so that overharvesting of this species will not lead to their extinction and consequently, the loss of this medicinal source (Alves and Rosa, 2013).

Currently, there is no study that directly address the possible ergogenic or anti-fatigue functions of tendon of deer liquid (TD). Therefore, this study seeks to evaluate the beneficial health effects of a 6-week TD supplementation in humans. This study was performed in accordance with our previously established experimental models to investigate the effects of physiological, physical adaptation and physical activities (Huang et al., 2017; Huang et al., 2018).

## 2. Methods

### 2.1. Preparation of tendon of sika deer liquid (TD)

Tendon of sika deer liquid (TD, Batch number: 43884216883) was provided by Dong Ao Deer Industry Group (Jilin, China). The deer's tendon meat was sealed in the can, stirred five times a day, soaked for 30 days in a solution of wine, water, sugar, polygonatum, wolfberry, scutellaria, clove, raspberry, Coix seed, anise, and tendon of deer. After 30 days, the extract was filtered and merged with the extract residue. After clarification, the extract is combined with the residue, sucrose is added and stirred till it dissolves, and extract is sealed again and left to stand for 15 days before filtration. TD was lyophilized by freeze-drying to obtain a powder extract. The TD used is a commercially available preparation that contains a large amount of collagen, a variety of amino acids, chondroitin sulfate, peptides, lipids, calcium, phosphorus and magnesium. Based on a previous supplement study, the daily recommended dose of TD in humans is 66.67 mg/kg (Huang et al., 2018).

### 2.2. Study design

This single center, randomized, placebo-controlled, double-blind, parallel group trial was approved by the Joint Institutional Review Board of Jilin Sport University (Changchun, China; JLSU-IRB no. 2018002). Subjects used in this study were volunteers from Jilin Sport University (JLSU). The subjects gave informed consent for inclusion before enrolment into the study which was conducted in accordance with the Declaration of Helsinki. After enrolment, subjects were randomly allocated to 2 groups: Tendon of sika deer liquid (TD) or placebo (glucose liquid) group. Each group ( $n = 8$ ) consumed TD or placebo at 50 mL/day daily before breakfast for 6 consecutive weeks (Fig. 1). Both TD and placebo were isocaloric at 105 kcal/day. Subjects attended 2 study visits on Day 0 (pre-test) and Day 42 (post-test). The post-test visit was arranged after the last supplementation. Body composition and effect on exercise performance were measured at these visits.

### 2.3. Subjects

Sixteen male Jilin Sport University free boxing club players volunteered to participate in this study. All subjects undergo regular free boxing training program and individuals were excluded from the study if they had any known metabolic disorders, heart/cardiopulmonary diseases, diabetes, thyroid disease, hypogonadism, hepatorenal disease, musculoskeletal disorders, neuromuscular/neurological diseases, autoimmune diseases, cancer, peptic ulcers or anemia. Subjects were asked to refrain from any aerobic or anaerobic exercise training while keeping their normal dietary pattern and daily caloric intake under control during the experimental period. Nutritional supplements including

certain types of protein, antioxidants, creatine and steroid supplementation were disallowed. Subjects were randomly assigned to the placebo or TD group and the basic characteristics of age ( $20.4 \pm 1.0$  vs.  $20.1 \pm 0.7$  years), height ( $175.3 \pm 3.9$  vs.  $174.1 \pm 2.9$  cm) and weight ( $64.3 \pm 3.5$  vs.  $63.8 \pm 3.9$  kg) did not significantly differ before and after the study.

#### 2.4. Endurance drop vertical jumps (DVJs) with kinetic and kinematic analysis

All subjects had to complete and familiarize themselves with the test protocol and specific jumping techniques one week before the exercise measurements. The drop-landing tasks was conducted from a 50 cm height. The subjects performed 200 counts DVJs with 60 s intervals between each jump. The subjects all wore the same kind of running shoes. Before the test protocol was carried out, the subjects had to warm up by running for 10 min on the treadmill. The subject stood on box and immediately performed the vertical drop-landing task as quickly as possible, with maximum force. There was a 60 s static recovery between each trial. Subjects were instructed to keep their hands on their waist and step off the platform using their dominant leg. The participants were asked to land using their natural landing style with both feet contacting the ground as symmetrically as possible. The motion simulation is shown in Fig. 1.

#### 2.5. Kinetic and kinematic data collection

A motion capture system (BTS DX400, BTS Bioengineering, Milano, Italy) consisting of ten infrared video cameras collected marker trajectories at a sampling rate of 200 Hz. Two force plates (BTS P6000, BTS Bioengineering, Milano, Italy) measured GRFs data at a sampling rate of 400 Hz. Motion and force plate were time synchronised. Twenty-one retro-reflective markers (19 mm in diameter) defined a seven-segment rigid link model of the lower limb, according to the Helen Hayes Marker set. The jump characteristics were measured 160, 170, 180, 190 and 200 DVJs. Force and marker trajectories from each trial were processed with a smoothing spline and with a 10 Hz cut-off frequency. Vertical ground reaction force was used to identify the time at initial contact with the ground (IC) and at toe off from the jump (TO). The foot contact and take off during the contact phase was determined using a 10 N vertical ground reaction force (vGRF) threshold. The jumping height (H) was calculated using the formula:  $H = gT^2/8$ . The peak vertical ground reaction force (PVGRF) were defined as the maximum PVGRF during the IC and the TO was normalized by body weight (BW). The side-to-side peak vertical ground reaction force (PVGRF) difference was calculated using the following formula:  $|PVGRF_{dominant\ leg} - PVGRF_{non\ dominant\ leg}|$ . The results from the pre-test and post-test were calculated using an average of 5 DVJs.

#### 2.6. Exhausted endurance exercise challenge

All subjects were asked to record their dietary intake and to consume similar foods during the study period. Subjects ate a standardized breakfast of 393 kcal (containing energy as 61.7% carbohydrate, 11.7% protein, and 26.6% fat) in the evening before each test day, thereby minimizing the impact of differences in food/caloric intake on physiological homeostasis. Subjects were pretreated with placebo or TD for 6 weeks before the post exercise performance test, given 1 h after the last consumption of study product. Ventilatory expired gases were obtained during exercise via a face mask using a breath-by-breath respiratory gas analysis system (Schiller ergo-spirometry unit with Ganshorn Power Cube gas analysis). Respiratory gas exchange variables were produced automatically over a 10 s average. Ventilatory threshold was identified by the computerized V-slope method (Katz et al., 1992) and this was cross-checked and confirmed by an experienced observer, in conjunction with plots of ventilatory equivalents and end tidal gas

tensions for  $VO_2$  and  $VCO_2$  (Meyer et al., 2005; Myers et al., 2010). Subjects were told to avoid any strenuous physical activity 3 days before the initial exercise test for  $VO_2$  max assessment. The speed and grade of the treadmill simultaneously increased every 3 min until volitional fatigue in accordance with the Bruce protocol (Bruce et al., 1973). Before and after the exhausted endurance exercise challenge, the biochemical levels of lactate, ammonia ( $NH_3$ ), creatine kinase (CK) and glucose were assessed using the Selectra Pro XL analyzer (Vita lab, Netherlands).

#### 2.7. Clinical biochemistry

At the end of experiment, blood samples were taken after subjects had fasted for at least 8 h. Biochemical levels of aspartate aminotransferase (AST), alanine aminotransferase (ALT), alkaline phosphatase (ALP), lactic dehydrogenase (LDH), creatine kinase (CK), albumin, total protein (TP), blood urea nitrogen (BUN), uric acid (UA), glucose, total cholesterol (TC), triglycerides (TG), high-density lipoprotein (HDL) and low-density lipoprotein (LDL) were assessed using a Beckman Coulter AU5800 autoanalyzer (Beckman Coulter Inc., Brea CA, USA).

#### 2.8. Anthropometric measurements

At the begin and end of experiment, all subjects arrived at the laboratory in the morning for anthropometric measurements including body height (cm), body weight (kg), body-mass index (BMI;  $kg/m^2$ ), basal metabolic rates (BMR), free fat mass (FFM, kg), body fat percentage (%), water content percentage (%) and bone salts (kg). Standing body height was measured without shoes or socks to the nearest 0.1 cm with a height meter mounted on the wall. BW, FFM, body fat, water content and bone salts were measured by a bioelectrical impedance instrument (CH18, HUAWEI Technologies Co., Ltd., Shenzhen, China) using standard methods to assess the body composition.

#### 2.9. Statistical analysis

Statistical analyses were performed using SPSS version 18.0 software (SPSS, Chicago, IL, USA). Data is expressed as the mean  $\pm$  SD. A mixed design two-way analysis of variance (ANOVA) (supplementation  $\times$  time) was used to compare the variables of biochemistry, body composition and exercise performance. A  $p$ -value  $< 0.05$  was considered statistically significant. A post-hoc independent-repeated  $t$ -test was used to determine significance of the main effect or interaction effect.

### 3. Results

#### 3.1. Effects of supplements on biochemical variables

Biochemical results at the indicated points of the experiment can provide clinical information about the physiological adaptation status of TD supplementation. We categorized different parameters according to physiological functions (Table 1). At the pre-test assessment, all biochemical indexes were no significant different with the placebo or TD groups. When we investigated the hepatic indexes AST and ALT, only AST showed significant time effects ( $F(3,28) = 2.299$ ,  $p = 0.015$ ). The TD group did not exhibit a significant AST change compared with placebo at the post-test. We examined for changes in the injury indexes ALP, LDH and CK. LDH showed significant time effect ( $F(3,28) = 7.867$ ,  $p < 0.0001$ ), however BUN, a fatigue-related parameter, was not significantly affected by TD supplementation ( $F(3,28) = 1.671$ ,  $p = 0.05$ ). The nutrition-related indexes albumin, total protein (TP) and glucose were also examined. Albumin and glucose showed significant time effects ( $F(3,28) = 5.290$ ,  $p = 0.029$ ,  $F =$



**Table 1**  
Biochemical analysis with TD supplementation at the end of the experiment.

Parameter	Treatment	Pre-test	Post-test	p values		
				Main effect (Sup.)	Main effect (Times)	Interaction (Sup. x Times)
AST (U/L)	Placebo	23.9 ± 5.0	19.6 ± 5.2	0.835	0.015	0.805
	TD	24.7 ± 5.2	19.6 ± 4.8			
ALT (U/L)	Placebo	20.9 ± 8.1	18.8 ± 11.6	0.142	0.372	0.906
	TD	17.2 ± 3.7	14.5 ± 3.8			
ALP (U/L)	Placebo	119.5 ± 17.9	122.9 ± 43.5	0.366	0.344	0.211
	TD	119.9 ± 27.4	99.6 ± 25.0			
LDH (U/L)	Placebo	185.8 ± 17.0 <sup>b</sup>	145.9 ± 12.5 <sup>a</sup>	0.320	< 0.0001	0.254
	TD	184.8 ± 21.8 <sup>b</sup>	161.0 ± 24.6 <sup>a</sup>			
Albumin (g/dL)	Placebo	49.3 ± 1.4	47.8 ± 1.9	0.117	0.029	0.614
	TD	49.9 ± 1.4	49.0 ± 1.3			
TP (g/L)	Placebo	81.6 ± 3.1 <sup>b</sup>	76.8 ± 3.9 <sup>a</sup>	0.420	0.770	0.002
	TD	78.0 ± 2.1	81.0 ± 3.4 <sup>*</sup>			
BUN (mmol/L)	Placebo	5.4 ± 1.0	5.0 ± 0.7	0.714	0.046	0.474
	TD	5.5 ± 0.9	4.6 ± 1.1			
CK (U/L)	Placebo	308 ± 108 <sup>b</sup>	173 ± 36 <sup>a</sup>	0.575	< 0.0001	0.299
	TD	323 ± 117 <sup>b</sup>	124 ± 39 <sup>a</sup>			
Glucose (mg/dL)	Placebo	94.3 ± 5.4	98.9 ± 6.2	0.714	0.005	0.325
	TD	92.9 ± 4.0 <sup>a</sup>	102.0 ± 8.8 <sup>b</sup>			
TG (mg/dL)	Placebo	70.9 ± 10.5	91.5 ± 10.1	0.412	0.059	0.387
	TD	71.2 ± 33.3	79.1 ± 18.8			
TC (mg/dL)	Placebo	154 ± 18	154 ± 20	0.252	0.721	0.730
	TD	161 ± 29	166 ± 23			
HDL (mg/dL)	Placebo	51 ± 9	50 ± 9	0.116	0.252	0.147
	TD	50 ± 4	58 ± 7			
LDL (mg/dL)	Placebo	90 ± 16	91 ± 14	0.873	0.736	0.920
	TD	90 ± 24	93 ± 18			

Data is expressed as mean ± SD,  $n = 8$  subjects/group. The post-test was assessed after 6 weeks of TD supplementation. The main effect of supplementation (Sup.) was examined for the TD and placebo groups, and the main effect of time was assessed at two time points (pre-test, post-test). The statistical analysis is a two-way ANOVA with a  $p$ -value < 0.05 considered significant. The pos-hoc test was a repeated Student's  $t$ -test between groups at the same time point, and significance (\*) was set at an alpha level of 0.05. Different letters (a, b) next to the values in the same row (within group) indicate a significant difference at  $p < 0.05$ . AST, aspartate aminotransferase; ALT, alanine aminotransferase; ALP, alkaline phosphatase; LDH, lactic dehydrogenase; CK, creatine kinase; TP.

(3,28) = 3.473,  $p = 0.005$ ), but TD supplementation did not significantly change albumin and glucose levels. TP supplementation shown significant interaction effect ( $F(3,28) = 4.157$ ,  $p = 0.002$ ) and compared to placebo, the TD group exhibited a significant increase in the TP (1.05-fold,  $p = 0.036$ ) at the post-test timepoint. The lipid-related parameters TG, TC, HDL and LDL were not significantly increased or decreased by TD supplementation. When we examined the data further, we realized that the significant time effects of AST, LDH, albumin, CK and glucose were because all the subjects were in the off-season period, thus the training programs were designed towards recover, causing these injury-related indexes to show time-effect decrease. Our data shows that TP could be increased by TD supplementation, suggesting that TD may be a good consideration as a nutrient supplement to improve serum total protein levels.

### 3.2. Effects of supplementation on body composition profiles

**Table 2** shows the body weight (BW), body mass index (BMI), free fat mass (FFM), fat mass, water content and bone salts content for the placebo and TD groups as assessed pre- and post-test. The mean height of the subjects in the placebo and TD group was  $175.3 \pm 3.9$  cm and  $174.1 \pm 2.9$  cm, respectively (data not shown). At the pre-test assessment, the body composition of the subjects in the TD group was not significantly different from the placebo group for BW ( $p = 0.8788$ ), BMI ( $p = 0.9836$ ), FFM ( $p = 0.5370$ ), fat mass ( $p = 0.7762$ ), water content ( $p = 0.5350$ ) and bone salts ( $p = 0.5294$ ). At the end of the 6-week supplementation, both TD and placebo groups were assessed again for the same parameters. The post-test BW ( $p = 0.9170$ ), BMI ( $p = 0.9615$ ), FFM ( $p = 0.5755$ ), fat mass ( $p = 0.7327$ ), water content ( $p = 0.8376$ ) and bone salts ( $p = 0.7264$ ) were again no different in the 2 groups. The data also showed no significant difference in main (supplementation, times) or interaction effects (supplementation x times). The results

suggest that TD supplementation did not significantly affect body composition.

### 3.3. Effects of supplementation on endurance drop vertical jumps (DVJs) training programs

Drop vertical jumps (DVJs) have been commonly used in plyometric training programs (Table 3). Our results show that TD group was able to increase the jumps height ( $p = 0.002$ ) compared with the placebo group following supplementation. There was a significance in interaction effects (supplementation x times,  $p = 0.042$ ) in the jump heights. The increase in jump height was due to the enhancement of endurance exercise performance by TD supplementation. The post-test analysis showed that the peak vertical ground reaction force (PVGRF), an index of the exercise explosiveness, was significantly increased ( $p = 0.018$ ) by TD supplementation. Both the supplementation effect ( $p = 0.0496$ ) and the interaction effect (supplementation x times,  $p = 0.032$ ) were significantly different in PVGRF. The knee injury index and side-to-side PVGRF difference was significantly decreased ( $p = 0.0003$ ) by TD supplementation. Taken together, our results suggest that 6-week TD supplementation increased the height and reduced the risk of injury on the drop jumps.

### 3.4. Effects of TD on physiological characteristics after exhausted endurance exercise

The endurance capacity was measured by an exhaustive treadmill test (Fig. 2a). The exhaustive times of  $12.0 \pm 0.8$  min and  $16.2 \pm 1.4$  min for the placebo and TD groups, respectively, reflect a significant difference ( $F(1, 14) = 53.027$ ,  $p < 0.0001$ ). The TD group had a 1.35-fold increase in exhaustive times compared to the placebo group. Fig. 2b shows the maximal oxygen consumption ( $\text{VO}_2 \text{ max}$ ) of

**Table 2**  
General characteristics of the body composition.

Characteristic	Treatment	Pre-test	Post-test	p values		
				Main effect (Sup.)	Main effect (Times)	Interaction (Sup. x Times)
Weight (kg)	Placebo	64.3 ± 3.5	64.4 ± 3.5	0.826	0.848	0.901
	TD	63.8 ± 3.9	64.2 ± 3.8			
BMI (kg/m <sup>2</sup> )	Placebo	22.2 ± 1.2	22.3 ± 1.2	0.533	0.517	0.622
	TD	21.7 ± 1.6	22.2 ± 1.3			
BMR (kcal/day)	Placebo	1388 ± 41	1395 ± 41	0.970	0.536	0.822
	TD	1384 ± 42	1398 ± 31			
FFM (kg)	Placebo	55.1 ± 1.4	55.4 ± 1.2	0.145	0.241	0.453
	TD	55.5 ± 1.8	56.7 ± 2.0			
Fat Mass (%)	Placebo	15.0 ± 3.6	16.1 ± 3.8	0.524	0.869	0.275
	TD	15.6 ± 3.1	14.0 ± 3.0			
Water content (kg)	Placebo	49.4 ± 1.8	49.2 ± 1.4	0.992	0.704	0.977
	TD	49.4 ± 2.3	49.1 ± 1.5			
Bone salts (kg)	Placebo	2.84 ± 0.29	2.84 ± 0.35	0.139	0.139	0.139
	TD	2.84 ± 0.59 <sup>a</sup>	3.28 ± 0.33 <sup>b</sup>			

Data is expressed as mean ± SD,  $n = 8$  subjects/group. The post-test was assessed after 6 weeks of supplementation, one day after the last administration. The main effect of supplementation (Sup.) refers to the TD and placebo groups, and the main effect of time was the two-time point assessments (pre-test, post-test). The statistical analysis is a two-way ANOVA and  $p$  values of  $< 0.05$  were considered to be significantly different. The post-hoc test was performed by a repeated Student's  $t$ -test between groups at the same time point and significance (\*) was set at an alpha level of 0.05. Data in the same row (within group) followed by different letters (a, b) indicate significant difference at  $p < 0.05$ .

$2.4 \pm 0.6$  and  $3.7 \pm 0.5$  L/min in the placebo and TD groups, respectively. The  $\text{VO}_2$  max of the TD group is significantly higher ( $F(1,14) = 22.378$ ,  $p = 0.0003$ , 1.55-fold) than the placebo group. We also calculate the  $\text{VO}_2$  max (mL/kg/min) by Cross-Validation Reference using different weights adjusted for BW (Fig. 2c). The  $\text{VO}_2$  max were  $36.3 \pm 11.6$  mL/kg/min and  $57.4 \pm 4.9$  mL/kg/min in the placebo and TD groups, respectively. TD group also had a  $\text{VO}_2$  max that is significantly higher by 1.58-fold ( $F(1,14) = 22.403$ ,  $p = 0.0003$ ) than the placebo group. Fig. 2d shows the  $\text{O}_2$  pulse, an important index for oxygen consumed per heart beat during exercise. The  $\text{O}_2$  pulses were  $12.6 \pm 3.5$  mL/beat and  $18.5 \pm 2.6$  mL/beat, respectively, for the placebo and TD groups. The  $\text{O}_2$  pulses was 1.47-fold higher ( $F(1,14) = 14.533$ ,  $p = 0.002$ ) in the TD than placebo group. Fig. 2 e-f shows the initial heart rate and maximum heart rate during exhausted exercise and both of them were not significant differently between the placebo and TD groups. Taken together, our results show that 6 weeks of TD supplementation was able to improve the exercise performance and physiological characteristics compared to the placebo group.

### 3.5. Effects of supplementation on serum lactate, ammonia, glucose and CK levels after exhausted endurance exercise challenge

Muscle fatigue after exercise can be evaluated by biochemical

indicators including lactate, ammonia, glucose and CK levels (Chen et al., 2014). Lactate can be converted back to pyruvic acid for the aerobic production of ATP, or two lactic acid molecules can combined in the liver to form glucose, with the accumulated lactate causing fatigue during exercise (Cabrera et al., 1999). Before the exhaustive treadmill test, lactate, ammonia, glucose and CK levels were not significantly different between the placebo and TD groups (Fig. 3). After the exhausted treadmill test, the lactate levels in the placebo and TD groups were  $11.2 \pm 1.4$  and  $12.0 \pm 0.0$  mmol/L, respectively. The lactate levels in the placebo and TD groups were not significantly differ after the treadmill test, but both of them were significantly ( $p < 0.0001$ ) higher after the test (Fig. 3a). Peripheral and central fatigue levels are related to increased ammonia levels during exercise. Serum ammonia levels in the placebo and TD groups were not significantly different after treadmill testing (Fig. 3b). Serum glucose levels in the placebo and TD groups were  $108.1 \pm 12.9$  and  $134.6 \pm 13.2$  mg/dL, respectively with the TD group higher by 1.25-fold ( $p < 0.0001$ ) than the placebo group (Fig. 3c).

Serum CK is an important clinical biomarker for muscle damage such as muscular dystrophy, severe muscle breakdown, myocardial infarction, autoimmune myositis and acute renal failure. CK activities in the placebo and TD groups were not significantly different at  $126 \pm 29$  and  $126 \pm 41$  U/L, respectively after the exhausted

**Table 3**  
Effect of TD supplementation on drop vertical jumps (DVJs) with kinetic and kinematic data.

Characteristic	Treatment	Pre-test	Post-test	p values		
				Main effect (Sup.)	Main effect (Times)	Interaction (Sup. x Times)
Vertical Jump Height	Placebo	30.9 ± 6.0	30.8 ± 5.2	0.079	0.044	0.042
	TD	30.4 ± 4.4 <sup>a</sup>	37.2 ± 3.5 <sup>b*</sup>			
PVGRF	Placebo	3.8 ± 0.6	3.6 ± 0.5	0.050	0.26	0.036
	TD	3.7 ± 0.5 <sup>a</sup>	4.3 ± 0.5 <sup>b*</sup>			
Side-to-side PVGRF difference	Placebo	3.8 ± 0.9	3.7 ± 1.0	0.053	0.020	0.032
	TD	3.9 ± 0.8 <sup>b</sup>	2.5 ± 0.8 <sup>a</sup>			

1. The post-test was assessed after 6 weeks of supplementation.

2. The main effect of supplementation (Sup) refers to the TD and placebo treatment and the main effect of time was assessed by 2 time-points (pre- and post-test). Data is expressed as mean ± SD for  $n = 8$  in each group. Statistical analysis was using a two-way ANOVA with a  $p$  value  $< 0.05$  indicating significant difference. The post-hoc test was performed by a repeated Student's  $t$ -test between groups at the same time point and significance (\*) set at an alpha level of 0.05. PVGRF: Peak vertical ground reaction force.

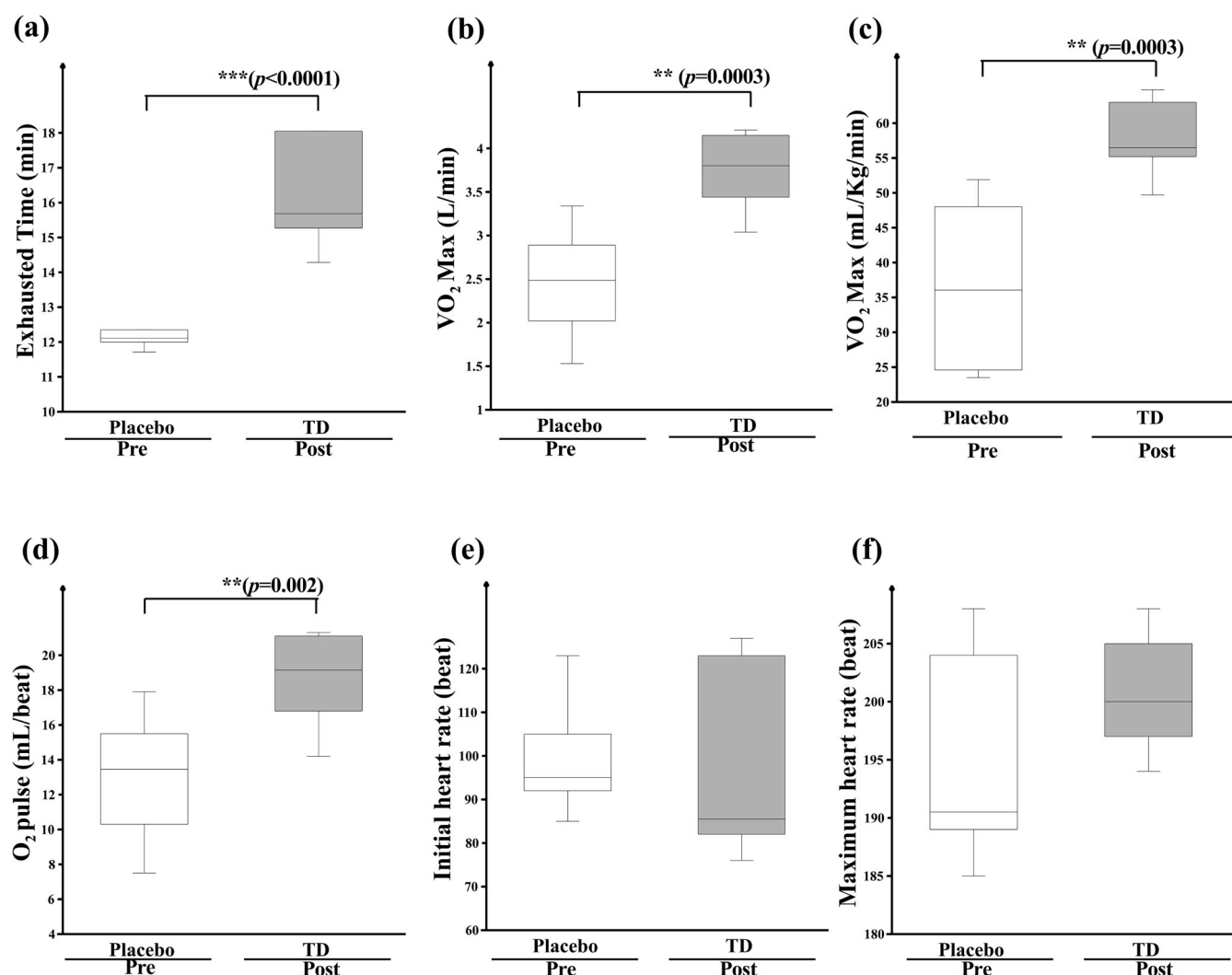


**Fig. 2.** Whisker box plots for the effect of a 6-week TD supplementation on physiological characteristics of (a) exhausted time, (b) maximal oxygen consumption ( $\text{VO}_2$  max), (c)  $\text{VO}_2$  max ( $\text{mL/kg/min}$ ), (d) oxygen pulse, (e) initial heart rate and (f) maximum heart rate after an exhausted exercise challenge. The box plot upper and lower brackets represents  $\pm 1.58 \times \text{interquartile range}$ . Subjects consumed either TD or placebo for 6 weeks and 1 h following the last administration, an exhausted exercise challenge test was carried out. Data is expressed as mean  $\pm$  SD with 8 subjects in each group. Significance (\*) was set at  $p < 0.05$ , (\*\*)  $p < 0.005$ ; (\*\*\*)  $p < 0.0005$  by a one-way ANOVA.

treadmill test (Fig. 3d). Compared to the placebo, TD supplementation was able to increase glucose level after the exhaustive treadmill challenge, possibly acting as an ergogenic supplement for fatigue recovery and improving endurance exercise performance.

#### 4. Discussion

TD is a liquid nutritional supplement that is commonly used in Northeast Asia as a Chinese medicine for various health benefits and remedies. In the current clinical study, we find that TD could significantly improve TP levels (Table 1). The higher the protein quality, the smaller the amount of protein necessary to satisfy our biological protein requirements (Schaafsma, 2005). As an animal-based food, TD can provide a higher quality of protein. Additionally, TD supplementation has no adverse effect on body composition with 6 weeks of supplementation (Table 2).

Exercise can lead to excessive production of reactive oxygen species (ROS) through many pathways and inhibiting the strength of skeletal muscle, resulting in fatigue, lipid and protein peroxidation damage, and affecting the physical performance (Sung et al., 2016). Animals, eggs, fishes, tendon of deer, chicken essence and plants are sources of bioactive peptides, with many protein hydrolysates and peptides

exhibiting health-related properties e.g. anti-oxidative functions (Zain and Syedsahiljamalulail, 2003). Some dipeptides and tripeptides may also be absorbed by enterocytes (Nagai et al., 2014; Stevens, 1992), although the effect of dynamic exercise or exercise training on amino acid absorption has not been extensively explored.

Asymmetrical lower limb biomechanical patterns arise from quadriceps strength deficits in the leg (Ithurburn et al., 2015; Schmitt et al., 2015). Side-to-side imbalances in neuromuscular strength, flexibility and coordination are important predictors of increased injury risk. When the strength between the muscles and the recruitment pattern is unbalanced, it will easily lead to more dynamic control on one side of the leg. Excessive use of the dominant foot will put more pressure on the knee joint, causing the non-dominant leg to be unable to absorb shock effectively (Hewett et al., 2010). The results from our study show that the group receiving TD supplementation is able to decrease side-to-side PVGRF difference after 200 DVJs. The dominant leg may potentially place both limbs at an increased risk of anterior cruciate ligament (ACL) injury. The non-dominant leg may be compromised in its ability to manage average force and torque, affecting the dominant leg due to increased dependence and increased loading. (Ford et al., 2003). In our study, the subjects in both the placebo and TD groups were fatigued, but only the TD group showed an increase in the height of the drop

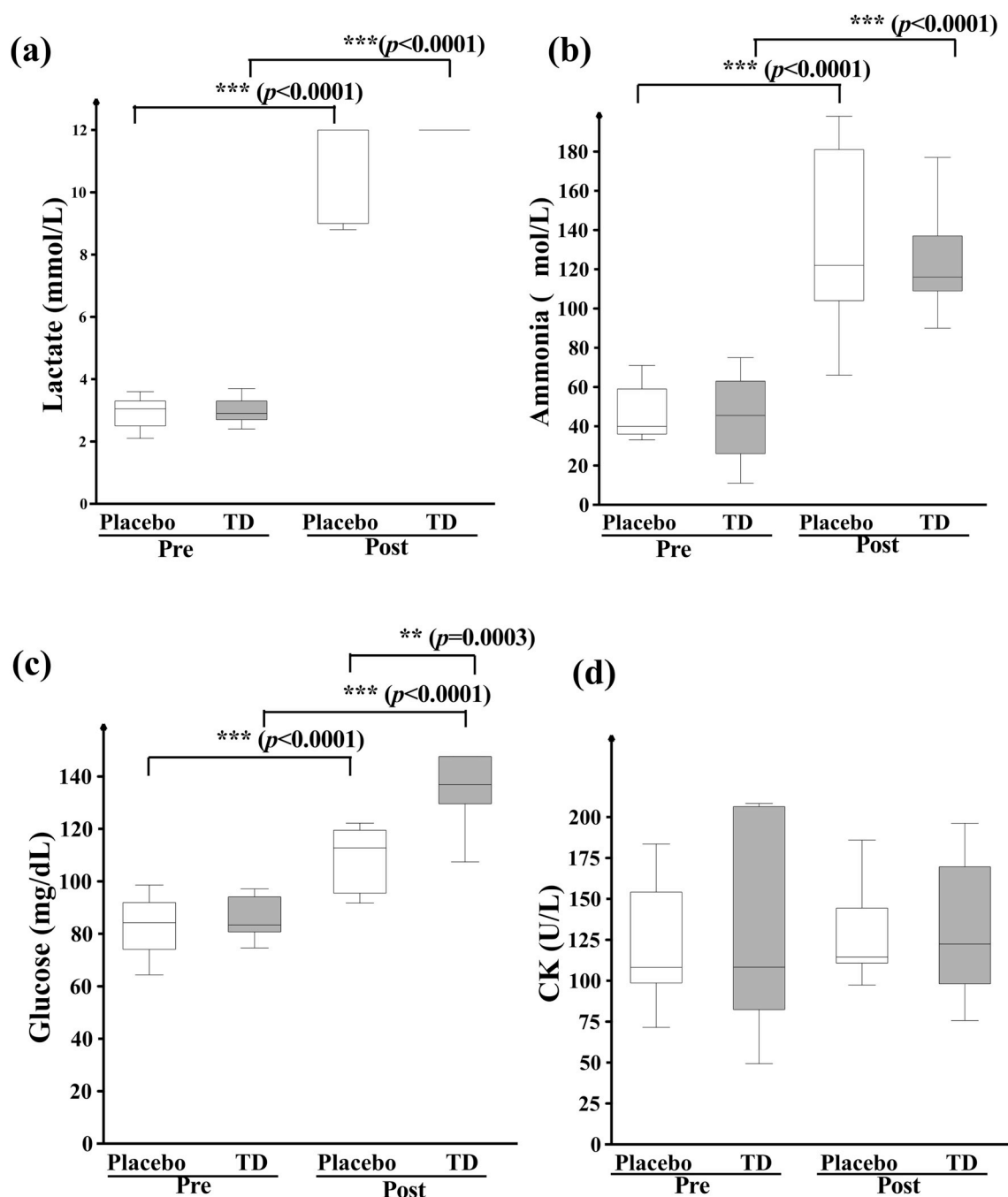


**Fig. 3.** Whisker box plots showing the effect of a 6-week TD supplementation on serum levels of (a) lactate, (b) ammonia, (c) glucose and (d) creatine kinase (CK) after an acute exhaustive exercise challenge. The box plot upper and lower brackets represents  $\pm 1.58 \times$  interquartile range. Subjects consumed either TD or placebo for 6 weeks and 1 h following the last administration, an exhaustive exercise treadmill challenge test was carried out. Data is expressed as mean  $\pm$  SD with 8 subjects in each group. Significance (\*) is set at  $p < 0.05$ , (\*\*)  $p < 0.005$ ; (\*\*\*)  $p < 0.0005$  by two-way ANOVA.

vertical jumps. Taken together, the study shows that a 6-week TD supplementation could enhance exercise performance in drop vertical jump height and decrease side-to-side PVGRF difference to reduce the risk of injury on drop jumps.

Physical adaptation occurs during the recovery process in response to the exercise performed. The amount, timing, intake and appropriate type of food, fluids and supplements could efficiently promote optimal health and performance with different training intensities (Thomas et al., 2016). The positive relationship between muscle contraction, oxygen consumption ( $VO_2$ ) and blood flow indicate that the convection and diffusion of oxygen from the vasculature is intimately related to energy expenditure. Exercise of larger muscles is associated with a

greater absolute workload and maximal oxygen consumption level ( $VO_{2\max}$ ). Maximum aerobic capacity expressed as  $VO_{2\max}$ , is regarded as a very good single indicator of maximal endurance and aerobic physical fitness (Bacon et al., 2013). Oxygen pulse ( $O_2$  pulse) is an important index of cardiovascular efficiency, defined as the ratio of oxygen consumption to heart rate and expressed as the volume of oxygen ejected from the ventricles with each cardiac contraction. In humans, oxygen pulse during exercise reflects the maximal aerobic capacity (Oliveira et al., 2011). We found that after 6 weeks of supplementation, the TD group exhibited higher  $VO_{2\max}$ ,  $O_2$  pulse and longer exhausted time after the exhausted treadmill challenge compared with the placebo group.

The glucose level after exhausted exercise was also significantly elevated, possibly for energy utilization benefit. During prolonged heavy exercise in the absence of carbohydrate supplementation, blood glucose levels decline and limit the muscle glucose uptake, leading to reduced exercise performance (McConell et al., 1994). TD supplementation was able to increase serum glucose levels after the exhausted exercise challenge, possibly acting as an ergogenic supplement for athletes to achieve potential ergogenic benefits.

Zanker and Swaine (2000) had previously shown that when energy availability is reduced, both insulin and the serum concentration of type I procollagen carboxy-terminal propeptide (PICP), a marker of bone type I collagen synthesis, declined linearly (Zanker and Swaine, 2000). When trained male runners performed intensive exercise while restricting their dietary energy intake by 50% in an experimental protocol designed to deplete their muscle glycogen stores, PINP concentrations declined by 30% in 3 days. This causal relationship between insulin and bone type I collagen synthesis and dose-response effects of energy availability on PICP and insulin, was also observed in a separate streptozotocin-induced diabetic mice model (Lu et al., 2003). Our study shows that supplementation of TD could affect serum glucose content during exhaustive exercise. It is possible that the abundance of amino acids in TD and other supplements/nutrients is responsible for increasing serum glucose during prolonged endurance exercise. TD supplementation regulates energy homeostasis by downregulating triglyceride levels to increase exercise performance. We observed beneficial effects of TD in decreasing TG levels to increase the serum glucose level. The results show that TD decreases the intramyocellular triglyceride (IMTG) stores and ensures an alternative fuel to muscle glycogen. IMTG could be used as a fuel substrate during prolonged exercise. TG offers an alternative to glycogen for energy in the endurance-trained athlete (Johnson et al., 2004).

Although athletes are increasingly turning to the use of these nutrients in a purified form rather than relying on obtaining them from foods, TD has the advantage of being a Traditional Chinese medicine (TCM) derived from conventional natural food. Its ability to improve both health and performance suggests that it has the potential to be used as a nutritional supplement for exercise. Our study shows that six weeks supplementation of TD was sufficient to improve the endurance exercise performance, and the physiological, biochemical variables, fatigue profile after exercise. Additionally, risk of injury during endurance training was also reduced with TD supplementation.

In China and Japan, the conservation status of “wild” sika deer is strictly enforced by law. One of the ways to tackle the issue of conservation has been to breed these sika deer. Some sika deer are bred in enclosures where their primary purpose is to be used as Traditional Chinese Medicine (TCM). There are some species of sika deer that are mainly used in medicine, including *Cervus dybowskii*, *Cervus nippon hortulorum* and *Cervus nippon taiouanus*. In recent years, urbanization and greater demand for traditional medicines have resulted in an increase in harvesting of animals medicine from rural areas, leading to a depletion of the rural resource base where certain species are vulnerable to over-exploitation (Alves et al., 2013). In the Van Vliet et al. study, several pathogens carried by bushmeat were found to be zoonotic and potentially transmissible to humans through consumption or exposure of body fluids and feces (Van Vliet et al., 2017). In order to replace the negative impact of bush meat consumption on human health, one could investigate possible replacements to sika deer or develop innovative ways for sika deer handling, conservation and processing. There is currently a lack of studies investigating whether bovids are possible replacements of the sika deer. However, in the Ledesma-Feliciano study, the authors found the relationship between zootherapeutic products and their target diseases, providing evidence for the possible replacement of wild animals by domestic animals (Ledesma-Feliciano et al., 2018). Bovid is among the animal species most frequently used in traditional folk medicine. According to historical documents, bovids have been used in traditional medicines since

ancient times (Alves et al., 2011). Thus, one practical way to reduce the negative impact on the environment may be to investigate the possibility of using bovids as alternatives.

## 5. Conclusions

Deer tendon is a Traditional Chinese Medicine known to have strengthening and repairing properties towards muscles and bones, showing promise for application in the nutritional supplement industry. Sika deer is regarded to have adaptogenic-like properties in Traditional Chinese Medicine, as it is considered a tonic of top grade quality (Zhu, 1998). Sika deer is a “hot” or “yang” tonic, used to treat “cold” diseases (Aramwit and Wirotsaengthong, 2013). These “yang” tonics were also called “qi-supplementing medicines”, “yang-supplementing medicines” or “blood-supplementing medicines (Liao et al., 2018) and have the following functions: enriching and activating blood by promoting the secretion of erythropoietin and inducing the production of stimulatory factors, e.g. macrophage colonies, to activate blood (Liao et al., 2018; Zhu, 1998). Although there is often a lack of information and study, making it difficult to quantitate the active compounds in TD, the main active principles of TD are collagen with a content of 82.12% (Zhang et al., 2014). The collagen peptide have health-promoting effects, such as enhances cutaneous wound healing and reduce the intercellular free radicals to protect the human (Sato, 2017).

To our knowledge, this is the first study examining the effect of supplementation of tendon of deer (TD) in a population of athletes on exercise performance and risk training injury. In this current study, we find that TD is able to improve exercise performance by increasing the height of the vertical jumps, enhance  $\text{VO}_2$  max levels and increase endurance exercise time. Also, it appears to reduce the risk of musculoskeletal injury, reduce the levels of fatigue-related markers and increase serum glucose levels after an acute exhaustive exercise. Taken together, our results suggest that TD has potential for use as a supplement taken in conjunction with appropriate diet for athletes on endurance programs.

## Availability of data and materials

Data are all contained within the paper.

## Author contributions

ILW and YMC designed the experiments. ILW, JS, and YMC carried out the supplement preparation and laboratory experiments. ILW, CYH and YMC analyzed the data, interpreted the results, prepared figures and wrote the manuscript. CYH, CCH, YW and YMC contributed reagents, materials and the analysis platforms.

## Conflicts of interest

All authors declare that they have no conflicts of interest with regard to the contents of this article.

## Funding

This work was supported by Chang Gung Memorial Hospital Grants (CMRPF1G0172). Research on Teaching Reform of Vocational Education and Adult Education in Jilin Province- Muscle simulation training system development (grant number: 2018ZCZ043).

## Acknowledgments

The authors thank Dong Ao Deer industry group (Jilin, China) for providing guidance and information on TD and its production process.



## Abbreviations

TD	Tendon of deer
ALT	alanine aminotransferase
AST	aspartate aminotransferase
CK	creatine kinase
LDH	lactate dehydrogenase
TP	total protein
CK	creatine kinase
TP	total protein
BUN	blood urea nitrogen
UA	uric acid
TC	total cholesterol
TG	triglycerides
HDL	high-density lipoprotein
LDL	low-density lipoprotein
DVJs	drop vertical jumps
PVGRF	peak vertical ground reaction force

## Appendix A. Supplementary data

Supplementary data to this article can be found online at <https://doi.org/10.1016/j.jep.2019.112119>.

## References

- Alves, R.R.N., Barboza, D., Rilke, R., Souto, S., de Medeiros, W., Mourão, J.d.S., 2011. Utilization of bovids in traditional folk medicine and their implications for conservation. *Environ. Res. J.* 5 (4), 547–562.
- Alves, R.R.N., Rosa, I.L., 2013. Introduction: toward a plural approach to the study of medicinal animals. In: Alves, R., Rosa, I. (Eds.), *Animals in Traditional Folk Medicine*. Springer, Berlin, Heidelberg, pp. 1–9.
- Alves, R.R.N., Rosa, I.L., Albuquerque, U.P., Cunningham, A.B., 2013. Medicine from the wild: an overview of the use and trade of animal products in traditional medicines. In: Alves, R., Rosa, I. (Eds.), *Animals in Traditional Folk Medicine*. Springer, Berlin, Heidelberg, pp. 25–42.
- Aramwit, P., Wirotsaengthong, S., 2013. Overview of commonly used Chinese herbs. *J. Med. Plants Res.* 7 (16), 998–1014.
- Bacon, A.P., Carter, R.E., Ogle, E.A., Joyner, M.J., 2013. VO2max trainability and high intensity interval training in humans: a meta-analysis. *PLoS One* 8 (9), e73182.
- Bruce, R.A., Kusumi, F., Hosmer, D., 1973. Maximal oxygen intake and nomographic assessment of functional aerobic impairment in cardiovascular disease. *Am. Heart J.* 85 (4), 546–562.
- Cabrera, M.E., Saidel, G.M., Kalhan, S.C., 1999. Lactate metabolism during exercise: analysis by an integrative systems model. *Am. J. Physiol.* 277 (5), R1522–R1536.
- Chen, Y.M., Tsai, Y.H., Tsai, T.Y., Chiu, Y.S., Wei, L., Chen, W.C., Huang, C.C., 2014. Fucoidan supplementation improves exercise performance and exhibits anti-fatigue action in mice. *Nutrients* 7 (1), 239–252.
- Cong, W., Qin, S.Y., Meng, Q.F., Zou, F.C., Qian, A.D., Zhu, X.Q., 2016. Molecular detection and genetic characterization of *Toxoplasma gondii* infection in sika deer (*Cervus nippon*) in China. *Infect. Genet. Evol.* 39, 9–11.
- Ford, K.R., Myer, G.D., Hewett, T.E., 2003. Valgus knee motion during landing in high school female and male basketball players. *Med. Sci. Sport. Exerc.* 35 (10), 1745–1750.
- Garthe, I., Maughan, R.J., 2018. Athletes and supplements: prevalence and perspectives. *Int. J. Sport Nutr. Exerc. Metab.* 28 (2), 126–138.
- Hewett, T.E., Ford, K.R., Hoogenboom, B.J., Myer, G.D., 2010. Understanding and preventing ACL injuries: current biomechanical and epidemiologic considerations - update 2010. *N Am J Sports Phys Ther* 5 (4), 234–251.
- Huang, C.C., Chen, Y.M., Kan, N.W., Chao, H.L., Ho, C.S., Hsu, M.C., 2014. Cornu cervi pantotrichum supplementation improves exercise performance and protects against physical fatigue in mice. *Molecules* 19 (4), 4669–4680.
- Huang, S.W., Hsu, Y.J., Lee, M.C., Li, H.S., Yeo, P.C.W., Lim, A.L., Huang, C.C., 2018. In vitro and in vivo functional characterization of essence of chicken as an ergogenic aid. *Nutrients* 10 (12).
- Huang, W.C., Chang, Y.C., Chen, Y.M., Hsu, Y.J., Huang, C.C., Kan, N.W., Chen, S.S., 2017. Whey protein improves marathon-induced injury and exercise performance in elite track runners. *Int. J. Med. Sci.* 14 (7), 648–654.
- Huang, W.C., Hsu, Y.J., Li, H., Kan, N.W., Chen, Y.M., Lin, J.S., Hsu, T.K., Tsai, T.Y., Chiu, Y.S., Huang, C.C., 2018. Effect of *Lactobacillus plantarum* TWK10 on improving endurance performance in humans. *Chin. J. Physiol.* 61 (3), 163–170.
- Huang, W.C., Lin, C.L., Chiu, C.C., Lin, Y.T., Huang, W.K., Huang, H.Y., Huang, C.C., 2014. Chicken essence improves exercise performance and ameliorates physical fatigue. *Nutrients* 6 (7), 2681–2696.
- Ithurburn, M.P., Paterno, M.V., Ford, K.R., Hewett, T.E., Schmitt, L.C., 2015. Young athletes with quadriceps femoris strength asymmetry at return to sport after anterior cruciate ligament reconstruction demonstrate asymmetric single-leg drop-landing mechanics. *Am. J. Sports Med.* 43 (11), 2727–2737.
- Johnson, N.A., Stannard, S.R., Thompson, M.W., 2004. Muscle triglyceride and glycogen in endurance exercise: implications for performance. *Sport. Med.* 34 (3), 151–164.
- Katz, S.D., Berkowitz, R., LeJemtel, T.H., 1992. Anaerobic threshold detection in patients with congestive heart failure. *Am. J. Cardiol.* 69 (19), 1565–1569.
- Knapik, J.J., Steelman, R.A., Hoedebecke, S.S., Austin, K.G., Farina, E.K., Lieberman, H.R., 2016. Prevalence of dietary supplement use by athletes: systematic review and meta-analysis. *Sport. Med.* 46 (1), 103–123.
- Ledesma-Feliciano, C., Hagen, S., Troyer, R., Zheng, X., Musselman, E., Slavkovic Lukic, D., Franke, A.M., Maeda, D., Zielonka, J., Munk, C., Wei, G., VandeWoude, S., Lochelt, M., 2018. Replacement of feline foamy virus bet by feline immunodeficiency virus vif yields replicative virus with novel vaccine candidate potential. *Retrovirology* 15 (1), 38.
- Liao, L.Y., He, Y.F., Li, L., Meng, H., Dong, Y.M., Yi, F., Xiao, P.G., 2018. A preliminary review of studies on adaptogens: comparison of their bioactivity in TCM with that of ginseng-like herbs used worldwide. *Chin. Med.* 13, 57.
- Lu, H., Kraut, D., Gerstenfeld, L.C., Graves, D.T., 2003. Diabetes interferes with the bone formation by affecting the expression of transcription factors that regulate osteoblast differentiation. *Endocrinology* 144 (1), 346–352.
- McConnell, G., Fabris, S., Proietto, J., Hargreaves, M., 1994. Effect of carbohydrate ingestion on glucose kinetics during exercise. *J. Appl. Physiol.* 77 (3), 1537–1541 1985.
- Meyer, T., Lucia, A., Earnest, C.P., Kindermann, W., 2005. A conceptual framework for performance diagnosis and training prescription from submaximal gas exchange parameters—theory and application. *Int. J. Sports Med.* 26 (Suppl. 1), S38–S48.
- Momaya, A., Fawal, M., Estes, R., 2015. Performance-enhancing substances in sports: a review of the literature. *Sport. Med.* 45 (4), 517–531.
- Myers, J., Goldsmith, R.L., Keteyian, S.J., Brawner, C.A., Brazil, D.A., Aldred, H., Ehrman, J.K., Burkhead, D., 2010. The ventilatory anaerobic threshold in heart failure: a multicenter evaluation of reliability. *J. Card. Fail.* 16 (1), 76–83.
- Nagai, T., Suzuki, N., Tanoue, Y., Kai, N., 2012. Collagen from tendon of yezo sika deer (*Cervus nippon yezoensis*) as by-product. *Food Nutr. Sci.* 3 (01), 72.
- Nagai, T., Tanoue, Y., Kai, N., Suzuki, N., 2014. Collagen hydrolysates derived from Yezo sika deer (*Cervus nippon yezoensis*) tendon have highly health-promoting potentials. *Int. Food Res. J.* 21 (4).
- Oliveira, R.B., Myers, J., Araujo, C.G., 2011. Long-term stability of the oxygen pulse curve during maximal exercise. *Clinics* 66 (2), 203–209.
- Peeling, P., Binnie, M.J., Goods, P.S.R., Sim, M., Burke, L.M., 2018. Evidence-based supplements for the enhancement of athletic performance. *Int. J. Sport Nutr. Exerc. Metab.* 28 (2), 178–187.
- Prokopov, I.A., Kovaleva, E.L., Minaeva, E.D., Pryakhina, E.A., Savin, E.V., Gamayunova, A.V., Pozharitskaya, O.N., Makarov, V.G., Shikov, A.N., 2019. Animal-derived medicinal products in Russia: current nomenclature and specific aspects of quality control. *J. Ethnopharmacol.* 240, 111933.
- Qin, S.Y., Zhang, X.X., Cong, W., Zhou, D.H., Wang, J.L., Yin, M.Y., Tan, Q.D., Zhao, Q., Zhu, X.Q., 2014. Seroprevalence and risk factors of *Toxoplasma gondii* infection in domestic sika deer (*Cervus nippon*) in northeastern China. *Acta Trop.* 140, 184–187.
- Sato, K., 2017. The presence of food-derived collagen peptides in human body-structure and biological activity. *Food Funct.* 8 (12), 4325–4330.
- Schaafsma, G., 2005. The Protein Digestibility-Corrected Amino Acid Score (PDCAAS)—a concept for describing protein quality in foods and food ingredients: a critical review. *J. AOAC Int.* 88 (3), 988–994.
- Schmitt, L.C., Paterno, M.V., Ford, K.R., Myer, G.D., Hewett, T.E., 2015. Strength asymmetry and landing mechanics at return to sport after anterior cruciate ligament reconstruction. *Med. Sci. Sport. Exerc.* 47 (7), 1426–1434.
- Slesinski, M.J., Subar, A.F., Kahle, L.L., 1995. Trends in use of vitamin and mineral supplements in the united state: the 1987 and 1992 national health interview surveys. *J. Am. Diet. Assoc.* 95 (8), 921–923.
- Stevens, B.R., 1992. Vertebrate intestine apical membrane mechanisms of organic nutrient transport. *Am. J. Physiol.* 263 (3 Pt 2), R458–R463.
- Sung, D., Kim, S., Kim, J., An, H., So, W.-Y., 2016. Role of l-carnitine in sports performance: focus on ergogenic aid and antioxidant. *Sci. Sport.* 31 (4), 177–188.
- Thomas, D.T., Erdman, K.A., Burke, L.M., 2016. American college of sports medicine joint position statement. Nutrition and athletic performance. *Med. Sci. Sport. Exerc.* 48 (3), 543–568.
- Tseng, S.H., Sung, H.C., Chen, L.G., Lai, Y.J., Wang, K.T., Sung, C.H., Wang, C.C., 2012. Effects of velvet antler with blood on bone in ovariectomized rats. *Molecules* 17 (9), 10574–10585.
- Van Vliet, N., Moreno Calderón, J.L., Gomez, J., Zhou, W., Fa, J.E., Golden, C., Alves, R.R.N., Nasi, R., 2017. Bushmeat and human health: assessing the evidence in tropical and sub-tropical forests. *Ethnobiol. Conserv.* 6 (3), 1–45.
- Whiting, M.J., Williams, V.L., Hibbitts, T.J., 2013. Animals traded for traditional medicine at the Faraday market in South Africa: species diversity and conservation implications. In: Alves, R., Rosa, I. (Eds.), *Animals in Traditional Folk Medicine*. Springer, Berlin, Heidelberg, pp. 421–473.
- Wu, H., Wan, Q.-H., Fang, S.-G., 2004. Two genetically distinct units of the Chinese sika deer (*Cervus nippon*): analyses of mitochondrial DNA variation. *Biol. Conserv.* 119 (2), 183–190.
- Xu, R., Wei, S., Zhou, G., Ren, J., Liu, Z., Tang, S., Cheung, P.C.K., Wu, X., 2018. Multiplex TaqMan locked nucleic acid real-time PCR for the differential identification of various meat and meat products. *Meat Sci.* 137, 41–46.
- Zain, A.M., Syedsahiljamalulail, S., 2003. Effect of taking chicken essence on stress and cognition of human volunteers. *Malays J. Nutr.* 9 (1), 19–29.
- Zanker, C.L., Swaine, I.L., 2000. Responses of bone turnover markers to repeated endurance running in humans under conditions of energy balance or energy restriction. *Eur. J. Appl. Physiol.* 83 (4–5), 434–440.
- Zha, D., Xing, X., Yang, F., 2010. A multiplex PCR assay for fraud identification of deer products. *Food Control* 21 (10), 1402–1407.

- Zhang, H., Dong, Y., Qi, B., Liu, L., Zhou, G., Bai, X., Yang, C., Zhao, D., Zhao, Y., 2014. Preventive effects of collagen Peptide from deer sinew on bone loss in ovariectomized rats. *Evid Based Complement Alternat Med* 2014, 627285.
- Zhang, L.Z., Xin, J.L., Zhang, X.P., Fu, Q., Zhang, Y., Zhou, Q.L., 2013. The anti-osteoporotic effect of velvet antler polypeptides from *Cervus elaphus* Linnaeus in ovariectomized rats. *J. Ethnopharmacol.* 150 (1), 181–186.
- Zhu, Y.-P., 1998. *Chinese Materia Medica: Chemistry, Pharmacology and Applications*. CRC press, Boca Raton, Florida, USA.



## Novel secoeunicellins produced by an octocoral *Cladiella* sp

Zhi-Jun Zhang<sup>a,b,1</sup>, Yi-Hsuan Wang<sup>c,1</sup>, Shu-Rong Chen<sup>d</sup>, Bo-Rong Peng<sup>b</sup>, San-Nan Yang<sup>e</sup>,  
Chiung-Chih Hu<sup>b</sup>, Lee-Shing Fang<sup>f,g</sup>, Tsong-Long Hwang<sup>c,h,i,j,\*</sup>, Ping-Jyun Sung<sup>a,b,d,k,l,\*</sup>

<sup>a</sup> Graduate Institute of Marine Biology, National Dong Hwa University, Pingtung 944, Taiwan

<sup>b</sup> National Museum of Marine Biology and Aquarium, Pingtung 944, Taiwan

<sup>c</sup> Graduate Institute of Natural Products, College of Medicine, Chang Gung University, Taoyuan 333, Taiwan

<sup>d</sup> Graduate Institute of Natural Products, College of Pharmacy, Kaohsiung Medical University, Kaohsiung 807, Taiwan

<sup>e</sup> Department of Pediatrics, E-DA Hospital, School of Medicine, College of Medicine, I-SHOU University, Kaohsiung 840, Taiwan

<sup>f</sup> Center for Environmental Toxin and Emerging-Contaminant Research, Cheng Shiu University, Kaohsiung 833, Taiwan

<sup>g</sup> Super Micro Mass Research and Technology Center, Cheng Shiu University, Kaohsiung 833, Taiwan

<sup>h</sup> Research Center for Chinese Herbal Medicine, Research Center for Food and Cosmetic Safety, Graduate Institute of Healthy Industry Technology, College of Human Ecology, Chang Gung University of Science and Technology, Taoyuan 333, Taiwan

<sup>i</sup> Chinese Herbal Medicine Research Team, Healthy Aging Research Center, Chang Gung University, Taoyuan 333, Taiwan

<sup>j</sup> Department of Anaesthesiology, Chang Gung Memorial Hospital, Taoyuan 333, Taiwan

<sup>k</sup> Chinese Medicine Research and Development Center, China Medical University Hospital, Taichung 404, Taiwan

<sup>l</sup> Department of Marine Biotechnology and Resources, National Sun Yat-sen University, Kaohsiung 804, Taiwan

### ARTICLE INFO

#### Article history:

Received 22 July 2019

Revised 10 October 2019

Accepted 17 October 2019

Available online 18 October 2019

#### Keywords:

Secoeunicellin

Octocoral

*Cladiella*

Anti-inflammatory

### ABSTRACT

Two novel 6,7-secoeunicellins, cladiueunicellins W (**1**) and X (**2**), along with a known eunicellin, klymollin Y (**3**), were isolated from an octocoral identified as *Cladiella* sp. The structures of secoeunicellins **1** and **2** were elucidated by spectroscopic methods. **1** is the first secoeunicellin possessing a  $\gamma$ -lactone ring and **2** represents the first secoeunicellin possessing two tetrahydrofuran moieties. Secoeunicellin **2** displayed significant inhibitory effects on the generation of superoxide anions and the release of elastase. These results implied that the methoxy group at C-6 in **2** plays an important role in determining the activity of these compounds.

© 2019 Elsevier Ltd. All rights reserved.

### Introduction

As part of our ongoing studies into the isolation of novel substances of diverse structures from marine invertebrates collected in the waters off Taiwan, at the intersection of the Kuroshio current and the South China Sea surface current, a series of interesting eunicellin-based diterpenoids (2,11-cyclized cembranoids) were obtained from various octocorals belonging to the genus *Cladiella* [1]. Recently, our chemical examination using NMR-directed investigation of octocoral *Cladiella* sp. (family Alcyoniidae) resulted in the isolation of two novel 6,7-secoeunicellins, cladiueunicellins W (**1**) and X (**2**), along with a known metabolite, klymollin Y (**3**) (Fig. 1) [2]. In this paper, we describe the isolation, structural elucidation and anti-inflammatory activities of eunicellins **1–3**.

### Results and discussion

Cladiueunicellin W (**1**) was isolated as a colorless oil that gave an  $[M + Na]^+$  ion peak at  $m/z$  357.20378 in HRESIMS, indicating the molecular formula  $C_{20}H_{30}O_4$  (calcd. for  $C_{20}H_{30}O_4 + Na$ , 357.20363) (6° of unsaturation). IR absorptions at 1768 and  $1714\text{ cm}^{-1}$  suggested the presence of  $\gamma$ -lactone and ketonic groups. Inspection of the  $^{13}\text{C}$  NMR and DEPT spectra of **1** revealed the presence of four methyls, five  $\text{sp}^3$  methylenes, one  $\text{sp}^2$  methylene, six  $\text{sp}^3$  methines (including two oxymethines), one  $\text{sp}^3$  oxygenated quaternary carbon, one  $\text{sp}^2$  quaternary carbon and two carbonyl carbons (including one ketonic and one ester carbonyl) (Table 1). Therefore, the remaining three degrees of unsaturation identified **1** as a tricyclic compound.  $^1\text{H}$  NMR data of **1** (Table 1) showed a methyl at  $\delta_{\text{H}}$  2.16 (3H, s,  $\text{H}_3$ -16) attached to a carbonyl carbon, a tertiary methyl attached to an oxygenated carbon ( $\delta_{\text{H}}$  1.35, 3H, s,  $\text{H}_3$ -15) and two secondary methyls ( $\delta_{\text{H}}$  0.98, 0.76, each 3H, d,  $J = 7.2\text{ Hz}$ ,  $\text{H}_3$ -19 and  $\text{H}_3$ -20) of an isopropyl moiety. In addition, a suite of resonances of proton signals at  $\delta_{\text{H}}$  2.19 (1H, ddd,  $J = 12.0, 7.6, 1.2\text{ Hz}$ ,

\* Corresponding authors at: National Museum of Marine Biology and Aquarium, Pingtung 944, Taiwan.

E-mail addresses: [htl@mail.cgu.edu.tw](mailto:htl@mail.cgu.edu.tw) (T.-L. Hwang), [pjsung@nmmba.gov.tw](mailto:pjsung@nmmba.gov.tw) (P.-J. Sung).

<sup>1</sup> These authors contributed equally to this work.

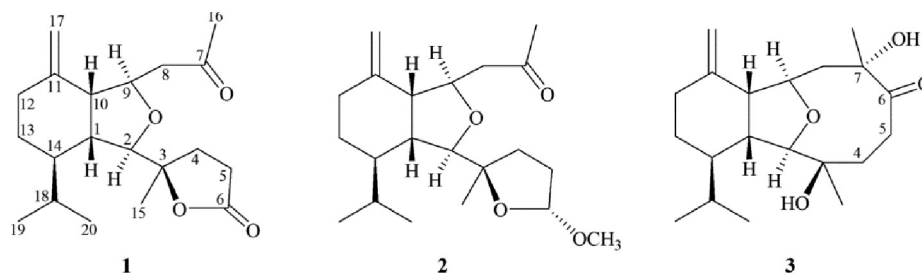


Fig. 1. Structures of cladienicellins W (1), X (2) and klymollin Y (3).

**Table 1**  
 $^1\text{H}$  (400 MHz,  $\text{CDCl}_3$ ) and  $^{13}\text{C}$  (100 MHz,  $\text{CDCl}_3$ ) NMR data for secoeunicellins **1** and **2**.

C/H	<b>1</b>	<b>2</b>
	$\delta_{\text{H}}$ (J in Hz)	$\delta_{\text{H}}$ (J in Hz)
1	2.19 ddd (12.0, 7.6, 1.2)	2.05 m
2	3.79 d (1.2)	3.82 br s
3		
4	2.44 m; 1.86 m	2.08 m; 1.49 m
5	2.67 m; 2.50 m	2.13 m; 1.92 m
6		4.98 dd (5.6, 2.0)
7		
8	2.46 m; 2.57 m	2.53 dd (16.0, 2.8); 2.78 dd (16.0, 8.4)
9	4.32 ddd (10.8, 8.8, 2.4)	4.33 ddd (8.4, 7.2, 2.8)
10	2.60 m	2.64 dd (10.8, 7.2)
11		
12 $\alpha/\beta$	2.05 m; 2.26 ddd (14.4, 3.2, 3.2)	2.06 m; 2.25 ddd (14.0, 3.2, 3.2)
13	1.74 dq (12.8, 3.2); 1.04 qd (12.8, 3.2)	1.74 dq (12.8, 3.2); 1.03 qd (12.8, 2.8)
14	1.43 m	1.48 m
15	1.35 s	1.11 s
16	2.16 s	2.20 s
17a/b	4.78 dd (2.0, 2.0); 4.74 dd (2.0, 2.0)	4.76 dd (2.4, 1.6); 4.66 dd (2.0, 1.6)
18	1.67 m	1.81 m
19	0.98 d (7.2)	0.97 d (6.8)
20	0.76 d (7.2)	0.74 d (6.8)
6-OCH <sub>3</sub>		3.40 s
	$\delta_{\text{C}}$ Mult.	$\delta_{\text{C}}$ Mult.
	44.7 (CH)	45.4 (CH)
	89.2 (CH)	88.4 (CH)
	87.1 (C)	86.7 (C)
	31.6 (CH <sub>2</sub> )	31.6 (CH <sub>2</sub> )
	30.1 (CH <sub>2</sub> )	32.3 (CH <sub>2</sub> )
	178.0 (C)	106.0 (CH)
	207.4 (C)	208.3 (C)
	47.7 (CH <sub>2</sub> )	47.6 (CH <sub>2</sub> )
	76.0 (CH)	75.8 (CH)
	52.2 (CH)	52.3 (CH)
	144.8 (C)	146.0 (C)
	31.4 (CH <sub>2</sub> )	31.2 (CH <sub>2</sub> )
	25.2 (CH <sub>2</sub> )	25.4 (CH <sub>2</sub> )
	43.1 (CH)	43.1 (CH)
	24.5 (CH <sub>3</sub> )	24.0 (CH <sub>3</sub> )
	30.7 (CH <sub>3</sub> )	31.0 (CH <sub>3</sub> )
	112.0 (CH <sub>2</sub> )	111.0 (CH <sub>2</sub> )
	27.7 (CH)	27.4 (CH)
	21.9 (CH <sub>3</sub> )	22.0 (CH <sub>3</sub> )
	15.2 (CH <sub>3</sub> )	15.2 (CH <sub>3</sub> )
		55.5 (CH <sub>3</sub> )

H-1), 2.60 (1H, m, H-10), 3.79 (1H, d,  $J = 1.2$  Hz, H-2) and 4.32 (1H, ddd,  $J = 10.8, 8.8, 2.4$  Hz, H-9), and carbon signals at  $\delta_{\text{C}}$  89.2 (CH-2), 76.0 (CH-9), 52.2 (CH-10) and 44.7 (CH-1), indicated the presence of a tetrahydrofuran moiety.

From the COSY spectrum, the proton sequences from H<sub>2</sub>-4/H<sub>2</sub>-5, H<sub>2</sub>-8/H-9/H-10/H-1/H-14/H<sub>2</sub>-13/H<sub>2</sub>-12, H-14/H-18/H<sub>3</sub>-19 and H-18/H<sub>3</sub>-20 were established (Fig. 2). These data, together with key HMBC between protons and quaternary carbons, such as H-1, H-2, H<sub>2</sub>-4, H<sub>2</sub>-5, H<sub>3</sub>-15/C-3; H<sub>2</sub>-8, H<sub>3</sub>-16/C-7; H-10, H<sub>2</sub>-12, H<sub>2</sub>-13, H<sub>2</sub>-17/C-11; and H<sub>2</sub>-4, H<sub>2</sub>-5/C-6 (Fig. 2), led to the establishment of the 6,7-secoeunicellin skeleton of **1**. Furthermore, an exocyclic double bond at C-11 was established from HMBC between H<sub>2</sub>-17/C-10, C-11, C-12; H-10/C-17; and H<sub>2</sub>-12/C-17. The C-15 methyl group was positioned at C-3 according to HMBC from H<sub>3</sub>-15 to C-2, C-3 and C-4.

Based on previous studies, naturally-occurring eunicellin-based diterpenoids from soft corals belonging to the genus *Cladiella* have H-1 *cis* to H-10, and are assigned as  $\beta$ -oriented, as shown in eunicellin derivatives. [3] In the NOESY experiment for **1** (Fig. 3), H-1 was correlated with H-10 and H<sub>3</sub>-20, suggesting that H-1, H-10 and the isopropyl group are situated on the same face as the  $\beta$  protons. A small coupling constant was detected between H-1 and H-2 ( $J = 1.2$  Hz), and no correlation between these two protons was identified in the NOESY experiment, indicating that H-2 should be  $\alpha$ -oriented. H<sub>3</sub>-15 showed a correlation with H-2, suggesting the  $\alpha$ -orientation of the C-15 methyl at C-3. A correlation was found between H-9 and H-14, but not with H-10, indicating that H-9 was  $\alpha$ -oriented. Based on the above findings, the relative configurations of the stereogenic centers of seco-eunicellin **1** were elucidated as 1*R*\*,2*R*\*,3*R*\*,9*R*\*,10*R*\*,14*R*\*.

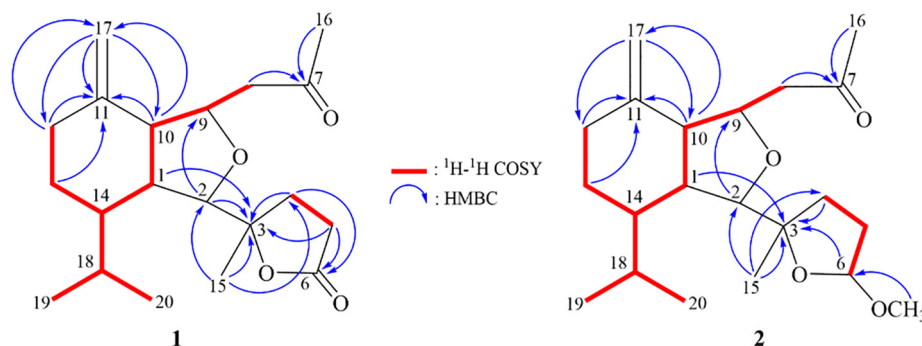


Fig. 2. COSY correlations and selective HMBC correlations of **1** and **2**.

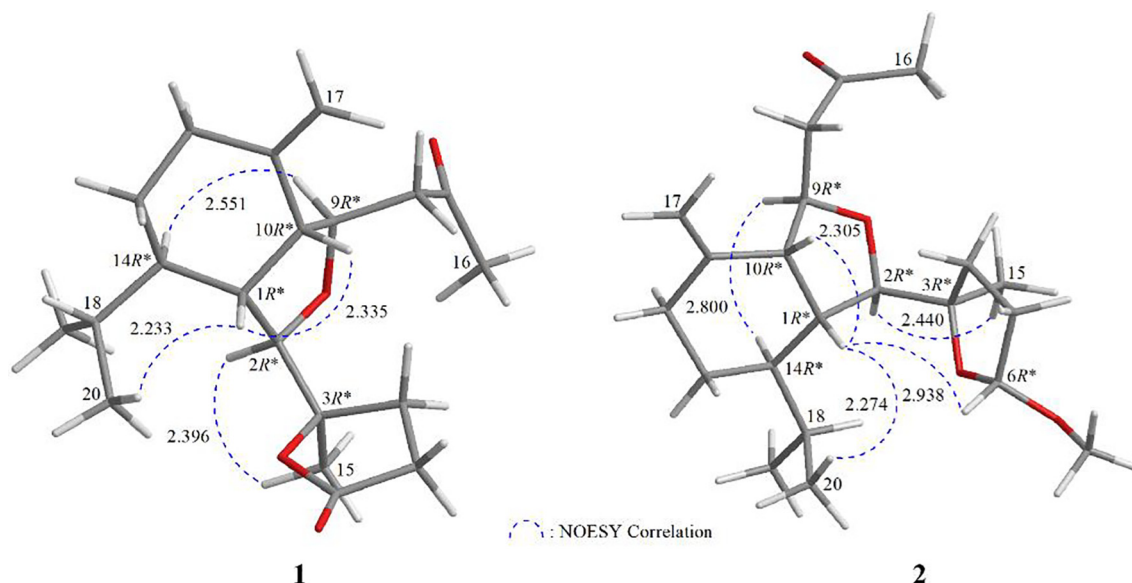


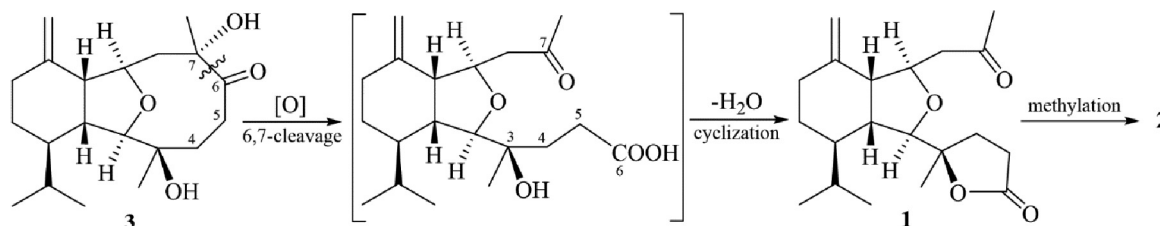
Fig. 3. Stereoviews of **1** and **2** (generated by computer modeling) and calculated distances (Å) between selected protons with key NOESY correlations.

The HRESIMS of **2** (cladieunicellin X) exhibited a pseudomolecular ion peak at  $m/z$  373.23477  $[M + Na]^+$ , consistent with the molecular formula  $C_{21}H_{34}O_4$  and implying five degrees of unsaturation. By comparing the NMR data of **2** with those of **1** (Table 1), it was found that the  $\gamma$ -lactone ring in **1** was converted to a tetrahydro-2-methoxyfuran moiety in **2**. This was further evidenced by the HMBC from the methoxy proton ( $\delta_H$  3.40) to C-6 ( $\delta_C$  106.0) and the absence of a  $\gamma$ -lactone carbonyl carbon in **2** (Fig. 2). In the NOESY experiment, the oxymethine proton H-6 ( $\delta_H$  4.98) showed a correlation with H-1 ( $\delta_H$  2.05), indicating that the methoxy group at C-6 was  $\alpha$ -oriented, and that the stereogenic carbons of **2** were assigned as  $1R^*, 2R^*, 3R^*, 6R^*, 9R^*, 10R^*, 14R^*$  (Fig. 3). The absolute stereochemistry of **2** was determined by comparing the experimental electronic circular dichroism (ECD) spectrum with the computer-generated ECD spectra. The ECD spectra of two stereoisomers,  $1R, 2R, 3R, 6R, 9R, 10R, 14R$ -**2** and  $1S, 2S, 3S, 6S, 9S, 10S, 14S$ -**2**, were calculated. The experimental ECD spectrum of **2** was consistent with the trend of the calculated ECD spectrum of  $1R, 2R, 3R, 6R, 9R, 10R, 14R$ -**2** (Fig. S19). From the

suite of spectroscopic data, **2** was unambiguously identified as cladieunicellin X. As secoeunicellin **1** and **2** were isolated along with **3** (klymollin Y) from the same organism, and the absolute configuration of **3** had been determined [2]. It was reasonable on biogenetic grounds to assume that **1** and **2** had the same absolute configuration as **3**. Therefore, based on above findings, the configurations of the stereogenic centers of **1** were confirmed as  $1R, 2R, 3R, 6R, 9R, 10R, 14R$ .

The biosynthetic pathway of secoeunicellin analogues is outlined in Scheme 1. The 6,7-secoeunicellins **1** and **2** might be derived from **3**, and the latter might subsequently undergo carbon-carbon bond cleavage, oxidation, dehydration and methylation to produce the carbon skeletons of **1** and **2**.

An *in vitro* anti-inflammatory activity assay was performed using human neutrophils, and the results demonstrated that secoeunicellin **2** showed significant inhibitory effects on the generation of superoxide anions and the release of elastase (Table 2). These results implied that the methoxy group at C-6 in **2** plays an important role in determining the activity of these compounds.



Scheme 1. Plausible biogenetic pathway of secoeunicellins **1** and **2**.

Table 2  
Inhibitory effects of eunicellins **1–3** on superoxide anion generation and elastase release by human neutrophils in response to fMet-Leu-Phe/Cytochalasin B.

Compound	Superoxide Anions			Elastase		
	IC <sub>50</sub> (μM) <sup>a</sup>	Inh % (10 μM)		IC <sub>50</sub> (μM) <sup>a</sup>	Inh % (10 μM)	
<b>1</b>	7.18 ± 1.20	6.57 ± 1.48	*	7.83 ± 0.83	3.88 ± 1.84	**
<b>2</b>		67.96 ± 8.42	**		63.60 ± 7.06	***
<b>3</b>		6.90 ± 1.82	*		14.34 ± 5.99	

Percentage of inhibition (Inh %) at 10 μM concentration. Results are presented as means ± S.E.M. ( $n = 3$ ). \* $P < 0.05$ , \*\* $P < 0.01$ , \*\*\* $P < 0.001$  compared with the control (fMLF/CB) or basal (solvent, DMSO). <sup>a</sup>Concentration necessary for 50% inhibition (IC<sub>50</sub>).



## Experimental

### General experimental procedures

Melting points of natural products were determined using Fargo apparatus and the values were uncorrected. Optical rotation values were measured using a Jasco P-1010 digital polarimeter. IR spectra were obtained with a Thermo Scientific Nicolet iS5 FT-IR spectrophotometer. ECD spectra were recorded on a Jasco J-815 CD spectrometer. NMR spectra were recorded on a 400 MHz Jeol ECZ NMR spectrometer using the residual  $\text{CHCl}_3$  signal ( $\delta_{\text{H}}$  7.26 ppm) and  $\text{CDCl}_3$  ( $\delta_{\text{C}}$  77.1 ppm) as the internal standards for  $^1\text{H}$  and  $^{13}\text{C}$  NMR, respectively; coupling constants ( $J$ ) are presented in Hz. ESIMS and HRESIMS were recorded using a Bruker 7 Tesla solarix FTMS system. Column chromatography was carried out with silica gel (230–400 mesh, Merck). TLC was performed on plates pre-coated with Kieselgel 60  $\text{F}_{254}$  (0.25-mm-thick, Merck), then sprayed with 10%  $\text{H}_2\text{SO}_4$  solution followed by heating to visualize the spots. Normal-phase HPLC (NP-HPLC) was performed using a system comprised of a Hitachi L-7100 pump and a Rheodyne 7725i injection port. A semi-preparative normal-phase column (Supelco Ascentis Si Cat#581515-U, 25 cm  $\times$  21.2 mm 5  $\mu\text{M}$ , Sigma-Aldrich) was used for NP-HPLC.

### Animal material

Specimens of *Cladiella* sp. [4] used for this study were collected in the Penghu Archipelago waters, Taiwan, in May 2017. A voucher specimen was deposited in the National Museum of Marine Biology and Aquarium (voucher no.: NMMBA-TWSC-17032), Taiwan.

### Extraction and isolation

Freeze-dried and sliced bodies (wet/dry weight = 570.3/202.8 g) of the coral specimen were prepared and extracted with a 1:1 mixture of MeOH and  $\text{CH}_2\text{Cl}_2$  to give 25.8 g of crude extract, which was partitioned between EtOAc and  $\text{H}_2\text{O}$  to obtain 16.8 g of the EtOAc extract. The EtOAc extract was then placed in a silica gel column and eluted with gradients of *n*-hexane/EtOAc (100% *n*-hexane–100% EtOAc, stepwise) to furnish 16 fractions (fractions A–P). Fractions E–I were combined and further chromatographed in a silica gel column and eluted with gradients of *n*-hexane/EtOAc (50:1–100% EtOAc, stepwise) to afford 31 subfractions (fractions E1–E31). Fraction E11 was then separated by normal-phase HPLC (NP-HPLC) using a mixture of *n*-hexane,  $\text{Me}_2\text{CO}$  and EtOAc (16:1:2.5) as the solvent to obtain 8 subfractions (fractions E11A–E11H). Fraction E11B was then separated by NP-HPLC using a mixture of *n*-hexane,  $\text{Me}_2\text{CO}$ , and EtOAc (17:1:2; at a flow rate of 2.0 mL/min) to afford **2** (2.0 mg). Fraction E17 was further separated by NP-HPLC using a mixture of *n*-hexane,  $\text{Me}_2\text{CO}$  and EtOAc (6:0.5:1; at a flow rate of 2.0 mL/min) to afford **1** (1.6 mg). Fractions E18 and E19 were combined and purified by NP-HPLC using a mixture of *n*-hexane,  $\text{Me}_2\text{CO}$  and EtOAc (9:0.5:2.5; at a flow rate of 2.0 mL/min) to afford **3** (6.0 mg).

Cladieunicellin W (**1**): Colorless oil;  $[\alpha]_{\text{D}}^{20}$  –21 (c 0.05,  $\text{CHCl}_3$ ), IR (ATR)  $\nu_{\text{max}}$  ( $\text{cm}^{-1}$ ) 1768, 1714;  $^1\text{H}$  NMR (400 MHz,  $\text{CDCl}_3$ ) and  $^{13}\text{C}$  NMR (100 MHz,  $\text{CDCl}_3$ ): see Table 1; ESIMS  $m/z$  357  $[\text{M} + \text{Na}]^+$ ; HRESIMS  $m/z$  357.20378 (calcd. for  $\text{C}_{20}\text{H}_{30}\text{O}_4 + \text{Na}$ , 357.20363).

Cladieunicellin X (**2**): Colorless oil;  $[\alpha]_{\text{D}}^{20}$  +12 (c 0.10,  $\text{CHCl}_3$ ), IR (ATR)  $\nu_{\text{max}}$  ( $\text{cm}^{-1}$ ) 1715;  $^1\text{H}$  NMR (400 MHz,  $\text{CDCl}_3$ ) and  $^{13}\text{C}$  NMR

(100 MHz,  $\text{CDCl}_3$ ): see Table 1; ESIMS  $m/z$  373  $[\text{M} + \text{Na}]^+$ ; HRESIMS  $m/z$  373.23477 (calcd. for  $\text{C}_{21}\text{H}_{34}\text{O}_4 + \text{Na}$ , 373.23493).

Klymollin Y (**3**): White amorphous powder; mp 194–195 °C;  $[\alpha]_{\text{D}}^{20}$  –30 (c 0.29,  $\text{CHCl}_3$ ) ( $[\alpha]_{\text{D}}^{20}$  –33 (c 0.43,  $\text{CHCl}_3$ )) [2]; IR (ATR)  $\nu_{\text{max}}$  ( $\text{cm}^{-1}$ ) 3444, 1694;  $^1\text{H}$  NMR (400 MHz,  $\text{CDCl}_3$ ) and  $^{13}\text{C}$  NMR (100 MHz,  $\text{CDCl}_3$ ) data were found to be in agreement with previous study [2]; ESIMS  $m/z$  359  $[\text{M} + \text{Na}]^+$ .

### ECD calculations

The lowest energies of 1R,2R,3R,6R,9R,10R,14R-**2** and 1S,2S,3S,6S,9S,10S,14S-**2** were calculated and the data analyzed using Gaussian 09 software (Gaussian Inc., Wallingford, CT, USA). Density functional theory (DFT) at the B3LYP/6-31G(d) level in the gas phase was used to obtain the restricted conformation. The minimal energies of 20 conformers were computed using the time-dependent density functional theory (TDDFT) methodology at the B3LYP/6-311++G(d,p) level. The final ECD files were generated using GaussSum 2.2.5 software with a bandwidth  $\sigma$  of 0.5 eV. The calculated ECD and experimental ECD curves were drawn using Excel.

### Superoxide anion generation and elastase release by human neutrophils

Human neutrophils were obtained by means of dextran sedimentation and Ficoll centrifugation [5]. Measurements of elastase release and superoxide anion generation were carried out according to previously described procedures [6–7]. Briefly, superoxide anion production was assayed by monitoring the superoxide dismutase-inhibitable reduction of ferricytochrome c. Elastase release experiments were performed using MeO-Suc-Ala-Ala-Pro-Valp-nitroanilide as the elastase substrate.

### Acknowledgments

This research was supported by grants from the National Museum of Marine Biology and Aquarium; the National Dong Hwa University; and the Ministry of Science and Technology (Grant Nos MOST 106-2320-B-291-001-MY3 and 107-2320-B-291-001-MY3), Taiwan, awarded to P.J.S.

### Appendix A. Supplementary data

Supplementary data to this article can be found online at <https://doi.org/10.1016/j.tetlet.2019.151300>.

### References

- [1] K.Y. Peng, N.F. Chen, Z.C. Chen, K.H. Tsui, Z.H. Wen, Y.D. Su, Y.C. Chang, Y.H. Chen, M.C. Lu, L.S. Fang, J.J. Chen, T.Y. Wu, Y.C. Wu, P.J. Sung, *Tetrahedron Lett.* 57 (2016) 4239–4242.
- [2] F.Y. Chang, U. Chokkalingam, C.J. Tai, C.Y. Huang, W.C. Wei, N.S. Yang, J.H. Su, P.J. Sung, J.H. Sheu, *Tetrahedron* 72 (2016) 192–198.
- [3] P. Radhika, *Biochem. Syst. Ecol.* 34 (2006) 781–789.
- [4] F.M. Bayer, *Proc. Biol. Soc. Wash.* 94 (1981) 902–947.
- [5] T.L. Hwang, H.W. Hung, S.H. Kao, C.M. Teng, C.C. Wu, S.J. Cheng, *Mol. Pharmacol.* 64 (2003) 1419–1427.
- [6] H.P. Yu, P.W. Hsieh, Y.J. Chang, P.J. Chung, L.M. Kuo, T.L. Hwang, *Free Radic. Biol. Med.* 50 (2011) 1737–1748.
- [7] T.L. Hwang, C.C. Wang, Y.H. Kuo, H.C. Huang, Y.C. Wu, L.M. Kuo, Y.H. Wu, *Biochem. Pharmacol.* 80 (2010) 1190–1200.



## Full length article

Asiatic acid, an active substance of *Centella asiatica*, presynaptically depresses glutamate release in the rat hippocampusCheng Wei Lu<sup>b,d</sup>, Tzu Yu Lin<sup>b,d</sup>, Su Jane Wang<sup>a,c,\*</sup>, Shu Kuei Huang<sup>b</sup><sup>a</sup> School of Medicine, Fu Jen Catholic University, No.510, Zhongzheng Rd., Xinzhuang Dist., New Taipei City, Taiwan, 24205<sup>b</sup> Department of Anesthesiology, Far-Eastern Memorial Hospital, Pan-Chiao District, New Taipei City, Taiwan, 22060<sup>c</sup> Research Center for Chinese Herbal Medicine, College of Human Ecology, Chang Gung University of Science and Technology, Taoyuan City, Taiwan<sup>d</sup> Department of Mechanical Engineering, Yuan Ze University, Taoyuan, Taiwan, 320

## ARTICLE INFO

## Keywords:

Asiatic acid  
Glutamate release  
Voltage-dependent calcium channels  
Protein kinase C  
Hippocampus  
Presynaptic inhibition

## ABSTRACT

Inhibiting glutamate release can reduce neuronal excitability and is recognized as a key mechanism of anti-epileptic drugs. In this study, by using isolated nerve terminal (synaptosome) and slice preparations, we investigated the effect of asiatic acid, a triterpene isolated from *Centella asiatica* with antiepileptic activity, on glutamate release in the hippocampus of rats. In hippocampal synaptosomes, application of asiatic acid resulted in a concentration-dependent inhibition of 4-aminopyridine-evoked glutamate release. This inhibitory action was dependent on extracellular calcium, blocked by inhibiting the vesicular transporter, but was unaffected by inhibiting the glutamate transporter. In addition, asiatic acid decreased the 4-aminopyridine-induced increase in the intraterminal calcium and failed to alter the synaptosomal potential. Furthermore, the asiatic acid-mediated release inhibition was significantly suppressed by the N- and P/Q-type calcium channel inhibitor  $\omega$ -conotoxin MVIIC or protein kinase C inhibitor GF109203X. Western blotting data in synaptosomes also revealed that asiatic acid reduced 4-aminopyridine-induced phosphorylation of protein kinase C. In hippocampal slices, asiatic acid decreased the frequencies of spontaneous excitatory postsynaptic currents without changing their amplitudes and glutamate-activated currents in CA3 pyramidal neurons. We also observed that asiatic acid significantly suppressed 4-aminopyridine-induced burst firing. These data suggest that, in rat hippocampal nerve terminals, asiatic acid attenuates the calcium influx via N- and P/Q-type calcium channels, subsequently suppressing protein kinase C activity and decreasing glutamate release.

## 1. Introduction

Epilepsy is a chronic brain disease that has been estimated to affect about 60 million people worldwide (Schmidt and Sillanpaa, 2012; Fisher et al., 2014). The use of antiepileptic drugs is the primary therapy for treating epilepsy. However, current antiepileptic drugs have numerous adverse effects, and 20%–30% of patients exhibit only partial or no response to these drugs (Perucca and Gilliam, 2012; Löscher et al., 2013). Accordingly, the discovery of a novel antiepileptic drug with better efficacy and fewer side effects is of fundamental importance.

Natural products from herbs have contributed significantly in antiepileptic drug discovery and development (Mukerjee and Wahil, 2006; Zhao et al., 2018; Emilie et al., 2019). *Centella asiatica* (L.) Urban (Apiaceae) is widely used in Asia as a medicinal herb (Gohil et al., 2010; Orhan, 2012). The health properties of *Centella asiatica* have been extensively studied, especially with respect to its neuroprotective and

antiepileptic activity (Visweswari et al., 2010a, 2010b; Lokanathan et al., 2016). This medicinal plant contains several active constituents, the principal one being asiatic acid (Fig. 1A), which is a triterpenoid (Nasir et al., 2011). Evidence has revealed that asiatic acid can freely penetrate through the blood-brain barrier (Raval et al., 2015) and possess antioxidant, anti-inflammatory, cognitive-enhancing, neuro-protective, and antiepileptic properties (Nasir et al., 2011; Chao et al., 2016; Loganathan and Thayumanavan, 2018; Park et al., 2017; Wang et al., 2018b).

The relevance of excitatory neurotransmitter glutamate to epilepsy and antiepileptic mechanisms is receiving growing attention (Chapman, 2000; Lason et al., 2013). Glutamate levels are elevated in patients with epilepsy (Cavus et al., 2016a, 2016b) and lower in those taking antiepileptic medications (Kalviainen et al., 2003; Kammerer et al., 2011). Thus, interventions for inhibiting glutamate release could be a potential approach in the treatment of epilepsy. The antiepileptic effects of

\* Corresponding author. School of Medicine, Fu Jen Catholic University, 510, Chung-Cheng Rd., Hsin-Chuang, New Taipei, Taiwan, 4205.

E-mail address: [med0003@mail.fju.edu.tw](mailto:med0003@mail.fju.edu.tw) (S.J. Wang).

<https://doi.org/10.1016/j.ejphar.2019.172781>

Received 26 June 2019; Received in revised form 25 October 2019; Accepted 4 November 2019

Available online 07 November 2019

0014-2999/ © 2019 Elsevier B.V. All rights reserved.

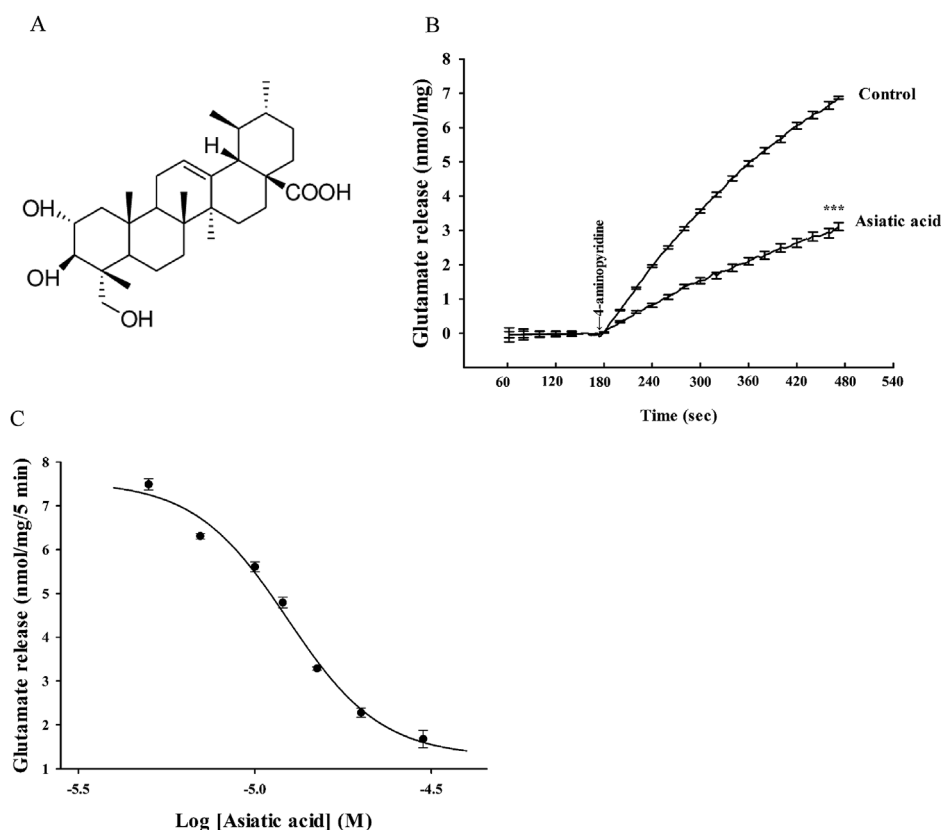


**Fig. 1.** Asiatic acid inhibits the 4-aminopyridine-evoked glutamate release in rat hippocampal synaptosomes. (A) Chemical structure of asiatic acid. (B) Glutamate release was evoked by the addition of 4-aminopyridine (1 mM) in the absence (control) or in the presence of asiatic acid (15  $\mu$ M). (C) Dose-response curve, showing the effect of asiatic acid (5–30  $\mu$ M) on 4-aminopyridine-evoked glutamate release. Data are mean  $\pm$  S.E.M. ( $n = 5-11$ ). \*\*\* $P < 0.001$  compare with control.

several agents with glutamate release inhibiting property such as vinpocetine, propylparaben, carbamazepine, and lamotrigine, have been reported in various animal models (Sitges et al., 2011; Deng et al., 2013). Although the antiepileptic effect of asiatic acid has been demonstrated (Umka et al., 2016; Wang et al., 2018b), whether asiatic acid influences glutamate release remains unknown. This work therefore investigates the effect and possible mechanisms of asiatic acid on glutamate release in the hippocampus of rats using isolated nerve terminal (synaptosome) and brain slice preparations. The mechanisms examined include intraterminal calcium concentration, nerve terminal membrane potential, nerve terminal calcium channel and protein kinase activity, as well as spontaneous excitatory postsynaptic currents.

## 2. Materials and methods

### 2.1. Chemicals

7-chloro-5-(2-chlorophenyl)-1,5-dihydro-4,1-benzothiazepin-2(3H)-one (CGP37157), dantrolene, DL-threo- $\beta$ -benzyloxyaspartate (DL-TBOA),  $\omega$ -conotoxin MVIIC, and GF109203X were purchased from Tocris Cookson (Bristol, UK). Fura-2-acetoxy-methyl ester (Fura-2-AM) and 3', 3', 3'-Dipropylthiadiazocarbocyanine iodide [DiSC<sub>3</sub>(5)] were purchased from Invitrogen (Carlsbad, CA, USA). Asiatic acid, 4-aminopyridine, tetrodotoxin, bicuculline, and all other chemicals were purchased from Sigma-Aldrich Co. (St. Louis, MO, USA).

### 2.2. Animals

Male Sprague-Dawley rats (14–23 days old and 150–200 g) were purchased from BioLASCO, Taiwan. Animals were housed in acrylic cage (40 cm  $\times$  25 cm  $\times$  26 cm) on a 12 h light/dark cycle under regulated temperature and humidity and fed with standard diet and water ad libitum. The experiments on animals have been approved by the Institutional Animal Care and Use Committee at the Fu Jen Catholic

University (AE10561).

### 2.3. Preparation of synaptosomes

Synaptosomes were isolated from rat hippocampus as previously reported (Wang et al., 2018a). Briefly, the hippocampus was homogenized in medium containing 320 mM sucrose (pH 7.4) and centrifuged (2 min, 3,000 g at 4  $^{\circ}$ C). The supernatant was gently placed on a 2 ml Percoll discontinuous gradients (3%, 10%, and 23% Percoll) and centrifuged at 32,500 g for 7 min at 4  $^{\circ}$ C. Synaptosomes placed between the 10% and the 23% Percoll bands was subsequently collected and diluted in 30 ml Hepes-buffered medium (5 mM KCl, 140 mM NaCl, 1.2 mM Na<sub>2</sub>HPO<sub>4</sub>, 5 mM NaHCO<sub>3</sub>, 1 mM MgCl<sub>2</sub>·6H<sub>2</sub>O, 10 mM glucose and 10 mM Hepes at pH 7.4) before centrifuged at 27,000 g for 10 min. The pellets were resuspended in 3 ml Hepes-buffered medium and the protein content was determined by the Bradford assay.

### 2.4. Glutamate release assay

Glutamate release from synaptosomes (0.5 mg of total protein) re-suspended in 2 ml of Hepes-buffered medium was assayed by on-line fluorimetry (Nicholls et al., 1987; Wang et al., 2014). Release was triggered with 4-aminopyridine (1 mM) and examined by measuring the increase of fluorescence (excitation and emission wavelengths of 340 and 460 nm, respectively) at 2 s intervals. The released glutamate was calculated by the addition of glutamate (5 nmol) at the end of each experiment. Data was expressed as nmol glutamate per mg synaptosomal protein (nmol/mg).

### 2.5. Membrane potential measurement using DiSC<sub>3</sub>(5)

Synaptosomes were resuspended in 2 ml Hepes-buffered medium and incubated for 3 min at 37  $^{\circ}$ C. DiSC<sub>3</sub>(5) (5  $\mu$ M) was then added and allowed a 5 min equilibration. DiSC<sub>3</sub>(5) fluorescence was monitored at

646 and 674 nm (Åkerman et al., 1987). Data were collected at 2 s intervals.

## 2.6. Cytosolic free $\text{Ca}^{2+}$ concentration ( $[\text{Ca}^{2+}]_C$ )

Synaptosomes were preincubated in Hepes-buffered medium containing Fura-2-AM (5  $\mu\text{M}$ ) and  $\text{CaCl}_2$  (0.1 mM) for 30 min at 37 °C as previously described (Lin et al., 2013). After incubation, synaptosomes were centrifuged at 3000 g for 30 s and the pellet was resuspended in HBM containing  $\text{CaCl}_2$  (1.2 mM). Fluorescence was measured at 340 and 505 nm and data were collected at 5 s intervals. The  $[\text{Ca}^{2+}]_C$  (nM) was calculated using equations described previously (Gryniewicz et al., 1985).

## 2.7. Immunoblotting assay

Proteins (20  $\mu\text{g}$ ) were separated by 10% SDS-PAGE, 12% polyacrylamide, and then transferred onto polyvinylidene difluoride membranes. For immunoblotting, membranes were blocked in Tris-buffered saline containing 5% skimmed milk and incubated with primary antibodies (anti-phospho-PKC 1:2000 or anti- $\beta$ -actin 1:5000; Cell Signaling Technology, MA, USA) overnight at 4 °C. After extensive wash and incubation with peroxidase-conjugated goat anti-rabbit secondary antibody (1:5000; Santa Cruz, CA, USA), immunoreactivity was detected by using the chemiluminescence Western blot detection system.

## 2.8. Brain slice preparation and electrophysiological recordings

Hippocampal slices were prepared as previously described (Chang et al., 2015). In brief, the brain of 14–23-day-old male rat was rapidly removed from the skull after decapitation. The brain was cut into 300- $\mu\text{m}$ -thick transverse hippocampal slices using a vibratome (VT1000S, Leica, Germany). The slices were then maintained in artificial cerebrospinal fluid comprising (in mM) 117 NaCl, 2.5  $\text{CaCl}_2$ , 4.7 KCl, 1.2  $\text{MgCl}_2$ , 1.2  $\text{NaH}_2\text{PO}_4$ , 25  $\text{NaHCO}_3$ , 11 glucose and saturated with 95%  $\text{O}_2$ –5%  $\text{CO}_2$  (pH 7.4, 300 mOsm) at 37 °C for 1 h before recording.

Brain slices were transferred to an immersion recording chamber mounted on the stage of an upright microscope (Olympus BX51W1, Tokyo, Japan), and continuously perfused with gassed artificial cerebrospinal fluid (1–2 ml/min). Patch electrode were pulled from borosilicate glass (outer diameter, 1.5 mm; internal diameter, 0.86 mm; Harvard, apparatus, Holliston, MA, USA) by using a micropipette puller (P87, Sutter Instruments, Novato, CA, USA) with a resistance of 2–5 M $\Omega$  and then filled with internal solution containing (in mM) 135 K-glucuronate, 0.3  $\text{Na}_3\text{GTP}$ , 2  $\text{MgCl}_2$ , 0.1 EGTA, 20 KCl, 4  $\text{Na}_2\text{ATP}$ , and 10 HEPES (pH 7.3 with KOH, 280 mOsm). Pyramidal neurons in the hippocampal CA3 region were visually identified using an infrared differential interference contrast microscope equipped with a 40  $\times$  water immersion objective (Olympus, Tokyo, Japan). Whole-cell recordings in voltage clamp or current clamp mode were performed using an Axopatch 200B amplifier (Axon Instruments, Foster City, CA, USA) connected to a Digidata 1500 interface (Axon). Cells were used only when access resistance (8–30 M $\Omega$ ) did not change by > 20% throughout the experiment. Synaptic currents were low-pass filtered at 2 kHz, digitized, and stored on desks using pCLAMP 10.0 software (Molecular Devices, Union City, CA, USA).

## 2.9. Data analysis

Data were presented as mean  $\pm$  S.E.M. The data reported were analyzed by the unpaired Student's t-test or by one-way ANOVA.  $P < 0.05$  was considered significant.

## 3. Results

### 3.1. Asiatic acid inhibits the glutamate release evoked by 4-aminopyridine in rat hippocampal synaptosomes

To examine the presynaptic action of asiatic acid specifically, first we tested the effect of asiatic acid on glutamate release from hippocampal synaptosomes. We depolarized synaptosomes with the  $\text{K}^+$  channel blocker 4-aminopyridine that opens voltage-dependent calcium channels and induces glutamate release (McMahon and Nicholls, 1991). When hippocampal synaptosomes were exposed to 4-aminopyridine (1 mM) in the presence of  $\text{CaCl}_2$  (1.2 mM), the release of glutamate was increased. Application of asiatic acid (15  $\mu\text{M}$ ) caused an depression of 4-aminopyridine-induced release of glutamate by about 56% [ $t(14) = 45.6$ ,  $P < 0.001$ ] (Fig. 1B). This release inhibition was concentration-dependent with an  $\text{IC}_{50}$  of about 13  $\mu\text{M}$  (Fig. 1C). Asiatic acid (15  $\mu\text{M}$ ) did not alter the basal release.

### 3.2. Effect of extracellular calcium chelation, bafilomycin A1, and DL-TBOA on asiatic acid-mediated release inhibition in synaptosomes

In Fig. 2, in the presence of calcium-free medium containing 300  $\mu\text{M}$  EGTA, the glutamate release evoked by 4-aminopyridine was decreased by 74% [ $F(2,12) = 390.0$ ,  $P < 0.001$ ]. This 4-aminopyridine-induced calcium-independent glutamate release was not affected by asiatic acid (15  $\mu\text{M}$ ) ( $P = 0.95$ ). On the other hand, the glutamate transporter blocker DL-TBOA (10  $\mu\text{M}$ ) increased 4-aminopyridine (1 mM)-induced release of glutamate ( $P < 0.001$ ). In the presence of DL-TBOA (10  $\mu\text{M}$ ), asiatic acid (15  $\mu\text{M}$ ) still produced a significant depression on the glutamate release induced by 4-aminopyridine [ $F(2,12) = 52.5$ ,

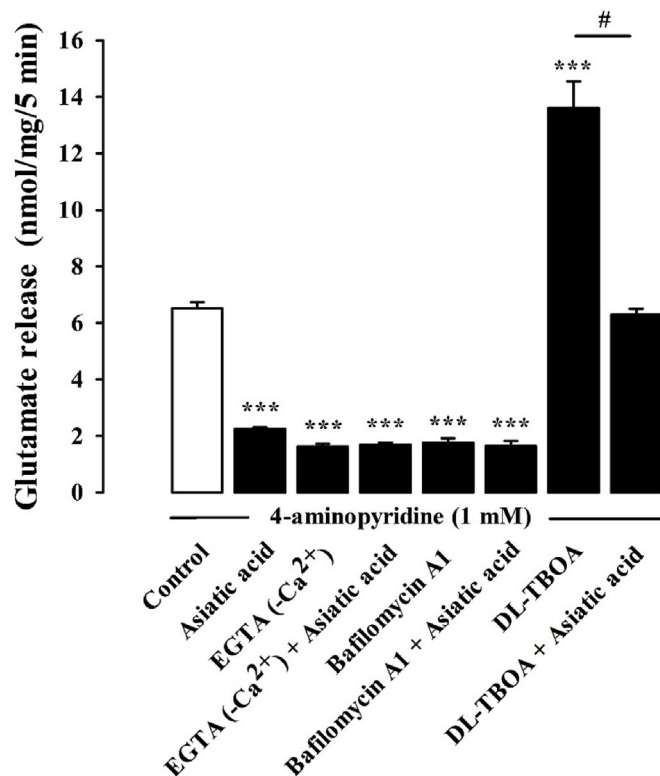


Fig. 2. Effect of EGTA 300  $\mu\text{M}$  (external calcium omission), the glutamate transporter blocker DL-TBOA 10  $\mu\text{M}$ , and the vesicular transporter inhibitor bafilomycin A1 0.1  $\mu\text{M}$  on the asiatic acid (15  $\mu\text{M}$ )-mediated inhibition of 4-aminopyridine-evoked glutamate release. Each column is mean  $\pm$  S.E.M. ( $n = 5$ ). \*\*\* $P < 0.001$  compare with control. # $P < 0.05$  compare with DL-TBOA-treated group.



**Table 1**Effect of asiatic acid on synaptosomal membrane potential and cytosolic free  $\text{Ca}^{2+}$  concentration ( $[\text{Ca}^{2+}]_c$ ) in rat hippocampal synaptosomes.

	$[\text{Ca}^{2+}]_c$ (nM)			Membrane potential (fluorescence units)		
	Basal	4-aminopyridine	n	Basal	4-aminopyridine	n
Control	1146.2 $\pm$ 4.8	196.3 $\pm$ 3.9 <sup>a</sup>	5	0.4 $\pm$ 0.1	37.2 $\pm$ 2.3 <sup>a</sup>	5
Asiatic acid	1140.9 $\pm$ 6.2	162.8 $\pm$ 5.7 <sup>b</sup>	5	0.5 $\pm$ 0.1	36.3 $\pm$ 2.0	5

a,  $P < 0.001$  versus the control group; b,  $P < 0.001$  versus the 4-AP group.

$P < 0.001$ , Fig. 2]. By contrast, the vesicular transporter inhibitor bafilomycin A1 (0.1  $\mu\text{M}$ ) decreased the glutamate release induced by 4-aminopyridine (1 mM) [ $F(2,12) = 232.2$ ,  $P < 0.001$ ]. In the presence of bafilomycin A1, however, asiatic acid (15  $\mu\text{M}$ ) failed to decrease 4-aminopyridine-induced glutamate release further ( $P = 0.89$ , Fig. 2). DL-TBOA and bafilomycin A1 did not alter the basal release.

### 3.3. Effect of asiatic acid on the synaptosomal membrane potential and $[\text{Ca}^{2+}]_c$

Table 1 shows that DiSC<sub>3</sub>(5) fluorescence was increased by 4-aminopyridine (1 mM) [ $t(8) = -15.7$ ,  $P < 0.001$ ] and this increase was unaffected in the presence of asiatic acid (10  $\mu\text{M}$ ) [ $t(8) = 0.28$ ,  $P = 0.79$ ]. In addition, 4-aminopyridine (1 mM) caused a rise in  $[\text{Ca}^{2+}]_c$  to a plateau level. Application of asiatic acid (15  $\mu\text{M}$ ) had no effect on the basal  $\text{Ca}^{2+}$  levels, but caused an 56% decreased in the 4-aminopyridine-induced rise in  $[\text{Ca}^{2+}]_c$  [ $t(8) = 4.31$ ,  $P < 0.001$ ] (Table 1).

### 3.4. Effect of $\omega$ -conotoxin MVIIC, CGP37157, and dantrolene on asiatic acid-mediated release inhibition in synaptosomes

In Fig. 3, the glutamate release induced by 4-aminopyridine (1 mM) was reduced when the N- and P/Q-type  $\text{Ca}^{2+}$  channel blocker  $\omega$ -conotoxin MVIIC (4  $\mu\text{M}$ ) was added [ $F(2,15) = 779.9$ ,  $P < 0.001$ ]. In the presence of  $\omega$ -conotoxin MVIIC (4  $\mu\text{M}$ ), asiatic acid (15  $\mu\text{M}$ ) decreased 4-aminopyridine-induced glutamate release only by 8.7% which was significantly less than when asiatic acid was applied alone (56%;  $P < 0.05$ ). In addition, the ryanodine-sensitive receptor antagonist dantrolene (10  $\mu\text{M}$ ), known to inhibit  $\text{Ca}^{2+}$  release from endoplasmic reticulum stores, reduced the glutamate release induced by 4-aminopyridine (1 mM) ( $P < 0.001$ ). In the presence of dantrolene, asiatic acid (15  $\mu\text{M}$ ) could still effectively reduced release. A statistical difference was observed between the release after dantrolene alone and after the dantrolene and asiatic acid treatment [ $F(2,13) = 337.1$ ,  $P < 0.001$ ]. Similar result was also obtained with the mitochondrial  $\text{Na}^+/\text{Ca}^{2+}$  exchange inhibitor CGP37157 [ $F(2,13) = 207.3$ ,  $P < 0.001$ ].

### 3.5. Contribution of protein kinase C to the asiatic acid-mediated release inhibition

Fig. 4A shows that GF109203X (10  $\mu\text{M}$ ), the specific inhibitor of protein kinase C, decreased the glutamate release induced by 4-aminopyridine (1 mM) [ $F(2,13) = 305.8$ ,  $P < 0.001$ ]. When GF109203X (10  $\mu\text{M}$ ) and asiatic acid (15  $\mu\text{M}$ ) were applied simultaneously, the release inhibition was not different from the GF109203X alone ( $P = 1$ ). In addition, Fig. 4B shows that 4-aminopyridine (1 mM) significantly increased protein kinase C phosphorylation in hippocampal synaptosomes ( $P < 0.001$ ). This 4-aminopyridine-increased phosphorylation was also decreased in the presence of asiatic acid (15  $\mu\text{M}$ ) [ $F(2,12) = 18.5$ ,  $P < 0.001$ ].

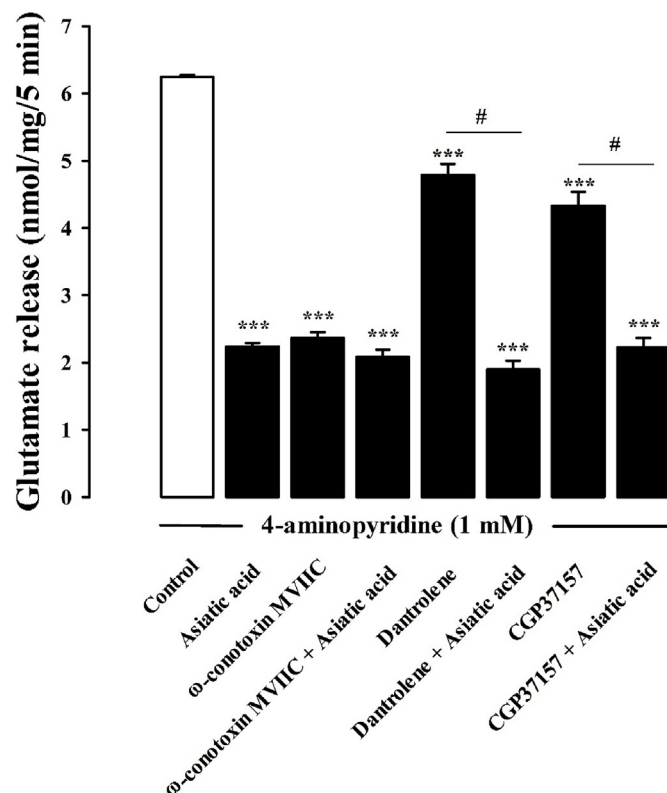
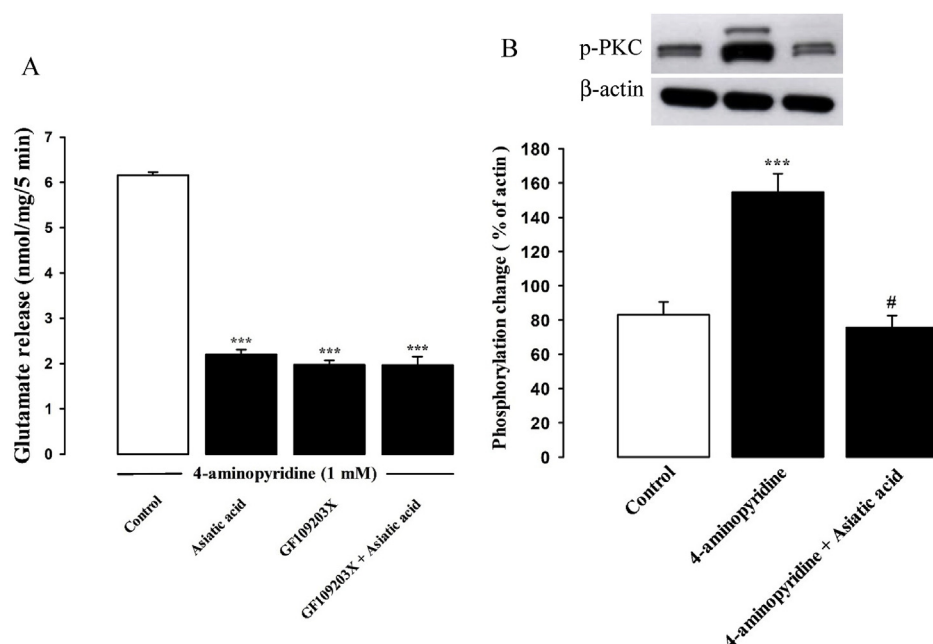


Fig. 3. Effect of N- and P/Q-type  $\text{Ca}^{2+}$  channel blocker  $\omega$ -conotoxin MVIIC 4  $\mu\text{M}$  or intracellular  $\text{Ca}^{2+}$  release inhibitors dantrolene 10  $\mu\text{M}$  and CGP37157 10  $\mu\text{M}$  on the asiatic acid (15  $\mu\text{M}$ )-mediated inhibition of 4-aminopyridine-evoked glutamate release. Each column is mean  $\pm$  S.E.M. ( $n = 5-6$ ). \*\*\* $P < 0.001$  compare with control. # $P < 0.05$  compare with dantrolene- or CGP37157-treated group.

### 3.6. Effect of asiatic acid on spontaneous and miniature excitatory postsynaptic currents in hippocampal slices

Whole-cell voltage clamp ( $V_h = -70$  mV) was used to record spontaneous excitatory postsynaptic currents (sEPSCs) in the presence of bicuculline (20  $\mu\text{M}$ ; the  $\gamma$ -aminobutyric acid type A receptor antagonist). As shown in Fig. 5A, superfusion of asiatic acid (15  $\mu\text{M}$ ) for 10 min produced a detectable changes in sEPSCs. Quantification of the results further reveals that asiatic acid produced a significant decrease in the sEPSC frequency [ $t(8) = 12.8$ ,  $P < 0.001$ ], but it had no effect on the sEPSC amplitude [ $t(8) = 0.63$ ,  $P = 0.55$ ] (Fig. 5B). On the other hand, we recorded miniature excitatory postsynaptic currents (mEPSCs) in the presence of bicuculline 20  $\mu\text{M}$  and tetrodotoxin (1  $\mu\text{M}$ ;  $\text{Na}^+$  channel blocker). Similar to the sEPSCs results, superfusion of asiatic acid (15  $\mu\text{M}$ ) produced a reduction in mEPSC frequency [ $t(8) = 5.75$ ,  $p < 0.001$ ] without any significant change in mEPSC amplitude [ $t(8) = 0.07$ ,  $P = 0.94$ ] (Fig. 6A and B).





**Fig. 4.** Decreased protein kinase C activation involves in the asiatic acid-mediated inhibition of 4-aminopyridine-evoked glutamate release in hippocampal synaptosomes. (A) Effect of the protein kinase C inhibitor GF109203  $\times$  10  $\mu$ M on the asiatic acid (15  $\mu$ M)-mediated inhibition of 4-aminopyridine-evoked glutamate release. (B) Effect of asiatic acid (15  $\mu$ M) on the activation of protein kinase C. The expression levels of p-protein kinase C and  $\beta$ -actin in synaptosomes were determined by western blotting. Each column is mean  $\pm$  S.E.M. (n = 5–7). \*\*\*p < 0.001 compare with control. #P < 0.05 compare with 4-AP alone.

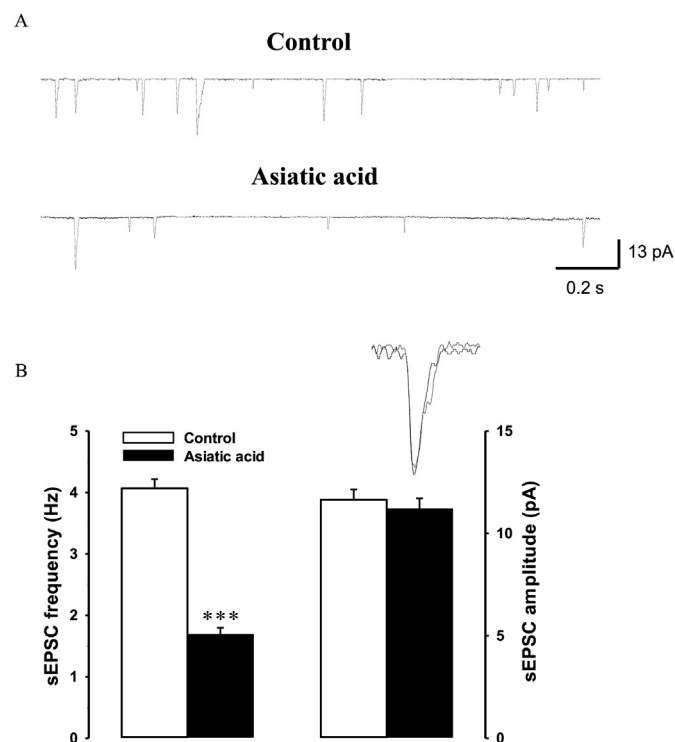


**Fig. 5.** Effect of asiatic acid on sEPSCs in rat hippocampal CA3 pyramidal neurons. (A) Sample traces recorded before and after exposure to asiatic acid (15  $\mu$ M, 10 min). (B) Quantification of the changes in the sEPSC frequency and amplitude before (control) and after asiatic acid. Inset, traces illustrating quanta events. Data are mean  $\pm$  S.E.M. (n = 5). \*\*\*P < 0.001 compare with control.

### 3.7. Effect of asiatic acid on glutamate-induced currents in hippocampal slices

In Fig. 7, a direct postsynaptic effect of asiatic acid on glutamate-induced currents ( $I_{Glu}$ ) was determined by exogenously applied glutamate (100  $\mu$ M). In the presence of tetrodotoxin (0.5  $\mu$ M), application of glutamate (100  $\mu$ M) induced an inward current. No significant

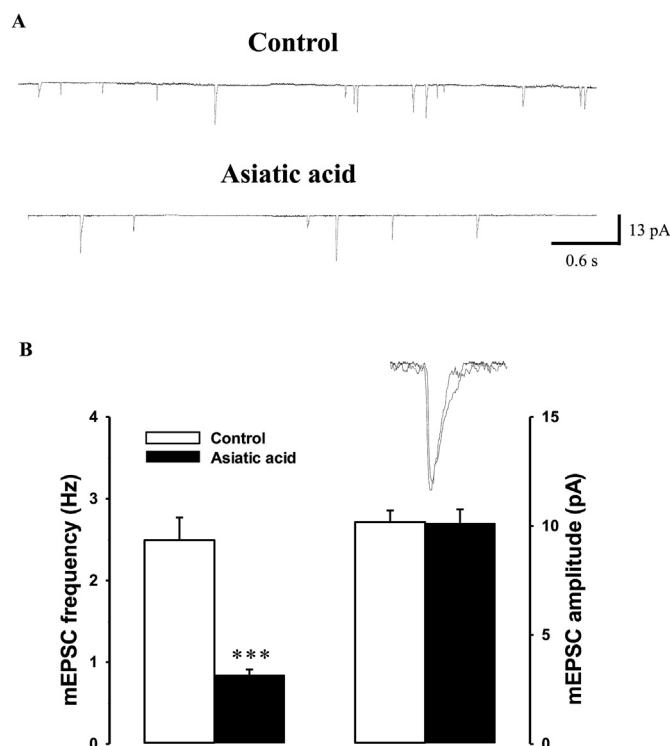


**Fig. 6.** Effect of asiatic acid on mEPSCs in rat hippocampal CA3 pyramidal neurons. (A) Sample traces recorded before and after exposure to asiatic acid (15  $\mu$ M, 10 min). (B) Quantification of the changes in the mEPSC frequency and amplitude before (control) and after asiatic acid. Inset, traces illustrating quanta events. Data are mean  $\pm$  S.E.M. (n = 5). \*\*\*P < 0.001 compare with control.

alterations in the postsynaptic glutamate response were observed in the presence of asiatic acid (15  $\mu$ M) [t(8) = 0.01, P = 0.99].

### 3.8. Effect of asiatic acid on the burst firing induced by 4-aminopyridine in hippocampal slices

In the final part of this work, to further evaluate the consequences of

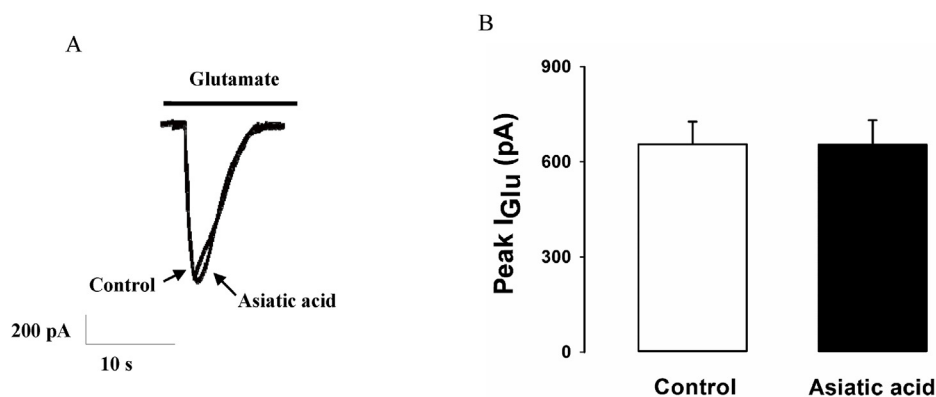


**Fig. 7.** Effect of asiatic acid on glutamate-induced postsynaptic currents ( $I_{Glu}$ ) in rat hippocampal CA3 pyramidal neurons. Sampled  $I_{Glu}$  and average peak  $I_{Glu}$  before (control) and after exposure to asiatic acid (15  $\mu$ M, 10 min). Data are mean  $\pm$  S.E.M. (n = 5). \*\*\*P < 0.001 compare with control.

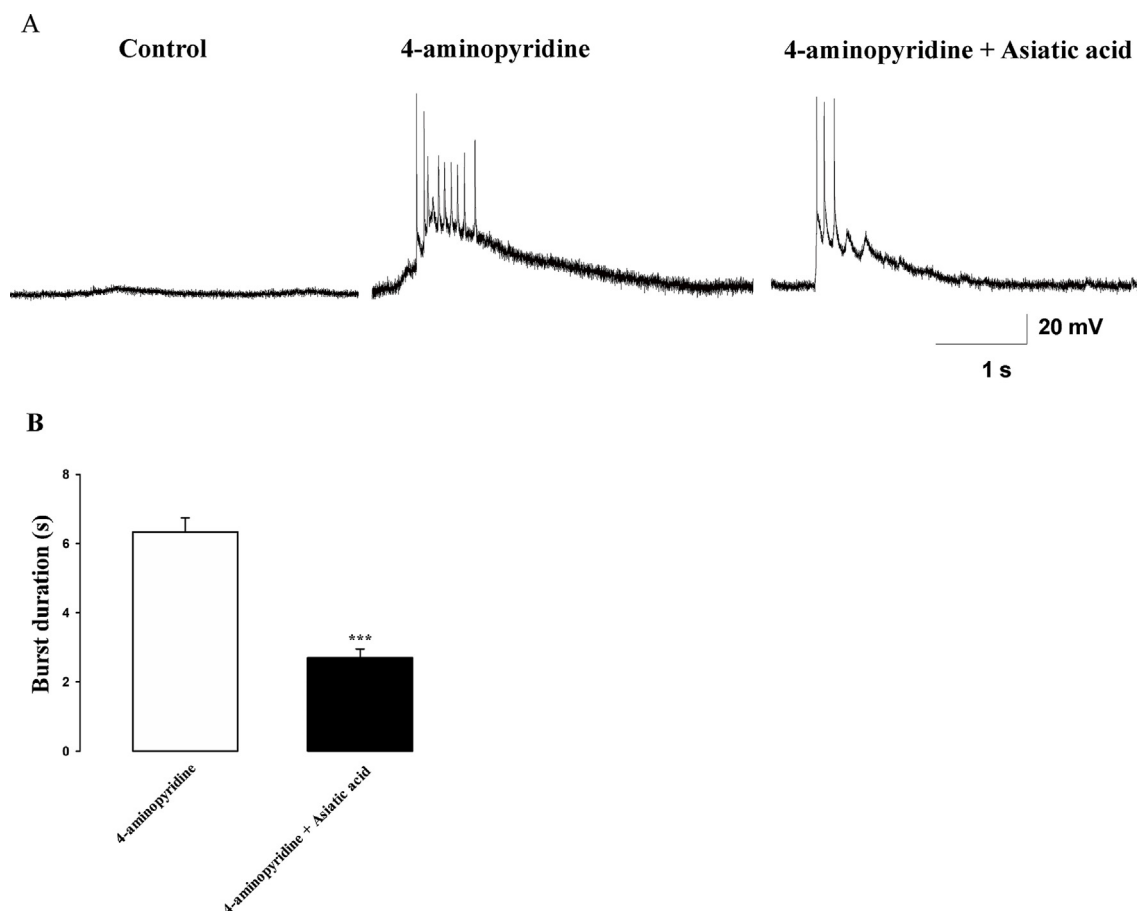


**Fig. 8.** Effect of asiatic acid on 4-aminopyridine-induced burst firing in rat hippocampal CA3 pyramidal neurons. (A) Sampled burst firing in control, 4-aminopyridine (100  $\mu$ M), and 4-aminopyridine (100  $\mu$ M) + asiatic acid (15  $\mu$ M). Asiatic acid was added 10 min after the application of 4-aminopyridine. (B) Bar graphs represent the mean  $\pm$  S.E.M. of the burst duration (n = 6). Duration of burst responses was measured as the time from the initial depolarization to 90% of its decay phase. \*\*\*P < 0.001 versus 4-aminopyridine group.

the inhibition of glutamatergic synaptic activity using asiatic acid, we performed current-clamp recording to examine the effect of asiatic acid on 4-aminopyridine-induced burst firing in CA3 neurons. In Fig. 8A after 10 min application of 100  $\mu$ M 4-aminopyridine, neurons generated spontaneous burst discharges. 10 min after application of asiatic acid (15  $\mu$ M), the burst duration induced by 4-aminopyridine was decreased by an average of 57.2%  $\pm$  2.8% [control, 6.3  $\pm$  0.4 s; asiatic acid, 2.7  $\pm$  0.3 s; t(10) = 7.5, P < 0.001; Fig. 8B].

#### 4. Discussion

Herbal plants and their bioactive compounds are attractive sources for the development of novel drugs and have been suggested to produce promising results for treating epilepsy (Zhao et al., 2018). Asiatic acid is a triterpene isolated from *Centella asiatica* and has been reported to display antiepileptic activity (Umka et al., 2016; Wang et al., 2018b). In the current study, we are particularly interested in investigating the relation between asiatic acid and the modulation of glutamate release, considering that an increased glutamate concentration in the

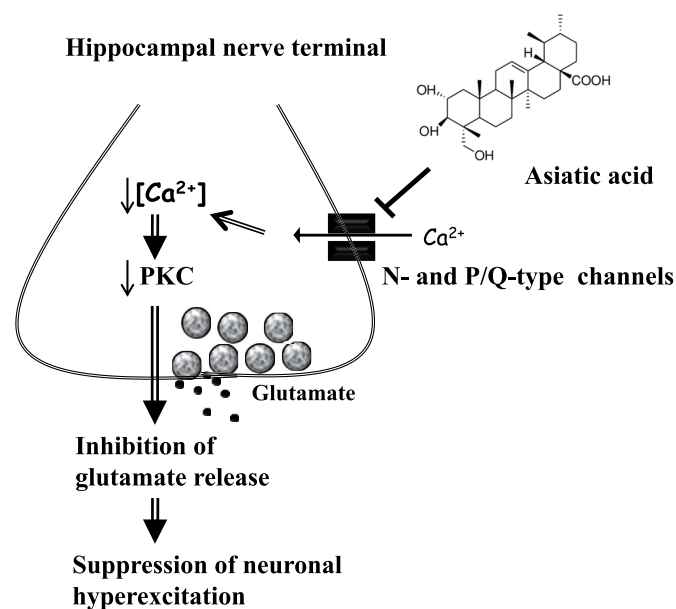


**Fig. 9.** Potential mechanisms by which asiatic acid inhibits glutamate release from rat hippocampal nerve terminals. Asiatic acid decreases the  $Ca^{2+}$  influx through N- and P/Q-type  $Ca^{2+}$  channels, which subsequently reduces protein kinase C activity to cause a decrease in glutamate release and neuronal hyperexcitation.

hippocampus has been observed in patients with epilepsy (Cavus et al., 2016a, 2016b). Furthermore, inhibiting glutamate release can reduce neuronal excitability and is recognized as a key mechanism of anti-epileptic drugs (<https://www.ncbi.nlm.nih.gov/pmc/articles/PMC2801216/>, Cunningham et al., 2004; Deng et al., 2013). Therefore, the study of the effect of asiatic acid on glutamate release is of great value.

Using hippocampal nerve terminal preparations, we discovered that asiatic acid inhibited glutamate release. This presynaptic inhibition could be ascribed to a reduction in the nerve terminal excitability or a direct inhibition of voltage-dependent calcium channels affecting the calcium influx (Nicholls, 1998). The results obtained in the present study indicated that asiatic acid inhibits 4-aminopyridine-induced glutamate release primarily by a decreased calcium entry via the N- and P/Q-type calcium channels, and this effect is not result from a decrease in the nerve terminal depolarization. First, the asiatic acid-mediated release inhibition was dependent on extracellular calcium, persisted in the presence of the glutamate transporter inhibitor, and blocked by the vesicular transporter inhibitor. Since depolarization-induced release of glutamate release can be sustained by different mechanisms including exocytosis and reversal of the glutamate transporter (Nicholls et al., 1987), our data suggest that asiatic acid inhibits 4-AP-evoked glutamate release by affecting the  $Ca^{2+}$ -dependent component of release rather than the  $Ca^{2+}$ -independent efflux due to the reversal of the glutamate transporter. Second, the membrane potential was unaffected by asiatic acid. Third, asiatic acid significantly reduced the sustained elevation in  $[Ca^{2+}]_i$  induced by 4-aminopyridine. This result is consistent with another work that showed that asiatic acid decreases the kainic acid-induced increase in intracellular calcium levels in PC12 cells (Wang et al., 2018b). Finally, the ability of asiatic acid to depress 4-aminopyridine-evoked glutamate release was abolished by inhibiting of N- and P/Q-type calcium channels, which are coupled to glutamate release from the nerve terminals (Millan and Sanchez-Prieto, 2002; Ladera et al., 2009; Lin et al., 2013). However, the asiatic acid-mediated release inhibition was not affected by dantrolene, an inhibitor of intracellular  $Ca^{2+}$  release from the endoplasmic reticulum, and CGP37157, a membrane-permeant blocker of mitochondrial  $Na^+/Ca^{2+}$  exchange, indicating that reduced calcium release from endoplasmic

reticulum and mitochondria was not involved in the action of asiatic acid. Although our observation suggests that the suppression of voltage-dependent calcium channels is involved in the asiatic acid-mediated release inhibition, how asiatic acid suppresses the activity of voltage-dependent calcium channels remains to be determined. Furthermore, the effect of asiatic acid was not completely abolished by the blockage of N- and P/Q-type calcium channels. The possibility that asiatic acid inhibits glutamate release by a mechanism other than suppressing N- and P/Q-type calcium channels cannot be ruled out.

During glutamate exocytotic process, some signal transduction pathways are activated, especially the protein kinase C cascade (Coffey et al., 1993; Millan et al., 2003). It was demonstrated that depolarization-induced increase in  $[Ca^{2+}]_i$  enhances protein kinase C activation and glutamate exocytosis (Coffey et al., 1993, 1994). In this study, the inhibitory action of asiatic acid on calcium influx may subsequently attenuate the protein kinase C activation to cause a decrease in evoked glutamate release. Concerning this hypothesis, we observed that the protein kinase C inhibitor GF109203X was sufficient to abolish the asiatic acid-mediated release inhibition. Furthermore, asiatic acid significantly decreased the phosphorylation of protein kinase C induced by 4-aminopyridine in synaptosomes.

In addition to the synaptosomal findings, we also discovered that asiatic acid reduced the frequency but not the amplitude of sEPSCs or mEPSCs in recordings from hippocampal slices. Generally, a reduction in the frequency of spontaneous release events is thought to reflect presynaptic effect, whereas a reduction in the amplitude normally suggests a decrease in postsynaptic sensitivity to the transmitter (Edwards, 2007). Therefore, our data indicate that the asiatic acid-mediated release inhibition is caused by a reduction in the probability of presynaptic glutamate release and not by a reduction in postsynaptic receptor sensitivity. This conclusion is supported by our observation that asiatic acid had no effect on exogenous glutamate-activated postsynaptic currents. On the other hand, we also observed that asiatic acid significantly suppressed the burst firing evoked by 4-aminopyridine in CA3 neurons; this effect is similar to the effect of the antiepileptic drugs carbamazepine and valproate (Smyth et al., 2002; Martín and Pozo, 2004). Based on these findings, we indicated that the suppression of burst firing by asiatic acid is due to a reduction of glutamate release, which decreased activation of glutamate receptor would lead to attenuate the depolarization of membrane potential which in turn reduces the level of neuronal hyperexcitation (Fig. 9). In consequence, our finding suggests that asiatic acid might prevent the generation and propagation of abnormal firing during epileptic seizures and these actions might possibly participate in the antiepileptic effect of asiatic acid. Mechanistically, drugs that are effective against generalized tonic-clonic and partial seizures usually inhibit sustained high-frequency repetitive firing of action potential by enhancing  $Na^+$  channel inactivation (Macdonald and Kelly, 1995). In this study, the possibility that asiatic acid acted by blocking  $Na^+$  channels, thereby inhibiting glutamate release could not be ruled out. On the other hand, other neurotransmitters are involved in the controlling of neuronal excitability besides glutamate. For example,  $\gamma$ -aminobutyric acid (GABA) is the primary inhibitory neurotransmitter in the brain producing inhibition through GABA<sub>A</sub> and GABA<sub>B</sub> receptors. The chloride channel of the GABA<sub>A</sub> receptor is responsible for the rapid hyperpolarization, and activation of GABA<sub>A</sub> receptor induces opening of chloride channel and subsequent hyperpolarization, which can result in a decrease of neuronal excitability (Solomon et al., 2019). Whether asiatic acid affects GABA release remains to be elucidated by additional studies.

The concentration (15  $\mu$ M) of asiatic acid used to depress glutamate release in the present work is consistent with that used in other studies. For example, asiatic acid, at a concentration of 20  $\mu$ M, attenuated methamphetamine- or kainic acid-induced neuroinflammation and neurotoxicity in human neuroblastoma dopaminergic SH-SY5Y cells and PC12 cells (Park et al., 2017; Wang et al., 2018b). In vivo studies have also reported that asiatic acid, at 20–75 mg/kg, exhibits cognition-

enhancing activity (Nasir et al., 2011; Sirichoat et al., 2015) and attenuates brain dysfunction induced by ischemia-, middle cerebral artery occlusion-, aluminum chloride-, or quinolinic acid (Lee et al., 2014; Loganathan and Thayumanavan, 2018; Ahmad et al., 2019). Furthermore, the administration of high dose of asiatic acid (165 mg/kg) does not produce any significant toxicity in rats (Krishnamurthy et al., 2009). Thus, the dose of asiatic acid we used may be considered safe.

In conclusion, the present experiments demonstrate that asiatic acid, an active constituent of *Centella asiatica*, presynaptically depresses glutamate release in the hippocampus. This finding not only reveals a action model of asiatic acid in the brain, but may also help explain its antiepileptic effect. Further investigations and clinical trials are warranted.

## Declaration of competing interest

The authors declare no conflict of interest.

## Acknowledgements

This research was supported by grants from the Ministry of Science and Technology (MOST 106-2320-B-030-002 MY3) and Far Eastern Memorial Hospital (FEMH-2017-D-003; FEMH-2017-C-008), Taiwan.

## References

- Ahmad Rather, A., Justin-Thenmozhi, A., Manivasagam, T., Saravanababu, C., Guillemin, G.J., Essa, M.M., 2019. Asiatic acid attenuated aluminum chloride-induced tau pathology, oxidative stress and apoptosis via AKT/GSK-3 $\beta$  signaling pathway in wistar rats. *Neurotox. Res.* 35, 955–968.
- Åkerman, K.E., Scott, I.G., Heikkilä, J.E., Heinonen, E., 1987. Ionic dependence of membrane potential and glutamate receptor-linked responses in synaptoneurosome as measured with a cyanine dye, DiSC-2(5). *J. Neurochem.* 48, 552–559.
- Cavus, I., Romanyshyn, J.C., Kennard, J.T., Farooque, P., Williamson, A., Eid, T., Spencer, S.S., Duckrow, R., Dziura, J., Spencer, D.D., 2016a. Elevated basal glutamate and unchanged glutamine and GABA in refractory epilepsy: microdialysis study of 79 patients at the yale epilepsy surgery program. *Ann. Neurol.* 80, 35–45.
- Cavus, I., Widi, G.A., Duckrow, R.B., Zaveri, H., Kennard, J.T., Krystal, J., Spencer, D.D., 2016b. 50 Hz hippocampal stimulation in refractory epilepsy: higher level of basal glutamate predicts greater release of glutamate. *Epilepsia* 57, 288–297.
- Chang, Y.C., Lin, T.Y., Lu, C.W., Wang, C.C., Wang, Y.C., Peter Chou, S.S., Wang, S.J., 2015. Apigenin, a natural flavonoid, inhibits glutamate release in the rat hippocampus. *Eur. J. Pharmacol.* 762, 72–81.
- Chao, P.C., Lee, H.L., Yin, M.C., 2016. Asiatic acid attenuated apoptotic and inflammatory stress in the striatum of MPTP-treated mice. *Food. Funct.* 7, 1999–2005.
- Chapman, A.G., 2000. Glutamate and epilepsy. *J. Nutr.* 130, 1043S–1045S.
- Coffey, E.T., Sihra, T.S., Nicholls, D., 1993. Protein kinase C and the regulation of glutamate exocytosis from cerebrocortical synaptosomes. *J. Biol. Chem.* 268, 21060–21065.
- Coffey, E.T., Herrero, I., Sihra, T.S., Sánchez-Prieto, J., Nicholls, D.G., 1994. Glutamate exocytosis and MARCKS phosphorylation are enhanced by a metabotropic glutamate receptor coupled to a protein kinase C synergistically activated by diacylglycerol and arachidonic acid. *J. Neurochem.* 63, 1303–1310.
- Cunningham, M.O., Woodhall, G.L., Thompson, S.E., Dooley, D.J., Jones, R.S., 2004. Dual effects of gabapentin and pregabalin on glutamate release at rat entorhinal synapses in vitro. *Eur. J. Neurosci.* 20, 1566–1576.
- Deng, Y., Wang, M., Jiang, L., Ma, C., Xi, Z., Li, X., He, N., 2013. A comparison of extracellular excitatory amino acids release inhibition of acute lamotrigine and topiramate treatment in the hippocampus of PTZ-kindled epileptic rats. *J. Biomed. Nanotechnol.* 9, 1123–1128.
- Edwards, R.H., 2007. The neurotransmitter cycle and quantal size. *Neuron* 55, 835–858.
- Emilie, A., François, C., Geneviève, B., Mayoura, B., Jérémy, J., Jaime, L., Voa, R., Pierre-Marie, P., Farid, B., 2019. Herbal medicine for epilepsy seizures in Asia, Africa and Latin America: a systematic review. *J. Ethnopharmacol.* 234, 119–153.
- Fisher, R.S., Acevedo, C., Arzimanoglou, A., Bogacz, A., Cross, J.H., Elger, C.E., Engel Jr., J., Forsgren, L., French, J.A., Glynn, M., Hesdorffer, D.C., Lee, B.I., Mathern, G.W., Moshé, S.L., Perucca, E., Scheffer, I.E., Tomson, T., Watanabe, M., Wiebe, S., 2014. ILAE official report: a practical clinical definition of epilepsy. *Epilepsia* 55, 475–482.
- Gohil, K.J., Patel, J.A., Gajjar, A.K., 2010. Pharmacological review on *Centella asiatica*: a potential herbal cure-all. *Indian J. Pharm. Sci.* 72, 546–556.
- Gryniewicz, G., Poenie, M., Tsien, R.Y., 1985. A new generation of Ca<sup>2+</sup> indicators with greatly improved fluorescence properties. *J. Biol. Chem.* 260, 3440–3450.
- Kälviäinen, R., Halonen, T., Pitkänen, A., Riekkinen, P.J., 2003. Amino acid levels in the cerebrospinal fluid of newly diagnosed epileptic patients: effect of vigabatrin and carbamazepine monotherapies. *J. Neurochem.* 60, 1244–1250.
- Kammerer, M., Brawek, B., Freiman, T., Jackisch, R., Feuerstein, T.J., 2011. Effects of antiepileptic drugs on glutamate release from rat and human neocortical synaptosomes. *Naunyn-Schmiedeberg Arch. Pharmacol.* 383, 531–542.
- Krishnamurthy, R.G., Senut, M.C., Zemke, D., Min, J., Frenkel, M.B., Greenberg, E.J., Yu, S.W., Ahn, N., Goudreau, J., Kassab, M., Panickar, K.S., Majid, A., 2009. Asiatic acid, a pentacyclic triterpene from *Centella asiatica*, is neuroprotective in a mouse model of focal cerebral ischemia. *J. Neurosci. Res.* 87, 2541–2550.
- Ladera, C., Martín, R., Bartolomé-Martín, D., Torres, M., Sánchez-Prieto, J., 2009. Partial compensation for N-type Ca<sup>2+</sup> channel loss by P/Q-type Ca<sup>2+</sup> channels underlines the differential release properties supported by these channels at cerebrocortical nerve terminals. *Eur. J. Neurosci.* 29, 1131–1140.
- Lasof, W., Chlebicka, M., Rejdak, K., 2013. Research advances in basic mechanisms of seizures and antiepileptic drug action. *Pharmacol. Rep.* 65, 787–801.
- Lee, K.Y., Bae, O.N., Weinstock, S., Kassab, M., Majid, A., 2014. Neuroprotective effect of asiatic acid in rat model of focal embolic stroke. *Biol. Pharm. Bull.* 37, 1397–1401.
- Lin, T.Y., Lu, C.W., Huang, S.K., Wang, S.J., 2013. Tanshinone IIA, a constituent of Danshen, inhibits the release of glutamate in rat cerebrocortical nerve terminals. *J. Ethnopharmacol.* 147, 488–496.
- Loganathan, C., Thayumanavan, P., 2018. Asiatic acid prevents the quinolinic acid-induced oxidative stress and cognitive impairment. *Metab. Brain Dis.* 33, 151–159.
- Lokanathan, Y., Omar, N., Ahmad Puzi, N.N., Saim, A., Hj Idrus, R., 2016. Recent updates in neuroprotective and neuroregenerative potential of *Centella asiatica*. *Malays. J. Med. Sci.* 23, 4–13.
- Löscher, W., Klitgaard, H., Twyman, R.E., Schmidt, D., 2013. New avenues for anti-epileptic drug discovery and development. *Nat. Rev. Drug Discov.* 12, 757–776.
- Macdonald, R.L., Kelly, K.M., 1995. Antiepileptic drug mechanism of action. *Epilepsia* 36, S19–S28.
- Martín, E.D., Pozo, M.A., 2004. Valproate reduced synaptic activity increase induced by 4-aminopyridine at the hippocampal CA3-CA1 synapse. *Epilepsia* 45, 436–440.
- McMahon, H.T., Nicholls, D.G., 1991. Transmitter glutamate release from isolated nerve terminals: evidence for biphasic release and triggering by localized Ca<sup>2+</sup>. *J. Neurochem.* 56, 86–94.
- Millán, C., Sánchez-Prieto, J., 2002. Differential coupling of N- and P/Q-type calcium channels to glutamate exocytosis in the rat cerebral cortex. *Neurosci. Lett.* 330, 29–32.
- Millán, C., Torres, M., Sánchez-Prieto, J., 2003. Co-activation of PKA and PKC in cerebrocortical nerve terminals synergistically facilitates glutamate release. *J. Neurochem.* 87, 1101–1111.
- Mukerjee, P., Wahil, A., 2006. Integrated approaches towards drug development from Ayurveda and other Indian system of medicine. *J. Ethnopharmacol.* 103, 25–35.
- Nasir, M., Habsah, M., Zamzuri, I., Rammes, G., Hasnan, J., Abdullah, J., 2011. Effects of asiatic acid on passive and active avoidance task in male Sprague–Dawley rats. *J. Ethnopharmacol.* 134, 203–209.
- Nicholls, D.G., 1998. Presynaptic modulation of glutamate release. *Prog. Brain Res.* 116, 15–22.
- Nicholls, D.G., Sihra, T.S., Sanchez-Prieto, J., 1987. Calcium-dependent and-independent release of glutamate from synaptosomes monitored by continuous fluorimetry. *J. Neurochem.* 49, 50–57.
- Orhan, I.E., 2012. *Centella asiatica* (L.) Urban: from traditional medicine to modern medicine with neuroprotective potential. *Evid. Based Complement Altern. Med.* 2012, 946259.
- Park, J.H., Seo, Y.H., Jang, J.H., Jeong, C.H., Lee, S., Park, B., 2017. Asiatic acid attenuates methamphetamine-induced neuroinflammation and neurotoxicity through blocking of NF- $\kappa$ B/STAT3/ERK and mitochondria-mediated apoptosis pathway. *J. Neuroinflammation* 14, 240.
- Perucca, P., Gilliam, F.G., 2012. Adverse effects of antiepileptic drugs. *Lancet Neurol.* 11, 792–802.
- Raval, N., Mistry, T., Acharya, N., Acharya, S., 2015. Development of glutathione-conjugated asiatic acid-loaded bovine serum albumin nanoparticles for brain-targeted drug delivery. *J. Pharm. Pharmacol.* 67, 1503–1511.
- Schmidt, D., Sillanpää, M., 2012. Evidence-based review on the natural history of the epilepsies. *Curr. Opin. Neurol.* 25, 159–163.
- Sirichoat, A., Chaijaroonkhanarak, W., Prachaney, P., Pannangrong, W., Leksomboon, R., Chaichun, A., et al., 2015. Effects of asiatic acid on spatial working memory and cell proliferation in the adult rat hippocampus. *Nutrients* 7, 8413–8423.
- Sitges, M., Sanchez-Tafolla, B., Chiu, L., Aldana, B., Guarneros, A., 2011. Vinpocetine inhibits glutamate release induced by the convulsive agent 4-aminopyridine more potently than several antiepileptic drugs. *Epilepsy Res.* 96, 257–266.
- Smyth, M.D., Barbaro, N.M., Baraban, S.C., 2002. Effects of antiepileptic drugs on induced epileptiform activity in a rat model of dysplasia. *Epilepsy Res.* 50, 251–264.
- Solomon, V.R., Tallapragada, V.J., Chebib, M., Johnston, G.A.R., Hanrahan, J.R., 2019. GABA allosteric modulators: an overview of recent developments in non-benzodiazepine modulators. *Eur. J. Med. Chem.* 171, 434–461.
- Umka, W.J., Sirichoat, A., Chaijaroonkhanarak, W., Prachaney, P., Pannangrong, W., Pakdeechote, P., Sripanidkulchai, B., Wigmore, P., 2016. Asiatic acid prevents the deleterious effects of valproic acid on cognition and hippocampal cell proliferation and survival. *Nutrients* 8, 303.
- Visweswari, G., Prasad, K.S., Chetan, P.S., Lokanatha, V., Rajendra, W., 2010a. Evaluation of the anticonvulsant effect of *Centella asiatica* (gotu kola) in pentylenetetrazol-induced seizures with respect to cholinergic neurotransmission. *Epilepsy Behav.* 17, 332–335.
- Visweswari, G., Siva Prasad, K., Lokanatha, V., Rajendra, W., 2010b. The antiepileptic effect of *Centella asiatica* on the activities of Na<sup>+</sup>/K<sup>+</sup>, Mg<sup>2+</sup> and Ca<sup>2+</sup>-ATPases in rat brain during pentylenetetrazol-induced epilepsy. *Indian J. Pharmacol.* 42, 82–86.
- Wang, C.C., Kuo, J.R., Huang, S.K., Wang, S.J., 2018. Metabotropic glutamate 7 receptor agonist AMN082 inhibits glutamate release in rat cerebral cortex nerve terminal. *Eur. J. Pharmacol.* 823, 11–18.
- Wang, C.C., Kuo, J.R., Wang, S.J., 2014. Dimebon, an antihistamine drug, inhibits glutamate release in rat cerebrocortical nerve terminals. *Eur. J. Pharmacol.* 734, 67–76.
- Wang, Z., Mong, M.C., Yang, Y.C., Yin, M.C., 2018. Asiatic acid and maslinic acid attenuated kainic acid-induced seizure through decreasing hippocampal inflammatory and oxidative stress. *Epilepsy Res.* 139, 28–34.
- Zhao, Z., He, X., Ma, C., Wu, S., Cuan, Y., Sun, Y., Bai, Y., Huang, L., Chen, X., Gao, T., Zheng, X., 2018. Excavating anticonvulsant compounds from prescriptions of traditional Chinese medicine in the treatment of epilepsy. *Am. J. Chin. Med.* 46, 707–737.



## Research Article

# ***Helminthostachys zeylanica* Water Extract Ameliorates Airway Hyperresponsiveness and Eosinophil Infiltration by Reducing Oxidative Stress and Th2 Cytokine Production in a Mouse Asthma Model**

**Wen-Chung Huang,<sup>1,2</sup> Nai-Chun Ting,<sup>3</sup> Yu-Ling Huang,<sup>4</sup> Li-Chen Chen<sup>1,2,5</sup> ,  
Chwan-Fwu Lin<sup>1,6,7</sup> , and Chian-Jiun Liou<sup>2,8</sup> **

<sup>1</sup>Graduate Institute of Health Industry Technology, Research Center for Food and Cosmetic Safety, and Research Center for Chinese Herbal Medicine, College of Human Ecology, Chang Gung University of Science and Technology, Taoyuan City 33303, Taiwan

<sup>2</sup>Division of Allergy, Asthma, and Rheumatology, Department of Pediatrics, Chang Gung Memorial Hospital, Linkou, Guishan Dist., Taoyuan City 33303, Taiwan

<sup>3</sup>Graduate Institute of Clinical Medical Sciences, Chang Gung University, Taoyuan City 33303, Taiwan

<sup>4</sup>National Research Institute of Chinese Medicine, Ministry of Health and Welfare, Beitou, Taipei, Taiwan

<sup>5</sup>Department of Pediatrics, New Taipei Municipal Tu Cheng Hospital, Chang Gung Memorial Hospital and Chang Gung University, Taiwan

<sup>6</sup>Department of Cosmetic Science, Research Center for Food and Cosmetic Safety, and Research Center for Chinese Herbal Medicine, College of Human Ecology, Chang Gung University of Science and Technology, Taoyuan City 33303, Taiwan

<sup>7</sup>Department of Anesthesiology, Chang Gung Memorial Hospital, Linkou, Guishan Dist., Taoyuan City 33303, Taiwan

<sup>8</sup>Department of Nursing, Division of Basic Medical Sciences, Research Center for Chinese Herbal Medicine, Chang Gung University of Science and Technology, Taoyuan City 33303, Taiwan

Correspondence should be addressed to Li-Chen Chen; [lcchen@adm.cgmh.org.tw](mailto:lcchen@adm.cgmh.org.tw), Chwan-Fwu Lin; [cflin@mail.cgust.edu.tw](mailto:cflin@mail.cgust.edu.tw), and Chian-Jiun Liou; [ccliu@mail.cgust.edu.tw](mailto:ccliu@mail.cgust.edu.tw)

Received 21 May 2020; Revised 26 September 2020; Accepted 29 October 2020; Published 2 December 2020

Academic Editor: Cristina Contreras

Copyright © 2020 Wen-Chung Huang et al. This is an open access article distributed under the Creative Commons Attribution License, which permits unrestricted use, distribution, and reproduction in any medium, provided the original work is properly cited.

*Helminthostachys zeylanica* is a traditional folk herb used to improve inflammation and fever in Taiwan. Previous studies showed that *H. zeylanica* extract could ameliorate lipopolysaccharide-induced acute lung injury in mice. The aim of this study was to investigate whether *H. zeylanica* water (HZW) and ethyl acetate (HZE) extracts suppressed eosinophil infiltration and airway hyperresponsiveness (AHR) in asthmatic mice, and decreased the inflammatory response and oxidative stress in tracheal epithelial cells. Human tracheal epithelial cells (BEAS-2B cells) were pretreated with various doses of HZW or HZE (1 µg/ml–10 µg/ml), and cell inflammatory responses were induced with IL-4/TNF-α. In addition, female BALB/c mice sensitized with ovalbumin (OVA), to induce asthma, were orally administered with HZW or HZE. The result demonstrated that HZW significantly inhibited the levels of proinflammatory cytokines, chemokines, and reactive oxygen species in activated BEAS-2B cells. HZW also decreased ICAM-1 expression and blocked monocytic cells from adhering to inflammatory BEAS-2B cells *in vitro*. Surprisingly, HZW was more effective than HZE in suppressing the inflammatory response in BEAS-2B cells. Our results demonstrated that HZW significantly decreased AHR and eosinophil infiltration, and reduced goblet cell hyperplasia in the lungs of asthmatic mice. HZW also inhibited oxidative stress and reduced the levels of Th2 cytokines in bronchoalveolar lavage fluid. Our findings suggest that HZW attenuated the pathological changes and inflammatory response of asthma by suppressing Th2 cytokine production in OVA-sensitized asthmatic mice.



## 1. Introduction

Allergic asthma is a complex airway inflammatory disease, where antigens stimulate and induce airway hyperresponsiveness (AHR), activated leukocyte infiltration, and airway mucosal hyperplasia [1, 2]. During acute attacks of asthma, patients suddenly coughed, wheezed, and experienced chest tightness, shortness of breath, and dyspnea [3]. When an allergen is inhaled into airways, it stimulates the epithelial cells to release inflammatory cytokines and mediators for respiratory inflammation [3]. In addition, airway epithelial cells secrete chemokines to attract more inflammatory immune cells and infiltrate into lung tissues, causing a more severe inflammatory response [4]. Furthermore, inflamed epithelial cells are accompanied by oxidative damage to epithelial cells and lung tissue, as well as increased activation of immune cells to destruct lung function [5, 6]. In particular, infiltrate of pulmonary macrophages and neutrophils can induce oxygen-dependent cytotoxic effects to release more  $O_2^-$  against the invasion of allergens [7]. Moreover, the oxidizing substance released by those immune cells also causes pulmonary oxidative damage [8]. Therefore, reducing the inflammation and oxidative damage of airways would improve symptoms during the development of asthma in patients.

Recent studies found that the allergen-stimulated Th2 cell activity of the lungs could be an important mechanism in the development of chronic asthma [9]. Th2 cells could secrete IL-4, IL-5, and IL-13 to trigger asthma symptom, including increased eosinophil infiltration and AHR [4, 10]. Therefore, blocking the activity of Th2 cells may ameliorate asthma in patients.

Current clinical strategies include treatment with asthma medications that contain acute attack medication and prevention medication [11]. Smooth muscle vasodilators that reduce the airway contraction and allow patients to breathe can be effective in severe asthma. Moreover, patients may use oral corticosteroids for maintenance and prevention of asthma attacks [12]. The dosage of oral corticosteroids is slight with few serious side effects [13]. Steroids are immunosuppressants and inhibit the function of Th1 and Th2 cells [14]. Therefore, the general public is not treated with steroid drugs for asthma.

Traditional Chinese medicine, yoga, qigong, and homeopathy are very common alternative medicines [15]. Chinese medicine has widely been used for thousands of years, and there have been many herbal formulas, including Ding Chuan Tang and Xiao-Qing-Long-Tang, used to improve asthma symptoms in China and Taiwan [16–18]. These herbal formulas contained ephedra, which contains ephedrine that predominantly reduced smooth muscle contraction in asthmatic patients [19]. Yet, ephedrine is a refined amphetamine and may endanger the health of teenagers [20]. Hence, scholars and practitioners have studied and dispensed alternative herbal formulas to replace those traditional formulas. Many scholars found that other herbal formulas could attenuate AHR and eosinophil infiltration by suppressing the activity of Th2 cells in asthmatic mice, including MSSM-002 and Danggui Buxue Tang [21, 22].

*Helminthostachys zeylanica* (L.) Hook. (Ophioglossaceae) is a common anti-inflammatory folk herb in Taiwan and has been used to improve inflammatory diseases and as an antipyretic [23]. Ugonin K was isolated from *H. zeylanica* and had anti-inflammatory effects in lipopolysaccharide-(LPS-) stimulated macrophages [24]. *H. zeylanica* extracts could also decrease MMP-9 expression and the inflammatory response in bradykinin-induced brain astrocytes [25]. We also found that water extract of *H. zeylanica* could reduce LPS-induced acute lung injury [26]. However, it is not clear whether *H. zeylanica* could attenuate the inflammatory response of airways and improve asthma symptoms. In this study, we investigated whether the *H. zeylanica* ethyl acetate (HZE) extract and water (HZW) extract could reduce AHR and eosinophil infiltration in asthmatic mice, and decrease oxidative stress and inflammatory response in tracheal epithelial cells.

## 2. Materials and Methods

**2.1. *H. zeylanica* Extraction.** The roots of *H. zeylanica* were collected from Taipei, Taiwan, in July 2013. The plant was identified by comparison with the voucher specimen (NRICM-99-003) already deposited at the herbarium of National Research Institute of Chinese Medicine, Taiwan. The roots of *H. zeylanica* (1000 g) were heated with ethanol at 50°C for 4 h. After evaporation of the solvent, the ethanol extract was partitioned between water and ethyl acetate to give water extract (HZW: 23.8 g, yield 2.38%) and ethyl acetate extract (HZE: 14.2 g, yield 1.42%).

**2.2. HPLC Analysis of HZW.** HZW (7.1 mg) was dissolved in 2 ml methanol and responded by ultrasonic wave for 10 minutes at 25°C. After the filtration through a 0.45  $\mu$ m polyvinylidene fluoride membrane, the filtrate was injected into the Agilent 1100 series HPLC (10  $\mu$ l) system. The separation was performed on a COSMOSIL 5C<sub>18</sub>-AR-II column (5  $\mu$ m, 250  $\times$  4.6 mm, i.d.), which was eluted at a flow rate of 1.0 ml/min with a mobile phase gradient of A–B (A = H<sub>2</sub>O (0.05% formic acid), B = MeOH) varying as follows: 0–10 min: 90–80% A, 10–20% B; 10–40 min: 80–0% A, 20–100% B; and 40–50 min: 0–0% A, 100–100% B. The UV detection wavelength was set at 254 nm. The two standards are quercetin-3-O- $\beta$ -D-glucopyranosyl-4'-O- $\beta$ -D-glucopyranosyl-(1  $\rightarrow$  2)- $\beta$ -D-glucopyranoside (compound 1) and quercetin-4'-O- $\beta$ -D-glucopyranosyl-(1  $\rightarrow$  2)- $\beta$ -D-glucopyranoside (compound 2) [27].

**2.3. HZW and HZE Treatment of BEAS-2B Cells.** HZW was dissolved in PBS and HZE was dissolved in DMSO. The concentration of these stock solutions was 10 mg/ml. There was  $\leq$ 0.1% DMSO in the experimental culture medium. BEAS-2B cells (American Type Culture Collection, Manassas, VA, USA) were seeded in DMEM/F12 medium in cultured plates. The cells were pretreated with HZW or HZE (1–10  $\mu$ g/ml) for 1 h, and then treated with 10 ng/ml TNF- $\alpha$  and 10 ng/ml IL-4 for 24 h. The supernatants were collected, and cytokines or chemokines were detected using specific ELISA kits. Cell viability was measured using the MTT assay, and

the results were determined by the absorbance values at 570 nm using a microplate reader (Multiskan FC, Thermo, Waltham, MA, USA).

**2.4. Detection of Reactive Oxygen Species (ROS) Production.** BEAS-2B cells were stimulated with TNF- $\alpha$ /IL-4 and treated with HZW or HZE in 96-well plates for 24 h. Cells were then treated with 2',7'-dichlorofluorescein diacetate (DCFH-DA) (Catalog No. D6883; Sigma, St. Louis, MO, USA) for 30 min as described previously [28, 29]. Cells were then lysed for detection of ROS using a multimode microplate reader (BioTek Synergy HT, Bedfordshire, United Kingdom).

**2.5. Cell-Cell Adhesion Assay.** BEAS-2B cells were treated with various doses of HZW or HZE for 1 h and then stimulated with TNF- $\alpha$ /IL-4 for 24 h in 6-well plates as described previously [30, 31]. THP-1 cells (Bioresource Collection and Research Center, Taiwan) were treated with calcein-AM solution (Catalog No. C1359; Sigma) at 37°C for 30 min, and THP-1 cells were cocultured with BEAS-2B cells at 37°C for 30 min. Finally, THP-1 cells adhered to BEAS-2B cells were measured using fluorescence microscopy (Olympus, Tokyo, Japan).

**2.6. Experimental Animals.** The animals used in this study were 6- to 8-week-old female BALB/c mice, obtained from the National Laboratory Animal Center in Taiwan. Water and food were provided ad libitum, and mice were housed at constant temperature and humidity environment, and maintained on a 12 h light/dark cycle at the Animal Center of Chang Gung University, Taiwan. Animal experimental procedures were approved by the Laboratory Animal Care Committee of Chang Gung University of Science and Technology (IACUC approval number: 2013-001).

**2.7. Allergy Sensitization and Drug Treatment.** Asthma was induced in mice by 50  $\mu$ g ovalbumin (OVA) (Catalog No. A5503; Sigma) and 0.8 mg aluminum hydroxide (Thermo, Rockford, IL, USA) in 200  $\mu$ l normal saline via intraperitoneal injection on days 1-3 and 14, as described previously [32]. Mice were challenged and exposed with aerosolized 2% OVA using an ultrasonic nebulizer (DeVilbiss Pulmo-Aide 5650D, USA) for 20 min on days 14, 17, 20, 23, and 27. From day 14 to day 27, the mice were orally administered with saline (N and OVA groups), HZW, or HZE for 14 consecutive days. In every independent experiment, mice were divided into six groups (of 10 mice each): (1) normal control mice (N group) sensitized with normal saline; (2) OVA-sensitized control mice (OVA group) sensitized with OVA; (3-5) experimental group mice sensitized with OVA and orally administered with 1 mg/kg, 5 mg/kg, or 10 mg/kg HZW or HZE (named HZW1, HZW5, and HZW10 or HZE1, HZE5, and HZE10, respectively); and (6) prednisolone control (P group) OVA-sensitized mice orally administered with 5 mg/kg prednisolone.

**2.8. Measurement of AHR.** On day 28, the AHR of mice was measured to evaluate airway function via various inhaled doses of methacholine, as described previously [33]. All mice inhaled aerosolized methacholine (0-40 mg/ml) for 3 min,

respectively. A single-chamber, whole-body plethysmograph (Buxco Electronics, Troy, NY, USA) was used to record the values of enhanced pause (Penh), a measurement of AHR.

**2.9. Serum Collection and Splenocyte Cultures.** On day 29, mice were anesthetized with 4% isoflurane (Aesica, Queenborough, UK), and blood was collected from the orbital vascular plexus and centrifuged at 6000 rpm for 5 min at 4°C. The serum was collected to measure OVA-specific antibodies that were detected by ELISA as previously described [28]. Next, mice were sacrificed by CO<sub>2</sub> asphyxiation. Their splenocytes were isolated and cultured with 100  $\mu$ g/ml OVA in RPMI 1640 medium for 5 continuous days. The levels of cytokines in the supernatants were assayed as previously described [32].

**2.10. Bronchoalveolar Lavage Fluid (BALF) and Cell Collection.** Mice were anesthetized using 4% isoflurane, and BALF was collected as described previously [34]. Briefly, the mice were incubated with an indwelling needle into the trachea, and the lungs were washed three times using 1 ml normal saline. The supernatant was collected to detect the levels of cytokines and chemokines by ELISA. Additionally, Giemsa stain (Catalog No. GS500; Sigma) was used to stain cells for measuring cell counts and differentiated cell morphology.

**2.11. Histologic Analysis of Lung Tissue.** Lung tissues were embedded in paraffin and cut into 6  $\mu$ m thick sections. Hematoxylin and eosin (HE) staining was used to observe the eosinophil infiltration of the lungs. Eosinophil infiltration inflammatory index used fivepoint scoring system as described previously [35]. Briefly, the degree of cell infiltration was scored as follows: 0, no cell; 1, a few cells; 2, a ring of inflammatory cells of one cell layer; 3, a ring of inflammatory cells of two to four cell layers; and 4, a ring of inflammatory cells > four cell layers. Furthermore, periodic acid-Schiff (PAS) staining was used to evaluate goblet cell hyperplasia of the trachea as described previously [28]. The lung tissue slide was deparaffinized and stained with periodic acid solution for 5 min. Next, the slide was washed and added with Schiff's reagent for 15 min. Finally, hematoxylin solution was added, and the goblet cells were observed using a light microscope (Olympus, Tokyo, Japan).

**2.12. Glutathione (GSH) Assay.** A glutathione assay kit was used to determine the glutathione levels of the lungs, according to the manufacturer's instructions (Catalog No. CS0260; Sigma). 50 mg lung tissues was homogenized by homogenizer (FastPrep-24, MP Biomedicals, Santa Ana, CA, United States). The sample was centrifuged, and supernatant detected the level of total glutathione, including reduced GSH and glutathione disulfide using a multimode microplate reader (BioTek Synergy HT, Bedfordshire, United Kingdom).

**2.13. Malondialdehyde (MDA) Assay.** The lipid peroxidation assay kit (Catalog No. MAK085; Sigma) was used to evaluate the MDA level of the lungs, according to manufacturer's instructions. Lung tissues were homogenized by homogenizer (FastPrep-24, MP Biomedicals, Santa Ana, CA, United

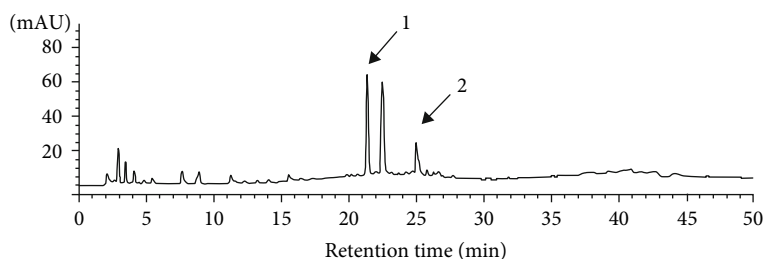


FIGURE 1: HPLC chromatograms of *H. zeylanica* water (HZW) extract. 1: quercetin-3-*O*- $\beta$ -D-glucopyranosyl-4'-*O*- $\beta$ -D-glucopyranosyl-(1  $\rightarrow$  2)- $\beta$ -D-glucopyranoside; 2: quercetin-4'-*O*- $\beta$ -D-glucopyranosyl-(1  $\rightarrow$  2)- $\beta$ -D-glucopyranoside.

States). The supernatant was treated with perchloric acid for protein precipitation. The tissue solution was centrifuged and collected supernatant to detect MDA expression by a multimode microplate reader (BioTek Synergy HT).

**2.14. Lung RNA Isolation and Real-Time PCR.** Lung tissues were homogenized and RNA extracted with TRIzol reagent (Catalog No. 15596026; Life Technologies, Carlsbad, CA, USA), as described previously [34, 36]. We used RNA to synthesize cDNA and a spectrofluorometric thermal cycler (iCycler; Bio-Rad) to investigate specific gene expression. The reaction cycling conditions were as follows: preincubated samples at 95°C for 10 min. Next, the PCR was performed as 40 cycles of 95°C for 15 seconds and 60°C for 1 minute.

**2.15. ELISA.** Cytokines, chemokines, and ICAM-1 were detected in the BALF and supernatants of cell cultures using specific ELISA kits, according to the manufacturer's instructions (R&D Systems, Minneapolis, MN, USA), as previously described [33]. Serum OVA-IgE and OVA-IgG1 were measured with specific ELISA kits (BD Biosciences). The OVA-IgG1 standard curve was used to calculate the units of IgG1, and the levels of OVA-IgE were determined by OD 450.

**2.16. Statistical Analysis.** Statistical analyses were performed with SPSS v19 (SPSS, Chicago, IL, USA). Animal experiment results were analyzed by one-way analysis of variance (ANOVA), followed by the Dunnett and post hoc test for multiple comparisons. Between two groups, an unpaired Student *t*-test was used in cell experiment. Statistical significance was set at  $P < 0.05$ , and the results were expressed as the mean  $\pm$  standard error of the mean (SEM) from three independent experiments.

### 3. Results

**3.1. HZW Inhibited the Levels of Cytokines and Chemokines in Inflammatory BEAS-2B Cells.** The HPLC fingerprint of *H. zeylanica* water (HZW) extract (Figure 1) showed compound 1 and compound 2 elute at 21.2 and 25.2 minutes, which was specific enough to be used for the identification of *H. zeylanica* [27]. The cytotoxicity of HZW and HZE in BEAS-2B cells was determined by MTT assay. Cell viability was not significantly affected by the doses of HZW or HZE  $\leq 10 \mu\text{g/ml}$  (Figures 2(a) and 2(b)). Therefore, in this current experiment, we used HZW and HZE doses from  $1 \mu\text{g/ml}$  to  $10 \mu\text{g/ml}$  *in vitro*. We used TNF- $\alpha$ /IL-4 to stimulate inflam-

mation in BEAS-2B cells to evaluate the anti-inflammatory effect of HZW and HZE. Our experimental results demonstrated that HZW could significantly reduce the levels of IL-6 and IL-8 at 5 and  $10 \mu\text{g/ml}$  (Figures 2(c) and 2(d)). We also found that HZW significantly reduced eotaxin (CCL11 and CCL24) production at 5 and  $10 \mu\text{g/ml}$  (Figures 2(e) and 2(f)). However, HZE was not as effective at reducing eotaxins and proinflammatory cytokines, although  $10 \mu\text{g/ml}$  HZE could significantly inhibit IL-6, IL-8, and CCL11 production. We also found that the  $10 \mu\text{g/ml}$  HZW group significantly decreased the levels of IL-6, IL-8, CCL11, and CCL24 compared with the  $10 \mu\text{g/ml}$  HZE group. Thus, HZW was better in reducing the inflammatory response than HZE.

**3.2. HZW Regulated ROS Production in BEAS-2B Cells.** BEAS-2B cells were treated with HZW or HZE and then stimulated with TNF- $\alpha$ /IL-4. Cells were lysed and detected with ROS using a multimode microplate reader. We found HZW decreased the ROS levels more than HZE in TNF- $\alpha$ /IL-4-activated BEAS-2B cells (Figure 3(a)).

**3.3. HZW Reduced Monocytic Cell Adhesion to BEAS-2B Cells.** HZW significantly suppressed the levels of intercellular adhesion molecule 1 (ICAM-1) compared with HZE in TNF- $\alpha$ /IL-4-activated BEAS-2B cells (Figure 3(b)). Additionally, HZW reduced the THP-1 cells that adhered to inflammatory BEAS-2B cells (Figures 3(c) and 3(d)), while HZE did not.

**3.4. HZW Improved AHR and Reduced the Inflammatory Cells in the BALF of OVA-Sensitized Mice.** AHR is one of the important features of asthma. It mainly evaluates the respiratory function when allergen or stimulus induces to increase sensitivity and reactivity of airways [37]. The AHR assay result showed that OVA-sensitized mice have Penh values that are increased in a dose-dependent manner compared with the normal mice. At  $40 \text{ mg/ml}$  methacholine, the HZW groups had significantly reduced the value of Penh compared with the OVA group (Figure 4(a)) (HZW1:  $6.22 \pm 0.56$ ,  $P = 0.08$ ; HZW5:  $5.01 \pm 0.30$ ,  $P < 0.01$ ; HZW10:  $4.18 \pm 0.38$ ,  $P < 0.01$  vs. OVA:  $7.68 \pm 0.39$ ). In HZE-treated OVA-sensitized mice, only HZE10 could suppress Penh values compared with the OVA group (Figure 4(c)) (HZE1:  $7.33 \pm 0.35$ ,  $P = 0.75$ ; HZE5:  $6.74 \pm 0.73$ ,  $P = 0.31$ ; HZE10:  $5.68 \pm 0.38$ ,  $P < 0.05$  vs. OVA:  $8.58 \pm 0.44$ ). Prednisolone-treated OVA-sensitized mice also significantly inhibited the Penh values compared to the OVA group mice. We also

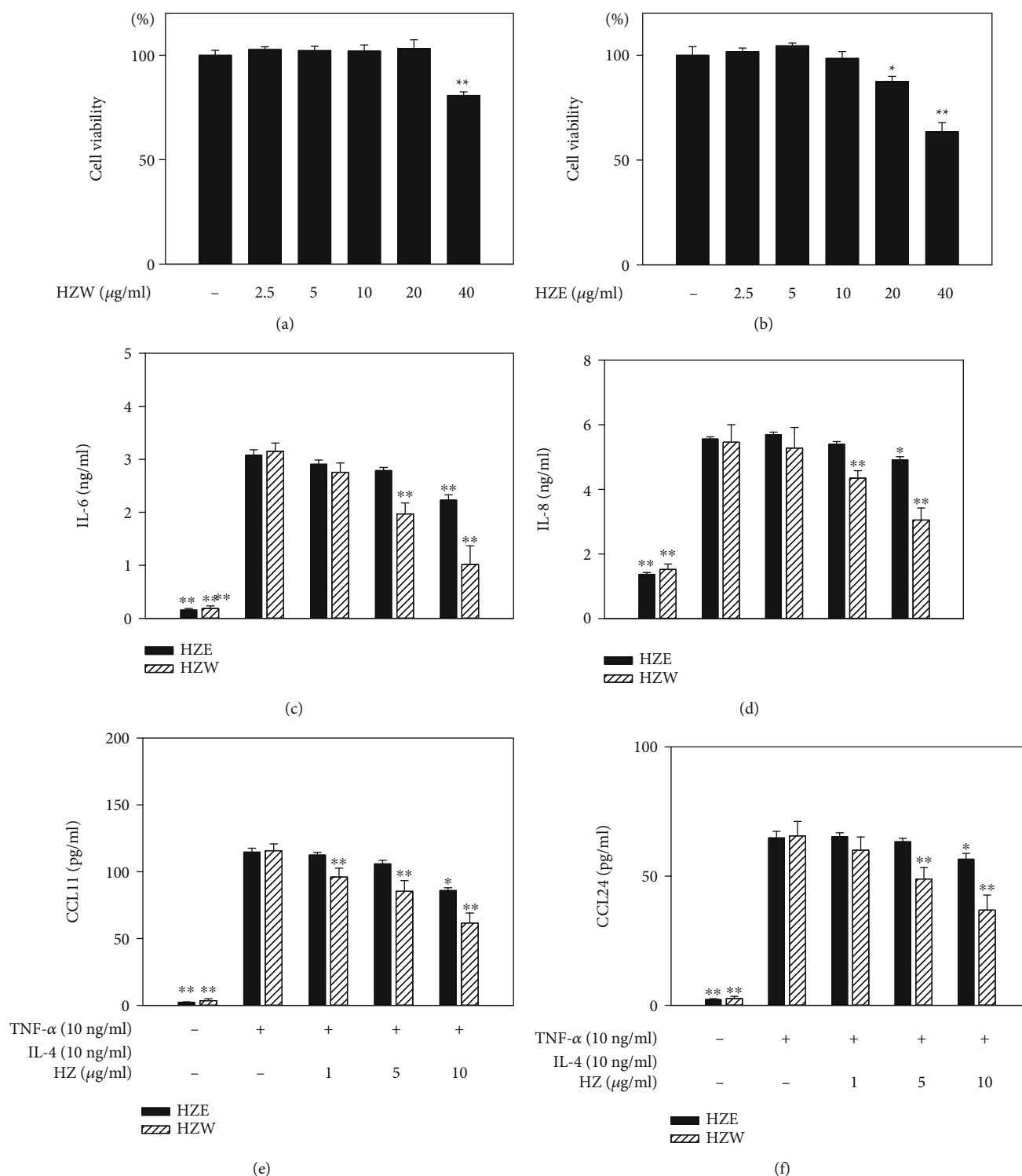


FIGURE 2: The effects of HZW and HZE on cytokine and chemokine productions in BEAS-2B cells. Cell viability of (a) HZW and (b) HZE in BEAS-2B cells. The levels of IL-6 (c), IL-8 (d), CCL11 (e), and CCL24 (f) were measured by ELISA. All data are presented as the mean  $\pm$  SEM. \* $P < 0.05$  and \*\* $P < 0.01$  compared with BEAS-2B cells stimulated with TNF- $\alpha$ /IL-4. HZ: *Helminthostachys zeylanica*. HZW was dissolved in PBS and HZE was dissolved in DMSO. Hence, vehicle HZE experiment contained 0.1% DMSO in medium and vehicle HZW experiment did not contain DMSO in medium.

investigated whether HZW and HZE could suppress inflammatory cells in the BALF of asthmatic mice. The result showed that HZW5 and HZW10 could significantly inhibit

eosinophils and total cells compared with the OVA group (Figure 4(b)). However, HZE did not significantly inhibit eosinophils and total cells compared with the OVA group



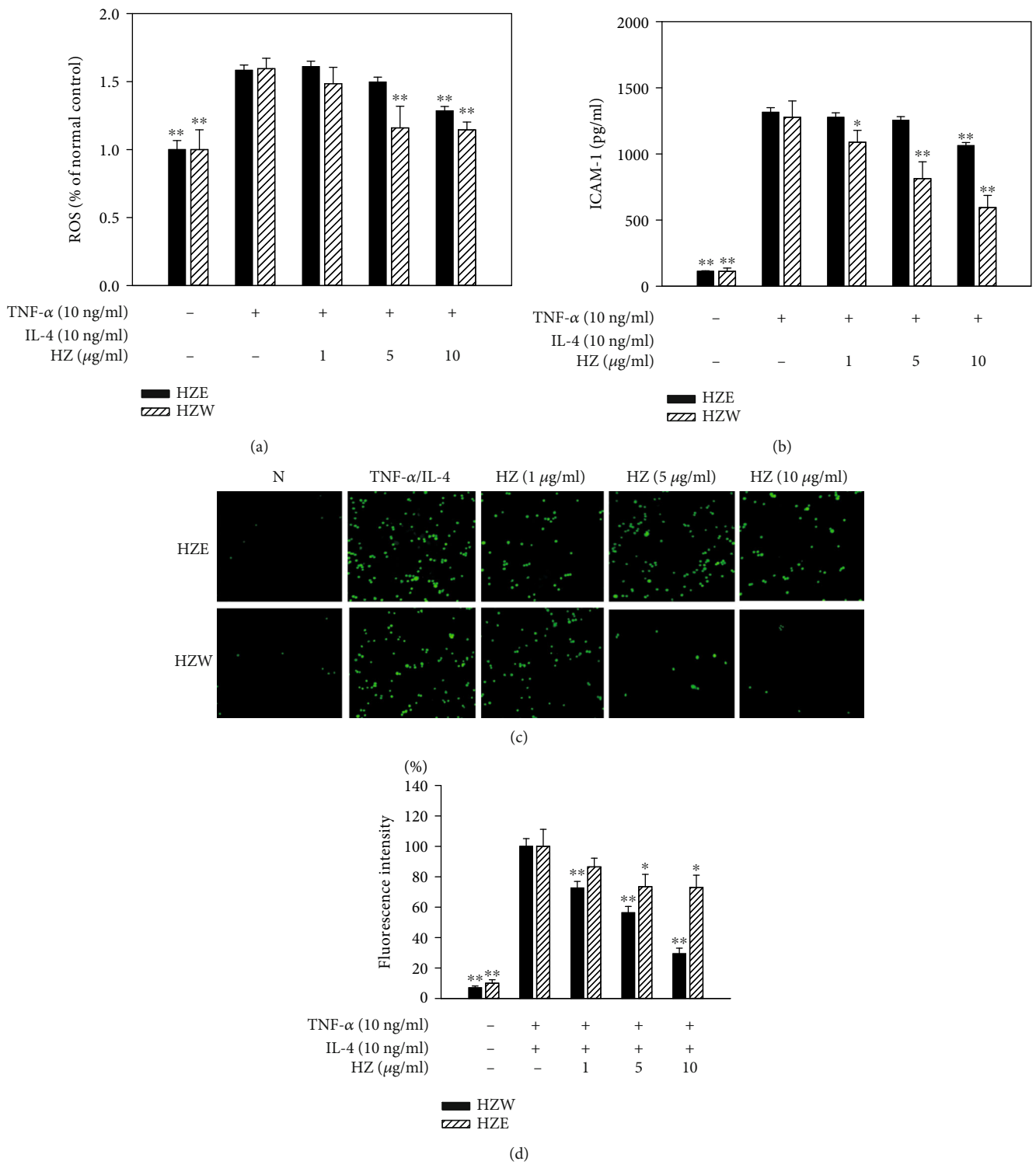


FIGURE 3: HZW and HZE inhibited ROS and THP-1 cell adherence to the activated BEAS-2B cells. (a) Percentage of ROS detected in cells treated with HZW or HZE compared with TNF- $\alpha$ /IL-4-activated BEAS-2B. (b) The levels of ICAM-1, detected by ELISA, in BEAS-2B cells activated with TNF- $\alpha$ /IL-4. (c) Fluorescence microscopy images of THP-1 cells labeled with calcein-AM and mixed with normal (N) and TNF- $\alpha$ /IL-4-activated BEAS-2B cells, in the absence or presence of HZW or HZE. HZ: *Helminthostachys zeylanica*. (d) Fluorescence intensity of THP-1 cell adhesion to BEAS-2B cells. The data are presented as the mean  $\pm$  SEM. \* $P < 0.05$  and \*\* $P < 0.01$  compared with BEAS-2B cells stimulated with TNF- $\alpha$ /IL-4.

(Figure 4(d)). Prednisolone-treated OVA-sensitized mice also significantly inhibited eosinophils and total cells compared to the OVA-sensitized mice. Hence, we only analyzed

how HZW ameliorates the effects of inflammation, oxidation, and the immune mechanism of asthma in the animal model.



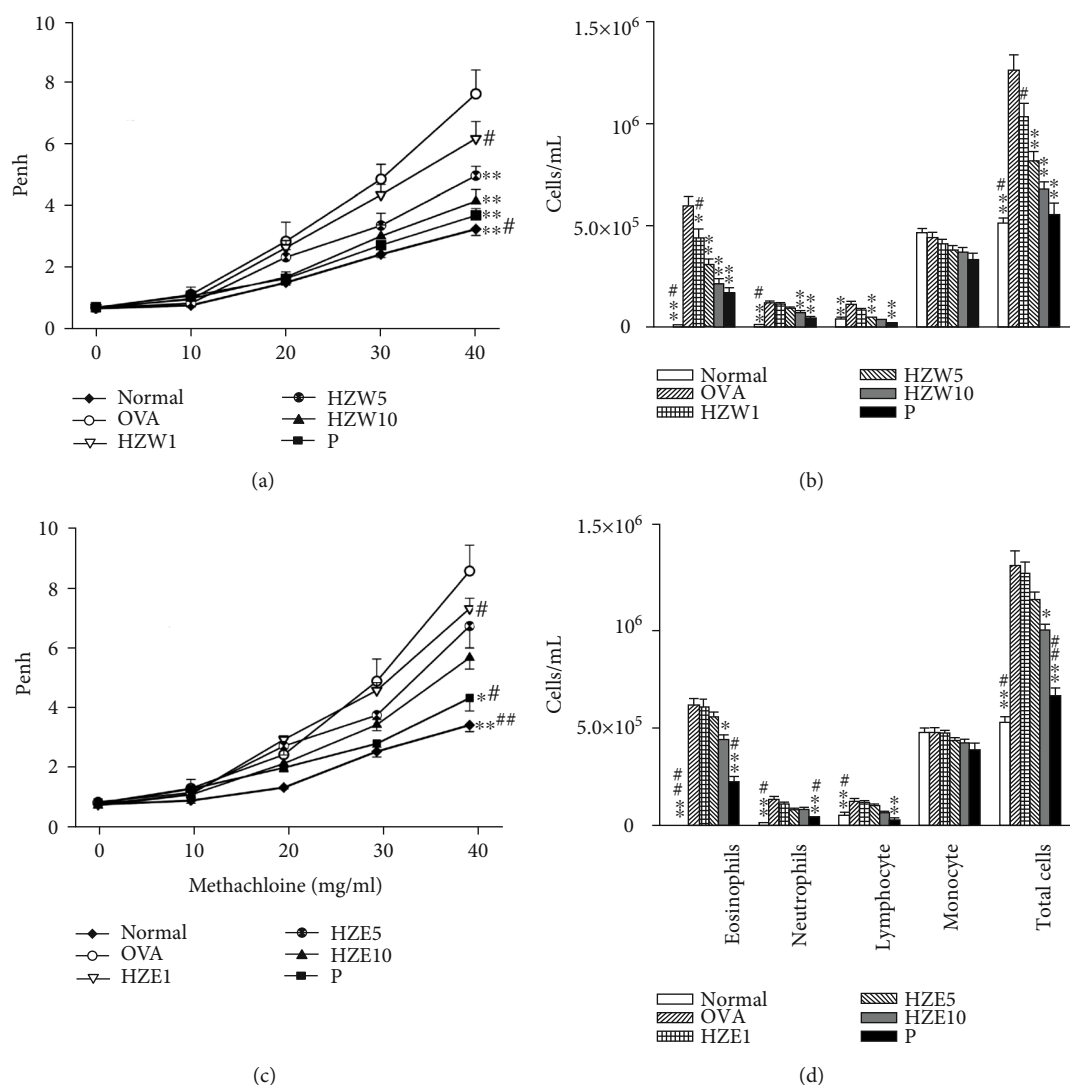


FIGURE 4: Effect of HZW or HZE on AHR and cell counts in the BALF of asthmatic mice. The AHR (Penh values) was measured after inhalation of increasing methacholine doses (10–40 mg/ml) in normal (N) and OVA-stimulated (OVA) mice, treated with or without HZW (a) or HZE (c) ( $n = 10$  mice/group, measured in three independent experiments). The numbers of inflammatory cells and total cells in the BALF from OVA-sensitive mice, treated with or without HZW (b) or HZE (d). All data are presented as the mean  $\pm$  SEM. \* $P < 0.05$  and \*\* $P < 0.01$  compared with the OVA control group. # $P < 0.05$  and ## $P < 0.01$  compared to the HZW10 or HZE10 group. Prednisolone (P) control orally administered with 5 mg/kg prednisolone as positive control.

**3.5. HZW Regulated the MDA and GSH Levels in the Lungs.** Asthma attacks would induce oxidative stress for causing lung cell damage [38]. We found that OVA-sensitized mice had significantly enhanced the MDA levels and reduced GSH production in lung tissue compared with normal mice (Figures 5(a) and 5(b)). HZW suppressed MDA and increased the GSH levels compared with OVA mice.

**3.6. HZW Attenuated Eosinophil Infiltration and Goblet Cell Hyperplasia in the Lungs.** In the lungs, infiltration of inflammatory cells is an important factor to cause pulmonary inflammation [39]. There were more eosinophils infiltrating between the blood vessels and bronchus of the lungs in OVA-sensitive mice than normal mice, and HZW could suppress eosinophil infiltration of the lungs in asthmatic mice (Figure 6). The PAS staining also showed HZW could

decrease goblet cell hyperplasia of airways compared with OVA-sensitive mice (Figure 7).

**3.7. HZW Regulated Cytokine and Chemokine Expression in BALF and Lung Tissue.** To analyze the levels of proinflammatory cytokine and Th2-associated cytokines in BALF, cytokines and chemokines were detected using ELISA. We found that HZW-treated mice had significantly suppressed the TNF- $\alpha$  levels compared with OVA-sensitized mice (Figure 8). HZW also significantly reduced IL-6, CCL11, IL-4, IL-5, and IL-13 compared with the OVA group, but did not decrease the levels of CCL24 in the BALF of asthmatic mice. The gene expression in lung tissues measured by real-time PCR demonstrated that HZW significantly reduced COX-2, CCL11 (not CCL24), ICAM-1, MUC5AC, IL-4, IL-5, and IL-13 gene expression compared with OVA-

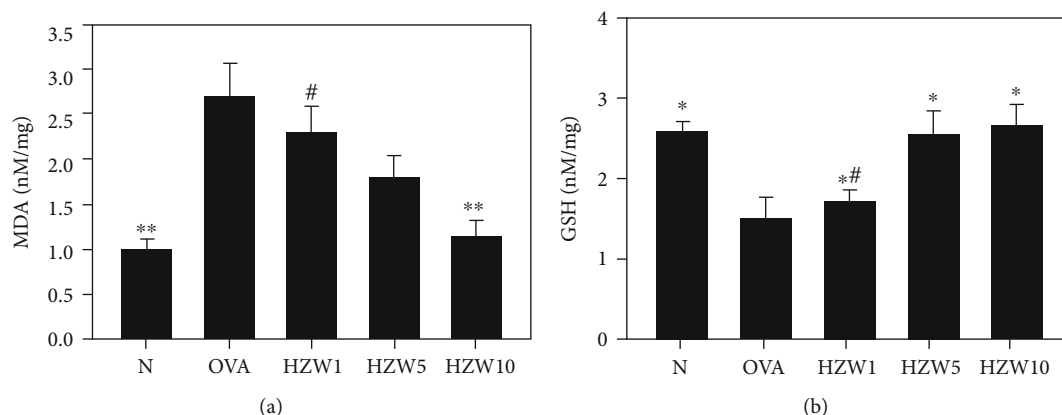


FIGURE 5: The effects of HZW on oxidative stress factors. The MDA level (a) and GSH activity (b) were measured in the lung tissues of mice. Data are presented as the mean  $\pm$  SEM. \* $P$  < 0.05 and \*\* $P$  < 0.01 compared with the OVA control group. # $P$  < 0.05 compared to the HZW10 group.

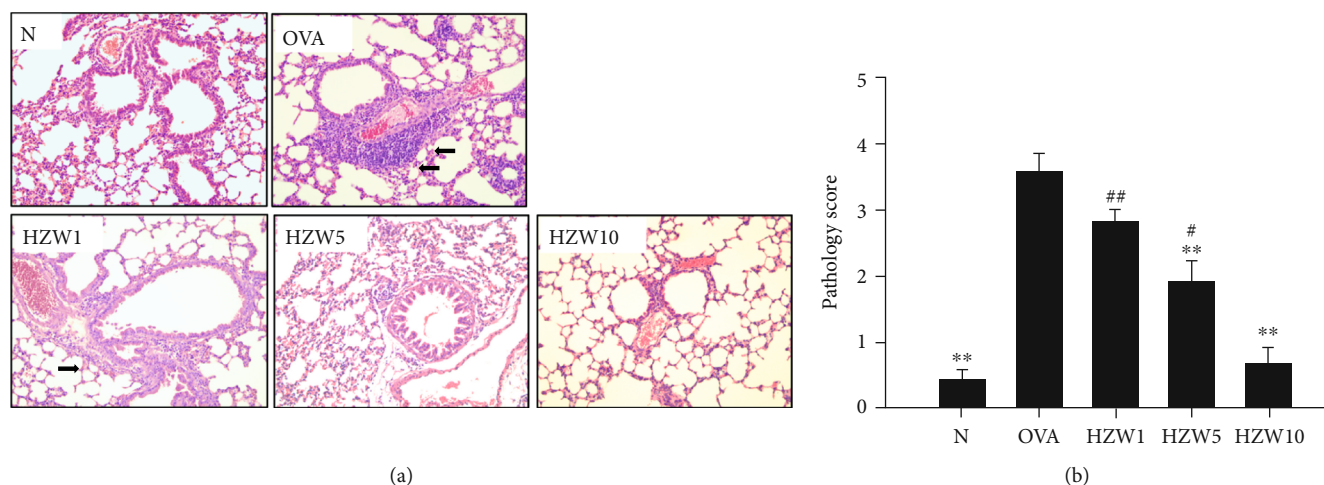


FIGURE 6: The effect of HZW on eosinophil infiltration of lung tissue in OVA-sensitized mice. (a) Hematoxylin and eosin staining of lung sections (6  $\mu$ m) observed eosinophil infiltration (200x magnification). Eosinophils were indicated with arrows. (b) The scoring of inflammation *via* pathological evaluation in lung sections. Data are presented as the mean  $\pm$  SEM. \* $P$  < 0.05 and \*\* $P$  < 0.01 compared with the OVA control group. # $P$  < 0.05 and ## $P$  < 0.01 compared to the HZW10 group.

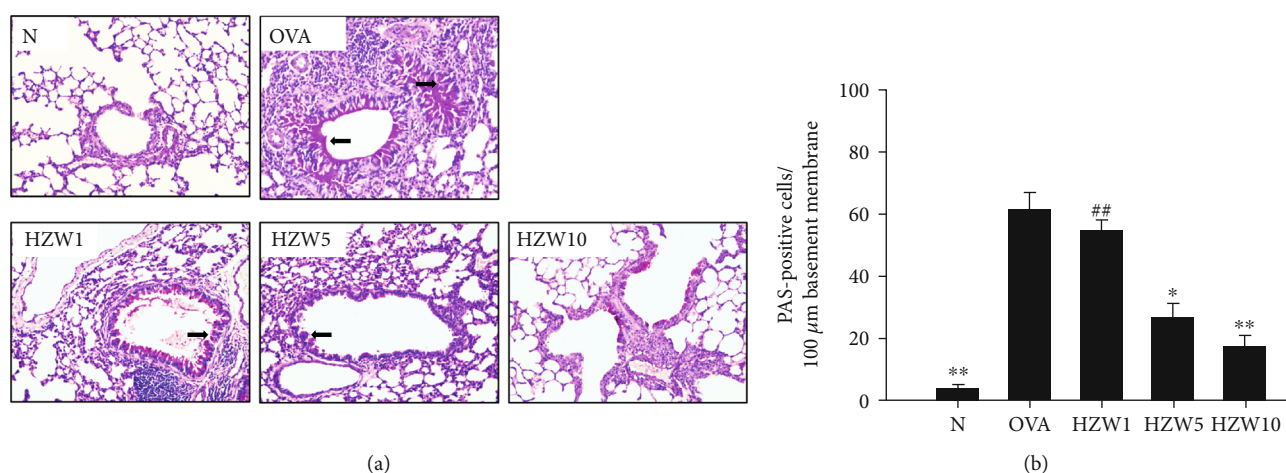


FIGURE 7: The effects of HZW on goblet cell hyperplasia in the lung tissue of OVA-sensitized mice. (a) Lung sections (6  $\mu$ m) were stained with PAS to observe goblet cell hyperplasia (200x magnification). Goblet cells were indicated with arrows. (b) Results expressed as the number of PAS-positive cells per 100  $\mu$ m of the basement membrane. Data are presented as the mean  $\pm$  SEM. \* $P$  < 0.05 and \*\* $P$  < 0.01 compared with the OVA control group. ## $P$  < 0.01 compared to the HZW10 group.

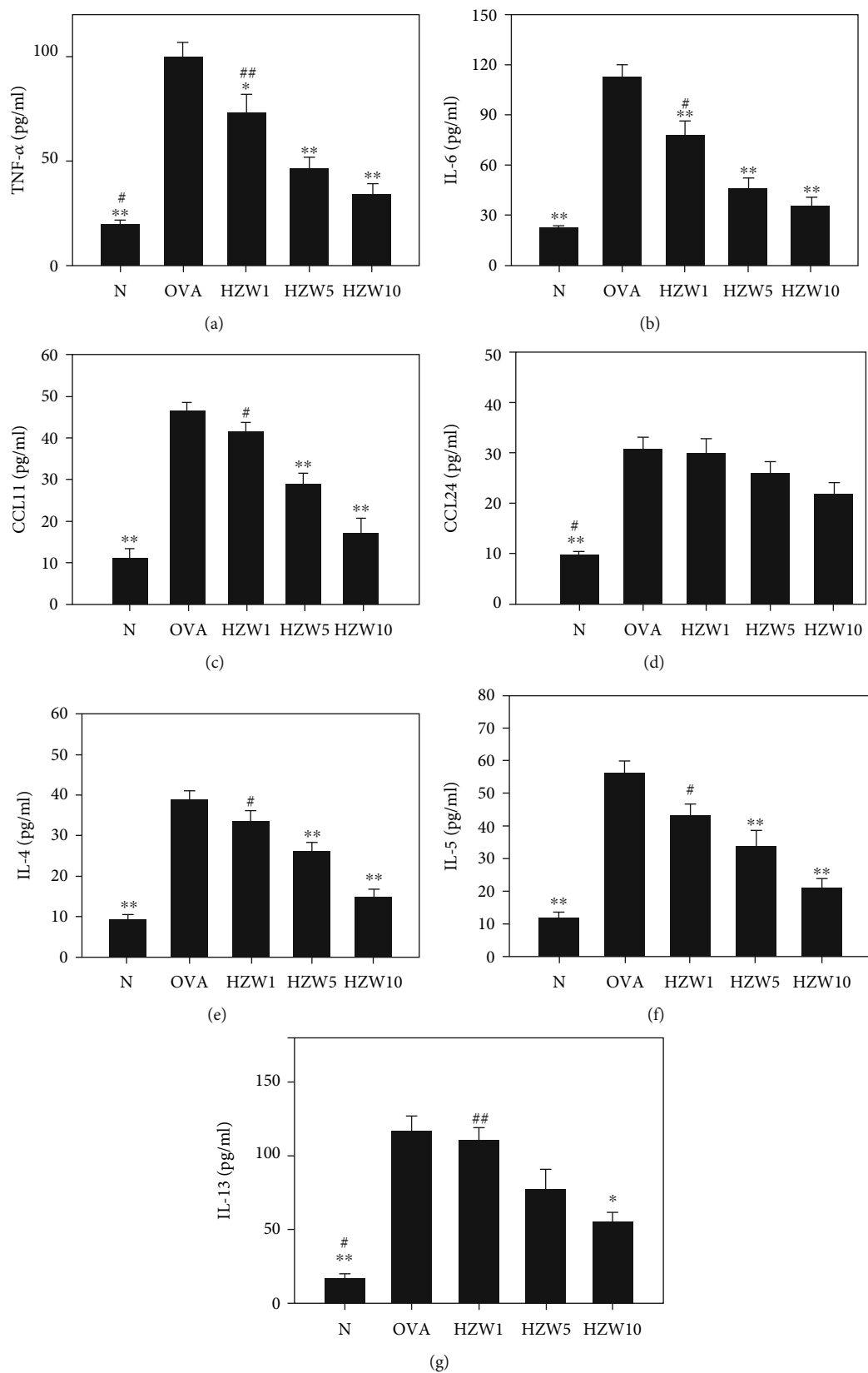


FIGURE 8: The effects of HZW on the levels of cytokines and chemokines in the BALF. The concentrations of TNF- $\alpha$  (a), IL-6 (b), CCL11 (c), CCL24 (d), IL-4 (e), IL-5 (f), and IL-13 (g) were measured by ELISA. All data are presented as the mean  $\pm$  SEM. \* $P$  < 0.05 and \*\* $P$  < 0.01 compared with the OVA control group. # $P$  < 0.05 and ## $P$  < 0.01 compared to the HZW10 group.

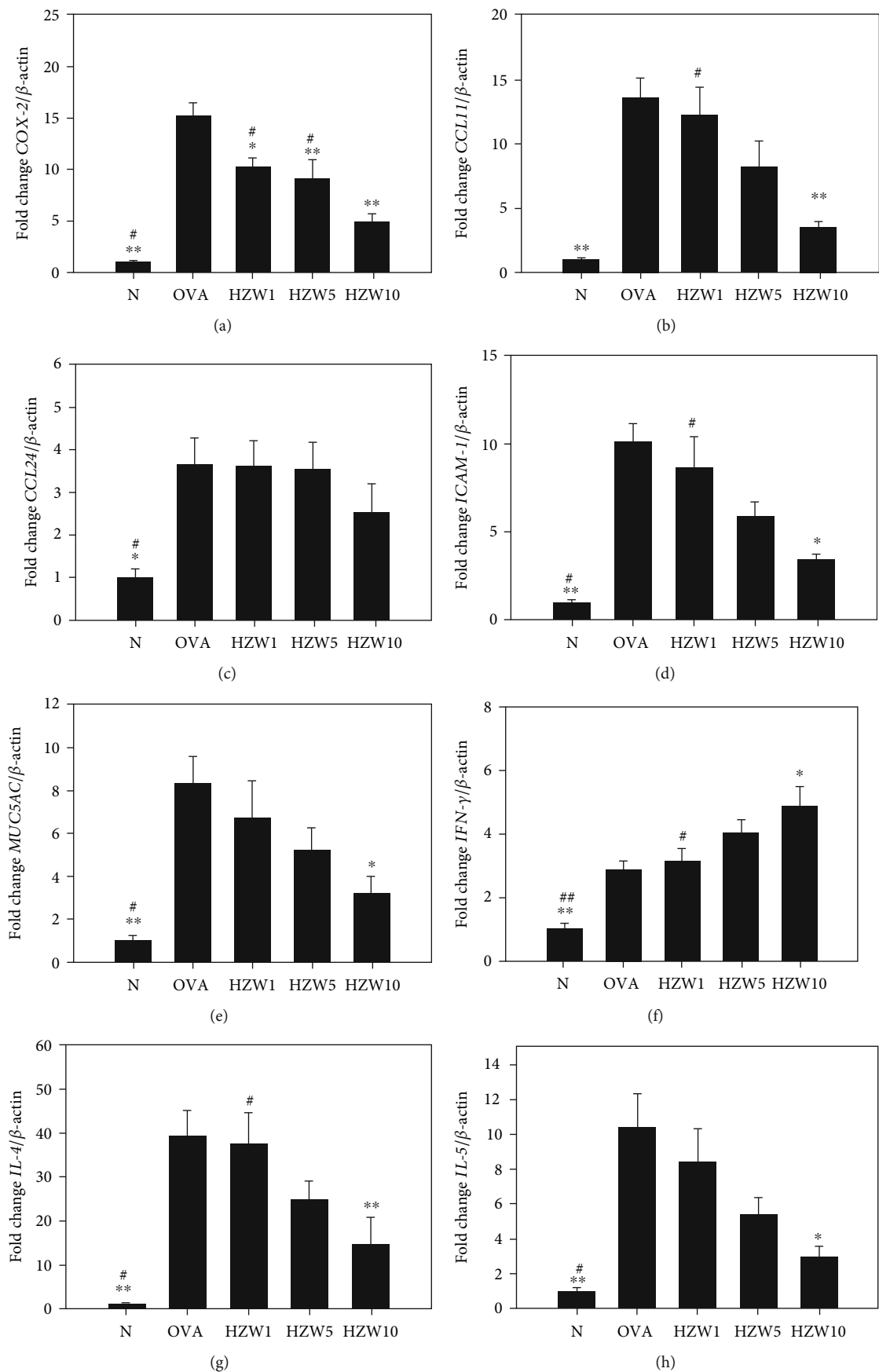


FIGURE 9: Continued.

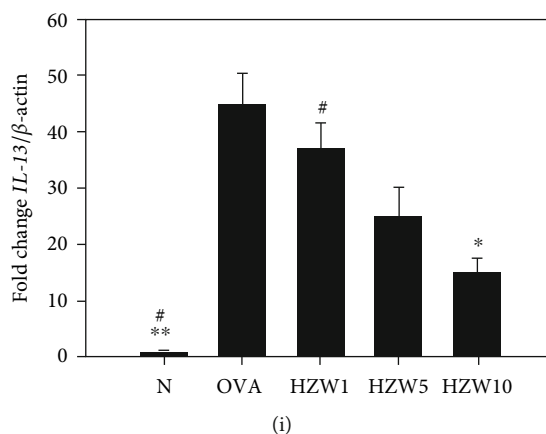


FIGURE 9: Effects of HZW on gene expression of cytokines, chemokines, and inflammatory mediators in the lungs. The gene expression levels of COX-2 (a), CCL11 (b), CCL24 (c), ICAM-1 (d), MUC5AC (e), IFN- $\gamma$  (f), IL-4 (g), IL-5 (h), and IL-13 (i) were determined by real-time PCR of RNA extracted from the lung tissues of normal (N) and OVA-stimulated (OVA) mice, treated with or without HZW. Fold changes in expression were measured relative to  $\beta$ -actin expression (internal control). Data are presented as the mean  $\pm$  SEM. \* $P < 0.05$  and \*\* $P < 0.01$  compared with the OVA control group. # $P < 0.05$  and ## $P < 0.01$  compared to the HZW10 group.

sensitized mice (Figure 9). However, HZW also increased IFN- $\gamma$  gene expression in asthmatic mice.

**3.8. HZW Regulated the Antibody and Cytokine Levels in Serum and Splenocytes.** To analyze the levels of OVA-specific antibodies in serum, HZW significantly attenuated the OVA-IgG1 and OVA-IgE levels compared with OVA-sensitized mice (Figures 10(a) and 10(b)). We also analyzed the levels of Th2-associated cytokines in splenocyte culture supernatants and found that mice treated with HZW10 had significantly reduced the levels of IL-4, IL-5, and IL-13 (Figures 10(c)–10(e)). Moreover, HZW increased the IFN- $\gamma$  levels compared with OVA-sensitized mice (Figure 10(f)).

#### 4. Discussion

Previous studies confirmed that *H. zeylanica* could improve liver damage in Wistar rats [40]. Previously, we found that HZW could also decrease inflammatory responses in lung tissues from LPS-treated mice [26]. In this current study, we found that HZW is more effective than HZE to reduce inflammatory response and decrease the ROS levels in TNF- $\alpha$ /IL-4-activated BEAS-2B cells. Also, HZW inhibited THP-1 cell adherence to inflammatory BEAS-2B cells more than HZE. We thought that HZW fraction should contain the main substance or compound that inhibited the inflammatory response of human tracheal epithelial cells. In the present study, we found that HZW significantly reduced oxidative stress and suppressed Th2-associated cytokines and chemokines in BALF. HZW could also inhibit the gene expression of inflammatory chemokines and cytokines in lung tissues. In addition, HZW significantly attenuated tracheal goblet cell hyperplasia, eosinophil infiltration of the lungs, and ameliorated AHR in asthmatic mice. Furthermore, HZW decreased the levels of Th2 cytokines in splenocyte culture medium and OVA-specific IgE in serum.

Recently, a study demonstrated that ugonin J and ugonin K were the main flavonoids of HZE [26]. A previous study

found that HZW analyzed with HPLC, and the UV detection wavelength was set at 254 nm. HZW could be isolated two bioactivity compounds, including quercetin-4- $O$ - $\beta$ -D-glucopyranosyl-(1  $\rightarrow$  2)- $\beta$ -D-glucopyranoside and quercetin-3- $O$ - $\beta$ -D-glucopyranosyl-4- $O$ - $\beta$ -D-glucopyranosyl-(1  $\rightarrow$  2)- $\beta$ -D-glucopyranoside [27]. These two pure compounds could suppress production of nitric oxide and proinflammatory cytokines in LPS-stimulated macrophage [27]. We thought that these two compounds should also have the potential to ameliorate respiratory inflammation and AHR and in asthmatic mice.

Asthma is a respiratory inflammatory disease. When patients inhale allergens, they stimulate an inflammatory response of airway epithelial cells [3]. Those epithelial cells then secrete inflammatory cytokines and chemokines for invasions of foreign substances [6]. Our experimental findings that HZW is effective at reducing the IL-6 levels in inflammatory tracheal epithelial cells suggest it may help prevent the development of lung inflammation in asthmatic patients. Asthmatic mice, treated with HZW, had suppressed the levels of IL-6 and TNF- $\alpha$  in BALF, and also reduced gene expression of inflammatory mediators (COX-2) in the lungs. Hence, HZW is a good natural plant extract with an anti-inflammatory effect in asthmatic mice.

During the asthma development process, immune cells and epithelial cells induce oxidative stress leading to lung tissue damage [41]. Researchers have found that patients could regulate oxidative stress, reduce allergic inflammation, and suppress asthma by taking an antioxidant supplement [42]. A previous study found that oral administration of high dose vitamin C could reduce inflammation and oxidative stress of the lungs and eosinophilic infiltration of BALF in OVA-sensitized mice [43]. Licochalcone A and quercetin also were found that could improve asthma by suppressing ROS and inflammation in OVA-induced asthmatic mice [44, 45]. Therefore, antioxidants have great potential to improve asthma symptoms. The antioxidant enzyme GSH can provide oxidation protection by reducing oxidative damage



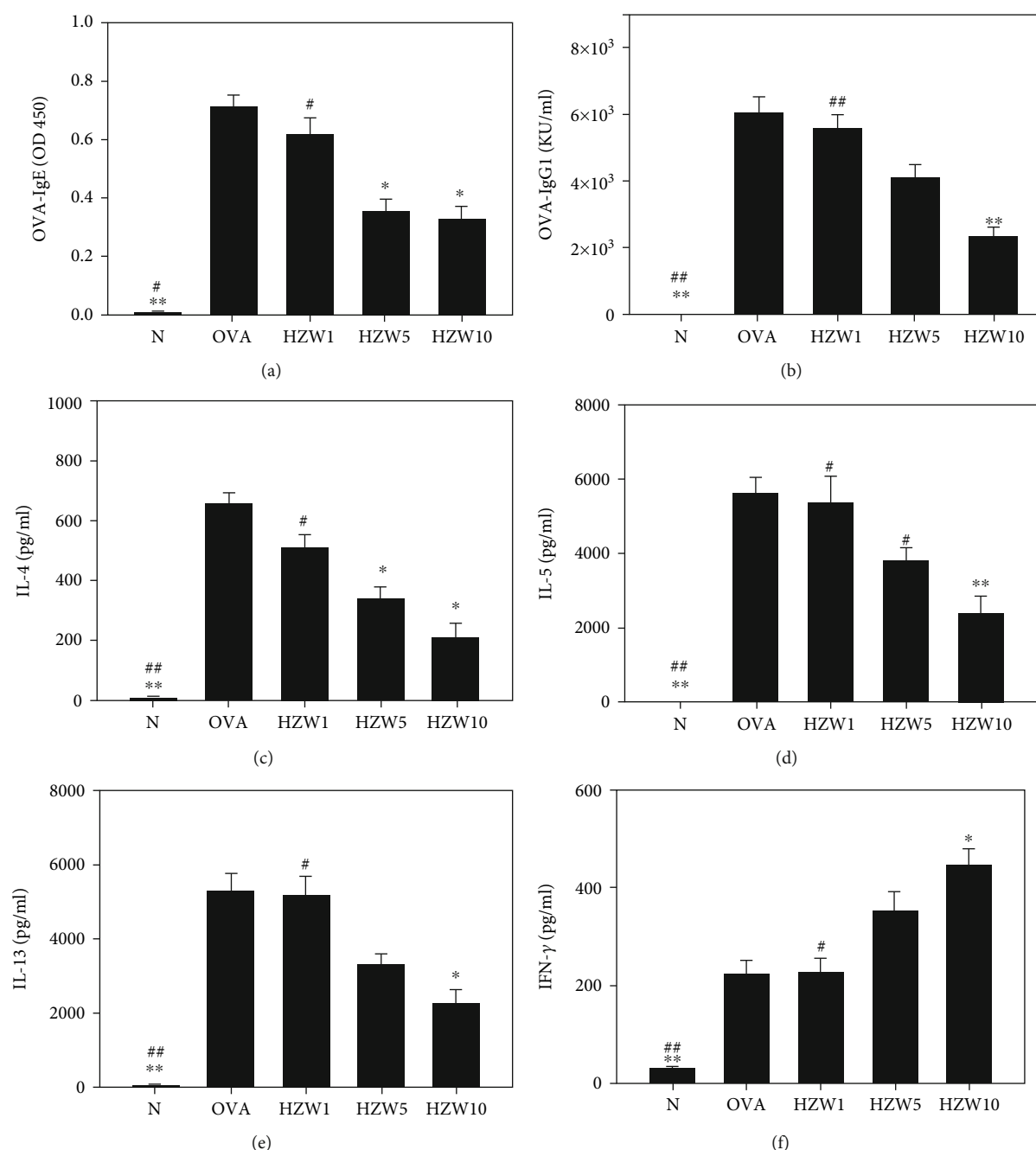


FIGURE 10: Effect of HZW on the levels of the OVA-specific antibodies and cytokines. HZW reduced the levels of OVA-IgE (a) and OVA-IgG1 (b) in serum as well as IL-4 (c), IL-5 (d), IL-13 (e), and IFN- $\gamma$  (f) produced by OVA-activated splenocytes. All data are presented as the mean  $\pm$  SEM. \* $P$  < 0.05 and \*\* $P$  < 0.01 compared with the OVA control group. # $P$  < 0.05 and ## $P$  < 0.01 compared to the HZW10 group.

and the chronic inflammatory response in the lungs of asthmatic mice [38]. Lipid peroxidation influences cellular function via oxidative damage and eventually leads to cell death [38]. Our results showed that HZW could effectively reduce ROS in tracheal epithelial cells and decrease the levels of MDA, a lipid peroxidation marker, in the lung tissue in asthmatic mice. Furthermore, HZW increased GSH expression to increase the protective effects against oxidative damage. Hence, HZW was effective at reducing lung damage by suppressing oxidative stress in asthmatic mice.

Excessive Th2 cytokines exacerbate the pathology response of asthma by increasing AHR, goblet cell hyperplasia, excessive mucus secretion, and inflammatory cell infiltration [4, 46]. Previous studies also found that IL-13 could aggravate AHR in asthmatic mice, causing shortness of breath and bronchoconstriction [1]. In clinical asthma cases, there are high IL-13 levels observed in BALF that induce AHR and difficulty of breathing [47]. Another study found that IL-13 knockout mice did not have significantly increased AHR compared with wild-type asthmatic mice [48]. We

found that HZW could significantly decrease IL-13 gene expression in the lungs and the IL-13 levels in BALF, and improve AHR in asthmatic mice. Furthermore, Th2 cells secrete excess IL-4 to induce B cell activation and secretion of more IgE to bind to the IgEεRI receptor of mast cells [3]. When patients inhale allergens, they form a complex with IgE and mast cells to induce mast cell activation and release histamine and leukotrienes, causing severe lung inflammation and allergic responses [6]. We found that HZW could significantly decrease the IL-4 levels and suppress OVA-specific IgE production in serum. These results confirm that HZW was effective at reducing the acute inflammatory response of airways and decreasing allergic response in asthmatic mice.

When combined with IL-13, IL-4 can promote goblet cell hyperplasia of the airway, and those goblet cells secrete excessive mucus leading to airway obstruction, breathing difficulties, and even death in asthmatic patients [18]. A previous study found that IL-4 or IL-13 knockout mice did not significantly increase goblet cell hyperplasia of the airway compared with wild-type asthmatic mice [9]. Here, we demonstrated that HZW reduced IL-4 and IL-13 production and decreased goblet cell hyperplasia in lung tissue, and also suppressed Muc5Ac gene expression in the lungs for improved mucus secretion.

Recently, a study demonstrated that active Th2 cells release more IL-5 to induce eosinophil proliferation and differentiation from the bone marrow [39]. In asthmatic patients, airway epithelial cells also secrete more eotaxins (CCL11, CCL24, and CCL26) to attract eosinophils that migrate into the lung tissue [6]. Eosinophils release more inflammatory substances, including eosinophil cationic protein and eosinophil peroxidase, to cause lung inflammation and oxidation damage in lung tissue [24]. HZW could significantly suppress CCL11 and IL-5 expression in the lungs and BALF, and also decrease the levels of CCL11 and CCL24 in inflammatory tracheal epithelial cells for reduced eosinophil differentiation and attraction to lung tissue. Hence, we thought that HZW mainly reduced CCL11 secretion of the lungs to decrease eosinophil infiltration in the lungs of asthmatic mice. In addition, HZW reduced ICAM-1 expression of tracheal epithelial cells that adhere to eosinophils and migrate into lung tissue to reduce the inflammation and allergic response in the lungs. In the current study, we confirmed that HZW inhibited the activity of Th2 cells, reducing lung inflammation and allergic reactions in asthmatic mice.

Steroids are clinical drugs for treating or preventing asthma [12]. However, steroids interfered with the function of immune cells and inhibited the expression of Th1 and Th2 cells [14]. Interferon- $\gamma$ , a Th1 cytokine, would suppress expression in asthmatic patient. In the present study, the gene expression of lung tissues demonstrated that HZW could increase IFN- $\gamma$  gene expression in asthmatic mice. Clinical trials found that herbal formulas, Ding Chuan Tang and ASHMI, reduced asthma symptoms and improved respiratory function by regulating the activity of Th1/Th2 cells [17, 49]. In this study, HZW inhibited allergic reactions and improved lung inflammation in asthmatic mice. Interestingly, HZW did not suppress the activity of Th2 and Th1 cells

as steroids. In steroid-resistant asthmatic patients, tracheal epithelial cells would release IL-8, thereby attracting more neutrophils into the lungs to cause serious inflammatory reactions. Our study found that the levels of IL-8 attenuated after BEAS-2B cells treated with HZW, indicating that HZW might reduce the inflammatory response in asthmatic patients.

In conclusion, our results demonstrated that HZW, but not HZE, significantly suppressed AHR, mucus hypersecretion, and eosinophil infiltration via blocked Th2 cytokine production in asthmatic mice. HZW also reduced oxidative stress and inflammation to prevent lung damage and maintain the function of the respiratory system. Thus, HZW may potentially ameliorate inflammation and antioxidative stress in asthma.

## Abbreviations

AHR:	Airway hyperresponsiveness
BALF:	Bronchoalveolar lavage fluid
DCFH-DA:	2',7'-Dichlorofluorescein diacetate
GSH:	Glutathione
HE:	Hematoxylin and eosin staining
HZW:	<i>Helminthostachys zeylanica</i> water
HZE:	<i>Helminthostachys zeylanica</i> ethyl acetate extracts
LPS:	Lipopolysaccharide
OVA:	Ovalbumin
MDA:	Malondialdehyde
PAS:	Periodic acid-Schiff
Penh:	Enhanced pause
ROS:	Reactive oxygen species.

## Data Availability

The data used to support the findings of this study are included with the article.

## Conflicts of Interest

The authors declare that there are no conflicts of interest.

## Authors' Contributions

WCH, NCT, CFL, and CJL are responsible for the experimental design and performance. WCH, NCT, YLH, and LCC are responsible for the data analysis and interpretation. LCC, CFL, and CJL are responsible for drafting the manuscript. Wen-Chung Huang and Nai-Chun Ting contributed equally to this work.

## Acknowledgments

This study was supported in part by grants from the Chang Gung Memorial Hospital (CMRPF1C0203, CMRPF1H0042, CMRPF1F0051-3, and CMRPF1J0031-3), the Chang Gung University of Science and Technology (EZRP3F0271 and ZRRPF3H0121), and the Ministry of Science and Technology in Taiwan (106-2320-B-255-007-MY3 and MOST-108-2320-B-255-001).

## References

- [1] S. Rayees, F. Malik, S. I. Bukhari, and G. Singh, "Linking GATA-3 and interleukin-13: implications in asthma," *Inflammation Research*, vol. 63, no. 4, pp. 255–265, 2014.
- [2] E. Leinaar, A. Alamian, and L. Wang, "A systematic review of the relationship between asthma, overweight, and the effects of physical activity in youth," *Annals of Epidemiology*, vol. 26, no. 7, pp. 504–510.e6, 2016.
- [3] A. Ray, M. Raundhal, T. B. Oriss, P. Ray, and S. E. Wenzel, "Current concepts of severe asthma," *The Journal of Clinical Investigation*, vol. 126, no. 7, pp. 2394–2403, 2016.
- [4] A. KleinJan, "Airway inflammation in asthma: key players beyond the Th2 pathway," *Current Opinion in Pulmonary Medicine*, vol. 22, no. 1, pp. 46–52, 2016.
- [5] P. S. Hiemstra, P. B. McCray Jr., and R. Bals, "The innate immune function of airway epithelial cells in inflammatory lung disease," *The European Respiratory Journal*, vol. 45, no. 4, pp. 1150–1162, 2015.
- [6] C. M. Lloyd and S. Saglani, "Epithelial cytokines and pulmonary allergic inflammation," *Current Opinion in Immunology*, vol. 34, pp. 52–58, 2015.
- [7] O. Ciepiela, M. Ostafin, and U. Demkow, "Neutrophils in asthma—a review," *Respiratory Physiology and Neurobiology*, vol. 209, pp. 13–16, 2015.
- [8] A. Auerbach and M. L. Hernandez, "The effect of environmental oxidative stress on airway inflammation," *Current Opinion in Allergy and Clinical Immunology*, vol. 12, no. 2, pp. 133–139, 2012.
- [9] J. W. Steinke and M. G. Lawrence, "T-cell biology in immunotherapy," *Annals of Allergy, Asthma, and Immunology*, vol. 112, no. 3, pp. 195–199, 2014.
- [10] R. Keyhanmanesh, R. Rahbarghazi, M. R. Aslani, M. Hassanpour, and M. Ahmadi, "Systemic delivery of mesenchymal stem cells condition media in repeated doses acts as magic bullets in restoring IFN- $\gamma$ /IL-4 balance in asthmatic rats," *Life Sciences*, vol. 212, pp. 30–36, 2018.
- [11] J. E. Fergusson, S. S. Patel, and R. F. Lockey, "Acute asthma, prognosis and treatment," *The Journal of Allergy and Clinical Immunology*, vol. 139, no. 2, pp. 438–447, 2017.
- [12] A. Arabkhazaeli, S. J. H. Vijverberg, C. K. van der Ent, J. A. M. Raaijmakers, and A. H. Maitland-van der Zee, "High incidence of oral corticosteroids prescriptions in children with asthma in early childhood," *The Journal of Asthma*, vol. 53, no. 10, pp. 1012–1017, 2016.
- [13] P. J. Barnes, "Glucocorticosteroids: current and future directions," *British Journal of Pharmacology*, vol. 163, no. 1, pp. 29–43, 2011.
- [14] J. M. Rodriguez, M. Monsalves-Alvarez, S. Henriquez, M. N. Llanos, and R. Troncoso, "Glucocorticoid resistance in chronic diseases," *Steroids*, vol. 115, pp. 182–192, 2016.
- [15] C. E. Ward and A. P. Baptist, "Characteristics of complementary and alternative medicine (CAM) use among older adults with asthma," *The Journal of Asthma*, vol. 53, no. 5, pp. 546–552, 2016.
- [16] F. Liu, N. X. Xuan, S. M. Ying, W. Li, Z. H. Chen, and H. H. Shen, "Herbal medicines for asthmatic inflammation: from basic researches to clinical applications," *Mediators of Inflammation*, vol. 2016, Article ID 6943135, 12 pages, 2016.
- [17] C. K. Chan, M. L. Kuo, J. J. Shen, L. C. See, H. H. Chang, and J. L. Huang, "Ding Chuan Tang, a Chinese herb decoction, could improve airway hyper-responsiveness in stabilized asthmatic children: a randomized, double-blind clinical trial," *Pediatric Allergy and Immunology*, vol. 17, no. 5, pp. 316–322, 2006.
- [18] S. D. Wang, L. J. Lin, C. L. Chen et al., "Xiao-Qing-Long-Tang attenuates allergic airway inflammation and remodeling in repetitive Dermatogoides pteronyssinus challenged chronic asthmatic mice model," *Journal of Ethnopharmacology*, vol. 142, no. 2, pp. 531–538, 2012.
- [19] H. M. Wang, S. K. Lin, C. H. Yeh, and J. N. Lai, "Prescription pattern of Chinese herbal products for adult-onset asthma in Taiwan: a population-based study," *Annals of Allergy, Asthma, and Immunology*, vol. 112, no. 5, pp. 465–470, 2014.
- [20] M. K. Lee, B. W. Cheng, C. T. Che, and D. P. Hsieh, "Cytotoxicity assessment of Ma-huang (Ephedra) under different conditions of preparation," *Toxicological Sciences*, vol. 56, no. 2, pp. 424–430, 2000.
- [21] X. M. Li, C. K. Huang, T. F. Zhang et al., "The Chinese herbal medicine formula MSSM-002 suppresses allergic airway hyperreactivity and modulates TH1/TH2 responses in a murine model of allergic asthma," *The Journal of Allergy and Clinical Immunology*, vol. 106, no. 4, pp. 660–668, 2000.
- [22] C. C. Lin, C. J. Liou, C. Y. Chiang, W. Y. Huang, and W. C. Huang, "Danggui Buxue Tang attenuates eosinophil infiltration and airway hyperresponsiveness in asthmatic mice," *Annals of Allergy, Asthma, and Immunology*, vol. 107, no. 6, pp. 501–509, 2011.
- [23] L. H. Su, Y. P. Li, H. M. Li et al., "Anti-inflammatory prenylated flavonoids from *Helminthostachys zeylanica*," *Chemical & Pharmaceutical Bulletin*, vol. 64, no. 5, pp. 497–501, 2016.
- [24] C. H. Lee, Y. L. Huang, J. F. Liao, and W. F. Chiou, "Ugonin K promotes osteoblastic differentiation and mineralization by activation of p38 MAPK- and ERK-mediated expression of Runx2 and osterix," *European Journal of Pharmacology*, vol. 668, no. 3, pp. 383–389, 2011.
- [25] H. L. Hsieh, S. H. Yang, T. H. Lee, J. Y. Fang, and C. F. Lin, "Evaluation of anti-inflammatory effects of *Helminthostachys zeylanica* extracts via inhibiting bradykinin-induced MMP-9 expression in brain astrocytes," *Molecular Neurobiology*, vol. 53, no. 9, pp. 5995–6005, 2016.
- [26] C. J. Liou, Y. L. Huang, W. C. Huang, K. W. Yeh, T. Y. Huang, and C. F. Lin, "Water extract of *Helminthostachys zeylanica* attenuates LPS-induced acute lung injury in mice by modulating NF- $\kappa$ B and MAPK pathways," *Journal of Ethnopharmacology*, vol. 199, pp. 30–38, 2017.
- [27] Y. L. Huang, C. C. Shen, Y. C. Shen, W. F. Chiou, and C. C. Chen, "Anti-inflammatory and antiosteoporosis flavonoids from the rhizomes of *Helminthostachys zeylanica*," *Journal of Natural Products*, vol. 80, no. 2, pp. 246–253, 2017.
- [28] W. C. Huang, L. W. Fang, and C. J. Liou, "Phloretin attenuates allergic airway inflammation and oxidative stress in asthmatic mice," *Frontiers in Immunology*, vol. 8, p. 134, 2017.
- [29] W. C. Huang, P. Y. Gu, L. W. Fang, Y. L. Huang, C. F. Lin, and C. J. Liou, "Sophoraflavanone G from *Sophora flavescens* induces apoptosis in triple-negative breast cancer cells," *Phyto-medicine*, vol. 61, p. 152852, 2019.
- [30] W. C. Huang, C. L. Lai, Y. T. Liang, H. C. Hung, H. C. Liu, and C. J. Liou, "Phloretin attenuates LPS-induced acute lung injury in mice via modulation of the NF- $\kappa$ B and MAPK pathways," *International Immunopharmacology*, vol. 40, pp. 98–105, 2016.

- [31] H. L. Peng, W. C. Huang, S. C. Cheng, and C. J. Liou, "Fisetin inhibits the generation of inflammatory mediators in interleukin-1 $\beta$ -induced human lung epithelial cells by suppressing the NF- $\kappa$ B and ERK1/2 pathways," *International Immunopharmacology*, vol. 60, pp. 202–210, 2018.
- [32] W. C. Huang, C. C. Chan, S. J. Wu et al., "Matrine attenuates allergic airway inflammation and eosinophil infiltration by suppressing eotaxin and Th2 cytokine production in asthmatic mice," *Journal of Ethnopharmacology*, vol. 151, no. 1, pp. 470–477, 2014.
- [33] C. J. Liou, C. Y. Cheng, K. W. Yeh, Y. H. Wu, and W. C. Huang, "Protective effects of casticin from *Vitex trifolia* alleviate eosinophilic airway inflammation and oxidative stress in a murine asthma model," *Frontiers in Pharmacology*, vol. 9, p. 635, 2018.
- [34] C. J. Liou, Y. R. Lai, Y. L. Chen, Y. H. Chang, Z. Y. Li, and W. C. Huang, "Matrine attenuates COX-2 and ICAM-1 expressions in human lung epithelial cells and prevents acute lung injury in LPS-induced mice," *Mediators of Inflammation*, vol. 2016, Article ID 3630485, 12 pages, 2016.
- [35] S. Myou, A. R. Leff, S. Myo et al., "Blockade of inflammation and airway hyperresponsiveness in immune-sensitized mice by dominant-negative phosphoinositide 3-kinase-TAT," *The Journal of Experimental Medicine*, vol. 198, no. 10, pp. 1573–1582, 2003.
- [36] S. Colicino, D. Munblit, C. Minelli, A. Custovic, and P. Cullinan, "Validation of childhood asthma predictive tools: a systematic review," *Clinical and Experimental Allergy*, vol. 49, no. 4, pp. 410–418, 2019.
- [37] C. B. Charron and S. Pakhale, "The role of airway hyperresponsiveness measured by methacholine challenge test in defining asthma severity in asthma-obesity syndrome," *Current Opinion in Allergy and Clinical Immunology*, vol. 16, no. 3, pp. 218–223, 2016.
- [38] S. H. Fatani, "Biomarkers of oxidative stress in acute and chronic bronchial asthma," *The Journal of Asthma*, vol. 51, no. 6, pp. 578–584, 2014.
- [39] S. Saglani and C. M. Lloyd, "Eosinophils in the pathogenesis of paediatric severe asthma," *Current Opinion in Allergy and Clinical Immunology*, vol. 14, no. 2, pp. 143–148, 2014.
- [40] S. R. Suja, P. G. Latha, P. Pushpangadan, and S. Rajasekharan, "Evaluation of hepatoprotective effects of *Helminthostachys zeylanica* (L.) Hook against carbon tetrachloride-induced liver damage in Wistar rats," *Journal of Ethnopharmacology*, vol. 92, no. 1, pp. 61–66, 2004.
- [41] Y. Ma, A. Ge, W. Zhu et al., "Morin attenuates ovalbumin-induced airway inflammation by modulating oxidative stress-responsive MAPK signaling," *Oxidative Medicine and Cellular Longevity*, vol. 2016, Article ID 5843672, 13 pages, 2016.
- [42] J. M. Gostner, K. Becker, F. Ueberall, and D. Fuchs, "The good and bad of antioxidant foods: an immunological perspective," *Food and Chemical Toxicology*, vol. 80, pp. 72–79, 2015.
- [43] P. Bansal, S. Saw, D. Govindaraj, and N. Arora, "Intranasal administration of a combination of choline chloride, vitamin C, and selenium attenuates the allergic effect in a mouse model of airway disease," *Free Radical Biology and Medicine*, vol. 73, pp. 358–365, 2014.
- [44] W. C. Huang, C. Y. Liu, S. C. Shen et al., "Protective effects of licochalcone A improve airway hyper-responsiveness and oxidative stress in a mouse model of asthma," *Cells*, vol. 8, no. 6, p. 617, 2019.
- [45] H. J. Park, C. M. Lee, I. D. Jung et al., "Quercetin regulates Th1/Th2 balance in a murine model of asthma," *International Immunopharmacology*, vol. 9, no. 3, pp. 261–267, 2009.
- [46] Z. W. Gu, Y. X. Wang, and Z. W. Cao, "Neutralization of interleukin-17 suppresses allergic rhinitis symptoms by down-regulating Th2 and Th17 responses and upregulating the Treg response," *Oncotarget*, vol. 8, no. 14, pp. 22361–22369, 2017.
- [47] K. Hirahara and T. Nakayama, "CD4+ T-cell subsets in inflammatory diseases: beyond the Th1/Th2 paradigm," *International Immunopharmacology*, vol. 28, no. 4, pp. 163–171, 2016.
- [48] S. L. Hall, T. Baker, S. Lajoie et al., "IL-17A enhances IL-13 activity by enhancing IL-13-induced signal transducer and activator of transcription 6 activation," *The Journal of Allergy and Clinical Immunology*, vol. 139, no. 2, pp. 462–471.e14, 2017.
- [49] K. Kelly-Pieper, S. P. Patil, P. Busse et al., "Safety and tolerability of an antiasthma herbal formula (ASHMI) in adult subjects with asthma: a randomized, double-blinded, placebo-controlled, dose-escalation phase I study," *The Journal of Alternative and Complementary Medicine*, vol. 15, no. 7, pp. 735–743, 2009.

## Article

# Synthesis and Thermal Characteristic of Liquid Crystalline Polyoxetane Containing Trans-Stilbene Side Group

Li-Chuan Wu <sup>1</sup>, Cheng-Chih Chen <sup>2</sup> and Chih-Hung Lin <sup>2,3,\*</sup> 

<sup>1</sup> Department of Applied Chemistry and Material Sciences, Fooyin University, 151 Jinxue Road, Daliao, Kaohsiung City 83102, Taiwan; SC023@fy.edu.tw

<sup>2</sup> Center for General Education, Chang Gung University of Science and Technology, 261 Wen-Hwa 1st Road, Kwei-Shan, Tao-Yuan 33303, Taiwan; ccchen@gw.cgust.edu.tw

<sup>3</sup> Research Center for Food and Cosmetic Safety and Research Center for Chinese Herbal Medicine, Chang Gung University of Science and Technology, Kweishan, Tao-Yuan 33303, Taiwan

\* Correspondence: chlin@mail.cgust.edu.tw or chihhung5622@gmail.com

Received: 21 December 2019; Accepted: 6 January 2020; Published: 10 January 2020



**Abstract:** A series of fourteen liquid crystalline monomers and polyoxetanes containing trans-biphenyl side group have been successfully synthesized. The thermal and mesomorphic properties of monomers (1M~14M) and polymers (1P~14P) are measured using DSC, POM, and X-ray. All of the series monomers present enantiotropic smectic H and smectic G phase and the series polymers show enantiotropic smectic A phase which three polymers contained exhibit smectic E. Polyoxetanes have been used as a cationic ring-opening polymerization of oxetane monomers bearing a pendant trans-stilbene mesogenic unit including different spacer length and terminal alkyl length.

**Keywords:** polyoxetane; liquid crystal; stilbene

## 1. Introduction

The first thermotropic side-chain liquid crystalline polymers were synthesized by Finkelmann and Rehage [1,2]. They had already understood the main factors in the formation of the liquid crystal phase of compounds. The liquid crystal properties of the compound were affected by the backbone liquid crystal structure, the mesogenic unit, the tail group, and the spacer length. The side-chain liquid crystal polymer integrated the properties of the liquid crystal and the polymer properties. They had potential applications in optical data storage, piezoelectric transducer, nonlinear optics, and gas or liquid chromatography stationary phases [3–7].

In the past few decades, a large number of side-chain liquid crystal polymers had been synthesized [8–10]. They combined the many different backbone types (such as methacrylates, acrylates, siloxanes, epoxides, ethylenes, etc.) and the vast number of mesogenic units available. Kawakami et al. reported the first example of a cationic ring-opening polymerized side-chain liquid crystalline polyoxetane [11–16].

According to the experimental results, polyoxetane flexibility had more than polyacrylate and polymethacrylate. The polymerization of the side-chain liquid crystalline polyoxetane molecular weight distribution (MWD) is less than 1.3.

The purpose of this research is to show the synthesis of a new series of side-chain liquid crystalline polyoxetanes containing the trans-stilbene mesogenic side group. The effects of terminal alkyl length and spacer length on the properties of mesophases exhibited are discussed.



## 2. Materials and Methods

### 2.1. Instruments

$^1\text{H}$ -NMR (400 MHz) spectra were measured using a Bruker AM 400 instrument (Bruker, Daltonik, Germany). The thermal transitions and the anisotropic textures were measured using a Carl-Ziess Axiphot polarized optical microscope (Carl-Ziess, Jena, Germany) and a Mettler FP82 hot stage (Mettler, Switzerland). Differential scanning calorimeter (DSC) was recorded on a Seiko SSC/5200 (Seiko, New Castle, DE, USA) with determined compounds of thermal transitions and thermodynamic parameters equipped with a cooling accessory. Thermal stability was measured using a Seiko TG/DTA 200 thermal gravimetric analyzer (Seiko, New Castle, DE, USA). X-ray diffraction by liquid crystals was measured using a Riraku powder diffractometer (Riraku, Austin, TX, USA).

### 2.2. Synthesis

The intermediates and targets compound synthetic routes were represented in Scheme 1. TLC and  $^1\text{H}$ -NMR spectroscopy were verified as the chemical structures and purity of the intermediates and target compounds. The synthesis methods and analysis of each product are described below.

3-[(3-Bromopropoxy)methyl]-3-methyloxetane (**1a**)

3-[(4-Bromobutoxy)methyl]-3-methyloxetane (**1b**)

3-[(5-Bromopentoxy)methyl]-3-methyloxetane (**1c**)

3-[(6-Bromohexoxy)methyl]-3-methyloxetane (**1d**)

3-[(12-Bromododecoxy)methyl]-3-methyloxetane (**1e**)

All five compounds were prepared by the same method. Taking compound **1d** as an example, the synthesis is described below.

3-(Hydroxymethyl)-3-methyloxetane (10.0 g, 0.098 mol), dibromohexane (73.2 g, 0.299 mol), and hexane (120 mL) was added to a stirred solution of sodium hydroxide (64.7 g, 1.618 mol) in 150 mL of water. Then, tetrabutylammonium bromide (1.0 g) was added to the solution. The solution was stirred for 12 h at room temperature, then heated to reflux for 0.5 h. The reaction solution cooled to room temperature, 1000 mL of water was added, and the organic layer was extracted three times with hexane. The extraction solution was dried through anhydrous magnesium sulfate and after removal of the solvent under reduced pressure. The crude product was purified by distillation, to yield 20.85 g (80.3%) of a colorless transparent liquid.  $^1\text{H}$ -NMR (300 MHz,  $\text{CDCl}_3$ ,  $\delta$ , ppm): 1.30 (s, 3H,  $-\text{CH}_3$  on the oxetane ring), 1.46–1.90 (m, 8H,  $-\text{OCH}_2(\text{CH}_2)_4\text{CH}_2-$ ), 3.39–3.48 (m, 6H,  $-\text{CH}_2\text{OCH}_2(\text{CH}_2)_4\text{CH}_2\text{Br}$ ), 4.34, 4.51 (AB quartet, each 2H,  $-\text{CH}_2-\text{O}$  on the oxetane ring).

3-[[3-(4-Hydroxybenzaldehyde)propoxy]methyl]-3-methyl oxetane (**2a**)

3-[[4-(4-Hydroxybenzaldehyde)butoxy]methyl]-3-methyl oxetane (**2b**)

3-[[5-(4-Hydroxybenzaldehyde)pentoxy]methyl]-3-methyl oxetane (**2c**)

3-[[6-(4-Hydroxybenzaldehyde)hexoxy]methyl]-3-methyl oxetane (**2d**)

3-[[12-(4-Hydroxybenzaldehyde)dodecanoxy]methyl]-3-methyl oxetane (**2e**)

4-Butoxy-benzaldehyde (**3a**)

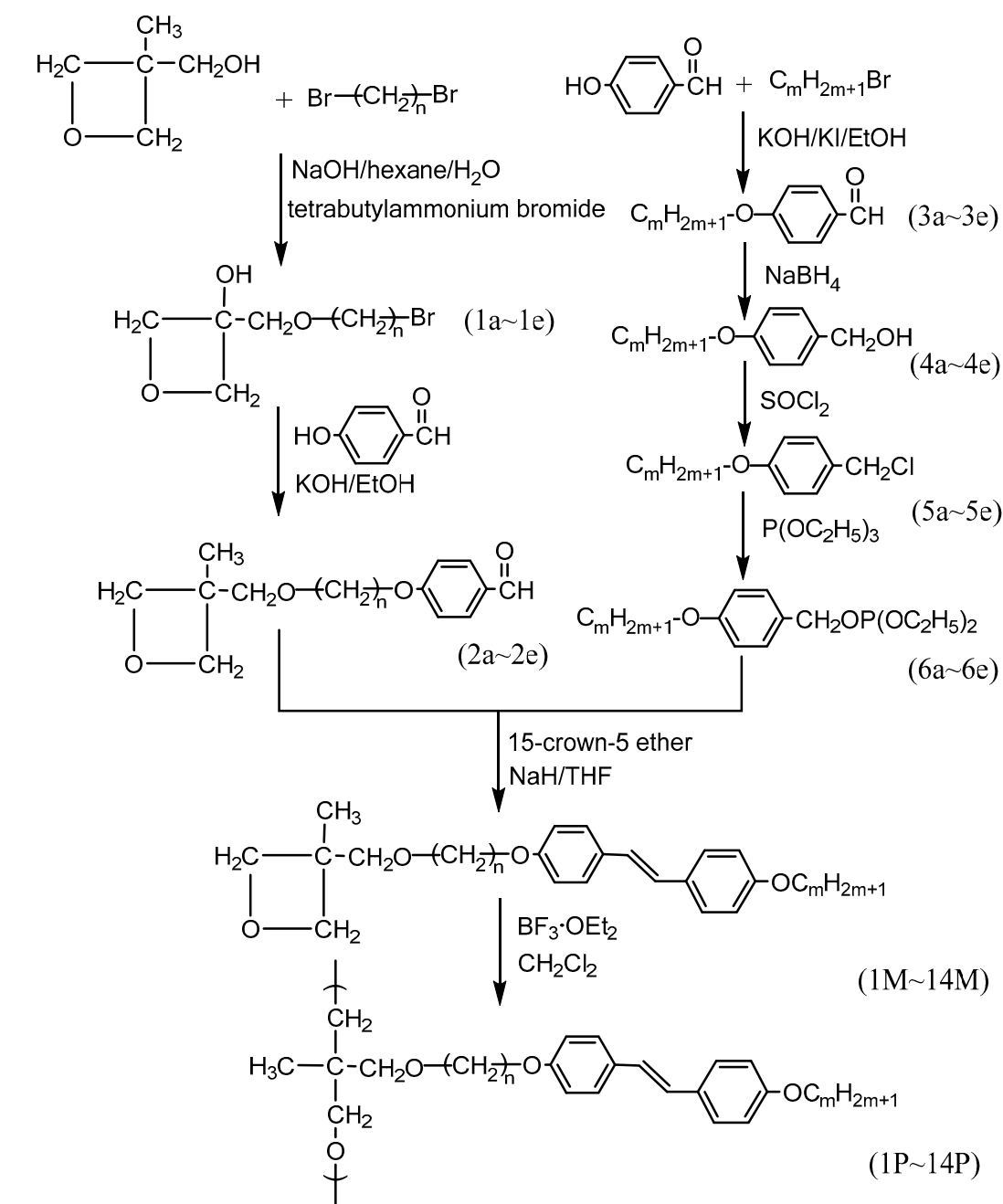
4-Pentoxy-benzaldehyde (**3b**)

4-Hexoxy-benzaldehyde (**3c**)

4-Heptoxy-benzaldehyde (**3d**)

4-Octoxy-benzaldehyde (**3e**)

All ten compounds were prepared by the same method. Taking compound **2d** as an example, the synthesis is described below.



monomer	1M	2M	3M	4M	5M	6M	7M	8M	9M	10M	11M	12M	13M	14M
polymer	1P	2P	3P	4P	5P	6P	7P	8P	9P	10P	11P	12P	13P	14P
n	3	4	5	6	6	6	6	6	6	12	12	12	12	12
m	1	1	1	1	4	5	6	7	8	4	5	6	7	8

Scheme 1. Synthesis of monomers 1M~14M and polymers 1P~14P.

4-Hydroxybenzaldehyde (4.45 g, 0.036 mol) was added to a stirred solution of potassium hydroxide (2.04 g, 0.036 mol) and potassium iodide (0.2 g) in 100 mL of 95% ethanol. Compound **1d** (8.00 g, 0.030 mol) was added dropwise after the solution mentioned above was refluxed for 1 h. The solution refluxed for 12 h and then cooled to room temperature. The solution was extracted with water and ethyl acetate. The extraction solution was washed with 10% KOH solution three times and dried through anhydrous magnesium sulfate. After removal of the solvent under reduced pressure, the crude product

was purified by column chromatography on silica gel using ethyl acetate/hexane as eluent to yield 2.42 g (82.5%) of light yellow liquid.  $^1\text{H-NMR}$  (300 MHz,  $\text{CDCl}_3$ ,  $\delta$ , ppm): 1.30 (s, 3H,  $-\text{CH}_3$  on the oxetane ring), 1.40–1.82 (m, 8H,  $-\text{OCH}_2(\text{CH}_2)_4\text{CH}_2-$ ), 3.46 (m, 4H,  $-\text{CH}_2\text{O}-$ ), 4.04 (t, 2H,  $-\text{CH}_2-\text{OPh}$ ), 4.33, 4.49 (AB quartet, each 2H,  $-\text{CH}_2-\text{O}$  on the oxetane ring), 6.96 (d, 2H, aromatic protons), 7.81 (d, 2H, aromatic protons), 9.87 (s, 1H, aldehyde protons).

4-Butoxy-benzyl alcohol (**4a**)

4-Pentoxo-benzyl alcohol (**4b**)

4-Hexoxy-benzyl alcohol (**4c**)

4-Heptoxy-benzyl alcohol (**4d**)

4-Octoxy-benzyl alcohol (**4e**)

Taking compound **4c** as an example, the synthesis is described below.

A solution of sodium tetrahydridoborate (3.28 g, 0.087 mol) in 2 mL of 0.45 N sodium hydroxide with 28 mL water was slowly added dropwise to 4-Hexoxy-benzaldehyde (14.9 g, 0.072 mol) with methanol (150 mL) solution. The solution was stirred 3 h at room temperature. Remove most of the methanol by distillation. The solution was extracted with ether and aqueous of dilute acid solution (50 mL). The organic phase was washed with 2% aqueous of sodium bicarbonate, saturated aqueous of sodium chloride, and dried through anhydrous magnesium sulfate. The crude product was purified by column chromatography on silica gel using n-hexane/ethyl acetate as eluent to yield 13.8 g (92.1%) of colorless liquid.  $^1\text{H-NMR}$  (300 MHz,  $\text{CDCl}_3$ ,  $\delta$ , ppm): 0.89 (t, 3H,  $-\text{CH}_3$ ), 1.31–1.80 (m, 8H,  $-\text{OCH}_2(\text{CH}_2)_4\text{CH}_3$ ), 3.96 (t, 2H,  $-\text{OCH}_2(\text{CH}_2)_4-$ ), 4.66 (s, 2H,  $\text{Ph}-\text{CH}_2\text{Cl}$ ), 6.89 (d, 2H, aromatic protons), 7.30 (d, 2H, aromatic protons).

4-Butoxy-benzyl chloride (**5a**)

4-Pentoxo-benzyl chloride (**5b**)

4-Hexoxy-benzyl chloride (**5c**)

4-Heptoxy-benzyl chloride (**5d**)

4-Octoxy-benzyl chloride (**5e**)

All five compounds were prepared by the same method. Taking compound **5c** as an example, the synthesis is described below.

4-Hexoxy-benzyl alcohol (5 g, 0.024 mol) was reacted with excess thionyl chloride (15 mL, 0.0206 mol) in 50 mL of methylene chloride. The solution was stirred at ice bath for 6 h. Then, added with water (30 mL) into the solution. The organic phase was washed with 10% aqueous of sodium bicarbonate, saturated aqueous of sodium chloride, and dried through anhydrous magnesium sulfate. The crude product was purified by column chromatography on silica gel using n-hexane/ethyl acetate as eluent to yield 4.58 g (84.3%) of light-yellow liquid.  $^1\text{H-NMR}$  (300 MHz,  $\text{CDCl}_3$ ,  $\delta$ , ppm): 0.89 (t, 3H,  $-\text{CH}_3$ ), 1.31–1.80 (m, 8H,  $-\text{OCH}_2(\text{CH}_2)_4\text{CH}_3$ ), 3.96 (t, 2H,  $-\text{OCH}_2(\text{CH}_2)_4-$ ), 4.66 (s, 2H,  $\text{Ph}-\text{CH}_2\text{Cl}$ ), 6.89 (d, 2H, aromatic protons), 7.30 (d, 2H, aromatic protons).

Diethyl[(4-butoxy)benzyl]phosphonate (**6a**)

Diethyl[(4-pentoxo)benzyl]phosphonate (**6b**)

Diethyl[(4-hexoxy)benzyl]phosphonate (**6c**)

Diethyl[(4-heptoxy)benzyl]phosphonate (**6d**)

Diethyl[(4-octoxy)benzyl]phosphonate (**6e**)

All five compounds were prepared by the same method. Taking compound **6c** as an example, the synthesis is described below.

4-Hexoxy-benzyl chloride (5.00 g, 0.022 mol) was injected by triethyl phosphite (11.0 g, 0.066 mol) with a syringe under nitrogen. The reaction mixture was refluxed for 12 h, then, was purified by distillation under reduced pressure to yield 5.89 g (81.6%) of colorless liquid.  $^1\text{H-NMR}$  (300 MHz,  $\text{CDCl}_3$ ,  $\delta$ , ppm): 0.89 (t, 3H,  $-\text{CH}_3$ ), 1.22 (m, 6H,  $\text{P}(\text{OCH}_2\text{CH}_3)_2$ ), 1.31–1.79 (m, 8H,  $-\text{OCH}_2(\text{CH}_2)_4\text{CH}_3$ ), 3.05 (d, 2H,  $\text{PCH}_2\text{Ph}$ ), 3.93–4.01 (m, 6H,  $-\text{OCH}_2(\text{CH}_2)_4-$  and  $\text{P}(\text{OCH}_2\text{CH}_3)_2$ ), 6.89 (d, 2H, aromatic protons), 7.30 (d, 2H, aromatic protons).

3-[3-(Trans-4'-methoxystilben-4-yloxy)propoxymethyl]-3-methyl oxetane (**1M**)

3-[4-(Trans-4'-methoxystilben-4-yloxy)butoxymethyl]-3-methyl oxetane (**2M**)  
 3-[5-(Trans-4'-methoxystilben-4-yloxy)pentoxymethyl]-3-methyl oxetane (**3M**)  
 3-[6-(Trans-4'-methoxystilben-4-yloxy)hexoxymethyl]-3-methyl oxetane (**4M**)  
 3-[6-(Trans-4'-butoxystilben-4-yloxy)hexoxymethyl]-3-methyl oxetane (**5M**)  
 3-[6-(Trans-4'-pentoxystilben-4-yloxy)hexoxymethyl]-3-methyl oxetane (**6M**)  
 3-[6-(Trans-4'-hexoxystilben-4-yloxy)hexoxymethyl]-3-methyl oxetane (**7M**)  
 3-[6-(Trans-4'-heptoxystilben-4-yloxy)hexoxymethyl]-3-methyl oxetane (**8M**)  
 3-[6-(Trans-4'-octoxystilben-4-yloxy)hexoxymethyl]-3-methyl oxetane (**9M**)  
 3-[12-(Trans-4'-butoxystilben-4-yloxy)dodecoxymethyl]-3-methyl oxetane (**10M**)  
 3-[12-(Trans-4'-pentoxystilben-4-yloxy)dodecoxymethyl]-3-methyl oxetane (**11M**)  
 3-[12-(Trans-4'-hexoxystilben-4-yloxy)dodecoxymethyl]-3-methyl oxetane (**12M**)  
 3-[12-(Trans-4'-heptoxystilben-4-yloxy)dodecoxymethyl]-3-methyl oxetane (**13M**)  
 3-[12-(Trans-4'-octoxystilben-4-yloxy)dodecoxymethyl]-3-methyl oxetane (**14M**)

All fourteen monomers **1M**–**14M** were prepared by the same method. Taking monomer **7M** as an example, the synthesis is described below.

Sodium hydride (0.33 g, 0.013 mol) dissolved in dry THF (50 mL) on the brown flask, 13-crown-5-ether (30 mg) was added to react under nitrogen in the ice bath. Then, a solution of compound **2d** (2.52 g, 0.008 mol) and compound **6d** (2.6 g, 0.008 mol) was added dropwise to a stirred mixture. The reaction mixture was stirred for 12 h at room temperature. The reaction solution mixture was poured into ice water. The solution was filtered, the remaining yellow solid was recrystallized from dimethyl formamide to yield 1.62 g of light-yellow solid.

The  $^1\text{H}$ -NMR spectrometer, the product yield, and element analysis of monomers **1M**–**14M** were as follows.

Compound **1M**: Yield: 40.7%;  $^1\text{H}$ -NMR (300 MHz,  $\text{CDCl}_3$ ,  $\delta$ , ppm): 1.28 (s, 3H,  $-\text{CH}_3$  on the oxetane ring), 2.03 (t, 2H,  $-\text{OCH}_2\text{CH}_2-$ ), 3.48 (s, 2H,  $-\text{CH}_2\text{O}(\text{CH}_2)_3-$ ), 3.62 (t, 2H,  $-\text{CH}_2\text{OCH}_2-$ ), 3.80 (s, 3H,  $-\text{PhOCH}_3$ ), 4.04 (t, 2H,  $-\text{CH}_2\text{CH}_2\text{OPh}$ ), 4.32, 4.48 (AB quartet, each 2H,  $-\text{CH}_2-$  on the oxetane ring), 6.84, 7.38 (m, 6H, 4H, stilbene protons); element analysis: Calc. for  $\text{C}_{23}\text{H}_{28}\text{O}_4$ : C 75.00, H 7.61, O 17.39; found C 75.00, H 7.75, O 17.25%.

Compound **2M**: Yield: 38.6%;  $^1\text{H}$ -NMR (300 MHz,  $\text{CDCl}_3$ ,  $\delta$ , ppm): 1.31 (s, 3H,  $-\text{CH}_3$  on the oxetane ring), 1.79 (m, 4H,  $-\text{OCH}_2(\text{CH}_2)_2-$ ), 3.49 (t, 4H,  $-\text{CH}_2\text{OCH}_2-$ ), 3.82 (s, 3H,  $-\text{PhOCH}_3$ ), 3.98 (t, 2H,  $-\text{CH}_2\text{CH}_2\text{OPh}$ ), 4.34, 4.50 (AB quartet, each 2H,  $-\text{CH}_2-$  on the oxetane ring), 6.85, 7.39 (m, 6H, 4H, stilbene protons); element analysis: Calc. for  $\text{C}_{24}\text{H}_{30}\text{O}_4$ : C 75.39, H 7.85, O 16.75; found C 75.46, H 7.99, O 16.45%.

Compound **3M**: Yield: 33.4%;  $^1\text{H}$ -NMR (300 MHz,  $\text{CDCl}_3$ ,  $\delta$ , ppm): 1.34 (s, 3H,  $-\text{CH}_3$  on the oxetane ring), 1.58–1.87 (m, 6H,  $-\text{OCH}_2(\text{CH}_2)_3-$ ), 3.51 (t, 4H,  $-\text{CH}_2\text{OCH}_2-$ ), 3.85 (s, 3H,  $-\text{PhOCH}_3$ ), 3.99 (t, 2H,  $-\text{CH}_2\text{CH}_2\text{OPh}$ ), 4.38, 4.53 (AB quartet, each 2H,  $-\text{CH}_2-$  on the oxetane ring), 6.85, 7.43 (m, 6H, 4H, stilbene protons); element analysis: Calc. for  $\text{C}_{25}\text{H}_{32}\text{O}_4$ : C 75.76, H 8.08, O 16.16; found C 75.52, H 8.15, O 16.33%.

Compound **4M**: Yield: 30.8%;  $^1\text{H}$ -NMR (300 MHz,  $\text{CDCl}_3$ ,  $\delta$ , ppm): 1.31 (s, 3H,  $-\text{CH}_3$  on the oxetane ring), 1.47–1.85 (m, 8H,  $-\text{OCH}_2(\text{CH}_2)_4-$ ), 3.46 (t, 4H,  $-\text{CH}_2\text{OCH}_2-$ ), 3.81 (s, 3H,  $-\text{PhOCH}_3$ ), 3.99 (t, 2H,  $-\text{CH}_2\text{CH}_2\text{OPh}$ ), 4.34, 4.50 (AB quartet, each 2H,  $-\text{CH}_2-$  on the oxetane ring), 6.87, 7.26 (m, 6H, 4H, stilbene protons); element analysis: Calc. for  $\text{C}_{26}\text{H}_{34}\text{O}_4$ : C 76.10, H 8.29, O 15.61; found C 75.82, H 8.47, O 15.71%.

Compound **5M**: Yield: 40.6%;  $^1\text{H}$ -NMR (300 MHz,  $\text{CDCl}_3$ ,  $\delta$ , ppm): 0.96 (t, 3H,  $-\text{CH}_2-\text{CH}_3$ ), 1.31 (s, 3H,  $-\text{CH}_3$  on the oxetane ring), 1.47–1.80 (m, 12H,  $-\text{OCH}_2(\text{CH}_2)_2\text{CH}_3$ ;  $-\text{OCH}_2(\text{CH}_2)_4\text{CH}_2-$ ), 3.46 (t, 4H,  $-\text{CH}_2\text{OCH}_2-$ ), 3.94 (t, 4H,  $-\text{CH}_2-\text{OPh}-$ ), 4.35, 4.51 (AB quartet, each 2H,  $-\text{CH}_2-$  on the oxetane ring), 6.86, 7.39 (m, 6H, 4H, stilbene protons); element analysis: Calc. for  $\text{C}_{29}\text{H}_{40}\text{O}_4$ : C 76.99, H 8.85, O 14.16; found C 77.03, H 9.02, O 13.95%.

Compound **6M**: Yield: 36.7%;  $^1\text{H}$ -NMR (300 MHz,  $\text{CDCl}_3$ ,  $\delta$ , ppm): 0.91 (t, 3H,  $-\text{CH}_2-\text{CH}_3$ ), 1.31 (s, 3H,  $-\text{CH}_3$  on the oxetane ring), 1.41–1.79 (m, 14H,  $-\text{OCH}_2(\text{CH}_2)_3\text{CH}_3$ ;  $-\text{OCH}_2(\text{CH}_2)_4\text{CH}_2-$ ), 3.45 (t, 4H,  $-\text{CH}_2\text{OCH}_2-$ ), 3.94 (t, 4H,  $-\text{CH}_2-\text{OPh}-$ ), 4.35, 4.50 (AB quartet, each 2H,  $-\text{CH}_2-$  on the oxetane

ring), 6.86, 7.39 (m, 6H, 4H, stilbene protons); element analysis: Calc. for  $C_{30}H_{42}O_4$ : C 77.25, H 9.01, O 13.73; found C 77.21, H 9.15, O 13.64%.

Compound **7M**: Yield: 41.0%;  $^1H$ -NMR (300 MHz,  $CDCl_3$ ,  $\delta$ , ppm): 0.91 (t, 3H,  $-CH_2-CH_3$ ), 1.31–1.80 (m, 19H,  $-CH_3$  on the oxetane ring,  $-OCH_2(CH_2)_4CH_3$ ,  $-OCH_2(CH_2)_4CH_2-$ ), 3.46 (t, 4H,  $-CH_2OCH_2-$ ), 3.94 (t, 4H,  $-CH_2-OPh-$ ), 4.35, 4.50 (AB quartet, each 2H,  $-CH_2-$  on the oxetane ring), 6.86, 7.39 (m, 6H, 4H, stilbene protons); element analysis: Calc. for  $C_{31}H_{44}O_4$ : C 77.50, H 9.17, O 13.33; found C 77.47, H 9.26, O 13.27%.

Compound **8M**: Yield: 40.6%;  $^1H$ -NMR (300 MHz,  $CDCl_3$ ,  $\delta$ , ppm): 0.88 (t, 3H,  $-CH_2-CH_3$ ), 1.26–1.80 (m, 21H,  $-CH_3$  on the oxetane ring,  $-OCH_2(CH_2)_5CH_3$ ,  $-OCH_2(CH_2)_4CH_2-$ ), 3.46 (t, 4H,  $-CH_2OCH_2-$ ), 3.95 (t, 4H,  $-CH_2-OPh-$ ), 4.35, 4.50 (AB quartet, each 2H,  $-CH_2-$  on the oxetane ring), 6.86, 7.39 (m, 6H, 4H, stilbene protons); element analysis: Calc. for  $C_{32}H_{46}O_4$ : C 77.73, H 9.31, O 12.96; found C 77.60, H 9.40, O 13.00%.

Compound **9M**: Yield: 38.6%;  $^1H$ -NMR (300 MHz,  $CDCl_3$ ,  $\delta$ , ppm): 0.87 (t, 3H,  $-CH_2-CH_3$ ), 1.26–1.82 (m, 23H,  $-CH_3$  on the oxetane ring,  $-OCH_2(CH_2)_6CH_3$ ,  $-OCH_2(CH_2)_4CH_2-$ ), 3.46 (t, 4H,  $-CH_2OCH_2-$ ), 3.94 (t, 4H,  $-CH_2-OPh-$ ), 4.35, 4.50 (AB quartet, each 2H,  $-CH_2-$  on the oxetane ring), 6.86, 7.39 (m, 6H, 4H, stilbene protons); element analysis: Calc. for  $C_{33}H_{48}O_4$ : C 77.95, H 9.45, O 12.60; found C 77.92, H 9.54, O 12.54%.

Compound **10M**: Yield: 34.7%;  $^1H$ -NMR (300 MHz,  $CDCl_3$ ,  $\delta$ , ppm): 0.96 (t, 3H,  $-CH_2-CH_3$ ), 1.29–1.79 (m, 27H,  $-CH_3$  on the oxetane ring,  $-OCH_2(CH_2)_2CH_3$ ,  $-OCH_2(CH_2)_{10}CH_2-$ ), 3.43 (t, 4H,  $-CH_2OCH_2-$ ), 3.96 (t, 4H,  $-CH_2-OPh-$ ), 4.35, 4.50 (AB quartet, each 2H,  $-CH_2-$  on the oxetane ring), 6.86, 7.39 (m, 6H, 4H, stilbene protons); element analysis: Calc. for  $C_{35}H_{52}O_4$ : C 78.36, H 9.70, O 11.94; found C 78.22, H 9.80, O 11.98%.

Compound **11M**: Yield: 39.1%;  $^1H$ -NMR (300 MHz,  $CDCl_3$ ,  $\delta$ , ppm): 0.91 (t, 3H,  $-CH_2-CH_3$ ), 1.27–1.78 (m, 29H,  $-CH_3$  on the oxetane ring,  $-OCH_2(CH_2)_3CH_3$ ,  $-OCH_2(CH_2)_{10}CH_2-$ ), 3.43 (t, 4H,  $-CH_2OCH_2-$ ), 3.94 (t, 4H,  $-CH_2-OPh-$ ), 4.34, 4.50 (AB quartet, each 2H,  $-CH_2-$  on the oxetane ring), 6.86, 7.39 (m, 6H, 4H, stilbene protons); element analysis: Calc. for  $C_{36}H_{54}O_4$ : C 78.54, H 9.82, O 11.64; found C 78.26, H 9.90, O 11.84%.

Compound **12M**: Yield: 24.1%;  $^1H$ -NMR (300 MHz,  $CDCl_3$ ,  $\delta$ , ppm): 0.90 (t, 3H,  $-CH_2-CH_3$ ), 1.26–1.79 (m, 31H,  $-CH_3$  on the oxetane ring,  $-OCH_2(CH_2)_4CH_3$ ,  $-OCH_2(CH_2)_{10}CH_2-$ ), 3.43 (t, 4H,  $-CH_2OCH_2-$ ), 3.94 (t, 4H,  $-CH_2-OPh-$ ), 4.34, 4.50 (AB quartet, each 2H,  $-CH_2-$  on the oxetane ring), 6.86, 7.39 (m, 6H, 4H, stilbene protons); element analysis: Calc. for  $C_{37}H_{56}O_4$ : C 78.72, H 9.93, O 11.35; found C 78.40, H 10.05, O 11.55%.

Compound **13M**: Yield: 27.4%;  $^1H$ -NMR (300 MHz,  $CDCl_3$ ,  $\delta$ , ppm): 0.87 (t, 3H,  $-CH_2-CH_3$ ), 1.26–1.77 (m, 33H,  $-CH_3$  on the oxetane ring,  $-OCH_2(CH_2)_5CH_3$ ,  $-OCH_2(CH_2)_{10}CH_2-$ ), 3.44 (t, 4H,  $-CH_2OCH_2-$ ), 3.95 (t, 4H,  $-CH_2-OPh-$ ), 4.35, 4.49 (AB quartet, each 2H,  $-CH_2-$  on the oxetane ring), 6.85, 7.38 (m, 6H, 4H, stilbene protons); element analysis: Calc. for  $C_{38}H_{58}O_4$ : C 78.90, H 10.03, O 11.07; found C 78.73, H 10.11, O 11.16%.

Compound **14M**: Yield: 34.7%;  $^1H$ -NMR (300 MHz,  $CDCl_3$ ,  $\delta$ , ppm): 0.89 (t, 3H,  $-CH_2-CH_3$ ), 1.29–1.81 (m, 35H,  $-CH_3$  on the oxetane ring,  $-OCH_2(CH_2)_6CH_3$ ,  $-OCH_2(CH_2)_{10}CH_2-$ ), 3.46 (t, 4H,  $-CH_2OCH_2-$ ), 3.94 (t, 4H,  $-CH_2-OPh-$ ), 4.35, 4.50 (AB quartet, each 2H,  $-CH_2-$  on the oxetane ring), 6.86, 7.39 (m, 6H, 4H, stilbene protons); element analysis: Calc. for  $C_{39}H_{60}O_4$ : C 79.05, H 10.14, O 10.81; found C 78.92, H 10.20, O 10.88%.

### 2.3. Synthesis of Polymers **1P**–**14P**

In this study, all the polymers were synthesized by cationic ring-opening polymerization. The preparation of polymer is described below. Under nitrogen, dichloromethane was dried by calcium hydride and was distilled just prior to use. Boron trifluoride ether complex (freshly distilled) was used as an initiator. Under nitrogen, a solution of monomer (0.5 mmol) and dichloromethane (5 mL) was cooled to 0 °C and the initiator of 2% mol with respect to monomer was injected with a syringe. The reaction solution mixture was stirred at 0 °C for 24 h. Then, the resulting polymers were



precipitated in methanol and purified further by dissolving in dichloromethane and then precipitating in ethanol repeatedly. The absence of monomer was checked by  $^1\text{H}$ -NMR and GPC.

### 3. Results and Discussion

This study intends to explore the liquid crystalline monomers of oxetane and liquid crystalline polyoxetane. Among the compounds of these monomers and polymers, spacer length and terminal chain length have influences on the thermal properties and mesophase. The molecular structure and the general synthetic procedures of the series of monomers are shown in Scheme 1, and all the products are examined by the nuclear magnetic resonance spectrometer and elemental analyzer in order to verify the correction of the molecular structure. There is one most important part among all the monomers in terms of using nuclear magnetic resonance spectrometer, that is oxetane in which the hydrogen, located on two carbons being beside the oxygen atoms, is the split from AB quartet, and it will gradually be disappearing after the ring-opening polymerization.

Monomers are composed of trans-stilbene as a mesogenic unit, their spacers length include several different alkyl chains ( $n = 3, 4, 5, 6, 12$ ) and links with the terminals of different alkoxy length ( $m = 1, 4, 5, 6, 7, 8$ ). Moreover, there are fourteen monomers (**1M~14M**) in this series, and their structures are exhibited in Scheme 1.

All monomers (**1M~14M**) used  $\text{BF}_3 \cdot \text{OEt}_2$  as an initiator to carry out the ring-opening polymerization and successfully synthesized a series of brand-new side-chain liquid crystalline polymers (**1P~14P**), and their structures and their synthesis procedures are listed in Scheme 1.

The thermal and mesomorphic properties of monomers (**1M~14M**) and polymers (**1P~14P**) are measured using DSC, POM, and X-ray. The phase transition temperature and enthalpy changed of monomers **1M~14M** are reported in Table 1. The series of monomers (**1M~14M**) reveal enantiotropic smectic H and smectic G phases.

There is no obvious regularity in the change of the phase transition temperature of the monomer **1M~4M**, although the length of the spacer changes. This phenomenon may be affected by the volume of oxetane.

Table 1 illustrates the representative phase transition temperature of monomers **5M~9M** (containing six methylene units spacer length). As can be seen from Table 1 the tendency toward mesomorphic temperature range increase by increasing the length of alkoxy terminal group (**5M** is  $2.6^\circ\text{C}$ , **6M** is  $3.3^\circ\text{C}$ , **7M** is  $2.1^\circ\text{C}$ , **8M** is  $20.6^\circ\text{C}$ , **9M** is  $38.1^\circ\text{C}$ ). In addition, when the length of the terminal groups become shorter, the transition temperature of liquid crystalline will gradually overlap with the isotropic temperature. **5M~7M** are observed by POM, only the tiny transition of liquid crystalline phases can be seen. There is a tendency for the isotropic temperature to lower down the temperature from  $136.4$  to  $118.0^\circ\text{C}$  when the length of terminal alkoxy is changed from  $m = 4$  to  $m = 8$ . **10M~14M** (containing twelve methylene units spacer length) finds that the length of terminal alkoxy becomes larger, and the mesogenic temperature range becomes smaller (**10M** is  $77.9^\circ\text{C}$ , **11M** is  $56.9^\circ\text{C}$ , **12M** is  $32.2^\circ\text{C}$ , **13M** is  $22.6^\circ\text{C}$ , **14M** is  $16.0^\circ\text{C}$ ). This is the opposite result as compared with that of monomers **5M~9M**. This result may be due to the flexible spacer with a too larger length. From the above result, it is found that the mesomorphic temperature range has a great relationship with the spacer length.

Taking **9M** for an example, the dendritic growth pattern is developed at the temperature of  $116.1^\circ\text{C}$  during the cooling scanning process, then mosaic platelets (Figure 1A) is formed at the temperature of  $115.6^\circ\text{C}$ . At last, the liquid crystalline mesophase includes a Zig-Zag line shown at the diagram of mosaic platelets (Figure 1B) at the temperature of  $82.6^\circ\text{C}$ . This characteristic is a transition phenomenon from smectic G phases to smectic H phases. In addition, in the X-ray test, Figure 2 presents the X-ray diffraction diagrams obtained from the powder sample of **9M** at  $54.6^\circ\text{C}$ . The diffraction diagram presents a sharp first-order reflection at  $34.53^\circ$ , which is a layer of the length of smectic phase, and there are three diffraction peaks of  $4.513$ ,  $4.240$ , and  $3.995^\circ$  in terms of the wider angles. Most of the X-ray diffraction studies performed on the SH phase indicate that it has

a structure equivalent to that of the SE phase, except that the molecules have their long axes tilted concerning the normal to the layer planes. From the description of the phase as being of the SE type, it must be assumed that the molecules adopt an orthorhombic close-packing in a plane at right angles to the molecular long axes. Hence, because of the tilt, the pseudo-hexagonal net becomes even more distorted, and the phase has a monoclinic structure. According to the research of Volino, Dianoux and Hervet [17], the results of the X-ray test and the diagram represent smectic H phase.

**Table 1.** Phase transition temperature and thermodynamic parameters of monomers 1M~14M.

Compound	Phase Transitions, °C (Corresponding Enthalpy Changes, Kcal/mol)	
	heating	cooling
1M	$S_H$ 108.5(–) <sup>a</sup> $S_G$ 117.1(4.63) $I$	$I$ 111.6(–4.73) $S_G$ 102.0(–) <sup>a</sup> $S_H$
2M	$S_H$ 121.3(–) <sup>a</sup> $S_G$ 124.5(3.92) $I$	$I$ 120.9(–3.82) $S_G$ 116.0(–) <sup>a</sup> $S_H$
3M	$S_H$ 90.0(–) <sup>a</sup> $S_G$ 118.0(3.68) $I$	$I$ 113.0(–3.90) $S_G$ 81.6(–) <sup>a</sup> $S_H$
4M	$S_H$ 109.3(–) <sup>a</sup> $S_G$ 114.3(3.97) $I$	$I$ 104.9(–4.40) $S_G$ 101.6(–) <sup>a</sup> $S_H$
5M	$S_H$ 132.1(–) <sup>a</sup> $S_G$ 136.4(6.94) $I$	$I$ 132.6(–7.37) $S_G$ 130.0(–) <sup>a</sup> $S_H$
6M	$S_H$ 130.8(–) <sup>a</sup> $S_G$ 132.2(8.05) $I$	$I$ 130.6(–8.20) $S_G$ 127.3(–) <sup>a</sup> $S_H$
7M	$S_H$ 124.8(–) <sup>a</sup> $S_G$ 126.2(4.77) $I$	$I$ 123.9(–5.10) $S_G$ 121.8(–) <sup>a</sup> $S_H$
8M	$S_H$ 121.9(–) <sup>a</sup> $S_G$ 122.8(9.52) $I$	$I$ 117.6(–7.77) $S_G$ 97.7(–0.72) $S_H$
9M	$S_H$ 97.0(0.72) $S_G$ 118.0(5.81) $I$	$I$ 114.2(–6.37) $S_G$ 76.1(–0.29) $S_H$
10M	$S_H$ 66.1(0.73) $S_G$ 131.6(7.19) $I$	$I$ 126.7(–7.45) $S_G$ 48.8(–0.77) $S_H$
11M	$S_H$ 64.0(1.29) $S_G$ 119.8(5.06) $I$	$I$ 114.9(–5.14) $S_G$ 58.0(–1.02) $S_H$
12M	$S_H$ 81.7(–) <sup>a</sup> $S_G$ 116.6(8.08) $I$	$I$ 110.0(–7.59) $S_G$ 77.8(–) <sup>a</sup> $S_H$
13M	$S_H$ 97.1(–) <sup>a</sup> $S_G$ 121.2(8.86) $I$	$I$ 115.8(–9.84) $S_G$ 93.2(–) <sup>a</sup> $S_H$
14M	$S_H$ 106.4(–) <sup>a</sup> $S_G$ 123.5(14.0) $I$	$I$ 119.1(–13.6) $S_G$ 103.1(–) <sup>a</sup> $S_H$

$S_A$  = smectic A,  $S_E$  = smectic E,  $I$  = isotropic. <sup>a</sup> determined by optical polarizing microscopic observation.

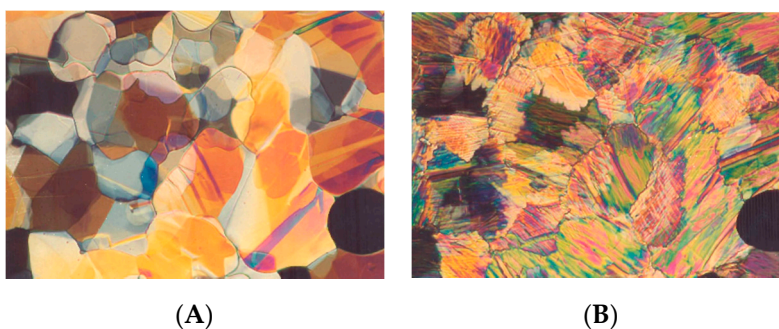


**Figure 1.** Optical polarizing micrographs displayed by monomer 9M upon cooling from isotropic phase. (A) The smectic G mosaic platelets texture obtained at 115.6 °C (320×). (B) The smectic H zig-zag line texture obtained at 82.6 °C (320×).

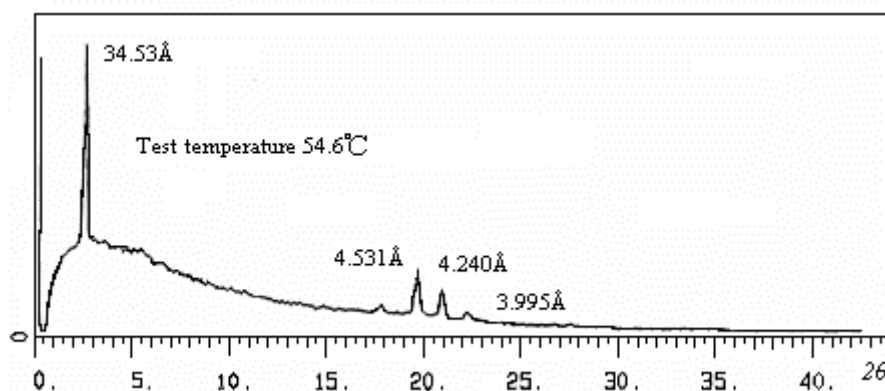


Figure 2. X-ray diffraction trace of 9M.

Table 2 reports the thermal transition and thermodynamic parameters of polymers **1P**–**14P**. Polymers **1P**–**4P** and **6P**–**11P** exhibit enantiotropic smectic A phase, **5P** and **12P**–**14P** show enantiotropic smectic A and smectic E phase. Figure 3A,B exhibits the texture of polymer **14P** by optical polarizing micrograph. Figure 3A shows a focal conic fan texture of smectic A phase at 172.6 °C. Figure 3B displays the fissure focal cone fan shape of the texture of smectic E phase at 152.2 °C, while the temperature is cooling to 120 °C, the texture does not change except in the bigger crack. Therefore, it can be a regular liquid crystalline smectic texture of crystallization. Seen from Table 2, polymers (**1P**–**4P**) that contain a short flexible spacer ( $n = 3\sim6$ ) and only one methyl terminal group show smectic A phase. Polymers (**5P**–**9P**, six methylene units spacer length; **10P**–**14P**, twelve methylene units spacer length) have different length of alkoxy terminal groups ( $m = 4\sim8$ ). Their isotropic temperature and liquid crystalline transition temperature exhibits the same tendency. The isotropic temperature of **5P** and **10P** ( $m = 4$ ) is especially high, maybe four alkoxy terminal groups can be easily arranged. **6P**–**9P** and **11P**–**14P** ( $m = 5\sim8$ ) polymers increase in isotropic temperature with the length of the alkoxy terminal group. **11P**–**14P** more than **6P**–**10P** formed the regular liquid crystalline phase because they have a long flexible spacer.

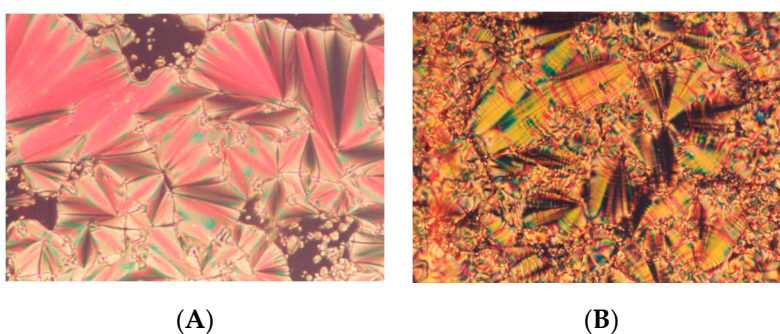


Figure 3. Optical polarizing micrographs displayed by polymer **14P** upon cooling from the isotropic phase. (A) The smectic A focal-conic texture obtained at 172.6 °C (320×). (B) The smectic E banded focal-conic texture obtained at 152.2 °C (320×).

The synthesized polymers (**1P**–**14P**) cannot be solved in an organic solvent (such as hexane, toluene, m-cresol, methanol, dichloromethane, acetone, ethyl acetate, THF, DMF, DMSO) under room temperature. During the ring-opening polymerization, the stilbene group might be cross-linked, because the total amount of H was decreased from the NMR spectrum after the polymerization, which might also cause the poor solubility of the synthesized polymer. In this study, **7P** and **14P** were selected for measuring molecular weight under the higher temperature of GPC, in which the solvent of m-cresol was used, and the test temperature of 85 °C was set. The molecular weight of **7P** is  $M_n = 4031$ ,  $M_w = 5107$ ,  $DPI = 1.266$ . The molecular weight of **14P** is  $M_n = 3666$ ,  $M_w = 5052$ ,

DPI = 1.378. The results are presented as a ring-polymerization reaction by BF<sub>3</sub>·OEt<sub>2</sub>, the molecular weight of the obtained polymer is not high, but its dpi is small, as expected. The structure of the polymers is comb-like, and polystyrene was used as the standard of GPC, the test results from using GPC would be lower. However, in fact, the molecule weight should be higher.

**Table 2.** Phase transition temperature and thermodynamic parameters of polymers **1P**–**18P**.

Compound	Phase Transitions, °C (Corresponding Enthalpy Changes, Kcal/mol)	
	heating	cooling
<b>1P</b>	$K174.1(-)^a S_A$	$178.0(4.08) I$ $I 173.6(-3.82) S_A$ $170.2(-)^a K$
<b>2P</b>	$K185.1(-)^a S_A$	$189.7(4.98) I$ $I 186.6(-4.90) S_A$ $178.6(-)^a K$
<b>3P</b>	$K156.0(-)^a S_A$	$152.2(4.52) I$ $I 146.6(-4.56) S_A$ $135.4(-)^a K$
<b>4P</b>	$K121.5(-)^a S_A$	$126.7(2.93) I$ $I 125.7(-2.61) S_A$ $115.8(-)^a K$
<b>5P</b>	$K171.0(-)^a S_E$	$188.5(-)^a S_A$ $193.1(5.26) I$ $I 191.6(-4.83) S_A$ $187.4(-)^a S_E$ $168.5(-)^a K$
<b>6P</b>	$K166.4(-)^a S_A$	$176.8(7.44) I$ $I 172.6(-6.99) S_A$ $167.0(-)^a K$
<b>7P</b>	$K168.4(-)^a S_A$	$179.5(8.53) I$ $I 174.6(-7.66) S_A$ $170.1(-)^a K$
<b>8P</b>	$K168.7(-)^a S_A$	$179.7(7.80) I$ $I 173.8(-7.60) S_A$ $166.3(-)^a K$
<b>9P</b>	$K174.0(-)^a S_A$	$183.9(7.27) I$ $I 176.4(-6.80) S_A$ $167.3(-)^a K$
<b>10P</b>	$K169.8(-)^a S_A$	$183.8(6.76) I$ $I 177.3(-7.11) S_A$ $165.4(-)^a K$
<b>11P</b>	$K_1 69.7(0.38) K_2 90.4(0.27) K_3 133.7(-)^a S_A$	$138.6(6.78) I$ $I 130.4(-7.29) S_A$ $122.4(-)^a K_2$ $61.5(-0.55) K_1$
<b>12P</b>	$K_1 84.6(0.46) K_2 126.7(1.81) S_E$	$162.1(-)^a S_A$ $167.9(0.19) I$ $I 164.4(-0.53) S_A$ $159.6(-)^a S_E$ $123.1(-0.29) K_2$ $61.6(-0.53) K_1$
<b>13P</b>	$K_1 93.9(1.42) K_2 161.4(-)^a S_E$	$167.3(-)^a S_A$ $175.3(6.88) I$ $I 168.8(-7.19) S_A$ $163.1(-)^a S_E$ $158.5(-)^a K_2$ $89.3(-0.88) K_1$
<b>14P</b>	$K_1 101.0(1.12) K_2 164.5(-)^a S_E$	$169.4(-)^a S_A$ $177.4(7.08) I$ $I 171.6(-7.18) S_A$ $164.8(-)^a S_E$ $161.6(-)^a K_2$ $98.2(-0.67) K_1$

$S_A$  = smectic A,  $S_E$  = smectic E,  $I$  = isotropic,  $K$  = crystal. <sup>a</sup> determined by optical polarizing microscopic observation.

#### 4. Conclusions

In this study, a series of fourteen liquid crystalline monomers and polyoxetanes containing trans-biphenyl side group are successfully synthesized. It is known from the results that the liquid crystal phase transition temperature, the isotropic temperature, the stability of the liquid crystal phase, and the type of the liquid crystal all have a great influence on both the length of the soft spacer and the length of the terminal alkyl group. It is found that the difference in the length of the soft spacer and the length of the terminal alkyl group affect the monomer or polymer. When the length of the soft spacer and the length of the terminal alkyl group are increased, the liquid crystal phase formed is polymorphism of mesophases, such as **14M** shows  $S_H$  and  $S_G$ , **14P** shows  $S_A$  and  $S_E$ , and has a relatively stable liquid crystal phase.

**Author Contributions:** Conceptualization, C.-H.L. and L.-C.W.; methodology, C.-C.C. and L.-C.W.; validation, C.-H.L. and L.-C.W.; formal analysis, C.-H.L.; data curation, C.-H.L.; writing—original draft preparation, C.-H.L. and L.-C.W.; writing—review and editing, C.-H.L.; funding acquisition, C.-C.C. and C.-H.L. All authors have read and agreed to the published version of the manuscript.

**Funding:** This research was funded by Chang Gung University of Science and Technology EZRPF3I0051.

**Acknowledgments:** The authors are grateful for Chang Gung University of Science and Technology.

**Conflicts of Interest:** The authors declare no conflict of interest.

## References

1. Finkelmann, H.; Rehage, G. Investigations on liquid crystalline polysiloxanes, Optical properties of cholesteric phases and influence of the flexible spacer on the mobility of the mesogenic groups. *Makromol. Chem. Rapid Commun.* **1980**, *1*, 733–740. [\[CrossRef\]](#)
2. Finkelmann, H.; Rehage, G. Investigations on liquid crystalline polysiloxanes, Cholesteric homopolymers—Synthesis and optical characterization. *Makromol. Chem. Rapid Commun.* **1982**, *3*, 859–864. [\[CrossRef\]](#)
3. Janini, G.M.; Laub, R.J.; Shaw, T.J. Synthesis and properties of high temperature mesomorphic polysiloxane (MEPSIL) solvents. Amide, ester and Schiff's base linked systems. *Makromol. Chem. Rapid Commun.* **1985**, *6*, 57–63. [\[CrossRef\]](#)
4. Bradshaw, J.S.; Schregenberger, C.; Chang, K.H.C.; Markides, K.E.; Lee, M.L. Synthesis and chromatographic properties of polysiloxane stationary phases containing biphenylcarboxylate ester liquid-crystalline side groups. *J. Chromatogr. A* **1986**, *358*, 95–106. [\[CrossRef\]](#)
5. Lin, C.H. Cholesteric Liquid Crystalline Copolymers for Gas Chromatographic Separation of Polycyclic Aromatic Compounds. *Adv. Mater. Sci. Eng.* **2012**, *2012*. [\[CrossRef\]](#)
6. Kaempfer, G. Special Polymers for Data Memories. *Polym. J.* **1987**, *19*, 257–268. [\[CrossRef\]](#)
7. Coles, H.J.; Simon, R. Side chain polysiloxane liquid crystals and their behaviour in electric fields. *Polymer* **1986**, *27*, 811–816.
8. Wang, R.; Wang, Z.G. Theory of Side-Chain Liquid Crystal Polymers: Bulk Behavior and Chain Conformation. *Macromolecules* **2010**, *43*, 10096–10106. [\[CrossRef\]](#)
9. Zhang, B.Y.; Meng, F.B.; He, X.Z.; Lin, D.A. Synthesis and characterization of side chain liquid crystalline polymers exhibiting cholesteric and blue phases. *Liq. Cryst.* **2005**, *32*, 1161–1167. [\[CrossRef\]](#)
10. Reddy, G.S.M.; Jayaramudu, J.; Ray, S.S.; Varaprasad, K.; Sadiku, E.R. Side Chain Liquid Crystalline Polymers: Advances and Applications. *Liq. Cryst. Polym.* **2015**, *2*, 389–415.
11. Kawakami, Y.; Takahashi, K. Smectic liquid crystalline polyoxetane with novel mesogenic group. *Polym. Bull.* **1991**, *25*, 439–442. [\[CrossRef\]](#)
12. Kawakami, Y.; Takahashi, K.; Hibino, H. Synthesis of liquid crystalline polymers with a polyoxetane main chain. *Macromolecules* **1991**, *24*, 4531–4537. [\[CrossRef\]](#)
13. Kawakami, Y.; Nishiguchi, K.T.S.; Toida, K. Synthesis and thermal transition of side-chain liquid crystalline polyoxetanes having laterally attached mesogenic group. *Polym. Int.* **1993**, *31*, 35–40. [\[CrossRef\]](#)
14. Kawakami, Y.; Kishimoto, N. Synthesis of new disiloxane-containing polymers. *Proc. Jpn. Acad.* **1998**, *74*, 41–45. [\[CrossRef\]](#)
15. Campo, A.D.; Bello, A.; Perez, E.; Benavente, R. Liquid crystalline polyoxetanes with two mesogens in the side chain separated by a flexible spacer. *Ferroelectrics* **2000**, *243*, 137–144. [\[CrossRef\]](#)
16. Lee, J.W.; Oh, D.K.; Yelamaggad, C.V.; Nagamani, S.A.; Jin, J.I. Ferroelectric liquid crystalline polyoxetanes bearing chiral dimesogenic pendants. *J. Mater. Chem.* **2002**, *12*, 2225–2230. [\[CrossRef\]](#)
17. Volino, F.; Dianoux, A.J.; Hervet, H.J. Neutron Quasi-Elastic Scattering Study of Rotational Motions in the Smectic C, H and VI Phases of Terephthal-Bis-Butyl-Antline (TBBA). *J. Phys.* **1976**, *37*, 55–64. [\[CrossRef\]](#)



© 2020 by the authors. Licensee MDPI, Basel, Switzerland. This article is an open access article distributed under the terms and conditions of the Creative Commons Attribution (CC BY) license (<http://creativecommons.org/licenses/by/4.0/>).



## Research Article

# Luteolin Attenuates IL-1 $\beta$ -Induced THP-1 Adhesion to ARPE-19 Cells via Suppression of NF- $\kappa$ B and MAPK Pathways

Wen-Chung Huang<sup>1,2</sup>, Chian-Jiun Liou<sup>2,3</sup>, Szu-Chuan Shen<sup>4</sup>, Cindy Hu<sup>5,6</sup>,  
Chien-Yu Hsiao<sup>6,7</sup> and Shu-Ju Wu<sup>6,7</sup>

<sup>1</sup>Graduate Institute of Health Industry Technology, Research Center for Food and Cosmetic Safety, College of Human Ecology, Chang Gung University of Science and Technology, Taoyuan City 33303, Taiwan

<sup>2</sup>Division of Allergy, Asthma, and Rheumatology, Department of Pediatrics, Chang Gung Memorial Hospital, Linkou, Taoyuan City 33303, Taiwan

<sup>3</sup>Department of Nursing, Division of Basic Medical Sciences, Research Center for Chinese Herbal Medicine, and Graduate Institute of Health Industry Technology, Chang Gung University of Science and Technology, Taoyuan 33303, Taiwan

<sup>4</sup>Graduate Program of Nutrition Science, National Taiwan Normal University, 88 Ting-Chow Rd, Sec 4, Taipei, Taiwan

<sup>5</sup>Department of Cosmetic Science, College of Human Ecology, Chang Gung University of Science and Technology, Guishan Dist., Taoyuan City 33303, Taiwan

<sup>6</sup>Department of Dermatology, Aesthetic Medical Center, Chang Gung Memorial Hospital, Linkou, Taoyuan City 33303, Taiwan

<sup>7</sup>Department of Nutrition and Health Sciences, Research Center for Chinese Herbal Medicine, College of Human Ecology, Chang Gung University of Science and Technology, Taoyuan City 33303, Taiwan

Correspondence should be addressed to Chien-Yu Hsiao; [nulycopene@gmail.com](mailto:nulycopene@gmail.com) and Shu-Ju Wu; [sjwu@mail.cgust.edu.tw](mailto:sjwu@mail.cgust.edu.tw)

Received 8 June 2020; Revised 23 July 2020; Accepted 4 August 2020; Published 16 October 2020

Academic Editor: Carla Sipert

Copyright © 2020 Wen-Chung Huang et al. This is an open access article distributed under the Creative Commons Attribution License, which permits unrestricted use, distribution, and reproduction in any medium, provided the original work is properly cited.

Cytokine-induced endothelial dysfunction leads to inflammation and vascular adhesion molecule production in retinal pigment epithelium (RPE) cells. Inflammation is a critical mediator in retinal degeneration (RD) diseases, including age-related macular degeneration (AMD), and RD progression may be prevented through anti-inflammatory activity in RPE cells. The flavonoid polyphenol luteolin (LU) has anti-inflammatory and antidiabetes activities, but its effects regarding retinal protection remain unknown. Here, we examined the ability of luteolin to alleviate markers of inflammation related to RD in cytokine-primed ARPE-19 cells. We found that luteolin decreased the levels of interleukin- (IL-) 6, IL-8, soluble intercellular adhesion molecule-1 (sICAM-1), and monocyte chemoattractant protein-1 (MCP-1) and attenuated adherence of the human monocytic leukemia cell line THP-1 to IL-1 $\beta$ -stimulated ARPE-19 cells. Luteolin also increased anti-inflammatory protein heme oxygenase-1 (HO-1) levels. Interestingly, luteolin induced protein kinase B (AKT) phosphorylation, thus inhibiting nuclear factor- (NF-)  $\kappa$ B transfer from cytoplasm into the nucleus and suppressing mitogen-activated protein kinase (MAPK) inflammatory pathways. Furthermore, cotreatment with MAPK inhibitors and luteolin decreased inflammatory cytokine and chemokine levels, and further suppressed THP-1 adhesion. Overall, these results provide evidence that luteolin protects ARPE-19 cells from IL-1 $\beta$ -stimulated increases of IL-6, IL-8, sICAM-1, and MCP-1 production by blocking the activation of MAPK and NF- $\kappa$ B signaling pathways, thus ameliorating the inflammatory response.

## 1. Introduction

The retinal pigment epithelium (RPE) is a single layer of pigment cells, which is in close contact with photoreceptors and maintains visual function [1]. RPE exposure to ultraviolet/

visible light leads to oxidative stress and chronic inflammation in the retinal tissue. Inflammation clearly plays a role in the development of age-related macular degeneration (AMD), which is a cause of severe irreversible visual impairment in elderly persons and in diabetic retinopathy [2, 3]. A

variety of factors promote retinal tissue degeneration and AMD progression, including genetic and environmental factors, aging, and oxidative stress [4]. AMD involves reduced photoreceptor cells and retinal pigment epithelium dysfunction in the macula and can be classified as “dry AMD” or “wet/exudative/neovascular AMD.” Compared to neovascular AMD, dry AMD has a higher incidence, but involves less vision degradation and is thus less frequently a cause of “blindness” [5, 6]. Neovascular AMD is characterized by excessive choroidal neovascularization (CNV) under the retina, leading to retinal edema and even detachment, thereby causing vision loss. Notably, dry AMD can potentially evolve into neovascular AMD, leading to irreversible vision loss [7, 8]. Therefore, the best means of avoiding vision deterioration in elderly persons and cases of diabetic retinopathy is to prevent macular degeneration.

Available data suggest that a number of inflammatory cytokines and chemokines are elevated in the serum or ocular tissue of AMD patients—including interleukin-6 (IL-6), IL-8, monocyte chemoattractant protein (MCP-1), and intercellular adhesion molecule (ICAM-1) [9–11]. Notably, IL-6 levels are increased in the intraocular fluids of patients with neovascular AMD compared to controls, and findings suggest that IL-6 and IL-8 are proangiogenic in AMD progression [12, 13]. Intraocular MCP-1 is a chemokine for monocyte recruitment, and ICAM-1 is an adhesion molecule that facilitates leukocyte transmigration. Studies have reported that elevated MCP-1 levels contribute to subfoveal neovascular membrane development and the degree of macular edema in eyes with exudative AMD and that elevated soluble ICAM-1 (sICAM-1) levels are correlated with choroidal neovascularization [13, 14]. Inflammatory mediators, including chemokines and cytokines, can upregulate ICAM-1 expression. IL-6 could directly or indirectly activate the leukocytes to induce retinal inflammation. It has been found that MCP-1 recruits leukocytes to sites of injury and activates ICAM-1; thus, ICAM-1 induced leukocyte-endothelial interactions and promoted leukocyte migration into extravascular locations involved in the inflammatory response [14, 15]. More studies found that IL-8 and MCP-1 could attract neutrophils and monocytes to migrate into inflammatory tissues. IL-1 $\beta$  is a proinflammatory cytokine and promotes the upregulation of chemokines in RPE as model of focal retinal degeneration [15]. In the present study, we evaluated the ability of the luteolin to modulate inflammation in ARPE-19 cells-THP-1 monocytes interactions. The levels of the inflammatory cytokines IL-6, IL-8, MCP-1, and ICAM-1 in ocular tissue are significantly associated with exudative AMD occurrence and progression [4]. Moreover, IL-1 $\beta$  activates inflammatory-related pathways, including nuclear factor- (NF-)  $\kappa$ B and mitogen-activated protein kinase (MAPK) signaling, thus enhancing the production of the proinflammatory mediators MCP-1, IL-6, cyclooxygenase-2 (COX-2), and inducible nitric oxide synthase (iNOS). Proinflammatory mediators are closely associated with the development and progression of retinal degenerative diseases [15, 16].

Luteolin (Lu), 3',4',5,7-tetrahydroxyflavone, is a flavonoid polyphenolic compound found in numerous vegetables

(e.g., celery, carrots, broccoli, and peppers), fruits (e.g., apple, mango, blueberry, peaches, and prunes), and herbs (e.g., chrysanthemum flowers and *Taraxacum mongolicum*) [17–20]. In previous studies, it was demonstrated that luteolin shows anti-inflammatory, anticancer, neuroprotective, and antiviral properties in vitro and in animal models [21–25]. Thus, luteolin has been investigated for potential use in the treatment of obesity [26] and obesity-related diseases and for antidiabetic [27–29] and neuroprotective therapies [30, 31]. In ophthalmological research, luteolin protects against oxidative stress-related damage and decreases inflammation in ARPE-19 cells [32, 33]. Luteolin is protective against diabetes-induced progression of retinopathy and reportedly inhibits expressions of the inflammation-related markers NF- $\kappa$ B and IL-1 $\beta$ , decreases levels of the lipid peroxidation product malondialdehyde (MDA), and increases the antioxidant glutathione (GSH) in diabetes-induced oxidative stress in the retina [34]. These findings indicate the potential to use luteolin for prevention and treatment of retinal inflammatory diseases.

Based on the available data, we speculate that IL-6, IL-8, MCP-1, and sICAM-1 could be target molecules for AMD therapy or prevention. In the present study, we aimed to assess the mechanisms underlying the luteolin-induced anti-inflammatory effects in ARPE-19 cells stimulated by the proinflammatory cytokine IL-1 $\beta$  (Figure 1).

## 2. Materials and Methods

**2.1. Materials.** Luteolin ( $\geq 98\%$  purity by TLC), cell counting kit-8 assays (CCK-8), and DAPI solution were purchased from Sigma-Aldrich (St. Louis, MO, USA). Human recombinant proinflammatory cytokine IL-1 $\beta$  and enzyme-linked immunosorbent assay (ELISA) kits were purchased from R&D Systems (Minneapolis, MN, USA). The inhibitors PD98059, SP600125, SB202190, and Bay 117082 were purchased from Enzo Life Sciences (Farmingdale, NY, USA). Antibodies against  $\beta$ -actin, COX-2, iNOS, HO-1, AKT, and phosphorylated- (phospho-) AKT were purchased from Santa Cruz Biotechnology (Santa Cruz, CA, USA). Antibodies against JNK, ERK, p38, phospho-JNK, phospho-ERK, and phospho-p38 were purchased from Millipore (Billerica, MA, USA).

**2.2. Preparation of Luteolin and Cell Culture.** Luteolin was dissolved in dimethyl sulfoxide (DMSO) to prepare a 100 mM stock solution, which was stored at  $-20^{\circ}\text{C}$ . The final culture medium had a DMSO concentration of  $\leq 0.1\%$ , as previously described [16]. The ARPE-19 human retinal pigment epithelial cell line was purchased from Bioresource Collection and Research Center (BCRC, Taiwan) and cultured in Dulbecco's modified Eagle's medium (DMEM)/F-12 medium (Invitrogen-Gibco, Paisley, Scotland) containing 10% heat-inactivated fetal bovine serum (FBS; Invitrogen-Gibco) and penicillin G (100 U/mL), streptomycin (100  $\mu\text{g/mL}$ ), and gentamycin (50 ng/mL). Cells were subcultured every 2–3 days at  $37^{\circ}\text{C}$  in a humidified atmosphere of 5%  $\text{CO}_2$ . ARPE-19 cells ( $2 \times 10^5$ ) were pretreated with or without various luteolin concentrations (1–30  $\mu\text{M}$ ) for 1 h,

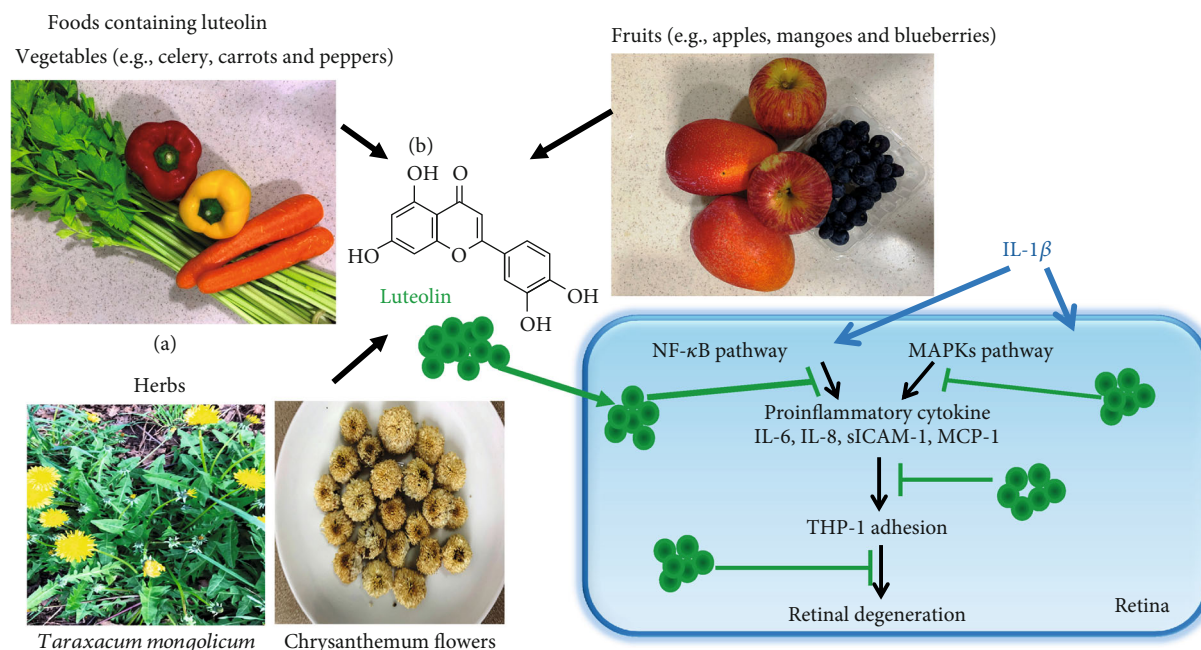


FIGURE 1: Experimental abstract. (a) Foods containing luteolin. (b) The structure of luteolin. (c) Pathways likely related to the anti-inflammatory activity of luteolin in IL-1 $\beta$ -stimulated ARPE-19 cells.

and then, IL-1 $\beta$  (1  $\mu$ g/mL) was added. After 24 h, the ARPE-19 cells were lysed for western blot analysis, and the media samples were subjected to ELISA analysis. The THP-1 human monocytic leukemia cell line was obtained from American Type Culture Collection (Manassas, VA, USA). THP-1 cells were cultured in RPMI 1640 medium (Gibco) containing FBS (10%) at 37°C in a humidified atmosphere of 5% CO<sub>2</sub> and subcultured every 3–4 days.

**2.3. Cell Viability Assay.** We assessed the inhibitory effect of luteolin on cell viability using CCK-8 kits (Sigma-Aldrich) as described previously [35]. Cells were seeded at 10<sup>5</sup> cells/well into 96-well plates and treated with luteolin at concentrations of 1–100  $\mu$ M for 24 h. After treatment, the CCK-8 solution was added, and the plates were incubated at 37°C for 2 h. Finally, cell viability was measured at 450 nm using a microplate reader (Multiskan FC; Thermo, Waltham, MA, USA). The CCK-8 assay with each concentration was carried out in triplicate, and cell viability was reported as a percentage relative to the cells without luteolin treatment.

**2.4. ELISA Assay.** ARPE-19 cells (10<sup>5</sup> cells/mL) were pretreated without or with various luteolin concentrations (1–30  $\mu$ M) in 24-well plates for 1 h. Then IL-1 $\beta$  (1 ng/mL) was added, and the cells were cultured for 24 h. Specific ELISA kits were used to measure the levels of IL-6, IL-8, MCP-1, and ICAM-1 in the supernatants, following the manufacturers' instructions. The OD at 450 nm was determined using a microplate reader (Multiskan FC; Thermo).

**2.5. Preparation of Total Proteins.** ARPE-19 cells (8 cells/mL) were pretreated with or without luteolin (1–30  $\mu$ M) for 1 h. In 6-well plates, the cells were then stimulated with or without IL-1 $\beta$  (1 ng/mL) for 24 h to evaluate total protein content,

or for 30 min to evaluate phosphorylated protein content. Cells were harvested with 300  $\mu$ L lysis buffer (50 mM Tris-HCl, pH 7.4; 1 mM EDTA; 150 mM NaCl; 1 mM DTT; 0.5% NP40; and 0.1% sodium dodecyl sulfate (SDS)) containing protease inhibitor cocktail and phosphatase inhibitors (Sigma, St. Louis, MO, USA). The BCA assay kit (Pierce) was used to quantitate all protein concentrations.

**2.6. Western Blot Analysis.** Protein samples were separated on 10% SDS polyacrylamide gels and then transferred to polyvinylidene fluoride (PVDF) membranes (Millipore, Billerica, MA, USA). Next, the PVDF membranes were incubated overnight at 4°C with specific primary antibodies against  $\beta$ -actin (Sigma), COX-2, iNOS, HO-1, AKT, pAKT (Santa Cruz, CA, USA), JNK, pJNK, p38, and pp38 (Cell Signaling Technology, Danvers, MA, USA). Then, the membranes were washed three times with tris-buffered saline with Tween 20 (TBST) buffer and incubated with secondary antibodies at room temperature for 1 h. Proteins were detected using Luminol/Enhancer solution (Millipore), and signals were detected using the BioSpectrum 600 system (UVP, Upland, CA, USA) to quantitate protein bands.

**2.7. Monocyte Adhesion Assay.** In the first step, AREP19 cells (2  $\times$  10<sup>5</sup> cells/mL) were pretreated with luteolin (1, 3, 10, and 30  $\mu$ M) or inhibitors (10  $\mu$ M SP600125, 10  $\mu$ M PD98059, 10  $\mu$ M SB202190, or 5  $\mu$ M Bay 11-7082) for 1 h in DMEM medium. THP-1 cells (5  $\times$  10<sup>5</sup> cells/mL) were labeled with fluorescent dye (5  $\mu$ M calcein-AM) in RPMI-1640 medium at 37°C for 30 min in the dark and then washed by centrifugation. Second, the labeled THP-1 cells were cocultured with the ARPE-19 cells in plates for 1 h, and then, the cells were washed three times with PBS to remove nonadherent THP-1



cells. Finally, the extent of adhesion of THP-1 cells to ARPE19 cells was observed under fluorescence microscope (4 per view; magnification,  $\times 200$ ; Olympus Corporation, Tokyo, Japan). The control groups were treated with IL-1 $\beta$  alone, and all experiments were repeated three times.

**2.8. Immunofluorescence Staining.** ARPE19 cells were seeded into 6-well plates until reaching 50–60% confluence and pretreated with or without luteolin (1, 3, 10, and 30  $\mu$ M) for 1 h, followed by addition of IL-1 $\beta$  for 15 min. Then, the medium was suctioned out, and the cells were washed with PBS. The cells were fixed with 4% (*w/v*) paraformaldehyde and incubated with anti-NF- $\kappa$ B p65 antibody overnight at 4°C. The next day, the medium was removed, and the cells were washed with PBS and then incubated with secondary antibodies at room temperature for 1 h. Then, the cells were washed 2–3 times with PBS, followed by the addition of fluorescent dye (BODIPY493/503 or BODIPY581/591). The cells were again washed with PBS to remove the dye, and 4',6-diamidino-2-phenylindole (DAPI; Sigma) was added to stain the nucleus. Finally, images were acquired using a fluorescence microscope (Olympus, Tokyo, Japan).

**2.9. Statistical Analysis.** Image Lab software (Bio-Rad) was used to quantify the intensity of western blot bands, and ImageJ software (W. Rasband, NIH, USA) to determine the numbers of THP-1 cells in the adhesion assay. Data were presented as the mean  $\pm$  standard deviation (SD) from at least three independent experiments. Statistical analyses included one-way analysis of variance (ANOVA) followed by the Tukey's post hoc test. A *p* value of  $< 0.05$  was considered significant.

### 3. Results

**3.1. Luteolin Inhibited Inflammatory Mediator Expression and Increased Anti-Inflammatory Protein HO-1 Expression in IL-1 $\beta$ -Stimulated ARPE19 Cells.** First, we performed a CCK-8 assay to assess luteolin cytotoxicity in ARPE-19 cells. Luteolin concentrations of  $\leq 50$   $\mu$ M showed no significant cytotoxicity in ARPE-19 cells, while cell numbers were significantly reduced at concentrations of  $\geq 100$   $\mu$ M (Figure 2(a)). Therefore, all subsequent experiments were performed using 1–30  $\mu$ M luteolin. ARPE-19 cells were seeded in 6-well plates, treated with luteolin, and then stimulated with 1 ng/mL IL-1 $\beta$ . Compared with IL-1 $\beta$  alone, additional treatment with luteolin at  $\geq 1$   $\mu$ M significantly inhibited expression of the inflammatory mediator iNOS (Figures 2(b) and 2(c)) but did not significantly inhibit COX-2 expression (data not shown). Notably, compared with IL-1 $\beta$  alone, treatment with 1 and 30  $\mu$ M luteolin significantly increased expression of the anti-inflammatory protein HO-1 (Figures 2(d) and 2(e)). Previous studies have indicated that AKT activation may contribute to inhibiting the NF- $\kappa$ B inflammatory pathway in inflammation-related diseases [36]. Our results showed that luteolin at  $\geq 1$   $\mu$ M enhanced the expression of phosphorylated AKT proteins in IL-1 $\beta$ -stimulated ARPE19 cells compared with in cells treated with IL-1 $\beta$  alone (Figures 2(f) and 2(g)).

**3.2. Luteolin Inhibited Inflammation-Related Cytokines and Attenuated THP-1 Cell Adherence to IL-1 $\beta$ -Stimulated ARPE-19 Cells.** ARPE-19 cells were pretreated with luteolin (1, 3, 10, or 30  $\mu$ M) for 1 h, and then, 1 ng/mL IL-1 $\beta$  was added for 24 h. IL-1 $\beta$  treatment alone significantly stimulated ARPE19 cells to release cytokines and chemokines compared with control cells. Luteolin at concentrations of 10 and 30  $\mu$ M significantly inhibited the IL-1 $\beta$ -induced release of IL-6 and IL-8 and decreased the levels of the cell adhesion molecule sICAM-1. Additionally, treatment with 30  $\mu$ M luteolin significantly decreased MCP-1 levels compared to treatment with IL-1 $\beta$  alone (Figures 3(a)–3(d)). Since luteolin concentrations of  $\geq 10$   $\mu$ M strongly inhibited sICAM-1 levels, we further investigated whether luteolin attenuated THP-1 cell adhesion to IL-1 $\beta$ -stimulated ARPE-19 cells. Pretreatment with luteolin significantly inhibited THP-1 cell adherence to IL-1 $\beta$ -stimulated ARPE-19 cells, compared to samples treated with IL-1 $\beta$  alone (Figures 3(e) and 3(f)).

**3.3. Luteolin Inhibited NF- $\kappa$ B Activation to Suppress THP-1 Cell Adherence to IL-1 $\beta$ -Stimulated ARPE-19 Cells.** We observed that luteolin significantly increased AKT activation (Figures 2(f) and 2(g)), and pAKT has previously been associated with inhibition of the NF- $\kappa$ B inflammatory pathway [37]. Therefore, we evaluated whether luteolin inhibited NF- $\kappa$ B in relation to the suppression of THP-1 cell adherence to IL-1 $\beta$ -stimulated ARPE-19 cells. Cells were pretreated with or without luteolin (1–30  $\mu$ M) for 1 h, then stimulation with IL-1 $\beta$  (1 ng/mL) for 15 min, to investigate whether luteolin inhibited NF- $\kappa$ B p65 translocation. Immunofluorescence staining revealed that luteolin at  $\geq 10$   $\mu$ M suppressed NF- $\kappa$ B p65 translocation from the cytoplasm into the nucleus and that the p65 subunit was retained in the cytoplasm in IL- $\beta$ -activated ARPE-19 cells (Figure 4(a)). Then, we evaluated whether luteolin inhibited I $\kappa$ B phosphorylation. Treatment with luteolin at  $\geq 1$   $\mu$ M significantly inhibited phosphorylated I $\kappa$ B expression, compared with IL-1 $\beta$  alone (Figure 4(b)). We further investigated whether luteolin decreased THP-1 cell adherence to ARPE-19 cells via inhibition of NF- $\kappa$ B p65 activation. First, ARPE-19 cells were pretreated with either luteolin (10  $\mu$ M) or Bay 11-7082 (5  $\mu$ M) for 1 h and then stimulated with IL-1 $\beta$ . Second, these pretreated ARPE-19 cells were cocultured with labeled THP-1 cells. Our results showed that both luteolin and Bay 11-7082 pretreatment significantly inhibited THP-1 cell adherence to IL-1 $\beta$ -stimulated ARPE-19 cells compared to cells treated with IL-1 $\beta$  alone (Figures 4(b) and 4(c)).

**3.4. Luteolin Blocked MAPK Inflammatory Pathways and MAPK Inhibitors Decreased THP-1 Cell Adherence to IL-1 $\beta$ -Stimulated ARPE-19 Cells.** We next evaluated whether luteolin inhibited MAPK phosphorylation and if this was related to the decreased THP-1 cell adherence to IL-1 $\beta$ -stimulated ARPE-19 cells. First, cells were pretreated with luteolin (1–30  $\mu$ M) for 1 h and then incubated with IL-1 $\beta$  (1 ng/mL) for 30 min or 24 h to evaluate the expression of MAPK signaling proteins. Our results showed that luteolin at  $\geq 3$   $\mu$ M significantly decreased phosphorylated c-JUN N-

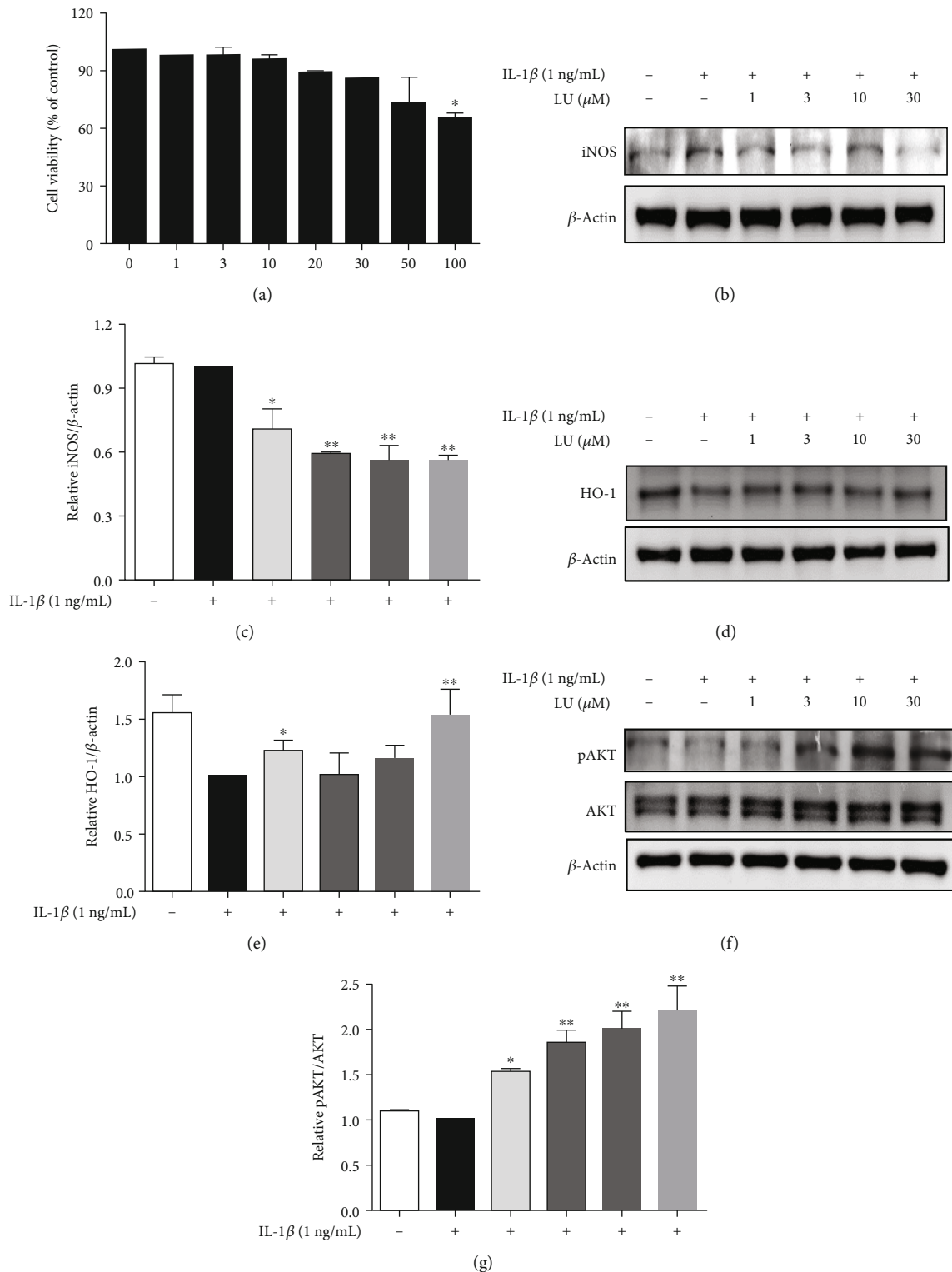


FIGURE 2: Luteolin inhibited inflammatory mediator expression and increased anti-inflammatory protein HO-1 expression in IL-1 $\beta$ -stimulated ARPE19 cells. (a) Cell viability of ARPE19 cells treated with various luteolin (LU) concentrations (0–100  $\mu$ M). Cells were pretreated with luteolin for 1 h, then stimulated with IL-1 $\beta$  (1 ng/mL) for 24 h. (b) Cells were pretreated with different LU doses and then incubated with IL-1 $\beta$  (1 ng/mL) for 30 min or 24 h. Western blots show iNOS protein expression. (c) The fold-change in iNOS protein expression was measured relative to  $\beta$ -actin expression. (d) Western blots show HO-1 protein expression. (e) The fold-change in HO-1 protein expression was measured relative to  $\beta$ -actin expression. (f) Western blots show phosphorylated AKT protein expression. (g) The fold-change in pAKT protein expression was measured relative to AKT expression. Data represent the mean  $\pm$  SD. \* $p$  < 0.05, \*\* $p$  < 0.01, compared to ARPE-19 cells stimulated with IL-1 $\beta$  alone.



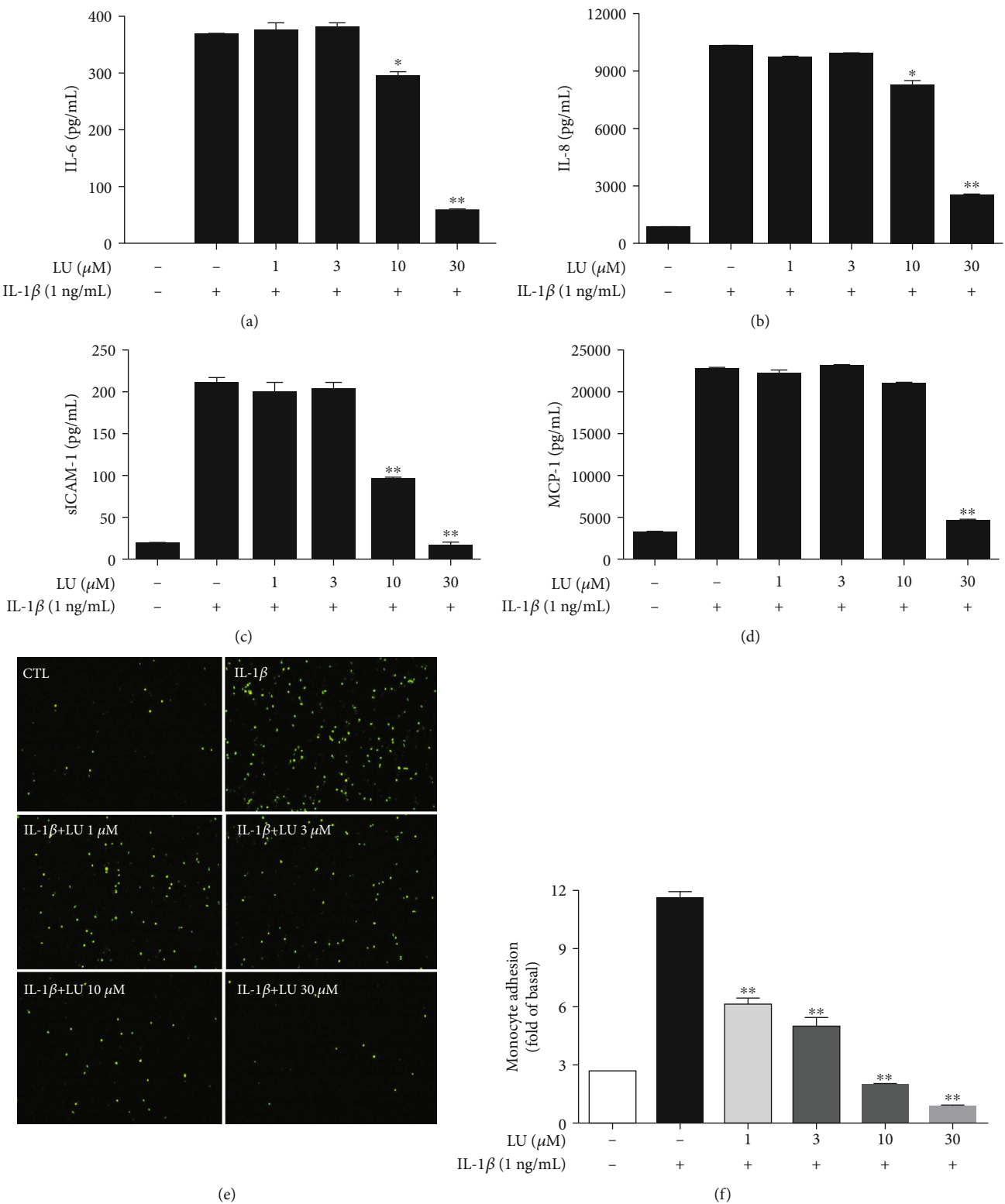


FIGURE 3: Luteolin inhibited inflammation-related cytokine expression and attenuated THP-1 cell adherence to IL-1 $\beta$ -stimulated ARPE-19 cells. Cells were pretreated with different doses of luteolin (LU) and then incubated with IL-1 $\beta$  (1 ng/mL) for 24 h. ELISA results showed the levels of (a) IL-6, (b) IL-8, (c) sICAM-1, and (d) MCP-1. (e) LU significantly suppressed THP-1 cell adherence to IL-1 $\beta$ -stimulated ARPE-19 cells. Fluorescent-labeled THP-1 cells (green) were cocultured with control (CTL) or IL-1 $\beta$ -stimulated ARPE-19 cells in the absence or presence of the indicated LU concentrations. (f) The fluorescence intensity revealed THP-1 cell adherence to IL-1 $\beta$ -stimulated ARPE-19 cells, which was used to quantify calcein-AM fluorescence. The data represent the mean  $\pm$  SD.  $*p < 0.05$ ,  $**p < 0.01$ , compared to ARPE-19 cells stimulated with IL-1 $\beta$  alone.

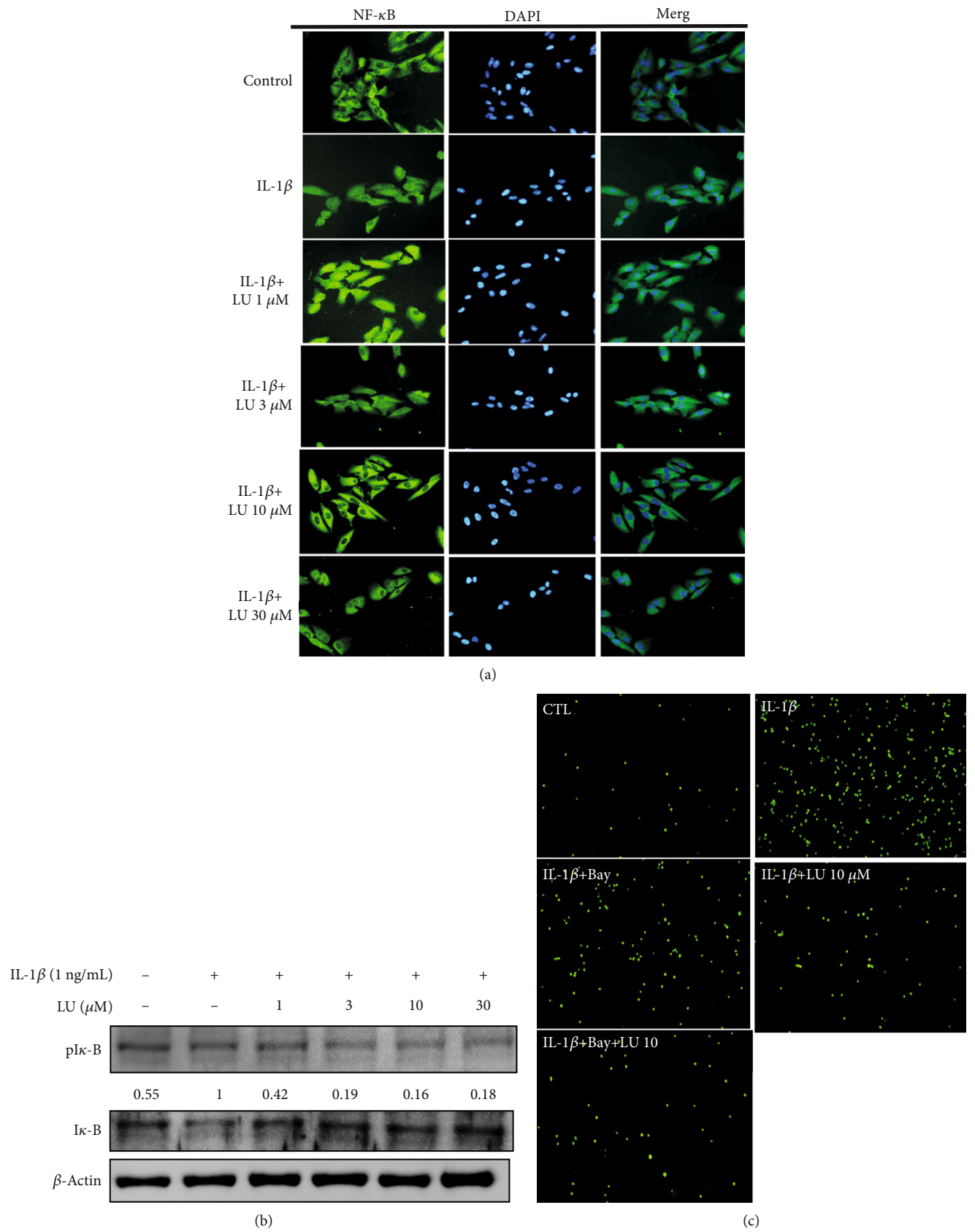


FIGURE 4: Continued.

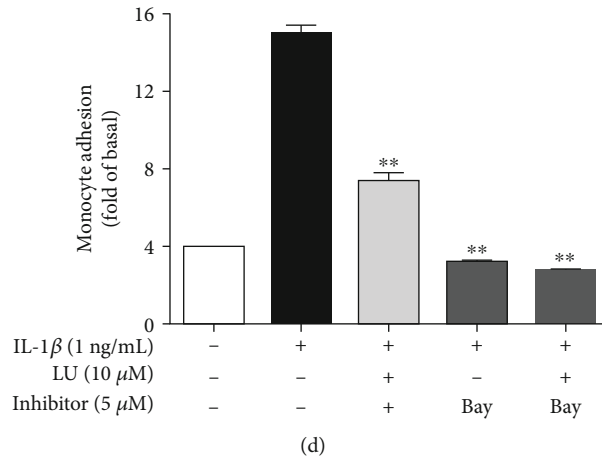


FIGURE 4: Luteolin inhibited NF- $\kappa$ B activation and thereby suppressed THP-1 cell adherence to IL-1 $\beta$ -stimulated ARPE-19 cells. Cells were pretreated with different doses of luteolin (LU) and then incubated with IL-1 $\beta$  (1 ng/mL) for 15 min. NF- $\kappa$ B p65 translocation was evaluated by immunofluorescence staining. Green: location of the p65 subunit. Blue: DAPI for nuclear staining. (a) DAPI staining revealed that luteolin attenuated NF- $\kappa$ B p65 translocation in IL-1 $\beta$ -stimulated ARPE-19 cells. (b) Western blots show the levels of phosphorylated I $\kappa$ B protein expression. (c) Luteolin suppressed THP-1 adhesion. ARPE-19 cells were pretreated with 10  $\mu$ M luteolin or 5  $\mu$ M Bay 117082 for 1 h and then cocultured with labeled THP-1 cells. (d) Fluorescence intensity showed THP-1 cell adhesion to IL-1 $\beta$ -stimulated ARPE-19 cells, which was used to quantify calcein-AM fluorescence. Data represent the mean  $\pm$  SD. \*\* $p$  < 0.01, compared to ARPE-19 cells stimulated with IL-1 $\beta$  alone.

terminal kinase (pJNK) 1/2 expression, luteolin at  $\geq 10$   $\mu$ M significantly decreased phosphorylated extracellular signal-regulated kinase (pERK) 1/2 expression, and luteolin at  $\geq 3$   $\mu$ M significantly decreased phosphorylated p38 protein expression (Figures 5(a), 5(b), 6(a), 6(b), 7(a), and 7(b)). We further evaluated whether the MAPK-inhibiting effects of luteolin were associated with decreased THP-1 adherence to ARPE-19 cells. ARPE-19 cells were pretreated with 10  $\mu$ M luteolin and/or 10  $\mu$ M of the JNK inhibitor SP60012, the ERK1/2 inhibitor PD98059, or the p38 inhibitor SB202190 for 1 h, followed by incubation with IL-1 $\beta$  (1 ng/mL) for 24 h. All tested pretreatments decreased THP cell adherence to ARPE-19 cells. Moreover, combined pretreatment with luteolin plus SP60012 or luteolin plus SB202190 resulted in significantly greater reductions of THP-1 adhesion compared to treatment with any of these agents alone (Figures 5(c), 5(d), 6(c), 6(d), 7(c), and 7(d)).

**3.5. MAPK Inhibitors Mediated the Levels of Cytokines and Chemokines in IL-1 $\beta$ -Stimulated ARPE-19 Cells.** We observed that luteolin significantly decreased the release of IL-6, IL-8, sICAM-1, and MCP-1 in IL-1 $\beta$ -stimulated ARPE-19 cells (Figures 3(a)–3(d)), as well as significantly suppressed MAPK pathways (Figures 5(a), 5(b), 6(a), 6(b), 7(a), and 7(b)). Next, we investigated whether MAPK inhibitors could attenuate the IL-1 $\beta$ -stimulated production of the inflammatory cytokines IL-6, IL-8, and MCP-1. ARPE-19 cells were pretreated with luteolin and/or MAPK inhibitors (10  $\mu$ M SB202190, 10  $\mu$ M PD98059, or 10  $\mu$ M SP600125) for 1 h and then incubated with 1 ng/mL IL-1 $\beta$  for 24 h. Interestingly, the pretreatment with MAPK inhibitors and luteolin significantly reduced the levels of IL-6, IL-8, sICAM-1, and MCP-1 in IL-1 $\beta$ -stimulated ARPE-19 cells (Figures 8(a)–8(d)). These results suggested that in IL-1 $\beta$ -stimulated ARPE-19 cells, luteolin suppressed the expression

of IL-6, IL-8, sICAM-1, and MCP-1 by influencing the phosphorylation of p38, ERK1/2, and JNK1/2.

#### 4. Discussion

In many retinal degenerative (RD) diseases, the pathogenesis is inflammation-induced, involving the recruitment and activation of microglia and macrophages, the expression of inflammatory mediators (COX-2 and iNOS), and photoreceptor cell death. The proinflammatory cytokine IL-1 $\beta$  triggers inflammatory responses and attracts inflammatory cells to migrate into the retina, promoting retinal impairment and degeneration in RD diseases [38, 39]. Numerous studies reported that IL-1 $\beta$  activates the expression of other proinflammatory cytokines and modulates chemokine expression. Proinflammatory cytokines can target and induce retinal inflammation in RD pathogenesis [36, 37] and the phytochemical luteolin has excellent anti-inflammatory properties [32, 33]. Therefore, here we performed a detailed exploration of the anti-inflammatory effects of luteolin in IL-1 $\beta$ -stimulated ARPE19 cells.

Prior studies have indicated that the cytokines IL-6 and IL-8 are proangiogenic, while the chemokine MCP-1 and cell adhesion molecule ICAM-1 facilitate leukocyte transmigration into ocular tissue, in AMD development and progression [4, 12–14]. Elevated IL-1 $\beta$  levels in the vitreous or retina lead to photoreceptor cell death in retinal detachment patients and in a mouse model, while reduced IL-1 $\beta$  levels inhibit photoreceptor cell death [40]. In the present study, we demonstrated that luteolin significantly inhibited cytokine and chemokine release in IL-1 $\beta$ -stimulated ARPE-19 cells (Figures 3(a)–3(d)). Prior studies have also shown that ICAM-1 is upregulated in response to inflammatory mediators and mediates leukocyte adhesion and transmigration on the RPE, while decreased ICAM-1 levels can suppress

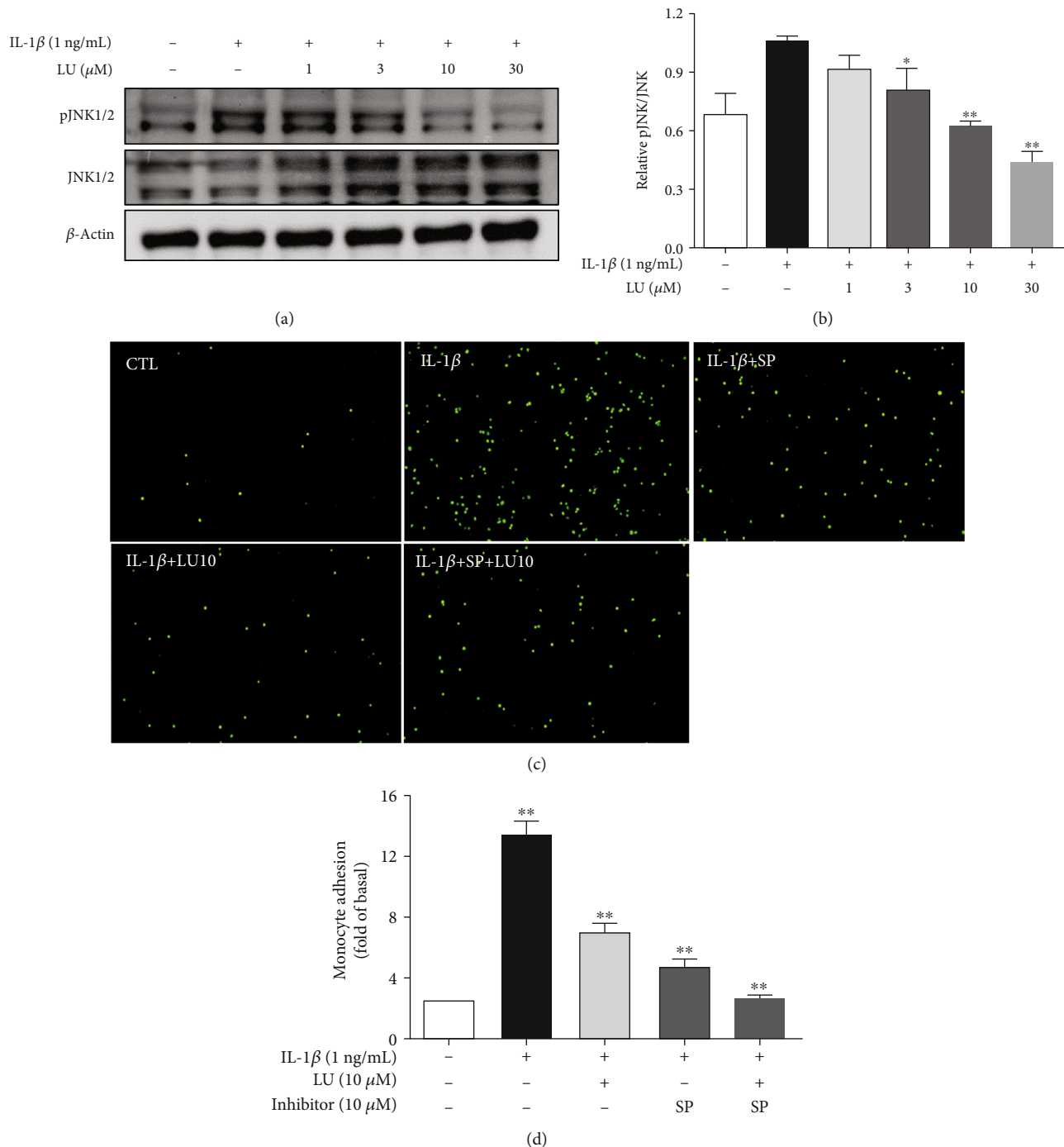


FIGURE 5: Luteolin blocked JNK phosphorylation, and the JNK inhibitor SP60012 (SP) decreased THP-1 cell adherence to IL-1 $\beta$ -stimulated ARPE-19 cells. (a) Western blots show the levels of phosphorylated JNK protein expression. (b) The fold-change in pJNK protein expression was measured relative to JNK expression. (c) ARPE-19 cells were pretreated with 10  $\mu$ M luteolin or JNK inhibitor (SP600125) for 1 h and then cocultured with labeled THP-1 cells. (d) The fluorescence intensity was used to quantify calcein-AM fluorescence. Data represent the mean  $\pm$  SD. \* $p$  < 0.05, \*\* $p$  < 0.01, compared to ARPE-19 cells stimulated with IL-1 $\beta$  alone.

monocyte adhesion in RPE cells [41, 42]. Here, we demonstrated that luteolin inhibited sICAM-1 levels and attenuated THP-1 cell adhesion to IL-1 $\beta$ -stimulated ARPE-19 cells (Figure 3(e)). We also found that luteolin significantly inhibited iNOS protein expression and increased HO-1 protein expression (Figures 2(b) and 2(d)). These findings support

that luteolin is indeed an anti-inflammatory phytochemical that can attenuate proinflammatory cytokine-induced inflammation in ARPE-19 cells.

IL-1 $\beta$  activation of NF- $\kappa$ B signaling is closely associated with RD diseases [15, 16] and pAKT is related to inhibition of the NF- $\kappa$ B inflammatory pathway [36]. Previous studies

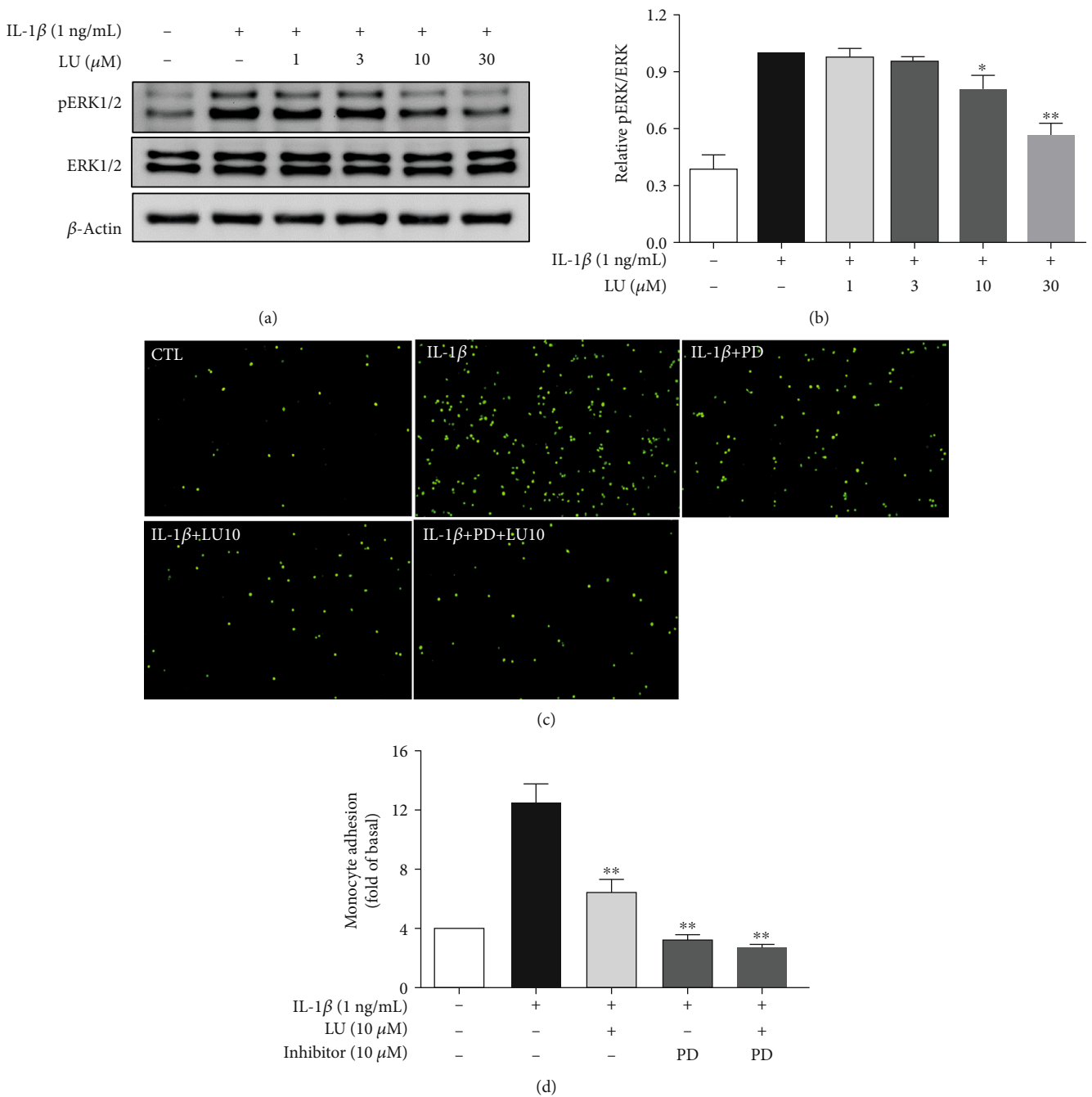


FIGURE 6: Luteolin blocked ERK phosphorylation and the ERK inhibitor PD98059 (PD) decreased THP-1 cell adherence to IL-1 $\beta$ -stimulated ARPE-19 cells. (a) Western blots show levels of phosphorylated ERK protein expression. (b) The fold-change in pERK protein expression was measured relative to ERK expression. (c) ARPE-19 cells were pretreated with 10  $\mu$ M luteolin or ERK inhibitor (PD98059) for 1 h and then cocultured with labeled THP-1 cells. (d) The fluorescence intensity was used to quantify calcein-AM fluorescence. Data represent the mean  $\pm$  SD. \* $p$  < 0.05, \*\* $p$  < 0.01, compared to ARPE-19 cells stimulated with IL-1 $\beta$  alone.

show that IL-1 $\beta$ -activates NF- $\kappa$ B, resulting in its translocation from the cytoplasm into the nucleus, followed by induction of cytokine and chemokine expressions in ARPE-19 cells [43]. Our present results showed that luteolin promoted AKT phosphorylation (Figures 2(f) and 2(g)), inhibited NF- $\kappa$ B p65 activation, and suppressed THP-1 cell adhesion (Figure 4). These findings suggest that luteolin promotes

AKT phosphorylation to block NF- $\kappa$ B p65 activation and thereby suppresses THP-1 cell adherence to IL-1 $\beta$ -stimulated ARPE-19 cells. Many studies have indicated that MAPK signaling plays an important role in AMD [44]. We observed that luteolin decreased the expression levels of IL-6, IL-8, sICAM-1, and MCP-1 in IL-1 $\beta$ -stimulated ARPE-19 cells. Thus, we further investigated whether luteolin attenuated



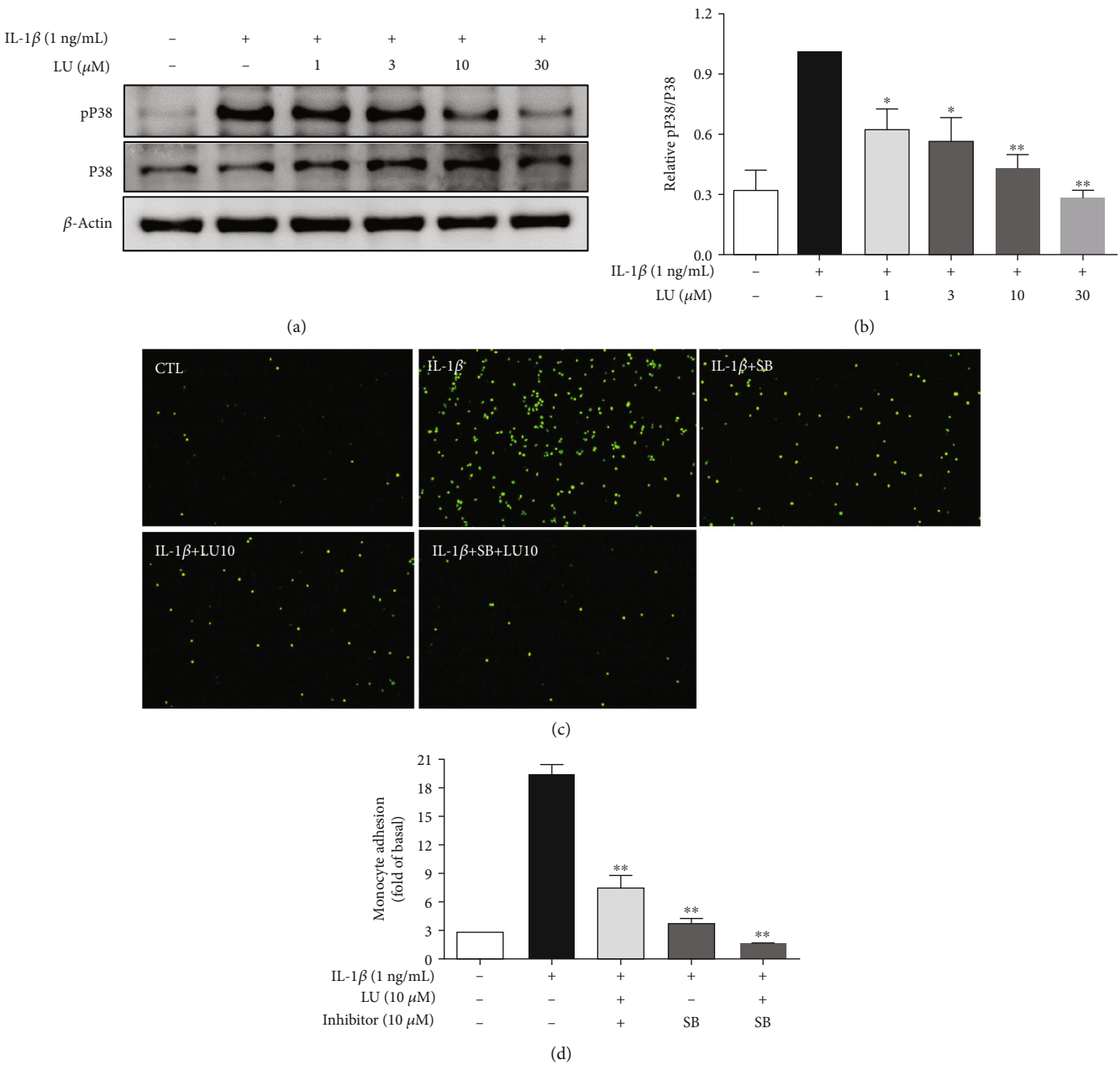


FIGURE 7: Luteolin blocked P38 phosphorylation, and the P38 inhibitor SB202190 (SB) decreased THP-1 cell adherence to IL-1 $\beta$ -stimulated ARPE-19 cells. (a) Western blots show levels of phosphorylated P38 protein expression. (b) The fold-change in pP38 protein expression was measured relative to P38 expression. (c) ARPE-19 cells were pretreated with 10  $\mu$ M luteolin or P38 inhibitor (SB203580) for 1 h and then cocultured with labeled THP-1 cells. (d) The fluorescence intensity was used to quantify calcein-AM fluorescence. Data represent the mean  $\pm$  SD. \* $p$  < 0.05, \*\* $p$  < 0.01, compared to ARPE-19 cells stimulated with IL-1 $\beta$  alone.

inflammation by suppressing MAPK pathways. Our results demonstrated that luteolin significantly inhibited the phosphorylation of the MAPKs JNK 1/2, ERK 1/2, and p38, supporting that luteolin may block MAPK pathways to decrease production of IL-6, IL-8I, sICAM-1, and MCP-1 (Figures 5(a), 5(b), 6(a), 6(b), 7(a), and 7(b)).

Human and animal studies have demonstrated that specific MAPK inhibitors may be potential therapeutic targets for RD disease treatment [44]. To explore the importance of individual MAPKs, we used the MAPK inhibitors SP600125 (JNK 1/2 inhibitor), PD98059 (ERK 1/2 inhibitor),

and SB202190 (P38), individually and as cotreatments with luteolin in IL-1 $\beta$ -stimulated ARPE-19 cells. We found that luteolin and MAPK inhibitors decreased THP-1 cell adherence to IL-1 $\beta$ -stimulated ARPE-19 cells (Figures 5(c), 5(d), 6(c), 6(d), 7(c), and 7(d)). We further found that these MAPK inhibitors attenuated the IL-1 $\beta$ -stimulated production of the inflammatory cytokines IL-6, IL-8, sICAM-1, and MCP-1 (Figures 8(a)–8(d)). These results suggested that luteolin blocked MAPK pathways and inhibited the expression of inflammation-related cytokines—thereby suppressing THP-1 adhesion.

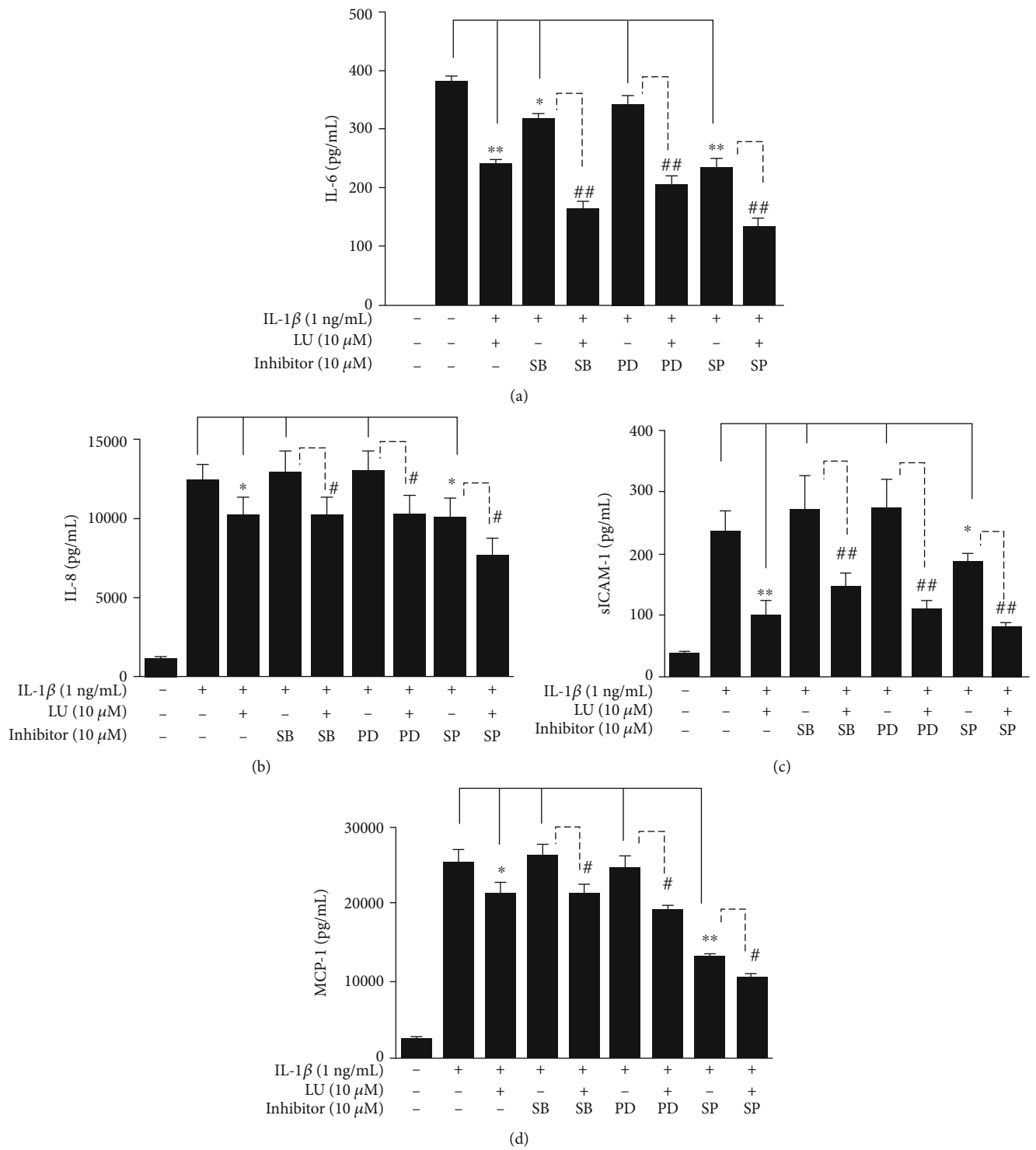


FIGURE 8: MAPK inhibitors mediated the expression levels of cytokines and chemokines in IL-1 $\beta$ -stimulated ARPE-19 cells. ARPE-19 cells were treated with MAPK inhibitors (10  $\mu$ M SB203580 (SB), 10  $\mu$ M PD98059 (PD), or 10  $\mu$ M SP600125 (SP)) with or without 10  $\mu$ M luteolin and then incubated with IL-1 $\beta$  for 24 h. ELISA results showed the levels of (a) IL-6, (b) IL-8, (c) sICAM-1, and (d) MCP-1. Data represent the mean  $\pm$  SD. \* $p$  < 0.05, \*\* $p$  < 0.01, compared to ARPE-19 cells stimulated with IL-1 $\beta$  alone. # $p$  < 0.05, ## $p$  < 0.01, compared to IL-1 $\beta$ -stimulated ARPE-19 cells pretreated with only MAPK inhibitor.

5. Conclusions

Our present data demonstrate that luteolin suppressed pro-inflammatory cytokine-induced retinal pigment epithelium

(RPE) inflammation via inactivation of the NF- $\kappa$ B pathway in IL-1 $\beta$ -stimulated ARPE-19 cells. Moreover, cotreatment with MAPK inhibitors plus luteolin attenuated THP-1 cell adhesion to IL-1 $\beta$ -stimulated ARPE-19 cells. Importantly,

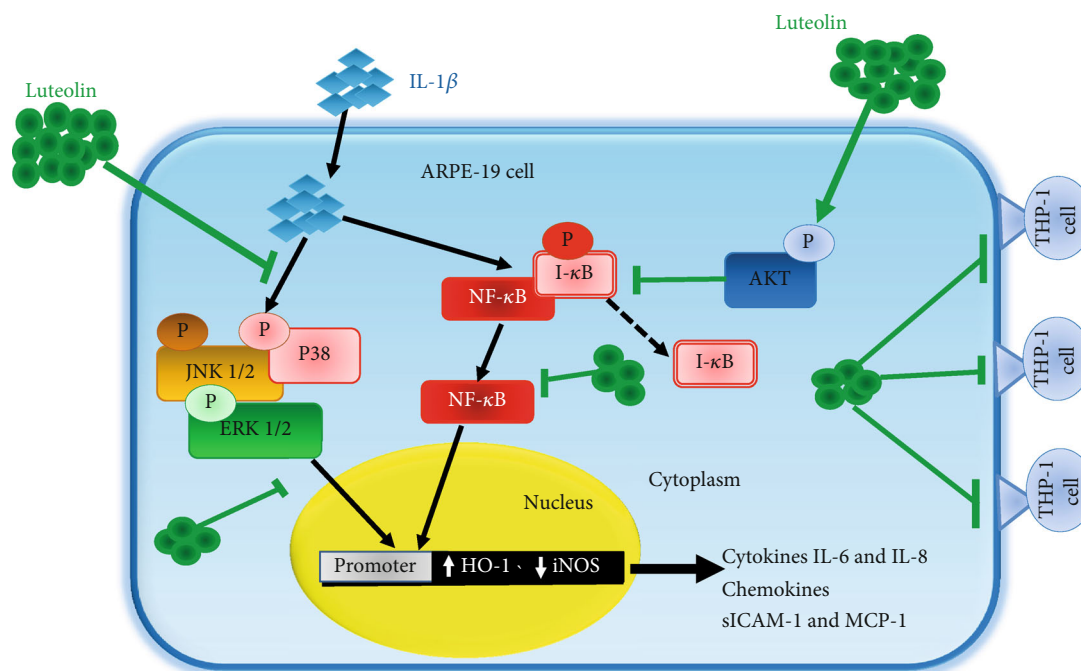


FIGURE 9: Model explaining the mechanisms via which luteolin inhibits IL-1 $\beta$ -induced inflammation in ARPE-19 cells. Luteolin promotes AKT phosphorylation, thus mediating the NF- $\kappa$ B and MAPK pathways, leading to decreased release of inflammatory-related cytokines, and thereby suppressing THP-1 cell adhesion to IL-1 $\beta$ -stimulated ARPE-19 cells. Luteolin also increases expression of the anti-inflammatory protein HO-1 and inhibits iNOS protein expression.

luteolin significantly reduced the expression levels of IL-6, IL-8, sICAM-1, and MCP-1 in IL-1 $\beta$ -stimulated ARPE-19 cells. Taken together, our findings suggest that luteolin blocks MAPK pathways, thus decreasing the expression levels of IL-6, IL-8, sICAM-1, and MCP-1, and thereby suppressing THP-1 cell adhesion to IL-1 $\beta$ -stimulated ARPE-19 cells (Figure 9). We conclude that the natural agent luteolin may ameliorate inflammation-induced retinal degeneration-related disorders via inhibition of the NF- $\kappa$ B and MAPK pathways in IL-1 $\beta$ -stimulated ARPE19 cells.

## Abbreviations

RPE:	Retinal pigment epithelium cells
RD:	Retinal degeneration
AMD:	Age-related macular degeneration
ARPE-19 cells:	Human retinal pigment epithelial cells
LU:	Luteolin
IL-1 $\beta$ :	Interleukin-1 $\beta$
IL-6:	Interleukin-6
IL-8:	Interleukin-8
sICAM-1:	Soluble intercellular adhesion molecule-1
MCP-1:	Monocyte chemoattractant protein-1
HO-1:	Heme oxygenase-1
AKT:	Protein kinase B
iNOS:	Inducible nitric oxide synthase
NF- $\kappa$ B:	Nuclear factor- $\kappa$ B
MAPK:	Mitogen-activated protein kinase
ELISA:	Enzyme-linked immunosorbent assay
JNK:	c-JUN N-terminal kinase
ERK:	Extracellular signal-regulated kinase.

## Data Availability

The data used to support the findings of this study are available from the corresponding author upon request.

## Conflicts of Interest

The authors declare that there is no conflict of interests regarding the publication of this paper.

## Authors' Contributions

Wen-Chung Huang and Chian-Jiun Liou are equal contributors to the work.

## Acknowledgments

This research was supported by grants from the Chang Gung Memorial Hospital (CMRPF1G0203, CMRPF1J0041), Ministry of Science and Technology (MOST 108-2320-B-255-004-), and Chang Gung University of Science and Technology (ZRRPF3J0081) of Taiwan.

## References

- [1] O. Strauss, "The retinal pigment epithelium in visual function," *Physiological Reviews*, vol. 85, no. 3, pp. 845–881, 2005.
- [2] S. Datta, M. Cano, K. L. Ebrahimi, L. Wang, and J. T. Handa, "The impact of oxidative stress and inflammation on RPE degeneration in non-neovascular AMD," *Progress in Retinal and Eye Research*, vol. 60, pp. 201–218, 2017.

- [3] H. Xu, M. Chen, and J. V. Forrester, "Para-inflammation in the aging retina," *Progress in Retinal and Eye Research*, vol. 28, no. 5, pp. 348–368, 2009.
- [4] J. E. Knickelbein, C. C. Chan, H. N. Sen, F. L. Ferris, and R. B. Nussenblatt, "Inflammatory mechanisms of age-related macular degeneration," *International Ophthalmology Clinics*, vol. 55, no. 3, pp. 63–78, 2015.
- [5] W. al-Zamil and S. A. Yassin, "Recent developments in age-related macular degeneration: a review," *Clinical Interventions in Aging*, vol. 12, pp. 1313–1330, 2017.
- [6] R. Chou, T. Dana, C. Bougatsos, S. Grusing, and I. Blazina, "Screening for impaired visual acuity in older adults: updated evidence report and systematic review for the US Preventive Services Task Force," *JAMA*, vol. 315, no. 9, pp. 915–933, 2016.
- [7] S. Hajar, A. al Hazmi, M. Wasli, A. Mousa, and M. Rabi, "Prevalence and causes of blindness and diabetic retinopathy in Southern Saudi Arabia," *Saudi Medical Journal*, vol. 36, no. 4, pp. 449–455, 2015.
- [8] A. Biesemeier, T. Taubitz, S. Julien, E. Yoeuruk, and U. Schraermeyer, "Choriocapillaris breakdown precedes retinal degeneration in age-related macular degeneration," *Neurobiology of Aging*, vol. 35, no. 11, pp. 2562–2573, 2014.
- [9] S. Cao, A. Ko, M. Partanen et al., "Relationship between systemic cytokines and complement factor H Y402H polymorphism in patients with dry age-related macular degeneration," *American Journal of Ophthalmology*, vol. 156, no. 6, pp. 1176–1183, 2013.
- [10] R. Klein, C. E. Myers, K. J. Cruickshanks et al., "Markers of inflammation, oxidative stress, and endothelial dysfunction and the 20-year cumulative incidence of early age-related macular degeneration: the Beaver Dam Eye Study," *JAMA Ophthalmology*, vol. 132, no. 4, pp. 446–455, 2014.
- [11] J. M. Seddon, S. George, B. Rosner, and N. Rifai, "Progression of age-related macular degeneration: prospective assessment of C-reactive protein, interleukin 6, and other cardiovascular biomarkers," *Archives of Ophthalmology*, vol. 123, no. 6, pp. 774–782, 2005.
- [12] H. Miao, Y. Tao, and X. X. Li, "Inflammatory cytokines in aqueous humor of patients with choroidal neovascularization," *Molecular Vision*, vol. 18, pp. 574–580, 2012.
- [13] J. B. Jonas, R. A. Jonas, M. Neumaier, and P. Findeisen, "Cytokine concentration in aqueous humor of eyes with diabetic macular edema," *Retina*, vol. 32, no. 10, pp. 2150–2157, 2012.
- [14] J. B. Jonas, Y. Tao, M. Neumaier, and P. Findeisen, "Monocyte chemoattractant protein 1, intercellular adhesion molecule 1, and vascular cell adhesion molecule 1 in exudative age-related macular degeneration," *Archives of Ophthalmology*, vol. 128, no. 10, pp. 1281–1286, 2010.
- [15] E. Brint, T. Kamradt, and S. L. Doyle, "Editorial: IL-1 family members in health and disease," *Frontiers in Immunology*, vol. 10, no. 2596, 2019.
- [16] Y. Dong, C. Qian, G. Wan, P. Yan, S. Liang, and J. Wang, "Schizandrin A protects human retinal pigment epithelial cell line ARPE-19 against HG-induced cell injury by regulation of miR-145," *Molecular Therapy - Nucleic Acids*, vol. 19, pp. 42–49, 2020.
- [17] A. K. Pandurangan and N. M. Esa, "Luteolin, a bioflavonoid inhibits colorectal cancer through modulation of multiple signaling pathways: a review," *Asian Pacific Journal of Cancer Prevention*, vol. 15, no. 14, pp. 5501–5508, 2014.
- [18] K. H. Miesan and S. Mohamed, "Flavonoid (myricetin, quercetin, kaempferol, luteolin, and apigenin) content of edible tropical plants," *Journal of Agricultural and Food Chemistry*, vol. 49, no. 6, pp. 3106–3112, 2001.
- [19] T. Sun, Z. Xu, C.-T. Wu, M. Janes, W. Prinyawiwatkul, and H. K. No, "Antioxidant activities of different colored sweet bell peppers (*Capsicum annuum* L.)," *Journal of Food Science*, vol. 72, no. 2, pp. S98–102, 2007.
- [20] Y. Luo, P. Shang, and D. Li, "Luteolin: a flavonoid that has multiple cardio-protective effects and its molecular mechanisms," *Frontiers in Pharmacology*, vol. 8, 2017.
- [21] N. Aziz, M. Y. Kim, and J. Y. Cho, "Anti-inflammatory effects of luteolin: a review of in vitro, in vivo, and in silico studies," *Journal of Ethnopharmacology*, vol. 225, pp. 342–358, 2018.
- [22] M. Imran, A. Rauf, T. Abu-Izneid et al., "Luteolin, a flavonoid, as an anticancer agent: a review," *Biomedicine & Pharmacotherapy*, vol. 112, article 108612, 2019.
- [23] S. F. Nabavi, N. Braid, O. Gortzi et al., "Luteolin as an anti-inflammatory and neuroprotective agent: a brief review," *Brain Research Bulletin*, vol. 119, pp. 1–11, 2015.
- [24] T. C. Theoharides, "COVID-19, pulmonary mast cells, cytokine storms, and beneficial actions of luteolin," *BioFactors*, vol. 46, no. 3, pp. 306–308, 2020.
- [25] H. Yan, L. Ma, H. Wang et al., "Luteolin decreases the yield of influenza A virus in vitro by interfering with the coat protein I complex expression," *Journal of Natural Medicines*, vol. 73, no. 3, pp. 487–496, 2019.
- [26] C. Horvath and C. Wolfrum, "Feeding brown fat: dietary phytochemicals targeting non-shivering thermogenesis to control body weight," *The Proceedings of the Nutrition Society*, vol. 15, pp. 1–19, 2020.
- [27] Y. Zhang, Y. Wang, X. Li et al., "WSF-7 inhibits obesity-mediated PPAR $\gamma$  phosphorylation and improves insulin sensitivity in 3T3-L1 adipocytes," *Biological and Pharmaceutical Bulletin*, vol. 43, no. 3, pp. 526–532, 2020.
- [28] Y. Baek, M. N. Lee, D. Wu, and M. Pae, "Luteolin reduces adipose tissue macrophage inflammation and insulin resistance in postmenopausal obese mice," *The Journal of Nutritional Biochemistry*, vol. 71, pp. 72–81, 2019.
- [29] Q. Zhang, E. Gonzalez de Mejia, D. Luna-Vital et al., "Relationship of phenolic composition of selected purple maize (*Zea mays* L.) genotypes with their anti-inflammatory, anti-adipogenic and anti-diabetic potential," *Food Chemistry*, vol. 289, pp. 739–750, 2019.
- [30] S. Park, D. S. Kim, S. Kang, and H. J. Kim, "The combination of luteolin and l-theanine improved Alzheimer disease-like symptoms by potentiating hippocampal insulin signaling and decreasing neuroinflammation and norepinephrine degradation in amyloid- $\beta$ -infused rats," *Nutrition Research*, vol. 60, pp. 116–131, 2018.
- [31] F. Ali and Y. H. Siddique, "Bioavailability and pharmacotherapeutic potential of luteolin in overcoming Alzheimer's disease," *CNS & Neurological Disorders - Drug Targets (Formerly Current Drug Targets - CNS & Neurological Disorders)*, vol. 18, no. 5, pp. 352–365, 2019.
- [32] M. Hytti, N. Piippo, E. Korhonen, P. Honkakoski, K. Kaarniranta, and A. Kauppinen, "Fisetin and luteolin protect human retinal pigment epithelial cells from oxidative stress-induced cell death and regulate inflammation," *Scientific Reports*, vol. 5, article 17645, no. 1, 2016.

- [33] M. Hytti, D. Szabó, N. Piippo et al., “Two dietary polyphenols, fisetin and luteolin, reduce inflammation but augment DNA damage-induced toxicity in human RPE cells,” *The Journal of Nutritional Biochemistry*, vol. 42, pp. 37–42, 2017.
- [34] H. Lu, Y. Chen, X. B. Sun, B. Tong, and X. H. Fan, “Effects of luteolin on retinal oxidative stress and inflammation in diabetes,” *RSC Advances*, vol. 5, no. 7, pp. 4898–4904, 2015.
- [35] W. C. Huang, H. H. Su, L. W. Fang, S. J. Wu, and C. J. Liou, “Licochalcone A inhibits cellular motility by suppressing E-cadherin and MAPK signaling in breast cancer,” *Cells*, vol. 8, no. 3, p. 218, 2019.
- [36] Y. Wooff, S. M. Man, R. Aggio-Bruce, R. Natoli, and N. Fernando, “IL-1 family members mediate cell death, inflammation and angiogenesis in retinal degenerative diseases,” *Frontiers in Immunology*, vol. 10, p. 1618, 2019.
- [37] Y. C. Lin, H. C. Kuo, J. S. Wang, and W. W. Lin, “Regulation of inflammatory response by 3-methyladenine involves the coordinative actions on Akt and glycogen synthase kinase  $\beta$  rather than autophagy,” *The Journal of Immunology*, vol. 189, no. 8, pp. 4154–4164, 2012.
- [38] X. He, D. Sun, S. Chen, and H. Xu, “Activation of liver X receptor delayed the retinal degeneration of rd1 mice through modulation of the immunological function of glia,” *Oncotarget*, vol. 8, no. 19, pp. 32068–32082, 2017.
- [39] C. A. Dinarello, “Overview of the IL-1 family in innate inflammation and acquired immunity,” *Immunological Reviews*, vol. 281, no. 1, pp. 8–27, 2018.
- [40] K. Kataoka, H. Matsumoto, H. Kaneko et al., “Macrophage- and RIP3-dependent inflammasome activation exacerbates retinal detachment-induced photoreceptor cell death,” *Cell Death & Disease*, vol. 6, no. 4, article e1731, 2015.
- [41] P. Thichanpiang, S. J. Harper, K. Wongprasert, and D. O. Bates, “TNF- $\alpha$ -induced ICAM-1 expression and monocyte adhesion in human RPE cells is mediated in part through auto-crine VEGF stimulation,” *Molecular Vision*, vol. 20, pp. 781–789, 2014.
- [42] L. Yang, R. M. Froio, T. E. Sciuto, A. M. Dvorak, R. Alon, and F. W. Luscinskas, “ICAM-1 regulates neutrophil adhesion and transcellular migration of TNF- $\alpha$ -activated vascular endothelium under flow,” *Blood*, vol. 106, no. 2, pp. 584–592, 2005.
- [43] X. Chen, R. Han, P. Hao et al., “Nepetin inhibits IL-1 $\beta$  induced inflammation via NF- $\kappa$ B and MAPKs signaling pathways in ARPE-19 cells,” *Biomedicine & Pharmacotherapy*, vol. 101, pp. 87–93, 2018.
- [44] S. V. Kyosseva, “Targeting MAPK signaling in age-related macular degeneration,” *Ophthalmology and Eye Diseases*, vol. 8, pp. 23–30, 2016.





# Oligochitosan modified albumin as plasmid DNA delivery vector: Endocytic trafficking, polyplex fate, in vivo compatibility

Monika Kumari<sup>a</sup>, Chi-Hsien Liu<sup>a,b,c,d,\*</sup>, Wei-Chi Wu<sup>d,e</sup>

<sup>a</sup> Department of Chemical and Materials Engineering, Chang Gung University, 259, Wen-Hwa First Road, Kwei-Shan, Tao-Yuan 333, Taiwan

<sup>b</sup> Research Center for Chinese Herbal Medicine and Research Center for Food and Cosmetic Safety, College of Human Ecology, Chang Gung University of Science and Technology, 261, Wen-Hwa First Road, Taoyuan, Taiwan

<sup>c</sup> Department of Chemical Engineering, Ming Chi University of Technology, 84, Gung-Juan Road, New Taipei City, Taiwan

<sup>d</sup> Department of Ophthalmology, Chang Gung Memorial Hospital, Linkou, 5, Fu-Hsing Street, Taoyuan, Taiwan

<sup>e</sup> College of Medicine, Chang Gung University, 259, Wen-Hwa First Road, Taoyuan, Taiwan

## ARTICLE INFO

### Article history:

Received 2 August 2019

Received in revised form 15 September 2019

Accepted 16 September 2019

Available online 5 October 2019

### Keywords:

Albumin  
Oligochitosan  
Gene delivery  
Trafficking

## ABSTRACT

Cationic macromolecules condense DNA into small nanoparticles and form polyplex. The composition of the polyplex determines the endocytic process, the intracellular routing and the fate of the polyplex. Previously, oligochitosan-modified vectors with different protein moieties are used as gene delivery vector and the types of protein moiety can influence the endosome escape ability and transfection efficiency. Among the modified vectors, oligochitosan-modified bovine serum albumin (BSA) showed 90% transfection efficiency compared to the modified zein and ovalbumin. These data encouraged us to investigate the mechanism of internalization involved in the superior transfection efficiency of modified BSA/ plasmid polyplex. The effect of specific endocytic inhibitors was studied in two adherent cell lines. The caveolae-mediated and lipid-mediated pathways play a significant role in the polyplex internalization. Next, a colocation of polyplex with lysosome was investigated in the presence of LysoTracker using confocal microscopy. Up to 70% of polyplex successfully escaped the lysosome without degradation. Four non-adherent cell lines showed above than 60% transfection efficiency at an optimized vector/plasmid ratio. Moreover, no significant hemolytic effect was observed up to 500 µg/mL of cationic BSA, indicating no detectable cell membrane disruption. Overall, the hybrid biomacromolecule showed good intracellular delivery and safety in a mice model.

© 2019 Published by Elsevier B.V.

## 1. Introduction

Gene therapy is gaining considerable interest for curing both acquired and inherited diseases. The design of vectors offers significant amelioration for the delivery of a desired sequence of DNA into the nucleus of the target cell without degradation [1]. Traditionally, there are two types of DNA delivery vectors: viral and non-viral. Recently, the synthesis of a non-viral vector was found to enhance gene delivery efficiency and cell viability by forming polyplex. Polyplexes are formed through the electrostatic interaction between the positively charged polymers with negatively charged plasmids into small, condensed nanoparticles. Therefore, a non-viral vector consisting of positive charges, such as cationic

\* Corresponding author at: Department of Chemical and Materials Engineering, Chang Gung University, 259, Wen-Hwa First Road, Kwei-Shan, Tao-Yuan 333, Taiwan.

E-mail addresses: [mkumari.biotech@gmail.com](mailto:mkumari.biotech@gmail.com) (M. Kumari), [CHL@mail.cgu.edu.tw](mailto:CHL@mail.cgu.edu.tw) (C.-H. Liu).

polymer and lipids, provides a potential tool to study the gene delivery approach into target cells [2]. However, the major limitation of a non-viral vector is its low transfection efficiency due to its multiple barriers, such as the binding of nanoparticles to the cell surface and its process (i.e., endosome escape ability and transport into the nucleus of the target cells) [3,4]. Besides, the cellular uptake mechanism is poorly understood. The mechanism of the cellular uptake pathway requires a detailed investigation to improve the transfection efficiency of designed vectors. Previous studies demonstrate that endocytosis is the major pathway for the cellular uptake mechanism of the cationic macromolecule and thus enhances the gene delivery efficiency [5].

Typically, the endocytic pathways are divided into two types: phagocytosis and pinocytosis. Further, pinocytosis is sub-divided into three classes: clathrin-mediated endocytosis (CME), clathrin-independent endocytosis (CIE), and macropinocytosis. The intracellular fate of polyplex followed by each endocytic pathway varies with the involvement of specific proteins [6]. The CME uptakes polyplex by forming clathrin-coated pits and then travels from

early to late endosomes. Finally, the late endosome fuse with the lysosomes and eventually release the polyplex in endo-lysosomes compartment [7]. The CIE is subdivided into two types: caveolae-independent and caveolae-mediated endocytosis (CvME). The polyplex via caveolae-mediated pathway comes through the formation of small flask-shaped invaginations called caveolae in the plasma membrane [8]. To study the mechanisms, different endocytic inhibitors are used such as chlorpromazine (CPZ), genistein, and methyl- $\beta$ -cyclodextrin related to CME, CvME, and lipid-mediated pathways. Each inhibitor utilizes distinct mechanism and has its own key feature to block the specific pathway. CPZ inhibition involves the loss of clathrin and AP2a adaptor complex from the cell surface and their artificial assembly on endosomal membranes [9]. The treatment with genistein inhibits the activity of Src kinase for caveolin 1 phosphorylation [10]. The role of the endosome-lysosome system is elucidated using lysosomotropic agents like monensin and PVP [11]. Monensin blocks the endocytosis pathway by disrupting the Golgi complex and lysosome function [12,13]. PVP is an agent related to the intracellular vesicular swelling due to osmosis. It also decreases the function of lysosome enzymes and restricts the fusion of lysosomes with polyplex [14]. The intracellular delivery of polyplex also differs depending upon the physical nature of the complexes, such as their type of conjugation, size, and stability. The degree of successful transfection is influenced by cell metabolism and varies for different types of cells. Indeed, the recent literature has indicated that the internalization route taken by polyplex plays an important role in successful gene delivery [15]. Rejman et al. suggested that the CvME pathway shows a high endosome escape ability with good transfection efficiency compared with CME pathways [16]. An excess amount of glucosamine in a chitosan-based gene delivery system helps to internalized polyplex via endocytic pathways [17]. Peng et al. found that CvME has gained significant attention for gene delivery applications, as it prevents the degradation of nanoparticles by lysosomal enzyme [18]. Therefore, several authors have made numerous efforts to design a vector that can be internalized via CvME pathways and driven toward efficient transfection efficiency [3]. Recently we prepared a protein-OC cationic vector with different protein moieties like bovine serum albumin (BSA), zein, and ovalbumin (OVA) via Schiff base formation. The obtained transfection efficiency of BSA-OC (up to 95%) was higher than zein-OC (up to 84%) and OVA-OC (up to 70%) in a serum-free condition [19,20]. These data generated a curiosity to investigate the cellular uptake pathway and intracellular distribution of BSA-OC/pDNA polyplex.

Herein, the DNA complexation and releasing ability of three synthesized vectors was investigated. Meanwhile, the cell lines for recombinant protein production, i.e., CHO-K1 and HEK 293T, were used to understand the roles of endocytic pathways involved for the delivery of pDNA by BSA-OC vectors. In the presence of different endocytic inhibitors, the intracellular distribution of polyplex and the integrity of endo-lysosomal membrane after polyplex transfection were visualized by confocal microscopy. The gene transfection efficiency in three different suspended cell lines and their biocompatibility were discussed. Finally, the blood biocompatibility of polyplexes was observed and their gene delivery to the mice was also used to evaluate the potential applicability of the developed vector.

## 2. Materials and methods

### 2.1. Materials

The oligochitosan (OC, average MW = 662 g/mol, degree of deacetylation >90%) was obtained from Yaizu Suisan Kagaku

Industry. Hoechst 33342, trypsin-EDTA, glutaraldehyde, chlorpromazine (CPZ), sodium azide, genistein, monensin, fluorescein isothiocyanate (FITC), ethidium bromide (EtBr), polyvinylpyrrolidone (PVP), and acridine orange were purchased from Sigma-Aldrich (St. Louis, MO, USA). Methyl- $\beta$ -cyclodextrin was acquired from Wako Pure Chemical Industries, Ltd. (Osaka, Japan). Rhodamine B was obtained from Acros Organics (PA, USA). LysoTracker Red was purchased from Molecular Probes/Invitrogen (Eugene, Oregon, USA). Plasmid tdTomato was obtained from Addgene (plasmid 30530). Plasmid EGFP-C3 (size 4.7 kb) was procured from Takara Bio (Shiga, Japan). Both plasmids were amplified in *Escherichia coli* strain DH-5 $\alpha$  and purified from the cell pellets using a purification kit (GeneMark, Taipei, Taiwan). Fetal bovine serum (FBS) was purchased from Biological Industries (Haemek, Israel). All reagents were used without further purification.

### 2.2. Cell culture

HEK 293T, CHO-K1, and the hybridoma cells (BCRC 60427 and BCRC 60252) were obtained from the Bioresource Collection and Research Center (BCRC, Hsinchu, Taiwan). HEK 293T and CHO-K1 are adherent cell lines, were cultured in Dulbecco's modified Eagle's medium-high glucose supplemented with 10% FBS. BCRC 60252 was maintained in RPMI-1640 medium supplemented with 10% FBS. The hybridoma cell line (CRL-1754) was obtained from American Type Culture Collection (Manassas, VA, USA). BCRC 60427 and CRL-1754 were maintained in serum-free CD Hybridoma medium supplemented with 8 mM L-glutamine (Sigma). The subculture of adherent cell lines was performed when cells had 80% of confluence using trypsin-EDTA. Four non-adherent cell lines were passaged every four days to maintain an exponential growth phase. All cells were maintained in a humidified air atmosphere at 37 °C with 5% CO<sub>2</sub>. The cell morphology and growth were monitored daily using a light microscope. The cell density and viability were determined using the Beckman Coulter counter (MS3 model) and the trypan blue staining.

### 2.3. Synthesis of the protein-OC vector and formation of polyplex

The protein (BSA, zein, or OVA) was cross-linked with OC in the presence of glutaraldehyde via the one-step process. The detail synthesis procedure was reported in our previous publication [19]. Briefly, the mixture of protein, OC, and glutaraldehyde was reacted for 2 h at room temperature. Finally, the free aldehyde group was quenched by the addition of 0.1 mg/mL glycine and vortexed for 30 min. The unreacted reagents were removed by washing twice with deionized water using the 50 kDa cutoff Vivaspin tube through the centrifugation technique to obtain the purified vectors.

### 2.4. DNA binding and stability test of the synthesized vector

The DNA binding and stability of all three synthesized vectors was investigated using EtBr assay and agarose gel electrophoresis assay. The DNA binding affinity was studied by EtBr assay as follows. Briefly, EtBr (0.2  $\mu$ g) was mixed with pDNA (0.2  $\mu$ g) and total volume was maintained to 50  $\mu$ L by using the water with a 5-min incubation. The vector (10–60  $\mu$ g) was mixed with EtBr-DNA solution (total volume 100  $\mu$ L) and incubated at different time duration to form complexes. EtBr displacement from DNA in the presence of a synthesized vector was recorded by fluorescence spectroscopy (Molecular Devices Spectramax i3x spectrophotometer (Sunnyvale, CA, USA)) into a 96 well black plate. The fluorescence intensity was measured at the excitation and emission of 516 nm and 605 nm. EtBr and DNA-EtBr fluorescence was also measured at the same condition as controls [21].

$$\text{Percentage of EtBr and DNA binding} = \frac{F_{\text{obs}} - F_0}{F_{\text{DNA}} - F_0} * 100$$

where,  $F_0$ ,  $F_{\text{DNA}}$ , and  $F_{\text{obs}}$  represent the fluorescence intensities of only EtBr, EtBr-DNA complex and EtBr-DNA complex with the vector respectively. The stability and releasing ability of DNA was investigated in the presence of anionic molecules i.e., heparin. Briefly, 10  $\mu\text{L}$  of the prepared polyplex at a weight ratio of 60:1 was exposed to 8  $\mu\text{g}/\mu\text{L}$  of heparin for 2 h at 37 °C. The disintegration of polyplexes was visualized by using the agarose electrophoresis.

## 2.5. Quantitative measurement for the uptake of polyplexes

For cellular uptake analysis, BSA-OC was labeled with rhodamine dye (Rh). CHO-K1 and HEK 293T cells were seeded into 48-well plate containing sterile coverslip at a density of  $5 \times 10^4$ . After 90% confluence, the cells were treated with polyplex containing the Rh-labeled BSA-OC vector for 3 h. After completion of incubation times, the cells were washed with PBS and the nuclei of the cells were labeled with Hoechst 33342. Finally, the coverslip was sealed with the acrylic glue in glass slide before examining in the confocal microscopy. The quantitative analysis of confocal micrograph was performed by using IN Cell Analyzer 1000 software.

## 2.6. Transfection efficiency and cellular uptake analysis in presence of endocytic inhibitor

The transfection and cellular uptake efficiency of BSA-OC/pDNA polyplex were examined in CHO-K1 and HEK 293T cells in the presence of different endocytic inhibitors. The cells were seeded in 48 well plates at a density of  $5 \times 10^4$  and after 90% confluence, the cells treated with polyplex and endocytic inhibitor for 3 h. Subsequently, the transfection medium was replaced with fresh 10% DMEM medium and further incubated for another 24 h. Finally, the cells were washed with PBS and nuclei of the cells were stained with Hoechst. The cellular uptake and transfection efficiency were calculated by using IN Cell Analyzer 1000 software.

Transfection efficiency (%)

$$= \frac{\text{Blue count with green fluorescence}}{\text{Blue count}} * 100$$

## 2.7. Intracellular trafficking of the polyplexes

The cells were seeded onto the glass coverslip in the 48-well culture plate as described above. For intracellular distribution of BSA-OC, the polyplex was prepared by using FITC labeled BSA-OC vector at a weight ratio of 60:1 and incubated for 3 h. After completion of the incubation period, the cells were treated with diluted LysoTracker Red DND (50 nM) in DMEM medium for 30 min. Following LysoTracker incubation, the cells were treated as stated previously for confocal imaging. The image was captured at excitation and emission wavelength of 488 nm and 560 nm for LysoTracker Red and further, the percentage of lysosome escape ability was calculated by using IN Cell Investigator software. Complex colocalization with LysoTracker Red is defined as:

Complex colocalization(%)

$$= \frac{\text{Area containig green and red fluorescence}}{\text{Area containig green fluorescence}} * 100$$

## 2.8. Endo-lysosome membrane integrity

Lysosome membrane integrity of treated cells with BSA-OC was investigated by acridine orange staining. The cells were seeded

onto 48-well culture plate containing glass coverslip as described above. The cells were incubated with BSA-OC/pDNA polyplex for 3 h and later treated with 10  $\mu\text{M}$  acridine for 15 min. Finally, cells were washed with PBS and nuclei were stained with Hoechst. The cells were visualized by the confocal microscopy and the cell images were analyzed with IN Cell Analyzer 1000.

## 2.9. Study of transfection efficiency in suspended cell lines

For suspended cells,  $1 \times 10^6$  cells were transfected in duplicates and the cell viability was maintained above 95% before transfection. The prepared polyplexes at a different weight ratio (10:1 to 60:1) were mixed to cells and incubated for 3 h. After the incubation time, the medium containing polyplex was removed by centrifugation at 12,000 rpm for 5 min. After centrifugation, the supernatant was discarded, and fresh medium was added to each well and incubated for another 24 h. At the end of incubation time, the cells were washed with PBS and fixed with ethanol/acetic acid solution and the nucleus was stained with Hoechst 33342. Following washing with PBS, the cells were mixed with Dako. A coverslip was covered and sealed by acrylic glue at the edge of the coverslip. Finally, the GFP expression and cell morphology were analyzed by IN Cell Analyzer 1000 microscope according to the above-stated protocol. The cell viability was also calculated by the automated investigation of the nuclear count (Hoechst filter; blue count):

$$\text{Cell viability(\%)} = \frac{\text{Blue count of treated cells}}{\text{Blue count of control cells}} * 100$$

## 2.10. Blood cell hemolysis

Freshly isolated mice blood cells were diluted with PBS (1:100 times) and treated with BSA-OC/pDNA polyplex at different weight ratios ranged from 10:1 to 300:1. Each weight ratio of prepared polyplex (100  $\mu\text{L}$ ) was then mixed with 100  $\mu\text{L}$  of diluted blood separately, and incubated at 37 °C for 2 h. After the incubation period, the tubes were centrifuge at 1000 rpm for 3 min. Finally, 100  $\mu\text{L}$  of supernatant was added to each well of the 96-well plate. Reading was taken at 576 nm by using a BioTek microplate reader. The blood cells mixed with sodium phosphate buffer was considered as a negative control (0% hemolysis), while cells treated with 0.1% v/v Triton X-100 was considered as a positive control (100% hemolysis). Percentage of hemolysis was calculated as follows:

$$\text{Hemolysis(\%)} = \frac{(OD_{\text{polyplex}} - OD_{\text{negative control}})}{(OD_{\text{positive control}} - OD_{\text{negative control}})} * 100$$

## 2.11. Biocompatibility of polyplexes in the in vivo condition

Four-week-old CD1 (ICR) male mice were purchased from Bio-lasco Biotechnology Co., Ltd. (Taipei, Taiwan). All experiments involving the use of mice were performed in accordance with protocols approved by the “Animal Care and Use Committee” of Chang Gung Memorial Hospital (Approval Numbers: CGU107-125). Control group of mice were intravenously injected with 200  $\mu\text{L}$  of PBS, 200  $\mu\text{g}$  of vector, and 90  $\mu\text{g}$  of DNA, separately. Whereas the experimental group of mice was intravenously injected with 200  $\mu\text{L}$  of prepared polyplexes. Two different concentration of vector (60  $\mu\text{g}$  and 90  $\mu\text{g}$ ) mixed with 60  $\mu\text{g}$  of DNA, separately, to prepare the desired weight ratio of vector/DNA, i.e., 1:1 and 1.5:1. The ventral position of mice was observed at different duration after injection (2 days, 3 days, and 7 days) by using the IVIS Lumina II imaging system. The exposure time was fixed to 0.5 s.

### 3. Results and discussion

#### 3.1. BSA-OC characterization and DNA condensation assay

Particle size of the non-viral vectors plays a significant role in the cellular uptake and intracellular trafficking of polyplex. Generally, proteins are very sensitive to pH solution which affecting their conformation, surface charge, size, and stability [22,23]. Fig. S1 represents the particle size and polydispersity index (PDI) of BSA-OC vector, which showed that the particle size decreased by increasing the pH value from acidic to a basic condition. The result that particle size increased slightly at pH 9 may be due to the aggregation of the vector near its isoelectric point (i.e. 8.34). When the zeta potential reaches zero around the isoelectric point, the interaction between molecules increases and prone to aggregation [24]. Furthermore, the increase in particle size at lower pH value indicates the protonated form of amine group which further limit the physical contact due to charge repulsion and thus form the larger nanoparticles. The deprotonation of amine groups has occurred at higher pH condition and thus decreased the particle size and PDI value [25]. The larger particle size at lower pH value also indicates the high buffering capacity caused from the accumulation of  $H^+$  ions. The nanoparticles absorb more protons triggering an inflow of chlorine ion. The flow of ions brings more fluid inside the endosomal vesicles leading to its breakdown and release of DNA into the cytoplasm. Simultaneously, the increase in particle size may also indicate the reduced interaction of vector with the DNA molecules and thus facilitate the DNA release from vector after the endosomal escape [26]. They reported that the smallest particle size and PDI value at pH 7 was the most suitable for the formation of polyplex and for gene delivery application. The smaller particle size could easily interact with the biological membranes due to large amount of surface to volume ratio [27]. Many studies revealed that the size and uniform dispersity of nanoparticle governs the cellular uptake efficiency and low PDI values indicate the uniformity of the nanoparticle [28,29]. Nano-carriers around 200 nm tend to form complexes that can enter the cells without damaging the cell membrane surface [30,31].

The cellular uptake mechanism of polyplex can influence the efficiency of gene expression by affecting the intracellular fate of the internalized nanoparticles [32]. The OC modified proteins can provide good gene transfection efficiency with low cytotoxicity. The transfection efficiency of these hybrid vectors depends on the weight ratio, amount of DNA, temperature effect, incubation time, and the presence of serum. A detailed investigation is requiring to understand the reasons of the high transfection efficiency using the cationic proteins. Therefore, we compared the DNA condensation and releasing ability of three vectors (i.e., BSA-OC, zein-OC, and OVA-OC) and then systematically investigated the internalization mechanism. The DNA binding affinity of the vector was analyzed through an EtBr retardation assay. The decrease in the relative fluorescence intensity of an EtBr-DNA complex following the addition of vector indicates the excellent formation of vector-pDNA polyplex. The interaction of EtBr-DNA complex with vector displaces the EtBr molecule from a double strand of DNA and further DNA associates with the vector, which decreases the fluorescence intensity of the EtBr-DNA complex. The higher reduction in fluorescence intensity indicates more condensation of DNA by the vector. In general, it has been reported that the increasing amount of polycations or amine contents reduces the fluorescence intensity of EtBr-DNA complex, which indicates the binding strength of polycation-DNA complex [33]. Our EtBr data also indicated that by increasing the concentration of the vector from 10  $\mu$ g to 60  $\mu$ g, the relative intensity of the EtBr-DNA complex decreases significantly, indicating that the positive charge of the vector interacts with

a negative charge of DNA (Table S1). Moreover, zein-OC and BSA-OC showed higher fluorescence quench than that of OVA-OC at the 300:1 ratio. This may be due to the larger zeta potentials of zein-OC ( $21.2 \pm 0.2$  mV) and BSA-OC ( $6.6 \pm 2$  mV) than OVA-OC ( $4.6 \pm 4.8$  mV). Similarly, Sun et al. indicated that the binding and release of DNA from the vector regulates the gene transfection efficiency [34].

The positively charged carriers condense DNA tightly and impede the release of DNA in the intracellular environment, which in turn reduces the gene transfection efficiency. Therefore, the DNA-releasing ability from the polyplex was analyzed in the presence of heparin using agarose gel electrophoresis. Heparin is a stronger anionic macromolecule that competes with the DNA binding site and releases the weaker anionic molecules, such as nucleic acid from the polyplex. The release of pDNA from the unpacking polyplex helps to correlate with the gene transfection efficiency [35]. In addition, the defective release of DNA after condensation also lowers the transfection efficiency of polyplex. As shown in Fig. S2, polyplex formed at a weight ratio of 60:1 showed the complete condensation of DNA by all three synthesized vectors, as no free DNA band was present. Moreover, the treatment with heparin manifests the release of DNA from all three polyplexes. Interestingly, the DNA disassociated from the vector was placed in the same position as naked DNA, which indicates the good condition of DNA. However, the released DNA from OVA-OC showed a faint band. In the case of zein-OC, some amount of DNA was still entrapped with the vector and has not been completely released. This may be due to the high surface charge of zein-OC tightly condensed the DNA and impedes the complete release of DNA. Compared with zein-OC and OVA-OC, BSA-OC was proven as an ideal vector that exhibited a good balance between DNA binding and release. Therefore, we chose the BSA-OC as the candidate for further mechanistic investigation. Besides, the appropriate binding strength between the vector and DNA complex may prompt the DNA-releasing ability and help to estimate the gene transfection efficiency in intracellular conditions. We investigated the mechanism of the BSA-OC vector for intracellular delivery and identified the key pathway driving the transfection.

#### 3.2. Quantitative measurement for the uptake of polyplexes

To explore the cellular uptake of 150 nm of BSA-OC/pDNA polyplex with a 25 mV surface potential, the vector was labeled with rhodamine. The cellular uptake mechanism and intracellular trafficking of polyplex is a key step in the successful transfection. This process is also influenced by constituents of the designed vector, type of modification, cell type, and culture medium [26]. The uptake analysis of BSA-OC was performed in two different epithelial cell lines, i.e., CHO-K1 and HEK 293T. The cells were incubated with rhodamine-labeled BSA-OC/pDNA polyplex for increasing time intervals, and Hoechst was used as a fluorescent stain for the cell nuclei to determine the intracellular fate of polyplex using a confocal microscope. At each time point, HEK 293T exhibited more intense red fluorescence than CHO-K1, indicating that the internalization rates of polyplex was faster in HEK 293T cells (Fig. 1). Previously, we demonstrated that HEK 293T showed high gene transfection efficiency as compared to CHO-K1 and HaCat cell lines at a weight ratio of 60:1. This may be due to the presence of mannose receptor on the surface of HEK 293T cells, which ease the interaction of OC molecules with the cell membrane [19]. Confocal microscopy image indicated that the polyplex was distributed into the cytosol and minimum level of cellular uptake was observed after 0.5 h of the incubation period. The uptake of polyplex was increased up to 2-fold at 2 h as compared to 1 h and then reached a plateau in Fig. 1(a). The distribution of rhodamine-labeled vector



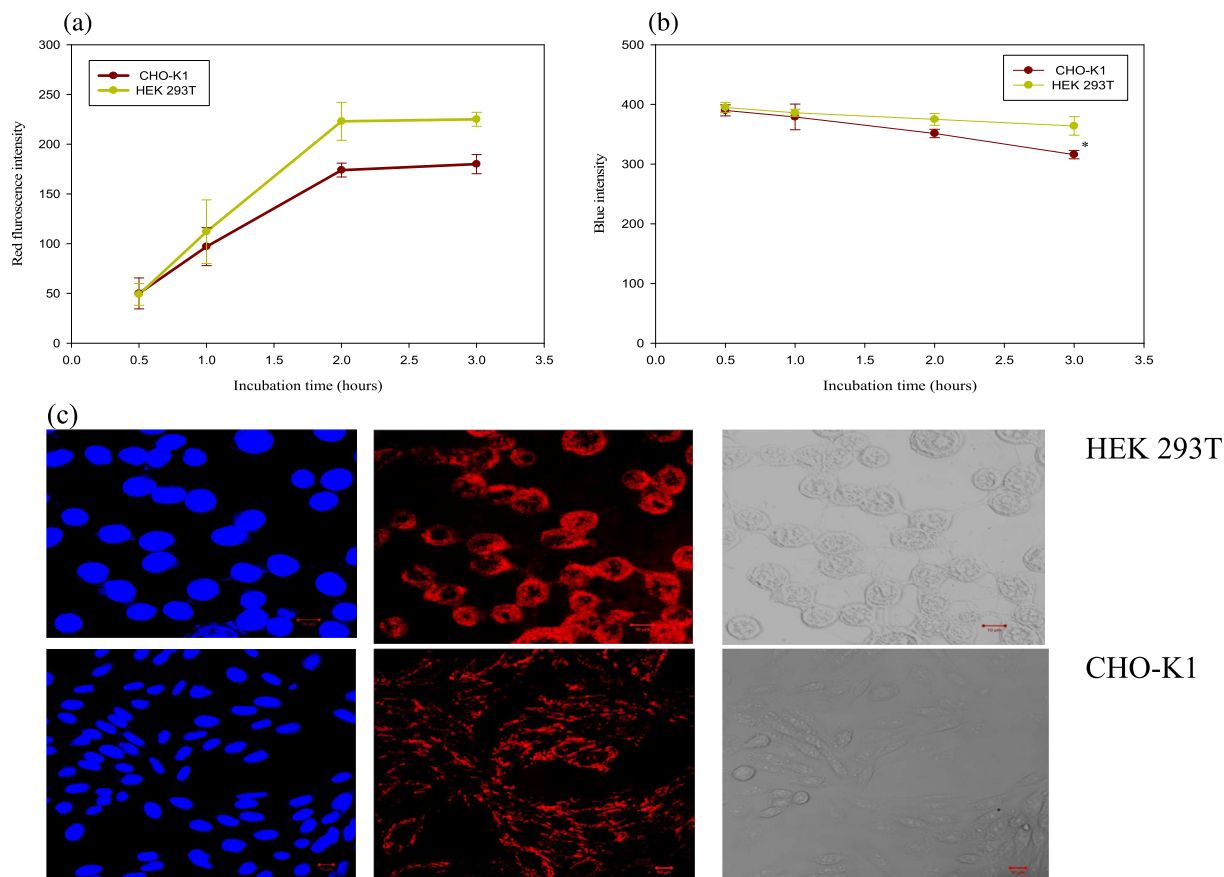


**Fig. 1.** Effect of incubation time on cellular uptake efficiency of Rh-labeled BSA-OC/pDNA polyplex. (a) red fluorescence intensity, (b) blue fluorescence intensity, (c) confocal microscopy image of HEK 293T and CHO-K1 cells incubated with polyplex for 3 h. The red and blue fluorescence intensity was quantified from individual cells by IN Cell Investigator software. Measurements were effectuated in duplicate with error bars representing the standard deviation. Stars (\*) indicate the significant difference as compared with 0.5 h of incubation time. The scale bar is 10 μm in the photos.

in cytoplasm suggests that the BSA-OC was able to cross the cell membrane barrier and to enter into the nucleus successfully. The uptake of polyplex has reached a plateau in both cell lines after 2 h of incubation time indicating that the sufficient nanoparticles are internalized and saturation of binding sites at the cell surface. Perumal et al. demonstrated that the key step for the internalization process of cationic dendrimers is the ionic interaction of proteoglycans present on the cell membrane with cationic dendrimers. The uptake of cationic dendrimers affects the adsorptive endocytosis process and this process saturates after one hour due to the limitation of membrane binding sites [36]. Therefore, it is important to maintain an adequate incubation time in which a maximal rate of cellular uptake is achieved.

The cell nuclei were labeled with Hoechst and the blue fluorescence intensity was used to analyze the toxicity of the vector. Hoechst 33342, a non-intercalating dye that binds to dsDNA of the nuclei, emits blue fluorescence at 350 nm of the excitation wavelength. The blue fluorescence intensity of the Hoechst is directly proportionate to the chromatin state in cells that provide an understanding of cellular conditions and the physiological characteristics of cells that reflect cellular viability [37]. As shown in Fig. 1(b), no significant difference was observed in the blue intensity with increasing time duration for HEK 293T cells, but for CHO-K1 the intensity was slightly reduced after 2 h of treatment. The data suggested that BSA-OC was a safe carrier to transfer genetic material into the mammalian cell lines.

### 3.3. Cellular uptake and internalization mechanism using endocytic inhibitors

Macromolecules are internalized into cells by a variety of mechanisms and their intracellular fates are usually relevant with the uptake pathways. Generally, cationic gene delivery carriers are internalized into cells via the endocytosis pathway as indicated in Table 1. To understand the internalization route of BSA-OC/pDNA polyplex, two cell lines (CHO-K1 and HEK 293T) were treated with a defined endocytic inhibitor to block the specific endocytic pathways and analyzed by IN Cell Analyzer 1000. The cell viability of endocytic inhibitor in the presence of polyplex was tested using the WST-1 assay according to a custom-developed protocol. As shown in Fig. 2(c), the cells treated with polyplex were considered controls, showing no significant difference from those treated with both endocytic inhibitor and polyplex. The data indicated that there were non-cytotoxic effects of endocytic inhibitors. Later, the BSA-OC/pDNA polyplex uptake and transfection efficiency were studied in the presence of endocytic inhibitor. Prior to endocytic study, treatment with sodium azide was performed to understand the role of energy (ATP)-dependent pathways. The presence of sodium azide significantly reduced the transfection efficiency and cellular uptake efficiency for both cell lines, which indicate that the endocytosis is the dominant pathway for the internalization of BSA-OC/pDNA polyplex. The treatment with CPZ increased the cellular uptake and transfection efficiency of the polyplex, which suggest



**Table 1**

The internalization pathways followed by modified nanoparticles in literature.

Nanoparticle composition	Particle size	Cell line	Pathway	Transfection efficiency	Ref
i. Self-branched and trisaccharide-substitutes chitosan oligomer (SBTCO),	76 nm	HeLa cells	CvME	30%	[43]
ii. Linear chitosan (LCO)	69 nm		CME and CvME	5%	
i. Hydrophobically modified glycol chitosan (HGC)	359 nm	HeLa cells	CvME, CME, and macropinocytosis	Uptake of HGC nanoparticle was 23% higher than GC	[44]
ii. Glycol chitosan (GC)	310 nm		Not mentioned.		
Alginate-chitosan nanoparticles	157 nm	293 T, COS7, and CHO cells	CME and CvME.	293 T- 15–20%, COS7- 1–3%, CHO—negligible	[45]
Human serum albumin-DOTAP DOPE/DNA (HSA-lipoplexes)	–	HeLa cells	CME and endo-lysosome system.	1.2 *10 <sup>4</sup> luciferase (ng)/total protein (mg)	[46]
i. Zein-OC	382 nm	CHO-K1 and HEK	CvME and Lipid-mediated pathways.	84%	[20]
ii. OVA-OC	110 nm	293T cells		70%	
BSA-OC	120 nm	CHO-K1 and HEK 293T cells	CvME pathway.	90%	This study

that the CPZ increased the compensatory pathways. However, the treatment with genistein significantly decreased the cellular uptake and transfection efficiency for both CHO and HEK cell lines. Inhibition data in the presence of CPZ and genistein indicate that the CvME plays a major role in the internalization of polyplex in both cell lines. The reduction of cellular uptake and transfection efficiency for both cell lines by methyl- $\beta$ -cyclodextrin (60%) confirmed the role of cholesterol (Fig. 2(a) and (b)). This result also suggests that the transportation of polyplex is not dependent on the endosome-lysosome system and internalized via caveolae-mediated pathway by avoiding the chance of pDNA degradation in lysosomes. The treatment with an endosome-lysosome acidification inhibitor can increase the transfection efficiency of lipopolyplexes by protecting the degradation of plasmid DNA in lysosomes [38]. The impacts of six endocytic inhibitors on cellular internalization are summarized in Table 2. Fig. 2(d), (e) illustrates the cell images of gene expression and the rhodamine labeled polyplex uptake by CHO-K1 and HEK 293T cells in presence of endocytic inhibitors. The inhibitor of the CvME pathway, genistein, could specifically hinder the GFP expression and polyplex uptake using ATP as the energy. We now believe that the high gene transfection efficiency of BSA-OC/pDNA polyplex is due to the involvement of the CvME pathway.

#### 3.4. Intracellular trafficking of the polyplexes

The caveolae-mediated pathway can escape the endo-lysosome compartments and thus deliver the DNA cargo without degradation [39]. But, it is completely not proven that polyplex internalized via caveolar vesicle could always escape the endo-lysosome degradation. Because a few studies demonstrate that in some cases caveosome vesicles can fuse with acidic compartments and polyplex faces the low pH condition [40]. Hill et al. have stated that the decrease level of caveolar coat protein (i.e., cavin) expression in caveolin leads to diffuse of caveolin in the plasma membrane and become internalized into the endo-lysosome compartment [41]. However, the internalization route and endosome escape ability of polyplex play a significant role in enhancing transfection efficiency [42]. Therefore, the intracellular distribution of BSA-OC/pDNA polyplex in both cell lines was studied by confocal microscopy. To understand the intracellular distribution of polyplex, the BSA-OC vector, cell nuclei, and lysosome were labeled with FITC, Hoechst, and LysoTracker Red. The FITC-labeled BSA-OC was used to prepare polyplex with pDNA. Fig. 3(a) and (b) represented the merged image of FITC labeled BSA-OC/pDNA polyplex with acidic organelles dye (LysoTracker Red). The quantitative

analysis of confocal images suggested that more than 70% of polyplex escaped the lysosome in both cell lines in Fig. 3(c). Thus, most of the polyplexes escape the endosome and prevent polyplex degradation by lysosome enzymes. In addition, the results of acidification inhibitors on transfection efficiency and uptake pathways demonstrate the importance of the endosome-lysosome system as a gene carrier. The treatment with acidification inhibitors, such as monensin and PVP, shows no inhibition effect on transfection efficiency, suggesting that acid organelles did not play a role in the transport process of polyplex. The acidic lysosomal compartment was not involved in the internalization of polyplex and was thus internalized via a neutral pH condition through the caveolar pathway in both cell lines.

#### 3.5. Evaluation of endo-lysosome membrane integrity

To investigate the endo-lysosomal membrane integrity of CHO-K1 and HEK 293T cells after treatment with the BSA-OC vector, the acridine orange (AO) staining technique was used. AO is a lysosomotropic weak base and cell-permeable dye that shows diffuse green fluorescence in an uncharged state. The protonated form of AO shows red fluorescence when it accumulates in acidic compartments. The distribution of red and green fluorescence intensity in the organelles helps to understand the lysosome membrane integrity [47]. As previously reported, cells treated with AO exhibit red fluorescence in the endosome and diffuse green fluorescence in the cytoplasm in low pH conditions. An increase in orange-red fluorescence indicates cell apoptosis [48]. Klimazewska-Wisniewska et al. performed AO staining to study cell autophagy. Upon treatment with drugs, such as fisetin and paclitaxel, the A549 cells undergo autophagy and show high red fluorescence intensity compared to positive control cells, representing an increase in acidic vesicular organelles (AVOs) [49]. As shown in Fig. 4(a) and (b), cells transfected with BSA-OC/pDNA polyplex slightly increased the red fluorescence intensity and had no significant difference from the controls. The cells transfected with BSA-OC/pDNA polyplex did not induce the formation of AVOs. The cells transfected with Fe3O4@SiO2-SS-PEI/siRNA show high colocalization of red and green fluorescence, confirming efficient endosomal disruption and the efficient release of siRNA [50]. In the present study, HEK 293T cells show high entrapment of polyplex with lysosomes (30%) compared to CHO-K1 (20%), which may disrupt lysosomes from releasing the entrapped polyplex and further increase the red fluorescence intensity of HEK 293T after staining with AO. The data suggest that BSA-OC is safe to transfer genetic material into mammalian cells.

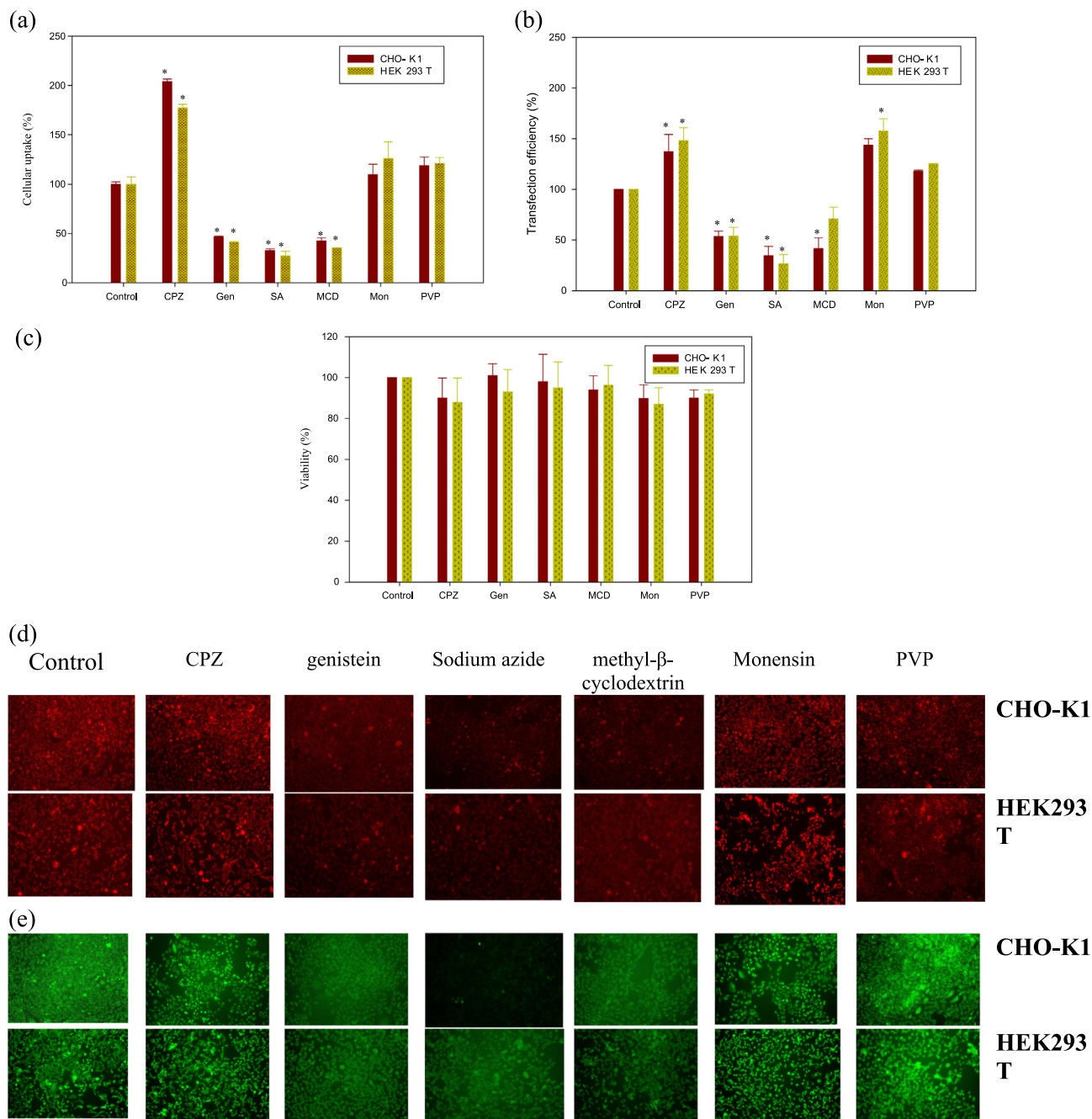


**Fig. 2.** Effect of the endocytic inhibitor on (a) cellular uptake efficiency, (b) transfection efficiency, (c) cell viability, (d) images of cells transfected with rhodamine labeled BSA-OC/pDNA polyplex, and (e) images of cells transfected by pEGFP-C3 plasmid. Measurements were in duplicate with error bars representing the standard deviation. Stars (\*) indicate the significant difference as compared with control.

**Table 2**  
Summary of endocytic inhibitor on cellular uptake using BSA-OC polyplex.

Inhibitor	Function	Concentration	Cellular uptake CHO HEK	
Chlorpromazine	Clathrin-mediated endocytosis inhibitor	30 $\mu$ M	+	+
Genistein	Caveolae-mediated endocytosis inhibitor	200 $\mu$ M	-	-
Sodium azide	Active transport inhibitor	1%	-	-
Methyl- $\beta$ -cyclodextrin	Cholesterol dependence endocytosis inhibitor	10 mM	-	-
Monensin	Block transport from Golgi complex to plasma membrane.	3 $\mu$ M	$\pm$	$\pm$
Polyvinylpyrrolidone	Intracellular vesicular swelling	1 mg/ml	$\pm$	$\pm$

Symbol (+) sign indicates the cellular uptake increased after treatment with a particular endocytic inhibitor as compared with control. Symbol (-) sign indicates the transfection efficiency decreased. Symbol ( $\pm$ ) indicates no significant difference as compared with control.

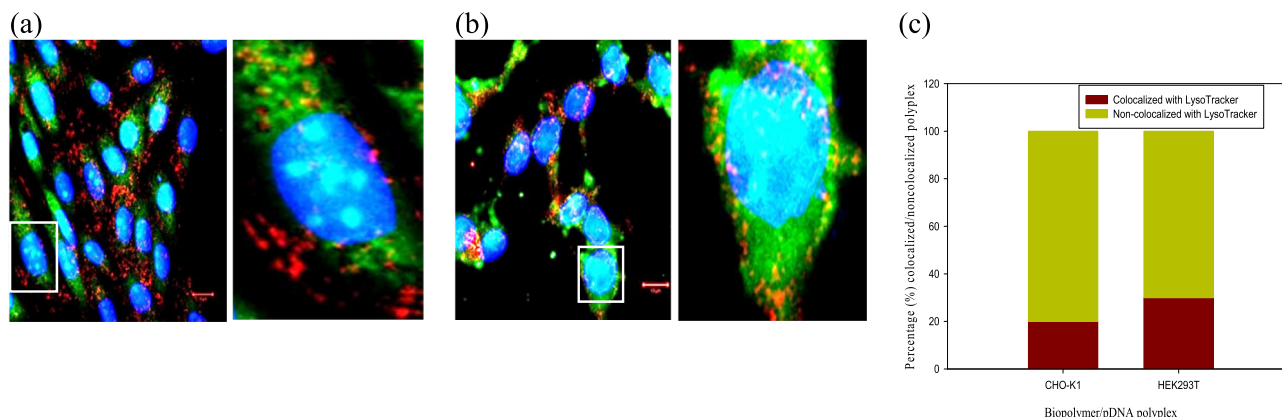


**Fig. 3.** Confocal microscopy image of the intracellular distribution of BSA-OC/pDNA polyplexes with LysoTracker in (a) CHO-K1, (b) HEK 293T cells, (c) Confocal images of both cell lines were quantified by IN Cell Investigator software. The scale bar is 10  $\mu$ m. The white box indicated the zoomed region of the cells showing colocalization. Blue fluorescence indicated the nuclei stained with Hoechst 33342. Green fluorescence indicated the FITC-labeled OC-modified proteins, and red fluorescence indicated the lysosome stained with LysoTracker Red.

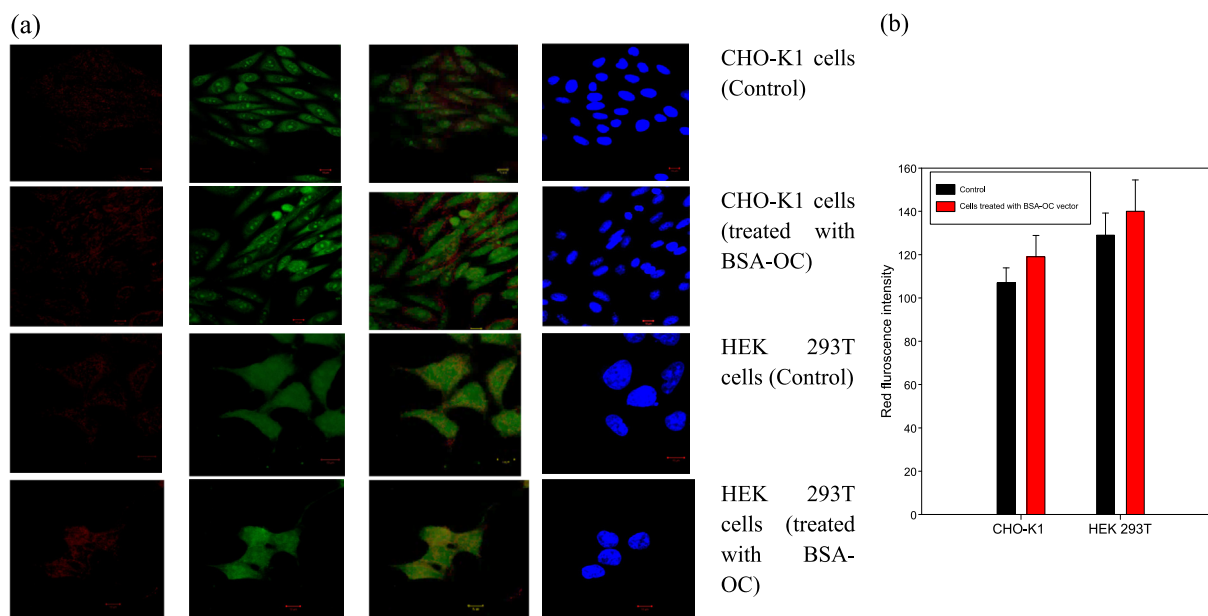


**Fig. 4.** Endosome-lysosomes membrane disruption study by using acridine orange. (a) Confocal image of cells treated with acridine orange in presence/absence of BSA-OC vector. (b) Confocal images of both cell lines were quantified by IN Cell Investigator software. The scale bar is 10  $\mu$ m.

### 3.6. Transfection in suspended cell lines

Transfection in a suspended cell line remains a major challenge. The most common reason for low transfection efficiency in suspended cells is the low attachment ability of polyplex to the cell membrane [51]. To date, many different approaches have been designed to deliver genetic material into a suspended cell line [52]. We found that BSA-OC/pDNA polyplex showed a high endosome escape ability and gene transfer efficiency in the adherent cell line. Therefore, we decided to test the transfection efficiency in a suspended cell line using BSA-OC/pDNA polyplex. Hattori et al. showed that the reverse transfection procedure shows high transfection efficiency and cell viability compared to the forward transfection procedure. In this procedure, the cells and transfection complex mixed together at the time of seeding cells in the plate [53]. We chose the reverse transfection to transfect a lymphoma cell line (BCRC 60252) and hybridoma cells (BCRC 60427 and CRL-1754). Fig. 5 shows the transfection efficiency of BSA-OC vector/pDNA polyplex at various weight ratios from 10:1 to 60:1.

The weight ratio was defined as different concentrations of the vector (10  $\mu$ g to 60  $\mu$ g) with 1  $\mu$ g DNA per well. By increasing the weight ratio, the transfection efficiency was increased and reached the maximal 80%. BCRC 60252 cells showed high gene transfer efficiency in 40:1 and 60:1 compared to hybridoma cells. Many authors have designed different techniques to transfect the suspended cells, such as droplet electroporation and laser irradiation [51,52]. But the obtained transfection efficiency and cell viability remain unsatisfactory (the transfection efficiency was in the range of 60–72% and cell viability was 70–75%). Furthermore, BSA-OC/pDNA polyplex could transfect three suspended cell lines with >85% cell viability (Fig. 5). The benefits of using the BSA-OC vector as a non-viral gene delivery vector are its simplicity, easy conjugation, high transfection efficiency, and high gene expression.

### 3.7. Blood cell hemolysis

One of the major drawbacks of using the cationic polymer as a gene delivery vector for clinical purposes is the non-specific

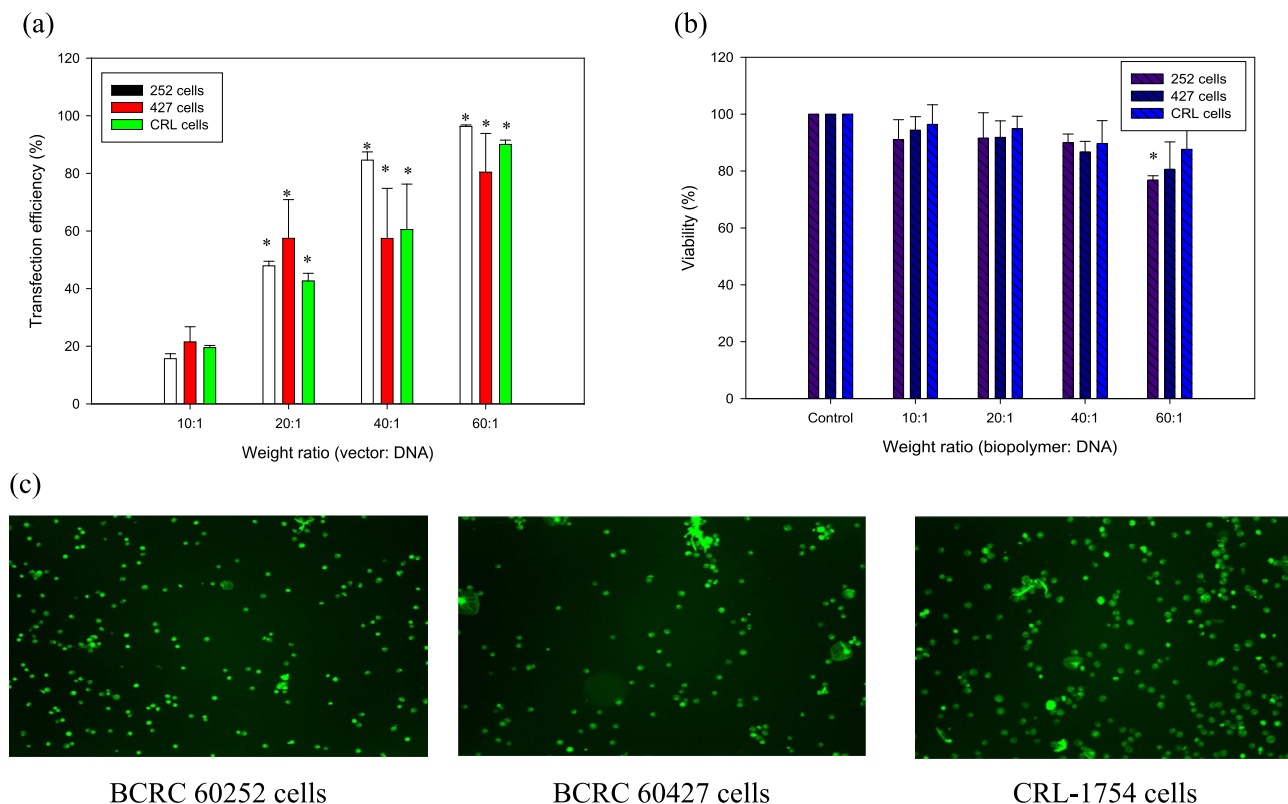


**Fig. 5.** GFP expression in suspended cells transfected by BSA-OC/pDNA polyplexes at various weight ratios (a) percentage of GFP-expressing cells, (b) cell viability after transfection, and (c) fluorescence images of BCRC60252, BCRC 60427, and CRL-1754 cells transfected at a weight ratio of 60:1. The images were obtained at a magnification of 10 $\times$ . Measurements were effectuated in duplicate with error bars representing the standard deviation. Stars (\*) indicate the significant difference as compared with the weight ratio of 10:1.

interaction of the polymer with red blood cells (RBCs) that causes the aggregation of RBCs and the risk of ischemic stroke [54]. The interaction of negatively charged blood components with positively charged macromolecules causes cell lysis and releases the hemoglobin from RBCs [55]. Therefore, it is essential to test the suitability of the cationic macromolecule when it interacts with the cell membrane with no damaging effect. We tested the hemolytic activity of BSA-OC/pDNA polyplex at different weight ratios (10:1–300:1) using mice blood. Triton X-100 (0.1%) and sodium phosphate buffer (pH 7.4) were used as a positive control and a negative control, respectively. The treatment of blood with Triton X-100 is considered 100% hemolysis, while treatment with sodium phosphate buffer is considered 0% hemolysis. As shown in Fig. 6, by increasing the weight ratio from 60:1 to 300:1, the percentage of hemolysis increased from 2% to 34%, and no significant hemolytic effects were observed up to 100:1 (500  $\mu$ g/mL of BSA-OC), indicating no detectable membrane disruption of the red blood cell. The BSA-OC vector showed high bio-compatibility toward blood cells and could be used for gene delivery using parenteral administration.

### 3.8. Biocompatibility of polyplexes in the *in vivo* condition

High transfection efficiency and endosome escape ability of the BSA-OC vector were obtained in the *in vitro* condition. The gene transfer ability was impeded in the *in vivo* condition due to the presence of inhibitory biological fluid and the extracellular barrier [56]. The efficiency of BSA-OC vector for gene delivery in an *in vivo* environment was examined using fluorescent tdTomato as a reporter gene. Two different vector/DNA ratios, i.e., 1:1 and 1.5:1, were injected intravenously into CD1 (ICR) mice via a tail vein injection. The size and zeta potential of two polyplexes was around  $250 \pm 23$  nm and  $28 \pm 3$  mV, respectively. Additionally, a mouse

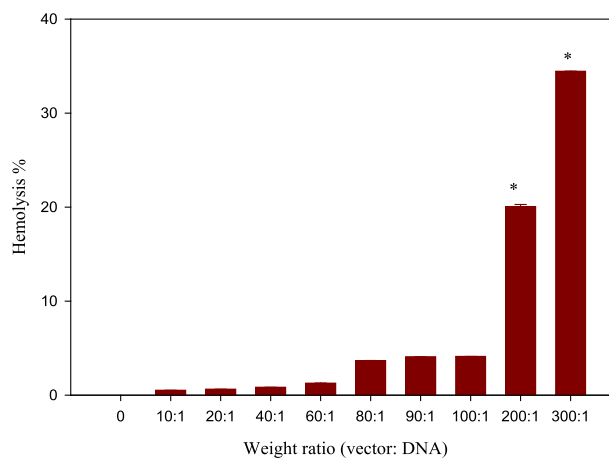


**Fig. 6.** Hemolytic activity of BSA-OC vector/pDNA polyplex at different weight ratio against RBCs. The polyplexes were prepared by mixing increasing concentration of vector from 10  $\mu$ g to 300  $\mu$ g with 1  $\mu$ g of pDNA. Stars (\*) indicate the significant difference ( $p < 0.01$ ) as compared with the weight ratio of 10:1.

injected with a high dosage of the vector (200  $\mu$ g) was used to study the biocompatibility of the vector. Mice individually injected with DNA (90  $\mu$ g) and PBS were used as the controls. As shown in Fig. 7(a) and (b), a high level of tdTomato expression was observed in the 1:1 polyplex in the liver containing the reticulo-endothelial system compared to that of 1.5:1 polyplex. The high tdTomato expression in RES organ is might be due to the interaction of OC molecules with the mannose receptors of liver non-parenchymal cells. The mixing ratio plays a significant role in successful transfection efficiency. Song et al. mentioned that a slight excess of



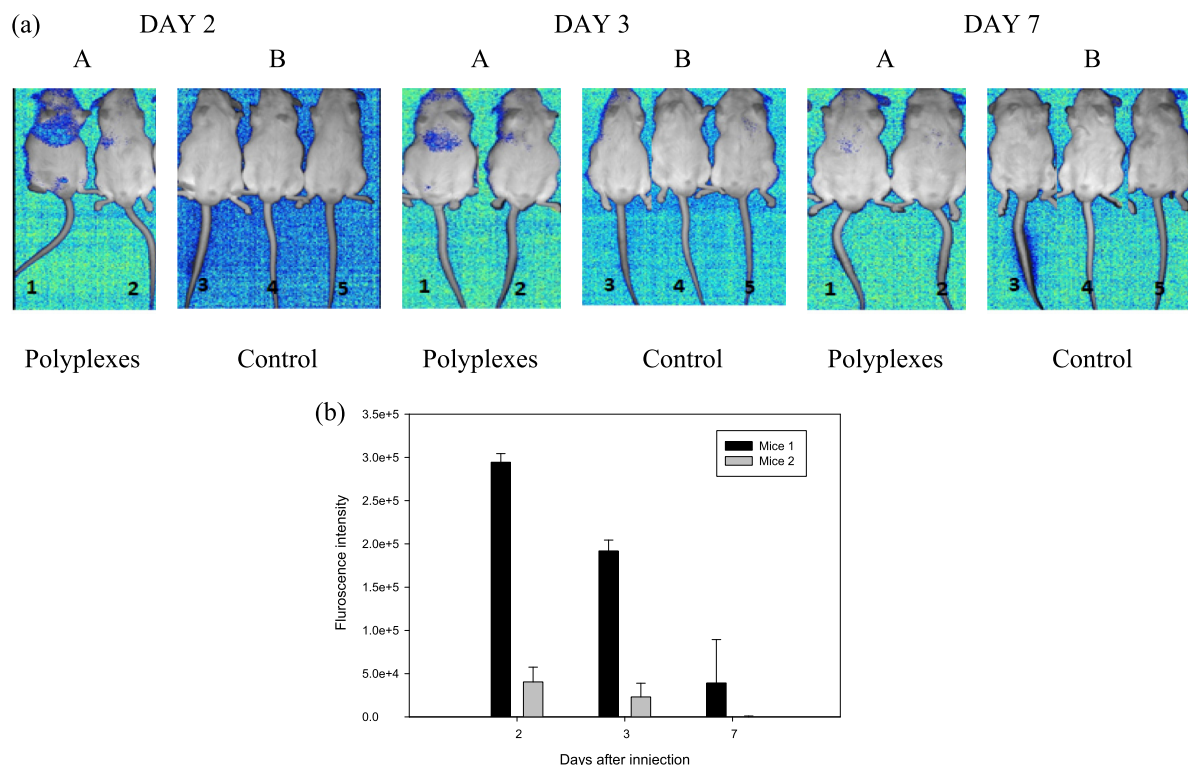


**Fig. 7.** *In vivo* bioluminescence imaging of CD1 mice with intravenous injection of polyplex sample. (a) Panel A is mice injected with prepared polyplex at a weight ratio of BSA-OC/pDNA polyplex (1) 60  $\mu$ g vector/60  $\mu$ g pDNA, and (2) 90  $\mu$ g vector/60  $\mu$ g pDNA; using tdTomato as a reporter gene. Panel B is the control mice injected with (3) vector only (200  $\mu$ g), (4) DNA only (90  $\mu$ g), and (5) PBS only. The mice were imaged using the IVIS spectrum after post-injection at a different time point (Day 2, 3, and 7), (b) quantitative estimation of tdTomato expression by using Image J software (mice 1: 60  $\mu$ g vector/60  $\mu$ g pDNA; mice 2: 90  $\mu$ g vector/60  $\mu$ g pDNA).

positive charge is suitable for gene transfection [57]. However, the large positive charge retards the release of DNA from the complex and showed lower gene expression. By increasing the injection time period, the fluorescence expression was decreased significantly. The fluorescence of tdTomato expression in control mice was not detected; this indicated that even a high dose of DNA alone cannot show fluorescent protein expression and will be degraded in an *in vivo* condition. One week after polyplex injection, the mouse did not show any sign of apparent weakness and spontaneous animal death, suggesting the biocompatibility of the vector *in vivo* environment. In conclusion, the data demonstrate that BSA-OC is a biocompatible vector for gene delivery.

#### 4. Conclusion

EtBr and agarose gel assay showed that BSA-OC had a good DNA condensation ability and a high DNA-releasing capacity compared to zein-OC and OVA-OC. The data confirm the hypothesis that the type of protein moiety influenced the surface charge of the vector and in thus balancing the good correlation between the DNA binding and release capacity. Further, the internalization data indicated that the caveolae/lipid-mediated pathway was the dominant pathway for the uptake of BSA-OC/pDNA polyplex in both cell lines CHO-K1 and HEK 293T. The colocalization of polyplex with Lyso-Tracker illustrates that BSA-OC/pDNA polyplex showed 70% endosome escape ability in the tested cells. By studying the endosome membrane integrity of BSA-OC, this vector delivered the gene without inducing cell death or apoptosis in all tested cell lines. The developed transfection process for suspended cell lines showed high gene expression with good cell viability using BSA-OC/pDNA polyplex. Furthermore, the hemolysis percentage was less than 2% at the 500  $\mu$ g/mL of BSA-OC and showed good gene

expression in the *in vivo* condition. Our data demonstrate the synthesized BSA-OC vector is a promising candidate for plasmid delivery application.

#### Declaration of Competing Interest

The authors declare that they have no conflict of interest.

#### Acknowledgements

We express gratitude to Ministry of Science and Technology, Taiwan (MOST 106-2221-E-182-050, 108-2221-E-182-039), Chang Gung University, Taiwan (BMRP 758) and Chang Gung Memorial Hospital, Taiwan (2J0161, 2H0071, 2H0072) for funding and supporting this research.

#### Appendix A. Supplementary data

Supplementary data to this article can be found online at <https://doi.org/10.1016/j.ijbiomac.2019.09.121>.

#### References

- [1] C.L. Grigsby, K.W. Leong, Balancing protection and release of DNA: tools to address a bottleneck of non-viral gene delivery, *J. R. Soc. Interface* 7 (Suppl 1) (2010) S67–S82.
- [2] M. Ramamoorthi, A. Narvekar, Non viral vectors in gene therapy – an overview, *J. Clin. Diagnostic Res.*: JCDR 9 (1) (2015) GE01–GE06.
- [3] F.C. Pérez-Martínez, J. Guerra, I. Posadas, V. Ceña, Barriers to non-viral vector-mediated gene delivery in the nervous system, *Pharm. Res.* 28 (8) (2011) 1843–1858.
- [4] P. Agrawal, R.P. Singh Sonali, L. Kumari, G. Sharma, B. Koch, C.V. Rajesh, A.K. Mehata, S. Singh, B.L. Pandey, M.S. Muthu, TPGS-chitosan cross-linked targeted nanoparticles for effective brain cancer therapy, *Mater. Sci. Eng., C* 74 (2017) 167–176.



- [5] J. Du, B. Li, P. Zhang, Y. Wang, Cationized bovine serum albumin as gene carrier: Influence of specific secondary structure on DNA complexibility and gene transfection, *Colloids Surf. B. Biointerfaces* 143 (2016) 37–46.
- [6] G. Sahay, D.Y. Alakhova, A.V. Kabanov, Endocytosis of nanomedicines, *J. Control. Release* 145 (3) (2010) 182–195.
- [7] N.L. Ross, E.V. Munsell, C. Sabanayagam, M.O. Sullivan, Histone-targeted polyplexes avoid endosomal escape and enter the nucleus during postmitotic redistribution of ER membranes, *Molecular Therapy. Nucleic Acids* 4 (2) (2015) e226.
- [8] C. Van den Broeke, T. Jacob, H.W. Favoreel, Rho'ing in and out of cells: viral interactions with Rho GTPase signaling, *Small GTPases* 5 (2014) e28318.
- [9] D. Dutta, J.G. Donaldson, Search for inhibitors of endocytosis: intended specificity and unintended consequences, *Cellular Logistics* 2 (4) (2012) 203–208.
- [10] H. Wang, A.X. Wang, K. Aylor, E.J. Barrett, Caveolin-1 phosphorylation regulates vascular endothelial insulin uptake and is impaired by insulin resistance in rats, *Diabetologia* 58 (6) (2015) 1344–1353.
- [11] G. Misinzio, P.L. Delputte, H.J. Nauwynck, Inhibition of endosome-lysosome system acidification enhances porcine coronavirus 2 infection of porcine epithelial cells, *J. Virol.* 82 (3) (2008) 1128–1135.
- [12] C.L. Chen, W.H. Hou, I.H. Liu, G. Hsiao, S.S. Huang, J.S. Huang, Inhibitors of clathrin-dependent endocytosis enhance TGF $\beta$  signaling and responses, *J. Cell Sci.* 122 (Pt 11) (2009) 1863–1871.
- [13] R. Pohlmann, S. Kruger, A. Hasilik, K. von Figura, Effect of monensin on intracellular transport and receptor-mediated endocytosis of lysosomal enzymes, *Biochem. J.* 217 (3) (1984) 649–658.
- [14] K. Ciftci, R.J. Levy, Enhanced plasmid DNA transfection with lysosomotropic agents in cultured fibroblasts, *Int. J. Pharm.* 218 (1–2) (2001) 81–92.
- [15] W. Wang, T. Naolou, N. Ma, Z. Deng, X. Xu, U. Mansfeld, C. Wischke, M. Gossen, A.T. Neffe, A. Lendlein, Polydepsipeptide block-stabilized polyplexes for efficient transfection of primary human cells, *Biomacromolecules* 18 (11) (2017) 3819–3833.
- [16] J. Rejman, A. Bragioni, M. Conese, Role of clathrin- and caveolae-mediated endocytosis in gene transfer mediated by lipo- and polyplexes, *Mol. Ther.* 12 (3) (2005) 468–474.
- [17] R.K. Keswani, M. Lazebnik, D.W. Pack, Intracellular trafficking of hybrid gene delivery vectors, *J. Control. Release* 207 (2015) 120–130.
- [18] S.F. Peng, M.T. Tseng, Y.C. Ho, M.C. Wei, Z.X. Liao, H.W. Sung, Mechanisms of cellular uptake and intracellular trafficking with chitosan/DNA/poly(gamma-glutamic acid) complexes as a gene delivery vector, *Biomaterials* 32 (1) (2011) 239–248.
- [19] M. Kumari, C.-H. Liu, W.-C. Wu, Efficient gene delivery by oligochitosan conjugated serum albumin: facile synthesis, polyplex stability, and transfection, *Carbohydr. Polym.* 183 (2018) 37–49.
- [20] M. Kumari, C.-H. Liu, W.-C. Wu, Protein moiety in oligochitosan modified vector regulates internalization mechanism and gene delivery: polyplex characterization, intracellular trafficking and transfection, *Carbohydr. Polym.* 202 (2018) 143–156.
- [21] R. Mehta, R. Kumari, P. Das, A.K. Bhowmick, Synthesis and characterization of a biocompatible monotyrosine-based polymer and its interaction with DNA, *J. Mater. Chem. B* 2 (37) (2014) 6236–6248.
- [22] N.A. Kim, I.B. An, D.G. Lim, J.Y. Lim, S.Y. Lee, W.S. Shim, N.-G. Kang, S.H. Jeong, Effects of pH and buffer concentration on the thermal stability of etanercept using DSC and DLS, *Biol. Pharm. Bull.* 37 (5) (2014) 808–816.
- [23] K. Talley, E. Alexov, On the pH-optimum of activity and stability of proteins, *Proteins* 78 (12) (2010) 2699–2706.
- [24] T.L. Moore, L. Rodriguez-Lorenzo, V. Hirsch, S. Balog, D. Urban, C. Jud, B. Rothen-Rutishauser, M. Lattuada, A. Petri-Fink, Nanoparticle colloidal stability in cell culture media and impact on cellular interactions, *Chem. Soc. Rev.* 44 (17) (2015) 6287–6305.
- [25] Y.L. Chiu, S.C. Chen, C.J. Su, C.W. Hsiao, Y.M. Chen, H.L. Chen, H.W. Sung, pH-triggered injectable hydrogels prepared from aqueous N-palmitoyl chitosan: in vitro characteristics and in vivo biocompatibility, *Biomaterials* 30 (28) (2009) 4877–4888.
- [26] J. Singh, D. Michel, J.M. Chitanda, R.E. Verrall, I. Badea, Evaluation of cellular uptake and intracellular trafficking as determining factors of gene expression for amino acid-substituted gemini surfactant-based DNA nanoparticles, *J. Nanobiotechnol.* 10 (2012) 7.
- [27] S.A.A. Rizvi, A.M. Saleh, Applications of nanoparticle systems in drug delivery technology, *Saudi Pharm. J.* 26 (1) (2018) 64–70.
- [28] S. Prabha, G. Arya, R. Chandra, B. Ahmed, S. Nimesh, Effect of size on biological properties of nanoparticles employed in gene delivery, *Artif. Cells Nanomed. Biotechnol.* 44 (1) (2016) 83–91.
- [29] L. Shang, K. Nienhaus, G.U. Nienhaus, Engineered nanoparticles interacting with cells: size matters, *J. Nanobiotechnol.* 12 (2014), 5–5.
- [30] W.T. Godbey, K.K. Wu, A.G. Mikos, Size matters: molecular weight affects the efficiency of poly(ethyleneimine) as a gene delivery vehicle, *J. Biomed. Mater. Res.* 45 (3) (1999) 268–275.
- [31] D. Fischer, T. Bieber, Y. Li, H.P. Elsasser, T. Kissel, A novel non-viral vector for DNA delivery based on low molecular weight, branched polyethylenimine: effect of molecular weight on transfection efficiency and cytotoxicity, *Pharm. Res.* 16 (8) (1999) 1273–1279.
- [32] D. Pozzi, C. Marchini, F. Cardarelli, H. Amenitsch, C. Garulli, A. Bifone, G. Caracciolo, Transfection efficiency boost of cholesterol-containing lipoplexes, *Biochimica et biophysica acta* 1818 (9) (2012) 2335–2343.
- [33] F. Nouri, H. Sadeghpour, R. Heidari, A. Dehshahri, Preparation, characterization, and transfection efficiency of low molecular weight polyethylenimine-based nanoparticles for delivery of the plasmid encoding CD200 gene, *Int. J. Nanomedicine* 12 (2017) 5557–5569.
- [34] Y. Sun, H. Liu, T. Yang, L. Lang, L. Cheng, H. Xing, L. Yang, P. Ding, Amphoteric poly(amido amine)s with adjustable balance between transfection efficiency and cytotoxicity for gene delivery, *Colloids Surf. B: Biointerfaces* 175 (2019) 10–17.
- [35] T. Ganbold, S. Han, A. Hasi, H. Baigude, Receptor-mediated delivery of therapeutic RNA by peptide functionalized curdlan nanoparticles, *Int. J. Biol. Macromol.* 126 (2019) 633–640.
- [36] O.P. Perumal, R. Inapagolla, S. Kannan, R.M. Kannan, The effect of surface functionality on cellular trafficking of dendrimers, *Biomaterials* 29 (24–25) (2008) 3469–3476.
- [37] D.F. Gilbert, G. Erdmann, X. Zhang, A. Fritzsche, K. Demir, A. Jaedicke, K. Muehlenberg, E.E. Wanker, M. Boutros, A novel multiplex cell viability assay for high-throughput RNAi screening, *PLoS One* 6 (12) (2011) e28338.
- [38] J. Gu, J. Hao, X. Fang, X. Sha, Factors influencing the transfection efficiency and cellular uptake mechanisms of Pluronic P123-modified polypropyleneimine/pDNA polyplexes in multidrug resistant breast cancer cells, *Colloids Surfaces B, Biointerfaces* 140 (2016) 83–93.
- [39] P. Foroozandeh, A.A. Aziz, Insight into cellular uptake and intracellular trafficking of nanoparticles, *Nanoscale Res. Lett.* 13 (1) (2018), 339–339.
- [40] K. von Gersdorff, N.N. Sanders, R. Vandenbroucke, S.C. De Smedt, E. Wagner, M. Ogris, The internalization route resulting in successful gene expression depends on both cell line and polyethylenimine polyplex type, *Mol. Ther.* 14 (5) (2006) 745–753.
- [41] M.M. Hill, M. Bastiani, R. Luetterforst, M. Kirkham, A. Kirkham, S.J. Nixon, P. Walser, D. Abankwa, V.M.J. Oorschot, S. Martin, J.F. Hancock, R.G. Parton, PTRF-Cavin, a conserved cytoplasmic protein required for caveola formation and function, *Cell* 132 (1) (2008) 113–124.
- [42] S.M. Caroline Diana, M.R. Rekha, Efficacy of vinyl imidazole grafted cationized pullulan and dextran as gene delivery vectors: a comparative study, *Int. J. Biol. Macromol.* 105 (2017) 947–955.
- [43] Z. Garaiova, S.P. Strand, N.K. Reitan, S. L  lu, S.   St  rset, K. Berg, J. Malm  , O. Folasire, A. Bj  rk  y, C. de L. Davies, Cellular uptake of DNA–chitosan nanoparticles: the role of clathrin- and caveolae-mediated pathways, *Int. J. Biol. Macromol.* 51 (5) (2012) 1043–1051.
- [44] H.Y. Nam, S.M. Kwon, H. Chung, S.-Y. Lee, S.-H. Kwon, H. Jeon, Y. Kim, J.H. Park, J. Kim, S. Her, Y.-K. Oh, I.C. Kwon, K. Kim, S.Y. Jeong, Cellular uptake mechanism and intracellular fate of hydrophobically modified glycol chitosan nanoparticles, *J. Controlled Release* 135 (3) (2009) 259–267.
- [45] K.L. Douglas, C.A. Piccirillo, M. Tabrizian, Cell line-dependent internalization pathways and intracellular trafficking determine transfection efficiency of nanoparticle vectors, *Eur. J. Pharm. Biopharm.* 68 (3) (2008) 676–687.
- [46] S. Simoes, V. Slepishkin, P. Pires, R. Gaspar, M.C. Pedrosa de Lima, N. Duzgunes, Human serum albumin enhances DNA transfection by lipoplexes and confers resistance to inhibition by serum, *Biochimica et Biophysica Acta* 1463 (2) (2000) 459–469.
- [47] P. Karna, S. Zughaier, V. Pannu, R. Simmons, S. Narayan, R. Aneja, Induction of reactive oxygen species-mediated autophagy by a novel microtubule-modulating agent, *J. Biol. Chem.* 285 (24) (2010) 18737–18748.
- [48] K. Nagahama, T. Utsumi, T. Kumano, S. Maekawa, N. Oyama, J. Kawakami, Discovery of a new function of curcumin which enhances its anticancer therapeutic potency, *Sci. Rep.* 6 (2016) 30962.
- [49] A. Klimaszewska-Wisniewska, M. Halas-Wisniewska, T. Tadrowski, M. Gagat, D. Grzanka, A. Grzanka, Paclitaxel and the dietary flavonoid fisetin: a synergistic combination that induces mitotic catastrophe and autophagic cell death in A549 non-small cell lung cancer cells, *Cancer Cell Int.* 16 (1) (2016) 10.
- [50] L. Zhang, Y. Li, J.C. Yu, K.M. Chan, Redox-responsive controlled DNA transfection and gene silencing based on polymer-conjugated magnetic nanoparticles, *RSC Adv.* 6 (76) (2016) 72155–72164.
- [51] D.J. Im, S.-N. Jeong, Transfection of Jurkat T cells by droplet electroporation, *Biochem. Eng. J.* 122 (2017) 133–140.
- [52] C. Yao, F. Rudnitski, G. Huttman, Z. Zhang, R. Rahmanzadeh, Important factors for cell-membrane permeabilization by gold nanoparticles activated by nanosecond-laser irradiation, *Int. J. Nanomed.* 12 (2017) 5659–5672.
- [53] Y. Hattori, Y. Yoshiike, M. Honda, H. Ohno, H. Onishi, Evaluation of small interfering RNA delivery into cells by reverse transfection in suspension with cationic liposomes, *Pharmacol. Pharmacy* 08 (2017) 12.
- [54] K. Sarkar, A. Chatterjee, G. Chakraborti, P.P. Kundu, Blood compatible N-maleyl chitosan-graft-PAMAM copolymer for enhanced gene transfection, *Carbohydr. Polym.* 98 (1) (2013) 596–606.
- [55] S.M. Noh, M.O. Park, G. Shim, S.E. Han, H.Y. Lee, J.H. Huh, M.S. Kim, J.J. Choi, K. Kim, I.C. Kwon, J.-S. Kim, K.-H. Baek, Y.-K. Oh, Pegylated poly-L-arginine derivatives of chitosan for effective delivery of siRNA, *J. Control. Release* 145 (2) (2010) 159–164.
- [56] M.G. Katz, A.S. Fargnoli, R.D. Williams, C.R. Bridges, Gene therapy delivery systems for enhancing viral and nonviral vectors for cardiac diseases: current concepts and future applications, *Hum. Gene Ther.* 24 (11) (2013) 914–927.
- [57] Y.K. Song, D. Liu, Free liposomes enhance the transfection activity of DNA/lipid complexes in vivo by intravenous administration, *Biochimica et biophysica acta* 1372 (1) (1998) 141–150.

Available online at [www.sciencedirect.com](http://www.sciencedirect.com)

ScienceDirect

Biomedical Journal

journal homepage: [www.elsevier.com/locate/bj](http://www.elsevier.com/locate/bj)

## Review Article

# Understanding the role of neutrophils in acute respiratory distress syndrome

Shun-Chin Yang<sup>a,b</sup>, Yung-Fong Tsai<sup>c,d</sup>, Yen-Lin Pan<sup>e</sup>,  
Tsong-Long Hwang<sup>b,c,f,g,\*</sup>

<sup>a</sup> Department of Anesthesiology, Taipei Veterans General Hospital and National Yang-Ming University, Taipei, Taiwan

<sup>b</sup> Graduate Institute of Natural Products, College of Medicine, Chang Gung University, Taoyuan, Taiwan

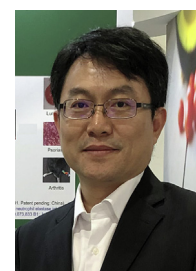
<sup>c</sup> Department of Anesthesiology, Chang Gung Memorial Hospital at Linkou, Taoyuan, Taiwan

<sup>d</sup> Graduate Institute of Clinical Medical Sciences, College of Medicine, Chang Gung University, Taoyuan, Taiwan

<sup>e</sup> Department of Pharmacy, Cheng Hsin General Hospital, Taipei, Taiwan

<sup>f</sup> Research Center for Chinese Herbal Medicine, Research Center for Food and Cosmetic Safety, and Graduate Institute of Health Industry Technology, College of Human Ecology, Chang Gung University of Science and Technology, Taoyuan, Taiwan

<sup>g</sup> Department of Chemical Engineering, Ming Chi University of Technology, New Taipei City, Taiwan



## ARTICLE INFO

## Article history:

Received 23 July 2020

Accepted 8 September 2020

Available online xxx

## Keywords:

ARDS

Neutrophil

Inflammation

## ABSTRACT

Acute respiratory distress syndrome (ARDS) is difficult to treat and is associated with a high mortality rate. The most severe form of coronavirus disease 2019 (COVID-19) also leads to life-threatening ARDS. Neutrophil counts are positively correlated with disease severity in ARDS. Neutrophil activation not only plays a significant role in immune defense against infections, but also causes tissue damage and leads to inflammatory diseases. Activated neutrophils rapidly migrate to inflamed lung tissue, releasing toxic granular contents and generating neutrophil extracellular traps. In the last few decades, it has become apparent that neutrophils occupy a central role in ARDS pathology. In this review, we summarize the neutrophil inflammatory responses and their relationships to ARDS. According to the current literature, understanding the function of neutrophils may be helpful in the treatment of ARDS.

Acute respiratory distress syndrome (ARDS) is a life-threatening respiratory condition with an increasing incidence rate, ranging from 20 to 40%, and a mortality rate of approximately 40% [1,2]. On account of the outbreak of

coronavirus disease 2019 (COVID-19), 29–42% COVID-19 patients developed ARDS and 15–52% of COVID-19 ARDS cases resulted in fatality [3,4]. Initially, the American-European Consensus Conference for ARDS defined acute lung injury

\* Corresponding author. Graduate Institute of Natural Products, College of Medicine, Chang Gung University, 259, Wenhua 1st Rd., Gueishan, Taoyuan 333, Taiwan.

E-mail address: [htl@mail.cgu.edu.tw](mailto:htl@mail.cgu.edu.tw) (T.-L. Hwang).

Peer review under responsibility of Chang Gung University.

<https://doi.org/10.1016/j.bj.2020.09.001>

2319-4170/© 2020 Chang Gung University. Publishing services provided by Elsevier B.V. This is an open access article under the CC BY-NC-ND license (<http://creativecommons.org/licenses/by-nc-nd/4.0/>).

(ALI) and ARDS as separate conditions. ALI was regarded as a less severe presentation of ARDS [5]. The Berlin definition of ARDS was updated, classified into mild, moderate, and severe grades based on the pulmonary oxygenation level. Due to its similarity to mild ARDS, ALI was removed from the Berlin definition [6]. The clinical symptoms and signs of ARDS are characterized by hypoxemia, marked diffuse bilateral pulmonary infiltrates, and extensive pulmonary edema. Studies of histological events of ARDS demonstrated that pulmonary edema is induced by increased vascular permeability, followed by protein-rich fluid in the alveolar space and accumulation of activated immune cells. The diffuse alveolar damage and accumulated immune cells lead to compromised gas exchange and respiratory failure [7,8]. Neutrophil infiltration in inflamed lung is a hallmark of ARDS [9]. Activated neutrophils trigger oxidative stress, release proteases, and form neutrophil extracellular traps (NETs), resulting in lung damage. However, neutrophils also play a role in the repair of inflamed lung tissues. Neutrophils are involved in the proliferation of type II pneumocytes during the repair phase after inflammatory lung injury [10]. It has been reported that neutropenia does not result in improved recovery in ARDS patients [11,12]. Although numerous studies have explored the pathogenesis of ARDS, there is still a lack of consensus regarding ARDS progression and effective pharmacotherapeutic treatment. Understanding the functional implications of neutrophils will allow exploration of applicable therapeutic strategies to reduce neutrophil-induced inflammatory lung injury. This review will focus on the roles of neutrophils and related immune products associated with ARDS.

## Overview of lung inflammatory injury

The pathogenesis of ARDS is complex and classified as direct or indirect. Most commonly, direct injury results from infectious damage to lung tissue. The causes of lung injury by infectious stimuli are not fully known. Pneumococcus and influenza A virus originally infect bronchial epithelium, induce upper airway and alveolar damage, recruit neutrophils and macrophages, and amplify cytokine and chemokine production [13,14]. Severe acute respiratory syndrome coronavirus 2 (SARS-CoV-2) infects pulmonary tissues, resulting in accumulation of massive amounts of immune cells and leads to an inflammatory cytokine storm. In COVID-19 ARDS patients, cytokine storm is a common characteristic. Patients with COVID-19 ARDS have elevated plasma levels of inflammatory cytokines, including interleukin (IL)-1 $\beta$ , IL-6, IL-8, granulocyte colony-stimulating factor, interferon gamma, and tumor necrosis factor alpha (TNF- $\alpha$ ). An excess of inflammatory cytokines further causes immune cell infiltration into inflamed lungs to induce alveolar damage and diminish lung function [3,15,16]. Another cause of direct lung injury is mechanical tissue damage, such as pulmonary contusion and inhalation of injurious materials. Pulmonary contusions primarily contribute to ARDS in traumatic patients by priming the innate immune response and enhancing the activity of toll-like receptor 4 resulting in excess production of pro-inflammatory mediators [17,18]. Additionally, indirect

pulmonary injuries can be explained by the “2-hit hypothesis” which states that an inflammatory response related to extra-pulmonary area stimulus (first hit) is followed by systemic inflammatory response (second hit) that can induce lung injury. Common triggers of indirect lung injury induced by systemic inflammatory response include sepsis, shock, acute pancreatitis, bone fracture, and massive blood transfusion [19,20]. It has been shown that severe systemic inflammatory response resulting from sepsis produces numerous circulating inflammatory mediators. These mediators reach the bronchial and alveolar tissues and activate resident macrophages that attract inflammatory cells. Excess recruitment of immune cells not only occludes lung microcirculation but also releases cytotoxic products to damage surrounding tissues [21,22]. Moreover, the pathogenesis of transfusion-related acute lung injury (TRALI) occurs through antibody-dependent mechanisms. The first hit contributes to the underlying inflammatory condition of the patient. The second hit is related to antibodies in the transfused blood product [23]. Neutrophils are thought to mediate the development of TRALI. The antibodies from transfused blood components bind to the pulmonary endothelium followed by accumulation and activation of neutrophils. Activated neutrophils undergo respiratory burst and release ROS, release proteolytic enzymes by degranulation, and form NETs, which further contribute to lung inflammation [24].

## Role of neutrophils in ARDS

Our research, along with other studies, has provided insights into the pathogenic role of neutrophils in various inflammatory states, including sepsis and ARDS [25,26]. Neutrophils are the first immune cells recruited to the site of inflammation following stimulation by chemotactic factors released from damaged pulmonary tissues. Both exogenous and endogenous inflammatory stimuli can be recognized by specific receptors of human neutrophils. This further promotes the recruitment and activation of circulating neutrophils. These activated neutrophils produce several cytotoxic products, including ROS, granular enzymes, NETs, and various pro-inflammatory cytokines [27]. Moreover, these immune products trigger several chemotactic signals to induce positive feedback, further enhancing inflammation. The overwhelming activation of neutrophils contributes to surrounding tissue damage and even lung dysfunction [Fig. 1] [28]. In COVID-19 ARDS patients, higher counts of neutrophil are observed and represent a predictor of poor outcome [29]. Therefore, strategies to diminish neutrophils in lung tissue, including decreasing neutrophil recruitment and impairing neutrophil immune functions, have been predicted to attenuate lung injury.

## Neutrophil recruitment in ARDS

Neutrophil migration from the circulatory system into inflamed lung tissue can be initiated by both infectious and sterile inflammatory stimuli. Neutrophils attach to the vascular endothelium, and then migrate following a

chemokine gradient [30]. These chemoattractive signals are recognized by local immune cells, which produce inflammatory mediators that further boost neutrophil recruitment. In ARDS, endothelial cells activate and capture circulating neutrophils [31,32]. Neutrophils are sequestered through selectin-mediated binding, triggering “inside-out” activation of integrins, such as CD11a/CD18, which binds to intercellular adhesion molecules (ICAMs) from the endothelium [33].

Neutrophil rolling is a form of migration along the endothelial wall and is facilitated by specialized structure like membrane extensions and uropods. The rolling neutrophils become flattened and polarized to generate the forward-moving force, and then slowly crawl along the endothelial cells [34]. This slow rolling, or crawling, delays the neutrophils’ passage through the inflammatory tissue. This phenomenon augments neutrophil recruitment through chemokine signaling. Crawling neutrophils can either pass between the endothelial cells or through them to exit the vessel lumen. Finally, the migrating neutrophils detach from the vessel wall and move into the inflamed respiratory tissues [35–37].

Once activated, pulmonary neutrophils exhibit various immune responses, including increased nicotinamide adenine dinucleotide phosphate (NADPH) oxidase activity and release of proteolytic enzymes [38,39]. Overwhelming NADPH oxidase activity and proteolytic enzyme release are associated with surrounding respiratory tissue damage. Therefore, strategies to reduce neutrophil migration may be useful in the alleviation of pulmonary tissue damage [40,41]. Consistently, several chemical compounds were shown to diminish neutrophil migration in animal models. Decreasing neutrophil recruitment decreases production of cytotoxic

mediators [42,43], whereas increased neutrophils in pulmonary tissue demonstrably contributes to the pathogenesis of ARDS. Notably, studies of human and animals with neutropenia and ARDS showed poor recovery [11,12]. Evidences that neutrophils promoted both pulmonary inflammation and repair explain these findings. Neutrophils participate in the remodeling of damaged lung tissue through release of MMP-9 and the Wnt/ $\beta$ -catenin pathway [44,45]. The role of neutrophil recruitment in ARDS is complex and still needs to be explored.

### ARDS and neutrophil oxidative stress

In response to infectious and sterile stimuli, neutrophils contribute to the progression of ARDS through the assembly and activation of the ROS-producing NADPH oxidase complex (NOX2) [46,47]. NOX2, located on the membrane, reduces oxygen into superoxide anion and releases it outside the cell. Superoxide anion is highly reactive and spontaneously dismutates into a more stable hydrogen peroxide ( $H_2O_2$ ).  $H_2O_2$  can pass through cell membrane and distribute to either extracellular or intracellular areas. The enzyme myeloperoxidase uses  $H_2O_2$  to produce a series of more reactive products, including hydroxyl radicals and hypochlorous acid [48,49]. ROS are harmful to pulmonary tissues, indicating that reducing ROS production is beneficial to mitigate lung inflammatory injury [50,51]. SARS-CoV-2 infections cause redox imbalance and induce ROS accumulation. Oxidative stress produced from downregulation of superoxide dismutase 3 expression in lung tissues is observed in elderly patients with

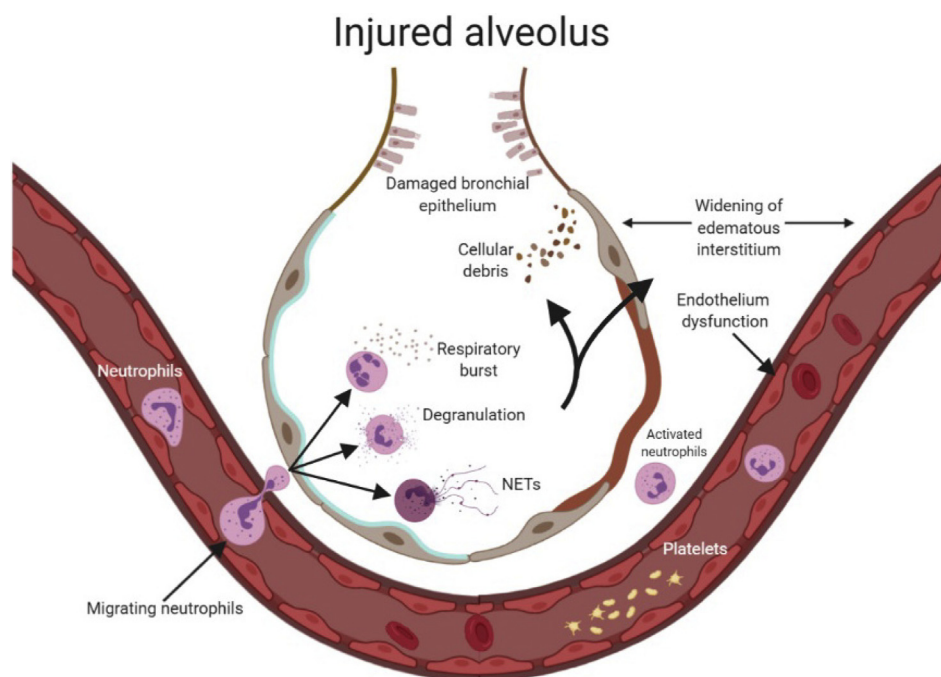


Fig. 1 Schematic diagram of neutrophil-mediated lung injury. Neutrophils migrate to inflamed lung tissue. This is followed by respiratory burst, degranulation, and NET formation in an injured alveolus. These immune responses lead to bronchial epithelial damage, cell debris production from dying cells attracting more immune cells, and endothelium dysfunction causing widening of edematous interstitium, further impairing oxygenation.



COVID-19, and the oxidative damage is closely related to poor outcome in elderly COVID-19 patients [52,53].

Several mechanisms of ROS are known. First, ROS directly damages the DNA of target cells. Previous research has shown that ROS produced from activated neutrophils induces oxidative DNA damage in respiratory epithelial cells [54,55]. Moreover, hyperoxia with 95% oxygen induces either neutrophil influx or oxidative DNA damage in neonate lung epithelial cells [56]. Second, ROS triggers peroxidation of lipid membranes, thus contributing to target cell lysis. The products of lipid peroxidation are also used as a measure of the level of tissue injury. In animal lung injury models, the level of lipid peroxidation was related to the severity of pulmonary tissue injury [57,58]. Third, ROS induces intracellular protein phosphorylation and transcription factor activation to promote the release of pro-inflammatory mediators. For instance, mitogen-activated protein (MAP) kinases can be activated by ROS to mediate cell death in response to stress, suggesting that the phosphorylation of MAP kinases have a major role in promotion of lung inflammatory injury [59,60]. Moreover, ROS triggers the activation of NF- $\kappa$ B, an important transcription factor that controls pro-inflammatory mediator release, to augment lung inflammatory injuries [61,62]. Research on the anti-oxidant  $\alpha$ -tocopherol showed that ROS production and related expression of NF- $\kappa$ B in activated neutrophils was decreased, and lung inflammatory injury was ameliorated in the presence of  $\alpha$ -tocopherol [63]. Similarity, another study showed that paraquat, an oxidant inducer, triggered ROS generation and release of inflammatory mediators, such as TNF- $\alpha$ , and IL-1 $\beta$ . The mechanisms of paraquat to heighten lung inflammation included activation of Jun N-terminal kinase (JNK) MAP kinase and NF- $\kappa$ B [64]. ROS damages the pulmonary endothelium, which is the barrier between the blood and vessels. Intracellular calcium signals are activated by ROS to increase endothelium permeability during pulmonary inflammatory process [65,66]. Cooperatively, neutrophil oxidative stress induces pulmonary endothelial and epithelial barrier dysfunctions. Barrier dysfunction increases neutrophil infiltration into lung tissues, and then these accumulated pulmonary neutrophils secrete several cytotoxic agents followed by worsening of pulmonary tissue damage, further enhancing the progression of ARDS [67].

#### ARDS and neutrophil degranulation

Neutrophil granules contain both pro- and anti-inflammatory substances that can be released to kill pathogens or for remodeling tissues. This process is called degranulation [68,69]. Neutrophils release membrane-bound vesicles, which contain various types of cytoplasmic granules associated with the progression of ARDS. The primary granules (also known as azurophilic granules) contain myeloperoxidase and many proteolytic proteins, including neutrophil elastase and cathepsin G. These granular proteins play major roles in microbicidal responses [70]. The secondary granules contain proteins that degrade the extracellular matrix. The tertiary granules contain few antimicrobials but store several metalloproteases [71,72]. During the inflammatory process, signals from receptors on the plasma membrane are transduced to the cytoplasm, which trigger the delivery of granule-

associated proteins to the cell surface and secretion of their contents out of the cells. The regulation mechanisms are numerous, including calcium signaling, src family kinases, MAP kinases, and GTPase-related signaling [73,74].

Neutrophilic infiltration into respiratory inflammatory tissues is a means of defending the host against pathogens, however, overwhelming extracellular release of neutrophil granular enzymes have been implicated in triggering collateral pulmonary tissue damage in ARDS [75,76]. Neutrophil elastase is a primary granular proteolytic enzyme and impacts lung inflammatory injury. Elastase can degrade pulmonary extracellular matrix proteins and cleave epithelial-cadherin to break respiratory cell-cell adhesion. Moreover, elastase has been shown to damage pulmonary vascular endothelial glycocalyx during the pulmonary inflammatory process [77–79]. Myeloperoxidase, the other primary granular enzyme, catalyzes H<sub>2</sub>O<sub>2</sub> to produce toxic ROS, which has been demonstrated to be a local mediator of alveolar damage [80]. The family of matrix metalloproteinases (MMPs) are released from the secondary and tertiary granules. Previous research showed that the expression of MMPs was correlated with the progression of ARDS. The enhanced expression of MMPs was related to inflammation-induced endothelial injury and impaired oxygenation in ARDS [81,82]. Another study revealed that MMP inhibitors suppressed MMP expression in plasma and lung tissue, decreased inflammatory mediator release, and attenuated lung inflammatory injury [83,84].

#### ARDS and NET formation

NETs are extracellular fibrous net-like structures, which have neutrophil granular proteins, such as myeloperoxidase or neutrophil elastase, coated on the backbone structures of DNA [85,86]. The mechanisms that induce NET formation have been explored, but signaling pathways involved are not completely understood. Raf/MEK/Erk signaling is activated to induce ROS production in the process of NET formation. Upon activation, the granular enzymes, myeloperoxidase and elastase, are released into the nucleus to induce nuclear disintegration. These granular enzymes coupled with PAD4 trigger chromatin decondensation and release. This mixture of granular enzymes and chromatin is expelled, followed by cell membrane rupture [87–89].

NETs are thought to be part of an innate immune mechanism for pathogen clearance; however, there are increasing concerns about the potential of NETs to initiate and propagate inflammatory damages in host tissues. Interestingly, both sterile and infective inflammations promote NET formation. During sterile inflammation, the components of NETs were found in lung and plasma of TRALI patients and mice. Treatment with DNase 1 decreased NET formation and lung injury [90,91]. Moreover, NET formation was observed in ventilator-induced lung injury. Previous human and animal studies showed that NET formation in the alveolar space was higher in bronchoalveolar lavage fluid from subjects with ventilator-induced ARDS. However, decreasing NET formation was not related to the shortening of mechanical ventilation [92–94]. During infective inflammation, NETs captured respiratory syncytial virus or influenza virus particles in patients and mice with respiratory infection. Nevertheless, cumulative



NET formation not only obstructed small airways, but also damaged alveolar–capillary to induce lung inflammatory injury [95–97]. The characteristics of lung tissue in ARDS demonstrated intensive neutrophil infiltration of lung tissue and NETs entwined with alveoli were exhibited in infected mice. The progression of inflammation further induced alveolar damage and pulmonary edema. Treatment with DNase I degraded NETs and reduced inflammatory cytokines, indicating that decreasing NET formation ameliorated lung injury and improved survival [98–100].

The severity and mortality of COVID-19 ARDS are correlated to higher neutrophil counts and NET level [29,101]. NETs play a significant role in producing a cytokine storm [102,103]. Furthermore, NETs have the ability to trigger immunothrombosis. The pulmonary capillary from patients with COVID-19 ARDS is filled with microthrombus and NETs. Microthrombi and fibrin deposition in lungs results in reduced oxygenation and further induces ARDS in COVID-19 patients [104–106].

## Conclusion

Although neutrophil immune responses are involved in ARDS, many questions remain unanswered. Neutrophils produce pro-inflammatory mediators and also augment inflammatory damage, implying that targeting neutrophils is a potential therapeutic for ARDS and COVID-19. However, on the basis of evidence supporting the fact that neutropenia does not attenuate ARDS, perhaps neutrophils play different roles in various phases of acute inflammation. The eventual goal is to determine when and how neutrophil activation is beneficial so as to tilt the balance toward benefit rather than harm.

## Conflicts of interest

The authors declare no competing financial interests.

## Acknowledgements

This research was supported by the grants from the Ministry of Science Technology (MOST 107-2320-B-075-001-MY3, MOST 108-2320-B-255-003-MY3, MOST 109-2327-B-182-002, and MOST 109-2327-B-255-001). The funders had no role in the study design, data collection and analysis, decision to publish, or preparation of the manuscript.

## REFERENCES

- [1] Pham T, Rubenfeld GD. Fifty years of research in ARDS. The epidemiology of acute respiratory distress syndrome. A 50th birthday review. *Am J Respir Crit Care Med* 2017;195:860–70.
- [2] Sigurdsson MI, Sigvaldason K, Gunnarsson TS, Moller A, Sigurdsson GH. Acute respiratory distress syndrome: nationwide changes in incidence, treatment and mortality over 23 years. *Acta Anaesthesiol Scand* 2013;57:37–45.
- [3] Huang C, Wang Y, Li X, Ren L, Zhao J, Hu Y, et al. Clinical features of patients infected with 2019 novel coronavirus in Wuhan, China. *Lancet* 2020;395:497–506.
- [4] Wu C, Chen X, Cai Y, Xia J, Zhou X, Xu S, et al. Risk factors associated with acute respiratory distress syndrome and death in patients with coronavirus disease 2019 pneumonia in Wuhan, China. *JAMA Intern Med* 2020;180:1–11.
- [5] Bernard GR, Artigas A, Brigham KL, Carlet J, Falke K, Hudson L, et al. The American-European Consensus Conference on ARDS. Definitions, mechanisms, relevant outcomes, and clinical trial coordination. *Am J Respir Crit Care Med* 1994;149:818–24.
- [6] Force ADT, Ranieri VM, Rubenfeld GD, Thompson BT, Ferguson ND, Caldwell E, et al. Acute respiratory distress syndrome: the Berlin Definition. *J Am Med Assoc* 2012;307:2526–33.
- [7] Papazian L, Calfee CS, Chiumello D, Luyt CE, Meyer NJ, Sekiguchi H, et al. Diagnostic workup for ARDS patients. *Intensive Care Med* 2016;42:674–85.
- [8] Bourenne J, Carvelli J, Papazian L. Evolving definition of acute respiratory distress syndrome. *J Thorac Dis* 2019;11:S390–3.
- [9] Zemans RL, Matthay MA. What drives neutrophils to the alveoli in ARDS? *Thorax* 2017;72:1–3.
- [10] Paris AJ, Liu Y, Mei J, Dai N, Guo L, Spruce LA, et al. Neutrophils promote alveolar epithelial regeneration by enhancing type II pneumocyte proliferation in a model of acid-induced acute lung injury. *Am J Physiol Lung Cell Mol Physiol* 2016;311:L1062–75.
- [11] Yacoub AT, Mojica L, Jones L, Knab A, Alrabaa S, Greene J. The role of corticosteroids in adult respiratory distress syndrome caused by viridans group streptococci bacteremia in neutropenic patients. *Mediterr J Hematol Infect Dis* 2014;6:e2014055.
- [12] Mokart D, van Craenenbroeck T, Lambert J, Textoris J, Brun JP, Sannini A, et al. Prognosis of acute respiratory distress syndrome in neutropenic cancer patients. *Eur Respir J* 2012;40:169–76.
- [13] Gotts JE, Bernard O, Chun L, Croze RH, Ross JT, Nessler N, et al. Clinically relevant model of pneumococcal pneumonia, ARDS, and nonpulmonary organ dysfunction in mice. *Am J Physiol Lung Cell Mol Physiol* 2019;317:L717–36.
- [14] Shah RD, Wunderink RG. Viral pneumonia and acute respiratory distress syndrome. *Clin Chest Med* 2017;38:113–25.
- [15] Yelleswaram S, Smith P, Burn T, Covington M, Juvekar A, Li Y, et al. Inhibition of cytokine signaling by ruxolitinib and implications for COVID-19 treatment. *Clin Immunol* 2020;218:108517.
- [16] McElvaney OJ, McEvoy N, McElvaney OF, Carroll TP, Murphy MP, Dunlea DM, et al. Characterization of the inflammatory response to severe COVID-19 illness. *Am J Respir Crit Care Med* 2020;202:812–21.
- [17] Hoth JJ, Martin RS, Yoza BK, Wells JD, Meredith JW, McCall CE. Pulmonary contusion primes systemic innate immunity responses. *J Trauma* 2009;67:14–21.
- [18] Daurat A, Millet I, Roustau JP, Maury C, Taourel P, Jaber S, et al. Thoracic Trauma Severity score on admission allows to determine the risk of delayed ARDS in trauma patients with pulmonary contusion. *Injury* 2016;47:147–53.
- [19] Eworuke E, Major JM, Gilbert McClain LI. National incidence rates for acute respiratory distress syndrome (ARDS) and ARDS cause-specific factors in the United States (2006–2014). *J Crit Care* 2018;47:192–7.
- [20] Hoegl S, Burns N, Angulo M, Francis D, Osborne CM, Mills TW, et al. Capturing the multifactorial nature of ARDS - "Two-hit" approach to model murine acute lung injury. *Phys Rep* 2018;6:e13648.

- [21] Deitch EA. Gut-origin sepsis: evolution of a concept. *Surgeon* 2012;10:350–6.
- [22] Whitney JE, Zhang B, Koterba N, Chen F, Bush J, Graham K, et al. Systemic endothelial activation is associated with early acute respiratory distress syndrome in children with extrapulmonary sepsis. *Crit Care Med* 2020;48:344–52.
- [23] Roubinian N. TACO and TRALI: biology, risk factors, and prevention strategies. *Hematology Am Soc Hematol Educ Program* 2018;2018:585–94.
- [24] Jongerius I, Porcelijn L, van Beek AE, Semple JW, van der Schoot CE, Vlaar APJ, et al. The role of complement in transfusion-related acute lung injury. *Transfus Med Rev* 2019;33:236–42.
- [25] Polverino E, Rosales-Mayor E, Dale GE, Dembowski K, Torres A. The role of neutrophil elastase inhibitors in lung diseases. *Chest* 2017;152:249–62.
- [26] Yang SC, Chang SH, Hsieh PW, Huang YT, Ho CM, Tsai YF, et al. Dipeptide HCH6-1 inhibits neutrophil activation and protects against acute lung injury by blocking FPR1. *Free Radic Biol Med* 2017;106:254–69.
- [27] Yang SC, Chen PJ, Chang SH, Weng YT, Chang FR, Chang KY, et al. Luteolin attenuates neutrophilic oxidative stress and inflammatory arthritis by inhibiting Raf1 activity. *Biochem Pharmacol* 2018;154:384–96.
- [28] Aulakh GK. Neutrophils in the lung: "the first responders". *Cell Tissue Res* 2018;371:577–88.
- [29] Liu Y, Du X, Chen J, Jin Y, Peng L, Wang HHX, et al. Neutrophil-to-lymphocyte ratio as an independent risk factor for mortality in hospitalized patients with COVID-19. *J Infect* 2020;81:e6–12.
- [30] Williams AE, Jose RJ, Mercer PF, Brealey D, Parekh D, Thickett DR, et al. Evidence for chemokine synergy during neutrophil migration in ARDS. *Thorax* 2017;72:66–73.
- [31] Zindel J, Kubes P. DAMPs, PAMPs, and LAMPs in immunity and sterile inflammation. *Annu Rev Pathol* 2020;15:493–518.
- [32] Vassallo A, Wood AJ, Subburayalu J, Summers C, Chilvers ER. The counter-intuitive role of the neutrophil in the acute respiratory distress syndrome. *Br Med Bull* 2019;131:43–55.
- [33] Lam FW, Da Q, Guillory B, Cruz MA. Recombinant human vimentin binds to P-selectin and blocks neutrophil capture and rolling on platelets and endothelium. *J Immunol* 2018;200:1718–26.
- [34] Hind LE, Vincent WJ, Huttenlocher A. Leading from the back: the role of the uropod in neutrophil polarization and migration. *Dev Cell* 2016;38:161–9.
- [35] Proebstl D, Voisin MB, Woodfin A, Whiteford J, D'Acquisto F, Jones GE, et al. Pericytes support neutrophil subendothelial cell crawling and breaching of venular walls in vivo. *J Exp Med* 2012;209:1219–34.
- [36] Matsumoto M, Hirata T. Moesin regulates neutrophil rolling velocity in vivo. *Cell Immunol* 2016;304–305:59–62.
- [37] Maas SL, Soehnlein O, Viola JR. Organ-specific mechanisms of transendothelial neutrophil migration in the lung, liver, kidney, and aorta. *Front Immunol* 2018;9:2739.
- [38] Zhao C, Itagaki K, Gupta A, Odom S, Sandler N, Hauser CJ. Mitochondrial damage-associated molecular patterns released by abdominal trauma suppress pulmonary immune responses. *J Trauma Acute Care Surg* 2014;76:1222–7.
- [39] Endo D, Fujimoto K, Hirose R, Yamanaka H, Homme M, Ishibashi KI, et al. Genetic phagocyte NADPH oxidase deficiency enhances nonviable *Candida albicans*-induced inflammation in mouse lungs. *Inflammation* 2017;40:123–35.
- [40] Qin X, Zhu G, Huang L, Zhang W, Huang Y, Xi X. LL-37 and its analog FF/CAP18 attenuate neutrophil migration in sepsis-induced acute lung injury. *J Cell Biochem* 2019;120:4863–71.
- [41] Faller S, Hausler F, Goefl A, von Itter MA, Gyllenram V, Hoetzel A, et al. Hydrogen sulfide limits neutrophil transmigration, inflammation, and oxidative burst in lipopolysaccharide-induced acute lung injury. *Sci Rep* 2018;8:14676.
- [42] Chen CY, Tsai YF, Huang WJ, Chang SH, Hwang TL. Propofol inhibits endogenous formyl peptide-induced neutrophil activation and alleviates lung injury. *Free Radic Biol Med* 2018;129:372–82.
- [43] Baudiss K, de Paula Vieira R, Cicko S, Ayata K, Hossfeld M, Ehrat N, et al. C1P attenuates lipopolysaccharide-induced acute lung injury by preventing NF-kappaB activation in neutrophils. *J Immunol* 2016;196:2319–26.
- [44] Blazquez-Prieto J, Lopez-Alonso I, Amado-Rodriguez L, Huidobro C, Gonzalez-Lopez A, Kuebler WM, et al. Impaired lung repair during neutropenia can be reverted by matrix metalloproteinase-9. *Thorax* 2018;73:321–30.
- [45] Zemans RL, Briones N, Campbell M, McClendon J, Young SK, Suzuki T, et al. Neutrophil transmigration triggers repair of the lung epithelium via beta-catenin signaling. *Proc Natl Acad Sci USA* 2011;108:15990–5.
- [46] Nguyen GT, Green ER, Mecas J. Neutrophils to the ROScues: mechanisms of NADPH oxidase activation and bacterial resistance. *Front Cell Infect Microbiol* 2017;7:373.
- [47] Teixeira G, Szyndralewicz C, Molango S, Carnesecchi S, Heitz F, Wiesel P, et al. Therapeutic potential of NADPH oxidase 1/4 inhibitors. *Br J Pharmacol* 2017;174:1647–69.
- [48] Winterbourn CC, Kettle AJ, Hampton MB. Reactive oxygen species and neutrophil function. *Annu Rev Biochem* 2016;85:765–92.
- [49] Pak O, Sydykov A, Kosanovic D, Schermuly RT, Dietrich A, Schroder K, et al. Lung ischaemia-reperfusion injury: the role of reactive oxygen species. *Adv Exp Med Biol* 2017;967:195–225.
- [50] Wagner J, Strosing KM, Spassov SG, Lin Z, Engelstaedter H, Tacke S, et al. Sevoflurane posttreatment prevents oxidative and inflammatory injury in ventilator-induced lung injury. *PloS One* 2018;13:e0192896.
- [51] Nadeem A, Siddiqui N, Al-Harbi NO, Attia SM, AlSharari SD, Ahmad SF. Acute lung injury leads to depression-like symptoms through upregulation of neutrophilic and neuronal NADPH oxidase signaling in a murine model. *Int Immunopharm* 2017;47:218–26.
- [52] Abouhashem AS, Singh K, Azzazy HME, Sen CK. Is low alveolar type II cell SOD3 in the lungs of elderly linked to the observed severity of COVID-19? *Antioxid Redox Signal* 2020;33:59–65.
- [53] Silvagno F, Vernone A, Pescarmona GP. The role of glutathione in protecting against the severe inflammatory response triggered by COVID-19. *Antioxidants* 2020;9:624.
- [54] Gould NS, White CW, Day BJ. A role for mitochondrial oxidative stress in sulfur mustard analog 2-chloroethyl ethyl sulfide-induced lung cell injury and antioxidant protection. *J Pharmacol Exp Ther* 2009;328:732–9.
- [55] Park JS, Park YJ, Kim HR, Chung KH. Polyhexamethylene guanidine phosphate-induced ROS-mediated DNA damage caused cell cycle arrest and apoptosis in lung epithelial cells. *J Toxicol Sci* 2019;44:415–24.
- [56] Auten RL, Whorton MH, Nicholas Mason S. Blocking neutrophil influx reduces DNA damage in hyperoxia-exposed newborn rat lung. *Am J Respir Cell Mol Biol* 2002;26:391–7.
- [57] Binder CJ, Papac-Milicevic N, Witztum JL. Innate sensing of oxidation-specific epitopes in health and disease. *Nat Rev Immunol* 2016;16:485–97.
- [58] Fukuhara K, Nakashima T, Abe M, Masuda T, Hamada H, Iwamoto H, et al. Suplatast tosilate protects the lung against

- hyperoxic lung injury by scavenging hydroxyl radicals. *Free Radic Biol Med* 2017;106:1–9.
- [59] Usatyuk PV, Vepa S, Watkins T, He D, Parinandi NL, Natarajan V. Redox regulation of reactive oxygen species-induced p38 MAP kinase activation and barrier dysfunction in lung microvascular endothelial cells. *Antioxid Redox Signal* 2003;5:723–30.
- [60] Dias-Freitas F, Metelo-Coimbra C, Roncon-Albuquerque Jr R. Molecular mechanisms underlying hyperoxia acute lung injury. *Respir Med* 2016;119:23–8.
- [61] Jiang K, Guo S, Yang C, Yang J, Chen Y, Shaikat A, et al. Barbaloin protects against lipopolysaccharide (LPS)-induced acute lung injury by inhibiting the ROS-mediated PI3K/AKT/NF-kappaB pathway. *Int Immunopharm* 2018;64:140–50.
- [62] Wang J, Huang J, Wang L, Chen C, Yang D, Jin M, et al. Urban particulate matter triggers lung inflammation via the ROS-MAPK-NF-kappaB signaling pathway. *J Thorac Dis* 2017;9:4398–412.
- [63] Rocksen D, Ekstrand-Hammarstrom B, Johansson L, Bucht A. Vitamin E reduces transendothelial migration of neutrophils and prevents lung injury in endotoxin-induced airway inflammation. *Am J Respir Cell Mol Biol* 2003;28:199–207.
- [64] Shen H, Wu N, Wang Y, Han X, Zheng Q, Cai X, et al. JNK inhibitor SP600125 attenuates paraquat-induced acute lung injury: an in vivo and in vitro study. *Inflammation* 2017;40:1319–30.
- [65] Di A, Mehta D, Malik AB. ROS-activated calcium signaling mechanisms regulating endothelial barrier function. *Cell Calcium* 2016;60:163–71.
- [66] Liu XY, Xu HX, Li JK, Zhang D, Ma XH, Huang LN, et al. Neferine protects endothelial glycocalyx via mitochondrial ROS in lipopolysaccharide-induced acute respiratory distress syndrome. *Front Physiol* 2018;9:102.
- [67] Kellner M, Noonepalle S, Lu Q, Srivastava A, Zemskov E, Black SM. ROS signaling in the pathogenesis of acute lung injury (ALI) and acute respiratory distress syndrome (ARDS). *Adv Exp Med Biol* 2017;967:105–37.
- [68] Lacy P. Mechanisms of degranulation in neutrophils. *Allergy Asthma Clin Immunol* 2006;2:98–108.
- [69] Mollinedo F. Neutrophil degranulation, plasticity, and cancer metastasis. *Trends Immunol* 2019;40:228–42.
- [70] Bedouhene S, Dang PM, Hurtado-Nedelec M, El-Benna J. Neutrophil degranulation of azurophil and specific granules. *Methods Mol Biol* 2020;2087:215–22.
- [71] Soehnlein O. Multiple roles for neutrophils in atherosclerosis. *Circ Res* 2012;110:875–88.
- [72] Pham CT. Neutrophil serine proteases: specific regulators of inflammation. *Nat Rev Immunol* 2006;6:541–50.
- [73] Miranda-Ribera A, Lecchi C, Bronzo V, Scaccabarozzi L, Sartorelli P, Franciosi F, et al. Down-regulatory effect of alpha 1-acid glycoprotein on bovine neutrophil degranulation. *Comp Immunol Microbiol Infect Dis* 2010;33:291–306.
- [74] Armstrong CL, Miralda I, Neff AC, Tian S, Vashishta A, Perez L, et al. Filifactor alocis promotes neutrophil degranulation and chemotactic activity. *Infect Immun* 2016;84:3423–33.
- [75] Rebetz J, Semple JW, Kapur R. The pathogenic involvement of neutrophils in acute respiratory distress syndrome and transfusion-related acute lung injury. *Transfus Med Hemother* 2018;45:290–8.
- [76] Moraes TJ, Zurawska JH, Downey GP. Neutrophil granule contents in the pathogenesis of lung injury. *Curr Opin Hematol* 2006;13:21–7.
- [77] Mebratu YA, Tesfaigzi Y. IL-17 plays a role in respiratory syncytial virus-induced lung inflammation and emphysema in elastase and LPS-injured mice. *Am J Respir Cell Mol Biol* 2018;58:717–26.
- [78] Suzuki K, Okada H, Takemura G, Takada C, Kuroda A, Yano H, et al. Neutrophil elastase damages the pulmonary endothelial glycocalyx in lipopolysaccharide-induced experimental endotoxemia. *Am J Pathol* 2019;189:1526–35.
- [79] Boxio R, Wartelle J, Nawrocki-Raby B, Lagrange B, Malleret L, Hirche T, et al. Neutrophil elastase cleaves epithelial cadherin in acutely injured lung epithelium. *Respir Res* 2016;17:129.
- [80] Aratani Y. Myeloperoxidase: its role for host defense, inflammation, and neutrophil function. *Arch Biochem Biophys* 2018;640:47–52.
- [81] Fligiel SE, Standiford T, Fligiel HM, Tashkin D, Strieter RM, Warner RL, et al. Matrix metalloproteinases and matrix metalloproteinase inhibitors in acute lung injury. *Hum Pathol* 2006;37:422–30.
- [82] Zinter MS, Delucchi KL, Kong MY, Orwoll BE, Spicer AS, Lim MJ, et al. Early plasma matrix metalloproteinase profiles. A novel pathway in pediatric acute respiratory distress syndrome. *Am J Respir Crit Care Med* 2019;199:181–9.
- [83] Wang CT, Zhang L, Wu HW, Wei L, Xu B, Li DM. Doxycycline attenuates acute lung injury following cardiopulmonary bypass: involvement of matrix metalloproteinases. *Int J Clin Exp Pathol* 2014;7:7460–8.
- [84] Albaiceta GM, Gutierrez-Fernandez A, Garcia-Prieto E, Puente XS, Parra D, Astudillo A, et al. Absence or inhibition of matrix metalloproteinase-8 decreases ventilator-induced lung injury. *Am J Respir Cell Mol Biol* 2010;43:555–63.
- [85] Van Avondt K, Hartl D. Mechanisms and disease relevance of neutrophil extracellular trap formation. *Eur J Clin Invest* 2018;48:e12919.
- [86] Brinkmann V, Reichard U, Goosmann C, Fauler B, Uhlemann Y, Weiss DS, et al. Neutrophil extracellular traps kill bacteria. *Science* 2004;303:1532–5.
- [87] Hakkim A, Fuchs TA, Martinez NE, Hess S, Prinz H, Zychlinsky A, et al. Activation of the Raf-MEK-ERK pathway is required for neutrophil extracellular trap formation. *Nat Chem Biol* 2011;7:75–7.
- [88] Papayannopoulos V. Neutrophil extracellular traps in immunity and disease. *Nat Rev Immunol* 2018;18:134–47.
- [89] Burgerer SS, Schroder K. Neutrophil extracellular traps in host defense. *Cold Spring Harb Perspect Biol* 2020;12:a037028.
- [90] Caudrillier A, Kessenbrock K, Gilliss BM, Nguyen JX, Marques MB, Monestier M, et al. Platelets induce neutrophil extracellular traps in transfusion-related acute lung injury. *J Clin Invest* 2012;122:2661–71.
- [91] Thomas GM, Carbo C, Curtis BR, Martinod K, Mazo IB, Schatzberg D, et al. Extracellular DNA traps are associated with the pathogenesis of TRALI in humans and mice. *Blood* 2012;119:6335–43.
- [92] Bendib I, de Chaisemartin L, Granger V, Schlemmer F, Maitre B, Hue S, et al. Neutrophil extracellular traps are elevated in patients with pneumonia-related acute respiratory distress syndrome. *Anesthesiology* 2019;130:581–91.
- [93] Yildiz C, Palaniyar N, Otulakowski G, Khan MA, Post M, Kuebler WM, et al. Mechanical ventilation induces neutrophil extracellular trap formation. *Anesthesiology* 2015;122:864–75.
- [94] Mikacenic C, Moore R, Dmyterko V, West TE, Altemeier WA, Liles WC, et al. Neutrophil extracellular traps (NETs) are increased in the alveolar spaces of patients with ventilator-associated pneumonia. *Crit Care* 2018;22:358.
- [95] Cortjens B, de Boer OJ, de Jong R, Antonis AF, Sabogal Pineros YS, Lutter R, et al. Neutrophil extracellular traps cause airway obstruction during respiratory syncytial virus disease. *J Pathol* 2016;238:401–11.

- [96] Juliana A, Zonneveld R, Plotz FB, van Meurs M, Wilschut J. Neutrophil-endothelial interactions in respiratory syncytial virus bronchiolitis: an understudied aspect with a potential for prediction of severity of disease. *J Clin Virol* 2020;123:104258.
- [97] Ashar HK, Mueller NC, Rudd JM, Snider TA, Achanta M, Prasanthi M, et al. The role of extracellular histones in influenza virus pathogenesis. *Am J Pathol* 2018;188:135–48.
- [98] Liu S, Su X, Pan P, Zhang L, Hu Y, Tan H, et al. Neutrophil extracellular traps are indirectly triggered by lipopolysaccharide and contribute to acute lung injury. *Sci Rep* 2016;6:37252.
- [99] Gan TT, Yang YL, Hu F, Chen XC, Zhou JW, Li Y, et al. TLR3 regulated poly I:C-induced neutrophil extracellular traps and acute lung injury partly through p38 MAP kinase. *Front Microbiol* 2018;9:3174.
- [100] Lefrancais E, Mallavia B, Zhuo HJ, Calfee CS, Looney MR. Maladaptive role of neutrophil extracellular traps in pathogen-induced lung injury. *JCI Insight* 2018;3:e98178.
- [101] Terpos E, Ntanas-Stathopoulos I, Elalamy I, Kastiris E, Sergeantanis TN, Politou M, et al. Hematological findings and complications of COVID-19. *Am J Hematol* 2020;95:834–47.
- [102] Barnes BJ, Adrover JM, Baxter-Stoltzfus A, Borczuk A, Cools-Lartigue J, Crawford JM, et al. Targeting potential drivers of COVID-19: neutrophil extracellular traps. *J Exp Med* 2020;217:e20200652.
- [103] Zuo Y, Yalavarthi S, Shi H, Gockman K, Zuo M, Madison JA, et al. Neutrophil extracellular traps in COVID-19. *JCI Insight* 2020;5:e138999.
- [104] Whyte CS, Morrow GB, Mitchell JL, Chowdary P, Mutch NJ. Fibrinolytic abnormalities in acute respiratory distress syndrome (ARDS) and versatility of thrombolytic drugs to treat COVID-19. *J Thromb Haemost* 2020;18:1548–55.
- [105] Zhang H, Zhou P, Wei Y, Yue H, Wang Y, Hu M, et al. Histopathologic changes and SARS-CoV-2 immunostaining in the lung of a patient with COVID-19. *Ann Intern Med* 2020;172:629–32.
- [106] Middleton EA, He XY, Denorme F, Campbell RA, Ng D, Salvatore SP, et al. Neutrophil extracellular traps (NETs) contribute to immunothrombosis in COVID-19 acute respiratory distress syndrome. *Blood* 2020;136:1169–79.





## Characterisation of teaghrelin-like principles from Assam tea cultivated in Thailand

Yue-Chiun Li<sup>a,b,\*</sup>, Chutima Tanapichatsakul<sup>b,c,\*</sup>, Patcharee Pripdeevech<sup>c</sup>,  
Tsong Long Hwang<sup>d,e,f</sup>, Ping-Chung Kuo<sup>a</sup> and Jason T. C. Tzen<sup>b</sup>

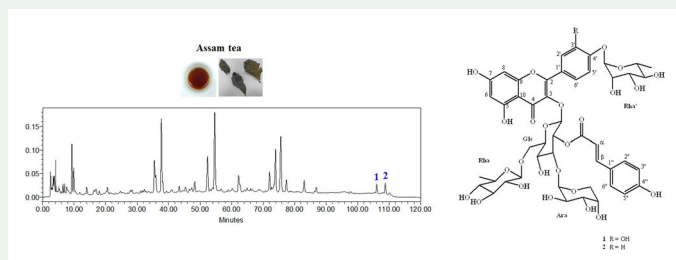
<sup>a</sup>School of Pharmacy, College of Medicine, National Cheng Kung University, Tainan, Taiwan;

<sup>b</sup>Graduate Institute of Biotechnology, National Chung-Hsing University, Taichung, Taiwan; <sup>c</sup>School of Science, Mae Fah Luang University, Thailand; <sup>d</sup>Graduate Institute of Natural Products, School of Traditional Chinese Medicine, College of Medicine, Chang Gung University, Taoyuan, Taiwan;

<sup>e</sup>Research Center for Industry of Human Ecology, Research Center for Chinese Herbal Medicine, Graduate Institute of Health Industry Technology, College of Human Ecology, Chang Gung University of Science and Technology, Taoyuan, Taiwan; <sup>f</sup>Department of Anesthesiology, Chang Gung Memorial Hospital, Taoyuan, Taiwan

### ABSTRACT

Teaghrelins were identified as unique acylated flavonoid tetraglycosides and firstly reported in Chin-shin oolong tea. In the present study, two new teaghrelin-like compounds (**1** and **2**) were purified and characterised from Assam tea varieties collected in Thailand. Their chemical structures were constructed by the spectroscopic and spectrometric analysis. These two teaghrelin-like compounds were also not supposed to exhibit significant ghrelin receptor affinity according to the structural comparison with those teaghrelin-like compounds previously reported. In addition, compounds **1** and **2** did not display notable anti-inflammatory activity in human neutrophils assay.



### ARTICLE HISTORY

Received 24 February 2020

Accepted 30 May 2020

### KEYWORDS


*Camellia sinensis* var. *assamica*; Assam tea; acylated flavonoid tetraglycoside; spectroscopic and spectrometric analysis; ghrelin receptor affinity

## 1. Introduction

The leaves of diversified *Camellia* species are usually produced as various tea products that are the most popular beverage in the world through different fermentation

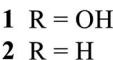
**CONTACT** Ping-Chung Kuo ✉ [z10502016@email.ncku.edu.tw](mailto:z10502016@email.ncku.edu.tw); Jason T. C. Tzen ✉ [tctzen@dragon.nchu.edu.tw](mailto:tctzen@dragon.nchu.edu.tw)

\*These authors contributed equally to this work.

 Supplemental data for this article can be accessed at <https://doi.org/10.1080/14786419.2020.1779715>.

© 2020 Informa UK Limited, trading as Taylor & Francis Group





Assam tea is a popular beverage and accompanies great economic value. For example, in India, around 256,000 tons of tea were exported and corresponding to a value of 786 million USD (BASIC, 2019). In northern Thailand, *Camellia sinensis* var.

*assamica* (Assam tea) and *C. sinensis* var. *sinensis* (Chinese tea) are the most common tea species (Dorkbuakaew et al. 2016; Khanongnuch et al. 2017). *C. sinensis* var. *assamica* is usually used to produce black tea and traditional ‘miang tea’, which possesses significant bioactivities (Dorkbuakaew et al. 2016; Khanongnuch et al. 2017). Twelve wild tea samples of *C. sinensis* var. *assamica* (Tzen-T12U01 ~ 12-2015) were collected from different regions in northern Thailand and analyzed preliminarily by HPLC (results were shown in Figure S1). According to our data, the extract of one tea cultivar (sample 5) contained relatively more abundant catechin derivatives which may be related to the presence of teaghrelin-like compounds, and some significant peaks could be observed in the regions of retention time at 100–110 min. Therefore, in the present study, we focussed on the purification of this tea sample and two new teaghrelin-like compounds were characterised through the comprehensive spectroscopic and spectrometric analysis.

## 2. Results and discussion

Compound **1** was isolated as optically active yellow solid with mp 214–215 °C and  $[\alpha]_D^{25} = -159$ . The molecular formula was determined as  $C_{47}H_{54}O_{26}$  by a sodium adduct ion peak at  $m/z$  1057.2758 in the HR-ESI-MS analytical data. The UV absorption maxima at 316 and 267 nm indicated the presence of a flavone skeleton (Mabry et al. 1970). The IR absorption bands at 3396 and  $1594\text{ cm}^{-1}$  corresponded with the presence of hydroxy and carbonyl groups. The  $^1\text{H-NMR}$  spectrum of **1** revealed ABX-coupled aromatic protons at  $\delta$  7.65 (1H, d,  $J = 2.5\text{ Hz}$ , H-2'), 7.59 (1H, dd,  $J = 8.5, 2.5\text{ Hz}$ , H-6') and 7.25 (1H, d,  $J = 8.5\text{ Hz}$ , H-5') and supported the trisubstituted B-ring. The flavone substructure was also suggested by the two *meta*-coupled broad singlets at  $\delta$  6.34 (1H, br s, H-8) and 6.16 (1H, br s, H-6). Furthermore, a set of proton signals at  $\delta$  7.68 (1H, d,  $J = 16.0\text{ Hz}$ , H- $\beta$ ), 7.45 (2H, d,  $J = 9.0\text{ Hz}$ , H-2'', -6''), 6.81 (2H, d,  $J = 9.0\text{ Hz}$ , H-3'', -5'') and 6.37 (1H, d,  $J = 16.0\text{ Hz}$ , H- $\alpha$ ) indicated the presence of *trans*-4-hydroxycinnamic acid moiety. In addition, D-glucose, L-rhamnose, L-arabinose, and L-rhamnose were identified by the  $^{13}\text{C-NMR}$  and DEPT analytical data (Table S1), and referenced to the corresponding coupling constants of anomeric protons at  $\delta$  5.56 (1H, d,  $J = 8.0\text{ Hz}$ ), 4.55 (1H, d,  $J = 1.5\text{ Hz}$ ), 4.33 (1H, d,  $J = 7.0\text{ Hz}$ ), and 5.56 (1H, d,  $J = 2.0\text{ Hz}$ ) (Manir et al. 2012), the configurations of sugar units were determined as  $\beta$ ,  $\alpha$ ,  $\alpha$ , and  $\alpha$ , respectively. The significant  $^2J$ - and  $^3J$ -HMBC correlation peaks from Glc H-1 to C-3, from Glc H-2 to *p*-coumaroyl C=O, from Rha H-1 to Glc C-6, from Ara H-1 to Glc C-3, and from Rha' H-1 to C-4' (as shown in Figure S2) established the connectivity of sugar moieties. The complete chemical structure elucidation of **1** was fully constructed by HMBC and NOESY experiments (Figure S2). Comparison of **1** with our published report (Li et al. 2019; Kuo et al. 2020), the spectral data of **1** is very similar to those published compounds but the different linkage of sugar moieties were observed. Conclusively, the structure of **1** was assigned as quercetin 3-*O*-[2''-*O*-(*E*)-*p*-coumaroyl][ $\alpha$ -L-arabinopyranosyl(1 $\rightarrow$ 3)- $\alpha$ -L-rhamnopyranosyl(1 $\rightarrow$ 6)]- $\beta$ -D-glucoside 4'- $\alpha$ -L-rhamnoside (Figure 1).

The chemical structure of **2** is similar to **1** but one oxygen atom less in the structure, which was evidenced by HR-ESI-MS analytical data ( $C_{47}H_{54}O_{25}$ ). The flavone

skeleton was determined as kaempferol based on the  $^1\text{H}$ -NMR spectral data, including  $\delta$  8.06 (2H, d,  $J=9.0$  Hz, H-2', 6'), 7.19 (2H, d,  $J=9.0$  Hz, H-3', 5'), 6.36 (1H, d,  $J=2.0$  Hz, H-8), and 6.17 (1H, d,  $J=2.0$  Hz, H-6), respectively. The sugar moieties of **2** were also identified as D-glucose, L-rhamnose, L-arabinose, and L-rhamnose according to the  $^{13}\text{C}$ -NMR and DEPT analysis (Manir et al. 2012), and as those in **1**, their configurations were determined as  $\beta$ ,  $\alpha$ ,  $\alpha$ , and  $\alpha$ , respectively. The connectivity of sugar fragments and complete assignments of all the proton and carbon signals of **2** were constructed by the comprehensive HMBC and NOESY experimental data as shown (Figure S2). Therefore, the chemical structure of **2** was established as kaempferol 3-O-[2''-O-(*E*)-*p*-coumaroyl][ $\alpha$ -L-arabinopyranosyl(1 $\rightarrow$ 3)- $\alpha$ -L-rhamnopyranosyl(1 $\rightarrow$ 6)]- $\beta$ -D-glucoside 4'- $\alpha$ -L-rhamnoside (Figure 1).

Recently our group had isolated several teaghrelin-like compounds from the natural sources. Compounds **3** and **4** were firstly characterised as teaghrelins in Chinshin oolong tea (Figure S3) (Lo et al. 2014). Furthermore, two similar compounds but different sugar moieties at C-3 of glucoside, were purified from Shy-jih-chuen oolong tea (**5** and **6**, as shown in Figure S3) (Li et al. 2019). Growth hormone-releasing peptide 6 (GHRP-6) is a synthetic analogue of ghrelin and could stimulate growth hormone secretion of rat primary anterior cells. Compounds **3-6** were demonstrated the similar stimulation with GHRP-6 in cell assay and could be combined to ghrelin receptor through the simulation results of molecular modelling and docking (Lo et al. 2014; Hsieh et al. 2015; Li et al. 2019). In addition, compounds **7** and **8** were identified in Jinxuan oolong tea (Kuo et al. 2020) and as compared with compounds **3-6**, one sugar moiety at C-3 of glucoside was disappeared but one more rhamnose was attached at the C-4' position of flavone basic skeleton. In our group a similar compound **9** was isolated from the wild tea cultivar collected from Liouguei, Kaohsiung, Taiwan, and its structure was characterized as one rhamnose substituted at the C-4' position of kaempferol backbone and two sugar moieties at C-3 of glucoside and C-3 of rhamnoside were vanished, respectively, which was previously reported and named trivially as camellikaempferoside B (**9**, as shown in Figure S3) (Yang et al. 2016).

According to the molecular docking results reported by our group, the attachment of a coumaroyl group was critical for binding to ghrelin receptor. However, the extra rhamnosyl substitution on the flavonoid backbone seemed to hinder its docking to ghrelin receptor (Hsieh et al. 2015). In the present research, two new teaghrelin-like compounds **1** and **2** were purified from *C. sinensis* var. *assamica* and their structures were similar to compounds **7-9** but lacking a glucose in C-3 of rhamnoside and one more arabinose attached to C-3 of glucoside. Nevertheless, the C-4' rhamnose substitution on the flavone skeleton of **1** and **2** may lead to unpractical ghrelin affinity. In addition, cellular model in isolated human neutrophils was used to evaluate the anti-inflammatory potential of the two new teaghrelin-like compounds **1** and **2** for their inhibitory effects on superoxide anion generation and elastase release by human neutrophils in response to *N*-formyl-L-methionyl-L-leucyl-L-phenylalanine/cytochalasin B (fMLF/CB) (Yu et al. 2011; Yang et al. 2013). However, compounds **1** and **2** did not display the significant anti-inflammatory bioactivity (Table S2).

### 3. Experimental

#### 3.1. General

The melting points was recorded on a WRX-4 melting-point apparatus without correction. Optical rotations were recorded on a Jasco P-2000 digital polarimeter. The UV spectra were obtained by a Hitachi U-2001 UV/Vis spectrometer. The IR spectra were examined with a Jasco P-2000 digital polarimeter.  $^1\text{H}$ -,  $^{13}\text{C}$ -, and 2D NMR spectra were recorded on the Bruker AV-500 spectrometers. Chemical shifts are shown in  $\delta$  values (ppm) with tetramethylsilane as an internal standard. The ESI-MS data were obtained on Shimadzu LC-8040 systems, and HR-ESI-MS were taken on a JEOL JMS-700 spectrometer (operated in the positive-ion mode). Column chromatography (CC) was performed on Sephadex LH-20 (Sigma-Aldrich) and LiChroprep® RP-18 gel (Sigma-Aldrich). High-performance liquid chromatography (HPLC) was performed on a Waters model 600E series pumping system equipped with a Waters 2996 photodiode array detector, and a Waters 717plus auto sampling system at ambient temperature. Waters fraction collector III was used for purification of teaghrelins.

#### 3.2. Chemicals and materials

All chemicals were purchased from E. Merck Co. (Merck KGaA, Darmstadt, Germany) unless stated otherwise. High-performance liquid chromatography (HPLC)-grade acetonitrile was bought from Fisher Scientific (Fair Lawn, NJ). Acetic acid (99.7%) was obtained from J. T. Baker (Mallinckrodt Baker, Inc., Phillipsburg, NJ). Methanol was purchased from Aencore Chemical PTY, LTD (Surrey Hills, Australia). Deuterated solvent methanol- $\text{d}_4$  was purchased from Sigma-Aldrich Co. (St. Louis, MO). Purified water was afforded by a Millipore clear water purification system (Direct-Q, Millipore, Billerica, MA). All the studied tea samples (samples 1–12, Tzen-T12U01 ~ 12-2015) were identified by Dr. Jason T.C. Tzen before extraction and analysis. A voucher specimen (Tzen-T12U05-2015) has been deposited in the Herbarium of Graduate Institute of Biotechnology, National Chung-Hsing University, Taichung, Taiwan.

#### 3.3. Extraction and isolation

Each wild tea sample (100 g) was immersed with 1 L 50% ethanol aqueous solution and sonicated for 30 min. After extraction for 3 times, the combined filtrates were concentrated in vacuo to obtain a brownish syrup. The crude extract was purified on a Sephadex LH-20 column and eluted with a step gradient of water and methanol (30, 40, 50, 60, 70, 80 and 100%) to afford seven fractions. The third and fourth fractions (50 and 60%) were combined and subjected to LiChroprep® RP-18 gel column eluted with water and a step gradient of methanol (40, 50, 60, 65, 70, 80 and 100%) to afford seven subfractions. The fourth subfraction (65%) was further purified by reversed-phase HPLC system with a Synchronis C18 column ( $250 \times 4.6$  mm,  $5\ \mu\text{m}$ ) to give **1** (1.3 mg) and **2** (3.4 mg). The mobile phase consisted of (A) acetonitrile and (B) water containing 0.5% acetic acid using a gradient elution of 5% A at 0 min, 20% A at 0–10 min, 30% A at 10–50 min, 5% A at 50–60 min, and ready for next collection. The

flow rate was 1.0 mL/min and each injection was 20  $\mu$ L at ambient temperature. The two acylated flavonoid tetraglycosides were monitored by the UV absorbance at 320 nm.

### 3.3.1. Quercetin 3-O-[2''-O-(E)-p-coumaroyl][ $\alpha$ -L-arabinopyranosyl(1 $\rightarrow$ 3)- $\alpha$ -L-rhamnopyranosyl(1 $\rightarrow$ 6)]- $\beta$ -D-glucoside 4'- $\alpha$ -L-rhamnoside (1)

Yellow solid; melting point: 213.5–215.0 °C (CH<sub>3</sub>OH);  $[\alpha]_D^{25}$  –159 (c 0.1, CH<sub>3</sub>OH); UV (CH<sub>3</sub>OH)  $\lambda_{\max}$  (log  $\epsilon$ ): 316 (4.45), 267 (4.35) nm; IR (neat)  $\nu_{\max}$  3396, 2922, 1594, 1509, 1448, 1363, 1259, 1164, 1072 cm<sup>–1</sup>; <sup>1</sup>H NMR and <sup>13</sup>C NMR, see Table S1; ESI-MS (*rel. int.* %)  $m/z$  1057 ([M + Na]<sup>+</sup>, 100); HR-ESI-MS  $m/z$  1057.2758 [M + Na]<sup>+</sup> (calcd for C<sub>47</sub>H<sub>54</sub>NaO<sub>26</sub>, 1057.2801).

### 3.3.2. Kaempferol 3-O-[2''-O-(E)-p-coumaroyl][ $\alpha$ -L-arabinopyranosyl(1 $\rightarrow$ 3)- $\alpha$ -L-rhamnopyranosyl(1 $\rightarrow$ 6)]- $\beta$ -D-glucoside 4'- $\alpha$ -L-rhamnoside (2)

Yellow solid; melting point: 201.4–203.7 °C (CH<sub>3</sub>OH);  $[\alpha]_D^{25}$  –119 (c 0.3, CH<sub>3</sub>OH); UV (CH<sub>3</sub>OH)  $\lambda_{\max}$  (log  $\epsilon$ ): 313 (4.38), 267 (4.26) nm; IR (neat)  $\nu_{\max}$  3411, 2928, 1651, 1604, 1509, 1250, 1171, 1072 cm<sup>–1</sup>; <sup>1</sup>H NMR and <sup>13</sup>C NMR, see Table S1; ESI-MS (*rel. int.* %)  $m/z$  1041 ([M + Na]<sup>+</sup>, 100); HR-ESI-MS  $m/z$  1041.2844 [M + Na]<sup>+</sup> (calcd for C<sub>47</sub>H<sub>54</sub>NaO<sub>25</sub>, 1041.2852).

## Acknowledgements

The authors gratefully acknowledge the use of 500NMR of the machine equipment belonging to the Instrument Center of National Cheng Kung University.

## Disclosure statement

No potential conflict of interest was reported by the authors.

## Funding

The present research was supported by a grant from the Ministry of Science and Technology, Taiwan (MOST 108-2622-8-005-002-TB1 awarded to JTC Tzen).

## References

- Bureau for the Analysis of Societal Impacts for Citizen information (BASIC). 2019. Study of Assam tea value chains. Available from: [https://www.tandf.co.uk/journals/authors/style/reference/tf\\_CSE.pdf](https://www.tandf.co.uk/journals/authors/style/reference/tf_CSE.pdf).
- Chen TY, Wang MMC, Hsieh SK, Hsieh MH, Chen WY, Tzen JTC. 2018. Pancreatic lipase inhibition of strictinin isolated from Pu'er tea (*Camellia sinensis*) and its anti-obesity effects in C57BL6 mice. *J Funct Foods*. 48:1–8.
- Dorkbuakaew N, Ruengnet P, Pradmeeteekul P, Nimkamnerd J, Nantitanon W, Thitipramote N. 2016. Bioactive compounds and antioxidant activities of *Camellia sinensis* var. *assamica* in different leave maturity from Northern Thailand. *Int Food Res J*. 23:2291–2295.
- Harbowy ME, Balentine DA, Davies AP, Cai Y. 1997. Tea chemistry. *Crit Rev Plant Sci*. 16(5): 415–480.




- Hsieh SK, Lo YH, Wu CC, Chung TY, Tzen JTC. 2015. Identification of biosynthetic intermediates of teaghrelins and teaghrelin-like compounds in oolong teas, and their molecular docking to the ghrelin receptor. *J Food Drug Anal.* 23(4):660–670.
- Katiyar SK, Mukhtar H. 1996. Tea in chemoprevention of cancer: epidemiologic and experimental studies review. *Int J Oncol.* 8(2):221–238.
- Khanongnuch C, Unban K, Kanpiengjai A, Saenjum C. 2017. Recent research advances and ethno-botanical history of *miang*, a traditional fermented tea (*Camellia sinensis* var. *assamica*) of northern Thailand. *J Ethn Foods.* 4(3):135–144.
- Kuo PC, Li YC, Wu RH, Tzen JTC. 2020. Characterization of teaghrelin-like compounds from tea cultivars. *Nat Prod Res.* 34, in press.
- Li YC, Wu CJ, Lin YC, Wu RH, Chen WY, Kuo PC, Tzen JTC. 2019. Identification of two teaghrelins in Shy-jih-chuen oolong tea. *J Food Biochem.* 43(4):e12810.
- Lo YH, Chen YJ, Chang CI, Lin YW, Chen CY, Lee MR, Lee VS, Tzen JTC. 2014. Teaghrelins, unique acylated flavonoid tetraglycosides in Chin-shin oolong tea, are putative oral agonists of the ghrelin receptor. *J Agric Food Chem.* 62(22):5085–5091.
- Mabry TJ, Markham KR, Thomas MB. 1970. The ultraviolet spectra of flavones and flavonols. In: *The systematic identification of flavonoids*. New York: Springer-Verlag; p. 45.
- Manir MM, Kim JK, Lee BG, Moon SS. 2012. Tea catechins and flavonoids from the leaves of *Camellia sinensis* inhibit yeast alcohol dehydrogenase. *Bioorg Med Chem.* 20(7):2376–2381.
- Obboh G, Ogunsuyi OB, Ogunbadejo MD, Adefegha SA. 2016. Influence of gallic acid on  $\alpha$ -amylase and  $\alpha$ -glucosidase inhibitory properties of acarbose. *J Food Drug Anal.* 24(3):627–634.
- Saha RK, Takahashi T, Kurebayashi Y, Fukushima K, Minami A, Kinbara N, Ichitani M, Sagesaka YM, Suzuki T. 2010. Antiviral effect of strictinin on influenza virus replication. *Antiviral Res.* 88(1):10–18.
- Yang SC, Chung PJ, Ho CM, Kuo CY, Hung MF, Huang YT, Chang WY, Chang YW, Chan KH, Hwang TL. 2013. Propofol inhibits superoxide production, elastase release, and chemotaxis in formyl peptide-activated human neutrophils by blocking formyl peptide receptor 1. *J Immunol.* 190(12):6511–6519.
- Yang S, Liu W, Lu S, Tian YZ, Wang WY, Ling TJ, Liu RT. 2016. A novel multifunctional compound camellikaempferoside B decreases A $\beta$  production, interferes with A $\beta$  aggregation, and prohibits A $\beta$ -mediated neurotoxicity and neuroinflammation. *ACS Chem Neurosci.* 7(4):505–518.
- Yu HP, Hsieh PW, Chang YJ, Chung PJ, Kuo LM, Hwang TL. 2011. 2-(2-Fluorobenzamido)benzoate ethyl ester (EFB-1) inhibits superoxide production by human neutrophils and attenuates hemorrhagic shock-induced organ dysfunction in rats. *Free Radic Biol Med.* 50(12):1737–1748.
- Yukihiko H. 2012. Elucidation of physiological functions of tea catechins and their practical applications. *J. Food Drug Anal.* 20:296–300.

ORIGINAL ARTICLE



## Astragaloside IV suppresses inflammatory response via suppression of NF- $\kappa$ B, and MAPK signalling in human bronchial epithelial cells

Hsi-Lung Hsieh<sup>a,b,\*</sup>, Shih-Hai Liu<sup>c,\*</sup>, Ya-Ling Chen<sup>d</sup>, Chien-Yi Huang<sup>e</sup> and Shu-Ju Wu<sup>f,g</sup> 

<sup>a</sup>Department of Nursing, Division of Basic Medical Sciences, Research Center for Chinese Herbal Medicine, and Graduate Institute of Health Industry Technology, Chang Gung University of Science and Technology, Taoyuan City, Taiwan; <sup>b</sup>Department of Neurology, Chang Gung Memorial Hospital, Linkou, Taoyuan City, Taiwan; <sup>c</sup>School of Medicine, Taipei Medical University, Taipei, Taiwan; <sup>d</sup>School of Nutrition and Health Sciences, Taipei Medical University, Taipei, Taiwan; <sup>e</sup>Department of Trauma and Emergency Surgery, Chang Gung Memorial Hospital, Linkou, Taoyuan City, Taiwan; <sup>f</sup>Department of Nutrition and Health Sciences, Research Center for Chinese Herbal Medicine, Chang Gung University of Science and Technology, Taoyuan City, Taiwan; <sup>g</sup>Aesthetic Medical Center, Department of Dermatology, Chang Gung Memorial Hospital, Linkou, Taoyuan, Taiwan

### ABSTRACT

**Context:** Astragaloside IV isolated from *Astragalus membranaceus* (Fisch.), which was reported to have anti-tumor, anti-asthma, and suppressed cigarette smoke-induced lung inflammation in mice.

**Objectives:** This study investigated whether astragaloside IV reduced the expression of inflammatory mediators and oxidative stress in BEAS-2B cells.

**Methods:** BEAS-2B cells treated with astragaloside IV, and then stimulated with TNF- $\alpha$  or TNF- $\alpha$ /IL-4. The levels of cytokine and chemokine were analysed with ELISA and real-time PCR.

**Results:** Astragaloside IV significantly inhibited the levels of CCL5, MCP-1, IL-6 and IL-8. Astragaloside IV also reduced ICAM-1 expression for blocked THP-1 monocyte adhesion to BEAS-2B cells. Furthermore, astragaloside IV attenuated the phosphorylation of MAPK, and reduced the translocation of p65 into the nucleus. Astragaloside IV could increase the expression of HO-1 and Nrf2 for promoting the oxidant protective effect.

**Conclusion:** Astragaloside IV has an anti-inflammatory and oxidative effect via regulated NF- $\kappa$ B, MAPK and HO-1/Nrf2 signalling pathways in human bronchial epithelial cells.

### ARTICLE HISTORY

Received 20 September 2019  
Revised 13 January 2020  
Accepted 3 February 2020  
Published online 13 February 2020

### KEYWORDS

Astragaloside IV; bronchial epithelial cells; inflammation; MAPK; NF- $\kappa$ B



### Introduction

Asthma is a common chronic inflammatory disease of the respiratory system, and asthma attacks are characterised by bronchoconstriction and difficulty breathing (Aghasafari *et al.* 2019). Allergens and microorganisms stimulated the activation of bronchial epithelial cells for induced inflammatory response, and secreted excess mucus to cause airway obstruction (Ferguson *et al.* 2017). Recent studies found that activated T cells and inflamed macrophages in the lungs released high levels of TNF- $\alpha$  and then stimulate the bronchial epithelial cells to secrete more inflammatory cytokines and chemokines (Lloyd and Saglani 2015, Parulekar *et al.* 2016). These inflamed cells will induce more severe airway inflammation and cause airway remodelling to alter respiratory function in asthmatic patients (Kudo *et al.* 2013). Therefore, inflamed bronchial epithelial cells play an important role in the pathological features of asthma attacks.

Invasion of the respiratory tract by microorganisms will induce the innate immune system of airways (Hiemstra *et al.* 2015). The activation of macrophages released TNF- $\alpha$  to cause airway inflammation, and even induced lower respiratory tract symptoms such as pneumonia (KleinJan 2016).

Allergens will also stimulate the activation of Th2 cells to release excessive Th2-related cytokines, causing respiratory allergies and inflammatory reactions, and even induce the development of asthma symptoms (Noval Rivas and Chatila 2016). Therefore, inhalation of excessive microorganisms or allergens by asthmatic patients will induce excessive production of inflammatory cytokines in respiratory system to stimulate the inflammatory response of the airways. Previous studies also found that Th2 cells released IL-4 to combine with TNF- $\alpha$  would stimulate the tracheal epithelial cells to secrete more eotaxins for attracted more eosinophils infiltration in lung (Huang and Liou 2012). Those activated eosinophils would cause more serious inflammation and allergic reactions in the respiratory system.

Inflammatory cytokines stimulated the activation of tracheal epithelial cells to cause the activation of NF- $\kappa$ B pathway, and translocated inflammatory messages into the nucleus to initiate inflammatory gene expressions (Hinz and Scheidereit 2014). Furthermore, inflammation could induce the activation of MAPK signal pathway to attract c-Jun transcription factor into the nucleus for triggering inflammation-associated gene expression (Cargnello and Roux 2011). Inflammatory cytokines also stimulated the oxidative stress

**CONTACT** Shu-Ju Wu  [sjwu@mail.cgu.edu.tw](mailto:sjwu@mail.cgu.edu.tw)  Department of Nutrition and Health Sciences, Research Center for Chinese Herbal Medicine, Chang Gung University of Science and Technology, No.261, Wenhua 1st Rd., Guishan Dist., Taoyuan City 33303, Taiwan

\*These authors contributed equally to this article.

of tracheal epithelial cells (Laforgia *et al.* 2018). Previous studies found that oxidative stress would increase the damage and apoptosis of cells in tracheal epithelial cells to affect the function of the respiratory tract (Zahiruddin *et al.* 2018). Therefore, blocking the inflammation and oxidative stress of tracheal epithelial cells would have a chance to restore normal function of the respiratory system.

*Astragalus membranaceus* is mainly grown in China. Traditional Chinese medicine uses *A. membranaceus* as an important herbal medicine for promoted qi expression (Bai *et al.* 2018). In recent years, scholars discovered that *A. membranaceus* has the ability to regulate immunity (Huang, Luo, *et al.* 2019). Astragaloside IV was isolated from *A. membranaceus*, and astragaloside IV was thought that could inhibit inflammatory response of macrophage via blocked NF- $\kappa$ B, MAPK signalling pathways (Li *et al.* 2017). Astragaloside IV induced apoptosis and arrested cell proliferation in cancer cells (Cheng *et al.* 2014, Jiang *et al.* 2017). Astragaloside IV could also attenuate cigarette smoke-induced lung inflammation in mice (Meiqian *et al.* 2018). Moreover, researchers also found that astragaloside IV could reduce the airway inflammatory response via blocked the excessive activation of Th2 cells in asthmatic mice (Du *et al.* 2008, Qiu *et al.* 2014). However, astragaloside IV regulated inflammatory response in tracheal epithelial cells is elusive. In this study, we evaluated the anti-inflammatory and anti-oxidation effect of astragaloside IV and the signalling mechanism of the NF- $\kappa$ B, MAPK and HO-1 pathways in bronchial epithelial cells.

## Materials and methods

### Cell line and culture medium

BEAS-2B cells purchased from the American Type Culture Collection (ATCC, USA), and cultured in DMEM/F12 medium (Invitrogen-GibcoTM, Paisley, Scotland) containing 10% FBS (Biological Industries, Haemek, Israel) and 100 U/mL penicillin and streptomycin. THP-1 cell line was purchased from the Bioresource Collection and Research Centre (BCRC, Taiwan), and cultured in RPMI 1640 medium (Invitrogen-GibcoTM). Cells were incubated in an atmosphere of 5% CO<sub>2</sub> at 37 °C, and cells subcultured twice each week.

### Cell viability assay

Figure 1(A) showed the chemical structures of astragaloside IV ( $\geq 98\%$  by HPLC), and was purchased from Sigma-Aldrich (Sigma, St. Louis, MO, USA). Cell viability was measured using the cell counting kit-8 assay kit (CCK-8, Sigma) to determine living cells, as previously described (Huang, Su, *et al.* 2019). Briefly, BEAS-2B cells seeded in 96-well plates, and treated with various concentration of astragaloside IV for 24 h. Cells treated with CCK-8 solution, and cell viability was assayed using a microplate reader (Multiskan FC, Thermo, Waltham, MA, USA).

### Western immunoblot analysis

BEAS-2B cells seeded in 6-well plates, and starved for overnight. Next, cells treated with astragaloside IV (0–100  $\mu$ M) for 1 h, and then stimulated with 10 ng/mL TNF- $\alpha$  24 h to detect total protein expression. Furthermore, cell stimulated with 10 ng/mL TNF- $\alpha$  30 min to detect protein phosphorylation. Cell proteins extracted using protein lysis buffer, and nuclear protein were separated by NE-PER<sup>TM</sup> Nuclear and Cytoplasmic Extraction Kit (Thermo Scientific, Rockford, IL, USA).

Proteins were separated on 10% SDS acrylamide gels, and proteins transferred onto polyvinylidene fluoride membranes, as previously described (Huang, Chen, *et al.* 2018, Huang, Huang, *et al.* 2019, Huang, Peng, *et al.* 2019). The membranes were incubated with primary antibodies, including HO-1, I $\kappa$ B- $\alpha$ , phosphorylated-I $\kappa$ B- $\alpha$ , Lamin B1, Nrf2 (Santa Cruz, CA, USA),  $\beta$ -actin (Sigma), ERK1/2, phosphorylated-ERK 1/2, ICAM-1, p38, phosphorylated-p38, JNK, phosphorylated-JNK, (Cell Signalling Technology, MA, USA). Then, the membranes incubated with secondary antibodies, and protein signals were expressed by Luminol/Enhancer solution and detected using the BioSpectrum 600 system (UVP, Upland, CA, USA).

### Elisa

BEAS-2B cells ( $10^5$  cell/mL) were seeded in 24-well plates, and cells treated with astragaloside IV (0–100  $\mu$ M) for 1 h, and then stimulated with 10 ng/mL TNF- $\alpha$  or 10 ng/mL TNF- $\alpha$ /10 ng/mL IL-4 for 24 h. The culture supernatants detected CCL11, CCL5, CCL24, ICAM-1, IL-6, IL-8, and MCP-1 using specific ELISA kits (R&D, Minneapolis, MN, USA), as previously described (Liou *et al.* 2018). Protein expressions were measured at 450 nm with a microplate reader (Multiskan FC, Thermo). Furthermore, MAPK inhibitors, including ERK inhibitor PD98059, p38 inhibitor SB203580, and JNK inhibitor SP600125 (Enzo Life Sciences, Inc., Farmingdale, NY, USA), combined with astragaloside IV to detect ICAM-1 protein expression of cell culture medium by ELISA.

### RNA isolation and quantitative real-time PCR analysis

BEAS-2B cells treated with astragaloside IV (0–100  $\mu$ M), and stimulated with 10 ng/mL TNF- $\alpha$  for 4 h. RNA was extracted and cDNA synthesised using the cDNA synthesis kit (Bio-Rad, San Francisco, CA, USA), as previously described (Liou *et al.* 2019). The gene expression was detected using SYBR Green Master Mix (Bio-Rad), and experimental condition of gene amplification: pre-incubated at 95 °C for 10 min, followed by 40 cycles of 95 °C for 15 s and 60 °C for 1 min using a spectrofluorometric thermal cycler (iCycler; Bio-Rad).

### Cell-cell adhesion assay

BEAS-2B cells were seeded in 24-well plates, and treated with astragaloside IV and stimulated with or without 10 ng/mL TNF- $\alpha$  for 24 h, as previously described (Huang, Liu, *et al.* 2019). THP-1 cells ( $10^7$ /mL) were treated with calcein

AM reagent (Sigma), and co-cultured with BEAS-2B cells. Attached THP-1 cells were assayed with fluorescence microscopy (Olympus, Tokyo, Japan).

### Determination of ROS production

BEAS-2B cells treated with astragaloside IV, and stimulated with TNF- $\alpha$  for 24 h. Cells incubated with 2',7'-dichlorofluorescein diacetate (DCFH-DA) and lysed to detect ROS levels using the Multi-Mode microplate reader (BioTek synergy HT) as described previously (Huang *et al.* 2017, Huang, Gu, *et al.* 2019). Additionally, intracellular ROS observed using fluorescence microscopy (Olympus).

### Statistical analysis

The results were analysed with one-way analysis and Dunnett's test. Data are presented as the mean  $\pm$  SD of at least three independent experiments. Statistical significance was set at  $p < .05$ .

## Results

### Astragaloside IV suppressed inflammatory mediators in BEAS-2B

The cytotoxicity of astragaloside IV in BEAS-2B cells was determined using the CCK8 assay. Astragaloside IV did not demonstrate significant cytotoxic effects at concentration  $\leq 100 \mu\text{M}$ , and subsequent experiments used astragaloside IV at 10–100  $\mu\text{M}$  concentrations (Figure 1(B)). 100  $\mu\text{M}$  astragaloside IV did not also demonstrate significant cytotoxic effects in 10 ng/mL TNF- $\alpha$  or 10 ng/mL TNF- $\alpha$ /IL-4 induced BEAS-2B cells (Figure 1(C)). BEAS-2B cells seeded in 24-well plates, and cells treated with astragaloside IV, and then stimulated with 10 ng/mL TNF- $\alpha$ . The result demonstrated that astragaloside IV could significantly decrease the levels of IL-6, IL-8, MCP-1, and CCL5 compared to TNF- $\alpha$ -activated BEAS-2B cells in a concentration-dependent manner (Figure 1(D–G)). Real-time PCR assays showed that astragaloside IV significantly also decreased IL-6, IL-8, MCP-1, and CCL5 gene expression compared to TNF- $\alpha$ -activated BEAS-2B cells (Figure 2). Previously, researchers found that IL-4 combined with TNF- $\alpha$  could induce eotaxin (CCL11, CCL24 and CCL26) secretions in BEAS-2B cells (Huang *et al.* 2017). In this study, we found

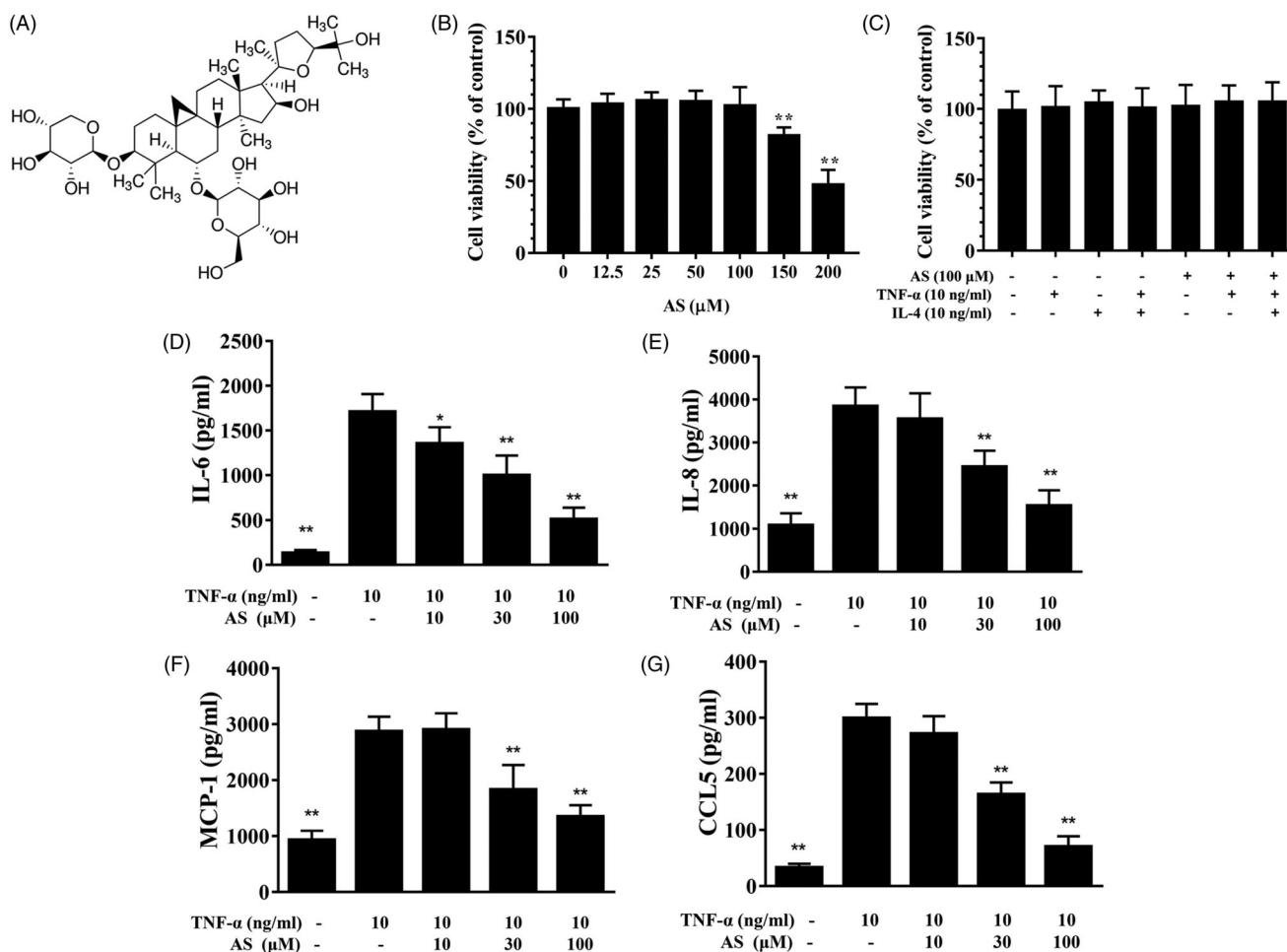


**Figure 1.** Astragaloside IV inhibited production of proinflammatory cytokines and chemokines in TNF- $\alpha$ -activated BEAS-2B cells. (A) Chemical structure of astragaloside IV. (B) Cell viability of BEAS-2B cells treated with the indicated astragaloside IV (AS) concentrations (0–200  $\mu\text{M}$ ) for 24 h. Cells were pre-treated with the indicated doses of astragaloside IV for 1 h, then stimulated with TNF- $\alpha$  (10 ng/mL) for 24 h. (C) Cell viability of TNF- $\alpha$  or TNF- $\alpha$ /IL-4 stimulated BEAS-2B cells treated with 100  $\mu\text{M}$  astragaloside IV for 24 h. In (C) and (D), the data represented mean  $\pm$  SD; \*\* $p < .01$ , compared to normal BEAS-2B cells. ELISA results showed the levels of (D) IL-6, (E) IL-8, (F) MCP-1, and (G) CCL5. The data represented mean  $\pm$  SD; \* $p < .05$ , \*\* $p < .01$ , compared to BEAS-2B cells stimulated with TNF- $\alpha$  alone.

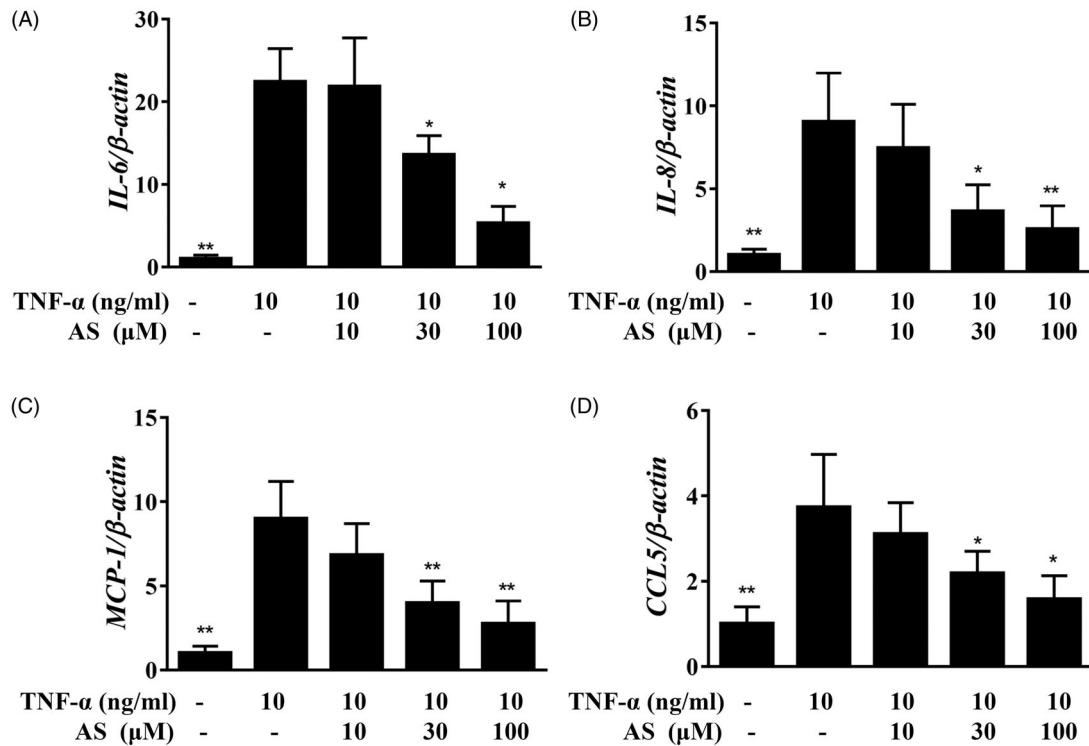


**Figure 2.** Astragaloside IV inhibited the gene expressions of proinflammatory cytokines and chemokines. Cells were treated with astragaloside IV (AS), then stimulated with TNF- $\alpha$  (10 ng/ml) for 4 h. Real-time RT-PCR results showed expression levels of *IL-6*, *IL-8*, *MAP-1*, and *CCL5*. The fold expression levels were calculated relative to the level of  $\beta$ -actin (internal control). The data represented mean  $\pm$  SD; \* $p$  < .05, \*\* $p$  < .01, compared to BEAS-2B cells stimulated with TNF- $\alpha$  alone.

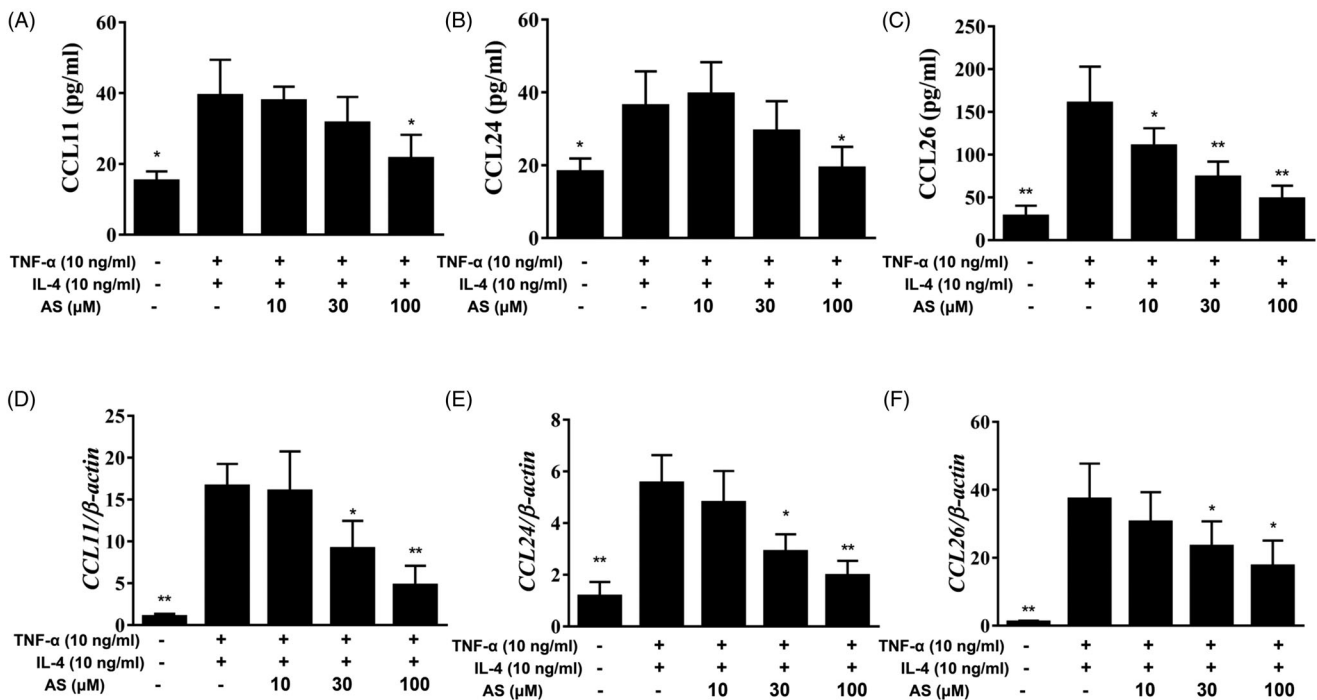


**Figure 3.** Astragaloside IV reduced productions of eotaxin in TNF- $\alpha$ /IL-4-stimulated BEAS-2B cells. Cells were pre-treated with astragaloside IV (AS) for 1 h and then stimulated with TNF- $\alpha$  (10 ng/ml) and IL-4 (10 ng/ml) for 24 h. (A–C) ELISA results showed the levels of CCL11, CCL24, and CCL26. (D–F) Cells were treated with astragaloside IV (AS), then stimulated with TNF- $\alpha$  (10 ng/ml) and IL-4 (10 ng/ml) for 4 h. Real-time RT-PCR results showed expression levels of *CCL11*, *CCL24*, and *CCL26*. The fold expression levels were calculated relative to the level of  $\beta$ -actin (internal control). The data represented the mean  $\pm$  SD; \* $p$  < .05, \*\* $p$  < .01, compared to BEAS-2B cells stimulated with TNF- $\alpha$ /IL-4.

that astragaloside IV suppressed the levels of CCL11, CCL24, and CCL26 in TNF- $\alpha$ /IL-4-stimulated BEAS-2B cells (Figure 3(A–C)). Real-time PCR assay also showed that

astragaloside IV could significantly reduce CCL11, CCL24, and CCL26 gene expression compared to TNF- $\alpha$ /IL-4-stimulated BEAS-2B cells (Figure 3(D–F)).



### Astragaloside IV suppressed MUC5AC and ICAM-1 expression

Real-time PCR showed that astragaloside IV could reduce the gene expression of *ICAM-1* and *MUC5AC* in TNF- $\alpha$ -activated BEAS-2B cells (Figure 4(A–B)). ELISA and Western blot assays also showed that astragaloside IV significantly decreased ICAM-1 expression compared to TNF- $\alpha$ -activated BEAS-2B cell (Figure 4(C–E)). Next, we also found that astragaloside IV significantly reduced THP-1 cell adherence to TNF- $\alpha$ -activated BEAS-2B cell (Figure 4(F)).

### Effect of astragaloside IV on phosphorylation of NF- $\kappa$ B and MAPK pathways in BEAS-2B cells

Astragaloside IV could reduce I $\kappa$ B- $\alpha$  protein degradation and suppress I $\kappa$ B- $\alpha$  phosphorylation compared to TNF- $\alpha$ -activated BEAS-2B cell (Figure 5(A,B)). We found that normal BEAS-2B cells, the NF- $\kappa$ B p65 subunit would keep in the cytoplasm. However, TNF- $\alpha$ -activated BEAS-2B cell increased p65 expressions in the nucleus. Interestingly, astragaloside IV could reduce p65 translocation into the nucleus compared to

TNF- $\alpha$ -activated BEAS-2B cell (Figure 5(A,C,D)). Furthermore, astragaloside IV significantly also decreased phosphorylation of ERK1/2, JNK and p38 compared to BEAS-2B cells stimulated with TNF- $\alpha$  alone (Figure 6). Moreover, when astragaloside IV treated with MAPK inhibitors, ICAM-1 expression significantly suppressed more effectively compared to astragaloside IV treated with TNF- $\alpha$ -activated BEAS-2B cells (Figure 7).

### Effect of astragaloside IV on ROS production

Fluorescence microscopy observed ROS result showed that astragaloside IV could decrease intracellular ROS expression compared to BEAS-2B cells stimulated with TNF- $\alpha$  alone (Figure 8(A,B)). Next, BEAS-2B cells treated with DCFH-DA, and the result showed that astragaloside IV also could attenuate ROS expression in TNF- $\alpha$  stimulated BEAS-2B cells (Figure 8(C)). Moreover, astragaloside IV could promote HO-1 expression in the cytoplasm and increase Nrf2 translocation into the nucleus compared to TNF- $\alpha$ -activated BEAS-2B cell (Figure 8(D–F)).

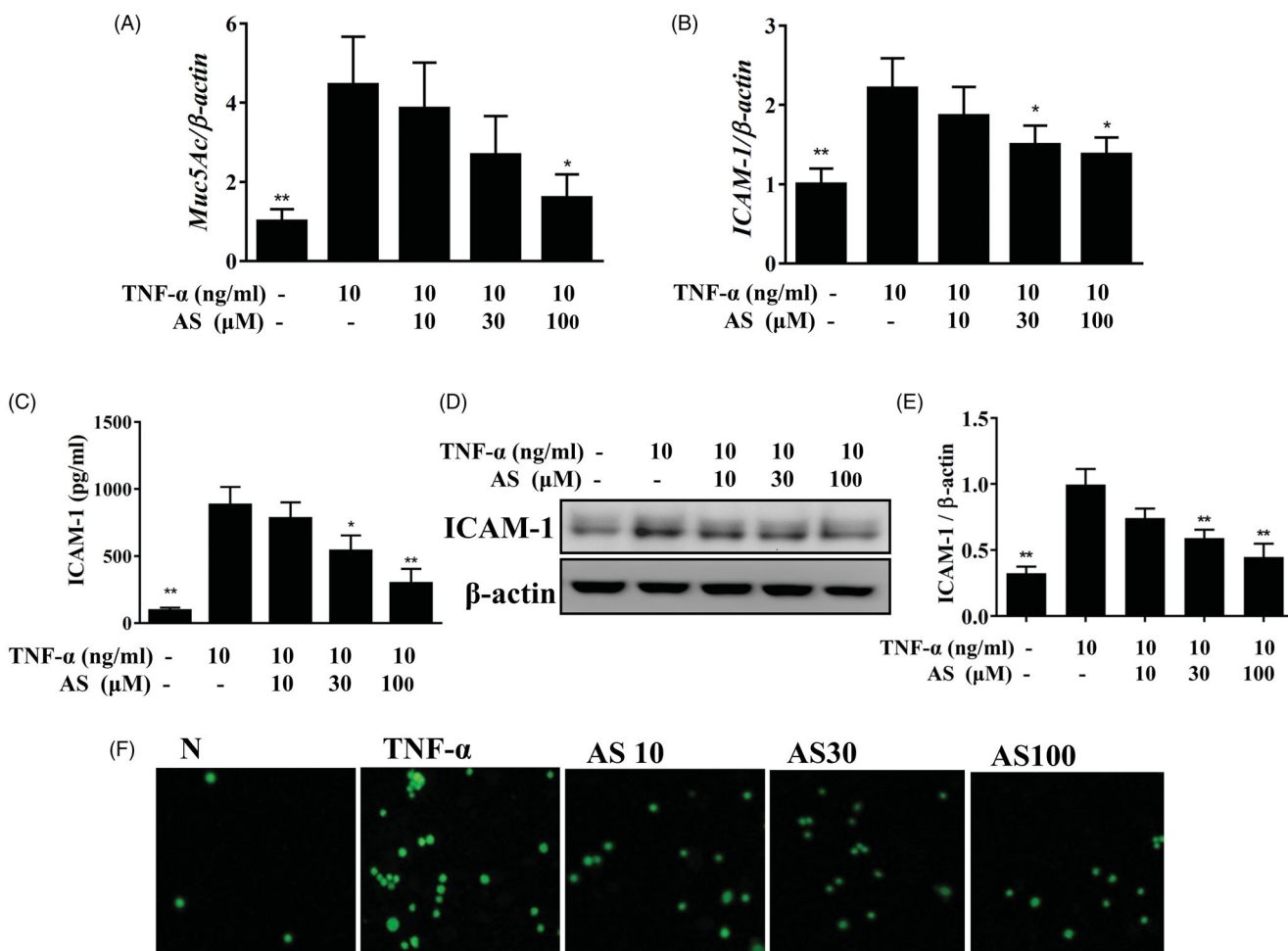


**Figure 4.** Astragaloside IV (AS) inhibited production of MUC5AC and ICAM-1 in TNF- $\alpha$ -stimulated BEAS-2B cells. Real-time RT-PCR results showed expression levels of (A) *MUC5AC* and (B) *ICAM-1*. The fold-changes in expression levels were calculated relative to the level of  $\beta$ -actin (internal control). (C) ELISA and (D) Western blot results showed dose dependent inhibition of ICAM-1 production. (E) The fold-change in the expression of ICAM-1 protein was measured relative to the expression of  $\beta$ -actin. (F) Fluorescent-labeled THP-1 cells (green) were co-cultured with unstimulated (N) or TNF- $\alpha$ -stimulated BEAS-2B cells in the absence and presence of the indicated astragaloside IV (AS) concentrations. After washing, adherent THP-1 cells remained attached to BEAS-2B cells. The data represented the mean  $\pm$  SD; \* $p$  < .05, \*\* $p$  < .01, compared to BEAS-2B cells stimulated with TNF- $\alpha$  alone.

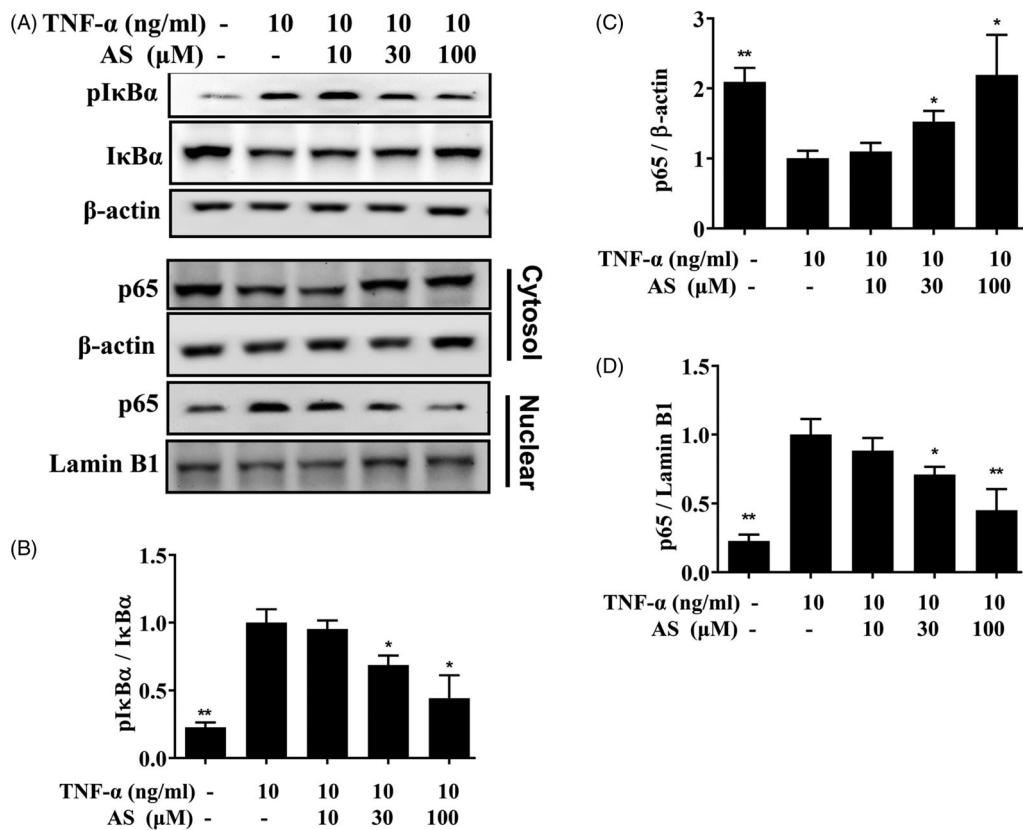


**Figure 5.** Inhibitory effects of astragaloside IV on the nuclear translocation of NF- $\kappa$ B in BEAS-2B cells. Cells were pre-treated with different doses of astragaloside IV (AS), and then incubated with TNF- $\alpha$  (10 ng/mL) for 30 min. (A) Representative Western blot showed the effects of astragaloside IV on TNF- $\alpha$ -induced NF- $\kappa$ B pathway expression. (B) The fold-change in the expression of pI $\kappa$ B $\alpha$  protein was measured relative to the expression of I $\kappa$ B $\alpha$ . (C) The fold-change in the expression of p65 protein was measured relative to the expression of  $\beta$ -actin. (D) The fold-change in the expression of p65 protein was measured relative to the expression of lamin B1. The data represented the mean  $\pm$  SD; \* $p$  < .05, \*\* $p$  < .01, compared to BEAS-2B cells stimulated with TNF- $\alpha$  alone.

## Discussion

Tracheal epithelial cells are a very important barrier to protect the respiratory tract (Paplińska-Goryca *et al.* 2013). When invaded by allergens, bacteria or viruses, it may irritate the immune cells of the airway and release inflammation-associated cytokines to stimulate the inflammatory response of epithelial cells (Kudo *et al.* 2013). Inflammatory tracheal epithelial cells also released more inflammatory cytokines and chemokines to exacerbate the inflammatory effects of the respiratory system and caused the damage of lung tissue cells (Lloyd and Saglani 2015). In addition, inflamed tracheal epithelial cells also released more mucus to block the airway for caused difficulty breathing (Aghasafari *et al.* 2019). Therefore, reducing the inflammatory response of tracheal epithelial cells should reduce the progression of respiratory diseases. In this current study, we simulated that the activated immune cells released TNF- $\alpha$  to stimulate inflammation of tracheal epithelial cells. This cell model evaluated whether astragaloside IV has the ability to inhibit the inflammatory response of bronchial epithelial cells. The results of the experiment showed that astragaloside IV could reduce the secretion of inflammatory cytokines and chemokines in TNF- $\alpha$ -stimulated BEAS-2B cells, inhibited eotaxin productions, and reduced the ICAM-1 expression to attach immune cells. We also found that astragaloside IV inhibited inflammatory

responses by inhibiting NF- $\kappa$ B and MAPK signal pathway, and astragaloside IV also attenuated the oxidative stress of inflammatory bronchial epithelial cells. Therefore, astragaloside IV has the ability to inhibit the inflammation and oxidation of inflammatory bronchial epithelial cells.

Previous studies found that astragaloside IV could inhibit airway hyperresponsiveness and reduce inflammation in the lungs of asthmatic mice (Jin *et al.* 2017). Astragaloside IV also reduced the levels of IL-6 and TNF- $\alpha$  in bronchoalveolar lavage fluid of asthmatic mice (Du *et al.* 2008). The lungs of asthmatic patients exhibit high levels of TNF- $\alpha$ , which is produced mainly from activated macrophages (de Groot *et al.* 2019). These inflammatory cytokines stimulated the activation and inflammation of bronchial epithelial cells to release more inflammatory cytokines and chemokines for caused cell oxidative stress and cell damage (Lloyd and Saglani 2015). Therefore, astragaloside IV reduced the release of IL-6 from inflammatory BEAS-2B cells, which contributed to improve inflammation in the lungs.

In addition, astragaloside IV also reduced the secretion of IL-8 in TNF- $\alpha$  activated BEAS-2B cells. IL-8 is a chemokine to attract the neutrophils to the inflammatory tissue (Ciepiela *et al.* 2015). In LPS-induced lung injury experiments could trigger more neutrophils infiltration into the lungs, and those activated neutrophils released inflammatory mediators to cause inflammation and oxidative damage of the lungs

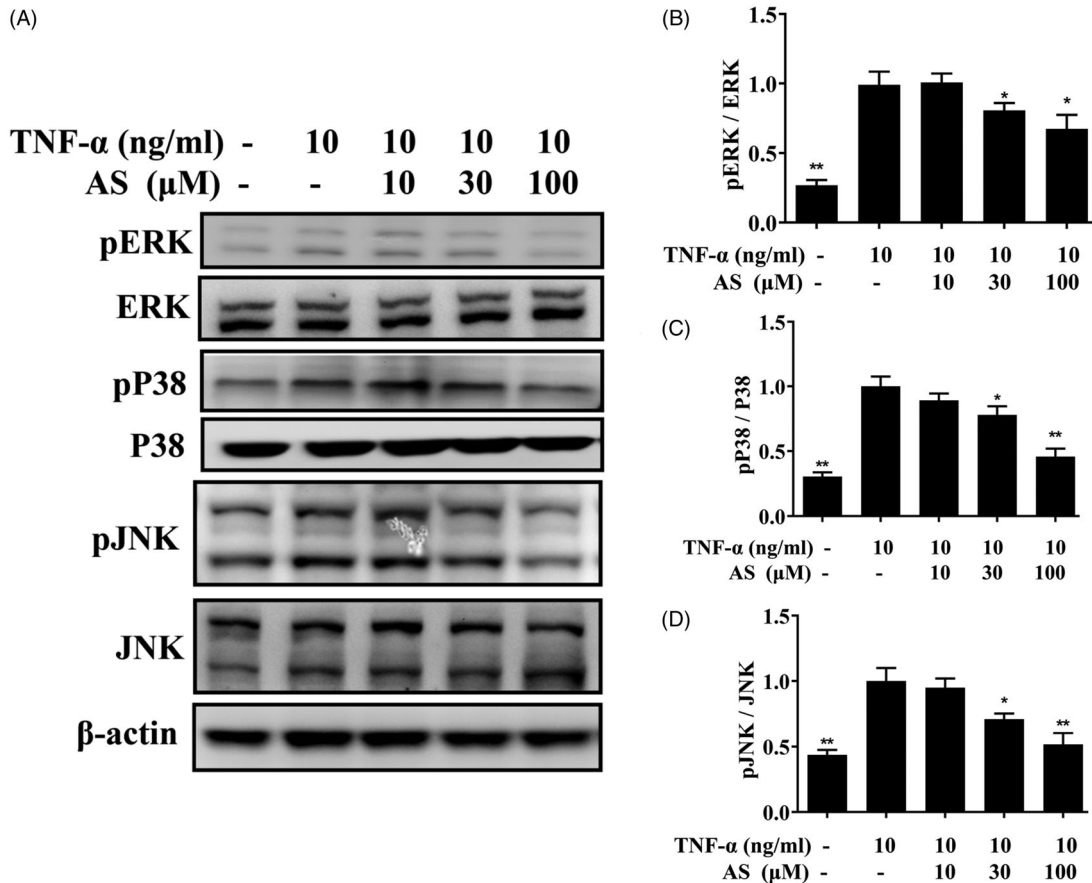


**Figure 6.** Effect of astragaloside IV on TNF- $\alpha$ -induced phosphorylation of MAPK pathway molecules. (A) Western blots showed phosphorylated levels of ERK, JNK, and p38 proteins. (B) The fold-change in the expression of pERK protein was measured relative to the expression of ERK. (C) The fold-change in the expression of pP38 protein was measured relative to the expression of p38. (D) The fold-change in the expression of pJNK protein was measured relative to the expression of JNK. The data represented the mean  $\pm$  SD; \* $p$  < .05, \*\* $p$  < .01, compared to BEAS-2B cells stimulated with TNF- $\alpha$  alone.

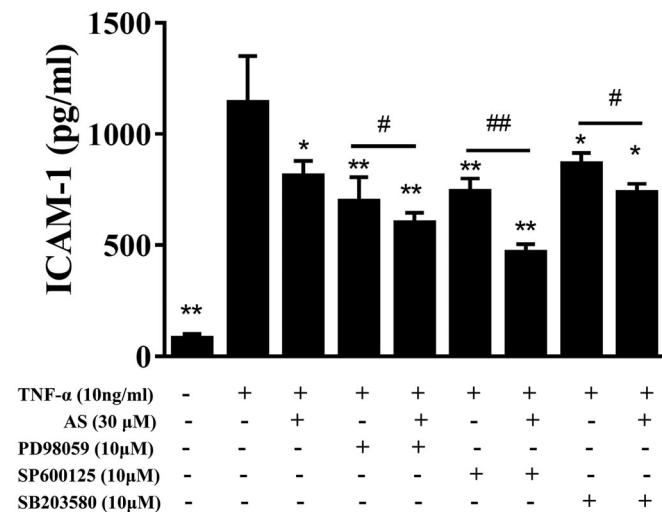


**Figure 7.** Inhibitory effects of MAPK inhibitors and astragaloside IV on TNF- $\alpha$ -induced ICAM-1 expression in BEAS-2B cells. BEAS-2B cells were treated with MAPK inhibitors (10  $\mu$ M PD98059, 10  $\mu$ M SP600125, or 10  $\mu$ M SB203580) with or without 30  $\mu$ M astragaloside IV, followed by TNF- $\alpha$  stimulation for 24 h. ELISA results showed ICAM-1 production levels. The data represented the mean  $\pm$  SD; \* $p$  < .05, \*\* $p$  < .01, compared to BEAS-2B cells stimulated with TNF- $\alpha$  alone. # $p$  < .05, ## $p$  < .01, compared to MAPK inhibitor treated with TNF- $\alpha$ -activated BEAS-2B cells.

(An *et al.* 2012). Previous studies also found that administration of astragaloside IV could reduce IL-6 and TNF- $\alpha$  levels of bronchoalveolar lavage fluid in LPS-induced lung injury mice

model (Huang and Li 2016). Therefore, we believed that astragaloside IV inhibited IL-8 expression in bronchial epithelial cells and has an improved effect on lung inflammation in patients with acute lung injury.

Previous experiments found that TNF- $\alpha$  stimulation could not induce eotaxin secretions, but TNF- $\alpha$  and IL-4 co-stimulated BEAS-2B cells, which enhanced the eotaxin expressions (Liou *et al.* 2016). Eotaxins can attract eosinophils migration and infiltrate into the lungs in asthma patients (Drake *et al.* 2018). When the lungs infiltrate a large number of activated eosinophils, these eosinophils will release more inflammation and allergen mediators for causing lung inflammatory and allergy response in asthma patients (Yancey *et al.* 2017). We found that astragaloside IV could inhibit the expression of CCL11, CCL24 and CCL26 in TNF- $\alpha$ /IL-4 stimulated BEAS-2B cells. Therefore, astragaloside IV has the ability to reduce the eosinophil infiltration in the lungs of asthma patients, which improved the development of asthmatic diseases.

Previous studies found that resveratrol inhibited airway hyperresponsiveness and eosinophil infiltration of lung in OVA-sensitized asthmatic mice through the inhibition of NF- $\kappa$ B and MAPK pathways (Jiang *et al.* 2019). Astragaloside IV could also reduce airway inflammation by blocking the mTORC1 pathway in asthmatic mice (Jin *et al.* 2017). Many previous experiments demonstrated that activation of NF- $\kappa$ B

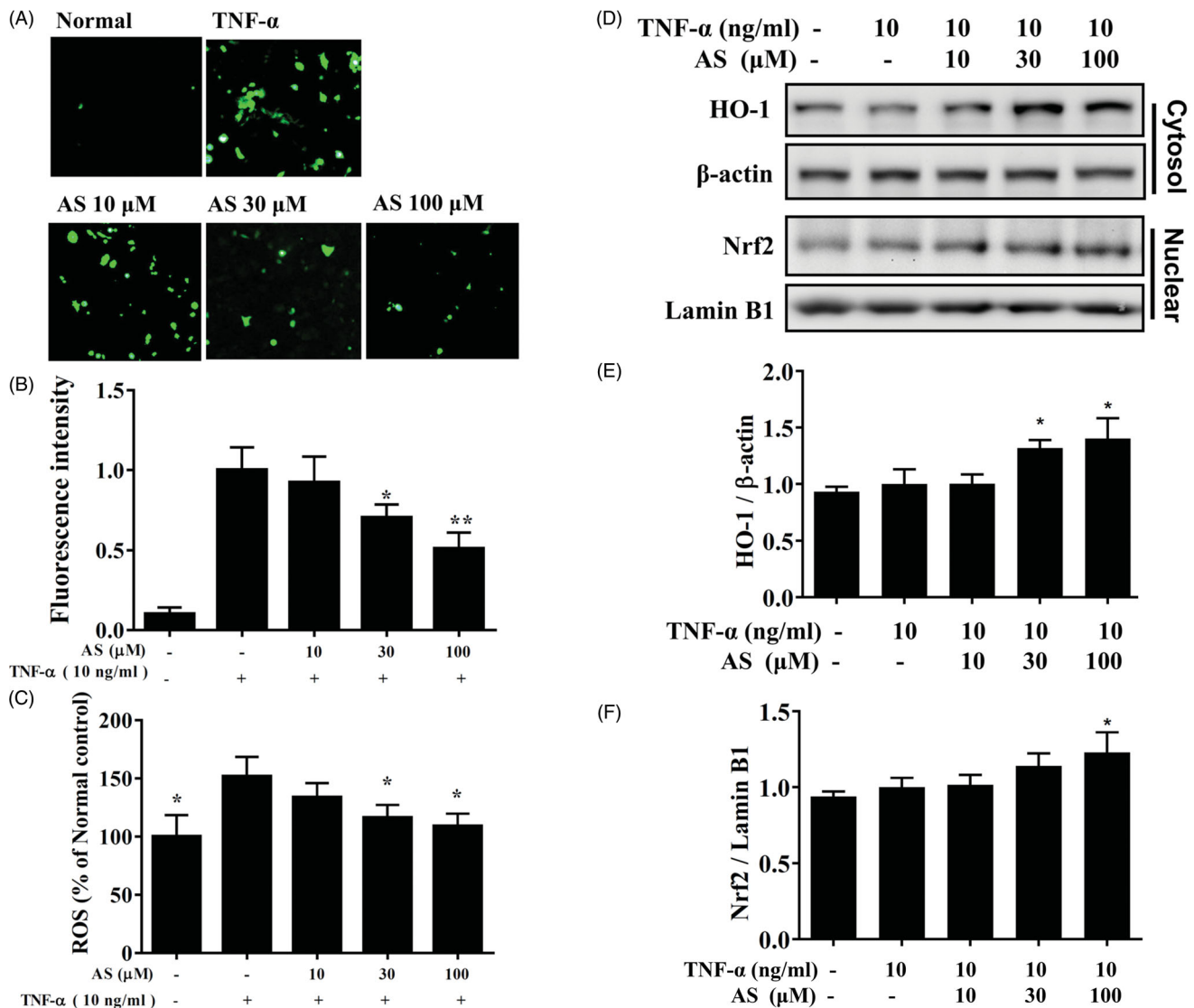


**Figure 8.** Effects of astragaloside IV (AS) on ROS production in activated BEAS-2B cells. (A) Fluorescence microscopy images of intracellular ROS. (B) Fluorescence intensity of intracellular ROS. (C) Percentages of ROS detected in TNF- $\alpha$ -activated BEAS-2B cells in the absence or presence of astragaloside IV compared to TNF- $\alpha$ -activated BEAS-2B cells. (D) Western blots showed the levels of HO-1, and Nrf2 proteins. (E–F) The fold-change in the expression of HO-1 and Nrf2 protein was measured relative to the expression of  $\beta$ -actin and lamin B, respectively. Three independent experiments were analysed and the data presented as mean  $\pm$  SD. \* $p < .05$ , \*\* $p < .01$  compared to BEAS-2B cells stimulated with TNF- $\alpha$ .

and MAPK signalling pathways would enhance the expression of chemokines, inflammatory cytokines, and cell surface adhesion molecules in tracheal and lung epithelial cells (Lloyd and Saglani 2015, Huang, Lai, *et al.* 2016, Huang, Wu, *et al.* 2018). In the NF- $\kappa$ B signal pathway of uninflammatory bronchial epithelial cells, I $\kappa$ B can hold NF- $\kappa$ B heterodimer protein (p65 and p50), and keep NF- $\kappa$ B protein in cytoplasm (Hinz and Scheidereit 2014). When TNF- $\alpha$  stimulated BEAS-2B cells, I $\kappa$ B would be phosphorylated and release two subunits of NF- $\kappa$ B (p65 and p50) translocation into the nucleus to bind to the promoter of the inflammatory-associated gene and induce inflammatory gene expressions. Furthermore, astragaloside IV reduced neuroinflammation through regulated NF- $\kappa$ B pathway in mice (Song *et al.* 2018). Our results demonstrated that astragaloside IV could significantly decrease I $\kappa$ B phosphorylation and NF- $\kappa$ B translocation into the nucleus in TNF- $\alpha$ -activated BEAS-2B cells. Hence, we found that astragaloside IV significantly reduced the gene

expressions of ICAM-1, CCL5, MCP1, IL-8 and IL-6 compared to TNF-activated BEAS-2B cell. Recent studies showed that activation of the MAPK signalling pathway also induced inflammatory gene expression and caused ICAM-1 gene expression (Huang, Wu, *et al.* 2018, Cheng *et al.* 2019). Previous research findings, conjugated linoleic acids combined with MAPK inhibitors more suppressed ICAM-1 expression and decreased THP-1 cell adherence to TNF- $\alpha$ -activated BEAS-2B cell (Huang, Tu, *et al.* 2016). Hence, we thought that astragaloside IV could decrease inflammatory response through suppressing the activation of NF- $\kappa$ B and MAPK signal pathways in TNF- $\alpha$ -activated BEAS-2B cell.

Chronic inflammation also induced oxidative stress to release more free radicals for caused cell and tissue destruction (Rogers and Cismowski 2018). Previous studies demonstrated that oxidative stress could stimulate more sputum secretion in the airways and injure bronchial epithelial cells (Antus 2016). We found that astragaloside IV had the ability



to attenuate ROS levels in inflammatory BEAS-2B cells. Previous research findings, astragaloside IV could ameliorate liver injuries via activating Nrf2/HO-1 pathway in mice (Li *et al.* 2018). Astragaloside IV also reduced acute kidney injury in mice through activation of Nrf2 and suppression of NF- $\kappa$ B signal pathway (Yan *et al.* 2017). In this current study, astragaloside IV also promoted nuclear Nrf2 expression for increasing HO-1 protein production in TNF- $\alpha$ -activated BEAS-2B cell. Therefore, astragaloside IV had a protective effect against oxidation stress to preserve the function of bronchial epithelial cells.

## Conclusion

Our results demonstrated that astragaloside IV could suppress chemokine and proinflammatory cytokine expressions via suppressing MAPK and NF- $\kappa$ B pathways in bronchial epithelial cells. Astragaloside IV also reduced ICAM-1 expression and suppressed immune cell adhesion to bronchial epithelial cells, and increased HO-1/Nrf2 expressions for promoted antioxidant effect. We suggested that astragaloside IV was an effective anti-inflammatory and anti-oxidation natural compound that could be used to improve airway inflammatory diseases.

## Disclosure statement

No potential conflict of interest was reported by the author(s).

## Funding

This study was supported in part by grants from the Chang Gung Memorial Hospital [CMRPF1G0203, CMRPF1F0123, CMRPF1F0132, CMRPF1H0051, CMRPF1H0052, and CMRPF1I0041], the Ministry of Science and Technology in Taiwan [MOST107-2320-B-255-003 and MOST 108-2320-B-255-004], and Chang Gung University of Science and Technology [ZRRPF3H0131].

## ORCID

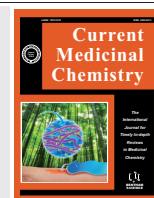
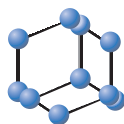
Shu-Ju Wu  <http://orcid.org/0000-0002-7771-2167>

## References

- Aghasafari, P., George, U., and Pidaparti, R., 2019. A review of inflammatory mechanism in airway diseases. *Inflammation research*, 68 (1), 59–74.
- An, L., *et al.*, 2012. Heme oxygenase-1 system, inflammation and ventilator-induced lung injury. *European Journal of Pharmacology*, 677, 1–4.
- Antus, B., 2016. Oxidative stress markers in sputum. *Oxidative medicine and cellular longevity*, 2016, 1–12.
- Bai, C.Z., *et al.*, 2018. Preparation of *Astragalus membranaceus* lectin and evaluation of its biological function. *Biomedical reports*, 9, 345–349.
- Cargnello, M., and Roux, P.P., 2011. Activation and function of the MAPKs and their substrates, the MAPK-activated protein kinases. *Microbiology and molecular biology reviews*, 75 (1), 50–83.
- Cheng, X., *et al.*, 2014. Astragaloside IV inhibits migration and invasion in human lung cancer A549 cells via regulating PKC- $\alpha$ -ERK1/2-NF- $\kappa$ B pathway. *International immunopharmacology*, 23 (1), 304–313.
- Cheng, S.C., *et al.*, 2019. Quercetin inhibits the production of IL-1 $\beta$ -induced inflammatory cytokines and chemokines in ARPE-19 cells via the MAPK and NF- $\kappa$ B signaling pathways. *International journal of molecular sciences*, 20 (12), 2957.
- Ciepiela, O., Ostafin, M., and Demkow, U., 2015. Neutrophils in asthma—a review. *Respiratory Physiology and Neurobiology*, 209, 13–16.
- De Groot, L.E.S., *et al.*, 2019. Oxidative stress and macrophages: driving forces behind exacerbations of asthma and chronic obstructive pulmonary disease? *American journal of physiology-lung cellular and molecular physiology*, 316 (2), L369–L384.
- Drake, M.G., *et al.*, 2018. Eosinophil and airway nerve interactions in asthma. *Journal of Leukocyte biology*, 104 (1), 61–67.
- Du, Q., *et al.*, 2008. Inhibitory effects of astragaloside IV on ovalbumin-induced chronic experimental asthma. *Canadian journal of physiology and pharmacology*, 86 (7), 449–457.
- Ferguson, J.E., Patel, S., and Lockey, R.F., 2017. Acute asthma, prognosis and treatment. *Journal of Allergy and Clinical immunology*, 139 (2), 438–447.
- Hiemstra, P.S., Mccray, P.B., Jr., and Bals, R., 2015. The innate immune function of airway epithelial cells in inflammatory lung disease. *European respiratory journal*, 45 (4), 1150–1162.
- Hinz, M. and Scheidereit, C., 2014. The I $\kappa$ B kinase complex in NF- $\kappa$ B regulation and beyond. *EMBO Reports*, 15 (1), 46–61.
- Huang, W.C., Chen, Y.L., *et al.*, 2018. Ginkgolide C reduced oleic acid-induced lipid accumulation in HepG2 cells. *Saudi pharmaceutical journal*, 26 (8), 1178–1184.
- Huang, W.C., Fang, L.W., and Liou, C.J., 2017. Phloretin attenuates allergic airway inflammation and oxidative stress in asthmatic mice. *Frontiers in immunology*, 8, 134.
- Huang, W.C., Gu, P.Y., *et al.*, 2019. Sophoraflavanone G from *Sophora flavescens* induces apoptosis in triple-negative breast cancer cells. *Phytomedicine*, 61, 152852.
- Huang, W.C., Huang, C.H., *et al.*, 2019. Topical spilanthol inhibits MAPK signaling and ameliorates allergic inflammation in DNCB-induced atopic dermatitis in mice. *International journal of molecular sciences*, 20 (10), 2490.
- Huang, W.C., Lai, C.L., *et al.*, 2016. Phloretin attenuates LPS-induced acute lung injury in mice via modulation of the NF- $\kappa$ B and MAPK pathways. *International immunopharmacology*, 40, 98–105.
- Huang, R., and Li, M., 2016. Protective effect of Astragaloside IV against sepsis-induced acute lung injury in rats. *Saudi pharmaceutical journal*, 24 (3), 341–347.
- Huang, W.C., and Liou, C.J., 2012. Dietary acacetin reduces airway hyper-responsiveness and eosinophil infiltration by modulating eotaxin-1 and th2 cytokines in a mouse model of asthma. *Evidence-based complementary and alternative medicine*, 2012, 1–11.
- Huang, W.C., Liu, C.Y., *et al.*, 2019. Protective effects of licochalcone A improve airway hyper-responsiveness and oxidative stress in a mouse model of asthma. *Cells*, 8 (6), 617.
- Huang, H., Luo, S.H., *et al.*, 2019. Immunomodulatory activities of proteins from *Astragalus membranaceus* waste. *Journal of the science of food and agriculture*, 99 (8), 4174–4181.
- Huang, W.C., Peng, H.L., *et al.*, 2019. Spilanthol from traditionally used *Spilanthes acmella* enhances AMPK and ameliorates obesity in mice fed high-fat diet. *Nutrients*, 11, 991.
- Huang, W.C., Su, H.H., *et al.*, 2019. Licochalcone A inhibits cellular motility by suppressing E-cadherin and MAPK signaling in breast cancer. *Cells*, 8 (3), 218.
- Huang, W.C., Tu, R.S., *et al.*, 2016. Conjugated linoleic acids suppress inflammatory response and ICAM-1 expression through inhibition of NF- $\kappa$ B and MAPK signaling in human bronchial epithelial cells. *Food & function*, 7 (4), 2025–2033.
- Huang, W.C., Wu, L.Y., *et al.*, 2018. Spilanthol inhibits COX-2 and ICAM-1 expression via suppression of NF- $\kappa$ B and MAPK signaling in interleukin-1 $\beta$ -stimulated human lung epithelial cells. *Inflammation*, 41 (5), 1934–1944.
- Jiang, H., *et al.*, 2019. Resveratrol protects against asthma-induced airway inflammation and remodeling by inhibiting the HMGB1/TLR4/NF- $\kappa$ B pathway. *Experimental and therapeutic medicine*, 18, 459–466.



- Jiang, K., et al., 2017. Astragaloside IV inhibits breast cancer cell invasion by suppressing Vav3 mediated Rac1/MAPK signaling. *International immunopharmacology*, 42, 195–202.
- Jin, H., et al., 2017. Astragaloside IV Ameliorates airway inflammation in an established murine model of asthma by inhibiting the mTORC1 signaling pathway. *Evidence-based complementary and alternative medicine*, 2017, 1–10.
- Kleinjan, A., 2016. Airway inflammation in asthma: key players beyond the Th2 pathway. *Current opinion in pulmonary medicine*, 22 (1), 46–52.
- Kudo, M., Ishigatsubo, Y., and Aoki, I., 2013. Pathology of asthma. *Frontiers in microbiology*, 4, 263.
- Laforgia, N., et al., 2018. The role of oxidative stress in the pathomechanism of congenital malformations. *Oxidative medicine and cellular longevity*, 2018, 1–12.
- Li, L., et al., 2018. Astragaloside IV attenuates acetaminophen-induced liver injuries in mice by activating the Nrf2 signaling pathway. *Molecules*, 23, pii:E2032.
- Li, Y., et al., 2017. Immune regulation mechanism of Astragaloside IV on RAW264.7 cells through activating the NF-kappaB/MAPK signaling pathway. *International immunopharmacology*, 49, 38–49.
- Liou, C.J., et al., 2018. Protective effects of casticin from *Vitex trifolia* alleviate eosinophilic airway inflammation and oxidative stress in a murine asthma model. *Frontiers in pharmacology*, 9, 635.
- Liou, C.J., et al., 2016. Matrine attenuates COX-2 and ICAM-1 expressions in human lung epithelial cells and prevents acute lung injury in LPS-induced mice. *Mediators of inflammation*, 2016, 1–12.
- Liou, C.J., et al., 2019. Protective effects of licochalcone a ameliorates obesity and non-alcoholic fatty liver disease via promotion of the Sirt-1/AMPK pathway in mice fed a high-fat diet. *Cells*, 8 (5), 447.
- Lloyd, C.M., and Saglani, S., 2015. Epithelial cytokines and pulmonary allergic inflammation. *Current opinion in immunology*, 34, 52–58.
- Meiqian, Z., Leying, Z., and Chang, C., 2018. Astragaloside IV inhibits cigarette smoke-induced pulmonary inflammation in mice. *Inflammation*, 41 (5), 1671–1680.
- Noval Rivas, M., and Chatila, T.A., 2016. Regulatory T cells in allergic diseases. *Journal of allergy and clinical immunology*, 138 (3), 639–652.
- Paplińska-Goryca, M., et al., 2013. The expression of the eotaxins IL-6 and CXCL8 in human epithelial cells from various levels of the respiratory tract. *Cellular and molecular biology letters*, 18 (4), 612–630.
- Parulekar, A.D., Diamant, Z., and Hanania, N.A., 2016. Role of T2 inflammation biomarkers in severe asthma. *Current opinion in pulmonary medicine*, 22 (1), 59–68.
- Qiu, Y.Y., et al., 2014. Protective effects of astragaloside IV against ovalbumin-induced lung inflammation are regulated/mediated by T-bet/GATA-3. *Pharmacology*, 94 (1–2), 51–59.
- Rogers, L.K., and Cismowski, M.J., 2018. Oxidative stress in the lung – the essential paradox. *Current opinion in toxicology*, 7, 37–43.
- Song, M.T., et al., 2018. Astragaloside IV ameliorates neuroinflammation-induced depressive-like behaviors in mice via the PPARgamma/NF-kappaB/NLRP3 inflammasome axis. *Acta Pharmacologica sinica*, 39 (10), 1559–1570.
- Yan, W., et al., 2017. Renoprotective mechanisms of Astragaloside IV in cisplatin-induced acute kidney injury. *Free radical research*, 51, 669–683.
- Yancey, S.W., et al., 2017. Biomarkers for severe eosinophilic asthma. *Journal of allergy and clinical immunology*, 140 (6), 1509–1518.
- Zahiruddin, A.S., Grant, J.A., and Sur, S., 2018. Role of epigenetics and DNA-damage in asthma. *Current opinion in allergy and clinical immunology*, 18 (1), 32–37.



# Natural Polymers Based Hydrogels for Cell Culture Applications

Gils Jose<sup>1</sup>, K.T. Shalumon<sup>1,\*</sup> and Jyh-Ping Chen<sup>1,2,3,4,\*</sup>

<sup>1</sup>Department of Chemical and Materials Engineering, Chang Gung University, Kwei-San, Taoyuan 33302, Taiwan; <sup>2</sup>Department of Plastic and Reconstructive Surgery and Craniofacial Research Center, Chang Gung Memorial Hospital, Kwei-San, Taoyuan 33305, Taiwan; <sup>3</sup>Research Center for Food and Cosmetic Safety, Research Center for Chinese Herbal Medicine, Chang Gung University of Science and Technology, Kwei-San, Taoyuan 33302, Taiwan; <sup>4</sup>Department of Materials Engineering, Ming Chi University of Technology, Tai-Shan, New Taipei City 24301, Taiwan

**Abstract:** It is well known that the extracellular matrix (ECM) plays a vital role in the growth, survival and differentiation of cells. Though two-dimensional (2D) materials are generally used as substrates for the standard *in vitro* experiments, their mechanical, structural, and compositional characteristics can alter cell functions drastically. Many scientists reported that cells behave more natively when cultured in three-dimensional (3D) environments than on 2D substrates, due to the more *in vivo*-like 3D cell culture environment that can better mimic the biochemical and mechanical properties of the ECM. In this regard, water-swollen network polymer-based materials called hydrogels are highly attractive for developing 3D ECM analogs due to their biocompatibility and hydrophilicity. Since hydrogels can be tuned and altered systematically, these materials can function actively in a defined culture medium to support long-term self-renewal of various cells. The physico-chemical and biological properties of the materials used for developing hydrogel should be tunable in accordance with culture needs. Various types of hydrogels derived either from natural or synthetic origins are currently being used for cell culture applications. In this review, we present an overview of various hydrogels based on natural polymers that can be used for cell culture, irrespective of types of applications. We also explain how each hydrogel is made, its source, pros and cons in biological applications with a special focus on regenerative engineering.

## ARTICLE HISTORY

Received: October 07, 2018  
Revised: August 15, 2019  
Accepted: August 20, 2019

DOI:  
10.2174/0929867326666190903113004



CrossMark

**Keywords:** Hydrogels, natural polymers, cell culture, extracellular matrix, three-dimensional culture, regeneration, tissue engineering.

## 1. INTRODUCTION

### 1.1. Hydrogels: Definition and History

Hydrogels are physically or chemically cross-linked polymer matrices capable of swelling by absorbing large amounts of water or biological fluids [1]. Peppas *et al.* defined hydrogels as water-swollen cross-linked polymeric structures having covalent bonds produced by the reaction of one or more co-monomers, physically cross-linked due to chain entanglements, having hydrogen bonds or strong Van der Waals interactions between chains, or crystallites bringing together two or

more macromolecular chains [2]. Recently, hydrogels have been defined as a multi-component system consisting of a three-dimensional (3D) network of polymer chains and water that fills the space between macromolecules [3]. In a rheological way, hydrogels can be defined as aqueous solutions of hydrophilic polymers at low or moderate concentrations where no substantial entanglement of chains occurs and normally demonstrate Newtonian behavior. The ability for a hydrogel to absorb water arises from its hydrophilic functional groups such as amino, carboxyl and hydroxyl groups. These groups are attached to the polymeric backbone, whereas its cross-linked structure found in-between network chains is responsible for their resistance to dissolution, excellent control over the crosslink density and mechanical stability [3-5]. The cross-linked structure of hydrogels is attained either by strong chemical bonds or by permanent or temporary physical entan-

\*Address correspondence to these authors at the Department of Chemical and Materials Engineering, Chang Gung University, Kwei-San, Taoyuan 333, Taiwan; Tel: +886-3-2118800; Fax: +886-3-2118668; E-mails: [jpchen@mail.cgu.edu.tw](mailto:jpchen@mail.cgu.edu.tw); [shalumon@gmail.com](mailto:shalumon@gmail.com)

lements and is characterized by junctions or tie points. This can also be accomplished by micro crystallite formation and weak interactions such as hydrogen bonds. Thus, hydrogels can be considered as a binary phase system consisting of a solid phase and a liquid phase. The 3D solid polymeric network phase of the hydrogels is derived from extremely hydrophilic monomers that are ultimately turned into insoluble materials as a result of cross-linking [6]. This solid phase is responsible for the soft elastomeric mechanical properties endowed to the hydrogel when the liquid phase is imbibed into the polymer network [7, 8]. Hydrogels typically may contain 50 to 90 percent of water depending on preparation and degree of crosslinking. The presence of high water content provides excellent biocompatibility and high drug encapsulation capacity to the hydrogels [9]. The hydrogels have become an interesting topic since poly(hydroxyethyl methacrylate) (pHEMA) hydrogel was reported by Wichterle and Lim for the first time in 1960 with the ambitious goal of using them in permanent contact with human tissues [10]. Due to the hydrophilic and biocompatible character, the application of hydrogels was extended by Lim and Sun through their influential work in 1980, which demonstrates the successful application of calcium alginate microcapsules for cell encapsulation [11]. Followed by this in the 1980s, Yannas and coworkers incorporated natural polymers such as collagen and shark cartilage into hydrogels for use as artificial burn dressings [12]. Subsequently, there has been a tremendous upsurge in the research and development of hydrogels for various applications, including biodegradable materials for drug delivery [13-15], sensors [16, 17], contact lenses [18, 19], purification [20] *etc.*

Hydrogels can be classified into different groups based on their sources, preparation methods, crosslinking properties, delivery methods, degradability, and so on. Based on the source of materials used, hydrogels can be classified into synthetic or natural ones. The hydrogels made from naturally occurring polymers can be categorized as natural hydrogels, showing good biocompatibility and lower cytotoxicity. These materials are either components of natural extracellular matrix (ECM) or show similarities in properties to natural ECM. Due to this characteristic feature, natural hydrogels can promote cell adhesion, proliferation and new tissue regeneration. Although the biological characteristics are excellent, some hydrogels made of natural polymers are usually associated with poor mechanical strength and only can be applied to non-weight-bearing sites. On the contrary, the hydrogels from synthetic polymers offer great mechanical properties, but possess

poor biological properties. Due to the versatility and tunability, hydrogels based on both natural and synthetic polymers have been of great interest to encapsulation of cells. Most recently, such hydrogels have become attractive to the new field of 'tissue engineering' as matrices for regeneration of a wide variety of tissues and organs. In order to balance the properties of various hydrogels, physical or chemical modifications (functionalization, crosslinking and/or copolymerization) can be employed. Improvement in internal specific functional groups, hydrogen bonding, and electrostatic interaction of hydrogel materials can increase their bioactivity, strength and toughness and thereby expanding the scope for clinical use. Depending on the charges on the bound groups, hydrogels may be cationic, anionic or neutral. On the basis of the crosslinking technique used during gel formation, hydrogels can be classified as physically crosslinked and chemically crosslinked hydrogels. Among these, physical crosslinking is achieved *via* processes such as hydrophobic association, crystallization, chain aggregation, polymer chain complexion and hydrogen bonding. Physically crosslinked hydrogels have gained more attention for applications in biomedical fields as they do not require any toxic chemicals for the crosslinking and processing. On the other hand, a chemical hydrogel is prepared *via* chemical covalent crosslinking. As it is made of very strong covalent bonding, it is very difficult to dissolve a chemical hydrogel in any solvents.

Based on the chemical/physical structure, hydrogels can be classified as (1) homo-polymers, (2) copolymers, (3) semi-interpenetrating networks and (4) interpenetrating networks. Homo-polymers refer to polymer networks derived from single species of a monomer with a crosslinked skeletal structure based on the nature of the monomer and polymerization technique. Copolymeric hydrogels are composed of two types of monomer in which at least one is hydrophilic in nature, arranged in block or alternating configuration, along the chain of the polymer network. If a linear polymer penetrates another crosslinked network without any other chemical bonds, it is called a semi-interpenetrating network. The multi-polymer interpenetrating polymer network (IPN) hydrogel is an important class of hydrogel, having a network system made of two independent cross-linked synthetic and/or natural polymer components. The interlocked structure of the cross-linked IPN components is believed to ensure stability of the bulk and surface morphology. According to the biodegradability, hydrogels could be classified as biodegradable hydrogel and non-biodegradable hydrogel. Considering the improvements observed in hydro-

gels, they can be categorized into three different generations. The first generation of hydrogels comprises various crosslinking procedures involving the chemical modifications of a monomer or a polymer with an initiator. When the classification moves to the second generation of hydrogels, these materials upgrade to a group that can alter their properties in response to the changes of surrounding stimuli. And finally, the stereo complexed hydrogels cross-linked by other physical interactions can be categorized as the third generation of hydrogels.

Hydrogels have become a hot topic for many years due to their versatile properties and the possibility to modify their structure to tune their properties. As a result, in-depth researches have been conducted on hydrogels in order to utilize their properties for various applications. Interestingly, hydrogel networks can alter its mechanical and morphological characteristics based on physical conditions of the surrounding environment. In addition, its properties can be modified by varying the preparation conditions including monomer concentrations and monomer to crosslinker ratios. However, a significant disadvantage of hydrogels is their low mechanical strength, handling difficulties and sterilization issues. There are both advantages and disadvantages in the use of hydrogels in tissue engineering, and the latter will need to be surpassed to make hydrogels useful in this exciting field. The improvements during the years have largely influenced application possibilities of hydrogels by rendering their versatility. The hydrogel technologies may be applied to hygienic products, agriculture, drug delivery systems, sealing, coal dewatering, artificial snow, food additives, pharmaceuticals, biomedical applications, tissue engineering and regenerative medicine, diagnostics, wound dressing, separation of biomolecules or cells, barrier materials to regulate biological adhesions, and biosensors.

In this review, we will discuss various natural polymer-based hydrogels intended for cell culture applications. It also includes critical design parameters of hydrogels to be considered during cell culture applications.

## 1.2. Hydrogels for Biological Applications

Owing to their biocompatibility, flexibility in fabrication, variable composition and desirable physical characteristics, hydrogels have been used widely for various biomedical applications including in stem cell and cancer research, cell therapy, tissue engineering scaffolds immunomodulation, *in vitro* diagnostics and drug delivery [21-23]. For example, various biode-

gradable polymeric hydrogels having sensitivity to various stimuli in the body have been widely used for biomedical applications, such as drug/protein delivery and tissue engineering. For various hydrogels that interrupt its equilibrium in response to a small temperature change, which induces sol-gel transition, they can be used for drug delivery applications. This includes the thermo-reversible poly(ethylene glycol) (PEG)-grafted chitosan hydrogel for the same use. Another class of stimuli sensitive hydrogels is the one responsive to variations of the pH of the environment. Cross-linked gelatin/pectin hydrogels belong to this category that undergoes equilibrium swelling and *in vitro* release of the model drug mannitol in response to variations in the environmental pH values. Hydrogels have also found applications in the preparation of biosensors which can act as supports for immobilization of enzymes. These biosensors can detect biological events either based on changes in their swelling properties in response to the biological interactions or by the help of receptors that can detect biological interactions.

In order to exploit hydrogels for biomedical applications, they should possess adequate mechanical strength for cell immobilization, attachment, and tissue formation. Moreover, it should have a high porosity for the efficient transport of nutrients and oxygen. In addition, the hydrogel should attain the shape of the required surfaces very easily, which could also be considered as an added benefit to enhance its applications in biomedical fields. In this context, selection of attractive biomaterials and relevant fabrication methods plays crucial roles in developing ideal hydrogels for biomedical applications. Application of various polymeric materials for the fabrication of hydrogels is of great interest due to their high mechanical strength, which is important for tissue engineering applications [24]. Depending on the source of materials that have been exploited to prepare hydrogels, hydrogels can be classified into either natural or synthetic polymer-based. The typical natural polymers used for the fabrication of hydrogels include chitosan [25-28], collagen or gelatin [29], alginate [30, 31], hyaluronic acid [32, 33], heparin [34], chondroitin sulfate [35], dextran [36], starch [37], gelatin [38], cellulose [39] and DNA [40].

Due to their structural similarity with the macromolecule-based components of the body, hydrogels have found lots of applications in tissue engineering. Hydrogels designed for use as tissue engineering scaffolds may contain pores large enough to accommodate living cells, or they may be designed to dissolve or de-

grade away, releasing growth factors and creating pores into which living cells may penetrate and proliferate. Certain hydrogel materials also carry mucoadhesive or bioadhesive properties, which in turn support cell adhesion and cell proliferation. Many natural polymers based hydrogels have the capacity to mimic natural ECM in terms of their biocompatibility, permeability to oxygen and nutrients, as well as their tissue-like viscoelastic properties; and hence hydrogels have been used to support and assist restoration of various tissues such as bone, cartilage, nerve, blood vessel and skin.

### 1.3. Advantages of Natural Polymers Based Hydrogels

Although both natural and synthetic polymer-based hydrogels offer various advantages including high mechanical properties, processibility and stability, natural polymer-based hydrogels dominate in the bioactive properties such as versatility, biocompatibility and ability to degrade *in vivo* [41]. Compared with synthetic polymers, natural polymers perform a diverse set of functions including better cellular interactions and thus allowing them to enhance tissue performance [42]. Moreover, for natural polymers, it is easier to covalently incorporate cell membrane receptor and peptide ligands to stimulate adhesion, spreading and growth of cells within the hydrogel matrix. The property of proteins to act as structural materials and their function as polysaccharides in membranes are selected examples for the aforementioned characteristics of natural polymers. Another characteristic property of natural polymeric hydrogels is their ability to hold cells and drugs in their structure and to carry them to specific sites in a controlled manner. In addition, the presence of reactive sites in natural polymers to favor various modifications involving ligand conjugation and crosslinking, has widened their applications in biomedical fields. The clinical applications of natural polymer-based hydrogels have gained much attention due to their minimal stimulation to inflammatory or immunological responses of the host tissues.

## 2. PROPERTIES OF HYDROGELS

The properties of hydrogels, both material and biological properties, have a significant role in determining the response of cells. As a result, some aspects of hydrogels like biodegradability, stiffness, morphology, and by-product toxicity play a key role in cell differentiation and proliferation. The following section discusses the properties of the hydrogels to be considered for cell culture applications.

### 2.1. Factors Influencing Hydrogel Properties

Hydrogels are illustrious for their swelling behavior, which represents their ability to absorb a large amount of water or biological fluids. This swelling behavior is accomplished through the surface attack and the subsequent penetration of a thermodynamically compatible solvent that is in contact with the gel. Swelling can be defined as a continuous process of transition from an un-solvated glassy or partially rubbery state to a relaxed rubbery region [43]. When solvent molecules come into contact with the hydrogel, the polymer chains present in the gel undergo certain rearrangements and finally result in swelling. These rearrangements in the polymer chain can be attained by interactions with the solvent, constituents of solutions or among the chains themselves [44].

The swelling process of hydrogels is completed through a series of stages including primary bounding of water, secondary bounding of water and total bounding of water. The primary bounding of water is the first stage of swelling in which the water molecules come into contact with the hydrogel first and hydrate the polar and hydrophilic groups of hydrogel. As a result, the hydrophilic regions of the gels become wet due to the accumulation of water in the surroundings. This is followed by the interaction of water molecules with the hydrophobic groups present in the gel which results in hydrophobically bound water or secondary bound water. In the third stage of swelling, both primary and secondary bound water are combined together to form the total bound water. When the hydrogels become totally bound with water and the intake of additional water molecules into the network chains becomes easier with the osmotic driving force, the polymeric network shows infinite dilution. The hydrogel in its dry or un-solvated stage exists as a glassy phase and after swelling, it turns to a flexible rubbery state. In general, these two phases are separated by a moving boundary that can alter its phase at any stage. As a porous hydrogel comes into contact with a solvent, the pores in the gel will start to expand and allow solvent molecules to penetrate the crosslinked gel structure. Due to inability to promote water penetration, substances in the glassy phase are extremely slow in diffusing through the hydrogel network, while substances located in the outer rubbery phase can penetrate into the system very easily, as the rubbery phase can support the penetration of solvents through its flexible structure. These changes involved in the swelling process could be visualized so as to understand the mechanisms involved in the whole process. Indeed, a previous study has developed a tech-



nique for the real-time visualization of dynamic deformation profiles during gel swelling processes [45]. The swelling behavior of hydrogels can be measured using various protocols as this measurement in turn indicates the network hydrophilicity and crosslinking density.

The water-absorbing and retaining properties of hydrogels depend on the types and properties of the hydrophilic monomers and/or polymers used for preparation. Hence, the material properties, degree of crosslinking and the nature of swelling medium can be altered to control the swelling properties of hydrogels. In addition to this, the polymers can be modified with some hydrophilic chains to increase the hydrophilic nature of the material. The addition of a swelling agent into a hydrogel is an alternative way to enhance its water penetration properties [2]. In general, increasing the hydrophilicity of the hydrogel and decreasing the crosslinking density will result in higher water absorption and swelling ratio. The swelling behavior of hydrogels can be explained based on various theories. Detailed understanding of the mechanism of equilibrium swelling and rubber elasticity could be used to explain the steps involved in hydrogel swelling. The following part describes both these theories and their relationship with hydrogel swelling in detail.

The water swelling behavior of hydrogels is very beneficial in various applications. Hence, numerous studies have been conducted to explain and modify the swelling behavior of hydrogels. The equilibrium swelling behavior of polymer networks was initially developed by Flory and Rehner, and various models were developed in subsequent years based on their model. According to this theory, the state of equilibrium swelling of a polymer network (immersed in a solvent) is obtained when the solvent inside the network is in thermodynamic equilibrium with the outside. The theory also explains that the gels are neutral and have tetrafunctionally crosslinked polymer network chains and exhibit a Gaussian distribution. When a polymer network comes in contact with aqueous solutions or biological fluids, the water starts penetrating the gel due to the thermodynamic compatibility of the polymer chains and water. When the hydrogel starts to swell by absorption of water, it starts generating an elastic force against the fluid environment. These two forces start to oppose each other during the swelling process and the swelling of crosslinked polymer chains will reach equilibrium in a fluidic environment with the elastic or retractile force of the polymer chains themselves to contract. These two forces can be balanced by each other in terms of the Gibbs free energy as:

$$\Delta G_{total} = \Delta G_{elastic} + \Delta G_{mixing}$$

Where  $\Delta G_{elastic}$  comes from the elastic stored forces in the extended polymer chains contained in the gel networks;  $\Delta G_{mixing}$  is the result of mixing.

Hydrogels under mechanical stress can exhibit a range of responses from rapid elastic recovery, following applied stress or strain to a time-dependent recovery approaching viscous behavior. At temperatures below the glass transition temperature ( $T_g$ ), hydrogels can undergo a transition away from the rubbery state to a viscoelastic phase due to a slow rearrangement of polymer segments under deformation. The phase transition of the material is highly dependent on various mechanical properties, including creep, stress relaxation and dynamic loading, and hence it is very important to consider the mechanical properties of hydrogels prior to fabrication [46]. Hydrogel scaffolds used for tissue engineering applications are fabricated with a higher porosity to facilitate cell proliferation. Due to this higher porosity, water molecules can easily penetrate the structure and plasticize the gel. The plasticization of the gel matrix leads to a reduction in its glass transition temperature well below the environmental temperature of 37°C, which is required for cell culture. This lower glass transition temperature of these hydrogels helps to maintain a rubbery state in culture conditions, and hence it can absorb water to enhance the swelling behaviors [47].

The properties of hydrogels, which directly influence their potential applications in biomedical fields, depend mainly on the gelation and the biodegradation of hydrogels. The term ‘gelation’ refers to the linking of different macromolecular chains together to form very large-branched crosslinked structures. Depending on the nature of the starting material, the gelation process results in the formation of water-insoluble products with various crosslinking densities. Hydrogels consist of a mixture of two components, a soluble branched polymer containing hydrophilic group called ‘sol’ and branched polymer structure with decreased solubility called ‘gel’. The duration of crosslinking procedure results in increased density of branched polymers and decreased solubility, but higher mechanical strength and structural stability. Depending on the nature of polymer selected for gel formation, the gelation can be carried out either by physical linking (physical gelation) or by chemical linking (chemical gelation). Among these, physical gelation can be initiated by a variation in temperature or pH as well as by the photopolymerization technique. In this method, an alteration in any of the above mentioned physical properties leads

to an increase in the viscosity of the material, which finally results in gel formation. Depending on material properties, an increase or decrease in temperature increases the viscosity of the material. Some materials can undergo phase transition from solution state to gel state with a decrease in temperature. Agarose is a specific example of this category [48]. However, some other materials such as cellulose derivatives can undergo gelation with an increase in temperature. In case of methylcellulose and hydroxypropylcellulose, the gelation process is carried out at a higher temperature as the polymer-polymer interaction becomes more prominent at higher temperatures [49]. Similarly, alterations in the pH environment of certain polymers result in instant gel formation. Chitosan-based hydrogels can be fabricated through instant gelation process in the presence of acetic acid, which can enhance the retention and engraftment of adipose-derived stem cells [50]. In comparison to the thermal and pH-sensitive hydrogels, photo-polymerization technique converts liquid monomer solutions into a gel by exposure to light. The light-induced gelation technique is considered to be beneficial owing to its high polymerization and conversion rate as well as its possibility to cause gelation only at irradiated sites [51]. Gelatin-methacrylate (GelMA), comprised of the modified natural ECM component gelatin, is a photopolymerizable hydrogel that promotes cell binding and cell proliferation in the micro-fabricated structure [52]

## 2.2. Properties of Hydrogels for Biological Applications

### 2.2.1. Biocompatibility

Biocompatibility is one of the most critical parameters to be considered while designing hydrogels for biological applications such as tissue engineering. It relates to the hydrogel's ability to exist within the body without damaging adjacent cells so that limited or no immunological, toxic, or foreign body responses should occur in the body. Otherwise, it would lead to significant scarring or elicit a response that detracts from its desired function. Biocompatibility is defined as "the ability of a material to function with an appropriate host response in a specific application" [53]. The term biocompatibility not only refers to the compatibility of a hydrogel, but also to the nontoxicity of the degradation products formed out of it, and the toxic chemicals that are used for polymerization and crosslinking of the hydrogel. To be a biocompatible material, these by-products must be metabolized into harmless products that can be excreted through renal filtration. If the con-

version of these toxic chemicals is incomplete, it may lead to inflammatory response from the hydrogel and thereby generates immune responses. As a result, it is important to purify the gels after synthesis in order to remove all toxic chemicals involved in the whole preparation process. The purification of hydrogels can be carried out by various processes including solvent washing and dialysis [54].

In general, biocompatibility can be classified into two subcategories namely biosafety and bio-functionality. Among these, biosafety refers to the property of the material, which did not cause any negative impacts such as cytotoxicity, mutagenesis and carcinogenesis on the host tissues as well as on the surrounding tissues. On the other hand, bio-functionality describes the ability of the material to perform the task that is assigned to it. In order to improve the biocompatibility of polymeric materials and thereby to enhance the interaction between the material and the host tissues, a hydrogel scaffold for implantation can be coated with various biocompatible materials. Various naturally occurring materials such as collagen, chitosan and alginate can be incorporated with the hydrogel to enhance its biocompatibility by utilizing the similarity of these coating materials with different biological materials.

### 2.2.2. Stiffness

Stiffness is an extensive property of a solid body which can be defined as the "extent to which it resists deformation in response to an applied force". It represents an important class of properties that need to be considered while designing a material for biomedical application. Stiffness of ECM plays a key role in controlling the mobility of cells within it, which in turn regulates various cell functions such as adhesion, migration and proliferation. The relationship between a hydrogel's stiffness and cellular behaviors has been discussed in various articles. One study reported the culturing of epidermal stem cells and mesenchymal stem cells on hydrogels of varying stiffness and protein anchorage densities. The study concluded that substrates of different stiffness have differing protein anchorage densities and configurations, which can regulate stem cell fates [55]. In another study, a correlation between hydrogel stiffness and cell migration was discussed, where physical properties of the hydrogel as a cellular environment that can directly affect epithelial growth as well as guide cell migration were demonstrated [56]. The cell migration is highly dependent on hydrogel stiffness and hence cells can easily migrate from one region of the hydrogel to the another. Based

on the hydrogel stiffness, most adherent cells will migrate to stiffer regions within a hydrogel. The stiffness of a hydrogel thus has the capacity to regulate the forces generated and/or imposed on the cell's actin cytoskeleton and it can further modulate cell differentiation [57].

As stiffness plays a significant role in the regulation of stem cell fate, it is recommended to modify the stiffness of hydrogels for better cell culture applications. Since polymer concentration and crosslinking density determine the stiffness of hydrogel, these parameters should also be adjusted to obtain the optimum stiffness required for cell culture needs. In addition to this, the mechanical properties of hydrogels also depend on many other factors including the source of the polymer, method of processing, concentration and type of crosslinking agent and gelling environment. Nonetheless, an increase in crosslinking density of hydrogel network will most likely result in an increase in its stiffness, mechanical properties and structural stability, while a reduction of its permeability and swelling behavior.

### 2.2.3. Porosity and Pore Size

In general, porosity is described as a morphological feature of a material that is characterized by the presence of cavities inside the bulk. The application of a material for biomedical and tissue engineering use is governed by the porosity of the material as it influences the properties as well as the viability of cells. Based on the characteristics of hydrogels, the definition of porosity can be modified as the maximum size of solutes that can diffuse in a hydrogel and is represented by the mesh size that quantifies the average space available between the polymer chains. Hydrogels have been recognized for various biomedical applications due to their high porosity that can facilitate the efficient transport of nutrients, carbon dioxide and oxygen within the system. The high porosity of a polymeric hydrogel also leads to high specific surface area and tenability, which in turn alter the rate of cell survival, distribution, proliferation, and interconnection [58]. The porosity also influences the swelling characteristics of the hydrogel. If the hydrogel is with smaller mesh size, it will lead to lower swelling and higher modulus and vice versa. The mechanical properties of hydrogels represent a direct relationship with the porosity and hence hydrogels with less porous structure possess higher mechanical strength. Although with higher structural stability, a hydrogel with lower porosity is not recommended for cell culture applications as it will show reduced cell migration characteristics as well as reduced nutrient supply to the cell. Similarly, very large pore

size is also not recommended for hydrogel scaffolds, as the cell-matrix interaction decreases when the diameter of cell does not match with the pore size.

The porosity of a hydrogel is a key factor when designing a hydrogel for cell culture applications as it determines its capacity to provide adequate transport of nutrients, waste products, and gases throughout the scaffold. In addition to this, pores are important in providing enough space for the spreading of cells, which in turn supports cell migration and cell proliferation. This property becomes prominent in using a biodegradable hydrogel as the scaffolding material, which gradually increases its porosity in concomitant with gel degradation [59]. As a result, the hydrogel scaffold may provide enough space to stimulate cell spreading, migration, proliferation, and then vascularization [60]. This character of a biomaterial is crucial in revascularization of tissues, as the porous structure allows vessel infiltration without the need for highly intensive matrix degradation. As porosity of hydrogel is determined by the crosslinking intensity of its polymer chains, the presence of non-crosslinked polymer chains in the hydrogel will result in an increased pore size, while the existence of polymer chain entanglements will result in pore size reduction. When the pore size of the hydrogel is slightly smaller than the size of a typical mammalian cell, the cell-matrix interaction increases and thus results in cell migration and cell proliferation without degrading the hydrogel scaffold.

Since pore size and porosity of hydrogels influence cell behavior, it is important to determine them before moving to application. The porosity of a hydrogel can be predicted by the Flory-Rehner theory, which describes the thermodynamics of the equilibrium swelling of a crosslinked polymer network in a fluidic environment. Based on the entropy of mixing of a solvent and a crosslinked polymer network, the Flory-Rehner equation states that the average molecular weight between crosslinks in polymeric networks is closely related to the polymer volume fraction in the swollen state. In addition to this, various experimental techniques are also available to determine the pore size of a hydrogel. These experimental techniques include mercury intrusion porosimetry (MIP), fluorescence microscopy and scanning electron microscopy (SEM). Among these, MIP is commonly used as the standard method for porosity measurement. The pore size distribution of a hydrogel is influenced by three factors; concentration of chemical cross-links in polymer strands, concentration of physical entanglements of the polymer strands and net charge of the polyelectrolyte hydrogel. The concen-

tration of cross-linker is inversely related to the pore size of the hydrogels and is influenced by the ratio between the cross-linker and monomer concentration during hydrogel preparation. Similarly, the concentration of physical entanglement is determined by the initial concentration of all polymerizable monomers in the aqueous solution, and the porosity decreases with an increase in physical entanglement. Finally, the net charge of a hydrogel is determined by the initial concentration of anionic and cationic monomers used for polymerization. Although various techniques have been introduced for fabrication of porous hydrogels, it is very important to make sure that the biocompatibility of the materials is still maintained irrespective of the methods used [61].

#### 2.2.4. Biodegradation

The tendency of a hydrogel scaffold to undergo controlled breakdown has a strong influence on cell migration, proliferation, differentiation and morphology of the newly formed tissue. This can be considered a key property to be considered while designing a hydrogel material for tissue replacement and for degradation-mediated biomolecule delivery. In hydrogels, the biodegradation is accomplished through the principles of dissolution, hydrolysis, enzymatic degradation and photo-degradation [62]. As the degradation characteristics required for individual experiments vary from one to another, it is necessary to consider the rate of degradation before designing biodegradable hydrogels. For example, the hydrogel design for certain tissue engineering applications including articular cartilage or corneal replacement may not require complete scaffold degradation, and hence semi-permanent or permanent scaffolds can be used to replace the functions of damaged tissues. The degradation of a hydrogel scaffold can be accomplished through a series of chain cleavages induced by various mechanisms including hydrolysis, oxidation, and photo-degradation. Additionally, degradation of hydrogels in a biological environment can occur through the entry of water and subsequent swelling of cross-linked polymer chains. This can also be achieved through biological processes like enzymatic digestion using collagenase, lysozyme and N-acetyl- $\beta$ -D-glucosaminidase for chitosan-gelatin hydrogel scaffolds. Degradability of hydrogel is an important parameter to consider as it affects cell proliferation and cell behavior including motility and spreading. This property of a material to degrade in controlled manner can be employed for the regeneration of various tissues within the body, including bone regeneration. This can be improved further by incorporating various side

groups within the polymer backbone too. A study conducted with mouse mesenchymal stem cells reveals that the cells can only spread in RGD-modified hyaluronic acid (HA)-based hydrogel with degradable characteristics [63]. The basic reason for this phenomenon is that degradation provides the space for cell stretching and proliferation especially for hydrogels having a smaller pore size. Hence it is necessary to control the degradability of hydrogels to mimic the breakdown characteristics of living tissues.

Degradability of hydrogels can be modified by tailoring cleavable groups through various mechanisms like hydrolysis, where the modifications are introduced into the polymer backbone or crosslinks. Incorporating ECM components such as collagen and HA into hydrogels is an alternative method to attain the degradable characteristics of natural ECM during cell proliferation. Anseth group incorporated hydrolytically cleavable groups into polyethylene glycol (PEG) hydrogel networks and found a correlation between the degradation profile and the production and distribution of collagen from encapsulated chondrocytes [64].

#### 2.2.5. Cell Adhesion

Bio-adhesion can be defined widely as a diverse phenomenon that allows the materials to adhere to biological surfaces. In the aspect of cell culture, bio-adhesion is considered as a key property that regulates various fundamental behaviors of cells, including survival, differentiation, proliferation and migration. In all biological processes, cell adhesion is considered as the fundamental property and this critically alters the morphology and biological functions of the cells.

The adhesion of cells is mainly controlled by two structures named focal adhesion and the actomyosin cytoskeleton. Among these, focal adhesion is a type of adhesive contact between the cell and ECM. The adhesion between the material and the biological surfaces depends on various factors such as surface morphology, chemical interactions, physiological factors and physical-mechanical interactions. The focal adhesion is connected with the cytoskeleton through the interaction of the transmembrane proteins with their extracellular ligands and intracellular multiprotein assemblies. These structures can control both mechanical and biochemical signaling. Interactions between the cell surface and the ECM occur through the binding of cell surface receptors to specific amino acid sequences in extracellular proteins.

Interestingly, the activity and dynamics of many adhesion molecules appear to be force dependent, for

which contractile forces generated by the actin fibers can induce conformational changes that ultimately trigger signaling pathways. As cell adhesion is the fundamental requirement of bioengineering, it is necessary to choose the materials having bio-adhesive properties for hydrogel design. Although many natural polymers based hydrogels such as fibrin or collagen inherently exhibit bio-adhesive properties, most other hydrogels do not. Therefore, tailoring bioactive scaffold is necessary for cell culture applications. An interesting way to produce a bioactive scaffold is the addition of biological components to a polymeric material.

#### 2.2.6. Surface Characteristics

The properties of hydrogel surface play an important role in determining its applications in cell culture, as these properties have an influence on cell attachment and cell proliferation. These surface properties are not limited to the morphology, but also the surface chemistry, and surface roughness. Till now, many studies have been reported to discuss the relationship between material surface characteristics and cell attachment. The topographical properties of materials have been analyzed extensively with mammalian cells to evaluate their impact on cell behavior, and study results pointed towards their direct influence on attachment, proliferation and differentiation. For example, a study by Foley *et al.* demonstrated that rat PC12 cells are sensitive to the topographical features of the substrate. They addressed the relationship between nerve cells and surface properties and confirm the role of incorporation of nanoscale topographic features on the biomaterials towards axon regeneration [65]. Various other studies also suggest that the incorporation of nanoscale features on the surface of a material is advantageous in creating the features of ECM as well as in controlling cell behavior, cell growth and cell proliferation [66]. Another study conducted to evaluate bone response towards topography shows that surface topography influences the rate at which bone is formed adjacent to the surface. This study also reveals that polished materials with very smooth and homogeneous surface have lower bone formation characteristics [67]. Roughness is also categorized as a topographical property, which is defined as randomly produced topography. The literature explains that the influence of the surface roughness on cell attachment depends on cell types used for the experiment. Although most cells prefer to attach on a rough surface, certain cells like periodontal ligament fibroblasts prefer smoother surfaces.

In addition to surface topography, surface chemistry also influences the cellular responses towards the hydrogel. In order to understand the fundamental goals of modern biomaterial's surface science, it is necessary to understand the influence of interfacial chemistry on cell behavior. The application of materials containing charged ions or the incorporation of ions onto the material surface has a great impact on cellular response. Endothelial cells are the best example reported in many studies to show the influence of surface chemistry on cell attachment. One example available in the literature is the modification of hyaluronic acid (HA) with heparin to fabricate a hydrogel that can support the formation of an endothelial layer on the surface. The experiments conducted with endothelial progenitor cells (EPCs) show that heparin-containing HA hydrogels allow the adhesion and spreading of EPCs on the hydrogel surface. This is due to the electrostatic interactions with proteins and growth factors developed from the strong ionic nature of heparin [68]. The studies conducted with materials having different surface charges concluded the hydrophilic surface nature if net charge is positive or negative while neutral charges denote the hydrophobic nature. Among the ionic materials, surfaces with net negative charge have lower cell attachment and growth in comparison with positively charged surfaces. Alginate hydrogels bearing negative surface charge are one among this and show lower cell attachment although they could be copolymerized with other polymers to obtain a positive surface charge. Alginate hydrogel copolymerized with poly-L-lysine (PLL) used for culture of HepG2 cells is an example for the modification of hydrogel surface to obtain a surface charge that supports cell attachment. In addition, the surface charge of the materials plays a crucial role in creating an environment with varying surface tension and surface energy, which have an influence on cell attachment. An old study in 1984 proved decreased cell attachment with a decrease in surface energy [69]. The concept of physical and chemical interactions between the hydrogel surface and cell surface is represented in Fig. (1). As mentioned above, the response of cells towards biomaterials is significantly influenced by the surface texture and other surface properties of the material. Therefore, improving surface properties of hydrogels is a good approach for successful cell culture on these materials. Various approaches including thin film deposition and immobilizations of adhesive molecules can be employed to fabricate hydrogel materials with varying surface chemistries to support cell attachment.



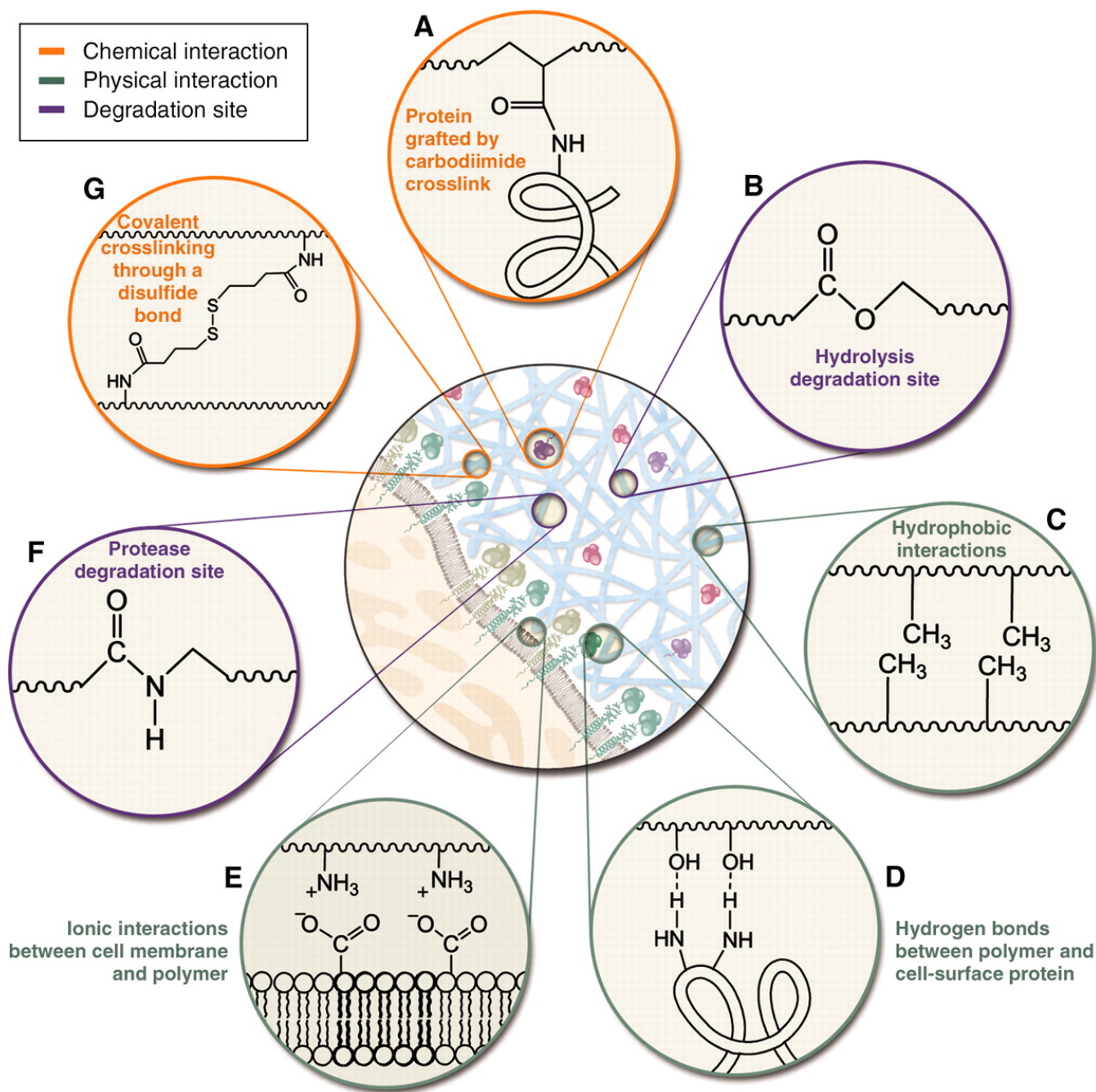


**Fig. (1).** Illustration of various chemical and physical interactions underlying the complexity of a cell-compatible hydrogel and its cellular interface. Reproduced with permission from reference [70].

### 2.2.7. Vascularization

The capacity to support vascularization or vessel formation is a strong requirement of tissue engineering scaffolds, as this vascular network is necessary to support enough quantities of oxygen and other nutrients to all the cells within the tissue. However, due to the lack of efficient strategies to support vascularization and also due to the large size of generated tissues, the sup-

ply of an adequate amount of nutrients and oxygen to the cells especially to the cells in the middle part of the tissue is challenging [71]. Due to this slow vessel formation within the tissues, the cells belonging to these areas are forced to survive in the absence of any supplements, and that may adversely affect cell properties and subsequently lead to cell death. Vascularization is controlled by various properties of biomaterials including mechanical, chemical and physical properties, and

among these, the role of physical properties outweighs the role of the other two for faster vessel generation. The porosity of hydrogels as well as the interconnection between the pores is very crucial for the ingrowth of blood vessels. Various groups conducted research works on the evaluation of the relationship between pore size and vascularization. The results suggested different pore sizes could lead to different blood vessel formation ability, with an approximate pore size of 200  $\mu\text{m}$ , deemed suitable for this function [72]. The materials with the optimum pore size to support cell ingrowth, cell distribution and vascularization can be fabricated using various techniques including gas forming, porogen leaching and electrospinning. In addition to this, interconnected pores were introduced in the system by polymerizing the biomaterials around the template followed by the template removal [73]. Apart from material property management, many other strategies are also available to promote vascularization. The blood vessel ingrowth after implantation can be improved by the addition of angiogenic factors, which include vascular endothelial growth factor (VEGF), platelet-derived growth factor (PDGF), transforming growth factor- $\beta$  (TGF- $\beta$ ) and angiopoietin-1 (Ang-1). In this approach, the addition of these angiogenic factors helps scaffolds to motivate the vasculature from the surrounding host tissues to scaffold interior to obtain vascularization required for the tissue. Another approach to induce vascularization in scaffold is the addition of endothelial cells to the tissues during *in vitro* culture. This approach applies the concept that endothelial cells are able to form pre-vascular network which can support the vascularization in the tissues. This approach of introducing pre-vascularization using the co-culture method has been discussed for various tissues including skeletal muscle, cardiac muscle, skin and bone. The study, conducted to assess the establishment of pre-vascularization on bone tissues using co-cultured endothelial cells and osteoblasts, disclosed the possibilities to generate pre-vascularization prior to implantation, as well to increase the rate of vascularization of the biomaterial after implantation [74].

### 3. HYDROGELS FOR CELL CULTURE

The application of 3D scaffolds for cell culture has gained increased attention recently, due to their ability to proliferate cells with better properties. This enhancement in the structural as well as in the biological properties is acquired from the better cell-cell and cell-matrix interactions, which lead to better cell signaling. Though various biomaterials are available for fabricating 3D scaffolds, hydrogels have gained more attention

due to their similarity with the naturally occurring ECM. Native ECM is generally formed either by secretion from resident cells or by de-cellularization of cells from different organs. These ECM are capable of providing biochemical and structural support for the surrounding tissues and can enhance the proliferation and properties of the cells. Other than this, hydrogels also show various properties similar to the native ECM including their porous structure, degradability and flexibility [75]. The ECM is composed of a variety of proteins and polysaccharides to enhance cellular interactions and tissue structure. As a result, it can transfer nutrients and growth factors to the cells through diffusion and that in turn regulates cell functions. A method to culture embryonic stem cells in 3D, highly porous, biomimetic polymer scaffolds to generate neural, hepatic and mesenchymal tissues was reported [76].

As mentioned in the previous sections, the hydrogels used to mimic the native ECM must have properties such as biocompatibility, biodegradability, and mechanical stability [77]. Compared to synthetic polymers, the properties of natural polymer-based hydrogels were found to have similarity with native ECM. Among the various attractive properties, the high water absorbing capacity, biocompatibility, and easiness in fabrication put natural polymer-based hydrogels in front row for cell culture. Although these natural polymers have attractive features, it is necessary to tune these properties based on their application. The modification of hydrogels to control their degradation characteristics and the subsequent diffusion of nutrients and growth factors as well as to control tissue regeneration is very important in increasing applications of hydrogels in tissue engineering. For example, in a work by Loessner and co-workers, the gelatin methacrylamide (GelMA)-based hydrogels were synthesized by combining the biocompatibility of natural matrices with the reproducibility, stability and modularity of synthetic biomaterials for *in vitro* and *in vivo* spheroid-based models for ovarian cancer. Later, these scaffolds provided better results in both *in vitro* and animal experiments. Thus, natural polymer-based hydrogels tuned for better properties are a better choice for cell culture applications.

The ECM is the extracellular component of natural tissues that provides structural support to the cells as well as performing various other important functions. Hydrogels in tissue engineering must meet a number of design criteria to mimic the ECM and consequently to function appropriately and promote new tissue formation. These hydrogel scaffolds, for instance, should

provide a 3D architecture for cell growth [78]. A cell-compatible hydrogel is characterized by its ability to control specific molecular interactions at the cell-material interface. These include biological interactions such as receptor-ligand chemistry that mediate cell adhesion and mesenchymal migration, bound or soluble molecule interactions facilitating proteolytic biodegradation or transcriptional events that govern cell phenotype, as well as focal adhesion interactions with compliant or rigid substrates to transmit mechanical stresses to cells. Bioactivity also needs to be considered while designing hydrogels for cell culture applications as this property can control various biological events in the body based on endogenous cell recruitment, local morphogenesis and controlled cell differentiation.

#### 4. HYDROGEL FABRICATION

Hydrogels are polymer networks having hydrophilic properties, which can be prepared from monomers, pre-polymers or existing hydrophilic polymers by various mechanisms. The synthesis of hydrogels from the monomer involves the mechanisms of crosslinking or free radical polymerization. When the monomers containing hydrophilic groups were added with multifunctional crosslinkers, the monomers either crosslink each other or initiate free radical polymerization to form hydrogels with interesting mechanical and biological properties. Low molecular weight hydrophilic polymers or oligomers can also be used for the preparation of hydrogels. Selective chemical crosslinking of hydrophilic polymers results in the formation of a hydrogel. One very well-known example of selective chemical crosslinking is the formation of gelatin hydrogel using polyaldehyde as a crosslinking agent. The crosslinking of gelatin can also be carried out using carbodiimide (EDC) and *N*-hydroxysuccinimide (NHS) [79]. Physical entanglement of polymer chains as in gelatin and agarose is also capable of producing 3D networks. To initiate chemical crosslinking, it is necessary to introduce a low molecular weight crosslinking agent together with a polymer into the reaction mixture. Although many crosslinking agents and initiators are available for the preparation of hydrogels from monomers, oligomers and polymers, their chemical nature and toxicity remain challenging while choosing these chemicals for the preparation of hydrogels for biomedical applications.

Based on the characteristics needed for the hydrogels, various fabrication methods have been reported for the preparation of hydrogels from different monomers and polymers. A slight modification in the solvent

casting, particulate leaching and gas foaming methods has been well characterized and studied. The gas-forming method is a commonly used technique to fabricate porous hydrogel scaffolds by incorporating foaming agents that can produce the bubbles inside the material scaffold during the polymerization process. Various types of foaming agents have been used for the in situ bubble generation to facilitate the formation of a porous structure within the scaffold. Among these, carbon dioxide ( $\text{CO}_2$ ) bubble-generating foaming agents such as sodium bicarbonate ( $\text{NaHCO}_3$ ), ammonium bicarbonate ( $\text{NH}_4\text{HCO}_3$ ) and potassium carbonate ( $\text{K}_2\text{CO}_3$ ) are commonly used for this fabrication technique. The studies suggest that when the biomaterial incorporated with  $\text{NH}_4\text{HCO}_3$  undergoes solvent evaporation process, the foaming agent undergoes decomposition to produce carbon dioxide and ammonia gas bubbles. The bubbles produced in this way can create well inter-connected pores in the resultant scaffolds [80]. Freeze drying is another method frequently applied for hydrogel preparation. It is based on sublimation process where the polymer is dissolved in a suitable solvent at the desired concentration, followed by freezing and lyophilizing to remove the solvent. The process of fabricating hydrogels using a similar but different method based on the freezing and thawing mechanism is known as cryogelation. Since the gelation happens at sub-zero temperatures, cryogelation occurs along with ice crystal formation, which in turn, can influence the porosity and interconnected pore structure. The influence of cryogelation on pore structure was evaluated elsewhere using chitosan-agarose-gelatin as the material for cryogelation. The study allowed the material to freeze at  $-12^\circ\text{C}$ , resulting in the formation of ice crystals in the gel, which, after melting, formed an interconnected porous structure [81]. Generally, this method operates at higher temperatures than freeze-drying and does not require sublimation of ice crystals in a vacuum. Thus, this technique reduces the expense of energy compared with freeze-drying to obtain scaffolds with high porosity and interconnectivity. An additional advantage is that the pore size can be controlled by adjusting the freezing rate and the pH value. However, its long processing time and smaller pore sizes have been marked as limitations of this method. Various other polymerization techniques are also employed to synthesize hydrogels and mostly through copolymerization/crosslinking methods. Methods like free-radical polymerization, in-situ polymerization and photo-polymerization have been well documented and reported for the fabrication of polymer hydrogels. These methods are mainly used when the

polymer hydrogels contain more than one polymeric constituent in their structure so that the other polymers can easily be incorporated using above techniques. For polymers with a double bond in their structure, free-radical polymerization and photopolymerization can be followed and for a copolymeric hydrogel, in-situ polymerization can be employed. Microfluidics is another important emerging technology for making hydrogels, where hydrogels with uniform pore size, porosity, complex patterns and reproducible 3D structure can be made through this method. In addition to the above discussed techniques, electrospinning can also be used to fabricate hydrogel fibers having a high surface area and porosity with varying thickness. Fibrous scaffolds were used in cell culture applications due to their mechanical and porous characteristics that can promote cellular adhesion. In a study, HA-based electrospun hydrogels were fabricated after modifying HA to make it capable to undergo enzymatic degradation. These electrospun hydrogels, crosslinked through photo-polymerizable peptides were found to be replica of ECM and are applicable in biomedical applications [82].

## 5. STERILIZATION OF HYDROGEL

The development and applications of hydrogels have gained increasing attention in the last few decades, but the sterility of these materials is a great concern while using them for the applications involving direct contact with cells and tissues. The term sterility is described as the absence of viable microorganisms in the material and hence the process of killing microorganisms present in the material is termed as sterilization. This process is used to avoid the chances of contamination from various microorganisms including bacteria, yeasts, and viruses. While exposing a material for sterilization, it is very important to maintain its structural and biochemical properties to ensure further application of this material. Due to the sensitivity of biomaterials to many sterilization techniques, it is very challenging to select a proper sterilization process that does not alter properties of biomaterials after the sterilization.

Based on the nature of techniques used for the sterilization, these can be classified as physical, chemical and physicochemical methods. Among these, heat sterilization is considered as the common technique used for biomedical samples and this includes both steam heating and dry heating. Steam heating is the process in which the material is exposed to steam under pressure in an autoclave. In this method, the material is kept at

temperature ranging from 121-124°C for 15 min [83]. During this process, all air present in the autoclave is replaced with steam and this steam at controlled temperature is used to sterilize the system. The process is then finished with the drying phase which involves steam evacuation. Compared to steam heating technique, dry heating does not require steam but a higher temperature and longer processing time. Heat sterilization technique has become famous due to its capacity to make sure the death of all the microorganisms present in the material. On the contrary, the application of a high temperature for a longer duration may result in the degradation of the material. In order to eliminate longer processing time and material exposure to higher temperature, radiation technique can be used as an alternative to heat sterilization. In this method, materials were exposed to ionizing radiations such as gamma radiation and ultra-violet radiation. As the irradiation has a higher penetration capacity, these techniques result in decontamination of the biomaterial at a shorter time period. Gamma radiation is described previously as the best suited method for biological tissues, and hence this technique was used in many allografts for sterilization [84]. Another technique used to sterilize biomaterials is the chemical method, which uses both liquid chemicals and gaseous chemicals to kill microorganisms. Gas sterilization technique is found to be an interesting sterilization technique that can be used for materials that degrade under exposure to radiation and temperature. Different types of gases are available for the sterilization of biomaterials. Among them, ethylene oxide is commonly used in gas sterilization. Moreover, many other gases including ozone and hydrogen peroxide can also be used for sterilization of biomaterials. Some studies suggest that dense gases can also be used for sterilization. A study describes the application of dense carbon dioxide gas for the sterilization of soft PEG hydrogels, which may lead to a safe sterilization technique that can be useful for sterilization of soft biomedical implants [85]. Washing the materials with various liquid chemicals can be summarized as liquid sterilization. Treatments with different types of alcohols such as ethanol and isopropyl alcohol are very commonly used methods in this category. Iodine treatment at an ambient temperature is also considered for sterilization which can kill microorganisms through oxidation, ionization and membrane immobilization mechanisms.

In addition to all the above-mentioned techniques, many other methods including filtration are also available for sterilization of biomaterials. Compared to other materials, hydrogel sterilization is little complicated as



it contains a high amount of water. As a result, sterilization without proper optimization and preparation may lead to degradation of the material. Hence the sterilization technique as well as the conditions for sterilizing hydrogels before cell culture must be optimized based on the material's properties to avoid post-sterilization complications.

## 6. NATURAL POLYMERS BASED HYDROGELS

Hydrogels made from natural polymers can be subcategorized into polysaccharides, proteins, bacterial polyesters and polynucleotides. The basic concepts of biocompatible hydrogels, their requirements for better cell interactions, and most commonly reported hydrogels from natural polymers for cell culture are schematically shown in Fig. (2).

### 6.1. Polysaccharides

Polysaccharides are considered as potential materials for cell culture and tissue engineering applications due to their adaptiveness to form hydrogels. Hydrogel formation depends on the chemical structures of the polysaccharides involved. The mechanism of gelation takes place through hydrogen bonding or intermolecular electrostatic interactions. A large molecule made of smaller monosaccharide units is a polysaccha-

ride. These small monomers bound together through special enzymes to form large sugar polymers *via* glycosidic bonds and the individual monosaccharides are known as residues. These are also called glycans. If all the monosaccharides are the same, then they are called homopolysaccharides, while others are known as heteropolysaccharides. Depending on the type of monosaccharide and connecting carbon in the attached monosaccharide, it can be divided into linear and branched polysaccharides. Based on the structure, polysaccharides display various functions in nature including energy storage, cellular messaging, tissue engineering, regeneration and many other biomedical applications [86, 87]. When covalently bonded to proteins or lipids, polysaccharides become glycoconjugates and glycolipids or glycoproteins and can be used to send signals between and within cells. Proteins targeting to specific sites could be tagged with certain polysaccharides too. In the following sections, we elaborate on different types of polysaccharide materials that have been extensively studied as hydrogel platforms for cell culture purposes.

#### 6.1.1. Chitin

Chitin exists in many different species with arthropod shells being the most accessible sources. The structure of chitin is a linear high molecular weight crystal-

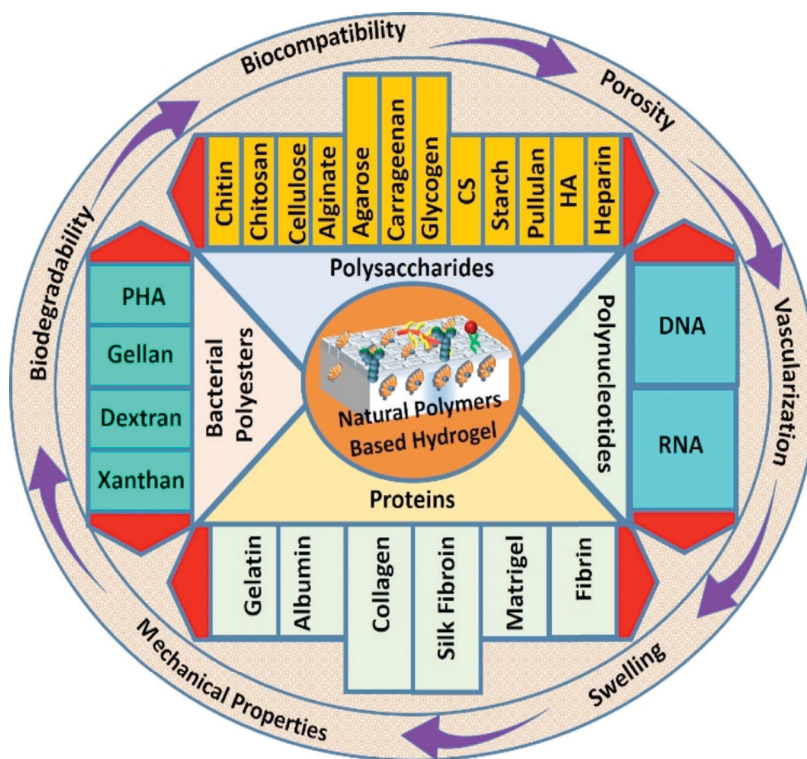


**Fig. (2).** Schematic representation of the basic concepts of biocompatible hydrogels, their requirements for better cell interactions, and most commonly reported hydrogels from natural polymers for cell culture.



line polysaccharide with the basic repeating unit being N-acetyl-D-glucosamine consisting of  $\beta$ -(1 $\rightarrow$ 4) linked D-glucose. Chitin has three crystalline forms known as  $\alpha$ ,  $\beta$  and  $\gamma$ , where  $\alpha$ -chitin is the most common type. Chitin and chitosan-based materials have been thoroughly used for various biomedical applications due to their extreme biocompatibility and adaptability. An early report [88] proves the advantage of composite porous hydrogel matrix of hydroxyapatite (HAP)-chitin for bone formation when cultured with rabbit mesenchymal stem cells. The chitin-HAP matrix containing pre-differentiated osteoblasts proved the effect of the porous matrix towards bone formation through *in vivo* rabbit implantation. In another study,  $\beta$ -chitin/nanohydroxyapatite (nHAP) hydrogel was prepared by freeze-drying approach from a mixture of  $\beta$ -chitin and nHAP in different concentrations. The obtained scaffolds had 70-80% porosity with well-defined interconnected porous structure having a swelling ratio of 15 to 20, controlled biodegradation and enhanced protein adsorption. When cultured with MG63, Vero, NIH3T3 and HDF cells, these hydrogel scaffolds displayed good cytocompatibility with well-improved cell attachment and proliferation [89]. In a separate study, a novel biodegradable, thermosensitive and injectable carboxymethyl chitin hydrogel was developed for 3D cell culture, where it could be easily tuned by varying the degree of carboxymethylation to make it appropriate for cell encapsulation at room temperature. When cultured with HeLa cells, the cells were proliferated and self-assembled to form 3D multicellular spheroids with high cell activity. COS-7 cells encapsulated within this *in-situ* forming hydrogel also showed cell survival and proliferation to confirm the potential of the hydrogels for 3D cell culture and biomedical applications [90]. Composite chitin hydrogels were also prepared through a combined approach of nHAP and chitin where their bio-compatibility for tissue regeneration was confirmed through cell culture experiments using fibroblast-like COS-7 cells [91]. Composite chitin hydrogels were also prepared in the form of  $\alpha$ -chitin/nHAP and cell viability, attachment and proliferation were examined using different cell lines to confirm the biocompatibility [92]. In 2008, Suzuki and co-workers developed  $\beta$ -chitin/chitosan sponges and cultured them with rabbit chondrocytes to observe high cell seeding efficiencies in the sponge (close to 98%) and confirmed the formation of a cartilage-like layer in the chondrocytes-sponge constructs that was similar to hyaline cartilage [93]. Most recently, a hydroxypropyl chitin-based hydrogel was formed by *in-situ* cross-linking through Diels-Alder reaction and provided a 3D

thermosensitive system for cell culture use. Cultured cells within the hydrogel showed sustainable proliferation and formation of multicellular spheroids. Further *in vivo* examination revealed their favorable injectability, *in-situ* thermogelation and good biocompatibility [94]. It should be noted that applications of chitin hydrogels are not only limited to cell culture. It could also be extended to wound dressings, cell cavity chambers, cosmetics, water purification, membranes and food additives.

#### 6.1.2. Chitosan

Chitosan is a linear polysaccharide composed of randomly distributed  $\beta$ -linked D-glucosamine and N-acetyl-D-glucosamine units, which is derived from shrimps, crabs and insects. Apart from other polysaccharides, chitosan is a highly basic polysaccharide carrying high positive charges in physiological condition and chitosan-based hydrogels are widely used for biomedical applications such as in tissue engineering [95], drug delivery [96] and cancer diagnosis [97]. Due to its good biocompatibility, low toxicity and mechanical properties, chitosan can be tuned to match native ECM. It was reported that chitosan hydrogels prepared from aqueous N-palmitoyl chitosan could support mouse 3T3 fibroblast culture and later *in vivo* studies proved the potential for cell delivery [98]. Richardson *et al.* developed chitosan/glycerophosphate hydrogels for clinical use for the regeneration of degenerated intervertebral disc. Mesenchymal stem cells (MSCs) seeded in hydrogels secreted both proteoglycans and collagens in a ratio which closely resembled that of nucleus pulposus (NP) cells [99]. An injectable chitosan/starch/ $\beta$ -glycerol phosphate hydrogel was cultured with chondrocytes and cells to maintain the chondrogenic phenotype during culture [100]. In another work, the primary amine groups in chitosan scaffolds underwent carbodiimide-mediated modification with RGD to facilitate cell adhesion [101]. In a similar way, photocrosslinkable chitosan was modified with both azide and lactose moieties and fabricated into a biological adhesive hydrogel for regeneration of soft tissues using human skin fibroblasts, coronary endothelial cells and smooth muscle cells [102].

#### 6.1.3. Cellulose

Cellulose is the most abundant biopolymer found in green plants, marine animals, algae, and bacteria. It shows good biocompatibility, low cytotoxicity, biodegradability, and sustainability to be used in various applications in the biomedical field using cellulosic materials. Chemically, D-glucose units in cellulose are connected with  $\beta$ -(1 $\rightarrow$ 4) glycosidic bonds with hydroxyl

groups arranged in an equatorial disposition. The stiff rod-like molecular chain conformation with strong intra- and intermolecular hydrogen bonding interactions results in crystalline fibrous materials. Cellulose can be used to make hydrogels for various biomedical applications using cellulose-based matrices or through composites incorporating nano-cellulose. Unlike other water-soluble polysaccharides, a separate cross-linking network is required for cellulose to fabricate a hydrogel [103]. Due to the inherent properties, cellulose based-hydrogel matrices are widely used for various biomedical applications in recent time. Cellulose hydrogels are generally prepared by the crosslinking of aqueous solutions of cellulose ethers such as ethylcellulose, methylcellulose, sodium carboxymethyl cellulose or hydroxypropyl methylcellulose. Thermo-responsive hydrogels are normally prepared from methylcellulose due to its hydrophobic-hydrophilic equilibrium by slightly varying temperature around its critical value [104]. Another group reported the effect of cellulose hydrogel on cellular biocompatibility without added growth factors, where cellular polarization and differentiation of human hepatic cell lines HepG2 were observed for 3D liver cell culture [105]. In a different approach, bacterial cellulose secreted by *Gluconacetobacter xylinus* was explored as a novel scaffold material for cartilage regeneration using chondrocytes [106]. Hydrogels with self-healing and shear-thinning properties have been used in a number of preclinical studies to provide protection during the injection stage and also to promote cell retention post-transplantation. An injectable system containing methylcellulose/hyaluronan hydrogel proved better-transplanted cell retention of induced pluripotent stem cell-derived oligodendrocytes for retinal and spinal cord therapies [107]. Cellulose-based hydrogels have also been used for various other applications including full-thickness wound healing using keratinocytes and fibroblasts [108], bone regeneration using MSCs [109], central nervous system repair using L929 mouse fibroblasts [110] and also as a model 3D cell culture platform for human pluripotent stem cells [111].

#### 6.1.4. Alginate

Alginate is a polysaccharide extracted from seaweeds, which is a natural anionic polymer electrolyte composed of two monosaccharides of  $\alpha$ -L-guluronic acid and  $\beta$ -D-mannuronic acid. It is abundant in nature, inexpensive and biocompatible. Alginate forms hydrogels through ionic bonding interaction between the carboxylate group in alginate backbone and a cationic cross-linking agent [112]. Divalent and trivalent cations may exist in the hydrogels and calcium-alginate

hydrogels are widely used in gel forms. Alginate hydrogels are widely used in biomaterials, as for example, their potential has been widely explored in tissue engineering and drug delivery and also as a model ECM for biological studies [113]. One of the disadvantages of natural materials is poor mechanical properties and limited cell adhesion [27]. When cells do not possess the receptors for alginate, the latter requires some modifications by conjugating with signaling molecules to promote cell-matrix interaction for the proliferation and differentiation of some cells within alginate hydrogels. Therefore, the poor adhesion property of alginate-based hydrogels was improved by Mooney and co-workers by using RGD peptides for culture of mouse skeletal myoblasts [112]. Material properties such as stiffness and porosity show an effect on the cell's fate and the stress relaxation of alginate-based hydrogels may regulate stem cell fate and activity. The hydrogel with faster relaxation property accommodates better in cell spreading, differentiation and proliferation than slower relaxation. In a separate study, a group of researchers developed a hybrid hydrogel comprised of alginate and poly(ethylene glycol) diacrylate to achieve a scaffold with toughness greater than natural cartilage for culture of MSCs [114]. The effectiveness of RGD-alginate hydrogel in the improvement of retinal tissue development using human pluripotent stem cells was also reported [115]. The potential use of alginate hydrogels in combination with cells is directly related to the ability to tailor and control the type and degree of cell-matrix interactions, which can be attained by covalently conjugating alginate with heparin binding peptides (HBP), peptide sequences *via* the non-integrin receptor syndecan for HBP, or integrins for ECM peptides [116]. The importance of RGD in alginate has been widely tested on RGD-coupled alginate (NovaMatrix<sup>®</sup>) using non-tumorigenic origin lung fibroblasts (Chinese hamster), myoblasts (murine), fibroblasts (embryonic, murine), kidney epithelial cells (canine) as well as carcinoma/adenocarcinoma origin human cell lines of cervix, ovarian, colon, colorectal, lung, prostate, breast, pancreas and leukemia [117]. Alginate hydrogels were thoroughly studied for their use as cell delivery vehicles for neo-cartilage formation [118], bone formation through transplanted calvarial osteoblasts [119] and regeneration of other tissues [120].

#### 6.1.5. Agarose

Agarose, also known as agar, is a naturally occurring biocompatible linear polysaccharide having 1,4-linked 3,6-anhydro- $\alpha$ -L-galactose and 1,3-linked- $\beta$ -D-galactose derivatives, which easily dissolves in water

upon moderate heating and forms a gel at room temperature. It has slow degradability, poor injectability, lower cell adhesiveness and high hydrophilicity but its adaptiveness for cell culture applications can be attained through polymer blending. Agarose turns into gel during cooling cycle through the formation of intermolecular hydrogen bonds, which result in the aggregation of double helices through anhydrous bridges. The viscoelastic properties of agarose are based on the degree of desulfation, molar mass and solution concentration. The elastic moduli of agarose gels range between  $\sim 1$  kPa to few thousand kPa, which is similar to the stiffness range of natural tissues [121]. Since native agarose has inert nature-lacking bioactive signals, blending with proteins and introducing cell-adhesion peptides into agarose, is a suitable method to enhance cell attachment. Nonetheless, agarose hydrogel possesses high water absorptivity and adequate permeation of oxygen and nutrients for cell growth, differentiation and proliferation [122]. The endothelial and salivary gland cells grown on stiff agarose gels showed capillary-like and acini-like morphologies [123], while soft agarose gels resulted in adipogenesis and neurogenesis. Numerous studies were conducted to evaluate the application of agarose hydrogels in biomedical applications including tissue engineering [124], chondrogenesis using MSCs for cartilage defect repair [125], reducing immunosuppression in diabetic disease treatment using insulin-producing porcine islets.

#### 6.1.6. Chondroitin Sulfate

Chondroitin sulfate (CS) is a glycosaminoglycan derivative containing alternating units of  $\beta$ -1,4-linked glucuronic acid and  $\beta$ -1,3-N-acetyl-D-glucosamine. It has a sulfated position on two different residues and classified into four major types. It is one of the major components in the ECM and provides mechanical resistance for certain tissues like cartilage to external compression. CS is generally extracted from cow trachea, pig ear or nose cartilage and shark cartilage. It is highly water-soluble and thus limits its use alone in the solid-state for biomedical applications. However, CS could be implemented for various applications by combining with other polymers. Its anionic nature allows easy interaction with cationic molecules to form interesting structures and thereby, augmenting its overall ability to function as a cell interacting molecule. Being one of the major components of the cartilage ECM, it possesses beneficial biological properties suitable for cartilage regeneration [126]. A modified version of CS, methacrylate chondroitin sulfate has been shown to support the chondrogenic differentiation of stem cells

[127]. Due to its inherent properties, CS has been mostly used in the cartilage tissue engineering applications. One study proved that a combination of CS and chitosan could aid chondrogenesis when bovine primary articular chondrocytes were seeded onto a thin layer of CS-chitosan hydrogel [128]. In another study, CS combined with chitosan resulted in good attachment and proliferation of seeded osteoblasts for bone formation [129]. Thermo-responsive hydrogels made of CS are also suitable for 2D and 3D cell culture using HEK 293 cells.

#### 6.1.7. Hyaluronic Acid

Hyaluronic acid (HA) or hyaluronan is an immunoneutral polysaccharide consisting of non-sulfated glycosaminoglycan with alternating disaccharide units of  $\beta$ (1,4)-D-glucuronic acid- $\beta$ (1,3)-N-acetyl-D-glucosamine. It is the only non-sulfated glycosaminoglycan distributed widely throughout connective, epithelial, and neural tissues in the body, which is in clinical use for many years. HA has a linear shape molecular structure and negative charges, made up of two sugars glucuronic acid and N-acetyl glucosamine and linked through alternating  $\beta$ -1,4 and  $\beta$ -1,3 glycosidic bonds. It is one of the major constituents of the ECM and has a prominent role in cell motility, wound healing, cellular signaling, matrix organization and angiogenesis [130]. The major sources of HA are rooster combs and *Streptococcus bacterium*. It is soluble in water and resistant to enzymatic degradation but can be modified to esters through the esterification of its carboxylic groups which enhances its processability to turn into membranes, spheres, and different porous structures. Carboxylic acid, hydroxyl, or N-acetyl groups in HA can be used for chemical modification to fabricate materials with desired functional groups. Being easily injectable, HA has been used in the cosmetic industry and tissue engineering and related approaches using human adipose-derived stem cells [131]. The hydrogel formed by crosslinking HA conjugates containing thiol functional groups with PEG vinyl sulfone *via* Michael addition has shown good cartilage regeneration ability when cultured with chondrocytes [132]. In another study, the migration and proliferation of mouse MSCs in HA hydrogel was found to increase with respect to the concentration of cell binding ligand [63]. Bone regeneration efficiency of acrylated HA-bone morphogenetic protein-2 hydrogel scaffold in combination with MSCs for rat calvarial bone defect repair was shown by Kim and his co-workers [133]. HA hydrogels were also reported to be ideal for various biomedical applications including skin regeneration using human fibroblasts

and keratinocytes, hepatocyte culture, as hybrid cardiac grafts, for blood vessel ingrowth and neural tissue development [134]. Hyaluronic acid-based 3D printable bio-ink for tissue engineering applications has been proven recently using bone cells, where the ink was printed in good flexible shape [135].

#### 6.1.8. Glycogen

Glycogen is a high molecular weight polysaccharide found in the liver and muscle of animals and has a critical role in energy storage. It contains about 30,000 glucose residues, where most of the glucose units are interlinked through  $\alpha$ -1,4 glycosidic linkages to result in a highly branched structure. Glycogen can be modified using various methods such as free radical polymerization, copper-catalyzed alkyne-azide cycloaddition and oxidative ring-opening to introduce a variety of bioactive species for therapeutic applications [136]. It has a spherical glycogenin protein core with a diameter of 50 nm and molecular weight of 400 kDa to few millions of Daltons. Considering the advantages of glycogen, it has multiple roles in drug delivery and other pharmaceutical applications [137]. Reports prove that glycogen hydrogel with multivalent binding sites of lectins could be used for targeting prostate cancer cells. Cationic enzymatically synthesized glycogen encapsulated with tetraphenyl porphine sulfonate was found to be effective for ovarian cancer cells compared to free drug dosage [138]. A nanogel with and without 5-fluorouracil was prepared from functionalized glycogen recently and found to be non-toxic towards MG-63 cancer cells when used alone, while the 5-fluorouracil-loaded nanogel kills the cancer cells effectively [139]. Glycogens have found applications as suitable materials for wound dressing applications. From biological testing, glycogen hydrogel microfibers were found to be highly porous, hydrophilic, readily functionalizable and nontoxic to human osteoblast-like MG63 cells. Collagen film crosslinked with oxidized glycogen also showed high *in vitro* cytocompatibility in cultures of human fibroblasts [140, 141].

#### 6.1.9. Starch

Starch is an odorless, tasteless white powder composed of two polymeric carbohydrates called amylose and amylopectin, in which the latter is in higher percentage in common types of cereal endosperm starches. The concentration of amylose and amylopectin in starch varies with type and source with an approximation of 20-25% and 75-80% respectively. Amylopectin contains chains of  $\alpha$ -D-glucopyranosyl units connected through (1 $\rightarrow$ 4) linkages with 5-6% of (1 $\rightarrow$ 6) bonds at the branch points while amylose has (1 $\rightarrow$ 4) linked  $\alpha$ -

D-glucopyranosyl units. Starch is generally insoluble in water or alcohol but can be dispersed in water upon heating. During cooling, the viscosity of starch increases due to the physical crosslinking of hydrogen bonds and forms of hydrogel. They are biodegradable, biocompatible and exhibit distinct structural forms and properties to be used in a variety of applications including food, cosmetics, thickening agent, paper and adhesives. In cell-based approach, starch is abundantly used for cartilage and bone-related research. One research group demonstrated the use of chondrocytes on starch-poly(caprolactone) to test the effect of dynamic culture on chondrocyte function and ECM synthesis [142]. Prior to this, the same group conducted an extensive study on corn starch-based materials through different methods [143, 144]. Cell culture with osteoblasts on starch/cellulose acetate scaffolds further proved the biocompatibility of the scaffold as a biomaterial while the biochemical assays demonstrated that cells maintained the osteogenic phenotype throughout the experiment [145]. The effect of starch/gelatin ratio on the *in vitro* response of MSCs was evaluated recently, where starch-rich hydrogels displayed the strongest osteogenic differentiation [146]. In a study reported this year, zwitterionic starch-based hydrogels were developed through thiolene crosslinking and cultured with brown adipose-derived stem cells. The hydrogels provided an effective 3D environment for maintaining the “stemness” of stem cells and effectively maintained their spontaneous cardiomyogenic differentiation capacity [147]. Hybrid hydrogel made of N-succinyl chitosan-dialdehyde starch was studied earlier for its cytocompatibility using human gingival fibroblast cells [148] while the potential of starch-based scaffolds for the proliferation and osteogenic differentiation of rat bone marrow stromal cells has also been revealed [149].

#### 6.1.10. Pullulan

Pullulan is a water-soluble polysaccharide obtained from the fermentation broth of *Aureobasidium pullulans*, containing maltotriose units connected by  $\alpha$ -1,6 glycosidic units. It can be prepared by fermentation of simple sugars and chemically modified to produce derivatives that are either less water-soluble or even completely insoluble. Characteristic glycosidic linkages give rise to the unique properties of pullulan while chemical modification can change its water solubility, viscosity or pH sensitivity by introducing functionally reactive groups. Pullulan has a range of applications such as a food additive, oxygen barrier, blood plasma substitute, adhesive film *etc.* Recently, pullulan was reported to be useful for various biomedical applica-

tions including wound healing, tissue engineering, targeted drug and gene delivery. In 2018, a study reported the preparation of an *in situ* forming and injectable CS/pullulan hydrogel with suitable gelation time and mechanical properties for cartilage tissue engineering. When chondrocytes were encapsulated, the hydrogel showed good viability and yielded a high content of cartilage ECM [126]. In another work, pullulan hydrogels were reinforced with nHAP and poly(3-hydroxybutyrate) fibers containing 3 wt% nHAP to enhance the compressive modulus of the scaffold by 10 fold. A double deposition method was followed to deposit hydroxyapatite on pore walls for rapid and uniform coating throughout the 3D scaffolds. Culturing of the human osteoprogenitor cell line (MG-63) on the hydrogel confirmed the potential of mineralized pullulan-based composite scaffolds in non-load-bearing bone tissue engineering application [150]. Salt-induced phase inversion technique was used to fabricate highly modifiable dermal-like pullulan-collagen composite hydrogels. It imitated the critical aspects of the structural chemistry of native skin. *In vitro* studies using human fibroblasts, murine MSCs and endothelial cells proved the cell viability while *in vivo* studies using the murine model improved wound closure [151]. Pullulan mixed with collagen was developed for skin tissue regeneration and *in vitro* tested with NIH3T3 fibroblast cells for biocompatibility. The potential of the hydrogel for wound healing was further proved through *in vivo* experiments on rat model [152]. Enzymatically cross-linked carboxymethylated pullulan/CS hydrogel [153] and pullulan microbeads combined with cellulose-based hydrogel for regenerating intervertebral disc [154] also demonstrate the biocompatible nature of pullulan based hydrogels. The latest study revealed the development of a high strength hydrogel of pullulan dialdehyde by crosslinking with gelatin, which was proved to be non-cytotoxic by treating with MC3T3 cells [155].

#### 6.1.11. Carrageenan

Carrageenan is a natural-origin polymer that closely mimics one of the most important constituents of native tissue ECM (glycosaminoglycan). It is a linear, water-soluble, sulfated anionic polysaccharide extracted from marine red algae of the class *Rhodophyceae*, with high flexibility and capability to form a variety of different gels at room temperature through helical structure assembly. Carrageenan can be divided based on its basic structure, with alternating  $\alpha$ -(1-3)-D-galactose-4-sulfate and  $\beta$ -(1-4)-3,6-anhydro-D-galactose being called kappa-carrageenan ( $\kappa$ -carrageenan) while iota-

carrageenan (iota-carrageenan) differs from  $\kappa$ -carrageenan by an additional sulphate group at C2 of the 1,4-linked galactose unit. Lambda-carrageenan ( $\lambda$ -carrageenan) has a third sulfate group at C6 of the 1,4-linked galactose unit. In gelation chemistry,  $\kappa$ -carrageenan produces rigid gels while iota-carrageenan results in soft gels.  $\lambda$ -carrageenan has a unique property of gelation only when mixed with proteins. Carrageenans have been widely used as stabilizing agents and emulsifiers in the food and pharmaceutical industries.  $\kappa$ -carrageenan has been proposed as a potential candidate for tissue engineering due to its good mechanical properties, gelation characteristics and resemblance to natural glycosaminoglycans. Taking advantage of the inherent thixotropic behavior,  $\kappa$ -carrageenan has been used as an injectable matrix to deliver macromolecules and cells for minimally invasive therapies. A study reported the use of novel composite of collagen/hydroxyapatite/ $\kappa$ -carrageenan for bone tissue engineering using mouse embryonic fibroblasts and confirmed biocompatible and suitable for bone replacement [156]. Another recent research evaluated the potential of injectable hydrogel prepared from carrageenan and hydroxyapatite nanorods as bone grafts [157]. Blending carrageenan with other biopolymers also gives rise to ideal hydrogel designs. Osteogenic differentiation and survival of adipose-derived stem cells were confirmed in  $\lambda$ -carrageenan/chitosan/gelatin hydrogels due to the presence of -OH, -COOH, -NH<sub>2</sub> and -SO<sub>3</sub>H functional groups [158]. In a separate study,  $\kappa$ -carrageenan/iron oxide hydrogel provided tailorable physical properties for chondrogenic differentiation of stem cells. When cultured with human adipose-derived stem cells, iron oxide magnetic nanoparticles improved the stability of hydrogel and increased gene expression of chondrogenic markers [159]. When carrageenan hydrogel was combined with TGF- $\beta$ 1 and stem cells, the growth factor-induced chondrocyte differentiation, proliferation and proteoglycans synthesis were observed, which proved to be a promising strategy for cartilage regeneration [160].

Other related biocompatible polysaccharides derived from seaweeds include fucoidan, laminarin and ulvan. They could also be easily processed to make hydrogels suitable for cell culture. Fucoidan-based hydrogels were prepared through chemical cross-linking and reported to be used for endothelial cell culture for vascular tissue engineering [161], while ulvan hydrogels incorporated with alkaline phosphatase fabricated through photo-crosslinking improved cellular activity [162].



### 6.1.12. Heparin

Heparin and heparin sulfate are linear polysaccharides, synthesized from a common precursor proteoglycan. Heparin and heparin sulfate have a linear polysaccharide structure with 1→4 linked disaccharide repeating units of uronic acid and glucosamine residues with varying degrees of sulfation and N-acetylation. Heparin is produced only from mast cells while heparin sulfate is found in most tissues. Heparin was discovered long back and well known as a blood anticoagulant due to its ability to bind to the serine protease inhibitor antithrombin and thus to inactivate thrombin. Heparin and heparin sulfate bind with proteins through electrostatic, hydrophobic interactions and hydrogen bonding, using the secondary structure. Heparin is isolated from the sources such as porcine intestine, natural tissues and bovine lung and the obtained heterogeneous portion has an average molecular weight of about 15 kDa. The presence of sulfate and carboxylate groups contributes to an overall negative charge, and thereby, allows interactions with numerous proteins, proteases, growth factors and chemokines. Such affinity of heparin for protein or growth factor has been employed in the design of engineered scaffolds for tissue regeneration or bioengineering. Apart from its applications in thrombogenicity, heparin can be combined with other biopolymers for its delivery. Modified heparin compounds were also used for direct cell differentiation. Heparin based hydrogels could be divided into various categories such as physically crosslinked heparin hydrogels, protein or peptide heparin crosslinked hydrogels, growth factor crosslinked hydrogels, chemically crosslinked heparin hydrogels, photo-crosslinked hydrogels, hydrogels formed *via* Michael-type addition reactions, hydrogels crosslinked through amide coupling and hydrogels prepared through enzyme-mediated crosslinking [163]. Heparin is also a good anti-cancer agent after the internalization into cancer cells [164]. Heparin has the ability to control angiogenic activity by preventing fibroblast growth factor (FGF)-induced endothelial cell migration and proliferation [165]. When modified with heparin, scaffolds could suppress non-specific protein absorption and at the same time, growth factors can promote cell attachment and proliferation [166]. Heparin modified materials are also capable of directing embryonic stem cell-derived neural progenitor cells differentiation with the help of growth factors *in vitro* and *in vivo*, after spinal cord injury [167, 168]. Heparin with thiol-functionalization was reacted with PEG-diacrylate to form a hydrogel and encapsulated with fibroblasts to prove the non-toxic characteristics [169]. In a separate study, thiolated heparin and diacrylated

PEG hydrogel were prepared for 3D cell culture and heparin was found to accelerate chondrocyte proliferation while maintaining chondrogenic phenotype for cartilage regeneration [170].

## 6.2. Proteins

Proteins are commonly used in the fabrication of hydrogels due to their unique properties. The chemistry of ECM has to be considered while designing a hydrogel since it surrounds cells in tissues. Suitable mechanical integrity for hydrogel is another relevant factor. ECM mainly contains proteoglycan filaments, collagen fibers and elastin. The function of collagen fibers is to provide tensile strength and durability for the surrounding tissue. Elastin assists the stretching and recoil of the ECM network and proteoglycan binds water and growth factors to give compression resistance. While preparing hydrogel scaffold with good cell adhesion, proliferation, and differentiation, the role of proteins cannot be neglected. It has critical roles in biomaterials through cell, growth factor and surface binding. In short, protein-based hydrogels are considered to be promising materials for various biomedical uses due to their high water content, tunable viscoelasticity, biocompatibility and injectability. The following part reviews the major protein molecules used for hydrogel fabrication, their structure, properties and examples of their applications.

### 6.2.1. Collagen

Collagen is one of the major components of ECM protein found in mammalian tissues responsible for important mechanical functions throughout the body. It is more abundantly observed in articular and bone tissues and plays a major role in functioning. The most common motifs in the amino acid sequence of collagen are glycine-proline-X and glycine-X-hydroxyproline, where X is any amino acid other than glycine, proline or hydroxyproline. It has a unique helix structure with three left-handed polypeptide helices intertwined together into a right-handed triple helix and peptide bonds crosslink adjacent helices at the ends of each helix. It can bind and release cellular mediators such as cytokines and growth factors. Collagen can be crosslinked through both physical and chemical methods, in which the former will generally result in reversible hydrogels with poor mechanical properties. At the same time, chemical crosslinking could lead to the fabrication of hydrogel with better physical properties. Collagen is one of the widely studied protein molecules for biomedical uses due to its unique characteristics. Considering biomedical aspects, collagen has widely been

used for bone and cartilage regeneration [171]. In an early study, collagen was bio-printed along with VEGF-releasing fibrin hydrogel scaffolds and murine neural stem cells (C17.2) for neural stem cell culture. The collagen caused morphological changes and migration of the printed C17.2 cells towards the fibrin gel to give > 90% cell viability [172]. Recently, the effect of collagen hydrogel in bone tissue engineering was verified through co-culture of MSCs and endothelial cells [173]. Most recent studies reported the fabrication of a hybrid silk fibroin/collagen hydrogel with tunable gelation and improved physical-biological properties to encapsulate human MSCs for cell delivery and tissue engineering in a wide spectrum of soft to hard tissues [174]. Cell cultured in collagen hydrogels were used alone or in combination with other components for numerous biomedical uses including wound healing [175], hepatic tissue development, skeletal muscle repair and tendon-ligament healing [176].

### 6.2.2. Gelatin

Gelatin is a mixture of polypeptides and proteins formed as a result of irreversible hydrolysis of collagen. There are two types of gelatin called type A and type B. The type A gelatin is obtained by acid hydrolysis while type B is produced through basic (alkali) hydrolysis of collagen. Alternatively, gelatin can also be extracted from the scales of fish and insects. The properties of gelatin vary with respect to the source and extraction method; and therefore gelatin from insects has different properties than commercial gelatin. It is a polydisperse peptide with high molecular weight and popular for food and biomedical use due to its gelling and thickening characteristics. Gelatin hydrogels can be crosslinked through physical or chemical methods. However, gelatin gels have low thermal stability, poor mechanical strength and faster degradation rates. It requires chemical crosslinking for mechanical stability to be used for cell culture related studies. The covalent bonds through chemical crosslinking could not only strengthen gelatin gels but also inhibit faster degradation. Similar to collagen, gelatin is also widely used in pharmaceuticals, cosmetics, foods, and in various biomedical applications due to its viscoelastic properties to act as a gelling agent, a thickener, or a stabilizer. One research group combined thiolated-gelatin with PEG-diacrylate to synthesize a hydrogel and the obtained hydrogel revealed improved cell spreading and showed better cell entrapment (neonatal human dermal fibroblasts) compared to physically incorporated gelatin in PEG hydrogel [177]. Previously, the research group of Khademhosseini reported directed endothelial

cell morphogenesis in micro-patterned gelatin methacrylate hydrogels. It was observed that the cells aligned and organized within the micro-patterned constructs and cord structures with organized actin fibers and circular/elliptical cross-sections were obtained [178]. Another study fabricated a fibroin-gelatin 3D tissue hydrogel construct with optimized rheology, secondary silk-gelatin bioink conformations, temporally controllable gelation strategies and printing parameters. Maximum cell viability and multi-lineage differentiation of the encapsulated human nasal inferior turbinate tissue-derived mesenchymal progenitor cells were observed and the strategy offered suitable method for direct printing of spatially customized anatomical architecture in a patient-specific manner [179]. A biomimetic gelatin hydrogel containing methacrylated dextran-graft-lysine is found to be useful for 3D smooth muscle cell culture and hence gelatin-based hydrogels are also useful in vascular tissue engineering and regeneration [180].

### 6.2.3. Albumin

Serum albumin is the protein found in vertebrate blood and it is the most abundant protein in blood plasma. In case of human serum albumin, it is produced in the liver and constitutes about half of the serum protein. It is the most abundant protein in blood plasma with 66 kDa molecular weight and water-soluble nature. It is also widely used as a critical component in therapeutic products due to its versatility as a drug carrier. Considering the similarity with ECM of tissues, biological hydrogels are extensively used in medical applications. Serum albumin hydrogels could be synthesized through intermolecular cross-linking through thermal or chemical means. Studies reveal that the electrostatic charges on albumin can be modified through solution pH change and further denaturation of the original protein structure exposes the hydrophobic regions. Kevin and co-workers proved that the newly exposed regions thus created could lead to biological hydrogel formation. An earlier study reported the combination of PEG and serum albumin as hydrogel matrix for enzyme immobilization in a mice model. Post-operative evaluation suggested the formation of a thin fibrous capsule around the implant site with limited inflammatory tissues [181]. Later, L-asparaginase was immobilized into the same PEG-albumin hydrogel to evaluate the *in vivo* performance. Another application of albumin is in the development of bio-adhesives based on the combination of albumin and adhesion compounds, which is approved for the limited use in the repair of aortic dissection [182]. Subia and co-

workers synthesized silk fibroin-albumin blended nanoparticles loaded with methotrexate through the desolvation method, which could be internalized by cells. The methotrexate-loaded nanoparticles displayed better encapsulation efficiency and drug loading ability. Cell viability assay using feline fibroblast cells (AH927) demonstrated that the silk fibroin-albumin nanoparticles did not affect the viability and biocompatibility of cells and could be a promising candidate for drug and bioactive molecules delivery [183]. A self-derived albumin hydrogel with pH and redox-sensitivity was reported in a recent study where the concentration of albumin and pH value tailored the physical, mechanical and biological properties of the hydrogel. Cyto-compatibility was confirmed using NIH3T3 fibroblasts while the hemo-compatibility assessment was performed using red blood cells. Such type of albumin hydrogel could potentially be useful for the preparation of scaffolds, microspheres and nanoparticles [184].

#### 6.2.4. Fibrin

Fibrin is a naturally occurring protein originated by thrombin-initiated aggregation of insoluble polypeptide chains of fibrinogen and then into a network of fibrils. It is the key protein involved in blood clotting, and the first biomaterial used to prevent bleeding and promote wound healing. Fibrin has a unique polymerization mechanism and network architecture, which allows the development of a wide array of soft substrates such as an injectable scaffold in tissue engineering or as a tissue culture model to study cellular behavior in a 3D environment. Effects of different thrombin concentrations for the structural characterization of 3D cell-cultured fibrin hydrogels were also studied. Fibrin gels have nonlinear elasticity and impressive stiffness to resist larger deformations and thereby work ideally as hemostatic plugs and as matrices for cell migration and wound healing. The filaments in a fibrin network are the softest in nature with large deformability and stiffness without a break. Fibrin naturally contains cell-binding sites, and therefore, does not require additional chemistry to introduce these sites for 2D and 3D cell culture studies. It can easily bind with many clot components and growth factors such as fibronectin and HA but its poor mechanical strength hinders its applicability in hard tissue replacement. Recently, a fibrin scaffold possessing integrin-binding sites adjacent to growth factor-binding sites with synergistic effects was used for bone regeneration [185]. The fibrin and cell surface integrin interaction occurs through two pairs of Arg-Gly-Asp (RGD) sites and one pair of AGDV. The

application of fibrin hydrogel has been reported in numerous studies and thus claims its candidacy for applications in medicine and bioengineering. When culturing with tumor cells, fibrin gels can also control the differentiation and proliferation rates of the cells through a mechanical method for cell targeting [186]. One research group prepared fibrin gels as a base matrix for incorporating non-glycosylated bone morphogenetic protein-2 (BMP-2), and its efficiency of bone healing in rat and dog models was confirmed [187]. The soft nature of fibrin gel is also proven to be ideally useful as a matrix model for neurons, where they usually reside in very soft tissues such as the brain [188]. In another study, fibrin gels were combined with biodegradable knitted fabric and neonatal rat heart cells to develop hybrid cardiac constructs with suitable mechanical properties for *in vitro* loading studies and *in vivo* implantation. After 1 week *in vitro* cell culture, the construct displayed a 5-fold increase in collagen content and maintenance of stiffness which was not observed in cell-free constructs. *In vivo* studies for 3 weeks exhibited the presence of cardiomyocytes and blood vessel ingrowth [189]. Fibrin gels also have been successfully used for the regeneration of cartilage tissues using chondrocytes [190], for angiogenesis in cardiovascular tissue engineering, for cord blood transplantation and for collagen-fibrin interpenetrating network fabrication for 3D cell culture [191].

#### 6.2.5. Silk Fibroin

Silks are natural structural proteins extracted from insects like spiders and worms. The silk produced from silkworm (*Bombyx mori*) is called silk fibroin. The quantity of silk fibroin acquired from each insect depends on the nutritional intake and environmental conditions. Silk contains two proteins, fibroin and sericin. It has a semi-crystalline nature with the major amino acids being tyrosine, glycine, serine, and alanine. Silk fibers contain up to 80% of silk fibroin and the remaining is made up of sericin, wax, and hydrocarbons. Fibroin has light (~26 kDa) and heavy chain (~390 kDa) polypeptides in 1:1 ratio connected through a disulfide bridge. The sericin is hydrophilic in nature and surrounded by fibroin. Silk should be boiled in alkaline solution at 120°C for at least 1 h to obtain pure fibroin and further solubilization and purification are necessary before its use as a biomaterial. Silk fibroin forms  $\beta$ -sheets from repeated amino acid sequence GAGAGS and becomes water-insoluble. Hydrophobic interactions within the protein chains in fibroin are responsible for the formation of silk fibroin hydrogels. Gelation can be enhanced by increasing temperature, decreasing

pH, by addition of a hydrophilic polymer or a change in fibroin concentration. Silk fibroin shows good mechanical and chemical properties and hence could be used as an excellent material for a variety of applications including cosmetics, food additives, transdermal drug delivery and scaffolds. Being an excellent biocompatible material with controlled degradation, it was also used to fabricate hydrogels for biomedical applications by integrating novel biological features. Silk fibroin hydrogel was combined with poly(D,L-lactide-glycolide) and tested *in vitro* and *in vivo*. These studies proved the biodegradability of the silk fibroin gels and showed the absence of inflammatory effects. Excellent bone regeneration observed *in vivo* in the rabbit cancellous model showed that silk fibroin hydrogels are potentially useful as synthetic injectable biomaterials for bone healing applications [192]. In 2015, Alexander and co-workers reported the preparation of transparent and nanostructured silk fibroin hydrogels with tunable mechanical characteristics for mimicking corneal tissue. Biocompatibility of the nanostructured silk fibroin hydrogels was tested and confirmed using human dermal fibroblasts. The culturing of human corneal epithelial cells on the hydrogel surface not only assured the important biological properties but also resulted in the formation of an epithelium without changing gel transparency [193]. The fundamental studies on the biocompatibility of silk fibroin were reported earlier in 2004, where silk fibroin hydrogels were prepared with and without glycerol. Cytotoxicity tests using human osteoblast-like cells indicated that both gels were non-cytotoxic, but cells showed faster proliferation on silk fibroin with glycerol but faster differentiation on silk fibroin hydrogel alone, which promoted *in situ* bone regeneration [194]. The use of fibroin hydrogel sponge and collagen gel for *in vitro* cartilage regeneration was studied by a group of researchers in 2003, where the hydrogel sponges were formed by phase separation. Chondrocytes were harvested from rabbits and cultured on both hydrogel sponges to observe well-defined cartilage tissue formation with higher sulfated glycosaminoglycan and cell density on fibroin hydrogel sponge compared to collagen gel [195].

#### 6.2.6. Matrigel

The Matrigel<sup>®</sup> matrix is a gelatinous protein mixture secreted by Engelbreth-Holm-Swarm (EHS) mouse sarcoma cells. This hydrogel is manufactured and marketed by leading biomedical companies and it has resemblance with the complex extracellular environment found in many tissues and therefore deemed ideal as a substrate for cell culture. It is an adequate platform for

the culture of polarized cells, promoting the differentiation of various cell types such as beta islets, hepatocytes, neurons, smooth muscle cells, endothelial and epithelial cells. In the high protein concentration grade, it provides greater matrix stiffness and scaffold integrity for *in vivo* cell delivery. In the growth factor-reduced pattern, it provides a more highly defined basement. A recent article described the use of Matrigel-alginate (1:1) hydrogel 3D construct to obtain a structurally stable and biologically active substrate for breast cancer cell culture. When human aggressive breast cancer cells were cultured, cells exhibited peculiar cytoskeleton shapes and nuclear fragmentation, characteristic of their malignancy with invadopodia expression. Moreover, cells mimicked a completely new 3D *in vitro* model of the very precursor steps of metastasis [196]. *In vitro* response of chondrocytes in Matrigel compared to other hydrogels of collagen, agarose and alginate was also studied earlier to establish its potential in cell culture [197]. Effects of Matrigel-coated Ca/P coating on bone cell behavior and cartilage repair by Ad-hBMP7-transfected chondrocytes on Matrigel scaffold were studied [198]. Matrigel can also aid the development of cell culture microenvironments for every specific culture needs. When trunk neural crest cells were cultured with different Matrigel lots in 2D and 3D environments, all analyzed Matrigel lots were equally efficient in allowing the appearance of glial cells, neurons, melanocytes, smooth muscle cells and chondrocytes. However, chondrocytes were found predominantly in the 3D microenvironment, whereas smooth muscle cells were almost exclusively located in the 2D microenvironment. Glial cells were present in both the environments, but with broader quantities on the 2D surface. Melanocytes and neurons were equally distributed in both 2D and 3D microenvironments, but with distinct morphologies [199]. Apart from above mentioned hydrogels, there are few more rarely explored protein-based hydrogels, like soy proteins, zein, wheat gluten, lecithin, gliadin, legumin *etc.*, which are useful for various biomedical needs including cell culture [200, 201].

#### 6.3. Bacterial Polyesters

Bacterial polyesters are biodegradable polymers that are synthesized by unbalanced growth of various bacteria, including *Bacillus megaterium*, *Wautersia eutropha* and *Pseudomonas*. These natural polymers with good mechanical stability have gained considerable attention in hydrogel synthesis due to their hydrolysable ester bonds. Due to their biodegradability, biocompatibility and non-toxicity, these polyester-based hydrogels have gained considerable attention as a drug

carrier in the biomedical industry. Starting from the rediscovery of polyhydroxy butyrate in late 1950s, bacterial polyesters have become a hot topic, and led to the successful discovery of many other types of microbial polyesters. In the following section, we discuss various members of this family that have been used for hydrogel fabrication.

### 6.3.1. Polyhydroxyalkanoates

Polyhydroxyalkanoates (PHAs), produced by an extensive variety of microorganisms can be considered as the family of biodegradable polyesters, which are biocompatible, biodegradable and non-toxic. Polyhydroxyalkanoates can be classified on the basis of carbon chain length of the polymers as short chain-length hydroxyalkanoic acids (SCL-PHAs) with 4 to 5 carbons in one repeating PHA unit, and medium chain-length hydroxyalkanoic acids (MCL-PHAs). The former one consists of poly(3-hydroxybutyrate) (PHB), poly(3-hydroxyvalerate) (PHV) and their copolymer poly(3-hydroxybutyrate-co-3-hydroxyvalerate) (PHBV), whereas the latter one includes poly(3-hydroxyoctanoate) (PHO) and poly(3-hydroxynonanoate) (PHN). Among different classes of PHAs available, PHB, the first PHAs discovered by the French scientist Lemoigne in 1926 in *Bacillus megaterium* is considered as the most widely accepted member of this family [202]. It is a linear, and homo-chiral thermoplastic bio-polyester that degrades to produce the endogenous ketone named 3-hydroxybutyric acid. Owing to the biodegradability attained through the hydrolysis involving the cleavage of esters bonds and their ability to promote sustainable development, PHAs were applied for various biomedical applications. These applications include the bioactive agent delivery, hard tissue replacement and tissue engineering. Although it is biodegradable, their advanced therapeutic applications in delivering bioactive agents were restricted by their incredibly high stability. Due to this high scaffold stability, the degradation of scaffolds and related drug release properties was not very satisfactory. Hence in order to solve the abovementioned problem, PHAs were modified with water-soluble functionalities to improve their biological behavior and thereby, widening their applications in various tissue engineering areas as poly(hydroxyl-butyrate-valerate) copolymers (PHBV) is another class of PHAs, which is a copolymer of PHB and PHV. PHBV is copolymer with slower biodegradation properties, and hence it has lot of applications in tissue engineering field especially for the controlled delivery of drugs as well as growth factors [203]. In addition to biodegradability and biocompati-

bility, a PHBV copolymer contains optical activity and thermo-plasticity which make this compound attractive in the biomedical field. Moreover, piezoelectric character of PHBV, which converts a mechanical stimulus into electrical charge can influence the cellular processes such as migration, proliferation and differentiation [204]. Polyhydroxyalkanoates were found to be biocompatible with cell adhesion characteristics. Different PHAs including PHB and PHBV were analyzed for their cell adhesion behavior and the results obtained for all the materials were satisfactory. In a study, the PHB scaffolds were analyzed using two cell lines, an osteosarcoma cell line and an epithelial cell line, to understand the effect of structural alterations in components of cell adhesion. They observed structural alterations in the cells cultured on PHB [205]. In another study, the influence of modified PHB on cell properties including cell attachment, morphology and proliferation, was analyzed using L929 mouse fibroblast cells as a model cell line and significant cell attachment was observed [206].

### 6.3.2. Suberin

Suberin is a composite biopolyester consisting of a polyaliphatic domain in association with a polyaromatic domain found in the suberized cell walls of higher plants, where it plays the fundamental role of a protective barrier between the organism and its environment. This lipid-based polyester contains long-chain fatty acid and glycerol, in which suberin acid is the fatty acid involved in its production. Suberin is a wax-like material consisting of a polyaliphatic domain and a polyaromatic domain. Among these, the polyaromatic domain that is located within the primary cell wall is mainly derived from ferulic acid. The polyaliphatic domain is located in between the primary cell wall and cell membrane, and is a biopolyester primarily composed of oxygenated fatty acid derivatives. The polyaliphatic domain is mainly responsible for the barrier function of suberin for water and solutes. Due to the antimicrobial properties, suberin fatty acids (SFAs) have been employed in biomedical applications, especially for wound treatment. In one particular study, suberin polymer was depolymerized by alkali solvent extraction, and the resulted SFA was combined with polyvinylpyrrolidone and chloramphenicol to produce electrospun fibers for wound healing application [207].

### 6.3.3. Gellan

Gellan, a linear anionic heteropolysaccharide produced by *Pseudomonas elodea* is a gelling agent wide-



ly used in food, biomedicine and pharmaceutical industry. It is composed of a tetrasaccharide repeating units of (1,3)- $\beta$ -D-glucose, (1,4)- $\beta$ -D-glucuronic acid, (1,4)- $\beta$ -D-glucose and (1,4)- $\alpha$ -L-rhamnose [208]. Gellan is available as acetylated and deacetylated compounds and both these compounds have the capacity to form thermo-reversible gels with different mechanical properties upon temperature decrease. The deacetylated form of gellan molecule known as gellan gum has a wide range of applications in biomedical fields. Recently, the FDA approved gellan gum has been receiving particular attention for tissue engineering applications due to its good mechanical and biological properties [209]. These naturally occurring polymers were accepted worldwide as a material for hydrogel preparation. Aqueous solutions of gellan turn into transparent, heat-resistant and acid-resistant gels with a decrease in temperature through a mechanism involving changes in the conformation of gellan chains from random coil to helix [210, 211]. The net negative charge on this polymer is attained from the carboxylic groups present in the glucuronic acid residues, which function as the key factor that promotes hydrogel formation. The characteristics of a gellan gum solution during the gelation process depend on its chemical nature and quantity of cations present. Gellan solutions may contain divalent cations or monovalent cations and the one containing divalent cations is able to promote the gelation much more strongly than monovalent cations. In the case of monovalent cations, the gelation is attained mainly as the result of the electrostatic repulsion between the ionized carboxylate groups on the gellan gum chains and hence the gelation is not as strong as the other one. Due to their stability and biological properties, gellan hydrogels have been used in various cell culture applications. One example of the application of gellan hydrogels in cell culture was demonstrated in a previous study in which gellan hydrogels were used to culture MC3T3 pre-osteoblastic cells [212]. In addition, gellan gum-based hydrogels have been used widely in various tissue engineering applications including bone, cartilage, spinal cord and neural tissue engineering [213]. Although gellan hydrogels show many advantages, their mechanical performance is not good enough for certain applications. Hence in order to enhance the mechanical performance and *in vitro* stability of gellan gum-based hydrogels, the polymer should be modified with various chemicals. The modification of glycidyl methacrylate by nucleophilic substitution reaction using hydroxyl and carboxyl groups in its structure prior to crosslinking is one method used to improve the properties of gellan. Modification with the methacry-

late group resulted in an improvement of the mechanical properties of the gel. In another study, gellan gum modified with poly(capro-lactone) as well as with HA showed improvements in the properties of gellan, which broadened its applications in tissue engineering field. In this way, hydrogels based on both gellan gum and modified gellan gum offer great opportunities as a material for cell culture.

#### 6.3.4. Dextran

Dextran is a highly water-soluble extracellular bacterial polysaccharide consisting of linear  $\alpha$ -1,6-linked glucopyranose with some degree of 1,3 branching [214]. This polymer produced in sucrose rich environment by *Lactobacillus*, *Leuconostoc* or *Streptococcus* can be converted into hydrogels through either physical or chemical crosslinking. Since dextran hydrogels are soft and flexible, these can be applied to burn wound treatment, where the hydrogel scaffold facilitates early inflammatory cell infiltration that leads to its rapid degradation, promoting the infiltration of angiogenic cells in the healing wounds. Dextran is a biodegradable compound and is metabolized by various dextranases present in various parts of the body including liver, spleen and colon. Dextran-based hydrogels can be synthesized by both physical and chemical crosslinking methods. Chemically cross-linked dextran hydrogels can be prepared by reacting a polymer with suitable crosslinking agents like diisocyanate and epichlorohydrin. Physically cross-linked polymers can be obtained through ionic interactions or hydrophobic interactions. Among these, physically crosslinked hydrogels have more applications in cell culture as it is formed without any crosslinking agents. The micro-carrier made from crosslinked dextran is available commercially as Sephadex, which has been used for cell culture applications since 1960s. In an experiment, Stenekes and co-workers applied crystallization technique to convert the aqueous solution of dextran into gel, in which gelation was attained through intramolecular hydrogen bonding [215]. Dextran is commonly used in biomedical field as an antithrombotic solution and as a drug delivery system. Although it has applications in cell culture, certain disadvantages of this material made modification of this material with some other materials necessary to achieve the desired properties. One example for such modification is grafting of cell adhesion peptides on low protein-binding dextran monolayer surfaces to stimulate the *in vitro* spreading of endothelial cells, fibroblasts, and smooth muscle cells. In another study, injectable hydrogels were prepared by crosslinking of dextran-tyramine and heparin-tyramine,

and the obtained hydrogels were used as for culture of chondrocytes. In this study, the heparin was incorporated to the hydrogel to enhance cartilage regeneration, and the results were satisfactory to explain potential of this hydrogel for cartilage tissue engineering [216]. Dextran-acrylate based hydrogel scaffolds can also be used for vascular differentiation of human embryonic stem cells, by crosslinking with RGD macromer by UV crosslinking. Methacrylate derivatives of dextran are another example of crosslinked dextran hydrogels that can undergo gelation through free radical polymerization in the presence of an initiator. These gels were used to culture human fibroblasts, and the results confirm that these dextran hydrogels are biocompatible for cell proliferation [217].

### 6.3.5. Xanthan

Xanthan is a high molecular weight anionic microbial polysaccharide produced by *Xanthomonas campestris* from sugar cane, corn or their derivatives. It consists of a cellulosic backbone of D-glucose, having side chains of D-mannosyl, and D-glucuronyl acid residues in which some of the inner and terminal mannoses may be substituted by acetate and pyruvate groups [218]. Being a high molecular weight exopolysaccharide having branched polymeric chains, xanthan has good water-solubility and excellent biocompatibility and is largely used as a thickener in food, cosmetics and drilling fluids. This water-soluble polysaccharide having non-Newtonian and pseudoplastic behavior can alter apparent viscosity significantly with time and/or shear rate [219]. The transition of a xanthan solution to disordered chain conformation at elevated temperatures and low ionic strength leads to the formation of gels. Due to its non-toxicity and excellent biocompatibility, xanthan hydrogels were used as a platform for cell culture applications. In a study, KB and HEK 293 cells were cultured to investigate the cytotoxicity of injectable xanthan gum hydrogels, and the results verified excellent biocompatibility of the material [220]. In another study, the *in vitro* behavior of xanthan hydrogels was analysed using the MG63 human osteosarcoma cell line. The study was performed using nanostructured hydrogel of gellan and xanthan containing dexamethasone disodium phosphate-encapsulated chitosan nanoparticles, where osteogenic differentiation and augmented bone regeneration were demonstrated [221]. The modification of xanthan gum with gellan and chitosan helps to mimic the viscoelastic properties of the natural ECM, and thereby provides a new route for preparing a xanthan-based hydrogel for cell culture.

### 6.3.6. Other Bacterial Polyesters

In addition to all the above mentioned bacterial polyesters, many other polymers belonging to this category are available for the applications in cell culture. Cutin, a biopolyester composed of hydroxyl and epoxy fatty acids is one of the examples. Cutin could be obtained from plants and it acts as a barrier between the aerial parts of higher plants and their environment. This amorphous polyester is composed of hydroxylated fatty acids and glycerol and shows hydrophobic character. It is arranged in the cuticles of plants to act as a unique barrier as well as to give hydrophobic and mechanical properties to the cuticular layer that in turn regulates multiple biological functions of plants [222]. The biological functions regulated by cutin barrier include resistance to biotic and abiotic stress, plant growth and development, water repellence and exchange of water and gas between plants and their environments. In addition to this, the layer of cutin can provide protection against UV radiation and subsequent maintenance of both polar and hydrophobic molecules. Based on the bio-functional properties of cuticular components, these polymers have gained various applications in biomedical fields. In order to widen their applications, these materials can be coupled with several genetic tools such as RNA interfaces, transfer DNA and targeting induced local lesions in genomes using various techniques [223].

Another example of the biopolyester is welan gum. Welan gum is a water-soluble anionic exopolysaccharide produced by the gram-negative microorganism named *Sphingomonas* sp. This non-gelling polysaccharide is composed of tetrasaccharide repeating units, with no side chains. The extracellular polysaccharide contains l-mannose, l-rhamnose, D-glucose, and D-glucuronic acids, and is primarily promoted for its excellent stability towards pH changes and shear, as well as for withholding its viscosity at even higher temperatures. Unlike many other bacterial polyesters, this material shows no gel-like behavior and especially does not show any characteristic changes in temperature range from 10 to 100°C [224]. Nonetheless, most of the applications are distributed in the petroleum industry and cement manufacturing and till now there is no reported use of welan gum in the field of biomedical engineering.

### 6.4. Polynucleotides

Polynucleotides are the class of biopolymers composed of long chains of nucleotides monomers joined together by ester linkages between the phosphoryl

group of nucleotide and the hydroxyl group of the sugar component of the neighboring nucleotide. The monomer unit of polynucleotides called nucleotides is an organic molecule that serves as the building block of nucleic acids, DNA and RNA. Nucleotides are made up of three main components; a nitrogenous base, a sugar component, and phosphate group(s). Polynucleotide based hydrogels are of interest for cell culture, which can be discussed based on the nature of the five-carbon sugar into DNA type and RNA type.

#### 6.4.1. DNA

Deoxyribonucleic acid (DNA) which is composed of the nucleotides adenine (A), cytosine (C), guanine (G) and thymine (T), forms double or triple strands with its complementary base pairs *via* hydrogen bonding and stacking of its bases [225]. Nucleic acids are polymers of nucleotides that are well known as genetic materials. DNA is a remarkable polymer that can be manipulated by a large number of molecular tools including enzymes. As a biomacromolecule, it is not only a bio-responsive entity but also a polymer that can be designed and modified by employing enzymatic and/or chemical methods. Traditionally, DNA is utilized as a carrier for genetic information. In material science, DNAs are considered as programmable and predictable polymers due their double helix structure consisting of purine and pyrimidine base pairs [226]. DNA-based hydrogels present several remarkable features including stability, flexibility and precise programmability. Under certain conditions, self-assembled DNA hydrogels can be achieved through sequence design, and DNA can also be incorporated into polymers to form DNA-hybrid hydrogels. In 2006, Luo and coworkers first reported the construction of a hydrogel entirely made from branched DNA *via* an enzymatic reaction [227]. In another work, an aptamer-functionalized DNA hydrogel was prepared for protein detection by incorporating inorganic nanomaterials such as gold nanoparticles and quantum dots as signal indicators. In this work, DNA hydrogel was designed with Y-shaped DNA and aptamer linker through simple DNA self-assembly and resulted in hydrogels having various advantages including biocompatibility, controllability, and ease of synthesis and modification [228]. Later in 2015, the same group demonstrated that the DNA hydrogels can be used successfully for 3D living cell bioprinting [229]. DNA can be synthesized in large quantities by an automated solid-phase technique and can also be modified with many functional groups, such as acrydite, amino, carboxyl and thiol, which can react with other functional moieties. With the development

of phosphoramidite chemistry, most DNA modifications can be incorporated by programming.

As a naturally occurring material, DNA based hydrogels show biocompatible and biodegradable characteristics. Moreover, due to their ability to attain any shape, DNA hydrogels can be molded into any size and shape with maximum precision and accuracy. In addition, they could be loaded with drugs, proteins and even living cells, which could be released over time upon degradation of the DNA hydrogel [230]. In DNA hydrogels, either change in environmental conditions or occurrence of an external stimulus changes the DNA structure, which, in turn, affects the properties of the hydrogel including its optical properties and surface properties. Thermo-responsive DNA hydrogels are one class of this category, which takes advantage of the hybridization between complementary base pairs of DNA and the thermal dissociation characteristics. Succinimide copolymers-based DNA hydrogel is considered as the first thermo-responsive DNA hydrogel. The succinimidyl ester group covalently immobilizes 5'-terminal-amino-modified DNAs to the side chains of a linear polymer, and the resulting copolymers remain in the solution phase. When the crosslinker DNAs, *i.e.* DNA strands complementary to the polymer-DNA, are added to the solution, they hybridize with polymer-DNAs and transform the linear polymers into a gel state.

#### 6.4.2. RNA

The ribonucleic acid, RNA, is a high molecular weight single stranded biopolymer consisting of five carbon and oxygen atoms. It is composed of repeating nucleotide units of ribose sugar, phosphate group and nitrogenous base. The structure of RNA consists of a reactive hydroxyl ( $-OH$ ) group on the second carbon atom which makes this material capable of undergoing hydrolysis [231]. It exhibits a phase separation-like behavior and undergoes structural rearrangements. RNAs can be divided into various classes such as messenger RNA (mRNA), transfer RNA (tRNA) and ribosomal RNA. mRNA is a type of RNA that carries the "message" of the DNA to the cytoplasm of cells in order to produce protein in the amino acid sequences specified by the mRNA. tRNA is a short-chain type of RNA present in cells that carries specific amino acids to regulate the formation of a protein with a specific amino acid. Finally, ribosomal RNA, the component of ribosomes, acts at a nonspecific site of mRNA and makes polypeptides.

RNA has found lots of biomedical applications, including gene therapy. In recent years RNA interference

has become an important strategy for gene therapy which can focus on specific genes. RNAs were also used for bone regeneration. In a recent study, the *in vivo* efficacy of cmRNA encoding BMP-2 for bone regeneration application in rats was evaluated, and the study suggested that the prepared cmRNA-containing scaffold is a powerful tool for stimulating bone regeneration [232]. Due to the stiff structure and relatively low spatial charge density, it is difficult to form stable and compact nano-complexes out of RNA. Recently RNAs have gained attention due to their capacity to form the self-assembled hydrogel structures out of it. The siRNA hydrogels prepared by Hong and co-workers through the crosslinking between siRNA and polyethyleneimine resulted in hydrogel containing inter- and intramolecular networks, demonstrating excellent structural stability during intracellular translocation [233]. In another study, a self-assembled dual-color RNA-triple-helix structure comprising two miRNAs was fabricated to provide outstanding capability to synergistically cure tumor. The final structure obtained was able to chemically interact and adhere to natural tissue amines in the tumor and resulted in 90% tumor shrinkage in two weeks after the gel implantation [234].

The chemical structure and properties of major natural polymers are shown in Table 1.

## 7. CHALLENGES AND FUTURE PERSPECTIVES

Even though various successful clinical translations of several engineered tissues have been done, relevant challenges are still associated with the use of hydrogel scaffolds. The use of various natural polymers made the mimicking of ECM much closer, but is not adequate enough to completely replace the functions associated with cellular response and regeneration. Although high water content and porosity of natural polymer-based hydrogels can provide aqueous environment for nutrient transport as required for cell growth, the difficulty in isolating these materials from biological tissues limits its versatility. In addition to this, the handling difficulties, lower mechanical properties and difficulties to sterilize the sample also act as obstacles for their widespread applications in cell culture and tissue engineering field. On the contrary, due to the excellent bioactive properties such as better cell interaction, biodegradation and biocompatibility, any modifications of their properties as well as in their fabrication techniques may result in excellent materials having various

applications in tissue engineering field. Even with better fabrication techniques and methods, hydrogels still lack the ability to maintain spatial and temporal control for homogenous cell distribution and growth. Poor cell penetration caused due to inadequate or non-interconnected hydrogel porosity is another concern. Even with many successful single tissue regeneration strategies, fabrication of a multi-tissue phase hydrogel and its associated unique ECM structure development is underway. A suitable co-culturing mechanism for hydrogel-based bi-phasic tissue development needs more attention in future studies. Due to the swollen or flexible nature, natural polymer-based hydrogels pose much inferior mechanical strength than those made of synthetic polymers and thereby inappropriate to use in load-bearing applications using respective precursor cells. Difficulties in making pre-vascularization inducing channels during hydrogel fabrication often lead to loss of both viability and function of the seeded cells.

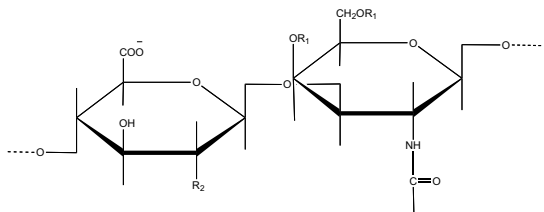
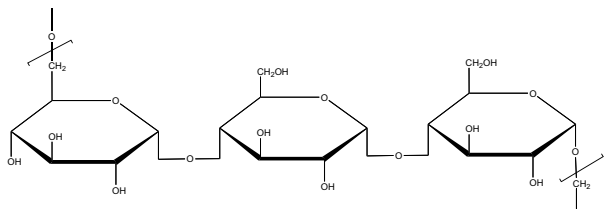
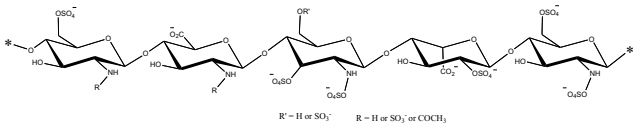
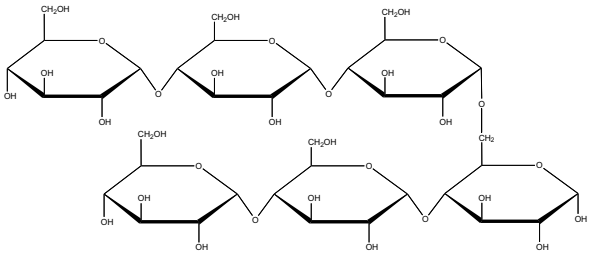
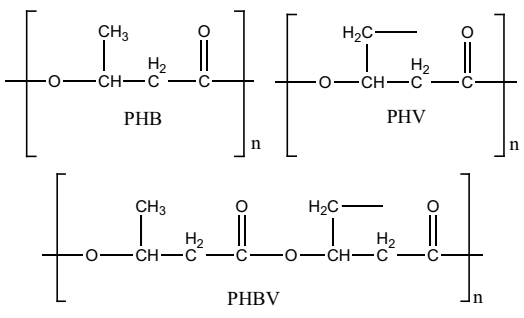
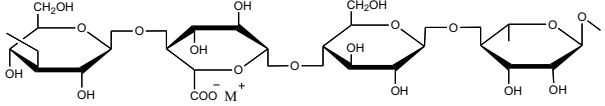
Apart from the above facts, natural polymer based hydrogels still face difficulties in characterization of cell response. Isolation and visualization of cells cultured on or within hydrogel scaffold are the two important steps involved in the analysis of cell responses. Although the isolation of RNA and proteins from cells grown on a hydrogel scaffold is similar to that seeded in the conventional plastic and glass surfaces, the scraping of cells from hydrogel may be found to be more difficult. Moreover, the separation of cells embedded in the hydrogel requires physical/enzymatic disruption and hence it is necessary to perform the procedures with maximum care to maintain the integrity of intracellular components. In many cases, the addition of undesirable buffer after cell culture may be involved for hydrogel solubilization when separating cells from these materials. Nonetheless, MCF-7 cells cultured on peptide hydrogel were isolated from the scaffold by mixing it with minimum essential medium [235]. Lowering the temperature of the system and thereby disrupting the gel matrix is another method used for the isolation of cells from some hydrogels. This method can be applied to separate cells from Matrigel hydrogels, as these materials exhibit a liquid state at lower temperatures. On the other hand, the alginate-based hydrogels require dissolving buffer to disrupt its structure. Enzymatic degradation of hydrogel is another method, and this can be applied for many hydrogels based on naturally derived materials such as collagen, fibrin and HA.

**Table 1.** The chemical structure and properties of major natural polymers.

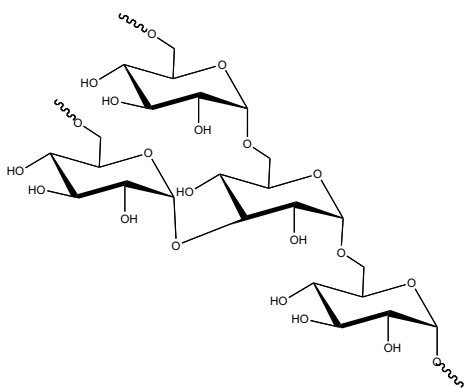
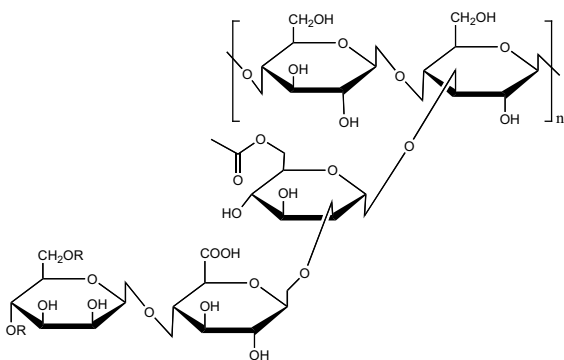
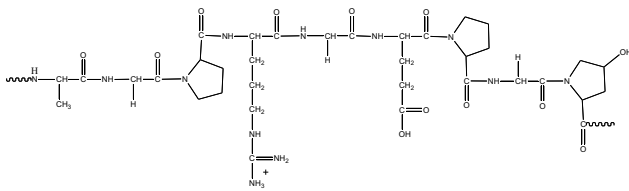
Name of Polymers	Chemical Structure	Properties
Chitin		<ul style="list-style-type: none"> <li>• Extreme biocompatibility and adaptability.</li> <li>• Degree of carboxymethylation can be varied to make it appropriate for cell encapsulation at room temperature.</li> </ul>
Chitosan		<ul style="list-style-type: none"> <li>• Properties can be tuned to match native ECM.</li> <li>• Carries high positive charges in physiological condition.</li> </ul>
Cellulose		<ul style="list-style-type: none"> <li>• Good biocompatibility.</li> <li>• Low toxicity.</li> <li>• Good mechanical properties.</li> </ul>
Agarose		<ul style="list-style-type: none"> <li>• Slow degradability.</li> <li>• Poor injectability.</li> <li>• Lower cell adhesiveness.</li> <li>• High hydrophilicity.</li> <li>• Adaptiveness for cell culture and applications can be attained through polymer blending.</li> </ul>
Carrageenan		<ul style="list-style-type: none"> <li>• Closely mimics constituents of native tissue ECM (glycosaminoglycans).</li> <li>• Good mechanical properties.</li> <li>• Good gelation characteristics.</li> </ul>
Glycogen		<ul style="list-style-type: none"> <li>• High molecular weight polysaccharide.</li> <li>• Has a spherical glycogenin protein core.</li> <li>• Contains multivalent binding sites of lectins.</li> </ul>

(Table 1) contd....



Name of Polymers	Chemical Structure	Properties
Chondroitin Sulphate	 <p><math>R_1 = \text{SO}_3^- \text{ or } \text{H}</math>  <math>R_2 = \text{OH or SO}_3^- \text{ (minor)}</math></p>	<ul style="list-style-type: none"> <li>One of the major components in the ECM.</li> <li>Highly water-soluble.</li> <li>The anionic nature allows easy interaction with cationic molecules to form interesting structures.</li> </ul>
Pullulan		<ul style="list-style-type: none"> <li>Water-soluble polysaccharide.</li> <li>Biocompatible.</li> <li>Water solubility, viscosity or pH sensitivity can be altered by chemical modifications.</li> </ul>
Heparin	 <p><math>R' = \text{H or SO}_3^- \quad R = \text{H or SO}_3^- \text{ or COCH}_3</math></p>	<ul style="list-style-type: none"> <li>Blood anticoagulant due to its ability to inactivate thrombin.</li> <li>Has the ability to control angiogenic activity.</li> </ul>
Starch		<ul style="list-style-type: none"> <li>Generally insoluble in water or alcohol, but can be dispersed in water upon heating.</li> <li>Viscosity increases upon cooling and forms hydrogel by physical crosslinking.</li> </ul>
Polyhydroxy-alkanoate (PHA)	 <p>PHB      PHV      PHBV</p>	<ul style="list-style-type: none"> <li>Biocompatible.</li> <li>Biodegradable.</li> <li>Non-toxic.</li> <li>Piezoelectric character influence the cellular processes such as migration, proliferation and differentiation.</li> </ul>
Gellan		<ul style="list-style-type: none"> <li>Capacity to form thermo-reversible gels upon temperature decrease.</li> <li>Good mechanical and biological properties.</li> </ul>

(Table 1) contd....

Name of Polymers	Chemical Structure	Properties
Dextran		<ul style="list-style-type: none"> <li>• Highly water-soluble.</li> <li>• Soft and flexible.</li> <li>• Biodegradable, and metabolized by various dextranases present in various parts of the body.</li> </ul>
Xanthan		<ul style="list-style-type: none"> <li>• Good water solubility.</li> <li>• Excellent biocompatibility.</li> <li>• Have non-Newtonian and pseudo-plastic behavior.</li> </ul>
Gelatin		<ul style="list-style-type: none"> <li>• Polydisperse peptide with a high molecular weight.</li> <li>• Excellent gelling and thickening characteristics.</li> <li>• Faster degradation rate.</li> <li>• Low thermal and mechanical properties.</li> </ul>

For the cell culture studies that require in situ cell imaging, hydrogel films can be fabricated on glass coverslips to enable high-resolution imaging. Cells cultured on these 2D hydrogels can often be processed for immunohistochemistry in the same fashion as cells cultured by a conventional method. However, due to their water-rich and polymeric natures, hydrogels are very sensitive to the histology procedures. As a result, it is necessary to provide care in order to make sure that the staining and washing steps do not disturb the attachment of hydrogel to coverslips. During this process, the chances for the covalent attachment of a hydrogel to glass slide are very high, and hence coverslip silanization can be used to avoid the possibility of this covalent binding. In addition, although the procedure used during the staining of the cells seeded on the hydrogel is similar to the conventional procedures, it is important

to extend the incubation time and mechanical agitation in order to make sure the diffusion of the chemicals into the interior parts of the hydrogels. This extra care during the experiments will result in the complete staining of cells in the hydrogel. The histology samples of hydrogels can be prepared by various techniques including standard paraffin processing and cryo-sectioning [236]. Among these, standard paraffin processing has some limitations including the possibilities of hydrogel collapse, which makes it very difficult to prepare samples using this technique. Cryo-sectioning is an alternative way for the histology sample preparation. Although cryo-sectioning can overcome some limitations of paraffin processing, the quality of hydrogel cryosections tends to be poor due to various factors including the size of the specimen, the density, susceptibility to chemicals, enzymatic reactions *etc.* Thus, the

studies and experiments suggest that the successful visualization of cellularized hydrogel scaffold is a challenging process that requires process optimization and skills. Taken together, hydrogels that can resolve the above-mentioned challenges will be an ideal candidate for various biomedical applications including cell culture.

## CONCLUSION

Hydrogels have attained considerable global scientific attention due to their use in a wide range of fields stemming from their versatility in composition, easiness of preparation, and tunable resulting physical properties. The soft nature, tunable molecule targeting affinity, biocompatibility, stimulus-responsive physicochemical changes, adjustable biodegradability through combined approach and controllable cross-linked density of hydrogels have made them crucial for applications in various biomedical uses including cell culture, tissue engineering and drug delivery. Since hydrogels are more likely to mimic the mechanical, biological, chemical and interfacial functions of native ECM, natural polymers based hydrogels are widely enrolled in combination with numerous types of cells to evaluate the interactions intended for use in cell delivery, drug elution or most abundantly in tissue regeneration. In this review, we attempt to give an overall view of the background of natural polymers based hydrogels, their definition and properties with swelling mechanism and gelation. The functional and biological requirements for the cellular interactions such as surface characteristics, stiffness, porosity, biocompatibility, biodegradation, cell adhesion and vascularization were also extensively explained with special reference to hydrogel fabrication and sterilization. Various natural polymers based hydrogels like polysaccharides, proteins, bacterial polyesters and polynucleotides are thoroughly presented here with extended illustration for the characterization of hydrogels and their future perspectives. Thus, this review has given an extensive survey on the overall picture of the natural polymers based hydrogels, their source and properties, requirements for biological uses and reported cases of cell culture uses.

## LIST OF ABBREVIATIONS

ECM	= Extracellular Matrix
2D	= Two-dimensional
3D	= Three-dimensional
pHEMA	= Poly(hydroxyethyl methacrylate)
IPN	= Interpenetrating Polymer Network

PEG	= Poly(ethylene glycol)
DNA	= Deoxyribonucleic Acid
RNA	= Ribonucleic Acid
Tg	= Glass Transition Temperature
GelMA	= Gelatin-methacrylate
MIP	= Intrusion Porosimetry
SEM	= Scanning Electron Microscopy
RGD	= Arg-Gly-Asp
HA	= Hyaluronic Acid
EPCS	= Progenitor Cells
PLL	= Poly-L-lysine
VEGF	= Vascular Endothelial Growth Factor
PDGF	= Platelet-derived Growth Factor
TGF- $\beta$	= Transforming Growth Factor- $\beta$
Ang-1	= Angiopoietin-1
EDC	= 1-ethyl-3-(3-dimethylaminopropyl)carbodiimide hydrochloride
NHS	= N-hydroxysuccinimide
HAP	= Hydroxyapatite
MSCs	= Mesenchymal Stem Cells
NP	= Nucleus Pulposus
nHAP	= Nanohydroxyapatite
HBP	= Heparin Binding Peptides
CS	= Chondroitin Sulfate
FGF	= Fibroblast Growth Factor
BMP-2	= Bone Morphogenetic Protein-2
EHS	= Engelbreth-holm-swarm
PHAs	= Polyhydroxyalkanoates
SCL-PHAs	Short Chain-length Hydroxyalkanoic Acids
MCL-PHAs	Medium Chain-length Hydroxyalkanoic Acids
PHB	= Poly(3-hydroxybutyrate)
PHV	= Poly(3-hydroxyvalerate)
PHBV	= Poly (3-hydroxybutyrate-co-3-hydroxyvalerate)
PHO	= Poly(3-hydroxyoctanoate)
PHN	= Poly(3-hydroxynonanoate)

PHBV	= Poly(hydroxyl-butyrates-valerate)
SFAs	= Suberin Fatty Acids
UV	= Ultraviolet
mRNA	= Messenger RNA
tRNA	= Transfer RNA
rRNA	= Ribosomal RNA

## CONSENT FOR PUBLICATION

Not applicable.

## FUNDING

We would like to acknowledge the financial support from the Ministry of Science and Technology, Taiwan, ROC (MOST106-2314-B-182-013-MY2) and Chang Gung Memorial Hospital, Taiwan, ROC (BMRP249, CMRPD2G0141 and CMRPD2G0142).

## CONFLICT OF INTEREST

The authors declare no conflict of interest, financial or otherwise.

## ACKNOWLEDGEMENTS

Declared none.

## REFERENCES

- [1] Kopecek, J. Polymer chemistry: swell gels. *Nature*, **2002**, 417(6887), 388-389, 391.  
<http://dx.doi.org/10.1038/417388a> PMID: 12024197
- [2] Peppas, N.A.; Bures, P.; Leobandung, W.; Ichikawa, H. Hydrogels in pharmaceutical formulations. *Eur. J. Pharm. Biopharm.*, **2000**, 50(1), 27-46.  
[https://doi.org/10.1016/S0939-6411\(00\)00090-4](https://doi.org/10.1016/S0939-6411(00)00090-4) PMID: 10840191
- [3] Ahmed, E.M. Hydrogel: Preparation, characterization, and applications: a review. *J. Adv. Res.*, **2015**, 6(2), 105-121.  
<http://dx.doi.org/10.1016/j.jare.2013.07.006> PMID: 25750745
- [4] Hoffman, A.S. Hydrogels for biomedical applications. *Adv. Drug Deliv. Rev.*, **2002**, 54(1), 3-12.  
[http://dx.doi.org/10.1016/S0169-409X\(01\)00239-3](http://dx.doi.org/10.1016/S0169-409X(01)00239-3) PMID: 11755703
- [5] Hennink, W.E.; van Nostrum, C.F. Novel crosslinking methods to design hydrogels. *Adv. Drug Deliv. Rev.*, **2002**, 54(1), 13-36.  
[http://dx.doi.org/10.1016/S0169-409X\(01\)00240-X](http://dx.doi.org/10.1016/S0169-409X(01)00240-X) PMID: 11755704
- [6] Shi, Z.; Gao, X.; Ullah, M.W.; Li, S.; Wang, Q.; Yang, G. Electroconductive natural polymer-based hydrogels. *Biomaterials*, **2016**, 111, 40-54.  
<http://dx.doi.org/10.1016/j.biomaterials.2016.09.020> PMID: 27721086
- [7] Chang, C.; Zhang, L. Cellulose-based hydrogels: present status and application prospects. *Carbohydr. Polym.*, **2011**, 84(1), 40-53.  
<http://dx.doi.org/10.1016/j.carbpol.2010.12.023>
- [8] Calvert, P. Hydrogels for soft machines. *Adv. Mater.*, **2009**, 21(7), 743-756.  
<http://dx.doi.org/10.1002/adma.200800534>
- [9] Li, J.; Mooney, D.J. Designing hydrogels for controlled drug delivery. *Nat. Rev. Mater.*, **2016**, 1(12), 16071.  
<http://dx.doi.org/10.1038/natrevmats.2016.71> PMID: 29657852
- [10] Wichterle, O.; Lim, D. Hydrophilic gels for biological use. *Nature*, **1960**, 185, 117.  
<http://dx.doi.org/10.1038/185117a0>
- [11] Lim, F.; Sun, A.M. Microencapsulated islets as bioartificial endocrine pancreas. *Science*, **1980**, 210(4472), 908-910.  
<http://dx.doi.org/10.1126/science.6776628> PMID: 6776628
- [12] Yannas, I.V.; Lee, E.; Orgill, D.P.; Skrabut, E.M.; Murphy, G.F. Synthesis and characterization of a model extracellular matrix that induces partial regeneration of adult mammalian skin. *Proc. Natl. Acad. Sci. USA*, **1989**, 86(3), 933-937.  
<http://dx.doi.org/10.1073/pnas.86.3.933> PMID: 2915988
- [13] Bajpai, A.K.; Shukla, S.K.; Bhanu, S.; Kankane, S. Responsive polymers in controlled drug delivery. *Prog. Polym. Sci.*, **2008**, 33(11), 1088-1118.  
<http://dx.doi.org/10.1016/j.progpolymsci.2008.07.005>
- [14] Wu, D.-Q.; Wang, T.; Lu, B.; Xu, X.-D.; Cheng, S.-X.; Jiang, X.-J.; Zhang, X.-Z.; Zhuo, R.-X. Fabrication of supramolecular hydrogels for drug delivery and stem cell encapsulation. *Langmuir*, **2008**, 24(18), 10306-10312.  
<http://dx.doi.org/10.1021/la8006876> PMID: 18680318
- [15] Nugent, M.J.D.; Higginbotham, C.L. Preparation of a novel freeze thawed poly(vinyl alcohol) composite hydrogel for drug delivery applications. *Eur. J. Pharm. Biopharm.*, **2007**, 67(2), 377-386.  
<http://dx.doi.org/10.1016/j.ejpb.2007.02.014> PMID: 17398082
- [16] Lee, Y.-J.; Braun, P.V. Tunable inverse opal hydrogel pH sensors. *Adv. Mater.*, **2003**, 15(7-8), 563-566.  
<http://dx.doi.org/10.1002/adma.200304588>
- [17] Sorber, J.; Steiner, G.; Schulz, V.; Guenther, M.; Gerlach, G.; Salzer, R.; Arndt, K.-F. Hydrogel-based piezoresistive pH sensors: investigations using FT-IR attenuated total reflection spectroscopic imaging. *Anal. Chem.*, **2008**, 80(8), 2957-2962.  
<http://dx.doi.org/10.1021/ac702598n> PMID: 18303919
- [18] Katsoulos, C.; Karageorgiadis, L.; Vasileiou, N.; Mousafeiropoulos, T.; Asimellis, G. Customized hydrogel contact lenses for keratoconus incorporating correction for vertical coma aberration. *Ophthalmic Physiol. Opt.*, **2009**, 29(3), 321-329.  
<http://dx.doi.org/10.1111/j.1475-1313.2009.00645.x> PMID: 19422564
- [19] Yasuda, H. Biocompatibility of nanofilm-encapsulated silicone and silicone-hydrogel contact lenses. *Macromol. Biosci.*, **2006**, 6(2), 121-138.  
<http://dx.doi.org/10.1002/mabi.200500153> PMID: 16416462
- [20] Ha, E.-J.; Kim, Y.-J.; An, S.S.A.; Kim, Y.-R.; Lee, J.-O.; Lee, S.-G.; Paik, H.J. Purification of His-tagged proteins using Ni<sup>2+</sup>-poly(2-acetamidoacrylic acid) hydrogel. *J. Chromatogr. B Analyt. Technol. Biomed. Life Sci.*, **2008**, 876(1), 8-12.  
<http://dx.doi.org/10.1016/j.jchromb.2008.10.020> PMID: 18980866
- [21] Singh, A.; Peppas, N.A. Hydrogels and scaffolds for immunomodulation. *Adv. Mater.*, **2014**, 26(38), 6530-6541.

- <http://dx.doi.org/10.1002/adma.201402105> PMID: 25155610
- [22] Wang, C.; Varshney, R.R.; Wang, D.A. Therapeutic cell delivery and fate control in hydrogels and hydrogel hybrids. *Adv. Drug Deliv. Rev.*, **2010**, 62(7-8), 699-710. <http://dx.doi.org/10.1016/j.addr.2010.02.001> PMID: 20138940
- [23] Oh, E.J.; Park, K.; Kim, K.S.; Kim, J.; Yang, J.A.; Kong, J.H.; Lee, M.Y.; Hoffman, A.S.; Hahn, S.K. Target specific and long-acting delivery of protein, peptide, and nucleotide therapeutics using hyaluronic acid derivatives. *J. Control Rel.*, **2010**, 141(1), 2-12. <https://doi.org/10.1016/j.jconrel.2009.09.010> PMID: 19758573
- [24] Singh, M.R.; Patel, S.; Singh, D. *Nanobiomaterials in Soft Tissue Engineering*; Grumezescu, A.M., Ed.; William Andrew Publishing, **2016**, pp. 231-260. <http://dx.doi.org/10.1016/B978-0-323-42865-1.00009-X>
- [25] Jin, R.; Moreira Teixeira, L.S.; Dijkstra, P.J.; Karperien, M.; van Blitterswijk, C.A.; Zhong, Z.Y.; Feijen, J. Injectable chitosan-based hydrogels for cartilage tissue engineering. *Biomaterials*, **2009**, 30(13), 2544-2551. <http://dx.doi.org/10.1016/j.biomaterials.2009.01.020> PMID: 19176242
- [26] Moura, M.J.; Figueiredo, M.M.; Gil, M.H. Rheological study of genipin cross-linked chitosan hydrogels. *Biomacromolecules*, **2007**, 8(12), 3823-3829. <http://dx.doi.org/10.1021/bm700762w> PMID: 18004810
- [27] Qu, X.; Wirsén, A.; Albertsson, A.C. Novel pH-sensitive chitosan hydrogels: swelling behavior and states of water. *Polymer (Guildf.)*, **2000**, 41(12), 4589-4598. [http://dx.doi.org/10.1016/S0032-3861\(99\)00685-0](http://dx.doi.org/10.1016/S0032-3861(99)00685-0)
- [28] Vrana, N.E.; Liu, Y.; McGuinness, G.B.; Cahill, P.A. Characterization of poly(vinyl alcohol)/chitosan hydrogels as vascular tissue engineering scaffolds. *Macromol. Symp.*, **2008**, 269(1), 106-110. <http://dx.doi.org/10.1002/masy.200850913>
- [29] Shen, Z.-S.; Cui, X.; Hou, R.-X.; Li, Q.; Deng, H.-X.; Fu, J. Tough biodegradable chitosan-gelatin hydrogels via *in situ* precipitation for potential cartilage tissue engineering. *RSC Advances*, **2015**, 5(69), 55640-55647. <http://dx.doi.org/10.1039/C5RA06835E>
- [30] Bidarra, S.J.; Barrias, C.C.; Granja, P.L. Injectable alginate hydrogels for cell delivery in tissue engineering. *Acta Biomater.*, **2014**, 10(4), 1646-1662. <http://dx.doi.org/10.1016/j.actbio.2013.12.006> PMID: 24334143
- [31] Chan, A.W.; Whitney, R.A.; Neufeld, R.J. Semisynthesis of a controlled stimuli-responsive alginate hydrogel. *Biomacromolecules*, **2009**, 10(3), 609-616. <http://dx.doi.org/10.1021/bm801316z> PMID: 19196004
- [32] Dorsey, S.M.; McGarvey, J.R.; Wang, H.; Nikou, A.; Arama, L.; Koomalsingh, K.J.; Kondo, N.; Gorman, J.H., III; Pilla, J.J.; Gorman, R.C.; Wenk, J.F.; Burdick, J.A. MRI evaluation of injectable hyaluronic acid-based hydrogel therapy to limit ventricular remodeling after myocardial infarction. *Biomaterials*, **2015**, 69, 65-75. <http://dx.doi.org/10.1016/j.biomaterials.2015.08.011> PMID: 26280951
- [33] Bhattacharyya, S.; Guillot, S.; Dabboue, H.; Tranchant, J.-F.; Salvétat, J.-P. Carbon nanotubes as structural nanofibers for hyaluronic acid hydrogel scaffolds. *Biomacromolecules*, **2008**, 9(2), 505-509. <http://dx.doi.org/10.1021/bm7009976> PMID: 18186607
- [34] Sim, H.J.; Thambi, T.; Lee, D.S. Heparin-based temperature-sensitive injectable hydrogels for protein delivery. *J. Mater. Chem. B. Mater. Biol. Med.*, **2015**, 3(45), 8892-8901. <http://dx.doi.org/10.1039/C5TB01399B>
- [35] Wang, F.; Li, Z.; Khan, M.; Tamama, K.; Kuppusamy, P.; Wagner, W.R.; Sen, C.K.; Guan, J. Injectable, rapid gelling and highly flexible hydrogel composites as growth factor and cell carriers. *Acta Biomater.*, **2010**, 6(6), 1978-1991. <http://dx.doi.org/10.1016/j.actbio.2009.12.011> PMID: 20004745
- [36] Van Tomme, S.R.; Hennink, W.E. Biodegradable dextran hydrogels for protein delivery applications. *Expert Rev. Med. Devices*, **2007**, 4(2), 147-164. <http://dx.doi.org/10.1586/17434440.4.2.147> PMID: 17359222
- [37] Li, X.; Xu, S.; Pen, Y.; Wang, J. The swelling behaviors and network parameters of cationic starch-g-acrylic acid/poly(dimethyldiallylammonium chloride) semi-interpenetrating polymer networks hydrogels. *J. Appl. Polym. Sci.*, **2008**, 110(3), 1828-1836. <http://dx.doi.org/10.1002/app.28581>
- [38] Gattás-Asfura, K.M.; Weisman, E.; Andreopoulos, F.M.; Micic, M.; Muller, B.; Sirpal, S.; Pham, S.M.; Leblanc, R.M. Nitrocinnamate-functionalized gelatin: synthesis and "smart" hydrogel formation via photo-cross-linking. *Biomacromolecules*, **2005**, 6(3), 1503-1509. <http://dx.doi.org/10.1021/bm049238w> PMID: 15877371
- [39] Chang, C.; Duan, B.; Cai, J.; Zhang, L. Superabsorbent hydrogels based on cellulose for smart swelling and controllable delivery. *Eur. Polym. J.*, **2010**, 46(1), 92-100. <http://dx.doi.org/10.1016/j.eurpolymj.2009.04.033>
- [40] Ma, Y.; Mao, Y.; An, Y.; Tian, T.; Zhang, H.; Yan, J.; Zhu, Z.; Yang, C.J. Target-responsive DNA hydrogel for non-enzymatic and visual detection of glucose. *Analyst (Lond.)*, **2018**, 143(7), 1679-1684. <http://dx.doi.org/10.1039/C8AN00010G> PMID: 29512663
- [41] Boudriot, U.; Dersch, R.; Greiner, A.; Wendorff, J.H. Electrospinning approaches toward scaffold engineering—a brief overview. *Artif. Organs*, **2006**, 30(10), 785-792. <http://dx.doi.org/10.1111/j.1525-1594.2006.00301.x> PMID: 17026578
- [42] Dhandayuthapani, B.; Yoshida, Y.; Maekawa, T.; Kumar D.S. Polymeric scaffolds in tissue engineering application. A review. *International Journal of Polymer Science*, **2011**, 2011, 19. <https://doi.org/10.1155/2011/290602>
- [43] Frisch, H.L. Diffusion in polymers. *Journal of Applied Polymer Science*; Crank, J.; G. S., Park, Eds.; Academic Press, London and New York, **1970**, 14(6), 1657. <https://doi.org/10.1002/pol.1969.160071204>
- [44] Ehrenhofer, A.; Elstner, M.; Wallmersperger, T. Normalization of hydrogel swelling behavior for sensoric and actuatoric applications. *Sens. Actuators B. Chem.*, **2018**, 255, 1343-1353. <http://dx.doi.org/10.1016/j.snb.2017.08.120>
- [45] Achilleos, E.C.; Prud'Homme, R.K.; Christodoulou, K.N.; Gee, K.R.; Kevrekidis, I.G. Dynamic deformation visualization in swelling of polymer gels. *Chem. Eng. Sci.*, **2000**, 55(17), 3335-3340. [http://dx.doi.org/10.1016/S0009-2509\(00\)00002-6](http://dx.doi.org/10.1016/S0009-2509(00)00002-6) PMID: 1600031
- [46] Anseth, K.S.; Bowman, C.N.; Brannon-Peppas, L. Mechanical properties of hydrogels and their experimental determination. *Biomaterials*, **1996**, 17(17), 1647-1657. [http://dx.doi.org/10.1016/0142-9612\(96\)87644-7](http://dx.doi.org/10.1016/0142-9612(96)87644-7) PMID: 8866026



- [47] Slaughter, B.V.; Khurshid, S.S.; Fisher, O.Z.; Khademhosseini, A.; Peppas, N.A. Hydrogels in regenerative medicine. *Adv. Mater.*, **2009**, *21*(32-33), 3307-3329. <http://dx.doi.org/10.1002/adma.200802106> PMID: 20882499
- [48] Jeong, B.; Kim, S.W.; Bae, Y.H. Thermosensitive sol-gel reversible hydrogels. *Adv. Drug Deliv. Rev.*, **2002**, *54*(1), 37-51. [http://dx.doi.org/10.1016/S0169-409X\(01\)00242-3](http://dx.doi.org/10.1016/S0169-409X(01)00242-3) PMID: 11755705
- [49] Bekturov, E.A. *Speciality Polymers*; Springer Berlin Heidelberg: Berlin, Heidelberg, **1981**, pp. 99-147. [http://dx.doi.org/10.1007/3-540-10554-9\\_11](http://dx.doi.org/10.1007/3-540-10554-9_11)
- [50] Alimirzaei, F.; Farahani, E. V.; Ghiaseddin, A.; M, S.; Pouri, Gharavi, N. Z. pH-sensitive chitosan hydrogel with instant gelation for myocardial regeneration. *J. Tissue Sci. Eng.* **2017**, *8*(3), 212. doi: 10.4172/2157-7552.1000212
- [51] Yao, H.; Wang, J.; Mi, S. Photo processing for biomedical hydrogels design and functionality: a review. *Polymers (Basel)*, **2017**, *10*(1), 11. <http://dx.doi.org/10.3390/polym10010011> PMID: 30966045
- [52] Nichol, J.; Koshy, S.; Bae, H.; Hwang, C.; Yamanlar, S.; Khademhosseini, A. Cell-laden microengineered gelatin methacrylate hydrogels. *Biomaterials*, **2010**, *31*(21), 5536-44. <http://dx.doi.org/10.1016/j.biomaterials.2010.03.064> PMID: 20417964
- [53] Fournier, E.; Passirani, C.; Montero-Menei, C.N.; Benoit, J.P. Biocompatibility of implantable synthetic polymeric drug carriers: focus on brain biocompatibility. *Biomaterials*, **2003**, *24*(19), 3311-3331. [http://dx.doi.org/10.1016/S0142-9612\(03\)00161-3](http://dx.doi.org/10.1016/S0142-9612(03)00161-3) PMID: 12763459
- [54] He, X.; Wei, B.; Mi, Y. Aptamer based reversible DNA induced hydrogel system for molecular recognition and separation. *Chem. Commun. (Camb.)*, **2010**, *46*(34), 6308-6310. <http://dx.doi.org/10.1039/c0cc01392g> PMID: 20672164
- [55] Trappmann, B.; Baker, B.M.; Polacheck, W.J.; Choi, C.K.; Burdick, J.A.; Chen, C.S. Matrix degradability controls multicellularity of 3D cell migration. *Nat. Commun.*, **2017**, *8*(1), 371. <http://dx.doi.org/10.1038/s41467-017-00418-6> PMID: 28851858
- [56] Saez, A.; Ghibaudo, M.; Buguin, A.; Silberzan, P.; Ladoux, B. Rigidity-driven growth and migration of epithelial cells on microstructured anisotropic substrates. *Proc. Natl. Acad. Sci. USA*, **2007**, *104*(20), 8281-8286. <http://dx.doi.org/10.1073/pnas.0702259104> PMID: 17488828
- [57] Engler, A.J.; Sen, S.; Sweeney, H.L.; Discher, D.E. Matrix elasticity directs stem cell lineage specification. *Cell*, **2006**, *126*(4), 677-689. <http://dx.doi.org/10.1016/j.cell.2006.06.044> PMID: 16923388
- [58] Eckert, R.L.; Rorke, E.A. Molecular biology of keratinocyte differentiation. *Environ. Health Perspect.*, **1989**, *80*, 109-116. <http://dx.doi.org/10.1289/ehp.8980109> PMID: 2466639
- [59] Fan, C.; Wang, D.A. macroporous hydrogel scaffolds for three-dimensional cell culture and tissue engineering. *Tissue Eng. Part B Rev.*, **2017**, *23*(5), 451-461. <http://dx.doi.org/10.1089/ten.teb.2016.0465> PMID: 28067115
- [60] Sokic, S.; Christenson, M.; Larson, J.; Papavasiliou, G. *In situ* generation of cell-laden porous MMP-sensitive PEG-DA hydrogels by gelatin leaching. *Macromol. Biosci.*, **2014**, *14*(5), 731-739. <http://dx.doi.org/10.1002/mabi.201300406> PMID: 24443002
- [61] Annabi, N.; Nichol, J.W.; Zhong, X.; Ji, C.; Koshy, S.; Khademhosseini, A.; Dehghani, F. Controlling the porosity and microarchitecture of hydrogels for tissue engineering. *Tissue Eng. Part B Rev.*, **2010**, *16*(4), 371-383. <http://dx.doi.org/10.1089/ten.teb.2009.0639> PMID: 20121414
- [62] Norris, S.C.P.; Delgado, S.M.; Kasko, A.M. Mechanically robust photodegradable gelatin hydrogels for 3D cell culture and *in situ* mechanical modification. *Polym. Chem.*, **2019**, *10*(23), 3180-3193. <http://dx.doi.org/10.1039/C9PY00308H>
- [63] Lei, Y.; Gojini, S.; Lam, J.; Segura, T. The spreading, migration and proliferation of mouse mesenchymal stem cells cultured inside hyaluronic acid hydrogels. *Biomaterials*, **2011**, *32*(1), 39-47. <http://dx.doi.org/10.1016/j.biomaterials.2010.08.103> PMID: 20933268
- [64] Bryant, S.J.; Bender, R.J.; Durand, K.L.; Anseth, K.S. Encapsulating chondrocytes in degrading PEG hydrogels with high modulus: engineering gel structural changes to facilitate cartilaginous tissue production. *Biotechnol. Bioeng.*, **2004**, *86*(7), 747-755. <http://dx.doi.org/10.1002/bit.20160> PMID: 15162450
- [65] Foley, J.D.; Grunwald, E.W.; Nealey, P.F.; Murphy, C.J. Cooperative modulation of neuritegenesis by PC12 cells by topography and nerve growth factor. *Biomaterials*, **2005**, *26*(17), 3639-3644. <http://dx.doi.org/10.1016/j.biomaterials.2004.09.048> PMID: 15621254
- [66] Kim, Y.; Abuefilat, A.Y.; Hoo, S.P.; Al-Abboodi, A.; Liu, B.; Ng, T.; Chan, P.; Fu, J. Tuning the surface properties of hydrogel at the nanoscale with focused ion irradiation. *Soft Matter*, **2014**, *10*(42), 8448-8456. <http://dx.doi.org/10.1039/C4SM01061B> PMID: 25225831
- [67] Larsson, C.; Thomsen, P.; Lausmaa, J.; Rodahl, M.; Kaseemo, B.; Ericson, L.E. Bone response to surface modified titanium implants: studies on electropolished implants with different oxide thicknesses and morphology. *Biomaterials*, **1994**, *15*(13), 1062-1074. [http://dx.doi.org/10.1016/0142-9612\(94\)90092-2](http://dx.doi.org/10.1016/0142-9612(94)90092-2) PMID: 7888577
- [68] Camci-Unal, G.; Nichol, J.W.; Bae, H.; Tekin, H.; Bischoff, J.; Khademhosseini, A. Hydrogel surfaces to promote attachment and spreading of endothelial progenitor cells. *J. Tissue Eng. Regen. Med.*, **2013**, *7*(5), 337-347. <http://dx.doi.org/10.1002/term.517> PMID: 22223475
- [69] Baier, R.E.; Meyer, A.E.; Natiella, J.R.; Natiella, R.R.; Carter, J.M. Surface properties determine bioadhesive outcomes: methods and results. *J. Biomed. Mater. Res.*, **1984**, *18*(4), 337-355. <http://dx.doi.org/10.1002/jbm.820180404> PMID: 6736072
- [70] Seliktar, D. Designing cell-compatible hydrogels for biomedical applications. *Science*, **2012**, *336*(6085), 1124-1128. <http://dx.doi.org/10.1126/science.1214804> PMID: 22654050
- [71] Carmeliet, P.; Jain, R.K. Angiogenesis in cancer and other diseases. *Nature*, **2000**, *407*(6801), 249-257. <http://dx.doi.org/10.1038/35025220> PMID: 11001068

- [72] Druecke, D.; Langer, S.; Lamme, E.; Pieper, J.; Ugarkovic, M.; Steinau, H.U.; Homann, H.H. Neovascularization of poly(ether ester) block-copolymer scaffolds *in vivo*: long-term investigations using intravital fluorescent microscopy. *J. Biomed. Mater. Res. A*, **2004**, *68*(1), 10-18. <http://dx.doi.org/10.1002/jbm.a.20016> PMID: 14661244
- [73] Marshall, A.J.; Ratner, B.D. Quantitative characterization of sphere-templated porous biomaterials. *AIChE J.*, **2005**, *51*(4), 1221-1232. <http://dx.doi.org/10.1002/aic.10390>
- [74] Unger, R.E.; Sartoris, A.; Peters, K.; Motta, A.; Migliaresi, C.; Kunkel, M.; Bulnheim, U.; Rychly, J.; Kirkpatrick, C.J. Tissue-like self-assembly in cocultures of endothelial cells and osteoblasts and the formation of microcapillary-like structures on three-dimensional porous biomaterials. *Biomaterials*, **2007**, *28*(27), 3965-3976. <http://dx.doi.org/10.1016/j.biomaterials.2007.05.032> PMID: 17582491
- [75] Zhang, L.; Webster, T.J. Nanotechnology and nanomaterials: Promises for improved tissue regeneration. *Nano Today*, **2009**, *4*(1), 66-80. <http://dx.doi.org/10.1016/j.nantod.2008.10.014>
- [76] Liu, H.; Roy, K. Biomimetic three-dimensional cultures significantly increase hematopoietic differentiation efficacy of embryonic stem cells. *Tissue Eng.*, **2005**, *11*(1-2), 319-330. <http://dx.doi.org/10.1089/ten.2005.11.319> PMID: 15738685
- [77] Reis, L.A.; Chiu, L.L.Y.; Liang, Y.; Hyunh, K.; Momen, A.; Radisic, M. A peptide-modified chitosan-collagen hydrogel for cardiac cell culture and delivery. *Acta Biomater.*, **2012**, *8*(3), 1022-1036. <http://dx.doi.org/10.1016/j.actbio.2011.11.030> PMID: 22155066
- [78] El-Sherbiny, I.M.; Yacoub, M.H. Hydrogel scaffolds for tissue engineering: progress and challenges. *Glob. Cardiol. Sci. Pract.*, **2013**, *2013*(3), 316-342. <http://dx.doi.org/10.5339/gcsp.2013.38> PMID: 24689032
- [79] Kuijpers, A.J.; van Wachem, P.B.; van Luyn, M.J.A.; Engbers, G.H.M.; Krijgsveld, J.; Zaat, S.A.J.; Dankert, J.; Feijen, J. *In vivo* and *in vitro* release of lysozyme from cross-linked gelatin hydrogels: a model system for the delivery of antibacterial proteins from prosthetic heart valves. *J. Control. Release*, **2000**, *67*(2-3), 323-336. [http://dx.doi.org/10.1016/S0168-3659\(00\)00221-2](http://dx.doi.org/10.1016/S0168-3659(00)00221-2) PMID: 10825564
- [80] Kim, T.K.; Yoon, J.J.; Lee, D.S.; Park, T.G. Gas foamed open porous biodegradable polymeric microspheres. *Biomaterials*, **2006**, *27*(2), 152-159. <http://dx.doi.org/10.1016/j.biomaterials.2005.05.081> PMID: 16023197
- [81] Kumar, A.; Mishra, R.; Reinwald, Y.; Bhat, S. Cryogels: freezing unveiled by thawing. *Mater. Today*, **2010**, *13*(11), 42-44. [http://dx.doi.org/10.1016/S1369-7021\(10\)70202-9](http://dx.doi.org/10.1016/S1369-7021(10)70202-9)
- [82] Wade, R.J.; Bassin, E.J.; Rodell, C.B.; Burdick, J.A. Protease-degradable electrospun fibrous hydrogels. *Nat. Commun.*, **2015**, *6*, 6639. <http://dx.doi.org/10.1038/ncomms7639> PMID: 25799370
- [83] McDonnell, G.E.; Sheard, D. *In A Practical Guide to Decontamination in Healthcare*. Wiley-Blackwell, **2015**, 460.
- [84] Singh, R.; Singh, D.; Singh, A. Radiation sterilization of tissue allografts: a review. *World J. Radiol.*, **2016**, *8*(4), 355-369. <http://dx.doi.org/10.4329/wjr.v8.i4.355> PMID: 27158422
- [85] Karajanagi, S.S.; Yoganathan, R.; Mammucari, R.; Park, H.; Cox, J.; Zeitels, S.M.; Langer, R.; Foster, N.R. Application of a dense gas technique for sterilizing soft biomaterials. *Biotechnol. Bioeng.*, **2011**, *108*(7), 1716-1725. <http://dx.doi.org/10.1002/bit.23105> PMID: 21337339
- [86] Bačáková, L.; Novotná, K.; Pařízek, M. Polysaccharides as cell carriers for tissue engineering: the use of cellulose in vascular wall reconstruction. *Physiol. Res.*, **2014**, *63*(Suppl. 1), S29-S47. PMID: 24564664
- [87] Slock, J.A.; Stahly, D.P. Polysaccharide that may serve as a carbon and energy storage compound for sporulation in *Bacillus cereus*. *J. Bacteriol.*, **1974**, *120*(1), 399-406. <http://dx.doi.org/10.1128/JB.120.1.399-406.1974> PMID: 4214355
- [88] Ge, Z.; Baguenard, S.; Lim, L.Y.; Wee, A.; Khor, E. Hydroxyapatite-chitin materials as potential tissue engineered bone substitutes. *Biomaterials*, **2004**, *25*(6), 1049-1058. [http://dx.doi.org/10.1016/S0142-9612\(03\)00612-4](http://dx.doi.org/10.1016/S0142-9612(03)00612-4) PMID: 14615170
- [89] Sudheesh Kumar, P.T.; Srinivasan, S.; Lakshmanan, V.-K.; Tamura, H.; Nair, S.V.; Jayakumar, R.  $\beta$ -Chitin hydrogel/nano hydroxyapatite composite scaffolds for tissue engineering applications. *Carbohydr. Polym.*, **2011**, *85*(3), 584-591. <http://dx.doi.org/10.1016/j.carbpol.2011.03.018>
- [90] Liu, H.; Liu, J.; Qi, C.; Fang, Y.; Zhang, L.; Zhuo, R.; Jiang, X. Thermosensitive injectable in-situ forming carboxymethyl chitin hydrogel for three-dimensional cell culture. *Acta Biomater.*, **2016**, *35*, 228-237. <http://dx.doi.org/10.1016/j.actbio.2016.02.028> PMID: 26911882
- [91] Chang, C.; Peng, N.; He, M.; Teramoto, Y.; Nishio, Y.; Zhang, L. Fabrication and properties of chitin/hydroxyapatite hybrid hydrogels as scaffold nanomaterials. *Carbohydr. Polym.*, **2013**, *91*(1), 7-13. <http://dx.doi.org/10.1016/j.carbpol.2012.07.070> PMID: 23044099
- [92] Kumar, P.T.S.; Srinivasan, S.; Lakshmanan, V.-K.; Tamura, H.; Nair, S.V.; Jayakumar, R. Synthesis, characterization and cytocompatibility studies of  $\alpha$ -chitin hydrogel/nano hydroxyapatite composite scaffolds. *Int. J. Biol. Macromol.*, **2011**, *49*(1), 20-31. <http://dx.doi.org/10.1016/j.ijbiomac.2011.03.006> PMID: 21435350
- [93] Suzuki, D.; Takahashi, M.; Abe, M.; Sarukawa, J.; Tamura, H.; Tokura, S.; Kurahashi, Y.; Nagano, A. Comparison of various mixtures of  $\beta$ -chitin and chitosan as a scaffold for three-dimensional culture of rabbit chondrocytes. *J. Mater. Sci. Mater. Med.*, **2008**, *19*(3), 1307-1315. <http://dx.doi.org/10.1007/s10856-007-3245-9> PMID: 17851736
- [94] Bi, B.; Ma, M.; Lv, S.; Zhuo, R.; Jiang, X. In-situ forming thermosensitive hydroxypropyl chitin-based hydrogel crosslinked by Diels-Alder reaction for three dimensional cell culture. *Carbohydr. Polym.*, **2019**, *212*, 368-377. <http://dx.doi.org/10.1016/j.carbpol.2019.02.058> PMID: 30832869
- [95] Ji, C.; Khademhosseini, A.; Dehghani, F. Enhancing cell penetration and proliferation in chitosan hydrogels for tissue engineering applications. *Biomaterials*, **2011**, *32*(36), 9719-9729. <http://dx.doi.org/10.1016/j.biomaterials.2011.09.003> PMID: 21925727

- [96] Bhattarai, N.; Gunn, J.; Zhang, M. Chitosan-based hydrogels for controlled, localized drug delivery. *Adv. Drug Deliv. Rev.*, **2010**, 62(1), 83-99.  
<http://dx.doi.org/10.1016/j.addr.2009.07.019> PMID: 19799949
- [97] Han, H.D.; Song, C.K.; Park, Y.S.; Noh, K.H.; Kim, J.H.; Hwang, T.; Kim, T.W.; Shin, B.C. A chitosan hydrogel-based cancer drug delivery system exhibits synergistic anti-tumor effects by combining with a vaccinia viral vaccine. *Int. J. Pharm.*, **2008**, 350(1-2), 27-34.  
<http://dx.doi.org/10.1016/j.ijpharm.2007.08.014> PMID: 17897800
- [98] Chiu, Y.L.; Chen, S.C.; Su, C.J.; Hsiao, C.W.; Chen, Y.M.; Chen, H.L.; Sung, H.W. pH-triggered injectable hydrogels prepared from aqueous N-palmitoyl chitosan: *in vitro* characteristics and *in vivo* biocompatibility. *Biomaterials*, **2009**, 30(28), 4877-4888.  
<http://dx.doi.org/10.1016/j.biomaterials.2009.05.052> PMID: 19527916
- [99] Richardson, S.M.; Hughes, N.; Hunt, J.A.; Freemont, A.J.; Hoyland, J.A. Human mesenchymal stem cell differentiation to NP-like cells in chitosan-glycerophosphate hydrogels. *Biomaterials*, **2008**, 29(1), 85-93.  
<http://dx.doi.org/10.1016/j.biomaterials.2007.09.018> PMID: 17920676
- [100] Ngoenkam, J.; Faikrua, A.; Yasothornsrikul, S.; Viyoch, J. Potential of an injectable chitosan/starch/beta-glycerol phosphate hydrogel for sustaining normal chondrocyte function. *Int. J. Pharm.*, **2010**, 391(1-2), 115-124.  
<http://dx.doi.org/10.1016/j.ijpharm.2010.02.028> PMID: 20206248
- [101] Ho, M.H.; Wang, D.M.; Hsieh, H.J.; Liu, H.C.; Hsien, T.Y.; Lai, J.Y.; Hou, L.T. Preparation and characterization of RGD-immobilized chitosan scaffolds. *Biomaterials*, **2005**, 26(16), 3197-3206.  
<http://dx.doi.org/10.1016/j.biomaterials.2004.08.032> PMID: 15603814
- [102] Ono, K.; Saito, Y.; Yura, H.; Ishikawa, K.; Kurita, A.; Akaike, T.; Ishihara, M. Photocrosslinkable chitosan as a biological adhesive. *J. Biomed. Mater. Res.*, **2000**, 49(2), 289-295.  
[http://dx.doi.org/10.1002/\(SICI\)1097-4636\(200002\)49:2<289::AID-JBM18>3.0.CO;2-M](http://dx.doi.org/10.1002/(SICI)1097-4636(200002)49:2<289::AID-JBM18>3.0.CO;2-M) PMID: 10571917
- [103] Cheng, Y.; Luo, X.; Payne, G.F.; Rubloff, G.W. Biofabrication: programmable assembly of polysaccharide hydrogels in microfluidics as biocompatible scaffolds. *J. Mater. Chem.*, **2012**, 22(16), 7659-7666.  
<http://dx.doi.org/10.1039/c2jm16215f>
- [104] Contessi, N.; Altomare, L.; Filipponi, A.; Farè, S. Thermo-responsive properties of methylcellulose hydrogels for cell sheet engineering. *Mater. Lett.*, **2017**, 207, 157-160.  
<http://dx.doi.org/10.1016/j.matlet.2017.07.023>
- [105] Bhattacharya, M.; Malinen, M.M.; Lauren, P.; Lou, Y.R.; Kuisma, S.W.; Kanninen, L.; Lille, M.; Corlu, A. Nanofibrillar cellulose hydrogel promotes three-dimensional liver cell culture. *J. Control Release*, **2012**, 164(3), 291-298.  
<https://doi.org/10.1016/j.jconrel.2012.06.039> PMID: 22776290
- [106] Svensson, A.; Nicklasson, E.; Harrah, T.; Panilaitis, B.; Kaplan, D.L.; Brittberg, M.; Gatenholm, P. Bacterial cellulose as a potential scaffold for tissue engineering of cartilage. *Biomaterials*, **2005**, 26(4), 419-431.  
<http://dx.doi.org/10.1016/j.biomaterials.2004.02.049> PMID: 15275816
- [107] Führmann, T.; Tam, R.Y.; Ballarin, B.; Coles, B.; Elliott Donaghue, I.; van der Kooy, D.; Nagy, A.; Tator, C.H.; Morshead, C.M.; Shoichet, M.S. Injectable hydrogel promotes early survival of induced pluripotent stem cell-derived oligodendrocytes and attenuates longterm teratoma formation in a spinal cord injury model. *Biomaterials*, **2016**, 83, 23-36.  
<http://dx.doi.org/10.1016/j.biomaterials.2015.12.032> PMID: 26773663
- [108] Loh, E.Y.X.; Mohamad, N.; Fauzi, M.B.; Ng, M.H.; Ng, S.F.; Mohd Amin, M.C.I. Development of a bacterial cellulose-based hydrogel cell carrier containing keratinocytes and fibroblasts for full-thickness wound healing. *Sci. Rep.*, **2018**, 8(1), 2875.  
<http://dx.doi.org/10.1038/s41598-018-21174-7> PMID: 29440678
- [109] Raucci, M.G.; Alvarez-Perez, M.A.; Demitri, C.; Sannino, A.; Ambrosio, L. Proliferation and osteoblastic differentiation of hMSCs on cellulose-based hydrogels. *J. Appl. Biomater. Funct. Mater.*, **2012**, 10(3), 302-307.  
<http://dx.doi.org/10.5301/JABFM.2012.10366> PMID: 23242882
- [110] Zhuo, F.; Liu, X.; Gao, Q.; Wang, Y.; Hu, K.; Cai, Q. Injectable hyaluronan-methylcellulose composite hydrogel crosslinked by polyethylene glycol for central nervous system tissue engineering. *Mater. Sci. Eng. C*, **2017**, 81, 1-7.  
<http://dx.doi.org/10.1016/j.msec.2017.07.029> PMID: 28887951
- [111] Lou, Y.R.; Kanninen, L.; Kuisma, T.; Niklander, J.; Noon, L.A.; Burks, D.; Urtti, A.; Yliperttula, M. The use of nanofibrillar cellulose hydrogel as a flexible three-dimensional model to culture human pluripotent stem cells. *Stem Cells Dev.*, **2014**, 23(4), 380-392.  
<http://dx.doi.org/10.1089/scd.2013.0314> PMID: 24188453
- [112] Rowley, J.A.; Madlambayan, G.; Mooney, D.J. Alginate hydrogels as synthetic extracellular matrix materials. *Biomaterials*, **1999**, 20(1), 45-53.  
[http://dx.doi.org/10.1016/S0142-9612\(98\)00107-0](http://dx.doi.org/10.1016/S0142-9612(98)00107-0) PMID: 9916770
- [113] Augst, A.D.; Kong, H.J.; Mooney, D.J. Alginate hydrogels as biomaterials. *Macromol. Biosci.*, **2006**, 6(8), 623-633.  
<http://dx.doi.org/10.1002/mabi.200600069> PMID: 16881042
- [114] Hong, S.; Sycks, D.; Chan, H.F.; Lin, S.; Lopez, G.P.; Guilak, F.; Leong, K.W.; Zhao, X. 3D printing of highly stretchable and tough hydrogels into complex, cellularized structures. *Adv. Mater.*, **2015**, 27(27), 4035-4040.  
<http://dx.doi.org/10.1002/adma.201501099> PMID: 26033288
- [115] Hunt, N.C.; Hallam, D.; Karimi, A.; Mellough, C.B.; Chen, J.; Steel, D.H.W.; Lako, M. 3D culture of human pluripotent stem cells in RGD-alginate hydrogel improves retinal tissue development. *Acta Biomater.*, **2017**, 49, 329-343.  
<http://dx.doi.org/10.1016/j.actbio.2016.11.016> PMID: 27826002
- [116] Hsiong, S.X.; Huebsch, N.; Fischbach, C.; Kong, H.J.; Mooney, D.J. Integrin-adhesion ligand bond formation of preosteoblasts and stem cells in three-dimensional RGD presenting matrices. *Biomacromolecules*, **2008**, 9(7), 1843-1851.  
<http://dx.doi.org/10.1021/bm8000606> PMID: 18540674
- [117] Andersen, T.; Auk-Emblem, P.; Dornish, M. 3d cell culture in alginate hydrogels. *Microarrays (Basel)*, **2015**, 4(2), 133-161.  
<http://dx.doi.org/10.3390/microarrays4020133> PMID: 27600217

- [118] Grimmer, J.F.; Gunnlaugsson, C.B.; Alsberg, E.; Murphy, H.S.; Kong, H.J.; Mooney, D.J.; Weatherly, R.A. Tracheal reconstruction using tissue-engineered cartilage. *Arch. Otolaryngol. Head Neck Surg.*, **2004**, *130*(10), 1191-1196. <http://dx.doi.org/10.1001/archotol.130.10.1191> PMID: 15492167
- [119] Alsberg, E.; Anderson, K.W.; Albeiruti, A.; Franceschi, R.T.; Mooney, D.J. Cell-interactive alginate hydrogels for bone tissue engineering. *J. Dent. Res.*, **2001**, *80*(11), 2025-2029. <http://dx.doi.org/10.1177/00220345010800111501> PMID: 11759015
- [120] Alsberg, E.; Anderson, K.W.; Albeiruti, A.; Rowley, J.A.; Mooney, D.J. Engineering growing tissues. *Proc. Natl. Acad. Sci. USA*, **2002**, *99*(19), 12025-12030. <http://dx.doi.org/10.1073/pnas.192291499> PMID: 12218178
- [121] Normand, V.; Lootens, D.L.; Amici, E.; Plucknett, K.P.; Aymard, P. New insight into agarose gel mechanical properties. *Biomacromolecules*, **2000**, *1*(4), 730-738. <http://dx.doi.org/10.1021/bm005583j> PMID: 11710204
- [122] Sánchez-Salcedo, S.; Nieto, A.; Vallet-Regí, M. Hydroxyapatite/ $\beta$ -tricalcium phosphate/agarose macroporous scaffolds for bone tissue engineering. *Chem. Eng. J.*, **2008**, *137*(1), 62-71. <http://dx.doi.org/10.1016/j.cej.2007.09.011>
- [123] Yamada, Y.; Hozumi, K.; Aso, A.; Hotta, A.; Toma, K.; Katagiri, F.; Kikkawa, Y.; Nomizu, M. Laminin active peptide/agarose matrices as multifunctional biomaterials for tissue engineering. *Biomaterials*, **2012**, *33*(16), 4118-4125. <http://dx.doi.org/10.1016/j.biomaterials.2012.02.044> PMID: 22410171
- [124] Campos, F.; Bonhome-Espinosa, A.B.; García-Martínez, L.; Durán, J.D.; López-López, M.T.; Alaminos, M.; Sánchez-Quevedo, M.C.; Carriel, V. *Ex vivo* characterization of a novel tissue-like cross-linked fibrin-agarose hydrogel for tissue engineering applications. *Biomed. Mater.*, **2016**, *11*(5), 055004. <http://dx.doi.org/10.1088/1748-6041/11/5/055004> PMID: 27680194
- [125] Huang, C.Y.; Reuben, P.M.; D'Ippolito, G.; Schiller, P.C.; Chung, H.S. Chondrogenesis of human bone marrow-derived mesenchymal stem cells in agarose culture. *Anat. Rec. A Discov. Mol. Cell. Evol. Biol.*, **2004**, *278*(1), 428-436. <http://dx.doi.org/10.1002/ar.a.20010> PMID: 15103737
- [126] Li, T.; Song, X.; Weng, C.; Wang, X.; Sun, L.; Gong, X.; Yang, L.; Chen, C. Self-crosslinking and injectable chondroitin sulfate/pullulan hydrogel for cartilage tissue engineering. *Applied Materials Today*, **2018**, *10*, 173-183. <http://dx.doi.org/10.1016/j.apmt.2017.12.002>
- [127] Varghese, S.; Hwang, N.S.; Canver, A.C.; Theprungsirikul, P.; Lin, D.W.; Elisseeff, J. Chondroitin sulfate based niches for chondrogenic differentiation of mesenchymal stem cells. *Matrix Biol.*, **2008**, *27*(1), 12-21. <https://doi.org/10.1016/j.matbio.2007.07.002> PMID: 17689060
- [128] Sechriest, V.F.; Miao, Y.J.; Niyibizi, C.; Westerhausen-Larson, A.; Matthew, H.W.; Evans, C.H.; Fu, F.H.; Suh, J.K. GAG-augmented polysaccharide hydrogel: a novel biocompatible and biodegradable material to support chondrogenesis. *J. Biomed. Mater. Res.*, **2000**, *49*(4), 534-541. [http://dx.doi.org/10.1002/\(SICI\)1097-4636\(20000315\)49:4<534::AID-JBM12>3.0.CO;2-#](http://dx.doi.org/10.1002/(SICI)1097-4636(20000315)49:4<534::AID-JBM12>3.0.CO;2-#) PMID: 10602087
- [129] Park, Y.J.; Lee, Y.M.; Lee, J.Y.; Seol, Y.J.; Chung, C.P.; Lee, S.J. Controlled release of platelet-derived growth factor-BB from chondroitin sulfate-chitosan sponge for guided bone regeneration. *J. Control. Release*, **2000**, *67*(2-3), 385-394. [http://dx.doi.org/10.1016/S0168-3659\(00\)00232-7](http://dx.doi.org/10.1016/S0168-3659(00)00232-7) PMID: 10825569
- [130] Li, Y.; Rodrigues, J.; Tomás, H. Injectable and biodegradable hydrogels: gelation, biodegradation and biomedical applications. *Chem. Soc. Rev.*, **2012**, *41*(6), 2193-2221. <http://dx.doi.org/10.1039/C1CS15203C> PMID: 22116474
- [131] Domingues, R.M.A.; Silva, M.; Gershovich, P.; Betta, S.; Babo, P.; Caridade, S.G.; Mano, J.F.; Motta, A.; Reis, R.L.; Gomes, M.E. Development of injectable hyaluronic acid/cellulose nanocrystals bionanocomposite hydrogels for tissue engineering applications. *Bioconjug. Chem.*, **2015**, *26*(8), 1571-1581. <http://dx.doi.org/10.1021/acs.bioconjchem.5b00209> PMID: 26106949
- [132] Jin, R.; Moreira Teixeira, L.S.; Krouwels, A.; Dijkstra, P.J.; van Blitterswijk, C.A.; Karperien, M.; Feijen, J. Synthesis and characterization of hyaluronic acid-poly(ethylene glycol) hydrogels via Michael addition: An injectable biomaterial for cartilage repair. *Acta Biomater.*, **2010**, *6*(6), 1968-1977. <http://dx.doi.org/10.1016/j.actbio.2009.12.024> PMID: 20025999
- [133] Kim, J.; Kim, I.S.; Cho, T.H.; Lee, K.B.; Hwang, S.J.; Tae, G.; Noh, I.; Lee, S.H.; Park, Y.; Sun, K. Bone regeneration using hyaluronic acid-based hydrogel with bone morphogenic protein-2 and human mesenchymal stem cells. *Biomaterials*, **2007**, *28*(10), 1830-1837. <http://dx.doi.org/10.1016/j.biomaterials.2006.11.050> PMID: 17208295
- [134] Zacchi, V.; Soranzo, C.; Cortivo, R.; Radice, M.; Brun, P.; Abatangelo, G. *In vitro* engineering of human skin-like tissue. *J. Biomed. Mater. Res.*, **1998**, *40*(2), 187-194. [http://dx.doi.org/10.1002/\(SICI\)1097-4636\(199805\)40:2<187::AID-JBM3>3.0.CO;2-H](http://dx.doi.org/10.1002/(SICI)1097-4636(199805)40:2<187::AID-JBM3>3.0.CO;2-H) PMID: 9549613
- [135] Noh, I.; Kim, N.; Tran, H.N.; Lee, J.; Lee, C. 3D printable hyaluronic acid-based hydrogel for its potential application as a bioink in tissue engineering. *Biomater. Res.*, **2019**, *23*(1), 3. <http://dx.doi.org/10.1186/s40824-018-0152-8> PMID: 30774971
- [136] Gopinath, V.; Saravanan, S.; Al-Maleki, A.R.; Ramesh, M.; Vadivelu, J. A review of natural polysaccharides for drug delivery applications: special focus on cellulose, starch and glycogen. *Biomed. Pharmacother.*, **2018**, *107*, 96-108. <http://dx.doi.org/10.1016/j.biopha.2018.07.136> PMID: 30086465
- [137] Perrone, M.; Lopalco, A.; Lopodota, A.; Cutrignelli, A.; Laquintana, V.; Douglas, J.; Franco, M.; Liberati, E.; Russo, V.; Tongiani, S.; Denora, N.; Bernkop-Schnurch, A. Preactivated thiolated glycogen as mucoadhesive polymer for drug delivery. *Eur. J. Pharm. Biopharm.*, **2017**, *119*, 161-169. <https://doi.org/10.1016/j.ejpb.2017.06.011> PMID: 28610879
- [138] Engelberth, S.A.; Hempel, N.; Bergkvist, M. Cationic dendritic starch as a vehicle for photodynamic therapy and siRNA co-delivery. *J. Photochem. Photobiol. B*, **2017**, *168*, 185-192. <http://dx.doi.org/10.1016/j.jphotobiol.2017.02.013> PMID: 28237436

- [139] Patra, P.; Seesala, V.S.; Das, D.; Panda, A.B.; Dhara, S.; Pal, S. Biopolymeric nanogel derived from functionalized glycogen towards targeted delivery of 5-fluorouracil. *Polym. (Guildf.)*, **2018**, *140*, 122-130.  
<http://dx.doi.org/10.1016/j.polymer.2018.02.015>
- [140] Rousseau, C.F.; Gagnieu, C.H. *In vitro* cytocompatibility of porcine type I atelocollagen crosslinked by oxidized glycogen. *Biomaterials*, **2002**, *23*(6), 1503-1510.  
[http://dx.doi.org/10.1016/S0142-9612\(01\)00276-9](http://dx.doi.org/10.1016/S0142-9612(01)00276-9) PMID: 11829447
- [141] Rabyk, M.; Hruby, M.; Vetrik, M.; Kucka, J.; Proks, V.; Parizek, M.; Konefal, R.; Krist, P.; Chvatil, D.; Bacakova, L.; Slouf, M.; Stepanek, P. Modified glycogen as construction material for functional biomimetic microfibers. *Carbohydr. Polym.*, **2016**, *152*, 271-279.  
<http://dx.doi.org/10.1016/j.carbpol.2016.06.107> PMID: 27516273
- [142] Oliveira, J.T.; Crawford, A.; Mundy, J.M.; Moreira, A.R.; Gomes, M.E.; Hatton, P.V.; Reis, R.L. A cartilage tissue engineering approach combining starch-polycaprolactone fibre mesh scaffolds with bovine articular chondrocytes. *J. Mater. Sci. Mater. Med.*, **2007**, *18*(2), 295-302.  
<http://dx.doi.org/10.1007/s10856-006-0692-7> PMID: 17323161
- [143] Elvira, C.; Mano, J.F.; San Román, J.; Reis, R.L. Starch-based biodegradable hydrogels with potential biomedical applications as drug delivery systems. *Biomaterials*, **2002**, *23*(9), 1955-1966.  
[http://dx.doi.org/10.1016/S0142-9612\(01\)00322-2](http://dx.doi.org/10.1016/S0142-9612(01)00322-2) PMID: 11996036
- [144] Gomes, M.E.; Godinho, J.S.; Tchalamov, D.; Cunha, A.M.; Reis, R.L. Alternative tissue engineering scaffolds based on starch: processing methodologies, morphology, degradation and mechanical properties. *Mater. Sci. Eng. C*, **2002**, *20*(1), 19-26.  
[http://dx.doi.org/10.1016/S0928-4931\(02\)00008-5](http://dx.doi.org/10.1016/S0928-4931(02)00008-5)
- [145] Salgado, A.J.; Gomes, M.E.; Chou, A.; Coutinho, O.P.; Reis, R.L.; Hutmacher, D.W. Preliminary study on the adhesion and proliferation of human osteoblasts on starch-based scaffolds. *Mater. Sci. Eng. C*, **2002**, *20*(1), 27-33.  
[http://dx.doi.org/10.1016/S0928-4931\(02\)00009-7](http://dx.doi.org/10.1016/S0928-4931(02)00009-7)
- [146] Van Nieuwenhove, I.; Salamon, A.; Adam, S.; Dubruel, P.; Van Vlierberghe, S.; Peters, K. Gelatin- and starch-based hydrogels. Part B: *In vitro* mesenchymal stem cell behavior on the hydrogels. *Carbohydr. Polym.*, **2017**, *161*, 295-305.  
<http://dx.doi.org/10.1016/j.carbpol.2017.01.010> PMID: 28189242
- [147] Dong, D.; Hao, T.; Wang, C.; Zhang, Y.; Qin, Z.; Yang, B.; Fang, W.; Ye, L.; Yao, F.; Li, J. Zwitterionic starch-based hydrogel for the expansion and "stemness" maintenance of brown adipose derived stem cells. *Biomaterials*, **2018**, *157*, 149-160.  
<http://dx.doi.org/10.1016/j.biomaterials.2017.12.011> PMID: 29272722
- [148] Kamoun, E.A. N-succinyl chitosan-dialdehyde starch hybrid hydrogels for biomedical applications. *J. Adv. Res.*, **2016**, *7*(1), 69-77.  
<http://dx.doi.org/10.1016/j.jare.2015.02.002> PMID: 26843972
- [149] Gomes, M.E.; Ribeiro, A.S.; Malafaya, P.B.; Reis, R.L.; Cunha, A.M. A new approach based on injection moulding to produce biodegradable starch-based polymeric scaffolds: morphology, mechanical and degradation behaviour. *Biomaterials*, **2001**, *22*(9), 883-889.  
[http://dx.doi.org/10.1016/S0142-9612\(00\)00211-8](http://dx.doi.org/10.1016/S0142-9612(00)00211-8) PMID: 11311006
- [150] Amrita, ; Arora, A.; Sharma, P.; Katti, D.S. Pullulan-based composite scaffolds for bone tissue engineering: Improved osteoconductivity by pore wall mineralization. *Carbohydr. Polym.*, **2015**, *123*, 180-189.  
<http://dx.doi.org/10.1016/j.carbpol.2015.01.038> PMID: 25843850
- [151] Wong, V.W.; Rustad, K.C.; Galvez, M.G.; Neofytou, E.; Glotzbach, J.P.; Januszyk, M.; Major, M.R.; Sorkin, M.; Longaker, M.T.; Rajadas, J.; Gurtner, G.C. Engineered pullulan-collagen composite dermal hydrogels improve early cutaneous wound healing. *Tissue Eng. Part A*, **2011**, *17*(5-6), 631-644.  
<http://dx.doi.org/10.1089/ten.tea.2010.0298> PMID: 20919949
- [152] S, I.; A. V, B.; Velswamy, P.; T. S, U.; Perumal, P.T., Design and development of a piscine collagen blended pullulan hydrogel for skin tissue engineering. *RSC Advances*, **2016**, *6*(63), 57863-57871.  
<http://dx.doi.org/10.1039/C6RA03578G>
- [153] Chen, F.; Yu, S.; Liu, B.; Ni, Y.; Yu, C.; Su, Y.; Zhu, X.; Yu, X.; Zhou, Y.; Yan, D. An injectable enzymatically crosslinked carboxymethylated pullulan/chondroitin sulfate hydrogel for cartilage tissue engineering. *Sci. Rep.*, **2016**, *6*, 20014.  
<http://dx.doi.org/10.1038/srep20014> PMID: 26817622
- [154] Henry, N.; Clouet, J.; Fragale, A.; Griveau, L.; Chédeville, C.; Véziers, J.; Weiss, P.; Le Bideau, J.; Guicheux, J.; Le Visage, C. Pullulan microbeads/Si-HPMC hydrogel injectable system for the sustained delivery of GDF-5 and TGF- $\beta$ 1: new insight into intervertebral disc regenerative medicine. *Drug Deliv.*, **2017**, *24*(1), 999-1010.  
<http://dx.doi.org/10.1080/10717544.2017.1340362> PMID: 28645219
- [155] Zhang, L.; Liu, J.; Zheng, X.; Zhang, A.; Zhang, X.; Tang, K. Pullulan dialdehyde crosslinked gelatin hydrogels with high strength for biomedical applications. *Carbohydr. Polym.*, **2019**, *216*, 45-53.  
<http://dx.doi.org/10.1016/j.carbpol.2019.04.004> PMID: 31047081
- [156] Feng, W.; Feng, S.; Tang, K.; He, X.; Jing, A.; Liang, G. A novel composite of collagen-hydroxyapatite/kappa-carrageenan. *J. Alloys Compd.*, **2017**, *693*, 482-489.  
<http://dx.doi.org/10.1016/j.jallcom.2016.09.234>
- [157] González, J.I.; Ossa, C.P.O. Injectability Evaluation of Bone-Graft Substitutes Based on Carrageenan and Hydroxyapatite Nanorods. In: *The Minerals, Metals & Materials Series*. Springer, Cham, **2017**, pp. 33-46.  
[https://doi.org/10.1007/978-3-319-52132-9\\_4](https://doi.org/10.1007/978-3-319-52132-9_4)
- [158] Li, J.; Yang, B.; Qian, Y.; Wang, Q.; Han, R.; Hao, T.; Shu, Y.; Zhang, Y.; Yao, F.; Wang, C. Iota-carrageenan/chitosan/gelatin scaffold for the osteogenic differentiation of adipose-derived MSCs *in vitro*. *J. Biomed. Mater. Res. B Appl. Biomater.*, **2015**, *103*(7), 1498-1510.  
<http://dx.doi.org/10.1002/jbm.b.33339> PMID: 25449538
- [159] Popa, E.G.; Santo, V.E.; Rodrigues, M.T.; Gomes, M.E. Magnetically-responsive hydrogels for modulation of chondrogenic commitment of human adipose-derived stem cells. *Polymers (Basel)*, **2016**, *8*(2), 28.  
<http://dx.doi.org/10.3390/polym8020028> PMID: 30979122
- [160] DeLise, A.M.; Fischer, L.; Tuan, R.S. Cellular interactions and signaling in cartilage development. *Osteoarthritis Cartilage*, **2000**, *8*(5), 309-334.  
<http://dx.doi.org/10.1053/joca.1999.0306> PMID: 10966838
- [161] Thébaud, N-B.; Pierron, D.; Bareille, R.; Le Visage, C.; Letourneur, D.; Bordenave, L. Human endothelial progeni-



- tor cell attachment to polysaccharide-based hydrogels: a pre-requisite for vascular tissue engineering. *J. Mater. Sci. Mater. Med.*, **2007**, 18(2), 339-345.  
<http://dx.doi.org/10.1007/s10856-006-0698-1> PMID: 17323167
- [162] Dash, M.; Samal, S.K.; Bartoli, C.; Morelli, A.; Smet, P.F.; Dubruel, P.; Chiellini, F. Biofunctionalization of ulvan scaffolds for bone tissue engineering. *ACS Appl. Mater. Interfaces*, **2014**, 6(5), 3211-3218.  
<http://dx.doi.org/10.1021/am404912c> PMID: 24494863
- [163] Liang, Y.; Kiick, K.L. Heparin-functionalized polymeric biomaterials in tissue engineering and drug delivery applications. *Acta Biomater.*, **2014**, 10(4), 1588-1600.  
<http://dx.doi.org/10.1016/j.actbio.2013.07.031> PMID: 23911941
- [164] Linhardt, R.J. Heparin-induced cancer cell death. *Chem. Biol.*, **2004**, 11(4), 420-422.  
<http://dx.doi.org/10.1016/j.chembiol.2004.04.001> PMID: 15123235
- [165] García-Fernández, L.; Halstenberg, S.; Unger, R.E.; Aguilar, M.R.; Kirkpatrick, C.J.; San Román, J. Anti-angiogenic activity of heparin-like polysulfonated polymeric drugs in 3D human cell culture. *Biomaterials*, **2010**, 31(31), 7863-7872.  
<http://dx.doi.org/10.1016/j.biomaterials.2010.07.022> PMID: 20674006
- [166] Rohman, G.; Baker, S.C.; Southgate, J.; Cameron, N.R. Heparin functionalisation of porous PLGA scaffolds for controlled, biologically relevant delivery of growth factors for soft tissue engineering. *J. Mater. Chem.*, **2009**, 19(48), 9265-9273.  
<http://dx.doi.org/10.1039/b911625g>
- [167] Willerth, S.M.; Rader, A.; Sakiyama-Elbert, S.E. The effect of controlled growth factor delivery on embryonic stem cell differentiation inside fibrin scaffolds. *Stem Cell Res. (Amst.)*, **2008**, 1(3), 205-218.  
<http://dx.doi.org/10.1016/j.scr.2008.05.006> PMID: 19383401
- [168] Johnson, P.J.; Tatara, A.; Shiu, A.; Sakiyama-Elbert, S.E. Controlled release of neurotrophin-3 and platelet-derived growth factor from fibrin scaffolds containing neural progenitor cells enhances survival and differentiation into neurons in a subacute model of SCI. *Cell Transplant.*, **2010**, 19(1), 89-101.  
<http://dx.doi.org/10.3727/096368909X477273> PMID: 19818206
- [169] Tae, G.; Kim, Y.-J.; Choi, W.-I.; Kim, M.; Stayton, P.S.; Hoffman, A.S. Formation of a novel heparin-based hydrogel in the presence of heparin-binding biomolecules. *Biomacromolecules*, **2007**, 8(6), 1979-1986.  
<http://dx.doi.org/10.1021/bm0701189> PMID: 17511500
- [170] Kim, M.; Shin, Y.; Hong, B.H.; Kim, Y.J.; Chun, J.S.; Tae, G.; Kim, Y.H. *In vitro* chondrocyte culture in a heparin-based hydrogel for cartilage regeneration. *Tissue Eng. Part C. Methods*, **2010**, 16(1), 1-10.  
<http://dx.doi.org/10.1089/ten.tec.2008.0548> PMID: 19327003
- [171] Liu, M.; Zeng, X.; Ma, C.; Yi, H.; Ali, Z.; Mou, X.; Li, S.; Deng, Y.; He, N. Injectable hydrogels for cartilage and bone tissue engineering. *Bone Res.*, **2017**, 5, 17014.  
<http://dx.doi.org/10.1038/boneres.2017.14> PMID: 28584674
- [172] Lee, Y.B.; Polio, S.; Lee, W.; Dai, G.; Menon, L.; Carroll, R.S.; Yoo, S.S. Bio-printing of collagen and VEGF-releasing fibrin gel scaffolds for neural stem cell culture. *Exp. Neurol.*, **2010**, 223(2), 645-652.  
<http://dx.doi.org/10.1016/j.expneurol.2010.02.014> PMID: 20211178
- [173] Nguyen, B.B.; Moriarty, R.A.; Kamalidinov, T.; Etheridge, J.M.; Fisher, J.P. Collagen hydrogel scaffold promotes mesenchymal stem cell and endothelial cell coculture for bone tissue engineering. *J. Biomed. Mater. Res. A*, **2017**, 105(4), 1123-1131.  
<http://dx.doi.org/10.1002/jbm.a.36008> PMID: 28093887
- [174] Buitrago, J.O.; Patel, K.D.; El-Fiqi, A.; Lee, J.-H.; Kundu, B.; Lee, H.-H.; Kim, H.-W. Silk fibroin/collagen protein hybrid cell-encapsulating hydrogels with tunable gelation and improved physical and biological properties. *Acta Biomater.*, **2018**, 69, 218-233.  
<http://dx.doi.org/10.1016/j.actbio.2017.12.026> PMID: 29410166
- [175] Moraes, P.R.F.S.; Saska, S.; Barud, H.; Lima, L.R.d.; Martins, V.C.A.; Plepis, A.M.G.; Ribeiro, S.J.L.; Gaspar, A.M.M. bacterial cellulose/collagen hydrogel for wound healing. *Mater. Res.*, **2016**, 19, 106-116.  
<http://dx.doi.org/10.1590/1980-5373-MR-2015-0249>
- [176] Yang, Z.; Cao, H.; Gao, S.; Yang, M.; Lyu, J.; Tang, K. effect of tendon stem cells in chitosan/ $\beta$ -glycerophosphate/collagen hydrogel on achilles tendon healing in a rat model. *Med. Sci. Monit.*, **2017**, 23, 4633-4643.  
<http://dx.doi.org/10.12659/MSM.906747> PMID: 28951538
- [177] Fu, Y.; Xu, K.; Zheng, X.; Giacomini, A.J.; Mix, A.W.; Kao, W.J. 3D cell entrapment in crosslinked thiolated gelatin-poly(ethylene glycol) diacrylate hydrogels. *Biomaterials*, **2012**, 33(1), 48-58.  
<http://dx.doi.org/10.1016/j.biomaterials.2011.09.031> PMID: 21955690
- [178] Nikkhah, M.; Eshak, N.; Zorlutuna, P.; Annabi, N.; Castello, M.; Kim, K.; Dolatshahi-Pirouz, A.; Edalat, F.; Bae, H.; Yang, Y.; Khademhosseini, A. Directed endothelial cell morphogenesis in micropatterned gelatin methacrylate hydrogels. *Biomaterials*, **2012**, 33(35), 9009-9018.  
<http://dx.doi.org/10.1016/j.biomaterials.2012.08.068> PMID: 23018132
- [179] Das, S.; Pati, F.; Choi, Y.J.; Rijal, G.; Shim, J.H.; Kim, S.W.; Ray, A.R.; Cho, D.W.; Ghosh, S. Bioprintable, cell-laden silk fibroin-gelatin hydrogel supporting multilineage differentiation of stem cells for fabrication of three-dimensional tissue constructs. *Acta Biomater.*, **2015**, 11, 233-246.  
<http://dx.doi.org/10.1016/j.actbio.2014.09.023> PMID: 25242654
- [180] Liu, Y.; Chan-Park, M.B. A biomimetic hydrogel based on methacrylated dextran-graft-lysine and gelatin for 3D smooth muscle cell culture. *Biomaterials*, **2010**, 31(6), 1158-1170.  
<http://dx.doi.org/10.1016/j.biomaterials.2009.10.040> PMID: 19897239
- [181] D'Urso, E.M.; Jean-François, J.; Doillon, C.J.; Fortier, G. Poly(ethylene glycol)-serum albumin hydrogel as matrix for enzyme immobilization: biomedical applications. *Artif. Cells Blood Substit. Immobil. Biotechnol.*, **1995**, 23(5), 587-595.  
<http://dx.doi.org/10.3109/10731199509117973> PMID: 8528452
- [182] Reece, T.B.; Maxey, T.S.; Kron, I.L. A prospectus on tissue adhesives. *Am. J. Surg.*, **2001**, 182(2)(Suppl.), 40S-44S.  
[http://dx.doi.org/10.1016/S0002-9610\(01\)00742-5](http://dx.doi.org/10.1016/S0002-9610(01)00742-5) PMID: 11566476

- [183] Subia, B.; Kundu, S.C. Drug loading and release on tumor cells using silk fibroin-albumin nanoparticles as carriers. *Nanotechnology*, **2013**, *24*(3), 035103. <http://dx.doi.org/10.1088/0957-4484/24/3/035103> PMID: 23262833
- [184] Raja, S.T.K.; Thiruselvi, T.; Mandal, A.B.; Gnanamani, A. pH and redox sensitive albumin hydrogel: A self-derived biomaterial. *Sci. Rep.*, **2015**, *5*, 15977. <http://dx.doi.org/10.1038/srep15977> PMID: 26527296
- [185] Schmoekel, H.G.; Weber, F.E.; Schense, J.C.; Grätz, K.W.; Schawalder, P.; Hubbell, J.A. Bone repair with a form of BMP-2 engineered for incorporation into fibrin cell in-growth matrices. *Biotechnol. Bioeng.*, **2005**, *89*(3), 253-262. <http://dx.doi.org/10.1002/bit.20168> PMID: 15619323
- [186] Liu, J.; Tan, Y.; Zhang, H.; Zhang, Y.; Xu, P.; Chen, J.; Poh, Y.C.; Tang, K.; Wang, N.; Huang, B. Soft fibrin gels promote selection and growth of tumorigenic cells. *Nat. Mater.*, **2012**, *11*(8), 734-741. <http://dx.doi.org/10.1038/nmat3361> PMID: 22751180
- [187] Schmoekel, H.; Schense, J.C.; Weber, F.E.; Gratz, K.W.; Gnagi, D.; Muller, R.; Hubbell, J.A. Bone healing in the rat and dog with nonglycosylated BMP-2 demonstrating low solubility in fibrin matrices. *J. Orthop. Res.*, **2004**, *22*(2), 376-381. [https://doi.org/10.1016/S0736-0266\(03\)00188-8](https://doi.org/10.1016/S0736-0266(03)00188-8) PMID: 15013099
- [188] Janmey, P.A.; Winer, J.P.; Weisel, J.W. Fibrin gels and their clinical and bioengineering applications. *J. R. Soc. Interface*, **2009**, *6*(30), 1-10. <https://doi.org/10.1098/rsif.2008.0327> PMID: 18801715
- [189] Boublik, J.; Park, H.; Radisic, M.; Tognana, E.; Chen, F.; Pei, M.; Vunjak-Novakovic, G.; Freed, L.E. Mechanical properties and remodeling of hybrid cardiac constructs made from heart cells, fibrin, and biodegradable, elastomeric knitted fabric. *Tissue Eng.*, **2005**, *11*(7-8), 1122-1132. <http://dx.doi.org/10.1089/ten.2005.11.1122> PMID: 16144448
- [190] Passaretti, D.; Silverman, R.P.; Huang, W.; Kirchhoff, C.H.; Ashiku, S.; Randolph, M.A.; Yaremchuk, M.J. Cultured chondrocytes produce injectable tissue-engineered cartilage in hydrogel polymer. *Tissue Eng.*, **2001**, *7*(6), 805-815. <http://dx.doi.org/10.1089/107632701753337744> PMID: 11749736
- [191] Rowe, S.L.; Stegemann, J.P. Interpenetrating collagen-fibrin composite matrices with varying protein contents and ratios. *Biomacromolecules*, **2006**, *7*(11), 2942-2948. <http://dx.doi.org/10.1021/bm0602233> PMID: 17096517
- [192] Fini, M.; Motta, A.; Torricelli, P.; Giavaresi, G.; Nicoli Aldini, N.; Tschon, M.; Giardino, R.; Migliaresi, C. The healing of confined critical size cancellous defects in the presence of silk fibroin hydrogel. *Biomaterials*, **2005**, *26*(17), 3527-3536. <http://dx.doi.org/10.1016/j.biomaterials.2004.09.040> PMID: 15621243
- [193] Mitropoulos, A.N.; Marelli, B.; Ghezzi, C.E.; Applegate, M.B.; Partlow, B.P.; Kaplan, D.L.; Omenetto, F.G. transparent, nanostructured silk fibroin hydrogels with tunable mechanical properties. *ACS Biomater. Sci. Eng.*, **2015**, *1*(10), 964-970. <http://dx.doi.org/10.1021/acsbiomaterials.5b00215>
- [194] Motta, A.; Migliaresi, C.; Faccioni, F.; Torricelli, P.; Fini, M.; Giardino, R. Fibroin hydrogels for biomedical applications: preparation, characterization and *in vitro* cell culture studies. *J. Biomater. Sci. Polym. Ed.*, **2004**, *15*(7), 851-864. <http://dx.doi.org/10.1163/1568562041271075> PMID: 15318796
- [195] Aoki, H.; Tomita, N.; Morita, Y.; Hattori, K.; Harada, Y.; Sonobe, M.; Wakitani, S.; Tamada, Y. Culture of chondrocytes in fibroin-hydrogel sponge. *Biomed. Mater. Eng.*, **2003**, *13*(4), 309-316. PMID: 14646046
- [196] Cavo, M.; Caria, M.; Pulsoni, I.; Beltrame, F.; Fato, M.; Scaglione, S. A new cell-laden 3D Alginate-Matrigel hydrogel resembles human breast cancer cell malignant morphology, spread and invasion capability observed "*in vivo*". *Sci. Rep.*, **2018**, *8*(1), 5333. <http://dx.doi.org/10.1038/s41598-018-23250-4> PMID: 29593247
- [197] Miao, Z.; Lu, Z.; Wu, H.; Liu, H.; Li, M.; Lei, D.; Zheng, L.; Zhao, J. Collagen, agarose, alginate, and Matrigel hydrogels as cell substrates for culture of chondrocytes *in vitro*: a comparative study. *J. Cell. Biochem.*, **2018**, *119*(10), 7924-7933. <http://dx.doi.org/10.1002/jcb.26411> PMID: 28941304
- [198] Maxian, S.H.; Di Stefano, T.; Melican, M.C.; Tiku, M.L.; Zawadsky, J.P. Bone cell behavior on Matrigel-coated Ca/P coatings of varying crystallinities. *J. Biomed. Mater. Res.*, **1998**, *40*(2), 171-179. [http://dx.doi.org/10.1002/\(SICI\)1097-4636\(199805\)40:2<171::AID-JBM1>3.0.CO;2-I](http://dx.doi.org/10.1002/(SICI)1097-4636(199805)40:2<171::AID-JBM1>3.0.CO;2-I) PMID: 9549611
- [199] Ramos-Hryb, A.B.; Da-Costa, M.C.; Trentin, A.G.; Calloini, G.W. Matrigel supports neural, melanocytic and chondrogenic differentiation of trunk neural crest cells. *Int. J. Dev. Biol.*, **2013**, *57*(11-12), 885-890. <http://dx.doi.org/10.1387/ijdb.130206gw> PMID: 24623080
- [200] Chien, K.B.; Chung, E.J.; Shah, R.N. Investigation of soy protein hydrogels for biomedical applications: materials characterization, drug release, and biocompatibility. *J. Biomater. Appl.*, **2014**, *28*(7), 1085-1096. <http://dx.doi.org/10.1177/0885328213497413> PMID: 23900448
- [201] Demir, M.; Ramos-Rivera, L.; Silva, R.; Nazhat, S.N.; Boccaccini, A.R. Zein-based composites in biomedical applications. *J. Biomed. Mater. Res. A*, **2017**, *105*(6), 1656-1665. <http://dx.doi.org/10.1002/jbm.a.36040> PMID: 28205372
- [202] Zinn, M.; Witholt, B.; Egli, T. Occurrence, synthesis and medical application of bacterial polyhydroxyalkanoate. *Adv. Drug Deliv. Rev.*, **2001**, *53*(1), 5-21. [http://dx.doi.org/10.1016/S0169-409X\(01\)00218-6](http://dx.doi.org/10.1016/S0169-409X(01)00218-6) PMID: 11733115
- [203] Chen, W.; Tong, Y.W. PHBV microspheres as neural tissue engineering scaffold support neuronal cell growth and axon-dendrite polarization. *Acta Biomater.*, **2012**, *8*(2), 540-548. <http://dx.doi.org/10.1016/j.actbio.2011.09.026> PMID: 22005329
- [204] Sultana, N.; Khan, T.H. *In vitro* degradation of PHBV scaffolds and nHA/PHBV composite scaffolds containing hydroxyapatite nanoparticles for bone tissue engineering. *J. Nanomater.*, **2012**, *2012*, 12. <http://dx.doi.org/10.1155/2012/190950>
- [205] Nebe, B.; Forster, C.; Pommerenke, H.; Fulda, G.; Behrend, D.; Bernewski, U.; Schmitz, K.-P.; Rychly, J. Structural alterations of adhesion mediating components in cells cultured on poly- $\beta$ -hydroxy butyric acid. *Biomaterials*, **2001**, *22*(17), 2425-2434.

- http://dx.doi.org/10.1016/S0142-9612(00)00430-0 PMID: 11511040
- [206] Chang, H.M.; Wang, Z.H.; Luo, H.N.; Xu, M.; Ren, X.Y.; Zheng, G.X.; Wu, B.J.; Zhang, X.H.; Lu, X.Y.; Chen, F.; Jing, X.H.; Wang, L. Poly(3-hydroxybutyrate-co-3-hydroxyhexanoate)-based scaffolds for tissue engineering. *Braz. J. Med. Biol. Res.*, **2014**, *47*(7), 533-539. http://dx.doi.org/10.1590/1414-431X20143930 PMID: 25003631
- [207] Tamm, I.; Heinämäki, J.; Laidmäe, I.; Rammo, L.; Paaver, U.; Ingebrigtsen, S.G.; Škalko-Basnet, N.; Halenius, A.; Yliruusi, J.; Pitkänen, P.; Alakurtti, S.; Kogermann, K. Development of suberin fatty acids and chloramphenicol-loaded antimicrobial electrospun nanofibrous mats intended for wound therapy. *J. Pharm. Sci.*, **2016**, *105*(3), 1239-1247. http://dx.doi.org/10.1016/j.xphs.2015.12.025 PMID: 26886306
- [208] Jansson, P-E.; Lindberg, B.; Sandford, P.A. Structural studies of gellan gum, an extracellular polysaccharide elaborated by *Pseudomonas elodea*. *Carbohydr. Res.*, **1983**, *124*(1), 135-139. http://dx.doi.org/10.1016/0008-6215(83)88361-X
- [209] Carlfors, J.; Edsman, K.; Petersson, R.; Jorvning, K. Rheological evaluation of Gelrite in situ gels for ophthalmic use. *Eur. J. Pharm. Sci.*, **1998**, *6*(2), 113-119. https://doi.org/10.1016/S0928-0987(97)00074-2 PMID: 9795027
- [210] Kani, K.; Horinaka, J.-I.; Maeda, S. Effects of monovalent cation and anion species on the conformation of gellan chains in aqueous systems. *Carbohydr. Polym.*, **2005**, *61*(2), 168-173. http://dx.doi.org/10.1016/j.carbpol.2005.04.011
- [211] Matsuoka, S.; Huang, Z.; Watanabe, T. Structural change of polymer chains of gellan monitored by circular dichroism. In: *Physical Chemistry and Industrial Application of Gellan Gum. Progress in Colloid and Polymer Science*. Nishinari, K., Ed.; Springer Berlin Heidelberg: Berlin, Heidelberg, **1999**, Vol. 114, pp. 92-97. https://doi.org/10.1007/3-540-48349-7\_13
- [212] Moxon, S.R.; Smith, A.M. Controlling the rheology of gellan gum hydrogels in cell culture conditions. *Int. J. Biol. Macromol.*, **2016**, *84*, 79-86. http://dx.doi.org/10.1016/j.ijbiomac.2015.12.007 PMID: 26683878
- [213] Koivisto, J.T.; Joki, T.; Parraga, J.E.; Pääkkönen, R.; Ylä-Outinen, L.; Salonen, L.; Jönkkäri, I.; Peltola, M.; Ihala, T.O.; Narkilahti, S.; Kellomäki, M. Bioamine-crosslinked gellan gum hydrogel for neural tissue engineering. *Biomed. Mater.*, **2017**, *12*(2), 025014. http://dx.doi.org/10.1088/1748-605X/aa62b0 PMID: 28233757
- [214] Ahmed, R.Z.; Siddiqui, K.; Arman, M.; Ahmed, N. Characterization of high molecular weight dextran produced by *Weissella cibaria* CMGDEX3. *Carbohydr. Polym.*, **2012**, *90*(1), 441-446. http://dx.doi.org/10.1016/j.carbpol.2012.05.063 PMID: 24751063
- [215] Stenekes, R.J.H.; Talsma, H.; Hennink, W.E. Formation of dextran hydrogels by crystallization. *Biomaterials*, **2001**, *22*(13), 1891-1898. http://dx.doi.org/10.1016/S0142-9612(00)00375-6 PMID: 11396895
- [216] Jin, R.; Moreira Teixeira, L.S.; Dijkstra, P.J.; van Blitterswijk, C.A.; Karperien, M.; Feijen, J. Chondrogenesis in injectable enzymatically crosslinked heparin/dextran hydrogels. *J. Control. Release*, **2011**, *152*(1), 186-195. http://dx.doi.org/10.1016/j.jconrel.2011.01.031 PMID: 21291927
- [217] Hennink, W.E.; Talsma, H.; Borchert, J.C.H.; De Smedt, S.C.; Demeester, J. Controlled release of proteins from dextran hydrogels. *J. Control. Release*, **1996**, *39*(1), 47-55. http://dx.doi.org/10.1016/0168-3659(95)00132-8
- [218] Bueno, V.B.; Bentini, R.; Catalani, L.H.; Petri, D.F.S. Synthesis and swelling behavior of xanthan-based hydrogels. *Carbohydr. Polym.*, **2013**, *92*(2), 1091-1099. http://dx.doi.org/10.1016/j.carbpol.2012.10.062 PMID: 23399133
- [219] Kumar, A.; Rao, K.M.; Han, S.S. Application of xanthan gum as polysaccharide in tissue engineering: a review. *Carbohydr. Polym.*, **2018**, *180*, 128-144. http://dx.doi.org/10.1016/j.carbpol.2017.10.009 PMID: 29103488
- [220] Liu, Z.; Yao, P. Injectable shear-thinning xanthan gum hydrogel reinforced by mussel-inspired secondary cross-linking. *RSC Advances*, **2015**, *5*(125), 103292-103301. http://dx.doi.org/10.1039/C5RA17246B
- [221] Sehgal, R.R.; Roohani-Esfahani, S.I.; Zreikat, H.; Banerjee, R. Nanostructured gellan and xanthan hydrogel depot integrated within a baghdadite scaffold augments bone regeneration. *J. Tissue Eng. Regen. Med.*, **2017**, *11*(4), 1195-1211. http://dx.doi.org/10.1002/term.2023 PMID: 25846217
- [222] Baker, E.A.; Martin, J.T. Cutin of plant cuticles. *Nature*, **1963**, *199*, 1268. http://dx.doi.org/10.1038/1991268a0
- [223] Petit, J.; Bres, C.; Mauxion, J.P.; Bakan, B.; Rothan, C. Breeding for cuticle-associated traits in crop species: traits, targets, and strategies. *J. Exp. Bot.*, **2017**, *68*(19), 5369-5387. PMID: 29036305
- [224] Tako, M.; Kiriaki, M. Rheological properties of welan gum in aqueous media. *Agric. Biol. Chem.*, **1990**, *54*(12), 3079-3084. https://doi.org/10.1080/00021369.1990.10870465
- [225] Nagahara, S.; Matsuda, T. Hydrogel formation via hybridization of oligonucleotides derivatized in water-soluble vinyl polymers. *Polym. Gels Netw.*, **1996**, *4*(2), 111-127. http://dx.doi.org/10.1016/0966-7822(96)00001-9
- [226] Zhang, F.; Yan, H. DNA self-assembly scaled up. *Nature*, **2017**, *552*(7683), 34-35. http://dx.doi.org/10.1038/d41586-017-07690-y
- [227] Um, S.H.; Lee, J.B.; Park, N.; Kwon, S.Y.; Umbach, C.C.; Luo, D. Enzyme-catalysed assembly of DNA hydrogel. *Nat. Mater.*, **2006**, *5*(10), 797-801. http://dx.doi.org/10.1038/nmat1741 PMID: 16998469
- [228] Zhang, L.; Lei, J.; Liu, L.; Li, C.; Ju, H. Self-assembled DNA hydrogel as switchable material for aptamer-based fluorescent detection of protein. *Anal. Chem.*, **2013**, *85*(22), 11077-11082. http://dx.doi.org/10.1021/ac4027725 PMID: 24138007
- [229] Li, C.; Faulkner-Jones, A.; Dun, A.R.; Jin, J.; Chen, P.; Xing, Y.; Yang, Z.; Li, Z.; Shu, W.; Liu, D.; Duncan, R.R. Rapid formation of a supramolecular polypeptide-DNA hydrogel for in situ three-dimensional multilayer bioprinting. *Angew. Chem. Int. Ed. Engl.*, **2015**, *54*(13), 3957-3961. http://dx.doi.org/10.1002/anie.201411383 PMID: 25656851
- [230] Wu, Y.; Li, C.; Boldt, F.; Wang, Y.; Kuan, S.L.; Tran, T.T.; Mikhalevich, V.; Förtsch, C.; Barth, H.; Yang, Z.; Liu, D.; Weil, T. Programmable protein-DNA hybrid hydrogels for

- the immobilization and release of functional proteins. *Chem. Commun. (Camb.)*, **2014**, 50(93), 14620-14622.  
<http://dx.doi.org/10.1039/C4CC07144A> PMID: 25311614
- [231] Wilkinson, K.A.; Vasa, S.M.; Deigan, K.E.; Mortimer, S.A.; Giddings, M.C.; Weeks, K.M. Influence of nucleotide identity on ribose 2'-hydroxyl reactivity in RNA. *RNA*, **2009**, 15(7), 1314-1321.  
<http://dx.doi.org/10.1261/rna.1536209> PMID: 19458034
- [232] Elangovan, S.; Khorsand, B.; Do, A.V.; Hong, L.; Dewerth, A.; Kormann, M.; Ross, R.D.; Sumner, D.R.; Allamargot, C.; Salem, A.K. Chemically modified RNA activated matrices enhance bone regeneration. *J. Control Release*. **2015**, 218, 22.  
<https://doi.org/10.1016/j.jconrel.2015.09.050> PMID: 26415855
- [233] Hong, C.A.; Kim, J.S.; Lee, S.H.; Kong, W.H.; Park, T.G.; Mok, H.; Nam, Y.S. Reductively dissociable siRNA-polymer hybrid nanogels for efficient targeted gene silencing. *Adv. Funct. Mater.*, **2013**, 23(3), 316-322.  
<http://dx.doi.org/10.1002/adfm.201200780>
- [234] Conde, J.; Oliva, N.; Atilano, M.; Song, H.S.; Artzi, N. Self-assembled RNA-triple-helix hydrogel scaffold for microRNA modulation in the tumour microenvironment. *Nat. Mater.*, **2016**, 15(3), 353-363.  
<http://dx.doi.org/10.1038/nmat4497> PMID: 26641016
- [235] Huang, H.; Ding, Y.; Sun, X.S.; Nguyen, T.A. Peptide hydrogelation and cell encapsulation for 3D culture of MCF-7 breast cancer cells. *PLoS One*, **2013**, 8(3), e59482.  
<http://dx.doi.org/10.1371/journal.pone.0059482> PMID: 23527204
- [236] Ruan, J.L.; Tulloch, N.L.; Muskheli, V.; Genova, E.E.; Mariner, P.D.; Anseth, K.S.; Murry, C.E. An improved cryosection method for polyethylene glycol hydrogels used in tissue engineering. *Tissue Eng. Part C Methods*, **2013**, 19(10), 794-801.  
<http://dx.doi.org/10.1089/ten.tec.2012.0460> PMID: 23448137

Available online at [www.sciencedirect.com](http://www.sciencedirect.com)

ScienceDirect

Biomedical Journal

journal homepage: [www.elsevier.com/locate/bj](http://www.elsevier.com/locate/bj)

## Short review

## G6PD: A hub for metabolic reprogramming and redox signaling in cancer

Hung-Chi Yang<sup>a,\*\*</sup>, Arnold Stern<sup>b</sup>, Daniel Tsun-Yee Chiu<sup>c,d,\*</sup><sup>a</sup> Department of Medical Laboratory Science and Biotechnology, Yuanpei University of Medical Technology, Hsinchu, Taiwan<sup>b</sup> New York University School of Medicine, New York, NY, USA<sup>c</sup> Research Center for Chinese Herbal Medicine, Graduate Institute of Health Industry Technology, College of Human Ecology, Chang Gung University of Science and Technology, Taoyuan, Taiwan<sup>d</sup> Department of Pediatric Hematology/Oncology, Chang Gung Memorial Hospital at Linkou, Taoyuan, Taiwan

## ARTICLE INFO

## Article history:

Received 17 April 2020

Accepted 2 August 2020

Available online xxx

## Keywords:

Cancer

Oncogene

G6PD

Metabolic reprogramming

Redox

Oxidative stress

## ABSTRACT

Metabolic hubs play a major role in the initiation and development of cancer. Oncogenic signaling pathways drive metabolic reprogramming and alter redox homeostasis. G6PD has potential oncogenic activity and it plays a pivotal role in cell proliferation, survival and stress responses. Aberrant activation of G6PD via metabolic reprogramming alters NADPH levels, leading to an antioxidant or a pro-oxidant environment which can either enhance DNA oxidative damage and genomic instability or initiate oncogenic signaling. Nutrient deprivation can rewire metabolism, which leads to mutations that determine a cancer cell's fate. Deregulated G6PD status and oxidative stress form a vicious cycle, which paves the way for cancer progression. This review aims to update and focus the potential role of G6PD in metabolic reprogramming and redox signaling in cancer.

## The redox role of G6PD

The study of glucose-6-phosphate dehydrogenase (G6PD) began in earnest following the discovery that certain anti-malarial drugs cause hemolysis in patients with G6PD deficiency [1]. G6PD is the first and rate-limiting enzyme of the oxidative branch of the pentose phosphate pathway (PPP). Traditionally, G6PD has been considered as an antioxidant enzyme with a

major biochemical function in the anabolic metabolism of ribose 5-phosphate for nucleotide synthesis and the regeneration of the reduced form of nicotinamide adenine dinucleotide phosphate (NADPH) for reductive lipid biosynthesis and the regeneration of glutathione (GSH) to detoxify reactive oxygen species (ROS). However, the prooxidant role of G6PD in generating ROS via NADPH oxidase (NOX) has also gained much attention. NOX generates ROS to exert its microbicidal action, also known as the cytotoxic effect, in phagocytic cells, whereas

\* Corresponding author. Research Center for Chinese Herbal Medicine, Graduate Institute of Health Industry Technology, College of Human Ecology, Chang Gung University of Science and Technology, Taoyuan, 33043, Taiwan.

\*\* Corresponding author.

E-mail addresses: [hcyang@mail.ypu.edu.tw](mailto:hcyang@mail.ypu.edu.tw) (H.-C. Yang), [dtychiu@mail.cgu.edu.tw](mailto:dtychiu@mail.cgu.edu.tw) (D.T.-Y. Chiu).

Peer review under responsibility of Chang Gung University.

<https://doi.org/10.1016/j.bj.2020.08.001>

2319-4170/© 2020 Chang Gung University. Publishing services by Elsevier B.V. This is an open access article under the CC BY-NC-ND license (<http://creativecommons.org/licenses/by-nc-nd/4.0/>).

Please cite this article as: Yang H-C et al., G6PD: A hub for metabolic reprogramming and redox signaling in cancer, Biomedical Journal, <https://doi.org/10.1016/j.bj.2020.08.001>



the NOX-derived ROS can serve as signaling molecules for promoting cellular activities in many non-phagocytic cells, also known as the cyto-regulatory effect [2].

G6PD-derived NADPH has a substantial impact on cellular oxidative and nitrosative stress/damage responses and on cellular growth and proliferation. However, how G6PD acts as a double-edged sword in modulating the cellular redox status which affects cellular, especially in altering cellular metabolism in cancer biology has not been extensively reviewed. The modulation of the redox status by G6PD during cancer development is the primary focus of this review.

### The role of G6PD in cancer development and resistance to cancer therapies

G6PD can be considered as having oncogenic activity because it is required for growth and survival in both normal and transformed cells. Its function is essential in cell survival and embryonic development through redox sensitive mechanisms [3]. Lower than normal levels of G6PD activity predisposes cells to pre-mature senescence and cell death, while severe G6PD deficiency results in teratogenesis and embryonic lethality [4]. Aberrant activation of G6PD causes elevated ROS leading to uncontrolled cell growth and differentiation [5]. Changes in G6PD activity up-regulates anti-apoptotic factors and down-regulates cell cycle proteins in human melanoma mouse xeno-grafts [6]. Increased G6PD activity and the increased ratio of pentose monophosphate to hexose monophosphate have been found during the late G1 and S phase in human colon cancer cells [7]. Deregulation of long noncoding RNA (LncRNA) is linked to an impaired cell cycle, cell proliferation, and cancer. Reduced levels of the LncRNA growth arrest-specific transcript 5 (GAS5), a tumor suppressor, is associated with cancer aggressiveness [8]. Knockdown of GAS5 induces G1/S cell cycle progression through up-regulation of cyclin and Bcl-2

expression. Reduced GAS5 up-regulates G6PD and NOX4, resulting in an imbalanced redox environment in multiple myeloma cells [9]. The LncRNA protein disulfide isomerase family A member 3 pseudogene 1 (PDIA3P) regulates growth and chemotherapy resistance in multiple myeloma through interacting with c-Myc, a sequence-specific DNA-binding protein required for cell cycle progression. The interaction enhances PDIA3P transactivation. This results in its binding to the G6PD promoter, leading to an increase in G6PD activity and the PPP flux [10]. Phosphorylation of G6PD by a mitotic regulator polo-like kinase1 (Plk1) promotes G6PD dimer formation and coordinates PPP flux and cell cycle progression in cancer cell proliferation [11].

The notion of G6PD having potential oncogenic activity is not unprecedented. Hyperactive G6PD activity has been found in many types of cancer cells and is linked to the characteristics of cancer cells, including transformation, metastasis and resistance to treatment [12]. G6PD up-regulation can serve as a surrogate marker for cancer staging and is an indicator of a poor prognosis [13]. Metabolic flux and labelling analysis reveals that nearly all pyruvate is produced from glycolysis and not the PPP in non-transformed breast cancer cells [14]. Increased PPP flux and doubled production of ribose are found in transformed and metastatic breast cancer cells compared to non-transformed cells. Consistent with the altered metabolic flux through the PPP, G6PD is a major contributor to invasion and migration in hepatocellular carcinoma [15]. G6PD is increased at the later but not the early stage of breast cancer brain metastasis as found by proteomics [16]. Transketolase of the non-oxidative branch of the PPP is considered as a hallmark of metastasis [17]. This contradiction suggests that differential metabolic flux may be determined by different progression stages in specific cancers.

That G6PD has potential oncogenic activity originates from the observation that G6PD is an angiogenic factor [18]. G6PD modulates endothelial cell growth, migration and capillary formation mediated by vascular endothelial growth factor (VEGF)-stimulated eNOS activity and nitric oxide generation [19]. Impaired vessel outgrowth from the thoracic aorta is found in G6PD-deficient mouse. The nonreceptor tyrosine kinase Src has many roles in cancer, including cell survival, proliferation, adhesion, angiogenesis, and migration. C-Src phosphorylates hexokinases HK1 and HK2, and promotes glycolysis leading to tumorigenesis and metastasis [20]. C-Src also directly phosphorylates G6PD and regulates VEGF-mediated endothelial cell responses [21].

G6PD activity may be critical for the response to radiotherapy and chemotherapy in cancer cells [22–24]. G6PD-derived endogenous reductants, such as NADPH and GSH, determine whether or not cancer cells are sensitive or resistant to apoptosis when stressed. Simultaneous use of inhibitors of glycolysis and G6PD, 2-deoxy-D-glucose (2-DG) and 6-aminonicotinamide (6-AN) respectively, enhances radiation damage selectively in malignant cells by a mechanism involving non-coordinated expression of antioxidant enzymes [23]. Accumulation of reactive oxygen species (ROS), reduced NADPH/NADP<sup>+</sup> and GSH/GSSG ratios have been observed in these cells 24 h after irradiation. Overexpression of the onco-gene Inhibitor of differentiation-1 (ID1) is associated with a poor prognosis and plays a role in chemotherapy and

**Table 1 Proteins regulating G6PD/PPP activity or flux.**

Protein	Regulation	Reference
<b>Transcription factor</b>		
HIF	Up	[36]
Nrf-2	Up	[41]
Snail	Up	[70]
TAp73	Up	[53]
TP53	Down	[46]
<b>Kinase</b>		
ATM	Up	[56]
AKT	Up	[59]
c-Src	Up	[20]
PI3K	Up	[59]
PAK4	Up	[47]
PLK-1	Up	[11]
Cyclin D3-CDK6	Up	[33]
AMPK	Down	[64]
<b>Others</b>		
ID1	Up	[26]
mTORC1	Up	[66]
TGFβ1	Up	[29]
PDIA3P	Up	[10]
TIGAR	Up	[76]
PTEN	Down	[62]

radiotherapy resistance [25]. Knockdown of Id1 reduces NADPH and G6PD activity and increases ROS. Reduction of ID1 also decreases cell proliferation and induces apoptosis in oxaliplatin-resistant hepatocellular carcinoma (HCC) cells [26].

G6PD can affect the efficacy of cancer drugs leading to drug resistance. Overexpression of G6PD and G6PD mRNA is a poor prognostic indicator in patients with colorectal cancer (CRC). G6PD knockdown reduces NADPH/NADP<sup>+</sup> and GSH/GSSG ratios as well as the H<sub>2</sub>O<sub>2</sub> level in CRC cell lines [27]. G6PD suppression through RNAi against G6PD or NRF2 prevents oxaliplatin-induced apoptosis in CRC cells. G6PD knockdown also increases oxaliplatin sensitivity in both CRC cell line-based and patient-derived xenograft (PDX) models [27]. The production of lactate and other acidic metabolites due to increased G6PD and glycolysis causes an extracellular acidic microenvironment which favors cancer invasiveness by interrupting the action of weak base anti-cancer drugs [28]. G6PD expression is responsible for cisplatin resistance in non-small cell lung cancer (NSCLC) cells. Transforming growth factor beta 1 (TGFβ1) induces G6PD activity by activating transcription of the forkhead box protein M1-high mobility group AT-hook 1-G6PD (FOXN1-HMGA1-G6PD) pathway [29]. While exogenous TGFβ1 confers resistance to cisplatin, disruption of the TGFβ1-FOXN1-HMGA1-G6PD axis sensitizes NSCLC cells to the drug. Over expression of G6PD contributes to the development of multi-drug resistance (MDR) in cancer cells. Compared to doxorubicin-sensitive human colon cancer cells, doxorubicin-resistant cells have increased GSH, MDR-related proteins (MRPs) expression and doxorubicin clearance [30]. These findings indicate that G6PD participates in the metabolism or the detoxification of xenobiotics and anti-cancer drugs through a redox-regulated pathway [31].

### Modulation of G6PD by oncogenic and metabolic regulators

The hallmark of cancer is the preference of glycolysis for glucose utilization rather than oxidative phosphorylation even in the presence of oxygen. This is known as aerobic glycolysis or the Warburg effect [32]. Cancer cells utilize a large amount of glucose compared to normal cells and convert it to lactate, which is excreted. The advantage to cancer cells lies in rapid production of ATP via glycolysis for cell proliferation and the accumulation of glycolytic intermediates for cell growth. This enables cancer cells with a capacity to outcompete normal cells even in adverse conditions. This unique feature may be related to the upstream regulation of G6PD by oncogenic and/or metabolic regulators.

Cyclins and cyclin-dependent kinases (CDKs) are cell cycle components important for that affect cell proliferation and metabolism. Phosphofructokinase, platelet (PFKP), the main isoform of PFK-1, is phosphorylated and inactivated by cyclin D3-CDK6 [33]. PFKP suppression results in the movement of glycolytic intermediates towards the PPP and the serine pathway. Depletion of cyclin D3-CDK6 reduces NADPH and GSH, while increasing ROS in T-acute lymphoblastic leukemia (T-ALL) cells. Supplementation with NAC or a SOD mimetic scavenges ROS and protects T-ALL cells from apoptosis. These

findings indicate that the metabolic reprogramming of the PPP is associated with cell survival and redox homeostasis.

Hypoxia-inducible factor (HIF) is an important metabolic regulator associated with G6PD [Table 1]. HIF, the central regulator of oxygen homeostasis, modulates angiogenesis by affecting endothelial cells, including cell survival and proliferation, cell invasion and glucose metabolism. The glycolytic end products, including pyruvate and lactate, stimulate the accumulation of HIF-1α [34]. Activation of G6PD by hypoxia is implicated in cancer cells and pulmonary remodeling [35,36]. Chronic exposure of hypoxia induced by cobalt chloride and dimethylxylglycine up-regulates G6PD gene expression in rat adrenal gland cells [37]. Increased G6PD and HIF-1 expression in glutamate-induced neural stem/progenitor cells in the rat mature retina suggests that PPP flux controls the fate of neural stem/progenitor cells [38].

Nuclear factor erythroid 2-related factor 2 (Nrf2), a basic leucine zipper (bZIP) transcription factor, which maintains cellular redox homeostasis and protects cells from oxidative stress, is another factor closely related to G6PD. The inactive form of Nrf2 is maintained in the cytosol by ubiquitination through Kelch-like ECH-associated protein 1 (Keap1) and Cullin 3. Oxidative stress disrupts the Keap1-Cul3 ubiquitination followed by the translocation of Nrf2 into the nucleus. Overexpression of Nrf2 has been found in cancer cells [39]. Suppression of Nrf2 and overexpression of Keap1 down-regulates the PPP enzymes, including G6PD and transketolase in metastatic breast cancer cells [40]. G6PD is required for Nrf2-dependent tumor proliferation mediated by the constitutive expression of Phosphoinositide 3-kinases (PI3Ks)-Akt. Overexpression of Nrf2 and knockdown of Keap1 enhance G6PD and HIF-1 expression in breast cancer cells. Mechanistically, Nrf-2 up-regulates Notch1 through the G6PD/HIF-1 pathway. Nrf2 activates antioxidant enzymes, up-regulates several oncogenes unrelated to antioxidant function, down-regulates lipid metabolic enzymes as well as interacting with microRNAs (miRNA) [41]. miR-1 and miR-206 suppress G6PD expression in cervical cancer cells by targeting the 3' UTR sequence [42,43]. Continuous activation of Nrf2 decreases miR-1 and miR-206 expression, leading to enhancement of G6PD activity and PPP flux [44].

The involvement of G6PD in cancer can be mediated by factors affecting the cell cycle, such as the tumor suppressor TP53 (p53). p53 is a transcription factor for inducing cell cycle arrest, apoptosis and maintaining genomic stability. It regulates cell survival and cell death through post-translational modification and intracellular redox status [45]. p53 is also the most frequently mutated gene in many cancers. p53 regulates the PPP by directly binding to G6PD, preventing its dimerization [46]. The p21-activated kinases 4 (PAK4) is up-regulated during cancer development, thereby supporting cancer cell proliferation. PAK4 binds to murine double minute 2 (Mdm2), an inhibitor of p53. PAK4 interacts with G6PD and enhances G6PD activity through promoting the degradation and ubiquitination of p53 in colon cancer cells [47]. It has been proposed that cancer-associated p53 mutations lift the restriction of G6PD and activate PFK-1, resulting in enhanced PPP flux and glycolysis, respectively [48]. The glycolytic enzyme phosphoglycerate mutase 1 (PGAM1) is frequently up-regulated in cancer cells lacking p53 [49]. PGAM1, catalyzing 3-

phosphoglycerate (3-PG) to 2-phosphoglycerate (2-PG), is required for cancer cell proliferation and tumor growth. Knockdown of PGAM1 inhibits PPP flux and leads to the accumulation of 3-PG, which suppress 6-phosphogluconate dehydrogenase (6PGD) but not G6PD [50]. In a comparative study using a bioprocessing culture, an inverse correlation of differential protein expression of G6PD and PGAM1 has been found in Chinese hamster ovary cells [51].

A structural homolog of p53, Tap73 is also an upstream regulator of G6PD. Tap73 plays a key role in the support of proliferation and promotion of the Warburg effect in cancer cells [52]. Unlike p53, there are rare mutations found in Tap73. Tap73 can transactivate p53-targeted genes, including G6PD. Tap73 deficiency induced-defective growth can be rescued by G6PD overexpression in human osteosarcoma epithelial cells, human lung cancer cells and mouse embryonic fibroblasts [53]. The inhibition of Ras-Tap73-G6PD signaling by Zoledronic acid, a therapeutic for bone disorders, suppresses G6PD activity and cell proliferation in bladder cancer cells [54]. These findings suggest a central role for G6PD in cancer cell proliferation and metabolism regulated by Tap73.

G6PD can participate in cancer development via Ataxia telangiectasia mutated (ATM) kinase which is required for regulating the cell cycle and for repairing double strand breaks (DSBs) [55]. Upon DNA damage, ATM phosphorylates Hsp27 and stimulates G6PD activity, promoting nucleotide synthesis for the repair of DSB [56]. Mutations of FMS-like tyrosine kinase 3 (FLT3) frequently trigger cell proliferation and survival in acute myeloid leukemia (AML) [57]. Failure of achieving long-term remission by FLT3 inhibitors in treating AML is ascribed to FLT3 mutation-derived resistance. Inactivation of ATM or its effector G6PD increases sensitivity to apoptosis induced by an FLT3 inhibitor [58].

Other oncoproteins linking G6PD with cancer include phosphoinositide 3-kinases (PI3Ks) which are involved in cellular transformation and cancer development. Mutations of the p110 alpha subunit of PI3K (PIK3CA) induces downstream AKT signaling and supports growth factor-independent proliferation. PI3K enhances glycolysis by up-regulating expression of the glucose transporter and phosphofructokinase activity through the PI3K/AKT pathway. Insulin-induced G6PD expression is rapamycin-sensitive and is transcriptionally regulated by the PI3K/AKT pathway in hepatocytes [59]. G6PD status is also regulated by the AKT pathway in bladder cancer cells. G6PD knockdown enhances apoptosis, and reduces ROS accumulation and the phosphorylated AKT/AKT ratio [60]. The phosphatase and tensin homologue (PTEN), a p53-targeted tumor suppressor, negatively regulates PI3K. The mutation and loss-of-function of PTEN is implicated in heritable and sporadic cancers [61]. PTEN suppresses the PPP by interrupting pre-mRNA splicing of G6PD in liver cancer cells [62].

An additional cell cycle regulator associated with G6PD in cancer development is AMP-activated protein kinase (AMPK). AMPK affects cell growth and energy metabolism. AMPK senses intracellular ATP changes and restores ATP through phosphorylation of downstream targets, such as acetyl CoA carboxylase (ACC), 3-hydroxy-3-methyl-glutaryl-CoA reductase (HMG-CoA), mTOR complex 1 (mTORC1) and p53 [63]. AMPK negatively regulates G6PD expression [64]. Upon

metabolic stress, AMPK suppresses protein synthesis and cell proliferation by inhibiting mTOR, thereby preserving energy and cellular resources. Overexpression of G6PD is correlated with elevated mTORC1 activity, which in turn is correlated with a poor prognosis in acute myeloid leukemia [65]. mTORC1 enhances the expression of G6PD through the sterol regulatory element-binding protein (SREBP) in human embryonic kidney cells [66].

## Involvement of G6PD in metabolic reprogramming upon stress and DNA damage

Cell survival depends on the adaptation to stress. Oxidative stress depletes the NADPH pool and alleviates the inhibition of G6PD leading to the activation of the PPP which is inhibited during normal growth through suppressing G6PD by NADPH [67]. Different metabolic requirements, such as ATP or NADPH or ribose, can switch on a distinct mode of metabolic flux [68]. Cancer cells need ribose more than ATP or NADPH for rapid growth in nutrient sufficient conditions but may need equal amounts of NADPH and ribose for proliferation. However, NADPH and ATP are required more than ribose in cancer cells under stress. Solid tumors detached from the extracellular matrix activate apoptotic pathways. Matrix detachment causes depletion of ATP and glucose as well as increased oxidative stress. To survive, cancer cells rewire metabolic flux to produce additional ATP and NADPH for meeting their energy needs as well as for balancing oxidative stress, respectively. Matrix detachment enhances G6PD expression [69]. Suppression of G6PD by siRNA knockdown or chemical inhibitors (DHEA, 6-AN) decreases glucose uptake and ATP and increases oxidative stress in detached breast cancer cells. The rescue of detachment-induced phenotypes by oncogene ErbB2 expression requires G6PD through the activation of PI3K and stabilization of the EGFR. Matrix detachment-induced energy reprogramming in breast cancer cells can also be reversed by the antioxidant N-acetyl-L-cysteine (NAC), a GSH precursor, or activation of AMPK [64]. Snail (SNAI1), a transcriptional repressor, regulates the epithelial-mesenchymal transition (EMT) in cancer cells. Knockdown of SNAI1 sensitizes cancer cells in a way that leads to their demise under metabolic stress, such as glucose deprivation [70]. SNAI1 inhibits glycolysis and redirects glucose to the PPP by suppression of PFKP in breast cancer cells.

Upon nutritional and genotoxic stress, cancer cells rewire metabolism from glycolysis to the PPP to obtain a sufficient supply of reductants such as NADPH to detoxify ROS. G6PD is activated rapidly for maximizing NADPH production in skin fibroblasts and keratinocytes during short-term oxidant and UV exposure [71]. Knockdown of G6PD renders sensitivity to oxidant-induced cell death in liver cancer cells [72]. Regeneration of GSH is impaired in G6PD-deficient liver cancer cells, and is worsened by treatment with the oxidant, diamide [73]. Upon diamide treatment, several metabolic pathways, including energy and amino acid metabolism, are affected. Diamide-enhanced NAD kinase activity is a compensatory action leading to an accumulation of NADPH in G6PD-deficient liver cancer cells [74]. NAC rescues diamide-induced cell death and GSH depletion in G6PD-deficient cells, suggesting that



G6PD is required for cell survival by maintaining an intracellular reductant environment and energy metabolism.

Beyond the contribution of genetics such as the buildup of multiple mutations in cancer, this disease has recently been considered as a metabolic disease shaped by the network between tumor cells and their surrounding environment. Metabolic reprogramming in cancer cells can be attributed to genotoxic insult-derived DNA damage, nutrient insufficiency, and impaired DNA repair. A network of DNA damage response (DDR) pathways has been established for maintaining genomic integrity. These include DNA repair, damage tolerance and cell-cycle checkpoint pathways [75]. DDR is involved in driving metabolic reprogramming regulated by ATM and ataxia telangiectasia and Rad3-related (ATR) kinases. ATM induces G6PD to generate NADPH and ribose in order to counteract the genotoxic stress [56]. p53 regulates the cell cycle, DNA repair and apoptosis by transactivation of downstream DDR genes at the promoter region. Induction of TP53-inducible glycolysis and apoptosis regulator (TIGAR) by p53 suppresses glycolysis and redirects glucose to the PPP [76]. In contrast to the traditional view that oncogenic mutations reprogram cancer cell metabolism, the unique microenvironment derived from rewired metabolism may lead to a rise of mutations. The availability of essential nutrients affects the fate of cancer cells by directly regulating mutations that control their survival or demise. Folate deficiency causes chromosome breaks by incorporating excessive uracil into DNA. It increases the risk of colorectal cancer [77]. Glucose depletion leads to mutations in the KRAS pathway in colorectal cancer cells [78].

DNA damage and repair pathways are critical in cancer development and cancer cell therapy [79]. Dysregulation of these pathways not only enhances genomic instability and the mutation rate, but also increases cancer heterogeneity [80,81]. This could result in the regulation of the DNA repair pathway by adding substrates from metabolic intermediates to nucleic acids and chromatin [82]. PPP-derived ribose is the main precursor for the synthesis of purines and pyrimidines. Genetic insult and hypoxia-induced DNA damage mediated by TIGAR can be reversed by supplementing human liver cancer cells with ribose [83].

Amino acid and metabolite levels determine the availability of intracellular nucleotides and influence the DNA repair pathway. Glutamine is essential for producing the intermediates inosine monophosphate and uridine monophosphate for purine and pyrimidine synthesis, respectively [84]. Deoxyribonucleotide triphosphate (dNTP) synthesis is dependent on the consumption of glucose and glutamine. Knockdown of ATM increases glucose and glutamine consumption, which is a characteristic of cancer cell metabolism. Nucleotide depletion-induced replication stress is important in cancer cell initiation. Cancer cells inactivate ATM in response replication stress by rewiring cellular metabolism to the PPP through p53-mediated G6PD up-regulation [85]. ROS is implicated in the relationship between metabolism and the DNA repair pathways. Increased ROS causes DNA oxidative damage by inducing single strand breaks. These lesions interrupt DNA replication and doubles DNA strand breaks [86]. Intracellular ROS-scavenging molecules and enzymes are required for counteracting DNA damage caused by ROS. G6PD-

derived NADPH is the main source for regenerating GSH, which is synthesized from cysteine, glycine and glutamate. Decreased levels of glutamate due to diminished glutamate dehydrogenase (GDH-1) activity, which relies on NADPH, is associated with impaired NADPH generating enzymes, including G6PD and IDH1 [87]. GSH peroxidase detoxifies peroxide compounds and oxidizes GSH. The regeneration to the reduced form of GSH is catalyzed by NADPH-dependent GSH reductase. Another source of NADPH comes from one-carbon metabolism, which includes the serine synthesis pathway and the glycine cleavage system (GCS). Cancer cells alter these pathways to maintain one carbon donors for cellular proliferation [88]. Serine hydroxymethyltransferases (SHMTs) convert serine to glycine and generate methylene-THF. Methylene tetrahydrofolate dehydrogenases (MTHFDs) utilize NADP as a substrate to produce NADPH. Like G6PD, several enzymes of the serine synthesis pathway are directly regulated by Nrf2, including activating transcription factor 4 (ATF4), phosphoglycerate dehydrogenase (PHGDH), and phosphoserine aminotransferase 1 (PSAT1) [89].

## Summary

Deregulated metabolism has long been considered as secondary to genomic abnormalities in cancer development. New evidence indicates that genetic alterations reprogram metabolic pathways by activating oncogenes or dampening tumor suppressor genes. G6PD, the core enzyme of the PPP, is closely linked to the development of cancer. Activated G6PD is exploited by cancer cells as a powerful weapon for proliferation and survival in an unfavorable environment. Ribose, NADPH and GSH, products of G6PD, are strategically utilized by cancer cells during growth, invasion, and metastasis as well as resistance to therapy. These measures enable cancer cells to tackle the cause of stress, which include oxygen deprivation, nutrient deficiency, ROS, RNS and DNA injury. Therapeutically, targeting G6PD in cancer cells is of great interest. However, the lack of a specific inhibitor hinders therapeutic development. A comprehensive understanding of the role of G6PD in the metabolism and in the redox regulation of tumorigenesis and cancer progression will provide a basis for establishing an additional and novel approach in the treatment of cancer.

## Conflicts of interest

The authors declare no conflict of interest.

## Acknowledgments

This review article is made possible by grants from the Ministry of Science and Technology, Taiwan [MOST108-2320-B-264-002 and MOST109-2320-B-264-001-MY2 to HCY; MOST108-2320-B-255-005 and MOST109-2320-B-255-009 to DTYC] and grant from Chang Gung Memorial Hospital, Taiwan [CMRPF1J0072 to DTYC].

## REFERENCES

- [1] Ho HY, Cheng ML, Chiu DT. G6PD—an old bottle with new wine. *Chang Gung Med J* 2005;28:606–12.
- [2] Yang HC, Cheng ML, Ho HY, Chiu DT. The microbicidal and cytoregulatory roles of NADPH oxidases. *Microb Infect* 2011;13:109–20.
- [3] Yang HC, Wu YH, Liu HY, Stern A, Chiu DT. What has passed is prolog: new cellular and physiological roles of G6PD. *Free Radic Res* 2016;50:1047–64.
- [4] Longo L, Vanegas OC, Patel M, Rosti V, Li H, Waka J, et al. Maternally transmitted severe glucose 6-phosphate dehydrogenase deficiency is an embryonic lethal. *EMBO J* 2002;21:4229–39.
- [5] Yang HC, Wu YH, Yen WC, Liu HY, Hwang TL, Stern A, et al. The redox role of G6PD in cell growth, cell death, and cancer. *Cells* 2019;8.
- [6] Hu T, Zhang C, Tang Q, Su Y, Li B, Chen L, et al. Variant G6PD levels promote tumor cell proliferation or apoptosis via the STAT3/5 pathway in the human melanoma xenograft mouse model. *BMC Canc* 2013;13:251.
- [7] Vizan P, Alcarraz-Vizan G, Diaz-Moralli S, Solovjeva ON, Frederiks WM, Cascante M. Modulation of pentose phosphate pathway during cell cycle progression in human colon adenocarcinoma cell line HT29. *Int J Canc* 2009;124:2789–96.
- [8] Yu Y, Hann SS. Novel tumor suppressor lncRNA growth arrest-specific 5 (GAS5) in human cancer. *OncoTargets Ther* 2019;12:8421–36.
- [9] Chen L, Yang H, Yi Z, Jiang L, Li Y, Han Q, et al. LncRNA GAS5 regulates redox balance and dysregulates the cell cycle and apoptosis in malignant melanoma cells. *J Canc Res Clin Oncol* 2019;145:637–52.
- [10] Yang X, Ye H, He M, Zhou X, Sun N, Guo W, et al. LncRNA PDIA3P interacts with c-Myc to regulate cell proliferation via induction of pentose phosphate pathway in multiple myeloma. *Biochem Biophys Res Commun* 2018;498:207–13.
- [11] Ma X, Wang L, Huang, Li Y, Yang D, Li T, et al. Polo-like kinase 1 coordinates biosynthesis during cell cycle progression by directly activating pentose phosphate pathway. *Nat Commun* 2017;8:1506.
- [12] Riganti C, Gazzano E, Polimeni M, Aldieri E, Ghigo D. The pentose phosphate pathway: an antioxidant defense and a crossroad in tumor cell fate. *Free Radic Biol Med* 2012;53:421–36.
- [13] Pu H, Zhang Q, Zhao C, Shi L, Wang Y, Wang J, et al. Overexpression of G6PD is associated with high risks of recurrent metastasis and poor progression-free survival in primary breast carcinoma. *World J Surg Oncol* 2015;13:323.
- [14] Richardson AD, Yang C, Osterman A, Smith JW. Central carbon metabolism in the progression of mammary carcinoma. *Breast Canc Res Treat* 2008;110:297–307.
- [15] Lu M, Lu L, Dong Q, Yu G, Chen J, Qin L, et al. Elevated G6PD expression contributes to migration and invasion of hepatocellular carcinoma cells by inducing epithelial-mesenchymal transition. *Acta Biochim Biophys Sin* 2018;50:370–80.
- [16] Chen EI, Hewel J, Krueger JS, Tiraby C, Weber MR, Kralli A, et al. Adaptation of energy metabolism in breast cancer brain metastases. *Canc Res* 2007;67:1472–86.
- [17] Tseng CW, Kuo WH, Chan SH, Chan HL, Chang KJ, Wang LH. Transketolase regulates the metabolic switch to control breast cancer cell metastasis via the alpha-ketoglutarate signaling pathway. *Canc Res* 2018;78:2799–812.
- [18] Zhang C, Zhang Z, Zhu Y, Qin S. Glucose-6-phosphate dehydrogenase: a biomarker and potential therapeutic target for cancer. *Anticancer Agents Med Chem* 2014;14:280–9.
- [19] Leopold JA, Walker J, Scribner AW, Voetsch B, Zhang YY, Loscalzo AJ, et al. Glucose-6-phosphate dehydrogenase modulates vascular endothelial growth factor-mediated angiogenesis. *J Biol Chem* 2003;278:32100–6.
- [20] Zhang J, Wang S, Jiang B, Huang L, Ji Z, Li X, et al. c-Src phosphorylation and activation of hexokinase promotes tumorigenesis and metastasis. *Nat Commun* 2017;8:13732.
- [21] Pan S, World CJ, Kovacs CJ, Berk BC. Glucose 6-phosphate dehydrogenase is regulated through c-Src-mediated tyrosine phosphorylation in endothelial cells. *Arterioscler Thromb Vasc Biol* 2009;29:895–901.
- [22] Yang CA, Huang HY, Lin CL, Chang JG. G6PD as a predictive marker for glioma risk, prognosis and chemosensitivity. *J Neuro Oncol* 2018;139:661–70.
- [23] Sharma PK, Bhardwaj R, Dwarakanath BS, Varshney R. Metabolic oxidative stress induced by a combination of 2-DG and 6-AN enhances radiation damage selectively in malignant cells via non-coordinated expression of antioxidant enzymes. *Canc Lett* 2010;295:154–66.
- [24] Cheng AJ, Chiu DT, See LC, Liao CT, Chen IH, Chang JT. Poor prognosis in nasopharyngeal cancer patients with low glucose-6-phosphate-dehydrogenase activity. *Jpn J Canc Res* 2001;92:576–81.
- [25] Ponz-Sarvisé M, Nguewa PA, Pajares MJ, Agorreta J, Lozano MD, Redrado M, et al. Inhibitor of differentiation-1 as a novel prognostic factor in NSCLC patients with adenocarcinoma histology and its potential contribution to therapy resistance. *Clin Canc Res* 2011;17:4155–66.
- [26] Yin X, Tang B, Li JH, Wang Y, Zhang L, Xie XY, et al. ID1 promotes hepatocellular carcinoma proliferation and confers chemoresistance to oxaliplatin by activating pentose phosphate pathway. *J Exp Clin Canc Res* 2017;36:166.
- [27] Ju HQ, Lu YX, Wu QN, Liu J, Zeng ZL, Mo HY, et al. Disrupting G6PD-mediated Redox homeostasis enhances chemosensitivity in colorectal cancer. *Oncogene* 2017;36:6282–92.
- [28] Glunde K, Guggino SE, Solaiyappan M, Pathak AP, Ichikawa Y, Bhujwalla ZM. Extracellular acidification alters lysosomal trafficking in human breast cancer cells. *Neoplasia* 2003;5:533–45.
- [29] Zhang R, Tao F, Ruan S, Hu M, Hu Y, Fang Z, et al. The TGFbeta1-FOXM1-HMGA1-TGFbeta1 positive feedback loop increases the cisplatin resistance of non-small cell lung cancer by inducing G6PD expression. *Am J Transl Res* 2019;11:6860–76.
- [30] Polimeni M, Voena C, Kopecka J, Riganti C, Pescarmona G, Bosia A, et al. Modulation of doxorubicin resistance by the glucose-6-phosphate dehydrogenase activity. *Biochem J* 2011;439:141–9.
- [31] Lin HR, Wu CC, Wu YH, Hsu CW, Cheng ML, Chiu DT. Proteome-wide dysregulation by glucose-6-phosphate dehydrogenase (G6PD) reveals a novel protective role for G6PD in aflatoxin B(1)-mediated cytotoxicity. *J Proteome Res* 2013;12:3434–48.
- [32] Warburg O. On the origin of cancer cells. *Science* 1956;123:309–14.
- [33] Wang H, Nicolay BN, Chick JM, Gao X, Geng Y, Ren H, et al. The metabolic function of cyclin D3-CDK6 kinase in cancer cell survival. *Nature* 2017;546:426–30.
- [34] Schito L, Semenza GL. Hypoxia-inducible factors: master regulators of cancer progression. *Trend Canc* 2016;2:758–70.
- [35] Chettimada S, Gupta R, Rawat D, Gebb SA, McMurtry IF, Gupta SA. Hypoxia-induced glucose-6-phosphate dehydrogenase overexpression and -activation in pulmonary



- artery smooth muscle cells: implication in pulmonary hypertension. *Am J Physiol Lung Cell Mol Physiol* 2015;308:L287–300.
- [36] Yi W, Clark PM, Mason DE, Keenan MC, Hill C, Goddard 3rd WA, et al. Phosphofructokinase 1 glycosylation regulates cell growth and metabolism. *Science* 2012;337:975–80.
- [37] Gao L, Mejias R, Echevarria M, Lopez-Barneo J. Induction of the glucose-6-phosphate dehydrogenase gene expression by chronic hypoxia in PC12 cells. *FEBS Lett* 2004;569:256–60.
- [38] Tokuda K, Baron B, Yamashiro C, Kuramitsu Y, Kitagawa T, Kobayashi M, et al. Up-regulation of the pentose phosphate pathway and HIF-1 $\alpha$  expression during neural progenitor cell induction following glutamate treatment in rat ex vivo retina. *Cell Biol Int* 2020;44:137–44.
- [39] Leinonen HM, Kansanen E, Polonen P, Heinaniemi M, Levonen AL. Dysregulation of the Keap1-Nrf2 pathway in cancer. *Biochem Soc Trans* 2015;43:645–9.
- [40] Zhang HS, Zhang ZG, Du GY, Sun HL, Liu HY, Zhou Z, et al. Nrf2 promotes breast cancer cell migration via up-regulation of G6PD/HIF-1 $\alpha$ /Notch1 axis. *J Cell Mol Med* 2019;23:3451–63.
- [41] Zimta AA, Cenariu D, Irimie A, Magdo L, Nabavi SM, Atanasov AG, et al. The role of Nrf2 activity in cancer development and progression. *Cancers* 2019;11:1755.
- [42] Cui J, Pan Y, Wang J, Liu Y, Wang H, Li H. MicroRNA-206 suppresses proliferation and predicts poor prognosis of HR-HPV-positive cervical cancer cells by targeting G6PD. *Oncol Lett* 2018;16:5946–52.
- [43] Hu T, Chang YF, Xiao Z, Mao R, Tong J, Chen B, et al. miR-1 inhibits progression of high-risk papillomavirus-associated human cervical cancer by targeting G6PD. *Oncotarget* 2016;7:86103–16.
- [44] Singh A, Happel C, Manna SK, Acquah-Mensah G, Carrero J, Kumar S, et al. Transcription factor NRF2 regulates miR-1 and miR-206 to drive tumorigenesis. *J Clin Invest* 2013;123:2921–34.
- [45] Eriksson SE, Ceder S, Bykov VJN, Wiman KG. p53 as a hub in cellular redox regulation and therapeutic target in cancer. *J Mol Cell Biol* 2019;11:330–41.
- [46] Jiang P, Du W, Wang X, Mancuso A, Gao X, Wu M, et al. p53 regulates biosynthesis through direct inactivation of glucose-6-phosphate dehydrogenase. *Nat Cell Biol* 2011;13:310–6.
- [47] Zhang X, Zhang X, Li Y, Shao Y, Xiao J, Zhu G, et al. PAK4 regulates G6PD activity by p53 degradation involving colon cancer cell growth. *Cell Death Dis* 2017;8:e2820.
- [48] Bensaad K, Tsuruta A, Selak MA, Vidal MN, Nakano K, Bartrons R, et al. TIGAR, a p53-inducible regulator of glycolysis and apoptosis. *Cell* 2006;126:107–20.
- [49] Huang K, Liang Q, Zhou Y, Jiang LL, Gu WM, Luo MY, et al. A novel allosteric inhibitor of phosphoglycerate mutase 1 suppresses growth and metastasis of non-small-cell lung cancer. *Cell Metabol* 2019;30:1107–19.e8.
- [50] Hitosugi T, Zhou L, Elf S, Fan J, Kang HB, Seo JH, et al. Phosphoglycerate mutase 1 coordinates glycolysis and biosynthesis to promote tumor growth. *Canc Cell* 2012;22:585–600.
- [51] Meleady P, Doolan P, Henry M, Barron N, Keenan J, O'Sullivan F, et al. Sustained productivity in recombinant Chinese hamster ovary (CHO) cell lines: proteome analysis of the molecular basis for a process-related phenotype. *BMC Biotechnol* 2011;11:78.
- [52] Li L, Li L, Li W, Chen T, Bin Z, Zhao L, et al. TAp73-induced phosphofructokinase-1 transcription promotes the Warburg effect and enhances cell proliferation. *Nat Commun* 2018;9:4683.
- [53] Du W, Jiang P, Mancuso A, Stonestrom A, Brewer MD, Minn AJ, et al. TAp73 enhances the pentose phosphate pathway and supports cell proliferation. *Nat Cell Biol* 2013;15:991–1000.
- [54] Wang X, Wu G, Cao G, Yang L, Xu H, Huang J, et al. Zoledronic acid inhibits the pentose phosphate pathway through attenuating the Ras-TAp73-G6PD axis in bladder cancer cells. *Mol Med Rep* 2015;12:4620–5.
- [55] Williams RM, Yates LA, Zhang X. Structures and regulations of ATM and ATR, master kinases in genome integrity. *Curr Opin Struct Biol* 2020;61:98–105.
- [56] Cosentino C, Grieco D, Costanzo V. ATM activates the pentose phosphate pathway promoting anti-oxidant defence and DNA repair. *EMBO J* 2011;30:546–55.
- [57] Daver N, Schlenk RF, Russell NH, Levis MJ. Targeting FLT3 mutations in AML: review of current knowledge and evidence. *Leukemia* 2019;33:299–312.
- [58] Gregory MA, D'Alessandro A, Alvarez-Calderon F, Kim J, Nemkov T, Adane B, et al. ATM/G6PD-driven redox metabolism promotes FLT3 inhibitor resistance in acute myeloid leukemia. *Proc Natl Acad Sci U S A* 2016;113:E6669–78.
- [59] Wagle A, Jivraj S, Garlock GL, Stapleton SR. Insulin regulation of glucose-6-phosphate dehydrogenase gene expression is rapamycin-sensitive and requires phosphatidylinositol 3-kinase. *J Biol Chem* 1998;273:14968–74.
- [60] Chen X, Xu Z, Zhu Z, Chen A, Fu G, Wang Y, et al. Modulation of G6PD affects bladder cancer via ROS accumulation and the AKT pathway in vitro. *Int J Oncol* 2018;53:1703–12.
- [61] Lee YR, Chen M, Pandolfi PP. The functions and regulation of the PTEN tumour suppressor: new modes and prospects. *Nat Rev Mol Cell Biol* 2018;19:547–62.
- [62] Hong X, Song R, Song H, Zheng T, Wang J, Liang Y, et al. PTEN antagonises Tc1/hnRNP-mediated G6PD pre-mRNA splicing which contributes to hepatocarcinogenesis. *Gut* 2014;63:1635–47.
- [63] Herzig S, Shaw RJ. AMPK: guardian of metabolism and mitochondrial homeostasis. *Nat Rev Mol Cell Biol* 2018;19:121–35.
- [64] Yang L, He Z, Yao J, Tan R, Zhu Y, Li Z, et al. Regulation of AMPK-related glycolipid metabolism imbalances redox homeostasis and inhibits anchorage independent growth in human breast cancer cells. *Redox Biol* 2018;17:180–91.
- [65] Poulain L, Sujobert P, Zylbersztejn F, Barreau S, Stuani L, Lambert M, et al. High mTORC1 activity drives glycolysis addiction and sensitivity to G6PD inhibition in acute myeloid leukemia cells. *Leukemia* 2017;31:2326–35.
- [66] Duvel K, Yecies JL, Menon S, Raman P, Lipovsky AI, Souza AL, et al. Activation of a metabolic gene regulatory network downstream of mTOR complex 1. *Mol Cell* 2010;39:171–83.
- [67] Christodoulou D, Kuehne A, Estermann A, Fuhrer T, Lang P, Sauer U. Reserve flux capacity in the pentose phosphate pathway by NADPH binding is conserved across kingdoms. *Science* 2019;19:1133–44.
- [68] Cho ES, Cha YH, Kim HS, Kim NH, Yook JI. The pentose phosphate pathway as a potential target for cancer therapy. *Biomol Ther* 2018;26:29–38.
- [69] Schafer ZT, Grassian AR, Song L, Jiang Z, Gerhart-Hines Z, Irie HY, et al. Antioxidant and oncogene rescue of metabolic defects caused by loss of matrix attachment. *Nature* 2009;461:109–13.
- [70] Kim NH, Cha YH, Lee J, Lee SH, Yang JH, Yun JS, et al. Snail reprograms glucose metabolism by repressing phosphofructokinase PFKP allowing cancer cell survival under metabolic stress. *Nat Commun* 2017;8:14374.
- [71] Kuehne A, Emmert H, Soehle J, Winnefeld M, Fischer F, Wenck H, et al. Acute activation of oxidative pentose phosphate pathway as first-line response to oxidative stress in human skin cells. *Mol Cell* 2015;59:359–71.

- [72] Yang HC, Cheng ML, Hua YS, Wu YH, Lin HR, Liu HY, et al. Glucose 6-phosphate dehydrogenase knockdown enhances IL-8 expression in HepG2 cells via oxidative stress and NF-kappaB signaling pathway. *J Inflamm* 2015;12:34.
- [73] Gao LP, Cheng ML, Chou HJ, Yang YH, Ho HY, Chiu DT. Ineffective GSH regeneration enhances G6PD-knockdown Hep G2 cell sensitivity to diamide-induced oxidative damage. *Free Radic Biol Med* 2009;47:529–35.
- [74] Ho HY, Cheng ML, Shiao MS, Chiu DT. Characterization of global metabolic responses of glucose-6-phosphate dehydrogenase-deficient hepatoma cells to diamide-induced oxidative stress. *Free Radic Biol Med* 2013;54:71–84.
- [75] Lama-Sherpa TD, Shevde LA. An emerging regulatory role for the tumor microenvironment in the DNA damage response to double-strand breaks. *Mol Canc Res* 2020;18:185–93.
- [76] Wang J, Duan Z, Nugent Z, Zou JX, Borowsky AD, Zhang Y, et al. Reprogramming metabolism by histone methyltransferase NSD2 drives endocrine resistance via coordinated activation of pentose phosphate pathway enzymes. *Canc Lett* 2016;378:69–79.
- [77] Ames BN. DNA damage from micronutrient deficiencies is likely to be a major cause of cancer. *Mutat Res* 2001;475:7–20.
- [78] Yun J, Rago C, Cheong I, Pagliarini R, Angenendt P, Rajagopalan H, et al. Glucose deprivation contributes to the development of KRAS pathway mutations in tumor cells. *Science* 2009;325:1555–9.
- [79] Kiwerska K, Szyfter K. DNA repair in cancer initiation, progression, and therapy-a double-edged sword. *J Appl Genet* 2019;60:329–34.
- [80] Ma J, Setton J, Lee NY, Riaz N, Powell SN. The therapeutic significance of mutational signatures from DNA repair deficiency in cancer. *Nat Commun* 2018;9:3292.
- [81] Andor N, Maley CC, Ji HP. Genomic instability in cancer: teetering on the limit of tolerance. *Canc Res* 2017;77:2179–85.
- [82] Reid MA, Dai Z, Locasale JW. The impact of cellular metabolism on chromatin dynamics and epigenetics. *Nat Cell Biol* 2017;19:1298–306.
- [83] Yu HP, Xie JM, Li B, Sun YH, Gao QG, Ding ZH, et al. TIGAR regulates DNA damage and repair through pentosephosphate pathway and Cdk5-ATM pathway. *Sci Rep* 2015;5:9853.
- [84] Natarajan SK, Venneti S. Glutamine metabolism in brain tumors. *Cancers* 2019;11:1628.
- [85] Aird KM, Worth AJ, Snyder NW, Lee JV, Sivanand S, Liu Q, et al. ATM couples replication stress and metabolic reprogramming during cellular senescence. *Cell Rep* 2015;11:893–901.
- [86] Anand SK, Sharma A, Singh N, Kakkar P. Entrenching role of cell cycle checkpoints and autophagy for maintenance of genomic integrity. *DNA Repair* 2020;86:102748.
- [87] Yang HC, Yu H, Liu YC, Chen TL, Stern A, Lo SJ, et al. IDH-1 deficiency induces growth defects and metabolic alterations in GSPD-1-deficient *Caenorhabditis elegans*. *J Mol Med (Berl)* 2019;97:385–96.
- [88] Yang M, Vousden KH. Serine and one-carbon metabolism in cancer. *Nat Rev Canc* 2016;16:650–62.
- [89] Lee SB, Sellers BN, DeNicola GM. The regulation of NRF2 by nutrient-responsive signaling and its role in anabolic cancer metabolism. *Antioxidants Redox Signal* 2018;29:1774–91.



Contents lists available at ScienceDirect

## Materials Science &amp; Engineering C

journal homepage: [www.elsevier.com/locate/msec](http://www.elsevier.com/locate/msec)

# A bioactive multi-functional heparin-grafted aligned poly (lactide-co-glycolide)/curcumin nanofiber membrane to accelerate diabetic wound healing

Han Tsung Liao<sup>a,b</sup>, Yu-Tin Lai<sup>a</sup>, Chang-Yi Kuo<sup>a</sup>, Jyh-Ping Chen<sup>a,b,c,d,\*</sup>

<sup>a</sup> Department of Chemical and Materials Engineering, Chang Gung University, Kwei-San, Taoyuan 33302, Taiwan, ROC

<sup>b</sup> Department of Plastic and Reconstructive Surgery and Craniofacial Research Center, Chang Gung Memorial Hospital, Chang Gung University School of Medicine, Kwei-San, Taoyuan 33305, Taiwan, ROC

<sup>c</sup> Research Center for Food and Cosmetic Safety, Research Center for Chinese Herbal Medicine, Chang Gung University of Science and Technology, Kwei-San, Taoyuan 33302, Taiwan, ROC

<sup>d</sup> Department of Materials Engineering, Ming Chi University of Technology, Tai-Shan, New Taipei City 24301, Taiwan, ROC

## ARTICLE INFO

## Keywords:

Wound healing  
Nanofibers  
Curcumin  
Heparin  
Wound dressing  
Poly(lactide-co-glycolide)

## ABSTRACT

Curcumin is reported to possess excellent efficacy to treat wounds that exhibit impaired healing. Heparin shows high affinity for many growth factors that are key biological mediators during the wound healing process. In this study, we aimed to prepare wound dressing membranes, for sustained release of an exogenous factor curcumin as well as sequestering endogenous growth factors at the wound site, to promote wound healing in diabetic rats. Toward this end, we prepared aligned curcumin-loaded poly(lactide-co-glycolide) (PLGA) nanofiber membranes (PC NFMs), followed by high density surface grafting of heparin to fabricate PLGA/curcumin (PCH) NFMs. Both PC and PCH NFMs show high tensile strength, low cytotoxicity and suitable water vapor transmission rate for application as wound dressings. Nonetheless, the PCH NFM shows higher curcumin release rate than PC due to enhanced hydrophilicity, which leads to higher cell migration rate and induced oxidative stress protection of HS68 fibroblast cells in vitro. In vivo study indicated the PCH exhibits the fastest wound closure rate among all membranes with accelerated re-epithelization rate, higher angiogenesis rate and more collagen deposition at the wound site. The accelerated and better skin tissue regeneration could be suggested to correlate with the multi-functionality of nanofibers, where grafted heparin attracting and stabilizing the growth factors important for wound healing in situ, together with relieving the high oxidative stress and the inflammatory cascade from released curcumin during diabetic wound healing.

## 1. Introduction

A wound dressing may provide physical protection, antibacterial function, exudate management and healing acceleration of the wound. However, conventional dressing materials may restrict wound healing from the secondary trauma during dressing removal or infection caused by excessive exudate [1]. In contrast, nanofiber membranes (NFMs) with their high surface area and microporous structure may attract fibroblasts toward the wound bed to start the wound healing signaling pathway, where cells can excrete collagen, angiogenic factors and growth factors for repair of damaged tissue [2]. In addition, the open structure offered by microporous NFMs provides good drainage of exudates and reduces the risk of secondary infection [3].

The electrospinning process can directly process biocompatible polymers into nanofibers by using an electrical charge to draw very fine fibers from a polymer solution [4]. The characteristic of electrospun NFMs could be manipulated by controlling process parameters such as voltage, flow rate, polymer concentration and solvent composition [5]. In order to provide physical cues for cell attachment, an aligned fiber orientation could replace the random orientation of typical electrospun nanofibers. Indeed, aligned nanofiber scaffold represent a unique group of fibrous scaffolds that could induce a particular cell orientation response, which will be suitable for regeneration of tendons, skin, muscle and nerve tissues with the anisotropic structure of these tissues [6,7]. From in vitro cell culture, aligned nanofiber scaffolds were found to exhibit higher cell proliferation rate compared with the random ones

\* Corresponding author at: Department of Chemical and Materials Engineering, Chang Gung University, Kwei-San, Taoyuan 33302, Taiwan, ROC.

E-mail address: [jpchen@mail.cgu.edu.tw](mailto:jpchen@mail.cgu.edu.tw) (J.-P. Chen).

<https://doi.org/10.1016/j.msec.2020.111689>

Received 21 April 2020; Received in revised form 23 October 2020; Accepted 27 October 2020

Available online 1 November 2020

0928-4931/© 2020 Elsevier B.V. All rights reserved.

with fiber alignment strengthening the interactions between cells and fibers in the longitudinal fiber direction [8]. The substrate morphology could also change the expression of matrix components (elastin, collagen and fibronectin) of fibroblasts [9]. For wound healing, it is thus possible to affect the process of wound closure in a spatial manner, using topographical cues offered by aligned NFMs, to result in faster wound closure rate [10]. A previous study showed that aligned nanofibers promote cell migration and wound healing, where contact guidance of cytoskeletal filaments via aligned nanostructure was postulated to be responsible for change in cell behavior [11].

After physical or chemical damage to the skin, the wound healing process involves four steps including hemostasis, inflammation, cell proliferation and remodeling [12]. In the hemostatic phase, the blood vessels contract to accelerate hemostasis and coagulation. Platelets and fibrin during blood clotting release platelet-derived growth factor (PDGF) and transforming growth factor beta 1 (TGF- $\beta$ 1) to recruit fibroblasts, endothelial cells and macrophages [12]. Macrophages are then stimulated to secrete cytokines, including fibroblast growth factor 2 (FGF-2). The production of FGF-2 is essential for angiogenesis during the wound healing process [13]. During the inflammation phase, vascular contraction promotes vascular permeability, leading to the intrusion of neutrophils, macrophages, and lymphocytes as well as eliminating the bacteria and necrotic tissue by reactive oxygen species (ROS) [14]. Excessive ROS causes damage to normal cells, which places endogenous antioxidants such as superoxide dismutase (SOD) and glutathione peroxidase (GPx) to play a critical role in ROS homeostasis. It is generally agreed that fibroblasts are widely required to secrete collagen for cell proliferation and neovascular formation [15]. The collagen at the wound is rearranged and the angiogenesis process is terminated afterward during the remodeling phase. In addition, the recycle of collagen is subsequently mediated by collagenase, with excessive collagen at the injured site prone for rigid scar formation in the end.

Poly(lactic-co-glycolic acid) (PLGA) is one of the polymers that are approvable by the U.S. Food and Drug Administration (FDA) for clinical use in wound dressing materials due to its biocompatibility and biodegradability. Previously, PLGA powder was found to promote angiogenesis and accelerate healing of excisional skin wounds, which was ascribed to sustained local release of exogenous lactate from PLGA [16]. Nonetheless, surface modification of PLGA is deemed necessary to improve its hydrophilicity for biomedical applications [17]. Specifically, surface grafting of bioactive molecules to fiber surface could enhance the hydrophilicity in addition to increase the functionality of PLGA NFMs [18].

Curcumin is a polyphenolic compound obtained from tumeric, the powdered root of *Curcuma longa*. It has been used for the treatment of common cold, skin diseases, abdominal spasms and inflammation, and is also employed as a dietary herbal supplement [19]. Specifically, a PLGA/curcumin nanofiber membrane has been reported to be effective for the treatment of carcinoma [20]. Recently, various topical formulations of curcumin have been developed to deliver curcumin at wounded sites and showed excellent efficacy to promote impaired wound healing [21]. The accelerated wound healing was suggested to be due to enhanced migratory ability of cells in the wound bed, improved neovascularization and efficient free radical scavenging activity [22]. Previous studies also show that curcumin has anti-inflammatory and anti-tumor activity by regulating the expression of interleukin-8, tumor necrosis factor- $\alpha$ , cyclooxygenase and lipoxygenase [23]. In addition, increasing number of studies indicate that curcumin decreases ROS and inflammation both in vitro and in vivo through mediation of the nuclear factor- $\kappa$ B (NF $\kappa$ B) pathway [24,25]. Taking advantage of the antioxidant and anti-inflammatory properties, curcumin-loaded nanofiber was shown to increase the wound closure rate in diabetic mice [26]. An additional benefit offered by curcumin for accelerated wound healing was suggested to be due to the regulation of collagen synthesis [27]. Furthermore, polyethyleneimine-carboxymethyl chitosan/pDNA-

angiogenin nanoparticles/cellulose nanocrystals/curcumin/PLGA composite NFMs were prepared to prevent local infection and promote skin regeneration in infected full-thickness burn wounds [28].

The extracellular matrix (ECM), with glycoaminoglycans (GAGs) as primary components, is a natural reservoir of many growth factors, where GAGs can bind, stabilize and promote the actions of various growth factors [29]. For instance, heparan sulfate in the ECM could bind with heparin-binding growth factors, which is critical for accumulation of growth factors in cell vicinity, protection of growth factors from degradation and proper cell signaling functions. In particular, heparin, a highly sulfated GAG, possesses structural domains exhibiting affinity to various growth factors. Heparin is well known for its capabilities to bind and enhance the functions of pro-angiogenic growth factors such as vascular endothelial growth factor (VEGF) and fibroblast growth factor 2 (FGF-2) through their heparin-binding domains [30]. With this growth factor binding activity, nanofiber surface decorated with heparin chains was found to induce new blood vessel formation in a rat model, which could not be achieved using bolus heparin injections or heparin delivered by using collagen gel matrix [31]. As supplement growth factors have been incorporated in many matrices (including nanofibers) to accelerate wound healing [32], endogenous growth factors secreted during different phases of wound healing could be also sequestered and stabilized by heparin at the wound bed for better wound healing outcomes. This was demonstrated in a previous study where soluble heparin/chitosan complex was reported to recruit the growth factor to the epidermis and subsequently enhance wound healing [33]. Therefore, nanofiber surface grafted with heparin may also be used as a physical cue to attract the locally produced growth factors and fortify the activity of endogenous growth factors by sequestering and localizing these growth factors produced in situ. Conjugating heparin moieties to a wound dressing material for sequestering the endogenous growth factors may lead to a new therapeutic angiogenesis modality to promote wound healing without exogenous proteins delivery by maximizing the action of endogenous pro-angiogenic growth factors at the wound site [34].

In this study, we start by hypothesizing a multi-functional wound dressing could be designed as a mechanical support to accelerate diabetic wound healing. Toward this end, we first prepared aligned PLGA/curcumin (PCH) NFMs, followed by surface grafting of high density heparin to provide bio-guidance for attracting endogenous growth factors as well as facilitating curcumin release, which could serve as an exogenous factor for wound healing. We first investigate the physico-chemical characteristics of the NFMs, followed by in vitro cell culture, and finally carry out diabetic wound healing in rats to study the mechanism and the efficacy of wound healing exerted by the designed NFMs.

## 2. Experimental section

### 2.1. Materials

Poly(lactic-co-glycolic acid) (PLGA) with a lactide-to-glycolide ratio of 50:50 (intrinsic viscosity = 0.42 dL/g) was provided by Green Chemical Inc. (Taipei, Taiwan). Poly(ethylene glycol) diamine HCl salt (PEG diamine, H<sub>2</sub>N-PEG-NH<sub>2</sub>, M<sub>w</sub> = 3500) was purchased from JenKem Company (Plano, TX, USA). Curcumin, 1-(3-dimethylaminopropyl)-3-ethylcarbodiimide (EDC), N-hydroxysuccinimide (NHS), heparin sodium salt from porcine intestinal mucosa and mouse anti- $\beta$ -actin monoclonal antibody were purchased from Sigma-Aldrich (St. Louis, MO, USA). N, N-Dimethylformamide (DMF) and tetrahydrofuran (THF) were purchased from Tedia (Fairfield, OH, USA). CellTiter 96® AQueous One Solution Cell Proliferation Assay Kits was obtained from Promega Co. (Madison, WI, USA). 2-(N-morpholino)ethanesulfonic acid, Dulbecco's modified Eagle's medium (DMEM), HyClone fetal bovine serum (FBS), penicillin/streptomycin, Ultra V Block, DAB Quanto Chromogen and ABsolute q-PCR SYBR Green Mix were purchased from Thermo



Fisher Scientific (Waltham, MA, USA). Total RNA Isolation Kit was purchased from GeneDireX Corporation (Miaoli, Taiwan). Maxime RT PreMix Kit was purchased from iNtRON Biotechnology Co. (Kyungki-Do, Korea). DC™ Protein Assay kit was purchased from Bio-Rad (Hercules, CA, USA).

## 2.2. Preparation of NFMs

Electrospun PLGA NFMs and PLGA/curcumin (PC) NFMs were prepared using 27%(w/w) PLGA and 26%(w/w) PLGA/1.3%(w/w) curcumin in a mixed solvent system of DMF and THF (1:1 volume ratio). The polymer solution was pumped from a syringe fitted with a 23-gauge needle (internal diameter = 0.37 mm) at 0.7 mL/h. The applied voltages were 15 kV and 20 kV for PLGA and PC NFMs, respectively. Aligned nanofibers were collected with a grounded rotational drum rotating at 3500 rpm. The drum surface was covered with an aluminum foil and placed 10 cm from the needle tip for collecting the electrospun nanofibers. The environment during electrospinning was controlled at ~25 °C and ~40% relative humidity. The PLGA/curcumin/heparin (PCH) NFM was prepared with EDC/NHS as the coupling agent for covalent binding of heparin to plasma-treated PC (PC-plasma) NFM, which contained abundant carboxyl (-COOH) groups on fiber surface [35]. In brief, PC was subjected to plasma treatment with a DC-pulsed O<sub>2</sub> plasma reactor using a SPIK 1000A oxygen plasma generator (MELEC GmbH, Baden, Germany) at 200 mTorr and 600 V for 60 s to obtain PC-plasma NFMs. PEG diamine was subsequently grafted by reacting PC-plasma NFM with EDC (6.4 M), NHS (4.3 M) and PEG diamine in pH 7 MES buffer (0.5 M) for 24 h (NH<sub>2</sub>/COOH molar ratio = 5) to obtain PC-NH<sub>2</sub> NFMs. Heparin was subsequently grafted to PC-NH<sub>2</sub> using similar EDC/NHS coupling chemistry in pH 7 MES buffer with 12.5 nmol heparin per mg of NFM-NH<sub>2</sub> to obtain PCH NFMs.

## 2.3. Characterization of NFMs

### 2.3.1. Determination of carboxylic acid group, primary amine group and heparin in NFMs

The amount of carboxylic groups introduced to PC-plasma NFM after plasma treatment was determined from the Toluidine Blue O (TBO) assay, assuming TBO complexed with carboxyl groups in 1:1 molar ratio. A 1 × 1 cm NFM was weighed and reacted with 1 mL TBO solution (0.5 mM) for 5 h at room temperature. After washing with 0.1 mM NaOH, the NFM was dried completely in a vacuum oven at 37 °C. The TBO complexed to -COOH was desorbed with 2 mL 50% acetic acid and the solution absorbance was determined at 633 nm using a UV-VIS spectrophotometer. The amount of -COOH was determined from a standard curve prepared from solutions with known TBO concentrations. The amount of primary amine groups introduced to PC-NH<sub>2</sub> NFM by grafting PEG diamine was determined by the o-phthalaldehyde (OPA) method using a UV-VIS spectrophotometer at 340 nm [36]. The amount of heparin conjugated to PCH was determined using a 5 µg/mL TBO solution prepared in 0.01 M HCl at 632 nm [37].

### 2.3.2. X-ray photoelectron spectroscopy (XPS) analysis

The surface chemical composition of NFMs was detected by a PHI 1600 ESCA photoelectron spectrometer (Physical Electronics; Chanhassen, MN, USA) equipped with a multichannel detector and a spherical capacitor analyzer to perform high-resolution X-ray photoelectron spectroscopy (XPS). The X-ray source was a magnesium anode operated at 15 kV and 400 W, and the pressure in the analysis chamber was maintained at  $2 \times 10^{-6}$  Pa. Using symmetrical Gaussian peak shapes and integrated background subtraction, the relative percentages of carbon atoms in different carbon functional groups was determined from the high resolution C1s spectra by fixing the peak positions according to tabulated chemical shifts during the curve fitting process.

### 2.3.3. Electron microscopy analysis

Scanning electron microscopy (SEM) (JEOL LSM 5410) was used to determine the orientation and the diameters of nanofibers. The diameters were calculated from 100 fibers chosen randomly from 10 SEM images using the ImageJ software (NIH, Bethesda, MD, USA). The orientation of nanofibers was calculated from the distribution of fiber angles of 100 fibers, which was obtained fiber orientation relative to a defined vertical direction (taken as 0°) within -90 to 90°. A field emission scanning electron microscope (FE-SEM) (Hitachi S5000) was used to study the detailed surface morphology of the nanofibers.

### 2.3.4. Water contact angle and water vapor transmission rate

The water contact angle of a NFM was determined at 25 °C using a FTA-125 contact angle/surface tension instrument (First Ten Angstroms; Portsmouth, VA, USA). The NFM was cut into 1 × 1 dimensions and loaded into a specimen holder. The images were taken within 3 s when a water drop was dropped on NFM surface, from both parallel and perpendicular directions to the axis of the aligned fiber. All reported contact angles were averaged over three measurements for three replicate NFM samples using distilled deionized (DDI) water.

The water vapor transmission rate (WVTR) was determined using a custom-made evaporimeter following ASTM E96-90 [38]. Briefly, a closed glass chamber in a 37 °C incubator was maintained at a relative humidity within  $73 \pm 5\%$  using saturated magnesium chloride solution in the chamber. A cup filled with 10 g of deionized (DI) water was covered by a NFM and placed in the chamber. Evaporation of water through the NFM was monitored from the lost weight of water in the cup due to permeation of water vapor through the membrane, from which WVTR (g/m<sup>2</sup>/day) was calculated.

### 2.3.5. Mechanical tensile testing

The mechanical properties of NFMs were evaluated by uniaxial tensile testing with a Tinius Olsen H1KT universal tensile testing machine. Each sample was in 50 × 10 mm rectangular dimension and vertically mounted by holding ends with two mechanical grippers and leaving a 3-cm gauge length for mechanical loading. The load-deformation value was recorded using a 10 N load cell at 5 mm/min deforming rate up to 30 mm maximum elongation length. The tensile stress at break, tensile strain at break and Young's modulus were calculated from the recorded stress-strain curve.

### 2.3.6. Curcumin release rates

The release of curcumin from NFMs was determined by immersing ~100 mg NFM discs (0.5 cm × 0.5 cm) in a 10 mL sample vial filled with 5 mL phosphate buffered saline (PBS) or 70% PBS/30% ethanol. The vial was shaken at 150 rpm in a 37 °C incubator. At predetermined time, the solution was completely removed from the vial and replenished with equal volume of fresh solution as before to continue the drug release study. The amount of curcumin released was determined from the solution absorbance (OD) by an ELISA microplate reader (BioTek, Winooski, VT) at 420 nm using a standard curve prepared from solutions with known curcumin concentrations.

## 2.4. In vitro studies

### 2.4.1. Cytotoxicity

Human skin fibroblast cell (HS68) purchased from the Bioresource Collection and Research Centre (Taiwan) was used for cell culture. Cytotoxicity of the material was examined from cell viability test by following ISO 10993-5. A 2 × 2 cm NFM was extracted with 1 mL of cell culture medium (DMEM with 10% FBS and 1% penicillin/streptomycin) at 37 °C for 24 h. HS68 fibroblasts were seeded ( $2.5 \times 10^3$  cells/well) in 24-well tissue culture plate and cultured with the extract at 37 °C and 5% CO<sub>2</sub>. Cell viability was monitored on day 1 and 3 from MTS assays using CellTiter 96® Aqueous One Solution Cell Proliferation Assay Kits. Fresh cell culture medium was used as a control.



#### 2.4.2. Cellular response of fibroblasts to NFMs

HS68 fibroblasts were seeded onto disk-shaped NFMs (1.5 cm diameter) in 24-well culture plates at a density of  $1 \times 10^5$  cells/well and cultured with cell culture medium (90% DMEM with 10% FBS and 1% penicillin/streptomycin) at 37 °C in a humidified CO<sub>2</sub> incubator. On day 3, the morphology of cells was observed by SEM and cell viability was examined by Live/Dead cell viability assays. The cell-seeded NFM was washed with PBS and cells were stained with the Live/Dead Viability/Cytotoxicity kit for mammalian cells (Thermo Fisher Scientific) and observed under a confocal laser scanning microscope (Zeiss LSM 510 Meta) at 490/515 nm for live cells and 535/617 nm for dead cells. For SEM observation, the cell-seeded NFMs were rinsed by PBS, followed by fixation with 2.5% glutaraldehyde at 4 °C for 2 h. The sample went through a stepwise dehydration process using 50%, 70%, 80%, 90% and 95% ethanol before immersing in absolute ethanol for 30 min. After drying, the sample was coated with gold and subject to SEM analysis.

#### 2.4.3. Migration of fibroblasts for wound healing

A NFM (2 × 2 cm) was extracted with 1 mL of cell culture medium at 37 °C for 48 h and the extract was collected for in vitro wound healing assays. Human fibroblast HS68 (2 × 10<sup>3</sup> cells) were seeded into a Culture-Insert 2 Well in  $\mu$ -Dish (IB 80206, ibidi GmbH, Martinsried, Germany) placed in a 35-mm culture dish. After cell attachment for 24 h, the Culture-Insert was removed to create a cell-free gap for observation of cell migration. For in vitro wound healing/migration assay, the medium was replaced by the extraction medium and cell migration into the gap was monitored by taking photos under an inverted microscope after 24 and 48 h. To analyze the gap closure rate, the sample was fixed in 100% formaldehyde for 1 h prior to staining with 0.04% (w/v) Giemsa solution for 30 min. The gap closure rate was calculated from the cell-free gap area determined by the PAX-it software (Villa Park, IL, USA), with relative cell migrated area (%) =  $(1 - GA_t/GA_0) \times 100$ , where  $GA_0$  and  $GA_t$  denote the initial gap area and the gap area at time  $t$ , respectively.

#### 2.4.4. Cytoprotective effects under high oxidative stress

After extracting a NFM (2 × 2 cm) with 1 mL cell culture medium at 37 °C for 48 h, the extract was collected to determine the cytoprotective effects of curcumin-loaded NFM under conditions of high oxidative stress environment occurred at a diabetic wound site. HS68 cells were seeded in 24-well culture plates at a density of  $2.5 \times 10^3$  cells/well and cultured with 1 mL extract medium containing 1% H<sub>2</sub>O<sub>2</sub> and cultured in a 5% CO<sub>2</sub> incubator at 37 °C for 24 h. At the end of the incubation time, the viability of cells was evaluated using the MTS assay. The cell viability was normalized to the blank sample without adding hydrogen peroxide in each group, which was taken as 100%.

### 2.5. In vivo studies

#### 2.5.1. Wound model and wound closure rates

All animal protocols were approved by the Institutional Animal Care and Use Committee of Chang Gung University. The streptozotocin-induced diabetic wound model in Sprague-Dawley (SD) rats was used for in vivo evaluation of wound closure. Male fifteen-week-old SD rats (LASCO, Taipei, Taiwan) weighing ~250 g were made hyperglycemic by intraperitoneal injections of 80 mg/kg body weight of streptozotocin (in pH 4.5 sodium citrate buffer). Whole blood was withdrawn from the tail vein on day 3, 10 and 17 after injection and the plasma glucose concentration was monitored using a blood glucose monitor. Only rats that had two consecutive fasting blood glucose levels higher than 250 mg/dL on day 10 and 17 were considered diabetic and used in the study. After complete anesthetization by intraperitoneal injection of Zoletil-50 and Rompun, two full-thickness wounds were created on each side of the dorsal area of a SD rat. A full-thickness wound to the deep fascia was made by excising the skin using a sterile square template in 1.5 cm × 1.5 cm dimension. The aseptic technique was followed throughout the

entire experiment period. Each wound created was covered with a 2 cm × 2 cm UV-sterilized gauze (control), or PLGA, PC or PCH NFMs. Afterward, the wounded area was covered with Tegaderm (3 M, USA) and adhesive fabric tape (BSN medical, France) was applied to prevent the rat from removing the NFM or gauze. All rats were returned to the housing and maintained with normal food and water. On day 3, 7 and 14 post-treatment, dressings were removed from four rats and animals were sacrificed with an overdose of intravenous sodium pentobarbital. The wounds were digitally photographed by maintaining identical optical zoom throughout the experiments. For quantitative evaluation, the wounds were replicated on a transparent tracing paper after tracing the wound border covered with epithelium. The paper was scanned, followed by analyzing the wound size with the ImageJ software (National Institute of Health, Bethesda, MD, USA). The wound closure rate was calculated based on the percentage closure of the original wound as relative wound size (%) =  $WA_t/WA_0 \times 100$ , where  $WA_0$  and  $WA_t$  denote the initial wound area and the wound area at time  $t$ , respectively. Dorsal skin tissue was dissected from the sacrificed rat and subject to histological and qPCR analysis. The granulation tissue in the wound and the sub-epidermal tissue in normal skin were used for the qPCR analysis.

#### 2.5.2. Histology and immunohistochemistry

The excised skin tissue of rat sacrificed on day 14 was harvested for hematoxylin-eosin (H&E), Masson's trichrome and immunohistochemical (IHC) analysis. For histological analysis, samples were immersed in 10% formaldehyde, followed by dehydration and embedding in paraffin. The samples were sectioned into 4- $\mu$ m thickness and subject to H&E, Masson's trichrome and  $\alpha$ -smooth muscle actin ( $\alpha$ -SMA) IHC staining after deparaffinization. For IHC staining, Ultra V Block was used to diminish nonspecific binding for 5 min, followed by incubation with 1:200 diluted  $\alpha$ -SMA primary antibody (rabbit anti- $\alpha$ -SMA polyclonal antibody, Abcam ab5694) for 24 h at 4 °C. Samples were then rinsed with PBST and incubated with N-Histofine simple stain rat MAX PO (MULTI) for 30 min at room temperature. The color was developed with DAB reagent (30  $\mu$ L of DAB Quanto Chromogen in 1 mL of DAB Quanto Substrate) prior to counterstaining by hematoxylin. The images were taken under an IX-71 inverted optical microscope and semi-quantitative analysis was carried out with the PAX-it software based on stained area. Six randomly selected fields from microscopic observation were examined and used to calculate the area percentage of  $\alpha$ -SMA positive vessels.

#### 2.5.3. Quantitative real-time polymerase chain reaction (qRT-PCR) analysis

The RNA of tissue samples was extracted and reverse transcribed into cDNA by using Total RNA Isolation Kit and Maxime RT PreMix Kit according to manufacturer's protocols. The cDNA was mixed with the SYBR Green RT-PCR kit before using a CFD-3120 Mini Option detection system (Bio-Rad, Hercules, CA, USA) for quantitative real-time polymerase chain reaction (qRT-PCR). Glyceraldehyde 3-phosphate dehydrogenase (GAPDH) was used as the housekeeping gene. The relative mRNA expression of GPx and NF $\kappa$ B was determined using the  $2^{-\Delta\Delta Ct}$  relative quantification method.

### 2.6. Statistical analysis

All results were presented as mean  $\pm$  standard deviation (SD). One-way analysis of variance (ANOVA) LSD test was used for statistical analysis and significant level was set at  $p < 0.05$ .

## 3. Results and discussion

### 3.1. Characterization of PLGA, PC and PCH NFMs

To achieve the goal of engineering a multi-functional nanofibrous wound dressing, we prepared aligned PLGA, PC and PCH NFMs under well-controlled electrospinning conditions, including optimized flow

rate, voltage, tip-to-collector distance and collector rotational speed. To achieve high heparin grafting ratio, PC NFMs were successively subjected to plasma treatment (PC-plasma NFMs), one-ended conjugation with PEG diamine (PC-NH<sub>2</sub> NFMs) and heparin grafting (PCH NFMs) as shown schematically in Fig. 1A. By choosing appropriate electrospinning parameters, aligned PLGA or PC with uniform and bead-free nanofibers could be obtained with similar surface morphology to PCH NFMs as shown from SEM images (Fig. 1B). The membrane thickness of PLGA, PC and PCH NFMs were  $190 \pm 24$  nm,  $185 \pm 6$  nm and  $220 \pm 16$  nm, respectively. The average fiber diameter and fiber orientation (average fiber angle) showed no significant difference among PLGA, PC and PCH NFMs (Table 1).

As the water contact angle is expected to be anisotropy for aligned fibers, the water contact angles were measured from two different orientations, parallel or perpendicular to the axis of aligned fibers (Fig. 1C). In contrast to randomly oriented nanofibers, where water wetting is isotropic, aligned nanofibers in uniaxial arrays leads to an asymmetric surface topography and consequently to different water contact angle measured along a direction parallel or perpendicular to the oriented fiber longitudinal axis (Table 1) [39]. The low contact angle from direction perpendicular to the fiber orientation is a result of preferential spreading of the droplet along the nanofibers due to roughness enhanced wetting as there are no barriers to the contact line motion that would cause pinning [40]. The water contact angle of PCH NFM from each direction decreased significantly when compared with that of PLGA or PC (Table 1), with no significant difference between them. This indicates that heparin grafting increased membrane hydrophilicity by introducing abundant hydrophilic heparin molecules to fiber surface (Fig. 1A). Furthermore, the difference in contact angles measured from different directions only changed substantially for PCH due to its higher hydrophilicity compared with PLGA or PC NFMs (Table 1).

Chemical analysis was used to confirm successful chemical change after the chemical modification of nanofibers as shown in Fig. 1A. After plasma treatment,  $2.99 \pm 0.09$  nmol -COOH was found per mg of PC-plasma NFM. Using excess PEG diamine to react with -COOH on PC-plasma, we can assure one-ended covalent binding of PEG diamine to

**Table 1**

The fiber diameter, fiber angle, water contact angle and water vapor transmission rate of NFMs. The water contact angles are shown for direction parallel or perpendicular to the fiber alignment axis.

NFM	Average fiber diameter (nm)	Average fiber angle (°)	Contact angle (°)		Water vapor transmission rate (g/m <sup>2</sup> /d)
			Parallel	Perpendicular	
PLGA	$461 \pm 109$	$90 \pm 7$	$94.3 \pm 4.6$	$93.9 \pm 3.3$	$456.5 \pm 10.1$
PC	$459 \pm 105$	$91 \pm 5$	$100.6 \pm 4.9$	$87.7 \pm 3.7$	$452.5 \pm 12.8$
PCH	$479 \pm 129$	$91 \pm 13$	$64.3 \pm 7.8^{*,\&}$	$35.8 \pm 9.8^{*,\&}$	$450.4 \pm 7.8$

\*  $p < 0.05$  compared to PLGA.

&  $p < 0.05$  compared to PC.

PC-plasma, leaving the other -NH<sub>2</sub> end group to react with -COOH in heparin. The amount of -NH<sub>2</sub> introduced to PC-NH<sub>2</sub> was determined to be  $1.06 \pm 0.14$  nmol/mg NFM using the OPA method to quantitatively determine the primary amine groups on fiber surface. The last step in Fig. 1A is critical to conjugate abundant heparin for exerting binding affinity toward endogenous growth factors. Using an optimal solution pH and heparin concentration during the conjugation step, we successfully achieved high loading of heparin on fiber surface at  $1.14 \pm 0.06$  nmol/mg NFM. This value was at least one order of magnitude higher than those reported before for heparin immobilization to different PLGA scaffolds, which was 0.096 pmol/mg for PLGA microspheres [41] and  $0.069 \pm 0.004$   $\mu$ mol/mg for PLGA yarn [42]. This high grafting density of heparin on PCH would facilitate guiding endogenous growth factors to the wound bed to promote wound healing..

Undoubtedly, more sophisticated morphological and chemical analyses of NFMs are needed. To meet this need, we use FE-SEM to observe the fiber surface morphology change from PC to PCH. As shown in Fig. 2, the original PC nanofibers showed smooth surface morphology. Plasma treatment introduced change of fiber surface morphology in PC nanofiber as expected. Nonetheless, further grafting with PEG diamine and

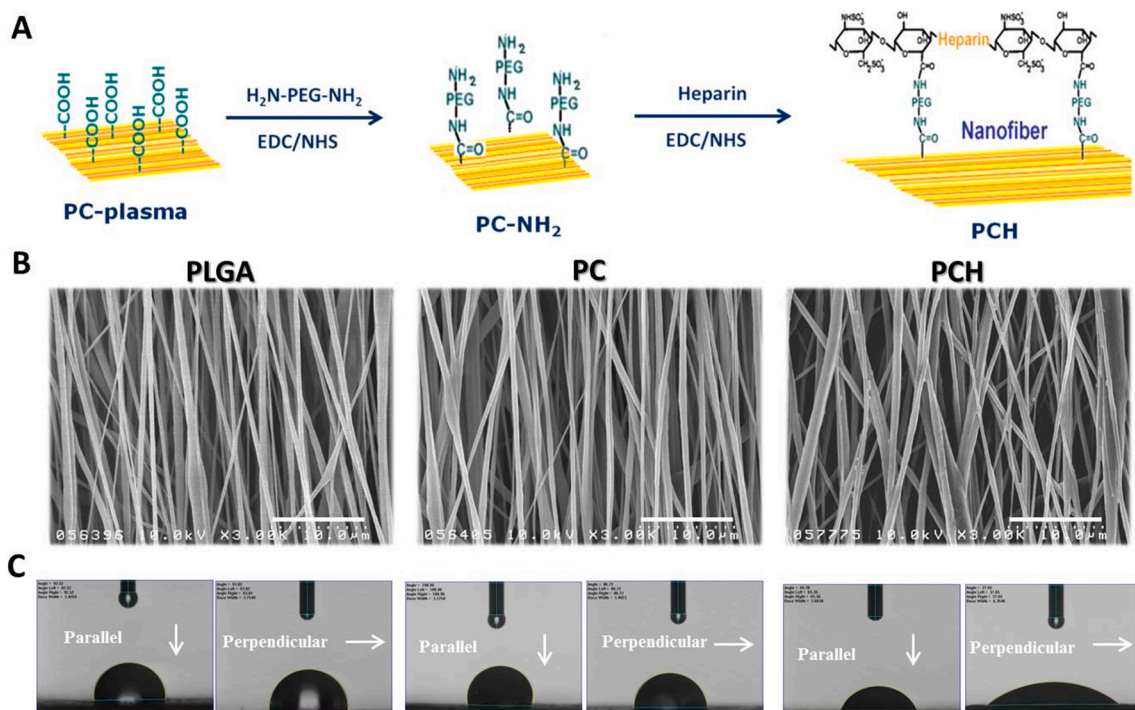


**Fig. 1.** (A) The schematic diagram showing the steps involved in preparing PCH NFMs. The SEM images (bar = 10  $\mu$ m) (B) and optical micrographs of water droplets in direction parallel and perpendicular to the fiber alignment axis of PLGA, PC and PCH nanofibers (C).

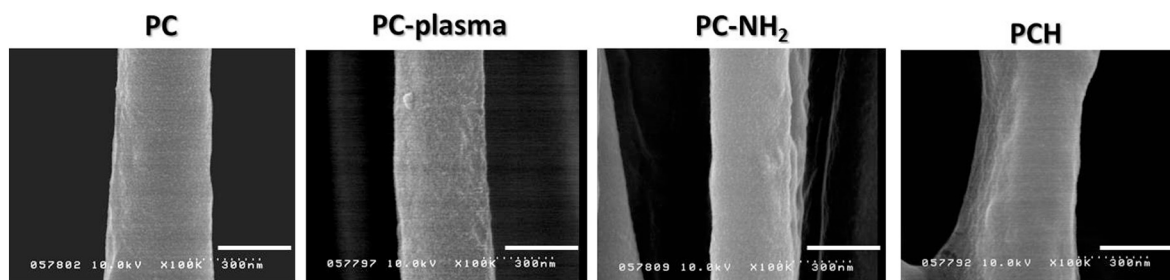


Fig. 2. The FE-SEM micrographs of PC, PC-plasma, PC-NH<sub>2</sub> and PCH NFMs. Bar = 300 nm.

heparin immobilization resulted in change of surface morphology of PC-NH<sub>2</sub> and PCH back to the smooth surface observed for PC. This is due to masking of surface roughness from grafted macromolecules on fiber surface, albeit with little change of fiber diameter. This surface morphology change is different from our previous report when gelatin was immobilized to plasma-treated PLLA nanofibers using the same crosslinking agent (EDC), which showed scattered particles of gelatin molecules distributed along the nanofiber surface as well as increased fiber diameter and surface roughness [35]. Although the average fiber diameter did not significantly change after heparin grafting from SEM images (Table 1), we could still observe a distinctive thin surface layer outside of PCH fiber from the FE-SEM image (Fig. 2). Undoubtedly, such difference could be attributed to different chemical structure between heparin and gelatin. Unlike gelatin, heparin molecules could not be crosslinked with each other on fiber surface using EDC/NHS (Fig. 1A), which leads to a thin coating of heparin on PCH fiber surface and smooth fiber surface morphology.

The surface chemical composition of NFMs was studied by XPS. As shown from the survey scan spectra in Fig. 3A, the XPS spectra had two separated peaks corresponding to C1s (285 eV) and O1s (532 eV). A distinct N1s peak at 400 eV in the spectrum of PC-NH<sub>2</sub> indicates that amine groups were successfully introduced onto fiber surface with the N atomic percentage being 2.2%. The N1s peak also appeared in PCH as expected with increased N atomic percentage (4.0%) due to nitrogen atoms in heparin. Additional Na1s, S2s and S2p peaks appeared in PCH NFMs (0.9% Na and 0.9% S atomic percentage) with the use of sodium heparin in this study. Furthermore, high resolution XPS C1s spectra are shown for all NFMs in Fig. 3B–F and the fractions of different carbon functional groups are given in Table 2. The spectrum from PLGA shows three components at 285, 286.8 and 289.9 eV, corresponding to C–C, C–O and O=C–O bonds in the chain (Fig. 3B) [43]. From the spectrum for PC, same peaks exist but the C–C peak increased while the C–O peak decreased as curcumin is less abundant in O (Fig. 3C). For PC-plasma, the saturated hydrocarbon C–C C1s peak decreased after plasma treatment, with concomitant increase in the peak intensity of C–O (from 33.7% to 35.2%) and O=C–O (from 28.2% to 32.7%), which could be attributed to the increase in carboxyl groups and the introduction of oxygen functionalities on fiber surface (Fig. 3D) [35]. Both PC-NH<sub>2</sub> (Fig. 3E) and PCH (Fig. 3F) revealed a new peak at 286.3 eV, which corresponds to the amide carbon in NH–C=O. This was accompanied by a decrease in the O=C–O peak from 32.7% to 11.5% for PC-NH<sub>2</sub> and further to 6.2% for PCH. Taken together, the XPS analysis confirms introduction of primary amine groups on fiber surface, which react with carboxyl groups of heparin for amide bond formation.

### 3.2. Water vapor permeation and mechanical properties of NFMs

Maintaining moisture is important during wound healing and a potential wound dressing should provide a suitable water vapor transmission rate (WVTR) to prevent excessive dehydration during wound healing. Toward this end, water loss from a NFM was determined in a well-controlled environment (Fig. 4A), from which the WVTR was

calculated within 2 h to 30 h. A similar WVTR was observed among all NFMs (Table 1), suggesting PLGA, PC and PCH NFMs are endowed with similar capability to maintain suitable moisture with the microporous structure of 1 to 2  $\mu\text{m}$  pore size (Fig. 1B). The water vapor permeability of a wound dressing should prevent both excessive dehydration as well as buildup of exudate. Therefore, the dressing material should control the water loss from a wound due to evaporation at an optimal rate [44]. It has been reported that the evaporative water losses for normal skin, burns and granulating wounds at close to skin temperature (35 °C) are  $204 \pm 12$ ,  $279 \pm 26$  and  $5138 \pm 202$  g/m<sup>2</sup> per day, respectively [45]. It could be also noted from Table 1 that the WVTR of all NFMs are  $\sim 450$  g/m<sup>2</sup> per day, which is close to the value for wet human skin (350 g/m<sup>2</sup>/day) and dry human skin (215 g/m<sup>2</sup>/day) [46]. Comparing with the WVTRs of commercial sponge-type wound dressings, such as Biobrane II (1565 g/m<sup>2</sup>/day) and HYAFF 11p75 (2327 g/m<sup>2</sup>/day), the functional NFM could reduce WVTR. On the other hand, the NFM has higher WVTR from its macroporous fiber structure when compared with a commercial film type PU wound dressing (Tegaderm®, WVTR = 62 g/m<sup>2</sup>/day). Taken together, the NFMs engineered here are deemed suitable to provide adequate moisture control for the wound and prevent excessive wound dehydration for an appropriate milieu during wound healing.

A wound dressing material should also provide good mechanical strength to withstand stretching and abrasion during application. From tensile mechanical testing, typical stress vs. strain curves are shown in Fig. 4B, from which the tensile strain at break, tensile stress at break and Young's modulus was compared in Table 3 for different NFMs. Overall, the incorporation of curcumin (PC) significantly raised the mechanical strength (ultimate stress and Young's modulus) of the NFM without influencing its flexibility and stretchability (ultimate strain). Even subject to further plasma treatment and grafting reactions, PCH is evident to retain or improve the preferred mechanical property of PC, to be useful as a membrane-type material for wound dressing application.

### 3.3. Release of curcumin and biocompatibility of NFMs

The release profile of curcumin from PC and PCH NFMs was first studied in PBS solution. As shown in Fig. 5A, slow release of curcumin was found for both NFMs and the cumulative release was only 13.5% (PC) and 21% (PCH) after 500 h due to the sparingly soluble nature of curcumin in water ( $\sim 0.6$   $\mu\text{g/mL}$ ) [47]. Nonetheless, the drug release from PCH is consistently and significantly higher, which could be correlated with the higher hydrophilic nature of PCH, as shown from the contact angle difference in Table 1. To confirm that curcumin could reach quantitative release disregarding the solubility limit, we also tested curcumin release in 70% PBS/30% ethanol solutions (Fig. 5B). A distinctive burst release was observed with 49% and 62% cumulative release of curcumin in 12 h was found for PCH and PC, respectively. The release percentage increased with time and plateaued at 95% for PCH and 92% for PC, without showing significant difference as expected.

In order to determine whether the released curcumin exerted any cytotoxicity, human HS68 fibroblasts were cultured in 24 h extraction medium of a NFM and the relative cell viability was determined by MTS



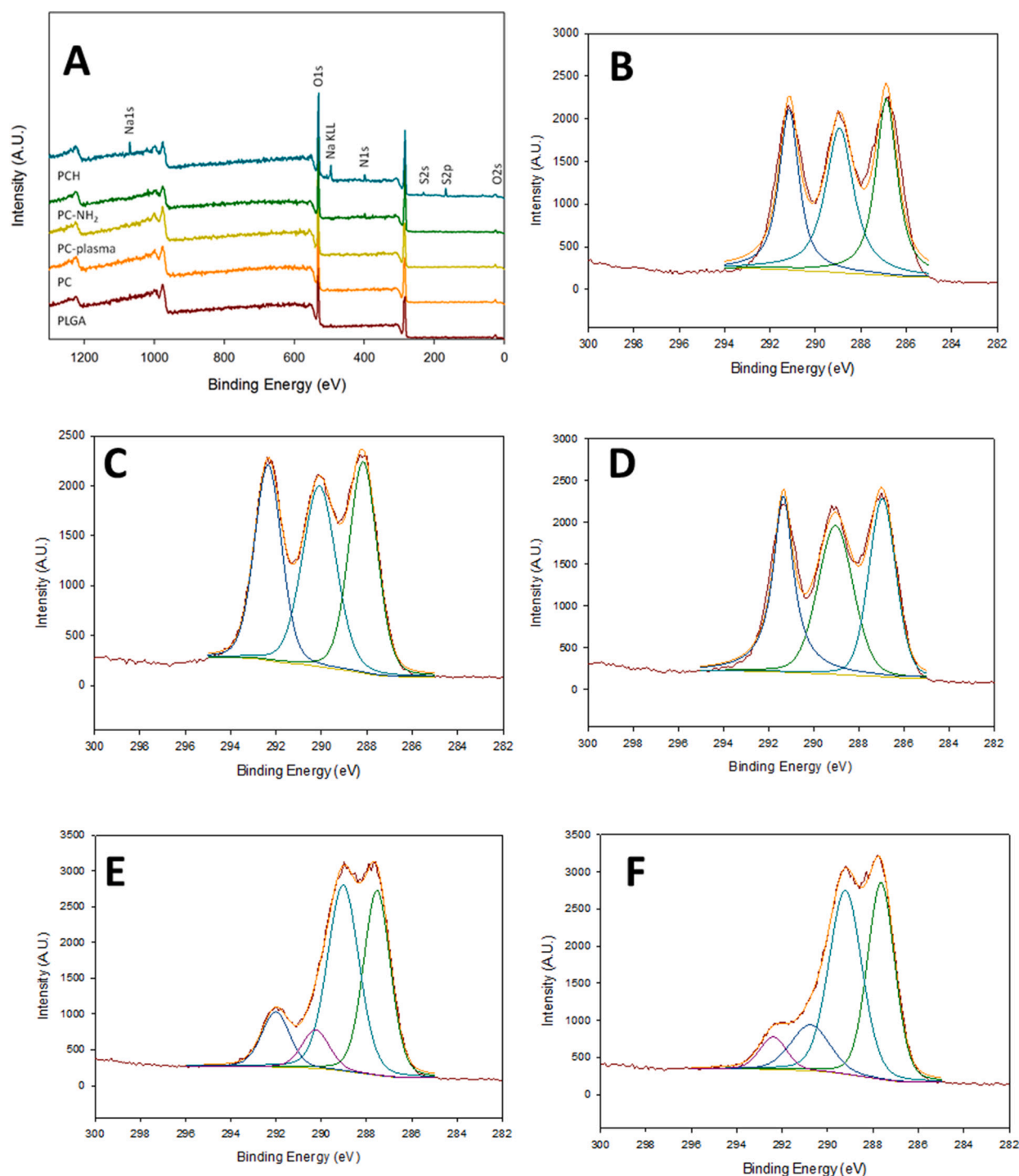


Fig. 3. The XPS survey scan spectra of different NFMs (A) and the XPS C1s spectra of PLGA (B), PC (C), PC-plasma (D), PC-NH<sub>2</sub> (E) and PCH (F) NFMs.

**Table 2**  
Fraction of carbon functional groups from high resolution C1s XPS peaks.

NFM	C—H ~285 eV (%)	C—O ~286.8 eV (%)	O—C=O ~289.9 eV (%)	NH—C=O ~286.3 eV (%)
PLGA	34.4	36.7	28.9	0.0
PC	38.1	33.7	28.2	0.0
PC-plasma	32.1	35.2	32.7	0.0
PC-NH <sub>2</sub>	36.9	43.7	11.5	7.9
PCH	38.2	43.0	6.2	12.6

assays. Fig. 6A shows cells cultured in the extraction medium of PC and PCH showed significantly reduced relative cell viability compared to curcumin-free PLGA NFM. No significant difference in cell viability was found between PC and PCH, since similar curcumin concentration was expected in the 24 h extraction medium from the drug release study in PBS (Fig. 5A). Curcumin is known to exhibit a wide range of pharmacological effects including anti-inflammatory, antioxidant and anti-carcinogenic activities, which is known to be concentration dependent. In a dose-dependent manner, curcumin can induce apoptosis in a wide variety of cells and down-regulate transcription factors such as NFκB [48]. Previous studies indicate that the cytotoxic effect of

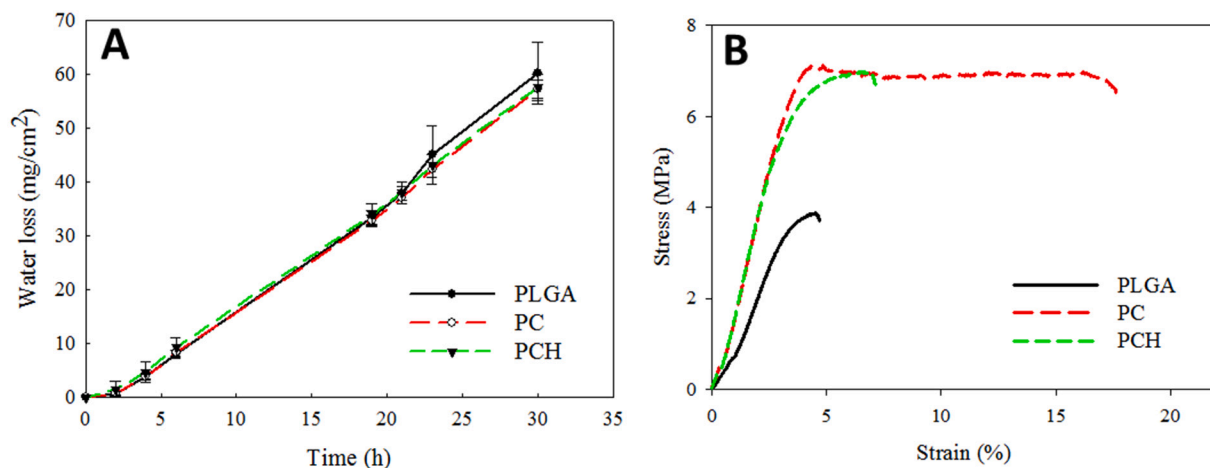


Fig. 4. The water vapor transmission rates (A) and the stress vs. strain curves (B) of PLGA, PC and PCH NFMs from tensile mechanical testing.

Table 3

The mechanical properties of PLGA, PC and PCH NFMs.

NFM	Tensile stress at break (MPa)	Tensile strain at break (%)	Young's modulus (MPa)
PLGA	3.82 ± 0.56	4.60 ± 0.19	125.95 ± 24.45
PC	7.04 ± 0.76*	4.81 ± 0.20	181.45 ± 20.31*
PCH	7.25 ± 0.65*	5.93 ± 0.57*,&	198.97 ± 16.98*

\*  $p < 0.05$  compared to PLGA.

&  $p < 0.05$  compared to PC.

curcumin was exhibited only at high concentrations ( $\sim 25 \mu\text{M}$ ) where less than 50% cell survival was found [49]. However, with more than 70% viable cells shown in Fig. 6A, we could confirm the low cytotoxicity of both curcumin-loaded NFMs, which is also consistent with a previous report that gradual release of curcumin from NFMs induced low cytotoxicity to fibroblasts [50].

Further experiments followed to elucidate membrane biocompatibility by seeding HS68 fibroblasts on different NFMs and cultured for 72 h before Live/Dead staining and SEM observation. As expected, fibroblasts showed high cell viability when cultured on all NFMs with minimum dead cells (red) distributed within a large number of viable cells (green) (Fig. 6B). More dead cells were found in PCH as more curcumin was released in 72 h (Fig. 5A). From SEM observation, there was no discernible change in cell morphology, with well-spread cells showing flat and spindle-like morphology and lamellipodia, endorsing the high biocompatibility of NFMs toward HS68 cell even when loaded with

curcumin (Fig. 6C). It could be also confirmed that attached cells were oriented in the direction of fiber alignment with elongated shape when cells proliferated in the direction of fiber alignment (Fig. 6B and C). Previous studies indicated aligned nanofiber scaffold could shorten the time for wound healing during skin tissue reconstruction due to the “contact-guided” effects of nanofiber orientation on cells [51]. In addition, aligned electrospun nanofibers also improve type I collagen expression with a higher degree of organization of collagen fibers secreted by fibroblast cells attached to aligned nanofibers [52].

#### 3.4. Migration of fibroblasts and protective effects under high oxidative stress

To confirm the released curcumin could promote cell migration, in vitro wound healing test was studied. Fig. 7A illustrates the curcumin-loaded NFMs (PC and PCH) enhanced HS68 migration at both time points compared with the control (medium) and the curcumin-free PLGA NFMs. Specifically, the quantitative analysis results shown in Fig. 7B indicate the area occupied by migrated cells in PC and PCH group increased by 3.1 and 5.6 folds, respectively, compared to control after 24 h. Similarly, PC and PCH groups showed 1.3 to 1.4 folds increase in recovered area after 48 h. Comparing PC and PCH, the faster curcumin release profile of PCH in PBS leads to higher curcumin in the 48 h extraction medium and significantly enhanced cell migration rate at 24 h (Fig. 5A). No significant difference between PC and PCH was found at 48 h as it is close to the end of the wound healing assay. Cells cultured with the extraction medium of PLGA did not show any significant effect

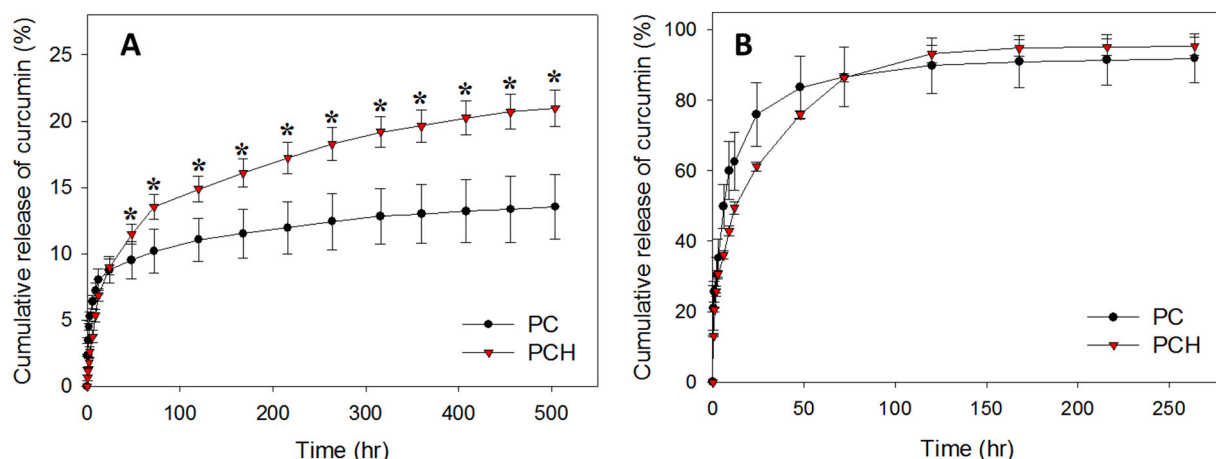
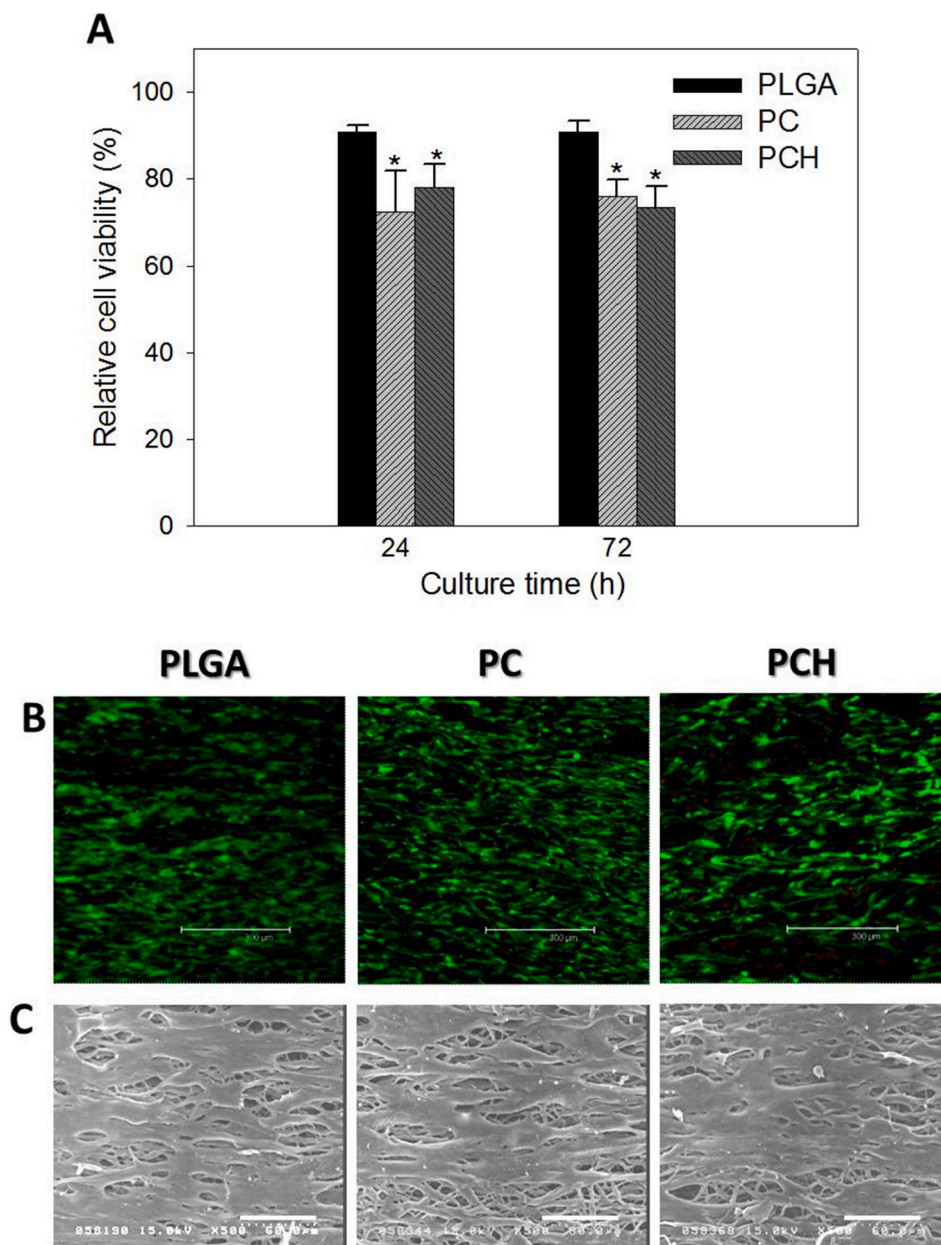


Fig. 5. The release profiles of curcumin from PC and PCH NFMs in PBS (A) and 70% PBS/30% ethanol (B). \* $p < 0.05$  compared with PC.





**Fig. 6.** Biocompatibility of NFMs by culture of fibroblasts with 24 h extraction medium of NFMs for 1 and 3 days (A) and culture of fibroblasts on NFMs for 3 days and subject to Live/Dead staining (B, bar = 300  $\mu$ m) or SEM observation (C, bar = 60  $\mu$ m). The cell viability in (A) was determined by MTS assays and reported as relative cell viability with cell culture medium taken as 100%. \* $p < 0.05$  compared with PLGA. (For interpretation of the references to color in this figure, the reader is referred to the web version of this article.)

to promote cell migration when compared to the control at both time points. These results are consistent with a recent study where wound healing capability was measured with human fibroblasts using curcumin-loaded gelatin nanofibers. The wound closure rate of human fibroblasts from wound scratch assay in vitro was found to be 26.6 and 14.4% for control and 0.003% curcumin after 48 h, respectively [53]. Taken together, the cell migration results suggest that curcumin released from PC and PCH will retain its bioactivity to enhance cell migration in vitro and also endorse the use of PCH over PC to shorten the required time for wound healing in vivo.

To evaluate the anti-oxidant effect and the free radical-quenching ability of curcumin-loaded nanofibers in reference to the beneficial effect on diabetic wound healing, we further evaluate the inhibition of cell death due to the oxidative stress induced by hydrogen peroxide. HS68 fibroblasts were cultured in 48 h extraction medium of NFM and supplemented with 1%  $H_2O_2$  to simulate the high oxidative stress. The cell viability determined by MTS assays in Fig. 7C shows the  $H_2O_2$ -induced oxidative stress caused damage to cells and reduced the relative cell viability to ~53% in both control and PLGA groups when compared to

the non-oxidative stress condition in the absence of hydrogen peroxide. However, the  $H_2O_2$ -induced oxidative stress damage was effectively alleviated, and the cell viability drastically elevated in the PC and PCH groups. Indeed, the relative cell viability in both PC and PCH groups was above 80% and significantly higher than those in the control and PLGA groups. The PCH also significantly enhanced the protective effect over PC due to more pronounced power to alleviate the oxidative stress, which improves cell viability under the high oxidative stress, as more curcumin was released in the 48 h extraction medium (Fig. 5A). Hydrogen peroxide is known to elicit excessive intracellular ROS, which lead to mitochondria and cell membrane damage and eventually cell apoptosis. The pronounced protective effect of PCH on proliferative fibroblasts, which are damaged by  $H_2O_2$ -induced supra-oxidative stress in vitro, underlines the modality of PCH to accelerate re-epithelialization during diabetes wound healing in vivo [54].

### 3.5. Diabetic wound healing in rats

To further verify whether aligned NFMs could accelerate diabetes

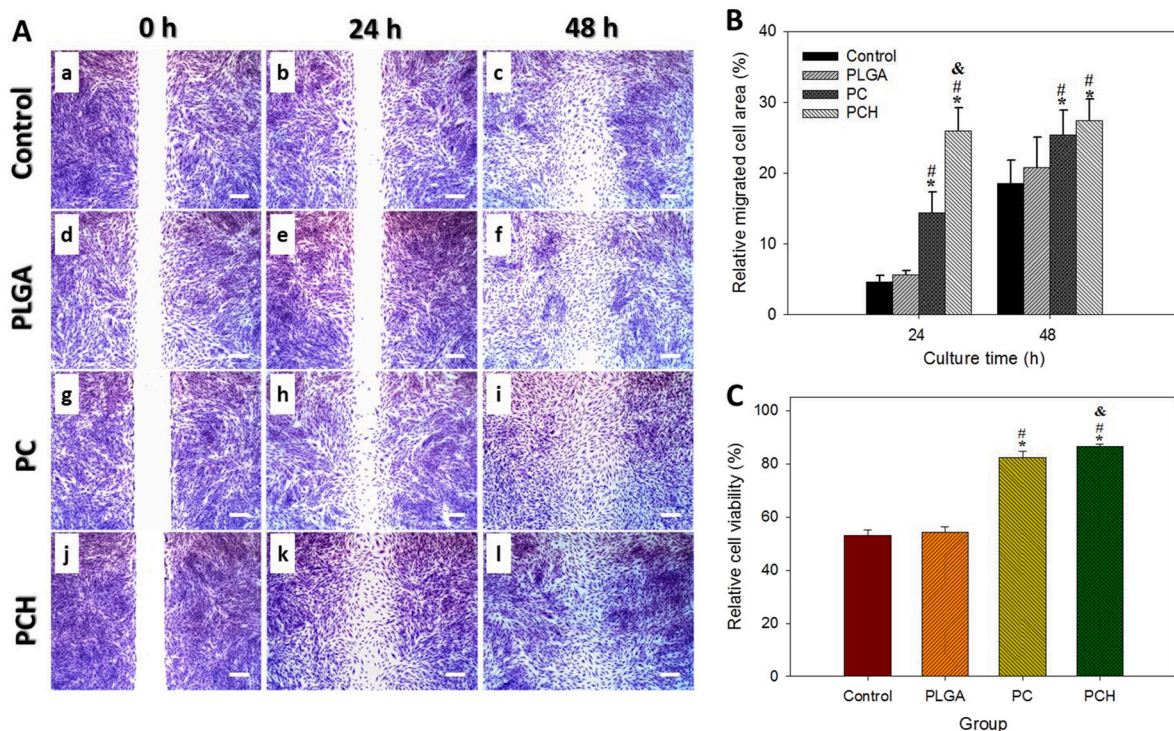


**Fig. 7.** In vitro wound healing assays from migration of HS68 fibroblasts after cultured with cell culture medium (control, a–c), 48 h extraction medium of PLGA (d–f), PC (g–i) or PCH NFM (j–l). The microscopic images of stained cells after cultured with the extraction medium for 24 and 48 h are shown in (A) (bar = 200  $\mu$ m), from which the relative migrated cell area was quantified using an image analysis software based on initial wound area at 0 h (B). (C) The relative cell viability of HS68 fibroblasts by MTS assays after cultured in cell medium (control), 48 h extraction medium of PLGA, PC or PCH NFM for 24 h in the presence of 1% hydrogen peroxide. The cell viability was taken as 100% in the absence of hydrogen peroxide for each group. \* $p < 0.05$  relative to control, # $p < 0.05$  relative to PLGA, & $p < 0.05$  relative to PC.

wound healing and to explore whether the combination of heparin grafting and curcumin controlled release could promote wound healing, an in vivo wound healing study was carried out using streptozotocin-induced diabetic SD rats. The healing rates of critical size wounds created in diabetic SD rats were evaluated after individually covering the wound with gauze (control), PLGA, PC or PCH NFMs (Fig. S1A, supplementary materials). The dressing was removed from the wound at day 3, 7 and 14 post-treatment for gross observation of wounds (Fig. S1B, supplementary materials). The wound area was estimated by image analysis from the gross view images taken from the wound area (Fig. 8A). The wound closure rate was compared among treatment groups using NFMs and the control group using gauze after normalizing the remaining wound size with the respective initial wound size. In accordance with the significant effect of curcumin-loaded NFMs in vitro, the diabetic wounds treated with PC and PCH showed faster wound healing rate compared with control and PLGA groups, with PCH NFM providing the best outcomes of wound healing. As shown in Fig. 8B, as early as 3 days post-treatment, PCH and PC significantly decrease the area of the wound to  $58.3 \pm 5.5\%$  and  $58.1 \pm 3.6\%$ , respectively, which are significantly less than the control ( $66.2 \pm 4.9\%$ ). The wound healing effect of all NFM-treated groups showed significant improvement over the control on day 7 with the PCH NFM group starting to show significant difference from the PLGA group. On day 14, the combined effect of curcumin and heparin manifest themselves in the PCH group, which significantly improved the wound healing rate over PC (with curcumin only). The wound size is in the order of PCH ( $13.9 \pm 6.6\%$ ) < PC ( $20.5 \pm 0.9\%$ ) < PLGA ( $27.4 \pm 4.4\%$ ) < gauze ( $37.1 \pm 6.6\%$ ), with significant difference among groups.

Interestingly, the PLGA NFM shows improved wound healing with significant contraction of wound size when compared with control gauze after day 7, which is in accordance with a previous report that released lactate from PLGA could promote wound healing [27]. It is also possible

the aligned nanofiber orientation can facilitate migration of fibroblasts and keratinocytes from the wound area peripheral to the center and promote re-epithelization and collagen deposition to shorten the wound healing time [55]. Encapsulation of curcumin in nanomaterials were shown to be an efficient and promising approach to maximize wound healing efficacy of curcumin [56]. Various topical formulations of curcumin such as films, fibers, emulsion, hydrogels and different nano-formulations were shown to deliver curcumin in a sustained way at the wounded site to improve the therapeutic effects [57]. Curcumin-loaded poly( $\epsilon$ -caprolactone) (PCL) nanofibers was demonstrated to increase the rate of wound closure in a diabetic mice model [58]. Mice treated with curcumin-loaded PCL nanofibers showed 80% wound closure, compared with only 60% wound closure in mice treated with PCL nanofibers on day 10. PLGA nanoparticles encapsulating curcumin could accelerate the wound healing in a full thickness excisional wound healing mouse model where PLGA–curcumin nanoparticles showed a two-fold higher wound healing activity compared to that of PLGA or curcumin [59]. Using electrospun curcumin-loaded PCL/gum tragacanth nanofibers for wound healing in diabetic rats, the pathological study showed that the nanofibers lead to markedly faster wound closure rate. Well-formed granulation tissues dominated by fibroblast proliferation, collagen deposition, complete early regenerated epithelial layer and formation of sweat glands and hair follicles were found after 15 days [60].

Although PC and PCH NFMs showed better wound healing due to their respective therapeutic activities, PCH accelerated the healing more profoundly than PC due to additive activity of released curcumin and add-on growth factor sequestering ability of heparin. These data suggested accelerated wound healing with aligned PLGA nanofibers compared with the control from the early phase of wound healing, which could be further improved by incorporating the exogenous therapeutic factor curcumin. Overall, the multi-functional PCH NFM is deemed as the most effective treatment for the diabetic wound to



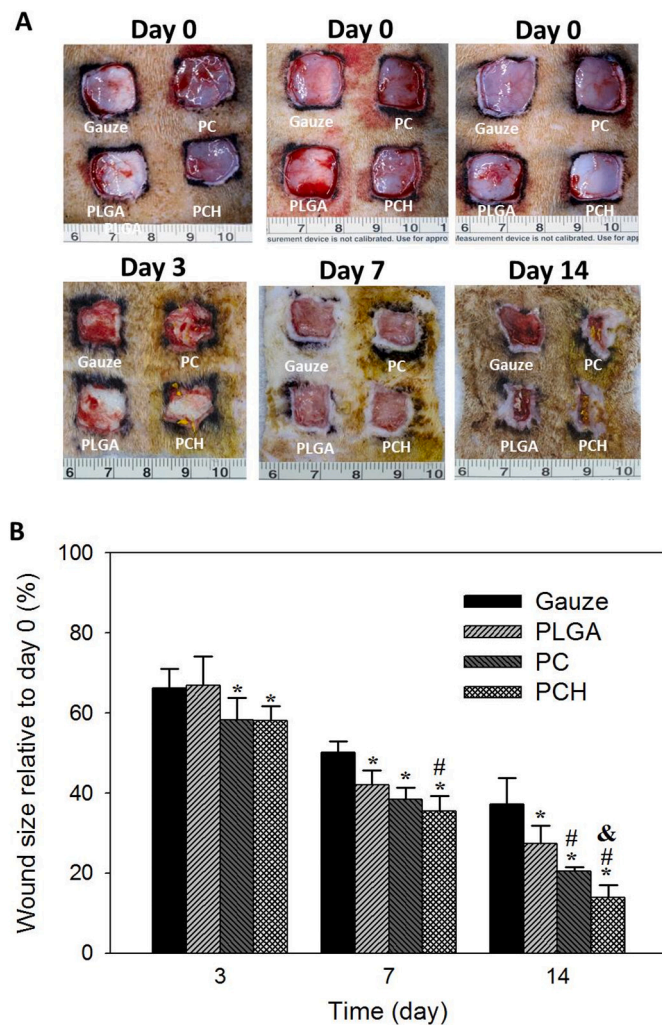


**Fig. 8.** (A) Wound closure for diabetic rats treated with gauze (control), PLGA, PC or PCH NFMs on day 0, 3, 7 and 14. (B) The relative wound size was determined from image analysis of the wound area from traced wound border covered with epithelium for each treatment and normalized to the initial wound area on day 0 ( $n = 4$ ). \* $p < 0.05$  relative to control, # $p < 0.05$  relative to PLGA, & $p < 0.05$  relative to PC.

effectively accelerate wound healing by reducing wound size to less than 14% of its original size in diabetic rats within 14 days. Undoubtedly, this trend is in accordance with our original objective by sequestering endogenous growth factors around the wound area through the action of grafted heparin in NFM, which must be subject to further examination through protein expression analysis of the healed wound tissues.

### 3.6. Histological analysis of wounds

At the final time point (day 14), skin tissue samples were harvested and examined by hematoxylin and eosin (H&E) staining for general observation of skin layers, Masson's trichrome staining to study the extent of collagen deposition and immunohistochemistry (IHC) analysis of  $\alpha$ -SMA expression (Fig. 9). Representative wound histology from HE stains for all groups showed clear differences in the extent of re-epithelialization and granulation tissue formation in the wounds after different treatments. The stratum corneum, stratum spinosum and stratum basale were differentiable in the PC and PCH groups, suggesting that the skin had partially recovered from the injury (Fig. 9A). Specifically, complete re-epithelialization and differentiated epithelium characterized by well-developed epidermis layers were shown in

wounds subjected to PCH NFM treatment, which clearly differed from less-differentiated epidermis in wounds treated with PC or epithelial incompleteness accompanied by fibrinous debris in wounds of control group and PLGA groups (Fig. 9A). Indeed, a loose crust of dermal layers and poor epithelium were evident in the control and PLGA groups while PC and PCH groups demonstrated a varied degree of migration of the epithelium over the dermis, granulation tissue formation and dermal remodeling. The PCH group showed complete re-epithelialization of the wound with well-formed and differentiated epithelium and significant increased deposition of connective tissue. Furthermore, more stratified epidermal layers were observed in PCH where papilla basement membrane was also observed as signs of well-defined dermal-epidermal junctions. The PCH group also showed neo-vascular structure compared to other groups.

The Masson trichrome stain could reveal the extent of collagen deposition in addition to the alignment of collagen fiber after wound healing. When stained with Masson's trichrome, keratin and muscle fiber were stained in red while collagen in blue. The Masson's trichrome staining clearly indicates increased collagen expression in the PCH group, with a dermal layer much closer in appearance to that of normal skin (Fig. 9B). Furthermore, neovascular structure was also visualized in PCH group from the H&E and Masson's trichrome staining. The neo-vessel formation in the newly formed skin tissue is expected to promote the vascularization in the damaged tissue for faster wound healing.

$\alpha$ -SMA is a marker for myofibroblasts that are largely responsible for wound contraction and production of ECM components such as collagen [61]. TGF- $\beta$ 1 is considered to be the major growth factor directly promoting myofibroblast development by inducing expression of  $\alpha$ -SMA, which are "fine-tuned" by cooperative or antagonistic growth factors [62]. Besides myofibroblasts,  $\alpha$ -SMA is also expressed by pericytes, which wrap around the endothelial cells lining the capillaries and are required for the maturation of blood vessels [63]. Therefore, the expression of  $\alpha$ -SMA marker in wounded tissue is deemed important for blood vessel maturation and wound contraction [64]. Increased  $\alpha$ -SMA expression by myofibroblasts and pericytes is shown for all groups from IHC staining of  $\alpha$ -SMA on day 14 (Fig. 9C). Indeed,  $\alpha$ -SMA-positive myofibroblasts in PCH group arranged more orderly and compactly than other groups, indicating the early differentiation of fibroblasts into myofibroblasts. The vascularization of wounds examined from IHC staining for  $\alpha$ -SMA also revealed extensive staining of blood vessel walls in the PCH treated wounds, indicating early blood vessel formation not present in other groups (Fig. 9C). Quantitative analysis of IHC staining images from image analysis indicated the area percentage of  $\alpha$ -SMA positive vessels in PCH group ( $17.4 \pm 4.0\%$ ) is significant higher than that associated with other groups, which is 5.8, 3.6 and 1.9 folds that of gauze ( $3.0 \pm 0.8\%$ ), PLGA ( $4.9 \pm 2.0\%$ ) and PC ( $9.4 \pm 0.9\%$ ) (Fig. 9D). As the vascularized area was significantly increased after PCH treatment, this heparin grafted membrane would be beneficial for critical wound healing originated from its growth factor sequestering ability. It could be suggested that PCH may enhance vessel formation and accelerate diabetic wound healing by sequestering and stabilizing growth factors such as TGF- $\beta$ 1 and FGF-2. By high density grafting heparin onto the surface of biodegradable nanofibers, sequestering, stabilization and release of endogenous growth factors could be expected in the wound as the matrix degrades in vivo.

### 3.7. Anti-inflammatory effect from qRT-PCR

Diabetic wounds are characterized by prolonged inflammation and oxidative stress originated from the hyperglycemic microenvironment, which will prevent the diabetic wound from transferring to the next proliferation phase with the prolonged inflammation phase [65]. The high oxidative stress environment in diabetic wounds also impair macrophage and neutrophil function in the inflammation phase, impair keratinocytes for delayed re-epithelialization and impair fibroblasts and vascular endothelial cells for insufficient granulation tissue and

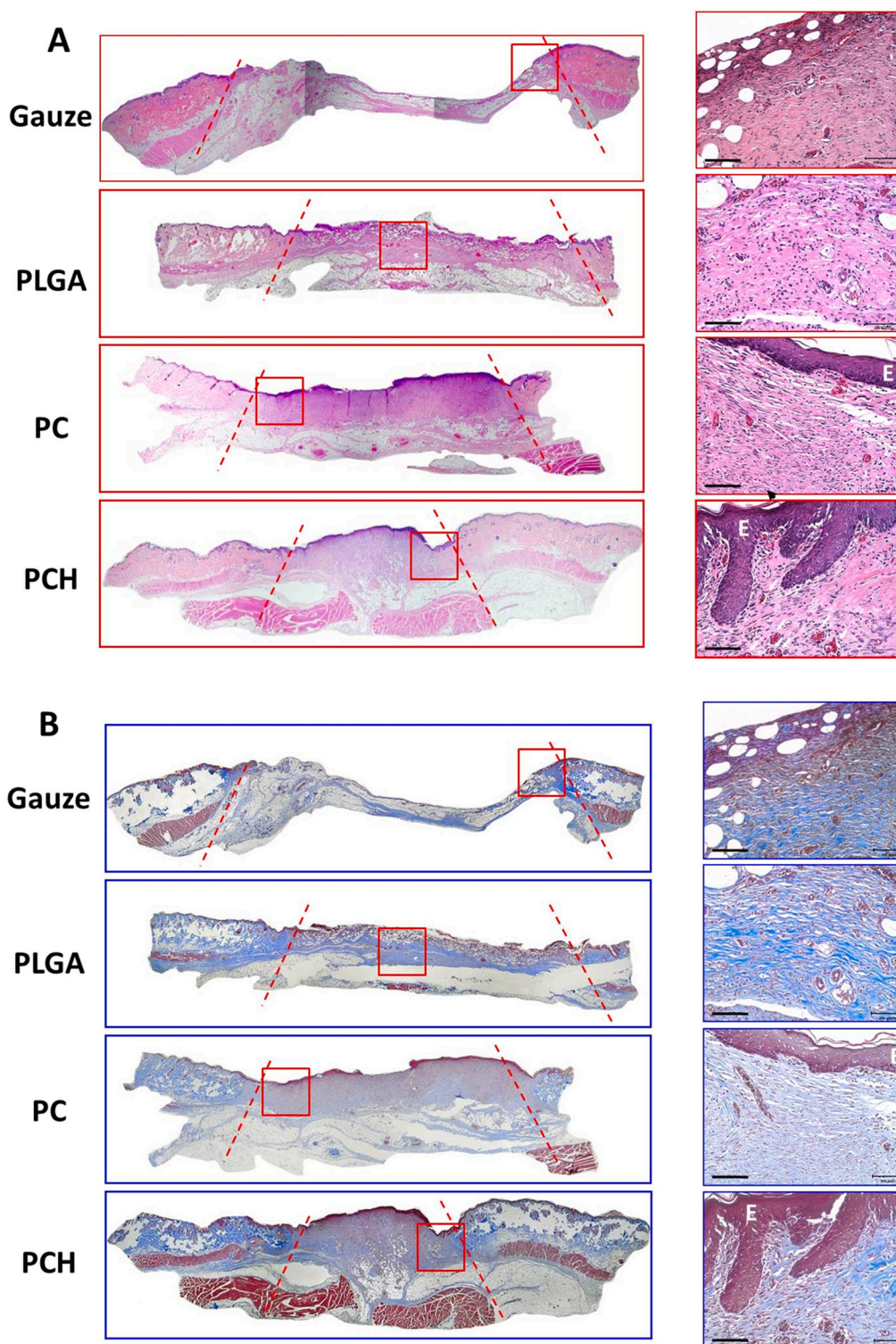


**Fig. 9.** Histological evaluation of wounds treated with gauze (control), PLGA, PC and PCH NFMs for 14 days by H&E (A) and Masson's trichrome staining (B) (bar = 100  $\mu$ m, E, epidermis). A low power image of each wound is shown with dotted lines indicating the boundary of created wound. A high power image taken from the rectangle in the low power image is shown to the right. White arrows in (A) indicate vessels perfused by blood. Images of immunohistochemical (IHC) staining (C) and the area percentage of  $\alpha$ -SMA positive vessels (D) on day 14 (bar = 100  $\mu$ m, V, vessel, L, lumen, M, myofibroblast, \* $p$  < 0.05; \*\* $p$  < 0.01). (For interpretation of the references to color in this figure, the reader is referred to the web version of this article.)

ischemia. As a dressing material for diabetic wound treatment must have anti-oxidative stress and anti-inflammation function, we evaluate the relative mRNA expression of the anti-oxidative enzyme glutathione peroxidase (GPx) and the transcription factor involved in cellular

inflammation response (NF $\kappa$ B) in wound tissues by qRT-PCR. This could verify whether released curcumin from PC or PCH NFM could retain its function in vivo for accelerated diabetic wound healing. As shown in Fig. 10, significant down regulation of GPx and NF $\kappa$ B gene expression



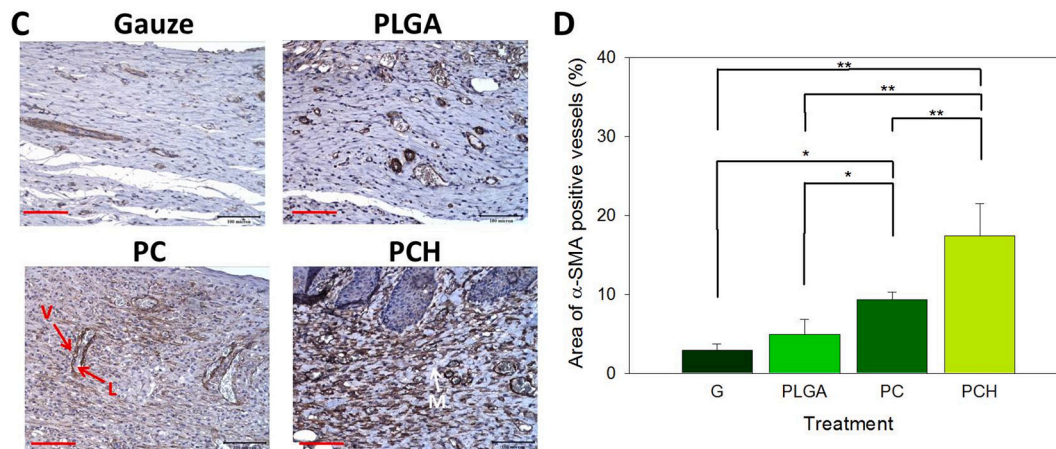


Fig. 9. (continued).

were found for PC and PCH compared to control and PLGA, which showed no significant difference between them on day 3 and 14 post-treatment. This reveals the sustained release of curcumin from the curcumin-containing PC and PCH NFMs can successfully quench ROS to enable reduction of GPx expression and mediate inflammation by regulating the PI3K/AKT/NF $\kappa$ B pathway.

Oxidative stress is a part of the wound physiology arising from the high cellular proliferation, migration and infiltration activities. The anti-oxidative enzymes like GPx can regulate the peroxidation rate and ROS generation at wounded area [66]. The low expression of GPx suggested that curcumin in PC and PCH NFMs may directly reduce the ROS level and indirectly inhibit the synthesis of endogenous antioxidant, which is consistent with previous findings [24,27]. Inflammation phase of the injury produced tremendous ROS, and it is possible to induce damage and lead to neoplastic transformation [67]. The successful quenching of ROS by released curcumin thus also leads to down-regulation of NF $\kappa$ B, which is a well-known transcription factor triggering the production of inflammatory cytokines by enhancing the inflammation pathway. Therefore, the results of GPx and NF $\kappa$ B relative mRNA expression underline the importance of sustained release of curcumin from PC to reduce inflammation throughout the wound healing process. This effect was further augmented, shown from accelerated wound closure in PCH, after additional benefit provided by heparin to justify the choice of PCH NFM as the best multi-functional wound dressing membrane. Overall, the PCH NFM exhibited the highest wound healing rate by

downregulating anti-oxidative enzymes and inflammatory marker gene expression and accelerating re-epithelialization, angiogenesis and collagen deposition in diabetes wound sites. The underlying mechanism may relate to the anti-oxidative stress and anti-inflammation effects of PCH, which demonstrates improved curcumin release rate after heparin grafting, for alleviating non-healing diabetic wounds. This will transfer the long-term inflammation phase into the proliferation phase to promote wound healing during diabetes wound healing [68]. The overall microenvironment change at wound sites induced by PCH therefore promoted a faster healing process for diabetic wounds.

#### 4. Conclusions

In this study, we employ nanotechnology-based engineering strategy to design electrospun NFMs as a multi-functional wound dressing material to accelerate diabetic wound healing. By taking advantage of the combined effects of curcumin and heparin, we designed functional aligned nanofibers by combining the exogenous effect from controlled delivery of curcumin and the endogenous effect from sequestered growth factors. The PC NFM is endowed with the intrinsic wound healing benefits provided by the base material PLGA, the aligned fiber orientation and the drug curcumin. This could be further programmed to provide specific binding sites for endogenous growth factors by surface grafting of high density heparin to fiber surface in PCH NFM to accelerate diabetic wound healing. With the high tensile strength, low

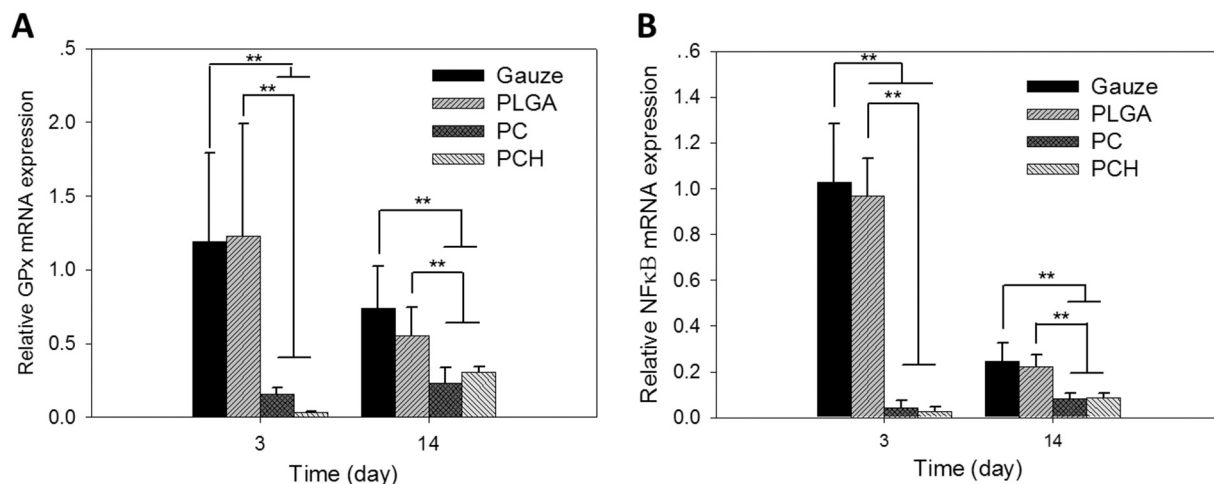


Fig. 10. Quantitative real-time PCR analysis of anti-inflammatory markers GPx (A) and NF $\kappa$ B (B) relative mRNA levels in skin tissue extracts of healed wounds of diabetic rats on day 3 and day 14 after treatment with gauze (control), PLGA, PC and PCH NFMs. Values are means  $\pm$  SD (n = 4). \* $p$  < 0.05, \*\* $p$  < 0.01.



cytotoxicity and suitable water vapor transmission rate, the PCH NFM was deemed as a suitable wound dressing material. Furthermore, as heparin surface grafting leads to higher curcumin release rate, PCH provides additional advantage such as higher migration ability and higher induced oxidative stress protection of HS68 fibroblast cells in vitro. In vivo study indicated the PCH NFM exhibits the fastest wound closure rate among all NFMs with accelerated re-epithelization, higher angiogenesis and collagen deposition at the wound site. Overall, this study suggests a promising nanofiber membrane to improve the clinical efficacy of diabetic wound healing by combining the heparin-induced endogenous factor (growth factors) and the exogenous factor (curcumin), which is expected to provide a basis for future development of material-based therapeutics.

Supplementary data to this article can be found online at <https://doi.org/10.1016/j.msec.2020.111689>.

### Declaration of competing interest

The authors declare that they have no known competing financial interests or personal relationships that could have appeared to influence the work reported in this paper.

### Acknowledgments

The authors would like to thank the Ministry of Science and Technology of Taiwan (ROC) (MOST106-2314-B-182-013-MY2) and Chang Gung Memorial Hospital (CMRPD2I0041, CMRPD2I0042 and BMRP249) for financially supporting this research.

### References

- J.S. Boateng, K.H. Matthews, H.N. Stevens, G.M. Eccleston, Wound healing dressings and drug delivery systems: a review, *J. Pharm. Sci.* 97 (8) (2008) 2892–2923.
- J.-P. Chen, G.-Y. Chang, J.-K. Chen, Electrospun collagen/chitosan nanofibrous membrane as wound dressing, *Colloids Surf. A Physicochem. Eng. Asp.* 313–314 (2008) 183–188.
- J.P. Chen, Y. Chiang, Bioactive electrospun silver nanoparticles-containing polyurethane nanofibers as wound dressings, *J. Nanosci. Nanotechnol.* 10 (11) (2010) 7560–7564.
- S.-H. Chen, Y. Chang, K.-R. Lee, J.-Y. Lai, A three-dimensional dual-layer nano/microfibrous structure of electrospun chitosan/poly(D,L-lactide) membrane for the improvement of cytocompatibility, *J. Membr. Sci.* 450 (2014) 224–234.
- M.S. Khil, D.I. Cha, H.Y. Kim, I.S. Kim, N. Bhattarai, Electrospun nanofibrous polyurethane membrane as wound dressing, *J. Biomed. Mater. Res. B Appl. Biomater.* 67 (2) (2003) 675–679.
- J. Xie, M.R. MacEwan, A.G. Schwartz, Y. Xia, Electrospun nanofibers for neural tissue engineering, *Nanoscale* 2 (1) (2010) 35–44.
- C.H. Chen, S.H. Chen, C.Y. Kuo, M.L. Li, J.P. Chen, Response of dermal fibroblasts to biochemical and physical cues in aligned polycaprolactone/silk fibroin nanofiber scaffolds for application in tendon tissue engineering, *Nanomaterials* (Basel, Switzerland) 7 (8) (2017).
- S. Zhong, W.E. Teo, X. Zhu, R.W. Beuerman, S. Ramakrishna, L.Y. Yung, An aligned nanofibrous collagen scaffold by electrospinning and its effects on in vitro fibroblast culture, *J. Biomed. Mater. Res.* A 79 (3) (2006) 456–463.
- K.D. Andrews, J.A. Hunt, Upregulation of matrix and adhesion molecules induced by controlled topography, *J. Mater. Sci. Mater. Med.* 19 (4) (2008) 1601–1608.
- M. Ottosson, A. Jakobsson, F. Johansson, Accelerated wound closure - differently organized nanofibers affect cell migration and hence the closure of artificial wounds in a cell based in vitro model, *PLoS One* 12 (1) (2017), e0169419.
- S. Patel, K. Kurpinski, R. Quigley, H. Gao, B.S. Hsiao, M.M. Poo, S. Li, Bioactive nanofibers: synergistic effects of nanotopography and chemical signaling on cell guidance, *Nano Lett.* 7 (7) (2007) 2122–2128.
- T. Velnar, T. Bailey, V. Smrkolj, The wound healing process: an overview of the cellular and molecular mechanisms, *J. Int. Med. Res.* 37 (5) (2009) 1528–1542.
- S. Werner, A novel enhancer of the wound healing process: the fibroblast growth factor-binding protein, *Am. J. Pathol.* 179 (5) (2011) 2144–2147.
- T. Kurahashi, J. Fujii, Roles of antioxidative enzymes in wound healing, *J. Dev. Biol.* 3 (2) (2015) 57.
- R.F. Diegelmann, M.C. Evans, Wound healing: an overview of acute, fibrotic and delayed healing, *Front. Biosci.* 9 (2004) 283–289.
- P.E. Porporato, V.L. Payen, C.J. De Saedeleer, V. Pr  at, J.-P. Thissen, O. Feron, P. Sonveaux, Lactate stimulates angiogenesis and accelerates the healing of superficial and ischemic wounds in mice, *Angiogenesis* 15 (4) (2012) 581–592.
- H. Park, K.Y. Lee, S.J. Lee, K.E. Park, W.H. Park, Plasma-treated poly(lactic-co-glycolic acid) nanofibers for tissue engineering, *Macromol. Res.* 15 (3) (2007) 238–243.
- J. Sharma, M. Lizu, M. Stewart, K. Zygula, Y. Lu, R. Chauhan, X. Yan, Z. Guo, E. Wujcik, S. Wei, Multifunctional Nanofibers towards active biomedical therapeutics, *Polymers* 7 (2) (2015) 186.
- S.J. Hewlings, D.S. Kalman, Curcumin: a review of its effects on human health, *Foods* (Basel, Switzerland) 6 (10) (2017).
- M. Sampath, R. Lakra, P. Korrapati, B. Sengottuvelan, Curcumin loaded poly (lactic-co-glycolic) acid nanofiber for the treatment of carcinoma, *Colloids Surf. B: Biointerfaces* 117 (2014) 128–134.
- D. Akbik, M. Ghadiri, W. Chrzanowski, R. Rohanizadeh, Curcumin as a wound healing agent, *Life Sci.* 116 (1) (2014) 1–7.
- X. Dai, J. Liu, H. Zheng, J. Wichmann, U. Hopfner, S. Sudhop, C. Prein, Y. Shen, H.-G. Machens, A.F. Schilling, Nano-formulated curcumin accelerates acute wound healing through Dkk-1-mediated fibroblast mobilization and MCP-1-mediated anti-inflammation, *NPG Asia Materials* 9 (3) (2017) e368.
- K.M. Shanmugam, G. Rane, M.M. Kanchi, F. Arfuso, A. Chinnathambi, E.M. Zayed, A.S. Alharbi, K.B. Tan, P.A. Kumar, G. Sethi, The multifaceted role of curcumin in cancer prevention and treatment, *Molecules* 20 (2) (2015).
- C. Mohanty, M. Das, S.K. Sahoo, Sustained wound healing activity of curcumin loaded oleic acid based polymeric bandage in a rat model, *Mol. Pharm.* 9 (10) (2012) 2801–2811.
- C. Buhrmann, A. Mobasher, F. Busch, C. Aldinger, R. Stahlmann, A. Montaseri, M. Shakibaei, Curcumin modulates nuclear factor kappaB (NF-kappaB)-mediated inflammation in human tenocytes in vitro: role of the phosphatidylinositol 3-kinase/Akt pathway, *J. Biol. Chem.* 286 (32) (2011) 28556–28566.
- N. Fereydooni, M. Darroudi, J. Movaffagh, A. Shahroodi, A.E. Butler, S. Ganjali, A. Sahebkar, Curcumin nanofibers for the purpose of wound healing, *J. Cell. Physiol.* 234 (2019) 5537–5554.
- M. Panchatcharam, S. Miriyala, V.S. Gayathri, L. Suguna, Curcumin improves wound healing by modulating collagen and decreasing reactive oxygen, *Mol. Cell. Biochem.* 290 (2006) 87–96.
- Y. Mo, Y. Zhang, B. Cheng, Y. Ahang, Controlled dual delivery of angiogenin and curcumin by electrospun nanofibers for skin regeneration, *Tissue Eng. A* 23 (13–14) (2017) 597–608.
- R. Sasisekharan, R. Raman, V. Prabhakar, Glycomics approach to structure-function relationships of glycosaminoglycans, *Annu. Rev. Biomed. Eng.* 8 (1) (2006) 181–231.
- D.L. Rabenstein, Heparin and heparan sulfate: structure and function, *Nat. Prod. Rep.* 19 (3) (2002) 312–331.
- K. Rajangam, H.A. Behanna, M.J. Hui, X. Han, J.F. Hulvat, J.W. Lomasney, S. I. Stupp, Heparin binding nanostructures to promote growth of blood vessels, *Nano Lett.* 6 (9) (2006) 2086–2090.
- H.J. Lai, C.H. Kuan, H.C. Wu, J.C. Tsai, T.M. Chen, D.J. Hsieh, T.W. Wang, Tailored design of electrospun composite nanofibers with staged release of multiple angiogenic growth factors for chronic wound healing, *Acta Biomater.* 10 (10) (2014) 4156–4166.
- D.K. Kweon, S.B. Song, Y.Y. Park, Preparation of water-soluble chitosan/heparin complex and its application as wound healing accelerator, *Biomaterials* 24 (9) (2003) 1595–1601.
- Y. Niu, Q. Li, Y. Ding, L. Dong, C. Wang, Engineered delivery strategies for enhanced control of growth factor activities in wound healing, *Adv. Drug Deliv. Rev.* 146 (2018) 190–208.
- J.P. Chen, C.H. Su, Surface modification of electrospun PLLA nanofibers by plasma treatment and cationized gelatin immobilization for cartilage tissue engineering, *Acta Biomater.* 7 (1) (2011) 234–243.
- J.P. Chen, P.C. Yang, Y.H. Ma, S.J. Tu, Y.J. Lu, Targeted delivery of tissue plasminogen activator by binding to silica-coated magnetic nanoparticle, *Int. J. Nanomedicine* 7 (2012) 5137–5149.
- G. Rohman, S.C. Baker, J. Southgate, N.R. Cameron, Heparin functionalisation of porous PLGA scaffolds for controlled, biologically relevant delivery of growth factors for soft tissue engineering, *J. Mater. Chem.* 19 (48) (2009) 9265–9273.
- H.M. Jeong, B.K. Ahn, B.K. Kim, Temperature sensitive water vapour permeability and shape memory effect of polyurethane with crystalline reversible phase and hydrophilic segments, *Polym. Int.* 49 (12) (2000) 1714–1721.
- H. Wu, R. Zhang, Y. Sun, D. Lin, Z. Sun, W. Pan, P. Downs, Biomimetic nanofiber patterns with controlled wettability, *Soft Matter* 4 (12) (2008) 2429–2433.
- G. Morello, R. Manco, M. Moffa, L. Persano, A. Camposeo, D. Pisignano, Multifunctional polymer nanofibers: UV emission, optical gain, anisotropic wetting, and high hydrophobicity for next flexible excitation sources, *ACS Appl. Mater. Interfaces* 7 (39) (2015) 21907–21912.
- H.J. Chung, H.K. Kim, J.J. Yoon, T.G. Park, Heparin immobilized porous PLGA microspheres for angiogenic growth factor delivery, *Pharm. Res.* 23 (8) (2006) 1835–1841.
- S. Bae, M.J. DiBalsi, N. Meilinger, C. Zhang, E. Beal, G. Korneva, R.O. Brown, K. G. Kornev, J.S. Lee, Heparin-eluting electrospun nanofiber yarns for antithrombotic vascular sutures, *Appl. Mater. Interfaces* 10 (10) (2018) 8426–8435.
-   . Kiss, I. Bert  ti, E.I. Vargha-Butler, XPS and wettability characterization of modified poly(lactic acid) and poly(lactic/glycolic acid) films, *J. Colloid Interface Sci.* 245 (1) (2002) 91–98.
- F.L. Mi, S.S. Shyu, Y.B. Wu, S.T. Lee, J.Y. Shyong, R.N. Huang, Fabrication and characterization of a sponge-like asymmetric chitosan membrane as a wound dressing, *Biomaterials* 22 (2) (2001) 165–173.
- L.O. Lamke, G.E. Nilsson, H.L. Reithner, The evaporative water loss from burns and the water-vapor permeability of grafts and artificial membranes used in the treatment of burns, *Burns* 3 (3) (1977) 159–165.

- [46] L. Ruiz-Cardona, Y.D. Sanzgiri, L.M. Benedetti, V.J. Stella, E.M. Topp, Application of benzyl hyaluronate membranes as potential wound dressings: evaluation of water vapour and gas permeabilities, *Biomaterials* 17 (16) (1996) 1639–1643.
- [47] G.H. Shin, J. Li, J.H. Cho, J.T. Kim, H.J. Park, Enhancement of curcumin solubility by phase change from crystalline to amorphous in Cur-TPGS nanosuspension, *J. Food Sci.* 81 (2) (2016) N494–N501.
- [48] M. Notoya, H. Nishimura, J.T. Woo, K. Nagai, Y. Ishihara, H. Hagiwara, Curcumin inhibits the proliferation and mineralization of cultured osteoblasts, *Eur. J. Pharmacol.* 534 (1–3) (2006) 55–62.
- [49] A. Scharstuhl, H.A. Mutsaers, S.W. Pennings, W.A. Szarek, F.G. Russel, F. A. Wagener, Curcumin-induced fibroblast apoptosis and in vitro wound contraction are regulated by antioxidants and heme oxygenase: implications for scar formation, *J. Cell. Mol. Med.* 13 (4) (2009) 712–725.
- [50] M.J. G. M.S. W. T. Lu, L.C. T. C.A. F. N.L. S, Curcumin-loaded poly( $\epsilon$ -caprolactone) nanofibres: diabetic wound dressing with anti-oxidant and anti-inflammatory properties, *Clin. Exp. Pharmacol. Physiol.* 36 (12) (2009) 1149–1156.
- [51] H.N. Kim, Y. Hong, M.S. Kim, S.M. Kim, K.Y. Suh, Effect of orientation and density of nanotopography in dermal wound healing, *Biomaterials* 33 (34) (2012) 8782–8792.
- [52] J. Xie, M.R. Macewan, W.Z. Ray, W. Liu, D.Y. Siewe, Y. Xia, Radially aligned, electrospun nanofibers as dural substitutes for wound closure and tissue regeneration applications, *ACS Nano* 4 (9) (2010) 5027–5036.
- [53] S.K. Sukumaran, R.J. Vadakketkuttikal, H. Kanakath, Comparative evaluation of the effect of curcumin and chlorhexidine on human fibroblast viability and migration: an in vitro study, *Journal of Indian Society of Periodontology* 24 (2) (2020) 109–116.
- [54] S. Patel, S. Srivastava, M.R. Singh, D. Singh, Mechanistic insight into diabetic wounds: pathogenesis, molecular targets and treatment strategies to pace wound healing, *Biomed. Pharmacother.* 112 (2019) 108615.
- [55] H. Hasmad, M.R. Yusof, Z.R. Mohd Razi, R.B. Hj Idrus, S.R. Chowdhury, Human amniotic membrane with aligned electrospun fiber as scaffold for aligned tissue regeneration, *Tissue Engineering. Part C, Methods* 24 (6) (2018) 368–378.
- [56] Z. Hussain, H.E. Thu, S.-F. Ng, S. Khan, H. Katas, Nanoencapsulation, an efficient and promising approach to maximize wound healing efficacy of curcumin: a review of new trends and state-of-the-art, *Colloids Surf. B: Biointerfaces* 150 (2017) 223–241.
- [57] C. Mohanty, S.K. Sahoo, Curcumin and its topical formulations for wound healing applications, *Drug Discov. Today* 22 (10) (2017) 1582–1592.
- [58] J.G. Merrell, S.W. McLaughlin, L. Tie, C.T. Laurencin, A.F. Chen, L.S. Nair, Curcumin-loaded poly( $\epsilon$ -caprolactone) nanofibres: diabetic wound dressing with anti-oxidant and anti-inflammatory properties, *Clin. Exp. Pharmacol. Physiol.* 36 (12) (2009) 1149–1156.
- [59] K.K. Cherredy, R. Coco, P.B. Memvanga, B. Ucar, A. des Rieux, G. Vandermeulen, V. Pr  at, Combined effect of PLGA and curcumin on wound healing activity, *J. Control. Release* 171 (2) (2013) 208–215.
- [60] M. Ranjbar-Mohammadi, S. Rabbani, S.H. Bahrami, M.T. Joghataei, F. Moayer, Antibacterial performance and in vivo diabetic wound healing of curcumin loaded gum tragacanth/poly( $\epsilon$ -caprolactone) electrospun nanofibers, *Mater. Sci. Eng. C* 69 (2016) 1183–1191.
- [61] I.A. Darby, B. Laverdet, F. Bont  , A. Desmouli  re, Fibroblasts and myofibroblasts in wound healing, *Clin. Cosmet. Investig. Dermatol.* 7 (2014) 301–311.
- [62] B. Hinz, Formation and function of the myofibroblast during tissue repair, *J. Investig. Dermatol.* 127 (3) (2007) 526–537.
- [63] G. Bergers, S. Song, The role of pericytes in blood-vessel formation and maintenance, *Neuro-Oncology* 7 (4) (2005) 452–464.
- [64] R.J. Bodnar, L. Satish, C.C. Yates, A. Wells, Pericytes: a newly recognized player in wound healing, *Wound Repair Regen.* 24 (2) (2016) 204–214.
- [65] C.-C.E. Lan, C.-S. Wu, S.-M. Huang, I.H. Wu, G.-S. Chen, High-glucose environment enhanced oxidative stress and increased interleukin-8 secretion from keratinocytes: new insights into impaired diabetic wound healing, *Diabetes* 62 (7) (2013) 2530–2538.
- [66] A.M. Rasik, A. Shukla, Antioxidant status in delayed healing type of wounds, *Int. J. Exp. Pathol.* 81 (4) (2000) 257–263.
- [67] H. Steiling, B. Munz, S. Werner, M. Brauchle, Different types of ROS-scavenging enzymes are expressed during cutaneous wound repair, *Exp. Cell Res.* 247 (2) (1999) 484–494.
- [68] Y. Han, Y. Jiang, Y. Li, M. Wang, T. Fan, M. Liu, Q. Ke, H. Xu, Z. Yi, An aligned porous electrospun fibrous scaffold with embedded asiatic acid for accelerating diabetic wound healing, *J. Mater. Chem. B* 7 (40) (2019) 6125–6138.

## Research Article

# Functional Redox Proteomics Reveal That *Salvia miltiorrhiza* Aqueous Extract Alleviates Adriamycin-Induced Cardiomyopathy via Inhibiting ROS-Dependent Apoptosis

Yu-Chiang Hung,<sup>1</sup> Pei-Wen Wang<sup>2</sup>,<sup>3</sup> Tung-Yi Lin,<sup>3</sup> Pei-Ming Yang,<sup>4,5</sup> Jyh-Sheng You,<sup>6</sup> and Tai-Long Pan<sup>6,7,8</sup>

<sup>1</sup>Department of Chinese Medicine, College of Medicine, Kaohsiung Chang Gung Memorial Hospital and Chang Gung University, Kaohsiung, Taiwan

<sup>2</sup>Department of Medical Research, China Medical University Hospital, China Medical University, Taichung, Taiwan

<sup>3</sup>Department of Traditional Chinese Medicine, Chang Gung Memorial Hospital, Keelung, Taiwan

<sup>4</sup>TMU Research Center of Cancer Translational Medicine, Taipei Medical University, Taipei, Taiwan

<sup>5</sup>Graduate Institute of Cancer Biology and Drug Discovery, College of Medical Science and Technology, Taipei Medical University, Taipei, Taiwan

<sup>6</sup>School of Traditional Chinese Medicine, Chang Gung University, Taoyuan, Taiwan

<sup>7</sup>Liver Research Center, Chang Gung Memorial Hospital, Taoyuan, Taiwan

<sup>8</sup>Research Center for Chinese Herbal Medicine and Research Center for Food and Cosmetic Safety, College of Human Ecology, Chang Gung University of Science and Technology, Taoyuan, Taiwan

Correspondence should be addressed to Pei-Wen Wang; [pwwang5105@hotmail.com](mailto:pwwang5105@hotmail.com) and Tai-Long Pan; [pan@mail.cgu.edu.tw](mailto:pan@mail.cgu.edu.tw)

Received 8 July 2020; Revised 14 August 2020; Accepted 19 August 2020; Published 10 September 2020

Academic Editor: Peeter Karihtala

Copyright © 2020 Yu-Chiang Hung et al. This is an open access article distributed under the Creative Commons Attribution License, which permits unrestricted use, distribution, and reproduction in any medium, provided the original work is properly cited.

The anticancer agent adriamycin (ADR) has long been recognized to induce a dose-limiting cardiotoxicity, while *Salvia miltiorrhiza* (SM) is a Chinese herb widely used for the treatment of cardiovascular disorders and its aqueous extract (SMAE) has shown anticancer as well as antioxidant effects. In the current study, we aimed at investigating the synergistic effect and potent molecular mechanisms of SMAE with a focus on the cardioprotective benefit observed under ADR adoption. Histopathological analysis indicated that SMAE could substantially alleviate cardiomyopathy and cell apoptosis caused by ADR. Meanwhile, the two-dimensional electrophoresis (2-DE) oxyblots demonstrated that SMAE treatment could effectively reduce carbonylation of specific proteins associated with oxidative stress response and various metabolic pathways in the presence of ADR. SMAE application also showed protective efficacy against ADR-mediated H9c2 cell death in a dose-dependent manner without causing any cytotoxicity and significantly attenuated the reactive oxygen species production. Particularly, the simultaneous administration of ADR and SMAE could remarkably suppress the growth of breast cancer cells. We also noticed that there was a marked upregulation of detoxifying enzyme system in the presence of SMAE, and its exposure also contributed to an increase in Nrf2 and HO-1 content as well. SMAE also amended the ERK/p53/Bcl-xL/caspase-3 signaling pathways and the mitochondrial dysfunction, which eventually attribute to apoptotic cathepsin B/AIF cascades. Correspondingly, both the ERK1/2 inhibitor (U0126) and pan-caspase inhibitor (Z-VAD-FMK) could at least partially abolish the ADR-associated cytotoxicity in H9c2 cells. Collectively, these results support that ROS apoptosis-inducing molecule release is closely involved in ADR-induced cardiotoxicity while SMAE could prevent or mitigate the causative cardiomyopathy through controlling multiple targets without compromising the efficacy of chemotherapy.

## 1. Introduction

The anthracycline antibiotic adriamycin (ADR), also known as doxorubicin, is the commonly used chemotherapeutic agent for the treatment of various cancers. However, the severe cardiotoxicity of ADR greatly restricts its clinical utilization [1, 2]. Although ADR-related injury appears to be multifactorial and complicated, oxidative stress and mitochondrial dysfunction have been proposed to majorly account for the pathogenesis of ADR-induced cardiomyopathy [3–6]. Moreover, cardiomyocytes apoptosis can be a pivotal event by which ADR causes deterioration of cardiac system but the detailed molecular mechanisms still remain unclear. Several chemical agents have been used to prevent the ADR-induced cardiotoxicity; nevertheless, treatment with these drugs is known to have certain disadvantages. Dexrazoxane (DXR), for example, is the only FDA-approved drug for treating ADR-associated cardiomyopathy; however, it might increase the risk of infection, myelosuppression, and second primary malignancies [7, 8]. Therefore, the development of alternative cardioprotectants with low toxicity is urgently needed for cancer survivors.

A great amount of effort has been made towards perfecting the clinical applications of herbal medicine that are frequently used in combination to improve the therapeutic efficacy [9]. Of note, *Salvia miltiorrhiza* (SM) has been prescribed for treating cardiovascular disorders since a long time [10]. The water-soluble components extracted from SM including salvianolic acids A, B, and C have garnered much interest as a multitargeted therapy owing to their antioxidant effects on free radicals. Additionally, *Salvia miltiorrhiza* aqueous extract (SMAE) has been utilized widely for the treatment of coronary heart disease, atherosclerosis, and ischemic cardiovascular diseases [11, 12]. Our previous research has also revealed that SMAE provides a protective effect against adriamycin- (ADR-) induced cardiomyopathy and hepatic damage [13]. However, the molecular pathways associated with the SMAE-mediated advantageous effect in managing the cardiotoxicity resulting from ADR treatment have not been thoroughly investigated. Herein, we used animal and cellular models to verify whether ADR-induced cardiomyopathy could be relieved by SMAE and also evaluate the synergistic effect on cancer cells.

ROS generation caused by ADR administration would disturb the normal redox balance and produce huge oxidative stress, which subsequently stimulates the carbonylation of specific groups of proteins involved in physiological dysfunction and induces cardiomyocyte apoptosis [14–16]. The most largely studied oxidative stress-caused by a modification of proteins is the formation of carbonyl groups which can react with 2,4-dinitrophenylhydrazine (DNP) and are discovered by redox proteomics [17, 18]. The appearance of carbonylated proteins has been considered as a hallmark of ROS-induced change of protein which might be helpful to predict novel targets for the diagnosis and prognosis of diseases. Furthermore, the functional “signature network” analyzed with MetaCore™ pathway generates global cellular mechanisms underlying different protein levels and imitates

signaling pathways based on the integration of molecular and clinical information [19].

The present study has shed light on the cellular mechanisms involved with SMAE, exhibiting its protective effect and inhibition of ADR-induced cardiomyopathy. Additionally, our findings should offer an opportunity to execute novel therapeutic strategies and sensitive markers for the clinical usage of ADR.

## 2. Materials and Methods

**2.1. Materials.** Specific antibodies to GAPDH, SOD, catalase, p53, Nrf2, and HO-1 were purchased from Santa Cruz (Santa Cruz, CA, USA). Monoclonal antibodies to  $\beta$ -actin were obtained from Millipore (Burlingame, CA, USA). Polyclonal antibodies to caspase-3, -9, PARP, Bax, Bcl-xL, phospho-p53, ERK, and phospho-ERK were purchased from Cell Signaling (Beverly, MA, USA). U0126 and Z-VAD-FMK were obtained from Enzo Life Science (New York, NY, USA).

**2.2. Prepare the Extract of *Salvia miltiorrhiza*.** The air-dried roots of cultivated *Salvia miltiorrhiza* Bunge (Labiateae) were purchased from a Traditional Chinese Medicine dispensary in Taiwan and authenticated by the experts in pharmacognosy. The preparation of *Salvia miltiorrhiza* aqueous extract (SMAE) was as reported by the method of Liu [20]. Briefly, the hot-water extract was prepared by boiling the dried roots with distilled water for 5 hr. The concentration used in each experiment was calculated upon the dry weight of the SMAE extract (mg/mL), which was resuspended in freshly prepared double distilled and deionized water as purified by the Milli-Q filtration system (Millipore).

**2.3. ADR-Induced Heart Failure on Animal Model.** Male Wistar rats, body weight 250–300 g, were maintained on a normal rat chow diet. The rats were randomly divided into three groups: CTL, ADR, and ADR plus SMAE. Five rats that received ready-to-use ADR (Adriablastina RD 10 mg-INS-040731, Pfizer Inc.) were administered by intraperitoneal injection in six equal doses (each containing 3 mg/kg ADR) over a period of 2 weeks, with a total cumulative dose of 18 mg/kg ADR, and five CTL rats were injected with an identical volume of normal saline. Five rats were administered with 100 mg/kg/day of SMAE via oral delivery with ADR injections. At the end of the 5-week posttreatment period, the heart was removed and separately stored for histomorphologic examination and protein expression analysis [13]. Thereby, we utilized the short-term model to evaluate cardiotoxicity, while a previous study had shown that 10 mg/kg ADR application would result in 80% mortality [21], which was consistent with our findings. The rats were treated according to the Ethical Guidelines of the Animal Center, and the experimental protocol was reviewed and approved by the Institutional Animal Care and Use Committee of Chang Gung University (CGU08-61).

**2.4. Histology and Immunohistochemistry.** The heart tissue fixed by 5% neutral buffered formalin was immersed in paraffin and then sliced into 5  $\mu$ m sections. The sample slices were stained with Masson's trichrome (MT) for a histological



assessment. Immunohistochemistry with caspase 3 was applied to specimens as previously described [22]. The histological changes were observed by using optical microscopy (Olympus BX51, Japan) in nonconsecutive, randomly chosen 400 $\times$  histological fields. The digital photomicrographs were then processed with DP-72.

**2.5. TUNEL Assay.** Apoptosis was assessed by terminal deoxynucleotidyl transferase-mediated dUTP biotin nick end labeling (TUNEL) using ApopTag<sup>®</sup> Plus Peroxidase in situ Apoptosis Detection Kit (Millipore) according to the manufacturer's instructions. The slides were counterstained with hematoxylin and mounted. The numbers of stained and unstained cells were then counted from randomly chosen fields per slide within a high-power field ( $\times 400$  magnification) under an Olympus BX50 microscope [22].

**2.6. Two-Dimensional Polyacrylamide Gel Electrophoresis (2-D PAGE).** The procedure has been reported previously [23]. Proteins (150  $\mu$ g for 2-DE oxyblot or 250  $\mu$ g for silver stain) were solubilized in the rehydrated buffer and applied onto 13 or 18 cm Immobiline DryStrip 3-10NL on the IPGphor IEF System (GE Healthcare). The running conditions of the IEF (isoelectric focusing) follow 30 V, 12 h; 100 V, 1 h; 250 V, 1 h; 500 V, 0.5 h; 1,000 V, 0.5 h; 4,000 V, 0.5 h; and 8,000 V, up to 80 kVh.

**2.7. Derivatization of Protein Carbonyls and DNP Immunostaining.** IPG strips were incubated in 2 N HCl with 10 mM DNPH at 25°C for 15 min after IEF; strips were then washed with 2 M Tris-Base/30% glycerol for 15 min [24]. The IPG strips were used for molecular weight-dependent separation of proteins by SDS-PAGE and transferred the protein blotting to a membrane which was incubated overnight at 4°C with the anti-DNP antibody in TBST containing 5% milk. The blots were washed and incubated goat anti-rabbit IgG HRP conjugate for 2 hrs. Enhanced chemiluminescence (PerkinElmer, CA, USA) was used for detection.

**2.8. In-Gel Enzymatic Digestion and Mass Spectrometry.** Spots of interest were excised and in-gel digested with trypsin according to previously described procedures [25]. Monoisotopic peptide masses were assigned and used for database searches with the MASCOT search engine (<http://www.matrixscience.com>) (Matrix Science, London). Search parameters were set as follows: a maximum allowed peptide mass error of 50 ppm and consideration of one incomplete cleavage per peptide.

**2.9. Biological Network Analysis Using MetaCore<sup>™</sup>.** Apply MetaCore<sup>™</sup> software (vers. 5.2 build 17389, GeneGo, St. Joseph, MI, USA) to reveal associated ontological classes and relevant pathways, which were represented among the proteins identified by the 2-DE and peptide mass fingerprint [25].

**2.10. Cell Culture and MTT Assay.** Rat cardiomyoblast-derived H9c2 cell was purchased from the Food Industry Research and Development Institute. The H9c2 and MCF-7 cells were maintained in DMEM medium containing 10%

fetal bovine serum (FBS) at 37°C in a humidified atmosphere of 5% CO<sub>2</sub>. Cell viability was determined by MTT. A total of  $1 \times 10^4$  cells were seeded in 24-well plates for 24 hours (h) and made quiescent by incubating in medium containing 0.2% FBS overnight. After treating with various concentrations (0, 0.3125, 0.625, 1.25, 2.5, 5, and 10 mg/mL) of SMAE for 48 h, isopropanol solution mixed with tetrazolium salt was added to the wells and incubated for additional 4 h at 37°C [26]. The optical density of the dissolved material was measured spectrophotometrically at 570 nm, and assays were performed in triplicate.

**2.11. Image Analysis for Generation of Intracellular ROS under SMAE Application.**  $2 \times 10^3$  H9c2 cells were seeded in a slide chamber, grown to 60% confluence, and cultured in serum-free DMEM medium overnight. Cells were then incubated with 2.5 mg/mL of SMAE for 6 h. Carboxy-H<sub>2</sub>DCFDA (4  $\mu$ M, dissolved in PBS) was added to the wells and incubated for 30 min at 37°C. To terminate the reaction, the cells were washed with PBS twice. Next, 500  $\mu$ L culture medium was added to each well and incubated for 20 min at 37°C. The cells were observed and photographed using a fluorescent microscope (Olympus BX51) under the DP72 Photo-Image system. Image-Pro<sup>®</sup> plus 4.5 (Media Cybernetics, Bethesda, MD) image analysis software was used to quantify image signals [27].

**2.12. Western Blot Analysis.** Samples proteins were isolated by cell lysis buffer (Cell Signaling, MA, USA) and measured using the Bradford Protein Assay Kit (AMRESCO, OH, USA). Total proteins were separated with 10% SDS-polyacrylamide gel electrophoresis and transferred to PVDF membrane (PALL). Next, the blots were incubated with specific primary antibody overnight at 4°C after blocking and further incubated with a peroxidase-labeled anti-mice or -rabbit IgG for 2 h; blots were then washed and incubated goat anti-rabbit and anti-mouse IgG (Chemicon) HRP conjugate for 2 hrs. Enhanced chemiluminescence (PerkinElmer, USA) was used for signal detection. The level of expression of  $\beta$ -actin was used as a gel loading control [27].

**2.13. Statistical Analysis.** All values were presented as the mean  $\pm$  SD. Statistical analysis of the mean values was carried out with the ANOVA test using SPSS software (SPSS Inc., Chicago, IL, USA). Differences were considered as being significant at  $p < 0.05$ .

### 3. Results

**3.1. Effects of SMAE on the Pathological Characteristics, Caspase-3 Level, and Apoptosis in ADR-Exposed Cardiomyocyte of Rats.** Drug-caused cardiotoxicity has become a critical issue linked to the therapeutic efficiency. Given that the protective effects of SMAE were evaluated by the extent of collagen accumulation and death of cardiomyocyte *in vivo*. As shown in Figure 1(a), ADR-applied hearts showed moderate damage characterized with collagen accumulation as detected by the use of Masson's trichrome staining, while the morphology of control tissue remained normal. Conversely, the rats which were simultaneously subjected to



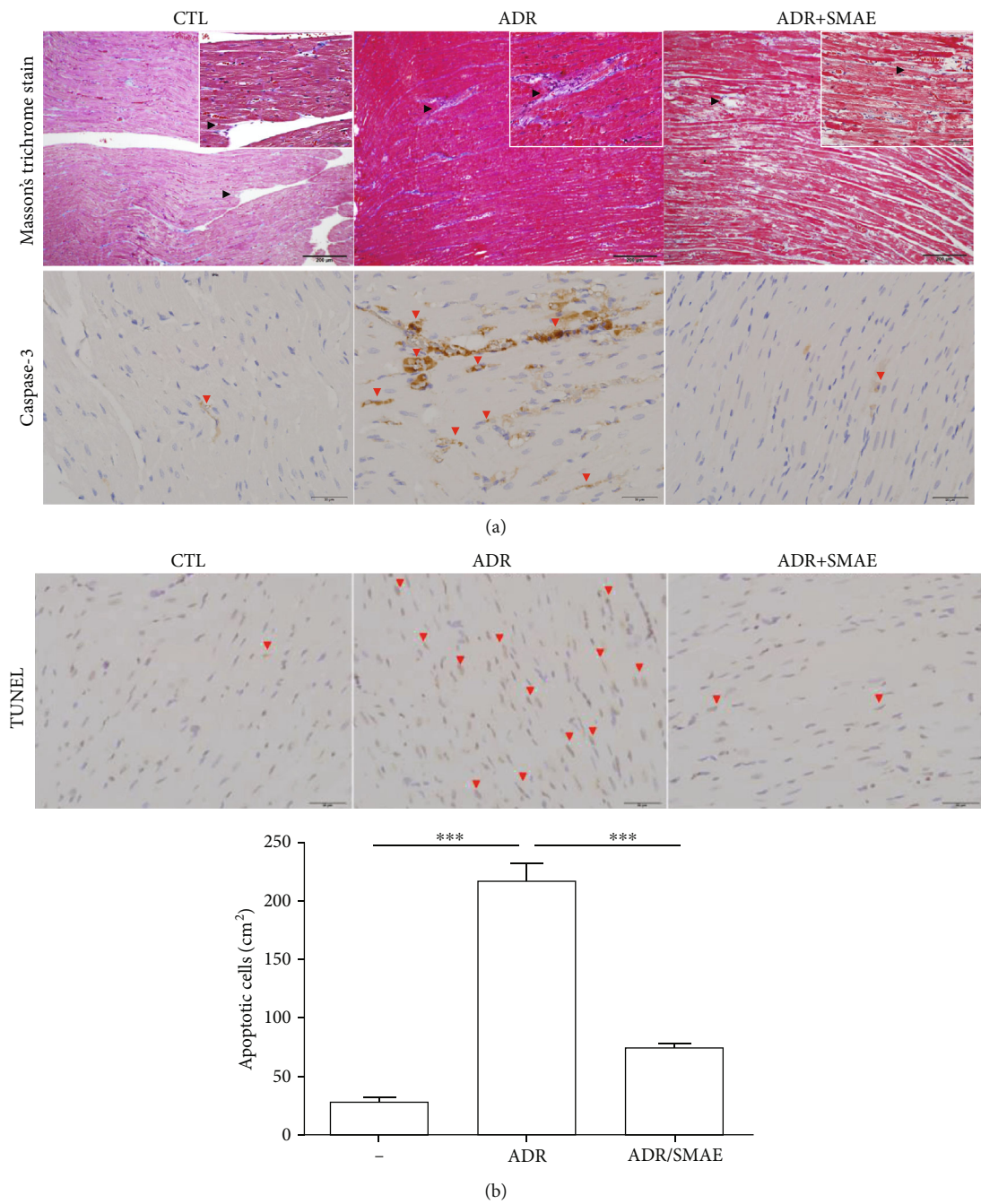


FIGURE 1: (a) Upper panels: histologic examination of heart tissue by Masson's trichrome staining and immunohistochemical analysis for control group, ADR-treated group, and ADR+SMAE group. The positive signals showing blue color demonstrated an accumulation of collagen and were zoomed in by white squares (indicated by black arrows; original magnification:  $\times 200$ ). Lower panels: the regions with differently expressed caspase-3 were indicated by red arrows. Original magnification:  $\times 400$ . (b) Terminal deoxynucleotidyl transferase dUTP nick end labeling (TUNEL) experiment was performed with immunohistochemical examination of rat heart, and the red arrows indicated TUNEL-positive signals. The quantification of the TUNEL-positive cardiomyocytes per cm<sup>2</sup> in various treatments was shown by bar chart. Data are mean  $\pm$  SD (\*\* $p < 0.001$ ).

SMAE and ADR treatment presented normal heart histological characteristics, and no sign of cardiac fibrogenesis was detected. Furthermore, cardiomyocytes apoptosis as a consequence of ADR exposure was also evaluated, which was characterized by the presence of altered heart foci. The immunohistochemistry examination showed that they

stained positively for caspase-3. In contrast, caspase-3 signal was rarely identified in samples treated with SMAE. Meanwhile, the terminal deoxynucleotidyl transferase-mediated dUTP biotin nick end labeling (TUNEL) results showed significantly increased cell death in the ADR-applied samples compared with the control; reversely, a minor apoptotic

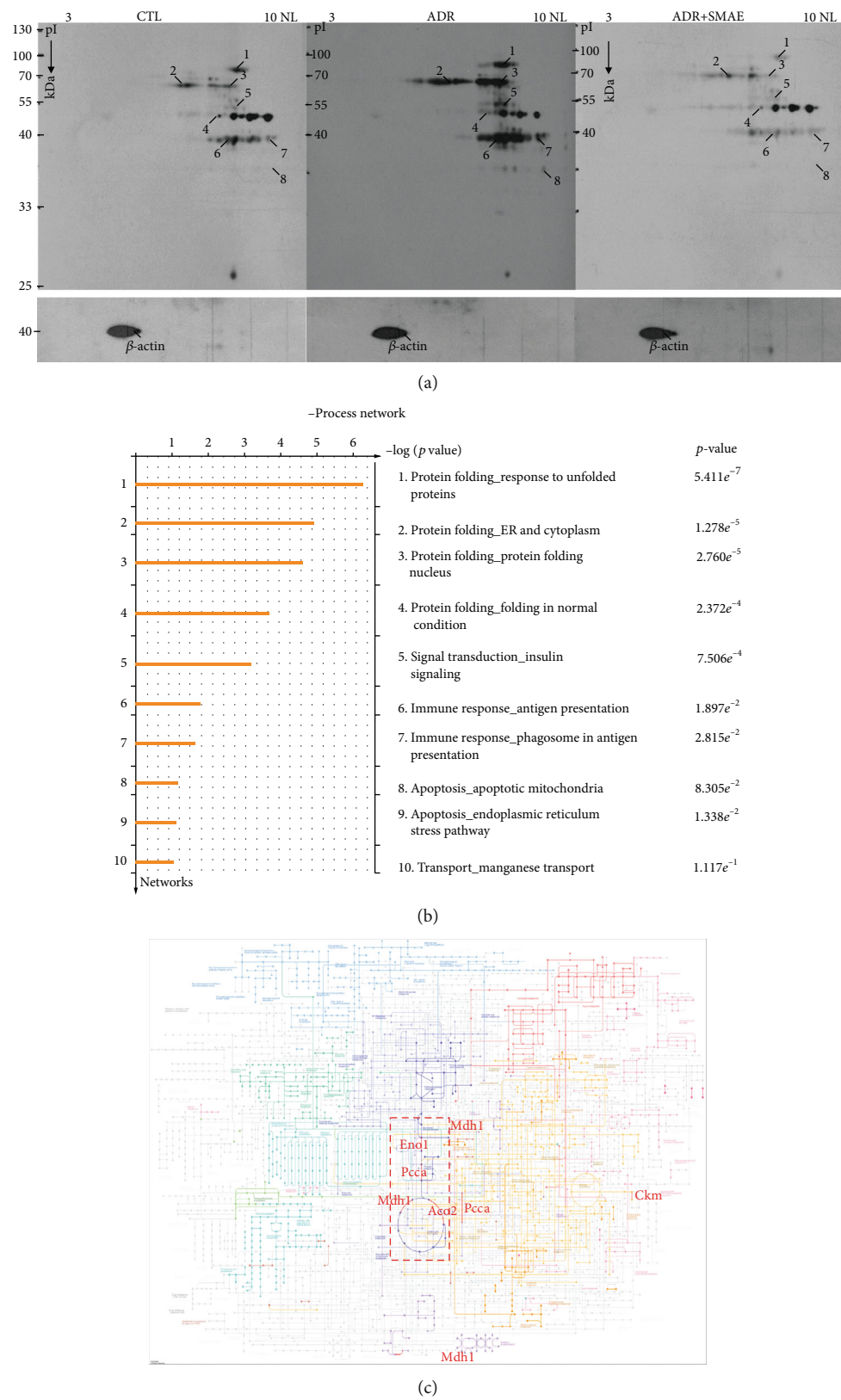


FIGURE 2: (a) Images of the 2-DE oxyblot. Analysis of protein oxidation levels in DNP-derivatized cellular proteins among the control group, ADR-treated group, and ADR+SMAE group. A significant reduction in the carbonylation levels of proteins are identified in the ADR+SMAE-applied group compared to the ADR group. (b) Top-ranked pathways from the GeneGo MetaCore™ pathway analysis. Pathways were ranked according to *p* values, and bars represent the inverse log of the *p* value. (c) The KEGG analysis indicated that several metabolisms processed in mitochondria were affected under the ADR treatments.

TABLE 1: List of identified oxidation of proteins in rat heart tissue.

Spot no.	Protein name	Accession number	Mw/pI	Score (coverage) <sup>1</sup>	Match fragment	Location	Function
1	ACON	Q9ER34	86.121/7.87	175 (37%)	23	Mitochondrion	Catalyzes the isomerization of citrate to isocitrate via cis-aconitate.
2	GRP75	P48721	74.097/5.97	189 (49%)	24	Mitochondrion	May play a role in the control of cell proliferation and cellular aging.
3	PCCA	P14882	82.198/7.59	113 (32%)	16	Mitochondrion matrix	This is one of the 2 subunits of the biotin-dependent propionyl-CoA carboxylase (PCC), a mitochondrial enzyme involved in the catabolism of odd chain fatty acids, branched-chain amino acids isoleucine, threonine, methionine, and valine and other metabolites.
4	ENOA	P04764	47.440/6.16	171 (54%)	18	Cytoplasm or cell membrane.	Multifunctional enzyme that, as well as its role in glycolysis, plays a part in various processes such as growth control, hypoxia tolerance and allergic responses.
5	ALDH2	P11884	56.966/6.63	125 (36%)	14	Mitochondrion matrix	An aldehyde + H <sub>2</sub> O + NAD <sup>+</sup> = a carboxylate + H <sup>+</sup> + NADH
6	KCRM	P00564	43.246/6.58	78 (26%)	9	Cytoplasm.	Creatine kinase isoenzymes play a central role in energy transduction in tissues with large, fluctuating energy demands, such as skeletal muscle, heart, brain, and spermatozoa.
7	ODPA	P26284	43.883/8.49	56 (20%)	8	Mitochondrion matrix	The pyruvate dehydrogenase complex catalyzes the overall conversion of pyruvate to acetyl-CoA and CO <sub>2</sub> , and thereby links the glycolytic pathway to the tricarboxylic cycle.
8	MDHM	P04636	36.117/8.93	84 (42%)	12	Mitochondrion matrix	(S)-malate + NAD <sup>+</sup> = H <sup>+</sup> + NADH + oxaloacetate

<sup>1</sup>SwissProt 2020\_02 (562253 sequences; 202348262 residues).

signal was detected in the ADR/SMAE-treated group (Figure 1(b)), implying a strong protection of SMAE against ADR-induced cardiocytotoxicity.

**3.2. Detection of the Protein Carbonylation with 2-DE Oxyblot and Functional Network Analysis.** Oxidative modification of proteins resulting from ADR application has been implicated as one of the leading causes of cardiac cell death. Meanwhile, carbonylation of proteins due to oxidative modification has been reported to impair their normal function in various metabolic processes. In our present study, changes in oxidized proteins among different groups were delineated by 2-DE oxyblots. The extent of protein oxidation was dramatically upregulated in the ADR group with respect to the control sample. Interestingly, there was a remarkably decreasing tendency for the protein carbonylation in the ADR/SMAE group, indicating that SMAE could effectively scavenge ROS induced by ADR (Figure 2(a)). The protein spots with significant and meaningful changes were indicated by Arabic numerals and were subjected to a PMF analysis after using MALDI-TOF mass spectrometry. Table 1 summarizes the detailed results obtained after using the MASCOT database searching. The individual carbonylated proteins separated by 2-DE analysis were normalized according to the intensity of the proteins. The eight targeted proteins which were uncovered by 2-DE oxyblot analysis were further dissected

with the MetaCore™ software to elucidate the intracellular events and the mechanisms associated with ADR-related heart injury. The biological networks were built based on the uploaded proteins, and the biological process was appointed to each network as shown in Figure 2(b). The specific interaction pathways showed that differentially expressed proteins under the influence of ADR and SMAE administration were majorly involved in the following cellular pathways: protein folding response to unfolded proteins ( $p = 5.411 \times 10^{-7}$ ), protein folding in ER and cytoplasm ( $p = 1.278 \times 10^{-5}$ ), and apoptosis in mitochondria ( $p = 8.305 \times 10^{-2}$ ). The  $p$  value demonstrates the significance of the assigned GO process on the basis of assembly size as compared with the subnetworks derived from the input protein list. According to the KEGG pathway analysis, glyoxylate and dicarboxylate metabolism, TCA cycle, pyruvate metabolism, and carbon metabolism were largely impaired due to ROS-mediated cell apoptosis and protein degradation (Figure 2(c)).

**3.3. Evaluation of Protective Effect of SMAE against the Cytotoxicity Observed in ADR-Applied H9c2 Cells.** To verify the drug safety and pharmaceutical effects of SMAE in vitro, cell viability was investigated by MTT assays. At first, H9c2 cells were treated with 0~10 mg/mL SMAE for 48 h, and cell viability was not affected under 2.5 mg/mL

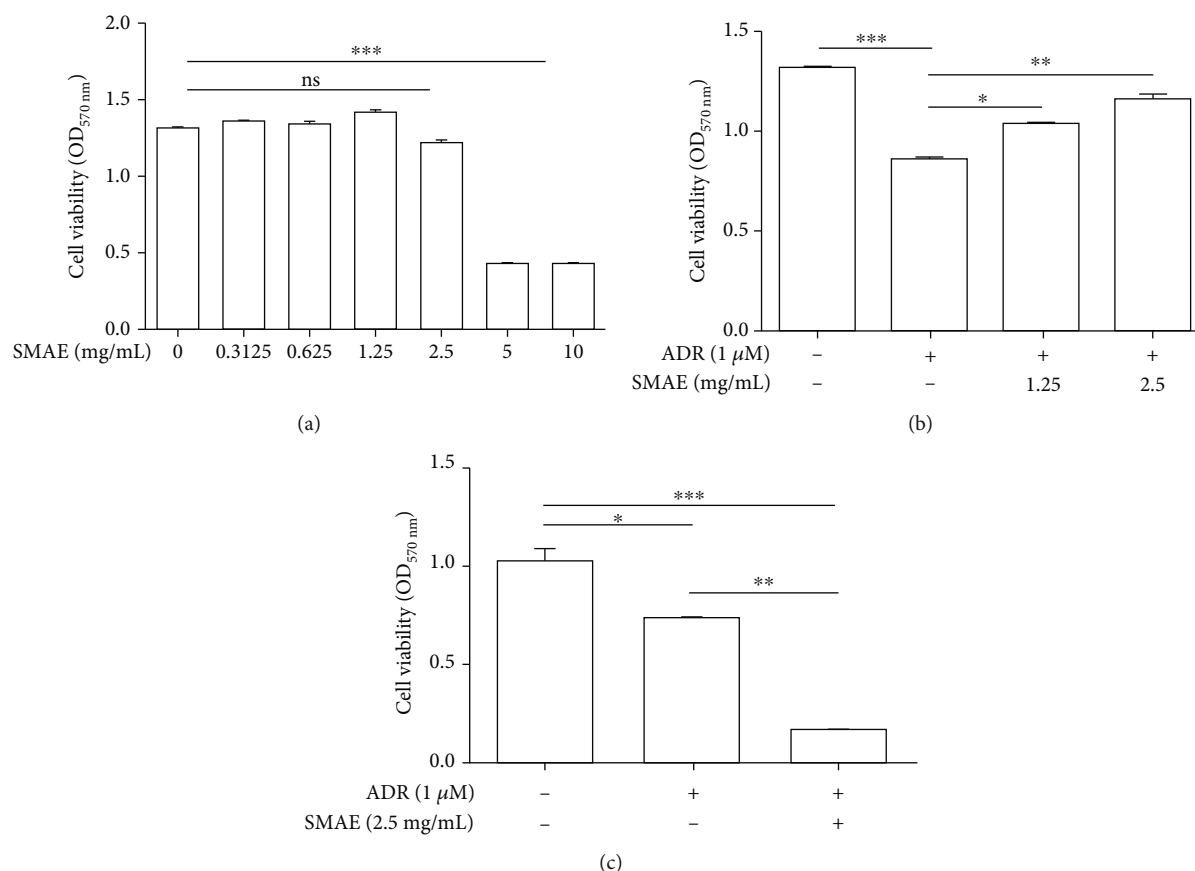


FIGURE 3: (a) Safety of SMAE extract upon H9c2 cell viability was measured by the MTT assays. H9c2 cells were treated with various concentrations of SMAE (*x*-axis). Data are mean  $\pm$  SD of three independent experiments, carried out in triplicate (ns means no significance, \*\*\* $p$  < 0.001). (b) Viability of H9c2 cell was determined with or without 1 micro M ADR under exposure to 1.25 and 2.5 mg/mL SMAE, respectively. The quantified results were indicated by the bar chart. Results represent the mean  $\pm$  SD of three independent experiments (\* $p$  < 0.05, \*\* $p$  < 0.01, \*\*\* $p$  < 0.001). (c) Synergistic effect of ADR and SMAE upon breast cancer cell (MCF-7) was determined with or without 1 micro M ADR under exposure to 2.5 mg/mL SMAE. The quantified results were indicated by the bar chart. Results represent the mean  $\pm$  SD of three independent experiments (\* $p$  < 0.05, \*\* $p$  < 0.01, \*\*\* $p$  < 0.001).

(Figure 3(a)). Next, SMAE application could effectively attenuate the cell death caused by the ADR exposure in a dose-dependent fashion (Figure 3(b)). The above response analysis highlighted that the optimal concentration of SMAE should be 2.5 mg/mL, while SMAE could effectively abolish the ADR-mediated cytotoxicity without causing any damage to cardiomyocytes.

**3.4. Detection of Synergistic Cytotoxic Activities of ADR and SMAE in Breast Cancer Cells.** The synergistic cytotoxic activities of ADR and SMAE were tested on the breast cancer cell line (MCF-7). The results demonstrated that SMAE could enhance the inhibitory effects of ADR, which was used to treat breast cancer. The findings suggested that the simultaneous administration of SMAE followed by chemotherapeutic agent treatment was better than the individual drug intervention (Figure 3(c)).

**3.5. The Effect of SMAE on Cellular ROS Production and on Antioxidant Enzymes.** Since ADR application creates an excessive amount of ROS, oxidative modification of biological molecules such as DNA and protein in the cytosol might

induce consecutive apoptosis. Dichlorofluorescein (DCF) fluorescent intensity (Figure 4(a)) showed that ADR treatment promoted intracellular ROS production within 6 hours compared with the control group while treatment with 2.5 mg/mL SMAE could largely reduce the oxidative stress. We also assessed the content of oxidative stress markers, including catalase and superoxide dismutase (SOD) in the H9c2 cells. Again, treatment conducted with SMAE could significantly promote the catalase and SOD content compared with the control group as well as with the ADR-exposed subjects, thus protecting the liver against ROS damage (Figure 4(b)). To further elucidate the molecular mechanism related to the regulation of the antioxidant enzymes, Nrf2 and HO-1 which act as the predominant contributors for the activation of the antioxidant system were determined by western blot analysis. In line with this result, ADR exposure remarkably suppressed Nrf2 and HO-1 expression as compared to the control, while SMAE treatment synchronously stimulated the levels of Nrf2 and HO-1 in a dose-dependent manner (Figure 4(c)).  $\beta$ -Actin was used as a loading control. These findings suggest that SMAE could effectively repeal ADR-mediated ROS generation.



**3.6. SMAE Modulates the Molecular Pathways of Apoptosis Induced by ADR.** To further address the signaling events underlying the apoptotic response of H9c2 cells after exposure to ADR with or without SMAE application, we investigated the MAPK cascades which might trigger downstream signaling such as p53 pathway associated with apoptosis induction. The peaks of phosphorylated ERK1/2 and p53 protein induction were detected at 24 hours following 1  $\mu$ M of ADR treatment compared to the control, while exposure to SMAE dramatically inhibited ERK1/2 and p53 phosphorylation which was stimulated by ADR. Total ERK1/2 and p53 content showed no significant changes over time (Figure 5(a)). In parallel with the result mentioned above, the ERK1/2 inhibitor (10  $\mu$ M U0126) moderately suppressed ERK1/2 and p53 phosphorylation, which was stimulated by ADR while administration of SMAE with U0126 significantly arrested the levels of ERK1/2 and p53 phosphorylation, which reflects that SMAE could restore the ADR-caused apoptosis via ERKs/p53 signaling transduction pathway (Figure 5(b)). The increased expression of p53 is associated with Bcl-2 family genes, which elicit the cytochrome c release, activation of caspase-9 and caspase-3, and eventually cell apoptosis. Furthermore, we demonstrated that the pretreatment of SMAE with or without U0126 significantly induced the Bcl-xL/Bax ratio, which was negatively accompanied by cytochrome c release into the cytoplasm and coordinately inhibited the cell apoptosis (Figure 5(c)). In line with our findings, we measured the signaling marker proteins, caspase-3, and PARP by western blot analysis. Active forms of caspase-3 and cleaved PARP (89 kDa) were increased under the treatment of ADR, whereas the application of SMAE with or without U0126 almost completely blocked the activation of these apoptotic proteins as shown in Figure 5(d). As expected, we demonstrated that SMAE combined with or without the pan-caspase inhibitors (z-VAD-FMK) could also effectively attenuate ADR-induced apoptosis associated with a cleavage of PARP (Figure 5(e)). These results showed that the antiapoptotic effect of SMAE may be involved in modulating p53 signaling and Bcl-xL through ERK-dependent pathways. According to the abovementioned findings, a pan-caspase inhibitor could not entirely arrest ADR-induced cell death, which was manifested by cleavage of PARP. It raised the possibility that SMAE could attenuate the cardiomyotoxicity through another pathway such as the cathepsin B/apoptosis-inducing factor- (AIF-) dependent event. Western blotting results showed that ADR treatment stimulated the level of cathepsin B but significantly suppressed AIF while SMAE strongly inhibiting the expression of cathepsin B, and a corresponding increase in the levels of AIF was observed (Figure 5(f)).

## 4. Discussion

Adriamycin (ADR) is a well-established and highly effective antineoplastic agent used to treat several cancers such as breast cancer and leukemia. The clinical application of ADR has been hindered as it has caused various cardiac disorders characterized by a broad spectrum of symptoms [16, 28]. It has been reported that approximately 10% of patients

exposed to ADR or its derivatives will develop cardiac complications after the cessation of chemotherapy. In this regard, the herbal medicine which has been widely used for heart protection or treatment of cancers may serve as a promising cardioprotective strategy against ADR-elicited cardiomyopathy [9, 29, 30]. Here, we have revealed the protective function and underlying molecular mechanisms of SMAE against ADR-induced cardiotoxicity *in vivo* and *in vitro*.

The *in vivo* results represented that ADR exposure initiates cardiomyopathy and stimulates specific genes involved in the apoptotic process such as the caspase-3 signaling pathway, which was verified by the reduction of cell growth under ADR treatment. SMAE exposure could ameliorate heart fibrogenesis and restore the cell survival via eliminating the expression of caspase-3 without causing any cytotoxicity to cardiomyocytes. Most importantly, SMAE utilization does not affect the efficacy of anticancer drugs but strongly suppresses the viability of cancer cells to exhibit a synergistic effect.

Growing evidence shows that ROS plays a critical role in ADR-mediated cardiocytotoxicity and the accumulation of ROS in mitochondria will finally result in cell apoptosis and will have an impact on cellular metabolism [31]. Hence, the inhibition or removal of ROS may be utilized for alleviating the heart injury caused by the ADR treatment. Particularly, SMAE comprises of several bioactive components including salvianolic acids (A and B), caffeic acid, 3,4-dihydroxyphenyl lactic acid (danshensu), and tanshinone and is confirmed to have antioxidant, anti-inflammatory, and anticancer effects [13, 32, 33]. The results have demonstrated that SMAE administration significantly restricted the production of carbonylated protein and oxidative stress induced by ADR application as shown in 2-DE oxyblot and DCF analysis. It has also been demonstrated that SMAE could induce Nrf2, which activates the Nrf2 –ARE pathway to stimulate the expression of multiple antioxidant enzymes such as HO-1. Accordingly, SMAE can prevent oxidative damage by elevating the levels of SOD and catalase in the ADR-exposed H9c2 cells. Taken together, these results imply that SMAE at least partially attenuated ADR-induced cardiomyopathy via regulating the protein carbonylation as well as the antioxidant system to relieve the ROS-mediated apoptosis.

The most striking feature observed in 2-DE oxyblot analysis is that lots of mitochondrial proteins showed significant and meaningful changes in redox state under different treatments modality. It is well-established that biomolecule oxidation is closely linked to a series of pathological events; the accumulation of redox-dependent posttranslational modification of certain key proteins would lead to ER stress and subsequent activation of the mitochondrial apoptotic pathway. The heart is one of the highest ATP-consuming organs and most of ATP is generated by the mitochondria through primarily oxidative phosphorylation [34–38]. Furthermore, network analysis has suggested that ADR-caused heart damage is majorly caused by impaired protein folding due to oxidative stress and mitochondrial dysfunction. Intertwined with this, the specific proteins including ACON, GRP75, PCCA, ENOA, KCRM, ODP, and MDHC which are mostly associated with critical metabolic processes in



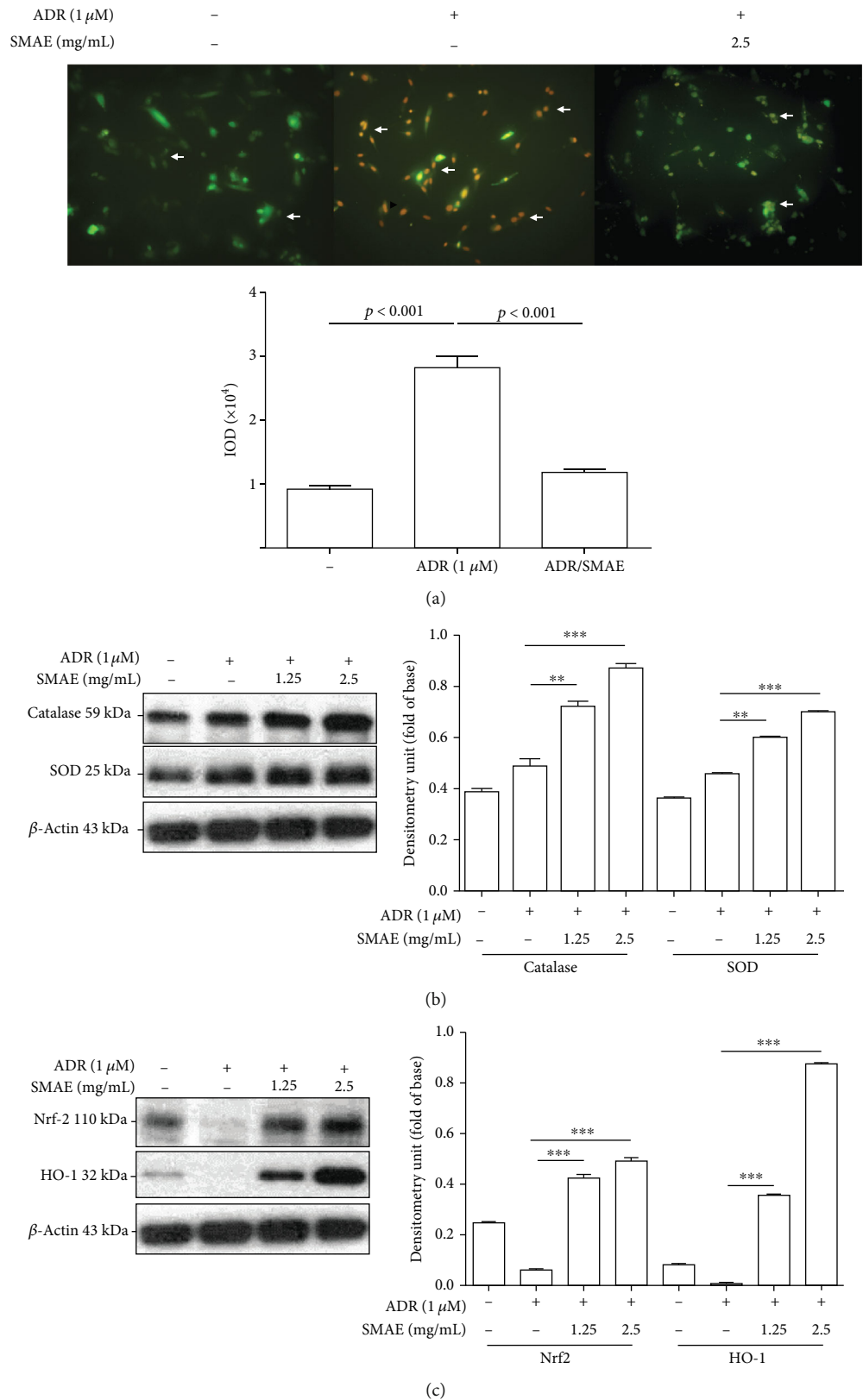


FIGURE 4: (a) H9c2 cells were incubated with or without 1 micro M ADR and 2.5 mg/mL SMAE. The DCF fluorescence signal was observed under a fluorescence microscope and demonstrated by arrows. (b) Validation of changes in protein expression after different treatments. Protein levels of catalase and SOD were determined by a Western blot analysis. (c) The expression of Nrf2 and HO-1 was evaluated with Western blot analysis.  $\beta$ -Actin was used as an internal control. The quantified results were indicated by the bar chart and represent the mean  $\pm$  SD of three independent experiments. (\*\* $p < 0.01$ , \*\*\* $p < 0.001$ ).

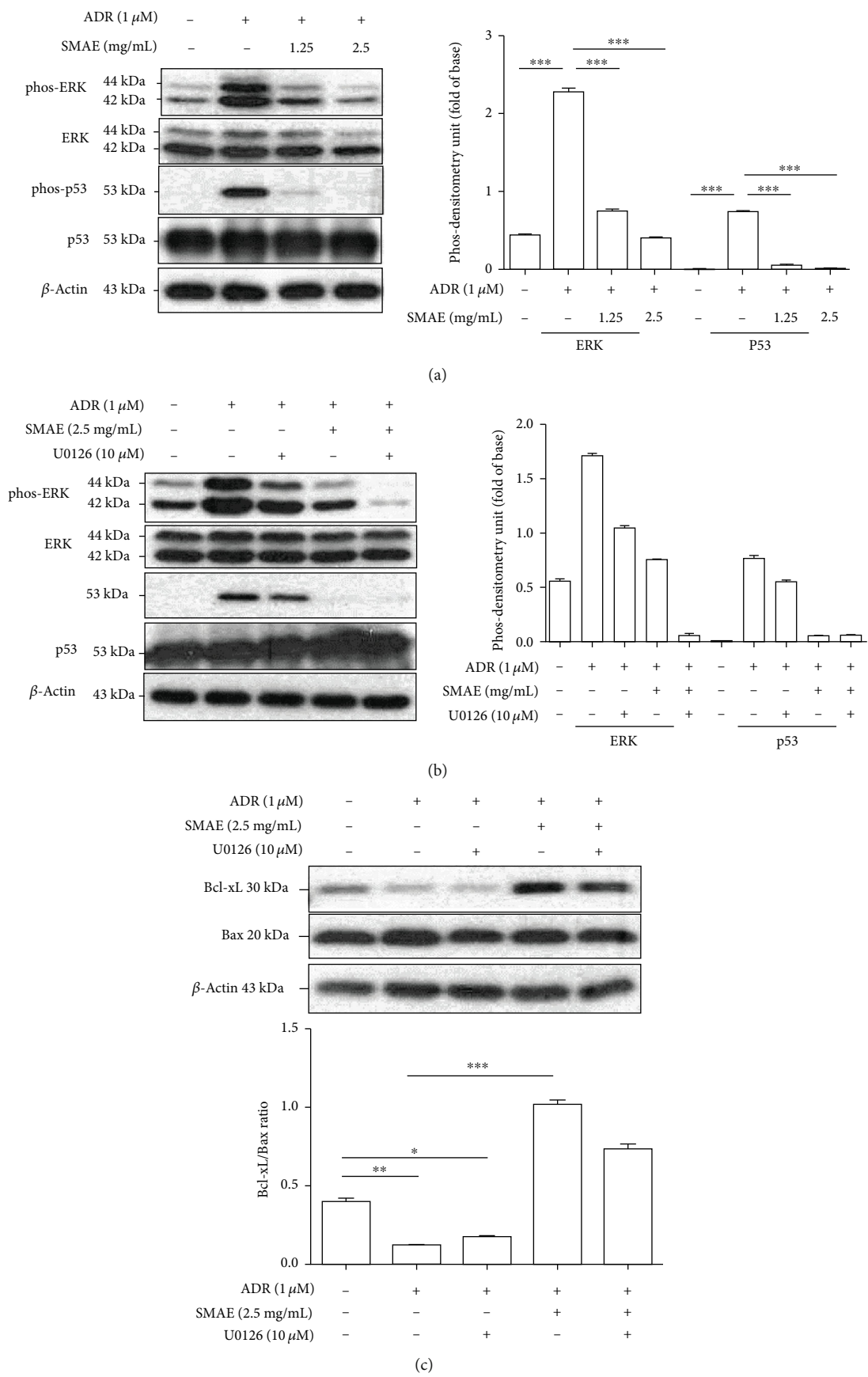


FIGURE 5: Continued.

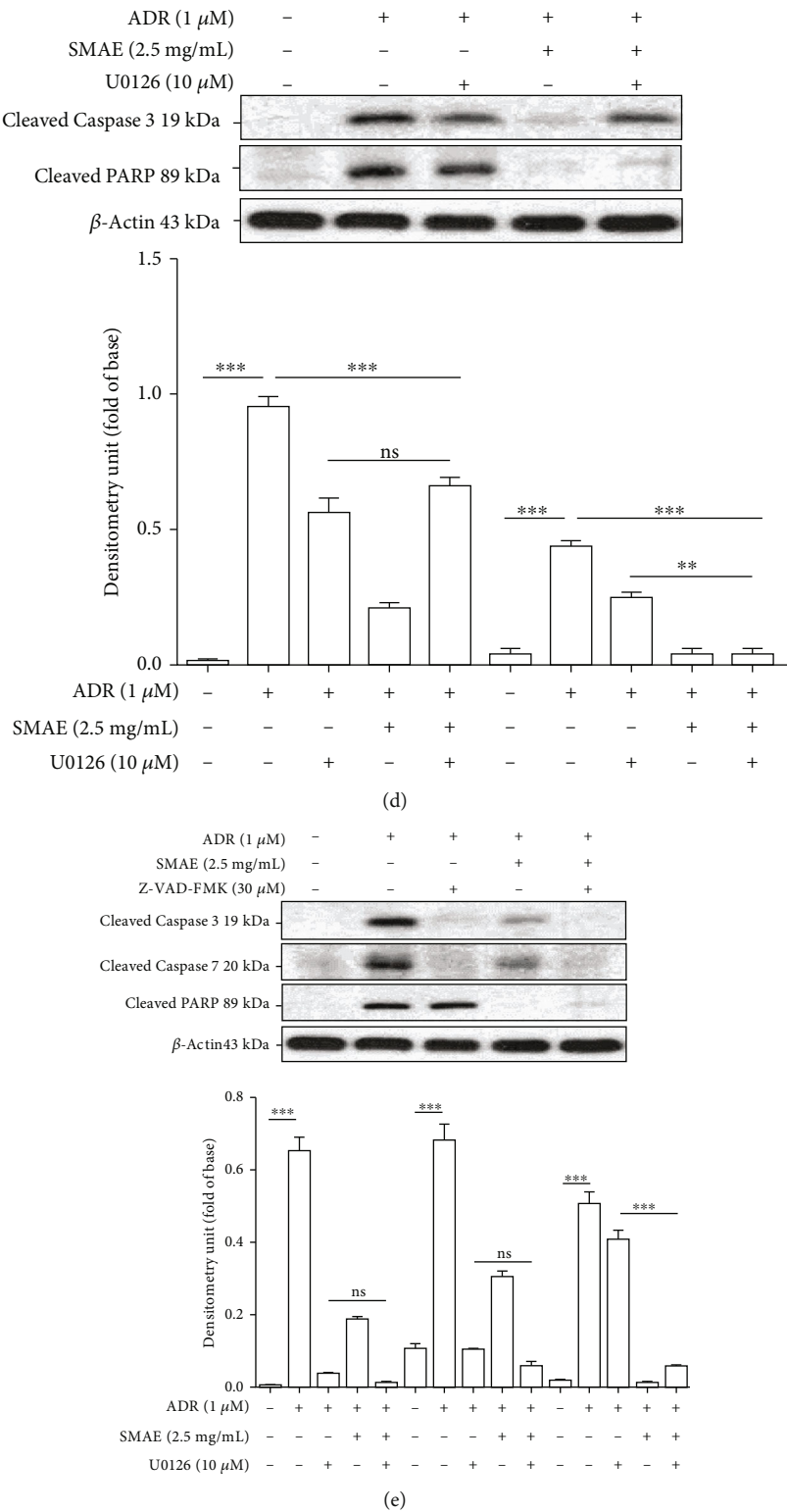


FIGURE 5: Continued.

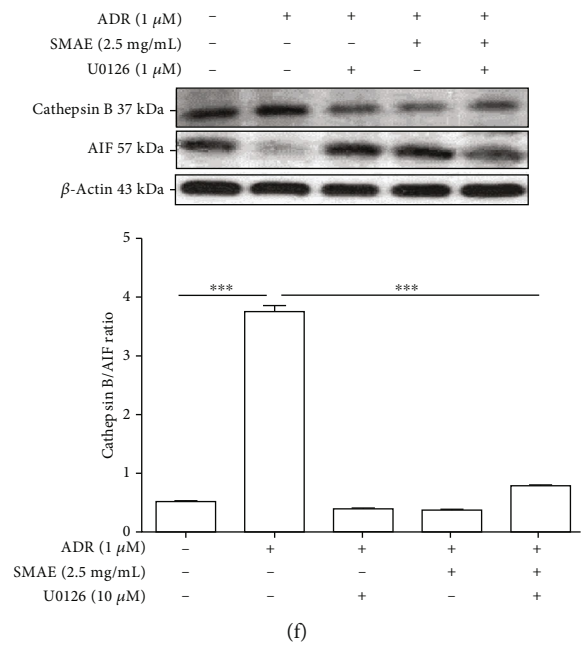


FIGURE 5: (a) Western blot analysis for phosphorylation and total protein levels of ERK1/2 and p53 with different treatments. The phosphorylation levels of ERK1/2 and p53 were normalized by total protein levels. Results represent the mean  $\pm$  SD of three independent experiments ( $***p < 0.001$ ). GAPDH was applied as the loading control. (b) Cells were preincubated with or without U0126 for 0.5 h and then treated with or without ADR and SMAE for 24 h. The phosphorylation levels of ERK1/2 and p53 were normalized by total protein levels.  $\beta$ -Actin was used as an internal control. Results represent the mean  $\pm$  SD of three independent experiments. (c) The protein levels of Bcl-xL and Bax with or without treatments of U0126, ADR, and SMAE were determined by western blotting assays. Density ratio of Bcl-xL over Bax was measured by densitometer, and  $\beta$ -actin was used as an internal control. The quantified results were indicated by the bar chart. (d) Cleavage of caspase-3 and PARP with or without treatments of U0126, ADR, and SMAE was determined by western blotting assays.  $\beta$ -actin was used as an internal control. The quantified results were indicated by the bar chart. (e) Cleavage of caspase-3 and PARP with or without treatments of Z-VAD-FMK (30  $\mu$ M), ADR, and SMAE was determined by western blotting assays.  $\beta$ -Actin was used as an internal control. The quantified results were indicated by the bar chart. (f) SMAE efficacy on protection against ADR induced cathepsin B/AIF-mediated apoptosis. The quantified results were indicated by the bar chart. Results represent the mean  $\pm$  SD of three independent experiments ( $***p < 0.001$ ).

mitochondria are highly oxidatively modified under ADR application, leading to cardiomyopathy, whereas SMAE treatment could remarkably abolish the oxidative stress via promoting the antioxidant capacity and therefore maintaining the normal physiological function of cardiomyocytes. These findings clearly explain that the heart is the most vulnerable organ which is greatly impacted by ADR application. Of these proteins, aconitase (ACON) that is considered as a biomarker for oxidative stress and serves as an intramitochondrial sensor of redox status participates in the tricarboxylic acid (TCA) cycle [39]. Previous reports have indicated that the decrease in ACON activity is related to specific disorders [40]. In our study, ACON was seen to be highly carbonylated after ADR treatment and caused functional impairment, whereas oxidative modification was reversed under the SAME administration, suggesting its involvement and protective role in the management of ADR-induced toxicity occurring in cardiac mitochondria. Similarly, the PCCA protein is responsible for the formation of carboxybiotin upon the hydrolysis of ATP in the TCA cycle [41]. Enzyme function was impacted by oxidative modification caused by ADR while SMAE exposure attenuated the degree of carbonylation of PCCA to retain normal characteristics. Pyruvate dehydrogenase complex (ODPA) irre-

versibly decarboxylates pyruvate to acetyl coenzyme A, thereby linking glycolysis to the TCA cycle and defining a critical step in cellular bioenergetics [42]. It was noticed that ADR elicited ROS, which resulted in protein damage via carbonylation, which ultimately caused an obstacle for energy production in mitochondria. In accordance with the network analysis result, it was evident that the ADR application would interfere with particular metabolic pathways which are crucial to maintain heart functions including glyoxylate metabolism, TCA cycle, and pyruvate metabolic process. Moreover, the most oxidizable proteins are largely linked to these metabolisms. The glucose-regulated protein 75 (GRP75), belongs to the family of chaperone protein, is particularly sensitive to oxidative stress, and reduces the toxicity by oxidation itself [43]. Current evidences have indicated that the oxidation of specific chaperons could induce the apoptosis in cells to offer a checkpoint after oxidative injury. Herein, much less carbonylated GRP75 presents the possible roles of SMAE treatment in the preventive effect against ROS-mediated damage to the cardiomyocytes. In summary, increases in the production of ROS due to ADR application are significantly greater than those that can be neutralized by intracellular antioxidant defenses and result in the generation of huge oxidative stress, finally leading to apoptosis of

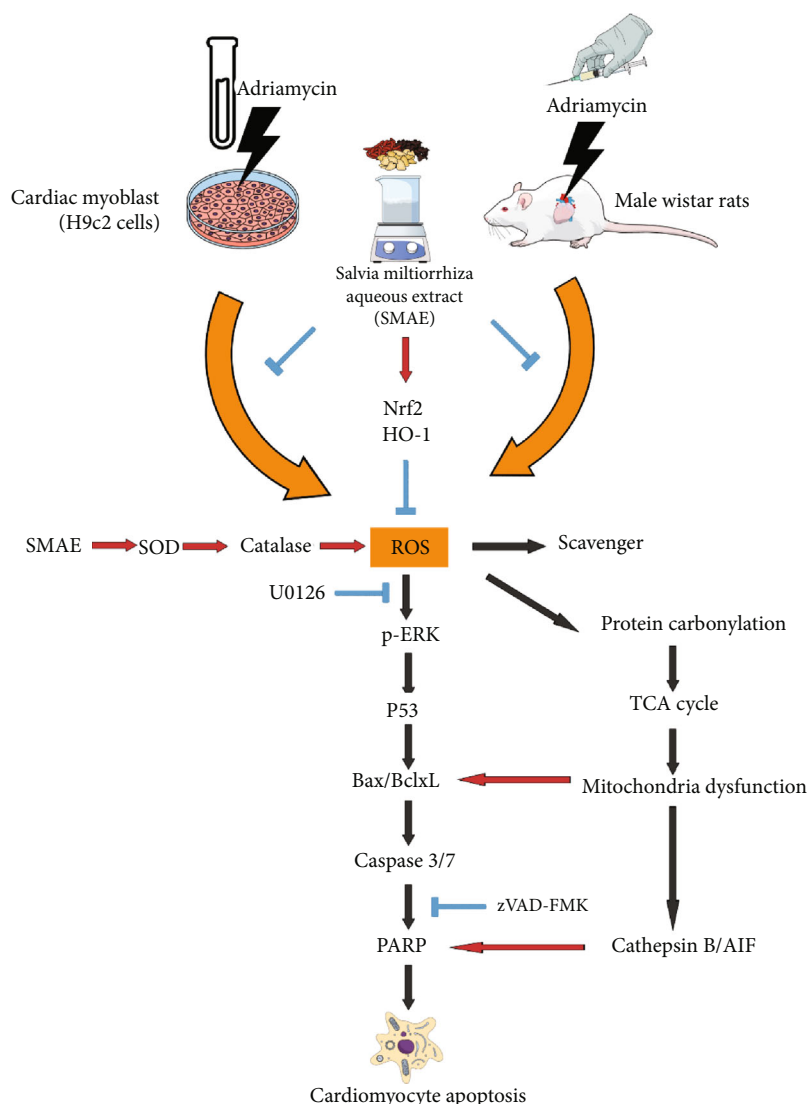


FIGURE 6: Schematic diagram of ADR-mediated cardiomyopathy through suppression of antioxidant enzymes and inducing oxidative modification of specific proteins involved in mitochondria metabolism. SMAE application could protect the heart cells against ADR damage via enhancement of antioxidant system as well as inhibition of ERK/p53- and cathepsin B/AIF-mediated apoptotic cascades.

cardiomyocytes. Of the various oxidative injuries, protein carbonylation has been considered as a potential mechanism involved in mitochondrial dysfunction, metabolic defects, and the exact contribution of carbonylation-induced dysfunction of these proteins to overall heart deficit.

Moreover, the ERK signaling pathways are proposed to be involved in NF- $\kappa$ B transactivation during oxidative stress in myoblasts [44]. As indicated in the previous investigation, ERK phosphorylation may contribute to the initiation of p53-dependent mechanisms, which stimulate the levels of the proapoptotic Bax protein and inhibit bcl-2 expression [45]. In the current study, ERK activation followed by p53 phosphorylation, cleavage of caspase3/7, and PARP were also performed in the western blotting data. Particularly, individual administration of U0126 or Z-VAD-FMK could not entirely block the cleavage of PARP; nevertheless, pretreatment with SMAE as well as U0126 totally attenuated ADR-induced ERK1/2 phosphorylation, Bcl-xL/Bax ratio, and sub-

sequent activation of PARP. Similarly, cotreatment of SMAE and inhibitor Z-VAD-FMK performed the powerful ability to absolutely suppress the caspase protein activation and PARP cleavage, an irreversible step toward apoptosis. These findings suggest that SMAE could protect against the ADR-caused cardiomyocyte apoptosis via multiple mechanisms except the ERK/p53/PARP signaling pathway. Consistently, SMAE treatment could also prevent ADR-caused cell death via cathepsin B-initiated partial extrinsic apoptotic cascade accompanied by the nuclear translocation of AIF, which emphasizes the important roles of mitochondria in ADR-induced cardiotoxicity as well as the protective function of SMAE.

Overall, it is clearly seen that the SMAE administration provides protection against ADR-induced cardiotoxicity via activating antioxidant enzymes and Nrf2/HO-1 signaling cascades. The apoptosis mediated by protein carbonylation and subsequent mitochondria dysfunction is diminished by



SMAE application, while SMAE also inhibits ERK/p53 signaling pathway, which in turn downregulates the Bcl-xL/Bax protein ratio leading to cytochrome c release followed by caspase protein activation and PARP cleavage. In addition to the caspase-dependent pathway, the SMAE application could regulate the cathepsin B/AIF cascade and relieve the ADR-caused cell death (Figure 6). Our study offers an insight into the molecular mechanisms of ADR-related apoptosis taking place in cardiomyocytes and presents the potent clinical implication of herbal medicine which can be used for treating cancers along with the ADR administration, which is associated with the serious side effect of cardiotoxicity.

## Data Availability

(1) The Western blotting and gel image data used to support the findings of this study have been deposited in the database of Chinese medicine laboratory in Chang Gung University. (2) The Western blotting and gel image data used to support the findings of this study are included within the article. (3) The Western blotting and gel image data used to support the findings of this study are available from the corresponding author upon request.

## Conflicts of Interest

The authors declare no conflicts of interest.

## Authors' Contributions

Yu-Chiang Hung and Pei-Wen Wang designed the protocol and prepared the manuscript; Tung-Yi Lin, Jyh-Sheng You, and Tai-Long Pan helped in conducting the experiment; Pei-Ming Yang helped in performing the statistical analysis; Tai-Long Pan was in charge of the whole experiment and proofreading of the manuscript.

## Acknowledgments

This work was supported by a grant from the Ministry of Science and Technology for Yu-Chiang Hung (MOST108-2320-B-182-022), for Pei-Wen Wang (MOST109-2320-B-039-040), and for Tai-Long Pan (MOST108-2320-B-182-024-MY3) and Chang Gung Memorial Hospital (CMRPD1J0191, BMRP445), Taiwan.

## References

- [1] C. Carvalho, R. Santos, S. Cardoso et al., "Doxorubicin: the good, the bad and the ugly effect," *Current Medicinal Chemistry*, vol. 16, no. 25, pp. 3267–3285, 2009.
- [2] B. Kalyanaraman, "Teaching the basics of the mechanism of doxorubicin-induced cardiotoxicity: have we been barking up the wrong tree?," *Redox Biology*, vol. 29, p. 101394, 2020.
- [3] Y. Octavia, C. G. Tocchetti, K. L. Gabrielson, S. Janssens, H. J. Crijns, and A. L. Moens, "Doxorubicin-induced cardiomyopathy: from molecular mechanisms to therapeutic strategies," *Journal of Molecular and Cellular Cardiology*, vol. 52, no. 6, pp. 1213–1225, 2012.
- [4] D. Cappetta, A. De Angelis, L. Sapio et al., "Oxidative stress and cellular response to doxorubicin: a common factor in the complex milieu of anthracycline cardiotoxicity," *Oxidative Medicine and Cellular Longevity*, vol. 2017, Article ID 1521020, 13 pages, 2017.
- [5] K. Renu, V. G. Abilash, P. B. Tirupathi Pichiah, and S. Arunachalam, "Molecular mechanism of doxorubicin-induced cardiomyopathy – An update," *European Journal of Pharmacology*, vol. 818, pp. 241–253, 2018.
- [6] V. Schwach, R. H. Slaats, and R. Passier, "Human pluripotent stem cell-derived cardiomyocytes for assessment of anticancer drug-induced cardiotoxicity," *Front Cardiovasc Med.*, vol. 7, p. 50, 2020.
- [7] S. M. Swain and P. Vici, "The current and future role of dexrazoxane as a cardioprotectant in anthracycline treatment: expert panel review," *Journal of Cancer Research and Clinical Oncology*, vol. 130, no. 1, pp. 1–7, 2004.
- [8] P. Reichardt, M. D. Tabone, J. Mora, B. Morland, and R. L. Jones, "Risk-benefit of dexrazoxane for preventing anthracycline-related cardiotoxicity: re-evaluating the European labeling," *Future Oncology*, vol. 14, no. 25, pp. 2663–2676, 2018.
- [9] Z. Wang, F. Qi, Y. Cui et al., "An update on Chinese herbal medicines as adjuvant treatment of anticancer therapeutics," *Bioscience Trends*, vol. 12, no. 3, pp. 220–239, 2018.
- [10] M. Y. Tsai, W. L. Hu, C. C. Lin et al., "Prescription pattern of Chinese herbal products for heart failure in Taiwan: a population-based study," *International Journal of Cardiology*, vol. 228, pp. 90–96, 2017.
- [11] Z. M. Li, S. W. Xu, and P. Q. Liu, "Salvia miltiorrhiza Burge (Danshen): a golden herbal medicine in cardiovascular therapeutics," *Acta Pharmacologica Sinica*, vol. 39, no. 5, pp. 802–824, 2018.
- [12] J. Ren, L. Fu, S. H. Nile, J. Zhang, and G. Kai, "Salvia miltiorrhiza in treating cardiovascular diseases: a review on its pharmacological and clinical applications," *Frontiers in Pharmacology*, vol. 10, p. 753, 2019.
- [13] J. S. You, T. L. Pan, and Y. S. Lee, "Protective effects of Danshen (Salvia Miltiorrhiza) on adriamycin-induced cardiac and hepatic toxicity in rats," *Phytotherapy Research*, vol. 21, no. 12, pp. 1146–1152, 2007.
- [14] M. Stërba, O. Popelová, A. Vávrová et al., "Oxidative stress, redox signaling, and metal chelation in anthracycline cardiotoxicity and pharmacological cardioprotection," *Antioxidants & Redox Signaling*, vol. 18, no. 8, pp. 899–929, 2013.
- [15] M. Songbo, H. Lang, C. Xinyong, X. Bin, Z. Ping, and S. Liang, "Oxidative stress injury in doxorubicin-induced cardiotoxicity," *Toxicology Letters*, vol. 307, pp. 41–48, 2019.
- [16] N. Wenningmann, M. Knapp, A. Ande, T. R. Vaidya, and S. Ait-Oudhia, "Insights into doxorubicin-induced cardiotoxicity: molecular mechanisms, preventive strategies, and early monitoring," *Molecular Pharmacology*, vol. 96, no. 2, pp. 219–232, 2019.
- [17] C. Lennicke, J. Rahn, N. Heimer, R. Lichtenfels, L. A. Wessjohann, and B. Seliger, "Redox proteomics: methods for the identification and enrichment of redox-modified proteins and their applications," *Proteomics*, vol. 16, no. 2, pp. 197–213, 2016.
- [18] G. Colombo, M. L. Garavaglia, E. Astori et al., "Protein carbonylation in human bronchial epithelial cells exposed to cigarette smoke extract," *Cell Biology and Toxicology*, vol. 35, no. 4, pp. 345–360, 2019.

- [19] P. W. Wang, Y. C. Cheng, Y. C. Hung et al., "Red raspberry extract protects the skin against UVB-induced damage with antioxidative and anti-inflammatory properties," *Oxidative Medicine and Cellular Longevity*, vol. 2019, Article ID 9529676, 14 pages, 2019.
- [20] K. Liu, J. W. Zhang, X. G. Liu et al., "Correlation between macroscopic characteristics and tissue-specific chemical profiling of the root of *Salvia miltiorrhiza*," *Phytomedicine*, vol. 51, pp. 104–111, 2018.
- [21] T. Nakahara, T. Tanimoto, A. D. Petrov, K. Ishikawa, H. W. Strauss, and J. Narula, "Rat model of cardiotoxic drug-induced cardiomyopathy," *Methods in Molecular Biology*, vol. 1816, pp. 221–232, 2018.
- [22] T. L. Pan, T. H. Wu, P. W. Wang et al., "Functional proteomics reveals the protective effects of saffron ethanolic extract on hepatic ischemia-reperfusion injury," *Proteomics*, vol. 13, no. 15, pp. 2297–2311, 2013.
- [23] J. Y. Fang, P. W. Wang, C. H. Huang, M. H. Chen, Y. R. Wu, and T. L. Pan, "Skin aging caused by intrinsic or extrinsic processes characterized with functional proteomics," *Proteomics*, vol. 16, no. 20, pp. 2718–2731, 2016.
- [24] P. W. Wang, T. Y. Lin, Y. C. Hung et al., "Characterization of fibrinogen as a key modulator in patients with Wilson's diseases with functional proteomic tools," *International Journal of Molecular Sciences*, vol. 20, no. 18, p. 4528, 2019.
- [25] T. L. Pan, P. W. Wang, C. C. Huang, C. T. Yeh, T. H. Hu, and J. S. Yu, "Network analysis and proteomic identification of vimentin as a key regulator associated with invasion and metastasis in human hepatocellular carcinoma cells," *Journal of Proteomics*, vol. 75, no. 15, pp. 4676–4692, 2012.
- [26] T. L. Pan, P. W. Wang, Y. L. Leu, T. H. Wu, and T. S. Wu, "Inhibitory effects of *Scutellaria baicalensis* extract on hepatic stellate cells through inducing G2/M cell cycle arrest and activating ERK-dependent apoptosis via Bax and caspase pathway," *Journal of Ethnopharmacology*, vol. 139, no. 3, pp. 829–837, 2012.
- [27] P. W. Wang, Y. C. Hung, T. Y. Lin et al., "Comparison of the biological impact of UVA and UVB upon the skin with functional proteomics and immunohistochemistry," *Antioxidants*, vol. 8, no. 12, p. 569, 2019.
- [28] J. V. McGowan, R. Chung, A. Maulik, I. Piotrowska, J. M. Walker, and D. M. Yellon, "Anthracycline chemotherapy and cardiotoxicity," *Cardiovascular Drugs and Therapy*, vol. 31, no. 1, pp. 63–75, 2017.
- [29] A. Hosseini and A. Sahebkar, "Reversal of doxorubicin-induced cardiotoxicity by using phytotherapy: a review," *J Pharmacopuncture*, vol. 20, no. 4, pp. 243–256, 2017.
- [30] C. H. Huang, H. P. Chang, S. Y. Su et al., "Traditional Chinese medicine is associated with a decreased risk of heart failure in breast cancer patients receiving doxorubicin treatment," *Journal of Ethnopharmacology*, vol. 229, pp. 15–21, 2019.
- [31] J. M. Berthiaume and K. B. Wallace, "Adriamycin-induced oxidative mitochondrial cardiotoxicity," *Cell Biology and Toxicology*, vol. 23, no. 1, pp. 15–25, 2007.
- [32] L. Wang, X. Zhang, J. Y.-W. Chan et al., "A novel danshensu derivative prevents cardiac dysfunction and improves the chemotherapeutic efficacy of doxorubicin in breast cancer cells," *Journal of Cellular Biochemistry*, vol. 117, no. 1, pp. 94–105, 2016.
- [33] Y. S. Lin, Y. C. Shen, C. Y. Wu et al., "Danshen improves survival of patients with breast cancer and dihydroisotanshinone I induces ferroptosis and apoptosis of breast cancer cells," *Frontiers in Pharmacology*, vol. 10, p. 1226, 2019.
- [34] F. S. Carvalho, A. Burgeiro, R. Garcia, A. J. Moreno, R. A. Carvalho, and P. J. Oliveira, "Doxorubicin-induced cardiotoxicity: from bioenergetic failure and cell death to cardiomyopathy," *Medicinal Research Reviews*, vol. 34, no. 1, pp. 106–135, 2014.
- [35] Z. V. Varga, P. Ferdinandy, L. Liaudet, and P. Pacher, "Drug-induced mitochondrial dysfunction and cardiotoxicity," *American Journal of Physiology. Heart and Circulatory Physiology*, vol. 309, no. 9, pp. H1453–H1467, 2015.
- [36] A. T. Akhmedov, V. Rybin, and J. Marín-García, "Mitochondrial oxidative metabolism and uncoupling proteins in the failing heart," *Heart Failure Reviews*, vol. 20, no. 2, pp. 227–249, 2015.
- [37] F. L. Sheeran and S. Pepe, "Mitochondrial bioenergetics and dysfunction in failing heart," *Advances in Experimental Medicine and Biology*, vol. 982, pp. 65–80, 2017.
- [38] S. Ichihara, Y. Suzuki, J. Chang et al., "Involvement of oxidative modification of proteins related to ATP synthesis in the left ventricles of hamsters with cardiomyopathy," *Scientific Reports*, vol. 7, no. 1, p. 9243, 2017.
- [39] O. V. Lushchak, M. Piroddi, F. Galli, and V. I. Lushchak, "Aconitase post-translational modification as a key in linkage between Krebs cycle, iron homeostasis, redox signaling, and metabolism of reactive oxygen species," *Redox Report*, vol. 19, no. 1, pp. 8–15, 2013.
- [40] J. Talib and M. J. Davies, "Exposure of aconitase to smoking-related oxidants results in iron loss and increased iron response protein-1 activity: potential mechanisms for iron accumulation in human arterial cells," *Journal of Biological Inorganic Chemistry*, vol. 21, no. 3, pp. 305–317, 2016.
- [41] P. Wongkittichote, N. Ah Mew, and K. A. Chapman, "Propionyl-CoA carboxylase - a review," *Molecular Genetics and Metabolism*, vol. 122, no. 4, pp. 145–152, 2017.
- [42] W. Sun, Q. Liu, J. Leng, Y. Zheng, and J. Li, "The role of pyruvate dehydrogenase complex in cardiovascular diseases," *Life Sciences*, vol. 121, pp. 97–103, 2015.
- [43] Y. C. Hung, P. W. Wang, T. L. Pan, G. Bazylak, and Y. L. Leu, "Proteomic screening of antioxidant effects exhibited by radix *Salvia miltiorrhiza* aqueous extract in cultured rat aortic smooth muscle cells under homocysteine treatment," *Journal of Ethnopharmacology*, vol. 124, no. 3, pp. 463–474, 2009.
- [44] G. Abdelhamid and A. O. S. El-Kadi, "Buthionine sulfoximine, an inhibitor of glutathione biosynthesis, induces expression of soluble epoxide hydrolase and markers of cellular hypertrophy in a rat cardiomyoblast cell line: roles of the NF- $\kappa$ B and MAPK signaling pathways," *Free Radical Biology & Medicine*, vol. 82, pp. 1–12, 2015.
- [45] J. Liu, W. Mao, B. Ding, and C. S. Liang, "ERKs/p 53 signal transduction pathway is involved in doxorubicin-induced apoptosis in H9c2 cells and cardiomyocytes," *American Journal of Physiology. Heart and Circulatory Physiology*, vol. 295, no. 5, pp. H1956–H1965, 2008.



Contents lists available at ScienceDirect

## Bioorganic Chemistry

journal homepage: [www.elsevier.com/locate/bioorg](http://www.elsevier.com/locate/bioorg)

# Antiinflammatory triterpenoids from the fruiting bodies of *Fomitopsis pinicola*

Ping-Chung Kuo<sup>a,1</sup>, Shih-Huang Tai<sup>b,1</sup>, Ching-Che Hung<sup>c</sup>, Tsong-Long Hwang<sup>d,e,f</sup>,  
Liang-Mou Kuo<sup>g,h</sup>, Sio Hong Lam<sup>a</sup>, Kun-Ching Cheng<sup>i</sup>, Daih-Huang Kuo<sup>j</sup>, Hsin-Yi Hung<sup>a,\*</sup>,  
Tian-Shung Wu<sup>a,j,\*</sup>

<sup>a</sup> School of Pharmacy, College of Medicine, National Cheng Kung University, Tainan 70101, Taiwan

<sup>b</sup> Departments of Surgery and Anesthesiology, and Institute of Biomedical Engineering, National Cheng Kung University, Medical Center and Medical School, Tainan 701, Taiwan

<sup>c</sup> Department of Chemistry, National Cheng Kung University, Tainan 70101, Taiwan

<sup>d</sup> Graduate Institute of Natural Products, College of Medicine, Chinese Herbal Medicine Research Team, Healthy Aging Research Center, Chang Gung University, Taoyuan 333, Taiwan

<sup>e</sup> Department of Anesthesiology, Chang Gung Memorial Hospital, Taoyuan 333, Taiwan

<sup>f</sup> Research Center for Chinese Herbal Medicine, Research Center for Industry of Human Ecology, Graduate Institute of Health Industry Technology, College of Human Ecology, Chang Gung University of Science and Technology, Taoyuan 333, Taiwan

<sup>g</sup> Department of General Surgery, Chang Gung Memorial Hospital at Chia-Yi, 613, Taiwan

<sup>h</sup> School of Medicine, College of Medicine, Chang Gung University, Taoyuan 333, Taiwan

<sup>i</sup> Taiwan Sugar Research Institute, Tainan 70176, Taiwan

<sup>j</sup> Department of Pharmacy, College of Pharmacy and Health Care, Tajen University, Pingtung 907, Taiwan

## ARTICLE INFO

## Keywords:

*Fomitopsis pinicola*

Fomitopsidaceae

Triterpenoid

Antiinflammatory

## ABSTRACT

Twelve undescribed lanostane-type triterpenes, and twenty-two known triterpenes were isolated and identified from a medicinal bracket fungus *Fomitopsis pinicola* (Sw.) P. Karst. The structures of these compounds were determined by spectroscopic and spectrometric analyses. The antiinflammatory potential of thirty-two triterpene compounds was evaluated using neutrophils as an assay model, and pinicolasin J was the most potent inhibitor of superoxide anion generation and elastase release, with IC<sub>50</sub> values of 1.81 ± 0.44 and 2.50 ± 0.64 μM, respectively. This study provides scientific insight into the nutritional supplement value and medicinal development of *Fomitopsis pinicola*.

## 1. Introduction

*Fomitopsis pinicola* (Sw.) P. Karst (Fomitopsidaceae), widely distributed in East Asia and Central Europe, is a type of red-banded polypore growing on decaying logs including *Abies* and *Betula* species [1]. *F. pinicola* was traditionally used for the treatment of headache, nausea, liver problems, hemorrhage, and inflammation [2]. Modern pharmacological studies demonstrated that the chloroform extract of *F. pinicola* possesses antitumor activities, and alkaline extracts are rich in polysaccharides with antihyperglycemic effects [3–6]. The reported principle compounds purified from *F. pinicola* were mostly classified as steroids and triterpenoids [2]. Minor compounds included diterpenoids, sesquiterpenoids, and coumarins [2]. The lanostanoid derivatives had

antimicrobial activity against *Bacillus subtilis* in a TLC bioassay [7]. Moreover, twelve glycosidic triterpenes demonstrated to have antiinflammatory activity mediated by cyclooxygenase-2 inhibition. Among them, fomitocide E had the IC<sub>50</sub> value of 0.15 μM, while clinically used NSAID indomethacin had the IC<sub>50</sub> of 0.6 μM [8]. Moreover, ergosterol identified in the chloroform extract was shown to have proapoptotic characteristics and inhibited the migration of SW-480 cells [9]. In 2019, thirty-five lanostane-type triterpenoids were evaluated their cytotoxicity against five cancer cell lines. Five most potent compounds were cytotoxic with the IC<sub>50</sub> values ranging from 3.92 to 28.51 μM [10]. Our previous study reported isolation of twelve sesquiterpenoids with herbertainoid-like structure from the titled fungi, and the most effective compound demonstrated significant inhibition of superoxide anion

\* Corresponding authors at: School of Pharmacy, College of Medicine, National Cheng Kung University, Tainan, Taiwan.

E-mail addresses: [z10308005@email.ncku.edu.tw](mailto:z10308005@email.ncku.edu.tw) (H.-Y. Hung), [tswu@mail.ncku.edu.tw](mailto:tswu@mail.ncku.edu.tw) (T.-S. Wu).

<sup>1</sup> The authors contributed equally to this work.

<https://doi.org/10.1016/j.bioorg.2020.104562>

Received 14 November 2020; Received in revised form 12 December 2020; Accepted 12 December 2020

Available online 16 December 2020

0045-2068/© 2020 Elsevier Inc. All rights reserved.



generation and elastase release with the IC<sub>50</sub> values of  $0.81 \pm 0.15$  and  $0.74 \pm 0.12$   $\mu$ M, respectively [11]. Neutrophils are important immune cells predominantly involved in innate immunity. Upon invasion of the microorganisms, acute inflammation is initiated, and reactive oxygen species (ROS) and lysosomal enzymes (e.g., elastase) are released from neutrophils to kill the microorganisms. If neutrophils persist beyond the acute inflammation phase, chronic inflammation may develop leading to various diseases [12]. Therefore, to continue the identification of antiinflammatory agents for drug discovery, we re-investigated the triterpenoids from *F. pinicola* and examined superoxide anion generation and elastase release from human neutrophils for discovering more antiinflammatory natural leads. Bioassay-guided fractionation of the ethanol extract of *F. pinicola* resulted in the identification of thirty-four triterpenoids. Among them, twelve previously undescribed triterpenoids were characterized using IR, 1D, and 2D NMR spectroscopic analyses as well as MS spectrometric data.

## 2. Material and methods

### 2.1. General experimental procedures

Optical rotations were measured using a JASCO P-2000 digital polarimeter. UV spectra were recorded at room temperature using a U-0080-D UV-Vis spectrophotometer. IR spectra were obtained with a PerkinElmer FT-IR Spectrum RX I spectrophotometer. <sup>1</sup>H and <sup>13</sup>C NMR spectra were recorded on a Bruker AV III 400 NMR spectrometer. Chemical shifts are shown in  $\delta$  values (ppm) with tetramethylsilane as an internal standard. The ESIMS and HRESIMS were recorded using a Bruker APEX II FT-MS spectrometer (positive-ion mode). ECD spectra were obtained on a JASCO J-720 spectrometer. Column chromatography (CC) was performed on silica (70–230 mesh and 230–400 mesh, Merck) and Diaion HP-20 (Mitsubishi) gels. High-performance liquid chromatography (HPLC) was performed on a Shimadzu LC-20AT series pump system equipped with a Shimadzu SPD-20A UV-Vis detector and a SIL-10AF autosampling system at ambient temperature using a RP-18 column (Ascentis C18, 5  $\mu$ m, 20 mm  $\times$  25 cm).

### 2.2. Fungus material

The fruiting bodies of *Fomitopsis pinicola* (Sw.) P. Karst (Fomitopsideaceae) were collected in July 2012 at Qilai Mountain in Hualien, Taiwan. The fungus material was identified by Prof. Jin-Bin Wu, Institute of Pharmaceutical Chemistry and Department of Pharmacy, China Medical University, Taichung, Taiwan. A voucher specimen (TSWU-20130711) was deposited in the School of Pharmacy, National Cheng Kung University, Tainan, Taiwan.

### 2.3. Extraction and isolation

The fresh fruiting bodies (13.7 kg) were cut into small pieces and refluxed with ethanol for 8 h three times by Jen Li biotech company. The ethanol was removed and evaporated in vacuo to yield 3320 g dried extract. The ethanol extract (1 kg) was subjected to column chromatography on Diaion HP-20 with a step gradient of water-methanol to give 6 fractions (FP-1 ~ FP-6). Ethanol extract (10 g) separated under the same conditions was used in the bioassay testing. Fraction FP-6 (500 g) was fractionated by silica gel chromatography (IPA-acetone = 15:1) to give 11 fractions. Fr. FP-6-2 was subjected to another silica gel chromatography eluted with hexane-acetone (15:1) to give 12 fractions. FP-6-2-10 was subjected to silica gel chromatography and eluted with hexane-acetone (3:1) to yield 7 fractions. Then, fraction FP-6-2-10-1 was further purified by semipreparative HPLC (MeOH-H<sub>2</sub>O-HCOOH = 67:33:0.1) using an Ascentis C18 column to obtain pinicolasin E (**5**, 2.6 mg), pinicolasin G (**7**, 3.1 mg), pinicolasin H (**8**, 1.9 mg), pinicolasin K (**11**, 6.9 mg), pinicolasin M (**13**, 1.8 mg), and fomipinic acid D (**18**, 16.7 mg). Fraction FP-6-2-10-2 was also purified by semipreparative HPLC

eluted with MeOH-H<sub>2</sub>O-HCOOH (77:23: 0.1) to yield pinicolasin D (**4**, 36.6 mg), pinicolasin L (**12**, 10.1 mg), fomipinic acid D (**18**, 4.5 mg), 3 $\beta$ -acetoxy-15 $\alpha$ -hydroxylanosta-8,24-dien-21-oic acid (**19**, 6.5 mg), and 3 $\alpha$ -pachimic acid (**28**, 41.0 mg). Fraction FP-6-2-10-3 was fractionated by semipreparative HPLC eluted with MeOH-H<sub>2</sub>O-HCOOH (67:33:0.1) to yield pinicolasin D (**4**, 25.2 mg), pinicolasin I (**9**, 2.9 mg), fomipinic acid C (**17**, 19.1 mg), piptolinic acid D (**24**, 17.3 mg), pachymic acid (**29**, 4.5 mg), 3-epidehydropachymic acid (**30**, 21.9 mg), polyporenic acid C (**33**, 14.8 mg), and daedaleanic acid A (**34**, 1.8 mg). Fraction FP-6-2-10-5 was further purified by semipreparative HPLC eluted with MeOH-H<sub>2</sub>O-HCOOH (80:20: 0.1) to yield 3 $\beta$ -acetyl-16 $\alpha$ -hydroxy-trametenolic acid (**20**, 3.4 mg), and polyporenic acid C (**33**, 1.7 mg).

Fraction FP-6-2-10-3 was purified by silica gel CC eluted with DCM-MeOH (69:1) to get 9 subfractions, and subfraction 5 was purified by semipreparative HPLC eluted with CH<sub>3</sub>CN-H<sub>2</sub>O-HCOOH (53:47:0.1) to yield pinicolasin B (**2**, 17.4 mg), pinicolasin C (**3**, 1.5 mg), pinicolasin F (**6**, 19.6 mg), pinicolasin J (**10**, 5.2 mg), pinicolic acid E (**21**, 20.1 mg), 16 $\alpha$ -hydroxy-3-oxolanosta-7,9(11),24-trien-21-oic acid (**22**, 26.1 mg), and polyporenic acid C (**33**, 14.8 mg). Additionally, subfraction 7 was subjected to semipreparative HPLC eluted with MeOH-H<sub>2</sub>O-HCOOH (70:30: 0.1%) to obtain pinicolasin A (**1**, 3.1 mg), 16 $\alpha$ -hydroxy-trametenolic acid (**15**, 1.9 mg), 16 $\alpha$ -hydroxy-3-oxolanosta-7,9(11),24-trien-21-oic acid (**22**, 2.1 mg), 6 $\alpha$ ,16 $\alpha$ -dihydroxy-3-oxolanosta-7,9(11),24-trien-21-oic acid (**23**, 5.5 mg), 3 $\alpha$ ,16 $\alpha$ -hydroxy-lanosta-7,9(11),24-trien-21-oic acid (**25**, 3.8 mg), tumulosic acid (**27**, 9.6 mg), 6 $\alpha$ -hydroxypolyporenic acid C (**32**, 8.9 mg), and polyporenic acid C (**33**, 14.8 mg).

#### 2.3.1. Pinicolasin A (**1**)

Colorless powder;  $[\alpha]_D^{25} + 0.4$  (c 0.07, MeOH); UV (MeOH)  $\lambda_{\max}$  (log  $\epsilon$ ) 324 (0.8), 211 (1.2) nm; ECD (MeOH) (Mol. CD) 324 (−1.2), 273 (1.6), 222 (2.4) nm; IR (KBr)  $\nu_{\max}$  3731, 2928, 2873, 1699, 1455, 1377, 1260, 1020, 756 cm<sup>−1</sup>; <sup>1</sup>H and <sup>13</sup>C NMR, see Table 1; HRESIMS  $m/z$  491.3130 ([M+Na]<sup>+</sup> calcd for C<sub>30</sub>H<sub>44</sub>O<sub>4</sub>Na, 491.3131).

#### 2.3.2. Pinicolasin B (**2**)

Colorless powder;  $[\alpha]_D^{25} - 2.3$  (c 0.1, MeOH); UV (MeOH)  $\lambda_{\max}$  (log  $\epsilon$ ) 324 (0.3), 208 (0.8) nm; ECD (MeOH) (Mol. CD) 362 (0.5), 272 (1.4), 208 (2.5) nm; IR (KBr)  $\nu_{\max}$  3378, 2963, 2873, 1731, 1715, 1567, 1415, 1248, 1031, 755 cm<sup>−1</sup>; <sup>1</sup>H and <sup>13</sup>C NMR, see Table 1; HRESIMS  $m/z$  489.2976 ([M+Na]<sup>+</sup> calcd for C<sub>30</sub>H<sub>42</sub>O<sub>4</sub>Na, 489.2975).

#### 2.3.3. Pinicolasin C (**3**)

Colorless powder;  $[\alpha]_D^{25} - 37.3$  (c 0.05, MeOH); UV (MeOH)  $\lambda_{\max}$  (log  $\epsilon$ ) 208 (0.9) nm; ECD (MeOH) (Mol. CD) 309 (−1.4), 213 (2.7) nm; IR (KBr)  $\nu_{\max}$  3518, 2928, 2851, 1731, 1616, 1434, 1379, 1028, 755 cm<sup>−1</sup>; <sup>1</sup>H and <sup>13</sup>C NMR, see Table 1; HRESIMS  $m/z$  493.3291 ([M+Na]<sup>+</sup> calcd for C<sub>30</sub>H<sub>46</sub>O<sub>4</sub>Na, 493.3288).

#### 2.3.4. Pinicolasin D (**4**)

Colorless powder;  $[\alpha]_D^{25} + 5.4$  (c 0.08, MeOH); UV (MeOH)  $\lambda_{\max}$  (log  $\epsilon$ ) 211 (1.3) nm; ECD (MeOH) (Mol. CD) 211 (1.6) nm; IR (KBr)  $\nu_{\max}$  3688, 2946, 1716, 1601, 1425, 1373, 1254, 1182, 757 cm<sup>−1</sup>; <sup>1</sup>H and <sup>13</sup>C NMR, see Table 1; HRESIMS  $m/z$  537.3551 ([M+Na]<sup>+</sup> calcd for C<sub>32</sub>H<sub>50</sub>O<sub>5</sub>Na, 537.3551).

#### 2.3.5. Pinicolasin E (**5**)

Colorless powder;  $[\alpha]_D^{25} - 24.5$  (c 0.09, MeOH); UV (MeOH)  $\lambda_{\max}$  (log  $\epsilon$ ) 210 (1.2) nm; ECD (MeOH) (Mol. CD) 307 (−3.3) nm; IR (KBr)  $\nu_{\max}$  3699, 2948, 1734, 1607, 1449, 1372, 1247, 1032, 755 cm<sup>−1</sup>; <sup>1</sup>H and <sup>13</sup>C NMR, see Table 1; HRESIMS  $m/z$  535.3395 ([M+Na]<sup>+</sup> calcd for C<sub>32</sub>H<sub>48</sub>O<sub>5</sub>Na, 535.3394).

#### 2.3.6. Pinicolasin F (**6**)

Colorless powder;  $[\alpha]_D^{25} - 2.4$  (c 0.3, MeOH); UV (MeOH)  $\lambda_{\max}$  (log  $\epsilon$ ) 208 (1.1) nm; ECD (MeOH) (Mol. CD) 222 (0.7) nm; IR (KBr)  $\nu_{\max}$

**Table 1**

<sup>1</sup>H and <sup>13</sup>C NMR Spectroscopic Data of Compounds 1–7 [ $\delta$  (multi.,  $J$  in Hz) in ppm; <sup>a</sup> <sup>1</sup>H and <sup>13</sup>C NMR data were measured in CD<sub>3</sub>OD at 400 and 100 MHz. <sup>b</sup> <sup>1</sup>H and <sup>13</sup>C NMR data were measured in CDCl<sub>3</sub> at 400 and 100 MHz]

	1 <sup>a</sup>		2 <sup>a</sup>		3 <sup>a</sup>		4 <sup>b</sup>		5 <sup>b</sup>		6 <sup>b</sup>		7 <sup>a</sup>	
position	δ <sub>C</sub>	δ <sub>H</sub>	δ <sub>C</sub>	δ <sub>H</sub>	δ <sub>C</sub>	δ <sub>H</sub>	δ <sub>C</sub>	δ <sub>H</sub>	δ <sub>C</sub>	δ <sub>H</sub>	δ <sub>C</sub>	δ <sub>H</sub>	δ <sub>C</sub>	δ <sub>H</sub>
1	36.9	2.02 (m) 1.41(br dd, 13.8, 3.6)	36.7	2.06 (m) 1.41 (m)	36.8	1.78 (dd, 12.4, 3.7) 1.25 (m)	30.8	1.40 (m)	35.1	1.72 (m) 1.32 (m)	32.1	1.51 (m)	30.4	1.72 (m) 1.64 (m)
2	28.5	1.92 (m) 1.74 (m)	28.4	1.92 (m) 1.76 (dd, 12.6, 4.0)	28.5	2.08 (m) 1.63 (dd, 8.0, 3.4) 6.2)	23.3	1.85 (m) 1.63 (d, 6.2)	24.0	1.70 (m) 1.66 (m)	24.3	1.91 (m) 1.64 (m)	23.1	1.92 (m) 1.76 (t, 3.3)
3	77.6	3.21 (dd, 11.9, 4.3)	77.6	3.23 (dd, 12.1, 4.4)	79.7	3.17 (dd, 8.2, 8.0)	77.8	4.66 (t, 2.9)	80.6	4.50 (dd, 11.6, 4.3)	79.9	4.68 (t, 2.9)	77.9	4.69 (t, 2.4)
4	42.9	–	43.0	–	40.1	–	36.7	–	37.8	–	37.9	–	36.5	–
5	153.0	–	154.1	–	51.9	1.08 (m)	51.1	1.43 (t, 2.9)	50.3	1.16 (dd, 10.4, 1.7)	46.9	1.54 (d, 13.7)	44.2	1.51 (dd, 10.0, 5.8)
6	119.7	6.02 (d, 6.8)	119.6	6.07 (d, 7.0)	19.4	1.75 (m) 1.58 (m)	17.9	1.47 (m)	17.9	1.70 (d, 3.4)	19.2	1.58 (m)	22.8	2.09 (m)
7	117.4	5.56 (d, 6.8)	118.6	5.62 (d, 7.0)	27.2	1.97 (m)	26.5	2.24 (m) 2.13 (m)	26.8	1.99 (d, 6.9)	27.4	2.06 (m)	115.5	5.50 (t, 3.5)
8	141.7	–	139.2	–	133.2	–	132.9	–	131.6	–	135.9	–	139.4	–
9	147.8	–	148.3	–	137.5	–	135.4	–	135.8	–	135.9	–	146.1	–
10	42.1	–	42.4	–	38.5	–	36.9	–	37.1	–	38.2	–	37.5	–
11	121.4	5.47 (s)	121.4	5.59 (s)	28.1	2.04 (m)	20.6	2.04 (m) 1.90 (m)	20.1	2.03 (m)	21.6	2.04 (m)	122.2	5.40 (d, 6.1)
12	37.7	2.21 (m) 1.97 (m)	37.1	2.70 (m) 2.16 (m)	29.8	1.98 (m) 1.64 (m)	29.5	1.82 (m) 1.36 (dd, 12.9, 4.7)	28.6	1.54 (d, 11.3)	30.3	1.78 (d, 9.4) 1.46 (m)	35.0	2.46 (m) 2.01 (d, 5.4)
13	45.7	–	43.7	–	44.7	–	44.9	–	43.5	–	47.0	–	42.5	–
14	49.6	–	45.1	–	45.3	–	51.4	–	44.0	–	49.5	–	44.3	–
15	44.3	2.20 (d, 9.4) 1.53 (d, 13.3)	47.2	2.16 (d, 18.2) 2.36 (d, 18.2)	47.5	2.39 (d, 18.5) 1.90 (d, 18.5)	73.3	4.24 (dd, 9.8, 5.7)	46.3	2.34 (d, 18.4) 1.94 (d, 18.4)	43.7	2.19 (dd, 13.7, 8.6) 1.28 (d, 13.0)	46.4	2.40 (d, 18.8) 2.13 (d, 18.4)
16	77.9	4.06 (t, 7.4)	219.3	2.63 (d, 10.5)	220.5	–	38.0	1.96 (t, 6.4) 1.77 (m)	218.0	–	77.8	4.03 (t, 7.2)	217.2	–
17	57.6	2.15 (m)	58.5	2.63 (d, 10.5)	58.7	2.55 (d, 9.9)	45.8	2.23 (m)	57.0	2.56 (t, 9.7)	57.5	2.03 (m)	57.0	2.62 (t, 10.0)
18	17.8	0.70 (s)	17.2	0.80 (s)	17.4	0.88 (s)	16.3	0.80 (s)	19.1	0.85 (s)	17.9	0.78 (s)	16.6	0.73 (s)
19	36.0	1.26 (s)	36.2	1.31 (s)	19.6	1.03 (s)	18.8	0.98 (s)	16.5	1.01 (s)	19.5	1.03 (s)	22.5	1.02 (s)
20	49.4	2.40 (m)	49.9	2.42 (m)	49.6	2.55 (d, 9.9)	47.2	2.22 (m)	43.6	2.55 (m)	48.8	2.37 (td, 8.7, 3.1)	43.3	2.57 (dd,10.2, 3.2)
21	180.0	–	181.4	–	179.6	–	181.7	–	179.1	–	180.7	–	179.3	–
22	33.5	1.89 (m) 1.64 (m)	32.7	2.43 (m) 1.50 (m)	32.5	2.42 (m) 1.54 (m)	32.4	1.53 (m)	30.8	2.45 (m) 1.62 (m)	33.5	1.83 (dd, 13.1, 2.9) 1.64 (m)	30.9	2.49 (m)
23	27.5	2.07 (m) 1.97 (m)	27.3	2.00 (dd, 11.9, 3.9)	21.3	1.97 (m)	25.8	1.96 (t, 6.4)	25.9	1.99 (d, 7.0)	27.3	2.08 (m) 1.94 (t, 8.0)	25.9	2.03 (d, 9.7) 1.64 (m)
24	125.5	5.15 (t, 7.0)	125.2	5.14 (t, 6.6)	125.2	5.13 (t, 7.4)	123.3	5.08 (t, 7.0)	123.6	5.12 (t, 5.8)	125.3	5.15 (t, 6.5)	123.3	5.14 (t, 7.0)
25	132.6	–	132.9	–	132.8	–	132.5	–	132.3	–	132.8	–	132.4	–
26	17.9	1.61 (s)	17.9	1.61 (s)	17.8	1.60 (s)	17.7	1.58 (s)	17.7	1.59 (s)	17.9	1.60 (s)	17.7	1.53 (s)
27	26.0	1.67 (s)	26.1	1.68 (s)	26.0	1.68 (s)	25.7	1.68 (s)	25.7	1.67 (s)	26.0	1.68 (s)	25.7	1.68 (s)
28	28.2	1.19 (s)	28.2	1.21 (s)	28.7	0.99 (s)	27.5	0.86 (s)	27.9	0.89 (s)	28.5	0.90 (s)	27.8	0.89 (s)
29	25.9	1.14 (s)	26.0	1.15 (s)	16.2	0.82 (s)	21.8	0.91 (s)	17.0	0.89 (s)	22.4	0.95 (s)	22.4	1.00 (s)
30	26.5	1.09 (s)	26.2	1.08 (s)	25.3	1.09 (s)	17.0	0.98(s)	25.0	1.07 (s)	25.6	1.14 (s)	25.7	1.11 (s)
31														
1'							170.8	–	171.1	–	172.4		170.8	–
2'							21.3	2.07 (s)	21.3	2.06 (s)	46.0	2.70 (m)	21.3	2.05 (s)
3'											70.9	–		
4'											28.1	1.37 (s)		
5'											46.6	2.71 (m)		
6'											173.2	–		
6'-OCH <sub>3</sub>											52.1	3.66 (s)		
	8 <sup>b</sup>		9 <sup>b</sup>		10 <sup>b</sup>		11 <sup>a</sup>		12 <sup>b</sup>		13 <sup>b</sup>			
position	δ <sub>C</sub>	δ <sub>H</sub>	δ <sub>C</sub>	δ <sub>H</sub>	δ <sub>C</sub>	δ <sub>H</sub>	δ <sub>C</sub>	δ <sub>H</sub>	δ <sub>C</sub>	δ <sub>H</sub>	δ <sub>C</sub>	δ <sub>H</sub>	δ <sub>C</sub>	δ <sub>H</sub>
1	35.2	1.99 (m) 1.52 (m)	30.6	1.62 (dd, 5.0, 3.0) 1.58 (m)	31.9	1.76 (m) 1.72 (m)	30.2	1.44 (m)	30.8	1.64 (m) 1.39 (m)	30.4	1.70 (m) 1.64 (m)		
2	24.1	1.74 (m)	23.1		24.1		26.5		23.3		23.0			

(continued on next page)



Table 1 (continued)

position	8 <sup>b</sup>		9 <sup>b</sup>		10 <sup>b</sup>		11 <sup>a</sup>		12 <sup>b</sup>		13 <sup>b</sup>	
	$\delta_C$	$\delta_H$	$\delta_C$	$\delta_H$	$\delta_C$	$\delta_H$	$\delta_C$	$\delta_H$	$\delta_C$	$\delta_H$	$\delta_C$	$\delta_H$
				1.90 (m)		2.08 (m)		1.85 (m)		1.82 (m)		1.91 (m)
				1.73 (m)		1.72 (m)		1.65 (m)		1.62 (m)		1.72 (m)
3	80.5	4.52 (dd, 11.3, 4.9)	78.0	4.67 (t, 2.8)	80.0	4.70 (t, 2.5)	77.8	4.67 (t, 2.6)	77.8	4.66 (br s)	77.9	4.69 (t, 2.9)
4	37.5	–	36.5	–	37.7	–	36.7	–	36.7	–	36.5	–
5	49.2	1.21 (dd, 10.9, 4.6)	44.0	1.48 (dd, 11.4, 4.1)	45.8	1.54 (d, 13.7)	45.2	1.50 (m)	45.1	1.41 (m)	44.2	1.52 (dd, 9.8, 6.1)
6	22.8	2.12 (m)	22.7	2.09 (m)	24.0	1.55 (t, 7.5)	17.8	1.64 (m)	17.9	1.62 (m)	22.8	2.07 (m)
7	122.1	5.48 (d, 2.2)	121.5	5.85 (d, 5.4)	121.8	5.50 (t, 5.1)	23.2	1.46 (t, 2.3)	26.5	1.47 (m)	122.2	5.50 (t, 4.0)
8	139.5	–	140.5	–	143.5	–	131.3	–	132.9	–	139.4	–
9	145.9	–	146.0	–	147.1	–	136.0	–	135.4	–	146.1	–
10	37.6	–	37.3	–	38.6	–	37.1	–	36.9	–	37.5	–
11	116.0	5.39 (d, 5.2)	115.5	5.29 (d, 6.5)	117.2	5.37 (d, 4.6)	20.1	2.10 (m)	20.6	2.03 (d, 8.2)	115.5	5.41 (d, 6.3)
12	34.9	2.47 (m)	36.1	2.26 (m)	36.9	2.26 (m)	28.7	2.03 (d, 7.9)	29.4	1.95 (m)	34.9	2.44 (d, 17.7)
13	42.4	–	44.3	–	45.7	–	43.5	–	44.9	–	42.5	–
14	44.2	–	51.7	–	50.0	–	44.0	–	51.5	–	44.3	–
15	46.4	2.39 (d, 13.1)	74.4	4.31 (dd, 9.8, 5.8)	44.5	2.20 (dd, 13.6, 7.4)	46.3	2.35 (d, 18.2)	73.3	4.25 (dd, 9.7, 5.7)	46.4	2.37 (d, 18.3)
16	217.2	–	38.8	1.98 (m)	77.6	4.03 (t, 7.0)	217.9	1.96 (d, 18.2)	38.0	1.95 (m)	217.2	–
17	57.0	2.61 (t, 10.1)	45.6	1.79 (d, 5.8)	57.7	2.15 (m)	57.1	1.48 (d, 13.6)	45.7	1.78 (m)	56.9	2.12 (dd, 10.6, 6.0)
18	16.6	0.72 (s)	16.2	2.26 (m)	17.7	0.64 (s)	17.0	4.03 (t, 7.0)	16.6	0.81 (s)	16.6	0.75 (s)
19	22.7	1.01 (s)	17.3	2.26 (m)	22.9	1.03 (s)	18.8	4.03 (t, 7.0)	18.8	0.98 (s)	22.5	0.97 (s)
20	43.3	2.56 (dd, 10.1, 2.9)	46.9	2.26 (m)	48.6	2.38 (td, 9.9, 2.1)	43.7	2.56 (td, 9.7, 2.8)	47.1	2.25 (m)	43.3	2.65 (t, 10.0)
21	178.7	–	180.2	–	180.5	–	179.9	2.65 (m)	180.6	–	178.3	–
22	30.8	2.45 (m)	32.5	1.54 (m)	33.4	1.85 (m)	29.3	2.65 (m)	30.9	1.66 (m)	29.4	1.74 (m)
23	25.9	2.05 (m)	25.8	1.68 (m)	27.4	1.68 (m)	32.0	1.73 (m)	31.8	1.87 (d, 7.9)	32.0	2.01 (d, 6.4)
24	123.3	5.13 (t, 7.5)	123.2	1.98 (m)	125.2	2.04 (m)	154.7	2.04 (t, 7.7)	154.9	–	154.7	–
25	132.4	–	132.5	1.96 (m)	132.8	1.96 (m)	33.6	2.26 (sep, 2.6)	33.8	2.20	33.6	2.27 (sep, 6.5)
26	17.7	1.59 (s)	17.7	5.08 (t, 6.6)	17.9	1.60 (m)	21.9	1.01 (d, 5.4)	21.8	1.00 (d, 6.5)	21.7	1.02 (d, 2.2)
27	25.7	1.68 (s)	25.7	1.58 (s)	26.0	1.68 (s)	21.8	1.03 (d, 5.2)	21.8	1.02 (d, 6.3)	21.8	1.03 (d, 1.9)
28	28.0	0.89 (s)	27.8	1.68 (s)	28.7	0.91 (s)	27.5	0.87 (s)	27.5	0.86 (s)	27.8	0.89 (s)
29	16.9	0.96 (s)	22.6	0.87 (s)	23.2	1.03 (s)	21.7	0.92 (s)	21.7	0.91 (s)	22.4	1.00 (s)
30	25.8	1.06 (s)	22.5	0.98 (s)	26.7	1.10 (s)	25.0	0.99 (s)	17.0	0.99 (s)	26.0	1.12 (s)
31				0.99 (s)			107.1	1.13 (s)	107.0	4.77 (s)	107.2	4.78 (s)
1'	171.0	–	170.9	–	172.4	–	170.8	4.74 (s)	170.8	4.67 (s)	170.8	4.75 (s)
2'	21.3	2.07 (s)	21.3	2.04 (s)	46.0	2.69 (m)	21.3	2.07 (s)	21.4	2.07 (s)	21.3	2.06 (s)
3'					70.9	–						
4'					28.2	1.35 (s)						
5'					46.5	2.68 (m)						
6'					173.2	–						
6'-OCH <sub>3</sub>					52.1	3.64 (s)						

<sup>1</sup>H and <sup>13</sup>C NMR Spectroscopic Data of Compounds 8–13 [ $\delta$  (multi.,  $J$  in Hz) in ppm; <sup>a</sup><sup>1</sup>H and <sup>13</sup>C NMR data were measured in CD<sub>3</sub>OD at 400 and 100 MHz. <sup>b</sup><sup>1</sup>H and <sup>13</sup>C NMR data were measured in CDCl<sub>3</sub> at 400 and 100 MHz]

3507, 2954, 1725, 1602, 1443, 1375, 1353, 1210, 1013, 756 cm<sup>-1</sup>; <sup>1</sup>H and <sup>13</sup>C NMR, see Table 1; HRESIMS  $m/z$  653.4025 ([M+Na]<sup>+</sup> calcd for C<sub>37</sub>H<sub>58</sub>O<sub>8</sub>Na, 653.4024).

### 2.3.7. Pinicolasin G (7)

Colorless powder; [ $\alpha$ ]<sub>D</sub><sup>25</sup> – 46.9 (c 0.1, MeOH); UV (MeOH)  $\lambda_{\max}$  (log  $\epsilon$ ) 241 (1.6), 207 (0.8) nm; ECD (MeOH) (Mol. CD) 224 (1.5) nm; IR (KBr)  $\nu_{\max}$  3447, 2936, 1729, 1597, 1441, 1377, 1248, 1184, 755 cm<sup>-1</sup>; <sup>1</sup>H and <sup>13</sup>C NMR, see Table 1; HRESIMS  $m/z$  533.3236 ([M+Na]<sup>+</sup> calcd for C<sub>32</sub>H<sub>46</sub>O<sub>5</sub>Na, 533.3237).

### 2.3.8. Pinicolasin H (8)

Colorless powder; [ $\alpha$ ]<sub>D</sub><sup>25</sup> – 18.6 (c 0.06, MeOH); UV (MeOH)  $\lambda_{\max}$

(log  $\epsilon$ ) 241 (1.7), 208 (1.1) nm; ECD (MeOH) (Mol. CD) 305 (–2.0), 235 (0.5) nm; IR (KBr)  $\nu_{\max}$  3445, 2934, 1732, 1596, 1448, 1374, 1247, 1032, 754 cm<sup>-1</sup>; <sup>1</sup>H and <sup>13</sup>C NMR, see Table 2; HRESIMS  $m/z$  533.3238 ([M+Na]<sup>+</sup> calcd for C<sub>32</sub>H<sub>46</sub>O<sub>5</sub>Na, 533.3238).

### 2.3.9. Pinicolasin I (9)

Colorless powder; [ $\alpha$ ]<sub>D</sub><sup>25</sup> + 26.3 (c 0.06, MeOH); UV (MeOH)  $\lambda_{\max}$  (log  $\epsilon$ ) 242 (1.3), 208 (0.8) nm; ECD (MeOH) (Mol. CD) 232 (1.7) nm; IR (KBr)  $\nu_{\max}$  3445, 2948, 1715, 1681, 1647, 1456, 1376, 1248, 1033, 756 cm<sup>-1</sup>; <sup>1</sup>H and <sup>13</sup>C NMR, see Table 2; HRESIMS  $m/z$  535.3392 ([M+Na]<sup>+</sup> calcd for C<sub>32</sub>H<sub>48</sub>O<sub>5</sub>Na, 535.3394).

**Table 2**

Inhibitory Effects of Isolated Compounds on Superoxide Anion Generation and Elastase Release in Human Neutrophils in Response to fMLP/CB.

Compound	IC <sub>50</sub> (μM) <sup>a</sup>	
	Superoxide anion generation	Elastase release
1	4.32 ± 0.22	>10
2	>10	>10
4	>10	>10
5	2.25 ± 0.22	2.87 ± 0.27
6	4.77 ± 0.97	6.66 ± 0.30
7	2.42 ± 0.08	2.67 ± 0.34
8	4.05 ± 1.03	4.84 ± 0.82
9	>10	>10
10	1.81 ± 0.44	2.50 ± 0.64
11	4.61 ± 0.51	3.51 ± 0.45
12	>10	>10
14	4.97 ± 0.56	6.40 ± 1.11
15	>10	>10
16	2.13 ± 0.41	2.83 ± 0.59
17	5.20 ± 1.69	6.74 ± 0.30
18	2.57 ± 0.78	3.30 ± 1.06
19	6.87 ± 0.58	>10
20	4.15 ± 0.29	2.46 ± 0.31
21	>10	>10
22	>10	>10
23	>10	>10
24	6.03 ± 0.61	>10
25	4.38 ± 0.86	5.86 ± 1.53
26	>10	>10
27	>10	>10
28	>10	4.73 ± 1.00
29	6.11 ± 1.20	>10
30	>10	5.38 ± 1.44
31	>10	>10
32	>10	>10
33	>10	>10
34	2.86 ± 0.62	3.42 ± 0.66
Genistein	1.62 ± 0.14	35.95 ± 1.53

<sup>a</sup> Concentration corresponding to 50% inhibition. The results are presented as the mean ± SEM (n = 3–5).**2.3.10. Pinicolasin J (10)**

Colorless powder;  $[\alpha]_D^{25} = 2.4$  (c 0.3, MeOH); UV (MeOH)  $\lambda_{\max}$  (log  $\epsilon$ ) 239 (1.9), 212 (1.3) nm; ECD (MeOH) (Mol. CD) 219 (3.3) nm; IR (KBr)  $\nu_{\max}$  3495, 2949, 2885, 1737, 1714, 1441, 1377, 1206, 1029, 756  $\text{cm}^{-1}$ ;  $^1\text{H}$  and  $^{13}\text{C}$  NMR, see Table 2; HRESIMS  $m/z$  651.3870  $[\text{M}+\text{Na}]^+$  calcd for  $\text{C}_{37}\text{H}_{56}\text{O}_8\text{Na}$ , 651.3867).

**2.3.11. Pinicolasin K (11)**

Colorless powder;  $[\alpha]_D^{25} = 64.6$  (c 0.1, MeOH); ECD (MeOH) (Mol. CD) 306 (−4.8) nm; IR (KBr)  $\nu_{\max}$  3700, 2953, 1733, 1609, 1453, 1375, 1247, 1182, 755  $\text{cm}^{-1}$ ;  $^1\text{H}$  and  $^{13}\text{C}$  NMR, see Table 2; HRESIMS  $m/z$  549.3549  $[\text{M}+\text{Na}]^+$  calcd for  $\text{C}_{33}\text{H}_{50}\text{O}_5\text{Na}$ , 549.3550).

**2.3.12. Pinicolasin L (12)**

Colorless powder;  $[\alpha]_D^{25} = 0.3$  (c 0.3, MeOH); IR (KBr)  $\nu_{\max}$  3687, 2949, 1716, 1454, 1375, 1250, 1180, 1054, 755  $\text{cm}^{-1}$ ;  $^1\text{H}$  and  $^{13}\text{C}$  NMR, see Table 2; HRESIMS  $m/z$  551.3709  $[\text{M}+\text{Na}]^+$  calcd for  $\text{C}_{33}\text{H}_{52}\text{O}_5\text{Na}$ , 551.3707).

**2.3.13. Pinicolasin M (13)**

Colorless powder;  $[\alpha]_D^{25} = 31.3$  (c 0.06, MeOH); UV (MeOH)  $\lambda_{\max}$  (log  $\epsilon$ ) 242 (0.8), 205 (0.4) nm; ECD (MeOH) (Mol. CD) 305 (−3.1), 228 (1.5) nm; IR (KBr)  $\nu_{\max}$  3701, 2957, 2883, 1733, 1607, 1376, 1246, 1182, 757  $\text{cm}^{-1}$ ;  $^1\text{H}$  and  $^{13}\text{C}$  NMR, see Table 2; HRESIMS  $m/z$  547.3395  $[\text{M}+\text{Na}]^+$  calcd for  $\text{C}_{33}\text{H}_{48}\text{O}_5\text{Na}$ , 547.3394).

**2.4. Human neutrophil preparation**

A standard method of dextran sedimentation was used to isolate

neutrophils prior to centrifugation on a Ficoll Hypaque gradient and hypotonic lysis of erythrocytes. Whole blood of healthy donors (20–30 years of age) was withdrawn by venipuncture; the protocol was approved by Chang Gung Memorial Hospital (IRB protocol number: 102-1595A3) review board. Before use, purified neutrophils were maintained at 4 °C in a  $\text{Ca}^{2+}$ -free Hank's balanced salt solution (HBSS) at pH 7.4. [13]

**2.5. Superoxide anion generation measurement**

Reduction of ferricytochrome *c* be inhibited by superoxide dismutase (SOD) was used to develop the superoxide anion generation assay. Each test compound or an equal volume of vehicle (0.1% DMSO, negative control) was incubated for 5 min with neutrophils ( $6 \times 10^5$  cells/mL) equilibrated in the presence of 0.5 mg/mL ferricytochrome *c* and 1 mM  $\text{Ca}^{2+}$  at 37 °C for 2 min. Cells were initially incubated with cytochalasin B (CB, 1 μg/mL) for 3 min; then, neutrophils were activated by *N*-formyl-L-methionyl-L-leucyl-L-phenylalanine (fMLF, 100 nM). The changes in absorbance due to reduction of ferricytochrome *c* at 550 nm were continuously monitored in a double-beam spectrophotometer equipped with a six cell positioning system (Hitachi U-3010, Tokyo, Japan) under constant stirring. Calculations were based on the differences in the reduction with and without SOD (100 U/mL) divided by the extinction coefficient for the reduction of ferricytochrome *c* ( $\epsilon = 21.1/\text{mM}/10 \text{ mm}$ ). Genistein was used as a positive control [13].

**2.6. Elastase release assay**

Degranulation of azurophilic granules was determined by elastase release as described previously. MeO-Suc-Ala-Ala-Pro-Val-*p*-nitroanilide was used as the elastase substrate. Neutrophils ( $6 \times 10^5$  cells/mL) equilibrated in the presence of MeO-Suc-Ala-Ala-Pro-Val-*p*-nitroanilide (100 μM) at 37 °C for 2 min were incubated with the test compounds or an equal volume of the vehicle (0.1% DMSO, negative control) for 5 min. Cells were activated by 100 nM fMLF and 0.5 μg/mL CB, and changes in absorbance at 405 nm were continuously monitored to measure elastase release. The results are expressed as the percentage of elastase release relative to the values detected in the fMLF/CB-activated drug-free control system. Genistein was used as a positive control [13].

**2.7. Statistical analysis**

The results are expressed as the mean ± SEM. Calculations of 50% inhibitory concentrations (IC<sub>50</sub>) were performed using a computer (PHARM/PCS v.4.2). Statistical comparison between the groups was performed using the Student's *t* test. Values of *p* less than 0.05 were considered statistically significant.

**3. Results and discussion**

The fruiting bodies of *F. pinicola* were extracted with ethanol, and the resulting crude extract was subjected to column chromatography, preparative TLC, and HPLC to afford twelve previously undescribed triterpenoids (1–4, 6–13, Fig. 1) and twenty-two known compounds. The structures of 1–13 were determined as described below.

Compound 1 was isolated as colorless powder with a pseudomolecular formula  $\text{C}_{30}\text{H}_{44}\text{O}_4\text{Na}$  on the basis of HRESIMS  $[\text{M}+\text{Na}]^+$ ,  $m/z$  491.3130. Its  $^1\text{H}$  NMR spectrum revealed seven methyl singlets at  $\delta_{\text{H}}$  0.70 (s), 1.09 (s), 1.14 (s), 1.19 (s), 1.26 (s), 1.61 (s), and 1.67 (s), three conjugated double bond proton signals at  $\delta_{\text{H}}$  5.47 (br s), 5.56 (d,  $J = 6.8$  Hz), and 6.02 (d,  $J = 6.8$  Hz), one olefinic proton at  $\delta_{\text{H}}$  5.15 (t,  $J = 7.0$  Hz), and two oxygenated methines at  $\delta_{\text{H}}$  3.21 (dd,  $J = 11.9, 4.3$  Hz) and 4.06 (t,  $J = 7.4$  Hz). In its  $^{13}\text{C}$  and DEPT-135 NMR spectra, thirty carbons were observed including seven methyls, six methylenes, eight olefinic carbons, two oxygenated methines, and one carboxylic acid. In the HMBC spectral analysis of 1 (Fig. 2), conjugated tri-ene system was

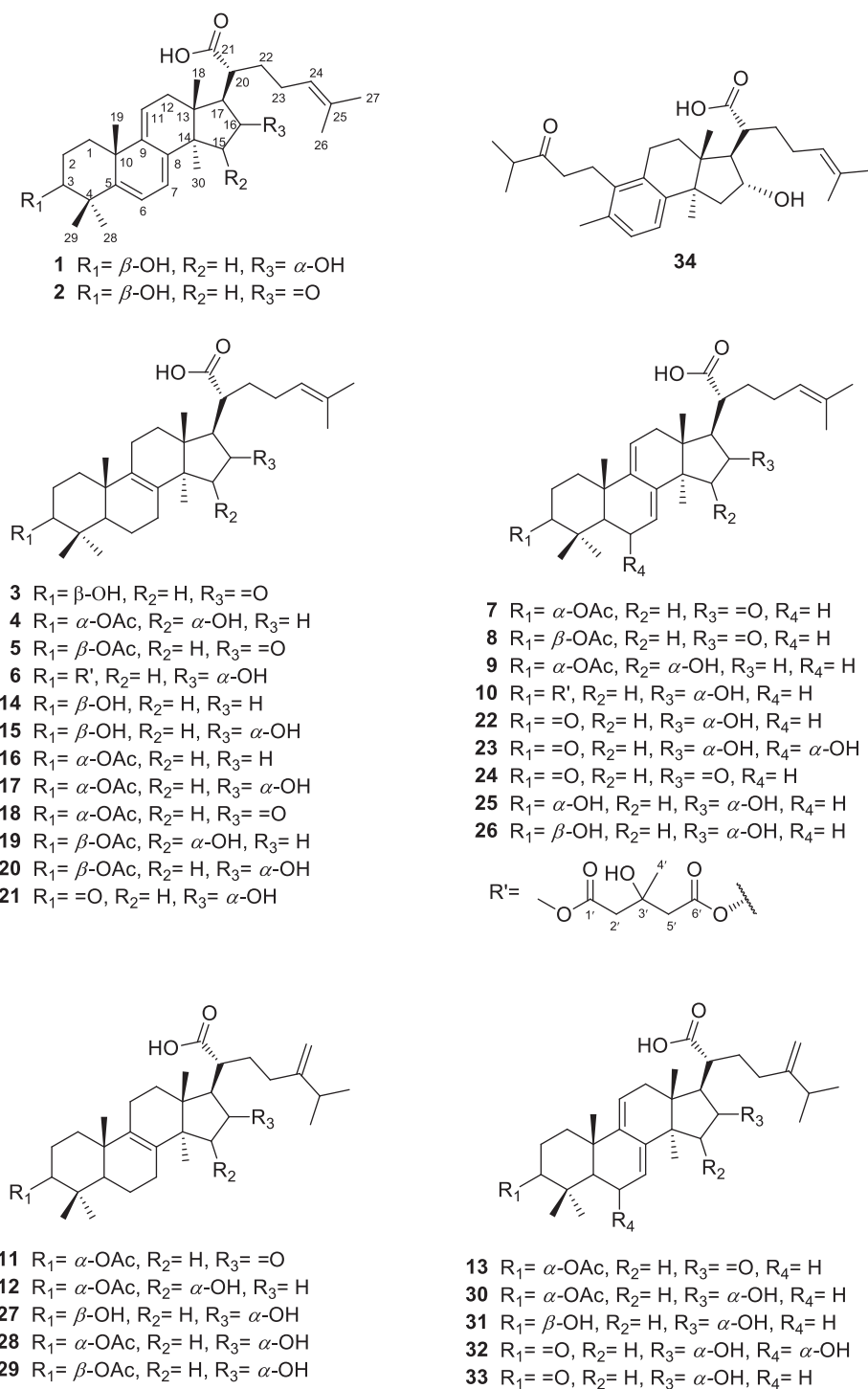


Fig. 1. Structures of triterpenes (1–34) isolated from *Fomitopsis pinicola*.

proposed according to the observed correlations of H-6 ( $\delta_{\text{H}}$  6.02, d,  $J = 6.8$  Hz) to C-4 ( $\delta_{\text{C}}$  42.9), C-8 ( $\delta_{\text{C}}$  141.7), and C-10 ( $\delta_{\text{C}}$  42.1); H-7 ( $\delta_{\text{H}}$  5.56, d,  $J = 6.8$  Hz) to C-5 ( $\delta_{\text{C}}$  153.0), C-9 ( $\delta_{\text{C}}$  147.8), and C-14 ( $\delta_{\text{C}}$  49.6); and H-11 ( $\delta_{\text{H}}$  5.47, br s) to C-7 ( $\delta_{\text{C}}$  117.4). Another carbon–carbon double bond was assigned to  $\Delta^{24,25}$  due to HMBC correlations of H-24 ( $\delta_{\text{H}}$  5.15, t,  $J = 7.0$  Hz) to C-26 ( $\delta_{\text{C}}$  17.9), and H-26 ( $\delta_{\text{H}}$  1.61, s)/H-27 ( $\delta_{\text{H}}$  1.67, s) to C-24 ( $\delta_{\text{C}}$  125.5) and C-25 ( $\delta_{\text{C}}$  132.6). Moreover, a lanostane type triterpene skeleton was constructed based on other HMBC correlations from H-18 ( $\delta_{\text{H}}$  0.70, s) to C-12 ( $\delta_{\text{C}}$  37.7), C-13 ( $\delta_{\text{C}}$  45.7), and C-14 ( $\delta_{\text{C}}$  49.6); from H-19 ( $\delta_{\text{H}}$  1.26, s) to C-1 ( $\delta_{\text{C}}$  36.9), C-5 ( $\delta_{\text{C}}$  153.0), C-9 ( $\delta_{\text{C}}$  147.8), and C-10

( $\delta_{\text{C}}$  42.1); from H-28 ( $\delta_{\text{H}}$  1.19, s)/H-29 ( $\delta_{\text{H}}$  1.14, s) to C-3 ( $\delta_{\text{C}}$  77.6), C-4 ( $\delta_{\text{C}}$  42.9), and C-5 ( $\delta_{\text{C}}$  153.0); and from H-30 ( $\delta_{\text{H}}$  1.09, s) to C-8 ( $\delta_{\text{C}}$  141.7), C-13 ( $\delta_{\text{C}}$  45.7), C-14 ( $\delta_{\text{C}}$  49.6), C-15 ( $\delta_{\text{C}}$  44.3), respectively. Two oxygenated methines at  $\delta_{\text{H}}$  3.21 (dd,  $J = 11.9$ , 4.3 Hz) and 4.06 (t,  $J = 7.4$  Hz) were proposed to be at C-3 and C-16 according to their HMBC correlations [H-3/C-1 ( $\delta_{\text{C}}$  36.9); H-16/C-14 ( $\delta_{\text{C}}$  49.6)]. Further, combining with COSY correlation of H-2 ( $\delta_{\text{H}}$  1.92, 1.74)/H-3 ( $\delta_{\text{H}}$  3.21), H-6 ( $\delta_{\text{H}}$  6.02)/H-7 ( $\delta_{\text{H}}$  5.56), H-11 ( $\delta_{\text{H}}$  5.47)/H-12 ( $\delta_{\text{H}}$  1.97), H-16 ( $\delta_{\text{H}}$  4.06)/H-17 ( $\delta_{\text{H}}$  2.15), H-17 ( $\delta_{\text{H}}$  2.15)/H-20 ( $\delta_{\text{H}}$  2.40), H-20 ( $\delta_{\text{H}}$  2.40)/H-22 ( $\delta_{\text{H}}$  1.89), and H-23 ( $\delta_{\text{H}}$  2.07, 1.97)/H-24 ( $\delta_{\text{H}}$  5.15), the structure of

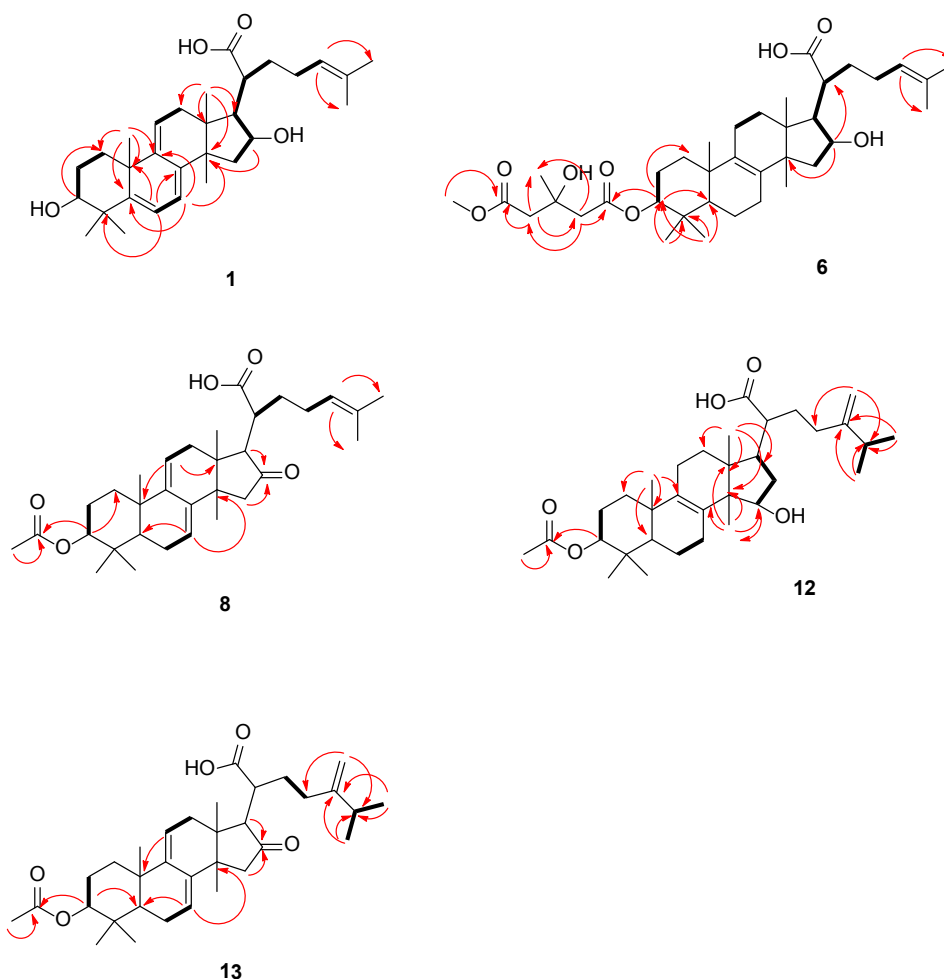


Fig. 2. Key HMBC (→,  $^1\text{H} \rightarrow ^{13}\text{C}$ ) and COSY (↔) correlation of **1**, **6**, **8**, **12**, and **13**.

3,16-dihydroxy-lanosta-5,7,9 (11),24-tetraen-21-oic acid skeleton was built. An  $\alpha$  (axial) orientation of H-3 ( $\delta_{\text{H}}$  3.21, dd,  $J = 11.9, 4.3$  Hz) was indicated by its large vicinal coupling constant values. The data of the literature indicate that H-3 can be in  $\alpha$  orientation if the proton splitting pattern is a doublet of doublet ( $J = 11\text{--}12$  and  $3\text{--}4$  Hz) or a triplet ( $J = 7\text{--}8$  Hz) [14–17], while H-3 is in  $\beta$  orientation with smaller coupling constant (both  $J = 3\text{--}4$  Hz). [18] NOE effects between H-3 and H-28<sub>eq</sub> also supported the H-3 $\alpha$  orientation. Moreover, the NOE correlations of H-18<sub>ax</sub>/H-16 and H-18<sub>ax</sub>/H-20 indicated the stereochemistry of substitutions at C-13, –16, and –20 to be  $\beta$ ,  $\alpha$ , and  $\alpha$ , respectively, as shown in Fig. 3 [19–21]. Further, NOESY correlation between H-16 and H-22 ( $\delta_{\text{H}}$  1.89) could partially support 20R configuration. Other 2D spectral experimental data confirmed the structure of **1** to be 3 $\beta$ ,16 $\alpha$ -dihydroxy-lanosta-5,7,9,24-tetraen-21-oic acid, and the compound was named trivially as pinicolasin A.

Pinicolasin B (**2**), also a colorless powder, had a pseudomolecular formula  $\text{C}_{30}\text{H}_{42}\text{O}_4\text{Na}$  on the basis of HRESIMS ( $[\text{M}+\text{Na}]^+$ ,  $m/z$  489.2976). The IR spectrum of **2** had absorption peaks at 3378 (OH), 1731 (ketone), and 1715 (carboxylic acid)  $\text{cm}^{-1}$ . The  $^1\text{H}$ ,  $^{13}\text{C}$ , and 2D NMR spectra of **2** were very similar to those of **1**. The minor differences included the lack of one oxygenated proton signal ( $\delta_{\text{H}}$  4.06, H-16) in **1** and the presence of a quaternary carbonyl carbon ( $\delta_{\text{C}}$  219.3) in **2**. According to the HMBC spectral analysis, this quaternary carbon was assigned to be C-16 based on the correlations of H-15 ( $\delta_{\text{H}}$  2.16 and 2.36) and H-17 ( $\delta_{\text{H}}$  2.63) with C-16. Moreover, similar to **1**, conjugated tri-ene system was observed based on HMBC correlations of H-6 ( $\delta_{\text{H}}$  6.07, d,  $J = 7.0$  Hz) to C-4 ( $\delta_{\text{C}}$  43.0), C-8 ( $\delta_{\text{C}}$  139.2), and C-10 ( $\delta_{\text{C}}$  42.4); H-7 ( $\delta_{\text{H}}$  5.62, d,  $J = 7.0$  Hz) to C-5 ( $\delta_{\text{C}}$  154.1), C-9 ( $\delta_{\text{C}}$  148.3), and C-14 ( $\delta_{\text{C}}$  45.1); and H-

11 ( $\delta_{\text{H}}$  5.59, s) to C-7 ( $\delta_{\text{C}}$  118.6). Large vicinal coupling constant values of H-3 ( $\delta_{\text{H}}$  3.23, dd,  $J = 12.1, 4.4$  Hz) implied a  $\alpha$  (axial) orientation. In the NOESY spectrum of **2**, NOE correlations were observed between H-3 ( $\delta_{\text{H}}$  3.23)/H-28<sub>eq</sub> ( $\delta_{\text{H}}$  1.21) and H-17 $\alpha$  ( $\delta_{\text{H}}$  2.63)/H-30 ( $\delta_{\text{H}}$  1.08) thus confirming the structure of **2** as 3 $\beta$ -hydroxy-16-oxo-lanosta-5,7,9,24-tetraen-21-oic acid.

The molecular formula of **3** was  $\text{C}_{30}\text{H}_{46}\text{O}_4$  on the basis of HRESIMS analytical data ( $[\text{M}+\text{Na}]^+$ ,  $m/z$  493.3291). Its IR spectrum showed absorption peaks at 3518 (OH), 1731 (ketone), and 1715 (carboxylic acid)  $\text{cm}^{-1}$ . Comparison of the  $^1\text{H}$  NMR spectra of **2** and **3** indicated that three conjugate double bond proton signals disappeared, and only one olefinic proton at  $\delta_{\text{H}}$  5.13 (t) was present in **3**. Furthermore,  $^{13}\text{C}$  NMR spectrum had four olefinic carbons ( $\delta_{\text{C}}$  125.2, 132.8, 133.2, and 137.5); these two double bonds were assigned to be C-24/C-25 and C-8/C-9, respectively, according to their HMBC correlations of H-19 ( $\delta_{\text{H}}$  1.03)/C-9 ( $\delta_{\text{C}}$  137.5), H-30 ( $\delta_{\text{H}}$  1.09)/C-8 ( $\delta_{\text{C}}$  133.2), and H-27 ( $\delta_{\text{H}}$  1.68)/C-24 ( $\delta_{\text{C}}$  125.2) and C-25 ( $\delta_{\text{C}}$  132.8). Additionally, a carbonyl carbon ( $\delta_{\text{C}}$  220.5) was assigned to be at C-16 due to the HMBC correlations from H-15 ( $\delta_{\text{H}}$  2.39, 1.90) to C-16 ( $\delta_{\text{C}}$  220.5) and H-30 ( $\delta_{\text{H}}$  1.09) to C-15 ( $\delta_{\text{C}}$  47.5). Moreover, the configuration of H-3 was assigned to be  $\alpha$  according to the coupling pattern (t,  $J = 7.3$  Hz). NOESY spectra of **3** also supported  $\alpha$  orientation of H-3 based on the NOE correlation between H-3 ( $\delta_{\text{H}}$  3.17) and H-28<sub>eq</sub> ( $\delta_{\text{H}}$  0.99). The structure of **3** was built as 3 $\beta$ -hydroxy-16-oxo-lanosta-8,24-dien-21-oic acid, and this compound was named pinicolasin C.

The molecular formula of pinicolasin D (**4**) was  $\text{C}_{32}\text{H}_{50}\text{O}_5$  on the basis of HRESIMS analytical data ( $[\text{M}+\text{Na}]^+$ ,  $m/z$  537.3551). The  $^1\text{H}$  and  $^{13}\text{C}$  NMR spectra of **4** are very similar to those of **3** except that C-15 carbonyl in **3** was absent and an oxygenated methine ( $\delta_{\text{H}}$  4.24) was

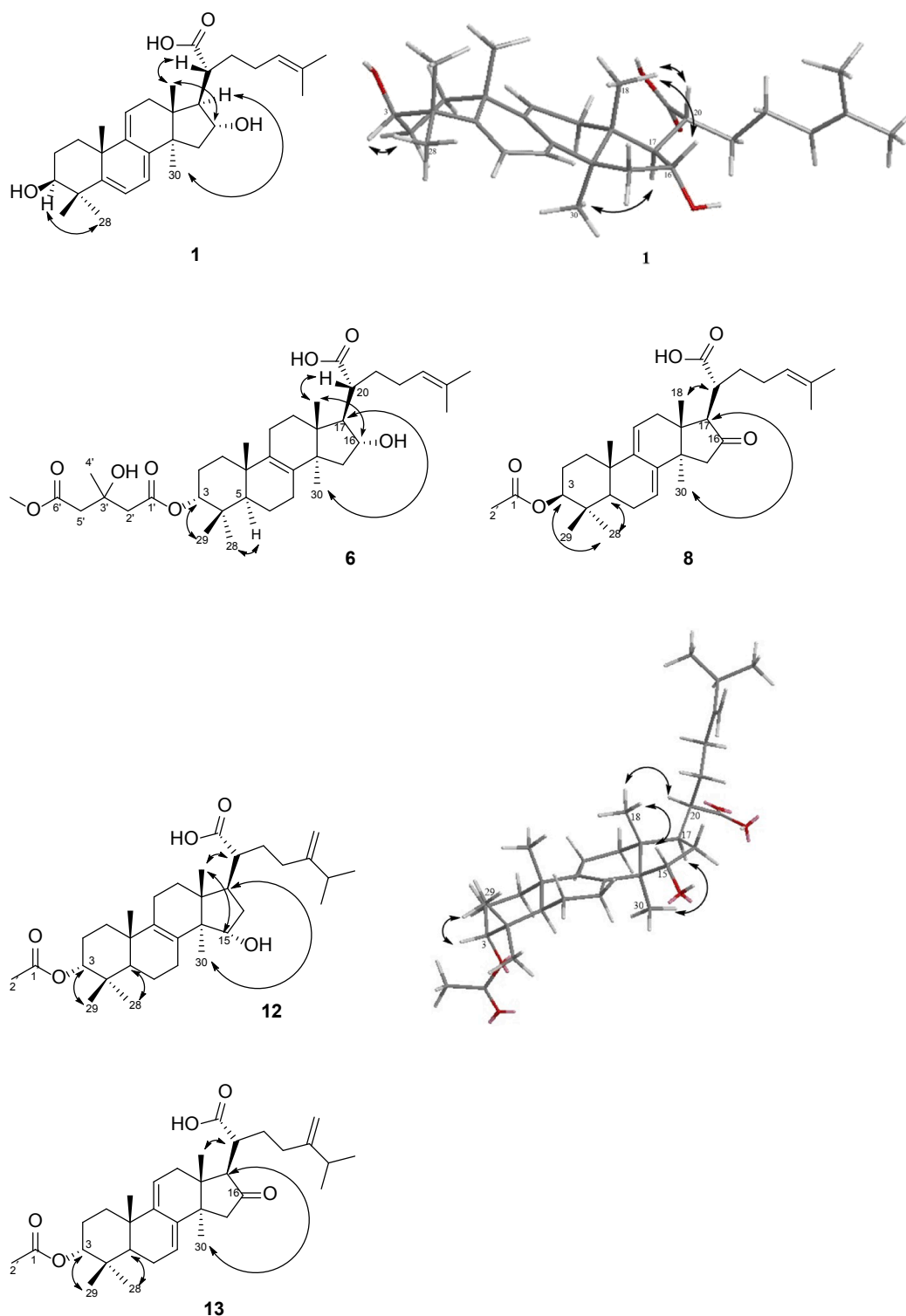


Fig. 3. Key NOESY ( $\leftrightarrow$ ,  $^1\text{H} \rightarrow ^1\text{H}$ ) correlation of **1**, **6**, **8**, **12**, and **13**.

present. This methine was assigned to be H-15 based on the HMBC correlation from H-15 ( $\delta_{\text{H}}$  4.24) to C-30 ( $\delta_{\text{C}}$  17.0). Moreover, an acetyl group was detected ( $\delta_{\text{H}}$  2.07,  $\delta_{\text{C}}$  21.3 and  $\delta_{\text{C}}$  170.8) and was connected to the C-3 hydroxyl group according to the HMBC spectral analysis in which H-3 ( $\delta_{\text{H}}$  4.66) correlated with C-1' ( $\delta_{\text{C}}$  170.8), thus confirming a 3-acetoxy-15-hydroxy-lanosta-8,24-dien-21-oic acid structure [22]. The orientation of H-3 was assigned to be  $\beta$  according to the typical chemical shift (C-3 at  $\delta_{\text{C}}$  77.8) and coupling pattern (br s). Moreover, OH-15 was

in  $\alpha$  orientation based on the NOE effect between H-15 $\beta$  ( $\delta_{\text{H}}$  4.24) and H-18 $_{\text{ax}}$  ( $\delta_{\text{H}}$  0.80). Thus, the structure of **4** was determined to be 3 $\alpha$ -acetoxy-15 $\alpha$ -hydroxy-lanosta-8,24-dien-21-oic acid.

The HRESIMS spectrum of pinicolasin E (**5**) had an  $[\text{M}+\text{Na}]^+$  ion peak at  $m/z$  535.3395 consistent with a pseudomolecular formula of  $\text{C}_{32}\text{H}_{48}\text{O}_5\text{Na}$ . Detailed analysis of  $^1\text{H}$  and  $^{13}\text{C}$  spectra indicated the presence of acetoxy signals of  $\delta_{\text{H}}$  2.06,  $\delta_{\text{C}}$  21.3, and  $\delta_{\text{C}}$  171.1, two olefinic signals of  $\delta_{\text{C}}$  123.6, 131.6, 132.3, and 135.8, and one additional carbonyl



signal of 217.2. The HMBC spectrum of **5** confirmed that the acetoxy was at C-3 position and two olefinic signals was proposed to be  $\Delta^{8,9}$  and  $\Delta^{24,25}$  based on the observed HMBC correlations of H-19 ( $\delta_H$  1.01) to C-9 ( $\delta_C$  135.8) and C-10 ( $\delta_C$  37.1); H-7 ( $\delta_H$  1.99) to C-8 ( $\delta_C$  131.6); H-30 ( $\delta_H$  1.07) to C-8 ( $\delta_C$  131.6); H-24 ( $\delta_H$  5.13) to C-26 ( $\delta_C$  17.8) and C-27 ( $\delta_C$  26.0); H-26 ( $\delta_H$  1.60) to C-24 ( $\delta_C$  125.2); and H-27 ( $\delta_H$  1.68) to C-24 ( $\delta_C$  125.2). In addition, the carbonyl is located at C-16 based on correlations of H-15 ( $\delta_H$  1.94, 2.34) and H-17 ( $\delta_H$  2.56) with C-16 ( $\delta_C$  217.2), suggesting a 3-acetoxy-16-oxo-lanosta-8,24-dien-21-oic acid skeleton. Moreover, the orientation of H-3 was assigned to be  $\alpha$  according to the typical shift of C-3 ( $\delta_C$  80.6) and coupling constants (dd,  $J = 11.6, 4.3$  Hz). Therefore, the structure of **5** was established as 3 $\beta$ -acetoxy-16-oxo-lanosta-8,24-dien-21-oic acid. This compound has just been reported as Formipinic acid **6** [20].

Pinicolasin F (**6**) had a pseudomolecular formula of  $C_{37}H_{58}O_8Na$  on the basis of HRESIMS ( $[M+Na]^+$ ,  $m/z$  653.4025). Comparison of the  $^1H$  and  $^{13}C$  spectra of **6** with those of **4** indicated the presence of a 4-carboxymethyl-3-hydroxy-3-methylbutanoyloxy substitution based on the proton signals of H-2' ( $\delta_H$  2.70, m), H-4' ( $\delta_H$  1.37, s), H-5' ( $\delta_H$  2.71, m), and OMe-6' ( $\delta_H$  3.66, s), and also on the carbon signals of C-1' ( $\delta_C$  172.4), C-2' ( $\delta_C$  46.0), C-3' ( $\delta_C$  70.9), C-4' ( $\delta_C$  28.1), C-5' ( $\delta_C$  46.6), C-6' ( $\delta_C$  173.2), and OMe-6' ( $\delta_C$  52.1) [10]. Its HMBC spectrum showed correlations of H-3 ( $\delta_H$  4.68) with C-1' ( $\delta_C$  172.4), H-2' with C-1'/C-4'/C-5', H-4' with C-2'/C-3'/C-5', H-5' with C-2'/C-4'/C-6', and OMe-6' with C-6' supporting C-3 substitution pattern. Furthermore, an oxygenated methine ( $\delta_H$  4.03) was assigned to be at C-16 according to the HMBC correlations from H-16 ( $\delta_H$  4.03) to C-14 ( $\delta_C$  49.5) and C-20 ( $\delta_C$  48.8). Finally, NOESY spectrum of **6** showed correlations of H-3 $\beta$  ( $\delta_H$  4.68) with H-29 $\alpha$  ( $\delta_H$  0.95) and H-16 $\beta$  ( $\delta_H$  4.03) with H-18 $\alpha$  ( $\delta_H$  0.78) concluded the structure of **6** as 3 $\alpha$ -[4'-carboxymethyl-3'-hydroxy-3'-methylbutanoyloxy]-16 $\alpha$ -hydroxy-lanosta-8,24-dien-21-oic acid.

The molecular formula of **7** was determined as  $C_{32}H_{46}O_5$  according to its HRESIMS analytical data ( $[M+Na]^+$ ,  $m/z$  533.3236). Its IR spectrum had absorption peaks at 3447 (OH), 1729 (ketone), and 1597 (conjugate double bonds)  $cm^{-1}$ . The conjugate double bond was assigned to C-7/C-8/C-9/C-11 based on the proton signals of H-7 ( $\delta_H$  5.50, t,  $J = 3.5$  Hz) and H-11 ( $\delta_H$  5.40, d,  $J = 6.1$  Hz) and carbon signals of C-7 ( $\delta_C$  115.5), C-8 ( $\delta_C$  139.4), C-9 ( $\delta_C$  146.1) and C-11 ( $\delta_C$  122.2), respectively. Moreover, HMBC spectrum of **7** confirmed the assignment based on the correlations of H-7 ( $\delta_H$  5.50)/C-5 ( $\delta_C$  44.2) and C-14 ( $\delta_C$  44.3), H-11 ( $\delta_H$  5.40)/C-10 ( $\delta_C$  37.5), and C-13 ( $\delta_C$  42.5), H-19 ( $\delta_H$  1.02)/C-9 ( $\delta_C$  146.1), and H-30 ( $\delta_H$  1.11)/C-8 ( $\delta_C$  139.4). In addition, 3-acetoxy substitution was assigned based on the chemical shifts of H-2' ( $\delta_H$  2.05, s), C-1' ( $\delta_C$  170.8), and C-2' ( $\delta_C$  21.3), and also by the HMBC correlations from H-2' to C-1', and from H-3 to C-1'. Furthermore, H-3 $\beta$  ( $\delta_H$  4.69, t,  $J = 2.4$  Hz) with smaller coupling constant had NOE correlation with H-29 $\alpha$  ( $\delta_H$  1.00) in the NOESY spectrum indicating 3-acetoxy to be in  $\alpha$  orientation [23]. Another carbonyl group was assigned to be at C-16 based on the HMBC correlations of H-15 ( $\delta_H$  2.16, 2.40) and H-17 ( $\delta_H$  2.62) with C-16 ( $\delta_C$  217.2). Therefore, the structure of **7** was constructed as 3 $\alpha$ -acetoxy-16-oxo-lanosta-7,9 (11),24-trien-21-oic acid, and it was assigned a trivial name pinicolasin G.

The molecular formula of **8** was also determined as  $C_{32}H_{46}O_5$ , which was the same as that of **7**, indicating that **8** was an isomer of **7**. The 1D NMR signals of **8** were also very similar to those of **7**. The majority of the difference was the H-3 signal ( $\delta_H$  4.52, dd,  $J = 11.3, 4.9$  Hz;  $\delta_C$  80.5) on A ring. A previous study indicated the splitting pattern of H-3 $\alpha$  to be a doublet of doublet ( $J = 11-12$  and  $3-4$  Hz) or a triplet ( $J = 7-8$  Hz), and the chemical shift of C-3 carbon was at  $\delta_C$  75-78 ppm. [10] Additionally, H-3 $\alpha$  had correlation with H-28 $_{eq}$  ( $\delta_H$  0.89) in its NOESY spectrum. Moreover, HMBC spectrum of **8** revealed structure of 3-acetoxy-16-oxo-lanosta-7,9 (11),24-trien-21-oic acid according to correlations of H-3 ( $\delta_H$  4.52)/C-1 ( $\delta_C$  35.2)/C-5 ( $\delta_C$  49.2) and C-1' ( $\delta_C$  171.0), H-7 ( $\delta_H$  5.48)/C-5 ( $\delta_C$  49.2) and C-14 ( $\delta_C$  44.2), H-11 ( $\delta_H$  5.39)/C-10 ( $\delta_C$  37.6), and C-13 ( $\delta_C$  42.4), H-18 ( $\delta_H$  0.72)/C-12 ( $\delta_C$  34.9)/C-13 ( $\delta_C$  42.4)/C-14 ( $\delta_C$  44.2) and C-17 ( $\delta_C$  57.0), H-19 ( $\delta_H$  1.02)/C-1 ( $\delta_C$  35.2)/C-5 ( $\delta_C$  49.2)/C-9 ( $\delta_C$

146.1) and C-10 ( $\delta_C$  37.6), H-24 ( $\delta_H$  5.13)/C-26 ( $\delta_C$  17.7)/C-27 ( $\delta_C$  25.7), H-26 ( $\delta_H$  1.59) and H-27 ( $\delta_H$  1.68)/C-24 ( $\delta_C$  123.3) and C-25 ( $\delta_C$  132.4), H-28 ( $\delta_H$  0.89) and H-29 ( $\delta_H$  0.96)/C-3 ( $\delta_C$  80.5)/C-4 ( $\delta_C$  37.5) and C-5 ( $\delta_C$  49.2), H-30 ( $\delta_H$  1.11)/C-8 ( $\delta_C$  139.4)/C-13 ( $\delta_C$  42.4) and C-14 ( $\delta_C$  44.2) and H-2' ( $\delta_H$  2.07)/C-1' ( $\delta_C$  171.0). Therefore, **8** was established as 3 $\beta$ -acetoxy-16-oxo-lanosta-7,9 (11),24-trien-21-oic acid, and was named as pinicolasin H.

Pinicolasin I (**9**) has a molecular formula of  $C_{32}H_{48}O_5$  based on the sodiated pseudomolecular ion peak at  $m/z$  535.3392 ( $[M+Na]^+$ ) in the HRESIMS analysis. Comparison of  $^1H$  and  $^{13}C$  NMR spectra of **9** with those of **7** indicated that the majority of the signals were similar except the presence of an oxygenated methine ( $\delta_H$  4.31, dd,  $J = 9.8, 5.8$  Hz;  $\delta_C$  74.4) and the disappearance of a carbonyl signal ( $\delta_C$  217.2). Therefore, a skeleton of 3-acetoxy-hydroxy-lanosta-7,9 (11),24-trien-21-oic acid was confirmed [24]. The position of the additional hydroxyl group was assigned at C-15 based on HMBC correlations of H-15 ( $\delta_H$  4.31) with C-8 ( $\delta_C$  140.5) and C-30 ( $\delta_C$  22.5). In addition, H-15 had an NOE effect with H-18 $\alpha$  ( $\delta_H$  0.69) indicating the  $\beta$  orientation of H-15. The orientation of H-3 was assigned to be  $\beta$  via the chemical shift of C-3 ( $\delta_C$  78.0) and the splitting pattern of H-3 (t,  $J = 2.8$  Hz). Moreover, NOE effect of H-3 ( $\delta_H$  4.67) with H-29 $\alpha$  ( $\delta_H$  0.98) also confirmed the  $\beta$  orientation of H-3. Thus, the structure of **9** was concluded to be 3 $\alpha$ -acetoxy-15 $\alpha$ -hydroxy-lanosta-7,9 (11),24-trien-21-oic acid.

Pinicolasin J (**10**) was purified as a white powder with a molecular formula of  $C_{37}H_{56}O_8$  on the basis of HRESIMS analytical data ( $[M+Na]^+$ ,  $m/z$  651.3870). detailed analysis of its  $^1H$  and  $^{13}C$  NMR spectra revealed a lanosta-7,9,24-trien-21-oic acid skeleton [25] and the same side chain, 4-carboxymethyl-3-hydroxy-3-methylbutanoyl as that in **6** was observed based on the proton signals at  $\delta_H$  2.69 (d,  $J = 2.8$  Hz), 1.35 (s), 2.68 (d,  $J = 4.3$  Hz), and 3.64 (s) and the carbon signals at  $\delta_C$  172.4, 46.0, 70.9, 28.2, 46.5, 173.2, and 52.1 [10]. HMBC spectral analysis confirmed the linkage via H-3 with C-1'/C-2', H-2' with C-4'/C-5', H-5' with C-2'/C-4'/C-6', OMe-6' with C-6', and H-4' with C-2'/C-3'/C-5', respectively. Moreover, H-3 $\beta$  ( $\delta_H$  4.70, t,  $J = 2.5$  Hz) with smaller coupling constant had NOE correlation with H-29 $\alpha$  ( $\delta_H$  1.03) in the NOESY spectrum indicating the  $\alpha$  linkage of the side chain [10]. Additionally, 16 $\alpha$ -hydroxy substitution was assigned based on the HMBC correlations from H-16 ( $\delta_H$  4.03, t,  $J = 7.0$  Hz) to C-14 ( $\delta_C$  50.0) and C-20 ( $\delta_C$  48.6), and the observed NOE effect between H-16 and H-18 $\alpha$  ( $\delta_H$  0.64). Thus, the structure of **10** was confirmed as 3 $\alpha$ -[4'-carboxymethyl-3'-hydroxy-3'-methylbutanoyloxy]-16 $\alpha$ -hydroxy-lanosta-7,9 (11),24-trien-21-oic acid.

The molecular formula of **11** was assigned as  $C_{33}H_{50}O_5$  based on the HRESIMS analytical data ( $[M+Na]^+$ ,  $m/z$  549.3549). Its  $^1H$  and  $^{13}C$  NMR spectra had the typical acetoxy signals at  $\delta_H$  2.07 and  $\delta_C$  170.8, 21.3. The remaining signals consisted of seven methylenes, ten methylenes including a terminal methylene ( $\delta_H$  4.77, s;  $\delta_H$  4.74, s;  $\delta_C$  107.1), five methines including one oxygenated signal ( $\delta_H$  4.67, t,  $J = 2.6$  Hz), and nine quaternary carbons including two carbonyl signals ( $\delta_C$  217.9 and 179.9). Analysis of the terminal methylene revealed a lanostane-type  $C_{31}$  triterpenoid basic skeleton based on the HMBC correlations of H-31 ( $\delta_H$  4.77 and 4.74) with C-23 ( $\delta_C$  32.0), C-24 ( $\delta_C$  154.7), C-25 ( $\delta_C$  33.6) [10,26]. Moreover, C-16 carbonyl was determined according to the HMBC correlations of H-15 ( $\delta_H$  1.96, 2.35)/C-16 ( $\delta_C$  217.9) and H-17 ( $\delta_H$  2.60, t,  $J = 9.7$  Hz)/C-16. Additionally, the chemical shift and splitting pattern of H-3 ( $\delta_H$  4.67, t,  $J = 2.6$  Hz) and C-3 ( $\delta_C$  77.8) indicated the  $\beta$  orientation of H-3. Therefore, **11** was confirmed as 3 $\alpha$ -acetoxy-16-oxo-lanosta-8,24 (31)-dien-21-oic acid.

Pinicolasin L (**12**) had a molecular formula of  $C_{33}H_{52}O_5$  deduced from HRESIMS pseudomolecular ion peak at  $m/z$  551.3709. Its  $^1H$  and  $^{13}C$  NMR had the signals characteristic for a lanostane-type  $C_{31}$  triterpenoid [10,26]. Comparison of its spectra with those of **11** revealed the presence of one additional hydroxyl in **12** and disappearance of the carbonyl signal detected in **11** confirming a skeleton of 3-acetoxy-hydroxy-lanosta-8,24(31)-dien-21-oic acid. The hydroxyl functionality was determined to be at C-15 based on the HMBC correlation from H-15

( $\delta_{\text{H}}$  4.25) to C-30 ( $\delta_{\text{C}}$  17.0), and H-15 was in the  $\beta$  orientation due to the NOE effect of H-15/H-18<sub>ax</sub> ( $\delta_{\text{H}}$  0.81). Furthermore, NOE effect was detected between H-3 ( $\delta_{\text{H}}$  4.66) and H-29<sub>ax</sub> ( $\delta_{\text{H}}$  0.91) indicating the  $\beta$  orientation of H-3. Moreover, the NOE correlations of H-18<sub>ax</sub>/H-15 and H-18<sub>ax</sub>/H-20 indicated the orientation of substitutions at C-13, -15, and -20 to be  $\beta$ ,  $\alpha$ , and  $\alpha$ , respectively, as shown in Fig. 3. Consequently, the structure of **12** was confirmed as 3 $\alpha$ -acetoxy-15 $\alpha$ -hydroxy-lanostan-8,24(31)-dien-21-oic acid.

The HRESIMS analytical data of **13** ( $[\text{M}+\text{Na}]^+$ ,  $m/z$  547.3395) established its molecular formula as C<sub>33</sub>H<sub>48</sub>O<sub>5</sub>. Its IR spectra had absorption peaks at 3701 (OH), 1733 (carbonyl) and 1607 (conjugated double bonds) cm<sup>-1</sup>. Based on the <sup>1</sup>H and <sup>13</sup>C NMR signals of  $\delta_{\text{H}}$  4.78 (1H, s),  $\delta_{\text{H}}$  4.75 (1H, s), and  $\delta_{\text{C}}$  107.2 and comparison of its spectra with those of **12** and **7**, a lanostane-type C<sub>31</sub> triterpenoid skeleton was confirmed [10,26]. Combination of the IR and NMR spectral signals of  $\delta_{\text{H}}$  5.50 (1H, t,  $J$  = 4.0 Hz) and 5.41 (1H, d,  $J$  = 6.3 Hz) and four olefinic carbons ( $\delta_{\text{C}}$  122.2, 139.4, 146.1 and 111.5),  $\Delta^{7,8}$  and  $\Delta^{9,11}$  were assigned. Detailed HMBC analytical results also supported this assignment via the correlations from H-7( $\delta_{\text{H}}$  5.50) to C-5 ( $\delta_{\text{C}}$  44.2) and C-14 ( $\delta_{\text{C}}$  44.3); from H-11 ( $\delta_{\text{H}}$  5.41) to C-10 ( $\delta_{\text{C}}$  37.5) and C-13 ( $\delta_{\text{C}}$  42.5); from H-19 ( $\delta_{\text{H}}$  0.97) to C-9 ( $\delta_{\text{C}}$  146.1); and from H-30 ( $\delta_{\text{H}}$  1.12) to C-8 ( $\delta_{\text{C}}$  139.4), respectively. Moreover, a typical 3-acetoxy group and a C-16 carbonyl group were detected by 2D-NMR experimental analysis. Its NOESY spectrum had a correlation between H-3 $\beta$  ( $\delta_{\text{H}}$  4.69,  $t$ ,  $J$  = 2.9 Hz) and H-29<sub>ax</sub> ( $\delta_{\text{H}}$  1.00) supporting a 3 $\alpha$ -acetoxy substitution. Thus, **13** was confirmed as 3 $\alpha$ -acetoxy-16-oxo-lanosta-7,9,24(31)-trien-21-oic acid, and was trivially named as pinicolasin M.

In addition to these thirteen undescribed triterpenoids, twenty-one known constituents were identified, including trametenolic acid **B** (**14**), 16 $\alpha$ -hydroxytrametenolic acid (**15**), 3 $\alpha$ -acetoxy-lanosta-8,24-dien-21-oic acid (**16**), fomipinic acid **C** (**17**), 3 $\alpha$ -acetoxy-16-oxolanosta-8,24-dien-21-oic acid (**18**), 3 $\beta$ -acetoxy-15 $\alpha$ -hydroxylanosta-8,24-dien-21-oic acid (**19**), 3 $\beta$ -acetyl-16 $\alpha$ -hydroxytrametenolic acid (**20**), pinicolic acid **E** (**21**), 16 $\alpha$ -hydroxy-3-oxolanosta-7,9(11),24-trien-21-oic acid (**22**), 6 $\alpha$ ,16 $\alpha$ -dihydroxy-3-oxolanosta-7,9(11),24-trien-21-oic acid (**23**), pipitolinic acid **D** (**24**), 3 $\alpha$ ,16 $\alpha$ -dihydroxylanosta-7,9(11),24-trien-21-oic acid (**25**), 3 $\beta$ ,16 $\alpha$ -dihydroxylanosta-7,9(11),24-trien-21-oic acid (**26**), tumulosic acid (**27**), 3 $\alpha$ -pachymic acid (**28**), pachymic acid (**29**), 3-*epi*-dehydro-pachymic acid (**30**), dehydrotumulosic acid (**31**), 6 $\alpha$ -hydroxy-poly-porenic acid **C** (**32**), poly-porenic acid **C** (**33**) and daedaleanic acid **A** (**34**) (references are provided in Supporting Information). The anti-inflammatory activities of the thirty-two compounds isolated in sufficient quantity were evaluated in a human neutrophil cell model to test their inhibition of the production of superoxide anion and elastase in human neutrophils activated with *N*-formyl-L-methionyl-L-leucyl-L-phenylalanine/cytochalasin B (fMLF/CB). Compound **10** with a 4-carboxymethyl-3-hydroxy-3-methyl-butanoyl side chain had the most potent antiinflammatory activity with the IC<sub>50</sub> of 1.81  $\pm$  0.44  $\mu\text{M}$  for inhibition of superoxide anion generation and the IC<sub>50</sub> of 2.50  $\pm$  0.64  $\mu\text{M}$  for inhibition of elastase release. Compound **6** with the same side chain also demonstrated good inhibition of superoxide anion generation with the IC<sub>50</sub> of 4.77  $\pm$  0.97  $\mu\text{M}$  and inhibition of elastase release with the IC<sub>50</sub> of 6.66  $\pm$  0.30  $\mu\text{M}$  for; the reference compound was genistein (IC<sub>50</sub> 1.62  $\pm$  0.14  $\mu\text{M}$  for superoxide anion generation and IC<sub>50</sub> of 35.95  $\pm$  1.53  $\mu\text{M}$  for inhibition of elastase release). Generally, C-3 carbonyl-bearing compounds had inferior antiinflammatory activity. Differences in the receptor-binding mode or different mechanisms of action may account for these results because no clear structure-activity relationship was observed.

#### 4. Conclusions

Thus, a total of thirty-four triterpenoids, including twelve undescribed compounds, were isolated from *Fomitopsis pinicola* (Sw.) P. Karst. Their structures were characterized by spectroscopic and spectrometric analyses as C<sub>30</sub> or C<sub>31</sub> lanostane-type triterpenoids. Antiinflammatory

activity of thirty-two purified compounds was tested using superoxide anion generation and elastase release as biomarkers. Compound **10** with a 4-carboxymethyl-3-hydroxy-3-methyl-butanoyl side chain had the most potent antiinflammatory activity for inhibition of superoxide anion generation and elastase release. Among all the tested isolates, compounds with C-3 carbonyl had inferior antiinflammatory activity and compounds with a 4-carboxymethyl-3-hydroxy-3-methyl-butanoyl side chain had good antiinflammatory activity. This study provides evidence supporting the use of *Fomitopsis pinicola* in nutritional supplements and as a lead in drug discovery.

#### Declaration of Competing Interest

The authors declare that they have no known competing financial interests or personal relationships that could have appeared to influence the work reported in this paper.

#### Acknowledgements

This study was sponsored by the Ministry of Science and Technology, Taiwan. Authors are thankful to Chang Gung Memorial Hospital (CMRPD1B0281~3, CMRPF1D0442~3, CMRPF 1F0011~3, CMRPF1F0061~3 and BMRP450 granted to T.-L.H.) for the partial financial support of the present study. Thanks Dr. He-Ping Chen at School of Pharmaceutical Sciences, South-Central University for Nationalities for correcting some mistakes.

#### Appendix A. Supplementary material

Supplementary data to this article can be found online at <https://doi.org/10.1016/j.bioorg.2020.104562>.

#### References

- [1] J.-E. Haight, G.A. Laursen, J.A. Glaeser, D.L. Taylor, Phylogeny of *Fomitopsis pinicola*: a species complex, *Mycologia* 108 (2016) 925–938.
- [2] U. Grienke, M. Zöll, U. Peintner, J.M. Rollinger, European medicinal polypores – a modern view on traditional uses, *J. Ethnopharmacol.* 154 (2014) 564–583.
- [3] D. Choi, S.-S. Park, J.-L. Ding, W.-S. Cha, Effects of *Fomitopsis pinicola* extracts on antioxidant and antitumor activities, *Biotechnol. Bioprocess Eng.* 12 (2007) 516–524.
- [4] S.I. Lee, J.S. Kim, S.H. Oh, K.Y. Park, H.G. Lee, S.D. Kim, Antihyperglycemic effect of *Fomitopsis pinicola* extracts in streptozotocin-induced diabetic rats, *J. Med. Food* 11 (2008) 518–524.
- [5] W.-S. Cha, J.-L. Ding, H.-J. Shin, J.-S. Kim, Y.-S. Kim, D. Choi, H.-D. Lee, H.-B. Kang, C.-W. Lee, Effect of *Fomitopsis pinicola* extract on blood glucose and lipid metabolism in diabetic rats, *Korean J. Chem. Eng.* 26 (2009) 1696–1699.
- [6] K.S. Bishop, Characterisation of extracts and anti-cancer activities of *Fomitopsis pinicola*, *Nutrients* 12 (2020) 609–619.
- [7] A.C. Keller, M.P. Maillard, K. Hostettmann, Antimicrobial steroids from the fungus *Fomitopsis pinicola*, *Phytochemistry* 41 (1996) 1041–1046.
- [8] K. Yoshikawa, M. Inoue, Y. Matsumoto, C. Sakakibara, H. Miyatake, H. Matsumoto, S. Arihara, Lanostane triterpenoids and triterpene glycosides from the fruit body of *Fomitopsis pinicola* and their inhibitory activity against COX-1 and COX-2, *J. Nat. Prod.* 68 (2005) 69–73.
- [9] Y. Wang, X. Cheng, P. Wang, L. Wang, J. Fan, X. Wang, Q. Liu, Investigating migration inhibition and apoptotic effects of *Fomitopsis pinicola* chloroform extract on human colorectal cancer SW-480 cells, *PLoS one* 9 (2014), e101303.
- [10] X.R. Peng, H.G. Su, J.H. Liu, Y.J. Huang, X.Z. Yang, Z.R. Li, L. Zhou, M.H. Qiu, C30 and C31 triterpenoids and triterpene sugar esters with cytotoxic activities from edible mushroom *Fomitopsis pinicola* (Sw. Ex Fr.) Krast, *J. Agric. Food Chem.* 67 (2019) 10330–10341.
- [11] S.-H. Tai, P.-C. Kuo, C.-C. Hung, Y.-H. Lin, T.-L. Hwang, S.H. Lam, D.-H. Kuo, J.-B. Wu, H.-Y. Hung, T.-S. Wu, Bioassay-guided purification of sesquiterpenoids from the fruiting bodies of *Fomitopsis pinicola* and their anti-inflammatory activity, *RSC Adv.* 9 (2019) 34184–34195.
- [12] K.M. Pietrosimone, P. Liu, Contributions of neutrophils to the adaptive immune response in autoimmune disease, *World J. Transl. Med.* 4 (2015) 60–68.
- [13] S.C. Yang, P.J. Chung, C.M. Ho, C.Y. Kuo, M.F. Hung, Y.T. Huang, W.Y. Chang, Y. W. Chang, K.H. Chan, T.L. Hwang, Propofol inhibits superoxide production, elastase release, and chemotaxis in formyl peptide-activated human neutrophils by blocking formyl peptide receptor 1, *J. Immunol.* 190 (2013) 6511–6519.
- [14] T. Kamo, M. Asanoma, H. Shibata, M. Hirota, Anti-inflammatory lanostane-type triterpene acids from *Piptoporus betulinus*, *J. Nat. Prod.* 66 (2003) 1104–1106.

- [15] Z. Tohtahon, J.J. Xue, J.X. Han, Y.S. Liu, H.M. Hua, T. Yuan, Cytotoxic lanostane triterpenoids from the fruiting bodies of *Piptoporus betulinus*, *Phytochemistry* 143 (2017) 98–103.
- [16] L. Zhou, Y.C. Zhang, L.A. Gapter, H. Ling, R. Agarwal, K.Y. Ng, Cytotoxic and anti-oxidant activities of lanostane-type triterpenes isolated from *Poria cocos*, *Chem. Pharm. Bull. (Tokyo)* 56 (2008) 1459–1462.
- [17] T. Akihisa, T. Hori, H. Suzuki, T. Sakoh, 24 $\beta$ -Methyl-5 $\alpha$ -cholest-9(11)en-3 $\beta$ -ol, two 24 $\beta$ -alkyl- $\Delta^{5,7,9(11)}$ -sterols and other 24 $\beta$ -alkylsterols from *Chlorella vulgaris*, *Phytochemistry* 31 (1992) 1769–1772.
- [18] T. Akihisa, W.C.M.C. Kokke, J.A. Krause, D.S. Eggleston, S. Katayama, Y. Kimura, T. Tamura, 5-Dehydrokarounidiol [D:C-Friedo-oleana-5,7,9(11)-triene-3 $\alpha$ ,29-diol], a novel triterpene from *Trichosanthes kirilowii* Maxim, *Chem. Pharm. Bull.* 40 (1992) 3280–3283.
- [19] M. Uklya, T. Akihisa, H. Tokuda, M. Hirano, M. Oshikubo, Y. Nobukuni, Y. Kimura, T. Tai, S. Kondo, H. Nishino, Inhibition of tumor-promoting effects by poricoic acids G and H and Other lanostane-type triterpenes and cytotoxic activity of poricoic acids A and G from *Poria cocos*, *J. Nat. Prod.* 65 (2002) 462–465.
- [20] J. Zhang, B. Chen, J. Liang, J. Han, L. Zhou, R. Zhao, H. Liu, H. Dai, Lanostane triterpenoids with PTP1B inhibitory and glucose-uptake stimulatory activities from mushroom *Fomitopsis pinicola* collected in North America, *J. Agric. Food Chem.* 68 (2020) 10036–10049.
- [21] I. Sofrenić, B. Anđelković, N. Todorović, T. Stanojković, L. Vujisić, M. Novaković, S. Milosavljević, V. Tešević, Cytotoxic triterpenoids and triterpene sugar esters from the medicinal mushroom *Fomitopsis betulina*, *Phytochemistry* 181 (2021), 112580.
- [22] Y.-M. Ying, W.-G. Shan, L.-W. Zhang, Y. Chen, Z.-J. Zhan, Lanostane triterpenes from *Ceriporia lacerate* HS-ZJUT-C13A, a fungal endophyte of *Huperzia serrata*, *Helvetica Chimica Acta* 96 (2013) 2092–2097.
- [23] M. Hirotani, I. Asaka, C. Ino, T. Furuya, M. Shiro, Ganoderic acid derivatives and ergosta-4,7,22-triene-3,6-dione form *Ganoderma lucidum*, *Phytochemistry* 26 (1987) 2797–2803.
- [24] T. Tai, T. Shingu, T. Kikuchi, Y. Tezuka, A. Akahori, Isolation of lanostane-type triterpene acids having an acetoxyl group from sclerotia of *Poria cocos*, *Phytochemistry* 40 (1995) 225–231.
- [25] K.H. Lai, M.C. Lu, Y.C. Du, M. El-Shazly, T.Y. Wu, Y.M. Hsu, A. Henz, J.C. Yang, A. Backlund, F.R. Chang, Y.C. Wu, Cytotoxic lanostanoids from *Poria cocos*, *J. Nat. Prod.* 79 (2016) 2805–2813.
- [26] T. Shingu, T. Tai, A. Akahori, A lanostane triterpenoid from *Poria cocos*, *Phytochemistry* 31 (1992) 2548–2549.

## Research Paper

# Berberine Inhibits Pro-inflammatory Cytokine-induced IL-6 and CCL11 Production via Modulation of STAT6 Pathway in Human Bronchial Epithelial Cells

Jason Ma<sup>1\*</sup>, Cheng-Chi Chan<sup>2\*</sup>, Wen-Chung Huang<sup>3,4,5</sup> and Ming-Ling Kuo<sup>1,4,5</sup>✉

1. Department of Microbiology and Immunology, Graduate Institute of Biomedical Sciences, College of Medicine, Chang Gung University, Taoyuan, Taiwan.
2. Cancer Vaccine and Immune Cell Therapy Core Laboratory, Chang Gung Immunology Consortium, Chang Gung Memorial Hospital, Linkou, Taoyuan, Taiwan.
3. Graduate Institute of Health Industry Technology, Research Center for Food and Cosmetic Safety, College of Human Ecology, Chang Gung University of Science and Technology, Taoyuan City, Taiwan.
4. Research Center for Chinese Herbal Medicine, College of Human Ecology, Chang Gung University of Science and Technology, Taoyuan City, Taiwan.
5. Division of Allergy, Asthma, and Rheumatology, Department of Pediatrics, Chang Gung Memorial Hospital, Taoyuan, Taiwan.

\*These authors contributed equally to this work.

✉ Corresponding author: Dr. Ming-Ling Kuo, Department of Microbiology and Immunology, College of Medicine, Chang Gung University, 259 Wen-Hwa 1st Road, Kwei-Shan, Tao-Yuan, TAIWAN. TEL: 886-3-2118800, ext 3319, FAX: 886-3-2118293, E-mail: mingling@mail.cgu.edu.tw.

© The author(s). This is an open access article distributed under the terms of the Creative Commons Attribution License (<https://creativecommons.org/licenses/by/4.0/>). See <http://ivyspring.com/terms> for full terms and conditions.

Received: 2020.02.27; Accepted: 2020.05.29; Published: 2020.06.08

## Abstract

Berberine is an isoquinoline alkaloid isolated from various Chinese herbs that has potential of anti-inflammatory, anti-lipidemic, anti-neoplastic, and anti-diabetic activity. In this study, we evaluated the anti-inflammatory efficacy of berberine on allergic airway inflammation by targeting epithelial cells. Allergic airway inflammation driven by T helper 2 (Th2)-type immunity is characterized by airway hyperresponsiveness, elevated IgE production, and eosinophilic infiltration. For eosinophil recruitment, major chemoattractant CCL11 (eotaxin-1) was secreted by lung epithelial cells. BEAS-2B cells, a human bronchial epithelial cell line, were pre-treated with berberine and then activated by IL-4 plus TNF- $\alpha$ . The viability of BEAS-2B cells was assessed. Expression levels of IL-6 and CCL11 were determined using ELISA and real-time PCR. The signaling pathways of MAP kinases, NF- $\kappa$ B, and STAT6 were analyzed by western blot. Berberine treatment ( $\leq 1 \mu$ M) didn't significantly affect the viability of BEAS-2B cells with or without IL-4 plus TNF-stimulation. Berberine significantly inhibited the secretion of IL-6 and CCL11 from pro-inflammatory cytokine-activated BEAS-2B cells. NF- $\kappa$ B and MAP kinase pathways were seemingly unaffected in BEAS-2B cells with berberine treatment. Significant reduction of nuclear STAT6 protein expression in activated BEAS-2B cells with berberine treatment was observed. Current study reveals that berberine has inhibitory effect in pro-inflammatory cytokine-activated BEAS-2B cells through reducing IL-6 and CCL11 production, which is possibly modulated by suppressing STAT6 signaling pathway.

Key words: Berberine, cytokines, asthma, eotaxin, epithelial cell

## Introduction

Asthma is one of the major public health concerns worldwide, with high prevalence and economic burden [1]. Asthma is a chronic inflammatory airway disease characterized by airflow obstruction, persistent inflammation, and airway hyperresponsiveness (AHR) to common environmental aero-allergens [2]. Asthmatic patients exhibit elevated allergen-specific IgE, mucus hypersecretion, and eosinophilia in the lungs. Most

treatments for asthma are based on western medicine, such as  $\beta$ 2-adrenergic receptor agonists, anti-IgE blockers, and corticosteroids combined with a long-acting bronchodilator, but only provide temporary alleviation of the symptoms [3]. In addition, steroids have certain side effects and some patients do not favorably respond to this treatment. Nevertheless, traditional Chinese medicines are reported to have



improved or curative effects in clinical trials for allergic diseases including asthma [4].

Airway epithelium acts as the first defense barrier against environmental stimuli by secreting numerous chemokines, cytokines and growth factors to recruit and activate a variety of immune cells including CD4<sup>+</sup> T helper 2 (Th2) cells, mast cells, and eosinophils [5]. Th2 cytokines, especially interleukin (IL)-4, IL-5, and IL-13, and other inflammatory mediators secreted by eosinophils and mast cells are primarily thought to orchestrate pathological features of asthma [6]. CCL11 (eotaxin-1), the most potent chemokine for eosinophil movement, is secreted by bronchial epithelial and endothelial cells and its receptor, CCR3, is highly expressed on eosinophils [7]. CCL11 is also verified to activate eosinophils by eliciting the release of RNase and cell-free granules [8]. Significant increase of CCL11 levels is detected in blood, sputum, and exhaled breath condensate (EBC) of asthmatic patients compared with healthy subjects [9]. Moreover, the disruption of CCL11 gene expression effectively reduces tissue eosinophilia [10]. Therefore, the reduction of eosinophil recruitment by inhibiting CCL11 expression in the lungs might have therapeutic potential for asthma.

The level of pro-inflammatory cytokine IL-6 was elevated in asthma patients [11]. A large variety of cells can produce IL-6, including cells from innate immune system, endothelial cells, fibroblasts, epithelial cells, etc. [12]. IL-6 functions as a growth factor for B cells and also contributes to CD4 T cells differentiation [13]. The presence of IL-6 promotes autocrine IL-4 production by activating STAT3 and ERK pathway [14], IL-5 production by p38 pathway, with the help of IL-2 signaling [15], and further enhances Th2 differentiation through an auto-feedback loop. Nonetheless, elevation of IL-6 is also correlated with elevated level of IL-13 and increased in asthma patients [16]. Taken together, targeting IL-6 may alleviate asthmatic responses by obstructing Th2 differentiation.

Previous papers showed that IL-4 and tumor necrosis factor (TNF)- $\alpha$  can stimulate the fibroblasts of nasal polyps to produce eotaxin-1 [17, 18]. Similarly, other evidences reveal that IL-4 plus TNF- $\alpha$  triggers the eotaxin secretion of human bronchial epithelial cells, BEAS-2B [19]. The activation of eotaxin gene expression is regulated by NF- $\kappa$ B and STAT6 in human airway epithelial cells upon IL-4 activation [19]. NF- $\kappa$ B pathway is also involved in regulating diverse inflammatory cytokine genes including IL-1 $\beta$  and TNF- $\alpha$  that re-stimulate immune cells and epithelial cells to exacerbate the inflammation [20]. With TNF- $\alpha$ , MAP kinases, which comprise the extracellular signal-regulated kinases (ERK), the p38

MAP kinases, and the c-Jun NH2-terminal kinases (JNK), can also be activated [21]. MAP kinase signaling pathways transduce a variety of extracellular signals that mediate cellular functions implicated in proliferation, differentiation, inflammation, and apoptosis [22].

Previous studies have reported that berberine, an alkaloid extracted from various traditional Chinese herbs, has pharmacological effects on intestinal bacteria, parasites, cardiovascular and cerebrovascular diseases, lowering blood sugar, and cancer [23]. In respiratory tract infections, berberine has been confirmed to suppress inflammatory agents, such as IL-1 $\beta$  and TNF- $\alpha$  by inhibiting I $\kappa$ B degradation in human lung cells [24]. Several papers also indicate that berberine decreases the inflammatory response by repressing the inflammation cytokine expression in colonic macrophages and epithelial cells or retinal pigment epithelial cells by down-regulating transcription factor NF- $\kappa$ B or the MAP kinase pathways [25, 26]. Based on these evidences, berberine is seemingly capable of suppressing the inflammatory responses.

In present study, we applied BEAS-2B cells, a human bronchial epithelial cell line, as an *in vitro* model to examine the anti-inflammatory efficacy of berberine on pro-inflammatory cytokine-stimulated epithelial cells. NF- $\kappa$ B, STAT6 and MAP kinases signaling pathways involved in modulating eotaxin gene expression are assessed.

## Materials and Methods

### Materials

Figure 1A shows the chemical structure of berberine chloride ( $\geq 98\%$  purity by TLC; Sigma-Aldrich). A stock solution of 20 mM berberine was prepared in DMSO (Sigma-Aldrich). The final DMSO concentration did not exceed 0.1% in the culture medium.

### Cell culture and berberine treatment

Human bronchial epithelial cells (BEAS-2B CRL-9609 cell line, ATCC) were cultured in Dulbecco's Modified Eagle Medium/Nutrient mixture F-12 (DMEM/F12) medium (Gibco) containing 10% fetal bovine serum (FBS, Gibco) and 1% penicillin/streptomycin (Gibco). Cells were seeded in 6-well plates ( $2 \times 10^6$  cells) or 24-well plates ( $4 \times 10^5$  cells) at 37 °C in a humidified 5% CO<sub>2</sub> atmosphere. Berberine chloride (Sigma-Aldrich) was dissolved in DMSO (Sigma-Aldrich), where same amount of DMSO for dissolving berberine was used as control for comparison. BEAS-2B cells were treated with or without different concentrations of berberine for 16-18 hours. After pre-treatment, BEAS-2B cells were



stimulated with IL-4 (20 ng/ml) (Peprotech) plus TNF- $\alpha$  (5 ng/ml) (Peprotech) and culture supernatants were harvested after 6 hours and 24 hours to detect IL-6 and CCL11 levels by ELISA assay. For inhibition assays, 10  $\mu$ M of JNK inhibitor-SP600125 (Enzo) and ERK inhibitor-PD-98059 (Enzo) were added one hour before cytokine stimulation and culture supernatants were harvested after 24 hours for IL-6 and CCL11 detection.

### Cell viability assay

BEAS-2B cells ( $2 \times 10^5$  cells) were seeded in a 48-well plate overnight and then were pre-treated with various concentrations of berberine or DMSO for 16–18 hours. After pre-treatment, cells were stimulated without or with IL-4 and TNF- $\alpha$  for 24 hours and the viability was analyzed by Cell Counting-kit 8 (CCK-8) (Sigma-Aldrich). Briefly, after the supernatants were harvested, cells were washed with 1 ml PBS and then CCK-8 was added into each well to incubate at 37 °C in a humidified 5% CO<sub>2</sub> atmosphere for 4 hours. Supernatants were transferred into a 96-well plate after incubation. Absorbance was measured on an ELISA reader at 450 nm (SpectraMax).

### Enzyme-linked immunosorbent assay

Culture supernatants were harvested following 6

or 24 hours of IL-4 and TNF- $\alpha$  stimulation. The levels of IL-6 and CCL11 (DuoSet ELISA kit, R&D systems) were determined by ELISA according to the manufacturer's instructions.

### RNA isolation and real-time polymerase chain reaction

RNA samples were collected at 3, 6, 12 and 24 hours after cytokine stimulation. Total RNA was extracted using TRIzol reagent (Invitrogen). Reverse transcription was performed by oligo-dT primers and M-MLV reverse transcriptase (Invitrogen). The mRNA expression of GAPDH, IL-6, and CCL11 were amplified by specific primers: 5'-GCAAATTCATGG CACCG-3' for GAPDH forward primer and 5'-TCGC CCCACTGATTTTGG-3' for GAPDH reverse primer; 5'-CCAATCTGGATTCAATGAGGAG-3' for IL-6 forward primer and 5'-GGTCAGGGGTGGTTATTGC ATC-3' for IL-6 reverse primer; 5'-AAAGCTCACACC TTCAGCCT-3' for CCL11 forward primer and 5'-TTT CTGGGGACATTTGCCAC-3' for CCL11 reverse primer. For real-time PCR, the reaction was performed by Lightcycler® 96 system (Roche) with iQ™ SYBR green supermix (Bio-rad). The relative expression of each gene was calculated by normalizing to the expression of GAPDH.

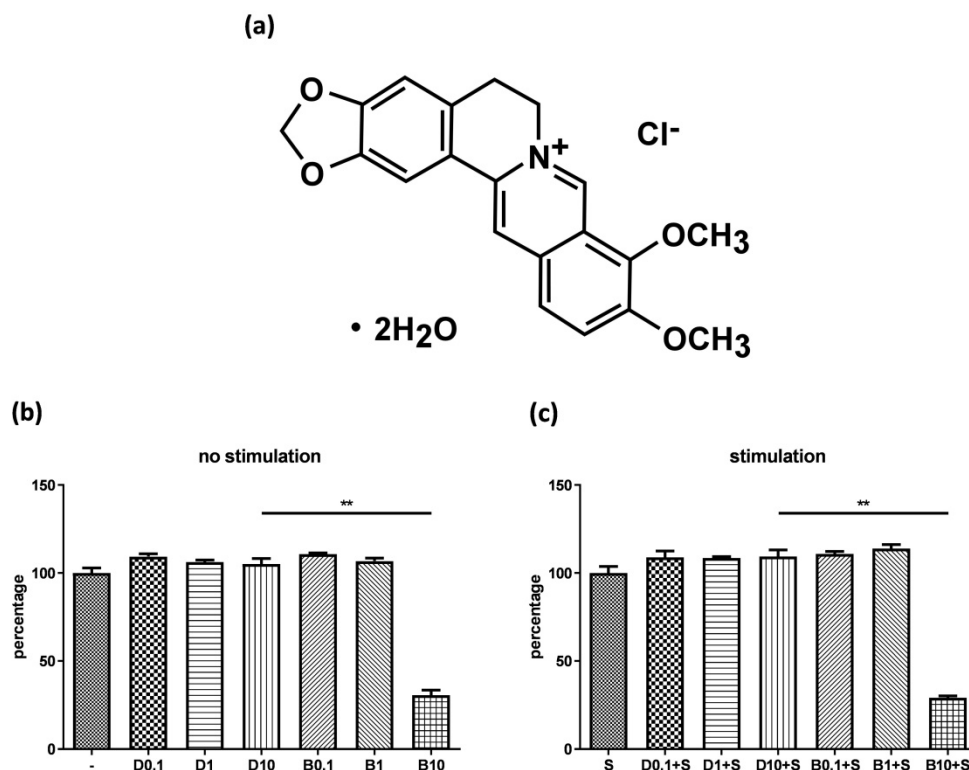


**Figure 1. Cytotoxicity of berberine on human bronchial epithelial cell line.** (A) The chemical structure of berberine. BEAS-2B cells were cultured in the 48-well plates overnight and then were treated with different concentrations of berberine (0.1  $\mu$ M to 10  $\mu$ M) or equal volume of DMSO for 16 to 18 hours. Subsequently, drug pre-treated cells were stimulated (A) without or (B) with pro-inflammation cytokines for 24 hours. The cell viability was analyzed by CCK-8 assay. The percentage was calculated by comparing the O.D. value with cell only group. Data are presented as mean  $\pm$  SEM (n= 6). S, pro-inflammation cytokine stimulation; D, DMSO; B, berberine. The number indicated the concentration ( $\mu$ M) of berberine or DMSO. \*\*P<0.01.

## The extraction of total cell, cytoplasm and nucleus protein

For total cell protein extraction, protein samples were collected at indicated time point after cytokine stimulation. Cells were lysed in cell lysis buffer containing 1 mM  $\text{Na}_3\text{VO}_4$ , 1 mM Tetraisoole, 25X diluted protease inhibitor, 5  $\mu\text{M}$   $\text{MgCl}_2$ , 20  $\mu\text{M}$  Tris-HCl, 50  $\mu\text{M}$  NaCl, 20% NP-40 on ice for 30 min. Cell lysates were centrifuged at 12,000 g for 30 min at 4 °C and the supernatants were harvested for western blot analysis. For cytoplasm and nucleus protein extraction, cell extracts were collected using Nuclear and Cytoplasmic Extraction Reagent kit (NE-PER kit) (Pierce Biotechnology) according to the manufacturer's instructions. Protein concentrations were determined using a BCA protein assay (Pierce Biotechnology) for western blot analysis.

## Western blot analysis

Protein samples (20  $\mu\text{g}$ ) were separated on sodium dodecyl sulfate-polyacrylamide gel, transferred to nitrocellulose membrane (Millipore) at 50 mA for 30 min and blocked in Tris-buffered saline with 0.1% Tween 20 (TBST) containing 5% BSA at room temperature for 1 hour. The blots were incubated with primary antibodies (rabbit anti-human antibody) to JNK, phosphorylated JNK, ERK, phosphorylated ERK, p38, phosphorylated p38, I $\kappa$ B, phosphorylated I $\kappa$ B, p65, STAT6, and phosphorylated STAT6, primary antibodies (mouse anti-human antibody) for  $\beta$ -actin and p38, and primary antibodies (goat anti-human antibody) for PCNA (Cell Signaling) overnight at 4 °C. Secondary antibodies conjugated with horseradish peroxidase were incubated for 2 hours. Finally, the blots were developed by using the Immobilon Western chemiluminescent HRP substrate (Millipore).

## Statistical analysis

Results are presented as mean  $\pm$  SEM. Significance was assessed using a two-tailed *P*-value calculated by the Mann-Whitney U test. *P* < 0.05 is considered significant. All graphs were generated and statistical analyses performed using GraphPad Prism 8.0 software.

## Results

### Determine berberine concentration for BEAS-2B without significant cytotoxic effect

Before examining anti-inflammatory efficacy of berberine, we evaluated whether berberine has cytotoxicity on BEAS-2B cell line. Cells were pre-treated with different concentrations of berberine (0.1  $\mu\text{M}$ -10  $\mu\text{M}$ ) or DMSO as control. Cells were

stimulated with or without IL-4 plus TNF- $\alpha$  for activation and cell viability was assayed. The data indicated berberine at 1  $\mu\text{M}$  or lower concentrations didn't affect the viability of BEAS-2B cells with or without pro-inflammatory cytokine stimulation compared with DMSO control (Figure 1B and C). Berberine had certain cytotoxic effect on BEAS-2B cells when treated with berberine higher than 10  $\mu\text{M}$  (Figure 1 and data not shown). Corresponded concentrations of DMSO control to berberine had no toxicity on BEAS-2B cells. Thus, in subsequent experiments, we used 1  $\mu\text{M}$  berberine to evaluate the anti-inflammatory effect of berberine on BEAS-2B cells.

### Berberine significantly reduced the production of IL-6 and CCL11 in pro-inflammatory cytokine-activated BEAS-2B cells

To assess the role of berberine on suppressing inflammatory mediators in bronchial epithelial cells, BEAS-2B cells were stimulated with IL-4 plus TNF- $\alpha$  for 6 and 24 hours. BEAS-2B cells without pro-inflammatory cytokine stimulation secreted low levels of IL-6 (Figure 2A and B) and CCL11 (Figure 2C and D). Significant amounts of IL-6 and CCL11 were detected in BEAS-2B cells after IL-4 plus TNF- $\alpha$  stimulation. Berberine (1  $\mu\text{M}$ ) significantly suppressed the protein levels of IL-6 (Figure 2A and B) and CCL11 (Figure 2C and D) in stimulated BEAS-2B cells compared to untreated group.

To carefully examine the gene expression, total RNA were collected from stimulated BEAS-2B cells with berberine pre-treatment at different time points and the gene expression of IL-6 and CCL11 were analyzed by real-time PCR (Figure 3). Obvious RNA expression of IL-6 and CCL11 were detected in BEAS-2B cells with pro-inflammatory cytokine stimulation (Figure 3A and B). Berberine treatment reduced the expression levels of IL-6 and CCL11 genes in stimulated BEAS-2B cells, which is consistent with cytokine secretion pattern. These results indicated that reduced inflammatory mediators (IL-6 and CCL11) in response to berberine pre-treatment may alleviate activated BEAS-2B cells-mediated airway inflammation.

### Significant reduction of nuclear STAT6 protein expression in activated BEAS-2B cells with berberine treatment

To investigate possible mechanisms involved in berberine-suppressed cytokine production, we first dissected the expression of STAT6 in BEAS-2B cells. Previous studies demonstrated that eotaxin-1 (CCL11) can be secreted from airway epithelial cells and fibroblasts after IL-4 plus TNF- $\alpha$  stimulation [17]. The

activation of STAT6 pathways play a pivotal role in regulating the expression of CCL11 gene [19]. We analyzed cytoplasmic and nuclear STAT6 in activated cells with or without berberine treatment by western blotting (Figure 4A). In both cytoplasm (Figure 4B) and nucleus (Figure 4C), lower STAT6 protein expression was observed after berberine treatment in activated BEAS-2B cells, while significantly decreased STAT6 protein was detected 6 hours after stimulation in the nucleus. Phosphorylated STAT6 expression was also decreased in nucleus after 60 minutes (Figure S1). These results suggest that berberine may reduce the expression of nuclear STAT6 protein in activated BEAS-2B cells to suppress the CCL11 production.

### Effect of berberine on MAP kinase pathways in activated BEAS-2B cells

To investigate how berberine suppressed IL-6 production in activated BEAS-2B cells, the expression and activity of MAP kinases and NF- $\kappa$ B were examined. The expression of p-JNK1/JNK1, p-JNK2/JNK2, p-ERK1/ERK1, and p-ERK2/ERK2 were detected in BEAS-2B cells with IL-4 plus TNF- $\alpha$  stimulation (Figure 5A and 6A). The expression levels of JNK and ERK proteins were not different between

each group after stimulation (Figure 5A and 6A). Relative expression levels of p-JNK1/JNK1 remains no change after berberine treatment, while p-JNK2/JNK2 (Figure 5B) was elevated 15 minutes after stimulation but later was recovered (Figure 5C). On the other hand, p-ERK1/ERK1, and p-ERK2/ERK2 (Figure 6B and C) were elevated in activated BEAS-2B cells with berberine treatment compared to untreated groups, but did not show significant difference. No significant differences were detected in p38 protein expression in activated BEAS-2B cells with or without berberine treatment and p-p38 expression levels were undetectable among the different groups (data not shown). We confirmed this result by adding JNK inhibitor or ERK inhibitor into berberine-treated and cytokine-activated BEAS-2B cells. The level of IL-6 (Figure S2A) and CCL11 (Figure S2B) were still suppressed in berberine treated group after using JNK and ERK inhibitors. Thus, berberine did not obviously affect the MAP kinase pathways of activated BEAS-2B cells. Also, berberine did not influence the expression levels of I $\kappa$ B (Figure 7B), p-I $\kappa$ B (Figure 7C) or p65 (Figure 7D), a subunit of NF- $\kappa$ B, in activated BEAS-2B cells.

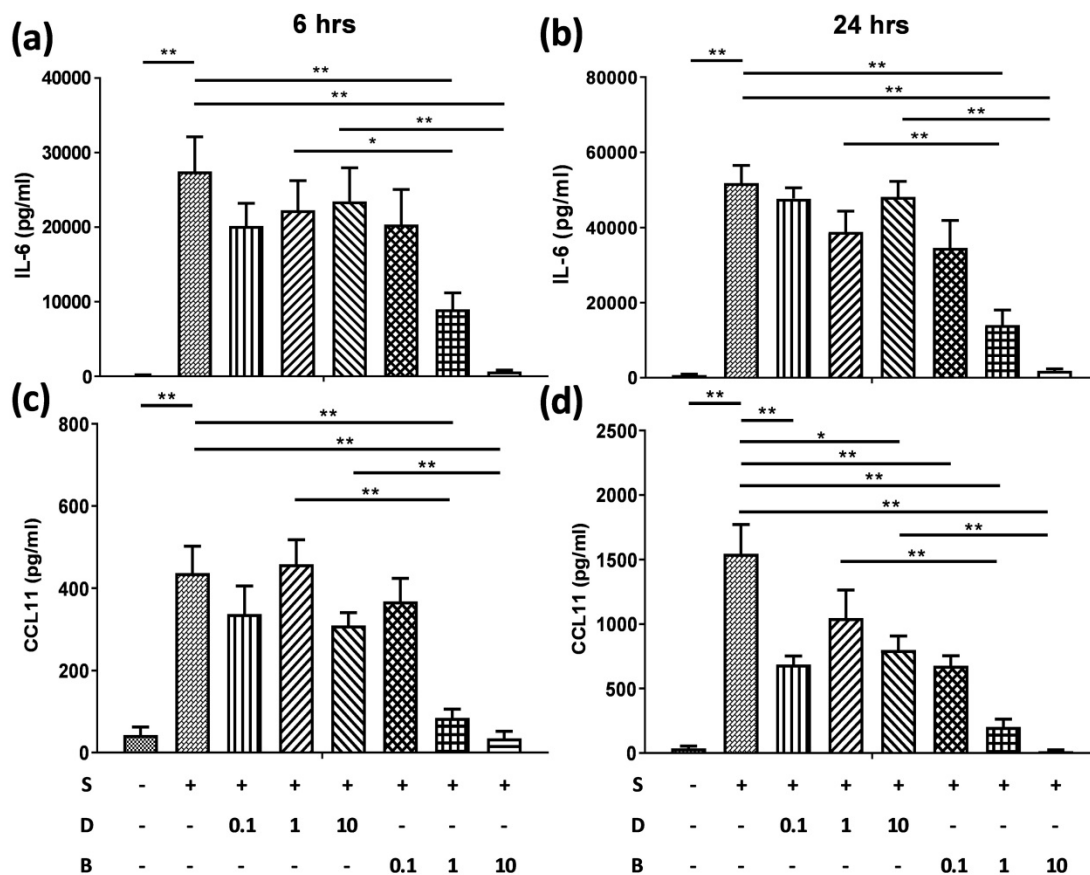


**Figure 2. Berberine pre-treatment suppressed pro-inflammatory cytokine-induced IL-6 and CCL11 production in the BEAS-2B cells.** BEAS-2B cells were seeded in the 48-well plate and treated with berberine (0.1  $\mu$ M to 10  $\mu$ M) or DMSO (control group) overnight. Cells with berberine pre-treatment were activated without or with IL-4 plus TNF- $\alpha$  for 6 and 24 hours. Culture supernatants were harvested and measured for (A, B) IL-6 and (C, D) CCL11 using ELISA. Data are presented as mean  $\pm$  SEM (n= 6). S, pro-inflammation cytokine stimulation; D, DMSO; B, berberine. The number indicated the concentration ( $\mu$ M) of berberine or DMSO. \*P<0.05; \*\*P<0.01.

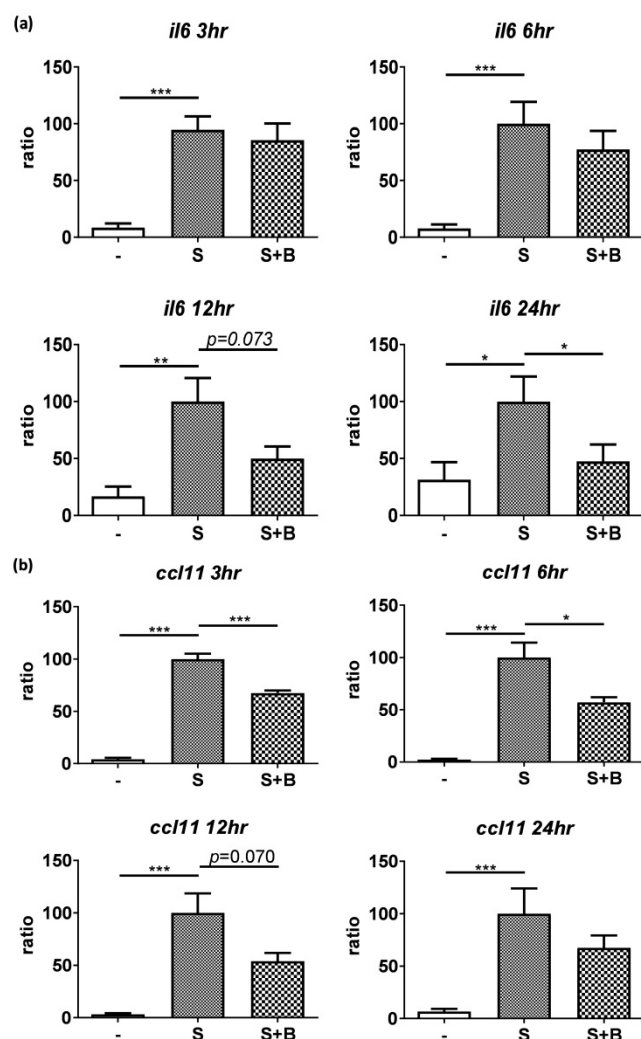


**Figure 3. Expression levels of IL-6 and CCL11 gene were reduced in pro-inflammatory cytokine-stimulated BEAS-2B cells with berberine pre-treatment.** Total RNA was extracted from IL-4 plus TNF- $\alpha$ -activated BEAS-2B cells pre-treated with berberine (1  $\mu$ M) at 3, 6, 12, and 24 hours. The RNA expression levels of (A) IL-6 and (B) CCL11 detected by real-time PCR, normalized with GAPDH and compared with stimulation group (n=7). Data are presented as mean  $\pm$  SEM. -, cell only; S, pro-inflammatory cytokine stimulation; B, berberine. \* $P$ <0.05, \*\* $P$ <0.01, \*\*\*  $P$ <0.001.

## Discussion

Allergic asthma is a chronic inflammatory disease of the airways that has become a global public health issue to result in a considerable burden on health services and expensive costs. The bronchial epithelium is recognized as a regulator of the initiation and maintenance of allergic airway inflammation [5]. Despite a growing number of pharmaceutical and immunotherapy strategies for asthma, the development of effective and long-term immunomodulatory approach has been difficult. In many Asian countries, traditional Chinese medicine is routinely used as maintenance of daily health care or as complementary treatment for conventional

Western medicine. Many evidences showed that traditional Chinese herb medicine has improved or therapeutic efficacy in allergic diseases, such as asthma, atopic dermatitis, and food allergy [27-29]. Here, our results demonstrated that berberine is capable of suppressing the secretion of IL-6 and CCL11 in pro-inflammatory cytokine-activated BEAS-2B cells, human airway epithelial cells. The inhibition of pro-inflammatory cytokine-induced IL-6 and CCL11 production by berberine may cause by reduction of nuclear STAT6 expression in activated cells. Consequently, berberine may be applied as a candidate for the improvement or treatment of allergic asthma.

Corticosteroids and bronchodilators are the most common treatment of asthma [30]. However, a few asthmatic patients respond poorly to these drugs or require higher doses to control the symptoms that lead to certain side-effects [31]. Some patients seek to improve asthma symptoms using alternative medicine, including Chinese herbal medicine, yoga, homeopathy, and even urine therapy [32]. Ma Xing Gan Shi Tang, Xiao Qing Long Tang, and Ding Chuan Tang are popular asthmatic complementary and alternative treatments which can modulate Th2 cell-driven airway inflammation [29, 33, 34]. However, these herbal formulas contain *Ephedra spp.*, which contains ephedrine, causes excitement and unwanted side effects [35]. Hence, other Chinese herbal formulas, single components, or pure compound extracts have been proved to relieve or treat the asthmatic symptoms, such as phloretin [36], ASHMI [37], MSSM-002 [38], and CVT-E002 [39]. ASHMI, which is composed by *Sophora flavescens*, *Glycyrrhiza uralensis*, and *Ganoderma lucidum*, suppresses AHR, airway eosinophilia, and Th2 cell-secreted cytokines in asthmatic mice [37]. ASHMI was also successfully applied for the Phase I of clinical trial to ameliorate FEV1, peak expiratory flow, and serum IgE levels [40]. Extract from plants or compounds also have therapeutic effects on asthma. For example, extracts of *Nigella sativa* or purple passion fruit peel were also reported to reduce asthmatic symptoms like cough, wheeze, and shortness of breath in asthmatic patients [41, 42]. Baicalin, a flavonoid compound isolated from *Scutellaria baicalensis*, was reported to suppress STAT3 expression and promotes FoxP3 expression to alleviate asthmatic symptoms in mice [43]. Therefore, single components or pure compound extracts from various Chinese herbs are able to serve as an attractive approach to modulate allergic asthma.



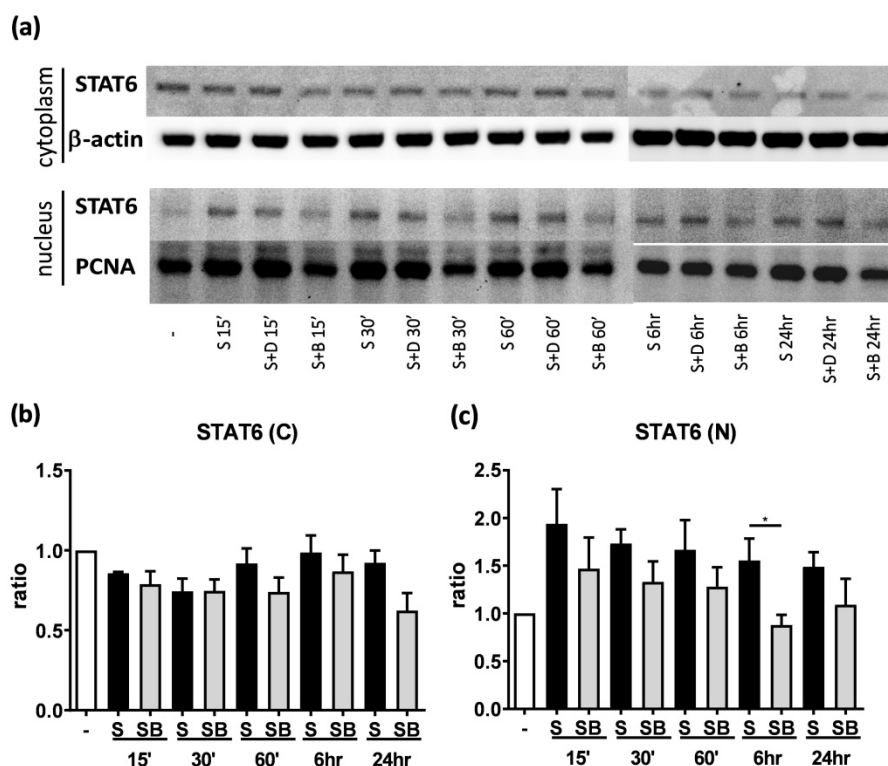


**Figure 4. Berberine down-regulates STAT6 protein expression in nucleus with pro-inflammatory cytokine stimulated BEAS-2B cells.** Cells with berberine (1  $\mu$ M) treatment were harvested on the indicated time points after IL-4 plus TNF- $\alpha$  stimulation and cytoplasm and nucleus proteins were extracted. (A) Expression levels of cytoplasm and nucleus STAT6 proteins were analyzed using western blotting (20  $\mu$ g per sample).  $\beta$ -actin and PCNA expression was used as an internal control. The relative quantity of (B) cytoplasm STAT6 (n=4) and (C) nucleus STAT6 (n=7) was normalized to  $\beta$ -actin and PCNA, respectively. Results are presented as mean  $\pm$  SEM. \* $P$ <0.05. -, cell only; S, pro-inflammation cytokine stimulation; D, DMSO, B, berberine.

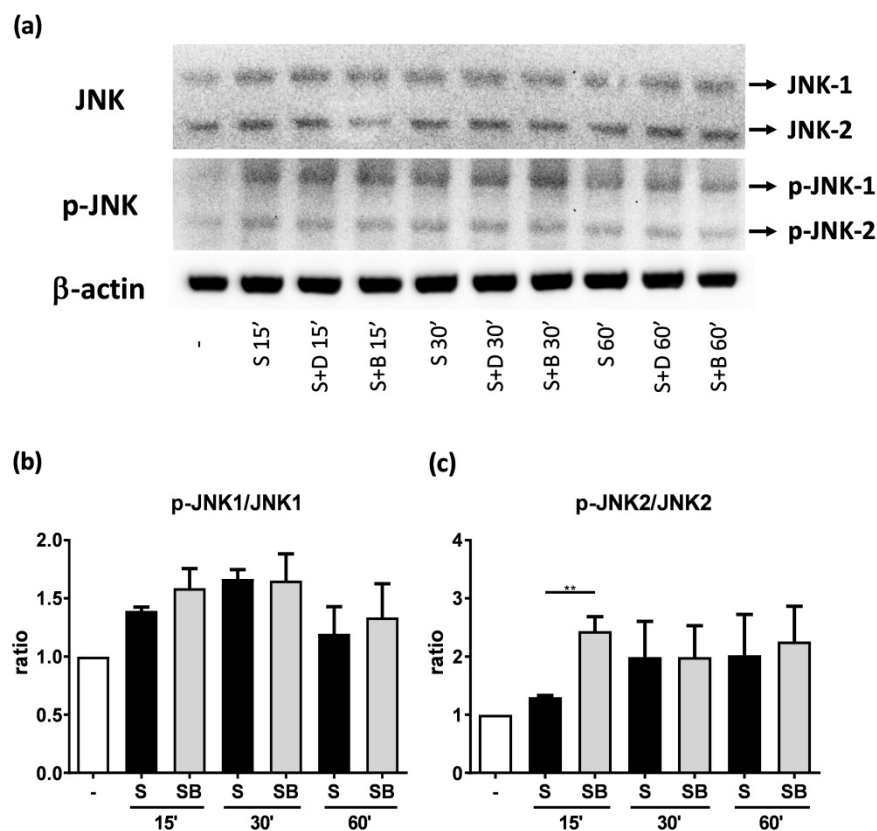


**Figure 5. JNK and p-JNK protein expression of activated BEAS-2B cells pre-treated with or without berberine.** Total cell proteins were collected at 15, 30, and 60 min of pro-inflammatory cytokine stimulation in BEAS-2B cells with berberine (1  $\mu$ M) pre-treatment. (A) Expression levels of JNK and p-JNK proteins were analyzed using western blotting (20  $\mu$ g per sample). The relative quantity of (B) p-JNK1 and (C) p-JNK2 was normalized to JNK1 and JNK2, respectively.  $\beta$ -actin expression was used as an internal control. Results are presented as mean  $\pm$  SEM of six independent experiments. -, cell only; S, pro-inflammation cytokine stimulation; D, DMSO, B, berberine.



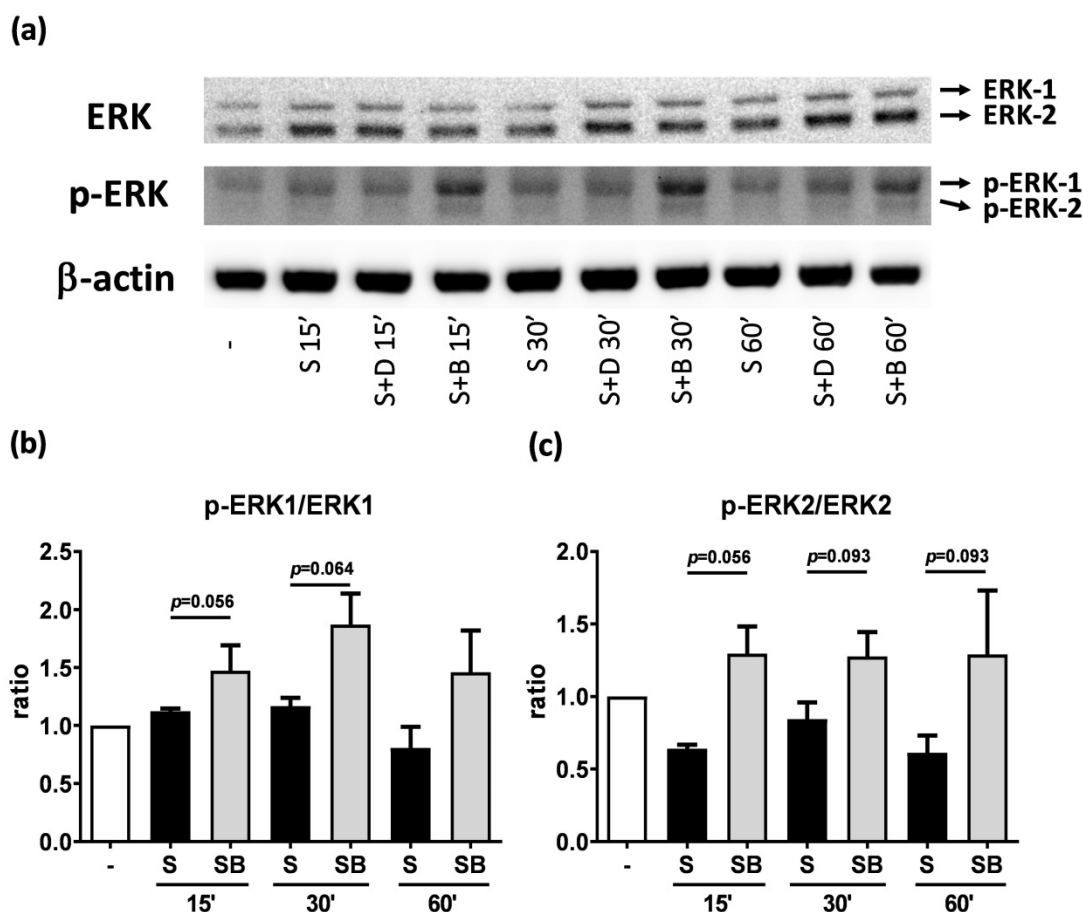


**Figure 6. Western blot analysis of ERK and p-ERK in pro-inflammatory cytokine stimulated BEAS-2B cells with berberine pre-treatment.** Total cell proteins were collected at 15, 30, and 60 min of IL-4 plus TNF- $\alpha$  stimulation in BEAS-2B cells with berberine (1  $\mu$ M) pre-treatment. (A) Expression levels of ERK and p-ERK proteins were analyzed using western blotting (20  $\mu$ g per sample). The relative quantity of (B) p-ERK1 and (C) p-ERK2 was normalized to ERK1 and ERK2, respectively.  $\beta$ -actin expression was used as an internal control. Results are presented as mean  $\pm$  SEM of six independent experiments. -, cell only; S, pro-inflammation cytokine stimulation; D, DMSO, B, berberine.

Alkaloid-containing plants have been used as medicine for animal and human starting from 4000 years ago. Alkaloids and derived species have been widely used to treat a variety of illnesses [44]. Berberine, an isoquinoline alkaloid that can be extracted from various Chinese herbs such as *Coptis chinensis*, *Hydrastis canadensis*, *Berberis aristata* and others, has potential of anti-inflammatory, anti-lipidemic, anti-neoplastic, and anti-diabetic activity [23, 45]. A previous study showed that berberine (100  $\mu$ M) was not toxic to A-549, U-937, and HFL-1 cell lines [24]. Our results indicate that berberine has dose-dependent cytotoxicity in BEAS-2B cells, although berberine at lower than 1  $\mu$ M is innocuous. At this concentration, berberine significantly reduced the secretion of IL-6 and CCL11 in IL-4 plus TNF- $\alpha$ -activated BEAS-2B cells. The activation of eotaxin-1 gene expression in IL-4 plus TNF- $\alpha$ -stimulated airway epithelial cells and fibroblasts was regulated by activating JAK1/3-STAT6 pathway [19]. After phosphorylation, STAT6 form homodimers and enter the nucleus [46]. A report has demonstrated that berberine inhibits IL-2

induced JAK3 phosphorylation in monoarthritis rats [47]. In our results, berberine significantly repressed the expression of nuclear STAT6 in activated BEAS-2B cells and reduces CCL11 levels. In ovalbumin (OVA)-induced rat model of asthma, berberine has been reported to relieve inflammatory cell infiltration, lung inflammation, and IgE production [48]. The suppressive effects on the airway inflammation might be mediated through the inhibition of NF- $\kappa$ B signaling pathway by berberine treatment. Berberine blocks the caspase1/NF- $\kappa$ B pathway to reduce thymic stromal lymphopoietin (TSLP) production in human mast cell line, HMC-1 cells [49]. However, in activated BEAS-2B cells, berberine didn't decrease the expression levels of I $\kappa$ B and NF- $\kappa$ B (p65 subunit). Berberine was also proposed to induce the production of IL-12 p40 by activating p38 MAP kinase in mouse macrophages [50]. In ARPE-19 cells, IL-6 secretion was stimulated by TNF- $\alpha$  through p38 MAP kinase, while berberine down-regulated the phosphorylation of p38 MAP kinase [26]. Although JNK and ERK might be elevated after berberine treatment, we demonstrated that the decrease of IL-6 and CCL11

(a)

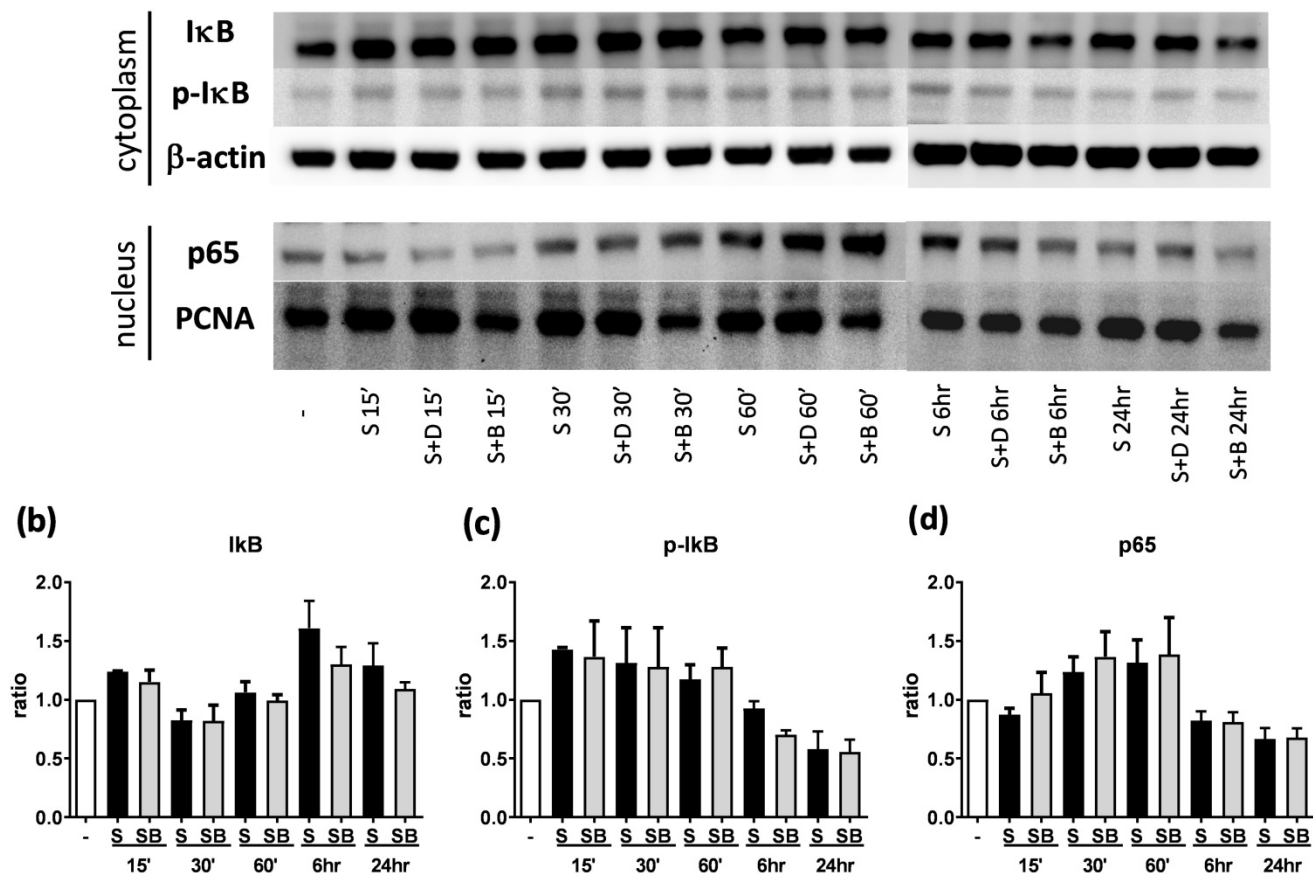


**Figure 7.** Western blot analysis of IκB, p-IκB, and p65 in pro-inflammatory cytokine stimulated BEAS-2B cells with berberine pre-treatment. Total cell proteins were collected at 15 min, 30 min, 60 min, 6 hours, and 24 hours of IL-4 plus TNF-α stimulation in BEAS-2B cells with berberine (1 μM) pre-treatment. (A) Expression levels of IκB, p-IκB, and p65 proteins were analyzed using western blotting (20 μg per sample). The relative quantity of (B) IκB (n=6), (C) p-IκB (n=3) and (D) nucleus p65 (n=6) was normalized to β-actin and PCNA, respectively. β-actin and PCNA expression was used as an internal control. Results are presented as mean ± SEM. -, cell only; S, pro-inflammation cytokine stimulation; D, DMSO; B, berberine.

were not caused by JNK or ERK activation by adding MAP kinase inhibitors. Thus, whether berberine is able to ameliorate the asthmatic symptoms by reducing IL-6 and CCL11 secretion of airway epithelial cells *in vivo* is needed to further investigate. In conclusion, berberine perhaps is able to relieve airway inflammation by suppressing cytokine and chemokine production of epithelial cells.

## Abbreviations

Th, T helper; IL, Interleukin; AHR, Airway hyperresponsiveness; EBC, Exhaled breath condensate; TNF, Tumor necrosis factor; MAPK, Mitogen-activated protein kinase; NF-κB, Nuclear factor-kappa B; IκB, Inhibitor of kappa B; JNK, c-Jun NH2-terminal kinase; ERK, Extracellular signal-regulated kinase; DMSO, Dimethyl sulfoxide; CCK-8, Cell Counting-kit 8; TSLP, Thymic stromal lymphopoietin; OVA, Ovalbumin.

## Supplementary Material

Supplementary figures and tables.

<http://www.medsci.org/v17p1464s1.pdf>

## Acknowledgments

This work was supported in part by a grant from Ministry of Science of Technology, Taiwan (R.O.C.): MOST 107-2320-B-182-005-MY3; and grants from Chang Gung Memorial Hospital: CMRPG1A0071~3, CMRPG1E0011~3, CMRPG1G0021, CMRPD1I0081~2, and BMRP 362.

## Competing Interests

The authors have declared that no competing interest exists.

## References

- To T, Stanojevic S, Moores G, Gershon AS, Bateman ED, Cruz AA, et al. Global asthma prevalence in adults: findings from the cross-sectional world health survey. *BMC Public Health*. 2012; 12: 204.
- Holgate ST. Innate and adaptive immune responses in asthma. *Nature Medicine*. 2012; 18: 673-83.

3. Lambrecht BN, Hammad H. The airway epithelium in asthma. *Nature Medicine*. 2012; 18: 684-92.
4. Li J, Zhang F, Li J. The immunoregulatory effects of traditional Chinese medicine on treatment of asthma or asthmatic inflammation. *The American Journal of Chinese Medicine*. 2015; 43: 1059-81.
5. Lloyd CM, Saglani S. Epithelial cytokines and pulmonary allergic inflammation. *Current Opinion in Immunology*. 2015; 34: 52-8.
6. Lloyd CM, Hessel EM. Functions of T cells in asthma: more than just T(H)2 cells. *Nature Reviews Immunology*. 2010; 10: 838-48.
7. Smit JJ, Lukacs NW. A closer look at chemokines and their role in asthmatic responses. *European Journal of Pharmacology*. 2006; 533: 277-88.
8. Shamri R, Melo RC, Young KM, Bivas-Benita M, Xenakis JJ, Spencer LA, et al. CCL11 elicits secretion of RNases from mouse eosinophils and their cell-free granules. *FASEB Journal*. 2012; 26: 2084-93.
9. Wu D, Zhou J, Bi H, Li L, Gao W, Huang M, et al. CCL11 as a potential diagnostic marker for asthma? *The Journal of Asthma*. 2014; 51: 847-54.
10. Wu CJ, Huang WC, Chen LC, Shen CR, Kuo ML. Pseudotyped adeno-associated virus 2/9-delivered CCL11 shRNA alleviates lung inflammation in an allergen-sensitized mouse model. *Human Gene Therapy*. 2012; 23: 1156-65.
11. Yokoyama A, Kohno N, Fujino S, Hamada H, Inoue Y, Fujioka S, et al. Circulating interleukin-6 levels in patients with bronchial asthma. *American Journal of Respiratory and Critical Care Medicine*. 1995; 151: 1354-8.
12. Rincon M, Irvin CG. Role of IL-6 in asthma and other inflammatory pulmonary diseases. *International Journal of Biological Sciences*. 2012; 8: 1281-90.
13. Scheller J, Chalaris A, Schmidt-Arras D, Rose-John S. The pro- and anti-inflammatory properties of the cytokine interleukin-6. *Biochimica et Biophysica Acta*. 2011; 1813: 878-88.
14. Rincon M, Anguita J, Nakamura T, Fikrig E, Flavell RA. Interleukin (IL)-6 directs the differentiation of IL-4-producing CD4<sup>+</sup> T cells. *Journal of Experimental Medicine*. 1997; 185: 461-9.
15. Heijink IH, Vellenga E, Borger P, Postma DS, de Monchy JG, Kauffman HF. Interleukin-6 promotes the production of interleukin-4 and interleukin-5 by interleukin-2-dependent and -independent mechanisms in freshly isolated human T cells. *Immunology*. 2002; 107: 316-24.
16. Neveu WA, Allard JL, Raymond DM, Bourassa LM, Burns SM, Bunn JY, et al. Elevation of IL-6 in the allergic asthmatic airway is independent of inflammation but associates with loss of central airway function. *Respiratory Research*. 2010; 11: 28.
17. Hoeck J, Woisetschlager M. STAT6 mediates eotaxin-1 expression in IL-4 or TNF-alpha-induced fibroblasts. *Journal of Immunology*. 2001; 166: 4507-15.
18. Yoshifuku K, Matsune S, Ohori J, Sagara Y, Fukuiwa T, Kurono Y. IL-4 and TNF-alpha increased the secretion of eotaxin from cultured fibroblasts of nasal polyps with eosinophil infiltration. *Rhinology*. 2007; 45: 235-41.
19. Matsukura S, Stellato C, Plitt JR, Bickel C, Miura K, Georas SN, et al. Activation of eotaxin gene transcription by NF-kappa B and STAT6 in human airway epithelial cells. *Journal of Immunology*. 1999; 163: 6876-83.
20. Gloire G, Legrand-Poels S, Piette J. NF-kappaB activation by reactive oxygen species: fifteen years later. *Biochemical Pharmacology*. 2006; 72: 1493-505.
21. Sabio G, Davis RJ. TNF and MAP kinase signalling pathways. *Seminars in Immunology*. 2014; 26: 237-45.
22. Chang L, Karin M. Mammalian MAP kinase signalling cascades. *Nature*. 2001; 410: 37-40.
23. Cicero AF, Baggioni A. Berberine and its role in chronic disease. *Advances in Experimental Medicine and Biology*. 2016; 928: 27-45.
24. Lee CH, Chen JC, Hsiang CY, Wu SL, Wu HC, Ho TY. Berberine suppresses inflammatory agents-induced interleukin-1beta and tumor necrosis factor-alpha productions via the inhibition of IkappaB degradation in human lung cells. *Pharmacological Research*. 2007; 56: 193-201.
25. Yan F, Wang L, Shi Y, Cao H, Liu L, Washington MK, et al. Berberine promotes recovery of colitis and inhibits inflammatory responses in colonic macrophages and epithelial cells in DSS-treated mice. *American Journal of Physiology Gastrointestinal and Liver Physiology*. 2012; 302: G504-14.
26. Wang Q, Qi J, Hu R, Chen Y, Kijlstra A, Yang P. Effect of berberine on proinflammatory cytokine production by ARPE-19 cells following stimulation with tumor necrosis factor-alpha. *Investigative Ophthalmology & Visual Science*. 2012; 53: 2395-402.
27. Li XM. Traditional Chinese herbal remedies for asthma and food allergy. *The Journal of Allergy and Clinical Immunology*. 2007; 120: 25-31.
28. Chan CC, Liou CJ, Xu PY, Shen JJ, Kuo ML, Len WB, et al. Effect of dehydroepiandrosterone on atopic dermatitis-like skin lesions induced by 1-chloro-2,4-dinitrobenzene in mouse. *Journal of Dermatological Science*. 2013; 72: 149-57.
29. Chan CK, Kuo ML, Shen JJ, See LC, Chang HH, Huang JL. Ding Chuan Tang, a Chinese herb decoction, could improve airway hyper-responsiveness in stabilized asthmatic children: a randomized, double-blind clinical trial. *Pediatric Allergy and Immunology*. 2006; 17: 316-22.
30. Castro-Rodriguez JA, Rodrigo GJ. A systematic review of long-acting beta2-agonists versus higher doses of inhaled corticosteroids in asthma. *Pediatrics*. 2012; 130: e650-7.
31. Luhadia SK. Steroid resistant asthma. *The Journal of The Association of Physicians of India*. 2014; 62: 38-40.
32. Mark JD. Integrative medicine and asthma. *Pediatric Clinics of North America*. 2007; 54: 1007-23; xii.
33. Kao ST, Yeh TJ, Hsieh CC, Shiau HB, Yeh FT, Lin JG. The effects of Ma-Xing-Gan-Shi-Tang on respiratory resistance and airway leukocyte infiltration in asthmatic guinea pigs. *Immunopharmacology and Immunotoxicology*. 2001; 23: 445-58.
34. Wang SD, Lin LJ, Chen CL, Lee SC, Lin CC, Wang JY, et al. Xiao-Qing-Long-Tang attenuates allergic airway inflammation and remodeling in repetitive Dermatogoides pteronyssinus challenged chronic asthmatic mice model. *Journal of Ethnopharmacology*. 2012; 142: 531-8.
35. Fleming RM. Safety of ephedra and related anorexic medications. *Expert Opinion on Drug Safety*. 2008; 7: 749-59.
36. Huang WC, Fang LW, Liou CJ. Phloretin attenuates allergic airway inflammation and oxidative stress in asthmatic mice. *Frontiers in Immunology*. 2017; 8: 134.
37. Busse PJ, Schofield B, Birmingham N, Yang N, Wen MC, Zhang T, et al. The traditional Chinese herbal formula ASHMI inhibits allergic lung inflammation in antigen-sensitized and antigen-challenged aged mice. *Annals of Allergy, Asthma & Immunology*. 2010; 104: 236-46.
38. Li XM, Huang CK, Zhang TF, Teper AA, Srivastava K, Schofield BH, et al. The chinese herbal medicine formula MSSM-002 suppresses allergic airway hyperreactivity and modulates TH1/TH2 responses in a murine model of allergic asthma. *The Journal of Allergy and Clinical Immunology*. 2000; 106: 660-8.
39. Ebeling C, Wu Y, Skappak C, Gordon JR, Ilarraza R, Adamko DJ. Compound CVT-E002 attenuates allergen-induced airway inflammation and airway hyperresponsiveness, in vivo. *Molecular Nutrition & Food Research*. 2011; 55: 1905-8.
40. Kelly-Pieper K, Patil SP, Busse P, Yang N, Sampson H, Li XM, et al. Safety and tolerability of an antiasthma herbal formula (ASHMI) in adult subjects with asthma: a randomized, double-blinded, placebo-controlled, dose-escalation phase I study. *Journal of Alternative and Complementary Medicine*. 2009; 15: 735-43.
41. Watson RR, Zibadi S, Rafatpanah H, Jabbari F, Ghasemi R, Ghafari J, et al. Oral administration of the purple passion fruit peel extract reduces wheeze and cough and improves shortness of breath in adults with asthma. *Nutrition Research*. 2008; 28: 166-71.
42. Boskabady MH, Javan H, Sajady M, Rakhshandeh H. The possible prophylactic effect of Nigella sativa seed extract in asthmatic patients. *Fundamental and Clinical Pharmacology*. 2007; 21: 559-66.
43. Xu L, Li J, Zhang Y, Zhao P, Zhang X. Regulatory effect of baicalin on the imbalance of Th17/Treg responses in mice with allergic asthma. *Journal of Ethnopharmacology*. 2017; 208: 199-206.
44. Vafa Amiria MH. Alkaloids as drug leads - A predictive structural and biodiversity-based analysis. *Phytochemistry Letters*. 2014; 10: xlvi-lxii.
45. Tillhon M, Guaman Ortiz LM, Lombardi P, Scovassi AI. Berberine: new perspectives for old remedies. *Biochemical Pharmacology*. 2012; 84: 1260-7.
46. Shen CH, Stavnezer J. Interaction of stat6 and NF-kappaB: direct association and synergistic activation of interleukin-4-induced transcription. *Molecular and Cellular Biology*. 1998; 18: 3395-404.
47. Kim BH, Kim M, Yin CH, Jee JG, Sandoval C, Lee H, et al. Inhibition of the signalling kinase JAK3 alleviates inflammation in monoarthritic rats. *The British Journal of Pharmacology*. 2011; 164: 106-18.
48. Li Z, Zheng J, Zhang N, Li C. Berberine improves airway inflammation and inhibits NF-kappaB signaling pathway in an ovalbumin-induced rat model of asthma. *The Journal of Asthma*. 2016; 53: 999-1005.
49. Moon PD, Choi IH, Kim HM. Berberine inhibits the production of thymic stromal lymphopoietin by the blockade of caspase-1/NF-kappaB pathway in mast cells. *International Immunopharmacology*. 2011; 11: 1954-9.
50. Kang BY, Chung SW, Cho D, Kim TS. Involvement of p38 mitogen-activated protein kinase in the induction of interleukin-12 p40 production in mouse macrophages by berberine, a benzodioxolquinolizine alkaloid. *Biochemical Pharmacology*. 2002; 63: 1901-10.

## RUMPELLOLIDE K, A NOVEL C-3/8 ETHER LINKAGE CARYOPHYLLANE FROM *RUMPELLA ANTIPATHES*

Hsu-Ming Chung,<sup>a,†</sup> Yu-Ming Chang,<sup>b,†</sup> Wei-Hsien Wang,<sup>c</sup> Jih-Jung Chen,<sup>d</sup>  
Tsong-Long Hwang,<sup>e,f,g,h,\*</sup> and Ping-Jyun Sung<sup>c,i,j,k,l,\*</sup>

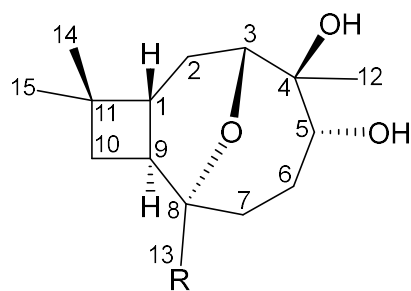
<sup>a</sup> Department of Applied Chemistry, National Pingtung University, Pingtung 900393, Taiwan. <sup>b</sup> Department of Neurosurgery, Kaohsiung Chang Gung Memorial Hospital and Chang Gung University College of Medicine, Kaohsiung 833401, Taiwan. <sup>c</sup> Department of Marine Biotechnology and Resources, National Sun Yat-sen University, Kaohsiung 804201, Taiwan. <sup>d</sup> Faculty of Pharmacy, School of Pharmaceutical Sciences, National Yang-Ming University, 112304, Taipei, Taiwan. <sup>e</sup> Research Center for Chinese Herbal Medicine, Research Center for Food and Cosmetic Safety, Graduate Institute of Healthy Industry Technology, College of Human Ecology, Chang Gung University of Science and Technology, Taoyuan 333324, Taiwan. <sup>f</sup> Graduate Institute of Natural Products, College of Medicine, Chang Gung University, Taoyuan 333323, Taiwan. <sup>g</sup> Chinese Herbal Medicine Research Team, Healthy Aging Research Center, Chang Gung University, Taoyuan 333323, Taiwan. <sup>h</sup> Department of Anaesthesiology, Chang Gung Memorial Hospital, Taoyuan 333423, Taiwan. <sup>i</sup> National Museum of Marine Biology and Aquarium, Pingtung 944401, Taiwan. <sup>j</sup> Graduate Institute of Marine Biology, National Dong Hwa University, Pingtung 944401, Taiwan. <sup>k</sup> Chinese Medicine Research and Development Center, China Medical University Hospital, Taichung 404394, Taiwan. <sup>l</sup> Graduate Institute of Natural Products, Kaohsiung Medical University, Kaohsiung 807378, Taiwan.

E-mail: htl@mail.cgu.edu.tw, pjsung@nmmmba.gov.tw

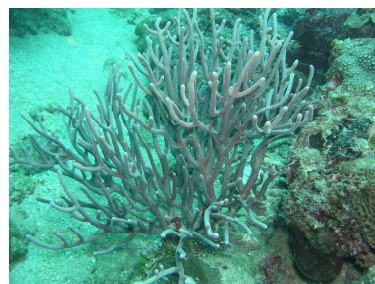
<sup>†</sup> These authors contributed equally to this work.

**Abstract** – Chemical examination of *RumPELLa antipathes*, collected in the waters of Taiwan, led to the isolation of a novel caryophyllane sesquiterpenoid, rumPELLolide K (**1**), with a C-3/8 ether linkage. The structure of **1** was established by spectroscopic analysis and this compound displayed inhibitory effects on the generation of superoxide anions and the release of elastase by human neutrophils.

The octocorals belonging to the genus *Rumphella* (family Gorgoniidae)<sup>1</sup> were found to be a rich source of caryophyllane sesquiterpenoids<sup>2–6</sup> and steroids,<sup>7</sup> and the compounds of these two types from *Rumphella* were found to exhibit antibacterial activity,<sup>2,3</sup> anti-inflammatory activity,<sup>4,5</sup> and cytotoxicity.<sup>7</sup> In our continuing studies of *R. antipathes*, a new caryophyllane sesquiterpenoid, rumphellolide K (**1**), was isolated (Chart 1). Herein, we described the isolation, structural characterization, and bioactivity of **1**.



**1:** R = Me, **2:** R = H



*R. antipathes*

**Chart 1.** Structures of rumphellolides K (**1**) and G (**2**), and a picture of *Rumphella antipathes*

Rumphellolide K (**1**) was isolated as a colorless oil that showed a sodiated adduct ion peak in its HRESIMS at  $m/z$  277.1779 ( $M + Na$ )<sup>+</sup>, accounted for the molecular formula, C<sub>15</sub>H<sub>26</sub>O<sub>3</sub> (Calcd for C<sub>15</sub>H<sub>26</sub>O<sub>3</sub> + Na, 277.1780) (unsaturation degrees = 3). Comparison of the <sup>1</sup>H NMR and DEPT data (Table 1) with the molecular formula indicated that there must be two exchangeable protons, requiring the presence of two hydroxy groups and this deduction was supported by a broad absorption in the IR spectrum at  $\nu_{max}$  3397 cm<sup>-1</sup>. From the <sup>13</sup>C NMR data of **1** (Table 1), there are no olefinic carbon and carbonyl group were observed. Thus, **1** must be a tricyclic compound.

**Table 1.** <sup>1</sup>H and <sup>13</sup>C NMR data for caryophyllane **1**

Position	$\delta_H$ (J in Hz) <sup>a</sup>	$\delta_C$ , <sup>b</sup> type
1	2.05 m	40.7, CH <sup>c</sup>
2/2'	2.06 m; 1.53 m	34.6, CH <sub>2</sub>
3	3.86 dd (7.6, 1.2)	78.6, CH
4		81.4, C
5	4.12 dd (10.0, 4.8)	69.4, CH
6	1.69 m	25.0, CH <sub>2</sub>
7/7'	1.82 m; 1.56 m	28.4, CH <sub>2</sub>
8		74.0, C
9	1.88 ddd (10.8, 10.8, 8.0)	48.2, CH
10/10'	1.48 dd (10.0, 8.0); 1.16 dd (10.8, 10.0)	35.3, CH <sub>2</sub>
11		35.7, C
12	1.28 s	23.3, Me
13	1.06 s	29.7, Me
14	1.03 s	30.2, Me
15	1.01 s	21.2, Me

<sup>a</sup> Spectra recorded at 400 MHz in CDCl<sub>3</sub> at 25 °C. <sup>b</sup> Spectra recorded at 100 MHz in CDCl<sub>3</sub> at 25 °C. <sup>c</sup> Multiplicity deduced by DEPT spectra.



The COSY spectrum of **1** enabled the determination of structural units, H-1/H<sub>2</sub>-2/H-3, H-5/H<sub>2</sub>-6/H<sub>2</sub>-7, H-9/H-1, and H-9/H<sub>2</sub>-10, which were assembled with the assistance of an HMBC experiment (Figure 1). The HMBC between protons and quaternary carbons, permitted elucidation of the main carbon skeleton of **1**. However, no correlation was observed between H-3 ( $\delta_{\text{H}}$  3.86) and C-8 oxygenated quaternary carbon at  $\delta_{\text{C}}$  74.0 in the HMBC experiment, so the cyclic ether ring between C-3/8 or C-4/8 cannot be determined by this method. Previous study showed that the NMR values of CH<sub>2</sub>-2, CH-3, C-4, CH-5, and Me-12 resonating in a caryophyllane analogue, rumphellolide G (**2**) (Chart 1),<sup>3</sup> with a C-3/8 ether bridge moiety, are similar with those of **1**, suggested that the position of ether bridge in **1** should be assigned between C-3 and C-8 by chemical shift changes for deuterium-induced <sup>13</sup>C NMR spectrum (Table 2). Thus, the remaining hydroxy groups were attached at C-4 (an oxygenated quaternary carbon resonating at  $\delta_{\text{C}}$  81.4) and C-5 (an oxymethine resonating at  $\delta_{\text{C}}$  69.4), respectively, as indicated by the key COSY correlations and characteristic NMR signals analysis, although the hydroxy protons for OH-4 and OH-5 were not observed in the <sup>1</sup>H NMR spectrum of **1**.

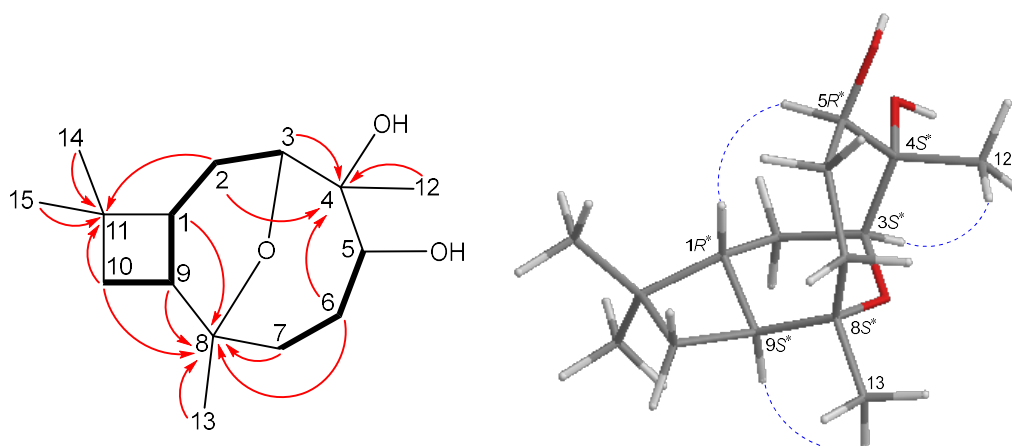


**Figure 1.** Key COSY (—), HMBC (→), and protons with NOESY (---) correlations of **1**

**Table 2.** Key NMR data for caryophyllanes **1** and **2**

Position	<b>1</b>		<b>2</b>	
	$\delta_{\text{H}}$ (J in Hz) <sup>a</sup>	$\delta_{\text{C}}$ , <sup>b</sup> type	$\delta_{\text{H}}$ <sup>a</sup>	$\delta_{\text{C}}$ , <sup>b</sup> type
2/2'	2.06 m; 1.53 m	34.6, CH <sub>2</sub> <sup>c</sup>	2.10 m; 1.56 m	34.9, CH <sub>2</sub>
3	3.86 dd (7.6, 1.2)	78.6, CH	3.90 m	79.0, CH
4		81.4, C		81.9, C
5	4.12 dd (10.0, 4.8)	69.4, CH	4.17 m	69.8, CH
12	1.28 s	23.3, Me	1.29 s	23.0, Me

<sup>a</sup> Spectra recorded at 400 MHz in CDCl<sub>3</sub> at 25 °C. <sup>b</sup> Spectra recorded at 100 MHz in CDCl<sub>3</sub>. <sup>c</sup> Multiplicity deduced by DEPT spectra.

The stereochemistry of **1** was determined by correlations observed in a NOESY experiment (Figure 1) and by vicinal proton coupling constants. The *trans* geometry of H-9 ( $\delta_{\text{H}}$  1.88) and H-1 ( $\delta_{\text{H}}$  2.05) is indicated by a 10.8 Hz coupling constant between these two ring juncture protons, and H-9 and H-1 were assigned as  $\alpha$ - and  $\beta$ -oriented protons, respectively, in **1**. In the NOESY experiment, H-9 showed a NOE correlation

with H<sub>3</sub>-13, indicating that C-13 methyl having an equatorial direction in the tetrahydropyran ring by molecular modeling analysis. H-1 exhibited a strong NOE interaction with H-5, suggesting that the hydroxy group at C-5 was placed on the  $\alpha$ -orientation. Moreover, H-3 showed an NOE correlation with H<sub>3</sub>-12, but not with H-1, suggesting that these protons were in  $\alpha$ -orientation at C-3 and C-4, respectively. Therefore, the configurations of stereogenic centers of **1** were elucidated as 1*R*\*,3*S*\*,4*S*\*,5*R*\*,8*S*\*, and 9*S*\*. As caryophyllane **1** was isolated along with rumphellaone A, a novel 4,5-*seco*-caryophyllane sesquiterpenoid from the same target organism, *R. antipathes*,<sup>8</sup> and the structure, including the absolute configuration, of rumphellaone A, was further confirmed by synthetic methods.<sup>9–11</sup> Therefore, it is reasonable on biogenetic grounds to conclude that caryophyllane **1** has the same absolute configuration as that of rumphellaone A,<sup>9–11</sup> and the configurations of the stereogenic carbons of **1** should be elucidated as 1*R*,3*S*,4*S*,5*R*,8*S*, and 9*S*. Rumphellolide K (**1**) represents the first caryophyllane-related sesquiterpenoid possessing a C-3/C-8 ether bridge moiety and this compound was found to exhibit 10.36 and 10.91% inhibitory effects on human neutrophils superoxide anions generation and elastase release, respectively, at a concentration of 10  $\mu$ g/mL.

## EXPERIMENTAL

**General Experimental Procedures.** Optical rotations were measured using a Jasco P-1010 digital polarimeter. IR spectra were measured on a Thermo Scientific Nicolet iS5 FT-IR spectrophotometer. NMR spectra were taken on a Varian NMR Mercury Plus spectrometer operating at 400 MHz for <sup>1</sup>H and 100 MHz for <sup>13</sup>C in CDCl<sub>3</sub> using the residual CHCl<sub>3</sub> signal ( $\delta_{\text{H}}$  7.26 ppm) and CDCl<sub>3</sub> ( $\delta_{\text{C}}$  77.1 ppm) as the internal standard for <sup>1</sup>H and <sup>13</sup>C NMR, respectively; coupling constants (*J*) are given in Hz. ESIMS and HRESIMS were recorded using a Bruker APEX II FTMS system. Column chromatography was carried out with silica gel (230–400 mesh, Merck). TLC was performed on plates precoated with Kieselgel 60 F<sub>254</sub> (0.25-mm-thick, Merck), then sprayed with 10% H<sub>2</sub>SO<sub>4</sub> solution followed by heating to visualize the spots. Normal-phase HPLC (NP-HPLC) was performed using a system comprised of a Hitachi L-7100 pump, a Hitachi L-7455 photodiode array detector, a Rheodyne 7725i injection port, and a semi-preparative normal-phase column (Supelco Ascentis Si, Cat #:581514-U, 25 cm  $\times$  10 mm, 5  $\mu$ m; Sigma-Aldrich).

**Animal Material.** Specimens of *R. antipathes* were collected in May 2004 by hand with SCUBA divers off the coast of Southern Taiwan. A voucher specimen was deposited in the National Museum of Marine Biology and Aquarium, Taiwan (NMMBA-TWGC-010).

**Extraction and Isolation.** *R. antipathes* (wet/dry weight = 402/144 g) were sliced and then extracted with a solvent mixture of methanol and dichloromethane (1:1). The extract was partitioned between ethyl acetate and H<sub>2</sub>O. The EtOAc layer (1.23 g) was then applied on silica gel column and eluted with gradients of *n*-hexane/EtOAc (from 25:1 to 100% EtOAc) to furnish 29 subfractions. Among them, fraction 22 was further purified by NP-HPLC, using a solvent mixture of dichloromethane/EtOAc (10:1) to yield 13 fractions 22A–

22M. Fraction 22M was further purified by semi-preparative NP-HPLC using a solvent mixture of dichloromethane and acetone to give **1** (2.3 mg, 10:1).

**Rumphellolide K (1):** colorless oil;  $[\alpha]_D^{26} -14$  (*c* 0.1, CHCl<sub>3</sub>); IR  $\nu_{\max}$  3397, 2948, 1457, 1037 cm<sup>-1</sup>; <sup>1</sup>H (CDCl<sub>3</sub>, 400 MHz) and <sup>13</sup>C (CDCl<sub>3</sub>, 100 MHz) NMR data, see Table 1; ESIMS *m/z* 277 (M + Na)<sup>+</sup>; HRESIMS *m/z* 277.1779 (Calcd for C<sub>15</sub>H<sub>26</sub>O<sub>3</sub> + Na, 277.1780).

**Anti-inflammatory Test.** Human neutrophils were obtained from healthy human volunteers and were isolated by Ficoll centrifugation and dextran sedimentation. Purified neutrophils were re-suspended in calcium (Ca<sup>2+</sup>)-free Hank's balanced salt solution (HBSS) buffer at pH 7.4, and were maintained at 4 °C before use. For superoxide anion generation assay, neutrophils (6 × 10<sup>5</sup> cell/mL) were equilibrated in ferricytochrome c (0.6 mg/mL) and Ca<sup>2+</sup> (1 mM) at 37 °C for 5 min and incubated with DMSO (0.1%) or tested compounds for another 5 min.<sup>12</sup> Cells were activated with fMLF (0.1 μM) for 10 min after the priming with CB (1 μg/mL) for 3 min. The change in absorbance was monitored continuously at 550 nm with a spectrophotometer (Hitachi U-3010). For elastase release assay, neutrophils (6 × 10<sup>5</sup> cell/mL) were equilibrated in MeO-Suc-Ala-Ala-Pro-Val-p-nitroanilide (100 μM) and Ca<sup>2+</sup> (1 mM) at 37 °C for 5 min and incubated with DMSO (0.1 %) or test compounds for another 5 min. Cells were activated with fMLF (0.1 μM) for 10 min after the priming with CB (0.5 μg/mL) for 3 min. The change in absorbance was monitored continuously at 405 nm with a spectrophotometer.<sup>12</sup> The results are recorded as the mean ± SEM of three measurements. The inhibition % was measured at 10 μM concentration of each compound and IC<sub>50</sub> values were estimated from dose-response curves. Statistical analysis using Student's t-tests with SigmaPlot (Systat Software).

## ACKNOWLEDGEMENTS

This research was supported by grants from the National Museum of Marine Biology and Aquarium; the National Dong Hwa University; and the Ministry of Science and Technology, Taiwan (MOST 106-2320-B-291-001-MY3, 107-2320-B-291-001-MY3, and 109-2320-B-291-001-MY3).

## REFERENCES AND NOTES

1. F.M. Bayer, *Proc. Biol. Soc. Wash.*, 1981, **94**, 902.
2. P.-J. Sung, L.-F. Chuang, J. Kuo, J.-J. Chen, T.-Y. Fan, J.-J. Li, L.-S. Fang, and W.-H. Wang, *Chem. Pharm. Bull.*, 2007, **55**, 1296.
3. P.-J. Sung, L.-F. Chuang, T.-Y. Fan, H.-N. Chou, J. Kuo, L.-S. Fang, and W.-H. Wang, *Chem. Lett.*, 2007, **36**, 1322.
4. T.-L. Hwang, Y.-D. Su, W.-P. Hu, L.-F. Chuang, and P.-J. Sung, *Heterocycles*, 2009, **78**, 1563.

5. P.-J. Sung, Y.-D. Su, T.-L. Hwang, L.-F. Chuang, H.-M. Chung, J.-J. Chen, J.-J. Li, L.-S. Fang, and W.-H. Wang, *Chem. Lett.*, 2009, **38**, 282.
6. C.-C. Lin, H.-M. Chung, Y.-D. Su, B.-R. Peng, W.-H. Wang, T.-L. Hwang, Y.-C. Wu, and P.-J. Sung, *Nat. Prod. Commun.*, 2017, **12**, 1835.
7. F.-Z. Yin, M. Yang, S.-W. Li, M.-J. Wu, X.-J. Huan, Z.-H. Miu, H. Wang, and Y.-W. Guo, *Steroids*, 2020, **155**, 108558.
8. H.-M. Chung, Y.-H. Chen, M.-R. Lin, J.-H. Su, W.-H. Wang, and P.-J. Sung, *Tetrahedron Lett.*, 2010, **51**, 6025.
9. T. Hirokawa and S. Kuwahara, *Tetrahedron*, 2012, **68**, 4581.
10. B. Ranieri, C. Obradors, M. Mato, and A.M. Echavarren, *Org. Lett.*, 2016, **18**, 1614.
11. J.C.Beck, C.R. Lacker, L.M. Chapman, and S.E. Reisman, *Chem. Sci.* 2019, **10**, 2315.
12. P.-J. Chen, I.-L. Ko, C.-L. Lee, H.-C. Hu, F.-R. Chang, Y.-C. Wu, Y.-L. Leu, C.-C. Wu, C.-Y. Lin, C.-Y. Pan, Y.-F. Tsai, and T.-L. Hwang, *EBioMedicine*, 2019, **40**, 528.



Article

# The Inhibitory Effects of Gold Nanoparticles on VEGF-A-Induced Cell Migration in Choroid-Retina Endothelial Cells

Chi-Ming Chan <sup>1,2</sup>, Chien-Yu Hsiao <sup>3,4</sup>, Hsin-Ju Li <sup>1</sup>, Jia-You Fang <sup>5</sup> , Der-Chen Chang <sup>6</sup>  
and Chi-Feng Hung <sup>1,7,8,\*</sup>

<sup>1</sup> School of Medicine, Fu-Jen Catholic University, New Taipei City 24205, Taiwan; chancm@mail.fju.edu.tw (C.-M.C.); sakumanatsumi@gmail.com (H.-J.L.)

<sup>2</sup> Department of Ophthalmology, Cardinal Tien Hospital, New Taipei City 23148, Taiwan

<sup>3</sup> Department of Nutrition and Health Sciences, Research Center for Food and Cosmetic Safety, and Research Center for Chinese Herbal Medicine, College of Human Ecology, Chang Gung University of Science and Technology, Taoyuan 33303, Taiwan; moztart@gw.cgust.edu.tw

<sup>4</sup> Aesthetic Medical Center, Department of Dermatology, Chang Gung Memorial Hospital, Taoyuan 33305, Taiwan

<sup>5</sup> Pharmaceuticals Laboratory, Graduate Institute of Natural Products, Chang Gung University, Taoyuan 33303, Taiwan; fajy@mail.cgu.edu.tw

<sup>6</sup> Department of Mathematics and Statistics and Department of Computer Science, Georgetown University, Washington, DC 20057, USA; Chang@georgetown.edu

<sup>7</sup> Ph.D. Program in Pharmaceutical Biotechnology, Fu-Jen Catholic University, New Taipei City 24205, Taiwan

<sup>8</sup> MS Program in Transdisciplinary Long Term Care, Fu-Jen Catholic University, New Taipei City 24205, Taiwan

\* Correspondence: skin@mail.fju.edu.tw; Tel.: +886-2-2905-3911; Fax: +886-2-2905-2095

Received: 27 November 2019; Accepted: 20 December 2019; Published: 23 December 2019



**Abstract:** Background: Vascular endothelial growth factor (VEGF) is upregulated by hypoxia and is a crucial stimulator for choroidal neovascularization (CNV) in age-related macular degeneration and pathologic myopia, as well as retinal neovascularization in proliferative diabetic retinopathy. Retinal and choroidal endothelial cells play key roles in the development of retinal and CNV, and subsequent fibrosis. At present, the effects of gold nanoparticles (AuNPs) on the VEGF-induced choroid-retina endothelial (RF/6A) cells are still unknown. In our study, we investigated the effects of AuNPs on RF/6A cell viabilities and cell adhesion to fibronectin, a major ECM protein of fibrovascular membrane. Furthermore, the inhibitory effects of AuNPs on RF/6A cell migration induced by VEGF and its signaling were studied. Methods: The cell viability assay was used to determine the viability of cells treated with AuNPs. The migration of RF/6A cells was assessed by the Transwell migration assay. The cell adhesion to fibronectin was examined by an adhesion assay. The VEGF-induced signaling pathways were determined by western blotting. Results: The 3-(4,5-Dimethylthiazol-2-yl)-2,5-diphenyltetrazolium bromide (MTT) viability assay revealed no cytotoxicity of AuNPs on RF/6A cells. AuNPs inhibited VEGF-induced RF/6A cell migration in a concentration-dependent manner but showed no significant effects on RF/6A cell adhesion to fibronectin. Inhibitory effects of AuNPs on VEGF-induced Akt/eNOS were found. Conclusions: These results suggest that AuNPs are an effective inhibitor of VEGF-induced RF/6A cell migration through the Akt/eNOS pathways, but they have no effects on their cell viabilities and cell adhesion to fibronectin.

**Keywords:** gold nanoparticles (AuNPs); vascular endothelial growth factor (VEGF); cell migration; Akt; endothelial nitric oxide synthase (eNOS); choroidal and retinal neovascularization



## 1. Introduction

Angiogenesis is the physiological process involving the growth of new blood vessels from existing vasculature [1]. It plays a central role in cancer and various ischemic diseases [2,3]. Vascular endothelial growth factor (VEGF) is upregulated by hypoxia during ischemia [4] and is a major stimulatory factor for choroidal neovascularization (CNV) in age-related macular degeneration [5,6] and high myopia [7], as well as retinal neovascularization in diabetic retinopathy [6]. Retinal and choroidal endothelial cells play key roles in the development of retinal and choroidal neovascularization, and subsequent fibrosis.

The migration of endothelial cells (EC) is a notable and key step in angiogenesis [8], but the detailed signaling molecules responsible for this migration are still under investigation. Although numerous factors affect EC migration, the influence of VEGF has received considerable attention from researchers, as VEGF is widely used as a signaling molecule for the induction of EC migration [9,10].

Gold nanoparticles (AuNPs) have been shown to be the material of choice of many diagnostic platforms. Their unique electronic, biocompatible, and molecular-recognition properties of small-sized AuNPs broaden the potential of gold in several fields of application [11]. Gold nanoparticles displayed an anti-angiogenic effect. They induce nanostructural reorganization of VEGFR2 on the human umbilical vascular endothelial cells (HUVEC) to repress angiogenesis [12]. Moreover, AuNPs can significantly inhibit HepG2-conditioned medium (HepG2-CM) activated HUVEC proliferation and migration through the down-regulation of VEGF activity and disruption of cell morphology [13]. AuNPs were shown to inhibit VEGF-induced migration in HUVEC [14] and laser-induced CNV in mice [15]. Fabrication of resveratrol-coated gold nanoparticles can increase the retinal pigment epithelium-derived factor and decrease the VEGF-1 in streptozotocin-induced diabetic rats [16]. However, the effects of AuNPs on the choroid-retina endothelial (RF/6A) cells viability and VEGF-induced RF/6A cell migration are still unknown.

In the present study, we investigated the inhibitory effect of AuNPs on VEGF-induced RF/6A cell migration and the possible underlying mechanisms involved. These mechanisms include the influence of AuNPs on RF/6A cell viability, cell adhesion, and Akt/endothelial nitric oxide synthase (eNOS) pathway activation.

## 2. Results

### 2.1. AuNPs Showed No Cytotoxicity on RF/6A Cells

To eliminate the possibility that AuNPs have an effect on RF/6A cell migration through their effects on cell viability, cell viability was determined by MTT assays. As shown in Figure 1, the treatment of AuNPs (1, 2, and 4 ppm) did not change cell viability in MTT assays. These data show that AuNPs have no cytotoxicity to RF/6A cells and their effects on cell migration did not result from the reduction of cell viability.

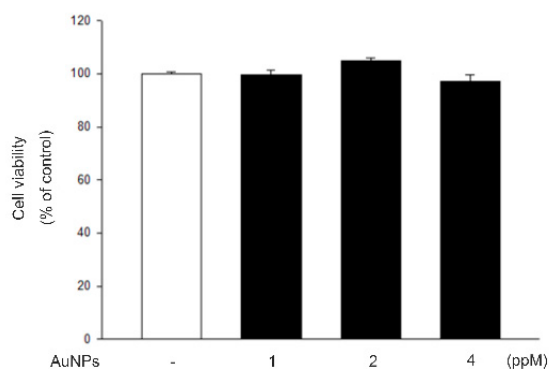


**Figure 1.** Viability of RF/6A cells was not influenced by AuNPs. The cells were treated with different concentrations of AuNPs for 24 h after being starved for 24 h. Cell viability was determined by the 3-(4,5-Dimethylthiazol-2-yl)-2,5-diphenyltetrazolium bromide (MTT) assay. The results are expressed as a percentage of control and represent the mean  $\pm$  standard errors (SE) of four independent experiments.

## 2.2. AuNPs Suppressed VEGF-Induced RF/6A Cell Migration

To decide the inhibitory activities of AuNPs on RF/6A cell migration, we carried out the Transwell migration assays. The data indicate that cell migration of RF/6A was increased by VEGF, and this effect was prominently inhibited by the preincubation of VEGF with AuNPs in a concentration-dependent manner. However, AuNPs had no effect on basal RF/6A cell migration without the treatment of VEGF (Figure 2).

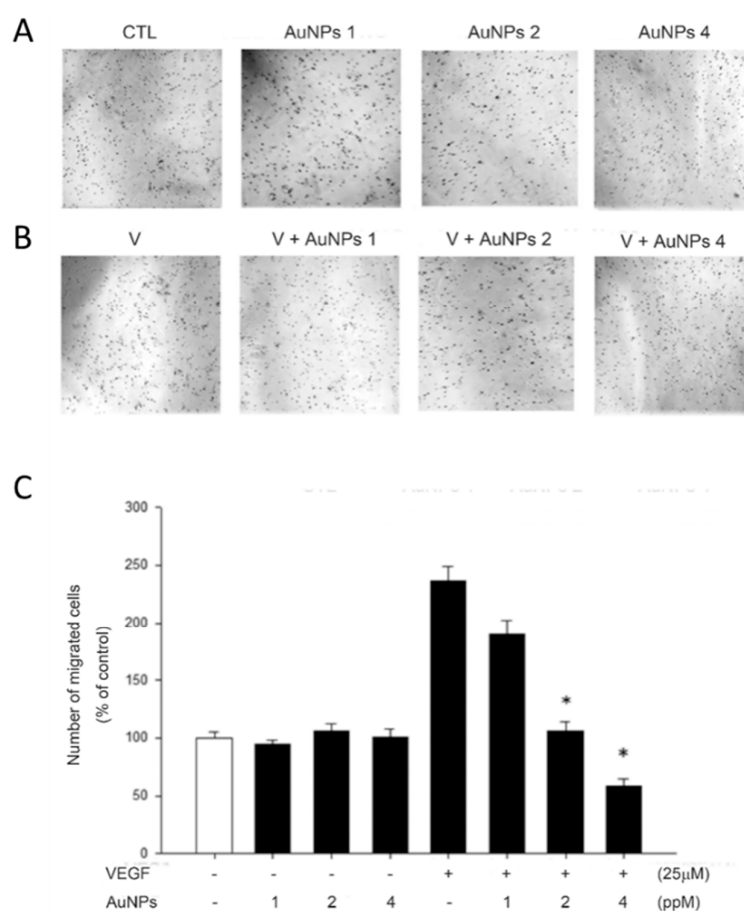


**Figure 2.** AuNPs suppress VEGF-induced cell migration in RF/6A cells by the Transwell migration assay. The Transwell inserts were coated with fibronectin (0.3 mg). RF/6A cells ( $5 \times 10^4$  in 200  $\mu$ L) were

seeded in the upper chamber in the absence or presence of AuNPs. The inserts were assembled in the lower chamber, which was filled with 600  $\mu$ L serum-free medium without VEGF, (A) containing VEGF (25 ng/mL), (B) and preincubated with various concentrations of AuNPs for 30 min at 37 °C. After incubating for 5 h at 37 °C, fixation was performed. RF/6A cells that migrated to the underside of the filter membrane were photographed (A, B) and counted by phase-contrast light microscope under high power field (magnification, 100 $\times$ ); (C) All experiments were conducted in duplicates, and similar results were repeated four times. The results are expressed as a percentage of control and represent the mean  $\pm$  standard errors (SE) of the eight experiments. \*  $p < 0.05$  significantly differs from VEGF-stimulated cells (the fifth bar).

### 2.3. AuNPs Had No Effect on RF/6A Cell Adhesion

To decide whether AuNPs suppressed RF/6A cell migration by interfering with their attachment to fibronectin, we conducted the effect of AuNPs on RF/6A cell adhesion with fibronectin-coated. As shown in Figure 3, the adhesion number was not affected by the treatment of AuNPs. These data suggest that the suppression of AuNPs on RF/6A cell migration was not produced by interference with the attachment of the cells to fibronectin.

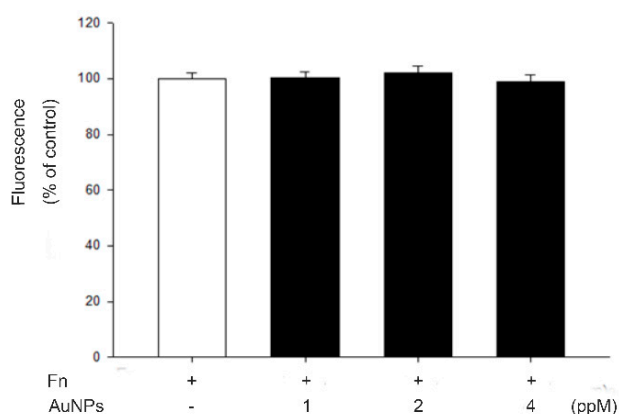


**Figure 3.** Cell adhesion of RF/6A cells was not influenced by AuNPs. BCECF-labeled cells were treated with DMSO or nanogold for 30 min. They were then seeded and allowed to adhere to plates with precoated fibronectin (fn) (15  $\mu$ g/mL) at 37 °C for 1 h. Fluorescence was measured using excitation and an emission wavelength of 485 and 535 nm, respectively. The results are expressed as a percentage of control and represent the mean  $\pm$  standard errors (SE) of three independent experiments.

### 2.4. AuNPs Suppressed VEGF-Induced Akt and eNOS Phosphorylation

To decide whether VEGF-induced signaling pathways are influenced by AuNPs, the level of phosphorylation of Akt and eNOS was determined by Western blotting. Figure 4 indicates that Akt and eNOS phosphorylation were enhanced by the treatment of VEGF. Preincubation with AuNPs produced the decrease of VEGF-induced PI3K and Akt phosphorylation in a dose-dependent manner.

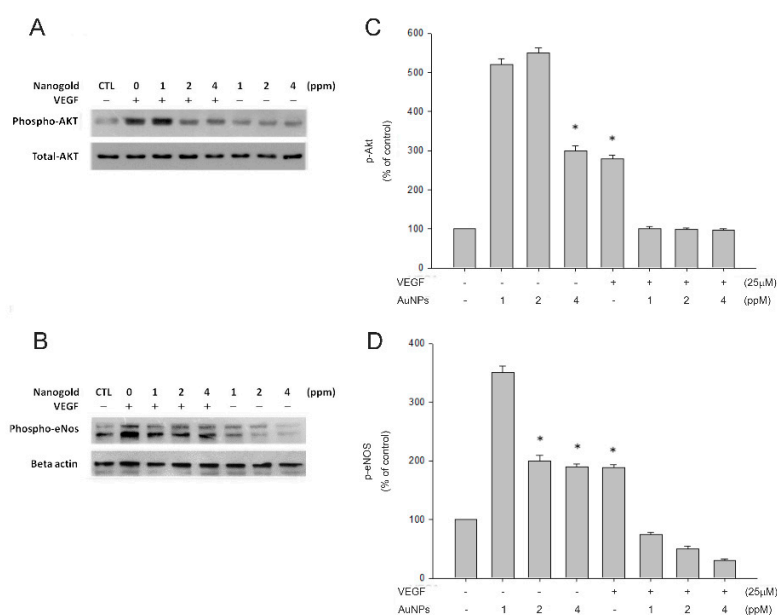


**Figure 4.** VEGF-induced protein kinase B (Akt) and endothelial nitric oxide synthase (eNOS) phosphorylations were inhibited by AuNPs. RF/6A cells were preincubated with the indicated concentrations of AuNPs (1, 2, 4 ppm) and incubated with or without VEGF (25 ng/mL) at 37 °C for 30 min, the cells were collected, and their lysates were analyzed by Western blot analysis. The changes in phosphorylated Akt and eNOS expression were evaluated (A,C). The quantitative data of western blot are shown below the panels, which are expressed as a percentage of control and represent the mean  $\pm$  standard errors (SE) of the three independent experiments (B,D). \*  $p < 0.05$  significantly differs from VEGF-stimulated cells (the second bar) (B,D).

### 3. Discussion

Angiogenesis is the physiological process of forming new blood vessels from preexisting vasculature. Physiological angiogenesis is highly regulated during wound repair [17,18]. Pathological choroidal and retinal angiogenesis are the leading causes of blindness, including age-related macular degeneration and diabetic retinopathy [19,20]. In angiogenesis, a serial process participated with several cells that include proteolytic degradation of the extracellular matrix, followed by migration and proliferation of capillary endothelial cells, pericyte recruitment, and assembly of the mature vessel [21]. The angiogenic process is regulated by a tight balance between pro-, and anti-angiogenic agents and vascular endothelial growth factor (VEGF) plays a critical regulatory role [22]. It is physiologically required for regulating proliferation and assembling endothelial cells during vasculogenesis, as well as for their maintenance and survival throughout the lifetime of blood vessels [23]. However, under subtle pathological alterations, abnormal angiogenesis with retinal and choroidal microvascular alterations have been observed during PDR, high myopia, and neovascular AMD [24–26].

AuNPs have been explored with a high expectation as they are effective and promising agents to improve the diagnosis and treatment of cancer [27–29]. Gold nanoparticles downregulate cellular cascades of interleukin-1 $\beta$ -induced pro-inflammatory response [30], and topical application of AuNPs decreases intraocular oxidative damage and inflammation [31]. Besides, AuNPs can effectively inhibit matrix metalloproteinase activity without causing cytotoxicity or inflammation [32]. AuNPs induce oxidative stress in mouse fibroblast, and the cells trigger the autophagic pathways as a survival mechanism to avoid cell death [33]. Gold nanoparticles can also inhibit retinal neovascularization through autophagy [34]. AuNPs can interrupt the crosstalk of tumor microenvironment and endothelial cells through the blockade of VEGF-VEGFR2 signaling during angiogenesis [35]. Under flow exposure conditions, anti-intercellular adhesion molecule-1 (ICAM-1) AuNPs can activate leukocyte adhesion receptors in tumor necrosis factor (TNF)-activated shear stress-adapted endothelial cells [36].

Many studies showed that AuNPs do not affect cell viabilities in several cell types [37], but some studies demonstrated their toxic effects [38,39]. The effect of AuNPs on choroid-retina endothelial cell viability is still unknown. Our study demonstrated that there are no toxic effects on RF/6A cell viabilities by AuNPs. Endothelial cell migration is essential to angiogenesis [40]. This motile and directional process is controlled by chemotactic, the directional migration toward a gradient of soluble chemoattractant; haptotaxis, the directional migration toward a gradient of immobilized ligands; and mechanotaxis, the directional migration generated by mechanical forces [41]. During angiogenesis, endothelial cell migration is integrated as a result of the above three mechanisms. In this study, we found that AuNPs significantly inhibit VEGF-induced choroid-retinal endothelial RF/6A cell migration without any signs of cytotoxicity as well.

Fibronectin is the main structural component of internal/outer collagenous and the elastic layer of Bruch's membrane [42]. It is also one of the serum autoantibody biomarkers for neovascular age-related macular degeneration [43]. In epiretinal membranes of vitreoproliferative retinopathy and proliferative diabetic retinopathy under immunohistochemical study, fibronectin is a major component in the extracellular matrix [44]. Under the retinal ischemic conditions, fibronectin is upregulated [45]. It is required for endothelial cell migration and tube morphogenesis and plays an important role during retinal and choroidal neovascularization [46]. However, our results indicate that AuNPs does not affect choroid-retinal endothelial RF/6A cell adhesion to fibronectin.

The PI3K/Akt pathway provides essential signaling for cell survival and proliferation. Signaling from different eNOS agonists, such as VEGF, insulin, and estrogen can affect eNOS activity through the PI3K/AKT pathway [47–49]. It has been reported that activations of the survival signal PI3K/Akt pathway and the endothelial-specific eNOS/NO pathway were closely associated with vascular remodeling and angiogenesis [50,51]. However, whether AuNPs affects the biological properties of choroid-retinal endothelial cells and the role of Akt/eNOS signaling pathway in VEGF-induced migration, have remained poorly understood. In the present study, we determined the effects of AuNPs on the VEGF/Akt/eNOS signaling pathway on choroid-retinal endothelial RF/6A cell migration. The results showed that AuNPs suppressed VEGF-induced activation of the Akt/eNOS signaling pathway during these processes.

## 4. Material and Methods

### 4.1. Materials

Gold nanoparticles (AuNPs) were purchased from Gold NanoTech Inc. (Taipei, Taiwan) [52]. The synthesis methods of AuNPs have been described in our previous study [53]. The size of the AuNPs we used in this study was 3–5 nm (SA20130129b). Phenylmethanesulfonyl fluoride (PMSF), bovine serum albumin (BSA), leupeptin, aprotinin, sodium fluoride (NaF), and sodium orthovanadate were purchased from Sigma-Aldrich (St Louis, MO, USA). Antibodies (Ab) raised against phospho-eNOS and eNOS were from Santa Cruz Biotechnology (Santa Cruz, CA, USA). Abs raised against phospho-Akt and Akt were from Cell Signaling Technology, Inc. (Beverly, MA, USA).

### 4.2. Cell Cultures

The rhesus macaque choroid-retinal endothelial cell line RF/6A derived from the choroid-retina of a rhesus macaque fetus was purchased from Food Industry Research and Development Institute (Hsinchu, Taiwan). The cells were maintained in RPMI 1640 Medium (Gibco, Carlsbad, CA, USA) supplemented with 10% fetal bovine serum (FBS, Gibco) and 1% penicillin/streptomycin (Hyclone, UT, USA) at 37 °C, 5% CO<sub>2</sub> and 95% humidified air. For most of the experiments, cells reaching a 90–95% of confluence were synchronized for 24 h by serum starvation before they were subjected to further analysis.



#### 4.3. Nanogold Treatment and VEGF Incorporation

AuNPs were dissolved by distilled water in a series of dilutions. In Transmigration assays and the Western blot analysis, the 25 ng/mL of vascular endothelial growth factor (VEGF) were incorporated with different concentrations of AuNPs in the serum-free RPMI 1640 medium in culturing RF/6A cells at 37 °C for 30 min.

#### 4.4. Transmigration Assays

By using a modified Boyden chamber model (Transwell apparatus, 8.0 mm pore size, Costar), the migration ability of RF/6A cell were demonstrated as previously described [54]. Briefly, the lower surface of the semi-permeable membrane was coated with 0.3 mg of fibronectin for 30 min in the laminar flow hood. Different concentrations of AuNPs were added to the lower chamber, which was filled with 0.6 mL of serum-free RPMI 1640 medium or 25 ng/mL VEGF-containing medium.  $2.5 \times 10^5$ /mL RF/6A cells were added to the upper chamber. Inserts were removed after 5 h, and the inner side was wiped with cotton swabs. Cells at the lower chamber were fixed and stained with 0.5% toluidine blue in 4% paraformaldehyde (PFA). The migrated cells were photographed and counted as the number of stained cells per  $\times 100$  field (high power field, HPF) under a phase-contrast microscope (Leica DMIL1) and photographed.

#### 4.5. Viability Assays

The cell viability was detected by the 3-(4,5-dimethylthiazol-2-yl)-2,5-diphenyltetrazolium bromide (MTT) assay. Briefly, different concentrations of AuNPs were preincubated with RF/6A cells for 24 h in 96-well plates. After a brief wash with medium, 0.5 mg/mL MTT was added and incubated at 37 °C for 4 h to measure the amount of living and metabolically active cells. MTT was metabolized by mitochondrial dehydrogenases to a purple formazan dye, with the light absorbance at 570 nm. The absorbance was detected by a spectrophotometer and was proportional to cell viability.

#### 4.6. Cell Adhesion Assays

The 50  $\mu$ L of fibronectin (15  $\mu$ g/mL in PBS, pH 7.4) was used to coat 96-well plates at 37 °C for 24 h. After gentle washed with PBS three times, the plates were blocked by 100 mg/mL bovine serum albumin (Sigma-Aldrich, St Louis, MO, USA) in PBS at room temperature for 1 h to avoid nonspecific binding to fibronectin. Afterward, RF/6A cells were labeled with 10 mg/mL BCECF/AM for 30 min at 37 °C in serum-free RPMI 1640 medium. After brief washed with the serum-free medium twice, the labeled cells were resuspended to a density of  $1.0 \times 10^5$  and incubated with different concentrations of AuNPs in the serum-free RPMI 1640 medium for further 30 min at 37 °C. Then, the suspended cells were plated onto 96-well plates with 100  $\mu$ L serum-free cell culture medium at 37 °C for 1 h. The nonadherent cells were removed from the plate by washing with PBS for three times and aspirated. The number of adhered cells in the 96-well plates was measured by the Wallac Victor 3 1420 multilabel counter (Perkin Elmer, Turku, Finland) at an excitation and emission wavelength of 485 and 535 nm.

#### 4.7. Preparation of Cell Lysates for Western Blots

The RF/6A cells were cultured on 6 cm dishes until 90–95% confluent and changed into a serum-free RPMI 1640 medium for 24 h. Various concentrations of nanogold mixed with or without VEGF (25 ng/mL) at 37 °C for 30 min in serum-free medium were added to the cells. After 30 min of incubation, cell were washing with PBS twice and lysing with sonication and centrifugation at 14,000 g for 10 min at 4 °C in the radioimmunoprecipitation assay buffer. The supernatant was removed and the concentration of protein was quantified by a Pierce protein assay kit (Pierce, Rockford, IL, USA). Total protein was separated by electrophoresis on 10% SDS–polyacrylamide gels. The protein bands were then transferred onto polyvinylidene fluoride (PVDF) membrane and probed with the antibodies against the phosphorylation of Akt and eNOS. Signals were detected by enhanced chemiluminescence

(Chemiluminescence Reagent Plus from NEN, Boston, MA, USA). The PVDF membrane was stripped at 60 °C for 30 min with a stripping buffer for staining internal control.

#### 4.8. Statistical Analysis

All results were analyzed with SigmaPlot for Windows (Version 10.00, Chicago, IL, USA). Data are shown as mean  $\pm$  standard error (SE) of four experiments. The *t*-test was performed to determine the difference between groups. A value of  $p < 0.05$  was considered statistically significant.

### 5. Conclusions

As VEGF is a key mediator and upregulated in many ocular angiogenic diseases such as proliferative diabetic retinopathy and wet-type age-related macular degeneration, anti-VEGF therapy is the current main strategy of treatment. Our studies provide the mechanism of AuNPs on the inhibitory effects of the VEGF-induced RF/6A cell migration through the suppression of Akt/eNOS phosphorylation. However, AuNPs show no cytotoxic effects on the RF/6A cells. Moreover, AuNPs do not affect the normal physiological functions of RF/6A cell adhesion to fibronectin. These studies provide important insight into further research on the effects of AuNPs in RF/6A cells and the possible beneficial effect on the suppression of angiogenesis by AuNPs in ocular angiogenic diseases.

**Author Contributions:** Formal analysis, C.-F.H.; Funding acquisition, C.-M.C. and D.-C.C.; Investigation, C.-F.H.; Methodology, C.-M.C., C.-Y.H. and J.-Y.F.; Resources, C.-Y.H.; Writing—original draft, C.-M.C.; Writing—review & editing, C.-F.H., H.-J.L. and D.-C.C. All authors have read and agreed to the published version of the manuscript.

**Funding:** This work was supported by the research grants from the National Science Council and from Cardinal Tien Hospital, Taipei, Taiwan (CTH-102-1-2A30, CTH-104-1-2B05). The fourth author is partially supported by an United States National Science Foundation grant DMS-1408839 and a McDevitt Endowment Fund at Georgetown University.

**Conflicts of Interest:** The authors declare no conflict of interest.

### References

- Okamoto, T.; Usuda, H.; Tanaka, T.; Wada, K.; Shimaoka, M. The Functional Implications of Endothelial Gap Junctions and Cellular Mechanics in Vascular Angiogenesis. *Cancers* **2019**, *11*, 237. [\[CrossRef\]](#)
- Apte, R.S.; Chen, D.S.; Ferrara, N. VEGF in Signaling and Disease: Beyond Discovery and Development. *Cell* **2019**, *176*, 1248–1264. [\[CrossRef\]](#)
- Zuazo-Gaztelu, I.; Casanovas, O. Unraveling the Role of Angiogenesis in Cancer Ecosystems. *Front. Oncol.* **2018**, *8*, 248. [\[CrossRef\]](#)
- Moreira-Soares, M.; Coimbra, R.; Rebelo, L.; Carvalho, J.; Travasso, R.D. Angiogenic Factors produced by Hypoxic Cells are a leading driver of Anastomoses in Sprouting Angiogenesis—a computational study. *Sci. Rep.* **2018**, *8*, 8726. [\[CrossRef\]](#)
- Ehrenberg, M.; Benny, O. Evolving multidimensional pharmacological approaches to CNV therapy in AMD. *Curr. Eye. Res.* **2018**, *43*, 147–154. [\[CrossRef\]](#)
- Campbell, M.; Doyle, S.L. Current perspectives on established and novel therapies for pathological neovascularization in retinal disease. *Biochem. Pharmacol.* **2019**, *164*, 321–325. [\[CrossRef\]](#)
- Teo, K.Y.; Ng, W.Y.; Lee, S.Y.; Cheung, C.M. Management of Myopic Choroidal Neovascularization: Focus on Anti-VEGF Therapy. *Drugs* **2016**, *76*, 1119–1133. [\[CrossRef\]](#)
- Kick, K.; Nekolla, K.; Rehberg, M.; Vollmar, A.M.; Zahler, S. New View on Endothelial Cell Migration: Switching Modes of Migration Based on Matrix Composition. *Arterioscler. Thromb. Vasc. Biol.* **2016**, *36*, 2346–2357. [\[CrossRef\]](#)
- Tang, Y.; Zhou, X. Antagonistic effects of exogenous Slit2 on VEGF-induced choroidal endothelial cell migration and tube formation. *Exp. Ther. Med.* **2019**, *17*, 2443–2450. [\[CrossRef\]](#)
- Lu, C.L.; Shyu, J.F.; Wu, C.C.; Hung, C.F.; Liao, M.T.; Liu, W.C.; Zheng, C.M.; Hou, Y.C.; Lin, Y.F.; Lu, K.C. Association of Anabolic Effect of Calcitriol with Osteoclast-Derived Wnt 10b Secretion. *Nutrients* **2018**, *10*, 1164. [\[CrossRef\]](#)

11. Jahangirian, H.; Kalantari, K.; Izadiyan, Z.; Rafiee-Moghaddam, R.; Shameli, K.; Webster, T.J. A review of small molecules and drug delivery applications using gold and iron nanoparticles. *Int. J. Nanomedicine* **2019**, *14*, 1633–1657. [\[CrossRef\]](#)
12. Pan, Y.; Ding, H.; Qin, L.; Zhao, X.; Cai, J.; Du, B. Gold nanoparticles induce nanostructural reorganization of VEGFR2 to repress angiogenesis. *J. Biomed. Nanotechnol.* **2013**, *9*, 1746–1756. [\[CrossRef\]](#)
13. Pan, Y.; Wu, Q.; Liu, R.; Shao, M.; Pi, J.; Zhao, X.; Qin, L. Inhibition effects of gold nanoparticles on proliferation and migration in hepatic carcinoma-conditioned HUVECs. *Bioorg. Med. Chem. Lett.* **2014**, *24*, 679–684. [\[CrossRef\]](#)
14. Pan, Y.; Wu, Q.; Qin, L.; Cai, J.; Du, B. Gold nanoparticles inhibit VEGF165-induced migration and tube formation of endothelial cells via the Akt pathway. *Biomed. Res. Int.* **2014**, *2014*, 418624. [\[CrossRef\]](#)
15. Roh, Y.J.; Rho, C.R.; Cho, W.K.; Kang, S. The Antiangiogenic Effects of Gold Nanoparticles on Experimental Choroidal Neovascularization in Mice. *Invest. Ophthalmol. Vis. Sci.* **2016**, *57*, 6561–6567. [\[CrossRef\]](#)
16. Dong, Y.; Wan, G.; Yan, P.; Qian, C.; Li, F.; Peng, G. Fabrication of resveratrol coated gold nanoparticles and investigation of their effect on diabetic retinopathy in streptozotocin induced diabetic rats. *J. Photochem. Photobiol. B.* **2019**, *195*, 51–57. [\[CrossRef\]](#)
17. Lilly, A.J.; Mazan, A.; Scott, D.A.; Lacaud, G.; Kouskoff, V. SOX7 expression is critically required in FLK1-expressing cells for vasculogenesis and angiogenesis during mouse embryonic development. *Mech. Dev.* **2017**, *146*, 31–41. [\[CrossRef\]](#)
18. DiPietro, L.A. Angiogenesis and wound repair: When enough is enough. *J. Leukoc. Biol.* **2016**, *100*, 979–984. [\[CrossRef\]](#)
19. Ved, N.; Hulse, R.P.; Bestall, S.M.; Donaldson, L.F.; Bainbridge, J.W.; Bates, D.O. Vascular endothelial growth factor-A165b ameliorates outer-retinal barrier and vascular dysfunction in the diabetic retina. *Clin. Sci. (Lond.)* **2017**, *131*, 1225–1243. [\[CrossRef\]](#)
20. Mesquita, J.; Castro-de-Sousa, J.P.; Vaz-Pereira, S.; Neves, A.; Passarinha, L.A.; Tomaz, C.T. Vascular endothelial growth factors and placenta growth factor in retinal vasculopathies: Current research and future perspectives. *Cytokine Growth Factor Rev.* **2018**, *39*, 102–115. [\[CrossRef\]](#)
21. Logsdon, E.A.; Finley, S.D.; Popel, A.S.; Mac Gabhann, F. A systems biology view of blood vessel growth and remodelling. *J. Cell. Mol. Med.* **2014**, *18*, 1491–1508. [\[CrossRef\]](#)
22. Karaman, S.; Leppanen, V.M.; Alitalo, K. Vascular endothelial growth factor signaling in development and disease. *Development* **2018**, *145*, dev151019. [\[CrossRef\]](#)
23. Shibuya, M. Vascular endothelial growth factor and its receptor system: Physiological functions in angiogenesis and pathological roles in various diseases. *J. Biochem.* **2013**, *153*, 13–19. [\[CrossRef\]](#)
24. Pakzad-Vaezi, K.; Mehta, H.; Mammo, Z.; Tufail, A. Vascular endothelial growth factor inhibitor use and treatment approach for choroidal neovascularization secondary to pathologic myopia. *Expert Opin. Biol. Ther.* **2016**, *16*, 873–881. [\[CrossRef\]](#)
25. Gucciardo, E.; Loukovaara, S.; Salven, P.; Lehti, K. Lymphatic Vascular Structures: A New Aspect in Proliferative Diabetic Retinopathy. *Int. J. Mol. Sci.* **2018**, *19*, 4034. [\[CrossRef\]](#)
26. Wang, L.; Lee, A.Y.; Wigg, J.P.; Peshavariya, H.; Liu, P.; Zhang, H. miRNA involvement in angiogenesis in age-related macular degeneration. *J. Physiol. Biochem.* **2016**, *72*, 583–592. [\[CrossRef\]](#)
27. Ning, L.; Zhu, B.; Gao, T. Gold Nanoparticles: Promising Agent to Improve the Diagnosis and Therapy of Cancer. *Curr. Drug Metab.* **2017**, *18*, 1055–1067. [\[CrossRef\]](#)
28. Singh, P.; Pandit, S.; Mokkapat, V.; Garg, A.; Ravikumar, V.; Mijakovic, I. Gold Nanoparticles in Diagnostics and Therapeutics for Human Cancer. *Int. J. Mol. Sci.* **2018**, *19*, 1979. [\[CrossRef\]](#)
29. Peng, J.; Liang, X. Progress in research on gold nanoparticles in cancer management. *Medicine* **2019**, *98*, e15311. [\[CrossRef\]](#)
30. Sumbayev, V.V.; Yasinska, I.M.; Garcia, C.P.; Gilliland, D.; Lall, G.S.; Gibbs, B.F.; Bonsall, D.R.; Varani, L.; Rossi, F.; Calzolari, L. Gold nanoparticles downregulate interleukin-1beta-induced pro-inflammatory responses. *Small* **2013**, *9*, 472–477. [\[CrossRef\]](#)
31. Pereira, D.V.; Petronilho, F.; Pereira, H.R.; Vuolo, F.; Mina, F.; Possato, J.C.; Vitto, M.F.; de Souza, D.R.; da Silva, L.; da Silva Paula, M.M.; et al. Effects of gold nanoparticles on endotoxin-induced uveitis in rats. *Invest. Ophthalmol. Vis. Sci.* **2012**, *53*, 8036–8041. [\[CrossRef\]](#)

32. Hashimoto, M.; Sasaki, J.I.; Yamaguchi, S.; Kawai, K.; Kawakami, H.; Iwasaki, Y.; Imazato, S. Gold Nanoparticles Inhibit Matrix Metalloproteases without Cytotoxicity. *J. Dent. Res.* **2015**, *94*, 1085–1091. [\[CrossRef\]](#)
33. Gioria, S.; Chassaigne, H.; Carpi, D.; Parracino, A.; Meschini, S.; Barboro, P.; Rossi, F. A proteomic approach to investigate AuNPs effects in Balb/3T3 cells. *Toxicol. Lett.* **2014**, *228*, 111–126. [\[CrossRef\]](#)
34. Shen, N.; Zhang, R.; Zhang, H.R.; Luo, H.Y.; Shen, W.; Gao, X.; Guo, D.Z.; Shen, J. Inhibition of retinal angiogenesis by gold nanoparticles via inducing autophagy. *Int. J. Ophthalmol.* **2018**, *11*, 1269–1276.
35. Zhang, Y.; Xiong, X.; Huai, Y.; Dey, A.; Hossen, M.N.; Roy, R.V.; Elechalawar, C.K.; Rao, G.; Bhattacharya, R.; Mukherjee, P. Gold Nanoparticles Disrupt Tumor Microenvironment—Endothelial Cell Crosstalk to Inhibit Angiogenic Phenotypes in vitro. *Bioconjug. Chem.* **2019**, *30*, 1724–1733. [\[CrossRef\]](#)
36. Klingberg, H.; Loft, S.; Oddershede, L.B.; Moller, P. The influence of flow, shear stress and adhesion molecule targeting on gold nanoparticle uptake in human endothelial cells. *Nanoscale* **2015**, *7*, 11409–11419. [\[CrossRef\]](#)
37. Aueviriyavit, S.; Phummiratch, D.; Maniratanachote, R. Mechanistic study on the biological effects of silver and gold nanoparticles in Caco-2 cells—induction of the Nrf2/HO-1 pathway by high concentrations of silver nanoparticles. *Toxicol. Lett.* **2014**, *224*, 73–83. [\[CrossRef\]](#)
38. Sun, H.; Jia, J.; Jiang, C.; Zhai, S. Gold Nanoparticle-Induced Cell Death and Potential Applications in Nanomedicine. *Int. J. Mol. Sci.* **2018**, *19*, 754. [\[CrossRef\]](#)
39. Pitchaimani, A.; Nguyen, T.D.T.; Koirala, M.; Zhang, Y.; Aryal, S. Impact of cell adhesion and migration on nanoparticle uptake and cellular toxicity. *Toxicol. In Vitro* **2017**, *43*, 29–39. [\[CrossRef\]](#)
40. Senger, D.R.; Davis, G.E. Angiogenesis. *Cold Spring Harb. Perspect. Biol.* **2011**, *3*, a005090. [\[CrossRef\]](#)
41. Lamalice, L.; Le Boeuf, F.; Huot, J. Endothelial cell migration during angiogenesis. *Circ. Res.* **2007**, *100*, 782–794. [\[CrossRef\]](#) [\[PubMed\]](#)
42. Nita, M.; Grzybowski, A.; Ascaso, F.J.; Huerva, V. Age-related macular degeneration in the aspect of chronic low-grade inflammation (pathophysiological parainflammation). *Mediators Inflamm.* **2014**, *2014*, 930671. [\[CrossRef\]](#) [\[PubMed\]](#)
43. Morohoshi, K.; Patel, N.; Ohbayashi, M.; Chong, V.; Grossniklaus, H.E.; Bird, A.C.; Ono, S.J. Serum autoantibody biomarkers for age-related macular degeneration and possible regulators of neovascularization. *Exp. Mol. Pathol.* **2012**, *92*, 64–73. [\[CrossRef\]](#) [\[PubMed\]](#)
44. Ioachim, E.; Stefanitou, M.; Gorezis, S.; Tsanou, E.; Psilas, K.; Agnantis, N.J. Immunohistochemical study of extracellular matrix components in epiretinal membranes of vitreoproliferative retinopathy and proliferative diabetic retinopathy. *Eur. J. Ophthalmol.* **2005**, *15*, 384–391. [\[CrossRef\]](#)
45. Reinhard, J.; Renner, M.; Wiemann, S.; Shakoob, D.A.; Stute, G.; Dick, H.B.; Faissner, A.; Joachim, S.C. Ischemic injury leads to extracellular matrix alterations in retina and optic nerve. *Sci. Rep.* **2017**, *7*, 43470. [\[CrossRef\]](#)
46. Miller, C.G.; Budoff, G.; Prenner, J.L.; Schwarzbauer, J.E. Minireview: Fibronectin in retinal disease. *Exp. Biol. Med.* **2017**, *242*, 1–7. [\[CrossRef\]](#)
47. Long, Y.; Xia, J.Y.; Chen, S.W.; Gao, C.L.; Liang, G.N.; He, X.M.; Wu, J.; Jiang, C.X.; Liu, X.; Huang, W.; et al. ATP2B1 gene Silencing Increases Insulin Sensitivity through Facilitating Akt Activation via the Ca(2+)/calmodulin Signaling Pathway and Ca(2+)-associated eNOS Activation in Endothelial Cells. *Int. J. Biol. Sci.* **2017**, *13*, 1203–1212. [\[CrossRef\]](#)
48. Hohmann, N.; Xia, N.; Steinkamp-Fenske, K.; Forstermann, U.; Li, H. Estrogen Receptor Signaling and the PI3K/Akt Pathway Are Involved in Betulinic Acid-Induced eNOS Activation. *Molecules* **2016**, *21*, 973. [\[CrossRef\]](#)
49. Sharma, S.; Guru, S.K.; Manda, S.; Kumar, A.; Minto, M.J.; Prasad, V.D.; Sharma, P.R.; Mondhe, D.M.; Bharate, S.B.; Bhushan, S. A marine sponge alkaloid derivative 4-chloro fascaplysin inhibits tumor growth and VEGF mediated angiogenesis by disrupting PI3K/Akt/mTOR signaling cascade. *Chem. Biol. Interact.* **2017**, *275*, 47–60. [\[CrossRef\]](#)
50. Namkoong, S.; Kim, C.K.; Cho, Y.L.; Kim, J.H.; Lee, H.; Ha, K.S.; Choe, J.; Kim, P.H.; Won, M.H.; Kwon, Y.G.; et al. Forskolin increases angiogenesis through the coordinated cross-talk of PKA-dependent VEGF expression and Epac-mediated PI3K/Akt/eNOS signaling. *Cell. Signal.* **2009**, *21*, 906–915. [\[CrossRef\]](#)
51. Xing, Y.; Lai, J.; Liu, X.; Zhang, N.; Ming, J.; Liu, H.; Zhang, X. Netrin-1 restores cell injury and impaired angiogenesis in vascular endothelial cells upon high glucose by PI3K/AKT-eNOS. *J. Mol. Endocrinol.* **2017**, *58*, 167–177. [\[CrossRef\]](#) [\[PubMed\]](#)

52. Yen, H.J.; Hsu, S.H.; Tsai, C.L. Cytotoxicity and Immunological Response of Gold and Silver Nanoparticles of Different Sizes. *Small* **2009**, *5*, 1553–1561. [[CrossRef](#)] [[PubMed](#)]
53. Lu, P.H.; Li, H.J.; Chang, H.H.; Wu, N.L.; Hung, C.F. Gold nanoparticles induce cell death and suppress migration of melanoma cells. *J. Nanopart. Res.* **2017**, *19*, 342. [[CrossRef](#)]
54. Chan, C.M.; Chang, H.H.; Wang, V.C.; Huang, C.L.; Hung, C.F. Inhibitory effects of resveratrol on PDGF-BB-induced retinal pigment epithelial cell migration via PDGFRbeta, PI3K/Akt and MAPK pathways. *PLoS ONE* **2013**, *8*, e56819.



© 2019 by the authors. Licensee MDPI, Basel, Switzerland. This article is an open access article distributed under the terms and conditions of the Creative Commons Attribution (CC BY) license (<http://creativecommons.org/licenses/by/4.0/>).



HETEROCYCLES, Vol. 100, No. 6, 2020, pp. 857 - 870. © 2020 The Japan Institute of Heterocyclic Chemistry  
Received, 27th December, 2019, Accepted, 28th January, 2020, Published online, 7th February, 2020  
DOI: 10.3987/REV-19-925

## SURVEY OF BRIARANE-TYPE DITERPENOIDS – PART VII

Yu-Hsin Chen,<sup>a†</sup> Hsien-Kuo Chin,<sup>b,ct</sup> Bo-Rong Peng,<sup>a</sup> You-Ying Chen,<sup>a</sup>  
Chiung-Chin Hu,<sup>a</sup> Li-Guo Zheng,<sup>a</sup> Thanh-Hao Huynh,<sup>a</sup> Tung-Pin Su,<sup>a</sup> Yi-Lin  
Zhang,<sup>a</sup> Zhi-Hong Wen,<sup>b</sup> Tsong-Long Hwang,<sup>d,e,f,g\*</sup> Yang-Chang Wu,<sup>h\*</sup> and  
Ping-Jyun Sung<sup>a,b,i,j,k\*</sup>

<sup>a</sup> National Museum of Marine Biology and Aquarium, Pingtung 94450, Taiwan.

<sup>b</sup> Department of Marine Biotechnology and Resources, National Sun Yat-sen University, Kaohsiung 80424, Taiwan. <sup>c</sup> Division of Cardiovascular Surgery, Department of Surgery, Kaohsiung Armed Forces General Hospital, 80284, Taiwan. <sup>d</sup> Research Center for Chinese Herbal Medicine, Research Center for Food and Cosmetic Safety, Graduate Institute of Healthy Industry Technology, College of Human Ecology, Chang Gung University of Science and Technology, Taoyuan 33303, Taiwan. <sup>e</sup> Graduate Institute of Natural Products, College of Medicine, Chang Gung University, Taoyuan 33302, Taiwan. <sup>f</sup> Chinese Herbal Medicine Research Team, Healthy Aging Research Center, Chang Gung University, Taoyuan 33302, Taiwan. <sup>g</sup> Department of Anaesthesiology, Chang Gung Memorial Hospital, Taoyuan 33305, Taiwan. <sup>h</sup> Graduate Institute of Integrated Medicine, College of Chinese Medicine, China Medical University, Taichung 40402, Taiwan. <sup>i</sup> Graduate Institute of Marine Biology, National Dong Hwa University, Pingtung 94450, Taiwan. <sup>j</sup> Chinese Medicine Research and Development Center, China Medical University Hospital, Taichung 40447, Taiwan. <sup>k</sup> Graduate Institute of Natural Products, Kaohsiung Medical University, Kaohsiung 80708, Taiwan.

E-mail: htl@mail.cgu.edu.tw, yachwu@gmail.com, pjsung@nmmba.gov.tw

<sup>†</sup>These authors contributed equally to this work.

**Abstract** – The structures, names, bioactivities, and references of 78 briarane-type natural products, including 56 new metabolites, isolated between 2017 and 2019 are summarized in this review article. All the briarane diterpenoids mentioned in this review were isolated from the octocorals Alcyonacea belonging to genus *Briareum*; the Gorgonacea belonging to genus *Junceella* and

*Subergorgia*; and the Pennatulacea belonging to genus *Anthoptilum*. Some of these compounds exhibited potentially biomedical activities, including anti-inflammatory activity, antiviral activity, and cytotoxicity.

## 1. INTRODUCTION

Following previous review articles from our research group focused on marine-origin briarane-type natural products,<sup>1–6</sup> this review covers the literature from 2017 to 2019, and describes 78 naturally-occurring briarane-related diterpenoids (including 56 new metabolites), all of which are characterized by the presence of a  $\gamma$ -lactone moiety fused to a bicyclo[8.4.0] ring system, obtained from various octocorals, including *Briareum excavatum*, *Briareum violaceum*, *Junceella fragilis*, *Subergorgia suberosa*, and *Anthoptilum grandiflorum*. Many of these compounds exhibited bioactivities *in vitro*, which might indicate a potential for use in biomedical applications. This survey of briarane-related compounds is presented taxonomically according to genus and species.

## 2. ALCYONACEA

### 2-1. *Briareum excavatum* (family Briareidae)

In 1977, the first briarane diterpenoid, briarein A, was isolated from the Caribbean octocoral *B. asbestinum*,<sup>7</sup> and since then *Briareum* played the most important role to produce briarane-type natural products. In 2017, four new briaranes, briarenols B–E (1–4) (Figure 1), were isolated from *B. excavatum*, collected off the waters of Taiwan, and the structures of briaranes 1–4 were established by interpretation of spectroscopic data.<sup>8,9</sup> It is interesting to note that 1 was found to enhance the expression of iNOS and COX-2 (158 and 132%, respectively)<sup>8</sup> than those of its 12-*O*-*n*-butyryl analogue, briarenolide ZII (5) (47 and 90%, respectively),<sup>8,10</sup> at a concentration of 10  $\mu$ M. It means that the size of functional groups at C-12 could influence the bioactivity. Briarenols D (3) and E (4) reduced the levels of iNOS to 78 and 67%, at a concentration of 10  $\mu$ M, respectively, and 3 showed an inhibitory effect on the release of elastase with an IC<sub>50</sub> value of 4.65  $\mu$ M.<sup>9</sup>

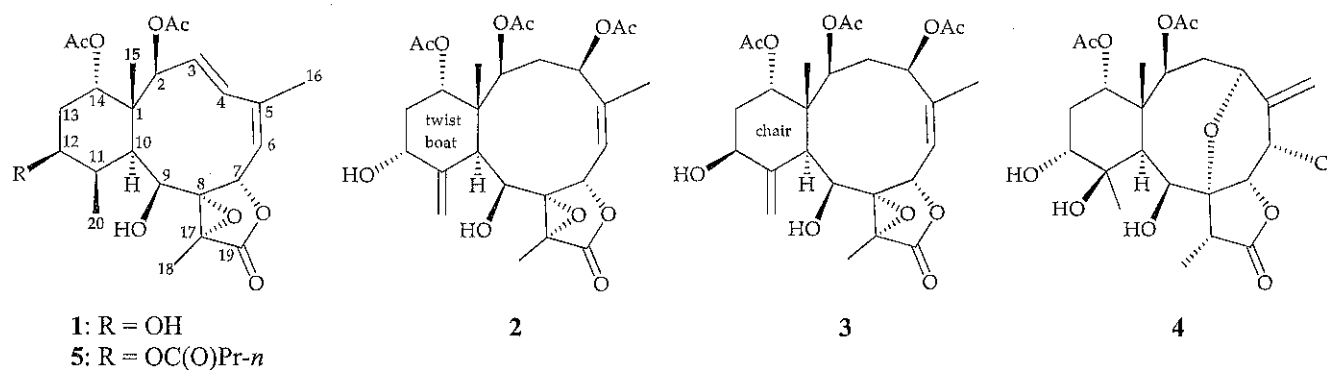
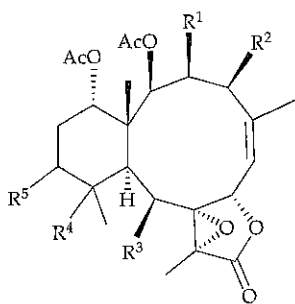


**Figure 1.** Structures of briarenols B–E (1–4) and briarenolide ZII (5)

## 2-2. *Briareum violaceum*

In continuing studies of the chemical constituents of a cultured-type octocoral *B. violaceum*, 14 new briarane derivatives, briaviolides K–X (6–19),<sup>11–15</sup> as well as four known briaranes, excavatolide Z (20),<sup>13,16</sup> brianthein W (21),<sup>14,17,18</sup> excavatolides B (22) and E (23) (Figure 2),<sup>15,19,20</sup> were obtained, and the structures of new briaranes 6–19 were determined based on analysis of their spectroscopic data. In the anti-inflammatory activity test, briaviolide L (7) showed activity against the expressions of iNOS and COX-2 to 47 and 62%, respectively, but briaviolide K (6) was found to be inactive, indicating that the activity of these two compounds is dependent on the stereochemistry of 11-hydroxy group.<sup>11</sup> Furthermore, by comparison the inhibitory effects on the release of iNOS of 7 (47%) with that of briaviolide O (10) (11%),<sup>11,12</sup> suggested that the 4 $\beta$ -acetoxy group in 10 will enhance the inhibitory activity on the release of iNOS. It is also interesting to note that briaviolide Q (12) reduced the level of iNOS to 26% and its analogue, excavatolide Z (20),<sup>16</sup> was found to be more weak (66%), indicating the length of the acyl group at C-12 could influence the bioactivity.<sup>13</sup> Furthermore, briaviolide S (14) showed an inhibitory effect on the generation of superoxide anion with an IC<sub>50</sub> value of 5.37  $\mu$ M<sup>14</sup> and excavatolide B (22) could be potential use as a therapeutic agent through the inhibition of osteoclastogenesis in rheumatoid arthritis.<sup>21</sup> Briarane 22 was also found to enhance contextual memory retrieval in both wild-type and *Ca<sub>v</sub>3.2<sup>-/-</sup>* mice via repressing the delayed rectifier potassium current in the hippocampus.<sup>22</sup> The absolute configurations for the known briaranes, brianthein W (21), excavatolides B (22) and E (23) were determined by single-crystal X-ray diffraction analysis in later studies,<sup>14,15</sup> and as briaranes 6–20 were obtained along with briaranes 21–23 from the same target organism, *B. violaceum*, it is reasonable on biogenetic grounds to assume that briaranes 6–23 have the same configuration as the C-15 methyl group *trans* to H-10, in briarane-related natural products.



- 6: R<sup>1</sup> = R<sup>2</sup> = H, R<sup>3</sup> = OAc, R<sup>4</sup> =  $\beta$ -OH, R<sup>5</sup> =  $\alpha$ -OC(O)Pr-*n*  
 7: R<sup>1</sup> = R<sup>2</sup> = H, R<sup>3</sup> = OAc, R<sup>4</sup> =  $\alpha$ -OH, R<sup>5</sup> =  $\alpha$ -OC(O)Pr-*n*  
 8: R<sup>1</sup> = H, R<sup>2</sup> = R<sup>3</sup> = OAc, R<sup>4</sup> =  $\alpha$ -H, R<sup>5</sup> =  $\alpha$ -OC(O)Pr-*n*  
 10: R<sup>1</sup> = H, R<sup>2</sup> = R<sup>3</sup> = OAc, R<sup>4</sup> =  $\alpha$ -OH, R<sup>5</sup> =  $\alpha$ -OC(O)Pr-*n*  
 11: R<sup>1</sup> = R<sup>2</sup> = H, R<sup>3</sup> = OAc, R<sup>4</sup> =  $\beta$ -OH, R<sup>5</sup> =  $\alpha$ -OAc  
 12: R<sup>1</sup> = R<sup>2</sup> = H, R<sup>3</sup> = OH, R<sup>4</sup> =  $\beta$ -OH, R<sup>5</sup> =  $\alpha$ -OC(O)(CH<sub>2</sub>)<sub>4</sub>Me  
 17: R<sup>1</sup> = H, R<sup>2</sup> = OH, R<sup>3</sup> = OAc, R<sup>4</sup> =  $\beta$ -OH, R<sup>5</sup> =  $\alpha$ -OC(O)Pr-*n*  
 20: R<sup>1</sup> = R<sup>2</sup> = H, R<sup>3</sup> = OH, R<sup>4</sup> =  $\beta$ -OH, R<sup>5</sup> =  $\alpha$ -OC(O)Pr-*n*  
 22: R<sup>1</sup> = OC(O)Pr-*n*, R<sup>2</sup> = H, R<sup>3</sup> = OAc, R<sup>4</sup> =  $\alpha$ -H, R<sup>5</sup> =  $\beta$ -OH  
 23: R<sup>1</sup> = R<sup>2</sup> = H, R<sup>3</sup> = OH, R<sup>4</sup> =  $\alpha$ -H, R<sup>5</sup> =  $\beta$ -OH

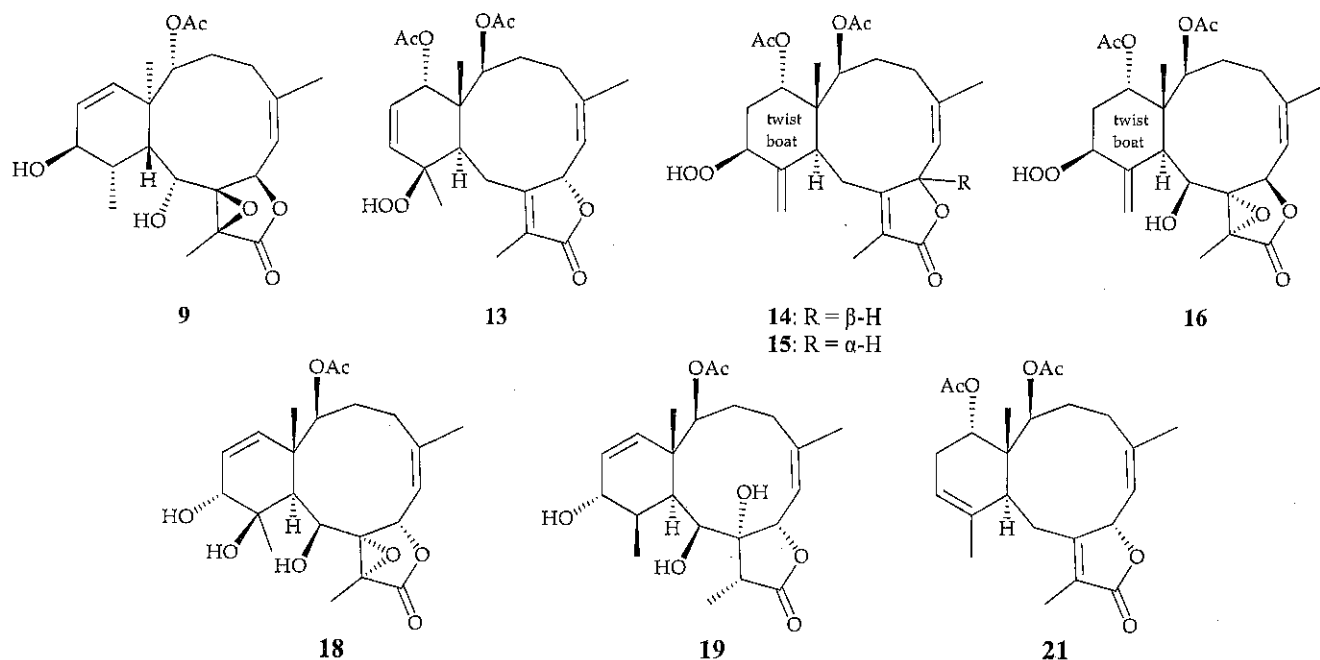


**Figure 2.** Structures of briaviolides K–X (6–19), excavatolides Z (20), B (22), E (23), and brianthein W (21)

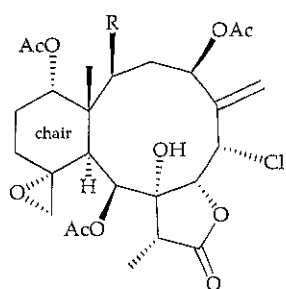
### 3. GORGONACEA

#### 3-1. *Junceella fragilis* (family Ellisellidae)

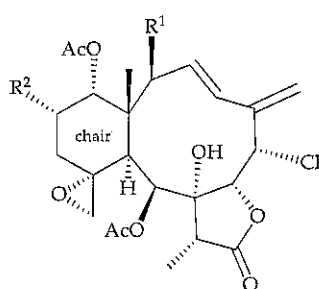
In 2017, 21 new briaranes, including fragilolides B–Q (24–39),<sup>23</sup> 3-deacetylpraelolide (40), 13 $\alpha$ -acetoxy-3-deacetylpraelolide (41), 13 $\alpha$ -acetoxy-2-deacetylpraelolide (42), 13 $\alpha$ -acetoxy-3-deacetyljunceellin (43), and 13 $\alpha$ -acetoxy-2-deacetyljunceellin (44),<sup>24</sup> along with three known briaranes, frajunolides H (45)<sup>23,25</sup> and N (46),<sup>23,26</sup> fragilide J (= 2-deacetylpraelolide) (47),<sup>24,27</sup> and a mixture of known metabolites 3-deacetyljunceellin (48) and 2-deacetyljunceellin (49),<sup>24,28</sup> were produced by *J. fragilis*, collected off the inner coral reef in Hainan Island, China (Figure 3).<sup>23,24</sup> Structures of briaranes 24–49 were elucidated by spectroscopic methods and by comparison the spectroscopic data of these compounds with those reported previously. Acetylation of 40 and 47 yield a crystal product, praelolide (50),<sup>24,25,28–43</sup> and its structure, including the absolute configuration of 50, was further confirmed by a single-crystal X-ray diffraction analysis.<sup>24</sup> As the naturally-occurring briaranes 24–49 were isolated from the same organism, it is reasonable on biogenetic grounds to assume that briaranes 24–49 have the same configuration as that of 50 (praelolide).

Frajunolide H (45) was found to show cytotoxicity toward Hep G2 (human hepatocellular carcinoma), SMMC-7721 (human papillomavirus-related endocervical adenocarcinoma), BGC-823 (human papillomavirus-related endocervical adenocarcinoma), HGC-27 (human gastric carcinoma), MGC-803 (human mucinous gastric adenocarcinoma), NCI-H1650 (human minimally invasive lung adenocarcinoma), A2780 (human ovarian carcinoma), and PA-1 (human ovarian mixed germ cell tumor)

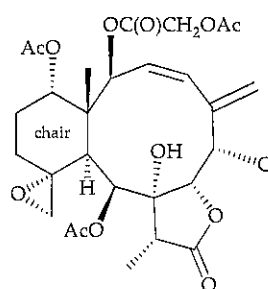
with  $IC_{50}$  values 0.89, 0.61, 2.10, 0.61, 1.97, 6.47, 1.18, and 0.42  $\mu$ M, respectively, and fragilolides D (26), G (29), I (31), L (34), and P (38), and frajunolide N (46) exhibited 19.4, 31.3, 37.3, 30.2, 26.4, and 21.1% selective inhibitory effects toward hepatitis B e-antigen (HBeAg) at a concentration of 10  $\mu$ M, respectively.<sup>23</sup> It is interesting to note that compounds 40 and 47; 41 and 42; 43 and 44; 48 and 49 were obtained as equilibrium mixtures, respectively, and at a dose of 50  $\mu$ M, the mixtures of 40 and 47; 41 and 42; 43 and 44; and 48 and 49, exerted inhibitory activities against the NO production with inhibitory rates of 39.4, 46.4, 42.7, and 36.3%, respectively.<sup>24</sup>



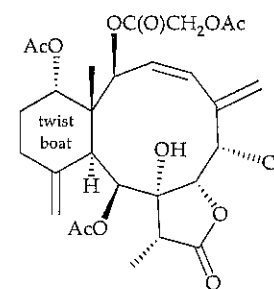
24: R = OC(O)Et  
46: R = OAc



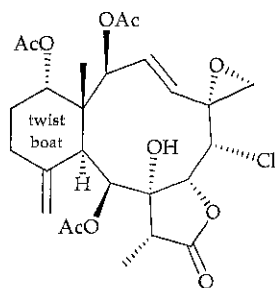
25: R<sup>1</sup> = OC(O)Et, R<sup>2</sup> = OAc  
26: R<sup>1</sup> = OAc, R<sup>2</sup> = H



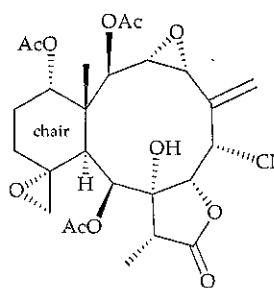
27



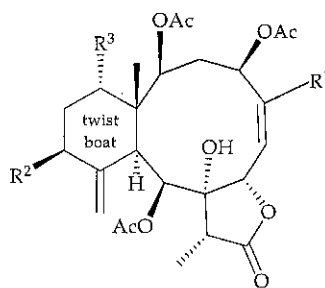
28



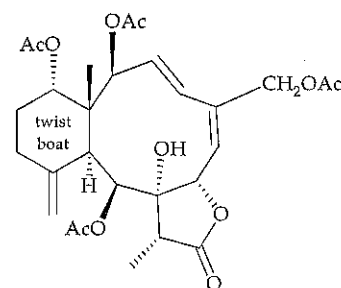
29



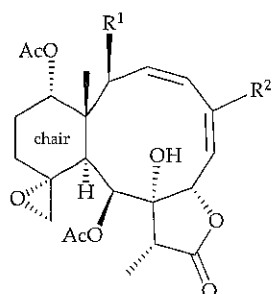
30



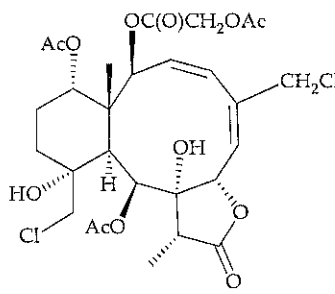
31: R<sup>1</sup> = Me, R<sup>2</sup> = R<sup>3</sup> = OAc  
32: R<sup>1</sup> = Me, R<sup>2</sup> = H, R<sup>3</sup> = OC(O)Bu-*i*  
33: R<sup>1</sup> = CH<sub>2</sub>Cl, R<sup>2</sup> = H, R<sup>3</sup> = OAc



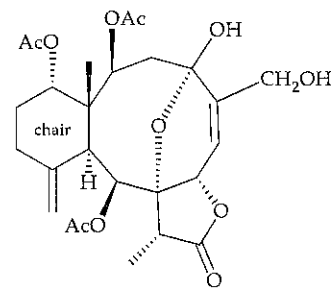
34



35: R<sup>1</sup> = OC(O)CH<sub>2</sub>OAc, R<sup>2</sup> = CH<sub>2</sub>OAc  
36: R<sup>1</sup> = OC(O)CH<sub>2</sub>OC(O)Bu-*i*, R<sup>2</sup> = CH<sub>2</sub>OAc  
37: R<sup>1</sup> = OC(O)CH<sub>2</sub>OC(O)Bu-*i*, R<sup>2</sup> = CH<sub>2</sub>Cl



38



39



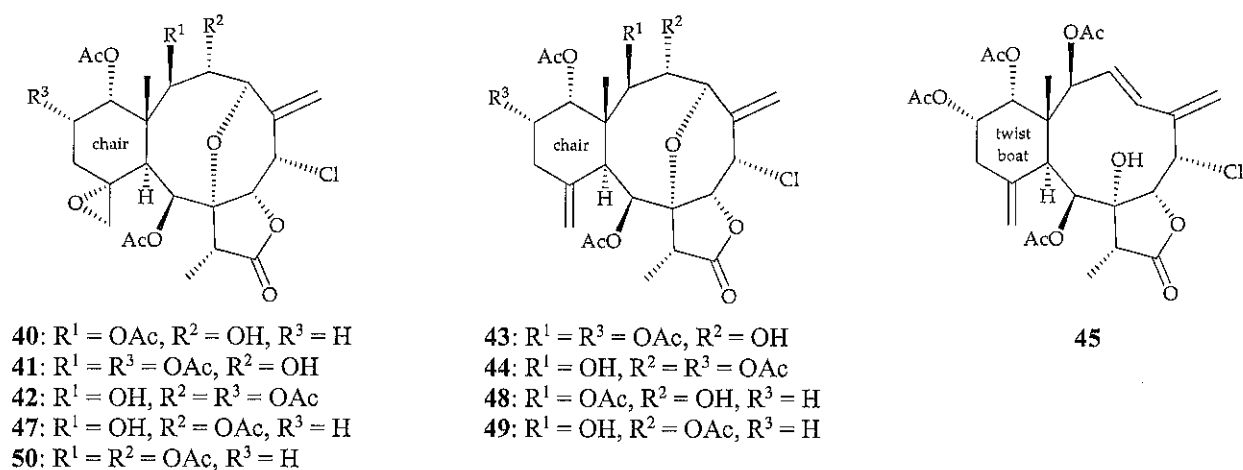


**Figure 3.** Structures of fragilolides B–Q (24–39), 3-deacetylpraelolide (40), 13 $\alpha$ -acetoxy-3-deacetylpraelolide (41), 13 $\alpha$ -acetoxy-2-deacetylpraelolide (42), 13 $\alpha$ -acetoxy-3-deacetyljunceellin (43), and frajunolide N (46), fragilide J (47), 3-deacetyljunceellin (48), 2-deacetyljunceellin (49), and praelolide (50)

In addition, 14 new briaranes, (+)-12-*epi*-fragilide G (51)<sup>44</sup> and fragilides K–W (52–64),<sup>43,45–48</sup> as well as nine known briaranes, praelolide (50) (Figure 3),<sup>24,25,28–43</sup> gemmacolides V (65) and X (66),<sup>41,43</sup> juncins P (67),<sup>36,43</sup> Z (68),<sup>46,49</sup> and ZI (69),<sup>43,49</sup> junceellin (70),<sup>25,28,31–40,42,45,48,50,51</sup> robustolide F (71),<sup>46,52,53</sup> and junceellonoid D (72),<sup>37,48,54</sup> were isolated from *J. fragilis*, collected off the waters of Taiwan (Figure 4).<sup>43–48</sup> The structures of all isolates 50–72 were established by spectroscopic methods and the absolute configuration of junceellin (70) was further confirmed by a single-crystal X-ray diffraction analysis.<sup>45,51</sup> Fragilides S (60) and T (61) are the first two briaranes known to possess 8 $\alpha$ -hydroxy and 17 $\beta$ -methyl groups in the  $\gamma$ -lactone moieties.<sup>47</sup> Briarane 51 was found to be the enantiomer of (–)-12-*epi*-fragilide G (73)<sup>55</sup> and 73 showed a 74.5% inhibitory effect on human neutrophils in terms of the generation of superoxide anions at a concentration of 20  $\mu\text{M}$ , but briarane 51 was not active. This result implied that the configurations of 51 and 73 played an important role in determining the activity.<sup>44</sup> Anti-inflammatory activity analysis showed that (+)-12-*epi*-fragilide G (51), fragilides L (53), S (60), U (62), and W (64), gemmacolide X (66), juncin ZI (69), and junceellin (70) inhibited iNOS expression to 54.7, 49.1, 61.2, 55.9, 28.6, 36.2, 43.3, 33.7%,<sup>43,44,47,48</sup> and gemmacolides V (65) and X (66) elicited reduction of COX-2 to 47.5 and 43.6%, at a concentration of 10  $\mu\text{M}$ , in LPS-stimulated murine macrophage-like RAW264.7 cells, respectively.<sup>43</sup> Briarane 68 (juncin Z) showed a 25.6% inhibitory effect on the generation of superoxide anions by human neutrophils at a concentration of 10  $\mu\text{M}$ .<sup>46</sup>

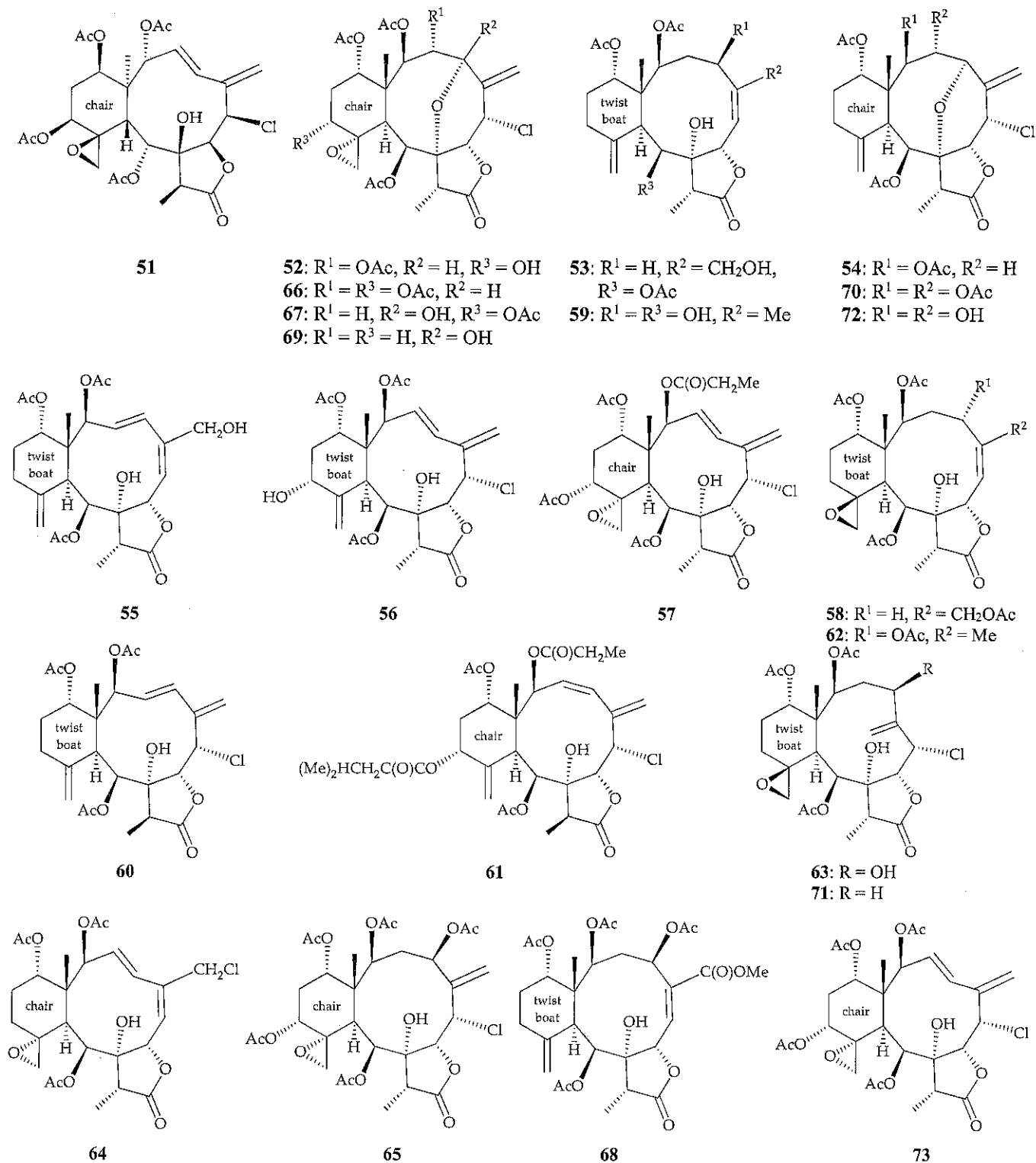


**Figure 4.** Structures of (+)-12-*epi*-fragilide G (**51**), fragilides K–W (**52**–**64**), gemmacolides V (**65**) and X (**66**), juncins P (**67**), Z (**68**), and ZI (**69**), junceellin (**70**), robustolide F (**71**), junceellonoid D (**72**), and (–)-12-*epi*-fragilide G (**73**)

### 3-2. *Subergorgia suberosa* (family Subergorgiidae)

In 2014, Sun *et al.* reported the isolation of five known briaranes, brianthein W (**21**) (Figure 2),<sup>14,17,18</sup> funicolide E (**74**),<sup>56</sup> 9-deacetylbriareolide H (**75**),<sup>18,57,58</sup> 9-deacetylstylatulide lactone (**76**),<sup>18</sup> and

umbraculolide A (**77**),<sup>32,59</sup> from the South China Sea gorgonian coral, *S. suberosa* (Figure 5).<sup>60</sup> Structural determination of known briaranes **21** and **74–77** were conducted using spectroscopic methods and by comparison with the spectral data previously reported in literature. The hydroxy group at C-7 in briarane **74** shown in ref.<sup>60</sup> should be revised as  $\alpha$ -oriented as shown in Figure 5. An exocyclic double bond between C-11/20 was existed in umbraculolide A (**77**),<sup>32,59</sup> and based on this finding, the structure for umbraculolide A that shown in ref.<sup>60</sup> also should be revised as shown in Figure 5. Briarane **75** exhibited cytotoxicity toward A549 (human epithelial lung carcinoma) cells with an  $IC_{50}$  value of 26.7  $\mu M$ .<sup>60</sup>

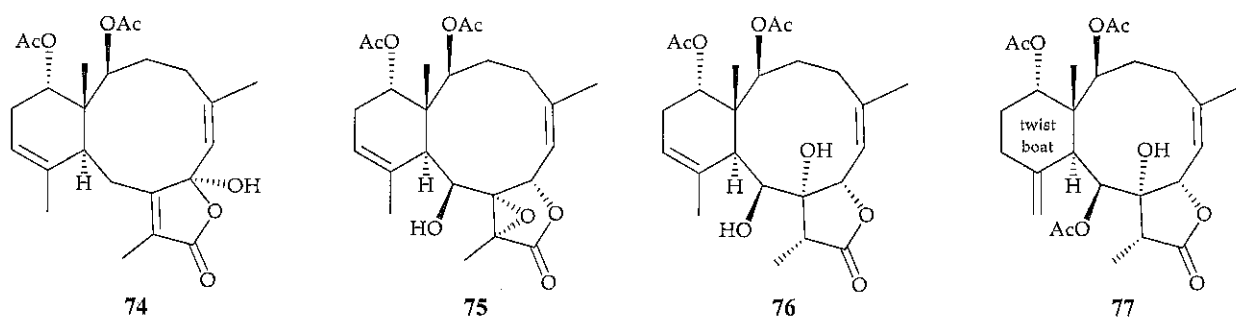


**Figure 5.** Structures of funicolide E (**74**), 9-deacetylbriareolide H (**75**), 9-deacetylstylatulide lactone (**76**), and umbraculolide A (**77**)

#### 4. PENNATULACE

##### 4-1. *Anthoptilum grandiflorum* (family Anthoptilidae)

Investigation of the chemical constituents of *A. grandiflorum*, collected off the north of Burdwood Bank by trawling on the R/V Nathaniel B. Palmer, the U.S. Antarctic Programs' research ship, afforded three novel briaranes, bathyptilones A–C (**78–80**) (Figure 6).<sup>61</sup> The structures, including the absolute configurations of briaranes **78–80** were elucidated by interpretation of spectroscopic methods, and further confirmed by single-crystal X-ray diffractions analysis. Briarane **78** showed cytotoxicity toward NTREA-2 (NT2) (human malignant pluripotent embryonal carcinoma) with an  $IC_{50}$  of 29 nM and briarane **80** was found to be more inactive in terms of cytotoxicity toward NT2 cells, indicating that the cytotoxicity of these compounds are largely dependent on the functional group at C-7.

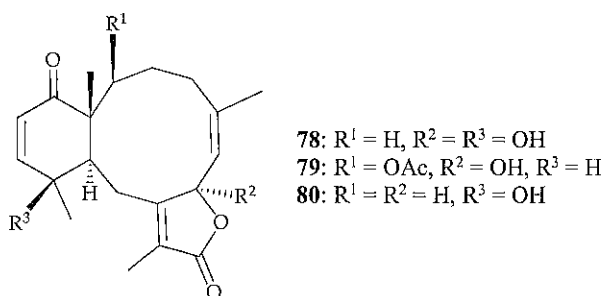


**Figure 6.** Structures of bathyptilones A–C (**78–80**)

## 5. CONCLUSIONS

In the past three years, 78 briarane-type diterpenoids, including 56 new metabolites have been prepared from soft corals belonging to the orders Alcyonacea, Gorgonacea, and Pennatulacea and compounds of this type have been demonstrated to possess various bioactivities, for example, excavatolide B (**22**) has been proven to show anti-inflammatory and to enhance contextual memory retrieval and bathyptilone A (**78**) showed potential cytotoxicity. Because of the structural diversity and biomedical bioactivities, there have been little synthetic work on briarane analogues.<sup>62–65</sup> It is interesting to note that most briaranes, excepting bathyptilones A–C (**78–80**), reported as having been isolated between 2017 and 2019 were all collected from octocorals distributed in the South China Sea.

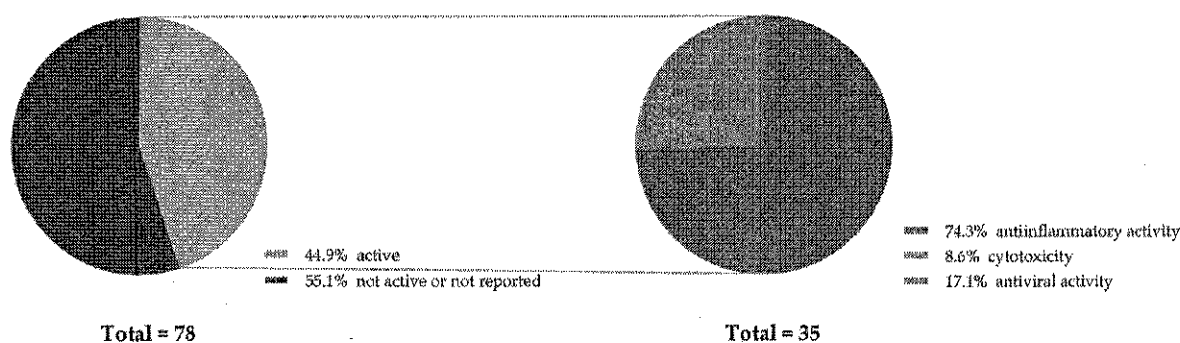


**Figure 7.** Numbers of briarane-type diterpenoids between 2017–2019 and their biomedical activities

## ACKNOWLEDGMENTS

This research was supported by grants from the National Museum of Marine Biology and Aquarium; the National Dong Hwa University; and the Ministry of Science and Technology (Grant Nos. MOST 106-2320-B-291-001-MY3 and 107-2325-B-291-001-MY3), Taiwan, awarded to Ping-Jyun Sung.

## REFERENCES AND NOTES

1. P.-J. Sung, J.-H. Sheu, and J.-P. Xu, *Heterocycles*, 2002, **57**, 535.
2. P.-J. Sung, P.-C. Chang, L.-S. Fang, J.-H. Sheu, W.-C. Chen, Y.-P. Chen, and M.-R. Lin, *Heterocycles*, 2005, **65**, 195.
3. P.-J. Sung, J.-H. Sheu, W.-H. Wang, L.-S. Fang, H.-M. Chung, C.-H. Pai, Y.-D. Su, W.-T. Tsai, B.-Y. Chen, M.-R. Lin, and G.-Y. Li, *Heterocycles*, 2008, **75**, 2627.
4. P.-J. Sung, J.-H. Su, W.-H. Wang, J.-H. Sheu, L.-S. Fang, Y.-C. Wu, Y.-H. Chen, H.-M. Chung, Y.-D. Su, and Y.-C. Chang, *Heterocycles*, 2011, **83**, 1241.
5. J.-H. Sheu, Y.-H. Chen, Y.-H. Chen, Y.-D. Su, Y.-C. Chang, J.-H. Su, C.-F. Weng, C.-H. Lee, L.-S. Fang, W.-H. Wang, Z.-H. Wen, Y.-C. Wu, and P.-J. Sung, *Mar. Drugs*, 2014, **12**, 2164.

6. Y.-D. Su, J.-H. Su, T.-L. Hwang, Z.-H. Wen, J.-H. Sheu, Y.-C. Wu, and P.-J. Sung, *Mar. Drugs*, 2017, **15**, 44.
7. J. E. Burks, D. van der Helm, C. Y. Chang, and L. S. Ciereszko, *Acta Cryst.*, 1977, **B33**, 704.
8. M.-J. Li, Y.-D. Su, Z.-J. Liao, Z.-H. Wen, J.-H. Su, Y.-C. Wu, and P.-J. Sung, *Nat. Prod. Commun.*, 2017, **12**, 221.
9. N.-F. Chen, Y.-D. Su, T.-L. Hwang, Z.-J. Liao, K.-H. Tsui, Z.-H. Wen, Y.-C. Wu, and P.-J. Sung, *Molecules*, 2017, **22**, 475.
10. Y.-D. Su, C.-S. Sung, Z.-H. Wen, Y.-H. Chen, Y.-C. Chang, J.-J. Chen, L.-S. Fang, Y.-C. Wu, J.-H. Sheu, and P.-J. Sung, *Int. J. Mol. Sci.*, 2016, **17**, 79.
11. J.-H. Xu, K.-H. Lai, Y.-D. Su, Y.-C. Chang, B.-R. Peng, A. Backlund, Z.-H. Wen, and P.-J. Sung, *Mar. Drugs*, 2018, **16**, 75.
12. J.-H. Xu, Y.-C. Chang, G.-Q. Li, Z.-H. Wen, Y.-C. Wu, and P.-J. Sung, *Phytochem. Lett.*, 2018, **27**, 129.
13. T.-C. Tsai, J.-H. Xu, M.-J. Li, J.-J. Chen, J.-H. Su, Y.-C. Wu, Z.-H. Wen, and P.-J. Sung, *Nat. Prod. Commun.*, 2018, **13**, 1235.
14. J.-W. Yao, W.-C. Chi, J.-H. Xu, G.-H. Lee, M. Y. Chiang, B.-R. Peng, N.-C. Lin, C.-C. Hu, L.-S. Fang, G.-Q. Li, Y.-C. Chang, T.-L. Hwang, and P.-J. Sung, *Tetrahedron*, 2019, **75**, 1510.
15. J.-W. Yao, W.-C. Chi, G.-H. Lee, J.-H. Su, T.-L. Hwang, Y.-J. Wu, T.-R. Su, J.-H. Sheu, and P.-J. Sung, *Tetrahedron*, 2019, **75**, 3751.
16. J.-H. Sheu, P.-J. Sung, J.-H. Su, G.-H. Wang, C.-Y. Duh, Y.-C. Shen, M. Y. Chiang, and I.-T. Chen, *J. Nat. Prod.*, 1999, **62**, 1415.
17. J. H. Cardellina II, T. R. James Jr., M. H. M. Chen, and J. Clardy, *J. Org. Chem.*, 1984, **49**, 3398.
18. J.-H. Sheu, P.-J. Sung, L.-H. Huang, S.-F. Lee, T. Wu, B.-Y. Chang, C.-Y. Duh, L.-S. Fang, K. Soong, and T.-J. Lee, *J. Nat. Prod.*, 1996, **59**, 935.
19. J.-H. Sheu, P.-J. Sung, M.-C. Cheng, H.-Y. Liu, L.-S. Fang, C.-Y. Duh, and M. Y. Chiang, *J. Nat. Prod.*, 1998, **61**, 602.
20. P.-J. Sung, M.-R. Lin, Y.-D. Su, M. Y. Chiang, W.-P. Hu, J.-H. Su, M.-C. Cheng, T.-L. Hwang, and J.-H. Sheu, *Tetrahedron*, 2008, **64**, 2596.
21. Y.-Y. Lin, Y.-H. Jean, H.-P. Lee, S.-C. Lin, C.-Y. Pan, W.-F. Chen, S.-F. Wu, J.-H. Su, K.-H. Tsui, J.-H. Sheu, P.-J. Sung, and Z.-H. Wen, *Mar. Drugs*, 2017, **15**, 9.
22. I. Y. Huang, Y.-L. Hsu, C.-C. Chen, M.-F. Chen, Z.-H. Wen, H.-T. Huang, and I. Y. Liu, *Mar. Drugs*, 2018, **16**, 405.
23. W. Cheng, M. Ji, X. Li, J. Ren, F. Yin, L. van Ofwegen, S. Yu, X. Chen, and W. Lin, *Tetrahedron*, 2017, **73**, 2518.



24. W. Cheng, X. Li, F. Yin, L. van Ofwegen, and W. Lin, *Chem. Biodivers.*, 2017, **14**, e1700053.
25. C.-C. Liaw, Y.-C. Shen, Y.-S. Lin, T.-L. Hwang, Y.-H. Kuo, and A.T. Khalil, *J. Nat. Prod.*, 2008, **71**, 1551.
26. C.-C. Liaw, Y.-H. Kuo, Y.-S. Lin, T.-L. Hwang, and Y.-C. Shen, *Mar. Drugs*, 2011, **9**, 1477.
27. S.-H. Wang, Y.-C. Chang, M. Y. Chiang, Y.-H. Chen, T.-L. Hwang, C.-F. Weng, and P.-J. Sung, *Chem. Pharm. Bull.*, 2010, **58**, 928.
28. N. K. Kubota, Y. Kobayashi, H. Iwamoto, Y. Fukazawa, and Y. Uchio, *Bull. Chem. Soc. Jpn.*, 2006, **79**, 634.
29. Y. Luo, K. Long, and Z. Fang, *Acta Sci. Nat. Univ. Sunyatseni*, 1983, (1), 83.
30. J. Dai, Z. Wan, Z. Rao, D. Liang, Z. Fang, Y. Luo, and K. Long, *Sci. Sin. B*, 1985, **28**, 1132.
31. J. Shin, M. Park, and W. Fenical, *Tetrahedron*, 1989, **45**, 1633.
32. C. Subrahmanyam, R. Kulatheeswaran, and R. S. Ward, *J. Nat. Prod.*, 1998, **61**, 1120.
33. M. García, J. Rodríguez, and C. Jiménez, *J. Nat. Prod.*, 1999, **62**, 257.
34. P.-J. Sung, T.-Y. Fan, L.-S. Fang, S.-L. Wu, J.-J. Li, M.-C. Chen, Y.-M. Cheng, and G.-H. Wang, *Chem. Pharm. Bull.*, 2003, **51**, 1429.
35. P.-J. Sung, T.-Y. Fan, M.-C. Chen, L.-S. Fang, M.-R. Lin, and P.-C. Chang, *Biochem. Syst. Ecol.*, 2004, **32**, 111.
36. S.-H. Qi, S. Zhang, H. Huang, Z.-H. Xiao, J.-S. Huang, and Q.-X. Li, *J. Nat. Prod.*, 2004, **67**, 1907.
37. S.-H. Qi, S. Zhang, Y.-M. Wen, Z.-H. Xiao, and Q.-X. Li, *Helv. Chim. Acta*, 2005, **88**, 2349.
38. Y.-M. Wen, S.-H. Qi, and S. Zhang, *Nat. Prod. Res. Dev.*, 2006, **18**, 234.
39. J. Yang, S. Zhang, S.-H. Qia, J.-Y. Pan, Y.-Q. Qiu, S.-H. Tao, H. Yin, and Q.-X. Li, *Biochem. Syst. Ecol.*, 2007, **35**, 770.
40. J.-F. Sun, H. Huang, X.-Y. Chai, X.-W. Yang, L. Meng, C.-G. Huang, X.-F. Zhou, B. Yang, J. Hu, X.-Q. Chen, H. Lei, L. Wang, and Y. Liu, *Tetrahedron*, 2011, **67**, 1245.
41. C. Li, M.-P. La, H. Tang, W.-H. Pan, P. Sun, K. Krohn, Y.-H. Yi, L. Li, and W. Zhang, *Bioorg. Med. Chem. Lett.*, 2012, **22**, 4368.
42. W. Zhou, J. Li, H.-C. E, B.-S. Liu, H. Tang, W. H. Gerwick, H.-M. Hua, and W. Zhang, *Mar. Drugs*, 2014, **12**, 589.
43. L.-G. Zheng, Y.-C. Chang, C.-C. Hu, Z.-H. Wen, Y.-C. Wu, and P.-J. Sung, *Molecules*, 2018, **23**, 1510.
44. L.-G. Zheng, Y.-C. Chang, J.-J. Chen, Z.-H. Wen, T.-L. Hwang, and P.-J. Sung, *Heterocycles*, 2018, **96**, 1601.
45. C.-C. Lin, W.-F. Chen, G.-H. Lee, Z.-H. Wen, L.-S. Fang, Y.-H. Kuo, C.-Y. Lee, and P.-J. Sung, *Heterocycles*, 2019, **98**, 984.

46. C.-C. Lin, J.-H. Su, W.-F. Chen, Z.-H. Wen, B.-R. Peng, L.-C. Huang, T.-L. Hwang, and P.-J. Sung, *Molecules*, 2019, **24**, 2487.
  47. Y.-Y. Chen, L.-S. Fang, Y.-H. Chen, B.-R. Peng, T.-P. Su, T.-H. Huynh, F.-Y. Lin, C.-C. Hu, N.-C. Lin, Z.-H. Wen, J.-J. Chen, C.-Y. Lee, J.-W. Wang, and P.-J. Sung, *Mar. Drugs*, 2019, **17**, 534.
  48. T.-P. Su, C.-H. Yuan, Y.-M. Jhu, B.-R. Peng, Z.-H. Wen, Y.-J. Wu, T.-Y. Wu, H.-W. Liu, and P.-J. Sung, *Mar. Drugs*, 2019, **17**, 706.
  49. S.-H. Qi, S. Zhang, P.-Y. Qian, Z.-H. Xiao, and M.-Y. Li, *Tetrahedron*, 2006, **62**, 9123.
  50. Y. Lin and K. Long, *Acta Sci. Nat. Univ. Sunyatseni*, 1983, (2), 46.
  51. J. Yao, J. Qian, H. Fan, K. Shih, S. Huang, Y. Lin, and K. Long, *Acta Sci. Nat. Univ. Sunyatseni*, 1984, (1), 83.
  52. C. Tanaka, Y. Yamamoto, M. Otsuka, J. Tanaka, T. Ichiba, G. Marriott, R. Rachmat, and T. Higa, *J. Nat. Prod.*, 2004, **67**, 1368.
  53. P.-J. Sung, M. Y. Chiang, W.-T. Tsai, J.-H. Su, Y.-M. Su, and Y.-C. Wu, *Tetrahedron*, 2007, **63**, 12860.
  54. P.-J. Sung, S.-H. Wang, M. Y. Chiang, Y.-D. Su, Y.-C. Chang, W.-P. Hu, C.-Y. Tai, and C.-Y. Liu, *Bull. Chem. Soc. Jpn.*, 2009, **82**, 1426.
  55. Y.-C. Chang, T.-L. Hwang, S.-K. Huang, L.-W. Huang, M.-R. Lin, and P.-J. Sung, *Heterocycles*, 2010, **81**, 991.
  56. A. Guerriero, M. D'Ambrosio, and F. Pietra, *Helv. Chim. Acta*, 1995, **78**, 1465.
  57. B. F. Bowden, J. C. Coll, and G. M. König, *Aust. J. Chem.*, 1990, **43**, 151.
  58. E. O. Pordesimo, F. J. Schmitz, L. S. Ciereszko, M. B. Hossain, and D. van der Helm, *J. Org. Chem.*, 1991, **56**, 2344.
  59. C. Subrahmanyam, S. Ratnakumar, and R. S. Ward, *Tetrahedron*, 2000, **56**, 4585.
  60. D.-W. Sun, M. Liu, F. Cao, C. Wang, and C.-Y. Wang, *Chem. Nat. Compd.*, 2017, **53**, 185.
  61. S. A. L. Thomas, A. Sanchez, Y. Kee, N. G. Wilson, and B. J. Baker, *Mar. Drugs*, 2019, **17**, 513.
  62. A. J. Hall, S. P. Roche, and L. M. West, *Org. Lett.*, 2017, **19**, 576.
  63. N. G. Moon and A. M. Harned, *Org. Biomol. Chem.*, 2017, **15**, 1876.
  64. M. T. Crimmins, Y. Zhang, and P. S. Williams, *Org. Lett.*, 2017, **19**, 3907.
  65. N. G. Moon and A. M. Harned, *R. Soc. Open Sci.*, 2018, **5**, 172280.
-

Article

# 11 $\beta$ ,20 $\beta$ -Epoxybriaranes from the Gorgonian Coral *Junceella fragilis* (Ellisellidae)

Tung-Pin Su <sup>1,2,†</sup>, Tsu-Jen Kuo <sup>3,4,5,†</sup>, San-Nan Yang <sup>6</sup>, Gene-Hsiang Lee <sup>7</sup>, Yen-Tung Lee <sup>8,9,10</sup>, Yi-Chen Wang <sup>11</sup>, Jih-Jung Chen <sup>12</sup> , Zhi-Hong Wen <sup>4</sup> , Tsong-Long Hwang <sup>13,14,15,16,\*</sup>  and Ping-Jyun Sung <sup>1,2,4,17,18,\*</sup> 

<sup>1</sup> Graduate Institute of Marine Biology, National Dong Hwa University, Pingtung 94450, Taiwan; g3xz84120@yahoo.com.tw

<sup>2</sup> National Museum of Marine Biology and Aquarium, Pingtung 94450, Taiwan

<sup>3</sup> Department of Stomatology, Kaohsiung Veterans General Hospital, Kaohsiung 81362, Taiwan; tsujenkuo@gmail.com

<sup>4</sup> Department of Marine Biotechnology and Resources, National Sun Yat-sen University, Kaohsiung 80424, Taiwan; wzhang@mail.nsysu.edu.tw

<sup>5</sup> Department of Dental Technology, Shu-Zen Junior College of Medicine and Management, Kaohsiung 82144, Taiwan

<sup>6</sup> Department of Pediatrics, E-DA Hospital, School of Medicine, College of Medicine, I-SHOU University, Kaohsiung 82445, Taiwan; y520729@gmail.com

<sup>7</sup> Instrumentation Center, National Taiwan University, Taipei 10617, Taiwan; ghlee@ntu.edu.tw

<sup>8</sup> Division of Natural Products, Graduate Institute of Biomedical Sciences, College of Medicine, Chang Gung University, Taoyuan 33302, Taiwan; b9105008@stmail.cgu.edu.tw

<sup>9</sup> Department of Cosmetic Science, College of Human Ecology, Chang Gung University of Science and Technology, Taoyuan 33303, Taiwan

<sup>10</sup> Department of Chinese Medicine, MacKay Memorial Hospital, Taipei 10449, Taiwan

<sup>11</sup> Division of Cardiology, Department of Internal Medicine, Kaohsiung Armed Forces General Hospital, Kaohsiung 80284, Taiwan; cvyc.wang@gmail.com

<sup>12</sup> Faculty of Pharmacy, School of Pharmaceutical Sciences, National Yang-Ming University, Taipei 11221, Taiwan; chenjj@ym.edu.tw

<sup>13</sup> Research Center for Chinese Herbal Medicine, Research Center for Food and Cosmetic Safety, Graduate Institute of Healthy Industry Technology, College of Human Ecology, Chang Gung University of Science and Technology, Taoyuan 33303, Taiwan

<sup>14</sup> Graduate Institute of Natural Products, College of Medicine, Chang Gung University, Taoyuan 33302, Taiwan

<sup>15</sup> Chinese Herbal Medicine Research Team, Healthy Aging Research Center, Chang Gung University, Taoyuan 33302, Taiwan

<sup>16</sup> Department of Anaesthesiology, Chang Gung Memorial Hospital, Taoyuan 33305, Taiwan

<sup>17</sup> Chinese Medicine Research and Development Center, China Medical University Hospital, Taichung 40447, Taiwan

<sup>18</sup> Graduate Institute of Natural Products, Kaohsiung Medical University, Kaohsiung 80708, Taiwan

\* Correspondence: htl@mail.cgu.edu.tw (T.-L.H.); pjsung@nmmba.gov.tw (P.-J.S.); Tel.: +886-3-211-8800 (ext. 5523) (T.-L.H.); +886-8-882-5037 (P.-J.S.); Fax: +886-3-211-8506 (T.-L.H.); +886-8-882-5087 (P.-J.S.)

† These authors contributed equally to this work.

Received: 18 March 2020; Accepted: 30 March 2020; Published: 31 March 2020



**Abstract:** Two 11,20-epoxybriaranes, including a known compound, juncenolide K (**1**), as well as a new metabolite, fragilide X (**2**), have been isolated from gorgonian *Junceella fragilis* collected off the waters of Taiwan. The absolute configuration of juncenolide K (**1**) was determined by single-crystal X-ray diffraction analysis for the first time in this study and the structure, including the absolute configuration of briarane **2** was established on the basis of spectroscopic analysis and compared with that of model compound **1**. One aspect of the stereochemistry of the known compound **1** was

revised. Briarane **2** was found to enhance the generation of inducible nitric oxide synthase (iNOS) and cyclooxygenase-2 (COX-2) release from RAW 264.7 cells.

**Keywords:** *Junceella fragilis*; fragilide; briarane; juncenolide; X-ray; iNOS; COX-2

## 1. Introduction

Gorgonian corals of the genus *Junceella* (family Ellisellidae) [1–3] were proven to be the most important flagship species to produce 11,20-epoxybriarane diterpenoids, a chemical marker for the octocorals belonging to the family Ellisellidae [4,5] and the compounds of this type demonstrate a wide spectrum of biological properties, such as anti-inflammatory activity [6–20], immunomodulatory activity [21], insecticidal activity [22], cytotoxicity [23–32], anti-viral activity [6,33], anti-fouling activity [34–37], antifeedant [35], and anti-microbial activity [28,29,32,38–40]. From the specimens of *J. fragilis* (Ridley 1884) collected off the waters of Taiwan, an area with high biodiversity at the intersection of the Kuroshio current and the South China Sea surface current, we have isolated two briaranes, including a known compound juncenolide K (**1**) [13], along with a new briarane–fragilide X (**2**), featuring an 11,20-epoxy moiety in their structures (Figure 1). A pro-inflammatory assay was employed to assess the activity of these isolates on the release of inducible nitric oxide synthase (iNOS) and cyclooxygenase-2 (COX-2) from RAW 264.7 macrophage cells.

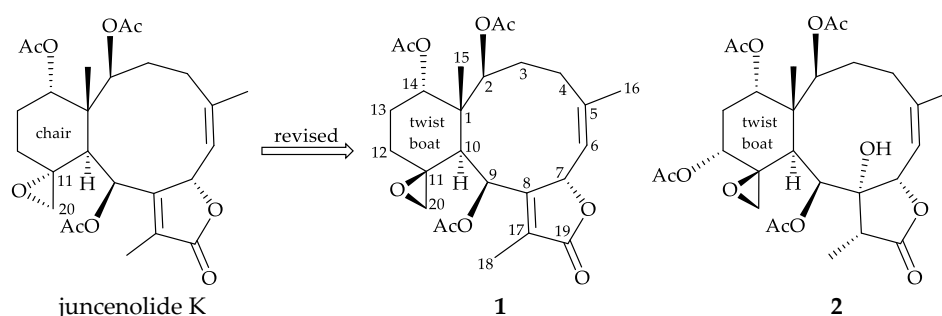


**Figure 1.** The structures of juncenolide K and its revised structure (**1**) and fragilide X (**2**).

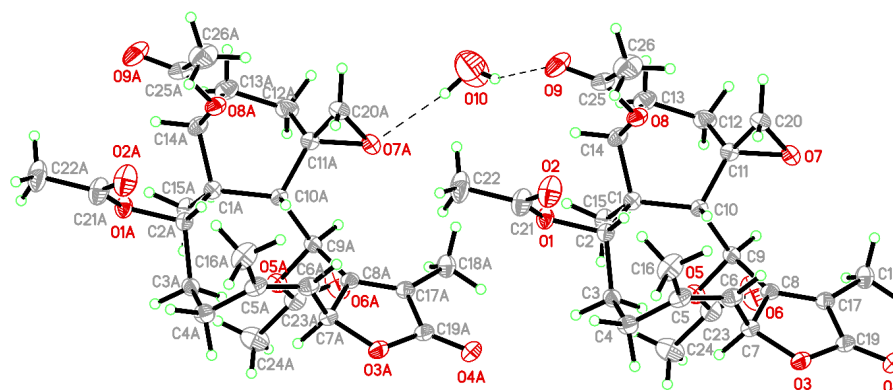
## 2. Results and Discussion

Compound **1** was isolated as a colorless prism that showed a sodiated adduct ion  $[M + Na]^+$  at  $m/z$  513.20949 in the (+)-high-resolution electrospray ionization mass spectrum (HRESIMS) analysis. The result revealed that **1** had a molecular formula of  $C_{26}H_{34}O_9$  (calculated for  $C_{26}H_{34}O_9 + Na$ , 513.20950) (unsaturation degrees = 10). The NMR chemical shifts for **1** and its proton coupling data are identical to those reported for juncenolide K [13] (Table 1). Juncenolide K was initially assigned possessing an 11 $\alpha$ ,20 $\alpha$ -epoxy configuration, and the cyclohexane ring was reported to exist with a chair conformation, but on the basis of our study of juncenolide K by a single-crystal X-ray diffraction analysis (Figure 2) and spectroscopic analysis (Table 1 and Figure 3) (Supplementary Materials, Figures S1–S14), it appears that the 11,20-epoxy group in **1** was found to be 11 $\beta$ ,20 $\beta$ -oriented and **1** possesses a cyclohexane ring in twist-boat form. The X-ray structure shows the twist-boat conformation of the cyclohexane ring in **1** and the Oak Ridge Thermal Ellipsoid Plot (ORTEP) diagram (Figure 2) showed that the absolute configurations of the stereogenic centers of **1** are 1S,2S,7S,9S,10S,11S and 14S (Flack parameter  $x = 0.07(5)$ ).

**Table 1.**  $^1\text{H}$  and  $^{13}\text{C}$  NMR ( $\text{CDCl}_3$ ) data for juncenolide K and briarane 1.

Position	Juncenolide K <sup>a</sup>		1	
	$\delta_{\text{H}}$ (J in Hz) <sup>b</sup>	$\delta_{\text{C}}$ , <sup>c</sup> type	$\delta_{\text{H}}$ (J in Hz) <sup>d</sup>	$\delta_{\text{C}}$ , <sup>e</sup> type
1		46.0, C		46.0, C
2	4.74 br s	74.1, CH	4.72 br s	74.1, CH
3	2.53–2.59 m; 1.74–1.80 m	31.3, $\text{CH}_2$	2.56 m; 1.74 m	31.3, $\text{CH}_2$
4	2.60–2.66 m; 2.20–2.26 m	29.1, $\text{CH}_2$	2.60 m; 2.22 m	29.1, $\text{CH}_2$
5		143.0, C		143.0, C
6	5.01 d (8.5)	124.7, CH	4.99 d (8.4)	124.8, CH
7	5.51 d (8.5)	77.2, CH	5.50 d (8.4)	77.1, CH
8		155.8, C		155.8, C
9	6.54 d (7.0)	66.5, CH	6.52 d (7.2)	66.6, CH
10	2.63–2.68 m	40.5, CH	2.64 br d (7.2)	40.5, CH
11		59.7, C		59.7, C
12	2.30–2.36 m; 1.10–1.16 m	22.9, $\text{CH}_2$	2.31 m; 1.12 m	22.9, $\text{CH}_2$
13	2.11–2.17 m; 1.80–1.86 m	23.8, $\text{CH}_2$	2.10 m; 1.82 m	23.8, $\text{CH}_2$
14	4.80 d (3.5)	73.9, CH	4.79 d (3.6)	73.9, CH
15	1.16 s	15.8, $\text{CH}_3$	1.15 s	15.9, $\text{CH}_3$
16	2.01 s	27.0, $\text{CH}_3$	1.99 s	27.0, $\text{CH}_3$
17		127.5, C		127.4, C
18	2.01 s	9.3, $\text{CH}_3$	1.99 s	9.3, $\text{CH}_3$
19		173.6, C		173.6, C
20a/b	2.60–2.66 m; 2.46–2.52 m	58.2, $\text{CH}_2$	2.62 br s; 2.48 br s	58.2, $\text{CH}_2$
OAc-2		170.7, C		170.7, C
	2.01 s	21.0, $\text{CH}_3$	2.00 s	21.0, $\text{CH}_3$
OAc-9		168.9, C		168.9, C
	2.12 s	21.6, $\text{CH}_3$	2.11 s	21.7, $\text{CH}_3$
OAc-14		169.8, C		169.8, C
	1.96 s	20.9, $\text{CH}_3$	1.95 s	20.9, $\text{CH}_3$

<sup>a</sup> Data were reported by Wang et al., see ref. [13]. <sup>b</sup> 500 MHz, <sup>c</sup> 125 MHz, <sup>d</sup> 400 MHz, <sup>e</sup> 100 MHz.

**Figure 2.** The Oak Ridge Thermal Ellipsoid Plot (ORTEP) of 1.

Fragilide X (**2**) was isolated as an amorphous powder and displayed a sodiated adduct ion  $[\text{M} + \text{Na}]^+$  at  $m/z$  589.22576 in the (+)-HRESIMS, indicating a molecular formula  $\text{C}_{28}\text{H}_{38}\text{O}_{12}$  (calculated for  $\text{C}_{28}\text{H}_{38}\text{O}_{12} + \text{Na}$ , 589.22555) (unsaturation degrees = 10). Absorption peaks at  $3333\text{ cm}^{-1}$ ,  $1773\text{ cm}^{-1}$ , and  $1742\text{ cm}^{-1}$  in the IR spectrum indicate hydroxy,  $\gamma$ -lactone, and ester groups, respectively. Analysis of the  $^1\text{H}$ ,  $^{13}\text{C}$  NMR, and distortionless enhancement by polarization transfer (DEPT) spectra, together with the molecular formula, suggested that there must be an exchangeable proton. The  $^{13}\text{C}$  NMR spectrum (Table 2), in combination with DEPT, HSQC, and HMBP spectra, revealed the presence of five esters including four acetoxy groups ( $\delta_{\text{C}}$  21.6, 21.0, 20.9, 20.7,  $4 \times \text{CH}_3$ ;  $\delta_{\text{C}}$  170.6, 169.8, 169.4, 169.2,  $4 \times \text{C}$ ) and a lactone moiety ( $\delta_{\text{C}}$  176.2), and a trisubstituted olefin ( $\delta_{\text{C}}$  143.8, C-5; 120.8, CH-6). Based on the  $^{13}\text{C}$  NMR data and numbers of unsaturation, **2** was established as a tetracyclic diterpenoid. The



presence of an exocyclic epoxy group was confirmed from the signals of an oxygenated quaternary carbon at  $\delta_C$  62.3 (C-11) and an oxymethylene at  $\delta_C$  53.9 (CH<sub>2</sub>-20). The chemical shifts of oxymethylene protons at  $\delta_H$  3.20 (1H, d,  $J$  = 4.4 Hz, H-20a) and 2.90 (1H, d,  $J$  = 4.4 Hz, H-20b) further supported the presence of this group. Moreover, a methyl singlet, two methyl doublets (including a vinyl methyl), three pairs of  $sp^3$  methylene protons, two  $sp^3$  methine protons, five oxymethine protons, an  $sp^2$  methine proton, four acetate methyls, and a hydroxy proton were observed in the  $^1H$  NMR spectrum (Table 2).

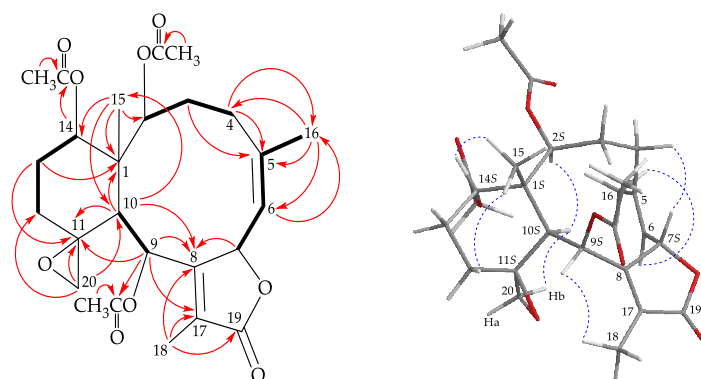


**Figure 3.** The COSY (—) correlations, selective HMBC correlations (---), and selective protons with key NOESY (·····) correlations of **1**.

**Table 2.**  $^1H$  and  $^{13}C$  NMR (CDCl<sub>3</sub>) data for **2**.

Position	$\delta_H$ <sup>a</sup> ( $J$ in Hz)	$\delta_C$ , <sup>b</sup> Type
1		46.8, C
2	4.74 d (4.8)	74.4, CH
3 $\alpha$ / $\beta$	1.67 m; 2.43 ddd (16.0, 16.0, 4.4)	32.1, CH <sub>2</sub>
4 $\alpha$ / $\beta$	2.52 br d (16.0); 2.07 m	28.7, CH <sub>2</sub>
5		143.8, C
6	5.61 br d (10.0)	120.8, CH
7	5.14 dd (10.0, 1.2)	77.7, CH
8		80.2, C
9	5.67 d (5.6)	67.3, CH
10	2.58 d (5.6)	39.9, CH
11		62.3, C
12	5.40 dd (8.4, 8.4)	62.0, CH
13 $\alpha$ / $\beta$	1.58 m; 2.70 m	32.6, CH <sub>2</sub>
14	4.85 d (4.4)	73.6, CH
15	1.16 s	15.3, CH <sub>3</sub>
16	2.03 d (1.2)	28.1, CH <sub>3</sub>
17	2.35 q (7.2)	42.3, CH
18	1.15 d (7.2)	6.7, CH <sub>3</sub>
19		176.2, C
20a/b	3.20 d (4.4); 2.90 d (4.4)	53.9, CH <sub>2</sub>
OH-8	4.57 d (1.2)	
OAc-2		170.6, C
	2.01 s	21.0, CH <sub>3</sub> <sup>c</sup>
OAc-9		169.2, C
	2.22 s	21.6, CH <sub>3</sub>
OAc-12		169.4, C
	1.98 s	20.7, CH <sub>3</sub> <sup>c</sup>
OAc-14		169.8, C
	2.02 s	20.9, CH <sub>3</sub> <sup>c</sup>

<sup>a</sup> 400 MHz, <sup>b</sup> 100 MHz, <sup>c</sup> Data exchangeable.

The  $^1\text{H}$  NMR coupling information in the correlation spectroscopy analysis enabled the determination of five different spin systems, H-2/H<sub>2</sub>-3/H<sub>2</sub>-4, H-6/H-7, H-9/H-10, H-12/H<sub>2</sub>-13/H-14, and H-17/H<sub>3</sub>-18, which were assembled with the assistance of an HMBC experiment (Figure 4). The HMBC correlations between protons and quaternary carbons, such as H-2, H-3 $\beta$ , H-10, H-13 $\alpha$ , H-14, H<sub>3</sub>-15 to C-1; H<sub>2</sub>-4, H-7, H<sub>3</sub>-16 to C-5; H-7, H-9, H-10, H-17, H<sub>3</sub>-18 to C-8; H-9, H-10, H-12, H<sub>2</sub>-20, H<sub>2</sub>-13 to C-11; and H-17, H<sub>3</sub>-18 to C-19, respectively, permitted elucidation of the carbon skeleton of **2**. A methyl at C-5 was confirmed by the HMBC correlations between H<sub>3</sub>-16 to C-4, C-5, and C-6; and further confirmed by an allylic coupling between H-6/H<sub>3</sub>-16 ( $J = 1.2$  Hz). The methyl group Me-15 on C-1 was substantiated by the HMBC correlations from H<sub>3</sub>-15 to C-1, C-2, C-10, C-14; and H-2, H-10 to C-15, respectively. The epoxy group at C-11/20 was confirmed by the HMBC correlations between H<sub>2</sub>-20 to C-10, C-11, C-12. The hydroxy group at C-8 was deduced from the HMBC correlations of a hydroxy proton at  $\delta_{\text{H}}$  4.57 to C-7, C-8, and C-9. Moreover, HMBC correlations from the oxymethine protons at  $\delta_{\text{H}}$  4.74 (H-2), 5.67 (H-9), 5.40 (H-12), and 4.85 (H-14) to the acetate carbonyls at  $\delta_{\text{C}}$  170.6, 169.2, 169.4, and 169.8, placed the acetate groups on C-2, C-9, C-12, and C-14, respectively.

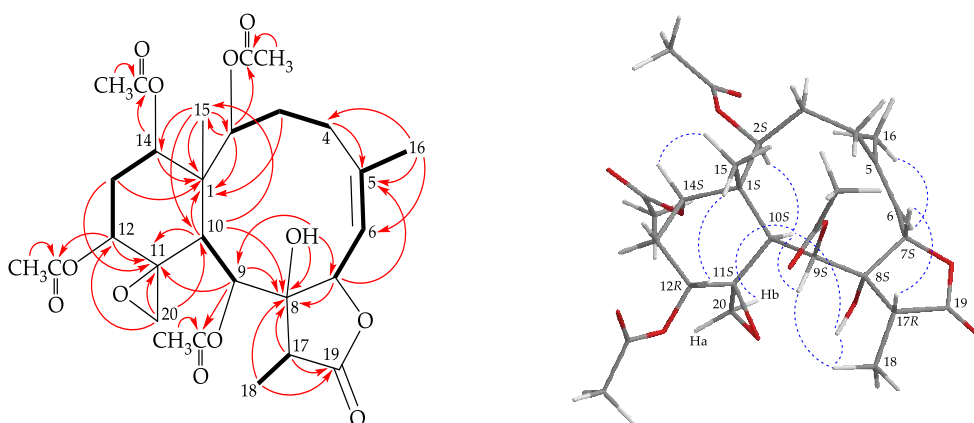


**Figure 4.** The COSY (—) correlations, selective HMBC correlations (---), and selective protons with key NOESY (·····) correlations of **2**.

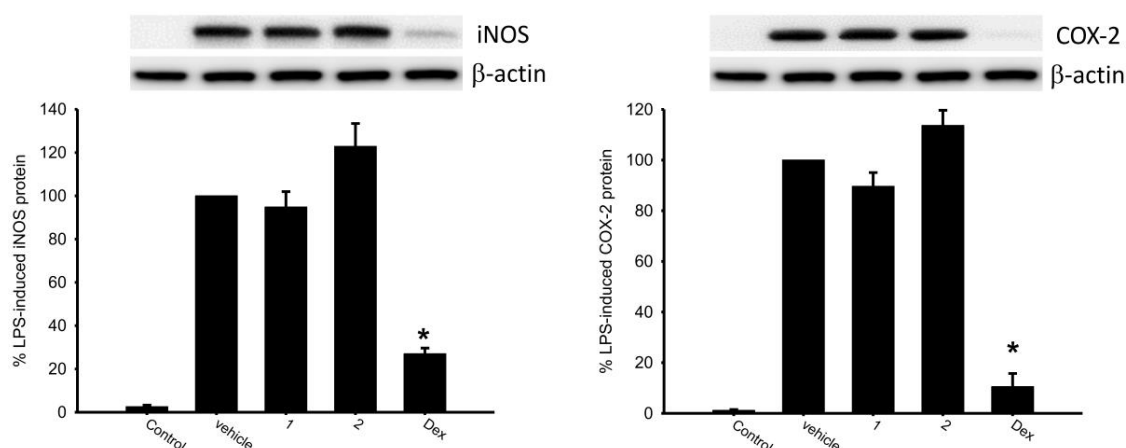
The stereochemistry of **2** was determined by NOE correlations observed in a NOESY experiment (Figure 4) and possible biogenetic considerations. The NOE correlations of H-10/H-2, H-10/OH-8, H-10/H-9, and H-10/H-20b indicated that these protons are situated on the same face of the structure and were assigned as the  $\alpha$  protons since the C-15 methyl is the  $\beta$ -substituent at C-1. Meanwhile, correlations of H<sub>3</sub>-15/H-12 and H<sub>3</sub>-15/H-14 indicated that H-12 and H-14 were  $\beta$ -oriented, and the cyclohexane ring may exhibit a twist-boat conformation. The NOESY spectrum showed a correlation from H-6 to H<sub>3</sub>-16, revealing the *Z* geometry of the C-5/6 double bond. H<sub>3</sub>-18 exhibited correlations to OH-8 and H-9, suggesting the  $\alpha$ -orientation of Me-18 at C-17. H-7 displayed a correlation with H-17, which confirmed that these two protons were  $\beta$ -oriented at C-7 and C-17, respectively. As briarane **2** was isolated along with **1** from the same organism, it is reasonable on biogenetic grounds to assume that **2** possessed the same absolute configuration as that of **1**. Therefore, the configurations of the stereogenic carbons of **2** should be assigned as 1*S*,2*S*,7*S*,8*S*,9*S*,10*S*,11*S*,12*R*,14*S*, and 17*R* (Supplementary Materials, Figures S15–S29).

The effects of briaranes **1** and **2** on the release of iNOS and COX-2 from lipopolysaccharide (LPS)-stimulated RAW 264.7 macrophage cells were assessed (Table 3 and Figure 5). It is interesting to note that **2** at 10  $\mu\text{M}$  enhanced the release of iNOS and COX-2 to 122.87% and 113.65%, respectively, as compared to results of the cells stimulated with LPS only.

**Table 3.** Effects of briaranes **1** and **2** on lipopolysaccharide (LPS)-induced pro-inflammatory iNOS and COX-2 protein expression in macrophages.

Compound	iNOS	COX-2	$\beta$ -Actin
	Expression (% of LPS)		
Control	2.59 $\pm$ 0.65	1.14 $\pm$ 0.34	100.15 $\pm$ 7.70
LPS	100.00 $\pm$ 0.00	100.00 $\pm$ 0.00	100.00 $\pm$ 0.00
<b>1</b>	94.81 $\pm$ 7.11	89.59 $\pm$ 5.45	101.09 $\pm$ 1.91
<b>2</b>	122.87 $\pm$ 10.53	113.65 $\pm$ 6.00	99.50 $\pm$ 1.64
Dexamethasone	26.99 $\pm$ 2.66	10.52 $\pm$ 5.23	99.02 $\pm$ 1.53

Data were normalized to those of cells treated with LPS alone, and cells treated with dexamethasone were used as a positive control. Data are expressed as the mean  $\pm$  standard error of the mean (SEM) ( $n = 3$ ).

**Figure 5.** Western blotting showed that briarane **2** enhanced the expression of iNOS and COX-2. Data were normalized to the cells treated with LPS only, and cells treated with dexamethasone (Dex) (10  $\mu$ M) were used as a positive control. Data are presented as the mean  $\pm$  SEM ( $n = 3$ ). \* Significantly different from cells treated with LPS ( $p < 0.05$ ).

### 3. Materials and Methods

#### 3.1. General Experimental Procedures

NMR spectra were recorded on a 400 MHz Jeol NMR (model ECZ 400S, Tokyo, Japan) spectrometer using the residual  $\text{CHCl}_3$  signal ( $\delta_{\text{H}}$  7.26 ppm) and  $\text{CDCl}_3$  ( $\delta_{\text{C}}$  77.1 ppm) as internal references for  $^1\text{H}$  and  $^{13}\text{C}$  NMR, respectively. ESIMS and HRESIMS were obtained from a Bruker mass spectrometer with 7 Tesla magnets (model: Solarix FTMS system, Bremen, Germany). Column chromatography, HPLC, IR spectra, and optical rotation values were performed according to our earlier research [19].

#### 3.2. Animal Material

The specimens coral *J. fragilis* were collected in July 2019 by hand, using self-contained underwater breathing apparatus (SCUBA) off the coast of Orchid Island (Lanyu Island), Taiwan. The samples were stored in a  $-20^\circ\text{C}$  freezer until extraction. A voucher specimen was deposited in the National Museum of Marine Biology and Aquarium (NMMBA) (voucher no.: NMMBA-TW-GC-2019-017). This organism was identified by comparison with previous descriptions [1–3].

#### 3.3. Extraction and Isolation

Sliced bodies (wet/dry weight = 1125 g/588 g) of the coral specimen were prepared and extracted with a mixture of methanol (MeOH) and dichloromethane ( $\text{CH}_2\text{Cl}_2$ ) (1:1) to give a crude extract (29.0 g) which was partitioned between ethyl acetate (EtOAc) and  $\text{H}_2\text{O}$ . The EtOAc extract (17.0 g) was then applied to a silica gel column chromatograph (C.C.) (500 g) and eluted with gradients of hexanes/acetone

(stepwise from 50:1 (3000 mL)-30:1 (3000 mL)-20:1 (3000 mL)-10:1 (3000 mL)-5:1 (3000 mL)-4:1 (3000 mL)-3:1 (3000 mL)-2:1 (3000 mL)-1:1 (3000 mL)-1:2 (3000 mL)) to furnish fractions A–J. Fraction F (913.9 mg) was separated on silica gel C.C. and eluted with gradients of hexanes/acetone (stepwise from 20:1 (2400 mL)-15:1 (2400 mL)-10:1 (2400 mL)-8:1 (2400 mL)-6:1 (2400 mL)-4:1 (2400 mL)-2:1 (2400 mL)-1:1 (2400 mL) to furnish fractions F1–F8. Fraction F5 was further separated by silica gel C.C. with a mixture of hexanes/acetone (10:1 to 1:1, stepwise) to afford fractions F5A–F5F. Afterward, fraction F5C was separated by normal-phase HPLC (NP-HPLC) using a mixture of CH<sub>2</sub>Cl<sub>2</sub> and acetone (10:1) to yield fractions F5C1–F5C4. Fraction F5C2 was purified by NP-HPLC using a mixture of *n*-hexane and EtOAc (2:1; at a flow rate = 2.0 mL/min) to afford **1** (32.4 mg). Fraction G was applied to a silica gel C.C. and eluted with a mixture of hexanes/acetone (3:1) to furnish fractions G1–G6. Fraction G4 was separated by silica gel C.C. using a mixture of CH<sub>2</sub>Cl<sub>2</sub> and acetone (20:1) to afford fractions G4A–G4F. Fraction G4E was separated by NP-HPLC using a mixture of *n*-hexane/EtOAc/acetone (5:2:1) to yield fractions G4E1–G4E5. Fraction G4E4 was purified by NP-HPLC using a mixture of CH<sub>2</sub>Cl<sub>2</sub> and acetone (10:1) to afford fractions G4E4A–G4E4C. Fraction G4E4A was separated by reverse-phase HPLC (RP-HPLC) using a mixture of acetonitrile and H<sub>2</sub>O (55:45; at a flow rate = 4.0 mL/min) to obtain **2** (0.7 mg).

Juncenolide K (**1**): Colorless crystals;  $[\alpha]_D^{26}$  −90 (*c* 1.62, CHCl<sub>3</sub>) (ref. [13]  $[\alpha]_D$  −85 (*c* 0.2, CH<sub>2</sub>Cl<sub>2</sub>)); IR (ATR)  $\nu_{\max}$  2926, 1746, 1728, 1372, 1251, 1216, 759 cm<sup>−1</sup>; <sup>1</sup>H (400 MHz, CDCl<sub>3</sub>) and <sup>13</sup>C (100 MHz, CDCl<sub>3</sub>) NMR data, see Table 1; ESIMS: *m/z* 513 [M + Na]<sup>+</sup>; HRESIMS: *m/z* 513.20949 (calcd. for C<sub>26</sub>H<sub>34</sub>O<sub>9</sub> + Na, 513.20950).

Fragilide X (**2**): Amorphous powder;  $[\alpha]_D^{25}$  +232 (*c* 0.23, CHCl<sub>3</sub>); IR (KBr)  $\nu_{\max}$  3333, 2942, 1773, 1742, 1374, 1219, 756 cm<sup>−1</sup>; <sup>1</sup>H (400 MHz, CDCl<sub>3</sub>) and <sup>13</sup>C (100 MHz, CDCl<sub>3</sub>) NMR data, see Table 2; ESIMS: *m/z* 589 [M + Na]<sup>+</sup>; HRESIMS: *m/z* 589.22576 (calcd. for C<sub>28</sub>H<sub>38</sub>O<sub>12</sub> + Na, 589.22555).

### 3.4. Single-Crystal X-ray Crystallography of Juncenolide K (**1**)

Suitable colorless prisms of **1** were obtained from a solution of MeOH and petroleum ether. The crystal (0.255 × 0.233 × 0.114 mm<sup>3</sup>) belongs to the orthorhombic system, space group *P*2<sub>1</sub>2<sub>1</sub>2<sub>1</sub> (#19), with *a* = 9.8842(2) Å, *b* = 15.5702(2) Å, *c* = 17.0502(3) Å, *V* = 2624.01(8) Å<sup>3</sup>, *Z* = 4, *D*<sub>calcd</sub> = 1.264 Mg/m<sup>3</sup>, λ (Cu Kα) = 1.54178 Å. Intensity data were measured on a Bruker D8 Venture diffractometer up to  $\theta_{\max}$  of 75.0°. All 12,468 reflections were collected. The structure was solved by direct methods and refined by a full-matrix least-squares procedure [41,42]. The refined structural model converged to a final *R*1 (the *R*-value, is the agreement between the calculated and observed models) = 0.0396; *wR*2 (*wR*2 is similar to *R*1, but refers to squared *F*-values) = 0.1090 for 5385 observed reflections [*I* > 2σ(*I*)] and 335 variable parameters. The absolute configuration was determined by the Flack parameter *x* = 0.07(5) [43,44]. Crystallographic data for the structure of juncenolide K (**1**) were deposited with the Cambridge Crystallographic Data Center (CCDC) as supplementary publication number CCDC 1973681 [45].

### 3.5. In Vitro Inflammatory Assay

Murine RAW 264.7 macrophages were obtained from the American Type Culture Collection (ATCC; No. TIB-71). Inflammation in macrophages was induced by incubating them for 16 h in a medium containing only LPS (0.01 µg/mL) without compounds. For the anti-inflammatory activity assay, compounds (10 µM) were added to the cells 5 min before LPS challenge. The cells were then washed with ice cold phosphate-buffered saline (PBS), lysed in ice-cold lysis buffer (50 mM Tris, pH 7.5, 150 mM NaCl, 1% Triton X-100, 100 µg/mL phenylmethylsulfonyl fluoride, 1 µg/mL aprotinin), and then centrifuged at 20,000× *g* for 30 min at 4 °C. The supernatant was decanted from the pellet and retained for Western blot analysis of pro-inflammation inducible nitric oxide synthase (iNOS) and cyclooxygenase-2 (COX-2) protein expression. Protein concentrations were determined using the detergent compatible (DC) protein assay kit (Bio-Rad, Hercules, CA, USA). Western blotting was performed according to the method described in a previous study [46]. An equal volume of sample

buffer (2% 2-mercaptoethanol, 2% sodium dodecyl sulfate (SDS), 0.1% bromophenol blue, 10% glycerol, and 50 mM Tris-HCl (pH 7.2)) was added to the samples, and the protein lysates were loaded onto a 10% SDS-polyacrylamide gel. Electrophoresis was carried out at 150 V for 90 min. After electrophoresis, gels were transferred overnight at 4 °C in transfer buffer (380 mM glycine, 50 mM Tris-HCl, 1% SDS and 20% methanol) onto a polyvinylidene difluoride membrane (PVDF; Immobilon-P, Millipore Corp. (0.45 µm pore size)). The PVDF membrane was first blocked with 5% non-fat dry milk in Tris-buffered saline containing 0.1% Tween (TTBS; 20 mM Tris-HCl, 0.1% Tween 20, and 137 mM NaCl (pH 7.4)) and incubated overnight at 4 °C with the primary antibodies for iNOS, COX-2, and β-actin proteins. Anti-iNOS and anti-COX-2 antibodies were purchased from Cayman Chemical Company (Ann Arbor, MI, USA). A horseradish peroxidase-conjugated secondary antibody was used for detection. It was obtained from Jackson ImmunoResearch Laboratories (West Grove, PA, USA). The bound antibodies were detected by chemiluminescence (Millipore Corp.). The images were obtained using the UVP BioChem Imaging System, and the LabWorks 4.0 software (UVP, Upland, CA, USA) was used to quantify the relative densities.

#### 4. Conclusions

*J. fragilis* has been demonstrated to have a wide structural diversity of briarane-type diterpenoids that possess various potential bioactivities. In our continued study on *J. fragilis*, a previously unreported 11,20-epoxybriarane, fragilide X (2), along with a known briarane, juncenolide K (1) were isolated. Revision of the structure and absolute configuration of juncenolide K (1) was confirmed by a single-crystal X-ray diffraction analysis. In the present study, a pro-inflammatory assay was employed to assess the activity of isolates, and fragilide X (2) was found to enhance the release of iNOS and COX-2, respectively.

**Supplementary Materials:** Supplementary Materials are available online at <http://www.mdpi.com/1660-3397/18/4/183/s1>. HRESIMS, IR, 1D (<sup>1</sup>H, <sup>13</sup>C NMR and DEPT spectra), and 2D (HSQC, HMBC, COSY, and NOESY) NMR spectra of juncenolide K (1) and fragilide X (2), and X-ray Crystallography of 1.

**Author Contributions:** Conceptualization, J.-J.C., Z.-H.W., T.-L.H., and P.-J.S.; investigation, T.-P.S., T.-J.K., S.-N.Y., G.-H.L., Y.-T.L., and Y.-C.W.; writing—original draft preparation, T.-P.S., T.-J.K., and P.-J.S.; writing—review and editing, T.-L.H. and P.-J.S. All authors have read and agreed to the published version of the manuscript.

**Funding:** This research was supported by grants from the National Museum of Marine Biology and Aquariums; the National Dong Hwa University; the Ministry of Science and Technology, Taiwan (grant numbers: MOST 106-2320-B-291-001-MY3 and 107-2320-B-291-001-MY3) awarded to Ping-Jyun Sung.

**Conflicts of Interest:** The authors declare no conflicts of interest.

#### References

1. Bayer, F.M. Key to the genera of octocorallia exclusive of Pennatulacea (Coelenterata: Anthozoa), with diagnoses of new taxa. *Proc. Biol. Soc. Wash.* **1981**, *94*, 902–947.
2. Bayer, F.M.; Grasshoff, M. The genus group taxa of the family Ellisellidae, with clarification of the genera established by J.E. Gray (Cnidaria: Octocorallia). *Senckenb. Biol.* **1994**, *74*, 21–45.
3. Chen, C.-C.; Chang, K.-H. Gorgonacea (Coelenterata: Anthozoa: Octocorallia) of Southern Taiwan. *Bull. Inst. Zool. Acad. Sin.* **1991**, *30*, 149–181.
4. Chung, H.-M.; Wang, Y.-C.; Tseng, C.-C.; Chen, N.-F.; Wen, Z.-H.; Fang, L.-S.; Hwang, T.-L.; Wu, Y.-C.; Sung, P.-J. Natural product chemistry of gorgonian corals of genus *Junceella*—Part III. *Mar. Drugs* **2018**, *16*, 339, and review articles in this series. [[CrossRef](#)] [[PubMed](#)]
5. Su, Y.-M.; Fan, T.-Y.; Sung, P.-J. 11,20-Epoxybriaranes from the gorgonian coral *Ellisella robusta* (Ellisellidae). *Nat. Prod. Res.* **2007**, *21*, 1085–1090. [[CrossRef](#)] [[PubMed](#)]
6. Shin, J.; Park, M.; Fenical, W. The juncellolides, new anti-inflammatory diterpenoids of the briarane class from the Chinese gorgonian *Junceella fragilis*. *Tetrahedron* **1989**, *45*, 1633–1638. [[CrossRef](#)]
7. Sheu, J.-H.; Chen, Y.-P.; Hwang, T.-L.; Chiang, M.Y.; Fang, L.-S.; Sung, P.-J. Juncellolides J-L, 11,20-epoxybriaranes from the gorgonian coral *Junceella fragilis*. *J. Nat. Prod.* **2006**, *69*, 269–273. [[CrossRef](#)] [[PubMed](#)]



8. Shen, Y.-C.; Chen, Y.-H.; Hwang, T.-L.; Guh, J.-H.; Khalil, A.T. Four new briarane diterpenoids from the gorgonian coral *Junceella fragilis*. *Helv. Chim. Acta* **2007**, *90*, 1391–1398. [[CrossRef](#)]
9. Sung, P.-J.; Chen, Y.-P.; Su, Y.-M.; Hwang, T.-L.; Hu, W.-P.; Fan, T.-Y.; Wang, W.-H. Fragilide B: A novel briarane-type diterpenoid with a *S-cis* diene moiety. *Bull. Chem. Soc. Jpn.* **2007**, *80*, 1205–1207. [[CrossRef](#)]
10. Sung, P.-J.; Lin, M.-R.; Su, Y.-D.; Chiang, M.Y.; Hu, W.-P.; Su, J.-H.; Cheng, M.-C.; Hwang, T.-L.; Sheu, J.-H. New briaranes from the octocorals *Briareum excavatum* (Briareidae) and *Junceella fragilis* (Ellisellidae). *Tetrahedron* **2008**, *64*, 2596–2604. [[CrossRef](#)]
11. Sung, P.-J.; Pai, C.-H.; Su, Y.-D.; Hwang, T.-L.; Kuo, F.-W.; Fan, T.-Y.; Li, J.-J. New 8-hydroxybriarane diterpenoids from the gorgonians *Junceella juncea* and *Junceella fragilis* (Ellisellidae). *Tetrahedron* **2008**, *64*, 4224–4232. [[CrossRef](#)]
12. Hwang, T.-L.; Lin, M.-R.; Tsai, W.-T.; Yeh, H.-C.; Hu, W.-P.; Sheu, J.-H.; Sung, P.-J. New polyoxygenated briaranes from octocorals *Briareum excavatum* and *Ellisella robusta*. *Bull. Chem. Soc. Jpn.* **2008**, *81*, 1638–1646. [[CrossRef](#)]
13. Wang, S.-S.; Chen, Y.-H.; Chang, J.-Y.; Hwang, T.-L.; Chen, C.-H.; Khalil, A.T.; Shen, Y.-C. Juncenolides H–K, new briarane diterpenoids from *Junceella juncea*. *Helv. Chim. Acta* **2009**, *92*, 2092–2100. [[CrossRef](#)]
14. Chang, Y.-C.; Hwang, T.-L.; Huang, S.-K.; Huang, L.-W.; Lin, M.-R.; Sung, P.-J. 12-*epi*-Fragilide G, a new briarane-type diterpenoid from the gorgonian coral *Ellisella robusta*. *Heterocycles* **2010**, *81*, 991–996. [[CrossRef](#)]
15. Wang, S.-H.; Chang, Y.-C.; Chiang, M.Y.; Chen, Y.-H.; Hwang, T.-L.; Weng, C.-F.; Sung, P.-J. Chlorinated briarane diterpenoids from the sea whip gorgonian corals *Junceella fragilis* and *Ellisella robusta* (Ellisellidae). *Chem. Pharm. Bull.* **2010**, *58*, 928–933. [[CrossRef](#)]
16. Chang, J.-Y.; Liaw, C.-C.; Fazary, A.E.; Hwang, T.-L.; Shen, Y.-C. New briarane diterpenoids from the gorgonian coral *Junceella juncea*. *Mar. Drugs* **2012**, *10*, 1321–1330. [[CrossRef](#)]
17. Cheng, W.; Li, X.; Yin, F.; van Ofwegen, L.; Lin, W. Halogenated briarane diterpenes with acetyl migration from the gorgonian coral *Junceella fragilis*. *Chem. Biodivers.* **2017**, *14*, e1700053. [[CrossRef](#)]
18. Zheng, L.-G.; Chang, Y.-C.; Hu, C.-C.; Wen, Z.-H.; Wu, Y.-C.; Sung, P.-J. Fragilides K and L, new briaranes from the gorgonian coral *Junceella fragilis*. *Molecules* **2018**, *23*, 1510. [[CrossRef](#)]
19. Su, T.-P.; Yuan, C.-H.; Jhu, Y.-M.; Peng, B.-R.; Wen, Z.-H.; Wu, Y.-J.; Wu, T.-Y.; Liu, H.-W.; Sung, P.-J. Fragilides U–W: New 11,20-epoxybriaranes from the sea whip gorgonian coral *Junceella fragilis*. *Mar. Drugs* **2019**, *17*, 706. [[CrossRef](#)]
20. Zheng, L.-G.; Chang, Y.-C.; Chen, J.-J.; Wen, Z.-H.; Hwang, T.-L.; Sung, P.-J. (+)-12-*epi*-Fragilide G, a new chlorinated briarane from the sea whip gorgonian coral *Junceella fragilis*. *Heterocycles* **2019**, *96*, 1601–1609.
21. Hamann, M.T.; Harrison, K.N.; Carroll, A.R.; Scheuer, P.J. Briarane diterpenes from Micronesian gorgonians. *Heterocycles* **1999**, *42*, 325–331.
22. El Sayed, K.A.; Dunbar, D.C.; Perry, T.L.; Wilkins, S.P.; Hamann, M.T.; Greenplate, J.T.; Wideman, M.A. Marine natural products as prototype insecticidal agents. *J. Agric. Food Chem.* **1997**, *45*, 2735–2739. [[CrossRef](#)]
23. Shen, Y.-C.; Lin, Y.-C.; Chiang, M.Y. Juncenolide A, a new briarane from the Taiwanese gorgonian *Junceella juncea*. *J. Nat. Prod.* **2002**, *65*, 54–56. [[CrossRef](#)] [[PubMed](#)]
24. Shen, Y.-C.; Lin, Y.-C.; Ko, C.-L.; Wang, L.-T. New briaranes from the Taiwanese gorgonian *Junceella juncea*. *J. Nat. Prod.* **2003**, *66*, 302–305. [[CrossRef](#)] [[PubMed](#)]
25. Tanaka, C.; Yamamoto, Y.; Otsuka, M.; Tanaka, J.; Ichiba, T.; Marriott, G.; Rachmat, R.; Higa, T. Briarane diterpenes from two species of octocorals, *Ellisella* sp. and *Pteroeides* sp. *J. Nat. Prod.* **2004**, *67*, 1368–1373. [[CrossRef](#)] [[PubMed](#)]
26. Qi, S.-H.; Zhang, S.; Wen, Y.-M.; Xiao, Z.-H.; Li, Q.-X. New briaranes from the South China Sea gorgonian *Junceella fragilis*. *Helv. Chim. Acta* **2005**, *88*, 2349–2354. [[CrossRef](#)]
27. Sun, J.-F.; Huang, H.; Chai, X.-Y.; Yang, X.-W.; Meng, L.; Huang, C.-G.; Zhou, X.-F.; Yang, B.; Hu, J.; Chen, X.-Q.; et al. Dichotellides A–E, five new iodine-containing briarane type diterpenoids from *Dichotella gemmacea*. *Tetrahedron* **2011**, *67*, 1245–1250. [[CrossRef](#)]
28. Li, C.; La, M.-P.; Sun, P.; Kurtan, T.; Mandi, A.; Tang, H.; Liu, B.-S.; Yi, Y.-H.; Li, L.; Zhang, W. Bioactive (3*Z*,5*E*)-11,20-epoxybriara-3,5-dien-7,18-olide diterpenoids from the South China Sea gorgonian *Dichotella gemmacea*. *Mar. Drugs* **2011**, *9*, 1403–1418. [[CrossRef](#)]
29. Li, C.; La, M.-P.; Tang, H.; Pan, W.-H.; Sun, P.; Krohn, K.; Yi, Y.-H.; Li, L.; Zhang, W. Bioactive briarane diterpenoids from the South China Sea gorgonian *Dichotella gemmacea*. *Bioorg. Med. Chem. Lett.* **2012**, *22*, 4368–4372. [[CrossRef](#)]

30. Li, C.; Jiang, M.; La, M.-P.; Li, T.-J.; Tang, H.; Sun, P.; Liu, B.-S.; Yi, Y.-H.; Liu, Z.; Zhang, W. Chemistry and tumor cell growth inhibitory activity of 11,20-epoxy-3Z,5(6)E-diene briaranes from the South China Sea gorgonian *Dichotella gemmacea*. *Mar. Drugs* **2013**, *11*, 1565–1582. [[CrossRef](#)]
31. La, M.-P.; Li, J.; Li, C.; Tang, H.; Liu, B.-S.; Sun, P.; Zhuang, C.-L.; Li, T.-J.; Zhang, W. Briarane diterpenoids from the gorgonian *Dichotella gemmacea*. *Mar. Drugs* **2014**, *12*, 6178–6189. [[CrossRef](#)] [[PubMed](#)]
32. Li, C.; La, M.-P.; Tang, H.; Sun, P.; Liu, B.-S.; Zhuang, C.-L.; Yi, Y.-H.; Zhang, W. Chemistry and bioactivity of briaranes from the South China Sea gorgonian *Dichotella gemmacea*. *Mar. Drugs* **2016**, *14*, 201. [[CrossRef](#)] [[PubMed](#)]
33. Cheng, W.; Ji, M.; Li, X.; Ren, J.; Yin, F.; van Ofwegen, L.; Yu, S.; Chen, X.; Lin, W. Fragilolides A–Q, norditerpenoid and briarane diterpenoids from the gorgonian coral *Junceella fragilis*. *Tetrahedron* **2017**, *73*, 2518–2528. [[CrossRef](#)]
34. Qi, S.-H.; Zhang, S.; Qian, P.-Y.; Xiao, Z.-H.; Li, M.-Y. Ten new antifouling briarane diterpenoids from the South China Sea gorgonian *Junceella juncea*. *Tetrahedron* **2006**, *62*, 9123–9130. [[CrossRef](#)]
35. Qi, S.H.; Zhang, S.; Qian, P.Y.; Xu, H.H. Antifeedant and antifouling briaranes from the South China Sea gorgonian *Junceella juncea*. *Chem. Nat. Compd.* **2009**, *45*, 49–54. [[CrossRef](#)]
36. Sun, J.-F.; Han, Z.; Zhou, X.-F.; Yang, B.; Lin, X.; Liu, J.; Peng, Y.; Yang, X.-W.; Liu, Y. Antifouling briarane type diterpenoids from South China Sea gorgonians *Dichotella gemmacea*. *Tetrahedron* **2013**, *69*, 871–880. [[CrossRef](#)]
37. Zhang, M.-Q.; Zhao, J.; Liu, H.-Y.; Cao, F.; Wang, C.-Y. Briarane diterpenoids from gorgonian *Dichotella gemmacea* collected from the South China Sea. *Chem. Nat. Compd.* **2016**, *52*, 945–947. [[CrossRef](#)]
38. Li, C.; La, M.-P.; Li, L.; Li, X.-B.; Tang, H.; Liu, B.-S.; Krohn, K.; Sun, P.; Yi, Y.-H.; Zhang, W. Bioactive 11,20-epoxy-3,5(16)-diene briarane diterpenoids from the South China Sea gorgonian *Dichotella gemmacea*. *J. Nat. Prod.* **2011**, *74*, 1658–1662. [[CrossRef](#)]
39. Murthy, Y.L.N.; Mallika, D.; Rajack, A.; Reddy, G.D. A new antifungal briarane diterpenoid from the gorgonian *Junceella juncea* Pallas. *Bioorg. Med. Chem. Lett.* **2011**, *21*, 7522–7525. [[CrossRef](#)]
40. Kapustina, I.I.; Kalinovskii, A.I.; Dmitrenok, P.S.; Kuz'mich, A.S.; Nedashkovskaya, O.I.; Grebnev, B.B. Diterpenoids and other metabolites from the Vietnamese gorgonians *Lophogorgia* sp. and *Junceella* sp. *Chem. Nat. Compd.* **2014**, *50*, 1140–1142. [[CrossRef](#)]
41. Sheldrick, G.M. SHELXT-Integrated space-group and crystal-structure determination. *Acta Crystallogr.* **2015**, *A71*, 3–8. [[CrossRef](#)] [[PubMed](#)]
42. Sheldrick, G.M. Crystal structure refinement with SHELXL. *Acta Crystallogr.* **2015**, *C71*, 3–8.
43. Flack, H.D. On enantiomorph-polarity estimation. *Acta Crystallogr.* **1983**, *A39*, 876–881. [[CrossRef](#)]
44. Flack, H.D.; Bernardinelli, G. Absolute structure and absolute configuration. *Acta Crystallogr.* **1999**, *A55*, 908–915. [[CrossRef](#)] [[PubMed](#)]
45. CCDC homepage. Available online: <http://www.ccdc.cam.ac.uk/conts/retrieving.html>.
46. Chen, C.-H.; Chen, N.-F.; Feng, C.-W.; Cheng, S.-Y.; Hung, H.-C.; Tsui, K.-H.; Hsu, C.-H.; Sung, P.-J.; Chen, W.-F.; Wen, Z.-H. A coral-derived compound improves functional recovery after spinal cord injury through its antiapoptotic and anti-inflammatory effects. *Mar. Drugs* **2016**, *14*, 160. [[CrossRef](#)]



© 2020 by the authors. Licensee MDPI, Basel, Switzerland. This article is an open access article distributed under the terms and conditions of the Creative Commons Attribution (CC BY) license (<http://creativecommons.org/licenses/by/4.0/>).

# Polyethylene Glycol-Coated Graphene Oxide Loaded with Erlotinib as an Effective Therapeutic Agent for Treating Nasopharyngeal Cancer Cells

This article was published in the following Dove Press journal:  
*International Journal of Nanomedicine*

Ming-Ying Lan<sup>1,2</sup>

Yen-Bin Hsu<sup>1,2</sup>

Ming-Chin Lan<sup>3,4</sup>

Jyh-Ping Chen<sup>5-8</sup>

Yu-Jen Lu<sup>9</sup>

<sup>1</sup>Department of Otolaryngology-Head and Neck Surgery, Taipei Veterans General Hospital, Taipei, Taiwan; <sup>2</sup>School of Medicine, National Yang-Ming University, Taipei, Taiwan; <sup>3</sup>Department of Otolaryngology-Head and Neck Surgery, Taipei Tzu Chi Hospital, Buddhist Tzu Chi Medical Foundation, New Taipei City, Taiwan; <sup>4</sup>School of Medicine, Tzu Chi University, Hualien, Taiwan; <sup>5</sup>Department of Chemical and Materials Engineering, Chang Gung University, Taoyuan, Taiwan;

<sup>6</sup>Department of Plastic and Reconstructive Surgery and Craniofacial Research Center, Chang Gung Memorial Hospital, Taoyuan, Taiwan; <sup>7</sup>Research Center for Food and Cosmetic Safety, Research Center for Chinese Herbal Medicine, College of Human Ecology, Chang Gung University of Science and Technology, Taoyuan, Taiwan;

<sup>8</sup>Department of Materials Engineering, Ming Chi University of Technology, Taipei, Taiwan; <sup>9</sup>Department of Neurosurgery, Chang Gung Memorial Hospital Linkou Medical Center and College of Medicine, Chang Gung University, Taoyuan, Taiwan

Correspondence: Yu-Jen Lu  
Department of Neurosurgery, Chang Gung Memorial Hospital Linkou Medical Center and College of Medicine, Chang Gung University, Taoyuan, Taiwan  
Email alexlu0416@gmail.com

Jyh-Ping Chen  
Department of Chemical and Materials Engineering, Chang Gung University, Taoyuan, Taiwan  
Email jpchen@mail.cgu.edu.tw

**Introduction:** Nasopharyngeal carcinoma (NPC) is a common cancer in southern China and Taiwan, and radiation therapy combined with or without chemotherapy is its mainstay treatment. Although it is highly sensitive to radiotherapy, local recurrence and distant metastasis remain difficult unsolved problems. In recent years, graphene oxide (GO) has been found to be a promising novel anticancer drug carrier. Here, we present our designed functionalized GO, polyethylene glycol-coated GO (GO-PEG), as a drug carrier, which was loaded with erlotinib and showed promising anticancer effects on NPC cells.

**Methods:** The effects of GO-PEG-erlotinib on the proliferation, migration, and invasion of NPC cells were investigated by WST-8 assay, wound healing assay, and invasion assay, respectively. RNA sequencing was conducted and analyzed to determine the molecular mechanisms by which GO-PEG-erlotinib affects NPC cells.

**Results:** Our results showed that GO-PEG-erlotinib reduced NPC cell viability in a dose-dependent manner and also inhibited the migration and invasion of NPC cells. The RNA sequencing revealed several related molecular mechanisms.

**Conclusion:** GO-PEG-erlotinib effectively suppressed NPC cell proliferation, migration, and invasion, likely by several mechanisms. GO-PEG-erlotinib may be a potential therapeutic agent for treating NPC in the future.

**Keywords:** nasopharyngeal carcinoma, anti-cancer, graphene oxide, erlotinib, drug carrier

## Introduction

Nasopharyngeal carcinoma (NPC) is very rare in western countries but is one of the most common cancers in southern Asian with annual incidence around 20–30/100,000.<sup>1,2</sup> Due to its deep location inside the nasal cavity and vague symptoms, most NPC patients have been diagnosed at an advanced stage.<sup>2</sup> The etiology of NPC has been proved to be closely related to several factors, including genetic, Epstein-Barr virus exposure, environmental, and dietary factors.<sup>1–4</sup> During development of the disease, viral infection and multiple somatic genetic and epigenetic changes synergistically disrupt normal cell function, thus contributing to NPC pathogenesis.<sup>3–8</sup> Radiotherapy is the foundation of curative treatment for NPC, and chemotherapy is usually combined with radiotherapy for advanced cases.<sup>9</sup> Although NPC is highly radiosensitive and chemosensitive with an optimal 5-year survival of over 80%, the treatment of patients with locoregionally advanced disease remains problematic due to locoregional failure and distant metastasis. Besides, patients often suffer from systemic toxicity or related complications of

chemotherapy. To reach a better outcome for NPC treatment, the refinement of current treatment modalities is of importance.

The recent development of novel materials, especially nanoparticles, having the advantages of large surface area-to-volume ratio and small size, enables them to carry small compounds with high efficiency. Graphene and its derivatives have drawn much attention in pharmaceutical sciences as carriers for targeted drug delivery in cancer diagnosis and treatment.<sup>10–13</sup> Graphene is an allotrope of carbon in the form of a one-atom-thick, two-dimensional, atomic-scale, hexagonal lattice, with high thermal conductivity, excellent mechanical properties, and large surface areas.<sup>14</sup> There are several members of the graphene family, including graphene oxide (GO), reduced graphene oxide (RGO), and graphene quantum dots (GQDs), that have been used in materials science, nanotechnology, and biomedicine. The combination of biomolecules, such as DNA, peptides, proteins, enzymes, carbohydrates, and viruses, with graphene-based materials offers a promising method to fabricate novel graphene-biomolecule hybrid nanomaterials with unique functions in drug delivery, cancer treatment, tissue engineering, biosensors, bioimaging, energy materials, and other nanotechnological applications.<sup>15–20</sup>

Erlotinib, a tyrosine kinase inhibitor (TKI) acting on the epidermal growth factor receptor (EGFR), was demonstrated in 2004 to be effective for locally advanced or metastatic non-small cell lung cancer (NSCLC) and, in combination with gemcitabine, for locally advanced or metastatic pancreatic cancer.<sup>21</sup> Currently, there is little information regarding its usage in NPC. Previously, an *in vitro* study showed that erlotinib has a role as an enhancer of radiation therapy in NPC.<sup>22</sup> However, a Phase II trial conducted on patients with recurrent and/or metastatic NPC revealed no efficacy of erlotinib as maintenance therapy after gemcitabine-platinum chemotherapy.<sup>23</sup>

Our previous works have prioritized several crucial NPC targets and identified many potential drugs for treating NPC.<sup>24,25</sup> Erlotinib is one of our potential drugs and was selected to be loaded on specific functionalized graphene to investigate its anticancer effect. The RNA sequencing was conducted to reveal related molecular mechanisms. The goal is to develop drugs with better anticancer activity but lower toxicity for possible future clinical applications in NPC patients.

## Materials and Methods

### Preparation of Graphene Oxide (GO)

The raw materials of graphite platelet (model xGnP) measuring 100  $\mu\text{m}$  in width and 5–15 nm in thickness were obtained from XG Sciences Inc (East Lansing, MI). Acrylic acid, potassium persulfate, sulfuric acid ( $\text{H}_2\text{SO}_4$ , 98%), sodium sulfate ( $\text{Na}_2\text{SO}_4$ ), potassium permanganate ( $\text{KMnO}_4$ ), hydrogen peroxide solution ( $\text{H}_2\text{O}_2$ ), and ammonia solution were purchased from Showa Chemical Co (Tokyo, Japan). Preparation of GO followed the modified Hummers' method (Figure 1).<sup>26</sup> One gram of graphite platelet and 23 mL of  $\text{H}_2\text{SO}_4$  (98%) were added into a 250 mL flask under magnetic stirring for 12 hours, followed by slow addition of 3 g of  $\text{KMnO}_4$  in an ice bath while keeping the temperature below 20°C. After stirring for 30 minutes, the flask was heated to 35–40°C and continually stirred for 30 minutes. The temperature of the solution was increased to 65–80°C with continued stirring for 45 minutes, followed by addition of 46 mL of deionized water. Then, the temperature of the solution was increased to 98–105°C and stirred for 30 minutes. After cooling for 1 hour at room temperature, 140 mL of deionized water and 10 mL 10%  $\text{H}_2\text{O}_2$  were added to the solution and incubated for 5 minutes at 35–40°C. The solution was centrifuged at 10,000 rpm and washed using 5% HCl solution 2–3 times. Then, deionized water was used to wash the precipitate several times to neutralize it. The precipitate was collected and subject to ultrasonication using an Ultrasonic Liquid Processor 2020 from Misonix (Farmingdale, NY) and filtered with Acrodisc 25 mm syringe filters (0.2  $\mu\text{m}$  Supor membrane). GO collected in the filtrate was subjected to further modification.

### Preparation of PEGylated GO (GO-PEG)

GO-polyethylene glycol (GO-PEG) was made following the method below. Briefly, the PBS was added to GO solution and sonicated for 1 hour. After cooling at room temperature, DSPE-PEG- $\text{CH}_3$  was added to the solution. The solution was then sonicated for 1 hour in an ice bath. Finally, the solution was centrifuged at high speed for 1 hour and the supernatant was removed. All GO materials were then dispersed in sterilized deionized water to prepare the stock solution (0.5 or 1 mg/mL) for later characterization and experiments.

### Characterization of GO Materials

(i) Fourier transform infrared spectroscopy (FTIR)



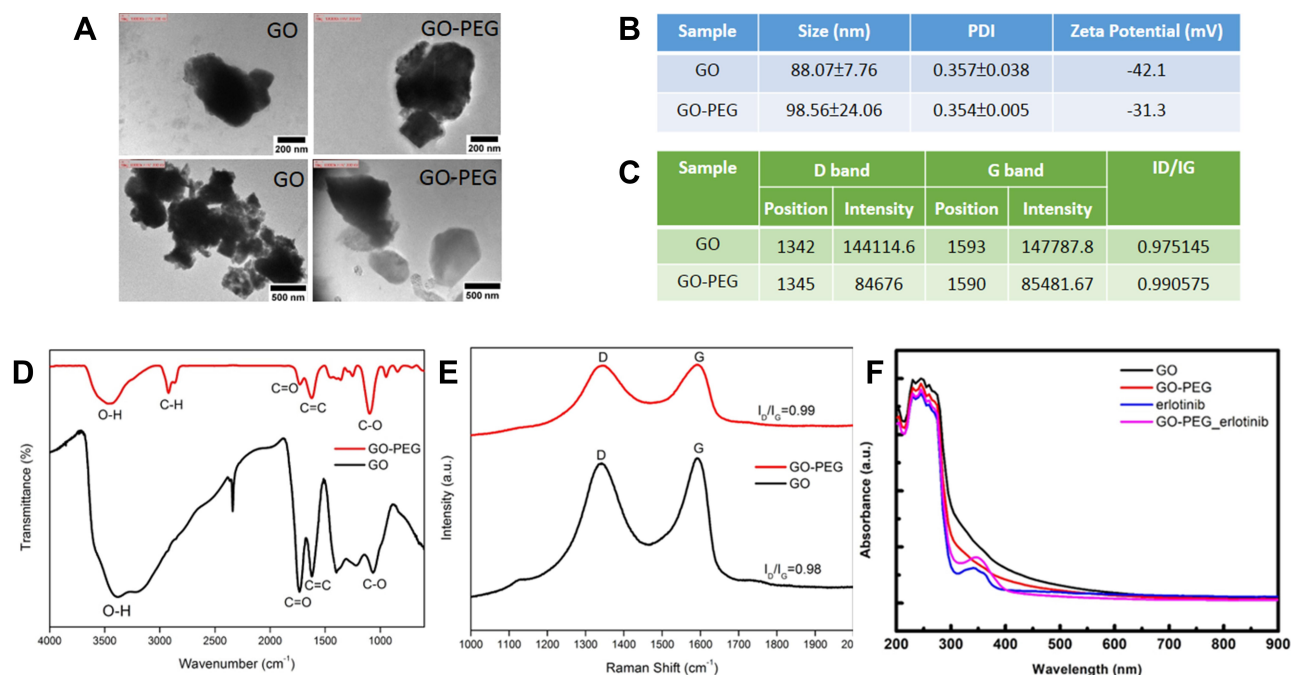


**Figure 1** Characterizations of GO and GO-PEG. **(A)** TEM images of GO and GO-PEG. **(B)** The table lists the measurements of size and zeta potential of GO and GO-PEG analyzed by DLS. **(C)** The intensity of D and G band of GO and GO-PEG in Raman spectra. **(D)** The infrared spectrum of GO and GO-PEG by FTIR shows that PEG was successfully conjugated on GO. **(E)** Raman spectra of GO and GO-PEG. **(F)** Absorbance of GO, GO-PEG, erlotinib, and GO-PEG-erlotinib analyzed by UV-Vis spectrophotometer.

**Abbreviation:** PDI, polydispersity index.

FTIR (Bruker Tensor 27) was used to obtain an infrared spectrum of absorption or emission of the GO and functionalized GO materials.

#### (ii) Dynamic light scattering (DLS) and zeta potential

The sizes of GO and GO-PEG were respectively measured by the zetasizer (Zetasizer Nano ZS90, Malvern).

#### (iii) TEM

Transmission electron microscopy (TEM; JEM-2100, JEOL, Japan) was utilized to determine the structure of the GO materials. The TEM samples were prepared by depositing a small drop of solution onto a carbon-coated copper electron microscopy grid and then dried at room temperature.

#### (iv) Raman spectroscopy

Raman spectra were collected using a Micro-Raman Spectrometer (PTT-EL) equipped with a 532nm laser and a 10X objective. The Raman spectra integration time was 20 sec for each location.

## Drug Loading Study

To prepare GO-PEG loaded with erlotinib (GO-PEG-erlotinib), 200 µg erlotinib was mixed with different concentrations of GO-PEG in 1 mL ddH<sub>2</sub>O. The suspension was rotated at 35 rpm at room temperature overnight and then centrifuged for 1 hour. The supernatant was removed and the concentration of erlotinib in the solution was analyzed by UV-Vis Spectrophotometer (Beckman Coulter DU730) at 735, 333, and 371 nm. The weight of drug loaded on GO-PEG was calculated by mass balance from the amount of drug initially added and the amount of drug in the supernatant. The drug entrapment efficiency (EE) (%) is defined as (weight of drug loaded on GO-PEG / weight of drug initially added) × 100. The drug loading efficiency (LE) (%) is defined as (weight of drug loaded on GO-PEG / weight of GO-PEG) × 100.

## Drug Release Study

GO-PEG-erlotinib was placed into the microtubes with 1 mL phosphate-buffered saline (PBS) at pH 7.4 and 5.5, respectively. The drug release was assumed to start as soon as the microtubes were placed into the incubator at 37°C. The microtube was under constant shaking. At particular time intervals, all supernatant was withdrawn from the



microtube for characterization after centrifugation and washing. The microtube was replenished with the same volume of PBS to continue the drug release study. The concentration of erlotinib released from the functionalized GO-PEG-erlotinib complex was determined using a UV-Vis Spectrophotometer (Beckman Coulter DU730). The drug release percentage was calculated from the cumulative amount of drug released after normalizing with amount of loaded drug.

## Cellular Uptake Study

To determine intracellular uptake of GO-PEG, NPC TW01 cells (10,000 cells/mL) were cultured in 2 mL DMEM supplemented with 10% FBS in 35 mm diameter plates. Cells were grown in a humidified incubator at 37°C under 5% CO<sub>2</sub> for 48 hours. To prepare fluorescent GO-PEG, 95  $\mu$ L of 2 mg/mL FITC-NHS (5/6-carboxyfluorescein succinimidyl ester) was mixed with 1 mL of 1 mg/mL GO-PEG solution and then vortexed at 25°C for 1 hour in the dark. The above solution was then mixed with 19  $\mu$ L of 42mM Glycine and then vortexed at 25°C for 60 minutes in the dark. After centrifugation and washing with 1x PBS, GO-PEG-FITC was re-dispersed in 1 mL ddH<sub>2</sub>O. Cells were then incubated with GO-PEG-FITC (20  $\mu$ L) in 100  $\mu$ L of minimum essential medium for 6 hours. The medium was then removed, and the cells were washed with 1 mL of Hank's balanced salt solution and then fixed with fresh ethanol for 5 minutes at room temperature. The cells were washed three times with Hank's balanced salt solution and analyzed by a laser confocal microscope (Olympus FV10i).

## NPC Cell Culture

The NPC cell line TW01 was kindly provided by Dr. Lin CT (Department of Pathology and Graduate Institute of Pathology, College of Medicine, National Taiwan University, Taiwan). The cell line was derived from primary nasopharyngeal tumors of Chinese patients with de novo NPC.<sup>27,28</sup> The use of the NPC cell line was approved by the institutional review board of the Taipei Veterans General Hospital. The NPC cell line was maintained in DMEM with 10% FBS at 37°C under 5% CO<sub>2</sub>.

## In vitro Cytotoxicity Assay

Cell viability of the exposed cells was determined using the Cell Counting Kit-8 (Sigma-Aldrich, St. Louis, USA), according to the manufacturer's instructions. After seeding cells at a concentration of 2000 cells/well in 100  $\mu$ L

culture medium in a 96-well microplate for 24 hours, cells were washed with PBS twice and exposed with GO, GO-PEG, erlotinib, and GO-PEG-erlotinib for various concentrations in a humidified atmosphere (37°C and 5% CO<sub>2</sub>) for 2–3 days. Then, the cells were incubated with 10  $\mu$ L CCK-8 cell proliferation reagent for 2 hours. Optical density was measured using a microplate reader (Spectral Max250) at 450 nm.

## Wound Healing Assay

Cells were plated in 6-well plates. When the cells grew into full confluency, a wound was created on the monolayer cells by scraping a gap using a micropipette tip after cells had been treated with control and GO-PEG-erlotinib for 20 hours. The speed of wound closure was compared between GO-PEG-erlotinib treated groups and the control group. Photographs were taken under 100 $\times$  magnifications using phase contrast microscopy immediately after wound incision and at 20 hours later.

## Cell Invasion Assay

A Transwell cell culture chamber (Millipore, Bedford, MA, USA) with a 6.5-mm-diameter polycarbonate filter (8  $\mu$ m pore size) was coated with Matrigel, dried, and reconstituted at 37°C with culture medium. Culture medium containing 10% FBS was placed in the lower chamber (24-well plates). Then, the cells at  $1 \times 10^5$  cells per chamber were added to the upper chamber in serum-free DMEM. After 48 hours of incubation with control, GO-PEG, erlotinib or GO-PEG-erlotinib at 37°C, the suspended media in the lower chamber were removed. The cells that had invaded the lower side of the filter were fixed in methanol and stained with DAPI. The number of cells that passed through the pores into the lower chamber was counted under a fluorescent microscope (five fields per chamber).

## RNA-Seq Analysis

Total RNA from NPC cell lines treated with or without GO-PEG-erlotinib (2.15  $\mu$ g/mL) for 72 hours was extracted with RNeasy Mini Kit (Qiagen, Germany) according to the manufacturer's protocol. RNA was subjected to RNA-Seq analysis on BGISEQ-500 system by Tri-I Biotech, Inc. Briefly, the RNA was sheared and reverse transcribed using random primers to obtain cDNA used for library construction. We performed sequencing on prepared library<sup>29</sup> and filtered all the generated raw sequencing reads to get clean reads stored as

FASTQ format.<sup>30</sup> We used Bowtie2 and HISAT to map clean reads to reference genes and genome, respectively.<sup>31,32</sup> Gene expression level (FPKM) was quantified by RSEM.<sup>33</sup> We used the DEseq2 method to screen out differentially expressed genes between two groups with fold change  $\geq 2$  and adjusted P value  $\leq 0.05$ .<sup>34</sup> Gene ontology (GO) and pathway annotation and enrichment analyses were based on the GO Database (<http://www.geneontology.org/>) and KEGG pathway database (<http://www.genome.jp/kegg/>), respectively. We then used the Ingenuity Pathway Analysis (IPA) to assign biological functions to genes and network analysis using the Ingenuity Pathways Knowledge Base (Ingenuity Systems, Inc., Redwood City, CA, USA).

## Statistical Analysis

All experiments were carried out in triplicate, and at least three independent experiments were performed. The results are presented as the means  $\pm$  SDs. Statistical comparisons of multigroup data were analyzed by ANOVA, followed by Scheffe's post-test using SPSS 12.0 software (SPSS Inc. Chicago, IL). A value of  $p < 0.05$  indicated statistical significance.

## Results

We prepared GO and GO-PEG from the raw materials of graphite platelet followed the modified Hummers' method. We characterized the GO and GO-PEG using several tools, including the TEM, FTIR, DLS, and Raman spectroscopy. The TEM images showed the irregular morphology of GO and GO-PEG (Figure 1A) in the solution. Compared to GO-PEG, GO forms small clusters more readily in the solution. From the TEM images, GO-PEG showed better dispersibility in water. Moreover, no contaminating particles were found on the surface of both GO and GO-PEG, which revealed great purity of these two materials in the solution (data not shown). We further used the DSL to measure the size of GO and GO-PEG, which were 88 nm and 96 nm in average, respectively (Figure 1B). DLS is a technique in physics that can be used to determine the size-distribution profile of small particles in suspension or polymers in solution. The polydispersity index (PDI) is used to describe the degree of "non-uniformity" of a distribution. PDI between 0 and 0.35 means narrow size-distribution of particles. The PDI of GO and GO-PEG were 0.357 and 0.354, respectively. ZP (zeta potential) measurements represent the surface charge of the materials. The ZP of GO and GO-PEG were  $-42.1$  and  $-31.1$ ,

respectively (Figure 1B). The FTIR was used to obtain an infrared spectrum of absorption or emission of the GO and functionalized GO materials, which revealed that PEG was successfully conjugated on GO (Figure 1D). Raman spectroscopy was performed using a Micro-Raman Spectrometer (PTT-EL) equipped with a 532nm laser. Raman spectroscopy can provide substantial information about nanostructure defect type, domain size, impurity element, etc. A G-band at around  $1575\text{cm}^{-1}$  in the Raman spectra represents the  $\text{sp}^2$ -hybridized carbon structure of GO, while a D-band at around  $1355\text{cm}^{-1}$  appears when the carbon structure exhibits small defects or edges. The intensity ratio (intensity of the D-band/intensity of the G-band, ID/IG) represents the structural integrity of GO. GO and GO-PEG had similar ID/IG values, indicating that PEGylation did not destroy the aromatic structures of GO (Figure 1C and E). Absorbance of GO, GO-PEG, erlotinib, and GO-PEG-erlotinib analyzed by UV-Vis spectrophotometer is shown in Figure 1F.

We then conducted the drug loading and release studies, which are essential for evaluating a drug delivery system. The drug loading efficiency (LE) and encapsulation efficiency (EE) of erlotinib-loaded GO-PEG were about 80%, and 38%, respectively (Figure 2A). On average,  $46.5 \pm 9.58$   $\mu\text{g}$  erlotinib was loaded on  $141.39 \pm 9.45$   $\mu\text{g}$  GO-PEG when 200  $\mu\text{g}$  erlotinib was mixed with 200  $\mu\text{g}$  GO-PEG. In regard to drug release testing, the release rate of GO-PEG-erlotinib at pH 5 at 5 hours was 93.01%; at 24 hours was 95.88%; and at 72 hours was 98.99%. The release rate of GO-PEG-erlotinib at pH 7 at 5 hours was 63.38%; at 24 hours was 68.33%; and at 72 hours was 76.74% (Figure 2A). In order to duplicate the physiological temperature, a temperature of  $37^\circ\text{C}$  was selected for the drug release response. A pH of 7.4 corresponds to the physiological pH of normal cells, while a pH of 5.5 corresponds to acidic cancer environments, and also within endosomes after internalization. Figure 2B shows that the cumulative release profile of erlotinib from the GO-PEG is pH-dependent, in which erlotinib release is enhanced at pH 5.5.

To determine intracellular uptake of GO-PEG, NPC TW01 cells were cultured and incubated with FITC-labeled GO-PEG suspension for 6 hours. The identification of GO-PEG was made possible by the green fluorescence signals from FITC-labeled GO-PEG (Figure 3). The green fluorescence of FITC-labeled GO-PEG mostly appears in the cytoplasm of NPC TW01 cells. It is supposed that GO-PEG accumulating in the cytoplasm is via endocytosis.

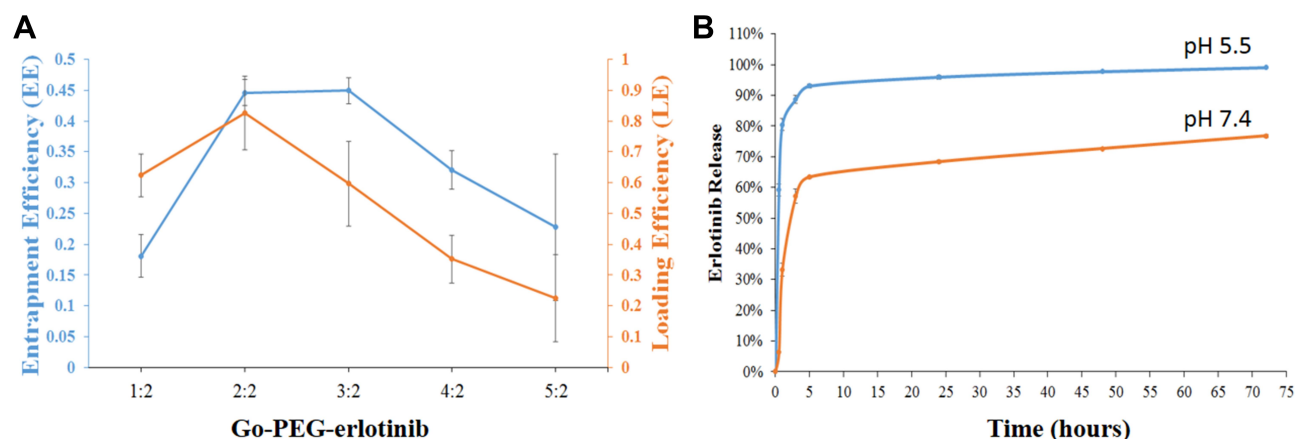


**Figure 2** (A) The drug loading efficiency (LE) and encapsulation efficiency (EE) of erlotinib-loaded GO-PEG. (B) The drug release test of GO-PEG-erlotinib in pH 7.4 and 5.5.

We then tested the GO and GO-PEG on NPC cells. Both GO and GO-PEG showed mild cytotoxicity on NPC cells at a concentration below 10  $\mu\text{g/mL}$ . The erlotinib was further tested for cytotoxicity. Erlotinib seems to have little cytotoxicity effect on NPC cells; the  $\text{IC}_{50}$  at 72 hours is around 100  $\mu\text{g/mL}$  (data not shown). However, GO-PEG-erlotinib has great cytotoxicity with the  $\text{IC}_{50}$  at 72 hours being 2.12  $\mu\text{g/mL}$  (Figure 4). This indicates that GO-PEG might be a promising drug delivery vehicle for erlotinib in NPC treatment.

The migration of NPC TW01 cells with or without GO-PEG-erlotinib was assessed by a wound healing assay. More cells migrated to the denuded area of the wound in the control group than to the cells treated with 0.7 and 2.15  $\mu\text{g/mL}$  GO-PEG-erlotinib at 20 hours after the creation of the wound (Figure 5). The results indicated that GO-PEG-erlotinib inhibited the migration of NPC cells. To investigate whether GO-PEG-erlotinib could inhibit cell invasion, cell invasion assays were conducted. The number of migrating cells was significantly reduced after treatment with 2.15  $\mu\text{g/mL}$  GO-PEG-erlotinib (Figure 6).

To identify differentially expressed genes, the RNA-Seq of the NPC cell lines treated with and without 2.15  $\mu\text{g/mL}$  GO-PEG-erlotinib for 72 hours were compared. A p-value  $<0.05$  was considered statistically significant. In regard to GO-PEG-erlotinib, a total of 1455 genes were differentially expressed by at least two-fold, with 623 upregulated and

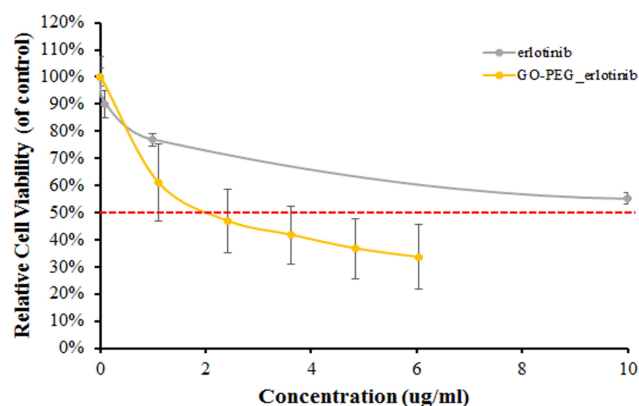


**Figure 4** Cell viability of NPC TW01 after treatment with erlotinib and GO-PEG-erlotinib at various concentrations. Cell viability was determined after incubating with erlotinib or GO-PEG-erlotinib for 72 hours.

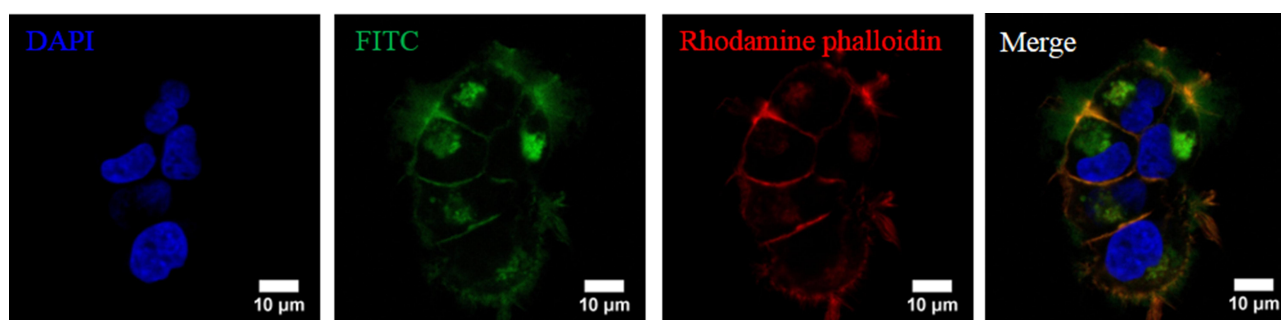


**Figure 3** Confocal microscopy images of NPC TW01 cells after treatment with FITC-labeled GO-PEG for 6 hours.

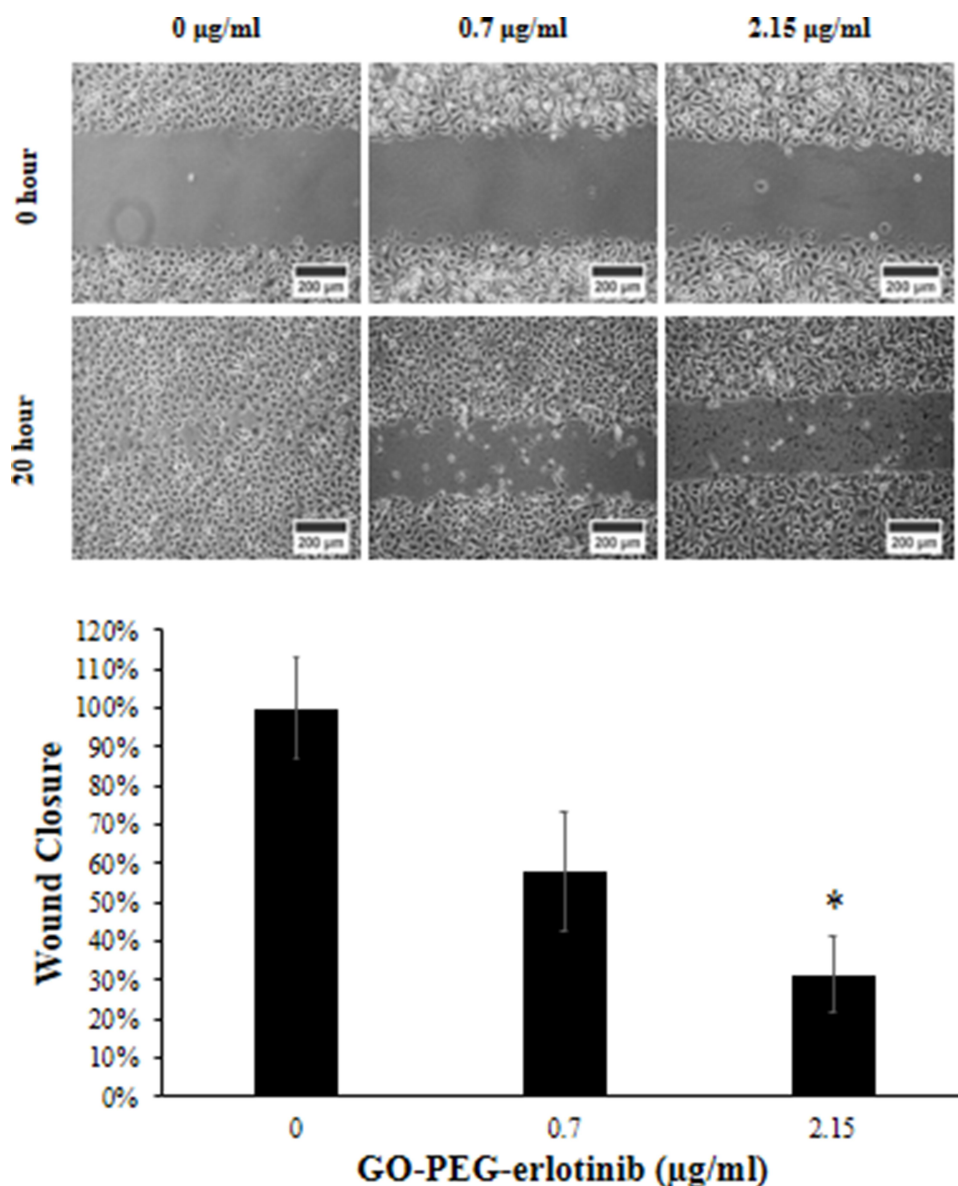


**Figure 5** GO-PEG-erlotinib reduces cell migration in NPC TW01 cells. More cells migrated to the denuded area of the wound in the control group (left) compared to the cells treated with 0.7 µg/mL GO-PEG-erlotinib (middle) and 2.15 µg/mL GO-PEG-erlotinib (right) at 20 hours after the creation of the wound. \* $p < 0.05$  compared with the control group by ANOVA.

832 downregulated genes. The data were then analyzed using the IPA functional analysis tool. Several networks and interactomes were created according to the biological functions of the genes and were ranked by the number of significantly expressed genes they contained. The top 10 upregulated and downregulated molecules and the top 10 upstream regulators in RNA-Seq analysis of NPC cells treated with GO-PEG-erlotinib are listed in Table 1. Further study of these top molecules will be conducted in the future to elucidate their roles in the mechanism of GO-PEG-erlotinib on NPC cells. Table 2 lists the top 5 associated networks of genes involved in the effect of GO-PEG-

erlotinib on NPC cells. Figure 7 shows the top-ranked network identified by IPA analysis in GO-PEG-erlotinib.

The KEGG pathway analysis of GO-PEG-Erlotinib on NPC cells is shown in Figure 8. There are seven branches for KEGG pathways: cellular processes, environmental information processing, genetic information processing, human disease (for animals only), metabolism, and organismal systems.

## Discussion

EGFR has been found to be overexpressed in 73% to 89% of NPC patients, which causes decreased overall

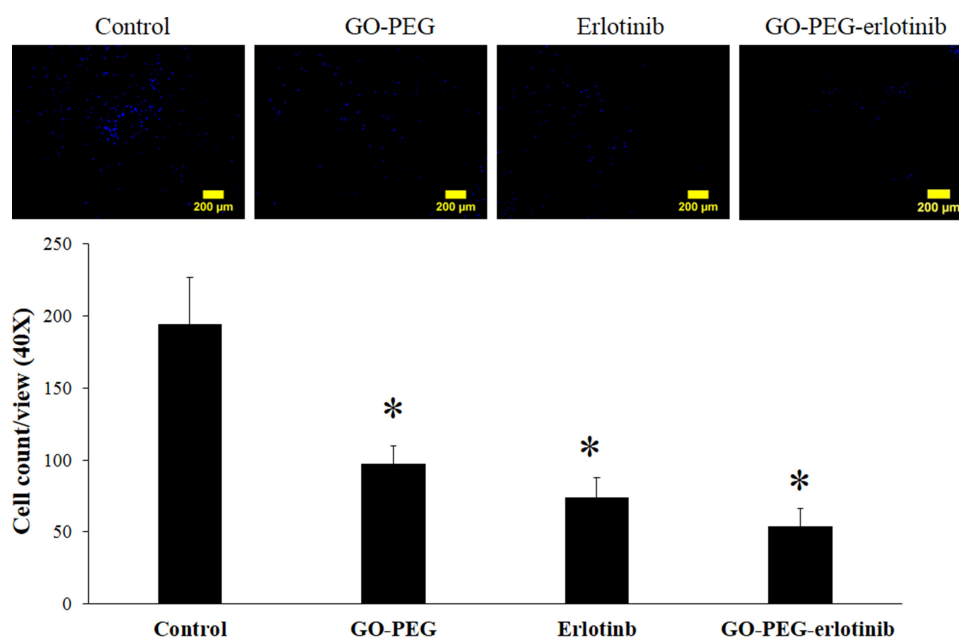


**Figure 6** GO-PEG-erlotinib inhibits cell invasion in NPC TW01 cells. Matrigel invasion assays of NPC TW01 cells showed that the invasion ability of NPC cells was reduced after treatment with 2.15 µg/mL GO-PEG-erlotinib, 2.15 µg/mL erlotinib, and 6.45 µg/mL GO-PEG for 48 hours. \* $p < 0.05$  compared with the control group by ANOVA.

survival and an increased risk of metastasis.<sup>35–37</sup> Several studies have shown that high EGFR expression is correlated with poor locoregional control and overall survival, but not distant metastasis-free survival (DMFS).<sup>38,39</sup> Erlotinib, an EGFR inhibitor, has been shown to be effective for NSCLC and pancreatic cancer, but without much study regarding its effect in head and neck cancer patients or in NPC patients.<sup>21</sup> A randomized phase II trial showed that the addition of erlotinib to cisplatin and radiotherapy did not confer additional tumor response or patient survival of 204 late-stage HNSCC patients.<sup>40</sup> Previously, a phase II trial conducted on patients with recurrent and/or metastatic NPC revealed

no efficacy of erlotinib as maintenance therapy after gemcitabine-platinum chemotherapy.<sup>23</sup>

Zheng et al recently identified serine protease inhibitor Kazal-type 6 (SPINK6) as a functional regulator of NPC metastasis via EGFR signaling, and erlotinib was revealed to reverse SPINK6-induced NPC cell migration and invasion in vitro, as well as inhibiting SPINK6-induced metastasis in vivo.<sup>41</sup> In our study, we found erlotinib has little cytotoxicity effect on NPC cells with the IC<sub>50</sub> at 72 hours being around 100 µg/mL, which may explain the relative unresponsiveness of erlotinib in clinical NPC patients. However, GO-PEG-erlotinib indeed showed good cytotoxicity on NPC cells with the IC<sub>50</sub> at 72 hours being

**Table 1** The Top 10 Upregulated and Downregulated Genes and Their Corresponding Upstream Regulators in RNA-Seq Analysis of NPC Cells Treated with GO-PEG-Erlotinib

Rank	Upregulated Gene	Expression Value	Downregulated Gene	Expression Value
1	<i>CHAC1</i>	4.279	<i>SNAI1</i>	−4.054
2	<i>RGPD4</i>	3.225	<i>ART5</i>	−3.982
3	<i>KRCC1</i>	3.046	<i>NPTX1</i>	−3.880
4	<i>ELAC1</i>	2.941	<i>HIST1H2BJ</i>	−3.774
5	<i>BORCS8-MEF2B</i>	2.755	<i>ART1</i>	−3.474
6	<i>CYP1A1</i>	2.755	<i>SLC6A12</i>	−3.434
7	<i>FGFBP3</i>	2.592	<i>SLC17A7</i>	−3.313
8	<i>C7orf25</i>	2.576	<i>KCNE1B</i>	−3.311
9	<i>SPRN</i>	2.483	<i>KLHL41</i>	−3.261
10	<i>MAGI2</i>	2.478	<i>SUCNR1</i>	−3.232



**Table 2** The Top 5 Associated Networks Involved in the Effect of GO-PEG-Erlotinib on NPC Cells Identified by IPA

Rank	Molecules	Associated Network Functions
1	34	Cardiovascular Disease, Hematological Disease, Hereditary Disorder
2	34	Cellular Development, Embryonic Development, Hair and Skin Development and Function
3	32	Cell Death and Survival, Cell-mediated Immune Response, Cellular Function and Maintenance
4	31	Reproductive System Development and Function, Cancer, Organismal Injury and Abnormalities
5	31	Endocrine System Development and Function, Molecular Transport, Small Molecule Biochemistry

2.12 ug/mL. We calculated the drug LE and EE of erlotinib-loaded GO-PEG was about 80%, and 38%, respectively, and the release rate of GO-PEG-erlotinib was enhanced at pH 5.5, corresponding to the acidic cancer environments in endosomes after internalization. Most tumor cells have high metabolic activity, which contributes to their more acidic intracellular pH.<sup>42</sup> Thus, an internalized graphene-based drug with pH-responsive characteristics, like GO-PEG-erlotinib in our study, can specifically release the drug at tumor sites.<sup>11</sup> Moreover, our results

show that GO-PEG-erlotinib not only reduced NPC cell viability in a dose-dependent manner but also inhibited the migration and invasion of NPC cells. The relatively moderate drug loading and the pH-sensitive release of erlotinib suggest that GO-PEG is a potential drug delivery vehicle for cancer therapy,<sup>43,44</sup> and that GO-PEG is a promising drug delivery vehicle for erlotinib in NPC treatment.

Graphene-based materials immobilize various biomolecules through either noncovalent adsorption, such as  $\pi$ - $\pi$  stacking, hydrogen bonds, and electrostatic interaction; or

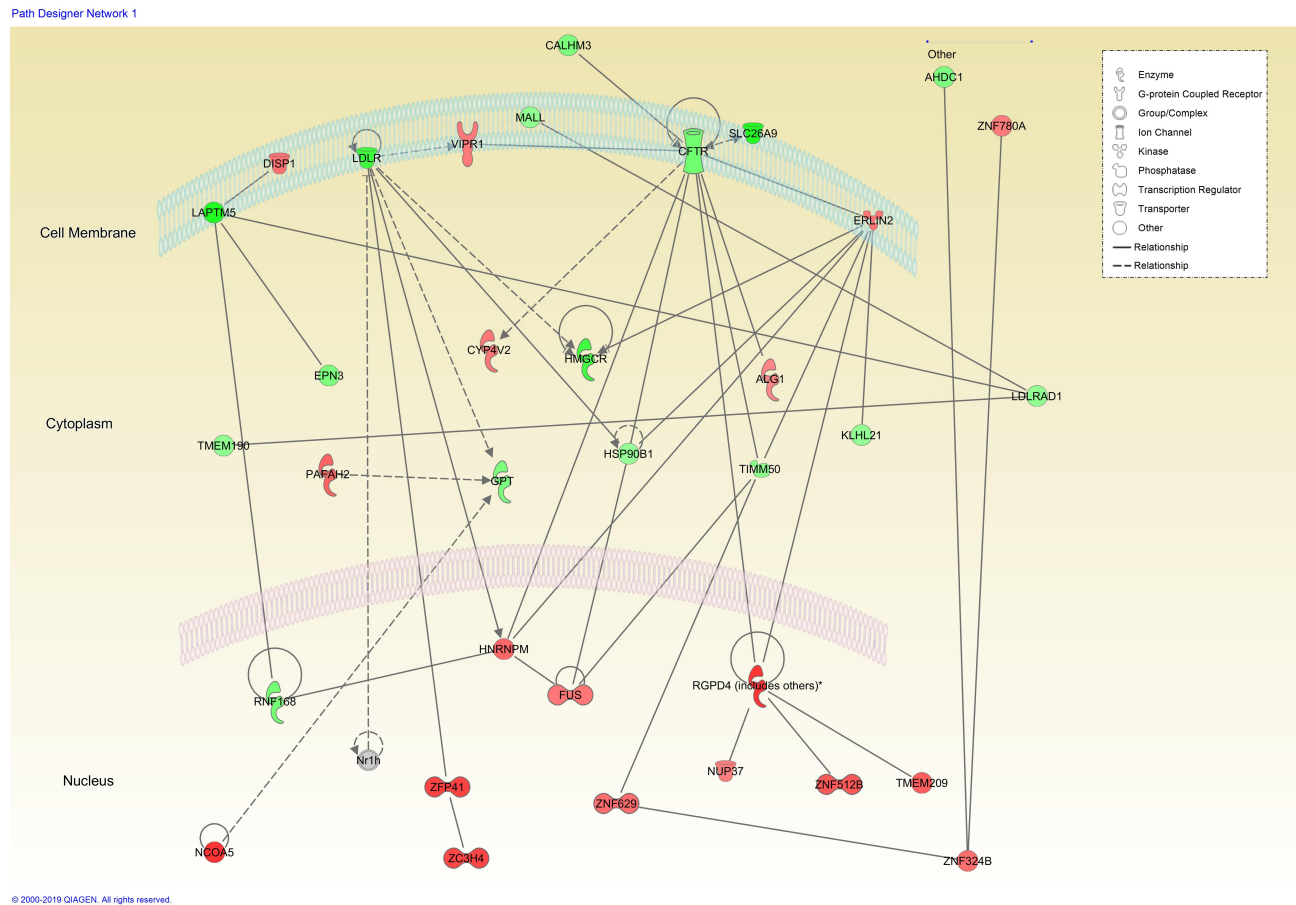


**Figure 7** The top-ranked network identified by IPA analysis in GO-PEG-erlotinib study. The top-ranked network, which includes 34 genes, is related to cardiovascular disease, hematological disease, and hereditary disorder. The genes shaded in red are upregulated, and genes shaded in green are downregulated. All shaded genes are statistically significant, as indicated by the statistical analysis. A dotted line indicates an indirect interaction between the two gene products, and a solid line represents a direct interaction.

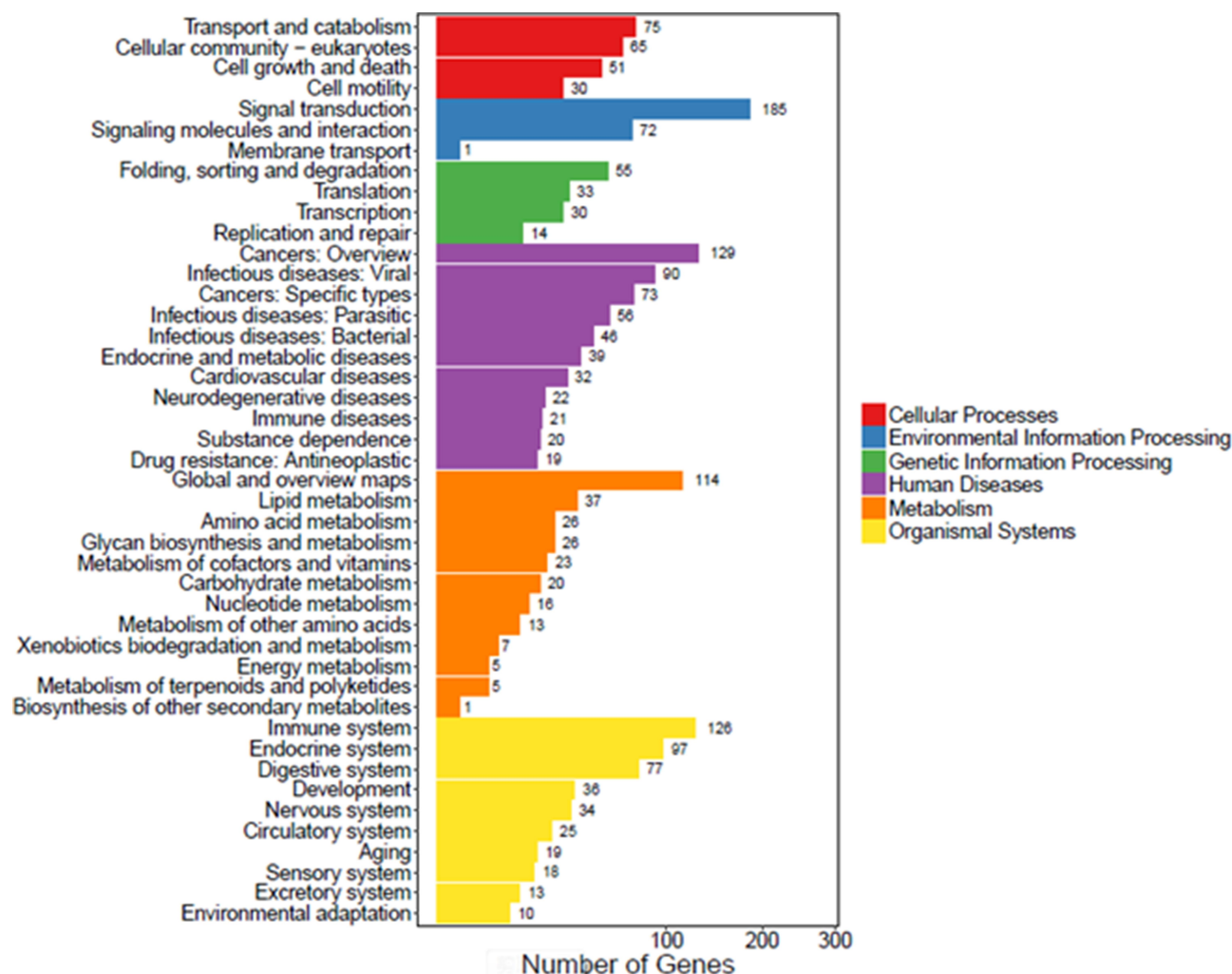


**Figure 8** KEGG pathway analysis of GO-PEG-erlotinib on NPC cells. There are seven branches for KEGG pathways: cellular processes, environmental information processing, genetic information processing, human disease, metabolism, and organismal systems.

covalent binding by their enriched oxygen functional groups.<sup>15</sup> They offer a high surface to weight ratio, a high possibility for surface modification, high drug-loading efficiency, a pH-responsive drug-delivery mechanism, and photothermal effects compared to other drug delivery systems.<sup>18,45,46</sup> Graphene is characterized by a pure carbon, an aromatic network providing an open surface for noncovalent interaction with biomolecules, while GO has many epoxides, carboxyl, and hydroxyl groups on its basal plane and edges which can bind with biomolecules via covalent, electrostatic, and hydrogen bond interactions.<sup>43,44</sup>

Most drugs binding on GO are based on noncovalent interactions. For example, chemotherapeutic drugs possessing aromatic ring structures, such as doxorubicin, camptothecin, and SN-38, bind on GO through  $\pi$ - $\pi$  stacking.<sup>47</sup> Various methods have been developed to

functionalize GO for improving its drug carrier function. Lui et al found that GO functionalized with polyethylene glycol (PEG) can carry water-insoluble cancer drugs such as camptothecin and SN38 and showed pH-dependent drug release behavior.<sup>48</sup> Besides, functionalized GO can enter mammalian cells, and thus it is a reasonable drug carrier. Moreover, the hydrophilic groups on both sides of GO make it stable in physiologic solutions while carrying drugs. In our study, intracellular uptake of FITC-labeled GO-PEG in NPC cells was clearly observed under confocal microscopy, which suggested that GO-PEG accumulating in the cytoplasm is via endocytosis. Finally, GO-PEG-erlotinib showed much better cytotoxicity on NPC cells than erlotinib alone, demonstrating that GO-PEG is a promising drug carrier for possible usage in NPC treatment in the future.

In recent years, several studies have focused on graphene and its derivatives as potential drug carriers for cancer therapy. Yang et al used a chemical coprecipitation method, not only adding Fe<sub>3</sub>O<sub>4</sub> magnetic nanoparticles onto graphene but also decorating it with folic acid as a targeting ligand. The drug-loaded graphene selectively killed breast cancer cells with released doxorubicin.<sup>45</sup> Zhang et al designed the drug carrier with low drug resistance rate but high cytotoxic efficacy by adding positive-charged polyethylenimine (PEI) onto the doxorubicin-loaded graphene which can adsorb negative-charged Bcl-2 siRNA.<sup>49</sup> Lu et al modified the GO surface with abundant polyacrylic acid (PAA) chains, which can react with BCNU through carbodiimide-mediated amide bond formation to increase drug loading. The PAA–GO–BCNU showed promising anticancer efficacy in in vitro study.<sup>47</sup> Yin et al functionalized GO with PEI and (PEG) as a plasmid-based Stat3 siRNA carrier, which showed a significant regression in tumor growth and tumor weight of mouse malignant melanoma growth in vivo.<sup>50</sup> Yang et al developed epidermal growth factor receptor (EGFR) antibody-conjugated PEGylated nanographene oxide (PEG-NGO) carrying epirubicin (EPI) that was able to target the tumor and kill the cancer cells by its triple-therapeutics (growth signal blocking, chemotherapy, photothermal therapy). The synergistic-targeted treatment simultaneously enhances the local drug concentration and performs ultra-efficient tumor suppression to significantly prolong survival in mice. This novel drug delivery platform overcomes the problems of low accumulation of most chemotherapeutic agents in tumor tissue and multidrug resistance (MDR) in current cancer treatment.<sup>51</sup> Recently, Pei et al developed cisplatin and doxorubicin dual-drug-loaded PEGylated nano-graphene oxide which exhibited significantly increased anticancer effect than the single drug delivery system.<sup>52</sup> Wang et al synthesized folate-modified GO/PEI siRNA nanocomplexes which successfully targeted ovarian cancer cells in vitro.<sup>53</sup> Shirvalilou et al developed magnetic NGO as a drug carrier for improving glioma-targeted iodo-2-deoxyuridine (IUDR) delivery and imaging.<sup>54</sup>

By conducting RNA-Seq analysis and following IPA analysis, the top 10 upregulated and top 10 downregulated molecules after GO-PEG-erlotinib treatment on NPC cells were identified (Table 1). Some of these molecules have been reported to be associated with carcinogenesis and prognosis in other types of cancers. CHAC1 (ChaC glutathione-specific gamma-glutamylcyclotransferase 1) plays a role in the regulation of glutathione levels and oxidative

balance in cells and is also a proapoptotic component of the unfolded protein response (UPR).<sup>55,56</sup> Activation of CHAC1 has been reported to induce cell apoptosis and decrease cell proliferation in human head and neck squamous cell cancer cell lines.<sup>57</sup> CYP1A1 (cytochrome P450 family 1 subfamily A member 1) is located at the endoplasmic reticulum. It can metabolize some polycyclic aromatic hydrocarbons to carcinogenic intermediates. This gene has been found to be associated with lung, prostate, and cervical cancer risks.<sup>58–60</sup> SNAI1 (snail family transcriptional repressor 1) proteins primarily act as transcriptional repressors.<sup>61</sup> It can induce epithelial-to-mesenchymal transition (EMT) in colorectal and lung cancer cells.<sup>62,63</sup> NPTX1 (neuronal pentraxin 1) belongs to the long pentraxin family of protein and is highly expressed in the central nervous system.<sup>64</sup> It is also involved in the regulation of apoptosis in some types of cells.<sup>65,66</sup> Recently, some studies found that NPTX1 may be involved in the progression of lung, pancreatic, and colon cancers.<sup>67–69</sup>

Recently, several ligands have been used in cancer targeted therapies, such as biotin, transferrin, and folate.<sup>70,71</sup> Montazerabadi et al functionalized curcumin-loaded dendritic magnetite nanocarriers with folate, which generated a thermo-chemotherapeutic effect on folate receptor-expressed cancer cells.<sup>72</sup> Zeiniazade et al used folate-conjugated gold nanoparticles for targeted nano-photo-thermal therapy.<sup>73</sup> Because of the high surface-area-to-volume ratio of nanocarriers, designing novel drug carriers with multiple targeting ligands are feasible ways to increase their antitumor effect.<sup>71</sup> In the future, we will further modify GO-PEG-erlotinib with specific ligands to induce selective cancer cell death.

Our study revealed that GO-PEG is a promising drug carrier for erlotinib with the advantages of high drug loading and pH-dependent controlled release. GO-PEG-erlotinib reduced NPC cell viability in a dose-dependent manner, and also inhibited the migration and invasion of NPC cells. The RNA sequencing revealed important molecules and several related molecular mechanisms. Further studies will be needed in the future.

## Conclusion

GO-PEG-erlotinib effectively suppressed NPC cell proliferation, migration, and invasion, and presented a better anticancer effect than free drugs. Several molecules and mechanisms were involved. GO-PEG-erlotinib may be a potential therapeutic agent for treating NPC in the future.

## Acknowledgments

This research was supported by grants from the Ministry of Science and Technology (MOST106-2314-B-075-035-MY3-2) to MYL and (MOST107-2314-B-182-020) to YJL. The authors thank the Clinical Research Core Laboratory at Taipei Veterans General Hospital for facility support.

## Disclosure

The authors report no conflicts of interest for this work.

## References

1. Cho WC. Nasopharyngeal carcinoma: molecular biomarker discovery and progress. *Mol Cancer*. 2007;6:1.
2. Lu JJ, Cooper JS, Lee AW. *Nasopharyngeal Cancer: Multidisciplinary Management*. Springer Science & Business Media; 2010.
3. Tao Q, Chan AT. Nasopharyngeal carcinoma: molecular pathogenesis and therapeutic developments. *Expert Rev Mol Med*. 2007;9(12):1–24.
4. Chou J, Lin YC, Kim J, et al. Nasopharyngeal carcinoma—review of the molecular mechanisms of tumorigenesis. *Head Neck*. 2008;30(7):946–963. doi:10.1002/hed.20833
5. Lee YC, Hwang YC, Chen KC, et al. Effect of Epstein-Barr virus infection on global gene expression in nasopharyngeal carcinoma. *Funct Integr Genomics*. 2007;7(1):79–93. doi:10.1007/s10142-006-0035-2
6. Chen X, Liang S, Zheng W, Liao Z, Shang T, Ma W. Meta-analysis of nasopharyngeal carcinoma microarray data explores mechanism of EBV-regulated neoplastic transformation. *BMC Genomics*. 2008;9:322. doi:10.1186/1471-2164-9-322
7. Bruce JP, Yip K, Bratman SV, Ito E, Liu FF. Nasopharyngeal cancer: molecular landscape. *J Clin Oncol*. 2015;33(29):3346–3355. doi:10.1200/JCO.2015.60.7846
8. Dai W, Zheng H, Cheung AK, Lung ML. Genetic and epigenetic landscape of nasopharyngeal carcinoma. *China Clin Oncol*. 2016;5(2):16. doi:10.21037/cco.2016.03.06
9. Gooi Z, Richmon J, Agrawal N, et al. AHNS series - Do you know your guidelines? Principles of treatment for nasopharyngeal cancer: a review of the national comprehensive cancer network guidelines. *Head Neck*. 2017;39(2):201–205. doi:10.1002/hed.24635
10. Ghanbarzadeh S, Hamishehkar H. Application of graphene and its derivatives in cancer diagnosis and treatment. *Drug Res (Stuttg)*. 2017;67(12):681–687. doi:10.1055/s-0042-115638
11. Gu Z, Zhu S, Yan L, Zhao F, Zhao Y. Graphene-based smart platforms for combined cancer therapy. *Adv Mater*. 2019;31(9):e1800662. doi:10.1002/adma.201800662
12. Liu J, Dong J, Zhang T, Peng Q. Graphene-based nanomaterials and their potentials in advanced drug delivery and cancer therapy. *J Control Release*. 2018;286:64–73. doi:10.1016/j.jconrel.2018.07.034
13. de Melo-diogo D, Lima-Sousa R, Alves CG, Costa EC, Louro RO, Correia IJ. Functionalization of graphene family nanomaterials for application in cancer therapy. *Colloids Surf B Biointerfaces*. 2018;171:260–275. doi:10.1016/j.colsurfb.2018.07.030
14. Novoselov KS, Geim AK, Morozov SV, et al. Electric field effect in atomically thin carbon films. *Science*. 2004;306(5696):666–669. doi:10.1126/science.1102896
15. Li D, Zhang W, Yu X, Wang Z, Su Z, Wei G. When biomolecules meet graphene: from molecular level interactions to material design and applications. *Nanoscale*. 2016;8(47):19491–19509. doi:10.1039/C6NR07249F
16. Gurunathan S, Kim JH. Synthesis, toxicity, biocompatibility, and biomedical applications of graphene and graphene-related materials. *Int J Nanomedicine*. 2016;11:1927–1945.
17. Rahmanian N, Eskandani M, Barar J, Omid Y. Recent trends in targeted therapy of cancer using graphene oxide-modified multifunctional nanomedicines. *J Drug Target*. 2017;25(3):202–215.
18. Yang K, Feng L, Liu Z. Stimuli responsive drug delivery systems based on nano-graphene for cancer therapy. *Adv Drug Deliv Rev*. 2016;105(Pt B):228–241. doi:10.1016/j.addr.2016.05.015
19. Zhang B, Wang Y, Zhai G. Biomedical applications of the graphene-based materials. *Mater Sci Eng C Mater Biol Appl*. 2016;61:953–964. doi:10.1016/j.msec.2015.12.073
20. Gulzar A, Yang P, He F, et al. Bioapplications of graphene constructed functional nanomaterials. *Chem Biol Interact*. 2017;262:69–89. doi:10.1016/j.cbi.2016.11.019
21. Xu MJ, Johnson DE, Grandis JR. EGFR-targeted therapies in the post-genomic era. *Cancer Metastasis Rev*. 2017;36(3):463–473. doi:10.1007/s10555-017-9687-8
22. Zhang HH, Yuan TZ, Li J, et al. Erlotinib: an enhancer of radiation therapy in nasopharyngeal carcinoma. *Exp Ther Med*. 2013;6(4):1062–1066. doi:10.3892/etm.2013.1245
23. You B, Le Tourneau C, Chen EX, et al. A Phase II trial of erlotinib as maintenance treatment after gemcitabine plus platinum-based chemotherapy in patients with recurrent and/or metastatic nasopharyngeal carcinoma. *Am J Clin Oncol*. 2012;35(3):255–260. doi:10.1097/COC.0b013e31820dbdce
24. Lan MY, Chen CL, Lin KT, et al. From NPC therapeutic target identification to potential treatment strategy. *Mol Cancer Ther*. 2010;9(9):2511–2523.
25. Lan MY, Yang WL, Lin KT, et al. Using computational strategies to predict potential drugs for nasopharyngeal carcinoma. *Head Neck*. 2014;36(10):1398–1407.
26. Hummers Jr WS, Offeman RE. Preparation of graphitic oxide. *J Am Chem Soc*. 1958;80(6):1339.
27. Lin CT, Wong CI, Chan WY, et al. Establishment and characterization of two nasopharyngeal carcinoma cell lines. *Lab Invest*. 1990;62(6):713–724.
28. Lin CT, Chan WY, Chen W, et al. Characterization of seven newly established nasopharyngeal carcinoma cell lines. *Lab Invest*. 1993;68(6):716–727.
29. Huang J, Liang X, Xuan Y, et al. A reference human genome dataset of the BGISEQ-500 sequencer. *Gigascience*. 2017;6(5):1–9.
30. Cock PJ, Fields CJ, Goto N, Heuer ML, Rice PM. The Sanger FASTQ file format for sequences with quality scores, and the Solexa/Illumina FASTQ variants. *Nucleic Acids Res*. 2010;38(6):1767–1771.
31. Kim D, Langmead B, Salzberg SL. HISAT: a fast spliced aligner with low memory requirements. *Nat Methods*. 2015;12(4):357–360. doi:10.1038/nmeth.3317
32. Langmead B, Salzberg SL. Fast gapped-read alignment with Bowtie 2. *Nat Methods*. 2012;9(4):357–359. doi:10.1038/nmeth.1923
33. Su CY, Fu D, Lu AY, et al. Transfer printing of graphene strip from the graphene grown on copper wires. *Nanotechnology*. 2011;22(18):185309. doi:10.1088/0957-4484/22/18/185309
34. Love MI, Huber W, Anders S. Moderated estimation of fold change and dispersion for RNA-seq data with DESeq2. *Genome Biol*. 2014;15(12):550.
35. Chua DT, Nicholls JM, Sham JS, Au GK. Prognostic value of epidermal growth factor receptor expression in patients with advanced stage nasopharyngeal carcinoma treated with induction chemotherapy and radiotherapy. *Int J Radiat Oncol Biol Phys*. 2004;59(1):11–20. doi:10.1016/j.ijrobp.2003.10.038
36. Sheen TS, Huang YT, Chang YL, et al. Epstein-Barr virus-encoded latent membrane protein 1 co-expresses with epidermal growth factor receptor in nasopharyngeal carcinoma. *Jpn J Cancer Res*. 1999;90(12):1285–1292. doi:10.1111/j.1349-7006.1999.tb00710.x



37. Ma BB, Poon TC, To KF, et al. Prognostic significance of tumor angiogenesis, Ki 67, p53 oncoprotein, epidermal growth factor receptor and HER2 receptor protein expression in undifferentiated nasopharyngeal carcinoma—a prospective study. *Head Neck*. 2003;25(10):864–872. doi:10.1002/hed.10307
38. Ooft ML, Braunius WW, Heus P, et al. Prognostic significance of the EGFR pathway in nasopharyngeal carcinoma: a systematic review and meta-analysis. *Biomark Med*. 2015;9(10):997–1010. doi:10.2217/bmm.15.68
39. Sun W, Long G, Wang J, Mei Q, Liu D, Hu G. Prognostic role of epidermal growth factor receptor in nasopharyngeal carcinoma: a meta-analysis. *Head Neck*. 2014;36(10):1508–1516.
40. Martins RG, Parvathaneni U, Bauman JE, et al. Cisplatin and radiotherapy with or without erlotinib in locally advanced squamous cell carcinoma of the head and neck: a randomized phase II trial. *J Clin Oncol*. 2013;31(11):1415–1421. doi:10.1200/JCO.2012.46.3299
41. Zheng LS, Yang JP, Cao Y, et al. SPINK6 promotes metastasis of nasopharyngeal carcinoma via binding and activation of epithelial growth factor receptor. *Cancer Res*. 2017;77(2):579–589. doi:10.1158/0008-5472.CAN-16-1281
42. Kato Y, Ozawa S, Miyamoto C, et al. Acidic extracellular microenvironment and cancer. *Cancer Cell Int*. 2013;13(1):89. doi:10.1186/1475-2867-13-89
43. Zhu Y, Murali S, Cai W, et al. Graphene and graphene oxide: synthesis, properties, and applications. *Adv Mater*. 2010;22(35):3906–3924.
44. Wang Y, Li Z, Wang J, Li J, Lin Y. Graphene and graphene oxide: biofunctionalization and applications in biotechnology. *Trends Biotechnol*. 2011;29(5):205–212. doi:10.1016/j.tibtech.2011.01.008
45. Yang X, Wang Y, Huang X, et al. Multi-functionalized graphene oxide based anticancer drug-carrier with dual-targeting function and pH-sensitivity. *J Mater Chem*. 2011;21(10):3448–3454. doi:10.1039/C0JM02494E
46. Yang K, Zhang S, Zhang G, Sun X, Lee ST, Liu Z. Graphene in mice: ultrahigh in vivo tumor uptake and efficient photothermal therapy. *Nano Lett*. 2010;10(9):3318–3323. doi:10.1021/nl100996u
47. Lu YJ, Yang HW, Hung SC, et al. Improving thermal stability and efficacy of BCNU in treating glioma cells using PAA-functionalized graphene oxide. *Int J Nanomedicine*. 2012;7:1737–1747.
48. Liu Z, Robinson JT, Sun X, Dai H. PEGylated nanographene oxide for delivery of water-insoluble cancer drugs. *J Am Chem Soc*. 2008;130(33):10876–10877.
49. Zhang L, Lu Z, Zhao Q, Huang J, Shen H, Zhang Z. Enhanced chemotherapy efficacy by sequential delivery of siRNA and anticancer drugs using PEI-grafted graphene oxide. *Small*. 2011;7(4):460–464. doi:10.1002/smll.201001522
50. Yin D, Li Y, Lin H, et al. Functional graphene oxide as a plasmid-based Stat3 siRNA carrier inhibits mouse malignant melanoma growth in vivo. *Nanotechnology*. 2013;24(10):105102. doi:10.1088/0957-4484/24/10/105102
51. Yang HW, Lu YJ, Lin KJ, et al. EGRF conjugated PEGylated nanographene oxide for targeted chemotherapy and photothermal therapy. *Biomaterials*. 2013;34(29):7204–7214. doi:10.1016/j.biomaterials.2013.06.007
52. Pei X, Zhu Z, Gan Z, et al. PEGylated nano-graphene oxide as a nanocarrier for delivering mixed anticancer drugs to improve anticancer activity. *Sci Rep*. 2020;10(1):2717. doi:10.1038/s41598-020-59624-w
53. Wang Y, Sun G, Gong Y, Zhang Y, Liang X, Yang L. Functionalized folate-modified graphene oxide/PEI siRNA nanocomplexes for targeted ovarian cancer gene therapy. *Nanoscale Res Lett*. 2020;15(1):57. doi:10.1186/s11671-020-3281-7
54. Shirvalilou S, Khoei S, Khoei S, Raoufi NJ, Karimi MR, Shakeri-Zadeh A. Development of a magnetic nano-graphene oxide carrier for improved glioma-targeted drug delivery and imaging: in vitro and in vivo evaluations. *Chem Biol Interact*. 2018;295:97–108. doi:10.1016/j.cbi.2018.08.027
55. Mungrue IN, Pagnon J, Kohannim O, Gargalovic PS, Lusis AJ. CHAC1/MGC4504 is a novel proapoptotic component of the unfolded protein response, downstream of the ATF4-ATF3-CHOP cascade. *J Immunol*. 2009;182(1):466–476. doi:10.4049/jimmunol.182.1.466
56. Crawford RR, Prescott ET, Sylvester CF, et al. Human CHAC1 protein degrades glutathione, and mRNA induction is regulated by the transcription factors ATF4 and ATF3 and a Bipartite ATF/CRE regulatory element. *J Biol Chem*. 2015;290(25):15878–15891.
57. Joo NE, Ritchie K, Kamarajan P, Miao D, Kapila YL. Nisin, an apoptogenic bacteriocin and food preservative, attenuates HNSCC tumorigenesis via CHAC1. *Cancer Med*. 2012;1(3):295–305. doi:10.1002/cam4.35
58. Liu Y, Li X, Zhang B, et al. CYP1A1 methylation mediates the effect of smoking and occupational polycyclic aromatic hydrocarbons co-exposure on oxidative DNA damage among Chinese coke-oven workers. *Environ Health*. 2019;18(1):69. doi:10.1186/s12940-019-0508-0
59. Zhu W, Liu H, Wang X, et al. Associations of CYP1 polymorphisms with risk of prostate cancer: an updated meta-analysis. *Biosci Rep*. 2019;39(3). doi:10.1042/BSR20181876.
60. Sengupta D, Guha U, Mitra S, Ghosh S, Bhattacharjee S, Sengupta M. Meta-analysis of polymorphic variants conferring genetic risk to cervical cancer in indian women supports CYP1A1 as an important associated locus. *Asian Pac J Cancer Prev*. 2018;19(8):2071–2081.
61. Jagle S, Busch H, Freihen V, et al. SNAIL1-mediated downregulation of FOXA proteins facilitates the inactivation of transcriptional enhancer elements at key epithelial genes in colorectal cancer cells. *PLoS Genet*. 2017;13(11):e1007109. doi:10.1371/journal.pgen.1007109
62. Ye X, Tam WL, Shibue T, et al. Distinct EMT programs control normal mammary stem cells and tumour-initiating cells. *Nature*. 2015;525(7568):256–260. doi:10.1038/nature14897
63. You J, Li M, Cao LM, et al. Snail1-dependent cancer-associated fibroblasts induce epithelial-mesenchymal transition in lung cancer cells via exosomes. *QJM*. 2019;112(8):581–590. doi:10.1093/qjmed/hcz093
64. Schlimgen AK, Helms JA, Vogel H, Perin MS. Neuronal pentraxin, a secreted protein with homology to acute phase proteins of the immune system. *Neuron*. 1995;14(3):519–526. doi:10.1016/0896-6273(95)90308-9
65. Schwartz D, Coute Y, Brunner Y, Wollheim CB, Sanchez JC. Modulation of neuronal pentraxin 1 expression in rat pancreatic beta-cells submitted to chronic glucotoxic stress. *Mol Cell Proteomics*. 2012;11(8):244–254. doi:10.1074/mcp.M112.018051
66. Guzeloglu-Kayisli O, Basar M, Shapiro JP, et al. Long-acting progestin-only contraceptives enhance human endometrial stromal cell expressed neuronal pentraxin-1 and reactive oxygen species to promote endothelial cell apoptosis. *J Clin Endocrinol Metab*. 2014;99(10):E1957–1966. doi:10.1210/jc.2014-1770
67. Zhou C, Qin Y, Xie Z, et al. NPTX1 is a novel epigenetic regulation gene and associated with prognosis in lung cancer. *Biochem Biophys Res Commun*. 2015;458(2):381–386. doi:10.1016/j.bbrc.2015.01.124
68. Yue W, Wang T, Zachariah E, et al. Transcriptomic analysis of pancreatic cancer cells in response to metformin and aspirin: an implication of synergy. *Sci Rep*. 2015;5:13390. doi:10.1038/srep13390
69. Mori Y, Olaru AV, Cheng Y, et al. Novel candidate colorectal cancer biomarkers identified by methylation microarray-based scanning. *Endocr Relat Cancer*. 2011;18(4):465–478. doi:10.1530/ERC-11-0083
70. Mehdizadeh A, Pandesh S, Shakeri-Zadeh A, et al. The effects of folate-conjugated gold nanorods in combination with plasmonic photothermal therapy on mouth epidermal carcinoma cells. *Lasers Med Sci*. 2014;29(3):939–948. doi:10.1007/s10103-013-1414-2



71. Pérez-Herrero E, Fernández-Medarde A. Advanced targeted therapies in cancer: drug nanocarriers, the future of chemotherapy. *Eur J Pharm Biopharm.* 2015;93:52–79. doi:10.1016/j.ejpb.2015.03.018
72. Montazerabadi A, Beik J, Irajirad R, et al. Folate-modified and curcumin-loaded dendritic magnetite nanocarriers for the targeted thermo-chemotherapy of cancer cells. *Artif Cells Nanomed Biotechnol.* 2019;47(1):330–340. doi:10.1080/21691401.2018.1557670
73. Zeinizade E, Tabei M, Shakeri-Zadeh A, et al. Selective apoptosis induction in cancer cells using folate-conjugated gold nanoparticles and controlling the laser irradiation conditions. *Artif Cells Nanomed Biotechnol.* 2018;46(sup1):1026–1038. doi:10.1080/21691401.2018.1443116

### International Journal of Nanomedicine

Dovepress

### Publish your work in this journal

The International Journal of Nanomedicine is an international, peer-reviewed journal focusing on the application of nanotechnology in diagnostics, therapeutics, and drug delivery systems throughout the biomedical field. This journal is indexed on PubMed Central, MedLine, CAS, SciSearch®, Current Contents®/Clinical Medicine,

Journal Citation Reports/Science Edition, EMBase, Scopus and the Elsevier Bibliographic databases. The manuscript management system is completely online and includes a very quick and fair peer-review system, which is all easy to use. Visit <http://www.dovepress.com/testimonials.php> to read real quotes from published authors.

Submit your manuscript here: <https://www.dovepress.com/international-journal-of-nanomedicine-journal>